Bharat Bhushan   *Coordinating Editor*

Dan Luo

Scott R. Schricker

Wolfgang Sigmund

Stefan Zauscher   *Editors*

Handbook of Nanomaterials Properties

INCLUDED IN
SPRINGERMATERIALS.COM

Springer

Handbook of Nanomaterials Properties

Bharat Bhushan • Dan Luo
Scott R. Schricker • Wolfgang Sigmund
Stefan Zauscher
Editors

Handbook of Nanomaterials Properties

With 627 Figures and 69 Tables

Springer

Editors
Bharat Bhushan
Nanoprobe Laboratory for
Bio- & Nanotechnology and Biomimetics
The Ohio State University
Columbus, OH, USA

Dan Luo
Department of Biological and
Environmental Engineering
Cornell University
Ithaca, NY, USA

Scott R. Schricker
Division of Restorative, Prosthetic and
Primary Care
College of Dentistry
The Ohio State University
Columbus, OH, USA

Wolfgang Sigmund
Department of Materials Science and
Engineering
Gainesville, Florida, USA

Stefan Zauscher
Department of Mechanical Engineering and
Materials Science
Duke University
Durham, NC, USA

Printed on acid-free paper

Preface

Nanomaterials are becoming increasingly important because of their unique properties. Although extensive research has been done in this field, it still lacks a comprehensive reference work that presents data on properties of different nanomaterials. This *Handbook of Nanomaterials Properties* is an authoritative and comprehensive reference covering all properties of nanomaterials available both commercially and being developed in various labs with some level of reproducibility. The properties being reported should be relevant to all researchers across various industries and related scientific disciplines. This is the first single reference work that brings together the various properties with wide breadth and scope.

The handbook contains chapters on individual nanomaterials containing various properties available in the literature. Contextual text about the processing, size, etc., has been added to make property information meaningful. The handbook covers all types of materials including inorganic, organic, biological, and hybrid materials. The morphologies and nanostructures of all kinds are covered including nanowires, nanotubes, nanorods, nanoparticles, and nanosheets.

The handbook is aimed at researchers and students who need reliable sources to find relevant information/data for their work. Such an electronic platform – with its advanced search functionalities – should be an invaluable resource for anyone working with these materials. To make the book completely searchable (using advanced search functions), each chapter of the book is thoroughly indexed and annotated – right down to the chemical composition of the material as well as its properties and applications.

The handbook is a part of Springer's database on materials called Springer-Materials (which also contains the Landolt-Börnstein book series). It is an online database on materials and their properties. Currently, SpringerMaterials is the largest database of its kind and contains over 100,000 documents on approximately 250,000 chemical substances. SpringerMaterials contains over 400 volumes of the Landolt-Börnstein book series and over 277,000 data sheets on structure/diffraction data, phase diagrams, and physical properties and other databases.

The chapters have been solicited by five coeditors – B. Bhushan, D. Luo, S. Schricker, W. Sigmund, and S. Zauscher. We thank chapter authors for providing state-of-the-art chapters. Finally, we thank acquisitions editors Sharon George and Michael Klinge and development editor Martin Mueller.

Prof. Bharat Bhushan
Coordinating Editor

About the Editors

Dr. Bharat Bhushan is an Ohio Eminent Scholar and The Howard D. Winbigler Professor in the College of Engineering, and the Director of the Nanoprobe Laboratory for Bio- & Nanotechnology and Biomimetics (NLB^2) at the Ohio State University, Columbus, Ohio. He is also serving as an ASME Science & Technology Policy Fellow, House Committee on Science, Space & Technology, United States Congress, Washington, DC. He holds two M.S., a Ph.D. in Mechanical Engineering/Mechanics, an MBA, and two honorary and two semi-honorary doctorates. His research interests include fundamental studies with a focus on scanning probe techniques in the interdisciplinary areas of bio/nanotribology, bio/nanomechanics, and bio/nanomaterials characterization and applications to bio/nanotechnology, and biomimetics. He has authored 8 scientific books, 90+ handbook chapters, 800+ scientific papers (h index, 68+; ISI Highly Cited Researcher in Materials Science since 2007 and in Biology and Biochemistry since 2013; ISI Top 5% Cited Authors for *Journals in Chemistry* since 2011), and 60+ scientific reports. He has also edited 50+ books and holds 19 U.S. and foreign patents. He is co-editor of Springer *NanoScience and Technology* Series and *Microsystem Technologies*. He has organized various international conferences

and workshops. He is the recipient of numerous prestigious awards and international fellowships including the Alexander von Humboldt Research Prize for Senior Scientists, Max Planck Foundation Research Award for Outstanding Foreign Scientists, and the Fulbright Senior Scholar Award. He is a member of various professional societies, including the International Academy of Engineering (Russia). He has previously worked for various research labs including IBM Almaden Research Center, San Jose, CA. He has held visiting professorship at University of California at Berkeley, University of Cambridge, UK, Technical University Vienna, Austria, University of Paris, Orsay, ETH Zurich and EPFL Lausanne. He is currently a visiting professor at University of Southampton, UK, University of Kragujevac, Serbia, Tsinghua University, China, Harbin Institute, China, and KFUPM, Saudi Arabia.

Dr. Dan Luo is currently Professor in the Department of Biological and Environmental Engineering at Cornell University. He is also a faculty member for the field of Biomedical Engineering and Kavli Institute at Cornell for Nanoscale Science. Dr. Luo obtained his B.S. in Biological Sciences from the University of Science and Technology of China and his Ph.D. in Molecular, Cellular and Developmental Biology from The Ohio State University in 1997. He carried out his postdoctoral training in Chemical Engineering at Cornell under Prof. Mark Saltzman. Dr. Luo joined Cornell faculty as an Assistant Professor in 2001, obtained tenure in 2007, and was promoted to full professorship in 2011.

He is a recipient of the National Science Foundation's CAREER Award, the Cornell Provost's Award for Distinguished Scholarship, the SUNY (New York State) Chancellor's Award for Excellence in Scholarship and Creative Activities,

the Journal of Materials Chemistry Editorial Board Award, New York State Faculty Development Award ("Distinguished Professor"), College Award for Outstanding Accomplishments in Basic Research, and Bill and Melinda Gates Foundation Point-of-Care Diagnostics Grand Challenge Award.

Dr. Luo's group has published close to 100 papers and patents with more than 15 in the *Nature*-series journals. Dr. Luo serves as an associate editor or an editorial board member for eight international journals and has given approximately 200 invited talks worldwide since 2001. He was also selected three times by undergraduate students as a Cornell outstanding educator. In 2013, Dr. Luo was elected as a College Fellow of the American Institute of Medical and Biological Engineering (AIMBE).

Dr. Scott Schricker is an Associate Professor at The Ohio State University, College of Dentistry. He earned his B.S. in polymer science at The Pennsylvania State University in 1991 and went on to earn his Ph.D. in Organic Chemistry in 1997 at the University of California, Santa Barbara, with Prof. Fred Wudl. In 1997 he joined Prof. Bill Culbertson's research group at The Ohio State University, College of Dentistry, as a postdoctoral researcher. He joined the faculty at the College in 2001 and became an Associate Professor in 2007. The focus of his research has been utilizing synthetic polymer chemistry to develop novel dental materials and biomaterials. In particular, his focus has been on polymeric restorative materials including glass-ionomer cements, composite resins and maxillofacial prosthetics. In addition, Dr. Schricker has worked on developing nanoscale block copolymer materials to control protein adhesion and adsorption. He has published over 50 peer-reviewed journal articles, review articles and book chapters and also holds a patent.

Wolfgang Sigmund is Professor of Materials Science at the University of Florida, USA. He is a fellow of ASM international and EURASC. He studied chemistry at the University of Heidelberg in Germany, got his doctorate at the University of Mainz for work done at the Max-Planck Institute of polymer research with Prof. G. Wegner. After postdoc and visiting professor positions at the University of Florida in the USA, Universidade de Pernambuco in Brazil, and RIKEN in Japan, he worked at the Powder Metallurgical Laboratory within the Max-Planck Institute of Metals Research where he was deputy director for the associated University of Stuttgart institute of nonmetallic inorganic materials. In 1999 he accepted a position as professor at the University of Florida in Gainesville. He also held a guest professor position at Hanyang University in South Korea from 2009 to 2013. He has published more than 200 articles and patents. His current work focuses on fabrication and processing of nanomaterials using electrospinning and surface science.

Stefan Zauscher Sternberg Family Professor of Mechanical Engineering and Materials Science, and of Biomedical Engineering and Chemistry, Durham, NC, USA

Dr. Stefan Zauscher is the Sternberg Family Professor of Mechanical Engineering and Materials Science at Duke University. He received his Ph.D. in Materials Science from the University of Wisconsin-Madison in 2000. Dr. Zauscher is an expert in (bio)surface and interface science, where a large portion of his research is focused on fabrication and characterization of surface-confined biomolecular and polymeric micro- and nanostructures and the necessary methodologies to manipulate these structures at the nanoscale. Within this broad research scope his research crosses disciplinary boundaries. He has authored over 100 scientific papers and book chapters (h index, 29). He is also a co-investigator and the Director for Education and Outreach in the recently NSF funded Triangle Materials Research Science and Engineering Center (MRSEC). Dr. Zauscher has organized several international conferences, and served as the Chair for the Biomaterial Interfaces Division of the AVS, and is the Chair of the 2014 Gordon Research Conference (GRC) in Biointerface Science. Dr. Zauscher is the recipient of numerous awards, including an NSF Faculty Early Career Development Award, the ICCES Outstanding Young Investigator Award, the 2012 Capers and Marion McDonald Award for Excellence in Teaching and Research, and he is a Fellow of the Bass Society at Duke University.

Contents

Volume 2

Contributors

Angelo Accardo Nanostructures Department, Italian Institute of Technology, Genoa, Italy

Olga Albert ERC Advanced Grant Research Group at the Institute for Physiological Chemistry, University Medical Center of the Johannes Gutenberg University Mainz, Mainz, Germany

Paolo Allia Applied Science and Technology Department, Politecnico di Torino, Torino, Italy

Esther Amstad Department of Physics, School of Engineering and Applied Sciences, Harvard University, Cambridge, MA, USA

Peter M. Anderson Department of Materials Science and Engineering, The Ohio State University, Columbus, OH, USA

Jennifer S. Andrew Department of Materials Science and Engineering, University of Florida, Gainesville, FL, USA

Mathieu Artus Department of Chemistry and Chemical Biology, McMaster Univeristy, Hamilton, ON, Canada

A. J. Atanacio Solar Energy Technologies, School of Computing, Engineering and Mathematics, University of Western Sydney, Penrith, NSW, Australia

Australian Nuclear Science and Technology Organisation, Kirrawee DC, NSW, Australia

Brandon Aubie Biointerfaces Institute, McMaster University, Hamilton, ON, Canada

Shereen S. Azer Division of Restorative, Prosthetic and Primary Care Dentistry, The Ohio State University College of Dentistry, Columbus, OH, USA

Wolfgang Bacsa Centre d'Elaboration des Matériaux et d'Etudes Structurales (CEMES), UPR-8011 CNRS, University of Toulouse, Toulouse, France

Tad Bak Solar Energy Technologies, School of Computing, Engineering and Mathematics, University of Western Sydney, Penrith, NSW, Australia

Manuel Bañobre-López International Iberian Nanotechnology Laboratory (INL), Braga, Portugal

Rohit Bhandari University Institute of Pharmaceutical Sciences, Panjab University, Chandigarh, India

Bharat Bhushan Nanoprobe Laboratory for Bio- & Nanotechnology and Biomimetics (NLBB), The Ohio State University, Columbus, OH, USA

John D. Brennan Department of Chemistry and Chemical Biology, McMaster Univeristy, Hamilton, ON, Canada

Dorothea Brüggemann School of Physics and CRANN, Trinity College Dublin, Dublin, Ireland

Department of New Materials and Biosystems, Max Planck Institute for Intelligent Systems, Stuttgart, Germany

Markus J. Buehler Laboratory for Atomistic and Molecular Mechanics (LAMM), Department of Civil and Environmental Engineering, Massachusetts Institute of Technology, Cambridge, MA, USA

Center for Computational Engineering, Massachusetts Institute of Technology, Cambridge, MA, USA

Giancarlo Canavese Center for Space Human Robotics@PoliTO, Istituto Italiano di Tecnologia, Torino, Italy

Patrizio Candeloro BioNEM Laboratories, Department of Experimental and Clinical Medicine, University Magna Graecia of Catanzaro, Catanzaro, Italy

Changhong Cao Department of Mechanical and Industrial Engineering, University of Toronto, Toronto, ON, Canada

Santino D. Carnevale Materials Science and Engineering Department, The Ohio State University, Columbus, OH, USA

John S. Carpenter Materials Science and Technology Division, Los Alamos National Laboratory, Los Alamos, NM, USA

Valentina Cauda Center for Space Human Robotics@PoliTO, Istituto Italiano di Tecnologia, Torino, Italy

Shu-Wei Chang Laboratory for Atomistic and Molecular Mechanics (LAMM), Department of Civil and Environmental Engineering, Massachusetts Institute of Technology, Cambridge, MA, USA

Elisabeth Charlaix Laboratoire interdisciplinaire de physique, Université Grenoble 1, CNRS, Grenoble, France

Yi Chen Department of Chemical Engineering, Faculty of Engineering, Monash University, Clayton, VIC, Australia

The Melbourne Centre for Nanofabrication, Clayton, VIC, Australia

Wenlong Cheng Department of Chemical Engineering, Faculty of Engineering, Monash University, Clayton, VIC, Australia

The Melbourne Centre for Nanofabrication, Clayton, VIC, Australia

Angelica Chiodoni Center for Space Human Robotics@PoliTO, Istituto Italiano di Tecnologia, Torino, Italy

Alessandro Chiolerio Center for Space Human Robotics@PoliTO, Istituto Italiano di Tecnologia, Torino, Italy

Manohar Chirumamilla Nanostructures Department, Italian Institute of Technology, Genoa, Italy

Seon-Jin Choi Department of Materials Science and Engineering, Korea Advanced Institute of Science and Technology (KAIST), Yuseong-gu, Daejeon, Republic of Korea

Wonbong Choi Department of Materials Science and Engineering, University of North Texas, Denton, TX, USA

Nitin Choudhary Department of Materials Science and Engineering, University of North Texas, Denton, TX, USA

Dewei Chu University of New South Wales, School of Materials Science and Engineering, Sydney, NSW, Australia

Maria Laura Coluccio BioNEM Laboratories, Department of Experimental and Clinical Medicine, University Magna Graecia of Catanzaro, Catanzaro, Italy

David S. Courson Department of Materials Science and Engineering, North Carolina State University, Raleigh, NC, USA

Stephen L. Craig Chemistry Department, Duke University, Durham, NC, USA

Si Amar Dahoumane Department of Chemistry and Chemical Biology, McMaster Univeristy, Hamilton, ON, Canada

Gobind Das Nanostructures Department, Italian Institute of Technology, Genoa, Italy

Massey de Los Reyes Australian Nuclear Science and Technology Organization, Lucas Heights, Australia

Johann P. de Silva School of Physics and CRANN, Trinity College Dublin, Dublin, Ireland

Bohua Dong Division of Nanobiomedicine, Suzhou Institute of Nano-Tech and Nano-Bionics, Chinese Academy of Sciences, Suzhou, Jiangsu, China

Ashish Dubey Department of Electrical Engineering and Computer Sciences, Center for Advanced Photovoltaics, DEH 219, South Dakota State University, Brookings, SD, USA

Kathy L. Elias Division of Orthodontics, College of Dentistry, The Ohio State University, Columbus, OH, USA

Walter Escoffier Laboratoire National des Champs Magnétiques Intenses, INSA UPS UJF CNRS, UPR 3228, Université de Toulouse, Toulouse, France

Nicole A. Estrich Department of Materials Science and Engineering, North Carolina State University, Raleigh, NC, USA

Enzo Di Fabrizio Physical Science & Engineering Division, King Abdullah University of Science and Technology, Thuwal, Kingdom of Saudi Arabia

Tobin Filleter Department of Mechanical and Industrial Engineering, University of Toronto, Toronto, ON, Canada

Emmanuel Flahaut Centre Inter-universitaire de Recherche et d'Ingénierie sur les Matériaux (CIRIMAT), UMR-5085 CNRS-UPS-INP, Institut Carnot, Université de Toulouse, Toulouse cedex 9, France

Rossana Gazia Center for Space Human Robotics@PoliTO, Istituto Italiano di Tecnologia, Torino, Italy

Francesco Gentile BioNEM Laboratories, Department of Experimental and Clinical Medicine, University Magna Graecia of Catanzaro, Catanzaro, Italy

Michael D. Gram Department of Materials Science and Engineering, The Ohio State University, Columbus, OH, USA

Liangran Guo Department of Biomedical and Pharmaceutical Sciences, College of Pharmacy, The University of Rhode Island, Kingston, RI, USA

Gautam Gupta Center for Integrated Nanotechnologies, Los Alamos National Laboratory, Los Alamos, NM, USA

Carol K. Hall Department of Chemical and Biomolecular Engineering, North Carolina State University, Raleigh, NC, USA

Wei Han NSF Research Triangle Materials Research Science and Engineering Center, Durham, NC, USA

Department of Biomedical Engineering, Duke University, Durham, NC, USA

James M. Harris NSF Research Triangle Materials Research Science and Engineering Center, Durham, NC, USA

Department of Biomedical Engineering, Duke University, Durham, NC, USA

Blake-Joseph Helka Department of Chemistry and Chemical Biology, McMaster Univeristy, Hamilton, ON, Canada

Yike Huang Pennsylvanian State University, University Park, PA, USA

Sookhyun Hwang Department of Materials Science and Engineering, University of North Texas, Denton, TX, USA

Mihail Ionescu Australian Nuclear Science and Technology Organisation, Kirrawee DC, NSW, Australia

Linnea K. Ista Center for Biomedical Engineering, Department of Chemical and Nuclear Engineering, University of New Mexico, Albuquerque, NM, USA

Esmaiel Jabbari Department of Chemical Engineering, Swearingen Engineering Center, Rm 2C11, University of South Carolina, Columbia, SC, USA

Andreas Janshoff Institute of Physical Chemistry, University of Göttingen, Göttingen, Germany

Indu Pal Kaur University Institute of Pharmaceutical Sciences, Panjab University, Chandigarh, India

Do-Gyoon Kim Division of Orthodontics, College of Dentistry, The Ohio State University, Columbus, OH, USA

Il-Doo Kim Department of Materials Science and Engineering, Korea Advanced Institute of Science and Technology (KAIST), Yuseong-gu, Daejeon, Republic of Korea

Roman Krahne Nanostructures Department, Italian Institute of Technology, Genoa, Italy

Uma Maheswari Krishnan Centre for Nanotechnology and Advanced Biomaterials (CeNTAB), School of Chemical & Biotechnology, SASTRA University, Thanjavur, India

Priyadharshini Kumaraswamy Centre for Nanotechnology and Advanced Biomaterials (CeNTAB), School of Chemical & Biotechnology, SASTRA University, Thanjavur, India

Thomas H. LaBean Department of Materials Science and Engineering, North Carolina State University, Raleigh, NC, USA

Christophe Laurent Centre Inter-universitaire de Recherche et d'Ingénierie sur les Matériaux (CIRIMAT), UMR-5085 CNRS-UPS-INP, Institut Carnot, Université de Toulouse, Toulouse cedex 9, France

Thomas D. Lazzara Institute of Organic and Biomolecular Chemistry, University of Göttingen, Göttingen, Germany

Polytechnique Montreal, 2900 boul, Édouard–Montpetit, Université de Montréal Campus 2500, Montréal, Québec, Canada

Liliane Léger Laboratoire de physique des solides, Université Paris-Sud – CNRS, Orsay, France

S. Leroy Institut Lumière Matière, Université Lyon 1 – CNRS, Villeurbanne, France

Chunyan Li Division of Nanobiomedicine, Suzhou Institute of Nano-Tech and Nano-Bionics, Chinese Academy of Sciences, Suzhou, Jiangsu, China

Lin Li Department of Metallurgical and Materials Engineering, The University of Alabama, Tuscaloosa, AL, USA

Linying Li NSF Research Triangle Materials Research Science and Engineering Center, Durham, NC, USA

Department of Biomedical Engineering, Duke University, Durham, NC, USA

Qing Li Department of Mechanical Engineering and Materials Science, Center for Biologically Inspired Materials and Material Systems, and Duke University, Durham, NC, USA

Yajuan Li Department of Biomedical and Pharmaceutical Sciences, College of Pharmacy, The University of Rhode Island, Kingston, RI, USA

Carlo Liberale Nanostructures Department, Italian Institute of Technology, Genoa, Italy

Paul Logan Department of Physics, Arizona State University, Tempe, AZ, USA

Gabriel P. López NSF Research Triangle Materials Research Science and Engineering Center, Durham, NC, USA

Department of Biomedical Engineering, Duke University, Durham, NC, USA

Department of Mechanical Engineering and Materials Science, Duke University, Durham, NC, USA

M. Arturo López-Quintela Departments of Physical Chemistry and Applied Physics, University of Santiago de Compostela, Santiago de Compostela, Spain

Wei Lu Department of Biomedical and Pharmaceutical Sciences, College of Pharmacy, The University of Rhode Island, Kingston, RI, USA

School of Pharmacy, Fudan University, Shanghai, China

Bruno Machado Laboratoire de Chimie de Coordination-ENSIACET, UPR-8241 CNRS, Université de Toulouse, Toulouse, France

Dave Maharaj Nanoprobe Laboratory for Bio- & Nanotechnology and Biomimetics (NLBB), The Ohio State University, Columbus, OH, USA

Peter Majewski Division of Information Technology, Engineering and the Environment, School of Engineering, Mawson Institute, University of South Australia, Mawson Lakes, Australia

Jacob Majikes Department of Materials Science and Engineering, North Carolina State University, Raleigh, NC, USA

Martin Malmsten Department of Pharmacy, Uppsala University, Uppsala, Sweden

Diego Manfredi Center for Space Human Robotics@PoliTo, Istituto Italiano di Tecnologia, Torino, Italy

Alexandria N. Marchi Department of Biomedical Engineering, Duke University, Durham, NC, USA

Piotr E. Marszalek Department of Mechanical Engineering and Materials Science, Center for Biologically Inspired Materials and Material Systems, and Duke University, Durham, NC, USA

Paola Martino Politronica Inkjet Printing S.r.l, Torino, Italy

Emmanuelle Martinot Laboratoire de physique des solides, Université Paris-Sud – CNRS, Orsay, France

Amanda Mcguire Department of Chemistry and Physics, Armstrong Atlantic State University, Savannah, GA, USA

Ermanno Miele Nanostructures Department, Italian Institute of Technology, Genoa, Italy

Sarah S. Mikhail Division of Restorative, Prosthetic and Primary Care Dentistry, The Ohio State University College of Dentistry, Columbus, OH, USA

Seyedsina Moeinzadeh Department of Chemical Engineering, Swearingen Engineering Center, Rm 2C11, University of South Carolina, Columbia, SC, USA

Marc Monthioux Centre d'Elaboration des Matériaux et d'Etudes Structurales (CEMES), UPR-8011 CNRS, University of Toulouse, Toulouse, France

Werner E. G. Müller ERC Advanced Grant Research Group at the Institute for Physiological Chemistry, University Medical Center of the Johannes Gutenberg University Mainz, Mainz, Germany

Roberto C. Myers Materials Science and Engineering Department, The Ohio State University, Columbus, OH, USA

Jessica A. Nash Department of Materials Science and Engineering, North Carolina State University, Raleigh, NC, USA

Janusz Nowotny Solar Energy Technologies, School of Computing, Engineering and Mathematics, University of Western Sydney, Penrith, NSW, Australia

Clifford Padgett Department of Chemistry and Physics, Armstrong Atlantic State University, Savannah, GA, USA

Manuel Palacio Western Digital

Simone Panaro Nanostructures Department, Italian Institute of Technology, Genoa, Italy

Zehra Parlak Department of Mechanical Engineering and Material Science, Duke University, Durham, NC, USA

Ronnie Pedersen Duke University, Durham, NC, USA

Xihong Peng School of Letters and Sciences, Arizona State University, Mesa, AZ, USA

Carmem S. Pfeifer Oregon Health and Science University, School of Dentistry, Portland, OR, USA

Y. Piñeiro Departments of Physical Chemistry and Applied Physics, University of Santiago de Compostela, Santiago de Compostela, Spain

Samuele Porro Center for Space Human Robotics@PoliTO, Istituto Italiano di Tecnologia, Torino, Italy

Christophe Poulard Laboratoire de physique des solides, Université Paris-Sud – CNRS, Orsay, France

Remo Proietti Zaccaria Nanostructures Department, Italian Institute of Technology, Genoa, Italy

Pascal Puech Centre d'Elaboration des Matériaux et d'Etudes Structurales (CEMES), UPR-8011 CNRS, University of Toulouse, Toulouse, France

Georgios Pyrgiotakis Department of Environmental Health, Harvard School of Public Health, Boston, USA

Xuefeng Qian School of Chemistry and Chemical Engineering, State Key Laboratory of Metal Matrix Composites, Shanghai Jiao Tong University, Shanghai, China

Qiquan Qiao Department of Electrical Engineering and Computer Sciences, Center for Advanced Photovoltaics, DEH 219, South Dakota State University, Brookings, SD, USA

Vijayakumar Rajamanickam Nanostructures Department, Italian Institute of Technology, Genoa, Italy

Bertrand Raquet Laboratoire National des Champs Magnétiques Intenses, INSA UPS UJF CNRS, UPR 3228, Université de Toulouse, Toulouse, France

Erik Reimhult Department of Nanobiotechnology, Institute for Biologically Inspired Materials, University of Natural Resources and Life Sciences Vienna, Vienna, Austria

Frédéric Restagno Laboratoire de physique des solides, Université Paris-Sud – CNRS, Orsay, France

José Rivas International Iberian Nanotechnology Laboratory (INL), Braga, Portugal

Ignazio Roppolo Center for Space Human Robotics@PoliTO, Istituto Italiano di Tecnologia, Torino, Italy

Won-Hee Ryu Department of Materials Science and Engineering, Korea Advanced Institute of Science and Technology (KAIST), Yuseong-gu, Daejeon, Republic of Korea

Shayla Sawyer Electrical, Computer, and Systems Engineering Department, Rensselaer Polytechnic Institute, Troy, NY, USA

Zackary N. Scholl Program in Computational Biology and Bioinformatics, Duke University, Durham, NC, USA

Scott R. Schricker Division of Restorative, Prosthetic and Primary Care Dentistry, The Ohio State University Columbus, Columbus, OH, USA

Heinz C. Schröder ERC Advanced Grant Research Group at the Institute for Physiological Chemistry, University Medical Center of the Johannes Gutenberg University Mainz, Mainz, Germany

Philippe Serp Laboratoire de Chimie de Coordination-ENSIACET, UPR-8241 CNRS, Université de Toulouse, Toulouse, France

Swaminathan Sethuraman Centre for Nanotechnology and Advanced Biomaterials (CeNTAB), School of Chemical & Biotechnology, SASTRA University, Thanjavur, India

Dali Shao Electrical, Computer, and Systems Engineering Department, Rensselaer Polytechnic Institute, Troy, NY, USA

Stefano Stassi Center for Space Human Robotics@PoliTO, Istituto Italiano di Tecnologia, Torino, Italy

Claudia Steinem Institute of Organic and Biomolecular Chemistry, University of Göttingen, Göttingen, Germany

Yu Sun Department of Mechanical and Industrial Engineering, University of Toronto, Toronto, ON, Canada

Fu Tang Department of Physics, Arizona State University, Tempe, AZ, USA

Anna Tarakanova Laboratory for Atomistic and Molecular Mechanics (LAMM), Department of Civil and Environmental Engineering, Massachusetts Institute of Technology, Cambridge, MA, USA

Andrea Toma Nanostructures Department, Italian Institute of Technology, Genoa, Italy

Qing Tu Department of Mechanical Engineering and Material Science, Duke University, Durham, NC, USA

Richar Villey Institut Lumière Matière, Université Lyon 1 – CNRS, Villeurbanne, France

Qiangbin Wang Division of Nanobiomedicine, Suzhou Institute of Nano-Tech and Nano-Bionics, Chinese Academy of Sciences, Suzhou, Jiangsu, China

Xiaohong H. Wang ERC Advanced Grant Research Group at the Institute for Physiological Chemistry, University Medical Center of the Johannes Gutenberg University Mainz, Mainz, Germany

National Research Center for Geoanalysis, Beijing, China

Yong Wang Pennsylvanian State University, University Park, PA, USA

Tad Whiteside Savannah River National Laboratory, Aiken, SC, USA

Bernhard Wolfrum Institute of Bioelectronics (PGI–8/ICS–8), Forschungszentrum Jülich, Jülich, Germany

IV. Institute of Physics, RWTH Aachen University, Aachen, Germany

Xuezhong Wu College of Mechatronics Engineering and Automation, National University of Defense Technology, Changsha, China

Xiang Xi College of Mechatronics Engineering and Automation, National University of Defense Technology, Changsha, China

Zeyu Xiao David H. Koch Institute for Integrative Cancer Research, Massachusetts Institute of Technology, Cambridge, MA, USA

Hockin H. K. Xu Biomaterials & Tissue Engineering Division, Department of Endodontics, Prosthodontics and Operative Dentistry, University of Maryland School of Dentistry, Baltimore, MD, USA

Xiaoming Xu Division of Biomaterials, Department of Comprehensive Dentistry & Biomaterials, Louisiana State University Health Sciences Center School of Dentistry, New Orleans, LA, USA

Jatinder Vir Yakhmi Homi Bhabha National Institute, Mumbai, India

Wenjuan Yang Department of Chemical Engineering, Faculty of Engineering, Monash University, Clayton, VIC, Australia

The Melbourne Centre for Nanofabrication, Clayton, VIC, Australia

Jiantao Zai School of Chemistry and Chemical Engineering, State Key Laboratory of Metal Matrix Composites, Shanghai Jiao Tong University, Shanghai, China

Stefan Zauscher Department of Mechanical Engineering and Material Science, Duke University, Durham, NC, USA

Properties of Carbon Nanotubes

1

Marc Monthioux, Emmanuel Flahaut, Christophe Laurent,
Walter Escoffier, Bertrand Raquet, Wolfgang Bacsa, Pascal Puech,
Bruno Machado, and Philippe Serp

Keywords

Bioapplications • Chemisorption • Cytotoxicity • Ecotoxicity • Mechanical •
Multi-wall carbon nanotubes • Nanotexture • Optical • Physisorption • Properties •
Single-wall carbon nanotubes • Structure • Texture • Thermal • Transport

Introduction

Carbon nanotubes are certainly the most studied nanomaterials ever, considering
the cumulated number of papers devoted to them since the 1990s (Fig. 1.1). Only
graphene will possibly overcome nanotubes in this regard one day, specifically
because of the boosting effect of the Nobel Prize dedicated to it in 2010. But it
cannot be ignored that carbon nanotubes are primarily based on graphene, and

M. Monthioux (✉) • W. Bacsa • P. Puech
Centre d'Elaboration des Matériaux et d'Etudes Structurales (CEMES), UPR-8011 CNRS,
University of Toulouse, Toulouse, France
e-mail: marc.monthioux@cemes.fr; wolfgang.bacsa@cemes.fr; pascal.puech@cemes.fr

E. Flahaut • C. Laurent
Centre Inter-universitaire de Recherche et d'Ingénierie sur les Matériaux (CIRIMAT), UMR-5085
CNRS-UPS-INP, Institut Carnot, Université de Toulouse, Toulouse cedex 9, France
e-mail: flahaut@chimie.ups-tlse.fr; laurent@chimie.ups-tlse.fr

W. Escoffier • B. Raquet
Laboratoire National des Champs Magnétiques Intenses, INSA UPS UJF CNRS, UPR 3228,
Université de Toulouse, Toulouse, France
e-mail: walter.escoffier@lncmi.cnrs.fr; bertrand.raquet@lncmi.cnrs.fr

B. Machado • P. Serp
Laboratoire de Chimie de Coordination-ENSIACET, UPR-8241 CNRS, Université de Toulouse,
Toulouse, France
e-mail: bruno.machado@ensiacet.fr; philippe.serp@ensiacet.fr

Fig. 1.1 Number of research
papers published every year
from 1990 to 2008 devoted to
fullerenes, carbon nanotubes,
and graphenes, respectively.
The 'SCI' plot reveals the
trend of the overall scientific
literature for comparison
(Modified from [1],
completed with [2])
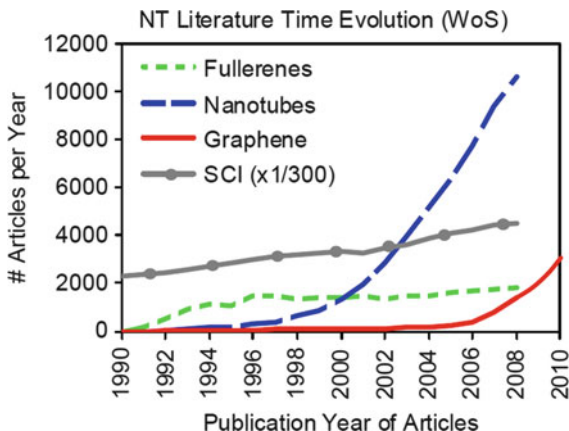
understanding carbon nanotube properties (and any other graphene-based materials indeed) requires describing graphene properties first.

Carbon nanotubes are built from sp^2-hybridized carbon atoms assembled via very short σ-bonds as hexagonal rings (that chemists call aromatic cycles), with the rings assembled according to a planar periodic lattice looking like a single-atom-thick hexagonal pavement, the otherwise-named graphene mentioned above (Fig. 1.2).

As a consequence of the hybridization state, each of the carbon atoms involved in graphene has an unpaired electron (π-electron) which has no reason to bond to one of its three neighbors preferably to another and therefore remain unlocalized. The presence of unlocalized electrons on the graphene surface is responsible for the **amazing electrical conductivity** in the graphene plane. It also maintains the C–C distance at the very short value of 0.142 nm (the same as that of genuine C=C double bonds, so-called π-bonds, which is even shorter than the C–C bond in diamond – 0.154 nm) which ensures the **extremely high mechanical resistance** of graphene and makes it the strongest material ever. The very short distance between atoms within cycles, the periodicity of their distribution, and the presence of the cloud of delocalized electrons are favorable features for phonon propagation, providing the graphene plane with **high thermal conductivity**.

As any periodic display of atoms, the perfect graphene lattice may be affected by structural defects, which consist in (i) vacancies and (ii) heterocycles, i.e., penta-gons, heptagons, and, more scarcely, octagons, for citing the energetically viable ones only (indeed, the constrains brought to bond angles in heterocycles with respect to the 120° bond angle in the aromatic ring decrease the stability of the ring). Heterocycles are particularly important as they generate severe and permanent curvatures in the graphene plane. For instance, adding one pentagon or one heptagon is enough to deform a planar graphene into a Chinese hat or a saddle horse, respectively [3], and the most well-known example of the effect of heterocycles is probably that of fullerenes, which can be described as a graphene closed into a sphere-like surface because it contains twelve pentagons [4]. It is worth noting that, when combined as close neighbors, the curving effect of a given

$$\vec{OA} = \vec{C}_h = n\vec{a}_1 + m\vec{a}_2$$

$$= \frac{a\sqrt{3}}{2}\vec{x} + \frac{a}{2}\vec{y} \quad \text{and} \quad \vec{a}_2 = \frac{a\sqrt{3}}{2}\vec{x} - \frac{a}{2}\vec{y} \quad \text{where} \quad a = 2.46 \,\overset{\circ}{A}$$

$$d = \frac{|\vec{C}_h|}{\pi} = \frac{a_{cc}\sqrt{3(n^2 + m^2 + nm)}}{\pi}$$

$$\text{where} \quad 1.41 \overset{\circ}{A} \leq a_{cc} \leq 1.44 \,\overset{\circ}{A}$$

$$\text{(graphite)} \qquad (C_{60})$$

$$\cos\theta = \frac{2n+m}{2\sqrt{n^2 + m^2 + nm}}$$
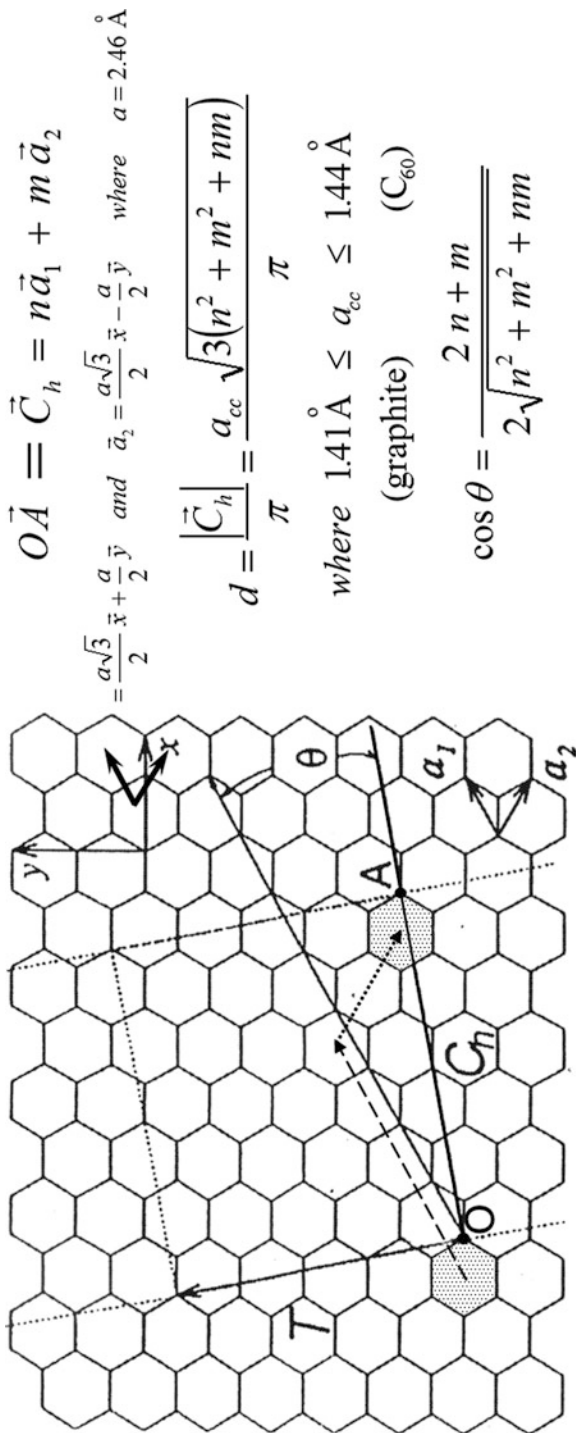
Fig. 1.2 Starting from a graphene lattice, a nanotube is obtained by rolling the graphene over itself, for instance, in the direction OA (which will determine the helicity angle θ), in such a way that, e.g., the atom in O superimposes to the atom in A (which determines the diameter $d = |C_h/\pi|$). The resulting tube is identified by the indices (n, m) where n and m are the number of rings that have to be crossed in the path from O to A while following the directions of the lattice vectors a_1 and a_2. In this case, the resulting tube is (4, 2) (Adapted from [8])

number of pentagons is compensated by the same number of heptagons, so that the graphene recovers planarity with only slight remaining deformations. Another consequence of the presence of heterocycles is to disrupt the perfect balance of the lattice symmetry, inducing the π-electrons of the carbon atoms involved to generate localized C=C double bonds instead of contributing to the π-electron cloud. Localized C=C double bonds and strains enhance the overall chemical reactivity and generate preferred sites for chemical reactions, otherwise quite limited except at the graphene edge.

Then, piling up graphenes on top of each other is of course possible, and it is the way genuine graphite is built, as well as most of sp^2-carbon-based materials indeed. As there are no more electrons available per atom, the only bonding possibility between stacked graphenes is to share their π-electron clouds, which results in a weak bonding strength, in the range of van der Waals forces (7 kJ mol^{-1} vs. 524 kJ mol^{-1} for the in-plane C–C bond). It also results in graphene-graphene distances which cannot be shorter than 0.3354 nm (i.e., the stacking distance in genuine graphite) but which can be much higher, e.g., 0.344 nm, for perfect but turbostratically stacked graphenes [5] (see below) and up to 0.4 nm or more in carbon material precursors [6]. This severely affects the mechanical, thermal, and electrical properties in the direction perpendicular to the graphene stacking plane.

From the quick picture above, it is now easy to understand that all the properties of carbon nanotubes will tightly depend on the number, perfection, and orientation of the graphenes that they are made with, mostly with respect to the elongation axis.

Describing Carbon Nanotubes

Carbon Nanotubes as Graphene-Based Objects

The simplest carbon nanotube, so-called single-wall carbon nanotubes (SWCNTs), can be described as a graphene rolled into a cylinder and closed at both ends by half fullerenes (therefore containing six pentagons each; see section 'Introduction') having the appropriate diameter. Of course, the graphene can be rolled up following various directions with respect to the symmetries of the graphene lattice, and, as described in Fig. 1.2, each SWCNT is identified by a set of two indices n and m that characterize them univocally [7], with a simple geometrical relationship between the nanotube diameter, the helicity angle, and the (n, m) indices.

A whole variety of carbon nanotubes with various helicity are thereby generated (Fig. 1.3). Meanwhile, whatever the (n, m) indices, SWCNTs can only exhibit a single morphology, that of a flexible nanofilament, with branching as the only possible – yet scarce – alternative. On the other hand, the only structural defects that can affect the SWCNT lattice are the same as for graphene, i.e., vacancies and heterocycles (see section 'Introduction'). Depending on their nature (pentagon, heptagon, and octagon), number, combination, and location, they can induce various kinds of distortion to the SWCNT morphology, either almost unnoticeable (e.g., in case of 5–7 ring pair) or severe (e.g., knee, diameter constriction).
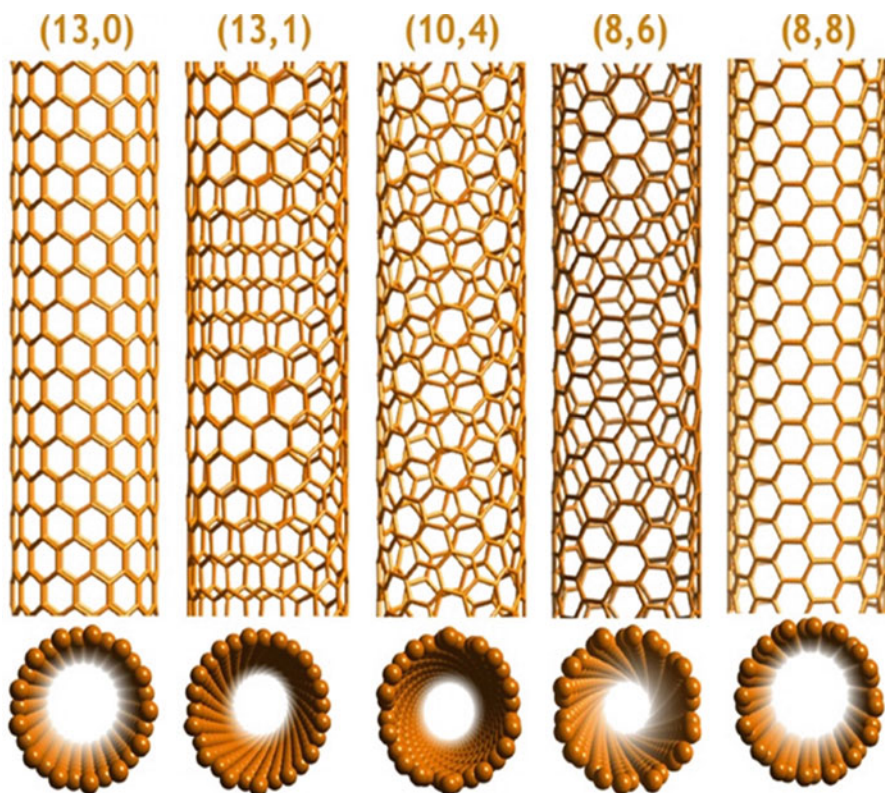
Fig. 1.3 Examples of single-wall carbon nanotubes with various helicities [9]. By reference to the cross-sectional edge aspect, $(n, 0)$ SWNTs are of so-called 'zigzag' type – here: $(13, 0)$– and (n, n) are of so-called 'armchair' type – here: $(8, 8)$. Both families are achiral since they exhibit symmetry planes in directions both parallel and perpendicular to the nanotube elongation axis. All other nanotube types are chiral and do not exhibit any symmetry plane

Much more complex to describe are so-called – yet improperly – 'multi-wall carbon nanotubes' (MWCNTs) whose wall is made of stacked graphenes, as they are subjected to large **morphological**, **textural**, **nanotextural**, and **structural** variations [10] which cannot affect SWCNTs. MWCNT morphologies can be straight, coiled, conical, branched, etc.

For each of those morphologies, a variety of textures may exist, with some modeled in Fig. 1.4.

In addition, nanotextural variations occur due to the presence of various in-plane (e.g., heterocycles) and out-of-plane (e.g., screw dislocations) defects which induce distortions within graphene stacks, in various extent, as illustrated in Fig. 1.5.

Defect-induced distortions as shown in Fig. 1.5 can be healed upon thermal treatment as the regular structural path for the carbonization then graphitization processes [15] or, on the contrary, can be provoked by any physical or chemical
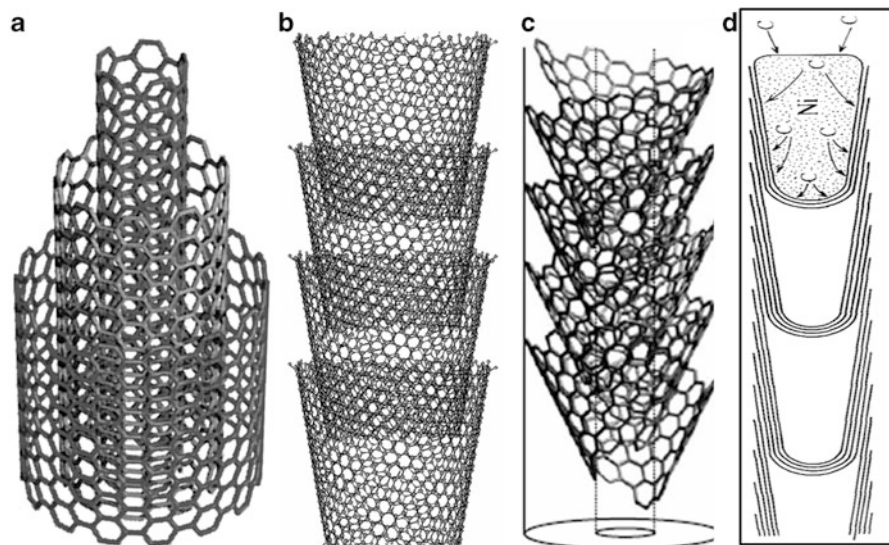
Fig. 1.4 Examples of multi-wall carbon nanotubes exhibiting various inner textures among the most frequent, all demonstrated in the literature. (**a**) is the so-called 'concentric' texture [11], actually made of SWCNTs of increasing diameters concentrically assembled; (**b**) and (**c**) are two possibilities for the so-called 'herringbone' texture: (**b**) is made of stacked, truncated graphene-based cones (Adapted from [12]); (**c**) is made of a single ribbonlike graphene helically wrapped over itself (Adapted from [13]). (**d**) is one possibility of the so-called 'bamboo' texture (From [14]), for which graphenes can be displayed perpendicular to the nanotube axis, thereby locally closing up the inner nanotube cavity. The bamboo texture does not exist by itself; it has to be combined with another (concentric or herringbone as exampled)

L_1 Average length of the stiff fringes
L_2 Average length of the continuous (yet distorted) fringes
N   Average number of fringes within the coherent graphene stacks
β   Average misorientation angle
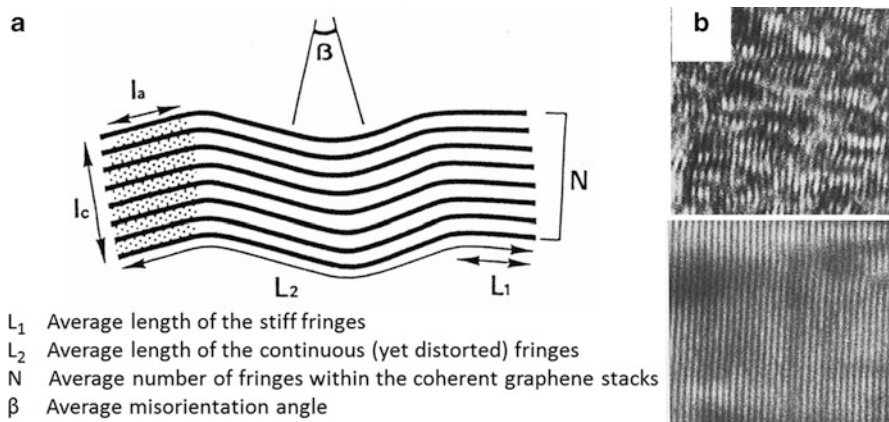
Fig. 1.5 Explanation of what nanotextural variation is, with (**a**) the various parameters to describe it, and (**b**) two examples (lattice fringe resolution transmission electron microscopy) of graphene stacks with different nanotextural order, increasing from *top* to *bottom*

Fig. 1.6 X-ray diffraction profiles typical of (**a**) an ensemble of SWCNTs of similar diameters and therefore arranged into a bundle according to a hexagonal lattice in cross section. The periodicities revealed by the diffraction spots are different from that of other crystallized forms of carbon, indicating that such a material (a SWCNT bundle) is a genuine carbon allotrope; (**b**) X-ray diffraction profiles typical of (*top*) a powder of MWCNTs and (*bottom*) a powder of genuine graphite flakes. Both show the 00*l* spots generated by the stacking sequence. However, the fact that graphenes are coherently stacked with orientation relationships in graphite gives rise to three-indices hkl diffraction spots with *h* and/or *k* $\neq 0$ and *l* $\neq 0$, whereas the fact that graphenes are not coherently stacked in MWCNTs gives rise to two-indices *hk* diffraction spots only
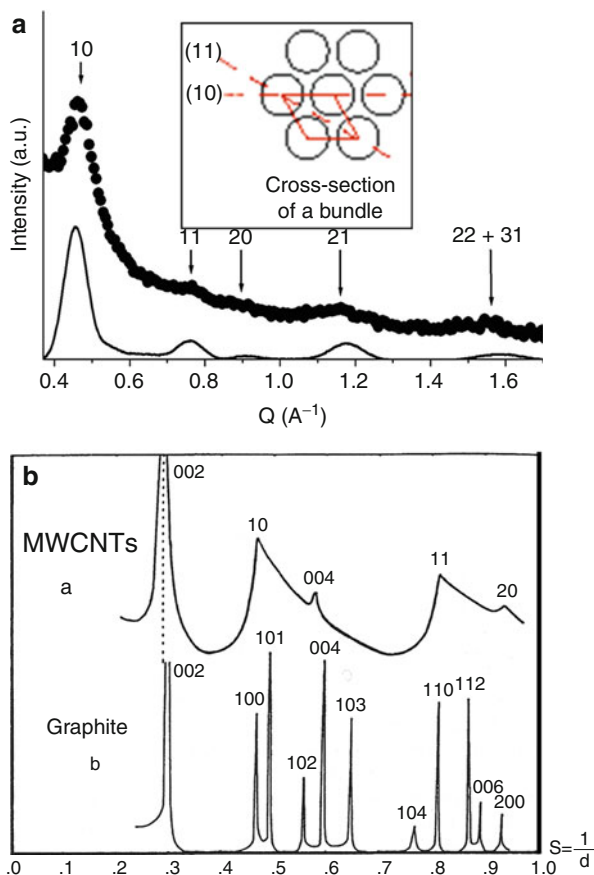
process able to alter the structure, e.g., irradiation (by neutrons, UV photons, ions, electrons [16], etc.) or partial oxidation (by heating up in air [17], soaking in concentrated nitric acid [18], etc.).

Carbon Nanotubes as Crystals

The structure of individual SWCNTs as described by Figs. 1.2 and 1.3 relates to that of macromolecules rather than that of crystals. On the other hand, van der Waals forces tend to make them agglomerate into bundles. If the SWCNTs involved in the bundles exhibit similar diameters (which is frequent), they spontaneously arrange according to a hexagonal lattice [19]; hence, they form one of the carbon allotropes (along with graphite, diamond, fullerite, lonsdaleite, etc.) – sometimes called 'nanotubulite' – since such an arrangement of SWCNTs generates specific period-icities and related diffraction spots (Fig. 1.6a).

On the contrary, the structure of individual MWCNTs relates to that of crystals instead of macromolecules. Because they are graphene-based materials, the
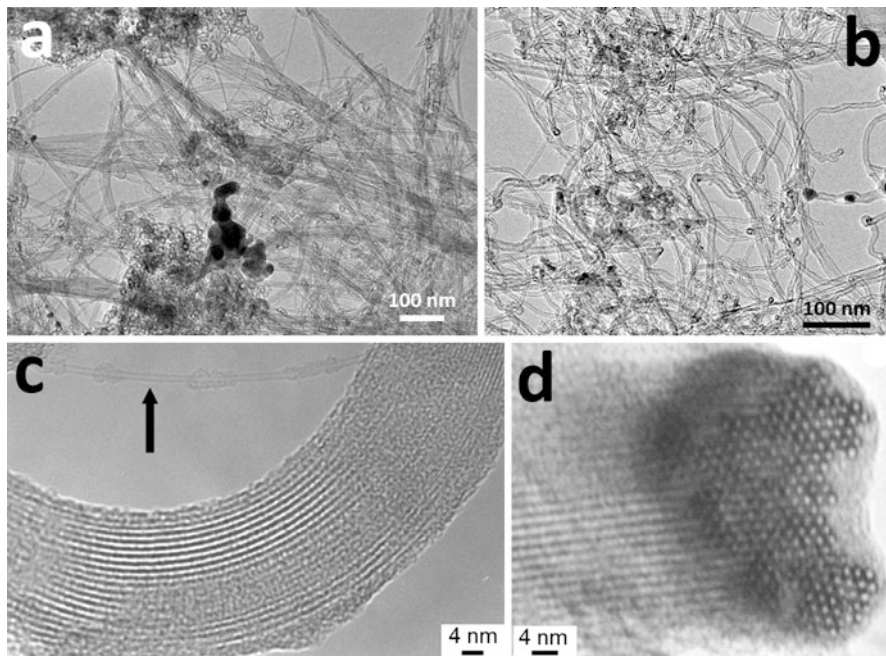
Fig. 1.7 TEM images of carbon nanotubes. Low magnification images showing entangled nanofilaments for (**a**) a SWCNT material and (**b**) a MWCNT material. (**c**) Higher magnification image showing that each nanofilament from (**a**) is actually a SWCNT bundle. An individual SWCNT is *arrowed* (From [20]). (**d**) A SWCNT bundle oriented with respect to the TEM electron beam so that the bundle cross section shows up, revealing the periodic (*hexagonal*) display of the SWCNTs (From [20])

MWCNT structure then tends towards that of genuine graphite (Fig. 1.6b, bottom). However, the way graphenes are stacked in MWCNTs prevents them to follow the ABAB Bernal stacking type typical of graphite, either because of the graphene curvature, for instance (e.g., in concentric-type MWCNTs, where the lattices of two successive nanotubes, yet perfect, cannot superimpose coherently over a long range), or because of the low-grade nanotexture. Therefore, instead of being exactly superimposed with only a back-and-forth shift with a direction and shift length equal to that of C $=$ C bond (the so-called ABAB or Bernal stacking, as in genuine graphite), graphenes in MWCNTs are stacked incoherently or with random orientation, giving rise to the so-called turbostratic structure (Fig. 1.6b, top).

Carbon Nanotubes as Seen by Transmission Electron Microscopy (TEM)

As seen by relatively low magnification TEM, a powder of standard carbon nanotubes, whatever the type (SWCNTs or MWCNTs), appears as a bunch of more or less entangled nanofilaments (Fig. 1.7a, b), eventually added with the
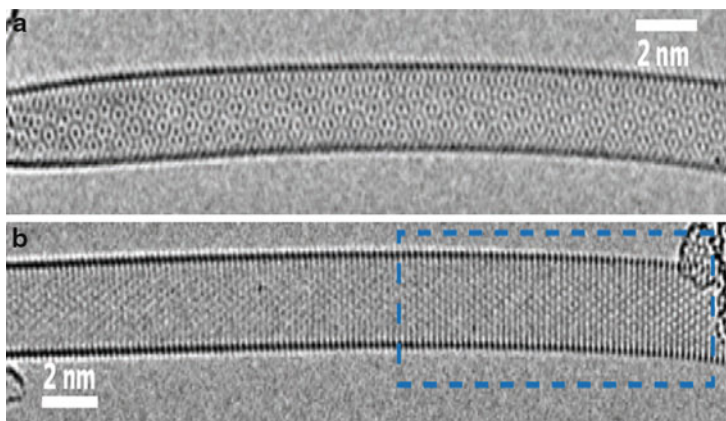
Fig. 1.8 Atomically resolved TEM images of SWCNTs (electron energy was down to 80 keV to reduce knock-on damages). (**a**) is a (18, 8) SWCNT, hence of chiral type. The chirality induces moiré effects due to the interference between the *top* and *bottom* lattices which are slightly rotated with respect to each other due to the helicity, as observed in Fig. 1.3 for the exampled chiral tube models. (**b**) is obviously a zigzag type SWCNT, here (28, 0). Because of the bending of the SWCNT, a strain deformation of the C–C bond of 1.6 % was able to be measured in the blue-framed area [22]

impurities (amorphous carbon, carbon shells, fullerenes, catalyst particles, etc.) that are inherited from the various synthesis processes [20], unless the material is previously purified (usually by oxidizing treatments [21]).

In case of SWCNTs, magnifying the image further reveals that filaments are actually SWCNT bundles (Fig. 1.7c, d), with individual SWCNTs sometimes showing up over short lengths (Fig. 1.7c, arrow). Because of their simple structure and absence of texture and nanotexture, SWCNTs only appear as two parallel lines that are the trace of the SWCNT wall, which exhibit more contrast because it is the location where the number of atoms to be superimposed in the path direction of the electron beam is the highest (similarly to atom columns in crystals). At that point, only limited information can be obtained, such as the tube diameters (with few % accuracy).

Then it requires even higher magnification and aberration-corrected TEM with atomic resolution to see more (Fig. 1.8), such as the atom positions in the SWCNT wall that relate to SWCNT type and indeed allow identifying their (n, m) indices, ideally by carrying-out diameter measurements and 2D fast Fourier transform, combined with image simulations. For instance, locally measuring C–C bond strain then becomes possible [22], although such investigations are no longer a routine.

Van der Waals attractions between MWCNTs are not as strong as between SWCNTs, due to the fact that π-electrons at the MWCNT surface are already partly involved in graphene-graphene interactions and other factors that relate to the MWCNT texture and nanotexture.

A consequence is that MWCNTs tend to remain individualized even for a small number of graphenes in the wall, say, beyond 3–4 graphenes, considering the concentric type. High magnification TEM is then able to reveal the inner display
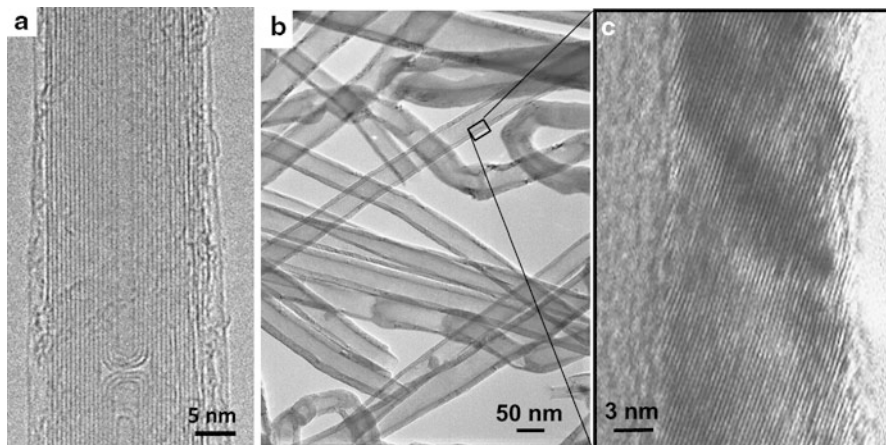
Fig. 1.9 TEM images of (**a**) a MWCNT exhibiting a combined concentric-bamboo texture, using lattice fringe resolution conditions; (**b**) a bunch of MWCNTs seen at low magnification, whose high magnification of a portion of the wall in lattice fringe mode imaging (**c**) reveals that they are of the herringbone texture type

of graphenes and to identify the texture type (Fig. 1.9). Then further magnification in lattice fringe imaging conditions will reveal the nanotexture, as exampled in Fig. 1.5b. On the other hand, going further down in resolution for imaging MWCNTs usually does not bring much more regarding their characterization because of the amount of incoherent information which is cumulated in the direction of the electron beam, unless the number of stacked graphenes making their wall is limited to, say, less than 5 or other specific cases.

Transport and Magnetotransport Properties

The electronic transport and magnetotransport properties of carbon nanotubes depend on many of their physical parameters such as the electrochemical potential, the number of shells, the diameter, the length, as well as the degree of disorder, to cite only a few examples. Indeed, some of these parameters strongly affect the electronic band structure which constitutes the basics for understanding their transport properties. We shall first briefly review the main theoretical issues relevant for understanding the electronic transport [23–26] in a single-walled carbon nanotube before opening the subject to more complex systems and scrutinizing the most relevant transport and magnetotransport phenomena. As reminded in section 'Describing Carbon Nanotubes' (Fig. 1.2), a single-walled carbon nanotube is described by the couple of indices (*n, m*) which relate to the orientation of the chiral vector. This orientation sets the main features of the electronic band structure which consists of multiple 1D sub-bands sliced from the 2D graphene band structure itself. The chiral vector defines the slicing orientation, so that there are
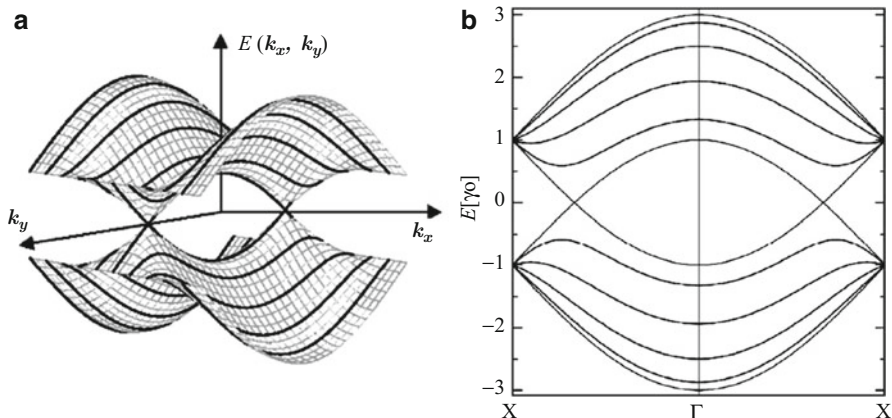
Fig. 1.10 (**a**) Band structure of a (5, 5) carbon nanotube using the band-folding scheme. The *bold lines* represent the slicing of the graphene band structure. (**b**) Energy dispersion of bands for a (5, 5) carbon nanotube in the conventional representation. Notice that the valence and conduction bands touch at zero energy so that this particular (*armchair*) nanotube is metallic (Adapted from [23])

as many possible set of 1D sub-bands as there are possible m/n ratios (e.g., an infinite number). Even if the band structure of any (n, m) carbon nanotube is unique, one can distinguish two main categories into which they can be classified. On the one hand, if $n - m = 3i$ (where i is an integer, including $i = 0$), carbon nanotubes show a very small band gap (of the order of a few tens of meV) so that their electronic behavior can be considered as metallic at room temperature. This small gap scales as $1/(2R)^2$ (where R is the radius of the nanotube) and originates from curvature effects. On the other hand, all the nanotubes which do not satisfy the above condition exhibit a semiconducting behavior [27, 28]. It can be demonstrated that the size of the gap varies as $Eg(eV) = E_{11}^{SC} \sim 0.8/2R(nm)$. In addition, it is worth mentioning that armchair nanotubes with $n = m$ do not show any gap and are therefore always metallic (Fig. 1.10).

The transport properties of any system are related to their electronic structure at the Fermi energy. In pristine carbon nanotube, the Fermi energy is expected to lie in between the highest occupied sub-band and the lowest unoccupied one. However, in practice, residual doping is observed so that the carbon nanotubes are inevitably populated in excess either with electrons or holes. Experimentally, one is able to control the position of the Fermi energy within the band structure using a gate electrode which ensures a capacitive coupling with the carbon nanotube [29]. It provides a way to continuously modify the doping at wish, using electrostatic effects. Experimentally, the gate-voltage dependence of the conductance of a carbon-nanotube-based device can be used to distinguish between semiconducting and metallic ones: the conductance should vanish when the Fermi energy is tuned within the gap in the former case, whereas it should always read nonzero value for the latter case, respectively.

The electronic transport in carbon nanotubes can be anticipated using the Landauer formula for quasi one-dimensional system, which provides a way to measure the transmission of electrons through the device via its conductance G:

$$G = \frac{g.e^2}{h} . \sum_{-\infty}^{+\infty} \int \frac{df(E - E_F)}{dE} . T_i(E) . dE$$

The index i is related to the ith 1D sub-band at the Fermi energy while $df.(E-E_F)/dE$ is the derivative of the Fermi function evaluated at the Fermi energy. The quantity $T_i(E)$ defines the transmission coefficient of the ith sub-band. Therefore, one notes that for $T_i(E) = 1$ (ballistic transport and transparent contacts), the conductance of each sub band reads $G_i = g.G_0$ where $G_0 = e^2/h$ is the conductance quantum and the factor g stands for the degeneracy of the electronic states ($g = 2$ when considering spin degeneracy). For a perfect SWCNT at zero temperature, one is able to work out the conductance of the system simply by counting the number of sub-bands below the Fermi energy and multiplying this number by $g.G_0$. This simple approach is unique to 1D system where the carrier group velocity cancels the contribution of the density of states in the general formula of the conductance. In experimental conditions, the transmission coefficient $T_i(E)$ is not unity but depends on disorder as well as the contact resistances between the carbon nanotubes and the metallic electrodes [30]. In the classical or diffusive regime, these two contributions adds incoherently so that the total resistance of the device reads $R = R_c + R_t$. The contact resistance R_c is always higher that $h/4.e^2$, whereas the nanotube resistance $R_t = h/4$. $e^2 \times (L/l)$ in case of uniform disorder distributed along the length L of the nanotube (here, l is the mean free path of the charge carrier with $l \ll L$ in the diffusive regime). We note that, because the density of states is symmetric between positive and negative energies, the conduction of carbon nanotubes shows an ambipolar behavior. However, it does not necessarily mean that the transport properties are also symmetric with respect to the charge of the involved carriers, as the conductance is sensitive to scattering and to the work function at the contacts, which both may differ for electrons and holes. The most prominent example concerns the creation of Schottky barriers at the interface between semiconducting carbon nanotubes and metallic electrodes [31]. Depending on the nature of the metallic electrodes, the nanotube characteristics, as well as environmental factors (doping), a large barrier may limit electron injection while hole-type carriers can be injected at no energy cost, and vice versa. One may notice, however, that since the energy gap depends on the tube radius, it is easier to achieve good electrical contact for large diameter carbon nanotubes rather than for small diameter ones [32]. On the other hand, as stated earlier, the presence of disorder can also drastically affect the conductance [33, 34]. We distinguish three main sources of disorder. First, localized defects such as vacancies or substitutions set on atomic scale and lead to large scattering momentum transfer of the charge carriers. Second, the presence of doping impurities adsorbed onto the nanotubes or located at their vicinity (e.g., substrate) creates long-range scattering potentials which also contribute to the total resistance of the device [35]. Finally, mechanical deformations such as strains and twists are

responsible for local band gap and therefore limit the conductance. The simultaneous presence of many types of disorder makes it difficult to decipher the exact contribution of each of them in a realistic experiment. Nevertheless, when backscattering is considered, the long-range and short-range disorders are expected to affect the charge carriers in different ways as explained below [36]. We first distinguish intra-valley and inter-valley backscattering processes. The former results in a transition between electronic states of opposite momentum which belong to the same valley, whereas the latter involves counter-propagating modes belonging to both K and K' valleys. Intra-valley scattering requires a small momentum transfer and is therefore expected to occur when long-range disorder is present. On the other hand, inter-valley scattering occurs only from atomically sharp defects. It has been demonstrated that intra-valley scattering is forbidden for metallic nanotubes due to the perfect orthogonality between the initial (bonding) and final (anti-bonding) states that occur in the linear $E(k)$ dispersion relation at zero energy [37]. For semiconducting carbon nanotubes, however, the backscattering probability is restored due to the massive character of the dispersion relation. Such sensitiveness to scattering translates into an estimate of the mean free paths, which have been found to be larger in metallic nanotubes (a few micrometers) as compared to semiconducting ones.

SWCNTs constitute an ideal playground when investigating quantum transport phenomena at low temperature. As described earlier, ballistic transport is certainly the most well-known one [38] and occurs in very clean systems with nearly perfect transmittance at the source and drain electrodes. In this regime, the conductance is quantized by steps of ge^2/h as the Fermi energy is swept among the 1D sub-bands and by steps of e^2/h when the full degeneracy is lifted (by, e.g., a large transverse electric field). But such nano-objects, because of their nearly perfect crystallinity, are also much more suitable for investigating the confinement of the electronic wave functions. One can cite, for example, the Coulomb blockade effect when the carbon nanotube is considered as a quantum dot coupled via highly reflecting tunnel barriers to the electrodes [39, 40]. In this regime, the energy levels are discrete and the system has nonzero conductance only for special sets of drain-source and gate voltages (Fig. 1.11a). In nanotube quantum dots, the charging energy E_c depends on the nanotube capacitance but is typically of the order of a few meV for the most common devices. It corresponds to the energy required to add one new electron to the dot and must, for the Coulomb blockade effect to occur, be larger than the thermal broadening $\approx k_B T$. Hence, such a conduction regime is only visible at cryogenic temperature. On the other hand, when the transmittance of the contacts is high, carbon nanotubes can act as an electronic Fabry-Perot cavity and hold standing electronic waves which modulate the conductivity [41]. Constructive interferences between the forward and backward waves occur when $\delta\varphi = k_{//} \times 2L = 2.\pi.n$ where $\delta\varphi$ represents the phase difference of the electronic waves, n is the order of the resonance, and L is the nanotube length. Assuming a linear dispersion relation in the vicinity of the Fermi energy, the corresponding energy level spacing reads $\Delta\varepsilon = h.v_F.\delta k_{//} = (h.v_F.\pi)/L$. Therefore, the Fabry-Perot regime can experimentally be observed as a periodic modulation of the conductance
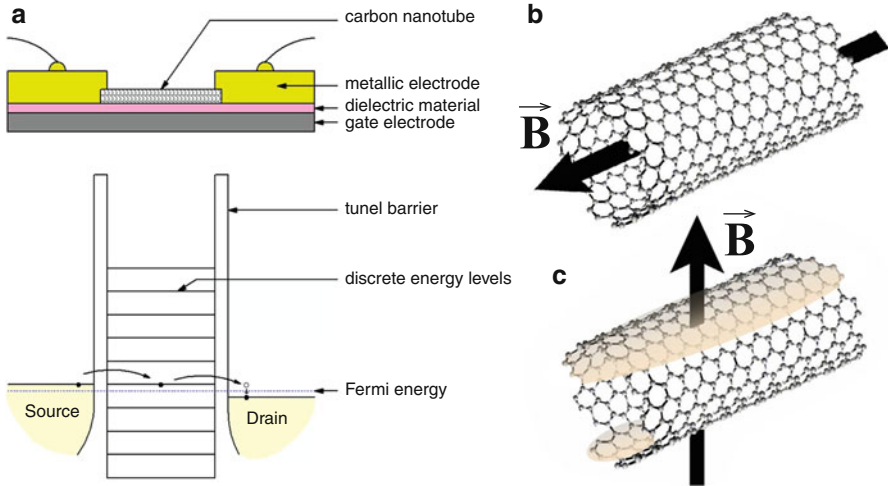
Fig. 1.11 (**a**) The nanotube is viewed as a quantum dot with quantized energy levels. The subsequent Coulomb blockade regime is achieved when tunnel barriers (very low transparency) develop at the contacts. The system shows nonzero conductance only when a quantized energy level is aligned with the source potential. (**b**) and (**c**) Two different experimental configurations for investigating the magnetotransport properties of carbon nanotubes: the magnetic field is applied either parallel or perpendicular to the tube axis. In the latter case, the wave function is localized at the top and bottom of the nanotube, as represented with the colored regions

as the energy of the device is changed by $\Delta\varepsilon$ using, e.g., a gate voltage. It is worth insisting that this effect can only take place at low temperature in order to reach the coherent regime ($L\varphi \geq L$) and in rather clean nanotubes, so that interference effects are not blurred by thermal broadening or disorder.

In addition to individual SWCNTs, SWCNT bundles or MWCNTs can also be found. In both cases, the transport properties are affected by the coupling between the shells and/or between the adjacent nanotubes [42, 43]. Commensurate MWCNTs (concentric type) usually distinguish from non-commensurate ones by the occurrence of a common unit cell for all shells in the former case [33]. In the regime of ballistic conduction, the total conductance of commensurate MWCNTs can be estimated by simply adding the conductance of the individual entities that compose the system since the coupling strength is usually weak (e.g., van der Waals interactions). On the other hand, for non-commensurate carbon nanotubes (or in the presence of disorder), the inter-shell coupling strength is reinforced. Electrons experience multiple scattering along the length of the nanotube as well as a tunnel transfer between radially consecutive shells, so that the transport becomes effectively diffusive for long enough systems. Beyond the above-mentioned generalities, transport in MWCNTs is complicated and strongly depends on the position of the Fermi energy. For technical reasons, the exact knowledge of the helicity of each of the concentric tubes is difficult to address while simultaneously performing transport experiments, so that the theoretical models developed for MWCNTs still suffer from a lack of experimental confirmation.

Magnetotransport (Fig. 1.11b, c) constitutes an efficient tool for investigating the electronic properties of carbon nanotubes [44, 45]. Indeed, following the Einstein relation $\sigma = e^2.\rho_{(E,B)}.D_{(E,B)}$ where the conductivity is the product of both the density of states and the diffusion coefficient, respectively, both the quantum interferences and the modifications of band structure are expected upon applying a magnetic field [46]. In disordered systems and at low temperature, one readily observes some reproducible fluctuations of the conductance as the magnetic field is varied. The mean amplitude of the fluctuations is of the order of e^2/h when $L\varphi$ approaches L, and this effect is referred to as universal conductance fluctuations (note that any external parameter, such as a gate voltage, would yield similar results). The presence of static disorder brings about a complex pattern of interfering electronic waves within the system, so that the transport probability of an electron from source to drain is affected. The application of a magnetic field randomizes the relative phases of the involved wave functions so that the aforementioned interference picture is replaced by a new one, which translates into a new value of the conductance. The visibility of conductance fluctuations depends on the coherence length $L\varphi$, which characterizes the mean distance an electron can travel before its quantum phase is randomized. This length relies on temperature, static disorder, and electron interactions which limit its range. One special class of quantum interference concerns loop-like paths and their time-reversal counterparts. It has been shown that constructive interference occurs so that the backscattering probability is actually enhanced. The application of a weak magnetic field breaks out this scheme and implies a positive magnetoconductance superimposed with the aforementioned conductance fluctuations. However, under certain conditions, the tubular nature of carbon nanotubes sets up new phenomena when the magnetic field is applied parallel to the tube axis [47]. Indeed, if the nanotube circumference C is longer than the elastic mean free path but lower than the coherence length $L\varphi$, it has been demonstrated that additional Φ_0 periodic oscillations develop in the conductance of the device as a function of the magnetic field (here, $\Phi_0 = h/e$ in the magnetic flux quantum). However, if the mean free path is larger than the circumference of the nanotube, but lower than the coherence length, then the magnetoconductance displays Φ_0 periodic oscillations in contrast to the previous case. Although difficult to decipher, this effect should not be mistaken with field-induced modifications of the band structure, which also manifest as Φ_0 periodic oscillations of the conductance. In the latter case, however, the amplitude of the oscillations is expected to be large at low temperature and to persist even at high temperature. Theoretically, the magnetic field is taken into account through the Peierls substitution in the Hamiltonian of the system. Within the band-folding scheme, it has been demonstrated that the Pierls substitution brings about a shift of the set of 1D sub-bands slicing the graphene band structure. Therefore, as the magnetic field is varied, the 1D sub-bands successively pass and escape the K and/or K' points of the first Brillouin zone so that the system alternates between a metallic behavior and a semiconducting behavior, respectively. The gap opening and closing is Φ_0-periodic, so that one should expect a typical period of conductance oscillation

of 13 T for a carbon nanotube of diameter 20 nm [48]. When a magnetic field is applied perpendicular to the tube axis, the electronic wave function becomes progressively localized around the top and bottom sides of the nanotube at low k-vectors, whereas the flanks of the nanotube develop chiral currents at large k-vectors. This condition holds when $C_h > 2.\pi.l_m$ (where l_m is the magnetic length) so that the formation of Landau levels affects and dominates the transport properties [49, 50]. In this regime, e.g., under sufficiently strong magnetic field, an initial semiconducting or metallic nanotube cannot be distinguished as they acquire the same transport properties.

Optical Properties

Optical properties of carbon nanotubes depend on size and shape. The one-dimensional shape of carbon nanotubes leads to singularities (Van Hove) in the electronic density of states. As a result, the optical response of carbon nanotubes is highly wavelength dependent. Small diameter carbon nanotubes can be semiconducting or metallic, leading to optical properties which depend on structural parameters such as the helical indices (n, m), the number of walls, or the length of the tube. The optical response of the tubes is strongly polarization dependent and is the highest when the polarization of light is parallel to the tube axis. Nanotubes can be used to polarize light or they can act as antennas in the near infrared (IR) and visible spectral range [51]. The optical investigation of individual tubes can be carried out at wavelengths near the electronic excitations energies or using interference substrates to detect spectroscopic signals [52–55]. Individual tubes can also be detected by modulation of the position of the focal point [56]. Tip-enhanced Raman spectroscopy (TERS) is probably the most powerful technique to observe individual tubes with high spatial and spectroscopic resolution [57].

The electronic transitions between two Van Hove singularities through optical absorption lead to electron-hole pairs which form excitons. Excitons in carbon nanotubes have exceptionally large binding energies (300 meV) and their formation is due to strong electronic interaction in one dimension [58]. The energy of the excitons is inversely proportional to the tube diameter and depends on nanotube environment. SWCNTs, once formed, agglomerate strongly and prevent the radiative decay of excitons. By using surfactant solutions or polymers, SWCNTs can be dispersed and individualized. Individualized SWCNTs show interesting photoluminescent properties. When detecting the photoluminescent signal as a function of excitation energy, the optical emission observed can be associated to tubes with particular n and m values. Thus photoluminescence excitation spectroscopy (PLE) has become a powerful tool for analyzing SWCNT solutions to reveal the (n,m) distribution of nanotubes. Bachilo et al. [59, 60] have determined the electronic transition energies from the luminescence of semiconducting tubes surrounded by a surfactant, sodium dodecyl sulfate, in 2002. The electronic transitions energies can be also derived by resonant Raman scattering [61, 62]. Using resonant

Table 1.1 Parameters for the electronic transition energies [63]. Values for metallic SWCNTs are from [64]

p	1	2	3	4	5	6
Energy	$E_{11}{}^{SC}$	$E_{22}{}^{SC}$	$E_{11}{}^{M}$	$E_{33}{}^{SC}$	$E_{44}{}^{SC}$	$E_{22}{}^{M}$
β_p with mod(2n + 1, 3) = 1	0.05	0.14	0.3	0.42	0.4	0.6
β_p with mod(2n + 1, 3) = 2	−0.07	−0.19	−0.19	−0.42	−0.4	−0.6
γ_p	0	0	0	0.305	0.305	0.305

Raman scattering, it is possible to determine in addition the transition energies of metallic tubes. In 2007, Araujo et al. [63] proposed the following general expression for the electronic transition energies:

$$E_{ii}(p,d) = \frac{\beta_p \cos(3\theta)}{d^2} + a\frac{p}{d}\left[1 + b\log\left(\frac{c}{p/d}\right)\right] + \frac{\gamma_p}{d}$$

where $a = 1.049$ eV.nm, $b = 0.456$, $c = 0.821$ nm^{-1}, p is the index of the optical transition, and d, $a_{c\text{-}c}$, and θ are the tube diameter, the carbon-carbon bond length, and the helicity angle respectively, which are related as described in Fig. 1.2. According to the authors, the values for the terms β_p and γ_p are as reported in Table 1.1.

Plotting the transition energies of nanotubes as a function of the diameter is referred as the 'Kataura plot' [65]. Photoluminescence from SWCNTs can be used to make them visible in solutions using conventional optical microscopy [66]. Effects of the environment, tube defects, tube length, or diffusion properties can be studied by analyzing changes in the photoluminescence signal. Measurements of the photoluminescence signal using time-resolved spectroscopy give information about the lifetime of the excited states and its decay mechanism [67]. Initially, the luminescence quantum yield was relatively low (1 %) but was found to depend on the tube environment and number of defects as well as the (n,m) indices. Some studies investigated the influence of oxygen on luminescence quantum yield. By reducing the amount of oxygen in the proximity of the tubes using organic molecules, it was possible to increase the quantum efficiency by 20 % [68]. This sensitivity of SWCNTs to the environment can be used to dope carbon nanotubes and control the type of charge carrier. By doping individual SWCNTs with electrons and holes, their recombination leads to an emission of photons. Electroluminescence of SWCNTs was then demonstrated. Inversely, the same device can be used as photon detector [69]. Such devices are truly molecular devices in which the diameter of each nanotube is atomically precise. SWCNTs can thus be used to convert electrical signals in optical signals or vice versa. Whereas these are highly desirable optoelectronic properties, positioning at low cost individual SWCNTs with selected diameters on given locations remains a major challenge. In future, it is thought that mass processing of carbon nanotubes for such applications might become possible using self-organization.

Table 1.2 Values for c_1 and c_2 from the literature

c_1	c_2	d(nm)	Individualization	Reference	Year
244.6	**0**	**1–3**	On Si	Jorio et al. [70]	2001
223.5	12.5	0.6–1.1	Sodium dodecyl sulfate (SDS)	Bachilo et al. [59]	2002
214.4	18.7	0.7–1.2	SDS	Telg et al. [62]	2004
218.3	15.9	0.7–1.2	SDS	Fantini et al. [61]	2004
204	27	1.4–3	Suspended between metallic contacts	Meyer et al. [71]	2005

The electronic transition energies can also be observed in optical absorption spectra of SWCNTs and double-wall carbon nanotubes (DWCNTs) when individualized in solutions with surfactants. The transition energies of semiconducting tubes are very similar in absorption and emission spectra. For metallic tubes, only the absorption can be detected as the decay of the exciton is non-radiative.

Inelastic light scattering or Raman scattering is particularly useful to analyze carbon nanotubes. The energy of the **radial breathing mode** (RBM) is inversely proportional to the diameter and falls within the low energy range of the Raman spectrum when exciting near optical transition energies. The following relation for the energy of the radial breathing mode as a function of the SWCNT diameter is used in the 1–2 nm range:

$$\omega_{\mathrm{RBM}}\left(\mathrm{cm}^{-1}\right) = \frac{c_1}{d(\mathrm{nm})} + c_2$$

The values for the constants c_1 and c_2 as determined experimentally are listed in Table 1.2:

Using a linear chain model, a relation for the frequency of the radial breathing mode can be derived as follows [72]:

$$\omega_{\mathrm{RBM}}\left(\mathrm{cm}^{-1}\right) = \omega_G \frac{a}{d} = \frac{224}{d(\mathrm{nm})}$$

where ω_G is the frequency of the Raman **G band**, a is the interatomic distance, and d is the tube diameter. This shows that the RBM frequency is directly related to that of the Raman G band, which is also subjected to a shift of its frequency with tube diameter but in a lesser extent than RBM. The Raman G band at around 1,590 cm^{-1} corresponds to the stretching vibration of the C–C bond in the primitive unit cell of graphene and split in two bands for SWCNTs, the **G$^+$** and **G$^-$ bands**, due to stretching vibrations along and perpendicular to the tube axis. More precisely, because of electron-phonon coupling, G$^+$ vibration is along the tube axis for semi-conducting SWCNTs and perpendicular to the tube axis for metallic SWCNTs. For metallic tubes (M) and semiconducting tubes (SC), the following approximate relations have been derived for the frequency of both G bands as a function of tube diameter [73]:

$$\omega_{G+}(M) = \omega_{G+}(SC) = 1,592\left(\mathrm{cm}^{-1}\right)$$

and

$$\omega_{G-}(SC) = 1,592 - 32.6/d^{1.4}$$

$$\omega_{G-}(M) = 1,592 - 64.6/d^{1.4}$$

The Raman spectrum of nanotubes also shows a band in the 1,350 cm^{-1} frequency range referred to as the **D band** (ω_D) which is due to a double resonance scattering phenomenon induced by the presence of structural defects [74]. The location of this band is wavelength dependent and shifts by 50–60 cm^{-1} eV^{-1}.

The **intensity ratio of D over G bands** for a given excitation energy can be used to obtain a relative measure of the number of defects present in the tube walls [75]. The relation proposed by Knight and White [76] is still often used: $L_a = 4.4/(I_D/I_G)$ where I is the intensity with an excitation wavelength at 488 nm and L_a the in-plane dimension of the defect-free graphene.

The overtone **2D band** (also called G' in the literature sometimes), located at $2.\omega_D$, is also intense and can be fitted with a single Lorentzian line shape for SWCNTs with a half width at half maximum (HWHM) of 15 cm^{-1}. For DWCNTs and MWCNTs, the shape of the 2D band is different and the HWHM is larger.

Tip-enhanced resonant Raman scattering (TERS) of carbon nanotubes has been particularly successful as mentioned above to observe individual SWCNTs. TERS allowed mapping carbon nanotubes at a resolution of 20 nm in 2003 [57]. The enhanced electric field in the vicinity of a sharp gold tip is used to overcome the classical diffraction limit and allows at the same time to record optical spectra at nanometer-scale resolution. The G and D bands of nanotubes have been thoroughly studied using TERS. The length scale of the D-band scattering near defects in individual metallic nanotubes [77] has been observed, and it was found that the D-band scattering process is extended of about 2 nm which is similar to what was observed for graphene [78].

With DWCNTs, the Raman spectrum is different from that of SWCNTs in the G and 2D band range (Fig. 1.12). The G$^+$ for the inner tube is located at 1,580 cm^{-1}, while the G$^+$ of the outer tube remains at 1,592 cm^{-1} leading to a broad G band [79, 80]. Moreover, the G$^-$ of the outer tubes is responsible for a shoulder at the lower frequency side of the G band. The G$^-$ of the inner tube falls is in the 1,530 cm^{-1} range.

The G band features are also different for MWCNTs, for which the G band is broad and is at the same spectral position as for graphite (1,580 cm^{-1}). Indeed, MWCNTs have larger diameters and the transition energies are therefore smaller and fall in the infrared spectral region ($E_{11}^{SC}(\text{eV}) \approx \frac{0.8}{d(\text{nm})}$, $d \approx 10$ nm). Consequently, no large optical cross-sectional enhancement is observed in the visible spectral region. This optical signal is similar to that of graphite. A shoulder at higher energy side corresponds to the **D' band** attributed to defect-induced intra-valley double resonance scattering. The frequency of the D' band is also dependent on the excitation energy. The D' frequency increases when excited in the red spectral region. On the other hand, the 2D band for MWCNTs remains controversial. It is not clear how the interaction between the walls, which can depend on diameter,

Fig. 1.12 Raman spectra for the *G* band of *MWCNT*, *DWCNT*, and *SWCNT* (By courtesy of V. Tishkova, CEMES)
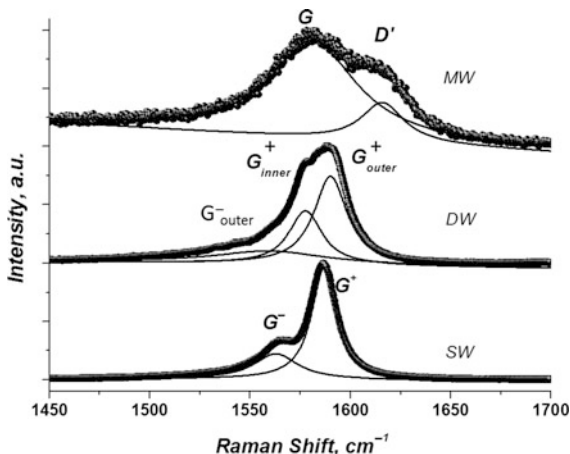
affects the line shape of the 2D band. Finally, the RBMs of adjacent tubes are coupling and have not been observed for MWCNTs except for MWCNTs made of few, small diameter tubes [81]. MWCNTs also often contain more defects, giving rise to a large D band, although MWCNTs grown by the electric arc discharge method can have a much lower number of defects [82].

When attempting to reveal the presence of nanotubes in a polymer matrix or in a biological tissue, the whole surrounding material contributes to the Raman spectrum as any form of sp^2-bonded carbons gives rise to a spectral band in the Raman G band region. The Raman D band is then the only available indicator of the presence of CNTs. The 2D band can also be used provided the quality of the tube is high. The D band intensity is larger when using a laser excitation in the red or infrared spectral region [83].

Photoluminescence and electroluminescence properties of carbon nanotubes are very promising. Optical methods are particularly powerful in observing carbon nanotubes in different environments, mapping the spatial distribution of CNTs in various matrices, probing electronic resonances, and providing a number of structural information such as diameter, helical indices, and defect quantification.

Thermal Properties

The comparison of CNTs with graphite makes one expect a very high thermal conductivity along the CNT axis but a much lower radial component in the case of MWCNTs [84]. The theoretical analytical approaches to specific heat and thermal conductivity are fairly complex [85]. The transport of thermal energy in CNTs is assumed to occur via a phonon conduction mechanism, which is influenced by several parameters and processes such as the number of phonon active modes, the boundary surface scattering, the length of the phonon free path, and the inelastic umklapp scattering [86, 87]. Phonon modes form a continuum at room temperature,

and phonon quantization manifests itself in CNTs at very low temperatures (below 8 K) [88–90]. Both the theoretical predictions and the experimental data are scattered over one order of magnitude. The reported thermal conductivities (κ) at room temperature are in the range 400–6,000 W mK^{-1} for SWCNTs [91–94] and in the range 300–3,000 W mK^{-1} for MWCNTs, depending on the type of CNTs, defect proportion, sample purity, and the measurement or simulation method.

SWCNT helicity determines the size of the band gap, which has a strong influence on the mechanism of heat conduction by phonons or electrons [95–97]. κ at 300 K is predicted to be approximately inversely proportional to the diameter of a SWCNT [98] and to increase with SWCNT length, at least for very short ones (typically from 5 to 500 nm) [99–101]. κ is thus expected to be constant when the length is longer than the phonon mean free path, which is thought to be relatively long ($\sim$500 nm for a MWCNT and even longer for a SWCNT [102–105]. For MWCNTs, κ at room temperature decreases as the diameter increases, actually as the number of walls increases. Vacancies and Stone-Thrower-Wales defects induce a scattering effect [106, 107] and therefore reduce κ, which is another reason why MWCNTs show κ values lower than for SWCNTs.

The measurement of κ on individual CNTs was done by different ways, including using a suspended micro-thermometer device on which a CNT was grown [102, 108–110] and using a T-junction sensor [111], the 3-ω method [112], and a non-contact method based on the shifts observed in Raman spectra [113]. κ was also deduced from electrical measurements on individual CNTs [101, 114]. Although it is best to measure κ, diameter, and helicity on the same CNT [115], measurements were also carried out on bundles, mats, sheets, and films [88, 116–119]. The measured values are usually two orders of magnitude lower than for individual CNTs (i.e., in the range 10–40 W mK^{-1}), which is attributed to high thermal contact resistance, which itself is difficult to measure [103, 113]. The room temperature κ of a CNT fiber (yarn, strand) 10 µm in diameter is 60 ± 20 W mK^{-1} and decreases with increasing diameter [120]. Recently, 1.5 mm long CNT fibers were reported to show an average κ value of 380 ± 15 W mK^{-1} [121]. This value doubles (635 W mK^{-1}) by doping with iodine and remains unchanged after annealing at 600 °C.

CNTs have been considered as fillers for thermally conductive composites, notably polymer-matrix composites [122]. However, large interfacial thermal resistance between the CNTs and the surrounding polymer matrix hinders the phonon transfer, resulting in κ values much lower than anticipated. CNT functionalization is readily used in order to favor CNT dispersion, but it is worth remembering that although covalent bonds can favor phonon transferring between the CNT and the polymer [123], the impact of disrupted π conjugation is expected to be strong because each covalent functionalization site scatters electrons and phonons [123, 124]. Non-covalent functionalization does not damage the CNT structure, but the forces between the wrapping molecules and the CNT may be very weak, possibly leading to high interfacial thermal resistances [125].

Early theoretical and experimental studies revealed an isotropic (axial/radial) coefficient of thermal expansion (CTE) for defect-free MWCNTs [84, 126]. XRD studies suggest that the CNT bundles have negative CTE at low temperature and

positive CTE at high temperature [127, 128]. An analytical method [129] predicts the same for both the axial and radial CTE for SWCNTs. The radial CTE is independent of the CNT chirality, but the axial CTE shows a strong dependence. However, another study [130] predicts that the axial CTE for SWCNTs is positive in the whole temperature range and that SWCNTs with smaller diameters have smaller radial CTE, resulting from the competition between bending vibration and radial breathing vibration.

Mechanical Properties

CNTs being obvious candidates as reinforcement components in ceramic-, metal- and polymer-matrix composites, their mechanical properties have been extensively investigated. The particularly strong bonding between the carbon atoms (sp^2 hybridization of the atomic orbitals) of the curved graphene sheet makes CNTs particularly stable against deformations. Numerous studies involving simulation and modeling techniques (reviewed in [131]) and direct and indirect measurements have been performed. Early works reported very different results for several reasons: differences in both modeling and experimental methods, measurements on individual versus bundled CNTs, and the use of different types of CNTs.

It is now accepted that the Young's modulus of a SWCNT is of the order of 1 TPa [132–136]. Very little influence of the number of walls was predicted [137], and indeed the measured Young's modulus for DWCNTs and triple-wall carbon nanotubes (TWCNTs) is in the range 0.73–1.33 TPa [138], as for some micrometer-sized carbon fibers [10, 20]. In the case of SWCNT bundles, shearing effects due to the weak inter-SWCNT cohesion give rise to a decrease by about one order of magnitude compared to an individual SWCNT: ca. 100 GPa is measured for SWCNT bundles [133, 139] and 50–115 GPa for DWCNT bundles [140]. Scattered results (0.27–0.95 TPa [135], 1 TPa [141]) were reported for MWCNTs, reflecting differences in texture (see Fig. 1.4) or the probable influence of defects [142, 143] or the emergence of a different bending mode, corresponding to a wavelike distortion (or ripple) of the inner side of the bent MWCNT [144]. Interestingly, CNTs which are so rigid are also capable to sustain large deformations over a certain stress. The flexibility is remarkable [145] and the bending may be fully reversible up to a critical angle as large as 110° for a SWCNT [146]. The elastic buckling makes them very resilient materials, enabling them to store or absorb considerable amounts of energy [147]. The competition between the van der Waals attraction forces and the elastic energy can provoke the flattening of the walls of two MWCNTs in contact with each other [148]. Compression and torsion forces can also provoke flattening and collapsing, forming a so-called nanoribbon [149]. The deformation of CNTs under pressure is well documented, notably for SWCNTs and DWCNTs ([150] and references therein). The first mechanical transition, corresponding to a modification of the outer wall cross section from circular to oval, could occur above 80 MPa for DWCNTs with an outer diameter of 4 nm [151].

The second one (collapsing) could occur above 540 MPa. The supporting effect of the internal tube pushes the collapsing pressure to higher values [79, 152, 153].

The theoretical maximum tensile strain (i.e., elongation) of a defect-free SWCNT is in the range 10–30 % [154–156], and the tensile strength could be as high as 100 GPa depending on its helicity [157, 158]. However, in practice SWCNT bundles achieve only 6 % [159, 160] and ca. 45 GPa [159] for tensile strain and strength, respectively (it is however worth noting that this is already seven times higher than the best high-strength carbon fibers, which were – until CNT arrive – the strongest materials ever [10]). It was shown that individual SWCNTs can undergo superplastic deformation at high temperatures, becoming nearly 280 % longer and 15 times narrower before breaking [161]. The superplastic deformation is the result of the nucleation and motion of kinks in the structure. The breaking strain (and tensile strength) of individual DWCNTs and TWCNTs were measured as 2.8 % (and 20 GPa) and 4.9 % (and 46 GPa), respectively [138] – although molecular dynamic (MD) simulations predict 28 % (and 160 GPa) for a DWCNT [162] – whereas the tensile strength of DWCNT bundles is in the range 3–13 GPa [140]. It was noted [138] that stepwise failure reduces the strength of the bundles due to the earlier failure of some CNTs in the bundle and thus that it is important for applications in composites that the CNTs in a bundle have similar strain-to-failures. Individual MWCNTs were measured to exhibit a strain-to-failure of 12 % and a tensile strength of 63 GPa [135]. Tensile strength values as high as 150 GPa [47] and over 110 GPa [163] have been measured for 'defect-free' MWCNTs (as compared to few GPa for manufactured micrometer-sized carbon fibers) [10, 20], in excellent agreement with the ultimate stress predicted by quantum mechanics for CNTs containing only an occasional vacancy defect. The authors [163] stress that this performance is made possible by omitting chemical treatments from the sample preparation process, thus preventing the formation of defects. Moreover, electron irradiation led to improvements in the maximum sustainable loads compared with non-irradiated samples of similar diameter, which is attributed to cross-linking between the walls.

MD simulation of the elastic and plastic deformation under axial tension of various CNTs ranging from a SWCNT to a four-walled armchair MWCNT revealed that fracture first takes place in the outermost layer [162]. When it has completely broken, the fracture begins in the next inner layer. This process will continue until the innermost layer completely breaks. Tensile-loading experiments on individual MWCNTs undergo the so-called 'sword-in-sheath' fracture mode, i.e., they break in the outer shells and then the inner core is pulled away [135, 163–165]. The barriers for the relative axial sliding of adjacent walls, and hence the corresponding shear strengths, are reported to be negligible in MWCNTs [166], and a shear strength equal to only 0.04 MPa was measured [167]. By contrast, ab initio calculations revealed that the shear strength for the relative axial sliding along a DWCNT and for their relative rotation about the axis is several orders of magnitude higher, reaching 215 MPa for the (9, 0)@(18, 0) DWCNT [168].

There has been lot of efforts put into the preparation of CNT fibers [169–171]. Very long (20 cm) SWCNT fibers with tensile strength of 1 GPa and Young's

modulus in the range 49–77 GPa were reported [172]. For DWCNT strands (diameters 3–20 μm, lengths 10 mm), the average tensile strength and Young's modulus were 1.2 GPa and 16 GPa, respectively [140]. Ropes of well-aligned MWCNTs (diameters 10 μm, lengths 2 mm) showed a tensile strength of 1.72 ± 0.64 GPa and an average Young's modulus of 450 ± 230 GPa [173]. Behabtu et al. [121] reported tensile strength of 1.0 ± 0.2 GPa, Young's modulus of 120 ± 50 GPa, and breaking elongation of 1.4 ± 0.5 % for ~20 mm long individual filaments cut from large spools (~100–500 m long). These authors stress out that CNT length, aspect ratio, and purity are keys to strength improvements, because of better CNT-CNT stress transfer and lower defect density. CNT orientation, graphitic (versus turbostratic) character, and number of walls are not as critical for attaining high strength, although a high degree or orientation tends to increase the modulus and a higher number of walls – as well as probably, a low nanotexture (see Fig. 1.5) – lowers the specific strength. A model [174] for the strength of pure CNT fibers shows that the axial stress in the CNTs is built up by stress transfer between adjacent CNTs through shear and is thus proportional to CNT length. Future developments in CNT-based fibers will stem from improvements in both the starting CNT and the processing and post-processing of the fibers [171].

Chemi- and Physisorption Properties

The hollow 1-D structure of CNTs is especially attractive for adsorption-related applications. As for any material, adsorption in/on CNTs is related to their surface physical and chemical properties. Surface area and porosity are important physical properties that influence the quality, utility, and handling of CNTs, which often must be carefully engineered to perform specific functions. Differences in the surface area and porosity of CNTs, which otherwise may have the same physical dimensions, can greatly influence their adsorption performances. Therefore, it is critically important that these characteristics be accurately determined and controlled. The surface chemistry of CNTs is governed by basal and edge carbon atoms, as well as by the presence of defects (i.e., as mentioned in section 'Introduction', structural carbon vacancies, and heterocycles). These imperfections and defects along the edges of graphene layers are the most active sites due to high densities of unpaired electrons. CNTs are usually associated with other nanotubes in bundles, fibers, films, papers, and so on, rather than individualized. Each of these has a specific range of porosities that determines its adsorption properties. In the following, we will address first the adsorption of various species over individual nanotubes, and the treatment of nanotubes as bundles will be discussed afterwards. We will focus our attention on (i) the description of the different types of sites for both physisorption and chemisorption, (ii) the adsorption on/in individual perfect CNTs, (iii) the importance of defects on the adsorption, and iv) the role of inter-tube voids on the porosity of these materials.
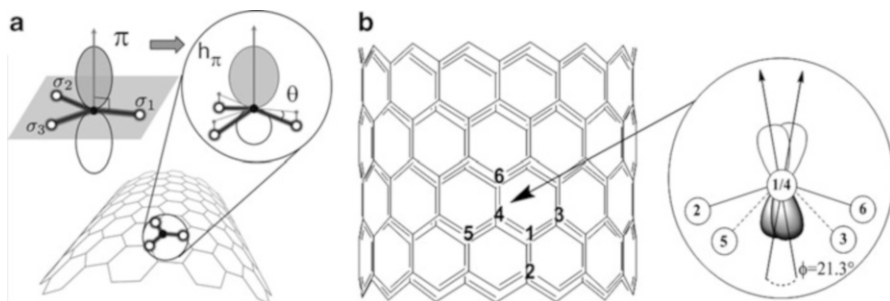
Fig. 1.13 (**a**) Diagram showing the π-orbital in planar graphene and its change into h_π under bending together with the pyramidalization angle θ. (**b**) The π-orbital misalignment angles Φ along the C_1–C_4

Individual Carbon Nanotubes

Defect-Free Structure

Because the electronic structure of SWCNTs strongly depends on the nanotube parameters, such as tube diameter and helicity (see sections 'Describing Carbon Nanotubes' and 'Transport and Magneto-Transport Properties'), it is expected that the latter will also affect strongly the adsorption. Additionally, the possibility to adsorb species on the convex (exohedral adsorption) or concave (endohedral adsorption) surface should be taken into account.

The nature and strength of the adsorption is directly correlated to carbon hybridization. In graphite, the four outer electrons of carbon form three sp^2 hybridized σ-bonds and one π-orbital, which give the conduction band six Fermi points and a linear dispersion around each of them. If a graphene sheet is rolled up into a structure such as a CNT, the orbital structure of carbon is altered because the bond length between carbon atoms decreases and the bond angle changes. The σ- and π-orbitals are no longer perpendicular to each other. An overlap of the π orbitals is introduced. As a consequence the parts of the π-orbitals inside and outside of a nanotube rearrange, in a way that the outer contribution is larger than the inner one (see Fig. 1.13a). The curvature induces a mixed state of σ- and π-orbitals, called rehybridization. Consequently, the π-orbital is always inclined by the hybridization angle $\delta = a/(2 \sqrt{3} d)$ (a is the length of the lattice unit vector and d is the tube diameter) relative to the direction normal to the tube surface [175]. This tilting angle is strongly dependent on the CNT diameter and helicity [176]. The graphene curvature introduces a misalignment of π-orbitals within the graphene sheet (Fig. 1.13b). The π-orbitals of a nanotube are not pointed directly towards the central axis of the nanotube, and some adjacent carbon π-orbitals have a misalignment angle, ϕ, between them. The π-orbitals of adjacent carbon atoms in a (10, 10) and a (5, 5) SWCNT have a π-orbital misalignments for the two different C–C bonds of $\phi = 0°$ and $10.4°$ for (10, 10) and $0°$ and $21.3°$ for (5, 5), respectively.

Fig. 1.14 Schematic representation of different binding sites of individual atoms adsorbed on a zigzag tube. H hollow (η^6), A axial, Z zigzag, T top, S substitution sites
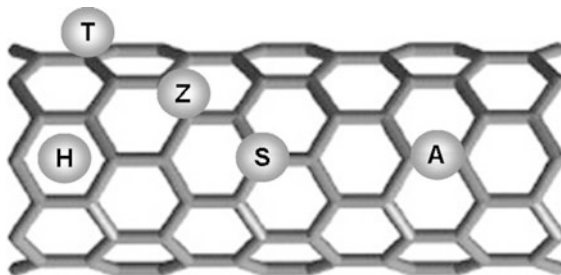
One of the crucial properties, which changes due to SWCNT curvature, is the ability to react with the surroundings. The rehybridization can also be explained by a mixture of sp^2 and sp^3 orbitals. While single sp^2 and sp^3 orbitals are saturated, the mixed state contains unsaturated orbitals. The mixing of a tetravalent sp^3 orbital with a trivalent sp^2 orbital leaves one hybrid orbital free for binding. The higher the ratio of the sp^3 contribution, the more free bonds exist and the higher the reactivity. The pyramidalization angle θ is used as an index for local reactivity (see Fig. 1.13a), which is sufficient for describing the curvature-induced shift in sp^2 hybridization. θ is the angle between the σ- and π-orbitals minus $90°$ ($\theta = 0°$ for the sp^2 hybridization). The tetrahedral sp^3 orbital has a pyramidalization angle of $19.5°$. This angle changes depending on the local mixture of sp^2 and sp^3 orbitals. The degree of hybridization $sp^{2+\eta}$ could be obtained, η being a number between 0 and 1. The comparison between different pyramidalization angles allows the comparison of reactivity, where a higher angle results in a larger reactivity. Thus, the degree of hybridization is highly curvature dependent, so that it is even possible to increase the reactivity by merely bending a SWCNT.

Finally, the SWCNT convex (outer) surface is chemically reactive because the convex arrangement of pyramidalized sp^2 carbon atoms is correctly disposed for the formation of chemical bonds with reagent species. For the same reason, the concave (inner) surface should be more inert and can withstand the presence of highly reactive species encapsulated within the nanotubes.

Adsorption of Single Atoms

The adsorption of single atoms on CNTs is mainly related to single metal atoms and alkali atoms, some light elements such as atomic hydrogen or lithium, and noble gases.

Adsorbed metal atoms can induce dramatic changes in the physical and chemical properties of the bare tube, either semiconducting or metallic [177]. Such a functionalization is of interest for three possible, insofar technologically important applications, namely, the fabrication of metallic nanowires, that of nanomagnets, and catalysis. The different adsorption sites on a zigzag SWCNT are depicted on Fig. 1.14.

Most of the adatoms studied in the literature yield the strongest binding at the η^6-H site. Ni, Pd, Pt, Cu, Ag, and Au seem to prefer the A site. Similar results were reported by Kusakabe et al. who modeled the adsorption of 25 metal atoms [178].

Although good conducting metals such as Zn, Cu, Ag, and Au form very weak bonds, transition-metal atoms such as Ti, Sc, Nb, and Ta are adsorbed with a relatively high binding energy [177]. Generally speaking, the curvature of the tube is a parameter that affects the binding strength [179, 180], with stronger binding on small diameter tube. In most cases, an individual transition-metal adatom gives rise to a band gap. Ti, which leads to a metal, appears to be the exception.

A systematic density functional theory (DFT) study of the $3d$ transition-metal interactions with planar and curved graphitic surfaces has also been reported [181]. Structurally, both graphene and (8, 0) SWCNT surfaces presented η^6 hollow adsorption sites (η^6-H site) with metals that mainly bound covalently and ionicity degrees that varied as expected with the metal electronegativity (charge transfer from metal to surface). It is clear that $3d$ transition-metal atoms, with the exception of Cr, Mn, and Cu, were chemisorbed onto graphene with a η^6 hollow geometry. Half-filled Cr and Mn and filled Cu $3d$ transition-metal atoms were physisorbed on these surfaces, and no energetically favored adsorption sites were predicted. In general, the binding energy increased as one moved in either direction away from the Cr/Mn couple of the $3d$ series.

First-principles calculations were performed to investigate the binding energies, geometric structures, and electronic properties of $4d$ transition-metal atoms adsorbed outside/inside SWCNTs [182]. For each transition-metal, the most energetically favorable site is the same for interior and exterior adsorptions. Interestingly, the equilibrium adsorption sites are sensitive to the atomic number of the transition-metal and can be classified into three types. Along the fifth row, the favorite positions are η^6-H site for elements from Y to Ru, off-center η^5-H site for Rh, and bridge A site for Pd. This is obviously related to the valence electron configurations. The early $4d$ atoms have more empty d states, which facilitate sp-d hybridization between carbon and transition-metal atoms. When the transition-metal atoms adsorb on a CNT, they show preferential binding to more carbon atoms; thus η^6-H site is the best choice. As the number of valence electrons increases, the bonding activity of metal atom becomes saturated and prefers to contact with less carbon atoms. Consequently, the location of Rh adatom inside and outside a (6, 6) CNT starts to deviate from the η^6-H site, and Pd atom with a completely filled d shell eventually adopts the bridge A site. When a Ru atom is adsorbed outside a CNT, the enriched π electrons due to the curvature effect enhance the hybridization between the π-electrons from carbon and the d electrons from Ru, leading to higher binding energy. As the tube diameter increases, the difference in electron densities inside and outside the CNT becomes smaller, and thus the binding energies on the two sides gradually approach the same asymptotic value of graphene. The amount of charge transfer from endohedral transition-metal atom to CNT is higher than that from the exohedral atom by a nearly constant shift of ∼0.5e. Such a difference in charge transfer regardless of the type of transition-metal atom relates to the different electrostatic potentials of the internal and external surfaces of CNTs due to the curvature effect. The magnitude of transition-metal-CNT charge transfer decreases with increasing atomic number. This trend can be correlated with the electronegativity difference between the transition-metal element and carbon.

In conclusion, the stable adsorption configuration and binding energy of the adatoms on CNTs are sensitive to the type of metal element and nanotube curvature, while the electronic properties depend on the valence electronic configuration of the metal atoms. The metal-CNT interaction results in considerable charge transfer accomplished by substantial modification of the electronic states of CNTs around the Fermi energy.

Alkali Atoms

Alkali-metal functionalized CNT-based materials are promising for nanoelectronics. Decreasing or modulating the work functions of CNTs is of great importance to control the interface properties between CNTs and other materials and considerably impacts device performance, including the field emission properties. Both experimental and theoretical calculations indicate that the work functions of CNTs are dramatically reduced upon alkali-metal (Li/K/Rb/Cs) adsorption, leading to a significant enhancement in the field emission [183]. For instance, in a (5,5) SWCNT whose metallic character may be turned into semi-conducting if capped and sufficiently short, the conduction properties can be back to metallic after alkali-metal adsorption. The work functions of the sidewalls of the CNTs are slightly higher than the axial work functions. The decrease in the work functions after adsorption of alkali-metal atoms was attributed to the elevation of Fermi levels and the decrease in vacuum levels induced by the electron transfer from the alkali-metal atom to the CNT [184].

Light Elements

Adsorption of light elements (H, Li) is related to energy applications. High performance electrical devices such as batteries based on CNTs, or hybrid materials, have been developed to promote Li adsorption, motivated by an increasing demand for better electrochemical materials with higher energy and power density. Based on first-principles calculations [185] and DFT calculations [186] on pristine SWCNTs, it has been reported that the dissociative adsorption of H_2 molecules is improbable due to very high energy barriers of about 2–3 eV. The dissociative chemisorption weakens carbon-carbon bonds, and the concerted effect of many incoming molecules with sufficient kinetic energies can lead to the scission of the nanotube. Molecular physisorption is predicted to be the most stable adsorption state. The physisorption energies outside the CNT are approximately 0.07 eV, whereas inside they can reach a value of 0.17 eV in a (5, 5) SWCNT. A DFT study of the interaction between atomic hydrogen and (5, 5) and (10, 0) SWCNT has shown a weak chemisorption in the outer wall [187]. A geometry relaxation produces a binding energy of about −1.5 eV. When SWCNTs are completely covered by hydrogen, the binding energy is enlarged by about 0.3 eV. From this study, a high sensitivity of the electronic structure to the presence of a H atom is reported.

The adsorption of lithium atoms on the surface of a (12, 0) SWCNT was investigated by using *ab initio* quantum chemical calculations [188]. For one atom adsorption, it was shown that the inside of this zigzag CNT is more favorable than the outside. Contradictory results were obtained in a DFT

study [189], where the authors also reported that binding energies tend to depend on the CNT configuration. After the lithium adsorption, charge is transferred from the Li atom to the CNT and the bond between Li and CNT has an ionic character [188]. The amount of charge transfer is larger for the *endo*-adsorption than for the *exo* and should be dependent on CNT curvature.

Noble Gases

Physisorption of noble gases is widely employed to study the structural and theoretical aspects of surface adsorption because the inertness of the noble gases typically excludes the possibility of chemical and polar interactions with the surface.

For helium, the difference of energy between the most favorable adsorption site (*H* site) and the less favorable one (top site *T*) characterizes the surface roughness. Its value, of the order of $3.45 \ 10^{-3}$ eV, is comparable to that of planar graphite [190]. The energy barriers for displacements of He atoms along the nanotube walls are of the order of $1.21 \ 10^{-3}$ eV, and the minimum energy of He-He interaction is $-0.86 \ 10^{-3}$ eV. Adsorption of noble gases (Ar, Kr, Xe) on metallic and semiconducting CNTs was investigated using the van der Waals density functional theory [191]. No difference was found in the adsorption between the metallic and semiconducting nanotubes, indicating that the adsorption energies for rare gases on CNTs are not strongly influenced by differences in the electronic structure of the nanotubes.

Adsorption of Other Gases

The adsorption of various gas molecules on SWCNTs is usually studied by first-principles calculations using density functional theory. The binding energy, tube-molecule distance, and charge transfers are generally investigated [192]. Atomistic modeling of gas adsorption in CNTs should be treated differently depending on the specific phenomena involved, either physical adsorption or chemical bonding. Sometimes, however, the classification of the phenomena studied in terms of physical or chemical adsorption is quite difficult due to the occurrence of strong polar interactions or weak charge transfer that makes uncertain the classification of the case under study. In these cases, the calculation of energetic quantities, such as the activation energy or the adsorption enthalpy, may help to get a clearer scenario, because it is expected that physical adsorption exhibits lower adsorption enthalpy values than the ones involved in chemical bonds [193].

Zhao et al. [194] studied the adsorption of various gas molecules on SWCNTs using first-principles method. The equilibrium tube-molecule distance, adsorption energy, and charge transfer for various molecules on $(10, 0)$, $(17, 0)$, and $(5, 5)$ SWCNTs were calculated. The results show that most of the studied molecules (except for NO_2 and O_2) are charge donors with small charge transfer (0.01–0.035e) and weak binding (≤ 0.2 eV). For these molecules, the adsorption can be identified as physisorption. For O_2 and NO_2, it shows that they both are charge acceptors with large charge transfer and adsorption energies. It also demonstrated that there is no clear dependence of adsorption on the tube size and chirality.

Adsorption of Organic Molecules

The outer surface of individual CNTs provides evenly distributed hydrophobic sites for organic chemicals. Hydrophobic interactions were emphasized in several studies that discussed protein, naphthalene, acidic herbicides, and streptavidin adsorption on CNTs [195]. If hydrophobic interactions are the only mechanism for the interactions between organic chemicals and CNTs, the adsorption can be predicted using the hydrophobic parameters of organic chemicals. However, this is not true for most cases. Other mechanisms include π-π interactions (between bulk π-systems on CNT surfaces and organic molecules with C=C double bonds or aromatic rings), hydrogen bonds (because of the functional groups on CNT surfaces), and electrostatic interactions (because of the charged CNT surface). Different adsorption mechanisms respond to the change of environmental conditions differently; thus, the relative contribution of an individual mechanism to the overall adsorption is of major importance to predict organic chemical adsorption on CNTs.

The most widely recognized influence of organic chemical functional groups on organic chemical-CNT interactions is on the electron-donor-acceptor (EDA) π-π interaction, i.e., the strength of π-π bond is highly dependent on functional groups attached to the benzene rings for organic chemicals. Because CNTs could be viewed as either electron-donors or acceptors, adsorption of either electron-acceptors (such as nitroaromatics) or electron-donors (such as phenols) on CNTs is expected to be stronger as compared to unsubstituted aromatic hydrocarbons. In addition, the tendency of a molecule to accept or donate electrons also determines the strength of the π-π bond, as in the case with strong charge donors over weak charge donors (such as 2,3-dichloro-5, 6-dicyano-1, 4-benzoquinone over benzene).

SWCNT Tip and Defective SWCNTs

Although most of the previous studies deal with the perfect surface of individual CNTs, it is worth noting that some works have been devoted to the reactivity of CNT tips. Although the contribution of the tips to adsorption in terms of specific surface area is negligible, it can be relevant at very low coverage or when studying field emission properties [196]. An interesting structural feature occurs near the ends of all CNTs from the closure of the graphene cylinders by the incorporation of topological defects such as pentagons in the hexagonal graphene lattice. Complex end structures can arise, for instance, conical-shaped sharp tips, due to the way pentagons are distributed near the ends for full closure, which is fully related to local reactivity [197]. It is suggested by theory that the ends of the tubes should have different electronic structure due to the presence of topological defects [198].

The presence of defects in SWCNT structure drastically affects all their properties such as transport, mechanical, magnetic, electronic, optical, or adsorptive [199, 200]. These defects, which can be seen as islands with elevated reactivity, can be produced naturally during growth and purification processes or can also be intentionally introduced to modify CNT properties. Under harsh conditions (purification and functionalization are commonly carried out with strong acids), the nanotubes are also attacked, resulting in the formation of defects on both the open-ended tips and sidewalls [201–203]. Among the most common defects are non-hexagonal rings,
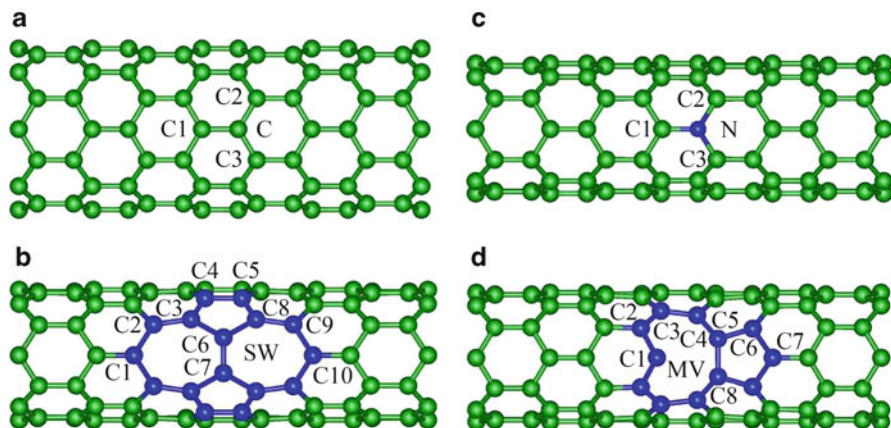
Fig. 1.15 Side view of (8, 0) nanotube structure (**a**) without deformation, (**b**) with a so-called Stone-Wales defect (whether this name is relevant [10] will not be discussed here), (**c**) with nitrogen atom as a substitutional impurity, and (**d**) with a mono-vacancy. The labels identify atoms of the defective sites (Adapted from [209])

namely, pentagons and heptagons (Fig. 1.15b). Other rings can also be temporarily observed at certain stages of the surface reconstruction, but they are found to rearrange by the Stone-Wales mechanism [204] into more stable ones. Heterocycles create a local disturbance (electrons are more concentrated around the double bonds involved in the defect instead of participating in the delocalized electron cloud above the graphene as usual), which serves as a reactive center for adsorption of various atoms, nanoparticles, or molecules [205–207]. Carbon atoms belonging to the tips are more reactive than those belonging to the sidewall of the nanotube, even in the presence of a Stone-Wales defect [208].

The influence of substitutional impurities (Fig. 1.15c) on adsorption will not be addressed in this chapter. Another common type of defect is vacancies (Fig. 1.15d). On such defects, the initial threefold symmetry is broken and a vacancy is formed. Removing a carbon atom leaves a vacant space with three dangling carbon bonds in the nanotube network [210]. The triplet state is slightly more stable than the singlet state [211]. These three dangling bonds are unstable and undergo recombination to make a chemical bond between two of them forming a pentagon ring and one remaining dangling bond − in a nonagon ring [212]. The related single occupied molecular orbital, given in Fig. 1.16, clearly indicates the propensity of one carbon atom of the defect to be very reactive. The formation of a vacancy and its orientation depends on the radius and chirality of nanotubes. The dangling bond can also participate in the interaction with other molecules, as well as it can be the functionalization site of the nanotubes. Hence, it is clear that defect sites are of great influence on the adsorption process [213–215].

Shi et al. [216] studied the adsorption of ten different atoms (H, B, C, N, O, F, Si, P, Li, and Na) over Stone-Wales defects on SWCNT and observed that only the adsorption capacity of B, N, F, and Si would benefit from introducing this defect
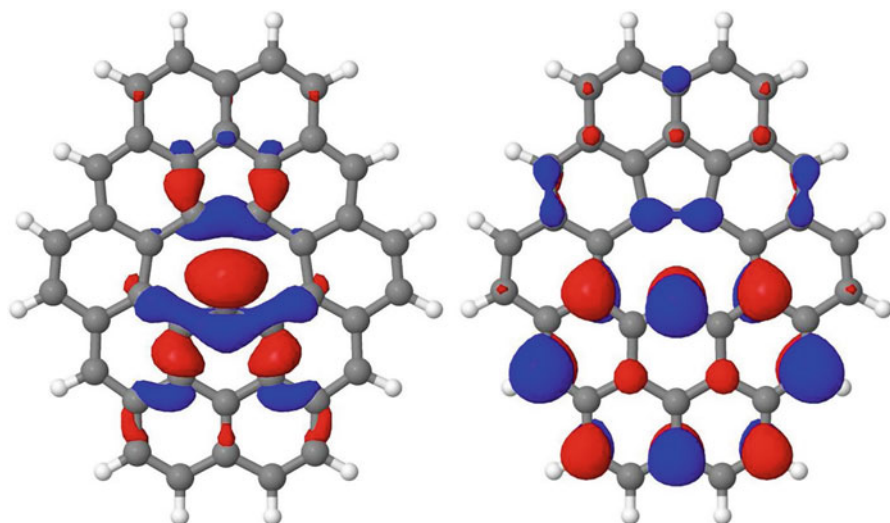
Fig. 1.16 Single occupied molecular orbitals in the lowest triplet state for a vacancy on a graphene sheet (From [211])

(the presence of a heptagon reduced the binding energy by about 0.5 eV). In another work by the same author [217], first-principles methods were applied to study the interaction of Stone-Wales defects in a SWCNT with eight other different metal atoms (Fe, Ni, Co, Ti, Cu, Al, Mg, and Mo). They found that there was no bonding between Mo and Ti and the SWCNT. On the other hand, Fe, Co, and Ni evidenced a strong attractive interaction with CNTs. In fact, these metals are the most frequently used as catalysts for growing CNTs.

Given the growing demand for noble metals, their scarce availability, and high cost, it is highly desirable that the catalytic activity conveyed by these atoms is as high as possible using the lowest amount of metal. For this reason, it is especially important to study the interaction of noble metals with the CNT surfaces. Kim et al. [218] used DFT calculations to study the defect-induced loading of Pt nanoparticles on CNTs. They observed that Pt atom could be strongly bound to the vacancy site (adsorption energy of –6.22 eV). Pt atom was stabilized by saturating the dangling bonds of adjacent carbon atoms in the vacancy.

Similarly, the presence of structural defects plays a significant role in the adsorption of gases on nanotubes. In general terms, a strong interaction is obtained whenever a gas molecule adsorbs over a defect on the nanotube surface (chemisorption), whereas a much weaker interaction (physisorption) is obtained when the same gas molecules interact with a perfect surface. This may relate to the literature contradiction about the quantity of hydrogen CNTs can uptake. This is mostly due to the fact that, up to now, the exact nature of the sites on which hydrogen activation takes place before they are adsorbed on the carbon atoms in the nanotubes is still unknown [219]. Lopez-Corral et al. [220] observed that H_2 adsorption occurred preferentially on C-defective sites. During hydrogen interaction with the

C-defective nanotube, the H–H bond was broken after adsorption on the parallel vacancy (adsorption energy value of 2.52 eV), representing a chemisorptive phenomenon. Gayathri and Geetha also observed a considerable increase in the adsorption binding energy of H_2 (in the order of 50 %) due to the presence of structural defects in SWCNTs [221].

One important application of adsorption in CNTs is gas sensing. It is based on the fact that the electrical conductivity of SWCNT changes dramatically upon exposure to some gaseous molecules. Among the most investigated are NH_3 and NO_2. DFT calculations were used by Tang and Cao [222] to investigate the effect of a Stone-Wales defects and vacancies on the interaction of NO_x (x = 1, 2, 3) with a semiconducting SWCNT. They found that the adsorption of NO_x on the mono-vacancy defect was more favorable energetically in comparison with the NO_x adsorption on the perfect CNT as well as the Stone-Wales defect. Such stronger interactions of NO_x with the vacancy defect were ascribed to the presence of a dangling bond (carbene-like reactivity).

Bundles of Carbon Nanotubes

As already noticed in section 'Describing Carbon Nanotubes', SWCNTs usually aggregate into bundles because of van der Waals interactions. Thus, it is most appropriate to discuss adsorption on CNTs samples not in terms of adsorption on individual nanotubes but in terms of adsorption on the outer or inner surfaces of such bundles. Most of the work has been analyzed in terms of a homogeneous bundle model. This model considers that bundles are constituted by infinitely long nanotubes of the same diameter, packed into perfect arrays. An alternative model, the heterogeneous bundle, has tubes of different diameters constituting the bundles. Diameter mismatch leads to the appearance of packing defects in the bundles, which give rise to interstitial channels with diameters larger than those found in the homogeneous bundles. Theoretical calculations have predicted that the molecule adsorption on the surface of or inside the SWCNT bundle (Fig. 1.17) is stronger than that on an individual tube [194]. A similar situation exists for MWCNTs, where adsorption could occur either on or inside the tube or between aggregated MWCNTs [223]. Considering closed-end SWCNTs, simple molecules can be adsorbed onto the walls of the outer nanotubes of the bundle and preferably on the external grooves (Fig. 1.17). In the first stages of adsorption (corresponding to the most reactive sites for adsorption), adsorption or condensation in the interstitial channels of the SWCNT bundles depends on the size of the molecule (and/or on the SWCNT diameters) and on their interaction energies [224–227]. However, opening of the tubes favors the adsorption of small gaseous molecules (including O_2, N_2, and H_2) onto the inner surface [228–230]. Nitrogen adsorption on open-ended SWCNT bundles was found to be three times larger than that on closed-ended bundles [231]. For hydrogen and other molecules like CO, CH_4, or CF_4, computational methods have shown that, for open SWCNTs, groove sites are energetically more favorable than surface sites [194, 227, 232–234].
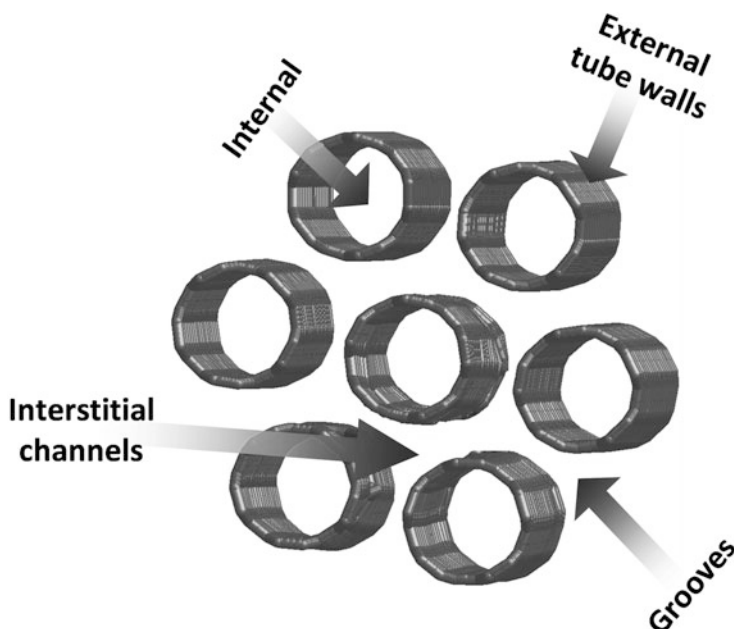
Fig. 1.17 Sketch of a SWCNT bundle illustrative of the different adsorption sites

Carbon Nanotubes and Biology

Because of the same reactivity properties as described in the previous section, carbon nanotubes may also exhibit strong interactions with biological systems. This may have some very positive effects that could be used for biomedical applications [235], but this may also lead to some adverse effects such as toxicity [236]. After describing how the functionalization of CNTs can modify their interactions with biological systems and in particular make them potentially exhibit some (at least partial) biodegradation, we will briefly review both the toxicity issue and the biomedical applications currently in development.

Biofunctionalization

Apart from morphological considerations (length, in particular), the way CNTs will behave in a biological environment mainly depends on their surface chemistry. The surface of CNTs may be functionalized as described previously, i.e., either covalently or non-covalently (simple adsorption of molecules, the interaction being enhanced in case of π-π stacking due to the intrinsically strong hydrophobic surface of pristine CNTs). Surface functionalization is usually aiming at giving new properties to the CNTs, but it could also occur spontaneously (especially non-covalently) as

soon as CNTs are exposed to biomolecules such as proteins. The goals of biofunctionalization can vary depending on the application. In most cases, functionalization is used to enhance the solubility/dispersibility of CNTs in water, facilitate their debundling, and stabilize them in the media. It is not the aim here to review all the different approaches proposed to functionalize CNTs [237]. Biofunctionalization is more often used either to target CNTs towards specific cells (e.g., cancer cells) or to enhance their circulation time in blood by limiting their interactions with the immune system (the adsorption of polyethylene glycol (PEG) molecules is generally used for this purpose [238]). The molecules used for targeting of course strongly depend on the goal to achieve. Examples include proteins [239], peptides [240, 241], polysaccharides [242], DNA [243], or polymers [244].

Biodegradation

The biodegradability of CNTs is strongly related to the toxicity issue. CNTs are usually relatively inert, and this is why covalent functionalization most often requires strongly oxidizing conditions to occur. However, biomolecules such as enzymes can, in some cases, degrade CNTs. This was first evidenced in vitro with a vegetal peroxidase, the horseradish peroxidase [245]. It was shown that this enzyme is only able to degrade oxidized SWCNTs (in fact, the CNTs used in this study not only were strongly oxidized but were also very short, which might also have played a role). Partial degradation of SWCNTs led to the formation of different organic compounds including oxidized aromatic hydrocarbons. However, the final product of the reaction was carbon dioxide. The potential relative toxicity of these intermediate products should be considered since some of these degradation compounds might be more deleterious than the original SWCNTs. A following paper by the same group described later the biodegradation of the same CNTs (i.e., strongly oxidized and very short) by the human myeloperoxidase [246], naturally produced by neutrophils, and by macrophages as well, yet to a lower extent. Again, it was shown that only this kind of CNTs could be fully metabolized in vitro but only in the presence of hypochlorite. In vivo, the partial biodegradation of the same CNTs was also evidenced. Again, in case of only partial degradation, the by-products might be much more toxic than the starting CNTs. Other works reported the partial degradation of amino-functionalized CNTs in the brain cortex [247], but to date, there is no clear evidence that oxidized or other kinds of functionalized CNTs can be completely biodegraded. Raw CNTs seem to be protected from this mechanism. The question of the biodegradation of CNTs is very important in terms of both biomedical applications and potential long-term toxicity and is clearly worth further investigation.

Potential Toxicity and Environmental Impact (Ecotoxicity)

CNTs come with a large variety of morphology (length, diameter, bundling), structure (number of walls, metallic or semiconducting electrical behavior), and purity, as this

has been described earlier in this chapter (section 'Describing Carbon Nanotubes'). All these parameters have some influence on their interaction with cells and thus on their toxicity. Short or entangled CNTs may be readily taken up by cells. This could occur in a passive way (passive diffusion or by piercing the cell membrane – especially if the CNTs are rigid enough – as kinds of nano-needles [235]) or via active mechanisms such as endocytosis [236] or phagocytosis. The exact mechanism will significantly depend on the characteristics of each sample, and different mechanisms may occur simultaneously depending on the kind of cell considered. The main route of exposure for CNTs is inhalation and concerns mainly workers (including researchers in laboratories). Most particles are usually cleared by the mucociliary escalator, but the smallest may reach the alveolar area. Long CNTs (at least beyond 15 μm) cannot be effectively treated by macrophages (this is called frustrated phagocytosis) and are thus likely to stay in the lungs. CNTs shorter than 4 μm should be able to translocate to other organs by leaving the lungs through the stomata (pores), but CNTs up to 10 μm which would be able to reach this area could not escape through the pores and would accumulate there, leading to continuous inflammation and potentially to mesothelioma in the long term [248]. There is no clear evidence today that CNTs may be able to penetrate through the skin, so this route of exposure is unlikely.

There are many difficulties with comparing the results of the toxicity studies published in the literature. There was initially a serious lack of characterization of the CNT samples used in toxicity studies [249]. Although there is currently a consensus that a minimum of characterization should be provided to be able to publish the results of toxicity studies [250], the relevance of methods recommended for other kinds of nanoparticles may be questioned in the specific case of CNTs. For example, the dynamic light scattering method commonly used to measure particle size distribution cannot be used with high aspect ratio nanoparticles such as CNTs. The wide variety of possible CNT samples brought by the variety of synthesis methods, chemical treatments (e.g., purification), and processing (leading to more or less agglomeration depending on factors such as whether surfactants are added or whether sonication is used – and if yes, which kind and conditions: bath, tip, power, time, etc.) must also be kept in mind. The choice of the dose unit is also a continuous matter of discussion: should it be the weight concentration? or the specific surface area? or the number of CNTs? Then, the other source of difficulties comes from the variety in biological models: most studies are performed in vitro using cancer cell lines from different organs (sometimes completely irrelevant in terms of potential exposure), because cancer cells are easier to culture and also to compare from one study to another. The number of studies performed on normal cells is much more limited, and the results highlight the differences in terms of sensitivity of these different kinds of cells (normal cells being more sensitive) [251]. There are similar discrepancies for in vivo investigations, with the variety of possible animal species and of exposure protocols (leading to preferential exposure to agglomerates or to better dispersed CNTs). Generally speaking, however, there is a consensus that there is often a dose-effect relationship and that the toxicity of CNTs is likely to be related to inflammation mechanisms (oxidative stress, activation of the inflammasome [252], etc.).

Finally, the environmental impact of CNTs is also to be taken into consideration due to the large and increasing number of commercial products in which they are included (mainly in composite materials and batteries). In the absence of specific regulation, CNT-containing materials may not be disposed of properly. For this reason, the investigation of the potential impact of CNTs on the different environmental compartments (soil, water) is very important. Initial studies focused on single compartments and generally revealed that biological species (worms, crustaceans, amphibian larvae, etc.) all interact with CNTs. In most cases, it seems that at low concentration (less than 10 mg L^{-1} in the case of studies in water), no significant effect is observed. CNTs transit through the gastrointestinal pathway without visible harm. Yet actual CNT concentrations in the environment are only available based on calculations so far (upon hypotheses on the transfer between air, soil, and water), they are expected to be few orders of magnitude below this value of 10 mg/L. However, at higher concentrations, some toxicity is generally noticed, which seems in most cases possible to correlate with 'mechanical' effects (perturbation of the digestion or the respiration, for example, not intrinsically related to the CNTs themselves but more to the presence of large amount of foreign material in the body). Here again, the question of sample preparation and its possible influence on the results is very important [253].

Positive Bioproperties (Biomedical Applications)

CNTs are promising candidates in the fields of drug delivery, diagnosis, and therapy [254]. Thanks to their needlelike shape, they possess an enhanced capacity to penetrate cellular membranes and have a superior flow dynamics compared to spherical nanoparticles and also the potential to carry multiple moieties at high density, thanks to their large specific surface area. CNTs are also flexible structures which might bend, thus allowing the interaction of functionalized CNTs with cells through multiple binding sites. Furthermore, it is also possible to take advantage of their tubular shape to simultaneously encapsulate a chosen biomedical payload in their hollow core while the external walls can be functionalized to render them dispersible, biocompatible, and even engineered for specific targets [244].

The intrinsic electronic (and optical) properties of CNTs also allow their monitoring (detection and imaging) in biological tissues by means of several spectroscopic techniques, including Raman, photoluminescence, and photoacoustic imaging [255]. Apart from imaging, SWCNTs exhibit some specific electronic properties that can be used for therapeutic purposes via photothermal therapy, since they strongly absorb light in the near-infrared and their emission range is within 800–2,000 nm, covering the whole transparency window of biological tissues (800–1,400 nm). Raman spectroscopy can also be used for imaging any kind of CNT in tissues.

Thanks to their easy penetration into cells, the use of CNTs could improve the targeted delivery of poorly water-soluble drugs, thus increasing the efficiency and reducing side effects [256]. CNTs could also be used as antibacterial coatings to eliminate resistant pathogens, although the efficiency strongly depends on both the

nature of the CNT samples and the kind of bacteria, as this could be expected from the results of the toxicity studies. Another promising application for CNTs is their use as substrate for tissue engineering and cell growth in general. As opposed to the toxicity which has been discussed earlier in the case of exposure of cells to individual CNTs or agglomerates, there is experimentally a good biocompatibility between CNT-coated surfaces and different cells such as osteoblasts [257] and neurons [258]. Especially in the case of neurons, the electrical conductivity of the CNTs, associated to their large specific surface area and thus high interaction with both cells and medium components, is expected to participate to the enhanced neuronal activity usually observed. There is thus currently an important research effort in the field of microelectrodes arrays, where CNTs offer a very interesting interface, increasing both the signal/noise ratio of the devices and their biocompatibility. Other bioapplications of CNTs are dealing with biosensors (generally based on electrochemical or field-effect transistors). Typical biological targets are enzymes, glucose, DNA, and proteins [259].

Conclusions

This too short chapter has just been able to show the emerged part of the iceberg that represents the whole knowledge gathered on the properties of carbon nanotubes since the 1990s. It requires reading many dedicated books [8, 20, 25, 55, 260–273] to figure out how deep and comprehensive this knowledge has become. Nowadays then, very little remain to discover regarding the intrinsic properties of pristine nanotubes. But a lot of work remains to do regarding the behavior of all kinds of nanotubes and all their possible avatars (so-called meta-nanotubes [273]) when interacting with various kinds of environment (matrices, atmospheres, dopants, etc.) and when subjected to various kinds of outer conditions and stresses (mechanical, thermal, magnetic, chemical, etc.). Even when modeling attempts have addressed related issues, different modeling principles do not necessarily provide consistent results. A good example for this is the estimate for the uptake of hydrogen by metallic-type SWCNTs [(10, 10) or (9, 9)] which was found to range from 14.3 wt% [274], or 3.3 wt% [275], to <0.5 wt% [276] for density functional theory, geometrical model, and quantum-mechanical molecular dynamics, respectively. Experimental confirmations are then needed in many instances because real systems are far from the simplified cases (from the point of view of the number of atoms, structural perfection, chemical complexity, etc.) considered in modeling in order to make it possible within reasonable time range and with using reasonable amount of computational resources. Finally, carbon nanotubes, which were considered as the most promising nanomaterials for revolutionizing our technological future until recently, have now to face the competition with graphene in many instances. Which one will hold its promises the most? Certainly, in relation to their respective superiorities in various domains, those two kin materials will end by being complementary regarding their use for the large panel of envisaged applications. But in order to find out, comparative property measurements will have to be carried out still for the next 10–15 years.

References

1. Marx W, Barth A (2010) Carbon nanotubes – a scientometric study. In: Marulanda JM (ed) Carbon nanotubes. InTech, Rijeka, pp 1–17
2. Lv PH, Wang GF, Wan Y et al (2011) Bibliometric trend analysis on global graphene research. Scientometrics 88:399–419
3. Sadoc JF, Mosseri R (1982) Order and disorder in amorphous, tetrahedrally coordinated semiconductors: a curved-space description. Phil Mag 45:467–483
4. Kroto HW, Heath JR, O'Brien SC et al (1985) C_{60} Buckminsterfullerene. Nature 318:162–163
5. Franklin RE (1951) The structure of graphitic carbons. Acta Cryst 4:253–261
6. Oberlin A, Boulmier JL, Villey M (1973) Electron microscopic study of kerogen microtexture. Selected criteria for determining the evolution path and evolution stage of kerogen. In: Durand B (ed) Kerogen. Technip, Paris, pp 191–241
7. Hamada N, Sawada SI, Oshiyama A (1992) New one-dimensional conductors, graphite microtubules. Phys Rev Lett 68:1579–1781
8. Dresselhaus MS, Dresselhaus G, Eklund PC (1996) Science of fullerenes and carbon nanotubes. Academic Press, San Diego
9. Noguez C (2006) Optical properties of nanostructures. http://www.fisica.unam.mx/cecilia/. Accessed 18 July 2011
10. Monthioux M (2012) Introduction to carbon nanotubes. In: Monthioux M (ed) Meta-nanotubes: synthesis, properties, and applications. Wiley-Blackwell, Chichester, pp 7–39
11. Iijima S (1991) Helical microtubules of graphite carbon. Nature 354:56–58
12. Oku T, Koi N, Suganuma K et al (2007) Formation and atomic structure of boron nitride nanotubes with a cup-stacked structure. Sol State Comm 143:331–336
13. Xu FF, Bando Y, Golberg D (2003) The tubular conical helix of graphitic boron nitride. New J Phys 5:118.1–118.16
14. Saito Y (1995) Nanoparticles and filled nanocapsules. Carbon 33:979–988
15. Oberlin A, Bonnamy S, Bourrat X et al (1986) Electron microscopic observations on carbonization and graphitization. In: Bacha JD, Newman JW, White JL (eds) Petroleum derived carbons, ACS symposium series. American Chemical Society, Washington, DC, pp 85–98
16. Banhart F (1999) Irradiation effects in carbon nanostructures. Rep Prog Phys 62:1181–1221
17. Cojean D, Monthioux M (1992) Unexpected behaviour of interfacial carbon in SiC/SiC composites during oxidation. Br Ceram Trans J 91:188–195
18. Rosca ID, Watari F, Uo M et al (2005) Oxidation of multiwalled carbon nanotubes by nitric acid. Carbon 43:3124–3131
19. Thess A, Lee R, Nikolaev P et al (1996) Crystalline ropes of metallic carbon nanotubes. Science 273:483–487
20. Monthioux M, Serp P, Flahaut E et al (2010) Introduction to carbon nanotubes. In: Bhushan B (ed) Nanotechnology handbook, 3rd edn (revised). Springer, Heidelberg, pp 47–118
21. Hou P-X, Liu C, Cheng H-M (2008) Purification of carbon nanotubes – a review. Carbon 46:2003–2025
22. Warner JH, Young NP, Kirkland AI et al (2011) Resolving strain in carbon nanotubes at the atomic level. Nature Mater 10:958–962
23. Charlier J-C, Blase X, Roche S (2007) Electronic and transport properties of nanotubes. Rev Mod Phys 79:677–732
24. Jorio A, Dresselhaus G, Dresselhaus MS (2007) Carbon nanotubes. Springer, Berlin
25. Loiseau A, Launois P, Petit P et al (2006) Understanding carbon nanotubes: from basics to applications. In: Lecturer notes physics, vol 677. Springer, Heidelberg
26. Ando T (2005) Theory of electronic states and transport in carbon nanotubes. J Phys Soc Jpn 74:777–817

27. Wilder JWG, Venema LC, Rinzler AG et al (1998) Electronic structure of atomically resolved carbon nanotubes. Nature 391:59–62
28. Odom TW, Huang J-L, Kim P et al (1998) Atomic structure and electronic properties of single-walled carbon nanotubes. Nature 391:62–64
29. Tans SJ, Verschueren ARM, Dekker C (1998) Room-temperature transistor based on a single carbon nanotube. Nature 393:49–52
30. Appenzeller J, Knoch J, Radosavljevic M et al (2004) Multimode transport in schottky-barrier carbon-nanotube field-effect transistors. Phys Rev Lett 92:226802
31. Chen Z, Appenzeller J, Knoch J et al (2005) The role of metal-nanotube contact in the performance of carbon nanotube field-effect transistors. NanoLett 5:1497–1502
32. Kim W, Javey A, Tu R et al (2005) Electrical contacts to carbon nanotubes down to 1 nm in diameter. Appl Phys Lett 87:173101
33. Triozon F, Roche S, Rubio A et al (2004) Electrical transport in carbon nanotubes: role of disorder and helical symmetries. Phys Rev B 69:121410
34. Latil S, Roche S, Mayou D et al (2004) Mesoscopic transport in chemically doped carbon nanotubes. Phys Rev Lett 92:256805
35. Woodside MT, McEuen PL (2002) Scanned probe imaging of single-electron charge states in nanotube quantum dots. Science 296:1098–1101
36. Ando T, Nakanishi T (1998) Impurity scattering in carbon nanotubes – absence of back scattering. J Phys Soc Jpn 67:1704–1713
37. McEuen PL, Bockrath M, Cobden DH et al (1999) Disorder, pseudospins, and backscattering in carbon nanotubes. Phys Rev Lett 83:5098–5101
38. Javey A, Guo J, Wang Q et al (2003) Ballistic carbon nanotube field-effect transistors. Nature 424:654–657
39. Buitelaar MR, Bachtold A, Nussbaumer T et al (2002) Multiwall carbon nanotubes as quantum dots. Phys Rev Lett 88:156801
40. Bezryadin A, Verschueren ARM, Tans SJ et al (1998) Multiprobe transport experiments on individual single-wall carbon nanotubes. Phys Rev Lett 80:4036–4039
41. Liang W, Bockrath M, Bozovic D et al (2001) Fabry-Perot interference in a nanotube electron waveguide. Nature 411:665–669
42. Hansson A, Stafström S (2003) Intershell conductance in multiwall carbon nanotubes. Phys Rev B 67:075406
43. Bourlon B, Miko C, Forró L et al (2004) Determination of the intershell conductance in multiwalled carbon nanotubes. Phys Rev Lett 93:176806
44. Roche S, Saito R (2001) Magnetoresistance of carbon nanotubes: from molecular to mesoscopic fingerprints. Phys Rev Lett 87:246803
45. Nanot S, Escoffier W, Lassagne B et al (2009) Exploring the electronic band structure of individual carbon nanotubes under 60 T. C R Phys 10:268–282
46. Aronov AG, Sharvin YV (1987) Magnetic flux effects in disordered conductors. Rev Mod Phys 59:755–779
47. Bachtold A, Strunk C, Salvetat J-P et al (1999) Aharonov-Bohm oscillations in carbon nanotubes. Nature 397:673–675
48. Coskun UC, Wei T-C, Vishveshwara S et al (2004) h/e magnetic flux modulation of the energy gap in nanotube quantum dots. Science 304:1132–1134
49. Nemec N, Cuniberti G (2006) Hofstadter butterflies of carbon nanotubes: pseudofractality of the magnetoelectronic spectrum. Phys Rev B 74:165411
50. Nanot S, Avriller R, Escoffier W et al (2009) Propagative landau states and Fermi level pinning in carbon nanotubes. Phys Rev Lett 103:256801
51. Wang Y, Kempa K, Kimball B et al (2004) Receiving and transmitting light-like radio waves: antenna effect in arrays of aligned carbon nanotubes. Appl Phys Lett 85:2607–2609
52. Ausserré D, Valignat M-P (2006) Wide-field optical imaging of surface nanostructures. NanoLett 6:1384–1388

53. Bacsa WS, Lannin JS (1992) Bilayer interference enhanced Raman scattering. Appl Phys Lett 61:19–21

54. Lambacher A, Fromherz P (2002) Luminescence of dye molecules on oxidized silicon and fluorescence interference contrast microscopy of biomembranes. J Opt Soc Am B 19:1435–1453

55. Reich S, Thomsen C, Maultzsch J (2004) Carbon nanotubes: basic concepts and physical properties. Wiley-VCH, Weinheim

56. Arbouet A, Christofilos D, Del Fatti N et al (2004) Direct measurement of the single-metal-cluster optical absorption. Phys Rev Lett 93:127401

57. Hartschuh A, Sánchez EJ, Xie XS et al (2003) High-resolution near-field Raman microscopy of single-walled carbon nanotubes. Phys Rev Lett 90:095503

58. Spataru CD, Ismail-Beigi S, Benedict LX et al (2004) Excitonic effects and optical spectra of single-walled carbon nanotubes. Phys Rev Lett 92:077402

59. Bachilo SM, Strano MS, Kittrell C et al (2002) Structure-assigned optical spectra of single-walled carbon nanotubes. Science 298:2361–2366

60. O'Connell MJ, Bachilo SM, Huffman CB et al (2002) Band gap fluorescence from individual single-walled carbon nanotubes. Science 297:593–596

61. Fantini C, Jorio A, Souza M et al (2004) Optical transition energies for carbon nanotubes from resonant Raman spectroscopy: environment and temperature effects. Phys Rev Lett 93:147406

62. Telg H, Maultzsch J, Reich S et al (2004) Chirality distribution and transition energies of carbon nanotubes. Phys Rev Lett 93:177401

63. Araujo PT, Doorn SK, Kilina S et al (2007) Third and fourth optical transitions in semiconducting carbon nanotubes. Phys Rev Lett 98:067401

64. Sfeir MY, Beetz T, Wang F et al (2006) Optical spectroscopy of individual single-walled carbon nanotubes of defined chiral structure. Science 312:554–556

65. Kataura H, Kumazawa Y, Maniwa Y et al (1999) Optical properties of single-wall carbon nanotubes. Synth Met 103:2555–2558

66. Tsyboulski DA, Rocha J-DR, Bachilo SM et al (2007) Structure-dependent fluorescence efficiencies of individual single-walled carbon nanotubes. NanoLett 7:3080–3085

67. Gambetta A, Manzoni C, Menna E et al (2006) Real-time observation of nonlinear coherent phonon dynamics in single-walled carbon nanotubes. Nat Phys 2:515–520

68. Ju SY, Kopcha WP, Papadimitrakopoulos F (2009) Brightly fluorescent single-walled carbon nanotubes via an oxygen-excluding surfactant organization. Science 323:1319–1323

69. Chen J, Perebeinos V, Freitag M et al (2005) Bright infrared emission from electrically induced excitons in carbon nanotubes. Science 310:1171–1174

70. Jorio A, Saito R, Hafner JH et al (2001) Structural (n, m) determination of isolated single wall carbon nanotubes by resonant Raman scattering. Phys Rev Lett 86:1118–1121

71. Meyer JC, Paillet M, Michel T et al (2005) Raman modes of index-identified freestanding single-walled carbon nanotubes. Phys Rev Lett 95:217401

72. Gerber IC, Puech P, Gannouni A et al (2009) Influence of nitrogen doping on the radial breathing mode in carbon nanotubes. Phys Rev B 79:075423

73. Jorio A, Souza Filho AG, Dresselhaus G et al (2002) G-band resonant Raman study of 62 isolated single-wall carbon nanotubes. Phys Rev B 65:155412

74. Thomsen C, Reich S (2000) Double resonant Raman scattering in graphite. Phys Rev Lett 85:5214–5217

75. Cançado LG, Jorio A, Martins Ferreira EH et al (2011) Quantifying defects in graphene via Raman spectroscopy at different excitation energies. NanoLett 11:3190–3196

76. Knight DS, White WB (1989) Characterization of diamond films by Raman spectroscopy. J Mater Res 4:385–393

77. Georgi C, Hartschuh A (2010) Tip-enhanced Raman spectroscopic imaging of localized defects in carbon nanotubes. Appl Phys Lett 97:143117

78. Cançado LG, Takai K, Enoki T et al (2006) General equation for the determination of the crystallite size La of nanographite by Raman spectroscopy. Appl Phys Lett 88:163106
79. Puech P, Hubel H, Dunstan DJ et al (2004) Discontinuous tangential stress in double wall carbon nanotubes. Phys Rev Lett 93:95506
80. Chen G, Bandow S, Margine ER et al (2003) Chemically doped double-walled carbon nanotubes: cylindrical molecular capacitors. Phys Rev Lett 90:257403
81. Bacsa RR, Flahaut E, Laurent C et al (2003) Narrow diameter double wall carbon nanotubes: synthesis and inelastic light scattering. New J Phys 5:131
82. Bacsa WS, Ugarte D, Châtelain A et al (1994) High-resolution electron microscopy and inelastic light scattering of purified multishelled carbon nanotubes. Phys Rev B 50:15473–15476
83. Tishkova V, Raynal P-I, Puech P et al (2011) Electrical conductivity and Raman imaging of double wall carbon nanotubes in a polymer matrix. Comp Sci Technol 71:1326–1330
84. Ruoff RS, Lorents DC (1995) Mechanical and thermal properties of carbon nanotubes. Carbon 33:925–930
85. Osman MA, Cummings AW, Srivastava D (2007) Thermal properties of carbon nanotubes. Topics Appl Phys 109:154–187
86. Maultzsch J, Reich S, Thomsen C et al (2002) Phonon dispersion of carbon nanotubes. Solid State Commun 121:471–474
87. Ishii H, Kobayashi N, Hirose K (2007) Electron-phonon coupling effect on quantum transport in carbon nanotubes using time-dependent wave-packet approach. Physica E 40:249–252
88. Hone J, Whitney M, Piskoti C et al (1999) Thermal conductivity of single-walled carbon nanotubes. Phys Rev B 59:R2514–R2516
89. Hone J, Batlogg B, Benes Z et al (2000) Quantized phonon spectrum of single-wall carbon nanotubes. Science 289:1730–1733
90. Yamamoto T, Watanabe S, Watanabe D (2004) Universal features of quantized thermal conductance of carbon nanotubes. Phys Rev Lett 92:075502/1–075502/4
91. Berber S, Kwon Y, Tomanek D (2000) Unusually high thermal conductivity of carbon nanotubes. Phys Rev Lett 84:4613–4616
92. Lindsay L, Broido DA, Mingo N (2009) Lattice thermal conductivity of single-walled carbon nanotubes: beyond the relaxation time approximation and phonon-phonon scattering selection rules. Phys Rev B 80:125407/1–125407/7
93. Osman MA, Srivastava D (2001) Temperature dependence of the thermal conductivity of single-wall carbon nanotubes. Nanotechnology 12:21–24
94. Gu Y, Chen Y (2007) Thermal conductivities of single-walled carbon nanotubes calculated from the complete phonon dispersion relations. Phys Rev B 76:134110/1–134110/9
95. Grujicic M, Cao G, Gersten B (2004) Atomic-scale computations of the lattice contribution to thermal conductivity of single-walled carbon nanotubes. Mater Sci Eng B 107:204–216
96. Ando T (2004) Carbon nanotubes and exotic transport properties. Physica E 22:656–661
97. Zhang W, Zhu Z, Wang F et al (2004) Chirality dependence of the thermal conductivity of carbon nanotubes. Nanotechnology 15:936–939
98. Cao JX, Yan XH, Xiao Y et al (2004) Thermal conductivity of zigzag single-walled carbon nanotubes: role of the Umklapp process. Phys Rev B 69:073407/1–073407/4
99. Maruyama SA (2002) Molecular dynamics simulation of heat conduction in finite length SWNTs. Physica B 323:193–195
100. Alaghemandi M, Algaer R, Böhm MC et al (2009) The thermal conductivity and thermal rectification of carbon nanotubes studied using reverse non-equilibrium molecular dynamics simulations. Nanotechnology 20:115704/1–115704/8
101. Chiu HY, Deshpande VV, Postma HWC et al (2005) Ballistic phonon thermal transport in multiwalled carbon nanotubes. Phys Rev Lett 95:226101/1–226101/4
102. Yu C, Shi L, Yao Z et al (2005) Thermal conductance and thermo-power of an individual single-wall carbon nanotube. Nano Lett 5:1842–1846

103. Prasher R (2008) Thermal boundary resistance and thermal conductivity of multi-walled carbon nanotubes. Phys Rev B 77:075424/1–075424/11
104. Chang CW, Okawa D, Garcia H et al (2008) Breakdown of Fourier's law in nanotube thermal conductors. Phys Rev Lett 101:075903/1–075903/4
105. Donadio D, Galli G (2007) Thermal conductivity of isolated and interacting carbon nanotubes: comparing results from molecular dynamics and the Boltzmann transport equation. Phys Rev Lett 99:255502/1–255502/4
106. Yamamoto T, Watanabe K (2006) Nonequilibrium Green's function approach to phonon transport in defective carbon nanotubes. Phys Rev Lett 96:255503/1–255503/4
107. Che J, Cagin T, Goddard WA (2000) Thermal conductivity of carbon nanotubes. Nanotechnology 11:65–69
108. Kim P, Shi L, Majumdar A et al (2001) Thermal transport measurements of individual multi-walled nanotubes. Phys Rev Lett 87:215502/1–215502/4
109. Small JP, Shi L, Kim P (2003) Mesoscopic thermal and thermoelectric measurements of individual carbon nanotubes. Solid State Commun 127:181–186
110. Yang DJ, Wang SG, Zhang Q et al (2004) Thermal and electrical transport in multi-walled carbon nanotubes. Phys Lett A 329:207–213
111. Fujii M, Zhang X, Xie H et al (2005) Measuring the thermal conductivity of a single carbon nanotube. Phys Rev Lett 95:065502/1–065502/4
112. Choi TY, Poulikakos D, Tharian J et al (2006) Measurement of the thermal conductivity of individual carbon nanotubes by the four-point three-ω method. Nano Lett 6:1589–1593
113. Li Q, Liu C, Wang X et al (2009) Measuring the thermal conductivity of individual carbon nanotubes by the Raman shift method. Nanotechnology 20:145702/1–145702/5
114. Pop E, Mann D, Wang Q et al (2006) Thermal conductance of an individual single-wall carbon nanotube above room temperature. Nano Lett 6:96–100
115. Pettes MT, Shi L (2009) Thermal and structural characterizations of individual single-, double-, and multi-walled carbon nanotubes. Adv Funct Mater 19:3918–3925
116. Mizel A, Benedict LX, Cohen ML et al (1999) Analysis of the low-temperature specific heat of multiwalled carbon nanotubes and carbon nanotube ropes. Phys Rev B 60:3264–3270
117. Yi W, Lu L, Zhang DL et al (1999) Linear specific heat of carbon nanotubes. Phys Rev B 59: R9015–R9018
118. Yang DJ, Zhang Q, Chen G et al (2002) Thermal conductivity of multi-walled carbon nanotubes. Phys Rev B 66:165440/1–165440/6
119. Aliev AE, Guthy C, Zhang M et al (2007) Thermal transport in MWCNT sheets and yarns. Carbon 45:2880–2888
120. Jakubinek MB, Johnson MB, White MA et al (2012) Thermal and electrical conductivity of array-spun multi-walled carbon nanotube yarns. Carbon 50:244–248
121. Behabtu N, Young CC, Tsentalovich DE et al (2013) Strong, light, multifunctional fibers of carbon nanotubes with ultrahigh conductivity. Science 339:182–186
122. Han Z, Fina A (2011) Thermal conductivity of carbon nanotubes and their polymer nanocomposites: a review. Prog Polymer Sci 36:914–944
123. Shenogin S, Bodapati A, Xue L et al (2004) Effect of chemical functionalization on thermal transport of carbon nanotube composites. Appl Phys Lett 85:2229–2231
124. Liu CH, Fan SS (2005) Effects of chemical modifications on the thermal conductivity of carbon nanotube composites. Appl Phys Lett 86:123106/1–123106/3
125. Mamunya Y, Boudenne A, Lebovka N et al (2008) Electrical and thermophysical behaviour of PVC-MWCNT nanocomposites. Compos Sci Technol 68:1981–1988
126. Bandow S (1997) Radial thermal expansion of purified multiwall carbon nanotubes measured by X-ray diffraction. Jpn J Appl Phys Part 2(36):1403–1405
127. Yosida Y (2000) High-temperature shrinkage of single-walled carbon nanotube bundles up to 1600 K. J Appl Phys 87:3338–3341
128. Maniwa Y, Fujiwara R, Kira H et al (2001) Thermal expansion of single-walled carbon nanotube (SWNT) bundles: x-ray diffraction studies. Phys Rev B 64:241402/1–241402/3

129. Jiang H, Liu B, Huang Y et al (2004) Thermal expansion of single wall carbon nanotubes. J Eng Mater Technol 126:265–270
130. Jiang JW, Wang JS, Li B (2009) Thermal expansion in single-walled carbon nanotubes and graphene: non-equilibrium Green's function approach. Phys Rev B 80:205429/1–205429/7
131. Shokrieh MM, Rafiee R (2010) A review of the mechanical properties of isolated carbon nanotubes and carbon nanotube composites. Mech Comp Mater 46:155–172
132. Treacy MMJ, Ebbesen TW, Gibson JM (1996) Exceptionally high Young's modulus observed for individual carbon nanotubes. Nature 381:678–680
133. Salvetat J-P, Briggs GAD, Bonard JM et al (1999) Elastic and shear moduli of single-walled carbon nanotube ropes. Phys Rev Lett 82:944–947
134. Krishnan A, Dujardin E, Ebbesen TW et al (1998) Young's modulus of single-walled nanotubes. Phys Rev B 58:14013–14019
135. Yu MF, Lourie O, Dyer MJ et al (2000) Strength and breaking mechanism of multiwalled carbon nanotubes under tensile load. Science 287:637–640
136. Tombler TW, Zhou C, Alexseyev L et al (2000) Reversible electromechanical characteristics of carbon nanotubes under local-probe manipulation. Nature 405:769–772
137. Lu JP (1997) Elastic properties of carbon nanotubes and nanoropes. Phys Rev Lett 79:1297–12300
138. Wei X, Chen Q, Peng LM et al (2009) Tensile loading of double-walled and triple-walled carbon nanotubes and their mechanical properties. J Phys Chem C 113:17002–17005
139. Li F, Cheng HM, Bai S et al (2000) Tensile strength of single-walled carbon nanotubes directly measured from their macroscopic ropes. Appl Phys Lett 77:3161–3163
140. Li Y, Wang K, Wei J et al (2005) Tensile properties of long aligned double-walled carbon nanotube strands. Carbon 43:31–35
141. Muster J, Burghard M, Roth S et al (1998) Scanning force microscopy characterization of individual carbon nanotubes on electrode arrays. J Vac Sci Technol 16:2796–2801
142. Sammalkorpi M, Krasheninnikov A, Kuronen A et al (2004) Mechanical properties of carbon nanotubes with vacancies and related defects. Phys Rev B 70:245416/1–245416/8
143. Mielke SL, Zhang S, Khare R et al (2007) The effects of extensive pitting on the mechanical properties of carbon nanotubes. Chem Phys Lett 446:128–132
144. Poncharal P, Wang ZL, Ugarte D et al (1999) Electrostatic deflection and electromechanical resonances of carbon nanotubes. Science 283:1513–1516
145. Després JF, Daguerre E, Lafdi K (1995) Flexibility of graphene layers in carbon nanotubes. Carbon 33:87–92
146. Iijima S, Brabec C, Maiti A et al (1996) Structural flexibility of carbon nanotubes. J Phys Chem 104:2089–2092
147. Demczyk BG, Wang YM, Cummings J et al (2002) Direct mechanical measurement of the tensile strength and elastic modulus of multiwalled carbon nanotubes. Mater Sci Eng, A 334:173–178
148. Ruoff RS, Tersoff J, Lorents DC et al (1993) Radial deformation of carbon nanotubes by Van der Waals forces. Nature 364:514–516
149. Chopra NG, Benedict LX, Crespi VH et al (1995) Fully collapsed carbon nanotubes. Nature 377:135–138
150. Aguiar AL, Capaz RB, Souza Filho AG et al (2012) Structural and phonon properties of bundled single- and double-wall carbon nanotubes under pressure. J Phys Chem C 116:22637–22645
151. Caillier C, Ayari A, Gouttenoire V et al (2010) An individual carbon nanotube transistor tuned by high pressure. Adv Funct Mater 20:3330–3335
152. Arvanitidis J, Christofilos D, Papagelis K et al (2005) Pressure screening in the interior of primary shells in double-wall carbon nanotubes. Phys Rev B 71:125404/1–125404/5
153. Aguiar AL, Barros EB, Capaz RB et al (2011) Pressure-induced collapse in double-walled carbon nanotubes: chemical and mechanical screening effects. J Phys Chem C 115:5378–5384

154. Buongiorno-Nardelli M, Yakobson BI, Bernholc J (1998) Mechanism of strain release in carbon nanotubes. Phys Rev B 57:R4277–R4280
155. Zhao QZ, Buongiorno-Nardelli M, Bernholc J (2002) Ultimate strength of carbon nanotubes: a theoretical study. Phys Rev B 65:144105/1–144105/6
156. Belytschko T, Xiao SP, Schatz GC et al (2002) Atomistic simulations of nanotube fracture. Phys Rev B 65:235430/1–235430/8
157. Ogata S, Shibutani Y (2003) Ideal tensile strength and band gap of single-walled carbon nanotubes. Phys Rev B 68:165409/1–165409/4
158. Mielke SL, Troya D, Zhang S et al (2004) The role of vacancy defects and holes in the fracture of carbon nanotubes. Chem Phys Lett 390:413–420
159. Walters DA, Ericson LM, Casavant MJ et al (1999) Elastic strain of freely suspended single-wall carbon nanotube ropes. Appl Phys Lett 74:3803–3805
160. Yu MF, Files BS, Arepalli S et al (2000) Tensile loading of ropes of single wall carbon nanotubes and their mechanical properties. Phys Rev Lett 84:5552–5555
161. Huang JY, Chen S, Wang ZQ et al (2006) Superplastic carbon nanotubes. Nature 439:281
162. Liew KM, He XQ, Wong CH (2004) On the study of elastic and plastic properties of multi-walled carbon nanotubes under axial tension using molecular dynamics simulation. Acta Mater 52:2521–2527
163. Peng B, Locascio M, Zapol P et al (2008) Measurements of near-ultimate strength for multiwalled carbon nanotubes and irradiation-induced crosslinking improvements. Nat Nanotechnol 3:626–631
164. Barber AH, Andrews R, Schadler LS et al (2005) On the tensile strength distribution of multiwalled carbon nanotubes. Appl Phys Lett 87:203106/1–203106/3
165. Yamamoto G, Suk JW, An JH et al (2010) The influence of nanoscale defects on the fracture of multi-walled carbon nanotubes under tensile loading. Diam Relat Mater 19:748–751
166. Lozovik YE, Popov AM (2007) Properties and nanotechnological applications of nanotubes. Phys Usp 50:749–761
167. Kis A, Jensen K, Aloni S et al (2006) Interlayer forces and ultralow sliding friction in multiwalled carbon nanotubes. Phys Rev Lett 97:025501/4–025501/4
168. Bichoutskaia E, Ershova OV, Lozovik YE et al (2009) Ab initio calculations of the walls shear strength of carbon nanotubes. Tech Phys Lett 35:666–669
169. Vigolo B, Penicaud A, Coulon C et al (2000) Macroscopic fibers and ribbons of oriented carbon nanotubes. Science 290:1331–1334
170. Dalton AB, Collins S, Muñoz E et al (2003) Super-tough carbon-nanotube fibres. Nature 423:702
171. Behabtu N, Green MJ, Pasquali M (2008) Carbon nanotube-based neat fibers. Nano Today 3:24–34
172. Zhu HW, Xu CL, Wu DH et al (2002) Direct synthesis of long single-walled carbon nanotube strands. Science 296:884–886
173. Pan ZW, Xie SS, Lu L et al (1999) Tensile tests of ropes of very long aligned multiwall carbon nanotubes. Appl Phys Lett 74:3152–3154
174. Vilatela JJ, Elliott JA, Windle AH (2011) A model for the strength of yarn-like carbon nanotube fibers. ACS Nano 5:1921–1927
175. Kleiner A, Eggert S (2001) Curvature, hybridization, and STM images of carbon nanotubes. Phys Rev B 64:113402
176. Yu O, Jing-Cui P, Hui W et al (2008) The rehybridization of electronic orbitals in carbon nanotubes. Chin Phys B 17:3123–3127
177. Durgun E, Dag S, Ciraci S et al (2004) Energetics and electronic structures of individual atoms adsorbed on carbon nanotubes. J Phys Chem B 108:575–582
178. Hosoya N, Kusakabe K, Maheswari SU (2011) Theoretical simulation of deformed carbon nanotubes with adsorbed metal atoms: enhanced reactivity by deformation. Jpn J Appl Phys 105101

179. Menon M, Andriotis AN, Froudakis GE (2000) Curvature dependence of the metal catalyst atom interaction with carbon nanotube walls. Chem Phys Lett 320:425–434
180. Chen G, Kawazoe Y (2006) Interaction between a single Pt atom and a carbon nanotube studied by density functional theory. Phys Rev B 73:125410
181. Valencia H, Gil A, Frapper G (2010) Trends in the adsorption of 3d transition metal atoms onto graphene and nanotube surfaces: a DFT study and molecular orbital analysis. J Phys Chem C 114:14141–14153
182. Gao H, Zhao J (2010) First-principles study of Ru atoms and clusters adsorbed outside and inside carbon nanotubes. J Chem Phys 132:234704
183. Xu S-F, Yuan G, Li C et al (2011) Modulation of the work function of capped single-walled carbon nanotube by alkali-metal adsorption: a theoretical study. J Phys Chem C 115:8928–8933
184. Xu S-F, Yuan G, Li C et al (2010) Work functions of capped (5, 5) and (9, 0) single-walled carbon nanotubes adsorbed with alkali-metal atoms. Appl Phys Lett 96:233111
185. Lee E-C, Kim Y-S, Jin Y-G et al (2002) First-principles study of hydrogen adsorption on carbon nanotube surfaces. Phys Rev B 66:073415
186. Alonso JA, Arellano JS, Molina LM et al (2004) Interaction of molecular and atomic hydrogen with single-wall carbon nanotubes. IEEE Trans Nanotech 3:304–310
187. Barone V, Heyd J, Scuseria GE (2004) Interaction of atomic hydrogen with single-walled carbon nanotubes: a density functional theory study. J Chem Phys 120:7169–7174
188. Senami M, Ikeda Y, Fukushima A et al (2011) Theoretical study of adsorption of lithium atom on carbon nanotube. AIP Adv 1:042106
189. Udomvech A, Kerdcharoen T, Osotchan T (2005) First principles study of Li and Li+ adsorbed on carbon nanotube: variation of tubule diameter and length. Chem Phys Lett 406:161–166
190. Firlej L, Kuchta B (2004) Helium adsorption in single wall carbon nanotubes-grand canonical Monte Carlo study. Colloids Surf A 241:149–154
191. Chen D-L, Al-Saidi W, Johnson K (2011) Noble gas adsorption on carbon nanotubes: insight from a van der Waals density functional study. In: American physical society meeting, March 21–25 Abstract #B31.008
192. Wang Y, Yeow JTW (2009) A review of carbon nanotubes-based gas sensors. J Sens Article ID:493904
193. Zollo G, Gala F (2012) Atomistic modeling of gas adsorption in nanocarbons. J Nanomater Article ID:152489
194. Zhao J, Buldum A, Han J et al (2002) Gas molecule adsorption in carbon nanotubes and nanotube bundles. Nanotechnology 13:195–200
195. Pan B, Xing B (2008) Adsorption mechanisms of organic chemicals on carbon nanotubes. Env Sci Technol 42:9005–9013
196. Chen C-W, Lee M-H, Clark SJ (2004) Gas molecule effects on field emission properties of single-walled carbon nanotube. Diamond Relat Mater 13:1306–1313
197. Suarez-Martinez I, Mittal J, Allouche H et al (2013) Fullerene attachment to sharp-angle nanocones mediated by covalent oxygen bridging. Carbon 54:149–154
198. Carroll DL, Redlich P, Ajayan PM et al (1997) Electronic structure and localized states at carbon nanotube tips. Phys Rev Lett 78:2811–2814
199. Charlier J-C (2002) Defects in carbon nanotubes. Acc Chem Res 35:1063–1069
200. Robinson JA, Snow ES, Badescu SC et al (2006) Role of defects in single-walled carbon nanotube chemical sensors. Nano Lett 6:1747–1751
201. Hamon MA, Hu H, Bhowmik P et al (2001) End-group and defect analysis of soluble single-walled carbon nanotubes. Chem Phys Lett 347:8–12
202. Mawhinney DB, Naumenko V, Kuznetsova A et al (2000) Surface defect site density on single walled carbon nanotubes by titration. Chem Phys Lett 324:213–216
203. Monthioux M, Smith BW, Burteaux B et al (2001) Sensitivity of single-wall carbon nanotubes to chemical processing: an electron microscopy investigation. Carbon 39:1251–1272

204. Stone AJ, Wales DJ (1986) Theoretical studies of icosahedral C_{60} and some related species. Chem Phys Lett 128:501–503
205. Bettinger HF (2005) The reactivity of defects at the sidewalls of single-walled carbon nanotubes: the Stone-Wales defect. J Phys Chem B 109:6922–6924
206. Picozzi S, Santucci S, Lozzi L et al (2004) Ozone adsorption on carbon nanotubes: the role of Stone-Wales defects. J Chem Phys 120:7147–7152
207. Yang SH, Shin WH, Kang JK (2006) Ni adsorption on Stone-Wales defect sites in single-wall carbon nanotubes. J Chem Phys 125:084705
208. Rivera JL, Rico JL, Starr FW (2007) Interaction of water with cap-ended defective and nondefective small carbon nanotubes. J Phys Chem C 111:18899–18905
209. Shtogun YV, Woods LM (2009) Electronic and magnetic properties of deformed and defective single wall carbon nanotubes. Carbon 47:3252–3262
210. Rossato J, Baierle RJ, Fazzio A et al (2005) Vacancy formation process in carbon nanotubes: first-principles approach. Nano Lett 5:197–200
211. Gerber I, Oubenali M, Bacsa R et al (2011) Theoretical and experimental studies on the carbon nanotube surface oxidation by nitric acid: interplay between functionalization and vacancy enlargement. Chem Eur J 17:11467–11477
212. Berber S, Oshiyama A (2006) Reconstruction of mono-vacancies in carbon nanotubes: atomic relaxation vs. spin polarization. Physica B 376–377:272–275
213. Chakrapani N, Zhang YM, Nayak SK et al (2003) Chemisorption of acetone on carbon nanotubes. J Phys Chem B 107:9308–9311
214. Hilding JM, Grulke EA (2004) Heat of adsorption of butane on multiwalled carbon nanotubes. J Phys Chem B 108:13688–13695
215. Ding D, Wang J, Cao Z et al (2003) Synthesis of carbon nanostructures on nanocrystalline Ni-Ni$_3$P catalyst supported by SiC whiskers. Carbon 41:579–582
216. Zhou LG, Shi SQ (2003) Adsorption of foreign atoms on Stone-Wales defects in carbon nanotube. Carbon 41:613–615
217. Meng FY, Zhou LG, Shi SQ et al (2003) Atomic adsorption of catalyst metals on Stone-Wales defects in carbon nanotubes. Carbon 41:2023–2025
218. Kim SJ, Park YJ, Ra EJ et al (2007) Defect-induced loading of Pt nanoparticles on carbon nanotubes. Appl Phys Lett 90:023114
219. Sankaran M, Viswanathan B (2006) The role of heteroatoms in carbon nanotubes for hydrogen storage. Carbon 44:2816–2821
220. Lopez-Corral I, Celis JD, Juan A et al (2012) DFT study of H_2 adsorption on Pd-decorated single walled carbon nanotubes with C-vacancies. Int J Hydrogen Ener 37:10156–10164
221. Gayathri V, Geetha R (2007) Hydrogen adsorption in defected carbon nanotubes. Adsorption 13:53–59
222. Tang S, Cao Z (2009) Defect-induced chemisorption of nitrogen oxides on (10, 0) single-walled carbon nanotubes: insights from density functional calculations. J Chem Phys 131:114706
223. Yang Q-H, Hou P-X, Bai S et al (2001) Adsorption and capillarity of nitrogen in aggregated multi-walled carbon nanotubes. Chem Phys Lett 345:18–24
224. Muris M, Dupont-Pavlovsky N, Bienfait M et al (2001) Where are the molecules adsorbed on single-walled nanotubes? Surf Sci 492:67–74
225. Hallock RB, Kahng YH (2004) Adsorption of helium and other gases to carbon nanotubes and nanotube bundles. J Low Temp Phys 134:21–30
226. Zhu J, Wang Y, Li W et al (2007) A density functional study of nitrogen adsorption in single-wall carbon nanotubes. Nanotechnology 18:095707
227. Heroux L, Krungleviciute V, Calbi MM et al (2006) CF$_4$ on carbon nanotubes: physisorption on grooves and external surfaces. J Phys Chem B 110:12597–12602
228. Fujiwara A, Ishii K, Suematsu H et al (2001) Gas adsorption in the inside and outside of single-walled carbon nanotubes. Chem Phys Lett 336:205–211

229. Yang CM, Kanoh H, Kaneko K et al (2002) Adsorption behaviors of HiPco single-walled carbon nanotube aggregates for alcohol vapors. J Phys Chem B 106:8994–8999
230. Iwata S, Sato Y, Nakai K et al (2007) Novel method to evaluate the carbon network of single-walled carbon nanotubes by hydrogen physisorption. J Phys Chem C 111:14937–14941
231. Yoo D-H, Rue G-H, Chan MHW et al (2003) Study of nitrogen adsorbed on open-ended nanotube bundles. J Phys Chem B 107:1540–1542
232. Matranga C, Bockrath B (2005) Hydrogen-bonded and physisorbed CO in single-walled carbon nanotube bundles. J Phys Chem B 109:4853–4864
233. Ellison MD, Crotty MJ, Koh D et al (2004) Adsorption of NH_3 and NO_2 on single-walled carbon nanotubes. J Phys Chem B 108:7938–7943
234. Albesa AG, Fertitta EA, Vicente JL (2010) Comparative study of methane adsorption on single-walled carbon nanotubes. Langmuir 26:786–795
235. Pantarotto D, Singh R, McCarthy D et al (2004) Functionalized carbon nanotubes for plasmid DNA gene delivery. Angew Chem Int Ed 43:5242–5246
236. Neves V, Heister E, Costa S et al (2010) Uptake and release of double-walled carbon nanotubes by mammalian cells. Adv Funct Mater 20:3272–3279
237. Tasis D, Tagmatarchis N, Bianco A et al (2006) Chemistry of carbon nanotubes. Chem Rev 106:1105–1136
238. Andersen AJ, Wibroe PP, Moghimi SM (2012) Perspectives on carbon nanotube-mediated adverse immune effects. Adv Drug Deliv Rev 64:1700–1705
239. Nel AE, Mädler L, Velego D et al (2009) Understanding biophysicochemical interactions at the nano–bio interface. Nature Mater 8:543–557
240. Walsh TR, Tomasio SM (2010) Investigation of the influence of surface defects on peptide adsorption onto carbon nanotubes. Mol BioSyst 6:1707–1718
241. Dieckmann GR, Dalton AB, Johnson PA et al (2003) Controlled assembly of carbon nanotubes by designed amphiphilic peptide helices. J Am Chem Soc 125:1770–1777
242. Star A, Steuerman DW, Heath JR et al (2002) Starched carbon nanotubes. Angew Chem Int Ed 41:2508–2512
243. Zheng M, Jagota A, Semke ED et al (2003) DNA-assisted dispersion and separation of carbon nanotubes. Nature Mater 2:338–342
244. Sanz V, Tilmacîu C, Soula B et al (2011) Chloroquine-enhanced gene delivery mediated by carbon nanotubes. Carbon 49:5348–5358
245. Allen BL, Kotchey GP, Chen Y et al (2009) Mechanistic investigations of horseradish peroxidase-catalyzed degradation of single-walled carbon nanotubes. J Am Chem Soc 131:17194–17205
246. Kagan VE, Konduru NV, Feng W et al (2010) Carbon nanotubes degraded by neutrophil myeloperoxidase induce less pulmonary inflammation. Nature Nanotech 5:354–359
247. Nunes A, Bussy C, Gherardini L et al (2012) In vivo degradation of functionalized carbon nanotubes after stereotactic administration in the brain cortex. Nanomedicine (Lond) 7:1485–1494
248. Donaldson K, Murphy F, Schinwald A et al (2011) Identifying the pulmonary hazard of high aspect ratio nanoparticles to enable their safety-by-design. Nanomedicine 6:143–156
249. Hurt RH, Monthioux M, Kane A (2006) Toxicology of carbon nanomaterials: status, trends, and perspectives. Carbon 44:1028–1033
250. Card JW, Magnuson BA (2010) A method to assess the quality of studies that examine the toxicity of engineered nanomaterials. Int J Toxicol 29:402–410
251. de Gabory L, Bareille R, Daculsi R et al (2011) Carbon nanotubes have a deleterious effect on the nose: the first in vitro data. Rhinology 49:445–452
252. Meunier E, Coste A, Olagnier D et al (2012) Double-walled carbon nanotubes trigger IL-1β release in human monocytes through the Nlrp3 inflammasome activation. Nanomedicine 8:987–995

253. Bourdiol F, Mouchet F, Perrault A et al (2013) Biocompatible polymer-assisted dispersion of multi walled carbon nanotubes in water, application to the investigation of their ecotoxicity using Xenopus laevis amphibian larvae. Carbon 54:175–191
254. Bianco A, Prato M (2003) Can carbon nanotubes be considered useful tools for biological applications? Adv Mater 15:1765–1768
255. Berciaud S, Cognet L, Lounis B (2008) Luminescence decay and the absorption cross section of individual single-walled carbon nanotubes. Phys Rev Lett 101:077402
256. Dolatabadi EN, Omidi J, Losic D (2011) Carbon nanotubes as an advanced drug and gene delivery nanosystem. Current Nanosci 7:297–314
257. Zhao B, Hu H, Mandal SK et al (2005) A bone mimic based on the self-assembly of hydroxyapatite on chemically functionalized single-walled carbon nanotubes. Chem Mater 17:3235–3241
258. Béduer A, Seichepine F, Flahaut E et al (2012) Elucidation of the role of carbon nanotube patterns on the development of cultured neuronal cells. Langmuir 28:17363–17371
259. Lin Y, Li H, Gu L et al (2008) Chemistry of carbon nanotubes. In: Basiuk EV (ed) Bioapplications of carbon nanotubes. American Scientific, Basiuk
260. Saito R, Dresselhaus G, Dresselhaus MS (1998) Physical properties of carbon nanotubes. Imperial College Press, London
261. Harris PJF (1999) Carbon nanotubes and related structures. Cambridge University Press, Cambridge
262. Tomanek D, Enbody RJ (eds) (2002) Science and applications of nanotubes. Kluwer, New York
263. Meyyapan M (ed) (2004) Carbon nanotubes; science and applications. CRC Press, Boca Raton
264. O'Connell MJ (ed) (2006) Carbon nanotubes: properties and applications. CRC Press/Taylor & Francis, Boca Raton
265. Gogotsi Y (ed) (2006) Nanotubes and nanofibers. CRC Press, Boca Raton
266. Jorio A, Dresselhaus MS, Dresselhaus G (2008) Carbon nanotubes. In: Topics in applied physics, vol 111, Springer, Heidelberg
267. Saito S, Zettl A (eds) (2008) Carbon nanotubes – quantum cylinders of graphene. Elsevier, Amsterdam
268. Harris PFJ (2009) Carbon nanotube science: synthesis, properties, and applications. Cambridge University Press, Cambridge
269. Yap YK (2009) B-C-N nanotubes and related nanostructures. In: Wang M, Waag A, Salamo G et al (eds) Lecture notes in Nanosc Science Technology, 6, Springer, Dordrecht
270. Guldi DM, Martin N (eds) (2010) Carbon nanotubes and related structures: synthesis, characterization, functionalization, and applications. Wiley-VCH, Weinheim
271. Naraghi M (ed) (2011) Carbon nanotubes – growth and applications. InTech, Rijeka
272. Bianco S (ed) (2011) Carbon nanotubes – from research to applications. InTech, Rijeka
273. Monthioux M (2012) Meta-nanotubes: synthesis, properties, and applications. Wiley-Blackwell, Chichester
274. Lee SM, Lee YH (2000) Hydrogen storage in single-walled carbon nanotubes. Appl Phys Lett 76:2877–2879
275. Dresselhaus MS, Williams KA, Eklund PC (1999) Advanced materials for energy storage – hydrogen adsorption in carbon materials. Mater Res Soc Bull 24:45–50
276. Cheng H, Pez GP, Cooper AC (2001) Mechanism of hydrogen sorption in single-walled carbon nanotubes. J Amer Chem Soc 123:5845–5846

Electronic Properties of Si and Ge Pure and Core-Shell Nanowires from First Principle Study

2

Xihong Peng, Fu Tang, and Paul Logan

Keywords

Band gap • Band structure • Effective mass • Ge nanowires • Intrinsic strain • Si nanowires • Si/Ge core-shell nanowires • Strain effect • Uniaxial strain • Work function

Introduction

The research area of nanoscale semiconductor structures including two-dimensional (2D) quantum well, 1D nanowires, and 0D quantum dot (see Fig. 2.1) has attracted extensive research efforts over the past several decades. Among them, group IV semiconductor nanowires such as Si and Ge nanowires have drawn a particular attention [1–17] due to their great potential in applications. These nanowires are expected to play a vital role as both interconnects and functional components in future mesoscopic electronic and optical devices including light-emitting diodes (LEDs) [1, 3], field-effect transistors (FETs) [5, 6], inverters [1, 7–9], photovoltaic cells [10–12], high-performance batteries [13, 14], and nanoscale sensors [7, 15–17]. The nanowires are also very interesting for fundamental research, since they provide an opportunity to test quantum mechanical concepts at the nanoscale level [18].

In experiments, researchers were able to grow semiconductor nanowires with diameters down to a few nanometers and lengths of tens of micrometers [4, 19–26]. In these nanowires, the electric carriers are confined in the lateral

X. Peng (✉)
School of Letters and Sciences, Arizona State University, Mesa, AZ, USA
e-mail: xihong.peng@asu.edu; xihongpeng@gmail.com

F. Tang • P. Logan
Department of Physics, Arizona State University, Tempe, AZ, USA
e-mail: tang2332@gmail.com; prlogan@gmail.com

Fig. 2.1 Schematics of nanostructures of 2D quantum well, 1D nanowire, and 0D quantum dot

direction of the wires, thus the quantum confinement effect is expected to play an important role. Unique properties due to the quantum confinement effect have been found in these nanowire structures.

This chapter provides a brief review of recent studies on Si and Ge pure and core-shell nanowires and summarizes the effects of size and strain on the electronic properties of the nanowires from first principles density-functional theory (DFT) calculations.

Si Nanowires

The quantum confinement effect in Si nanowires can be observed, for example, in photoluminescence (PL) studies, and the nanowires were found to exhibit substantial blueshift in the emission with a reduction of nanowire diameter [4, 5, 19, 27, 28]. For instance, Holmes et al. [19] have grown defect-free Si nanowires with nearly uniform diameter (4–5 nm) and length on the order of several micrometers using a supercritical fluid solution-phase approach. They observed visible band-edge PL which was strongly blueshifted from the bulk Si indirect band gap of 1.1 eV. It was also found that the wavelength of luminescence depends on not only the diameter, but also the crystalline orientation of the wires [19, 27, 28].

Si nanowires are attractive building blocks for future nanoelectronics, such as FETs [5, 6, 29], since the reduction in size of a device built from Si nanowires allows increased speed and computing power and gives greater device densities. For example, Cui et al. [6] reported that Si nanowire FET demonstrates high performance with increases in the average conductance from 45 to 800 nS and average mobility from 30 to 560 cm^2 V^{-1} s^{-1}. In addition, these authors also claimed that Si nanowires have a potential to substantially exceed conventional devices when one compares the transport parameters of scaled Si nanowire FET with those of a state-of-the-art planar metal-oxide-semiconductor FET (MOSFET), and hence could be the ideal (best so far) building blocks for future nanoelectronics.

Ge Nanowires

Compared to Si, Ge has some superior properties. For example, Ge has an indirect band gap of 0.66 eV, while the indirect band gap of Si is at a value of 1.12 eV. Ge also has a higher electron/hole mobility, i.e., $\mu_n = 3,800$ cm^{2}V^{-1}s^{-1} and

Fig. 2.2 Schematics of
a type II band alignment in the
Si/Ge heterostructure

Type II band alignment
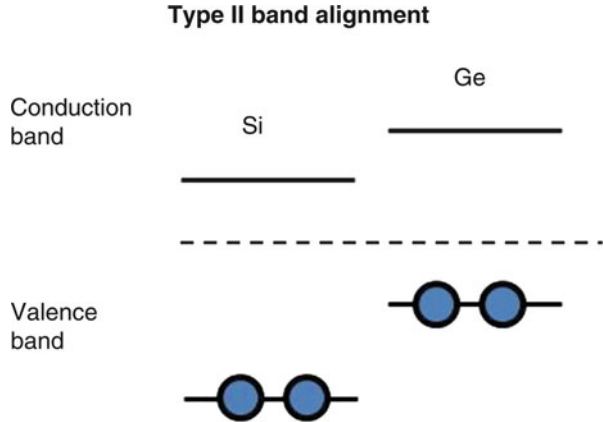
$\mu_p = 1{,}800$ cm^{2}V^{-1}s^{-1}, compared to $\mu_n = 1{,}500$ cm^{2}V^{-1}s^{-1} and $\mu_p = 450$ cm^{2}V^{-1}s^{-1} in Si at room temperature [23, 30, 31]. Ge has a much lower intrinsic resistivity of 46 Ω cm compared to $3.2 \times 10^5 \Omega$ cm in Si. Therefore, Ge offers appealing opportunities for advanced device scaling, such as low drive voltage and high drive currents for high-speed electronics [31]. However, the surface of Ge is very difficult to passivate, which could deteriorate the device functionality tremendously. From the point of view of nanoscale applications, the quantum confinement effect on Ge nanostructures is more prominent than on Si nanowires, which is essentially related to a much larger excitonic Bohr radius of 24.3 nm in Ge compared to 4.9 nm in Si. This makes Ge nanostructures with novel electronic properties more readily fabricated.

Ge nanowires can be synthesized with a diameter of a few nanometers [22–26]. They demonstrate strong quantum confinement effects as seen in PL studies [32]. Theoretically, researchers found that the band gaps of Ge nanowires are dependent on several factors, such as size [33–37], crystalline orientation [34–36, 38], surface chemistry [38, 39], and doping [38, 40, 41].

Core-Shell Nanowire Structure

Si/Ge nanowire heterostructures such as core-shell configurations [42–53] have drawn lots of research interest in recent years [44, 46–48, 51–63], in which factors, such as heterostructure composition and interface geometry, can be further manipulated to tune the electronic properties of the nanowires. In the core-shell heterostructure, the core can be either Si or Ge and the shell will be Ge or Si.

In such a heterostructure, a typical type II band alignment can be formed [48, 51–53, 64]. In Fig. 2.2, a schematic of a type II band offset is given. The valence band of the heterostructure is contributed by Ge, thus the charge of the valence band edge (VBE) is primarily located at Ge atoms. On the other hand, the conduction band of the heterostructure is contributed by Si; therefore the state

of the conduction band edge (CBE) is mainly located at Si atoms (details are illustrated in a later section focused on the core-shell structure). In this case, the hole and the electron are separated by materials, namely, the electron is in the Si composition and the hole is in Ge. With this natural separation of the electron and hole, a better conductance and higher mobility of charge carriers can be obtained, due to the band offset in the core-shell nanowires [44, 48, 57]. The unique band alignment enables the application of novel electronic devices [65]. The core-shell structures also render an interesting feature for photovoltaic applications. The separated charges in the core-shell nanowires are effectively collected along the radial direction, and the long axial length of the nanowires enables a high optical absorption [66].

The Electronic Property Tailoring-Strain Effect

Tailoring electronic properties of semiconductor nanowires has been critical for nanoscale applications [66–72]. Among various tailoring methods, size, surface passivation, and functionalization are most commonly adopted. Recently, mechanical strain [37, 52, 73, 74] has shown great potential to tune electronic properties of nanoscale semiconductors and is receiving increased attention. Adventitious strain is almost unavoidable experimentally, but more interesting cases come from intentionally introduced and controlled strains. One of the most prominent examples is the greatly enhanced mobility in the strained Si nanochannel [75, 76]. The band structures of semiconductor nanowires can be modulated effectively under a moderate strain, as shown recently [37, 42, 51–53, 64, 73, 77–83]. The approaches introducing strain include lattice mismatch, functional wrapping [84, 85], doping of material [86, 87], and direct mechanical application [74]. It was also found that the nanostructures can maintain integrity under a much higher strain than their bulk counterparts [51, 88], which dramatically expands the applicable strain strength to the nanostructures.

In our study, the effect of strain on the electronic properties of nanowires has been the focus, and the problems we tried to address include how strain works, along with other factors such as size to affect the properties of the nanowires. Si/Ge heterostructure systems are well known for possessing strain due to the lattice mismatch up to 4 % between Si and Ge. A famous example on such strain is the Ge self-assembly pseudomorphic nanodots on Si substrates. Various nanostructures such as springs and nanotubes were also produced through bilayer Si/Ge structures, which possess unique electronic and optical properties. The Si/Ge core-shell nanowires contain an intrinsic strain due to the lattice mismatch between Si and Ge, which serves as a good example for demonstrating the strain effect.

The rest of the chapter is organized in the following manner. In section 'Methods', the detailed theoretical methods are introduced. The results of pure Si and Ge nanowires are presented in section 'Pure Si and Ge Nanowires', in which the structural and electronic properties of the nanowires are discussed in detail. In section 'Si/Ge Core-Shell Nanowires', the properties of Si/Ge core-shell nanowires are introduced.

Methods

Theoretical methods, such as empirical tight-binding methods [89–93], k · p models [94–98], and density-functional theory (DFT) [99–101], provide detailed fundamental understanding of material properties, in addition to experimental studies. The advantage of first principles DFT calculations is that the key properties and behaviors of physical systems, including energies, structural, and electronic properties, can be readily predicted using Schrodinger's equation from quantum mechanics without having to rely on fitting parameters. First principles DFT calculations are applicable to solve problems across various fields, ranging from physics and chemistry to biology and material sciences. They are playing an essential role in modern scientific research and explorations.

In this project of Si/Ge nanowires, the DFT calculations were primarily performed to study the effects of size and strain on the electronic properties of the nanowires. In detail, the DFT code Vienna Ab-initial Simulation Package [102, 103] was used. The local density approximation was applied. Pseudo-potential plane wave approach was used with the kinetic energy cutoff of 300.0 eV. The core electrons were described using ultrasoft Vanderbilt pseudo-potentials [104]. The reciprocal space was sampled at $1 \times 1 \times 4$ using Monkhorst-Pack meshes. A total of 21 K points were included in the band structure calculations along the reciprocal direction Γ (0, 0, 0) to X (0, 0, 0.5) in the [110] direction. The dangling Si (Ge) bonds on the surface of the nanowires were saturated by hydrogen atoms with the initial bond lengths 1.47 and 1.51 Å for the Si-H and Ge-H bonds, respectively. These Si-H and Ge-H bonds were allowed to relax during geometry optimization. The lateral size of the cell is chosen so that the distance between the nanowire and its replica (due to periodic boundary conditions) is more than 10 Å, to minimize the interaction between nanowires.

The lattice constants along the axial [110] direction in the pure Si and Ge nanowires were initially set to be 3.862 and 3.977 Å, respectively. These values were derived from the bulk lattice constants of Si (5.461 Å) and Ge (5.625 Å), respectively, according to the following equation:

$$a_{\text{initial[110]}} = a_{\text{bulk[110]}} = \frac{a_{\text{bulk}}}{\sqrt{2}} \qquad (2.1)$$

In the studied Si/Ge core-shell nanowires, the core contains 30 atoms and the thickness of the shell varies. The initial lattice constant for a Si/Ge core-shell nanowire was set to follow that of shell composition. For example, if the shell composition is Si, the initial axial lattice constant of the core-shell nanowire was set to be 3.862 Å. If the shell is Ge, the axial lattice constant was initially set to be 3.977 Å. Such setting of the initial lattice constant using the shell composition is due to the fact that the studied Si/Ge core-shell nanowires generally have more atoms in the shell compared to that in the core. The axial lattice constants for all the nanowires, including the Si and Ge pure and core-shell nanowires, are then optimized through the technique of total energy minimization till the forces acting on atoms are less than 0.02 eV/Å.

The electronic properties of the nanowires, such as band gap and the effective masses of the electron and the hole, were then calculated by solving the Kohn-Sham equation within the frame of DFT. The band gap of a wire is defined by the energy difference between the CBE and the VBE. The effective masses of the electron and the hole can be readily calculated according to the formula

$$m^* = \hbar^2 \cdot \left[\frac{d^2 E}{dk^2} \right]^{-1} \tag{2.2}$$

from the band structure of the nanowires.

Once the geometry of a relaxed nanowire was obtained, uniaxial strain was then applied by rescaling the optimized axial lattice constant of the nanowire. For instance, a tensile strain of 2 % means the axial lattice and the z coordinates of the atoms in the nanowire were rescaled to 102 % of their original values, while a compressive strain of 2 % implies the axial lattice and the z coordinates were rescaled to 98 % of their original values. The positive values of strain refer to uniaxial expansion, while negative corresponds to the compression. For each strained nanowire, the lateral x and y coordinates were further relaxed through the technique of the total energy minimization. Our study showed that the electronic properties of the nanowire were affected significantly by the strain.

Pure Si and Ge Nanowires

The studied homogeneous Si and Ge nanowires were listed in Table 2.1. $N_{Si(Ge)}$ is the number of Si (Ge) atoms in a given wire; N_H represents the number of H atoms needed to saturate the surface dangling bonds in the nanowire; D is the diameter of the nanowire in the unit of Å. The values in the parentheses are for the Ge nanowires. Figure 2.3 gives the snapshots of the pure Si (Ge) nanowires with diameters up to $\sim$50 Å. Blue dots are Si (Ge) atoms and white are H atoms.

Axial Lattice Constants

The lattice constants in bulk Si and Ge are 5.461 and 5.625 Å, respectively, based on the simulation parameters mentioned in section 'Methods'. The initial axial lattice constants for the Si and Ge nanowires along the [110] direction were obtained using Eq. 2.1. This axial lattice constant was defined as the interplanar distance between two consecutive [110] planes in Si or Ge.

To optimize the axial lattice constant along the z-direction, a series of calculations were performed by scanning the lattice constant, and the total energy was collected with different lattice constants for a given wire. The total energy was

Table 2.1 A list of the studied homogeneous Si and Ge nanowires along the [110] direction. $N_{Si(Ge)}$ is the number of Si(Ge) atoms in a given wire; N_H represents the number of H atoms needed to saturate the surface dangling bonds; D is the diameter of a given wire (the values in the parentheses are for Ge wires); the fourth column is the optimized axial lattice constants of the wires (values in the parentheses are for Ge wires)

$N_{Si(Ge)}$	N_H	D (Å)	Axial lattice (Å)
16	12	10 (12)	3.912 (3.997)
42	20	16 (18)	3.900 (3.984)
76	28	22 (25)	3.892 (3.977)
110	32	27 (30)	3.881 (3.977)
172	44	33 (37)	3.881 (3.977)
276	52	43 (47)	3.862 (3.977)
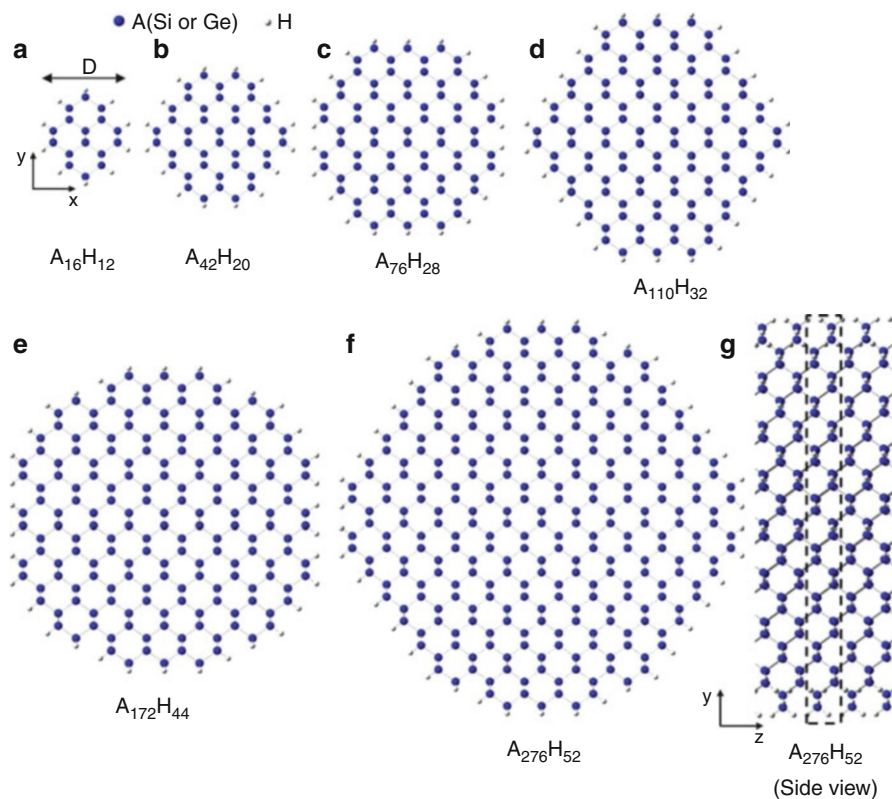
Fig. 2.3 Snapshots of Si (Ge) nanowires in the cross section of the wires and the side view. The composition of each wire in a unit cell is given. *Dashed rectangle* in (g) indicates a unit cell. *Blue dots* represent Si or Ge atoms and *white dots* for H

Fig. 2.4 The optimized
axial lattice constant of the
pure Si and Ge nanowires
along the [110] direction as
a function of the diameters of
the wires
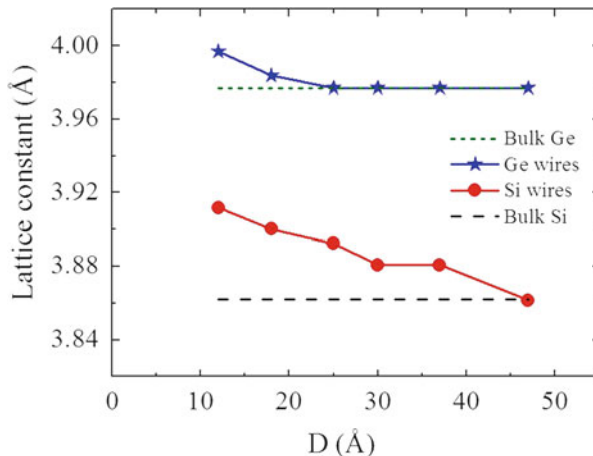
plotted as a function of the axial lattice constant, and the optimized axial lattice constant was then obtained through a parabolic fitting of the curve of energy-versus-lattice constant. For example, the optimized lattice constant for the Ge nanowire with a diameter of 12 Å was found to be 3.997 Å, which is greater than the initial value of 3.977 Å derived from the bulk Ge. This means that, compared to the bulk, the nanowire expands along the axial direction upon relaxation, which is in a good agreement with experimental data [32]. The optimized axial lattice constants for all studied pure Si and Ge nanowires are reported in the last column in Table 2.1 and also plotted in Fig. 2.4 as a function of the diameters of the nanowires.

In Fig. 2.4, it is clear that the lattice constants of the Si and Ge nanowires increase with decreasing wire diameter. The lattice constants of the nanowires approach their bulk counterparts as the size of the wire increases. For example, the lattice constant of Ge nanowires approaches its bulk value when the diameter of the wire is beyond the critical value of 20 Å. In the case of Si nanowires, this critical size is ∼40 Å, and beyond that size the axial expansion of the Si nanowires becomes negligible. The larger critical size for Si might be resulting from the stronger bond of Si. Although both Si and Ge crystals have diamond structures and tetrahedral networking, the Si-Si bonds are stronger than the Ge-Ge bonds. It costs more surface energy for Si to form the nanowire structure through breaking the Si bonds on the surface. This may account for the larger required size of the Si nanowires for the disappearance of axial expansion, in which extra surface energy is accommodated by the interior and saturation atoms without much change in the lattice constant.

Band Structure

Bulk Si and Ge are semiconductors with indirect band gaps. However, the Si and Ge nanowires along the [110] direction demonstrate direct band gaps
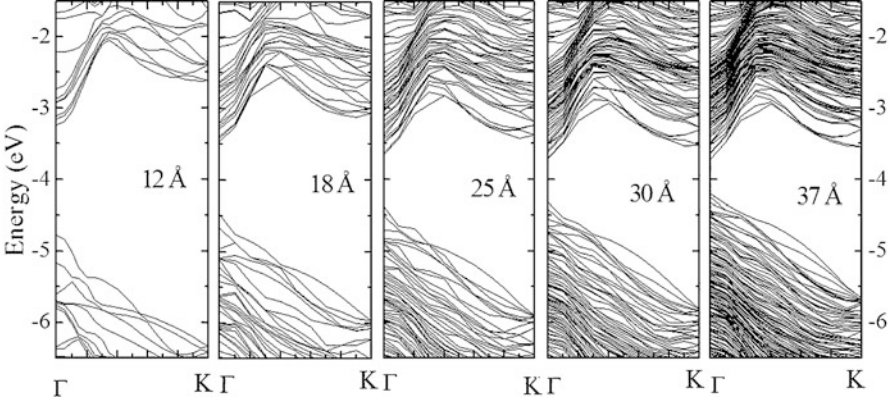
Fig. 2.5 The band structures of the Ge [110] nanowires with various diameters. The energies are referenced to the vacuum level

at Γ [27, 28, 33, 36, 38, 73]. As an example, the band structures of the Ge nanowires with various diameters are presented in Fig. 2.5. From the band structures, the Ge nanowires show direct band gaps with both the CBE and the VBE located at Γ, which is consistent with previous work [33, 36, 38]. The direct gap in the Si and Ge nanowires along the [110] direction can be readily understood from the zone-folding effect of the reciprocal space.

It is also interesting to observe that the band structures of the Si and Ge nanowires can be significantly modulated by externally applied strain. As an example, Fig. 2.6a shows the band structure of one Ge nanowire with and without strain. Black solid lines represent the band structure without strain; red dashed and blue dotted lines are the band structure for the tensile and compressive uniaxial strains, respectively. Generally, strain has dominant effects on the band structure near the Γ point and the energies are shifted evidently with strain. However, it has negligible effects on the wave vectors far away from Γ and results in a minimal energy shift under strain. The majority of electronic properties in a semiconductor are related to the CBE and VBE. Therefore, the energy variation of these two states with strain was particularly singled out and presented in Fig. 2.6b. From Fig. 2.6b, it is clear that the strain modifies the energies of the CBE and the VBE dramatically in the region near the Γ point and has negligible effect on shifting energies at the wave vectors far away from Γ.

A tight-binding model [105, 106] is applied to understand the strain effect on the electronic bands in Fig. 2.6. In this model, the wave function of a crystal is in a form of a block function, and the energy of the band can be expressed as

$$E(k) = E_v - \beta - \gamma \sum_{n,n} \cos\left(\vec{k} \cdot \vec{R}\right) \tag{2.3}$$

where the summation goes over those $\vec{R}$ of the nearest neighbors. To discuss the strain effect on the band structure, the energy can be further simplified as
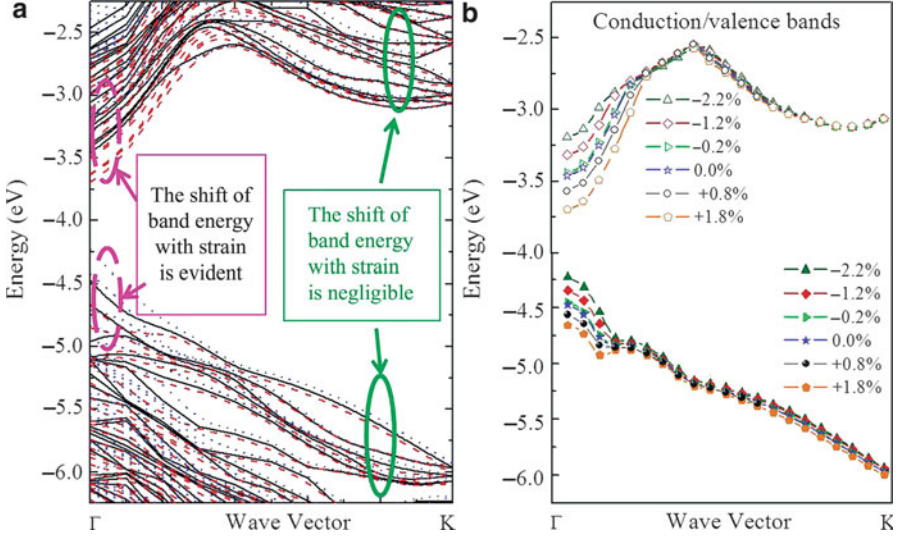
Fig. 2.6 (**a**) The effect of uniaxial strain on the band structure of the Ge nanowire with a diameter of 18 Å along the [110] direction. *Black solid lines* are the band structure without strain. *Red dashed* and *blue dotted lines* are for tensile and compressive strains, respectively. (**b**) The variations of the conduction and valence bands in the Ge nanowire with various values of strain

$$E(k) = E_v - \beta - 2\gamma \cos\left(\frac{k_{//}a}{2}\right) \tag{2.4}$$

where E_v is the energy of atomic orbitals, $k_{//}$ is the magnitude of the wave vector along the direction of the wire axis, β is a small quantity contributed by the energy correction near the position of the nucleus, γ is called the overlap integral and is another term of energy correction dependent on the overlap between orbitals centered at two neighboring atoms, and a is the lattice constant. For the Γ point ($k_{//} = 0$), the energy is

$$E(\Gamma) = E_v - \beta - 2\gamma \tag{2.5}$$

For the X point ($k_{//} = \frac{1}{2}\frac{2\pi}{a}$), the contribution from the overlap integral γ vanishes, and the energy is

$$E(X) = E_v - \beta \tag{2.6}$$

By applying strain to a Ge nanowire, the bond length between Ge atoms will be changed. Thus we expect a prominent modification of the γ value, while the variation of β is negligible due to its local nature. Referring to the above formulae of $E(\Gamma)$ and $E(X)$, strain will bring a more pronounced effect in the energy at Γ, compared to other wave vectors.

Fig. 2.7 The DFT-predicted band gap for the Si and Ge nanowires as a function of the wire diameter
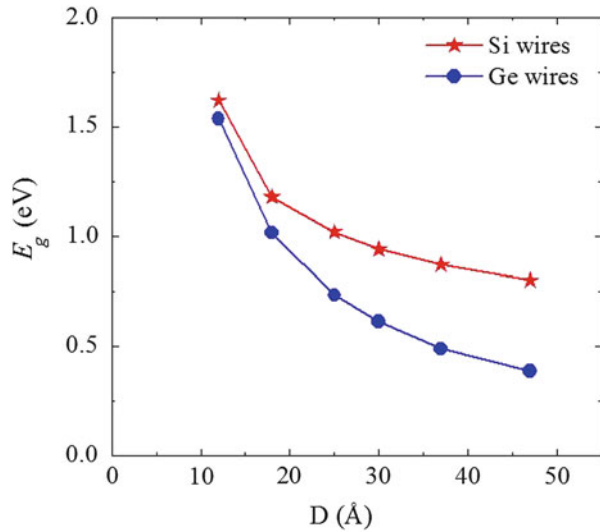
Band Gap

As mentioned before, the band gap of a nanowire is defined as the energy difference between the CBE and the VBE. The DFT-predicted band gaps for the Si and Ge wires are plotted in Fig. 2.7 as a function of the diameters of the nanowires. The band gap of the Si and Ge nanowires increases when the size of the wire is reduced. This effect is primarily due to quantum confinement. Our predicted size dependence of the band gap in the Si and Ge nanowires is in good agreement with the literature [27, 28, 33, 78] and the references within.

It is known that DFT underestimates the band gaps of semiconductors, while advanced GW method [107–110] can provide improved predictions. However, for the size of the nanowires investigated in the present work, GW is not applicable due to its extremely high computing cost. The present work is mainly focused on the variation of electronic properties under factors such as external strain and size. Previous studies [111] on Si nanoclusters showed that the energy gap calculated by DFT obeys a similar strain dependency as the optical gap predicted by the advanced configuration interaction method and the quasiparticle gap (defined as the difference of ionization potential and electron affinity). In addition, the band gap predicted by DFT demonstrates a similar size dependency as the optical gap obtained using GW and quantum Monte Carlo methods [27, 112–114]. Therefore, the band gap calculated by DFT should qualitatively predict the correct trends both with varying size and strain.

Uniaxial strain was applied to the Si and Ge nanowires to study the strain effect on their electronic properties. Figure 2.8 presents the strain effect on the band gap of the nanowires: the variation of band gaps as a function of uniaxial strain in several different sized Si and Ge nanowires. Positive strain refers to a uniaxial expansion
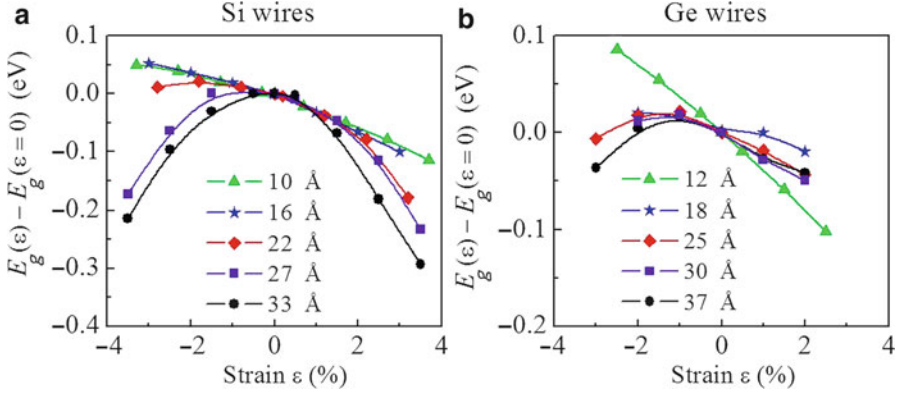
Fig. 2.8 The strain effect on the band gap for the (**a**) Si and (**b**) Ge nanowires. Positive strain refers to a uniaxial expansion, while negative strain corresponds to the compression

while negative strain corresponds to the compression. For example, for the Si (Ge) wire with a diameter of 10 (12) Å, the band gap variation with strain is almost linear, as shown by the green-triangle curves. The gap decreases with expansion and increases with compression. The gap variation with strain in the Si (Ge) wire with a diameter of 16 (18) Å diameter shows a similar linear relation (the blue-star curves). However, for the Si (Ge) wire with a diameter larger than 25 Å, the gap variation with strain exhibits a nearly parabolic behavior: the gap drops not only under expansion, but also under compression. This parabolic behavior is more evident for the larger wires. We conclude that the strain effect on the band gap in the Si (Ge) wires is strongly dependent on their size.

In order to understand this size dependence of the strain-gap relation in Fig. 2.8, the energy variation of the VBE and the CBE with strain was examined. As an example, the energy shifts of the CBE/VBE with strain in two different sized Si and Ge nanowires are presented in Fig. 2.9. It is clear that the energies of the CBE and the VBE in the smaller Si (Ge) wires are linear functions of strain. The energies of the CBE and the VBE decrease with expansion while increasing with compression. In addition, the slope of the CBE is slightly smaller (i.e., more negative) compared to that of the VBE plot. Since the band gap is given by the energy difference between the CBE and the VBE, the gap is also a nearly linear function of strain (see the corresponding curves in Fig. 2.8). However, for the larger Si and Ge wires, the energies of the CBE and the VBE are not linear functions with strain, as shown in Fig. 2.9. Generally, both energies of the CBE and the VBE are reduced under expansion and increased with compression. However, the curve of the CBE decreases faster than that of the VBE under expansion. On the other side, the curve of the CBE increases slower than that of the VBE under compression. This explains the nonlinear relation of the energy gap with strain for the larger nanowires presented in Fig. 2.8.
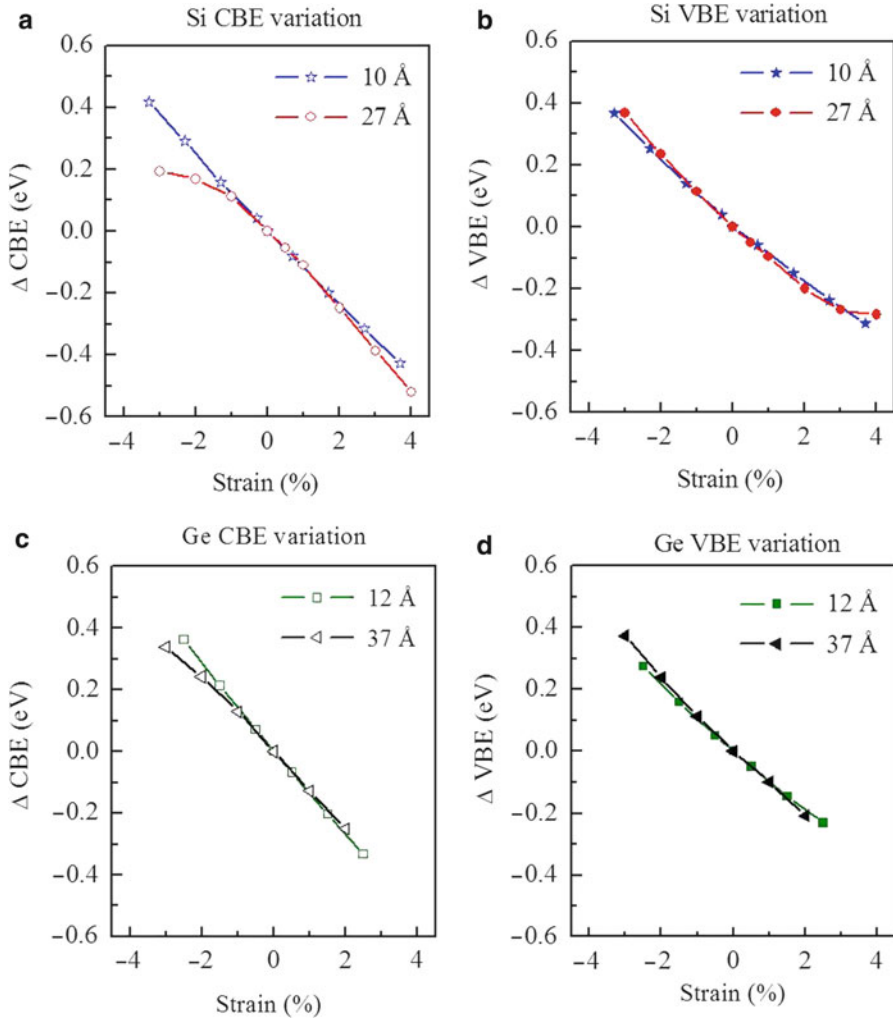
Fig. 2.9 The energy variation of the CBE and the VBE in the Si and Ge nanowires as a function of uniaxial strain

The detailed wave functions of the CBE and the VBE were explored to further understand the behaviors of the strain effects on their energies. As an example, the electron wave function contour plots of the VBE and the CBE in the cross section and the side views in a Ge nanowire are presented in Fig. 2.10. The orbitals of the VBE and the CBE have a bonding character – the electron cloud is mainly located in the intermediate regions shared by the Ge atoms. Once a uniaxial strain is applied to the nanowire, the bonds in the *x*- and *y*-directions will change due to the Poisson effect. For example, when a uniaxial tensile strain is applied, the lateral *xy*-plane
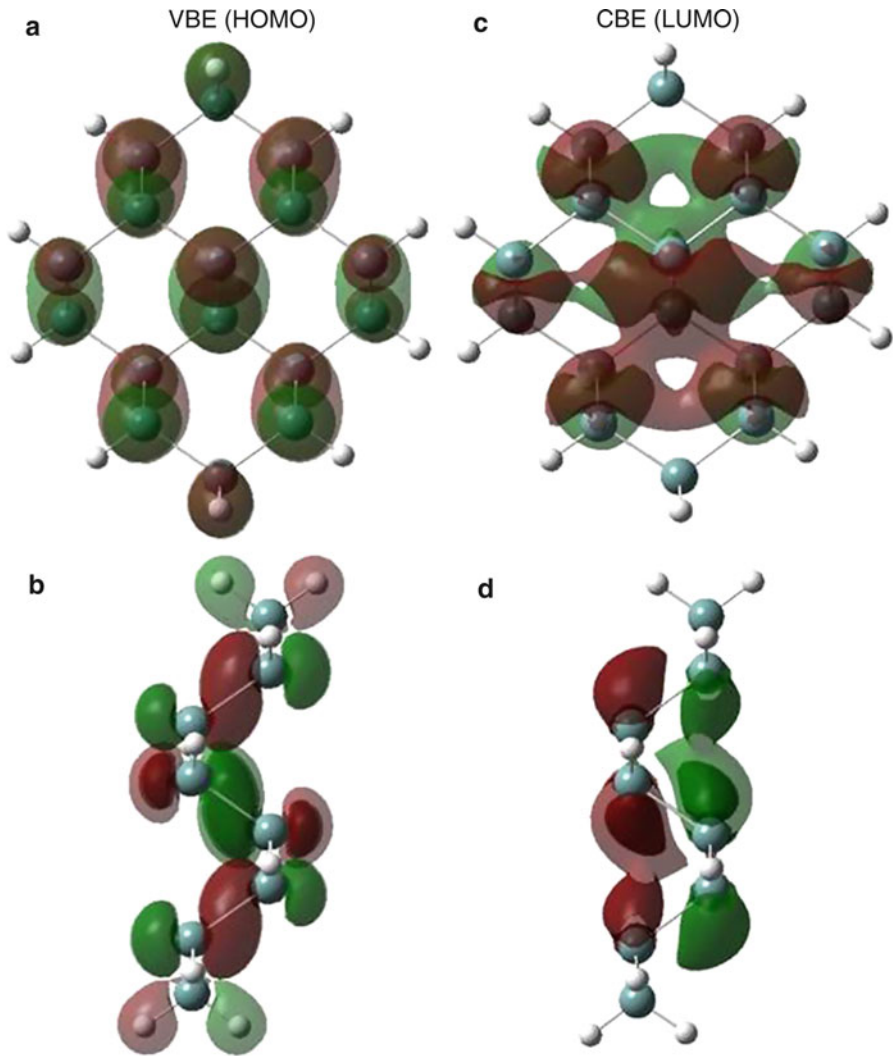
Fig. 2.10 The electron wave function contour plots at the isovalue of 0.02 eV/Å^3 for the VBE (*left*) and the CBE (*right*) in the 12 Å Ge nanowire viewed from the lateral *xy*-plane (*top*) and the side *yz*-plane (*bottom*). *Red* and *green* colors correspond to the positive and negative values of the wave function. *Blue dots* are Ge atoms, and *white* are H atoms

will bear a compressive strain, which means the distance of Ge atoms in the *xy*-plane will be reduced. The reduction of Ge-Ge bond lengths causes the electron cloud of the VBE and the CBE orbitals to be more effectively shared by Ge atoms. This effect results in an increased electron-nucleus Coulomb attraction, thus an appreciable decrease of energies of both the VBE and the CBE (the change in the electron–electron repulsion energy is relatively small). In contrast, with a uniaxial

compression, the lateral xy-plane experiences an expansive strain. With this expansion, energies of both the VBE and the CBE increase due to the decrease of electron-nucleus attraction. This explains the general variation trends of the energies of the VBE and the CBE with respect to strain in Fig. 2.9 – i.e., the energies of the VBE and the CBE increase with compression while decreasing with expansion. Figure 2.10 also shows that the orbital of the CBE is more delocalized than that of the VBE. Thus, the electron cloud of the CBE is more effectively shared by the Ge atoms in the xy-plane. As a result, the energy of the CBE is more sensitive to strain than that of the VBE. Therefore, the slope of the CBE curve in the 12 Å wire in Fig. 2.9 is slightly larger than that of the VBE curve.

For the Ge nanowire with a larger diameter of 37 Å, it was found that the curve of the CBE in Fig. 2.9 decreases faster than that of the VBE under expansion, while the curve of the CBE increases slower than that of the VBE under compression. This might result from the combined effects of energy-strain response and degeneracy release of band edges. If only the effect of strain is considered, one can expect a similar linear variation of the CBE and the VBE energies with strain as discussed for the smaller nanowire. However, for the larger wire, the band edges are degenerate due to the tetrahedral symmetry of the core Ge atoms. Under uniaxial strain, the Td symmetry of the core Ge atoms is broken and the degeneracy of the band edges is released. The splitting of the degenerated band edges causes the energies of the CBE and the VBE to vary as a parabolic function of strain [107]. That means the energy of the CBE decreases while that of the VBE increases with both expansion and compression [107]. Therefore, the curves for the larger wire in Fig. 2.9 may be understood from the combined effects of the energy-strain response and the degeneracy lifting of the band edges.

Effective Mass

The effective masses of the electron and the hole in the pure Si and Ge nanowires can be readily calculated according to Eq. 2.2 from their band structures. In detail, the energy dispersion curve near the Γ point of a given wire was calculated in the range of the wave vector from -0.1 to $+0.1$, where ± 0.1 is in units of $2\pi/a$ (a is the axial lattice constant). Then the curves of the energy dispersion around Γ are fitted using the second order polynomial

$$E = C_1 k^2 + C_2 k + C_3 \tag{2.7}$$

where

$$C_1 = \frac{1}{2}\left(d^2 E/dk^2\right) \tag{2.8}$$

Furthermore, the effective mass of the electron and the hole can be estimated through the relation

Table 2.2 The DFT-predicted effective masses of the electron and the hole for the Si and Ge nanowires. The values in the parentheses are for the Ge nanowires

$N_{Si(Ge)}$	N_H	D (Å)	m_e*	m_h*
16	12	10 (12)	0.14 (0.12)	0.17 (0.11)
42	20	16 (18)	0.14 (0.12)	0.17 (0.09)
76	28	22 (25)	0.14 (0.11)	0.26 (0.15)
110	32	27 (30)	0.15 (0.11)	0.29 (0.19)
172	44	33 (37)	0.18 (0.11)	0.36 (0.31)

$$m^* = \hbar^2/2C_1 \tag{2.9}$$

In Table 2.2, the calculated effective masses are reported. The effective mass of the electron is represented by m_e^*, while m_h^* is the effective mass of the hole, in the unit of free-electron mass m_e. For example, the effective mass of the electron m_e^* in the strain-free Si wires with diameters smaller than 25 Å is 0.14 m_e; it increases with size of the wire slightly. In general, the effective mass of the hole m_h^* increases with size in both Si and Ge wires. Note that a smaller effective mass of the charge carrier in a material implies a larger mobility of the charge carrier, thus increasing the operating speed of devices made from the material.

From Table 2.2, one can see that the effective mass of the hole decreases substantially when the size of the Si and Ge nanowires is reduced. In contrast, the effective mass of the electron is less sensitive to the size. Karanth and Fu [110] showed similar findings in their calculations of InP nanowires. The reduced effective mass of the hole in the ultrathin nanowires results from the quantum confinement effect in the nanowires. As the diameter of the Si (Ge) nanowire is reduced, the component of the wave vector perpendicular to the wire axis, $k_\perp$, becomes quantized and inversely proportional to the size of the nanowire [109]. In this way, $k_\perp$ always has a finite value. As a result, the CBE and the VBE will shift away from its bulk position. This causes a non-parabolic band curvature, enhancing the effective mass of the electron [109]. This effect of non-parabolicity is originated from the second order perturbation and is usually small, consistent with our calculations of the effective mass of the electrons in Table 2.2. For the hole, the situation is not the same. For example, in a bulk Ge crystal, the valence band is degenerated with the light hole and the heavy hole bands at Γ. When $k_\perp$ becomes quantized, this degeneration will be released. The energy of the heavy hole band may shift lower, compared to the energy of the light hole band. One possible reason for this is that for the heavy hole band, the overlap of the wave function in the direction perpendicular to the wire axis is significant [110]. In contrast, for the light hole band, the overlap in the perpendicular direction is small (see Fig. 2.10a), although this overlap is significant along the quantum wire axis as shown in Fig. 2.10b. A larger overlap of the wave function in the perpendicular direction implies a smaller effective mass in this direction ($m_{\perp\,eff}$). Since here the amount of energy downshift by the quantized $k_\perp$ is approximately [110]

$$\Delta E = \frac{\hbar^2 k_\perp{}^2}{m_{\perp eff}} \tag{2.10}$$

The energy of the heavy hole band, which has a smaller $m_{\perp eff}$, will be decreased more [110]. Consequently, the light hole band becomes the very top valence band at Γ of the nanowire and gives a smaller effective mass of the hole, compared with the value of the bulk crystal.

As mentioned before, the band structure of the Si and Ge nanowires can be significantly modified by applied uniaxial strain as shown in Fig. 2.6. To emphasize this, the conduction and the valence bands of Si and Ge wires near the region of the Γ point under different values of strain are presented in Fig. 2.11. It is clear that the curvature of the energy dispersion curve near Γ is drastically altered by strain. Therefore, the effective masses of the electron and the hole are expected to be tuned by strain. The strain effect on the effective masses of the electron and the hole in the studied pure Si and Ge nanowires are presented in Fig. 2.12. Taking the 37 Å Ge nanowire as an example (see its dispersion relation near Γ with different values of strain in Fig. 2.11b), the effective mass of the electron is increased to 0.166 m_e (increased by 55 %), while the effective mass of the hole is reduced to 0.133 m_e (decreased by 57 %) with a 2 % compressive strain. In contrast, under a 2 % expansive strain, the effective mass of the electron is decreased to 0.102 m_e (reduced by 4.7 %), while the effective mass of the hole increases dramatically to 1.139 m_e (increased by 270 %), resulting from the nearly flat energy dispersion relation in Fig. 2.11b, shown by the blue-pentagon curve.

From Fig. 2.12, the strain effect on the effective masses of the electron and the hole is also dependent on the size of nanowires. However, it shows a general trend. From Fig. 2.12a, c, the effective mass of the hole reduces under compression, while enhanced dramatically with a tensile strain. However, the effective mass of the electron in Fig. 2.12b, d increases rapidly with a compressive uniaxial strain, while decreasing mildly with a tensile strain.

Finally, it is necessary to briefly discuss the impact of surface passivation on the calculated electronic properties. In the present work, the surface dangling bonds of the Si and Ge wires are passivated by hydrogen atoms. From the contour plots of electronic wave functions near the Fermi level, the orbitals including the VBE and the CBE are mainly contributed by Si (Ge) atoms rather than H [111], as shown in Fig. 2.10a–d. This gives evidence that the reported results of the band gap and the effective masses of Si (Ge) nanowires are predominantly dependent on the diameter and strain rather than the surface H atoms. Experimentally, the surface of Si and Ge nanowires may be saturated by oxygen under an ambient condition. From previous studies of Si nanowires and quantum dots [112–116], this oxygen shell would bring surface states near the Fermi level. All electronic properties related to the surface states are expected to be different from that of H passivation. This effect of surface chemistry (beyond the scope of the present work) could be another tuning factor to modulate the electronic properties of semiconductor nanostructures.

Fig. 2.11 The conduction and the valence bands of (**a**) Si wire with a diameter of 27 Å and (**b**) Ge wire with a diameter of 37 Å at the near region of Γ are plotted under different values of strain
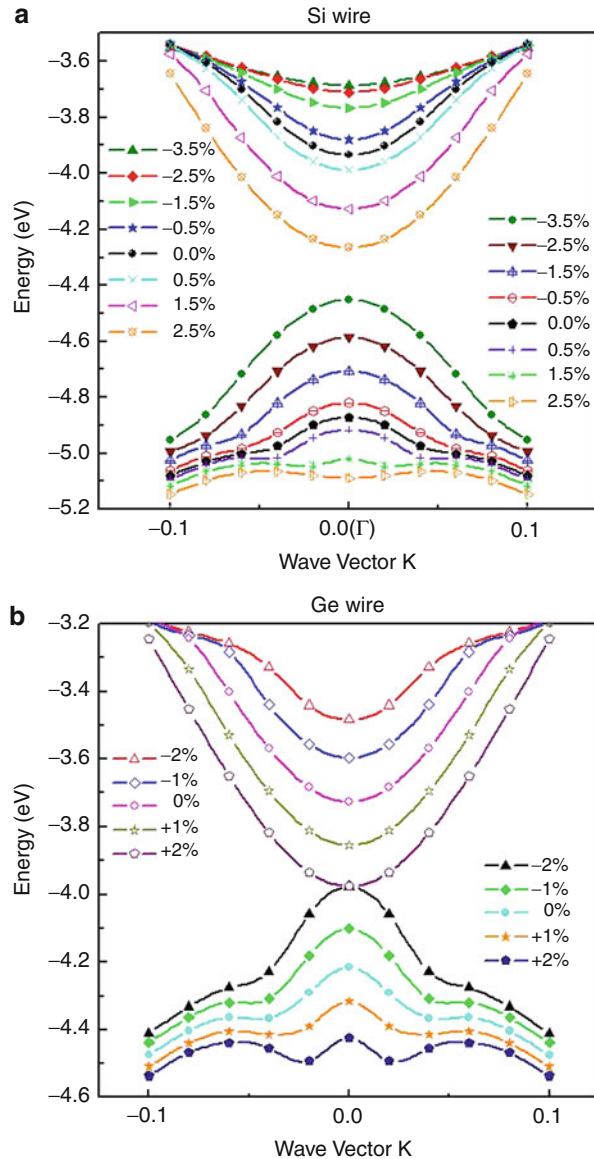
Si/Ge Core-Shell Nanowires

Si/Ge heterostructured core-shell nanowires possess an intrinsic strain due to the lattice mismatch between Si and Ge, which serves as a good example for demonstrating strain effect. We studied the Si/Ge core-shell nanowires with Si in the core and Ge in the shell (or vice versa). Table 2.3 lists the studied Si/Ge core-shell
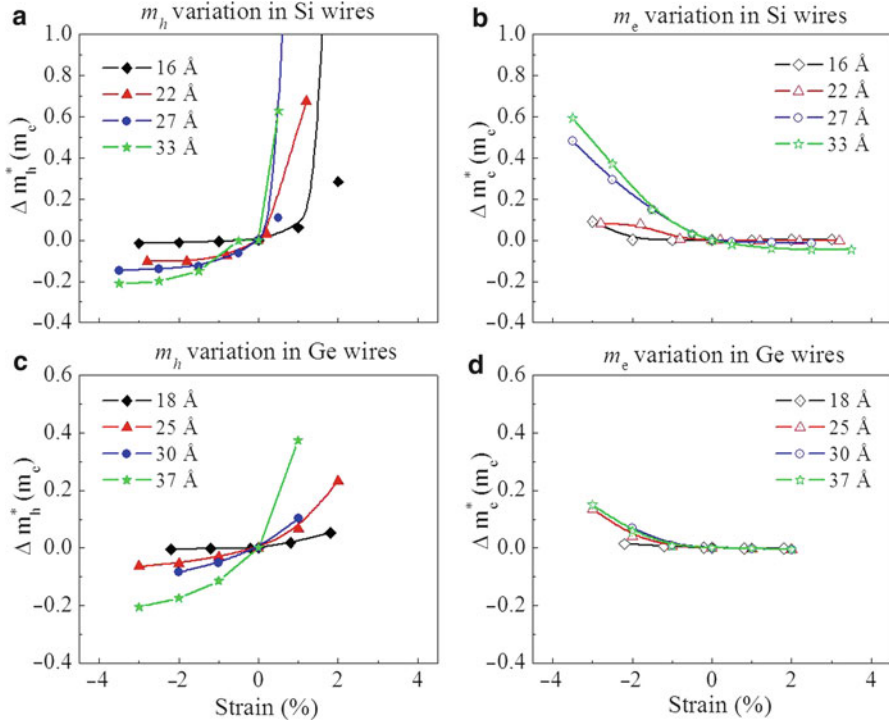
Fig. 2.12 The strain effect on the effective masses of the electron (*left*) and hole (*right*) in the Si (*top*) and the Ge (*bottom*) nanowires. The effective mass of the electron increases rapidly with compressive uniaxial strain, while decreasing mildly with tensile strain. However, the effective mass of the hole reduces under compression, while enhanced dramatically with tensile strain

Table 2.3 A list of the studied Si/Ge core-shell nanowires along the [110] direction. D is the diameter of a wire. N(core)/N(shell) is the number of the core/shell atoms in a given wire. N(H) is the number of H atoms needed to passivate the surface dangling bonds

D (Å)	N(core)	N(shell)	N(H)
25	30	46	28
30	30	80	32
37	30	142	44
47	30	246	52

nanowires along the [110] direction. D is the diameter of the core-shell nanowires; N(core)/N(shell) is the number of the core-shell atoms in a given wire; N(H) is the number of H atoms needed to passivate the surface dangling bonds. Figure 2.13 gives the snapshots of three core-shell nanowires with the diameters of 25, 37, and 47 Å, respectively. In all studied Si/Ge core-shell nanowires, the core contains 30 atoms and the thickness of the shell varies. The diameter of the core is roughly 15 Å.

a 25 Å - $Core_{30}Shell_{46}H_{28}$ **b** 37 Å - $Core_{30}Shell_{142}H_{44}$

c 47 Å - $Core_{30}Shell_{246}H_{52}$
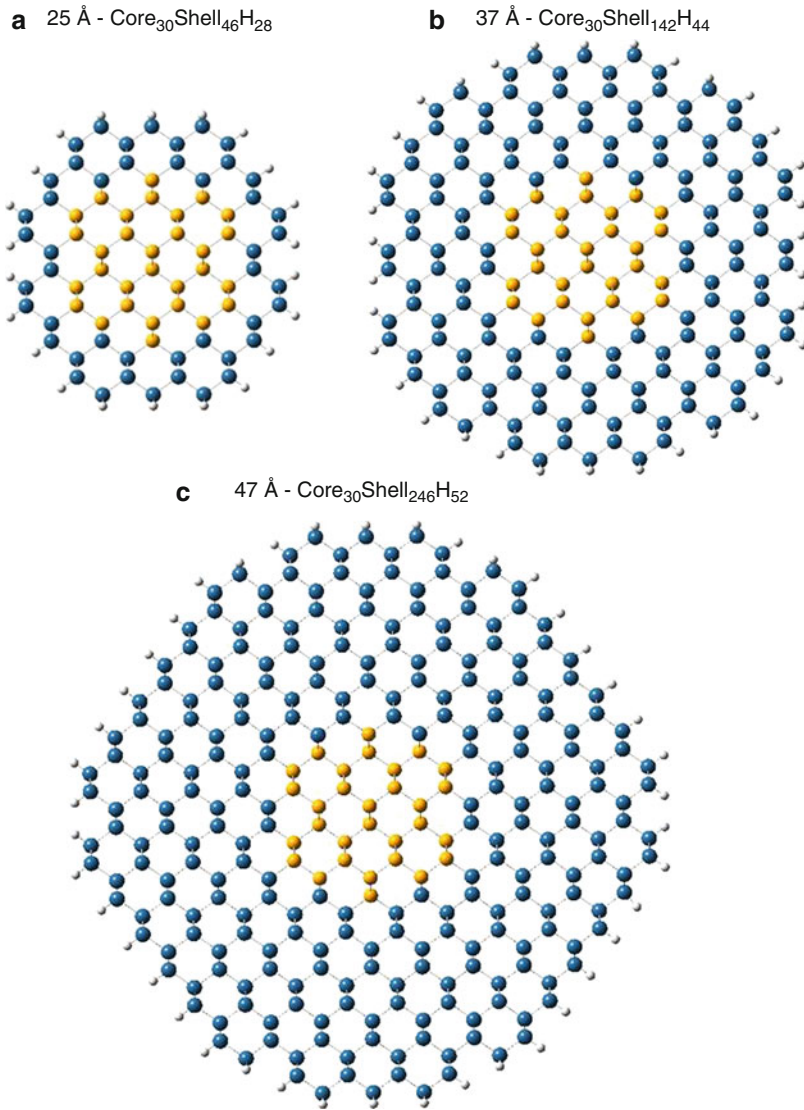
Fig. 2.13 Snapshots of the Si/Ge core-shell nanowires viewed from the cross section. The core atoms can be Si (Ge); thus the shell will be Ge (Si). *White dots* on the surface are H atoms

Structural Properties

Similar to the pure Si and Ge nanowires, the axial lattice constants of the Si/Ge core-shell nanowires were obtained through the technique of minimizing the total energy of the wire. The optimized lattice constants are reported in Table 2.4 and plotted as a function of the size of the nanowires in Fig. 2.14. It shows that the

Table 2.4 The calculated optimized axial lattice constants, intrinsic strain to the core and shell compositions in the relaxed Si/Ge core-shell nanowires

	D (nm)	a (nm)	$e_{intrinsic}$ to core (%)	$e_{intrinsic}$ to shell (%)
Si-core/Ge-shell	2.5	0.3917	1.5	−1.5
	3.0	0.3945	2.2	−0.8
	3.7	0.3965	2.7	−0.3
	4.7	0.3944	2.1	−0.8
Ge-core/Si-shell	2.5	0.3985	0.2	3.2
	3.0	0.3950	−0.7	2.3
	3.7	0.3931	−1.2	1.8
	4.7	0.3900	−1.9	1.0
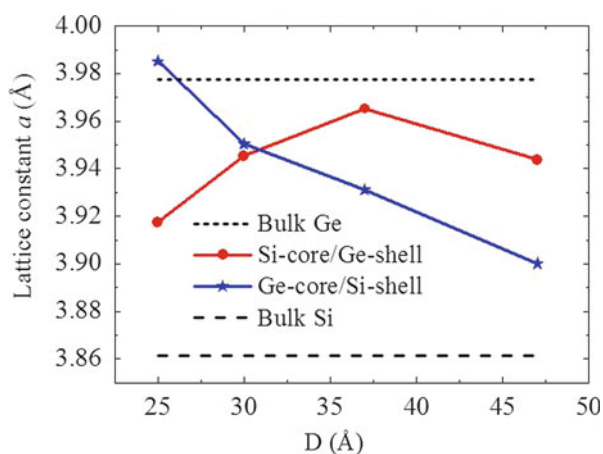
Fig. 2.14 The optimized axial lattice constant of the Si/Ge core-shell nanowires as a function of the wire diameter

lattice constant of the Si-core/Ge-shell nanowires generally increases with the diameter of the wire, from 3.917 Å for the 25 Å wire to 3.944 Å for the 47 Å wire. In addition, these lattice constants are smaller than 3.977 Å (derived from bulk Ge) but larger than 3.862 Å (derived from bulk Si), as shown in Fig. 2.14. These results are expected since a larger Si-core/Ge-shell wire contains more Ge atoms in the shell, thus the lattice constant generally increases with size. On the other hand, the lattice constant of the Ge-core/Si-shell nanowires decreases with the diameter of the wire, from 3.985 to 3.900 Å, and approaching that of bulk Si with a larger diameter.

It is interesting to note that the lattice constant for the smallest Ge-core/Si-shell wire with a diameter of 25 Å is even larger than 3.977 Å from bulk Ge (see Fig. 2.14). This is consistent with the findings in the above pure Si and Ge nanowires with H passivation [37, 73], in which small Si or Ge nanowires along the [110] direction were expanded upon relaxation, compared to their bulk lattice constants.

From Fig. 2.14, one notices that the lattice constants of the Si/Ge core-shell nanowires are, in general, larger than that of bulk Si but smaller than that of bulk Ge.

One can conclude that Ge composition in the core-shell nanostructure is intrinsically compressed, while the Si composition is under expansion. This intrinsic strain in the Si (Ge) composition was calculated according to the formula

$$\varepsilon_{\text{intrinsic}} = \left(a - a_{\text{bulk}[110]}\right)/a_{\text{bulk}[110]} \tag{2.11}$$

where a is the optimized lattice constant of the core-shell nanowire and $a_{\text{bulk}[110]}$ is the lattice constant of bulk Si or Ge along the [110] direction. The calculated intrinsic strain in both Si and Ge composition in the studied Si/Ge core-shell nanowires is reported in Table 2.4. This intrinsic strain creates an effect in the band gap, significantly countering the quantum confinement effect, as discussed later.

Band Structures

The Si/Ge core-shell nanowires also demonstrate a direct band gap at Γ [33, 36–38, 48, 51–53, 73], similar to that of pure Si and Ge wires. The band structures for the relaxed Si/Ge core-shell nanowires are presented in Fig. 2.15. In particular, the electronic states of the CBE and the VBE were further examined, since both determine the band gap. The contour plots of the charge density of the CBE and the VBE confirm that the band alignment in the Si/Ge core-shell nanowires is a type II. As an example, Fig. 2.16 shows the isovalue surfaces of the charge density of the VBE and the CBE in the nanowires with diameters of 25 and 37 Å. From the figures viewed in the cross sections (i.e., in the xy-plane), the charge of the VBE in the Si-core/Ge-shell wires is mainly distributed in the Ge-shell, while the charge of the CBE is mainly located in the Si-core, as shown in Fig. 2.16a, b. On the other hand, the charge of the VBE in the Ge-core/Si-shell wires is primarily in the Ge core, while the charge of the CBE is distributed in the Si shell, shown in Fig. 2.16c, d. In conclusion, the charge of the VBE is mainly concentrated in the Ge composition, while the CBE charge is in the Si composition, regardless of whether the nanowire is of a Si-core/Ge-shell or Ge-core/Si-shell structure [48, 51–53, 64].

This band alignment is also implied in the band structures. Examining the band edges at Γ in Fig. 2.15, one notices that for the Si-core/Ge-shell wires, as shown in Fig. 2.15a–d, the valence and lower occupied bands at Γ are generally close to each other, while the conduction band and higher unoccupied bands are considerably discrete. The discrete energies of the conduction band (contributed by Si composition) and neighboring unoccupied bands at Γ result from the fact that the Si atoms in the core are more significantly quantum confined compared to the Ge atoms in the shell. On the other hand, for the Ge-core/Si-shell wires in Fig. 2.15e–h, the space of the energy levels in the valence band (contributed by Ge composition) and neighbored occupied bands is larger than that of the conduction bands, mainly due to the fact that the Ge atoms in the core are more significantly confined.

External strain also shows a significant effect on tuning the band structures of the Si/Ge core-shell nanowires. As an example, the band structure of a 25 Å
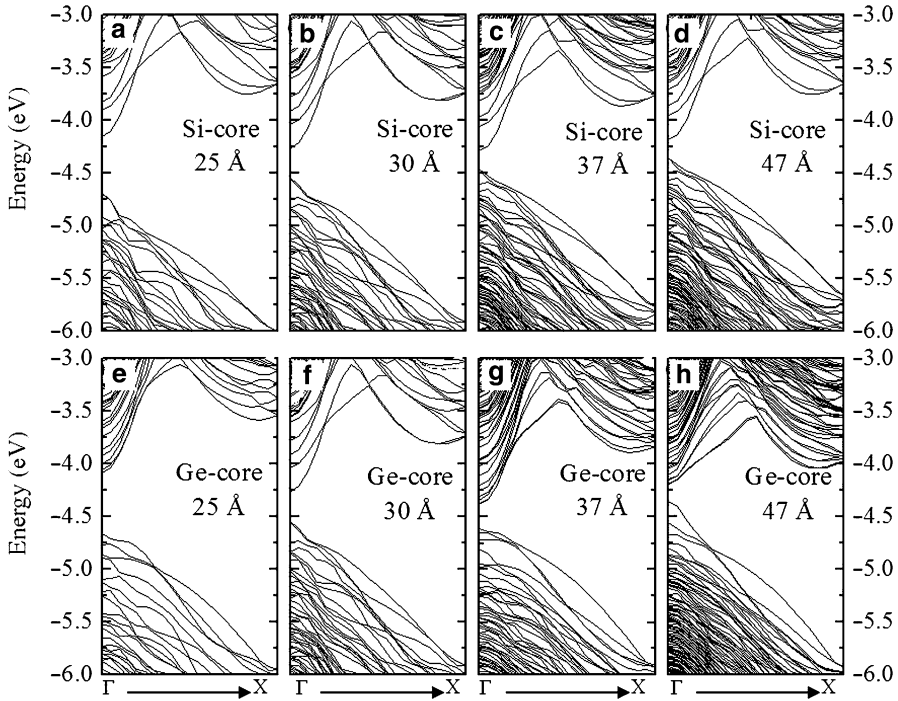
Fig. 2.15 The band structures of the Si/Ge core-shell nanowires at different composition and diameters. The energies are referenced to the vacuum level

Ge-core/Si-shell nanowires under different values of uniaxial strain is plotted in Fig. 2.17a–e. Examining the band edges, one finds that the energies of both the CBE and the VBE are decreased with tensile strain, while they are increased under compression. Interestingly, tensile strain shows a dramatic effect in the VBE. In Fig. 2.17d, e, the VBE is no longer located at Γ, implying a band gap transition from direct to indirect in the nanowire [53].

Band Gap

The DFT-predicted band gaps for the Si/Ge core-shell wires are reported in Table 2.5 and plotted as a function of the size of the wire in Fig. 2.18a. The band gap of the core-shell nanowires increases with reducing wire size, which is mainly due to the quantum confinement effect. The band gaps of the pure Si and Ge nanowires are also plotted in Fig. 2.18a for comparison. It is interesting to note that the band gap of the core-shell nanowires is smaller than that of both pure Si and Ge nanowires, at a given diameter. For example, the DFT gaps for the Si and Ge wires with the diameter of 25 Å are 1.02 eV and 0.73 eV [37, 73], respectively.
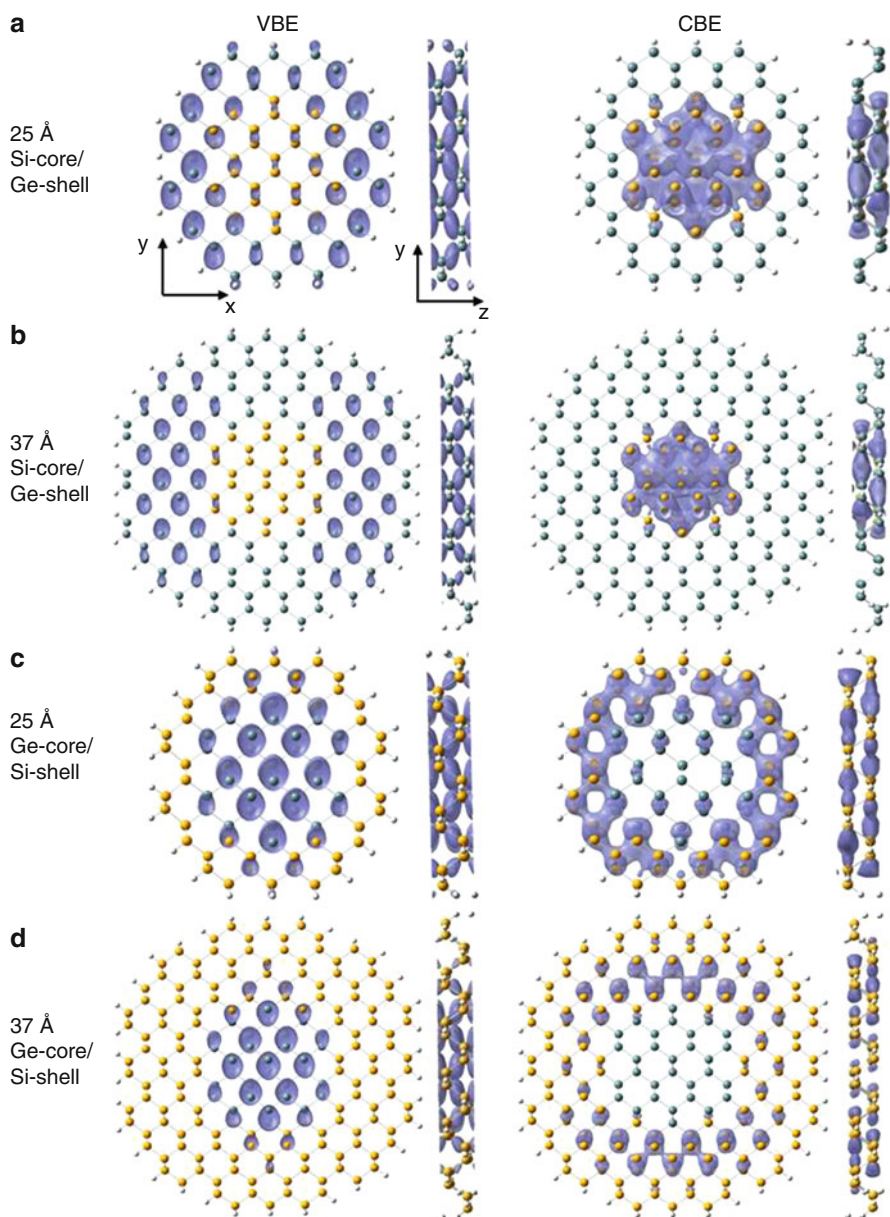
Fig. 2.16 The isovalue surfaces of the charge density of the VBE and the CBE in the Si/Ge core-shell nanowires. The *yellow*, *blue*, and *white dots* represent Si, Ge, and H atoms, respectively
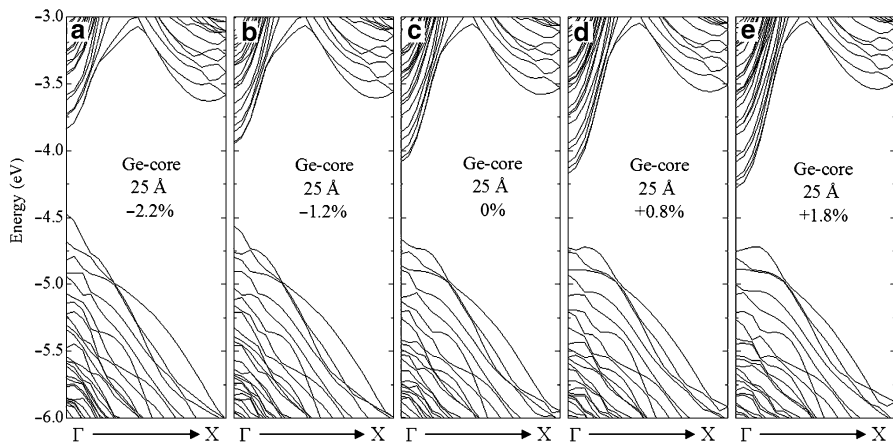
Fig. 2.17 The band structure of a 25 Å Ge-core/Si-shell nanowire under different values of uniaxial strain. The energies are referenced to the vacuum level

Table 2.5 The DFT-calculated band gap, effective masses of the electron and the hole, and work function in the relaxed Si/Ge core-shell nanowires

	D (nm)	E_g (eV)	m_e^* (m_e)	m_h^* (m_e)	ϕ (eV)
Si-core/Ge-shell	2.5	0.54	0.13	0.16	4.64
	3.0	0.29	0.13	0.21	4.55
	3.7	0.18	0.14	0.32	4.46
	4.7	0.13	0.14	0.26	4.38
Ge-core/Si-shell	2.5	0.58	0.14	0.21	4.66
	3.0	0.31	0.13	0.17	4.58
	3.7	0.23	0.14	0.74	4.61
	4.7	0.18	0.14	0.36	4.36

However the gaps for the Si/Ge core-shell wires are 0.58 eV(Ge-core) and 0.54 eV (Si-core), respectively, which are both smaller than that of the pure Si and Ge wires. Similar trends are also observed for other larger nanowires.

   To understand this reduced gap in the core-shell wires, the 30 Å Si-core/Ge-shell nanowire was examined as an example. The gap of the Si-core/Ge-shell wire was reduced by 0.3 eV compared to that of the pure Ge wire with a diameter of 30 Å. From the lattice constant and intrinsic strain reported in Table 2.4, the Si-core in the 30 Å Si-core/Ge-shell nanowire experiences a 2.2 % tensile strain, while the Ge-shell is contracted with a 0.8 % compressive strain. Since the CBE/VBE states in the core-shell wire are primarily contributed by Si/Ge composition, it is necessary to examine the CBE energy variation with strain in the pure Si nanowire of a diameter of 15 Å (represents the core) and the VBE energy variation with strain in
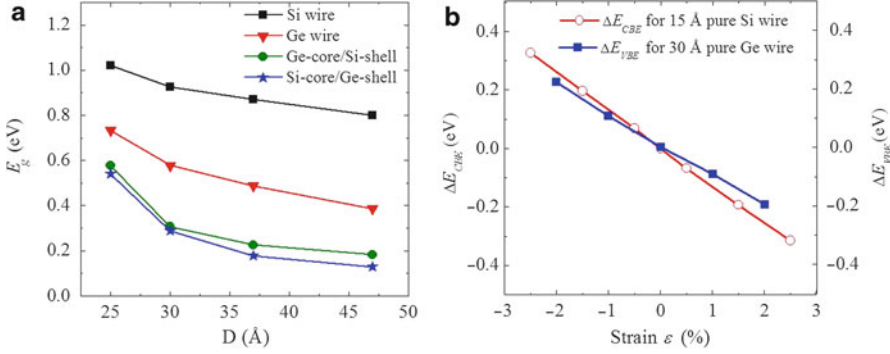
Fig. 2.18 (**a**) The band gap of the Si/Ge core-shell and pure Si and Ge nanowires as a function of the wire diameter. (**b**) The energy variation of the CBE (for a 15 Å pure Si wire representing the core) and the VBE (for a 30 Å pure Ge wire) with strain

the pure Ge nanowire of a diameter of 30 Å. The energy variations of the CBE and the VBE with strain is defined as

$$\Delta E_{CBE} = E_{CBE}(\varepsilon) - E_{CBE}(0)$$

$$\Delta E_{VBE} = E_{VBE}(\varepsilon) - E_{VBE}(0) \tag{2.12}$$

where $E_{VBE}(\varepsilon)/E_{CBE}(\varepsilon)$ and $E_{VBE}(0)/E_{CBE}(0)$ are energies of the VBE/CBE with and without strain, respectively. The results are shown in Fig. 2.18b. The CBE of the 15 Å Si wire is decreased by ~0.28 eV under a 2.2 % tensile strain. However, the VBE energy in the 30 Å Ge wire is increased about 0.8 eV with a 0.8 % compressive strain. This implies that the band gap in the 30 Å Si-core/Ge-shell nanowire will be reduced by 0.36 eV, compared to the pure 30 Å Ge wire. This estimated reduction in the band gap (0.36 eV) is close to the actual calculation (~ 0.3 eV). Similar qualitative behaviors are also observed in the Ge-core/Si-shell nanowires.

From the above analysis, one can see that the reduced band gap is closely related to the intrinsic strain of the core-shell wires. Amato and colleagues [49] also observed a reduced band gap in Si/Ge hetero nanowires, which form an explicit interface between Si and Ge regions. These authors explained the gap reduction using quantum confinement effects in the band edges. The quantum confinement effect may be able to explain the results in their ultrathin nanowires with diameters up to 16 Å. However, it is not able to explain our larger wires with a diameter up to 50 Å, where the quantum confinement effect is weaker. We argue that the reduction of the band gap in the Si/Ge core-shell nanowires is largely related to the intrinsic strain in the Si/Ge composition.

Effective Mass and Work Function

The calculated effective masses of the electron and the hole for the relaxed Si/Ge core-shell nanowires are reported in Table 2.5, where m_e^* represents the effective mass of the electron, while m_h^* is the effective mass of the hole, in the unit of free-electron mass m_e. The effective masses of the electron are 0.13 or 0.14 m_e, having a negligible change with size and the core-shell composition. In contrast, the effective mass of the hole is dependent on the wire size and composition.

It is of great importance to predict the work function of semiconducting nanowires, since it affects the band alignment in the nanowire/metal interfaces and displays an impact in the device performance [42]. The work function of a nanowire is defined as the energy difference between the Fermi and vacuum levels:

$$\phi = V_{vacuum} - E_{Fermi} \tag{2.13}$$

Usually in first principles DFT calculations, the Fermi level is set at the VBE. Since the electronic energies in the present calculations are referenced to the vacuum, the work function ϕ is simply

$$\phi = -E_{VBE} \tag{2.14}$$

The calculated work functions ϕ for the Si/Ge core-shell nanowires are reported in Table 2.5. The work function is in the range of 4.4 $\sim$ 4.6 eV, consistent with the reported work function of H-passivated Si nanowires along the [110] direction [42, 117]. In general, the work function of the nanowire decreases with increasing size. For example, the work function of the Si-core/Ge-shell nanowires reduces from 4.64 eV for the 25 Å wire to 4.38 eV for the 47 Å wire. For the Ge-core/Si-shell wires, it decreases from 4.66 eV in the 25 Å wire to 4.36 eV in the 47 Å wire. This general trend is also demonstrated in the band structures in Fig. 2.15. Since the band energies in Fig. 2.15 are referenced to the vacuum level, the energy of the VBE reflects the work function (with opposite sign). With increasing nanowire size, the VBE energies increase, implying that the work function decreases. This size dependence of the work function is also consistent with that of Si and Ge nanowires [42, 117].

Conclusion

First principles DFT calculations were performed to investigate the properties of Si and Ge pure and core/shell nanowires with a diameter up to 50 Å. It was found that the electronic properties of the nanowires, such as band structure, band gap, effective mass of charge carrier, and work function, are strongly dependent on the size of the nanowires which is primarily attributed to the quantum confinement effect. It was also found that strain, including both intrinsic and external strains, shows significant effects on tuning the electronic properties of the nanowires.

References

1. Cui Y, Lieber CM (2001) Functional nanoscale electronic devices assembled using silicon nanowire building blocks. Science 291:851–853
2. Canham LT (1990) Silicon quantum wire array fabrication by electrochemical and chemical dissolution of wafers. Appl Phys Lett 57:1046–1048
3. Hirschman KD, Tsybeskov L, Duttagupta SP, Fauchet PM (1996) Silicon-based visible light-emitting devices integrated into microelectronic circuits. Nature 384:338–341
4. Morales AM, Lieber CM (1998) A laser ablation method for the synthesis of crystalline semiconductor nanowires. Science 279:208–211
5. Koo SM, Fujiwara A, Han JP, Vogel EM, Richter CA, Bonevich JE (2004) High inversion current in silicon nanowire field effect transistors. Nano Lett 4:2197–2201
6. Cui Y, Zhong ZH, Wang DL, Wang WU, Lieber CM (2003) High performance silicon nanowire field effect transistors. Nano Lett 3:149–152
7. Cui Y, Wei QQ, Park HK, Lieber CM (2001) Nanowire nanosensors for highly sensitive and selective detection of biological and chemical species. Science 293:1289–1292
8. Rustagi SC, Singh N, Fang WW, Buddharaju KD, Omampuliyur SR, Teo SHG, Tung CH, Lo GQ, Balasubramanian N, Kwong DL (2007) CMOS inverter based on gate-all-around silicon-nanowire MOSFETs fabricated using top-down approach. Electron Device Lett IEEE 28:1021–1024
9. Wang D, Sheriff BA, Heath JR (2006) Complementary symmetry silicon nanowire logic: power-efficient inverters with gain. Small 2:1153–1158
10. Garnett E, Yang P (2010) Light trapping in silicon nanowire solar cells. Nano Lett 10:1082–1087
11. Garnett EC, Yang P (2008) Silicon nanowire radial p–n junction solar cells. J Am Chem Soc 130:9224–9225
12. Tsakalakos L, Balch J, Fronheiser J, Korevaar BA, Sulima O, Rand J (2007) Silicon nanowire solar cells. Appl Phys Lett 91:2331171–2331173
13. Chan CK, Peng H, Liu G, McIlwrath K, Zhang XF, Huggins RA, Cui Y (2008) High-performance lithium battery anodes using silicon nanowires. Nat Nanotechnol 3:31–35
14. Ruffo R, Hong SS, Chan CK, Huggins RA, Cui Y (2009) Impedance analysis of silicon nanowire lithium ion battery anodes. J Phys Chem C 113:11390–11398
15. Chen K-I, Li B-R, Chen Y-T (2011) Silicon nanowire field-effect transistor-based biosensors for biomedical diagnosis and cellular recording investigation. Nano Today 6:131–154
16. Shao MW, Shan YY, Wong NB, Lee ST (2005) Silicon nanowire sensors for bioanalytical applications: glucose and hydrogen peroxide detection. Adv Funct Mater 15:1478–1482
17. Hahm J, Lieber CM (2004) Direct ultrasensitive electrical detection of DNA and DNA sequence variations using nanowire nanosensors. Nano Lett 4:51–54
18. Hu JT, Odom TW, Lieber CM (1999) Chemistry and physics in one dimension: synthesis and properties of nanowires and nanotubes. Acc Chem Res 32:435–445
19. Holmes JD, Johnston KP, Doty RC, Korgel BA (2000) Control of thickness and orientation of solution-grown silicon nanowires. Science 287:1471–1473

20. Cui Y, Lauhon LJ, Gudiksen MS, Wang J, Lieber CM (2001) Diameter-controlled synthesis of single-crystal silicon nanowires. Appl Phys Lett 78:2214–2216
21. Ma DDD, Lee CS, Au FCK, Tong SY, Lee ST (2003) Small-diameter silicon nanowire surfaces. Science 299:1874–1877
22. Wu XY, Kulkarni JS, Collins G, Petkov N, Almecija D, Boland JJ, Erts D, Holmes JD (2008) Synthesis and electrical and mechanical properties of silicon and germanium nanowires. Chem Mater 20:5954–5967
23. Nguyen P, Ng HT, Meyyappan M (2005) Growth of individual vertical germanium nanowires. Adv Mater 17:549–553
24. Wang D (2007) Synthesis and properties of germanium nanowires. Pure Appl Chem 79:55
25. Dailey E, Drucker J (2009) "Seedless" vapor–liquid–solid growth of Si and Ge nanowires: the origin of bimodal diameter distributions. J Appl Phys 105:064317–064321
26. Wang D, Chang YL, Wang Q, Cao J, Farmer DB, Gordon RG, Dai H (2004) Surface chemistry and electrical properties of germanium nanowires. J Am Chem Soc 126:11602–11611
27. Zhao X, Wei CM, Yang L, Chou MY (2004) Quantum confinement and electronic properties of silicon nanowires. Phys Rev Lett 92:236805–236808
28. Vo T, Williamson AJ, Galli G (2006) First principles simulations of the structural and electronic properties of silicon nanowires. Phys Rev B 74:045116
29. Weber WM, Geelhaar L, Graham AP, Unger E, Duesberg GS, Liebau M, Pamler W, Chèze C, Riechert H, Lugli P, Kreupl F (2006) Silicon-nanowire transistors with intruded nickel-silicide contacts. Nano Lett 6:2660–2666
30. Jacoboni C, Canali C, Ottaviani G, Alberigi Quaranta A (1977) A review of some charge transport properties of silicon. Solid State Electron 20:77–89
31. Sze SJ (1981) Physics of semiconductor devices, 2nd edn. Wiley, New York
32. Audoit G, Mhuircheartaigh EN, Lipson SM, Morris MA, Blau WJ, Holmes JD (2005) Strain induced photoluminescence from silicon and germanium nanowire arrays. J Mater Chem 15:4809–4815
33. Beckman SP, Han J, Chelikowsky JR (2006) Quantum confinement effects in Ge [110] nanowires. Phys Rev B 74:165314
34. Bruno M, Palummo M, Marini A, Del Sole R, Olevano V, Kholod AN, Ossicini S (2005) Excitons in germanium nanowires: quantum confinement, orientation, and anisotropy effects within a first-principles approach. Phys Rev B 72:153310
35. Bruno M, Palummo M, Ossicini S, Del Sole R (2007) First-principles optical properties of silicon and germanium nanowires. Surf Sci 601:2707–2711
36. Arantes JT, Fazzio A (2007) Theoretical investigations of Ge nanowires grown along the [110] and [111] directions. Nanotechnology 18:295706–295710
37. Logan P, Peng XH (2009) Strain-modulated electronic properties of Ge nanowires: a first-principles study. Phys Rev B 80:115322
38. Medaboina D, Gade V, Patil SKR, Khare SV (2007) Effect of structure, surface passivation, and doping on the electronic properties of Ge nanowires: a first-principles study. Phys Rev B 76:205327
39. Kagimura R, Nunes RW, Chacham H (2007) Surface dangling-bond states and band lineups in hydrogen-terminated Si, Ge, and Ge/Si nanowires. Phys Rev Lett 98:026801–026805
40. Peelaers H, Partoens B, Peeters FM (2007) Properties of B and P doped Ge nanowires. Appl Phys Lett 90:263103–263105
41. Peelaers H, Partoens B, Peeters FM (2008) First-principles study of doped Si and Ge nanowires. Physica E 40:2169–2171
42. Leu PW, Svizhenko A, Cho K (2008) Ab initio calculations of the mechanical and electronic properties of strained Si nanowires. Phys Rev B 77:235305
43. Huang M, Boone C, Roberts M, Savage DE, Lagally MG, Shaji N, Qin H, Blick R, Nairn JA, Liu F (2005) Nanomechanical architecture of strained bilayer thin films: from design principles to experimental fabrication. Adv Mater 17:2860–2864

44. Goldthorpe IA, Marshall AF, McIntyre PC (2008) Synthesis and strain relaxation of Ge-core/Si-shell nanowire arrays. Nano Lett 8:4081–4086
45. Goldthorpe IA, Marshall AF, McIntyre PC (2009) Inhibiting strain-induced surface roughening: dislocation-free Ge/Si and Ge/SiGe core − shell nanowires. Nano Lett 9:3715–3719
46. Trammell TE, Zhang X, Li YL, Chen LQ, Dickey EC (2008) Equilibrium strain-energy analysis of coherently strained core-shell nanowires. J Cryst Growth 310:3084–3092
47. Musin RN, Wang XQ (2006) Quantum size effect in core-shell structured silicon-germanium nanowires. Phys Rev B 74:165308–165312
48. Yang L, Musin RN, Wang XQ, Chou MY (2008) Quantum confinement effect in Si/Ge core-shell nanowires: first-principles calculations. Phys Rev B 77:195325–195329
49. Amato M, Palummo M, Ossicini S (2009) Reduced quantum confinement effect and electron–hole separation in SiGe nanowires. Phys Rev B 79:201302
50. Xiang J, Lu W, Hu Y, Wu Y, Yan H, Lieber CM (2006) Ge/Si nanowire heterostructures as high-performance field-effect transistors. Nature 441:489–493
51. Peng XH, Logan P (2010) Electronic properties of strained Si/Ge core-shell nanowires. Appl Phys Lett 96:143119
52. Peng X-H, Tang F, Logan P (2011) Band structure of Si/Ge core–shell nanowires along the [110] direction modulated by external uniaxial strain. J Phys Condens Matter 23:115502
53. Peng X-H, Tang F, Logan P (2011) First principles study of Si/Ge core-shell nanowires – structural and electronic properties. In: Hashim A (ed) Nanowires – fundamental research. InTech, Croatia
54. Lauhon LJ, Gudiksen MS, Wang CL, Lieber CM (2002) Epitaxial core-shell and core-multishell nanowire heterostructures. Nature 420:57–61
55. Wu YY, Fan R, Yang PD (2002) Block-by-block growth of single-crystalline Si/SiGe superlattice nanowires. Nano Lett 2:83–86
56. Lu W, Xiang J, Timko BP, Wu Y, Lieber CM (2005) One-dimensional hole gas in germanium/silicon nanowire heterostructures. Proc Natl Acad Sci U S A 102:10046–10051
57. Kagimura R, Nunes RW, Chacham H (2007) Surface dangling-bond states and band lineups in hydrogen-terminated Si, Ge, and Ge/Si nanowires. Phys Rev Lett 98:026801–026805
58. Amato M, Palummo M, Ossicini S (2009) Reduced quantum confinement effect and electron–hole separation in SiGe nanowires. Phys Rev B 79:201302–201305
59. Hu JQ, Bando Y, Golberg D (2009) Novel semiconducting nanowire heterostructures: synthesis, properties and applications. J Mater Chem 19:330–343
60. Varahramyan KM, Ferrer D, Tutuc E, Banerjee SK (2009) Band engineered epitaxial Ge-Si$_x$Ge$_{1-x}$ core-shell nanowire heterostructures. Appl Phys Lett 95:033101–033103
61. Musin RN, Wang XQ (2005) Structural and electronic properties of epitaxial core-shell nanowire heterostructures. Phys Rev B 71:155318–155321
62. Yang JE, Jin CB, Kim CJ, Jo MH (2006) Band-gap modulation in single-crystalline Si$_{1-x}$Ge$_x$ nanowires. Nano Lett 6:2679–2684
63. Migas DB, Borisenko VE (2007) Structural, electronic, and optical properties of <001>−oriented SiGe nanowires. Phys Rev B 76:035440–035448
64. Huang S, Yang L (2011) Strain engineering of band offsets in Si/Ge core-shell nanowires. Appl Phys Lett 98:0931143
65. Amato M, Ossicini S, Rurali R (2010) Band-offset driven efficiency of the doping of SiGe core − shell nanowires. Nano Lett 11:594–598
66. Czaban JA, Thompson DA, LaPierre RR (2008) GaAs core − shell nanowires for photovoltaic applications. Nano Lett 9:148–154
67. Khayer MA, Lake RK (2008) Performance of n-type InSb and InAs nanowire field-effect transistors. IEEE Trans Electron Devices 55:2939–2945

68. Gallo EM, Chen G, Currie M, McGuckin T, Prete P, Lovergine N, Nabet B, Spanier JE (2011) Picosecond response times in GaAs/AlGaAs core/shell nanowire-based photodetectors. Appl Phys Lett 98:241113-3

69. Soci C, Zhang A, Bao XY, Kim H, Lo Y, Wang DL (2010) Nanowire photodetectors. J Nanosci Nanotechnol 10:1430–1449

70. Mi Z, Chang Y-L (2009) III-V compound semiconductor nanostructures on silicon: epitaxial growth, properties, and applications in light emitting diodes and lasers. J Nanophotonics 3:031602–031619

71. Tajik N, Peng Z, Kuyanov P, LaPierre RR (2011) Sulfur passivation and contact methods for GaAs nanowire solar cells. Nanotechnology 22:225402

72. Patolsky F, Zheng G, Lieber CM (2006) Nanowire sensors for medicine and the life sciences. Nanomedicine 1:51–65

73. Peng XH, Alizadeh A, Kumar SK, Nayak SK (2009) Ab-initio study of size and strain effects on the electronic properties of Si nanowires. Int J Appl Mech 1:483–499

74. Wang YG, Zhang QL, Wang TH, Han W, Zhou SX (2011) Improvement of electron transport in a ZnSe nanowire by in situ strain. J Phys D: Appl Phys 44:125301

75. Tezuka T, Sugiyama S, Mizuno T, Suzuki M, Takagi S-i (2001) A novel fabrication technique of ultrathin and relaxed SiGe buffer layers with high Ge fraction for sub-100 nm strained silicon-on-insulator MOSFETs. Jpn J Appl Phys 40:2866–2874

76. Ghani T, Armstrong M, Auth C, Bost M, Charvat P, Glass G, Hoffmann T, Johnson K, Kenyon C, Klaus J, McIntyre B, Mistry K, Murthy A, Sandford J, Silberstein M, Sivakumar S, Smith P, Zawadzki K, Thompson S, Bohr M (2003) A 90 nm high volume manufacturing logic technology featuring novel 45nm gate length strained silicon CMOS transistors. In: Electron devices meeting, 2003. IEDM '03 technical digest. IEEE international, Hillsboro, pp 11.6.1–11.6.3

77. Copple A, Ralston N, Peng X (2012) Engineering direct–indirect band gap transition in wurtzite GaAs nanowires through size and uniaxial strain. Appl Phys Lett 100:193108-4

78. Hong KH, Kim J, Lee SH, Shin JK (2008) Strain-driven electronic band structure modulation of Si nanowires. Nano Lett 8:1335–1340

79. Huang Z, Geyer N, Werner P, de Boor J, Gösele U (2011) Metal-assisted chemical etching of silicon: a review. Adv Mater 23:285–308

80. Rurali R (2010) Colloquium: structural, electronic, and transport properties of silicon nanowires. Rev Mod Phys 82:427–449

81. Wu Z, Neaton JB, Grossman JC (2009) Charge separation via strain in silicon nanowires. Nano Lett 9:2418–2422

82. Das K, Mondal SP, Dhar A, Ray SK (2007) Formation of Ge-based nanowires for nanoelectronic applications by vapor–liquid–solid mechanism. In: Physics of semiconductor devices, 2007. IWPSD 2007. International workshop on, pp 377–379

83. Peng Xihong, Copple Andrew (2013) Origination of the direct–indirect band gap transition in strained wurtzite and zinc-blende GaAs nanowires: a first principles study. Phys Rev B 87:115308

84. Thean A, Leburton JP (2001) Strain effect in large silicon nanocrystal quantum dots. Appl Phys Lett 79:1030–1032

85. Wu XL, Xue FS (2004) Optical transition in discrete levels of Si quantum dots. Appl Phys Lett 84:2808–2810

86. Seravalli L, Minelli M, Frigeri P, Allegri P, Avanzini V, Franchi S (2003) The effect of strain on tuning of light emission energy of InAs/InGaAs quantum-dot nanostructures. Appl Phys Lett 82:2341–2343

87. Mazzucato S, Nardin D, Capizzi M, Polimeni A, Frova A, Seravalli L, Franchi S (2005) Defect passivation in strain engineered InAs/(InGa)As quantum dots. Mater Sci Eng C 25:830–834

88. Hochbaum AI, Yang P (2009) Semiconductor nanowires for energy conversion. Chem Rev 110:527–546
89. Persson MP, Xu HQ (2002) Electronic structure of nanometer-scale GaAs whiskers. Appl Phys Lett 81:1309–1311
90. Persson MP, Xu HQ (2004) Electronic structure of [100]-oriented free-standing semiconductor nanowires. Nano Lett 4:2409–2414
91. Sanders GD, Chang Yia-Chung (1992) Theory of optical properties of quantum wires in porous silicon. Phys Rev B 45:9202–9213
92. Yorikawa H, Uchida H, Muramatsu S (1996) Energy gap of nanoscale Si rods. J Appl Phys 79:3619–3621
93. Harris C, O'Reilly EP (2006) Nature of the band gap of silicon and germanium nanowires. Physica E 32:341–345
94. Luttinger JM (1956) Quantum theory of cyclotron resonance in semiconductors: general theory. Phys Rev 102:1030–1041
95. Bir GL, Pikus GE (1974) Symmetry and strain-induced effects in semiconductors. Wiley, New York
96. Kishore VVR (2013) Electronic structure of core-shell nanowires. In: Physics. University of Antwerpen, Belgium
97. Cardona M, Pollak FH (1966) Energy-band structure of germanium and silicon: the k·p method. Phys Rev 142:530–543
98. Dietl T, Ohno H, Matsukura F (2001) Hole-mediated ferromagnetism in tetrahedrally coordinated semiconductors. Phys Rev B 63:195205
99. Hohenberg P, Kohn W (1964) Inhomogeneous electron gas. Phys Rev 136:B864–B871
100. Kohn W, Sham LJ (1965) Self-consistent equations including exchange and correlation effects. Phys Rev 140:1133–1138
101. Parr RG, Wang W (1989) Density-functional theory of atoms and molecules. Oxford University Press, New York
102. Kresse G, Furthmuller J (1996) Efficiency of ab-initio total energy calculations for metals and semiconductors using a plane-wave basis set. Comput Mater Sci 6:15–50
103. Kresse G, Furthmuller J (1996) Efficient iterative schemes for ab initio total-energy calculations using a plane-wave basis set. Phys Rev B 54:11169–11186
104. Vanderbilt D (1990) Soft self-consistent pseudopotentials in a generalized eigenvalue formalism. Phys Rev B 41:7892–7895
105. Ashcroft NW, Mermin ND (1976) Solid state physics, 1st edn. Thomson Learning, New York
106. Omar MA (1993) Elementary solid state physics. Addison-Wesley, New York
107. Peng XH, Alizadeh A, Bhate N, Varanasi KK, Kumar SK, Nayak SK (2007) First principles investigation of strain effects on the energy gaps in Si nanoclusters. J Phys Condens Matter 19:266212
108. Karanth D, Fu H (2006) Polarization ratio and effective mass in InP nanowires: effect of crystallographic axis. Phys Rev B 74:155312
109. Ekenberg U (1989) Nonparabolicity effects in a quantum well: sublevel shift, parallel mass, and Landau levels. Phys Rev B 40:7714–7726
110. Davies JH (1998) The physics of low-dimensional semiconductors. Cambridge University Press, Cambridge
111. Kholod AN, Shaposhnikov VL, Sobolev N, Borisenko VE, Arnaud D'AF, Ossicini S (2004) Orientation effects in the electronic and optical properties of germanium quantum wires. Phys Rev B 70:035317
112. Puzder A, Williamson AJ, Grossman JC, Galli G (2002) Surface chemistry of silicon nanoclusters. Phys Rev Lett 88:097401–097404
113. Puzder A, Williamson AJ, Grossman JC, Galli G (2002) Surface control of optical properties in silicon nanoclusters. J Chem Phys 117:6721–6729

114. Wolkin MV, Jorne J, Fauchet PM, Allan G, Delerue C (1999) Electronic states and luminescence in porous silicon quantum dots: the role of oxygen. Phys Rev Lett 82:197–200
115. Zhou Z, Brus L, Friesner R (2003) Electronic structure and luminescence of 1.1- and 1.4-nm silicon nanocrystals: oxide shell versus hydrogen passivation. Nano Lett 3:163–167
116. Tsutomu S-I, David EH, Ian WB (1999) Mechanism of photoluminescence of Si nanocrystals in SiO 2 fabricated by ion implantation: the role of interactions of nanocrystals and oxygen. J Phys Condens Matter 11:6595
117. Ng MF, Sim LY, Da HX, Jin HM, Lim KH, Yang SW (2010) Modulation of the work function of silicon nanowire by chemical surface passivation: a DFT study. Theor Chem Acc 127:689–695

Compositionally Graded III-Nitride Nanowire Heterostructures: Growth, Characterization, and Applications

3

Santino D. Carnevale and Roberto C. Myers

Keywords

Doping • Light-emitting diodes • Molecular beam epitaxy • Nanostructures • Nitrides • Polarization

Introduction

The aim of this chapter is to provide important background information necessary to understand the role of graded III-nitride nanowires in polarization-engineered devices. Several key topics will be covered. First, a brief explanation of the origin of polarization phenomena in III-nitrides will be provided, including the concept of polarization doping. It will become clear that moving away from a planar thin film geometry to nanowires allows full utilization of polarization charge in a given materials system. Second, background on the growth of III-nitride nanowires is provided, including growth maps and growth kinetics for nanowires grown by plasma-assisted molecular beam epitaxy. This is finally followed by a review of compositionally graded III-nitride nanowire heterostructures and their applications, for example, in ultraviolet light-emitting diodes.

Before covering these topics, we must explain the motivation for researching polarization-doped devices. The primary driving force for the interest in polarization doping comes out of the shortcomings of impurity doping. The vast majority of electronics devices are based on semiconductors with conductivity controlled by impurity doping. Since one of the most basic qualities of any semiconductor material is the ability to control its conductivity, impurity doping can be seen as

S.D. Carnevale (✉) • R.C. Myers

Materials Science and Engineering Department, The Ohio State University, Columbus, OH, USA
e-mail: carnevale.23@osu.edu; myers.1079@osu.edu

Fig. 3.1 Dopant ionization as a function of bandgap for a variety of semiconductors and impurities. Common semiconductors over a range of bandgaps are listed along the top of the plot (Data taken from [1, 2])
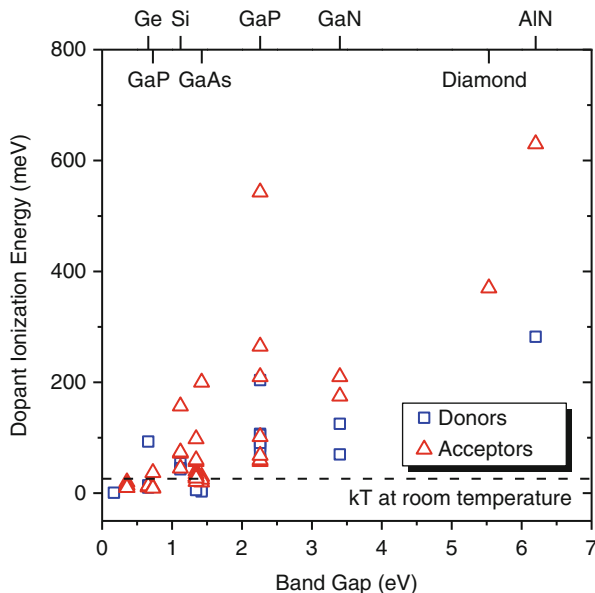
the basis for all semiconductor technology. For many decades controlling conductivity in this way has worked well, but there are two looming issues with impurity doping that must be addressed.

First, the push for new applications and increased performance in semiconductor-based devices has led to a search for new materials to use in these devices. This search has led to using wide bandgap semiconductors for specific applications such as ultraviolet light-emitting diodes and high power devices. Unfortunately, impurity doping is challenging in wide bandgap materials due to large donor and acceptor ionization energies, which tends to increase along with bandgap. This trend is shown in Fig. 3.1, which plots the ionization energy of donors and acceptors in a number of common semiconductors as a function of bandgap. In many cases, these levels become much larger than the thermal energy at room temperature, making it impossible to achieve high conductivity by impurity doping.

The second looming issue is related to aggressive semiconductor device scaling. Given that device sizes continue to decrease, the random position of dopants will eventually have a negative impact on device reliability once the critical dimensions are on the same scale as the average dopant-to-dopant distance. For a reasonable carrier density of 10^{17} cm^3, the average dopant atom spacing is 21 nm, approaching the critical dimension of current semiconductor devices. This phenomenon has been widely discussed as it pertains to the future of transistor technologies [3–5].

Thankfully, both of these issues can be addressed with polarization engineering. As will be covered in more detail later, polarization doping, used in conjunction with impurity doping, addresses the problem of thermal activation of dopants by

activating dopants using a polarization-induced electric field. Additionally, the use of polarization doping without supplemental impurity doping avoids random dopant fluctuation effects because, simply put, there are no intentional dopants. The following section provides background information necessary to understand how this can be achieved with polarization grading.

Polarization in III-Nitride Materials

Origin of Polarization in III-Nitrides

This section provides a brief overview of polarization in the III-nitrides. For more details handling this topic, the reader is referred to the book edited by Jena and Wood [6].

All semiconductors with a non-centrosymmetric crystal structure (e.g., zincblende or wurtzite) exhibit polarization-related effects. Non-centrosymmetric crystal structures are common in semiconductor materials; thus, polarization in semiconductors has a long history. For example, the magnitude of the spontaneous polarization was estimated in certain II–VI semiconductors as early as 1968 [7]. With the explosion of interest in III-nitride devices, since Nakamura et al. developed the blue LED and laser [8–10], polarization effects were recognized to play a dominate role in band engineering both in LED active regions composed of highly polarization distorted quantum wells and in charge (electron) accumulation layers occurring at interfaces in III-nitride heterostructures.

Comparing the polarization effects of the two common tetragonally coordinated binary compound crystal structures for semiconductors, zincblende and wurtzite, it is noted that while wurtzite exhibits spontaneous and piezoelectric polarization (i.e., the presence of a polarization under applied strain), zincblende only exhibits piezoelectric polarization. Most of this chapter will focus on spontaneous polarization because strain accommodation in graded nanowires will reduce the role of piezoelectric polarization.

A material exhibits spontaneous polarization when a polarization dipole exists in each unit cell of the material in its relaxed, equilibrium state. In the wurtzite structure, this occurs both due to a lack inversion symmetry in the crystal and a deviation in lattice parameters c and a from their ideal ratio (i.e., $c/a = (8/3)^{1/2}$). This deviation from the ideal ratio means there is a net displacement between cation and anion placement within the unit cell, creating a dipole. The stronger the ionic character of the bonds, the larger the polarization expected. For example, the ionic oxides $LiNbO_3$ and $BaTiO_3$ with perovskite crystal structure exhibit at least one order of magnitude larger spontaneous polarization than the less ionic solids ZnO and III-nitrides with wurtzite crystal structure; see Fig. 3.2. Like the nitrides, ZnO forms in the wurtzite structure, with a magnitude of spontaneous polarization somewhere roughly between that of AlN and GaN.

Given that a dipole contains a direction, the orientation of the dipole in each unit cell is determined by the crystallographic orientation of the material. In the wurtzite

Fig. 3.2 The magnitude of spontaneous polarization in a variety of materials [11]
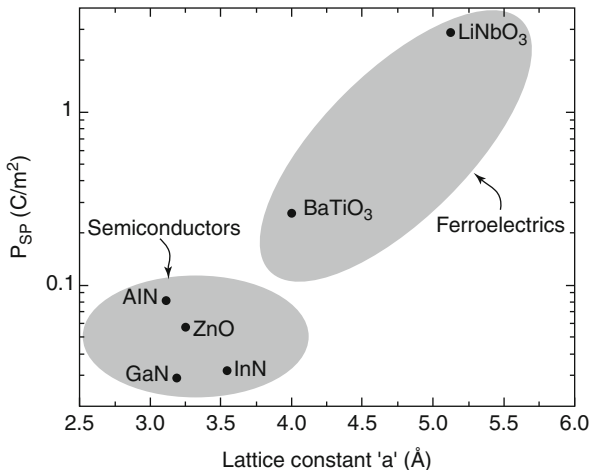
structure, [0001] points towards the $(-)$ end of the dipole and [000–1] the $(+)$ end of the dipole. Material grown along the [0001] is commonly referred to as Ga-face or metal-face in III-nitrides because the dangling N bond $(-$ end of dipole) along the c-direction is passivated by 3 Ga bonds per N atom during thin film growth. Along the [000–1] direction, the dangling Ga bond (+ end of dipole) along the c-axis is passivated with 3 N atoms per Ga and is subsequently called N-face.

Within a bulk crystal, polarization does not lead to net positive or negative charge because the charge imbalance from each dipole is canceled by adjacent dipoles. However, at the surfaces or interfaces of a crystal, bound polarization charge (ρ_π) occurs, due to the change in spontaneous polarization density (P_{sp}). The bound charge density in the material can be found using the following expression:

$$\rho_\pi(z) = \nabla \cdot P(z) \tag{3.1}$$

where $P(z)$ is the polarization density along the growth direction of the material, z.

In the case of a bulk single crystal with spontaneous polarization (Fig. 3.3), at the top and bottom free surfaces, there will be sheets of bound (immobile) charge that are positive on one end and negative on the other. This charge imbalance leads to an electric field in the semiconductor, dictated by Poisson's equation:

$$\nabla \cdot E = \rho/\varepsilon \tag{3.2}$$

where E is the electric field, ρ is charge density, and ε is the permittivity of the material. However, in a thick slab of material, the electric field will lead to a large voltage across the material. This voltage cannot be maintained, and so it must be screened by other charges (ρ_s). The possible mechanisms for screening this charge, including surface states or valence band electrons, are described in greater detail elsewhere [12].

Fig. 3.3 (a) Schematic showing a freestanding slab of GaN, (b) the polarization density of the slab and its surfaces, and (c) the resulting charge distribution, assuming the bound polarization charge at the two surfaces is fully screened
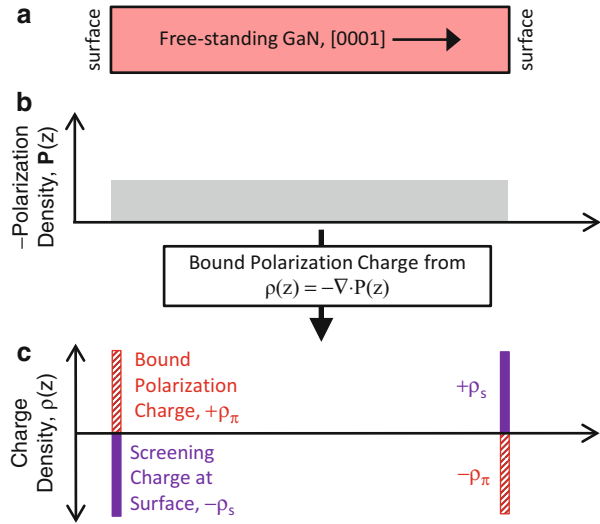
By forming a similar diagram for the case of AlGaN grown on GaN (Fig. 3.4), it becomes clear that a sheet of charge forms at the heterojunction interface. The magnitude of spontaneous polarization is different for AlGaN and GaN. Therefore, at the interface between the two, there is a step function in polarization density. This change in spontaneous polarization alone leads to a sheet of charge. Note that as in Fig. 3.3, there will also be some bound polarization charge at the surfaces of the material, but in Fig. 3.4, the GaN surface (or interface, if the GaN is grown heteroepitaxially) is intentionally neglected to focus on the charge near the GaN/AlGaN interface. This does not affect the present discussion because as in the previous case for freestanding GaN, the bound polarization charge at the surface is assumed to be screened. Additionally, the AlGaN is assumed to be strained to the GaN beneath it. This strain leads to added charge from piezoelectric polarization. In the specific case of metal-face AlN on GaN, the contributions from spontaneous and piezoelectric polarization both add net positive charge, but this might not be true for other heterostructure interfaces. That is, in some situations, the contributions from spontaneous and piezoelectric polarization create charge with opposite signs and therefore partially cancel out.

Because these materials are single crystalline semiconductors, charge density and location directly affect the charge neutrality equation, the resulting band edge diagrams, and the conductivity. That is, a net positive or negative bound charge results in a Coulombically attractive or repulsive potential for electrons or holes, respectively. Electrons or holes could diffuse in from a source (either intentionally supplied donors or acceptors or naturally occurring surface donors or acceptors). Thus, if the material in this example is Ga-face, the net bound polarization charge is positive and will result in a potential well for electrons at the AlGaN/GaN interface that will be compensated by electrons from ionized surface donor states (ρ_{sd}),
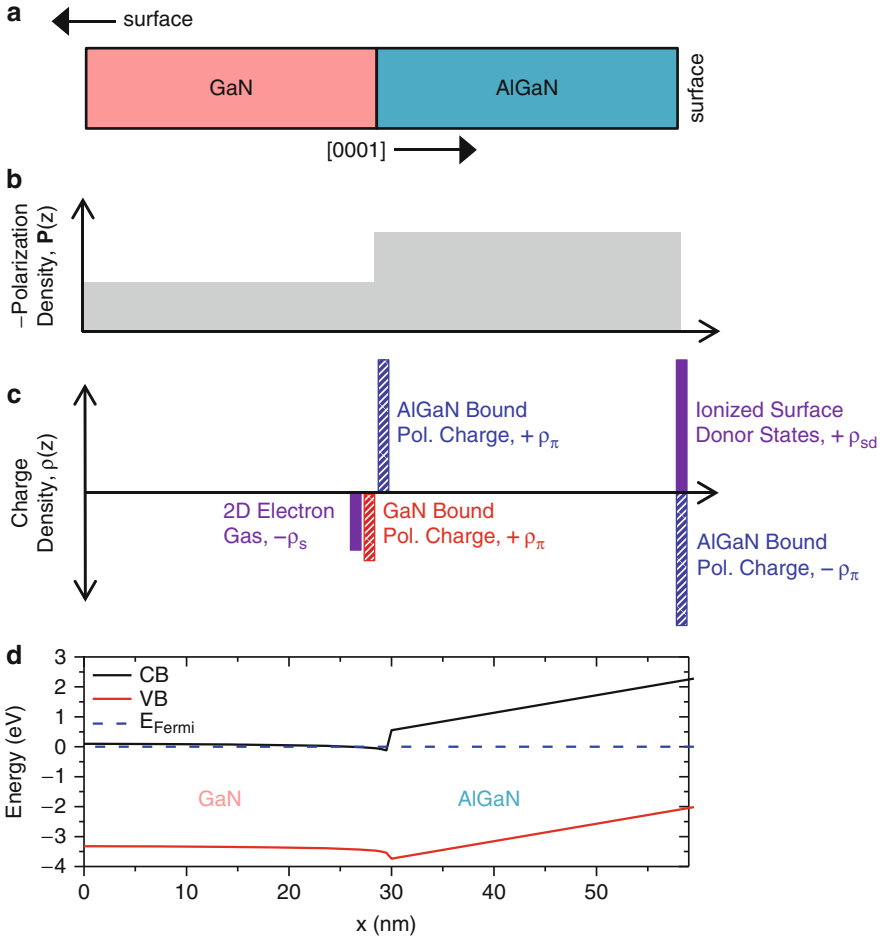
Fig. 3.4 (**a**) Schematic showing AlGaN grown on GaN (GaN surface on left is neglected for simplicity). (**b**) Change in polarization density across heterostructure interface. (**c**) Distribution of charge at the AlGaN/GaN interface and AlGaN surface. (**d**) A band diagram showing the formation of a 2D electron gas at the GaN/AlGaN

forming a two-dimensional electron gas (n_s). This situation results in local charge neutrality and the minimum energy state of the system. Polarization charge is often used in this way to form AlGaN/GaN high-electron-mobility transistors [13]. If the material is N-face, the bound charge is negative, and holes will compensate the charge at the interface, thus forming a two-dimensional hole gas.

If the heterostructure is not abrupt, the bound polarization charge at the interface will not be abrupt either. This is illustrated in Fig. 3.5. The stack of material depicted here starts with GaN, and then its composition is linearly graded by addition of Al along the [0001] direction. Because of discontinuities in the

Fig. 3.5 (**a**) Schematic showing material graded from GaN to AlN with surfaces neglected for simplicity. (**b**) Change in polarization density in the material. (**c**) Bound positive polarization charge and the 3D slab of electrons that screens the polarization charge. (**d**) The band diagram showing n-type graded AlGaN by polarization-induced doping
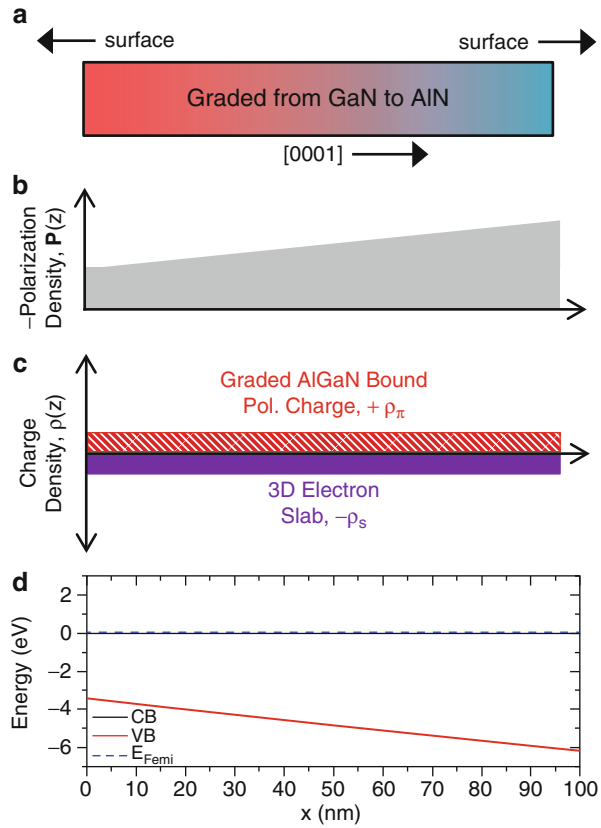
magnitude of spontaneous polarization between each unit cell, there is a small amount of net charge at the interface of each adjacent unit cell resulting in a three-dimensional region containing bound charge. Again, a positive bound charge would act as an attractive Coulombic potential (lowering of the band edges) leading to electronic conductivity throughout the graded region and a net free electron density (conduction band edge electrons), thus satisfying the charge neutrality equation. Such polarization-induced electron conductivity was first reported by Jena et al. [14]. In the case of a compositional gradient of increasing Al composition along [000–1], a bound negative charge would occur throughout the graded region leading to a repulsive potential for electrons (attractive to holes), thereby raising the band edges locally. However, because nitrides typically contain a substantial background donor density, polarization-induced hole conductivity is not expected to occur until the background donors are compensated. This has most likely lead to an inconsistency in the literature, with the first report of polarization-induced hole conductivity in graded AlGaN requiring compensating Mg acceptor doping [15], while a later report demonstrated p-type AlGaN through polarization-induced charge alone [16]. The technique described above, using

compositionally graded heterostructures to form three-dimension conducting slabs of material, is referred to as polarization-induced doping.

Benefits of Polarization-Induced Doping

There are several benefits to using polarization-induced doping instead of impurity doping. First, while impurities are usually used to increase electrical conductivity in semiconductors, this is accompanied by a reduction of charge carrier mobility. When a donor or acceptor is thermally ionized, electrons or holes occupy the bands, but a bound ion of opposite polarity is left behind. Charged impurity scattering from ionized donors and acceptors reduces the mobility of free carriers. Since the electrical conductivity of a material is given by

$$\sigma = q\left(n\mu_n + p\mu_p\right) \tag{3.3}$$

where σ is electrical conductivity, q is the charge of an electron, $n(p)$ is the electron (hole) concentration, and $\mu_n(\mu_p)$ is the electron (hole) mobility, a decrease in mobility will lead to smaller conductivity, if it were not more than offset by an increase in carrier concentration. One method to spatially separate the ionized donors and acceptors from the conducting region, referred to as modulation doping [17], utilizes electrons thermally ionized from donors doped within a wide bandgap material that diffuse into a lower bandgap region, thereby spatially separating the electron gas from the donor ions. Polarization-induced doping can also reduce ionized impurity scattering, by achieving conduction without the use of impurities at all. This means that charge concentration can be increased without a decrease in mobility, leading to overall higher conductivity. This was experimentally shown by Jena et al. [14]. In this work, Ga-face graded AlGaN layers were compared to impurity-doped GaN layers and found to be more highly conductive than the Si (donor)-doped GaN layers when graded from GaN to either $Al_{0.2}Ga_{0.8}N$ or $Al_{0.3}Ga_{0.7}N$ over 100 nm. The higher conductivity in the graded layers was due to an increase in both carrier concentrations and mobility. This serves as an important proof of concept that polarization-induced doping without the use of impurities can lead to higher material quality, highly conductive semiconductor layers in wide bandgap semiconductor ternary alloys.

As previously stated, a second benefit to using polarization-induced doping is that polarization charge can be used to activate impurity dopants. Recall that Fig. 3.1 shows the increase in dopant ionization energy as bandgap increases. In wide bandgap materials, the ionization energy is much larger than room temperature, thus making it difficult to ionize dopants and form highly conducting material. But if impurities are included in material with bound polarization charges ($-$ for acceptor doped or $+$ for donor doped), then dopants will be ionized by the
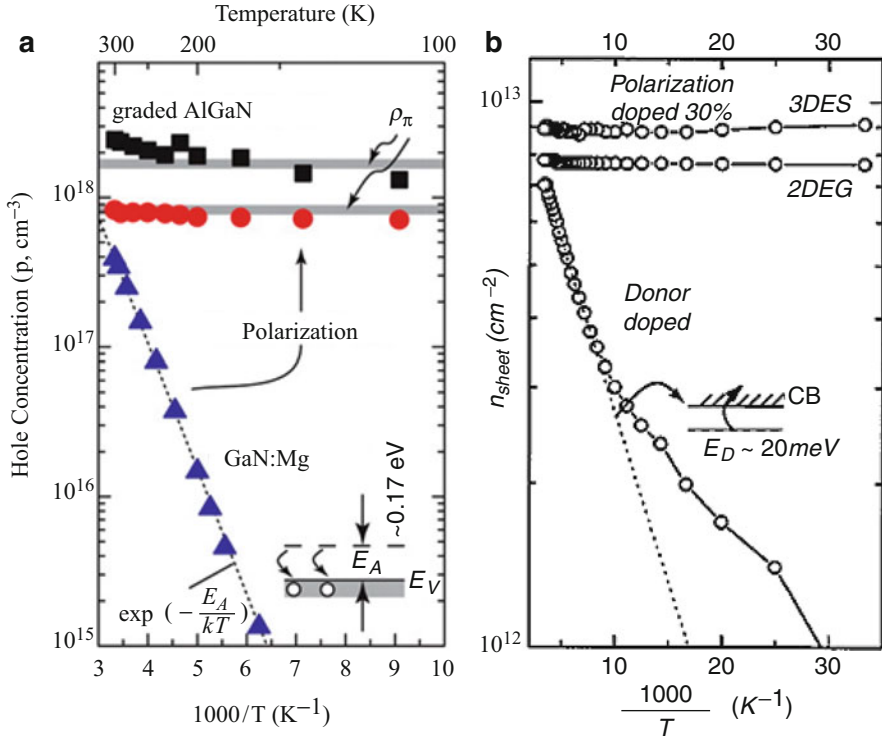
Fig. 3.6 Variable temperature Hall measurement of carrier concentration showing (**a**) p-type [15] and (**b**) n-type polarization-induced doping [14]

electric field induced by the Coulombic potential of the bound polarization charge. In essence the impurities are field ionized rather than thermally ionized. This was conclusively shown by the breakthrough work of Simon et al. [15]. By grading N-face material from GaN to low compositions of AlGaN and simultaneously doping with Mg (acceptors), they formed highly conducting p-type layers despite the very high ionization energy of Mg in AlGaN, which typically results in very low p-type conductivity. To prove that acceptors were not thermally ionized, variable temperature Hall measurements were used to measure hole concentrations in Mg-doped graded AlGaN and Mg-doped GaN. The results of this are shown in Fig. 3.6a, while similar measurements on polarization-induced n-type material from Jena et al. are also provided (Fig. 3.6b) for comparison. Hole concentration in the impurity-doped GaN (Fig. 3.6a, blue triangles) exponentially drops as temperatures is lowered following the expected Arrhenius dependence. But in the polarization-induced heterostructures (Fig. 3.6a, black squares and red circles), carrier concentration remains constant with respect to changes in temperature.

Given the trend shown in Fig. 3.1 and the fact that many wide bandgap semiconductors show strong polarization effects (e.g., GaN, AlN, ZnO), polarization-induced doping can play a key role in the formation of both n-type and p-type highly conductive wide bandgap materials.

Polarization-Engineered III-Nitride Devices

In this section a list of devices that utilize polarization in III-nitrides is presented. It should be noted that these devices do not strictly use polarization-induced doping in their design. Rather, they are polarization-engineered devices in a more general sense and are presented here to give the reader some conception of the wide range of possibilities that polarization opens up.

The most widely studied polarization-engineered device is the AlGaN/GaN high-electron-mobility transistor. These devices utilize the two-dimensional electron gas formed at an AlGaN/GaN interface to achieve extremely large carrier concentrations in the channel of the transistor. Many variations on the original AlGaN on GaN design [13] have been studied, such as replacing AlGaN with a layer of InAlN that is lattice matched to GaN [18] or using N-face instead of Ga-face material [19]. These devices are now commercially available, and in many ways, the success of these devices has pushed researchers into obtaining a better understanding of polarization in III-nitrides.

III-nitride tunnel junctions can greatly benefit from polarization effects. High-conductivity (quasi-ohmic) tunnel junctions are used to convert carrier type from electrons to holes, for example, in multijunction solar cells or in situations where one wishes to replace high-resistance p-type contacts with lower-resistance n-type contacts, which is often the case in III-nitrides. Tunnel junctions in the III-nitrides are more difficult to create than in most compound semiconductors in commercial use because large bandgaps and difficulty in doping generally lead to very wide depletion regions with large barrier heights that inhibit tunneling. To avoid this, recently a number of III-nitride tunnel junctions were reported that use polarization charge to greatly reduce the width of the depletion region and/or the energy barrier height for improved tunneling. The polarization charge can be induced using thin inserts of AlN [20, 21] or InGaN [22, 23].

In addition to these devices, there are a number of polarization-engineered devices proposed by Jena et al. including 'polarization-balanced' devices. A polarization-balanced device uses heterostructures of alloys that have the same magnitude of polarization but different bandgaps. For example, the alloys $Al_{0.65}In_{0.35}N$ and $In_{0.1}Ga_{0.9}N$ are polarization matched (assuming contributions from both spontaneous and piezoelectric polarization), so at an interface between the two, there will be no net charge. Jena et al. propose that these alloys can be used in the active region of a light-emitting diode, where $Al_{0.65}In_{0.35}N$ acts as the barriers for multiple $In_{0.1}Ga_{0.9}N$ quantum wells. These devices remove the band bending associated with III-nitride heterointerfaces that are not polarization

matched and could lead to improved LED performance due to improved overlap of the electron and hole envelope wave functions within each quantum well. Designs such as this show the great creativity a device engineer can use in designing a polarization-engineered device.

Additional devices specifically designed for use in III-nitride nanowires are discussed at the end of the following section.

Benefits of Nanowire Versus Planar Geometry

It should be clear that there are a great number of interesting possibilities offered through polarization engineering and polarization-induced doping. But with all of these possibilities come some difficulties, specifically with polarization-induced doping. In order to control conductivity with polarization-induced doping, it is necessary to linearly grade between two polarization mismatched materials. The amount of charge that results from the grading is given by Eq. 3.1. For the specific case of graded $Al_xGa_{1-x}N$, this can be simplified to

$$\rho_\pi(z) \sim 5 \times 10^{13} \times (x_2 - x_1)/d \qquad (3.4)$$

where x_1 and x_2 are the composition of Al at either end of the graded layer and d is the thickness of the graded layer (in centimeters) [15]. In order to maximize ρ_π, the layers should be graded over the largest possible range of compositions (i.e., maximize Δx) and over the smallest possible thickness (i.e., minimize d). However, in coherently strained epitaxial thin films (pseudomorphic), the range of compositions is limited by the lattice mismatch between the two polarization mismatched materials.

Polarization-induced doping in pseudomorphic graded AlGaN thin films has been shown by a number of publications [14–16, 24–27], but none have graded over more than 30 % of the compositions range (i.e., grading either from GaN to $Al_{0.3}Ga_{0.7}N$ or from AlN to $Al_{0.7}Ga_{0.3}N$). The range of compositions used in these experiments is limited by the amount of lattice mismatch between GaN and AlN. As the composition of the material is changed as the layer grows thicker, strain energy builds up until the layer eventually reaches a critical thickness. Above a critical thickness, the film strain relaxes through formation of defects in the material, usually substrate/film interface misfit dislocations connected to threading dislocations, but also by cracking [28]. The exact thickness at which the layer relaxes is determined by the compositions that it is graded between, with a larger range of compositions leading to a smaller critical thickness.

Figure 3.7 displays ρ_π in a graded AlGaN layer for different combinations of layer thickness and compositional range using Eq. 3.3 not including piezoelectric polarization. The dashed line in the plot shows the critical thickness for an abrupt interface of AlGaN on GaN, with values provided in Lee et al. [29]. The dotted line is the approximate critical thickness of an AlGaN layer graded to a given composition, assuming that the critical thickness in the graded layer is roughly twice the
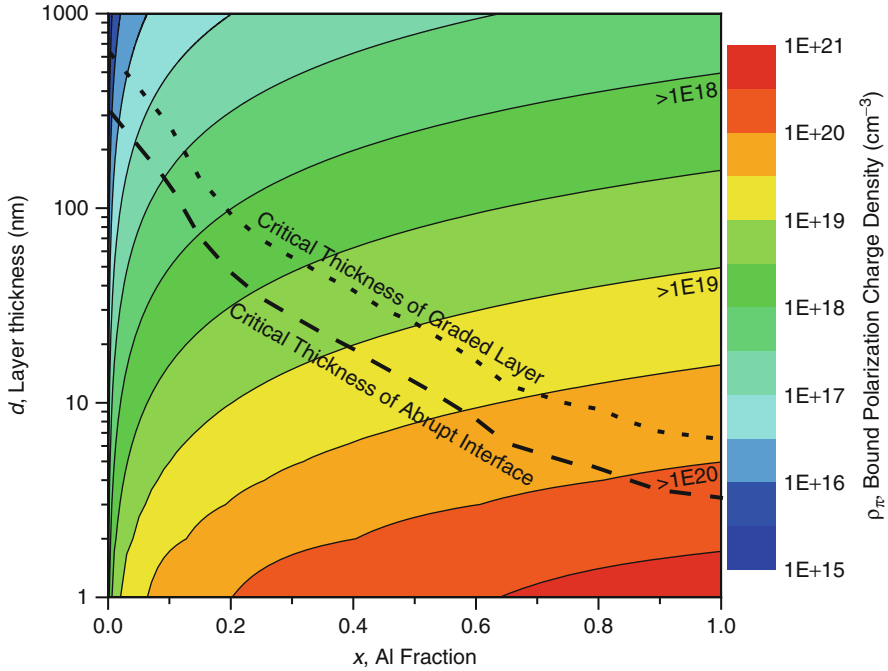
Fig. 3.7 Polarization charge due to spontaneous polarization as a function of layer thickness and Al fraction in a graded AlGaN layer. Critical thickness for abrupt interfaces is taken from Lee et al. [29]

critical thickness of a layer of the same composition with an abrupt interface. The dotted line should be taken as a very rough estimate of how critical thickness changes between abrupt and graded layers, and is only meant to show the correct trend. The only layers that are possible to form in planar material are those beneath the critical thickness line. Thus, there are structural limitations set on the kinds of polarization-doped layers that are possible to grow. Ideally, there would be a way to grade over any desired compositional range without worrying about reaching a critical thickness, so that the thickness of the layer and its electrical conductivity can be separately chosen.

Devices fabricated from nanowires instead of thin films are ideal for this purpose. Nanowires benefit from increased strain accommodation when compared to thin films. This means that heterostructures that cannot be formed without reaching a critical thickness in thin films are possible in nanowires. The enhanced strain accommodation is due to the free surface of the nanowire sidewalls, and the smaller the radius, the more strain accommodation can be expected [30–32]. The change in critical thickness with decreasing radius has been modeled, and it was found that at small enough radius, the critical thickness for strain relaxation diverges [32]. This makes nanowires particularly interesting for use in

polarization-engineered/polarization-doped devices. The following section describes two polarization-engineered devices specifically designed for use in III-nitride nanowires.

Polarization-Engineered Nanowire Devices

Possible applications for polarization-engineered devices were provided in section 'Polarization-Engineered III-Nitride Devices', but none of these devices were specific to nanowires. Two nanowire devices that make use of polarization are described below.

To our knowledge, we have published the only nanowire devices that utilize polarization-induced doping [33, 34]. The devices described in these works are polarization-induced nanowire light-emitting diodes (PINLEDs).

A schematic showing the design of PINLEDs and the associated band diagram is shown in Fig. 3.8a, b. The nanowires used in these devices are grown on n-Si(111) substrates. The bottom section of the nanowire is graded from GaN to AlN. As stated earlier, if the material polarity for the nanowire is Ga-face, this grading will result in n-type materials. The top section of the nanowire is graded from AlN back to GaN, which for Ga-face nanowires will provide p-type material. Here we see that just by simply linearly grading from GaN to AlN then back to GaN, a polarization-induced p-n junction has been formed. Each of these sections can optionally be doped with impurities (in which case the impurities are activated by the polarization) or dopant free (in which case mobile charge must come from the nanowires surface). In most of the devices formed so far, impurity doping has been included to achieve the highest carrier concentration possible in the device. In this way it is possible to form highly conducting AlGaN material, even with a high percentage of Al, by utilizing the polarization-induced activation, and not thermal activation, of dopants.

At the center of the nanowire, a thin section of lower bandgap material is inserted between the layers of AlN. This smaller bandgap material will form a quantum well that will aid in the recombination of electrons and holes injected into the center of the device. Because AlN has such a large bandgap (6.2 eV), it is possible to insert a wide range of alloys into the center of the nanowire and still have good confinement in the quantum well. To further insure this high level of confinement, a narrow section of intrinsic AlN is included on either side of the quantum well. Given the confinement in the active region, PINLEDs with different quantum wells should be able to emit nearly throughout the entire range of wavelengths obtainable in the AlGaN system (200 nm from AlN and 365 nm from GaN). To date PINLEDs have been fabricated that emit through a wide range in wavelengths, from 250 nm [33] to as high as 550 nm (using an InGaN quantum well). A selection of the emission wavelengths will be shown in section 'Characterization of Graded III-Nitride Nanowires'. Hopefully, with the highly conducting top and bottom layers of AlGaN and the ability to tune emission into the deep UV, PINLEDs could lead to higher-efficiency deep ultraviolet LEDs than what is possible with current technology.
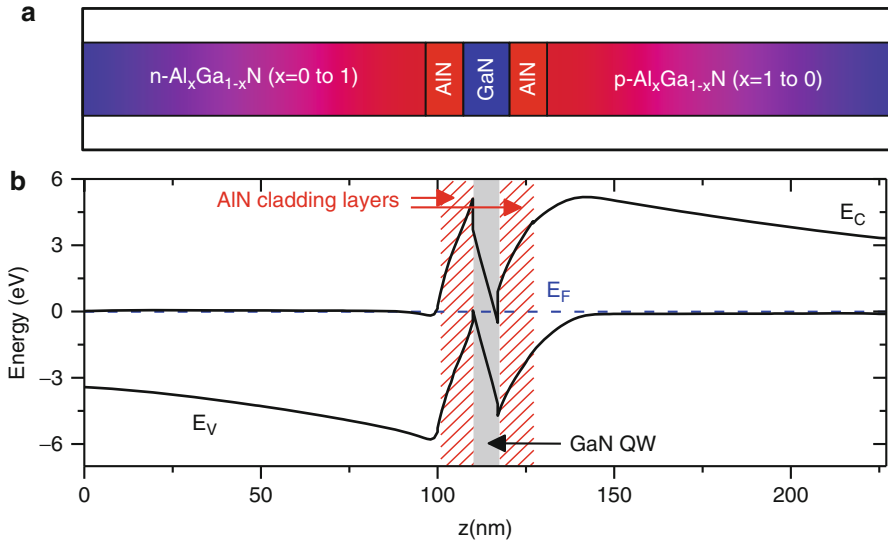
Fig. 3.8 (**a**) Schematic showing the change in composition along the length of a polarization-induced nanowire light-emitting diode (PINLED). (**b**) Energy band diagram of a PINLED

A second use of polarization engineering in nanowire devices is the use of graded InGaN nanowires in solar cells. Previous experimental [35, 36] and theoretical work [37] has focused on using InGaN in solar cells because it has a number of attractive characteristics: a bandgap range that spans the entire solar spectrum, high mobility [38], large saturation velocities, high absorption coefficient [39], and strong radiation resistance [40]. For all the previously stated reasons regarding strain accommodation, nanowire geometry allows for the formation of InGaN nanowire solar cells that do not contain strain-related defects. In addition to this, polarization engineering might help avoid some other difficulties faced in designing InGaN-based solar cells. For example, it is difficult to make contact to p-InGaN due to pinning of the Fermi level above the conduction band minimum at InGaN surfaces [41]; thus, p-GaN is used instead as a transparent contact layer. At an abrupt p-GaN/InGaN interface, strain in the structure will lead to reduced carrier collection in the solar cell, hence lowering efficiency. To avoid this, Sarwar and Myers have proposed the use of graded InGaN interfaces in place of abrupt GaN/InGaN interfaces [42]. Modeling has shown that by grading at the interface, the strain in the heterostructure is reduced by a factor of 6. The reduction in strain could lead to an increase in solar cell efficiency from <1 % to as high as 21 %. The key findings from this study are shown in Fig. 3.9.

Given the advantageous aspects of using graded nanowires in polarization-engineered and polarization-doped devices, the following section focuses on the growth of catalyst-free III-nitride nanowires by PAMBE.
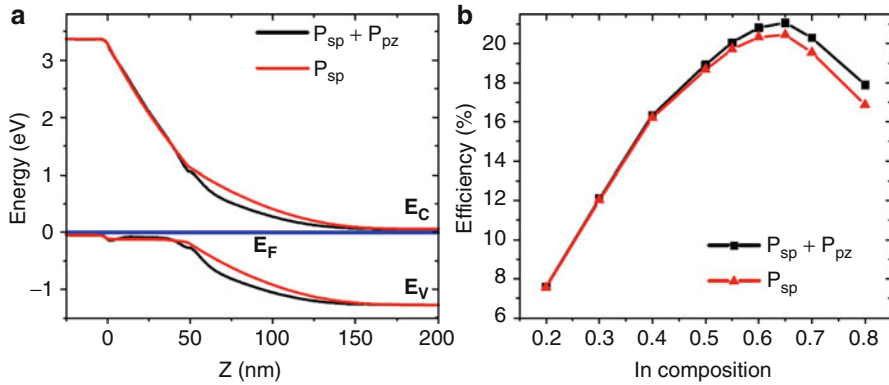
Fig. 3.9 Modeled (**a**) energy band diagram and (**b**) efficiency for an InGaN-based solar cell with a graded InGaN interface assuming contributions from only spontaneous polarization or both piezoelectric and spontaneous polarization [42]

Overview of Catalyst-Free III-Nitride Nanowire Growth by PAMBE

Since first grown by plasma-assisted molecular beam epitaxy (PAMBE) in 1997, self-assembled, catalyst-free, III-nitride nanowires have garnered a great deal of attention. This attention is well deserved since these nanowires have a number of attractive characteristics for use in optoelectronic devices. They grow on a variety of substrates, including Si(111) [43], Si(001) [44], and Al_2O_3 [45]. Photoluminescence and transmission electron microscopy (TEM) demonstrate that each nanowire grows fully relaxed and free of extended defects [46, 47]. This is an especially important aspect given that it is currently difficult to grow planar GaN without extended defects. Strain accommodation due to the nanowire free surface allows for the incorporation of lattice-mismatched materials into a single nanowire heterostructure that cannot be incorporated into a single planar heterostructure [30, 32]. GaN nanowires have also been formed using a vapor–liquid–solid growth mechanism [48–50] and on patterned substrates [51–53]. The majority of work in graded III-nitride nanowires for polarization-doping purposes has been completed with catalyst-free nanowires grown by PAMBE, so the catalyst-free method will be the primary focus of this text (Fig. 3.10).

General Growth Conditions and Growth Maps

Catalyst-free GaN nanowires grown by PAMBE are formed spontaneously. To achieve nanowire growth (as opposed to planar GaN growth), deposition is initiated on a bare substrate (usually Si(111)), and if the growth conditions in the PAMBE chamber are correct, nanowires will grow vertically with their c-axis perpendicular to the substrate's surface. Generally speaking, the conditions needed for nanowire growth are relatively high temperature (between 720 °C and 800 °C) and a ratio of
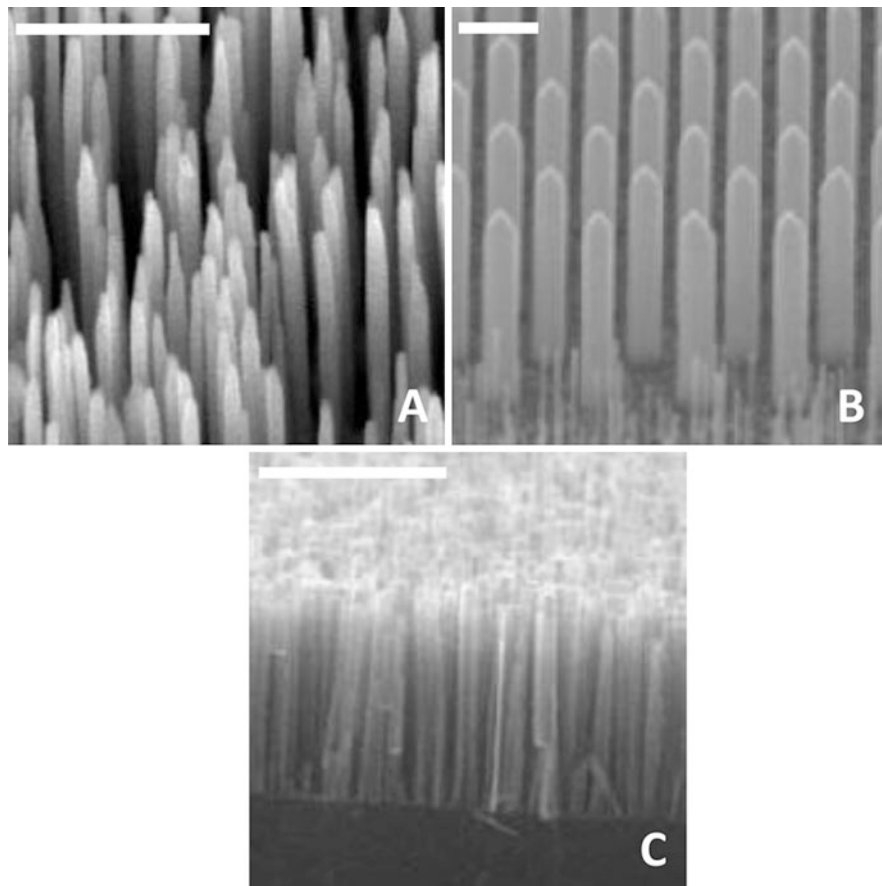
Fig. 3.10 GaN nanowires grown by PAMBE using (**a**) catalyst-assisted [50], (**b**) patterned-substrate [52], and (**c**) catalyst-free growth [54]. All scale bars are 500 nm

Ga flux to active N flux of <1 impinging on the substrate. These conditions are generally unfavorable for high-quality planar GaN epilayers [55]. While it is possible for nanowires to form in a wide range of growth conditions, tailoring nanowire characteristics (e.g., areal density, diameter) to the specific application requires close control of growth conditions. It is therefore important to relate these growth conditions to nanowire parameters, referred to as growth maps or growth phase diagrams, described below.

Nanowires have been demonstrated to require a limited substrate temperature range and Ga/N flux ratio. Fernandez-Garrido et al. [54] mapped out a growth phase diagram for nanowire growth on bare Si(111) substrates. This growth phase diagram is shown in Fig. 3.11a. They found that at too low of a temperature, nanowires will not form, possibly because Ga adatom mobility is too low in this region to nucleate nanowires. At too high of a temperature, there is no growth at all

Fig. 3.11 Growth phase diagrams for GaN nanowires grown on Si(111) by plasma-assisted molecular beam epitaxy published in (**a**) Fernandez-Garrido et al. [54] and (**b**) Carnevale et al. [56]
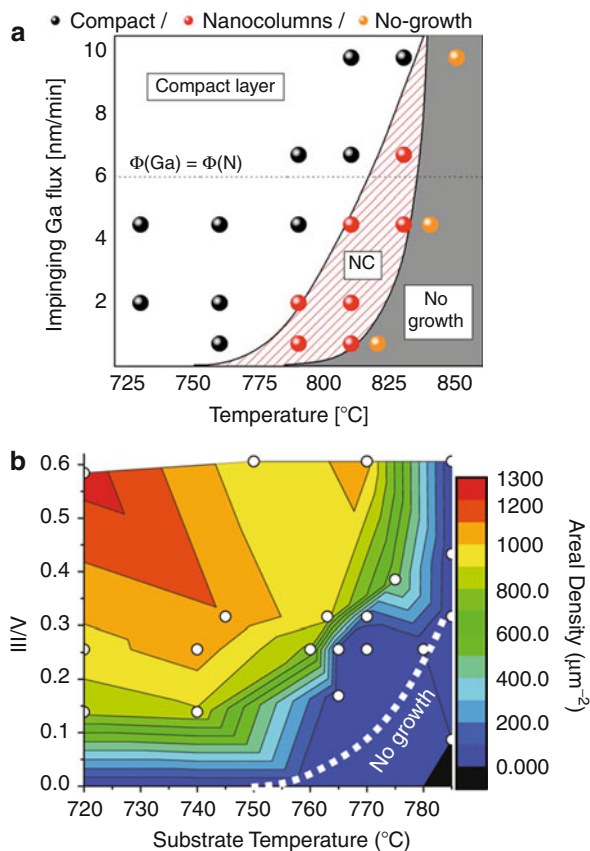
since the desorption of Ga adatoms and thermal decomposition of GaN will occur faster than the formation of GaN. III/V ratio usually needs to be below 1 (i.e., N-rich conditions), but at high enough temperatures, it is possible to still achieve nanowire growth even with a III/V greater than 1. This is possible because enough Ga desorbs from the surface so that the actual III/V conditions on the sample will be below stoichiometry even if the nominal III/V may be above stoichiometry.

We have published similar growth maps [56]. In this work, growth maps were established that not only show the area in which nanowires grow but also relate nanowire characteristics to growth conditions. The growth map relating nanowire density to growth conditions is shown in Fig. 3.11b. When comparing the two different maps, one notices that NW growth was achieved at much colder temperatures by Carnevale et al. The samples in each study were grown for different deposition times, which could affect the results. Carnevale et al. used deposition times of 30 min per sample, while Fernandez-Garrido et al. grew until NW density reached saturation. It is possible that some samples grown at lower temperatures will appear to grow as nanowires initially, but after a long deposition time will coalesce to some degree. After coalescence the nanowires might instead resemble

a semi-closed film rather than a group of individual nanowires. Regardless of the differences between these two results, it can safely be said that a general nanowire growth window has been outlined.

Nanowire Nucleation and Growth

Having explained the general growth conditions of GaN nanowires, at this point, one might naturally ask how these catalyst-free nanowires form in the first place. This question should be broken down into two smaller questions. First, what occurs during nanowire nucleation to give the structures their shape? Second, once the correct shape is achieved, why do nanowires prefer to grow vertically as deposition continues? Nucleation will be discussed first.

The most detailed accounts of nanowire nucleation have been provided in two separate papers by Consonni et al. [57, 58]. They used cross-section TEM images and reflection high-energy electron diffraction (RHEED) to study the initial stages of nucleation on Si(111) substrates with and without an AlN buffer layer.

When growing on AlN buffers, they found that nucleation occurs in distinct stages. First, small GaN clusters form on the substrate and grow into islands with spherical caps on top. As the islands continue growing, the shape of the islands changes from spherical caps to truncated pyramids and eventually into full pyramids. The facets of the pyramids continue to get steeper during deposition. Eventually, strain relaxation in the pyramids causes them to change shape from pyramids with steep facets into very short nanowires. The nanowires grow rapidly from this point on with no further change in shape. TEM images show that before the transition, pyramids have small misfit dislocations located beneath one side of the pyramid. After the transition, the misfit dislocation is seen directly underneath the center of the nanowire [57].

Consonni et al. performed a similar study for growth on Si(111) wafer with a SiN_x layer present on its surface [58]. SiN_x layers are commonly reported for GaN growth on bare Si substrates because active nitrogen nitridates the surface before nanowires start to form. In this study, they found that growth once again started with islands of GaN in the shape of spherical caps. After the caps reach a critical radius (5 nm for their specific growth conditions), the islands undergo a shape transformation to nanowires. In this paper, no intermediate pyramid shapes were observed. The authors point to two main driving forces for the transition from a spherical cap to the nanowires geometry. First, strain energy is reduced in the nanowire geometry compared to the cap. Second, there is a reduction in surface energy in the nanowire geometry due to the presence of low-energy c-plane (i.e., the nanowire tops) and m-plane (i.e., the sidewalls) surfaces, as compared to the high-index, and therefore high-energy planes on the surface of the spherical cap. Together, these studies go a long way towards understanding the nucleation of catalyst-free GaN nanowires.

Once the nanowire shape is obtained, why do the nanowires continue to grow vertically? The vertical growth of nanowires has been studied much more

Fig. 3.12 Vertical growth rate as a function of Ga cell temperature [60]
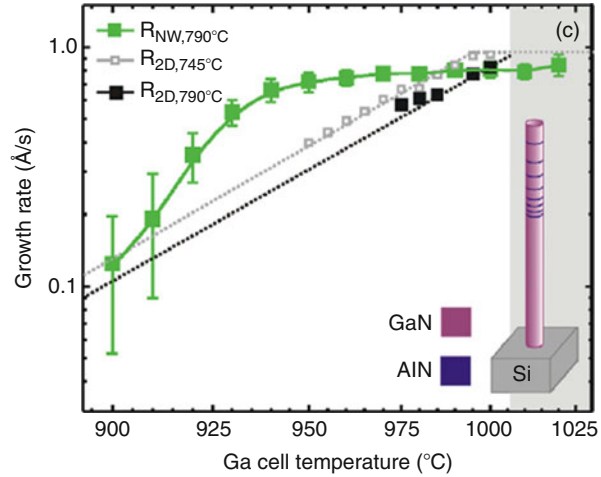
extensively than nucleation, so it is possible to pull together results from a number of different researchers to determine the vertical growth mechanism. In the first paper reporting the growth of GaN nanowires by PAMBE, Yoshizawa et al. [45] found that vertical growth rate increases with larger amounts of active N, which was interpreted as evidence that vertical growth must be Ga-rich. In other words, there are more Ga adatoms than N adatoms at nanowire tops. This relationship between active nitrogen and vertical growth was later reinforced by the work of Bertness et al. [59], who also found that vertical growth rate increases with more active nitrogen. Songmuang et al. [60] studied the effects of increased Ga flux on vertical growth rate and found that for a given small Ga flux, vertical growth rate was larger than the Ga-limited two-dimensional growth rate one would expect for the same flux (Fig. 3.12). Furthermore, as Ga flux increases, so does vertical growth rate, until it saturates at the N-limited growth rate. This saturation occurs at a flux that would normally lead to Ga-limited growth in a planar sample.

Taken together, these findings illustrate that the conditions for vertical growth (i.e., the amount of Ga at NW tops) are Ga-rich, even though the overall conditions of growth are N-rich. The commonly accepted explanation for this is that Ga adatoms diffuse up sidewalls to nanowire tops, while N adatoms do not (if they did, vertical growth would still be Ga limited). This conclusion was expounded by Debnath et al. [61] who showed that the length of GaN nanowires is inversely proportional to diameter plus a constant. This was previously shown in other III-V nanowires in which the diffusion of adatoms up sidewalls contributes to vertical growth [41, 42, 62]. The expression relating length and diameter is

$$l = C_1(1 + C_2/d) \tag{3.5}$$

where C_1 and C_2 are constants related to an individual sample. Notably, C_2 corresponds to twice the diffusion length of Ga adatoms on nanowire sidewalls.

This expression fits nanowire data very well, thus reinforcing the idea that vertical growth occurs due to the diffusion of Ga adatoms up nanowire sidewalls. Furthermore, it was shown that by increasing growth temperature and therefore Ga adatom mobility, more adatoms reach the tops of nanowires, thus increasing the ratio of vertical to lateral growth rate [56]. The exact reason that Ga adatoms move up the nanowire sidewalls and incorporate onto the tops is, to date, somewhat unclear. Ristic et al. [63] reasonably hypothesized that the greater number of dangling bonds on the c-plane tops will lead to a large difference in diffusion lengths between the tops and m-plane sidewalls of nanowires. This means the tops will act as a trap for adatoms, forcing the nanowire to preferentially grow vertically.

It is important to note that while nanowires do preferentially grow vertically, that does not result in zero lateral growth. Several groups have found that the ratio of vertical to lateral growth for GaN is in the range of 30:1 [64–66]. Further work has shown that the ratio of vertical to lateral growth rate for AlN deposition on top of nanowires is much lower than it is for GaN, approximately 4:1 [65, 66]. For AlN growth, the increased lateral rate is attributed to lower Al adatom mobilities. The explanation is that the adatoms will want to incorporate onto tops, but will incorporate onto sidewalls if the diffusion length is not large enough to reach the tops. This idea was used by Carnevale et al. [56] to grow coaxial AlN/GaN superlattices at extremely low growth temperatures to force GaN to incorporate laterally at the same rate as AlN. The difference in lateral incorporation rates between AlN and GaN will play an important role in the formation of graded nanowire heterostructures, which will be discussed in greater detail later.

Growth of Compositionally Graded AlGaN Nanowires

The two preceding sections have covered the basics of growing catalyst-free nanowires by PAMBE. Until now, this discussion has focused on the formation of homogenous nanowires, with only a brief mention of nanowire heterostructures. This section focuses on the formation of graded nanowire heterostructures, specifically graded AlGaN structures.

As was stated earlier, the nanowire deposition occurs under Ga-limited PAMBE conditions. This means that the growth rate is limited by the amount of Ga incorporating into the nanowires. Therefore, when forming an alloy, composition will simply be determined by the growth rate of one of the components of the alloy divided by the total growth rate. For example, suppose that during nanowire growth, the Al and Ga sources were opened at the same time, forming $Al_xGa_{1-x}N$. In this case, the x is determined by the following formula:

$$x = R_{AlN}/(R_{AlN} + R_{GaN}) \tag{3.6}$$

where R_{AlN} and R_{GaN} are the growth rates at a given flux for AlN and GaN, respectively. Therefore, to control the alloy composition, it is necessary to

control the flux of Ga and Al impinging on the sample, the same method used for growth of most III-V compound semiconductor MBE typically formed under V-rich conditions.

A few minor complicating factors should also be mentioned here. First, if the combined growth rate of AlN and GaN exceeds the N-limited growth rate, then Eq. 3.6 will no longer hold. That is, Eq. 3.6 assumes that the growth rate is Ga or metal limited. Above the N-limited growth rate, the composition will be determined by the competition of Ga and Al adatoms for active N. Therefore, one must choose impinging Ga and Al fluxes carefully when forming graded alloys. Second, the ratio of vertical growth for GaN and AlN is different. Therefore, to determine the composition of the material formed as a shell during deposition, the lateral growth rates should be used in Eq. 3.6. Because AlN forms at a higher rate laterally than does GaN, a shell of high composition $Al_xGa_{1-x}N$ will form during growth. In fact, it has been shown that the GaN lateral growth rate can be effectively reduced to zero through manipulation of growth conditions [56], so it is possible to form a shell of pure AlN during deposition, even though the center of the nanowires will contain the desired graded heterostructure vertically.

These complications aside, controlling the composition in a graded nanowire should amount to linearly changing the flux impinging on the substrate as deposition occurs. There are two ways of doing this, which are shown in Fig. 3.13. First, it is possible to change the amount of material leaving the Ga and Al sources in the PAMBE system. In almost all situations, effusion cells (or Knudsen cells) are used to provide a flux of Ga or Al in an MBE chamber. The flux of material leaving the cell is exponentially related to the temperature of the material in the cell. Therefore, to linearly change a given flux, the cell temperature must be logarithmically ramped as a function of time. This technique was previously employed to form graded AlGaN nanowires, but it has some drawbacks. To grade composition, the flux of one component must be increased while the other is decreased. This could leave one of the cells at the wrong temperature for the next section of the heterostructure. Also, one wishes to grade over increasingly shorter lengths; this would mean cooling and heating the cells at progressively higher rates. Heating a cell at an exceptionally high rate might damage the cell, and cooling the cell at an exceptionally high rate might not be feasible (once the cell is no longer receiving power, it will cool at its own rate). For these reasons, an alternative approach is needed.

The second way to control the composition is to pulse shutters that block the opening of the effusion cell and leave the cell temperature constant. The shutters provide control over which material is grown during any given stage of deposition. By pulsing the Al and Ga shutters, it is possible to control the composition of the resulting AlGaN. To make sure that composition is smoothly changed, the shutters are pulsed on the time scale needed to grow one monolayer of material (roughly 5 s). Thus, in each pulse, a partial monolayer of either GaN or AlN is formed, which overall will form AlGaN. Then by changing the duty cycle of each shutter over time, composition is linearly varied over time. By using shutter pulsing, the cell temperature never changes during growth, avoiding the problems described for the previous method of controlling composition.
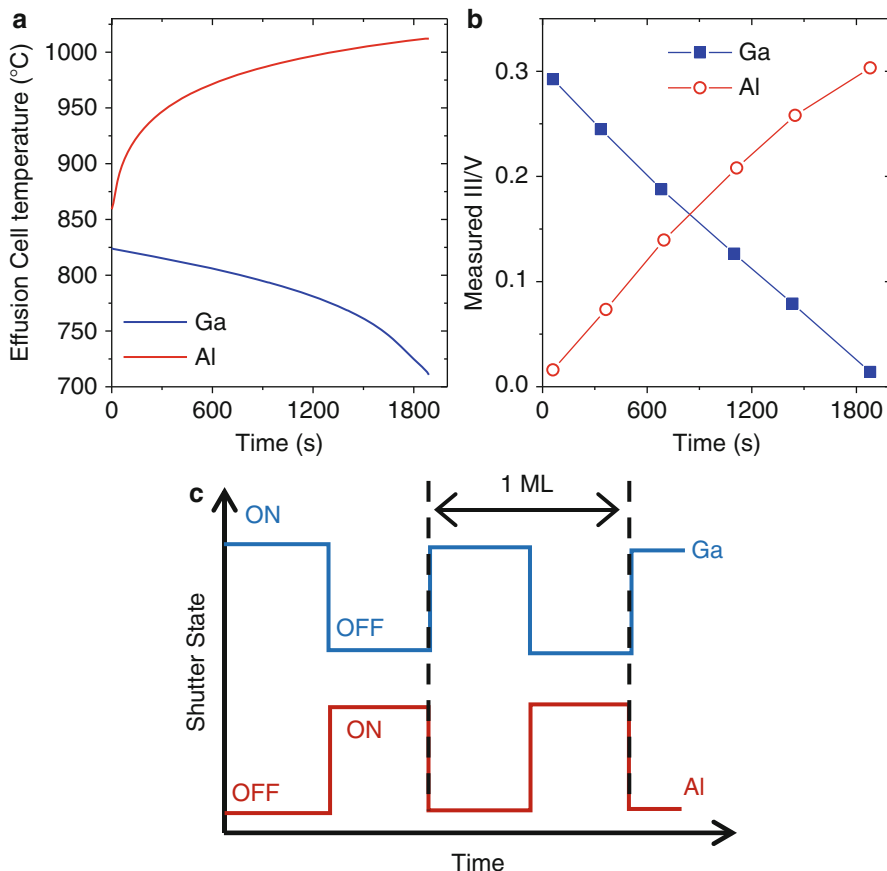
Fig. 3.13 (**a**) Effusion cell temperature versus time used to grow a graded AlGaN nanowire. (**b**) Linear increase and decrease in fluxes due to the change in temperatures from (**a**). (**c**) The duty cycle of Ga and Al shutters to control composition

Growth of Compositionally Graded InGaN Nanowires

The growth of graded InGaN structures can be carried out in much the same way as AlGaN nanowires, with a few modifications. First, InN is usually grown at much lower temperatures (~400 °C) than GaN. Therefore, substrate temperature will play a much larger role in the growth of graded InGaN nanowires than in GaN nanowires. Furthermore, there is a range of temperatures in which InN will decompose but In will not desorb from the surface. This is not the case for GaN, because at temperatures in which GaN decomposes, Ga also desorbs from the surface. Following from this, if the substrate temperature is not controlled appropriately, decomposing InGaN could lead to a buildup of excess In on the sample. This can potentially alter the control of the composition of the alloy.

A second difference involves the strain in graded InGaN structures. Recall that nanowire structures are preferred over planar structures because of enhanced strain accommodation in the former. This has allowed researchers to form many AlGaN nanowire heterostructures that cannot be formed in a planar structure. However, the lattice mismatch between GaN and AlN ($\sim$2 %) is much smaller than the lattice mismatch between GaN and InN ($\sim$11 %). The larger lattice mismatch in the latter has led to cracks in graded InGaN nanowires [67]. These nanowires were graded from InN to GaN. Due to the larger InN lattice parameter, grading to GaN causes a large amount of tensile strain in the nanowires and cracks form in the nanowires. These cracks were visible by scanning electron microscopy. This cracking can be avoided by grading from GaN to InN, thus replacing tensile strain with compressive strain. Even still, the main point to take away from this work is that even though strain accommodation in nanowires allows for the formation of structures that cannot be formed in thin films, there is a limit to how much strain can be accommodated in a graded nanowire. Future experimental work should certainly focus on how nanowire parameters like radius and length either enhance or diminish strain accommodation in graded nanowires. For the time being, the general assumption can be made that graded AlGaN nanowires should not result in cracked nanowires, while graded InGaN nanowires can certainly lead to cracking over large composition ranges.

Characterization of Graded III-Nitride Nanowires

Having discussed the specific growth of graded nanowires, we can now move to the characterization of these nanowires. This characterization comes in three forms, namely, electron microscopy, electronic measurements, and optical spectroscopy.

Scanning Transmission Electron Microscopy

Scanning transmission electron microscopy is an invaluable tool for the characterization of graded nanowires. In traditional thin film devices, a number of characterization techniques for probing material structure are available that are not available for nanowires. For example, x-ray diffraction is commonly used to determine the thickness and composition of different material layers in a heterostructure with high accuracy measurement of lattice constants through diffraction peaks. Unfortunately, this technique is not useful in characterizing the structure of most nanowire heterostructures since even though individual nanowires are single crystalline, an ensemble of nanowires on the same substrate exhibits random tilting, which broadens diffraction peaks beyond use. To fill this void, scanning transmission electron microscopy is used. Through STEM a wide range of characterization is possible, including the thickness and chemical composition of graded layers. Though there are a wide array of measurements that can be carried out with STEM, here we focus only on the ones that are most useful for characterizing graded nanowires.

Fig. 3.14 (**a**) STEM image in HAADF mode of a single PINLED [33]. (**b**) Image intensity as a function of length taken from (**a**). (**c**) EDXS data from an individual PINLED [33]. (**d**) EDXS data from a graded InGaN nanowire [67]
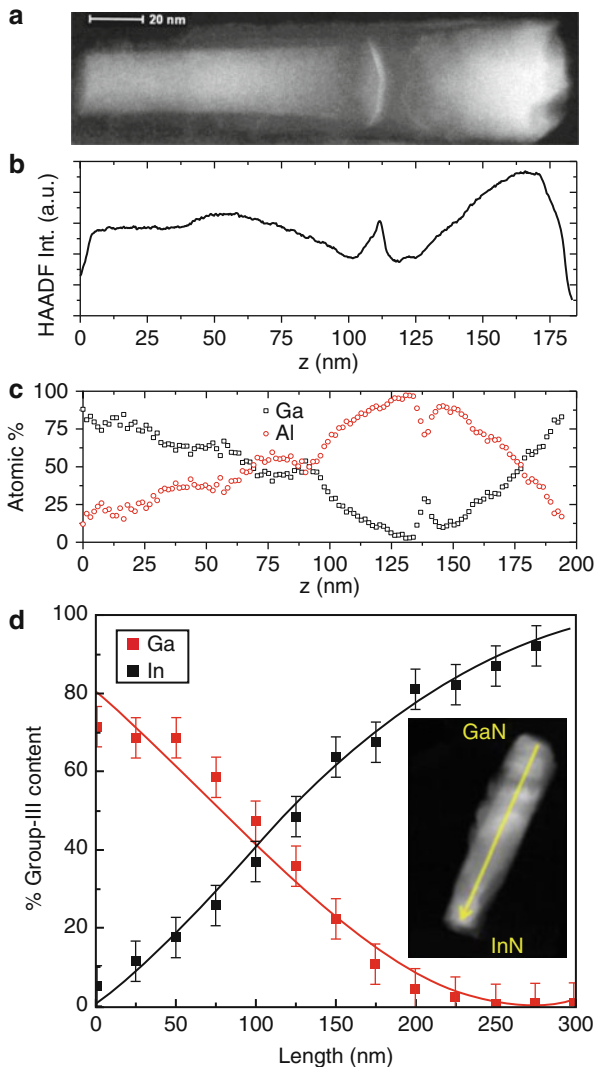
A sample STEM image taken in high-angle annular dark field (HAADF) mode is shown in Fig. 3.14. HAADF images include Z-contrast, with heavy elements showing up brighter and lighter elements showing up darker. This is useful in a number of ways. First, by plotting the intensity in the image as a function of length, it is possible to determine the general trend in chemical composition along the length of a single nanowire. Such a plot is shown in Fig. 3.14b. The intensity profile clearly shows the length of the first graded section, the quantum well at the center of the nanowire, and then the length of the top graded section. Through analyzing

many such nanowire images, it is possible to determine how closely the actual structure is in agreement with the target structure. This information can then be used in further growths to gain better agreement with the target structure. The HAADF image also reveals that there is a shell of high %Al AlGaN that covers the sidewalls of the nanowires. This is because AlN forms laterally at a higher rate than GaN under the conditions these nanowires were formed in. This shell also leads to a tapering in the more Ga-rich portions of the nanowire. This again is due to the presence of the shell. The shell forms during growth, and initially it is thin. When the nanowire grows vertically, newly deposited material will incorporate onto top of the shell, as well as the core resulting in the Ga-rich section of the nanowire being thicker. As the shell gets thicker during deposition, so then does the core Ga-rich section. Thus the tapered shape shown in Fig. 3.14 is achieved. None of these details about nanowire formation would be possible without electron microscopy.

In addition to the Z-contrast achieved through HAADF imaging, it is also possible to use energy dispersive x-ray spectroscopy (EDXS) to measure the chemical composition in the nanowires. Plots of chemical composition as a function of nanowire length in both graded AlGaN and InGaN nanowires are shown in Fig. 3.14c, d. It is clear in both of these cases that the chemical composition agrees with the HAADF intensity plot shown in Fig. 3.14b. However, there are some obvious difficulties with such measurements. From a device perspective, knowing the chemical composition through the center of the nanowire is most important. Unfortunately, the AlN shell described earlier will contribute to the measured chemical composition as the STEM samples through the entire depth of the nanowire. And since the thickness of the shell changes as a function of nanowire length, the contribution the shell makes to the measured composition is different at different points along the nanowire. This makes chemical composition determined by EDXS somewhat difficult to interpret, but these complications can be taken into account and chemical composition can be found. In the future, EDXS will likely be used as a tool to determine the composition of quantum wells at the center of graded nanowires used as LEDs. This will allow connections to be made between the light emitted from the nanowire and the composition of the material in the quantum well.

Finally, STEM imaging in annular bright field (ABF) mode has proven to be a useful technique for characterizing the material polarity of nanowires. In HAADF imaging it is possible to image the atomic columns containing Ga or Al, but not N. These images therefore cannot be used to determine the stacking sequence of Ga and N in the structure. Luckily, researchers recently showed that it is possible to image both Ga and N containing atomic columns using ABF mode [68]. Images of a GaN/AlN heterostructure taken in ABF mode are displayed in Fig. 3.15. This technique has been used to determine material polarity in a variety of materials, including GaAs, ZnO, and GaN. As stated in section 'Polarization in III-Nitride Materials', material polarity determines the sign of polarization-induced charge, and it is therefore extremely important to understand the material polarity in graded nanowire heterostructures.

Fig. 3.15 STEM images (**a**) HAADF and (**b, c**) ABF mode from de la Mata et al. used to image nanowire material polarity
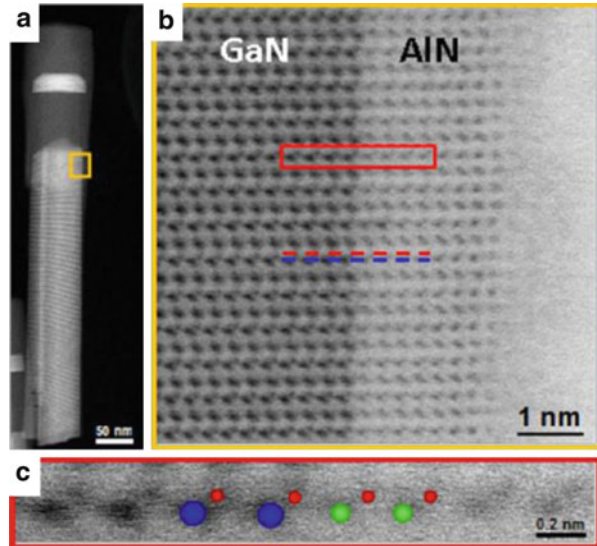
Electrical Characterization of Polarization-Induced Nanowire Light-Emitting Diodes

The electrical characterization of polarization-doped nanowire devices will be handled in this section. While graded AlGaN PINLEDs have been extensively studied, little work has been published on the use of graded InGaN nanowires in electrical devices. Therefore, this section, and the next, will focus solely on the characterization of graded AlGaN nanowire PINLEDs.

Once the nanowires are grown as described in the preceding section, they are processed in a very simple way to form LEDs. Top contacts are defined using standard photolithography techniques and electron beam evaporation of metals. Because the tops of the nanowires are assumed to be p-type, a thin Ni/Au contact is used to contact the nanowire tops. The Si substrate is used to make contact to the base of the nanowires. To do this, nanowires are removed from the surface of the Si with a diamond scribe, and a small piece of In is annealed onto the Si surface. Certainly more sophisticate methods have been used to form nanowire-based LEDs (including planarizing the nanowires [44] and coalescing the nanowire tops [69]), but this simple device design works surprisingly well in the early, proof-of-concept devices that have been reported.

The current voltage characteristics of a PINLED with a GaN quantum well are shown in Fig. 3.16a, b. A number of details should be pointed out. First, the device shows clear rectification, which provides strong evidence that the nanowire heterostructure indeed does form a p-n junction. Second, the device turns on under forward bias at ~4 V. Because the nanowire is made completely of AlGaN, one might have expected a higher turn on voltage. This is because AlGaN is usually a very resistive material, causing a large series resistance in the
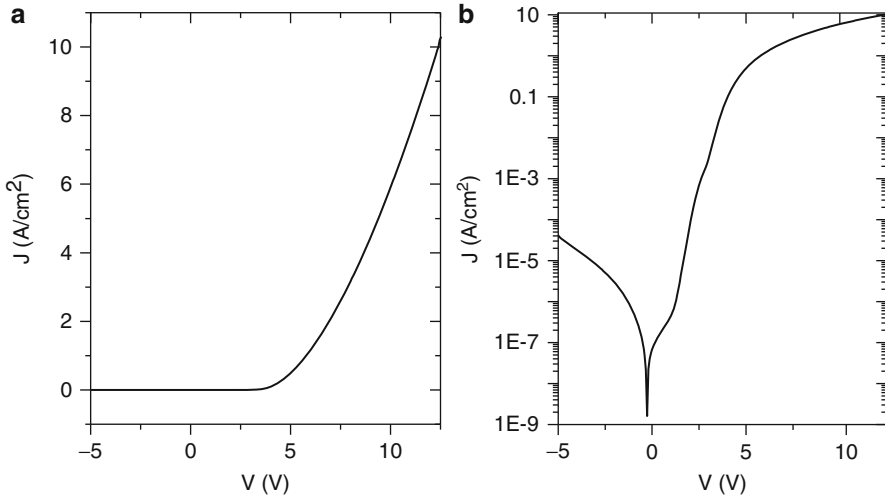
Fig. 3.16 Sample current density versus voltage characteristics for a PINLED device in (**a**) linear and (**b**) log scale [33]

device. This series resistance will push out the bias needed to turn on the device. Therefore, the fact that the device turns on at this relatively low voltage is an indication that the AlGaN material in the nanowires is highly conductive. Highly conductive AlGaN (especially p-AlGaN) is difficult to achieve through impurity doping alone; thus, the polarization charge in the graded sections must be increasing electrical conductivity in the nanowires.

To further show this, electrical measurements of PINLEDs with impurity doping were taken down to cryogenic temperatures. Recall that in previous experiments, variable temperature Hall measurements showed that polarization-induced charge does not freeze out at low temperatures (Fig. 3.6). This same phenomenon is seen in PINLEDs. Figure 3.17 shows the results of I-Vs measured as low as 15 K. The contour plot in Fig. 3.17a shows the measured current in the device as a function of voltage and temperature. In an impurity-doped device, one would expect an order of magnitude drop in conductivity as temperature is lowered due to carrier freeze out. There is some reduction in temperature seen in the PINLEDs, but it is less than one order of magnitude. This reduction is most likely due to thermally assisted tunneling in the nanowires [33]. To show this in another way, the current density in the device at a given voltage is plotted as function of temperature (Fig. 3.17b). Alongside this current density data are the predicted carrier concentrations for Si and Mg dopants in AlN and GaN as a function of temperature, given their respective ionization energies. The current density in the device at 10 V shows little change as a function of temperature compared to the many orders of magnitude change in carrier concentration one would expect in the dopants. This electrical characterization is important for showing that the dopants in these structures are indeed ionized using polarization.

Fig. 3.17 (**a**) Current density as a function of voltage and temperature in a PINLED device. (**b**) The measured current density in a PINLED at 10 V at variable temperatures [34]
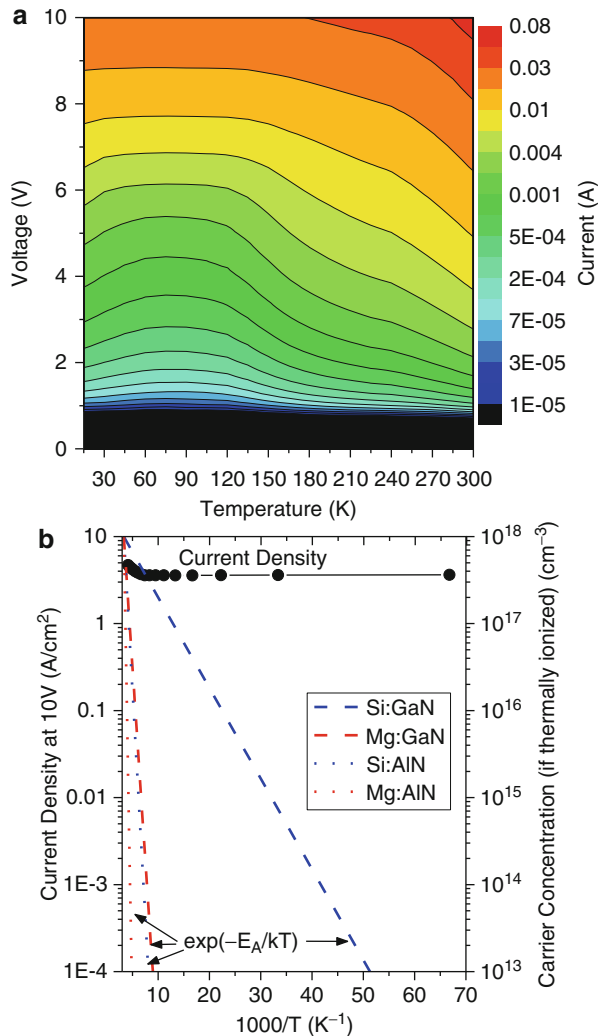
Finally, as stated above, the inclusion of dopants in this structure is optional. A comparison of the same devices with and without dopants is shown in Fig. 3.18. Three samples are grown with the same nanowire heterostructure, with the only difference being what dopants were included in the structure. In the first case, Si is included in the base of the nanowire, and Mg is included in the top of the nanowire, both chosen to reinforce the polarization-induced charge in nanowires assuming Ga-face polarity. In the second sample, Si is removed so that the only remaining dopants are Mg acceptors in the nanowire tops. Finally, a third sample is grown that contains no impurity doping in the graded sections. The I-V characteristics for these three samples are shown in Fig. 3.18. Clearly, the sample with dopants in both
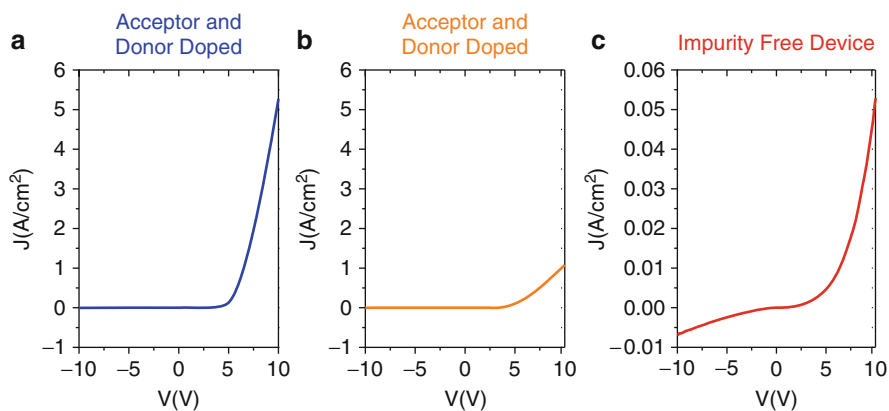
Fig. 3.18 Current density-voltage characteristics for different doping schemes in PINLED devices

graded sections is the most conductive, and when Si is removed from the device, there is a 5 times reduction in the current at a given voltage. The least conductive case occurs for the dopant-free device, which still shows rectification, but has roughly 100 times less current at a given voltage when compared to the device that includes dopants in both graded sections. This result indicates that in order to achieve the most conductive material, dopants should be added to the structure that reinforces the polarization-induced charge. This result also indicates that it is possible to achieve a p-n junction without the use of impurity dopants (i.e., with polarization-induced charge alone). However, this data does not by itself prove that a dopant-free p-n junction has been formed because other structures (e.g., a Schottky contact) might also provide rectification. Further proof that the dopant-free structures are indeed p-n junctions is provided in the following section.

Optical Characterization

The optical characterization is obviously of the utmost importance of any optoelectronic device. Of the many possible optical characterization techniques that are available to researchers (e.g., photoluminescence), electroluminescence (EL) measurements are the most important for characterizing an LED and will therefore be the focus of this section. In an EL measurement, the LED is operated at a number of progressively larger currents, and the emission spectra are recorded. From the spectra a number of important EL parameters are collected, including emission intensity, wavelength, and FWHM. Figure 3.19 displays this data for a PINLED with a GaN quantum well. EL intensity clearly increases as current increases (Fig. 3.16a, b), which is expected for an LED. Perhaps more interestingly, the peak emission energy blue shifts by a large amount as current increase (Fig. 3.19b, c). At low initial currents, the emission energy is 2.5 eV (496 nm), and as current increases,
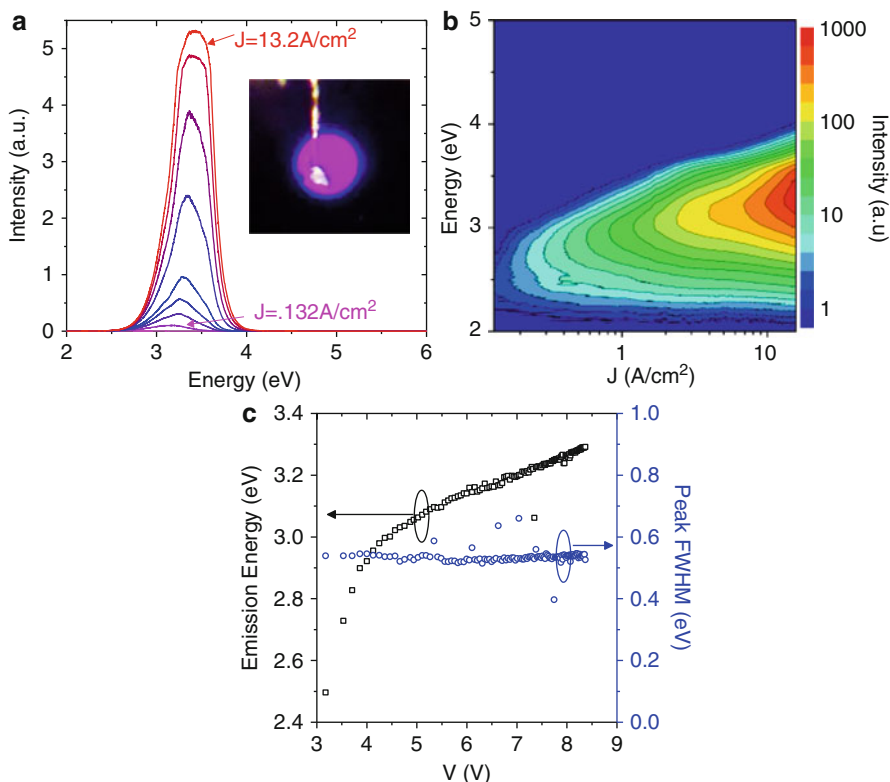
Fig. 3.19 (**a**) Electroluminescence (*EL*) spectra versus current density. (**b**) A contour plot of EL intensity as a function of current density. (**c**) Emission energy and full width at half maximum as a function of applied voltage [33]

the emission dramatically blue shifts by nearly 1 eV. This built-in red shift in the low-current emission is expected given the large polarization-induced quantum-confined Stark effect in the GaN quantum well [33]. The red shift in emission is particularly pronounced given that the GaN quantum well is surrounded by AlN cladding layers on either side, providing a large change in spontaneous polarization at the quantum well interfaces and hence a large amount of bound polarization charge at the interface.

As stated above, the AlN at the center of the nanowire provides a large bandgap that other smaller bandgap materials can be inserted into. PINLEDs have been grown with a range of AlGaN quantum wells. Emission from these devices is shown in Fig. 3.20. With a GaN quantum well, emission is centered at 365 nm, as expected. Progressively larger amounts of Al are then incorporated into the quantum well, shifting the EL emission deeper into the UV. The data shown here goes as deep as 282 nm. In addition to emission from AlGaN, an InGaN quantum well is also inserted into the active region, providing green emission at 563 nm.
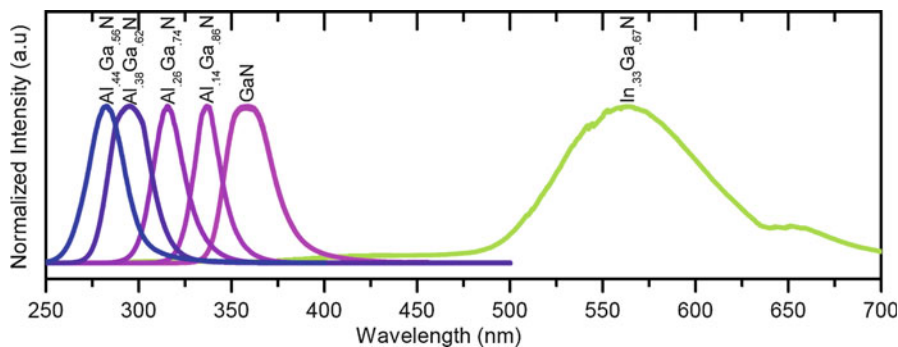
Fig. 3.20 Electroluminescence at a variety of wavelengths for PINLEDs with different AlGaN quantum wells
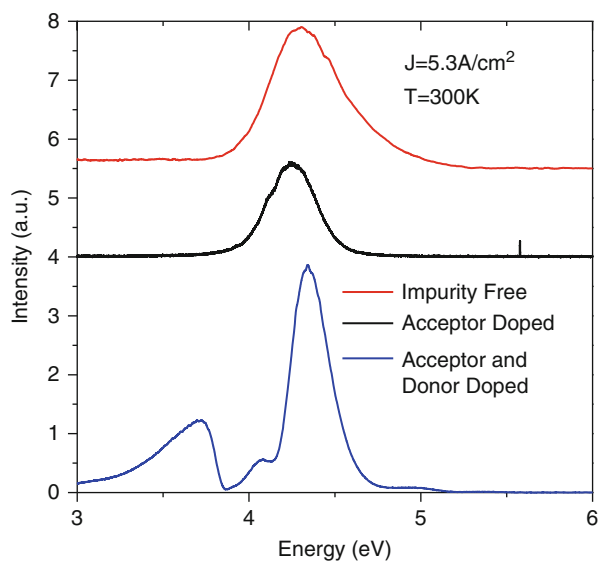
Fig. 3.21
Electroluminescence spectra
for PINLED devices with
different doping schemes [33]

Even though this is an impressively large range of emission, it should be possible to cover an even broader range by using higher percentages of Al and In in the AlGaN and InGaN quantum wells.

Finally, EL measurements are taken from the previously described set of samples that use different doping schemes (i.e., dopants in both graded section, doping in only p-type section, and no dopants in either section). All three samples in this study provide EL. At low operating currents the emission for these devices are comparable (Fig. 3.21). However, at higher currents, the emission from devices

with dopants increases more rapidly than the dopant-free device. This could perhaps be to due increased heating in the devices due to the more resistive nature of the dopant-free devices. Nevertheless, the fact that emission is seen in the dopant-free device decisively shows that electron–hole recombination is occurring in the nanowires that requires electron and hole injection. This coupled with the I-V characteristics from the previous section provides clear evidence that a p-n junction has been formed through the use of polarization-induced charge alone. In the specific application of LEDs, the current data suggests that dopants should be included in graded layers to reinforce the polarization-induced charge and obtain the highest carrier concentrations possible. However, this is not necessarily the case for all applications, so future devices and applications might benefit from the use of dopant-free polarization-induced conducting layers.

Conclusion

Polarization doping could solve the problem of achieving highly conductive material in many wide bandgap semiconductors. Due to their exceptionally high material quality and enhanced strain accommodation, nanowires are well suited to take full advantage of polarization doping. Structural characterization shows that it is possible to form heterostructures in nanowires that cannot be formed in planar devices. Electrical characterization shows that it is possible to achieve conduction in graded layers through either the activation of dopants or without the use of dopants at all. Finally, optical characterization shows that polarization-doped AlGaN nanowires are already being used to form LEDs that can emit through a wide range of wavelengths in the UV. Together, polarization doping in nanowires offers device designers many new options that are not available through impurity-doped, thin film-based devices. Given this, we might one day see a new class of devices, based on polarization-doped nanowires that can perform functions that other more traditional devices cannot.

References

1. NSM Archives – Physical Properties of Semiconductors (2004) http://www.ioffe.ru/SVA/NSM/Semicond/index.html 2013
2. Taniyasu Y, Kasu M, Makimoto T (2006) An aluminium nitride light-emitting diode with a wavelength of 210 nanometres. Nature 441:325
3. Keyes R (1975) Effect of randomness in distribution of impurity atoms on FET thresholds. Appl Phys 8:251
4. Asenov A (1998) Random dopant induced threshold voltage lowering and fluctuations in sub-0.1 μm MOSFET's: A 3-D "atomistic" simulation study. IEEE Trans Electron Devices 45:2505
5. Wong HSP, Taur Y, Frank DJ (1998) Discrete random dopant distribution effects in nanometer-scale MOSFETs. Microelectron Reliab 38:1447
6. Wood C, Jena D (eds) (2008) Polarization effects in semiconductors: from ab initio theory to device applications. Springer, New York

7. Ogawa T (1968) Estimation of spontaneous polarization of hexagonal ZnS, CdS and ZnO crystals. J Phys Soc Jpn 25:1126
8. Nakamua S, Mukai T, Senoh M (1991) High-power gan P-N-junction blue-light-emitting diodes. Jpn J Appl Phys Part 2 Lett 30:L1998
9. Nakamura S, Senoh M, Mukai T (1993) P-GaN/n-InGaN/n-GaN double-heterostructure blue-light-emitting diodes. Jpn J Appl Phys Part 2 Lett 32:L8
10. Nakamura S, Senoh M, Nagahama S et al (1996) InGaN-based multi-quantum-well-structure laser diodes. Jpn J Appl Phys Part 2 Lett 35:L74
11. Jena D, Alpay SP, Mantese JV (2008) Functionally graded polar heterostructures: New materials for multifunctional devices. In: Jena D, Wood C (eds) Polarization effects in semiconductors: from ab initio theory to device applications, 1st edn. Springer, New York
12. Mishra U, Singh J (2008) Semiconductor device physics and design. Springer, Dordrecht
13. Khan M, Bhattarai A, Kuznia J et al (1993) High-electron-mobility transistor based on a Gan-AlxGa1-xn heterojunction. Appl Phys Lett 63:1214
14. Jena D, Heikman S, Green D et al (2002) Realization of wide electron slabs by polarization bulk doping in graded III-V nitride semiconductor alloys. Appl Phys Lett 81:4395
15. Simon J, Protasenko V, Lian C et al (2010) Polarization-induced hole doping in wide-band-gap uniaxial semiconductor heterostructures. Science 327:60
16. Li S, Ware M, Wu J et al (2012) Polarization induced pn-junction without dopant in graded AlGaN coherently strained on GaN. Appl Phys Lett 101:122103
17. Dingle R, Stormer H, Gossard A et al (1978) Electron mobilities in modulation-doped semiconductor heterojunction super-lattices. Appl Phys Lett 33:665
18. Kuzmik J (2001) Power electronics on InAlN/(In)GaN: Prospect for a record performance. IEEE Electron Device Lett 22:510
19. Rajan S, Wong M, Fu Y et al (2005) Growth and electrical characterization of N-face AlGaN/GaN heterostructures. Jpn J Appl Phys Part 2 Lett Express Lett 44:L1478
20. Grundmann MJ, Mishra UK (2007) Multi-color light emitting diode using polarization-induced tunnel junctions. Physica Status Solidi C Curr Top Solid State Phys 4(7):4–2830
21. Simon J, Zhang Z, Goodman K et al (2009) Polarization-induced zener tunnel junctions in wide-band-gap heterostructures. Phys Rev Lett 103:026801
22. Krishnamoorthy S, Nath DN, Akyol F et al (2010) Polarization-engineered GaN/InGaN/GaN tunnel diodes. Appl Phys Lett 97:203502
23. Krishnamoorthy S, Park PS, Rajan S (2011) Demonstration of forward inter-band tunneling in GaN by polarization engineering. Appl Phys Lett 99:233504
24. Li S, Zhang T, Wu J et al (2013) Polarization induced hole doping in graded AlxGa1-xN (x=0.7 ∼ 1) layer grown by molecular beam epitaxy. Appl Phys Lett 102:062108
25. Rajan S, Xing HL, DenBaars S et al (2004) AlGaN/GaN polarization-doped field-effect transistor for microwave power applications. Appl Phys Lett 84:1591
26. Rajan S, DenBaars S, Mishra U et al (2006) Electron mobility in graded AlGaN alloys. Appl Phys Lett 88:042103
27. Simon J, Wang A, Xing HL et al (2006) Carrier transport and confinement in polarization-induced three-dimensional electron slabs: Importance of alloy scattering in AlGaN. Appl Phys Lett 88:042109
28. Matthews JW, Blakeslee AE (1974) Defects in epitaxial multilayers .1. Misfit dislocations. J Cryst Growth 27:118
29. Lee SR, Koleske DD, Cross KC et al (2004) In situ measurements of the critical thickness for strain relaxation in AlGaN/GaN heterostructures. Appl Phys Lett 85:6164
30. Thillosen N, Sebald K, Hardtdegen H et al (2006) The state of strain in single GaN nanocolumns as derived from micro-photoluminescence measurements. Nano Lett 6:704
31. Ertekin E, Greaney PA, Chrzan DC et al (2005) Equilibrium limits of coherency in strained nanowire heterostructures. J Appl Phys 97:114325
32. Glas F (2006) Critical dimensions for the plastic relaxation of strained axial heterostructures in free-standing nanowires. Phys Rev B 74:121302

33. Carnevale SD, Kent TF, Phillips PJ et al (2012) Polarization-induced pn diodes in wide-band-gap nanowires with ultraviolet electroluminescence. Nano Lett 12:915
34. Carnevale SD, Kent TF, Phillips PJ et al (2012) Graded nanowire ultraviolet LEDs by polarization engineering. Proc SPIE 8467:84670L–84671L
35. Jani O, Ferguson I, Honsberg C et al (2007) Design and characterization of GaN/InGaN solar cells. Appl Phys Lett 91:132117
36. Neufeld CJ, Toledo NG, Cruz SC et al (2008) High quantum efficiency InGaN/GaN solar cells with 2.95 eV band gap. Appl Phys Lett 93:143502
37. Hamzaoui H, Bouazzi A, Rezig B (2005) Theoretical possibilities of InxGa1-xN tandem PV structures. Solar Energy Mater Solar Cells 87:595
38. Hsu L, Jones RE, Li SX et al (2007) Electron mobility in InN and III-N alloys. J Appl Phys 102:073705
39. Muth JF, Lee JH, Shmagin IK et al (1997) Absorption coefficient, energy gap, exciton binding energy, and recombination lifetime of GaN obtained from transmission measurements. Appl Phys Lett 71:2572
40. Wu J, Walukiewicz W, Yu KM et al (2003) Superior radiation resistance of In1-xGaxN alloys: Full-solar-spectrum photovoltaic material system. J Appl Phys 94:6477
41. Li SX, Yu KM, Wu J et al (2005) Fermi-level stabilization energy in group III nitrides. Phys Rev B 71:161201
42. Sarwar ATMG, Myers RC (2012) Exploiting piezoelectric charge for high performance graded InGaN nanowire solar cells. Appl Phys Lett 101:143905
43. Sanchez-Garcia MA, Calleja E, Monroy E et al (1998) The effect of the III/V ratio and substrate temperature on the morphology and properties of GaN- and AlN-layers grown by molecular beam epitaxy on Si(111). J Cryst Growth 183:23
44. Guo W, Zhang M, Banerjee A et al (2010) Catalyst-free InGaN/GaN nanowire light emitting diodes grown on (001) silicon by molecular beam epitaxy. Nano Lett 10:3355
45. Yoshizawa M, Kikuchi A, Mori M et al (1997) Growth of self-organized GaN nanostructures on Al$_2$O$_3$(0001) by RF-radical source molecular beam epitaxy. Jpn J Appl Phys Part 2-Lett 36:L459
46. Bertness KA, Sanford NA, Barker JM et al (2006) Catalyst-free growth of GaN nanowires. J Electron Mater 35:576
47. Park YS, Lee SH, Oh JE et al (2005) Self-assembled GaN nano-rods grown directly on (111) Si substrates: Dependence on growth conditions. J Cryst Growth 282:313
48. Dong YJ, Tian BZ, Kempa TJ et al (2009) Coaxial group III-nitride nanowire photovoltaics. Nano Lett 9:2183
49. Qian F, Gradecak S, Li Y et al (2005) Core/multishell nanowire heterostructures as multicolor, high-efficiency light-emitting diodes. Nano Lett 5:2287
50. Geelhaar L, Cheze C, Weber WM et al (2007) Axial and radial growth of Ni-induced GaN nanowires. Appl Phys Lett 91:093113–093113-3
51. Calleja E, Ristic J, Fernandez-Garrido S et al (2007) Growth, morphology, and structural properties of group-III-nitride nanocolumns and nanodisks. Phys Status Solidi B-Basic Solid State Phys 244:2816
52. Kishino K, Sekiguchia H, Kikuchi A (2009) Improved Ti-mask selective-area growth (SAG) by rf-plasma-assisted molecular beam epitaxy demonstrating extremely uniform GaN nanocolumn arrays. J Cryst Growth 311:2063
53. Bertness KA, Sanders AW, Rourke DM et al (2010) Controlled nucleation of GaN nanowires grown with molecular beam epitaxy. Adv Funct Mater 20:2911
54. Fernandez-Garrido S, Grandal J, Calleja E et al (2009) A growth diagram for plasma-assisted molecular beam epitaxy of GaN nanocolumns on Si(111). J Appl Phys 106:126102
55. Koblmuller G, Wu F, Mates T et al (2007) High electron mobility GaN grown under N-rich conditions by plasma-assisted molecular beam epitaxy. Appl Phys Lett 91:221905–221905-3
56. Carnevale SD, Yang J, Phillips PJ et al (2011) Three-dimensional GaN/AlN nanowire heterostructures by separating nucleation and growth processes. Nano Lett 11:866

57. Consonni V, Knelangen M, Geelhaar L et al (2010) Nucleation mechanisms of epitaxial GaN nanowires: Origin of their self-induced formation and initial radius. Phys Rev B 81:085310
58. Consonni V, Hanke M, Knelangen M et al (2011) Nucleation mechanisms of self-induced GaN nanowires grown on an amorphous interlayer. Phys Rev B 83:035310–035310-8
59. Bertness KA, Roshko A, Sanford NA et al (2006) Spontaneously grown GaN and AlGaN nanowires. J Cryst Growth 287:522
60. Songmuang R, Ben T, Daudin B et al (2010) Identification of III-N nanowire growth kinetics via a marker technique. Nanotechnology 21:295605
61. Debnath RK, Meijers R, Richter T et al (2007) Mechanism of molecular beam epitaxy growth of GaN nanowires on Si(111). Appl Phys Lett 90:123117
62. Dubrovskii VG, Cirlin GE, Soshnikov IP et al (2005) Diffusion-induced growth of GaAs nanowhiskers during molecular beam epitaxy: Theory and experiment. Phys Rev B 71:205325–205325-6
63. Ristic J, Calleja E, Fernandez-Garrido S et al (2008) On the mechanisms of spontaneous growth of III-nitride nanocolumns by plasma-assisted molecular beam epitaxy. J Cryst Growth 310:4035
64. Songmuang R, Landre O, Daudin B (2007) From nucleation to growth of catalyst-free GaN nanowires on thin AlN buffer layer. Appl Phys Lett 91:251902
65. Calarco R, Meijers RJ, Debnath RK et al (2007) Nucleation and growth of GaN nanowires on Si(111) performed by molecular beam epitaxy. Nano Lett 7:2248
66. Tchernycheva M, Sartel C, Cirlin G et al (2007) Growth of GaN free-standing nanowires by plasma-assisted molecular beam epitaxy: structural and optical characterization. Nanotechnology 18:385306
67. Laskar MR, Carnevale SD, Sarwar ATMG et al (2013) Molecular beam epitaxy of graded-composition InGaN nanowires. J Electron Mater 42:863
68. de la Mata M, Magen C, Gazquez J et al (2012) Polarity assignment in ZnTe, GaAs, ZnO, and GaN-AlN nanowires from direct dumbbell analysis. Nano Lett 12:2579–2586
69. Kikuchi A, Kawai M, Tada M (2004) InGaN/GaN multiple quantum disk nanocolumn light-emitting diodes grown on (111)Si substrate. Jpn J Appl Phys Part 2-Lett Expr Lett 43:L1524

Mechanical Characterization of Graphene

4

Changhong Cao, Xuezhong Wu, Xiang Xi, Tobin Filleter,
and Yu Sun

Introduction

Graphene is a planar monolayer of strongly sp^2-bonded carbon atoms arranged into
a two-dimensional honeycomb lattice with a carbon–carbon bond length of
0.142 nm [1]. It was initially assumed not to exist in free state and was described
as 'academic material' [2] until 2004 when Novoselov et al. [3] successfully
separated single-layer graphene experimentally. It can be wrapped up into 0D
fullerenes, rolled into 1D nanotubes or stacked into 3D graphite (Fig. 4.1) [4].
Five typical methods are typically used to make graphene sheets which include [5]
(i) chemical vapor deposition (CVD) on metals, (ii) micromechanical exfoliation of
graphite, (iii) reduction of graphene oxide, (iv) epitaxial growth on large band gap
semiconductor S_iC, (v) and the creation of colloidal suspension.

In terms of mechanical properties, graphene is a super strong nanomaterial.
A suspended monolayer graphene sheet over circular holes on a Si substrate was
measured by AFM (atomic force microscopy) nano-indentation revealing that it
exhibits a Young's modulus of $\sim$1TPa and a critical failure stress and strain of

C. Cao (✉) • T. Filleter • Y. Sun

Department of Mechanical and Industrial Engineering, University of Toronto, Toronto,
ON, Canada
e-mail: changhongcao@hotmail.com; filleter@mie.utoronto.ca; sun@mie.utoronto.ca

X. Wu • X. Xi

College of Mechatronics Engineering and Automation, National University of Defense
Technology, Changsha, China
e-mail: www.67113@gmail.com; fordada@126.com
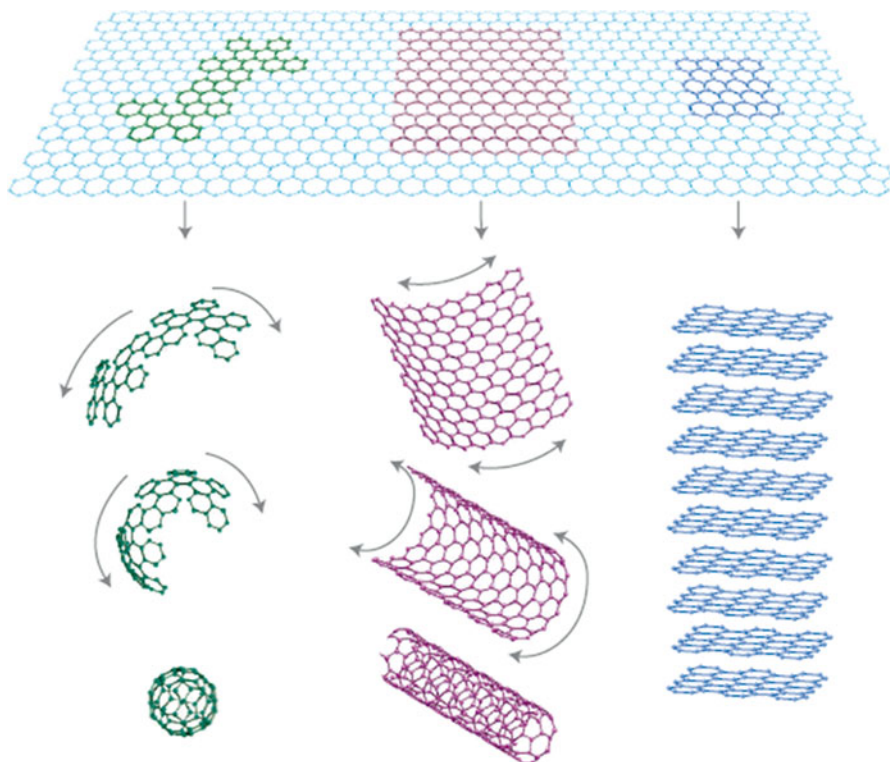
Fig. 4.1 Mother of all graphitic forms. Graphene is a 2D building material for carbon materials of all other dimensionalities. It can be wrapped up into 0D buckyballs, rolled into 1D nanotubes or stacked into 3D graphite (Figure/Caption reproduced (Adapted) with permission from Macmillan Publishers Ltd: [Nature Material] [4], Copyright (2007))

130GPa and 25 %, respectively [6]. These extraordinary mechanical properties, in addition to the well-documented beneficial electrical properties of graphene, have attracted a great deal of interest in areas such as nano-/microelectromechanical system (NEMS/MEMS) [7, 8], nanoelectronics [9, 10], as well as nanocomposites [11]. A detailed fundamental understanding of its mechanical properties is of importance in its application to a number of these fields, in particular nanocomposites and MEMS.

Mechanical Characterization Techniques

Optical microscopy, electron microscopy, AFM, and Raman spectroscopy have been applied to the mechanical characterization of graphene. Optical microscopy is used to image samples 'macro'scopically, and electron microscopy provides higher imaging resolutions down to nanometer and sub-nanometer scales, facilitating both structural and mechanical characterization of graphene samples. AFM is a standard

tool to obtain surface images of graphene and can also be applied in mechanical testing modes to measure mechanical properties such as Young's modulus, friction, and strength. Raman spectroscopy is used to investigate the vibrational properties of graphene and measure graphene thickness accurately, which is essential in the interpretation and analysis of graphene's mechanical behavior.

Optical microscopy is primarily used to detect graphene 'macro'scopically. Substrate design is of great importance in order to enhance the visibility of graphene under optical microscopy [12, 13]. Based on the Fabry–Perot interference mechanism, various materials have been employed to enhance imaging contrast. For example, a SiO_2 layer is usually created on the surface of a silicon substrate [14]. By adjusting the SiO_2 thickness to 90 or 300 nm, the intensity of the reflected light is at the maximum, which is also the maximum sensitivity of human eye [3]. In addition, 50 nm Si_3N_4 and 72 nm Ai_2O_3 substrates have also been used to improve the contrast of graphene [14, 15]. Additionally, fluorescence quenching microscopy (FQM) was used to image graphene, reduced graphene oxide (RGO), and graphene oxide (GO) for sample evaluation and manipulation so that the synthesis process can be improved [16].

Scanning electron microscopy (SEM) and transmission electron microscopy (TEM) are widely used in nanomaterials research. Similar to optical microscopy, an underlying substrate is needed for using SEM to image graphene sheets. The magnification of SEM is order of magnitude higher than that of optical microscopy typically achieving a spatial resolution on the order of tens to a few nms.

TEM is used to observe morphological and structural features of graphene and measure the number of graphene layers accurately. For samples in which the edges of graphene films fold back, the observation of these edges by TEM provides an accurate way to count the number of layers at multiple locations on the films, as shown in Fig. 4.2a [17]. In addition, TEM is often assisted with electron diffraction pattern analysis, which enables the observation of the crystal structure of graphene sheets [18] (Fig. 4.2b). Defects in graphene can also be detected by using this method [18]. However, it should be noted that the resolution of electron microscopy is limited by the accelerating voltage. High accelerating voltages can damage the monolayer of graphene. Aberration-corrected TEM has been reported to achieve a 1 Å resolution at an acceleration voltage of only 80 kV [19, 20].

Atomic force microscopy (AFM) can provide a direct way to observe the topography of single to few layer graphene films which are atomically thin. In theory, the thickness of a single layer of graphene is about 0.34 nm. However, due to the surface adsorption of graphene, the actual measured value consistently appears to be 0.8–1.2 nm. The number of layers can be obtained by measuring the thickness of a single-layer sheet, and it can be calculated according to [21]

$$N = \frac{P - X}{0.34} + 1$$

where N is the number of layers of graphene, P is the measured thickness, and X is the measured thickness of a single-layer graphene. Furthermore, AFM can be used
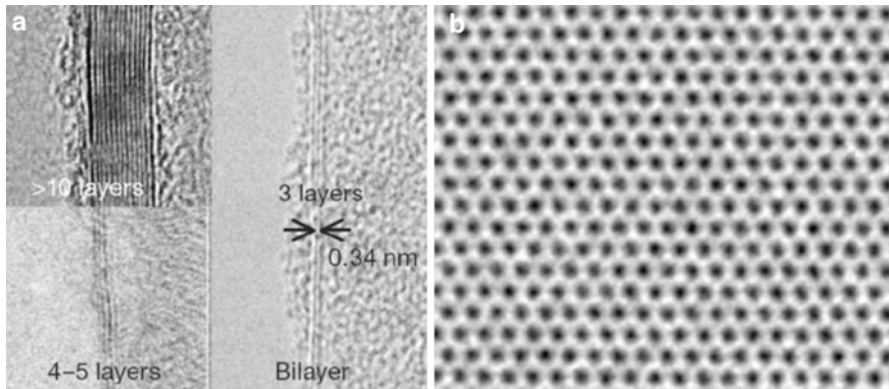
Fig. 4.2 TEM images: (**a**) Edges of graphene films (Figure/Adaption Reprinted (Adapted) by permission from Macmillan Publishers Ltd. on behalf of Cancer Research UK: [Nature] [17], Copyright (2009)) (**b**) Hexagonal pattern of the graphene structure (Figure/Caption Reprinted (adapted) with permission from [18], Copyright (2008) American Chemical Society)

to investigate the mechanical properties of graphene such as elastic modulus, tensile strength, bending stiffness, and friction. In this case, several mechanical testing modes of AFM are implemented including friction force microscopy (FFM), for determining the frictional characteristics of graphene [22–24], and AFM deflection for measuring elastic modulus and strength [6].

Raman spectroscopy provides a fast and nondestructive way to gain insight into the electron–phonon interactions in graphene. The frequency of scattered photons is changed due to the interaction of incident light and the material's molecular structure. Thus, the structural features of graphene can be identified, such as the number of graphene layers, the molecular structure, and defects in graphene [25]. Figure 4.3 shows the spectra of single-layer and double-layer graphene sheets [26]. Raman spectroscopy can also be used to measure the mechanical properties of graphene [27]. Mingyuan Huang et al. [28] presented Raman spectra of optical phonons in graphene monolayers under tunable uniaxial tensile stress. They showed that all the prominent bands exhibit significant red shifts and the resulting shift rates can be used to calibrate strain in graphene.

Mechanical Characterization of Graphene

Young's Modulus

Simulation

The elastic properties of graphene can be estimated by using numerical simulations, based on elasticity theory. It is known that graphene is a two-dimensional crystal of carbon atoms bonded by sp^2 hybridized bonds. Interatomic force field models for graphene thus can be built. Based on the continuum elasticity theory, a simple
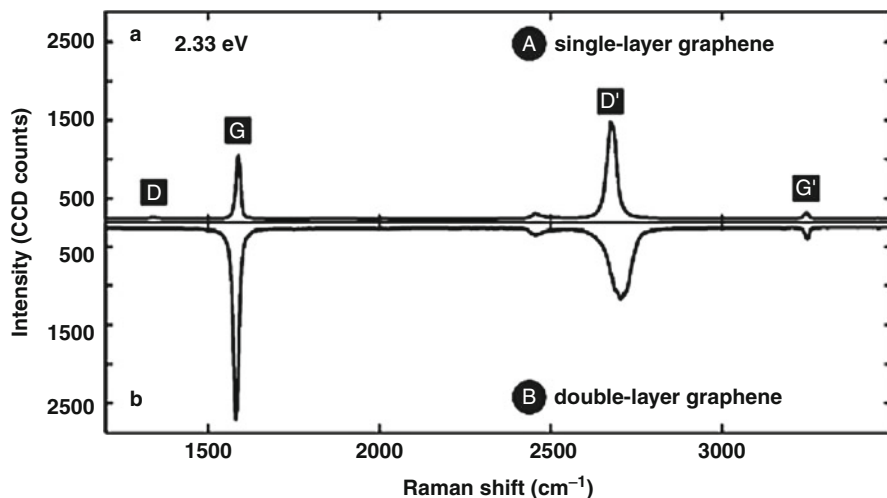
Fig. 4.3 Raman spectra of single and double layer grapheme (Figure/Caption Reprinted (adapted) with permission from [26], Copyright (2007) American Chemical Society)

Table 4.1 Graphene Young's modulus values from simulation studies

Graphene	
Study	E (TPa)
Continuum mechanics [31]	1.04
Molecular dynamics [32]	1.24
Molecular dynamics [33]	0.912
Molecular dynamics [34]	1.0913
Structural mechanics (amber model) [35]	1.305
Structural mechanics (Morse model) [35]	1.668

valence force field model was formulated by Keating [29] for semiconductors and then extended to graphene by Lobo [30]. Results predicting the Young's modulus of graphene were reported based on different modeling theories. Table 4.1 [31–35] summarizes these results from different simulation studies. It can be seen that with different modeling approaches, the Young's modulus values are close to 1 TPa.

Experiment

Reported experimental results of the Young's modulus are ~1.0 TPa [6] which is in good agreement with simulations. A suspended monolayer graphene sheet over circular holes on a Si substrate was measured using AFM nano-indentation (Fig. 4.4) [36]. The thickness of the graphene sample was accurately determined using contact mode AFM imaging [37]. AFM was also used to accurately resolve the small forces involved in deformation and friction of graphene [36, 38]. Young's modulus is calculated according to

$$\sigma = E\varepsilon + D\varepsilon^2$$

where σ is the stress, ε is the strain, and D is the third-order elastic modulus.

Elastic properties of graphene with different boundary conditions were also measured. Wong et al. [29] investigated the mechanical properties of suspended graphene drums via static deflection experiments. Deflection was detected using AFM, which is highly sensitive to topographical changes in the out-of-plane direction and can pick up height variations as small as 1 nm. The AFM scans provided information on both the peak displacement amplitude and the deflection mode shape of the drum structure. It was found that the structures have linear spring constants ranging from 3.24 to 37.4 N m^{-1} and could be actuated to about 18–34 % of their thickness before exhibiting nonlinear deflections [29]. The result indicates a Young's modulus value of 1TPa which agrees well with the results reported by Lee et al. [6].

Bending Stiffness

Simulation

Theoretical studies have suggested that the bending stiffness of graphene is critical to attain structural stability for suspended graphene sheets, which in turn affects their mechanical properties significantly [39–41]. Molecular mechanics simulations for graphene bending rigidity were reported through calculations of the strain energy for graphene sheets subjected to a point loading [42]. Based on the first-generation Brenner potential, an analytical form was derived for the bending modulus of monolayer graphene under infinitesimal bending curvature [43, 44], namely,

Fig. 4.5 Bending rigidity variation. (**a**) Variation of the bending rigidity with the size of square graphenes; (**b**) Variation of the bending rigidity with the shape of rectangular graphenes (Figure/Caption Reprinted (Adapted) from Physics Letter A [42], Copyright (2010), with permission from Elsevier)
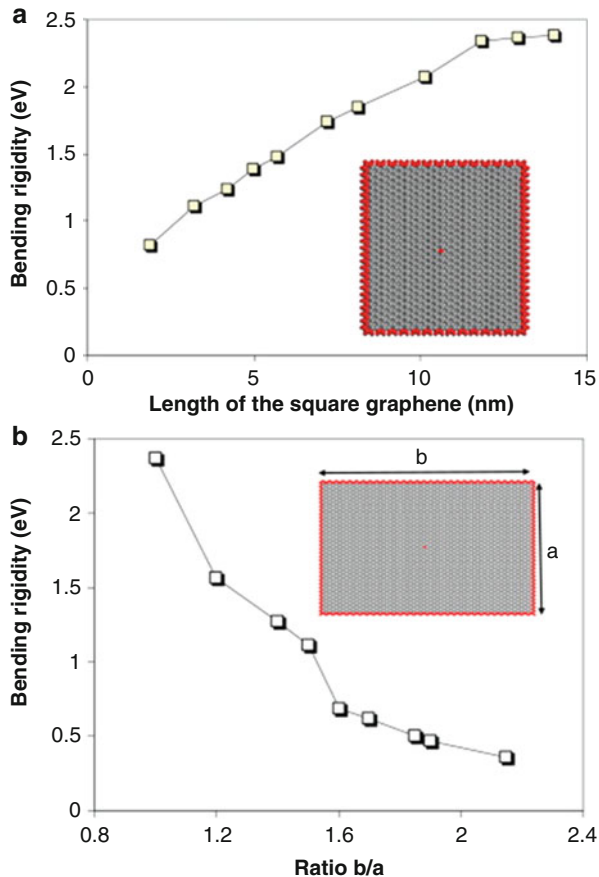
$$D_{\text{bending}} = \frac{\sqrt{3}}{2} \frac{\partial V_{ij}}{\partial \cos \theta_{ijk}} = \frac{1}{2} V(r_0) \frac{\partial b_{ij}}{\partial \theta_{ijk}}$$

where the interatomic potential takes the form

$$V_{ij} = V_R(r_{ij}) - \overline{b} V_A(r_{ij})$$

and $\overline{b} = (b_{ij} + b_{ji})/2$ is a function of the bond angles.

Simulation results show that the bending rigidity increases from a small value of 0.819 eV with the size of 1.87 nm to an asymptotic value of 2.385 eV for sheets with sizes larger than 12 nm. In addition, rigidity changes from the asymptotic value, 2.385 eV, for a square sheet to a smaller value, 0.360 eV, for a sheet with the shape ratio of $b/a = 2.15$, as shown in Fig. 4.5 [42].
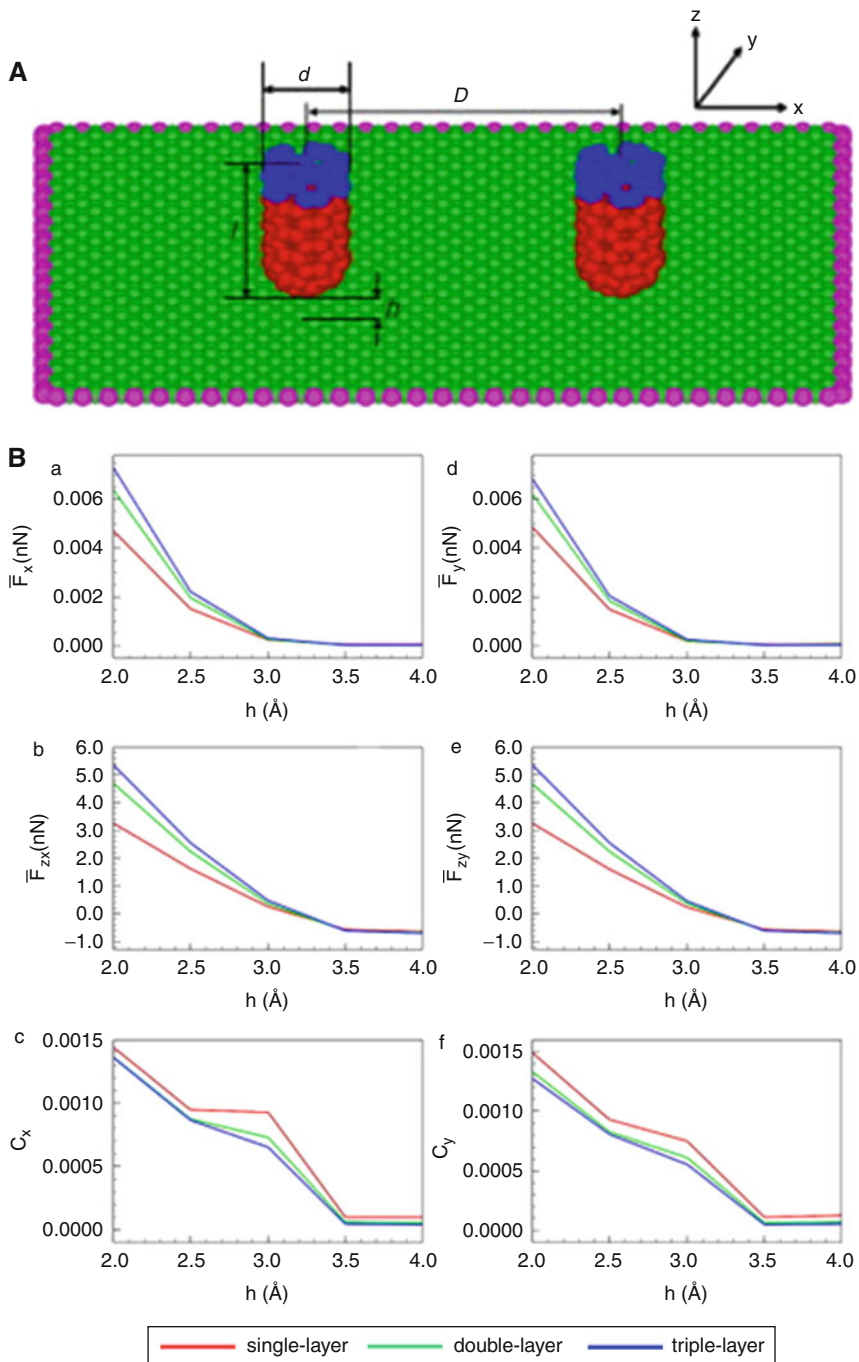
Fig. 4.6 (continued)

Experiment

While in-plane mechanical properties such as elastic modulus and strength of monolayer graphene have been deduced from experiments [6, 45], direct measurements of bending stiffness of monolayer graphene have not been reported. By using nano-indentation on suspended multilayer graphene flakes, the bending stiffness for 8–100 layers has been measured and determined to be in the range of 2×10^{-14} N m^{-2} $\times 10^{-11}$ N m^{-1} [46].

Friction

Simulation

Molecular dynamics simulations can also be applied to extract frictional properties of graphene. A probing tip using a short-capped single-walled carbon nanotube is able to capture the frictional characteristics and resolve the graphene lattice through measuring oscillatory lateral forces or normal forces. As shown in Fig. 4.6a [47], the graphene sheet (atoms are colored in red and blue) has a length l and a diameter d. The initial tip–surface distance is h, and the sliding distance is D. The atoms in blue are prescribed with a moving velocity while the atoms in red follow the molecular dynamics. The graphene sheet with lateral dimensions of 7.6×7.6 nm was placed horizontally with its boundary atoms (in pink) fixed and its interior atoms (in green) following the molecular dynamics. By averaging the oscillatory lateral force and normal force along the tip moving path, the friction coefficient was extracted [47].

Based on the simulation, it was found that the friction coefficient decreases with an increase in the initial tip–surface distance and the number of graphene layer [47]. The calculated results for the friction force $\overline{F}_x$ and the friction coefficient C_x at different initial tip–surface distances and the number of graphene layers are shown in Fig. 4.6b [47].

Experiment

The frictional properties of graphene can be measured using AFM under applied loads. Initially, the AFM tip is made to contact the specimen surface at a fixed normal load, and the friction force is measured over a distance for multiple cycles in which friction loops are recorded. Then, the applied load is varied, and the friction force is measured again for multiple applied loads. This process is repeated until the tip becomes detached from the specimen surface due to excessive negative loads and the relationship between normal force and frictional forces is determined [23, 24, 38].

Fig. 4.6 (**A**) Schematic of the probing interactions between the capped nanotube and graphene layer (**B**) Tip sliding along the x-direction, (**a**) the friction force (**c**) the friction coefficient; along the y-direction (**b**) the friction force (**d**) the friction coefficient (Figure/Caption Reprinted (Adapted) from Carbon [47], Copyright (2011), with permission from Elsevier)

Measurements down to single atomic sheets revealed that friction monotonically increased as the number of layers decreased for suspended graphene [23]; a similar trend revealed that monolayer epitaxial graphene on SiC exhibited higher friction than bilayer graphene, and the single and bilayer graphene reduced friction on the SiC substrate by a factor of $\sim$10 [24]. In another study, binding the graphene strongly to a mica surface suppressed the friction trend as a function of thickness [23, 24]. Li-Yu Lin et al. [38] investigated the friction and wear characteristics of multilayer graphene films deposited on a S_i substrate. The graphene films consisted of a few layers of carbon basal plane. The number of graphene layers was determined by AFM and Raman spectroscopy. It was found that graphene films exhibited much lower friction (from 0.36 to 0.62 nN) than bare Si surface (from 1.1 to 4.3 nN) when applied loads varied from 3 to 30 nN.

Strength and Fracture

Depending on single or polycrystalline nature, the fracture mechanisms of graphene can vary. For single crystalline graphene, the failure mechanism (take double vacancy as an example) by molecular dynamics simulation is illustrated in Fig. 4.7a [48]. Before the propagation of fracture, pentagons and heptagons initiate around the defects. As load increases, fracture disperses in the direction parallel to the loading direction. Two chains of atoms are formed at the region of the vacancy defects and the other two chains on the edges of the sheet during fracture propagation. The critical stress and critical strain relationship depends on the number of vacancy defects [48, 49]. As shown in Fig. 4.7b [48], a pristine single-layer graphene sheet has the highest ultimate strength and strain. The presence of vacancy defects can reduce these features of the graphene sheet. A single-layer graphene sheet with a single vacancy defect has a critical stress and strain reduction of 6.4 % and 9.7 %, respectively, compared with the pristine sheet. A reduction of 7.3 % and 11.46 % for a double vacancy defect graphene sheet was also estimated.

Simulation performed by Cao et al. [50] shows that for polycrystalline graphene, fracture initiates from either a grain boundary triple junction [Fig. 4.8a–d] or an array of vacancies on a preferential grain boundary [Fig. 4.8e–h] by unzipping atomic bonds along a preferential grain boundary. Crack propagation takes only 4.0 ps from crack initiation to the final failure of the entire sample. Furthermore, polycrystalline graphene exhibits 'flaw tolerance' as reported in the simulation study reported by Zhang et al. [51]. As illustrated in Fig. 4.9, fracture behavior of polycrystalline graphene can become insensitive to a preexisting flaw (hole or notch) below a critical length scale, which means that there is no stress concentration near the flaw site.

Experimental fracture behavior of graphene is relatively understudied. Research in experimentally revealing fracture mechanisms is a promising future field, which can significantly enhance the understanding of failure modes of graphene in various applications.
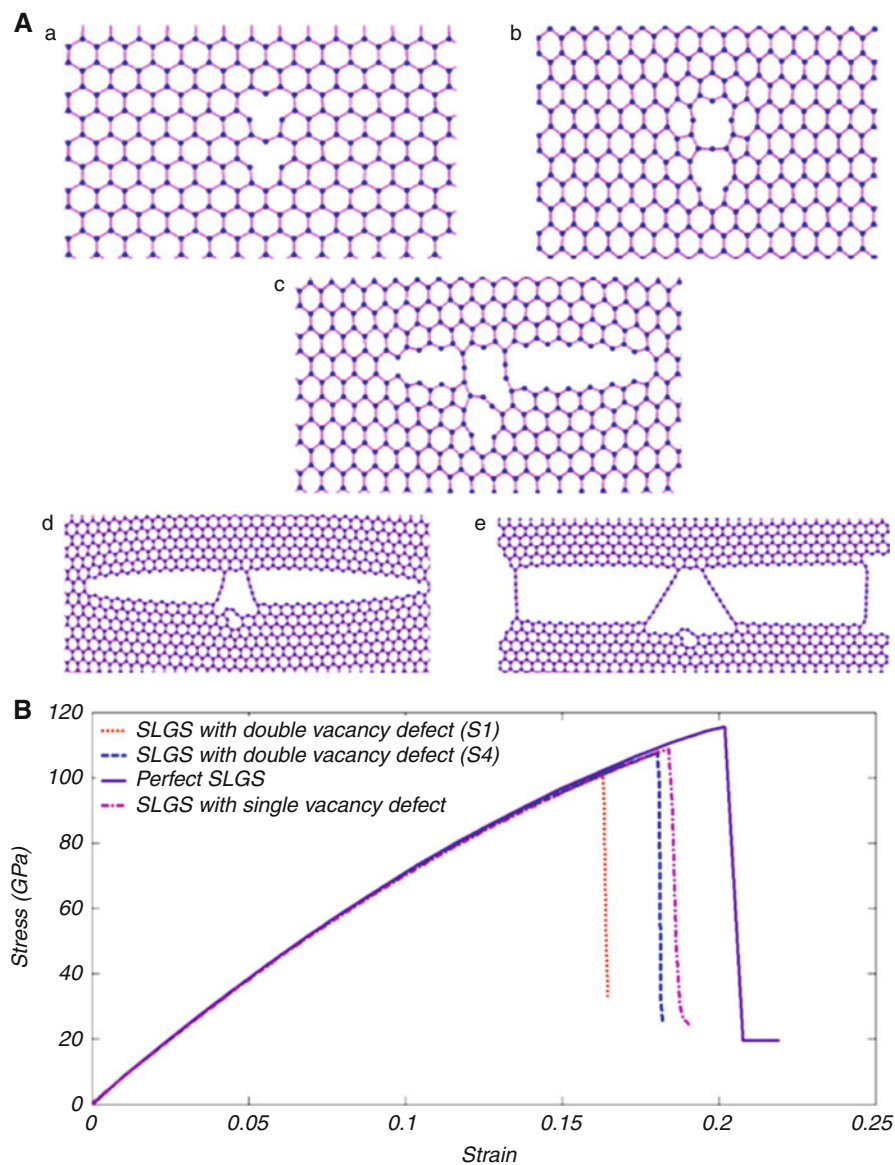
Fig. 4.7 (**A**) Failure process of a SLGS with double vacancy (shortest possible separation distance). (**a**) after initial relaxation, (**b**) formation of pentagons and heptagons at adjacent of the vacancies, (**c**) early stages of fracture propagation, (**d**) formation of two chains at the location of vacancy defects, and (**e**) formation of four chains. (**B**) Stress–strain curves of graphene sheets with double vacancies, single vacancy, and a perfect structure (Figures/Captions Reprinted (Adapted) from Solid State Communications [48], Copyright (2011), with permission from Elsevier)

Fig. 4.8 (**a–d**) Snapshots of the microstructure to show the unzipping mechanism leading to brittle inter-granular fracture. No significant out-of-plane displacement is observable. The *arrow* indicates the unzipping direction. (**e–h**) show the perforation mechanisms of separate nano-voids that cause the spontaneous initiation of crack (Figures/ Captions Reprinted (Adapted) with permission from [50], Copyright [2013], American Institute of Physics)
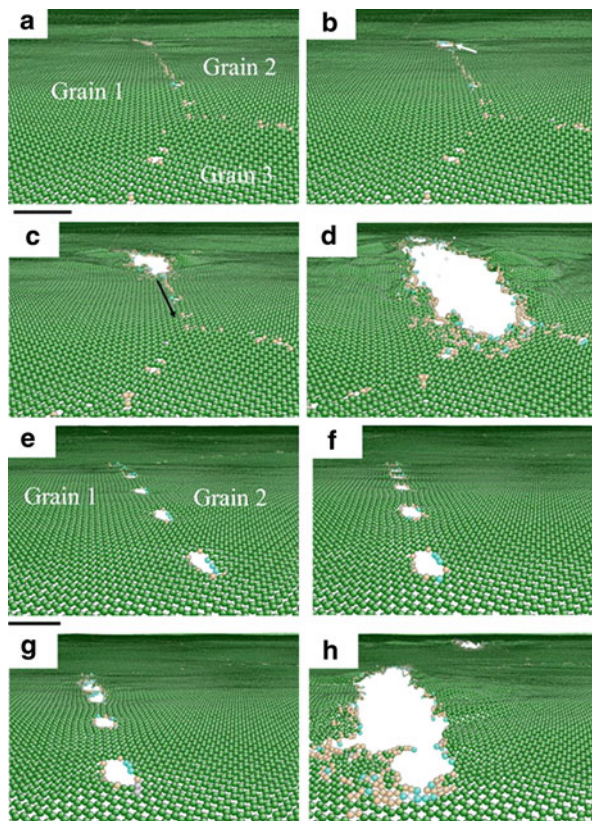
Fig. 4.9 Schematic shows the fracture behavior of the polycrystalline graphene can be insensitive to preexisting flaw (Figure/Caption Reprinted (adapted) with permission from [51], Copyright (2012) American Chemical Society)
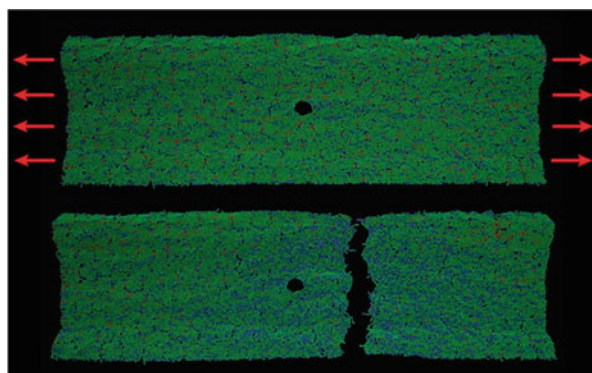
Summary

The synthesis, characterization, and applications of graphene are rapidly progressing. Mechanically, Young's modulus of mechanical exfoliated monolayer

graphene was determined to be $\sim$1.0TPa, and a critical failure stress and strain of 130 GPa and 25 % were measured, respectively; bending stiffness was reported only for 8–100 layers to be in the range between 2×10^{-14} N m^{-1} and 2×10^{-17} N m^{-1}; friction of graphene shows a trend that it monotonically increases as the number of layers decreases for suspended graphene and epitaxial graphene on S$_i$C; fracture behavior of graphene depends on its nature of crystalline. Simulation results show that polycrystalline graphene exhibits 'flaw tolerance'. However, debates over properties such as wear and shear modulus remain unsolved. In addition to the techniques this chapter described, MEMS devices which have micrometer-sized features can also be applied to study single-layer and multilayer graphene as they can bridge investigation of materials at the macro- and nanoscales. Although a number of MEMS devices have been developed for mechanical characterizing individual 1D nanomaterials, such as carbon nanotubes [52] and silicon nanowires [53], few devices exist for characterizing 2D nanomaterials such as graphene. In future work, the development of advanced experimental techniques and methodologies for interpreting data will produce more thorough mechanical characterization results and enable additional in-depth understanding of this important nanomaterial.

References

1. Weiss PR (1958) Band structure of graphite. The State University, New Brunswick
2. Fradkin E (1986) Critical behavior of disordered degenerate semiconductors. II. Spectrum and transport properties in mean-field theory. Phys Rev B 33(5):3263–3268
3. Novoselov KS, Geim AK, Morozov SV, Jiang D, Zhang Y, Dubonos SV, Grigorieva IV, Firsov AA (2004) Electric field effect in atomically thin carbon films. Science 306(5696):666–669
4. Geim AK, Novoselov KS (2007) The rise of graphene. Nat Mater 6(3):183–191
5. Park S, Ruoff RS (2009) Chemical methods for the production of graphenes. Nat Nanotechnol 4(4):217–224
6. Lee C, Wei XD, Kysar JW, Hone J (2008) Measurement of the elastic properties and intrinsic strength of monolayer graphene. Science 321(5887):385–388
7. Yang YT, Callegari C, Feng XL, Ekinci KL, Roukes ML (2006) Zeptogram-scale nanomechanical mass sensing. Nano Lett 6(4):583–586
8. Chen CY, Rosenblatt S, Bolotin KI, Kalb W, Kim P, Kymissis I, Stormer HL, Heinz TF, Hone J (2009) Performance of monolayer graphene nanomechanical resonators with electrical readout. Nat Nanotechnol 4(12):861–867
9. Shang NG, Papakonstantinou P, McMullan M, Chu M, Stamboulis A, Potenza A, Dhesi SS, Marchetto H (2008) Catalyst-free efficient growth, orientation and biosensing properties of multilayer graphene nanoflake films with sharp edge planes. Adv Funct Mater 18(21):3506–3514
10. Thevenot DR, Toth K, Durst RA, Wilson GS (1999) Electrochemical biosensors: definitions and classification. Pure Appl Chem 71(12):16
11. Stankovich S, Dikin DA, Dommett GHB, Kohlhaas KM, Zimney EJ, Stach EA, Piner RD, Nguyen ST, Ruoff RS (2006) Graphene-based composite materials. Nature 442(7100):282–286
12. Jung I, Pelton M, Piner R, Dikin DA, Stankovich S, Watcharotone S, Hausner M, Ruoff RS (2007) Simple approach for high-contrast optical imaging and characterization of graphene-based sheets. Nano Lett 7(12):3569–3575
13. Kamat PV (2010) Graphene-based nanoarchitectures. Anchoring semiconductor and metal nanoparticles on a two-dimensional carbon support. J Phys Chem Lett 1(2):520–527

14. Blake P, Hill EW, Neto AHC, Novoselov KS, Jiang D, Yang R, Booth TJ, Geim AK (2007) Making graphene visible. Appl Phys Lett 91(6):63124

15. Gao LB, Ren WC, Li F, Cheng HM (2008) Total color difference for rapid and accurate identification of graphene. ACS Nano 2(8):1625–1633

16. Kim J, Cote LJ, Kim F, Huang JX (2010) Visualizing graphene based sheets by fluorescence quenching microscopy. J Am Chem Soc 132(1):260–267

17. Kim KS, Zhao Y, Jang H, Lee SY, Kim JM, Ahn JH, Kim P, Choi JY, Hong BH (2009) Large-scale pattern growth of graphene films for stretchable transparent electrodes. Nature 457(7230):706–710

18. Meyer JC, Kisielowski C, Erni R, Rossell MD, Crommie MF, Zettl A (2008) Direct imaging of lattice atoms and topological defects in graphene membranes. Nano Lett 8(11):3582–3586

19. Gomez-Navarro C, Meyer JC, Sundaram RS, Chuvilin A, Kurasch S, Burghard M, Kern K, Kaiser U (2010) Atomic structure of reduced graphene oxide. Nano Lett 10(4):1144–1148

20. Girit CO, Meyer JC, Erni R, Rossell MD, Kisielowski C, Yang L, Park CH, Crommie MF, Cohen ML, Louie SG, Zettl A (2009) Graphene at the edge: stability and dynamics. Science 323(5922):1705–1708

21. Dan ZH, Xu Z, Xie (2011) Graphene: structure, fabrication method and characterization. Tsinghua University Press, Beijing

22. Li QY, Lee C, Carpick RW, Hone J (2010) Substrate effect on thickness-dependent friction on graphene. Phys Status Solidi B 247(11–12):2909–2914

23. Lee C, Li QY, Kalb W, Liu XZ, Berger H, Carpick RW, Hone J (2010) Frictional characteristics of atomically thin sheets. Science 328(5974):76–80

24. Filleter T, McChesney JL, Bostwick A, Rotenberg E, Emtsev KV, Seyller T, Horn K, Bennewitz R (2009) Friction and dissipation in epitaxial graphene films. Phys Rev Lett 102(8)

25. Ferrari AC, Meyer JC, Scardaci V, Casiraghi C, Lazzeri M, Mauri F, Piscanec S, Jiang D, Novoselov KS, Roth S, Geim AK (2006) Raman spectrum of graphene and graphene layers. Phys Rev Lett 97(18)

26. Graf D, Molitor F, Ensslin K, Stampfer C, Jungen A, Hierold C, Wirtz L (2007) Spatially resolved raman spectroscopy of single- and few-layer graphene. Nano Lett 7(2):238–242

27. Gong L, Kinloch IA, Young RJ, Riaz I, Jalil R, Novoselov KS (2010) Interfacial stress transfer in a graphene monolayer nanocomposite. Adv Mater 22(24):2694–2697

28. Huang M (2009) Studies of mechanically deformed single wall carbon nanotubes and graphene by optical spectroscopy. Columbia University

29. Wong CL, Annamalai M, Wang ZQ, Palaniapan M (2010) Characterization of nanomechanical graphene drum structures. J Micromech Microeng 20(11)

30. Kysar JW (2008) Direct comparison between experiments and computations at the atomic length scale: a case study of graphene. Sci Model Simul 15(1–3):143–157

31. Shokrieh MM, Rafiee R (2010) Prediction of Young's modulus of graphene sheets and carbon nanotubes using nanoscale continuum mechanics approach. Mater Des 31(2):790–795

32. Bu H, Chen Y, Zou M, Yi H, Bi K, Ni Z (2009) Atomistic simulations of mechanical properties of graphene nanoribbons. Phys Lett A Gen, At Solid State Phys 373(37):3359–3362

33. Tsai JL, Tu JF (2010) Characterizing mechanical properties of graphite using molecular dynamics simulation. Mater Des 31(1):194–199

34. Ni Z, Bu H, Zou M, Yi H, Bi K, Chen Y (2010) Anisotropic mechanical properties of graphene sheets from molecular dynamics. Phys B Condens Matter 405(5):1301–1306

35. Scarpa F, Adhikari S, Srikantha Phani A (2009) Effective elastic mechanical properties of single layer graphene sheets. Nanotechnology 20(6)

36. Lee C, Wei XD, Li QY, Carpick R, Kysar JW, Hone J (2009) Elastic and frictional properties of graphene. Phys Status Solidi B Basic Solid State Phys 246(11–12):2562–2567

37. Nemes-Incze P, Osvath Z, Kamaras K, Biro LP (2008) Anomalies in thickness measurements of graphene and few layer graphite crystals by tapping mode atomic force microscopy. Carbon 46(11):1435–1442

38. Jun L-YL, Dae-Eun K, Whan-Kyun K, Seong C (2011) Friction and wear characteristics of multi-layer graphene films investigated by atomic force microscopy. Surf Coat Technol 205:6
39. Fasolino A, Los JH, Katsnelson MI (2007) Intrinsic ripples in graphene. Nat Mater 6(11):858–861
40. Abedpour N, Neek-Amal M, Asgari R, Shahbazi F, Nafari N, Tabar MRR (2007) Roughness of undoped graphene and its short-range induced gauge field. Phys Rev B 76(19)
41. Kim EA, Neto AHC (2008) Graphene as an electronic membrane. EPL 84(5)
42. Wang Q (2010) Simulations of the bending rigidity of graphene. Phys Lett A 374(9):1180–1183
43. Arroyo M, Belytschko T (2004) Finite crystal elasticity of carbon nanotubes based on the exponential Cauchy-Born rule. Phys Rev B 69(11)
44. Huang Y, Wu J, Hwang KC (2006) Thickness of graphene and single-wall carbon nanotubes. Phys Rev B 74(24)
45. Bunch JS, Verbridge SS, Alden JS, van der Zande AM, Parpia JM, Craighead HG, McEuen PL (2008) Impermeable atomic membranes from graphene sheets. Nano Lett 8(8):2458–2462
46. Cranford SW, Buehler MJ (2011) Packing efficiency and accessible surface area of crumpled graphene. Phys Rev B 84(20)
47. Liu P, Zhang YW (2011) A theoretical analysis of frictional and defect characteristics of graphene probed by a capped single-walled carbon nanotube. Carbon 49(11):3687–3697
48. Ansari R, Motevalli B, Montazeri A, Ajori S (2011) Fracture analysis of monolayer graphene sheets with double vacancy defects via MD simulation. Solid State Commun 151(17):1141–1146
49. Khare R, Mielke SL, Paci JT, Zhang SL, Ballarini R, Schatz GC, Belytschko T (2007) Coupled quantum mechanical/molecular mechanical modeling of the fracture of defective carbon nanotubes and graphene sheets. Phys Rev B 75(7)
50. Cao A, Qu J (2013) Atomistic simulation study of brittle failure in nanocrystalline graphene under uniaxial tension. Appl Phys Lett 102(7)
51. Zhang T, Li XY, Kadkhodaei S, Gao HJ (2012) Flaw insensitive fracture in nanocrystalline graphene. Nano Lett 12(9):4605–4610
52. Espinosa HD, Bernal RA, Filleter T (2012) In situ TEM electromechanical testing of nanowires and nanotubes. Small 8(21):3233–3252
53. Yong Z, Xinyu L, Changhai R, Yan Liang Z, Lixin D, Yu S (2011) Piezoresistivity characterization of synthetic silicon nanowires using a MEMS device. J Microelectromech Syst 20(4):959–967

Nanostructured ZnO Materials: Synthesis, Properties and Applications

5

Valentina Cauda, Rossana Gazia, Samuele Porro, Stefano Stassi, Giancarlo Canavese, Ignazio Roppolo, and Alessandro Chiolerio

Introduction

Zinc oxide is a group II–VI compound semiconductor whose ionic nature resides at the borderline between covalent and ionic semiconductors [1]. It possesses promising catalytic, electrical, electronic, and optical properties [1]. The preparation and characterization of ZnO materials at nanometric scale, including the forms of nanowires, nanobelts, and nanoparticles, have recently attracted considerable attention due to their physical properties and potential applications [2, 3], e.g., solar cells and other electronic nanodevices.

The crystal structures featured by ZnO are *wurtzite* (Fig. 5.1a), *zinc blende* (Fig. 5.1b), and *rock salt* (or Rochelle salt) (here not shown). Under ambient conditions, the wurtzite symmetry is the most thermodynamically stable phase. The zinc blende structure can be stabilized only by growth on cubic substrates, and the rock salt or Rochelle salt (NaCl) structure may be obtained only at relatively high-pressure syntheses, as in the case of GaN [1]. ZnO is also known as zincite in the mineral form and is very rare in nature. The zincite presents the tetrahedral structure of ZnO_4 and has a wurtzite crystal structure.

The wurtzite structure is a hexagonal close-packed structure (Fig. 5.1), where each zinc atom is surrounded by a tetrahedron of four oxygen atoms and vice versa, thus forming an alternate combination of planes of oxygen and zinc atoms,

V. Cauda • R. Gazia • S. Porro • S. Stassi • G. Canavese • I. Roppolo • A. Chiolerio (✉)
Center for Space Human Robotics@PoliTO, Istituto Italiano di Tecnologia, Torino, Italy
e-mail: valentina.cauda@iit.it; rossana.gazia@iit.it; samuele.porro@iit.it; stefano.stassi@iit.it; giancarlo.canavese@iit.it; ignazio.roppolo@iit.it; alessandro.chiolerio@iit.it

137
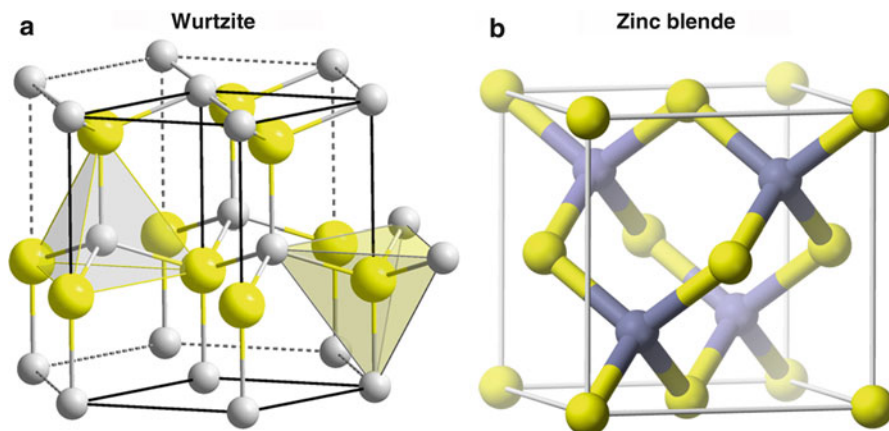
Fig. 5.1 ZnO different crystal structures

respectively. All tetrahedra are oriented in one direction, and their stacking produces the ZnO hexagonal symmetry. The major axis is symmetrically polar and results in a hemimorphic crystal structure, thus having different crystalline forms at each end of the crystallographic axis, without any transverse plane of symmetry nor center of symmetry. The typical crystal habit exhibits a basal (pedion) polar oxygen plane (001), a top tetrahedron corner-exposed polar zinc (001) face, and low-index faces (parallel to the c-axis) consisting of a nonpolar (100) face and C_6v symmetric ones. The 'low-symmetry' nonpolar faces with threefold coordinated atoms are the most stable ones, whereas the polar (001) faces show the highest surface energy, leading to higher growth rate of ZnO nanocrystals along the c-axis direction. Additionally, there is no center of inversion in the wurtzite crystal structure, and therefore an inherent asymmetry along the c-axis is present, allowing the anisotropic growth of the crystal along the [001] direction. Consequently, the theoretical and most stable crystal habit is a hexagonal prism elongated along the c-axis (Fig. 5.2). The tetrahedral coordination is typical of sp^3 covalent bonding, but these materials also have a substantial ionic character that tends to increase the bandgap beyond the one expected from the covalent bonding.

ZnO Main Properties

Zinc oxide (ZnO) is an n-type semiconductor material with promising catalytic, electronic [5], and optical properties. In the abovementioned fields, it possesses great potential because of its high electron mobility, high thermal conductivity, wide bandgap ($\sim$3.3 eV) [6], and large exciton-binding energy ($\sim$60 meV) [7] and exhibits UV absorption in the range 200–350 nm and emission in the near UV and visible range from 500 to 600 nm and piezoelectricity [8]. In addition, monocrystalline ZnO structures show a superior fatigue resistance, high isoelectric point and

Fig. 5.2 Crystal habit of wurtzite ZnO hexagonal rod (Reprinted with permission from [4], Copyright © 2009, Elsevier)

charge transfer properties, biocompatibility, and low impact on the environment at the end of life cycle.

As reported in the next paragraphs, ZnO nanomaterials are easy to fabricate, and raw materials and precursors are easily available.

The combination of semiconducting and piezoelectric properties has been addressed as the 'piezotronic effect' [9, 10], whereas the combination of optical and piezoelectric properties gives rise to the so-called piezo-phototronic effect [11]. Recently, ZnO nanostructures have been widely studied as gas [12, 13] and mechanical strain sensors [14], thanks to the high electromechanical coupling, as well as energy nanogenerators responding to mechanical deformation [2, 15, 16]. A reasonable power density has been generated from ZnO-based piezoelectric harvesting devices [17, 18].

ZnO Synthesis Techniques

From an experimental point of view, many methods have been employed for the growth of ZnO nanomaterials with different compositions and morphologies, such as vapor-phase transport processes [19–21], chemical vapor deposition (CVD) [22], metalorganic chemical vapor deposition (MOCVD) [23, 24], molecular beam

epitaxy (MBE) [25], pulsed laser deposition (PLD) [26], sputtering [27], and template-based method [28]. In particular, soft solution processes and wet chemical methods, such as electrodeposition technique [29, 30] and aqueous chemical growth [31, 32], provide the possibility of growing ZnO nanostructures at low temperature. In the following these techniques are discussed in details.

Liquid Phase Growth

In order to minimize the disadvantages of the high-temperature approaches to synthesize nanostructures, the sol–gel method has been extensively used to obtain various kinds of oxide materials due to its simplicity, cost-effective process, low-energy deposition method, the ease of control of chemical components and final composition, large area coating, and uniformity of thickness [31, 32]. When preparing nanostructured materials, such as thin films or nanostructures from a sol, the main factors affecting the final morphology, the crystalline structure, and thus the properties of the material are precursor concentration and the pH of the solution, aging time of sol [33] and, in case of an oriented growth of nanostructures on a substrate, the ZnO seed layer on the substrate [34], the layer's thickness, the structure and the preparation method, and the thermal treatment [35, 36].

In the sol–gel process, the precursors for the preparation of colloids or nanoparticles consist of a metal or metalloid element surrounded by various ligands [37]. The common precursors for zinc oxide include inorganic salts such as zinc nitrate $Zn(NO_3)_2$ and organic compounds such as zinc acetate $Zn(OOCCH_3)_2$ (also written as $Zn(OAc)_2$) which is a carboxylate, the class of precursors most widely used in sol–gel research.

The liquid phase synthesis or sol–gel method can be divided in three main families:

– Solution growth [38, 39], leading to nano- or micro-sized powders or colloids
– Hydrothermal or aqueous chemical growth [31, 34], thus leading to the anisotropic growth of vertically oriented nanowires on a substrate
– Template-based growth [28], using a porous matrix where the nanostructure growth takes place, filling the porosities of the template

Solution Growth: Sol–gel Hydrolysis and Condensation Method

Mono- or polycrystalline materials in the final form of powders or colloids can be easily obtained with this sol–gel approach [38, 40]. First the Zn-precursor hydrolyzes in a solvent (generally water or alcohols) forming Zn^{2+} ions which react with the OH- anions of a base present in the reaction mixture (generally sodium hydroxide, NaOH, or potassium hydroxide, KOH), to form different hydroxyl species [41], including $ZnOH^+(aq)$, $Zn(OH)_2(aq)$, $Zn(OH)_2(s)$, $Zn(OH)_3$-(aq), and $Zn(OH)_4^{2-}$ (as in Eq. 5.1). Further the intermediate $[Zn(OH)_4]^{2-}$ condenses into the oxide form (Eq. 5.2).
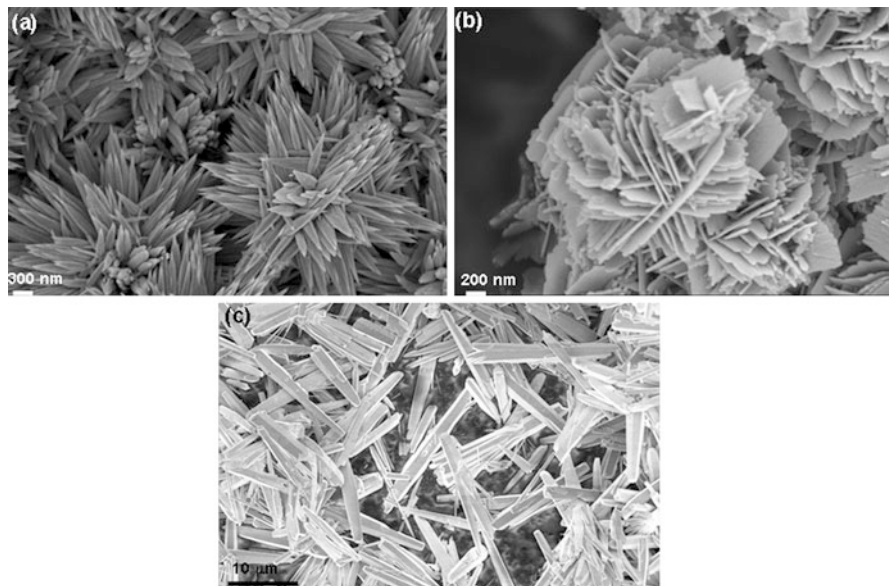
Fig. 5.3 Different ZnO particles morphologies obtained by sol–gel method: (**a**) multipods, (**b**) flower-like particles, (**c**) micro-wires

$$Zn^{2+} + 4OH^- \rightarrow \left[Zn(OH)_4\right]^{2-} \tag{5.1}$$

$$\left[Zn(OH)_4\right]^{2-} \rightarrow ZnO + H_2O + 2OH^- \tag{5.2}$$
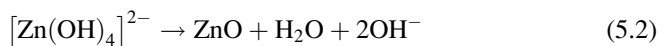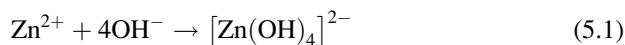
The overall reaction can be thus summarized in:

$$Zn^{2+} + 2OH^- \rightarrow ZnO + H_2O. \tag{5.3}$$
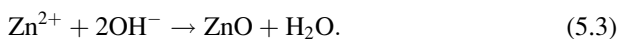
With this general approach, nano- and microparticles, multipods, wires, and rods have been reported in the literature [38, 40] (Fig. 5.3). Classical model explains the formation of nanoparticles in two phases: nucleation and growth [37]. The formation of tiny crystalline nuclei in supersaturated media leads to the genesis of particles. Thereafter the crystal grows under a process controlled by the mass transport and by the surface equilibrium of addition and removal (dissolution) of individual monomers, such as atoms, ions, or molecules. Under this equilibrium conditions, the driving force for dissolution increases with decreasing particle size. Thus, within an ensemble of particles with slightly different sizes, larger particles will grow at the cost of smaller ones. This mechanism is called Ostwald ripening [37] and is generally believed to be the main path for crystal growth.

An interesting approach is the so-called oriented attachment under hydrothermal conditions, where single-crystalline ZnO nanoparticles of few nanometers can coalesce forming anisotropic structures, i.e., nanorods [39]. As detailed before,

in the case of ZnO wurtzite structure, the crystal grows along the c-axis as this is known to have the largest growth rate [34]. This is also due to the fact that the corresponding crystallographic plane (001) is the most reactive surface as it is composed only of O or Zn atoms; in contrast, the other basal crystallographic planes are stoichiometric and therefore less reactive. This means that an oriented attachment of the nanoparticles takes place at the higher energetic plane, leading to partially fused dimers and oligomers to almost perfect nanorods.

Oriented Deposition by Aqueous Chemical Method on Substrates

One-dimensional free-standing single-crystal ZnO nanowires can be directly grown on a substrate by soft chemical methods, such as aqueous chemical growth [31], without the use of templates, catalysts, or surfactants. The aqueous chemical growth method involves the heating of an aqueous solution of Zn-salts or complexes at mild temperatures (generally below 100 °C) in a closed vessel, in the presence of a substrate, where the most used ones are silicon wafers, which can be coated with a conductive metallic layer, or glass slides, eventually with a thin conductive oxide layer, such as ITO (indium tin oxide) or FTO (fluorine-doped tin oxide). The aqueous chemical growth is advantageous since it does not require high-pressure containers and is also entirely recyclable, safe, and environmentally friendly because only water is commonly used as solvent [32]. Moreover, this process avoids the hazards related to the use of organic solvents and their potential toxicity. The residual salts obtained at the end of the process are easily washed out by water due to their high solubility. In most cases no additional heat or chemical treatment is necessary to obtain crystalline structures, which represents a significant improvement compared with surfactant-, template-, or membrane-based synthesis methods. Moreover, the aqueous chemical growth allows a full coverage of the substrate, also in the order of square centimeters, within few hours. The nanowires length can be thus opportunely tuned by varying the reaction time, which may be necessary for certain applications where tailoring the overall physical properties of the final device (e.g., semiconducting or piezoelectric properties) is of main interest [36].

It was often reported that highly vertically oriented and dense nanowires are obtained when starting from a crystalline ZnO thin films, used as seed layers [42]. Thus the nanowire growth synthesis involves the controlled heteronucleation of metal oxides in aqueous solutions.

The seed layer grows preferentially along the crystallographic c-axis, and it can be morphologically tuned by properly choosing the seed layer deposition method, the starting solution concentration, the annealing temperature, and so on [36]. There exist different coating techniques for the formation of thin films, and they can be selected according to the application requiring the seed layer to be grown. The control of the process parameters plays a key role since it can help to tune the deposition, uniformity, and thickness of the seed layer that could directly affect the orientation of the nanowire array. The most common coating techniques are drop casting, spin coating, and dip coating [36], but also sputter deposition of thin ZnO film is a well-established approach to prepare the seed layer [35]. According to Liu [43], the most important parameter to be controlled in the seed
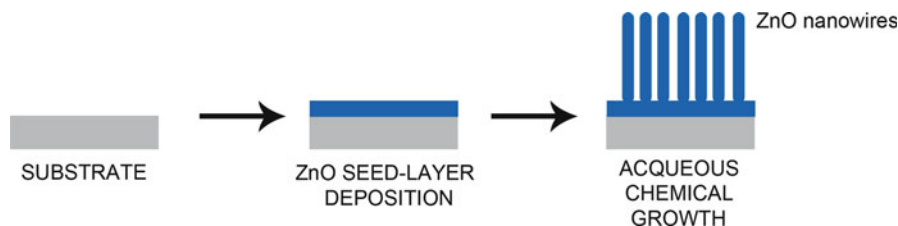
Fig. 5.4 Scheme of ZnO nanowires obtained by aqueous chemical growth
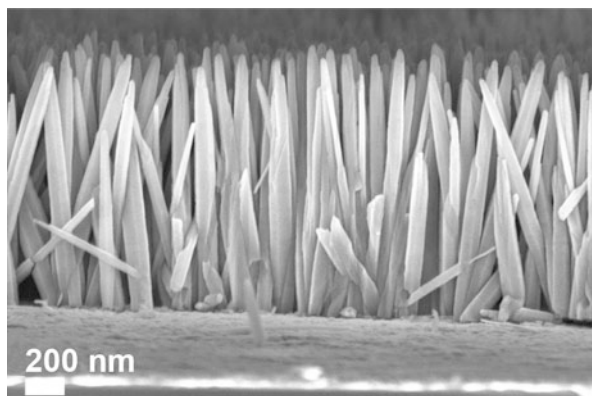
Fig. 5.5 ZnO vertical arrays of nanowires by aqueous chemical growth

layer preparation is the nucleation step, because it influences the overall crystallinity and thus the architecture of the ZnO thin film. After the film deposition, the seed layer has to be thermally treated, to transform the high free-energy solid phase (e.g., amorphous zinc) into the seed layer (e.g., hexagonal zinc oxide nanocrystal) through mass transfer of atoms. Figure 5.4 shows schematically the ZnO nanowires growing steps, which involve a coating step of the substrate with an amorphous zinc solution to form a seed layer, then transformed into ZnO nanocrystals by heating the coated substrate under controlled conditions and finally the aqueous chemical growth where the seed layer allows the nucleation and growth of ZnO nanowires.

Vertically oriented ZnO nanowires (as shown in Fig. 5.5) are synthesized by a chemical aqueous growth method according to the following reactions shown in Eqs. 5.3, 5.4, and 5.5:

$$Zn^{2+} + 2OH^- \leftrightarrow ZnO + H_2O \tag{5.3}$$

$$(CH_2)_6N_4 + 6H_2O \leftrightarrow 4NH_3 + 6HCHO \tag{5.4}$$

$$NH_3 + H_2O \leftrightarrow NH_3 \cdot H_2O \leftrightarrow NH_4^+ + OH^- \tag{5.5}$$
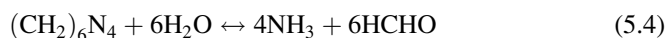
where the hexamethylenetetramine ($(CH_2)_6 N_4$ or HMT), NaOH, or NH_4OH is the most commonly used hydroxide sources. As seen in the previous paragraph,

Zn^{2+} can complex with OH^- to form different hydroxyl species [41], including $ZnOH^+$(aq), $Zn(OH)_2$(aq), $Zn(OH)_2$(s), $Zn(OH)_3$-(aq), and $Zn(OH)_4^{2-}$, thus solid ZnO crystals can grow on the preexisting seed-layer nuclei by the condensation of the hydroxyl groups with the hydroxyl complexes, or even new solid ZnO nuclei can be formed by dehydration of the hydroxyl species (Eq. 5.3). At the same time, the HMT hydrolyzes into formaldehyde and ammonia (Eq. 5.4) and acts as a pH buffer. It is slowly decomposed during the nanowires growth process to provide a continuous source of ammonium hydroxide (Eq. 5.5) and thereby supply the OH^-, which is needed on the reaction shown in Eq. 5.3 to lead the ZnO formation.

Generally, as there is a high degree of supersaturation in the reaction mixture with respect to ZnO, the ZnO formation is induced in the bulk solution, through homogeneous nucleation, and on the surface of preexisting nuclei. However, since only the formation of ZnO on the seed layer is desirable, the homogeneous nucleation of ZnO in the bulk solution should be avoided, as it would result in a fast depletion of reactants and shorter nanowire lengths. As an additional disadvantage, the ZnO nanowires grown on a substrate are easily contaminated by the ZnO precipitated out of the bulk solution, reducing the crystallographic quality of the sample. Some recent efforts have been carried out for reducing the homogeneous nucleation and promoting one-dimensional ZnO crystal growth, by maintaining relatively large growth rates and enhancement of anisotropic (one-dimensional NWs) nanostructure formation [31, 35, 36, 44]. This was achieved by adding capping agents, such as ammonium hydroxide and polyethylenimine (PEI), to the Zn^{2+} supersaturated growth solution, as proposed by Xu et al. [42]. Ammonium hydroxide substantially forms coordination complexes with the zinc ions Zn^{2+}, keeping them in solution and thus suppressing ZnO homogeneous nucleation. PEI is a cationic low molecular weight polymer able to preferentially adsorb to the polar (100) facets of ZnO clusters, thus inhibiting further crystal growth along these faces and inducing additional anisotropy for the growth along the longitudinal direction of the nanowires. In these conditions, it was possible to obtain ZnO wires with high aspect ratio growing on the seeded substrate at a reasonably high growth rate (approximately 0.02 μm per minute) [36]. The growth of even longer nanowires would require repeating the immersion of the substrates into fresh solution baths for several hours (Fig. 5.5).

Template Growth

Nanoporous materials used as a template to confine and grow guest materials also provide an easy way to obtain ZnO nanostructures. Several comprehensive reviews on this topic were already published [45, 46], showing that miniaturized, oriented, and anisotropic structures can be prepared by this approach starting from a material precursor or solution. Many porous materials have been used indeed to prepare ZnO nanostructures [28]. Among them, the most common are the anodic porous alumina [29, 47] (APA, with pores diameter ranging from 20 to 500 nm) and track-etched polycarbonate membrane [46] whereas, among the less common, mesoporous

silica [48] (i.e., micelle-templated porous SiO_2 with pore sizes of 2–15 nm), porous silicon, and carbon nanotubes can be mentioned [46]. All these templates usually contain very small cylindrical pores, and the empty spaces are filled with the desired material, which adopts the pore morphology, shape, and size to form regular nanostructures. Thus, by appropriately selecting monodispersed size distribution, as well as aligned and long pores of the templating matrix, ordered and monodispersed arrays of nanowires can be obtained.

The templating method generally requires the use of colloids, precursors solutions, or sols to fill the pores by simple wet impregnation or by electrodeposition [29, 49] of the charged species, i.e., Zn^{2+} cations. In this case, the template should be an electrical insulator. All these approaches are cheap and scalable to mass production, and one can obtain nanowires (NWs) when the material completely fills the pores of the template or nanotubes, if the material deposits to the pore walls of the template.

There are some fundamental requirements to get a successful impregnation, such as the template compatibility with the solution used, i.e., chemical and thermal inertness. However, some possible contamination can take place, such as the template dissolution during synthesis. In addition the solution must wet the pores, and the growth can proceed from the bottom to the top (possibly leading to diffusion limitation) or growth from the channel walls and proceed inwards (with the disadvantage of pore blockage). Therefore the major drawback of the templating approach is the difficulty to ensure the complete filling of the pores. Additionally polycrystalline ZnO nanowires are generally obtained, most of the times requiring a thermal treatment in order to obtain the crystal wurtzitic phase.

During electrodeposition [29, 49], an oriented diffusion of charged reactive species through the solution takes place by applying an external electric field. For electrodeposition, a standard three-electrode setup is typically used, with a saturated Ag/AgCl electrode as reference. The template is attached to the cathode in contact with the deposition solution, and the anode (generally Pt as the counter electrode) is placed in the deposition solution, parallel to the cathode. A constant voltage source is maintained in order to guarantee a constant driving force, or a constant current source is supplied to maintain a constant reaction rate. The Zn^{2+} cations diffuse through the template pores and are reduced by depositing on the cathode. The O_2 dissolved in the solution reduces at the cathode, as shown in Eq. 5.6

$$O_2 + 2H_2O + 4e^- \leftrightarrow 4OH^- \tag{5.6}$$
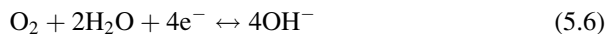
thus providing a source of OH^- [50] and raising the local pH value. The OH^- coordinates with Zn^{2+} and then the agglomerate undergoes dehydration to form ZnO, as summarized by Eq. 5.3. Nucleation takes place from the bottom of the template channels, and the charged species deposit onto the tip of the nucleating structures, resulting in continued growth of the nanowires inside the template channels (Fig. 5.6).

Fig. 5.6 ZnO nanowires
obtained upon (**a**)
electrodeposition and (**b**) wet
impregnation into porous
alumina matrices. The images
show the cross section of the
alumina membrane filled by
the ZnO material and in the
inset a top view of the
nanowires
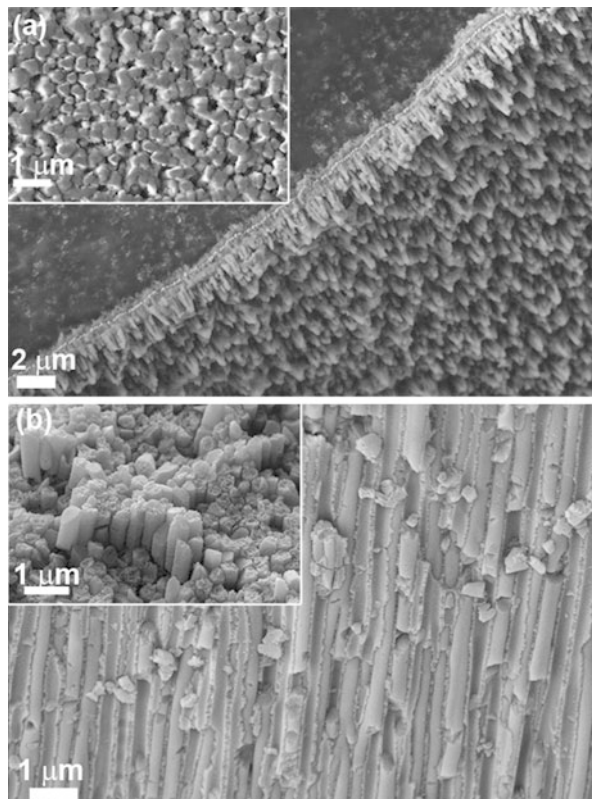
Thermally Activated Chemical Vapor Deposition

Among the large variety of techniques for the synthesis of ZnO nanostructures,
chemical vapor deposition is undoubtedly one of the most investigated. CVD is
a versatile vapor transport process, in which a solid material is deposited on
a heated surface following a chemical reaction in the vapor phase [51]. It is suitable
for the synthesis of a variety of materials (carbon, silicon, carbides, nitrides, oxides,
intermetallics, and many others) in many different forms (coatings, powders, fibers,
nanostructures, etc.) on substrates with various geometries (planar substrates, deep
recesses, holes, three-dimensional configurations, and so on). It generally provides
high deposition rates and good uniformity, and it is usually economical. Moreover,
CVD equipment does not require ultrahigh vacuum, and it is very flexible to process
variations and changes in composition of the grown materials. It has however the
disadvantage of being normally performed at relatively high temperatures, usually
not lower than 500 °C [52, 53]. CVD can be exploited either at atmospheric pressure
(APCVD) or low pressure (LPCVD). APCVD offers a very high deposition rate but
features low purity and poor uniformity. LPCVD improves uniformity and purity,
however, with higher temperatures and lower deposition rates than APCVD.

One of the simplest ways to activate reactive species in a CVD process is by heating them in a furnace. In thermally activated CVD, source materials are vaporized at high temperatures, while the desired products are condensed from the vapor phases in a cooler region of the reaction chamber, under conditions (temperature, pressure, atmosphere, substrate, etc.) tailored to form the desired products. In fact, the deposition is influenced by several process parameters (temperature, pressure, carrier gas, gas flow rate, substrate, and evaporation time), which need to be properly tuned before and during the thermal vaporization. The processes are usually carried out in a horizontal tube furnace, which is equipped with a quartz or alumina tube having ends sealed by rubber O-rings, a gas supply and control system, and a rotary pump (except for APCVD). In the case of LPCVD, pre-vacuum is normally not lower than $\sim 10^{-1}$ Pa. An inert gas is used as a carrier of reactive species coming from the source materials, which are normally loaded on an alumina boat positioned inside the working tube at a position where the temperature is usually slightly lower than its melting point. Substrates are placed downstream for collecting growth products, which may differ depending on the temperature of the collecting position and the distance from the source [54]. Depending on the choice of the source materials, oxygen is added to the inert gas stream at different concentrations, having influence on the volatility of the source, the stoichiometry of the vapor phase, and the formation of the products [55].

ZnO nanostructures can be grown by thermally activated CVD using either ZnO or metallic Zn source, with the addition of oxygen in the gas stream. The use of different ratios and mixtures of Zn and ZnO powders in the presence of oxygen under different growth temperatures changes the morphology and allows the formation of different nanostructures. For instance, nanobelts are typically grown using a ZnO powder source and a steady flow of oxygen, while nanotubes are believed to originate from nanorods which transform their shapes during elongation, due to partial sublimation of their cores [3]. A great variety of different ZnO crystal morphologies, such as nanowires, tetrapods, combs, springs, rings, trees, belts, and rods are generally found in different zones of vapor transport reactor [56, 57].

Several scientific works have reported the use of catalysts, such as nanoparticles of Au or other metals, deposited directly onto substrates to selectively grow nanorods and nanowires [20, 58–63]. In fact, on an amorphous surface or under lattice mismatching conditions, ZnO nanowires tend to grow in random directions. By pre-seeding substrates with catalysts, the nanostructures can be grown with a good control on size and homogeneity. For example, vertically aligned ZnO nanowires were grown on FeCrAl metal substrates using a thin pseudo-buffer layer, which was self-forming by annealing the FeCrAl metal substrate prior to growth [64]. Alternatively it was reported the use of 2 nm Au catalyst interlayers thermally evaporated onto silicon substrates, using a mixture of ZnO and carbon powders as source heated up to 900 °C in absence of oxygen in the gas stream [65].

However, the use of elements other than Zn as catalysts may induce undesired contaminations of nanocrystals and affect their properties. To avoid contamination, examples have been reported in the literature concerning the use of ZnO or Zn as

Fig. 5.7 Tilted SEM top
view of a ZnO nanowire array
grown from acetate-derived
seeds using APCVD at 650 °C
(scale bar 1 μm)
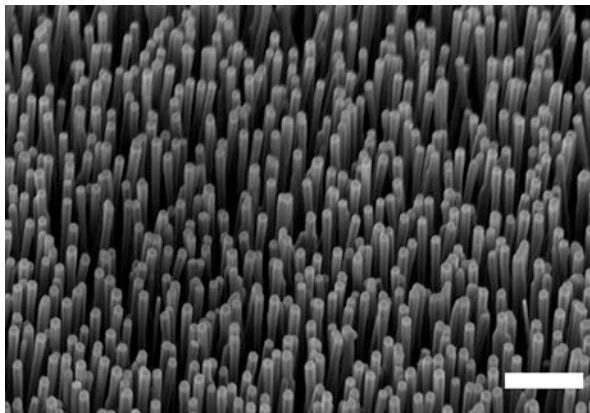
growth seeds for ZnO nanostructures. For instance, the decomposition or hydrolysis of zinc salts is an established route to the formation of ZnO colloids and nanocrystals in aqueous solution. This approach was used to form layers of ZnO nanocrystals, which can act as nucleation seeds for the CVD process, directly on a substrate by thermally decomposing zinc acetate at 350 °C [34]. In this way, the alignment of CVD-grown ZnO nanocrystals is substrate independent and occurs on flat surfaces regardless of their crystallinity or surface chemistry (Fig. 5.7). Moreover, this seeding method can be paired with nearly any ZnO growth technique, gas phase or solution phase (see also the paragraph "Oriented deposition by aqueous chemical method on substrates") [249].

Other works report the thermal CVD growth of vertically aligned ZnO nanowires on silicon/silicon dioxide substrates, with the use of a seed layer prepared by thermal treatment of a 30-nm-thick sputtered Zn layer [66]. The as-grown Zn film is thermally crystallized and oxidized to ZnO in a furnace at 400 °C in ambient air, forming a layer along the (002) plane. Also using this procedure, the growth direction of the nanowires depends on the seed layer crystallinity; therefore a good control of the seeding crystal orientation brings to deposition of well-aligned ZnO nanowires. The nanowires synthesized by this method have typical lengths of 1.0–5.0 μm and diameters of 50–100 nm and grow along the [002] direction.

The use of metallic Zn in place of ZnO powder as a source material for the synthesis was introduced in order to reduce the deposition temperature. As an example, several experiments from Calestani and coworkers were reported [67, 68], in which ZnO nanowires were grown by a self-catalyzed CVD method based on a combination of thermal evaporation and controlled oxidation. In those cases, metallic Zn served as both the source material and the catalyst for ZnO nanowires growth. The introduction of this metal layer allowed to achieve suitable and stable values of Zn overpressure on a large area (up to 20 cm^2), so that a selective growth of high-purity ZnO nanowires was reproducibly obtained on many substrates in each growth run. In the optimized process, a 10-μm-thick Zn overlayer was pre-deposited on alumina substrates, and the CVD process was carried out at a temperature of 650 °C in Ar/O$_2$ gas flow for 30 min, at atmospheric pressure (Fig. 5.8).
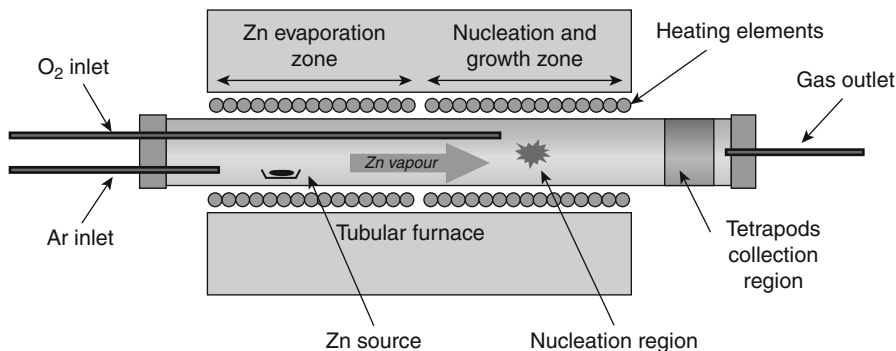
Fig. 5.8 Scheme of the APCVD synthesis reactor used in [68] (Reprinted from Sensors and Actuators B, 144, D. Calestani et al., Growth of ZnO tetrapods for nanostructure-based gas sensors, 472–478., Copyright (2010), with permission from Elsevier)

Authors also observed that several ZnO nanostructure morphologies are grown and found often mixed together (Fig. 5.9). By carefully selecting process parameters and the geometry of the deposition system, it is possible to separate the growth of nanowires from that of other nanostructures. In particular, ZnO tetrapods can be found downstream in the coldest zone of the reactor. These three-dimensional structures nucleate and grow while floating in the gas stream and accumulate at the end of the reaction tube, transported by the gas stream. As in the previous cases, structural analysis by XRD and TEM indicated that the nanowires and other nanostructures were made of ZnO single crystal in wurtzite hexagonal phase.

Several works report the use of thermal CVD to synthesize ZnO nanowires with modified values of the energy bandgap. In fact, ZnO high-energy bandgap can be tuned up in a wide range by doping with other materials [69]. The possibility of having both n-type and p-type ZnO nanowires is essential in order to fabricate electronic and optoelectronic devices. Wurtzite crystalline ZnO is naturally n-type and because of asymmetry in doping, synthesizing stable p-type ZnO is difficult. A possible way of introducing doping species during the deposition is the addition of doping species to the source material, for example, by using a mixed source of a chemical compound of phosphorus and ZnO powder and graphite powder, as reported in Refs. [70, 71]. In these cases, phosphorus-doped ZnO nanowires with high density and uniformity were grown in a LPCVD setup, at relatively high deposition temperature.

Sputter Deposition

The sputtering technique is among the most employed thin film deposition methods. In its simplest configuration, it exploits two electrodes (the cathode where the source material is placed and the anode represented by a substrate) placed in a vacuum chamber. A plasma is created in a gas by applying a polarization voltage
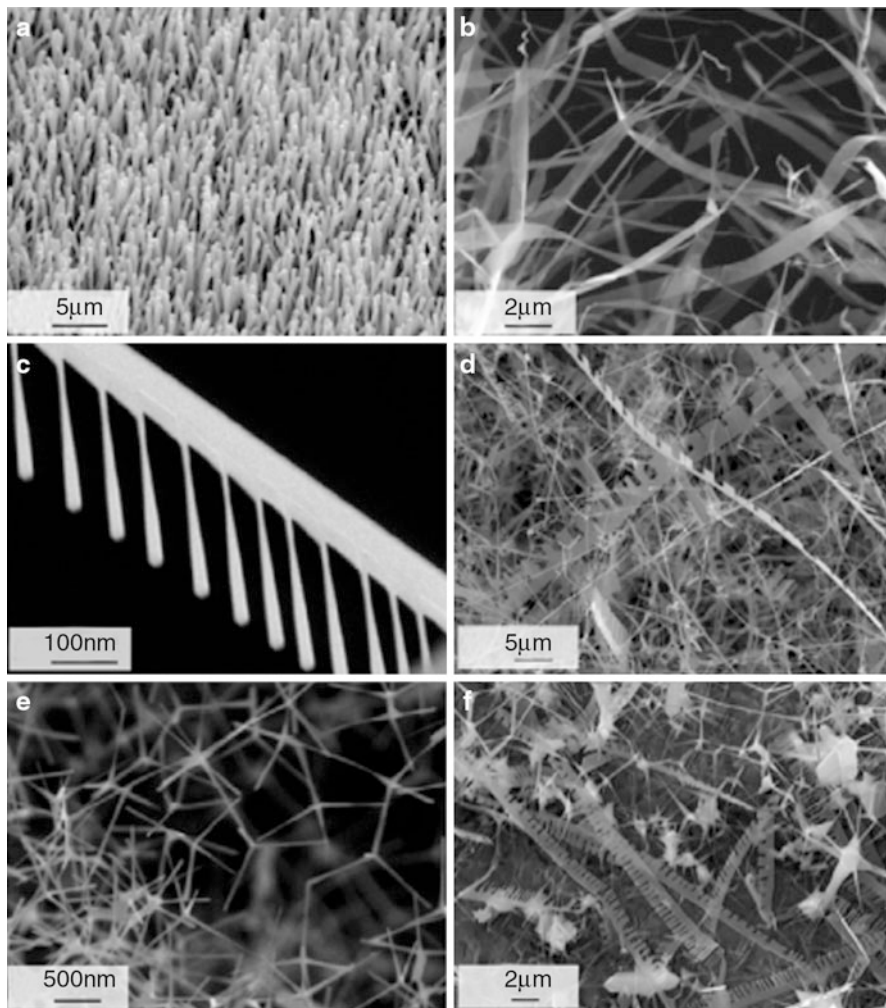
Fig. 5.9 SEM images of CVD-grown ZnO nanostructures: (**a**) nanorods with hexagonal cross section, (**b**) thin and large ribbons, (**c**) nanocombs, (**d**) tetrapods, (**e**) nanostructures mixed with tetrapods and powders, (**f**) nanostructures free of nanopowders and tetrapods [67] (Reprinted from Nanotechnology, 19 (2008) 325603, page 2, M. Zha et al., Large-area self-catalyzed and selective growth of ZnO nanowires, doi:10.1088/0957-4484/19/32/325603. © IOP Publishing. Reproduced by permission of IOP Publishing. All rights reserved)

between the electrodes. The polarization voltage can be a DC or a radio frequency (RF) voltage (usually at 13.56 MHz) and is chosen according to the nature of material to be grown. The ionized gas ions impact on the source material surface (usually called *target*) causing the removal of molecules that travel towards the substrate surface where they coalesce and grow as a thin film.

Fig. 5.10 FESEM micrograph of a ZnO thin film obtained by reactive magnetron sputtering deposition from a metallic target
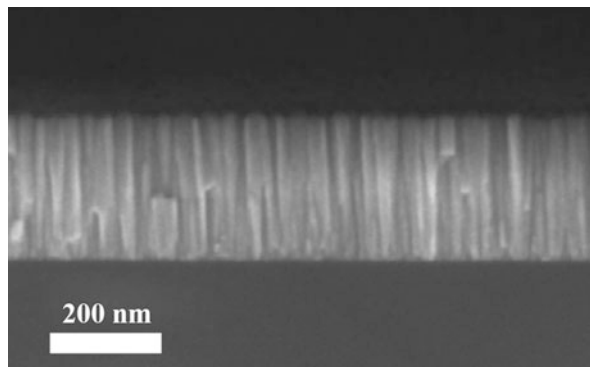
In the case of metallic thin films, a DC voltage is generally applied. The deposition of ceramic thin films, including ZnO films, requires particular conditions. As a first aspect to be considered, the ceramic materials have usually low conductivity. This behavior, in the case of DC polarization, causes a charge accumulation that would slowly reduce the ion acceleration towards the target with the creation of an electric field in opposition to that generated by the DC polarization. For this reason RF polarization is usually employed in the deposition of ceramic materials. A second aspect is related to the nature of the target material. An oxide material can be deposited as a thin film starting from either a metallic target or a ceramic target. In order to form an oxide material from a metallic target, oxygen has to be injected into the vacuum chamber in addition to the commonly used sputtering gas, i.e., argon. The concentration of oxygen is usually of few percent units, and it is responsible for the final stoichiometry of the deposited films. When a ceramic target is used, argon could be in principle the only gas inserted in the chamber, since oxygen is already present in the target material. However, oxygen is a volatile element, thus the resulting films obtained in an argon plasma can be oxygen deficient. For this reason a mixture of argon and oxygen is usually employed in order to compensate oxygen loss during the deposition process.

Many examples in literature [72–75] report on the reactive sputtering deposition (sputtering under reactive gas atmosphere) of dense or nanostructured zinc oxide films by means of the two approaches described above, although the formation of dense thin films is more likely to occur. In general, the use of ceramic targets promotes the growth of films with columnar structure and densely packed grains. An example of the typical morphology of a ZnO thin film obtained by reactive sputtering from ceramic target is reported in Fig. 5.10.

The deposition from Zn target is generally more favorable to the growth of porous ZnO films [73], and even nanowires formation [76] can occur with this method, although only particular system configurations (such as unbalanced sputtering systems) and conditions (especially oxygen partial pressure and RF power) have to be adopted. Moreover, other methods are more suitable for the synthesis of nanostructured ZnO since they can lead to highly ordered ZnO structures with a better control of the morphology. Therefore, in most cases, reactive sputtering is used for the growth of dense ZnO films.

ZnO films obtained by sputtering deposition grow in a polycrystalline form. They can exhibit different crystal orientations although a preferential *c*-axis orientation is often present even when grown at room temperature, i.e., without intentional heating supplied to the substrate. By accurately choosing the deposition conditions and the kind of substrate, the suppression of crystal orientations other than the [002] can be achieved. The ease of synthesizing *c*-axis-oriented ZnO films is an advantage when dealing with the fabrication of piezoelectric devices, since the piezoelectric coefficient in such films is maximized.

ZnO in the form of thin film is transparent and is characterized by unique electrical and optical properties that will be discussed in details later in this chapter. A way to easily tune these characteristics is to control the oxygen concentration in the gas mixture during the deposition process, since it regulates the oxygen incorporation in the films. Other parameters, such as substrate temperature and applied power, affect the final properties of ZnO films, and some examples will be given in below.

Classification of ZnO Nanostructures

From the morphological point of view, nanostructures can be categorized into four basic classes: 0D (i.e., nanoclusters and nanoparticles), 1D (i.e., nanotube, nanowires, nanorods, and nanobelts), 2D (i.e., nanoplates and layers), and 3D (i.e., nanotetrapods, nanoflowers) [77]. Other more exotic structures such as nanopropellers and nanorings can be tentatively ascribed to 3-D nanostructures. The deposition and growth methods have a profound impact on morphology and can be engineered to fabricate novel structures. In particular, the morphology is highly dependent on three parameters: source material composition, growth temperatures, and diffusion rates.

In the following paragraphs, the different morphologies of ZnO nanostructures and their main properties and applications are illustrated.

Nanoparticles Properties and Applications

Self-assembly synthesis methods are an important part of bottom-up techniques for the fabrication of small particles, employed as components in nanotechnology and material manufacturing. With this method, a profound control over the particle size, shape, and crystalline structure can be achieved.

ZnO nanoparticles are an excellent tool to design advanced structures with anisotropic properties. They have been widely employed in the literature as colloidal solutions for the preparation of thin films and seed layers for the further growth of vertically oriented nanowires; additionally they have been used as precursor for the 'oriented growth' of ZnO nanorods (as detailed in paragraph "Solution growth: Sol-gel hydrolysis and condensation method") [39]. One application is the anchoring of ZnO nanoparticles on other nanostructured and porous surfaces, mainly to enhance the luminescence properties [78, 79]. Another possibility to employ ZnO

nanoparticles is related to their use in medicine for drug delivery and anticancer agents [80]. The use of nanoparticles as filler of polymeric matrices leading to composite materials and their diverse applications will be discussed in paragraph "Hybrid materials containing ZnO nanofillers".

Nanorods, Nanowires, and Nanotubes: Properties and Applications

One-dimensional nanomaterials refer to nanowires, nanorods, nanofibers, nanocables, nanotubes, nanobelts, etc. which are elongated in one specific direction. Due to their unique optical and electronic properties, semiconducting ZnO nanowires or nanotubes are of crucial interest for the development of devices in nanoelectronics, chemical and biological sensing, energy conversion and storage (photovoltaic cells, batteries, capacitors, and hydrogen-storage devices), light-emitting diodes, catalysis, drug delivery, and piezoelectric energy nanogeneration [2, 32].

The aqueous chemical growth and CVD methods ensure that a great part of the nanowires obtained in an array are in direct contact with the substrate. In this way, ZnO nanowires provide a continuous pathway for electric carrier transport. This is an important feature for increasing the efficiency of future devices based on these kinds of nanomaterials [81]. Vertically oriented ZnO nanowires have good optoelectronic properties [18, 82], and thus they have been studied for the construction of light-emitting diodes and solar cells [83], including p-n junctions, dye-sensitized solar cells (DSC), and most recently for water splitting devices [84]. In addition, the piezoelectric and semiconducting properties of ZnO lead to possible applications as light, pH, and gas-sensing element [85–87], as well as to the construction of energy nanogenerators, as recently demonstrated by Wang and coworkers [17, 54]. These applications are briefly reviewed in the following paragraphs.

Gas Sensors

The large surface area of the ZnO 1-D nanostructures makes them attractive for gas and chemical sensing. Indeed the electrical conductivity of ZnO can be dramatically affected by the adsorption and desorption of gas species on their surface [88]. The first gas sensors based on ZnO were fabricated in the form of thin-film devices; however, compared with bulk and thin films, 1-D ZnO nanostructures have a higher aspect ratio and thus surface area, giving rise to a higher sensibility and selectivity to gas molecules.

The mechanism behind ZnO gas sensors is usually described by the change of electrical properties induced by the adsorption of gas molecules on the surface of ZnO [89, 90]. In general, undoped ZnO is naturally an n-type semiconductor due to oxygen vacancies acting as electron donors which supply electrons to the conduction band. In ambient air, some oxygen molecules are adsorbed on the surface of the ZnO and subsequently reduced to oxygen ions (O_2^-, O^-, and O^{2-}) by capturing

electrons from the ZnO conduction band, resulting in an increased electrical resistance [91]. When exposed to a reducing gas environment at moderate temperatures, the gas reacts with the adsorbed oxygen ions, releasing the trapped electrons back to the conduction band, thereby leading to an increased carrier concentration. Consequently, the resistance decreases under exposure to reducing agents such as ethanol (CH_2OH), acetone (C_3H_6O), ammonia (NH_3), carbon monoxide (CO), and hydrogen (H_2) [90, 92]. Wang et al. reported gas sensors based on hydrothermally synthesized ZnO nanowire arrays finding excellent sensitivity to H_2, NH_3, and CO [93]. A highly selective gas sensor based on dumbbell-like ZnO was reported by Qi et al. [94], showing high sensitivity to acetone; less sensitivity to ethanol, methanol (CH_3OH), and ammonia; and no sensitivity to CO, NO (nitrogen monoxide), NO_2 (nitrogen dioxide), CH_4 (methane), and H_2. Sensors based on single-crystalline ZnO nanoscrew drivers hydrothermally grown showed high sensitivity to hydrogen sulfide (H_2S) gas, exhibiting detection limits at ppb levels at 150 °C [95].

In addition, some researchers have been focused on improving the sensitivity of ZnO gas sensors by surface modification. Kakati et al. reported ZnO nanowires with an indium antimonide (InSb) surface modification. They found that the acetone sensitivity was significantly improved due to the reduced activation energy [96].

pH Sensors

The surface electrical charge density or electrode potential of ZnO changes with pH in electrolyte [97, 98]. The sensing mechanism for chemical adsorbates in piezoelectric materials originates from the compensation of the polarization-induced-bound surface charge by interaction with the polar molecules in the liquids. The pH response of metal oxide surfaces has been modeled by a number of groups in terms of formation of hydroxyl groups that lead to a pH-dependent net surface change with a resulting change in voltage drop at the semiconductor/liquid interface [99, 100]. Based on this principle, ZnO nanorods were used to fabricate a highly sensitive pH sensor on Ag-coated borosilicate glass Femtotio® II capillaries to detect the intracellular pH of a human fat cell [97]. Other authors [101] have shown pH-sensing devices based on single-ZnO nanorods with ohmic contacts at either ends, exhibiting large changes in current upon exposing the surface region to polar liquid electrolytes. The polar species led to a change of surface charges on the ZnO nanorod, producing a change in surface potential at the semiconductor/liquid interface, with a linear change in conductance between pH 2 and 12 of 8.5 nS/pH in the dark with a stable operation and a resolution of 0.1 pH over the entire pH range.

UV Sensors

ZnO has great potentialities for optical applications, such as UV detection. Soci et al. [102] have proposed that the high-sensitivity UV detection of ZnO nanowires is due to the presence of oxygen-related hole-trapping states at their surface.

Very recently Yang et al. [85] have proposed an enhancement of the UV sensitivity of single-ZnO nanowires by tuning the mechanical strain applied to it. Therefore the authors exploited the coupling of optical, mechanical, and electrical properties of ZnO nanowires. The photodetector device was built in a metal–semiconductor (ZnO)-metal configuration, guaranteeing a nonlinear conduction mechanism, thus a Schottky barrier between the nanowires and the metal electrode. The paper showed a deep investigation on photoconducting responses at different bending strains and excitation light intensities.

Field Emission Devices

ZnO 1-D nanostructure arrays are also efficient field emitters, thanks to their low work functions, high aspect ratios, high mechanical stabilities, and conductivities [103]. It has been also shown that the field emission efficiency can be improved by controlling the emitter density and aspect ratio [104–106]. Emitters that are too closely packed suffer from a screening effect, whereas emitters spaced too far apart approach the behavior of a thin film [107, 108]. Therefore, it is expected that there is an optimal density for achieving the best field emission performance. In particular it resulted that an emitter density of seven nanowires per μm^2 and a tapered tip morphology generated a high-field enhancement factor of 5,884 with a low turn-on field of 5.1 V μm^{-1} [109].

Field-Effect Transistors

ZnO nanorods and nanobelts have been successfully used for the fabrication of field-effect transistors (FETs). Arnold et al. [110] fabricated FETs by depositing dispersed ZnO nanobelts on predefined gold electrode arrays. A 120-nm-thick SiO_2 gate dielectric and a back gate electrode fabricated by evaporating gold on the p^+ Si side of the substrate were used. By forming metal electrode/nanostructure electrical contacts, a typical nanobelt FET showed a gate threshold voltage of -15 V, a switching ratio of nearly 100, and a peak conductivity of $1.25 \cdot 10^{-3}$ Ω^{-1} cm^{-1} [110]. In addition high-performance n-channel FETs with back gate geometry were also fabricated using e-beam lithography along with high-quality ZnO nanorods prepared by catalyst-free metalorganic vapor phase epitaxy (MOVPE) [111]. At room temperature, typical ZnO nanorod FETs exhibited good electrical characteristics with a transconductance of 140 nS and a mobility of 75 cm^2 V^{-1} s^{-1} (at a gate voltage of 2.4 V). This electron mobility is higher than that of the ZnO thin-film transistors [112], presumably due to high purity and low defect concentrations of single-crystal ZnO nanorods as a result of the employed catalyst-free growth method. ZnO nanowire FETs were also utilized for O_2 detection [113]. Single-crystal ZnO nanowires synthesized by CVD method were configured as FETs, and the adsorption of oxygen molecules was shown to cause the depletion of the FET channel. The chemisorbed oxygen on the ZnO surface at vacancy sites forms O^{2-},
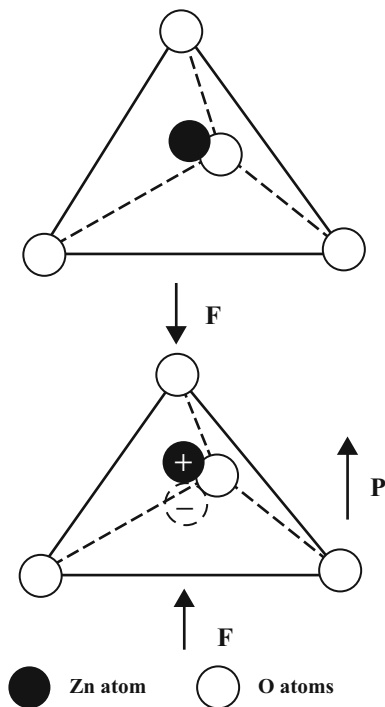
resulting in a surface charge depletion layer which leads to a reduction in the electrical conductivity. Moreover, detection sensitivity could be modulated by the gate voltage, and it was shown to increase with decreasing nanowire radius from 270 to 20 nm. The single-nanowire photoconductivity spectrum was also measured for these FETs, and the transconductance was observed to decrease with illumination. It was demonstrated that the nanowire FETs could be reversibly turned on and off by applying a switching illumination.

Piezoelectric Nanogenerators

One of the most significant properties of ZnO nanostructures is piezoelectricity, the ability of generating polar charges in dielectric crystals subjected to an external mechanical stress. The origin of the ZnO piezoelectricity is based on its non-centrosymmetric crystal structure, where the oxygen and zinc atoms are tetrahedrally bonded. Thus, the center of positive charge (Zn atom) and negative charges (O atoms) can be displaced due to an external pressure inducing a lattice deformation (Fig. 5.11), resulting in the creation of local dipole moments. If all of the tetrahedra in the crystal have the same orientation or some other mutual orientation that does not allow for a cancellation among the dipoles, the crystal will have a macroscopic dipole. The two opposite faces of the crystal have opposite electric charges, thus a macroscopic dipole moment appears over the whole crystal.

Several studies of Wang and coworkers have demonstrated that by deflecting vertically aligned ZnO nanowires or nanobelts using a conductive AFM tip, the nanoscale mechanical energy could be converted into electric energy exploiting the characteristic ZnO nanowires piezoelectric effect which make them quite suitable to be used in energy nanogenerators and harvesters [16, 115, 116]. In particular the authors obtained an effective piezoelectric coefficient d_{33} of ZnO nanobelt varying from 14.3 to 26.7 pm V^{-1}, depending on the frequency [115]. The values are much larger than that of the ZnO bulk (0 0 0 1) of 9.93 pm/V.

Dye-Sensitized Solar Cells

Dye-sensitized solar cells (DSCs) are among the most promising low-cost devices for the conversion of solar energy into electrical current. In general, the anodes of DSCs are made of TiO_2 in the form of films or nanostructures, although the use of other materials, such as SnO_2 or ZnO nanoparticles [117] deposited as a paste on a defined substrate and sintered to produce electrical continuity, has been proposed. The nanostructured film provides a large internal surface area that allows to load a high amount of dye molecules, which are responsible for solar light absorption. The strategy of increasing the photoelectrode surface area using ZnO nanorods has been widely investigated, because they provide direct electrical pathways ensuring the rapid collection of carriers generated throughout the device [118].

However, one of the new challenges for the scientists is to create innovative ZnO DSCs with improved efficiency. In particular, when the nanowires are closely spaced, approximately twice the exciton diffusion length (<40 nm) where recombination occurs, the rate of recombination is greatly reduced, thus enhancing the power conversion efficiency [21].

Porous and Dense ZnO Thin Films

Among ZnO morphologies, nanowires and nanorods are object of a great number of works. Arrays of nanowires, nanorods, or nanotubes supported by a substrate are often considered as porous structures. However, due to their unique properties and to the numerous fields of applications, a separate section has been dedicated to their description. For this reason the present paragraph will describe in details synthesis methods, properties, and applications concerning only ZnO-disordered porous structures and dense thin films.

Porous ZnO films

The synthesis of porous ZnO films can be performed by means of numerous methods, which can be classified in two main families: chemical and physical synthesis routes.

Among the chemical synthesis methods employed for the formation of porous layers, techniques such as self-assembled monolayer (SAM) [119], sol–gel synthesis [120], hydrothermal synthesis [121, 122], successive ionic layer adsorption and reaction (SILAR) method [123], and electrodeposition [124], sometimes associated to the use of templating elements [125], allow the formation of stable porous ZnO nanostructures.

Physical synthesis techniques, instead, are not as effective as the chemical routes to this task. Some examples of porous ZnO layers obtained by physical processes are given in paragraph "Sputter deposition". Nevertheless, the combination of different physical methods organized as successive steps allows the synthesis of porous structures. An example of this approach is represented by the method exploiting as first step the growth of a porous zinc layer by means of a physical vapor deposition (PVD) technique and as second step the thermal oxidation, occurring at relatively low temperature, of the metallic zinc layer, giving rise to a porous ZnO layer. The key point of this method lies in the fact that with PVD techniques it is easier to obtain porous layers of zinc, rather than porous films of ZnO. The explanation to this phenomenon can be found in the so called structure zone model, proposed by Movchan and Demchishin, and successively integrated by Thornton [126] first, and then by Jankowski and Hayes [127], and is mainly related to the effect of the combination of gas pressure and substrate temperature during the deposition process.

The PVD technique used in this two-step method to deposit porous Zn layers can be either thermal evaporation [128] or sputtering deposition using a substrate temperature of about 100 °C [129]. Only recently room temperature sputtering deposition of porous zinc layers, followed by oxidation, has been proposed [130], and the resulting ZnO morphology has been found to be basically independent of the kind of substrate used [131].

Porous films can also be obtained by oxidizing slices of zinc at about 380 °C [132]. However, in this case, the choice of the substrate is fixed.

Figure 5.12 reports the morphology of a ZnO film obtained by the sputtering deposition of a porous zinc film followed by a thermal oxidation in ambient air at 380 °C.

Due to the high surface-to-volume ratio, porous ZnO films have been successfully used for the fabrication of gas sensors [133]. Indeed, for a fixed substrate size, a higher amount of gas molecules can be adsorbed on the film surface with respect to a dense film. Since the mechanism of ZnO gas sensors resides in the variation of the electrical transport properties with oxygen sorption, a higher amount of gas adsorbed all over the bulk porosity causes a higher variation of the conduction in the material. Therefore, the sensing capability in porous layers is enhanced.

Films of porous ZnO are also employed as sensing layers in UV photodetectors. ZnO is a semiconductor with a bandgap of 3.37 eV [134], thus able to generate electron–hole couples when exposed to UV light. Moreover, the oxygen adsorbed on the surface in dark conditions under UV radiation is photodesorbed by capturing a photogenerated hole. Therefore the conduction in the material is further enhanced. The morphology in this case plays an important role, because the number of defects

Fig. 5.12 FESEM micrograph of a ZnO porous layer obtained by a two-step method (sputtering + thermal oxidation)
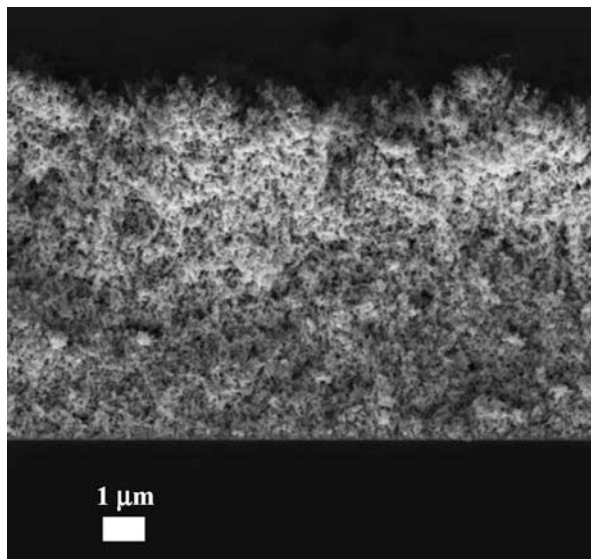
formed under UV light is higher for layers with high specific surface area. As a drawback the slow process of dissociative adsorption of OH^- groups at the optically generated defects contributes to a lowering of the photoconduction. Nevertheless this effect is not immediately observed, since it requires time for being appreciated and it occurs also when the layer of ZnO is dense.

In the field of solar energy harvesting, particularly for what concerns DSCs, photoanodes based on porous zinc oxide layers can provide photoconversion efficiencies as high as about 7 % [119, 135, 136], although TiO_2-based photoanodes still give the best performances (with efficiencies over 11 % [137]). Many efforts have been dedicated by several research groups to the study of nanostructured ZnO-based DSC photoanodes, since ZnO electronic transport and mobility properties are more favorable to the correct DSC operation than those of TiO_2, and, in addition, the advantage over TiO_2, represented by the ease of synthesizing ZnO nanostructures with a variety of shapes, can help tuning such properties [137]. In spite of these advantages, the degradation that ZnO undergoes when in contact with the dye-impregnating solution limits the dye loading in the photoanode. For this reason the photoconversion efficiency is still lower for ZnO-based photoanodes, and some alternatives are being investigated, such as the variation of the pH of the sensitizing solutions [135] or the introduction of TiO_2-ZnO core-shell structures, where TiO_2 can prevent the contact between ZnO and the sensitizing solution.

The possibility to obtain unique ZnO morphologies exhibiting very high surface-to-volume ratios has been successfully exploited also in the fabrication of biosensors. ZnO is a biocompatible material that has a high isoelectric point (IEP), suitable for the adsorption of low-IEP proteins or enzymes [138], and its bandgap and electrical properties facilitate the electron transfer of the enzymes immobilized on its surface [139]. Some works revealed that, when in the form of porous

nanostructure, ZnO further improves the electron transfer of the immobilized enzymes, thus enhancing the sensing capability of such sensors with respect to those based on solid nanospheres [139].

These unique electrical and optical properties, combined with the possibility to expose high surface area to air or different kinds of chemical or biological solutions, make porous ZnO a good candidate for a wide range of applications.

Dense ZnO Films

Unlike the porous ones, dense ZnO films can be grown by many physical vapor and chemical vapor deposition techniques. Among them pulsed laser deposition (PLD) [140, 141], sputtering [119, 142], CVD [143], metalorganic chemical vapor deposition (MOCVD) [144], and MBE [145] can be used for depositing thin films of ZnO on various substrates and with different crystalline characteristics. MOCVD and MBE can promote epitaxial growth of ZnO if a material with lattice constants close to those of ZnO is chosen as substrate. Films obtained with the other techniques are more likely to grow as polycrystalline layers. However, although random crystal orientation may be present in some cases, films textured along [002] direction can be easily obtained by means of all the abovementioned techniques by properly tuning the deposition conditions. This is an advantage when a maximization of the piezoelectric coefficient is desired.

As discussed in the previous section, the combination of morphology and material properties defines the fields of application of ZnO. The surface-to-volume ratio of dense films is much lower than in the case of porous nanostructures, thus lower performances are achieved in those applications requiring the impregnation of the material or a high specific surface area, as in the case of gas sensors or DSC photoanodes.

In spite of this drawback, dense films can still be employed in solar energy-harvesting or -sensing devices [146, 147].

Due to their electrical properties, high-quality crystalline and dense films of ZnO have been successfully employed for the fabrication of thin-film transistors (TFTs), which require high channel mobility [148, 149]. In addition to its electrical properties, ZnO films are transparent in the visible portion of the electromagnetic spectrum, and their use in TFTs opens a path towards transparent devices for display or other optoelectronic applications requiring transparent and fast response devices. Another advantage of the use of ZnO resides in the fact that high-quality polycrystalline ZnO thin films can be obtained at/close to the room temperature, thus allowing the deposition on polymer substrates, which can add flexibility to these devices.

The optical properties of ZnO films can be exploited for lasing operations. By pumping at a UV wavelength ZnO polycrystalline films deposited on glass, laser emission in the range of 385–390 nm can be appreciated [150].

ZnO thin film-based surface acoustic wave (SAW) [151] and film bulk acoustic resonator (FBAR) filters [152], usually employed for electronic telecommunication

purposes, are characterized by resonance frequencies of the order of the GHz and by high-electromechanical coupling coefficients. Since the resonance frequency can be strongly affected by the mass variation of the material, ZnO-based SAW devices and FBARs [153–155] have been successfully employed also as biosensors [156, 157] and gas sensors [158] able to detect the presence of biological molecules or gas adsorption on their surface.

An interesting configuration, involving ZnO films for sensing and actuation purposes, consists in the deposition of ZnO films on a cantilever. The piezoelectric material on the topside of a cantilever provides displacement sensing to the system and can at the same time replace the optical displacement sensing setup, that is not effective in the case of cantilever arrays. Another advantage is represented by the actuation capability of the piezoelectric film since, when polarized, it responds with a deformation that is in turn transferred to the cantilever. This configuration is useful when indentation or scratching operations are desired [142].

Although the limitation consisting in the lack of porosity that precludes their use when impregnation or exposure of large surface to air or solutions are required, ZnO dense films are versatile structures that allow to achieve valuable results in many applications.

Hybrid Materials Containing ZnO Nanofillers

In the latest years, hybrid materials with ZnO nanoparticles embedded in organic matrices were utilized in different fields, both for structural and functional applications. In the following paragraphs, a brief overview of the latest developments on these materials is reported, sorted according to the application.

Structural Application

Zinc oxide nanoparticles were used as reinforcement fillers for improving the structural properties of a wide range of polymers such as rubber [159], PP [160], PET [161], epoxy resin [162, 163], PMMA [164], polysulfone [165] and many others [166–170]. Also nanocomposites based on renewable sources were studied [171].

More specific studies were devoted in evaluating the enhancement in surface properties obtained by the addition of ZnO nanoparticles, e.g., scratch resistance (Chakraborty et al. in PMMA [172] and Bermúdez et al. in polycarbonate [173]), corrosion (Olad et al. in PVC [174] and Dhoke [175] et al. in waterborne resins [175]), and gas barrier [176]. Other applications were found in nanocomposites for wood protection [177–179] and phase-changing materials (PCM) [180].

Although ZnO is a well-known UV absorber and it was also used for UV-shielding materials, UV-curable ZnO hybrid materials were synthesized, maintaining high transparency in the visible range (Fig. 5.13). ZnO nanoparticles were principally incorporated in acrylic resins [181–186] but also in epoxy [187] and thiol-ene systems [188]. A particularly interesting application was reported by

Fig. 5.13 UV-cured acrylic/ZnO hybrid materials with high transparency (Reprinted from Ceramics International, 36(4), H.C. Huang, T.E. Hsieh, Preparation and characterizations of highly transparent UV-curable ZnO-acrylic nanocomposites, 1245–1251., Copyright (2010), with permission from Elsevier)
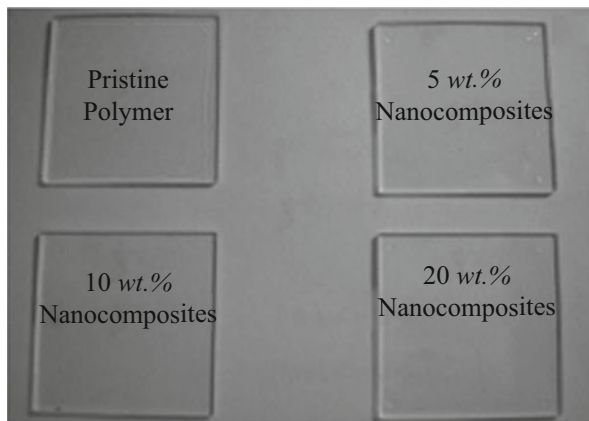
Schmitt on the use of ZnO nanoparticles both as filler and photoinitiator for acrylic resin UV curing [189].

At last, an extensive reviewing of nanohybrid materials of hyperbranched polymer and different metal oxides, among which zinc oxide, was recently reported by Hu et al. [190].

Optical Applications

ZnO nanoparticles are widely used as active filler for the modification of the optical properties of polymers. In this frame, the most common application is the use of ZnO for creating excellent UV-shielding materials. Hybrid materials were synthesized by embedding or creating in situ, by sol–gel technique, ZnO nanoparticles in different transparent polymeric resins such as PS [191], PMMA [192], PVDF [193], EVA [194], PLA [195], UV-curable resins [196], and copolymers [197, 198]. ZnO nanocomposites also exhibit resistance against ionizing radiations, thus opening application possibilities in this field [199]. A particular application related to UV-shielding properties of ZnO is in the cosmetic field for solar protection of the skin, as reviewed by Morabito et al. [200].

ZnO nanoparticles were utilized for modifying the optical properties of hosting matrices. Wong et al. [201] reported a method for tuning the refractive index of hybrid materials by different functionalization of ZnO nanoparticles. Moreover, PS-ZnO layers were used as scattering layers for improving the efficiency of OLED [202] and for obtaining structures with nonlinear optical properties [203, 204].

Hybrid Materials for Energy Applications

As already mentioned, ZnO is a wide bandgap semiconductor that, in the presence of a suitable radiation, is able to generate a photocurrent. This property

Fig. 5.14 Strain sensor based on PSS/PVA-ZnO (With kind permission from Springer Science+Business Media: Journal of Materials Science Zinc oxide nanoparticle-polymeric thin films for dynamic strain sensing, 46(1), 2010, 228–237, K.J. Loh)
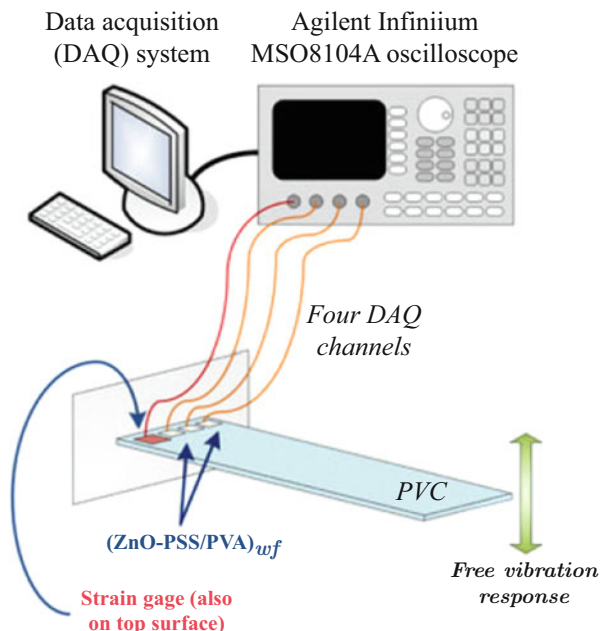
was widely exploited in the last years for synthesizing materials for solar energy application. ZnO hybrids materials were prepared employing poly (*N*-vinylcarbazole) [205, 206], poly(phenylene vinylene) copolymers [207–209], polyaniline [210], poly(3-hexylthiophene) [211, 212], polypyrrole [213], and poly(3,4-ethylenedioxythiophene) [214] as hosting matrices.

Recently Bouclé and Ackermann reported an extensive review of the state of the art and of the perspectives of hybrid materials containing ZnO for photovoltaic applications [215].

In the energy materials frame, some works are present in the literature regarding the use of ZnO hybrid materials for synthesizing ion conductive membranes as host matrices, such as PEO [216], gel-polymer electrolyte [217], and cellulose [218]. These materials could be employed as polymeric electrolytes in Li-ion batteries.

Sensors Based on ZnO Hybrid Materials

Many sensors exploit ZnO nanoparticles as active material due to their numerous potentialities. First of all, the photogeneration of charges occurring in ZnO hybrid materials under UV irradiation led to the use of such structures in UV sensors [86, 219, 220]. Nanocomposites were also used for preparing strain sensors (see Fig. 5.14) embedding ZnO nanowires in PDMS [221], PVA [222], or polyimide [223]. Another trend application is in gas [224, 225] and thermal sensors [226].
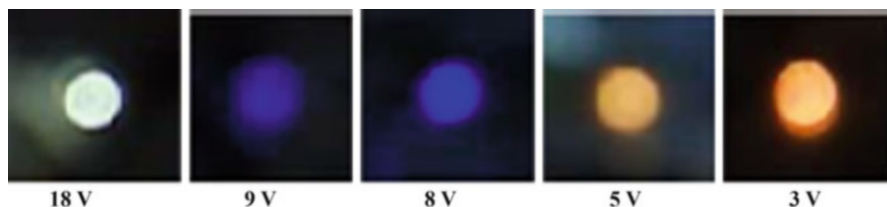
Fig. 5.15 PAM/ZnO electroluminescent device at different voltage applied (With kind permission from Springer Science+Business Media: Journal of Nanoparticle Research Blue electroluminescence nanodevice prototype based on vertical ZnO nanowire/polymer film on silicon substrate, 12(1), 2009, 169–176, Y. He, J. A. Wang, X. B. Chen, W. F. Zhang, X. Y. Zeng, Q. W. Gu)

At last there is a great interest for biological sensors, recently reviewed by Arya [227] and Pearton [228].

Light-Emitting Devices

In the last decade, ZnO-based light-emitting devices were largely studied due to the robust light emission of ZnO nanowires and colloids. The embedding of these nanoparticles in polymer matrices was largely studied in order to synthesize flexible and transparent light-emitting devices for optoelectronic applications (see Fig. 5.15). As hosting matrices, common polymers such as polymethylmethacrylate [229], polystyrene [230], poly(vinylalcohol) [231], and epoxy resins [232, 233] as well as specialty polymers such as polynorbornene [234], polyacrylamide [235], polydiacetylene [236], and MEh-PPV copolymers [237] were used. A recent review of hybrid organic–inorganic light-emitting devices was reported by Sessolo and Bolink [238].

As a different electrooptical materials, Fang et al. recently reported about novel supramolecular nanocomposites based on pyridine-functionalized ZnO in aryl-imidazo-phenanthrolines [239].

Other Applications

ZnO hybrid materials were used for other innovative applications such as piezo-electric materials taking advantage of the piezoelectric properties of ZnO nanoparticles, as reviewed by Wang et al. [2] For example, Prashanthi et al. recently reported about a piezoelectric nanocomposite based in photosensitive resin for MEMS applications [240] while Gullapalli et al. reported about a piezoelectric paper nanocomposite [241].

The last class of materials is represented by materials for bio-applications. In this frame it is possible to mention both materials for health care [242, 243] and materials for tissue engineering [244]. Other studies could be found in reviews from Brayner [245] and Kaiser [246].

Trends and Future Developments for Application of ZnO Nanostructures

Due to the unique properties of ZnO nanostructures, as described in the previous paragraphs, it is easy to imagine the importance of this material for future applications. In particular the combination of different properties of ZnO, such as the piezotronic [10] and the piezo-phototronic [11] effects in addition to the ease of fabrication and availability of raw materials and low impact on the environment at the end of life cycle, would enable in the near future the broad use of ZnO nanostructures.

The good compatibility of ZnO nanostructure fabrication with silicon-based processes that are the basis for MEMS and CMOS devices fabrication suggests an easy integration of nanodevices to obtain cost-effective multifunctional sensors (pressure, strain, UV light) [247] or hybrid energy harvesters able to collect both the energy of light and the energy carried by mechanical vibrations [248]. Process should be controlled in order to avoid contact with deionized water, due to a slight solubility of 2 mg/l, and with other strong acids such as Piranha solution. Finally, heat treatments at temperatures higher than 400 °C should be avoided in the fabrication process of MEMS devices, due to the sensitivity of the components to higher temperatures. Following these requirements, it would be possible to fabricate MEMS devices integrating ZnO nano-objects controlled in size, aspect, orientation, and properties.

Devices based on surface acoustic waves, for example, would require ZnO thin films deposited by means of RF sputtering. Applications for those devices are foreseen in microfluidic devices, where fluid movimentation, mixing, and eventually ejection may be obtained by a fine tuning of the supersonic wave pattern propagating on the surface of the thin ZnO film [153–155].

Chemical methods, using low-temperature wet techniques, will probably represent the best solution for large-scale, low-cost, and lower-quality nanostructures, for the high-volume segment of consumer flexible electronics, the fast growing market that will soon permeate society. Typical issues for the flexible electronics field are (i) low-cost flexible and disposable substrates, such as paper, polyethylene, polypropylene, polyester, and polyamide; (ii) low-temperature processes, compatible with the substrate; (iii) high-throughput fabrication technologies such as roll-to-roll printing, flexography, gravure, offset, screen printing; and (iv) low-speed devices based on polymeric semiconductors (<100 MHz).

An example of target device will be a flexible DSC panel, where both ZnO and TiO_2 are excellent candidates to support the organic photoactive materials [215].

For what concerns biosensing applications, it has been shown that ZnO nanostructures represent a preferred substrate for supporting sensing biomolecules (receptors) and for enhancing signal transduction and operational stability of the sensor. Once again the unique properties of ZnO (mainly semiconducting, piezoelectric, piezotronic and piezo-phototronics) will be exploited to fabricate cost-effective and reliable sensors for DNA or other biomolecule detection.

Besides these advanced applications in sensors and devices, ZnO nanoparticles are nowadays and will be in the future strongly demanded by cosmetics, in particular as filler for UV solar filters.

Scientific breakthroughs are still demanded, for what concerns the neutralization of the piezoelectric potential screening effect due to free carriers and the optimization and localization of those free carriers in the semiconductor.

References

1. Morkoç H, Özgür Ü (2009) Zinc oxide: fundamentals, materials and device technology. Wiley-VCH, Weinheim, Germany
2. Shen XS, Wang GZ, Hong X, Zhu W (2009) Nanospheres of silver nanoparticles: agglomeration, surface morphology control and application as SERS substrates. Phys Chem Chem Phys 11:7450–7454
3. Gomez JL, Tigli O (2013) Zinc oxide nanostructures: from growth to application. J Mater Sci 48:612–624
4. Wang ZL (2009) ZnO nanowire and nanobelt platform for nanotechnology. Mat Sci Eng R 64:33–71
5. Vayssieres L, Keis K, Hagfeldt A, Lindquist S-E (2001) Three-dimensional array of highly oriented crystalline ZnO microtubes. Chem Mater 13:4395–4398
6. Ozgur U, Alivov YI, Liu C, Teke A, Reshchikov MA, Dogan S, Avrutin V, Cho S-J, Morkoc H (2005) A comprehensive review of ZnO materials and devices. J Appl Phys 98:041301
7. Tian ZR, Voigt JA, Liu J, McKenzie B, McDermott MJ, Rodriguez MA, Konishi H, Xu H (2003) Complex and oriented ZnO nanostructures. Nat Mater 2:821–826
8. Wilson SA, Jourdain RPJ, Zhang Q, Dorey RA, Bowen CR, Willander M, Wahab QU, Al-hilli SM, Nur O, Quandt E, Johansson C, Pagounis E, Kohl M, Matovic J, Samel B, van der Wijngaart W, Jager EWH, Carlsson D, Djinovic Z, Wegener M, Moldovan C, Iosub R, Abad E, Wendlandt M, Rusu C, Persson K (2007) New materials for micro-scale sensors and actuators: an engineering review. Mater Sci Eng R 56:1–129
9. Zhang Y, Yan X, Yang Y, Huang Y, Liao Q, Qi J (2012) Scanning probe study on the piezotronic effect in ZnO nanomaterials and nanodevices. Adv Mater 24:4647–4655
10. Zhang Y, Liu Y, Wang ZL (2011) Fundamental theory of piezotronics. Adv Mater 23:3004–3013
11. Xu S, Guo W, Du S, Loy MMT, Wang N (2012) Piezotronic effects on the optical properties of ZnO nanowires. Nano Lett 12:5802–5807
12. Calestani D, Zha M, Mosca R, Zappettini A, Carotta MC, Natale VD, Zanotti L (2010) Growth of ZnO tetrapods for nanostructure-based gas sensors. Sens Actuat B 144:472–478
13. Kiasari NM, Servati P (2011) Dielectrophoresis-assembled ZnO nanowire oxygen sensors. IEEE Electron Device Lett 32:982–984
14. Desai AV, Haque MA (2007) Mechanical properties of ZnO nanowires. Sens Actuat A Phys 134:169–176
15. Xu S, Qin Y, Xu C, Wei Y, Yang R, Wang ZL (2010) Self-powered nanowire devices. Nat Nanotechnol 5:366–373
16. Wang ZL, Song J (2006) Piezoelectric nanogenerators based on zinc oxide nanowire arrays. Science 312:242–246
17. Wang ZL, Yang RS, Zhou J, Qin Y, Xu C, Hu YF, Xu S (2010) Lateral nanowire/nanobelt based nanogenerators, piezotronics and piezo-phototronics. Mat Sci Eng R 70:320–329
18. Wang ZL (2004) Zinc oxide nanostructures: growth, properties and applications. J Phys Condens Matter 16:R829
19. Huang MH, Wu Y, Feick H, Tran N, Weber E, Yang P (2001) Catalytic growth of zinc oxide nanowires by vapor transport. Adv Mater 13:113–116

20. Zhu Z, Chen T-L, Gu Y, Warren J, Osgood RM (2005) Zinc oxide nanowires grown by vapor-phase transport using selected metal catalysts: a comparative study. Chem Mater 17:4227–4234
21. Yu D, Trad T Jr, McLeskey JT, Craciun V, Taylor CR (2010) ZnO nanowires synthesized by vapor phase transport deposition on transparent oxide substrates. Nanoscale Res Lett 5:1333–1339
22. Wu JJ, Liu SC (2002) Catalyst-free growth and characterization of ZnO nanorods. J Phys Chem B 106:9546
23. Park WI, Kim DH, Jung SW, Yi GC (2002) Metalorganic vapor-phase epitaxial growth of vertically well-aligned ZnO nanorods. Appl Phys Lett 80:4232–4234
24. Yuan H, Zhang Y (2004) Preparation of well-aligned ZnO whiskers on glass substrate by atmospheric MOCVD. J Cryst Growth 263:119–124
25. Heo YW, Varadarajan V, Kaufman M, Kim K, Norton DP, Ren F, Fleming PH (2002) Site-specific growth of ZnO nanorods using catalysis-driven molecular-beam epitaxy. Appl Phys Lett 81:3046–3048
26. Sun Y, Fuge GM, Ashfold MNR (2004) Growth of aligned ZnO nanorod arrays by catalyst-free pulsed laser deposition methods. Chem Phys Lett 396:21–26
27. Chiou WT, Wu WY, Ting JM (2003) Growth of single crystal ZnO nanowires using sputter deposition. Diam Relat Mater 12:1841–1844
28. Bechelany M, Amin A, Brioude A, Cornu D, Miele P (2012) ZnO nanotubes by template-assisted sol–gel route. J Nanopart Res 14:980–987
29. Öztürk S, Tasaltın N, Kılınç N, Yüzer H, Öztürk ZZ (2010) Fabrication of ZnO nanowires at room temperature by cathodically induced sol–gel method. Appl Phys A 99:73–78
30. Ramirez D, Pauporte T, Gomez H, Lincot D (2008) Electrochemical growth of ZnO nanowires inside nanoporous alumina templates. A comparison with metallic Zn nanowires growth. Phys Stat Solid (a) 205:2371–2375
31. Xu S, Wang ZL (2011) One-dimensional ZnO nanostructures: solution growth and functional properties. Nano Res 4:1013–1098
32. Weintraub B, Zhou Z, Li Y, Deng Y (2010) Solution synthesis of one-dimensional ZnO nanomaterials and their applications. Nanoscale 2:1573–1587
33. Li Y, Xu L, Li X, Shen X, Wang A (2010) Effect of aging time of ZnO sol on the structural and optical properties of ZnO thin films prepared by sol–gel method. Appl Surf Sci 256:4543–4547
34. Greene LE, Law M, Tan DH, Montano M, Goldberger J, Somorjai G, Yang P (2005) General route to vertical ZnO nanowire arrays using textured ZnO seeds. Nano Lett 5:1231–1236
35. Laurenti M, Cauda V, Gazia R, Fontana M, Rivera V F, Bianco S, Canavese G (2013) Wettability control on ZnO nanowires driven by seed layer properties. Eur J Inorg Chem 2013:2520-2527
36. Rivera VF, Auras F, Motto P, Stassi S, Canavese G, Celasco E, Bein T, Onida B, Cauda V (2013) Length-dependent charge generation from vertical arrays of high-aspect ratio ZnO nanowires. Chem Eur J doi: 10.1002/chem.201204429 (in press)
37. Brinker CJ, Scherer GW (1990) The physics and chemistry of sol–gel processing. Academic, Boston
38. Chen P, Gu L, Xuea X, Songa Y, Zhua L, Cao X (2010) Facile synthesis of highly uniform ZnO multipods as the supports of Au and Ag nanoparticles. Mater Chem Phys 122:41–48
39. Pacholski C, Kornowski A, Weller H (2002) Self-assembly of ZnO: from nanodots to nanorods. Angew Chem Int Ed 41:1188–1191
40. Jiang P, Zhou J-J, Fang H-F, Wang C-Y, Wang ZL, Xie S-S (2007) Hierarchical shelled ZnO structures made of bunched nanowire arrays. Adv Funct Mater 17:1303–1310
41. Govender K, Boyle DS, Kenway PB, O'Brien P (2004) Understanding the factors that govern the deposition and morphology of thin films of ZnO from aqueous solution. J Mater Chem 14:2575–2591
42. Xu C, Shin P, Cao L, Gao D (2009) Preferential growth of long ZnO nanowire array and its application in Dye-sensitized solar cells. J Phys Chem C 114:125–129

43. Liu JP, Xu CX, Zhu GP, Li X, Cui YP, Yang Y, Sun XW (2007) Hydrothermally grown ZnO nanorods on self-source substrate and their field emission. J Phys D: Appl Phys 40:1906
44. Xu S, Wei Y, Kirkham M, Liu J, Mai W, Davidovic D, Snyder RL, Wang ZL (2008) Patterned growth of vertically aligned ZnO nanowire arrays on inorganic substrates at Low temperature without catalyst. J Am Chem Soc 130:14958–14959
45. Xia Y, Yang P, Sun Y, Wu Y, Mayers B, Gates B, Yin Y, Kim F, Yan H (2003) One-dimensional nanostructures: synthesis, characterization, and applications. Adv Mater 15:353–389
46. Cao G, Liu D (2008) Template-based synthesis of nanorod, nanowire, and nanotube arrays. Adv Colloid Interface Sci 136:45–64
47. Wang Z, Li HL (2002) Highly ordered zinc oxide nanotubules synthesized within the anodic aluminum oxide template. Appl Phys A 74:201–203
48. Coasne B, Mezy A, Pellenq RJM, Ravot D, Tedenac JC (2009) Zinc oxide nanostructures confined in porous silicas. J Am Chem Soc 131:2185–2198
49. Postels B, Bakin A, Wehmann H-H, Suleiman M, Weimann T, Hinze P, Waag A (2008) Electrodeposition of ZnO nanorods for device application. Appl Phys A 91:595–599
50. Elias J, Tena-Zaera R, Levy-Clement C (2008) Effect of the chemical nature of the anions on the electrodeposition of ZnO nanowire arrays. J Phys Chem C 112:5736–5741
51. Hornyak G (2009) Fundamentals of nanotechnology. CRC Press, Boca Raton
52. Powell CF (1966) Chemical vapor deposition. Wiley, New York
53. Pierson HO (1999) Handbook of chemical vapor deposition (CVD), principles, technology, and applications. William Andrew Publishing, Norwich/New York
54. Wang ZL (2004) Zinc oxide nanostructures: growth, properties and applications. J Phys Condens Mat 16:R829–R858
55. Dai ZR, Pan ZW, Wang ZL (2003) Novel nanostructures of functional oxides synthesized by thermal evaporation. Adv Funct Mater 13:9–24
56. Wang ZL (2004) Nanostructures of zinc oxide. Mat Today 7:26–33
57. Wang ZL (2007) The new field of nanopiezotronics. Mat Today 10:20–28
58. Li SY, Lin P, Lee CY, Tseng TY (2004) Field emission and photofluorescent characteristics of zinc oxide nanowires synthesized by a metal catalyzed vapor–liquid–solid process. J Appl Phys 95:3711–3716
59. Wang X, Li Q, Liu Z, Zhang J, Liu Z, Wang R (2004) Low-temperature growth and properties of ZnO nanowires. Appl Phys Lett 84:4941–4943
60. Yang Q, Tang K, Zuo J, Qian Y (2004) Synthesis and luminescent property of single-crystal ZnO nanobelts by a simple low temperature evaporation route. Appl Phys A 79:1847–1851
61. Xing YJ, Xi ZH, Zhang XD, Song JH, Wang RM, Xu J, Xue ZQ, Yu DP (2005) Thermal evaporation synthesis of zinc oxide nanowires. Appl Phys A 80:1527–1530
62. Lyu SC, Zhang Y, Ruh H, Lee H-J, Shim H-W, Suh E-K, Lee CJ (2002) Low temperature growth and photoluminescence of well-aligned zinc oxide nanowires. Chem Phys Lett 363:134–138
63. Shen G, Bando Y, Chen D, Liu B, Zhi C, Golberg D (2006) Morphology-controlled synthesis of ZnO nanostructures by a simple round-to-round metal vapor deposition route. J Phys Chem B 110:3973–3978
64. Ngo-Duc T, Singh K, Meyyappan M, Oye MM (2012) Vertical ZnO nanowire growth on metal substrates. Nanotechnology 23:194015
65. L-l Y, J-h Y, D-d W, Y-j Z, Y-x W, H-l L, H-g F, J-h L (2008) Photoluminescence and Raman analysis of ZnO nanowires deposited on Si(1 0 0) via vapor–liquid–solid process. Physica E 40:920–923
66. Cha SN, Song BG, Jang JE, Jung JE, Han IT, Ha JH, Hong JP, Kang DJ, Kim JM (2008) Controlled growth of vertically aligned ZnO nanowires with different crystal orientation of the ZnO seed layer. Nanotechnology 19:235601
67. Zha M, Calestani D, Zappettini A, Mosca R, Mazzera M, Lazzarini L, Zanotti L (2008) Large-area self-catalysed and selective growth of ZnO nanowires. Nanotechnology 19:325603

68. Calestani D, Zha M, Mosca R, Zappettini A, Carotta MC, Di Natale V, Zanotti L (2010) Growth of ZnO tetrapods for nanostructure-based gas sensors. Sens Actuators B 144:472–478

69. Heo YW, Ip K, Park SJ, Pearton SJ, Norton DP (2004) Shallow donor formation in phosphorus-doped ZnO thin films. Appl Phys A 78:53–57

70. Karamdel J, Dee CF, Saw KG, Varghese B, Sow CH, Ahmad I, Majlis BY (2012) Synthesis and characterization of well-aligned catalyst-free phosphorus-doped ZnO nanowires. J Alloys Compd 512:68–72

71. Hsu CL, Chang SJ, Lin YR, Tsai SY, Chen IC (2005) Vertically well aligned P-doped ZnO nanowires synthesized on ZnO-Ga/glass templates. Chem Commun (Camb) 28(28):3571–3573

72. Kar JP, Ham MH, Lee SW, Myoung JM (2009) Fabrication of ZnO nanostructures of various dimensions using patterned substrates. Appl Surf Sci 255:4087–4092

73. Sharma P, Mansingh A, Sreenivas K (2002) Ultraviolet photoresponse of porous ZnO thin films prepared by unbalanced magnetron sputtering. Appl Phys Lett 80:553–555

74. Saw KG, Lim YT, Tan GL, Hassan Z, Ibrahim K, Yam FK, Ng SS (2008) Effect of zinc on the growth mechanism of zinc oxide nanostructures in the nitrogen environment. J Phys D: Appl Phys 41:055506

75. Sundaram KB, Khan A (1997) Characterization and optimization of zinc oxide films by r.f. Magnetron sputtering. Thin Solid Films 295:87–91

76. Chiou W-T, Wu W-Y, Ting J-M (2003) Growth of single crystal ZnO nanowires using sputter deposition. Diamond Relat Mater 12:1841–1844

77. Pokropivny VV, Skorokhod VV (2007) Classification of nanostructures by dimensionality and concept of surface forms engineering in nanomaterial science. Mater Sci Eng C 27:990–993

78. Zhu Y, Elim HI, Foo YL, Yu T, Liu Y, Ji W, Lee JY, Shen Z, Wee ATS, Thong JTL, Sow CH (2006) Multiwalled carbon nanotubes beaded with ZnO nanoparticles for ultrafast nonlinear optical switching. Adv Mater 18:587–592

79. Lu Q, Wang Z, Li J, Wang P, Ye X (2011) Structure and photoluminescent properties of ZnO encapsulated in mesoporous silica SBA-15 fabricated by two-solvent strategy. Nanoscale Res Lett 4:646–654

80. Rasmussen JW, Martinez E, Louka P, Wingett DG (2010) Zinc oxide nanoparticles for selective destruction of tumor cells and potential for drug delivery applications. Expert Opin Drug Deliv 7:1063–1077

81. Law M, Goldberger J, Yang P (2004) Semiconductor nanowires and nanotubes. Annu Rev Mater Res 34:83–122

82. Hung CH, Whang WT (2003) A novel low-temperature growth and characterization of single crystal ZnO nanorods. Mater Chem Phys 82:705–710

83. Gonzale-Valls I, Lira-Cantu M (2009) Vertically-aligned nanostructures of ZnO for excitonic solar cells: a review. Energ Environ Sci 2:19–34

84. Kim G-S, Ansari SG, Seo H-K, Kim Y-S, Yang O-B, Shin H-S (2007) Hydrothermal growth of ZnO on annealed electrodeposited titanate film: influence of zinc nitrate and Methenamine. Appl Surf Sci 253:7197–7202

85. Yang Q, Guo X, Wang W, Zhang Y, Xu S, Lien DH, Wang ZL (2010) Enhancing sensitivity of a single ZnO micro-/nanowire photodetector by piezo-phototronic effect. ACS Nano 4:6285–6291

86. He YN, Zhang W, Zhang SC, Kang X, Peng WB, Xu YL (2012) Study of the photoconductive ZnO UV detector based on the electrically floated nanowire array. Sens Actuat A Phys 181:6–12

87. Kang BS, Ren F, Heo YW, Tien LC, Norton DP (2005) pH measurements with single ZnO nanorods integrated with a microchannel. Appl Phys Lett 86:112105

88. Seiyama T, Kato A, Fulishi K, Nagatani M (1962) A new detector for gaseous components using semiconductive thin films. Anal Chem 34:1502

89. Kwak G, Yong K (2008) Adsorption and reaction of ethanol on ZnO nanowires. J Phys Chem C 112:3036

90. An W, Wu X, Zeng XC (2008) Adsorption of O2, H2, CO, NH3, and NO2 on ZnO nanotube: a density functional theory study. J Phys Chem C 112:5747

91. Yamazoe N, Sakai G, Shimanoe K (2003) Oxide semiconductor gas sensors. Catal Surv Asia 7:63

92. Law JBK, Thong JTL (2008) Improving the NH3 gas sensitivity of ZnO nanowire sensors by reducing the carrier concentration. Nanotechnology 19:205502

93. Wang JX, Sun XW, Yang Y, Huang H, Lee YC, Tan OK, Vayssieres L (2006) Hydrother-mally grown oriented ZnO nanorod arrays for gas sensing applications. Nanotechnology 17:4995

94. Qi Q, Zhang T, Liu L, Zheng X, Yu Q, Zeng Y, Yang H (2008) Selective acetone sensor based on dumbbell-like ZnO with rapid response and recovery. Sens Actuators B 134:166

95. Wang D, Chu X, Gong M (2007) Hydrothermal growth of ZnO nanoscrewdriversand their gas sensing properties. Nanotechnology 18:185601

96. Kakati N, Jee SH, Kim SH, Lee HK, Yoon YS (2009) Sensitivity enhancement of ZnO nanorod gas sensors with surface modification by InSb thin film. Jpn J Appl Phys 48:105002

97. Al-Hilli SM, Willander M, Ost A, Stralfors P (2007) ZnO nanorods as an intracellular sensor for pH measurements. J Appl Phys 102:084304

98. Ogata K, Koike K, Sasa S, Inoue M, Yano M (2009) ZnO nanorod arrays on n-type Si(111) substrates for pH measurements. J Vac Sci Technol B 27:1684

99. Yales DE, Levine S, Healy TW (1974) Site-binding model of the electrical double layer at the oxide/water interface. J Chem Soc Faraday Trans 70:1807

100. Siu WM, Collold RSC (1979) Basic properties of the electrolyte—SiO2—Si system: Phys-ical and theoretical aspects. Electron devices. IEEE Trans 26:1805

101. Kang BS, Ren F, Heo YW, Tien LC, Norton DP, Pearton SJ (2005) pH measurements with single ZnO nanorods integrated with a microchannel. Appl Phys Lett 86:12105

102. Soci C, Zhang A, Xiang B, Dayeh SA, Aplin DPR, Park J, Bao XY, Lo YH, Wang D (2007) ZnO nanowire UV photodetectors with high internal gain. Nano Lett 7:1003

103. Gayen RN, Dalui S, Rajaram A, Pal AK (2009) Modulation of field emission properties of vertically aligned ZnO nanorods with aspect ratio and number density. Appl Surf Sci 255:4902

104. Bonard JM, Weiss N, Kind H, Stoeckli T, Forrò L, Kern K, Chatelain A (2001) Tuning the field emission properties of patterned carbon nanotube films. Adv Mater 13:184

105. Li XJ, Jiang WF (2007) Enhanced field emission from a nest array of multi-walled carbon nanotubes grown on a silicon nanoporous pillar array. Nanotechnology 18:065203

106. Banerjee D, Jo SH, Ren ZF (2004) Enhanced field emission of ZnO nanowires. Adv Mater 16:2028

107. Wang X, Zhou J, Lao C, Song J, Xu N, Wang ZL (2007) In situ field emission of density-controlled ZnO nanowire arrays. Adv Mater 19:1627

108. Nilsson L, Groening O, Emmenegger C, Kuettel O, Schaller E, Schlapbach L, Kind H, Bonard JM (2000) Scanning field emission from patterned carbon nanotube films. Appl Phys Lett 76:2071

109. Weintraub B, Chang S, Singamaneni S, Han WH, Choi YJ, Bae J, Kirkham M, Tsukruk VV, Deng Y (2008) Density-controlled, solution-based growth of ZnO nanorod arrays for enhanced field emission. Nanotechnology 19:435302

110. Arnold MS, Avouris P, Pan ZW, Wang ZL (2003) Field-effect transistors based on single semiconducting oxide nanobelts. J Phys Chem B 107:659

111. Park WI, Kim JS, Yi G-C, Bae MH, Lee H-J (2004) Fabrication and electrical characteristics of high-performance ZnO nanorod field-effect transistors. Appl Phys Lett 85:5052

112. Bae HS, Yoon MH, Kim JH, Im S (2003) Photodetecting properties of ZnO-based thin-film transistors. Appl Phys Lett 83:5313

113. Fan Z, Wang D, Chang P-C, Tseng W-Y, Lu JG (2004) ZnO nanowire field-effect transistor and oxygen sensing property. Appl Phys Lett 85:5923

114. Fan Z, Lu JG (2005) Zinc oxide nanostructures: synthesis and properties. J Nanosci Nanotechnol 5:1561–1573
115. Zhao MH, Wang ZL, Mao SX (2004) Piezoelectric characterization of individual zinc oxide nanobelt probed by piezoresponse force microscope. Nano Lett 4:587
116. Wang ZL (2007) Piezoelectric nanostructures: from novel growth phenomena to electric nanogenerators. MRS Bull 32:109
117. Law M, Greene LE, Johnson JC, Saykally R, Yang P (2005) Nanowire dye-sensitized solar cells. Nat Mater 4:455–459
118. Peng Q, Qin Y (2011) ZnO nanowires and their application for solar cells. In: Hashim A (ed) Nanotechnology and nanomaterials, Nanowires – implementations and applications. Intech Open, Rijeka, Croatia, pp 157–167
119. Kılıç B, Gür E, Tüzemen S (2012) Nanoporous ZnO photoelectrode for dye-sensitized solar cell. J Nanomater 2012:7
120. Wang J, Qi Y, Zhi Z, Guo J, Li M, Zhang Y (2007) A self-assembly mechanism for sol–gel derived ZnO thin films. Smart Mater Struct 16:2673
121. Yadav R, Pandey A, Sanjay S (2007) ZnO porous structures synthesized by CTAB-assisted hydrothermal process. Struct Chem 18:1001–1004
122. Zhou H, Fan T, Zhang D (2007) Hydrothermal synthesis of ZnO hollow spheres using spherobacterium as biotemplates. Micropor Mesopor Mat 100:322–327
123. Lupan O, Shishiyanu S, Chow L, Shishiyanu T (2008) Nanostructured zinc oxide gas sensors by successive ionic layer adsorption and reaction method and rapid photothermal processing. Thin Solid Films 516:3338–3345
124. Li G-R, Dawa C-R, Bu Q, Lu X-H, Ke Z-H, Hong H-E, Zheng F-L, Yao C-Z, Liu G-K, Tong Y-X (2007) Electrochemical self-assembly of ZnO nanoporous structures. J Phys Chem C 111:1919–1923
125. Yan H, Yang Y, Fu Z, Yang B, Xia L, Fu S, Li F (2005) Fabrication of 2D and 3D ordered porous ZnO films using 3D opal templates by electrodeposition. Electrochem Commun 7:1117–1121
126. Thornton JA (1977) High rate thick film growth. Annu Rev Mater Sci. 7:239–260
127. Jankowski AF, Hayes JP (2003) Sputter deposition of a spongelike morphology in metal coatings. J Vacuum Sci Technol A 21:422–425
128. Gupta RK, Shridhar N, Katiyar M (2002) Structure of ZnO films prepared by oxidation of metallic zinc. Mat Sci Semicon Proc 5:11–15
129. Kim S, Jeong M-C, Oh B-Y, Lee W, Myoung J-M (2006) Fabrication of Zn/ZnO nanocables through thermal oxidation of Zn nanowires grown by RF magnetron sputtering. J Cryst Growth 290:485–489
130. Gazia R, Chiodoni A, Bianco S, Lamberti A, Quaglio M, Sacco A, Tresso E, Mandracci P, Pirri CF (2012) An easy method for the room-temperature growth of spongelike nanostructured Zn films as initial step for the fabrication of nanostructured ZnO. Thin Solid Films 524:107–112
131. Gazia R, Canavese G, Chiodoni A, Lamberti A, Stassi S, Sacco A, Bianco S, Virga A, Tresso E, Pirri CF (2013) Novel spongelike nanostructured ZnO films: properties and applications. J Alloys Compd. doi:10.1016/j.jallcom.2013.01.149:
132. Gao W, Li ZW, Harikisun R, Chang SS (2003) Zinc oxide films formed by oxidation of zinc under low partial pressure of oxygen. Mater Lett 57:1435–1440
133. Hsueh T-J, Hsu C-L (2008) Fabrication of gas sensing devices with ZnO nanostructure by the low-temperature oxidation of zinc particles. Sens Actuators B 131:572–576
134. Wagner A, Bakin A, Otto T, Zimmermann M, Jahn B, Waag A (2012) Fabrication and characterization of nanoporous ZnO layers for sensing applications. Thin Solid Films 520:4662–4665
135. Lamberti A, Gazia R, Sacco A, Bianco S, Quaglio M, Chiodoni A, Tresso E, Pirri CF (2013) Coral-shaped ZnO nanostructures for dye-sensitized solar cell photoanodes. Prog Photovoltaics Res Appl. doi:10.1002/pip.2251.:n/a-n/a

136. Sacco A, Lamberti A, Gazia R, Bianco S, Manfredi D, Shahzad N, Cappelluti F, Ma S, Tresso E (2012) High efficiency dye-sensitized solar cells exploiting sponge-like ZnO nanostructures. Phys Chem Chem Phys 14:16203–16208

137. Yin X, Wang B, He M, He T (2012) Facile synthesis of ZnO nanocrystals via a solid state reaction for high performance plastic dye-sensitized solar cells. Nano Res 5:1–10

138. Zhang F, Wang X, Ai S, Sun Z, Wan Q, Zhu Z, Xian Y, Jin L, Yamamoto K (2004) Immobilization of uricase on ZnO nanorods for a reagentless uric acid biosensor. Anal Chim Acta 519:155–160

139. Lu X, Zhang H, Ni Y, Zhang Q, Chen J (2008) Porous nanosheet-based ZnO microspheres for the construction of direct electrochemical biosensors. Biosens Bioelectron 24:93–98

140. Dikovska AO, Atanasov PA, Vasileva C, Dimitrov IG, Stoyanchov TR (2005) Thin ZnO films produced by pulsed laser deposition. J Optoelectron Adv M 7:1329–1334

141. King SL, Gardeniers JGE, Boyd IW (1996) Pulsed-laser deposited ZnO for device applications. Appl Surf Sci 96–98:811–818

142. Shibata T, Unno K, Makino E, Ito Y, Shimada S (2002) Characterization of sputtered ZnO thin film as sensor and actuator for diamond AFM probe. Sens Actuat A Phys 102:106–113

143. Abduev A, Akhmedov A, Asvarov A, Omaev A (2012) Preferred oriented ZnO films growth on nonoriented substrates by CVD. J Phys Conf Ser 345:012046

144. Liu Y, Gorla CR, Liang S, Emanetoglu N, Lu Y, Shen H, Wraback M (2000) Ultraviolet detectors based on epitaxial ZnO films grown by MOCVD. J Electron Mater 29:69–74

145. Li H, Sang J, Liu C, Lu H, Cao J (2008) Microstructural study of MBE-grown ZnO film on GaN/sapphire (0001) substrate. Cent Euro J Phys 6:638–642

146. Choi D, Lee KY, Lee KH, Kim ES, Kim TS, Lee SY, Kim SW, Choi JY, Kim JM (2010) Piezoelectric touch-sensitive flexible hybrid energy harvesting nanoarchitectures. Nanotechnology 21:405503

147. Yadav HK, Sreenivas K, Gupta V (2007) Enhanced response from metal/ZnO bilayer ultraviolet photodetector. Appl Phys Lett 90:172113–172113

148. Ma AM, Gupta M, Chowdhury FR, Shen M, Bothe K, Shankar K, Tsui Y, Barlage DW (2012) Zinc oxide thin film transistors with Schottky source barriers. Solid-State Electron 76:104–108

149. Fortunato E, Goncalves A, Pimentel A, Barquinha P, Goncalves G, Pereira L, Ferreira I, Martins R (2009) Zinc oxide, a multifunctional material: from material to device applications. Appl Phys A 96:197–205

150. Cho S, Ma J, Kim Y, Sun Y, Wong GKL, Ketterson JB (1999) Photoluminescence and ultraviolet lasing of polycrystalline ZnO thin films prepared by the oxidation of the metallic Zn. Appl Phys Lett 75:2761–2763

151. Yoshino Y, Makino T, Katayama Y, Hata T (2000) Optimization of zinc oxide thin film for surface acoustic wave filters by radio frequency sputtering. Vacuum 59:538–545

152. Lee JB, Kim HJ, Kim SG, Hwang CS, Hong S-H, Shin YH, Lee NH (2003) Deposition of ZnO thin films by magnetron sputtering for a film bulk acoustic resonator. Thin Solid Films 435:179–185

153. Fu YQ, Garcia-Gancedo L, Pang HF, Porro S, Gu YW, Luo JK, Zu XT, Placido F, Wilson JIB, Flewitt AJ, Milne WI (2012) Microfluidics based on ZnO/nanocrystalline diamond surface acoustic wave devices. Biomicrofluidics 6:024105–024111

154. Pang HF, Fu YQ, Garcia-Gancedo L, Porro S, Luo J K, Placido F, Wilson JIB, Flewitt AJ, Milne WI, Zu XT (2013) Enhancement of microfluidic efficiency with nanocrystalline diamond interlayer in the ZnO-based surface acoustic wave device. Microfluidics Nanofluidics 15:377–386

155. Pang HF, Garcia-Gancedo L, Fu YQ, Porro S, Gu YW, Luo JK, Zu XT, Placido F, Wilson JIB, Flewitt AJ, Milne WI (2013) Characterization of the surface acoustic wave devices based on ZnO/nanocrystalline diamond structures. Phys Status Solidi A 210:1575–1583

156. Yan Z, Zhou XY, Pang GKH, Zhang T, Liu WL, Cheng JG, Song ZT, Feng SL, Lai LH, Chen JZ, Wang Y (2007) ZnO-based film bulk acoustic resonator for high sensitivity biosensor applications. Appl Phys Lett 90:143503–143503

157. Chen Y, Reyes P, Duan Z, Saraf G, Wittstruck R, Lu Y, Taratula O, Galoppini E (2009) Multifunctional ZnO-based thin-film bulk acoustic resonator for biosensors. J Electron Mater 38:1605–1611

158. Chen D, J-j W, Liu Q-X, Xu Y, Li D-H, Liu Y-J (2011) Highly sensitive ZnO thin film bulk acoustic resonator for hydrogen detection. J Micromech Microeng 21:115018

159. Kalaee M, Akhlaghi S, Mazinani S, Sharif A, Jarestani YC, Mortezaei M (2012) Effect of ZnO nanoparticles on kinetics of thermal degradation and final properties of ethylene-propylene-diene rubber systems. J Therm Anal Calorim 110:1407–1414

160. Kruenate J, Tongpool R, Panyathanmaporn T, Kongrat P (2004) Optical and mechanical properties of polypropylene modified by metal oxides. Surf Interface Anal 36:1044–1047

161. Gao W, Zhou B, Liu Y, Ma X, Liu Y, Wang Z, Zhu Y (2013) The influence of surface modification on the structure and properties of a zinc oxide-filled poly(ethylene terephthalate). Polym Int 62:432–438

162. Liu Y, Lin ZY, Lin W, Moon KS, Wong CP (2012) Reversible superhydrophobic-superhydrophilic transition of ZnO nanorod/epoxy composite films. Acs Appl Mat Inter 4:3959–3964

163. Ramezanzadeh B, Attar MM, Farzam M (2011) Effect of ZnO nanoparticles on the thermal and mechanical properties of epoxy-based nanocomposite. J Therm Anal Calorim 103:731–739

164. Demir MM, Castignolles P, Akbey Ã, Wegner G (2007) In-situ bulk polymerization of dilute particle/MMA dispersions. Macromolecules 40:4190–4198

165. Gaur MS, Singh PK, Suruchi CRS (2013) Structural and thermal properties of polysulfone-ZnO nanocomposites. J Therm Anal Calorim 111:743–751

166. Steele A, Bayer I, Loth E (2009) Inherently superoleophobic nanocomposite coatings by spray atomization. Nano Lett 9:501–505

167. Mallakpour S, Zeraatpisheh F (2012) The nanocomposites of zinc oxide/L-amino acid-based chiral poly(ester-imide) via an ultrasonic route: synthesis, characterization, and thermal properties. J Appl Polym Sci 126:1416–1424

168. Vural S, Koytepe S, Seckin T, Adiguzel I (2011) Synthesis, characterization, UV and dielectric properties of hexagonal disklike ZnO particles embedded in polyimides. Mater Res Bull 46:1679–1685

169. Wu KM, Imin P, Adronov A, Zhitomirsky I (2011) Electrophoretic deposition of poly [3-(3-N, N-diethylaminopropoxy)thiophene] and composite films. Mater Chem Phys 125:210–218

170. Yu JG, Yang JW, Liu BX, Ma XF (2009) Preparation and characterization of glycerol plasticized-pea starch/ZnO-carboxymethylcellulose sodium nanocomposites. Bioresour Technol 100:2832–2841

171. Anand A, Kulkarni RD, Gite VV (2012) Preparation and properties of eco-friendly two pack PU coatings based on renewable source (sorbitol) and its property improvement by nano ZnO. Prog Org Coat 74:764–767

172. Chakraborty H, Sinha A, Mukherjee N, Ray D, Protim Chattopadhyay P (2013) A study on nanoindentation and tribological behaviour of multifunctional ZnO/PMMA nanocomposite. Mater Lett 93:137–140

173. Bermudez MD, Brostow W, Carrion-Vilches FJ, Sanes J (2010) Scratch resistance of polycarbonate containing ZnO nanoparticles: effects of sliding direction. J Nanosci Nanotechnol 10:6683–6689

174. Olad A, Nosrati R (2013) Preparation and corrosion resistance of nanostructured PVC/ZnO-polyaniline hybrid coating. Prog Org Coat 76:113–118

175. Dhoke SK, Khanna AS, Sinha TJM (2009) Effect of nano-ZnO particles on the corrosion behavior of alkyd-based waterborne coatings. Prog Org Coat 64:371–382
176. Gupta S, Sindhu S, Varman KA, Ramamurthy PC, Madras G (2012) Hybrid nanocomposite films of polyvinyl alcohol and ZnO as interactive gas barrier layers for electronics device passivation. Rsc Adv 2:11536–11543
177. Cristea MV, Riedl B, Blanchet P (2011) Effect of addition of nanosized UV absorbers on the physico-mechanical and thermal properties of an exterior waterborne stain for wood. Prog Org Coat 72:755–762
178. Devi RR, Maji TK (2012) Effect of nano-ZnO on thermal, mechanical, UV stability, and other physical properties of wood polymer composites. Ind Eng Chem Res 51:3870–3880
179. Weichelt F, Emmler R, Flyunt R, Beyer E, Buchmeiser MR, Beyer M (2010) ZnO-based UV nanocomposites for wood coatings in outdoor applications. Macromol Mater Eng 295:130–136
180. Teng TP, Yu CC (2012) Characteristics of phase-change materials containing oxide nano-additives for thermal storage. Nanoscale Res Lett 7:1–10
181. De Hazan Y, Heinecke J, Weber A, Graule T (2009) High solids loading ceramic colloidal dispersions in UV curable media via comb-polyelectrolyte surfactants. J Colloid Interface Sci 337:66–74
182. Liao WJ, Gu AJ, Liang GZ, Yuan L (2012) New high performance transparent UV-curable poly(methyl methacrylate) grafted ZnO/silicone-acrylate resin composites with simultaneously improved integrated performance. Colloid Surfac A 396:74–82
183. Kim D, Jeon K, Lee Y, Seo J, Seo K, Han H, Khan S (2012) Preparation and characterization of UV-cured polyurethane acrylate/ZnO nanocomposite films based on surface modified ZnO. Prog Org Coat 74:435–442
184. Huang HC, Hsieh TE (2010) Preparation and characterizations of highly transparent UV-curable ZnO-acrylic nanocomposites. Ceram Int 36:1245–1251
185. Burunkova JA, Denisyuk IY, Semina SA (2011) Self-organization of ZnO nanoparticles on UV-curable acrylate nanocomposites. J Nanotech 2011:951036
186. Kim D, Jang M, Seo J, Nam K-H, Han H, Khan SB (2013) UV-cured poly(urethane acrylate) composite films containing surface-modified tetrapod ZnO whiskers. Compos Sci Technol 75:84–92
187. Ramezanzadeh B, Attar MM (2011) Characterization of the fracture behavior and viscoelastic properties of epoxy-polyamide coating reinforced with nanometer and micrometer sized ZnO particles. Prog Org Coat 71:242–249
188. Lenko D, Schlögl S, Temel A, Schaller R, Holzner A, Kern W (2013) Dual crosslinking of carboxylated nitrile butadiene rubber latex employing the thiol-ene photoreaction. J Appl Polym Sci A 129:2735–2743
189. Schmitt M (2012) ZnO nanoparticle induced photo-Kolbe reaction, fragment stabilization and effect on photopolymerization monitored by Raman–UV–vis measurements. Macromol Chem Phys 213:1953–1962
190. Hu XZ, Zhou L, Gao C (2011) Hyperbranched polymers meet colloid nanocrystals: a promising avenue to multifunctional, robust nanohybrids. Colloid Polym Sci 289:1299–1320
191. Tu Y, Zhou L, Jin YZ, Gao C, Ye ZZ, Yang YF, Wang QL (2010) Transparent and flexible thin films of ZnO-polystyrene nanocomposite for UV-shielding applications. J Mater Chem 20:1594–1599
192. Gowri VS, Almeida L, de Amorim MTP, Pacheco NC, Souto AP, Esteves MF, Sanghi SK (2010) Functional finishing of polyamide fabrics using ZnO-PMMA nanocomposites. J Mater Sci 45:2427–2435
193. Indolia AP, Gaur MS (2013) Optical properties of solution grown PVDF-ZnO nanocomposite thin films. J Polym Res 20:1–8
194. Kyprianidou-Leodidou T, Margraf P, Caseri W, Suter UW, Walther P (1997) Polymer sheets with a thin nanocomposite layer acting as a UV filter. Polym Adv Technol 8:505–512

195. Therias S, Larche JF, Bussiere PO, Gardette JL, Murariu M, Dubois P (2012) Photochemical behavior of polylactide/ZnO nanocomposite films. Biomacromolecules 13:3283–3291
196. Lü N, Lü X, Jin X, Lü C (2007) Preparation and characterization of UV-curable ZnO/polymer nanocomposite films. Polym Int 56:138–143
197. Ge JL, Zeng XF, Tao X, Li X, Shen ZG, Yun J, Chen JF (2010) Preparation and characterization of PS-PMMA/ZnO nanocomposite films with novel properties of high transparency and UV-shielding capacity. J Appl Polym Sci 118:1507–1512
198. Khrenov V, Klapper M, Koch M, Müllen K (2005) Surface functionalized ZnO particles designed for the Use in transparent nanocomposites. Macromol Chem Phys 206:95–101
199. Borjanovic V, Bistricic L, Mikac L, McGuire GE, Zamboni I, Jaksic M, Shenderova O (2012) Polymer nanocomposites with improved resistance to ionizing radiation. J Vacuum Sci Technol B 30:041803
200. Morabito K, Shapley NC, Steeley KG, Tripathi A (2011) Review of sunscreen and the emergence of non-conventional absorbers and their applications in ultraviolet protection. Int J Cosmet Sci 33:385–390
201. Wong MH, Guenther J, Sun LY, Blumel J, Nishimura R, Sue HJ (2012) Synthesis and fabrication of multifunctional nanocomposites: stable dispersions of nanoparticles tethered with short, dense and polydisperse polymer brushes in poly(methyl methacrylate). Adv Funct Mater 22:3614–3624
202. Nenna G, Del Mauro A D, Massera E, Bruno A, Fasolino T, Minarini C (2012) Optical properties of polystyrene-ZnO Nanocomposite scattering layer to improve light extraction in organic light-emitting diode. J Nanomater 2012:319398
203. Jeeju PP, Jayalekshmi S, Chandrasekharan K, Sudheesh P (2012) Size dependent nonlinear optical properties of spin coated zinc oxide-polystyrene nanocomposite films. Opt Commun 285:5433–5439
204. Jeeju PP, Jayalekshmi S, Chandrasekharan K, Sudheesh P (2013) Enhanced linear and nonlinear optical properties of thermally stable ZnO/poly(styrene)–poly(methyl methacrylate) nanocomposite films. Thin Solid Films 531:378–384
205. Li GW, Ni XY (2008) A novel photoconductive ZnO/PVK nanocomposite prepared through photopolymerization induced by semiconductor nanoparticles. Mater Lett 62:3066–3069
206. Li GW, Min GQ, Fei LC, Ni XY, Lu WQ (2009) One-step synthesis to photoelectric hybrid composite of N-vinylcarbazole-methyl acrylate copolymer and ZnO nanocrystals via nanocrystals-initiated polymerization. J Colloid Interface Sci 334:8–12
207. Wang MQ, Lian YQ, Wang XG (2009) PPV/PVA/ZnO nanocomposite prepared by complex precursor method and its photovoltaic application. Curr Appl Phys 9:189–194
208. Beek WJE, Wienk MM, Janssen RAJ (2005) Hybrid polymer solar cells based on zinc oxide. J Mater Chem 15:2985–2988
209. Geng HW, Guo Y, Peng RX, Han SK, Wang MT (2010) A facile route for preparation of conjugated polymer functionalized inorganic semiconductors and direct application in hybrid photovoltaic devices. Sol Energ Mat Sol C 94:1293–1299
210. Zhao YP, Cai ZS, Zhou ZY, Fu XL (2011) Fabrication of conductive network formed by polyaniline-ZnO composite on fabric surfaces. Thin Solid Films 519:5887–5891
211. Cheng K, Cheng G, Wang SJ, Fu DW, Zou BS, Du ZL (2010) Electron transport properties in ZnO nanowires/poly(3-hexylthiophene) hybrid nanostructure. Mater Chem Phys 124:1239–1242
212. Olson DC, Shaheen SE, Collins RT, Ginley DS (2007) The effect of atmosphere and ZnO morphology on the performance of hybrid poly(3-hexylthiophene)/ZnO nanofiber photovoltaic devices. J Phys Chem C 111:16670–16678
213. Chougule MA, Sen S, Patil VB (2012) Facile and efficient route for preparation of polypyrrole-ZnO nanocomposites: microstructural, optical, and charge transport properties. J Appl Polym Sci 125:E541–E547
214. Semaltianos NG, Logothetidis S, Hastas N, Perrie W, Romani S, Potter RJ, Dearden G, Watkins KG, French P, Sharp M (2010) Modification of the electrical properties of

PEDOT: PSS by the incorporation of ZnO nanoparticles synthesized by laser ablation. Chem Phys Lett 484:283–289

215. Bouclé J, Ackermann J (2011) Solid-state dye-sensitized and bulk heterojunction solar cells using TiO_2 and ZnO nanostructures: recent progress and new concepts at the borderline. Polym Int 61:355–373

216. Xiong H-M, Zhao X, Chen J-S (2001) New polymer–inorganic nanocomposites: PEO-ZnO and PEO-ZnO-LiClO$_4$ films. J Phys Chem B 105:10169–10174

217. Sellam HSA (2012) Enhanced zinc ion transport in gel polymer electrolyte: effect of nano-sized ZnO dispersion. J Solid State Electrochem 16:3105–3114

218. Bagheri M, Rabieh S (2012) Preparation and characterization of cellulose-ZnO nanocomposite based on ionic liquid ([C4mim]Cl). Cellulose 20:699–705

219. Jin YZ, Wang JP, Sun BQ, Blakesley JC, Greenham NC (2008) Solution-processed ultraviolet photodetectors based on colloidal ZnO nanoparticles. Nano Lett 8:1649–1653

220. Lao CS, Park M-C, Kuang Q, Deng Y, Sood AK, Polla DL, Wang ZL (2007) Giant enhancement in UV response of ZnO nanobelts by polymer surface-functionalization. J Am Chem Soc 129:12096–12097

221. Mai WJ, Liang ZW, Zhang L, Yu X, Liu PY, Zhu HM, Cai X, Tan SZ (2012) Strain sensing mechanism of the fabricated ZnO nanowire-polymer composite strain sensors. Chem Phys Lett 538:99–101

222. Loh KJ, Chang D (2011) Zinc oxide nanoparticle-polymeric thin films for dynamic strain sensing. J Mater Sci 46:228–237

223. Chen Q, Sun YY, Wang Y, Cheng HB, Wang QM (2013) ZnO nanowires-polyimide nanocomposite piezoresistive strain sensor. Sens Actuat A Phys 190:161–167

224. Chougule MA, Dalavi DS, Mali S, Patil PS, Moholkar AV, Agawane GL, Kim JH, Sen S, Patil VB (2012) Novel method for fabrication of room temperature polypyrrole-ZnO nanocomposite NO$_2$ sensor. Measurement 45:1989–1996

225. Hu XL, Gong JM, Zhang LZ, Yu JC (2008) Continuous size tuning of monodisperse ZnO colloidal nanocrystal clusters by a microwave-polyol process and their application for humidity sensing. Adv Mater 20:4845

226. He JH, Singamaneni S, Ho CH, Lin YH, McConney ME, Tsukruk VV (2009) A thermal sensor and switch based on a plasma polymer/ZnO suspended nanobelt bimorph structure. Nanotechnology 20:065502

227. Arya SK, Saha S, Ramirez-Vick JE, Gupta V, Bhansali S, Singh SP (2012) Recent advances in ZnO nanostructures and thin films for biosensor applications: review. Anal Chim Acta 737:1–21

228. Pearton SJ, Ren F, Wang YL, Chu BH, Chen KH, Chang CY, Lim W, Lin JS, Norton DP (2010) Recent advances in wide bandgap semiconductor biological and gas sensors. Prog Mater Sci 55:1–59

229. Chaurasia A, Wang L, Gan LH, Mei T, Li Y, Liang YN, Hu X (2013) Polymerothermal synthesis – a facile and versatile method towards functional nanocomposites. Eur Polym J 49:630–636

230. Chang CY, Tsao FC, Pan CJ, Chi G-C, Wang HT, Chen JJ, Ren F, Norton DP, Pearton SJ, Chen KH, Chen LC (2006) Appl Phys Lett 88:173503

231. Chen W, Huang G, Lu H, McCready DE, Joly AG, Bovin JO (2006) Utilizing nanofabrication to construct strong, luminescent materials. Nanotechnology 17:2595–2601

232. Yang Y, Li YQ, Fu SY, Xiao HM (2008) Transparent and light-emitting epoxy nanocomposites containing ZnO quantum dots as encapsulating materials for solid state lighting. J Phys Chem C 112:10553–10558

233. Li YQ, Yang Y, Fu SY, Yi XY, Wang LC, Chen HD (2008) Transparent and light-emitting epoxy super-nanocomposites containing ZnO-QDs/SiO(2) nanocomposite particles as encapsulating materials for solid-state lighting. J Phys Chem C 112:18616–18622

234. Li F, Zhang L, Chen YW (2012) Approach to cross-linked polynorbornene/ZnO nanocomposites through nitroxide-mediated free radical graft polymerization and in situ hydrolysis. Opt Mater 34:1563–1569

235. He Y, Wang JA, Chen XB, Zhang WF, Zeng XY, Gu QW (2010) Blue electroluminescence nanodevice prototype based on vertical ZnO nanowire/polymer film on silicon substrate. J Nanopart Res 12:169–176
236. Chanakul A, Traiphol N, Traiphol R (2013) Controlling the reversible thermochromism of polydiacetylene/zinc oxide nanocomposites by varying alkyl chain length. J Colloid Interface Sci 389:106–114
237. Neves AAR, Camposeo A, Cingolani R, Pisignano D (2008) Interaction scheme and temperature behavior of energy transfer in a light-emitting inorganic–organic composite system. Adv Funct Mater 18:751–757
238. Sessolo M, Bolink HJ (2011) Hybrid organic–inorganic light-emitting diodes. Adv Mater 23:1829–1845
239. Fang HP, Wu YH, Lin HC (2013) Synthesis and study of novel supramolecular nanocomposites containing aryl-imidazo-phenanthroline-based metallo-polymers (H-donors) and surface-modified ZnO nanoparticles (H-acceptors). Tetrahedron 69:293–301
240. Prashanthi K, Naresh M, Seena V, Thundat T, Rao VR (2012) A novel photoplastic piezoelectric nanocomposite for MEMS applications. J Microelectromech S 21:259–261
241. Gullapalli H, Vemuru VSM, Kumar A, Botello-Mendez A, Vajtai R, Terrones M, Nagarajaiah S, Ajayan PM (2010) Flexible piezoelectric ZnO-paper nanocomposite strain sensor. Small 6:1641–1646
242. Khan R, Kaushik A, Solanki PR, Ansari AA, Pandey MK, Malhotra BD (2008) Zinc oxide nanoparticles-chitosan composite film for cholesterol biosensor. Anal Chim Acta 616:207–213
243. Sanoop PK, Mahesh KV, Nampoothiri KM, Mangalaraja RV, Ananthakumar S (2012) Multifunctional ZnO-biopolymer nanocomposite coatings for health-care polymer foams and fabrics. J Appl Polym Sci 126:E232–E243
244. Amna T, Hassan MS, Sheikh FA, Lee HK, Seo KS, Yoon D, Hwang IH (2013) Zinc oxide-doped poly(urethane) spider web nanofibrous scaffold via one-step electrospinning: a novel matrix for tissue engineering. Appl Microbiol Biotechnol 97:1725–1734
245. Brayner R (2006) Current approaches in natural biopolymer- nanoparticle hybrid functional materials: from drug delivery to Bio-detection applications. Front Drug Des Discov 2:241–258
246. Kaiser J-P, Zuin S, Wick P (2013) Is nanotechnology revolutionizing the paint and lacquer industry? A critical opinion. Sci Tot Environ 442:282–289
247. Xu C, Pan C, Liu Y, Wang ZL (2012) Hybrid cells for simultaneously harvesting multi-type energies for self-powered micro/nanosystems. Nano Energ 1:259–272
248. Wang Y (2012) PhD Dissertation, Title "Simultaneous energy harvesting and vibration control via piezoelectric materials", Virginia Polytechnic Institute and State University, Blacksburg
249. Podrezova LV, Porro S, Cauda V, Fontana M, Cicero G (2013) Comparison between ZnO nanowires grown by chemical vapor deposition and hydrothermal synthesis. Appl Phys A. doi:10.1007/s00339-013-7838-5.

Nanosized Gold and Silver Spherical, Spiky, and Multi-branched Particles

6

Stefano Stassi, Valentina Cauda, Giancarlo Canavese,
Diego Manfredi, Ignazio Roppolo, Paola Martino, and
Alessandro Chiolerio

Keywords

Metal nanoparticles • Gold • Silver • Shape-controlled synthesis • Multi-branched particles • Surface plasmon resonance • Nanocomposites

Introduction

The worldwide interest in metal NPs rapidly grew in the last decades due to their electrical, optical, and chemical properties that allow their implementation as promising solution in several applications like catalysis, surface-enhanced Raman spectroscopy (SERS), nanoelectronics, photonics, and biological and physical sensing [1–9]. This wide range of possible applications is promoted by the possibility of tuning the intrinsic properties of metal nanostructures by controlling their shape and dimension [10]. For example, in catalysis the shape of NPs determines the exposed facets and the defects of the crystal (including corner and edges), modifying the reactivity and selectivity towards different chemical compounds [11, 12]. In fact, it was demonstrated that metal nanocrystals exposing high-index planes can exhibit a higher activity in breaking chemical bonds, therefore improving their catalytic performance. With regard to the optical properties, the morphology and the size of metal nanostructures influence the number and the width of the surface plasmon resonance peaks (SPR) and the intensity and spectral range of the SERS effect [13].

S. Stassi (✉) • V. Cauda • G. Canavese • D. Manfredi • I. Roppolo • A. Chiolerio
Center for Space Human Robotics@PoliTo, Istituto Italiano di Tecnologia, Torino, Italy
e-mail: stefano.stassi@iit.it; valentina.cauda@iit.it; giancarlo.canavese@iit.it; diego.manfredi@iit.it; ignazio.roppolo@iit.it; alessandro.chiolerio@iit.it

P. Martino
Politronica Inkjet Printing S.r.l, Torino, Italy
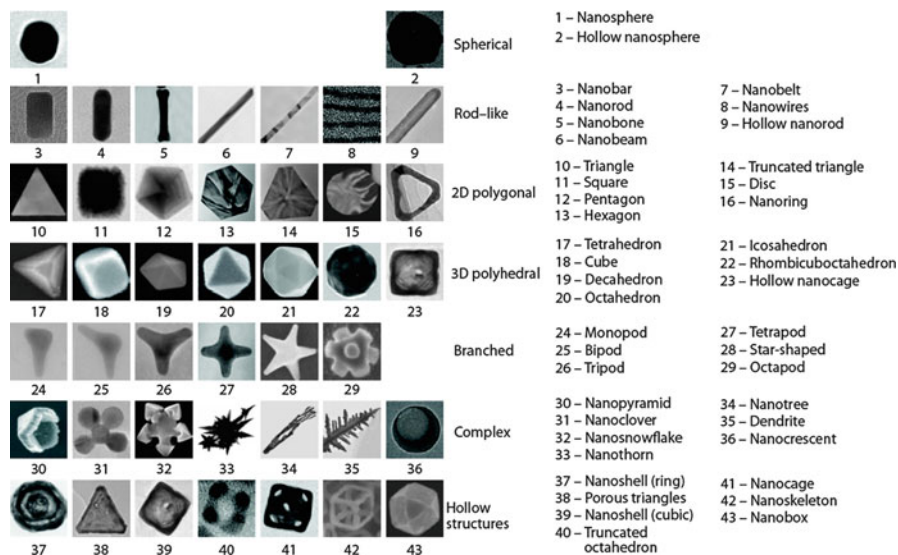
Fig. 6.1 Some examples of different obtainable morphology of metal NPs categorized by geometrical parameters (Reprinted by permission from Macmillan Publishers Ltd: Nature Nanotechnology [14]. Copyright 2011)

Therefore many efforts were spent in the development of innovative synthesis route to control the shape of the NPs and to investigate and tune the shape-dependent properties. In particular wet synthesis methods were implemented to obtain NPs with several different morphology as spheres, wires, rods, cubes, plates, belts, cages, polyhedral, meatballs, stars, thorns, snowflakes, flowers, combs, prisms, and several other interesting and odd shapes, some of which are reported in Fig. 6.1 [2, 6, 12, 14–22].

Despite the wide range of different shapes synthetically available, it remains challenging to obtain a high-yield production of these nanostructures and to design a synthesis route leading to different and controllable morphologies by tuning the reactant compositions [2]. Effective strategies were developed with solution-phase syntheses, using surfactants or polymers as capping agent. Their use has the potential of growing metallic nanocrystals in bulk quantities with a fine control on the final morphology. These amphiphilic organic compounds, composed by both hydrophobic and hydrophilic groups, have strong interaction with the metal atoms controlling the nucleation, the growth kinetics, and thus the final shape.

The key point in designing new synthesis procedures is the study and deep understanding of the growth mechanisms to select the chemical precursors, the utilization of seeds, and the physical stimuli (e.g., electromagnetic radiation field, temperature) allowing the accretion on the desired facets. All these parameters

control the nucleation and the growth kinetics. Investigation of shape and dimension variation of the metal nanocrystals during the succession of growing step relies on scanning electron microscopy (SEM) and transmission electron microscopy (TEM) techniques, allowing a visualization of the samples up to a sub-nanometric definition. For an exhaustive characterization of the NPs, energy dispersive spectroscopy (EDS/EDX), selected area electron diffraction (SAED), X-ray diffraction (XRD), and X-ray photoelectron spectroscopy (XPS) return fundamental information on the chemical composition and on the crystal structure of the samples, while nitrogen sorption measurements analyze the specific surface area, a fundamental parameter for catalytic applications.

This chapter is focused on gold and silver NPs, because of the easiness of synthesizing nanocrystals of these noble metals with various shapes and because of the wide range of applications. As an example, Au NPs are largely implemented in drug delivery systems because of their biocompatibility and of photothermal properties able to produce a localized heating effect. The antibacterial and antifungal activity of Ag NPs is widely exploited in the biotechnology, medical, and water-treatment fields [23]. Moreover both gold and silver NPs have narrow plasmon resonance and have affinity for binding to many biological molecules, a property that inspired several research projects and technological applications [3, 6, 24, 25].

Synthesis Methods

The synthesis of metal nanocrystals has been widely studied in the last decades. The formation process starting from the metal precursor and leading to the final nanocrystals can be roughly divided into three distinct stages: (i) nucleation, (ii) evolution of nuclei into seeds, and (iii) growth of seeds into the final nanocrystals [11]. Nucleation is the very first stage of any crystallization process, the nucleus consisting in a cluster of very few atoms and/or ions. Increasingly sophisticated theories were formulated and refined to simulate the nucleation process and understand it [26]. In the second step, the nuclei slightly grow through atom by atom addition to form a seed. The seed can grow in size through further addition of metal atoms, and thus the shape of the final nanocrystal is largely determined by the structure of the seed. Recently, much emphasis was put on controlling the size, the shape, and the crystallinity of metallic nanosized particles because catalytic, optical, magnetic, and electronic properties were demonstrated to be dimensionally sensitive [27–30]. The present research efforts are devoted not only in synthesizing spherical metal particles and stabilize them in a colloidal suspension but also in synthesizing anisotropic and/or multi-branched Au and Ag nanostructures. In the following sections, attention will be paid in describing the most important approaches to synthesize silver and gold nanocrystals and nanostructures with different morphologies.

Bottom-Up Self-Assembly Approach

In a typical solution-phase synthesis of metal nanocrystals, metal compounds or salts are commonly dissolved in a solvent. These precursors are in a higher oxidation state than the atomic metal species, thus during the reaction they are reduced to generate zerovalent atoms, i.e., the building blocks of a metal nanocrystal. Two synthetic pathways are at present under discussion. The first possibility is that the precursor compound is reduced into zerovalent atoms first, which then aggregate into nuclei and grow into nanocrystals. In the second possible reaction pathway, the unreduced metal species start forming nuclei and then are reduced to zerovalent metal species [11].

Generally this second reduction mechanism requires mild reducing agent and a high concentration of precursors. Under these conditions, the unreduced metal species forming nuclei cannot undergo to complete reduction into the zerovalent state. In this way the nanosized cluster surface of the forming material is terminated by positively charged metal ions, which are then able to coordinate to ligands or solvated by solvent molecules. Xia et al. [11] reported that this surface reactivity might be related to the capping effect of some ionic species such as Cl^-, Br^-, and citrate, as well as polymeric species, like polyvinylpyrrolidone, as we will expose in the next section.

In the synthesis of colloidal gold nanocrystals, the control on the shape is achieved by operating under either thermodynamic or kinetic control, thus by accurately tuning the nucleation and growth processes. Under thermodynamic control, a crystal in equilibrium tends to have the lowest surface energy for a given volume of material. Since the surface-to-volume ratio is high for an NP, the surface energy of the growing crystal plays a crucial role in determining the final morphology.

Kinetic control is obtained when the crystal formation is directed by a finite driving force, thus under conditions far away from the thermodynamic equilibrium. Under kinetically controlled synthesis, the reaction should proceed considerably slower than under normal conditions, thus by slowing down the precursor decomposition or reduction [11].

In kinetically controlled synthesis, mild reduction conditions have to be reached, using, for example, mild reducing agents, like L-ascorbic acid. It was also previously reported [18, 31] that an excess of L-ascorbic acid in the synthesis of gold nanocrystals promotes the anisotropic growth, thus producing particles with a branched shape. There are also evidences that upon increasing the molar ratio of the ascorbic acid to the gold source, the reduction efficiency is higher, thus increasing the nucleation rate of gold, forming several crystal domains with a smaller size, as evidenced by the increase in the number of protuberances. A final polycrystalline gold structure can be also obtained as the result of the subunit growth and aggregation of several small crystal domains.
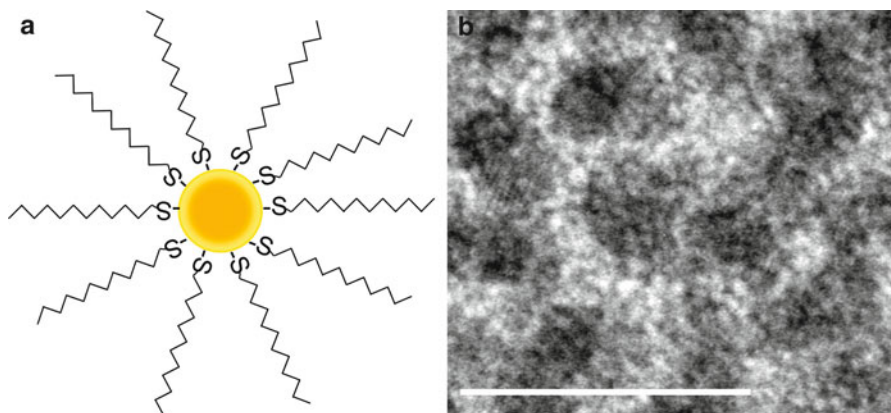
Fig. 6.2 (**a**) Scheme of a dodecanethiol-stabilized gold NP and (**b**) high-resolution transmission electron microscopy image (HRTEM), showing the single-crystalline structure of the NPs. Scale bar corresponds to 10 nm

Synthesis of monodisperse single-crystalline Au NPs as colloidal suspension in organic solvent has been widely reported [32–34]. To obtain the colloidal stability, these nanosized clusters of Au atoms are stabilized by a monolayer of chemisorbed alkanethiolate ligands and are reproducibly prepared in large quantities (see Fig. 6.2a). Dodecanethiolate-stabilized gold NPs (Au NPs) were prepared by some of us [22], according to a modified procedure reported in literature [35], by tuning the synthesis parameters to obtain a colloidal suspension with Au NPs of about 4 nm in diameter in toluene. Hydrogen tetrachloroaurate ($HAuCl_4 \cdot 3H_2O$), a typical precursor for gold structure, was used together with sodium borohydride ($NaBH_4$) as reducing agent. In the reported synthesis, dodecanethiol was also added to the mixture prior to the introduction of the reducing agent, thus for stabilizing the anionic $AuCl_4^-$ species. The reduction step was carried out for 1 h at −78 °C under stirring, thus under kinetic control in order to slow down the reducing rate of the gold species. These nanosized single-crystalline gold structures (as reported from the TEM image in Fig. 6.2b) showed surface plasmons and electron–hole pair excitations, which could act as energy acceptor and effectively suppressed the fluorescence of organic dye molecules. Actually the fluorescence emission of the dye could be quenched through transfer of the excitation energy to the metal surface, where the electron gas of the metal would dissipate this energy into the bulk through various scattering processes. This mechanism is usually effective only for distances lower than 8 nm and thus was efficiently used by the authors to probe the morphological and functional properties of dye-labeled nanosized materials [22].

Concerning the synthesis of silver nanocrystals, silver nitrate ($AgNO_3$) is the most commonly used precursor because of its good solubility in polar solvents. As a drawback, it shows a high sensitivity to light leading to significant effect on the nature of Ag species in solution. Cautions must be taken in the storing and handling of this precursor. Like other face-cubic-centered (fcc) metals, icosahedral and decahedral seeds and their corresponding nanocrystals are the thermodynamically favored products via the reduction route of silver nitrate.

Surfactant-Assisted Synthesis

The capping agents are chemical compounds, polymers, or even ionic species added purposely to a solution-phase synthesis in order to control the shape of a nanocrystal. Their use should be considered as a thermodynamic means of controlling the shape, since these molecules thermodynamically adsorb to specific crystal planes of the metal, thus reducing their surface free energies and stabilizing them [36]. For colloidal synthesis, shape control at the crystallographic level can be achieved by employing molecular adsorbates that selectively adsorb, lowering the surface energy of these planes and thus these facets. In this way, the free energies of the different crystallographic planes are modified, and thus their relative growth rates, inducing the addition of metal atoms on the non-capped surfaces. Despite the importance of surface capping agents in controlling the shape of a nanocrystal, the complete mechanism is not yet completely understood.

Actually, the mechanism for the adsorbate-directed synthesis of metal nanocrystals can be divided in two different approaches: (i) the directed growth-based synthesis and (ii) the oriented attachment-based synthesis. In the first mechanism, the crystal growth is blocked on the crystalline facets strongly bound to the capping molecules and promoted on the crystal planes where there is no or weak binding through continuous addition of metal atoms. On the other hand, metal nanocrystals can be shaped through an oriented attachment mechanism; the metal seeds are preformed with adsorbate molecules bound to the highest free energy planes. These capped seeds undergo oriented attachment along the crystal planes where there is no or weak binding.

A wide variety of molecules including surfactants, polymers, biomolecules, small organic molecules, and metal ions or atoms can be used as capping agents, thus directing the growth of gold and silver NPs, or other metallic nanocrystals, into certain shapes.

The use of polymeric capping agent, such as polyvinylpyrrolidone (PVP), is an alternative and effective approach to obtain high synthesis yield and to prepare NPs with several well-controlled morphology by varying the content of the chemical precursors. PVP is able to strongly bind with its oxygen atoms to the 100 facets of Ag [37]. This preferential chemisorption will cap then {100} facets, thus driving the addition of new Ag atoms to the other crystal facets.

Bromide, an ionic capping agent, shows a similar effect and is also able to selectively adsorb onto the {100} facets of Ag and Au nanocrystals, inducing the formation of nanocubes, rectangular nanobars, and octagonal nanorods [38]. With respect to PVP, bromide ions are quite smaller; thus the crystals obtained with this capping agent are less than 25 nm in size. In addition, under certain conditions, Br^- can even induce anisotropic growth transforming Ag nanocubes into nanobars with rectangular cross sections [39]. Ag nanoplates were prepared under kinetic control by slowing down the reduction, thus using a mild reducing agent such as OH-terminated PVP, ascorbic acid, or glycylglycine [40, 41].

In contrast to the silver nanocrystal systems, the binding of PVP to Au does not seem sufficiently strong to promote the formation of {100} facets and is probably due to differences in surface reactivity. In contrast, mild reductants including phenylenediamine, PVP, or glucose can lead to Au nanoplates when the reduction rate is substantially lowered, thus again under kinetic control. The nanoplates usually show hexagonal or triangular profiles [41].

Highly regular shapes of gold nanostars were obtained [12] in a water-free room-temperature synthesis assisted by deep-eutectic solvents (DES). DES are ionic solvents composed by a mixture of quaternary ammonium salts and hydrogen donors species, which shows a melting point much lower than those of the individual components [42]. Stassi et al. have reported on the use of choline chloride and urea in a 1:2 M ratio, leading to a eutectic mixture which is liquid at RT [12]. DES forms a highly structured 'supramolecular' solvent, due to the extended hydrogen-bond network in the liquid state, and is able to direct the shape-controlled synthesis of gold nanostructures in the form of highly pointed nanostars, without further addition of seeds or other capping agents. Therefore star-shaped gold NPs were obtained from the mild reduction of $HAuCl_4$ by L-ascorbic acid at RT in the DES as both solvent and capping agent. Other authors have reported the use of DES as a liquid template [43] and as a particle stabilizer [12] for the synthesis of shape-controlled gold NPs.

Seeded Growth

The seeded growth consists in the addition into the synthesis bath of preformed nanocrystals with well-defined facets. These seeds act as primary nucleation sites, so this growth could be considered starting from a heterogeneous nucleation. During crystal growth, the metal atoms could continuously add with the same crystal structure of the seed, leading to the so-called epitaxial process. This condition is achieved when the seeds have the same chemical nature as the added atoms, and this approach was commonly used to grow gold nanorods from Au seeds.

In contrast, heteroepitaxial growth can be achieved when the seeds are chemically different from the growth atoms. Heteroepitaxy is commonly used in gas-phase deposition to prepare heterostructures or junctions. Very recently, the heteroepitaxial seeded growth was also explored in the wet-chemistry domain [44, 45]. It is fundamental for obtaining heteroepitaxial growth that the seed shows a close lattice match with the added atoms. In contrast, in the presence of a large-lattice mismatch between the seed and the deposited atoms, for instance, 4.08 % in the case of growing Au nanocrystals on Pt seeds, the heteroepitaxial growth is not favored due to high strain energy, and crystals with unpredictable shapes, i.e., different from the seed one, can be obtained.

The seeded growth was reported in the literature as a powerful method to obtain shape-controlled gold NPs [46, 47]. First, small Au seeds were prepared via fast reduction route with a strong reducing agent. Further, the nanocrystal growth was induced on the surface of the seeds by adding new precursor ($HAuCl_4$) into the solution batch. Slow reduction with ascorbic acid then took place in the presence of a surfactant or polymeric stabilizers, like CTAB, to produce anisotropic Au nanorods and nanowires.

UV-Induced Synthesis of Gold and Silver NPs

Since the eighteenth century, gold and silver complexes, e.g., metal halides, are known as photosensitive compounds for photography applications. In fact light exposure of these materials leads to the generation of noble metal microparticles that were used in photography emulsion [48]. Therefore the synthesis of noble metal NPs induced by light irradiation is one of the most common ways to obtain gold and silver colloids and NPs.

Generally the reaction of photoreduction could be written as

$$M^+ + e^- \rightarrow M$$
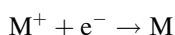
where M^+ is a metal ion in solution (that could be either Au or Ag, but also other noble metal ions), M is the corresponding metal atom, and e^- is a photogenerated free electron. Clearly, in order to have an efficient reaction, the two main issues are the presence of ions in solution and an efficient photogeneration of free electrons available for the reduction.

During the last 50 years, many studies were done by selecting different metal precursor and electron donors in order to be able to control both the dimension and the shape of the NPs synthesized. Looking in the past, in the 1970s, Hada worked on the synthesis of silver NPs in aqueous and alcohol solution by UV-induced photoreduction [49] taking advantage from the photooxidation of water and alcohols under a deep-UV irradiation. Nowadays the most common strategy for the synthesis of silver and gold NPs consists in utilizing photocleavable aromatic ketones that, under UV exposure, are able to photogenerate a radical that induces

Fig. 6.3 Gold nanoparticles synthesized by UV irradiation in presence of aromatic ketones (Reprinted from [53]. Copyrights (2009) © IUPAC)
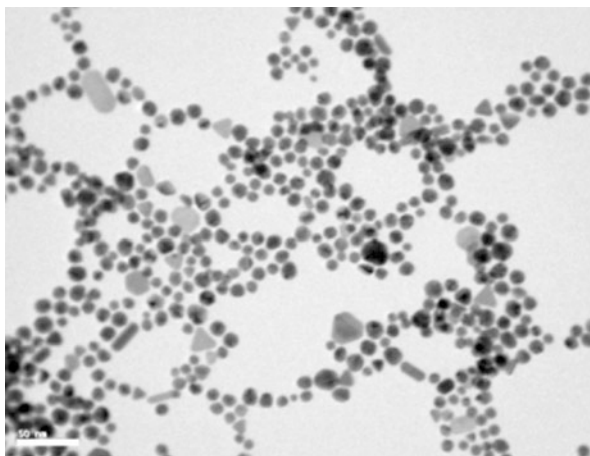
Fig. 6.4 Gold NPs grown on CdSe (Adapted from [63]. Copyright 2009 American Chemical Society)
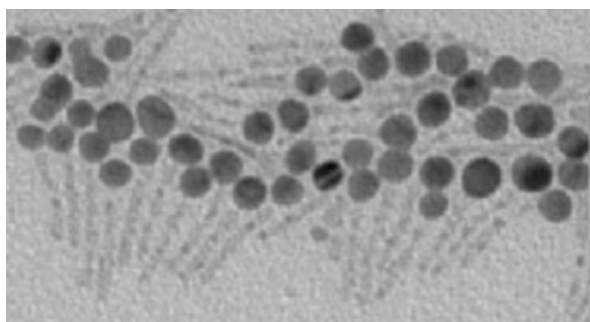
the photoreduction of silver [50–52]. Different conditions were studied, for example, by applying a magnetic field during the UV irradiation [53]. Recently Scaiano et al. reported a complete review explaining the photochemical background of the reaction and the effect of the different parameters on the shape of the NPs (see Fig. 6.3) [54]. Other studies were reported utilizing as photoreducing agent other molecules, such as acrylic monomers [55], controlling the pH in presence of sodium citrate [56], or using nonaqueous media [57]. It is important to underline that, by an appropriate choice of the metal precursor, it is possible to synthesize also NPs of alloys [58].

One other option that does not involve the use of organic compounds for the electron generation is to synthesize metal NPs in the presence of photoactive semiconductors which, under UV irradiation, are able to promote a free electron and then reducing the metal ions. The most investigated one was titanium dioxide [59–61], but also zinc oxide [62] and cadmium selenide (see Fig. 6.4) [63] were used.

The last important issue is the control of the shape. In a recent review Dong and Zhou reported about many parameters for the controlling of the shape of photogenerated gold NPs [64]. NPs of very different shape were synthesized: triangular [65], nanodisks [66], hexagonal [67], parallel rods [68], or as satellites of a greater silver NP [69].

NPs' Morphology and Characterization by Electron Microscopy

Electron microscopy has revolutionized our understanding of materials by completing the *processing-structure-properties* links down to atomistic levels. As widely recognized, the scanning electron microscope (SEM) permits the observation and characterization of materials from a nanometer to micrometer scale [70]. Three-dimensional images with high resolution of the surfaces of a very wide range of materials could be obtained thanks to the large depth of field, allowing different morphological features to be correctly interpreted and measured. On the other side, in order to find out exactly how nano-materials could be made, the new synthesis methods should be accompanied by atomic scale compositional and structural analysis. And for this matter, the transmission electron microscope (TEM) seems to be the perfect tool: it can give atomic-resolution images of materials and their defects, together with spectroscopic data and diffraction patterns from sub-nanometer regions [71]. According to [15], in recent years systematically organization of the morphology and architecture of metal crystals at microscale and nanoscale levels is a significant challenge: morphology influences not only the intrinsic properties of metal crystals but also their relevant applications in different fields. In particular, as reported by Wang et al. [17], sub-micrometer metallic particles of Au and Ag have unique optical properties in the visible and near-infrared (NIR) regions of the spectrum that are highly useful for a variety of applications, such as nanoscale optical components or devices, chemical and biomolecular sensing, medical imaging and photothermal therapy, and surface-enhanced spectroscopy. Moreover, metal conductive particles have recently gained attention as fillers for dielectric polymers to be used as piezoresistive composites for strain and pressure sensors [72]. In most of these applications, size, shape, and surface topography control of particles is essential not only to maximize their performances but also to fully exploit the potential of these remarkable nanoscale materials. Thus it is clear the fundamental role of electron microscopy to effectively put in practice this control.

As well-summarized in Fig. 6.1 [14], high-quality metallic NPs with tunable size and controllable shapes could be produced through wet-chemical synthesis techniques, in which careful optimization of the synthesis conditions allows rational control over NP sizes and morphologies. In the 'periodic table' of Fig. 6.1, each row illustrates a different level of dimensionality and complexity, including spherical and rodlike shapes, two-dimensional (2D) polygonal shapes, three-dimensional (3D) polyhedral shapes, branched structures, more complex
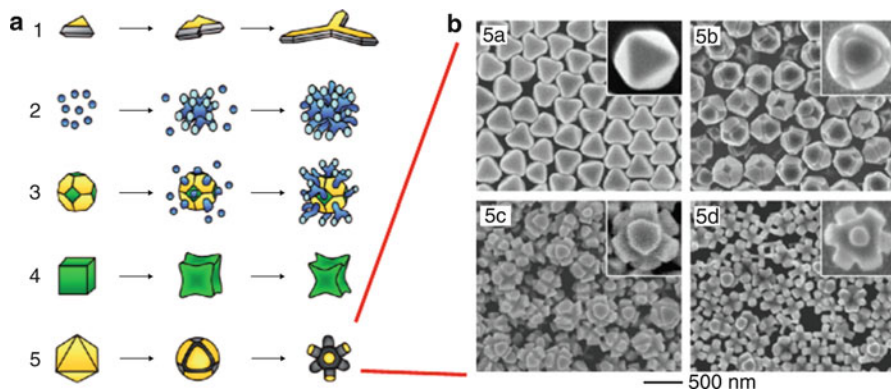
Fig. 6.5 (**a**) Various pathways that can lead to branched metal nanocrystals: *1* anisotropic overgrowth into a multipod, *2* aggregation-based growth into a nanodendrite, *3* aggregation-based growth in the presence of a foreign nanocrystal seed and formation of a bimetallic nanodendrite, *4* selective etching on the faces and edges coupled with overgrowth along the corners, *5* selective etching on the corners and edges. (**b**) SEM images showing the etching progress of octahedral Ag nanocrystals: *5-a* Ag octahedrons used as the starting material and *5-b–d* Ag nanocrystals obtained by exposing the octahedrons to increased concentrations of etchant (Reproduced from [74] with the permission of John Wiley and Sons)

structures, and hollow structures. In each row, the geometric order of the structures (in terms of aspect ratio, number of sides and facets, or number of branches) increases from left to right.

Among various possible morphologies that can be obtained from a metal nanocrystal, multipods are of particular interest: during the past decade, shape-controlled synthesis of colloidal metal nanocrystals in solution has advanced remarkably, and it is now possible to generate highly branched nanostructures for various metals, including Au and Ag, thanks to recent advances in synthetic approaches based on kinetically controlled overgrowth, aggregation-based growth, heterogeneous seeded growth, and selective etching (Fig. 6.5a). As an example, an interesting approach for multipod-shaped silver nanocrystals was recently reported by Yang and coworkers [73], who added an appropriate wet etchant to a suspension of the as prepared octahedral silver nanocrystals. The use of a relatively weak etchant made it possible to selectively etch the corners and edges of the octahedrons, resulting in the formation of octapod-shaped nanocrystals with the same symmetry of the starting octahedrons (Fig. 6.5b).

Recently, metal nanostructures with complex three-dimensional (3D) surface morphology, which are often referred in literature as nanoflowers or nanostars, have received considerable attention due to their excellent performances as catalysts and SERS substrates. Shuang Shen et al. [6] reported high-yield, controlled synthesis of Ag nanospheres that are formed by agglomeration of primary Ag NPs. They divided the silver nanospheres possible shapes into three types according to their surface morphology, as shown in Fig. 6.6: nanospheres with a relatively lower surface roughness, defined as 'shape 1'; nanospheres with platelike surface morphology,
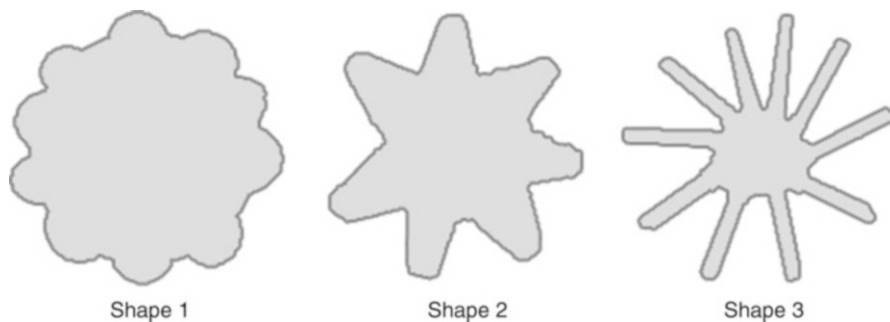
Fig. 6.6 Schematic illustration of the three types of Ag nanospheres
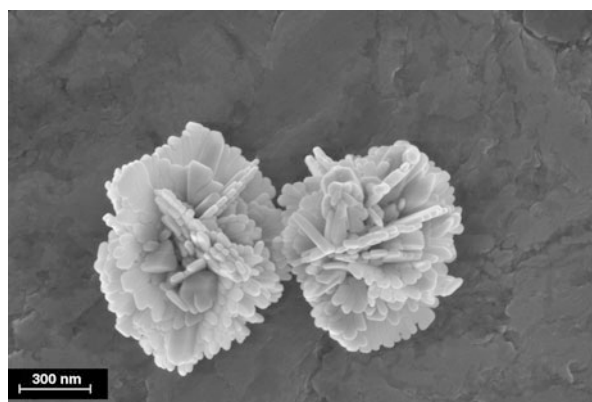
Fig. 6.7 FESEM images of silver desert roselike NPs

defined as 'shape 2'; nanospheres with more rough surfaces, with sharper edges and corners, defined as 'shape 3'.

According to Meng et al. [1], generally it is possible to distinguish between hierarchical microstructures with subunits at the nanoscale level and true fractal dendrites. All the hierarchical structures (HSs) are promising for catalysis, as SERS active substrates, and for super-hydrophobic coatings, but they are also attractive building blocks for advanced nanotechnological devices. In [1] an electrochemical approach to fabricate 3D flowerlike silver HSs on the surface of a Pt film electrode was also reported. Using a similar approach, silver 'desert roselike' NPs could be obtained. A high-magnification FESEM image of two flowerlike structures' flakes which seem to intersect mutually sometimes is reported in Fig. 6.7. All of the flakes have smooth surfaces, outwardly wavy edges, and uniform thickness. The average thickness of the flower flakes is 25 nm. Hong and coworkers [15] synthesized flowerlike Ag nanostructures in aqueous solution at room temperature in the aid of citric acid. More recently, Xionghu and Aixia [16] prepared silver crystals with different shapes such as spheres, flowerlike aggregates consisting of platelike petals, and hexagonal and triangle plates through a simple wet-chemical method.
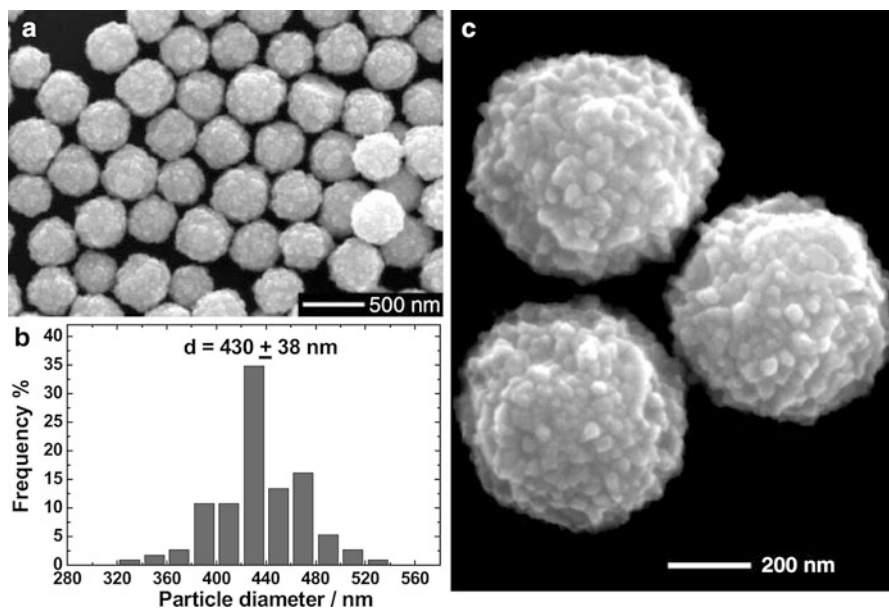
Fig. 6.8 (**a**) SEM image of the sub-micrometer meatball-like Au spheres with nanoscale surface roughness. (**b**) Histograms indicating the particle size distribution. (**c**) SEM image with higher resolution, revealing the surface topography of sub-micrometer Au particles (Reproduced from [17] with the permission of John Wiley and Sons)

Considering Au NPs, Wang et al. [17] fabricated sub-micrometer Au spheres with nanoscale surface roughness, the so-called meatball-like Au particles, through controlled reduction of chloroauric acid ($HAuCl_4$) by ascorbic acid in aqueous solution at room temperature. The colloidal meatball-like particles fabricated by this method exhibited nanoscale surface roughness (Fig. 6.8a) and also appear quite monodisperse, given their irregular surfaces. The size distribution reported in a histogram (Fig. 6.8b) was obtained from scanning electron microscopy (SEM) images of over 200 particles. The average particle size was 430 nm with a standard deviation of 38 nm. In Fig. 6.8c, a SEM image with higher magnification than the previous images is shown, revealing the surface topography of several individual particles. The surface of each particle is composed by a large number of randomly arranged, irregular nanoscale protrusions approximately 20–50 nm in size. Each particle appears to consist of many nanometer-sized, crystalline subunits with defined grain boundaries.

Recently much emphasis was put on controlling the shape of the metallic NPs, since the presence of nanosized sharp tips significantly alter the local field enhancement. It was reported [72] that highly regular shapes of gold nanostars were obtained in a water-free, room-temperature synthesis assisted by deep-eutectic solvents (DES). The experimental parameters for the above synthesis were modified in order to investigate the most reproducible and feasible reaction conditions

Dry Synthesis   Acqueous synthesis
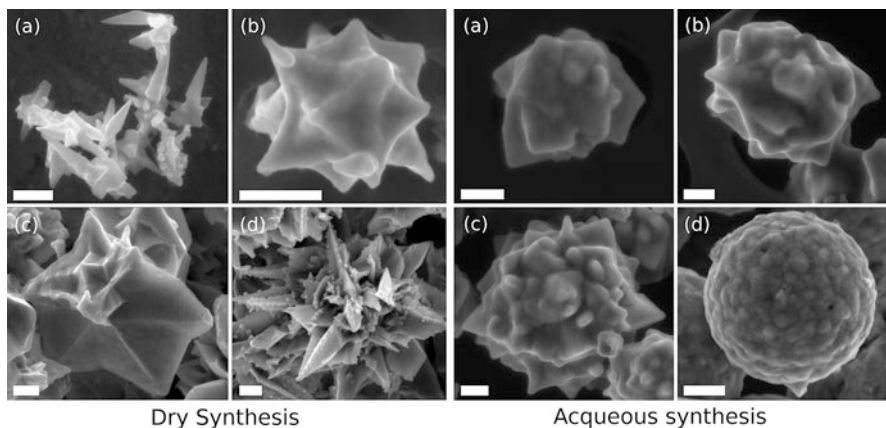
Fig. 6.9 Nanosized gold spiky particles, synthesized under dry conditions (panels on the *left*) and in presence of water [50 % (vol) H_2O, 50 % (vol) DES] (panels on the *right*) by using an ascorbic acid (AA)/hydrogen tetrachloroaurate ($HAuCl_4$) molar ratio of (**a**) 4:1, (**b**) 6:1, (**c**) 9:1, (**d**) 12:1. The scale bar is 200 nm in the dry synthesis image and 100 nm in the aqueous one (Reproduced from [72] with the permission of John Wiley and Sons)

for the preparation of spiky gold NPs. In particular, the relationship between the particle diameter, the protuberance size and shape, and the easiest and cost-effective reaction conditions were investigated. Under dry conditions, the obtained gold particles showed sharp tips, as reported in Fig. 6.9 from FESEM imaging [72]. By increasing the molar ratio of $AA/HAuCl_4$, the number, the height, and the length at the base of the tips increased, to form highly multi-branched gold nanostars, as shown in Fig. 6.9d – dry synthesis. In addition, the core size of the gold spiky particles also increased, starting from single sharp pyramids for the lower $AA/HAuCl_4$ ratio to bulkier core sizes. By substituting half of the DES volume with water in the synthetic batch, particles with a more pronounced spherical shape were obtained. This effect was even more evident upon increasing the ascorbic acid to gold source molar ratio (Fig. 6.9 – dry synthesis). Under these synthetic conditions, the core size of the gold particles increased, but not as much as in the previous synthesis. In addition, as the molar ratio of the reactants increased, the height and the length at the base of the tips at the gold surface strongly decreased. As also observed under dry conditions, the number of the protuberances also increased because of excess of L-ascorbic acid. Interestingly, with a ratio AA/HAuCl4 of 12:1, meatball gold NPs of about 500 nm in diameter were obtained with a rough surface. According to previous considerations, several small tips are present at the core surface (Fig. 6.9d – aqueous synthesis), and their growth in height and lateral size was completely prevented.

Using a similar synthesis route, Liao et al. [12] obtained star-shaped Au NPs with various interesting shapes and surface structure by adjusting the content of water in the DES solvent. In fact water plays a key role: without water, snowflake-like gold NPs with a very particular end-tips shapes were obtained, of about 300 nm
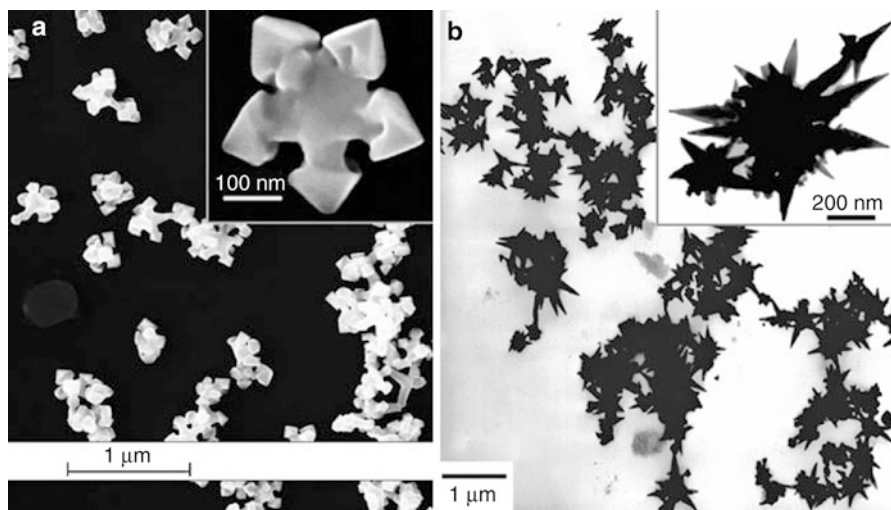
Fig. 6.10 (**a**) SEM images of the snowflake-like Au NPs; (**b**) TEM images of Au nanothorns (Reproduced from [12] with the permission of John Wiley and Sons)

in size, as reported in Fig. 6.10a. The ends of the NP branches form tetragonal micropyramids shaped, while using a large content of water in the DES led to the formation of nanothorns, as reported in Fig. 6.10b.

Properties of Nanostructured Gold and Silver Multi-branched Particles

NPs presenting spiky edges and tips on the surface show a very high sensitivity to local variation of the dielectric environment and a large enhancement of the electric field around the nanocrystal [75–77]. The field enhancement is normally obtained by the interaction between an incoming electromagnetic radiation and a surface plasmon. These collective oscillations of the metal electrons are confined to metal/dielectric boundary, such as the metal NP surface (where the dielectric medium is represented by air surrounding particles), and may interact with electromagnetic radiations of proper frequency. Since shape and size of NPs determine the electron confinement in the meta, surface plasmons are strongly influenced by NP structure. In this way the tips on the surface of spiky NPs work as 'hot spots' leading to the local electric enhancement effect. Therefore, spiky NPs find promising application in surface-enhanced Raman spectroscopy, as will be described later in this chapter.

The enhancement of the local electric field due to charge accumulation on the tips is also exploited in piezoresistive nanocomposites [72, 78], because it induces a large increase of the electrical conduction in the material.

The presence of narrow tips on the NPs surface has also strong effects on the catalytic properties. Multi-branched NPs with high-index facets, thus a high density

of atomic steps, ledges, and dangling bonds, exhibit an elevate catalytic activity with respect to other low-index facet nanostructures. However, it is very difficult to develop synthesis routes to obtain metal nanocrystals with high-index facets. Indeed the growth rate along the direction perpendicular to the high-index planes is normally much faster with respect to the low-index planes; thus it results in a relative elimination of the high-index planes during the crystal formation. Despite of these challenges, effective synthesis procedures to prepare metal spiky or dendritic NPs for the fabrication of electrodes with a high catalytic activity has been developed using deep-eutectic solvents [12] or an electrochemical route [79].

Highly reactive facets are also fundamental for the bactericidal effect of silver nanoparticles. Ag NPs are partially absorbed on the surface of the bacterial cell membrane altering essential function like respiration and permeability, while the NPs penetrating inside the bacteria damage DNA and vital enzymes [23, 80].

Applications

The applications of shape-controlled gold and silver nanocrystals are developing rapidly. Shaped nanocrystals can thus find promising applications in a wide range of fields including electronics, photonics, and plasmonics, as well as in catalysis, sensing, biology, and biomedicine. In the following, these techniques are discussed in details and reviewed.

Surface-Enhanced Raman Spectroscopy (SERS)

When irradiated by light of proper wavelength, the free electrons of a metal collectively oscillate in phase with the incident light, driven by the alternating electric field. This effect is known as surface plasmon resonance (SPR) [81], enabling effective scattering and absorption of light under a resonant condition. This gives, for example, to metal colloids, like Ag and Au, their brilliant colors. At the same time of the electron oscillation, the surface charges result polarized under light excitation. In the case of a metal NP, this generated charges cannot propagate as a wave along the flat surface as in bulk metals. They are in contrast confined to and concentrated on the NP surface; therefore this phenomenon is called localized surface plasmon resonance (LSPR) [81].

In these conditions, if organic molecules are adsorbed on the surface of metal NPs, the LSPR leads to intense local electric fields within a few nanometers from the particle surface and thus can be used for the enhancement of the Raman scattering cross sections of molecules. This would provide an enhanced 'fingerprint' spectrum of the molecule, rich of chemical information. This technique is widely known as surface-enhanced Raman scattering (SERS) [82–84] and was firstly demonstrated by Fleischman and Van Dyune in the 1970s.

It is also known that not only the nanosized dimension but also the shape of a nanocrystal affects its interaction with light. Therefore the intensity and position of LSPR peaks can be fine-tuned by shape control, and a significant Raman signal enhancement can be achieved by simply selecting nanocrystals with an appropriate shape. Signal enhancement of organic molecules is needed for detection of low-concentration analytes. Therefore the sensitivity of SERS can be greatly enhanced by many orders of magnitude by tailoring the shape of Ag and Au nanocrystals and thus their plasmonic features, i.e., the LSPR [85, 86]. Particularly, branched gold and silver nanocrystals with tips, such as stars, flowers, and dendrites, have attracted increasing interest for their application in SERS due to the enhanced plasmonic features [75, 87].

Gold and Silver Polymer Nanocomposites

In the latest years there is an increasing interest regarding the application of composites containing silver and gold NPs. There are two main strategies for the synthesis of these composite materials: the first (and most important one) consists in embedding the ex situ synthesized NPs in a polymeric matrix and the second by creating the NPs in situ, mainly by UV curing. In this paragraph the main applications of ex situ synthesized nanocomposites will be discussed, followed by the strategies for in situ synthesis, and at last innovative strategies for the synthesis of nanocomposite materials.

Nanocomposites by Direct Embedding of Silver and Gold NPs in Polymers
Biological Application
The main topic for gold and silver nanocomposites is in biological field. One of the most investigated properties of these materials is the antimicrobial activity. Silver nanocomposites with these characteristics were produced using, as polymeric matrix, cellulose [88], polyurethanes [89, 90], hydrogels [91], polyvinyl alcohol [92], and polysiloxanes [93]. Many other matrices were also used in textile applications, as recently reviewed by Dallas et al. [94] and by Dastjerdi et al. [95], and in water treatment as reviewed by Goyal et al. [96]. Other important fields are nanotheranostics [97–100], drug delivery [101, 102], tissue engineering [103–105], and cell imaging [106]. On the other side the emerging applications of these materials created the need of evaluating their toxicology and environment impact as recently reviewed by Zhao and Castranova [107] and Tolaymat et al. [108].

Conductive Nanocomposites
Embedding highly conductive nanofillers in polymer is a common strategy for producing conductive polymer nanocomposites. Even if evaluating the composite electrical resistivity is a common strategy for characterizing the noble
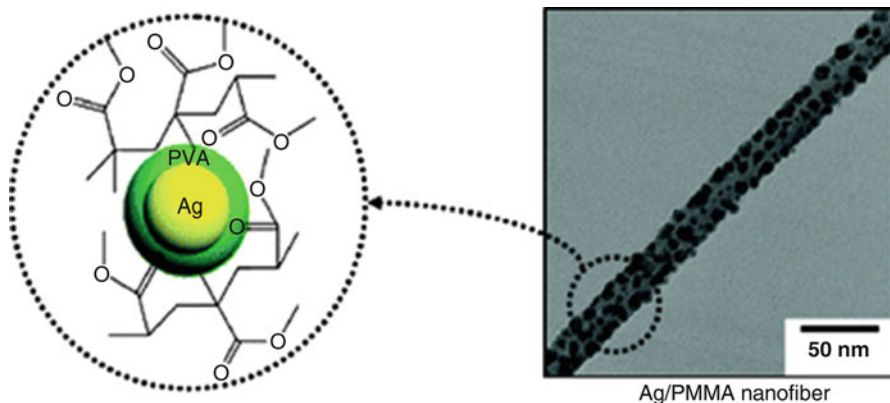
Fig. 6.11 PMMA fiber covered by PVA/AG nanoparticles (Reprinted from [94], Copyright (2011), with permission from Elsevier)

metal/polymer composites, in literature many works were reported regarding the application of these materials specifically for electrical purposes. Silver conductive nanocomposites were synthesized by embedding silver NPs of different shapes in diverse matrices as HDPE [109], PPMA [110], PVA [111, 112], bisphenol F diglycidyl ether [113], PVDF [114], and PDMS [78], but also in inks [115] and conductive polymers as PEDOT [116, 117]. Similar applications were found for gold nanocomposites by embedding them both in insulating polymer as PDMS [72, 78] or PS [118] and in conductive polymers as PANI [119] and polyindole [120].

Sensors

Different pressure and tactile sensors were produced using silver and gold as active fillers, mainly taking advantage from the electrical conductivity arisen from the nanocomposites upon mechanical stress variation. These nanocomposites were recently reviewed by Nambiar and Yeow [121] and Kotov [122]. Other sensors were based on the different electrical conductivity after gas [123] and molecule absorption [124] and for electrochemiluminescence sensors [125].

Optical Devices

The control of the shape and dimensions of gold and silver NPs leads to the ability in controlling the SPR of these NPs. Therefore by embedding these NPs into polymers, it is possible to synthesize nanocomposites with desired optical properties [126, 127]. In literature there are also present studies on polymeric optical diodes [128] recently reviewed by Nguyen [129].

Layer-by-Layer (LBL) Nanocomposite Materials

Layer-by-layer deposition is a technique that allows a precise control of structural organization of nanocomposite materials and thus allows to precisely tune the properties of the whole material. Layered nanocomposites containing
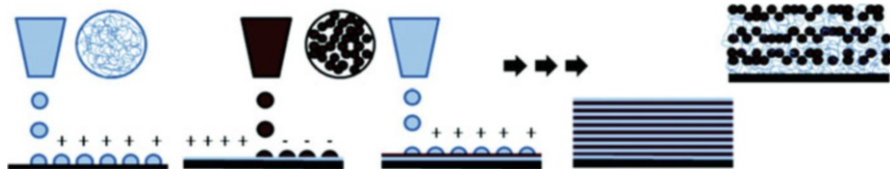
Fig. 6.12 Inkjet-printed LBL composite with gold NPs (Reprinted with the permission of [133]. Copyright 2010 American Chemical Society)

gold or silver nanocomposites were used in food packaging [130, 131], as well as for creating optically manipulated materials [132] or inkjet-printed electronic devices [133].

Other Applications

Gold or silver nanocomposites were generally used for improving the thermal stability of polymeric host matrices [134] and for synthesizing polymer nanocomposites with catalytic properties [135]. Also nanocomposites synthesized by UV curing were produced [136, 137]. Maity reported about the use of gold NPs as photoactivated heating systems in polymer composites [138].

In Situ UV Nanocomposites Synthesis

Homogeneous dispersion of metallic NPs in polymer matrix remains a critical issue for the nanocomposite preparation due to their high surface energy. A common strategy consists in functionalizing the surface of the NPs in order to make them dispersible in polymeric matrices. An alternative way developed in the last years envisages the direct dispersion of silver or gold precursors in photocurable monomers (often using also a cosolvent) and then, by UV irradiation, the simultaneous formation of the polymeric network and of the metal NPs already dispersed in the matrix. For the synthesis it is necessary to disperse a photosensitive metal precursor into the polymeric matrix. In the literature several studies are reported using silver hexafluoroantimonate (in acrylates [139–141], epoxies[142, 143], thiol-ene [144], and divinyl ethers [145] systems), also with engineered structures [146], using silver nitrate [147] for synthesizing silver nanocomposites, and using gold(III) chloride hydrate (in acrylates [140] and epoxies [148]) for the gold ones. The use of the light allows to create also very complex structures, such as periodic nanocomposites structure as reported by Smirnova et al. [149].

Non-conventional Synthesis of Nanocomposites

In this last section some innovative strategies for the synthesis of silver or gold nanocomposites are presented in order to illustrate possible future trends in this field. The first strategy regards the control of the shape of the NPs in solid bulk phase, meaning the control of the growing NPs by matrix parameters.

Trandafilović et al. reported about the synthesis of silver nanoplates in polyampholyte copolymers [150]. Jeon et al. studied the growth of NPs using PVP both as hosting matrix and reducing agent [151]. The growth of star-shaped gold NPs in block copolymer monolayer was studied by Suntivich et al. [151] while Kim et al. showed the synthesis of gold nanorods [152]. On the contrary, Hu et al. demonstrated the effect of gold NPs on the morphology of a PMMA/PS copolymer [153]. Mallick et al. reported on an interfacial reaction for the formation of gold-poly o-phenylenediamine composite [154].

Other approaches to in situ synthesize gold and silver NPs for the preparation of nanocomposites exploited the reducing effect on metal precursors by the curing agent of bicomponent PDMS [155, 156] or laser ablation of metal component in solution [157].

Finally, alternative interactions with the electromagnetic radiation were studied: Anyaogu et al. reported about the possible employ of functionalized gold NPs as UV photoinitiator for acrylic monomers polymerization [158], while Spano et al. showed the in situ synthesis of gold NPs by laser ablation in chitosan [159].

Tunnelling Conductive Fillers in Piezoresistive Composites

Recently, piezoresistive composite materials have found interesting applications in the fields of microsensors [160, 161], electromechanical devices, circuit breakers [162], and touchable sensitive screens and tactile sensors for robotics [163]. With respect to the commercially available devices, these composite systems can thus provide cheaper, faster, and more accurate alternatives. The properties of these materials could be tuned by varying the nature and morphology of the conductive particles, used as functional filler, and the type of polymeric matrix [164]. Several papers in the literature have indeed reported on piezoresistive composites prepared by incorporating different conductive fillers, mostly carbon structures (carbon black and nanotubes) and metal particles in an insulating polymer matrix (e.g., silicones, polyurethane, acrylics) [165]. By adjusting the amount and the type of the fillers, the composite can assume the electrical properties of an insulator up to the one of a good conductor. The conduction mechanism could be based on a percolation effect [166, 167], in the case of contact between the particles, or on a tunnelling mechanism [168, 169], when each conductive particle is separated from the others by a thin layer of insulating polymer representing the tunnelling barrier. In the piezoresistive composites based on tunnelling conduction mechanism, a small deformation due to an external load induces a huge change in the electrical conductivity [170, 171]. The applied mechanical strain induces a decrease of the polymer thickness between the particles, thus reducing the tunnelling barrier. In this way, the probability of tunnelling phenomena is increased, and a large reduction of the bulk electrical resistance takes place. The shape and the size of the filler particles in this kind of composite become a fundamental parameter to be adjusted as well as the filler type and amount. In particular, conductive particles showing sharp nanostructured tips at their surface lead to huge variations

of the electrical conduction of the overall composite material in response to a mechanical strain. This spiky morphology is indeed responsible for a local electric field enhancement [172] that considerably increases the tunnelling probability through the insulating barrier.

Several scientific works [170, 171, 173–175] have reported on the use of different metal microparticles as functional fillers. In order to drastically reduce the piezoresistive film thickness and to promote the integration with MEMS technologies, Stassi et al. recently reported on the application of gold NPs as conductive fillers in piezoresistive composites [72, 78]. The authors investigated how the morphological features of the nanostructured particles could influence the required amount of the fillers to obtain similar piezoresistive performances among different material compositions. In particular, highly pointed gold nanostars were synthesized in a room-temperature synthesis assisted by deep-eutectic solvents (DES), as shown in Fig. 6.9 [72]. These particular nanostructures were developed because of their high electrical conductivity and especially for the presence of nanosized sharp tips at their surface. These features generated an enhancement of the local electric field increasing the tunnelling probability between neighboring particles. The synthesized gold nanostars were dispersed in a PDMS matrix, and the prepared composite, with a thickness of 100 μm, was tested under different mechanical stress to evaluate the electric piezoresistance. The composite samples displayed a variation up to ten orders of magnitude of the electrical resistance under uniaxial pressure of 10 MPa, varying from a highly insulating state to a conductive one (Fig. 6.13).

Silver nanostructures were also studied and employed as conductive fillers for functional sensing composites. Recently, Hong et al. investigated the electrical and thermal conductivities of a silver flake/thermosetting polymer composite. The authors studied the influence of silver flake size, distribution and filler loading on the electrical volume resistivity, and thermal conductivity of the composite [15]. In particular, among many methods reported in the literature to synthesize silver NPs, including chemical reduction of silver ions in aqueous/nonaqueous solutions [176], template method [177], and photochemical reduction [178], the authors demonstrated that the flowerlike silver nanoarchitectures can be easily obtained in aqueous solution at room temperature in the presence of citric acid as anisotropic agent.

Ag- and Au-Based Inks for Inkjet Printing Flexible Electronics

Stabilized concentrated silver (Fig. 6.14) and gold NPs are well-known materials with novel properties and promising applications as pigments in inkjet inks for the preparation of metallic structures on various substrates because of their high electrical conductivity and resistance to oxidation.

Mainly Ag and Au NP-based inks for inkjet printing should meet some important requirements: for instance, they should not dry out and clog when in the printhead, they should have a good adhesion to the substrate with a limited coffee-ring effect

$$y=5,14*10^{11}e^{-2,17x}$$
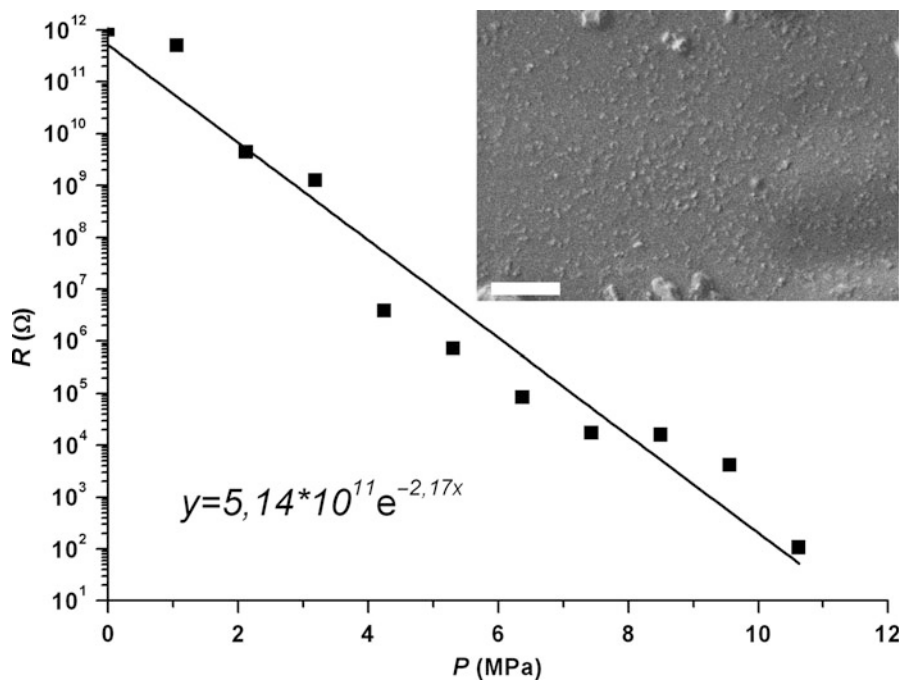
Fig. 6.13 Piezoresistive response of a PDMS-spiky gold nanostar composite. A FESEM image of the material is reported in the *inset* (the scale bar is 10 μm) (Reprinted from [72] with the permission of John Wiley and Sons)

and a reduction of particle aggregation, and they should be characterized by a suitable viscosity and surface tension.

Viscosity and surface tension are extremely important since they affect printing quality: they determine drop size, drop placement accuracy, satellite formation, and wetting of the substrate [180].

To this regard there are several approaches to formulate Ag- and Au-based inks for inkjet printing as well as many compounds. Compositions are specifically formulated for piezoelectric and thermal inkjet printing to produce low resistivity and high-resolution conductive traces on different substrates [179, 181, 182].

First of all conductive inks must contain an appropriate highly conductive metal precursor such as Ag, Cu, and Au NPs and a carrier vehicle. Most of them are water based: water is the main ink component and to limit contaminants, it must be as pure as possible.

Inks may also contain other additives such as humectants, binders, surfactants, and bactericides/fungicides. Additives are typically a small percentage with respect to the composition of the ink. They are used to tune ink properties or to add specific properties thus increasing its performance: it is important to have an ink formulation which is compatible with the particular inkjet system chosen for deposition, which in turn influences the interaction between NPs [183].

Fig. 6.14 (**a**) FESEM image of a water-based Ag NP ink deposited on a silicon substrate; panel (**b**) reports the NP diameter distribution as computed by a numerical routine (Reprinted from [179], copyright 2012, with permission from Elsevier)
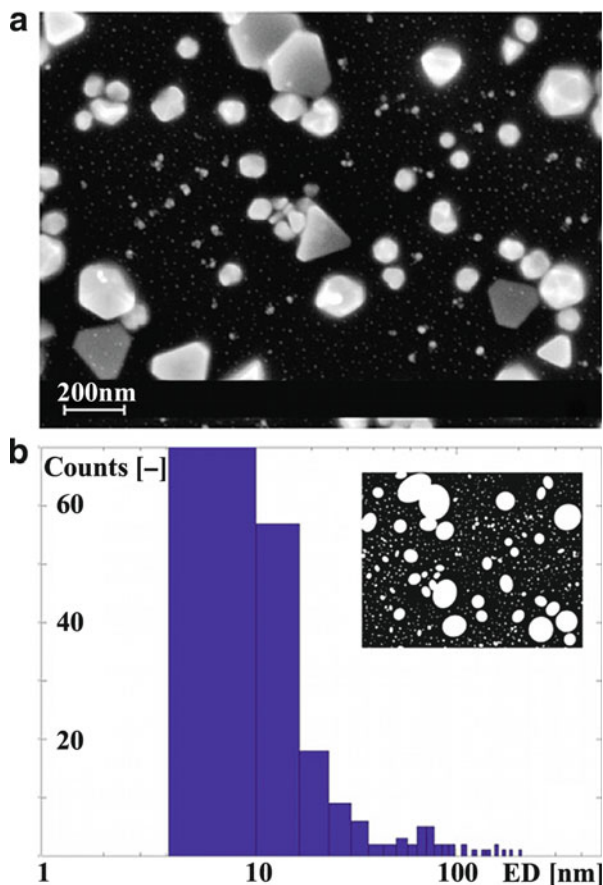
When the colloidal inks are used, to prevent agglomeration and precipitation of metal NPs, the formulation may contain dispersants to stabilize metal colloids. This allows to increase NP load to produce high-quality conductive inks. Two classes of compounds are used for this purpose: surfactants and polymers. These compounds interact with the surface of NPs and form a coating of variable composition and thickness. The resulting modified particle surfaces either attract or repel each other leading to flocculation or stabilization, respectively.

Humectants, including alcohols and glycols, are usually added to the ink as an additional vehicle or carrier for metal NPs. They may also be used to control the evaporation of the ink and to reduce the coffee-ring effect [184]. Most glycols are hygroscopic and can store moisture from the air.

Binder components are designed to facilitate the ink transfer to different substrates. They allow NPs to adhere to the substrate. Binders are typically resins that will remain on the substrate or surface along with the NPs.

Surfactants are added to adjust the surface tension of the resultant ink. Surfactants are molecules that contain both a hydrophilic and a hydrophobic portion. The addition of a surfactant to a water-based ink will have the result of drastically lowering the surface tension due to the orientation effects at interfaces caused by the hydrophilic and hydrophobic portions of the surfactant. If the surface tension of an ink is too high, the ink may not wet the cartridge correctly. A high surface tension also causes that the ink does not wet the substrate, giving poor results in terms of geometry reproduction [180].

Biocides and fungicides are added to eliminate growth of bacteria and fungi in the materials, even though with Ag conductive inks it is not necessary since silver NPs themselves have antibacterial properties.

In addition, inks should have a viscosity appropriate to the printing process. In order to adjust the viscosity to the desired value, a polymeric thickening agent can be used to increase it (e.g., the polyvinyl alcohol, PVA) [185]. In the case of piezoelectric printheads, the ink viscosity should be in the range of 5–20 cP, while thermal printheads require a viscosity from 1 to 5 cP.

After inkjet printing of a metal NP-based ink, in order to form a conductive printed pattern, particles must be sintered to create continuous connectivity between them and obtain electrical percolation. Sintering is the process of welding particles together at temperatures below the corresponding bulk metal melting point, involving surface diffusion phenomena rather than phase change between the solid and the liquid.

The conventional approach to sinter metal NPs is heating either with a hot plate or an oven driven by conduction/convection mechanisms (thermal sintering [186]).

The melting temperature of 1.5-nm-diameter gold NPs was experimentally found to be as low as 380 °C (melting point of bulk gold is 1,063 °C).

In addition to the thermal sintering, at present some emerging sintering techniques are studied and used such as laser-induced sintering [187], flash sintering (photonic sintering) [188], microwave oven sintering [189], and low-pressure Ar plasma sintering (plasma sintering [190]). Sintering can be also obtained by the addition of a positively charged polyelectrolyte such as poly(diallyldimethylammonium chloride) (PDAC) which promotes the coalescence of the NPs due to a decrease in their zeta potential (chemical sintering) [179, 191].

Conclusion

The important improvements in the shape-controlled synthesis field have raised the attention on metal NPs. Different chemical routes have been refined to obtain high-yield production and controllable and repeatable morphologies. An unprecedented possibility of tuning nanoscale and bulk material properties has been reached with these approaches leading to the exploitation of metal NPs in an extremely wide range of applications. Among noble metal NPs, gold and silver are the most

diffused and promising ones because of easiness of shaping different nanostructured morphologies. SERS, catalysis, pressure sensors, inkjet inks, bactericidal materials, and biosensors were analyzed in this chapter, some among the many emerging applications of nanostructured metal crystals.

References

1. Meng XK, Tang SC, Vongehr S (2010) A review on diverse silver nanostructures. J Mater Sci Technol 26:487–522
2. Wiley B, Sun Y, Mayers B, Xia Y (2005) Shape-controlled synthesis of metal nanostructures: the case of silver. Chem A Eur J 11:454–463
3. Jain PK, Huang X, El-Sayed IH, El-Sayed MA (2008) Noble metals on the nanoscale: optical and photothermal properties and some applications in imaging, sensing, biology, and medicine. Acc Chem Res 41:1578–1586
4. Hu M, Chen J, Li ZY, Au L, Hartland GV, Li X, Marquez M, Xia Y (2006) Gold nanostructures: engineering their plasmonic properties for biomedical applications. Chem Soc Rev 35:1084–1094
5. Xiao J, Qi L (2011) Surfactant-assisted, shape-controlled synthesis of gold nanocrystals. Nanoscale 3:1383–1396
6. Shen XS, Wang GZ, Hong X, Zhu W (2009) Nanospheres of silver nanoparticles: agglomeration, surface morphology control and application as SERS substrates. Phys Chem Chem Phys 11:7450–7454
7. Qin Y, Song Y, Sun N, Zhao N, Li M, Qi L (2008) Ionic liquid-assisted growth of single-crystalline dendritic gold nanostructures with a three-fold symmetry. Chem Mater 20:3965–3972
8. Maier SA, Brongersma ML, Kik PG, Meltzer S, Requicha AAG, Atwater HA (2001) Plasmonics – a route to nanoscale optical devices. Adv Mater 13:1501–1505
9. Huang X, El-Sayed IH, Qian W, El-Sayed MA (2006) Cancer cell imaging and photothermal therapy in the near-infrared region by using gold nanorods. J Am Chem Soc 128:2115–2120
10. Sau TK, Rogach AL, Jäckel F, Klar TA, Feldmann J (2010) Properties and applications of colloidal nonspherical noble metal nanoparticles. Adv Mater 22:1805–1825
11. Xia Y, Xiong Y, Lim B, Skrabalak SE (2009) Shape-controlled synthesis of metal nanocrystals: simple chemistry meets complex physics? Angew Chem Int Ed Engl 48:60–103
12. Liao H-G, Jiang Y-X, Zhou Z-Y, Chen S-P, Sun S-G (2008) Shape-controlled synthesis of gold nanoparticles in deep eutectic solvents for studies of structure-functionality relationships in electrocatalysis. Angew Chem Int Ed Engl 47:9100–9103
13. Barbosa S, Agrawal A, Rodríguez-Lorenzo L, Pastoriza-Santos I, Alvarez-Puebla RA, Kornowski A, Weller H, Liz-Marzán LM (2010) Tuning size and sensing properties in colloidal gold nanostars. Langmuir 26:14943–14950
14. Tan SJ, Campolongo MJ, Luo D, Cheng W (2011) Building plasmonic nanostructures with DNA. Nat Nanotechnol 6:268–276
15. Hong L, Li Q, Lin H, Li Y (2009) Synthesis of flower-like silver nanoarchitectures at room temperature. Mater Res Bull 44:1201–1204
16. Xionghui C, Aixia Z (2010) Preparation of microsized silver crystals with different morphologies by a wet-chemical method. Rare Metals 29:407–412
17. Wang H, Halas NJ (2008) Mesoscopic au "meatball" particles. Adv Mater 20:820–825
18. Burt J, Elechiguerra J, Reyesgasga J, Martinmontejanocarrizales J, Joseyacaman M (2005) Beyond Archimedean solids: star polyhedral gold nanocrystals. J Cryst Growth 285:681–691

19. Sau TK, Murphy CJ (2004) Room temperature, high-yield synthesis of multiple shapes of gold nanoparticles in aqueous solution. J Am Chem Soc 126:8648–8649

20. Zhao N, Wei Y, Sun N, Chen Q, Bai J, Zhou L, Qin Y, Li M, Qi L (2008) Controlled synthesis of gold nanobelts and nanocombs in aqueous mixed surfactant solutions. Langmuir 24:991–998

21. Xia Y, Li W, Cobley CM, Chen J, Xia X, Zhang Q, Yang M, Cho EC, Brown PK (2011) Gold nanocages: from synthesis to theranostic applications. Acc Chem Res 44:914–924

22. Cauda V, Schlossbauer A, Kecht J, Zuerner A, Bein T (2009) Multiple core-shell functionalized colloidal mesoporous silica nanoparticles. J Am Chem Soc 131:11361–11370

23. Morones JR, Elechiguerra JL, Camacho A, Holt K, Kouri JB, Ramírez JT, Yacaman MJ (2005) The bactericidal effect of silver nanoparticles. Nanotechnology 16:2346–2353

24. Daniel MC, Astruc D (2004) Gold nanoparticles: assembly, supramolecular chemistry, quantum-size-related properties, and applications toward biology, catalysis, and nanotechnology. Chem Rev 104:293–346

25. Jeong GH, Lee YW, Kim M, Han SW (2009) High-yield synthesis of multi-branched gold nanoparticles and their surface-enhanced Raman scattering properties. J Colloid Interface Sci 329:97–102

26. Auer S, Frenkel D (2001) Prediction of absolute crystal-nucleation rate in hard-sphere colloids. Nature 409:1020

27. Matijevic E (1996) Controlled colloid formation. Curr Opin Colloid Interface Sci 1:176–183

28. Schon G, Simon U (1995) A fascinating new field in colloid science: small ligand stabilized metall clusters and possible applications in microelectronics. Colloid Polym Sci 273:101–117

29. Weller H (1993) Colloidal semiconductor Q-particles: chemistry in the transition region between solid state and molecules. Angew Chem Int Ed 32:41–53

30. Murray CB, Kagan CR, Bawendi MG (1995) Self-organization of CdSe nanocrystallites into three-dimensional quantum dot superlattices. Science 270:1335–1338

31. Kuo C-H, Huang MH (2005) Synthesis of branched gold nanocrystals by a seeding growth approach. Langmuir 21:2012–2016

32. Brust M, Bethell D, Schiffrin DJ, Kiely CJ (1995) Novel gold-dithiol nano-networks with non-metallic electronic properties. Adv Mater 7:795–797

33. Hostetler MJ, Green SJ, Stokes JJ, Murray RW (1996) Monolayers in three dimensions: synthesis and electrochemistry of ω-functionalized alkanethiolate-stabilized gold cluster compounds. J Am Chem Soc 118:4212–4213

34. Leff DV, Ohara PC, Heath JR, Gelbart WM (1995) Thermodynamic control of gold nanocrystal size: experiment and theory. J Phys Chem 99:7036–7041

35. Hostetler MJ, Wingate JE, Zhong C-J, Harris JE, Vachet RW, Clark MR, Londono JD, Green SJ, Stokes JJ, Wignall GD, Glish GL, Porter MD, Evans ND, Murray RW, Royce W (1998) Alkanethiolate gold cluster molecules with core diameters from 1.5 to 5.2 nm: core and monolayer properties as a function of core size. Langmuir 14:17–30

36. Tao AR, Habas S, Yang PD (2008) Shape control of colloidal metal nanocrystals. Small 4:310

37. Sun Y, Mayers B, Herricks T, Xia Y (2003) Polyol synthesis of uniform silver nanowires: a plausible growth mechanism and the supporting evidence. Nano Lett 3:955

38. Xiong Y, Xia Y (2007) Shape-controlled synthesis of metal nanostructures: the case of palladium. Adv Mater 19:3385

39. Wiley BJ, Chen Y, McLellan J, Xiong Y, Li Z-Y, Ginger D, Xia Y (2007) Synthesis and optical properties of silver nanobars and nanorice. Nano Lett 7:1032

40. Washio I, Xiong Y, Yin Y, Xia Y (2006) Reduction by the end groups of Poly(vinyl pyrrolidone): a new and versatile route to the kinetically controlled synthesis of Ag triangular nanoplates. Adv Mater 18:1745

41. Xiong Y, Washio I, Chen J, Cai H, Li Z-Y, Xia Y (2006) Poly(vinyl pyrrolidone): a dual functional reductant and stabilizer for the facile synthesis of noble metal nanoplates in aqueous solutions. Langmuir 22:8563

42. Morrison HG (2009) Characterization of thermal behavior of deep eutectic solvents and their potential as drug solubilization vehicles. Int J Pharm 378:1–2

43. Parnham ER, Drylie EA, Wheatley PS, Slawin AMZ, Morris RE (2006) Ionothermal materials synthesis using unstable deep-eutectic solvents as template-delivery agents. Angew Chem Int Ed Engl 45:4962–4966

44. Chambers SA (1991) Epitaxial film crystallography by high-energy Auger and X-ray photoelectron diffraction. Adv Phys 40:357

45. Ledentsov NN, Ustinov VM, Shchulan VA, Koper PS, Alferov ZI, Bimbers D (1998) Quantum dot heterostructures: growth, properties, lasing. Semiconductors 32:343

46. Jana NR, Gearheart L, Murphy CJ (2001) Wet chemical synthesis of high aspect ratio cylindrical gold nanorods. J Phys Chem B 105:4065

47. Nikoobakht B, El-Sayed MA (2003) Preparation and growth mechanism of gold Nanorods (NRs) using seed-mediated growth method. Chem Mater 15:1957

48. Barbieri A, Accorsi G, Armaroli N (2008) Luminescent complexes beyond the platinum group: the d10 avenue. Chem Commun 19:2185–2193

49. Hada H, Yonezawa Y, Yoshida A, Kurakake A (1976) Photoreduction of silver ion in aqueous and alcoholic solutions. J Phys Chem 80:2728–2731

50. Sato T, Onaka H, Yonezawa Y (1999) Sensitized photoreduction of silver ions in the presence of acetophenone. J Photochem Photobiol A Chem 127:83–87

51. Itakura T, Torigoe K, Esumi K (1995) Preparation and characterization of ultrafine metal particles in ethanol by UV irradiation using a photoinitiator. Langmuir 11:4129–4134

52. Esumi K, Matsumoto T, Seto Y, Yoshimura T (2005) Preparation of gold-, gold/silver-dendrimer nanocomposites in the presence of benzoin in ethanol by UV irradiation. J Colloid Interface Sci 284:199–203

53. Scaiano JC, Aliaga C, Maguire S, Wang D (2006) Magnetic field control of photoinduced silver nanoparticle formation. J Phys Chem B 110:12856–12859

54. Scaiano JC, Billone P, Gonzalez CM, Maretti L, Marin ML, McGilvray KL, Yuan N (2009) Photochemical routes to silver and gold nanoparticles. Pure Appl Chem 81:635–647

55. Courrol LC, de Oliveira Silva FR, Gomes L (2007) A simple method to synthesize silver nanoparticles by photo-reduction. Colloids Surf A Physicochem Eng Asp 305:54–57

56. Yang S, Wang Y, Wang Q, Zhang R, Ding B (2007) UV irradiation induced formation of Au nanoparticles at room temperature: the case of pH values. Colloids Surf A Physicochem Eng Asp 301:174–183

57. Han MY, Quek CH (2000) Photochemical synthesis in formamide and room-temperature Coulomb staircase behavior of size-controlled gold nanoparticles. Langmuir 16:362–367

58. Esumi K, Wakabayashi M, Torigoe K (1996) Preparation of colloidal silver-palladium alloys by UV-irradiation in mixtures of acetone and 2-propanol. Colloids Surf A Physicochem Eng Asp 109:55–62

59. Hada H, Yonezawa Y, Saikawa M (1982) Photoreduction of silver in a titanium dioxide suspension. Bull Chem Soc Jpn 55:2010–2014

60. Yonezawa Y, Kometani N, Sakaue T, Yano A (2005) Photoreduction of silver ions in a colloidal titanium dioxide suspension. J Photochem Photobiol A Chem 171:1–8

61. Zhang H, Wang G, Chen D, Lv X, Li J (2008) Tuning photoelectrochemical performances of Ag-TiO$_2$ nanocomposites via reduction/oxidation of Ag. Chem Mater 20:6543–6549

62. Hada H, Tanemura H, Yonezawa Y (1978) Photoreduction of the silver ion in a zinc oxide suspension. Bull Chem Soc Jpn 51:3154–3160

63. Carbone L, Jakab A, Khalavka Y, Sönnichsen C (2009) Light-controlled one-sided growth of large plasmonic gold domains on quantum rods observed on the single particle level. Nano Lett 9:3710–3714

64. Dong SA, Zhou SP (2007) Photochemical synthesis of colloidal gold nanoparticles. Mater Sci Eng B Solid-State Mater Adv Technol 140:153–159

65. Jia H, Xu W, An J, Li D, Zhao B (2006) A simple method to synthesize triangular silver nanoparticles by light irradiation. Spectrochim Acta A Mol Biomol Spectrosc 64:956–960

66. Maillard M, Huang P, Brus L (2003) Silver nanodisk growth by surface plasmon enhanced photoreduction of adsorbed [Ag +]. Nano Lett 3:1611–1615

67. Taubert A, Arbell I, Mecke A, Graf P (2006) Photoreduction of a crystalline Au(III) complex: a solid-state approach to metallic nanostructures. Gold Bull 39:205–211

68. Tung HT, Song JM, Nien YT, Chen IG (2008) A novel method for preparing vertically grown single-crystalline gold nanowires. Nanotechnology 19:455603

69. Glover RD, Miller JM, Hutchison JE (2011) Generation of metal nanoparticles from silver and copper objects: nanoparticle dynamics on surfaces and potential sources of nanoparticles in the environment. ACS Nano 5:8950–8957

70. Goldstein J, Newbury D, Joy D, Lyman C, Echlin P, Lifshin E, Sawyer LC, Michael JR (2002) Scanning electron microscopy and X-ray microanalysis. Springer, New York

71. Williams DB, Carter CB (2009) Transmission electron microscopy: a textbook for materials science. Springer, New York

72. Stassi S, Cauda V, Canavese G, Manfredi D, Pirri CF (2012) Synthesis and characterization of gold nanostars as filler of tunneling conductive polymer composites. Eur J Inorg Chem 16:2669–2673

73. Mulvihill MJ, Ling XY, Henzie J, Yang P (2010) Anisotropic etching of silver nanoparticles for plasmonic structures capable of single-particle SERS. J Am Chem Soc 132:268–274

74. Lim B, Xia Y (2011) Metal nanocrystals with highly branched morphologies. Angew Chem Int Ed Engl 50:76–85

75. Senthil Kumar P, Pastoriza-Santos I, Rodríguez-González B, Javier García de Abajo F, Liz-Marzán LM (2008) High-yield synthesis and optical response of gold nanostars. Nanotechnology 19:015606

76. Khoury CG, Vo-Dinh T (2008) Gold nanostars for surface-enhanced Raman scattering: synthesis, characterization and optimization. J Phys Chem C 112:18849–18859

77. Nalbant Esenturk E, Hight Walker AR (2009) Surface-enhanced Raman scattering spectroscopy via gold nanostars. J Raman Spectrosc 40:86–91

78. Stassi S, Canavese G, Cauda V, Marasso SL, Pirri CF (2012) Evaluation of different conductive nanostructured particles as filler in smart piezoresistive composites. Nanoscale Res Lett 7:327

79. Xu X, Jia J, Yang X, Dong S (2010) A templateless, surfactantless, simple electrochemical route to a dendritic gold nanostructure and its application to oxygen reduction. Langmuir 26:7627–7631

80. Feng QL, Wu J, Chen GQ, Cui FZ, Kim TN, Kim JO (2000) A mechanistic study of the antibacterial effect of silver ions on *Escherichia coli* and *Staphylococcus aureus*. J Biomed Mater Res 52:662–668

81. Xia Y, Halas NJ (2005) Shape-controlled synthesis and surface plasmonic properties of metallic nanostructures. MRS Bull 30:338–348

82. Haynes CL, McFarland AD, Van Duyne RP (2005) Surface-enhanced: Raman spectroscopy. Anal Chem 77:338 A–346 A

83. Jeanmaire DL, Van Duyne RP (1977) Surface Raman spectroelectrochemistry Part I. Heterocyclic, aromatic, and aliphatic amines adsorbed on the anodized silver electrode. J Electroanal Chem 84:1–20

84. Fleischmann M, Hendra PJ, McQuillan AJ (1974) Raman spectra of pyridine adsorbed at a silver electrode. Chem Phys Lett 26:163–166

85. Virga A, Rivolo P, Descrovi E, Chiolerio A, Digregorio G, Frascella F, Soster M, Bussolino F, Marchiò S, Geobaldo F, Giorgis F (2012) SERS active Ag nanoparticles in mesoporous silicon: detection of organic molecules and peptide-antibody assays. J Raman Spectrosc 43:730–736

86. Chiolerio A, Virga A, Pandolfi P, Martino P, Rivolo P, Geobaldo F, Giorgis F (2012) Direct patterning of silver particles on porous silicon by inkjet printing of a silver salt via in-situ reduction. Nanoscale Res Lett 7:502

87. Huang T, Meng F, Qi L (2010) Controlled synthesis of dendritic gold nanostructures assisted by supramolecular complexes of surfactant with cyclodextrin. Langmuir 26:7582–7589

88. Sureshkumar M, Siswanto DY, Lee CK (2010) Magnetic antimicrobial nanocomposite based on bacterial cellulose and silver nanoparticles. J Mater Chem 20:6948–6955

89. Shah MSAS, Nag M, Kalagara T, Singh S, Manorama SV (2008) Silver on PEG-PU-TiO$_2$ polymer nanocomposite films: an excellent system for antibacterial applications. Chem Mater 20:2455–2460

90. Hsu SH, Tseng HJ, Lin YC (2010) The biocompatibility and antibacterial properties of waterborne polyurethane-silver nanocomposites. Biomaterials 31:6796–6808

91. Varaprasad K, Murali Mohan Y, Ravindra S, Narayana Reddy N, Vimala K, Monika K, Sreedhar B, Mohana Raju K (2010) Hydrogel-silver nanoparticle composites: a new generation of antimicrobials. J Appl Polym Sci 115:1199–1207

92. Bryaskova R, Pencheva D, Kale GM, Lad U, Kantardjiev T (2010) Synthesis, characterisation and antibacterial activity of PVA/TEOS/Ag-Np hybrid thin films. J Colloid Interface Sci 349:77–85

93. Dastjerdi R, Montazer M, Shahsavan S (2010) A novel technique for producing durable multifunctional textiles using nanocomposite coating. Colloids Surf B Biointerfaces 81:32–41

94. Dallas P, Sharma VK, Zboril R (2011) Silver polymeric nanocomposites as advanced antimicrobial agents: classification, synthetic paths, applications, and perspectives. Adv Colloid Interface Sci 166:119–135

95. Dastjerdi R, Montazer M (2010) A review on the application of inorganic nano-structured materials in the modification of textiles: focus on anti-microbial properties. Colloids Surf B Biointerfaces 79:5–18

96. Goyal AK, Johal ES, Rath G (2011) Nanotechnology for water treatment. Curr Nanosci 7:640–654

97. Gasparyan VK (2009) Gold and silver nanoparticles in bioassay, cell visualization and therapy. Curr Clin Pharmacol 4:159–163

98. Leung KCF, Xuan S, Zhu X, Wang D, Chak CP, Lee SF, Ho WKW, Chung BCT (2012) Gold and iron oxide hybrid nanocomposite materials. Chem Soc Rev 41:1911–1928

99. Rahman M, Ahmad MZ, Kazmi I, Akhter S, Afzal M, Gupta G, Jalees Ahmed F, Anwar F (2012) Advancement in multifunctional nanoparticles for the effective treatment of cancer. Expert Opin Drug Deliv 9:367–381

100. Wang LS, Chuang MC, Ho JA (2012) Nanotheranostics – a review of recent publications. Int J Nanomedicine 7:4679–4695

101. Li D, He Q, Li J (2009) Smart core/shell nanocomposites: intelligent polymers modified gold nanoparticles. Adv Colloid Interface Sci 149:28–38

102. Tang YH, Huang AYT, Chen PY, Chen HT, Kao CL (2011) Metallodendrimers and dendrimer nanocomposites. Curr Pharm Des 17:2308–2330

103. Ravichandran R, Sundarrajan S, Venugopal JR, Mukherjee S, Ramakrishna S (2012) Advances in polymeric systems for tissue engineering and biomedical applications. Macromol Biosci 12:286–311

104. Huang H, Yuan Q, Yang X (2005) Morphology study of gold-chitosan nanocomposites. J Colloid Interface Sci 282:26–31

105. Madhumathi K, Sudheesh Kumar PT, Abhilash S, Sreeja V, Tamura H, Manzoor K, Nair SV, Jayakumar R (2010) Development of novel chitin/nanosilver composite scaffolds for wound dressing applications. J Mater Sci Mater Med 21:807–813

106. Tang F, He F, Cheng H, Li L (2010) Self-assembly of conjugated polymer-Ag@SiO$_2$ hybrid fluorescent nanoparticles for application to cellular imaging. Langmuir 26:11774–11778

107. Zhao J, Castranova V (2011) Toxicology of nanomaterials used in nanomedicine. J Toxicol Environ Health B Crit Rev 14:593–632
108. Tolaymat TM, El Badawy AM, Genaidy A, Scheckel KG, Luxton TP, Suidan M (2010) An evidence-based environmental perspective of manufactured silver nanoparticle in syntheses and applications: a systematic review and critical appraisal of peer-reviewed scientific papers. Sci Total Environ 408:999–1006
109. Rybak A, Boiteux G, Melis F, Seytre G (2010) Conductive polymer composites based on metallic nanofiller as smart materials for current limiting devices. Compos Sci Technol 70:410–416
110. Kim WT, Jung JH, Kim TW, Son DI (2010) Current bistability and carrier transport mechanisms of organic bistable devices based on hybrid Ag nanoparticle-polymethyl methacrylate polymer nanocomposites. Appl Phys Lett 96:253301
111. Mahendia S, Tomar AK, Kumar S (2010) Electrical conductivity and dielectric spectroscopic studies of PVA-Ag nanocomposite films. J Alloys Compd 508:406–411
112. Gautam A, Ram S (2010) Preparation and thermomechanical properties of Ag-PVA nanocomposite films. Mater Chem Phys 119:266–271
113. Zhang R, Moon KS, Lin W, Wong CP (2010) Preparation of highly conductive polymer nanocomposites by low temperature sintering of silver nanoparticles. J Mater Chem 20:2018–2023
114. Chun KY, Oh Y, Rho J, Ahn JH, Kim YJ, Choi HR, Baik S (2010) Highly conductive, printable and stretchable composite films of carbon nanotubes and silver. Nat Nanotechnol 5:853–857
115. Pudas M, Hagberg J, Leppävuori S (2004) Gravure offset printing of polymer inks for conductors. Prog Org Coat 49:324–335
116. Zhu R, Chung CH, Cha KC, Yang W, Zheng YB, Zhou H, Song TB, Chen CC, Weiss PS, Li G, Yang Y (2011) Fused silver nanowires with metal oxide nanoparticles and organic polymers for highly transparent conductors. ACS Nano 5:9877–9882
117. Gaynor W, Burkhard GF, McGehee MD, Peumans P (2011) Smooth nanowire/polymer composite transparent electrodes. Adv Mater 23:2905–2910
118. Kim BY, Shim IB, Araci ZO, Scott Saavedra S, Monti OLA, Armstrong NR, Sahoo R, Srivastava DN, Pyun J (2010) Synthesis and colloidal polymerization of ferromagnetic Au-Co nanoparticles into Au-Co_3O_4 nanowires. J Am Chem Soc 132:3234–3235
119. Englebienne P, Van Hoonacker A (2005) Gold-conductive polymer nanoparticles: a hybrid material with enhanced photonic reactivity to environmental stimuli. J Colloid Interface Sci 292:445–454
120. Joshi L, Prakash R (2011) One-pot synthesis of polyindole-Au nanocomposite and its nanoscale electrical properties. Mater Lett 65:3016–3019
121. Nambiar S, Yeow JTW (2011) Conductive polymer-based sensors for biomedical applications. Biosens Bioelectron 26:1825–1832
122. Kotov N (2004) Membrane sensors: nanocomposites are stretched thin. Nat Mater 3:669–671
123. Hanisch C, Ni N, Kulkarni A, Zaporojtchenko V, Strunskus T, Faupel F (2011) Fast electrical response to volatile organic compounds of 2D Au nanoparticle layers embedded into polymers. J Mater Sci 46:438–445
124. Shan C, Yang H, Han D, Zhang Q, Ivaska A, Niu L (2010) Graphene/AuNPs/chitosan nanocomposites film for glucose biosensing. Biosens Bioelectron 25:1070–1074
125. Devadoss A, Spehar-Délèze AM, Tanner DA, Bertoncello P, Marthi R, Keyes TE, Forster RJ (2010) Enhanced electrochemiluminescence and charge transport through films of metallopolymer-gold nanoparticle composites. Langmuir 26:2130–2135
126. Jiang G, Hore MJA, Gam S, Composto RJ (2012) Gold nanorods dispersed in homopolymer films: optical properties controlled by self-assembly and percolation of nanorods. ACS Nano 6:1578–1588

127. Beyene HT, Chakravadhanula VSK, Hanisch C, Elbahri M, Strunskus T, Zaporojtchenko V, Kienle L, Faupel F (2010) Preparation and plasmonic properties of polymer-based composites containing Ag-Au alloy nanoparticles produced by vapor phase co-deposition. J Mater Sci 45:5865–5871

128. Hu X, Li Z, Zhang J, Yang H, Gong Q, Zhang X (2011) Low-power and high-contrast nanoscale all-optical diodes via nanocomposite photonic crystal microcavities. Adv Funct Mater 21:1803–1809

129. Nguyen TP (2011) Polymer-based nanocomposites for organic optoelectronic devices. A review. Surf Coat Technol 206:742–752

130. Duncan TV (2011) Applications of nanotechnology in food packaging and food safety: barrier materials, antimicrobials and sensors. J Colloid Interface Sci 363:1–24

131. Orozco VH, Kozlovskaya V, Kharlampieva E, López BL, Tsukruk VV (2010) Biodegradable self-reporting nanocomposite films of poly(lactic acid) nanoparticles engineered by layer-by-layer assembly. Polymer 51:4127–4139

132. Zhu Z, Senses E, Akcora P, Sukhishvili SA (2012) Programmable light-controlled shape changes in layered polymer nanocomposites. ACS Nano 6:3152–3162

133. Andres CM, Kotov NA (2010) Inkjet deposition of layer-by-layer assembled films. J Am Chem Soc 132:14496–14502

134. Chrissafis K, Bikiaris D (2011) Can nanoparticles really enhance thermal stability of polymers? Part I: an overview on thermal decomposition of addition polymers. Thermochim Acta 523:1–24

135. Yuan C, Luo W, Zhong L, Deng H, Liu J, Xu Y, Dai L (2011) Gold@Polymer nanostructures with tunable permeability shells for selective catalysis. Angew Chem Int Ed 50:3515–3519

136. Sangermano M, Perruchas S, Gacoin T, Rizza G (2008) Synthesis of Au@SiO$_2$ core/shell nanoparticles and their dispersion into an acrylic photocurable formulation: film preparation and characterization. Macromol Chem Phys 209:2343–2348

137. Sangermano M, Marchino A, Perruchas S, Gacoin T, Rizza G (2008) UV-cured nanostructured gold/acrylic coating. Macromol Mater Eng 293:964–968

138. Maity S, Bochinski JR, Clarke LI (2012) Metal nanoparticles acting as light-activated heating elements within composite materials. Adv Funct Mater 22:5259–5270

139. Chiolerio A, Sangermano M (2012) In situ synthesis of Ag-acrylic nanocomposites: tomography-based percolation model, irreversible photoinduced electromigration and reversible electromigration. Mater Sci Eng B Solid-State Mater Adv Technol 177:373–380

140. Sangermano M, Roppolo I, Camara VHA, Dizman C, Ates S, Torun L, Yagci Y (2011) Polysulfone/metal nanocomposites by simultaneous photoinduced crosslinking and redox reaction. Macromol Mater Eng 296:820–825

141. Chiolerio A, Vescovo L, Sangermano M (2010) Conductive UV-cured acrylic inks for resistor fabrication: models for their electrical properties. Macromol Chem Phys 211:2008–2016

142. Sangermano M, Yagci Y, Rizza G (2007) In situ synthesis of silver-epoxy nanocomposites by photoinduced electron transfer and cationic polymerization processes. Macromolecules 40:8827–8829

143. Vescovo L, Sangermano M, Scarazzini R, Kortaberria G, Mondragon I (2010) In-situ-synthetized silver/epoxy nanocomposites: electrical characterization by means of dielectric spectroscopy. Macromol Chem Phys 211:1933–1939

144. Colucci G, Celasco E, Mollea C, Bosco F, Conzatti L, Sangermano M (2011) Hybrid coatings containing silver nanoparticles generated in situ in a thiol-ene photocurable system. Macromol Mater Eng 296:921–928

145. Cook WD, Nghiem QD, Chen Q, Chen F, Sangermano M (2011) Simultaneous photoinduced silver nanoparticles formation and cationic polymerization of divinyl ethers. Macromolecules 44:4065–4071

146. Chiolerio A, Roppolo I, Sangermano M (2013) Radical diffusion engineering: tailored nanocomposite materials for piezoresistive inkjet printed strain measurement. RSC Adv 3:3446–3452

147. Nair JR, Ijeri VS, Gerbaldi C, Bodoardo S, Bongiovanni R, Penazzi N (2010) Novel self-directed dual surface metallisation via UV-curing technique for flexible polymeric capacitors. Org Electron Phys Mater Appl 11:1802–1808

148. Yagci Y, Sangermano M, Rizza G (2008) Synthesis and characterization of gold – epoxy nanocomposites by visible light photoinduced electron transfer and cationic polymerization processes. Macromolecules 41:7268–7270

149. Smirnova TN, Kokhtych LM, Kutsenko AS, Sakhno OV, Stumpe J (2009) The fabrication of periodic polymer/silver nanoparticle structures: In situ reduction of silver nanoparticles from precursor spatially distributed in polymer using holographic exposure. Nanotechnology 20:405301

150. Trandafilović LV, Luyt AS, Bibić N, Dimitrijević-Branković S, Georges MK, Radhakrishnan T, Djoković V (2012) Formation of nano-plate silver particles in the presence of polyampholyte copolymer. Colloids Surf A Physicochem Eng Asp 414:17–25

151. Jeon SH, Xu P, Zhang B, MacK NH, Tsai H, Chiang LY, Wang HL (2011) Polymer-assisted preparation of metal nanoparticles with controlled size and morphology. J Mater Chem 21:2550–2554

152. Kim JU, Cha SH, Shin K, Jho JY, Lee JC (2004) Preparation of gold nanowires and nanosheets in bulk block copolymer phases under mild conditions. Adv Mater 16:459–464

153. Hu S, Brittain WJ, Jacobson S, Balazs AC (2006) Selective ordering of surfactant modified gold nanoparticles in a diblock copolymer. Eur Polym J 42:2045–2052

154. Mallick K, Witcomb M, Scurrell M (2007) A novel synthesis route for a gold-polymer soft composite material. Phys Status Solid Rapid Res Lett 1:R1–R3

155. Scott A, Gupta R, Kulkarni GU (2010) A simple water-based synthesis of Au Nanoparticle/PDMS composites for water purification and targeted drug release. Macromol Chem Phys 211:1640–1647

156. Goyal A, Kumar A, Patra PK, Mahendra S, Tabatabaei S, Alvarez PJJ, John G, Ajayan PM (2009) In situ synthesis of metal nanoparticle embedded free standing multifunctional PDMS films. Macromol Rapid Commun 30:1116–1122

157. Kalyva M, Kumar S, Brescia R, Petroni S, La Tegola C, Bertoni G, De Vittorio M, Cingolani R, Athanassiou A (2013) Electrical response from nanocomposite PDMS-Ag NPs generated by in situ laser ablation in solution. Nanotechnology 24:035707

158. Anyaogu KC, Cai X, Neckers DC (2008) Gold nanoparticle photopolymerization of acrylates. Macromolecules 41:9000–9003

159. Spano F, Massaro A, Blasi L, Malerba M, Cingolani R, Athanassiou A (2012) In situ formation and size control of gold nanoparticles into chitosan for nanocomposite surfaces with tailored wettability. Langmuir 28:3911–3917

160. Govindaraju A et al (2005) Reinforcement of PDMS masters using SU-8 truss structures. J Micromech Microeng 15:1303

161. Mannsfeld SCB, Tee BCK, Stoltenberg RM, Chen CVHH, Barman S, Muir BVO, Sokolov AN, Reese C, Bao Z (2010) Highly sensitive flexible pressure sensors with microstructured rubber dielectric layers. Nat Mater 9:859–864

162. Harsaanyi G (2000) Polymer films in sensor applications: a review of present uses and future possibilities. Sens Rev 20:98–105

163. Shimojo M, Namiki A, Ishikawa M, Makino R, Mabuchi K (2004) A tactile sensor sheet using pressure conductive rubber with electrical-wires stitched method. IEEE Sens J 4:589–596

164. Strumpler R, Glatz-Reichenbach J (1999) Conducting polymer composites. J Electroceramics 3:329–346

165. Fu S-Y, Feng X-Q, Lauke B, Mai Y-W (2008) Effects of particle size, particle/matrix interface adhesion and particle loading on mechanical properties of particulate-polymer composites. Compos B Eng 39:933–961
166. Toker D, Azulay D, Shimoni N, Balberg I, Millo O (2003) Tunneling and percolation in metal-insulator composite materials. Phys Rev B 68:041403
167. Lundberg B, Sundqvist B (1986) Resistivity of a composite conducting polymer as a function of temperature, pressure, and environment: applications as a pressure and gas concentration transducer. J Appl Phys 60:1074–1079
168. Lantada AD, Lafont P, Sanz JLM, Munoz-Guijosa JM, Otero JE (2010) Quantum tunnelling composites: characterisation and modelling to promote their applications as sensors. Sens Actuators A Phys 164:46–57
169. Zhang XW, Zheng PY, Yi XQ (2000) Time dependence of piezoresistance for the conductor-filled polymer composites. J Polym Sci B Polym Phys 38:2739–2749
170. Bloor D, Donnelly K, Hands PJ, Laughlin P, Lussey D (2005) A metal–polymer composite with unusual properties. J Phys D: Appl Phys 38:2851–2860
171. Canavese G, Lombardi M, Stassi S, Pirri CF (2012) Comprehensive characterization of large piezoresistive variation of Ni-PDMS composites. Appl Mech Mater 110–116:1336–1344
172. Edgcombe CJ, Valdrè U (2001) Microscopy and computational modelling to elucidate the enhancement factor for field electron emitters. J Microsc 203:188–194
173. Ausanio G, Barone A, Campana C, Iannotti V, Luponio C, Pepe G, Lanotte L (2006) Giant resistivity change induced by strain in a composite of conducting particles in an elastomer matrix. Sens Actuators A Physl 127:56–62
174. Canavese G, Stassi S, Stralla M, Bignardi C, Pirri CF (2012) Stretchable and conformable metal–polymer piezoresistive hybrid system. Sens Actuators A Phys 186:191–197
175. Bloor D, Graham A, Williams EJ, Laughlin PJ, Lussey D (2006) Metal–polymer composite with nanostructured filler particles and amplified physical properties. Appl Phys Lett 88:102103
176. Sun Y, Mayers B, Xia Y (2003) Transformation of silver nanospheres into nanobelts and triangular nanoplates through a thermal process. Nano Lett 3:675–679
177. Chen S, Carroll DL (2002) Synthesis and characterization of truncated triangular silver nanoplates. Nano Lett 2:1003–1007
178. Lu HW, Liu SH, Wang XL, Qian XF, Yin J, Zhu ZK (2003) Silver nanocrystals by hyperbranched polyurethane-assisted photochemical reduction of Ag+. Mater Chem Phys 81:104–107
179. Chiolerio A, Cotto M, Pandolfi P, Martino P, Camarchia V, Pirola M, Ghione G (2012) Ag nanoparticle-based inkjet printed planar transmission lines for RF and microwave applications: considerations on ink composition, nanoparticle size distribution and sintering time. Microelectron Eng 97:8–15
180. Molesa S, Redinger DR, Huang DC, Subramanian V (2003) High-quality inkjet-printed multilevel interconnects and inductive components on plastic for ultra-low-cost RFID applications. Mater Res Soc Sympos Proc 769:253–258
181. Magdassi S, Bassa A, Vinetsky Y, Kamyshny A (2003) Silver nanoparticles as pigments for water-based ink-jet inks. Chem Mater 15:2208–2217
182. Bidoki SM, Lewis DM, Clark M, Vakorov A, Millner PA, McGorman D (2007) Ink-jet fabrication of electronic components. J Micromech Microeng 17:967–974
183. Tiberto P, Barrera G, Celegato F, Coisson M, Chiolerio A, Martino P, Pandolfi P, Allia P (2013) Magnetic properties of jet-printer inks containing dispersed magnetite nanoparticles. Eur Phys J B 86:173
184. Soltman D, Subramanian V (2008) Inkjet-printed line morphologies and temperature control of the coffee ring effect. Langmuir 24:2224–2231
185. Lichtenberger M (2004) Inks Water-based. www.eng.buffalo.edu/COurses/spring04/ce457_527/Matt.pdf

186. Lee HH, Chou KS, Huang KC (2005) Inkjet printing of nanosized silver colloids. Nano-technology 16:2436–2441
187. Chiolerio A, MacCioni G, Martino P, Cotto M, Pandolfi P, Rivolo P, Ferrero S, Scaltrito L (2011) Inkjet printing and low power laser annealing of silver nanoparticle traces for the realization of low resistivity lines for flexible electronics. Microelectron Eng 88:2481–2483
188. Bai JG, Creehan KD, Kuhn HA (2007) Inkjet printable nanosilver suspensions for enhanced sintering quality in rapid manufacturing. Nanotechnology 18:185701
189. Perelaer J, De Gans BJ, Schubert US (2006) Ink-jet printing and microwave sintering of conductive silver tracks. Adv Mater 18:2101–2104
190. Reinhold I, Hendriks CE, Eckardt R, Kranenburg JM, Perelaer J, Baumann RR, Schubert US (2009) Argon plasma sintering of inkjet printed silver tracks on polymer substrates. J Mater Chem 19:3384–3388
191. Kamyshny S, Steinke J, Magdassi S (2011) Metal-based inkjet inks for printed electronics. Open Appl Phys J 4:19–36

Magnetite and Other Fe-Oxide Nanoparticles

7

Alessandro Chiolerio, Angelica Chiodoni, Paolo Allia, and Paola Martino

Introduction

Magnetic NPs containing 3D transition metal oxides or relative mixtures are one of the most studied nanomaterials in view of their prospective, ubiquitous applications in quite different areas, the most important being biomedicine, sensor technology, and magnetic recording [1]. According to their usage, magnetic NPs are often either embedded in a diamagnetic solid [2] or dispersed in a fluid; in some cases they are surrounded by an outer shell of a diamagnetic material.

The magnetic properties of nanoparticles (NPs) are quite different from those of the corresponding bulk material and a detailed subsection will analyze them in detail. In a simplified picture, an ideal magnetic NP can be figured out as provided of a highly symmetrical body (e.g., spherical, ellipsoid, acicular) and characterized by a homogeneous magnetization provided by the ferro- (or ferri-) magnetic alignment of elementary magnetic moments, giving rise to a mesoscopic permanent

A. Chiolerio (✉) • A. Chiodoni
Center for Space Human Robotics@PoliTO, Istituto Italiano di Tecnologia, Torino, Italy
e-mail: alessandro.chiolerio@iit.it; angelica.chiodoni@iit.it

P. Allia
Applied Science and Technology Department, Politecnico di Torino, Torino, Italy
e-mail: paolo.allia@polito.it

P. Martino
Politronica Inkjet Printing S.r.l, Torino, Italy
e-mail: paola.martino@politronica.eu

magnetic moment associated to the particle. Of course this picture can be improved to account for the role played by the NP surface, whose chemical and magnetic properties can be quite different from those at the particle core.

Synthesis

Several methods have been employed to produce magnetite NPs. They can typically be grouped into two categories: *top-down* and *bottom-up* approaches.

The first approach, *top down*, involves the breaking down of the bulk material into nano-sized structures or particles, while the alternative approach, *bottom-up*, refers to the buildup of a material from the bottom: atom-by-atom, molecule-by-molecule, or cluster-by-cluster in a gas phase or in solution. The latter approach is far more popular and less expensive in the synthesis of NPs. A variety of 'bottom-up' synthesis methods have been developed and many reports have described efficient synthesis approaches to produce magnetic NPs with controllable size, morphology, composition, structure, biocompatibility, and magnetic properties.

The most common 'bottom-up' methods include coprecipitation reactions, polyol methods, microemulsion, sol–gel synthesis, thermal decomposition, hydrothermal and high temperature reactions, sonochemical synthesis, and flow injection synthesis.

The synthesis of magnetite nanocrystals is a complex process because their properties depend strongly on their dimensions. A critical point is to control magnetic grain size, morphology, and composition of NPs and to select a reproducible process to prepare NPs with homogeneous composition and narrow size distribution: fundamental characteristics in order to control magnetic properties. In the following paragraph some examples of 'bottom-up' preparation methods of magnetite NPs are briefly reported.

Synthesis by Coprecipitation

The coprecipitation method is probably the most conventional technique to obtain magnetic NPs, in particular iron oxides (Fe_3O_4 and γ-Fe_2O_3).

Magnetite NPs (Fe_3O_4) are usually synthesized mixing ferric and ferrous ions (1:2 M ratio) in a basic solution (pH range 8–14) according to the following reaction:

$$Fe^{2+} + 2Fe^{3+} + 8OH^- \rightarrow Fe_3O_4 + 4H_2O$$

The size and shape of magnetite NPs can be adjusted to change the nature of salts used as reagents (nitrates, chlorides, sulfates etc.), adjusting the pH, the reaction temperature, and the ion strength and tuning other parameters such as the stirring rate and the Fe^{2+}/Fe^{3+} ratio.

The main advantage of the coprecipitation method is the large amount of NPs synthesized, but this technique generates NPs with a wide particle size distribution. To obtain the control of particles size, chelating organic ions such as citric acid, oleic acid, and sodium dodecyl sulfate or polymer such as polyvinyl alcohol can be added in the reaction media. These molecules act as protecting agent, control the particle size, and improve the stability of magnetic NPs solution.

Since magnetite NPs are not so stable and very sensitive to oxidation, it is important to carry out the synthesis in a non-oxidizing environment (anaerobic condition) in order to avoid or slow down the transformation process from magnetite to maghemite (γ-Fe_2O_3) [3, 4].

Sonochemical Synthesis

Sonochemical technique is an efficient way for the synthesis of magnetite NPs. The physical phenomenon, which occurs when liquids are irradiated by ultrasonic mechanical waves, is acoustic cavitation: the formation, growth, and implosive collapse of bubbles in liquid medium. This phenomenon generates extremely high transient temperatures ($>$5,000 K), high local pressure (1,800 bars), and cooling rate in excess of 10^{10} K/s: extreme reaction conditions which lead to many unique properties of the synthesized particles such as unusually magnetic properties.

Sonochemical technique, thanks to its versatility, has been applied for the synthesis of various magnetic nanocomposites [5].

Sol–Gel Synthesis

Magnetite NPs have been successfully synthesized also by sol–gel methods. An important example of sol–gel process is the synthesis of magnetite NPs embedded in an inert, inorganic, transparent, and temperature-resistant silica matrix. This method has also been used to synthesized magnetite and maghemite thin films.

In sol–gel methods a chemical solution (*sol*) is the starting point and the solvent used is, generally, water.

Metal alkoxides and metal chloride are typical precursors; they undergo hydrolysis and polycondensation reaction to form a *sol* composed of NPs in solvent. The *sol* evolves in the *gel* phase consisting of an inorganic network in a liquid phase; after this step follows a drying process that removes the liquid phase.

The sol–gel approach offers several advantages such as good homogeneity, low cost, and high purity. It is usually used to control the microstructure and to eventually embed functional molecules within the sol–gel matrix. The particle size depends on several parameters: rate of hydrolysis and condensation, solution composition, pH, and temperature.

Sol–gel methods present, however, some disadvantages such as the contamination from by-products of reactions: after synthesis, a purification treatment of the products is required [3–5].
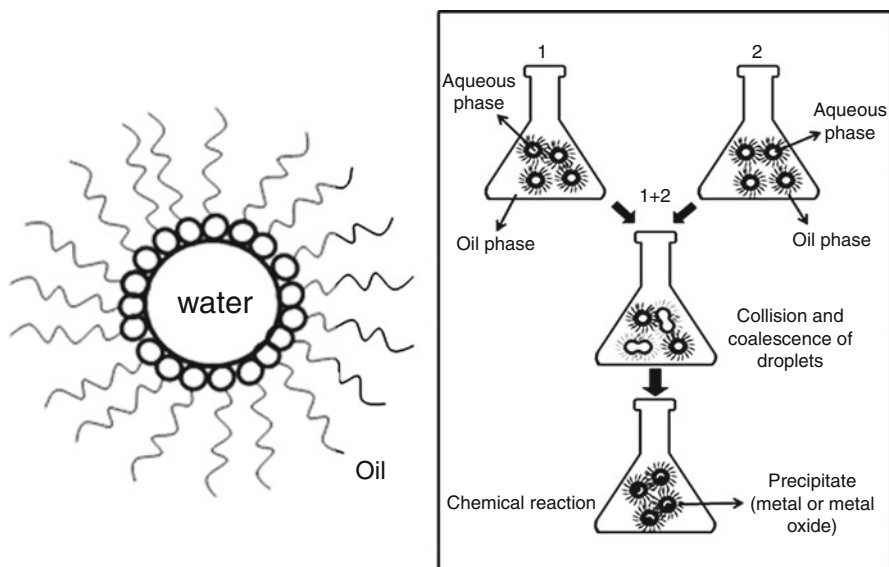
Fig. 7.1 Schematic drawing of a micelle and proposed mechanism for the formation of magnetic particles within micelle 'nanochamber'

Microemulsion Synthesis

A microemulsion is a thermodynamically stable mixture of two immiscible phases (water and oil) separated by the surfactant.

A surfactant, i.e., a molecule featuring both polar and nonpolar moieties, may dissolve in water or oil; when its concentration exceeds a minimum value, said critical micelle concentration (CMC), its molecules associate spontaneously to form aggregate micelles [6]. Microdroplets can be in the form of either oil-swollen micelles dispersed in the aqueous phase or water-swollen micelles dispersed in oil (reverse microemulsion) [7], driven by strong hydrophobic interactions of the hydrophobic tail (O/W micelle) or by hydrophilic interactions of the polar head (W/O micelle).

Micelles can be regarded as real 'nanoreactors' providing a suitable environment for controlled nucleation and growth. The mixing of two microemulsions containing appropriate reactants produces collisions between them in a very fast process (from 10 μs to 1 ms between collisions) and it is the limiting factor for particle growth, slow if compared to diffusion of reagents inside the nanoconfinement ('nanoreactor') (Fig. 7.1). The attractive interaction between droplets, which is responsible for the percolation process, is of great importance for the kinetics [6]. Water-in-oil microemulsion can be used to synthesize iron oxide, metallic iron NPs, and silica-coated iron oxide NPs employing several surfactant such as sodium dodecyl sulfate (SDS), cetyltrimethylammonium bromide (CTAB), and polyvinylpyrrolidone (PVP) [5].

Hydrothermal Synthesis

This method includes various wet-chemical technologies of crystallizing substances in a sealed container from the high temperature solution (generally 130–250 °C) at high vapor pressure (generally 0.3–4 MPa) that facilitates the interaction of precursors during synthesis. The process can be used to prepare many geometries, including thin films, bulk powders, single crystals, and nanocrystals; as an example, highly crystalline iron oxides NPs were prepared [4].

Particle size, shape distribution, and crystalline fraction are precisely controlled by tuning parameters such as temperature, pressure, and reaction time. This method takes advantage of the solubility of almost all inorganic substances in water at high temperatures and pressures and subsequent crystallization of the dissolved material from the fluid.

Rising the temperature brings to a different coordination of the water molecules, as well as a much higher vapor pressure. Reactant properties, including their solubility and reactivity, also change at higher temperatures. The solvent choice is not limited to water but includes also polar or nonpolar solvents, such as benzene, and the process is more appropriately called *solvothermal synthesis* [3].

Morphologies

In scientific research, the most diffused morphological and structural characterization tool for nanostructures is the transmission electron microscope (TEM). With this powerful instrument, it is possible to have at the same time information related to nanostructures size (TEM), shape (TEM), way to aggregate (TEM), crystalline orientation (Electron Diffraction, ED), crystalline quality (high-resolution TEM, HRTEM), and chemical composition (Energy Dispersive Spectroscopy, EDS, Electron Energy Loss Spectroscopy, EELS). Also scanning electron microscopy plays an important role in determining the morphology of nano materials down to some nm in size. The two techniques can be fruitfully combined to have an overall overview of the quality of the material synthesized. Other techniques can be used to investigate the morphology at the micro-nano scale, such as scanning probe microscopies (SPM), including atomic force microscopy, scanning tunnel microscopy, and magnetic force microscopy, and confocal microscopy. Low-energy electron microscopy (LEEM) is also used to study the evolution of the growth of crystals during thin films deposition. The morphological/structural characterizations coming from the microscopies can be combined with X-ray diffraction (XRD) to understand/confirm the crystalline quality of the different nanostructures. This comprehension of the crystalline structure of the materials has to be then correlated with their magnetic properties, from which depends their application in devices.

Each of the mentioned characterization techniques does not provide the exact description of the material, because the results depend on the type of interaction that the material has with the probe and on the scientist interpretation. In some cases, to have a good understanding of the material it is enough to use one single technique,

as TEM, that provides many of the information needed. In more complex situations, the cross-check with different techniques can help to properly reconstruct the properties of the material.

Iron can be found in nature in different crystalline and stoichiometric forms:

Oxides

- Iron(II) oxide, wüstite (FeO)
- Iron(II,III) oxide, magnetite (Fe_3O_4)
- Iron(III) oxide (Fe_2O_3)
- Alpha phase, hematite (α-Fe_2O_3), beta phase, (β-Fe_2O_3)
- Gamma phase, maghemite (γ-Fe_2O_3)
- Epsilon phase (ε-Fe_2O_3)

Hydroxides

- Iron(II) hydroxide ($Fe(OH)_2$)
- Iron(III) hydroxide ($Fe(OH)_3$), bernalite

Mixed oxide/Hydroxides

Iron(III) oxide-hydroxide
- Goethite (α-FeOOH)
- Akaganéite (β-FeOOH)
- Lepidocrocite (γ-FeOOH)
- Feroxyhyte (δ-FeOOH)
- Ferrihydrite ($Fe_5HO_8 \cdot 4H_2O$ approx)
- High-pressure FeOOH
- Schwertmannite (ideally $Fe_8O_8(OH)_6(SO) \cdot nH_2O$ or $Fe^{3+}_{16}O_{16}(OH,SO_4)_{12-13} \cdot 10\text{-}12H_2O$)[2]
- Green rust ($Fe^{III}_xFe^{II}_y(OH)_{3x+2y-z}(A^-)_z$; where A^- is Cl^- or $0.5SO_4^{2-}$)

Among them, the most interesting, from the application point of view, is magnetite, although for some application other Fe-based materials are found [8–10]. In recent years, due the increasing interest of magnetite in medicine and biology, a lot of work has been done to prepare core-shell structures able to better interact with the human body. Work has been done also to use magnetite in composite/hybrid materials for specific applications [2, 11–13].

In the following, some example of nanostructures divided in two sections, magnetite and core-shell structures, will be reported. The chosen examples are not exhaustive and do not have the intention to cover the entire literature on this topic, but they are reported just to help the discussion.

Magnetite

Fe_3O_4 is a crystal with face-centered cubic (FCC) structure. From the point of view of crystallography, single-crystalline Fe_3O_4 typically has octahedral shapes. However, what is found from the literature is that it is possible to control the preparation of magnetite in various sizes and shapes by properly choosing the starting chemicals and the synthesis route. It is possible to grow NPs, nanoplatelets, nanorod, nanowires, nanocubes, and hollow magnetite nanostructures, and it is also possible to grow thin films by using deposition methods as molecular beam epitaxy.

Depending on the stoichiometry and on the size, the magnetic properties can change noticeably. Many research groups implement the different synthesis route to obtain a material optimized for a specific application. Some time, the composition and magnetic behavior of the synthesized iron oxide nanostructures are directly related with their size, so that also the control of the kinematics in the synthesis becomes a key role to obtain the desired functional properties. For example, if the size of the magnetic particles is adequately small, each particle can be a single magnetic domain and exhibit superparamagnetic (SPM) properties.

As will be described in the application section, magnetite NPs have been long used in many industrial applications such as magnetic recording media, printing inks, magneto-rheological fluids, and sensors. Recently their applications have been more diversified to targeted drug delivery, contrast agents for magnetic resonance imaging (MRI), photonic crystals, and electrically conductive materials. In recent years, magnetite was also investigated as an anode material for Li-ion batteries because it has a high theoretical specific capacity, low cost, it is environmental friendly, and shows reasonable reduction/oxidation potentials. Fe_3O_4 also owns good electronic conductivity, which is considerably better than other transition metal oxides.

This broad range of possible applications explains the large number of scientific papers related with this material.

Nanoparticles (NPs)

NPs are the most diffused magnetite nanostructures in applications. They are prepared with different synthesis approaches, as already described in the previous section. Here we report on NPs prepared by means of the solvent-free thermal decomposition method [14] (Fig. 7.2 example 1), one-step thermal decomposition of an iron-urea complex in triethylene glycol [15] (Fig. 7.2 example 2), and solvothermal method [16] (Fig. 7.2 example 3).

In the third example, the authors report on particles size ranging between 5 and 10 nm, depending on the conditions. All the presented NPs exhibit a quasi-spherical shape, single-crystalline characteristic, and are monodispersed. In example 1 it is evident that change in size is due to the variations of synthesis conditions: depending on time and temperature, the NPs 5 nm in size, increasing up to 10 nm. Due to their size, all of them exhibit SPM characteristics.
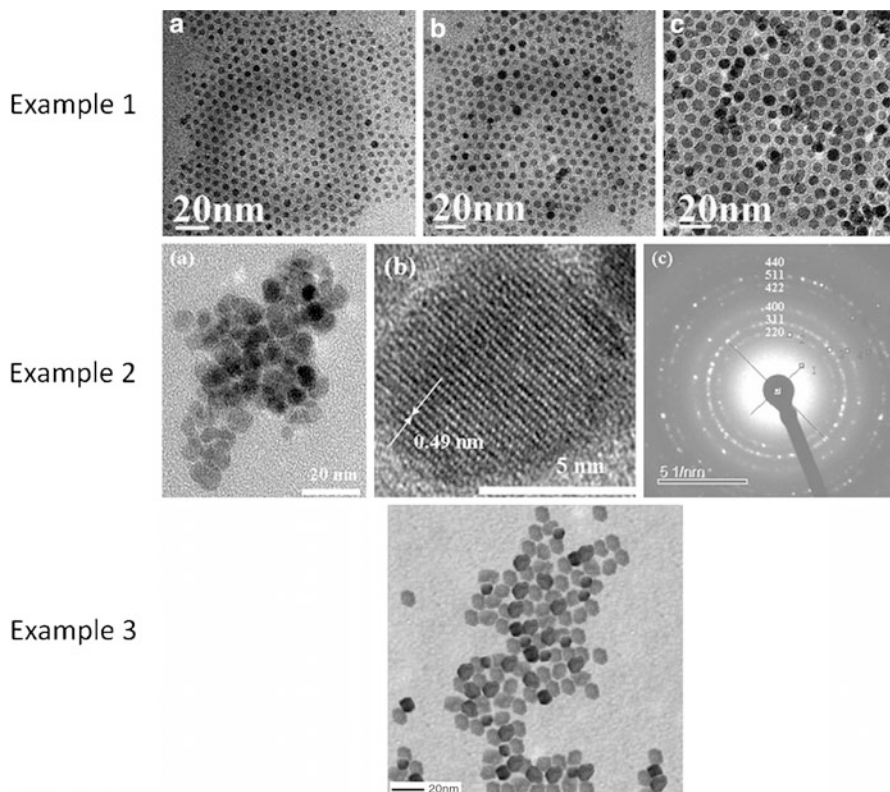
Fig. 7.2 TEM characterization of magnetite NPs. Example 1 shows the change in the size NPs while changing the synthesis conditions (Reprinted from [14], Copyright 2009, with permission from Elsevier). Example 2 shows the crystalline quality of the NPs (Reprinted from [15], Copyright 2012, with permission from Elsevier). Example 3 put in evidence the morphology of the NPs (Reprinted from [16], Copyright 2013, with permission from Elsevier)

Nanoplatelets

For this type of nanostructure, we report two different synthesis routes: ultrasonic irradiation, using FeSO4 and NaOH as reagents at low temperature [17], and solvothermal route, where ethylenediamine was used as the solvent and reducing agent [18]. In Fig. 7.3, a comparison between the two materials is reported.

In the first example [17], the authors claim that these 2-D Fe_3O_4 flakes are homogeneous in thickness with sharp crystallographic edges and a single-crystal structure. Because magnetite and maghemite have very similar lattice parameters, it's hard to distinguish between the two phases, also with X-ray diffraction (XRD). In this case, the authors used the X-ray photoelectron spectroscopy (XPS)
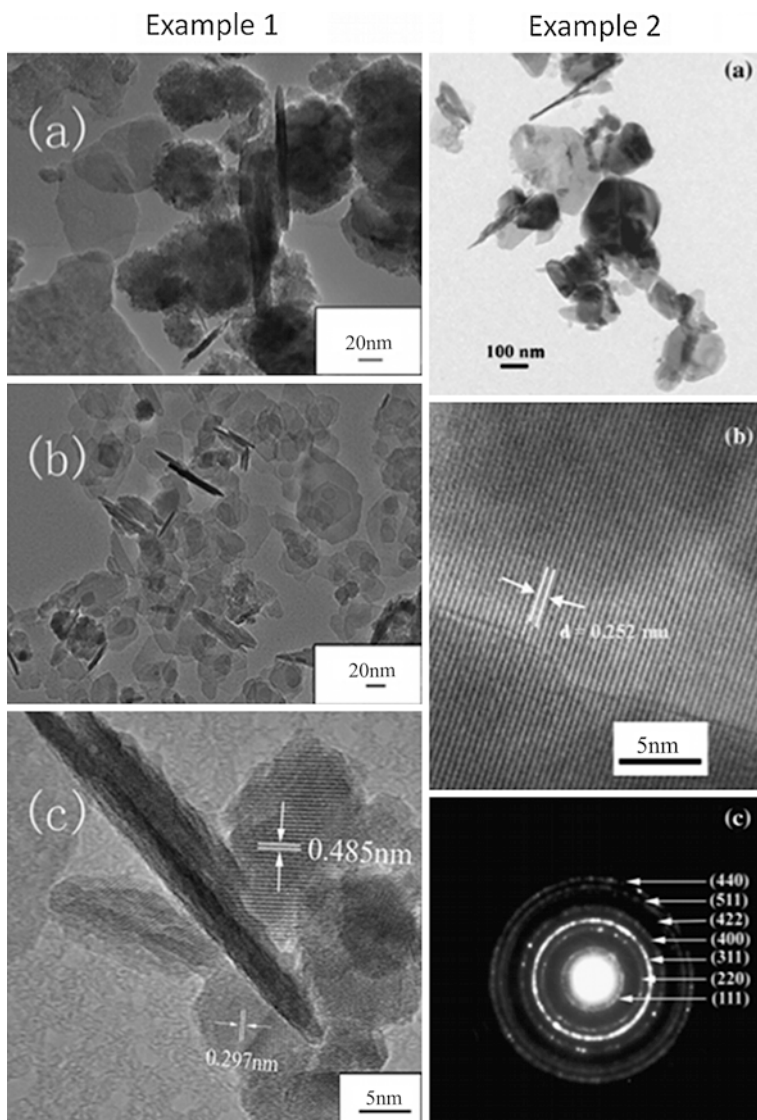
Fig. 7.3 TEM characterization of magnetite nanoplatelets. In Example 1, it is put in evidence the single-crystalline nature of the single flakes (Reprinted from [17], Copyright 2011, with permission from Elsevier). In Example 2, similar crystalline properties are exhibited (Reprinted from [18], Copyright 2009, with permission from Elsevier)

technique to distinguish between the two oxides. By considering the magnetic properties associated with these samples, the value of the saturation magnetizations Ms is relatively low compared to the bulk value. This is explained by the authors with (1) a nano-sized effect for ultrafine

magnetic particles that decrease Ms due to the small size of the final product and (2) contamination of the sample, causing a slight loss Ms.

In the second example [18], the authors report on Fe_3O_4 nanoplatelets with a thickness estimated to be 20 nm. The HRTEM images (Fig. 7.3) indicate that the magnetite nanoplatelets have well-defined crystallinity with a lattice spacing of 0.252 nm, which is in good agreement with the value of the {311} facet of bulk magnetite. The investigation on magnetic properties confirmed that these platelets exhibit values close to the bulk values of magnetite. In this second paper, the authors present also the results get without the introduction of the capping agent in the synthesis route: in this case, they obtained magnetite nanocubes instead of platelets. This strengthens the concept that by changing the synthesis route the obtained nanostructures can strongly change in morphology.

Nanorods

As example of nanorods, we report on two papers [19, 20]. In the first paper [19], the authors report on nanorods prepared via an oxidative ageing of $Fe(OH)_2$ in aqueous suspensions, characterized by a single crystal structure. In this paper, they present typical nanorod dimensions of ca. 500 nm in length and ca. 20 nm in diameter. These nanostructures are used in ferronematic liquid crystal colloids for use in magneto-optical devices. The authors studied the interaction between the magnetic material and the liquid crystal molecule in order to improve the magneto-optic response of the composite mixture.

In the second paper [20], the authors report on magnetite nanorods prepared by pulsed current electrochemical method, having 60 nm average diameters and 1,000 nm average lengths. The sample exhibits ferromagnetic behavior with a relatively high saturation magnetization, a little lower than that of the corresponding bulk. The nanorods result to be SPM. These nanostructures are used as adsorbent for removal of some heavy metal ions such as Fe, Pb, Zn, Ni, Cd, and Cu from aqueous solutions.

Thin Films

The thin film reported in the first example [21] is prepared by a reactive molecular beam epitaxy, by monitoring the growth in real time by low-energy electron microscopy (LEEM). In the second example [22], the film was prepared in UHV system containing a miniature molecular beam epitaxy system equipped with metal vapor sources, quartz thickness monitors, and a four-grid low-energy electron diffraction/Auger electron spectroscopy (LEED/AES) spectrometer to monitor thickness and composition. In both cases, the thin films were used to carefully study the magnetic properties of a 2D system, correlating the magnetic features with their thickness and establishing the limits of the material for application (Fig. 7.4).

Fig. 7.4 Example 1: LEEM images from a sequence acquired during the growth of the magnetite crystals. Panels (*a*)–(*c*) show the completion of the FeO layer, while the last frame shows the final film with magnetite crystals with well-defined edges (Reprinted from [21], Copyright 2012, with permission from Elsevier). Example 2: STM image of the Fe_3O_4 (001) surface taken in the constant current mode with *arrows* identifying antiphase boundaries of different types (Reprinted from [2], copyright 2011, with permission from Elsevier)
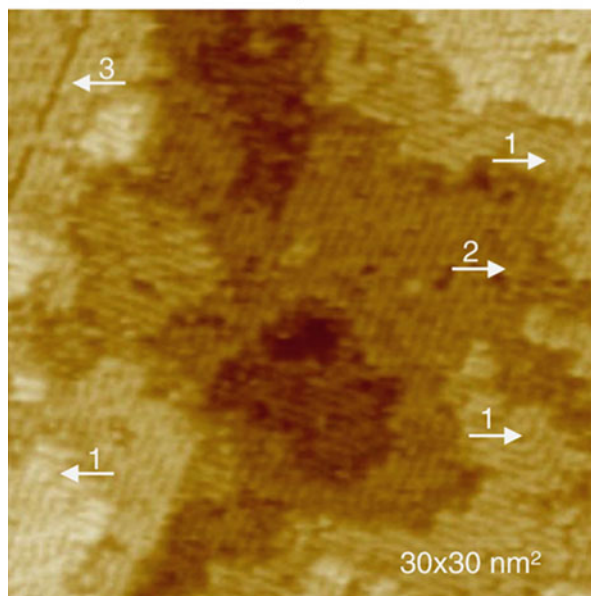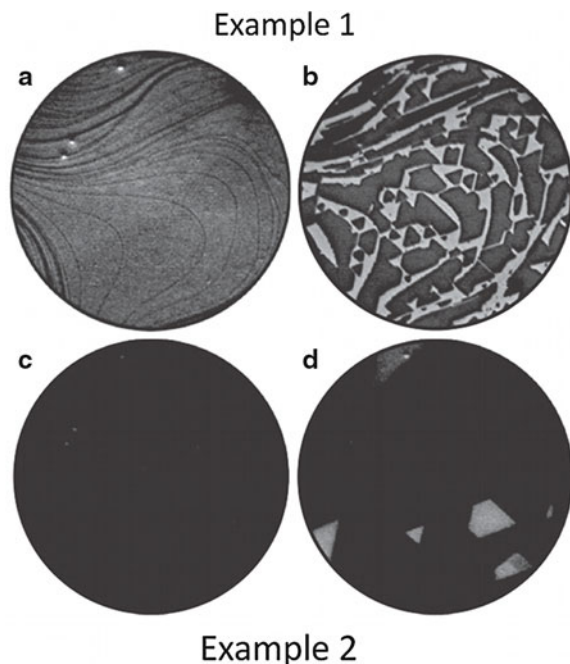
Hollow Nanospheres

We report here two papers related with hollow nanospheres. In the first paper [23], the authors prepared monodisperse Fe_3O_4 hollow spheres with a size of about

180 nm and core diameter of about 135 nm via solvothermal process without using any template. They observed by means of SEM and TEM that the single hollow sphere consists of many building blocks of smaller magnetite NPs. They exhibit ferromagnetic behavior with a saturation magnetization of about 81 emu g^{-1}.

In the second paper [24], the hollow Fe_3O_4 spheres were synthesized by a simple solvothermal process, with different diameters and shell thickness. As for the previous case, the shell of the hollow spheres exhibited porous structure composed of aggregated Fe_3O_4 NPs. Again, the reaction temperature and time have important effects on the morphology and particle sizes of the as-synthesized magnetite nanostructures. This particular geometry was proposed by the authors as anode materials in Li-ion batteries, because it has high theoretical specific capacity, low cost, environmentally benign, and reasonable reduction/oxidation potentials. They propose this hollow structure by considering the effect of three problems for magnetite in Li-ion batteries: low rate performance arising from kinetic limitations, poor cycling stability resulting from agglomerations, and large volume expansion occurring during cycling. By combing the hollow structures with specific conductive agents, the authors obtained good electrochemical performances.

Nanocubes

The nanocubes in the first example [25] are prepared via surfactant-free hydrothermal route; in this case, the morphological and structural characterizations put in evidence that they have a face-center-cubic (FCC) structure. As underlined for the other magnetite nanostructures, the morphology of Fe_3O_4 depends on the synthesis process, in this case, the contents of hydroxide ions, hydrazine hydrate, and reaction time. These crystals exhibit excellent magnetic properties, which make them useful in many applications (Fig. 7.5).

In the second example [26], the authors compare a one- and second-step liquid–liquid phase-transfer synthesis. In the one-step method, particles are synthesized in a biphasic medium where the particles are formed in the microdroplets and migrate to the organic phase simultaneously, whereas in the two-step method, particles are first prepared in an aqueous phase and subsequently transferred to the organic phase. They found that in the case of one-step protocol, the size and size distribution of the particles is dictated by the confinement within the water droplets in the water-organic emulsion. The magnetite nanocrystals have an average size less than 20 nm, smaller than the one obtained with the two-step method.

Peony Structures

These characteristic peony-like nanostructures were obtained by a low-temperature one-step aqueous method without any surfactant and calcination treatment [27]. In this case, the authors explain the obtained morphology by considering a self-assembling mechanism, starting from nanocubes and truncated nanocubes,
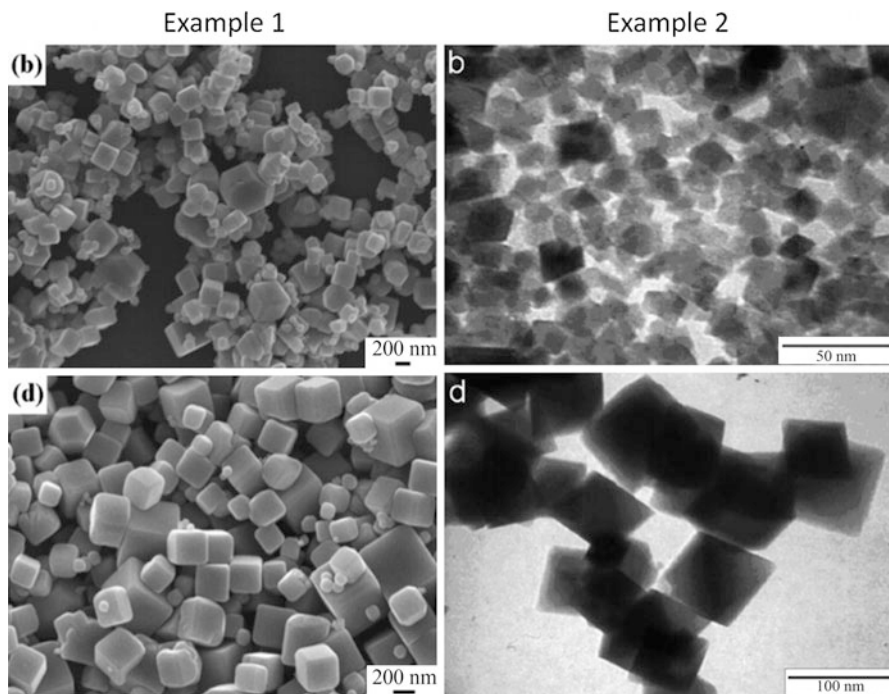
Fig. 7.5 Example 1: SEM images of Fe_3O_4 prepared with different pH values: (**b**) pH $= 8$ (**d**) pH $= 10$ (Reprinted from [25], Copyright 2011, with permission from Elsevier). Example 2: TEM images of magnetite particles synthesis via: (**b**) one-step method and (**d**) two-step method (Reprinted from [26], Copyright 2007, with permission from Elsevier)

moving to octahedra and finally to the peony structure. The sample exhibits a ferrimagnetic behavior. The Fe_3O_4 peony nanostructures are proposed by the authors as adsorbents in waste-water treatment and exhibit an excellent ability to remove Cr(VI) pollutant from aqueous solution.

Coral-Like Nanostructures

Magnetite nanostructure with coral-like morphology was synthesized by a simple glucose-assisted solvothermal method [28]. This hierarchical structure was deeply investigated with TEM. The authors put in evidence the different crystalline characteristics of the root and of the branches: the root seems to be composed of aggregated NPs of about 11 nm randomly oriented, while the branches (twigs) seem to be constituted by aggregation of more oriented NPs. The magnetic characterization of this complex structure puts in evidence that there is a conversion from ferromagnetic to super- paramagnetic when coral-like structures detach into single particles. The authors attribute the ferromagnetic behavior of the hierarchical magnetite to the oriented twigs.

Dodecahedron: Tetrakaidecahedral Nanostructures

Dodecahedral magnetite nanocrystals were fabricated using ethlenediamine tetra-acetic acid (EDTA)-mediated hydrothermal route [29]. The synthesis conditions, the time, and the kinematic play a crucial role in obtaining such a structure. By the scanning electron microscopy characterization, every facet of a dodecahedron nanocrystal is close to an isosceles triangle, with smooth surfaces. The size distribution of these dodecahedron nanocrystals is relatively uniform, some hundreds of nm in length. The sample results to be magnetic soft.

Tetrakaidecahedral Fe_3O_4 microcrystals were prepared with a two-step refluxing and calcination process [30]. The scanning electron microscopy put in evidence the morphology, made of eight hexagonal faces and six quadrilateral faces, about 2 mm, in diameter. The authors explain the obtained geometries in terms of difference in surface energy of the different facets of the nanostructure during the crystal growth.

Core-Shell Structures

In the following, two examples of core-shell nanostructures based on magnetite will be presented. The coating of magnetite is usually performed to make it more biocompatible or to reduce the possible NPs aggregation during the growth process.

In the first example [31], magnetite NPs were coated with inorganic silica layer via sol–gel process. Synthesis involves hydrolysis and condensation steps using tetraethylorthosilicate (TEOS) in methanol/polyethylene glycol (PEG) solution and ammonia catalyst. The authors describe a core-shell easily tunable in size through the alteration of the Fe_3O_4-to-TEOS ratio. As this ratio increases, the size decreases from 270 to 15 nm while maintaining a magnetite core of 12 nm, indicating a decrease in thickness of the silica coating. Although the silica coating systematically reduces the magnetite magnetic properties, all the core shells displayed ferromagnetic behavior. For this reason, the authors predict that these particles can induce heat generation under the application of a magnetic field and be amenable to use as thermo-seeds in the design of a hyperthermia systems for cancer treatment (Fig. 7.6).

In the second example [32], monodisperse oleic acid-coated Fe_3O_4 NPs with uniform size and shape obtained via a thermal decomposition of Fe(acac)3 in the presence of oleic acid (OA) are presented. It turns out that they are nearly monodisperse single-crystalline spherical NPs with a narrow size distribution, ranging from 20 to 32 nm. The thin OA layer constituting the shell has a thickness of about 3 nm. These core-shell structures exhibit paramagnetic property. The authors propose this coating process to address the issue of reducing aggregation during particle formation through van der Waals interparticle attractions, by using stabilizing agents, which can attach to the surface of the particles and provide spatial isolation in the synthesis process.
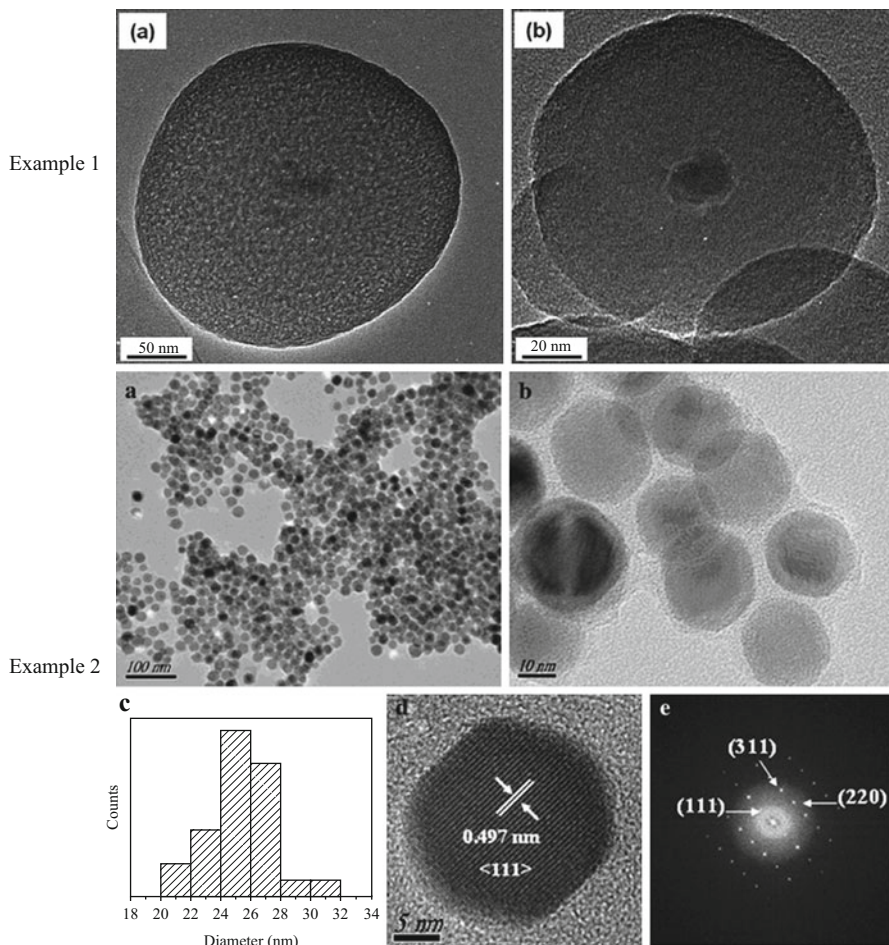
Fig. 7.6 Example 1: TEM images of silica-coated magnetite samples prepared with different silica concentrations. Nanoparticles were homogeneous in size and contained an MNP central core (*darker area*), as well as a silica layer of uniform thickness, thus exhibiting a core-shell structure (Reprinted from [31], Copyright 2012, with permission from Elsevier). Example 2: (**a**, **b**) TEM images showing the core-shell structure, (**c**) distribution of the particle size, (**d**) high-resolution TEM image of a single Fe_3O_4 nanoparticle, and (**e**) FFT pattern of the HRTEM image shown in panel (**d**) (Reprinted from [32], Copyright 2010, with permission from Elsevier)

Magnetic Properties

Magnetite NPs

Magnetic properties of magnetite NPs make this class of new materials very interesting for prospective applications in a variety of areas, ranging from high-tech ICTs (such as information storage, electronics, ferrofluid technology,

magnetic inks for printable electronics, magnetic tags) [33–36] to biomedical applications (magnetic heating, drug delivery), which are possibly the most promising ones nowadays [37–39], also because of the reduced toxicity of Fe-oxide NPs for living tissues. Magnetite NPs combine a fairly high saturation magnetization (typically, 60–90 emu/g, depending on size and consequent surface role [40]) associated with a magnetic anisotropy of the order of 1×10^5 erg/cm^3 in magnitude at room temperature (for magnetite NPs with a size larger than 5–6 nm, where surface anisotropy is not dominant [2]). As a consequence, their size and shape can be tailored to produce nanopowders exhibiting a wide range of hysteretic properties and coercive fields, including the (nearly) SPM state at room temperature; in addition, they display higher chemical stability and reduced toxicity with respect to pure metal particles. The current chemical routes to magnetite NP production, discussed elsewhere in this chapter, have notable advantages: (a) they are well established and provide reproducible outputs; (b) Fe-oxide NPs obtained by these techniques usually have a sufficiently narrow spread of sizes and shapes; (c) the NPs are covered of, or enveloped within, a nonmagnetic insulating organic shell which helps preventing NP aggregation by magnetic or electrostatic forces and avoids the formation of large NP agglomerates which respond coherently to a magnetic field by effect of interparticle contact interaction and enhanced magnetic exchange length [41].

The large amount of experimental results presently available in the literature does not allow one to draw a univocal picture of the magnetic properties of magnetite NPs. In fact, dealing with data and conclusions in apparent contrast is the rule rather than the exception for the reader. This can be explained as the effect of the wide variety of existing production methods, particle sizes, particle shapes, types of samples, degrees of interparticle interaction, and aggregation; as a consequence, it can be stated that the magnetic properties of magnetite NPs are not completely assessed yet. Better, it should be realized that it is hardly possible to give a figure of a magnetic quantity which could be taken as representative of all produced systems composed of or containing magnetite NPs. Almost paradoxically, the abundance of experimental results hinders a comprehensive picture to be given of the magnetic properties of NPs containing magnetite and/or other iron oxides. In this contribution, an attempt is made to point out some problems or interpretative difficulties which still need insight.

Magnetic Versus Real Size of Individually Responding NPs

At and around room temperature (RT), systems composed of or containing magnetite NPs exhibit magnetization loops which are usually – and perhaps hastily – called 'superparamagnetic' (SPM) [42, 43] on the basis of features checked by a single measurement (e.g., a slowly saturating behavior of the M(H) curve at high fields; very small – albeit usually nonzero – coercivity) without looking for further confirmation. Of course, a genuine SP behavior of any NP system is a carefully looked-for property because of its interest in biomedical [37] and fluidic [44] applications. However, it should be reminded that the only

way to firmly assess the SP character of a set of magnetic NPs is *at least* to do a complete study of isothermal magnetization loops down to low temperature *and* to measure the dc magnetic susceptibility after cooling with and without a magnetic field (FC/ZFC curves) [45].

As known, the NP volume in a standard SPM material can be obtained using (a) a fit of the magnetization curve to a Langevin function [46] or a discrete sum/convolution of Langevin functions [43] and (b) an estimate of the intrinsic magnetization of the magnetite NPs under consideration. As a matter of fact, both conditions are hardly fulfilled in real cases. Often the intrinsic magnetization of a magnetite NP is sensibly reduced with respect to the corresponding value in bulk magnetite (90 emu/g or 480 emu/cm^3 at room temperature [46]). Values lower by 10–30 % have been reported in the literature for magnetite NPs [40, 47]. Such a discrepancy is thought to originate from the increasingly dominant role of the NP surface, where symmetry breaking brings about highly disordered magnetic states. However, the first point (although often uncritically taken for granted) gives rise to problems too. In fact, fitting the measured loop to one or more Langevin curves (disregarding for the moment the residual magnetic hysteresis) is often easy to do with satisfactory results and provides a figure of an *effective* magnetic moment per NP. The actual significance of the obtained value is however debatable. In fact, if one applies the same procedure at a different temperature (significantly lower than RT but still well above blocking temperature; in most cases the region from 50 to 250 K is fine), the magnetic moment resulting from the fits is sensibly lower than the one measured at RT, which is physically implausible. As a matter of fact, the particle volume (or diameter) obtained starting from a single fit of RT experimental data to a Langevin function is typically smaller than the one obtained by X-ray scattering data analysis and/or direct observation by TEM; this discrepancy becomes even more marked if the saturation magnetization per particle is significantly lower than the bulk value.

As an example, Fig. 7.7 (bottom panel, blue shaded area) provides an estimate of the average NP diameter for a 10 phr dispersion of magnetite NPs in PEGDA (a photocured polymer), as obtained from standard Langevin-curve fits at different temperatures. According to X-ray analysis of the original nanopowder, the actual NP diameter is 8–9 nm with narrow dispersion around this figure. The maximum of the ZFC curve (top panel) is indeed sharp and occurs at 15 K; using a magnetocrystalline anisotropy constant in the range 1–2×10^5 erg/cm^3 (this typical value is appropriate at low temperatures for small to medium sized magnetite NPs [45, 46]), a diameter between 8 and 10 nm is obtained, in good agreement with the structural data.

This implies that the NPs have not become aggregate when dispersed in the polymer. However, the diameter estimated from Langevin-curve fits is systematically lower than the actual one, independent of the value of the spontaneous magnetization, which is not perfectly known (the limits of the shaded area correspond to two possible choices for the RT magnetization of 300 and 480 emu/cm^3, respectively) and decreases with decreasing T, indicating that an estimate of the size based upon Langevin-curve fits can be very misleading (in this example,
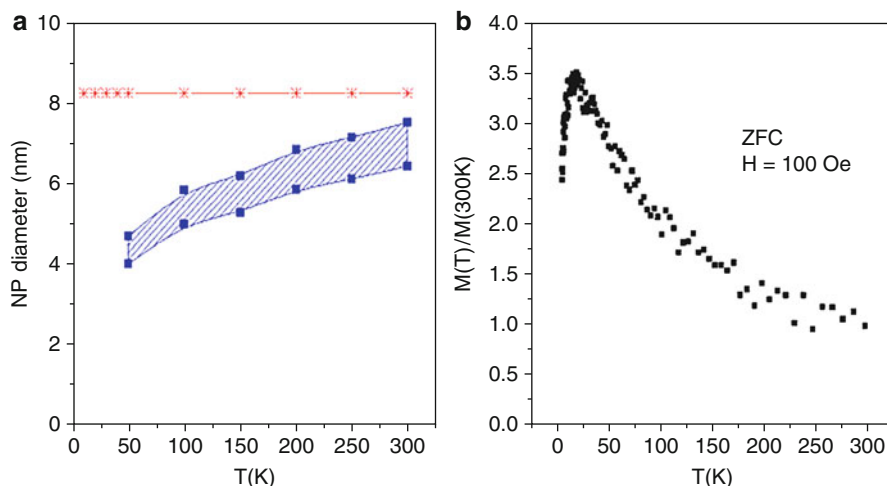
Fig. 7.7 (**a**) Dispersion of 8–10 nm magnetite NPs in PEGDA polymer. *Shaded* region: magnetic size as obtained by fitting the experimental M(H) curves to a Langevin function (boundaries represent two values of the spontaneous magnetization at RT); *red* symbols: magnetic NP diameter derived from the ISP model; (**b**) ZFC curve

the fitting procedure underestimates the real NP diameter up to a factor of two at 50 K, still well above the blocking temperature). A reason for this discrepancy will be given in section (c) below.

It can be concluded that often the size obtained from fits of RT magnetization curves to a Langevin function can only give an order-of-magnitude estimate of the real NP size. This applies to the case of dilute/dispersed systems, where particles are physically separated in space and no contact interactions exist.

Magnetic Response at Different Degrees of NP Aggregation

An entirely different category of problems emerges when the particles are touching and/or strongly interacting. In this case, the size estimated from magnetic measurements can be much larger than the actual size of a single particle, because the individual ordering unit which responds to a magnetic field is an aggregate of many particles rather than a single particle. This behavior is not collective in a strict sense: as a first approximation, the NP aggregates can be pictured as responding coherently to the magnetic field and to random magneto-mechanical torques originated by thermal disorder; each aggregate has its own magnetic moment (the vectorial sum of individual particle moments) which changes in direction rather than in magnitude by combined effect of temperature and magnetic field. As an example, let us consider the FC/ZFC curves of a magnetic powder obtained from a precursor alcoholic solution and a solid-state dispersion of the same magnetite NPs with average diameter of 15 nm (Fig. 7.8). In the former case (red symbols), the flat, featureless, well-separated curves indicate a bulk ferromagnetic response of the nanopowder [48], where the NPs have clearly lost their individual character to

Fig. 7.8 FC/ZFC curves for an aggregated nanopowder of 15 nm magnetite NPs (*red* symbols) and for a dispersion in epoxy resin (*blue* symbols). The mixing process substantially breaks the NP aggregates
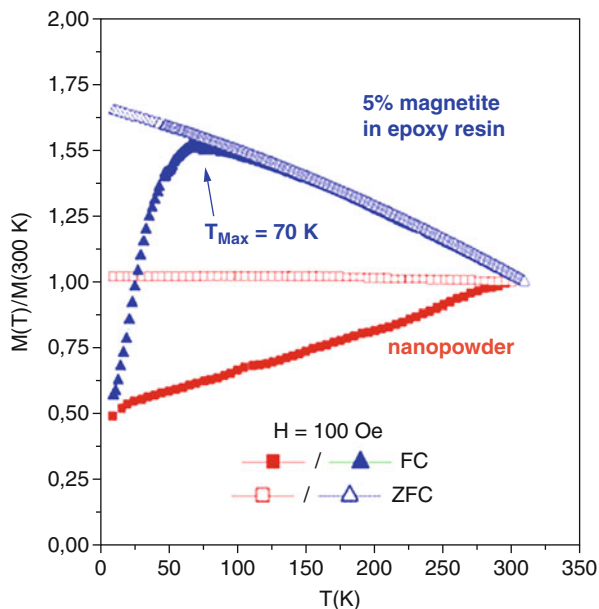
form much larger magnetic entities, while in the second case (blue symbols) the curves are perfectly superimposed at higher temperatures and exhibit all features typical of individual nearly SPM NPs undergoing low-T blocking. The maximum of the ZFC curve occurs at about 70 K, which is fully compatible with particles of 15 nm and a crystalline anisotropy of $1-2 \times 10^5$ erg/cm^3, as previously indicated. One can conclude that the mixing/stirring procedure has been able to break the electro-/magnetostatic bonds among NPs which existed in the nanopowder.

A similar behavior, coherent/collective on the local scale and incoherent/individual on the macroscopic scale, is sometimes checked by observing the displacement toward higher temperatures of the maximum of the ZFC curve with respect to the value one could expect from a system where the individual magnetic units are really single particles.

As a general rule, it can be stated that magnetic measurements should be preferably corroborated by structural/morphologic data in order to provide a sensible figure of the NP size.

Effect of the Environment on the Magnetic Behavior of Fe-Oxide NPs

Magnetite NPs prepared by chemical bottom-up routes usually occur either as dispersions in fluids (basically, water for particles surrounded by hydrophilic organic shells or a hydrocarbon such as *n*-hexane for particles surrounded by hydrophobic shells) or as a dried nanopowders (each NP being still surrounded by an organic shell). In a number of cases, the NPs are embedded in a nonmagnetic host, such as a polymeric material; this can be done in various ways, e.g., by mixing the magnetic ferrofluid suspension to a monomer which is later quickly

polymerized. Identical NPs (i.e., NPs obtained by the same batch, characterized by closely similar size, shape, and type of organic shell) can display very different magnetic properties in dependence of the environment where they are put in. It can be meaningless to attempt to associate a given magnetic response to all NPs coming from the same batch: their magnetic response is intimately associated with the type and nature of the specific sample being considered.

Actually, the same NP system can occur in very many forms: (a) as a fluid dispersion, (b) as a dried powder obtained from fluid dispersion in quasi-static conditions, (c) as a solid-state dispersion obtained adding and mixing the ferrofluid to a polymerizable fluid monomer, and (d) as a dried marker dynamically obtained by spraying the ferrofluid (acting as a magnetic ink) through a nozzle on a flat surface made of plastic or paper. The degree of NP aggregation changes markedly from case to case.

In ferrofluid systems, almost no hysteresis is typically observed at room temperature, and the system is often described as SP. However, attention should be paid to the fact that the absence of measurable hysteresis is not, by itself, a sufficient evidence for SPM: in dilute ferrofluids, the NPs are free or almost free to continuously rotate their axes around an external axis; therefore their magnetic moments reorient not only by the usual magnetization rotation against the NP's crystal axes but as a consequence of the physical rotation of the NP as a whole; this is enough to destroy the magnetic hysteresis. Therefore, the usual plain correspondences no hysteresis = SPM = small NPs should not be uncritically applied when NP suspensions are considered: the magnetic entities which reorient individually could be much larger than the estimate provided from the (apparent) absence of hysteresis. It is enough to freeze the fluid to get rid of the NPs' rotational degrees of freedom and see the hysteresis to reappear. As an example, Fig. 7.9 shows the coercivity of a fluid suspension of large Fe-oxide NPs (size slightly above 100 nm) that are not in the single-domain state and obviously not in the SP regime [49]. The room-temperature value of the coercivity is negligible; however, temperature-dependent hysteresis reappears below 250 K (in this case the freezing temperature of the aqueous solution of NPs surrounded by guar/xanthan gums being in the range 252–258 K, as indicated in the Figure). Even stronger effects should be observed for fluid dispersions of smaller NPs.

Let us now consider a ferrofluid containing 8 nm magnetite NPs sprayed through a nozzle onto a flat diamagnetic surface and look at the differences in the magnetic response between the original ferrofluid (ink) and the sprayed layer (print) [50]. The FC/ZFC curves of both materials are shown in Fig. 7.10 (the ferrofluid is actually frozen over almost all the measurement temperature range). The maximum of the ZFC curve is displaced toward higher temperatures and is broader in the ink with respect to the print. Using the value $K = 1–2 \times 10^5$ emu/cm^3 appropriate to the low-T region, the blocking temperature of 64 K (print) is compatible with an effective NP radius of 13–16 nm, i.e., somewhat larger than the real NP size, indicating some aggregation of NPs. However, the degree of NP aggregation is

Fig. 7.9 Apparent and real coercive field of Fe-oxide NPs (diameter >100 nm) in gum aqueous solution. The coercive field observed below freezing (*dashed* region) becomes vanishingly small in the fluid phase. The *dashed line* is a guide for the eye
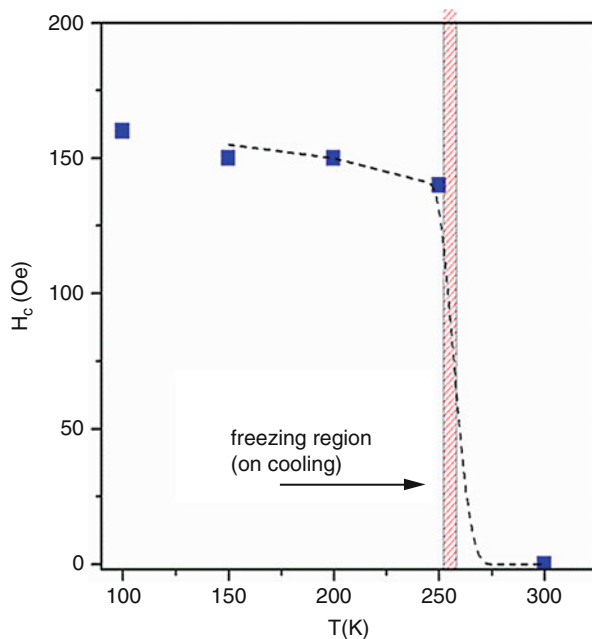
Fig. 7.10 FC/ZFC curves of a ferrofluid (ink) containing 8 nm magnetite NPs before and after jet printing onto paper (*blue/red* symbols, respectively). Spraying partially breaks small NP aggregates
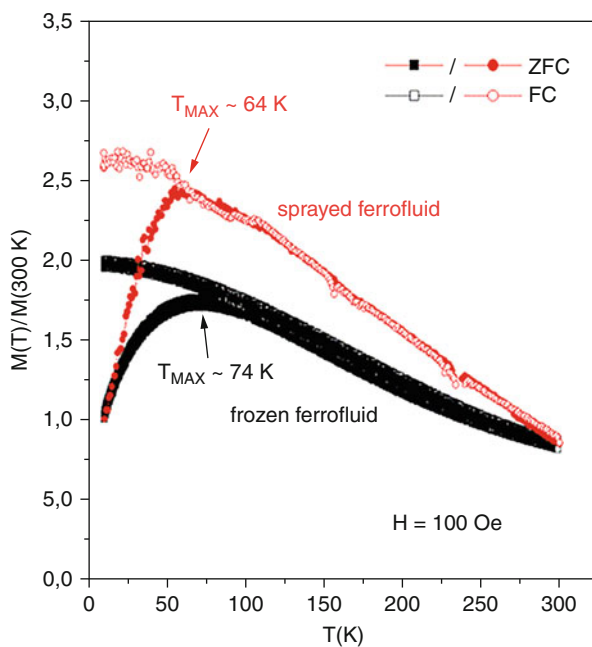
larger in the frozen ferrofluid, and a much wider distribution of sizes of the aggregates is present there, as indicated by the broader maximum. In addition, the increase in the magnetic signal related to magnetic moment unfreezing is weaker in the frozen ferrofluid owing to larger effective size of the individual magnetic units there.

Fe-Oxide NPs as Standard and Interacting SPM Materials

All magnetic NPs can magnetically interact in a variety of ways depending on their concentration and state of agglomeration. From this viewpoint, magnetite NPs are a very interesting subject of study, because they are often physically separated from each other by a diamagnetic spacer (e.g., the organic shell surrounding hem even in dried nanopowders or the nonmetallic, diamagnetic media where they can be dispersed). In NPs not in direct contact, the interparticle exchange interaction can be safely ruled out and the dipolar interaction is the most important energy contribution and can reach a strength comparable to that of the single-particle anisotropy energy.

There is a vast literature about isolated magnetic dipoles in solid-state systems. These can be associated either to single impurity atoms [51] or to NPs [52]. The temperature below which magnetic dipolar interaction is non-negligible is $N\mu^2/k$, where μ is the magnetic moment per atom (or particle). For atomic dipolar magnets, this is in the range 1–10 K [51]. However, in NP systems it can reach much larger values [51], indicating that dipolar effects cannot be neglected even at high temperatures.

There is no commonly accepted view about the effect of dipolar energy on magnetization. At low temperatures, a self-sustained ordered state could emerge; however, different approaches provide contrasting predictions which in turn critically depend on the dimensionality of the system, the arrangement of dipoles in space (whether crystalline or random), and the approximations done [52]; for 3D random systems of point dipoles, the dipolar interaction generally results in an increase of the blocking temperature, while a long-range magnetic ordering, either ferro- or antiferromagnetic-like, is predicted to exist above some critical volume fraction of freely rotating dipoles; on the contrary, an assembly of randomly oriented particles submitted to uniaxial anisotropy is unlikely to order [53].

When the temperature is high enough, dipolar systems are not expected to display self-sustained ordering; however, dipolar interactions still play a role and can be accounted for in various ways [43, 54]. One of the existing approaches is the ISP model [43, 55], describing a set of interacting NPs in the framework of a mean-field approach which introduces an interaction temperature T* while basically preserving the standard description of magnetization curves in terms of modified Langevin functions; in other words, the NP system is viewed as a modified SPM system, the so-called 'interacting superparamagnet'. The ISP approach is particularly suitable to account for the effect of dipolar interactions on nearly SPM NPs, i.e., in an intermediate region of temperatures where dipolar effects are not overcome by thermal disorder but are not largely predominant. The fictive temperature T* is related to a r.m.s. dipolar energy term ε_D through the relation

Fig. 7.11 Fictive interaction temperature T* as a function of measurement temperature for magnetite NPs of different size in different environments
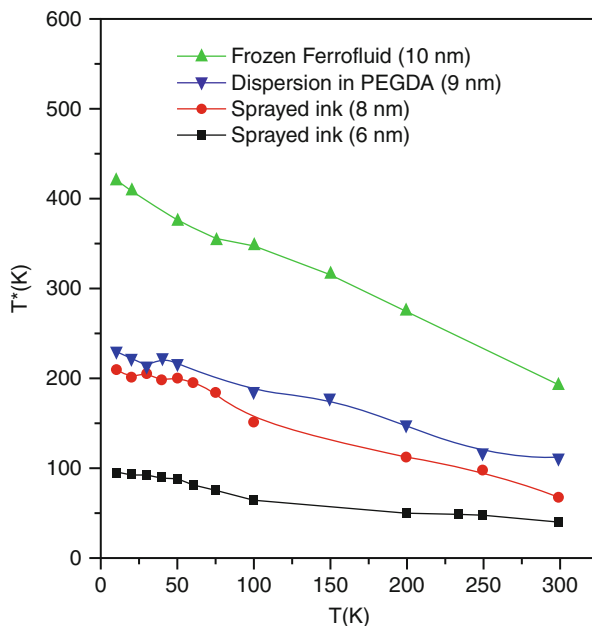
$T^* = \alpha\mu^2/d^3 = \alpha N\mu^2/k$ where α is a positive constant of the order of unit, μ is the true magnetic moment (as distinct from the apparent magnetic moment obtained from the standard SP fit of the M(H) curve to a Langevin function (see section (a) above)), d is the interparticle distance, and N is the number of NPs per unit volume. The adequacy of the ISP analysis is supported by the close correspondence of the true magnetic moments obtained from this model and the structural data. For instance, the horizontal line in Fig. 7.7, bottom panel, is the temperature-independent NP size obtained from the true magnetic moment of the magnetite NPs considered there; the value (8,3 nm) is perfectly in line with the results of X-ray analysis (8–9 nm).

The interacting SP is an intermediate state between the ideal SP regime and the blocked-particle regime [54]. When an ISP system is fitted to a standard Langevin curve, effective moments and an effective dipole density are obtained, according to specific transformation rules [55–57]. The dipolar temperature T* is weakly depending on measurement temperature because the true magnetic moment per particle μ changes with temperature by effect of thermally induced misalignment of individual spins. In Fig. 7.11, T* is plotted as function of temperature for different samples containing magnetite NPs; generally speaking, T* is particularly affected by the quadratic dependence on the NP size through μ (although the linear dependence on the NP concentration N plays a role too).

Recently, it has been pointed out that dipolar interactions have an inherently *dynamical* character, the dipolar field acting on each magnetic moment being a random variable of time [58]. The ISP model has been related to the kinetics of

thermally activated crossing of a randomly fluctuating energy barrier. The fluctuation of the dipolar field, which occurs at high rates at any finite temperature, adds to thermal effects and contributes to an increase of the disorder of magnetic moments, in contrast to the ordering effect of an applied magnetic field. This justifies introducing the additional dipolar temperature T^* in the ISP theory.

Magnetite NPs are an ideal ground to test in detail the scaling laws predicted for SP and ISP materials, because of their narrow size dispersion and of their easy dispersibility in different amounts within a diamagnetic, insulating host medium such as a polymer. As known, in a pure SP material the reduced magnetization M/M_s is predicted to scale with the ratio H/T. Such a scaling is usually observed at high temperatures only. On the other hand, the ISP model predicts that M/M_s scales with H/Ms in the ISP regime.

The actual degree of SP/ISP scaling can be figured out by introducing a suitable parameter $<\Delta>$ defined as the difference $\Delta(H) = [M(T_0,H)-M(T,H)]/M(T_0,H) \times 100$ averaged over the entire curve. Here T_0 is a reference temperature, T is the measurement temperature, and the point at $H = 0$ (where $M = 0$) is excluded. The behavior of $<\Delta>_{SP}$ and $<\Delta>_{ISP}$ is reported in Fig. 19 for magnetite NPs with 9 nm diameter and blocking temperature of about 15 K. The values $T_0 = 300$ K and $T_0 = 25$ K have been used for SP/ISP scaling, respectively.

Although above 25 K the system should be fully SP, the scaling law is actually followed at the higher temperatures only ($T > 200$ K); at lower temperatures, there is an increasing deviation of the experimental data away from the predicted master curve, as indicated by the increasingly positive values taken by $<\Delta>_{SP}$. On the other hand, $<\Delta>_{ISP}$ is zero or near to zero below about 100 K and increases at higher temperature.

In a sense, the $<\Delta>_{SP}$ and $<\Delta>_{ISP}$ curves are complementary to each other: the ISP scaling law is well followed below 100 K, while for higher temperatures the experimental curves increasingly deviate from the prediction.

It can be concluded that the ISP regime steadily and smoothly transforms into the SP regime with increasing temperature, without displaying any abrupt transition, or that the standard SP behavior can be viewed just as the limit of the ISP regime when T^* is negligible with respect to T. It is interesting to note that in this system the ratio T^*/T is predicted to be equal to 1 at $T = 120$ K (see inset in Fig. 7.12); when $T^* << T$ the material is in the SP regime and the standard SP scaling law is valid, while when $T^* \geq T$ the dipolar interactions cannot be neglected, the ISP regime applies and the ISP scaling law is followed. The transition between regimes occurs around the temperature T such that $T = T^*(T)$, extending however over an interval of ± 50 K.

Quasi-static Hysteretic Properties of Magnetite NPs

A common feature of magnetic NPs is the existence of low-temperature magnetic blocking effects. In the simplest picture an assembly of free, magnetically independent NPs is characterized by a high-temperature SPM state followed at lower temperatures by a magnetically blocked state emerging as a result of single-particle blocking by magnetic anisotropy. However, we have just seen

Fig. 7.12 Parameter $<\Delta>(T)$ measuring the deviation from the scaling laws predicted by the SP and ISP model for a nanopowder of 9 nm magnetite NPs (*black/red* symbols, respectively); when $<\Delta>=0$ the scaling law is perfectly followed. *Inset*: behavior of the ratio T*/T; ISP regime sets up when $T^* > T > 1$
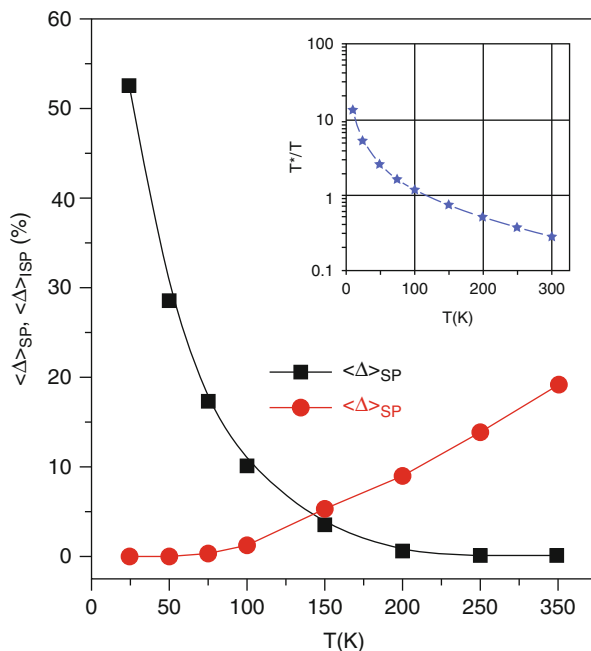
that the SP regime does not directly transform into the blocked state, because of the emergence of the ISP region.

In any case, single-particle blocking is usually associated with the appearance of a quasi-static magnetic hysteresis, as predicted by the Stoner-Wohlfarth (SW) model [42]. In principle, both SP and ISP regimes should be characterized by reversible, anhysteretic magnetic response of the NP system in quasi-static conditions, i.e., under a slowly varying field (typical magnetizing frequency in the range 10^{-2}–10 Hz). Bona fide SP particles can exhibit a dynamic hysteresis at high magnetizing frequency ($f > 50$ kHz) [59].

In fact, a small magnetic hysteresis is often found, in quasi-static conditions, even at room temperature. One common explanation for this is to ascribe the small hysteresis measured at high temperature to particles in the upper tail of the spread of sizes (often pictured as a single-mode – e.g., lognormal – distribution).

Magnetite NPs, characterized by rather narrow distribution functions, may be an interesting case to investigate. As a representative example, the coercive field of two systems of magnetite NPs with an average diameter of 15 nm is shown in Fig. 7.13, left panel. These are the same materials whose FC/ZFC curves were displayed in Fig. 7.13: one system is the original nanopowder; the other material is a photocured epoxy resin containing a 5 phr dispersion of the same NPs. The nanopowder exhibits a notable magnetic hysteresis up to room temperature, indicating the this system is very far from ideality; in fact, we know from FC/ZFC curve analysis that the units responding to the magnetic field are large NP agglomerates, not the individual particles themselves (Fig. 7.13, red symbols). On the other hand,
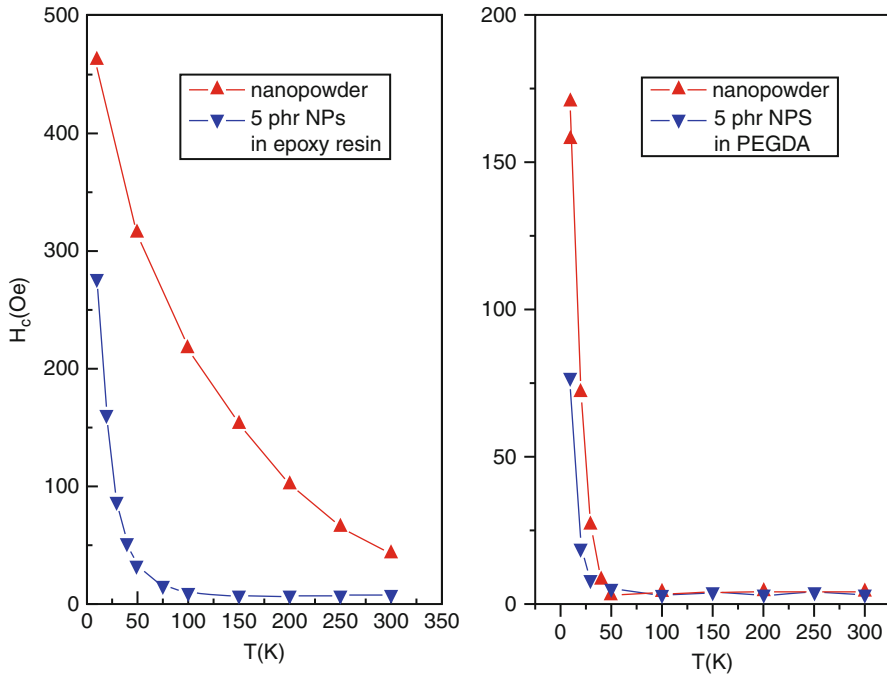
Fig. 7.13 *Left* panel: coercive field of an aggregated nanopowder of magnetite NPs (15 nm diameter) and of NPs dispersed in epoxy resin. *Right* panel: the same for a non-aggregated nanopowder of magnetite NPs (8–10 nm diameter) and for NPs dispersed in PEGDA polymer

the coercivity of the nanocomposite is essentially zero down to about 70–80 K (the small signal observed at high temperature merely corresponding to the intrinsic coercivity of the magnetic poles in the measuring setup) and displays a remarkably quick increase below that temperatures. We remind that the blocking temperature as measured from the ZFC curve is 70 K in this material (Fig. 7.7, blue curve), in perfect agreement with the temperature below which magnetic hysteresis sets up. The right panel of Fig. 7.13 shows similar curves for a 9–10 nm magnetite nanopowder and its 5 phr dispersion in PEGDA. Here the starting nanopowder is virtually non-aggregate, so the two curves are quite similar. The onset of magnetic hysteresis occurs here at a lower temperature (30–35 K) in agreement with the blocking temperature (30 K) measured from ZFC curve in the 5 phr dispersion. From this viewpoint, the simple blocking model seems to work very well for magnetite NPs.

Difficulties arise considering the shape of the hysteresis loop themselves. The standard SW model (in three as well as in two dimensions) fails to predict the slender, elongated shape of isothermal loops measured on magnetite NPs and other nanoparticulate magnetic systems. On the other hand, hysteresis is often observed at temperatures much higher than the blocking temperature. This is usually attributed to the tail of larger particles, which become blocked earlier

than the NP of average size. However, attempts to quantitatively describe the measured loops' shape on the basis of some model distribution function are usually ineffective. On the other hand, hysteresis loops with a very similar shape are measured in entirely different systems, such as arrays of interacting *electric* dipoles [60]. This may suggest that magnetic dipolar interaction plays a role in determining the hysteresis properties of magnetic NPs, in addition to or in competition with the usual SW mechanism; some interesting attempts to base this proposal on more solid grounds indeed exist, but no entirely satisfactory theory has been given so far [61, 62].

Hematite and Doped Hematite NPs

Pure hematite exhibits a spin-flip transition at the Morin temperature T_M [63]. At low temperatures, Fe^{3+} spins of pure bulk hematite are antiferromagnetically oriented along the c-axis of the hexagonal corundum cell [space group $D_{3d}^6(R\overline{3}c)$] [64]; a spin-flip transition occurs at the Morin temperature $T_M \cong 260$ K [63]; above T_M hematite becomes a canted antiferromagnet with Fe^{3+} spins now lying in the basal plane of the hexagonal cell. The Morin temperature marks the onset of spin-canted (or weak) ferromagnetism resulting from incomplete balance of canted spins. However, another ferromagnetic signal arising from defects of whatsoever origin in the crystal (hence termed *defect ferromagnetism*) can be usually observed in pure hematite both below and above T_M [65]. Both effects add to the dominant antiferromagnetic behavior, which is anisotropic in bulk hematite but isotropic in nanopowders.

The magnetic properties of hematite micro- and NPs have been recently elucidated [66]; the Morin transition temperature has been proven to be strongly dependent on the particle size, dropping to below 165 K for NPs below 100 nm in effective diameter.

Hematite NPs exhibit enhanced defect magnetism below T_M with respect to bulk crystals, presumably mostly arising from surface disorder. The FC/ZFC curve of pure hematite INPs with a radius of about 65 nm is shown in Fig. 7.14 (black symbols); the Morin transition is rather sharp and indicated by (1); the flat, featureless region 2 below T_M corresponds to standard defect ferromagnetism.

Defect Superparamagnetism in Hematite NPs Doped with Rare-Earth Ions

Hematite NPs doped with trivalent rare-earth ions such as Eu^{3+} have been recently produced [67]. Controlled replacement of Fe^{3+} ions by Eu^{3+} ions in nanometer-sized hematite particles entails a variety of structural, morphologic, and magnetic effects. Trivalent Eu cations bring about an expansion of the corundum-like with respect to pure hematite; on the other hand, the observed change in particle morphology with Eu doping originates from the hindering effect of Europium on particle growth along the [001] direction [67].

Fig. 7.14 FC/ZFC curves of pure hematite NPs (*black* symbols) and of Eu-doped hematite NPs (*red* symbols). Labels mark different magnetic regions or effects (see text)
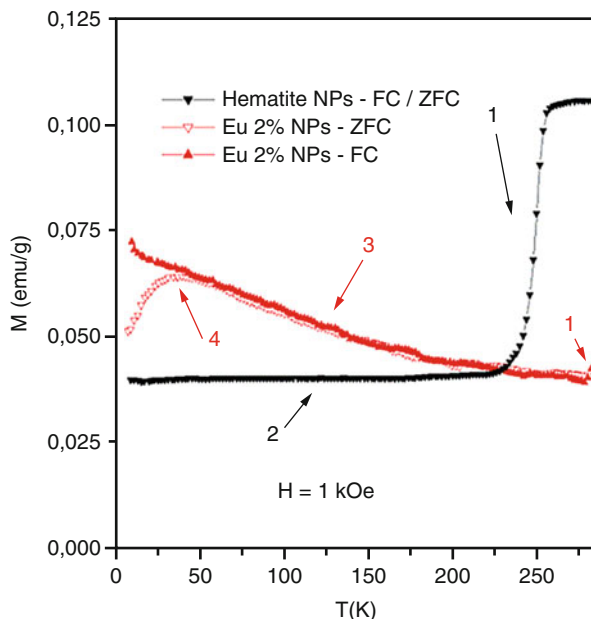
The magnetic properties of Eu-doped hematite NPs are notably affected by doping. The Eu^{3+} ions take place of Fe^{3+} ions within the NP cores; these ions can be thought of as having an intrinsic magnetic moment always lower than that of Fe^{3+} ions and variable with temperature (the ground state of this cation is nonmagnetic; a resident magnetic moment appears at finite temperatures by effect of population of low-lying excited levels). Dopant ions act to make the antiferromagnetic order of the host material weaker and give rise to a magnetic disorder in the NP cores which adds to defect magnetism mostly arising from NP surfaces. As a result, the net (uncompensated) magnetic moment per particle is enhanced.

A new effect termed *defect superparamagnetism* is observed in Eu-doped particles below T_M. The uncompensated moment generated in the NP core can randomly change direction under the influence of temperature, taking different equivalent directions perpendicular to the c-axis of the corundum cell separated by a low-energy barrier. Finally, the uncompensated moment becomes blocked below a temperature $T_B \cong 40$ K. This is shown in Fig. 7.14 (red symbols): below the Morin transition (region 1), a region typical of SPM NPs appears (region 3); finally, the uncompensated moment becomes blocked at low temperature (region 4).

Applications

Magnetic NPs in the SPM phase are attractive for biomedical applications, because they can be easily driven by a magnetic field. In fact an oscillating field makes them their 'free' moments to oscillate; an inhomogeneous field exerts a force on them,
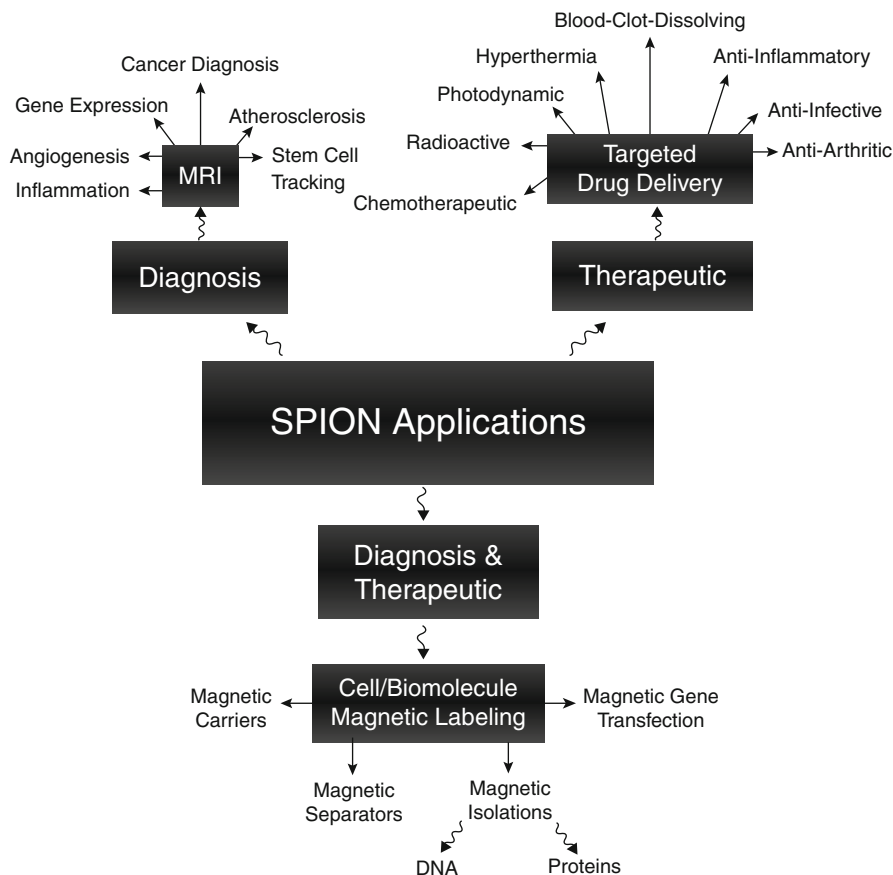
Fig. 7.15 Classification of SPIONs' applications (Reprinted from [68], Copyright 2011, with permission from Elsevier)

displacing them toward a target point, when placed in a liquid medium. Oscillating magnetic moments dissipate energy as heat and may effectively contribute in the local heating of organic tissue, exploited in hyperthermia applications where the heat is used in cancer therapy. In particular for what concerns this specific application oxides are preferred due to their greater biocompatibility with respect to metallic counterparts. Magnetic NPs may be properly functionalized with diamagnetic, organic shells in order to act as the portable inner core of a larger, multilayered particle aimed to a specific intra-body target where it can release specific drugs carried by the organic shell (drug delivery). Other applications of functionalized particles include cell separation and DNA reconnaissance. SuperParamagnetic Iron Oxide Nanoparticles (SPIONs) are biocompatible vehicles, used both in hyperthermia and drug delivery, with a proper surface architecture and conjugated targeting ligand/proteins (see Fig. 7.15).

SPIONs are targeted to the required area using external magnets, and after removal of this field the particles show no longer magnetic interaction. They typically have two configurations: a magnetic particle core (either magnetite or maghemite) coated by a biocompatible polymer or a porous biocompatible polymer containing SPIONs precipitated inside the pores. Another important application of SPIONs is in vivo biomedical imaging, including magnetic resonance imaging (MRI) as contrast agents [68].

In fact contrast agents in MRI have been developed to further increase the contrast between diseased and healthy tissues. Particles whose hydrodynamic radius is smaller than 40 nm have been called USPIO agents (ultrasmall particles of iron oxide) and have been suggested since they do not accumulate in the reticuloendothelial system as faster as their larger counterparts [69]. For this specific application, maghemite NPs are preferred to magnetite ones [70]. On the contrary, few works exist on the application of hematite NPs, whose toxicokinetic properties are under evaluation [71].

Another application of SPM transition metal oxide NPs is in ferrofluids, liquid suspensions containing a dispersion of functionalized NPs in a proper solvent (normally water, oil, or diester) [72]. Ferrofluids are stable under the effects of gravity and under the effects of an external magnetic field. Practical applications include rotary shaft seals, like the one of hard disk drives, where very fast rotation speeds are possible even at high differential pressure (50,000 rpm for noncontinuous operation); vibration damping, including voice coil resonance suppression in high fidelity loudspeakers; accelerometers for rugged environments, able to withstand 1,000 g and 125 °C; optical switches, exhibiting Faraday rotation in the dilute form; magnetic inks, or inkjettable formulations exhibiting magnetic properties [50].

Blocked NPs are interesting because they can be exploited as low-cost substitutes of more expensive high-coercivity materials in permanent magnet industry and in magnetic data storage [73]. While hard-disk magnetic memories are often based upon nanoparticulate media where the information can be safely stored owing to the high coercivity of the medium, low-density memories such as magnetic tape ones are still based on composite transition metal oxides: magnetite, maghemite, chromium dioxide, mixed composition. Their distribution is limited and in future they will be probably substituted with cheaper and faster solid-state devices. In this case, SPM is detrimental because it causes a loss of information. A major drawback of almost all techniques proposed so far to produce magnetic NPs is the lack of full control on their size, which results in a (more or less) broad size distribution. Considering how size matters in determining the magnetic properties of these magnetic nanomaterials, as we will see, it is apparent why many efforts of both fundamental and applied research are now aimed to develop preparation techniques resulting in monodisperse NP systems.

Concluding Remarks

NPs and composite nanomaterials containing magnetite and other Fe oxides are experiencing notable interest, high expectations, and robust growth. As it happens

for any popular subject, knowledge evolves much rapidly and something is lost in the process. Almost paradoxically, the plenty of experimental results and interpretations available in the recent literature and still continuously produced may hinder a comprehensive in-depth picture to be established. However, the progress in the knowledge of basic properties of these NPs, including of course magnetism, is stringently needed in order to transform prospective applications into real achievements.

References

1. Reiss G, Hutten A (2005) Magnetic nanoparticles: applications beyond data storage. Nat Mater 4:725–726
2. Allia P, Tiberto P, Coisson M, Chiolerio A, Celegato F, Vinai F, Sangermano M, Suber L, Marchegiani G (2011) Evidence for magnetic interactions among magnetite nanoparticles dispersed in photoreticulated PEGDA-600 matrix. J Nanopart Res 13:5615–5626
3. Laurent S, Forge D, Port M, Roch A, Robic C, Vander Elst L, Muller RN (2008) Magnetic Iron oxide nanoparticles: synthesis, stabilization, vectorization, physicochemical characterization and biological applications. Chem Rev 108:2064–2110
4. Wu W, He Q, Jiang C (2008) Magnetic iron oxide nanoparticles: synthesis and surface functionalization strategies. Nanoscale Res Lett 3:397–415
5. Teja AS, Koh PY (2009) Synthesis, properties and applications of magnetic iron oxide nanoparticles. Prog Cryst Growth Charact Mater 55:22–45
6. Capek I (2004) Preparation of metal nanoparticles in water-in-oil (w/o) microemulsions. Adv Colloid Interface Sci 110:49–74
7. Tavakoli A, Sohrabi M, Kargari A (2007) A review of methods for synthesis of nanostructured metals with emphasis on iron compounds. Chem Pap 61:151–170
8. Schlueter C, Lübbe M, Gigler AM, Moritz W (2011) Growth of iron oxides on Ag (111) – reversible Fe_2O_3/Fe_3O_4 transformation. Surf Sci 605:1986–1993
9. Baldokhin YV, Suzdalev IP, Prusakov VE, Burnazyan DA, Korneev VP, Kovalenko LV, Folmanis GE (2012) A study of nanostructures formed in the hydrogen reduction of $Fe(OH)_3$. Russ J Phys Chem B 6:81–88
10. Fei X, Shao Z, Chen X (2013) Hematite nanostructures synthesized by a silk fibroin-assisted hydrothermal method. J Mater Chem B 1:213–220
11. Bayat M, Yang H, Ko F (2011) Electromagnetic properties of electrospun Fe_3O_4/carbon composite nanofibers. Polymer 52:1645–1653
12. Zhan Y, Meng F, Yang X, Zhao R, Liu X (2011) Solvothermal synthesis and characterization of functionalized graphene sheets (FGSs)/magnetite hybrids. Mater Sci Eng B 176:1333–1339
13. Zhan Y, Meng F, Yang X, Liu X (2011) Magnetite-graphene nanosheets (GNs)/poly(arylene ether nitrile) (PEN): fabrication and characterization of a multifunctional nanocomposite film. Colloids Surf A Physicochem Eng Aspects 390:112–119
14. Maity D, Choo SG, Yi J, Ding J, Xue JM (2009) Synthesis of magnetite nanoparticles via a solvent-free thermal decomposition route. J Magn Magn Mater 321:1256–1259
15. Asuhan S, Wan HL, Zhao S, Deligeer W, Wu HY, Song L, Tegus O (2012) Water-soluble, mesoporous Fe_3O_4: synthesis, characterization, and properties. Ceram Int 38:6579–6584
16. Liu J, Wang L, Wang J, Zhang L (2013) Simple solvothermal synthesis of hydrophobic magnetic monodispersed Fe_3O_4 nanoparticles. Mater Res Bull 48:416–421
17. Cheng JP, Ma R, Shi D, Liu F, Zhang XB (2011) Rapid growth of magnetite nanoplates by ultrasonic irradiation at low temperature. Ultrason Sonochem 18:1038–1042
18. Liu XM, Kim JK (2009) Solvothermal synthesis and magnetic properties of magnetite nanoplatelets. Mater Lett 63:428–430

19. Podoliak N, Buchnev O, Bavykin DV, Kulak AN, Kaczmarek M, Sluckin TJ (2012) Magnetite nanorod thermotropic liquid crystal colloids: synthesis, optics and theory. J Colloid Interface Sci 386:158–166

20. Karami H (2013) Heavy metal removal from water by magnetite nanorods. Chem Eng J 219:209–216

21. Monti M, Santos B, Mascaraque A, Rodrıguez de la Fuente O, Niño MA, Mentes TO, Locatelli A, McCarty KF, Marco JF, de la Figuera J (2012) Magnetism in nanometer-thick magnetite. Phys Rev B 85:020404

22. Zajac M, Freindl K, Slezak T, Slezak M, Spiridis N, Wilgocka-Slezak D, Korecki J (2011) Electronic and magnetic properties of ultra-thin epitaxial magnetite films on MgO(001). Thin Solid Films 519:5588–5595

23. Deng Y, Zhang Q, Shi Z, Han L, Peng F, Chen G (2012) Synergies of the crystallinity and conductive agents on the electrochemical properties of the hollow Fe_3O_4 spheres. Electrochim Acta 76:495–503

24. Nguyen DT, Kim KS (2012) One-pot synthesis of multifunctional magnetite hollow nanospheres. 2012 International conference on biomedical engineering and biotechnology. doi:10.1109/iCBEB.2012.288

25. Yu X, Chen K (2011) A facile surfactant-free fabrication of single-crystalline truncated Fe_3O_4 cubes. Mater Sci Eng B 176:750–755

26. Abu Bakar M, Tan WL, Abu Bakar NHH (2007) A simple synthesis of size-reduce magnetite nano-crystals via aqueous to toluene phase-transfer method. J Magn Magn Mater 314:1–6

27. Wang J, Xia T, Wu C, Feng J, Meng F, Shi Z, Meng L (2012) Self-assembled magnetite peony structures with petal-like nanoslices: one-step synthesis, excellent magnetic and water treatment properties. RSC Adv 2:4220–4227

28. Qin Z, Jiao X, Chen D (2011) Preparation of coral-like magnetite through a glucose-assisted solvothermal synthesis. Cryst Eng Commun 13:4646–4651

29. Chen F, Gao Q, Hong G, Ni J (2008) Synthesis and characterization of magnetite dodecahedron nanostructure by hydrothermal method. J Magn Magn Mater 320:1775–1780

30. Guo C, Hu Y, Qian H, Ning J, Xu S (2011) Magnetite (Fe_3O_4) tetrakaidecahedral microcrystals: synthesis, characterization, and micro-Raman study. Mater Charact 62:148–151

31. Singh RK, Kim TH, Patel KD, Knowles JC, Kim HW (2012) Biocompatible magnetite nanoparticles with varying silica-coating layer for use in biomedicine: physico-chemical and magnetic properties, and cellular compatibility. J Biomed Mater Res A 100A:1734–1742

32. Li D, Jiang D, Chen M, Xie J, Wu Y, Dang S, Zhang J (2010) An easy fabrication of monodisperse oleic acid-coated Fe_3O_4 nanoparticles. Mater Lett 64:2462–2464

33. Sun S et al (2000) Monodisperse FePt nanoparticles and Ferromagnetic FePt nanocrystal superlattices. Science 287:1989–1992

34. Tang J et al (2001) Magnetic properties of nanocrystalline Fe_3O_4 films. J Appl Phys 89:7690–7692

35. Pu HT et al (2005) Towards high sedimentation stability: magnetorheological fluids based on CNT/Fe_3O_4 nanocomposites. Nanotechnology 16:1486–1489

36. Atarashi T, Shimoiizaka J (1990) On the preparation of the colored water-based magnetic fluids (red, yellow, blue and black). J Magn Magn Mater 85:3–6

37. Hofmann-Amtenbrink M et al (2009) Superparamagnetic nanoparticles for biomedical applications. In: Tan MC (ed) Nanostructured materials for biomedical applications. Transworld Research Network, Trivandrum, p 119

38. Kim DK et al (2001) Biomedical application of ferrofluids containing magnetite nanoparticles. Mat Res Soc Symp Proc 676:Y8.32.1

39. Tartaj P et al (2003) The preparation of magnetic nanoparticles for applications in biomedicine. J Phys D: Appl Phys 36:R182–R197

40. Dutta P et al (2009) Size dependence of magnetic parameters and surface disorder in magnetite nanoparticles. J Appl Phys 105:07B501/1–07B501/3

41. Del Bianco L, Hernando A, Fiorani D (2005) Exchange coupling in iron and iron/oxide nanogranular systems. In: Fiorani DP (ed) Surface effects in magnetic nanoparticles. Springer, Heidelberg, p 217
42. Coey JMD (2009) Magnetism and magnetic materials. Cambridge University Press, New York
43. Knobel M et al (2008) Superparamagnetism and other magnetic features in granular materials: a review on ideal and real systems. J Nanosci Nanotechnol 8:2836–2857
44. Husband B et al (2005) A superparamagnetic bead driven fluidic device. In: Cane C, Chiao J-C, Vidal Verdu F (eds) Smart sensors, actuators, and MEMS II, Proc. SPIE, The International Society for Optical Engineering, Canberra, ACT, Australia, vol 5836. pp 607–611
45. Hansen MF, Mørup S (1999) Estimation of blocking temperatures from ZFC/FC curves. J Magn Magn Mater 203:214–216
46. Cullity BD, Graham CD (2009) Introduction to magnetic materials. Wiley, Hoboken
47. Guardia P et al (2005) Surfactant effects in magnetite nanoparticles of controlled size. J Magn Magn Mater 316:e756–e759
48. Jimenez-Villacorta F, Prieto C (2008) Magnetic properties and interaction mechanisms of iron-based core–shell structures prepared by sputtering at low substrate temperatures. J Phys Condens Matter 20:085216/1–085216/10
49. Tosco T et al (2012) Zerovalent iron nanoparticles for groundwater remediation: surface and magnetic properties, colloidal stability, and perspectives for field application. In: Chiolerio A, Allia P (eds) Nanoparticles featuring electromagnetic properties: from science to engineering. Research Signpost, Trivandrum, p 201
50. Tiberto P, Barrera G, Celegato F, Coisson M, Chiolerio A, Martino P, Pandolfi P, Allia P (2013) Magnetic properties of jet-printer inks containing dispersed magnetite nanoparticles. Eur Phys J B. 86:1-6
51. Roser MR, Corruccini LR (1990) Dipolar ferromagnetic order in a cubic system. Phys Rev Lett 65:1064–1067
52. Panissod P, Drillon M (2002) Magnetic ordering due to dipolar interaction. In: Miller JS, Drillon M (eds) Magnetism: molecules to materials IV. Wiley-VCH, Weinheim, p 232
53. Zhang H, Widom M (1995) Spontaneous magnetic order in random dipolar solids. Phys Rev B 51:8951–8957
54. Dormann JL et al (1999) On the models for interparticle interactions in nanoparticle assemblies: comparison with experimental results. J Magn Magn Mater 202:251–257
55. Allia P et al (2001) Granular Cu-Co alloys as interacting superparamagnets. Phys Rev B 64:144420–1–144420–12
56. Knobel M et al (2004) Interaction effects in magnetic granular systems. Physica B Condens Matter 354:80–87
57. Franco V et al (2005) Relationship between coercivity and magnetic moment of superparamagnetic particles with dipolar interaction. Phys Rev B 72:174424–1–174424–10
58. Allia P, Tiberto P (2012) Dynamic effects of dipolar interactions on the magnetic behavior of magnetite nanoparticles. J Nanopart Res 13:7277–7293
59. Usov NA (2010) Low frequency hysteresis loops of superparamagnetic nanoparticles with uniaxial anisotropy. J Appl Phys 107:123909–1–123909–13
60. Fiory AT (1970) Electric dipole interactions among polar defects in alkali halides. Phys Rev B 4:614–627
61. Lu JJ et al (1999) Hysteretic behavior of magnetic particles with dipole interaction. J Appl Phys 85:5558–5560
62. Vasilakaki M et al (2012) Monte Carlo simulations on the magnetic behaviour of nanoparticle assemblies: interparticle interactions effects. In: Chiolerio A, Allia P (eds) Nanoparticles featuring electromagnetic properties: from science to engineering. Research Signpost, Trivandrum, p 105
63. Chikazumi S (1997) Physics of ferromagnetism. Oxford University Press, Oxford
64. Besser PJ et al (1967) Magnetocrystalline anisotropy of pure and doped Hematite. Phys Rev 153:632–642

65. Bowles J et al (2010) Interpretation of low-temperature data Part II: the Hematite Morin transition. IRM Q 20:1–10
66. Özdemir Ö et al (2008) Morin transition in hematite: size dependence and thermal hysteresis. G3 Geochem Geophys Geosyst 9:1–12
67. Freyria FS et al (2013) Eu-doped α-Fe_2O_3 nanoparticles with modified magnetic properties. J Solid State Chem. doi:10.1016/j.jssc.2013.03.018
68. Mahmoudi M, Sant S, Wang B, Laurent S, Sen T (2011) Superparamagnetic iron oxide nanoparticles (SPIONs): development, surface modification and applications in chemotherapy. Adv Drug Deliv Rev 63:24–46
69. Quiao R, Yang C, Gao M (2009) Superparamagnetic iron oxide nanoparticles: from preparations to in vivo MRI applications. J Mater Chem 19:6274–6293.
70. Veintemillas-Verdaguer S, del Puerto Morales M, Bomati-Miguel O, Bautista C, Zhao X, Bonville P, Pérez de Alejo R, Ruiz-Cabello J, Santos M, Tendillo-Cortijo FJ, Ferreirò J (2004) Colloidal dispersions of maghemite nanoparticles produced by laser pyrolysis with application as NMR contrast agent. J Phys D Appl Phys 37:2054–2059
71. Zhang W, Rittmann B, Chen Y (2011) Size effects on adsorption of hematite nanoparticles on *E. coli* cells. Environ Sci Technol 45:2172–2178
72. Popplewell J (1985) Technological applications of ferrofluids. Phys Technol 15:150–158
73. Gubin SP, Koksharov YA, Khomutov GB, Yurkov GY (2005) Magnetic nanoparticles: preparation, structure and properties. Russ Chem Rev 74(6):489–520

Hierarchical Self-Assembled Peptide Nano-ensembles

<div style="text-align:right">**8**</div>

Priyadharshini Kumaraswamy, Swaminathan Sethuraman, Jatinder Vir Yakhmi, and Uma Maheswari Krishnan

Introduction

Self-assembly is defined as a process where individual components form organized structures via specific and local interactions without any external intervention [1]. Molecular self-assembly is a spontaneous process where the molecular components organize into ordered structures through non-covalent interactions such as van der Waals, hydrophobic, capillary forces, electrostatic forces, or hydrogen bonds [2]. Although these interactions are relatively weak when compared to covalent bonds, they form reasonably stable higher-order structures through self-assembly due to the additive effect of these secondary forces. In other words, these self-assembled structures are thermodynamically more stable due to lower values of Gibbs free energy when compared to that of the individual components (building blocks). Since the underlying interactions are rather weak, any external stimulus can alter the self-assembled structures. However, once the stimulus is removed, they can revert back to their original structure. Molecular self-assembly is ubiquitous in nature, and it has evolved in many areas including chemical synthesis, nanotechnology, polymer

P. Kumaraswamy • S. Sethuraman • U.M. Krishnan (✉)
Centre for Nanotechnology and Advanced Biomaterials (CeNTAB), School of Chemical & Biotechnology, SASTRA University, Thanjavur, India
e-mail: darshini.kumaraswamy@gmail.com; swami@sastra.edu; umakrishnan@sastra.edu

J.V. Yakhmi
Homi Bhabha National Institute, Mumbai, India
e-mail: yakhmi@barc.gov.in

science and materials science, and engineering [3–9]. The molecular level self-assembly is a typical example of the 'bottom-up' approach where molecules in the sub-nm range come together to form assemblies that are in nm or bit larger in dimensions [10, 11]. Numerous self-assembling systems ranging from di- and tri-block copolymers, complex DNA structures, simple and complex proteins, and peptides have been developed [12–20]. Complex and intricate monodisperse structures can be obtained through self-assembly with high precision and reproducibility.

Self-Assembling Peptides

Biomolecules possess an inherent ability to form hierarchical self-assemblies in aqueous medium. Biomolecules such as proteins, deoxyribonucleic acid, and lipids have been widely investigated for their self-assembling properties [21–27]. In fact, these three biomolecules form the 'molecular trinity' of biomolecular self-assembly. Peptide systems have been especially popular self-assembling systems due to the large number of structures that can be generated by slight modification of the number and nature of amino acid residues in the sequence [8, 28, 29]. The stability, ease of synthesis, and controlled self-assembly regulated by various physicochemical parameters have resulted in the popularity of self-assembled peptide systems [30]. Since peptide self-assembly is a bottom-up process where amino acids form the building blocks, it is easy to introduce functionalities on the carboxyl or amine terminal groups, opening up the possibilities of a wide range of chemical interactions leading to specific functions. Though peptides containing naturally occurring L-amino acids have been widely investigated for their self-assembling characteristics, D-amino acid containing peptide systems have also been explored due to their stability against proteases [31]. Self-assembling peptides may vary in the number of amino acids starting from 2 to as high as 20. The simplest building block reported thus far is the dipeptide (diphenylalanine – FF) from the core recognition motif of Alzheimer's amyloid beta peptide [32]. This dipeptide is reported to form different structures based on the pH that is employed (Fig. 8.1). For instance, at a pH lower than the isoelectric point of the peptide, it forms nanofibrils, whereas at a pH higher than its isoelectric point, the peptide forms nanotubes [33].

Despite the numerous advantages of self-assembling peptides, there are several challenges associated with their use in biomedical applications, which include problems related to processability, control of size, functionalization, and stability in aqueous media [34]. For example, biosensing platforms employing self-assembling peptides require electric contacts between the self-assembled nanostructures and transducers, which become tedious due to the small dimensions involved. However, with the advancement in micro- and nanofabrication techniques, such problems are being overcome, paving the way for use of peptide nanostructures in molecular electronics. Another impediment
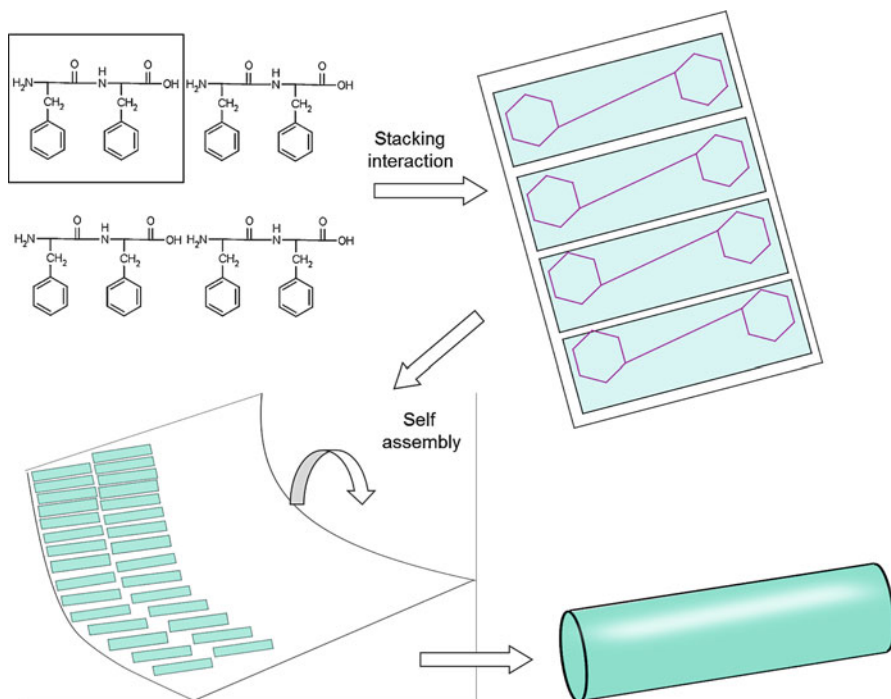
Fig. 8.1   Mechanism of formation of nanotubes by FF dipeptide

relates to the low conductivity of the self-assembled peptide nanostructures, which limits their use in sensing and diagnosis. However, by the introduction of conductive polymers, enzymes, and metallic particles, the electrical current conductivity can be enhanced [31, 35].

Factors Influencing Self-Assembly

The self-assembly process is influenced by many factors that can be grouped into any of the three categories, namely, environment-driven factors, substrate-driven factors, and peptide-driven factors.

Environment-Driven Factors

The pH, temperature, solvent, nature of ions, and ionic strength are factors that influence the self-assembly process. The pH of the medium alters the charge status on the peptide and hence the electrostatic forces between the peptide

molecules. For instance, the peptide STVIIE forms beta-sheets when its net charge is +1, whereas in its zwitterionic state, it forms random coils and it exists as a mixture of random coils and beta-sheets when the net charge is −1. This is because when the net charge is zero as in the zwitterionic form, the packing of the peptides could happen in many ways leading to an amorphous structure. The presence of a net charge gives directionality to the associations as well as determines the distance between the peptide chains [36]. The charge distribution in the peptide also influences the self-assembled structures formed. For example, when the peptides EAK 16-I (AEAKAEAKAEAKAEAK), EAK 16-II (AEAEAKAKAEAEAKAK), and EAK 16-IV (AEAEAEAEAKAKAKAK) were self-assembled, it was found that EAK 16-I and EAK 16-II formed fibrillar assemblies, while EAK 16-IV formed globular structures between pH 6.5 and 7.5 and fibrillar structures at other pH due to the neutralization of charges in the beta-sheet structures formed, which promotes aggregation at pH away from the neutral pH [37]. The nature of anion also was found to influence the structures formed by the EAK 16-II peptide in the presence of Cu^{2+} ions. While SO_4^{2-} caused formation of nanofibers, the monovalent Cl^- and NO_3^- caused formation of short fibrils with a mixture of alpha helix and random coils. This is due to the ability of the divalent sulfate anions to act as an electrostatic bridge between two lysine residues unlike the monovalent ions. Higher ionic strength of the medium contributes the shielding of the electrostatic charges on the ionizable groups present in the peptide sequence, thereby altering the critical aggregation concentration as well as the pH required for association or dissociation of the self-assembled structure [37]. Factors like the solvent polarity, surface tension, hydrogen bond-forming ability, and dielectric constant influence the peptide self-assembly and strength of the self-assembled structures. Introduction of methanol as cosolvent contributed to the formation of nanofibers of diphenylalanine (FF) on a glass substrate. This was attributed to the high hydrogen bond donor and acceptor property of methanol that promoted formation of highly crystalline nanofibers [38]. On increasing the methanol content, solvation of the peptide molecules occurred, which prevented aggregation of the solvated peptide. It was also observed that organic cosolvents with higher surface tension contributed to reduction in fiber dimensions to the nm range. The dielectric constant of the solvent has been found to influence the peptide substrate binding affinities [39].

Substrate-Driven Factors

The surface tension, hydrophobicity, and surface texture of the substrate influence the self-assembly process. Hydrophobic substrates promote better spreading of peptide sequences that have greater number of hydrophobic residues. Surface topography, on the other hand, directs the orientation as well as fiber dimensions. The dipeptide FF was found to self-assemble into nanofibers with a well-spread morphology on poly(vinyl chloride), whereas in silicon, which had a periodic rough

texture, finer fibers were observed along with vertically aligned hollow nanotubes of larger dimensions suggesting that the rough morphology retards the stacking interactions between the peptide molecules [34].

Peptide-Driven Factors

Peptide-driven factors that direct self-assembly are the number and nature of amino acid residues in the sequence, the isoelectric point, and the peptide concentration [40]. Aromatic residues led to the formation of rigid structures that possessed nanotape or nanoribbon morphology [41]. Reduction in the surface tension of the peptide molecule can lead to the formation of globular assemblies instead of fibrillar structures as observed with the peptide EAK 16-IV at neutral pH. Peptide aggregates are formed above a particular concentration known as critical aggregation concentration (cac), which in turn is dependent on the peptide sequence. Below the cac, the seeding and nucleation occur, while above cac, the aggregated ensembles are discernible [42]. In the case of surfactant-like peptide amphiphiles, if the surfactant number is between ⅓ and ½, then cylindrical micelles and nanofibers are observed (Fig. 8.2). However, if the surfactant number is between ½ and 1, then bilayer formation occurs. In the case of micelle-forming peptides, increase in the intermolecular cross-links has been found to reduce the curvature leading to the formation of cylindrical micelles as observed in the hexadecyl-modified peptide sequence CCCCGGG phosphoserine–RGD [43].

Classes of Self-Assembling Peptides

Peptides that self-assemble are amphiphilic and are classified based on their nature of self-assembly.

Molecular Lego Peptides

Peptide lego systems consist of both hydrophilic and hydrophobic residues that form beta-sheet structures and well-defined nanofiber matrices with an average pore size of 5–200 nm in aqueous solution. These peptides are termed as molecular lego peptides as they possess alternating charged and hydrophobic amino acids like the pegs and holes of lego blocks. For example, in the peptide RAD 16-I, the sequence is RADARADARADARADA, where R (arginine) is a cationic amino acid and D (aspartate) is an anionic amino acid. These oppositely charged amino acid residues are separated by a hydrophobic amino acid residue, alanine. The charge status of the peptide sequence will therefore be represented as (+ − + − + − + − + − + − + − + −), and such sequences are referred to as modulus I peptides. Similarly, modulus II (++− −++− −) and modulus III (+++− − −+++− − −) have also been reported based on their charge pattern.
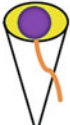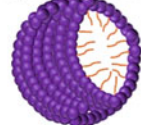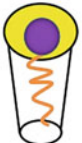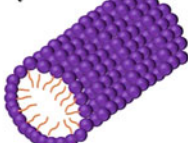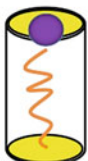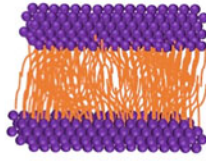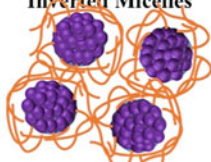
Critical Packing Parameter $(v/a_0 l_c)$	Critical Packing Shape	Structure formed
<1/3	Cone	Spherical Micelle
1/3–1/2	Truncated Cone	Cylindrical Micelle
1/2–1	Truncated Cone	Flexible Bilayers
~1	Cylinder	Planar Bilayers
>1	Inverted truncated Cone	Inverted Micelles

Fig. 8.2 Influence of surfactant number on the formation of self-assembled nanostructures

These peptides spontaneously form nanofibers of 10 nm length in the presence of cations of alkaline earth metals due to electrostatic forces. Since ionic interactions are involved in the self-assembly process, the molecular lego peptides readily form hydrogels [44]. The hexadecapeptide DAR 16-IV with the peptide sequence DADADADARARARARA has similar amino acid residues as RAD, with the only difference that the sequence of the charged amino acid residues varies. This difference is markedly reflected in the self-assembled structures formed by the two peptides. The self-assembled structures formed by DAR 16-IV can transform from an alpha helix to a beta-sheet depending on the pH, ionic strength, and temperature

of self-assembly. But, RAD 16-I does not form alpha helical structures under any condition. This is because in the case of RAD 16-I, if the peptide assumes an alpha helical structure, the positively charged side groups in arginine (R) will be repelled by the positively charged N-terminus, and the anionic aspartate (D) will experience electrostatic repulsion from the like-charged carboxylate in the C-terminus. Hence, it always remains in the beta-sheet form. In the case of DAR 16-IV, the negatively charged aspartate will stabilize the positive N-terminus, and the positively charged arginine will exhibit electrostatic attraction with the negative C-terminus when it adopts an alpha helical form. Thus the nature, number, and sequence of amino acids are critical parameters that determine the type of self-assembled structures that can be formed by peptides [45].

The molecular lego peptides are also known as ionic self-complementary peptides due to their pattern of electrostatic association that contribute to their stability. Zhang and his coworkers identified the first molecular lego peptide EAK-16 from a Z-DNA binding protein zuotin from yeast [36]. The ionic self-complementary peptides initially form beta-sheets, which later form a fibrous network, progressively by undergoing sol–gel transition. The substitution of a basic amino acid with another basic amino acid (for instance R with K) or an acidic amino acid with another acidic amino acid (e.g. D with E) does not bring about significant changes in the self-assembly pattern. However, substitution of an acidic amino acid with a basic amino acid and vice versa was found to alter the self-assembly pattern. Such structures were found to form beta-sheets but did not form higher-order structures. Substitution of the alanine residues with more hydrophobic residues such as leucine, valine, and isoleucine accelerates the self-assembly process [46].

Surfactant-Like Peptides

Surfactant-like peptides self-assemble either into nanotubes or nanovesicles [47–50] (Fig. 8.3). They are termed as surfactant-like due to the presence of a hydrophilic head comprising charged amino acids (lysine, arginine, glutamic acid, aspartic acid, etc.) and a hydrophobic segment comprising nonpolar amino acids (alanine, leucine, valine, etc.). Intermolecular hydrogen bonding plays a major role in determining the structures formed by the self-assembly of these peptides. Vauthey et al. were the first to design a self-assembling peptide that can self-assemble into nanotubes and nanovesicles [47]. Some common examples of surfactant-like peptides include A_6D, V_6D, V_6D_2, $L_6D_2 15$, and G_6D_2. These peptides initially self-assemble to form a bilayer, which later undergo further associations to form nanotubes.

The nature of the amino acids in the sequence has an important role in dictating the type of self-assembled structures formed. The peptide sequences A_6K and A_6D both formed nanotubes often exhibiting twisted tape or fibrillar morphology. A heptapeptide, namely, Ac-GAVILRR-NH_2, formed donut-like ring structures [46]. Peptides like V_6D_2, V_5DVD, and $V_4D_2V_2$ have been reported to form fibers, tapes, and twisted ribbons rather than nanotubes. The differences in the self-assembled
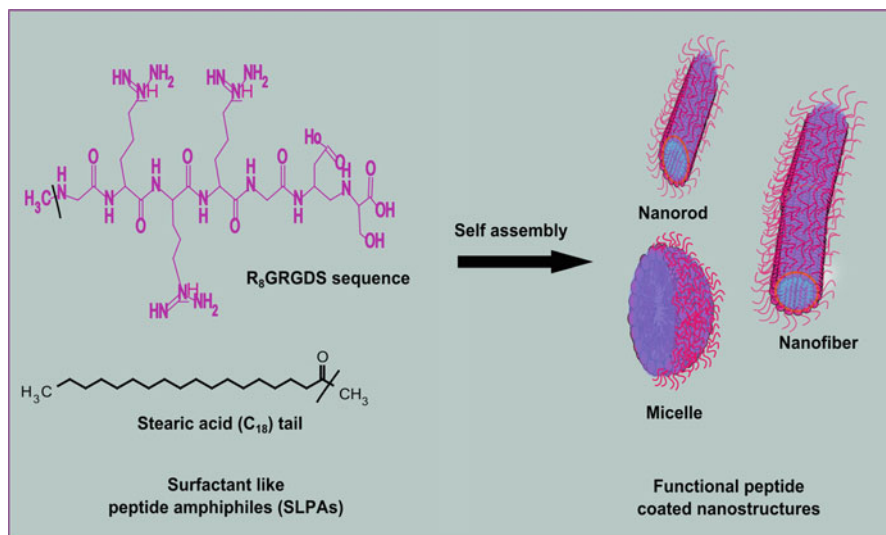
Fig. 8.3 Self-assembly of surfactant-like peptide amphiphiles (*SLPAs*) into various nanostructures

structures formed could be attributed to the variations in the packing density of the peptide aggregates [51]. The number of hydrophobic amino acids in each surfactant-like peptide also influences the final self-assembled structure. Three peptides A_3K, A_6K, and A_9K, with different hydrophobic chain lengths were investigated for their self-assembling properties [52]. While A_3K formed stacked bilayers, A_6K formed nanofibers and A_9K formed nanorods. The absence of higher-order structures in A_3K peptide was attributed to the absence of measurable critical aggregation concentration (cac), probably due to the short hydrophobic segment. Several surfactant-like peptides found in nature also exhibit similar self-assembling characteristics to form vesicular structures that may be relevant to prebiotic enclosures that sequester enzymes from their environment [53].

Lipid-Like Amphipathic Peptides

The lipid-like peptides are a subtype of surfactant-like peptides and consist of a hydrophilic head group and a tunable hydrophobic tail. Though the lipid-like peptides possess different composition, sequence, and packing, they share several similarities with phospholipids that self-assemble to form lipid bilayers. The length of the peptide is about 2.5 nm, which is comparable to natural phospholipids. Both systems self-assemble in water to form nanovesicles with an average diameter of 30–50 nm. A point of distinction between the two systems is in the nature of association between the individual components. In phospholipids, the acyl chains in the hydrophobic tails compactly pack together to displace water molecules
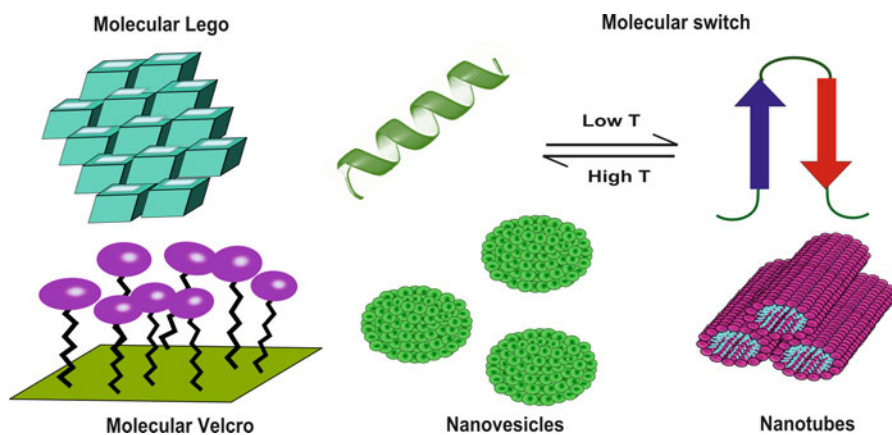
Fig. 8.4   Various self-assembled structures formed by carpet and switch peptides

from the interior and hydrophobic forces drive this process, which impedes formation of hydrogen bonds. However, in the case of lipid-like peptides, in addition to the hydrophobic tail packing, intermolecular hydrogen bonds are formed in the backbone. The presence of charged side chains in these peptides confers pH sensitivity as well as responsiveness to change in the ionic strength of the medium.

Carpet Peptides

Carpet peptides also known as molecular paint peptides were first developed by Zhang et al. [54]. These peptides can undergo self-assembly and form monolayers, a few nanometers thick on a surface. These peptides thus act as a carpet for the attachment of cells or they can trap other molecules, thereby providing molecular recognition (Fig. 8.4). These peptides consist of three segments. The first segment or head contains ligands that serve as molecular recognition motifs for cell surface receptors. The middle segment serves as a linker that allows the head to interact at a distance away from the surface and also provides certain degree of flexibility to the peptide structure. The last segment or tail enables covalent binding with the surface. These peptides are widely used to study cell–cell communication. The peptide sequence RGDAAAAAC is a typical example of a molecular paint peptide [54]. The RGD segment serves as a recognition motif for the cell surface receptors integrins and hence can promote cell adhesion. The five alanine residues (AAAAA) serve as linkers, while the lone cysteine residue can enable anchoring of the peptide to gold substrates through its sulfhydryl group. Similarly, the tetradecapeptide RADSRADSAAAAAC that also possesses a ligand (RADS) for cell recognition has been developed for painting gold surfaces [55].

Switch Peptides

The switch peptides possess a unique ability to transform its molecular structure in response to environmental stimuli. For example, the hexadecapeptide DAR16-IV can form beta-sheet structures at ambient temperatures but transforms to an alpha helix when the temperature or pH of the system is modified. This suggests that secondary structures of sequences flanked by the negative charges on N-terminus and positive charges on C-terminus may undergo drastic changes if the pH and temperature are changed. These peptides were converted to electronically responsive structures through incorporation of metal nanocrystals [56]. An undecapeptide with the sequence Ac-QQRFQWQFEQQ-NH$_2$ was found to self-assemble into structures with progressively increasing order – tapes, ribbons, fibrils, and finally fibers [57] (Fig. 8.4). The side chains of the glutamine (Q) residues involve in hydrogen bonding and promote formation of β-sheets. The arginine (R) and glutamate (E) residues facilitate electrostatic interactions with the complementary countercharges on the neighboring chains leading to stabilization of antiparallel β-sheets forming a tape-like structure. The phenylalanine (F) and tryptophan (W) residues contribute to hydrophobic forces that drive the formation of ribbons. In the ribbon-like morphology, two tapes associate face-to-face stabilized by the hydrophobic forces leading to a twist. At higher concentrations of the peptide, the ribbons stack together to form fibrils. The substitution of the glutamine residues with glutamate (E) in the peptide sequence induces pH responsiveness in the peptide. At acidic pH (<2), the glutamate residue is protonated and hence will exhibit associative interactions promoting the existence of a nematic phase. As the pH is increased, the glutamate residues get deprotonated, and hence greater repulsive forces are introduced leading to transformation of the nematic phase to an isotropic fluid phase. Thus the peptide acts as a molecular switch in response to pH changes by transforming reversibly between nematic and isotropic fluid phases.

Cyclic Peptides

The design of cyclic peptides, whose dimensions and assembly could be tailored as desired, was inspired from the tubular pores formed by the tobacco mosaic virus [58]. Ghadiri and his coworkers were the first to report the self-assembly of a rationally designed cyclic octapeptide cyclo(L-gln-D-ala-L-glu-D-ala-)$_2$ [59]. These cyclic peptides have alternating D- and L-amino acids, which interact through intermolecular hydrogen bonding to form an array of self-assembled nanotubes with an internal diameter of 7–8 Å (Fig. 8.5). The diameter of the tube depends on the number of amino acid residues forming the cyclic peptide. At alkaline pH, the carboxylate groups of glutamate residues become negatively charged as a result of deprotonation and prevent stacking associations due to strong electrostatic repulsive forces. At acidic pH, the carboxylate groups become protonated and hence favor association through extensive hydrogen bonding between the amide carbonyl and –NH– groups in the backbone. Each cyclic peptide forms a flat
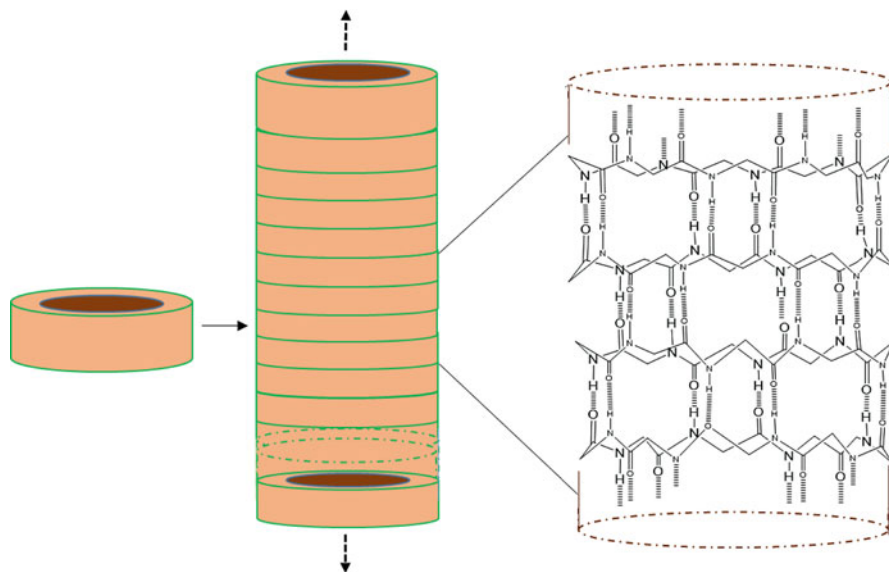
Fig. 8.5 Self-assembly of cyclic octapeptide lanreotide into nanotubes

ring that stacked over one another and is stabilized by hydrogen bonding resulting in a hollow nanotube. The side chains of the amino acids face the exterior of the tube to minimize steric repulsions. These side chains can also be functionalized to incorporate desired properties to the nanotubes. The cyclic octapeptide lanreotide NH_2-(D)naphthylalanine-Cys-Tyr-(D) Trp-Lys-Val-Cys-Thr-$CONH_2$, an analogue of somatostatin 14, also self-assembled into tubular structures with a diameter of 24 nm and length running to several microns [60].

Nucleopeptides

This category of peptides represents a hybrid molecule formed from oligonucleo-tides and amino acids. The sequence of both components influences the nature of self-assembly. Gour et al. have reported the self-assembly of a nucleopeptide formed by grafting the dipeptide FF to the 12-mer oligonucleotide with sequence CTCTCTCTCTTT [61]. The diphenylalanine (FF) is part of the core recognition motif of the amyloid peptide and self-assembles to fibrillar structures in its pristine state. However, the nucleopeptide formed using this peptide motif self-assembled to spherical structures, which may be attributed to the hydrogen bonding interac-tions and amphiphilicity of this hybrid molecule. Li et al. had developed nucleopeptides that self-assemble to form supramolecular hydrogels using the dipeptide FF conjugated to a nucleobase (A, G, T, or C). These nucleopeptides served as hydrogelators forming entangled nanofibers in water and could lead to many interesting biomedical applications [62, 63].

Peptide Amphiphiles (PA)

Peptide amphiphiles comprise of a hydrophilic head and hydrophobic tail that self-assemble in aqueous solution to form well-defined nanostructures like peptide bilayers, micelles, nanotubes, nanorods, and nanovesicles [64–66]. These molecules can be chemically modified easily to tailor their properties for specific applications such as cell adhesion and internalization. The mechanistic insights into the self-assembly of peptide amphiphiles using V_6D as a model have suggested that the peptide amphiphile initially self-assembles into a bilayer and then into a cyclic vesicular form that undergoes stacking to form nanotubes. It has also been suggested that higher-order structures could be obtained by interconnection of these tubes through three-way junctions [67]. Most of the peptide amphiphiles form beta-sheet containing nanofibrils that can be induced either by addition of divalent salts or by altering the pH of the solution. The divalent cations form an ion bridge leading to stronger intra- and interfibrillar associations. Experiments have revealed a high degree of solvation in the interior of the self-assembled structures formed by peptide amphiphiles [44]. Incorporation of a cysteine residue in a peptide sequence promotes reversible cross-linking of the peptide leading to modification of the stiffness of the peptide chain. Another strategy to impart amphiphilic character to the peptide sequence is to incorporate a fatty acyl chain to the N-terminus of a peptide sequence. The acyl chain contributes to the hydrophobic character to the peptide amphiphile. Using an elegant set of experiments, Lowik et al. demonstrated the influence of alkyl chain length on the self-assembly of the peptide GANPNAAG [68]. The peptide molecules modified with C_6, C_{10}, and C_{12} acyl chains self-assembled into random coils independent of temperature, while those containing C_{14} and C_{16} acyl chains underwent a transition from β-sheets to random coils on increasing the temperature. Increasing the acyl chain length contributes to enhanced hydrophobicity leading to differences in the thermal stability.

In a seminal work, Hartgerink et al. developed a peptide amphiphile with four distinct domains that self-assembled into cylindrical micelles in aqueous solution [69]. The N-terminus of the peptide sequence Cys-Cys-Cys-Cys-Gly-Gly-Gly-phosphoSer-Arg-Gly-Asp was modified with a 16-carbon alkyl chain that forms the hydrophobic component. The cysteine residues contribute to the formation of β-sheets and stabilize the self-assembled structure by covalent capture where superstructures are transformed into a supramolecule through covalent bonding. The disulphide bridges formed due to the oxidation of the cysteine residues confer rigidity to the supramolecular structure. Further, stabilization of the structure is provided through extensive hydrogen bonding. The glycine-rich segment forms the flexible spacer domain. The phosphoserine residue confers charge and hence pH responsiveness to the sequence, while the RGD serves as a recognition motif for cell adhesion. This peptide amphiphile associated at acidic pH and dissociated at alkaline pH (Fig. 8.6). Similar analogues have now been developed for many biological
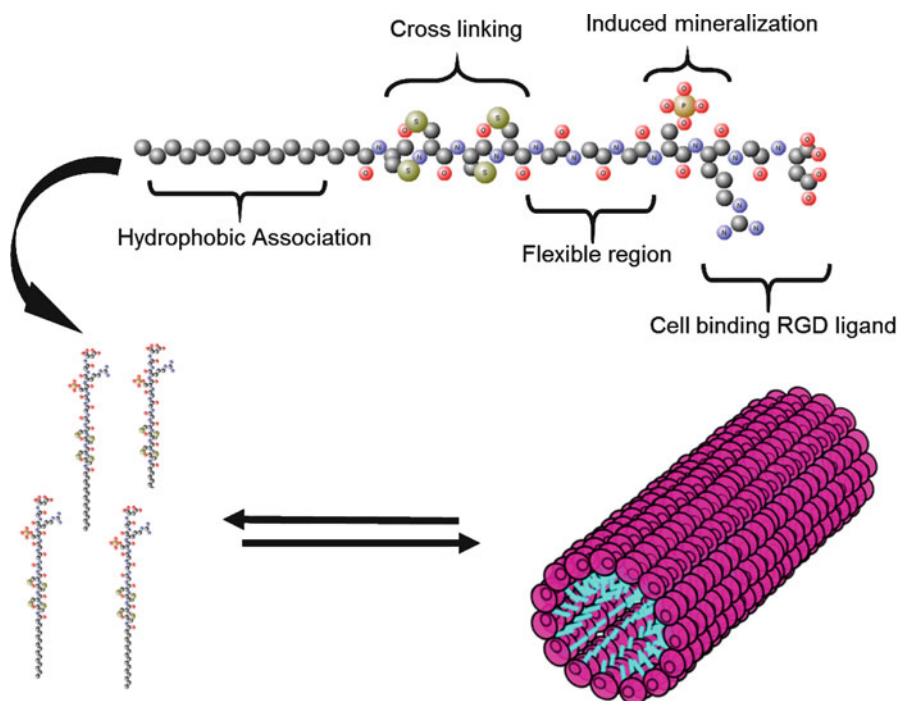
Fig. 8.6 Self-assembly of Hartgerink peptide

applications. Reverse peptide amphiphiles like C16O-VEVE with a free N-terminus were prepared using unnatural amino acid (ornithine, O) modified with a fatty acid chain and were mixed with conventional peptide amphiphiles containing free C-terminus. Such de novo designed peptide amphiphiles formed nanobelts [70]. A twisted nanoribbon morphology was observed when the cell adhesion motif RGD was incorporated in the C-terminus (C16O-VEVEGRGD).

Apart from normal method of peptide synthesis, recombinant DNA techniques have also been employed to produce two amphiphilic peptides, namely, $Ac\text{-}A_2V_2L_3WG_2\text{-}COOH$ and $Ac\text{-}A_2V_2L_3WG_7\text{-}COOH$, which self-assembled into nanovesicles [71].

Bolaamphiphilic Peptides

A bolaamphiphilic peptide consists of two hydrophilic terminals linked through a hydrophobic segment. This class of peptides derives its name from the South American hunting weapon that consists of two balls linked by a string. Stupp and his coworkers reported the self-assembly of a bolaamphiphilic peptide consisting of

Structure of a bolaamphiphile

n= 4 -13
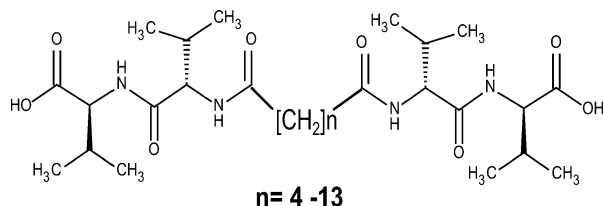
glycylglycine (GG) residues at either end linked through a 7-carbon acyl chain [72] (Fig. 8.7). The bolaamphiphilic peptides were pH responsive and formed helical ribbon-like structures at alkaline pH. The hydrophobicity of the acyl chain in the middle influences the twist in the structure so as to minimize contact with the polar environment. At acidic pH, the peptide self-assembles to form nanotubes presumably due to the additional hydrogen bonds formed through the protonated carboxylic groups of the amino acid residues.

Other Self-Assembled Peptide Structures

Crick, in 1953, first reported coiled-coil structures, commonly seen in many proteins. The major driving force is the hydrophobic interaction among the helices and a typical coiled structure consists of 2–5 left-handed alpha helices containing seven amino acid residues (heptad), each wrapped around each other to form a supercoil. According to the peptide Velcro (PV) hypothesis, there are three major requirements for formation of such structures [54]. The first and fourth residues must be hydrophobic to facilitate dimerization of the peptide chains along one face of the helix. The length of the hydrophobic side chain dictates the formation of dimers, trimers, or tetramers. Increasing hydrophobicity stabilizes the self-assembled structure through van der Waals' and hydrophobic interactions. The fifth and seventh amino acid residues should have charge to promote electrostatic interactions between the peptide chains. In order to facilitate attractive associations, it is important to have an acidic and a basic amino acid residue at these positions. Leucine zipper proteins and cartilage oligomeric matrix proteins exhibit such type of coiled-coil structures. A right-handed alpha helical coiled-coil structure has also been identified in tetrabrachion, a protein from the bacterial *Staphylococcus marinus*. This structure contains undecapeptide helices that possess a core filled with water, thereby exhibiting a different packing pattern with the hydrophobic and hydrophilic residues in the first, fourth, and eighth positions falling on the same face [73]. Apart from peptide Velcro where one strand of acidic amino acid residues mingles with other strand of basic residues to form a parallel heterodimer, Ryadnov et al. have designed belts and braces where two peptides are bound together by the third peptide of opposite charge. These belt and braces were used as a template to form colloidal gold particles and were commonly referred as peptide-mediated nanoparticle assembly [74]. Other types of self-assembled peptide systems include amphiphilic peptides in beta strand conformation which self-assemble into twisted

Table 8.1 List of peptide systems and their self-assembled structures

Peptide sequence	Study carried out
A_6D, V_6D, V_6D_2, L_6D_2	Formation of nanotubes [47]
G_4D_2, G_6D_2, G_8D_2, $G_{10}D_2$	Formation of nanotubes and vesicles [48]
V_6K, V_6K_2, V_3K	Adsorption at air/water interface used for DNA immobilization [75]
V_6K_2, L_6K_2, A_6K, V_6H, V_6K, H_2V_6, KV_6	Formation of nanotubes and vesicles [48]
Ac-A_6D-COOH and Ac-A_6K-COOH	Determination of critical aggregation concentration (cac) of particles formed during self-assembly [66]
Mixtures of Ac-A_6D-OH and Ac-A_6K-NH$_2$	Formation of twisted fibrils [76]
Ac-GA VILRR-NH$_2$	Formation of 'nanodonut' structures [46]
I_6K_2, L_6K_2, V_6K_2	Correlation of secondary structure with the morphology of nanostructures formed [67]
V_6D_2, V_5DVD, $V_4D_2V_2$	Influence of sequence and purity on self-assembly [51]
A_3K, A_6K, A_9K	Determination of cmc, self-assembled structures, correlation with its antibacterial activity [52]
A_6K	Elucidation of nanotube structure and its mechanism of formation [77, 78]
Ac-$A_2V_2L_3WG_2$-COOH and Ac-$A_2V_2L_3WG_7$-COOH	Formation of vesicles [71]
chol-H_5R_{10}, chol-$H_{10}R_{10}$ (chol denotes cholesterol)	Vehicles for delivering genes [79]
$A_{12}H_5K_{10}$, $A_{12}H_5K_{15}$, and H_5K_{10} (non-amphiphilic control)	Vehicles for delivering genes [80]
Ac-$(AF)_6H_5K_{15}$-NH$_2$	Vehicles used for delivering both drugs and genes [81]
NH$_2$-$I_5H_4R_8$-CONH$_2$, NH$_2$-$F_5H_4R_8$-CONH$_2$, NH$_2$-$W_5H_4R_8$-CONH$_2$, NH$_2$-H_4R_8-CONH$_2$	Vehicles for delivering genes [82]
chol-G_3R_6TAT, TAT = YGRKKRRQRRR	Antimicrobial activity [83]
A_6D and A_6K	Stabilization of G-protein-coupled receptor bovine rhodopsin against denaturation [82, 84]
Ac-V_6R_2-NH$_2$, Ac-V_6K_2-NH$_2$, Ac-A_6K-NH$_2$, Ac-I_6K_2-NH$_2$, Ac-A_6K-OH, DA_6-NH$_2$, Ac-V_6D_2-NH$_2$, Ac-A_6D-OH, KA_6-NH$_2$	Stabilization of protein complex photosystem-I and enhancement of activity [64]
H-K_3-[W^{D}L]$_3$-W-NH$_2$, H-CK_3-[W^{D}L]$_3$-W-NH2, Ac-[K(Ac)]$_3$-W-[W^{D}L]$_3$-W-NH$_2$, Ac-C[K(Ac)]$_3$-W-[W^{D}L]$_3$-W-NH$_2$, Ac-C(sl)[K(Ac)]$_3$-W-[W^{D}L]$_3$-W-NH$_2$, where sl denotes the spin label acetamidoproxyl	Micelle aggregation and formation of particles and beads [85]

tapes, helical dipolar peptides that undergo conformational change between a helix and beta-sheet similar to molecular switch, and surface binding peptides that form monolayers that are covalently bound to a surface. Table 8.1 gives a list of some of the major peptide systems investigated for their self-assembling properties.

Structure Manipulation

The formation of nanofibers can be promoted by peptides that have an ability to form beta-sheets. Presence of branched amino acid residues confers an ability to transform from a α-helical structure to a β-sheet depending on the nature of the medium [86]. The propensity of beta-sheet forming ability of peptide sequences can be retarded by introduction of proline residues at the N- and C-terminals. As proline lacks hydrogen bond-forming ability owing to its planar ring structure, it restricts the expansion of the beta-sheet network. This results in formation of straight nanofibers of about 80–130 nm in diameter and several mm long. The fine structure will show striations arising due to packing of tightly coiled alpha helical structures, especially if phenylalanine was one of the amino acid residues in the sequence. This is due to additional aromatic interactions contributed by phenylalanine. If phenylalanine was substituted by aliphatic hydrophobic residue such as isoleucine, the straight fibers formed revealed tape-like inner structures. Attempts to functionalize these nanofibers to impart biorecognition have been made using biotin conjugation at their N-terminus [87]. These biotin terminals can be used to tether molecules linked to anti-biotin molecules. However, such functionalization strategies resulted in a loss of the supramolecular assembly formed by the peptide.

Three main forces, namely, hydrophobic, hydrogen bonding, and coulombic forces, are mostly involved in controlling the self-assembly process [88]. A combination of hydrogen bonding, π–π interactions, and van der Waals' interactions promotes formation of columnar, disc-like aggregates, while hydrophobic effects and π–π stacking favor formation of 2D sheets and rectangular aggregates. Cross-linking between peptide chains leads to rigid rods, while cross-linking in micellar assemblies leads to reduction curvature, thereby forming cylindrical micelles. Rod-shaped structures can further stack to form columnar assemblies as their elongated, anisotropic geometry permits their preferential alignment along one spatial direction [89]. Hartgerink had employed three main design principles for customizing the peptide nanostructures that could be formed from cyclic peptide sequences [30, 59]. The cyclic peptide should contain only eight amino acid residues as shorter sequences lead to strained amide backbone, while longer sequences will be flexible. Steric interactions between the side chain and the backbone of the heterochiral alignment are prevented by designing the register of the stack in such a way that the rings will align with homochiral residues as their neighbors. Side chain–side chain interactions are manipulated using glutamine residues that play a major role in intra- and intermolecular hydrogen bonding interactions. Incorporation of non-peptide moieties into a self-assembled ensemble can lead to emergence of novel properties. For instance, the poor conductivity of self-assembled peptide nanostructures, which limits their use in sensing and diagnosis, can be overcome by the introduction of conductive polymers, enzymes, and metallic particles. Alignment and positioning of the peptide nanostructures on

a solid surface can be achieved through appropriate chemical modification of the substrate surface or peptide nanostructures, or both. Atomic force microscopy (AFM), dielectrophoresis, or optical tweezers have been employed for making appropriate connection between the self-assembled peptide nanostructures and transducers [90, 91]. Sedman et al. have used AFM as a thermomechanical lithographic tool to create indents and trenches in the self-assembled nanotubes formed by diphenylalanine and dinaphthylalanine, thus utilizing them as nanobarcodes [92]. Reches and Gazit have also tried manipulation of the peptide nanostructures using magnetic forces. Apart from modification, functionalization of the peptide nanostructures has been carried out by Rica and coworkers using dielectrophoresis (DEP) for the incorporation of antibody-functionalized peptide nanotube on top of gold electrodes for the development of label-free pathogen detection chip [72]. Schnarr et al. have created coiled-coil heterotrimeric assembly by employing electrostatic forces, and this molecular self-assembly is driven by the hydrophobic forces, while the building blocks were matched via electrostatic interactions [93].

Improving Stability of Peptide Self-Assembling Systems

Many attempts have been made to improve stability of the self-assembled ensembles through cross-linking or enhancing associative forces. Recently, self-assembled polymeric vesicles with enhanced stability, specificity, and tunability were formed from amphiphilic block copolymers with alternating hydrophilic and hydrophobic segments [44]. Introduction of a polypeptide chain in this amphiphilic block copolymer results in the formation of peptosomes [57, 94]. The peptide segments are mostly associated with the hydrophobic segments resulting in the self-assembly. The peptide WNVFDFLIVIGSIIDVILSE derived from the calcium channel forming protein CaIVS3 exhibits adhesive properties and thereby enhanced stability [95] due to the cohesive forces between the chains that are responsible for driving their association even in the absence of water. Gudlur et al. had designed two amphiphilic peptides with an oligolysine main chain (K_5). The α- and ε-amino groups were both modified with either the hydrophobic nonapeptide FLIVIGSII (h_9) or the hydrophobic pentapeptide FLIVI (h_5). These amphipathic lipid-like peptides when mixed in equimolar quantities (h_9h_5) spontaneously self-assembled to form vesicular structures in an aqueous medium. Differential scanning calorimetry studies on the h_9h_5 peptide vesicles indicated good thermal stability over a wide range of temperature, and no alteration in the structure was observed [95]. A peptide derived from human elastin consisting of hydrophobic repeats PGVGVA along with the cross-linking regions composed of polyalanine interspersed with lysine [96] formed highly insoluble nanofibers upon incubation at 37 °C. Once fibers were formed, the side chain of lysine is converted to an aldehyde by lysyl oxidase enzyme, which then reacts with neighboring primary amines to form

dehydrolysinonorleucine that then forms desmosine cross-links. These cross-linked fibers formed from a small peptide fragment of elastin exhibit good mechanical properties like resilience and strain at breaking point. Covalent capture is a recently developed strategy that integrates the design and synthesis features offered by non-covalent self-assembly along with structural integrity. This approach involves covalent bond formation for stabilizing the self-assembled supramolecular ensembles without significantly affecting their structure. The formation of covalent bonds can occur before or after self-assembly. The order of self-assembly and the covalent bond formation play an important role in determining the physical structure of the aggregate formed. If the covalent bond is formed before self-assembly, either there will be low yield or the desired molecular aggregate will not be formed. However, if the covalent bond is formed after self-assembly, the pre-organization of reacting species happens, and the covalent bond formation is also enhanced. Bilgicer et al. have employed the covalent capture method to dimerize two coiled peptides – one containing a leucine residue and the other an unnatural amino acid hexafluoro leucine at the same specific site [97]. The dimerization of the two peptide sequences containing the natural leucine and unnatural fluorinated leucine hydrophobic residues was achieved by incubating them in a glutathione buffer.

Characterization Tools

Characterization of the self-assembled peptide structures for their electrical, physical, and chemical properties is essential to determine their potential in applications. A wide range of characterization tools have been employed to elicit such information on the self-assembled structures (Table 8.2). This effort is intensifying as newer customized protocols become available with time to evaluate the performance and properties of novel peptide ensembles.

Microscopic Techniques

Different types of microscopic tools have been used to visualize the self-assemblies formed by peptides. Apart from forming nanostructures, self-assembled peptides also form micrometer scale structures that can be analyzed using polarized light, epifluorescence, and confocal microscopy [98]. While polarized light microscopy deals with birefringence and is employed to investigate the behavior of light-crystalline phases, epifluorescence and confocal microscopy are specific for the peptidic structures involving the fluorophores. Polarized light microscopy is used to identify various mesophases like nematic, cholesteric, and cubic involved in the lyotropic behavior of the nanostructures formed from the amino acid units.

Table 8.2 Information obtained from various characterization tools for peptides

Characterization technique	Information obtained
Dynamic light scattering (DLS)	Size of the nanostructures formed and investigation of the kinetics of self-assembly
Thioflavin T fluorescence	Determination of presence of beta-sheet structures. Employed in studying the mechanism of amyloid fibril formation
Surface plasmon resonance spectroscopy	Measurement of fibril growth and elongation
Atomic force microscopy	Investigation of the kinetics of self-assembly, conduct structure manipulation, determine the size and morphology of the nanostructures formed during the self-assembly
Diffraction studies	Nanofiber alignment and determination of cross β-sheet structures
Electron microscopy	Morphology of self-assembled structures
Gel electrophoresis	Determination of monomers and its subsequent polymerization into dimers, tetramers, and oligomers
Circular dichroism	Determination of secondary structure and transition between secondary structures during self-assembly process
Fourier transform infrared spectroscopy	Determination of beta-sheet structures

Epifluorescence Microscopy

Epifluorescence microscopy is a technique that is widely applied to biological systems. The sample is irradiated with electromagnetic radiation of a particular wavelength known as excitation wavelength and the longer wavelength that is emitted from the sample is then detected. In epifluorescence microscopy, both excitation and observation of the emission occur from above ('epi') the sample. This technique has been applied to detect both intrinsic fluorescence of the peptide structures and the emission from fluorophores linked to the peptide chains. The topography of the self-assembled structures formed by two amphiphilic peptidolipids derived from the 31–35 residues of the amyloid beta peptide (C_{18}-IIGLM-OH and C_{18}-IIGLM-NH$_2$) was observed using this technique [99]. Studies on the association between the FF nanotubes and pyrenyl derivatives have revealed that the final structure and its photophysical response are found to be dependent on the pH and the fluorophore concentration. When the pyrenyl concentration is low and when the pH is less or equal to 7, the structures formed are shorter and thinner, while at higher peptide concentrations and at alkaline pH, the fibrils formed are thicker [100]. These findings confirm that the final structure is due to the balance between electrostatic and hydrophobic forces. At lower pH, protonation of carboxyl groups of either pyrenyl chromophore or FF molecules occurs, and hence electrostatic interactions become weakened, while the aromatic π stacking between the aromatic rings of the pyrenyl structure dominates. At neutral pH, though the amino groups are protonated, the carboxyl groups of FF and pyrenyl

are not protonated, and hence only weak induced dipole interactions are favored. At alkaline pH, both carboxyl and amino groups are deprotonated, and hence electrostatic forces cannot compete with the hydrophobic forces resulting in side-chain contacts to form thicker fibrils [100].

Thioflavin Binding Assay

Thioflavin T (ThT) is a fluorescent molecule that binds to beta-sheet structures of peptide assemblies. The binding results in a red shift in the emission of thioflavin T from 342 to 442 nm. The presence of aromatic residues that contribute to π–π stacking interactions of the aromatic rings in ThT with the peptide causes a change in the charge distribution of ThT in its excited state causing the red shift [101]. The rigidity of the peptide structure and its flatness are additional factors that contribute to ThT binding. One of the limitations of ThT is its poor solubility in aqueous solvents. To overcome this issue, a sulfonated analogue thioflavin S (ThS) has been introduced with sulfonated groups [102]. Congo red is yet another fluorescent probe that has exhibited selective binding to the beta-sheets of amyloid and amyloid-like fibrils [103].

Confocal Laser Scanning Microscopy

Confocal laser scanning microscopes (CLSMs) provide high in-plane resolutions by restricting entry of out-of-focus light by employing a pinhole for illumination of a sample, thus making it an attractive tool for investigating peptide self-assemblies. They are mainly used in 3D reconstruction of images recorded at different slices along the z direction. The imaging of the peptide nanostructures formed has been accomplished by using confocal laser scanning microscopy (CLSM). FF microtubes labeled with rhodamine B were imaged using CLSM [104], and this technique has been used to identify the hydrophobic-rich and hydrophilic-rich regions by labeling FF structures with two fluorescence dyes, namely, rhodamine and phthalocyanine. Since rhodamine is relatively hydrophilic, it was localized in the inner core of the peptide assembly, which consists of hydrophilic clusters. Phthalocyanine was found in the hydrophobic external wall of FF nanostructures. The CLSM enabled visualization of both the hydrophilic and hydrophobic clusters by reconstructing the images in 3D. Similarly, the distribution of the peptide amphiphiles C_{16}-VVVAAAGGKLAKKLAKKLAKKLAK and C_{16}-VVVAAAKKK in a hyaluronic acid membrane was imaged using CLSM [105]. The peptide amphiphiles were modified with a fluorophore at the N-terminus to enable imaging. The z-sectioning served to understand the localization of the peptide self-assemblies within the membrane. The effect of the nanofibers formed by the self-assembly of glucagon-like peptide 1 (GLP-1) mimetic peptide amphiphiles on the cell viability and proliferation of rat insulinoma cells were investigated using CLSM. The CLSM

technique has been extensively used as a powerful tool to investigate cell morphology, migration, and proliferation. The influence of a self-assembled scaffold formed from an ionic complementary peptide modified with biorecognition motifs on the cell morphology, spreading, and migration was investigated using CLSM. The results indicated that the designer peptides modified with cell adhesion motif from osteopontin and signaling motif from osteogenic signaling peptide promoted excellent growth and proliferation of osteoblasts.

Atomic Force Microscopy

Scanning probe microscopies, especially the atomic force microscopy (AFM), have been widely used to investigate the geometry of the self-assembled nanostructures, to measure their conductivity, and to determine the Young's modulus and thermal stability of the structures under dry conditions. The AFM contains a probe attached to a flexible cantilever, and as the probe moves over the sample at a preset rate, the force of interactions between the probe tip and the sample surface is measured, and the topography of the sample is constructed. The deflections in the cantilever are recorded by monitoring the reflection of a laser beam focused on the cantilever and recorded through a photosensitive photodiode. This technique offers atomic level resolution and can be a very valuable tool in research on self-assembled structures. The probe tip, generally in the range of 10 nm, can be conducting or nonconducting and can be functionalized to investigate specific interactions. The material of the probe and its geometry are vital in determining its performance. The data acquisition in AFM can be made in the contact mode or noncontact mode or tapping mode. One of the challenges involved in using AFM technique is to study peptide self-assembly in solution as it requires sufficient adhesion with the substrate. Generally, AFM had been extensively employed to study the morphology of the aggregates formed by the self-assembly of peptides. Chaudhary et al. had investigated the propensity of two sequences derived from the amyloid tau protein Ac-VQIVYK-amide and Ac-QIVYK-amide to form beta-sheets in the presence of different solvents using AFM [106]. The results revealed that the Ac-VQIVYK-amide existed both as alpha helices and beta-sheets and the nature of the solvent was a key determinant of the form in which the peptide aggregates existed. The formation of the supramolecular assemblies by the peptide can also be monitored in a time-dependent manner using the AFM probe. Time-lapse liquid imaging of amyloid fibrils has been employed for kinetic studies on the rate of formation as well as morphological changes introduced in the amyloid peptide during the aggregation process under various self-assembling conditions [107].

For the determination of Young's modulus, the AFM tip is positioned on the top of the structure and pressed. From the force–distance curves, the Young's modulus can be directly derived using the theoretical model proposed by Niu et al. [108]. However, this model has a limitation since it depends on the type of

structure that can be assumed. For example, if it is a hollow structure rather than a solid, then the Young's modulus calculated using this model will exhibit significant deviations from the actual value. Knowles et al. have used another approach to understand the rigidity and mechanical strength of the self-assembled amyloid fibrils on mica substrate [109]. The topography of more than 900 fibrils was imaged using AFM and the shape fluctuations were used to compute the bending rigidity (C_B) of the fibrils. The cross-sectional moments of inertia (I) were computed for each fibril based on their height measured using AFM. The Young's modulus (Y) was then computed as $Y = C_B/I$. These values range between 2 and 14 GPa for most protein fibrils. The Young's modulus for the completely self-assembled amyloid fibrils falls in the range 13 and 42 GPa. The elastic modulus of the peptide assemblies can be further dissected into contributions from the backbone as well as the side chains, i.e. $Y = Y_{BB} + Y_{SC}$ where Y_{BB} and Y_{SC} are contributions from the peptide backbone and side chains, respectively. The computed results suggest that the contribution of the backbone interactions towards the elastic modulus is more than twice that of the side chains. In the case of amyloid fibrils, the contribution of Y_{BB} is about 74 %. It is also postulated that peptide structures with moduli greater than 22 GPa have significant contributions from the involvement of side chains in hydrogen bonding. In the absence of significant intermolecular hydrogen bonding in the peptide structures, the surface tension arising due to the hydrophobic and hydrophilic residues can also be employed to determine the Young's modulus using the relation $Y = 2\gamma/h$ where γ is the surface tension and h is the inter-sheet spacing with values in the range of 8 and 12 Å. For the observation of thermal stability of the nanostructures under dry conditions, the AFM tip is positioned above the structures and the position of the tip is monitored with increase in temperature. At a particular temperature, as the structure degenerates, the tip will move downward which gives an indication of the maximum temperature beyond which the nanostructure will lose its stability. Transthyretin fibrils have been examined for their stability after prolonged exposure to high temperatures using AFM, and it was found that the thermal stability of the pre-fibrillar aggregates was poor when compared to the fibrillar assemblies [110].

Electron Microscopy

Electron microscopic techniques, which include scanning and transmission electron microscopy, are commonly employed tools for imaging self-assembled structures. Focused ion beam milling techniques were also recently employed to characterize the nanostructures. Scanning electron microscopy (SEM) is usually used to determine the geometry of the nanostructure. However, the presence of any defects or cavities in the structure can be better visualized using transmission electron microscopy (TEM) where high-energy electrons pass through the nanostructures and the final image is reconstructed by mapping the intensities of electrons from each point in the sample. The more conducting regions in the sample will therefore appear dark when compared with regions with some resistance to the passage of electrons.

The imaging is usually done in ultrahigh vacuum of the order of 10^{-9} Pa. The main advantages of electron microscopy techniques when employed for visualizing the morphology of the peptide structures are ease of implementation, high magnification, resolution, and its ability to image a range of dimensions ranging from sub-nanometric to micrometric scales. These prospects are possible due to the smaller wavelength of electrons employed when compared to the visible light. The scanning electron microscopic technique when applied to nonconducting samples such as peptide nanostructures requires a thin coating of an inert metal such as platinum or gold to enable generation of the image. Otherwise, the electrons will remain on the surface of the sample making the visualization of the finer structures on the sample impossible. In the case of transmission electron microscopy, there is a restriction in the thickness of the sample that can be imaged. Samples less than 0.1 μm alone can be imaged using transmission electron microscopy, as thicker samples will not permit transmission of the electrons. It is not advisable to use accelerating voltages beyond 10 kV in scanning electron microscopy for analyzing peptide nanostructures. Similarly, in transmission electron microscopy, very high voltages will lead to damage of the peptide structures. Apart from giving information on the morphology of the aggregates, the dimensions of the individual self-assembled structures can also be obtained from the electron microscopy techniques. The thermal stability of the structure can also be investigated using SEM where after exposing the nanostructure to particular temperature, the structures can be imaged to observe any deformations postexposure to high temperature. The strength of the structure can be determined using SEM combined with FIB source (FIB – focused ion beam). The nanostructure is placed inside FIB SEM and the time taken to mill the sample is analyzed [111]. By comparing the time with the standard materials, the stability of the structure can be determined. The incorporation of metallic compounds in the peptide assemblies can be imaged using TEM. For instance, TEM was employed to determine the presence of CuO within the nanotubes due to the enhanced contrast provided by the metallic compounds [112]. Recently modified FF peptide nanotubes were used for the determination of the neurotransmitter dopamine. The FF nanotubes were modified with cyclic-tetrameric copper (II) species containing the ligand (4-imidazolyl)-ethylene-2-amino-1-ethylpyridine $[Cu_4(apyhist)_4]^{4+}$ (apyhist refers to the ligand 2-(1H-imidazol-4-yl)-N-(1-(pyridin-2-yl)ethylidene)ethanamine) in Nafion membrane on a glass carbon electrode. The morphology of the modified tubes imaged using scanning electron microscopy revealed tubular structures of thickness around 350–500 nm. The deposition of the Nafion membrane on the nanotubes was also clearly distinguished [113].

Circular Dichroism

Circular dichroism (CD) is a technique that is applied to optically active chiral molecules such as proteins and peptides. It is based on the principle of differential absorption of right and left circularly polarized light by the chiral

molecule. CD spectroscopy is an invaluable tool to identify the secondary structures adopted by a peptide during the self-assembly process. The exact location of the alpha helices or beta-sheets or random coils can be identified by this technique, and it provides information on the structural transformations that can occur during the self-assembly process under different conditions. Hauser et al. have used this technique to show that the self-assembly process proceeds through structural transition that may occur in three possible steps based on the peptide concentration [114]. The peptide monomers interact via antiparallel pairing which is followed by a structural transition to α-helical conformation. The peptide pairs assemble to form fibers and condense to form fibrils. The assembly of the peptide monomers serves as the nucleation step, which then proceeds to form fibrils via nucleation-dependent polymerization mechanism. The assembly of peptide monomers, however, requires a transition from random coil to α-helical conformation. Though it is reported that short peptides of 3–6 amino acids cannot form α-helical conformation, it is indeed possible above a threshold concentration. The CD spectra also demonstrated that at low concentrations, the peptides were stable up to 90°C and changed its random coiled structure as the temperature is increased from 25°C to 90°C. This change was reversed on cooling. However, once the fibril is formed, the peptide ensembles adopt β-turn structures, and no reversal in conformation is observed upon changing the temperature. Circular dichroism has also been widely used to study the kinetics involved in the formation of a peptide network. It was used to show that the beta-sheet structures progressively increase with concomitant reduction in helical coils in peptides with a propensity to form fibers [114]. Zhang et al. had reported that the ionic complementary peptide EAK16 formed a macroscopic membranous structure due to extensive beta-sheet formation [56]. The membrane formation propensity was retarded in the dodecapeptide EAK12, while the octapeptide EAK8 did not form membranous structure. Investigations with CD spectroscopy revealed that the EAK16 formed beta-sheets extensively, while EAK 12 had both alpha helix and beta-sheets and EAK8 had only random coils. Similarly CD spectroscopic studies on the self-assembly of KFE8 (FKFEFKFE) revealed the presence of left-handed double helical beta-sheets that could represent a new category of molecular materials.

X-Ray Diffraction

The properties of the peptide bond can be studied using X-rays. Linus Pauling and Robert Corey were the first to report the length of C–N bond in the peptide link. They also found that the peptide bond is planar, i.e. all the four atoms in the peptide bond are located in the same plane and the α-carbon atoms attached to the C and N are in *trans* conformation. The structural and functional

relationships in the fibrous protein in wool were established using X-ray diffraction patterns by William Astbury [115]. X-ray diffraction has been now employed to determine the crystal structure of any newly synthesized peptide. It has also been used to calculate the bond distances and bond angles between the moieties in the peptide. Based on the torsion angle measurements, it is also possible to predict the secondary structure conformation adopted by the peptide. Moreover, the forces that stabilize the crystal structure such as van der Waals and hydrogen bonding interactions can also be predicted. X-ray diffraction technique is also employed to determine the ultrastructural organization found in self-assembled peptide structures. Nanofibrillar arrangement results in characteristic diffraction patterns that reveal the presence of cross β-sheet structures. The meridional and equatorial reflections have been used to identify the amyloid structure. The spacing between the hydrogen-bonded β-strands results in meridional reflection at 4.7–4.8 Å, and the distance between the β-sheets contributes to an equatorial reflection at 10 and 11 Å [116]. The main challenge in employing X-ray diffraction techniques is that it is difficult to obtain pure crystals of many self-assembled structures. The X-ray data is usually obtained using a beam wavelength of 0.975 Å and an extremely small beam size of about 5 μm. Generally, the crystals need to be cooled to about 100 K for data recording. Localized radiation damage to the crystals could be avoided by illuminating the peptide crystals at different locations.

Computational Studies

Due to the high degree of complexity involved in understanding the mechanism of self-assembly, various theoretical and computational methods have also been employed. These techniques not only help in understanding the mechanism but also to design the new sequences with the selected properties for nanobiotechnological applications. In particular, molecular dynamic simulations have been used to monitor the dynamics and investigate the influence of mutations and solvent effects in the conformational transition from alpha helices into beta-sheet structures [117]. Various algorithms and theories have been developed to investigate the properties of complex biomolecular systems at different levels. Due to the high degree of complexity involved along with the small time scales, coarse-grained models were used to follow the actual process [118]. However, in this model, fine atomic details are neglected and only relevant degrees of freedom of peptide molecule are retained. Activation relaxation technique is a subcategory of the coarse-grained model, where the interactions among several peptide chains were simulated ab initio with no bias in original orientation and conformation. Molecular dynamics studies have now been employed to address peptide self-assembly [119]. These simulations have certain advantages such as ability to mimic the actual self-assembly of the peptide residues, reveal the structural

information at an atomic level of the peptide, and provide a dynamic molecular model at atomic level of ordered assembly. However, there are certain limitations associated with this technique, too, such as a limited resolution, strong dependency of the quality of predictions on the size of the peptide, and the limited number of peptide residues for which such predictions could be made. Several computational approaches have been used to predict the aggregation propensity of the proteins. For example, a computer program named TANGO considers the secondary structure and the desolvation penalty of the residues for calculating the aggregation propensity [120].

Other Techniques

All the techniques discussed thus far are used to characterize the nanostructures in dry conditions. However, stability of the structures differs when they are analyzed in wet conditions. To determine the stability of the nanostructures in wet conditions, they are submerged in aqueous solution, and the concentration of monomers is monitored with time using high-performance liquid chromatography (HPLC). The increase in the concentration of monomers with time is an indication that the nanostructures are dissolving in the medium and are, therefore, not stable. High-performance liquid chromatography has also been employed to identify impurities associated with the peptide after synthesis [121]. Microrheometry technique is widely used to perform measurement on weak hydrogels without affecting their structural components. The measurements are very fast, and the experiments are not affected by external factors as they carried out in a closed chamber. Recently, multiple particle-tracking microrheology experiments were used to follow the hydrogel formation by the peptide KFE8 [122]. Fourier transform infrared spectroscopy (FTIR) analysis reveals the presence of parallel or antiparallel beta-sheets and nature of hydrogen bonds in the self-assembled structures. Differential scanning calorimetry (DSC) and thermogravimetric analysis (TGA) are used to determine the effect of temperature on the self-assembled structures. While DSC gives information on the phase transition temperatures of the peptide assembly, TGA provides information on the degradation profile of the assemblies. Crystallographic studies have also been carried out to understand the mechanism of self-organization. Biocompatibility and immunogenicity of the self-assembled peptide structures have to be evaluated before their use in biological systems. Both in vitro and in vivo studies need to be carried out to evaluate the biocompatibility of a peptide assembly. The self-assembled structure fabricated using the *Fmoc*-diphenylalanine peptide was used as a scaffold to grow Chinese hamster ovary (CHO) cells. The cell viability analyzed using MTT assay showed that 90 % of the cells were viable, suggesting that the peptide scaffold is biocompatible. More in-depth biocompatibility and immunogenicity assessment is however necessary to eliminate any potential risk of using these structures for biomedical applications [123].

Applications of Self-Assembled Peptides

The unique reproducible structures obtained through self-assembly of peptide sequences have many interesting applications in biological and nonbiological fields. Figure 8.8 depicts multiple applications that can arise from a cyclic peptide. A few of them are highlighted in the following sections.

Peptide Nanostructures as Model Systems

Peptide systems that form nanofibrils similar to those formed by the amyloid beta peptide have been investigated extensively to understand the mechanism of formation of amyloid fibrils. Amyloid fibril formation has been implicated in a wide range of degenerative diseases like Alzheimer's, Parkinson's, type II diabetes, and other prion-related diseases [124–127]. The switch peptides have also been employed to find information about the interactions between the various proteins involved in the pathology of protein conformation diseases like scrapie, kuru, Huntington's, Parkinson's, and Alzheimer's disease [128, 129]. Amyloid fibrils are formed by various peptides such as the full-length human islet amyloid polypeptide (hIAPP), NFGSVQ peptide fragment from medin, and FF peptide from Alzheimer's amyloid beta peptide. NFGAIL a hexapeptide fragment from islet amyloid polypeptide is reported to form well-ordered amyloid fibrils
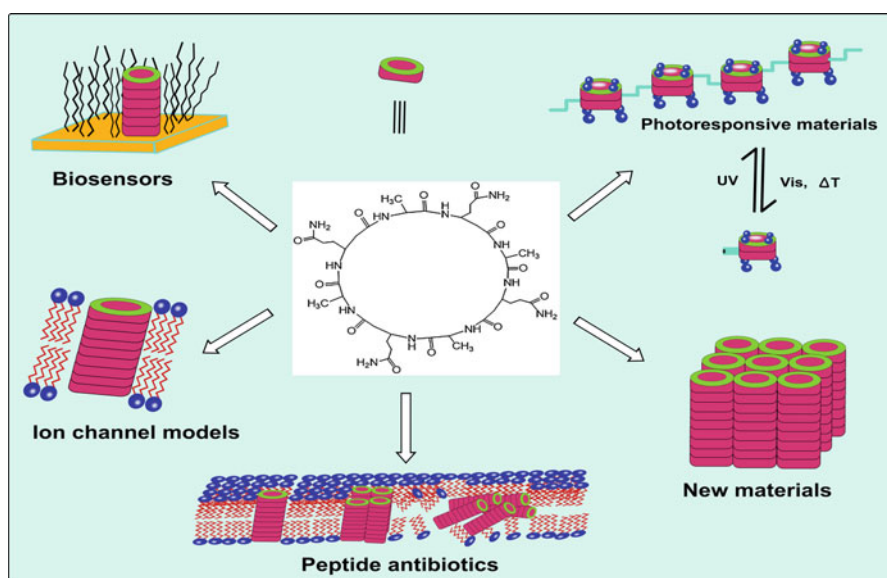
Fig. 8.8 Various biomedical applications of peptide nanotubes formed by cyclic peptide

which exactly mimics those formed by the parent peptide [130]. Two active amyloidogenic peptides, namely, NFLVH fragment of hIAPP and NFGSVQ fragment derived from aortic medial amyloid, also formed fibrils. Another peptide from the human calcitonin, namely, NH$_2$-DFNKF-COOH, is also reported to form amyloid fibrils similar to those formed by the parent protein [56]. A short truncated tetrapeptide, namely, NH$_2$-DFNK-COOH, also formed fibrils, which clearly shows there is no correlation between hydrophobicity and amyloidogenic potential since most of the short peptides are relatively hydrophilic. These results were further supported by Johansson et al., who studied charged tetrapeptides and proved hydrophobicity is not sufficient for fibril formation [131]. Peptide legos (RADA, EAK), peptide amphiphiles, bolaamphiphiles, peptide conjugates, ionic self-complementary peptides, and long-acting gonadotropin-releasing hormone have all been reported to self-assemble into amyloid fibril structure. Many peptides derived from the Alzheimer's amyloid beta peptide also been shown to form fibrils. These include AAKLVFF, KLVFFAE, ßAßAKLVFF, YYKLVFFC, FFKLVFF-PEG, FFKLVFF, Ac-KLVFFAE-NH$_2$, FF, and YYKLVFF-PEG [132–135]. It has been concluded that alternating binary patterns and the peptides with high beta-sheet propensity are prone to form amyloid structures. Gazit and coworkers have identified that aromatic amino acids play an important role in amyloid fibril formation through π–π stacking interactions [136]. Custom-made peptides used as model systems should possess strong electrostatic binding with the negatively charged lipid membranes and should exhibit structural transition from random coil to beta-sheet on binding to lipid membranes which initiates the association and the formation of oligomers and larger aggregates.

Apart from utilizing the self-assembling peptides to understand the pathological mechanism, it is also used to understand the functions and mechanisms of assembly of proteins like collagen. Tobacco mosaic virus (TMV) is also a form of supramolecular structure assembled from a single strand of mRNA along with many copies of identical coat proteins, which organize to form rod-like shape. This TMV has been used by Schlick et al. for the construction of nanoscale materials without disrupting its self-assembly [137]. Peptide molecules also have the ability to self-organize at the air–water interface, which are widely used for mineralization studies because of its resemblance to insoluble proteins found in nature.

Tissue Engineering Applications

Self-assembling peptides have gained considerable interest in the field of tissue engineering because functional tissue recovery has been observed in brain and heart lesions [138, 139]. One common example is the incorporation of cell adhesion motif RGD in the peptide sequence, which improves the cell adhesion onto the self-assembled structures formed by peptide amphiphiles. Collagen-mimetic peptide amphiphiles, which self-assemble into nanofibers that exactly mimic the structural and biological properties of the native collagen, have been widely used in tissue regeneration as natural collagen is immunogenic and

difficult to process [140]. Molecular lego peptides, such as RAD 16-I and EAK 16, have been used as scaffolds for neurite outgrowth, hepatocyte regeneration, etc. [146]. Chondrocytes encapsulated in a peptide scaffold using a self-assembled peptide with the sequence (Ac-KLDLKLDLKLDL-NH$_2$) exhibited excellent phenotype and secreted its own growth factors within 4 weeks of culture [147].

Drug Delivery Systems

Peptide nanovesicles have been employed as drug carriers and it is believed that these nanovesicles enter the cells via endocytosis mechanism and thus can deliver drugs, genes, etc. [95]. Hydrogelating self-assembling fibers (hSAFs) designed by Woolfson and group using coiled-coil assemblies had limited use as a drug delivery system due to the limitation of rapid drug release. However, this was overcome by incorporating an anionic polyelectrolyte in the cationic peptide [148]. Ghosh et al. designed a smart self-assembling peptide amphiphile that transforms from a linear or spherical form to fibrous form upon altering the pH for drug delivery and in vivo imaging applications [149].

Peptide Assemblies as Therapeutic Agents

The nanotubes formed by cyclic peptides comprising D- and L-amino acids serve as ion channels and form pores in the membranes leading to disruption of the cell architecture. As D-amino acids are taken up preferentially by microbes, these systems can function as effective antimicrobial agents which kill the microorganisms through formation of pores in the cell membrane, thereby causing osmotic collapse [150]. MacKay et al. have created a chimeric polypeptide consisting of an elastin-like polypeptide (ELP) fragment and a short cysteine-rich fragment for the treatment of cancer [151]. The drug conjugated with the cysteine residue drives the self-assembly that finally forms a drug-rich core and a hydrophilic peptide corona. Instead of a drug, the self-assembly can also be triggered by linking the hydrophobic cholesterol moieties with hydrophilic cell penetrating peptides consisting of six arginine residues. These peptide nanoparticles have antimicrobial properties and were shown to effectively terminate the bacterial growth in the infected brains of the rabbits. Beta-sheet-rich peptide nanofibers functionalized with B-cell and T-cell epitopes have been developed for immunization [152]. These functionalized nanofibers developed antibodies in mice when injected with saline, and the levels were comparable with those injected with complete Freund's adjuvant. Protection against the beta-sheet-rich peptide nanofibers lasted for a year and the antibody response is T-cell dependent. Recently, self-assembling peptide/protein nanoparticles have been used as antigen display systems for the development of vaccines. For example, a fragment of the surface protein of severe acute respiratory syndrome coronavirus (SARS-CoV) was incorporated in a self-assembling peptide nanofiber in the native trimeric coiled conformation [153].

Antibody formation was elicited when these peptide structures were injected into the mice, and the antibodies were conformation specific as determined by qualitative enzyme-linked immunosorbent assay.

Sensors

Peptide nanofibers have been extensively investigated as the next-generation biosensors where they are used both as a fabrication material and also as a component in the final system (BioFET) [86]. Nanotubes coated with proteins, nanocrystals, and metalloporphyrins by hydrogen bonding have been employed as chemical sensors. These nanotubes also served to improve the catalytic activity of the enzymes like lipase. Apart from using FF nanotubes as a template for the fabrication of nanowires, they have also been used for biosensing where FF nanotubes are deposited on the surface of screen-printed graphite and gold electrodes for improving the sensitivity. It is also reported that these electrodes exhibit greater sensitivity compared to those electrodes modified with carbon nanotubes. The possible reason may be that the FF nanotubes increase the functional surface area of the electrode. Electrical and magnetic fields have been used to align FF nanotubes. Apart from this, patterning of the FF tubes has been carried out using inkjet technology, machined by thermomechanical lithography via atomic force microscopy, manipulated and immobilized using dielectrophoresis, and arranged on the surfaces by low electron irradiation [31]. Nanotubes are also used in the detection of pathogens, neurotoxins, glucose, ethanol, and hydrogen peroxide and as an immunosensor [72]. Peptide nanofibers have been reported for the detection of copper, dopamine, *Yersinia pestis*, glucose, etc. [141, 154–155] (Fig. 8.9).

Other Applications

Amyloid-forming peptides are used in the field of nanoelectronics as nanowires. For example, FF nanotubes are used as a template for silver nanowires of diameter of approximately 20 nm. Switch peptides find application in molecular electronics by serving as a nanoswitch [142]. Ryu et al. developed photoluminescent peptide nanotubes by incorporating luminescent complexes composed of photosensitizers like salicylic acid. Kasotakis et al. employed self-assembled peptides as a scaffold for the introduction of metal-binding residues at specific locations within the structure [143]. An octapeptide from the fiber protein of adenovirus was used to design cysteine-containing octapeptides that can bind to silver, gold, and platinum nanoparticles. These metal-decorated fibers were employed in photodynamic therapy and also used in the development of surface-enhanced Raman-scattering biosensors for detecting DNA. Lipid-like peptides find application in solubilizing, stabilizing, and crystallizing membrane proteins, used for drug formulations and also as model systems for studying protein conformational diseases [144]. Velcro peptides have been mainly used to study cell–cell communication and cell behavior [145].
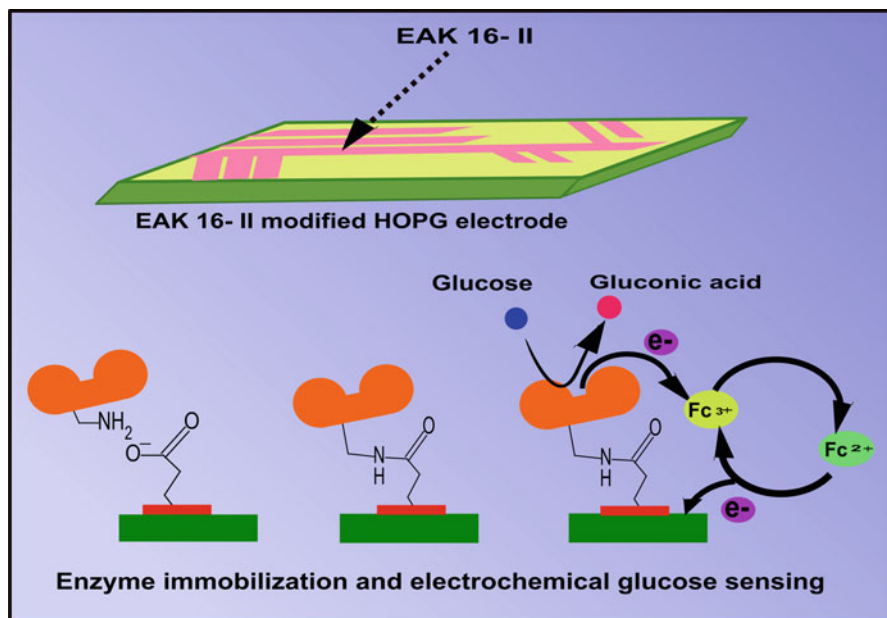
Fig. 8.9   Self-assembled EAK 16-II nanostructures used in electrochemical glucose sensing
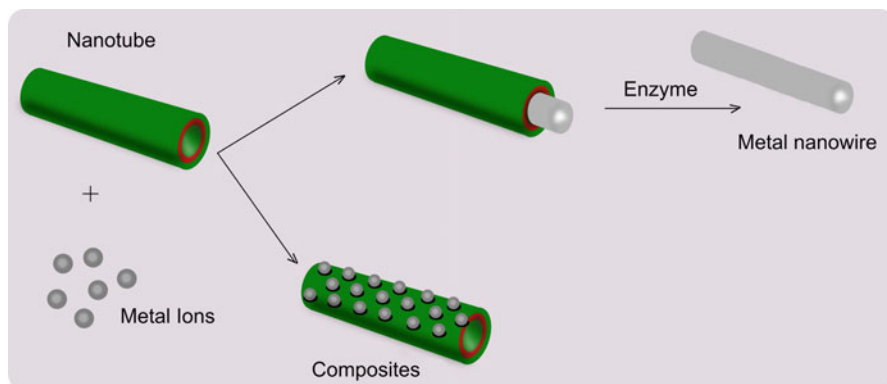
Fig. 8.10   Template-assisted synthesis of metal nanowire

FF nanotubes are used as an etching mask for the fabrication of silicon nanowires. It reduces fabrication time, cost, and use of aggressive chemicals. It is also possible to scale up these arrays of FF nanotubes by vapor deposition methods. Self-assembling peptide nanostructures have also been used as photosynthetic devices, and the peptide Ac-KLVFFAE-NH$_2$ is reported to form nanotubes.

Precise ordering of strong chromophores along the inner and outer walls of the nanotubes enables utilization of this peptide structure as nanoscale antennas and photosynthetic device [156]. The peptide nanofibers can also serve as a template for the growth of inorganic materials such as silver, gold, platinum, cobalt, nickel, and various semiconducting materials (Fig. 8.10).

Conclusions

An in-depth understanding of the molecular self-assembling mechanism of peptides and various stabilizing forces associated with the overall stability of the nanostructures formed by them is essential to design novel applications using these peptides. Various classes of self-assembling peptides have been developed that have led to emergence of novel applications in the fields of tissue engineering, drug delivery, electronics, etc. Different characterization tools have been designed to decipher the structural and functional aspects of the self-assembled peptide structures. The field of self-assembly continues to expand and has opened up new vistas for further research.

References

1. Harada A, Li J, Kamachi M (1993) Synthesis of a tubular polymer from threaded cyclodextrins. Nature 364:516–518
2. Yan X, Cui Y, Qi W et al (2008) Self-assembly of peptide-based colloids containing lipophilic nanocrystals. Small 4:1687–1693
3. Yan X, He Q, Wang K et al (2007) Transition of cationic dipeptide nanotubes into vesicles and oligonucleotide delivery. Angew Chem Int Ed 46:2431–2434
4. Yemini M, Reches M, Rishpon J et al (2005) Novel electrochemical biosensing platform using self-assembled peptide nanotubes. Nano Lett 5:183
5. Yan X, Zhu P, Li J (2010) Self-assembly and application of diphenylalanine based nanostructures. Chem Soc Rev 39:1877–1890
6. Bromley EH, Channon K, Moutevelis E et al (2008) Peptide and protein building blocks for synthetic biology: from programming biomolecules to self-organized biomolecular systems. ACS Chem Biol 3:38–50
7. Zhang S (2002) Emerging biological materials through molecular self-assembly. Biotechnol Adv 20:321–329
8. Zhang S (2003) Fabrication of novel materials through molecular self-assembly. Nat Biotechnol 21:1171–1178
9. Zhang S, Zhao X (2004) Design of molecular biological materials. Using peptide motifs. J Mater Chem 14:2082–2086
10. Zhao X, Zhang S (2004) Building from bottom up: fabrication of molecular materials using peptide construction motifs. Trends Biotechnol 22:470–476
11. Yu YC, Pakalns T, Dori Y et al (1997) Construction of biologically active protein molecular architecture using self-assembling peptide-amphiphiles. Methods Enzymol 289:571–587
12. Fields GB (1999) Induction of protein-like molecular architecture by self-assembly. Bioorg Med Chem 7:75–81
13. Kumar P (2010) Directed self-assembly: expectations and achievements. Nanoscale Res Lett 5:1367–1376

14. Yang Y, Khoe U, Wang X et al (2009) Designer self-assembling peptide nanomaterials. Nano Today 2:193–210
15. Mitchell JC, Harris JR, Malo J et al (2004) Self-assembly of chiral DNA nanotubes. J Am Chem Soc 126:16342–16343
16. Rothemund PW, Ekani-Nkodo A, Papadakis N et al (2004) Design and characterization of programmable DNA nanotubes. J Am Chem Soc 126:16344–16352
17. Schnur JM (1993) Lipid tubules: a paradigm for molecularly engineering structures. Science 262:1669–1676
18. Spector MS, Singh A, Massersmith PB et al (2001) Chiral self-assembly of nanotubules and ribbons from phospholipid mixtures. Nano Lett 1:375–378
19. Benner K, Klüfers P, Schuhmacher J (2003) Hydrogen-bonded sugar-alcohol trimmers as hexadentate silicon chelators in aqueous solution. Angew Chem Int Ed 42:1058–1062
20. Gattuso G, Menzer S, Nepogodiev SA et al (2003) Carbohydrate nanotubes. Angew Chem Int Ed 36:1451–1454
21. Aizenberg J, Fratzl P (2009) Biological and biomimetic materials. Adv Mater 21:387–388
22. Sanchez C, Arribart H, Guille MM (2005) Biomimetism and bioinspiration as tools for the design of innovative materials and systems. Nat Mater 4:277–288
23. Palmer LC, Newcomb CJ, Kaltz SR et al (2008) Biomimetic systems for hydroxyapatite mineralization inspired by bone and enamel. Chem Rev 108:4754–4783
24. Ariga K, Hill JP, Lee MV et al (2008) Challenges and breakthroughs in recent research on self-assembly. Sci Technol Adv Mater 9:014109
25. Nie Z, Kumacheva E (2008) Patterning surfaces with functional polymers. Nat Mater 7:277–290
26. Ajayaghosh A, Praveen VK, Vijayakumar C (2008) Organogels as scaffolds for excitation energy transfer and light harvesting. Chem Soc Rev 37:109–122
27. He Q, Duan L, Qi W et al (2008) Microcapsules containing a biomolecular motor for ATP biosynthesis. Adv Mater 20:2933–2937
28. Gazit E (2007) Self-assembled peptide nanostructures: the design of molecular building blocks and their technological utilization. Chem Soc Rev 36:1263–1269
29. Ulijn RV, Smith AM (2008) Designing peptide based nanomaterials. Chem Soc Rev 37:664–675
30. Jun HW, Paramonov SE, Dong H et al (2008) Tuning the mechanical and bioresponsive properties of peptide-amphiphile nanofiber networks. J Biomater Sci Polym Ed 19:665–676
31. Ghadiri MR, Granja JR, Milligan RA et al (1993) Self-assembling organic nanotubes based on a novel cyclic peptide architecture. Nature 366:324–327
32. Gazit E (2002) Role of π-π stacking in the self-assembly of amyloid fibrils. FASEB J 16:77–83
33. Kumaraswamy P, Lakshmanan R, Sethuraman S et al (2011) Self-assembly of peptides: influence of substrate, pH and medium on the formation of supramolecular assemblies. Soft Matter 7:2744–2754
34. Castillo-León J, Andersen KB, Svendsen WE (2011) Self–assembled peptide nanostructures for biomedical applications: advantages and challenges, biomaterials science and engineering, Prof. Rosario Pignatello (ed). ISBN: 978-953-307-609-6, InTech, DOI:10.5772/23322
35. Castillo J, Tanzi S, Dimaki M et al (2008) Manipulation of self-assembly amyloid peptide nanotubes by dielectrophoresis. Electrophoresis 29:5026–5032
36. Zhang S, Lockshin C, Herbert A et al (1992) Zuotin, a putative Z-DNA binding protein in *Saccharomyces cerevisiae*. EMBO J 11:3787–3796
37. López De La Paz M, Goldie K, Zurdo J et al (2002) De novo designed peptide-based amyloid fibrils. Proc Natl Acad Sci U S A 99:16052–16057
38. Ikeda M, Tanida T, Yoshi T et al (2011) Rational molecular design of stimulus-responsive supramolecular hydrogels based on dipeptides. Adv Mater 25:2819–2822
39. Han TH, Park JS, Oh JK et al (2008) Morphology control of one-dimensional peptide nanostructures. J Nanosci Nanotechnol 8:5547–5550

40. Kar K, Wang YH, Brodsky B (2008) Sequence dependence of kinetics and morphology of collagen model peptide self-assembly into higher order structures. Protein Sci 17:1086–1095
41. Fishwick CWG, Beevers AJ, Carrick LM et al (2003) Structures of helical beta-tapes and twisted ribbons: the role of side-chain interactions on twist and bend behavior. Nano lett 11:1475–1479
42. Fung SY, Keyes C, Duhamel J et al (2003) Concentration effect on the aggregation of a self-assembling oligopeptide. Bio Phys J 85:537–548
43. Khoe U, Yang Y, Zhang S (2009) Self-assembly of nanodonut structure from a cone-shaped designer lipid-like peptide surfactant. Langmuir 25:4111–4114
44. Zhao X, Zhang S (2006) Molecular designer self-assembling peptides. Chem Soc Rev 35:1105–1110
45. Hol WG, Halie LM, Sander C (1981) Dipoles of the alpha-helix and beta-sheet: their role in protein folding. Nature 294:532–536
46. Whitesides GM, Grzybowski B (2002) Self-assembly at all scales. Science 295:2418–2421
47. Vauthey S, Santoso S, Gong H et al (2002) Molecular self-assembly of surfactant-like peptides to form nanotubes and nanovesicles. Proc Natl Acad Sci USA 99:5355–5360
48. Santoso S, Hwang W, Hartman H et al (2002) Self-assembly of surfactant-like peptides with variable glycine tails to form nanotubes and nanovesicles. Nano Lett 2:687–691
49. von Maltzahn G, Vauthey S, Santoso S et al (2003) Positively charged surfactant-like peptides self-assemble into nanostructures. Langmuir 19:4332–4337
50. Yang S, Zhang S (2006) Self-assembling behavior of designer lipid-like peptides. Supramol Chem 18:389–396
51. Adams DJ, Holtzmann K, Schneider C et al (2007) Self-assembly of peptide surfactants. Langmuir 23:12729–12736
52. Xu H, Wang J, Han S et al (2009) Hydrophobic region induced transitions in self-assembled peptide nanostructures. Langmuir 25:4115–4123
53. Brack A, Orgel LE (1975) ß structures of alternating polypeptides and their possible prebiotic significance. Nature 256:383–387
54. Zhang S, Yan L, Altman M et al (1999) Biological surface engineering: a simple system for cell pattern formation. Biomaterials 20:1213–1220
55. Minor DL Jr, Kim PS (1996) Context-dependent secondary structure formation of a designed protein sequence. Nature 380:730–734
56. Altman M, Lee P, Rich A et al (2000) Conformational behavior of ionic self-complementary peptides. Protein Sci 9:1095–1105
57. Mart RJ, Osborne RD, Stevens MM et al (2006) Peptide-based stimuli-responsive biomaterials. Soft Matter 2:822–835
58. Ketchem RR, Hu W, Cross TA (1993) High-resolution conformation of gramicidin A in a lipid bilayer by solid-state NMR. Science 261:1457–1460
59. Hartgerink JD, Granja JR, Milligan RA et al (1996) Self-assembling peptide nanotubes. J Am Chem Soc 118:43–50
60. Valéry C, Paternostre M, Robert B et al (2003) Biomimetic organization: octapeptide self-assembly into nanotubes of viral capsid like dimension. Proc Natl Acad Sci USA 100:10258–10262
61. Gour N, Kedracki D, Safir I et al (2012) Self-assembling DNa-peptide hybrids:morphological consequences of oligopeptide grafting to a pathogenic amyloid fibrils forming dipeptide. Chem Commun 48:5440–5442
62. Raguse TL, Lai JR, LePlae PR et al (2001) ß-peptide helix bundles. Org Lett 3:3963–3966
63. Cheng RP, DeGrado WF (2002) Long-range interactions stabilize the fold of a non-natural oligomer. J Am Chem Soc 124:11564–11565
64. Das R, Kiley PJ, Sega M et al (2004) Integration of photosynthetic protein molecular complexes in solid-state electronic devices. Nano Lett 4:1079–1083
65. Kiley P, Zhao X, Vaughn M et al (2005) Self-assembling peptide detergents stabilize isolated photosystem I. PLoS Biol 3:1180–1186

66. Nagai A, Nagai Y, Qu H et al (2007) Dynamic behaviors of lipid-like self-assembling peptide A6D and A6K nanotubes. J Nanosci Nanotechnol 7:2246–2252
67. Baumann MK, Textor M, Reimhult E (2008) Understanding self-assembled amphiphilic peptide supramolecular structures from primary structure helix propensity. Langmuir 24:7645–7647
68. Löwik DW, Garcia-Hartjes J, Meijer JT et al (2005) Tuning secondary structure and self-assembly of amphiphilic peptides. Langmuir 21:524–526
69. Hartgerink JD, Beniash E, Stupp SI (2001) Self-assembly and mineralization of peptide-amphiphile nanofibers. Science 294:1684–1688
70. Cui H, Muraoka T, Cheetham AG et al (2009) Self-assembly of giant peptide nanobelts. Nano Lett 9:945–951
71. van Hell AJ, Costa CI, Flesch FM et al (2007) Self-assembly of recombinant amphiphilic oligopeptides into vesicles. Biomacromolecules 8:2753–2761
72. de la Rica R, Mendoza E, Lechuga LM et al (2008) Label-free pathogen detection with sensor chips assembled from peptide nanotubes. Angew Chem Int Ed 47:9752–9755
73. Peters J, Nitsch M, Kuhlmorgen B et al (1995) Tetrabrachion: a filamentous archaebacterial surface protein assembly of unusual structure and extreme stability. J Mol Biol 245(4):385–401
74. Ryadnov MG, Ceyhan B, Niemeyer CM et al (2003) Belt and braces: a peptide-based linker system of de novo design. J Am Chem Soc 125:9388–9394
75. Pan F, Zhao X, Perumal S et al (2010) Interfacial dynamic adsorption and structure of molecular layers of peptide surfactants. Langmuir 26:5690–5696
76. Khoe U, Yang YL, Zhang SG (2008) Synergistic effect and hierarchical nanostructure formation in mixing two designer lipid-like peptide surfactants. Macromol Biosci 8:1060–1067
77. Bucak S, Cenker C, Nasir I et al (2009) Peptide nanotube nematic phase. Langmuir 25:4262–4265
78. Castelletto V, Nutt DR, Hamley IW et al (2010) Structure of single-wall peptide nanotubes: in situ flow aligning X-ray diffraction. Chem Commun 46:6270–6272
79. Guo XD, Tandiono F, Wiradharma N et al (2008) Cationic micelles self-assembled from cholesterol-conjugated oligopeptides as an efficient gene delivery vector. Biomaterials 29:4838–4846
80. Wiradharma N, Khan M, Tong YW et al (2008) Self-assembled cationic peptide nanoparticles capable of inducing efficient gene expression in vitro. Adv Func Mater 18:943–951
81. Wiradharma N, Tong YW, Yang YY (2009) Self-assembled oligopeptide nanostructures for co-delivery of drug and gene with synergistic therapeutic effect. Biomaterials 30:3100–3109
82. Seow WY, Yang YY (2009) A class of cationic triblock amphiphilic oligopeptides as efficient gene delivery vectors. Adv Mater 21:86–90
83. Liu L, Xu K, Wang H et al (2009) Self-assembled cationic peptide nanoparticles as an efficient antimicrobial agent. Nat Nanotechnol 4:457–463
84. Matsumoto K, Koutsopoulos S, Vaughn M et al (2009) Designer peptide surfactants stabilize functional photosystem-I membrane complex in aqueous solution for extended time. J Phys Chem 115:75–83
85. Schuster TB, de Bruyn OD, Bordignon E et al (2010) Reversible peptide particle formation using a mini amino acid sequence. Soft Matter 6:5596–5604
86. Castillo J, Svendsen WE, Dimaki M (2011) Micro and nano techniques for the handling of biological samples. CRC Press, New York, 9781439827437
87. Reches M, Gazit E (2007) Biological and chemical decoration of peptide nanostructures via biotin-avidin interaction. J Nanosci Nanotechnol 7:2239–2245
88. Wooley KL, Moore JS, Wu C et al (2000) Novel polymers: molecular to nanoscale order in three-dimensions. Proc Natl Acad Sci U S A 97:11147–11148

89. Li C, Zhong K-L, Jin LY et al (2010) Supramolecular honeycomb and columnar assemblies formed by self-assembly of coil-rod-coil molecules with a conjugated rod segment. Macromol Res 18(8):800–805

90. Clausen CH, Dimaki M, Panagos SP et al (2011) Electrostatic force microscopy of self-assembled peptide structures. Scanning 33:201–207

91. Clausen CH, Jensen J, Castillo J et al (2008) Qualitative mapping of structurally different dipeptide nanotubes. Nano Lett 8:4066–4069

92. Sedman VL, Allen S, Chen X et al (2009) Thermomechanical manipulation of aromatic peptide nanotubes. Langmuir 25:7256–7259

93. Evans DF, Wennerstrom H (1994) The colloidal domain: where physics, chemistry, biology and technology meet. VCH Publishers, New York, p 515

94. Lu JR, Zhao XB, Yaseen M (2007) Biomimetic surfactants: biosurfactants. Curr Opin Colloid Interface Sci 12:60–67

95. Gudlur S, Sukthankar P, Gao J et al (2012) Peptide nanovesicles formed by the self-assembly of branched amphiphilic peptides. PLoS One 7:e45374

96. Miao M, Bellingham CM, Stahl RJ et al (2003) Sequence and structure determinants for the self-aggregation of recombinant polypeptides modeled after human elastin. J Biol Chem 278:48553–48562

97. Pei D, Schultz PG (1991) Engineering protein specificity: gene manipulation with semisynthetic nucleases. J Am Chem Soc 113:9391–9392

98. Ghadiri MR, Choi C (1990) Secondary structure nucleation in peptides. Transition metal ion stabilized alpha-helices. J Am Chem Soc 112:1630–1632

99. Bilgiçer B, Xing X, Kumar K (2001) Programmed self-sorting of coiled coils with leucine and hexafluoroleucine cores. J Am Chem Soc 123:11815–11816

100. da Silva ER, Liberato MS, de Souza MI et al (2012) Microscopy tools for investigating nano-to-mesoscale peptide assemblies. In: Méndez-Vilas A (ed) Current microscopy contributions to advances in science and technology. Formatex Research Center, Spain

101. Wang C, Li C, Ji X et al (2006) Peptidolipid as binding site of acetylcholinesterase: molecular recognition of paraoxon in Langmuir films. Langmuir 22:2200–2204

102. Martins TD, deSouza MI, Cunha BB et al (2011) Influence of pH and pyrenyl on the structural and morphological control of peptide nanotubes. J Phys Chem C 115:7906–7913

103. Voyer N (1996) Bioorganic chemistry. Top Curr Chem 184:1

104. Urbanc B, Cruz L, Le R et al (2002) Neurotoxic effects of thioflavin S-positive amyloid deposits in transgenic mice and Alzheimer's disease. Proc Natl Acad Sci USA 99:13990–13995

105. Khurana R, Uversky VN, Nielsen L et al (2001) Is congo red an amyloid-specific dye? J Biol Chem 276:22715–22721

106. Karstens T, Kobs K (1980) Rhodamine B and rhodamine 101 as reference substances for fluorescence quantum yield measurements. J Phys Chem 84:1871–1872

107. Chow LW, Bitton R, Webber MJ et al (2011) A bioactive self-assembled membrane to promote angiogenesis. Biomaterials 32:1574–1582

108. Chaudhary N, Singh S, Nagaraj R (2009) Morphology of self-assembled structures formed by short peptides from the amyloidogenic protein tau depends on the solvent in which the peptides are dissolved. J Pept Sci 15:675–684

109. Goldsbury C, Green J (2005) Time-lapse atomic force microscopy in the characterization of amyloid-like fibril assembly and oligomeric intermediates. Mol Biol 299:103–128

110. Niu L, Chen X, Allen S et al (2007) Using the bending beam model to estimate the elasticity of diphenylalanine nanotubes. Langmuir 23:7443–7446

111. Knowles TP, Oppenheim TW, Buell AK et al (2010) Nanostructured films from hierarchical self-assembly of amyloidogenic proteins. Nat Nanotechnol 5:204–207

112. Cardoso I, Goldsbury CS, Müller SA et al (2002) Transthyretin fibrillogenesis entails the assembly of monomers: a molecular model for in vitro assembled transthyretin amyloid-like fibrils. J Mol Biol 317:683–695

113. Larsen M, Andersen K, Svendsen W et al (2011) Self-assembled peptide nanotubes as an etching material for the rapid fabrication of silicon wires. BioNanoScience 1:31
114. Mu C, He J (2011) Confined conversion of CuS nanowires to CuO nanotubes by annealing-induced diffusion in nanochannels. Nanoscale Res Lett 6:150
115. Matos Ide O, Alves WA (2011) Electrochemical determination of dopamine based on self-assembled peptide nanostructure. ACS Appl Mater Interf 3:4437–4443
116. Hauser CA, Deng R, Mishra A et al (2011) Natural tri- to hexapeptides self-assemble in water to amyloid beta-type fiber aggregates by unexpected alpha-helical intermediate structures. Proc Natl Acad Sci U S A 108:1361–1366
117. Bernal JD (1963) William Thomas Astbury 1898–1961. Biograph Memory Fellow Roy Soc 9:1–35
118. Kumaraswamy P, Sethuraman S, Krishnan UM (2013) Hierarchical self-assembly of Tjernberg peptide at nanoscale. Soft Matter 9:2684–2694
119. Xu Y, Shen J, Luo X et al (2005) Conformational transition of amyloid beta-peptide. Proc Natl Acad Sci U S A 102(5):5403–5407
120. Bieler NS, Knowles TPJ, Frenkel D et al (2012) Connecting macroscopic observables and microscopic assembly events in amyloid formation using coarse grained simulations. Plos Comp Biol 8(10):e1002692
121. Colombo G, Soto P, Gazit E (2007) Peptide self-assembly at the nanoscale: a challenging target for computational and experimental biotechnology. Trends Biotechnol 25:211–218
122. Tartaglia GG, Cavalli A, Pellarin R et al (2005) Prediction of aggregation rate and aggregation-prone segments in polypeptide sequences. Protein Sci 14:2723–2734
123. Andersen KB, Castillo-Leon J, Hedström M et al (2011) Stability of diphenylalanine peptide nanotubes in solution. Nanoscale 3:994–998
124. Qin Z, Buehler MJ (2010) Molecular dynamics simulation of the α-helix to β-sheet transition in coiled protein filaments: evidence for a critical filament length scale. Phys Rev Lett 104:198304
125. Mahler A, Reches M, Rechter M et al (2006) Rigid self-assembled hydrogel composed of a modified aromatic dipeptide. Adv Mater 18:1365–1370
126. Sunde M, Blake CC (1998) From the globular to the fibrous state: protein structure and structural conversion in amyloid formation. Q Rev Biophys 31:1–39
127. Rochet JC, Lansbury PT Jr (2000) Amyloid fibrillogenesis: themes and variations. Curr Opin Struct Biol 10:60–68
128. Soto C (2001) Protein misfolding and disease; protein refolding and therapy. FEBS Lett 498:204–207
129. Gazit E (2002) The "correctly-folded" state of proteins: Is it a metastable state? Angew Chem Int Ed 41:257–259
130. Zhang S, Rich A (1997) Direct conversion of an oligopeptide from a ß-sheet to an α-helix: a model for amyloid formation. Proc Natl Acad Sci U S A 94:23–28
131. Tenidis K, Waldner M, Bernhagen J et al (2000) Identification of a penta- and hexapeptide of islet amyloid polypeptide (IAPP) with amyloidogenic and cytotoxic properties. J Mol Biol 295:1055–1071
132. Kamihira M, Naito A, Tuzi S et al (2000) Conformational transitions and fibrillation mechanism of human calcitonin as studied by high-resolution solid-state 13C NMR. Protein Sci 9:867–877
133. Tjernberg L, Hosia W, Bark N et al (2002) Charge attraction and beta propensity are necessary for amyloid fibril formation from tetrapeptides. J Biol Chem 277:43243–43246
134. Hamley IW, Castelletto V, Moulton C et al (2010) Self-assembly of a modified amyloid peptide fragment: pH responsiveness and nematic phase formation. Macromol Biosci 10:40–48
135. Dong J, Lu K, Lakdawala A et al (2006) Controlling amyloid growth in multiple dimensions. Amyloid 13:206–215
136. Childers WS, Mehta AK, Lu K et al (2009) Templating molecular arrays in amyloid's cross-beta grooves. J Am Chem Soc 131:10165–10172

137. Hamley IW, Krysmann MJ (2008) Effect of PEG crystallization on the self-assembly of PEG/peptide copolymers containing amyloid peptide fragments. Langmuir 24:8210–8214
138. Reches M, Gazit E (2006) Molecular self-assembly of peptide nanostructures: mechanism of association and potential uses. Curr Nanosci 2:105–111
139. Zhang S, Zhao X, Spirio L (2005) Puramatrix: Self-assembling peptide nanofiber scaffolds. In: Ma P, Elisseeff J (eds) Scaffolding in tissue engineering. CRC Press, Boca Raton, pp 217–238
140. Banwell EF, Abelardo ES, Adams DJ et al (2009) Rational design and application of responsive alpha-helical peptide hydrogels. Nat Mater 8:596–600
141. Zhang S (2012) Lipid-like self-assembling peptides. Acc Chem Res 45:2142–2150
142. Kyle S, Aggeli A, Ingham E et al (2009) Production of self-assembling biomaterials for tissue engineering. Trends Biotechnol 27:422–433
143. Liang Y, Guo P, Pingali SV et al (2008) Light harvesting antenna on an amyloid scaffold. Chem Commun 48:6522–6524
144. Schlick TL, Ding Z, Kovacs EW et al (2005) Dual-surface modification of the tobacco mosaic virus. J Am Chem Soc 127:3718–3723
145. Cheng TY, Chen MH, Chang WH et al (2013) Neural stem cells encapsulated in a functionalized self-assembling peptide hydrogel for brain tissue engineering. Biomaterials 34:2005–2016
146. Ghosh A, Haverick M, Stump K et al (2012) Fine-tuning the pH trigger of self-assembly. J Am Chem Soc 134:3647–3650
147. Ghadiri MR, Granja JR, Buehler LK (1994) Artificial transmembrane ion channels from self-assembling peptide nanotubes. Nature 369:301–304
148. MacKay JA, Chen M, McDaniel JR et al (2009) Self-assembling chimeric polypeptide-doxorubicin conjugate nanoparticles that abolish tumours after a single injection. Nat Mat 8:993–999
149. Babapoor S, Neef T, Mittelholzer C et al (2011) A novel vaccine using nanoparticle platform to present immunogenic M2e against avian influenza infection. Influenza Res Treat 2011:126794
150. Pimentel TA, Yan Z, Jeffers SA et al (2009) Peptide nanoparticles as novel immunogens: design and analysis of a prototypic severe acute respiratory syndrome vaccine. Chem Biol Drug Des 73:53–61
151. Viguier B, Zor K, Kasotakis E et al (2011) Development of an electrochemical metal-ion biosensor using self-assembled peptide nanofibrils. Appl Mater Interf 3:1594–1600
152. Sasso L, Vedarethinam I, Emneus J et al (2011) Self-assembled diphenylalanine nanowires for cellular studies and sensor applications. J Nanosci Nanotechnol 12:3077–3083
153. Men D, Zhang ZP, Guo YC et al (2010) An auto-biotinylated bifunctional protein nanowire for ultra-sensitive molecular biosensing. Biosens Bioelectron 26:1137–1141
154. Hamad- Schifferli K, Schwartz JJ et al (2002) Remote electronic control of DNA hybridization through inductive coupling to an attached metal nanocrystal antenna. Nature 415:152–155
155. Kasotakis E, Mossou E, Adler-Abramovich L et al (2009) Design of metal-binding sites onto self-assembled peptide fibrils. Biopolymers 92:164–172
156. Capito RM, Mata A, Stupp SI (2010) Self-assembling peptide-based nanostructures for regenerative medicine. Nanotechnology. doi:10.1002/9783527628155
157. Luo J, Tong YW (2011) Self-assembly of collagen-mimetic peptide amphiphiles into biofunctional nanofiber. ACS Nano 5:7739–7747
158. Cheng T-Y, Wu H-C, Huang M-Y et al (2013) Self-assembling functionalized nanopeptides for immediate hemostasis and accelerative liver tissue regeneration. Nanoscale 5:2734–2744

Nanostructure Formation in Hydrogels

9

Seyedsina Moeinzadeh and Esmaiel Jabbari

Introduction

Hydrogels are three-dimensional (3D) networks of cross-linked hydrophilic polymers (Fig. 9.1a). Owing to their hydrophilic nature, hydrogels can retain a large fraction of water in the equilibrium state without dissolving. Their water content is determined by the balance of osmotic forces, which leads to swelling, and elastic retraction forces of the network, which leads to the extension of chains between the cross-links. Owing to their high water content, hydrogels are permeable to small molecules like oxygen and glucose as well as larger molecules like peptides and proteins. However, the permeability depends on molecular size of the permeating molecule. Due to their high water content, high permeability, and resilience, hydrogels are used extensively as a substitute for soft tissues in medicine [1, 2]. Hydrogels have also been used as a vehicle or platform for drug delivery in pharmaceutical applications [3, 4]. Other major applications include soft contact lenses, sensing devices, and as water absorbent in oil recovery and agriculture [5–9]. Hydrogels can be divided into nanogels and micellar gels. Nanogels are further divided into physically cross-linked and chemically cross-linked. Micellar gels are further divided into synthetic-based and peptide-based micellar gels. The following three sections cover nanogels, synthetic micellar gels, and peptide-based micellar gels.

S. Moeinzadeh • E. Jabbari (✉)

Department of Chemical Engineering, Swearingen Engineering Center, Rm 2C11, University of South Carolina, Columbia, SC, USA
e-mail: jabbari@mailbox.sc.edu
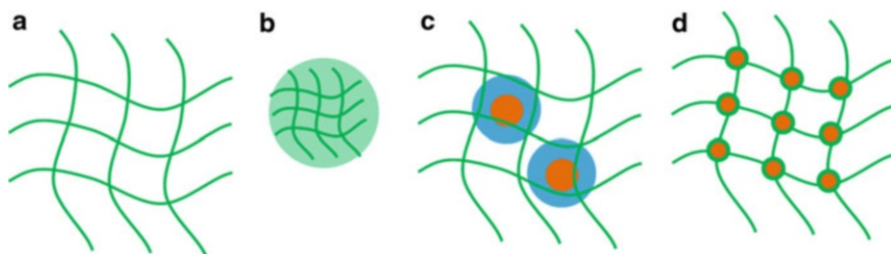
Fig. 9.1 (**a**) Schematic representation of the structure of a hydrogel with cross-linked macromer chains (*green*) forming an insoluble network; (**b**) schematic diagram of a cross-linked nanogel; (**c**) schematic diagram of a micelle embedded or incorporated in a hydrogel network (*green*). The micelle's hydrophobic core is shown in *brown* and its hydrophilic shell in contact with the hydrogel phase is shown in *blue*. The hydrophilic hydrogel chains (*green*) may be different from the hydrophilic chains that form the micelle shell; (**d**) schematic diagram of a bonded micellar gel with hydrophobic micelle cores (*brown*) surrounded by a dense layer of hydrophilic shell (*green*). The chains forming the dense hydrophilic shell are the same as the hydrogel chains

Nanogels

Nanogels are hydrated nanoparticles with <200 nm diameter that are thermodynamically stable and dispersible in an aqueous medium (Fig. 9.1b) [3, 10]. Due to their hydrophilic nature, nanogels are a promising vehicle for delivery of hydrophilic drugs. Nanogels can undergo gelation by physical or chemical cross-linking [3]. Physically cross-linked nanogels are produced by self-assembly of hydrophilic macromers by means of hydrophobic interactions, hydrogen bonding, or electrostatic interactions [11, 12]. Covalently cross-linked nanogels are formed by polymerization of hydrophilic monomers or cross-linking of preformed macromonomers in a water/oil microemulsion or using nanoimprint photolithography [3, 13, 14]. In the former approach, gelation is confined to the nanoscale using inverse microemulsion of an aqueous solution in an organic solvent. For example, nanogels with diameter of 20–50 nm are formed by redox polymerization of (3-acrylamidopropyl)-triethyl ammonium chloride as the monomer and N,N-methylenebisacrylamide as the cross-linker in a water/isooctane inverse microemulsion [15]. Nanogels of poly(D,L-lactic acid)-*b*-poly(ethylene glycol)-*b*-poly(D,L-lactic acid) were formed by photo-cross-linking of micelles formed in a THF/water microemulsion [16]. The resulting nanogels are spherical with 150–200 nm diameter and used for encapsulation of a hydrophobic drugs [16]. The water content of nanogels generally decreases with increasing hydrophobicity of the monomer/macromer, increasing cross-link density and decreasing charge density of the cross-linked network [3, 17]. Block copolymers of ethylene oxide (EO) and α-hydroxy acid (HA) with short EO and HA segments linked by fumarate units, hereafter referred to as poly(hydroxy acid-co-ethylene oxide fumarate) or PHEOF, are used to synthesize hydrolytically degradable nanogels [18, 19]. The relatively rigid unsaturated fumarate units play a significant role in micelle

formation as the less rigid acrylate units form larger particles. PHEOF nanogels are synthesized with L-lactide (PLEOF), glycolide (PGEOF), ε-caprolactone (PCEOF), and dioxanone (PDEOF) and their copolymers such as PLGEOF. Degradation rate and drug release rate are strongly correlated to α-hydroxy acid type. Dissipative particle dynamics (DPD) simulations show that nanogel formation is dominated by hydrophobic interactions between α-hydroxy acid segments of PHEOF macromers (Fig. 9.2a, b). The hydrophobic groups (α-hydroxy acid and fumarate linkers) aggregated and formed junctions on the scale of a few nanometers. The hydrophilic ethylene oxide segments of PHEOF and water molecules, which are attached to the hydrophobic junctions, occupy a large fraction of the nanogel volume. The degradation rate of the nanogel increased as the α-hydroxy acid monomer is changed from ε-caprolactone (C) to lactide (L) and lactide/glycolide (GL) (Fig. 9.2c). Nanogels with caprolactone (PCEOF) have the slowest degradation (many months), while those with 50:50 lactide:glycolide (PLGEOF) have the fastest degradation (few days, Fig. 9.2c). The release of a model compound, 1-(2-pyridylazo)-2-naphthol (PAN), encapsulated in the nanogels ranged from 4 days for 50:50 PLGEOF to 4 weeks for PLEOF and many months for PCEOF (Fig. 9.2d), consistent with degradation of the nanogels (Fig. 9.2c). The presence of a large fraction of water in the structure increases the drug-loading capacity of nanogels, compared with block-copolymer micelles [3]. The nanogel surface can be modified with bioactive peptides to facilitate self-assembly [20] or target to an organ or tissue [21, 22]. One drawback of nanogels is that biological molecules cannot be encapsulated in the nanogels in the process of nanogel formation because organic solvents are used to dissolve the macromers prior to dialysis and self-assembly [23–25]. This limitation is overcome by grafting the protein drug to the surface of the nanogels after dialysis and self-assembly [26].

Micellar Gels

Micellar gels are macroscale polymeric networks with nanoscale micellar structures as part of or incorporated into the network (Fig. 9.1c, d). Micellar gels are divided into micelle-incorporated gels (Fig. 9.1c), physically bonded micellar gels, and covalently bonded micellar gels (Fig. 9.1d).

Micelle-Incorporated Gels

In these gels, the preformed micelles are encapsulated in the hydrogel or they are covalently linked to the hydrogel network. The motivation behind incorporation in the gel is to immobilize and increase the micelle's residence time in the gel network while concurrently increasing the loading of hydrophobic drug in the hydrogel and extend the duration of drug release. In one study, core-cross-linked polyethylene glycol-*b*-poly ε-caprolactone (PEG-*b*-PCL) micelles were incorporated in poly (2-hydroxyethyl methacrylate) (pHEMA) hydrogels to reduce the drug burst release
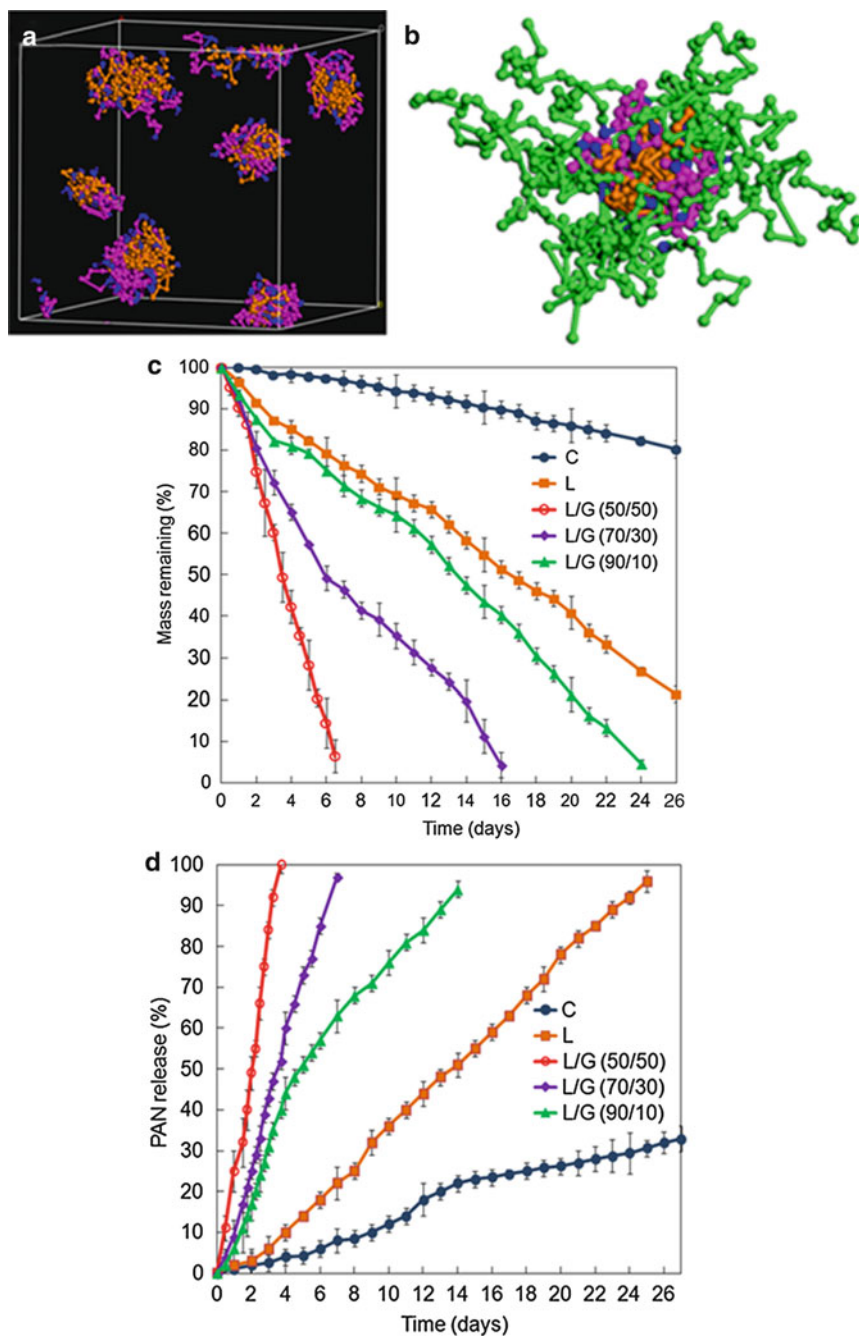
Fig. 9.2 (**a**) Dissipative particle dynamics (DPD) simulation of poly(lactide-glycolide-co-ethylene oxide) fumarate (PLGEOF) macromonomers in aqueous solution. *Brown*, *purple*, *blue*,

and extend duration of release [27]. In another study, micelles preloaded with the hydrophobic drug sirolimus were incorporated in a chitosan hydrogel to improve drug-loading efficiency (amount of drug per unit hydrogel volume) and decrease the initial burst release [28].

Physically Bonded Micellar Gels

A-B-A triblock copolymers are known to form micellar gels in selective solvents [29, 30]. These micelles are responsive to temperature and pH depending on the nature of 'A' and 'B' blocks. The formed micelles pack into an ordered phase at high concentrations (higher than 20 wt%) and form a gel when the 'A' block is solvophilic [29, 31]. However, when the 'B' block is solvophilic, gelation takes place by bridge formation between the micelles [32, 33]. Micelle formation in A-B-A triblock copolymers is illustrated schematically in Fig. 9.3. At low concentrations, the block copolymers are freely dissolved in the solvent. As the concentration exceeds the critical micelle concentration (CMC), the solvophobic 'A' blocks aggregate and form the core of the micelles and the solvophobic 'B' blocks form the shell or corona. Each macromer chain adopts one of four possible conformations: bridge, loop in which two chain ends are in the same micelle, tethered in which one chain end is free, and free chains (see Fig. 9.3). The probability of bridge formation as well as total number of bridges increases with increasing macromer concentration [34]. The increase in macromer concentration beyond a finite percolation threshold leads to the formation of a transient micellar network cross-linked by intermicellar bridges. Each bridge in a transient network has a finite residence time in the micelle. The residence time of a chain in a micelle can be estimated by rheometry via frequency sweep tests on the block copolymer solution. If 'f' is the frequency corresponding to the crossover of the storage (G') and loss modulus (G'') in the frequency sweep test (transient gelation point), the residence time of a bridge (τ) is given by [33]

$$\tau = \frac{1}{2\pi f}$$

The transient bridges act as permanent cross-links at times scales much longer than the measured residence time τ. At those time scales, G' is independent of

---

Fig. 9.2 (continued) and *green* beads show lactide, glycolide, ethylene oxide, and fumarate beads, respectively. Water beads are not shown in the image. The simulation shows that hydrophobic lactide, glycolide, and fumarate beads interact to form a nanogel; (**b**) cross section of one of the nanogels in (**a**) showing distribution of lactide, glycolide, fumarate, and ethylene oxide beads within a nanogel; effect of hydrophobic hydroxy acid segment type in poly(hydroxy acid-co-ethylene oxide) fumarate (PHEOF) macromonomer on mass loss (**c**) and release rate of a model compound (**d**) in PHEOF nanogels. The PHEOF hydrophobic segment in C, L, L/G(50/50), L/G (70/30), and L/G(90/10) is ε-caprolactone, L-lactide, 50:50 lactide:glycolide, 70:30 lactide: glycolide, and 90:10 lactide:glycolide, respectively. In (**d**) PAN is 1-(2-pyridylazo)-2-naphthol. Error bars in (**c**) and (**d**) correspond to mean ± SD for three experiments
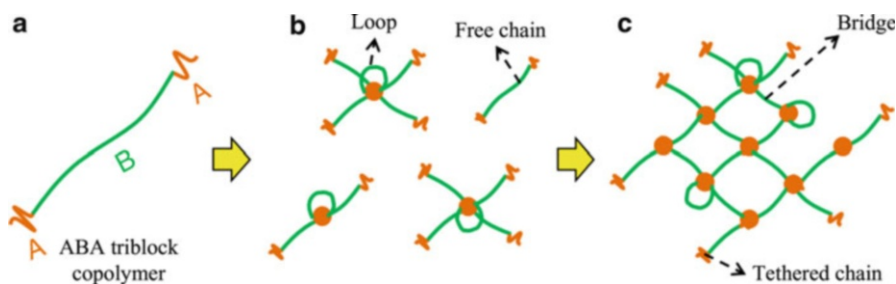
Fig. 9.3 (**a**) Schematic diagram of an A-B-A triblock copolymer with solvophilic block B (*green*) and solvophobic block A (*brown*); (**b**) conformation of chains in A-B-A triblock copolymer chains in solution and formation of micellar structure by aggregation of solvophobic A blocks; (**c**) formation of a physical network in a solution of A-B-A triblock copolymers by aggregation and micelle formation of solvophobic A blocks. Solvophilic (B block) and solvophobic (A block) segments of the copolymer are shown in *green* and *brown*, respectively

frequency and higher than G″ even at very low frequencies. Thus, τ serves as a good indicator of the stability of physical links in a transient network. The residence time τ is proportional to [35]

$$\tau \sim \gamma \cdot n^{2/3}$$

where γ is the effective interfacial tension between the micelle core and solution and n is the number of repeating units on the solvophobic segment of the macromer ('A' block). Therefore, stability of physical cross-links increases with increasing length of the solvophobic segment.

Covalently Bonded Micellar Gels

Micelle Formation in Hydrogel Precursor Solutions

A transient network of micelles is mechanically reinforced and permanently stabilized by the formation of covalent bonds within the core of the micelles. The confinement of the cross-linking reaction inside the micelle cores imparts unique features to the hydrogel. In the case of degradable hydrophobic segments, degradation of the hydrogel network is confined to the micellar domains. A degradable macromonomer is synthesized by chain extension of star 4-arm polyethylene glycol (PEG) with short hydroxyl acid segments such as L-lactide and termination of the arms with reactive acrylate groups. The macromonomer is denoted by SPELA-nLa where 'a' is the number of lactide monomers per macromonomer [36–38]. The length of the hydrophobic segments on each arm should be relatively short (<5 per arm) for the macromonomer to be soluble in aqueous solution. Otherwise the synthesized macromonomer will precipitate and phase separate in aqueous medium. Hydrophobic segments of SPELA macromonomers aggregate to form micelles in the hydrogel precursor solution interconnected by bridging arms (Fig. 9.4).
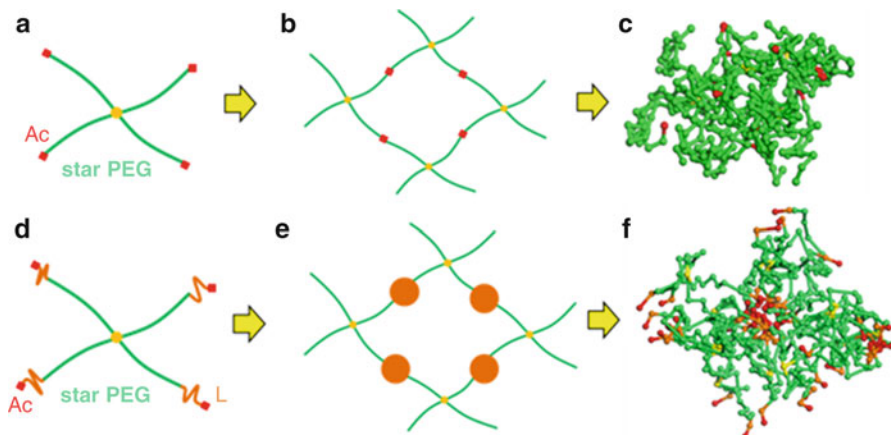
Fig. 9.4 Schematic representation of a star polyethylene glycol acrylate (PEGA) macromonomer (*top row*) precursor solution (**a**) that cross-links to form a network (**b**); (**c**) simulation of the distribution of acrylate groups (*red*) in PEGA macromonomer (*green*) by dissipative particle dynamics (DPD); (**d**) schematic representation of star poly(lactide-co-ethylene oxide) acrylate (SPELA) macromonomer (*bottom row*) precursor solution in which the hydrophobic lactide segments form micellar structures (*brown* in **e**); DPD simulation of the distribution of acrylate groups (*red*) in SPELA macromonomer (*green*) showing micelle formation (**f**) Micelle formation reduces the average distance between acrylate groups, leading to higher extent of cross-linking and faster gelation

Dissipative particle dynamics (DPD) simulation of the gel precursor solution shows that hydrophobic lactide segments and acrylate units form the core of micelles while PEG segments form the corona of micelles facing the aqueous solution [39]. According to DPD simulations, core radius of the micelles formed in SPELA precursor solutions increased from 1 to 3 nm when the number of lactide monomers on each macromonomer arm increased from 1 to 6 (2 to 12 repeating units) [39]. The aggregation number of a micelle or the average number of macromonomers incorporated in a micelle increased from 3 to 22 when the number of lactide monomers increased from 1 to 6. A similar increase in the micelle core size and aggregation number with increasing lactide segment length has been reported for linear PEG-PLA copolymers [40].

Gelation Kinetics of Micellar Gels

Time evolution of the shear storage modulus (G') for gelation of SPELA macromonomer as a function of number of lactide monomers (nL) is measured by rheometry (Fig. 9.5a). The intersection of storage and loss moduli (G'', not shown in Fig. 9.5a), where $G' = G''$, is the gelation time of the gel precursor solution. All time sweep tests exhibited a lag or induction time, a developing portion, and a plateau region [41]. However, length of each region as well as the final value of G' is affected by macromonomer structure, i.e., linear versus star
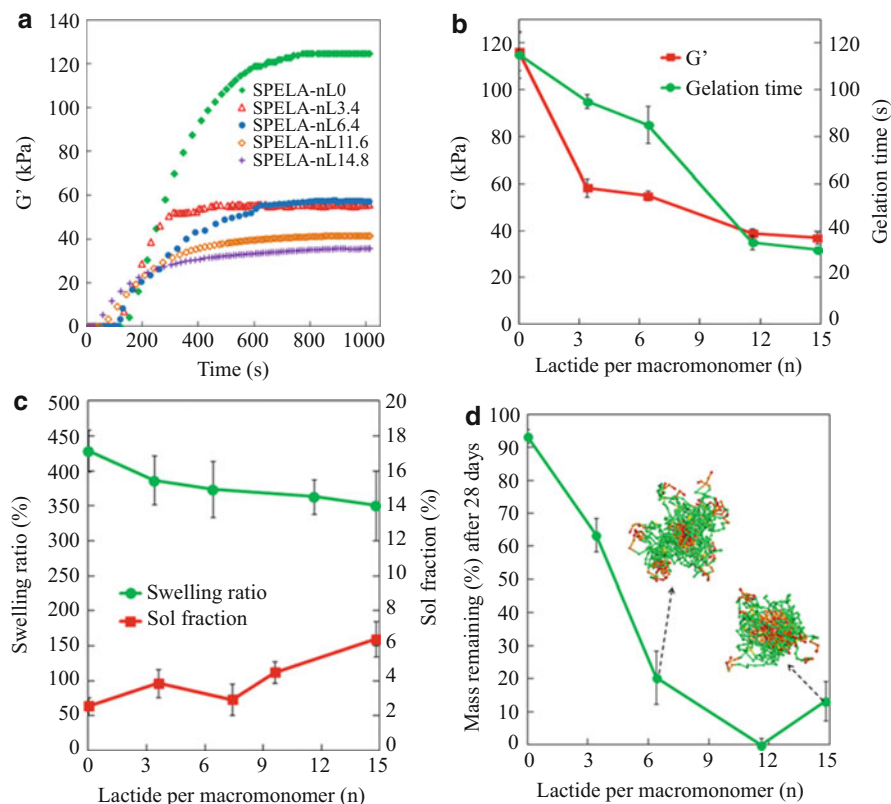
Fig. 9.5 (**a**) Evolution of the storage shear modulus in gelation of 20 wt% SPELA solution with time as a function of number of hydrophobic lactide monomers per macromonomer (n). *Green*, *red*, *blue*, *brown*, and *purple curves* correspond to n value of zero, 3.4, 6.4, 11.6, and 14.8, respectively; effect of number of lactide monomers per macromonomer (n) on storage modulus (*red*) and gelation time of 20 wt% SPELA macromonomers in aqueous solution; (**c**) effect of n on equilibrium water swelling ratio (*green*) and sol fraction of 20 wt% SPELA gel in aqueous solution; (**d**) effect of n on percent mass loss (100 − mass remaining) of 20 wt% SPELA gel after 28 days of incubation in aqueous medium. The insets in (**d**) are DPD simulations of the molecular structure of SPELA-nL6.4 and SPELA-nL14.8 micelles with *green*, *brown*, and *red* beads representing ethylene glycol, lactide, and acrylate beads in the macromonomers. Error bars in (**b–d**) correspond to mean ± SD for three experiments

and the number of lactides. The time for induction/lag time decreased with increasing n because the average distance between the reactive acrylate groups of the macromonomers decreased with increasing n. The slope and duration of the developing portion of the gelation curve decreased with increasing n, due to micelle formation by hydrophobic lactide segments. The effect of number of lactide monomers on plateau storage modulus (G′) and gelation time of 20 wt% SPELA precursor solutions is shown in Fig. 9.5b. G′ decreased from 116 to 37 kPa and gelation time decreased from 115 to 32 s when number

of lactide monomers per macromonomer increased from zero to 14.8, which is attributed to micelle formation by lactide segments. In the absence of micelles (SPELA-nL0 macromonomer), gelation time was significantly higher as the average distance between the uniformly distributed acrylate groups was greater than that with micelles. The localization of reactive acrylate groups in the micelles' core decreased the average distance between the acrylate groups. The lifetime of bridging arms in the micelles' core increased with increasing lactide segment length. Furthermore, simulation results of 20 wt% SPELA precursor solutions indicated that >98 % of the initiator molecules partitioned to the hydrophobic lactide core of the micelles in close proximity to the acrylates. Therefore, micelles dramatically reduced the average inter-acrylate and acrylate-initiator distances, leading to a significant increase in the rate of initiation and propagation of reactive acrylates. Those factors worked together to decrease gelation time with increasing lactide content of the macromonomer. With further increase in lactide content of SPELA macromonomer, mobility of acrylates in the hydrophobic micelles with very low water content decreased with increasing core size. Consequently, a fraction of acrylates were trapped in the micelles' core and did not react to form elastically active cross-links, which led to a decrease in hydrogel modulus.

The effect of number of lactide monomers per SPELA macromonomer on swelling ratio and sol fraction of SPELA gels is shown in Fig. 9.5c. The swelling ratio decreased slightly from 430 % to 350 % (77 % to 72 % water content) with increasing number of lactide monomers per SPELA macromonomer from zero to 14.8. Therefore, formation of micelles did not significantly affect the bulk water content of the gels. However, micelles due to their hydrophobicity repelled water molecules, which decreased the proximity of water molecules to degradable ester groups at the nanoscale. The redistribution of water and ester groups with micelle formation significantly affected the rate of hydrogel degradation (Fig. 9.5d). Mass loss of SPELA gels was affected by the number of ester units per macromonomer (2n for lactide where n is the number of lactide monomers) as well as the proximity of water molecules to ester units. Mass loss of 20 wt% SPELA gels increased from 7 % to 37 %, 80 %, and 100 % after 28 days of incubation when n increased from zero to 3.4, 6.4, and 11.6. Then, mass loss decreased from 100 % to 87 % with increasing n from 11.6 to 14.8, which was due to the formation of large micelles with reduced proximity of water molecules to ester groups in the micelles (see Fig. 9.5d).

Peptide-Based Gels

β-Sheet-Forming Peptide Gels

Self-complementary β-sheet-forming peptides consist of alternating repeat units of hydrophobic and ionic amino acids such as $(+O - O)_n$ or $(+O + O - O - O)_n$ where $+$, $-$, and O represent positively charged, negatively charged, and hydrophobic amino acids. The self-assembly of peptides to nanostructured gels is

governed by intermolecular hydrogen bonding between peptides' backbone in β-sheets, ionic interactions between the charged side chains on one side of β-sheets, and hydrophobic interactions between hydrophobic side chains at the other side of β-sheet [42–44]. For example, peptides with alternating arginine-alanine-aspartate (RAD) residues with 16 amino acids (RADA)$_4$ and (RARADADA)$_2$ with 1–10 mg/mL peptide concentration form fibrous gels with 10–20 nm fiber diameter in physiological medium or in salt solution [42]. Similarly designed peptides one with lysine (K), aspartic acid (D), and leucine (L) residues with 12 amino acids ((KLDK)$_3$) and another with alanine (A), glutamic acid (E), and lysine residues with 16 amino acids ((AEAEAKAK)$_2$) form gels at 0.1–1 % concentration [44, 45]. The designer peptides are used for adhesion of mammalian cells and encapsulation of chondrocytes. Rheological measurements show that the sol-gel transition in the β-sheet-forming peptide solutions is induced by increasing salt concentration to the critical coagulation concentration (CCC) where the salt ions screen the charged residues on the peptide [46]. The CCC decreases with increasing hydrophobicity of the side chains on the peptide [46]. Furthermore, aqueous solutions of a three-stranded β-sheet-forming peptide undergo thermoresponsive gelation [47] with a storage modulus (G′) of 8.5 kPa at 2 wt% concentration, pH 7.4, and 37 °C temperature after 60 min. The G′ of the aforementioned gel increased with increasing temperature [47].

Surfactant-Like Peptide Gels

The surfactant-like peptides have a hydrophilic head and a hydrophobic tail similar to a conventional surfactant. The peptides undergo self-assembly in aqueous solution to form micelles with different morphologies such as nanotubes, nanovesicles, and nanofibers [48, 49]. When the hydrophobic segment of a surfactant-like peptide is an alkyl chain, the structure is called peptide amphiphile (PA) [50]. The head (hydrophilic amino acids) can be rationally designed to tailor the self-assembly of the amphiphile through hydrogen bonding and electrostatic interactions. The self-assembled PA micelles generally have nanofiber morphology with highly packed alkyl chains in the core and radially aligned peptides exposed to the solution [51, 52]. For example, PA solutions with an alkyl tail of 16 carbon atoms and a head composed of 4 consecutive cysteines, 3 glycines, a serine, and a segment of arginine-glycine-aspartic acid (RGD) undergo self-assembly to form nanofibrous gels upon decreasing pH below 4 [53] with a fiber diameter of 7.6 nm and several micrometers length [53]. In another case, PAs composed of a C16 alkyl tail and a valine-alanine-glutamic acid ($V_3A_3E_3$) head are first annealed by heating to 80 °C followed by cooling to 25 °C and then calcium chloride is added to form an aligned fibrous gel [50]. The annealing process increased the gel stiffness by fourfolds [50].

The properties of the micellar gels from PAs are governed by several factors including hydrophobicity of the amino acids close to the tail end, flexibility of the amino acids, and the nature of the head's end-group [54]. For example, substitution

of more hydrophobic and bulkier amino acid residues in PAs leads to a decrease in gelation time [54]. A study on gelation of PAs based on glycine-threonine-alanine-glycine-leucine-isoleucine-glycine-glutamine (GTAGLIGQ) amino acid sequence demonstrate that the gel storage modulus decreases up to threefolds with the addition of model ligands at the end of the peptide [55].

References

1. Cushing MC, Anseth KS (2007) Hydrogel cell cultures. Science 316:1133–1134
2. Peppas NA, Lustig SR (1986) Solute Diffusion in Hydrophilic Network Structures. In: Hydrogels in Medicine and Pharmacy. I. Fundamentals. CRC Press, Boca Raton, FL
3. Kabanov AV, Vinogradov SV (2009) Nanogels as pharmaceutical carriers: finite networks of infinite capabilities. Angew Chem Int Ed 48:5418–5429
4. Hamidi M, Azadi A, Rafiei P (2008) Hydrogel nanoparticles in drug delivery. Adv Drug Deliv Rev 60:1638–1649
5. Buenger D, Topuz F, Groll J (2012) Hydrogels in sensing applications. Prog Polym Sci 37:1678–1719
6. Laftah WA, Hashim S, Ibrahim AN (2011) Polymer hydrogels: a review. Polym Plast Technol Eng 50:1475–1486
7. Abd El-Rehim HA (2006) Characterization and possible agricultural application of polyacryl-amide/sodium alginate crosslinked hydrogels prepared by ionizing radiation. J Appl Polym Sci 102:6088–6090
8. Zolfaghari R, Katbab AA, Nabavizadeh J et al (2006) Preparation and characterization of nanocomposite hydrogels based on polyacrylamide for enhanced oil recovery applications. J Appl Polym Sci 100:2096–2103
9. Kopecek J (2009) Hydrogels: from soft contact lenses and implants to self-assembled nanomaterials. J Polym Sci Part A Polym Chem 47:5929–5946
10. Yallapu MM, Jaggi M, Chauhan SC (2011) Design and engineering of nanogels for cancer treatment. Drug Discov Today 16:457–463
11. Yu SY, Yao P, Jiang M et al (2006) Nanogels prepared by self-assembly of oppositely charged globular proteins. Biopolymers 83:148–158
12. Doloud-Mahammed S, Couvreur P, Gref R (2007) Novel self-assembling nanogels: Stability and lyophilisation studies. Int J Pharmaceut 332:185–191
13. Pan GQ, Guo QP, Cao CB et al (2013) Thermo-responsive molecularly imprinted nanogels for specific recognition and controlled release of proteins. Soft Matter 9:3840–3850
14. Rolland JP, Maynor BW, Euliss LE et al (2005) Direct fabrication and harvesting of mono-disperse, shape-specific nanobiomaterials. J Am Chem Soc 127:10096–10100
15. Sahiner N, Godbey WT, McPherson GL et al (2006) Microgel, nanogel and hydrogel-hydrogel semi-IPN composites for biomedical applications: synthesis and characterization. Colloid Polym Sci 284:1121–1129
16. Lee WC, Li YC, Chu IM (2006) Amphiphilic poly(D, L-lactic acid)/poly(ethylene glycol)/poly(D, L-lactic acid) nanogels for controlled release of hydrophobic drugs. Macromol Biosci 6:846–854
17. McAllister K, Sazani P, Adam M et al (2002) Polymeric nanogels produced via inverse microemulsion polymerization as potential gene and antisense delivery agents. J Am Chem Soc 124:15198–15207

18. Mercado AE, He X, Xu WJ et al (2008) The release characteristics of a model protein from self-assembled succinimide-terminated poly(lactide-co-glycolide ethylene oxide fumarate) nanoparticles. Nanotechnology 19:325609
19. Sarvestani AS, Xu W, He X et al (2007) Gelation and degradation characteristics of in situ photo-crosslinked poly(L-lactid-co-ethylene oxide-co-fumarate) hydrogels. Polymer 48:7113–7120
20. Jabbari E, Yang X, Moeinzadeh S et al (2012) Drug release kinetics, cell uptake, and tumor toxicity of hybrid VVVVVVKK peptide-assembled polylactide nanoparticles. Eur J Pharm Biopharm 84:49–62
21. Jabbari E (2009) Targeted delivery with peptidomimetic conjugated self-assembled nanoparticles. Pharm Res 26:612–630
22. Vinogradov SV, Kohli E, Zeman AD (2006) Comparison of nanogel drug carriers and their formulations with nucleoside 5′-triphosphates. Pharm Res 23:920–930
23. He X, Ma J, Mercado AE et al (2008) Cytotoxicity of paclitaxel in biodegradable self-assembled core-shell poly(lactide-co-glycolide ethylene oxide fumarate) nanoparticles. Pharm Res 25:1552–1562
24. Mercado AE, Jabbari E (2010) Effect of encapsulation or grafting on release kinetics of recombinant human bone morphogenetic protein-2 from self-assembled poly(lactide-co-glycolide ethylene oxide fumarate) nanoparticles. Microsc Res Tech 73:824–833
25. Mercado AE, Ma J, He X et al (2009) Release characteristics and osteogenic activity of recombinant human bone morphogenetic protein-2 grafted to novel self-assembled poly (lactide-co-glycolide fumarate) nanoparticles. J Contr Rel 140:148–156
26. Mercado AE, Yang X, He X et al (2012) Effect of grafting BMP2-derived peptide to nanoparticles on osteogenic and vasculogenic expression of stromal cells. J Tissue Eng Regen Med. doi: 10.1002/term.1487
27. Lu CH, Mikhail AS, Wang XY et al (2012) Hydrogels containing core cross-linked block co-polymer micelles. J Biomater Sci Polym Ed 23:1069–1090
28. Chen MC, Tsai HW, Liu CT et al (2009) A nanoscale drug-entrapment strategy for hydrogel-based systems for the delivery of poorly soluble drugs. Biomaterials 30:2102–2111
29. Huynh CT, Nguyen MK, Lee DS (2011) Injectable block copolymer hydrogels: achievements and future challenges for biomedical applications. Macromolecules 44:6629–6636
30. Riess G (2003) Micellization of block copolymers. Prog Polym Sci 28:1107–1170
31. Cohn D, Lando G, Sosnik A et al (2006) PEO-PPO-PEO-based poly(ether ester urethane)s as degradable reverse thermo-responsive multiblock copolymers. Biomaterials 27:1718–1727
32. Kim HK, Shim WS, Kim SE et al (2009) Injectable in situ-forming ph/thermo-sensitive hydrogel for bone tissue engineering. Tissue Eng Part A 15:923–933
33. O'Lenick TG, Jin NX, Woodcock JW et al (2011) Rheological properties of aqueous micellar gels of a thermo- and ph-sensitive aba triblock copolymer. J Phys Chem B 115:2870–2881
34. Sanson N, Rieger J (2010) Synthesis of nanogels/microgels by conventional and controlled radical crosslinking copolymerization. Polym Chem 1:965–977
35. Nicolai T, Colombani O, Chassenieux C (2010) Dynamic polymeric micelles versus frozen nanoparticles formed by block copolymers. Soft Matter 6:3111–3118
36. Moeinzadeh S, Khorasani SN, Ma J et al (2011) Synthesis and gelation characteristics of photo-crosslinkable star poly (ethylene oxide-co-lactide-glycolide acrylate) macromonomers. Polymer 52:3887–3896
37. Moeinzadeh S, Barati D, He X et al (2012) Gelation characteristics and osteogenic differentiation of stromal cells in inert hydrolytically degradable micellar polyethylene glycol hydrogels. Biomacromolecules 13:2073–2086
38. Moeinzadeh S, Barati D, He X et al (2012) Response of marrow stromal cells to encapsulation in inert hydrolytically degradable polyethylene glycol hydrogels. J Tissue Eng Regen Med 6:209
39. Moeinzadeh S, Jabbari E (2012) Mesoscale simulation of the effect of a lactide segment on the nanostructure of star poly(ethylene glycol-co-lactide)-acrylate macromonomers in aqueous solution. J Phys Chem B 116:1536–1543

40. Posocco P, Fermeglia M, Pricl S (2010) Morphology prediction of block copolymers for drug delivery by mesoscale simulations. J Mater Chem 20:7742–7753
41. Sarvestani AS, He X, Jabbari E (2007) Viscoelastic characterization and modeling of gelation kinetics of injectable in situ cross-linkable poly(lactide-co-ethylene oxide-co-fumarate) hydrogels. Biomacromolecules 8:406–415
42. Holmes TC, de Lacalle S, Su X et al (2000) Extensive neurite outgrowth and active synapse formation on self-assembling peptide scaffolds. Proc Natl Acad Sci USA 97:6728–6733
43. Zhang SG, Holmes T, Lockshin C et al (1993) Spontaneous assembly of a self-complementary oligopeptide to form a stable macroscopic membrane. Proc Natl Acad Sci USA 90:3334–3338
44. Zhang SG, Holmes TC, Dipersio CM et al (1995) Self-complementary oligopeptide matrices support mammalian-cell attachment. Biomaterials 16:1385–1393
45. Kisiday J, Jin M, Kurz B et al (2002) Self-assembling peptide hydrogel fosters chondrocyte extracellular matrix production and cell division: Implications for cartilage tissue repair. Proc Natl Acad Sci USA 99:9996–10001
46. Caplan MR, Schwartzfarb EM, Zhang SG et al (2002) Control of self-assembling oligopeptide matrix formation through systematic variation of amino acid sequence. Biomaterials 23:219–227
47. Rughani RV, Salick DA, Lamm MS et al (2009) Folding, self-assembly, and bulk material properties of a de novo designed three-stranded beta-sheet hydrogel. Biomacromolecules 10:1295–1304
48. Santoso S, Hwang W, Hartman H et al (2002) Self-assembly of surfactant-like peptides with variable glycine tails to form nanotubes and nanovesicles. Nano Lett 2:687–691
49. Vauthey S, Santoso S, Gong HY et al (2002) Molecular self-assembly of surfactant-like peptides to form nanotubes and nanovesicles. Proc Natl Acad Sci USA 99:5355–5360
50. Zhang SM, Greenfield MA, Mata A et al (2010) A self-assembly pathway to aligned monodomain gels. Nature Mater 9:594–601
51. Hartgerink JD, Beniash E, Stupp SI (2002) Peptide-amphiphile nanofibers: a versatile scaffold for the preparation of self-assembling materials. Proc Natl Acad Sci USA 99:5133–5138
52. Luo JN, Tong YW (2011) Self-assembly of collagen-mimetic peptide amphiphiles into biofunctional nanofiber. ACS Nano 5:7739–7747
53. Hartgerink JD, Beniash E, Stupp SI (2001) Self-assembly and mineralization of peptide-amphiphile nanofibers. Science 294:1684–1688
54. Niece KL, Czeisler C, Sahni V et al (2008) Modification of gelation kinetics in bioactive peptide amphiphiles. Biomaterials 29:4501–4509
55. Anderson JM, Andukuri A, Lim DJ et al (2009) Modulating the gelation properties of self-assembling peptide amphiphiles. ACS Nano 3:3447–3454

Nanomanipulation and Nanotribology of Nanoparticles and Nanotubes Using Atomic Force Microscopy

10

Dave Maharaj and Bharat Bhushan

Keywords

Nano-objects • Nanomanipulation • Nanotribology • Friction • Wear

Introduction

Nanoparticles and nanotubes have been investigated for applications that require controlled manipulation and targeting in biomedicine and the oil industry and tribology on the macro- to nanoscale. Knowledge of interfacial friction and wear is important for determining their suitability for various applications.

In controlled manipulation and targeting, applications include but are not limited to use in targeted drug delivery and chemical sensors in the identification of oil, removal of contaminants, and enhanced oil recovery (EOR). Au, Fe_2O_3, polymer, and Si nano-objects have been studied in targeted drug delivery [12, 14, 19, 31]. Figure 10.1a shows a nanoparticle loaded with a therapeutic drug and functionalized with a biomolecule (ligand), which selectively attaches to receptors in a cancer cell. The drug is then released as the nanoparticle diffuses into the diseased cell resulting in cell death. In applications requiring chemical sensors, nanoparticles and nanotubes including oxidized carbon black coated with oil-detecting agents and composites of collagen and superparamagnetic iron oxide nanoparticles have been used [2, 28, 36, 41]. Figure 10.1b shows an example of nanoparticles being used as a chemical sensor in oil detection. Oxidized carbon black nanoparticles with a polyvinyl alcohol shell are coated with an oil-detecting agent, $2,2',5,5'$-tetrachlorobiphenyl (PCB). The release of this agent on contact with

D. Maharaj • B. Bhushan (✉)

Nanoprobe Laboratory for Bio- & Nanotechnology and Biomimetics (NLBB), The Ohio State University, Columbus, OH, USA

e-mail: Bhushan.2@osu.edu
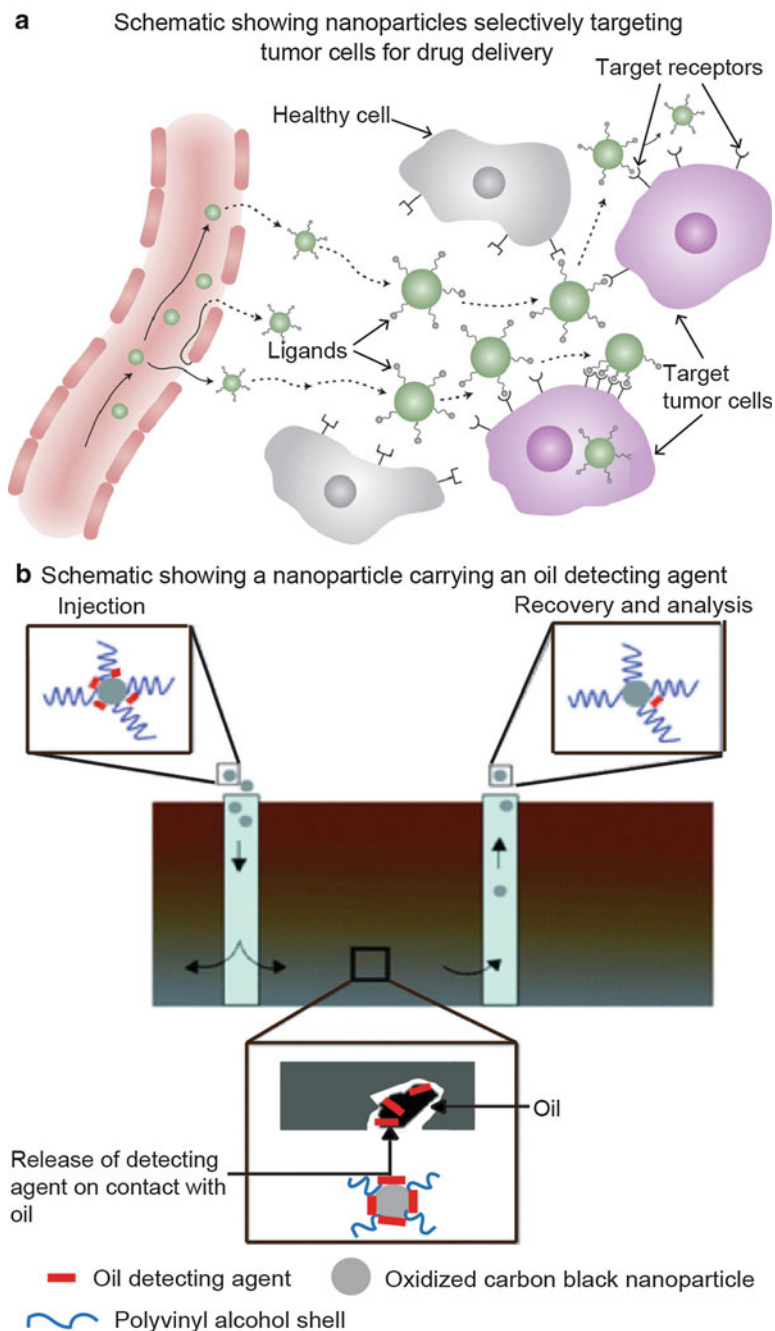
Fig. 10.1 Schematics (**a**) of a drug carrying nanoparticles targeting cancer cells and releasing their therapeutic payload resulting in death of the cancer cell [19] (**b**) showing the process of oil

hydrocarbons is used as an indication of the presence of oil, on nanoparticle recovery [2]. In both of these applications, low friction in liquid medium is of interest. In manipulation studies with an AFM under dry conditions, several groups have demonstrated the contact area and relative humidity dependence of friction force [11, 25, 29, 30, 35]. Studies carried out in liquid environments have shown reductions in friction force [25–27].

For tribological applications on the micro-/nanoscale, increasing the lifetime and efficiency of individual components of systems is crucial to the commercialization of micro-/nanoelectromechanical systems (MEMS/NEMS) [3]. Adhesive and friction forces, which are surface area dependent, become more significant as surface to volume ratio increases. With MEMS/NEMS devices, the initial start-up forces and torques needed become high, which can hinder device operation and reliability [4]. The choice of a suitable lubricant on these scales becomes crucial.

Nanoparticles including Au, carbon nanohorns (CNH), Fe_2O_3, Sb, MoS_2, and WS_2; nanorods including ZnS, ZnO, and $AgVO_3$; and nanotubes including MoS_2, WS_2, and carbon nanotubes (CNT) have been studied in tribological applications on the macro- to nanoscale. Studies have been carried out in dry conditions on the macroscale [5, 25–27, 32, 39], microscale using a surface force apparatus (SFA) [43, 45], and the nanoscale using an AFM [11, 18, 22, 24–27, 29, 30, 35, 38, 40]. In liquid conditions studies have also been carried out on the macroscale [5, 9, 10, 16, 17, 20, 21, 25–27, 33], microscale, using an SFA [1, 15], and nanoscale using an AFM [25–27, 34].

In nanotribological studies using an AFM, reductions in friction and wear were observed when Au, silica, and CNH nanoparticles and MoS_2 and WS_2 nanotubes were used as lubricants in dry conditions [25–27, 30]. Further reductions in friction and wear were obtained when nano-objects were submerged in water, dodecane, and glycerol [25–27]. Reductions in friction and wear as a result of the presence of nano-objects are believed to occur through rolling, sliding, and dragging of nano-objects as depicted in Fig. 10.2a–c with CNH nanoparticles as an example. Nano-objects made of lamellar materials can also reduce friction and wear through the exfoliation and tribofilm formation as shown in Fig. 10.2d, e. In the case of CNH nanoparticles, the additional roughness provided by the nanohorns can further reduce the contact area of the nanoparticles. This together with their low meniscus force contribution to adhesion further enhances the ability to reduce friction and wear [27].

To characterize friction forces and understand the mechanism of friction and wear reduction of nano-objects, nanoscale studies have been carried in both single- and multiple-nano-object contact using an AFM. In single-nano-object contact studies, nano-objects are pushed laterally using an AFM tip and provide

Fig. 10.1 (continued) detection with nanoparticles. The carbon black nanoparticles are coated with an oil-detecting agent. After injection into the ground, the agent is released on contact with hydrocarbons and this is used as an indication of the presence of oil on recovery and analysis of the nanoparticle [2]
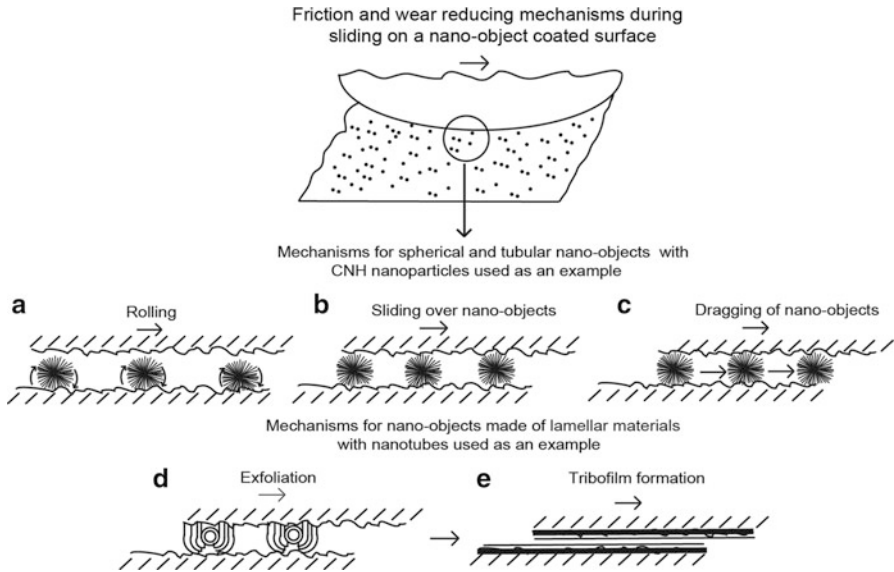
Fig. 10.2 Schematic of friction and wear reducing mechanism of nano-object-coated surface by (**a**) rolling, (**b**) sliding over nano-objects, (**c**) dragging of nano-objects, (**d**) exfoliation, and (**e**) tribofilm formation. Carbon nanohorns (*CNH*) are used as an example for mechanisms (**a**) through (**c**), and WS_2 and MoS_2 nanotubes are used as an example for mechanisms (**d**) through (**e**) [27]

understanding of the nature of the friction mechanism. Multiple-nano-object contact studies simulate the ensuing contacts experienced when nano-objects are introduced for the purpose of friction and wear reduction.

This chapter will present an overview of friction and wear of Au and CNH nanoparticles and MoS_2 and WS_2 nanotubes in dry and submerged-in-liquid environments.

Single- and Multiple-Nano-object Contact

In this section, results from experiments in single- and multiple-nano-object contact are presented for dry conditions and submerged-in-liquid conditions for water, dodecane, and glycerol [25–27]. In single-nano-object contact, as shown in Fig. 10.3a as an example, a sharp tip with a nominal radius of 15 nm was used to push the nano-object laterally. In multiple-nano-object contact as shown in Fig. 10.3b as an example, a glass sphere attached to an AFM tip was used to slide over several nano-objects [27]. The friction forces are presented for Au 30, Au 90, and CNH nanoparticles and MoS_2 and WS_2 nanotubes. In addition, wear data on the nanoscale with and without addition of nanoparticles and nanotubes are also presented. Morphological characterization of the nano-objects and wear scars are also shown.
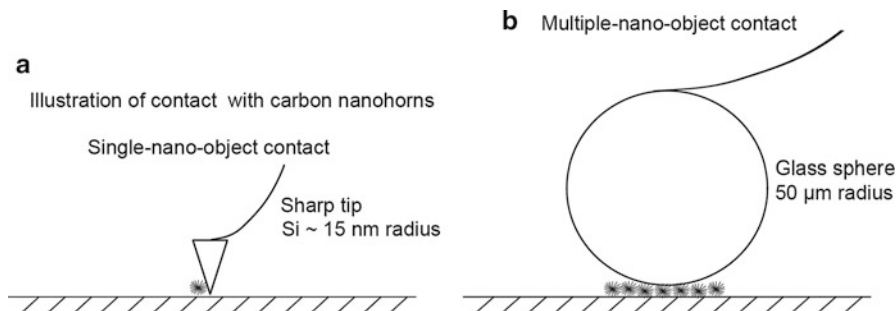
Fig. 10.3 Schematics of (**a**) a sharp tip pushing a nano-object in single-nano-object contact and (**b**) a glass sphere sliding over several nano-objects in multiple-nano-object contact [27]

Single-Nano-object Contact: Lateral Manipulation of Nano-objects over a Silicon Substrate in Dry and Submerged-in-Liquid Environments

For single-nano-object contact under dry conditions, a sharp tip was used to push the nano-objects in the lateral direction [25–27]. For both Au 90 and CNH nanoparticles which are spherical in nature, the manipulation can involve rolling, sliding, and rotation about the vertical axis [38]. In the case of the MoS_2 and WS_2 nanotubes, manipulation can involve rolling, sliding, as well as in-plane rotation which occurs at a pivot point. This can happen when the nanotubes are not pushed directly at the center of its length. Similar observations were found for manipulations of carbon nanotubes on mica and graphite [13].

Figure 10.4 shows the friction forces during nanoparticle manipulation for Au 30 and Au 90 nanoparticles under dry and submerged-in-water conditions [25]. Here scale effects on friction and wear are of interest. The data shows that Au 90 exhibit higher friction forces compared to Au 30. As discussed by Maharaj and Bhushan [25], the normal load acting on the nanoparticle is due only to the mass of the nanoparticle since it is pushed from the side and the friction force is the result of adhesion between the nanoparticle and the silicon substrate. The adhesive force can include van der Waals forces under both dry and submerged-in-water conditions and meniscus forces under dry conditions. In this regime the friction force is not proportional to the normal load since it is dependent on the contact area. The friction force in this case, for single-nanoparticle contact of spherical shapes is proportional to (normal load)$^{2/3}$ [4, 30, 37, 46]. The normal load comprises the external normal load and the adhesive force. Since the adhesive force is dependent on surface area, it is expected that the larger Au 90 nanoparticles will have a higher friction force compared to the smaller Au 30 nanoparticles and this is confirmed from the results shown in Fig. 10.4a, b for both dry and submerged-in-water conditions.

Figure 10.4b presents the result of measurements of the average friction force for Au 30 and Au 90 nanoparticles submerged in water. A normal load of 1 nN was

Fig. 10.4 Friction force for Au 30 and Au 90 nanoparticles on the silicon substrate during manipulation, at normal loads of (**a**) 300 nN in air and (**b**) 1 nN in water. The vertical scale has been magnified for data in water (Adapted from Maharaj and Bhushan [25])
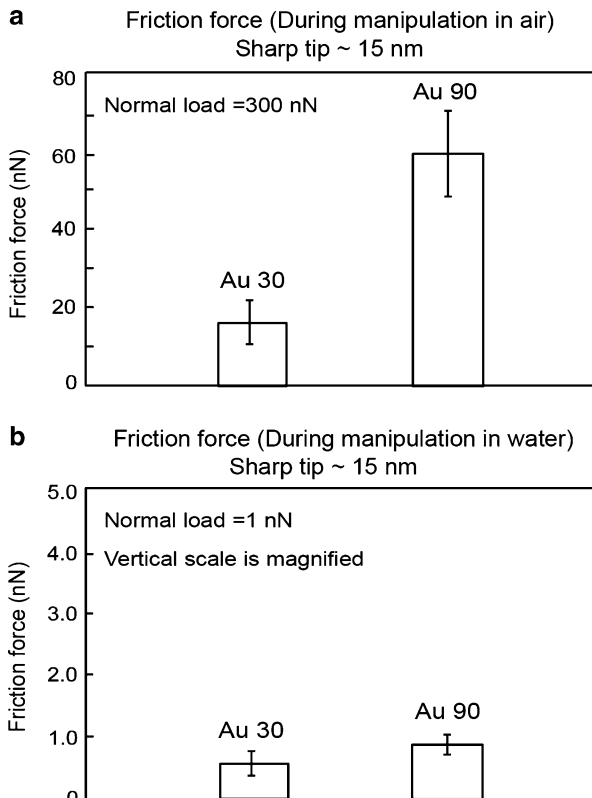
used during manipulation as partial images cannot be obtained at higher load. This is sufficient since the nanoparticles are weakly adhered to the substrate and can be easily moved during the manipulation process and is discussed in further detail by Maharaj and Bhushan [25]. The adhesive forces are due to van der Waals interactions since there are no meniscus bridges formed under submerged-in-water conditions. The lower friction forces in the submerged-in-water condition compared to the dry condition can thus be attributed to the elimination of meniscus forces and sliding on a surface of low shear strength.

Figure 10.5 presents the results for the average friction forces for Au 90 and CNH nanoparticles and MoS_2 and WS_2 nanotubes under dry and submerged-in-liquid environments [26, 27]. Here material effects on friction and wear are of interest.

The friction force data for the nanoparticles and nanotubes in dry conditions are shown in Fig. 10.5a. There is an overall trend towards lower friction forces for the CNH nanoparticles and MoS_2 and WS_2 nanotubes compared to Au 90 nanoparticles. In the case of the nanotubes, it is not believed that exfoliation and tribofilm formation are responsible for the lower values as discussed by Maharaj and Bhushan [26, 27]. Here the nanotubes are pushed from the side, and there is no external pressure acting on the nanotubes to cause them to exfoliate.

Fig. 10.5 Friction force for Au 90 and CNH nanoparticles and MoS$_2$ and WS$_2$ nanotubes on the silicon substrate during manipulation, at normal loads of (**a**) 300 nN in air and (**b**) 1 nN in liquids. The vertical scale is magnified for data in liquids [27]
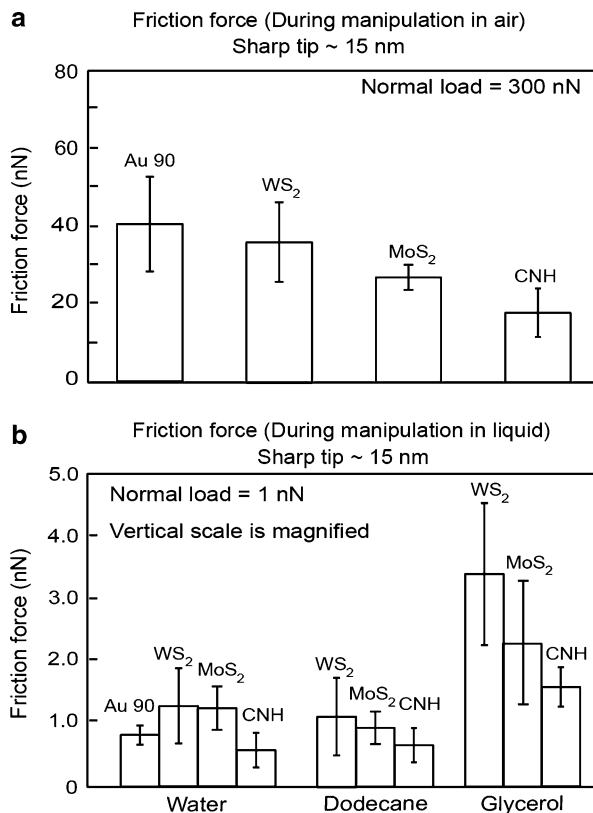
The higher friction force observed for the Au 90 nanoparticles is due to attractive
(adhesive) meniscus forces from water vapor in the atmosphere that condenses
around the contact area of the nanoparticles and silicon substrate. As discussed by
Maharaj and Bhushan [27], these attractive forces are larger on materials with
higher work of adhesion (W_a). Table 10.1 gives the work of adhesion for thin films
of Au, MoS$_2$ and WS$_2$, and graphene with their corresponding contact angles. W_a is
calculated from the Dupré equation, given as

$$W_a = \gamma_l(1 + \cos\theta) \tag{10.1}$$

In this equation, γ_l is the surface tension or free surface energy of a liquid which
is the additional energy available at the surface of the liquid due to fewer bonds with
neighboring atoms and molecules [3]. A value of 72 mN/m at 25 °C is used for
water [23] in this calculation. The static water contact angle, θ, is the angle between
the water droplet and the substrate surface [3]. Higher work of adhesion means
more work has to be done to separate the solid–liquid interface which contributes to
greater attractive meniscus forces [3]. The work of adhesion is highest with Au
films and lowest with graphene films. It is expected that since Au 90 nanoparticles

Table 10.1 Work of adhesion for thin films of Au, MoS_2, WS_2, and graphene in contact with water

Films	Water contact angle, θ (°)	Work of adhesion, W_a (mN/m²)
Au	50[a]	118
MoS_2	75[b]	91
WS_2	93[c]	68
Graphene	127[d]	29

[a]Cayre and Paunov [8]
[b]Fuerstenau and Han [47]
[c]Zhang et al. [44]
[d]Wang et al. [42]

will have a higher work of adhesion compared to CNH nanoparticles and MoS_2 and WS_2 nanotubes, the meniscus force contribution to adhesion will be greater. This increased adhesion accounts for the higher friction force observed with the Au 90 nanoparticles. For the CNH nanoparticles, it is believed that the reduced contact area, due to the roughness provided by the nanohorns and the reduced meniscus force contribution, is responsible for the lowest observed friction forces [27].

Figure 10.5b presents the friction forces for the nanoparticles and nanotubes submerged-in-liquid conditions. In liquids, the adhesive forces are due to van der Waals interactions since there are no meniscus bridges being formed under the submerged-in-liquid condition. The lower friction forces under the submerged-in-liquid conditions compared to the dry conditions can be attributed to the elimination of meniscus forces and nanoparticles and nanotubes sliding on a low shear strength surface. Similar to dry conditions, exfoliation of MoS_2 and WS_2 nanotubes does not occur, and there is no contribution from tribofilm formation. The lowest friction forces occur with the CNH nanoparticles due to the low contact area provided by the roughness of the nanohorns. The highest friction force occurs in glycerol, which has the highest viscosity of the liquids used and therefore the greatest contribution to viscous drag force. Even though dodecane has a greater viscosity than water, it is still not sufficiently high enough to give a significant contribution to drag forces on the nano-objects or the AFM tip, which explains the similarity in friction forces observed for both liquids with and without nanoparticles and nanotubes.

Multiple-Nano-object Contact Sliding of a Glass Sphere over Several Nano-objects in Dry and Submerged-in-Liquid Conditions

Nanoscale Friction

In multiple-nano-object contact, the effect of the normal load acting on the nanoparticles and nanotubes between two surfaces was studied to determine the effects on the friction force. Figure 10.6 summarizes the coefficient of friction under dry and submerged-in-water conditions for Au 30 and Au 90. Here scale effects on friction and wear are of interest. Maharaj and Bhushan [25] showed that the coefficients of friction were lower for sliding under submerged-in-water

Fig. 10.6 Coefficients of friction for both dry and water conditions, with and without Au particles. Friction forces are lower for sliding on nano-objects in all conditions with lowest values obtained in water conditions (Adapted from Maharaj and Bhushan [25])
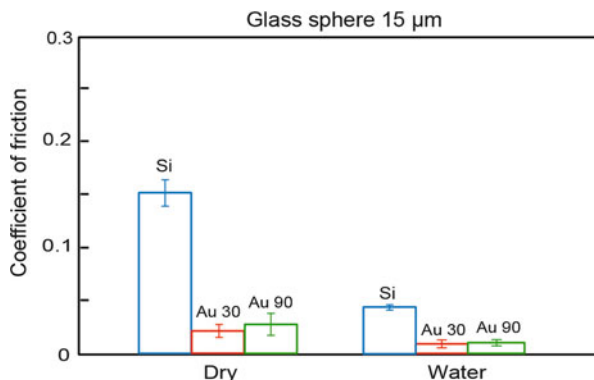
conditions as compared to sliding in dry conditions for both nano-object-coated and uncoated surfaces. The coefficient of friction is also lower for sliding on Au 30 nanoparticles compared to Au 90. This is expected since the lateral manipulation of the nanoparticles resulted in lower friction forces for Au 30 nanoparticles compared to Au 90. The difference is more pronounced under the dry conditions compared to sliding under water conditions. This occurs since, under the submerged conditions, the nanoparticles and cantilever are completely covered by water, and the meniscus force contribution to the friction force is eliminated. One must also consider that, since the glass sphere is glued to the cantilever, the addition of the epoxy could contribute to an increased stiffness (k) of the cantilever, making it less sensitive to detecting changes in the lateral friction force signal, especially for sliding in water where friction force signals are lower [25].

It has also been demonstrated that sliding on multiple asperities on nanopatterned surfaces [7] results in the reduction of friction. In this particular case, the asperities are immobile, and reduction occurs as a result of the reduced contact area. For sliding on Au nanoparticles, coefficient of friction reduction can be attributed to the mobility of the nanoparticles in addition to the reduced contact area. It is expected that as the glass sphere comes into contact with the Au nanoparticles, some of them will be deformed, since the larger nanoparticles will be encountered first and experience the highest contact pressures, due to fewer particles supporting the normal load. The resulting friction reduction mechanism can thus be attributed to the reduced contact area, the sliding over deformed nanoparticles, and individual nanoparticles sliding with the glass sphere. It is also possible for some rolling to take place as the sphere encounters a greater number of nanoparticles, and the contact pressure is reduced, leading to undeformed nanoparticles which may roll between the surface. In addition to elimination of meniscus forces, the presence of a liquid film between the glass sphere and the silicon substrate provides a low shear strength interface [6] which also contributes to the reduction in the coefficient of friction.

Figure 10.7 summarizes the coefficient of friction for Au 90 and CNH nanoparticles and MoS_2 and WS_2 nanotubes in dry and submerged-in-liquid conditions [26, 27]. Here material effects on friction and wear are of interest.
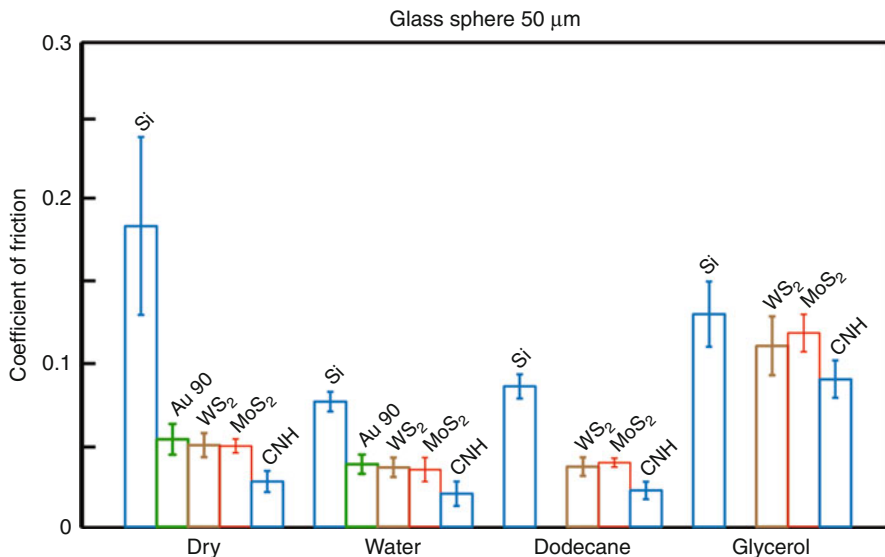
Fig. 10.7 Coefficients of friction for both dry and submerged-in-liquid conditions, with and without nano-objects. Friction forces are lower for sliding on nano-objects in all conditions with lowest values obtained in water conditions (Adapted from Maharaj and Bhushan [27])

In general, sliding on nano-objects results in lower coefficients of friction for all cases compared to sliding on the silicon substrate.

In dry conditions, the coefficient of friction data for the CNH nanoparticles and the MoS_2 and WS_2 nanotubes are generally lower than the Au 90 nanoparticles. As in the case of single-nano-object contact, with the Au 90 nanoparticle there is a higher meniscus force contribution to friction compared to the CNH nanoparticles and MoS_2 and WS_2 nanotubes. Exfoliation and tribofilm formation of the nanotubes, as shown in Fig. 10.2d, e, are not believed to occur due to the low contact pressure as discussed by Maharaj and Bhushan [26, 27]. This is evident in the similar coefficients of friction obtained for the Au 90 nanoparticles and MoS_2 and WS_2 nanotubes under dry and water conditions.

In macroscale experiments (not shown) using a ball-on-flat tribometer, Maharaj and Bhushan [27] slid a sapphire sphere over nanoparticle and nanotube-coated and uncoated silicon substrates for 500 cycles under a normal load of 200 mN in dry conditions. In these experiments MoS_2 and WS_2 nanotubes exhibited lower coefficients of friction compared to Au 90 with the lowest coefficient of friction observed with CNH nanoparticles. SEM micrographs taken of the wear scars showed crushed MoS_2 and WS_2 nanotubes which occurs due to the high contact pressure, and this is believed to be responsible for some exfoliation and tribofilm formation in dry conditions. The tribofilm provides a low shear strength surface for sliding and contributes to lower friction. With the CNH nanoparticles, the reduced contact area, as a result of the roughness of the nanohorns, and low meniscus force contribution are responsible for the low friction forces.

In submerged-in-liquid conditions, the coefficients of friction were lower compared to dry conditions. For water, as the meniscus forces are eliminated, the coefficient of friction data shows very little difference for Au 90 nanoparticles and MoS_2 and WS_2 nanotubes. The CNH nanoparticles have the lowest coefficient of friction in all liquid conditions due to the reduced contact area. The highest friction force and coefficient of friction occurs in glycerol, which has the highest viscosity and therefore results in a greater contribution from viscous drag force similar to single-nano-object contact followed by dodecane. The elimination of the meniscus forces together with sliding on surface of low shear strength as mentioned earlier results in lower coefficients of friction compared to dry conditions.

Nanoscale Wear

For a potential lubricant to be considered effective, it must not only be able to reduce the coefficient of friction, but also protect the underlying surface. Figure 10.8 summarizes the wear data for sliding on Si and Si coated with Au 90 and CNH nanoparticles and MoS_2 and WS_2 nanotubes [26, 27]. Typical wear data for nanoparticles are shown for 1, 10, and 100 cycles at a normal load of 20 μN under dry conditions, using CNH as an example. Wear data for Si and all nanoparticles and nanotubes are shown for 100 cycles in Fig. 10.8b. A 20 × 20 μm area is imaged to show wear scars which were created over a 10 × 10 μm area. Topography maps along with corresponding height profiles are also shown.

After 1 cycle the CNH nanoparticles are just beginning to be pushed out of the wear area. After 10 cycles the CNH nanoparticles are pushed out of the wear area and agglomerate around the edges of the wear scar. Similar observations were made for the other nano-objects for 1 and 10 cycles and are not shown here. For the uncoated silicon substrate after 100 cycles, a small amount of material is removed with a wear depth of approximately 0.25 nm as seen in the height profile. For the coated surfaces, very few nanoparticles and nanotubes remain in the wear area for MoS_2 and WS_2 nanotubes, while for CNH and Au 90 nanoparticles, they are completely removed after 100 cycles.

Figure 10.9 shows SEM micrographs of the wear scars in dry conditions (first row) after 100 cycles [26, 27]. Magnified micrographs of the areas within the squares are shown in the second row as indicated by the vertical arrows. In the magnified micrographs, agglomerated Au 90 and CNH nanoparticles and broken MoS_2 and WS_2 nanotubes are pointed out by arrows within each micrograph. Agglomeration and breaking of the nanoparticles and nanotubes can occur during the wear process. In the case of the MoS_2 and WS_2, broken nanotubes can also result, while samples are being prepared during sonication as they collide with one another. Since there is no evidence for crushed nanotubes from the SEM micrographs, it is unlikely that exfoliation of MoS_2 and WS_2 nanotubes would occur. It is not expected that there would be protection of the substrate from wear due to tribofilm formation.

It is believed, since the nanoparticles and nanotubes remain in the wear area after 1 cycle, that the damage of the silicon surface should be less than that of an initially uncoated substrate. This occurs since the nanoparticles and nanotubes are believed
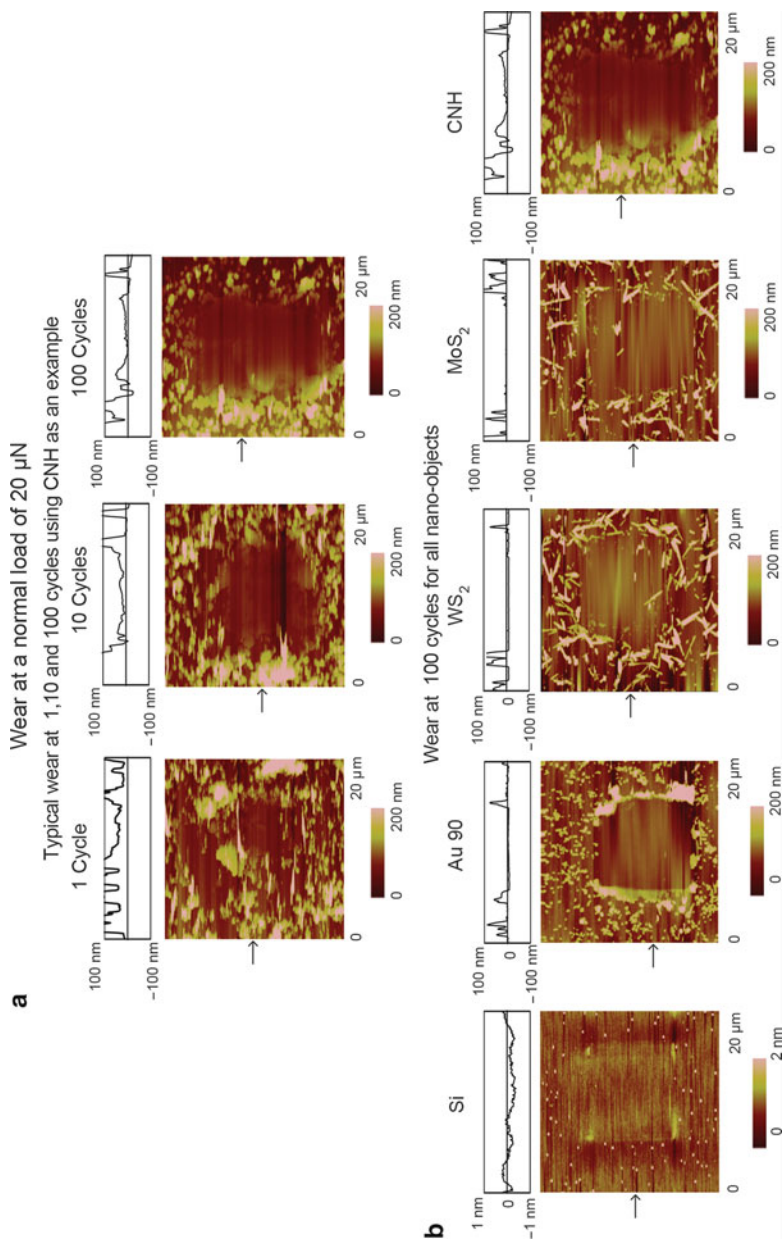
Fig. 10.8 Topography maps and 2D profiles, at sections shown by the *arrows*, after sliding at 1, 10, and 100 cycles with CNH at a normal load of 20 µN on Si and Si coated with CNH nanoparticles as an example (*first row*). Topography maps and 2D profiles, at sections shown by the *arrows*, after sliding at 100 cycles for Si and Si coated with Au and CNH nanoparticles and MoS₂ and WS₂ nanotubes (*second row*) (Adapted from Maharaj and Bhushan [27])

Fig. 10.9 SEM micrographs of nanoscale wear scars for Au 90 and CNH nanoparticles and MoS$_2$ and WS$_2$ nanotubes in dry conditions after 100 cycles at a normal load of 20 μN (*first row*). The nano-objects within the squares are magnified and the *vertical arrows* point to those micrographs in the *second row*. The magnified micrographs show agglomerated Au 90 and CNH nanoparticles and broken MoS$_2$ and WS$_2$ nanotubes as indicated by *arrows* within the micrographs [27]

to roll and slide between the glass sphere and the substrate which promotes facile shearing of the two surfaces, in addition to the reduced contact area provided by the nano-objects. For the CNH nanoparticles, the reduction in contact area due to the roughness provided by the nanohorns is expected to further reduce wear. After 100 cycles, it is therefore expected that the greatest wear occurs on the bare silicon substrate and the presence of nanoparticles and nanotubes does provide protection of the substrate with the least wear occurring with the CNH nanoparticles.

Conclusions

In this chapter an overview of friction and wear on the nanoscale was presented. Au and carbon nanohorn (CNH) nanoparticles and MoS_2 and WS_2 nanotubes have been investigated for their effect on friction and wear in dry and liquid conditions in water, dodecane, and glycerol. Studies presented were conducted in both single- and multiple-nano-object contacts with the aid of an AFM. For single-nanoparticle contact, when scale effects were compared, it was shown that friction force was greater for Au 90 compared to Au 30 in both dry and submerged-in-water conditions. When material effects were compared, the lowest friction forces were obtained with the CNH nanoparticles compared to Au nanoparticles and MoS_2 and WS_2 nanotubes. This is due to the reduced contact area provided by the roughness of the nanohorns and low meniscus force contribution in dry conditions. Lower friction forces occur in submerged-in-liquid conditions compared to dry conditions due to elimination of meniscus force and sliding on a low shear strength surface among the various liquids. The highest friction forces occur in glycerol due to high viscosity.

For multiple-nano-object contact, sliding over nanoparticles and nanotubes reduced coefficients of friction compared to sliding on the bare silicon substrate due to reduced contact area and rolling and sliding among the various nanoparticles and nanotubes in dry conditions. Similar scale effects were observed as in single-nano-object contact with Au nanoparticles. When material effects were compared, the lowest coefficient of friction occurs with the CNH nanoparticles compared to the other nano-objects due to the mechanisms mentioned for single-nano-object contact in dry conditions. In liquid conditions the coefficient of friction was lower compared to dry conditions due to the mechanisms mentioned for single-nano-object contact. In nanoscale wear experiments in dry conditions, the addition of nanoparticles and nanotubes prevents the glass sphere from coming directly into contact with the surface and reduces the wear of the substrate through possible rolling and sliding of the nanoparticles and nanotubes.

In macroscale studies (not shown), sliding over the various nanoparticles and nanotubes reduced friction and wear due to the mechanisms mentioned in multiple-nano-object contact on the nanoscale. Additionally, in dry conditions, sliding on the nanotubes reduced the coefficient of friction and the wear due to exfoliation and tribofilm formation.

In this chapter studies on nanomanipulation of nanoparticles and nanotubes in dry and liquid environments to determine friction forces have been presented and will aid in better design of applications requiring controlled manipulation and targeting of nanoparticles and nanotubes. Nanotribological studies have been presented and demonstrate the ability of nanoparticles and nanotubes to reduce friction and wear in dry and liquid environments.

References

1. Akbulut M, Belman N, Golan Y, Israelachvili JN (2006) Frictional properties of confined nanorods. Adv Mater 18:2589–2592
2. Berlin JM, Yu J, Lu W, Walsh EE, Zhang L, Zhang P, Chen W, Kan AT, Wong MS, Tomson MB, Tour JM (2011) Engineered nanoparticles for hydrocarbon detection in oil-field rocks. Energy Environ Sci 4:505–509
3. Bhushan B (ed) (2010) Springer handbook of nanotechnology, 3rd edn. Springer, Heidelberg
4. Bhushan B (ed) (2011) Nanotribology and nanomechanics, I and II, 3rd edn. Springer, Heidelberg
5. Bhushan B, Gupta BK (1991) Handbook of tribology: materials, coatings, and surface treatments. McGraw-Hill, New York
6. Bhushan B, Sundararajan S (1998) Micro/nanoscale friction and wear mechanisms of thin films using atomic force and friction force microscopy. Acta Mater 46:3793–3804
7. Burton Z, Bhushan B (2005) Hydrophobicity, adhesion and friction properties of nanopatterned polymers and scale dependence for MEMS/NEMS. Nano Lett 5:1607–1613
8. Cayre OJ, Paunov VN (2004) Contact angles of colloid silica and gold particles at air–water and oil–water interfaces determined with the gel trapping technique. Langmuir 20:9594–9599
9. Cizaire L, Vacher B, Mogne T, Le Martin JM, Rapoport L, Margolin A, Tenne R (2002) Mechanisms of ultra-low friction by hollow inorganic fullerene-like MoS_2 nanoparticles. Surf Coat Technol 160:282–287
10. St Dennis JE, Jin K, John VT, Pesika NS (2011) Carbon microspheres as ball bearings in aqueous-based lubrication. ACS Appl Mater Interfaces 3:2215–2218
11. Dietzel D, Monninghoff GS, Jansen L, Fuchs H, Ritter C, Scharwz UD, Schirmeisen A (2007) Interfacial friction obtained by lateral manipulation of nanoparticles using atomic force microscopy techniques. J Appl Phys 102:084306
12. Duncan R (2003) The dawning era of polymer therapeutics. Nat Rev Drug Discov 2:347–360
13. Falvo MR, Taylor RM II, Helser A, Chi V, Brooks FP Jr, Washburn S, Superfine R (1999) Nanometre-scale rolling and sliding of carbon nanotubes. Nature 397:236–238
14. Ferrari M (2005) Cancer nanotechnology: opportunities and challenges. Nat Rev Cancer 5:161–171
15. Gourdon D, Yasa M, Godfrey Alig AR, Li Y, Safinya CR, Israelachvili JN (2004) Mechanical and structural properties of $BaCrO_4$ nanorod films under confinement and shear. Adv Funct Mater 14:238–242
16. Greenberg R, Halperin G, Etsion I, Tenne R (2004) The effect of WS_2 nanoparticles on friction reduction in various lubrication regimes. Tribol Lett 17:179–186
17. Hu HS, Dong JX, Chen GX (1998) Study on antiwear and reducing friction additive of nanometer ferric oxide. Tribol Int 31:355–360
18. Hui X, Regnier S (2012) High-efficiency automated nanomanipulation with parallel imaging/manipulation force microscopy. IEEE Trans Nanotechnol 11:21–33
19. Irvine DJ (2011) Drug delivery: one nanoparticle, one kill. Nat Mater 10:342–343
20. Joly-Pottuz L, Dassenoy F, Belin M, Vacher B, Martin JM, Fleischer N (2005) Ultralow-friction and wear properties of $IF-WS_2$ under boundary lubrication. Tribol Lett 18:477–485

21. Kalin M, Kogovšek J, Remškar M (2012) Mechanisms and improvements in the friction and wear behavior using MoS_2 nanotubes as potential oil additives. Wear 280–281:36–45

22. Lahouij I, Dassenoy F, de Knoop L, Martin J-M, Vacher B (2011) In situ TEM observation of the behavior of an individual fullerene-like MoS_2 nanoparticle in a dynamic contact. Tribol Lett 42:133–140

23. Lide DR (ed) (2009) CRC handbook of chemistry and physics, 90th edn. CRC Press, Boca Raton

24. Lüthi R, Meyer E, Haefke H, Howald L, Gutmannsbauer W, Güntherodt H-J (1994) Sled-type motion on the nanometer scale: determination of dissipation and cohesive energies of C60. Science 266:1979–1981

25. Maharaj D, Bhushan B (2012) Effect of spherical Au nanoparticles on nanofriction and wear reduction in dry and liquid environments. Beilstein J Nanotechnol 3:759–772

26. Maharaj D, Bhushan B (2013) Effect of MoS_2 and WS_2 nanotubes on nanofriction and wear reduction in dry and liquid environments. Tribol Lett 49:323–339

27. Maharaj D, Bhushan B (2013) Effect of carbon nanohorns on nanofriction and wear reduction in dry and liquid environments. J Colloid Interface Sci 400:147–160

28. Matteo C, Candido P, Vera R, Francesca V (2012) Current and future nanotech applications in the oil industry. Am J Appl Sci 9:784–793

29. Mougin K, Gnecco E, Rao A, Cuberes MT, Jayaraman S, McFarland EW, Haidara H, Meyer E (2008) Manipulation of gold nanoparticles: influence of surface chemistry, temperature, and environment (vacuum versus ambient atmosphere). Langmuir 24:1577–1581

30. Palacio M, Bhushan B (2008) A nanoscale friction investigation during manipulation of nanoparticles in controlled environments. Nanotechnology 19:315710

31. Panyala NR, Pena-Mendez EM, Havel J (2009) Gold and nano-gold in medicine: overview, toxicology and perspectives. J Appl Biomed 7:75–91

32. Rapoport L, Lvovsky M, Lapsker I, Leshinsky V, Volovik Y, Feldman Y, Zak A, Tenne R (2001) Slow release of fullerene-like WS_2 nanoparticles as a superior solid lubrication mechanism in composite matrices. Adv Eng Mater 3:71–75

33. Rapoport L, Nepomnyashchy O, Lapsker I, Verdyan A, Soifer Y, Popovitz-Biro R, Tenne R (2005) Friction and wear of fullerene-like WS_2 under severe contact conditions: friction of ceramic materials. Tribol Lett 19:143–149

34. Resch R, Lewis D, Meltzer S, Montoya N, Koel BE, Madhukar A, Requicha AA, Will P (2000) Manipulation of gold nanoparticles in liquid environments using scanning force microscopy. Ultramicroscopy 82:135–139

35. Ritter C, Heyde M, Stegemann B, Rademann K, Schwarz UD (2005) Contact-area dependence of frictional forces: moving adsorbed antimony nanoparticles. Phys Rev B 71:085405

36. Ryoo S, Rahmani AR, Yoon KY, Prodanovic M, Kotsmar C, Milner TE, Huh C (2012) Theoretical and experimental investigation of the motion of multiphase fluids containing paramagnetic nanoparticles in porous media. J Petrol Sci Eng 81:129–144

37. Schwarz UD, Zwörner O, Köster P, Wiesendanger R (1997) Quantitative analysis of the frictional properties of solid materials at low loads. I. Carbon compounds. Phys Rev B 56:6987–6996

38. Sitti M (2004) Atomic force microscope probe based controlled pushing for nanotribological characterization. IEEE/ASME Trans Mechatron 9:343–349

39. Tanaka A, Umeda K, Yudasaka M, Suzuki M, Ohana T, Yumura M, Iijima S (2005) Friction and wear of carbon nanohorn-containing polyimide composites. Tribol Lett 19:135–142

40. Tevet O, Von-Huth P, Popovitz-Biro R, Rosentsveig R, Wagner HD, Tenne R (2011) Friction mechanism of individual multilayered nanoparticles. Proc Natl Acad Sci U S A 108:19901–19906

41. Thanikaivelan P, Narayanan NT, Pradhan BK, Ajayan PM (2012) Collagen based magnetic nanocomposites for oil removal applications. Sci Rep 2:230. doi:10.1038/srep00230
42. Wang S, Zhang Y, Abidi N, Cabrales L (2009) Wettability and surface free energy of graphene films. Langmuir 25:11078–11081
43. Zhang J, Zhang J (2013) Surfactant inducing phase change of ZnO nanorods to low friction. Tribo Lett 49:77–83
44. Zhang S, Zeng XT, Tang ZG, Tan MJ (2002) Exploring the antisticking properties of solid lubricant thin films in transfer molding. Int J Mod Phys B 16:1080–1085
45. Singh DP, Polychronopoulou K, Rebholz C, Aouadi SM (2010) Room temperature synthesis and high temperature frictional study of silver vanadate nanorods. Nanotechnology 21:325601
46. Bhushan B (2013) Introduction to tribology, 2nd ed. Wiley, New York
47. Fuerstenau MC, Han KN (ed) (2003) Principles of mineral processing, society for mining, metallurgy, and exploration (SME). Littleton, Colorado

Fabrication, Properties and Applications of Gold Nanopillars

11

Dorothea Brüggemann, Bernhard Wolfrum, and Johann P. de Silva

Introduction

Nanotechnology has brought forward the design of various gold nanostructures with a vast variety of different nanoarchitectures. The outstanding optical properties of gold nanoparticles and flower or waxberry-like gold nanostructures – a result of surface-plasmon oscillations – have made these nanomaterials very attractive for applications in sensing, diagnostics, or photothermal therapeutics [1, 2]. Lying gold nanorods fabricated via chemical synthesis exhibited excellent properties for optical imaging or plasmonic waveguide applications [3, 4]. Biosensing devices have benefited hugely from the biocompatibility and excellent electronic properties of

D. Brüggemann (✉)
School of Physics and CRANN, Trinity College Dublin, Dublin, Ireland

Department of New Materials and Biosystems, Max Planck Institute for Intelligent Systems,
Stuttgart, Germany
e-mail: brueggemann@is.mpg.de

B. Wolfrum
Institute of Bioelectronics (PGI-8/ICS-8), Forschungszentrum Jülich, Jülich, Germany

IV. Institute of Physics, RWTH Aachen University, Aachen, Germany
e-mail: b.wolfrum@fz-juelich.de

J.P. de Silva
School of Physics and CRANN, Trinity College Dublin, Dublin, Ireland
e-mail: j.desilva@physics.org

nanoporous gold and gold nanoflakes as low-impedance electrodes [5–7] or gold microspines for cell recordings and improved cell adhesion [8, 9].

The sensitivity of biosensors and plasmonic devices can be increased with nanostructures of high aspect ratios: this makes vertical gold nanopillars excellent candidates for these applications. To date, nanopillars have already been produced from a large variety of materials, ranging from polymers [10], silicon [11], SiO_2 [12, 13], and GaAs [14] to various metallic nanopillars such as copper [15, 16], platinum [17], nickel [18, 19], and silver [20]. Gold nanopillars in particular have several advantages over other metallic nanopillars: they are chemically inert, biocompatible, and offer various possible surface functionalizations via thiol coupling, for example [21]. Furthermore, gold nanopillars combine excellent optical properties based on surface-plasmon resonance and also outstanding electronic properties. Several methods such as template-assisted synthesis, various microfabrication techniques, and less well-known approaches have been established to fabricate gold nanopillars. The geometry and long-range order of gold nanopillar arrays can be tailored by these different fabrication techniques. However, to date gold nanopillars have only been produced in a research laboratory environment and are not yet commercially available.

In this chapter we present established and novel techniques for the fabrication of gold nanopillars (Template-Assisted Synthesis to Other Fabrication Techniques) and also focus on the prepatterning of these nanostructures (Fabrication of Prepatterned Nanopillars). Furthermore, we shall discuss the versatile material properties of gold nanopillars (Mechanical Stability to Electrochemical Properties) and their potential for various surface modifications (Self-Assembled Monolayer Coatings to Metal Oxide Coatings) and metamaterials (Metamaterials). From these attributes a wide application range for gold nanopillars has evolved, and here we discuss recent applications of gold nanopillars in the fields of biosensing (Biosensing Employing Nanopillar Electrodes) and plasmonic devices (Gold Nanopillars in Plasmonic Devices).

Fabrication Methods

Various fabrication techniques have already been implemented for the fabrication of gold nanopillars. Most commonly, gold is electrochemically deposited onto nanoporous templates with vertical nanochannels. This simple fabrication method yields good reproducibility of gold nanopillars with a versatile range of geometries and aspect ratios combined with low costs [22, 23]. Often gold nanopillars are also produced by focused ion beam (FIB) milling or nanoimprint lithography (NIL). Microfabrication equipment is required for these techniques, which increases the cost of gold nanopillars fabricated by such methods. Conversely, very precise geometries with high reproducibility over a large surface area can be facilitated when microfabrication techniques are used. FIB-machined gold nanopillars especially can be produced with a larger range of diameters and lengths than other common methods (see Table 11.1) [24]. Electron beam lithography can also be employed for the fabrication of gold nanopillars; in this approach a photoresist is

Table 11.1   Range of possible nanopillar geometries for various fabrication methods

Fabrication method	Diameter (nm)	Height (nm)	Features	References
Anodic aluminum oxide template-assisted deposition	15–200	100–8,000	Simple, low-cost method with high reproducibility and large geometry range	[40–43]
Focused ion beam milling	50–8,000	30 to 11,000	Direct pillar fabrication with large geometry range and very high reproducibility, high costs	[28, 62]
Nanoimprint lithography	100–1,100	50–4,000	Coating of polymer casts is common, high costs	[20, 63, 69–71]
Electron beam lithography	50–200	50–285	Combination with metal deposition, good reproducibility, high costs	[25, 45]

prestructured to serve as a mask, and gold is subsequently deposited onto this mask to obtain nanopillars [25, 26]. Despite good reproducibility this method is not widely used due to the high costs that are involved. Two rare fabrication methods, which have only been introduced recently, are the assembly of gold nanoparticles into pillars using a polymer mask [27] and decomposition from an organometallic precursor [28].

Established and novel fabrication methods for gold nanopillars and the resulting geometries are presented in this section. We also focus on prepatterning approaches for the production of localized pillars with long-range order.

Template-Assisted Synthesis

The use of nanoporous template materials for the fabrication of vertical metal nanowires was first established by Possin in 1970 [29], where he used track-etched mica membranes to produce indium, tin, and zinc nanowires of 40 nm diameter and up to 15 μm length. At this stage, the fabrication of gold nanopillars was not yet possible, but other metal, organic, and polymer nanopillars were subsequently produced via template synthesis. In the following years template-assisted nanopillar synthesis has been developed further, and other template materials were introduced [30].

Template Materials

Several template materials may be used in the fabrication of gold nanopillars: the most common templates with cylindrical pores of uniform diameter are anodic aluminum oxide and track-etched polymer membranes. Other template materials with a nanochannel architecture are, for example, glass, silica aerogels, titania, or mesoporous zeolites [22, 31, 32]. The pore diameter and distribution in the respective nanoporous template material determines the resulting pillar geometry and arrangement.

Nanoporous anodic aluminum oxide (AAO) membranes are fabricated from aluminum in a very efficient and low-cost anodization process with polyprotic acids such as oxalic, sulfuric, or phosphoric acid [33]. The self-assembled parallel nanochannels grow perpendicularly to the surface with uniform pore sizes and lengths, which can exceed 100 μm [34]. By adjusting anodization voltage, time, and pH value of the acid, the pore geometries can be controlled accurately. These variations yield pore diameters ranging from only 4 nm up to several hundred nanometers, and pore densities can reach up to 10^{11} pores per cm^2 [31]. Furthermore, AAO membranes are commercially available with a limited number of pore sizes (such as Anopore^{TM} from Whatman or Unikera^{TM} from Synkera Technologies) [22].

Track-etched polymer membranes, also known as nuclear track filters or screen membranes, are fabricated through heavy ion bombardment of polymer sheets such as polycarbonate (PC) or polyester [31]. Subsequently, the ion tracks are chemically etched to transform the damaged area into a hollow nanochannel. Cylindrical and cone-shaped pores can be achieved via this step, which is controlled by the chemical nature of the etchant, KOH or HF, for example, concentration, temperature, or the total etch time [35]. The etch rate of the membrane material and the presence of any surfactants are also important parameters [36]. The ion bombardment results in nanopores that are slightly tilted with respect to the surface of the sheets [22]. Pore diameters between 10 nm and tens of microns may be produced by ion bombardment and track etching, and pore densities up to 10^9 pores per cm^2 are possible [30, 37]. These membranes are also available commercially for a wide range of filtering applications (Nucleopore$^®$ from PCI Scientific, Poretics$^®$ from Sphaero Q, Cyclopore^{TM} from Whatman, Osmonics from Lenntech, Isopore^{TM} from Millipore) [31].

Microfabricated masks are another template material that can be used for the synthesis of gold nanopillars: the advantage here is that the nanochannel architecture can be adjusted very precisely by controlling the process parameters, thus enabling the fabrication of localized gold nanopillars with long-range order (see section 'Fabrication of Prepatterned Nanopillars').

Deposition Techniques
Electrochemical Deposition

Two decades after the first metal nanopillars were produced by Possin et al., the electrochemical deposition of gold nanopillars into nanoporous AAO templates [38] and track-etched membranes [39] was presented by Martin et al. for the first time. To obtain gold nanopillars electrochemically via template synthesis, one side of the nanoporous membranes is coated with a gold film by sputtering or thermal evaporation. This film serves as a cathode in the subsequent electroplating step [22]. After depositing gold the AAO membrane is dissolved (in KOH, for instance), to obtain freestanding gold nanopillars (see Fig. 11.1). In this process the geometry of the nanoporous template determines the dimensions of the resulting nanopillars. The nanopillar length depends on the
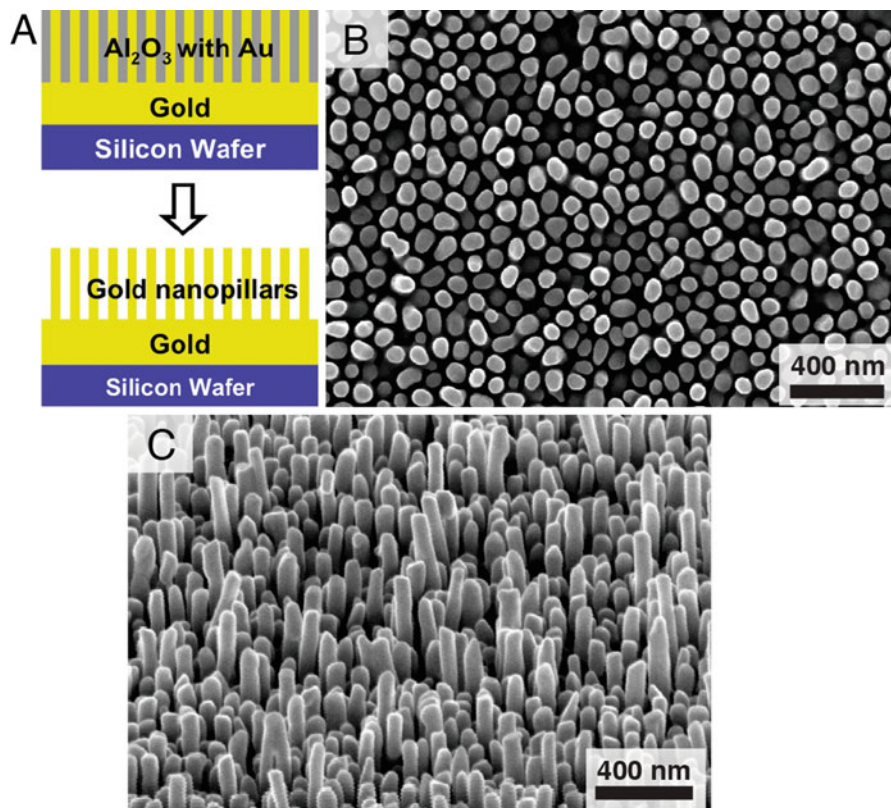
Fig. 11.1 (**A**) Schematic view of gold nanopillars fabricated via electrochemical template synthesis. After gold has been deposited into the nanochannels of an AAO membrane, the template is removed, thus yielding freestanding gold nanopillars (**B**) and (**C**) scanning electron micrograph of gold nanopillars prepared via electrochemical deposition into AAO membranes, in both plan and tilted projections

membrane thickness and can be accurately controlled by the amount of gold deposited, i.e., by varying the deposition time. Tailoring the pillar height enables the fabrication of gold nanostructures with variable aspect ratios (length to diameter), which is important for the optical properties of nanostructured metals [23], for example. Gold nanopillars that are electrodeposited onto AAO membranes have been fabricated with diameters between 15 nm [40] and 200 nm [41] and heights ranging from 100 nm [42] to 8 μm [43] (see Table 11.1).

Martin et al. found that electrochemical deposition of gold into AAO pores yields two different nanostructures depending on the presence of an organocyanide molecular anchor. When an anchor such as (2-cyanoethyl) triethoxysilane is attached to the pore walls, the formation of hollow gold tubules takes place, whereas the absence of any molecular anchors results in the growth

of solid Au nanopillars [38]. This modification of the pore walls with a silane derivative was reported as pore-wall-modified electrodeposition [37].

After 2000 electrodeposition of gold into photoresist masks was presented by Greer et al. [44] and Nagel et al. [45]. In Greer's work the pillars were relatively large with diameters in the micrometer range, whereas Nagel produced pillars of 100 nm in diameter and 285 nm in height. Today, electrochemical deposition of gold nanopillars onto different template materials is well established and widely used for applications such as cell interfaces [46, 47], plasmonic devices [48], and electrodes for glucose detection [43, 49–51].

Electroless Plating

Electroless gold plating is a very simple and versatile fabrication method for vertical gold nanostructures that was introduced by Menon et al. in 1995 [52]. The templates for electroless deposition do not need to be electronically conductive because they do not serve as functioning electrodes: thus, nonconducting nanostructured polymer membranes are used, for example [22, 31]. In this approach a catalyst is required, which acts as a molecular anchor at the pore walls; Martin et al. used Sn^{2+} to sensitize the membrane [30]. In the following redox reaction involving $AgNO_3$, Ag nanoparticles are deposited at the pore walls: when this coated membrane is placed in a gold plating bath, the Ag particles are galvanically displaced as Au is the more noble metal [52]. The metal deposition starts at the pore walls and proceeds uniformly down through the complete pore length. Thus, nanopillars up to 10 μm can be deposited, longer than nanotubes resulting from other template-assisted methods. Depending on the pore length of the polymer template, the production of longer gold nanopillars up to 50 μm is possible [37]. For short deposition times hollow metal tubules are obtained, whereas longer deposition times of up to 48 h lead to the formation of solid gold pillars [31, 53]. Gold nanotubes or pillars with diameters from 10 nm [52, 54] to 460 nm [55, 56] have been prepared by electroless plating. Currently, this method is primarily applied to the fabrication of gold electrodes with hollow nanotubes or solid nanopillars [42, 56–59].

Physical Vapor Deposition

Physical vapor deposition (PVD) into track-etched polycarbonate membranes was considered by Brumlik et al. as another fabrication method for gold nanostructures [37]. However, they did not obtain solid gold nanorods with this technique but rather hollow tubules, which they subsequently strengthened electrochemically. Anandan et al. also used PVD to prepare silicon nanopillars from AAO templates [60]: when Si wires were exposed to water to test applicability in biosensors, severe bending of the nanostructures due to capillary forces occurred (see section 'Mechanical Stability'). They concluded that PVD would not be a suitable fabrication method for gold nanopillars used in biosensing applications as this method results in nanopillars of insufficient mechanical strength. Instead, cost-effective electrochemical template synthesis was recommended, which resulted in more mechanically stable gold nanorods.

Focused Ion Beam Milling

Focused ion beam (FIB) fabrication techniques involve the use of a beam of heavy ions, typically Ga+, to selectively and nonreactively etch a surface [61]. The technique may be used to trace geometric patterns on the tens of a nanometer scale, depending on the quality of the control systems of the particular instrument. The finesse of the resultant structures is typically limited by the quality of the ion optics, the Gaussian distribution of the incident focused ion beam, parameters and systems used to trace the design, and thermal- and charge-induced drift of the sample image position. Charge compensation using a local electron flood gun can act to mitigate image drift and distortion to a certain extent, while sectioning for depth profiling can be performed by the formation and polishing of a trench [61]. Reactive gas may be injected for local etching, as well as deposition of metal such as platinum in order to provide a scaffold for nanostructures that might otherwise be damaged during sectioning.

Dual-beam instruments combine a scanning electron microscopy (SEM) and FIB column to permit in situ forming and imaging by both ion and electron beams; the FIB column is commonly mounted at an oblique angle to the vertical SEM column, permitting concurrent SEM and FIB manipulation at an appropriately eucentric position on the sample. Ion beam imaging may be implemented as an alternative microscopy contrast to that of SEM, but one must be aware that sample etching occurs concurrently, and thus one must optimize parameters to avoid sample degradation [61]. A schematic example of the dual-beam FIB setup is shown in Fig. 11.2 below, where the main features of the apparatus are highlighted.

FIB milling is well suited to the manufacture of gold nanopillars, including individual pillars for mechanical testing, and arrays of pillars for device style applications [24, 62–65]. A multistep FIB milling procedure has been developed that is suitable for the fabrication of gold nanopillars of complex geometries [28]. Seeding of pattern array positions or templates for epitaxially grown structures is also possible by FIB methods, as regular arrays can be laid down on a surface with a high degree of automation. The diameter of FIB-milled gold nanopillars may range from 50 nm [28] to 8 μm [62] and thus spans a much larger range than template-assisted synthesis. With 30 nm [28] to 11 μm [62] the height range is comparable (see Table 11.1).

Negative issues that could arise during the use of FIB fabrication techniques include the implantation of heavy ions, the formation of defects, and an amorphous surface layer [44, 61, 66]. The nature of such an amorphous layer and precipitation of gallium at the sample surface has been investigated by Lehrer et al. [67], where they found the implantation depth depends on the energy of the incident ions and may be up to 70 nm below the surface. With regard to milled nanopillar structures, one should also be aware of lateral contamination due to redistribution of sputtered gallium and sample particulates from the milling process.

Fig. 11.2 Schematic of a dual-beam FIB/SEM setup, illustrating a vertical SEM column and tilted FIB column, both incident on a eucentric working area on the sample
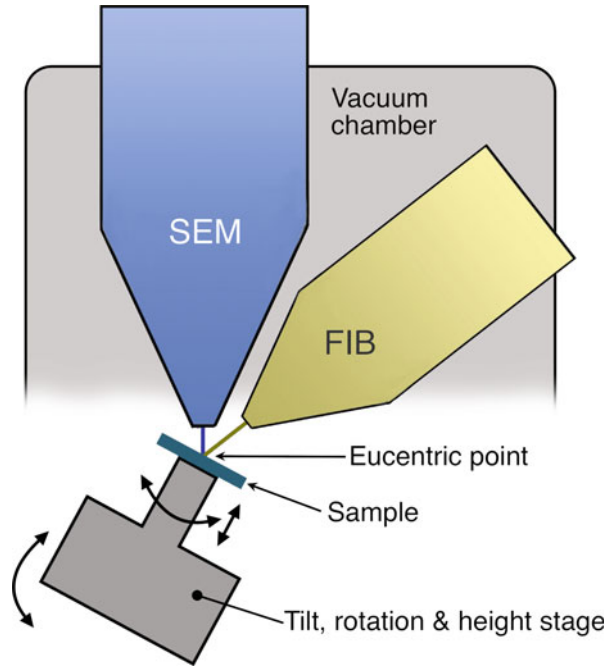
Nanoimprint Lithography

Nanoimprint lithography (NIL) by both hot and cold embossing is another promising route to the fabrication of uniform nanostructures over large areas. One generally considers the imprint of a high-stiffness, nanopatterned mold into a soft layer under the influence of pressure and/or temperature, either directly over a single area or in a roll-to-roll process [68]. By such methods one can rapidly produce large nanopatterned areas with applications in the field of biology, photoresists, and photonics, for example [69]. The malleability of gold facilitates NIL embossing as a feasible method for the production of gold nanopillars; the lithographic imprinting of gold by a prefabricated patterned master (e.g., by lithographic writing onto silicon) can produce high-fidelity nanopillars for various applications [20, 63, 70, 71]. A wide range of geometries are feasible depending on the quality of replication; to date gold nanopillars were fabricated via NIL in a much narrower geometry range than FIB-milled nanopillars (see Table 11.1). The diameters of imprinted gold pillars range from 100 to 1,100 nm with heights between 50 and 4,000 nm.

For certain applications imprinted gold nanopillars may be modified after the imprinting process. Gao et al. fabricated a large array of 300 nm diameter gold nanopillars with 1:1 aspect ratio via NIL, which they subsequently coated with Fe_2O_3 to enable plasmonic applications [71]. It is also possible to deposit gold onto

polymeric nanopillars produced by NIL in order to form active systems for plasmonic sensing [72, 73]. Nakamoto et al. fabricated nanopillar-hole structures for plasmonic nanogap devices [70], where nanoholes consisting of polyethylene terephthalate were fabricated via NIL followed by sputtering gold into the holes. This process led to the formation of one nanopillar in each hole, due to selective gold deposition at the base of the hole and upper edge of the surrounding polymer. Almost defectless nanopillar-hole pairs were fabricated over an area of several square millimeters. Nanopillar height and the gap between pillar and hole could be controlled by tuning the hole depth and sputtering time.

Other Fabrication Techniques

Gold nanopillars can also be fabricated by electron beam (e-beam)-induced decomposition of an organometallic precursor [28]. Dhawan et al. used an e-beam to dissociate gold from the precursor gas dimethyl Au (III) fluoro acetylacetonate. The necessary ionization energy was in the range of the secondary electrons (between 5 and 50 eV), generated when the glass substrate was exposed to a focused e-beam. The glass substrate was coated with either indium tin oxide (ITO) or Ti, as the negative surface charge of uncoated glass would deflect the e-beam. Linear arrays of gold nanopillars, with diameters between 40 and 70 nm and spacing between 15 and 30 nm, were fabricated by this process. In future developments, such linear gold nanopillar arrays on coated glass could find applications as plasmonic waveguides.

A novel fabrication method for gold nanopillars based on the assembly of Au nanoparticles was recently presented by Cetin et al. [27]: a mask of poly(methyl methacrylate) (PMMA) on a gold substrate was structured by e-beam lithography to form nanopores; these nanopores were subsequently filled with gold nanoparticles suspended in deionized water (see Fig. 11.3). By applying an electric field, the nanoparticles were fused together to form nanopillars, and upon removal of the PMMA mask by dissolution with acetone, freestanding gold nanopillars with diameters between 50 and 100 nm and heights up to 400 nm remained. Changing the mask geometry will also enable the assembly of Au nanoparticles into pillars of other dimensions. Appropriate applications for such Au nanopillars would be in optical trapping or biosensing nanoplasmonic devices, for instance.

Fabrication of Prepatterned Nanopillars

Often, the fabrication of gold nanopillars is combined with a patterning method to create arrays of gold nanopillars with specific geometric constraints and long-range order. A simple approach for the fabrication of localized gold nanopillars is the combination of e-beam lithography and metal deposition. Zin et al. used this approach to produce gold nanopillars on Si wafers that were prestructured by e-beam lithography of a PMMA resist followed by a lift-off process [25]. The resulting gold
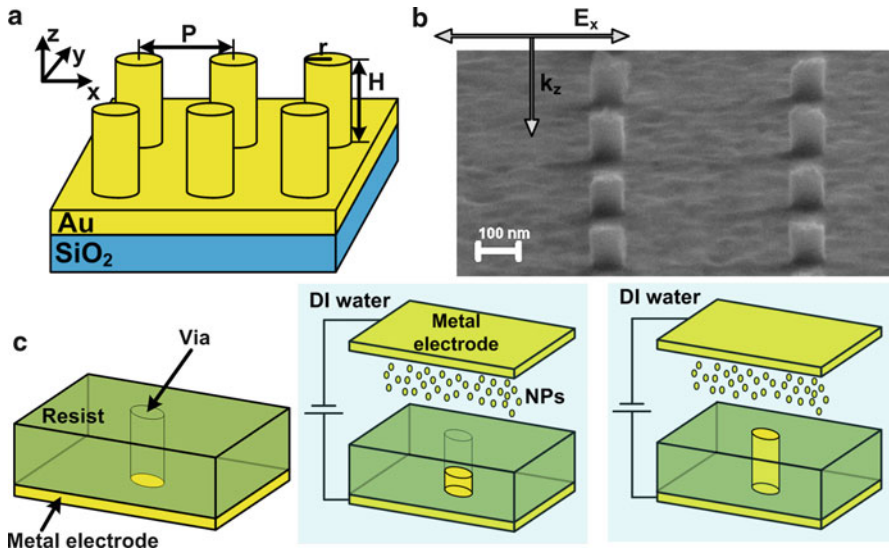
Fig. 11.3 Gold nanopillars prepared by assembly of gold nanoparticles. (**a**) Geometry of the nanopillar arrays. (**b**) SEM image of the nanopillar array with radius 50 nm, height 100 nm, and pitch 500 nm. The direction of propagation and polarization of the illumination source is indicated in the figure. (**c**) Fabrication process of the nanopillar arrays (Reprinted with permission from [27], copyright 2011 AIP Publishing LLC)

nanopillars had diameters ranging from 50 to 200 nm, where the height was maintained at 50 nm. Due to the prepatterning of the Si wafer, periodic arrangements of pillar bundles were achieved with grating constants from 50 to 200 nm. These patterns could be fabricated with a precision of 20 nm on a large scale up to $10 \times 10 \ \mu m^2$. Nagel et al. also used this approach to create a cubic lattice of single-gold nanopillars with a height of 285 nm and a diameter of 100 nm [45]; the pitch of this lattice was adjusted to 250 nm.

Combining imprint or lithography methods with template-assisted synthesis also enables the fabrication of localized gold nanopillars at predefined positions on a substrate. This technique has been employed for the production of large-scale nano- and micropatterned gold nanopillar arrays on silicon substrates [74]. First, Si wafers were coated with 500 nm of aluminum, onto which different micropatterns were imprinted using silicon stamps that were prestructured by lithography combined with reactive ion etching (RIE). After transferring the micropattern onto the Al film, anodization was carried out to obtain nanoporous AAO membranes, which were electrochemically filled with Au at the predefined positions. The resulting gold nanopillars were 35 nm in diameter and 300 nm high.

Later, Matéfi-Tempfli et al. realized the growth of localized gold nanopillars by combining template-assisted deposition onto AAO templates with two different photolithography methods [75]. In one approach AAO membranes were prepared on a confluent gold layer, subsequently coated with 100 nm of SiN, and finally

Fig. 11.4 Scanning electron micrograph of localized single nanowires in a matrix arrangement, fabricated by the masking of the supported nanoporous alumina surface using e-beam lithography. Image courtesy of A. Vlad (unpublished)
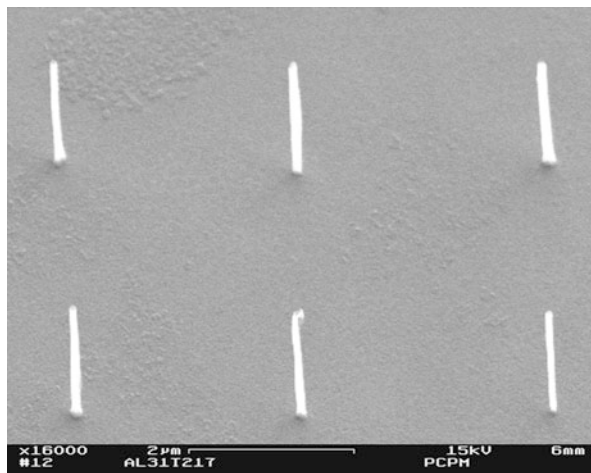
PMMA was deposited on the SiN and prestructured by e-beam lithography. After resist development and RIE, the SiN layer was patterned and gold was deposited into the selectively opened nanopores. This technique exhibited a very high precision, which allowed for the production of freestanding gold nanopillars at widely spaced, predefined positions, as can be seen in Fig. 11.4.

In an alternate fabrication method, a gold layer upon a Si wafer was prestructured via lithography before Al was deposited and anodized to obtain nanopores. During the subsequent electrochemical gold deposition, the pillars only grew on the localized conducting parts of the underlayer [75].

Recently, Weber et al. adapted this lithography approach of a metal layer under the AAO membrane by depositing a sandwich structure of a gold film, a titanium barrier, and an upper gold film on Si [76]. Circular gold patches with diameters from 100 to 600 nm were patterned on the upper gold layer using e-beam lithography into a PMMA resist followed by a lift-off step. Subsequently, an Al film was deposited and anodized, followed by electrochemical filling of the AAO nanopores yielding gold nanopillars in the predefined circular positions. The rest of the surface was masked by the Ti barrier layer meaning the associated pores were not filled with gold. Prestructuring of the underlying gold substrate could also be achieved by FIB milling, as suggested by Einsle et al. [77]. Certain areas of the gold layer may be removed with the ion beam, and the size of these areas could be adjusted to the diameter of single AAO pores. Subsequent aluminum deposition, anodization, and pore filling yielded gold nanopillar arrays with scalable pillar densities and tailored heights.

A combination of e-beam lithography and template stripping to fabricate localized areas of gold nanopillars was recently introduced by Wang et al. [78]. In this approach, a silicon template was produced by e-beam lithography and RIE, followed by the deposition of 500 nm gold and 1,000 nm copper. The copper layer was topped by single-crystal silicon, which was then used to strip the gold structure from the underlying template [48]. The resulting single gold nanopillars of diameter 280 nm

and a height of 130 nm were extremely regular in shape and of a smoother surface than gold nanopillars fabricated by the standard lift-off process [78]. As an illustration of the application of these gold nanostructures, plasmonic trapping of small polystyrene particles was demonstrated by Wang et al. [48, 78].

Properties

Gold nanopillars have been found to exhibit a wide range of material properties, combining excellent optical properties, based on surface-plasmon resonance (SPR), as well as good electrical conductivity. Due to their chemical inertness, gold nanopillars are also biocompatible and favorable as biointerfaces. In this section we present a detailed overview of the versatile properties of gold nanopillars.

Mechanical Stability

Mechanical properties of nanoscale structures are well known to deviate from those of the bulk, exhibiting size effects across a wide range of properties [62]. Nanopillars fabricated of metal and dielectric materials, in both amorphous and microcrystalline states, generally fall under the banner of 'smaller is stronger' [44]. The result of this size effect is that metallic nanopillars often exhibit mechanical properties of an increased magnitude: typically the moduli (relating elastic properties) and yield strength (the minimum stress required to induce plastic deformation) both increase with respect to the accepted bulk values, the mechanisms for which shall be considered further in this section.

Uniaxial compression testing of individual gold nanopillars has been accomplished to a high level of accuracy using instrumented nanoindenter apparatus [63, 65], as shown in Fig. 11.5, for example: a diamond flat punch of a diameter larger than the pillar is brought into conformal contact with the pillar in a load-controlled regime, while load–displacement data are gathered during loading to compressive failure. This 'smaller is stronger' refrain is ably demonstrated to be valid for gold nanopillars tested under uniaxial compression: the ultimate compressive yield stress has been shown to increase from the bulk value of around 30 MPa to as high as 800 MPa, an effect that has been attributed to dislocation starvation [24, 66]. Other size effects are also manifested: for example, it has been demonstrated for both as-produced and prestrained/annealed gold nanopillars that the yield stress is reduced (typically by up to around 50 %) by prestraining, an effect not seen in the bulk and a result of increased dislocation density and reduced flow stress [64]. No significant differences were found when comparing gold nanopillars produced by FIB milling and NIL fabrication methods with regard to mechanics and scaling behavior [63].

The mechanical stability of gold nanopillars is particularly important for applications where they are exposed to electrolytes or buffer solutions, such as in biocompatibility studies, for example. Anandan et al. used a water droplet test to
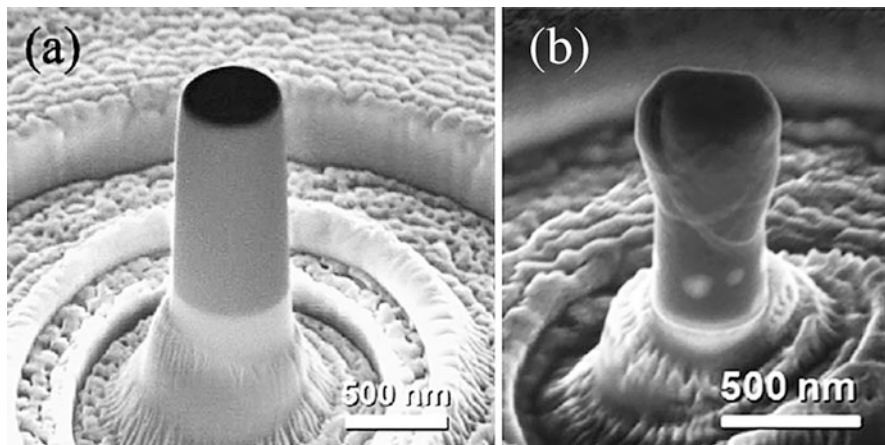
Fig. 11.5 Scanning electron micrographs illustrating the uniaxial compression testing of a FIB milling-fabricated Au nanopillar in an instrumented nanoindenter (**a**) prior to, and (**b**), post compression: the slip boundaries that form at the surface propagate across the pillar causing failure (Reproduced from [64], copyright 2009 Elsevier Ltd.)

study how gold nanorods behave in a liquid environment [60]. The pillars were fabricated via AAO template synthesis and were of 150 nm in diameter and 4.5 μm high, thus yielding an aspect ratio of 30. After the AAO template was removed, the nanopillars showed slight bunching at the free ends. The subsequent water droplet tests did not deform the pillars any further; Anandan et al. concluded that the pillar bending occurred due to capillary forces between the nanostructures and the electrolyte. For gold nanopillars with aspect ratios below 30, no deformation was observed: thus, gold nanopillars of lower aspect ratios exhibit a higher resistance to bending, which is important in cell culture or electrochemical studies where the nanopillars are exposed to liquids (see sections 'Biocompatibility' and 'Electrochemical Properties').

Crystalline Microstructure

Gold nanopillar volumes are sufficiently small such that one may turn to molecular dynamic (MD) simulations to provide some information on the anomalous behavior observed in nanopillar mechanics. MD simulations of defect-free gold nanopillars of only a few nanometers in diameter indicate that dislocations are nucleated on the exterior surface of the nanopillar [79]. Similarly, simulations of dislocation motion through single nanopillars with diameters below 10 nm have shown that when the diameter falls below a certain critical length scale, the onset of slippage (dislocation motion within a crystal plane) is governed only by the free surface rather than the bulk of the pillar [80]. Bulk metallic glass nanopillars – amorphous states of metal with no crystalline structure – exhibit a lesser magnitude of size effect on the yield strength compared to microcrystalline metallic nanopillars [81]. The Young's modulus of

multishell gold nanowires under compression is shown to increase with decreasing radius by MD simulation [82]. Simulations also indicate that the formation of nanotwinned grain boundaries in gold nanopillars – where the atomic structure is mirrored on either side of the boundary – results in an increase of mechanical strength [83].

The crystalline structure, orientation, and grain boundaries within gold nanopillars may be experimentally probed by suitable techniques, including scanning and transmission electron microscopy (SEM and TEM), X-ray diffraction (XRD), and photon correlation spectroscopy (PCS). TEM was utilized by Lancon et al. to show that incommensurate surfaces at <100> slip boundaries in gold nanopillars lead to frictionless sliding at that boundary [65]. Schneckenburger et al. showed with high resolution TEM that electrochemically deposited gold nanowires with <111> orientation had a homogenous, monocrystalline and low defect nature [153]. Crystalline gold nanotubes and nanorods with <111> orientation on titanium foils were also analyzed by Wang et al. using TEM and XRD to study the respective growth mechanisms in PC templates [154]. Shin et al. and Cherevko et al. used energy-dispersive X-ray spectroscopy, field emission SEM, and XRD to characterize the surface morphology and chemical composition of gold nanopillar arrays for electrochemical sensor applications [49, 51]. Similar techniques were used by Forrer et al. to characterize gold nanowire arrays formed by template synthesis [42].

Crystal orientation plays a significant role in the mechanics of gold nanopillars: for example, the onset of plasticity in <111>−oriented gold nanopillars is shown by atomistic simulation to depend on the binding of the surface atoms [84]. Diao and coworkers have studied the yield mechanisms in gold nanowires by atomistic simulation and show that nanowires yield via the propagation of <112> dislocations [85, 86]. Further MD simulations by Weinberger and Cai comparing body-centered cubic (BCC) and face-centered cubic (FCC) gold pillars indicate that single dislocations may multiply within a BCC micropillar but not an FCC pillar [87].

Plasmonic and Optical Characteristics

Surface-plasmon resonance is a property commonly observed in metals, whereby the electrons at the surface oscillate collectively in response to incident light. Gold is strongly plasmonically active, and the frequencies at which the plasmon resonance interacts with the incident light may be tuned via control of nanoscopic length scales. One may witness this effect in gold nanoparticle suspensions, whereby with decreasing particle diameter the observed color of the nanoparticle suspension becomes distinctly blue and then red, depending on the wavelengths of light absorbed by the plasmonic interaction [1].

The same degree of control over surface-plasmon interaction may be replicated by patterning gold with nanopillars of various diameters. Plasmonically active gold nanopillar arrays – with the requisite varying diameters – may be formed by the nanoimprinting of gold nanoparticles from a PDMS stamp, as demonstrated by Liang et al. [69]. Wurtz et al. proposed the use of plasmonic properties of gold

nanorod arrays for ultrafast optical device applications [88]. Furthermore, gold nanopillar surfaces are suitable for forming surface-plasmon traps and waveguides, as presented in recent studies [28, 48, 71]. Metamaterials, such as AAO membranes with embedded gold nanopillars (see section 'Metamaterials'), can also be applied to non-plasmonic optical applications: Pollard and coworkers have, for instance, demonstrated a number of applications utilizing the optical extinction spectra of such metamaterials by experiment and theoretical modeling [40, 89].

Biocompatibility

During the past few years, cell-nanostructure interfaces have become increasingly important in various nanobiotechnology applications, including cell signaling for improved cell adhesion and the development of novel implant materials [90, 91]. All these applications require the respective nanomaterial to be biocompatible so cells may adhere to the nanotopography showing vital growth.

Gold nanopillars have been found to exhibit biocompatibility towards several cell types. The first cell culture experiments on gold nanopillars were presented in 2007 by Haq et al. using the neuron precursor cell line of rat pheochromocytoma (PC-12) [92]. The nanopillars were fabricated using electrodeposition onto AAO templates of 200 nm in diameter, 2 μm high and spaced 70 nm apart, dimensions comparable to the size of cellular filopodia. A poly-L-lysine coating on top of a self-assembled monolayer (see section 'Self-Assembled Monolayer Coatings') was used to promote cell adhesion, and the PC-12 cells were found to adhere and proliferate on the coated nanopillars. However, the cells developed fewer and shorter neurites on the nanopillar substrates than on smooth reference surfaces, indicating the PC-12 cells were spatially aware of the underlying nanotopography. In future, gold nanopillar substrates may act as a useful tool in controlling neurite development in neurons.

In a later study gold nanopillar electrode arrays of 8–20 μm in diameter were coated with the protein fibronectin (see section 'Protein Modifications') and used for extracellular recordings from the cardiac muscle cell line HL-1 [46]. The gold nanopillars were of 300–400 nm in height and 60 nm in diameter. In this geometry the pillars supported tight adhesion of HL-1 cells, while the cell membranes also followed the underlying nanotopography. The distance between cell membrane and pillar tips was found to be ≤ 100 nm, as shown in Fig. 11.6. However, the membrane did not bend around the pillars or incorporate the nanostructures in any way. When the same pillar geometry was used for large-scale gold nanopillar arrays in detailed cell adhesion studies, HL-1 cells protruded into the inter-pillar cavities with diameters below 100 nm for the first time [47]. Furthermore, gold nanopillars were found to support vital growth and tight adhesion of the human embryonic cell line HEK 293. Gaps between pillar tips and HEK cell membranes were low, with distances generally below 200 nm. It was also observed that not only did cells react to the underlying nanotopography but bending of the nanopillars also occurred with HL-1 and HEK cells adhered to the arrays; nanostructure bending was presumably driven by cell adhesion forces.

Fig. 11.6 Tight adhesion of
HL-1 cells to gold nanopillars.
(**a**) Overview on the
cell-nanopillar interface.
(**b**) Detailed view of the
HL-1 cell membrane
protruding into the inter-pillar
regions (Reproduced from
[47], copyright 2012
Inderscience)
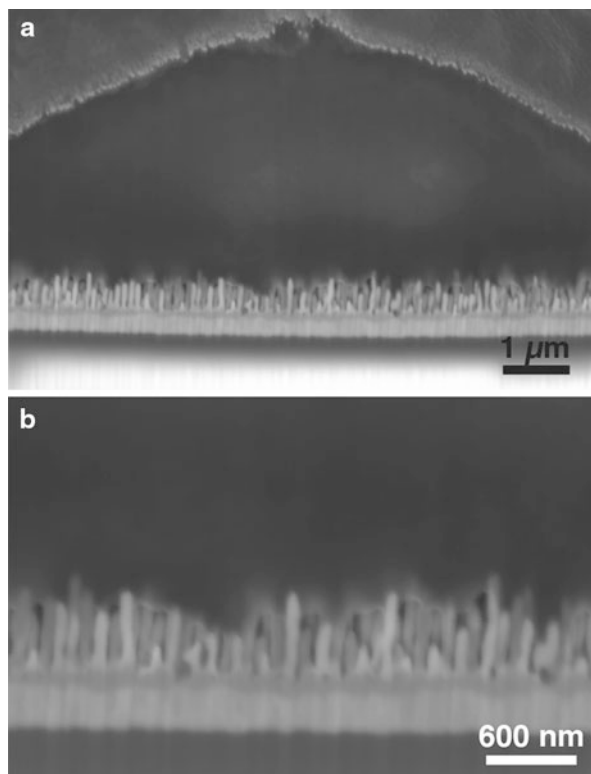
When primary cortical rat embryonic neurons (RCN) were grown on gold
nanopillar arrays that had been coated with distinct self-assembled monolayers
(see section 'Self-Assembled Monolayer Coatings'), a different scenario was
observed [47]. Adhesion and viability of RCN were unexpectedly low with large
distances between neuronal cell bodies and nanopillars. Actin assembly in the
neuronal growth cones was modified on gold nanopillars, thus indicating changes
in the neuronal cytoskeleton leading to a reduction in adhesion. These observations
were independent of the respective self-assembled monolayer coating; thus, it was
assumed that the nanopillar geometry is the key parameter for neuronal adhesion
and proliferation. Changes in the geometry might enable vital neuronal cell growth
on gold nanopillars in future studies.

Electrochemical Properties

Over the last decades, the development of new micro- and nanoscale electrode
designs has been largely motivated by electrochemical investigations. For example,
studies on neuronal chemical communication, such as the observation of vesicular
neurotransmitter release from individual cells, require the use of tiny electrodes to

achieve the desired spatial resolution on a (sub)cellular level [93–95]. Apart from the benefit of performing localized electrochemical experiments, such as the investigation of single cells, nanoscale electrodes allow the exploration of fundamental electrochemical phenomena, due to the fast diffusive processes that occur on the nanometer scale. The possibility to fabricate and employ such electrodes has facilitated the study of rapid electron-transfer reactions that are not accessible using conventional macroelectrodes [96, 97]. Furthermore, the small dimensions and associated small interface capacitances of such electrodes make it possible to carry out electrochemical measurements in highly resistive media and to observe phenomena on a submicrosecond time scale [98–100]. First band electrodes that were confined at least in one dimension to the nanoscale were developed and tested during the 1980s by several groups [101–103]. Since then, a huge variety of different approaches for both fabricating and applying nanoscale electrodes has been implemented [104–108]. In this context, not only the size of the electrodes but also the distance between individual electrodes has been scaled to the nanometer range. This is particularly interesting for redox-cycling applications, where closely spaced electrodes are independently biased to subsequently reduce and oxidize a molecule of interest [109]. The electrochemical amplification associated with redox cycling on the nanoscale has been exploited in a variety of applications, including scanning electrochemical microscopy (SECM) [110–116] and the electrochemical detection of single molecules [117–122]. On-chip redox cycling techniques for electrochemical sensing applications can profit from versatile nanofabrication technologies [123]. In the future, individually addressable nanopillar electrodes might further advance the implementation of highly efficient redox cycling concepts for electrochemical applications.

Metal nanopillars fabricated by template deposition as described above (see section 'Template-Assisted Synthesis') fall into a special category of nanoelectrode ensembles [52]. Typically, all nanoelectrodes are addressed at the same time, and template materials that exhibit densely packed nanostructures, such as AAO membranes, result in pillar arrangements whose distances lie in the submicrometer regime. Consequently, in most electrochemical experiments the diffusive field of individual pillar electrodes will overlap, as shown in Fig. 11.6, where various different diffusion mechanisms are depicted. The resulting 'macroscopic' diffusion layer and steady-state Faradaic currents are dominated by the geometric aspects of the electrode itself and not by the individual structure of the nanopillars. Macroscopic nanopillar modified electrodes thus exhibit 'classical' peak-shaped voltammograms, instead of the diffusion-limited sigmoidal shapes observed with individual ultramicro- or nanoelectrodes that exhibit radial diffusion profiles (see Fig. 11.7). However, there is a striking difference between conventional planar and nanopillar modified macroelectrodes. As the mass transport at the tip of an individual nanopillar is enhanced, kinetic effects of the electrode reactions play a greater role compared to reactions occurring at a planar surface. This makes it possible to study fast electrode kinetics not accessible in experiments employing planar macroelectrodes. Furthermore, if the shafts of the nanopillars are insulated, then the overall exposure of the electrode material to the electrolyte is strongly reduced without altering the geometric
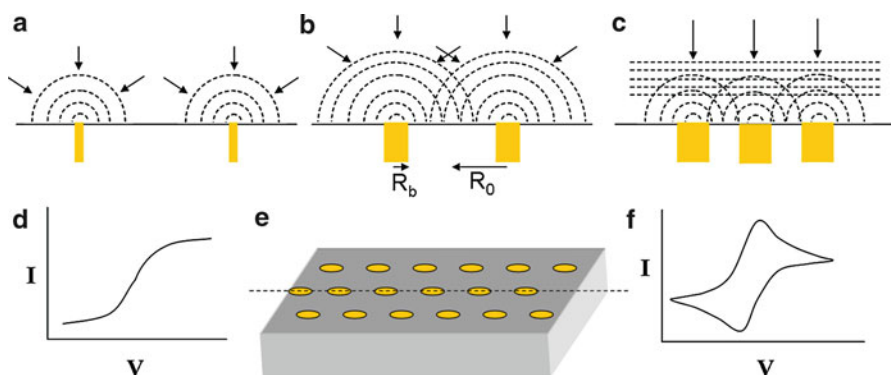
Fig. 11.7 Schematic of electrode ensembles of different size and density showing (**a**) radial diffusion, (**b**) overlapping radial diffusion, and (**c**) planar diffusion. (**d** and **f**) Cyclic voltammograms for the diffusion scenario in (**a**) and (**c**), respectively. (**e**) Electrode ensemble with metal electrodes represented by yellow circles surrounded by gray insulating material. Microelectrode radius, R_b, and diffusion zone radius, R_0, are shown (Reprinted with permission from [134], copyright 2008 American Chemical Society)

dimensions of the electrode. As a result, we obtain a decrease of the double-layer capacitance and corresponding increase in the electrode impedance, which reduces the background noise in current measurements. Additionally, the low capacitance yields fast response times without compromising the sensitivity of the electrode via an effective geometric area reduction. Martin and coworkers have exploited this effect in their pioneering work on gold nanoelectrode ensembles [52, 124]. They demonstrated a reduction of the detection limit for redox-active molecules exhibiting fast electron-transfer kinetics by three orders of magnitude at a gold nanoelectrode ensemble. A variety of approaches based on this principle and related techniques have evolved since then, not only with gold nanopillars but also with carbon nanotubes, magnetic nanowires, or polymeric and semiconductor nanostructures [54, 58, 59, 125–135]. While most of these methods aim at increasing the ratio of Faradaic to capacitive currents, some applications do require the opposite, namely, the presence of a large interfacial capacitance at small geometric dimensions. This is particularly interesting for highly localized voltage measurements of electrophysiological signals such as extracellular recordings of action potentials from single cells. Gold nanopillar electrodes can also meet this requirement if the shafts and not only the tips are exposed to the electrolyte solution [42, 46, 50, 136–138]. Such a configuration effectively lowers the electrode impedance without altering its geometric size and can additionally enhance the coupling between cell and electrode. In fact, this and similar concepts are currently pursued for the development of novel neurotechnology interfaces [5, 7, 8, 46, 47, 138–142]. Other applications of gold nanopillars make use of exposed pillars to increase the apparent electrode kinetics, or the loading capacity for specific enzymes, to improve the electrochemical sensing performance [41, 50]. Electrochemical characteristics of different studies on gold nanopillars are summarized in Table 11.2.

Table 11.2 Electrochemical properties of gold nanopillar electrode systems with different geometries

Nanopillar geometry	Electrochemical characteristics	References
Gold nanowire arrays, electropolished in 1 M H_2SO_4 (100–800 nm long, tip diameters of 30–80 nm)	Measured by cyclic voltammetry in Na_2SO_4, gold nanowires show a surface increase factor of 90 compared to flat gold electrodes	Forrer et al. [42]
Gold nanopillar microelectrodes (8–20 μm diameter) with pillars of 300–400 nm length and 60 nm diameter	Impedance of gold nanopillars in NaCl is reduced by one order of magnitude compared to planar gold electrodes	Brüggemann et al. [46]
Gold nanorod electrodes on flexible polyimide film: pillar diameter of 50–200 nm and height between 300 nm and 1 μm	Impedance of gold nanorods in NaCl is 25 times lower than the impedance of planar gold electrodes	Zhou et al. [138]
Gold nanopillars of 150 nm diameter with 4.5 μm height	Charging currents in Na_2SO_4 are 38 times higher than for flat gold electrodes. With the redox-active molecule $K_4Fe(CN)_6$, a sevenfold increase in sensitivity compared to flat gold electrodes is obtained	Anandan et al. [60]
Gold nanopillars with 150 nm diameter and heights between 1 and 6 μm	Sensitivity of nanopillar electrodes to the redox molecule $K_4Fe(CN)_6$ in Na_2SO_4 is increased by a factor of two compared to flat gold	Anandan et al. [50]
Gold nanopillars with 50 nm diameter and 200 nm height	Surface increase factors between 1.5 and 11.3 for different capacity and charge transfer-based systems	Schröper et al. [136]
Gold nanopillars of 200 nm diameter and 4 to 22.5 μm length on microelectrodes (10 to 40 μm diameter)	At 1 kHz impedance is reduced by a factor of 89.5	Nick et al. [156]

Functionalization and Surface Modification

A variety of surface functionalization methods have been introduced for gold nanopillars to facilitate their use in applications such as biosensors and cell interfaces. Established surface modifications ranging from self-assembled monolayers, proteins, and polymers to metal oxides are presented in this section. Furthermore, we discuss gold nanopillars that have been incorporated into other materials to form metamaterials with novel properties.

Self-Assembled Monolayer Coatings

Self-assembled monolayers (SAMs) can reproducibly immobilize, orientate, and organize biomolecules on various metal surfaces through different functional head groups. SAMs are widely employed as anchoring molecules for modifications of gold nanopillars in cell culture and biosensing applications.

Table 11.3 Overview on self-assembled monolayers, which have previously been used to modify gold nanopillars for various applications

Self-assembled monolayer	Applications	References
2-Mercaptoethylamine 3-Mercaptopropionic acid	Enzyme electrode fabrication for amperometric detection of glucose and H_2O_2	Delvaux et al. [55, 56, 143]
3-Mercaptopropionic acid 11-Mercaptoundecanoic acid	Glucose sensing: reaction kinetics and influence of SAM chain length Biotin/avidin detection system	Anandan et al. [41, 50, 144]
2-Mercaptoethylamine, coated with poly-L-lysine	Growth promoting coating for PC-12 cells	Haq et al. [92]
$HS(CH_2)_{11}NH_2$ and mixed monolayer consisting of $HS(CH_2)_{11}EG_3$ and HS $(CH_2)_{11}EG_6NH_2$	Growth and adhesion promoting coating for neuronal cell cultures	Brüggemann et al. [47]
2-Mercaptoethylamine as substrate for gold nanopillars	Electrochemical sensors	Wang et al. [145] and Shin et al. [51]
11-Mercaptoundecanoic acid	Immobilization of the redox protein cytochrome c for electrochemical studies	Schröper et al. [136]
Thiophenol	Surface-enhanced Raman scattering sensors	Caldwell et al. [152]
10-Carboxyl-1-decanethiol	Highly sensitive plasmonic biosensors	Saito et al. [72]

For gold in particular, alkanethiol SAMs are used, which form a strong covalent bond via chemisorption of an –SH group [21]. Because of this strong bond, it is not possible to remove SAM coatings from gold surfaces and as such they cannot be reused. When used in biosensors, SAMs prevent the close approach of solvents to the electrode surface, which results in a reduction of non-faradaic background currents [56]. The various different SAM molecules applied to gold nanopillars by several research groups are summarized in Table 11.3.

Delvaux et al. first reported the SAM modification of gold nanotube electrodes that had been deposited by electroless plating into track-etched PC membranes. They used a thiolated SAM of 2-mercaptoethylamine (MPE, cysteamine) and 3-mercaptopropionic acid (MPA) to introduce amine and carboxylic functionalities onto Au nanotubes by chemisorption [55, 143]. Aminated MPE layers were activated by the linking agent glutaraldehyde that couples to the enzyme glucose oxidase (GOx), which is responsible for breaking down sugar into its metabolites within cells. The terminal carboxylic acid groups of MPA gold pillars were modified with the activating agents 1-ethyl-3-(3-dimethylaminopropyl) hydrochloride (EDC) and *N*-hydroxysuccinimide (NHS), which enabled further coupling of the MPA-modified nanotubes to GOx. By this procedure it was possible, for the first

time, to covalently immobilize GOx to gold nanoelectrodes [143]. In a later study MPA and MPE monolayers on gold nanotubes were also used to bind the enzyme horseradish peroxidase (HRP) to gold nanostructures for the amperometric detection of hydrogen peroxidase (H_2O_2) [56].

Anandan et al. used MPA-modified gold nanopillars from template synthesis with GOx to study reaction kinetics and mass transport during glucose sensing [50]. By introducing the longer SAM 11-mercaptoundecanoic acid (MUA), they were able to examine in detail how the chain length of the absorbed SAMs affects the sensitivity of glucose detection [41]. GOx was covalently bound to MPA- and MUA-modified gold nanopillars with EDC and NHS. The long MUA chains were found to assemble in a more orderly fashion, with a higher degree of surface coverage and less defects than the shorter MPA chains. However, MPA exhibited a higher sensitivity in glucose detection due to a reduced electron-transfer resistance compared to the long MUA chains. MUA SAMs could also be modified with avidin, which enabled the use of MUA-coupled gold nanopillars as a highly sensitive biotin/avidin test system [144]. An alternative to using SAM-modified gold pillars for GOx functionalization is the conducting polymer polypyrrole (PPy). In a recent study films of GOx/PPy were also electropolymerized onto gold nanopillars to enable glucose detection (see section 'Polymer Functionalization') [43].

Cell cultures are another application area for SAM-modified gold nanopillars. Cysteamine monolayers on gold pillars were coated with the protein poly-L-lysine (PLL) by Haq et al. to promote adhesion and growth of the neuronal cell line pheochromocytoma (PC-12) [92]. In a further study two different kinds of SAMs were used to functionalize gold nanopillars for the growth of primary cortical rat neurons: $HS(CH_2)_{11}NH_2$ and a mixed monolayer consisting of $HS(CH_2)_{11}EG_3$ and $HS(CH_2)_{11}EG_6NH_2$ [47]. Both SAMs yielded a vital neuronal cell growth in short-time cell cultures up to 4 days. However, in cultures lasting up to 10 days, the SAM-coated gold nanopillars were not found to support adhesion and proliferation of the neuronal cells, while planar gold substrates with identical SAMs yielded good cell adhesion and proliferation (see section 'Biocompatibility').

SAM modification of gold nanopillars has also been used for other concepts: in a novel approach a monolayer of cysteamine on a planar gold substrate functioned as an anchor layer for the AAO template synthesis of gold nanopillars of uniform height and diameter [51, 145]. A possible application for gold nanopillars grown on SAMs are electrochemical sensors. In electrochemical studies carboxy-terminated monolayers such as MUA were also employed to immobilize redox proteins such as cytochrome c on gold nanopillar surfaces [136]. Moreover, SAMs were reported to improve the surface-enhanced Raman scattering (SERS) of different nanopillar materials that had been modified with gold capping layers. Thiophenol was, for instance, used as a modification for gold-capped Si nanowires in SERS applications [152]. Recently, gold-capped polymer nanopillars of cycloolefin (COP) were functionalized with 10-carboxyl-1-decanethiol to develop a plasmonic detection system for human immunoglobulin [72] (see section 'Gold Nanopillars in Plasmonic Devices').
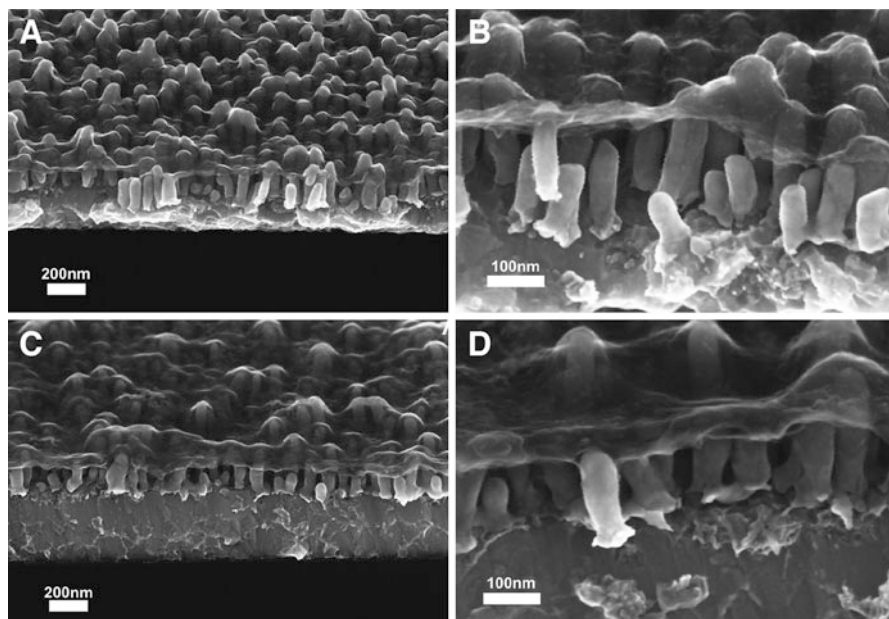
Fig. 11.8 Cross-sectional SEM images of Au nanopillar samples spin coated with PEDOT/PSS. (**A**) and (**B**) show a 28 nm film and (**C**) and (**D**) a 120 nm film in overview and close up. The thinner film adapts better to corrugations of nanopillars than the thicker one resulting in a higher surface roughness for the thinner film (Reprinted with permission from [137], copyright 2011 John Wiley & Sons Inc.)

Polymer Functionalization

Polymer modifications of gold nanopillars have been introduced for many different applications; the conducting polymer PPy was used as an alternative to SAM-modified gold nanopillars for the functionalization with GOx, for example [43]. In this study films of GOx/PPY were electropolymerized onto gold nanopillars for glucose sensing. Another conductive polymer for gold nanopillar modifications is poly(3,4-ethylenedioxythiophene) stabilized with polystyrene sulfonic acid (PEDOT/PSS) [137]. Sanetra et al. spin coated thin PEDOT/PSS films onto gold nanopillars with thicknesses ranging from 30 to 120 nm, completely covering the nanopillars as can be seen in the cross-sectional SEM images in Fig. 11.8. The impedance of these polymer-coated gold nanopillars was reduced by a factor of 2.5 compared to planar gold. In future applications biocompatible conductive polymers could facilitate the use of gold nanopillars as biosensors with improved chemical properties and reduced impedance.

A novel concept of gold-capped polymer nanopillars was recently presented by Saito et al. [72]: an AAO template was used to produce cycloolefin polymer (COP) nanopillars via thermal nanoimprint lithography (NIL) followed by sputter coating of a gold layer of 24–96 nm thick. When the tips of the gold nanopillars were coated with

a 10-carboxyl-1-decanethiol SAM, these structures could be used as biosensors for human immunoglobulin. Since NIL offers the advantage of mass production of polymer nanopillars with reproducible geometries, Saito et al. suggested that gold-capped COP nanopillars will be suitable for industrial and commercial applications in plasmonic biosensing (see section 'Gold Nanopillars in Plasmonic Devices').

Protein Modifications

Protein coatings have been tested for cell culture applications of gold nanopillars alongside SAM modifications (see section 'Biocompatibility'). Recently, gold nanopillar electrodes were coated with fibronectin to enable vital growth and extra-cellular recordings of the cardiac muscle cell line HL-1 [46, 47]. For cell cultures of human embryonic kidney cells (HEK 293) on gold nanopillars, a modification with PLL was employed, also yielding vital cell growth. Furthermore, PLL has been used as surface modification for cysteamine-coated gold nanopillars to support vital growth and neurite development of PC-12 cells [92]. One advantage of protein coatings versus SAM modifications is that these coatings may be selectively removed with enzymes such as trypsin. This procedure enables the reuse of the underlying gold nanopillar substrates for further cell culture experiments.

In an alternative application of gold nanopillar arrays, a protein-based functionalization strategy was developed to immobilize CdSe-ZnS quantum dots on the pillar tips. Using e-beam lithography and PMMA masks, gold nanoarrays were produced with very precise diameters and interspacing [25]. Three molecules of gold-binding peptide (GBP) formed a consecutive biomolecular linker that was modified with biotin at one end. Streptavidin-modified CdSe-ZnS quantum dots were then coupled to the biotin end of the linker producing structures suitable for surface-plasmon-enhanced fluorescence applications.

Metal Oxide Coatings

A coating of iron oxide was recently deposited onto gold nanopillars through e-beam evaporation [71]. Pillars were coated with 90 nm of Fe_2O_3 using metallic Fe followed by annealing in oxygen. The Fe_2O_3-coated nanopillars were employed as thin-film electrodes for photocatalytic water splitting. Apart from the use of Fe_2O_3 coatings, future experiments could be performed with photoactive materials with wider band gaps such as WO_3 and TiO_2, in combination with nanopillars from other plasmonic metals such as Ag, Al, or Pd.

Metamaterials

Gold nanopillars have also been incorporated into other materials to form composites with tailored properties. A very simple approach to forming such a

Fig. 11.9 Electrochemically deposited gold nanopillars of 200 nm height in a nanoporous AAO template
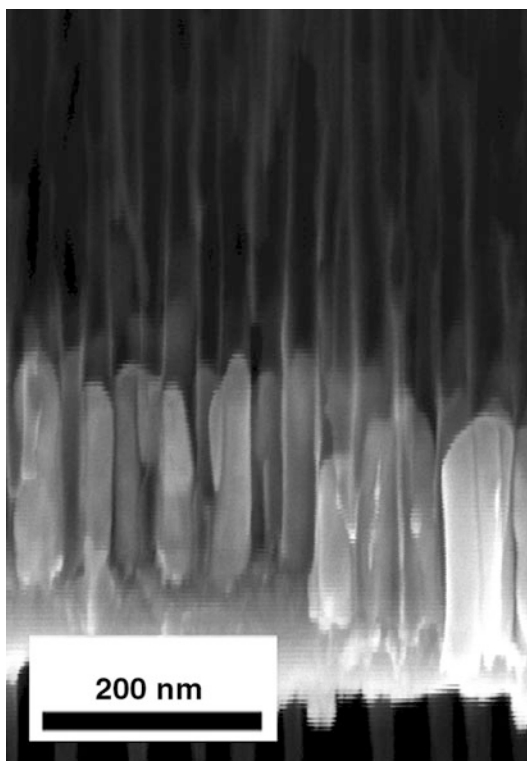
metamaterial is the use of template-synthesized gold nanopillars where the AAO membrane is not removed (see Fig. 11.9) [23, 146, 147, 155]. These composites were shown to be transparent in the visible range of the electromagnetic spectrum, and the color of the composite could be tailored by adjusting the diameter of the nanopillars in the AAO membrane [23]. Such AAO/Au metamaterials were also used for plasmonic biosensing with the streptavidin-biotin affinity model [155] and as microhole array electrodes [147]. In later studies AAO/Au composites on glass or silicon substrates and associated optical properties were investigated in more detail, and their application as plasmonic metamaterials with subpicosecond response times was suggested [40, 88, 89].

Composites of polymers and gold nanostructures have also been studied, such as polyester (PES) membranes with embedded gold nanotubes filled with a conductive polymer [148]. The metamaterial was biotinylated to enable coupling with streptavidin-coated microspheres. This model system demonstrated that microtubes could be used as building blocks for the self-assembly of supramolecular architectures. A composite of PC templates and gold nanopillars has also been presented, where a PC-gold composite was etched by O_2 plasma to selectively remove the polymer surface, thus exposing the ends of the gold nanopillars [149]. Since the etch rate of gold is much lower than for the surrounding PC template, the length of

the exposed nanopillars is adjustable by tuning of the plasma etch time. An application of this metamaterial may be nanostructured gold electrodes with tunable surface areas, for instance.

Applications

Gold nanopillars offer outstanding electrochemical and optical properties, good biocompatibility, and a large variety of surface modifications. Because of these excellent properties, they have, for instance, been employed as electrodes in biosensors and into plasmonic devices. We present an overview of recent applications of gold nanopillars within these fields and compare and contrast their respective performance.

Biosensing Employing Nanopillar Electrodes

Electrodes of gold nanopillars were first presented by Menon et al., who used electroless deposition to produce gold nanoelectrode ensembles with individual electrode diameters as small as 10 nm [52] (see section 'Electrochemical Properties'). Several applications of gold nanopillar electrodes in biomolecular sensors and for cell signaling followed this pioneering study. Different gold nanopillar electrode systems with their applications and performance characteristics are summarized in Table 11.4.

Brunetti et al. presented biosensors with hollow gold nanotubes formed by electroless plating. They used gold nanostructures with diameters of 38 nm to develop biosensors based on the enzymes phenothiazine and methylviologen [59]. The resulting nanotube devices exhibited detection limits up to an order of magnitude lower than the detection limit of gold macroelectrodes. With Azure A and Azure B as electron-transfer mediators, the detection limit was as low as 0.12 μM, and for methylviologen 0.2 μM was measured. A later voltammetry study used these nanotube electrodes for trace amounts of (ferrocenylmethyl) trimethylammonium hexafluorophosphate (TMAFc$^+$ PF$_6^-$) and the protein cytochrome c [58]. The sensors in this work consisted of 4.8×10^6 nanoelectrodes over a total surface of 0.005 square centimeters: detection limits were 0.02 μM for FA$^+$ and 0.03 μM for cytochrome c. These results opened the path to (bio) sensing applications with gold nanopillars in the submicromolar concentration for the first time.

Today gold nanopillar electrodes are frequently used for the detection of glucose, which has become a model system to study the performance of nanoelectrodes. In amperometric measurements Delvaux et al. first studied the response of β-glucose to gold nanotube biosensors. Hollow gold nanotubes were modified with MPE and MPA to anchor the enzyme GOx above them; in glucose sensing these enzyme-modified gold nanoelectrodes showed a sensitivity of 400 nA mM^{-1} cm^{-2} [143]. In a later study, glucose sensitivities between 50 and

Table 11.4 Performance of gold nanopillars in various biosensing applications

Sensing device	Application	Sensing performance	References
Gold nanodisk electrodes with 10 nm diameter	Voltammetric detection of the redox-active molecule TMAFc$^+$	Detection limit was reduced by three orders of magnitude compared to gold macroelectrodes	Menon et al. [52]; Wirtz et al. [54]
Nanoelectrode ensemble of hollow gold nanotubes	Enzyme detection	Detection limits: 0.12 μM for Azure A and Azure B, 0.2 μM for methylviologen	Brunetti et al. [59]
Nanoelectrode ensemble of hollow gold nanotubes	Voltammetric detection of trace analytes	Detection limits: 0.02 μM for TMAFc$^+$, 0.03 μM for cytochrome c	Moretto et al. [58]
Hollow gold nanotubes with MPE or MPA as anchor for GOx	Amperometric detection of glucose	Sensitivity: 400 nA mM^{-1} cm^{-2}	Delvaux et al. [143]
		Sensitivity: 50–130 nA mM^{-1} cm^{-2} Detection limit: 2×10^{-4} M	Delvaux et al. [55]
Hollow gold nanotubes: bare and with MPE or MPA as anchor for HRP	Amperometric H$_2$O$_2$ detection	Bare nanotubes: Sensitivity of 14 μA μM^{-1}	Delvaux et al. [56]
		HRP-modified nanotubes: Sensitivity: 9.5 μA μM^{-1} for MPE and 11.3 μA μM^{-1} for MPA Detection limit: 4×10^{-6} M	
Solid gold nanopillars with GOx on MPA	Amperometric glucose sensing	Sensitivity: 3.13 μA mM^{-1} cm^{-2}	Anandan et al. [50]
Solid gold nanopillars with MPA and MUA for GOx immobilization	Amperometric glucose detection	MPA modification: Sensitivity of 2.68 μA μM^{-1} cm^{-2}	Anandan et al. [41]
		MUA functionalization: Sensitivity of 0.09 μA μM^{-1} cm^{-2}	
Solid gold nanopillars with GOx/PPY	Amperometric glucose sensing	Sensitivity: 36 μA μM^{-1} cm^{-2}	Gangadharan et al. [43]
Solid gold nanopillars without any modification	Nonenzymatic glucose detection: voltammetric and amperometric sensing	Voltammetric detection Sensitivity: 41.9 μA mM^{-1} cm^{-2} Detection limit: below 3×10^{-5} M	Cherevko et al. [49]
		Amperometric sensing Sensitivity: 309.0 μA mM^{-1} cm^{-2} Detection limit: 5×10^{-5} M	
Solid gold nanopillars with avidin on MUA	Avidin-based biotin sensor	Detection limit: 1 ng/ml Sensitivity: 159.0–845.1 Ω(ng)$^{-1}$ ml mm^{-2} (EIS), 0.521–4.196 (mFng)$^{-1}$ ml mm^{-2} (CV)	Lee et al. [144]
Microelectrodes with solid gold nanopillars	Extracellular signaling with heart muscle cells	Peak-to-peak	Brüggemann et al. [46]
	Signal recording from neurons	Signal amplitudes up to 10 times higher than with planar electrodes	Nick et al. [156]

130 nA mM^{-1} cm^{-2} were reported, where the detection limit was down to just 0.2 mM, and a high reproducibility with standard deviations below 4 % was achieved [55]; at 25 s the response time to the glucose injection was also reasonably fast. Even in the presence of interfering molecules such as ascorbic or uric acid, a linear relationship between glucose concentration and measured current was found for a glucose concentration range between 0.2 and 30 mM.

These same hollow gold nanoelectrodes were used for the amperometric detection of H$_2$O$_2$ with and without SAM functionalization. In the presence of a hydroquinone mediator (H$_2$Q), bare gold nanotubes yielded a sensitivity of 14 µA mM^{-1}, while flat gold macroelectrodes only offered 0.41 µA mM^{-1} [56]. When the gold nanotubes were modified with MPE and MPA, respectively, the enzyme HRP was immobilized on top of them. These HRP nanoelectrodes yielded a slightly lower sensitivity than bare nanotubes, approximately 10 µA mM^{-1} for both SAMs. The lower sensitivity was explained as a decrease of the active surface area during SAM modification and enzyme immobilization. Nevertheless, detection limits down to 4×10^{-6} M were measured for HRP-SAM nanotubes compared to 8×10^{-4} M for flat gold electrodes. When the interfering molecules uric and ascorbic acid or acetaminophen were introduced, the HRP-SAM nanoelectrodes showed the highest selectivity for H$_2$O$_2$. Besides their outstanding biosensing performance, these enzyme-modified gold nanotubes have the advantages of low cost, ease of fabrication, fast response time, and good reproducibility.

Anandan et al. later studied the role of reaction kinetics and mass transport in glucose sensing for nanoelectrodes with solid gold nanopillars of different heights (1, 2.5 and 6 µm) [50]. The pillars were of 150 nm in diameter and were functionalized with MPA and loaded with GOx. When 2.5 and 6 µm high nanopillars were wetted during the functionalization process, the nanostructures displayed a slight bunching deformation due to capillary interaction compounded by the reduced flexure rigidity of the higher pillars. The sensitivity of the functionalized pillars to glucose in amperometric current measurements was 0.91, 1.8, and 3.13 µA mM^{-1} cm^{-2} for the 1, 2.5, and 6 µm tall pillars, respectively. The highest sensitivity value for 6 µm high pillars was 12 times greater than the reference result for a flat gold electrode (0.27 µA mM^{-1} cm^{-2}) and almost 8 times greater than the value Delvaux previously reported for hollow gold nanotubes [143]. It was also observed that the larger pillars exhibited longer response times to glucose injection. In another study Anandan et al. investigated the influence of SAM chain length on the sensitivity of glucose detection by functionalizing gold nanopillars with MPA and MUA. The shorter MPA SAM resulted in a higher sensitivity in glucose detection (2.68 µA mM^{-1} cm^{-2}) than the longer-chain MUA (0.09 µA mM^{-1} cm^{-2}) [41]. Since the GOx-catalyzed glucose oxidation is controlled by the position of the redox center relative to the electrode surface, sensitivity also depends on the chain length of the SAM layer: for this reason gold nanopillars with the longer MUA SAM chain exhibited reduced sensing performance compared to MPA. This trend was confirmed for planar gold modified with MPA and MUA, yielding 0.47 and 0.05 µA mM^{-1} cm^{-2}, respectively.

Gold nanopillars of 150 nm in diameter and heights ranging from 1 to 8 µm were also modified with films of GOx/PPY for improved glucose detection (see section 'Polymer Functionalization') [43]. These functionalized nanoelectrodes exhibited maximal sensitivities of 36 µA cm^{-2} mM^{-1} for 6 µm high nanopillars, the highest glucose sensitivity of gold nanopillar devices reported thus far. Moreover, the sensitivity was about 12 times higher than the value Anandan et al. previously reported for nanopillars of the same geometry functionalized with MPA and GOx [50].

Nonenzymatic glucose detection was recently presented for gold nanopillars of 70 nm diameter [49]. This study compared the voltammetric detection via cyclic voltammetry (CV) and differential pulse voltammetry with amperometric glucose sensing. Voltammetry yielded a sensitivity of 41.9 µA mM^{-1} cm^{-2} with a detection limit below 30 µM and a linear detection range up to 20 mM. For amperometric detection a linear correlation with the glucose concentration was found in the range of 1–10 mM. The sensitivity in this regime was very high at 309.0 µA mM^{-1} cm^{-2}, where a detection limit of 50 µM glucose was reported. Au nanopillar electrodes also showed good long-term stability, being utilized for up to two months with storage at ambient conditions. For practical applications, and because of the increased sensitivity, the use of amperometric gold nanopillar sensors was positively recommended in this study.

Gold nanopillar biosensors have also been applied as biotin detectors by anchoring an avidin functionalization onto MUA [144]. This setup was used for voltammetric detection and electrical impedance spectroscopy (EIS) of biotin diluted in phosphate-buffered saline (PBS) solution. The detection range for this avidin-based sensor was 1–50 ng/ml, while in CV experiments the sensitivity ranged from 0.5 to 4.2 (mF ng)$^{-1}$ ml mm^{-2}, corresponding to a 27–221 times increase over planar gold sensors. The sensitivity in EIS measurements was between 159 and 845 Ω(ng)$^{-1}$ ml mm^{-2}, an increase by a factor of 10.8–57.6 compared to planar gold electrodes. Overall, EIS measurements were more sensitive than CV in discriminating small changes due to surface adsorption of different molecules.

Recently, microelectrodes were modified with gold nanopillars (60 nm diameter, 300–400 nm height) to record action potentials from HL-1 cells [46]. The cells were cultivated on arrays of 64 pillar-modified electrodes with a fibronectin coating and diameters ranging from 8 to 20 µm. Due to the large surface area, the impedance of the nanopillar electrodes was strongly decreased compared to smooth electrodes. As a result, increased action potentials were measured yielding maximal peak-to-peak amplitudes of up to 1.5 mV with RMS noise levels of 6–7 µV. Compared to planar gold microelectrodes, the pillar electrodes yielded up to 100 % greater signal amplitudes. Nick et al. modified microelectrodes with even larger gold nanopillars, which were between 4 and 22.5 µm high. In cell culture experiments with neurons these sensors yielded signal amplitudes which were up to ten times higher than with planar gold electrodes [156]. In the future nanopillar electrodes with tailored geometries and larger heights in particular might also enable the recording of intracellular signals, similar to the concept of gold microspines as introduced by Hai et al. [8].

Table 11.5 Performance characteristics of plasmonic applications with gold nanopillars

Plasmonic device	Application	Performance characteristics	References
Polymer nanopillars with gold caps, SAM coating, and goat IgG	Plasmonic biosensor for human IgG	Detection limit: 1 ng/ml (corresponds to 6.7 pM)	Saito et al. [72]
Solid gold nanopillars with CdSe-ZnS quantum dots on protein linkers	Fluorescence applications	Fifteen-fold increase in surface-plasmon-enhanced fluorescence	Zin et al. [25]
Solid gold nanopillars with Fe_2O_3 coating	Electrodes for catalytic water splitting	50 % increase in photocurrent density compared to planar electrodes	Gao et al. [71]
Ag/Au nanodisks on top of HSQ nanoposts	High-resolution printing and optical data storage	Printing at the limit of visible-light imaging with a resolution of 100,000 dpi	Kumar et al. [151]
Solid gold nanopillar arrays	Plasmonic nano-tweezer	Stable trapping of polystyrene beads with 110 nm diameter	Wang et al. [78]
Gold-capped silicon nanopillars	SERS-based biochemical sensors	Enhancement factors of up to 1.2 × 10^8	Caldwell et al. [152]
Poly(3-hexylthiphene) and [6,6]-phenyl C61 butyric acid methyl ester with gold nanopillars	Organic photovoltaic device	Peak enhancement of 60 % at a wavelength of 675 nm	Tsai et al. [26]
AAO/Au composite	Plasmonic biosensing with streptavidin-biotin	Detection limit of 300nM for biotin, corresponding to two orders of magnitude better than SPR sensors with continuous films	Kabashin et al. [155]
Solid gold nanopillar array	Optical detection of protein adsorption	Detection of lysozyme and bovine serum albumine: sensitivity of 246 ± 12 nm wavelength shift per refractive index unit	Pallarola et al. [157]

Gold Nanopillars in Plasmonic Devices

Gold nanopillars that have been implemented into plasmonic sensing devices also contribute to improved sensing performance (see Table 11.5). Pallarola et al. fabricated electrically active gold nanopillar arrays from PC membranes, which they used for the optical detection of protein adsorption. With nanopillars of approximately 100 nm diameter and 1.9 μm in height they could influence the adsorption kinetics of lysozyme and bovine serum albumine by electrochemical modulation [157]. Recently, polymer nanopillars from COP (40 and 65 nm in diameter) were modified with gold caps to create plasmonic sensors for human IgG. The gold caps were coated with a 10-carboxyl-1-decanethiol SAM, followed by a functionalization with goat antihuman IgG [72]. For the optical absorbance of the anti-IgG-immobilized Au-capped nanopillars, a linear detection range up to
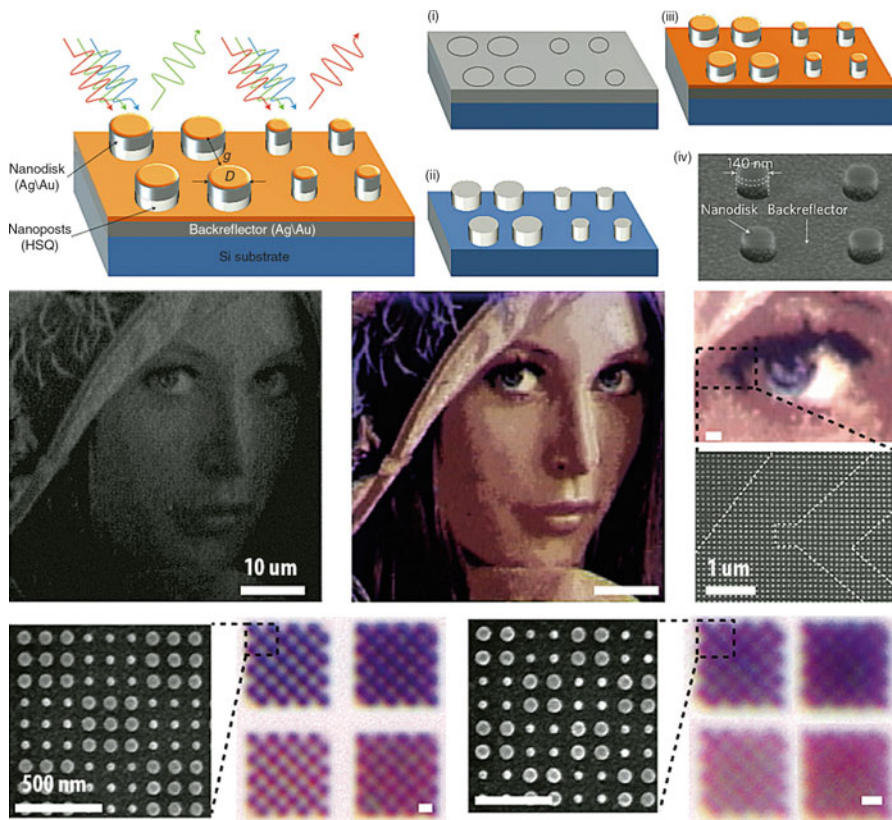
Fig. 11.10 Geometry-controlled, gold-coated HSQ/aluminum nanopillars are used to produce color images with a resolution of up to 100,000 dpi (Reproduced from [151], copyright 2012 Nature Publishing Group)

100 µg/ml was found. These gold nanopillar sensors displayed a detection limit of only 1 ng/ml, which corresponds to 6.7 pM IgG. In a previous study on plasmonic IgG sensors with horizontal gold nanorods 50 nm long and 15 nm in diameter, the detection limit was found to be only about 1 nM [150]. Thus, vertical gold nanostructures – even when only capped by gold – exhibit a superior binding capacity and sensitivity compared to lying nanorods.

Gold nanopillars were recently modified with CdSe-ZnS quantum dots for fluorescence applications by using a molecular biotin-streptavidin linker [25]. This arrangement yielded an increase in surface-plasmon-enhanced photoluminescence; up to a factor of 15 was achieved for 50 nm tall nanopillar arrays with 100 nm diameter and a grating constant of 100 nm. The fluorescence increase was also found to depend on the length of the molecular spacer between the quantum dots and pillar tips, where 16 nm was the optimum spacer length in this study. The biotin-streptavidin affinity model was also used by Kabashin et al. to demonstrate

plasmonic biosensing with gold nanopillars embedded in AAO templates [155]. The AAO/Au metamaterial yielded a detection limit of 300 nM for biotin and was shown to be two orders of magnitude better than conventional SPR sensors with continous films.

By coating gold nanopillars with Fe_2O_3, thin-film electrodes were designed that could be used for plasmon-enhanced photocatalytic water splitting [71]. With an oxide layer of 50 nm, the photocurrent density was enhanced by 50 % compared to planar electrodes. This enhancement was attributed to the increased optical absorption, which originated from surface-plasmon resonances and photonic-mode light trapping in the nanostructures.

Gold coating of hydrogen silsesquioxane (HSQ)/aluminum nanopillars formed on a backside reflecting material such as aluminum can be applied to the creation of some rather spectacular color images [151]. As shown in Fig. 11.10, the reproduction of color spectra is achieved by selective tuning of the plasmonically active nanopillar dimensions to form pixels of the desired color. Such a methodology has possible applications in the creation of imprinted color features on various media or for security purposes. Nakamoto et al. also fabricated nanopillar-hole structures for plasmonic nanogap devices [70], while linear arrays of gold nanopillars have been demonstrated to act as plasmonic waveguides through coupling of plasmons [28]. Wang et al. utilized plasmon trapping with gold nanopillars to form optical tweezers for the manipulation of small particles. With this design they were able to trap and rotate polystyrene spheres with diameters down to 110 nm [48, 78]. Gold-capped silicon nanopillar arrays were fabricated by Caldwell et al. for use in SERS-based chemical sensors, and thiophenol SAM showed an enhancement factor of over eight orders of magnitude greater than the bare-structured surface [152]. Furthermore, gold nanopillar arrays have recently been used in prototype organic photovoltaic devices to improve their performance. The novel solar cells exhibited an increased quantum efficiency between 640 and 720 nm compared to devices without nanopillars; at 675 nm the peak enhancement was around 60 % [26].

References

1. Eustis S, El-Sayed MA (2006) Why gold nanoparticles are more precious than pretty gold: noble metal surface plasmon resonance and its enhancement of the radiative and nonradiative properties of nanocrystals of different shapes. Chem Soc Rev 35(3):209–217
2. Duan GT et al (2006) Electrochemically induced flowerlike gold nanoarchitectures and their strong surface-enhanced Raman scattering effect. Appl Phys Lett 89(21):211905–3
3. Murphy CJ et al (2005) Anisotropic metal nanoparticles: synthesis, assembly, and optical applications. J Phys Chem B 109(29):13857–13870
4. Kim F et al (2008) Chemical synthesis of gold nanowires in acidic solutions. J Am Chem Soc 130(44):14442–14443
5. Seker E et al (2010) The fabrication of low-impedance nanoporous gold multiple-electrode arrays for neural electrophysiology studies. Nanotechnology 21(12):125504
6. Nishio K, Masuda H (2011) Anodization of gold in oxalate solution to form a nanoporous black film. Angew Chem Int Ed 50(7):1603–1607

7. Kim JH et al (2010) Surface-modified microelectrode array with flake nanostructure for neural recording and stimulation. Nanotechnology 21(8):85303

8. Hai A, Shappir J, Spira ME (2010) In-cell recordings by extracellular microelectrodes. Nat Methods 7(3):200–202

9. Panaitov G et al (2011) Fabrication of gold micro-spine structures for improvement of cell/device adhesion. Microelectron Eng 88(8):1840–1844

10. Choi MK et al (2011) Simple fabrication of asymmetric high-aspect-ratio polymer nanopillars by reusable AAO templates. Langmuir 27(6):2132–2137

11. Schmidt MS, Hübner J, Boisen A (2012) Large area fabrication of leaning silicon nanopillars for surface enhanced raman spectroscopy. Adv Mater 24(10):OP11–OP18

12. Xie C et al (2010) Noninvasive neuron pinning with nanopillar arrays. Nano Lett 10(10):4020–4024

13. Xie C et al (2011) Vertical nanopillars for highly localized fluorescence imaging. Proc Natl Acad Sci USA 108(10):3894–3899

14. Lin A et al (2012) Extracting transport parameters in GaAs nanopillars grown by selective-area epitaxy. Nanotechnology 23(10):105701

15. Jang D et al (2012) Deformation mechanisms in nanotwinned metal nanopillars. Nat Nanotechnol 7(9):594–601

16. Anandan V, Rao YL, Zhang G (2005) Nanopillar arrays with superior mechanical strength and optimal spacing for high sensitivity biosensors. NSTI-Nanotech 3

17. Yang M et al (2006) Platinum nanowire nanoelectrode array for the fabrication of biosensors. Biomaterials 27(35):5944–5950

18. Vlad A et al (2008) Nanowire-decorated microscale metallic electrodes. Small 4(5):557–560

19. Tian JH et al (2011) Fabrication of high density metallic nanowires and nanotubes for cell culture studies. Microelectron Eng 88(8):1702–1706

20. Buzzi S et al (2008) Metal direct nanoimprinting for photonics. Microelectron Eng 85(2):419–424

21. Ulman A (1996) Formation and structure of self-assembled monolayers. Chem Rev 96(4):1533–1554

22. Hulteen JC, Martin CR (1997) A general template-based method for the preparation of nanomaterials. J Mater Chem 7(7):1075–1087

23. Foss CA et al (1992) Optical-properties of composite membranes containing arrays of nanoscopic gold cylinders. J Phys Chem 96(19):7497–7499

24. Greer JR, Nix WD (2005) Size dependence of mechanical properties of gold at the sub-micron scale. Appl Phys A 80(8):1625–1629

25. Zin MT et al (2009) Surface-plasmon-enhanced fluorescence from periodic quantum dot arrays through distance control using biomolecular linkers. Nanotechnology 20(1):015305

26. Tsai SJ et al (2010) Effect of gold nanopillar arrays on the absorption spectrum of a bulk heterojunction organic solar cell. Opt Express 18(Suppl 4):A528–A535

27. Cetin AE et al (2011) Monopole antenna arrays for optical trapping, spectroscopy, and sensing. Appl Phys Lett 98(11):111110–111113

28. Dhawan A et al (2009) Fabrication of nanodot plasmonic waveguide structures using FIB milling and electron beam-induced deposition. Scanning 31(4):139–146

29. Possin GE (1970) A method for forming very small diameter wires. Rev Sci Instrum 41(5):1684640–1684642

30. Martin CR (1996) Membrane-based synthesis of nanomaterials. Chem Mater 8(8):1739–1746

31. Huczko A (2000) Template-based synthesis of nanomaterials. Appl Phys A Mater Sci Process 70(4):365–376

32. Ghicov A, Schmuki P (2009) Self-ordering electrochemistry: a review on growth and functionality of TiO_2 nanotubes and other self-aligned MOx structures. Chem Commun 20(20):2791–2808

33. Diggle JW, Downie TC, Goulding CW (1969) Anodic oxide films on aluminum. Chem Rev 69(3):365–405

34. Sulka GD (2008) Highly ordered anodic porous alumina formation by self-organized anodizing. In: Eftekhari A (ed) Nanostructured materials in electrochemistry. Wiley, Weinheim, pp 1–116

35. Fischer BE, Spohr R (1983) Production and use of nuclear tracks – imprinting structure on solids. Rev Mod Phys 55(4):907–948

36. Apel P (2001) Track etching technique in membrane technology. Radiat Meas 34(1–6):559–566

37. Brumlik CJ, Menon VP, Martin CR (1994) Template synthesis of metal microtubule ensembles utilizing chemical, electrochemical, and vacuum deposition techniques. J Mater Res 9(5):1174–1183

38. Brumlik CJ, Martin CR (1991) Template synthesis of metal microtubules. J Am Chem Soc 113(8):3174–3175

39. Martin CR (1991) Template synthesis of polymeric and metal microtubules. Adv Mater 3(9):457–459

40. Evans P et al (2006) Growth and properties of gold and nickel nanorods in thin film alumina. Nanotechnology 17(23):5746

41. Anandan V, Gangadharan R, Zhang G (2009) Role of SAM chain length in enhancing the sensitivity of nanopillar modified electrodes for glucose detection. Sensors (Basel) 9(3):1295–1305

42. Forrer P et al (2000) Electrochemical preparation and surface properties of gold nanowire arrays formed by the template technique. J Appl Electrochem 30(5):533–541

43. Gangadharan R, Anandan V, Zhang G (2008) Optimizing the functionalization process for nanopillar enhanced electrodes with GOx/PPY for glucose detection. Nanotechnology 19(39):395501

44. Greer JR, Oliver WC, Nix WD (2005) Size dependence of mechanical properties of gold at the micron scale in the absence of strain gradients. Acta Mater 53(6):1821–1830

45. Nagel PM et al (2012) Surface plasmon assisted electron acceleration in photoemission from gold nanopillars. Chem Phys 414:106–111

46. Brüggemann D et al (2011) Nanostructured gold microelectrodes for extracellular recording from electrogenic cells. Nanotechnology 22(26):265104

47. Brüggemann D et al (2012) Adhesion and survival of electrogenic cells on gold nanopillar array electrodes. Int J Nano Biomater 4(2):108–127

48. Wang K, Crozier KB (2012) Plasmonic trapping with a gold nanopillar. Chemphyschem 13(11):2639–2648

49. Cherevko S, Chung CH (2009) Gold nanowire array electrode for non-enzymatic voltammetric and amperometric glucose detection. Sensor Actuator B Chem 142(1):216–223

50. Anandan V et al (2007) Role of reaction kinetics and mass transport in glucose sensing with nanopillar array electrodes. J Biol Eng 1:5

51. Shin C, Shin W, Hong H-G (2007) Electrochemical fabrication and electrocatalytic characteristics studies of gold nanopillar array electrode (AuNPE) for development of a novel electrochemical sensor. Electrochim Acta 53(2):720–728

52. Menon VP, Martin CR (1995) Fabrication and evaluation of nanoelectrode ensembles. Anal Chem 67(13):1920–1928

53. Demoustier-Champagne S, Delvaux M (2001) Preparation of polymeric and metallic nanostructures using a template-based deposition method. Mater Sci Eng C 15(1–2):269–271

54. Wirtz M, Martin CR (2003) Template-fabricated gold nanowires and nanotubes. Adv Mater 15(5):455–458

55. Delvaux M, Demoustier-Champagne S, Walcarius A (2004) Flow injection amperometric detection at enzyme-modified gold nanoelectrodes. Electroanalysis 16(3):190–198

56. Delvaux M, Walcarius A, Demoustier-Champagne S (2004) Electrocatalytic H_2O_2 amperometric detection using gold nanotube electrode ensembles. Anal Chim Acta 525(2):221–230

57. Krishnamoorthy K, Zoski CG (2005) Fabrication of 3D gold nanoelectrode ensembles by chemical etching. Anal Chem 77(15):5068–5071
58. Moretto LM, Pepe N, Ugo P (2004) Voltammetry of redox analytes at trace concentrations with nanoelectrode ensembles. Talanta 62(5):1055–1060
59. Brunetti B et al (2000) Electrochemistry of phenothiazine and methylviologen biosensor electron-transfer mediators at nanoelectrode ensembles. J Electroanal Chem 491(1–2):166–174
60. Anandan V, Rao YL, Zhang G (2006) Nanopillar array structures for enhancing biosensing performance. Int J Nanomedicine 1(1):73–79
61. Reyntjens S, Puers R (2001) A review of focused ion beam applications in microsystem technology. J Micromech Microeng 11:287–300
62. Volkert CA, Lilleodden ET (2006) Size effects in the deformation of sub-micron Au columns. Philos Mag 86(33–35):5567–5579
63. Dietiker M et al (2011) Deformation behavior of gold nano-pillars prepared by nanoimprinting and focused ion-beam milling. Acta Mater 59(5):2180–2192
64. Lee SW, Han SM, Nix WD (2009) Uniaxial compression of fcc Au nanopillars on an MgO substrate: the effects of prestraining and annealing. Acta Mater 57(15):4404–4415
65. Lancon F et al (2010) Superglide at an internal incommensurate boundary. Nano Lett 10(2):695–700
66. Greer JR, Nix WD (2006) Nanoscale gold pillars strengthened through dislocation starvation. Phys Rev B 73(24):245410
67. Lehrer C et al (2000) Defects and gallium – contamination during focused ion beam micro machining. In: IEEE conference proceedings: ion implantation technology, 2000. Conference on Ion Implantation Technology, Alpbach, 2000. pp 695–698
68. Ahn SH, Guo LJ (2008) High-speed roll-to-roll nanoimprint lithography on flexible plastic substrates. Adv Mater 20:2044–2049
69. Liang C-C et al (2011) Plasmonic metallic nanostructures by direct nanoimprinting of gold nanoparticles. Opt Express 19(5):4768–4776
70. Nakamoto K, Kurita R, Niwa O (2011) Arrays of metallic nanopillars in holes for plasmonic devices. In: 15th international conference on miniaturized systems for chemistry and life sciences, Seattle
71. Gao H et al (2012) Plasmon-enhanced photocatalytic activity of iron oxide on gold nanopillars. ACS Nano 6(1):234–240
72. Saito M et al (2012) Novel gold-capped nanopillars imprinted on a polymer film for highly sensitive plasmonic biosensing. Anal Chem 84(13):5494–5500
73. Kubo W, Fujikawa S (2010) Au double nanopillars with nanogap for plasmonic sensor. Nano Lett 11(1):8–15
74. Wolfrum B et al (2006) Fabrication of large-scale patterned gold-nanopillar arrays on a silicon substrate using imprinted porous alumina templates. Small 2(11):1256–1260
75. Mátéfi-Tempfli S et al (2009) Nanowires and nanostructures fabrication using template methods: a step forward to real devices combining electrochemical synthesis with lithographic techniques. J Mater Sci Mater Electron 20(1):249–254
76. Weber D et al (2011) Large-scale patterning of gold nanopillars in a porous anodic alumina template by replicating gold structures on a titanium barrier. J Nanosci Nanotechnol 11(2):1293–1296
77. Einsle JF et al (2012) Directed self-assembly of nanorod networks: bringing the top down to the bottom up. Nanotechnology 23(50):505302
78. Wang K et al (2011) Trapping and rotating nanoparticles using a plasmonic nano-tweezer with an integrated heat sink. Nat Commun 2:469
79. Zepeda-Ruiz LA et al (2007) Mechanical response of freestanding Au nanopillars under compression. Appl Phys Lett 91(10):101907-3
80. Rabkin E, Srolovitz DJ (2007) Onset of plasticity in gold nanopillar compression. Nano Lett 7:101–107

81. Ye JC et al (2010) Extraction of bulk metallic-glass yield strengths using tapered micropillars in micro-compression experiments. Intermetallics 18(3):385–393
82. Lin JS, Ju SP, Lee WJ (2005) Mechanical behavior of gold nanowires with a multishell helical structure. Phys Rev B 72(8):085448
83. Afanasyev KA, Sansoz F (2007) Strengthening in gold nanopillars with nanoscale twins. Nano Lett 7(7):2056–2062
84. Rabkin E, Srolovitz DJ (2006) Onset of plasticity in gold nanopillar compression. Nano Lett 7(1):101–107
85. Diao J et al (2006) Atomistic simulations of the yielding of gold nanowires. Acta Mater 54(3):643–653
86. Diao JK, Gall K, Dunn ML (2004) Yield strength asymmetry in metal nanowires. Nano Lett 4(10):1863–1867
87. Weinberger CR, Cai W (2008) Surface-controlled dislocation multiplication in metal micropillars. Proc Natl Acad Sci USA 105(38):14304–14307
88. Wurtz GA et al (2011) Designed ultrafast optical nonlinearity in a plasmonic nanorod metamaterial enhanced by nonlocality. Nat NanoTechnol 6(2):107–111
89. Pollard RJ et al (2009) Optical nonlocalities and additional waves in epsilon-near-zero metamaterials. Phys Rev Lett 102(12):127405
90. Spatz JP, Geiger B (2007) Molecular engineering of cellular environments: cell adhesion to nano digital surfaces. In: Yu-Li W, Dennis ED (eds) Methods in cell biology. Academic, New York, pp 89–111
91. Curtis ASG et al (2001) Substratum nanotopography and the adhesion of biological cells. Are symmetry or regularity of nanotopography important? Biophys Chem 94(3):275–283
92. Haq F et al (2007) Neurite development in PC12 cells cultured on nanopillars and nanopores with sizes comparable with filopodia. Int J Nanomedicine 2(1):107–115
93. Wightman RM (1981) Microvoltammetric electrodes. Anal Chem 53(9):1125A–1134A
94. Wightman RM (2006) Probing cellular chemistry in biological systems with microelectrodes. Science 311(5767):1570–1574
95. Cans A-S, Ewing AG (2011) Highlights of 20 years of electrochemical measurements of exocytosis at cells and artificial cells. J Solid State Electr 15(7–8):1437–1450
96. Smith C, White H (1993) Theory of the voltammetric response of electrodes of submicron dimensions – violation of electroneutrality in the presence of excess supporting electrolyte. Anal Chem 65(23):3343–3353
97. Bond AM, Oldham KB, Zoski CG (1989) Steady-state voltammetry. Anal Chim Acta 216:177–230
98. Conyers JL, White HS (2000) Electrochemical characterization of electrodes with submicrometer dimensions. Anal Chem 72(18):4441–4446
99. Amatore C, Maisonhaute E (2005) When voltammetry reaches nanoseconds. Anal Chem 77(15):303A–311A
100. Baltes N et al (2004) Imaging concentration profiles of redox-active species with nanometric amperometric probes: effect of natural convection on transport at microdisk electrodes. Angew Chem Int Ed 43(11):1431–1435
101. Wehmeyer KR, Deakin MR, Wightman RM (1985) Electroanalytical properties of band electrodes of submicrometer width. Anal Chem 57(9):1913–1916
102. Bond AM, Henderson TLE, Thormann W (1986) Theory and experimental characterization of linear gold microelectrodes with submicrometer thickness. J Phys Chem 90(13):2911–2917
103. Morris RB, Franta DJ, White HS (1987) Electrochemistry at platinum bane electrodes of width approaching molecular dimensions: breakdown of transport equations at very small electrodes. J Phys Chem 91(13):3559–3564
104. Arrigan DWM (2004) Nanoelectrodes, nanoelectrode arrays and their applications. Analyst 129(12):1157–1165

105. Dudin PV et al (2011) Electrochemistry at nanoscale electrodes: individual single-walled carbon nanotubes (SWNTs) and SWNT-templated metal nanowires. ACS Nano 5(12):10017–10025

106. Rassaei L, Singh PS, Lemay SG (2011) Lithography-based nanoelectrochemistry. Anal Chem 83(11):3974–3980

107. Cox JT, Zhang B (2012) Nanoelectrodes: recent advances and new directions. In: Cooks RG, Yeung ES (eds) Annual review of analytical chemistry, vol 5. Annu Rev, Palo Alto, pp 253–272

108. Oja SM, Wood M, Zhang B (2013) Nanoscale electrochemistry. Anal Chem 85(2):473–486

109. Sanderson DG, Anderson LB (1985) Filar electrodes: steady-state currents and spectroelectrochemistry at twin interdigitated electrodes. Anal Chem 57(12):2388–2393

110. Bard AJ et al (1989) Scanning electrochemical microscopy. Introduction and principles. Anal Chem 61(2):132–138

111. Macpherson JV, Unwin PR (2000) Combined scanning electrochemical-atomic force microscopy. Anal Chem 72(2):276–285

112. Sun P, Laforge FO, Mirkin MV (2007) Scanning electrochemical microscopy in the 21st century. Phys Chem Chem Phys 9(7):802–823

113. Edwards MA et al (2006) Scanning electrochemical microscopy: principles and applications to biophysical systems. Physiol Meas 27(12):R63–R108

114. Amemiya S et al (2008) Scanning electrochemical microscopy. In: Annual review of analytical chemistry. Annal Reviews, Palo Alto, pp 95–131

115. Schulte A, Nebel M, Schuhmann W (2010) Scanning electrochemical microscopy in neuroscience. Annu Rev Anal Chem 3(1):299–318

116. Takahashi Y et al (2012) Topographical and electrochemical nanoscale imaging of living cells using voltage-switching mode scanning electrochemical microscopy. Proc Natl Acad Sci 109(29):11540–11545

117. Fan F-RF, Bard AJ (1995) Electrochemical detection of single molecules. Science 267(5199):871–874

118. Fan F-RF, Kwak J, Bard AJ (1996) Single molecule electrochemistry. J Am Chem Soc 118(40):9669–9675

119. Sun P, Mirkin MV (2008) Electrochemistry of individual molecules in zeptoliter volumes. J Am Chem Soc 130(26):8241–8250

120. Zevenbergen MA et al (2011) Stochastic sensing of single molecules in a nanofluidic electrochemical device. Nano Lett 11(7):2881–2886

121. Singh PS et al (2012) Stochasticity in single-molecule nanoelectrochemistry: origins, consequences, and solutions. ACS Nano 6(11):9662–9671

122. Lemay SG et al (2012) Single-molecule electrochemistry: present status and outlook. Acc Chem Res 46(2):369–377

123. Kätelhön E, Wolfrum B (2012) On-chip redox cycling techniques for electrochemical detection. Rev Anal Chem 31(1):7–14

124. Hulteen JC, Menon VP, Martin CR (1996) Template preparation of nanoelectrode ensembles – achieving the "pure-radial" electrochemical-response limiting case. J Chem Soc Faraday Trans 92(20):4029–4032

125. Martin CR, Mitchell DT (1999) Template-synthesized nanomaterials in electrochemistry. In: Bard AJ, Rubinstein I (eds) Electroanalytical chemistry, vol 21. Marcel Dekker, New York, pp 1–74

126. Jeoung E et al (2001) Fabrication and characterization of nanoelectrode arrays formed via block copolymer self-assembly. Langmuir 17(21):6396–6398

127. Li J et al (2002) Novel three-dimensional electrodes: electrochemical properties of carbon nanotube ensembles. J Phys Chem B 106(36):9299–9305

128. Schmid G (2002) Materials in nanoporous alumina. J Mater Chem 12(5):1231–1238

129. Cheng WL, Dong SJ, Wang EK (2002) Gold nanoparticles as fine tuners of electrochemical properties of the electrode/solution interface. Langmuir 18(25):9947–9952
130. Ugo P, Moretto LM, Vezza F (2002) Ionomer-coated electrodes and nanoelectrode ensembles as electrochemical environmental sensors: recent advances and prospects. Chemphyschem 3(11):917–925
131. Yamada K, Gasparac R, Martin CR (2004) Electrochemical and transport properties of templated gold/polypyrrole-composite microtube membranes. J Electrochem Soc 151(1): E14–E19
132. Lin YH et al (2004) Glucose biosensors based on carbon nanotube nanoelectrode ensembles. Nano Lett 4(2):191–195
133. Koehne J et al (2004) The fabrication and electrochemical characterization of carbon nanotube nanoelectrode arrays. J Mater Chem 14(4):676–684
134. LaFratta CN, Walt DR (2008) Very high density sensing arrays. Chem Rev 108(2):614–637
135. Ugo P et al (2010) Diffusion regimes at nanoelectrode ensembles in different ionic liquids. Electrochim Acta 55(8):2865–2872
136. Schröper F et al (2008) Analyzing the electroactive surface of gold nanopillars by electro-chemical methods for electrode miniaturization. Electrochim Acta 53(21):6265–6272
137. Sanetra N et al (2011) Low impedance surface coatings via nanopillars and conductive polymers. Physica Status Solidi A 208(6):1284–1289
138. Zhou H-B et al (2009) Integration of Au nanorods with flexible thin-film microelectrode arrays for improved neural interfaces. J Microelectromech Syst 18(1):88–96
139. Hai A et al (2009) Spine-shaped gold protrusions improve the adherence and electrical coupling of neurons with the surface of micro-electronic devices. J R Soc Interface 6(41):1153–1165
140. Hai A et al (2009) Changing gears from chemical adhesion of cells to flat substrata toward engulfment of micro-protrusions by active mechanisms. J Neural Eng 6(6):066009
141. Nam Y (2012) Material considerations for in vitro neural interface technology. MRS Bulletin 37(6):566–572
142. Spira ME, Hai A (2013) Multi-electrode array technologies for neuroscience and cardiology. Nat Nanotechnol 8(2):83–94
143. Delvaux M, Demoustier-Champagne S (2003) Immobilisation of glucose oxidase within metallic nanotubes arrays for application to enzyme biosensors. Biosens Bioelectron 18(7):943–951
144. Lee S-J, Anandan V, Zhang G (2008) Electrochemical fabrication and evaluation of highly sensitive nanorod-modified electrodes for a biotin/avidin system. Biosens Bioelectron 23(7):1117–1124
145. Wang X-Y et al (2004) Direct electrochemical fabrication of metallic nanopillar array on Au electrode surface by the template technique. Chem Lett 33(8):982–983
146. Wang Z, Su YK, Li HL (2002) AFM study of gold nanowire array electrodeposited within anodic aluminum oxide template. Appl Phys A 74(4):563–565
147. Brumlik CJ, Martin CR, Tokuda K (1992) Microhole array electrodes based on microporous alumina membranes. Anal Chem 64(10):1201–1203
148. Sapp SA, Mitchell DT, Martin CR (1999) Using template-synthesized micro- and nanowires as building blocks for self-assembly of supramolecular architectures. Chem Mater 11(5):1183–1185
149. Yu S et al (2003) Nano wheat fields prepared by plasma-etching gold nanowire-containing membranes. Nano Lett 3(6):815–818
150. Mayer KM et al (2008) A label-free immunoassay based upon localized surface plasmon resonance of gold nanorods. ACS Nano 2(4):687–692
151. Kumar K et al (2012) Printing colour at the optical diffraction limit. Nat Nanotechnol 7(9):557–561

152. Caldwell JD et al (2011) Plasmonic nanopillar arrays for large-area, high-enhancement surface-enhanced Raman scattering sensors. ACS Nano 5(5):4046–4055
153. Schneckenburger M et al (2012) Cross-sectional characterization of electrodeposited, monocrystalline Au nanowires in parallel arrangement. Small 8(22):3396–3399
154. Wang H-W et al (2006) Standing [111] gold nanotube to nanorod arrays via template growth. Nanotechnology 17(10):2689–2694
155. Kabashin AV et al (2009) Plasmonic nanorod metamaterials for biosensing. Nat Mater 8 (11):867–871
156. Nick C et al. (2013) High aspect ratio gold nanopillars on microelectrodes for neural interfaces. Microsyst Technol
157. Pallarola D et al. (2013) Real-time monitoring of electrochemical controlled protein adsorption by a plasmonic nanowire based sensor. Chem Comm 49:8326–8328

Stabilization and Characterization of Iron Oxide Superparamagnetic Core-Shell Nanoparticles for Biomedical Applications

12

Erik Reimhult and Esther Amstad

Keywords

Colloidal stability • MRI • NP • PEG • Polymer grafting • SPION • Surface functionalization

Introduction

Superparamagnetic iron oxide NPs, with core diameters between 3 and 15 nm, are used in a rapidly expanding number of research and practical applications in the biomedical field; the most common includes magnetic cell labeling [1, 2], separation [3], and tracking [3], for therapeutic purposes in hyperthermia [4, 5] and drug delivery [6] and for diagnostic purposes most prominently as contrast agents for magnetic resonance imaging (MRI) [7–9]. There are also many applications for smart hybrid materials functionalized with nanoparticle constituents for which superparamagnetic nanoparticles are an interesting alternative to provide a built-in actuator for heating or mechanical movement on the nanoscale.

Magnetic materials such as Co generally have higher saturation magnetization (M_s) than iron oxide [10] and would therefore serve as more efficient magnetic transducers or sensors. Biomedical applications are, however, constrained by the need for low toxicity and for regulatory approval. Iron oxide nanoparticles have a decisive advantage for biomedical applications [11], since they dissolve in a mild

E. Reimhult (✉)

Department of Nanobiotechnology, Institute for Biologically Inspired Materials, University of Natural Resources and Life Sciences Vienna, Vienna, Austria
e-mail: erik.reimhult@boku.ac.at

E. Amstad

Department of Physics, School of Engineering and Applied Sciences, Harvard University, Cambridge, MA, USA
e-mail: esther.amstad@seas.harvard.edu

acidic environment found, for instance, in lysosomes. The resulting Fe^{3+} ions can be fed into the natural iron storage, which is 3–5 g of iron for an adult human [12, 13]. Thus, the additional amount of iron released from dissolved iron oxide NPs is negligible if iron oxide NP concentrations in the µg/kg body weight range are injected [14].

To allow dispersion of NPs in a matrix or liquid, especially in aqueous media and at physiologic salt concentrations, the common strategy is to surround the NP core with an organic polymer shell of so-called dispersants. NPs without a dispersant shell will rapidly aggregate through strong, mainly dipolar, interactions with themselves and with other molecules in solution. The presence of polymeric bio-molecules such as proteins and saccharides with diverse surface physicochemical properties, ubiquitous in biological environments, strongly drives agglomeration and precipitation of clusters of nanoparticles through surface adsorption, bridging, and depletion interactions. The dispersant shell of NPs in biomedical applications not only prevents the direct aggregation of the NPs but also screens all interactions of the nanoparticle core with the biological molecules present in the environment that indirectly can induce agglomeration.

Commercially available superparamagnetic iron oxide NPs intended for magnetic labeling, cell separation purposes, and as MR contrast agents are typically stabilized with sugars such as dextran or synthetic polymers such as silicone [15]. These polymers used with molecular weights >10 kDa have a moderate affinity to the NP surface [16]. The resulting shell consisting of flexible polymers prevents NP cores from close interactions with other particles and proteins. This requires polymers to bind to the particle core, to be highly hydrated, and to induce repulsive interactions with proteins and other biomolecules. Due to the moderate affinity to iron oxide of these high molecular weight dispersants and the lack of a defined anchoring group, they often enwrap and cluster multiple iron oxide NP cores by direct physisorption to multiple NP surfaces. This results in poor control over cluster size (Fig. 12.1a) [17–20]. Furthermore, the dynamic rearrangement of the polymer shell results in a constantly changing interface of the nanoparticle.

An alternative strategy to disperse particles is to use a dispersant shell with low M_w (<10 kDa) where the polymer spacers are covalently bound to the nanoparticle core using an anchor that has high affinity for the NP surface (Fig. 12.1b). The anchors covalently linked to one end of the polymer chain assure an orientation of the polymer spacer and allow the use of polymer spacers with freely chosen properties, such as maximum hydration and protein repulsion, since the requirement to bind to the nanoparticle core can be relaxed. Using only one or closely spaced anchor groups ensures that these dispersants can bind to one NP core only. The resulting core-shell NPs can thus be divided into four components: the core, the anchor, the spacer, and optional surface functionalities (Fig. 12.1b). Each of these components can independently be adjusted through the modular buildup and defined geometry, rendering such NPs very versatile for a multitude of applications [21]. An important advantage resulting from the modular and controlled buildup is that the hydrodynamic size of the NPs can be precisely controlled, which
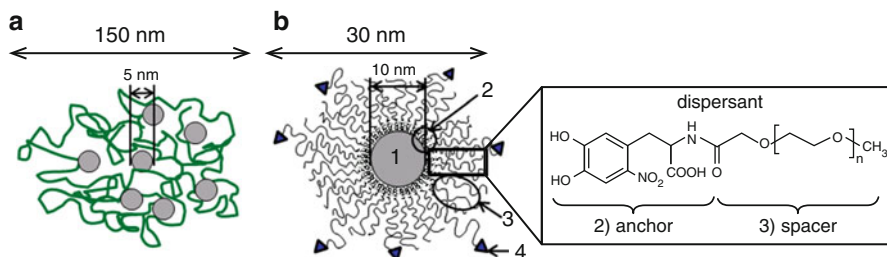
Fig. 12.1 Steric stabilization of iron oxide NPs. (**a**) Schematic of commercially available iron oxide-based MR contrast agents such as Feridex and Endorem. Superparamagnetic iron oxide NPs are coated with physisorbed high molecular weight dispersants such as dextran. The poor binding affinity of dextran leads to its reversible adsorption on the iron oxide NP surface. Furthermore, multiple iron oxide cores are embedded in one cluster. The resulting hydrodynamic diameter is many times larger than the core diameter. (**b**) Superparamagnetic iron oxide NPs stabilized with low M_w dispersants result in core-shell iron oxide NPs. These NPs can be divided into four components, namely, (*1*) core, (*2*) anchors, (*3*) spacers, and optionally (*4*) functionalities

is in contrast to NPs with dispersant shells consisting of physisorbed high M_w polymers. Furthermore, the well-defined assembly of dispersants at the NP surface enables controlled surface presentation of functionalities.

The size of NPs, their stability, dispersant shell thickness, and control over functionalities presented at the NP surface are the factors that determine NP performance in the demanding environment of a biological fluid [22, 23]. The structure of the dispersant shell which is determined by how it is assembled or synthesized will therefore control the performance of the NPs for their biomedical applications. An understanding of the influence of the type and assembly of dispersants on the NP surface and development of new types of dispersants are thus of pivotal importance for improving the performance of next-generation superparamagnetic NPs for imaging, drug delivery, and other demanding applications in biological fluids.

This chapter describes different aspects of NP stability, from its practical definition to its implementation. One goal is to link the understanding of the requirements on the molecular and nanoscale structure to different techniques by which they can be realized and to discuss their respective pros and cons. A critical point in nanoparticle research that is often not sufficiently appreciated in research focused on the clinical application of NPs is the challenge to characterize their actual physicochemical properties and structure. This includes the characterization of nanomaterials in an aqueous environment where most standard high-resolution imaging and chemical characterization techniques require specialized and demanding sample preparations. The definition and investigation of the colloidal stability of NPs might appear simple, but we will argue that it requires a comprehensive set of complementary characterization techniques. A careful reading of the literature also reveals that the meaning of stability

often varies from one paper to another and possibly from one subfield to another. We therefore also discuss the de facto definitions of NP stability to be found in the literature. After these general aspects, we describe how superparamagnetic iron oxide NPs are modified with dispersants of low and high surface affinity and M_w. Special attention is given to the selection of binding groups to tether the dispersants to the nanoparticle core, so-called anchors. This special attention is merited by the importance of anchors for the stability of the controlled surface modification. The synthesis of magnetic nanoparticle cores is treated in ▶ Chap. 7, "Magnetite and Other Fe-Oxide Nanoparticles," by Chiolerio et al. and will therefore not be discussed in this chapter. After establishing the different approaches to steric stabilization, we detail how dispersants have been optimized to gain close control over iron oxide NP stability, size, and functionalities by independently considering the influences of anchors and spacers. We also provide insights into the influence of the stability of superparamagnetic iron oxide NPs, and therefore the strategy for the stabilization and functionalization of iron oxide NP, on their magnetic properties. For a thorough review on the application of magnetic nanoparticles in the biomedical field, we refer to ▶ Chap. 15, "Magnetic Nanoparticles for Biomedical Applications," by Rivas et al., which complements the description of the design procedure of superparamagnetic nanoparticles in this chapter.

Characterization of Nanoparticles

Thorough characterization is essential to closely control the assembly of dispersants on the NP surface and to understand its influence on the size distribution, stability, and functionality of NPs. The optimal NP design can only be achieved if the detailed structure of the core-shell NPs is known in addition to the identification and quantification of the core-shell NP constituents. This is a challenging task given that the NP core and the dispersants used to encapsulate it are of similar size, but the methods used to characterize nanoscale inorganic particles and polymers are by necessity different and not always compatible. In practice we seek information on polymer shell thickness, polymer packing density, core size distribution, core morphology, and core surface roughness. We want to relate these properties to the assembly of dispersants into the shell and ultimately to NP colloidal stability in the biological environment and to presentation of functionality and functional groups.

The core size, size distribution, and morphology can be characterized with a combination of different techniques such as transmission electron microscopy (TEM) [24], X-ray diffraction (XRD) [24], and scattering techniques such as small-angle X-ray scattering (SAXS) [25] and small-angle neutron scattering (SANS) [26, 27]. The hydrodynamic diameter of dispersed NPs is defined as the effective diameter of the NP when diffusing in water; it is typically understood as the sum of the core diameter and twice the shell thickness. It can be assessed with scattering techniques, e.g., dynamic and static light scattering (DLS and SLS) [28], SANS [27], and X-ray disc centrifugation (XDC) [29].

The packing density of dispersants can be quantified with thermogravimetry analysis (TGA) [21, 30] and SANS [27]. To verify that only dispersants are adsorbed on the NP surface rather than impurities or capping agents such as oleic acid, and thus to assign the mass loss measured with TGA to the dispersants adsorbed on the NP surface, the chemical composition of stabilized NPs must be analyzed; this can be done with different techniques such as Fourier transform infrared (FTIR) spectroscopy [30, 31] or less common with X-ray photoelectron spectroscopy (XPS) [21]. To extract information about the packing density and density profile of dispersants from SANS results, it is highly beneficial to do contrast variation experiments, where the contrast of the core and shell are varied by changing the ratio of protonated to deuterated solvents and thus varying the scattering length density of the solvent [32]. Alternatively, information about the packing density of dispersants on the surfaces of NPs can be extracted from SANS results acquired with polarized neutrons [27]. Furthermore, the dispersant density profile can be assessed with SANS measurements [33].

Because of the different advantages and disadvantages of each characterization technique, it is highly beneficial to characterize NPs with multiple, complementary methods. However, attention has to be paid to the precise meaning of the results if results obtained with different methods are compared. Differences and artifacts can be introduced, for example, through different weighting of sizes, model-dependent extraction of parameters, and sample preparation protocols. Such aspects can lead to substantial differences in the quantification of a physical property of the NPs with different techniques.

Scattering techniques reveal intensity-weighted averages ($I(q) \propto r^6$) and are thus sensitive to the presence of large NPs and clusters in a sample. X-ray diffraction (XRD) reveals volume-weighted averages ($\propto r^3$), while TEM allows direct visualization of number-weighted ($\propto r$) structures. A comparison between TEM results and scattering data even for only slightly polydisperse samples can therefore yield a discrepancy that is created by the different intrinsic weighting functions if the weighting is not explicitly taken into account. The unskewing of the weighting is however only possible if the core size distribution is known. Scattering data are therefore more sensitive to the presence of even small proportion of aggregates and yield larger average sizes.

TEM reveals direct and at first glance model-independent information. Preparation of NP samples for TEM is done through drying on, e.g., carbon-supported TEM grids, unless TEM samples are prepared with cryo-preparation techniques. Drying of NP dispersions can introduce artifacts such as NP agglomeration and inhomogeneous assembly of NPs of different sizes. Furthermore, it leads to collapse of the dispersant layer that makes it impossible to accurately determine the thickness of the wet shell even if the coating can be visualized with TEM [34]. A complication with interpreting TEM data is that the apparent simplicity of measuring sizes from an image can obscure the fact that a choice of size is performed on the basis of image contrast. Instead of judging by eye, which often produces biased and arbitrary choices, an algorithm can be

applied that makes consistent choices of particle size based on image contrast and also allows automated image analysis to collect better statistics. In addition, such image analysis tools, like the freely available Pebbles [35], can improve the determination of the size beyond the direct image contrast by using knowledge of the particle symmetry to fit the grayscale image. NPs analyzed with this algorithm are slightly larger than they appear for most people doing the same measurement by eye. Despite the introduction of a model to interpret the data, automated analysis of TEM images retains the advantage that particle sizes and histograms are compiled on the single particle level.

Scattering techniques allow analyzing NPs directly in dispersion and are therefore less prone to sample preparation artifacts and better suited to determine the thicknesses of the shell. However, they require model-dependent data analysis that is performed on the entire ensemble. SANS and SAXS data are fitted with form factors and, if required by particle-particle interactions, with superimposed structure factors. The form factors assume a certain structure and size distribution of the evaluated objects. Therefore, accurately done, the data analysis requires detailed prior knowledge about the shape and structure of the analyzed objects. If the quality of the scattering data is sufficient, the dispersant shell density profile can be obtained by comparing scattering data to a set of models. However, the concentration of NPs can critically affect the outcome of scattering results. If the concentration of NPs is high, multiple scattering produces severe artifacts in light scattering results [36]. SANS and SAXS data acquired on highly concentrated NP dispersions typically include a structure factor contribution that is convoluted with the form factor [37]. While the form factor describes the size distribution and shape of NPs, the structure factor is influenced by inter-particle interactions, clustering, and assembly of NPs. Because multiple scattering and structure factor contributions can significantly influence scattering results, it is very important to prepare samples such that effects of the NP concentration on the scattering results can be excluded or appropriately accounted for. The low scattering signal obtained from dilute core-shell particle samples, which mainly comprise weakly scattering, highly hydrated polymer shells, requires very long data acquisition times to obtain high-resolution data. This is seldom possible due to the restrictions on the facilities that can acquire SANS and SAXS data; a detailed experimental determination of the shell structure is therefore elusive.

Dynamic light scattering using commercial benchtop instruments is often applied to determine the hydrodynamic size of core-shell NPs in solution. DLS does not directly analyze the scattering of the particle to obtain its structure, but instead the time-correlation of the scattering intensity which relates to the Brownian motion to the hydrodynamic size of the NPs. The commercial versions of this method are best suited for dilute samples of strongly scattering objects with sizes in the 100 nm range. The NPs to be analyzed should be homogeneous and absorb neither light nor fluoresce. Unfortunately, magnetic nanoparticles and in particular iron oxide nanoparticles strongly absorb light; this compromises the reliability of DLS size measurements. Qualitatively it might be used to track changes in aggregation using the scattering intensity, which is sensitive to the size, as well as

the hydrodynamic size to assess the colloidal stability of the nanoparticle dispersion. This is particularly useful to assess the influence of external parameters, such as a change in temperature, on the stability of NPs [21].

The fact that the analysis of data acquired with scattering techniques is model dependent renders a comparison to data acquired with complementary, model-independent, or less model-sensitive techniques highly advantageous. The comparison of the quantification of NP parameters obtained using scattering techniques with quantification measured with model-independent techniques allows checking the validity of the model assumed to analyze scattering data.

The value of characterizing NPs with different, complementary techniques can be exemplified by the determination of the packing density of dispersants and their density profile. These parameters can be measured and quantified with SANS. However, to analyze SANS data, a form factor that comprises assumptions about the core-shell structure of the NPs including the dispersant density profile has to be applied to analyze the scattering data.

The ratio of the mass of organic to inorganic materials can be quantified with TGA, although no information on the density profile can be obtained. To ensure that the mass loss of organic molecules measured with TGA can exclusively be assigned to dispersants rather than to impurities or remaining capping agents, further chemical analysis on the stabilized NPs such as FTIR or XPS is required [21]. However, also after excluding the influences of impurities, the determination of dispersant grafting density by TGA is very sensitive to assumptions and further input data. The determination of the grafting density requires normalizing the measured ratio of organic to inorganic mass to the surface area of the NPs, using a distribution of the molecular weight of the dispersant. The surface area of the nanoparticles is only known if the size distribution of the cores is known. Since the surface-to-volume ratio of nanoparticles is very high, even small errors in the size distribution of NP cores propagate to large uncertainties in the grafting density. Furthermore, this normalization is almost always performed for assumed smooth and spherical cores. Depending on the synthesis method, the cores can have highly irregular, faceted, or rough morphologies; the surface area of NP cores is therefore often underestimated. Also, the poor statistics obtained from TEM images does not allow for an accurate assessment of the size distribution of the cores in a scattering sample as described above. This information must be obtained iteratively by fitting scattering data with form factors that agree with the shape and morphology of NPs seen in TEM images. Therefore, the dispersant packing density and density profile on NPs can only be revealed if NPs are characterized with multiple methods, such as SANS, TGA, TEM, and FTIR spectroscopy in concert.

Nanoparticle Stability

NPs are stable if the inter-particle potential (U_{tot}) has an energy barrier that is high compared to $k_B T$. In a first approximation, U_{tot} of NPs contains four contributions, the attractive van der Waals and magnetic potentials and the repulsive electrostatic

and steric potentials [38, 39]. These potentials can be calculated if the core radius, shell thickness, saturation magnetization, zeta potential, and dispersant density profile are known [38–40]. Considering the four main contributions to U_{tot}, NPs can be electrostatically or sterically stabilized. Optionally, the two stabilization methods can be combined. Electrostatic NP stabilization is only effective at low ion concentrations where the Debye screening length is on the order of tens of nm and at pHs far above or below the isoelectric point (IEP) of NPs. However, biomedical applications require good stability of NPs under high salt concentrations and over a range of pHs. The macromolecules, predominantly proteins, present in a biological fluid also contain both positively and negatively charged residues; typically they are zwitterionic and carry opposite charges in patches on the protein surface. To avoid interactions of NPs with these macromolecules, NPs must be sterically stabilized [41, 42] and the colloidal stability of the resulting core-shell NPs has to be evaluated for biomedical applications.

The interaction potentials of NPs cannot be measured directly due to the limited resolution of the techniques developed for such investigations on microparticles. Hence, in practice, the term 'stability' has been used with very different meaning in the literature on NPs, mostly without explicit acknowledgment of these differences. NPs are often considered stable if they do not visibly precipitate over a finite period of time [43, 44]. A thorough characterization of NP dispersions, e.g., with scattering techniques allows to define NP stability more precisely.

The importance of the technique and conditions used to characterize NP stability was exemplified on poly(ethylene glycol)-hydroxydopamine (PEG-hydroxydopamine)-stabilized superparamagnetic iron oxide NPs. PEG (0.55 kDa)-hydroxydopamine-stabilized iron oxide NPs were stable for more than a year if stored dispersed and analyzed at RT [21]. However, PEG (5 kDa)-hydroxydopamine-stabilized iron oxide NPs agglomerated if they were subjected to multiple filtrations (Fig. 12.2) [21]. If dispersants adsorb reversibly at the NP surface, dispersants adsorbed on the NP surface are in equilibrium with unbound dispersants in solution. If NP dispersions are filtered, free dispersants are removed. To reestablish the equilibrium in the NP dispersion, some dispersants adsorbed at the NP surface desorb, leading to a lower dispersant packing density at the NP surface. The dispersant packing density at the NP surface decreases with increasing number of filtration steps. If the dispersant packing density at the NP surface drops below a critical value, NPs start to agglomerate [45]. The fact that PEG (5 kDa)-hydroxydopamine-stabilized iron oxide NPs agglomerated after filtration indicates that hydroxydopamine adsorbs reversibly on Fe_3O_4 surfaces. However, if the dispersant packing density at the NP surface is sufficiently high under the conditions NP dispersions are stored, then NPs remain long term stable even if they are stabilized with reversibly binding anchors such as hydroxydopamine.

Applications of superparamagnetic iron oxide NPs in vitro in cell cultures and in vivo always include high dilutions of NP dispersions. Therefore, reversible dispersant adsorption that leads to agglomeration of iron oxide NPs can have severe adverse consequences for these applications. Once injected into a living
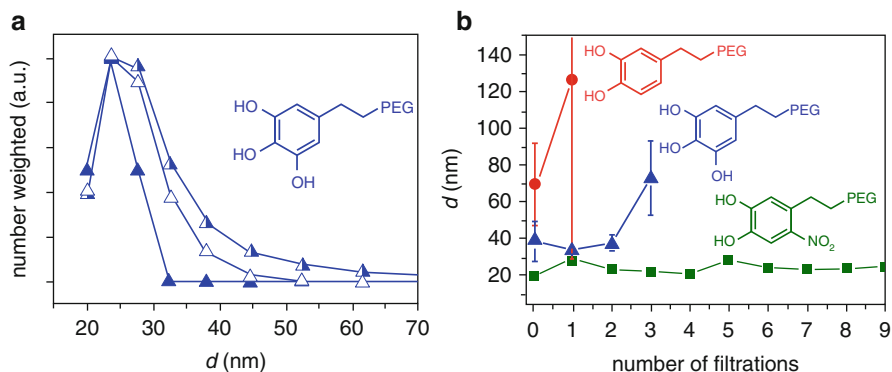
Fig. 12.2 Characterization of the stability of superparamagnetic iron oxide NPs. The stability of superparamagnetic iron oxide NPs was measured with DLS at 25 °C. (**a**) The hydrodynamic diameter of PEG (0.55 kDa)-hydroxydopamine stabilized iron oxide NPs as-stabilized (-▲-), after storage for 1 year in PBS (-▲-) and after storing them for 20 months in HEPES (-△-).[21] (Copyright Wiley-VCH Verlag GmbH & Co. KGaA. Reproduced with permission). (**b**) The stability of superparamagnetic iron oxide NPs was evaluated as a function of the number of filtrations performed to remove excessive dispersants of iron oxide NPs stabilized with PEG (5 kDa)-nitrodopamine (-■-), PEG(5 kDa)-hydroxydopamine (-▲-), and PEG (5 kDa)-dopamine (-●-). [21] (Nano letters by American Chemical Society. Reproduced with permission of AMERICAN CHEMICAL SOCIETY in the format Journal via Copyright Clearance Center) While PEG-hydroxydopamine stabilized iron oxide NPs were stable at RT for more than 20 months, they started to agglomerate after excessive dispersants were removed by more than two filtrations. This indicates that superparamagnetic iron oxide NPs agglomerate upon dilution and will lead to adverse consequences if applied in vivo

body, agglomeration of NPs is difficult to assess because the size of NPs can no longer be measured. Additionally, once NPs are exposed to cells or injected into the body, agglomeration of NPs is convoluted with other effects such as exposure to many different proteins that might adsorb to the NPs or even displace reversibly anchored dispersants. The result is a poorly defined system. An accurate analysis of this system such as a study of the efficiency of targeting NPs to desired locations by the addition of ligands to the NP shell is difficult. The effects caused by engineering the surface of core-shell NPs are convoluted with effects caused by uncontrolled NP agglomeration and nonspecific protein adsorption on the NP surface. This illustrates the necessity to characterize NPs stringently, especially if they are intended for biomedical applications. Thus, also for NPs that are shown colloidally stable under dilute conditions with the dispersants remaining tethered to the core, the in vivo colloidal stability must be assessed by studying the NP tendency to aggregate in dilute solutions of serum or cell media. It is particularly important to understand the colloidal stability in serum where sticky macromolecules are present, which can compete with the dispersants for access to the core surface and, if adsorbed to the NP, induce a cascade of interactions from nonspecific bridging of particles to signaling and opsonization.

Steric Stabilization of Iron Oxide Nanoparticles Using Polymer Shells

Nanoparticles that have to be stable in aqueous media containing high concentrations of ions must be sterically stabilized [41, 42]. Steric stabilization relies on polymers, so-called dispersants, which surround NP cores. Dispersants with a high affinity to the solvent they are dissolved in provide a sufficiently thick shell around the NP core to overcome the attractive van der Waals and magnetic potentials. They therefore impart long-term colloidal stability under dilute conditions, at high salt concentrations, and at elevated temperatures. Dispersants used to sterically stabilize superparamagnetic iron oxide NPs can be divided into two groups. One group of dispersants are high molecular weight polymers consisting of repeat units that have a low affinity to the surface of iron oxide NPs. This leads to reversible adsorption of the dispersant. The other group of dispersants typically consists of a high affinity anchor that is covalently linked to a low molecular weight (M_w) spacer, usually below 10 kDa.

Physisorption of High M_w Dispersants

Superparamagnetic iron oxide NPs used for clinical applications are currently most often coated with high M_w polymers such as dextran [46], alginate [47], chitosan [48], poly(vinyl amine) (PVA) [49–51] or poly(acrylic acid) (PAA) [52], or by electrostatically adsorbing charged polymers like poly(ethylene imine) (PEI) to which subsequently a layer of poly(ethylene oxide)-*b*-poly(glutamic acid) (PEO-PGA) can be adsorbed [53]. These polymers lack a well-defined high affinity anchor that irreversibly bind them to the surface of iron oxide NPs and typically have a molecular weight >10 kDa [9]. Therefore, such dispersants often encapsulate multiple cores within one cluster, and the resulting hydrodynamic cluster radius is many times larger than the radius of individual cores [18–20]. The weak physisorption of the stabilizing polymer dispersants compromises iron oxide NP stability [54], leads to protein adsorption onto the core particle, and drastically decreases blood circulation time if applied in vivo [55]. The poorly defined interface of such NPs also prevents controlled functionalization in terms of number and presentation of ligands [54].

One solution to this problem is to cross-link the enwrapping polymer [56]. However, this renders control over the thickness of the dispersant layer difficult, and the resulting hydrodynamic diameter was much larger than that of single cores [56]. Additionally, epichlorohydrin, the cross-linking agent used to cross-link the dextran in these studies, is classified as cancerogenic, mutagenic, and reproxotic [57, 58], which could limit its clinical use.

Grafting of Low M_w Dispersants

An attractive approach to obtain core-shell NPs with control over size, interfacial stability, and the presentation of functional groups at the surface in a defined manner is to use low M_w dispersants that consist of one well-defined anchor covalently linked to a spacer polymer (Fig. 12.1b). Low M_w dispersants can be bound to NP surfaces either through the 'grafting to' or the 'grafting from' technique (Fig. 12.3). For the latter approach, initiators are covalently bound to the NP surface. Spacers can subsequently be grown in situ, by different polymerization routes, such as through radical polymerization (Fig. 12.3a) [59, 60]. The grafting density of dispersants is determined by the density of anchors with initiator groups at the NP surface. This results in a highest packing density of dispersants and excellent NP stability.

Although the 'grafting from' technique results in a high packing density of dispersants, it has some inherent drawbacks. The characterization of dispersants and control over the dispersant polydispersity and the shell thickness are difficult, despite that the use of living polymerization should ensure excellent control over chain length. Controlled polymerization is difficult to scale up to large volumes and in the presence of high concentrations of nanoparticles, which might affect the polymerization conditions. Furthermore, functionalization of stabilized NPs with different ligands or other functional units and controlling the density of functional groups presented at the NP interface are challenging [61].

Low M_w dispersants synthesized prior to their adsorption on the NP surface can be characterized with conventional chemical characterization methods. They can be grafted to the NP surface without performing in situ chemistry by using suitable anchors (Fig. 12.3b). This self-assembly approach has the advantage that it is cost-effective, has high reproducibility, and is easy to scale up. The thickness of the dispersant layer can be controlled by the spacer configuration, packing density, and M_w of the dispersant. The density of one or multiple ligands presented at the surface can be tailored by co-adsorbing differently functionalized dispersants in one or several subsequent assembly steps [21, 62]. Polymers adsorbed through the 'grafting to' approach pack at a significantly lower density on flat surfaces than the polymers adsorbed through the 'grafting from' approach [61]. This difference is a result of that steric repulsion of dispersants already adsorbed on surfaces; it hinders the grafting of additional dispersants and thus limits the maximum grafting density. By contrast, the maximum packing density of dispersants using 'grafting from' the surface is limited only by the footprint of the anchor [63, 64]. At a highly curved interface of a NP, the lateral steric repulsion of grafted polymers is reduced due to the rapidly increasing free volume available to dispersants with increasing distance from the core. Therefore, the difference in grafting densities of surfaces modified through the 'grafting from' and the 'grafting to' approaches is expected to decrease with increasing surface curvature (Fig. 12.4). However, it still limits the maximum M_w of dispersants that can be grafted to the surface at a given packing density.
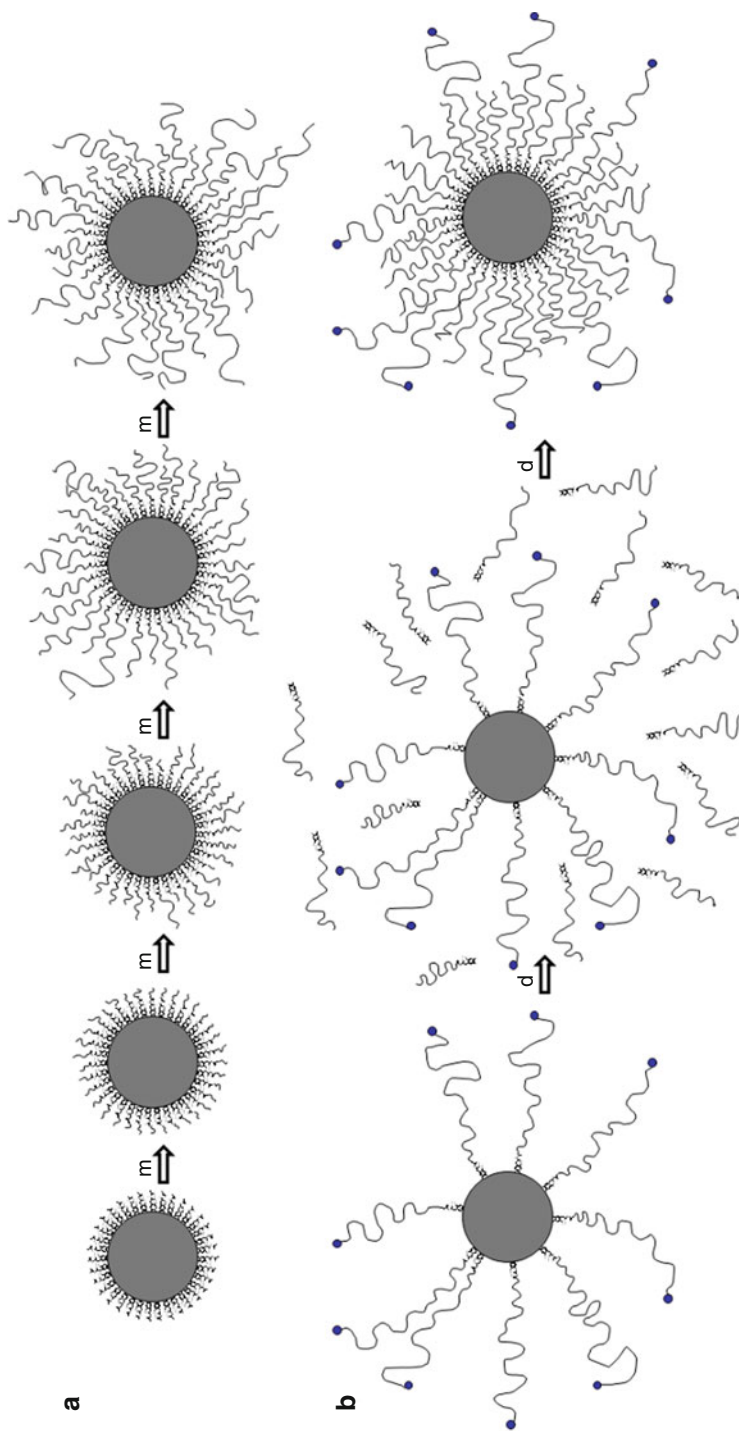
Fig. 12.3 Modifying iron oxide NP surfaces with low M_w dispersants. Low M_w dispersants can be (**a**) grafted from and (**b**) grafted to the NP surface. If low M_w dispersants are grafted from the NP surfaces, initiators are firmly bound to the NP surface. After monomers (m) were added to the NP dispersion, dispersants are grown in situ, typically through a radically initiated chemical reaction. Dispersants grown in situ are densely packed on the NP surface; however, control over the length of dispersants, their polydispersity, and density of functionalities presented at the NP surface is difficult. Alternatively,
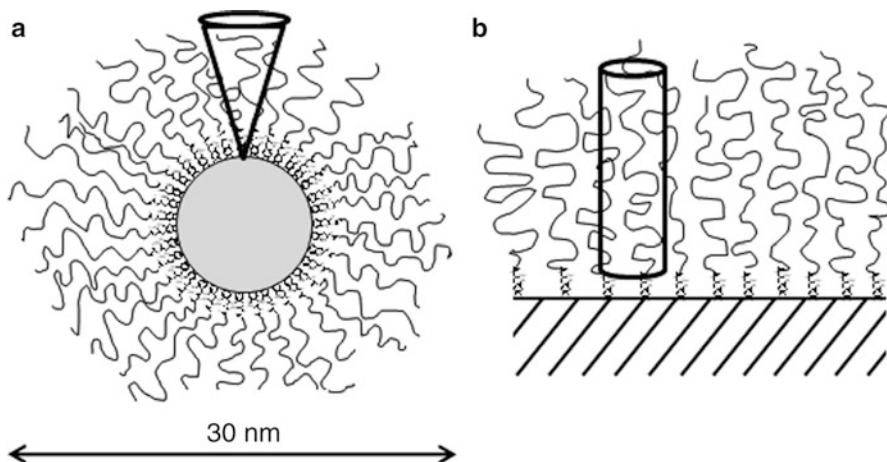
Fig. 12.4 Free volume of dispersants. The free volume of dispersants adsorbed on (**a**) NPs and (**b**) flat surfaces. While the free volume of dispersants adsorbed on NPs increases conically with increasing distance to the NP surface, it remains constant for dispersants adsorbed on planar surfaces

Anchors

Low M_w dispersants have to firmly adhere to the NP surface through suitable anchors (Fig. 12.1b). Ideally, the binding affinity of anchors is high and its desorption rate k_{off} negligible. Naturally, anchors that meet these stringent requirements can be used both to immobilize initiators for 'grafting from' polymerization of dispersants and to graft polymer brushes to a NP surface. Typical anchors to modify surfaces of superparamagnetic iron oxide NPs described in the literature are catechol [65–68] or catechol derivatives [21, 69, 70], carboxy groups [71–73], phosphonates [72, 74, 75], and silanes [76–80].

Despite the importance of anchors for the NP stability and to define the density of functional units on a NP, the influence of the affinity of anchors to NPs has only been studied recently. Similar catechol anchor chemistries were shown to result in large variations in affinity to iron oxide; this translated into large differences in colloidal stability of superparamagnetic Fe_3O_4 NPs stabilized by low M_w PEG-based dispersants [21]. Due to the lack of characterization of anchor stability, only a few irreversibly binding anchors have been identified. The bulk of the

Fig. 12.3 (continued) dispersants (d) are synthesized prior to the adsorption on the NP surface. These dispersants are grafted to the NP surface. The resulting packing density of dispersants is lower than that of dispersants grafted from the surface of NPs. However, the grafting to approach allows for close control over the thickness of the dispersant shell and the density of functionalities presented at the NP surface. The latter is achieved by adsorbing a defined concentration of functionalized dispersants at the NP surface. The NP surface is subsequently backfilled with non-functionalized dispersants

literature on superparamagnetic iron oxide NP contrast agents thus uses NPs stabilized with *reversibly* binding dispersants, which often implies compromised colloidal stability.

Messersmith and coworkers demonstrated that the affinity of reversibly binding anchors can be significantly improved by designing multivalent anchors; they achieved high densities of polymer brushes that were grafted to flat surfaces [81]. The enhanced binding affinity could only be observed if the multiple binding groups were interconnected by sufficiently flexible linkers [81]; longer flexible linkers would be required to achieve the same improvement in binding affinity on the highly curved surface of a NP. The surface area occupied by multiple anchors is considerably larger than that of a single anchor, which might critically decrease the packing density of dispersants on highly curved surfaces. On these surfaces, the density of anchors might limit the maximum packing density of dispersants as the lateral steric repulsion of adjacent spacers is considerably lower than on flat surfaces [82].

Among the commonly described anchors, phosphonic acid has been reported to be too weak to replace carboxy groups from iron oxide NP surfaces [83]. Furthermore, carboxy groups were shown to be replaced by proteins [84] and compared unfavorably to catechols and nitrocatechols [21]. Silanes pose experimental difficulties in the assembly of dispersants on the surface of iron oxide NPs as they have to be adsorbed in water-free solvents, but anchor hygroscopic polymer spacers. Furthermore, they can cross-link which compromises the control over the assembly of silane anchored dispersants [85].

Inspired by the presence of catechols in organisms for fixation of metals and for surface adhesion, superparamagnetic iron oxide NPs have increasingly been surface modified using this chemical motif [86]. Because of the biological relevance of DOPA/Fe^{3+} and dopamine/Fe^{3+} complexes, their structure [87–89] and electronic interactions [90, 91] have been studied in detail. Despite their recent popularity, their suitability as anchors to stabilize iron oxide NPs is debated. Iron is well known to catalyze catechol oxidation leading to semiquinones, quinones, and eventually carboxy-containing products [92–94]. Oxidative degeneration of dopamine adsorbed on iron oxide NPs that results in a loss of the stability of NPs has also been reported [95], and recently, cryo-TEM images of PEG-dopamine stabilized Fe_3O_4 NPs revealed their agglomeration [96].

Already in 1976, it was noticed that electronegative substituents on the catechol ring strengthen the iron-catechol bond. The bond of nitrogen-substituted catechols (nitrocatechols) to iron ions remained unchanged for 24 h at 25 °C [97]; this is considered an irreversible bond. It was speculated that nitrocatechols can act as oxidizing agents which was assumed to be the reason for this exceptionally strong bond [97]. Detailed studies on the binding of nitrocatechols to iron ions revealed a significantly lower tendency to generate radicals for nitrocatechol/iron compared to catechol/iron complexes [98]. Based on complexation studies of these anchors with Fe^{3+}, the increased complexation strength of electronegatively substituted catechols compared to unsubstituted counterparts was related to the increased acidity of the former compounds [99, 100]. Recently, electron paramagnetic

resonance (EPR) studies on superparamagnetic iron oxide NPs coated with nitroDOPA revealed an enhanced electron density at nitroDOPA anchors and electron-depleted iron ions on the NP surface [70, 101]. To the contrary, dopamine is known to oxidize if adsorbed to iron oxide surfaces [95].

The strong complexation of nitrocatechols to Fe^{3+} ions and enhanced electron density at the nitroDOPA anchors have been shown to directly relate to the high stability of grafted polymer films when nitrocatechols are used as anchors. The stability of superparamagnetic iron oxide NPs with shells of PEG-nitroDOPA or PEG-nitrodopamine was shown to be much higher than that of iron oxide NPs stabilized with PEG-DOPA and PEG-dopamine [21]. Follow-up studies revealed that the binding affinity of anchors to the metal ion of oxides has to be optimized rather than maximized to achieve good stability of iron oxide NPs [70, 102], since the anchor with the highest binding affinity resulted in dissolution of the iron oxide cores.

Spacers

The spacer part of a dispersant (Fig. 12.1b) has to prevent that the NPs get into sufficient proximity for the van der Waals and magnetic interactions to dominate. If two sterically stabilized cores approach each other, the volumes of the respective polymer shells are confined. This reduces the entropy of dispersants and increases the osmotic pressure between NPs. The resulting repulsive potential critically depends on the density profile of dispersants, their packing density [103], binding reversibility, and the solvent quality with respect to the dispersants [104]. The design and optimization of sterically stabilized core-shell NPs would be greatly facilitated if these parameters were known. Only then can the inter-particle potentials be calculated [105, 106]. Recent theoretical investigations of density profiles of dispersants adsorbed on surfaces of NPs have been performed with models that are sufficiently similar to the relevant application examples to serve as a guide to further optimize core-shell NPs.

Polymer Density Profiles on Highly Curved Surfaces

The standard theories to study spherical brushes, i.e. brushes from interfaces that are curved on the length scale of the spacer, build on the framework originally developed by Alexander and de Gennes for planar brushes [105, 107–109]. Refinements of scaling and self-consistent field (SCF) models [110] led to the finding that polymer density profiles change from parabolic to step function as the brush grafting density is increased.

Early attempts to apply scaling theory to NPs resulted in a dispersant density profile decaying exponentially with increasing distance from the surface of NPs [111]; this is clearly different from the parabolic decay obtained on flat surfaces [112]. These attempts however neglected that the scaling approach and

the Derjaguin approximation fail if the dimensions of the solvated dispersant chain approach or exceed the core diameter, which is the case for sterically stabilized superparamagnetic iron oxide NPs. Applying SCF calculations [113, 114] and Monte Carlo (MC) simulations [115] to chains grafted to a surface of NPs allows extraction of more detailed information and has resulted in a different, more parabolic-like density profile with the core interface region depleted by free polymer end segments [116].

The assumption of negligible interchain penetration inherent to the models described above only holds for long chains and low packing densities. Short chains significantly interpenetrate adjacent chains; this alters the dispersant density profile. Deviations from the parabolic polymer density profile are seen for polymer chains shorter than 1,000 repeat units; they result in an earlier and gradual onset of repulsive inter-particle forces compared to inter-particle potentials calculated for parabolic polymer density profiles [117]. Furthermore, the dispersant density profile was predicted to undergo a smooth change from a parabolic decay at low surface curvatures and for small or stiff dispersants to a power law decay similar to that of star polymers as the curvature increased relative to the length of the polymer spacer [104, 118]. Recently, very good agreement between the power law decay of the density profile for star polymers and relevant model NPs with high grafting densities of linear polymers was shown using density functional theory calculations and coarse-grained molecular dynamics simulations [119]. Increasing the chain length or grafting density resulted in an increasingly sharp cut-off of the region with power law dependence, as well as a smeared out distribution of the free-end segments. As chain interpenetration starts, the interaction potential is only a few $k_B T$; by contrast, a very strong repulsion is obtained as the particles get close due to the rapidly increasing polymer density [120].

In summary, the lack of experimental data to evaluate the contradictory theoretical findings has led to an ongoing debate about the density profile of polymers adsorbed on highly curved surfaces. The lack of experimental data is a result of a lack of experimental techniques that can investigate with sub-nm resolution the structure and interaction potentials of polymers grafted to nanoparticles. Compounding this problem is the lack of experimental data on dispersants *irreversibly* grafted to highly curved surfaces. Reversible adsorption of dispersants introduces time-dependent changes to the grafting density and density profile of dispersants. The best suited experimental methods to assess the shell density profile are scattering techniques such as SANS, but any free desorbed dispersant will scatter and smear the information on the shell density profile. Thus, there are very few experimental investigations which directly relate to the theoretical work. Experimentally, it has been demonstrated that the colloidal stability is decreased as the PEG M_w is decreased for similar grafting densities [70]. A direct comparison to density profiles was however not shown. Another interesting recent finding was that iron oxide NPs also could be functionalized by nitrocatechol-anchored PEG-dendrimers, which should provide a different dispersant density profile to the standard linear polymer surface modifications [121]. It was shown that NPs remained colloidally stable if the PEG-dendrimers were irreversibly bound to the

NP surface and were at least second generation. A dendrimer is compact and rigid but provides a much higher EG density close to the surface than a linear PEG chain; this might be the reason for the observed stability. However, the thin shell did not completely screen the surface charge of the core and anchor region [121, 122]. The resulting additional electric double layer repulsion contributes to colloidal stability under the measurement conditions but would be detrimental for applications in the biomedical field. However, the possibility to use dendritic spacers to make ultra-small iron oxide NPs with a high degree of controlled functionalization is a tantalizing prospect that warrants more theoretical and experimental attention.

Effect of Shell Properties on Protein Resistance and In Vivo Response

Superparamagnetic iron oxide NPs intended for biomedical applications have to be colloidally stable and to resist adsorption of biomacromolecules such as proteins, a property often referred to as 'stealth'. It is a necessity for their successful application in vivo. If plasma proteins such as opsonins are adsorbed on the surface of NPs, NPs are taken up by macrophages, monocytes, and dendritic cells and thus initiate their clearance [123]. The requirement of resistance to protein adsorption precludes electrostatic stabilization, because most proteins express multiple charged groups on their surface. As a result, NPs must be sterically stabilized with a polymer shell for which proteins and other biomolecules have no affinity.

The most commonly used dispersant spacer that renders NPs stealth is poly(ethylene glycol) (PEG) [12, 20]. PEG-modified surfaces exhibit extremely low attractive van der Waals forces compared to other well-known water-soluble polymers due to the low refractive index of PEG [124]. Furthermore, protein adsorption onto highly hydrated polymers such as PEG leads to confinement of the polymer chains; the entropy decrease renders this adsorption energetically unfavorable [125]. A final factor contributing to the protein repellency of PEG is the ordering of water around PEG chains [126]; this prevents direct contact of PEG with proteins [127]. However, PEG is known to be prone to degeneration if applied in vivo [128, 129]. Possible alternatives exist; in vitro studies showed that poly (2-methyl-2-oxazoline) (pMOXA) has similar protein-repelling properties to PEG but is far less prone to degradation [130].

Nanoparticles must be stabilized with irreversibly grafted dispersants to ensure that the resistance of NPs to protein adsorption is correctly evaluated. A physisorbed surface coating can be partially replaced by adsorbing proteins. Such processes have to be excluded as the evaluation of protein resistance is mainly done by tracking nanoparticle size and the mass fraction of organic materials, which both can be insensitive to dispersant replacement.

Protein adsorption has been studied in detail on PEG-modified planar surfaces where quantitative surface-sensitive characterization techniques such as XPS and time-of-flight secondary ion mass spectroscopy (ToF-SIMS) can be used to chemically verify the presence and surface coverage of proteins [81, 131, 132].

It was found that protein adsorption decreases almost linearly with increasing density of ethylene glycol (EG) monomers at the surface. For a surface to be protein resistant, the EG surface densities must be >15–30 nm^{-2} [81, 131]. The existence of a threshold value for the EG density to render surfaces protein resistant has direct consequences for the packing density and the M_w of the grafted PEG chains, as they both linearly affect the projected EG surface density. A high packing density of PEG is especially crucial to prevent adsorption of small proteins, while the adsorption of large proteins is less sensitive to it [132–135]. Generally, protein resistance requires that the grafted PEG chains are in the so-called brush regime, in which the distance between adjacent chains is smaller than the Flory radius of the polymers [107, 136].

The PEG M_w and EG surface density are crucial parameters for the protein resistance and thus circulation time of NPs, as could be expected from the results for planar surfaces. However, the critical EG density above which NPs are protein resistant might be higher on highly curved surfaces of NPs than it is on flat surfaces. The high surface curvature of a NP leads to a conically increasing free volume for the PEG spacer and possibly a polynomially decreasing polymer density [119] with increasing distance from the surface of the NP core (Fig. 12.4). Thus, if coated with the same grafting density and M_w of PEG, proteins can come much closer to surfaces of NPs than to flat surfaces. This was exemplified in a study, where protein resistance of 100 nm diameter poly(lactic acid) (PLA) NPs stabilized with PEG (2 kDa) could only be obtained if the PEG packing density was ≥ 0.2 molecules/nm^2 [137]. For lower PEG packing densities, circulation times increased with increasing $M_w s$ of PEG due to an increased EG density [55]. Protein adsorption on 200 nm diameter PLA NPs could be significantly decreased if at least 5 wt% PEG (5 kDa) was added to the PLA NP surface [55]. At this concentration, PEG should be in the brush regime as the distance between two PEG chains was 1.4 nm [55], whereas the Flory radius of PEG (5 kDa) is 5.1 nm and the curvature of the core is rather low. However, due to steric repulsion and depending on the grafting method, the packing density of PEG might also decrease with increasing PEG M_w. A too low packing density of PEG in itself compromises the stability of NPs and sets an upper limit to the suitable M_w range [45]. Thus, grafting densities and $M_w s$ of PEG chains cannot be directly substituted for each other. Due to these reasons, PEG $M_w s$ in the range 1.9–5 kDa have been found optimal to disperse superparamagnetic iron oxide NPs intended for biomedical applications [70, 133, 138]. These NPs showed prolonged circulation times in vivo [139, 140].

Biodistribution: Relation to Nanoparticle Size and Stability

In addition to the surface chemistry, which determines the affinity of proteins to adsorb on NP surfaces, the fate of NPs in vivo is influenced by the size, shape [49, 141], and surface charge of NPs [142, 143]. While particles larger than 200 nm are rapidly cleared by the spleen, NPs smaller than 10–50 nm are generally removed from the body through extravasation and renal clearance [12, 57].

The optimal range of the hydrodynamic diameter for in vivo applications of intravenously injected NPs that require prolonged blood half-life times is therefore typically 10–100 nm.

Superparamagnetic iron oxide NPs stabilized with PEGylated dispersants and administered to nude mice have been reported to mainly end up in the liver and spleen if their size is 30–50 nm [144]. The clearance of PEGylated NPs was shown to depend on the affinity of the dispersant anchors to the NP surface [123, 145]. The circulation time was substantially prolonged for NPs stabilized with covalently attached compared to physisorbed PEG [55, 145]. The fast clearance of the latter NPs was assigned to the fact that proteins could replace physisorbed PEG; this results in an activation of clearing mechanisms.

Similar to PEG-stabilized superparamagnetic iron oxide NPs, dextran-coated, agglomerated iron oxide NPs accumulate in the liver and spleen. In addition to slow clearance and a tendency to agglomerate [146], NPs coated with dextran have also been shown to induce differentiation of monocytes into macrophages [54].

Effect of Shell Properties on Magnetic Properties

The magnitude of the magnetic response of a superparamagnetic iron oxide NP is determined by its saturation magnetization (M_s). The higher the saturation magnetization of superparamagnetic iron oxide NPs, the easier they can be magnetically separated and ferried to desired locations. A high M_s also locally induces a strong magnetic field gradient if a homogenous magnetic field is applied. The local perturbation of the magnetic field is responsible for the changed relaxivity, r_2, of surrounding water molecules measured in MRI. Thus, the higher the M_s of superparamagnetic iron oxide NPs, the more effective they are as magnetic resonance contrast agents [12].

The magnetic properties of NPs depend on the composition, size, and shape of their core [12]. However, M_s of superparamagnetic iron oxide NPs is always below that of the bulk material, and it decreases with decreasing size of the core [147]. This decrease has been assigned to surface anisotropy effects [148, 149], which become increasingly important as the surface-to-volume ratio increases with decreasing size of the NP cores.

Effect of Surface Modification on Saturation Magnetization of Superparamagnetic Iron Oxide Nanoparticles

The M_s has been shown to decrease if superparamagnetic iron oxide NPs are sterically stabilized [21, 150]. However, a direct comparison of stabilized and unstabilized superparamagnetic iron oxide NPs requires normalization of the M_s to the mass of iron oxide to account for the lower wt% of NP cores in NPs stabilized with dispersants compared to bare counterparts. The lower M_s of surface functionalized iron oxide NPs might be related to interactions of the anchors with

surface iron ions that influence the magnetism of the iron oxide NP surface layer [101, 102]. Therefore, improved stability of iron oxide NPs induced by irreversibly anchored dispersants might partially come at the expense of lower M_s values.

One common way to demonstrate good magnetic properties of stabilized superparamagnetic iron oxide NPs dispersed in solution is to show their attraction to a small tabletop magnet. However, individually stabilized superparamagnetic iron oxide NPs have too low M_s to be strongly attracted by a small tabletop magnet. In contrast, agglomerates are readily attracted by such magnets [21, 43]. Therefore, tests in which iron oxide NPs are rapidly cleared from aqueous solutions using tabletop magnets not only indicate good magnetization of the superparamagnetic iron oxide NPs but also poor NP stability.

Relaxivity

Superparamagnetic iron oxide NPs enhance contrast in MR images by changing the relaxation times r_1 and r_2 of adjacent water molecules [12]. The exchange rate of water molecules in the first hydration shell of superparamagnetic iron oxide NPs mainly determines r_1. Thus, r_1 depends on the accessibility of water molecules to the iron oxide core surface. Commercially available superparamagnetic iron oxide NPs are coated with reversibly adsorbing dextran that allows water to readily exchange also in close proximity to the iron oxide surface (Fig. 12.1a). However, stabilization of NPs with low M_w dispersants at high dispersant packing density reduces the accessibility of water molecules to the core surface. The anchor region might be dense and not sufficiently polar to allow direct contact of water molecules with the surface of iron oxide; this reduces the r_1 contrast of NPs stabilized with irreversibly bound dispersants [45] compared to NPs with a physisorbed dextran coating.

Increasing the size of iron oxide NPs increases r_2 [151, 152]. Furthermore, agglomeration and controlled cross-linking [153] have also been shown to increase r_2 [154, 155]. This was confirmed by Monte Carlo simulations [156, 157]. Thus, r_2 of individually stabilized superparamagnetic iron oxide NPs is lower than for NPs stabilized with a physisorbed dextran coating. However, low M_w dispersants that are firmly bound to the iron oxide NP surface through suitable anchors allow independent tuning of the diameter of the core and the thickness of the shell. This creates the possibility to increase r_2 without sacrificing the stability of iron oxide NPs, by increasing the size of the core up to the limit ($>10\,nm$) where iron oxide NPs become ferromagnetic. Therefore, individually stabilized superparamagnetic iron oxide NPs [45] can have r_2 values comparable to those of commercially available iron oxide-based MR contrast agents [14, 15] while the former have a hydrodynamic diameter many times smaller than the commercially available analogues.

The influence of the spacer region on the relaxivity is still debated [158, 159]. The hydrophilicity of the polymer shell was shown to influence r_2 values [159]. In the same study r_2 did not change systematically with the thickness of the shell of

superparamagnetic iron oxide NPs [159]. By contrast, r_2 was shown to decrease with shell thickness for NPs stabilized with PEG-based dispersants with molecular weights lower than 1 kDa in another study [158], whereas NPs stabilized with PEG dispersants with M_ws between 1 and 5 kDa had similar relaxivities. A caveat in comparing these studies is that it is questionable whether PEG spacers with $M_w < 1$ kDa result in stable NPs [70]. Thus, the dependence of r_2 on the thickness of the dispersant shell likely was affected by aggregation of NPs for dispersants with low molecular weights.

Specific Adsorption Rate (SAR)

The specific adsorption rate (SAR) determines how effectively NPs generate heat if they are exposed to an alternating magnetic field (AMF). The SAR is the most important property for the use of superparamagnetic iron oxide NPs in hyperthermia treatment or for triggering release of cargo encapsulated in thermoresponsive drug delivery vehicles [57].

For superparamagnetic NPs that have small magnetic anisotropies, the SAR at a fixed frequency v is proportional to the relaxation time τ of the NPs [57]. This relaxation time increases with increasing size of the core of NPs [160]; Thus, also the SAR increases with increasing size of NPs up to a critical diameter of the core d_{crit}. If $\tau > (2\pi v)^{-1}$, the Néel and/or Brownian relaxations of NPs cannot follow the alternating magnetic field and thus the SAR then rapidly decays with increasing τ and therefore size of NPs [57, 160].

The agglomeration of iron oxide NPs is known to increase the magnetic interparticle interactions [161]; this decreases Néel relaxation losses at frequencies typically used for SAR applications [162]. Thus, steric stabilization of individual iron oxide cores increases the SAR, as was experimentally shown on agglomerated and with poly(methyl methacrylate) (PMMA) stabilized superparamagnetic iron oxide NPs [162].

Surface Presentation of Ligands

Different types of untargeted superparamagnetic iron oxide NPs stabilized with weakly adsorbing high M_w dispersants, such as dextran, are FDA approved and used mainly as negative MR contrast agents to detect lesions in the liver and spleen [57]. Adding functional groups to the shell of NPs allows targeting in vitro and in vivo. Potential functional groups suited for targeting in biomedical applications are antibodies [163], peptides [79, 164–166], aptamers [167], DNA [153, 168] and RNA [169] sequences.

Reports where in vivo targeting of superparamagnetic iron oxide NPs is claimed are numerous. However, the vast majority of iron oxide NPs were targeted towards the liver, kidney or lymph nodes, locations they naturally end up during clearance [170]. Alternatively, iron oxide NPs were targeted to tumors and cancer

Fig. 12.5 Effect of functionalization on the size of superparamagnetic iron oxide NPs. (**a**) The dispersant shell consisting of amine terminated PEG-silanes [79] (Copyright Wiley-VCH Verlag
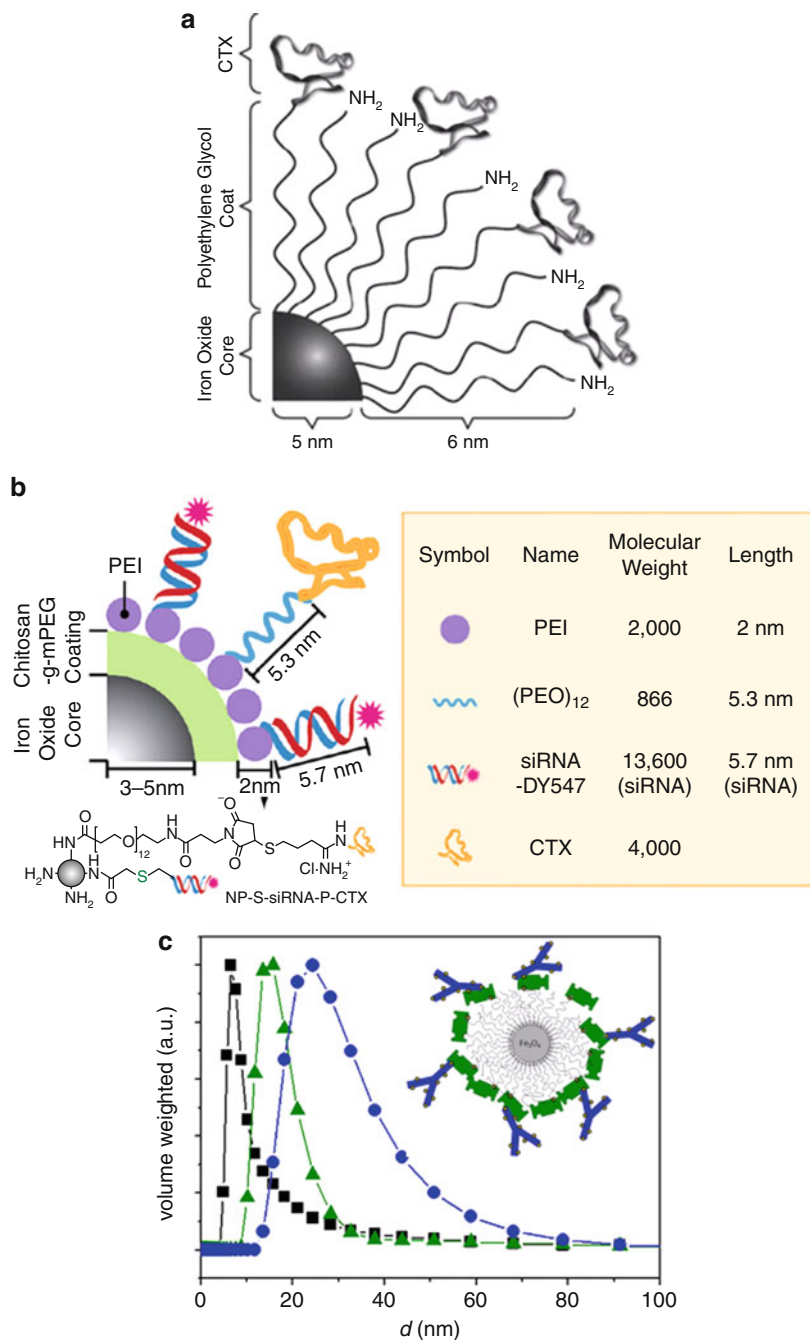
cells, where they naturally accumulate due to the enhanced permeation retention (EPR) effect [57, 171]. Proving specific targeting to such organs is therefore difficult as increased accumulation can occur also without specific binding to a target.

The targeting functionality has to be irreversible bound to the particle surface and accessible for binding; this requires covalent coupling to an irreversibly bound dispersant shell. Desorbed targeting ligands can block receptors before functionalized NPs reach these locations. In addition, loss of targeting moieties renders particles unable to bind. The density of ligands presented at the surface of NPs can be closely controlled if NPs are stabilized with low M_w dispersants; this is achieved by co-adsorbing functionalized and unfunctionalized dispersants to the NP surface [21]. By contrast, the serpentine, constantly changing conformation of physisorbed high M_w dispersants prevents efficient addition and controlled presentation of ligands at the interface of NPs [172].

Stealth properties are preserved best if the number of proteins in the ligand shell is minimized. This can be achieved by covalently linking ligands directly to the stealth PEG dispersant shell at a controlled density. Superparamagnetic iron oxide NPs functionalized with covalently bound ligands have typically been coated with dispersants such as dextran that lack well-defined anchors [163]; this renders a controlled surface presentation of functionalities difficult [166].

By contrast, a controlled presentation of ligands at the interface of NPs is possible if they are stabilized with low M_w dispersants such as PEG-silanes (Fig. 12.5a). This was demonstrated on iron oxide NPs functionalized with chlorotoxin [9, 79]. Their performance and uptake was subsequently studied in vitro in cell assays. A controlled surface presentation of ligands is thought to increase the targeting efficiency by decreasing the risk that ligands are buried in the dispersant shell. Furthermore, it allows for closer control over the hydrodynamic diameter of NPs upon functionalization and enables optimization of the number of ligands bound to one NP. The latter is important to ensure sufficient binding affinity while minimizing nonspecific interactions.

Because the hydrodynamic size of superparamagnetic iron oxide NPs significantly influences their uptake by cells [173], control over their hydrodynamic diameter upon functionalization is crucial. Ligands, such as antibodies and peptides are often comparable in size to the iron oxide NPs [169]. Their coupling can therefore significantly change the hydrodynamic size (Fig. 12.5).

Fig. 12.5 (continued) GmbH & Co. KGaA. Reproduced with permission) can be of comparable size to the iron oxide core. The hydrodynamic diameter of sterically stabilized NPs is therefore considerably larger than the size of the core. (**b**) Targeting ligands such as chlorotoxin, siRNA, and fluorophores can have a similar size to that of iron oxide cores. Therefore, the hydrodynamic radius of functionalized NPs can be significantly larger than that of unfunctionalized counterparts [169]. (Biomaterials by Biological Engineering Society. Reproduced with permission of PERGAMON in the format Journal via Copyright Clearance Center). (**c**) The increase in hydrodynamic diameter of iron oxide NPs upon coupling ligands to the dispersant shell is experimentally shown on superparamagnetic iron oxide NPs stabilized with PEG (5 kDa)-nitroDOPA that were further functionalized with neutravidin (*green*) followed by biotinylated antibodies (*blue*)

Ligands can also cross-link and cluster individually stabilized NPs if they carry multiple chemically reactive groups per NP (Fig. 12.5c); this significantly increases the hydrodynamic diameter and prevents elucidation of the effect of ligands on the biodistribution and clearance of functionalized NPs. Therefore, it is of highest importance to measure the hydrodynamic diameter and zeta potential of NPs before and after ligands are coupled to their shells. Differences in the biodistribution and clearance rate of NPs can only be unequivocally attributed to a targeting effect if the size and surface charge of NPs are not significantly altered by the attachment of ligands. Such careful studies were performed to demonstrate in vitro the specific binding of cRGD-functionalized iron oxide NPs to cancer cells [174].

An alternative very good way to elucidate binding specificity of NPs is to functionalize them with different peptide sequences of similar sizes and charges. A comparison of the binding of NPs functionalized with native and scrambled RGD sequences to cells allows assessment of the binding specificity of such NPs [164]. Superparamagnetic iron oxide NPs have most frequently been functionalized with peptides, since the small size of these ligands and the possibility to synthesize them offers easy and cost-effective functionalization. By contrast, only a few antibodies would be able to decorate a NP surface due to steric constraints. It has been shown that multivalent binding greatly enhances the targeting ability of NPs [165]. For this reason, and due to the reduced circulation time of antibody functionalized NPs, peptide and other low M_w molecules might be more promising targeting ligands for superparamagnetic iron oxide NPs than antibodies are [165].

It is important to thoroughly remove excess material after stabilization and functionalization of NPs since the excessive material will comprise biopolymers of similar size as the NPs. Rigorous purification is crucial but difficult to perform if the ligand shell is physisorbed and not cross-linked, as such NPs do not pass column purification and can be damaged by filtration and centrifuge purification. The need to pay attention to the difficulty to completely remove even the smallest ligands was exemplified in a study in which non-complexed ^{64}Cu could not be removed by centrifugation but required purification of iron oxide NPs by column separation [175].

Conclusions

The increasingly demanding and versatile requirements imposed on superparamagnetic iron oxide NPs intended for biomedical applications require close control over the size, structure and surface properties of NPs. The key requirement is colloidal stability under physiological conditions which can only be met if iron oxide NPs are sterically stabilized with dispersants that firmly and for practical purposes irreversibly bind to the surface of the NPs. Dispersants consisting of a suitable anchor covalently linked to a spacer have been shown to meet this stringent requirement.

Close control over the assembly of dispersants at the NP surface allows tuning of the size of the core and thickness of the shell independently. While the magnetic response of superparamagnetic iron oxide NPs is directly related to the size of the core, the stability of NPs and their biodistribution are controlled by the thickness, structure and properties of the shell. Thus, within the limit of superparamagnetic cores, magnetic response of individually stabilized iron oxide NPs can be maximized by increasing the size of the core without compromising their stability. This, however, is only possible if iron oxide NPs are stabilized with optimized dispersants that consist of an irreversibly binding anchor covalently linked to a spacer long enough to provide good steric stability but still small enough to allow high packing densities of dispersants at a sufficient distance from the surface of the core. If these requirements are fulfilled, individually stabilized superparamagnetic iron oxide NPs can be used as highly stable, well-dispersed NPs for a multitude of biomedical applications. End-grafted and irreversibly bound dispersants further allow for controlled functionalization of individually stabilized NPs. This is achieved by simply adjusting the molar ratio of differently functionalized and unfunctionalized dispersants that are grafted to the surface of iron oxide NPs.

In summary, the emerging modular approach to design iron oxide NPs greatly enhances the versatility of iron oxide NP platforms being developed for various biomedical applications. However, ensuring the effect of each functionalization step in this modular approach requires the application of a wide range of characterization techniques from multiple research fields. This inter-disciplinary expertise often is not accessible within one group or even one research environment and is therefore seldom performed in the study of a single NP material. Despite this challenge it is clear that the research and application of iron oxide core-shell NPs is approaching a state of maturity in the understanding of what characterization techniques and material parameters are of importance. We should therefore expect further breakthrough developments in the design of NPs for biomedical and other applications in the near future.

References

1. Lewin M, Carlesso N, Tung CH et al (2000) Tat peptide-derivatized magnetic nanoparticles allow in vivo tracking and recovery of progenitor cells. Nat Biotechnol 18:410–414
2. Pittet MJ, Swirski FK, Reynolds F et al (2006) Labeling of immune cells for in vivo imaging using magnetofluorescent nanoparticles. Nat Protoc 1:73–79
3. Wang DS, He JB, Rosenzweig N et al (2004) Superparamagnetic Fe2O3 Beads-CdSe/ZnS quantum dots core-shell nanocomposite particles for cell separation. Nano Lett 4:409–413
4. Halbreich A, Roger J, Pons JN et al (1998) Biomedical applications of maghemite ferrofluid. Biochimie 80:379–390
5. Pankhurst QA, Thanh NKT, Jones SK et al (2009) Progress in applications of magnetic nanoparticles in biomedicine. J Phys D-Appl Phys 42
6. Namdeo M, Saxena S, Tankhiwale R et al (2008) Magnetic nanoparticles for drug delivery applications. J Nanosci Nanotechnol 8:3247–3271
7. Weissleder R, Hahn PF, Stark DD et al (1987) MR imaging of splenic metastases – ferrite-enhanced detection in rats. Am J Roentgenol 149:723–726

 8. Weissleder R, Elizondo G, Wittenberg J et al (1990) Ultrasmall superparamagnetic iron-oxide – characterization of a new class of contrast agents for Mr imaging. Radiology 175:489–493
 9. McCarthy JR, Weissleder R (2008) Multifunctional magnetic nanoparticles for targeted imaging and therapy. Adv Drug Deliv Rev 60:1241–1251
10. Hutten A, Sudfeld D, Ennen I et al (2004) New magnetic nanoparticles for biotechnology. J Biotechnol 112:47–63
11. Duran JDG, Arias JL, Gallardo V et al (2008) Magnetic colloids as drug vehicles. J Pharm Sci 97:2948–2983
12. Krishnan KM (2010) Biomedical nanomagnetics: a spin through possibilities in imaging, diagnostics, and therapy. IEEE Trans Magn 46:2523–2558
13. Louie A (2010) Multimodality imaging probes: design and challenges. Chem Rev 110:3146–3195
14. Wang YXJ, Hussain SM, Krestin GP (2001) Superparamagnetic iron oxide contrast agents: physicochemical characteristics and applications in MR imaging. Eur Radiol 11:2319–2331
15. Jung CW, Jacobs P (1995) Physical and chemical-properties of superparamagnetic iron-oxide Mr contrast agents – ferumoxides, ferumoxtran, ferumoxsil. Magn Reson Imaging 13:661–674
16. Lin MM, Kim DK, El Haj AJ et al (2008) Development of Superparamagnetic Iron Oxide Nanoparticles (SPIONS) for translation to clinical applications. IEEE Trans Nanobioscience 7:298–305
17. Cengelli F, Maysinger D, Tschudi-Monnet F et al (2006) Interaction of functionalized superparamagnetic iron oxide nanoparticles with brain structures. J Pharmacol Exp Ther 318:108–116
18. Pardoe H, Chua-anusorn W, St Pierre TG et al (2001) Structural and magnetic properties of nanoscale iron oxide particles synthesized in the presence of dextran or polyvinyl alcohol. J Magn Magn Mater 225:41–46
19. Bautista MC, Bomati-Miguel O, Zhao X et al (2004) Comparative study of ferrofluids based on dextran-coated iron oxide and metal nanoparticles for contrast agents in magnetic resonance imaging. Nanotechnology 15:S154–S159
20. Basiruddin SK, Saha A, Pradhan N et al (2010) Advances in coating chemistry in deriving soluble functional nanoparticle. J Phys Chem C 114:11009–11017
21. Amstad E, Gillich T, Bilecka I et al (2009) Ultrastable iron oxide nanoparticle colloidal suspensions using dispersants with catechol-derived anchor groups. Nano Lett 9:4042–4048
22. Lu AH, Salabas EL, Schuth F (2007) Magnetic nanoparticles: synthesis, protection, functionalization, and application. Angew Chem Int Ed 46:1222–1244
23. Jun YW, Lee JH, Cheon J (2008) Chemical design of nanoparticle probes for high-performance magnetic resonance imaging. Angew Chem Int Ed 47:5122–5135
24. Sun SH, Zeng H, Robinson DB et al (2004) Monodisperse MFe2O4 (M = Fe, Co, Mn) nanoparticles. J Am Chem Soc 126:273–279
25. Thunemann AF, Rolf S, Knappe P et al (2009) In situ analysis of a bimodal size distribution of superparamagnetic nanoparticles. Anal Chem 81:296–301
26. Bonini M, Wiedemann A, Baglioni P (2006) Synthesis and characterization of magnetic nanoparticles coated with a uniform silica shell. Mater Sci Eng C-Biomim Supramol Syst 26:745–750
27. Butter K, Hoell A, Wiedenmann A et al (2004) Small-angle neutron and X-ray scattering of dispersions of oleic-acid-coated magnetic iron particles. J Appl Crystallogr 37:847–856
28. Degen P, Shukla A, Boetcher U et al (2008) Self-assembled ultra-thin coatings of octadecyltrichlorosilane (OTS) formed at the surface of iron oxide nanoparticles. Colloid Polym Sci 286:159–168
29. Cowles RJH (1999) Particle characterization for oil sand processing – 1: particle size measurements using a disc centrifuge. Pet Sci Technol 17:429–442

30. Roonasi P, Holmgren A (2009) A Fourier transform infrared (FTIR) and thermogravimetric analysis (TGA) study of oleate adsorbed on magnetite nano-particle surface. Appl Surf Sci 255:5891–5895

31. Chen S, Li Y, Guo C et al (2007) Temperature-responsive magnetite/PEO-PPO-PEO block copolymer nanoparticles for controlled drug targeting delivery. Langmuir 23:12669–12676

32. Zackrisson M, Stradner A, Schurtenberger P et al (2005) Small-angle neutron scattering on a core-shell colloidal system: a contrast-variation study. Langmuir 21:10835–10845

33. Dingenouts N, Seelenmeyer S, Deike I et al (2001) Analysis of thermosensitive core-shell colloids by small-angle neutron scattering including contrast variation. Phys Chem Chem Phys 3:1169–1174

34. Gelbrich T, Feyen M, Schmidt AM (2006) Magnetic thermoresponsive core-shell nanoparticles. Macromolecules 39:3469–3472

35. Mondini S, Ferretti AM, Puglisi A et al (2012) PEBBLES and PEBBLEJUGGLER: software for accurate, unbiased, and fast measurement and analysis of nanoparticle morphology from transmission electron microscopy (TEM) micrographs. Nanoscale 4:5356–5372

36. Zakharov P, Bhat S, Schurtenberger P et al (2006) Multiple-scattering suppression in dynamic light scattering based on a digital camera detection scheme. Appl Optics 45:1756–1764

37. Scheffold F, Mason TG (2009) Scattering from highly packed disordered colloids. J Phys Condens Matter 21:332102

38. Zhang QA, Thompson MS, Carmichael-Baranauskas AY et al (2007) Aqueous dispersions of magnetite nanoparticles complexed with copolyether dispersants: experiments and theory. Langmuir 23:6927–6936

39. Mefford OT, Vadala ML, Goff JD et al (2008) Stability of polydimethylsiloxane-magnetite nanoparticle dispersions against flocculation: interparticle interactions of polydisperse materials. Langmuir 24:5060–5069

40. Bevan MA, Petris SN, Chan DYC (2002) Solvent quality dependent continuum van der Waals attraction and phase behavior for colloids bearing nonuniform adsorbed polymer layers. Langmuir 18:7845–7852

41. Thanh NTK, Green LAW (2010) Functionalisation of nanoparticles for biomedical applications. Nano Today 5:213–230

42. Verma A, Stellacci F (2010) Effect of surface properties on nanoparticle-cell interactions. Small 6:12–21

43. Xiao ZP, Yang KM, Liang H et al (2010) Synthesis of magnetic, reactive, and thermoresponsive Fe3O4 nanoparticles via surface-initiated RAFT copolymerization of N-isopropylacrylamide and acrolein. J Polym Sci Part a-Polym Chem 48:542–550

44. Somaskandan K, Veres T, Niewczas M et al (2008) Surface protected and modified iron based core-shell nanoparticles for biological applications. New J Chem 32:201–209

45. Amstad E, Starmans LWE, Visbal MA et al Influence of the PEG Shell on the stability and magnetic properties of iron oxide nanoparticles (in preparation)

46. Gamarra LF, Amaro E, Alves S et al (2010) Characterization of the biocompatible magnetic colloid on the basis of Fe_3O_4 nanoparticles coated with dextran, used as contrast agent in magnetic resonance imaging. J Nanosci Nanotechnol 10:4145–4153

47. Ma HL, Qi XT, Maitani Y et al (2007) Preparation and characterization of superparamagnetic iron oxide nanoparticles stabilized by alginate. Int J Pharm 333:177–186

48. Park JH, Im KH, Lee SH et al (2005) Preparation and characterization of magnetic chitosan particles for hyperthermia application. J Magn Magn Mater 293:328–333

49. Mahmoudi M, Simchi A, Milani AS et al (2009) Cell toxicity of superparamagnetic iron oxide nanoparticles. J Colloid Interface Sci 336:510–518

50. Chastellain A, Petri A, Hofmann H (2004) Particle size investigations of a multistep synthesis of PVA coated superparamagnetic nanoparticles. J Colloid Interface Sci 278:353–360

51. Schopf B, Neuberger T, Schulze K et al (2005) Methodology description for detection of cellular uptake of PVA coated superparamagnetic iron oxide nanoparticles (SPION) in synovial cells of sheep. J Magn Magn Mater 293:411–418

52. Santra S, Kaittanis C, Grimm J et al (2009) Drug/dye-loaded, multifunctional iron oxide nanoparticles for combined targeted cancer therapy and dual optical/magnetic resonance imaging. Small 5:1862–1868

53. Thunemann AF, Schutt D, Kaufner L et al (2006) Maghemite nanoparticles protectively coated with poly(ethylene imine) and poly(ethylene oxide)-block-poly(glutamic acid). Langmuir 22:2351–2357

54. Shubayev VI, Pisanic TR, Jin SH (2009) Magnetic nanoparticles for theragnostics. Adv Drug Deliv Rev 61:467–477

55. Mosqueira VCF, Legrand P, Morgat JL et al (2001) Biodistribution of long-circulating PEG-grafted nanocapsules in mice: effects of PEG chain length and density. Pharm Res 18:1411–1419

56. Josephson L, Tung CH, Moore A et al (1999) High-efficiency intracellular magnetic labeling with novel superparamagnetic-tat peptide conjugates. Bioconjug Chem 10:186–191

57. Laurent S, Forge D, Port M et al (2008) Magnetic iron oxide nanoparticles: synthesis, stabilization, vectorization, physicochemical characterizations, and biological applications. Chem Rev 108:2064–2110

58. Corot C, Robert P, Idee JM et al (2006) Recent advances in iron oxide nanocrystal technology for medical imaging. Adv Drug Deliv Rev 58:1471–1504

59. Du BY, Mei AX, Tao PJ et al (2009) Poly[N-isopropylacrylamide-Co-3-(trimethoxysilyl)-propylmethacrylate] coated aqueous dispersed thermosensitive Fe_3O_4 nanoparticles. J Phys Chem C 113:10090–10096

60. Wang SX, Zhou Y, Guan W et al (2008) One-step copolymerization modified magnetic nanoparticles via surface chain transfer free radical polymerization. Appl Surf Sci 254:5170–5174

61. Zhao B, Brittain WJ (2000) Polymer brushes: surface-immobilized macromolecules. Prog Polym Sci 25:677–710

62. Bae KH, Kim YB, Lee Y et al (2010) Bioinspired synthesis and characterization of gadolinium-labeled magnetite nanoparticles for dual contrast T-1- and T-2-weighted magnetic resonance imaging. Bioconjug Chem 21:505–512

63. Nagase K, Kobayashi J, Okano T (2009) Temperature-responsive intelligent interfaces for biomolecular separation and cell sheet engineering. J R Soc Interface 6:S293–S309

64. Knoll W, Advincula RC (eds) (2011) Functional polymer films, vol 2. Wiley-VCH, Weinheim, Germany

65. Xie J, Xu CJ, Xu ZC et al (2006) Linking hydrophilic macromolecules to monodisperse magnetite (Fe_3O_4) nanoparticles via trichloro-s-triazine. Chem Mater 18:5401–5403

66. Xie J, Chen K, Lee H-Y et al (2008) Ultrasmall c(RGDyK)-coated Fe_3O_4 nanoparticles and their specific targeting to integrin alpha(v)beta3-rich tumor cells. J Am Chem Soc 130:7542–7543

67. Xu CJ, Xu KM, Gu HW et al (2004) Dopamine as a robust anchor to immobilize functional molecules on the iron oxide shell of magnetic nanoparticles. J Am Chem Soc 126:9938–9939

68. Gu HW, Yang ZM, Gao JH et al (2005) Heterodimers of nanoparticles: formation at a liquid-liquid interface and particle-specific surface modification by functional molecules. J Am Chem Soc 127:34–35

69. Amstad E, Isa L, Reimhult E (2011) Nitrocatechol dispersants to tailor superparamagnetic Fe_3O_4 nanoparticles. Chimia 64:826

70. Isa L, Amstad E, Textor M et al (2010) Self-assembly of iron oxide-poly(ethylene glycol) core-shell nanoparticles at liquid-liquid interfaces. Chimia 64:145–149

71. Yu S, Chow GM (2004) Carboxyl group (-CO_2H) functionalized ferrimagnetic iron oxide nanoparticles for potential bio-applications. J Mater Chem 14:2781–2786

72. White MA, Johnson JA, Koberstein JT et al (2006) Toward the syntheses of universal ligands for metal oxide surfaces: controlling surface functionality through click chemistry. J Am Chem Soc 128:11356–11357

73. Song HT, Choi JS, Huh YM et al (2005) Surface modulation of magnetic nanocrystals in the development of highly efficient magnetic resonance probes for intracellular labeling. J Am Chem Soc 127:9992–9993

74. Basly B, Felder-Flesch D, Perriat P et al (2010) Dendronized iron oxide nanoparticles as contrast agents for MRI. Chem Commun 46:985–987

75. Lalatonne Y, Paris C, Serfaty JM et al (2008) Bis-phosphonates – ultra small superparamagnetic iron oxide nanoparticles: a platform towards diagnosis and therapy. Chem Commun 22:2553–2555

76. Zhou Y, Wang SX, Ding BJ et al (2008) Modification of magnetite nanoparticles via surface-initiated atom transfer radical polymerization (ATRP). Chem Eng J 138:578–585

77. Forge D, Laurent S, Gossuin Y et al (2011) An original route to stabilize and functionalize magnetite nanoparticles for theranosis applications. J Magn Magn Mater 323:410–415

78. Sun CR, Du K, Fang C et al (2010) PEG-mediated synthesis of highly dispersive multifunctional superparamagnetic nanoparticles: their physicochemical properties and function in vivo. Acs Nano 4:2402–2410

79. Veiseh O, Gunn JW, Kievit FM et al (2009) Inhibition of tumor-cell invasion with chlorotoxin-bound superparamagnetic nanoparticles. Small 5:256–264

80. Larsen EKU, Nielsen T, Wittenborn T et al (2009) Size-dependent accumulation of PEGylated Silane-coated magnetic iron oxide nanoparticles in murine tumors. ACS Nano 3:1947–1951

81. Dalsin JL, Lin LJ, Tosatti S et al (2005) Protein resistance of titanium oxide surfaces modified by biologically inspired mPEG-DOPA. Langmuir 21:640–646

82. Corbierre MK, Cameron NS, Lennox RB (2004) Polymer-stabilized gold nanoparticles with high grafting densities. Langmuir 20:2867–2873

83. Kim M, Chen YF, Liu YC et al (2005) Super-stable, high-quality Fe$_3$O$_4$ dendron-nanocrystals dispersible in both organic and aqueous solutions. Adv Mater 17:1429

84. Chen ZP, Zhang Y, Xu K et al (2008) Stability of hydrophilic magnetic nanoparticles under biologically relevant conditions. J Nanosci Nanotechnol 8:6260–6265

85. Haensch C, Chiper M, Ulbricht C et al (2008) Reversible supramolecular functionalization of surfaces: terpyridine ligands as versatile building blocks for noncovalent architectures. Langmuir 24:12981–12985

86. Waite JH, Tanzer ML (1981) Polyphenolic substance of mytilus-edulis – novel adhesive containing L-dopa and hydroxyproline. Science 212:1038–1040

87. Lynch MW, Valentine M, Hendrickson DN (1982) Mixed-valence semi-quinone catecholate iron complexes. J Am Chem Soc 104:6982–6989

88. Heistand RH, Roe AL, Que L (1982) Dioxygenase models – crystal-structures of [N, N'-(1,2-phenylene)bis(salicylideniminato)](catecholato-O)iron(III) and Mu-(1,4-benzenediolato-O, O')-bis[N, N'-ethylenebis(salicylideniminato)iron(III)]. Inorg Chem 21:676–681

89. Attia AS, Bhattacharya S, Pierpont CG (1995) Potential for redox isomerism by quinone complexes of Iron(Iii). – studies on complexes of the Fe-III(N-N)(Dbsq)(Dbcat) series with 2,2′-bipyridine and N, N, N', N'-tetramethylethylenediamine coligands. Inorg Chem 34:4427–4433

90. Grillo VA, Hanson GR, Wang DM et al (1996) Synthesis, x-ray structural determination, and magnetic susceptibility, Mossbauer, and EPR studies of (Ph(4)P)(2)[Fe-2(Cat)(4)(H$_2$O)(2)]·6H(2)O, a catecholato-bridged dimer of iron(III). Inorg Chem 35:3568–3576

91. Girerd JJ, Boillot ML, Blain G et al (2008) An EPR investigation of the electronic structure of pseudo-octahedral and spin crossover catecholato-iron(III) complexes in the low-spin state. Inorg Chim Acta 361:4012–4016

92. Kalyanaraman B, Felix CC, Sealy RC (1985) Semiquinone anion radicals of catechol(amine) S, catechol estrogens, and their metal-ion complexes. Environ Health Perspect 64:185–198

93. Cox DD, Que L (1988) Functional models for catechol 1,2-dioxygenase – the role of the Iron (III) center. J Am Chem Soc 110:8085–8092

94. Emerson JP, Kovaleva EG, Farquhar ER et al (2008) Swapping metals in Fe- and Mn-dependent dioxygenases: evidence for oxygen activation without a change in metal redox state. Proc Natl Acad Sci U S A 105:7347–7352

95. Shultz MD, Reveles JU, Khanna SN et al (2007) Reactive nature of dopamine as a surface functionalization agent in iron oxide nanoparticles. J Am Chem Soc 129:2482–2487

96. Goldmann AS, Schodel C, Walther A et al (2010) Biomimetic mussel adhesive inspired clickable anchors applied to the functionalization of Fe_3O_4 nanoparticles. Macromol Rapid Commun 31:1608–1615

97. Galpin JR, Tielens LGM, Veldink GA et al (1976) Interaction of some catechol derivatives with iron atom of soybean lipoxygenase. FEBS Lett 69:179–182

98. Kawabata T, Schepkin V, Haramaki N et al (1996) Iron coordination by catechol derivative antioxidants. Biochem Pharmacol 51:1569–1577

99. Crisponi G, Remelli M (2008) Iron chelating agents for the treatment of iron overload. Coord Chem Rev 252:1225–1240

100. Nurchi VM, Pivetta T, Lachowicz JI et al (2009) Effect of substituents on complex stability aimed at designing new iron(III) and aluminum(III) chelators. J Inorg Biochem 103:227–236

101. Amstad E, Fischer H, Gehring AU et al (2011) Magnetic decoupling of surface Fe(3+) in magnetite nanoparticles upon Nitrocatechol-anchored dispersant binding. Chem A Eur J 17:7396–7398

102. Amstad E, Gehring AU, Fischer H et al (2011) Influence of electronegative substituents on the binding affinity of catechol-derived anchors to Fe(3)O(4) nanoparticles. J Phys Chem C 115:683–691

103. Fritz G, Schadler V, Willenbacher N et al (2002) Electrosteric stabilization of colloidal dispersions. Langmuir 18:6381–6390

104. Gast AP (1996) Structure, interactions, and dynamics in tethered chain systems. Langmuir 12:4060–4067

105. Witten TA, Pincus PA (1986) Colloid stabilization by long grafted polymers. Macromolecules 19:2509–2513

106. Vincent B, Edwards J, Emmett S et al (1986) Depletion flocculation in dispersions of sterically-stabilized particles (soft spheres). Colloid Surf 18:261–281

107. Degennes PG (1980) Conformations of polymers attached to an interface. Macromolecules 13:1069–1075

108. Milner ST, Witten TA, Cates ME (1988) Theory of the grafted polymer brush. Macromolecules 21:2610–2619

109. Zhulina EB, Borisov OV, Priamitsyn VA (1990) Theory of steric stabilization of colloid dispersions by grafted polymers. J Colloid Interface Sci 137:495–511

110. Shim DFK, Cates ME (1989) Finite extensibility and density saturation effects in the polymer brush. Journal De Physique 50:3535–3551

111. Alexander S (1977) Polymer adsorption on small spheres – scaling approach. Journal De Physique 38:977–981

112. Birshtein TM, Zhulina EB (1984) Conformations of star-branched macromolecules. Polymer 25:1453–1461

113. Dan N, Tirrell M (1992) Polymers tethered to curved interfaces – a self-consistent-field analysis. Macromolecules 25:2890–2895

114. Ball RC, Marko JF, Milner ST et al (1991) Polymers grafted to a convex surface. Macromolecules 24:693–703

115. Toral R, Chakrabarti A (1993) Monte-Carlo study of polymer-chains end-grafted onto a spherical interface. Phys Rev E 47:4240–4246

116. Li H, Witten TA (1994) Polymers grafted to convex surfaces – a variational approach. Macromolecules 27:449–457
117. Martin JI, Wang ZG (1995) Polymer brushes – scaling, compression forces, interbrush penetration, and solvent size effects. J Phys Chem 99:2833–2844
118. Lin EK, Gast AP (1996) Self consistent field calculations of interactions between chains tethered to spherical interfaces. Macromolecules 29:390–397
119. Lo Verso F, Egorov SA, Milchev A et al (2010) Spherical polymer brushes under good solvent conditions: molecular dynamics results compared to density functional theory. J Chem Phys 133:184901
120. Lo Verso F, Yelash L, Egorov SA et al (2011) Interactions between polymer brush-coated spherical nanoparticles: the good solvent case. J Chem Phys 135:214902
121. Gillich T, Acikgoz C, Isa L et al (2013) PEG-stabilized core-shell nanoparticles: impact of linear versus dendritic polymer shell architecture on colloidal properties and the reversibility of temperature-induced aggregation. ACS Nano 7:316–329
122. Isa L, Calzolari DCE, Pontoni D et al (2013) Core-shell nanoparticle monolayers at planar liquid-liquid interfaces: effects of polymer architecture on the interface microstructure. Soft Matter 9:3789–3797
123. Owens DE, Peppas NA (2006) Opsonization, biodistribution, and pharmacokinetics of polymeric nanoparticles. Int J Pharm 307:93–102
124. Jeon SI, Lee JH, Andrade JD et al (1991) Protein surface interactions in the presence of polyethylene oxide 1. Simplified theory. J Colloid Interface Sci 142:149–158
125. Bhat R, Timasheff SN (1992) Steric exclusion is the principal source of the preferential hydration of proteins in the presence of polyethylene glycols. Protein Sci 1:1133–1143
126. Feldman K, Hahner G, Spencer ND et al (1999) Probing resistance to protein adsorption of oligo(ethylene glycol)-terminated self-assembled monolayers by scanning force microscopy. J Am Chem Soc 121:10134–10141
127. Wang RLC, Kreuzer HJ, Grunze M (1997) Molecular conformation and solvation of oligo (ethylene glycol)-terminated self-assembled monolayers and their resistance to protein adsorption. J Phys Chem B 101:9767–9773
128. Roosjen A, de Vries J, van der Mei HC et al (2005) Stability and effectiveness against bacterial adhesion of poly(ethylene oxide) coatings in biological fluids. J Biomed Mater Res B Appl Biomater 73B:347–354
129. Shen MC, Martinson L, Wagner MS et al (2002) PEO-like plasma polymerized tetraglyme surface interactions with leukocytes and proteins: in vitro and in vivo studies. J Biomater Sci Polym Ed 13:367–390
130. Konradi R, Pidhatika B, Muhlebach A et al (2008) Poly-2-methyl-2-oxazoline: a peptide-like polymer for protein-repellent surfaces. Langmuir 24:613–616
131. Pasche S, De Paul SM, Voros J et al (2003) Poly(L-lysine)-graft-poly(ethylene glycol) assembled monolayers on niobium oxide surfaces: a quantitative study of the influence of polymer interfacial architecture on resistance to protein adsorption by ToF-SIMS and in situ OWLS. Langmuir 19:9216–9225
132. Michel R, Pasche S, Textor M et al (2005) Influence of PEG architecture on protein adsorption and conformation. Langmuir 21:12327–12332
133. Szleifer I (1997) Protein adsorption on surfaces with grafted polymers: a theoretical approach. Biophys J 72:595–612
134. Zahr AS, Davis CA, Pishko MV (2006) Macrophage uptake of core-shell nanoparticles surface modified with poly(ethylene glycol). Langmuir 22:8178–8185
135. Gessner A, Paulke BR, Muller RH et al (2006) Protein rejecting properties of PEG-grafted nanoparticles: Influence of PEG-chain length and surface density evaluated by two-dimensional electrophoresis and bicinchoninic acid (BCA)-proteinassay. Pharmazie 61:293–297

136. Kenworthy AK, Hristova K, Needham D et al (1995) Range and magnitude of the steric pressure between bilayers containing phospholipids with covalently attached Poly(ethylene glycol). Biophys J 68:1921–1936
137. Vittaz M, Bazile D, Spenlehauer G et al (1996) Effect of PEO surface density on long-circulating PLA-PEO nanoparticles which are very low complement activators. Biomaterials 17:1575–1581
138. Storm G, Belliot SO, Daemen T et al (1995) Surface modification of nanoparticles to oppose uptake by the mononuclear phagocyte system. Adv Drug Deliv Rev 17:31–48
139. Klibanov AL, Maruyama K, Torchilin VP et al (1990) Amphipathic polyethyleneglycols effectively prolong the circulation time of liposomes. FEBS Lett 268:235–237
140. Mori A, Klibanov AL, Torchilin VP et al (1991) Influence of the steric barrier activity of amphipathic poly(ethyleneglycol) and ganglioside GM1 on the circulation time of liposomes and on the target binding of immunoliposomes invivo. FEBS Lett 284:263–266
141. Decuzzi P, Pasqualini R, Arap W et al (2009) Intravascular delivery of particulate systems: does geometry really matter? Pharm Res 26:235–243
142. Dobrovolskaia MA, McNeil SE (2007) Immunological properties of engineered nanomaterials. Nat Nanotechnol 2:469–478
143. Gbadamosi JK, Hunter AC, Moghimi SM (2002) PEGylation of microspheres generates a heterogeneous population of particles with differential surface characteristics and biological performance. FEBS Lett 532:338–344
144. Tiefenauer LX, Tschirky A, Kuhne G et al (1996) In vivo evaluation of magnetite nanoparticles for use as a tumor contrast agent in MRI. Magn Reson Imaging 14:391–402
145. Harper GR, Davies MC, Davis SS et al (1991) Steric stabilization of microspheres with grafted polyethylene oxide reduces phagocytosis by rat Kupffer cells-invitro. Biomaterials 12:695–704
146. Lacava LM, Garcia VAP, Kuckelhaus S et al (2004) Long-term retention of dextran-coated magnetite nanoparticles in the liver and spleen. J Magn Magn Mater 272:2434–2435
147. Berkowit A, Schuele WJ, Flanders PJ (1968) Influence of crystallite size on magnetic properties of acicular gamma-Fe$_2$O$_3$ particles. J Appl Phys 39:1261
148. Dutta P, Pai S, Seehra MS et al (2009) Size dependence of magnetic parameters and surface disorder in magnetite nanoparticles. J Appl Phys 105:7B501
149. Krycka KL, Booth RA, Hogg CR et al (2010) Core-shell magnetic morphology of structurally uniform magnetite nanoparticles. Phys Rev Lett 104:207203
150. Vidal-Vidal J, Rivas J, Lopez-Quintela MA (2006) Synthesis of monodisperse maghemite nanoparticles by the microemulsion method. Colloid SurfA Physicochem Eng Asp 288:44–51
151. Jun YW, Huh YM, Choi JS et al (2005) Nanoscale size effect of magnetic nanocrystals and their utilization for cancer diagnosis via magnetic resonance imaging. J Am Chem Soc 127:5732–5733
152. Cheon J, Lee JH (2008) Synergistically integrated nanoparticles as multimodal probes for nanobiotechnology. Acc Chem Res 41:1630–1640
153. Josephson L, Perez JM, Weissleder R (2001) Magnetic nanosensors for the detection of oligonucleotide sequences. Angew Chem Int Ed 40:3204–3206
154. Berret JF, Schonbeck N, Gazeau F et al (2006) Controlled clustering of superparamagnetic nanoparticles using block copolymers: design of new contrast agents for magnetic resonance imaging. J Am Chem Soc 128:1755–1761
155. Seo SB, Yang J, Lee TI et al (2008) Enhancement of magnetic resonance contrast effect using ionic magnetic clusters. J Colloid Interface Sci 319:429–434
156. Brown KA, Vassiliou CC, Issadore D et al (2010) Scaling of transverse nuclear magnetic relaxation due to magnetic nanoparticle aggregation. J Magn Magn Mater 322:3122–3126
157. Matsumoto Y, Jasanoff A (2008) T-2 relaxation induced by clusters of superparamagnetic nanoparticles: Monte Carlo simulations. Magn Reson Imaging 26:994–998

158. LaConte LEW, Nitin N, Zurkiya O et al (2007) Coating thickness of magnetic iron oxide nanoparticles affects R-2 relaxivity. J Magn Reson Imaging 26:1634–1641
159. Duan HW, Kuang M, Wang XX et al (2008) Reexamining the effects of particle size and surface chemistry on the magnetic properties of iron oxide nanocrystals: new insights into spin disorder and proton relaxivity. J Phys Chem C 112:8127–8131
160. Rosensweig RE (2002) Heating magnetic fluid with alternating magnetic field. J Magn Magn Mater 252:370–374
161. Buscher K, Helm CA, Gross C et al (2004) Nanoparticle composition of a ferrofluid and its effects on the magnetic properties. Langmuir 20:2435–2444
162. Rovers SA, Dietz C, van der Poel LAM et al (2010) Influence of distribution on the heating of superparamagnetic iron oxide nanoparticles in Poly(methyl methacrylate) in an alternating magnetic field. J Phys Chem C 114:8144–8149
163. Tsourkas A, Shinde-Patil VR, Kelly KA et al (2005) In vivo imaging of activated endothelium using an anti-VCAM-1 magnetooptical probe. Bioconjug Chem 16:576–581
164. Kelly KA, Allport JR, Tsourkas A et al (2005) Detection of vascular adhesion molecule-1 expression using a novel multimodal nanoparticle. Circ Res 96:327–336
165. Montet X, Funovics M, Montet-Abou K et al (2006) Multivalent effects of RGD peptides obtained by nanoparticle display. J Med Chem 49:6087–6093
166. Martin AL, Hickey JL, Ablack AL et al (2010) Synthesis of bombesin-functionalized iron oxide nanoparticles and their specific uptake in prostate cancer cells. J Nanopart Res 12:1599–1608
167. Yigit MV, Mazumdar D, Kim HK et al (2007) Smart "Turn-on" magnetic resonance contrast agents based on aptamer-functionalized superparamagnetic iron oxide nanoparticles. Chembiochem 8:1675–1678
168. Cutler JI, Zheng D, Xu XY et al (2010) Polyvalent oligonucleotide iron oxide nanoparticle "Click" conjugates. Nano Lett 10:1477–1480
169. Veiseh O, Kievit FM, Fang C et al (2010) Chlorotoxin bound magnetic nanovector tailored for cancer cell targeting, imaging, and siRNA delivery. Biomaterials 31:8032–8042
170. Cho EC, Glaus C, Chen JY et al (2010) Inorganic nanoparticle-based contrast agents for molecular imaging. Trends Mol Med 16:561–573
171. Gindy ME, Prud'homme RK (2009) Multifunctional nanoparticles for imaging, delivery and targeting in cancer therapy. Expert Opin Drug Deliv 6:865–878
172. Sun C, Lee JSH, Zhang MQ (2008) Magnetic nanoparticles in MR imaging and drug delivery. Adv Drug Deliv Rev 60:1252–1265
173. Huang J, Bu LH, Xie J et al (2011) Effects of nanoparticle size on cellular uptake and liver MRI with polyvinylpyrrolidone-coated iron oxide nanoparticles. ACS Nano 4:7151–7160
174. Yu MK, Park J, Jeong YY et al (2010) Integrin-targeting thermally cross-linked superparamagnetic iron oxide nanoparticles for combined cancer imaging and drug delivery. Nanotechnology 21:415102
175. Jarrett BR, Gustafsson B, Kukis DL et al (2008) Synthesis of Cu-64-labeled magnetic nanoparticles for multimodal imaging. Bioconjug Chem 19:1496–1504

Bio-inorganic Nanomaterials for Biomedical Applications (Bio-silica and Polyphosphate)

13

Werner E. G. Müller, Olga Albert, Heinz C. Schröder,
and Xiaohong H. Wang

Keywords

Bio-polyphosphate • Bio-silica • Bone biomaterials • HA • Osteoporosis • Sponges

Introduction

In living organisms, four major groups of biominerals exist: (1) iron compounds, which are restricted primarily to Prokaryota; (2) calcium phosphates, found in Metazoa; (3) calcium carbonates, used by Prokaryota, Protozoa, Plantae, Fungi, and Metazoa; and (4) silica (opal), which is presented in sponges and diatoms. It is surprising that the occurrence of silica as a major skeletal element is restricted to some unicellular organisms and to sponges (Demospongiae and Hexactinellida) [1]. At present, it is not known why sponges have used silica as the biomineral to form one major innovation during the evolution from Protozoa to Metazoa, the hard skeleton. Since the transition from Protozoa to Metazoa is dated back 600–1,000 million years ago, it has been proposed that oxygen level, temperature, and seawater chemistry played a major role in this evolution. In particular, it was assumed that during the period of the appearance of sponges, the ocean was richer in sodium carbonate than in sodium chloride and that such a "soda ocean" had

W.E.G. Müller (✉) • O. Albert • H.C. Schröder
ERC Advanced Grant Research Group at the Institute for Physiological Chemistry, University Medical Center of the Johannes Gutenberg University Mainz, Mainz, Germany
e-mail: wmueller@uni-mainz.de

X.H. Wang (✉)
ERC Advanced Grant Research Group at the Institute for Physiological Chemistry, University Medical Center of the Johannes Gutenberg University Mainz, Mainz, Germany

National Research Center for Geoanalysis, Beijing, China
e-mail: wang013@uni-mainz.de

probably a pH above 9. Under such conditions, the concentration of silica, the dioxide form of silicon, was presumably higher in seawater than it is today [2, 3].

The formation of the skeleton is a multifaceted process and will be explained in an exemplary way for Porifera [4]. Even though these animals comprise the simplest body plan, their biomineral structure formation is already highly complex and by far not completely understood. Like in triploblasts, the diploblastic Porifera skeleton formation also has a pronounced effect on morphogenesis. As an example, if the animals are growing under unfavorable conditions that do not allow the formation of inorganic deposits (silica or calcium biominerals), the growth of the specimens is extremely suppressed [5]. Silica is the major constituent of sponge spicules in the classes Demospongiae and Hexactinellida. The spicules of these sponges are composed of hydrated, amorphous, noncrystalline silica. The secretion of spicules occurs in Demospongiae in specialized cells, the sclerocytes; there, silica is deposited around an organic filament. If the formation of siliceous spicules is inhibited, the sponge body collapses [6]. The synthesis of spicules is a rapid process; the 100 µm long megasclere are formed within 40 h. Inhibition studies revealed that skeletogenesis of siliceous spicules is enzyme mediated, more particularly, by an Fe^{++}-dependent enzyme. Recent studies revealed that the dominant enzyme that catalyzed the formation of monomeric to polymeric silica is catalyzed by an enzyme that belonged to the cathepsin subfamily and was termed silicatein (reviewed in: [7, 8]).

Bio-silica: An Osteogenically Active Natural Polymer

Bio-silica: An Enzymatic Product of Sponge Silicatein

The formation of siliceous spicules in sponges is genetically controlled; this process initiates the morphogenesis phase. Data demonstrated that at suitable concentrations, silicate induces genes, e.g., those encoding collagen, silicatein, and myotrophin. A major step forward in elucidating the formation of the siliceous spicules on a molecular level was the finding that the "axial organic filament" of siliceous spicules is in reality an enzyme, silicatein, which mediates the apposition of amorphous silica and hence the formation of spicules (reviewed in: [7, 9]).

The skeletal framework of the sponges is highly ordered. In the demosponge *Lubomirskia baicalensis* (Fig. 13.1a, b), it can be seen that the growth of the sponges proceeds in a radiate accretive manner, meaning that growth zones, which are highly ordered, are delimited by growth lines. These growth centers are constructed by an ordered arrangement of the spicules within the body. Most siliceous sponges are composed of megascleres (length > 10 µm) and microscleres (length < 10 µm). Some microscleres have a bizarre shape, while the megascleres usually have a long central rod with ends that in some cases are decorated with spines (Fig. 13.1d). Interestingly, the spicules have the enzyme silicatein both in the central hole, within the axial filament (Fig. 13.1c), and around the outer silica layers. The central core rod of the spicule is synthesized first by the
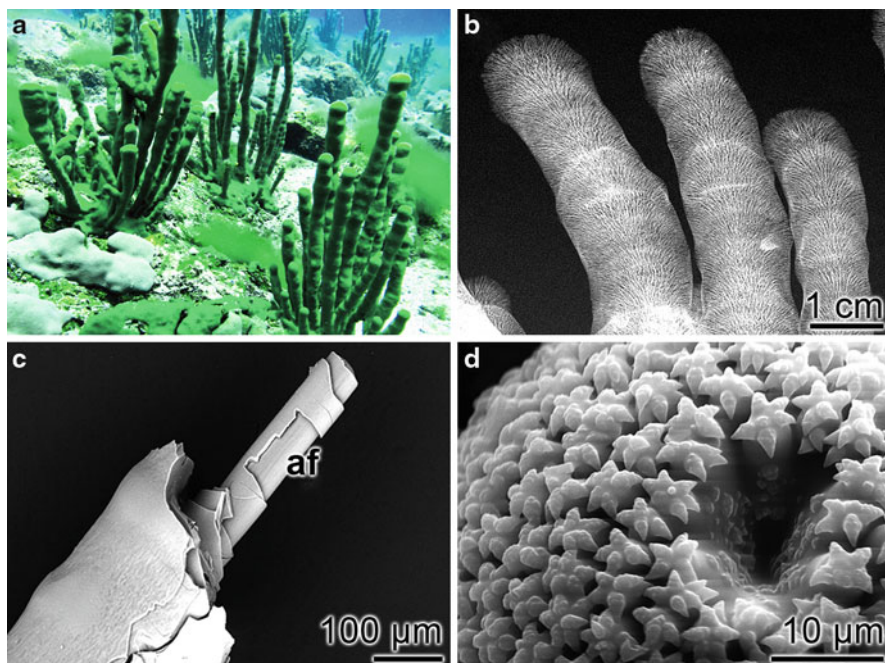
Fig. 13.1 The skeletal framework of the sponges is highly ordered. (**a**, **b**) Radiate accretive growth pattern seen in the skeletal arrangement of the spicules from the freshwater demosponge *Lubomirskia baicalensis*. (**a**) Photograph from the field [Lake Baikal], showing the 40–60 cm high sponge specimens. (**b**) X-ray image showing the orientation and pattern of spicule arrangement in *L. baicalensis*. (**c**) Scanning electron microscopic analysis of basal spicules from the hexactinellid *Hyalonema sieboldi* showing the concentric layers of silica layers by which they are built. The center of the spicule is composed of an organic/axial filament (*af*), which comprises of the silica-forming enzyme silicatein and forms the first hollow fiber. Around the first fiber structure, silicatein is deposited again and forms the second concentric layer. (**d**) A microsclere from the demosponge *Geodia cydonium*

silicatein fiber, which exists in the central hole around which a 1–3 μm thick siliceous hollow fiber is formed. This layer becomes surrounded by an organic silicatein layer, which synthesizes the second siliceous layer and so on. This process of growth is very reminiscent of the process of bone formation. A scheme outlining the growth phases of sponge spicules is shown in Fig. 13.2.

Silicon/Silicate Metabolism and Disorders in Human and Animals

The first report on the presence of silicon in a human body came from Schultz [10], who determined highest levels in tendons and aponeurosis. After this report [11], detailed and in-depth analyses have been performed which had
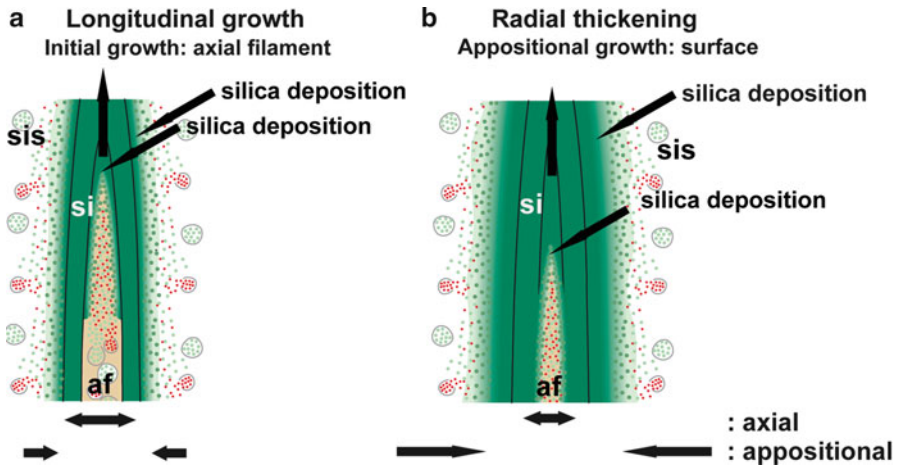
Fig. 13.2 The two growth phases of a spicule, after the release of the immature spicule into the extracellular space via evagination of a cell protrusion; (*1*) longitudinal elongation and (*2*) radial thickening. (**a**) Longitudinal elongation: Initially, the spicule is pushed away from the cell (sclerocyte) that initially has formed the spicule. This process is driven by an elongation of the cell protrusion and in turn an elongation of the axial filament (*af*) within the axial canal. In this phase, a narrowing of the axial canal takes place mediated by an enzymatic polycondensation via silicatein molecules that compose the axial filament; the spicule remains slim. (**b**) Radial thickening: The appositional layering of the growing spicule occurs in radial direction and is driven by silicatein that is released from silicasomes (sis) of cells that surround the growing spicule

been summarized more recently [12, 13]. The mineral taken up by the gastrointestinal tract is excreted via the kidney [14]. Uncharged orthosilicate species can readily pass the mucosa of the intestine and in turn also readily be excreted via the urine [15, 16]. Moreover, if the diet is low in calcium, silica will be more bioavailable [17], suggesting that calcium forms with silica insoluble salts in the lumen – or competes with silica for the same uptake channel.

With age, the uptake rate in human reduces which is attributed to a reduced gastric acid secretion into the stomach [18]. Even more important, silicate uptake and metabolism is also controlled by the hormonal status of humans [19]; during aging, these processes are impaired, due to a reduced hormone or thyroid activity. In general, silica is considered as a trace element that is contributing substantially to human well-being, to strengthen bone and to increase collagen synthesis, especially during aging [13]. In addition, this mineral causes beneficial effects on Alzheimer's disease, atherosclerosis, and prevents the development of atheromatous plaques. Since the studies of Loeper et al. [20], it is accepted that bio-silica is crucial for the functional formation of bone. This view is corroborated by recent biological and molecular biological data, which conclusively support the promoting role of bio-silica on differentiation of the osteoblasts from their precursor cells and strongly suggest the beneficial morphogenetic role during HA formation.

Osteoclasts/Osteoclast: Essential OPG-RANKL Ratio

Osteoporosis is a skeletal disease that is characterized by low, but progressive, bone mass reduction and by micro-architectural deterioration. This deterioration is paralleled with an increased bone fragility that can be followed by a susceptibility to bone fracture [21, 22]. The cellular basis for this disorder is an imbalance between cells, specialized in bone formation (osteoblasts) and those functioning during bone resorption (osteoclasts). Hence, this imbalance can be the result of an excessive bone resorption or a reduced bone formation. There is differentiation in osteoblast that originates from mesenchymal stem cells [23] and in osteoclast from hematopoietic stem cells [24], their in vivo functions are closely linked and differentiation level reciprocally controlled [3]. The major transcription factor, involved in the differentiation and proliferation of osteoprogenitor cells, is Runx2, a factor which is expressed in the mesenchymal stem cells and along the different stages of the osteoblast lineage [25]; Runx2 again is under the control of the bone morphogenetic protein 2 [26]. These inducer factors cause an increasingly stronger expression of genes encoding bone-specific alkaline phosphatase (b-ALP), collagen type I (COLI), osteopontin (OP), and more terminally also of bone sialoprotein (BSP) and osteocalcin (OC). The HA-producing osteoblast terminally differentiate to osteocytes and remain trapped in the HA deposits or undergo apoptosis [27]. Osteocytes in turn express sclerostin, which functions as a potent antagonist of BMP2; this effect can be counteracted by the parathyroid hormone [28].

Osteoclasts are multinucleated cells that originate from the hematopoietic lineage [29]. Those stem cells undergo differentiation and maturation in the presence of the macrophage colony-stimulating factor and also RANKL. As markers for the multinucleated osteoclasts, the tartrate-resistant acid phosphatase (TRAP), the calcitonin receptor (CTR), and the integrin $a_v b_3$ have been used [30].

There is a cytokine/receptor triad that crucially controls bone formation and bone remodeling: the receptor activator of NF-κB ligand (RANKL) with its receptor (RANK) and the endogenous decoy receptor osteoprotegerin (OPG) [31, 32]. RANKL is synthesized by the osteoblastic lineage cells and is essential for the differentiation of the cells involved in bone resorption, the osteoclasts. It binds to the cell surface receptor RANK, located on precursor and mature osteoclasts, and thereby promotes osteoclastogenesis. This receptor becomes activated by RANKL, which is expressed on osteoblasts, T cells, dendritic cells, and their precursors from where it can be released by specific proteases [33]. After binding of RANKL to RANK, the osteoclasts become activated and resorb bone, during which the cells have a close contact to the bone surface [34]. At this interface with the bone, via integrin $(a_v b_3)$, vesicles are formed that contain proton pumps and acid hydrolases (cathepsin K); they are inserted into the bone-apposed area under formation of a "ruffled border." A "resorptive hemivacuole" is formed between cell and bone, allowing the protons to dissolve HA of the bone. The intracellular pH is thought to be kept at a near-neutral level by chloride/bicarbonate exchange and the help of the carbonic anhydrase [35].

The activity and function of RANKL is controlled by OPG that is secreted by stromal cells and also osteoblasts [36]. The OPG scavenges RANKL by binding to it and neutralizes the function of the ligand. From these results, it is mandatory to conclude that any deregulation of the tuned expression of the RANKL/RANK/OPG system causes a disregulation of the tuned differentiation pathways of the osteoblasts as well as the osteoclasts and in turn impairs bone remodeling [31]. More specifically, OPG prevents bone resorption by binding to RANKL and abolishes the activation of the osteoclast via inhibition of the RANK pathway. Hence, the relative concentrations of RANKL and OPG in bone are the major determinants of bone mass and strength.

Osteoporosis: Imbalance of the OPG-RANKL Ratio

Osteoporosis is a systemic skeletal disorder that is characterized by vulnerable bone strength due to an impaired bone compactness leading to increased fracture risks [37, 38]. Bone strength depends on the structural and material integrity of bone, both of which are in turn dependent on the rate of bone turnover. Bone mineral density is a very useful indicator of fracture risk. In addition, the increased degradation product of COLI, the cross-linked telopeptide of COLI, and the increased activity of bone alkaline phosphatase (b-ALP) are the additional markers for the progression of osteoporosis. In biochemistry and molecular biology, the OPG-RANKL ratio is a reliable marker for the differentiations state of the osteoblasts and osteoclast. Overexpression of OPG had been shown to result in vivo in osteopetrosis "marble bone disease"-like symptoms, while OPG-knockout mice showed the phenotype of severe osteoporosis [39]. Initiated by findings, it is now well-established that RANKL/RANK interaction is crucial for differentiation and maintenance of osteoclast activity, and thus is fundamentally involved in the manifestation of osteoporosis [40].

Bio-silica: Regulators of the OPG-RANKL Ratio In Vitro

In vitro and in vivo studies have been performed to interfere with the age-correlated OPG-RANKL imbalance [41]. It has been found that the OPG-RANKL ratio is influenced by a series of substances, including hormones and cytokines. In the course of those studies, it could be established that treatment of osteoblasts with stimulators of osteoclast formation (e.g., vitamin D, PTH, prostaglandin E_2, or interleukin-11) upregulates the expression of *RANKL*. Substitutions with BMP2, interleukin-1β, or TNF-α increase the *OPG* mRNA steady-state level as well as the protein synthesis in fetal osteoblasts.

Since the discovery of the poriferan enzyme silicatein, catalyzing the formation of bio-silica, and the enlightenment of a common body plan from the sponges [Porifera] to the higher Metazoa, it became clear that bio-silica might display a common morphogenetic potential during skeleton formation in the animal kingdom. This proposition became a fact with the finding that bio-silica, a non-toxic
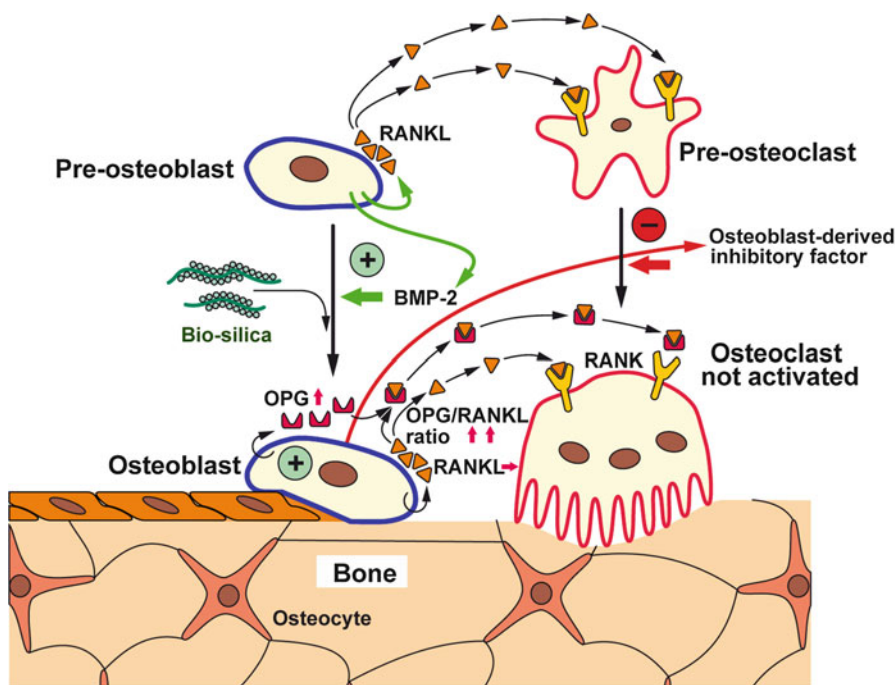
Fig. 13.3 Proposed effects of bio-silica on osteoblasts, osteoclasts, and their progenitor cells; schematic representation. Bio-silica causes an increased expression of OPG in osteoblasts. In addition, the differentiation of osteoblasts is induced and accelerated by BMP-2. It is assumed that in turn the osteoblasts acquire the potential to differentiate to osteocytes and to lining cells. Furthermore, OPG counteracts various effects of RANKL, a cytokine that induces pre-osteoclast maturation and osteoclast activation. Finally, it could be identified that the osteoblasts release a factor, the osteoblasts-derived inhibitory factor that strongly inhibits the proliferation of osteoclasts; the nature of this factor is not yet known

polymer, causes a significant shift of the OPG-RANKL ratio toward the steady-state level of OPG in vitro [42]. As cell system for the in vivo studies, the SaOS-2 cells, human osteogenic sarcoma cells, have been used. There bio-silica causes an increased gene expression of *OPG*, while the steady-state level of *RANKL* remains unchanged. This increased *OPG* expression was verified also on protein level, by application of an ELISA system and also by direct staining of the SaOS-2 with Alizarin Red S [42] (Fig. 13.3). Subsequently, it had to be clarified if bio-silica causes also a modulation of *BMP2* expression [42]. The answer is important for the comprehensive understanding of the differentiation/proliferation property of bio-silica. Again, by application of quantitative polymerase chain reaction analysis (qPCR), it became overt that bio-silica also induces the expression of the important cytokine BMP2. In continuation, we analyzed if bio-silica has an effect on the proliferation propensity of these cells in vitro. This question is important in order to assess the osteogenic potential of this inorganic polymer. Incorporation studies revealed [42] that the ratio between [^{3}H]dT incorporation into DNA and HA

formation was significantly higher in cells that grew on silicatein/biosilica-modified substrates. This latter finding is the first strong indication that the osteogenic potential of bio-silica is much more higher than merely an osteoconductive one. Following (1) the introduced definition [43], bio-silica can be considered to have an osteoinductive capability since it combines the expressed genes (proteins) required for the differentiation and (2) also the potential to increase proliferation of the osteogenic cells. In the mentioned contribution [42], it is also highlighted that the initial HA crystals might be formed intracellularly. In an ongoing attempt in our group, we studied the effect of bio-silica also on the *COL1* [collagen-I] expression (in preparation). The PCR data disclosed that in SaOS-2 cells the gene expression of this subtype I of the collagen family is almost in parallel upregulated with *BMP2*. These two aspects of the bio-silica effect on SaOS-2 cell in vitro suggest – or perhaps even show – that this polymer, bio-silica, has not only a potential to accelerate cell proliferation and differentiation on osteogenic cells in vitro but also has the capacity to provide and synthesize the matrix, the scaffold for the osteogenic cells (collagen type I), on which the differentiating cells can find their functional destination within a growing bone structure.

Hence, the biological effect caused by bio-silica combined the three building blocks required for a comprehensive compound/polymer in bone reconstruction/ remodeling, namely, induction of cell proliferation, direction of differentiation toward functionally bone-forming cells, and finally migration onto a fibrous scaffold whose formation is initiated and triggered by bio-silica as well (Fig. 13.3).

Bio-silica: Potential Mode of Action in Mammalian Tissue

Based on the elaborated data, it can be accepted that bio-silica displays a positive osteogenic activity not only in vitro but also in vivo. The above-mentioned data had been comprehensively confirmed recently [44]. It could be substantiated that bio-silica/ortho-silicate causes a beneficial and promising effect in future applications for bone diseases, e.g., osteoporosis. These confirmatory data had been elaborated with bone marrow stromal cells by showing that silica causes an upregulation of the bone-related, anabolic genes OPN, osteocalcin (OCN), and b-ALP, as well as of the expression of WNT and sonic hedgehog homolog (SHH) signaling-related genes [44].

The data reviewed by Jugdaohsingh [13] as well as our data [42, 45] together with those of Han et al. [44] allow the following first interpretation of a action mode of silica on cellular and subcellular level. Silica can be taken up by the oral route, then it can be transported to the bulky extracellular space of the connective tissue and very likely also into cells. In the extracellular space, ortho-silicate can be supposed to bind to Ca^{2+} ions which are abundant in the compartment where is rich in mucopolysaccharides [46]. Since Ca-silicates have a lower solubility compared to the respective Na^+ or K^+ salts [47], it can be accepted that Ca-silicates accumulate in the collagen-mucopolysaccharide fibrous scaffold (Fig. 13.4), where they can be mobilized again by changing the solubility product or by changing the pH milieu. In the extracellular space, polymeric silica can be hydrolytically

Fig. 13.4 Mitogenic effect of silica on bone cells. After taken up by the organism, silica is proposed to accumulate extracellularly around the collagen/mucopolysaccharides fibrous network. Perhaps there it is stored in the form of Ca-salt. After conversion of polysilicate into monomeric units, silica acts on the MAPK/ERK pathway, and likely also on the TGF-receptor signaling route and finally via the WNT/SHH differentiation/polarity way. As a consequence, the genes encoding the anabolic bone-forming mediators OPN, osteocalcin (OCN), and b-ALP are increasingly induced
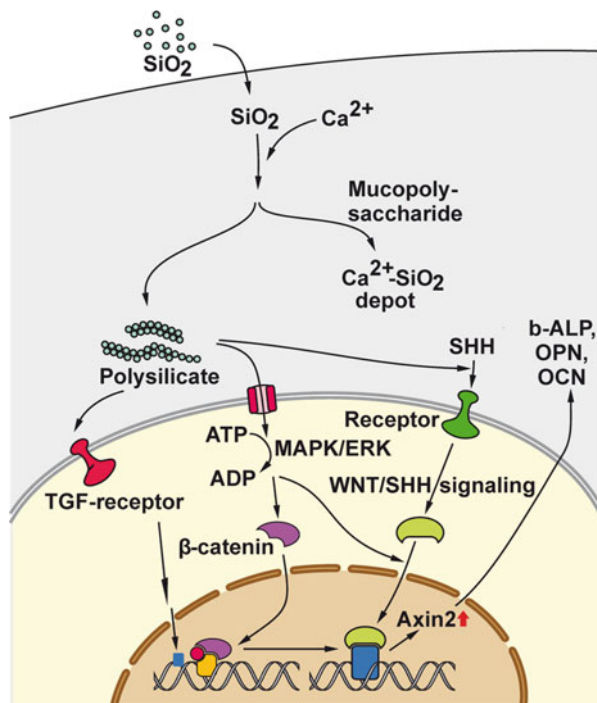
degraded to monomeric silica perhaps by cathepsins or by lowering the concentrations of the monomeric reactant, with respect to polysilica. The presumed uptake of ortho-silicate via an ion channel might be facilitated through the consumption of ATP. Intracellularly, silica is supposed to activate the MAPK-ERK pathway in osteoblast-like cells [48]; via this signaling pathway, the silica signal is translocated to the nucleus. Additionally – or flanking this pathway – silica has been described to enhance cellular differentiation and collagen production via the TGF pathway by binding TGF-1 to its cognate receptors [49]. Finally, data led to suggest that silica activates the WNT and SHH signaling pathways with Axin2 and β-catenin as the central molecules [44]. These proposed mechanisms favor the idea that silica acts on the different levels or pathways involved, primarily at the transcriptional level, of those genes that encode for proteins, stimulating bone anabolic metabolism, e.g., OCN, OPN, and b-ALP.

Polyphosphate: An Osteogenically Active Natural Polymer

Bio-polyphosphates: A Widespread Inorganic Polymer

Inorganic polymeric phosphate/polyphosphate (polyP) can be prepared chemically in the crystalline and the amorphous state [50–53], while in the inorganic nature

only the amorphous form of polyP was found [50, 51]. Chemically, polyP synthesis requires high temperature [54], while bacteria and animals are able to produce that polymer metabolically at ambient temperatures via kinases (see: [51]). The bio-polymer polyP, which is found in a wide range of organisms, including bacteria, fungi, algae, plants, and animals (see: [51]), is readily water-soluble in millimolar concentrations at chain lengths <100 phosphate units [55, 56]. The natural polyP is a linear polymer of phosphate residues linked together via anhydride linkages from tens to hundreds of units. In spite of the presence of phospho-anhydride bonds, the polymer is stable over wide temperature and pH ranges [51, 53]. PolyP is successfully used as food additive as well as base material for cosmetic products [57]. The nutritional benefit has been substantiated by animal experiments [58, 59]. As a multivalent anion, polyP binds to the essential cations of Ca, Mg, Mn, Fe, and Co (see: [51]); more specifically, polyP can act as a strong Ca^{2+} chelator and as an antioxidant [60].

The biological function of polyP has been studied in microorganisms (reviewed in: [61, 62]) and more recently also in animals (reviewed in: [51, 63]). It has been proposed that polyP acts as a storage substance of energy, as a chelator for metal cations, as a donor for sugar and adenylate kinase, and as an inducer of apoptosis, as well as it is involved in mineralization processes of bone tissue [53, 63–65]. Finally, some data have been presented that polyP might act as a modulator of gene expression. Results [66] suggest that in the osteoblast-like cell line, MC3T3-E1, polyP causes an increased gene expression of osteocalcin, osterix, bone sialoprotein, and tissue nonspecific alkaline phosphatase, all proteins known to be crucial for bone formation [67, 68]. The gene expression data in MC3T3-E1 cells have been obtained with 1 mM polyP [66, 69]. Till then, it is not clear whether polyP causes the increased skeletal mineralization in its polymeric form or as monomeric phosphates that are formed from polyP through hydrolysis by phosphatases [70]. The susceptibility of polyP for phosphatases is well established [71–73]. As one consequence of the enzymatic hydrolysis of polyP, a release of Ca^{2+} ions has been proposed; this cation is metabolically utilized during HA [hydroxyapatite] formation [50]. The possible modulating effect of phosphatases on the size of polyP is also notable with respect to a probable parallel effect of the enzyme on the amount of the extracellular ß-glycerophosphate, which is a well-established component required for biomineralization, for HA formation in mammalian cells in vitro [74]. Under in vivo conditions, ß-glycerophosphate is rapidly and virtually completely degraded to phosphate prior to or during the initial phase of mineralization [75].

PolyP: A Targeted Phosphate Donor for HA Formation

The initial study on the effect of polyP on bone formation was by Leyhausen et al. [64], who described that polyP exists at different chain lengths in the space adjacent to osteoblast-like cells in vitro and in vivo. Furthermore, they provided evidence that human osteoblast-like cells have the enzymatic machinery to

hydrolyze polyP [63]. Based on this contribution, recent studies focused on the effect of soluble polyP [polyP (Ca^{2+} salt)], on the role of alkaline phosphatase (ALP), in SaOS-2 cells. This enzyme had been implicated in phosphate metabolism in bone, due to its high levels and regional accumulation in areas of highest ossification [76]. In humans, four isoenzymes of ALP have been identified; three of them are expressed in a tissue-specific pattern in the intestine, the placenta, and germ cells, while the fourth is abundant in bone and liver (see: [77]). It has been proposed that bone ALP generates inorganic phosphate (P_i), which is needed for HA crystallization in the bone matrix [78], while in an alternative view it had been hypothesized that this enzyme hydrolyzes the mineralization inhibitor inorganic pyrophosphate (PP_i) in order to accelerate mineral precipitation and growth [79]. Surely the additive β-glycerophosphate, added to the bone cells during in vitro cultivation, is readily degraded to P_i. In turn, the proposition from the experiments performed and the goal for future in vivo experiments was to provide the first basis for a targeted application of polyP in vivo. We suggested to apply polyP to cells in vitro with the aim to clarify if the cell-associated bone ALP has the ability to hydrolyze the polymer at the spot, where P_i is required for the formation of the HA crystals [77].

Exposure of SaOS-2 cells to polyP (Ca^{2+} salt) was shown to efficiently replace β-glycerophosphate during the in vitro HA biomineralization process. That is to say, polyP causes a strong increase in the activity of the alkaline phosphatase and also an induction of the steady-state expression of this gene [77]. Furthermore, this study shows that polyP exposure causes HA crystallite deposition, a process which involves not just a single cell but a cluster of intimately interacting cells that form a common crystallite [80]. The second component required for the HA is Ca^{2+}. The availability of this cation strongly increases in the cytosol of SaOS-2 cells after exposure to polyP (Ca^{2+} salt) [77]. The osteogenic potential of polyP is even boosted by recent findings that polyP also causes an upregulation of the expression of *BMP2* in SaOS-2 cells and simultaneously causes an inhibition of the phosphorylation of IκBα, which is supposed to abolish RANKL-mediated NF-κB activation [81] in RAW 264.7 cells, osteoclast-like cells (Fig. 13.5).

These new data provide the in vitro evidence that polyP has the potential to contribute to the favored property of bio-silica to stimulate osteoblast differentiation and HA formation or even potentiate the polyP effect. The latter aspect appears to be likely since the action modes of the two natural inorganic polymers are different.

PolyP: Potential Action Mode in Mammalian Tissue

Since the discovery of high-polymeric inorganic polyphosphates in living organisms [82] and their metabolism [83, 84], the enzymes involved had been elucidated mainly by Kornberg and co-workers (reviewed in: [51, 85]). The enzymes which had been connected with the energy metabolism of polyP are polyphosphate
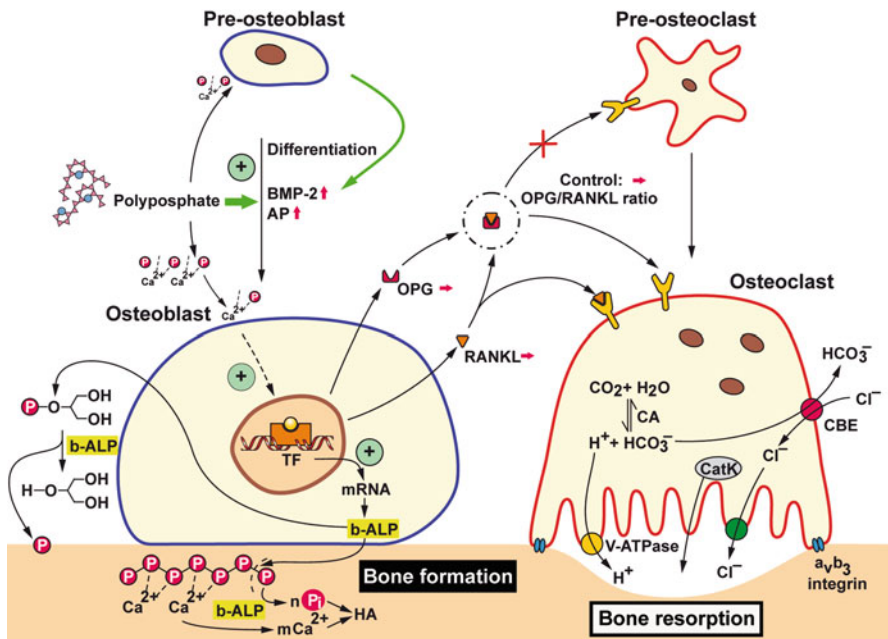
Fig. 13.5 Schematic representation summarizing the effect of bio-polyP, in the form of the Ca^{2+} salt, on the tuned interaction between osteoblasts [HA anabolic pathway] and osteoclasts [HA catabolic pathway]. It is outlined that bio-polyP supports the progression of precursor osteoblasts to mature osteoblasts by induction of the genes encoding BMP-2 (bone morphogenetic protein 2) and b-ALP (alkaline phosphatase), followed by the increased release of b-ALP. It is assumed that polyP activates a hypothetical TF (transcription factor). ALP hydrolyzes both polyP (Ca^{2+} salt) and β-GP (β-glycerophosphate). The CBE (chloride-bicarbonate exchanger) in concert with the CA (carbonic anhydrase) is involved in the homeostasis of the intracellular CO_2 concentration and pH level

kinase (PPK), polyphosphate:glucose-6-phosphotransferase, exopolyphosphatase, polyphosphate:adenosine monophosphate phosphotransferase, 1,3-diphospho-glycerate: polyphosphate phosphotransferase, tripolyphosphatase, polyphosphate glucokinase, and endopolyphosphatase (reviewed in: [51]). The PPKs had been considered as the key enzymes since they are capable of reversibly shift both energy and phosphate, storage or consumption, of phosphate energy control (reviewed in: [86]). The key enzymes had been discovered not only in prokaryotes but also in Metazoa [73]. The Ca^{2+} salt of polyP are less soluble compared to the Na^+ or K^+ salts (see: [53]); in turn the Ca^{2+} salts polyP are stored in vesicles, especially in vesicles of bone cells [87].

Released from the storage vesicles within bone or their neighboring cells, polyP is transported into the extracellular space, where it undergoes degradation to ortho-phosphate via the b-ALP [64, 77]. In this compartment, ortho-phosphate together with Ca^{2+} will serve as substrate for HA formation [77]. Since the initial sites of HA

Fig. 13.6 Schematic outline of the intracellular polyP metabolism, storage, and subsequent release to the extracellular space where ortho-phosphate serve with Ca^{2+} as substrates for HA synthesis
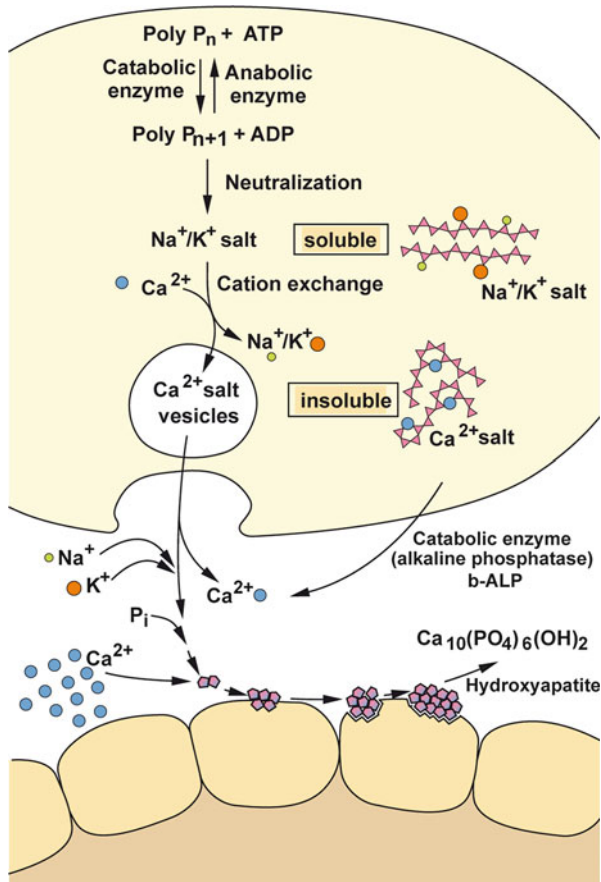
formation are present within cells [88], similar mobilization and deposition reaction can be proposed here also. A schematic outline of the polyP metabolism and the connection with HA deposition onto bone cells is given in Fig. 13.6.

Bio-silica and Polyphosphate: Two Novel Osteogenically Active Scaffold Materials?

Biocompatibility of the Bio-silica Scaffold: The biocompatibility of the bio-silica was excellent and no toxicity was determined in vitro, applying the MTT-viability assay. In addition, the requirement with respect to the porosity allowing a suitable assembly and growth of bone cells within the cavities of the scaffold was analyzed (reviewed in: [89, 90]). The histological examination revealed that the cells within the scaffold showed increased proliferation and differentiation and – after addition of the mineralization cocktail – formed larger HA crystals. Furthermore, the

bio-silica scaffolds provide a physiochemical-biomimetic environment that can be dissolved by the cells. These analyses supported the view that the porosity of the material is suitable for the infiltration of cells and for a physiological interaction of the cells within the cavities.

Bio-inorganic Bio-polyP Scaffold: In initial studies, we could demonstrate that the biogenically and morphogenetically active bio-polyP is a likewise ideal polymer to be used for building of scaffold materials (see: [90]). Especially the chemical properties to be soluble at physiological pH conditions as a salt with the cations Na^+ and K^+, while becoming insoluble with cation Ca^{2+}, polyP is assumed to be provided with the suitable property to undergo hardening after the 3D printing process. Furthermore, the Ca^{2+} salt of polyP is – like the Na^+ and K^+ salts – biologically active and causes an increased release of the cytokine BMP-2.

Future Direction: Application of Bio-silica and Bio-polyP in Bone Tissue Engineering: The advantages in utilizing synthetic bone scaffolds include the following: the elimination of disease transmission risk, fewer surgical procedures, a reduced risk of infection or immunogenicity, and especially abundance of synthetic scaffold materials. The basic challenge to develop a suitable synthetic scaffold is to mimic the complex physiological environment in which bone cells grow and differentiate. In a physiological framework, the bone cells find a suitable scaffold that allows their in-growth into a scaffold with the matching porosity where they can differentiate and communicate by signaling with the neighboring cells. Moreover, these cavities must allow the substrates for the osteoblasts to enter and to be available for the osteoid deposition, allow vascularization, and finally bone in-growth. It must be noted that the synthetic scaffolds provide the bone cells with the spatially gradient and temporally appropriate expression of the signals promoting osteogenicity and osteoinductivity, resulting in a homogeneous osseointegration.

Focusing on bone tissue engineering strategies, e.g., such as cell transplantation, acellular scaffolds and stem cell therapy, again the physiological regulatory network of cytokines and growth factors must be provided to the mesenchymal stems cells (MSCs) after the removal from the donor ex vivo. As sketched in Fig. 13.7, the MSCs are taken from the donor, often from the iliac crest, and seeded onto a scaffold, where they must be cultivated and expanded. Here a major hurdle must be overcome in a way that the cells can be stimulated in the growth medium with the factors triggering the pluripotent MSC into the differentiation direction toward osteoblasts, provided with the ability to deposit HA. For this process, it is important that the mineralization cocktail, dexamethasone, ascorbic acid, and β-glycerophosphate are added as the terminal "mineralization factors/substrates." The addition of these substances is straightforward, and their price cheap. However, the cultures must be additionally supplemented with the morphogens which have to be added at phase-specific and appropriate differentiation stages. Among these are the most relevant growth factors, the PDGFs, BMPs, IGFs, and TGF-βs. It would be ideal if the bone cells themselves, growing onto the artificial scaffold(s), produce these factors timely and spatially in a correct pattern to allow a functional differentiation of the bone cells. As outlined in Fig. 13.7 (upper panel), those factors have
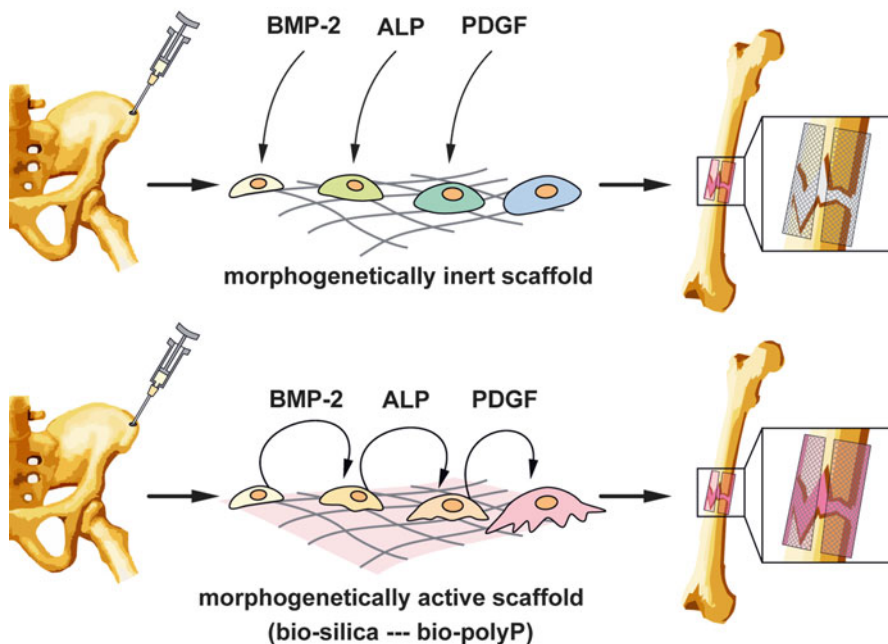
Fig. 13.7 Outline of a strategy [90] to prepare cell-populated scaffolds from cells, taken from, e.g., iliac crest, and cultivated ex vivo on either morphogenetically inert scaffold (*upper panel*) or morphogenetically active scaffold, prepared from bio-silica or bio-polyP (*lower panel*). While in cultures with the inert template, the cytokines/factors [BMP-2 (bone morphogenetic protein-2), ALP (alkaline phosphatase), and PDGF (platelet-derived growth factor)] are added from external sources (*upper panel*), at least BMP-2 and ALP are actively elicited from the cells, growing onto silica-based scaffolds, resulting in a directed differentiation of the osteoblast-precursor cells to functionally active osteoblasts (*lower panel*)

to be added to the cultures during the ex vivo expansion from external sources. This means that the scaffold is morphogenetically inert.

In conclusion, the available data gathered in the last years indicate that the natural inorganic polymers bio-silica and bio-polyP, both abundantly produced in deep-sea sponges, display inductive activity and elicit from the bone cells the morphogens/ligand molecules BMP-2 and RANKL and as a result cause a differentiation of the bone cells toward an anabolic, HA-forming status (Fig. 13.7; lower panel). Certainly these data are only the first step toward the development of a morphogenetically active polymer suitable to function alone as template/modulator for cells to grow to HA-forming osteoblasts ex vivo. Nevertheless, a thorough, continuous, and intensive elaboration of the model in this line to tailor a functional polymer with self-regulatory activity on the bone cells appears to be very encouraging. Animal trials are in progress.

References

1. Simpson TL (1984) The cell biology of sponges. Springer, New York
2. Müller WEG, Wiens M, Adell T, Gamulin V, Schröder HC, Müller IM (2004) Bauplan of Urmetazoa: basis for genetic complexity of Metazoa. Int Rev Cytol 235:53–92
3. Wang XH, Hu SX, Gan L, Wiens M, Müller WEG (2010) Sponges (Porifera) as living metazoan witnesses from the Neoproterozoic: biomineralization and the concept of their evolutionary success. Terra Nova 22:1–11
4. Müller WEG (2005) Spatial and temporal expression patterns in animals. In: Meyers RA (ed) Encyclopedia of molecular cell biology and molecular medicine, vol 13. Wiley-VCH, Weinheim, pp 269–309
5. Maldonado M, Carmona MC, Uriz MJ, Cruzado A (1999) Decline in Mesozoic reef-building sponges explained by silicon limitation. Nature 401:785–788
6. Müller WEG (2006) The stem cell concept in sponges (Porifera): metazoan traits. Semin Cell Dev Biol 17:481–491
7. Morse DE (1999) Silicon biotechnology: harnessing biological silica production to construct new materials. Trends Biotechnol 17:230–232
8. Wang XH, Schröder HC, Wang K, Kaandorp JA, Müller WEG (2012) Genetic, biological and structural hierarchies during sponge spicule formation: from soft sol-gels to solid 3D silica composite structures. Soft Matter 8:9501–9518
9. Müller WEG, Wang XH, Cui FZ, Jochum KP, Tremel W, Bill J, Schröder HC, Natalio F, Schloßmacher U, Wiens M (2009) Sponge spicules as blueprints for the biofabrication of inorganic–organic composites and biomaterials. Appl Microbiol Biotechnol 83:397–413
10. Schultz H (1901) Über den Kieselsäuregehalt menschlicher und thierischer Gewebe. Pflügers Arch Ges Physiol 84:67–100
11. Carlisle EM (1986) Silicon as an essential trace element in animal nutrition. In: Evered D, O'Connor M (eds) Silicon biochemistry, vol 121, CIBA foundation symposium. Wiley, Chichester, pp 123–136
12. Jugdaohsingh R, Anderson SHC, Tucker KL, Elliott H, Kiel DP, Thompson RPH, Powell JJ (2002) Dietary silicon intake and absorption. Am J Clin Nutr 75:887–893
13. Jugdaohsingh R (2007) Silicon and bone health. J Nutr Health Aging 11:99–110
14. Dobbie JW, Smith MJB (1986) Urinary and serum silicon in normal and uraemic individuals. In: Evered D, O'Connor M (eds) Silicon biochemistry, vol 121, Ciba foundation symposium. Wiley, Chichester, pp 194–208
15. Reffitt DM, Jugdoahsingh R, Thompson RPH, Powell JJ (1999) Silicic acid: its gastrointestinal uptake and urinary excretion in man and effects on aluminium excretion. J Inorg Biochem 76:141–147
16. Jugdaohsingh R, Reffitt DM, Oldham C, Day JP, Fifield LK, Thompson RP, Powell JJ (2000) Oligomeric but not monomeric silica prevents aluminum absorption in humans. Am J Clin Nutr 71:944–949
17. Nielsen FH (1991) Nutritional requirements for boron, silicon, vanadium, nickel, and arsenic: current knowledge and speculation. FASEB J 5:2661–2667

18. Anonymous (1974) Anticaking agents. Silicon dioxide and certain silicates. In: Toxicological evaluation of some food additives including anticaking agents, antimicrobials, antioxidants, emulsifiers and thickening agents. World Health Organisation, Geneva, pp 21–30

19. Charnot Y, Pérès G (1971) Modification de l'absorption et du métabolisme tissulaire du silicium en relation âvec l'age, le sehe et diverses glandes endocrines. Lyon Med 13:85

20. Loeper J, Goy-Loeper J, Rozensztajn L, Fragny M (1979) The antiatheromatous action of silicon. Atherosclerosis 33:397–408

21. Sambrook P, Cooper C (2006) Osteoporosis. Lancet 367:2010–2018

22. Lane NE, Yao W (2009) Developments in the scientific understanding of osteoporosis. Arthritis Res Ther 11:228

23. Bruedigam C, Eijken M, Koedam M, van de Peppel J, Drabek K, Chiba H, van Leeuwen JP (2010) A new concept underlying stem cell lineage skewing that explains the detrimental effects of thiazolidinediones on bone. Stem Cells 28:916–927

24. Hayase Y, Muguruma Y, Lee MY (1997) Osteoclast development from hematopoietic stem cells: apparent divergence of the osteoclast lineage prior to macrophage commitment. Exp Hematol 25:19–25

25. Hu R, Liu W, Li H, Yang L, Chen C, Xia ZY, Guo LJ, Xie H, Zhou HD, Wu XP, Luo XH (2011) A RUNX2/MIR-3960/MIR-2861 regulatory feedback loop during mouse osteoblast differentiation. J Biol Chem 286:12328–12339

26. Lee SJ, Kang SW, Do HJ, Han I, Shin DA, Kim JH, Lee SH (2010) Enhancement of bone regeneration by gene delivery of BMP2/Runx2 bicistronic vector into adipose-derived stromal cells. Biomaterials 31:5652–5659

27. Bellido T, Plotkin LI (2011) Novel actions of bisphosphonates in bone: preservation of osteoblast and osteocyte viability. Bone 49:50–55

28. Agholme F, Li X, Isaksson H, Ke HZ, Aspenberg P (2010) Sclerostin antibody treatment enhances metaphyseal bone healing in rats. J Bone Miner Res 25:2412–2418

29. Boyle WJ, Simonet WS, Lacey DL (2003) Osteoclast differentiation and activation. Nature 423:337–342

30. Cerri PS, Boabaid F, Katchburian E (2003) Combined TUNEL and TRAP methods suggest that apoptotic bone cells are inside vacuoles of alveolar bone osteoclasts in young rats. J Periodont Res 38:223–226

31. Boyce BF, Xing L (2008) Functions of RANKL/RANK/OPG in bone modeling and remodeling. Arch Biochem Biophys 473:139–146

32. Santini D, Schiavon G, Vincenzi B, Gaeta L, Pantano F, Russo A, Ortega C, Porta C, Galluzzo S, Armento G, La Verde N, Caroti C, Treilleux I, Ruggiero A, Perrone G, Addeo R, Clezardin P, Muda AO, Tonini G (2011) Receptor activator of NF-kB (RANK) expression in primary tumors associates with bone metastasis occurrence in breast cancer patients. PLoS One 6:e19234

33. Zhang S, Liu C, Huang P, Zhou S, Ren J, Kitamura Y, Tang P, Bi Z, Gao B (2009) The affinity of human RANK binding to its ligand RANKL. Arch Biochem Biophys 487:49–53

34. Fuller K, Ross JL, Szewczyk KA, Moss R, Chambers TJ (2010) Bone is not essential for osteoclast activation. PLoS One 5:e12837. doi:10.1371/journal.pone.0012837

35. Jansen IDC, Mardones P, Lecanda F, de Vries TJ, Recalde S, Hoeben KA, Schoenmaker T, Ravesloot JH, van Borren MMGJ, van Eijden TM, Bronckers ALJJ, Kellokumpu S, Medina JF, Everts V, Oude-Elferink RPJ (2009) Ae2a, b-deficient mice exhibit osteopetrosis of long bones but not of calvaria. FASEB J 23:3470–3481

36. Kearns AE, Khosla S, Kostenuik PJ (2008) Receptor activator of nuclear factor kappaB ligand and osteoprotegerin regulation of bone remodeling in health and disease. Endocr Rev 29:155–192

37. Kanis JA (1994) WHO Study Group. Assessment of fracture risk and its application to screening for postmenopausal osteoporosis: synopsis of a WHO report. Osteoporos Int 4:368–381

38. Felsenberg D, Boonen S (2005) The bone quality framework: determinants of bone strength and their interrelationships, and implications for osteoporosis management. Clin Ther 27:1–11
39. Bucay N, Sarosi I, Dunstan CR, Morony S, Tarpley J, Capparelli C, Scully S, Tan HL, Xu W, Lacey DL, Boyle WJ, Simonet WS (1998) Osteoprotegerin-deficient mice develop early onset osteoporosis and arterial calcification. Genes Dev 12:1260–1268
40. Raisz LG (2005) Pathogenesis of osteoporosis: concepts, conflicts, and prospects. J Clin Invest 115:3318–3325
41. Jabbar S, Drury J, Fordham JN, Datta HK, Francis RM, Tuck SP (2011) Osteoprotegerin, RANKL and bone turnover in postmenopausal osteoporosis. J Clin Pathol 64:354–357
42. Wiens M, Wang XH, Schröder HC, Kolb U, Schloßmacher U, Ushijima H, Müller WEG (2010) The role of biosilica in the osteoprotegerin/RANKL ratio in human osteoblastlike cells. Biomaterials 31:7716–7725
43. Albrektsson T, Johansson C (2001) Osteoinduction, osteoconduction and osseointegration. Eur Spine J 10:S96–S101
44. Han P, Wu C, Xiao Y (2013) The effect of silicate ions on proliferation, osteogenic differentiation and cell signalling pathways (WNT and SHH) of bone marrow stromal cells. Biomater Sci 1:379–392
45. Wiens M, Wang XH, Schloßmacher U, Lieberwirth I, Glasser G, Ushijima H, Schröder HC, Müller WEG (2010) Osteogenic potential of bio-silica on human osteoblast-like (SaOS-2) cells. Calcif Tissue Int 87:513–524
46. Schmidt UJ, Kranz D, Brüschke G, Kalbe I, Bollmann R (1969) Animal experiments (rats) on the calcium- and mucopolysaccharide content of the aortic wall in iron deficiency and iron overload following vitamin D2 poisoning. Z Gesamte Inn Med 24:414–415
47. Manzano H, Moeini S, Marinelli F, van Duin AC, Ulm FJ, Pellenq RJ (2012) Confined water dissociation in microporous defective silicates: mechanism, dipole distribution, and impact on substrate properties. J Am Chem Soc 134:2208–2215
48. Shie MY, Ding SJ, Chang HC (2011) The role of silicon in osteoblast-like cell proliferation and apoptosis. Acta Biomater 7:2604–2614
49. Li J, Wei L, Sun J, Guan G (2013) Effect of ionic products of di-calcium silicate coating on osteoblast differentiation and collagen production via TGF-beta1 pathway. J Biomater Appl 27:595–604
50. Omelon SJ, Grynpas MD (2008) Relationships between polyphosphate chemistry, biochemistry and apatite biomineralization. Chem Rev 108:4694–4715
51. Rao NN, Gómez-Garcıa MR, Kornberg A (2009) Inorganic polyphosphate: essential for growth and survival. Annu Rev Biochem 78:605–647
52. Liu G, Liu X, Yu J (2010) Ammonium polyphosphate with crystalline form V by ammonium dihydrogen phosphate process. Ind Eng Chem Res 49:5523–5529
53. Kulaev IS, Vagabov V, Kulakovskaya T (2004) The biochemistry of inorganic polyphosphates. Wiley, New York
54. Griffith EJ (1995) Phosphate fibers, Topics in applied chemistry. Springer, Berlin
55. Katchman BJ, Smith HE (1958) Diffusion of synthetic and natural polyphosphates. Arch Biochem Biophys 76:396–402
56. Van Wazer JR (1958) Phosphorus and its compounds: chemistry, vol 1. Interscience Publishers, New York
57. Omoto M, Imai T, Seki K, Nomura R, Otahara Y (1997) The effect on the bones of condensed phosphate when used as food additives: its importance in relation to preventive medicine. Environ Health Prev Med 2:105–116
58. Lee J, Park JB, Herr Y, Chung JH, Kwon YH (2008) The effect of polyphosphate on exophytic bone formation. J Korean Acad Periodontol 38:59–66
59. Lee BH, Kim MC, Choi SH, Lee YK (2009) Amorphous calcium polyphosphate bone regenerative materials based on calcium phosphate glass. Key Eng Mater 396–398:209–212

60. Shahidi F, Rubin LJ, Diosady LL, Kassam N, Fong JC, Li S, Wood DF (1986) Effect of sequestering agents on lipid oxidation in cooked meats. Food Chem 21:145–152
61. Kulaev IS (1979) The biochemistry of inorganic polyphosphates. Wiley, New York
62. Wood HG, Clark JE (1988) Biological aspects of inorganic polyphosphates. Annu Rev Biochem 57:235–260
63. Schröder HC, Müller WEG (1999) Inorganic polyphosphates. Biochemistry, biology, biotechnology, vol 23. Springer, Berlin/Heidelberg
64. Leyhausen G, Lorenz B, Zhu H, Geurtsen W, Bohnensack R, Müller WEG, Schröder HC (1998) Inorganic polyphosphate in human osteoblast-like cells. J Bone Miner Res 13:803–812
65. Schröder HC, Kurz L, Müller WEG, Lorenz B (2000) Polyphosphate in bone. Biochemistry (Moscow) 65:296–303
66. Usui Y, Uematsu T, Uchihashi T, Takahashi M, Takahashi M, Ishizuka M, Doto R, Tanaka H, Komazaki Y, Osawa M, Yamada K, Yamaoka M, Furusawa K (2010) Inorganic polyphosphate induces osteoblastic differentiation. J Dent Res 89:504–509
67. Sinha KM, Yasuda H, Coombes MM, Dent SYR, de Crombrugghe B (2010) Regulation of the osteoblast-specific transcription factor Osterix by NO66, a Jumonji family histone demethylase. EMBO J 29:68–79
68. Sun L, Blair HC, Peng Y, Zaidi N, Adebanjo OA, Wu XB, Wu XY, Iqbal J, Epstein S, Abe E, Moong BS, Zaidi M (2005) Calcineurin regulates bone formation by the osteoblast. Proc Natl Acad Sci USA 102:17130–17135
69. Hacchou Y, Uematsu T, Ueda O, Usui Y, Uematsu S, Takahashi M, Uchihashi T, Kawazoe Y, Shiba T, Kurihara S, Yamaoka M, Furusawa K (2007) Inorganic polyphosphate: a possible stimulant of bone formation. J Dent Res 86:893–897
70. Omelon S, Georgiou J, Henneman ZJ, Wise LM, Sukhu B, Hunt T, Wynnyckyj C, Holmyard D, Ryszard B, Grynpas MD (2009) Control of vertebrate skeletal mineralization by polyphosphates. PLoS ONE 4:e5634. doi:10.1371/journal.pone.0005634
71. Lorenz B, Marmé S, Müller WEG, Unger K, Schröder HC (1994) Preparation and use of polyphosphate-modified zirconia for purification of nucleic acids and proteins. Anal Biochem 216:118–126
72. Lorenz B, Müller WEG, Kulaev IS, Schröder HC (1994) Purification and characterization of an exopolyphosphatase activity from *Saccharomyces cerevisiae*. J Biol Chem 269:22198–22204
73. Lorenz B, Münkner J, Oliveira MP, Kuusksalu A, Leitão JM, Müller WEG, Schröder HC (1997) Changes in metabolism of inorganic polyphosphate in rat tissues and human cells during development and apoptosis. Biochim Biophys Acta 1335:51–60
74. Chung CH, Golub EE, Forbes E, Tokuoka T, Shapiro IM (1992) Mechanism of action of beta-glycerophosphate on bone cell mineralization. Calcif Tissue Int 51:305–311
75. Bellows CG, Heersche JNM, Aubin JE (1992) Inorganic phosphate added exogenously or released from β-glycerophosphate initiates mineralization of osteoid nodules *in vitro*. Bone Miner 17:15–29
76. Lorch IJ (1949) Alkaline phosphatase and the mechanism of ossification. J Bone Joint Surg 31:94–99
77. Müller WEG, Wang XH, Diehl-Seifert B, Kropf K, Schloßmacher U, Lieberwirth I, Glasser G, Wiens M, Schröder HC (2011) Inorganic polymeric phosphate/polyphosphate as an inducer of alkaline phosphatase and a modulator of intracellular Ca^{2+} level in osteoblasts (SaOS-2 cells) *in vitro*. Acta Biomater 7:2661–2671
78. Millan JL (2006) Alkaline phosphatases. Structure, substrate specificity and functional relatedness to other members of a large superfamily of enzymes. Purinergic Signal 2:335–341
79. Hessle L, Johnson KA, Anderson HC, Narisawa S, Sali A, Goding JW, Terkeltaub R, Millan JL (2002) Tissue nonspecific alkaline phosphatase and plasma cell membrane glycoprotein-1 are central antagonistic regulators of bone mineralization. Proc Natl Acad Sci USA 99:9445–9449

80. Nelson M, Balasundaram G, Webster TJ (2006) Increased osteoblast adhesion on nanoparticulate crystalline hydroxyapatite functionalized with KRSR. Int J Nanomedicine 1:339–334

81. Sung B, Murakami A, Oyajobi BO, Aggarwal BB (2009) Zerumbone abolishes RANKL-induced NF-kappaB activation, inhibits osteoclastogenesis, and suppresses human breast cancer-induced bone loss in athymic nude mice. Cancer Res 69:1477–1484

82. Liebermann L (1890) Nachweis der Metaphosphorsäure im Nuclein der Hefe. Pflugers Arch 47:155–160

83. Lohmann K (1928) Über das Vorkommen und den Umsatz von Pyrophosphat im Muskel. Naturwissensch 16:298

84. Langen P, Liss E (1958) Über Bildung und Umsatz der Polyphosphate der Hefe. Biochem Z 330:455–466

85. Rao NN, Kornberg A (1999) Inorganic polyphosphate: a molecule of many functions. In: Schröder HC, Müller WEG (eds) Progress in molecular and subcellular biology, vol 23. Springer, Heidelberg, pp 183–195

86. Achbergerová L, Nahálka J (2011) Polyphosphate – an ancient energy source and active metabolic regulator. Microb Cell Fact 10:63. doi:10.1186/1475-2859-10-63

87. Boonrungsiman S, Gentleman E, Carzaniga R, Evans ND, McComb DW, Porter AE, Stevens MM (2012) The role of intracellular calcium phosphate in osteoblast-mediated bone apatite formation. Proc Natl Acad Sci USA 109:14170–14175

88. Mahamid J, Sharir A, Gur D, Zelzer E, Addadi L, Weiner S (2011) Bone mineralization proceeds through intracellular calcium phosphate loaded vesicles: a cryo-electron microscopy study. J Struct Biol 174:527–535

89. Wang XH, Schröder HC, Wiens M, Ushijima H, Müller WEG (2012) Bio-silica and bio-polyphosphate: applications in biomedicine (bone formation). Curr Opin Biotechnol 23:570–578

90. Wang XH, Schröder HC, Feng QL, Draenert F, Müller WEG (2013) The natural inorganic polymers, biogenic polyphosphate (bio-polyP) and biogenic silica (bio-silica) as biomimetic scaffolds for bone tissue engineering: fabrication of a morphogenetically-active polymer. Marine Drugs 11:718–746

Lipids as Biological Materials for Nanoparticulate Delivery

14

Indu Pal Kaur, Rohit Bhandari, and Jatinder Vir Yakhmi

Keywords

Bioperformance • Characterization • Lipid types • Lipid nanoparticle • Preparation • Size and shape • Surfactants • Toxicity/safety

Introduction

The major impediment to the absorption of most of the pharmaceutically active therapeutics is their inherently skewed hydrophilic or lipophilic nature, while for an optimum absorption and bioavailability, a fair balance of the two is required. Most drugs, except those taken up by specialized transport mechanisms, either are not absorbed well from the GIT (hydrophilic) or are not wetted or dissolved (lipophilic) in the GIT fluid and hence experience low or incomplete bioavailability. Such molecules when formulated into lipid-based materials demonstrate promising biopharmaceutical performance [1–4]. Incorporation of hydrophilic active pharmaceutical ingredients (APIs) into these systems can help improve their uptake and biodistribution while the nanosize and the colloidal nature imparted to the lipophilic molecules overcomes their limited wettability/solubility. These lipid nanosystems also tend to protect the enclosed drug molecules from oxidation, photodecomposition, and hydrolytic or enzymatic degradation, both during storage and upon in vivo administration.

I.P. Kaur (✉) • R. Bhandari

University Institute of Pharmaceutical Sciences, Panjab University, Chandigarh, India
e-mail: indupalkaur@yahoo.co.in; bhandarirohit79@yahoo.co.in

J.V. Yakhmi
Homi Bhabha National Institute, Mumbai, India
e-mail: ya_kmi@yahoo.com

Further to it, they may also impart protection against drug–drug or pH–drug-induced interactions or inactivation [5]. These nanocarrier systems tend to be transported (i) across the gut via lymphatics [6, 7] overcoming first-pass metabolism encountered by the corresponding free drug; (ii) across biological membranes, including those of GIT, blood vessels, organs, and blood–brain barrier [8–10], via pinocytosis and transcytosis and also an active or passive uptake; and (iii) by inhibition of various efflux transporters including Pgp [11]. Lipid-based materials are also being exploited nowadays to avoid drug resistance and to regulate functional assortment of stem cells [5, 12, 13]. It is an ever-growing field of research, starting with fat emulsions for delivering parenteral nutrition in the past to the present day targeted delivery of drugs. Lipid-based nanosystems (LNs) constitute liposomes, SLNs, nanostructured lipid carriers, and self-nanoemulsifying drug delivery systems (SNEDDS). Use of lipids for improving the bioavailability and solubility of drugs and advantages like biocompatibility, lesser susceptibility to erosion phenomena, and slower water uptake makes them an ideal choice for delivering therapeutics in a controlled and targeted manner.

Classification and Type of Lipid-Based Nanomaterials

The lipid-based nanomaterials could be classified based on their physical state into solid lipid nanoparticles (SLNs, the one with a solid core), nanostructured lipid carriers (NLCs, system with an improved mobility due to use of low melting point lipid/oil in combination with the solid lipid), liposomes (bi- or multilayered systems incorporating aqueous spaces), and the spontaneously forming systems like self-microemulsifying (SMEDDS) or self-nanoemulsifying drug delivery systems (SNEDDS).

Solid Lipid Nanoparticle (SLNs)

Lipid nanoparticles (LNs) were first reported [14] in 1992 and have received considerable interest due to their ability to overcome the limitations of vesicular colloidal carriers [15–19], viz., liposomes and as an alternative to polymeric nanoparticles [20]. They are supposed to be identical to oil/water emulsion for parenteral nutrition, with the liquid lipid of the emulsion being replaced with the solid lipid [21].

SLNs can be prepared from fatty acids; mono-, di-, and triglycerides; and phospholipids, which are normal constituents of the human body and are thus biocompatible [22–24]. SLNs can efficiently incorporate lipophilic drugs [9, 25–27] because the latter can be incorporated easily within the lipid core. They are reported to be suitable for hydrophilic drug molecules too, though with a lesser entrapment efficiency [11, 28, 29].

Advantages of SLNs [2, 4, 29–31]

SLNs combine the advantages of polymeric nanoparticles, fat emulsions, and liposomes while, simultaneously avoiding their limitations or disadvantages as elaborated below:

1. The nanoparticles and the SLNs particularly those in the range of 120–200 nm are not taken up readily by the cells of the RES (reticuloendothelial system) and thus bypass liver and spleen filtration.
2. Controlled release of the incorporated drug can be achieved for up to several weeks. Further, by coating with or attaching ligands to SLNs, there is an increased scope of drug targeting.
3. LN formulations stable for up to 3 years have been developed [27]; this is of paramount importance with respect to the other colloidal carrier systems.
4. High drug payload achieved with SLNs versus a limited drug loading for polymeric nanoparticles is a highlight of these systems.
5. Excellent scalability and reproducibility of significant properties, in large batches, using a cost-effective high-pressure homogenization technique as the preparation procedure, is again an exclusive advantage with SLNs.
6. The feasibility of incorporating both hydrophilic and hydrophobic drugs.
7. The carrier lipids are biodegradable and hence safe for human consumption. This is especially relevant in reference to polymers or the monomers produced thereof with polymeric nanoparticles.
8. Avoidance of organic solvents during preparation of SLNs, which is otherwise a necessity for polymeric nanoparticles and in most instances of vesicular systems, is also an added advantage.

Nanostructured Lipid Carriers (NLCs)

Nanostructured lipid carriers (NLCs) are modified LNs, formed specifically with an aim of improving the entrapment/loading of drug(s) within the lipid phase by increasing the space for accommodating the drug. This is achieved by enhancing the lipid imperfections within these nanostructural carriers, thus introducing mobility in the lipid matrix by partially replacing the high-melting lipid with a low melting (liquid) alternative. NLCs are further differentiated into [32, 33]:

1. Type I NLCs formed by blending solid and liquid lipids together. They contain higher imperfections than their solid lipid counter parts, viz., SLNs.
2. Type II NLCs are similar to the type I except that the incorporated amount of liquid lipid/oil is much higher. Drug molecules are incorporated into both the phases but higher concentrations are usually observed in the liquid lipid phase.
3. Type III NLCs are formed by mixing two lipids, one solid and another liquid, in such a way that the lipids remain in an amorphous state, therefore preventing drug expulsion. These are rationally developed, more evolved, and useful NLCs. Advantages of NLCs [32, 34–36]:
1. Prevention of drug expulsion, very commonly observed with SLNs.
2. Modulating release, by controlling the proportion of liquid and solid lipids.
3. Enhanced drug-loading capacity, in comparison to SLNs, owing to the incorporation of mobile liquid lipid core.

Self-nanoemulsifying Drug Delivery System (SNEDDS)

Self-nanoemulsifying drug delivery systems (SNEDDS) are thermodynamically stable isotropic mixtures composed of oil, surfactant, cosurfactant, and drug, with a capacity to readily disperse in aqueous environment of the gastrointestinal tract by forming a fine o/w emulsion with a droplet size less than 100 nm under gentle agitation. SNEDDS can dramatically improve the bioavailability of lipophilic molecules and essential oils [37–39] by increasing drug solubilization and surface area, due to the small droplet size. The latter enhances permeation across the intestinal membrane and [37, 40] facilitates transcellular and paracellular absorption with the use of surfactants like Cremophor® [41]. Food effects which are usually observed with lipophilic drug molecules are significantly reduced by their incorporation into SNEDDS [37, 40]. The SNEDDS differ from their earlier counterparts, i.e., SMEDDS (Self-Microemulsifying Drug Delivery Systems) in terms of the narrow droplet size, which increases the effective interfacial surface area for drug absorption with consequent advantage of presenting the drug in a dissolved form exhibiting an enhanced bioavailability. The SNEDDS are administered as pre-concentrates, which readily form nanoemulsion when dispersed in the stomach or intestinal fluid. Normal motility of the GIT provides energy for nanoemulsification in contrast to SLNs, NLCs, or liposome in which case large amounts of external energy are required for their formation [42]. Hydrolysis of the liquid lipid of SNEDDS leads to an enhanced drug release and/or generation of mixed micelles containing the drug. Various process parameters that can affect the size and bioavailability of these SNEDDS like solubility of the drug in lipid/surfactant blends, nature of the lipid/surfactant pair, ratio of the lipid and surfactant, the surfactant concentration, and uniform droplet size distribution following self-emulsification are necessary and important components need to be monitored during development of SMEDDS or SNEDDS [43–47]. SNEDDS are usually made with the primary aim of improving the bioavailability of the hydrophobic drugs, and as such, they release the drug immediately on reaching the stomach/intestines. However, recently controlled release SNEDDS have also been formulated wherein the release has been modified by incorporating the nanoemulsion forming components into a tablet core and monitoring their release [48, 49].

Based on their physical state, SNEDDS are further classified into [50, 51]:

1. Liquid SNEDDS: These are waterless systems containing a mixture of surfactant, cosurfactant, and oils. These are the most common form of SNEDDS; however, the liquid nature of these systems often poses difficulty in their manufacturability and scalability.
2. Semisolid SNEDDS: These SNEDDS are also waterless systems like liquid SNEDDS but are freeze-dried to a semisolid consistency. These are formed either by using lipids that melt at body temperature or by use of gel-forming agents, which form a nanoemulsion by swelling in the GIT fluid.
3. Solid SNEDDS: Solid SNEDDS are relatively newer systems wherein the components required to form SNEDDS are adsorbed on to solids to form a solid dosage form like tablet, granules, or pellets. The solid SNEDDS offer advantages, over their earlier counterparts, like the absence of drug leakage,

leaching of components from the capsule shell, interaction with capsule shell components and difficulties in handling, machinability, and stability often encountered with liquid SNEDDS.

Advantages of SNEDDS [52–55]:

1. Improved physical and/or chemical stability upon long-term storage.
2. They can be filled into unit dosage forms like soft/hard gelatin capsules and hence are commercially viable and patient acceptable. SNEDDS can also overcome palatability issues of bitter drugs (in contrast to nanoemulsions) as they can be filled into capsules.
3. Reduced inter- and intra-subject variability and food effects.
4. Fast onset of action.
5. Reduction in dose.
6. Ease of manufacturability and scalability.

Although SNEDDS offer several advantages as outlined above, however they are not suitable for drugs, which tend to undergo pH-catalyzed or solution-state degradation. Further, they have a limited carrier capacity, in the sense that they tend to present a solubilized drug molecule at the mucosal surface, but do not carry it across these biological membranes. Free drug molecules have to fend for themselves against enzymatic degradation or metabolism in the GIT. Drugs also undergo the first-pass metabolism and normal clearance and mean residence time (MRT) within the body, intrinsic to them without any modification. It may also be said that the major application of SNEDDS is for poorly water-soluble drugs.

Liposomes

Liposomes are small vesicles of spherical shape with a closed bilayer structure, formed spontaneously when a phospholipid is dispersed in water. In addition to phospholipids they can be produced from cholesterols, nontoxic surfactants, sphingolipids, glycolipids, long-chain fatty acids, and even membrane proteins [56, 57]. Liposomes with different sizes, compositions, charge, and lamellarity to accommodate different drug candidates have been reported [30, 57]. Liposomes are composed of relatively biocompatible and biodegradable materials, and they consist of an aqueous volume entrapped by one or more bilayers of natural and/or synthetic lipids and thus serve as potential delivery systems for both hydrophilic and hydrophobic molecules. However, drug leakage due to an otherwise fluidized nature of the enclosing membrane, low drug loading because of limited space, and scale up issues are few hurdles which limit the success of these systems even after five decades of their discovery [57–59].

Liposomes can be classified in terms of [60–63]:

1. Composition and mechanism of intracellular delivery into five types as follows: (i) conventional liposomes, (ii) pH-sensitive liposomes, (iii) cationic liposomes, (iv) immunoliposomes, and (v) long-circulating liposomes
2. Size and number of bilayers, into one of three categories: (i) multilamellar vesicles, (ii) large unilamellar vesicles, and (iii) small unilamellar vesicles

Factors Influencing Characteristics and Biodistribution of Lipid Nanoparticles (LNs)

Effects of Hydrophobicity/Hydrophilicity of Drugs on Entrapment Efficiency

Intrinsic physicochemical properties of the drug can influence the characteristic like drug loading, entrapment efficiency, release, as well as stability of the nanoformulation. Entrapment efficiency (EE) is the ratio of the drug encapsulated within the nanoparticles and the total drug added and can be controlled by a number of factors. Both hydrophilic and hydrophobic materials can be incorporated with in lipid nanocarriers; however, a low EE always remains a concern for hydrophilic materials [9, 25, 26, 64–70]. To demonstrate the above, a series of aliphatic esters of the NSAID naproxen were synthesized and encapsulated within SLNs [71]. The authors observed that increasing lipophilicity of the synthesized naproxen esters primarily influenced their affinity for the solid lipid matrix and consequently affected the drug release from the developed SLNs. No significant change in particle size, surface charge, and stability was observed. It was also concluded that the alteration in lipophilicity of a highly lipophilic molecule is not expected to improve drug loading or retention in a lipid carrier. It may however result in drug expulsion, probably due to the increased lipophilicity and/or steric hindrance of the drug inside the lipid matrix [71].

Singh et al. prepared SLNs by a w/o/w double-emulsion solvent-evaporation method (using a combination of lipids). Individual lipids and their combinations were tried to entrap zidovudine (aqueous solubility 20.1 mg/ml) into SLNs, and a maximum entrapment efficiency of 27.34 ± 0.42 % was achieved when stearic acid was used as the lipidic component. A reduced EE ranging from 1.6 ± 0.04 % for a 1:3 ratio of tripalmitin/stearic acid to 6.93 ± 1.2 % with 3:1 tripalmitin/stearic acid was observed when different lipids were combined. The highly ordered crystal packing of triglycerides over fatty acids was cited as the most probable reason for the expulsion of hydrophilic drugs from the lipid matrix consequently resulting in a decrease in EE. The particle size for all the formulations was however very large ($\sim$700 nm) [72].

Doxorubicin-loaded SLNs with single and combination of fatty acid and cacao butter indicated a significant increase in entrapment efficiency with a 1:1 combination. The increase was attributed to the introduction of voids due to a disturbance in the organization within the lipid molecule. The authors also observed that the lipid solubility of the drug and the type and concentration of surfactants could influence the entrapment efficiency [73].

High entrapment efficiencies are however observed in general, with lipophilic molecules. Entrapment efficiencies as high as 99.70 %, with a small particle size ($\sim$50 nm), have been reported for isotretinoin-loaded Precirol ATO 5 SLNs [74]. Very recently, we have demonstrated a high entrapment efficiency of 84 % for a highly hydrophilic drug (Isoniazid, aqueous solubility 230 mg/ml) by introducing greater imperfections in the lipid matrix, with the use of a mixture of lipid and fatty acid [29].

Effects of Lipid Type on Nanoparticle Characteristics

Properties of the lipid may also affect EE, particle size, shape, and bioperformance of the final nanoparticulate system [75–77]. Martin et al. evaluated the role of lipids and surfactants in governing the final size and stability of LNs prepared by hot high-pressure homogenization (HPH). They characterized in terms of macroscopic appearance, particle size and optical single particle sizing, zeta potential, as well as physical state and polymorphism by differential scanning calorimetry. The authors observed that both, the type of lipid and the surfactant concentration, affected the macroscopic appearance, mean size, and colloidal stability of the LNs [78].

A study reporting the effect of lipid-based oral formulation on the plasma and tissue concentrations of amphotericin B in male rats demonstrated significant improvement in plasma and tissue concentration complemented, with a reduction in drug-induced renal toxicities following administration of triglyceride-rich oral formulations in contrast to the micellar system composed of sodium deoxycholate [79].

Muhlen et al. while trying to prepare etomidate and prednisolone SLNs observed that the drug loading varies with the type of lipid/matrix material used. They observed high EE (between 85 % and 99 %) for these hydrophobic drugs. The authors also observed a comparatively slow release of prednisolone from Compritol® 888 ATO SLNs in comparison to cholesterol SLNs and correlated the prolonged release to the chemical nature of the lipid matrix in addition to the processing parameters like temperature and type and concentration of the surfactant [80].

A combination of lipids can also be used for improving the EE of highly hydrophilic drugs. We prepared SLNs by varying the lipid types while keeping the method of preparation (microemulsification); the relative properties of constituent drug, lipid, surfactant, and cosurfactant; and other process variables constant. The lipid phase constituted either stearic acid or glyceryl behenate alone or varying combinations thereof. A significant increase in EE for the entrapped hydrophilic drug, isoniazid, with a 1:4 combination of stearic acid with glyceryl behenate was observed. The increase was attributed to the additive or synergistic nature of interaction of isoniazid with both the lipids. We for the first time pointed towards the usefulness of spectral techniques like FTIR and DSC for the systematic selection of excipients for preparing these lipid nanocarrier systems [81].

In another comparative study, SLNs and NLCs of nevirapine have been prepared using stearic acid and Compritol® 888 ATO, with the NLCs containing oleic acid in addition to stearic acid and Compritol® 888 ATO. The authors observed that the drug solubility in the lipid is an essential requirement for obtaining high EE and demonstrated that the preparation of SLNs with the addition of a lipid with low drug solubility into another showing a high drug solubility resulted in a decrease in EE. Interestingly, the authors observed that the drug lipid solubility was not the sole criteria, because addition of lipids with high drug solubility (one solid and another liquid) could also result in a decrease in EE, especially when the void spaces were reduced. The authors correlated the fluidity of the lipid core in NLCs as the reason behind an increased cumulative drug released compared to similarly prepared SLNs [36].

Effect of Process Variables on Particle Size

Vitorino et al. prepared SLNs using emulsification–solvent-evaporation method by applying a double factorial design to select the variables that result in a narrow particle size. Factors like lipid concentration, lipid/solvent ratio, and emulsifier concentrations were varied, and the authors observed that the increase in amount of solvent directly reduces the size irrespective of the type of the lipid and solvent, while varying amounts of emulsifier had no significant effect on the size [82].

Effect of Size and Shape on Biodistribution

The size and deformability of particles play a critical role in their clearance by the sinusoidal spleens of humans and rats. Particles must be either small or deformable enough to avoid the splenic filtration process at the interendothelial cell slits (IES) in the walls of venous sinuses [83, 84]. The IES in sinusoidal spleens provide resistance to flow through the reticular meshwork. The endothelial cells of the sinus wall have two sets of cytoplasmic filaments: a set of loosely associated tonofilaments and a set of filaments tightly organized into dense bands in the basal cytoplasm containing actin and myosin, which can probably vary the tension in the endothelial cells and, hence, the size of IES [85]. However, the slit size rarely exceeds 200–500 nm in width, even with an erythrocyte in transit [83]. Hence, retention of blood cells and blood-borne particles at the IES depends on their bulk properties, such as size, sphericity, and deformability. These cell slits are the sites where erythrocytes containing rigid inclusions (e.g., Heinz bodies, malarial plasmodia) are believed to be "pitted" of their inclusions, which are eventually cleared by the red pulp macrophages [86]. Therefore, the size of engineered long-circulatory particles should not exceed 200 nm ideally. If larger, then the particle must be deformable enough to pass the IES filtration. Alternatively, long-circulating rigid particles greater than 200 nm may act as splenotropic agents [84, 87].

The size and shape have also been demonstrated to influence the uptake of nanoparticles into cells. For example, for nanoparticles larger than 100 nm the highest uptake was observed with rod shapes, followed by spheres, cylinders, and cubes [88]. However, with sub-100-nm nanoparticles, spheres show an appreciable advantage over rods [89, 90]. The size-dependent uptake of nanoparticles is likely related to the so-called membrane-wrapping process which governs how a membrane encloses a particle [91]. It has been demonstrated that optimal endocytosis occurs when there is no ligand shortage on the nanoparticle surface and no localized receptor shortage on the cell surface [75, 92] and this "sweet spot" occurs with nanoparticles in the diameter range of 30–50 nm [75, 93–95]. The nanoparticles in 50 nm range are also demonstrated to generate sufficient free energy such that they can be internalized through membrane wrapping. Docking studies on single nanoparticles have demonstrated that nanoparticles smaller than 50 nm are actually not able to produce sufficient free energy which is necessary to wrap these nanoparticles on the surface of the membrane. Such small nanoparticles must be clustered together to gain access into the cell [2, 93].

Constituents of Lipid Nanoparticles

Lipid Matrix

Lipids are defined as hydrophobic or amphipathic small molecules that may originate entirely or in part by carbanion-based condensations of ketoacyl thioesters and/or by carbocation-based condensations of isoprene units [96]. Various commercially available and metabolic lipids (and their important characteristics) that are being employed for the preparation of lipid nanoparticles are enumerated in Table 14.1.

Emulsifiers/Surfactant/Cosurfactant

Emulsifiers are important constituents for preparing and stabilizing lipid nanoparticle dispersions or vesicular systems. The choice of the emulsifiers is a critical parameter as the charge, molecular weight, chemical structure, and the hydrophile–lipophile balance (HLB) of the emulsifiers govern the formation as well as the stability of the developed nanosystems. The amount and selection of an emulsifier should be based on the end use including the route of administration of the formulation. Different grades of polysorbates and PEGs have been reported widely for use with these systems [97–99].

The use of emulsifiers can also help nanoparticles for their specific and targeted delivery to specific organs like brain. A passive uptake by pinocytosis and endocytosis [100, 101] and an active uptake of these nanoparticulate systems by brain endothelial cells have been reported. The presence of hydrophilic polysorbate 80 on the outer coat of particles is documented to adsorb the circulating plasma apolipoprotein E (Apo E) such that they are selectively taken up by the ApoE receptors present at the blood–brain barrier (BBB) [102–105]. The hydrophilic polysorbate coating has also been demonstrated to assist the uptake of different nanoparticulate systems through the temporary opening of inulin spaces [106, 107].

The type of emulsifiers and its concentration governs the particle size of the lipid nanoparticles. The influence of the lipid type and the emulsifier on size has been demonstrated using different lipids (Precirol®, Compritol® 888 ATO, and Tripalmitin) and emulsifiers (Tween®80 and PVA) [82]. The authors concluded that the decrease in particle size was evident only up to a specific increase in emulsifier concentration and that an increase beyond this limiting concentration resulted in an increase in particle size. The probable reason put forth for this increase in particle size when emulsifier was incorporated at a concentration above a critical reported level was the higher degree of deposition of surfactants on the surface of these nanoparticles or because of bridging effect that promotes their aggregation. Table 14.2 defines some of the emulsifiers used for the preparation of lipid nanosystems.

Use of combinations of emulsifiers has also been tried specifically for CNS uptake of drugs. Koziara and Lockman evaluated SLNs when emulsifying wax; Brij 72/Brij 78 and/or polysorbate 80 was used as the surfactant combination.

Table 14.1 Commonly used and commercially available lipids for preparing lipid-based nanoparticles

Lipid class (reference)	Examples, CAS no.	Trade name/synonym	Melting point °C	HLB	Solubility	LD50 (mg/Kg BW)	Regulatory status
Saturated fatty acid [96, 106, 109–111]	Myristic acid, 544-63-8	Edenor C14 98-100	54	16	Soluble in ethanol, ether, and most organic solvents; solubility in water 0.02 g/l at 20 °C	Rat, oral:10	GRAS; FDA inactive ingredients; Nonparenteral medicines licensed in the UK
	Palmitic acid, 57-10-3	Emersol 140	58–63	15	Soluble in ethanol, ether, and most organic solvents; Insoluble in water at 20 °C	Rat, oral:10	GRAS; FDA inactive ingredients; Nonparenteral medicines licensed in the UK
	Stearic acid, 57-11-4	Pristerene, Hystrene; Industrene; Kortacid 1895	55–60	11–15	Soluble in ethanol, ether, and most organic solvents; Insoluble in water at 20 °C	Rat, oral:10	GRAS; Food additive in Europe; FDA inactive ingredients; Nonparenteral medicines licensed in the UK; Canadian list of acceptable non-medicinal ingredients

				Ethanol		
Arachidonic acid, 506-32-1	–	~49	–		Rat, oral:7.06	–
Lauric acid, 143-07-7	Wecoline 1295	44/48	16	4.81 mg/ml in water at 25°C. Very soluble in ether, ethanol (95 %), and methanol; soluble in acetone; slightly soluble in chloroform; miscible with benzene	Mouse, IV:131 Rat, oral:12,000	GRAS FDA food additive EPA TSCA Inventory
Unsaturated fatty acids Linoleic Acid, 60-33-3	Emersol 310; Emersol 315	–5	16	Freely soluble in ether; soluble in ethanol (95 %); miscible with dimethyl formamide, fat solvents, and oils	Mouse, i.p.280	GRAS Food additive in Europe and the USA
Oleic acid, 112-80-1	Priolene	7.5	15	Soluble in ethanol, ether and most organic solvents. Insoluble in water at 20 °C	Rat, oral:10	GRAS FDA inactive ingredients database Nonparenteral medicines in the UK Canadian list of acceptable non-medicinal ingredients

Table 14.1 (continued)

Lipid class (reference)	Examples, CAS no.	Trade name/synonym	Melting point °C	HLB	Solubility	LD50 (mg/Kg BW)	Regulatory status
Fatty alcohols [111]	Capric acid, 334-48-5	Decanoic acid	31.5	3–4	Practically insoluble in water (0.015 g/ 100 g at 20 °C); soluble in ethanol; ether; chloroform; benzene; carbon disulfide; dilute nitric acid, very soluble in acetone, benzene, ethyl ether	Rat, oral:3,320 Mouse, i. v.:129 Rabbit, dermal:>5,000	
	Myristyl alcohol, 112-72-1	Lanette wax, Nacol	38	–	Practically insoluble in water; soluble in ether, slightly soluble in ethanol (95 %)	Rabbit, Skin:7,100 Rat, oral: 33,000	FDA inactive ingredients database Included in nonparenteral medicines licensed in the UK

Palmityl alcohol, 36653-82-4	Speziol C16 Pharma; Tego Alkanol 16	42–52	Freely soluble in ethanol (95 %) and ether, solubility increasing with temperature; practically insoluble in water. Miscible when melted with fats, liquid and solid paraffins, and isopropyl myristate	Mouse, i.p.:1,600 Mouse, oral:3,200 Rat, i.p.:1,600 Rat, oral:5,000	FDA inactive ingredients database Nonparenteral medicines licensed in the UK Canadian list of acceptable non-medicinal ingredients
Stearyl alcohol, 112-92-5	Stenol; Tego Alkanol 18; Vegarol	59.4	– Soluble in chloroform, ethanol (95 %), ether, hexane, propylene glycol, benzene, acetone, and vegetable oils; practically insoluble in water	Rat, oral:20,000 Rat, oral >5,000–8,000 Rabbit dermal >3,000	FDA inactive ingredients database Included in nonparenteral medicines licensed in the UK Canadian list of acceptable non-medicinal ingredients

Table 14.1 (continued)

Lipid class (reference)	Examples, CAS no.	Trade name/synonym	Melting point °C	HLB	Solubility	LD50 (mg/Kg BW)	Regulatory status
	Oleyl alcohol, 143-28-2	Novol; Ocenol	13–19	–	Soluble in ethanol (95 %), and ether; practically insoluble in water	–	FDA inactive ingredients Database Included in nonparenteral medicines licensed in the UK Canadian list of acceptable non-medicinal ingredients
	Isoarachidyl alcohol, 5333-42-6	Jarcol 1-20; Jeecol ODD	<–20.0	–	Miscible with ethanol (95 %); practically insoluble in water	–	FDA inactive ingredients Database Included in nonparenteral medicines licensed in the UK. Canadian list of acceptable non-medicinal ingredients

Glycerolipids [106, 111–113]	Glyceryl behenate, 91052-55-0	Compritol® 888 ATO, glycerol behenate	65–70	2	Ethanol 96 °C: insoluble Chloroform, methylene chloride: soluble under heating conditions n-Hexane: insoluble Water: insoluble Mineral oils: insoluble	Mouse, oral:5,000	EP, USP/NF
	Glyceryl monooleate, 25496-72-4	Peceol; Priolube 1408; Stepan GMO; Tegin	35	3–4	Ethanol 96°: very soluble Chloroform, methylene chloride: easily soluble n-Hexane: insoluble Water: insoluble Mineral oils: very soluble	–	GRAS FDA inactive ingredients Database Nonparenteral medicines licensed in the UK Canadian list of acceptable non-medicinal ingredients

(continued)

Table 14.1 (continued)

Lipid class (reference)	Examples, CAS no.	Trade name/synonym	Melting point °C	HLB	Solubility	LD50 (mg/Kg BW)	Regulatory status
	Glyceryl monostearate, 31566-31-1	Imwitor 191; Imwitor 900	55–60	3.8	Soluble in hot ethanol, ether, chloroform, hot acetone, mineral oil, and fixed oils. Practically insoluble in water, but may be dispersed in water with the aid of a small amount of soap or other surfactant	Mouse, i.p.:200	GRAS; FDA inactive ingredients Database; Nonparenteral medicines licensed in the UK; Canadian list of acceptable non-medicinal ingredients
	Glyceryl palmitostearate, 8067-32-1	Precirol ATO 5	52–55	–	Freely soluble in chloroform and dichloromethane; practically insoluble in ethanol (95 %), mineral oil, and water	Rat, oral: >6,000	GRAS; FDA inactive ingredients Database; Canadian list of acceptable non-medicinal ingredients

Tristearin, 555-43-1	DYNASAN 118	55–73	–	Insoluble in water. Soluble in chloroform, carbon disulfide very soluble in acetone, benzene. soluble in ether, petroleum ether. Insoluble in ethanol	Rat, oral: >20,000	–
Glycerides [106, 111, 113, 114]	Medium-chain triglycerides, 73398-61-5	Bergabest; caprylic/capric triglyceride; Captex, Waglinol	–	Soluble in all proportions at 20°C in acetone, benzene, 2-butanone, carbon tetrachloride, chloroform, dichloromethane, ethanol, ethanol (95 %), ether, ethyl acetate, petroleum ether, special petroleum spirit (boiling range 80–110°C), propan-2-ol, toluene, and xylene. Miscible with long-chain hydrocarbons and triglycerides; practically insoluble in water	Mouse, i.v.:3,700; Mouse, oral:29,600; Rat, oral:33,300	GRAS; FDA inactive ingredients Database; Nonparenteral and parenteral medicines licensed in Europe; Canadian list of acceptable non-medicinal ingredients

Table 14.1 (continued)

Lipid class (reference)	Examples, CAS no.	Trade name/synonym	Melting point °C	HLB	Solubility	LD50 (mg/Kg BW)	Regulatory status
	Caprylic acid triglyceride, 538-23-8	Tricaprylin, Caprylic acid, Panasate 800; Rofetan GTC, Miglyol 808	9–10	7	Miscible with most organic solvents including ethanol (95 %). Captex 8000 is insoluble in water	Mouse, i.p. >27,800; Mouse, i.v.:3,700; Mouse, oral: 29,600 Mouse, s.c.:>27,800; Rat, i.p.:50; Rat, i.v.:4,000 Rat, oral:33,300	FDA inactive ingredients Database
Caprylocaproyl macrogolglycerides, 73398-61-5		Labrasol; macrogolglyceridorum caprylocaprates; PEG 400 caprylic/capric glycerides	<20	14	Dispersible in hot water; freely soluble in methylene chloride	–	EP, USP/NF
Lauroyl polyoxylglycerides, 57107-95-6		Gelucire 44/14; hydrogenated coconut oil PEG 1500 esters; hydrogenated palm/palm kernel oil PEG 300 esters; macrogolglyceridorum laureates	44	4 (PEG300), 14 (PEG1500)	Dispersible in hot water; freely soluble in methylene chloride	–	EP, USP/NF, USFA

	Synonyms			Solubility		Pharmacopoeia
Linoleoyl polyoxyl glycerides, 61789-25-1	Corn oil PEG 300 esters; Labrafil M2125CS; macrogolglyceridorum linoleates	<45	4	Practically insoluble but dispersible in water; freely soluble in methylene chloride	—	EP, USP/NF
Oleoylpoly oxylglycerides, 68424-61-3	Apricot kernel oil PEG 300 esters; Labrafil M1944CS; macrogolglyceridorum oleates; peglicol-5-oleate	<40	4	Practically insoluble but dispersible in water; freely soluble in methylene chloride	—	EP, USP/NF
Stearoylpol yoxylglycerides, 1323-83-7	Gelucire 50/13; hydrogenated palm oil PEG 1500 esters; macrogolglyceridorum stearates	50	13	Dispersible in warm water and warm liquid paraffin; soluble in warm ethanol; freely soluble in methylene chloride	—	EP, USP/NF
Triglyceride esters [106, 111, 115] Hard fat, 8002-74-2	Novata; semisynthetic glycerides; Suppocire; Wecobee; Witepsol	32–44	—	Freely soluble in carbon tetrachloride, chloroform, ether, toluene, and xylene; slightly soluble in warm ethanol; practically insoluble in water	—	EP/BP

(continued)

Table 14.1 (continued)

Lipid class (reference)	Examples, CAS no.	Trade name/synonym	Melting point °C	HLB	Solubility	LD50 (mg/Kg BW)	Regulatory status
Waxes	Anionic emulsifying wax, 8014-38-8	Collone HV; Crodex A; Cyclonette Wax; Lanette SX; Lanette W	49–54	–	Soluble in chloroform, ether and, on warming, in fixed oils and mineral oil. The PhEur 6.2 specifies that cetostearyl alcohol, emulsifying (type A and type B) are soluble in hot water giving an opalescent solution, practically insoluble in cold water and slightly soluble in ethanol (96 %). The BP 2009 specifies that emulsifying wax is practically insoluble in water (forms an emulsion); partly soluble in ethanol (96 %)	–	FDA inactive ingredients Included in nonparenteral medicines licensed in the UK Canadian list of acceptable non-medicinal ingredients

| Yellow beeswax, 8012-89-3 | Apifil; cera flava; E901; refined wax | 61–65 | – | – | Soluble in chloroform, ether, fixed oils, volatile oils, and warm carbon disulfide; sparingly soluble in ethanol (95 %); practically insoluble in water | GRAS Food additive in Europe. FDA inactive ingredients Database Nonparenteral medicines licensed in the UK Canadian list of acceptable non-medicinal ingredients |

"–": information not available

Table 14.2 Commonly used emulsifiers for preparing lipid-based nanoparticles [116–119]

Name	CAS number	HLB	Primary use Emulsifier (E)/co-emulsifier (CE)	LD50 (g/KG BW) Rat Oral	Rat i.p.	Rat i.v.	Mouse Oral	Mouse i.p.	Mouse i.v.
Polysorbate 20	9005-64-5	16.7	E	37.0	3.8	0.80	25.0	2.60	2.90
Polysorbate 60	9005-67-8	14.9	E	>60 ml/Kg		1.20			
Polysorbate 80	9005-65-6	15.0	E	>63.8	6.8	1,790.00	25.0	7.60	4.50
Poloxamer	9003-11-6	29.0	E	9.4	–	7.50	15.0	–	1.00
Lecithin	8002-43-5	4.0–9.0	E/CE	–	–	–	–	–	–
Phosphatidylcholine	26853-31-6	11.0	CE	0.98	–	–	0.3	–	–
Sodium cholate	361-09-1	18	CE	–	–	–	2.4	0.16	0.20
Sodium taurocholate	145-42-6	13.0–14.0	CE	0.31–0.45	–	–	–	–	–
Sodium deoxycholate	302-95-4	16.0	CE	1.37	0.12	0.15	1.05	0.04	0.11
Butanol	71-36-3	7–9.0	E/CE	0.79	1.12	0.31	2.68	0.25	0.38
Polyoxyl 23 lauryl ether/Brij 35	9002-92-0	17.0	CE	1.00	0.16	0.03	1.170	0.16	0.10
Tricaprylin/Miglyol	538-23-8	7.0	–	33.30	0.05	4.00	29.60	3.70	27.80

"–": information not available

Table 14.3 Miscellaneous need-based excipients for preparing lipid nanoparticles [4, 30, 117, 120]

Cryoprotectants	Trehalose	Mannitol
	Glucose	Glucose
	Mannose	Polyvinyl pyrrolidone (PVP)
	Maltose	Polyvinyl alcohol (PVA)
	Lactose	Gelatin
	Sorbitol	
Charge modifiers	Stearylamine	
	Dicetylphosphate	
	Dipalmitoyl phosphatidylcholine (DPPC)	
	Dimyristoyl phophatidyl glycerol (DMPG)	
Stealthing agents	Polyethyleneglycol	
	Poloxamer	
	Polysorbate 80	
Targeting ligand	Folic acid	
	Thiamine	
	Apolipoprotein E	
	LDL apoproteins	
	Tetra(ethylene glycol)ylated cationic ligands (TTMA)	
	Fluorogenic ligands (HSBDP)	
Preservatives	Thiomersal	
	Parabens	

No adverse effects on BBB integrity were observed upon use of these surfactants or surfactant mix by western blot analysis [108]. Other need-based excipients (Table 14.3) are also recommended for preparation of suitable lipid nanoparticles.

Methods of Preparing Lipid-Based Nanomaterials

Numerous methods have been reported in literature for the production of lipid nanoparticles; however, it is important to select a method which yields the desired particle size, entrapment, stability, and drug loading while taking into consideration the physicochemical properties like solubility of the drug in question.

Particle size can govern the penetration of the drug across biological membranes. Several researchers indicate the influence of lipid type (velocity of crystallization, hydrophilicity, and self-emulsifying properties of the lipid) on the particle size of LNs [24, 121–125]. Different particle sizes can be obtained by carefully selecting the excipients and method of preparation. The methods can be broadly classified as bottom-up and top-down. In the bottom up method, nanomaterials are prepared block by block [126]. This type of processes is faster and usually requires less energy and generates lesser waste. Commonly used methods to prepare LNs like solvent emulsification/evaporation, microemulsification, supercritical fluid, spray drying method, and double emulsification.

The top-down methods are those that start with a larger piece of material and reduce its size using techniques like etching, milling, or a combination of these [126]. These processes require more energy, generate more waste, and are complex and time consuming. Reliability of final product size is howsoever the major advantage of these processes. Commonly used and commercially available methods used to prepare lipid nanoparticles like high-pressure homogenization (hot and cold), ultrasonication, and high-pressure emulsification can all be classified under top-down approaches.

Some commonly used methods for preparation of LNs are described below:

High-Pressure Homogenization (HPH)

In this method a coarse pre-emulsion is formed by the combination of hot lipid phase with aqueous surfactant phase which is then passed through a narrow orifice under high pressure. The pre-emulsion/fluid is accelerated at very high speed over a small distance such that the particles are divided by the very high shear stress and cavitation forces into smaller particles. There are two modifications to this technique depending on the sensitivity of the active pharmaceutical ingredient (API) to temperature, i.e., hot HPH and cold HPH. Both the methods involve suspension or solubilization of the drug in the lipid followed by the dispersion of lipid containing the drug into an aqueous solution of the surfactant mix (coarse emulsion) which is then passed through the HPH.

In **hot homogenization**, the pre-emulsion is formed at 5–10 °C above the lipid melting point, by dispersing the hot lipid containing the drug in dissolved or dispersed states in hot aqueous surfactant solution at the same temperature which is passed through HPH while hot. Pressure, number of passes through the HPH and the orifice size monitor the final particle size of the nanodispersion. The product of this process is hot o/w emulsion, and the cooling of this emulsion leads to crystallization of the lipid and the formation of lipid nanoparticle [127].

In cold homogenization process, drug is incorporated into the melted lipid and the lipid melt is quickly cooled up to solidification. The latter is ground by a mortar mill. Obtained lipid microparticles are dispersed in a cold surfactant solution at room temperature or even at temperature distinctly below room temperature and passed through the HPH to form nanoparticles. The method has merit over hot homogenization, since, even during storage of the aqueous solid lipid dispersion, the EE remains unchanged. A comparison of hot versus cold homogenization is elaborated below (Fig. 14.1).

Ultrasonication or High-Speed Stirring/Homogenization

The main advantage of the method lies in the use of basic lab equipments which are easily accessible. However, the wide particle size distribution obtained by the method minimizes its expected usage. Furthermore, physical instabilities
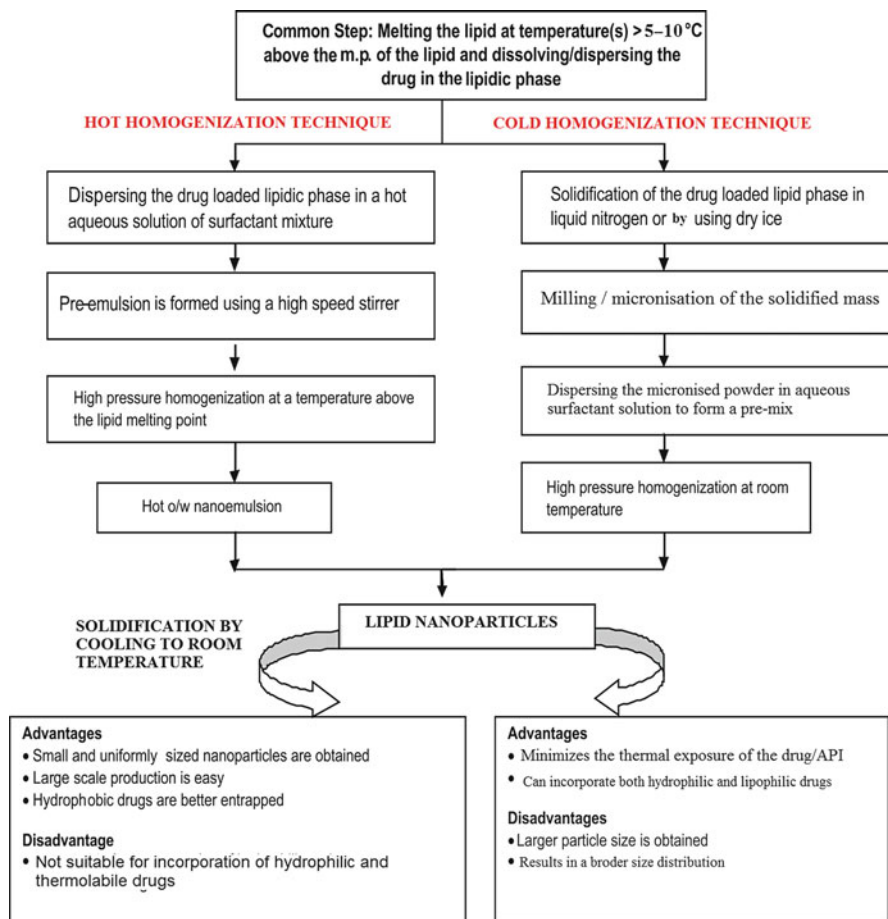
Fig. 14.1 Comparison of hot and cold homogenization techniques

(particle growth upon storage) and potential metal contamination due to ultrasonication may add to the shortcomings of the method. Thus, the technique is generally combined with high-speed stirring for making a stable formulation.

Solvent Emulsification/Evaporation

Production of LNs by emulsification involves the principle of precipitation [128]. The first step involves dissolution of lipid phase in water-immiscible organic solvent (cyclohexane) which is emulsified in an aqueous phase. Solvent evaporation upon stirring and precipitation of the lipid in the aqueous medium results in the formation of lipid nanoparticles. Siekmann and Westensen reported the formation of cholesterol acetate nanoparticles with mean particle size of 29 nm [129] using cholesterol acetate as model drug and lecithin/sodium glycocholate blend as the emulsifier.

Microemulsification

The method is based on controlled precipitation of a hot lipid microemulsion. Microemulsions are produced by stirring an optically transparent mixture at 65–700 rpm. The former are characteristically composed of a low melting fatty acid/lipid/wax, an emulsifier (polysorbate 20, polysorbate 60, soy phosphatidylcholine, and sodium taurodeoxycholate), a suitable co-emulsifier, and water. The hot microemulsion thus formed is dispersed in cold water (2–8 °C), while it is still hot under stirring. Typical volume ratios of the hot microemulsion to cold water are in the range of 1:25–1:50 [130, 131]. It is because of this dilution step that the achievable lipid contents are considerably lower in comparison with the HPH-based formulations. However, the particle size obtained by this method is small, significantly uniform, and not affected by varying the type of the lipid used [132].

Since the droplet structure is already contained in the microemulsion, therefore, no energy is required to achieve submicron particle sizes [133, 134]. We have recently reported [27, 135, 136] and filed patents on preparation of SLNs using much lower dilutions of 1:1–1:9 resulting in highly concentrated dispersions [137–139]. Formation of dilute dispersions, requiring an ultimate step of diafiltration or lyophilization, is one major limitation of SLNs prepared by the microemulsification process.

Various process parameters involved during preparation of SLNs by this technique affect the final properties of the developed SLNs like size, EE, and drug loading. Main process parameters that influence the final features of the nanodispersion include temperature of the microemulsion and water, the temperature gradient, and the hydrodynamics of mixing [140]. High-temperature gradients facilitate a rapid lipid crystallization and also prevent aggregation [64].

Supercritical Fluid

This technique for nanoparticle production has the advantage of producing lipid nanoparticles without the use of organic solvents [141, 142]. There are several variations to this platform technology for powder and nanoparticle preparations. Nanoparticles can be prepared by the rapid expansion of supercritical carbon dioxide solutions (RESS).

Spray Drying Method

It is a suitable and an economical alternative to lyophilization in order to transform aqueous nanoparticles dispersion into a solid product. This method however suffers from a major drawback of causing aggregation of particles due to high temperature, shear forces, and partial melting of the particle. Freitas and Muller [143] recommend the use of high-melting-point lipid (>70 °C) for spray drying. The best result was obtained with lipid nanoparticle concentration of 1 % in a solution of trehalose in water or 20 % trehalose in ethanol–water mixtures (10:90 v/v).

Membrane Contractor Technique

In this, **technique** the melted lipid is forced to pass through a membrane, to form small droplets upon contraction of the lipid membrane. The latter are washed away by the circulating aqueous phase at lipid melt temperature. The nanoparticles are formed by gradually cooling the hot aqueous phase to room temperature. Various process parameters like the pore size of the membrane, the surfactant type and concentration, aqueous-phase cross-flow velocity, and the lipid-phase pressure can affect the final characteristics of the nanoparticles. The method offers many advantages like scalability and an efficient control of size and shape. The method is however more suitable for hydrophobic drugs, generates SLNs at a slower rate, and results in a more polydisperse product owing to the slow rate of cooling [35, 144].

Characterization of lipid Nanoparticles

Size and Shape

Size of nanoparticles can be determined by techniques like photon correlation spectroscopy (PCS) also called dynamic light scattering (DLS). The PCS techniques determine the hydrodynamic diameter of the nanomaterial by measuring the dynamic light scattering of particle in Brownian movement.

The shape can be determined using transmission electron microscopy (TEM) and scanning electron microscopy (SEM) or field emission SEM (FESEM). For determination of shape using SEM, the nanomaterial has to be conductive such that it can transmit the electrons from its surface. However, the shape of the nonconductive nanomaterial can also be determined without necessarily coating it with conductive materials like gold/copper. In TEM analysis the shape of the particle is generated by the electrons transmitted through the nanoparticle. Further freeze fracture or internal structure analysis of the nanomaterials can also be performed using TEM or atomic force microscopy (AFM) [19].

Charge

Charge on the nanoparticles has been reported to influence their in vivo behavior. It is usually expressed in terms of zeta potential. The charged nanoparticles are taken up more rapidly by the cell membranes, which have an opposite charge on their surface or inside them in contrast to the neutral particles. However, binding of positively charged particles is reported to induce fluidity of the membranes. On the other hand, the binding of a negatively charged nanoparticle to the lipid bilayer induces gelation. No such effect of membrane fluidity or gelation is however, reported for neutral nanoparticles in the literature. The suitability of the latter is also supported for achieving an efficient brain delivery of therapeutics (Fig. 14.2)
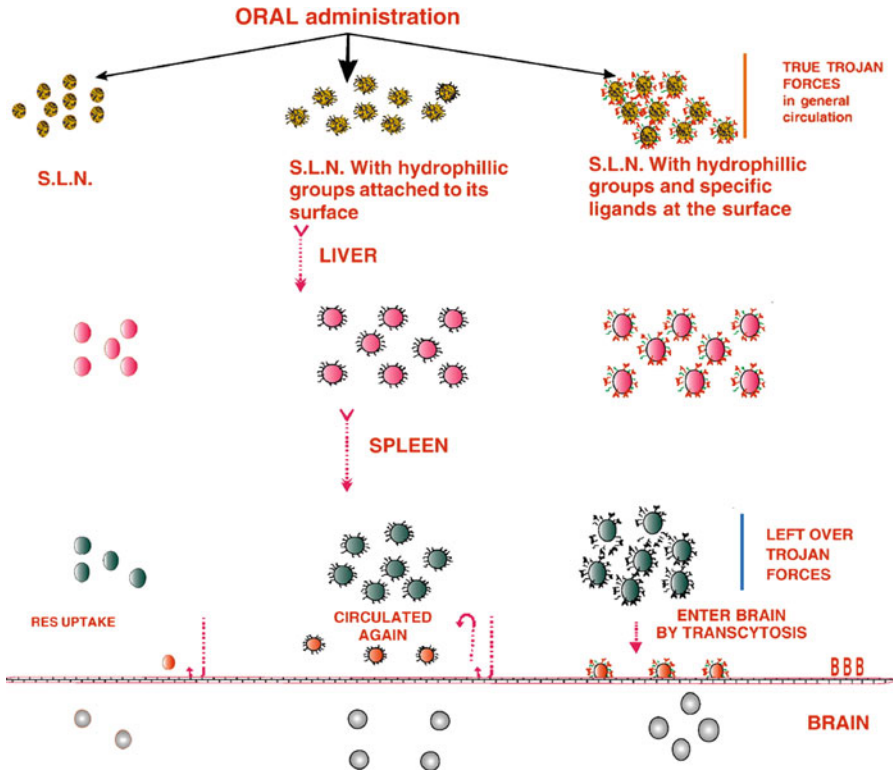
Fig. 14.2 ⬤ Uncoated SLNs, ⬤ SLNs coated with hydrophilic polymers like polysorbates, ⬤ SLNs coated with both hydrophilic polymer (like PEG), and a specific uptake linker monoclonal antibodies/thiamine/glucose. ⬤ Available SLNs in general circulation immediately after oral administration. ⬤ SLNs *left* after 1st metabolism. ⬤ SLNs *left* after encounter with another RES organ "spleen." ⬤ Final SLNs made available to the CNS after passing BBB. This figure shows the fate of different types of SLNs after oral administration. The SLN can bypass the RES removal because of their small particle size; moreover their RES detection could be further decreased by providing a hydrophilic coat, e.g., polysorbates, PEG, Poloxamer F 68, and Brij 78. This will result in an increased circulation time and thus higher chances to be taken up by the target organ. The nanoparticles statistically keep on circulating until the hydrophilic coating is dissolved, when they are either removed by the liver or taken up by the target organ. The hydrophilic coating prevents their interaction with the blood plasma proteins (opsonins) and thus with the membranes of macrophages. The binding of SLNs to the target site, e.g., the brain, can be improved by placing certain ligands, e.g., thiamine, onto their surface; these thiamine ligands could bind to the thiamine receptors and gain access to the brain by receptor-mediated transcytosis (Reproduced from our previous work *License number*: 3144920698114)

without acutely influencing the BBB integrity [145]. Similar observations for neutral isoniazid loaded SLNs for improved brain bioavailability were reported by us recently [2].

Charge on the nanoparticles also influences their circulation time, metabolism, clearance, and immune response as the circulating proteins instantaneously bind on
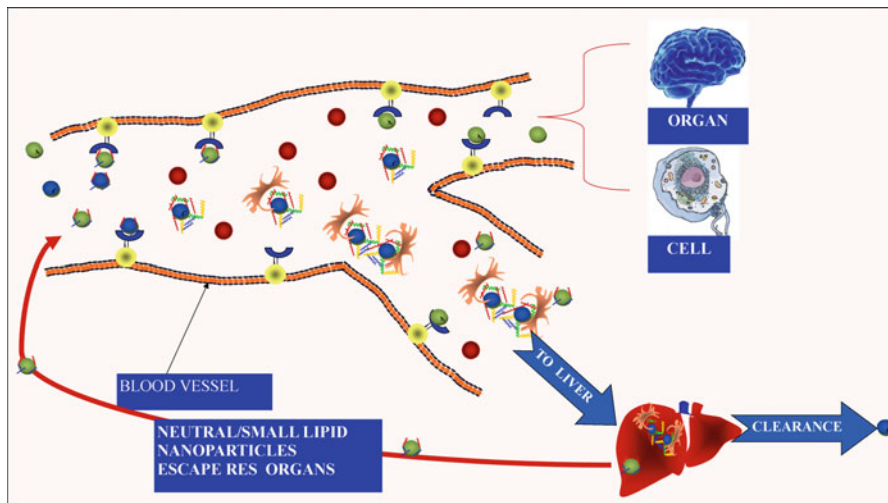
Fig. 14.3 Schematic representation of the biodistribution of lipid nanoparticles. ● Neutral/PEGylated lipid nanoparticles, ● Charged lipid nanoparticles, ● Opsonized lipid nanoparticles with surface adsorbed protein corona, ● Cluster of opsonized particles and their consequent detection by circulating macrophages/reticuloendothelial system, which presents them from liver for metabolism and elimination

the surface of the nanoparticles (Fig. 14.3) and tag them by forming a soft corona which can initiate elimination of particulates from the body within few minutes, by presenting them to the mononuclear phagocyte system (MPS) inside the liver and spleen (Fig. 14.2). The neutral nanoparticles are however expected to remain in circulation over a prolonged period as opsonization processes are not equally activated (as for their charged counter parts) for their removal from the body [75].

Degree of Crystallinity

SLNs can recrystallize as more than one distinct crystalline species/polymorphic form having different melting points, X-ray diffraction (XRD) patterns, and solubilities. Further, the polymorphic forms have different thermodynamic stability, lipid packing density, and drug incorporation rates, which can affect the drug loading, EE, and drug expulsion during storage [146].

The polymorphic states of the lipid can be determined using thermal analysis techniques (DSC and DTA) and XRD. The rate of crystallinity using DSC is estimated by comparing the melting enthalpy/g of the bulk material with that of the LNs dispersion while DTA differentiates the polymorphic forms based on the difference in melting points. The different polymorphic forms can be identified by correlation with the XRD data, which can identify specific polymorphic forms based on their crystal structure [140].

Drug Release Models

Although it is always desirable to have a predictable release profile from a nanomaterial, but attaining tunable release profiles for these systems is still a challenge. The release from the lipid nanomaterial is usually retarded because of its hydrophobic nature. Factors like lipid fluidity can however be exploited for controlling drug release from within those LNs by allowing water influxes [147].

A biocompatible vegetable oil (palm oil) has been used successfully to control the release of a highly hydrophilic molecule terbutaline sulfate, for pulmonary drug delivery by providing a coating on the lipid microspheres. Degradation of the oily layer proceeded the drug release step such that burst release, usually observed with hydrophilic drugs, was avoided and a sustained release was attained [148].

LNs can also be designed to trigger immediate drug release by judicious assortment of components. Lipids which form highly crystalline particles with a perfect lattice (e.g., monoacid triglycerides) lead to drug expulsion [149], while complex lipids being mixtures of mono-, di-, and triglycerides and also containing fatty acids of different chain length form less perfect crystals with many imperfections offering more space to accommodate drugs [29, 80]. LNs may also be suitably coated with a hydrogel or a water-insoluble oily layer to avoid burst release. Crystallization of the lipid in nanoparticles is different from the bulk material; lipid nanoparticles recrystallize at least partially in the α-form, whereas bulk lipids tend to recrystallize preferentially in the β′-modification and transform rapidly to the β-form [149]. Formation of stable modifications results in perfect lattice with minimal imperfections (e.g., formation of β′/β-modification) promoting drug expulsion. In general, the transformation is slower for long-chain than for short-chain triglycerides [70]. An optimal SLN carrier can be produced in a controlled way when a certain fraction of β′-form can be created and preserved during the storage time. The release of entrapped drug can also be harmonized by including thermosensitive materials like hydrogels within the lipid-based nanomaterials and the consequent release from these nanoparticles by controlling the gel to sol temperature-sensitive transformations [150, 151].

The drug either can be homogeneously mixed within the lipid matrix of nanoparticles or may be limited to the shell or core of the formed systems. The drug release from homogeneous matrix occurs either via diffusion from the lipid matrix or by degradation of lipid matrix in the gut [124, 152]. Drug-enriched shell is formed when the lipid precipitates faster than the drug, forming a drug-free core or a core with less drug content. This could also be because of the migration of the drug towards the surface due to higher solubility in the aqueous phase especially in the presence of surfactant and at elevated temperatures. However, as the temperature falls the drug tends to partition back towards the lipid phase from the aqueous phase resulting in the formation of a drug-enriched shell. This type of SLNs exhibits an initial phase of a burst release followed by a second phase of slow and controlled release. We have recently observed and proposed tri- or 4-phase releases for hydrophilic drugs (Fig. 14.4) [2].

In contrast, the drug-enriched core model is formed when the drug precipitation is faster than lipid during cooling of the nanoemulsion. This phenomenon is
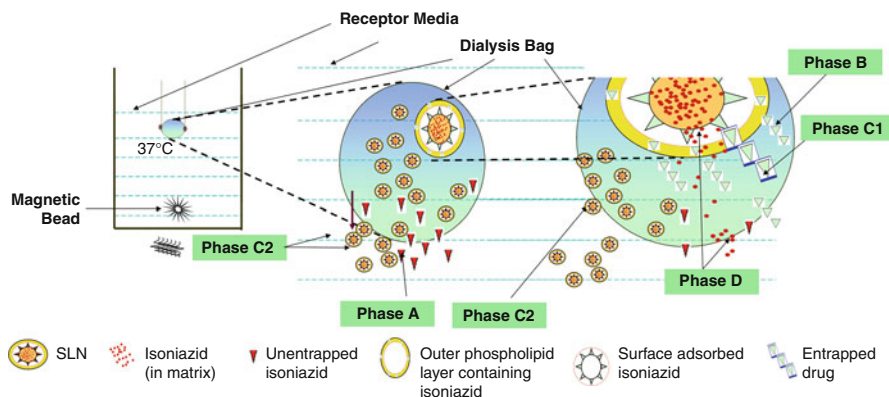
Fig. 14.4 Four-phasic drug release: phase A (free drug, *red triangle*), phase B (drug release from outer phospholipid membrane), phase C (release of surface adsorbed drug and small *solid lipid* nanoparticle), and phase D (drug release from matrix). *Blue triangles* represent entrapped drug (Reproduced from our previous published work [2] *License number*: *3144920492243*)

observed when the drug is dissolved at its saturation solubility in the lipid at production temperature. A drug precipitation from a supersaturated state occurs during cooling of the nanoemulsion. A prolonged drug release is generally observed from these SLNs [153]. The release profile and the amount of the drug in the drug-enriched core can be controlled by process variables like production temperature, surfactant type, and composition [154].

Tailoring of Lipid Nanomaterials Based on Route of Administration and the Target Organ

Nanomaterials are generally internalized by passive targeting due to their enhanced permeation and retention effects at the target site (viz., tumor). Other factors like leaky vasculature, higher metabolic rate, or level of oxygenation of the tissue may also potentiate this passive targeting. However, this passive internalization usually results in a lower uptake due to limited biorecognition and subsequent internalization. The biorecognition or active targeting of these nanomaterials can be achieved by attaching suitable ligands on their surface (Fig. 14.2). The ligand should have the right conformation, high affinity for the corresponding receptor, and should exhibit high cellular internalization [77].

Ligands or homing devices that specifically bind to the surface epitopes or receptors on the target sites can be coupled to the surface of these long-circulating nanocarriers. Certain cancer cells overexpress receptors like folic acid (in cancerous cells of epithelial origin) and low-density lipoproteins (LDL) as in B16 melanoma cell lines and peptide receptors (such as somatostatin analogues, vasoactive intestinal peptide, gastrin-related peptides, cholecystokinin, luteinizing hormone-releasing hormone). Attaching suitable ligands for these receptors on to the surface of nanoparticles

would thus result in their increased selectivity [155–157]. Some hydrophilic surfactants, in particular polysorbates, interact with the surface of the BBB [103, 158–160], showing effective delivery to the brain. Polysorbate-coated nanoparticles (but not PEG-coated) have shown a great promise for delivery to the brain. Adsorption of apolipoprotein E onto these surfactant-coated nanoparticles favors receptor-mediated uptake [28]. Allen et al. [161] postulated that the presence of specific ligands on the surface of nanoparticles could lead to their increased retention and a consequent uptake at the BBB. While attempting to prove their point, they prepared coated nanoparticles from Brij 78 and emulsifying wax, with thiamine ligand (linked to DSPE (1,2-distearoyl-sn-glycero-3-phosphoethanolamine) via a PEG spacer. The authors however could not achieve prolonged nanoparticle concentration which was attributed to a number of factors including insufficient thiamine ligand coating and a nonproductive binding of the thiamine ligand to the blood thiamine transporters [161]. Better interaction with brain endothelial cells and higher intracellular accumulation of sterically stabilized colloidal particles coupled to cationized albumin as compared to bovine serum albumin [162] is however reported. Further, the cationized albumin is taken up into the brain endothelia via a caveolae-mediated endocytic pathway.

Intact antibodies have been used as highly specific targeting agents with a high affinity towards their target. The antibodies act as guides for delivery of nanoparticles across the BBB [162]. Use of peptidomimetic antibodies which can bind to BBB transcytosis receptor and brain-targeted PEGylated immunonanoparticles is also being proposed, such that the delivery of entrapped actives into the brain parenchyma can be achieved without inducing BBB permeability alteration [97]. Similarly, delivery to the brain using nanoparticulate drug carriers in combination with the novel targeting principles of "differential protein adsorption (Pathfinder Technology)" has been reported [163]. The Pathfinder Technology exploits proteins in the blood, which adsorb onto the surface of intravenously injected carriers for targeting.

Polysorbate-stabilized SLNs for delivering drugs to the brain have been reported [99]. It was found that Apo CI and Apo CII inhibit the receptor-mediated binding of Apo E containing lipoproteins (such as β-very-low-density lipoprotein (VLDL)) to the LDL receptor. It would thus be advantageous to have a high Apo E/Apo CII ratio adsorbed on the particles to achieve brain targeting. Further it was found that the SLNs stabilized by polysorbate 80 adsorbed lowest amount of Apo CII [99]. Adsorption of polysorbate 80 onto the albumin nanoparticles has been demonstrated to result in transcytosis of the nanoparticles across the brain endothelium due to its interaction with apolipoprotein receptors [107]. Similar observations have been made by us for curcumin- and sesamol-loaded SLNs explored Alzheimer's in preclinical models of the disease [164], depression [165], stroke (EJPS), and menopause-induced neurological deficits [102].

SLNs prepared by double-emulsification method were utilized for investigating the release of 5-fluorouracil (5-FU) inside the colonic medium for local treatment of colon cancer. Developed system improved the uptake of anticancer drugs inside colon tumors [166]. Better tolerance and antitumor efficacy of docetaxel-loaded

hepatoma-targeted SLNs was observed in murine model bearing hepatoma. The studies on cellular uptake and biodistribution indicated that the better antitumor efficacy of the SLNs was attributed to both the increased accumulation of drug in tumor and higher cellular uptake by hepatoma cells. Further, local injection of loaded lipid nanoparticle local injections is also reported to reduce the toxicity and improve its safety and bioavailability [167].

Brain levels after i.v. administration of etoposide-loaded tripalmitin nanoparticles and etoposide solution were studied, and a relationship between the charge on the lipid nanoparticle and the brain drug levels was observed. Positively charged tripalmitin nanoparticles showed highest brain concentration (0.07 % of injected dose per gram of organ/tissue) when compared to similar negatively charged etoposide-incorporated tripalmitin nanoparticles (0.02 % of injected dose per gram of organ/tissue) and etoposide solution (0.01 % of injected dose per gram of organ/tissue) [168].

Although numerous trials for improving the internalization of nanoparticles using ligand mediated, active targeting can be found in literature but majority of them failed to define any efficacy over nontargeted nanomaterials [145]. Attributes like disruption of ligand structure or shielding from the target because of its altered orientation or nonspecific biomolecular adsorption from the environment (e.g., protein corona effect) were held responsible for their failure [77].

Toxicity of Lipid-Based Nanomaterials

Need for Toxicity Assessment

It has been well said by Paracelsus that all substances are poisons; the difference is in the dose [169]. The statement illustrates that the potential for harm of any substance is widespread and all chemicals could be toxic but the degree of harm that a chemical can inflict, on a human or any other living being, depends on the dose or the degree of exposure, as well as on other factors. In other words, the risk from a toxic hazard depends on the exposure and has to be assessed in terms of the advantages delivered versus toxic manifestations.

Physicochemical properties possessed by the drug within the nanoparticles are different from its free analogues, due to the extremely small size and large surface area such that they intimately interact with biological systems [170]. *Hence, it becomes pertinent to determine the toxicity of these systems.*

The basic objective of a toxicity assessment is to identify what adverse health effects a chemical may cause and how the appearance of these adverse events depends on the exposure level (dose). The toxic effects of a chemical frequently depend on the route of exposure (oral, inhalation, dermal) and the duration of exposure (sub-chronic, chronic, or lifetime). Thus, a full description of the toxic effects of a chemical includes a listing of what adverse health effects the chemical may cause and how the occurrence of these effects depends upon dose, route, and duration of exposure. Some examples of various studies carried out in this regard with LNs are reported below.

LNs are well tolerated in living systems, since they are made from physiological compounds. Silva et al. [171] studied the toxicity of SLNs (composed of glyceryl monostearate, 40–55 %) and risperidone-loaded LNs Caco-2 cells by (4, 5-dimthylthiazol-2-yl) 2, 5-diphenyl-tetrazolium bromide (MTT) assay. The results suggest that all the evaluated formulations were biocompatible with Caco-2 cells and hence are expected to be well tolerated in the GIT. SLNs comprising of two different lipids Dynasan 114 and Compritol® 888 ATO and polymeric nanoparticles prepared using polyalkylcyanoacylate or polylactic/glycolic acid (PLA/GA) and stabilized by poloxamers, polysorbate 80, soya lecithin, and sodium dodecylsulfate were evaluated for cytotoxicity against HL60 and human granulocyte [172]. No effect of lipid on viability of the cells was observed, whereas distinct differences were found for the surfactants. The authors correlated from the results that the binding of the surfactants to the SLNs markedly reduced their toxicity and an in general lower cytotoxicity of SLNs was observed in comparison to their polymeric counterparts [172]. Olbric et al. prepared SLNs of a hydrophilic drug diminazene diaceturate using stearic acid and lipid–drug conjugate (LDC) nanoparticles (stearic acid and oleic acid). The authors reported that both the LDC nanoparticles and SLNs showed signs of cytotoxicity during in vitro studies with human granulocytes while the same were not observed in vivo. The authors observed that the excipients and the drug could influence the individual toxicity of the components when formulated into SLNs. A reduced cytotoxicity of polysorbate 80 was observed when it was associated with SLNs, which was further reduced when a combination of two lipids was used. The cytotoxic potential of LDC nanoparticles prepared using stearic acid (solid lipid) and oleic acid (liquid lipid) was comparable to PBCA (polybutylcyanoacrylate) nanoparticles and was highest than PLA nanoparticles, while it was much lower for stearic acid nanoparticles containing polysorbate 80. An increase in cytotoxicity as a function of decreasing drug loading was also observed [65].

Further, in an attempt to counter the low bioavailability and concurrent renal toxicity of the antifungal drug amphotericin B, Risovic and Boyd [79] prepared lipid-based SNEDDs using Peceol and Intralipid A reduction in renal toxicity probably because of the low recoveries of amphotericin B in the kidneys that were observed [79].

The in vivo toxicity on the liver and the spleen of mice after i.v. injection of two lipid nanoparticle formulations composed of cetylpalmitate or Compritol® 888 ATO has been reported [173]. Even if cetylpalmitate is not a physiological wax, no accumulation was observed since its degradation is very rapid. On the contrary, Compritol® 888 ATO provoked a reversible liver and spleen weight increase, which was however reversible. The liver histological analyses revealed the presence of mononuclear cell infiltration, Kupffer cell hyperplasia, and liver cell necrosis. These effects were almost totally reversible 6 weeks, after the injection since neither inflammation nor fresh infiltrations were observed. Besides, the Compritol® 888 ATO loaded lipid nanoparticle injected dose was remarkably high, in fact, if correlated to the human body mass, the dose was equivalent to 100 g solid lipid mass administered six times by i.v. injection. In light of these considerations, the effects observed can be ascribed to the enormous dose administered, much larger than that theoretically needed for therapy [174].

Pharmacokinetic Behavior of Lipid-Based Nanomaterials

A perfect drug candidate for oral drug absorption should have high solubility and permeability. However, not all therapeutically active drugs possess these properties and thus tend to exhibit poor bioavailability [47]. Coadministration of such drugs with poor permeability, with high fat diet, has been reported to improve permeability [175] probably because of prolonged GIT residence, stimulation of lymphatic transport, stimulation of biliary and pancreatic secretions, enhanced intestinal wall permeability, reduced metabolism, reduced efflux, and alteration in mesenteric and liver blood flow [140]. Lipid-based formulations may thus reduce the inherent limitations of slow and incomplete dissolution of poorly soluble drugs, by facilitating the formation of solubilized phases, from which absorption may occur. Factors enumerated above may also enhance the transport of drugs loaded into LNs. Adhesive nature of LNs may also lead to enhanced GIT absorption of drugs and an improved absorption either due to the increased release of the drug at the site of adhesion or direct entry of the intact SLNs through the GIT [7, 10, 140, 176]. The majority of the drugs taken orally usually enter the systemic circulation through blood capillaries into the portal blood while the lipophilic compounds (log $P > 5$) reach systemic circulation via the lymphatics and as such bypass hepatic first-pass metabolism. The most common site of lymphatic transport is Peyer's patches, which are the most important structural units of gut-associated lymphoid tissue (GALT). GALT is characterized by M-cells that cover the lymphoid tissue and are specialized for endocytosis and transport into intraepithelial spaces and adjacent lymphoid tissue. LNs bind to the apical membrane of these M-cells and are rapidly internalized and ferried to the lymphocytes. The absorption through GALT is affected by various physical characteristics of the lipid nanomaterials like size, shape, specific surface area, surface charge, drug loading, interactions with gut contents, transit time, transport through mucosa, adhesion to epithelial surfaces, and aggregation of the particles in contact with the food content of the gut [6, 177].

A poorly water-soluble drug cryptotanshinone, when incorporated into SLNs prepared by an ultrasonic and HPH method, was found to show significantly improved relative bioavailability in comparison to its suspension in a pharmacokinetic study in rats. Enhanced bioavailability was attributed to the improved absorption of LNs formulations [178]. Similar bioavailability enhancement is also reported for pentoxifylline a highly water-soluble drug, post-incorporation into SLNs using homogenization–sonication technique [179].

A study in healthy volunteers demonstrated that plasma levels of curcumin after dosing of a solid lipid curcumin particle (SLCP) formulation at 650 mg of SLCP was 22.43 ng/ml while dosing an equal quantity of unformulated 95 % curcuminoids extract did not produce detectable levels in plasma [180]. Another study reported an enhancement in relative bioavailability of quercetin-loaded SLNs (QT-SLNs) by fivefolds in comparison to quercetin suspension. Further, their pharmacokinetic data revealed a prolonged T_{max} and mean residence time (MRT) for quercetin in rat plasma after oral administration. The enhanced bioavailability

by the SLNs was attributed to the direct uptake of nanoparticles through the GI tract, increased permeability by surfactants, and decreased degradation and clearance [181]. We have shown 32–155 times enhancement in bioavailability, in a multidose study of curcumin upon its incorporation into SLNs prepared by microemulsification [27]. An improvement in relative bioavailability of vinpocetine (VIN) in SLNs (prepared by ultrasonic-solvent emulsification technique) as compared with that of the VIN solution is also reported. The improved bioavailability was accredited to the effect of surfactant on the oral absorption of VIN with lipid nanoparticle formulations [182]. Superiority of SLNs to avoid the toxic effects of cyclosporine was established by a pharmacokinetic study, in pigs. The authors compared the pharmacokinetic profile of cyclosporine SLNs in comparison to the drug nanocrystals and a reference conventional formulation, i.e., Sandimmun Neoral/Optoral®. The lipid nanoparticle formulation avoided side effects by maintaining the blood concentrations below 1,000 ng/ml. Further, the LNs decreased the variations in cyclosporine A bioavailability, following oral administration, simultaneously avoiding the plasma peak typical of the conventional Sandimmun® formulation [183].

SLNs of a lipophilic drug nitrendipine were prepared for improving its bioavailability upon i.v. administration. SLNs were made using different triglycerides (tripalmitin, trimyristin, and tristearin), emulsifiers (soy lecithin), poloxamer 188, and charge modifiers (dicetyl phosphate, DCP, and stearylamine, SA). Upon i.v. administration of nitrendipine suspension and nitrendipine SLNs, the latter were found to be taken up to a greater extent by the brain and maintained high drug levels for 6 h as compared to only 3 h with nitrendipine suspension. The C_{max} of 3.2, 7.3, and 9.1 times was achieved with nitrendipine tripalmitin, nitrendipine tripalmitin dicetyl phosphate, and nitrendipine tripalmitin stearylamine SLNs when compared with nitrendipine suspension [184].

Wang et al. incorporated 3′, 5′-dioctanoyl –5-fluoro-2′-deoxyuridine into SLNs. The loaded SLNs and drug solution were administered intravenously and it was found that the AUC values achieved with SLNs were twofolds of that obtained by injecting free drug solution [185]. Intravenous injection of 1.3 mg/Kg of an anticancer drug camptothecin into mice resulted in significantly prolonged drug residence time in body when drug-loaded stearic acid LNs were administered compared with plain drug solution. An increase of fivefolds in plasma AUC and tenfolds in brain AUC which further increased on increasing the dose of camptothecin from 1.3 to 3.3 mg/Kg body weight (BW) by another 2.7-folds for plasma AUC and 2.6-folds for brain AUC was observed [186].

Antitubercular drugs such as rifampicin-, isoniazid-, pyrazinamide-loaded lipid nanoparticulate system prepared by emulsion solvent diffusion technique were able to decrease the dosing frequency and improve the patient compliance [187]. We report an increase of six times in plasma bioavailability and four times enhanced brain availability of isoniazid [2] upon incorporation into SLNs [135, 136] in rats. A significant improvement in the bioavailability and circulation of ofloxacin lipid nanoparticles was observed when ofloxacin was entrapped within SLNs [188].

Advances in Gene Delivery Using Lipid-Based Nanoparticles Drug Delivery

In the past decades, numerous gene delivery systems have been developed to transfect various cells in vitro and in vivo. However, a safe and efficient gene delivery vector remains an elusive challenge for effective human therapy.

LNs are presently being proposed widely, although their potential for in vivo gene delivery is yet to be established. The concept is however in its infancy and is hampered by various factors including nucleotide incorporation. One critical feature influencing nucleotide incorporation or binding is the zeta potential [189] which reflects charge force for nucleotide binding. Major advances have however been achieved with lipid-based nanocarriers sterically stabilized by poly(ethylene glycol) [190]. PEG-shielded nanoparticle is a robust and modestly effective system for systemic gene delivery. Although PEG has revolutionized the field of nanocarriers but cumulative experience has revealed that upon repeated administration, PEGylated nanocarriers lose their ability to circulate over long periods in the bloodstream [191].

The option of polylipid nanoparticle formulations using [192] polycationic lipids and cholesterol has now been documented for a more effective delivery. The morphology of these polylipid nanoparticles did not change significantly after interaction with genetic molecule, and its large carrying capacity allowed it to be saturated with negatively charged plasmid DNA. The polylipid nanoparticles also showed a good stability in the bloodstream and a higher transfection efficiency in vivo compared to other formulations of lipid nanoparticles [193].

Another option for gene delivery is polymer–lipid hybrid nanoparticles. Poly (ethylene glycol)–distearoylphosphatidylethanolamine-modified long-circulating polymer–lipid hybrid nanoparticles using the emulsifying solvent-evaporation method have been reported [194]. These hybrid nanoparticles showed higher transfection efficiency and acceptable cytotoxicity, which is beneficial for the development of nonviral gene transfer vector that has also been developed. A polymer–lipid nanoparticle (PLN) system has also been developed [195] for an intracellular delivery. These PLNs in their unconjugated form had nuclear-targeting capability in the absence of nuclear-localization signals. Therefore, PLNs could be manipulated easily via different type of targeting ligands and could potentially be used as a powerful tool for delivering drugs to specific cellular organelles [195].

Scientists around the globe are busy in designing and synthesizing new lipids and polymers for their improved delivery and targetability characteristics. Polyethylenimines are a series of synthetic polymers known for efficient gene delivery with high transfection efficiency [195].

Conclusion

It is now evident that lipid nanocarrier systems have brought about a revolutionary change in drug therapeutics. They are more convenient alternative to "new drug discovery" which is time consuming (launch of any new molecule takes almost

20–30 years) and costly (about 100 billion dollars/molecule). In contrast, packaging or remodeling of existing drug molecules of established therapeutic potential, using a lipid carrier system, can suitably address multiple issues like solubility, stability, permeability, metabolic degradation, fast clearance, and adverse effects limiting its effectiveness. In addition, the resulting product is protectable and commercializable because of the "newness" assigned to it.

However, this very "newness" adds trepidation to clinical translation of these nanoproducts. The latter requires stringent evaluation of various parameters; but regulatory guidelines for their evaluation, especially in terms of stability and toxicity, are yet missing. Significant differences, from existing guidelines for conventional products, are anticipated in terms of parameters and methods of assessment and also the acceptance criteria, majorly due to the complex nature of these systems. For example, the surface and edge reactivities leading to possible self-association (both reversible and irreversible) in terms of aggregation and agglomeration may be entirely different for a nanodisperse system. Similarly, stability of these systems needs to be evaluated in terms of both the entrapped and free drug (their amounts and ratios) and the product in its entirety including in vitro release, in addition to their interaction with serum/plasma proteins. Long-term toxicological repercussions of these nanoproducts are another concern, which may limit fruitful commercialization of these versatile products.

In view of the above considerations, industrial participation is restricted, as the required investment (in terms of man, money and time) may exceed the comfort zone of "risk-averse" pharma industry across the globe. Inspite of all this, several new nanoproducts have not only been launched but have also captured a substantial market, thus dampening unnecessary apprehensions associated with their use and application. The technology has opened newer vistas opportunities for public–private research partnerships. Options for extensive characterization by supporting growth in instrumentation and analytical techniques, newer production methodologies for narrow particle size distribution, and establishment of safer constituent materials and the carrier system in entirety are being amalgamated to result in their successful translation to the market as viable products (in terms of therapeutic benefits, safety, and commercialization).

References

1. Desai PP, Date AA, Patravale VB (2012) Overcoming poor oral bioavailability using nanoparticle formulations: opportunities and limitations. Drug Discov Today Technol 9:e87–e95
2. Bhandari R, Kaur IP (2013) Pharmacokinetics, tissue distribution and relative bioavailability of isoniazid-solid lipid nanoparticles. Int J Pharm 441:202–212
3. Xue M, Zhao Y, Li X-j, Jiang Z-z, Zhang L, Liu S-h, Li X-m, Zhang L-Y, Yang S-y (2012) Comparison of toxicokinetic and tissue distribution of triptolide-loaded solid lipid nanoparticles vs free triptolide in rats. Eur J Pharm Biopharm 47:713–717
4. Qi J, Lu Y, Wu W (2012) Absorption, disposition and pharmacokinetics of solid lipid nanoparticles. Curr Drug Metab 13:418–428

5. Singh H, Bhandari R, Kaur IP (2013) Encapsulation of rifampicin in a solid lipid nanoparticulate system to limit its degradation and interaction with isoniazid at acidic pH. Int J Pharm 446:106–111

6. Paliwal R, Rai S, Vaidya B, Khatri K, Goyal AK, Mishra N, Mehta A, Vyas SP (2009) Effect of lipid core material on characteristics of solid lipid nanoparticles designed for oral lymphatic delivery. Nanomedicine 5:184–191

7. Sanjula B, Shah FM, Javed A, Alka A (2009) Effect of poloxamer 188 on lymphatic uptake of carvedilol-loaded solid lipid nanoparticles for bioavailability enhancement. J Drug Target 17:249–256

8. Olivier JC (2005) Drug transport to brain with targeted nanoparticles. NeuroRx 2:108–119

9. Tabatt K, Kneuer C, Sameti M, Olbrich C, Müller RH, Lehr CM, Bakowsky U (2004) Transfection with different colloidal systems: comparison of solid lipid nanoparticles and liposomes. J Control Release 97:321–332

10. Trevaskis NL, Charman WN, Porter CJ (2008) Lipid-based delivery systems and intestinal lymphatic drug transport: a mechanistic update. Adv Drug Deliv Rev 60:702–716

11. Dong X, Mattingly CA, Tseng MT, Cho MJ, Liu Y, Adams VR, Mumper RJ (2009) Doxorubicin and paclitaxel-loaded lipid-based nanoparticles overcome multidrug resistance by inhibiting P-Glycoprotein and depleting ATP. Cancer Res 69:3918–3926

12. Chabra S, Ranjan M, Bhandari R, Kaur T, Aggrawal M, Puri V, Mahajan N, Kaur IP, Puri S, Sobti RC (2011) Solid lipid nanoparticles regulate functional assortment of mouse mesenchymal stem cells. J Stem Cells Regen Med 7:75–79

13. Hu C-MJ, Zhang L (2012) Nanoparticle-based combination therapy toward overcoming drug resistance in cancer. Biochem Pharmacol 83:1104–1111

14. Lucks JS, Müller RH, Konig B (1992) Solid lipid nanoparticles (SLN) – an alternative parenteral drug carrier system. Eur J Pharm Biopharm 38:33S

15. Kang KC, Lee CI, Pyo HB, Jeong NH (2005) Preparation and characterization of nano-liposomes using phosphatidylcholine. J Ind Eng Chem 11:847–851

16. Schwarz C, Mehnert W, Lucks JS, Muller RH (1994) Solid lipid nanoparticles for controlled drug delivery. I. Production, characterization and sterilization. J Control Release 30:83–96

17. Lee GS, Lee DH, Kang KC, Lee CI, Pyo HB, Choi TB (2007) Preparation and characterization of bis-ethylhexyloxyphenolmethoxyphenyltriazine (BEMT) loaded solid lipid nanoparticles (SLN). J Ind Eng Chem 13:1180–1187

18. Yang HJ, Cho WG, Park SN (2009) Stability of oil-in-water emulsions prepared using the phase inversion composition method. J Ind Eng Chem 15:331

19. Kaur IP, Bhandari R, Bhandari S, Kakkar V (2008) Potential of solid lipid nanoparticles in brain targeting. J Control Release 127:97–109

20. Jenning V, Lippacher A, Gohla SH (2002) Medium scale production of solid lipid nanoparticles (SLN) by high pressure homogenization. J Microencapsul 19:1–10

21. Cavalli R, Caputo O, Gasco MR (2000) Preparation and characterization of solid lipid nanospheres containing paclitaxel. Eur J Pharm Biopharm 10:305–330

22. Almeida AJ, Runge S, Miiller RH (1997) Peptide-loaded solid lipid nanoparticles (SLN): influence of production parameters. Int J Pharm 149:255–265

23. Rawat M, Manju S, Singh D, Saraf S (2008) Lipid carriers: a versatile delivery vehicle for proteins and peptides. Yakugaku Zasshi 128:269–280

24. Westesen K, Bunjas H, Koch MHJ (1997) Physicochemical characterization of lipid nanoparticles and evaluation of their drug loading capacity and sustained release potential. J Control Release 48:223–236

25. Hu L, Tang X, Cui F (2004) Solid lipid Nanoparticles. (SLNs) to improve oral bioavailability of poorly soluble drug. J Pharm Pharmacol 56:1527–1535

26. Lim S, Lee M, Kim C (2004) Altered chemical and biological activities of all-trans retinoic acid incorporated in solid lipid nanoparticle powders. J Control Release 100:53–61

27. Kakkar V, Singh S, Singla D, Kaur IP (2011) Exploring solid lipid nanoparticles to enhance the oral bioavailability of curcumin. Mol Nutr Food Res 55:495–503

28. Steiniger SC, Kreuter J, Khalansky AS, Skidan IN, Bobruskin AI, Smirnova ZS, Severin SE, Uhl R, Kock M, Geiger KD, Gelperina SE (2004) Chemotherapy of glioblastoma in rats using doxorubicin-loaded nanoparticles. Int J Cancer 109:759–767

29. Bhandari R, Kaur IP (2013) A method to prepare solid lipid nanoparticles with improved entrapment efficiency of hydrophilic drugs. Curr Nanosci 9:211–220

30. Lim SB, Banerjee A, Onyukel H (2012) Improvement of drug safety by the use of lipid-based nanocarriers. J Control Release 163:34–45

31. Ghadiri M, Fatemi S, Vatanara A, Doroud D, Najafabadi AR, Darabi M, Rahimi AA (2012) Loading hydrophilic drug in solid lipid media as nanoparticles: statistical modeling of entrapment efficiency and particle size. Int J Pharm 424:128–137

32. Radtke M, Souto EB, Muller R (2005) Nanostructured lipid carriers: a novel generation of solid lipid drug carriers. Pharm Technol Eur 17:45–50

33. Muchow M, Maincent P, Müller RH (2008) Lipid nanoparticles with a solid matrix (SLN®, NLC®, LDC®) for Oral Drug Delivery. Drug Dev Ind Pharm 34:1394–1405

34. Iqbal MA, Md S, Sahni JK, Baboota S, Dang S, Ali J (2012) Nanostructured lipid carriers system: recent advances in drug delivery. J Drug Target 20:813–830

35. Shidhaye SS, Vaidya R, Sutar S, Patwardhan A, Kadam VJ (2008) Solid lipid nanoparticles and nanostructured lipid carriers-innovative generations of solid lipid carriers. Curr Drug Deliv 5:324–331

36. Kuo YC, Chung JF (2011) Physicochemical properties of nevirapine-loaded solid lipid nanoparticles and nanostructured lipid carriers. Colloids Surf B Biointerfaces 83:299–306

37. Villar AMS, Naveros BC, Campmany ACC, Trenchs MAZ, Rocabert CB, Bellowa LH (2012) Design and optimization of self-nanoemulsifying drug delivery systems (SNEDDS) for enhanced dissolution of gemfibrozil. Int J Pharm 431:161–175

38. Constantinides PP (1995) Lipid microemulsions for improving drug dissolution and oral absorption: physical and biopharmaceutical aspects. Pharm Res 12:1561–1572

39. Zhao Y, Wang C, Chow AHL, Ren K, Gong T, Zhang Z, Zheng Y (2010) Self-nanoemulsifying drug delivery system (SNEDDS) for oral delivery of Zedoary essential oil: formulation and bioavailability studies. Int J Pharm 383:170–177

40. Wang Z, Sun J, Wang Y, Liu X, Liu Y, Fu Q, Meng P, He Z (2010) Solid self-emulsifying nitrendipine pellets: preparation and in vitro/in vivo evaluation. Int J Pharm 383:1–6

41. Basalious EB, Shawky N, Badr-Eldin SM (2010) SNEDDS containing bioenhancers for improvement of dissolution and oral absorption of lacidipine. I: development and optimization. Int J Pharm 391:203–211

42. Larsen AT, Ogbonna A, Abu-Rmaileh R, Abrahamsson B, Østergaard J, Müllertz A (2012) SNEDDS containing poorly water soluble cinnarizine; development and in vitro characterization of dispersion, digestion and solubilization. Pharmaceutics 4:641–665

43. Shah NH, Carvajal MT, Patel CI, Infield MH, Malick AW (1994) Self-emulsifying drug delivery systems (SEDDS) with polyglycolized glycerides for improving in vitro dissolution and oral absorption of lipophilic drugs. Int J Pharm 106:15–23

44. Pouton CW (1985) Self-emulsifying drug delivery systems: assessment of the efficiency of emulsification. Int J Pharm 27:335–348

45. Gershanik T, Benita S (2000) Self-dispersing lipid formulations for improving oral absorption of lipophilic drugs. Eur J Pharm Biopharm 50:179–188

46. Kommuru TR, Gurley B, Khan MA, Reddy IK (2001) Self-emulsifying drug delivery systems (SEDDS) of coenzyme Q10: formulation development and bioavailability assessment. Int J Pharm 212:233–246

47. Chakraborty S, Shukla D, Mishra B, Singh S (2009) Lipid-an emerging platform for oral delivery of drugs with poor bioavailability. Eur J Pharm Biopharm 73:1–15

48. Patil PR, Biradar SV, Paradkar AR (2009) Extended release felodipine self-nanoemulsifying system. AAPS PharmSciTech 10:515–523

49. Nazzal S, Khan MA (2006) Controlled release of a self-emulsifying formulation from a tablet dosage form: stability assessment and optimization of some processing parameters. Int J Pharm 315:110–121

50. Shanmugam S, Baskaran R, Balakrishnan P, Thapa P, Yong CS, Yoo BK (2011) Solid self-nanoemulsifying drug delivery system (S-SNEDDS) containing phosphatidylcholine for enhanced bioavailability of highly lipophilic bioactive carotenoid lutein. Eur J Pharm Biopharm 79:250–257

51. Nazzal S, Smalyukh II, Lavrentovich OD, Khan MA (2002) Preparation and in vitro characterization of a eutectic based semisolid self-nanoemulsified drug delivery system (SNEDDS) of ubiquinone: mechanism and progress of emulsion formation. Int J Pharm 235:247–265

52. Nielsen FS, Gibault E, Ljusberg-Wahren H, Arleth L, Pedersen JS, Müllertz A (2007) Characterization of prototype self-nanoemulsifying formulations of lipophilic compounds. J Pharm Sci 96:876–892

53. Nepal PR, Han HK, Choi HK (2010) Preparation and in vitro-in vivo evaluation of Witepsol H35 based self-nanoemulsifying drug delivery systems (SNEDDS) of coenzyme Q(10). Eur J Pharm Sci 39:224–232

54. Nielsen FS, Petersen KB, Müllertz A (2008) Bioavailability of probucol from lipid and surfactant based formulations in minipigs: influence of droplet size and dietary state. Eur J Pharm Biopharm 69:553–562

55. Date AA, Desai N, Dixit R, Nagarsenker M (2010) Self-nanoemulsifying drug delivery systems: formulation insights, applications and advances. Nanomedicine (Lond) 5:1595–1616

56. Grubber SM (1987) Liposomes: from biophysics to therapeutics. Marc Ostro (Ed.). Marcel Dekker: New York

57. Samad A, Sultana Y, Aqil M (2007) Liposomal drug delivery systems: an update review. Curr Drug Deliv 4:297–305

58. Johnston APR, Such GK, Ng SL, Caruso F (2011) Challenges facing colloidal delivery systems: from synthesis to the clinic. Curr Opin Colloid Interface Sci 16:171–181

59. Lee JS, Ankone M, Pieters E, Schiffelers RM, Hennink WE, Feijen J (2011) Circulation kinetics and biodistribution of dual-labeled polymersomes with modulated surface charge in tumor-bearing mice: comparison with stealth liposomes. J Control Release 155:282–288

60. Crommelin DJA, Daemen T, Scherphof GL, Vingerhoeds MH, Heeremans JLM, Kluft C, Storm G (1997) Liposomes: vehicles for the targeted and controlled delivery of peptides and proteins. J Control Release 46:165–175

61. Gabizon A, Goren D, Horowitz AT, Tzemach D, Lossos A, Siegal T (1997) Long-circulating liposomes for drug delivery in cancer therapy: a review of biodistribution studies in tumor-bearing animals. Adv Drug Deliv Rev 24:337–344

62. Sharma A, Sharma US (1997) Liposomes in drug delivery: progress and limitations. Int J Pharm 154:123–140

63. Aggarwal D, Kaur IP (2005) Improved pharmacodynamics of timolol maleate from a mucoadhesive niosomal ophthalmic drug delivery system. Int J Pharm 290:155–159

64. Cortesi R, Esposito E, Luca G, Nastruzzi C (2002) Production of lipospheres as carriers for bioactive compounds. Biomaterials 23:2283–2294

65. Olbrich C, Gessner A, Schröder W, Kayser O, Müller RH (2004) Lipid-drug conjugate nanoparticles of the hydrophilic drug diminazene-cytotoxicity testing and mouse serum adsorption. J Control Release 96:425–435

66. Jie L, Tao G, Changguang W, Zhirong Z, Zhirong Z (2007) Solid lipid nanoparticles loaded with insulin by sodium cholate-phosphatidylcholine-based mixed micelles: preparation and characterization. Int J Pharm 340:153–162

67. Morel S, Ugazio E, Cavalli R, Gasco MR (1996) Thymopentin in solid lipid nanoparticles. Int J Pharm 132:259–261

68. Reithmeier H, Herrmann J, Gopferich A (2001) Lipid microparticles as a parenteral controlled release device for peptides. J Control Release 73:339–350
69. Singh S, Dobhal AK, Jain A, Pandit JK, Chakraborty S (2010) Formulation and evaluation of solid lipid nanoparticles of a water soluble drug: zidovudine. Chem Pharm Bull 58:650–655
70. Nair R, Priya KV, Kumar KS, Badivaddin TM, Sevukarajan M (2011) Formulation and evaluation of solid lipid nanoparticles of water soluble drug: isoniazid. Int J Pharm Pharm Sci 3:1256–1264
71. Stancampiano AHS, Puglisi G, Pignatello R (2008) Effect of lipophilicity of dispersed drugs on the physicochemical and technological properties of solid lipid nanoparticles. Open Drug Deliv J 2:26–32
72. Singh S, Dobhal AK, Jain A, Pandit PK, Chakarborty S (2010) Formulation and evaluation of solid lipid nanoparticles of a water soluble drug: zidovudine. Chem Pharm Bull (Tokyo) 58:650–655
73. Kuo YC, Liang CT (2011) Catanionic solid lipid nanoparticles carrying doxorubicin for inhibiting the growth of U87MG cells. Colloids Surf B Biointerfaces 85:131–137
74. Liu J, Hu W, Chen H, Ni Q, Xu H, Yang X (2007) Isotretinoin-loaded solid lipid nanoparticles with skin targeting for topical delivery. Int J Pharm 328:191–195
75. Albanese A, Tang PS, Chan WCW (2012) The effect of nanoparticle size, shape, and surface chemistry on biological systems. Annu Rev Biomed Eng 14:1–16
76. Ugazio E, Marengo E, Pellizzaro C, Coradini D, Peira E, Daidone MG, Gasco MR (2001) The effect of formulation and concentration of cholesteryl butyrate solid lipid nanospheres (SLN) on NIH-H460 cell proliferation. Eur J Pharm Biopharm 52:197–202
77. Mahon E, Salvati A, Baldelli BF, Lynch I, Dawson KA (2012) Designing the nanoparticle-biomolecule interface for "targeting and therapeutic delivery". J Control Release 161:164–174
78. Martins S, Tho I, Ferreira DC, Souto EB, Brandl M (2011) Physicochemical properties of lipid nanoparticles: effect of lipid and surfactant composition. Drug Dev Ind Pharm 37:815–824
79. Risovic V, Boyd M, Choo E, Wasan KM (2003) Effects of lipid-based oral formulations on plasma and tissue amphotericin B concentrations and renal toxicity in male rats. Antimicrob Agents Chemother 47:3339–3342
80. Muhlen AZ, Schwarz C, Mehnert W (1998) Solid lipid nanoparticles for controlled drug delivery – drug release and release mechanism. Eur J Pharm Biopharm 45:149–155
81. Bhandari R, Kaur IP (2012) A method to prepare solid lipid nanoparticles with improved entrapment efficiency of hydrophilic drugs. Curr Nanosci 9:211–220
82. Vitorino C, Carvalho FA, Almeida AJ, Sousa JJ, Pais AACC (2011) The size of solid lipid nanoparticles: an interpretation from experimental design. Colloids Surf B Biointerfaces 84:117–130
83. Chen LT, Weiss L (1973) The role of the sinus wall in the passage of erythrocytes through the spleen. Blood 41:529–537
84. Moghimi SM, Porter CJH, Muir IS, Illum L, Davis SS (1991) Non-phagocytic uptake of intravenously injected microspheres in rat spleen: influence of particle size and hydrophilic coating. Biochem Biophys Res Commun 177:861–866
85. Drenckhahn D, Wagner J (1986) Stress fibers in the splenic sinus endothelium in situ: molecular structure, relationship to the extracellular matrix and contradictibility. J Cell Biol 102:1738–1747
86. Groom AC (1987) Microcirculation of the spleen: new concepts. Microvasc Res 34:269–289
87. Moghimi SM, Hunter C, Murray JC (2001) Long-circulating and target-specific nanoparticles:theory to practice. Pharmacol Rev 53:283–318
88. Gratton SE, Ropp PA, Pohlhaus PD, Luft JC, Madden VJ (2008) The effect of particle design on cellular internalization pathways. Proc Natl Acad Sci U S A 105:11613–11618
89. Qiu Y, Liu Y, Wang LM, Xu LG, Bai R (2010) Surface chemistry and aspect ratio mediated cellular uptake of Au nanorods. Biomaterials 31:7606–7619
90. Chithrani BD, Ghazani AA, Chan WC (2006) Determining the size and shape dependence of gold nanoparticle uptake into mammalian cells. Nano Lett 6:662–668

91. Gao H, Shi W, Freund LB (2005) Mechanics of receptor-mediated endocytosis. Proc Natl Acad Sci U S A 102:9469–9474
92. Yuan HY, Li J, Bao G, Zhang SL (2010) Variable nanoparticle-cell adhesion strength regulates cellular uptake. Phys Rev Lett 105:1381011–1381014
93. Chithrani BD, Chan WC (2007) Elucidating the mechanism of cellular uptake and removal of protein coated gold nanoparticles of different sizes and shapes. Nano Lett 7:1542–1550
94. Lu F, Wu SH, Hung Y, Mou CY (2009) Size effect on cell uptake in well-suspended, uniform mesoporous silica nanoparticles. Small 5:1408–1413
95. Jin H, Heller DA, Sharma R, Strano MS (2009) Size-dependent cellular uptake and expulsion of single-walled carbon nanotubes: single particle tracking and a generic uptake model for nanoparticles. ACS Nano 3:149–158
96. Fahy E, Cotter D, Sud M, Subramaniam S (2011) Lipid classification, structures and tools. Biochim Biophys Acta 1811:637–647
97. Harris JM, Chess RB (2003) Effect of pegylation on pharmaceuticals. Nat Rev Drug Discov 2:214–221
98. Oyewumi MO, Yokel RA, Jay M, Coakley T, Mumper RJ (2004) Comparison of cell uptake, biodistribution and tumor retention of folate coated and PEG coated gadolinium nanoparticles in tumor bearing mice. J Control Release 95:613–626
99. Goppert TM, Muller RH (2005) Polysorbate-stabilized solid lipid nanoparticles as colloidal carriers for intravenous targeting of drugs to the brain. Comparison of plasma protein adsorption patterns. J Drug Target 13:179–187
100. Zhang S, Li J, Lykotrafitis G, Bao G, Suresh S (2009) Size-dependent endocytosis of nanoparticles. Adv Mater 21:419–424
101. Panyam J, Labhasetwar V (2003) Dynamics of endocytosis and exocytosis of poly(D, L-Lactide-co-Glycolide) nanoparticles in vascular smooth muscle cells. Pharm Res 20:212–220
102. Kakkar V, Mishra AK, Chuttani K, Chopra K, Kaur IP (2011) Delivery of sesamol-loaded solid lipid nanoparticles to the brain for menopause-related emotional and cognitive central nervous system derangements. Rejuvenation Res 14:597–604
103. Ambruosi A, Gelperina S, Khalansky A, Tanski S, Theisen A, Kreuter J (2006) Influence of surfactants, polymer and doxorubicin loading on the anti-tumour effects of poly(butyl cyanoacrylate) nanoparticles in a rat glioma model. J Microencapsul 23:582–592
104. Iea B (2004) Negative preclinical results with stealth1 nanospheres encapsulated doxorubicin in an orthotopic murine brain tumor model. J Control Release 100:29–40
105. Alyautdin RN, Petrov VE, Langer K, Berthold A, Kharkevich DA, Kreuter J (1997) Delivery of loperamide across the blood brain barrier with polysorbate 80-coated polybutylcyanoacrylate nanoparticles. Pharm Res 14:325–328
106. Rowe RC, Sheskey PJ, Quinn ME (2009) Handbook of pharmaceutical excipients, 6th edn. Pharmaceutical Press, Greyslake
107. Zensi A, Begley D, Pontikis C, Legros C, Mihoreanu L, Wagner S, Büchel C, Briesen HV, Kreuter J (2009) Albumin nanoparticles targeted with apo E enter the CNS by transcytosis and are delivered to neurones. J Control Release 137:78–86
108. Koziara JM, Lockman PR, Allen DD, Mumper RJ (2003) In situ blood-brain barrier transport of nanoparticles. Pharm Res 20:1772–1778
109. www.mfc.co.jp downloaded from http://www.mfc.co.jp/english/productinfor.htm. Accessed 4 Apr 2013
110. Pasquali RC, Bregni C, Taurozzi MP (2009) New values of the required hydrophilic-lipophilic balance for oil in water emulsions of solid fatty acids and alcohols obtained from solubility parameter and dielectric constant values. J Dispers Sci Technol 30:328–331
111. HSDB (2013) Downloaded from http://toxnet.nlm.nih.gov/cgi-bin/sis/search/f?./temp/~10IcEv:1. Accessed 23 Feb 2013
112. Michael Ash IA (2007) Handbook of fillers, extenders, and diluents, 2nd edn. Synapse Information Resources, Endicott

113. Gattefossé (2013) Technical documents accessed from http://www.gattefosse.com/en/document-center/. Accessed 17 Feb 2013
114. www.sasoltechdata.com. Downloaded from www.sasoltechdata.com/.../Excipients_Pharmaceuticals.pdf. Accessed 9 Apr 2013
115. www.sasoltechdata.com/.../Excipients_Pharmaceuticals.pdf. Downloaded from www.sasoltechdata.com/.../Excipients_Pharmaceuticals.pdf. Accessed 9 Apr 2013
116. www.ntp.niehs.nih.gov. Downloaded from http://ntp.niehs.nih.gov/index.cfm?objectid=E8841408-BDB5-82F8-FC7F7D3E0F941C7E. Accessed 2nd Jan 2013
117. Severino P, Andreani T, SofiaMacedo A, Fangueiro JF, Santana MA, Silva AM, Souto EB (2012) Current state-of-art and new trends on lipid nanoparticles (SLN and NLC) for oral drug delivery. J Drug Deliv. doi:10.1155/2012/750891
118. Trotta M, Debernardi F, Caputo O (2003) Preparation of solid lipid nanoparticles by a solvent emulsification-diffusion technique. Int J Pharm 257:153–160
119. www.sigmaaldrich.com. Detergents properties and applications. Downloaded from www.sigmaaldrich.com/img/assets/.../Detergent_Selection_Table.pdf. Accessed 3 Jan 2013
120. Pedersen N, Hansen S, Heydenreich AV, Kristensen HG, Poulsen HS (2006) Solid lipid nanoparticles can effectively bind DNA, streptavidin and biotinylated ligands. Eur J Pharm Biopharm 62:155–162
121. Heiati H, Tawashi R, Phillips NC (1998) Drug retention and stability of solid lipid nanoparticles containing azidothymidine palmitate after autoclaving, storage and lyophilization. J Microencapsul 15:173–184
122. Bunjes H, Westesen K, Koch MHJ (1996) Crystallization tendency and polymorphic transitions in triglyceride nanoparticles. Int J Pharm 129:159–173
123. Cavalli R, Gasco MR, Morel S (1992) Behaviour of timolol incorporated in liposheres in the presence of a series of phosphate esters. STP Pharma Sci 2:514–518
124. Mehnert W, Mader K (2001) Solid lipid nanoparticles: production, characterization and applications. Adv Drug Deliv Rev 47:165–196
125. Siekmann B, Westesen K (1992) Submicron-sized parenteral carrier systems based on solid lipids. Pharm Pharmacol Lett 1:123–126
126. Thassu D, Pathak Y, Deleers M (2007) Nanoparticulate drug delivery systems: an overview in nanoparticulate drug delivery systems. Informa Healthcare, New York, pp 1–31
127. Wissing SA, Kayser O, Müller RH (2004) Solid lipid nanoparticles for parenteral drug delivery. Adv Drug Del Rev 56:1257–1272
128. Sjostrom B, Bergenstahl B (1992) Preparation of submicron drug particles in lecithin-stabilized o/w emulsions: I: Model studies of the precipitation of cholesteryl acetate. Int J Pharm 88:53–62
129. Siekmann B, Westesen K (1996) Investigations on solid lipid nanoparticles prepared by precipitation in o/w emulsions. Eur J Pharm Biopharm 43:104–109
130. Gasco MR (1993) Method for producing solid lipid microspheres having a narrow size distribution. US Patent 5250236
131. Muller RH (1990) Colloidal carriers for controlled drug delivery and targeting. Verlagsgesellschaft GmbH, Stuttgart
132. Cavalli R, Caputo O, Carlotti ME, Trotta M, Scarnecchia C, Gasco MR (1997) Sterilization and freeze drying of drug-free and drug-loaded solid lipid nanoparticles. Int J Pharm 148:47–54
133. Gasco MR (1997) Solid lipid nanospheres from warm micro-emulsions. Pharm Technol Eur 9:52–58
134. Boltri L, Canal T, Esposito PA, Carli F (1993) Evaluation of some critical formulation parameters: lipid nanoparticles. Proc Intern Symp Control Rel Bioact Mater 20:346–347
135. Kaur IP, Bhandari R (2012) Solid lipid nanoparticles entrapping hydrophilic/amphiphilic drug and a process for preparing the same. PCT application number: PCT/IN2012/000154 dated 5 March 2012

136. Kaur IP, Bhandari R (2012) Solid lipid nanoparticles entrapping hydrophilic/amphiphilic drug and a process for preparing the same. Indian patent application number: 127/DEL/2012, dated 13 Jan 2012
137. Kaur IP, Verma MK (2012) Solid nanolipidic particulates of retinoic acid and vitamin D3 with DCGI. Indian patent application number: 79/DEL/2012 dated 9 Jan 2012
138. Kaur IP, Singh M, Verma MK (2012) Oral nanocolloidal aqueous dispersion (NCD) of streptomycin sulfate. Indian patent application number: 3093/DEL/2012, dated 3 Jan 2012
139. Kaur IP, Verma MK (2013) A process for preparing solid lipid sustained release nanoparticles for delivery of vitamins. PCT application number: PCT/IB2013/050169, dated 9 Jan 2013
140. Das S, Chaudhury A (2011) Recent advances in lipid nanoparticle formulations with solid matrix for oral drug delivery. AAPS PharmSciTech 12:62–76
141. Kaiser CS, Rompp H, Schmidt PC (2001) Pharmaceutical applications of supercritical carbon dioxide. Pharmazie 56:907–926
142. Chen YJ, Jin RX, Zhou YQ, Zeng J, Zhang H, Feng QR (2006) Preparation of solid lipid nanoparticles loaded with Xionggui powder-supercritical carbon dioxide fluid extraction and their evaluation in vitro release. Zhongguo Zhong Yao Za Zhi 31:376–379
143. Freitas C, Muller RH (1998) Spray-drying of Solid lipid nanoparticles (SLN TM). Eur J Pharm Biopharm 46:145–151
144. Charcosset C, El-Harati A, Fessi H (2005) Preparation of solid lipid nanoparticles using a membrane contactor. J Control Release 108:112–120
145. Lockman PR, Oyewumi MO, Koziara JM, Roder KE, Mumper RJ, Allen DD (2003) Brain uptake of thiamine-coated nanoparticles. J Control Release 93:271–282
146. Manjunath K, Reddy JS, Venkateswarlu V (2005) Solid lipid nanoparticles as drug delivery systems. Methods Find Exp Clin Pharmacol 27:127–144
147. Thassu D, Pathak Y, Deleers M (2007) Nanoparticulate drug delivery systems: nanoengineering of drug delivery systems. Informa Healthcare, New York, pp 99–109
148. Cook RO, Pannu RK, Kellaway IW (2005) Novel sustained release microspheres for pulmonary drug delivery. J Control Release 104:79–90
149. Westesen K, Siekmann B, Koch MHJ (1993) Investigations on the physical state of lipid nanoparticles by synchrotron X-ray diffraction. Int J Pharm 93:189–199
150. Guo X, Xing Y, Zhang X, Li J, Mei Q, Zhang H, Chen C, Zhang Z, Cui F (2012) In vivo controlled release and prolonged antitumor effects of 2-methoxyestradiol solid lipid nanoparticles incorporated into a thermosensitive hydrogel. Drug Deliv 19:188–193
151. Guo X, Cui F, Xing Y, Mei Q, Zhang Z (2011) Investigation of a new injectable thermosensitive hydrogel loading solid lipid nanoparticles. Pharmazie 66:948–952
152. Muller RH, Mäder K, Gohla S (2000) Solid lipid nanoparticles (SLN) for controlled drug delivery – a review of the state of the art. Eur J Pharm Biopharm 50:161–177
153. zur Muhlen A, Schwarz C, Mehnert W (1998) Solid lipid nanoparticles (SLN) for controlled drug delivery – drug release and release mechanism. Eur J Pharm Biopharm 45:149–155
154. Muller RH, Mehnert W, Lucks JS, Schwarz C, Muhlen AZ, Weyhers H, Freitas C, Ruhl D (1995) Solid lipid nanoparticles (SLN) – an alternative colloidal carrier systems for controlled drug delivery. Eur J Pharm Biopharm 41:62–69
155. Pardridge WM (2002) Drug and gene targeting to the brain with molecular Trojan horses. Nat Rev Drug Discov 1:131–139
156. Tiwari SB, Amiji MM (2006) A review of nanocarrier based CNS delivery systems. Cur Drug Deliv 3:219–232
157. Xiang QY, Wang MT, Chen F, Gong T, Jian YL, Zhang ZR, Huang Y (2007) Lung-targeting delivery of dexamethasone acetate loaded solid lipid nanoparticles. Arch Pharm Res 30:519–525
158. Kreuter J (2001) Nanoparticles system for brain delivery of drugs. Adv Drug Deliv Rev 47:65–81

159. Petri B, Bootz A, Khalansky A, Hekmatara T, Müller R, Uhl R, Kreuter J, Gelperina S (2007) Chemotherapy of brain tumour using doxorubicin bound to surfactant-coated poly(butyl cyanoacrylate) nanoparticles: revisiting the role of surfactants. J Control Release 117:51–58

160. Iea B (2004) Negative preclinical results with stealth1 nanospheres encapsulated doxorubicin in an orthotopic murine brain tumor model. J Control Release 100:29–40

161. Allen DD, Lockman PR, Oyewumi MO, Koziara JM, Roder KE, Mumper RJ (2003) Brain uptake of thiamine-coated nanoparticles. J Control Release 93:271–282

162. Thole M, Nobmanna S, Huwyler J, Bartmann A, Fricker GJ (2002) Uptake of cationized albumin coupled liposomes by cultured porcine brain microvessel endothelial cells and intact brain capillaries. J Drug Target 10:337–344

163. Muller RH, Keck CM (2004) Challenges and solutions for the delivery of biotech drugs – a review of drug nanocrystal technology and lipid nanoparticles. J Biotechnol 113:151–170

164. Kakkar V, Kaur IP (2012) Evaluating potential of curcumin loaded solid lipid nanoparticles in aluminium induced behavioural, biochemical and histopathological alterations in mice brain. Food Chem Toxicol 49:2906–2913

165. Kakkar V, Kaur IP (2012) Antidepressant activity of curcumin loaded solid lipid nanoparticles (C-SLNs) in mice. Am J PharmTech Res 2:729–736

166. Yassin AEB, Anwer MK, Mowafy HA, El-Bagory IM, Bayomi MA, Alsarra IA (2010) Optimization of 5-fluorouracil solid-lipid nanoparticles: a preliminary study to treat colon cancer. Int J Med Sci 7:398–408

167. Lu B, Xiong S-B, Yang H, Yin X-D, Chao R-B (2006) Solid lipid nanoparticles of mitoxantrone for local injection against breast cancer and its lymph node metastases. Eur J Pharm Sci 28:86–95

168. Reddy JS, Venkateshwarlu V (2004) Novel delivery systems for drug targeting to the brain. Drugs Future 29:63–83

169. www.agius.com, http://www.agius.com/hew/resource/toxicol.htm. Accessed 5 May 2013

170. Zhao J, Castranova V (2011) Toxicology of nanomaterials used in nanomedicine. J Toxicol Environ Health B Crit Rev 14:593–632

171. Silva AC, González-Mira ME, Garcia ML, Egea MA, Fonseca J, Silva R (2011) Preparation, characterization and biocompatibility studies on risperidone-loaded solid lipid nanoparticles (SLN): high pressure homogenization versus ultrasound. Colloids Surf B Biointerfaces 86:158–165

172. Muller R, Ruhl D, Runge S, Sculze-Foster K, Mehenert W (1997) Cytotoxicity of solid lipid nanoparticles as a function of lipid matrix and the surfactant. Pharm Res 4:458–462

173. Weyhers H, Hahn WMH, Muller RH (1995) Solid lipid nanoparticles-determination of in vivo toxicity. First world meeting APGI/APV489-490

174. Blasi P, Giovagnoli S, Schoubben A, Ricci M, Rossi C (2007) Solid lipid nanoparticles for targeted brain drug delivery. Adv Drug Deliv Rev 59:454–477

175. Charman WN, Porter CJH, Mithani S, Dressman JB (1997) Physicochemical and physiological mechanisms for the effects of food on drug absorption: the role of lipids and pH. J Pharm Sci 86:269–282

176. Liversidge GG, Cundy KC (1995) Particle size reduction for improvement of oral bioavailability of hydrophobic drugs: I. Absolute oral bioavailability of nanocrystalline danazol in beagle dogs. Int J Pharm 125:91–97

177. Gasco MR (2007) Nanoparticulate drug delivery systems: gastrointestinal applications of nanoparticulate drug-delivery systems. Informa Healthcare, New York, pp 305–316

178. Hu L, Xing Q, Meng J, Shang C (2010) Preparation and enhanced oral bioavailability of cryptotanshinone-loaded solid lipid nanoparticles. AAPS PharmSciTech 11(2):582–587

179. Varshosaz J, Minayian M, Moazen E (2010) Enhancement of oral bioavailability of pentoxifylline by solid lipid nanoparticles. J Liposome Res 20:115–123

180. Gota VS, Maru GB, Soni TG, Gandhi TR, Kochar N, Agarwal MG (2010) Safety and pharmacokinetics of a solid lipid curcumin particle formulation in osteosarcoma patients and healthy volunteers. J Agric Food Chem 58:2095–2099
181. Li HL, Zhao XB, Ma YK, Zhai GX, Li LB, Lou HX (2009) Enhancement of gastrointestinal absorption of quercetin by solid lipid nanoparticles. J Control Release 133:238–244
182. Luo Y, Chen D, Ren L, Zhao X, Qin J (2006) Solid lipid nanoparticles for enhancing vinpocetine's oral bioavailability. J Control Release 114:53–59
183. Müller RH, Runge S, Ravelli V, Mehnert W, Thünemann AF, Souto EB (2006) Oral bioavailability of cyclosporine: Solid lipid nanoparticles (SLN®) versus drug nanocrystals. Int J Pharm 317:82–89
184. Manjunath K, Venkateshwarlu V (2006) Pharmacokinetics, tissue distribution and bioavailability of nitrendipine solid lipid nanoparticles after intravenous and intraduodenal administration. J Drug Target 14:632–645
185. Wang JX, Sun X, Zhang ZR (2002) Enhanced brain targeting by synthesis of 3′,5′-dioctanoyl-5-fluoro-2′-deoxyuridine and incorporation into solid lipid nanoparticles. Eur J Pharm Biopharm 54:285–290
186. Yang S, Zhu J, Lu Y, Liang B, Yang C (1999) Body distribution of camptothecin solid lipid nanoparticles after oral administration. Pharm Res 16:751–757
187. Pandey R, Sharma S, Khuller GK (2005) Oral solid lipid nanoparticle-based antitubercular chemotherapy. Tuberculosis 85:415–420
188. Xie S, Zhu L, Dong Z, Wang Y, Wang X, Zhou W (2011) Preparation and evaluation of ofloxacin-loaded palmitic acid solid lipid nanoparticles. Int J Nanomedicine 6:547–555
189. Huang L, Liu Y (2011) In vivo delivery of RNAi with lipid-based nanoparticles. Annu Rev Biomed Eng 13:507–530
190. Li W, Szoka FC (2007) Lipid based nanoparticles for nucleic acid delivery. Pharm Res 24:438–449
191. Mintzer MA, Simanek EE (2009) Nonviral vectors for gene delivery. Chem Rev 109:259–302
192. Nyunt MT, Dicus CW, Cui Y-Y, Yappert MC, Huser TR, Nantz MH, Wu J (2009) Physicochemical characterization of polylipid nanoparticles for gene delivery to the liver. Bioconjug Chem 20:2047–2054
193. Fan Y, Wu J (2013) Polylipid nanoparticle, a novel lipid-based vector for liver gene transfer. Gene Therapy - Tools and Potential Applications. Francisco Martin Molina (Ed.). InTech
194. Jian LI, Ying-ZI HE, Wen LI, Shen Y-Z, Y-R LI, Wang Y-F (2010) A novel polymer-lipid hybrid nanoparticle for efficient nonviral gene delivery. Acta Pharmacol Sin 31:509–514
195. Wang J, Ornek-Ballanco C, Xu J, Yang W, Yu X (2013) Preparation and characterization of vinculin-targeted polymer–lipid nanoparticle as intracellular delivery vehicle. Int J Nanomedicine 8:39–46

Magnetic Nanoparticles for Biomedical Applications

15

Manuel Bañobre-López, Y. Piñeiro, M. Arturo López-Quintela, and José Rivas

Keywords

Magnetic hyperthermia • Magnetic nanoparticles • Magnetic resonance imaging • Particle surface functionalization

Introduction

Nanotechnology emerged as a powerful discipline able to synthesize and manipulate materials at the nanoscale. The chemical and physical properties of bulk materials were found to drastically change when the particle size was reduced to the nanometer scale, basically due to the big increase of the surface-to-volume ratio. The discovery of these remarkably unique size-dependent chemical and physical properties allowed the development of new research areas that have led to important results in both fundamental and applied sciences. Most of these achievements have changed the way in which our society behaves nowadays. Even at the nanoscale, different materials structures can be found attending to their dimensionality (Fig. 15.1). In this chapter, we will focus on the applicability of magnetic nanoparticles, which are considered 3D materials with enhanced surface-to-volume ratio.

If within the vast world of nanotechnology we need to highlight one topic that resulted to be an authentic revolution in several areas of knowledge, this is the use of magnetic nanoparticles. During the last decades, magnetic nanoparticles have attracted much attention, since a big number of opportunities are

M. Bañobre-López (✉) • J. Rivas
International Iberian Nanotechnology Laboratory (INL), Braga, Portugal
e-mail: manuel.banobre@inl.int; jose.rivas@inl.int; jose.rivas@usc.es

Y. Piñeiro • M.A. López-Quintela
Departments of Physical Chemistry and Applied Physics, University of Santiago de Compostela, Santiago de Compostela, Spain
e-mail: y.pineiro.redondo@usc.es; malopez.quintela@usc.es

Fig. 15.1 Material structures
depending on their
dimensionality

Layers (2D)

Wires (1D)

Nanoparticles
(0D)
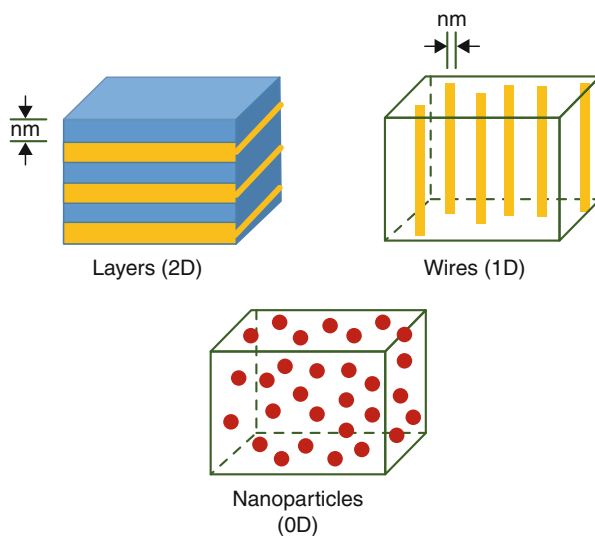
opened when their size-tunable magnetic properties are combined with other
size-dependent chemical or physical properties, i.e., optical, magneto-
resistance, thermoelectric and biocide properties, and surface functionalization
ability. Other research disciplines have noticed in the use of magnetic
nanoparticles a novel and original solution to many of their problems.
The collaboration of different areas of knowledge has been of fundamental
importance for the development of advanced magnetic nanosystems. Such
interdisciplinary motivated the design of multifunctional nanoparticles able to
fulfill several chemical and physical requirements needed for a given application
(Fig. 15.2). Nowadays, multifunctional particles play an important role in
different technological areas with potential applications in fields such as elec-
tronics [1], energy [2], and biomedicine [3]. Its research involves the
design, synthesis, and characterization of a wide variety of unconventional
magnetic nanoparticles and core-shell nanostructures. Depending on their com-
position, particle size and distribution, morphology, structure, and different
particle assemblies, magnetic nanoparticles have demonstrated a diverse range
of useful bioapplications going from magnetic resonance imaging,
magnetic separation, carriers for drug delivery to cell and tissue targeting or
hyperthermia [4–6].

The use of magnetic nanoparticles in nanomedicine implies the use of biocom-
patible nanoparticles, so different functionalization strategies can be carried out to
improve their biocompatible character, i.e., coating with organic or inorganic
compounds. Within the biocompatible magnetic nanoparticles, superparamagnetic
nanoparticles are especially interesting. At the nanometer scale, magnetic proper-
ties depend on the particle size. In a top-down approach, the reduction of the
particle size is accompanied of an energetically favorable destruction of magnetic

Fig. 15.2 Illustration of
a multifunctional nanoparticle
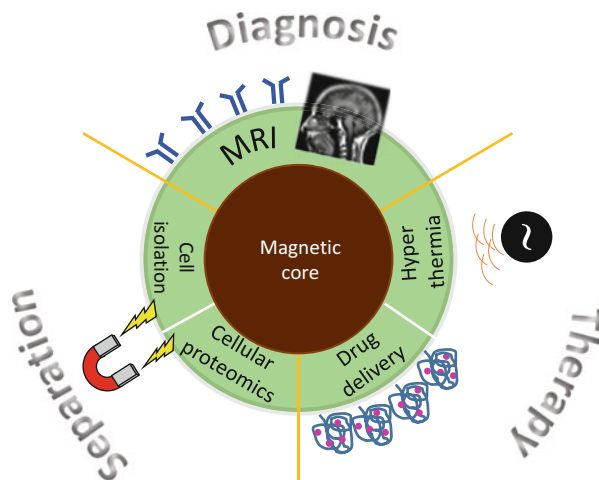
domain walls, in such a way that below a certain particle size, the formation of only one single domain is favored. The magnetic behavior of these single-domain particles is known as superparamagnetism, and it is basically characterized by having no coercive forces or remanence, what means that they exhibit nule magnetization when the applied magnetic field is removed. And this is of great importance in biomedicine, since it avoids the magnetic dipolar interaction between nanoparticles and so their aggregation.

Along this chapter, we will briefly describe the main chemical routes widely used to prepare magnetic nanoparticles. Several modifications and new methods are continuously emerging with the aim of (i) controlling more precisely the properties of the magnetic nanoparticles and (ii) searching more environmental friendly and less cost-effective procedures. We will focus on the most established methods and those general aspects settle out as their basis. Then, we will discuss about the importance of the particle functionalization for biomedical applications and which are the main strategies carried out with this purpose. Next sections will focus on the most researched applications of magnetic nanoparticles in the biomedical field, describing the basic principles of the techniques involved and reviewing the main related findings in those fields. Finally, a perspective with future considerations will be speculated.

Synthesis

The most used form of magnetic particles in nano-biomedicine is as aqueous colloidal dispersions. The colloidal stability depends strongly on the particle size and surface functionalization, so they should be sufficiently small to avoid the natural gravitation forces and preferentially show significant

electrostatic/steric particle interactions [7]. Inorganic nanometer-sized colloidal dispersions have been extensively used in many biomedical applications due to their contrasted good optical, electronic, and magnetic properties, which are dependent on their composition, particle size, and morphology [8, 9]. In order to guarantee reproducibility and high-quality performance, monodisperse nanoparticles in both size and shape are highly demanded. The synthesis is the most powerful tool to act over these parameters, and it will determine the particle size and distribution, morphology, surface activity, and, therefore, their chemical and physical properties. There are a lot of critical parameters involved in a chemical reaction that eventually will origin the desired product. Starting precursors, ion concentration, temperature, time, and atmosphere are only some of them, and depending on how much precisely we will control them we will have better or worse control in the final structure and related properties. The use of templates is also widely used for the synthesis of some materials with specific structures and properties. Some of them are used as nanoreactors in which the particle size can be controlled or limited by physical constrains, as in the case of microemulsions. Several functional materials can be also used as building blocks to form more complex systems that integrate different properties, as, for example, bimetallic alloy particles or core-shell structures [10].

Following, we will describe the most established methods for the synthesis of improved uniform magnetic nanoparticles, essentially involving solution techniques. We will mainly focus on those methods that can be used to obtain iron oxide nanoparticles, since due to their chemical stability, their well-known size-tunable physical properties, surface chemistry, and bio-compatibility, they are the most accepted candidate materials for in vivo applications.

Coprecipitation

Coprecipitation is the most popular method to synthesize iron oxide nanoparticles in a facile, fast, and scalable way. Either Fe_3O_4 (magnetite) or γ-Fe_2O_3 (maghemite) can be obtained from an aqueous solution containing Fe^{2+} and Fe^{3+} ions by addition of a base under inert atmosphere at room temperature or higher. There are several parameters that determine the final particle size, shape, and surface charge of the nanoparticles, such as the Fe^{2+}/Fe^{3+} salt precursors (nitrates, chorides, sulfates), the Fe^{2+}/Fe^{3+} ratio, pH, temperature, and ionic strength of the media. It is important to mention that magnetite nanoparticles are not very stable under ambient conditions and are easily oxidized to maghemite. However, from the magnetic point of view this is not a serious problem since maghemite is also a ferrimagnet with similar high saturation magnetization. The synthesis of magnetite nanoparticles with a controllable particle size and narrow distribution is highly desired for both in vivo (i.e., MRI, hyperthermia, drug delivery) and in vitro (i.e., biosensing, magnetic separation) biomedical applications.

Fig. 15.3 Classical model of LaMer and Dinegar for the mechanism of formation of uniform particles in solution
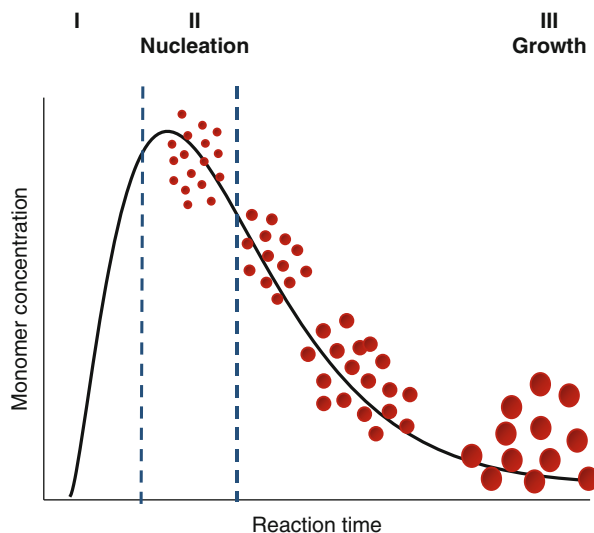
And, unfortunately, general coprecipitation methods lead to polydisperse nanoparticles. Due to the size-dependent magnetic properties, a broad particle size distribution will result in a wide range of blocking temperatures and, therefore, in a non-optimized magnetic behavior for those applications in which deviations from a superparamagnetic behavior are not recommended. In a general homogeneous precipitation a short burst of nucleation occurs when the concentration of constituent species reaches the supersaturation. Then, these nuclei grow uniformly to give rise to bigger nanoparticles [11] (Fig. 15.3). It is well known that the final particle monodispersity will depend on how these two processes develop. An efficient separation of the nucleation and nuclei growth stages, as well as a slow growth process, is needed to achieve high monodisperse nanoparticles.

However, other mechanisms involving simultaneous nucleation events and *Ostwald ripening* growth (continuous growth by diffusion) [12] and smaller particle *aggregation* [13, 14] have been also proposed to explain the formation of monodisperse nanoparticles. Other coprecipitation methods have been developed to achieve homogenous and monodisperse magnetite nanoparticles, i.e., from aqueous ferrous and ferric hydroxides by aggregation of the initial small particles originated in the hydroxide gel (*seed*-based methods).

The use of different organic coatings and additives has been a useful tool to increase the monodispersity of the magnetite/maghemite nanoparticles and also their biocompatibility, making them interesting for in vivo applications. Among a long list of stabilization agents, oleic acid (OA) [15, 16], polyacrylic acid (PAA) [17], polyethylene glycol (PEG) [18], polyvinyl alcohol (PVA) [19], polyvinylpyrrolidone (PVP) [20], polysaccharides [21, 22], and other synthetic polymers have been some of the most successfully used. It is important to

mention that all these coating agents or stabilizers can greatly affect the atomic structure at the particle surface and so preserve the spin alignment observed in the inner core [23].

Thermal Decomposition

The thermal decomposition of iron precursors at relatively high temperatures and in presence of appropriate surfactants improves significantly the crystallinity of iron oxide nanoparticles and leads to a better size and shape controlled particles with narrow size distributions. Basically, monodisperse magnetic nanocrystals between 4 and 20 nm can be synthesized through the thermal decomposition of organometallic compounds in high-boiling organic solvents containing stabilizing surfactants [9]. In the particular case of magnetite/maghemite nanoparticles, the commonest used organometallic precursors are iron pentacarbonyl [Fe(CO)$_5$], iron tri-acetylacetonate [Fe(acac)$_3$], and FeCup$_3$ (Cup: N-nitrosophenylhydroxylamine). Whereas in the first case (Fe in 0 valence) the reaction goes through the intermediate metal formation, that will be later on oxidized to magnetite by addition of a mild oxidant (trimethylamine oxide) [24], the synthesis using the Fe(acac)$_3$ as starting material leads directly to the maghemite nanoparticles [25, 26]. Maghemite nanocrystals between 4 and 10 nm were obtained by injection of FeCup3 solutions in octylamine into long-chain amines at 250–300 °C in octylamine.

In general, fatty acids, oleic acid, oleylamine, and hexadecylamine are commonly used as surfactants, whereas the use of a specific solvent depends on the solubility of the other reagents and the maximum temperature that will be raised during the reaction. Some representative examples of solvents used in this method are octylamine, phenyl ether, phenol ether, octyl ether, hexadecanediol, octadecene, 1-hexadecene, and 1-octadecene, among others, and the main characteristic of most of them is their high boiling temperature. For example, magnetite nanoparticles with sizes from 3 to 20 nm have been synthesized reaction of Fe(acac)$_3$ in phenyl ether in the presence of alcohol, oleic acid, and oleylamine at 265 °C [26]. It is especially interesting to mention a different approach developed by Park et al. [27], in which they use iron chloride [Fe(Cl)$_3$] and sodium oleate to generate an intermediate iron oleate complex that is later on decomposed at high temperatures between 240 °C and 320 °C.

However, all these experimental procedures lead to magnetic nanoparticles dispersible in organic solvents such as toluene or hexane. Different particle surface modification strategies have been developed to transfer after synthesis these organic-stabilized nanoparticles to aqueous solvents. For example, water-soluble magnetite nanoparticles have been directly prepared by thermal decomposition of FeCl$_3$·6H$_2$O and 2-pyrrolidone under reflux at 245 °C and also in similar conditions by addition of carboxyl-terminated poly(ethylene glycol) as coating agent [28, 29].

Although we have focused mainly on the synthesis of magnetite, thermal decomposition procedures in which metal-organic precursors are boiled at high temperatures in organic solvents can be extended to the synthesis of other metal

transition oxides (Fe, Mn, Co, Ni, Cr), metallic nanoparticles (Fe, Ni, Co), or alloys (CoPt$_3$, FePt) which could be also useful for specific biomedical applications [9]. Moreover, thermal decomposition has settled out as one of the best methods to prepare magnetic nanoparticles with a good control of the particle size and morphology.

Microemulsions

Everybody has experienced at some point the phenomenon that arises when two immiscible solvents are mixed (i.e., water and oil). However, the addition of a surfactant can stabilize the dispersion of one of the phases in the other. Surfactants are amphiphilic molecules with two well-differentiated parts: one hydrophobic and other hydrophilic. They are placed in the interface between the aqueous and the organic phases reducing the surface tension between them and allowing the stable dispersion of one phase within the other through the formation of different structures, such as small drops, cylinders, and layers, depending on the mass relation between the aqueous and organic phases and surfactant. Therefore, a *microemulsion* can be defined as a thermodynamically stable isotropic dispersion of two immiscible liquids where the microstructures are stabilized by an interfacial layer of surfactant molecules.

The *microemulsion* technique is a powerful method to prepare simple metallic and oxide NPs, as well as, core-shell and 'onion-like' NPs [30–32]. Although microemulsions cannot be considered as real templates, they constitute an elegant technique that provides a very good control of the final particle size. The reason for that is a complex interplay mainly between three parameters, namely, surfactant film flexibility, reactant concentration, and reactant exchange rate [33]. By adequately choosing these three parameters, one can get a homogeneous distribution of particle sizes down to few atoms. In the particular case of microemulsions, the diameter of the microdroplets typically ranges from 1 to 50 nm. The main physical properties of microemulsions are transparency (the structures are so small that there is no light dispersion), low viscosity, and high stability that avoid the phase separation with time. Depending on what phase is dispersed, microemulsions can be classified as water-in-oil (W/O) or oil-in-water (O/W) when the oil is dispersed in the aqueous phase. The most used in the synthesis of magnetic nanoparticles is the case of water-in-oil microemulsions, because it allows the aqueous microdroplets to behave as nanoreactors in which the reaction takes place. The size confinement created inside these cavities limits the particle nucleation, growth, and agglomeration.

In a typical procedure, nanoparticles will be obtained by mixing two identical W/O microemulsions containing the desired reactants dissolved in the aqueous phase inside the droplets, one of them with the metal ions of interest and the other with the reducing agent. The method is based on continuous collisions between microemulsions, followed by their coalescence and reactants exchange, that will start the reaction and eventually will give place to the formation of

Fig. 15.4 Schematic representation of a microemulsion reaction
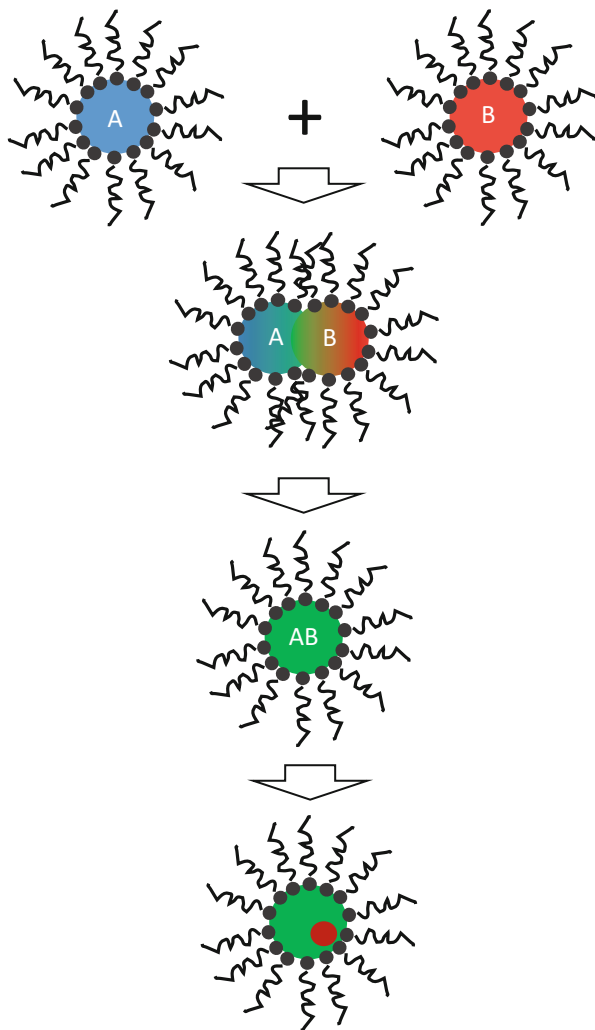
a precipitate inside the reverse micelles (Fig. 15.4). This precipitate can be extracted by adding acetone or ethanol, which breaks the droplets integrity, and then filtering or centrifuging the original mixture. The normal particle sizes that can be obtained by this method are below 20 nm and they can be controlled by the volume ratio of water to the organic solvent and amount of surfactant used. Some representative examples of microemulsion systems for the particular synthesis of magnetite can be found in the literature. For example, $FeCl_2$ and $FeCl_3$ chlorides can be hydrolyzed with ammonium hydroxide inside spherical drops of water-in-oil generated by AOT as surfactant in heptane as continuous phase to obtain magnetite nanoparticles of 4 nm [30]. Other similar microemulsions can be formed by using different surfactants (CTAB, SDS,

dodecylbenzenesulfonate (NaDBS)) and oil phases (octane, toluene, heptane, etc.). Also core-shell structures [34] and different particle shapes droplets [35] can be obtained through this method by an appropriate design of the dispersed reverse micelles [36, 37].

Although the microemulsion method is useful to synthesize monodispersed nanoparticles with different morphologies, the large volume of solvent that it needs, its low yield in comparison to the coprecipitation or thermal decomposition methods and the difficulty for an industrial scale-up are some of its main disadvantages.

Hydrothermal

The hydrothermal method is based on a solid-liquid-solution reaction in which a phase transfer and separation process occur at the solid-liquid and solid-solution interfaces along the reaction time. This method was reported by Li et al. [38], who synthesized high crystalline and water-soluble magnetite and ferrites by using FeCl$_3$ as iron source, ethylene glycol as high-boiling solvent and reducing agent, and sodium acetate and polyethylene glycol as electrostatic and steric stabilizers, respectively, to avoid the particle aggregation [39]. In a typical experiment, this multicomponent reaction mixture would be stirred and sealed in a teflon stainless autoclave that will be later heated up at temperatures around 200 °C for times up to 72 h. Depending on the reaction temperature and duration, the particle size and distribution would be modified. Although this method has been only a little explored for the synthesis of magnetic nanoparticles, it leads to high-quality structural and morphological particles.

Other solution-based techniques also used in the preparation of magnetic nanoparticles for biomedical applications are the *polyol* process, *pyrolysis*-related methods (laser and spray), *aerosol/vapor* methods, *sonochemical-assisted* methods, and *electrochemical* methods, in which the particle size can be tuned by applying a different current density [40].

Functionalization

Applications of magnetic nanoparticles in life sciences fields, such as biotechnology and biomedicine (diagnosis and therapy), imply the use of stable colloidal dispersions in which the nanoparticles are dispersed in different liquid mediums, i.e., blood, urine, physiologic and medium. The colloidal stability of these fluids depends mainly on two parameters: first, on the dimensions of the particles, which should be small enough to avoid their precipitation due to the gravitation forces and, second, on the charge and surface chemistry that determine the steric and coulombic repulsions [7]. All the magnetic nanoparticles used in biomedicine concerning in vivo applications must be properly coated or functionalized for several reasons: an adequate coating of the particle surface not only provides better

stability to the colloidal dispersions avoiding the formation of large aggregates but also prevents structural changes and biodegradation (i.e., oxidation, biological pH changes) that could irreversibly deteriorate their physicochemical properties when exposed to real physiological systems.

On other hand, one of the most important issues for the successful and efficient performance of magnetic nanoparticle-based systems in biomedical applications depends greatly on our ability to drive them to the area of interest, so a proper surface modification should allow attaching ligands for specific target recognition of the desired species (molecules, cells, tissues, or organs). There are several strategies of surface functionalization involving different coating agents that help us to get this goal. Among them, we can mention polymers, virus, antibodies (that recognize specifically proteins), aptamers (show high affinity to certain molecules), etc. Also many polymers and hydrogels have been widely used as coating agents of nanoparticles that allow binding drugs by covalent attachment, adsorption, or entrapment on the particle surface [41] and which will be released precisely in the area of interest under certain chemical or physical stimuli, either internally or externally induced (i.e., internal physiologic pH change or an application of an oscillating magnetic field for hyperthermia, respectively). In the particular case of magnetic nanoparticles, one of the most desirable administrations via would be by intravenous injection, so the additional creation of strong enough magnetic forces by permanent magnets could guide them to the target tissue, overcoming the blood flow forces naturally generated in the blood circulation system.

Additionally to the reasons described above, a suitable particle surface modification or coating is also a useful tool to improve their biocompatibility and nontoxicity, avoiding as much as possible the activation of the immune system agents. Attending only to considerations purely related to physical properties, there would be several materials with better magnetic specifications than iron oxides and which would show a better performance for many of the biomedical applications that have been mentioned here. However, the toxicity associated to these materials constitutes an important drawback. In a big extent, this toxicity is determined by the nature of the magnetic core. Magnetic materials with very good magnetic performance, such as Co or Ni, are considered non-useful for biomedical applications due to their proved toxicity [42, 43]. For this reason, the commonest materials used in biological applications are mostly iron oxides, such as magnetite, maghemite, and other ferrites, for which several protocols of particle surface functionalization have been already established for various biomedical applications [44].

Several multifunctional structures have been designed to improve the colloidal stability and the biocompatibility of magnetic nanoparticles for applications in biomedicine. Among them, we can emphasize core-shell nanostructures [10], in which the external layer does not only preserve the chemical and physical properties of the core against oxidation by oxygen or erosion by acids or bases but also increase the time stability avoiding agglomeration or precipitation and provides the nanoparticle with a more feasible surface to be further functionalized with organic and inorganic functional molecules and compounds. Coatings with organic shells involve polymers and surfactants, such as fatty acids or phospholipids [45–50],

whereas inorganic coatings include silica [51, 52], precious metals [53], or oxides [54]. In the case of ferrofluids the particle size and the surface properties are the main factors that determine the colloidal stability, so electrostatic or steric repulsions are often used to achieve highly stable colloidal dispersions. Surfactants and polymers can be chemically anchored or physically adsorbed to the nanoparticle surface to form single or double layers [55] that balance the attractive dipolar magnetic interactions and the van der Waals forces, which tend to aggregate magnetic nanoparticles in solution. Among others, some of the polymers having functional groups (carboxylic acids, phosphates, sulfates, etc.) that allow them to bind to the particle surface are poly(aniline), poly(pyrrol), poly(glycolic acid), poly (lactic acid), poly(ε-caprolactone), etc [56]. Some representative examples of stabilizations with polymers and surfactants involving iron oxides are peptizations of magnetite nanoparticles with tetramethylammonium hydroxide (TMAOH) [57], coatings with poly(aniline) in the presence of the oxidant ammonium peroxodisulfate [58], polystyrene coatings of ferrites nanoparticles [59], or coatings with poly(acrylic acid) shells [17]. The synthesis methods described in the literature to fabricate these stable core-shell structures is diverse, from coprecipitation and microemulsion methods [60] to oxidative polymerizations [58] or atom transfer radical polymerizations [59].

Regarding inorganic coatings, gold and silica protective shells are two of the most extensive researched coatings for biomedical applications. Gold shells have been mostly used to coat metallic iron nanoparticles [53], whereas silica coatings have been successfully applied also to iron oxides [9, 61]. Both gold and silica coatings have several advantages since they provide nanoparticles with an enhanced stability in aqueous solvents, they have an easy surface modification, and can control the interparticle interactions by variation of the shell thickness. Moreover, their low reactivity and its very well-known surface chemistry allow to introduce further functionalization and additional functionalities, what makes them very promising for targeting drug delivery, bio-labeling, and tissue or molecular imaging. Regarding their synthesis, the method commonly used for gold coatings imply the use of wet chemistry procedures in which $HClAu_4$ is used as starting material to coat iron nanoparticles previously reduced in microemulsions formed by CTAB as surfactant, 1-butanol as cosurfactant, and octane as continuous oil phase [53]. Also a coating of Au on the surface of Fe_3O_4 nanoparticles has been achieved by reducing $HAuCl_4$ in a chloroform solution of oleylamine [62]. In the case of silica coatings, the commonest experimental procedures to coat iron oxides nanoparticles involve the Stöber method and sol-gel processes [63, 64] which basically consist on a basic hydrolysis of tetramethyloxilane (TEOS) in aqueous solution at room temperature. The reaction between the oxide surface and silica takes place through the OH groups. By controlling the amount of TEOS added stepwise, the silica shell thickness can be modified [52]. Sometimes, the natural formation of a controlled oxidized shell under ambient conditions is a strategy to passive the particle surface and avoid further oxidization of the magnetic core. This is the case of iron nanoparticles that are oxidized under ambient conditions at room temperature to form core-shell iron/iron oxide nanoparticles [54]. The additional use of excess stabilizers provide core-shell

structures with extra chemical stability that preserves the high magnetic performance of the iron cores without increasing the cytotoxicity, making them useful for cellular MRI applications. In both organic and inorganic coatings, the protective shells allow further surface modifications, such as the addition of specific targeting ligands, dyes, or therapeutic agents, that make them suitable for MRI, hyperthermia-targeted therapies, drug delivery vectors, etc.

Moreover, the coating material determines in a great extent the biodistribution and the half-life of the magnetic nanoparticles in the blood circulation system without being phagocyted by cells belonging to the reticuloendothelial immune system. The surface charge also plays an important role in blood half-lives, being the neutral ones those recommended to extend circulation times. The development of longer circulating MNPs has allowed the imaging of particular pathologies, such as tumors and inflammatory and infectious issues.

An appropriate surface modification also provides active sites for subsequent functional conjugation with biological or chemical functional moieties [65–67]. Although we will not focus on specific biological functionalizations, since there is a considerable amount of them depending on the specific targeting and application, we would like to mention some of the commonest surface modification strategies to activate the reactivity of the particle surface for further targeted bioconjugation. As explained previously, iron oxides are the most used nanomaterials for biomedical applications because they are biocompatible and nontoxic and because they can be easily synthesized through coprecipitation of the Fe^{2+} and Fe^{3+} salts in basic medium. However, this method shows some drawbacks, such as the difficulty to obtain monodisperse particle size distributions. To solve this problem, other alternative methods have been successfully applied to obtain monodisperse iron oxide nanoparticles. The use of microemulsions as nanoreactors [68] and also organic chemical routes in which the nucleation of the nanoparticles takes place in organic solvents at high temperature [69] have been both the most successfully applied. However, nanoparticles synthesized in this way are normally stabilized by oleic acid and oleylamine and are strongly hydrophobic, so the most primary strategy to turn them into water-soluble colloidal dispersions useful for biomedical applications must be by surfactant addition or surfactant exchange. The former one consists in the addition of amphiphilic molecules containing both hydrophobic and hydrophilic moieties, in such a way that the hydrocarbon chain can form a bilayer with the hydrophobic component of the original one and the hydrophilic groups will be exposed to outside of the nanoparticles, rendering water soluble. On other hand, the ligand exchange is based on a direct replacement of the original stabilizer molecules by other amphiphilic ligands due to their stronger affinity by the particle surface (via a strong chemical bond), in such a way that the polar groups allow the phase transfer of the magnetic nanoparticles to aqueous solvents. Similarly, several amphiphilic polymers can be used to transfer hydrophobic magnetic nanoparticles from organic solvents to aqueous solutions. In order to avoid cluster formation by grafting of previously prepared polymers chains, a different approach was developed by which a polymer brush is growth directly from the particle surface. This requires the presence of ligands

onto the particle surface that act as initiators and induce the polymerization process. These ligands are attached to the surface by replacing the original stabilizers (usually oleic acid or oleylamine) by ligand exchange. In the particular case of iron oxides M. Lattuada et al. [70] used capping agents having one or more reactive carboxylic acid groups (that easily interact with the Fe^{3+} present in the particle surface) and are the ones responsible to induce the polymerization. The most widely used polymerization technique is the atom transfer radical polymerization (ATRP) [71, 72]. Also ring opening polymerization (ROP) [73] have been used to coat magnetic nanoparticles with biodegradable polyesters. Furthermore, by an appropriate selection of ligands and polymers, we will be able to provide the particle surface with different functional groups, including carboxylic acids, thiols, amines, and carbonyl, that will allow the immobilization of various biological moieties, such as peptides, proteins, and oligonucleotides. Some examples are carboxyl acid- and amine-terminated polyethylene glycol (PEG) ligands that allow to transfer hydrophobic nanoparticles from an organic solvent to an aqueous media and also the bioconjugation of biomolecules onto magnetic nanoparticles, i.e., chromones (cromoglycates) for drug delivery [48, 74], through, for example, the EDC/NHS amidation chemistry. Also organosilanes (amino-, carboxylic acid-PEG terminated silanes), bifunctional molecules (2, 3-dimercaptosuccinic, DMSA), carboxylated phospholipids, and variety of carboxylates, phosphates, phosphonates, or other multidentate ligands improved the stability and biocompatibility of nanoparticles, as well as specificity to target through bioconjugation with peptides or antibodies [45, 75, 76].

The surface modification described above is a requirement for the application of magnetic nanoparticles in biomedicine, since stable and water-soluble colloidal dispersions are required. Additionally, another objective of this initial surface modification is to leave reactive functional groups for further specific functionalization and so tailoring nanosystems for a targeted application. As it would be impossible to cover all the biological functionalizations existent, we recommend to the reader the review of Schladt et al. and its references [61].

Biomedical Applications

With the increasing development of nanotechnology, more ambitious challenges are being searched with the aim to provide society with better efficient solutions. Most of the nanoparticle-based in vivo applications are very demanding and need the fulfillment of several requirements in order to guarantee their medical efficiency. Therefore, the integration of several functionalities in one single platform has become one of the most motivating issues in nanotechnology for biomedical applications. With this aim, the so-called *theranostic* nanoparticles emerged [77], referring to multifunctional nanoparticles with the ability to play important roles in both *diagnosis* and *therapy* applications. In this sense, magnetic nanoparticle cores and their appropriate surface functionalization provide nanoparticles with a very helpful multifunctional character in applications such

as cell and tissue targeting, bone tissue engineering, targeting drug delivery, magnetic separation, hyperthermia, and MRI. These complex nanostructured magnetic systems have enhanced the efficiency in therapeutics applications compared to conventional drugs, as well as reduce the harmful side effects [78], In some extent, this has been allowed due to a more localized targeting inside the desired area of the body, as well as to a longer time of residence in the body before being expulsed by the reticuloendothelial system and their ability to overcome specific biological barriers because of their small size, shape, and surface functionalization chemistry.

To cover all the biomedical applications of magnetic nanoparticles would be too much ambitious, so in this chapter the authors have decided to focus on, from our point of view, two of the most researched and projecting applications: magnetic resonance imaging and magnetic hyperthermia. We will try to explain to the reader the fundamentals of these techniques and interesting remarks about the research that is being carried out on them.

Magnetic Resonance Imaging (MRI)

Magnetic resonance imaging (MRI) is a powerful noninvasive medical radiology technique that uses the nuclear magnetic resonance (NMR) principle to visualize not only internal tissues and organs of the human body but also to monitor biological processes with high spatial resolution and without the use of ionizing radiation of radiotracers. MRI has become a very powerful technique in medical diagnosis, and now it constitutes one of the most researched topics in biomedicine, although still some limitations related to its imaging sensitivity need to be further improved. For these reasons, the ongoing research is focused on the search and development of new MRI contrast agents able to enhance the imaging resolution and so broaden the range of related applications.

MRI is based on the alignment and precession of the nuclear spins of protons around a strong applied magnetic field. Then, an extra transverse radio-frequency pulse (RF) is applied that disturbs these protons spins from the direction of the magnetic field and modify their relaxation time in their process to return to their original and more favorable lower-energy state. Two independent relaxation pathways can be monitored to generate an MR image: longitudinal relaxation (T1 recovery) that involves the recovering of the decreased net magnetization in the direction of the applied magnetic field and the transverse relaxation (T2 decay) that involves the disappearance of the induced magnetization in the perpendicular direction to the applied magnetic field, both as consequence of the energy transfer and spin dephasing after the application of the RF pulse, respectively (Fig. 15.5).

The contrast that can be appreciated in MR images is the result of local variations of the T1 and/or T2 relaxation times in adjacent regions. In other words, the spin-spin interaction between water protons nuclei and bio-macromolecules in biological tissues can induce variations in the local magnetic field that greatly affects the spin relaxation times of the nuclear spins of the

**Fig. 15.5** Fundamentals of magnetic resonance imaging
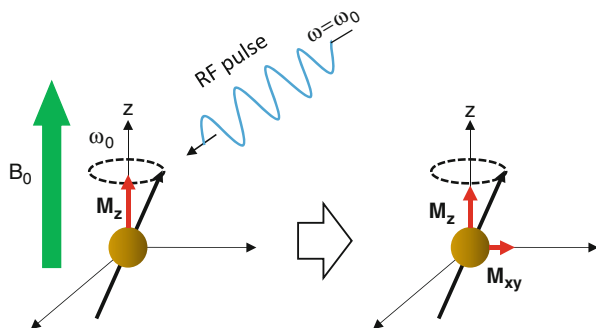
surrounding hydrogen atoms. This spin dephasing can be caused by a combination of local inhomogeneities in the magnetic field due to tissue-inherent factors (intrinsic molecular interactions) or external sources (subtle variations in the external magnetic field) [79]. When the dephasing process accounts for both intrinsic molecular interactions and extrinsic magnetic field inhomogeneities, the images produced are called T2*:

$$\frac{1}{T_{2^*}} = \frac{1}{T_2} + \gamma Bs \qquad (15.1)$$

where γBs represents the relaxation time caused by external field inhomogeneities. On the other hand, when the dephasing time accounts for the molecular interactions alone, it is called T2*-weighted (bright contrast).

MR contrast arises from proton density, as well as the chemical and physical nature of the tissues within the specimen. In most tissues, the variation of T1 and T2 between them is very small to observe good image contrast, so materials capable to enhance the contrast between the tissue of interest and the surrounding tissue are highly desired for clinical uses. These materials are called *contrast agents*, and depending over the relaxation process they act, they can be classified as T1 and T2 contrast agents, showing positive and negative contrast (bright and dark contrast, respectively). Currently, the most widely used clinical contrast agents are based on paramagnetic chelates of gadolinium [79, 80]. However, they present several drawbacks, such as short blood circulation times, poor detection sensitivity, and toxicity. These important issues resulted in the search of new and more efficient biocompatible contrast agents for MRI. In particular, those based on superpara-magnetic iron oxides nanoparticles have been intensively developed in the last years due to their tunable physicochemical properties with size, shape, composition, and assembly, showing relatively high saturation magnetization, suitable surface chemistry, and biocompatibility [81]. When placed in an external magnetic field, each magnetic nanoparticle creates a local magnetic field that, in turn, induce local field inhomogeneities in the surrounding areas. In this scenario, when water molecules diffuse within the periphery of the MNPs, the coherent precessions of surrounding water proton spins are perturbed (Fig. 15.6). The net effect is a change

Fig. 15.6 Effect of MNP on the MRI contrast signal
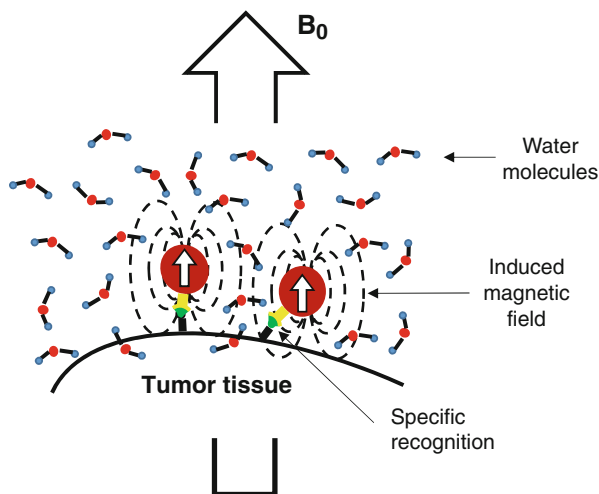
in the magnetic resonance signal, which is measured as a shortening of the longitudinal (T1, spin-lattice) and transverse (T2, spin-spin) relaxation times, amplifying the signal difference between lesions and healthy tissues. For a T1 shortening a close interaction between protons and contrast agents is required, which can be hindered by the chemical nature and thickness of the coating agent around the MNP. On the other hand, the T2 shortening is caused by the large susceptibility difference between the particles and surrounding medium resulting in microscopic magnetic field gradients [82]. In particular, when superparamagnetic iron oxide-based nanoparticles present in tissues are subjected to an external magnetic field, the large magnetic moments of the particles align in the field direction, in such a way that create large field gradients through which water protons diffuse [83]. The dipolar coupling between the magnetic moments of water protons and the magnetic moments of particles causes efficient spin dephasing and T2 relaxation leading to a decrease in signal intensity (negative contrast) [84, 85].

For example, Bae et al. and Yang et al. synthesized T1/T2 dual contrast agents through modifying Gd-DTPA molecules on the surface of magnetic iron oxide nanoparticles [86, 87], and Choi et al. designed a core-shell nanostructure $MnFe_2O_4@SiO_2@Gd_2O(CO_3)_2$ in which the T1 and T2 contrast materials were magnetically decoupled and their relaxivities simultaneously maximized by adjusting the thickness of the silica shell in between them [88]. However, ultrasmall iron oxide NPs (Fe_3O_4/Fe_2O_3) continue to be better promising candidates due to their improved biocompatibility and stabilization in aqueous solutions [89, 90]. Additionally, they are especially interesting because of their high resistance to proteins adsorption and surface modification, which allow them to overcome some physiological barriers [91]. Nowadays, we can find several commercial brands using superparamagnetic iron oxide nanoparticles based on dextran or carbohydrate coatings, such as Ferridex, Combidex, Resovist, and

AMI-288/gerumoxytrol. More recently, FeCo NPs showed better MRI contrast than iron oxide NPs, although still some toxicity-related issues remain unsolved [92].

The efficiency of the contrast agents can be described by its longitudinal and transversal relaxivities, r1 and r2, respectively, which are the proportionality constant of the measured rate of relaxation, R1 (1/T1) and R2 (1/T2), over a range of contrast agent concentration. So, accumulation of MNPs in tissues in a significant concentration will enhance the MR contrast by shortening the relaxation of water surrounding protons. In general, the relaxivities are determined by three key aspects of the magnetic nanoparticles: [93].

(i) Chemical composition: It can greatly affect the contrast-enhanced capability of the nanoparticles, since ion defects and ion doping in specific sites of the structural lattice can result in a significant change of the magnetic structure and, therefore, also in a modification of the magnetic properties. By doping Fe_3O_4 with different cations at the octahedral sites, the resulting ferrites exhibit different relaxivities according to their different mass magnetization. For example, Mn-doped ferrite nanoparticles, $MnFe_2O_4$, show higher magnetic moment per unit and relaxivity values as high as $358 \text{ mM}^{-1} \text{ s}^{-1}$ at 1.5 T [15]. Further Zn doping in the tetrahedral sites resulted in even higher saturation magnetization and, consequently, in an enhanced relaxivity of $860 \text{ mM}^{-1} \text{ s}^{-1}$ at 4.7 T [94].

(ii) Particle size and degree of aggregation: transverse relaxivity is directly proportional to the magnetic moment of the particle. The saturation magnetization of magnetic nanoparticles is strongly dependent of the particle size and distribution, among other factors such as shape or surface modification, is increasing as the particle size increases. Therefore, the enhanced MR contrast induced by nanostructured magnetic materials is directly correlated with the particle size. The relationship between the transverse relaxivity (r2) and particle size was studied in uniform-sized iron oxide nanoparticles and was found to increase from $106 \text{ mM}^{-1} \text{ s}^{-1}$ to $218 \text{ mM}^{-1} \text{ s}^{-1}$ when the particle size increases from 6 to 12 nm [95]. Another different approach to increase the cross section of magnetic nanoparticles and enhance the MR contrast properties by shortening T2-weighted relaxation time is to fabricate magnetic nanoclusters consisting of smaller nanoparticles or embedded in polymeric matrixes [96, 97].

The shortening in the longitudinal relaxation time T1 is rather due to a direct magnetic interaction between the magnetic atoms in the particle surface and the surrounding protons. For this reason, the relaxivity R1 depends more preferentially on the total surface area of the nanoparticles than on the particle size. Recently, enhanced T1 contrast was found in MnO nanoparticles when the particle size was decreased [98], and also higher surface-to-volume structures were obtained in which more active magnetic ions were exposed to water protons, exhibiting much higher R1 values [99].

(iii) Surface properties: the magnetic interactions between water and nanoparticles occur preferentially at the particle surface, so it is perfectly understandable that the use of capping agents that modify or functionalize the surface plays an important role in the magnetic properties and, therefore, in the MRI contrast enhancement. They affect the relaxation of the water molecules in several

ways, for example, favoring the diffusion of the protons to the magnetic core or also establishing hydrogen bindings. This is especially important in the nanoparticles used for in vivo experiments, since they must be biocompatible and show as low toxicity as possible. As mentioned above, there are a lot of coating materials and strategies commonly used to functionalize magnetic nanoparticles for in vivo applications. Regarding the MR imaging, hydrophobicity and shell thickness around the nanoparticle are two important factors that determine the efficiency of the enhanced MRI contrast [100, 101].

According to Koening-Keller model, the longitudinal (spin-lattice, energy exchange between water and paramagnetic ions) or transverse (spin-spin, dipolar magnetic interaction between the water proton spins and the magnetic moment of the nanoparticle) relaxivity R_i can be expressed as following [102]:

$$R_i = \frac{1}{T_i} = \frac{a}{d_{MNP}D}\gamma^2\mu^2 C_{MNP}J(\omega,\tau_D) \quad (i = 1, 2) \tag{15.2}$$

Where a is a constant, d_{MNP} is the diameter of the magnetic nanoparticle, D is the diffusion coefficient of water, μ is the magnetic moment of the nanoparticles, γ is the gyromagnetic ration of the water proton, C_{MNP} is the concentration of the nanoparticles, and $J(\omega,\tau_D)$ is the spectral density function.

Magnetic nanoparticles possess unique structural and magnetic properties that confer them with ability to interact with cells and biomolecules, making them very interesting platforms to be used in many biomedical applications. In particular, they have been carefully studied over the past few years as contrast agents for MRI applications, such as cancer imaging, cell migration, gene expression, angiogenesis, apoptosis, cardiovascular disease imaging, or molecular imaging [103]. High-resolution molecular and cellular imaging is one of the most promising applications of magnetic nanoparticles due to their powerful ability to diagnose diseases in early stages of progress, by combining molecular biology and in vivo imaging [104]. Advances in particle surface functionalization have provided nanoparticles with ligands having functional moieties able to recognize molecular and cellular targets. In this way, MNP-based molecular imaging offers a noninvasive visual representation beyond the vascular and tissue morphology imaging, providing a high-resolution monitoring of the expression and activity of specific molecules and biological processes at the cellular and molecular levels, such as in vivo cell tracking [105, 106] angiogenesis, metastasis, apoptosis detection [107, 108], and imaging of enzyme activities [109], that determine tumor behavior and response to therapy. Furthermore, these MNPs with targeted moieties can be also loaded with drugs, in such a way that they can recognize diseases (i.e., tumors) at molecular or cellular levels and play simultaneous diagnosis and treatment roles more efficiently that can be visually followed. For all of these characteristics, these multifunctional nanoplatforms become really helpful on cancer detection, allowing an individualized therapeutic treatment of the patient and drug development. It is important to remark the outstanding spatial resolution of MRI that, for example, in oncology

diagnosis applications, allows to detect millimeter-sized metastases, which is beyond the detection limit of other imaging techniques [110].

Hyperthermia

Hyperthermia refers to an abnormally high temperature found in a body, which can be of natural origin, as in any fever process, or be artificially produced to obtain therapeutical benefits. Induced hyperthermia goes back far in time to the Greek's and Roman's physicians who believed that they could cure any disease by controlling the body temperature [111].

This inspiration took concrete form in modern medicine through multiple techniques using extended sources, as infrared or microwave techniques, to help killing cancer cells by rising the body temperature above 42–45 °C. However, these approaches resulted to be nonspecific and provoked harmful secondary effects in the healthy tissues. This encouraged the search of new mechanisms capable of increasing the T of damaged areas while keeping healthy the rest of tissues. And one solution to this was found with magnetic hyperthermia and the use of magnetic nanoparticles. Magnetic hyperthermia allows to remotely induce local heat by means of the magnetic energy losses of MNP under an oscillating magnetic field. In other words, magnetic nanoparticles are able to transform electromagnetic energy into heat (Fig. 15.7). The frequencies of this oscillating magnetic field must be in the RF field, ranging from a few KHz and 1 MHz. Actually, it is a compromise between healthy radiation and a proper penetration depth into the human body, allowing the access to internal tissues and organs. It also avoids the deleterious physiological responses to high-frequency magnetic fields which include stimulation of the peripheral and skeletal muscles, cardiac stimulation, and arrhythmia [112]. It can be used with confidence for medical therapy if magnetic actuators fulfill the safety regulation requirement to be below a limiting value of $H \cdot f < 4.58 \cdot 10^8$ $A \cdot m^{-1} \cdot s^{-1}$ [113].

Basically, magnetic hyperthermia allows for [114, 115]:

(i) A localized heating of the nanoparticle-containing tissues
(ii) The selective killing of targeted cancer cells, which are thermally more sensitive than the healthy ones
(iii) A considerable reduction of many of the classical secondary effects: killing of healthy cells, long times of exposure to heating sources, or large doses of chemicals into patient's body

Although we will explain deeper the main mechanisms involved in the magnetic losses of magnetic nanoparticles that enable magnetic hyperthermia, we introduce here that they are basically three depending on the electric and magnetic properties of the materials:

(i) Eddy currents: induced in the material if this has appreciable conductivity.
(ii) Hysteresis losses: this is the main mechanism in nonconductive FM particles, involving magnetic domain creation and motion and extinction processes. In a simple approach, they can be easily quantified by the area under the MvsH hysteresis loop.

Fig. 15.7 Illustration of MNP-based hyperthermia
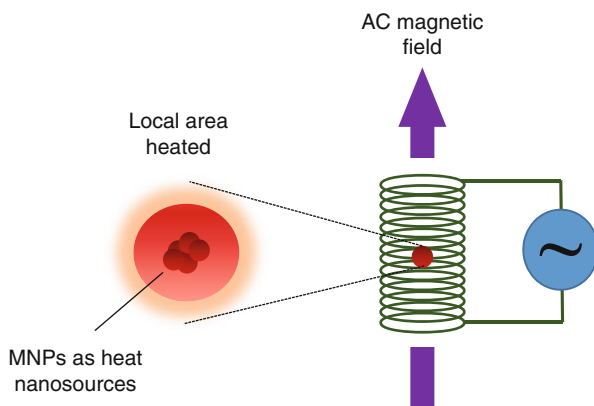
(iii) Brown and Néel relaxation times: these are the main mechanisms involved in dispersions consisting of superparamagnetic nanoparticles (particle sizes below the single-to-multidomain transition).

The use of superparamagnetic iron oxide nanoparticles is preferred in biomedical applications for several reasons: they are thought to be biocompatible and nontoxic, they show size-tunable magnetic properties with relatively high saturation magnetizations and noncoercive forces or remanence, preventing magnetic particle interactions and avoiding particle aggregation after removing the applied magnetic field.

The efficiency of MH applications depends on the instrumental parameters (externally applied magnetic field intensity and frequency) and the physicochemical properties of the colloidally stable nanosized systems (particle shape and size, distribution, concentration, embedding medium properties, or chemical, structural, and magnetic properties) [115–117] that have to be optimized for each specific application.

It is important to mention that magnetic hyperthermia as therapy has been successfully installed in some clinics and hospitals. This is the case of a setup developed in Germany [118], which comprises a clinical magnetic actuator together with a therapeutic ferrofluid of optimized iron oxide nanoparticles with an aminosilane coating that provides a fully operative clinical therapy for brain cancer in humans. It constitutes the first European approval for a medical product using magnetic nanoparticles for clinical purposes [4, 118].

Magnetic Hyperthermia Basis

The understanding of the relevant parameters which govern the magnetic hyperthermia performances of MNPs is crucial in order to maximize the heat release. Transformation of magnetic energy into heat can be analyzed in terms of specific absorption rate (SAR), (W/g^{-1}), or the specific loss power, SLP (W/m^{-3}), which are simply related by $\rho = m/V^{-1}$ $(g\,m^{-3})$ [112]. Experimentally this quantity is simply determined applying

thermodynamics by measuring the temperature increase of the system, which is related to the energy transferred to it by

$$Q = m \cdot C \cdot \Delta T = (m \cdot C + m_1 \cdot C_1) \Delta T \tag{15.3}$$

where C and C_1 are respectively the specific heat capacity per unit mass of the medium and magnetic material: $V_1 = m_1/\rho$. This quantity is related to magnetic power density, P, applied to the system by $Q/t = P \cdot V_1$, and leads to the experimental expression for SAR, which is easily determined by measuring the temperature increase of the system by

$$SAR = \frac{P \cdot V_1}{m_1} = \frac{P}{\rho} = \frac{(m \cdot C + m_1 \cdot C_1)}{m_1} \cdot \frac{\Delta T}{\Delta t} \tag{15.4}$$

Although the experimental determination of SAR is very simple, the challenge is to formulate it in terms of the applied magnetic excitation and the colloidal parameters of the ferrofluid in order to be able to optimize the performance for each precise application. The first approaches that attempt the quantification of SAR relay on the fact that small nonconducting MNPs respond linearly to the low-amplitude magnetic field excitations which are used in biomedical applications [119]. The well-known approach of Rosensweig [120] relays on this assumption and bases magnetic hyperthermia on relaxation processes for superparamagnetic (SPM) diluted ferrofluids and hysteretic dissipation in large FM-based ferrofluids. Since then, the limits of validity of the assumption of linear response have been questioned and on the last years new contributions to the field have been proposed under a more comprehensive view which intend to give a complete view of SAR produced by MNPs of any size, from SPM to FM [121, 122].

The Rosensweig's approach assumes that transformation of radio-frequency (RF) magnetic energy into heat by MNPs is due to different processes depending on the size: hysteresis losses due to magnetic domain and domain wall motion for multidomain nanoparticles, respectively [120]. And Néel and Brown relaxation mechanisms for single-domain SPM (superparamagnetic).

In multidomain particles (ferro- or ferrimagnetic), each magnetic domains has a definite direction of magnetization, which under the application of a magnetic field, changes promoting the growth of those domains with a magnetization direction along the applied magnetic field axis. This process, sketched in Fig. 15.8, is irreversible and energy losses take place as magnetization follows, in an hysteretic fashion, the cycles of the AC applied magnetic field. In this way, SAR can be easily calculated from experimental data as

$$P(H,f) = A_{hys}f \tag{15.5}$$

For particle sizes below the superparamagnetic (SPM) limit, no magnetization hysteresis appears and, therefore, no heating due to hysteresis losses occur. In this scenario, an externally applied magnetic field may produce two different effects:
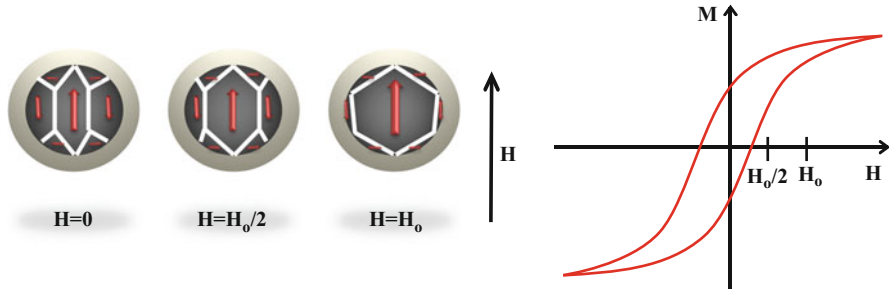
Fig. 15.8 (*left*) Magnetization grows in the direction of the applied magnetic field on multidomain MNPs (*right*) FM hysteresis loop responsible for the irreversible energy losses by reversal magnetization cycles
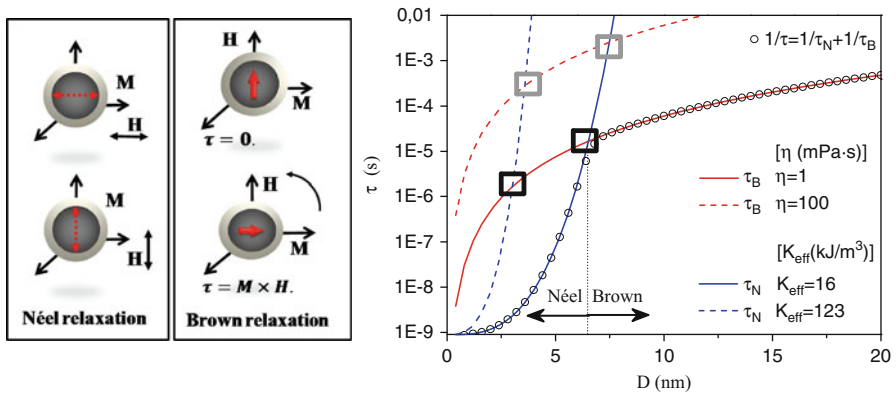
Fig. 15.9 (*left*) Néel and Brown relaxation mechanisms and (*right*) and characteristic times τ, τ_N, and τ_B as a function of NPs size calculated for magnetite parameters

(i) If it can overcome the energy barrier $E_b = KV$ of the particle, it will reorient internally M inside the crystal lattice. (ii) If, otherwise, the energy barrier is much higher, magnetization will remain in the direction minimum energy and the magnetic field will physically rotate the whole particle within the solvent following the torque, $\boldsymbol{\tau} = \boldsymbol{M} \times \boldsymbol{H}$ provoking the subsequent heat losses by reversal magnetization or friction, respectively.

These mechanisms, sketched in Fig. 15.9, are respectively known as Néel and Brown relaxations, with a characteristic times, τ_N and τ_B, defined by

$$\tau_N = \tau_0 \frac{\sqrt{\pi}}{2} \frac{\exp\left(\frac{K_{eff}V}{k_BT}\right)}{\left(\frac{K_{eff}V}{k_BT}\right)^{1/2}} \tag{15.6}$$

$$\tau_B = \frac{3\eta V_H}{k_B T} \tag{15.7}$$

where η is the viscosity of the solvent in which the particles are dispersed, k_B the Boltzmann constant, T the absolute temperature (K), V_H the hydrodynamic volume of the particle (including the nonmagnetic shell if exists), and V the magnetic volume of the core and K_{eff} effective anisotropy constant. Both mechanisms depend on particle size whereas only the Brownian contribution depends on the viscosity, η, of the embedding medium. Rosensweig assumed that both may contribute as processes occurring in parallel and their combination is accounted into an effective relaxation time $\frac{1}{\tau} = \frac{1}{\tau_B} + \frac{1}{\tau_N}$ to produce losses as follows:

$$P = \Delta U f = \frac{H_0^2 \mu_0^2 V M_s^2}{3 k_B T \tau} \frac{(2\pi f \tau)^2}{1 + (2\pi f \tau)} \tag{15.8}$$

In Figure 15.9 the Brown, Néel and effective relaxation times are illustrated by computing equations (15.6) and (15.7) for different experimental conditions: maghemite NPs with $K_{eff} = 16$ kJ/K and cobalt ferrite with $K_{eff} = 123$ kJ/K solved in water with $\eta_{water} = 1$ mPa·s and a viscous mixture $\eta_{water} = 100$ mPa·s at $T = 293$ K.

The crossover between both regimes ($\tau_N = \tau_B$), marked with squares in the figure, depends on the effective anisotropy and the viscosity of the solvent and determines which mechanism will prevail in each case. For example, strong magnets (higher K_{eff}) will show more contribution from Brown relaxation since anisotropy energy barrier is large and Néel relaxation will happen very much slowly (large τ_N). In addition for highly viscous fluids, Brown relaxation will be highly hindered, (large τ_B), and Néel relaxation will lead the heat release.

Parameters Influencing the Performance of MH in Biological Environments

In biological environments such as blood, tumor cells, or in the extracellular matrix which is a highly complex medium composed by many types of macromolecules, viscosity is high and largely variable compared to the usual water-based ferrofluids, $\eta(water) = [1]$ mPa·s, employed to validate the theoretical models of magnetic hyperthermia. For example, blood is three times more viscous than water, $\eta(blood) = [3,4]$ mPa·s [123], and in different cell locations viscosity can vary from low $\eta(cytoplasm) = [1,3]$ mPa·s, in the cytoplasm, up to large viscosity in extracell matrix $\eta(matrix) = 200$ mPa·s, i.e., SK-OV-3 ovarian cancer cells present viscosities among $\eta(SK\text{-}OV\text{-}3) = [120,260]$ mPa·s [124]. Therefore, an adequate experimental design of in vitro and in vivo MH applications requires a systematic study of the physicochemical parameters involved in the SAR performance, with values simulating the conditions of biological environments:

(i) Variable range of viscosities: $\eta = [1, 400]$ mPa·s.
(ii) MNPs are locally concentrated on the target location $\Phi = [0.1, 100]$ g/L^{-1}.
(iii) Small sizes to avoid the immune system $D = [1, 30]$ nm.

Despite of its limits of applicability, Rosensweig's model is mathematically more affordable than others and can be used to obtain general predictions about the influence of the physicochemical conditions on the heat release. There can be found in literature computations of SAR given by Eq. 15.8 Rosensweig [120, 125] varying widely the range of the parameters [126]. However, only brief results about the general behavior of SAR with respect to viscosity, particle size, concentration, and coating are presented here, since an exhaustive analysis of this subject is beyond the intention of this handbook. Therefore, within the Rosensweig model [120], there is generally predicted that (i) an optimum viscosity exists for which losses can be maximized, which remains nearly independent of the applied field magnitude but moves to lower values for large frequencies and large particles [125] and (ii) an optimum particle size (R and RH) exists which stands nearly independent of the applied field, although polydispersity widens the shape of the peak and its location and magnitude depend respectively on viscosity and frequency [125].

To find the location of the optimum viscosity or size, one can analyze the condition of maximum of losses:

$$2\pi f = {}^1\!/_{\tau_N\left(K_{eff},R\right)} + {}^1\!/_{\tau_B\left(\eta,R\right)} \tag{15.9}$$

This readily shows the intricate behavior among all parameters, which are in the origin of much part of the experimental controversies found in literature. In fact, depending on particular combinations of the experimental parameters, the profile of SAR can present a maximum, be flat, or even decay. In Figure 15.10, computations of normalized SAR versus viscosity η, for magnetite MNPs, illustrate how frequency and size can shift the maximum towards lower values of η when frequency is increased in Fig. 15.10 (left), or size is increased in Fig. 15.10 (right). However, for a different combination of experimental conditions, location of maximums or shape and magnitude of SAR can largely vary.

Reported SAR data [126], for dextran-coated magnetite based ferrofluids, show a significant dependence of losses with viscosity, from the lowest loss value $P = 57 \text{ W/g}^{-1}$ on $\eta = 1 \text{ mPa.s}$ to the maximum $P_{max} = 76 \text{ W/g}^{-1}$ on $\eta = 1.96 \text{ mPa·s}$. In another work [17], reported experimental data of polyacrylic acid-coated magnetite MNPs in water show a milder dependence on viscosity. The location of the maximum in this case was reported on $\eta = 17 \text{ mPa.s}$ with a loss value of SAR $= 37.2 \text{ W/g}^{-1}$. The decrease in SAR is due to the mechanical hindrance that increases with large viscosities producing a decay in the contribution of Brown relaxation. And, also marginal dependences on viscosity have been observed by Wang et al. [127], as reported in Table 15.1, for magnetite NPs ferrofluids in different solvents.

A further step was given by Fortin et al. [116, 128] in an interesting study made with γ-Fe$_2$O$_3$ maghemite and CoFe$_2$O$_4$ cobalt ferrite which were internalized into cultured tumor cells and exposed under MH. Both compositions entered with the same efficiency and were uptake by endosomes of 0.5 μm and confined there on high concentrations. In order to unravel the mechanism of the intracellular heating, sets of NPS with sizes in between $D = [7, 15]$ nm were dispersed in different

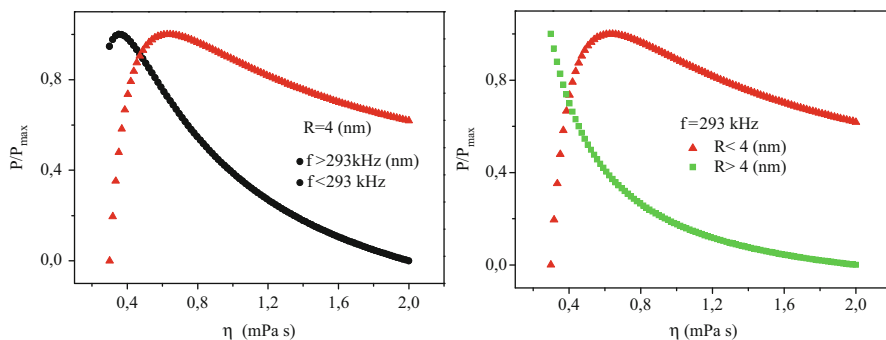**Fig. 15.10** Normalized losses obtained with simulations of Rosensweig's equation for different experimental conditions

Table 15.1 SAR data reported in Ref. [127] for magnetite ferrofluids showing the influence of solvents' viscosity

Core D (MNP)	η (mPa s) solvent				
	SAR (W/g^{-1})				
Magnetite 10 nm	0.545 Octane	0.586 Toluene	0.601 Benzene	0.696 Styrene	38.8 Oleic acid
	123	127	135	124	126

mixtures of water and glycerol covering large range of viscosities $\eta = [1, 1,000]$ mPa s and simulating different cell environments. In Fig. 15.11, it is only shown the behavior of SAR for small NPS of maghemite, $D = 7.1$ nm, and cobalt ferrite, $D = 9.7$ nm, although results for other sizes can be seen in Ref. [130]. Generally, SAR maghemite NPs shows to be independent of η into the experimental conditions while cobalt ferrite decays steeply for small sizes and afterwards presents a slight increase up to a plateau for large sizes. These results in combination with the fact that anisotropy constants for both materials are largely different, $K_{eff}(\gamma\text{-Fe}_2\text{O}_3) = 16$ kJ/m^{-3} and $K_{eff}(\text{Co Fe}_2\text{O}_4) = 123$ kJ/m^{-3}, allowed them to conclude that maghemite nanoparticle generates heat mostly by Néel relaxation and cobalt ferrite by Brown relaxation. And therefore, for intracellular environment, where viscosity is so large that Brown relaxation is mostly hindered, maghemite will be the most suitable material, since it mainly contributes with Néel relaxation (unaffected by viscosity). In fact, in their study maghemite NPS of 14 nm attain large losses, around 1,000 W/g^{-1}.

Another important parameter influencing the heating performance is size, through the intricate relationship reported above, Eq. 15.9. Experimental results show that SAR confirms Rosensweig's prediction, although, as it happens with viscosity, the location of the optimum size depends strongly on the rest of the experimental parameters. In Fig. 15.12, a compilation of different experimental data of the heat losses, SAR, reported in literature [125, 129, 130], is plotted for magnetite NPs with different sizes. It can be observed the

Fig. 15.11 SAR for small
NPS of maghemite,
$D = 7.1$ nm, and cobalt
ferrite, $D = 9.7$ nm, dispersed
in mixtures of water and
glycerol with $\eta = [1, 1{,}000]$
mPa s, plotted from
experimental data reported on
Fortin et al. [128]
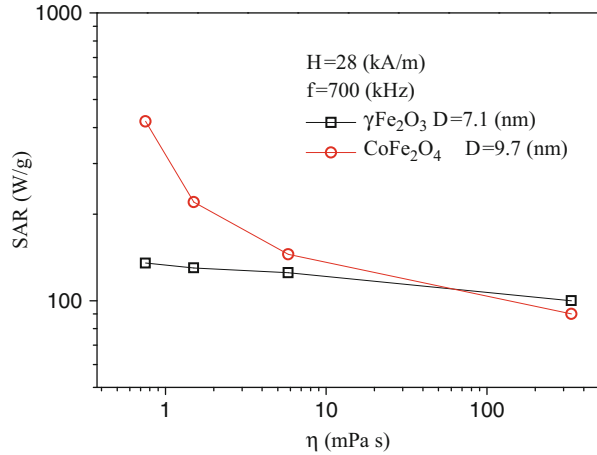
Fig. 15.12 Experimental
dependence of SAR with size
for magnetite NPs from data
reported in literature
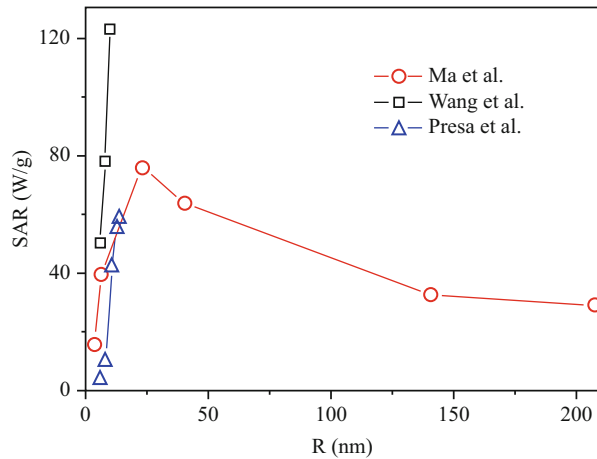
dependence on size, which for the experimental conditions in Ma et al. [129] the maximum of SAR is attained around 20 nm. For larger sizes the losses decrease mainly due to an increase volume (and so the anisotropy energy barrier), which makes the Néel relaxation process less effective.

Another example is given by Motoyama et al. [131] in Fig. 15.13, which shows the influence of particle size and frequency on the behavior of SAR (W/g^{-1}). SAR experimental data of a set of magnetite NPs were plotted versus the specific surface areas (SSA), which are directly related to particle size. The effect of frequency on the location and magnitude of the maximum of SAR for a fixed applied magnetic power (6 kW) are evident.

Since surface spins in typical 10 nm nanoparticles represent the third part of the total [132], the chemical environment of surface contributes importantly to the

Fig. 15.13 SAR (W/g^{-1}) data reported by Ref. [131] about a set of magnetite NPS with different specific surface areas (*SSA*), directly related to size, and under different frequencies and a total magnetic field power 6 kW
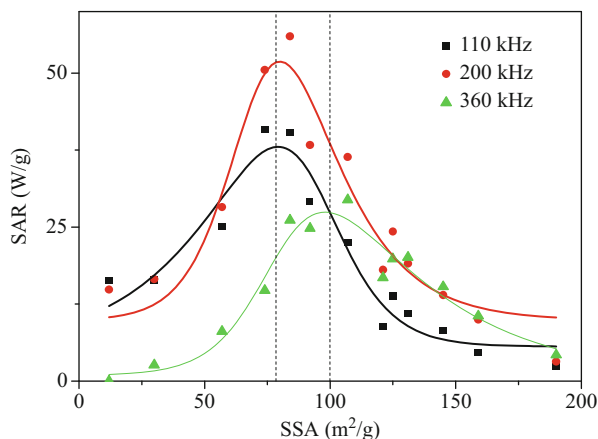
particle properties and the coating shell can affect the magnetic hyperthermia performance through different ways:

(i) By the magnetic interaction of spins between the NP surface and the coating agent, which can alter the inner spins configuration by exchange bias from the surface to the core [133].

(ii) Due to the shell thickness and the physical properties of the coating, which can hinder the heat transference from the inside of the particle to the outside or induce hydrodynamic hindrances.

Some of the influences of the coating are not computed into the Rosensweig's model, i.e., the thermal conductivity of the shell or the magnetic deviation produced to the core properties. Therefore, detailed experimental testing of the coating materials is needed before attempting to design hyperthermia applications. It has been reported by Guardia et al. [133] that very small magnetite NPs $D = [6,20]$ nm, coated with oleic acid, show a saturation magnetization, $M_{sat,}$ around 80 emu/g^{-1}, very close to the bulk value 82 emu/g^{-1}, larger than expected for small NPs. They attribute unexpectedly high value to the covalent bonding of oleic acid molecules to the surface of magnetite that attains to reduce the spin disorder at the surface. Interestingly, Wang et al. [127], in a different work, report SAR values for magnetite NPs, which we include in Table 15.2, coated with different materials, revealing that those coated with oleic acid present the best MH performance. This fact is in clear correspondence with the magnetic order enhancement that oleic acid provides to the NPs surface as measured by Guardia et al. [133].

On the other hand, surface spins may get pinned in a disordered state by the coating and by exchange bias effect, they also transfer some degree of frustration or disorder to the core spins, lowering the total magnetization of the nanoparticle. If this happens, the expected magnetic heating power will be worst. The effect of coating is crucial for drug delivery applications triggered by magnetic hyperthermia, since the effectiveness of the delivery depends of the magneto-thermal ability of the ensemble. Therefore, thermally active coating has to preserve the

Table 15.2 Effect of coating materials on SAR for magnetite NPs reported in Ref. [127]

Core D (MNP)	Surfactants SAR (W/g^{-1})			
Magnetite 10 nm	None	Amilosane	Oleic acid	Oleic acid + SDBS
	21	77	126	120
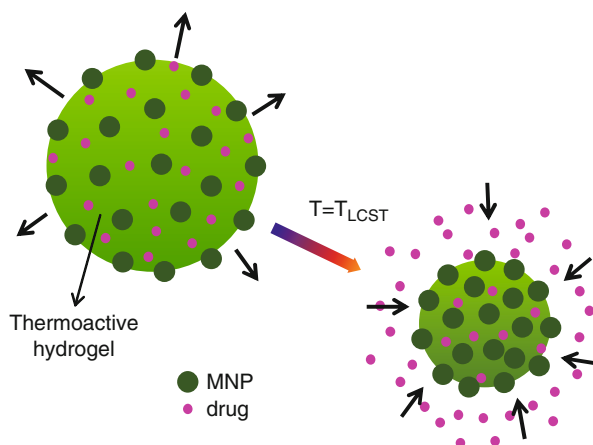
Fig. 15.14 Example of a drug delivery mechanism induced by magnetic hyperthermia

magnetic properties of the MNP core to be properly triggered by the magnetic action of the core. Poly-*N*-isopropylacrylamide (PNIPAM) is a biocompatible and thermo-reversible polymer able to generate hydrogels that undergo a coil to globule collapse for temperatures above 32 °C (which called the lower critical solution temperature LCST) [134]. The coil collapse can be exploited to expel substances (Fig. 15.14). In fact, conveniently loaded with therapeutic agents and magnetic cores, PNIPAM is the preferred candidate in drug delivery applications. Regmi et al. [135] have loaded PNIPAM/magnetite composites with mitoxantrone, an anticancer drug, and have succeeded to produce a controlled release of the drug by applying magnetic hyperthermia. By applying a magnetic field of 130 (Oe) and 380 kHz, on samples with different compositions in PNIPAM/magnetite loaded with mitoxantrone, they attained to produce a mild hyperthermia from 298 to 323 K in only 4 min and a controlled release of the drug up to the 4 % of the total [135].

Another source of controversy is the influence of magnetic material concentration on the MH performance. Obviously, below a certain concentration there is no appreciable temperature increase upon the application of a magnetic field over a ferrofluid. For biological environments this is a crucial factor for having success. Fortin et al. [128] incubated cancer cells with maghemite, with a proportion of 22.6 pg per cell, into pellets of 300 μL containing 20 million cells. For different percentages of magnetized cells Φ = [0, 20, 80, 100] %, by application of MH the temperature raised from T_{in} = 37 °C to T_f = [37.5, 38.5, 43, 44.5] °C.

However the controversy rises up for the concentration effects on the efficiency of the heating, SAR. Examples can be found in literature where for magnetite ferrofluids marginal dependences of SAR versus concentration are found (Uritzberea et al.) [136]; sharp losses are observed in Linh et al. [137], or even maximums of SAR depending on experimental conditions have been reported for iron NPs [138]. There is no common theoretical frame explaining this controversy, since it is a complex task involving the interplay of dipolar interactions on non-touching particles, exchange interactions in contacting NPs, anisotropy, and thermal energies.

Conclusions and Future Remarks

The development of the nanotechnology has allowed a drastic miniaturization of the materials and opened new frontiers for applications. The multidisciplinary approach carried out over the last decades to address fundamental and applied issues at the nanoscale have boosted the research on single nanoplatforms that are able to integrate several functionalities. This is the case of the so-called 'theranostic' nanoparticles in the biomedical field, which are able to carry out simultaneously diagnosis and therapeutic functions in diseased areas of the human body.

In this chapter we have focused on iron oxide-based nanoparticles, since they constitute the most widely accepted magnetic nanoparticles for in vivo biomedical applications due to their unique size-dependent magnetic properties, biocompatibility, and ability to be easily surface modified with both organic and inorganic coating agents. Therefore, a delicate design of structure, composition, and surface chemistry is essential to achieve the desired properties in MNP systems, such as chemical stability, specific target recognition (molecules, cells, diseased tissues), and/or multimodality, that will enable their efficient performance in final applications, such as hyperthermia and high MR imaging-contrast, both reviewed in this chapter as two of the main researched applications of magnetic nanoparticles in biomedicine. In general, the most efficient nanostructures for biomedical applications using magnetic nanoparticles consist of (i) a magnetic core responsible of the required magnetic behavior, (ii) water-soluble surface that provides them stability and compatibility in physiological fluids, and (iii) surface functionalized with bioactive ligands for specific targeting purposes. The design of these magnetic nanosystems is especially interesting in hyperthermia and MRI applications, as more efficient nanoheaters and contrast agents for MRI, respectively. The combination of adequate magnetic properties with a proper particle surface functionalization for specific target recognition not only will allow the detection of diseases in early stages of advance but also to monitor molecules and biological processes characteristic of specific evolution stages of the disease, as well as to provide a more localized therapeutic treatment (i.e., magnetically induced drug delivery) which effectiveness can be also followed in situ.

With the development of nanotechnology, novel physicochemical properties and applications have been emerging. Although it is difficult to speculate about what kind of new discoveries at the nanoscale the future will bring us, the logical advance in the particular case of magnetic nanoparticles for biomedical applications seem to be the development of multifunctional and more complex nanosystems able to more efficiently overcome several limitations that are being found today by using more simple structures. The knowledge achieved about the synthesis and nanoparticle surface functionalization has boosted the development of detection systems based on the ability of magnetic nanoparticles to recognize and attach specific targets. In the particular case of magnetic hyperthermia and MRI, the design of nanoparticle-based structures that combine a magnetic core and suitable functional moieties remains promising for a simultaneous high sensitivity detection and high space resolution for localized treatment and/or imaging. Actually, the combination of several materials with different magnetic properties in one single structure continues to be a challenge in order to obtain more efficient contrast agents that simultaneously enhance both T1 and T2 MR contrast. The accumulation of these systems in desired tissues and organs will allow us to focus more precisely in the damaged cells and leave healthy the surrounding ones. In the case of hyperthermia, a specific attachment of these heat nano-generators to the tissue of interest is essential. In this sense, the specificity shown by many toxins could be a very suitable driven force for targeting of these multifunctional nanosystems. It is also important to mention the use of hyperthermia technology as a promising tool for drug delivery systems, in which the drug release is achieved by a temperature increase magnetically induced.

However, a new world starts to be explored below nanometer scale: *atomic clusters*. In the last years, the synthesis of sub-nanometric metal clusters (Au, Ag, Cu) has been greatly investigated due to their amazing chemical, optical, and catalytic properties [139]. At this particle-size scale, their physicochemical behavior is dominated by quantum effects, which are responsible of a drastic change of their chemical, optical, and electrical properties (magnetism, photoluminescence, or catalytic activity). All these unique properties make sub-nanometric species very promising for biomedical applications. For example, their very small size could overcome problems related to overpass physiological barriers, whereas the possibility of having magnetic clusters could provide new original solutions for molecular MRI.

References

1. Ko SH, Park I, Pan H, Grigoropoulos CP, Pisano AP, Luscombe CK, Fréchet JMJ (2007) Direct nanoimprinting of metal nanoparticles for nanoscale electronics fabrication. Nano Lett 7(7):1869

2. Gibson RF (2010) A review of recent research on mechanics of multifunctional composite materials and structures. Compos Struct 92:2793
3. Bañobre-López M, Piñeiro-Redondo Y, De Santis R, Gloria A, Ambrosio L, Tampieri A, Dediu V, Rivas J (2011) Poly(caprolactone) based magnetic scaffolds for bone tissue engineering. J Appl Phys 109:07B313
4. Rivas J, Bañobre-López M, Piñeiro-Redondo Y, Rivas B, López-Quintela MA (2012) Magnetic nanoparticles for application in cancer therapy. J Magn Magn Mater 324:3499
5. Laurent S, Forge D, Port M, Roch A, Robic C, Vander Elst L, Muller RN (2008) Magnetic iron oxide nanoparticles: synthesis, stabilization, vectorization, physicochemical characterizations, and biological applications. Chem Rev 108(6):2064
6. Hadjipanayis CG, Bonder MJ, Balakrishnan S, Wang X, Mao H, Hadjipanayis GC (2008) Metallic iron nanoparticles for MRI contrast enhancement and local hyperthermia. Small 4(11):1925
7. Langer R (1990) New methods of drug delivery. Science 249(4976):1527
8. Bulte JWM, Modo MMJ (eds) (2008) Nanoparticles in biomedical imaging – emerging 1009 technologies and applications. Springer, New York
9. Lu AH, Salabas EL, Schüth F (2007) Magnetic nanoparticles: synthesis, protection, functionalization, and application. Angew Chem Int Ed 46(8):1222
10. Salgueiriño-Maceira V, Correa-Duarte MA (2007) Increasing the complexity of magnetic core/shell structured nanocomposites for biological applications. Adv Mater 19(23):4131
11. LaMer VK, Dinegar RH (1950) Theory, production and mechanism of formation of monodispersed hydrosols. J Am Chem Soc 72(11):4847
12. den Ouden CJJ, Thompson RW (1991) Analysis of the formation of monodisperse populations by homogeneous nucleation. J Colloid Interface Sci 143(1):77
13. Sugimoto T, Matijevic E (1980) Formation of uniform spherical magnetite particles by crystallization from ferrous hydroxide gels. J Colloid Interface Sci 74(1):227
14. Ocaña M, Rodriguez-Clemente R, Serna CJ (1995) Uniform colloidal particles in solution: formation mechanisms. Adv Mater 7(2):212
15. Lee J-H, Huh Y-M, Y-w J, J-w S, J-t J, Song H-T, Kim S, Cho E-J, Yoon H-G, Suh J-S, Cheon J (2007) Artificially engineered magnetic nanoparticles for ultra-sensitive molecular imaging. Nat Med 13:95
16. Cushing BL, Kolesnichenko VL, O'Connor CJ (2004) Recent advances in the liquid-phase syntheses of inorganic nanoparticles. Chem Rev 104(9):3893
17. Piñeiro-Redondo Y, Bañobre-López M, Pardiñas-Blanco I, Goya G, López-Quintela MA, Rivas J (2011) The influence of colloidal parameters on the specific power absorption of PAA-coated magnetite nanoparticles. Nano Res Lett 6:383
18. Zhang Y, Kohler N, Zhang M (2002) Surface modification of superparamagnetic magnetite nanoparticles and their intracellular uptake. Biomaterials 23(7):1553
19. Petri-Fink A, Chastellain M, Juillerat-Jeanneret L, Ferrari A, Hofmann H (2005) Development of functionalized superparamagnetic iron oxide nanoparticles for interaction with human cancer cells. Biomaterials 26(15):2685
20. D'Souza AJM, Schowen RL, Topp EM (2004) Polyvinylpyrrolidone-drug conjugate: synthesis and release mechanism. J Control Release 94(1):91
21. Berry CC, Wells S, Charles S, Aitchison G, Curtis ASG (2004) Cell response to dextran-derivatised iron oxide nanoparticles post internalisation. Biomaterials 25(23):5405
22. Bergemann C, Müller-Schulte D, Oster J, Brassard L, Lübbe AS (1999) Magnetic ion-exchange nano- and microparticles for medical, biochemical and molecular biological applications. J Magn Magn Mater 194(1–3):45
23. Rodríguez C, Bañobre-López M, Kolen'ko YV, Rodríguez B, Freitas P, Rivas J (2012) Magnetization drop at high temperature in oleic acid-coated magnetite nanoparticles. IEEE Trans Magn 48(11):3307

24. Hyeon T, Lee SS, Park J, Chung Y, Na HB (2001) Synthesis of highly crystalline and monodisperse maghemite nanocrystallites without a size-selection process. J Am Chem Soc 123(51):12798

25. Sun S, Zeng H (2002) Size-controlled synthesis of magnetite nanoparticles. J Am Chem Soc 124(28):8204

26. Sun S, Zeng H, Robinson DB, Raoux S, Rice PM, Wang SX, Li G (2004) Monodisperse MFe$_2$O$_4$ (M = Fe, Co, Mn) nanoparticles. J Am Chem Soc 126(1):273

27. Park J, An K, Hwang Y, Park J-G, Noh H-J, Kim J-Y, Park J-H, Hwang N-M, Hyeon T (2004) Ultra-large-scale syntheses of monodisperse nanocrystals. Nat Mater 3(12):891

28. Li Z, Sun Q, Gao M (2005) Preparation of water-soluble magnetite nanocrystals from hydrated ferric salts in 2-pyrrolidone: mechanism leading to Fe$_3$O$_4$. Angew Chem Int Ed 44(1):123

29. Hu F, Wei L, Zhou Z, Ran YL, Li Z, Gao M (2006) Preparation of biocompatible magnetite nanocrystals for in vivo magnetic resonance detection of cancer. Adv Mater 18(19):2553

30. López-Quintela MA, Rivas J (1993) Chemical reactions in microemulsions: a powerful method to obtain ultrafine particles. J Colloid Interface Sci 158(2):446

31. López-Quintela MA, Rivas J (1996) Nanoscale magnetic particles: synthesis, structure and dynamics. Curr Opinion Colloid Interface Sci 1(6):806

32. López-Quintela MA, Rivas J, Blanco MC, Tojo C (2003) Synthesis of nanoparticles in microemulsions. In: Liz Marzán LM, Kamat PV (eds) Nanoscale materials, vol 6. Kluwer Academic Plenum, Dordrecht, Netherlands, p 135

33. López-Quintela MA (2003) Synthesis of nanomaterials in microemulsions: formation mechanisms and growth control. Curr Opin Colloid Interface Sci 8(2):137

34. Boutonnet M, Kizling J, Stenius P (1982) The preparation of monodisperse colloidal metal particles from microemulsions. Colloids Surf A: Physicochem Eng Aspects 5(3):209

35. Woo K, Lee HJ, Ahn J-P, Park YS (2003) Sol–gel mediated synthesis of Fe$_2$O$_3$ Nanorods. Adv Mater 15(20):1761

36. Vidal J, Rivas J, López-Quintela MA (2006) Synthesis of monodisperse maghemite nanoparticles by the microemulsion method. Colloids Surf A Physicochem Eng Asp 288 (1–3):44

37. López-Pérez JA, López-Quintela MA, Mira J, Rivas J, Charles SW (1997) Advances in the preparation of magnetic nanoparticles by the microemulsion method. J Phys Chem B 101(41):8045

38. Wang X, Zhuang J, Peng Q, Li Y (2005) A general strategy for nanocrystal synthesis. Nature 437(7055):121

39. Deng H, Li X, Peng Q, Wang X, Chen J, Li Y (2005) Monodisperse magnetic single-crystal ferrite microspheres. Angew Chem Int Ed Engl 44(18):2782

40. Tartaj P, del Puerto-Morales M, Veintemillas-Verdaguer S, González-Carreño SCJ (2003) The preparation of magnetic nanoparticles for applications in biomedicine. J Phys D: Appl Phys 36:R182

41. Denizot B, Tanguy G, Hindre F, Rump E, Lejeune JJ, Jallet P (1999) Phosphorylcholine coating of iron oxide nanoparticles. J Colloid Interface Sci 209(1):66

42. Hansen T, Clermont G, Alves A, Eloy R, Brochhausen C, Boutrand JP, Gatti AM, Kirkpatrick CJ (2006) Biological tolerance of different materials in bulk and nanoparticulate form in a rat model: sarcoma development by nanoparticles. J R Soc Interface 3(11):767

43. Ahamed M (2011) Toxic response of nickel nanoparticles in human lung epithelial A549 cells. Toxicol In Vitro 25(4):930

44. Mehdaoui B, Meffre A, Lacroix L-M, Carrey J, Lachaize S, Gougeon M, Respaud M, Chaudret B (2010) Large specific absorption rates in the magnetic hyperthermia properties of metallic iron nanocubes. J Magn Magn Mater 322(19):L49

45. Deng M, Tu N, Bai F, Wang L (2012) Surface functionalization of hydrophobic nanocrystals with one particle per micelle for bioapplications. Chem Mater 24(13):2592

46. Euliss LE, Grancharov SG, O'Brien S, Deming TJ, Stucky GD, Murray CB, Held GA (2003) Cooperative assembly of magnetic nanoparticles and block copolypeptides in aqueous media. Nano Lett 3(11):1489

47. Liu X, Guan Y, Ma Z, Liu H (2004) Surface modification and characterization of magnetic polymer nanospheres prepared by miniemulsion polymerization. Langmuir 20(23):10278

48. Hong R, Fischer NO, Emrick T, Rotello VM (2005) Surface PEGylation and ligand exchange chemistry of FePt nanoparticles for biological applications. Chem Mater 17 (18):4617

49. Sahoo Y, Pizem H, Fried T, Golodnitsky D, Burstein L, Sukenik CN, Markovich G (2001) Alkyl phosphonate/phosphate coating on magnetite nanoparticles: a comparison with fatty acids. Langmuir 17(25):7907

50. Kim M, Chen Y, Liu Y, Peng X (2005) Super-stable, high-quality Fe_3O_4 dendron–nanocrystals dispersible in both organic and aqueous solutions. Adv Mater 17(11):1429

51. Kobayasi Y, Horie M, Konno M, Rodriguez-Gonzalez B, Liz-Marzan LM (2003) Preparation and properties of silica-coated cobalt nanoparticles. J Phys Chem B 107(30):7420

52. Lu Y, Yin Y, Mayers T, Xia Y (2002) Modifying the surface properties of superparamagnetic iron oxide nanoparticles through a sol−gel approach. Nano Lett 2(3):183

53. Liu Q, Xu Z, Finch JA, Egerton R (1998) A novel two-step silica-coating process for engineering magnetic nanocomposites. Chem Mater 10(12):3936

54. Cheong S, Ferguson P, Hermans IF, Jameson GNL, Prabakar S, Herman DAJ, Tilley RD (2012) Synthesis and stability of highly crystalline and stable iron/iron oxide core/shell nanoparticles for biomedical applications. Chem Plus Chem 77(2):135

55. Shen L, Laibinis PE, Hatton TA (1999) Bilayer surfactant stabilized magnetic fluids: synthesis and interactions at interfaces. Langmuir 15(2):447

56. Wan M, Li J (1998) Synthesis and electrical–magnetic properties of polyaniline composites. J Polym Sci A Polym Chem 36(15):2799

57. Massart R (1981) Preparation of aqueous magnetic liquids in alkaline and acidic media. IEEE Trans Magn MAG-17:1247

58. Deng J, Ding X, Zhang W, Peng Y, Wang J, Long X, Li P, Chan ASC (2002) Magnetic and conducting Fe_3O_4-cross-linked polyaniline nanoparticles with core-shell structure. Polymer 43:2179

59. Vestal CR, Zhang ZJ (2002) Effects of surface coordination chemistry on the magnetic properties of MnFe(2)O(4) spinel ferrite nanoparticles. J Am Chem Soc 124:14312

60. Dresco PA, Zaitsev VS, Gambino RJ, Chu B (1999) Preparation and properties of magnetite and polymer magnetite nanoparticles. Langmuir 15:1945

61. Schladt TD, Schneider K, Schild H, Tremel W (2011) Synthesis and bio-functionalization of magnetic nanoparticles for medical diagnosis and treatment. Dalton Trans 40:6315

62. Xu Z, Hou Y, Sun S (2007) Magnetic core/shell Fe_3O_4/Au and Fe_3O_4/Au/Ag nanoparticles with tunable plasmonic properties. J Am Chem Soc 129:8698

63. Stöber W, Fink A, Bohn EJ (1968) Controlled growth of monodisperse silica spheres in the micron size range. J Colloid Interface Sci 26:62

64. Tago T, Hatsuta T, Miyajima K, Kishida M, Tashiro S, Wakabayashi K (2002) Novel synthesis of silica-coated ferrite nanoparticles prepared using water-in-oil microemulsion. J Am Ceram Soc 85:2188

65. Medintz IL, Stewart MH, Trammell SA, Susumu K, Delehanty JB, Mei BC, Melinger JS, Blanco-Canosa JB, Dawson PE, Mattoussi H (2010) Quantum-dot/dopamine bioconjugates function as redox coupled assemblies for in vitro and intracellular pH sensing. Nat Mater 9:676

66. Dong A, Ye X, Chen J, Kang Y, Gordon T, Kikkawa JM, Murray CB (2011) A generalized ligand-exchange strategy enabling sequential surface functionalization of colloidal nanocrystals. J Am Chem Soc 133:998

67. Erathodiyil N, Ying JY (2011) Functionalization of inorganic nanoparticles for bioimaging applications. Acc Chem Res 44:925

68. Pileni MP (2001) Magnetic fluids: fabrication, magnetic properties, and organization of nanocrystals. Adv Func Mater 11(5):323

69. Sun SH, Zeng H, Robinson DB, Raoux S, Rice PM, Wang SX, Li GX (2004) Monodisperse MFe_2O_4 (M = Fe, Co, Mn) nanoparticles. J Am Chem Soc 126(1):273

70. Lattuada M, Alan Hatton T (2007) Functionalization of monodisperse magnetic nanoparticles. Langmuir 23:2158

71. von Werne T, Patten TE (2001) Atom transfer radical polymerization from nanoparticles: a tool for the preparation of well-defined hybrid nanostructures and for understanding the chemistry of controlled/"living" radical polymerizations from surfaces. J Am Chem Soc 123(31):7497

72. Marutani E, Yamamoto S, Ninjbadgar T, Tsujii Y, Fukuda T, Takano M (2004) Surface-initiated atom transfer radical polymerization of methyl mthacrylate on magnetic nanoparticles. Polymer 45(7):3321

73. Schmidt AM (2005) Magnetic core-shell nanoparticles by surface-initiated ring-opening polymerization of e-caprolactone. Macromol Rapid Commun 26(2):93

74. Wang B, Xu C, Xie J, Yang Z, Sun S (2008) pH controlled release of chromone from chromone-Fe_3O_4 nanoparticles. J Am Chem Soc 130:14436

75. Frey NA, Peng S, Cheng K, Sun S (2009) Magnetic nanoparticles: synthesis, functionalization, and applications in bioimaging and magnetic energy storage. Chem Soc Rev 38:2532

76. Xie J, Chen K, Lee H-Y, Xu C, Hsu AR, Peng S, Chen X, Sun S (2008) Ultrasmall c(RGDyK)-coated Fe_3O_4 nanoparticles and their specific targeting to integrin $\alpha v \beta_3$-rich tumor cells. J Am Chem Soc 130:7542

77. Ma X, Zhao Y, Liang X-J (2011) Theranostic nanoparticles engineered for clinic and pharmaceutics. Acc Chem Res 44(10):1114

78. Lübbe AS, Bergemann C, Riess H, Schriever F, Reichardt P, Possinger K, Matthias M, Dörken B, Herrmann F, Gürtler R, Hohenberger P, Haas N, Sohr R, Sander B, Lemke A-J, Ohlendorf D, Huhnt W, Huhn D (1996) Clinical experiences with magnetic drug targeting: a phase I study with 4´-epidoxorubicin in 14 patients with advanced solid tumors. Cancer Res 56:4686

79. Na HB, Song IC, Hyeon T (2009) Inorganic nanoparticles for MRI contrast agents. Adv Mater 21(21):2133

80. Caravan P, Ellison JJ, McMurry TJ, Lauffer RB (1999) Gadolinium(III) chelates as MRI contrast agents: structure, dynamics, and applications. Chem Rev 99:2293

81. Sun C, Du K, Fang C, Bhattarai N, Veiseh O, Kievit F, Stephen Z, Lee D, Zhang M (2010) PEG-mediated synthesis of highly dispersive multifunctional superparamagnetic nanoparticles: their physicochemical properties and function in vivo. ACS Nano 4(4):2402

82. Pankhurst QA, Connolly J, Jones SK, Dobson J (2003) Applications of magnetic nanoparticles in biomedicine. J Phys D: Appl Phys 36:R167

83. Stephen ZR, Kievit FM, Zhang M (2011) Magnetite nanoparticles for medical MR imaging. Mater Today 14:330

84. Corot C, Robert P, Idee JM, Port M (2006) Recent advances in iron oxide nanocrystal technology for medical imaging. Adv Drug Deliver Rev 58:1471

85. Sun C, Lee JSH, Zhang M (2008) Magnetic nanoparticles in MR imaging and drug delivery. Adv Drug Deliver Rev 60:1252

86. Bae KH, Lee K, Kim C, Park TG (2011) Surface functionalized hollow manganese oxide nanoparticles for cancer targeted siRNA delivery and magnetic resonance imaging. Biomaterials 32(1):176

87. Yang H, Zhuang Y, Sun Y, Dai A, Shi X, Wu D, Li F, Hu H, Yang S (2011) Targeted dual-contrast T1- and T2-weighted magnetic resonance imaging of tumors using multifunctional gadolinium-labeled superparamagnetic iron oxide nanoparticles. Biomaterials 32:4584

88. J-s C, Lee J-H, Shin T-H, Song H-T, Kim EY, Cheon J (2010) Self-confirming "AND" logic nanoparticles for fault-free MRI. J Amer Chem Soc 132:11015

89. Chambon C, Clement O, Leblanche A, Schoumanclaeys E, Frija G (1993) Superparamagnetic iron oxides as positive MR contrast agents: in vitro and in vivo evidence. J Magn Reson Imaging 11(4):509

90. Taboada E, Rodriguez E, Roig A, Oro J, Roch A, Muller RN (2007) Relaxometric and magnetic characterization of ultrasmall iron oxide nanoparticles with high magnetization. Evaluation as potential T1 magnetic resonance imaging contrast agents for molecular imaging. Langmuir 23(8):4583

91. Gref R, Minamitake Y, Peracchia MT, Trubetskoy V, Torchilin V, Langer R (1994) Biodegradable long-circulating polymeric nanospheres. Science 263:1600

92. Seo WS, Lee JH, Sun X, Suzuki Y, Mann D, Liu Z, Terashima M, Yang PC, McConnell MV, Nishimura DG, Dai H (2006) FeCo/graphitic-shell nanocrystals as advanced magnetic-resonance-imaging and near-infrared agents. Nat Mater 5:971

93. Huang J, Zhong X, Wang L, Yang L, Mao H (2012) Improving the magnetic resonance imaging contrast and detection methods with engineered magnetic nanoparticles. Theranostics 2(1):86

94. Jang JT, Nah H, Lee JH, Moon SH, Kim MG, Cheon J (2009) Critical enhancements of MRI contrast and hyperthermic effects by dopant-controlled magnetic nanoparticles. Angew Chem Int Ed 48:1234

95. Jun YW, Huh YM, Choi JS, Lee JH, Song HT, Kim S, Yoon S, Kim KS, Shin JS, Suh JS, Cheon J (2005) Nanoscale size effect of magnetic nanocrystals and their utilization for cancer diagnosis via magnetic resonance imaging. J Am Chem Soc 127:5732

96. Ai H, Flask C, Weinberg B, Shuai X, Pagel MD, Farrell D, Duerk J, Gao JM (2005) Magnetite-loaded polymeric micelles as ultrasensitive magnetic-resonance probes. Adv Mater 17:1949

97. Berret J-F, Schonbeck N, Gazeau F, El Kharrat D, Sandre O, Vacher A, Airiau M (2006) Controlled clustering of superparamagnetic nanoparticles using block copolymers: design of new contrast agents for magnetic resonance imaging. J Am Chem Soc 128:1755

98. Na HB, Lee JH, An K, Park YI, Park M, Lee IS, Nam D-H, Kim ST, Kim S-H, Kim S-W, Lim K-H, Kim K-S, Kim S-O, Hyeon T (2007) Development of a T1 contrast agent for magnetic resonance imaging using MnO nanoparticles. Angew Chem Int Ed 46(28):5397

99. Shin J, Anisur RM, Ko MK, Im GH, Lee JH, Lee IS (2009) Hollow manganese oxide nanoparticles as multifunctional agents for magnetic resonance imaging and drug delivery. Angew Chem Int Ed 48:321

100. Duan H, Kuang M, Wang X, Wang YA, Mao H, Nie S (2008) Reexamining the effects of particle size and surface chemistry on the magnetic properties of iron oxide nanocrystals: new insights into spin disorder and proton relaxivity. J Phys Chem C 112:8127

101. Tong S, Hou S, Zheng Z, Zhou J, Bao G (2010) Coating optimization of superparamagnetic iron oxide nanoparticles for high T2 relaxivity. Nano Lett 10:4607

102. Koenig SH, Kellar KE (1995) Theory of 1/T1 and 1/T2 NMRD profiles of solutions of magnetic nanoparticles. Magn Reson Med 34:227

103. Weissleder R, Moore A, Mahmood U, Bhorade R, Benveniste H, Chiocca E, Basilion JP (2000) In vivo magnetic resonance imaging of transgene expression. Nat Med 6:351

104. Jun YW, Lee JH, Cheon J (2008) Chemical design of nanoparticle probes for high-performance magnetic resonance imaging. Angew Chem Int Ed 47:5122

105. Bulte JWM, Douglas T, Witwer B, Zhang SC, Strable E, Lewis BK, Zywicke H, Miller B, van Gelderen P, Moskowitz BM, Duncan ID, Frank JA (2001) Magnetodendrimers allow endosomal magnetic labeling and in vivo tracking of stem cells. Nat Biotechnol 19:1141

106. de Vries IJM, Lesterhuis WJ, Barentsz JO, Verdijk P, van Krieken JH, Boerman OC, Oyen WJG, Bonenkamp JJ, Boezeman JB, Adema GJ, Bulte JWM, Scheenen TWJ, Punt CJA, Heerschap A, Figdor CG (2005) Magnetic resonance tracking of dendritic cells in melanoma patients for monitoring of cellular therapy. Nat Biotechnol 23:1407

107. Zhao M, Beauregard DA, Loizou L, Davletov B, Brindle KM (2001) Non-invasive detection of apoptosis using magnetic resonance imaging and a targeted contrast agent. Nat Med 7:1241

108. Schellenberger EA, Sosnovik D, Weissleder R, Josephson L (2004) Magneto/optical Annexin V, a multimodal protein. Bioconjugate Chem 15:1062
109. Sosnovik D, Weissleder R (2007) Emerging concepts in molecular MRI. Curr Opin Biotechnol 18:4
110. Harisinghani MG, Barentsz J, Hahn PF, Deserno WM, Tabatabaei S, van de Kaa CH, de la Rosette J, Weissleder R (2003) Noninvasive detection of clinically occult lymph-node metastases in prostate cancer. N Engl J Med 348:2491
111. Kapp DS, Hahn GM, Carlson RW (2000) Principles of hyperthermia. Decker, Ontario
112. Gü S (2004) Nanoparticles: from theory to application. Wiley-VCH, Weinheim
113. Mornet S, Vasseur S, Grasset F, Duguet E (2004) Magnetic nanoparticle design for medical diagnosis and therapy. J Mater Chem 14:2161
114. Andra W, Nowak H (1998) Magnetism in medicine: a handbook. Wiley-VCH, Berlin
115. Hergt R, Andra W, d'Ambly CG, Hilger I, Kaiser WA, Richter U, Schmidt HG (1998) Physical limits of hyperthermia using magnetite fine particles. IEEE Trans Magn 34:3745
116. Fortin JP, Wilhelm C, Servais J, Ménager C, Bacri JC, Gazeau F (2007) Size-sorted anionic iron oxide nanomagnets as colloidal mediators for magnetic hyperthermia. J Am Chem Soc 129:2628
117. Eggeman AS, Majetich SA, Farrell D, Pankhurst QA (2007) Size and concentration effects on high frequency hysteresis of iron oxide nanoparticles. IEEE Trans Magn 43:2451
118. magforce. www.magforce.com
119. Hergt R, Dutz S, Röder M (2008) Effects of size distribution on hysteresis losses of magnetic nanoparticles for hyperthermia. J Phys: Condens Matter 20:385214
120. Rosensweig RE (2002) Heating magnetic fluid with alternating magnetic field. J Magn Magn Mater 252:370
121. Hergt R, Dutz S, Ziesberger M (2010) Validity limits of the Néel relaxation model of magnetic nanoparticles for hyperthermia. Nanotecnology 21:015706
122. Carrey J, Mehdaoui B, Respaud M (2011) Simple models for dynamic hysteresis loop calculations of magnetic single-domain nanoparticles: Application to magnetic hyperthermia optimization. J Appl Phys 109:083921
123. Tefferi A (2003) A contemporary approach to the diagnosis and management of polycythemia vera. Curr Hematol Rep 2(3):237
124. Kuimova MK (2012) Mapping viscosity in cells using molecular rotors. Phys Chem Chem Phys 14(37):12671
125. Wang X, Tang J, Shi L (2010) Induction heating of magnetic fluids for hyperthermia treatment. IEEE Trans Mag 46:1043
126. Zhang LY, Gu HC, Wang XM (2007) Magnetite ferrofluid with high specific absorption rate for application in hyperthermia. J Mag Mag Mater 311:228
127. Wang X, Gu H, Yang Z (2005) The heating effect of magnetic fluids in an alternating magnetic field. J Magn Magn Mater 293:334
128. Fortin JP, Gazeau F, Wilhelm C (2008) Intracellular heating of living cells through Néel relaxation of magnetic nanoparticles. Biophys Lett 37:223
129. Ma M, Wu Y, Zhou J, Sun Y, Zhang Y, Gu N (2004) Size dependence of specific power absorption of Fe_3O_4 particles in AC magnetic field. J Magn Magn Mater 268:33
130. de la Presa P, Luengo Y, Multinger M, Costo R, Morales MP, Rivero G, Hernando A (2012) Study of heating efficiency as a function of concentration, size, and applied field in γ-Fe_2O_3 nanoparticles. J Phys Chem 116:25602
131. Motoyama J, Hakata T, Kato R, Yamashita N, Morino T, Kobayashi T, Honda H (2008) Hyperthermic treatment of DMBA-induced rat mammary cancer using magnetic nanoparticles. Biomagnetic Res Techn 6(4):1
132. Cótica LF, Santos IA, Girotto EM, Ferri EV, Coelho AA (2010) Surface spin disorder effects in magnetite and poly(thiophene)-coated magnetite nanoparticles. J Appl Phys 108:064325
133. Guardia P, Batlle-Brugal B, Roca AG, Iglesias O, Morales MP, Serna CJ, Labarta A, Batlle X (2007) Surfactant effects in magnetite nanoparticles of controlled size. J Magn Magn Mater 316:e756

134. Dionigi C, Piñeiro Y, Riminucci A, Bañobre-López M, Rivas J, Dediu V (2013) Regulating the thermal response of PNIPAM hydrogels by controlling the adsorption of magnetite nanoparticles. Appl Phys A (in press)
135. Regmi R, Bhattarai SR, Sudakar C, Wani CS, Cunningham R, Vaishnava PP, Naik R, Oupicky D, Lawes G (2010) Hyperthermia controlled rapid drug release from thermosensitive magnetic microgels. J Mater Chem 20:6158
136. Urtizberea A, Natividad E, Arizaga A, Castro M, Mediano A (2010) Specific absorption rates and magnetic properties of ferrofluids with interaction effects at low concentrations. J Phys Chem C 114:4916
137. Linh PH, Thach PV, Tuan NA, Thuan NC, Mahn DH, Phuc NX, Hong LV (2009) Magnetic fluid based on Fe_3O_4 nanoparticles: preparation and hyperthermia application. J Phys: Conf Ser 187:012069
138. Martinez-Boubeta C, Simeonidis K, Serantes D, Conde-Leborán I, Kazakis I, Stefanou G, Peña L, Galceran R, Balcells L, Monty C, Baldomir D, Mitrakas M, Angelakeris M (2012) Adjustable hyperthermia response of self-assembled ferromagnetic Fe-MgO core–shell nanoparticles by tuning dipole–dipole interactions. Adv Funct Mater 22(17):1
139. Calvo-Fuentes J, Rivas J, López-Quintela MA (2012) Synthesis of subnanometric metal nanoparticles. In: Bhushan B (ed) Encyclopedia of nanotechnology. Springer Verlag, Heidelberg, Germany, p 2639

Mechanical Properties of Nanostructured Metals

16

Peter M. Anderson, John S. Carpenter, Michael D. Gram, and Lin Li

Keywords

Dislocations • Mechanical properties • Multilayers • Nanocrystal • Plasticity

Polycrystals

This section is divided into four subsections. The subsection on synthesis and structure treats electrodeposition, severe plastic deformation, and mechanical alloying. It highlights features that affect mechanical properties such as texture, grain size and shape, internal stress, twinning, dislocations, and point defects. The mechanical properties subsection contrasts yield strength, ductility, strain hardening, strain-rate sensitivity, creep, and fatigue in conventional versus nanocrystalline metals. Underlying deformation mechanisms are then discussed in terms of deformation-mechanism maps and intragranular slip versus grain-boundary-mediated regimes. Finally, modeling and simulation approaches are presented in terms of atomistic versus continuum methods.

P.M. Anderson (✉) • M.D. Gram
Department of Materials Science and Engineering, The Ohio State University, Columbus, OH, USA
e-mail: anderson.1@osu.edu; gram.7@osu.edu

J.S. Carpenter
Materials Science and Technology Division, Los Alamos National Laboratory, Los Alamos, NM, USA
e-mail: carpenter@lanl.gov

L. Li
Department of Metallurgical and Materials Engineering, The University of Alabama, Tuscaloosa, AL, USA
e-mail: lin.li@eng.ua.edu

Synthesis and Structure

Nanocrystalline (NC) materials can be made by using five general approaches: solid-state processing, liquid-phase processing, vapor-phase processing, chemical synthesis, and electrochemical synthesis. The principal synthesis techniques include severe plastic deformation, mechanical attrition, mechanical alloying, crystallization from an amorphous phase, sputtering, electrodeposition, chemical vapor deposition, and physical vapor deposition. The three most common techniques are described.

Electrodeposition (ED)

Electrodeposition (ED) is a technique within the broader group of electrochemical synthesis methods. It offers significant advantages to synthesize NC materials [1, 2], including (1) production of a large variety of nanograin materials, including pure metals, alloys, and composite systems; (2) high quality with less porosity; (3) few size and shape limitations; (4) precise control of grain size; and (5) control of structure over length scales down to $\sim$ nm, providing potential benefits to mechanical performance, e.g. nanotwins [3].

Electrodeposited nickel is one of the first systematically studied NC metals and the superior properties motivated one of the first large-scale industrial applications of nanomaterials in the mid-1990s. Figure 16.1a–c shows respective bright-field, dark-field, and electron diffraction images for ED NC Ni with average grain size $d_{avg} = 10$ nm [2]. The bright-field and dark-field micrographs suggest negligible porosity and no abnormally large grains. The nonuniform intensity along the diffraction pattern rings indicates similar or preferred grain orientations, suggesting microtextures over small volumes. The resulting grain-size distribution in Fig. 16.1d can be approximated by a typical logarithmic normal distribution.

Alloying additions can promote grain-boundary (GB) segregation, which can be used to achieve thermodynamically stable or metastable states. Schuh and co-workers were able to systematically vary grain size over a broad 2–140 nm range by controlling the W composition in NC Ni–W alloys [4]. Figure 16.2 illustrates refinement of the NC structure with increasing W content. The plot in Fig. 16.2d shows a systematic decrease in average grain size (d_{avg}) with composition (at.% W), for both cathodic and reverse-pulse conditions. The symbols highlighted by the three arrows in Fig. 16.2d correlate to the specific bright-field images in Fig. 16.2a ($d_{avg} = \sim$100 nm, $\sim$2.5 at.% W), Fig. 16.2b ($d_{avg} = \sim$20 nm, $\sim$15 at.% W), and the high-resolution TEM image in Fig. 16.2c ($d = \sim$2–4 nm, $\sim$23 at.%W).

Electrodeposition can also produce hierarchical structures, e.g. Cu with submicron grain size and a high density of nm-scale twin boundaries [3]. These nanotwins improve both the mechanical strength and ductility, yet maintain high electric conductivity. This is shown in Fig. 16.4c (see section 'Strength and Ductility').
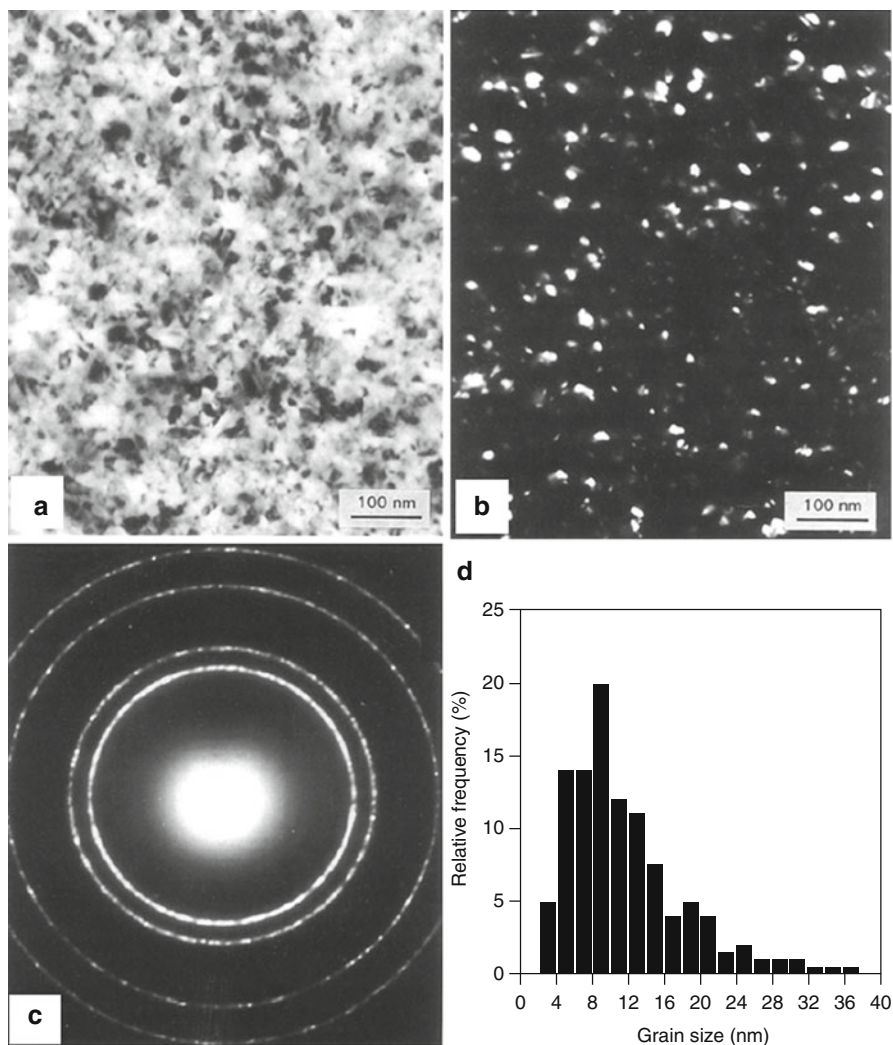
Fig. 16.1 (**a**) Bright-field, (**b**) dark-field, (**c**) electron diffraction pattern, and (**d**) grain-size distribution in nanocrystalline (NC) nickel, average grain size $d_{avg} \sim 10$ nm (Reprinted figure from [2] with permission from Springer copyright 1995)

Severe Plastic Deformation (SPD)

Severe plastic deformation (SPD) can be used to refine grain size from the micron to submicron/nanoscale. In principle, any method to introduce large plastic strain in metals may lead to a reduction in grain size. Two methods, developed by Valiev and co-workers, have contributed to the widespread use of SPD to process bulk ultrafine-grained materials [5]. They are (1) severe shear straining under high-pressure torsion (HPT) and (2) equal-channel angular pressing (ECAP). Both methods involve
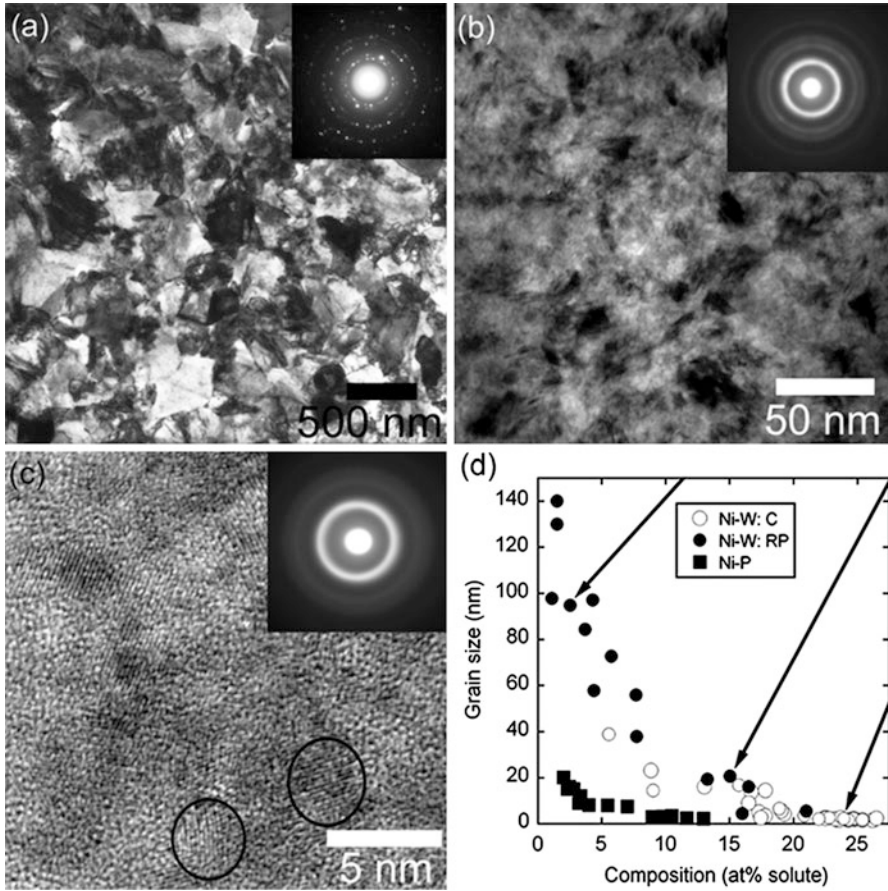
Fig. 16.2 (**a–c**) Bright-field TEM images and selected area diffraction patterns showing decreasing grain size with increasing solute content in Ni–W specimens. (**d**) Decrease in grain size *d* with increasing at.% W, in Ni–W specimens electrodeposited under cathodic (C) and periodic reverse-pulse (RP) current conditions. Data for the Ni–P system is also shown (Reprinted figure from [4] with permission from Elsevier copyright 2007)

hydrostatic pressure, thereby enabling large shear deformation, and also repeated deformation, thereby permitting large stored energy and grain refinement. SPD methods have been used to fabricate bulk nanostructured samples and billets out of different metals and alloys, including commercial alloys and intermetallics [5].

Although SPD can produce NC structures with $d_{avg} < 100$ nm, ultrafine-grain (UFG) structures with submicron grain size ($d_{avg} \sim 200$–500 nm) are more typical. The resulting microstructure is very dependent on deformation path and sequence, but generic features are (1) nonequilibrium GBs; (2) nanotwins, stacking faults, and intragranular cells [6]; (3) segregation clusters [7]; and (4) nanoparticles. These nanostructured elements within submicron grains can provide additional strengthening.

Mechanical Alloying (MA)

Mechanical alloying (MA) produces nanostructured materials via repeated deformation (welding, fracturing, and rewelding) of powder particles in a dry, high-energy ball. This severe deformation causes structural disintegration of a coarse-grained (CG) structure [8]. Advantages of MA relative to other methods include (1) ease of use, (2) ability to make large quantities of powders with smaller ultimate grain size than most other SPD methods, and (3) ability to incorporate 2nd phases or elements that stabilize grain size [9]. For instance, Chookajorn and Schuh [9] used MA to prepare NC W–Ti. Their thermodynamic models identified a W–Ti alloy (20 % Ti) to be thermodynamically stable in NC form. Indeed, a 20 nm grain size can be maintained at 1,100 °C for >1 week. Some drawbacks to MA are (1) introduction of defects and crack nucleation sites induced by deformation, (2) excessive coarsening, and (3) contamination due to abrasion of grinding media.

Mechanical Properties

Strength and Ductility

A striking feature of NC materials is their extraordinary strength compared to corresponding bulk materials. Grain refinement is a well-known strategy for strengthening. The yield strength σ_y of polycrystalline metals often is observed to increase with decreasing grain size d according to the empirical Hall–Petch (H–P) relationship:

$$\sigma_y = \sigma_0 + k_{HP}/d^{1/2} \qquad (\text{Hall–Petch relation}) \qquad (16.1)$$

where σ_0 is a reference stress as $d \to \infty$ (i.e. a single-crystal limit) and k_{HP} is the H–P coefficient. A physical basis for this behavior involves dislocation pileups at GBs. According to Eq. 16.1, metals with nanoscale grains should be much stronger than their CG counterparts, depending on the value of k_{HP}. Indeed, high strength and hardness values exceeding 1 GPa have been observed in NC metals.

Figure 16.3a summarizes experimental measurements of Cu yield strength as a function of grain size [10]. Two features are noted. First, k_{HP} in Eq. 16.1 decreases for $d < 100$ nm, based on the divergence of the blue line (data) and the green dashed line (extrapolated from the microcrystalline region). Second, when $d < 25$ nm ($d^{-1/2} = 0.2$ nm$^{-1/2}$), the trend in the plot becomes ambiguous. Some results suggest a plateau while others show a negative slope or 'inverse H–P' effect. The breakdown of the H–P relation has been attributed to a change in deformation mechanism, e.g. from strength controlled by dislocation pileups against GBs to that controlled by GB-mediated processes such as GB sliding or dislocation nucleation. Other data for Ni in Fig. 16.3b display a H–P relationship down to $d \sim 10$ nm [11, 12].
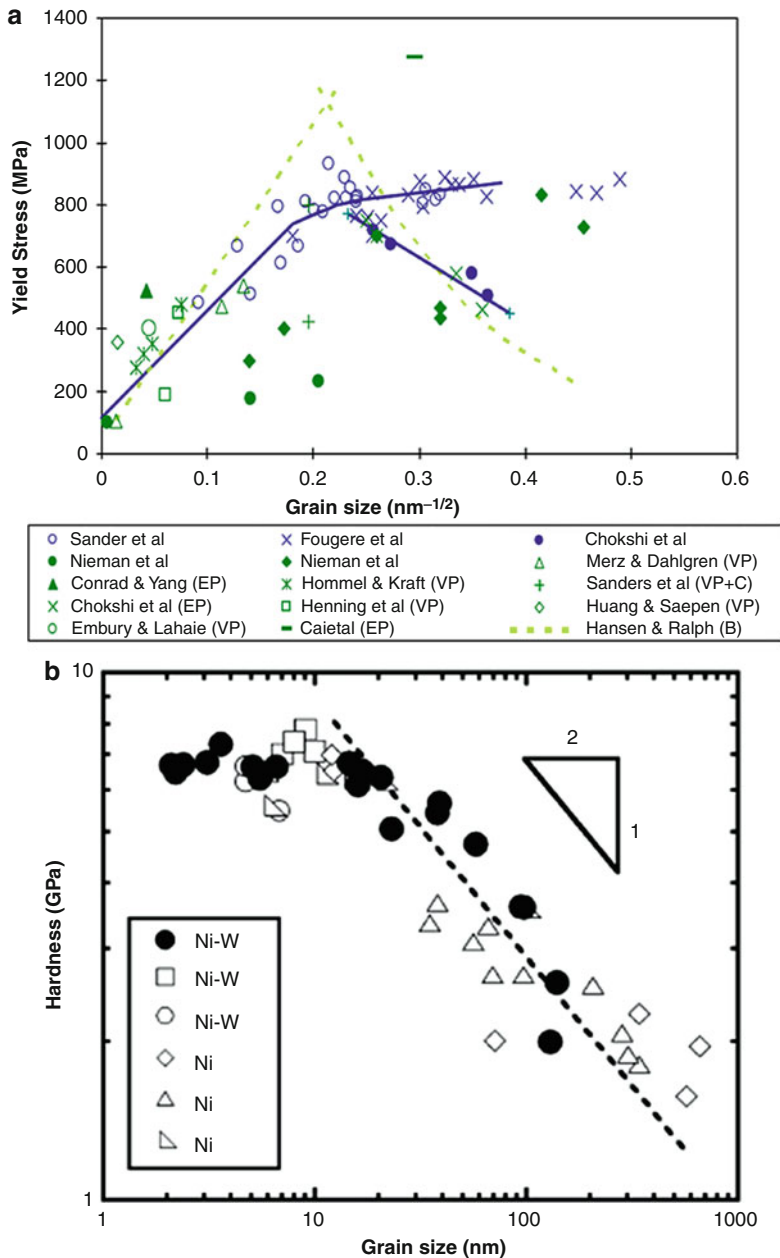
Fig. 16.3 (**a**) Yield strength versus (grain size)$^{-1/2}$ for Cu, from various sources. A different trend is observed in the nanocrystalline (NC) regime (Reprinted figure from [10] with permission from Elsevier copyright 2006). (**b**) Hardness versus grain size d for Ni and Ni–W alloys. A classical Hall–Petch relationship (indicated by the *dashed line*, slope = 2) is not obeyed for $d < 10$ nm (Reprinted figure from [4] with permission from Elsevier copyright 2007)

It is acknowledged that when $d \sim$ nm, GB processes are enhanced and may control plastic deformation. One issue under debate is the critical grain size at which the H–P relation breaks down. Computer simulations by Schiotz and Jacobsen report a maximum flow strength in Cu at $d_{\text{crit}} = 10–15$ nm, where the underlying deformation mechanism shifts from dislocation-mediated plasticity to GB sliding [13]. Further, Van Swygenhoven et al. [14] identify $d_{\text{crit}} \sim 8$ nm for Cu, below which the plastic deformation is dominated by GB sliding. Argon and Yip [15] propose a model demonstrating a 'strongest size', below which a GB shear mechanism kicks in.

Such a maximum strength, however, has not been fully confirmed experimentally. Trelewicz and Schuh [12] use nanoindentation to evaluate the deformation behavior of NC Ni–W alloys over the range $d_{\text{avg}} = 3$ to 150 nm. The results thus span the classical H–P regime and regions that deviate from the H–P trend. They observe H–P scaling to break down at $d_{\text{avg}} \sim 10–20$ nm. A marked transition to inhomogeneous, glass-like flow (i.e. shear banding) occurs at the smallest grain size approaching the amorphous limit. The rate and pressure dependence of deformation is found to be greatest at approximately the same d_{avg} for onset of the H–P breakdown. These experimental data support a mechanistic crossover into the amorphous metal regime.

Most basic studies of NC strengthening consider single-phase, single-element material. Strengthening can also be achieved using solutes and second-phase particles, which can play significant roles in stabilizing NC structures [9]. Nanotwin structures containing a high density of twin boundaries display considerable strength improvement yet retain good ductility [3].

Good ductility and ultrahigh strength at room temperature are desirable for structural applications. However, NC metals and alloys often suffer from limited ductility [16, 17]. Figure 16.4a provides representative data for tensile elongation to failure versus yield strength for NC metals [17]. Note that (1) ultrahigh strength in NC metals is achieved at the expense of ductility and (2) tensile elongation to failure <10 % for a majority of NC materials. Early NC materials displayed low ductility due to processing flaws and artifacts [18, 19]. However, lack of strain hardening and specimen geometry can also limit uniform tensile elongation. The grain size in NC metals is too small to involve intragranular dislocation interaction and entanglement [20]. Consequently, conventional strain hardening arising from dislocation storage is reduced dramatically. This intrinsic limitation promotes plastic instabilities such as shear band formation or necking. Three cases are presented that demonstrate enhancement of ductility in NC metals.

First, *an engineered grain-size distribution* can impart both high strength and ductility [20, 21]. Figure 16.4b displays the stress–strain behavior of Cu that is synthesized by heavy cold work and then post-processed via various thermal–mechanical treatments [22]. Case E shows that bimodal grain-size distributions can impart an optimal combination of strength and ductility. The corresponding TEM image (inset) shows large grains embedded in an ultrafine-grain/NC matrix, achieved by cold rolling to produce a fine-grain structure and then secondary recrystallization at 200 °C to obtain larger grains. The benefits of a bimodal
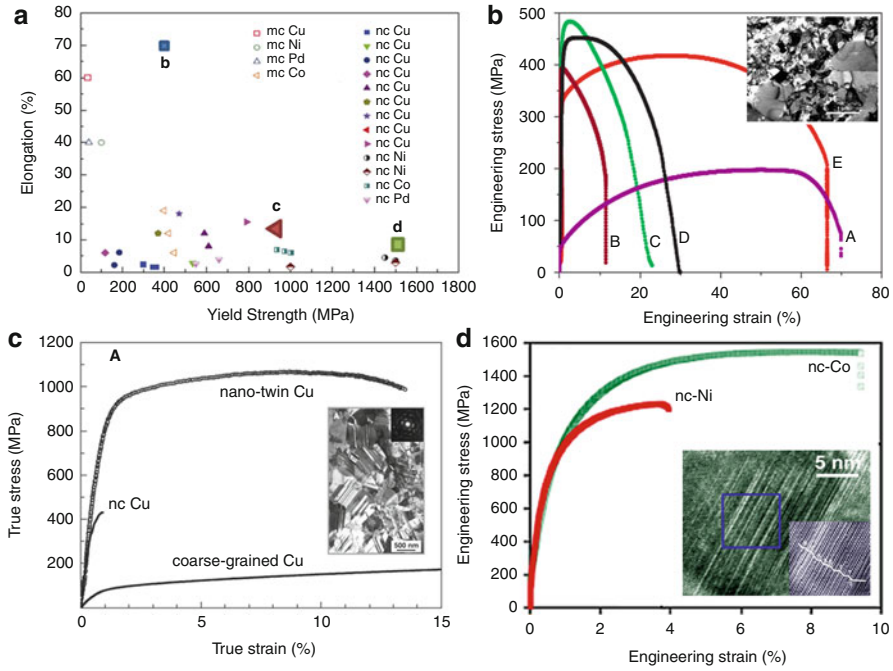
Fig. 16.4 (**a**) Tensile elongation to failure versus yield strength for NC metals (Reprinted figure from [17] with permission from Elsevier copyright 2007). (**b**–**d**) Stress–strain response for (**b**) UFG Cu with bimodal grain-size distribution synthesized by heavy cold work and then post-annealed (Reprinted figure from [22] with permission from Nature Publishing Group copyright 2007), (**c**) nanotwin Cu (Reprinted figure from [3] with permission from Elsevier copyright 2005), and (**d**) NC-Co with deformed twins (Reprinted figure from [29] with permission from The American Physical Society)

structure on ductility and strength have been demonstrated in many metal and alloy systems [23, 24]. An explanation in terms of micromechanisms is still under discussion. A general assumption is that large grains can work harden and suppress crack formation and/or propagation, while NC grains provide high strength and hardness [25].

Second, *growth twins* can impart enhanced ductility, as evidenced in nanotwinned Cu produced by Lu and co-workers [3]. Figure 16.4c shows that this material exhibits tensile strength ∼1 GPa, 10× that of a CG counterpart, yet it retains >10 % tensile ductility. The inset shows an ultrafine-grain structure with a high density of nanoscale growth twins. The twins create a lamellar structure within grains, with submicron dimensions parallel to the twin boundaries (the plastically soft direction) and nm dimensions transverse to twin boundaries (the plastically hard direction). Thus, dislocation glide/accumulation is easier parallel versus transverse to the twin boundaries. The work suggests a benefit to combined strength–ductility when general

high-angle GBs in NC metals are replaced with nanoscale coherent twin boundaries [26, 27].

Third, *designing NC metals with a propensity for deformation faults or twins* may improve combined strength/ductility. For example, Fig. 16.4d shows that NC-Co [28], a hexagonal close-packed material with a low stacking-fault energy, exhibits tensile strengths $\sim$2–3$\times$ that of CG counterparts, yet the strain to failure is $\sim$6–9 % [29]. This is attributed to a high density of thin ($\sim$10 nm) twins formed during deformation (inset, Fig. 16.4d). This suggests NC materials with low stacking-fault energy may be intrinsically more ductile. It offers a potential strategy to improve ductility in high stacking-fault metals – namely, to add secondary or tertiary elements to reduce stacking-fault energy and thus promote deformation faults.

Strain Hardening and Strain Recovery

Strain hardening – the capacity of a material to resist further plastic deformation – is a key factor to impart uniform tensile elongation in NC metals. In CG metals, strain hardening is attributed predominately to increased dislocation density and dislocation interactions within grains. In NC metals, dislocation content is stored predominately at grain boundaries and not inside grains, so that the apparent strain hardening behavior in NC metals deviates dramatically from that in CG metals.

Extraction of meaningful strain-hardening rates in NC metals is complicated by a potentially large residual stress state and grain-size distribution. In CG materials, the majority of grains are assumed to be plastically deforming at the macroscopic yield stress, where the macroscopic plastic strain is $\sim$0.2 %. However, Brandstetter et al. [30] found this assumption to be incorrect for NC Ni. Instead, the grain-size distribution produces a significant deviation in yield strength from grain to grain, thus extending the elastic–plastic regime [31]. In contrast, NC Al films with a more homogeneous grain-size distribution show a much sharper elastic–plastic transition [32].

Therefore, grain-size distribution must be taken into account when quantitative comparisons of 'strain hardening' are made. Strain hardening can be raised by increasing the width of the grain-size distribution [22] or texture [33], although doing so may simultaneously reduce the yield strength. In principle, a nonuniform residual stress state can also extend the elastic–plastic transition strain, even when grain size is uniform. A wide grain-size distribution in NC metals can also impart recovery of plastic strain [31]. Interrogation of UFG-NC Al by in situ synchrotron X-rays suggests that after compressive deformation, tensile residual stresses develop in the larger (UFG) grains, promoting backward dislocation glide, even at room temperature [34]. Experimental and computational results agree that an inhomogeneous stress distribution can also drive plastic strain recovery [35, 36].

Additional strategies to enhance strain hardening in NC metals include the introduction of growth twins, formation of deformation twins, and the elimination of flaws produced during synthesis [37–39].
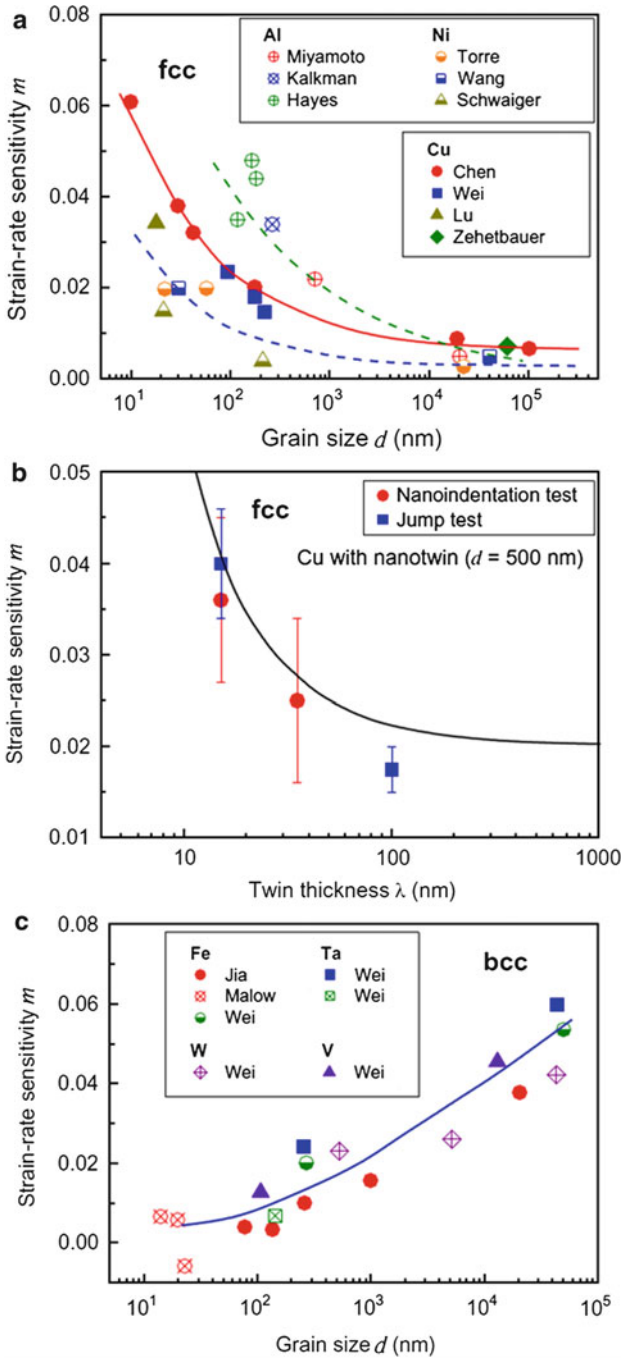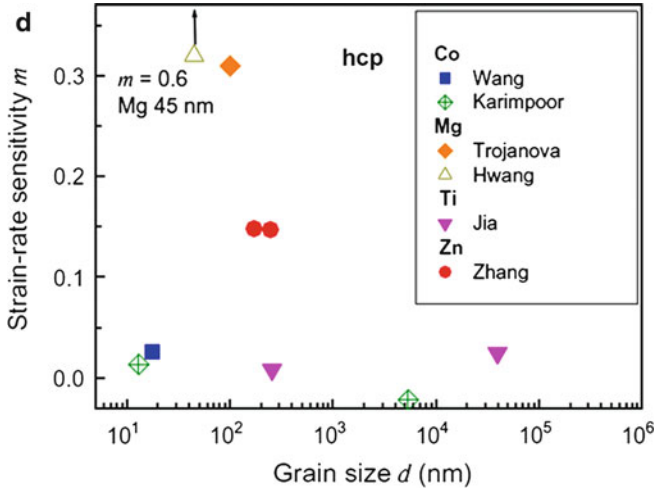
Fig. 16.5 (continued)

Fig. 16.5 (**a**) Strain-rate sensitivity of (**a–b**) FCC, (**c**) BCC, and (**d**) HCP metals as a function of grain size d or twin thickness λ. The *curve* in (**b**) is calculated using the GDAS model [51]; all other curves are visual guides (Reprinted figure from [40] with permission from Elsevier copyright 2012)

Strain-Rate Sensitivity

The dependence of the flow strength σ on the rate of strain $\dot{\varepsilon}$ is described by the strain-rate sensitivity:

$$m = \frac{d\ln\sigma}{d\ln\dot{\varepsilon}} \; \text{(strain-rate sensitivity)} \tag{16.2}$$

For $T < T_{\text{melt}}/3$, m is $\sim$0.01 for FCC metals and $\sim$0.1 for BCC metals with conventional, micron-scale grain size. Figure 16.5a [40] shows that m for several FCC metals increases monotonically with decreasing d_{avg}, with $m > 0.1$ for NC FCC metals [41–50]. Figure 16.5b shows similar trends for Cu with nanotwins [51]. The large m achieved in both cases can help suppress localization at large deformation rates. In contrast, Fig. 16.5c shows that m for BCC metals has the opposite dependence on grain size, with $m < 0.1$ for NC BCC metals [46, 52–57]. Figure 16.5d indicates that HCP metals have no distinct trend [28, 58–62]. Variation in m is due to variations in processing route, structure, purity, grain-size distribution, as well as loading method.

Indentation tests have been used to determine m by noting that hardness H is proportional to flow stress [63], so that σ in Eq. 16.2 can be replaced by H. Also, $\dot{\varepsilon} = \dot{h}/h$ is assumed, where h is the indentation depth. However, the validity of indentation tests at low strain rates has been called into question due to the accumulation of thermal drift over long test times. Attempts to circumvent this problem include indentation strain-rate jump tests (Fig. 16.5b); they furnish m values for NC Ni comparable to those from uniaxial compression [64].

Insight into the dominant deformation mechanism is often interpreted in terms of the activation volume for plastic deformation:

$$V = \frac{\sqrt{3}kT}{m\sigma} \;\text{(activation volume for plastic deformation)} \qquad (16.3)$$

where k is Boltzmann's constant and T is the absolute temperature. For CG FCC metals, $V \sim 100b^3$, which is the activation volume associated with cutting of forest dislocations. For NC FCC metals, $V \sim (1–20)b^3$, indicating a change in deformation mechanism [10]. Asaro and Suresh discuss several mechanisms and corresponding activation volumes [65]. They conclude that the dominant deformation mechanism cannot be determined unambiguously from activation volume data, due to the range of grain size in NC samples and the similarity of activation volumes for a number of deformation mechanisms. Deformation mechanisms in NC materials are discussed in more detail within the section 'Deformation Mechanisms'.

Wear Resistance

NC materials generally are often produced as films with large hardness. This suggests coating applications and motivates an interest in wear properties. During frictional sliding experiments, the microstructure in the vicinity of the worn surface may not be stable. Frictional sliding studies on NC Ni confirm this, showing significant grain coarsening in the sliding track [66]. Rupert and Schuh [67] systematically studied the wear response of NC Ni–W with d_{avg} ranging from 3 to 47 nm. Over this span, the H–P relation is known to break down and the dominant plastic deformation mechanism shifts from intra- to intergranular [67]. As d_{avg} decreases, the wear resistance of NC Ni–W alloys monotonically increases. Grain growth has indeed been observed when initial grain size is < 10 nm, yet the wear resistance of the finest NC materials is high. The repetitive sliding leads to a modest amount of grain growth and grain-boundary relaxation, which in turn leads to local hardening in the wear track. This evolution in microstructure can, in fact, improve the mechanical properties of the alloy. This fortuitous outcome might be exploited to integrate NC materials into mechanical systems.

Fatigue and Fracture

Quantifying damage tolerance in NC metals is essential for future applications as structural materials or coatings on engineering components. However, more conventional fatigue test methods present difficulties due to the small volume of NC metals produced. Further, variations in grain size, grain structure, and/or defect density complicate fatigue behavior [16]. Despite this, some general trends have emerged, primarily for FCC metals.

NC metals display enhanced fatigue lifetimes under stress-controlled conditions, based on S-N data (e.g. see the recent review [68]). Fatigue performance is controlled primarily by the initiation and propagation of fatigue cracks. Hanlon and colleagues [69, 70] show that NC metals have lower fatigue crack growth

thresholds but greater crack propagation. This is attributed to less tortuous crack paths and reduced crack closure (crack-tip plasticity). Thus, the enhanced fatigue lifetimes are attributed to greater resistance to crack initiation – an outcome of increased yield strength with grain refinement [71]. In CG metals, cracks can initiate from surface extrusions and intrusions caused by persistent slip bands [72]. Although surface defects are cited as crack initiation sites in NC metals, the persistent slip mechanism is thought to be suppressed in NC metals. Boyce and Padilla [73] suggest that crack initiation is preceded by the formation of highly coarsened grains, thus enabling the persistent slip mechanism. Also, internal defects and inclusions are recognized as crack initiation sites because NC metals have a reduced critical crack length [68].

During cyclic strain-controlled tests, NC Ni exhibits higher cyclic stresses than CG Ni, as well as cyclic softening [74–76]. Moser and colleagues [74] suggest that dislocation sources residing in grain boundaries are exhausted during the early hardening phase, allowing diffusional mechanisms to dominate at higher cycles. Consistent with this explanation and the enhanced strain-rate sensitivity of FCC NC metals, they report a reduction in strain amplitude with increased load-controlled frequency, perhaps indicating suppression of GB sliding or diffusional climb [68].

Deformation Mechanisms

The deviation of NC properties from extrapolations of classical scaling laws for CG metals has motivated extensive research into the underlying mechanisms. These deviations include increases in strain-rate sensitivity and strength as well as the controversial inverse H–P relation below a critical grain size. The large density of GB networks is expected to influence deformation mechanisms. Figure 16.6 shows a deformation-mechanism map by Yamakov et al. [77]. It is divided into three regions, based on fundamental physical processes observed in molecular dynamics simulations. Region I encompasses larger grain size and/or higher stacking-fault energy (SFE), where plastic deformation is dominated by full (perhaps extended) dislocations that nucleate from GBs and propagate across grains. Region II involves smaller grain size and/or lower SFE, where incomplete dislocations nucleate and propagate across grains. These generate stacking-faults within grains that inhibit subsequent dislocation propagation and cause strain hardening. Region III corresponds to the smallest grain size or lowest stress regime, where no dislocations are present and deformation is controlled by GB-mediated processes. These processes can involve coupled GB sliding and GB diffusion, producing an inverse H–P effect. However, this map is informed from MD simulations for which strain rates are unrealistically large (10^7–10^9 s^{-1}) [78, 79]. Thus, it is imperative to substantiate these results with experimental data. The following sections focus on dislocation nucleation from GBs and GB-medicated processes, with an emphasis on experimental observations and mechanistic model verification.
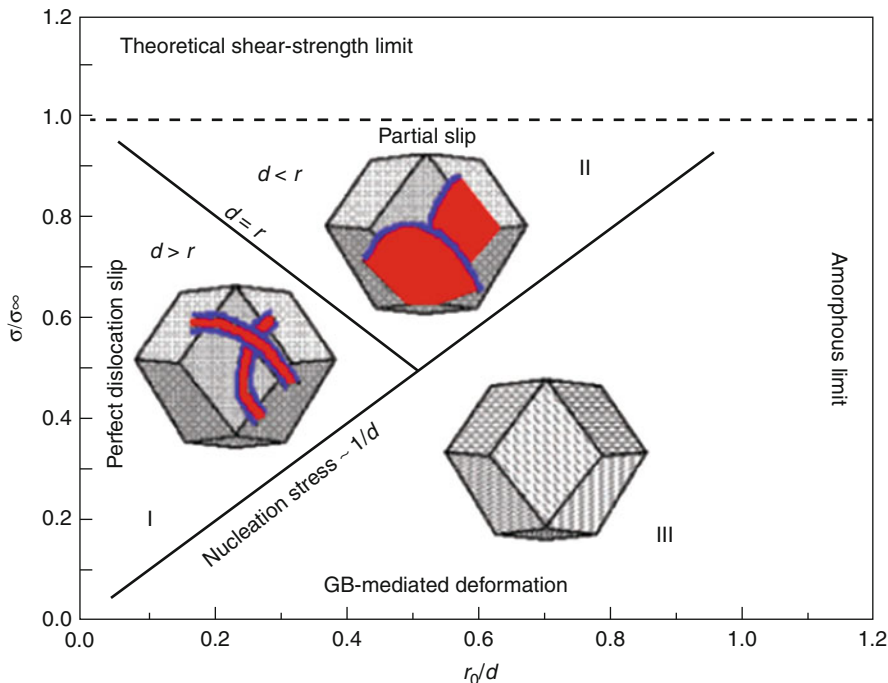
Fig. 16.6 Deformation-mechanism map for NC FCC metals at low temperature, based on MD simulations. Region I = intragranular slip of perfect dislocations, Region II = intragranular slip of partial dislocations, and Region III = GB-mediated deformation. Reduced units of stress (σ/σ_∞) and inverse grain size (r_0/d) are used, where σ_∞ and r_0 are functions of the stacking-fault energy and elastic properties (Reprinted figure from [77] with permission from Nature Publishing Group copyright 2004)

Intragranular Slip

Dislocation emission from GBs is substantiated by MD simulations, transmission electron microscopy (TEM), and in situ X-ray diffraction (XRD). In the simulations, a key deformation process is dislocation nucleation at a GB, glide across grain interiors that are free of obstacles, and absorption into the opposite GB. In this context, GBs act as dislocation sources as well as dislocation sinks [80]. Initial experimental studies have used ex situ TEM. Kumar et al. report isolated dislocations and evidence of sporadic dislocation networks in deformed Ni specimens ($d_{avg} \sim 30$ nm) [81]. However, the low dislocation density in grain interiors is unable to account for the magnitude of imposed plastic strain. In NC Ni, in situ XRD observations report peak broadening upon loading and reversal of the broadening upon unloading [82]. These results point to the lack of storage of dislocation debris after room-temperature deformation. Similar conclusions are reached in other TEM studies of many post-deformation NC specimen [83, 84].

Where do dislocations in NC metals go if they are the dominant carriers of plasticity? In situ TEM tensile testing of NC Ni by Hugo et al. [83] and Kumar et al. [81] indicate 'pervasive dislocation nucleation and motion' down to

Fig. 16.7 (**a**) HRTEM micrograph of a NC Ni grain after tensile testing at liquid nitrogen temperature. (**b**) Twin boundary indicated by an *arrow* in Region A. (**c**) Evidence of several full dislocations in Region B (Reprinted figure from [84] with permission from American Institute of Physics copyright 2006)
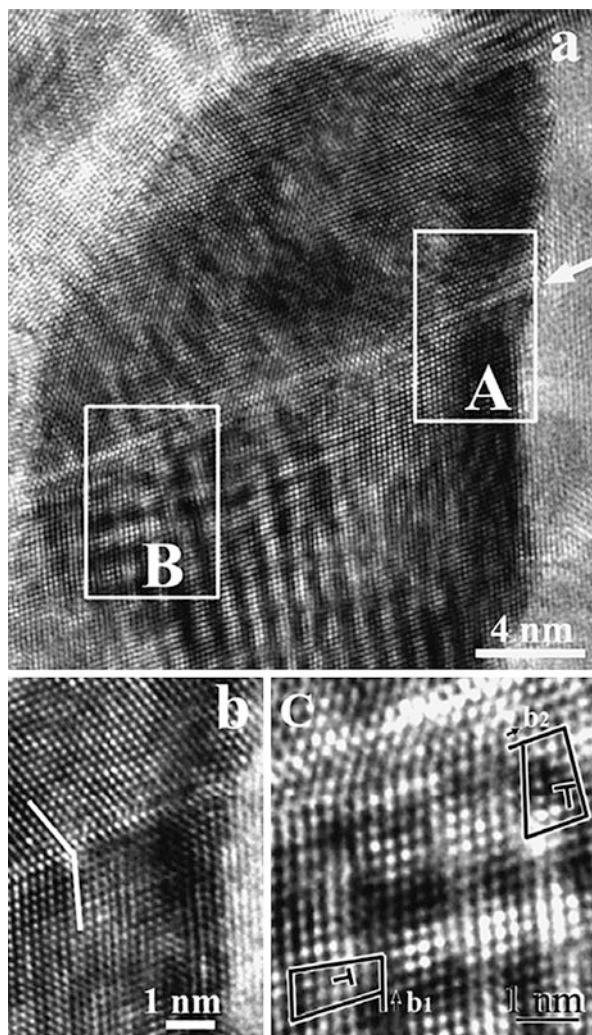
$d \sim 10$ nm. Also, Youseff et al. [85] provide evidence for dislocation pileups at GBs in NC Cu down to $d_{avg} = 30$ nm. Using high-resolution TEM (HRTEM) during in situ deformation of NC Ni, Shan [86] reports that full dislocations are frequently trapped near GBs for d as small as 5 nm. Further, GB relaxation processes produce dislocation absorption, recombination, and annihilation.

The formation of deformation twins and stacking-faults can contribute to NC deformation [87–89]. Deformation twins have been observed by TEM in NC Al [87], NC Cu, and NC Ni [89]. Wu and Zhu argue an inverse grain-size effect on twinning in NC FCC metals [88], so that twinning is more prevalent as d decreases. This trend is opposite to that in CG metals. Figure 16.7a is a HRTEM image of a deformation twin (white arrow) in a NC Ni grain after tensile deformation [84].

The twin boundary is clearly revealed in Fig. 16.7b, which is an enlarged view of Region A. These twins are believed to form during deformation and act as either sources or barriers to dislocations. Full dislocations have been activated and are found near the twin boundary, as shown in Fig. 16.7c.

Analytical models [65, 90] based on dislocation theory have been proposed to explain the operation of partial dislocations or twins in NC metals. The resolved shear stress at which a full dislocation is emitted from GBs can be calculated as

$$\tau = \frac{2\alpha G b}{d} \text{ (nucleation, full dislocation)} \tag{16.4}$$

where G is the elastic shear modulus, b is the magnitude of Burgers vector of a full dislocation, d is the grain size, and the coefficient α usually ranges between 0.5 and 1. On the other hand, the resolved shear stress to nucleate two partials can be expressed as [65, 90]

$$\tau = \frac{Gb}{3d} + \frac{d-s}{d}\frac{\gamma}{b} \text{ (nucleation, partial dislocation)} \tag{16.5}$$

where s is the equilibrium distance between two partials at zero applied stress and γ is the stacking-fault energy. As d approaches s, Eq. 16.5 predicts a smaller stress. For FCC metals for which $\gamma/Gb = 1/500 \sim 1/100$, Eqs. 16.4 and 16.5 predict that τ for partials is lower than that for full dislocations if $d < 50$ nm. Both equations also predict $\tau \sim 1/d$ instead of a $1/\sqrt{d}$ dependence predicted from dislocation pileup models. The crossover to partial dislocation nucleation reflects a simple concept that when $d < s$, the leading partial will traverse the grain before the trailing partial can nucleate. Furthermore, Zhu et al. conclude that s is much larger in the NC versus CG regime, based on a partial dislocation emission model [91]. This enhances the possibility of nucleating leading partials rather than full dislocations. It also rationalizes enhanced twining and stacking-fault formation during deformation of NC materials [88].

GB-Mediated Deformation

GB-mediated deformation is expected to be more important in NC metals due to a higher density of GBs. The $\tau \sim 1/d$ dependence in Eqs. 16.4 and 16.5 suggests that dislocation-mediated plasticity will require prohibitively large stress to operate as d decreases. In this regime, MD simulations reveal GB deformation involving GB sliding [92], Coble creep-like diffusive processes involving grain growth and coalescence [93], and GB migration via atomic shuffling [93]. Stress-coupled GB motion [94] is another possible GB-mediated mechanism, but it has not been established for NC metals.

Experimental observations of GB sliding and grain rotation in NC metals are controversial [95, 96] because individual and adjacent NC grains are difficult to image during in situ TEM. In contrast, postmortem TEM studies clearly indicate growth of deformed NC grains [97]. Gianola et al. conclude that grain growth can

be an active room-temperature deformation mode in abnormally ductile NC Al thin films, based on coupled micro-tensile thin-film testing, in situ synchrotron diffraction experiments, and postmortem TEM [98]. Legros and co-workers report stress-assisted grain growth at room temperature in NC Al films with initial average grain size $\sim$40–90 nm, using in situ TEM [99]. The grain growth appears to have preceded dislocation activity and involved GB migration and grain coalescence. Select grains were observed to grow to several times the film thickness, surrounded by a sea of NC grains with initial dimensions.

Figure 16.8 illustrates fast grain growth under stress in the vicinity of a crack originating from the right in this sequence [99]. Initially, (a) grains A and B were not connected but had already grown to 200–300 nm. Significant prior dislocation activity is evident based on visible dislocation loops and segments in these grains. Growth and coalescence commenced by the motion of the lower right part of grain A toward grain B (a–c) at a rate of 5–10 nm s^{-1}. This speed is two orders of magnitude greater than 'normal' GB speeds. Legros et al. argue that their observations are consistent with a shear-coupled GB motion model proposed by Cahn and co-workers [94]. More recent experiments by Rupert [100] have pinpointed shear stress as the driving force for mechanically induced grain growth. However the role of stress-driven GB migration and other GB deformation processes in governing mechanical behavior is still unclear.

To summarize, NC metals exhibit new deformation regimes that involve GBs as the primary sources and sinks for dislocations as well as diffusive and sliding phenomena. The fundamental data to relate stress, temperature, strain rate, and grain size are not developed sufficiently, so complete deformation-mechanism maps are not yet available. Indeed, the variation in grain size and the possibility of grain growth during deformation make this a particularly challenging task.

Modeling and Simulation

Molecular Dynamics Simulations

Deformation mechanisms of NC materials have been investigated extensively using MD simulations. These atomistic simulations provide the most widely accepted descriptions of NC deformation [13, 77, 92, 93, 101–104], which are characterized in terms of (1) GB-mediated and (2) dislocation-mediated processes. For GB-mediated modes, GB sliding is usually accompanied by atomic shuffling and stress-assisted free-volume migration [13, 92]. The processes that induce shear deformation along GB planes can also cause motion normal to GBs [94]. This deformation mode may contribute to stress-assisted grain growth during room-temperature NC deformation [99]. Further, triple junctions can move and collective GB sliding [92] and grain rotation may be required to satisfy compatibility.

Dislocation activity can be prevalent in the NC regime [101–104] but unlike CG metals, dislocations are controlled by interaction with GBs instead of other dislocations. A widely accepted picture is that dislocations nucleate at GBs, propagate across the entire grain, and are absorbed into GBs [103]. MD simulations of FCC
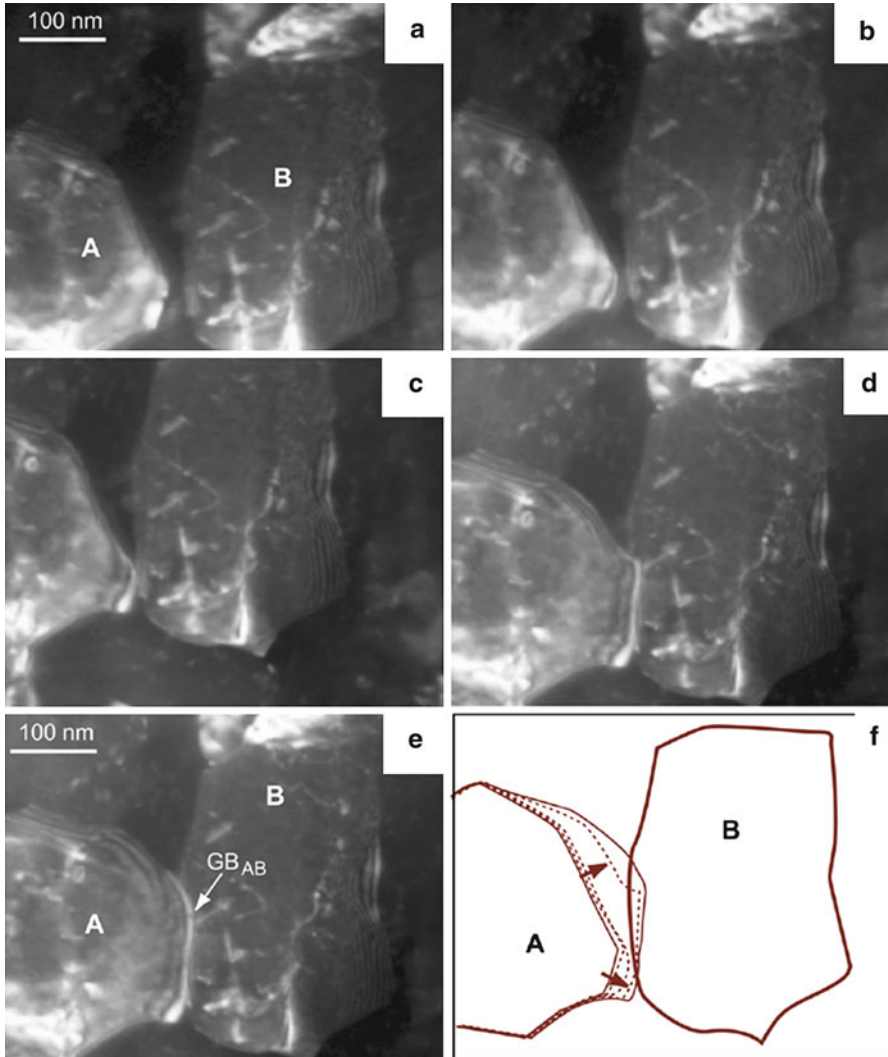
Fig. 16.8 In situ TEM observations of grain growth occurring by fast grain-boundary (*GB*) motion in stressed NC aluminum films at 300 K, at various times $t = $ (**a**) 0 s, (**b**) 1.2 s, (**c**) 18.16 s, (**d**) 29.04 s, and (**e**) 29.24 s. (**f**) Successive positions of the GB (Reprinted figure from [99] with permission from Elsevier copyright 2008)

metals show partial dislocation nucleation at GB stress concentrators. Leading and trailing partial dislocations may nucleate at different locations in a GB or even at different GBs. Trailing partials are not always observed if the simulated material has low stacking-fault energy or if the simulated time is too short [101, 102]. If a trailing partial is not nucleated, a twin fault may form by nucleation and propagation of a partial in an adjacent plane [89].
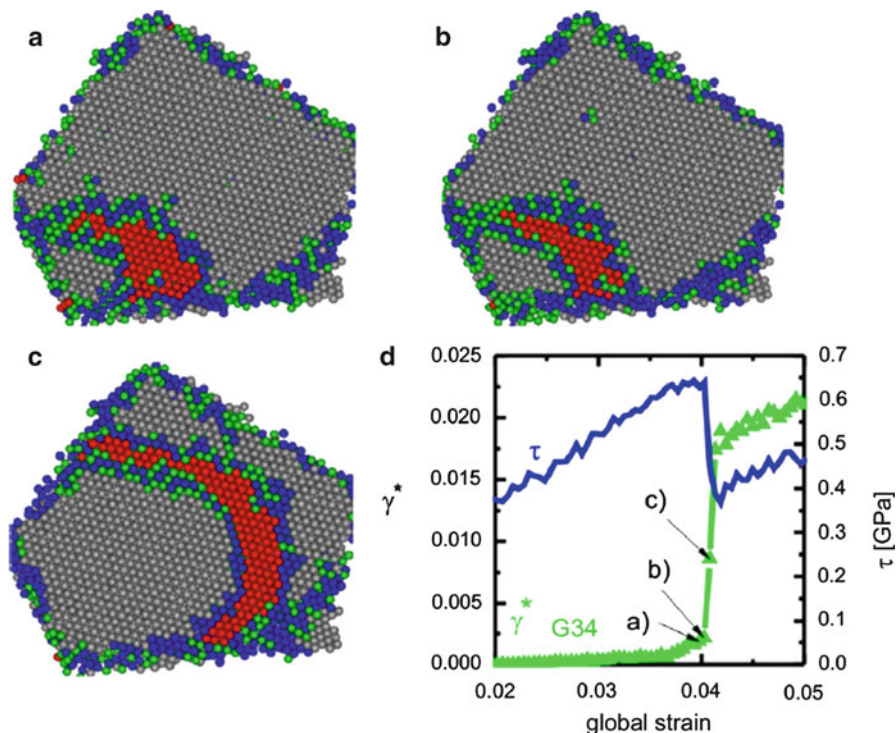
Fig. 16.9 MD simulations of intragranular slip showing grain cross section with (**a**) leading/trailing partial dislocations pinned at GBs and stacking-fault (*red atoms*), (**b**) continued GB pinning at higher stress, and (**c**) breakaway and unstable dislocation propagation across grain. (**d**) Grain-averaged resolved shear strain γ and shear stress τ versus applied global strain on the polycrystal (Reprinted figure from [104] with permission from Elsevier copyright 2008)

Expansion of a dislocation loop across a grain can be hindered if the loop is pinned at GB ledges, as shown in Fig. 16.9a from the MD simulations of Bitzek et al. [104]. The strength of the pinning site is influenced by the relative orientation of the Burgers vector to the GB ledge geometry. Depinning is both thermally and mechanically driven. At the critical state in Fig. 16.9b, the grain-averaged resolved shear stress on the slip plane reaches a maximum, and the loop propagates unstably across the grain, as shown in Fig. 16.9c. The grain-averaged plastic strain jumps by an amount $\propto b/d$ and the resolved shear stress spontaneously drops (Fig. 16.9d).

These analyses help inform meso- and continuum-scale simulations, which tend to operate at much larger length and time scales appropriate to experimental conditions.

Continuum Approaches

Continuum approaches to capture the mechanical response of NC metals can be categorized into (a) two-phase, (b) dislocation slip, and (c) grain-boundary types.

Two-phase models are motivated by an assumption that the volume fraction of GBs increases as grain size decreases. Dislocation and GB-mediated processes are weighted according to grain size. Fu et al. propose a 'core and mantle model' to investigate how yield stress depends on grain size in the NC regime [105]. The outer core represents material that work hardens in the vicinity of GBs, where multiple slip systems are activated to satisfy compatibility. The thickness t of the outer core is assumed to be $\propto d^{1/2}$. This introduces a new $1/d$ dependent term in the H–P equation, giving rise to a deviation from conventional H–P behavior at small d.

Wei and Anand [106] describe a model to study inelastic deformation and failure in FCC NC metals. Cohesive elements along the grain boundaries simulate GBs. The GB elements obey evolution equations for normal and tangential tractions across GBs, and the grain interior obeys a single-crystal plasticity relation. The volume fraction of 'GB phase' and the flow stress in the 'grain interior phase' are assumed to increase with decreasing d. The simulation results for NC Ni suggest a transition from 'grain interior' to 'GB shearing' deformation as d decreases from 50 to 10 nm. Further, low ductility in NC Ni is attributed to failure due to GB shearing and the resulting cavitation.

Asaro et al. adopt the concept of dislocation nucleation at GBs and calculate an athermal critical nucleation stress for full as well as partial lattice dislocations [65, 90]. The critical stress $\propto 1/d$, thus introducing a length scale. The resulting model predicts nucleation of partial rather than full dislocations for $d < 30$ nm in pure Ni. Zhu [107] extends this work by including a lognormal grain-size distribution and demonstrates how a variation in grain size affects the operative deformation mode. For example, partial dislocation emission is predicted to dominate in NC Ni with uniform $d = 20$ nm, but it switches to full dislocation emission if a large variation is present, i.e., a variance of ~100 in a lognormal grain-size distribution with mean $d = 20$ nm.

Wei and Gao describe a GB-mediated model with heterogeneous GB diffusion and sliding. This model is able to reproduce the extraordinary plastic recovery observed in NC Al thin films [108]. The grain interior is assumed to deform only by anisotropic elasticity and each GB is assigned either high or low values of diffusivity and sliding viscosity. This heterogeneous feature is essential to obtain required magnitudes of internal stress, which drives plastic recovery.

Li and Anderson propose a meso-scale 'quantized crystal plasticity' (QCP) model that is informed by the MD simulation results in Fig. 16.9, where dislocation depinning produces a spontaneous (~1 %) jump in grain-averaged plastic strain [35, 109]. A constitutive law similar to Fig. 16.9d is programmed into a crystal plasticity formalism where any of the 12 FCC slip systems in a NC grain spontaneously operates at a critical τ. Figure 16.10a shows a polycrystalline model with randomly oriented grains that are colored according to tensile Schmid factor. Figure 16.10b shows that the grain-averaged shear stress and plastic strain within individual grains evolve in a manner similar to the MD results in Fig. 16.9d. Several characteristic NC mechanical properties – enhanced strength, extended elastic–plastic strain, recoverable plastic strain – are captured provided there is a large grain-to-grain variation in critical τ. The simulations are applied to diffraction experiments on polycrystalline NC Ni specimens loaded in tension

Fig. 16.10 Quantized crystal plasticity (QCP) model. (**a**) Polycrystal model with $10 \times 10 \times 10$ grains, colored according to tensile Schmid factor. Inset shows the 'quantized' plastic shear strain in a grain, $\gamma_{target} \propto 1/d$, due to a single slip event. (**b**) Predicted evolution of local shear strain (*lower*) and local shear stress (*upper*) versus average plastic strain in the polycrystal (Reprinted figure from [35] with permission from Elsevier copyright 2009)
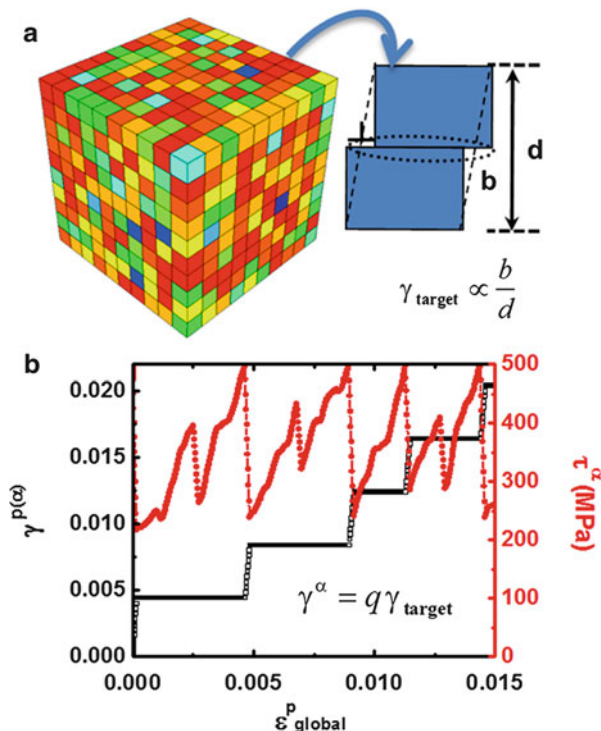
(Fig. 16.11a). Upon unloading, grains can take on a large statistical variation in residual stress (Fig. 16.11c) that does not correlate with Schmid factor (Fig. 16.11b). The predicted evolution in residual stress in <200> and other diffracting groups (Fig. 16.11d) captures trends from diffraction experiments [109]. The QCP simulations suggest that local yield in NC metals is not dictated primarily by local grain orientation (Schmid factor) as in CG metals, but rather by local pinning strength within grains. Further, they suggest a large distribution in pinning strength that is random, so that soft and hard grains exist within the same diffraction group (Fig. 16.11e–g). Such close coupling of simulations and mechanical and diffraction experiments offers a promising approach to study NC metals.

Multilayer Thin Films

Multilayer thin films are a special class of composite materials with two, nanometer length-scales – grain size and layer thickness. Both scales confine the mechanics and kinetics of deformation. Approaches to fabricate these composites range from bottom-up methods such as deposition to top-down methods such as severe plastic deformation. A key goal is to effectively control the distribution of heterophase interface densities, homophase grain-boundary densities, geometric distribution of
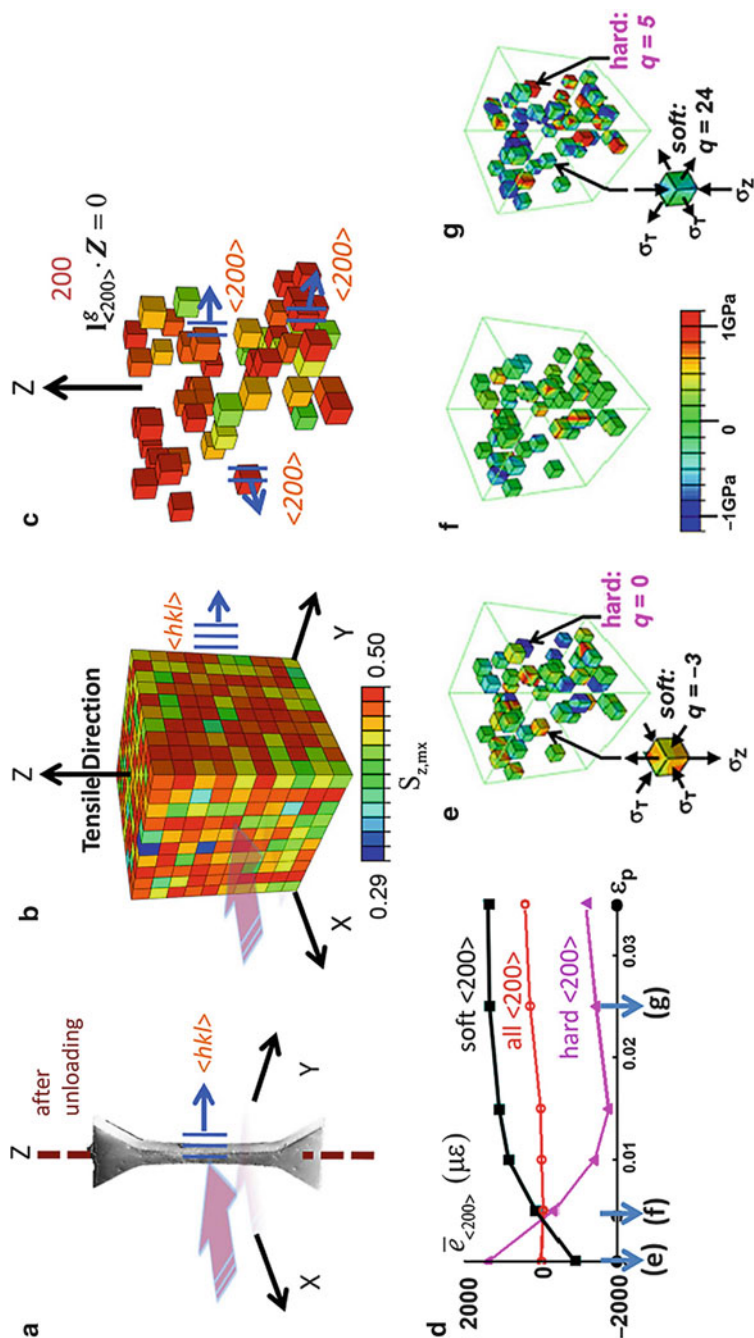
Fig. 16.11 (a) Diffraction experiment to measure transverse lattice strain $e_{<hkl>}$ in different $<hkl>$ groups in NC Ni with average grain size $d_{avg} \sim 30$ nm, after tensile unloading. Quantized crystal plasticity simulations showing (b) grain-to-grain distribution of Schmid factor in a polycrystal with no texture (*random*), (c) grains contributing to $\bar{e}_{<200>}$ predictions, and (d) $e_{<200>}$ versus imposed macrostrain. (e–g) Residual axial stress σ_z in $<200>$ grains at states (e), (f), and (g) in Fig. (d) (Reprinted figure from [109] with permission from Elsevier copyright 2012)

phases, and interfacial character. Multilayer thin films and nanostructured composites exhibit order-of-magnitude increases in strength compared to bulk constituents [110–113]. In some cases, they display increased ductility [112–114], resistance to radiation damage [115, 116], resistance to shock damage [117], and thermal stability [118–120]. Interfacial density, interfacial character, and internal stress state appear to control material behavior more so than the particular bulk properties of the constituent materials, as described in sections 'Mechanical Properties', 'Deformation Mechanisms', 'Modeling and Simulation'. Multilayer thin films are essentially miniature 'laboratories' to study the effects of interfaces and grain size on mechanical and physical properties. These results have motivated models of deformation mechanisms and strength to aid in the design of multilayer thin films and nanostructured composites.

This section addresses fabrication methods, mechanical properties, deformation mechanisms and modeling/simulation. This builds on an earlier review of the mechanical behavior of multilayers [121].

Synthesis and Structure

Physical Vapor Deposition (PVD)

Physical vapor deposition (PVD) is the most common approach to fabricate metallic multilayer thin films. PVD methods include evaporation [122–128], sputtering [122–128], and less commonly molecular beam epitaxy [129, 130]. These methods all rely on physical mechanisms to produce source atoms in the gaseous state, but differences in the physical mechanisms lead to disparities in thin-film quality and properties [131–133], including the potential to create amorphous metals [134]. Schematics of these processes are presented in Ohring [125].

Evaporation is a PVD method in which a heating source creates gaseous atoms that are then deposited onto a substrate [125, 126, 128]. The source is usually a crucible of pure metal that is heated resistively or with an electron beam. Electron beam heating is more common because it is not limited to particular materials and contamination is reduced [125]. The film can have a variety of growth patterns, depending on the chamber pressure and temperature difference between source and substrate [127, 131–134].

Multiple layers of different materials can be grown in a single chamber by sequentially baffling sources. Evaporative methods to deposit thin films are cheaper and often yield higher purity layers than sputtering [127]. Due to the physical mechanism of evaporation, however, the process is anisotropic and step coverage can be minimal [125]. Also, it is more difficult to achieve alloys of consistent and accurate composition using evaporative methods, leading to a preference for sputtering [127].

Sputtering relies on ionized gas to remove atoms from a source [127]. An inert noble gas (e.g. argon) is first ionized through collision with electrons. A bias voltage is used to accelerate the ionized gas toward a target containing the source material [125]. Source atoms are removed through collisions and they deposit onto
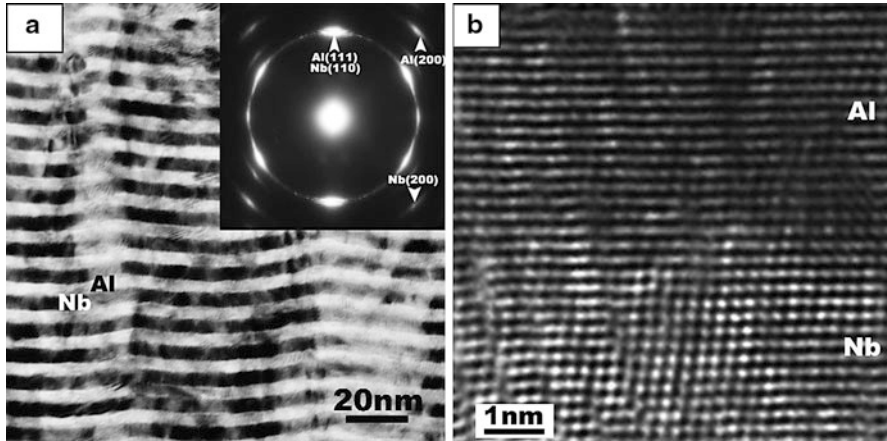
Fig. 16.12 (**a**) Waviness in an Al–Nb multilayered thin films arising from island growth mechanism described in [131, 132]. This effect intensifies with increasing film thickness. (**b**) Interfaces made via sputtering can be chemically and structurally sharp (Reprinted figure from [135] with permission from Elsevier copyright 2008)

a substrate within a low pressure chamber. The efficiency or 'yield' of deposition can be increased using a magnetic field above the target (i.e., magnetron sputtering). This keeps the electrons that ionize the argon gas close to the target material, ensuring that fewer electrons collect at the anode and heat the substrate. Like evaporative methods, the quality and structure of the film are controlled by the chamber pressure, the temperature difference between the anode and cathode, and rate of deposition [127].

Compared to other methods, sputtering creates a greater variety of impact angles of the sputtered atoms onto the substrate, because atom collisions are used remove target atoms [127]. This gives better coverage of defects and steps on the substrate surface [123]. Also, the substrate can be cleaned immediately before deposition by reversing the polarity of the substrate, or 'backsputtering' [127]. However, the impact energies of sputtered atoms are higher (3–10 eV) compared to evaporated atoms (0.2–0.26 eV), increasing the possibility of crystal damage [122, 127].

PVD for metallic multilayer fabrication is relatively slow compared to other methods and thus overall multilayer thickness is limited. Figure 16.12 shows magnetron sputtered Al–Nb multilayers with individual layer thickness $h \sim 5$ nm [135]. The waviness is attributed to an island growth phenomenon, explained in Refs. [127, 131, 132]. This waviness increases with continued deposition (increasing film thickness), introducing a microstructural length scale that can affect mechanical properties. The interfaces in Fig. 16.12 are chemically sharp and ordered, providing an idealized case for atomistic modeling. Achieving such sharp, ordered interfaces can be time consuming, since common metal deposition rates are $\sim 10^{-1}$ nm/s [135].

Electrodeposition (ED)

Electrodeposition (ED) uses an electric current to deposit pure metals from an aqueous, electrolytic solution. ED as a method to fabricate metallic multilayer thin films began $\sim$100 years ago with deposition of alternating Cu and Ni layers with individual layer thickness $h \sim 24$ μm by Blum [136]. ED is rarely used despite early use and technical ease. A primary use has been to grow multilayers with giant magnetoresistance (GMR) such as Cu–X, where X = Ni, Co, Ag, etc., or alloys thereof [137, 138]. The ED process is reviewed by Ross [139] and more recently by Bakonyi and Péter [140]. The latter includes >140 papers focused on the ED process, deposition conditions for Cu–X multilayers, the resulting microstructure, and the GMR effect. A conclusion is that ED multilayers show a diminished GMR effect compared to PVD multilayers. Despite this, a brief description follows because it underscores the relationship between microstructure and mechanical properties.

Electrodeposition or electroplating methods utilize one or more baths to deposit metals. For single-bath deposition, the electrolytic solution contains all of the metallic elements to be deposited [139, 140]. Agitation, current, and potential are used to control the deposition of individual metals from the solution. For multiple-bath deposition, the substrate is moved between separate baths containing different electrolytic solutions [139, 140]. Single-bath deposition is preferred since it minimizes movement of the substrate, but the electrochemistry of the two metals must be sufficiently different to discriminate them via agitation, current, and potential [139, 140]. Multiple-bath deposition offers a greater choice of metals to be deposited [139], yet the literature focuses primarily on optimizing the properties of Cu–X multilayers [140]. Figure 16.13a shows a cross-sectional view of an ED Cu–Ni multilayer, revealing a canted microstructure [141]. Figure 16.13b shows a plan-view image revealing a circular fiber morphology [142]. Yahalom et al. [143] report that interfaces in Cu–Ni ED multilayers are not atomically sharp and composition modulation leads to Cu-rich and Ni-rich layers. This contrasts with sharp composition modulation in PVD Cu–Ni multilayers deposited at low temperature [144].

Compared to PVD, ED offers a lower cost and faster low-temperature deposition method [139, 140]. The impurity concentration has been controlled, although this is limited primarily to Cu–X multilayers [139, 140]. The higher rates of deposition enable bulk production of material. However, extension of ED to other systems hinges on the control of nucleation and grain orientation – two factors that strongly affect the planarity and uniformity of multilayers.

Severe Plastic Deformation (SPD)

Severe plastic deformation (SPD) differs from PVD and ED in that it uses a top-down approach to achieve structural refinement [5, 145, 146]. An example is accumulative roll bonding (ARB) [147]. ARB has been limited primarily to the Cu–Nb system [148–150], where a distinct benefit is the immiscible nature of Cu and Nb even at elevated temperatures. Miscible multilayer systems such as Cu–Ni [151] are unlikely candidates, due to the strain and heat associated with ARB. Other ARB variables of interest include % reduction to achieve bonding, inter-rolling annealing temperature, and pre-bonding surface treatment [149].
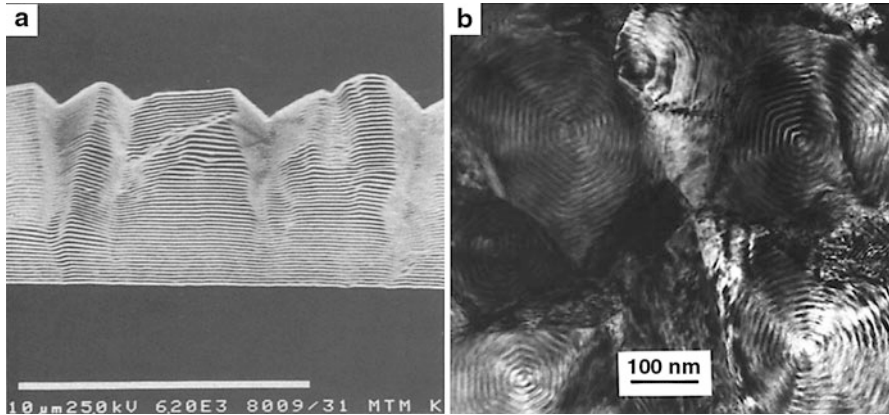
Fig. 16.13 (**a**) Cross-sectional SEM image of Cu–Ni multilayer with individual layer thickness $h = 100$ nm, showing canted effect (Reprinted figure from [141] with permission from The Electrochemical Society copyright 1994). (**b**) Plan-view TEM image of $Ni_{81}Cu_{19}$ (10 nm)/Cu (1.4 nm) multilayer, showing fiber texture (Reprinted figure from [142] with permission from The Electrochemical Society copyright 2000)

Another SPD method is repeated pressing and rolling. This originated at Kyoto University with the production of nanoscale multilayer Cu–Fe [152] and Fe–Ag [153] and it has since been demonstrated for Cu–Nb [154]. The two metals must be immiscible to suppress intermixing during an annealing step prior to pressing. Figure 16.14 shows that pressing and rolling can produce an epitaxial relationship between Fe and Ag layers [152]. Similar to ARB, the layer morphologies have imperfect planarity but do retain chemically sharp interfaces.

Diffusion bonding followed by cold rolling is another SPD method. Several plates are stacked and diffusion bonded at elevated temperature before subsequent cold rolling [155, 156]. This differs from ARB where bonding occurs during rolling. A limited number of systems have been investigated, primarily steel-brass [155, 156]. Individual layer thickness as small as $h \sim 15$ nm and substantial increases in strength beyond rule-of-mixtures values are possible, although the interfaces can be nonplanar, with incomplete layers [155, 156].

To summarize, SPD methods can be used to produce metallic multilayer thin films with nanoscale layers and chemically sharp interfaces. However, planar interfaces and controlled epitaxial orientation relationship between layers have been demonstrated in just a few systems. SPD is attractive for bulk production, but the systems must be immiscible and greater control of heterophase interface character and spacing is needed.

Mechanical Properties

Yield Strength/Hardness and Ductility
Original interest in metallic multilayer thin films emanated from the high values of experimentally measured yield strength obtained by decreasing layer thickness h [136].

Fig. 16.14 (**a**) Cross-sectional TEM of Fe–Ag multilayer fabricated via repeated pressing and rolling. *Arrow* indicates rolling direction. (**b**) HRTEM image showing the ordered nature of the interfaces and chemical sharpness (Reprinted figure from [153] with permission from the American Institute of Physics copyright 1997)
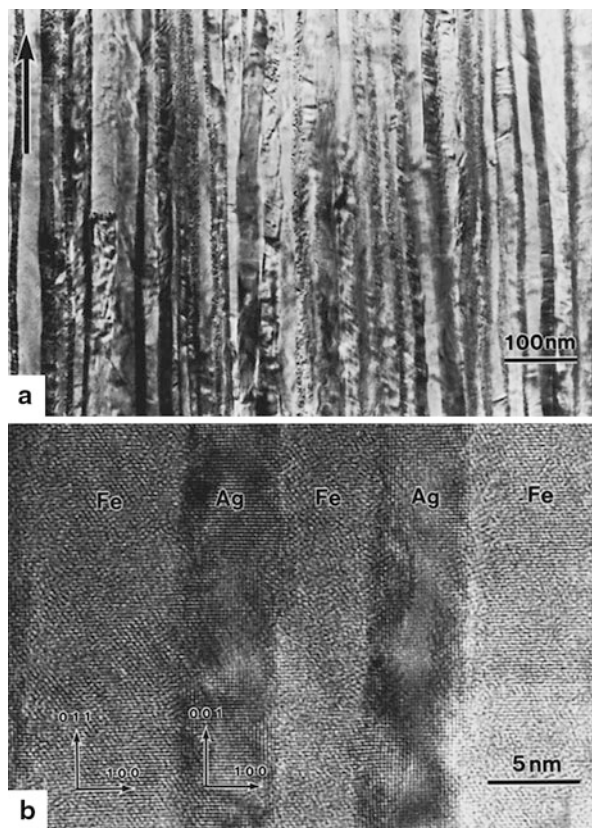
Fabrication and characterization methods were more limited in Blum's era, when the minimum layer thickness was $h \sim 25$ μm [136]. Today, the literature contains numerous references with h more than four orders of magnitude smaller, extending to ~10 atomic layers [135, 157–164]. This section focuses on nanoscale metallic multilayer thin films with $h < 50$ nm. Techniques to measure yield strength and hardness include microindentation [135], nanoindentation [157–166], tensile testing [167–169], and micropillar compression testing [112, 113, 164, 170–172]. However, these techniques focus on the composite yield strength. Recent work by Gram et al. outlines an elevated temperature X-ray diffraction-based technique to measure individual layer stress caused by the thermal expansion mismatch between a Cu–Ni multilayer thin film and a Si substrate [173]. Cu–Ni [136, 160, 167, 170, 174] and Cu–Nb [110, 112, 113, 157, 164, 175] are treated separately here due to extensive work on these two systems. The remaining metal-on-metal composite systems are treated afterward.

In 1921, Blum used ED Cu–Ni to study the effect of thin layers on strength [136]. Since then, PVD methods have yielded multilayers with polycrystalline layers [160] as well as near-single-crystal layers with an epitaxial relationship across interfaces [167, 170, 174]. Figure 16.15 compares hardness versus bilayer thickness for Cu–Ni
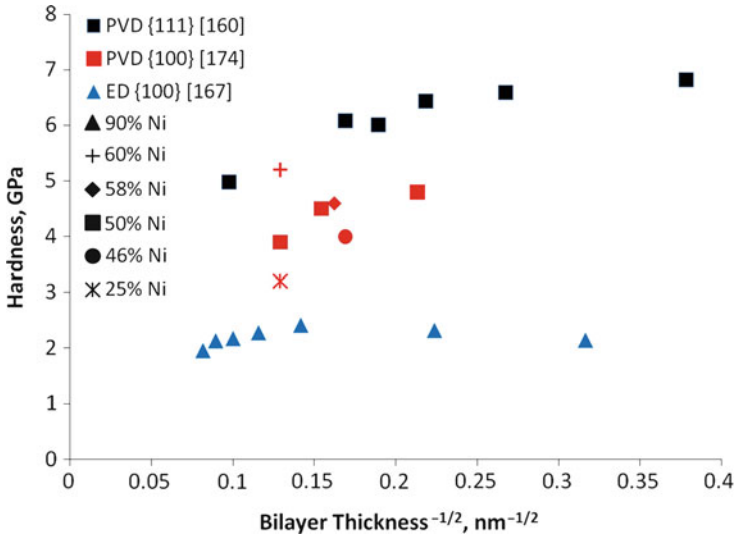
Fig. 16.15 Hardness for Cu–Ni multilayer thin films versus fabrication method (*ED* electrode-position, *PVD* physical vapor deposition), volume fraction of Ni, and interface orientation ({001} vs. {111} parallel to interfaces)

multilayer thin films, based on fabrication method, volume fraction of Ni, and orientation of the interfaces. Hardness of the ED Cu-Ni is obtained by multiplying reported tensile yield strengths by 2.7, as suggested by finite element modeling of homogeneous materials [176]. The hardness of ED {001} versus PVD {001} are different, despite similar layer thickness, interface sharpness, interface orientation [167, 174]. This suggests a discrepancy in the correlation between hardness and yield strength and/or the internal stress state of the multilayer. Interface orientation strongly affects hardness, as evidenced by comparison of PVD {111} versus PVD {001} in Fig. 16.15. The PVD {111} multilayer has a strong $<111>_{Cu} \parallel <111>_{Ni}$ orientation relationship normal to interfaces and the layers are polycrystalline [160]. The PVD {001} multilayer has a strong cube-on-cube or $<001>_{Cu} \parallel <001>_{Ni}$ orientation relationship with near-single-crystal layers [174]. Both were fabricated using PVD, but the sputtering parameters differed, so that internal stress state is possibly different (insufficient data exist to confirm this) [160].

Studies of the Cu–Nb system have incorporated multiple test methods while maintaining the same fabrication method and interface orientation [112, 157, 169]. Table 16.1 compares values based on tensile versus nanoindentation versus micropillar compression tests.

The good agreement in flow stress between test methods is encouraging. The loading axis differs: it is parallel to interfaces for the tensile data and perpendicular to interfaces for the micropillar compression and nanoindentation data.

Figure 16.16 presents hardness (*H*) data for a variety of bimetallic multilayer systems, focusing on data published in the past 10 years. The results convey that rigorous models are needed to interpret the complex interplay between

Table 16.1 Comparison of test method and the accompanying flow stress results for Cu–Nb multilayer thin films fabricated via PVD. For nanoindentation data, flow stress is determined as hardness/2.7

Bilayer thickness, nm	Volume fraction, %Ni	Flow stress, GPa	Testing method	Reference
80	0.5	1.55	Tensile testing	[169]
80	0.5	1.76	Micropillar compression	[113]
80	0.5	1.65	Nanoindentation	[157]
10	0.5	2.4	Micropillar compression	[112, 113]
10	0.5	2.4	Nanoindentation	[157]
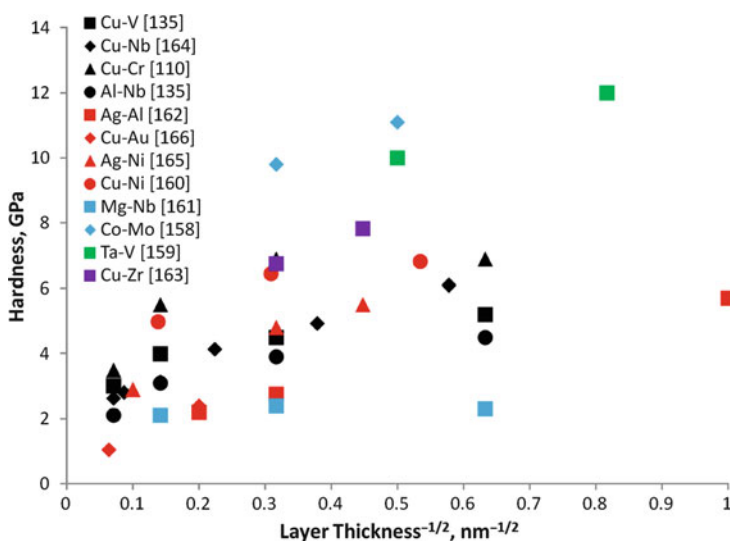
Fig. 16.16 Hardness versus individual layer thickness h for various A-B multilayer thin films with 50/50 volume fraction. Sources of data are indicated in legend. Colors are indicative of crystal structure pairing as defined in Table 16.2

fabrication-based variables such as internal stress state, epitaxial relationship, and interfacial structure. Two systems, Co–Mo [158] and Ta–V [159], exhibit superior strength. Table 16.2 compares H, crystal structure, Young's modulus (E), and fabrication method for cases with $h \sim 1$–5 nm and volume fraction $\sim 50/50$. The entries are ordered from smaller to larger E, based on a rule of mixtures. A key point is that H does not correlate with the bulk properties of the constituents. For example, the Co–Mo and Ta–V cases have similar H and h, yet E differs by nearly a factor of two. In general, increasing E does not necessarily increase H [158, 159]. More generally, multilayer strength and other properties derive from interfacial structure, bonding, defects, and internal stress.

Table 16.2 Comparison of peak hardness for a variety of systems, crystal structures, and fabrication methods

System (A/B)	Crystal structures (A/B)	Layer thickness, h nm	Hardness, H GPa	Rule-of-mixtures modulus, E GPa	Fabrication method	Reference
Al–Ag	FCC/FCC	1.0	5.7	72	Sputtering	[162]
Mg–Nb	HCP/BCC	2.5	2.3	74	Sputtering	[161]
Al–Nb	FCC/BCC	2.5	4.5	86	Sputtering	[135]
Cu–Nb	FCC/BCC	2.5	6.8	107	Sputtering	[157]
Cu–V	FCC/BCC	2.5	5.2	118	Sputtering	[135]
Ag–Ni	FCC/FCC	5.0	5.5	142	Sputtering	[165]
Ta–V	BCC/BCC	1.5	12	156	Sputtered	[159]
Cu–Ni	FCC/FCC	3.0	6.8	159	Evaporation	[160]
Cu–Cr	FCC/BCC	2.5	6.9	179	Sputtering	[110]
Co–Mo	HCP/BCC	4.0	11	270	Evaporation	[158]

Nominal strain to failure data for A/B multilayer thin films is limited since nanoindentation has been the primary mechanical test method. Figure 16.17 shows available data from tensile [167–169] and micropillar compression [112, 113, 164, 171, 172] tests. As expected, tensile tests have much smaller values than compression tests, reflecting that tensile failure often involves localization from area reduction and even crack nucleation from edge defects in thin films. In contrast, compression failure often involves shear localization in equiaxed samples machined from the film and loaded perpendicular to interfaces. Mara et al. [169] show that the strain at failure in tension compares well with the Considére criterion, if adapted for thin-sheet specimen [177, 178].

Figure 16.17 provides evidence that increases in flow stress are coupled to increases in strain to failure. These results run counter to a common trend that large strength and ductility are mutually exclusive [179]. Rolling studies on nanoscale Cu–Nb multilayers [149, 180] report rolling strains of >60 % with no material failure. This shows that nanolamellar composites can have both high flow stress and reasonable ductility if a compressive mean stress is present. Table 16.1 shows that different methods furnish similar flow strengths. The different flow strengths in Fig. 16.17 stem from differences in h and follow the trend observed in Fig. 16.16.

Strain-Rate Sensitivity

Trends in rate sensitivity (m) in multilayers are more complex than those of single-phase NC metals. Section 'Strain-Rate Sensitivity' shows opposing trends of m on grain size d, depending on crystal structure (i.e. BCC vs. FCC). For multilayer thin films, it is interesting to explore how m is influenced by dissimilar interfaces. Differences in testing and sample prep methodology make it difficult to compare results in the literature. In light of this, only a few cases are presented.

Mara et al. detail the results of rate jump tensile testing at 700 °C, on freestanding Cu–Nb multilayers with layer thicknesses of 75 nm/75 nm, 60 nm/60 nm, and
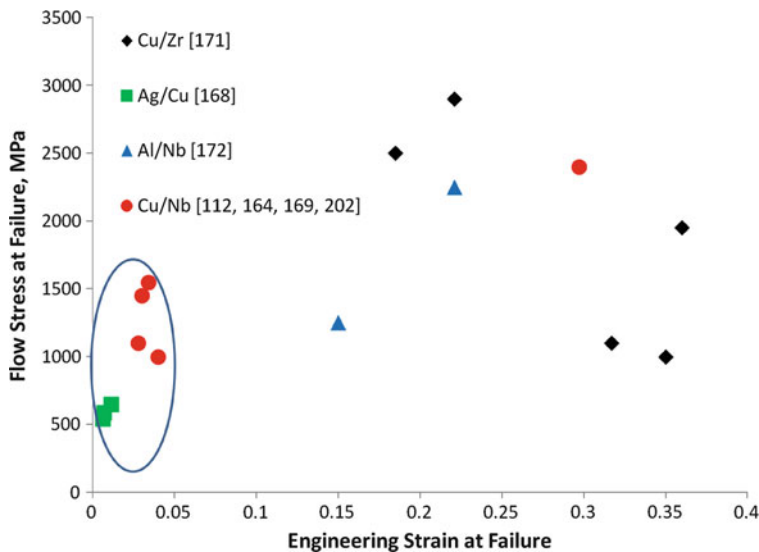
Fig. 16.17 Flow stress versus engineering strain at failure for various A-B multilayer thin films with 50/50 volume fraction. Individual layer thickness $h < 100$ nm for all cases. Flow stress tends to increase with engineering strain up to ~ 0.25. *Circle* indicates tensile data; remaining data are from micropillar compression tests

40 nm/40 nm [181]. Larger m values were observed at larger h and lower stress (i.e. lower strain rate). Larger values of $m \sim 0.5$ and evidence of grain pullout on fracture surfaces suggest a grain-boundary sliding deformation mechanism [181–183]. Smaller values of $m \sim 0.21$ were obtained for $h = 5$ μm and 0.5 μm, under power-law creep conditions at 600 °C and strain rates exceeding 10^{-7} s^{-1} [184].

Carpenter et al. [170] detail a different approach to study rate effects in Cu–Ni multilayers. Instead of fabricating thick films and removing them from the substrate for testing, a focused-ion beam was used to fabricate micron-size pillars. Rate jump compression tests were then performed using a flat punch indenter inside an instrumented indentation system. Resulting room-temperature values of m range from 0.013 to 0.020 as compressive stress increases from 660 to 1,800 MPa [170]. These m values are similar to those for NC FCC metals.

Other researchers have explored strain-rate sensitivity using strain-rate dependent indentation testing (Cu–Ta [185]) or indentation creep testing (Ag–Co [186], Ag–Fe [187], Cu–Ni [160], Cu–Cr, and Cu–Zr [40]). These test methods allow rapid measurement of m, but they are subject to complications due to the multiaxial stress state under an indenter [188] as well as thermal drift, which can be significant during long hold times [64]. Time-dependent microstructure evolution may generate additional complications [189]. Contrasting trends are reported: (1) m increases with h for all systems except Ag–Fe. The increasing sensitivity is potentially a result of a decreasing twin fraction in Cu [40] and/or Co at lower h. (2) Room-temperature

values of m reach $\sim$0.5 at longer (600 s) hold times in Ag–Co, Cu–Ni, and Ag–Fe, but $m < 0.04$ at shorter hold times (60 s) in Cu–Cr and Cu–Zr. This data requires more rigorous verification before conclusions can be deduced.

Residual Stress

In principle, yield in composite systems such as multilayer thin films depends on the magnitude of internal or residual stress in individual layers as well as the macroscopic stress imposed by the substrate on the film. The potentially large alternating (coherency) stresses caused by a mismatch in the stress-free lattice parameters of the layers can be an important strengthening mechanism [190]. Measurement of residual stress in single-phase thin films is relatively straightforward, and typically, it is accomplished using substrate curvature or X-ray diffraction-based techniques [191]. In multilayer thin films, the situation is more complicated, particularly if the film is attached to a substrate. In particular, force equilibrium in a direction parallel to the interfaces in an A/B multilayer requires [192]

$$\sigma_{\mathrm{f}} = \sigma_{\mathrm{A}} v_{\mathrm{A}} + \sigma_{\mathrm{B}} v_{\mathrm{B}} + N f / t_{\mathrm{f}} \qquad (16.6)$$

where σ_{f} and t_{f} are the respective macroscopic stress (parallel to interfaces) and thickness of the film, σ_{A} and σ_{B} are the respective in-plane stresses in A and B type layers, v_{A} and v_{B} are the corresponding volume fractions, N is the number of layers in the film, and f is the interfacial stress. The last quantity is the force per unit depth of film associated with elastic stretching of an A/B or B/A interface to the present configuration. Substrate curvature measurements can furnish σ_{f} but not σ_{A} and σ_{B}. X-ray diffraction measurements complement this by providing lattice strains in phases A and B, from which σ_{A} and σ_{B} can be obtained via Hooke's law. Interfacial stress can be obtained by combining these techniques (Ag–Ni [192], Au–Ni [193], Ag–Cu [194], Ni–Mo [195], Cu–W [196]) or by monitoring σ_{f} during deposition using in situ substrate curvature techniques (Ag–Cu [197]; Pd–Pt, Cu–Pd, Cu–Pt [198]). Another option is to combine measurements of σ_{f} for the multilayer film with σ_{A} and σ_{B} measurements based on tests of single A and B films (Cu–Cr [199], Cu/330 stainless steel [200]). An implicit assumption is that σ_{A} and σ_{B} values from single films approximate those in the multilayer. Finally, f can be determined using X-ray diffraction on freestanding thin films (Ag–Ni [201], Cu–Nb [202]).

Interface stress has also been calculated using atomistic approaches. Estimates using the embedded atom method [203] are smaller in magnitude than experimental values, except for Cu–Nb [202]. For Ag–Cu [194], the values differ in sign. Experimental values can have large differences in magnitude. For the same Ag–Cu multilayer, $f = -0.21$ N/m based on in situ substrate curvature measurements [197] versus $f = -3.19$ N/m based on a combined ex situ substrate curvature and X-ray diffraction technique [194]. Variation also arises when stress is determined from in-plane diffraction measurements based on stress-free lattice constants from bulk values (e.g. [192]) versus those from the $\sin^2 \Psi$ technique (e.g. [193]). See [204] for additional discussion related to the applicability of the $\sin^2 \Psi$ technique in multilayers [205] and the extent, if any, of intermixing [206].

Regardless of the technique or system, the contribution of interface stress f to film stress σ_f is not important for bilayer periods >10 nm. If $f = 3$ N/m is used in Eq. 16.6, for example, the interface stress term contributes ~ 60 MPa when the bilayer period is 50 nm but over 1 GPa when the bilayer period is <3 nm. Therefore, the primary concerns of residual stress related to the mechanical properties of multilayers are: (1) the interpretation of mechanical tests (specifically indentation) in the presence of significant film stress and (2) the contribution of coherency stress to multilayer strength.

Fatigue and Fracture

Fatigue testing of multilayers is limited. The limited sample volume from PVD and ED prohibit use of typical compact tension specimens, for example. Consequently, fatigue properties of multilayers have been investigated either as coatings [207] or using special thin-film fatigue techniques. Examples of the latter include compliant substrate testing [208], vibrating cantilever beams (for self-supported films) [209], and cantilevered microbeams cyclically deflected by a nanoindenter [210]. Fatigue and fracture behavior is couched in terms of crack initiation and crack propagation.

Fatigue crack initiation is suppressed in multilayers compared to bulk, regardless of the test method. For example, Cu fatigue specimens tested in a four-point rotating beam bending geometry displayed a significant improvement in fatigue life if a Cu–Ni multilayer coating was used, relative to a monolithic Cu or Ni coating or no coating [207]. Freestanding Cu–Nb multilayers tested in a vibrating cantilever beam geometry showed an order-of-magnitude increase in the stress amplitude for failure, compared to bulk Cu [211]. Fatigue crack initiation in Cu–Ni multilayers is suppressed as multilayer yield strength increases, based on work by Zhu et al. using polyamide-supported films [212]. No slip band intrusions and extrusions were reported in any of the multilayer fatigue tests [207, 211, 212]. This suggests a transition from bulk-like fatigue behavior to one controlled by individual dislocation and interface-mediated damage.

Fatigue crack propagation is a function of the variation in applied stress intensity, crack-tip shielding due to plastic deformation, and the ability to accommodate crack-tip dislocation activity without crack advance. The first quantity depends on the stress amplitude and crack length. Since crack initiation is expected in the less ductile of the two (A/B) layers [213], the stress intensity should scale with thickness of the less ductile layer [214]. Crack-tip shielding is dependent on the ability of interfaces and misfit dislocation content to aid or suppress plasticity, including effects on dislocation nucleation and suppression of dislocation propagation within the fracture process zone [215]. As layer thickness decreases, individual dislocation mechanisms dominate and misfit dislocations become less prevalent. It follows that as h decreases, a transition from an opening mode to a shear mode of fracture occurs (Cu-Ni [213], Cu–Cr [214], and Cu–Ta [216]). This transition is dependent on the relative fractions of the two phases [214].
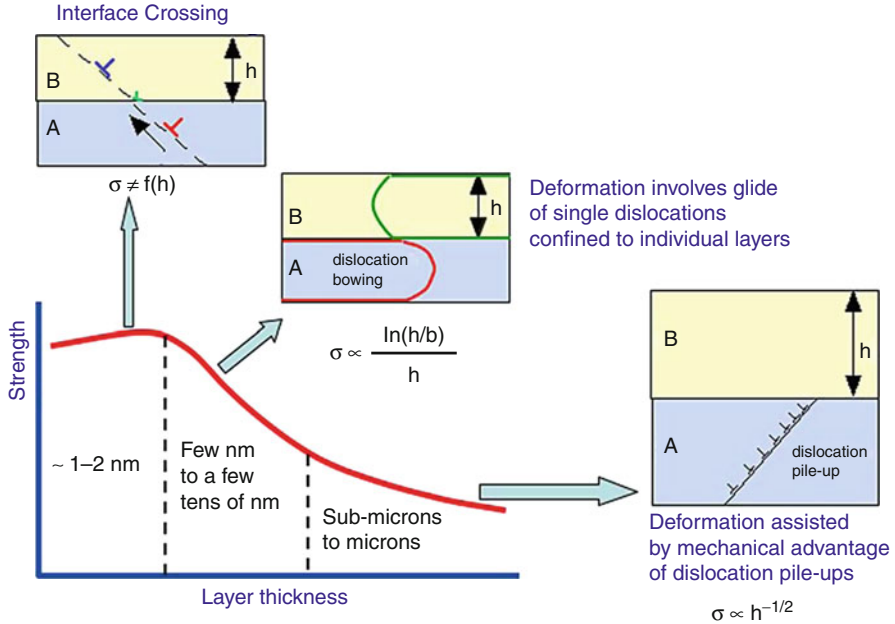
Fig. 16.18 Schematic of multilayer thin-film strength versus individual layer thickness h in A/B multilayer thin films. Inset images show controlling deformation mechanism (Reprinted figure from [157] with permission from Elsevier copyright 2005)

Deformation Mechanisms

The unusual combination of desirable properties in metallic nanolayered composites has inspired a large effort to understand the underlying deformation mechanisms. Misra et al. [157], building on previous experimental and theoretical work, produced Figure 16.18 to summarize the deformation regimes in metallic multilayer thin films as a function of individual layer thickness h. Each of the three regimes – Hall–Petch, single dislocation, and interface crossing – is discussed in sequence.

Hall–Petch Regime

The Hall–Petch (H–P) theory was motivated by experimental observations of increasing plastic strength with decreasing grain size d in metallic materials [217–219]. In the H–P theory, grain boundaries act as barriers to dislocation motion [217] due to discontinuities in slip plane, Burgers vector, stress state, and modulus at grain boundaries. At subcritical magnitudes of applied stress σ_a, dislocations nucleate at sources, glide, and pile up [218] against GBs. The number of dislocations in the pileup scales as $n_p \propto \sigma_a d$. The force on the leading dislocation at the GB scales as $f_p \propto \sigma_a^2 d$ and the stress in the vicinity of the pileup scales as $\sigma_p \propto \sigma_a d^{1/2}$. Eventually, f_p reaches a critical value f_c to push the leading dislocation across the

Fig. 16.19 Hardness versus $h^{-1/2}$ for various A-B multilayer thin films, where h = individual layer thickness. Data (*symbols*) follow a Hall–Petch trend (*solid lines*) at larger h. For $h < 50$ nm, the data depart from a Hall–Petch trend, implying a change in mechanism (Reprinted figure from [135] with permission from Elsevier copyright 2008)
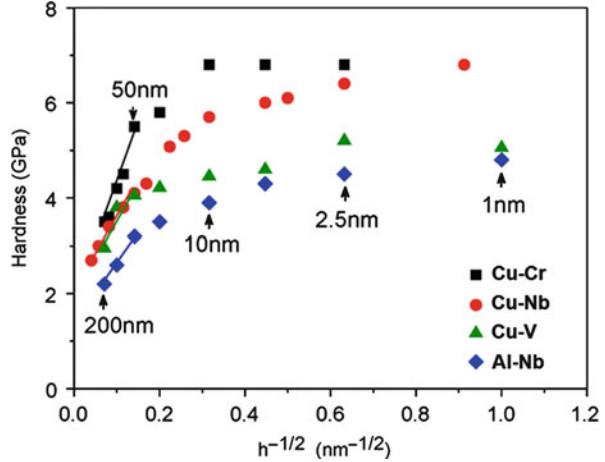
boundary or σ_p reaches a critical value to activate sources in the adjoining grain. Thus, the critical applied stress scales as the H–P relation (Eq. 16.1), where σ_0 is a reference stress yield strength in the limit $d \to \infty$. An excellent description of the H–P theory and the accompanying strengthening effect of smaller grain sizes is found in [219].

A simple extension to metallic multilayers is to use Eq. 16.1 with d replaced by layer thickness h:

$$\sigma_{\text{crit}} = \sigma_0 + k_{\text{HP}}/h^{1/2}, k_{\text{HP}} \propto (Gf_c)^{1/2} \qquad (7)$$

where G is an elastic shear modulus and f_c is the critical force for transmission across an interface. Figure 16.19 demonstrates that the H–P theory with $d = h$ fits the data for metallic multilayers at larger h (>100 nm) but it breaks down in the vicinity of $h \sim 50$ nm [135]. This breakdown occurs, in part, because Eq. 16.7 treats the number of dislocations n_p as a continuum, valid when $n_p \gg 1$. But other key issues are the nature of sources and interface structure. For $d \sim \mu$m or larger, dislocation sources within grain interiors are ubiquitous and operate at low stress. When $h \sim$ nm, sources shift to interfaces and the stress to operate them depends on interfacial structure, which is h-dependent. Second, the stress to glide dislocations within individual layers (confined layer slip) scales as $1/h$ [220]. A consequence is that σ_0 and f_c in Eq. 16.7 are h-dependent. These and other issues are discussed in [157, 221, 222].

Single-Dislocation Regime
Figure 16.19 demonstrates that strength increases with decreasing h down to at least $h \sim 2.5$ nm. The slope deviates further from the H–P prediction with decreasing h [135]. This continued strengthening has been described [157, 222] as an effect of confined layer slip (CLS) of single-dislocation loops within the confined geometry

Fig. 16.20 Schematic of confined layer slip (*CLS*) activity (see *middle regime* in Fig. 16.18). (**a**) CLS on a single slip system in layer A deposits dislocations at A/B interfaces, where they are trapped. (**b**) CLS on a second slip system (*2*) in layer A. (**c**) CLS on both systems (*1*) and (*2*) result in arrays (*3*) with a net 'edge' character. This affects subsequent CLS events (Reprinted figure from [157] with permission from Elsevier copyright 2005)
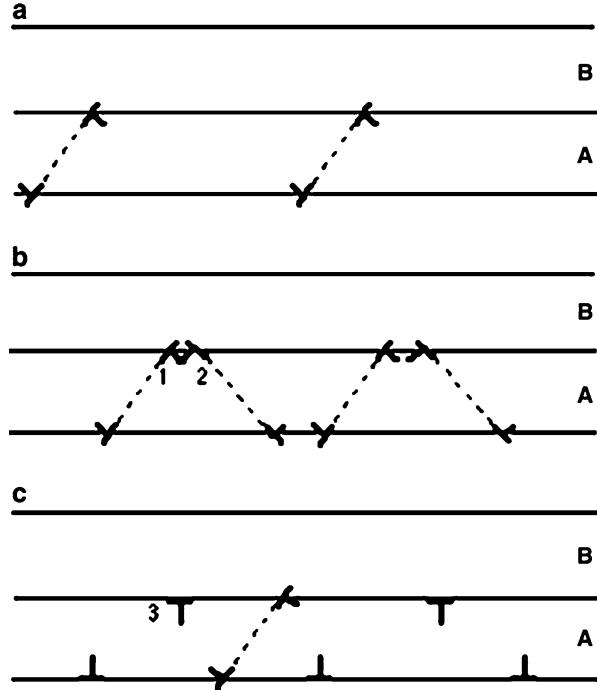
of multilayer thin films. The CLS theory relates the plastic strength of an individual layer to the shear stress to propagate Orowan-type (or hair pin) dislocation loops. These loops are shown experimentally to originate from existing threading dislocations, from interfaces, and from interactions with other dislocations [222–226]. Figure 16.20 presents a simple schematic of interface dislocations produced by CLS [157]. Note that two separate CLS events produce the equivalent of an edge dislocation at the interface. Figure 16.21 shows bowing of single-dislocation loops in Cu–Nb multilayers, leaving behind content, producing schematic dislocation structures as in Fig. 16.20a [227]. Figure 16.22 shows arrays dislocations produced by CLS activity in V–Ag multilayers, producing schematic dislocations as in Fig. 16.20c [228]. Earlier observations by Kramer and Foecke on ED Cu–Ni [224] coupled with more recent observations in various PVD multilayers [157, 227, 229] provide convincing evidence of CLS.

During CLS, the local resolved shear stress τ in the layer does work, $\tau bh\, \delta x$, when the loop advances by a distance δx parallel to the layers. For CLS to occur, this work must exceed the energy, $2e\, \delta x$, associated with depositing additional dislocation lines with energy per length e [198, 230–234]. This furnishes a critical stress $\tau_{CLS} = 2e/bh$. During fabrication via PVD, a mismatch in stress-free lattice parameter of the A/B layers, coupled with a driving force to create low energy, coherent interfaces, can lead to large in-plane stresses in layers [174]. At sufficiently large h, the condition $\tau > \tau_{CLS}$ is met and dislocations are deposited at interfaces [235]. The resulting dislocation arrays have been observed
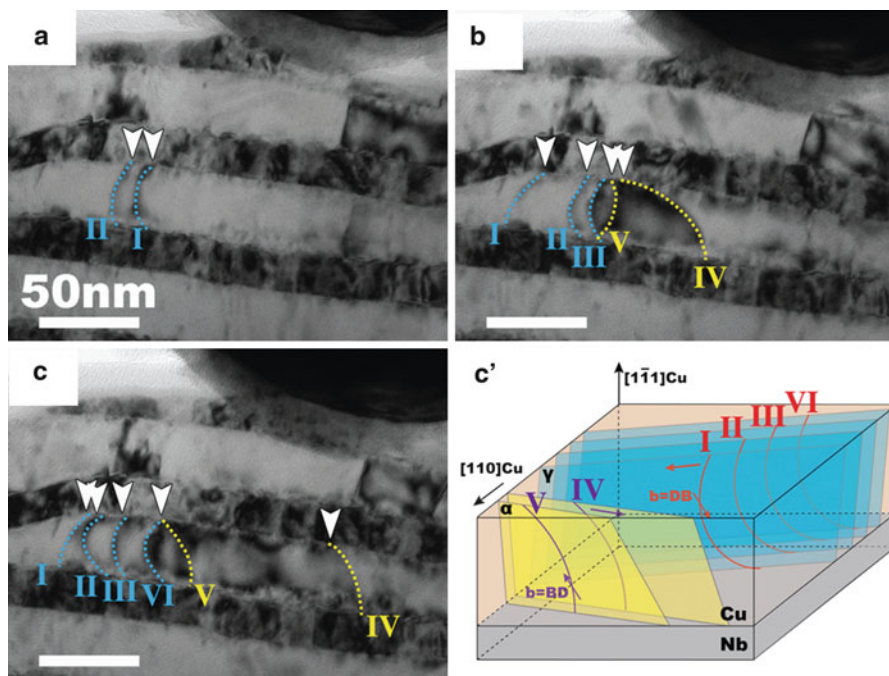
Fig. 16.21 In situ TEM micrographs showing confined layer slip (*CLS*) in a Cu–Nb multilayer thin film as deformation increases from (**a**) to (**c**). (**c'**) Schematic of resulting dislocation loop motion (Reprinted figure from [227] with permission from Cambridge University Press copyright 2012)

experimentally in single-crystal films of Cu [236–238]. Plan-view images in metallic multilayers confirm the concept of a critical thickness for CLS [239, 240]. The plastic strength of the composite is reached when both A and B layers yield. This might be achieved by independent CLS events in A and B layers, by transmission of slip across interfaces so that loops spanning multiple layers are formed, or by dislocation nucleation at interfaces into both A and B layers [110, 241, 242].

Several models for the stress at which the dislocation loops transmit into neighboring layers have been presented. In some cases, yield is defined by the macroscopic stress to eliminate an alternating tensile/compressive stress state between A/B layers, arising from a mismatch in the stress-free lattice parameters of A and B layers [223, 243, 244]. Other models require overcoming the energetic force on dislocations arising from a mismatch in elastic modulus between A and B layers [190]. Some models estimate the flow stress in multilayers based on the existing interfacial dislocation structure and internal stress state [174, 245]. Others combine internal stress state with continuity of slip planes across the interface [246, 247]. Deviations from estimates of strength due to lattice parameter and/or elastic modulus mismatch are sometimes attributed to an interfacial strength dependent on interfacial dislocation content, dislocation core spreading at interfaces, and continuity of slip

Fig. 16.22 High-resolution transmission electron micrograph of a V–Ag multilayer showing dislocation arrays at interfaces, produced by confined layer slip (*CLS*) (Reprinted figure from [228] with permission from Elsevier copyright 2011)
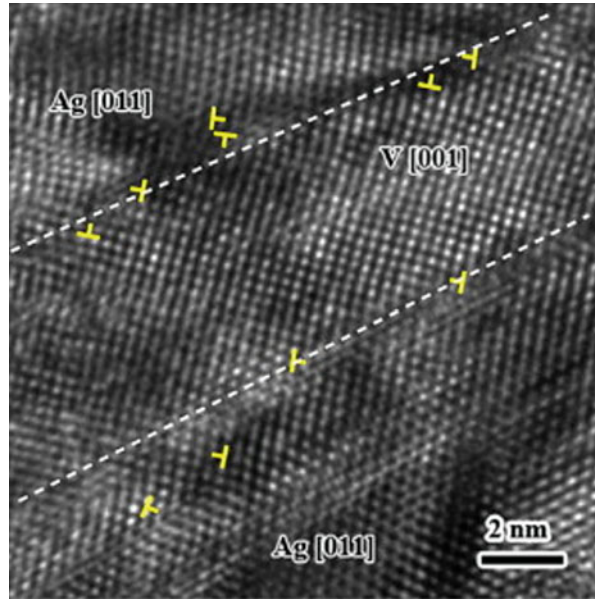
planes across interface [230, 231, 243, 248, 249]. Estimates of core spreading and other effects vary and are difficult to correlate with experimental data [230, 231, 243, 248]. At present, models based on the CLS theory largely ignore interdiffusion at interfaces and the polycrystalline nature of layers. Interdiffusion can create new phases near interfaces that may pin dislocations, for example.

Interface-Crossing Regime

Figure 16.18 indicates that when layer thickness $h < \sim 2$ nm, an interface crossing or dislocation transmission mechanism controls strength [1]. Hardness (H) plateaus [4] and may decrease for $h < \sim 1$ nm [37]. A variety of metallic multilayers display this trend with plateaus at various h [25, 40, 42, 43]. The saturation or plateau in H has been attributed to the stress τ_{CLS} ($= 2e/bh$) exceeding the stress for interfacial transmission [215, 250]. In that case, a single-dislocation loop will expand across multiple layers prior to CLS. This process is captured in simulations of dislocation loop expansion [251] using a 3D cellular automaton model of dislocations [252]. The decrease at $h < \sim 1$ nm has been attributed to nonlinear effects associated with layer thickness on the order of dislocation core width [215, 244, 253]. In this limit, dislocation line energy is averaged across layers. This, coupled with a dependence of interfacial structure on h, may decrease the stress for interfacial transmission at $h < \sim 1$ nm. The issue is complex, in that cases with wide dislocation cores, as predicted by atomistic modeling, may show little evidence of a hardness peak, while those with narrow cores may display hardness peaks [244, 253]. For $h < \sim 1$ nm, the effects of even small amounts of interdiffusion may have a pronounced effect on strength [253].

Modeling and Simulation

Atomistics

Metallic multilayer thin films derive their properties from the structure of interfaces and their interaction with mobile dislocations. Interface properties have been studied primarily with atomistic simulations, using the embedded atom method. However, density functional theory has been used in select cases to investigate nonmetal systems (Al–TiN [254]) and the effects of interfacial mixing (Al–Pd [255]).

Interfaces have been grouped into two categories: *transparent* if there is continuity of slip across interfaces and *opaque* if there is no continuity. Both types of interfaces impart significant strength increases to multilayers relative to bulk counterparts. However, atomistics show the strengthening mechanism is different for each case and that multilayer strength may benefit from a combination of both transparent and opaque interfaces [256–258].

For transparent interfaces such as epitaxial $Cu_{[001]}/Ni_{[001]}$ ([001] is the interface normal), geometrical barriers to transmission are absent, in the sense that a dislocation can glide across an interface and simply leave a step at the interface, with minimal residual dislocation content. Despite this, transparent interfaces increase the strength of multilayer thin films over that of bulk materials. This is shown in the experimental results in Fig. 16.16 and in atomistic simulations of indentation (Cu–Ni [259, 260] and Cu–Ag [261]) and scratch testing (Cu–Ni [262]). With minimal slip-plane misorientation, the strength of transparent A/B interfaces is attributed to a difference or 'mismatch' in (1) stress-free lattice parameter a_0, (2) elastic shear modulus G (Koehler barrier), (3) chemistry (stacking-fault mismatch) γ, and (4) Burgers vector b. The relative contribution of each has been studied in Cu–Ni and to a lesser extent in the Cu–Ag system, as presented below.

Lattice parameter mismatch $\Delta a_0/a_0$ is the dominant strengthening mechanism in multilayers with transparent interfaces [263]. It creates alternating compressive and tensile in-plane stress as atoms stretch or compress to match the lattice parameter of neighboring layers. Tension exists in layers with smaller a_0 and compression in ones with larger a_0 [244]. The magnitude of resolved stress increases with decreasing h according to $\tau = \tau_{CLS}$ ($=2e/bh$, section 'Single-Dislocation Regime'), reaching a maximum $\tau_{max} \sim G\,\Delta a_0/a_0 \sim$ GPa for $h < h_{crit}$. A superimposed applied stress (e.g. in-plane tension) will tend to increase the magnitude of stress in one layer (e.g. the tensile layer) and decrease it in the other (e.g. the compressive layer). When slip commences, it may be confined by oppositely signed in-plane stress in the adjoining layers. Macroyield is expected when the applied stress is sufficient to eliminate the alternating sign stress [263]. For $h > h_{crit}$, arrays of misfit dislocations are present and interfaces are semicoherent [264]. Here, strength is attributed to pockets of large coherency stress between misfit dislocations, as well as the stress field of discrete misfit dislocations [244].

Modulus mismatch $\Delta G/G$ can also be a significant barrier to dislocation transmission. Since the energy/length of a dislocation is proportional to shear modulus G, dislocations are attracted to reside in the lower modulus layer in an A/B system,

similar to attraction of dislocations to free surfaces. The extent of the attractive or repulsive 'image' force on the dislocation is dependent on the difference in dislocation line energy in A versus B layers and thus is proportional to the modulus mismatch [190, 265]. Atomistic simulations predict the barrier due to modulus mismatch in Cu–Ni multilayers to be $\sim$0.01 G and nearly independent of interface orientation and dislocation character [266]. The contribution drops as h approaches the dislocation core size, i.e. for $h < 10$ nm [266].

Chemical mismatch $\Delta\gamma/\gamma$ and Burgers vector mismatch $\Delta b/b$ contribute significantly less to interface strength. Chemical mismatch is typically studied in terms of the unstable stacking energy γ, the maximum energy/area of a slip plane as it is sheared. Dislocation line energy tends to increase with γ [219] so that a mismatch $\Delta\gamma$ can generate a force as the dislocation crosses an interface. Atomistic calculations suggest the contribution is relatively small (0.003 G) in Cu–Ni multilayers [266]. A mismatch in Burgers vector leads to the formation of interfacial line defects (dislocations and disconnections) when dislocations cross the interface. These defects interact with mobile dislocations to hinder successive interface slip on the same or adjacent slip systems, thereby work-hardening the interface and encouraging homogenous deformation [263]. Disconnections are predicted to offer little resistance to the initial dislocation crossing the interface, but do offer resistance to subsequent crossing [267].

Opaque interfaces are present in non-isostructural systems. Although opaque systems tend not to have large coherency stress, their strength tends to exceed that of transparent interfaces (Fig. 16.16) [268]. This is attributed to a low shear strength of the interface and resultant trapping of mobile dislocations [263]. Weak interfaces can be sheared by the stress field of an approaching dislocation, generating an attractive force that absorbs the dislocation. The core of the absorbed dislocation spreads into an intricate, non-planar pattern due to the low, nonuniform shear strength of the interface as shown in Fig. 16.23 [249]. Transmission requires compaction of the dislocation core to nucleate a mobile dislocation in the adjacent crystal [269]. It follows that lower interfacial shear strength requires a larger stress for transmission [247]. See the recent reviews [246, 270] and also section 'Continuum Methods' for continuum approaches.

Interfacial shear strength is a function of the bonding of the layer materials at the interface and their atomic arrangement. Using Cu/Nb as a model system and artificially changing the dilute heat of mixing, Wang et al. observed that a larger (more positive) heat of mixing leads to a lower interfacial shear strength [271]. In a separate study, Wang et al. showed that Cu/Nb interfaces with nearly degenerate energy have unique shear resistance and orientation dependence [269].

Interfacial sliding generates an attractive force on mobile dislocations and allows for core spreading in the interface [269, 271], thus hindering dislocation transmission [247]. However, atomistic simulations show that even at room temperature, dislocation climb can aid slip transmission [272]. Following compaction of the dislocation core, the transmitted dislocation can nucleate at a preferred location and on a slip system dependent on both geometry (Schmid factor) and interfacial structure [226, 273].
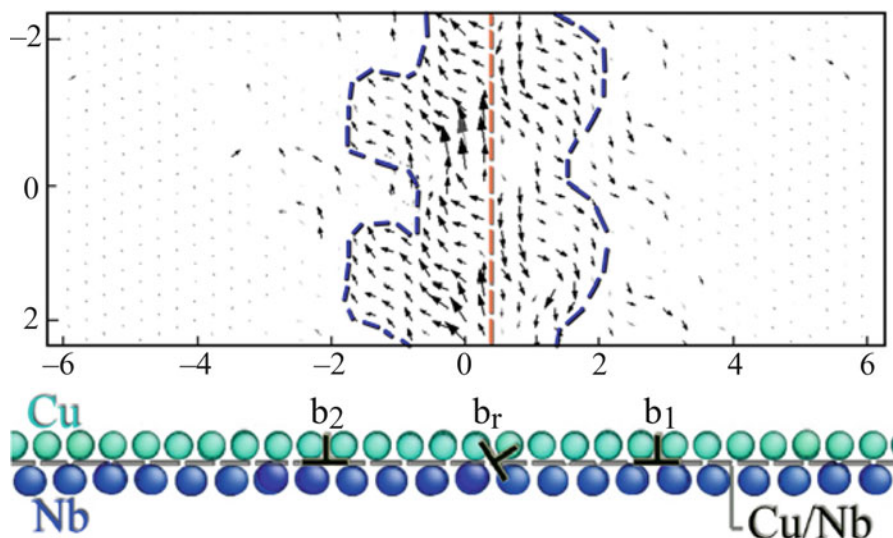
Fig. 16.23 (*lower*) Schematic of a Cu–Nb interface with a Kurdjumov–Sachs orientation relation, after a glide dislocation is absorbed into it. Dislocations b_1 and b_2 depict the extent of core spreading, and dislocation b_r depicts residual dislocation. (*upper*) Plan view of the interface, showing atomistic simulations of the vector field plot of disregistry across the interface plane. *Blue dashed lines* show extent of core spreading and orange dashed line shows residual dislocation (Reprinted figure from [249] with permission from Elsevier copyright 2009)

A related issue is the ability of misfit dislocations in non-isostructural systems to glide and climb. This allows them to act as sinks for point defects – for example, those generated by radiation [274] – and facilitate recovery of interfacial dislocations [272]. Knowledge of interfaces between point defects and interfaces has been expanded to non-planar interfaces and orientation relationships consistent with those formed by severe plastic deformation [275, 276].

Dislocation Dynamics

Discrete dislocation dynamics (DDD) simulations provide insight into dislocation interactions and the evolution of dislocation structure with deformation. Dislocations are discretized into segments and the Peach–Koehler force on each segment is computed based on the applied stress and stress from other segments and defects. A mobility function is used to determine the displacement of a dislocation segment during an iteration. The two main foci of DDD simulations are determining the stress required for a dislocation to cross an interface and the stress required to propagate dislocations in a confined layer slip (CLS) mode. At present, only FCC/FCC systems have been considered.

Atomistic simulations of FCC/FCC multilayers reveal that the two dominant impediments to interface crossing arise from lattice parameter mismatch and elastic modulus mismatch. Models by Verdier indicate that the number of dislocations in a
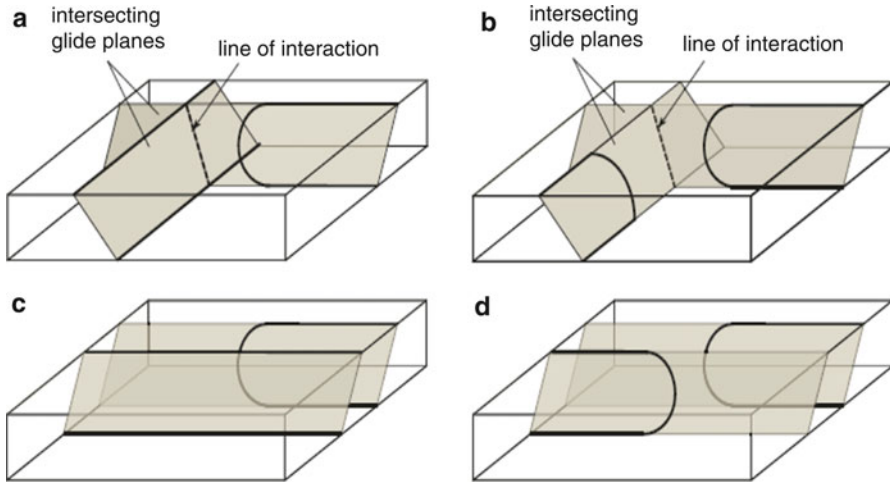
Fig. 16.24 Types of dislocation interactions during confined layer slip: (**a**) intersecting thread–misfit interaction, (**b**) intersecting thread–thread interaction, (**c**) parallel thread–misfit interaction, and (**d**) parallel thread–thread interaction (Reprinted figure from [280] with permission from Elsevier copyright 2009)

pileup decreases as layer thickness and/or interface strength decreases [242]. Keralavarma and Benzerga report that pileups can lead to significant hardening and a pronounced Bauschinger effect [277]. Anderson and Li [278] model crack propagation in multilayers using DDD to capture the plastic zone. They conclude that fracture toughness reduces with decreasing layer thickness h, but increases with increasing interface barrier strength. DDD simulations are usually limited to isotropic linear elasticity for simplicity. However, Ghoniem and Han developed line integral forms of the elastic field around dislocations in anisotropic multilayers to study the effect of image forces [279]. The effect of image forces is predicted to decrease strengthening between 10 and 20 nm, consistent with experimental Cu–Ni hardness data.

Strength during CLS is governed by inhibiting threading dislocation motion. Figure 16.24 shows four dislocation–dislocation interactions in thin films and multilayers that are generally responsible for strengthening: (a) intersection of a threading dislocation and interfacial misfit dislocations, (b) intersection of threading dislocations, (c) interaction of parallel thread and misfit dislocations, and (d) interaction of parallel threading dislocations [280]. Pant et al. treats the contribution of each interaction for passivated FCC films and concludes that no single interaction is dominant. Although the strength of thread–thread interactions could be greater, the strength of all four interactions depends strongly on the film thickness and plastic strain (i.e. dislocation density) [281]. Similar to Pant el at., Akasheh et al. report that neither intersecting nor parallel thread–misfit interactions can independently explain the measured dependence of strength on layer thickness in multilayers, even when coherency stress is included (no elastic modulus mismatch is included) [230, 231]. Large-scale DDD simulations

of passivated FCC films suggest all four interactions are important and contribute in an additive manner due to the inhomogeneous stress field that develops during relaxation [282]. The average magnitude and degree of fluctuation in the stress field which governs dislocation interactions is dependent on the misfit dislocation structure and therefore layer thickness [282, 283]. Similar large-scale DDD simulations have been developed for multilayers; however, no in-depth analysis has been presented [284].

Other numerical methods have been used to overcome drawbacks of the DDD method, although they suffer drawbacks of their own. The level set method more easily combines dislocation climb, cross-slip, and glide because it does not require explicit discretization of the dislocation [285]. Quek et al. use the level set method to show that threading dislocations on the same or intersecting slip planes form junctions that serve as barriers to dislocations, potentially creating pileups at high threading dislocation densities [286]. They also show that cross-slip of threading dislocations is much more prevalent in multilayer versus single-layer films. Using a misfit strain of 2 % and no modulus mismatch, they conclude that frequent cross-slip events lead to complex misfit dislocation structures that could provide significant strengthening in multilayers [287]. Cellular automaton-based methods allow reduced computational time at the expense coarse dislocation line discretization. Li and Anderson show that there is a critical layer thickness below which confined slip in single layers is not possible; rather, loops expand across multiple interfaces [288]. The phase field method is limited to small-scale simulations, but applications of it indicate that image forces in multilayers reduce the driving force for dislocation motion compared to single-layer films [289].

Although atomistic simulations are suited to describe complex dislocation core behavior and interaction with interfaces and grain boundaries, DDD provides a link between the atomistic and continuum scales and offers predictions of dislocation evolution in deforming multilayer thin films. Dislocation–dislocation interactions are predicted to impart large strength to multilayer thin films, and the overall evolution is a complex function of layer thickness and initial structure (inhomogeneous stress state). More large-scale DDD simulations are needed to understand the interplay of all these factors – including lattice parameter and modulus mismatch – on the strength of multilayers.

Continuum Methods

Continuum methods have been used to understand multilayer strength on the basis of dislocation generation and interaction but with significantly less computational effort. Empirical continuum models (discussed in section 'Deformation Mechanisms') typically require calibration to experiments and/or parameters from other simulations [157, 241]. Finite element simulations may be used in some cases to interpret experimental results or guide empirical models. Examples include indentation [290–292] and micropillar compression [293].

Confined layer slip (CLS) can be modeled by continuum dislocation approaches (see section 'Single-Dislocation Regime'). The process relieves coherency stress, changes interfacial structure, and thus affects dislocation nucleation and

propagation. As noted in section 'Atomistics', CLS can arise from lattice parameter mismatch [294]. Continuum models indicate that the critical thickness for CLS in multilayers exceeds that for single layers [295] and depends on the type of interfacial dislocation [296]. They can be used to quantify dislocation–dislocation interactions (Fig. 16.24), and they indicate that the resultant strain hardening [232, 297] or softening [297] depends on the dislocation character. Continuum models generally assume isotropic, homogeneous elasticity and lack kinetic effects.

The critical stress for dislocation transmission across interfaces has been studied using pileup, Peierls, and slipping interface models. Pileup models typically have assumed point-like sources for dislocations and examined how plastic strength depends on modulus mismatch, layer thickness, intermixing, pileup orientation, dislocation source properties, and interfacial barrier strength [221, 233, 298–301]. Plastic strength is predicted to increase with decreasing layer thickness and decreasing number of dislocations in a pileup. Deviations from Hall–Petch scaling occur when layer dimensions or interlayer grain size [250] restricts pileups to one or two dislocations. These models require estimates of source operation stress and interface barrier strength, either from experiments or other simulations.

Peierls models offer a simplified approach to study the qualitative interaction between interfaces and mobile dislocations, accounting for nonlinear core effects (see [302] for a recent review of the Peierls model and [303] for recent extensions). For systems with strong interfacial bonding (non-slipping interfaces), the transmission strength is predicted to have a complex dependence on modulus mismatch, coherency stress, and stacking-fault mismatch, all of which affect dislocation line energy near an interface [304]. Large interface transmission strength arises from abrupt changes in dislocation line energy. Surprisingly, interfaces with weak bonding provide large barriers to transmission because they delocalize dislocation cores and trap the dislocation in a low energy state [305–307]. The analysis is limited to straight screw dislocations in isotropic layers but is consistent with atomistic [247] and more recent 2D Green's function modeling [234].

Continuum models help interpret experimental data and infer macroscopic properties. For example, instrumented indentation is convenient but results are difficult to interpret due to complex stress states beneath the indenter. Both analytical [63, 308, 309] and finite element-based [310, 311] analyses for homogeneous materials are available to extract elastic–plastic properties from experimental data. These are frequently used for multilayers, yet finite element studies by Tan and Shen [290] show that hardness is significantly larger for a homogenous sample ($H_{homog.}$) versus a multilayer sample with the same average properties. This is demonstrated by finite element results in Fig. 16.25, showing extrusion of softer layers (layer B) directly under the indenter. The deviation is proportional to the difference in individual layer yield strengths and also depends on the internal stress state prior to indentation [312]. Indentation simulations for a metal–ceramic system (Al–SiC) show localized regions of tension unique to multilayers, consistent with crack locations in experiments [292]. Simulations also reveal plastic strain occurring during unloading, which could be detrimental to fatigue performance [313], and calls into question the common practice of extracting elastic modulus using the unloading curve in multilayer systems [314].
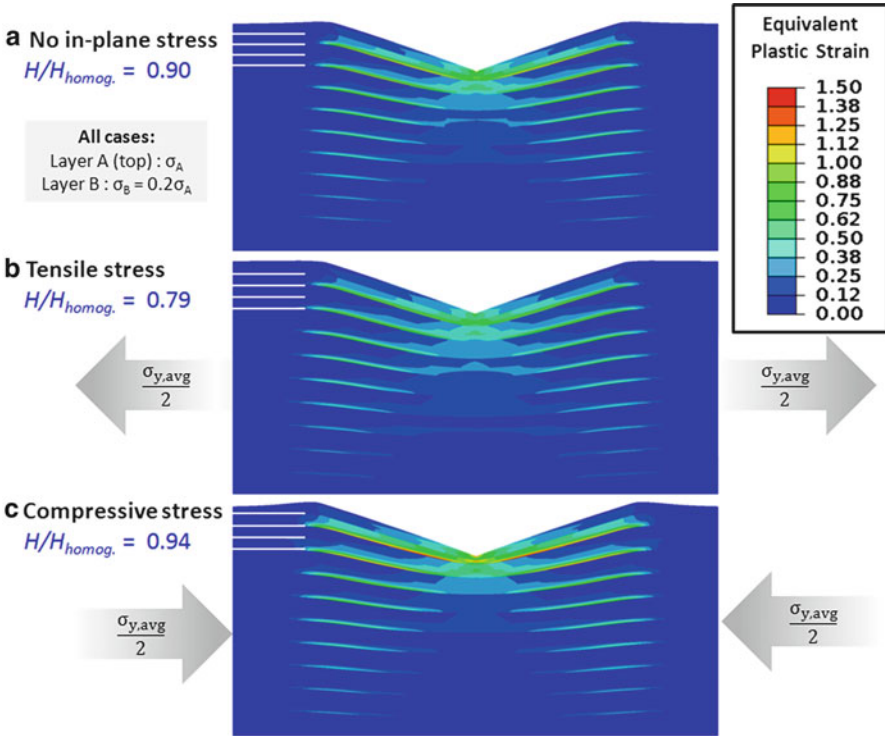
Fig. 16.25 Finite element simulations of the hardness H and contours of equivalent plastic strain due to indentation of an A/B multilayered thin film. The yield strength ratio $s_A:s_B = 5:1$. (**a**) $H < H_{homog}$, the value for a homogeneous, freestanding film with average yield strength and elastic properties. H/H_{homog} (**b**) decreases or (**c**) increases if an in-plane tensile or compressive stress is present during indentation, respectively

Continuum models also aid interpretation of micropillar compression tests. Pillar taper, misalignment of the pillar and platen, and pillar fillet radius are prevalent in experiments and cause deviations from an assumed uniform uniaxial compressive state. Finite element models have quantified these effects [315] and revel that finite element modeling is not only advantageous but in some cases necessary to interpret experiments [316–318]. To date, this approach has been applied only to Al–SiC multilayers [293, 319], where plastically soft Al layers are observed to extrude out during compression, in contrast to homogeneous pillars.

Overall, a hierarchy of simulation techniques exists, ranging from first-principles calculations of dislocation core structure, to atomistic studies of interface structure and barrier strength, to interface crossing and nucleation, to dislocation dynamics simulations of many-dislocation phenomena, to finite element and continuum approaches that capture sample geometry and time scales appropriate to macroscopic tests. Each of these techniques offers a useful contribution to understand deformation phenomena in multilayer thin films.

References

1. Erb U, Aust KT, Palumbo G (2007) Electrodeposited nanocrystalline metals, alloys and composites. In: Koch CC (ed) Nanostructured materials – processing, properties, and applications, 2nd edn. William Andrew, New York, pp 235–292

2. El-Sherik AM, Erb U (1995) Synthesis of bulk nanocrystalline nickel by pulsed electrode-position. J Mater Sci 30:5743–5749

3. Shen YF, Lu L, Lu QH, Jin ZH, Lu K (2005) Tensile properties of copper with nano-scale twins. Scripta Mater 52:989–994

4. Detor AJ, Schuh CA (2007) Tailoring and patterning the grain size of nanocrystalline alloys. Acta Mater 55:371–379

5. Valiev R, Islamgaliev R, Alexandrov I (2000) Bulk nanostructured materials from severe plastic deformation. Progress Mater Sci 45:103–189

6. Zhu YT, Liao XZ, Srinivasan SG, Lavernia EJ (2005) Nucleation of deformation twins in nanocrystalline face-centered-cubic metals processed by severe plastic deformation. J Appl Phys 98:034319

7. Liddicoat PV, Liao X-Z, Zhao Y, Zhu Y, Murashkin MY, Lavernia EJ, Valiev RZ, Ringer SP (2010) Nanostructural hierarchy increases the strength of aluminium alloys. Nat Commun 1:63

8. Suryanarayana C (2001) Mechanical alloying and milling. Prog Mater Sci 46:1–184

9. Chookajorn T, Murdoch HA, Schuh CA (2012) Design of stable nanocrystalline alloys. Science 337:951–954

10. Meyers MA, Mishra A, Benson DJ (2006) Mechanical properties of nanocrystalline materials. Prog Mater Sci 51:427–556

11. Schuh CA, Nieh TG, Iwasaki H (2003) The effect of solid solution W additions on the mechanical properties of nanocrystalline Ni. Acta Mater 51:431–443

12. Trelewicz JR, Schuh CA (2007) The Hall–Petch breakdown in nanocrystalline metals: a crossover to glass-like deformation. Acta Mater 55:5948–5958

13. Schiøtz J, Di Tolla FD, Jacobsen KW (1998) Softening of nanocrystalline metals at very small grain sizes. Nature 391:561–563

14. Van Swygenhoven H, Caro A, Farkas D (2001) Grain boundary structure and its influence on plastic deformation of polycrystalline FCC metals at the nanoscale: a molecular dynamics study. Scr Mater 44:1513–1516

15. Argon AS, Yip S (2006) The strongest size. Philos Mag Lett 86:713–720

16. Kumar K, Van Swygenhoven H, Suresh S (2003) Mechanical behavior of nanocrystalline metals and alloys. Acta Mater 51:5743–5774

17. Dao M, Lu L, Asaro RJ, De Hosson JTM, Ma E (2007) Toward a quantitative understanding of mechanical behavior of nanocrystalline metals. Acta Mater 55:4041–4065

18. Nieman GW, Weertman JR, Siegel RW (1991) Mechanical behavior of nanocrystalline Cu and Pd. J Mater Res 6:1012–1027

19. Sanders PG, Eastman JA, Weertman JR (1997) Elastic and tensile behavior of nanocrystalline copper and palladium. Acta Mater 45:4019–4025

20. Koch CC (2003) Optimization of strength and ductility in nanocrystalline and ultrafine grained metals. Scr Mater 49:657–662

21. Fang TH, Li WL, Tao NR, Lu K (2011) Revealing extraordinary intrinsic tensile plasticity in gradient nano-grained copper. Science 331:1587–1590

22. Wang Y, Chen M, Zhou F, Ma E (2002) High tensile ductility in a nanostructured metal. Nature 419:912–915

23. Lee Z, Witkin DB, Radmilovic V, Lavernia EJ, Nutt SR (2005) Bimodal microstructure and deformation of cryomilled bulk nanocrystalline Al–7.5 Mg alloy. Mater Sci Eng A 410–411:462–467

24. Zhilyaev AP, Nurislamova GV, Kim B-K, Baró MD, Szpunar JA, Langdon TG (2003) Experimental parameters influencing grain refinement and microstructural evolution during high-pressure torsion. Acta Mater 51:753–765

25. Wang YM, Ma E (2004) Three strategies to achieve uniform tensile deformation in a nanostructured metal. Acta Mater 52:1699–1709

26. Ma E, Wang YM, Lu QH, Sui ML, Lu L, Lu K (2004) Strain hardening and large tensile elongation in ultrahigh-strength nano-twinned copper. Appl Phys Lett 85:4932–4934

27. Dao M, Lu L, Shen YF, Suresh S (2006) Strength, strain-rate sensitivity and ductility of copper with nanoscale twins. Acta Mater 54:5421–5432

28. Karimpoor AA, Erb U, Aust KT, Palumbo G (2003) High strength nanocrystalline cobalt with high tensile ductility. Scr Mater 49:651–656

29. Wang YM, Ott RT, Hamza AV, Besser MF, Almer J, Kramer MJ (2010) Achieving large uniform tensile ductility in nanocrystalline metals. Phys Rev Lett 105:215502

30. Brandstetter S, Van Swygenhoven H, Van Petegem S, Schmitt B, Maaß R, Derlet PM (2006) From micro- to macroplasticity. Adv Mater 18:1545–1548

31. Rajagopalan J, Han JH, Saif MTA (2007) Plastic deformation recovery in freestanding nanocrystalline aluminum and gold thin films. Science 315:1831–1834

32. Rajagopalan J, Rentenberger C, Peter Karnthaler H, Dehm G, Saif MTA (2010) In situ TEM study of microplasticity and Bauschinger effect in nanocrystalline metals. Acta Mater 58:4772–4782

33. Rajagopalan J, Saif MTA (2011) Effect of microstructural heterogeneity on the mechanical behavior of nanocrystalline metal films. J Mater Res 26:2826–2832

34. Lonardelli I, Almer J, Ischia G, Menapace C, Molinari A (2009) Deformation behavior in bulk nanocrystalline-ultrafine aluminum: in situ evidence of plastic strain recovery. Scr Mater 60:520–523

35. Li L, Anderson PM, Lee M-G, Bitzek E, Derlet P, Swygenhoven HV (2009) The stress–strain response of nanocrystalline metals: a quantized crystal plasticity approach. Acta Mater 57:812–822

36. Koslowski M (2010) Effect of grain size distribution on plastic strain recovery. Phys Rev B 82:054110

37. Li H, Ebrahimi F (2004) Transition of deformation and fracture behaviors in nanostructured face-centered-cubic metals. Appl Phys Lett 84:4307–4309

38. Cheng S, Ma E, Wang YM, Kecskes LJ, Youssef KM, Koch CC, Trociewitz UP, Han K (2005) Tensile properties of in situ consolidated nanocrystalline Cu. Acta Mater 53:1521–1533

39. Wei H, Hibbard GD, Palumbo G, Erb U (2007) The effect of gauge volume on the tensile properties of nanocrystalline electrodeposits. Scr Mater 57:996–999

40. Niu JJ, Zhang JY, Liu G, Zhang P, Lei SY, Zhang GJ, Sun J (2012) Size-dependent deformation mechanisms and strain-rate sensitivity in nanostructured Cu/X (X = Cr, Zr) multilayer films. Acta Mater 60:3677–3689

41. Zehetbauer M, Seumer V (1993) Cold work hardening in stages IV and V of F.C.C. metals—I. Experiments and interpretation. Acta Metall Mater 41:577–588

42. Lu L, Li SX, Lu K (2001) An abnormal strain rate effect on tensile behavior in nanocrystalline copper. Scr Mater 45:1163–1169

43. Kalkman AJ, Verbruggen AH, Radelaar S (2002) High-temperature tensile tests and activation volume measurement of free-standing submicron Al films. J Appl Phys 92:6612–6615

44. Schwaiger R, Moser B, Dao M, Chollacoop N, Suresh S (2003) Some critical experiments on the strain-rate sensitivity of nanocrystalline nickel. Acta Mater 51:5159–5172

45. Hayes R, Witkin D, Zhou F, Lavernia E (2004) Deformation and activation volumes of cryomilled ultrafine-grained aluminum. Acta Mater 52:4259–4271

46. Wei Q, Cheng S, Ramesh KT, Ma E (2004) Effect of nanocrystalline and ultrafine grain sizes on the strain rate sensitivity and activation volume: fcc versus bcc metals. Mater Sci Eng A 381:71–79

47. Torre FD, Spätig P, Schäublin R, Victoria M (2005) Deformation behaviour and microstructure of nanocrystalline electrodeposited and high pressure torsioned nickel. Acta Mater 53:2337–2349

48. Wang YM, Hamza AV, Ma E (2006) Temperature-dependent strain rate sensitivity and activation volume of nanocrystalline Ni. Acta Mater 54:2715–2726

49. Chen J, Lu L, Lu K (2006) Hardness and strain rate sensitivity of nanocrystalline Cu. Scr Mater 54:1913–1918

50. Miyamoto H, Ota K, Mimaki T (2006) Viscous nature of deformation of ultra-fine grain aluminum processed by equal-channel angular pressing. Scr Mater 54:1721–1725

51. Gu P, Dao M, Asaro RJ, Suresh S (2011) A unified mechanistic model for size-dependent deformation in nanocrystalline and nanotwinned metals. Acta Mater 59:6861–6868

52. Malow TR, Koch CC, Miraglia PQ, Murty KL (1998) Compressive mechanical behavior of nanocrystalline Fe investigated with an automated ball indentation technique. Mater Sci Eng A 252:36–43

53. Jia D, Ramesh KT, Ma E (2003) Effects of nanocrystalline and ultrafine grain sizes on constitutive behavior and shear bands in iron. Acta Mater 51:3495–3509

54. Wei Q, Jiao T, Mathaudhu SN, Ma E, Hartwig KT, Ramesh KT (2003) Microstructure and mechanical properties of tantalum after equal channel angular extrusion (ECAE). Mater Sci Eng A 358:266–272

55. Wei Q, Kecskes L, Jiao T, Hartwig KT, Ramesh KT, Ma E (2004) Adiabatic shear banding in ultrafine-grained Fe processed by severe plastic deformation. Acta Mater 52:1859–1869

56. Wei Q, Jiao T, Ramesh KT, Ma E (2004) Nano-structured vanadium: processing and mechanical properties under quasi-static and dynamic compression. Scr Mater 50:359–364

57. Wei Q, Ramesh KT, Ma E, Kesckes LJ, Dowding RJ, Kazykhanov VU, Valiev RZ (2005) Plastic flow localization in bulk tungsten with ultrafine microstructure. Appl Phys Lett 86:101907

58. Jia D, Wang YM, Ramesh KT, Ma E, Zhu YT, Valiev RZ (2001) Deformation behavior and plastic instabilities of ultrafine-grained titanium. Appl Phys Lett 79:611–613

59. Hwang S, Nishimura C, McCormick P (2001) Deformation mechanism of nanocrystalline magnesium in compression. Scr Mater 44:1507–1511

60. Zhang X, Wang H, Scattergood RO, Narayan J, Koch CC, Sergueeva AV, Mukherjee AK (2002) Studies of deformation mechanisms in ultra-fine-grained and nanostructured Zn. Acta Mater 50:4823–4830

61. Wang YM, Ma E (2004) On the origin of ultrahigh cryogenic strength of nanocrystalline metals. Appl Phys Lett 85:2750–2752

62. Trojanová Z, Lukáč P, Száraz Z (2005) Deformation behaviour of nanocrystalline Mg studied at elevated temperatures. Rev Adv Mater Sci 10:437–441

63. Tabor D (1970) The hardness of solids. Rev Phys Technol 1:145

64. Maier V, Durst K, Mueller J, Backes B, Höppel HW, Göken M (2011) Nanoindentation strain-rate jump tests for determining the local strain-rate sensitivity in nanocrystalline Ni and ultrafine-grained Al. J Mater Res 26:1421–1430

65. Asaro RJ, Suresh S (2005) Mechanistic models for the activation volume and rate sensitivity in metals with nanocrystalline grains and nano-scale twins. Acta Mater 53:3369–3382

66. Jeong DH, Erb U, Aust KT, Palumbo G (2003) The relationship between hardness and abrasive wear resistance of electrodeposited nanocrystalline Ni–P coatings. Scr Mater 48:1067–1072

67. Rupert TJ, Schuh CA (2010) Sliding wear of nanocrystalline Ni–W: structural evolution and the apparent breakdown of Archard scaling. Acta Mater 58:4137–4148

68. Padilla HA II, Boyce BL (2010) A review of fatigue behavior in nanocrystalline metals. Exp Mech 50:5–23

69. Hanlon T, Kwon Y-N, Suresh S (2003) Grain size effects on the fatigue response of nanocrystalline metals. Scr Mater 49:675–680
70. Hanlon T, Tabachnikova ED, Suresh S (2005) Fatigue behavior of nanocrystalline metals and alloys. Int J Fatigue 27:1147–1158
71. Mughrabi H, Höppel HW (2010) Cyclic deformation and fatigue properties of very fine-grained metals and alloys. Int J Fatigue 32:1413–1427
72. Suresh S (1998) Fatigue of materials. Cambridge University Press, Cambridge
73. Boyce BL, Padilla HA II (2011) Anomalous fatigue behavior and fatigue-induced grain growth in nanocrystalline nickel alloys. Metall Mat Trans A 42:1793–1804
74. Moser B, Hanlon T, Kumar KS, Suresh S (2006) Cyclic strain hardening of nanocrystalline nickel. Scr Mater 54:1151–1155
75. Cheng S, Stoica AD, Wang X-L, Wang GY, Choo H, Liaw PK (2007) Fracture of Ni with grain-size from nanocrystalline to ultrafine scale under cyclic loading. Scr Mater 57:217–220
76. Cheng S, Xie J, Stoica AD, Wang X-L, Horton JA, Brown DW, Choo H, Liaw PK (2009) Cyclic deformation of nanocrystalline and ultrafine-grained nickel. Acta Mater 57:1272–1280
77. Yamakov V, Wolf D, Phillpot SR, Mukherjee AK, Gleiter H (2004) Deformation-mechanism map for nanocrystalline metals by molecular-dynamics simulation. Nat Mater 3:43–47
78. Cheng S, Spencer JA, Milligan WW (2003) Strength and tension/compression asymmetry in nanostructured and ultrafine-grain metals. Acta Mater 51:4505–4518
79. Lund AC, Schuh CA (2005) Strength asymmetry in nanocrystalline metals under multiaxial loading. Acta Mater 53:3193–3205
80. Frøseth AG, Derlet PM, Van Swygenhoven H (2004) Dislocations emitted from nanocrystalline grain boundaries: nucleation and splitting distance. Acta Mater 52:5863–5870
81. Kumar KS, Suresh S, Chisholm MF, Horton JA, Wang P (2003) Deformation of electrodeposited nanocrystalline nickel. Acta Mater 51:387–405
82. Budrovic Z, Swygenhoven HV, Derlet PM, Petegem SV, Schmitt B (2004) Plastic deformation with reversible peak broadening in nanocrystalline nickel. Science 304:273–276
83. Hugo RC, Kung H, Weertman JR, Mitra R, Knapp JA, Follstaedt DM (2003) In-situ TEM tensile testing of DC magnetron sputtered and pulsed laser deposited Ni thin films. Acta Mater 51:1937–1943
84. Wu X-L, Ma E (2006) Dislocations in nanocrystalline grains. Appl Phys Lett 88:231911
85. Youssef KM, Scattergood RO, Murty KL, Horton JA, Koch CC (2005) Ultrahigh strength and high ductility of bulk nanocrystalline copper. Appl Phys Lett 87:091904
86. Shan ZW, Wiezorek JMK, Stach EA, Follstaedt DM, Knapp JA, Mao SX (2007) Dislocation dynamics in nanocrystalline nickel. Phys Rev Lett 98:095502
87. Chen M, Ma E, Hemker KJ, Sheng H, Wang Y, Cheng X (2003) Deformation twinning in nanocrystalline aluminum. Science 300:1275–1277
88. Wu XL, Zhu YT (2008) Inverse grain-size effect on twinning in nanocrystalline Ni. Phys Rev Lett 101:025503
89. Zhu YT, Liao XZ, Wu XL (2012) Deformation twinning in nanocrystalline materials. Prog Mater Sci 57:1–62
90. Asaro RJ, Krysl P, Kad B (2003) Deformation mechanism transitions in nanoscale fcc metals. Philos Mag Lett 83:733–743
91. Liao XZ, Srinivasan SG, Zhao YH, Baskes MI, Zhu YT, Zhou F, Lavernia EJ, Xu HF (2004) Formation mechanism of wide stacking faults in nanocrystalline Al. Appl Phys Lett 84:3564
92. Van Swygenhoven H, Derlet PM (2001) Grain-boundary sliding in nanocrystalline fcc metals. Phys Rev B 64:224105
93. Wolf D, Yamakov V, Phillpot SR, Mukherjee A, Gleiter H (2005) Deformation of nanocrystalline materials by molecular-dynamics simulation: relationship to experiments? Acta Mater 53:1–40

94. Cahn JW, Mishin Y, Suzuki A (2006) Coupling grain boundary motion to shear deformation. Acta Mater 54:4953–4975
95. Shan Z, Stach EA, Wiezorek JMK, Knapp JA, Follstaedt DM, Mao SX (2004) Grain boundary-mediated plasticity in nanocrystalline nickel. Science 305:654–657
96. Ke M, Hackney SA, Milligan WW, Aifantis EC (1995) Observation and measurement of grain rotation and plastic strain in nanostructured metal thin films. Nanostructured Mater 5:689–697
97. Zhang K, Weertman JR, Eastman JA (2005) Rapid stress-driven grain coarsening in nano-crystalline Cu at ambient and cryogenic temperatures. Appl Phys Lett 87:061921
98. Gianola DS, Van Petegem S, Legros M, Brandstetter S, Van Swygenhoven H, Hemker KJ (2006) Stress-assisted discontinuous grain growth and its effect on the deformation behavior of nanocrystalline aluminum thin films. Acta Mater 54:2253–2263
99. Legros M, Gianola DS, Hemker KJ (2008) In situ TEM observations of fast grain-boundary motion in stressed nanocrystalline aluminum films. Acta Mater 56:3380–3393
100. Rupert TJ, Gianola DS, Gan Y, Hemker KJ (2009) Experimental observations of stress-driven grain boundary migration. Science 326:1686–1690
101. Van Swygenhoven H, Derlet PM, Hasnaoui A (2002) Atomic mechanism for dislocation emission from nanosized grain boundaries. Phys Rev B 66:024101
102. Van Swygenhoven H, Derlet PM, Frøseth AG (2004) Stacking fault energies and slip in nanocrystalline metals. Nat Mater 3:399–403
103. Van Swygenhoven H, Derlet PM, Frøseth AG (2006) Nucleation and propagation of dislocations in nanocrystalline fcc metals. Acta Mater 54:1975–1983
104. Bitzek E, Derlet PM, Anderson PM, Van Swygenhoven H (2008) The stress–strain response of nanocrystalline metals: a statistical analysis of atomistic simulations. Acta Mater 56:4846–4857
105. Fu H-H, Benson DJ, Meyers MA (2001) Analytical and computational description of effect of grain size on yield stress of metals. Acta Mater 49:2567–2582
106. Wei Y, Su C, Anand L (2006) A computational study of the mechanical behavior of nanocrystalline fcc metals. Acta Mater 54:3177–3190
107. Zhu B, Asaro RJ, Krysl P, Zhang K, Weertman JR (2006) Effects of grain size distribution on the mechanical response of nanocrystalline metals: part II. Acta Mater 54:3307–3320
108. Wei Y, Bower AF, Gao H (2007) Recoverable creep deformation due to heterogeneous grain-boundary diffusion and sliding. Scr Mater 57:933–936
109. Li L, Van Petegem S, Van Swygenhoven H, Anderson PM (2012) Slip-induced intergranular stress redistribution in nanocrystalline Ni. Acta Mater 60:7001–7010
110. Misra A, Verdier M, Lu Y, Kung H, Mitchell T, Nastasi M, Embury J (1998) Structure and mechanical properties of Cu-X (X = Nb, Cr, Ni) nanolayered composites. Scripta Mater 39:555–560
111. Clemens BM, Kung H, Barnett SA (1999) Mechanical behavior of nanostructured materials – structure and strength of multilayers. MRS Bull 24:20–26
112. Mara NA, Bhattacharyya D, Dickerson P, Hoagland RG, Misra A (2008) Deformability of ultrahigh strength 5 nm Cu/Nb nanolayered composites. Appl Phys Lett 92:231901
113. Mara NA, Bhattacharyya D, Dickerson P, Hoagland RG, Misra A (2009) Ultrahigh strength and ductility of Cu-Nb nanolayered composites. Mater Sci Forum 633–634:647–653
114. Misra A, Zhang X, Hammon D, Hoagland RG (2005) Work hardening in rolled nanolayered metallic composites. Acta Mater 53:221–226
115. Zhang X, Li N, Anderoglu O, Wang H, Swadener JG, Höchbauer T, Misra A, Hoagland RG (2007) Nanostructured Cu/Nb multilayers subjected to helium ion-irradiation. Nucl Instr Meth Phys Res B 261:1129–1132
116. Misra A, Demkowicz MJ, Zhang X, Hoagland RG (2007) The radiation damage tolerance of ultra-high strength nanolayered composites. J Miner Metals Mater Soc 59:62–65
117. Han WZ, Misra A, Mara NA, Germann TC, Baldwin JK, Shimada T, Luo SN (2011) Role of interfaces in shock-induced plasticity in Cu/Nb nanolaminates. Philos Mag 91:4172–4185

118. Misra A, Hoagland RG (2005) Effects of elevated temperature annealing on the structure and hardness of copper/niobium nanolayered films. J Mater Res 20:2046–2054

119. Anderoglu O, Misra A, Wang H, Zhang X (2008) Thermal stability of sputtered Cu films with nanoscale growth twins. J Appl Phys 103:094322

120. Zheng S, Beyerlein IJ, Carpenter JS, Kang K, Wang J, Han W, Mara NA (2013) High-strength and thermally stable bulk nanolayered composites due to twin-induced interfaces. Nat Commun 4:1696

121. Misra A (2006) Mechanical behavior of metallic nanolaminates. In: Hannink RHJ, Hill AJ (eds) Nanostructure control of materials. Woodhead, Cambridge, pp 146–176

122. Barnett SA, Shinn M (1994) Plastic and elastic properties of compositionally modulated thin films. Ann Rev Mater Sci 24:481–511

123. Smith D (1995) Thin-film deposition: principles and practice. McGraw Hill Professional, New York

124. Jankowski AF (1995) Metallic multilayers at the nanoscale. Nanostructured Mater 6:179–190

125. Ohring M (2001) Materials science of thin films, 2nd edn. Academic Press, San Diego

126. Seshan K (2012) Handbook of thin film deposition, 3rd edn. William Andrew, Oxford

127. Geng H (2005) Semiconductor manufacturing handbook, 1st edn. McGraw-Hill Professional, Blacklick

128. Mattox DM (2010) Handbook of physical vapor deposition (PVD) processing, 2nd edn. William Andrew, Norwich

129. Emmerson CM, Shen T-H, Evans SD, Allinson H (1996) A combined in situ optical reflectance–electron diffraction study of Co/Cu and Co/Au multilayers grown by molecular beam epitaxy. Appl Phys Lett 68:3740–3742

130. Westerwaal RJ, Slaman M, Broedersz CP, et al (2006) Optical, structural, and electrical properties of Mg_2NiH_4 thin films in situ grown by activated reactive evaporation. J Appl Phys 100:063518

131. Thompson CV (1990) Grain growth in thin films. Ann Rev Mater Sci 20:245–268

132. Thompson CV (2000) Structure evolution during processing of polycrystalline films. Ann Rev Mater Sci 30:159–190

133. Wuhrer R, Yeung WY (2004) A comparative study of magnetron co-sputtered nanocrystalline titanium aluminium and chromium aluminium nitride coatings. Scr Mater 50:1461–1466

134. Donohue A, Spaepen F, Hoagland RG, Misra A (2007) Suppression of the shear band instability during plastic flow of nanometer-scale confined metallic glasses. Appl Phys Lett 91:241905

135. Fu EG, Li N, Misra A, Hoagland RG, Wang H, Zhang X (2008) Mechanical properties of sputtered Cu/V and Al/Nb multilayer films. Mater Sci Eng A 493:283–287

136. Blum W (1921) The structure and properties of alternately deposited metals. Trans Am Electrochem Soc 40:307–320

137. Alper M, Attenborough K, Hart R, Lane SJ, Lashmore DS, Younes C, Schwarzacher W (1993) Giant magnetoresistance in electrodeposited superlattices. Appl Phys Lett 63:2144–2146

138. Schwarzacher W, Lashmore DS (1996) Giant magnetoresistance in electrodeposited films. IEEE Trans Magn 32:3133–3153

139. Ross CA (1994) Electrodeposited multilayer thin films. Ann Rev Mater Sci 24:159–188

140. Bakonyi I, Péter L (2010) Electrodeposited multilayer films with giant magnetoresistance (GMR): progress and problems. Prog Mater Sci 55:107–245

141. Haseeb ASMA, Celis JP, Roos JR (1994) Dual-Bath electrodeposition of Cu/Ni compositionally modulated multilayers. J Electrochem Soc 141:230–237

142. Tóth-Kádár E, Péter L, Becsei T, Tóth J, Pogány L, Tarnóczi T, Kamasa P, Láng G, Cziráki Á, Schwarzacher W (2000) Preparation and magnetoresistance characteristics of electrodeposited Ni-Cu alloys and Ni-Cu/Cu multilayers. J Electrochem Soc 147:3311–3318

143. Yahalom J, Tessier DF, Timsit RS, Rosenfeld AM, Mitchell DF, Robinson PT (1989) Structure of composition-modulated Cu/Ni thin films prepared by electrodeposition. J Mater Res 4:755–758
144. Liu Y, Bufford D, Wang H, Sun C, Zhang X (2011) Mechanical properties of highly textured Cu/Ni multilayers. Acta Mater 59:1924–1933
145. Valiev RZ, Estrin Y, Horita Z, Langdon TG, Zechetbauer MJ, Zhu YT (2006) Producing bulk ultrafine-grained materials by severe plastic deformation. J Miner Metals Mater Soc 58:33–39
146. Bachmaier A, Pippan R (2013) Generation of metallic nanocomposites by severe plastic deformation. Int Mater Rev 58:41–62
147. Saito Y, Utsunomiya H, Tsuji N, Sakai T (1999) Novel ultra-high straining process for bulk materials-development of the accumulative roll-bonding (ARB) process. Acta Mater 47:579–583
148. Lim SCV, Rollett AD (2009) Length scale effects on recrystallization and texture evolution in Cu layers of a roll-bonded Cu–Nb composite. Mater Sci Eng A 520:189–196
149. Carpenter JS, Vogel SC, LeDonne JE, Hammon DL, Beyerlein IJ, Mara NA (2012) Bulk texture evolution of Cu–Nb nanolamellar composites during accumulative roll bonding. Acta Mater 60:1576–1586
150. Wang J, Kang K, Zhang RF, Zheng SJ, Beyerlein IJ, Mara NA (2012) Structure and property of interfaces in ARB Cu/Nb laminated composites. J Miner Metals Mater Soc 64:1208–1217
151. Tayyebi M, Eghbali B (2013) Study on the microstructure and mechanical properties of multilayer Cu/Ni composite processed by accumulative roll bonding. Mater Sci Eng A 559:759–764
152. Huang B, Ishihara KN, Shingu PH (2001) Preparation of high strength bulk nano-scale Fe/Cu multilayers by repeated pressing-rolling. J Mater Sci Lett 20:1669–1670
153. Yasuna K, Terauchi M, Otsuki A, Ishihara KN, Shingu PH (1997) Bulk metallic multilayers produced by repeated press-rolling and their perpendicular magnetoresistance. J Appl Phys 82:2435
154. Shahabi HS, Manesh HD (2009) Micro-structural evaluation of Cu/Nb nano-layered composites produced by repeated press and rolling process. J Alloys Compd 482:526–534
155. Sahay SS, Ravichandran KS, Byrne JG (1996) Nanoscale brass/steel multilayer composites produced by cold rolling. Metall Mater Trans A 27:2383–2385
156. Kavarana FH, Ravichandran KS, Sahay SS (2000) Nanoscale steel-brass multilayer laminates made by cold rolling: microstructure and tensile properties. Scr Mater 42:947–954
157. Misra A, Hirth JP, Hoagland RG (2005) Length-scale-dependent deformation mechanisms in incoherent metallic multilayered composites. Acta Mater 53:4817–4824
158. Yang GH, Zhao B, Gao Y, Pan F (2005) Investigation of nanoindentation on Co/Mo multilayers by the continuous stiffness measurement technique. Surf Coat Technol 191:127–133
159. Jankowski AF, Hayes JP, Saw CK (2007) Dimensional attributes in enhanced hardness of nanocrystalline Ta–V nanolaminates. Philos Mag 87:2323–2334
160. Zhu XY, Liu XJ, Zong RL, Zeng F, Pan F (2010) Microstructure and mechanical properties of nanoscale Cu/Ni multilayers. Mater Sci Eng A 527:1243–1248
161. Ham B, Zhang X (2011) High strength Mg/Nb nanolayer composites. Mater Sci Eng A 528:2028–2033
162. Bufford D, Bi Z, Jia QX, Wang H, Zhang X (2012) Nanotwins and stacking faults in high-strength epitaxial Ag/Al multilayer films. Appl Phys Lett 101:223112
163. Zhang JY, Liu Y, Chen J, Chen Y, Liu G, Zhang X, Sun J (2012) Mechanical properties of crystalline Cu/Zr and crystal–amorphous Cu/Cu–Zr multilayers. Mater Sci Eng A 552:392–398
164. Beyerlein IJ, Mara NA, Wang J, Carpenter JS, Zheng SJ, Han WZ, Zhang RF, Kang K, Nizolek T, Pollock TM (2012) Structure–property-functionality of bimetal interfaces. J Miner Metals Mater Soc 64:1192–1207

165. Wen SP, Zong RL, Zeng F, Guo S, Pan F (2009) Nanoindentation and nanoscratch behaviors of Ag/Ni multilayers. Appl Surf Sci 255:4558–4562
166. Li YP, Zhu XF, Zhang GP, Tan J, Wang W, Wu B (2010) Investigation of deformation instability of Au/Cu multilayers by indentation. Philos Mag 90:3049–3067
167. Tench DM, White JT (1991) Tensile properties of nanostructured Ni-Cu multilayered materials prepared by electrodeposition. J Electrochem Soc 138:3757–3758
168. Huang H, Spaepen F (2000) Tensile testing of free-standing Cu, Ag and Al thin films and Ag/Cu multilayers. Acta Mater 48:3261–3269
169. Mara NA, Bhattacharyya D, Hoagland RG, Misra A (2008) Tensile behavior of 40 nm Cu/Nb nanoscale multilayers. Scr Mater 58:874–877
170. Carpenter JS, Misra A, Uchic MD, Anderson PM (2012) Strain rate sensitivity and activation volume of Cu/Ni metallic multilayer thin films measured via micropillar compression. Appl Phys Lett 101:051901
171. Zhang JY, Lei S, Liu Y, Niu JJ, Chen Y, Liu G, Zhang X, Sun J (2012) Length scale-dependent deformation behavior of nanolayered Cu/Zr micropillars. Acta Mater 60:1610–1622
172. Kim Y, Budiman AS, Baldwin JK, Mara NA, Misra A, Han SM (2012) Microcompression study of Al-Nb nanoscale multilayers. J Mater Res 27:592–598
173. Gram MD, Carpenter JS, Payzant EA, Misra A, Anderson PM. Forward and reverse plastic flow in nanoscale layers: results from heated diffraction studies. Mater Res Lett (submitted)
174. Carpenter JS, Misra A, Anderson PM (2012) Achieving maximum hardness in semi-coherent multilayer thin films with unequal layer thickness. Acta Mater 60:2625–2636
175. Carpenter JS, Zheng SJ, Zhang RF, Vogel SC, Beyerlein IJ, Mara NA (2013) Thermal stability of Cu–Nb nanolamellar composites fabricated via accumulative roll bonding. Philos Mag 93:718–735
176. Mata M, Anglada M, Alcalá J (2002) Contact deformation regimes around sharp indentations and the concept of the characteristic strain. J Mater Res 17:964–976
177. Onyewuenyi OA, Hirth JP (1982) Plastic instability in U-notched bend specimens of spheroidized AIS11090 steel. Metall Trans A 13:2209–2218
178. Argon AS (1973) Stability of plastic deformation. The Inhomogeneity of plastic deformation. ASM Seminar, pp 161–189
179. Valiev R (2002) Materials science: nanomaterial advantage. Nature 419:887–889
180. Anderson PM, Bingert JF, Misra A, Hirth JP (2003) Rolling textures in nanoscale Cu/Nb multilayers. Acta Mater 51:6059–6075
181. Mara NA, Tamayo T, Sergueeva AV, Zhang X, Misra A, Mukherjee AK (2007) The effects of decreasing layer thickness on the high temperature mechanical behavior of Cu/Nb nanoscale multilayers. Thin Solid Films 515:3241–3245
182. Mara N, Sergueeva A, Misra A, Mukherjee AK (2004) Structure and high-temperature mechanical behavior relationship in nano-scaled multilayered materials. Scripta Mater 50:803–806
183. Mara NA, Misra A, Hoagland RG, Sergueeva AV, Tamayo T, Dickerson P, Mukherjee AK (2008) High-temperature mechanical behavior/microstructure correlation of Cu/Nb nanoscale multilayers. Mater Sci Eng A 493:274–282
184. Lewis AC, Heerden DV, Weihs TP, Josell D (2003) Creep deformation in multilayered and microlaminate materials. J Miner Metals Mater Soc 55:34–37
185. Huang P, Wang F, Xu M, Lu TJ, Xu KW (2011) Strain rate sensitivity of unequal grained nano-multilayers. Mater Sci Eng A 528:5908–5913
186. Wen SP, Zeng F, Gao Y, Pan F (2006) Indentation creep behavior of nano-scale Ag/Co multilayers. Scr Mater 55:187–190
187. Zhu XY, Liu XJ, Zeng F, Pan F (2010) Room temperature nanoindentation creep of nanoscale Ag/Fe multilayers. Mater Lett 64:53–56
188. Josell D, Weihs TP, Gao H (2002) Diffusional creep: stresses and strain rates in thin films and multilayers. MRS Bull 27:39–44

189. Wang J, Anderson PM (2005) Pinch-off maps for the design of morphologically stable multilayer thin films with immiscible phases. Acta Mater 53:5089–5099
190. Koehler JS (1970) Attempt to design a strong solid. Phys Rev B 2:547
191. Freund LB, Suresh S (2003) Thin film materials: stress. Cambridge University Press, Defect Formation and Surface Evolution
192. Ruud JA, Witvrouw A, Spaepen F (1993) Bulk and interface stresses in silver-nickel multilayered thin films. J Appl Phys 74:2517–2523
193. Labat S, Gergaud P, Thomas O, Gilles B, Marty A (2000) Interdependence of elastic strain and segregation in metallic multilayers: an x-ray diffraction study of (111) Au/Ni multilayers. J Appl Phys 87:1172–1181
194. Berger S, Spaepen F (1995) The Ag/Cu interface stress. Nanostructured Mater 6:201–204
195. Bain JA, Chyung LJ, Brennan S, Clemens BM (1991) Elastic strains and coherency stresses in Mo/Ni multilayers. Phys Rev B 44:1184–1192
196. Girault B, Villain P, Le Bourhis E, Goudeau P, Renault P-O (2006) X-ray diffraction analysis of the structure and residual stresses of W/Cu multilayers. Surf Coat Technol 201:4372–4376
197. Shull AL, Spaepen F (1996) Measurements of stress during vapor deposition of copper and silver thin films and multilayers. J Appl Phys 80:6243–6256
198. Ramaswamy V, Nix WD, Clemens BM (2004) Coherency and surface stress effects in metal multilayers. Scr Mater 50:711–715
199. Misra A, Kung H, Mitchell TE, Nastasi M (2000) Residual stresses in polycrystalline Cu/Cr multilayered thin films. J Mater Res 15:756–763
200. Zhang X, Misra A (2004) Residual stresses in sputter-deposited copper/330 stainless steel multilayers. J Appl Phys 96:7173–7178
201. Josell D, Bonevich JE, Shao I, Cammarata RC (1999) Measuring the interface stress: silver/nickel interfaces. J Mater Res 14:4358–4365
202. Aydıner CC, Brown DW, Mara NA, Almer J, Misra A (2009) In situ x-ray investigation of freestanding nanoscale Cu–Nb multilayers under tensile load. Appl Phys Lett 94:031906
203. Gumbsch P, Daw M (1991) Interface stresses and their effects on the elastic moduli of metallic multilayers. Phys Rev B 44:3934–3938
204. Daniels BJ, Nix WD, Clemens BM (1994) Effect of structure, stress, strain, and alloying on the hardness of Fe(001)/Pt(001) epitaxial multilayers. MRS Symp Proceed 356:373–378
205. Chocyk D, Proszynski A, Gladyszewski G, Labat S, Gergaud P, Thomas O (2002) Stresses in multilayer systems: test of the sin2Ψ method. Adv Eng Mater 4:557–561
206. Clemens BM, Nix WD, Ramaswamy V (2000) Surface-energy-driven intermixing and its effect on the measurement of interface stress. J Appl Phys 87:2816–2820
207. Stoudt MR, Ricker RE, Cammarata RC (2001) The influence of a multilayered metallic coating on fatigue crack nucleation. Int J Fatigue 23(Suppl 1):215–223
208. Hommel M, Kraft O, Arzt E (1999) A new method to study cyclic deformation of thin films in tension and compression. J Mater Res 14:2373–2376
209. Wang Y-C, Hoechbauer T, Swadener JG, Misra A, Hoagland RG, Nastasi M (2006) Mechanical fatigue measurement via a vibrating cantilever beam for self-supported thin solid films. Exper Mech 46:503–517
210. Schwaiger R, Kraft O (1999) High cycle fatigue of thin silver films investigated by dynamic microbeam deflection. Scr Mater 41:823–829
211. Wang Y-C, Misra A, Hoagland RG (2006) Fatigue properties of nanoscale Cu/Nb multilayers. Scripta Mater 54:1593–1598
212. Zhu XF, Zhang GP (2009) Tensile and fatigue properties of ultrafine Cu–Ni multilayers. J Phys D Appl Phys 42:055411
213. Zhu XF, Zhang GP, Yan C, Zhu SJ, Sun J (2010) Scale-dependent fracture mode in Cu–Ni laminate composites. Philos Mag Lett 90:413–421
214. Zhang JY, Zhang X, Liu G, Zhang GJ, Sun J (2011) Dominant factor controlling the fracture mode in nanostructured Cu/Cr multilayer films. Mater Sci Eng A 528:2982–2987

215. Lashmore DS, Thomson R (1992) Cracks and dislocations in face-centered cubic metallic multilayers. J Mater Res 7:2379–2386
216. Zhu XF, Li YP, Zhang GP, Tan J, Liu Y (2008) Understanding nanoscale damage at a crack tip of multilayered metallic composites. Appl Phys Lett 92:161905
217. Hall EO (1951) The deformation and ageing of mild steel: III discussion of results. Proc Phys Soc B 64:747
218. Petch NJ (1953) The cleavage strength of polycrystals. J Iron Steel Inst 174:25–28
219. Hirth JP, Lothe J (1992) Theory of dislocations. Krieger, Malabar
220. Nix WD (1989) Mechanical properties of thin films. Metall Trans A 20:2217–2245
221. Friedman LH, Chrzan DC (1998) Scaling theory of the Hall–Petch relation for multilayers. Phys Rev Lett 81:2715–2718
222. Anderson PM, Foecke T, Hazzledine PM (1999) Dislocation-based deformation mechanisms in metallic nanolaminates. MRS Bull 24:27
223. Tu K, Mayer JW, Feldman LC (1992) Electronic thin film science: for electrical engineers and materials scientists. Macmillan, New York
224. Kramer DE, Foecke T (2002) Transmission electron microscopy observations of deformation and fracture in nanolaminated Cu-Ni thin films. Philos Mag A 82:3375–3381
225. Dehm G, Balk TJ, Edongué H, Arzt E (2003) Small-scale plasticity in thin Cu and Al films. Microelectron Engin 70:412–424
226. Zhang RF, Wang J, Beyerlein IJ, Germann TC (2011) Dislocation nucleation mechanisms from fcc/bcc incoherent interfaces. Scr Mater 65:1022–1025
227. Li N, Wang J, Misra A, Huang JY (2012) Direct observations of confined layer slip in Cu/Nb multilayers. Microsc Microanal 18:1155–1162
228. Wei QM, Li N, Mara N, Nastasi M, Misra A (2011) Suppression of irradiation hardening in nanoscale V/Ag multilayers. Acta Mater 59:6331–6340
229. Wei Q, Misra A (2010) Transmission electron microscopy study of the microstructure and crystallographic orientation relationships in V/Ag multilayers. Acta Mater 58:4871–4882
230. Akasheh F, Zbib HM, Hirth JP, Hoagland RG, Misra A (2007) Dislocation dynamics analysis of dislocation intersections in nanoscale metallic multilayered composites. J Appl Phys 101:084314
231. Akasheh F, Zbib HM, Hirth JP, Hoagland RG, Misra A (2007) Interactions between glide dislocations and parallel interfacial dislocations in nanoscale strained layers. J Appl Phys 102:034314
232. Nix WD (1998) Yielding and strain hardening of thin metal films on substrates. Scr Mater 39:545–554
233. Anderson PM, Li C (1995) Hall–Petch relations for multilayered materials. Nanostruct Mater 5:349–362
234. Chu HJ, Wang J, Beyerlein IJ, Pan E (2013) Dislocation models of interfacial shearing induced by an approaching lattice glide dislocation. Int J Plast 41:1–13
235. Embury JD, Hirth JP (1994) On dislocation storage and the mechanical response of fine scale microstructures. Acta Metall Mater 42:2051–2056
236. Mitlin D, Misra A, Radmilovic V, Nastasi M, Hoagland R, Embury DJ, Hirth JP, Mitchell TE (2004) Formation of misfit dislocations in nanoscale Ni–Cu bilayer films. Philos Mag 84:719–736
237. Mitlin D, Misra A, Mitchell TE, Hoagland RG, Hirth JP (2004) Influence of overlayer thickness on the density of Lomer dislocations in nanoscale Ni–Cu bilayer thin films. Appl Phys Lett 85:1686–1688
238. Mitlin D, Misra A, Mitchell TE, Hirth JP, Hoagland RG (2005) Interface dislocation structures at the onset of coherency loss in nanoscale Ni–Cu bilayer films. Philos Mag 85:3379–3392
239. Inglefield HE, Bochi G, Ballentine CA, O'Handley RC, Thompson CV (1996) Perpendicular magnetic anisotropy in epitaxial Cu/Ni/Cu/Si (001). Thin Solid Films 275:155–158

240. Misra A, Kung H, Hammon D, Hoagland RG, Nastasi M (2003) Damage mechanisms in nanolayered metallic composites. Int J Damage Mech 12:365–376
241. Misra A, Hirth JP, Kung H (2002) Single-dislocation-based strengthening mechanisms in nanoscale metallic multilayers. Philos Mag A 82:2935–2951
242. Verdier M (2004) Plasticity in fine scale semi-coherent metallic films and multilayers. Scr Mater 50:769–773
243. Lamm AV, Anderson PM (2004) Yield maps for nanoscale metallic multilayers. Scr Mater 50:757–761
244. Hoagland RG, Mitchell TE, Hirth JP, Kung H (2002) On the strengthening effects of interfaces in multilayer fcc metallic composites. Philos Mag A 82:643
245. Anderson PM, Carpenter JS (2010) Estimates of interfacial properties in Cu/Ni multilayer thin films using hardness data. Scripta Mater 62:325–328
246. Wang J, Misra A (2011) An overview of interface-dominated deformation mechanisms in metallic multilayers. Curr Opin Solid State Mater Sci 15:20–28
247. Wang J, Misra A, Hoagland RG, Hirth JP (2012) Slip transmission across fcc/bcc interfaces with varying interface shear strengths. Acta Mater 60:1503–1513
248. Was GS, Foecke T (1996) Deformation and fracture in microlaminates. Thin Solid Films 286:1–31
249. Wang J, Hoagland RG, Misra A (2009) Mechanics of nanoscale metallic multilayers: From atomic-scale to micro-scale. Scr Mater 60:1067–1072
250. Misra A, Verdier M, Kung H, Embury JD, Hirth JP (1999) Deformation mechanism maps for polycrystalline metallic multilayers. Scr Mater 41:973–979
251. Li Q, Anderson PM (2003) Dislocation confinement and ultimate strength in nanoscale metallic multilayers. MRS Symp Proc 791:Q5.19
252. Li Q, Anderson PM (2004) A three-dimensional cellular automaton model of dislocation motion in FCC crystals. Modell Simul Mater Sci Eng 12:929
253. McKeown J, Misra A, Kung H, Hoagland RG, Nastasi M (2002) Microstructures and strength of nanoscale Cu–Ag multilayers. Scripta Mater 46:593–598
254. Yadav SK, Ramprasad R, Misra A, Liu X-Y (2012) First-principles study of shear behavior of Al, TiN, and coherent Al/TiN interfaces. J Appl Phys 111:083505
255. Kong Y, Shen L, Proust G, Ranzi G (2011) Al–Pd interatomic potential and its application to nanoscale multilayer thin films. Mater Sci Eng A 530:73–86
256. Mastorakos IN, Zbib HM, Bahr DF (2009) Deformation mechanisms and strength in nanoscale multilayer metallic composites with coherent and incoherent interfaces. Appl Phys Lett 94:173114
257. Mastorakos IN, Bellou A, Bahr DF, Zbib HM (2011) Size-dependent strength in nanolaminate metallic systems. J Mater Res 26:1179–1187
258. Yan JW, Zhu XF, Zhang GP, Yan C (2013) Evaluation of plastic deformation ability of Cu/Ni/W metallic multilayers. Thin Solid Films 527:227–231
259. Saraev D, Miller RE (2006) Atomic-scale simulations of nanoindentation-induced plasticity in copper crystals with nanometer-sized nickel coatings. Acta Mater 54:33–45
260. Medyanik SN, Shao S (2009) Strengthening effects of coherent interfaces in nanoscale metallic bilayers. Comput Mater Sci 45:1129–1133
261. Li J, Lu H, Ni Y, Mei J (2011) Quasicontinuum study the influence of misfit dislocation interactions on nanoindentation. Comput Mater Sci 50:3162–3170
262. Cheng D, Yan ZJ, Yan L (2007) Misfit dislocation network in Cu/Ni multilayers and its behaviors during scratching. Thin Solid Films 515:3698–3703
263. Hoagland RG, Kurtz RJ, Henager CH Jr (2004) Slip resistance of interfaces and the strength of metallic multilayer composites. Scripta Mater 50:775–779
264. Henager CH Jr, Hoagland R (2004) A rebound mechanism for misfit dislocation creation in metallic nanolayers. Scr Mater 50:701–705
265. Kamat SV, Hirth JP (1990) Dislocation injection in strained multilayer structures. J Appl Phys 67:6844–6850

266. Rao SI, Hazzledine PM (2000) Atomistic simulations of dislocation–interface interactions in the Cu-Ni multilayer system. Philos Mag A 80:2011–2040

267. Henager CH Jr, Kurtz RJ, Hoagland RG (2004) Interactions of dislocations with disconnections in fcc metallic nanolayered materials. Philoso Mag 84:2277–2303

268. Wang J, Hoagland RG, Misra A (2008) Phase transition and dislocation nucleation in Cu–Nb layered composites during physical vapor deposition. J Mater Res 23:1009–1014

269. Wang J, Hoagland RG, Hirth JP, Misra A (2008) Atomistic simulations of the shear strength and sliding mechanisms of copper-niobium interfaces. Acta Mater 56:3109–3119

270. Demkowicz MJ, Wang J, Hoagland RG (2008) Interfaces between dissimilar crystalline solids. In: Hirth JP (ed) Dislocations in solids. Elsevier, Amsterdam, pp 141–205

271. Wang J, Hoagland RG, Liu XY, Misra A (2011) The influence of interface shear strength on the glide dislocation–interface interactions. Acta Mater 59:3164–3173

272. Wang J, Hoagland RG, Misra A (2009) Room-temperature dislocation climb in metallic interfaces. Appl Phys Lett 94:131910

273. Zhang RF, Wang J, Beyerlein IJ, Misra A, Germann TC (2012) Atomic-scale study of nucleation of dislocations from fcc–bcc interfaces. Acta Mater 60:2855–2865

274. Demkowicz MJ, Hoagland RG, Hirth JP (2008) Interface structure and radiation damage resistance in Cu-Nb multilayer nanocomposites. Phys Rev Lett 100:136102

275. Kang K, Wang J, Beyerlein IJ (2012) Atomic structure variations of mechanically stable fcc-bcc interfaces. J Appl Phys 111:053531

276. Kang K, Wang J, Zheng SJ, Beyerlein IJ (2012) Minimum energy structures of faceted, incoherent interfaces. J Appl Phys 112:073501

277. Keralavarma SM, Benzerga AA (2007) A discrete dislocation analysis of strengthening in bilayer thin films. Modell Simul Mater Sci Eng 15:S239

278. Anderson PM, Li C (1993) Crack-dislocation modeling of ductile-to-brittle transitions in multilayered materials. MRS Symp Proceed 308:731

279. Ghoniem NM, Han X (2005) Dislocation motion in anisotropic multilayer materials. Philos Mag 85:2809–2830

280. Fertig RS, Baker SP (2009) Simulation of dislocations and strength in thin films: a review. Prog Mater Sci 54:874–908

281. Pant P, Schwarz KW, Baker SP (2003) Dislocation interactions in thin FCC metal films. Acta Mater 51:3243–3258

282. Fertig RS III, Baker SP (2010) Dislocation dynamics simulations of dislocation interactions and stresses in thin films. Acta Mater 58:5206–5218

283. Fertig RS III, Baker SP (2011) Threading dislocation interactions in an inhomogeneous stress field: a statistical model. Scr Mater 65:384–387

284. Akasheh F, Zbib HM (2008) Multiscale modeling and simulation of deformation in nanoscale metallic multilayered composites. In: Kwon YW, Allen DH, Talreja R (eds) Multiscale modeling and simulation of composite materials and structures. Springer US, New York, pp 235–270

285. Quek SS, Xiang Y, Zhang YW, Srolovitz DJ, Lu C (2006) Level set simulation of dislocation dynamics in thin films. Acta Mater 54:2371–2381

286. Quek SS, Wu Z, Zhang Y-W, Xiang Y, Srolovitz DJ (2007) Dislocation junctions as barriers to threading dislocation migration. Appl Phys Lett 90:011905

287. Quek SS, Zhang YW, Xiang Y, Srolovitz DJ (2010) Dislocation cross-slip in heteroepitaxial multilayer films. Acta Mater 58:226–234

288. Li Q, Anderson PM (2005) Dislocation-based modeling of the mechanical behavior of epitaxial metallic multilayer thin films. Acta Mater 53:1121–1134

289. Wang YU, Jin YM, Khachaturyan AG (2003) Phase field microelasticity modeling of dislocation dynamics near free surface and in heteroepitaxial thin films. Acta Mater 51:4209–4223

290. Tan XH, Shen Y-L (2005) Modeling analysis of the indentation-derived yield properties of metallic multilayered composites. Compos Sci Technol 65:1639–1646

291. Tang G, Shen Y-L, Chawla N (2008) Plastic deformation during indentation unloading in multilayered materials. J Appl Phys 104:116102
292. Tang G, Shen Y-L, Singh DRP, Chawla N (2010) Indentation behavior of metal-ceramic multilayers at the nanoscale: numerical analysis and experimental verification. Acta Mater 58:2033–2044
293. Singh DRP, Chawla N, Tang G, Shen Y-L (2010) Micropillar compression of Al/SiC nanolaminates. Acta Mater 58:6628–6636
294. Frank FC, van der Merwe JH (1949) One-dimensional dislocations. I. static theory. Proc R Soc Lond A 198:205–216
295. Hirth JP, Feng X (1990) Critical layer thickness for misfit dislocation stability in multilayer structures. J Appl Phys 67:3343–3349
296. Feng X, Hirth JP (1992) Critical layer thicknesses for inclined dislocation stability in multilayer structures. J Appl Phys 72:1386–1394
297. Kreidler ER, Anderson PM (1996) Orowan-based deformation model for layered metallic materials. MRS Symp Proc 434:159–172
298. Chu X, Barnett SA (1995) Model of superlattice yield stress and hardness enhancements. J Appl Phys 77:4403–4411
299. Rao SI, Hazzledine PM, Dimiduk DM (1995) Interfacial strengthening in semi-coherent metallic multilayers. MRS Symp Proc 362:67
300. Friedman LH (2004) Towards a full analytic treatment of the Hall–Petch behavior in multilayers: putting the pieces together. Scr Mater 50:763–767
301. Fang L, Friedman LH (2007) Analytic treatment of metallic multilayer strength at all length scales: influence of dislocation sources. Acta Mater 55:1505–1514
302. Schoeck G (2005) The Peierls model: progress and limitations. Mater Sci Eng A 400–401:7–17
303. Shen Y, Cheng X (2009) Dislocation movement over the Peierls barrier in the semi-discrete variational Peierls framework. Scr Mater 61:457–460
304. Shen Y, Anderson PM (2007) Transmission of a screw dislocation across a coherent, non-slipping interface. J Mech Phys Solids 55:956–979
305. Anderson PM, Li Z (2001) A Peierls analysis of the critical stress for transmission of a screw dislocation across a coherent, sliding interface. Mater Sci Eng A 319–321:182–187
306. Shen Y, Anderson PM (2006) Transmission of a screw dislocation across a coherent, slipping interface. Acta Mater 54:3941–3951
307. Shehadeh MA, Lu G, Banerjee S, Kioussis N, Ghoniem N (2007) Dislocation transmission across the Cu/Ni interface: a hybrid atomistic–continuum study. Philos Mag 87:1513–1529
308. Oliver WC, Pharr GM (1992) An improved technique for determining hardness and elastic modulus using load and displacement sensing indentation experiments. J Mater Res 7:1564–1583
309. Oliver WC, Pharr GM (2004) Measurement of hardness and elastic modulus by instrumented indentation: advances in understanding and refinements to methodology. J Mater Res 19:3–20
310. Dao M, Chollacoop N, Van Vliet KJ, Venkatesh TA, Suresh S (2001) Computational modeling of the forward and reverse problems in instrumented sharp indentation. Acta Mater 49:3899–3918
311. Cheng Y-T, Cheng C-M (2004) Scaling, dimensional analysis, and indentation measurements. Mater Sci Eng R 44:91–149
312. Gram MD, Carpenter JS, Misra A, Anderson PM. Interpreting hardness data in nanoscale multilayer thin films (in preparation)
313. Shen Y-L, Blada CB, Williams JJ, Chawla N (2012) Cyclic indentation behavior of metal–ceramic nanolayered composites. Mater Sci Eng A 557:119–125
314. Tang G, Shen Y, Singh D, Chawla N (2008) Analysis of indentation-derived effective elastic modulus of metal-ceramic multilayers. Int J Mech Mater Des 4:391–398

315. Zhang H, Schuster BE, Wei Q, Ramesh KT (2006) The design of accurate micro-compression experiments. Scripta Mater 54:181–186
316. Shade PA, Wheeler R, Choi YS, Uchic MD, Dimiduk DM, Fraser HL (2009) A combined experimental and simulation study to examine lateral constraint effects on microcompression of single-slip oriented single crystals. Acta Mater 57:4580–4587
317. Kiener D, Motz C, Dehm G (2009) Micro-compression testing: a critical discussion of experimental constraints. Mater Sci Eng A 505:79–87
318. Schwaiger R, Weber M, Moser B, Gumbsch P, Kraft O (2012) Mechanical assessment of ultrafine-grained nickel by microcompression experiment and finite element simulation. J Mater Res 27:266–277
319. Lotfian S, Rodríguez M, Yazzie KE, Chawla N, Llorca J, Molina-Aldareguía JM (2013) High temperature micropillar compression of Al/SiC nanolaminates. Acta Mater. doi:10.1016/j.actamat.2013.04.013

Properties of Diamond Nanomaterials 17

Tad Whiteside, Clifford Padgett, and Amanda Mcguire

Introduction

Nanosized diamond represents an important division of carbon nanostructures and has a large number of potential uses in many areas of science and technology, such as molecular-scale computing devices, drug delivery, material coatings, and reinforcing agents in composite material. Diamond nanostructures are defined as sp^3-hybridized carbon atoms bound to other sp^3-hybridized carbon atoms whose size in the largest performance-sensitive dimension is typically less than 100 nm. Within this division of materials there exist three primary classes or '*dimensionalities*': pseudo-zero dimensional diamond nanoparticles, one-dimensional diamond nanowires, and two-dimensional diamond nanofilms. In this article, we present an overview of the sizes of the materials, their current and proposed uses, the methods of synthesis and characterization, and their various properties.

T. Whiteside (✉)
Savannah River National Laboratory, Aiken, SC, USA
e-mail: tad.whiteside@srnl.doe.gov

C. Padgett • A. Mcguire
Department of Chemistry and Physics, Armstrong Atlantic State University, Savannah, GA, USA
e-mail: clifford.padgett@armstrong.edu; am5232@students.armstrong.edu

Diamond Nanoparticles

Diamond nanoparticles typically range from 2 to 100 nm in size. They are created by multiple means and have many unique uses. Most diamond nanoparticles have a diamond (sp^3) carbon core and are surrounded by an amorphous (sp^2) carbon shell. These nanoparticles have found uses as reinforcing agents in composite material, as drug delivery systems, as biological imaging agents, and as catalysts.

Synthesis

Diamond nanoparticles have been synthesized using several techniques, such as explosive detonation, chemical vapor deposition, plasma vapor deposition, laser ablation, hydrodynamic cavitation, and irradiation of other forms of carbon with ions or electrons. Bulk synthesis of diamond nanoparticles is produced by detonation of explosives (containing excess carbon relative to the amount of oxygen present). In this process, diamond nanoparticles are synthesized in the high-pressure-high-temperature conditions found within the shock wave created during detonation. Under these conditions, diamond nanoparticles between 3 and 5 nm are typically found in the soot, which can be up to 80 % by weight in diamond nanoparticles [1–4].

Diamond nanoparticles have also been synthesized from carbon nanotubes and graphite under high-pressure-high-temperature methods [5]. Using these methods, diamond nanoparticles exhibit higher oxygen content than ones made from graphite (7.34 % vs. 5.8 %). It is believed that this is due to the carbon nanotube structure, which is more likely to contain oxygen than the structure of graphite [6]. As a result, the properties of these diamond nanoparticles may have enhanced biological applications [7].

Cavitation experiments have shown that diamond nanoparticles can be successfully created in a reproducible manner using a carbon-containing contact liquid. Hydrodynamic cavitation provides a new way to control impurities, defects, structure, size, and other properties. The physics of cavitation bubbles collapsing and of shock wave compression (detonation) is very similar and allows for investigation of the rapid cooling process in detonation experiments, which is known to be important in the formation of diamond nanoparticles [8]. The hydrodynamic cavitation of benzene generated diamond nanoparticles, which range from 5 to 20 nm, as well as aggregates of other carbon nanostructures [8].

Pulsed laser-induced liquid–solid interfacial reaction has been used to generate diamond nanoparticles in various shapes including cubic and hexagonal structures [9–14]. The mechanism of this laser-based material processing method for the nucleation and growth of the diamond nanoparticles is not well understood. The diamond nanoparticles form via the condensation of water on the ablated graphite, which is formed by a laser-induced plasma at the liquid–solid interface. This system reaches pressures in the range of 10–15 GPa and temperatures in the range of 4,000–5,000 K [10].

Characterization

Diamond nanoparticles are generally characterized in one of two states: either dispersed into a solution or incorporated into a composite material. The most common characterizing methods are microscopy (atomic force microscopy (AFM), scanning electron microscopy (SEM), and/or transmission electron microscopy (TEM)); spectroscopy (UV–vis, FTIR, and X-ray photoelectron spectroscopy (XPS)); and crystallography (X-ray diffraction (XRD)). Other characterization techniques, such as thermogravimetric analysis (TGA), have also been used.

AFM/SEM/TEM

AFM is used to probe the surface topography of the diamond nanoparticles [15, 16]. These results can characterize the diamond nanoparticle grain size in composite structures as well as the thickness and roughness of the composite film [16]. SEM and TEM images provide details of the morphologies (shape/structure) of the nanoparticles as well as their dispersion on the substrate or within a composite [15–21]. These images are used to examine how these morphologies change as synthesis methods change [20]. They are also used to characterize the impurities or other structures present within the composite materials [17].

UV–Vis

UV–vis spectroscopy is used to characterize diamond nanoparticle dispersions and films [17, 22, 23]. For diamond nanoparticles, the absorption dies off rapidly (transmittance increases) at wavelengths greater than 200 nm. When these particles are annealed at high (+1,000 K) temperatures, the diamond cores turn into fullerene-like carbon onions, and an absorption peak around 263 nm appears. This is due to the increase in sp^2 sites and a corresponding decrease in sp^3 sites [17, 22].

FTIR

FTIR spectroscopy is used to track the changes in functionalization of the surface of diamond nanoparticles as experimental conditions change [19, 24]. It is also used to measure the types of bonds formed between the nanoparticles and their surroundings [25]. For example, to determine if diamond nanoparticles are chemically bonded to ethylenediamine, there should be bands present in the FTIR spectra. If they are only adsorbed onto ethylenediamine, these bands will be missing. The FTIR spectra show the bands; thus, diamond nanoparticles bond to ethylenediamine [25].

XRD

The typical XRD pattern of diamond nanoparticles shows sharp peaks at approximately 42, 75, and 95 2θ which correspond to the (111), (220), and (311) facets of diamond; see Fig. 17.1 [7, 15, 16]. If the diamond nanoparticles are embedded in an amorphous matrix, the XRD peaks will be very broad or absent [16].

Fig. 17.1 XRD spectra of diamond nanoparticles
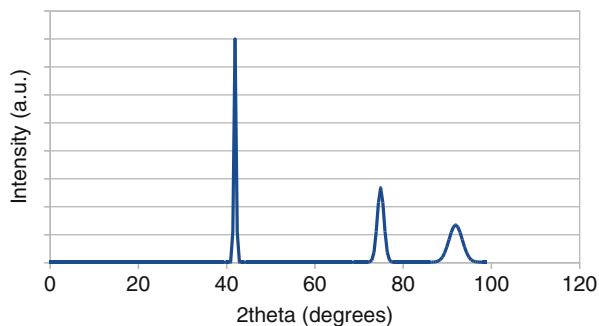
TGA

Thermogravimetric analysis is a complementary method to FTIR and is used to provide additional information in support of the description of the composition of functionalized diamond nanoparticles [24, 25].

Properties

Biological

Diamond nanoparticles have been conjugated with many different biomolecules, including nucleic acids, proteins, and biotins [26]. These conjugated systems retain much of their functionality and activity, and it has been shown that they can actively target specific cells and organs [26]. One example of this conjugation is the adsorption of the proteins albumin, γ-globulin, and lysozyme onto 5 nm and 100 nm diamond nanoparticles. This conjugation was measured using FTIR [27], and it was shown that these proteins most readily adsorb onto the 5 nm nanoparticles due to their larger surface area [27]. Additionally, this adsorption causes changes in the FTIR spectra, particularly those spectra of the 5 nm nanoparticles, which is most likely due to structural deformations of the adsorbed protein [27]. Diamond nanoparticles created from carbon nanotubes under high pressure and high temperature have more oxygen-containing functional groups than diamond nanoparticles prepared from graphite [7]. These nanoparticles have a negative charge of −27 mV and as such bond readily with dopamine. When these dopamine-diamond nanoparticles were placed in water, they formed a stable (2-day) suspension, compared to a diamond nanoparticle suspension which was only stable for 7 h [7]. Analysis via small-angle X-ray scattering spectroscopy suggests that the dopamine-diamond nanoparticles have an 11.4 % smaller surface interface than diamond nanoparticles [7].

Diamond nanoparticles are efficient biological imaging agents in that they are bright emitters with a high efficiency and do not exhibit photobleaching or blinking [26]. These properties allow the tracking of single particles within cells by the use of one- or two-photon excitation [26].

Diamond nanoparticles can be added to cells in concentrations up to $400\ \mu g\ mL^{-1}$ without showing reduction in activity [26]. The cytotoxicity of nanodiamond has also been measured against mitochondrial function, luminescent ATP production, osteoblast differentiation, and others. None of these processes show a reduction in cell viability [21, 26].

Chemical

When diamond nanoparticles are incorporated into a Ni-P composite, the composite structure has excellent corrosion resistance as compared to conventional Ni-P structures [16]. This is likely due to the nanodiamond particles lowering the chemical activity of the Ni-P film [16].

Mechanical

Diamond nanoparticles have been incorporated into liquid paraffin at 0.2 % by weight. This incorporation caused a decrease in the friction coefficient by approximately 0.01 (from 0.09 to 0.08) [19]. A similar decrease is seen when diamond nanoparticles are incorporated into Ni-P films and in TiO_2 films [15, 16]. In the TiO_2 films, when nanodiamond is added at more than 1 % by weight, the coefficient of friction increases. This is likely due to the synthesis technique used to create the diamond-TiO_2 composite [15].

Functionalizing the surface of diamond nanoparticles generally increases the stiffness and hardness of the material the functionalized nanodiamond is incorporated into. When diamond nanoparticles are doped with amines or carboxylic acid and mixed with an epoxy resin, these particles react with the resin to covalently incorporate the nanodiamond particle into the polymer network [25]. For 7 % by weight nanodiamond-amines, this incorporation improved the Young's modulus of the epoxy from 0.3 to 3.0 GPa and the hardness from 0.5 to 90 MPa [25]. For 7 % by weight nanodiamond-carboxylic acid, the Young's modulus increased to 2.0 GPa and the hardness increased to 30 MPa [25]. When diamond nanoparticles were incorporated into another polymer, poly(L-lactic acid) (PLLA), the Young's modulus was also observed to increase from 2.6 to 6.8 GPa at 7 % by weight nanodiamond [21]. The hardness also increased from 0.05 to 0.31 GPa [21]. When diamond nanoparticles are incorporated into Ni-P films, the hardness of those films is also observed to increase [16].

Optical

Diamond nanoparticles synthesized such that vacancies are next to nitrogen impurities create color centers that have strong fluorescence and are resistant to photobleaching [26, 28, 29].

Diamond nanoparticles are weak optical limiters (where the transmittance of a material reaches a constant value, even as light intensity increases) [17]. The transmittance of diamond nanoparticles is also limited through an applied voltage. In polymer-dispersed liquid crystals (PDLC), diamond nanoparticles limit the transmittance as a voltage is applied across the film [30]. For undoped PDLC,

the transmittance increases from 0 % to 60 % as the voltage increases to 100 V and then levels off as the voltage increases beyond 100 V [30]. For PDLC doped with 1 % by weight diamond nanoparticles, the transmittance increases to 40 % as voltage increases to 40 V and then levels off as the voltage is increased [30].

The refractive index of a poly(vinyl alcohol) (PVA) polymer film increases with increasing quantities of embedded diamond nanoparticles [23]. The refractive index increases linearly from 1.52 for pure PVA to 1.88 for 60 % by volume diamond nanoparticles [23]. These are similar results to those found in Vlaeva et al. [31]. In the work of Vlaeva et al. [31], the PVA's refractive index increases from 1.488 to 1.505 at 1 % by weight diamond nanoparticles [31].

Physical

When 0.67 % by weight diamond nanoparticles are added to an epoxy resin, the dielectric permittivity of the resin decreases by approximately 1.5 from 5.75 to 4.25 [18]. This decrease is due to the diamond nanoparticles causing an increase in the number of cross-links to be formed during the resin's curing process, thereby strengthening the resin and disabling its ability to orient under an applied electric field [18]. Similar results are noted when diamond nanoparticles are added to a benzocyclobutene film. In this case, the permittivity decreases from 2.65 to 2.5 to 2.25 as 0.5 % and 1.5 % by weight diamond nanoparticles are added to the mixture [20]. However, as the weight percent of diamond nanoparticles increases in the benzocyclobutene mixture, the relative permittivity increases. This is likely caused by the hydrophobicity of the benzocyclobutene and the surface properties of the diamond nanoparticles by creating an 'air gap' surrounding the nanoparticles [20].

Thermal

When diamond nanoparticles are incorporated into benzocyclobutene at more than 4 % by weight, an increase of thermal conductivity by 40 % is observed (from 0.23 to 0.34 W m^{-1} K^{-1}) [20].

As diamond nanoparticles are incorporated into a copper film, the thermal expansion coefficient of these films decreases, up to a 20 % by volume content of nanoparticles, after which it increases [32]. This increase is likely due to high specimen porosity and the low strength of the bond between the copper and diamond nanoparticles [32].

Diamond Nanowires

Diamond nanowires are generally defined as 'one-dimensional' structures primarily composed of sp^3-bonded carbon atoms arranged in a cylinder with a diameter size on the order of nanometers and a length which ranges from nanometers to microns. These materials are usually created through an etching process and can be functionalized to improve their bonding and use in composite materials.

While the use of diamond nanowires in applications is still at the experimental stage, they have many potential uses, including as components of molecular-scale computing devices, as reinforcing agents to be mixed with polymers, and as thermal management materials.

Synthesis

Diamond nanowires are created through a variety of techniques, primarily through etching diamond film or through the growth from diamond nucleation sites. The original description in the literature used air plasma to etch remove a polycrystalline diamond film coated with a molybdenum mask to form well-aligned, uniformly dispersed diamond nanowires up to 60 nm in diameter [33]. Another method creates diamond nanowires on the order of 50–200 nm in diameter and several microns in length by reactive-ion etching single-crystal diamond substrates using oxide or aluminum impurities within the substrate, each of which acts as a micro-mask [34]. Diamond nanowires can also be created by using gold nanodots as the etching mask in a hydrogen/argon plasma [35].

Most plasma-assisted etching methods use a mask to protect the carbon underneath the mask [33–35]. In 2009, a 'mask-free' process to fabricate an array of boron-doped diamond nanowires was reported. The described mechanism had boron oxide form on the surface of the film and then serve as the etching mask during this process [36]. However, it was later shown that diamond nanowire arrays could be fabricated using the same mask-free process without boron [37, 38]. In fact, very long aligned one-dimensional (submicron) diamond nanowires have been reported using mask-free processes from a polished polycrystalline substrate and oxygen plasma etching [39]. It should be noted that in the 'mask-free' etching process, the mask is generally self-generating. In the case of Lin et al. [39], the mask is Fe_2O_3, generated from the steel substrate holder.

A growth technique uses microwave plasma-assisted chemical vapor deposition with the aid of an anodic aluminum oxide template and 50 nm diamond nanoparticle nucleation sites to create arrays of polycrystalline diamond nanowires 300 nm in diameter and up to 5 μm long [40]. Smaller diamond nanowires have been synthesized using a hydrogen plasma posttreatment of multiwalled carbon nanotubes. This process resulted in single-crystalline diamond nanowires with diameters of 8–10 nm and lengths up to 200 nm. These diamond nanowires had a core-sheath structure with the outer shell being composed of amorphous carbon while the inner core was diamond. The nanowires grew along the (110) direction. The researchers proposed a growth mechanism similar to the silicon oxide-assisted growth mechanism seen in Si nanowires [41, 42]. Diamond nanowires have also been created from C_{60} fullerenes using high temperature and pressure in a multi-anvil apparatus. The individual diamond nanowires that make up the aggregates were 5–20 nm in diameter and longer than 1 μm [43]. Diamond nanowires with diameter in the range of 3–5 nm and lengths up to 200 nm have been synthesized from the hydrogen plasma posttreatment of nanocrystalline diamond films. In this

process, the diamond nanowires grow from graphite clusters that are created by the etching of carbon film (both diamond and non-diamond); these clusters then recrystallized to form nanodiamond which grew into the diamond nanowires [44]. Argon-rich microwave plasma chemical vapor deposition containing nitrogen and methane has been used to grow diamond nanowires on Si wafers [45]. This generally produces diamond nanowires covered by amorphous carbon, but improvements in the method have resulted in increased efficiency and the generation of graphite-coated single-crystalline diamond nanowires whose core was 2–5 nm in diameter and tens of nanometers long. The graphite encapsulation was variable in thickness and was enhanced by the content of nitrogen gas used [46].

Simulated Properties

Mechanical

Simulations of diamond nanowires with different diameters and with different crystal plane orientations ((111), (011), (001)) along the axis have been carried out to predict the elastic stiffness and tensile fracture force of these materials. The results from these simulations suggest that for diamond nanowires with a diameter greater than 6 nm, the elastic stiffness and tensile fracture force would exceed that of carbon nanotubes, depending on the axial orientation of the diamond nanowire [47].

Physical

With the aid of molecular modeling and a many-body bond order potential, the binding energy for several diamond nanowires with different axial orientations was calculated, and it was shown to be comparable to that of single-walled carbon nanotubes [47].

First principle calculations have been used to determine the thermodynamic stability of diamond nanowires and their preferred morphologies. The results from these calculations suggest that the (111) facets lead to partial graphitization and that bare (001) surfaces undergo dimer pairing surface reconstructions to reduce the number of radical sites. The (011) facets largely preserve the diamond structure and result in stable diamond nanowires [48]; in addition this morphology also had the smallest calculated heat of formation [49]. Other morphologies have been explored using a bond order potential by Brenner [50] to calculate the heat of formation for structures that represent the six different morphologies corresponding to the (001) and (011) principal axes and low-index facets [51]. These calculations showed that stability is based on a combination of surface and axis orientation, which is consistent with experimental observations of diamond nanowire growth in the (011) direction [41]. Simulations of the phase stability of diamond nanowires using a heat of formation model also predict that the stability is dependent on morphology and nanowire diameter. This indicates that diamond nanowires occupy a 'window of stability' that ranges from 3 to 9 nm in diameter [52].

Thermal

Molecular dynamics simulations were used to calculate the thermal conductivity of diamond nanowires and the results compared to those of carbon nanotubes, using the Brenner potential [50]. In these simulations, the dependency of the thermal conductivity on length, temperature, and boundary condition was examined and the thermal conductivity was found to be extremely dependent on the nanowire (or nanotube) length, especially at the shorter lengths. The thermal conductivity of a (10, 10) nanotube varied from 215 $W\,m^{-1}\,K^{-1}$, for a 50 nm periodic box length, to 831 $W\,m^{-1}\,K^{-1}$, for a 1 μm box. Simulations of the nanowires suggest they have a much lower thermal conductivity than carbon nanotubes. This is probably due to the increased number of scattering sites on the nanowire surfaces [53]. Calculations have also shown that thermal conductivity of diamond nanowires is less affected by surface functionalization than similarly sized carbon nanotubes and that above 3 % surface functionalization diamond nanowires are better thermal conductors than carbon nanotubes. This makes them valuable for building thermal management polymers [54].

Electronic

Density functional tight-binding calculations have been used to examine the electronic properties of diamond nanowires. The result of these calculations indicates that both of these materials may exhibit metallic and semiconducting electrical properties, depending on their morphology and size. The band gap energy for all large diamond nanowires (area greater than 150 $\mathring{A}^2$) was metallike with the gap energy equal to zero. Smaller nanowires had a band gap energy ranging from 0 to 0.60 eV, depending on size and morphology [48].

Measured Properties

Mechanical

The strength and hardness of aggregated diamond nanowires have been extrapolated from X-ray diffraction (XRD) data and measured using a Vickers-type indenter. The XRD data suggest that the density of aggregated diamond nanowires is 0.2–0.4 % higher than that of bulk diamond and their isothermal bulk modulus is 491 GPa (bulk diamond is 442 GPa). The indentation measurements indicate that the hardness of aggregated diamond nanowires exceeds 100 GPa. In addition, these diamond nanowires scratched the (111) faces of natural single-crystal diamond [43]. These measurements show that diamond nanowires have the lowest measured compressibility and are the densest of all carbon materials [43]. Aggregated diamond nanowires overcome many of the problems associated with the use of single-crystal diamond abrasives, such as the tendency to undergo graphitization at elevated temperature, low fracture toughness, and being directionally dependent for many of its physical properties. Aggregated diamond nanowires have a fracture toughness of 11 $MPa*m^{0.5}$, which exceeds that of both natural and synthetic diamonds (3–5 $MPa*m^{0.5}$) [55].

Aggregated diamond nanowire samples show the enhancement of wear resistance up to 300 % in comparison with commercially available polycrystalline diamonds; in addition, these diamond nanowires show no reaction with iron (to form iron carbide) that typically limits the use of diamond in the cutting of steel and other iron-containing alloys. This makes them extremely attractive materials for applications as super-abrasives [56].

Using indentation experiments and atomistic simulations, characteristic load–displacement curves have been generated and used to determine the mechanical properties of diamond nanowires. The results indicate these substances undergo elastic deformation during indentation, with the force exerted on the indenter varying as the depth raised to the power 1.6 [57]. The values from these experiments show that diamond nanowires have a similar value for hardness as diamond and the elastic modulus value exceeded that of diamond in some cases. The indentation measurements are very precise for diamond and diamond films; however, the measurements on aggregated diamond nanowires show large variation in the measured values due to inhomogeneity in the material [57].

Optical

The optical properties of diamond nanowires have been measured and compared to those of diamond and diamond films via Raman and infrared spectroscopy. In general, a strong peak around $1{,}332$ cm^{-1} (characteristic peak of diamond) and a broad peak around $1{,}500$–$1{,}600$ cm^{-1} are observed in the Raman spectrum of nanocrystalline diamond (corresponding to the (100) facet). The broadness of the peak is used to determine the size and purity of these nanowires and crystalline diamond [58].

Diamond Nanofilms

Diamond-like carbon (DLC) thin films are sheets of amorphous sp^2-bonded (graphite-like) carbon bound to crystalline phases of sp^3-bonded (diamond-like) carbon [59]. The size of the crystalline phases typically ranges from 5 to 50 nm, and the film's thickness is usually less than 100 nm. These films were first synthesized and characterized by Aisenberg and Chabot in the early 1970s and are typically created through chemical vapor deposition. The ratio of the sp^3 to sp^2 bonds in the carbon network determines the characteristics of the DLC films [59]. The sp^3-bonded carbons govern the mechanical properties and the sp^2-bonded carbons, which are near the Fermi level, control the electronic and optical properties [60]. Overall, these films have characteristics similar to that of macroscale diamond: optically transparent, large index of refraction, biocompatible, electrically insulating, high hardness, low friction, resistance to acid, and low dielectric constant [61].

The optical and electrical properties of DLC films make them ideal for magnetic storage media and optical coating applications. In addition, their mechanical properties of high hardness and low friction have led to much interest in using these films for coatings used in precision manufacturing and machining. After overcoming

substrate adhesion issues, many objects are now being coated with DLC films and used in areas ranging from metal cutting taps and extrusion dies to engine cam shafts and medical bone saws [62, 63]. Coating implantable medical devices with DLC films is routinely done due to their wear resistance and high biocompatibility. They have recently been fabricated as self-supporting foils at widths of less than 5 nm and used for laser-driven ion acceleration [64].

Synthesis

Many techniques have been used to create DLC films including ion beam deposition/sputter deposition (physical vapor deposition – PVD) [60, 61, 65–67], plasma-enhanced deposition from a hydrocarbon gas (chemical vapor deposition – CVD) [59, 68–77], cathodic arc [64, 78], laser ablation [79–81], and electrodeposition [82–85]. Based on a literature review, the simplest and most commonly used techniques in a research environment are CVD and electrodeposition. For commercial applications, a hybrid technique – known as closed-field unbalanced magnetron sputter ion plating – combines the PVD and CVD methods to create durable, high-quality DLC films.

The general method to create DLC films using CVD is to use glass, SnO_2-coated glass, or a monocrystalline Si wafer as the substrate. This substrate is kept at a low temperature (300–500 K) in a low-pressure (1–1,000 Pa) chamber. It is exposed to a precursor carbon source, such as methane or acetylene, and a carrier gas, like argon or nitrogen, in the presence of an energy source, such as a hot filament, microwave power, or a plasma arc discharge for less than 1 h. The ratio of carbon source to carrier gas is the primary mechanism that controls the film's creation and properties. However, these properties are also affected by the temperature, pressure, energy source, and deposition time. The CVD method is typically used to create films that range from 10 to 100 nm thick. The following references have complete details on individual experiments where the above parameters are varied and described in detail: [59, 60, 68–77, 86, 87].

When electrodeposition is used to create DLC films, the substrate is mounted at the anode and a graphite plate is mounted at the cathode within an electrolytic cell. The distance between the two plates is less than 10 mm. The electrolytic bath typically consists of an aqueous or liquid carbon source, such as methanol, DMSO, or acetic acid. The voltage used depends on the electrolytic solution and varies between 2.5 V and 800 V. The temperature of the solution is mild, ranging between 300 and 400 K. The deposition rate varies between 10 and 100 nm h^{-1}. The following references have complete experimental details: [82–85].

Characterization

DLC films are characterized using the standard techniques of microscopy and spectroscopy. The most common characterizing methods used are atomic force

microscopy (AFM), Raman spectroscopy, X-ray diffraction (XRD), and X-ray photoelectron spectroscopy (XPS). Other techniques, such as transmission electron microscopy (TEM) and scanning electron microscopy (SEM), are also used, but mainly to complement the results obtained by the previous methods.

AFM

AFM is used to determine the surface topographical information about the DLC films. AFM results also show that the substrate surface greatly influences the final DLC film topography [59]. For etched surface substrates, the final DLC film roughness decreases as deposition time increases. For substrates with a powder coating, the final DLC film roughness increased as deposition time increased. For both types of substrates, the final average surface roughness was between 20 and 50 nm [59]. This value is in keeping with the measured surface roughness by other researchers [64, 71, 75, 84].

SEM and TEM

SEM and TEM images provide details of the morphologies of the DLC films [68, 72, 74, 76, 83, 86]. Multiple SEM and TEM images can be used to examine how these morphologies change as synthesis methods change. In addition to morphologies, SEM can be used to analyze the films thickness [74, 86]. It is also used for DLC films containing dopants, to characterize the density and dispersion of the dopants [60, 85].

Raman

The composition of the DLC films can be characterized using Raman spectroscopy. A typical Raman spectrum of a DLC film has the general shape shown in Fig. 17.2. There are two distinctive primary peaks: the G-peak and the D-peak. The G-peak and D-peak terminology is from carbon nanotube (CNT) nomenclature, with the G-peak meaning 'graphitic-carbon' (sp^2 carbon) and the D-peak meaning 'disorder' (sp^3 carbon) because in CNTs, most of the atoms are sp^2 atoms and the tube ends or defects are sp^3 carbons. The G-peak occurs between 1,550 and 1,575 cm^{-1} and the intensity is a measure of the number of sp^2 sites within the film; the width of the G-peak is indicative of the environment of the sp^2 sites. A broad G-peak means the sp^2 sites are within the carbon matrix and are bonded to atoms with many different vibrational frequencies, such as sp^3 carbons and hydrogen. The D-peak occurs between 1,325 and 1,375 cm^{-1} and the intensity is a measure of the number of sp^3 sites within the film [85]. This peak also tends to be broad because the sp^3 carbons are bound to terminal hydrogens, other sp^3 carbons, sp^2 carbons, etc. The ratio of these peaks (I_D/I_G) is a measure of the amount of sp^3 sites in the carbon matrix and is used to categorize the DLC film [60]. The exact wave number of these peaks may shift due to the bonding environment [70]. There may be a peak near 1,150 cm^{-1}, which has been related to the calculated phonon density of states of diamond [68]. However, other groups have assigned it to transpolyacetylene [71], and, due to the noise in most spectra, this peak may not actually be present.

Fig. 17.2 Typical Raman spectra of DLC film obtained at 300 K
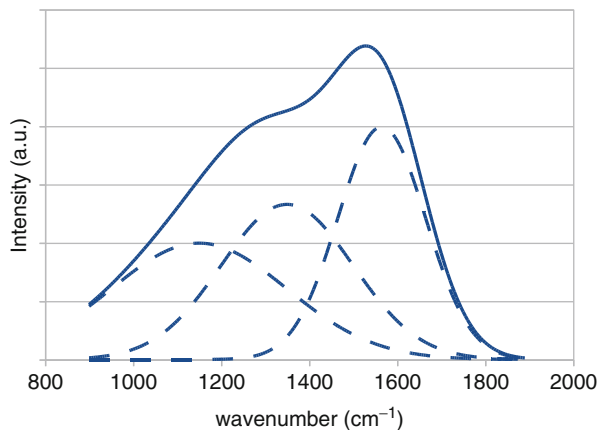
Fig. 17.3 XPS wide survey spectra of pure DLC
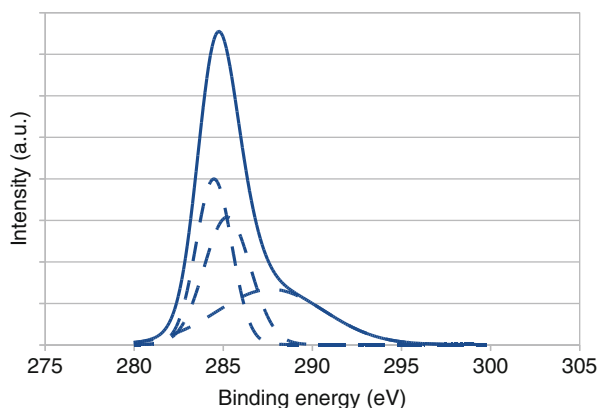
XPS

XPS is a useful technique to examine solid-state samples and provides an estimate of the chemical composition. A typical C_{1s} spectrum of a DLC film is shown in Fig. 17.3. The solid line is the measured values. The dashed lines are the deconvoluted peaks: the sp^2-hybridized peak is around 284.5 eV, the sp^3 hybridized is around 285 eV, and the peak around 287 is likely due to CO bonds formed by the air and the sample [67, 77, 83, 84].

XRD

The XRD patterns of the DLC films depend upon the growth conditions. A sample XRD pattern is shown in Fig. 17.4. If diamond is present, there will be peaks around 42 2θ for the (111) facet and around 75 2θ for the (220) facet. If there are no peaks, then the film is amorphous [70, 75].

Fig. 17.4 Example of XRD spectra showing cubic diamond planes of (111) and (220)
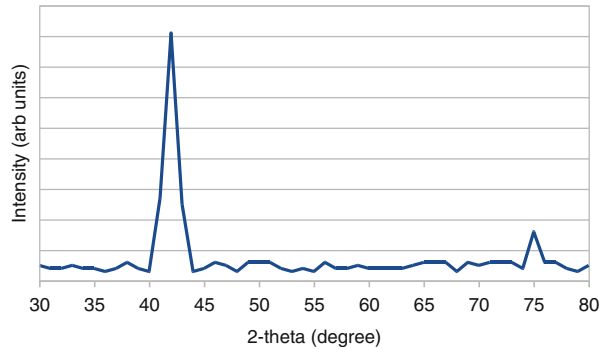
Properties

Biological

The antibacterial properties of copper-doped DLC films have been evaluated against *Escherichia coli* (*E. coli*) [76]. *E. coli* were cultured on pure substrate, DLC film, and copper-doped DLC films, and then the antibacterial activity was calculated according to Eq. 17.1.

$$\text{antibacterial\_rate} = 100 * (\text{num\_bacteria}_{\text{control}} - \text{num\_bacteria}_{\text{tested}}) / \text{num\_bacteria}_{\text{control}}$$

$$(17.1)$$

The DLC film had an antibacterial rate of 40 %, and both of the copper-doped plates had an antibacterial rate of 100 % [76].

DLC films also have good biocompatibility; studies have shown these films do not invoke inflammation or cytotoxicity [88, 89]. Also, due to their tribological properties, they minimize thrombogenicity by minimizing platelet adhesion and activation [88]. By doping the films with nitrogen, their biocompatibility is improved due to the nitrogen supporting the attachment and proliferation of cells [89].

Electronic

There has been much interest in using DLC films as possible field electron emitters (FE). An FE is a device that emits electrons induced by an electrostatic field. These devices are used in electron guns for FE microscopy and in FE flat panel displays. It was initially thought that since DLC films have a negative electron affinity, they have the potential to serve as an FE without special preparation [90]. DLC films with a large (80 %) fraction of sp^3 bonds have the lowest threshold field for electron emission, of about 10 V μm^{-1} [90]. However, it was later discovered that surface roughness, not electron affinity, controls the field emission effects [90]. Due to quality control issues with developing DLC films and the superior properties of carbon nanotubes, DLC films are not currently being considered for use in industrial applications.

Mechanical

The internal stress in a DLC film is calculated by measuring the curvature of the substrate and film. The average internal stress in pure DLC films is 2.9 GPa [70, 71, 86]. When doped with Cu [86] or La_2O_3 [70] or ionized [71], the stress decreases. This is likely due to relaxing the bonds at the sp^3-sp^2 grain boundary. The internal stress is related to adhesion, and it should be noted that as the internal stress decreases, the adhesion of the DLC film to the substrate increases.

The strength of the adhesion (critical load) between the DLC film and the substrate is measured using a scratch tester. The critical load depends on the coating adhesive, the cohesive strength, and the frictional force between the diamond stylus and the coating. The median critical load of DLC films is 64 mN [70, 71, 74, 86]. The critical load is increased through doping or increasing the ion exposure of the DLC films. These methods decrease internal stress and cause the formation of a transition layer between the substrate and DLC film [70, 71, 86].

The hardness (toughness) of a DLC film is measured by indentation tests. These are usually conducted at enough of a load to significantly deform the film and the substrate. Pure DLC films had a hardness between 13 and 80 GPa, with an average hardness of 22 GPa [60, 67, 69, 70, 74, 77, 86]. When these films are doped with metals or annealed, the hardness decreases. DLC films doped with Cu had a hardness of 16 Gpa [86]. When DLC films were doped with tungsten, the hardness was reduced to 18 GPa [67]. After annealing to more than 1,000 K for 1 min, the hardness decreased to 14 GPa [60]. Much of the hardness depends on the ratio of sp^3 to sp^2 carbon within the DLC, so doped or annealed films should have a lower hardness as these types of films have an altered sp^3 to sp^2 ratio.

The elastic modulus measures the stiffness of the DLC films. For typical DLC films, the elastic modulus is approximately 180 GPa [67, 77]. When dopants are added to the DLC films, the elastic modulus changes depending on how the dopants affect the matrix. In the case of tungsten, it decreases [67]; when titanium is added, the elastic modulus increases, and as more titanium is added, the elastic modulus begins to decrease [77]. For films that consist of large amounts of sp^3 carbon, the elastic modulus is approximately 265 GPa [74].

The friction coefficient can be calculated using several different methods. Using scratch tests, DLC films have a friction coefficient that ranges between 0.19 [67] and 0.095 [70]. A copper-doped DLC film against a stainless steel ball has a friction coefficient of 0.15 [83]. As the amount of doped metal increases, the friction coefficient decreases [67, 70, 83].

Optical Properties

DLC films have good transmittance in the visible and IR range of the spectrum; however, in the UV portion of the spectrum, the transmittance drops off sharply due to the onset of fundamental absorption at the band gap of crystalline diamond (220 nm); see Fig. 17.5 [65, 68, 85]. This high transmittance indicates the suitability of DLC films for use in optical windows. Doping the DLC films with Ni or Cu ions causes the transmittance to decrease by half [65, 85]; a similar drop is seen when the films are annealed [68].

Fig. 17.5 Transmittance spectrum of representative DLC film
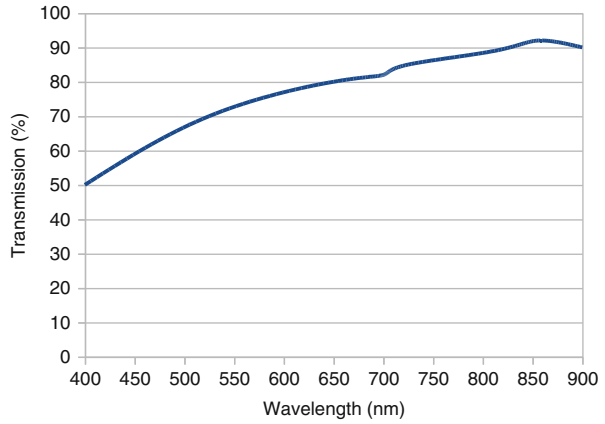
Fig. 17.6 Tauc plot showing extrapolated band gap
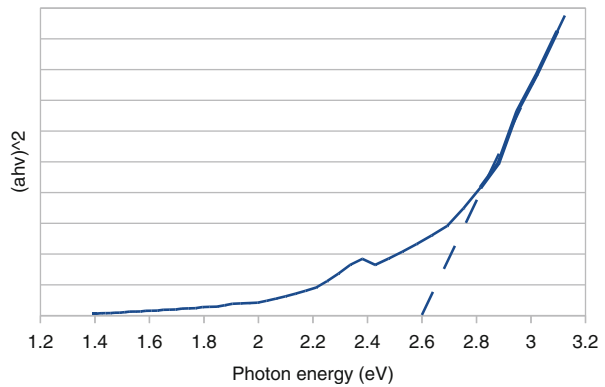
The optical band gap of DLC films can be calculated from the transmittance data, the Beer-Lambert law, and the Tauc relation [85]. The absorption coefficient, from the Beer-Lambert law, is given as Eq. 17.2:

$$a = \ln(1/\text{transmittance}) * (1/\text{path\_length}) \tag{17.2}$$

The optical band gap, E_g, is related to the absorption coefficient, a, by the Tauc relation, Eq. 17.3 [85]:

$$a = (A/h\nu)(h\nu - E_g) \tag{17.3}$$

In this equation, $h\nu$ is the incident photon energy and A is the constant of proportionality. The constant of proportionality differs for different transitions. To determine the band gap, a plot of $(ah\nu)^2$ versus $h\nu$ is created and the linear portion (near the transition energy) is extrapolated back to the x-intercept ($a = 0$);

see Fig. 17.6. This energy (hv) is the band gap. Since this technique depends on extrapolation, the estimated band gap can vary. For DLC films, the reported band gap is between 1.25 and 2.60 eV [65, 68, 85]. It is noted that the band gap decreases as the sp^3/sp^2 ratio decreases. The increase in sp^2 sites is indicative of graphitization within the films, which increases conductivity and hence reduces the band gap [68, 85].

References

 1. Dolmatov VY (2001) Detonation synthesis ultradispersed diamonds: properties and applications. Russ Chem Rev 17:687–708
 2. Gruen D, Shenderova O et al (2005) Synthesis, properties and applications of ultrananocrystalline diamond. Springer, Amsterdam
 3. Shenderova O, Gruen D (2006) Ultrananocrystalline diamond: synthesis properties and applications. William-Andrew Publishing, Norwich
 4. Shenderova OA, Zhirnov VV et al (2002) Carbon nanostructures. Crit Rev Solid State 27:227–356
 5. Novikov NV (1999) New trends in high-pressure synthesis of diamond. Diamond Relat Mater 8:1427–1432
 6. Lejosne J, Mercier G et al (2011) Low degree of functionalization of single-walled carbon nanotubes probed by highly sensitive characterization techniques. Carbon 49:3010–3018
 7. Que R, Shao M, Chen T et al (2011) Diamond nanoparticles with more surface functional groups obtained using carbon nanotubes as sources. J Appl Phys 110:054321/1–054321/4
 8. Voropaev S (2011) Cavitations synthesis of carbon nanostructures. J Phys Conf Ser 291:012028
 9. Yang GW, Wang JB, Liu QX (1998) Preparation of nano-crystalline diamonds using pulsed laser induced reactive quenching. J Phys Condens Matter 10:7923
10. Wang JB, Zhang CY, Zhong XL, Yang GW (2002) Cubic and hexagonal structures of diamond nanocrystals formed upon pulsed laser induced liquid–solid interfacial reaction. Chem Phys Lett 361:86
11. Liang CH, Shimizu Y, Sasaki T, Koshizaki N (2003) Synthesis of ultrafine SnO_{2a-x} nanocrystals by pulsed laser-induced reactive quenching in liquid medium. J Phys Chem B 107:9220
12. Liu QX, Wang CX, Zhang W, Yang GW (2003) Immiscible silver–nickel alloying nanorods growth upon pulsed-laser induced liquid/solid interfacial reaction. Chem Phys Lett 382:1
13. Yang GW, Wang JB (2000) Carbon nitride nanocrystals having cubic structure using pulsed laser induced liquid–solid interfacial reaction. Appl Phys A Mater Sci Process 71:343
14. Wang JB, Yang GW, Zhang CY, Zhong XL, Ren ZA (2003) Cubic-BN nanocrystals synthesis by pulsed laser induced liquid–solid interfacial reaction. Chem Phys Lett 367:10
15. Hanada K, Shoji T, Mayuzumi M et al (2004) Development of self-lubricating titania/diamond nanoparticle composite. Mater Sci Technol 20:1103–1108
16. Xu H, Yang Z, Li M-K et al (2005) Synthesis and properties of electroless Ni-P-nanometer diamond composite coatings. Surf Coat Technol 191:161–165
17. Koudoumas E, Kokkinaki O, Konstantaki M et al (2002) Onion-like carbon and diamond nanoparticles for optical limiting. Chem Phys Lett 357:336–340
18. Bilogurova L, Shevtsova M (2009) Investigation of the improvement of the physical and mechanical properties of polymer composite materials with nano-sized powders. Materialwiss Werkstofftech 40:331–333
19. Peng DX, Kang Y, Hwang RM et al (2009) Tribological properties of diamond and SiO_2 nanoparticles added in paraffin. Tribol Int 42:911–917
20. Gracias A, Tokranova N, Thelen BCM et al (2011) Influence of diamond nanoparticles on the thermal properties of benzocyclobutene (BCB). Phys Status Solidi A 208:684–690

21. Zhang Q, Mochalin VN, Neitzel I et al (2011) Fluorescent PLLA-nanodiamond composites for bone tissue engineering. Biomaterials 32:87–94

22. Tomita S, Fujii M, Hayashi S (2002) Optical extinction properties of carbon onions prepared from diamond nanoparticles. Phys Rev B Condens Matter 66:245424/1–245424/7

23. Ogata T, Yagi R, Nakamura N et al (2012) Modulation of polymer refractive indices with diamond nanoparticles for metal-free multilayer film mirrors. ACS Appl Mater Interfaces 4:3769–3772

24. Rozhkova NN, Gorlenko LE, Emel'yanova GI et al (2009) Effect of ozone on the structure and physicochemical properties of ultradisperse diamond and shungite nanocarbon elements. Pure Appl Chem 81:2093–2105

25. Mochalin VN, Neitzel I, Etzold BJM et al (2011) Covalent incorporation of aminated nanodiamond into an epoxy polymer network. ACS Nano 5:7494–7502

26. Fan J, Chu PK (2010) Group IV nanoparticles: synthesis, properties, and biological applications. Small 6:2080–2098

27. Perevedentseva EV, Su FY, Su TH et al (2010) Laser-optical investigation of the effect of diamond nanoparticles on the structure and functional properties of proteins. Quantum Electron 40:1089–1093

28. Cuche A, Sonnefraud Y, Faklaris O et al (2009) Diamond nanoparticles as photoluminescent nanoprobes for biology and near-field optics. J Lumin 129:1475–1477

29. Tizei LHG, Kociak M (2012) Spectrally and spatially resolved cathodoluminescence of nanodiamonds: local variations of the NV0 emission properties. Nanotechnology 23:175702/1–175702/8

30. Elouali M, Elouali FZ, Beyens C et al (2012) The effect of diamond nanoparticles on electro-optical properties of polymer dispersed liquid crystals. Mol Cryst Liq Cryst 561:136–144

31. Vlaeva I, Yovcheva T, Sainov S et al (2010) Optical properties of PVA films with diamond and titania nanoparticles. J Phys Conf Ser 253:012027/1–012027/6

32. Prosviryakov AS, Samoshina ME, Popov VA (2012) Structure and properties of composite materials based on copper strengthened with diamond nanoparticles by mechanical alloying. Met Sci Heat Treat 54:298–302

33. Baik E-S, Baik Y-J, Jeon D (2000) Aligned diamond nanowhiskers. J Mater Res 15:923–926

34. Ando Y, Nishibayashi Y, Sawabe A (2004) Nano-rods of single crystalline diamond. Diamond Relat Mater 13:633–637

35. Zou YS, Yang Y, Zhang WJ et al (2008) Fabrication of diamond nanopillars and their arrays. Appl Phys Lett 92:053105–053108

36. Wei M, Terashima C, Lv M et al (2009) Boron-doped diamond nanograss array for electrochemical sensors. Chem Commun 24:3624–3626

37. Szunerits S, Coffinier Y, Galopin E et al (2010) Preparation of boron-doped diamond nanowires and their application for sensitive electrochemical detection of tryptophan. Electrochem Commun 12:438–441

38. Coffinier Y, Galopin E, Szunerits S et al (2010) Preparation of superhydrophobic and oleophobic diamond nanograss array. J Mater Chem 20:10671–10675

39. Lin J-Y, Li Z-C, Chen C-Y et al (2011) Fabrication of submicron scale vertically aligned diamond rods by mask-free oxygen plasma etching. Diamond Relat Mater 20:922–926

40. Masuda H, Yanagishita T, Yasui K et al (2001) Synthesis of well-aligned diamond nanocylinders. Adv Mater 13:247–249

41. Sun L, Gong J, Zhu D et al (2004) Diamond nanowires from carbon nanotubes. Adv Mater 16:1849–1853

42. Gong JL, Sun LT, Zhu DZ et al (2006) Diamond nanowires from carbon nanotubes by hydrogen plasma treatment. Int J Nanosci 5:307–313

43. Dubrovinskaia N, Dubrovinsky L, Langenhorst F et al (2005) Nanocrystalline diamond synthesized from C60. Diamond Relat Mater 14:16–22

44. Rakha SA, Yu G, Zhou X et al (2009) Diamond nanowires from nanocrystalline diamond films. J Cryst Growth 311:3332–3336

45. Arenal R, Bruno P, Miller DJ et al (2007) Diamond nanowires and the insulator-metal transition in ultrananocrystalline diamond films. Phys Rev B 75:195431
46. Rakha SA, Yu G, Cao J et al (2010) Diamond-graphite nanowires produced by microwave plasma chemical vapor deposition. Diamond Relat Mater 19:284–287
47. Shenderova O, Brenner D, Ruoff RS (2003) Would diamond nanowires be stronger than fullerene nanotubes? Nano Lett 3:805–809
48. Ivanovskaya VV, Ivanovskii AL (2007) Atomic structure, electronic properties, and thermal stability of diamond-like nanowires and nanotubes. Inorg Mater 43:349–357
49. Barnard AS (2005) From nanodiamond to nanowires. In: Gruen DM, Shenderova O, Vul AY (eds) Synthesis, properties and applications of ultrananocrystalline diamond. Springer, Netherlands
50. Brenner DW, Shenderova OA, Harrison JA et al (2002) A second-generation reactive empirical bond order (REBO) potential energy expression for hydrocarbons. J Phys Condens Matter 14:783
51. Shenderova OA, Padgett CW, Hu Z et al (2005) Diamond nanowires. J Vac Sci Technol B Microelectron Nanometer Struct Process Meas Phenom 23:2457–2464
52. Barnard AS, Snook IK (2004) Phase stability of nanocarbon in one dimension: nanotubes versus diamond nanowires. J Chem Phys 120:3817–3821
53. Moreland JF, Freund JB, Chen G (2004) The disparate thermal conductivity of carbon nanotubes and diamond nanowires studied by atomistic simulation. Microscale Thermophys Eng 8:61–69
54. Padgett CW, Shenderova O, Brenner DW (2006) Thermal conductivity of diamond nanowires: molecular simulation and scaling relations. Nano Lett 6:1827–1831
55. Drory MD, Gardinier CF, Speck JS (1991) Fracture toughness of chemically vapor-deposited diamond. J Am Ceram Soc 74:3148–3150
56. Dubrovinskaia N, Dub S, Dubrovinsky L (2006) Superior wear resistance of aggregated diamond nanowires. Nano Lett 6:824–826
57. Richter A, Smith R, Dubrovinskaia N et al (2006) Mechanical properties of superhard materials synthesized at various pressure-temperature conditions investigated by nanoindentation. High Pressure Res 26:99–109
58. Zeng L, Peng H, Wang W et al (2008) Synthesis and characterization of diamond microcrystals and nanowires deposited by hot cathode direct current plasma chemical vapor deposition method. J Phys Chem C 112:6160–6164
59. Mousinho AP, Mansano RD, Salvadori MC (2010) Nanostructured diamond-like carbon films characterization. J Alloys Compd 495:620–624
60. Chung CK, Wu BH, Lai CW et al (2012) Nano silicon top-layer for composite-induced multiphasic enhancement of thermal stability of hardness of diamond-like carbon nanofilm at 900°C. Surf Coat Technol 206:4580–4584
61. Aisenberg S, Chabot R (1971) Ion-beam deposition of thin films of diamondlike carbon. J Appl Phys 42:2953–2958
62. Voevodin AA, Zabinski JS (1998) Superhard, functionally gradient, nanolayered and nanocomposite diamond-like carbon coatings for wear protection. Diamond Relat Mater 7:463–467
63. Hauert R, Patscheider J (2000) From alloying to nanocomposite - improved performance of hard coatings. Adv Eng Mater 2:247–259
64. Ma W, Liechtenstein VK, Szerypo J et al (2011) Preparation of self-supporting diamond-like carbon nanofoils with thickness less than 5 nm for laser-driven ion acceleration. Nucl Instrum Methods Phys Res A 655:53–56
65. Faizrakhmanov IA, Bazarov VV, Stepanov AL et al (2006) Effect of copper ion implantation on the optical properties and low-temperature conductivity of carbon films. Semiconductors 40:414–419
66. Wu W-Y, Ting J-M (2006) Growth and characteristics of metal-containing diamond-like carbon using a self-assembled process. Carbon 44:1210–1217

67. Bharathy PV, Yang Q, Kiran M et al (2012) Reactive bias target ion beam deposited W-DLC nanocomposite thin films – microstructure and its mechanical properties. Diamond Relat Mater 23:34–43
68. Sharda T, Rahaman MM, Nukaya Y et al (2001) Structural and optical properties of diamond and nano-diamond films grown by microwave plasma chemical vapor deposition. Diamond Relat Mater 10:561–567
69. Hayashi Y, Soga T (2004) Structural, optical and mechanical properties of nanostructure diamond synthesized by chemical vapor deposition. Tribol Int 37:965–974
70. Zhang Z, Lu X, Luo J et al (2007) Preparation and characterization of La$_2$O$_3$ doped diamond-like carbon nanofilms (I): structure analysis. Diamond Relat Mater 16:1905–1911
71. Palnitkar UA, Joseph PT, Niu H et al (2008) Adhesion properties of nitrogen ion implanted ultra-nanocrystalline diamond films on silicon substrate. Diamond Relat Mater 17:864–867
72. Wang C, Wang Q, Wang Z et al (2008) Nanocrystalline diamond embedded in hydrogenated fullerenelike carbon films. J Appl Phys 103:056110/1–056110/3
73. Luong JH, Male KB, Glennon JD (2009) Boron-doped diamond electrode: synthesis, characterization, functionalization and analytical applications. Analyst 134:1965–1979
74. Popov C, Favaro G, Kulisch W et al (2009) Influence of the nucleation density on the structure and mechanical properties of ultrananocrystalline diamond films. Diamond Relat Mater 18:151–154
75. Weng J, Xiong L, Wang J et al (2010) Effect of gas sources on the deposition of nano-crystalline diamond films prepared by microwave plasma enhanced chemical vapor deposition. Plasma Sci Technol 12:761–764
76. Chan Y-H, Huang C-F, Ou K-L et al (2011) Mechanical properties and antibacterial activity of copper doped diamond-like carbon films. Surf Coat Technol 206:1037–1040
77. Caschera D, Federici F, Pandolfi L et al (2011) Effect of composition on mechanical behaviour of diamond-like carbon coatings modified with titanium. Thin Solid Films 519:3061–3067
78. Brown IG (1998) Cathodic arc deposition of films. Annu Rev Mater Sci 28:243–269
79. Krishnaswamy J, Rengan A, Narayan J et al (1989) Thin-film deposition by a new laser ablation and plasma hybrid technique. Appl Phys Lett 54:2455–2457
80. Siegal MP, Barbour JC, Provencio PN et al (1998) Amorphous-tetrahedral diamondlike carbon layered structures resulting from film growth energetics. Appl Phys Lett 73:759–761
81. Foong YM, Hsieh J, Li X et al (2009) The study on the effect of erbium on diamond-like carbon deposited by pulsed laser deposition technique. J Appl Phys 106:064904/1–064904/8
82. Guo D, Cai K, Li L et al (2000) Preparation of hydrogenated diamond-like carbon films on conductive glass from an organic liquid using pulsed power. Chem Phys Lett 325:499–502
83. Huang L, Jiang H, Zhang J et al (2006) Synthesis of copper nanoparticles containing diamond-like carbon films by electrochemical method. Electrochem Commun 8:262–266
84. Wan S, Wang L, Xue Q (2010) Electrochemical deposition of sulfur doped DLC nanocomposite film at atmospheric pressure. Electrochem Commun 12:61–65
85. Pandey B, Hussain S (2011) Effect of nickel incorporation on the optical properties of diamond-like carbon (DLC) matrix. J Phys Chem Solids 72:1111–1116
86. Chen C-C, Hong FC-N (2005) Structure and properties of diamond-like carbon nanocomposite films containing copper nanoparticles. Appl Surf Sci 242:261–269
87. Hebert C, Ruffinatto S, Eon D et al (2013) A composite material made of carbon nanotubes partially embedded in a nanocrystalline diamond film. Carbon 52:408–417
88. Roy RK, Lee KR (2007) Biomedical applications of diamond-like carbon coatings: a review. J Biomed Mater Res B Appl Biomater 83:72–84
89. Liao WH, Lin CR, Wei DH et al (2012) Concurrent improvement in biocompatibility and bioinertness of diamond-like carbon films with nitrogen doping. J Biomed Mater Res A 100:3151–3156
90. Grill A (1998) Diamond-like carbon: state of the art. Diamond Relat Mater 8:428–434

Sensing the Mechanical Properties of Supported Micro- to Nano-elastic Films

18

Frédéric Restagno, Emmanuelle Martinot, Richar Villey, S. Leroy, Christophe Poulard, Elisabeth Charlaix, and Liliane Léger

---

Keywords

Adhesion • AFM • Boussinesq • Contact mechanics • DMT • Elastomer • Hertz • JKR • Load • PDMS • SFA • Soft probe • Surface force apparatus • Thin films

---

Introduction

Thin polymer films are widely used in a number of applications of our everyday life. Some of these applications, as for example, paints or surface coatings, are not too much demanding in terms of mechanical properties of the films. On the contrary, a number of other more technical situations do rely on a precise adjustment of the mechanical response of this polymer films. This is, for example, the case of the thin adhesive layers ensuring the cohesion in multilayers co-extruded packaging films used in the food industry or of any other polymer adhesive layer. This is also the case of the tribological layers of nanometric thickness used to protect the surface of the hard discs of our computers. In many of these applications, the knowledge and the fine adjustment of the mechanical properties of the polymer thin films are of primary importance. Measuring these mechanical properties remains however to a large extent a challenge, essentially because most of the known mechanical tests

F. Restagno (✉) • E. Martinot • C. Poulard • L. Léger
Laboratoire de physique des solides, Université Paris-Sud – CNRS, Orsay, France
e-mail: frederic.restagno@u-psud.fr; emmanuelle.martinot6@gmail.com; liliane.leger@u-psud.fr

R. Villey • S. Leroy
Institut Lumière Matière, Université Lyon 1 – CNRS, Villeurbanne, France
e-mail: richard.villey@univ-lyon1.fr

E. Charlaix
Laboratoire interdisciplinaire de physique, Université Grenoble 1, CNRS, Grenoble, France
e-mail: Elisabeth.Charlaix@ujf-grenoble.fr

are unable to only sense the mechanical response of the film itself, and leads to a mechanical response often largely dominated by that of the underlying substrate.

The problem is intrinsically related to the fact that most methods for characterizing the mechanical properties of a solid consist in imposing a certain deformation and measuring the corresponding force. For supported films, this can essentially be done by pushing locally on the surface of the film, using to do so another solid, in order to force the deformation and measure the resulting force. This implies first the formation of a contact between the pushing solid (the indenter) and the surface of the film, where adhesion forces develop and affect the measured force. These adhesion contributions depend on the size of the contact and thus need an additional measurement of the area of contact to be correctly accounted for. A full mechanical description of the contact, taking into account adhesion, needs to be used to be able to extract information on the mechanical properties of the solid tested. Second, the geometry of a supported thin film intrinsically implies a large degree of confinement of this film in the region of contact between the film and the indenter, as soon as the size of the contact is comparable or larger than the thickness of the film. For films with thicknesses below the micrometer range, it is not at all easy to achieve small enough contact areas so that one can be sure that the measured force is dominated by the mechanical response of the film.

The first step is to develop contact mechanics analysis taking into account adhesion and elastic deformation contributions. Such descriptions have been widely developed and tested in the past 50 years, in the case where both the solicited solid and the indenter could be considered as semi-infinite elastic media. This is the so-called JKR (Johnson, Kendall, and Roberts) [1] or DMT (Derjaguin, Müller, and Toporov) [2] descriptions of the contact that we shall briefly recall in the first part of this chapter. These descriptions necessitate a determination of the area of contact to allow one to determine independently with accuracy the composite elastic modulus of both solids at contact and the adhesion energy. These models, which are well confirmed by a number of experiments, will allow us to point out more precisely a thickness criteria (compared to the size of the contact) specifying when these descriptions will fail in accounting for the mechanical response of supported thin films [3, 4].

Then, several alternative routes can be (and have been) followed.

One can think decreasing drastically the size of the contact between the film and the indenter, in order to ensure that the size of the contact always remains much smaller than the film thickness. This is the route followed by people proposing micro or nano-indenters, such as, an AFM tip. Presenting the AFM or indenters technique is not the object of this book chapter but this technique has been often used to try to characterize thin films. Among them, we can cite [5–8] but an extensive literature exists on the subject that we do not detail here.

In the second section of this chapter, we shall examine an alternative route: it consists in keeping with indenter sizes allowing one to optically determine the size of the area of contact, along with developing attempts to analyze the mechanics of the stratified film plus substrate system, taking into account the finite thickness of the film, and the constraint imposed to the deformation field by the presence of the buried interface between the film and the supporting substrate. We shall review the

diverse attempts made along this line in the past 20 years, pointing out their benefits and their limitations. We shall concentrate our attention on the last one of these attempts, the semi-analytical approach proposed by E. Barthel [9, 10], and compare its predictions to series of experiments conducted on thin micrometric films of polydimethylsiloxane (PDMS) elastomers, which first allow to validate the Barthel's description and second to demonstrate the complexity and the difficulty of extracting an elastic modulus of the film itself from contact mechanics experiments on a supported film.

The third section of the present chapter will be devoted to the description of a totally different and recently proposed approach, based on the mechanical solicitation of the supported film by a liquid flow [11, 12]. The interest of this approach is that the strength of the mechanical solicitation can be varied in a very large range, without changing the nature of the fluid–film contact, i.e., without any change in adhesion forces (no solid–solid contact). We shall describe the surface force apparatus (SFA) based on the approach of a millimetric sphere to a plane surface, down to subnanometric distances, with a superimposed oscillation of the sphere having a subnanometric amplitude and a frequency chosen in the range one to several 10 Hz [13–15]. Such SFA experiments in the dynamic SFA mode constitute a highly sensitive nano-rheometer, which allows one to sense not only the properties of the fluid down to molecular confinements but also the mechanical characteristics of the involved solids. We shall discuss in details the advantages and the limitations of this new mode of test. We shall show that the mechanical response is indeed sensitive to the presence of a thin elastomer film deposited on one of the solid arms of the SFA machine, even for film thicknesses well below a micrometer.

An Introduction to Contact Mechanics

The description of elastic contacts between elastic solids is quite classical and has been presented in a number of books or review articles [3, 4, 16]. We briefly present here the main results necessary for the understanding of the rest of the chapter.

When two elastic solids are brought into contact, if they do not conform each other, they initially touch at a single point, and, under the action of a load (even very small), they deform in the vicinity of this point and develop a contact area. Increasing the applied load increases the size of this contact area. If the load remains small, the size of the contact area can remain small compared to the dimension of both solids, which can then be considered as semi-infinite on each side of the contact. A theory of the contact intends to predict the size of this contact area and to describe how it depends on the applied load. It also intends to predict the magnitude and the distribution of the stresses transmitted through the interface. Historically, this problem has been solved first for the contact between two semi-infinite elastic solids, postulating no adhesion forces at the contact [17]. This is the Hertz's theory of elastic contacts, classically described in mechanics textbooks, in terms of the elastic contact between two spheres or equivalently between a sphere and a plane. Then, adhesion forces have been introduced into the mechanical description. These adhesion interactions indeed do

manifest themselves: first they are responsible for a finite contact area under zero load, and second they are responsible for the finite negative load (tensile load) needed to separate the solids. Indeed, this pull-off load can be taken as a qualitative measurement of adhesive forces. Two different and opposing routes were first followed to incorporate adhesion forces into the problem. Derjaguin, Müller, and Toporov (DMT) [2] assumed that adhesion forces were acting in a small annular zone around the contact, outside of the contact, but without deforming the profile of the two solids, which remained Hertzian (the Young's modulus was assumed to be large enough so that the interaction forces between the two solids separated on the edge of the contact by a distance smaller than the range of these interactions were not strong enough to deform the solids outside of the contact). On the contrary, Johnson, Kendall, and Roberts (JKR) [1], who were attempting to explain experiments conducted on rather deformable solids (elastomers), assumed that adhesion forces were acting under the contact and were able to increase the area of contact compared to the Hertz solution, for a given load, just because in the region near the contact, the adhesion forces were able to pull the two solids into contact, at the price, of course of additional elastic deformations. Both approaches were predicting dependences of the pull-off force versus the adhesion energy and the reduced radius of the spheres, only differing for a numerical coefficient (2π for DMT and $\frac{3}{2}\pi$ for JKR in the case of a plane and a sphere). These two apparently contradictory descriptions were later reconciled by Maugis [4, 18] who, incorporating a reexamination of their results by Müller, Yushchenko, and Derjaguin [19] and similar ideas developed by Tabor [20], could demonstrate that indeed DMT and JKR were two limiting cases of the same theory, taking into account both adhesion and elasticity, and that the transition between these limiting cases was ruled by the magnitude of a parameter μ comparing the strength of adhesion and elastic terms. μ is given by $\mu = \frac{64}{3\pi} \left(\frac{4W^2R}{9\pi\varepsilon^3K^2} \right)^{1/3}$, with W the adhesion energy, R the reduced radius of the spheres into contact ($\frac{1}{R} = \frac{1}{R_1} + \frac{1}{R_2}$), and K the effective Young's modulus, related to the Young's modulus of each solid, E_1 and E_2 by $\frac{1}{K} = \frac{3}{4} \left(\frac{1-v_1^2}{E_1} + \frac{1-v_2^2}{E_2} \right)$. v_1 and v_2 are the Poisson's coefficients of each solid and ε fixes the range of the adhesive interactions, of the order of a molecular size. Maugis has proposed solutions for all values of μ [18].

In the following, we shall first briefly recall the main results of the Hertz description and then present in more detail the JKR approach, which will be the starting point of the developments of the analysis of supported thin films presented in section 'The JKR Test: Finite Size Effects and Role of Adhesion'.

Elastic Contact Between Two Large Elastic Spheres: The Hertz Approach

The problem of the contact between two elastic large half spheres has been solved by Hertz in 1881 [17]. Hertz solved the question of the stress distribution in the area of contact, the penetration depth (the approach of the two spheres), and the radius of

Fig. 18.1 Hertz problem. An elastic sphere of radius R is put in contact with a solid. P is the force applied on the sphere. a is the radius of the contact area. δ is the deformation of the sphere. The elastic sphere is characterized by its elastic properties (Young's modulus E, Poisson coefficient v)
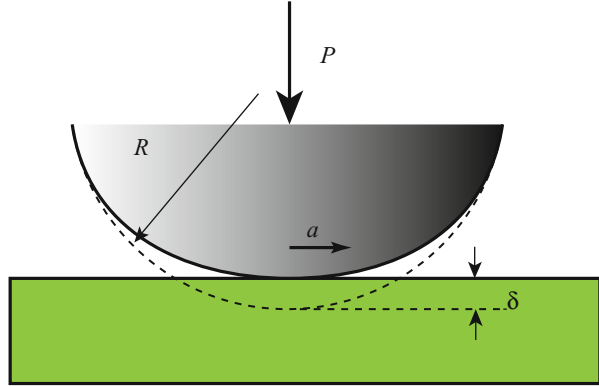
contact, as a function of the load. Before entering into more details, let us give simple scaling arguments to extract the main results of the Hertz description.

Consider an elastic sphere with a radius R and a Young's modulus E in contact with a semi-infinite plane non-deformable solid, as schematically presented in Fig. 18.1 (the problem would be exactly the same for the contact between two elastic solids, replacing in Eqs. 18.1, 18.2, and 18.3 below the radius of the sphere by the reduced radius of both spheres, yet specified above, and the effective modulus of the contact by the one given above too). Under the load P, a circular area of contact develops, with a radius a. A representative value of the stress is $\sigma = P/\pi a^2$, and a representative value of the strain is $\lambda = a/R$. Applying the Hooke's law, $\sigma = \lambda E$, one gets $a^3 \approx {}^{PR}\!/_E$. This tells us that the size of the area of contact grows like $P^{2/3}$, i.e., nonlinearly with the load.

Provided a and the deformation of the sphere, estimated by the change in distance of the two centers, δ, (the indentation depth) remain small in front of R, all deformations can be considered as small, and the deformations and the stress distribution can be calculated (see, for example, the detailed description of the calculation in reference [3]). The mains results of the Hertz approach are:

$$\delta = \frac{a^2}{R} \tag{18.1}$$

$$P = \frac{4}{3}\frac{E}{(1-v^2)}\frac{a^3}{R} = \frac{Ka^3}{R} \tag{18.2}$$

$$\delta = \frac{P^{2/3}}{K^{2/3}}\frac{1}{R^{1/3}} \tag{18.3}$$

with v the Poisson coefficient of the sphere and K the effective Young's modulus yet defined above in the case of the contact between two elastic spheres. The relations between the load and either the radius of contact or the indentation of the sphere are clearly nonlinear.
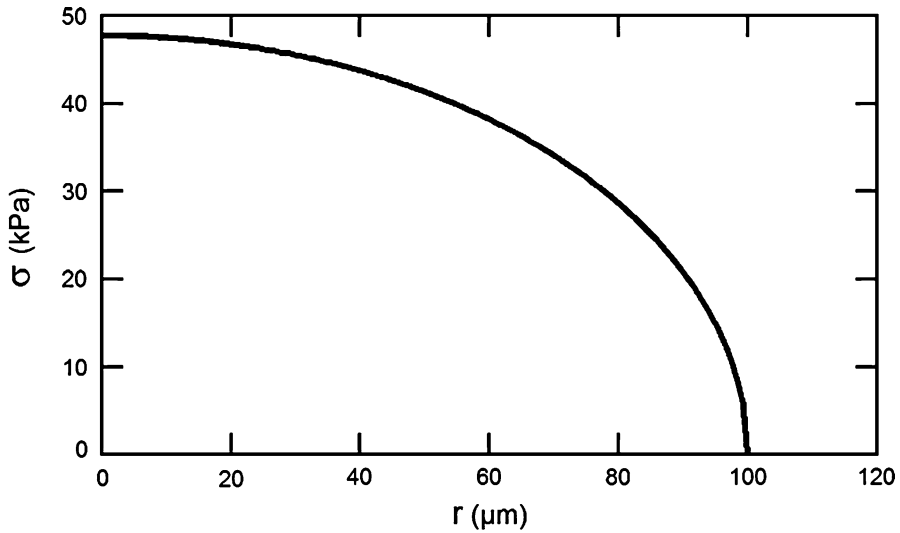
Fig. 18.2 Distribution of the normal stress $\sigma(r)$ in the Hertz contact (in Pa). $K = 1$ MPa, $R = 1$ mm, $a = 0.1$ mm

The full calculations of the stress and strain fields can be found in reference [3]. We just present here the main results of these calculations. The pressure distribution inside the contact if given, as a function of the radial coordinate r, by (Fig. 18.2):

$$\sigma(r) = \frac{3K}{2\pi R} a \left(1 - \frac{r^2}{a^2} \right)^{1/2} \tag{18.4}$$

Outside the contact, the displacement $u(r)$ of the surface of the sphere is given by:

$$u(r) = \frac{a^2}{\pi R} \left[\left(\frac{r^2}{a^2} - 1 \right)^{1/2} - \left(\frac{r^2}{a^2} - 2 \right) \tan^{-1} \left(\left(\frac{r^2}{a^2} - 1 \right)^{-1/2} \right) \right] \tag{18.5}$$

And the profile $z(r)$ of the deformed surface of the sphere outside the contact is:

$$z(r) = \frac{r^2}{2R} - \frac{a^2}{R} + u(r) \tag{18.6}$$

One can notice that the Hertz approach predicts that the elastic sphere joins the solid plane tangentially, as it is gently squeezed on the plane surface, with no additional stresses than elastic. This is schematically represented in Fig. 18.3.
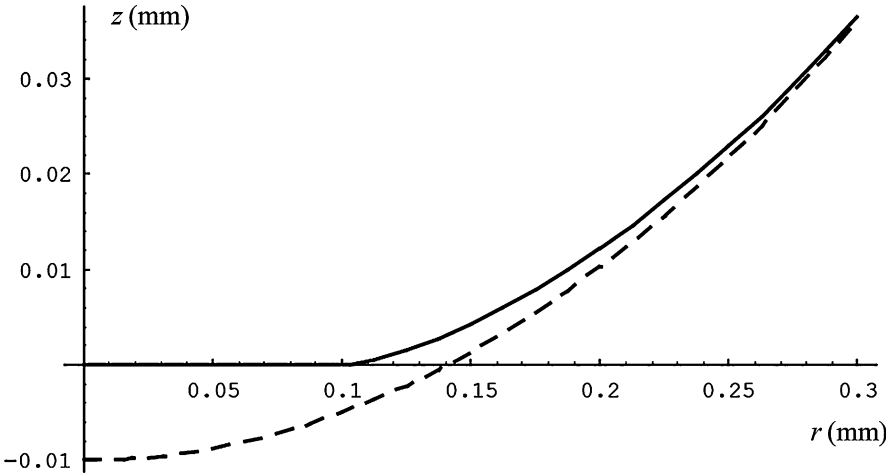
Fig. 18.3 Profile of the deformed sphere in the case of an Hertzian profile. The *dashed line* corresponds to the non-deformed surfaces. $R = 1$ mm, $a = 0.1$ mm
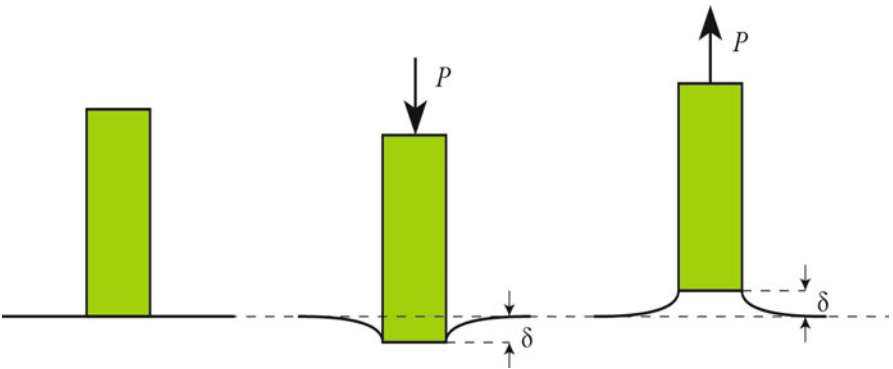
Fig. 18.4 Boussinesq geometry. A flat punch is put in contact with an elastic solid and submitted to the load P

It is also interesting to notice that the above results for the Hertz contact are totally different from what happens when a flat punch is pushed on a plane elastic solid, a problem known as the Boussinesq problem [3, 4] and schematically presented in Fig. 18.4.

There, the area of contact is fixed. The stress distribution is given by:

$$\sigma(r) = \frac{P}{2\pi a^2 \sqrt{1 - \frac{r^2}{a^2}}} \tag{18.7}$$

A singularity appears at the edge of the contact, where the stress diverges. Close to the edge of the contact, the stress can be expressed as:

$$\sigma(r) = \frac{K_1}{\sqrt{2\pi(a-r)}} \quad \text{with} \quad K_1 = \frac{P}{2a\sqrt{\pi a}}. \tag{18.8}$$

The vertical displacement of the surface outside the contact is given by:

$$u(r) = \frac{4}{3\pi K}\frac{P}{a}\sin^{-1}\left(\frac{a}{r}\right) = \frac{8}{3\pi K}K_1\sqrt{\pi a}\sin^{-1}\left(\frac{a}{r}\right) \tag{18.9}$$

And the indentation is proportional to the load:

$$\delta = \frac{2P}{3aK} \tag{18.10}$$

These two examples illustrate the importance of the geometry of the contact, and the complications introduced in the problem by the fact that, in general, the size of the contact area depends in a nonlinear manner on the load.

Adhesive Contact Between Two Elastic Spheres: The JKR Approach

As yet said, adhesion forces are present and can induce significant deviations to the contact behavior obtained by Hertz, especially when the elastic solids in contact are soft and deformable. When such is the case, adhesion forces induce noticeable deformations, especially close to the edge of the contact zone, and the profile of a soft sphere in contact with a non-deformable plane becomes quite different from the picture in Fig. 18.3.

The ideas at the origin of the development of the JKR description of adhesive contacts are the following: due to adhesion forces, the two solids in contact tend to deform and increase their area of contact, compared to the situation without adhesion (the Hertz case), for the same applied load (Fig. 18.5). In order to take adhesion forces into account, Johnson, Kendall, and Roberts [1] have proposed to consider the contact as the result of the superposition of a loading of a Hertz contact (no adhesion) up to a load allowing to reach the final area of contact characterized by a radius a and of a partial unloading by a flat punch (fixed area of contact), in order to attain the actually applied load (indeed, to form a contact with a given area, a smaller load needs be applied in the presence of adhesion forces than without such forces, as adhesion tends to push the surface against each other). The relation between the applied load and the radius of contact then contains an additional term, compared to that obtained by Hertz, and writes:

$$a^3 = \frac{R}{K}\left[P + 3\pi WR + \sqrt{6\pi WRP + (3\pi WR)^2}\right] \tag{18.11}$$
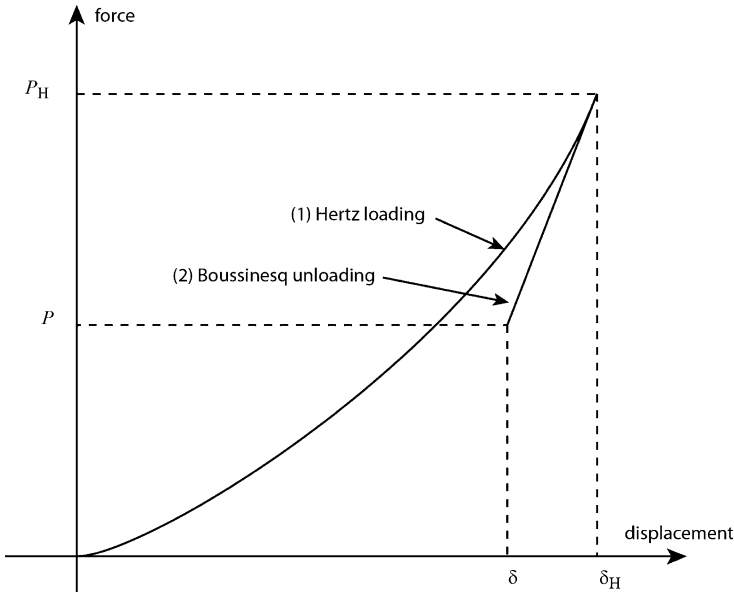
Fig. 18.5 Principle of the JKR calculation

With W the thermodynamic work of adhesion, i.e., the energy per unit area necessary to rupture the contact in a thermodynamic way. If for any reason the changes imposed to the area of contact, changing either the load or the distance between the sphere and the plane solid are not performed following a thermodynamic path (too quickly for example to proceed by successive quasi-equilibrium states), then W has to be replaced by what is commonly named G, the energy release rate. In many JKR experiments performed with elastomers, the loading can rather easily be performed in a quasi-thermodynamic manner (because the van der Waals interactions involved in the formation of the contact develop quasi instantaneously), but the unloading curves usually lead to G values larger than W, due to various dissipative processes taking place at polymer interfaces, as, for example, the interdigitation of pending polymer chains pertaining to each solid under the contact, during the time the contact has been established. Then, it costs more energy to rupture that contact than to form it. As these dissipative phenomena have sometime slow characteristic times, care has to be taken to consider that G can depend on the velocity at which the fracture rupturing the contact advances [21].

Equation 18.11 is the so-called JKR equation. It is accompanied by the companion relation between indentation, radius of contact, and load:

$$\delta = \frac{a^2}{3R} + \frac{2P}{3aK} \tag{18.12}$$
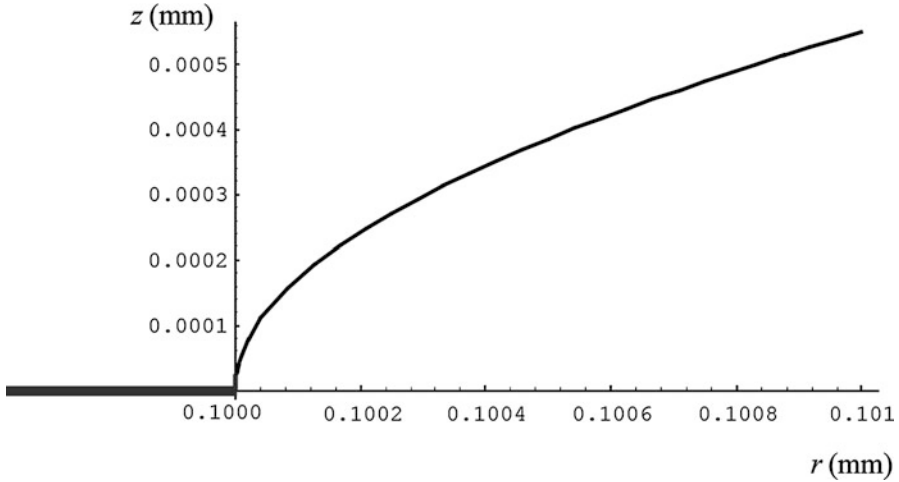
Fig. 18.6 Profile of the surfaces outside the contact zone predicted by Eq. 18.15. $K = 1$ MPa, $R = 1$ mm, $a = 0.1$ mm, and $W = 44$ m J m^{-2}

There is no simple explicit relation between the displacement and the load, but a, P, and δ must be related by the above relation, which is independent of the adhesion energy and represents an internal test of the validity of the JKR approach to analyze a given set of data.

Both the stress profile inside the zone of contact and the deformation of the surface outside the contact can be deduced from the superposition of the Hertz compression and the Boussinesq unloading. The results are given by:

$$\sigma(r) = \frac{K_1}{\sqrt{\pi a}} \frac{1}{\sqrt{1 - \frac{r^2}{a^2}}} - \frac{3aK}{2\pi R} \sqrt{1 - \frac{r^2}{a^2}} \tag{18.13}$$

$$u(r) = \frac{8}{3\pi K} K_1 \sqrt{\pi a} \sin^{-1}\left(\frac{a}{r}\right)$$
$$+ \frac{a^2}{\pi R}\left[\left(\frac{r^2}{a^2} - 1\right)^{\frac{1}{2}} - \left(\frac{r^2}{a^2} - 2\right)\tan^{-1}\left(\left(\frac{r^2}{a^2} - 1\right)^{-1/2}\right)\right] \tag{18.14}$$

The distance between the two surfaces outside the contact is given by:

$$z(r) = \frac{r^2}{2R} - \delta + u(r) \tag{18.15}$$

As shown in Fig. 18.6, the sphere now reaches the plane surface with a vertical tangent, illustrating the effect of the adhesion forces which pull the deformable

sphere to increase the size of the contact and gain some adhesion energy. This makes clear that the whole behavior of the solid in contact results from a balance between elastic and adhesion contributions.

In fact the JKR relation between a^3 and the load P (Eq. 18.11) is not easy to handle in the form presented above. It can be linearized by a good choice of scaled variables and rewritten as:

$$\frac{P}{\sqrt{6\pi a^3}} = K\frac{a^{3/2}}{R\sqrt{6\pi}} - \sqrt{WK} \qquad (18.16)$$

In the scaled units, $\frac{P}{\sqrt{6\pi a^3}}$ versus $\frac{a^{3/2}}{R\sqrt{6\pi}}$, if the JKR analysis of the contact is correct, the data should produce a straight line, with a slope equal to the compound reduced elastic modulus, K, and the intercept at origin equal to $\sqrt{WK}$, i.e., allowing one to measure the thermodynamic work of adhesion or the energy release rate if K is known. In order to conduct such an analysis of the data, one obviously needs to know the value of the radius of the sphere. In fact, the linearity of the data in the scaled units defined above constitutes a strong test of the validity of the JKR approach for a given experiment. It has allowed one to pinpoint that when the solids in contact could no longer be considered as semi-infinite elastic solids, the JKR analysis was no longer valid. These finite size effects are the object of the section 'The JKR Test: Finite Size Effects and Role of Adhesion'.

The JKR Test: Finite Size Effects and Role of Adhesion

Introduction

The JKR test [1, 22, 23], with a sphere put into contact with a semi-infinite elastic planar solid, as described above, is indeed an efficient tool to characterize both the adhesion energy of the two bodies in contact and the effective elastic modulus of the system. This effective elastic modulus is directly related to the elastic modulus of both solids, so that one can easily deduce one of the elastic modulii if the other one is known. Since the historical paper by Johnson, Kendall, and Robert [1], a large body of experimental data has been accumulated, showing the strength of this JKR description of the contact between two elastic bodies, provided adhesion forces remain localized inside the contact zone [22, 24]. As shown by Maugis [18], it is also possible to rationalize how one can transit from the JKR to the DMT [2] description, depending upon the value of the parameter $\mu = W^2R/K^2a^3$, which characterizes the ratio of adhesion to elastic contributions (W is the adhesion energy, R the radius of the sphere, K the compound reduced elastic modulus, and a the radius of the contact). For relatively soft solids, $\mu \gg 1$, adhesion dominates and the JKR description holds.

In fact, the experimental use of the JKR test has exploded after the important work by Whiteside and Chaudhury [25], as attested by the quasi-exponential increase with time after 1991 of the number of citations of the historical JKR paper.
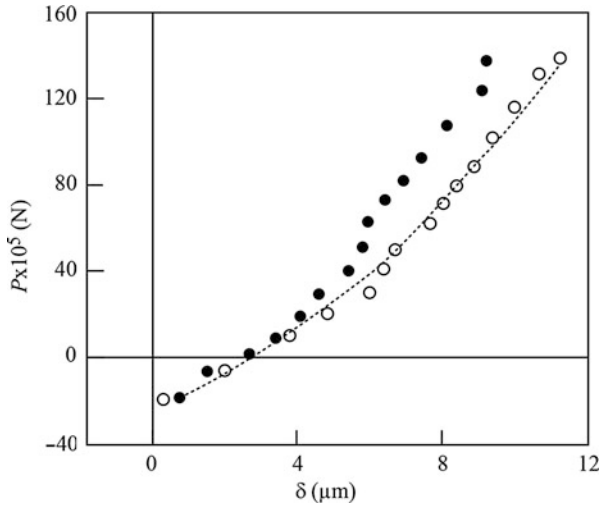
Fig. 18.7 Finite size effects due to the small dimensions of the microlens, in terms of load P versus displacement δ. The *full symbols* correspond to the experimental data with a PDMS sphere ($R = 1.1$ mm, $E = 1.27$ MPa) put into contact with a silicon wafer covered by a nanometric layer of adsorbed PDMS chains ($W = 42$ mJ m^{-2}). The *empty symbols* correspond to the measurements when a thick layer of PDMS is intercalated between the sphere and its holder. The line is a fit of the JKR Equation (Eq. 18.11) with no adjustable parameter (From Ref. [21])

In their seminal 1991 work, Whiteside and Chaudhury [25] proposed a simple and easy way to fabricate small semi-spherical lenses, with a radius of order of a millimeter and a very smooth surface (the surface roughness is fixed by the thermally excited capillary waves of the pre-cured elastomer liquid and thus remains in the subnanometric range). It consists in depositing pre-cured polydimethylsiloxane (PDMS) drops on a non-wetting surface, then curing these drops to form well crosslinked elastic solid hemispheres. These microlenses can be quite conveniently used to develop JKR tests allowing for relatively local measurements, as they easily lead to diameters of the contact area of order 100 μm. Quite soon after the use of these microlenses had been introduced, it appeared however that they could induce deviations from the JKR mechanics of the contact [21, 26], especially visible in the displacement versus load curves. An example [21] of such deviations is shown in Fig. 18.7.

Interestingly enough, it was found by Deruelle et al. [21] that these deviations could be suppressed by intercalating a 1 mm thick flat ribbon of the same elastomer as the lens between the lens and the rigid solid holder of that lens as depicted in Fig. 18.8. These experimental finding pointed out that finite size effects, coming from the finite thickness of the lens (typically half a millimeter), were able to seriously affect the mechanics of the contact. The origin of these deviations is easy to trace back: with a schematics of a JKR apparatus as shown in Fig. 18.8, the solid support of the lens imposes that the strain field vanishes to zero at the surface between the lens and this rigid support.
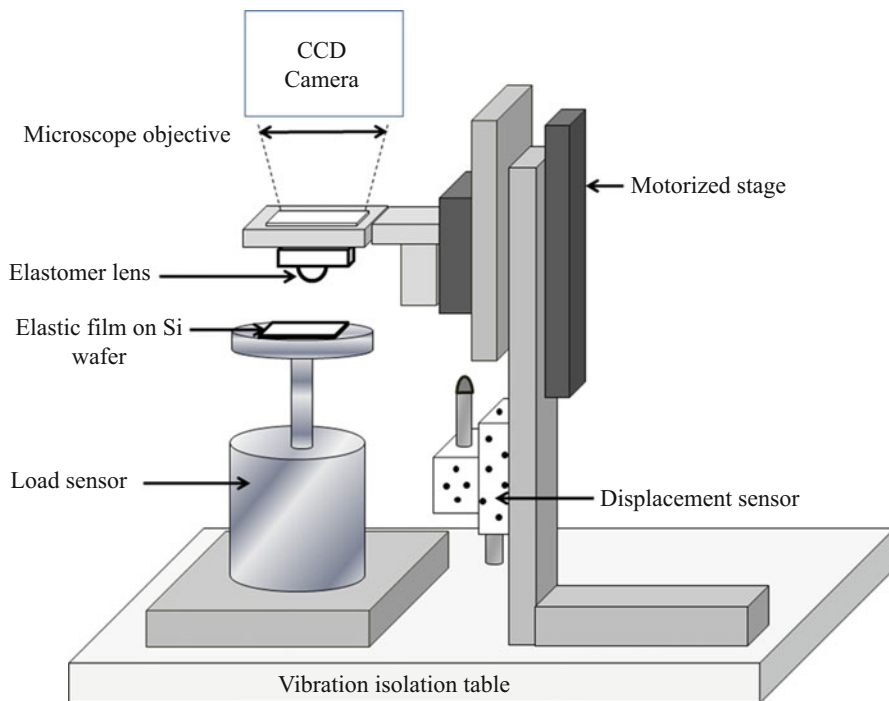
Fig. 18.8 Typical JKR apparatus setup. The motorized stage has a resolution of 0.00757 μm. A thick elastomer ribbon (1 mm) is placed between the elastomer lens and the rigid holder in order to avoid finite size effect in the elastomer lens

The strain field in an axisymmetric configuration can be analytically calculated along the symmetry axis for semi-infinite elastic bodies [27]. It appears that significant strain develops from the contact up to ten times the radius of contact along that symmetry axis. As soon as the thickness of the lens becomes smaller than ten times the radius of the contact, the presence of the interface between the lens and the holder, which imposes a zero boundary condition to the strain field, affects the whole strain field inside the lens and induces deviations to the JKR description. The presence of the lens/holder interface makes the lens appear more rigid than it is. If not correctly taken into account, such an effect will lead to incorrect determinations of the elastic modulus of the substrate or (and) incorrect estimations of the adhesion energy.

Deruelle et al. have proposed an efficient way of getting read of the finite size effects associated to the small dimensions of the microlens, through the intercalation of a flat thick ribbon made of the same elastomer as the lens, but it appears obvious that similar finite size effect should develop on either side of the contact, each time one of the elastic bodies in contact has a thickness smaller than ten times the radius of contact. This is particularly the case when dealing with supported thin elastic films or when the substrate is constituted of stratified sheets of various elastic properties, some of these sheets having a thickness smaller than ten times the radius of the contact. These two last situations are however quite important in practice, and

Fig. 18.9 Classical scaled JKR plot in the case of an elastic PDMS sphere ($K = 1,87$ MPa, $R = 912$ μm) in contact with a flat polyisoprene layer ($h = 1,52$ μm). The *straight dotted line* is the classical JKR adjustment (Eq. 18.16). A deviation from the *straight dashed line* is observed. The *full line* is an adjustment to the elastic foundation model developed by Tardivat et al. [27] (Data from [27])
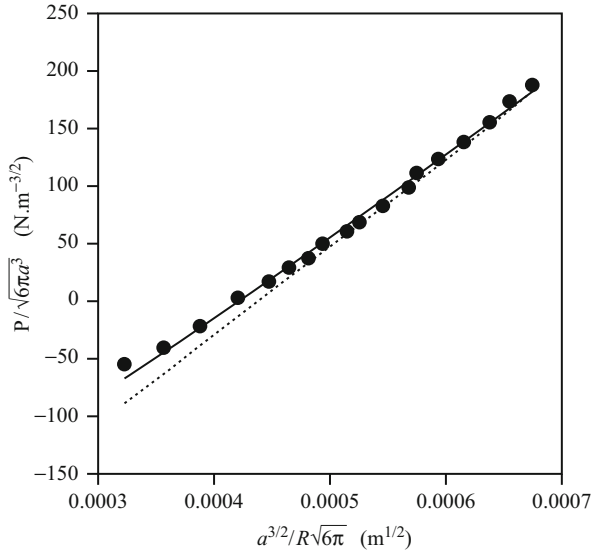
one would often like to have a good and easy way of characterizing the corresponding elastic properties. This is, for example, the case for supported polymer films such as the one used in coatings or more specifically for the thin mica sheet glued on a glass cylinder of a surface apparatus machine (SFA). An example of deviations to the JKR mechanics in the case of supported thin films is reported in Fig. 18.9. The linear representation of the JKR equation is used, so that the deviations can be easily observed.

Attempts of Mechanical Modeling of Finite Size Effects in Contact Mechanics Problems

A number of attempts have thus been made to try to quantify and to take into account these finite size effects in JKR like contacts, either starting from a rather practical or experimental point of view or trying to develop contact mechanics descriptions able to tackle the delicate question of the connection between deformations and stresses, in situations with intrinsically complex boundary conditions.

A first practical approach developed by Ahn and Shull [26], relied on the idea that finite size effects were changing the compliance of the system by a small amount, ΔC. Ahn and Shull proposed to correct the displacement versus load expression given by JKR, to first order in ΔC, and they extracted values of ΔC as a function of the parameters of the system from and adjustment of their data to this corrected expression. Tardivat et al. [28] attempted to describe soft elastic polybutadiene films deposited on a hard substrate (silicon wafer) as a series of independent springs under compression (this is the elastic foundation approach proposed by Johnson [1, 3], which neglects shear deformations). This allowed them to propose a correction to

the JKR expression of the force versus the radius of contact, introducing an effective elastic modulus which depends on the thickness of the film. This expression could account for the nonlinear observed normalized load versus normalized area of contact curve, as shown in Fig. 18.9, but the absolute value of the corresponding effective elastic modulus was not in agreement with the simple evaluations from the value of the bulk elastic modulus, meaning that it is certainly not correct to neglect the shear deformations. Sridhar et al. [29] have then developed a finite element analysis of the problem and obtained results in rather good agreement with the experimental data by Tardivat et al. [28] or by Flanigan et al. [30, 31], except for very small areas of contact. Similar approaches have also been proposed to tackle the important question of the analysis of indentation and nano-indentation data and are briefly reviewed in [32].

In parallel to the practical approaches summarized above, attempts to derive analytical contact mechanics solutions for layered elastic solids have also been proposed and applied to the problem of the contact between two elastic solids which indeed automatically forms a layered system. Solutions for nonadhesive contacts were first developed and then, more recently, for adhesive JKR like contacts. A review of existing analytical contact mechanics solutions for layered substrates can be found in [33]. The difficulty consists in expressing the relations between the strain and stress fields, taking correctly into account the boundary conditions at the various interfaces of the system.

Starting from the basic equations of elasticity and writing the boundary conditions at the interfaces between the layers, analytical expressions for the Fourier or Hankel transform of displacements and stresses can be obtained, for a prescribed distribution of surface stresses ([33] and reference included [1–14]).

As detailed in [32], for the system depicted in Fig. 18.10, where a rigid sphere indents a coated substrate, the Hankel transforms of the normal displacement at the surface, $u_1(r)$ and of the applied normal stress, $\sigma(r)$, are related by Eq. 18.1:

$$\bar{u}_1(\psi) = \frac{2}{E_1^*} \frac{X(\psi d)}{\psi} \bar{\sigma}(\psi) \qquad (18.17)$$

With E_1^* the reduced modulus of the film, defined by $E_1/(1 - v_1^2)$, with E_1 and v_1, respectively, the Young's modulus and the Poisson's ratio of the film, $X(\psi)$ is defined by:

$$X(\xi d) = \frac{1 + 4b\psi d e^{-2\xi d} - abe^{-4\psi d}}{1 - \left(a + b + 4b(\psi d)^2\right)e^{-2\psi d} + abe^{-4\psi d}} \qquad (18.18)$$

$$a = \frac{\alpha\gamma_0 - \gamma_1}{1 + \alpha\gamma_0}, b = \frac{\alpha - 1}{\alpha + \gamma_1}, \alpha = \frac{G_1}{G_0}, \gamma_1 = 3 - 4v_1, \gamma_0 = 3 - 4v_0 \qquad (18.19)$$

G_1 and G_0 denote, respectively, the shear modulus of the film and of the substrate, while v_0 is the Poisson's coefficient of the substrate. The ψ is the conjugated variable of r.

Fig. 18.10 Schematic description of the elastic indentation of a coated substrate by a rigid sphere. The layer is assumed to be perfectly bound to the substrate and the contact interface is frictionless. E_i and v_i are the Young's modulus and the Poisson's ratio of the substrate ($i = 0$) and the layer ($i = 1$)
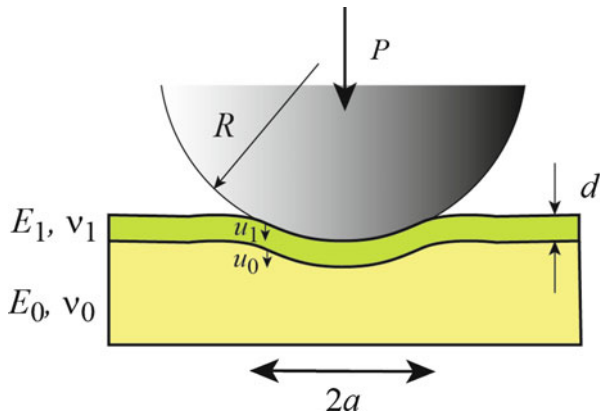
In Eq. 18.17, the quantities $\bar{u}_1(\xi)$ and $\bar{\sigma}(\xi)$ are the Hankel transforms of, respectively, the local displacements and the local stress, with the Hankel transform of a function $q(r)$ defined by:

$$\bar{q}(\xi) = \int_0^\infty r J_0(\xi r) q(r) dr \qquad (18.20)$$

With $J_0(x)$ the 0th order Bessel function of the first kind.

Equation 18.17 is quite general and contains potentially the answer to any contact mechanics problem involving elastic solids, provided one is able to solve it, inserting the correct boundary conditions of the given problem.

In fact, the difficult question is that of the inversion of this Green's tensor. The evaluation of the integral transforms can be made numerically, but then, one is often faced to very slow convergence of the numerical calculation, especially for the contact problem on a coated substrate, when the ratio of the supported film thickness to the radius of contact is small. Such a situation of high confinement is however the practically important one [32].

Perriot and Barthel [34] have developed a semi-analytical methodology which allows for the inversion of this Green's tensor in the real space. This approach has been used to provide exact solutions to the problem of the determination of the indentation versus the contact load when indenting a coated substrate[34] or the problem of the determination of the local stress and displacement fields inside the layered substrate [33].

More recently, a semi-analytical model of supported elastic films in adhesive contact with an elastic compliant sphere has been developed along these lines by Barthel [9] and provides predictions for the deviations to the JKR analysis of the contact behavior, even in highly confined conditions, i.e., when the contact radius is much larger than the thickness of the film.

These deviation from JKR solution are summarized in Eq. 18.21, which relates the applied load P, to the radius of contact, a, (in the scaled units of the linear JKR equation), but including the additional terms resulting from the presence of the thin supported elastic film:

$$\frac{P}{\sqrt{6\pi}\,a^{3/2}} = \frac{E_s^*}{2\sqrt{6}}\left(\frac{a^{3/2}}{\sqrt{\pi R}}\right)\Pi_0 - \sqrt{\frac{4wE_s^*}{3}}\frac{E_{eq}}{\Gamma} \qquad (18.21)$$

Here, the compound sphere-layer modulus is $E_s^{*\,-1} = E_f^{*\,-1} + E_l^{*\,-1}$. Π_0 is the normalized force for the adhesionless contact (along the lines of the JKR analysis, the solution is supposed to be a linear superposition of an adhesionless contact and of a flat punch, with the total force given by $P = P_0 + S\delta_{fp}$, with P_0 the force for the adhesionless contact, S the stiffness of the contact, and δ_{fp} the indentation of the flat punch), and Γ is the stress intensity factor at the crack tip, related to the adhesion energy W. E_{eq} is the normalized stiffness of the contact, defined by $S = 2aE_l^*E_{eq}$.

Indeed, the approach proposed by E. Barthel should in principle hold whatever the confinement and thus describe the transition from a JKR contact behavior dominated by the thin elastic film, when the contact radius is much smaller than the film thickness, to a JKR contact behavior dominated by the underlying rigid substrate when the contact radius becomes much larger than the film thickness and thus when the strain field largely spans the underlying substrate. Because of the potential importance of such a semi-analytical description of the contact between elastic layered solids, especially for supported elastic thin films under confinement tested through indentation experiments, it appeared necessary to test in details the validity of the Barthel's approach. We present below the results of a systematic investigation of the mechanical response of thin supported elastic films, tested in the JKR geometry, and we compare these data to the predictions of the Barthel's model.

Experimental Investigation of Finite Size Effects Observed in JKR Test on Supported Elastic Thin Films and Comparisons to the Barthel's Model

In order to evaluate the importance of finite size effects associated with the confinement of the thin elastic film intercalated between the elastic lens and the solid substrate of a JKR experiment and to examine the validity of the semi-analytical model proposed by E. Barthel [9], we have developed a systematic experimental investigation of the thickness dependence of the mechanical response of thin elastomer (cross-linked PDMS) films (in the thickness range few μm to few 100 μm) inserted in a JKR apparatus similar to the one presented in Fig. 18.8 and put into contact with microlenses of the same PDMS (Sylgard 184). The flat thin elastic films of various thicknesses were formed by controlled speed dip-coating
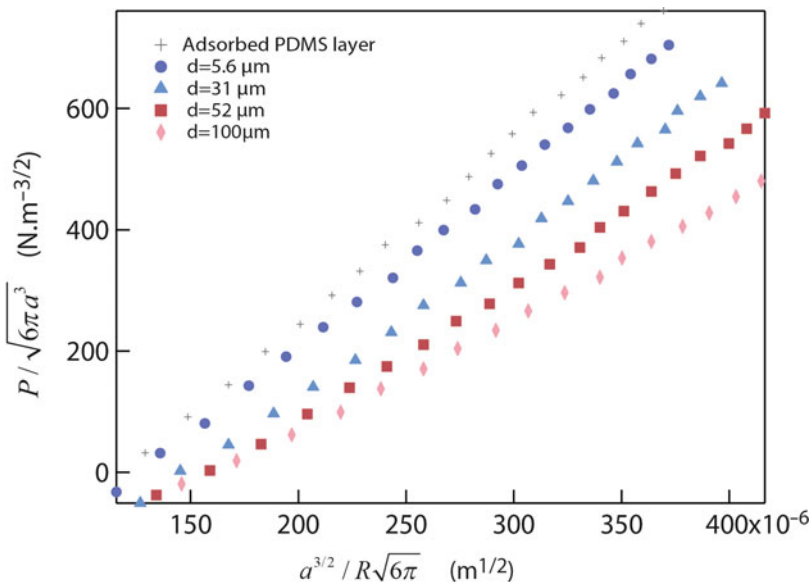
Fig. 18.11 Rescaled force P as a function of the rescaled radius of contact, a, (in the scaled units of the linear JKR plot, Eq. 18.16), between a PDMS sphere ($R = 0.612$ mm, $E = 1.73$ MPa) and a series of PDMS thin films supported by silicon wafers

method, slowly extracting a silicon wafer (previously cleaned by UV-Ozone treatment) from an uncured bath of Sylgard 184 mixture, and then curing overnight at 80 °C. The microlenses were formed by depositing drops of the uncured Sylgard mixture on a glass plate previously covered with a monolayer of fluorinated chlorosilane, so that the contact angle with PDMS was around 60°. The small drops were then cured overnight at 80 °C in a similar manner to the films. These drops are then detached from the silanated glass plate and transferred and attached to the JKR apparatus, intercalating between the lens holder and the lens a thick ribbon of the same PDMS film, in order to avoid important finite size effects due to the small size of the lens.

Typical results are presented in Fig. 18.11 and reported in the scaled units of the JKR analysis (see section 'An Introduction to Contact Mechanics'), for elastic film thicknesses ranging from 5 to 100 μm. For comparison, data for a nanometric film of adsorbed PDMS are also shown; in this latter case, the adhesion energy should be the same as that of the supported micrometric films (same PDMS–PDMS contact), but the nanometric film being always highly confined for contact radius in the 50 to several 100 μm range, the mechanics of the contact should be only sensitive to the silicon wafer high elastic modulus. We recall that, in the scaled units of the representation chosen here, a test of the validity of a JKR analysis is a straight line (which is indeed the case for the adsorbed layer – lens contact) and that the slope of the straight line gives a measurement of the composed elastic modulus of the contact. It is clear that the experiment is highly sensitive to the presence of
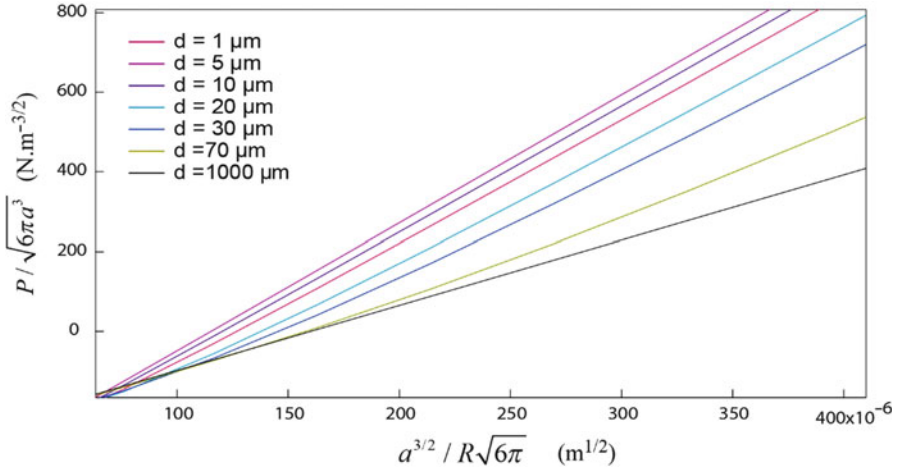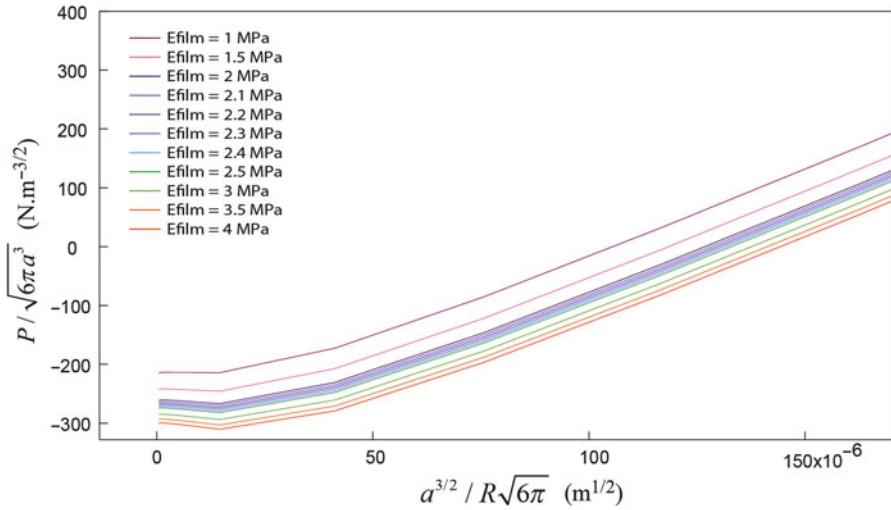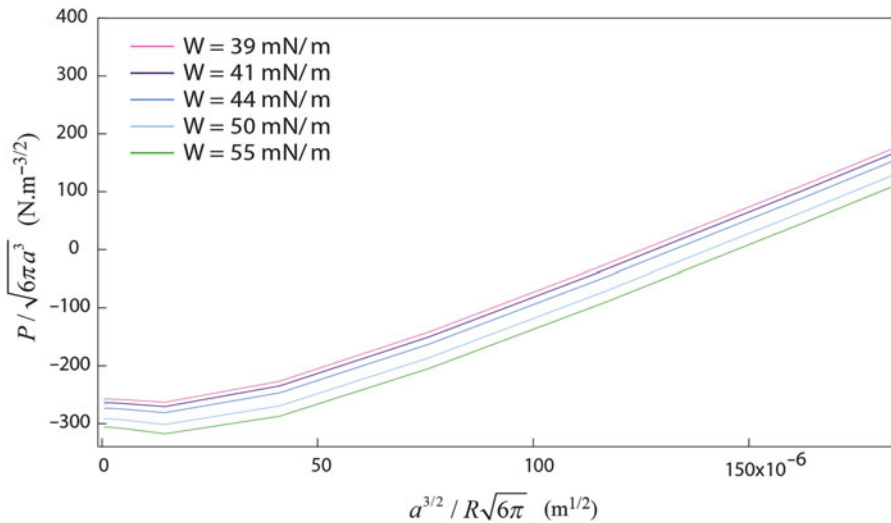
Fig. 18.12 Influence of the thin film thickness d on the load versus contact radius curves (in the classical JKR representation where the rescaled force $\frac{P}{\sqrt{6\pi a^3}}$ is plotted as a function of the rescaled radius $a^{3/2}/R\sqrt{6\pi}$) and computed from the Barthel's approach (Eq. 18.21). The curves are plotted in the case $E_f = 1.5$ MPa, $R = 0.6$ mm, $E_l = 1.86$ MPa, and an energy of adhesion $W = 48$ mNm^{-1}

a supported elastic film and that such soft film tends to decrease the slope of the scaled force versus the scaled radius, just because it decreases the stiffness of the contact. It is also clear that as soon as a micrometric film is present, the JKR analysis is no longer valid: the curves deviate from straight lines as a consequence of the change of state of confinement of the elastic thin film when the radius of contact changes.

Because Barthel's result relies on numerical resolutions, it is not easy to directly compare the experimental data to the prediction of the model. Also the number of system parameters entering into the model is rather large (at least, the adhesion energy, W, the radius of the lens, R, the Young's modulus of the lens, E_l and of the film, E_f, the thickness of the film, d, the Poisson coefficient of the lens and of the film, v_l and v_f, and the elastic modulus of the substrate, which was assumed to be infinite in all the following). We thus present in Figs. 18.12, 18.13, and 18.14 curves of the rescaled load versus the rescaled contact radius computed from Eq. 18.4 along with a numerical resolution of the mechanical equations allowing one to solve the problem in the Barthel's approach and to compute the various parameters, Π_0 and Γ. These series of curves have been obtained varying the elastic modulus of the supported film, at fixed thickness (Fig. 18.13), varying the adhesion energy, again at fixed thickness of the supported film (Fig. 18.14), and varying the thickness of the film at fixed elastic modulus and adhesion energy (Fig. 18.12). It is clear in all these figures that the curves are not straight lines, so that clear deviations from the simple JKR behavior are predicted. It is also clear that the curves are not so much sensitive to the exact value of either the elastic modulus or the adhesion energy. The sensitivity to the film thickness is however quite large, especially for rather small normalized contact radius, where the curves even cross each other.

Fig. 18.13 Influence of the Young's modulus of the film on the load versus contact radius curves (in the classical JKR representation where the rescaled force $\frac{P}{\sqrt{6\pi a^3}}$ is plotted as a function of the rescaled radius $a^{3/2}/R\sqrt{6\pi}$), in the Barthel's approach (Eq. 18.21). The curves are plotted in the case $d = 30$ μm, $R = 0.6$ mm, $E_l = 1.86$ MPa, and an energy of adhesion $W = 48$ mNm^{-1}

Fig. 18.14 Influence of the adhesion energy of the film on the load versus contact radius curves (in the classical JKR representation where the rescaled force $\frac{P}{\sqrt{6\pi a^3}}$ is plotted as a function of the rescaled radius $a^{3/2}/R\sqrt{6\pi}$) in the Barthel's approach (Eq. 18.21). The points are plotted in the case $d = 30$ μm, $R = 0.6$ mm, $E_l = 1.86$ MPa, and $E_f = 1.5$ MPa
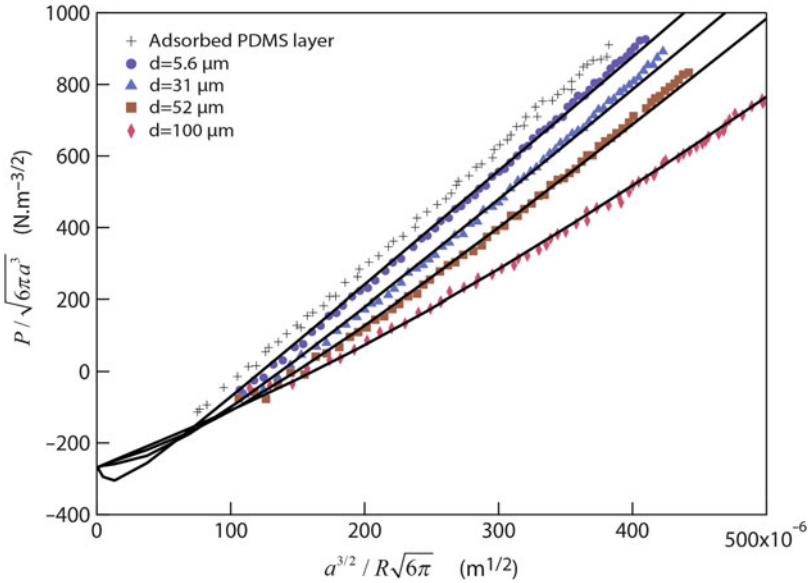
Fig. 18.15 Rescaled force $\frac{P}{\sqrt{6\pi a^3}}$ as a function of the rescaled radius of contact $a^{3/2}/R\sqrt{6\pi}$ between a PDMS sphere ($R = 0.612$ mm, $E = 1.73$ MPa). The *lines* correspond to the fit of the experimental data to the Barthel's prediction, with the Young's modulus of the film chosen equal to 1.5 MPa and the adhesion $W = 44$ mJ m^{-2}. The thickness d is adjusted to obtain the best fit and the corresponding value d_{fit} is compared to the independently measured value in Table 18.1

In Fig. 18.15, the experimental data presented in Fig. 18.11 are compared to the predictions of the Barthel's model, inserting in the computation reasonable parameters of the system for the elastic modulus of the film and the adhesion energy and letting float the thickness of the films. In Table 18.1, the film thicknesses evaluated from the best adjustment of the computed curves to the experimental data are compared to the actual independently measured thicknesses. One can see that the Barthel's model accounts quite correctly for the experimental data, thus, demonstrating the power of this approach.

Up to now, even if quite promising, the Barthel's approach for adhesive soft elastic contacts has not been explicated in terms of relations between load and indentation depth or indentation depth versus the size of the radius of contact. This would represent however an interesting extension of the description (and all theoretical ingredients are there), as the deviations due to finite size effects are more pronounced on the displacement versus load curves than on the radius of contact versus load curves. A full test of the validity of the Barthel's description would thus be easier to conduct in terms of displacement than in terms of radius of contact.

Table 18.1 Comparison between the best-fitted values of the film thicknesses d_f and the values d independently measured by optical reflectometry

$d_{\text{fit}}(\pm 0.5\ \mu\text{m})$	5,7	37,9	52,4	102
$d(\pm 0.4\ \mu\text{m})$	5,6	30	52	100

Summary

In this section, we have reviewed the consequences of mechanical confinement on the mechanical response, when a thin elastic film is squeezed between two adjacent elastic solids. We have shown that the whole mechanical response of the system could be deeply affected, so that the classical contact mechanics analysis could not be used to try to extract characteristic parameters of the contact such as the adhesion energy or an elastic modulus. This is of course of particular importance in a number of practical situations where one wants to characterize the mechanical properties of supported nano- or micro-thin films, using either macro or even nano contacts, such as in nano-indentation tests. We have seen that the deviations from the contact mechanics between two semi-infinite elastic media were progressively developing when increasing the size of the area of contact and were clearly important as soon as the radius of contact was a tens of the confined film thickness. Thus, the thinner the confined film, the more important the deviations from simple contact mechanics behavior are. We have shown that the recent developments in the mechanical description of the contacts proposed by E. Barthel could correctly account for series of JKR experiments on thin supported micrometric elastomer films, in the case of contact sizes in the 100 μm range. This quite promising approach right now has only been developed in terms of relations between contact area and load, but all theoretical ingredients are there to push it further and propose a description in terms of relation between load and indentation depth. This would give a mechanical description allowing one to take into account confinement effects in micro- or nano-indentation experiment. This is of particular importance as, in order to try to circumvent the difficulties linked to confinement and finite size effects, a clear tendency has been to try to decrease the size of the contact area, drastically decreasing the size of the probe used to form the contact (AFM tips, colloidal probe modified AFM, nano-indentation. . .).

Indeed, like for any mechanical test, the contact mechanics tests presented above rely on establishing the relation between stresses and strains. An intrinsic complication comes from the fact that changing the displacement (the indentation depth) not only changes the elastic energy involved but also the adhesion energy, just because the size of the contact also changes. Contact tests like JKR or indentation indeed involve a balance between adhesion and elastic deformations of both solids into contact. If one wants to extract with a reasonable accuracy an elastic modulus from such an experiment, one needs to correctly account for the adhesion contributions at each step of the experiment. *This is the main advantage of macro- or micro-JKR tests*, for *which direct visualizations of the area of contact are possible* and allow for a detailed test of the validity of the mechanical analysis

used, even if the number of system parameters involved in this mechanical analysis is rather large. Accessing the area of contact is not really easy for most indentation experiments, especially when the size of the indenter is decreased in order to decrease the size of the contact zone. It is then not always clear how far one can know that the mechanical analysis used is indeed correct for the given system investigated. In fact, depending on the way the contact is formed, these adhesion terms can seriously differ. For example, in nano-indentation experiments, the shape of the indenter needs to be known, in order to correctly estimate the involved adhesion energy. If the same indenter is used to test supported films of different thicknesses, the indentation depth will differ, due to confinement effects which will apparently rigidify the thinner films, decreasing the adhesion contributions. If an AFM cantilever is used, the bending of the cantilever may change the contact. *This question of correctly controlling the adhesion terms is an intrinsic complication of solid–solid contact*.

To circumvent these difficulties, we propose in the next section a new test, named the soft liquid probe, which allows, intercalating a simple liquid between the two solids squeezed against each other, to keep the adhesion (surface interaction terms) fixed, while applying to both solids through the liquid flow a changing and controlled stress field. The idea is that a liquid probe can be an alternative to the classical hard contact mechanics. More precisely the nano-hydrodynamic interaction between a sphere and a soft layer supported on a rigid substrate can provide a new, precise, and faithful method for measuring its absolute elastic properties.

The Soft-Probe Technique

The Flow Between Two Curved Surfaces

The Reynolds force. The liquid flow between a sphere of radius R and a plane is usually called the Reynolds flow [35–37]. Let us first summarize the main properties of this flow by deriving the force F[1] needed to approach the sphere to the plane at an instantaneous velocity dD/dt, where D is the distance measured between the apex of the sphere and the plane (see Fig. 18.16). We shall in this first section assume that the surfaces are sufficiently rigid so that all deformations of the surfaces due to surface forces are negligible.

When the radius of the sphere is large compared to the distance of closest approach between the surfaces, the flow of liquid at small Reynolds number can be described by the lubrication approximation [38]. In this approximation, it is assumed that locally the flow is similar to that between parallel plates. That is, the

---

[1] In this section the force acting in on the soft surface is F in order to avoid the confusion with the pressure P. The displacement field of the soft surface is ξ since we used the letter u for the fluid velocity as usually done in the lubrication equations.

Fig. 18.16 Coordinate
system to describe the flow
between a curved surface of
radius R and a flat plane
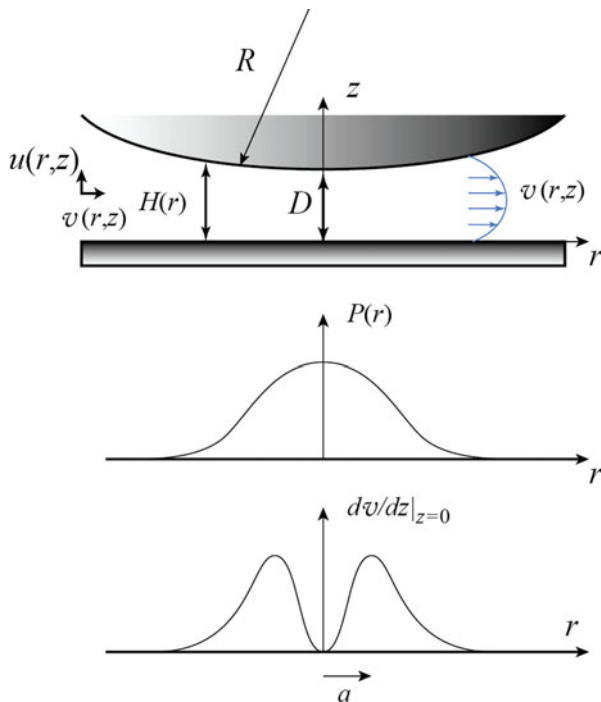
radial component of the velocity field $v(r,z)$ is large in comparison with the normal
component $u(r,z)$ and derivatives in the direction normal to the plane are dominant.
In this limit, the momentum equation for the velocity field $v(r,z)$ of a fluid of
viscosity η is parabolic and verifies:

$$v = \frac{1}{2\eta} z(z - H(r)) \frac{dP}{dr} \tag{18.22}$$

assuming the no-slip boundary condition $v(r,0) = v(r, H(r)) = 0$. If we combine this
result with the equation of continuity:

$$\frac{\partial u}{\partial z} = -\frac{1}{r} \frac{\partial}{\partial r} (rv) \tag{18.23}$$

Together with the boundary condition $u(r,0) = 0$, we can integrate once more
with respect to the vertical coordinate:

$$u = -\frac{1}{r} \frac{\partial}{\partial r} \left(\frac{r}{2\eta} \left(\frac{1}{3} z^3 - \frac{1}{2} z^2 H \right) \frac{dP}{dr} \right) \tag{18.24}$$

Noting that $u(H) = dD/dt$, one gets:

$$\frac{dD}{dt} = \frac{1}{12\eta} \frac{1}{r} \frac{\partial}{\partial r} \left(rH^3 \frac{dP}{dr} \right) \tag{18.25}$$

Using that $dP/dr = 0$ is finite at $r = 0$, Eq. 18.25 can be integrated to give:

$$P(r) = P(\infty) - 6\eta \frac{dD}{dt} \int_r^\infty \frac{sds}{H^3(s)} = P(\infty) - \frac{3\eta R}{H^2(r)} \frac{dD}{dt} \tag{18.26}$$

Here $P(\infty)$ is the ambient pressure at $r = \infty$. The pressure induced by the Reynolds flow is thus maximum in the center and decreases with the distance r. Noting the sphere surface can be approximated by a parabola, $H(r) = D + r^2/2R$, enables to calculate the shear rate:

$$\frac{\partial v}{\partial z} = -\frac{3r}{H^3(r)} (2z - H(r)) \frac{dD}{dt} \tag{18.27}$$

The shear rate is maximum at each surface, $z = 0$ and $z = H(r)$, where:

$$\frac{\partial v}{\partial z} \bigg|_{z=0} = -\frac{3r}{(D + r^2/2R)^2} \frac{dD}{dt} \tag{18.28}$$

This leads to an important feature of the Reynolds flow: the shear rate is maximum at a distance:

$$a = (2RD/3)^{1/2} \tag{18.29}$$

This distance a can be considered as the size over which the Reynolds flow applies. The hydrodynamic force F can be obtained by a simple integration of the pressure (Eq. 18.26):

$$F = \int_0^\infty 2\pi r \left(-\frac{3\eta R}{H^2(r)} \frac{dD}{dt} \right) dr = -\frac{6\pi\eta R^2}{D} \frac{dD}{dt} \tag{18.30}$$

If we assume that the flow applies a pressure over a typical size πa^2, the average pressure induced by the Reynolds flows is thus:

$$\overline{P} = \frac{9\eta R}{D^2} \frac{dD}{dt} \tag{18.31}$$

A fundamental property of the Reynolds flow is that it implies a force which diverges when the distance between the sphere and the plane decreases to zero.

To measure with a good precision the Reynolds force, it is possible to create an oscillating flow with a nanometric amplitude h_0 smaller than the confining distance D in order to stay in the linear regime ($h_0 \ll D$). The quantity of interest is the mechanical complex impedance $Z^*(D, \omega)$, which is the ratio of the dynamic hydrodynamic force $F(t) = Re[F_\omega e^{i\omega t}]$ acting on the plane at the excitation frequency, ω, to the amplitude h_0 of the sphere oscillations, $h_0 \cos(\omega t)$:

$$Z^*(D, \omega) = \frac{F_\omega}{h_0} \qquad (18.32)$$

For the classical Reynolds flow, the mechanical impedance is thus purely imaginary and writes:

$$Z^*(D, \omega) = -i\frac{6\pi\eta R^2\omega}{D} \qquad (18.33)$$

The inverse of the mechanical impedance is thus purely imaginary and increases linearly with the distance D.

Experimental verification. The first experimental validation of the Reynolds force down to nanometric confinement has been performed by D. Y. C. Chan and R. G. Horn in 1985 [36] using a surface forces apparatus developed by D. Tabor and J. Israelachvili [39, 40]. More recently, two questions have been addressed more specifically to know if the Reynolds force was always valid.

The first question is related to the validity of the Navier–Stokes (NS) equation down to nanometric confinement. As a matter of fact, for simple liquids, the continuum framework of hydrodynamics is apparently valid down to the nanometer scale. In other words, there is no expected deviation to the bulk NS equation for confinement larger than $\sim$1 nm. This very surprising result is actually suggested by a number of experimental and numerical simulations studies. On the experimental side, one may cite the pioneering work by Chan and Horn [36] and later by Georges et al. [41] using surface force apparatus (that will be described in the next section) and more recently and specifically for water the works by Klein et al. [42–45] and Riedo et al. [46] showing that water keeps its bulk properties down to 1–2 nm. A similar behavior was found for other liquids like octamethylcyclotetrasiloxane (OMCTS) [47, 48]. The threshold for applicability of continuum hydrodynamics was also investigated using molecular dynamics simulations of confined water and the same value of about 1 nm came out of the simulation results [49–52].

The second question was related to the validity of the no-slip boundary condition. Indeed, the question is to know if it is possible to apply the condition $v(r,0) = 0$ in the previous equation. An alternative to the sticky boundary condition is to consider a slip length b, which should be the distance below the solid surface for which the extrapolation of the fluid velocity profile vanishes (Fig. 18.17).

The Reynolds force in the presence of slip at the wall has been calculated by O. Vinogradova [53–55] and leads to a force:
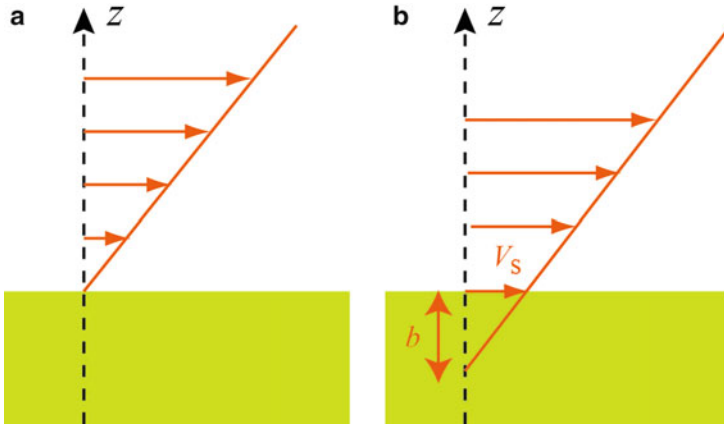
Fig. 18.17 (**a**) Flow of a liquid over a sticky surface. The fluid velocity at the surface is equal to zero. (**b**) Flow of a liquid over a slippy surface. The fluid velocity at the solid surface is not equal to zero. The slip length (**b**), also called the Navier length, is the extrapolation length of the velocity profile to zero velocity

$$F = -\frac{6\pi\eta R^2}{D}\frac{dD}{dt}f^* \quad \text{with } f^*$$

$$= \frac{1}{4}\left\{1 + \frac{6D}{4b}\left(\left(1 + \frac{D}{4b}\right)\ln\left(\left(1 + \frac{D}{4b}\right)\right) - 1\right)\right\} \quad (18.34)$$

The theoretical understanding of slippage has been the object of intense research over the last decade (see Ref. [56] for a review). It is now commonly accepted that the boundary condition on atomically smooth surfaces depends essentially on the structure of the liquid at the interface, itself determined by its interactions, its commensurability with the solid phase, and its global density [56, 57]. This has been confirmed by experimental verifications of Eq. 18.33 [56, 58–62] or by other techniques such as near-field laser velocimetry [63–65] or fluorescence correlation spectroscopy [66]. An important result is that the slip length is nanometric or of tens of nanometers but decreases with the roughness of the surfaces down to a molecular size or less in the case of surfaces with a nanometric roughness [67].

The 'Soft-Probe' Principle

When a liquid is forced to flow between deformable surfaces, the Reynolds flow has to be modified since the confining solids will be deformed by the flow as described in Fig. 18.18. More precisely we have studied the effect of supported film of thickness *d* supported on a rigid substrate. The thin film is characterized by its two elastic constants (*E*, the Young's modulus, and *v*, the Poisson's modulus). One has thus to take into account the displacement $\xi(r, t)$ of the surface at the distance *r* of the axis. We restrict here to the quasistatic limit and do not consider the elastic
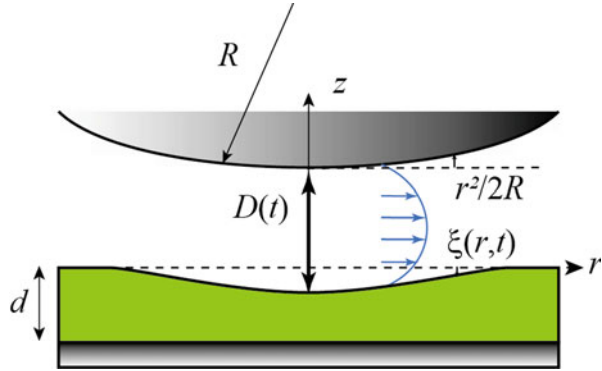
wave generated by the oscillating stress: this is adequate for layers of shear moduli
$G = E/2(1 + v)$ in the range of kilopascals or more, for which the relevant frequency
$\sqrt{G/2RD\rho_s}$ is much higher than the excitation frequency. The liquid film thickness
in the zone of interest is again given by the parabolic approximation:

$$H(r,t) = D + \frac{r^2}{2R} + h_0 \cos(\omega t) + \xi(r,t) \tag{18.35}$$

In the linear response regime, all the time-dependent quantities are harmonic
functions of time at the driving frequency: $\xi(r, t) = Re[\xi(r)e^{i\omega t}]$ and $P(r, t) =
Re[\delta P(r)e^{i\omega t}] + P_0$, where P_0 is the ambient pressure and $\xi(r)$ and $\delta P(r)$ are complex
amplitudes. The lubrication Eq. 18.23 can be linearized:

$$i\omega r(h_0 + \xi(r)) = \frac{1}{12\eta} \frac{\partial}{\partial r} \left(r \left(D + \frac{r^2}{2R} \right)^3 \frac{d\delta P}{dr} \right) \tag{18.36}$$

The tangential stress at the surface is negligible compared to the normal stress:
estimated in the case of a rigid surface, the ratio scales as $\frac{\sigma_T}{P(r)} \sim \sqrt{\frac{D}{R}} \ll 1$. Thus, one
needs only to consider the thin film response to the axyssymetric pressure acting on
its surface. This response has been calculated independently by Li and Chou [68]
and by Nogi and Kato [69], with a sticky boundary condition of the film on the
underlying substrate. The response relates the zeroth-order Hankel transforms of
the normal displacement $\xi(r)$ to the one of the pressure $\delta P(r)$ [11, 70]:

$$\check{\xi}(\psi) = \frac{2}{E^*} \frac{X(\psi d)}{\psi} \delta \check{P}(\psi) \tag{18.37}$$

Where $E^* = E/(1 - v^2)$ is the reduced Young's modulus and $X(\psi d)$ is the response
function given in [11]. The details of the calculation can be found in [11] and will not
be reproduced in this book. Note that Eq. 18.37 is the same equation as the Eq. 18.18,
introduced for the description of the elastic contact (Fig. 18.19).
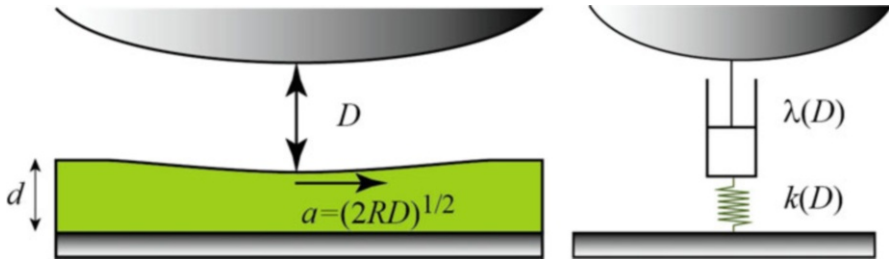
Fig. 31.19 Schematic *spring*-and-*dashpot* model equivalent to the 'soft probe'

We only summarize here the two regimes of interest: the incompressible thin film ($v = 1/2$) in the regime $d \ll \sqrt{2RD}$, which is the regime where the thin film is much thinner than the fluid probe radius a defined in Eq. 18.8, and the compressible film ($v = 0$) in the same regime $d \ll \sqrt{2RD}$. It is of interest to describe the theoretical predictions with a scaling semi-quantitative argument. At large distance, the hydrodynamic force acting on the supported thin film is weak and does not indent the elastomer significantly. The fluid probe acts as a dashpot of damping coefficient:

$$\lambda(D) = \frac{6\pi\eta R^2}{D} \tag{18.38}$$

The target surface responds with a stiffness $k(D)$. The mechanical impedance of this spring-and-dashpot in series is thus:

$$Z^*(D, \omega) = \frac{ik\lambda\omega}{k + i\lambda\omega} \tag{18.39}$$

This defines a critical distance D_c by $k(D_c) = \lambda(D_c)\omega$. The amplitude of the indentation is:

$$\xi = \frac{\overline{p}(D)}{k(D)} \tag{18.40}$$

where $\overline{p}(D) = \lambda(D)/k(D)\pi a^2$. Thus, the small indentation regime observed for $D \gg D_c$ corresponds to the case where $k(D) \gg \lambda(D)\omega$. A first-order development of the mechanical impedance thus leads to:

$$Z^*(D, \omega) \sim i\lambda\omega + \frac{(\lambda\omega)^2}{k} \tag{18.41}$$

In this regime, the elastic deformation of the thin layers gives only a small correction to the Reynolds Eq. 18.12.

When the distance D becomes lower than D_c, the flow separates in two regions. In a central region where the liquid thickness is lower than D_c, the liquid is clamped

by its viscosity and acts as a solid probe. The elastic indentation of the target fully accommodates for the sphere oscillations. Outside this region, the features of the Reynolds flow are recovered. The system is now a spring-and-dashpot in parallel, and the response saturates to:

$$Z^*(D, \omega) \sim k(D_c) + i\omega\lambda(D_c) \tag{18.42}$$

more or less close to its crossover value.

The Incompressible Thin Film ($\nu = 1/2$)

Calculating the stiffness $k(D)$. In the case of an incompressible film deposited on an incompressible substrate is possible. The thin film can deform only by an in-plane shear, and due to its incompressibility, the indentation ξ is compensated by an in-plane displacement $\zeta = RD\xi/d\sqrt{2RD}$. As the layer is clamped on the underlying substrate, this displacement induces a shear of order $\epsilon \sim \zeta/d$. The stored elastic energy is $\overline{p}\xi \sim \left(\frac{\mu\epsilon^2}{2}\right)a^2 d$, with $G = E/3$, and it determines the stiffness of the confined layer:

$$k(D) = \frac{\overline{p}}{\xi} \sim \frac{4\pi R^2 D^2 E}{3d^3} \tag{18.43}$$

This gives a critical distance defined by:

$$D_c = d(4\eta\omega/E)^{1/3} \tag{18.44}$$

The critical distance depends linearly of the thickness of the film and depends only on the one-third of its Young's modulus. For $D \gg D_c$, according to Eq. 18.42, we expect $Re[Z^*(D, \omega)] \sim D^{-4}$. Using a full numerical solution of Eq. 18.37, it is possible to obtain a theoretical value of $Z^*(D, \omega)$ which depends of the critical distance D_c via a tabulated function $g_{1/2}(x)$.

$$Z^*(D, \omega) = \frac{6\pi\eta R^2 \omega}{D_c} g_{1/2}\left(\frac{D}{D_c}\right) \tag{18.45}$$

The asymptotic values of $g_{1/2}(x)$ are the following:

$$\begin{aligned}
\lim_{x \to 0} g_{1/2}(x) &= 0.838\left(1 + i\sqrt{3}\right) \\
\lim_{x \to \infty} g_{1/2}(x) &= \frac{3}{10x^4} + \frac{i}{x}
\end{aligned} \tag{18.46}$$

Measuring the experimental values of $Z^*(D, \omega)$ and comparing the values to Eq. 18.45 thus lead to a precise determination of the critical distance D_c and then to the Young's modulus of the film.

The Compressible Thin Film ($v \neq 1/2$)

Calculating the stiffness $k(D)$ in the case of a compressible film deposited on an incompressible substrate is also possible. This configuration is formally equivalent to a compressible layer of thickness d under a uniaxial compression. The uniaxial compression modulus writes

$$E^{'} = E \frac{1 - v}{(1 - 2v)(1 + v)} \tag{18.47}$$

When the normal pressure $\bar{p}$ is applied, the compressible layer indents as $\xi = d\bar{p}/E^{'}$, and its effective stiffness is:

$$k(D) = \frac{E^{'}}{d} \pi a^2 = \frac{2\pi R D E^{'}}{d} \tag{18.48}$$

The associated critical distance is:

$$D_c = \left(8\eta\omega R d / E^{'} \right)^{1/2} \tag{18.49}$$

For $D \gg D_c$, according to Eq. 18.20, we expect $Re[Z*(D, \omega)] \sim D^{-3}$. Using a full numerical solution of Eq. 18.37, it is possible to obtain a theoretical value of $Z*(D, \omega)$ which depends of the critical distance D_c via a tabulated function $g_v(x)$.

$$Z^*(D,\omega) = \frac{6\pi\eta R^2\omega}{D_c} g_v \left(\frac{D}{D_c} \right) \tag{18.50}$$

The asymptotic values of $g_v(x)$ are the following:

$$\begin{aligned} \lim_{x\to 0} g_v(x) &= \sqrt{2/3}(1 + i) \\ \lim_{x\to\infty} g_v(x) &= \frac{1}{8x^3} + \frac{i}{x} \end{aligned} \tag{18.51}$$

Again, measuring the experimental values of $Z*(D, \omega)$ and comparing the values to Eq. 18.50 thus lead to a precise determination of the critical distance D_c and then to the uniaxial compression modulus. The Young's modulus or the Poisson modulus can then be determined but not independently.

Dynamic Surfaces Forces Apparatus

The 'soft-probe' technique can thus be used as soon as it is possible to measure the mechanical impedance. This is possible using either an atomic force microscope AFM or a surface force apparatus. In this book, we will illustrate the use of the SFA to measure the mechanical properties of supported thin films.

The most common SFA is the so-called interferometric SFA. It has been extensively described in the literature [40, 71]. In this technique, collimated white light is transmitted through the surfaces, which generally are atomically smooth mica. A thin metallic layer on the back side of each mica sheets acts as an optical mirror, producing sharp interference fringes of equal chromatic order (FECO) in the focal plane of an imaging spectrograph. Determination of FECO wavelengths allows the simultaneous determination of the surfaces separation, the refractive index of the interstitial medium, and the shape of the surfaces. A first limitation of this technique is the time needed for the analysis of the fringes pattern, which limits the temporal resolution to roughly 1 s. Moreover, the constraint that solid surfaces must be both transparent and optically smooth limits the practical choice of surfaces to mica, glass, or silica. These limitations may be avoided by reporting the measurement on mechanical parts rigidly fixed to surfaces. With such a geometry, contrary to the common interferometer-based SFA, the deflection of the force-measuring cantilever is directly measured. The two main advantages of such a design are the free choice of the solid surfaces and the possibility of using fast and accurate electronic or optic sensors.

Tonck and Georges [41, 72] have developed such an SFA machine using two capacitive sensors and Restagno et al. developed an SFA machine with a capacitive sensor for the relative displacement measurements and an interferometric sensor for the force measurement [13–15]. The latter is shown schematically in Fig. 18.20.

This apparatus measures the static and dynamic forces between two macroscopic surfaces, generally a plane and a sphere as a function of their relative displacement. An important feature is to allow only a pure translational motion of the surfaces. For this, the two surfaces are firmly clamped to two double cantilevers $C1$ and $C2$. These cantilevers prevent any rotation of the surfaces. The relative motion of the surfaces is obtained with the help of a translation stage, which pushes the extremity of the cantilever $C1$. This translation stage is composed of three elements. First, a 30 nm step micromotor is used for a rough positioning of the surfaces at the beginning of the experiments. The initial distance between the surfaces is typically between 1 and 3 mm. Second, fine displacements of the surfaces are performed by two piezoelectric actuators. The first one, driven with a voltage ramp, allows a 5 mm quasistatic approach or recede of the surfaces. The second one is driven with a sinusoidal voltage to add a small sinusoidal motion of amplitude h_0 of the order of a fraction of nanometer to the continuous motion.

The extremity of the second cantilever $C2$ is free so that the deflection of $C2$ measures the forces acting on it. A mirror, glued to C2 is included in an interferometer. The deflection x of the force cantilever C2 is measured with a differential interferometer based on the well-known Nomarski principle. This displacement is converted into a force using the mechanical response of the cantilever which can be modeled using a spring-and-dashpot model and precisely measured prior to any experiment.

The relative displacement of the surfaces is measured with a capacitive sensor which makes the measurements independent of the response of the two piezoelectric elements. For this purpose two 5 cm diameter duraluminium plates are
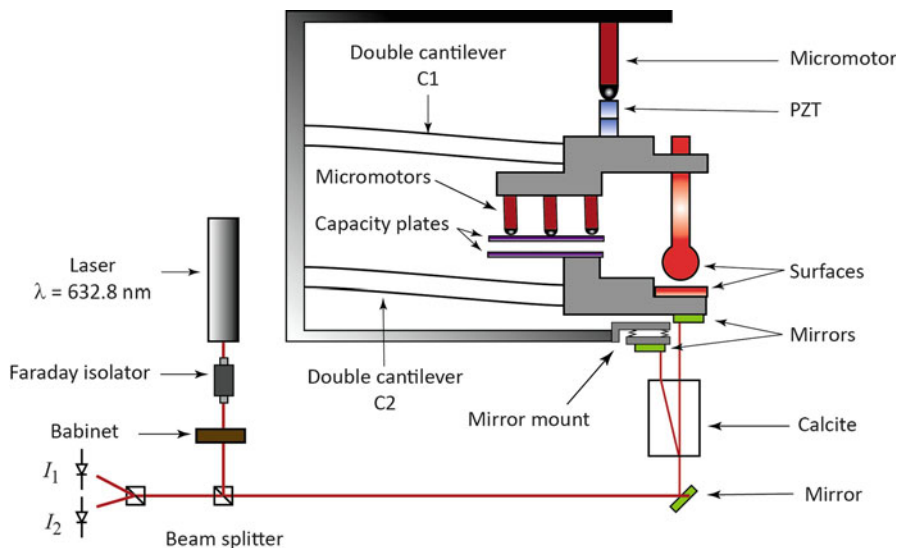
Fig. 18.20 Schematic of the dynamic SFA developed by Restagno et al.

connected to the cantilevers extremities and form a plane capacitor. The parallelism of the two plates is adjusted using three 30 nm step motors. The capacitor plate mounted on C2 is rigidly bound to the surface holder. The consequence is that during a cantilever deformation, the capacitor plate and the surface holder are translated on the same distance, whatever the cantilever deformation.
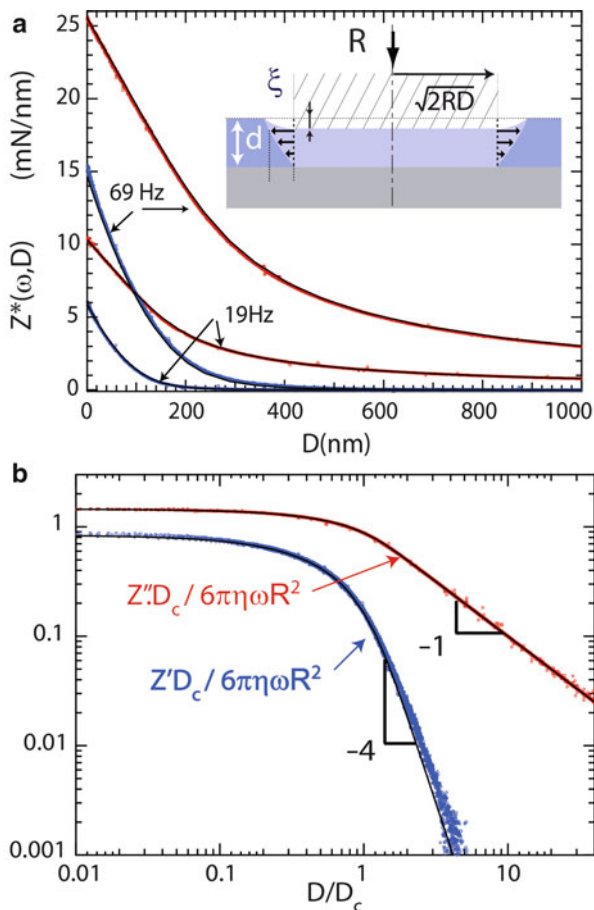
The plane displacement with respect to a rigid frame is measured by a Nomarski interferometer with a bandwidth of 1 kHz and a quasistatic (steady-state) resolution of 1 Å. With the classical C2 cantilever spring constant used in the experiments ($K \sim 2{,}000$ N/m), the quasistatic force resolution is 0.7 μN. The relative sphere-plane displacement D is measured with a bandwidth of 1 kHz and a quasistatic resolution of 1 Å. In dynamic measurements the harmonic components of these two displacements are measured in amplitude and phase by two double lock-in amplifiers SR830. Taking into account the noise level of the environment, resolutions, respectively, of 10 nN and 5 pm for the relative displacement are achieved in the frequency range 10–100 Hz.

Application of the 'Soft-Probe Technique'

Up to now, the 'soft-probe technique' has been tested only on thin PDMS films and thin bubble films which are two examples of respectively incompressible and compressible films.

A first example is a 4.4 μm crosslinked PDMS film studied with the SFA ($R = 3$ mm) using a glycerol-water mixture of viscosity 43 ± 2 mPa s as a probe. The thin film was deposited on a floated pyrex plane by spin coating a solution of

PDMS (30 % in heptane) mixed with the curing agent (Sylgard, Dow Corning, crosslinking ration 10:1). After deposition the samples were cured first at 150 °C for 1 h, and then at 75 °C over a night in an oven. The results are reported in Fig. 18.21. The force response shows a viscous regime at large distance and saturates at small distance as calculated theoretically. The agreement with the data obtained by fitting the single parameter D_c is excellent. In particular the model predicts $Z'(0)/Z''(0) = 1/\sqrt{3}$ as observed. More precisely we find cutoff values $D_c(19 \text{ Hz}) = 109 \pm 1$ nm and $D_c(69 \text{ Hz}) = 170 \pm 1$ nm. Their ratio equal to 0.647 is very close to the theoretical ratio $(19/69)^{1/3} = 0.651$. The derived value of the Young's modulus is $E = 1.3 \pm 0.1$ MPa. It is important to mention that the main uncertainty comes from the value of the film thickness $d = 4.4 \pm 0.1$ μm.

An example of compressible objects resting on a rigid surface has been obtained using an array of microbubbles embedded in the holes of a textured, hydrophobic surface (Fig. 18.21). The fluid probe was a water/glycerol mixture of 39 ± 2 mPa s. This configuration is formally equivalent to a compressible layer of thickness d and

Fig. 18.22 (**a**) The mechanical impedance $Z^*(\omega, D)$ in linear scales measured on a regular array of submicrometric bubbles embedded in the holes of a textured silanized silicon surface. *Red*: real part, *blue*: imaginary part. Two frequencies are superimposed: $f = 69$ Hz with $D_c = 320$ nm and $f = 19$ Hz (with $D_c = 624$ nm). The *black lines* are the theoretical predictions. (**b**) Normalized mechanical impedance $Z^*(\omega, D)D_c/6\pi\eta\omega R^2$ as a function of D in log-log scales. The *black lines* are plots of the theoretical function g_v
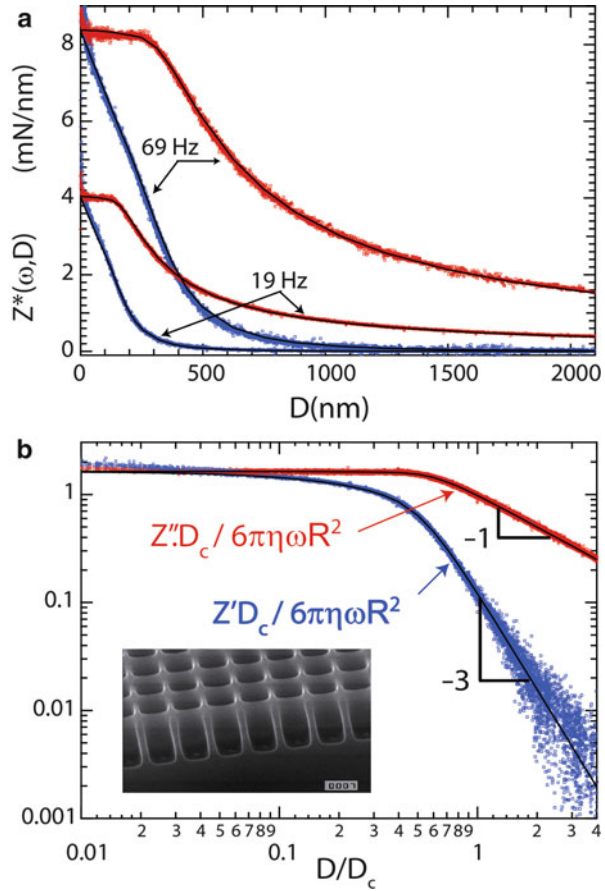
uniaxial compression modulus E'. Hence, again, the agreement with the experimental data shown in Fig. 18.22 is excellent. The values found for D_c at 19 and 69 Hz, 160 and 312 nm, allow to determine the stiffness $\frac{E'}{d} = (1.1 \pm 0.1) \times 10^{12}$ N m of the mattress of bubble. This value can be compared to a theoretical prediction using the elastic deformation of the bubbles [73].

Summary

In conclusion, we have introduced a new technique to measure the mechanical properties of micro- to nano-elastic films using hydrodynamic interactions at a nanoscale as a unique tool for the quantitative testing of small and soft elastic objects.

We have first briefly reviewed the main physical characteristics of the Reynolds flow which is the flow induced by the approach motion of a sphere close to a flat surface in the low Reynolds number limit and in the lubrication approximation.

This hydrodynamic interaction acts to push on the flat surface with an amplitude which depends on the distance between the sphere and the plane and with a characteristic lateral size which can also be modulated by the distance between the two objects. We have reviewed some past and recent results on the validity of this continuum mechanics approach down to molecular size.

In a second part, we have introduced more precisely the 'soft-probe' principle. If a Reynolds flow is applied on a thin supported elastic layer, it can act as an indenter. We have summarized the elastohydrodynamic calculation allowing to extract the mechanical properties of thin supported films from the measurement of the complex mechanical impedance of the fluid and the thin film.

We have illustrated the capability of this technique with two very different examples of thin films: a thin compressible film of air bubble trapped on a superhydrophobic surface and a thin incompressible film of elastomer. For each of these examples, quite different scaling laws were predicted. These two examples clearly demonstrate the strong potentialities of the soft probe. It would be interesting to develop its use in colloidal probe AFM in order to be able to increase the frequency range of this mechanical testing, allowing one to probe not only purely elastic but also viscoelastic supported thin films.

Conclusion

As mentioned in the introduction, thin supported elastic nano- or micrometric films are everywhere in our everyday life, and it is often of outmost importance for the quality of their function in a given application to be able to characterize precisely their mechanical properties. In the present chapter, we have reviewed the main experimental approaches developed along the years to access the mechanical characteristics of such supported thin films. Classical routes to do so are based on a mechanical analysis of the contact mechanics proposed by Johnson, Kendall, and Roberts, using either nanometric probes such as an AFM tip or a nanoindenter or micrometric hemispherical probes in the so-called JKR test. We have examined the fundamental reasons why the modeling of the contact between such probes and a supported thin film remains a quite difficult mechanical problem. We have briefly presented the successive contact mechanics models which have been proposed to take into account the observed apparent increased stiffness of these elastic films when they are confined between the supporting solid and the other solid (the indenter) used to squeeze them in order to deduce their mechanical properties from load versus deformation curves. We have put a special emphasis on the recent model developed by E. Barthel and discussed its confrontation to series of experimental results obtained through a JKR test of thin supported PDMS elastomer films solicited by a microlens made of the same PDMS. The good observed agreement between the experimental load versus radius of the area of contact curves, for all investigated thicknesses of the films, is certainly indicative of the strength of this model, which needs be further on explicited to describe indentation experiments, in the presence of adhesion.

An important conclusion that needs to be kept in mind by anyone wanting to measure the properties of supported thin films is that using a nanometric indenter is not a real route to be sure that mechanical confinement does not impact the measurement. Indeed, such nanometric probes usually do not permit to access to a precise knowledge of the contact area between the probe and the films, so that it is not easy to estimate the relative role of adhesion and elasticity in the observed behavior. On the other hand, using a macro- or millimetric indenter imposes to rely on a subtle mechanical model of the contact mechanics of adhesive coatings.

We then have presented an alternative technique to this solid–solid contact method. This is the so-called soft-probe technique in which rather than soliciting the thin films with a solid (the indenter), one uses the Reynolds flow induced by the oscillations of a sphere progressively brought in the proximity of the film surface to act as a gentle indenter. The interest of this new approach is twofold: first the adhesion terms are fixed and do not depend on the distance between the sphere and the film surface, as both solids are immersed in the liquid, so that no changes in contact area are induced by the change of the mechanical solicitation; second, the strength of the mechanical solicitation by the hydrodynamic flow can be varied and controlled in a large range. In order to exemplify the potential performances of this new technique, the characterization of the mechanical properties of thin micrometric thin PDMS elastomer films and those of a layer of air bubbles have been presented and discussed. This new test appears particularly interesting when confined very soft films need be tested.

References

1. Johnson KL, Kendall K, Roberts AD (1971) Surface energy and the contact of elastic solids. Proc R Soc Lond Math Phys Sci 324:301–313
2. Derjaguin BV, Muller VM, Toporov YP (1975) Effect of contact deformations on the adhesion of particles. J Colloid Interface Sci 53:314–326
3. Johnson KL (1987) Contact mechanics. Cambridge University Press, Cambridge
4. Maugis D (2000) Contact, adhesion and rupture of elastic solids. Springer, Berlin/New York
5. Wang D, Liang X-B, Liu Y-H et al (2011) Characterization of surface viscoelasticity and energy dissipation in a polymer film by atomic force microscopy. Macromolecules 44:8693–8697. doi:10.1021/ma201148f
6. Cappella B, Kaliappan S, Sturm H (2005) Using AFM force-distance curves to study the glass-to-rubber transition of amorphous polymers and their elastic-plastic properties as a function of temperature. Macromolecules 38:1874–1881
7. Gillies G, Prestidge CA, Attard P (2002) An AFM study of the deformation and nanorheology of cross-linked PDMS droplets. Langmuir 18:1674–1679
8. Lin L-Y, Kim D-E (2012) Measurement of the elastic modulus of polymeric films using an AFM with a steel micro-spherical probe tip. Polym Test 31:926–930. doi:10.1016/j.polymertesting.2012.06.012
9. Barthel E, Perriot A (2007) Adhesive contact to a coated elastic substrate. J Phys Appl Phys 40:1059–1067. doi:10.1088/0022-3727/40/4/021
10. Barthel E (2007) Adhesive contact of a compliant sphere to an elastic coated substrate: the thin film limit. J Adhes 83:729–739

11. Leroy S, Charlaix E (2011) Hydrodynamic interactions for the measurement of thin film elastic properties. J Fluid Mech 674:389–407. doi:10.1017/S0022112010006555

12. Leroy S, Steinberger A, Cottin-Bizonne C et al (2012) Hydrodynamic Interaction between a spherical particle and an elastic surface: a gentle probe for soft thin films. Phys Rev Lett. doi:10.1103/PhysRevLett.108.264501

13. Restagno F, Crassous J, Charlaix E, Monchanin M (2001) A new capacitive sensor for displacement measurement in a surface-force apparatus. Meas Sci Technol 12:16–22

14. Restagno F, Crassous J, Charlaix E et al (2002) A new surface forces apparatus for nanorheology. Rev Sci Instrum 73:2292–2297

15. Leroy S, Restagno F, Charlaix E (2009) Fine calibration of the residual dissipation in a surface forces apparatus using a capacitive sensor. Rev Sci Instrum 80:085103–085106

16. Georges J-M (2000) Frottement, usure et lubrification. Eyrolles-CNRS Editions, Paris

17. Hertz H (1881) Uber die BeruhrungfesterelastischerKorper (Sur le contact entre corps elastiques). J Reine Angew Math 92:156–171

18. Maugis D (1992) Adhesion of spheres: the JKR-DMT transition using a dugdale model. J Colloid Interface Sci 150:243–269

19. Muller V, Yushchenko V, Derjaguin B (1980) On the influence of molecular forces on the deformation of an elastic sphere and its sticking to a rigid plane. J Colloid Interface Sci 77:91–101

20. Tabor D (1977) Surface forces and surface interactions. J Colloid Interface Sci 58:2–13

21. Deruelle M, Hervet H, Jandeau G, Léger L (1998) Some remarks on JKR experiments. J Adhes Sci Technol 12:225–247

22. Shull KR (2002) Contact mechanics and the adhesion of soft solids. Mater Sci Eng R 36:1–45

23. Ebenstein DM, Wahl KJ (2006) A comparison of JKR-based methods to analyze quasi-static and dynamic indentation force curves. J Colloid Interface Sci 298:652–662. doi:10.1016/j.jcis.2005.12.062

24. Drelich J, Tormoen GW, Beach ER (2004) Determination of solid surface tension from particle-substrate pull-off forces measured with the atomic force microscope. J Colloid Interface Sci 280:484–497. doi:10.1016/j.jcis.2004.08.002

25. Chaudhury MK, Whitesides GM (1991) Direct measurement of interfacial interactions between semispherical lenses and flat sheets of poly(dimethylsiloxane) and their chemical derivatives. Langmuir 7:1013–1025

26. Ahn D, Shull KR (1998) Effects of substrate modification on the interfacial adhesion of acrylic elastomers. Langmuir 14:3646–3654

27. Amouroux N (1998) Étude des mécanismes de modulation de l'adhérence entre un élastomère silicone et un adhésif acrylique. Université Pierre et Marie Curie, Paris VI

28. Tardivat C, Hervet H, Leger L (2001) Adhesionevaluation for a stratified system in JKR geometry. J Adhes Sci Technol 15:1055–1078. doi:10.1163/156856101317035486

29. Sridhar I, Zheng ZW, Johnson KL (2004) A detailed analysis of adhesion mechanics between a compliant elastic coating and a spherical probe. J Phys Appl Phys 37:2886–2895. doi:10.1088/0022-3727/37/20/016

30. Flanigan CM, Shull KR (1999) Adhesive and elastic properties of thin gel layers. Langmuir 15:4966–4974. doi:10.1021/la9810556

31. Shull KR, Ahn D, Chen W-L et al (1998) Axisymmetric adhesion tests of soft materials. Macromol Chem Phys 199:489–511

32. Chateauminois A, Fretigny C, Gacoin E (2009) Mechanical properties of thin polymer films within contacts. In: Sinha S, Briscoe BJ (eds) Polymer tribology. Imperial College Press, London, pp 559–581

33. Fretigny C, Chateauminois A (2007) Solution for the elastic field in a layered medium under axisymmetric contact loading. J Phys Appl Phys 40:5418–5426

34. Perriot A, Barthel E (2004) Elastic contact to a coated half-space: effective elastic modulus and real penetration. J Mater Res 19:600–608. doi:10.1557/jmr.2004.19.2.600

35. Reynolds O (1886) On the theory of lubrication and its application to Mr. Beauchamp tower's experiments, including an experimental determination of the viscosity of olive oil. Proc R Soc Lond 40:191–203
36. Chan DYC, Horn RG (1985) The drainage of thin liquid films between solid surfaces. J Chem Phys 83:5311. doi:10.1063/1.449693
37. Hocking LM (1973) The effect of slip on the motion of a sphere close to a wall and of two adjacent spheres. J Eng Math 7:207
38. Guyon E, Hulin J-P, Petit L (1994) Hydrodynamique physique. Inter Editions/Edition du CNRS, Paris
39. Israelachvili J, Adams G (1978) Measurement of forces between two mica surfaces in aqueous electrolyte solutions in the range 0–100 nm. J Chem Soc Faraday Trans 74:975–1001
40. Israelachvili J (1992) Intermolecular & surface forces. Academic, London
41. Georges JM, Millot S, Loubet JL, Tonck A (1993) Drainage of thin liquid films between relatively smooth surfaces. J Chem Phys 98:7345–7360
42. Klein J, Kumacheva E (1998) Simple liquids confined to molecularly thin layers. I. Confinement-induced liquid-to-solid phase transitions. J Chem Phys 108:6996. doi:10.1063/1.476114
43. Klein J, Kumacheva E (1995) Confinement-induced phase transitions in simple liquids. Science 269:816–819
44. Klein J, Raviv U, Perkin S et al (2004) Fluidity of water and of hydrated ions confined between solid surfaces to molecularly thin films. J Phys Condens Matter 16:S5437–S5448
45. Perkin S, Chai L, Kampf N et al (2006) Forces between mica surfaces, prepared in different ways, across aqueous and nonaqueous liquids confined to molecularly thin films. Langmuir 22:6142–6152
46. Li T-D, Riedo E (2008) Nonlinear viscoelastic dynamics of nanoconfined wetting liquids. Phys Rev Lett. doi:10.1103/PhysRevLett.100.106102
47. Maali A, Cohen-Bouhacina T, Couturier G, Aime J (2006) Oscillatory dissipation of a simple confined liquid. Phys Rev Lett 96:086105. doi:10.1103/PhysRevLett.96.086105
48. Becker T, Mugele F (2003) Nanofluidics: viscous dissipation in layered liquid films. Phys Rev Lett 91(16):166104
49. Stevens MJ, Mondello M, Grest GS et al (1997) Comparison of shear flow of hexadecane in a confined geometry and in bulk. J Chem Phys 106:7303
50. Barrat J-L, Bocquet L (2007) Flow boundary conditions from nano- to micro-scales. Soft Matter 3:685
51. Gupta SA, Cochran HD, Cummings PT (1997) Shear behavior of squalane and tetracosane under extreme confinement. I. Model, simulation method, and interfacial slip. J Chem Phys 107:10316–10326
52. Bhushan B, Israelachvili JN, Landman U (1995) Nanotribology – friction, wear and lubrication at the atomic-scale. Nature 374:607–616
53. Vinogradova OI (1995) Drainage of a thin liquid film confined between hydrophobic surfaces. Langmuir 11:2213–2220
54. Vinogradova OI (2000) Elastohydrodynamic collision of two spheres allowing slip on their surfaces. J CollInterf Sci 221:1–12
55. Vinogradova OI (1998) Implication of hydrophobic slippage for the dynamic measurements of hydrophobic forces. Langmuir 14:2827–2837
56. Neto C, Evans DR, Bonaccurso E et al (2005) Boundary slip in Newtonian liquids: a review of experimental studies. Reports Prog Phys 68:2859–2897
57. Bocquet L, Charlaix E (2010) Nanofluidics, from bulk to interfaces. Chem Soc Rev 39:1073. doi:10.1039/b909366b
58. Cottin-Bizonne C, Cross B, Steinberger A, Charlaix E (2005) Boundary slip on smooth hydrophobic surfaces: Intrinsic effects and possible artifacts. Phys Rev Lett 94(5), 056102
59. Cottin-Bizonne C, Barrat J-L, Bocquet L, Charlaix E (2003) Low friction flows of liquids at nanopatterned interfaces. Nat Mater 2:237–240

60. Horn RG, Vinogradova OI, Mackay ME, Phan-Thien N (2000) Hydrodynamic slippage inferred from thin film drainage measurements in a solution of nonadsorbing polymer. J Chem Phys 112:6424–6433
61. Craig VSJ, Neto C, Williams DRM (2001) Shear-dependent boundary slip in an aqueous newtonian liquid. Phys Rev Lett 87:0545041–4
62. Bonaccurso E, Kappl M, Butt H-J (2002) Hydrodynamic force measurements: boundary slip of water on hydrophilic surfaces and electrokinetic effects. Phys Rev Lett 88(7), 076103
63. Schmatko T, Hervet H, Léger L (2005) Friction and slip at simple fluid-solid interfaces: the roles of the molecular shape and the solid-liquid interaction. Phys Rev Lett 94:244501
64. Pit R, Hervet H, Léger L (1999) Friction and slip of a simple liquid at a solid surface. Tribol Lett 7:147–152
65. Pit R, Hervet H, Léger L (2000) Direct experimental evidence of slip in hexadecane: solid interfaces. Phys Rev Lett 85:980–983
66. Lumma D, Best A, Gansen A et al (2003) Flow profile near a wall measured by double-focus fluorescence cross-correlation. Phys Rev E 67:056313
67. Schmatko T, Hervet H, Léger L (2006) Effect of nanometric-scale roughness on slip at the wall of simple fluids. Langmuir 22:6843–6850
68. Li J, Chou TW (1997) Elastic field of a thin-film/substrate system under an axisymmetric loading. Int J Solids Struct 34:4463–4478. doi:10.1016/S0020-7683(97)00053-X
69. Nogi T, Kato T (1997) Influence of a hard surface layer on the limit of elastic contact.1. Analysis using a real surface model. J Tribol Trans ASME 119:493–500. doi:10.1115/1.2833525
70. Gacoin E, Fretigny C, Chateauminois A et al (2006) Measurement of the mechanical properties of thin films mechanically confined within contacts. Tribol Lett 21:245–252
71. Bhushan B (2001) Modern tribology handbook. CRC Press, Boca Raton
72. Tonck A (1989) Developpement d'un appareil de mesure des forces de surface et de nanorheologie. École Centrale de Lyon
73. Steinberger A, Cottin-Bizonne C, Kleimann P, Charlaix E (2008) Nanoscale flow on a bubblemattress: effect of surface elasticity. Phys Rev Lett 100(13), 134501

Metal Structures as Advanced Materials in Nanotechnology

<div align="right">**19**</div>

Angelo Accardo, Remo Proietti Zaccaria, Patrizio Candeloro, Francesco Gentile, Maria Laura Coluccio, Gobind Das, Roman Krahne, Carlo Liberale, Andrea Toma, Simone Panaro, Ermanno Miele, Manohar Chirumamilla, Vijayakumar Rajamanickam, and Enzo Di Fabrizio

Introduction: The Importance of Metal Nanostructures as Advanced Materials

Metal nanostructures can play an important role in a variety of topics ranging from near-field imaging and tip spectroscopy (TERS or SPPERS) [1–10], surface-enhanced Raman spectroscopy (SERS) [11–13], to energy efficiency of devices such as solar panels or batteries [14], photocatalysis [15, 16], and electric transport [17]. The morphology of the metallic nanostructures must be tailored according to the chosen application, for example, metal nanoparticles can be well suited for SERS analysis while metallic thin films can be more suitable for solar harvesting.

A. Accardo (✉) • R. Proietti Zaccaria • G. Das • R. Krahne • C. Liberale • A. Toma • S. Panaro • E. Miele • M. Chirumamilla • V. Rajamanickam
Nanostructures Department, Italian Institute of Technology, Genoa, Italy
e-mail: angelo.accardo@iit.it; remo.proietti@iit.it; gobind.das@iit.it; roman.krahne@iit.it; carlo.liberale@iit.it; andrea.toma@iit.it; simone.panaro@iit.it; ermanno.miele@iit.it; manohar.chirumamilla@iit.it; vijayakumar.rajamanickam@iit.it

P. Candeloro • F. Gentile • M.L. Coluccio
BioNEM Laboratories, Department of Experimental and Clinical Medicine, University Magna Graecia of Catanzaro, Catanzaro, Italy
e-mail: patrizio.candeloro@unicz.it; gentile@unicz.it; mlcoluccio@gmail.com

E. Di Fabrizio
Physical Science & Engineering Division, King Abdullah University of Science and Technology, Thuwal, Kingdom of Saudi Arabia
e-mail: enzo.difabrizio@kaust.edu.sa

Morphology can also be tuned for enhancing the photo–chemi–electric properties of the nanostructures. For example, the catalytic performance strongly depends on the exposed area of the metallic nanostructure, while its photonic properties greatly depend on the resonance conditions which, in turn, are related to the geometrical characteristics of the nanostructure. Other examples of metallic structure, where the optical and electric properties are related to each other, are metallic photonic crystals which have applications in areas such as filters, optical switches, cavities, and efficient laser designs [18]. Such metallic crystals are particularly attractive because of their ability to control electronic and photonic resonances simultaneously. Therefore, such structures may open up further impressive possibilities for tailoring the light–matter interaction [19].

When it comes to choose an appropriate metal for realizing photo–chemi–electric nanodevices, two materials are among the most common choices: silver and gold. Silver nanostructures are best known for their morphology-dependent optical properties like surface plasmon resonances (SPRs). They also serve as very efficient substrates for SERS and are the most efficient catalyst for epoxidation of ethylene. Furthermore, silver is very often chosen for photo-applications in the visible range, ought to its low absorption. Similarly, gold nanostructures are very attractive due to their excellent chemical stability, bio-inertness, SPRs/SERS properties, and unique catalytic activity. These aspects are also the reason of using gold for photo-applications in the visible range, even though it shows a higher absorption peak than silver.

A number of techniques can be followed in order to realize metallic nanostructures; however, the fabrication of nanodevices can be categorized in two main groups: top-down and bottom-up. The former makes use of lithographic techniques in order to mold a 'brick' of material to the final desired product [20, 21], while the latter reaches the same goal by moving atoms or molecules into place by means of special tools such as atomic force microscope and scanning tunneling microscope [22], through self-organization techniques [23–29], or by means of alternative methods as the shadow mask deposition [30] or even by using DNA [31].

To date, the bottom-up nanoscale manufacturing is not as controllable as the top-down one which makes the latter approach the main choice for a number of applications, especially when reproducibility is an important issue. For this reason we shall mainly focus on this manufacturing method where techniques such as electron beam lithography and focus ion beam have been employed guaranteeing a reproducibility of devices down to the nanometers. In particular, in section 'Micro- and Nanofabrication Methods for Devices at the Nanoscale: Silver Nanoclusters, Metal Nanoparticles, and 3D Plasmonic Design' we will give a brief overview of representative microfabrication processes related to metal nanoparticles and nanostructures design followed, in section 'Characterization, Physical, and Chemical Properties of Metal Nanostructures as a Function of the Size, Shape, and Formation Conditions', by the description of a number of physical mechanisms related to nanoparticles aggregation at the nanoscale and nanowires templating. Finally, in section 'Properties, Specific Physical Effects of Metal Nanostructures, and the Case of Surface Plasmon Resonance', we will focus on the specific case of metal nanostructured plasmonic devices.

Micro- and Nanofabrication Methods for Devices at the Nanoscale: Silver Nanoclusters, Metal Nanoparticles, and 3D Plasmonic Design

Electroless Metal Deposition

A chemical/electroless deposition process is a novel deposition technique whereby metal ions are reduced as atoms and deposited on a solid surface, specifically a metal, a semiconductor, or also a plastic material. The electroless process is considered very attractive because it is of simple realization, it does not need expensive or specialized equipment, and it enables the contemporary fabrication of a great quantity of nanoparticles and then of patterned substrates. This makes it interesting for the large-scale production in electronic, catalysis, or optical devices fabrication. Furthermore, in nanotechnology, the great uniqueness of this method is that it allows precise control over the nucleation and growth of nanoparticles. In this technique, a metal salt precursor is reduced in solution in the presence of a stabilizing agent, which prevents aggregation and improves the chemical stability of the formed nanoparticles. Explicitly, metal ions are reduced to metals by a reducing agent that is simply an electron donor while the metal ions are electron acceptors. The reaction rate is often accelerated by a catalyst on which both the surface metal ions and the reducing agent are adsorbed to facilitate the transfer of electrons. Minute amounts of the deposited metal catalyze the reaction, and thus, the deposition itself becomes autocatalytic. Electroless deposition can therefore continue indefinitely, provided that the metal ions and the reducing agents are replenished [32]. Using electroless techniques, several metals may be deposited, including silver, gold, copper, nickel, or their alloys, thus obtaining thin films, sub-micrometric metallic structures, or nanoparticles [33–36].

In the particular case of electroless deposition, the reducing agent is the surface where the metal has to be deposited. A typical example is the silver deposition on a silicon substrate. The scheme of the silver electroless chemical reaction is briefly recapitulated in Figs. 19.1 and 19.2.

When a silicon substrate is dipped in a solution of fluoridric acid (HF) and silver nitrate ($AgNO_3$) (a typical composition is [HF] = 0.15 M and [$AgNO_3$] = 1 mM), silicon reduces silver ions to the metallic form, as described by the following chemical reaction [37–40]:

$$4Ag^+ + Si(s) + 6HF \rightarrow 4Ag^0 + H_2SiF_6 + 4H^+ \qquad (19.1)$$
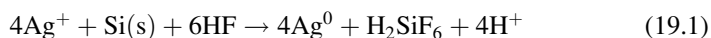
which can be separated into two half-cell reactions, that is, the Si oxidation at the anode

$$Si + 2H_2O \rightarrow SiO_2 + 4H^+ + 4e^- \qquad (19.2)$$
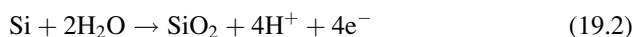
and the Ag reduction, at the cathode

Fig. 19.1 Schematic representation of an electroless process where metal ions (M^+) are reduced by the electrons given from oxidation of a reducing species (R)
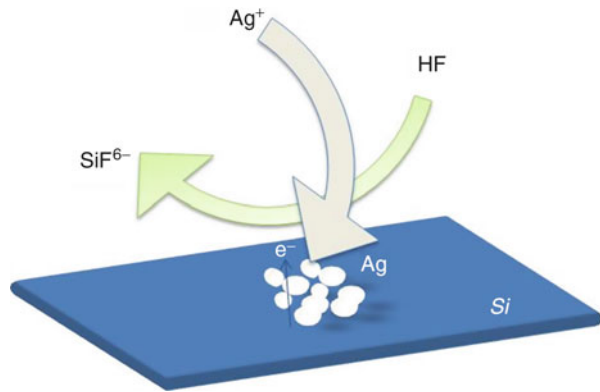

$$M^+ + R \rightarrow M + O$$
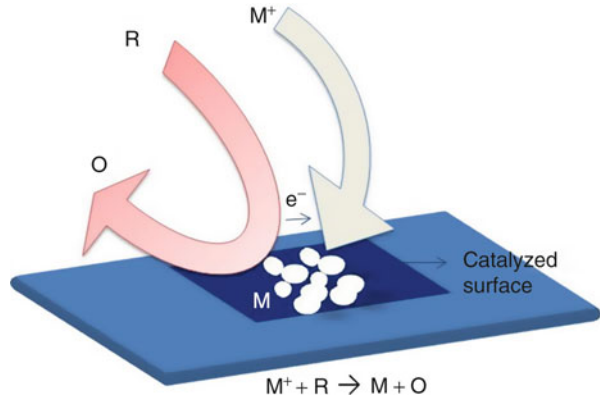
Fig. 19.2 Schematic representation of silver electroless deposition on a silicon substrate into a HF solution

$$Ag^+ + e^- \rightarrow Ag^0 \tag{19.3}$$

The role of HF in solution is to remove both the superficial silicon oxide (SiO_2) and the SiO_2 which is formed from silicon oxidation consequently to the electroless process. Upon the immersion in the fluoridric acid solution, the following reaction takes place:

$$SiO_2 + 6\,HF \rightarrow 2\,H^+ + SiF_6{}^{2-} + 2\,H_2O. \tag{19.4}$$
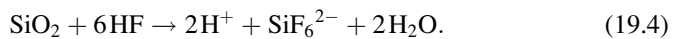
Here, the formation of Si–F superficial bonds is expected because thermodynamically favourable, nevertheless the acid environment of the solution causes a consistent polarization of $Si^{\delta+}$–$F^{\delta-}$ determining the weakening of the bulk Si–Si bonds. In these conditions, HF could easily react with the substrate, according to a nucleophilic attack, producing a hydrogenated silicon surface, as described by
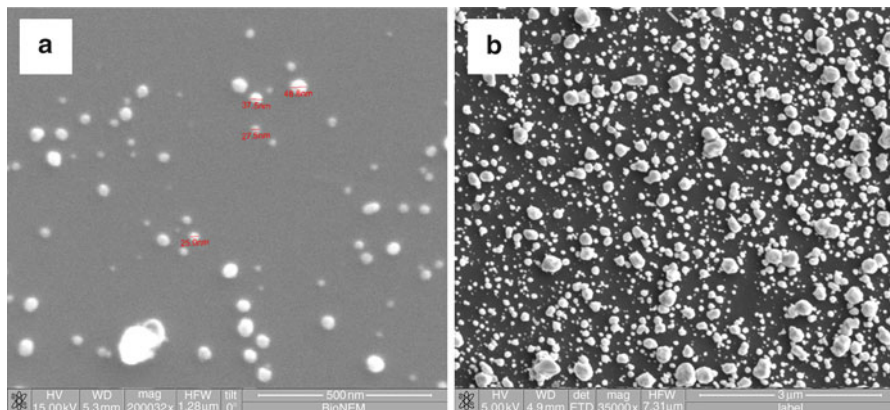
Fig. 19.3 SEM micrographs of silver deposition: (**a**) on a silicon surface, operative conditions HF 0.15 M AgNO$_3$ 1 mM 50 °C 1 min and (**b**) on a silicon surface, operative conditions HF 0.15 M AgNO$_3$ 1 mM 50 °C 5 min

$$Si_{bulk} - Si - Si^{\delta+} {}^- F^{\delta-} + HF \rightarrow Si_{bulk} - Si - H + F - Si - F. \tag{19.5}$$
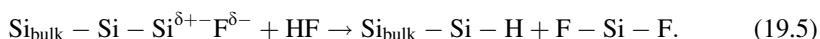
This hydrogenated silicon surface is inert to reactions with O$_2$, CO$_2$, CO, etc., while presenting a good reactivity with silver ions [38]. The presence of HF gives force to the deposition process and it is important for plating large surfaces.

The mechanism of metal deposition sees, on a first stage, the nanoparticles formation by the direct reaction of some silver ions with the silicon substrate, forming metallic nuclei. These Ag nuclei are strongly electronegative, and because of this, they attract other electrons from silicon bulk becoming negatively charged; then, new silver ions react with disposable electron on the silver grains, reducing to Ag^0 and thus inducing the growth of the original Ag nuclei [41]. An autocatalytic mechanism is therefore generated, which continues also when all the silicon surface has been covered by silver, until electrons can be attracted from the silicon bulk.

The morphology of electroless nanoparticles and their aggregates depends on a variety of factors, including the pH of solution, the temperature T of the system, the total time t of the process, and the metal concentration c in solution (Fig. 19.3).

The rate of the reactions is regulated by a balance between thermodynamics and kinetics, and these parameters are closely correlated [42]. In particular, the driving force of the charge exchange is the difference between the redox potentials of the redox species in solution. The redox potential at equilibrium could be calculated approximately by using the Nernst relationship:

$$E = E^0 + \frac{RT}{nF} \ln \frac{[Ox]}{[Red]} \tag{19.6}$$

in which E is equilibrium potential, R is the ideal gas constant 8.314 J K^{-1} mol^{-1}, F is the Faraday constant 96,500 C mol^{-1}, T is the absolute temperature, and

[Ox] and [Red] are the molarities of the oxidized and reduced species in solution, respectively.

Equation 19.6 for the metal ions becomes

$$E = E^0 + \frac{RT}{F} \ln[M^+].$$

Considering the total redox reaction of the process, the Nernst equation expresses the relation between the equilibrium constant (K_e) and the redox potential (ΔE):

$$\ln K_e = \frac{nF\Delta E}{RT} \tag{19.7}$$

This equation evidences parameters like the concentrations of the ions in solution and the temperature of the system. It influences also the reaction's yield and the shape and size of the metal nanoparticles aggregates.

These considerations make electroless deposition a technique interesting for the realization of nanoparticles aggregates of specific shape and size, by means of the regulation of the process parameters. Using different growth conditions, metal nanoparticle aggregates may therefore grow within well-defined patterns. Recent advances in nanofabrication techniques, especially electron beam lithography (EBL), focused ion beam (FIB), and two-photon lithography (2PL), have improved the fabrication of patterned substrates [43–45]. These techniques afford exact control over the shape and size of bidimensional (in the case of EBL), and sometimes three-dimensional (in the case of FIB and 2PL), patterns at the nanoscale [42, 46]. Electroless deposition represents indeed a good method for assembling metal nanocluster into lithographic patterns, with extreme precision (Fig. 19.4).

Examples of typical parameters of deposition for metals such as silver and gold are reported in Table 19.1.

Novel 3D Nanoscale Plasmonic Device Design

There have been many efforts through traditional lithography technique for 3D microfabrication techniques such as self-assembly, μ stereo, ink-jet printing, layer by layer, holography and phase mask, LIGA (lithography, electroplating, and molding), optical sintering, and electron/ion beam lithographies, which proved their significant potential with the following limitations: (i) periodicity, (ii) limited 3D complexity, and (iii) lack of mechanical constraints. Apparently, by adapting and/or integrating one or more lithographic modalities working on a different scale would overcome these limits and advance the 3D nano-biotech research by lifting up as 3D emerging techniques.

Here, we present novel integrated nanoplasmonic structures obtained by lithographic methods on an optical tweezers (OT)-based 3D micromanipulator [47].
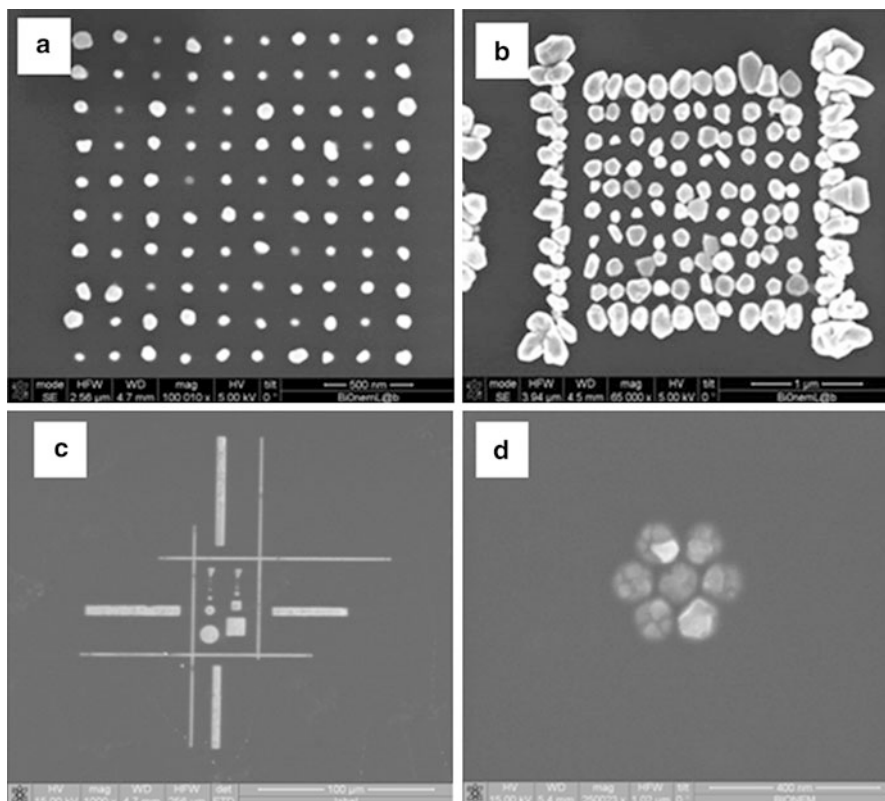
Fig. 19.4 SEM micrographs of metal deposition: (**a**) silver on a patterned silicon surface (*circular holes* with diameter 40 nm), operative conditions HF 0.15 M AgNO$_3$ 1 mM 50 °C 5 s; (**b**) silver on a patterned silicon surface (*circular holes* with diameter 40 nm), operative conditions HF 0.15 M AgNO$_3$ 0.05 mM 50 °C 50 s; (**c**) gold on a patterned silicon surface (*circular and quadrate holes*), operative conditions HF 0.15 M HAuCl$_4$ 1 mM 50 °C 3 min; and (**d**) silver on a patterned silicon surface (*structures with holes* of 100 nm diameter), operative conditions (i) first step HF 0.15 M 50 °C 1 min and (ii) second step AgNO$_3$ 0.003 mM 50 °C 40 s

Table 19.1 Typical parameters for silver and gold electroless deposition on silicon substrate	
Deposition solutions	
Silver: HF 0 ÷ 0,15 M, [AgNO$_3$] 0.1 ÷ 1 mM	
Gold: HF 0 ÷ 0,15 M, [HAuCl$_4$] 0.1 ÷ 1 mM	
Operative conditions	
T = 0 ÷ 50 °C, time = 10 ÷ 60 s	

The combination of different lithographic methods, also working on different scales, appears to be a very powerful strategy to increase the degrees of freedom for the fabrication of 3D micro- and nanostructures. These kinds of structures are of great interest, as they enable to add plasmonic functions to a probe that can be manipulated by using optical tweezers (OT) [48–52].

Fig. 19.5 Asymmetrical bead design
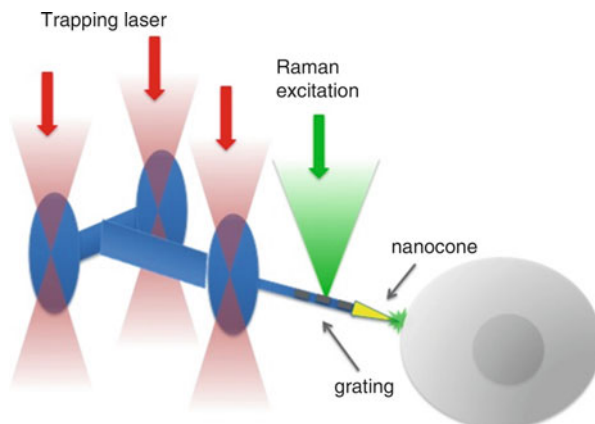
At first glance, the common spherical beads (most often polystyrene or silica beads) used with OT seem to be not the best structure or geometry on which to add a plasmonic probing part. An important drawback of the spherical beads is, in fact, related to the lack of an effective mechanism to fully control in the 3D space their orientation. This aspect is very important during the physical approach of the bead, carrying the plasmonic probe, to the sample to be measured. A second important issue comes from the observation that, when an optically trapped bead is close to a cell in suspension, the latter will be also attracted by the optical trap due to the closeness of the trapping point and the plasmon excitation point, preventing an accurate positioning of the plasmonic probing part with respect to the sample.

Because of these reasons, we choose to create an asymmetric bead with a larger main body, where it is optically trapped, and a long thin arm, on top of which there will be the plasmonic nanocone, which extends away from the position of the trapping laser focus. More precisely, we choose a design with three different trapping points and a protruding arm (a schematic of the asymmetrical beads and the optical traps is shown in Fig. 19.5).

These asymmetrical structures are fabricated by using the two-photon lithography (TPL) [53] method. This technique is intrinsically a 3D structuring process, since the photo-polymerizable resist is exposed only in the focus spot of an intense laser beam and relies on a straightforward process that allows creating structures that would be very complex or even impossible to fabricate with conventional lithographic methods [54, 55]. Moreover, as recently demonstrated, the spatial resolution attainable using TPL is sub-100 nm using laser wavelengths around 800 nm, which is well below the diffraction limit [56]. The custom made setup used for fabrication is schematized in Fig. 19.6.

A 100 fs pulse width, 80 MHz Ti–Sapphire laser oscillator (Tsunami, Spectra-Physics) is used as the excitation source for two-photon photopolymerization, and its central wavelength is tuned to around 720 nm. The output laser power at the back
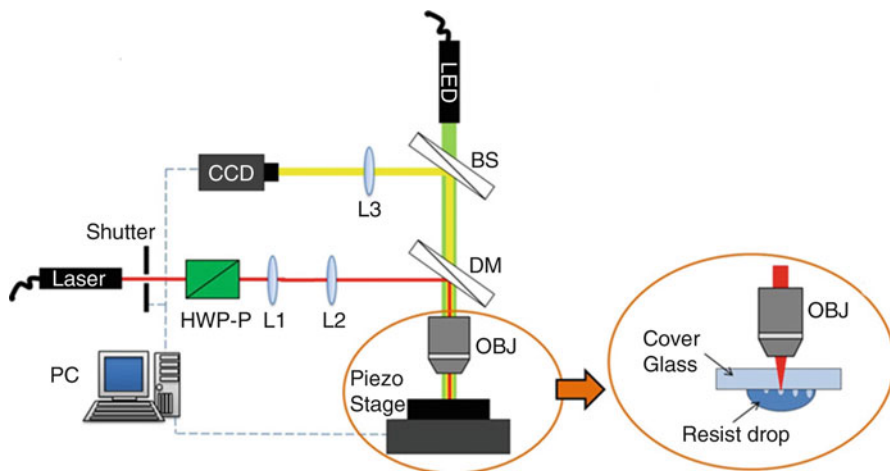
Fig. 19.6 Schematic of the two-photon lithography setup

focal plane of the microscope objective is controlled by using a variable attenuator made by an achromatic half-waveplate and a polarizer. The exposure time for each pixel is controlled through a computer-driven mechanical shutter. The beam is expanded and collimated by a telescope in order to obtain overfilling of the focusing microscope objective. Further, laser beam is reflected by a 45° dichroic mirror directly onto the objective back aperture. The dichroic mirror reflects most of the NIR laser beam and transmits part of the visible spectrum (400–550 nm) to a CCD camera which is used to check the position of the beam focus and for real-time monitoring of the photopolymerization process. The laser is focused by using a dry semi-apochromatic microscope objective (Olympus, LUCPlanFLN 60×, NA = 0.70) equipped with a spherical aberration correction collar.

A suitable coverslip holder is mounted on a xyz piezo stage (Tritor 101, Piezosystem Jena) for positioning in horizontal and vertical directions. The travel range of the piezo stage is 80 μm in each of the x, y, and z directions. A dedicated software, developed by our group, translates the structure points to piezo stage positions and controls the synchronization of the movements with the mechanical shutter, in order to achieve the desired local energy dose.

Two different photopolymers have been used for fabrication: the first is a commercial UV curing adhesive (NOA 63, Norland) with optimum sensitivity in the 350–400 nm range, whereas the second is an epoxy-based resin (SU-8, MicroChem). With NOA63, the process starts by depositing a drop of resist on a cover glass and letting it to achieve a mechanical equilibrium followed by a preexposure with a UV lamp done for a few seconds in order to increase the resin viscosity. The SU-8 requires spin coating of the resist on the coverslip, followed by a pre-bake procedure before starting the TPL fabrication.

The laser power (measured before the objective) is set to ∼6.5 mW. After exposure of all the point set defining the desired structures, the unpolymerized
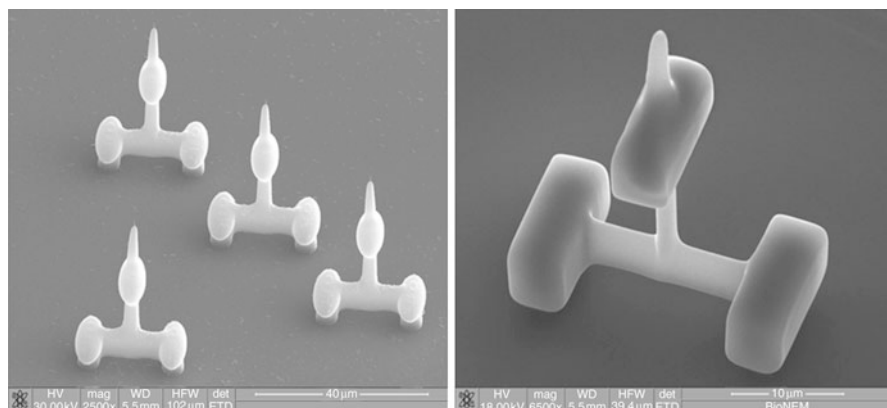
Fig. 19.7 Asymmetrical beads with ellipsoidal (*left*) and with rectangular (*right*) shape of the single composing beads (Picture kindly reprinted from Ref. [47])

resin is removed by developing in acetone for the NOA63 and developing in a proper solvent after a post-bake procedure for the SU-8. In Fig. 19.7, some SU-8 TPL-fabricated beads are shown. The high degree of control of the fabricated structure shape is evident from the ability to choose, e.g., among a rectangular or an ellipsoidal geometry for the single composing beads (see Fig. 19.7).

As a further step, a silver plasmonic nanocone is fabricated on top of the protruding arm, following the procedure described in section 'Microfabrication of Advanced Plasmonic Devices'. Figure 19.8a shows a SEM image of an asymmetrical bead on top of which a nanocone is fabricated.

Afterwards, to enable coupling of the excitation from a focused laser beam into an adiabatic plasmon polariton on the nanocone, a grating is fabricated by using a FIB milling (see section 'Microfabrication of Advanced Plasmonic Devices'). A final fabricated bead is shown in Fig. 19.8b. The presented device was trapped in our OT system, and full 3D manipulation (translation, rotation, and tilting) was successfully tested. The combination of OT and plasmonics could be used for membrane proteins study in living conditions.

Gold Nanocuboid Structures

Metallic nanocubes are intriguing plasmonic nanostructures due to their sharp corners (8 corners, 6 faces, and 12 ridges), where the maximum electric field is localized, and exhibit multipolar resonances [57]. Nanocubes show the focusing of strong plasmon field at the sharp corners and edges, which in turn leads to a dramatic increment in local electromagnetic (EM) field. In the present paragraph, fabrication and characterization of Au plasmonic nanocuboid structures were investigated by means of SERS and numerical simulations.
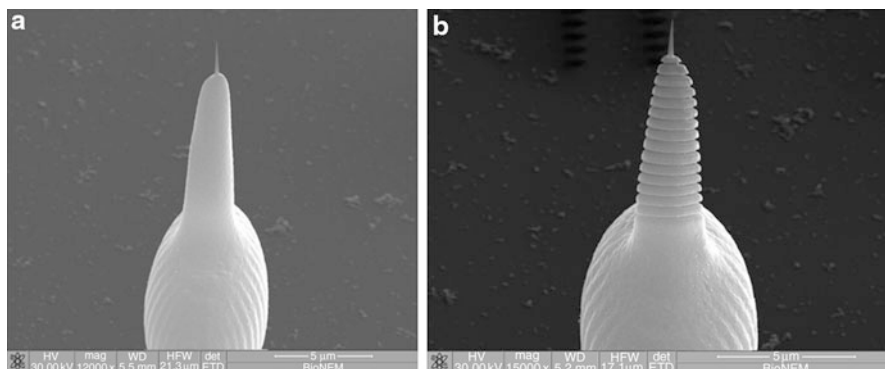
Fig. 19.8 (**a**) Silver nanocone fabricated on the protruding arm of the asymmetrical bead; (**b**) FIB-fabricated grating for plasmonic coupling of the nanocone (Picture kindly reprinted from Ref. [47])

Plasmonic Au nanocuboid structures [58] arranged in the form of 4×4 array by varying edge size from 40 to 70 nm with a stepsize of 5 nm were fabricated by electron beam lithography (EBL-Raith 150-Two) associated with lift-off techniques. The height of the nanostructures was fixed to 25 nm. The schematic representation of 4×4 array of Au nanocuboid structures with edge size L and interparticle separation (IPS) is represented in Fig. 19.9a. Figure 19.9b represents the typical normal-incidence scanning electron microscope (SEM) image of 4×4 array structures with $L = 70$ nm and IPS $= 20$ nm. Inset represents the magnified view of single nanocuboid structure, which emphasizes the morphological quality in terms of sharp edges and corners.

In order to investigate the effect of Au nanocuboid edge size on SERS intensity, SERS measurements were performed on 4×4 array of Au nanocuboid structures with various edge sizes by using Rhodamine-6G (R6G) molecules as analyte. A Renishaw inVia microRaman spectroscopy in backscattering geometry was used to analyze SERS substrate. Thermoelectrically cooled charge-coupled device (CCD) was used as a detector. The spectral resolution of the instrument was 1.1 cm^{-1}. The instrument is equipped with an excitation laser at 633 nm and a $150\times$ objective lens (NA $= 0.95$) of Leica microscope. The molecules were deposited on to the nanocuboid structures by means of chemisorption technique, in which the nanocuboid substrate was kept in R6G (10 μM) solution for 20 min (which allows the adsorption of R6G molecules to the metal surface) and then taken out and rinsed with deionized water in order to remove excess molecules. After rinsing, the nanocuboid substrate was dried with nitrogen gas and then SERS measurements were performed.

Typical reference Raman spectrum and SERS spectrum of 4×4 arrays of 55 nm Au nanocuboid structures are shown in Fig. 19.10a, blue and red trace, respectively. In order to avoid c-Si Raman peak centered at 521 cm^{-1} (first order) and the broad band around 965 cm^{-1} (second order), SERS spectra were acquired in the range of
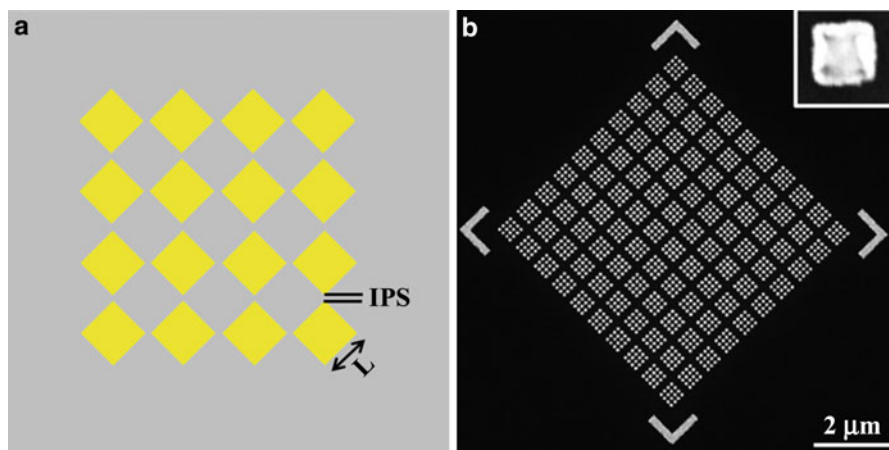
Fig. 19.9 (**a**) Schematic representation of 4 × 4 array of plasmonic Au nanocuboid structures with cuboid edge size *L* and interparticle separation *IPS*. (**b**) Normal-incidence SEM micrograph of 4 × 4 array of 65 nm Au nanocuboid structures with 20 nm IPS. Inset represents the magnified view of single nanocuboid structure (Picture kindly reprinted from Ref. [58])

$1,080–1,900$ cm^{-1}. The excitation laser power and integration time for reference Raman and SERS spectrum are represented in Fig. 19.10. The incident laser polarization was fixed parallel to the nanocuboid edge. SERS spectrum of R6g molecules on nanocuboid structures (red trace) shows distinct features of R6G. The major bands centered at $1,360$, $1,510$, and $1,649$ cm^{-1} were clearly seen in the spectrum and can be assigned to C–H bending, a combination of C–N stretching, C–H and N–H bending, and combination of ring stretching of the C–C vibration and C–H$_x$ bending of the xanthenes ring, respectively. The peak positions are in good agreement with [44]. Reference Raman spectrum (blue trace) shows the low intense peaks of R6G albeit the laser power and integration time (reported in Fig. 19.10a) were higher than the values used in SERS spectrum of nanocuboid structures. Inset in Fig. 19.10a represents the background Raman spectrum of Au nanocuboid structures taken before chemisorption of R6G molecules. No significant Raman features within the spectral range are observed, thus confirming the absence of surface contamination.

Figure 19.10b represents the variation of SERS intensity with respect to Au nanocuboid size at three different peak positions ($1,360$, $1,510$, and $1,649$ cm^{-1}). It is seen that SERS intensity increased with cuboid edge size in the range from 40 to 55 nm and then decreased with rise in cuboid edge size. LSPRs of metal nanoparticle/nanostructure are tunable throughout the visible and near-infrared region of the spectrum by simply acting on the nanoparticle topology [59, 60]. The maximum SERS enhancement can be observed by positioning the LSPR of metal nanostructure close to the excitation wavelength [61, 62]. Therefore, we can assume that the plot observed in Fig. 19.10b corresponds to the resonant

Fig. 19.10 (**a**) Typical reference Raman spectrum and SERS spectrum of 4×4 arrays of 55 nm edge size Au nanocuboid structures after depositing a monolayer of R6G, *blue* and *red* trace, respectively. Inset represents the background Raman spectrum coming from bare 55 nm Au cuboid structures. (**b**) Variation of SERS intensity as a function of cuboid edge size at 1,360, 1,510, and 1,649 cm^{-1} peak positions (Picture kindly reprinted from Ref. [58])
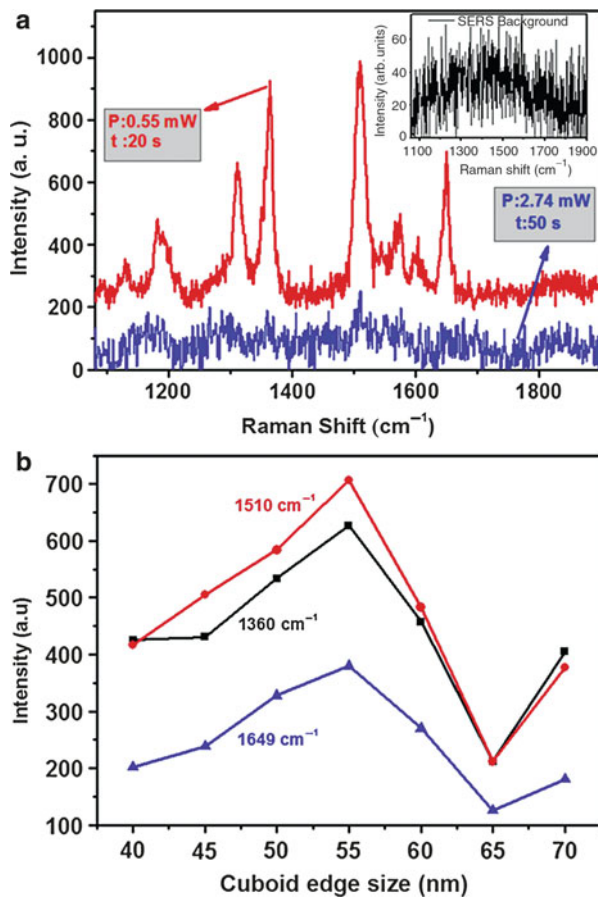
behavior of the nanocuboid structure, centered on $L = 55$ nm. The excitation of LSPR is one of the main mechanisms allowing for signal enhancement in Raman measurements. A similar behavior was observed in the past for nanocylinder structures [63]. SERS enhancement factor was calculated [64] by assuming that the molecules (closely packed) were deposited only on to the metal surface. By considering laser beam focal radius of 500 nm, the average SERS enhancement factor for the reference band centered at 1,510 cm^{-1} is about 10^4 with respect to flat Au marker. The reference band centered at 1,510 cm^{-1} is considered here to calculate the SERS enhancement factor owing to its high signal-to-noise ratio.

In order to understand the electric field distribution in nanocuboid array structures, numerical simulations (CST Microwave Studio) were performed on 4×4 array of Au nanocuboid structures with 55 nm edge size. CST allows the tetrahedral characterization of the geometry, which avoids the generation of fake peaks on curved surfaces. In order to obtain stationary results, convergence mesh analysis was applied. The dielectric constants of Si and Au employed in the present

Fig. 19.11 Electric field
distribution in *xy* plane with
a 633 nm excitation source
polarized at 45° with respect
to *x*-axis for 4 × 4 array of
55 nm Au cuboid structures
(Picture kindly reprinted from
Ref. [58])
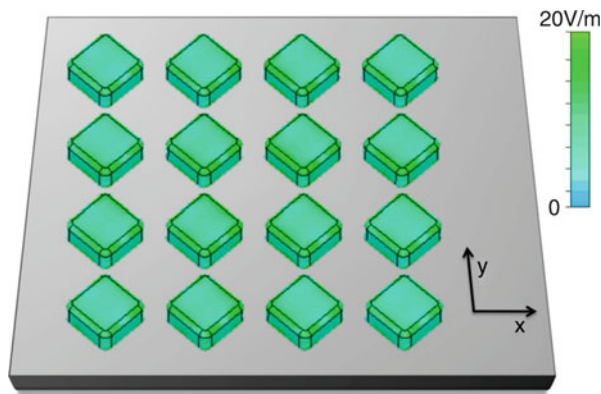
simulation were $\varepsilon_{Si} = 15.21$ and $\varepsilon_{Au} = -9.79 + 1.97i$ [65], respectively, for $\lambda = 633$ nm. The incident light is polarized along the nanocuboid edge (polarized at 45° with respect to x-axis). Amplitude of the electric field distribution, $|E|$, on the xy plane is shown in Fig. 19.11. The electric field distribution shows a maximum electric field of 20 V/m, localized at the corners of the nanocuboids. By considering the fact that the SERS enhancement is proportional to $|E|^4$ [66], we can conclude that theoretical calculations are supporting experimental results.

Plasmonic Au nanocuboid structures of 4 × 4 arrays with edge size ranging from 40 to 70 nm and with a stepsize of 5 nm were fabricated by EBL technique. Nanocuboid structure size was optimized with SERS by using R6G (10 μM) as analyte. Au nanocuboid structures with 55 nm edge size showed highest SERS intensity. The average SERS enhancement factor of $\sim 10^4$ is observed for 55 nm edge sized cuboid structures with respect to flat Au marker. Au nanocuboid substrate appears as a promising SERS device towards the capability of potential sensitivity for biological and chemical detection even at single-molecule level.

Characterization, Physical, and Chemical Properties of Metal Nanostructures as a Function of the Size, Shape, and Formation Conditions

The Physical Mechanisms of Metal Particles Aggregation at the Nanoscale

While the electroless deposition (see section 'Electroless Metal Deposition') revealed itself effective in forming supramolecular clusters of metal atoms, on the theoretical side the method still lacks an adequate formalization. The aim of this section is to expound on a diffusion-limited aggregation (DLA) model, that is a framework that can describe the aggregation of ions into ordered structures, and give a rationale in the design of devices that utilize rough metal surfaces and effects

thereof, including the very large area of SERS substrates. Moreover, it will be explained how nonconventional variables, including the fractal dimension, can intimately describe the nature of those aggregates with unprecedented accuracy. The new revolution in nanoscience, engineering, and technology is being driven by our ability to manipulate matter at the molecular, nanoparticle, and colloidal level to create designed structures. Using computer simulations and theoretical frameworks, we can discover the fundamental principles of how nanoscale systems behave.

Simulating the Formation of Ordered Superclusters of Metal Atoms

The mechanism of metal growth can be reproduced under the assumption of a diffusion-limited aggregation (DLA) process, where other atomic forces, including steric, electrical, and van der Waals, are instead neglected in the long range limit. This assumption holds true when diffusion dominates over chemical reaction or, equivalently, when the kinetics of metal reduction is extremely fast. The model makes it possible to decipher, at an atomic level, the rules governing the evolution of the growth front and to explore ways to tailor film morphology to obtain specific characteristics [67, 68].

DLA is a simulation method based on simple algorithms that is capable to provide valuable help in understanding natural process, in alternative to models that instead make use of analytical solution of equations [69]. Indeed, in many situations it is possible to model a system by entities that diffuse and occasionally react upon encounter each other. These systems are governed by two time scales: the diffusion time, which is the characteristic time required for two particles to meet, and the reaction time, which is the characteristic time for particles to react when held in proximity (within the reaction range) to each other. When the diffusion time dominates over the reaction time, the process is limited by diffusion. In this case, the immediate neighborhood of a particle is important, because reactions are very likely to take place once particles meet, and the kinetics is dominated by local fluctuations in the distribution of the particles.

DLA is formally regulated by certain rules which can be found, for example, in [67, 70, 71] and are recapitulated below. Proposed for the first time in the pioneering works of Witten and Sander in the early 1980s [67, 71], this numerical framework is very well understood and has been utilized, as for some examples, to reproduce the process of electrodeposition in single wells [72], to investigate the role of sedimentation and buoyancy on the kinetics of colloidal aggregation [73], to describe solute percolation in soils [74], to describe the early stages of thin-film growth at an atomistic scale [68], and to gain insight into physical phenomena including the annealing of defects in crystals [75] and the electron hole recombination [76].

The choice of using here a DLA model where diffusion dominates over chemical reactions is motivated by a number of observations, widely reported in literature, where electroless method produces dendritic nanostructures, with stems, branches, and leaves (Fig. 19.12a) [77, 78]. These fractal structures are generally observed in nonequilibrium growth processes, and DLA is one of the most suitable approaches
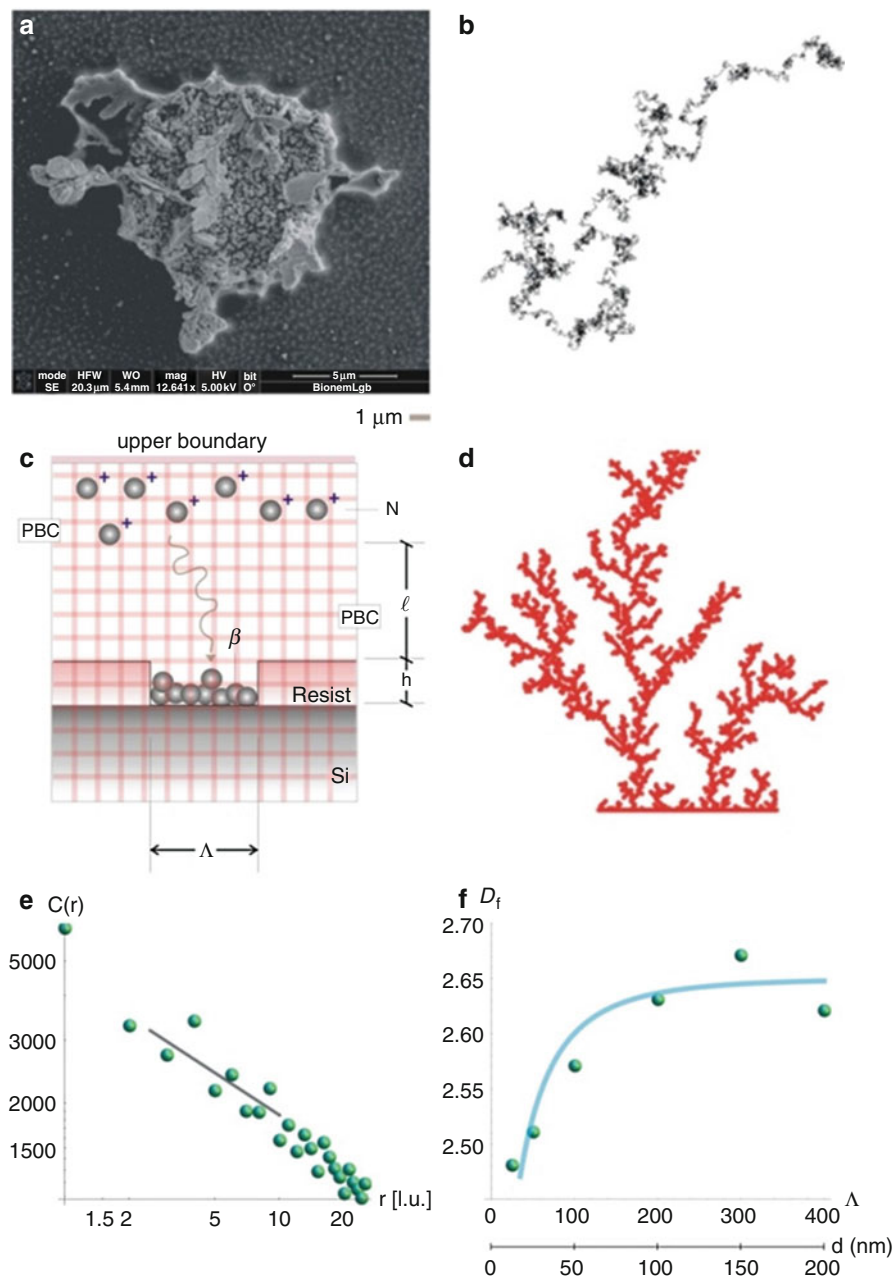
Fig. 19.12 SEM image of a supercluster of silver nanoparticles produced by electroless deposition, revealing a clear dendritic/fractal nature (**a**). Typical pattern of migration of a particle moving a stochastic, random walk: at any step, the probability distribution of the direction of movement is uniform or flat, with events equally likely to occur anywhere within the interval from 0 to 2 π (**b**). Schematic representation of the DLA process reproduced in a regular grid (**c**). The characteristic

for their description. As for an example, Liu and colleagues, while patterning silicon substrates with SERS silver nanograin islands using electroless deposition, observed that the deposition rate could be increased twofold by simply stirring the solution above the substrate, and this would indicate that the overall growth rate is diffusion limited [79]. Moreover, in recent papers describing the process of electroless deposition [32, 78], it is suggested that the formation mechanism of these silver dendritic nanostructures should be considered within the framework of a DLA model. In the model, the displacement of a metal ion, at any time, is arbitrary, and thus, the trajectory of the particles can be correctly described by a random walk, as to resemble a Brownian motion (Fig. 19.12b). Brownian motion is a continuous-time probabilistic process, and its use here is motivated by mathematical convenience and the accuracy of the model to describe an otherwise complex phenomenon. At very short time scales, the motion of a particle undergoing Brownian motion is dominated by its inertia, and its displacement will be linearly dependent on time, $\Delta x = v \tau$, and this can be reproduced or simulated in a regular grid (Fig. 19.12c) where particles are dislodged by the finite distance Δx in the time interval τ that is the mean time between collisions. The instantaneous velocity of the particles, v, is maintained constant during τ, and it would depend solely upon the energy of the system. The distribution of displacement probability of the Brownian particle itself is best described using a Gaussian density function, centered around the origin of the walk, that means that the most probable position of a particle after a sufficiently large number of steps is paradoxically its original position. The root mean square distance of the walk gives a measure of the extent of spread of the particle ensemble, and this would be proportional to time [80]:

$$\langle r^2 \rangle = \langle x^2 \rangle + \langle y^2 \rangle = 4Dt \qquad (19.8)$$

where x, y, and r are the Cartesian coordinates in the plane, while the celebrated Stokes–Einstein equation may be used to derive the diffusion coefficient D [81]:

$$D = \frac{k_b T}{6\pi\mu a} \qquad (19.9)$$

where k_b is the Boltzmann constant, T the absolute temperature of the system, μ the viscosity of the medium, and a is the diameter of a particle with mass m. D can be alternatively expressed in terms of Δx and τ as

Fig. 19.12 (continued) structure generated from the DLA model, the multibranched arrangement of particles recalls the dendrite, fractal nature that electroless grown systems reveal under certain growth conditions (**d**). Power spectrum density function of a numerical aggregate (**e**). The solid line recapitulates the DLA prediction of the fractal dimension of the silver nanoparticle aggregates as a function of pattern size, perfectly matching the experimental points (**f**)

Table 19.2 Physical variables and values thereof of the silver ion gas system considered for the particle growth

Variable	Symbol	Units	Value	Source
Mass of a silver ion	m	[Kg]	1.78×10^{-25}	Ref. [82]
Van der Waals size of a silver ion	R	[m]	$1{,}172 \times 10^{-12}$ m	Ref. [82]
Temperature of the system	T	[k]	323	–
Velocity of the ion	v	[m s^{-1}]	22	$\sqrt{k_b T/m}$
Viscosity of water at T = 323 K	μ	[Pa s]	0.3×10^{-3}	Ref. [82]
Diffusion coefficient	D	[m^{2}s]	1.5×10^{-9}	$k_b T/6\pi\mu a$
Mean path length	Δx	[nm]	0.5	$4D/v$
Time interval	τ	[s]	2.2×10^{-11}	$\Delta x/v$

$$D = \frac{\Delta x^2}{2\tau} = \frac{(v\,\tau)^2}{2\tau} = \frac{k_b T}{2m} \qquad (19.10)$$

where the kinetic theory of gases has been used for obtaining the right-hand term of Eq. 19.10 [80]. Notice that, on comparing Eqs. 19.2 and 19.3, given the results of the simulations, the behavior of the real system would be determined. In the equations above, the time parameter t is an estimate of an hypothetical true external time that a clock measures. The time interval τ can be considered as the simplest basis, or subunit, of this absolute time. An interaction, that is, the dislodgement of a metal ion by a lattice unit, takes the time τ, and the system cannot see or sense any time shorter than τ. To this extent, the total time can be discretized in τ units. τ is not arbitrary and instead depends on physically observable variables of the system, such as the temperature T, the mass m and diameter a of the dislodging ions, and the viscosity of the medium. These variables are linked together especially by relations Eqs. 19.2 and 19.10. For the present configuration, those variables assume prescribed values as recapitulated in Table 19.2.

A Case Study: Effect of Pattern Size

This concept was used in [70] to simulate the deposition of metal ions in a patterned silicon substrate, where the size of the pattern was varied over a significant range, namely, from few nanometers to some hundreds of nanometers. Consider, for ease of visualization, the scheme in Fig. 19.12c. At a distance l from the wells, N particles are simultaneously released in the system, where N should be chosen with care to reproduce the initial concentration of silver ions. At any cycle the particles move within a regular square pattern of cells by one lattice unit (l.u.), and thus, the mean path length is $\Delta x = 1$ (l.u.). At the side boundaries (i.e., the left and the right) of the domain, periodic boundary conditions (PBC) are imposed, and when an individual particle passes through one of those faces, it instantaneously reappears on the opposite face with the same velocity. In topological terms, the plane can be thought of as being mapped onto a torus; by doing so, an infinite perfect tiling of the system is simulated in the longitudinal direction, and this accounts for the fact that the area of the wells is small compared to the area above the wells. At the upper boundary of

the system, and at the side walls of the wells, a bouncing condition is imposed, whereby the particles which collide with those boundaries would rebound in an opposite direction. After a certain number of repetitions, a particle aggregate is thus formed as in Fig. 19.12d. The multibranched arrangement of particles recalls the dendrite, fractal nature that electroless grown systems reveal under certain growth conditions (Fig. 19.12a). On analyzing the fractal nature of those systems, the fundamental mechanisms of particle aggregation can be revealed. This can be accomplished by deriving the pair correlation function, the power spectrum, and consequently the fractal dimension D_f, of those lattices, as described in the following.

For the present configuration, the parameters of the simulations were adjusted as follows. The simulation was halted after a number of iterations $Ni = O (10^{10})$. The total number of particles N was held fixed, being N = 2,000.

This numerical procedure was verified against real nanoscale systems. Nanostructures were fabricated via electroless deposition. These comprise clusters or aggregates of silver NPs, clothed in the form of hemispheres, with a diameter ranging from $d \sim 20$ to $d \sim 200$ nm (Fig. 19.12f). The structures were imaged using SEM and AFM microscopy. From these profiles, a power spectrum was conveniently derived as described below, and the characteristic fractal dimensions, for each hemisphere, were accordingly determined. These are the mean values derived over multiple measurements and samples, with a small standard deviation, and are reported in the diagram of Fig. 19.12f. Notice that the fractal dimension increases monotonically for increasing d, that is, large structures are less uniform than small ones.

Those results were explained within the realm of DLA theory. The aggregates were produced where the initial seed length Λ is steadily changed from 25 to 400 (l.u.). Considering that, for the present configuration, the mean path length is about $\delta \sim 1/2$ nm the scale factor of the problem is 2, and thus, 25 (l.u.) would roughly correspond to 12.5 nm in the real system and 400 (l.u.) to 200 nm. Per each configuration, a pair correlation analysis was applied (Fig. 19.12e), whereby the fractal dimension D_f of the aggregates was derived. In Fig. 19.12f, the solid line represents the numerical DLA D_f as a function of Λ; in the same diagram, the markers in bright green correspond to the structures produced experimentally. The model recovers the experiments with advanced precision and accuracy and may be used to comprehend and design processes where advanced nanofabrication/characterization techniques are involved.

This DLA framework is *predictive* to the extent that gives the promise of describing the overall dynamics of aggregations of NPs. Specifically, this case study demonstrated that the process of NPs aggregation is size dependent, that is, a remarkable result, and especially, it was found that (i) for small systems, metal aggregates are continuous and homogeneous; (ii) for large systems, metal aggregates are discontinuous and less compact; (iii) the transition from small to large occurs at a size that, for the present configuration, is about $d \sim 50$ nm; and (iv) for sufficiently large systems, the internal structure of the clusters settles down to a steady state, that is, the growth is constant with d.

Deriving the Fractal Dimension of a Surface

Fractals are mathematical objects that are too irregular to be described by conventional geometry. They all retain, to different extents, certain properties that may be reviewed as follows: (i) they reveal details on arbitrarily small scales (fine structure), (ii) they can be generated (and thus described) by short algorithms (perhaps recursively), and (iii) they exhibit a *fractal* dimension D_f strictly greater than the classical topological dimension [83]. The latter property reserves particular attention, in that it claims that a surface, under a fractal point of view, may have a dimension D_f even greater than 2, and the more D_f is close to 3, the more the fractal set *fills* the space it is embedded in. The fractal dimension of the nanoparticles aggregates can be derived as described below.

Suppose to have an AFM profile of the substrate. This can be thoroughly processed to obtain the corresponding power spectrum density function C(q). C(q) delivers significant information regarding the fractal dimension and microstructure of the substrates at study, it is formally obtained as

$$C_{2D}(q) = \frac{1}{(2\pi)^2} \left(\int \langle z(\chi)z(o)e^{-iq\chi}d\chi^2 \rangle \right) \tag{19.11}$$

where $\chi = (x, y)$ is the planar coordinate; $z(\chi)$ is the surface profile measured from the average surface plane, defined as $\langle z \rangle = 0$; and q is the wave number, related to the characteristic wavelength λ as $q = 2\pi/\lambda$. The symbol $\langle \ldots \rangle$ stands for ensemble averaging over a collection of different surfaces with identical statistical properties. Since the 2D power spectrum density introduced above is impractical for comparison purposes, a 1D power spectrum density can be conveniently extracted using the FACA (fractal analysis by circular averaging) approach, as described in [84]. Considering the polar variables q and ψ ($q = (q_x^2 + q_y^2)^{1/2}$; $\psi = \arctan(q_y/q_x)$) in the plane (x, y) of interest, the power spectrum C(q) is derived as an average taken over every circumference Γ of radius q and origin ($q_x = 0$, $q_y = 0$), that is to say,

$$C(q) = \frac{1}{\Gamma} \oint_{\Gamma} C_{2D}(q_x, q_y)d\gamma = \frac{1}{2\pi} \int_0^{2\pi} C_{2D}(q\cos\psi, q\sin\psi)d\psi. \tag{19.12}$$

In the case of self-affine surfaces, for which a rescale in the planar coordinates x→bx and y→by is accompanied by a rescaling in the normal direction z ($b\chi$)→ $bHz(\chi)$, the power spectrum C(q) takes the form

$$C(q) = \frac{H}{2\pi} \left(\frac{h_o}{q_0} \right)^2 \left(\frac{q}{q_0} \right)^{-2(H+1)}, \text{for q} > q_o \tag{19.13}$$

where q_o is the lower cutoff wave number corresponding to an upper cutoff wavelength $\lambda_o = 2\pi/q_o$ and h_o is related to the Rrms roughness amplitude as $h_o = (2)^{1/2}$ Rrms. A self-affine fractal surface can be consequently univocally

identified by specifying the surface roughness (Rrms), the cutoff wave number q_o, and the coefficient H, known as the Hurst coefficient. In a log–log plot, the power spectrum density appears as a line with a slope β for $q > q_o$ (Fig. 19.12e). The slope β is related to the Hurst parameters as $\beta = 2(H + 1)$. The fractal dimension D_f of the surface can be derived from β or H as Df = (8-β)/2 or Df = 3-H. The fractal dimension D_f for a surface ranges from 2, representing a perfectly flat surface (Euclidean dimension of a surface), to 3, representing an extremely rough surface. For $D_f = 2.5$, the so-called Brownian surfaces are identified which have totally random and uncorrelated profiles.

Deriving the Fractal Dimension of a Diffusion-Limited Aggregation (DLA) Aggregate

The structure of clusters of occupied lattice sites (Fig. 19.12d) exhibits geometric scaling relationships which are characteristic of fractals and can be used to estimate an effective fractal dimensionality D_f. The fractal dimension is a parameter that can be used to describe intimately the topography of a variety of systems, especially at the nanoscales. The importance of D_f resides in the fact that it is used in the definition of certain parameters or properties which describe the deposit.

As, for an instance, the thickness T of the aggregate scales with the total number of deposited particles n, as [85]

$$T \sim n^{1/\left(D_f-1\right)} \tag{19.14}$$

the fractal dimension is also correlated to the distribution or number I of clusters with size S as a function of cluster size [85]:

$$I(S) \sim S^{-\left(1+1/D_f\right)} \tag{19.15}$$

Most importantly, the mean cluster size can be deduced and correlated to n via a very simple power law, being [86]

$$S \sim n^{D_f/\left(D_f-1\right)}, \tag{19.16}$$

and thus, given n, that can be easily calculated, the mean cluster size would be readily derived. Similarly to what described for real surfaces in the former paragraph, the fractal dimension of the numerical aggregates can be derived from their characteristic power spectrum density function C(q). Specifically, the power spectrum of a numerical data set can be determined from a pair correlation analysis. The pair correlation function g(r) is related to the probability of finding the center of a particle at a given distance r from the center of another particle. For short distances, this is related to how the particles are packed together. Here, we provide a simple algorithm following which g(r) may be calculated. One should choose and fix a value of dr sufficiently small. Therefore, for all the values of r considered for the analysis, the following steps of a procedure should be repeated: (i) count the

particles positioned at a distance comprised between r and r + dr from the reference particle. Those are all particles in a circular shell, with thickness dr, surrounding the reference particle. (ii) Divide your total count by the number of reference particles you considered. (iii) Divide this number by $2\pi r$ dr, that is, the area of the circular shell. This accounts for the fact that as r gets larger, for trivial reasons you find more particles with the given separation. (iv) Divide this by the particle number density. This ensures that g(r) = 1 for data with no structure. (v) The resulting value is the value of the pair correlation function at the specific distance r, g(r).

DNA Templating on Superhydrophobic Micropillar Surfaces for Nanowire Circuitry

In this section we will discuss the possibility to exploit the peculiar evaporation dynamics of liquid drops on superhydrophobic surfaces to obtain suspended nanowires with diameters below 100 nm and length in the mm range. The idea is the following: the retraction of a liquid droplet loaded with lambda DNA on a superhydrophobic surface consisting of an array of regular micropillars leads to suspended DNA strings or bundles that span regular patterns over the pillars [87]. In the next step, these DNA nanowire templates can be coated with metals, for example, by thermal gold evaporation, to obtain good electrical conductivity, and clever control of the DNA drop motion during drying can be employed to design complex patterns via evaporative self-assembly [88, 89]. Furthermore, optical functionality can be added to the nanowires by growing semiconductor nanocrystals on top of the gold coating, which we will demonstrate with ZnO. Such hybrid metal–semiconductor wires should have interesting properties for photodetection in the UV range, and the suspended nanowire geometry should provide a particularly large surface area for interaction with the environment. In the following we will describe the superhydrophobic surface fabrication, the DNA deposition to obtain the nanowire templates, the metallization, and finally the decoration with ZnO nanocrystals in detail.

The fabrication of the SU-8 micropillars involves a two-step approach composed by (i) an optical lithography phase to define the position of the microstructures and their development and (ii) a plasma process to cover the chip with a Teflon layer to make the surface superhydrophobic and/or to add a nanoroughness on the top of the micropillars to further enhance the non-wetting features and the anchoring of DNA nanowires.

The SU-8 resin contains eight epoxy groups per molecule which gives the polymer very high functionality. The high degree of cross-linking gives it good thermal stability (Tg > 200 °C). When fully processed, SU-8 creates a glass-like surface that is extremely hard and difficult to remove, which is due to its molecular structure that is formed during the exposure and post-exposure baking (PEB). Fully cross-linked SU-8 forms a ladder or H structure at the molecular level, and it is this repeating chemical chain which gives to the fully cured SU-8 its strength.

The micropillar structure is fabricated by first rinsing a Si wafer acetone, followed by IPA rinse (isopropyl alcohol) and drying with N_2. To remove solvent residues from surface, the wafer is then baked on a hot plate for 5/10 min at a temperature between 85 °C and 105 °C. SU-8 is then spin coated (1,500 RPM per 60 s) on the surface. Before exposure, the Si wafer coated with the SU-8 passes through a soft-baking (65 °C/5 min, 95 °C/40–45 min), which ensures the evaporation of the solvent and the densification of the film. For better results, ramping or stepping the soft bake temperature is performed. Indeed, lower initial bake temperatures allow the solvent to evaporate out of the film in a more controlled way. The following step is the exposure (15 s) during which UV radiation passes through the clear zones of the optical mask. After the exposure the sample is baked again (PEB, post exposure baking 65 °C/5 min, 95 °C/15 min) to selectively cross-link the exposed portions of the film. Finally, the sample is first immersed in a SU-8 developer (10 min), performing strong agitation to obtain high aspect ratio, and finally rinsed in IPA and dried by nitrogen.

The second step involves an ICP-RIE (inductive coupled plasma-reactive ion etch) plasma Teflon coating or a plasma nanotexturing + Teflon coating. In the first case, the sample is processed for 10 s in a plasma environment created by the injection of 85 sccm of C_4F_8 with a chamber pressure of 27 mT and an ICP/RF power of respectively 1 W and 600 W. In the second case, a plasma texturing precedes the Teflon coating and creates a nanoscale fibrillar structure on the top of the pillars enhancing the superhydrophobic features of the substrate. This plasma etch consist of a CF_4/O_2 flux (5/15 sccm) at pressure of 9.06 Pa and an ICP/RF power of respectively 100 W and 50 W for 10 min (Fig. 19.13).

The fabrication of ordered 1D organic nanostructures on a large scale is a challenging subject that holds promising spin-off in next generation high performance optoelectronic devices [90, 91]. Here, we show how ordered hexagonal arrays of SU-8 pillars with superhydrophobic behavior and three-phase wetting were exploited to obtain regular and controlled DNA wire arrays. Such surfaces allow the fine control of wire diameters and length by controlling the overall wetting behavior and the local surface–molecule–solvent interaction [92], in terms of shear viscosity and interaction time.

Double strand λ-DNA has been suspended in phosphate buffer solution (PBS) (50 ng/μl DNA in 1 % PBS volume). A drop of 4–7 μl has been deposited onto the superhydrophobic pillar surface, fabricated as above described. A three-phase contact (TPC) line was created, and a suitable contact time was chosen in order to trigger a gravity-driven DNA concentration gradient within the drop. This procedure allows the DNA molecule to get in contact and interact with the wetted features of the surface (top of the pillars). Once the wetting interface is created, the drop can be let to evaporate overnight [93]: in this process, the solvent evaporation induces changes in the drop/substrate wetting condition, which leads to a sequence of pinning and depinning processes from the pillars [87, 94]. Alternatively, a similar pinning/depinning process can be obtained by relative motion of the substrate with respect to the DNA solution droplet, which sensibly influences the shear flow conditions during the shrinking of the drop as reported by us previously [95].
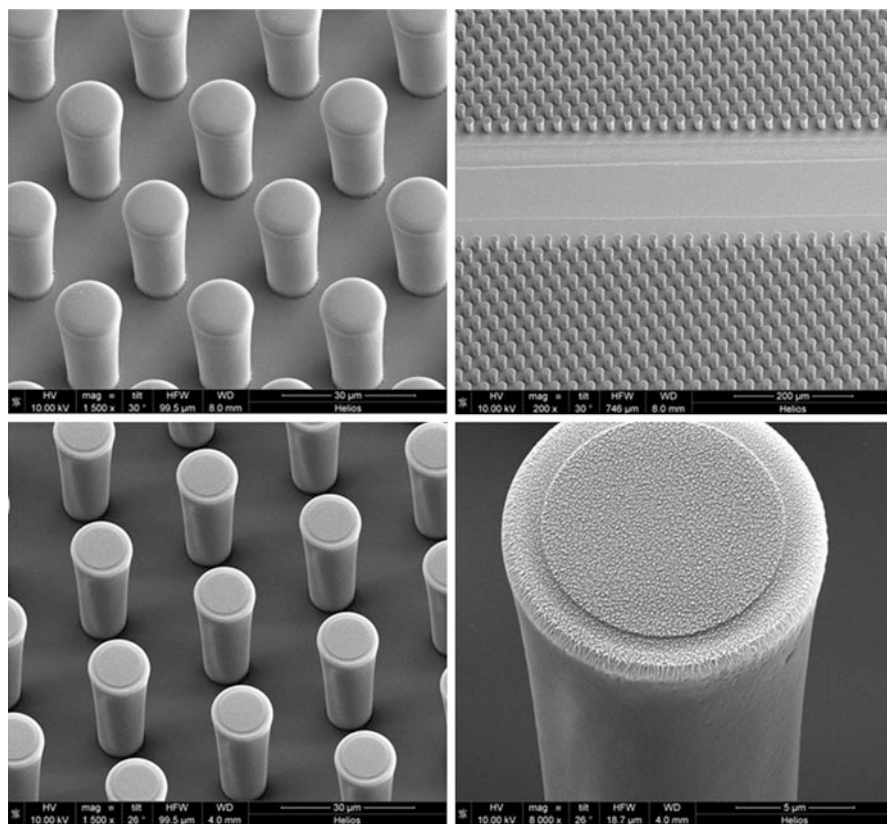
Fig. 19.13 SEM images of SU-8 micropillar arrays without (*up*) and with (*down*) the plasma nanotexturing on top

This dynamic process is similar to Langmuir–Blodgett preparation: once a tip was linked to the drop, a relative tangential motion was applied at the TPC with a velocity comprised between 100 and 600 um/s. While moving the drop/support contact line, DNA molecules were stretched and suspended between the pin points of the surface, i.e., the wetting features. The process yields an ordered and tunable array of 1D organic nanostructures consisting in DNA bundles. The forces responsible for the formation of the bundles were basically the capillary force F_c and the pulling force F_p necessary to pull a DNA molecule or bundles [87]. Capillary force involves surface tension at the contact line and liquid viscosity. Tuning the velocity it was possible to achieve a desired pulling force, thus selecting the diameters of DNA bundle to be stretched (Fig. 19.14).

Furthermore, the tuning of the direction of the TPC motion allows the fabrication of organic meshes and grids in a few simple steps (Fig. 19.15).

DNA bundles can serve as an optimal template for the cost-effective nanowire fabrication with large area coverage. The obtained 1D structures can be coated with
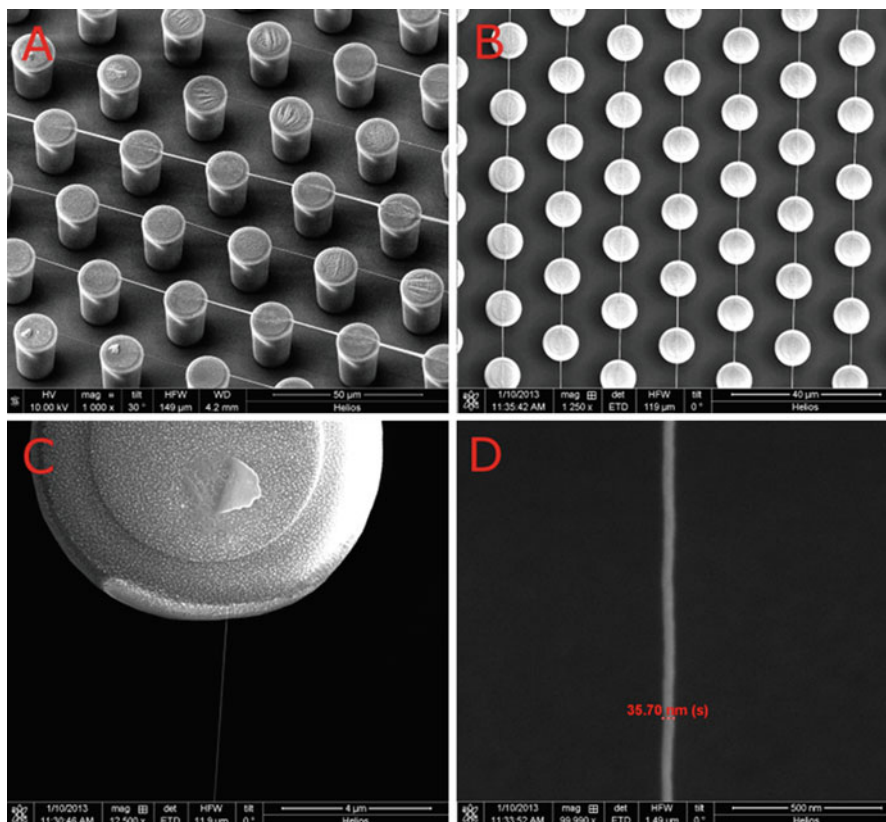
Fig. 19.14 SEM images of DNA filaments stretched and suspended on SU-8 micropillars. In (**a**) and (**b**), an overview of the surface and 1D DNA directional arrays is shown. In (**c**) and (**d**), a detail of the filament diameters is shown

metals by means of thermal evaporation resulting in conducting wires with controlled diameter that are suspended on an insulating pillar arrays with tailored periodicity and wire meshes. Such suspended nanowire networks are particularly attractive for sensing applications due to the large exposed surface area.

As proof of concept, we have deposited 30 nm of Au onto the above described nanowire templates by thermal evaporation. We used pillar structures with undercut lateral profiles to avoid electrical shortcuts between the electrical circuitry and the bottom of the substrate. We have performed electrical characterization of the suspended nanowires in between individual pillars by contacting neighboring pillars with tungsten micromanipulators (tip radius 5 μm). Typical current–voltage curves of a suspended Au-coated DNA nanowire with around 100 nm diameter suspended between pillars with 18 μm distance are shown in Fig. 19.16. At low bias, we observe ohmic behavior (red solid line in Fig. 19.16), as expected. If the bias voltage is increased to some hundreds of mV, the current gets into saturation

Fig. 19.15 SEM image of λ-DNA meshes obtained by crossing different TPC lines by support/drop motion
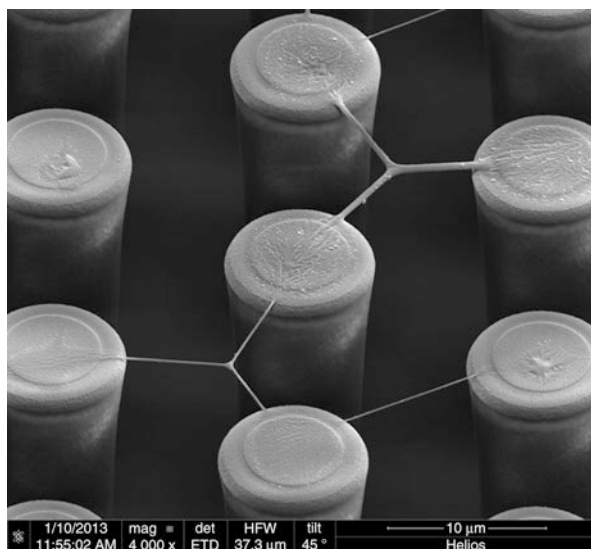
Fig. 19.16 Current–voltage curves of a suspended Au-coated DNA wire measured between two adjacent pillars: first, the solid red curve in a low bias regime was recorded, then the bias was increased until current saturation set in (*upper inset*), and after this, the IV was recorded again at low bias (*dashed black curve*), showing increased conductivity. The SEM image in the inset shows the Au-coated wires under test. The distance in between the pillars was 18 μm
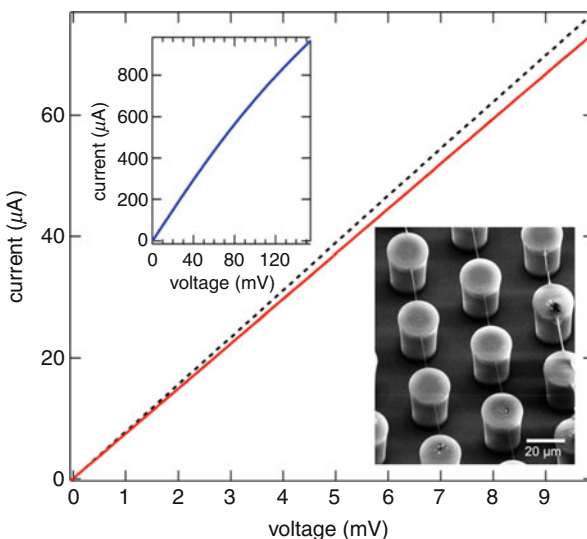
(upper inset), and upon further increase it will be burned [96]. The current saturation can be understood by nanowire heating due to the high current density (of the order of 10^8 A/cm^2). Interestingly, the nanowires demonstrate higher conductivity after being ramped into saturation as shown by the dashed line in Fig. 19.16. This can be rationalized by the annealing effect caused by the high current density that should lead to a more homogeneous Au film.
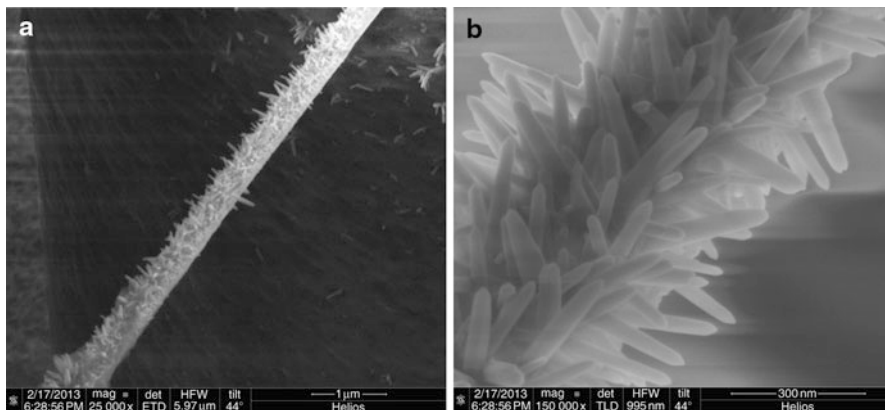
Fig. 19.17 ZnO nanocrystals hydrothermally grown on DNA bundles (**a**). In (**b**) a detail of radial symmetric ZnO nanocrystal growth is shown

Eventually, the nanowire templates can be decorated with other nanomaterials that have different functionality, or they can act as templates for nanocrystal growth. This approach opens new pathways for the fabrication of hybrid nanowire architectures for novel device applications, for example, optical sensors that could work in liquid environment.

In order to demonstrate the feasibility of this approach, we have used the Au-coated DNA nanowires as templates for zinc oxide (ZnO) crystals hydrothermal growth [97–99]. Figure 19.17 shows sections of such ZnO-decorated nanowires, evidencing that the ZnO grows in rodlike structures in radial direction, instead of a homogeneous layer. This spinose decoration results in an extremely high surface area that can be useful for sensing applications. In detail, we deposited a thin (20 nm) ZnO film by thermal evaporation on a chip with Au-coated DNA bundles in order to create a seed layer. Then, the sample containing the suspended Au–ZnO DNA wires was immersed in an aqueous solution of ZnO precursors (zinc nitrate, $Zn(NO_3)_2$ $6H_2O$ 25 mM; hexamethylenetetramine, (HTMA) 25 mM; and poly(ethyleneimine), (PEI) 6 mM) and kept at 90 °C for 40 min. Afterwards, the support was washed several times with DI water and gently blow-dried with nitrogen.

The obtained hybrid ZnO–Au (metal semiconductor) can be expected to show photocurrent when excited with laser light above the band gap of ZnO, thus in the UV spectral region. Here, the Au core should facilitate good electrical conduction, while the ZnO acts as the light-absorbing material. Furthermore, this hybrid architecture with very large ZnO surface area can also be interesting in solar cell applications in combination with a hole harvesting polymer matrix.

Properties, Specific Physical Effects of Metal Nanostructures, and the Case of Surface Plasmon Resonance

L-Shape Gap Nanoantenna Dimers Supporting Plasmon-Polariton Modes

The most remarkable property of plasmonic nanostructures consists in the easy coupling between electromagnetic (EM) radiation and *surface plasmon polaritons* (SPPs) [100]. In particular, when the dimensions of the systems under study are shorter than the incoming radiation wavelength, the quasi-static approximation well describes EM responses and the plasmonic modes supported by the structures can be defined as *localized surface plasmons* (LSPs) [101].

Sub-wavelength nanoantennas are typical nanostructure devices able to efficiently convert free propagating EM radiation into near-field EM energy, concentrated into sub-wavelength active regions called *hot spots* [102]. Such property, in visible (VIS) and near-infrared (NIR) spectral region, can be efficiently exploited for advanced spectroscopic techniques with particular applications in biosensing and biomolecular spectroscopy, in perspective to achieve the challenging single-molecule detection [103, 104]. In order to obtain an antenna-based device able to efficiently couple to light, generating an intense and localized hot spot, an optimal solution consists in putting two nanoantennas in close proximity [20].

When two sub-wavelength plasmonic nanostructures exposed to EM radiation are put at a mutual distance shorter than their typical dimensions, a strong overlapping occurs between their generated near-field *evanescent tails* [105]. In this condition, in analogy to the theory of molecular orbitals, Maxwell's equations admit for the coupled system two hybridized eigenmodes which result from the interaction between the unperturbed LSP modes supported by each nanostructure. The energies associated to such modes are respectively lower and higher than the degenerate energy level, and the difference between them depends upon the intensity of the interaction. The lower energy plasmonic mode is defined as *bonding* while the higher one is called *antibonding* [106].

By arranging nanoantenna dimers in an L-shape gap configuration (see Fig. 19.18a), it is possible to obtain a device supporting plasmon-polariton modes that are combinations of in-phase (bonding mode) and out-of-phase (antibonding mode) single antenna long-axis surface plasma oscillations. In the former case, charge distributions induce in the gap region an intense hot spot while in the latter one a 'zero-field spot' occurs in a plasmonic mode which can be referred to a nonzero dipolar momentum [107].

The crucial point on which the EM behavior of L-shape antennas device consists in the strong gap-induced coupling between the LSPs supported by each nanoantenna arm. Considering the VIS–NIR spectral region as working range of the device, the gaps between the apexes of antenna arms have to be around 10 nm in order to show appreciable hybridization of plasmonic states. In such perspective, the technique employed for the realization of L-shape antennas device has been *electron beam lithography* (EBL), a fabrication approach particularly addressed for
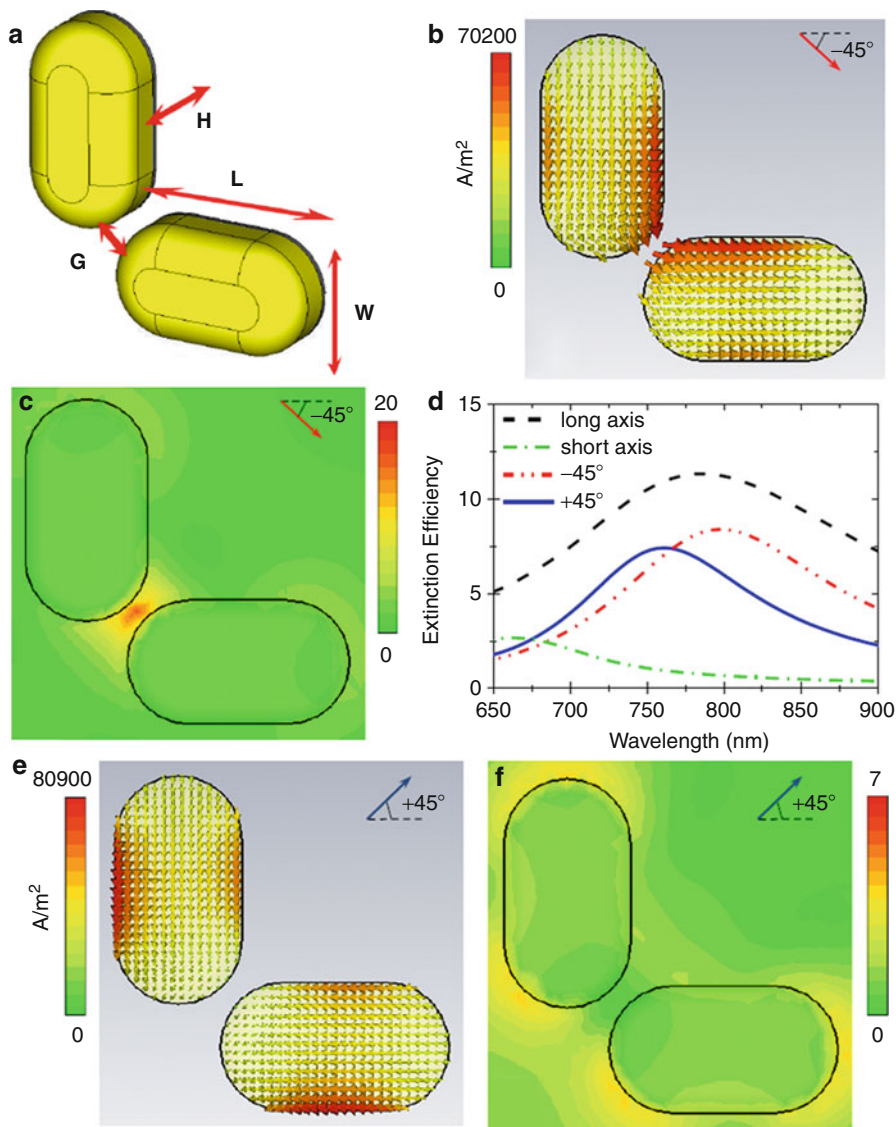
Fig. 19.18 (**a**) 3D sketch of L-shape antennas showing the geometrical parameters representative of the morphology (**b**, **c**) Respectively, current density and electric field intensity 2D plots for normal-incidence light polarized at $-45°$ valued at $\lambda = 810$ nm (**d**) Theoretical extinction efficiency spectra of L-shape antennas ($L = 190$ nm, $W = 110$ nm, $H = 60$ nm, and $G = 20$ nm) and of their single antenna arm; in *black dashed line* the long-axis reference extinction spectrum of single antenna, in *green dotted/dashed line* the short-axis reference extinction spectrum of single antenna, in red double-dotted/dashed line the L-shape antenna extinction spectrum for $-45°$ polarization, and in blue continuous line the L-shape antenna extinction spectrum for $+45°$ polarization (**e**, **f**) Respectively, current density and electric field intensity 2D plots for normal-incidence light polarized at $+45°$ valued at $\lambda = 760$ nm (Picture kindly reprinted from Ref. [107])

the achievement of high nanostructure accuracy and reproducibility over large areas (order of the mm^2). Such procedure involves several steps. Initially, a positive electronic resist (*polymethylmethacrylate* – PMMA) is spin coated on a CaF$_2$ (100) substrate, chosen for its high transparency in VIS–NIR spectral region. Afterwards, a thin Al layer is evaporated on the resist in perspective of preventing electron charging effects during the exposure process. Once the Al-coated resist layer has been prepared, the sample is exposed to an electronic beam accelerated to 20 KeV. Therefore, after the Al removal in KOH, the patterned resist is developed in a conventional MIBK/IPA solution in order to produce a positive mask. Hence, *physical vapor deposition* (PVD) at room temperature, respectively of 5 nm Ti as adhesion layer and 55 nm Au, is performed on the sample. Finally, the unexposed resist is removed with acetone and rinsed out in IPA. As result of the fabrication process, 40×40 μm^2 size matrices of L-shape antennas have been obtained with interparticle gaps equal to 20 nm (Fig. 19.19a–c).

In quasi-static approximation, L-shape nanoantennas support two pairs of hybridized long-axis LSP modes. In the former mode, charge distributions in both antenna arms flow in-phase in a convenient energetic configuration (Fig. 19.18b). Conversely, the latter mode presents charge distributions forced to contemporarily converge towards the gap in an inconvenient energetic configuration (Fig. 19.18e). As a consequence of that, moving from the bonding to the antibonding mode, the electric field generated within the gap region experiences a strong variation. In fact, from an intense hot spot occurring for the in-phase charges configuration, it is possible to see how the electric field appears completely nullified in the out-of-phase condition (Fig. 19.18c, f). Such two modes are both associable to nonzero dipolar momenta, whose orientations correspond to the lines forming angles respectively $\theta = -45°$ and $\theta = +45°$ with the horizontal antenna long axis. This fact implies that such modes are both able to efficiently couple to light, reemitting EM radiation in far-field. In particular, for incoming light polarized at $\theta = -45°$, it is possible to promote the bonding mode, activating the gap-induced hot spot in near-field and observing a correspondent single broad resonance peak in the extinction efficiency spectrum (red dashed/double-dotted curve in Fig. 19.18d). To the contrary, by rotating the polarization vector of a 90° angle ($\theta = +45°$), it is possible to suppress the bonding mode and consequently the hot spot in the gap region. In this way only the antibonding mode can be excited and observed in far-field as a broad resonance peak centered on a wavelength which is blue-shifted with respect to the bonding wavelength (blue continue curve in Fig. 19.18d).

As it is possible to verify in the extinction efficiency spectra reported in Fig. 19.18d, the peaks observed for L-shape antennas response at $\theta = \pm45°$ are definitely not related to single antenna short-axis LSPs, which instead occur in a different spectral region (green dashed/dotted curve in Fig. 19.18d), but conversely they result from the hybridization of single antenna long-axis LSPs (black dashed curve in Fig. 19.18d).

Such behavior has been verified by transmission spectroscopy for light polarized at $\theta = -45°$ and $\theta = +45°$, keeping in mind the relation between transmission and extinction efficiency:
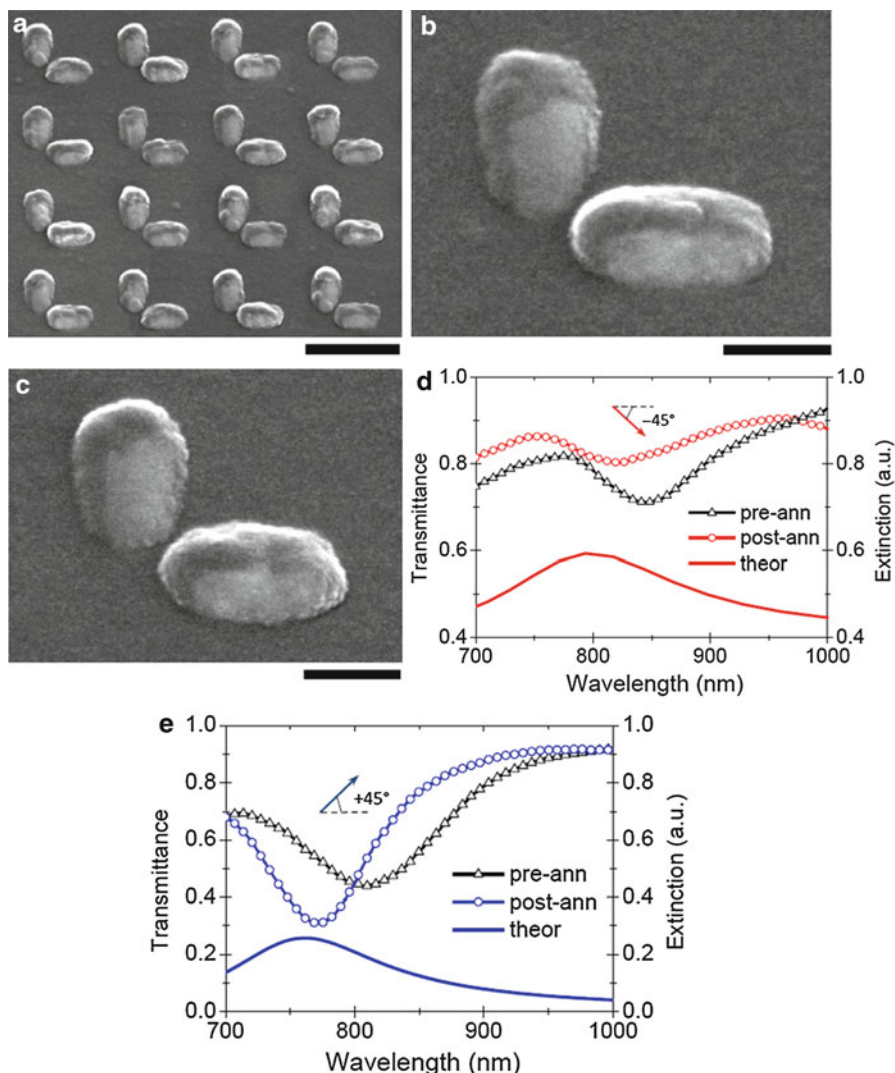
Fig. 19.19 (**a**) and (**b**) Representative SEM images, respectively, of 30° out-of-normal tilted L-shape antenna arrays and single L-shape antenna fabricated by EBL technique before annealing process (scale bars corresponding, respectively, to 400 and 100 nm). The nanostructure geometrical parameters are $L = 190$ nm, $W = 110$ nm, $H = 60$ nm, $G = 20$ nm, and $S = 100$ nm (**c**) Representative SEM image of 30° out-of-normal tilted L-shape antenna after 200 °C annealing (scale bar corresponding to 100 nm) (**d**) Transmission optical spectra of the L-shape antenna arrays before (*black curve with triangles*) and after annealing at 200 °C (*red curve with circles*) and theoretical extinction efficiency (*continuous red curve*) for normal-incidence light polarized at −45° (**e**) Transmission optical spectra of the L-shape antenna arrays before (*black curve with triangles*) and after annealing at 200 °C (*blue curve with circles*) and theoretical extinction efficiency (*continuous blue curve*) for normal-incidence light polarized at +45° (Picture kindly reprinted from Ref. [107])

$$Q_{ext} = \frac{A(1 - T_{rel})}{Na} \tag{19.17}$$

where 'A' is the area illuminated by the light spot, 'N' is the number of arrays elements inside of the spot, and 'a' is the area of L-shaped antenna projection on the plane where the polarization vector lies.

From a comparison between collected and calculated spectra, it is possible to find a good accordance, apart from a slight red-shift of measured resonance wavelengths with respect to theoretical ones (Fig. 19.19d, e). This fact suggests that the hybridization model, which determines the antibonding/bonding energy splitting, is correct even if applied to a system that is not ideal. In fact, as exhaustively described in literature [108], gold aggregates evaporated at room temperature present a nonuniform internal structure. They are organized in grains of about 30 nm size, mainly (111)-oriented, and electrons flowing through them experience multi-scattering effects that result in an additional contribution to their internal damping. More precisely, the damping factor of a gold polycrystalline nanostructure differs from the model system of the following quantity:

$$\Delta\Gamma = \Gamma_g - \Gamma_0 = \frac{1.37 v_F R}{D(1 - R)} \approx \frac{1}{D} \tag{19.18}$$

where 'v_F' is the Fermi velocity for gold, 'R' is the reflection coefficient of electron at the grain boundary, and 'D' is the average diameter of the grains.

Gold atoms within a polycrystalline aggregate at room temperature are 'frozen' in a metastable energetic configuration where the majority of them are organized in grains with an energetically convenient orientation, that is (111), and the remaining ones belong to grains with different orientations. Starting from such configuration and increasing the temperature, it is possible to make the (111)-oriented grains grow at the expense of the other grains, promoting an average grain growth and grain boundary migration. As confirmed by means of X-ray diffraction experiments (reported in [108]), which show the increasing of (111) peak both in intensity and sharpness as function of the *annealing* temperature, the average diameter of the grains increases from 30 nm at room temperature to 40 nm at 400 °C [108]. Therefore, from Eq. 19.2 it is possible to deduce how annealing process on polycrystalline gold aggregates makes the damping factor tend to the theoretically expected value. Finally, the reduction of the damping factor determines a general blue-shift in the LSP resonance (LSPR) wavelength and the shrinking of the resonance peak in the far-field spectrum.

In order to confirm such interpretation of the phenomenon involved, annealing has been performed on L-shape antennas at 200 °C observing a blue-shift of both the in-phase and out-of-phase resonances. The after-annealing transmission spectra collected and reported in Fig. 19.19d, e are in very good accordance with theoretical extinction spectra reconfirming the extra damping factor, introduced by the polycrystalline nature of the structures, as the origin of the resonances mismatch observed at room temperature.

Adiabatic Cones, Photonic Crystals, and Superhydrophobicity: A Versatile Tool for Chemical Mapping and Single-Molecule Detection

The main interest in the fabrication of nanoscaled tapered waveguides, such as metallic nanocones, is due to the fact that this kind of structures is predicted [109] and can actually [3] focus and concentrate the optical radiation energy at the nanometric scale. This phenomenon is of paramount importance since it offers the possibility to overcome the diffraction limit of light, and optical-based techniques, like Raman spectroscopy, can exploit this mechanism to achieve an unprecedented spatial resolution. This focusing effect can be achieved by excitation of surface plasmon polaritons propagating towards the tip of a tapered metal nanowaveguide, and, with proper geometric conditions, the surface plasmon polaritons adiabatically slow down and simultaneously increase the accompanying electromagnetic field.

Microfabrication of Advanced Plasmonic Devices

It is a crucial point that the nano-waveguide is properly shaped as a cone with an accurate control of the apex angle and of the curvature radius of the final tip.

These requirements make the standard micro- and nanofabrication techniques with top-down approach, such as the lithographic techniques, not suitable for the fabrication of these devices. In fact, lithographic techniques, for example, electron beam lithography (EBL), have the capability to achieve the necessary spatial resolution, but they are intrinsically 2D (two-dimensional) processes and not well suited for the 3D structures here required. In EBL processes, typically a 2D pattern is prepared with some CAD software and then replicated on a resist layer by means of a spatially selected electron beam exposure of the resist. After resist development, the 2D resist pattern is transferred to the substrate through an additive or subtractive process. In the additive process, some material, e.g., a thin metal layer, is deposited on the sample, and the final result is a 2D metal pattern; in the subtractive process, the resist pattern is used as a mask through which the material from the substrate is removed by means of an etching step, thus producing a 2D pattern in the material of the substrate (typically a Si substrate or similar). So the only 3D feature of this process is a 2D pattern with vertical walls. Such an approach makes very difficult to produce real 3D structures [110, 111], in which something more than a vertical wall is required. Even simple 3D solids, like a cone or a pyramid, is not a trivial task with standard lithographic techniques, and more in general whenever a tilted, bent, or curved shape is required the intrinsically 2D nanofabrication meets strong limitations.

In order to overcome these troubles, different nanofabrication techniques have to be pursued beside the standard 2D lithographic processes. More in detail, electron beam-induced deposition (EBID) combined with focused ion beam milling (FIBM) is exploited in the present case to produce metal cone-shaped nanodevices coupled to a photonic crystal (PC) optical cavity (Fig. 19.20).

Fig. 19.20 Photonic crystal array and cavity with metallic cone-shaped nano-waveguide in the middle of the cavity. The substrate is a 100 nm thick Si_3N_4 membrane in which air holes are produced by means of ion beam lithography (*IBL*). The nanocone is produced by means of electron beam-induced deposition (*EBID*) technique and is made of platinum carbon covered with an Ag thin layer (20 nm) (Picture kindly reprinted from cover page of Nature Nanotechnology (2010) [3])
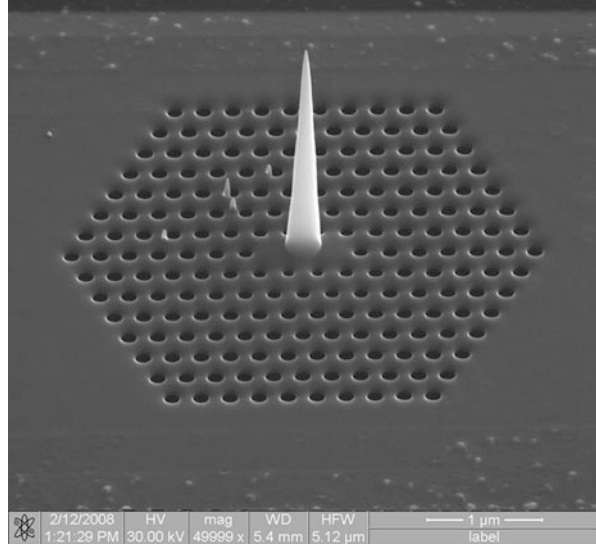
The working principle of FIBM is the same as EBL, but in this case, an ion beam is used instead of an electron beam. For the fabrication of this device, Ga^+ ions with an accelerating voltage of 30 kV are used to produce air holes in a thin Si_3N_4 membrane. So the Ga^+ ion beam is exploited to produce a real milling of the substrate with material removal. This effect is produced by physical bombardment of the substrate by the 'heavy' ions. In comparison, the 'light' electrons of EBL do not produce any milling effect but only destroy some molecular bonds in the polymeric chains of the resist, thus changing locally the chemical properties (such as the dissolution rate in presence of solvents) of the resist layer. The similarity of FIBM with EBL is that both the techniques are 2D fabrication processes in which a charged particle beam (ions or electrons) is focused on the sample surface and deflected over the sample in agreement with a CAD designed pattern. The difference is that in EBL, the 2D pattern reproduces a 2D change of the chemical properties of the resist, while in FIBM, in the present case of the device of Fig. 19.20, we use the Ga^+ ions to physically remove material from the substrate in agreement with the 2D pattern. This is made possible by the fact that the thickness of the Si_3N_4 substrate is a small one, in the 100 nm regime. The array of air holes produced in the substrate constitutes a photonic crystal [112, 113], and the three missing holes in the center of the array (where the base of the cone is placed) realize a photonic crystal optical cavity [114], termed L3. The whole array has triangular lattice geometry with lattice constant of 250 nm (Fig. 19.21) and the holes have 160 nm diameter size; these geometrical features make the PC and cavity tuned at a laser wavelength of $\lambda = 532$ nm.

Fig. 19.21 Si$_3$N$_4$ photonic crystal: the lattice of the air holes is a triangular one with lattice constant of 250 nm; the holes diameter is 160 nm. The thickness of the Si$_3$N$_4$ membrane is 100 nm
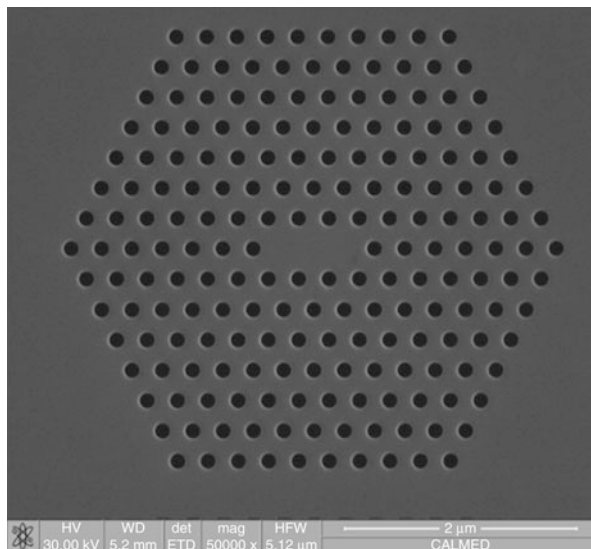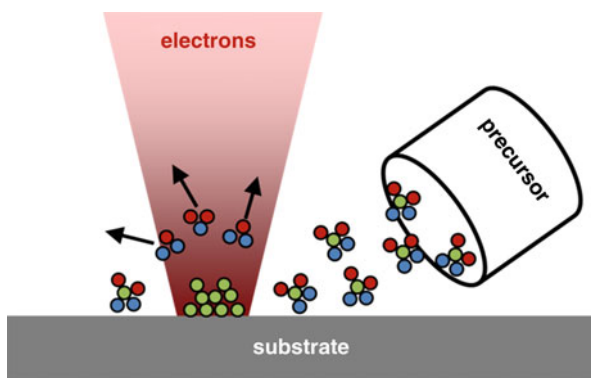

Fig. 19.22 Schematic representation of the electron beam-induced deposition (EBID). (CH$_3$)$_3$Pt(CpCH$_3$) molecules of the precursor gas are broken thus allowing for Pt deposition on the substrate

So far the employed technique is still a 2D fabrication process. The real 3D process is the fabrication of the cone-shaped nano-waveguide in the center of the PC structure. In order to achieve the result of Fig. 19.20, an EBID process is exploited. Electron beam-induced deposition [115] is a structuring technique capable of the same high spatial resolution typical of electron beam techniques, but with the advantage of some 3D capabilities. In EBID (Fig. 19.22), a gas of precursor molecules, in this case (CH$_3$)$_3$Pt(CpCH$_3$) (methylcyclo-pentadienyltrimethyl-platinum), is injected in the vacuum chamber in the proximity of the substrate surface.

The electron beam is focused on the same substrate, in the area where the gas is injected, and hits the molecules of the precursor gas. This bombardment causes the precursor molecules to be broken in more fragments and to release the Pt atom that soon is deposited on the substrate; the other fragments of the molecules are instead
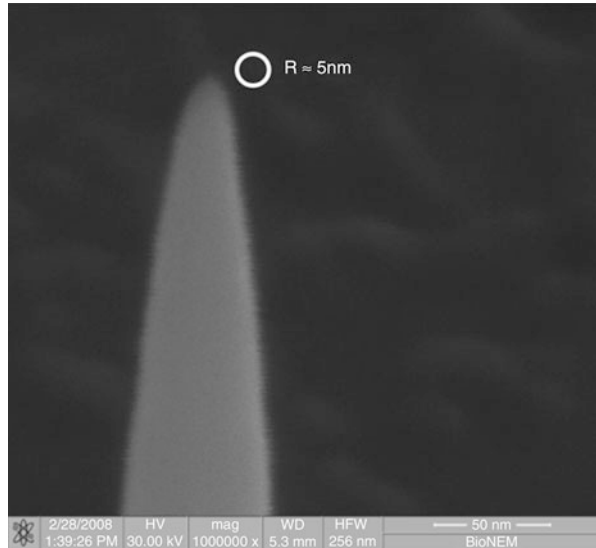
volatile ones and are pumped away by the vacuum system. The only disadvantage
of this mechanism is that the Pt deposition so induced is not of pure Pt, but carbon is
also deposited to a certain amount on the substrate. The Pt–C material deposited is
however a metallic one, since it is conductive both electrically and thermally. This
disadvantage mainly comes from the fact that the precursor molecules so far used in
EBID techniques are metallorganic materials. The minimum size of the deposited
material is comparable with the spot-size of the electron beam, thus being in the
more advanced equipments in the 10 nm range. The thickness of the deposited
material depends on the dwell time the electron beam is kept in a fixed position on
the substrate. So it is possible to deposit a first layer of Pt–C with a desired 2D shape
and subsequently to deposit the next layer starting from the previous one but with
a different 2D shape. The reiteration of this process allows for an easy fabrication of
3D structures. As a simple example, the cone-shaped nano-waveguides have been
fabricated as a vertical stack of disks with different diameters, starting from the
largest disk deposited directly on the Si_3N_4 substrate and going on with the smaller
disks deposited on the former ones. The process has been reiterated starting from
a disk with 300 nm diameter which constitutes the base of the cone and going up
towards smaller and smaller disks, till the last one which is constituted by a single
pixel and so ensures the smallest curvature radius at the tip apex (Fig. 19.23).

The final height of the cone is imposed to be 2.5 μm for geometrical reasons due
to surface plasmon-polariton adiabatic propagation along the cone.

Both the processes so far described, the FIBM and the EBID ones, have been
used to produce photonic crystal cavity and cone nano-waveguide on top of an
atomic force microscopy (AFM) cantilever. Commercially available Si_3N_4 with
600 nm standard thickness cantilevers have been used and locally thinned in the
area of the photonic crystal. The thinning process has been achieved by means of
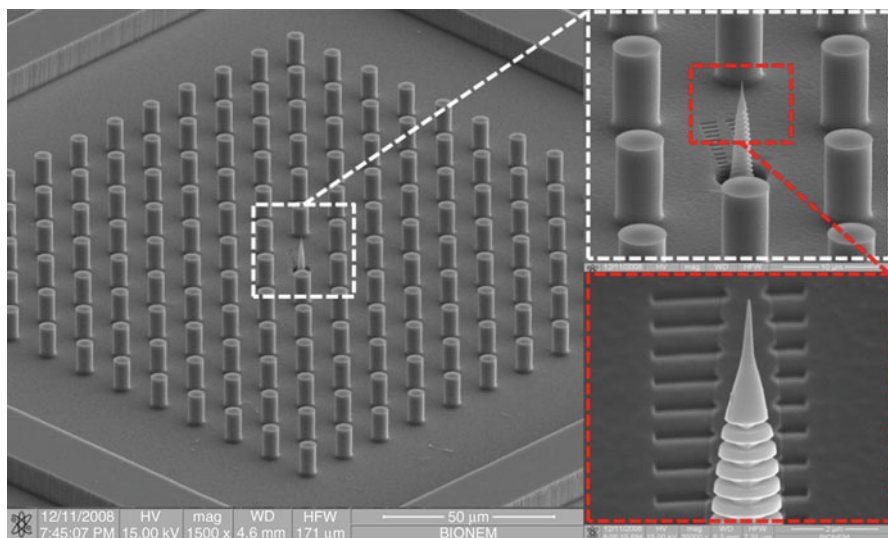
Fig. 19.24 Superhydrophobic chip with embedded a plasmonic metal cone-shaped nano-waveguide. One of the pillars of the superhydrophobic chip has been cone-reshaped by means of focus ion beam milling, and a coupling grating has been produced on one side of the cone using the same technique. Subsequently, a high-resolution plasmonic nano-waveguide has been fabricated on top of the reshaped pillar using electron beam-induced deposition (Picture kindly rearranged from Ref [93])

ion beam bombardment with large ions flux, and the area of the PC has been thinned down to 100 nm. Then, the PC has been realized by means of ion beam localized removal of material, thus opening air holes in the Si_3N_4 thinner area. Subsequently, the Pt–C cone has been fabricated in the middle of the PC optical cavity by means of EBID. A thin Ag layer (30 nm thickness) has been deposited over the sample and in particular over the cone, thus having a noble metal layer for the surface plasmon–polaritons propagation. Finally, the Ag layer has been removed only from the area of the photonic crystal, and not from the cone, with a gentle (small ion flux) ion beam bombardment of the PC surface. All these processes have been carried out using one only equipment, a FEI Nova Nanolab 600 dual beam system. This machine is, briefly speaking, constituted by two columns, an electron one along the vertical direction and a Ga^+ ions one that is tilted respect to the electrons one. The sample is mounted on a stage that can be tilted in the space, in order to have the sample perpendicular to the electron column or to the ion one, according to the column used for manufacturing the sample. The system is moreover equipped with a gas injection system that allows in the present case EBID in combination with the electron beam.

Similar plasmonic nano-waveguides have been also implemented in micropatterned superhydrophobic substrates. Micropatterned superhydrophobic substrates are made of regular arrays of pillars with typical dimensions in the 10 μm scale. As an example, the superhydrophobic pattern in Fig. 19.24 is

constituted by a triangular lattice of Si pillars with 5 µm diameter, 15 µm of lattice constant, and 50 µm of height.

Geometrical parameters can be adjusted in order to achieve higher contact angle once a drop of solution is deposited on the superhydrophobic surface. The superhydrophobic pattern is accomplished with standard, planar 2D lithographic techniques, made of optical lithography in combination with deep reactive ion etching process (Bosch process) [116]. Once produced, the superhydrophobic pattern has been processed using focus ion beam milling and electron beam-induced deposition. First of all the Si pillar in the middle of the pattern, which initially has a cylindrical shape, has been reshaped as a cone by means of FIBM: ion bombardment has been used to remove Si material from the cylindrical pillar until a cone is obtained. Subsequently, FIBM has been used to produce a far-field light coupling grating on one side of this large cone. The grating is necessary in order to couple the laser light coming from far-field with the plasmonic nano-waveguide (see further). At this point a plasmonic nanocone has been fabricated on top of the large cone by using EBID, as described above. It is worthy to say that the cone shaped from the cylindrical pillar by means of FIBM exhibits a regular cone shape, but the resolution achievable with this technique for the apex is much worse than the resolution of a cone produced by means of EBID. Finally, a thin Ag layer (20 nm) has been deposited on the whole sample area and obviously on the cone nano-waveguide, thus ensuring the presence of a noble metal layer for surface plasmon-polariton propagation.

Characterization of the Plasmonic Devices

As mentioned above, plasmonic cone-shaped nano-waveguides have attracted interest due to their ability to propagate and concentrate light beyond the diffraction limit. This fascinating effect is also accompanied by an increase of the propagating electromagnetic field as it approaches the apex tip, and smaller is the radius of curvature larger is the enhancing factor. Both these effects in turn produce significant advantages in optical-based techniques, such as Raman spectroscopy. In fact, by means of a proper use and configuration of the plasmonic nanocones, largely enhanced Raman signals can be recorded from very narrow areas, i.e., with spatial resolution higher than the spatial resolution imposed by the diffraction limit.

When laser light coming from the far-field is focused through an optical objective, the maximum spatial resolution achievable is of the order of half wavelength, and for visible light, we are in the 200–300 nm range. Instead, if light is properly coupled with the base of the plasmonic cone, surface plasmon polaritons are excited at the cone base and start to propagate along the cone towards the tip. Surface plasmon polaritons are oscillations of the electron gas within the metallic layer, which covers the nanocones (the 20 nm thick Ag layer), and these charge oscillations inside the metal layer are accompanied by an oscillating electromagnetic field just outside the metal surface. As predicted in Ref. [109], the surface plasmon-polariton experience, in the propagation along the cone, larger effective refractive index as they approach the apex. This in turn produces a slowing of their group velocity and consequently a plasmon accumulation occurs at the apex, with a high
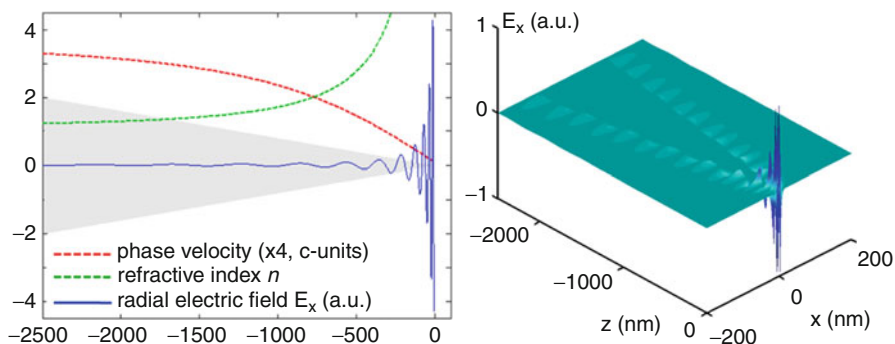
Fig. 19.25 Propagation of surface plasmon polaritons along the cone surface and plasmon accumulation at the tip of the cone. On the *left*, the behavior of both the effective refractive index and the phase velocity of the polaritons as a function of the position along the cone axis. The phase velocity goes to zero as the tip is approached. Also, the electric field in radial direction, termed E_x, calculated just outside of the cone, is reported as a function of the position along the cone axis: it is evident the strong enhancement achieved at the tip due to plasmon accumulation. On the *right*, a two-dimensional plot of the radial electric field: the field inside the cone is nearly zero and we have, just outside the cone, the electric field accompanying the plasmon polaritons. The enhancement is strongly localized around the tip of the cone, and the field soon decays as we move far from the tip (Picture kindly rearranged from Ref [3])

enhancement of the electric field which propagates along with the plasmon polaritons (Fig. 19.25).

The result is that the far-field light coupled to the base of the cone is concentrated in a narrow area comparable with the tip dimension, which is in the 2.5–5 nm range in the case of the cone shown in Fig. 19.20 and Fig. 19.23, much beyond the diffraction limit. Once at the tip, this electromagnetic field propagating with the surface polaritons decays again in free photons, due to the apex singularity. The resulting electromagnetic field can then produce Raman scattering from species very close to the tip, a Raman signal coming from a very narrow area which is of the same order of the tip size. As a result, it is possible to record Raman enhanced signals with a high spatial resolution, well beyond the diffraction limit.

This effect is strongly dependent on the geometry of the cone. First of all the cone has to produce an adiabatic compression of surface polaritons, thus meaning that the slope of the cone, i.e., the apex angle, has to be small enough to ensure a slowly varying effective refractive index. The other crucial point is the apex radius of curvature, which strongly affects the field enhancement. If we consider as field enhancement the ratio $|E_T|/|E_B|$, where E_T and E_B are respectively the electric field amplitudes at the tip and at the base of the cone, we obtain large enhancing factors only for tip radius below 5 nm (Fig. 19.26). Both these requirements are met by the cone fabricated on top of AFM cantilever (Figs. 19.20 and 19.23) and the cone embedded in the superhydrophobic surface (Fig. 19.24).

This working mechanism has been first demonstrated using the metal cone nano-waveguides fabricated on top of the AFM cantilever. Following the scheme
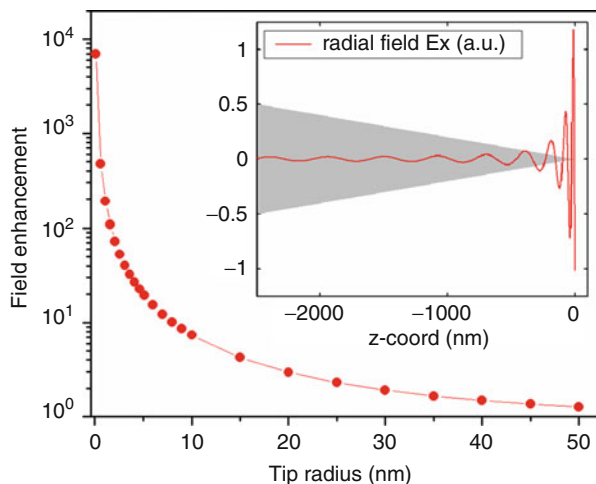
Fig. 19.26 Electric field enhancement at the cone tip as a function of the curvature radius of the tip itself. The calculations for the tip enhancement are based on the method proposed in Ref. [1]; the continuous line is just a guideline for eyes. As we can see from the graph, the curvature radius at the tip is a crucial parameter, and only for curvature radius below 10 nm significant enhancement factors are achieved. Keep in mind that Raman enhancement scales as the fourth power of the field enhancement factor (Picture kindly rearranged from Ref [3])

reported in Fig. 19.27, this device has been used to simultaneously record topographic and chemical data from a well-known sample [3]. The AFM cantilever has been mounted on an AFM machine and an infrared laser has been used to record the deflection of the AFM cantilever, thus recording the topography of the sample as usually done in AFM measurements. At the same time Raman measurements in transmission configuration are recorded. A laser light with wavelength $\lambda = 532$ nm has been focused on the photonic crystal cavity with a standard microscope condenser lens (numerical aperture NA = 0.35 and working distance of 70 mm), thus producing coupling between the far-field laser light and the base of the metal cone. Surface plasmon polaritons are excited at the base of the cone and propagate towards the tip, experiencing adiabatic slowing of the velocity and plasmon accumulation at the tip. This in turn produces a high enhancement of the electric field, which generates enhanced Raman signal from the sample that is close to the tip during the AFM measurement. Finally, the Raman signal is collected by a high numerical aperture objective placed at the bottom of the sample (immersion oil objective with NA = 1.4). This is made possible by the fact that the well-known sample is a transparent one and it consists of gratings of silicon nanocrystals having different pitches (from several micrometers to a sub-micrometer scale) obtained by laser melting of a silica substrate previously fabricated by plasma-enhanced chemical vapor deposition. The resulting sample is constituted by alternate stripes of SiO_x (taller) and Si (smaller) on a base of SiO_x substrate. The chemical mapping
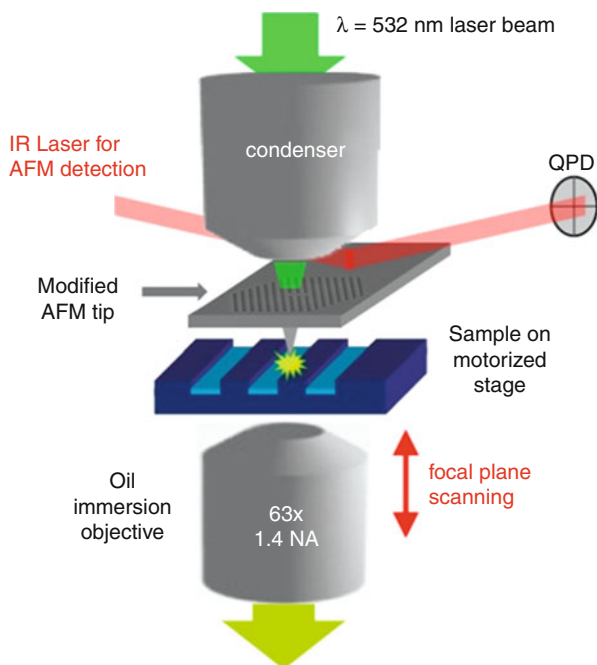
Fig. 19.27 Schematic picture of the experiment for simultaneous topographical and chemical mapping with high spatial resolution. An infrared laser is reflected by the *AFM* cantilever, and a quadrant photodiode (*QPD*) allows for measuring the cantilever deflection, thus measuring the topography of the sample as in *AFM* measurements. The tapping mode has been used for *AFM* recording. At the same time, a 532 nm wavelength laser is focused through a condenser lens on the photonic crystal cavity, thus exciting plasmon polaritons at the nanocone base. Polaritons propagate till the cone tip, where plasmon accumulation generates an intense and very narrow (below the diffraction limit) light spot. This light produces Raman scattering on the sample that is close to the tip, and the Raman signal is collected by a high numerical aperture objective, in transmission mode (Picture kindly reprinted from Ref. [3])

achieved by means of Raman spectroscopy depends on the fact that Si has a characteristic Raman peak at 520 cm^{-1} missing in SiO$_x$ material.

To test the spatial resolution of this device for chemical mapping, the best fabricated tapered waveguide with an apex radius of curvature of 2.5 nm has been used. In this case, the expected theoretical field enhancement is $\approx$100 (Raman enhancement $\approx 1 \times 10^8$). The AFM–Raman setup has been operated in tapping mode and wet conditions (in distilled water) to measure simultaneously the topography and Raman intensity map by scanning the sample and acquiring Raman data across the lithographic structures, point by point. Figure 19.28 shows the results of simultaneous topographic and chemical mapping: it is clear from the topographical data that we are crossing the edge between a SiO$_x$ stripe and a Si one, and at the same time, the collected Raman spectra show the transition between the distinctive Si spectra and the SiO$_x$ ones (collected spectral region between 400 and
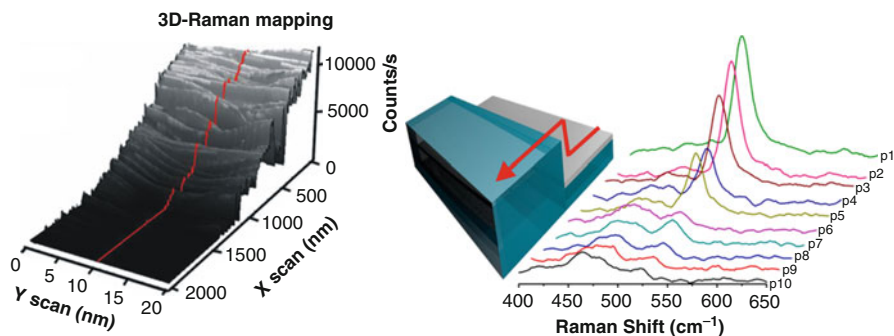
Fig. 19.28 Simultaneous topographic (*AFM*) and chemical (Raman spectroscopy) mapping of a test sample constituted by alternating stripes of SiO_x and Si with different height. On the *left* is the result of the topographic mapping, and on the *right* is the result of the chemical mapping. In the chemical mapping, the transition from Si, with a sharp Raman peak at 520 cm^{-1}, to SiO_x which exhibits a broader band at 480 cm^{-1} (and no Si peak) is clear. The scanning stepsize was 220 nm along the direction perpendicular to the stripes (Picture kindly reprinted from Ref. [3])

650 cm^{-1}). In Fig. 19.28, the AFM scan stepsize is 220 nm. A much higher spatial resolution acquisition is reported in Fig. 19.29, where the Si/SiO_x stripes have a much smaller pitch (at the sub-micrometer scale). In this case we center the Raman spectra at 520 cm^{-1} (collected spectral region between 500 and 540 cm^{-1}), and the presence of the peak at 520 cm^{-1} is an evidence of Si material. As we can see from the figure, as the topographical height of the sample decreases, the 520 cm^{-1} peak intensity increases, as expected when passing from SiO_x (taller) to Si (smaller) stripe. In this case the AFM scan stepsize is 7 nm, thus meaning that chemical mapping by means of an optical technique, Raman spectroscopy, has been achieved with a spatial resolution much beyond the diffraction limit of light.

As aforementioned, a similar device has been embedded also in a superhydrophobic pattern (Fig. 19.24) [93]. In this case the final goal is not the mapping of a surface, but the Raman-enhanced signal in a well-defined position. In this kind of device, a solution drop with a largely diluted solute is deposited on the superhydrophobic pattern. Due to the large contact angle, the drop of solution will stay only on the top of the pillars without wetting the bottom surface. As evaporation of the drop goes on, the diluted solute will be concentrated and finally released only on the top of few pillars. In the present case, where a sharp cone is present in the position of one of the pillar, the drop will concentrate the solute mainly on top of the cone apex, as thoroughly discussed in the supplementary material of Ref. [93]. Once the solution has been concentrated on top of this Raman enhancing antenna, it will be possible to detect very small starting concentrations, bringing molecules, which in the starting solution were not possible to probe, to a detectable level.

We have tested this device with a 1 fM lysozyme solution. More in details, a 160 nl droplet has been deposited on the superhydrophobic pattern
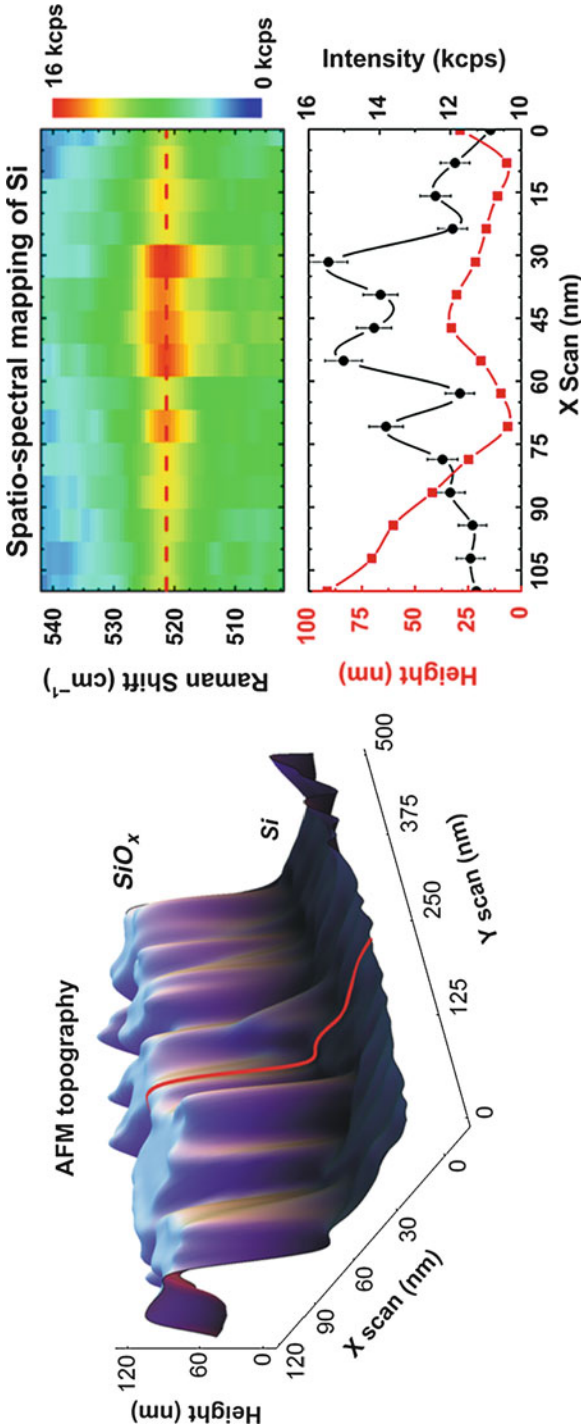
Fig. 19.29 Simultaneous topographic (*AFM*) and chemical (Raman spectroscopy) mapping of a test sample constituted by alternating stripes of SiO$_x$ and Si with different height. On the *left* is the result of the topographic mapping. On the *right* is a color intensity map (*top*) of the 520 cm^{-1} Raman peak, typical of Si, as a function of the position; in the *bottom*, a graph showed the peak intensity together with the height profile data, showing that the Si peak is present where the sample height is smaller (corresponding to the Si stripe). The scanning stepsize was 7 nm along the direction perpendicular to the stripes, much beyond the diffraction limit of light (Picture kindly reprinted from Ref. [3])
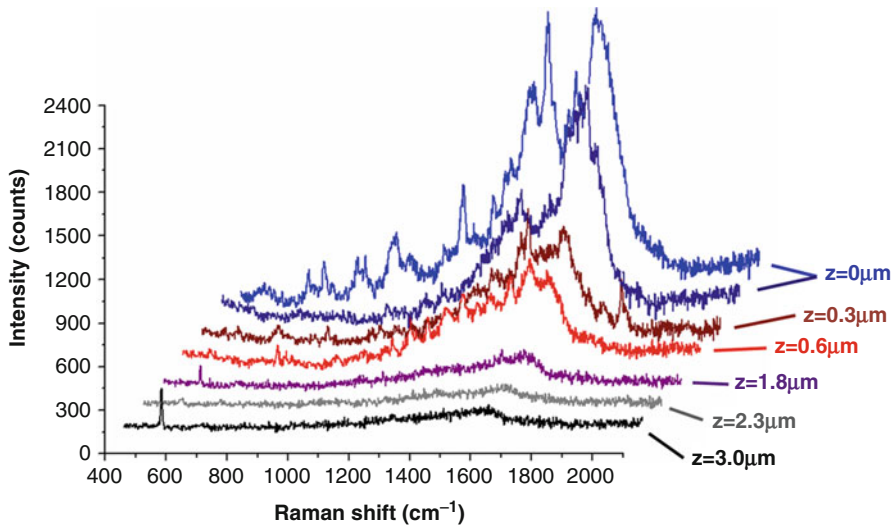
Fig. 19.30 Raman spectra recorded on 1 fM solution of lysozyme evaporated on top of a plasmonic cone-shaped nano-waveguide. The evaporation process took advantage of the presence of a micropatterned superhydrophobic surface. When the illumination and detection condition are the optimum, termed $z = 0$ μm, we have enhanced Raman signal with intense bands; as soon as we move far from the optimal conditions, the Raman bands soon decrease, and they are completely lost for z = 3.0 μm

by means of a microinjector coupled to a micromanipulator for aligning to the center of the pattern. At the end of the evaporation process that lasts few seconds due to the small amount of liquid, lysozyme accumulates on the silver cone. Only molecules very close to the tip are probed by Raman scattering, as the electric field enhancement soon decreases when moving from the tip apex. Far-field laser light at $\lambda = 532$ nm is coupled with the diffraction grating fabricated on one side of the largest Si cone (see Fig. 19.25). This excites surface plasmon polaritons in the thin silver layer, and they propagate till the cone apex. As before the cone is properly shaped in order to produce an adiabatic compression of polaritons with an enhanced electric field at the apex. For a tip with a curvature radius of 10 nm the expected amplification factor is ∼35, which leads to a Raman enhancement of 1.5×10^6. The few lysozyme molecules deposited on the tip are probed by means of this enhanced Raman scattering, as a function of the focused laser along the z direction (which is the one of the optical axis). The recorded Raman spectra exhibit intense Raman bands when the coupling with the grating and the detection conditions are optimized, named $z = 0$ μm (see Fig. 19.30). When moving far from the polaritons excitation, i.e., from the coupling with the grating, the Raman bands soon decrease, and in a 3 μm range from the optimal condition of illumination, the Raman signal is completely lost.

Large Area Ordered and Reproducible SERS Substrate Based on Anodic Porous Alumina Template

Surface-enhanced Raman spectroscopy (SERS), an analytical technique, gained a lot of attraction in recent years due to its application in a wide range of fields. However, some drawbacks, such as lack of SERS enhancement for large areas and existence of random distribution of the hot spots, made SERS substrates not employed very often. A few works, reported in the past, overcame the hindering concerns by producing plasmonic devices following different techniques such as nanosphere lithography [117] and hole-mask lithography [118]. Herein, a new technique based on a gold-coated anodic porous alumina (gold APA) template is proposed to fabricate a convenient large-area SERS substrate. The porosity, wall thickness, and pore size of the APA template can be modulated by different fabrication parameters such as the electrolyte solution and etching time [119].

APA substrates with periodic hexagonal structures were fabricated by following different protocols, which allowed us to obtain different pore diameters and pore wall thickness. The fabricated APA substrates were used as a template for the preparation of nano-patterned gold surface, obtained by gold film deposition of 25 nm thickness, covering the APA features. The novelty of this work relies on the fabrication of reproducible large-area SERS substrates with wall thickness and pore-size down to 15 and 36 nm, respectively [64, 120]. The surface morphology of the SERS device was investigated by means of scanning electron microscopy (SEM) whereas the functioning as a SERS substrate was examined for different fluorescent molecules (cresyl violet (CV) and rhodamine6G (Rd6G)) after depositing them by chemisorption technique. The gold APA substrates were demonstrated to be an effective universal SERS substrate for analytical purpose.

APA substrates were prepared at $+7\,°C$ bath temperature with electrolyte stirring with aluminum sheet (250 μm) as the anode and platinum as the cathode, in the same electrochemical cell configuration as explained [121] (see Fig. 19.31). Firstly, the Al foil was electro-polished in a 1:5 v/v aqueous solution of $HClO_4$:C_2H_5O-H. A fast anodization process (1 h) was carried out in aqueous solutions of different acids (phosphoric, oxalic, and sulfuric acid) in order to achieve different pore diameter/wall thickness. A periodic structure can be observed on aluminum surface after removing the anodic oxide layer using the solution of phosphoric acid and chromic acid. Further, slow anodization during overnight was performed to attain a homogeneously formed pore structures on the aluminum foil.

In this work, the substrates were categorized in three parts: (a) large pore-size APA substrate utilizing H_3PO_4 acid (APA_Ph) at 130 V, (b) medium-sized pore APA using $H_2C_2O_2$ (APA_Ox) at 40 V, and (c) small-sized pore APA using H_2SO_4 (APA_Sul) at 25 V.

In order to make APA substrate as plasmonic devices, gold with 25 nm thickness was thermally evaporated from a tungsten boat onto these substrates (APA_Ph, APA_Ox, and APA_Sul). The substance of interest was deposited over resulting gold-coated APA substrates (termed 'Au-APA_Ph,' 'Au-APA_Ox,' and 'Au-APA_Sul,' respectively) using a chemisorption technique. In this process,
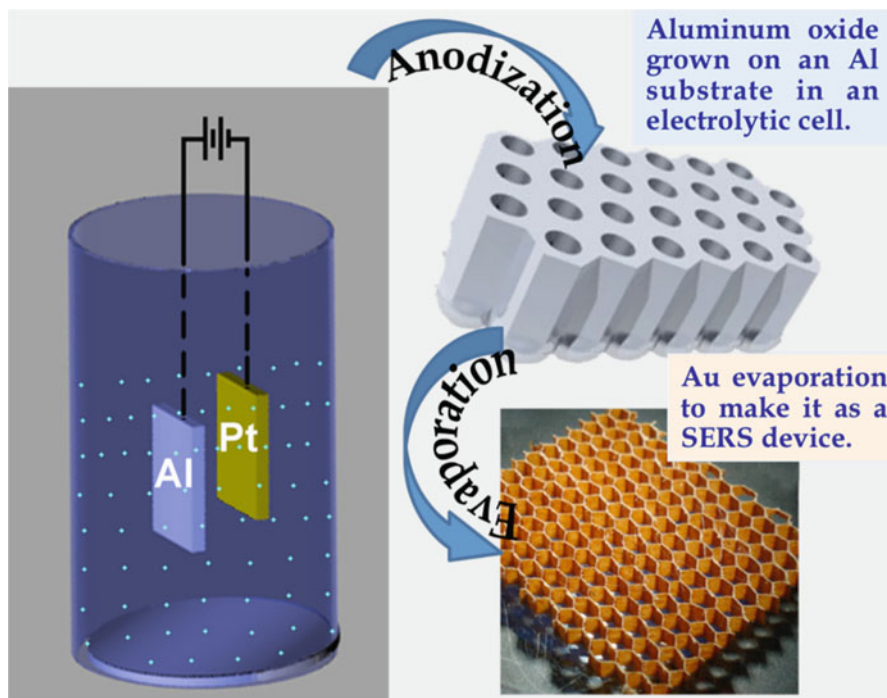
Fig. 19.31 Fabrication procedure of Au-APA substrate

the substrate was dipped into a solution containing the molecule of interest. After incubation, each substrate was removed from the solution and gently rinsed to remove excess molecules not attached directly to the metal surface. Thereafter, the samples were dried in N_2 flow and finally stored in a desiccator before SERS measurements. CV and Rd6G (10^{-6} M), fluorescent dyes, were employed as probe molecules.

SEM measurements (JSM-7500FA, Jeol, Japan) were also performed on the APA substrates, keeping a 15 kV acceleration voltage for the primary electron beam and collecting the topographic signal from the secondary electrons. For imaging of the specimens before gold coating the SEM was operated in low vacuum conditions (70–120 Pa residual chamber pressure) in order to prevent major static charging effects due to the impinging electron beam. A cartoon of honeycomb structure and SEM images of APA substrates before and after gold deposition are shown in Fig. 19.32.

SERS measurements were carried out by means of an inVia (Renishaw, New Mills, UK) microspectrometer, with a spectral resolution of 1.10 cm^{-1} with the help of a holographic grating of 1,800 grooves/mm. The samples were excited using the 633 nm laser wavelength (laser power 5.5–55 mW) in backscattering configuration through a $100\times$ objective (NA-0.90) and with an accumulation time of 20 s. Spectral data were analyzed using Renishaw WiRE software 3.0.
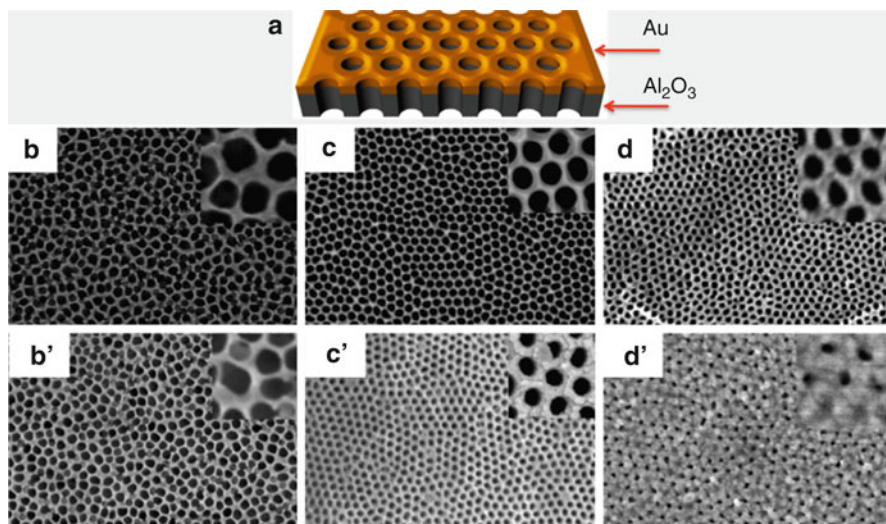
Fig. 19.32 (**a**) Cartoon image of Au-APA substrate. All the substrates before (**b–d**) and after (**b'–d'**) gold deposition are shown

SEM images of all the Au-APA samples before and after gold deposition are shown in Fig. 19.32b–d and Fig. 19.32b'–d', respectively. CV and Rd6G, fluorescent dye molecules, were deposited using chemisorption technique to investigate the SERS activity of Au-APA substrates. The optical absorption spectra of both the molecules are shown in Fig. 19.32a.

Firstly, Raman spectrum of the bare substrate before depositing any molecule was performed and found a Raman spectrum within the noise level without any Raman peak (shown in inset of Fig. 19.33b), confirming the substrate free of any contamination. SERS spectra of CV molecules, deposited over different Au-APA substrates, are shown in Fig. 19.33b. In all the SERS spectra of the CV molecule, performed on Au-APA substrates with different pore diameters (15–160 nm) and wall thicknesses (36–100 nm) (Fig. 19.33b), the characteristic vibrational bands of CV are observed in the spectral range of 300–1,300 cm^{-1} [122]. Intense Raman bands centered at around 348, 591, 675, and 1,186 cm^{-1} can be attributed to the out-of-plane skeleton deformation, combination of in-plane N–H$_2$ and ring bending, ring deformation, and combination of N–H$_2$ rocking and C–H$_x$ rocking, respectively [122, 123]. When the pore size/wall thickness of Au-APA substrate decreases from 160 nm/100 nm to 60 nm/40 nm, a significant increase in SERS intensity for the CV bands is observed with respect to the flat Au surface (inset of Fig. 19.33b). The band intensity, centered at 591 cm^{-1}, increases abruptly. It is shown in the inset of Fig. 19.33b the band intensity (591 cm^{-1}) variation for all the Au-APA substrates. It is found, finally, that when the pore size/wall thickness is around 100 nm/40 nm, the substrate behaves in its best conditions. SERS measurements were performed at different points of the large-area SERS device, showing
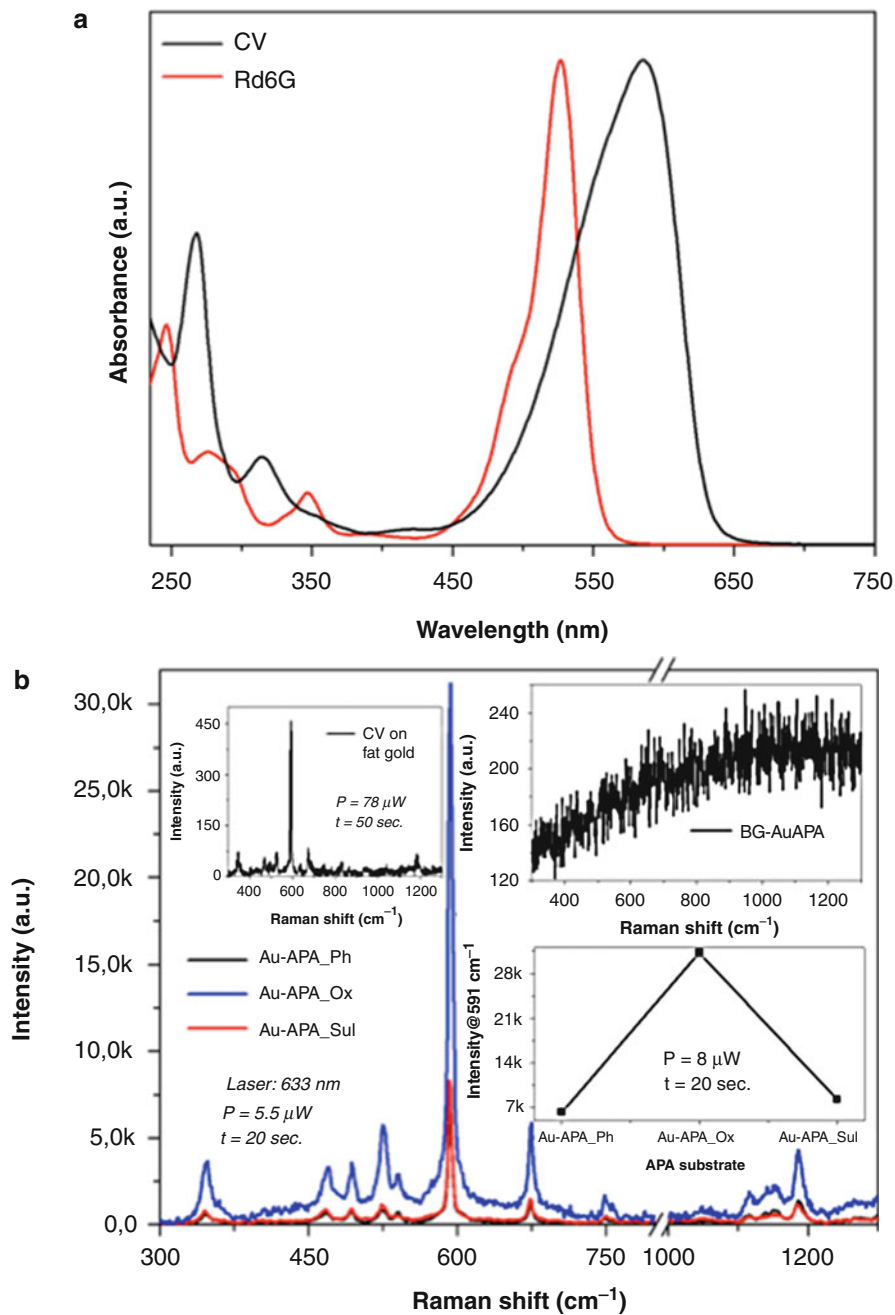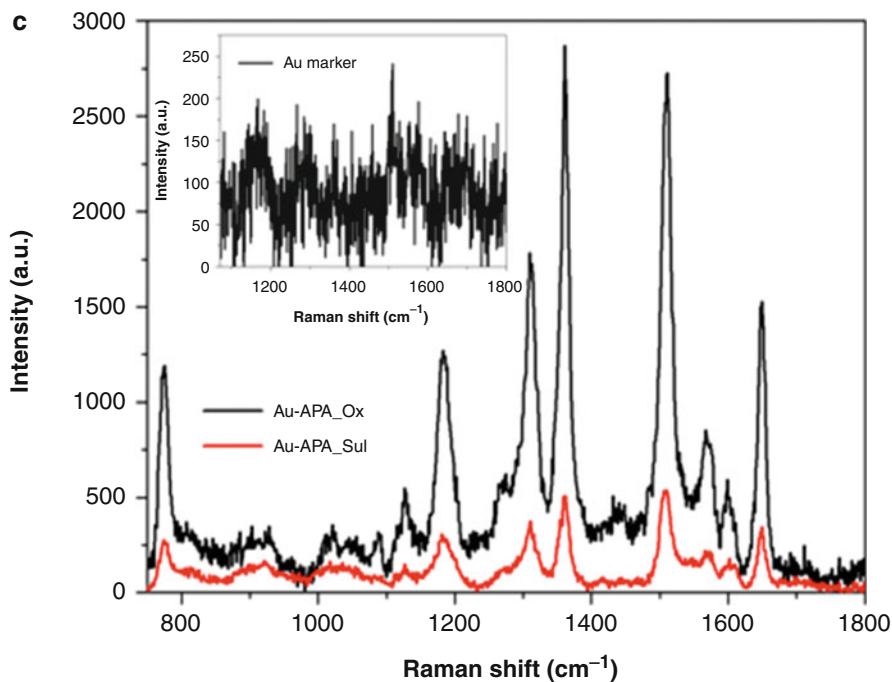
Fig. 19.33 (continued)

Fig. 19.33 (**a**) Optical absorption spectra for CV and Rd6G fluorescent molecules in the range of 230–750 nm. (**b**) SERS spectra of CV in the range of 300–1,300 cm^{-1}, deposited over all Au-APA substrates, in the inset bare SERS device Raman spectrum, reference measurement of CV on flat Au marker and the intensity variation of 591 cm^{-1} for all the Au-APA substrates are shown. (**c**) SERS spectra of Rd6G, deposited over Au-APA_Ox and Au-APA_Sul, are shown, in the inset, reference measurement of Rd6G deposited over Au marker is also shown

reproducible behavior of the device. This confirms the generation of hot spots in a controlled manner [64]. Considering this peak as a reference band to calculate the SERS enhancement factor, it is found to be around 10^4 with respect to the flat Au marker.

Furthermore, the substrates were investigated for Rd6G fluorescent dye molecule in order to demonstrate its efficiency for different molecules. Reference measurement for Rd6G molecule, deposited over flat Au marker, is shown in the inset of Fig. 19.33c. It shows few weak bands in the range of 1,000–1,800 cm^{-1}. SERS measurements were performed for the same, deposited over different Au-APA substrates (Fig. 19.33c). Figure 19.33 shows various characteristic peaks of Rd6G molecule within the spectral range [44, 124, 125]. In this case also, it is found that Au-APA_Ox is demonstrating its SERS enhancement much better than other Au-APA substrates.

To summarize, various home-built Au-APA substrates with varying pore size and wall thickness were utilized for large-area SERS substrates. CV and Rd6G fluorescent dye molecules were deposited using a chemisorption technique, through

which a monolayer of molecules can be achieved. It is observed that the AuAPA2 substrate (pore size = 59 ± 9, wall thickness = 40 ± 9) demonstrates the maximum SERS enhancement 'G'. The respective SERS enhancement factor 'G' is estimated to be 10^4 with respect to the flat Au marker. Additionally, the sensing efficacy of the fabricated SERS devices on different dyes and proteins (CV, Rd6G, and GFP in our case) opens the way for real application as a biosensor. Further research should be made in order to optimize 'G' on the basis of the substrate parameters of pore size, wall thickness, and thickness of the gold coating. The easy and inexpensive processing required for APA SERS fabrication would also make these substrates disposable, opening the way to their large-scale applications.

References

1. De Angelis F, Patrini M, Das G, Maksymov I, Galli M, Businaro L, Andreani LC, Di Fabrizio E (2008) A hybrid plasmonic-photonic nanodevice for label-free detection of a few molecules. Nano Lett 8:2321–2327
2. Zhang W, Cui X, Martin OJF (2009) Local field enhancement of an infinite conical metal tip illuminated by a focused beam. J Raman Spectrosc 40:1338–1342
3. De Angelis F, Das G, Candeloro P, Patrini M, Galli M, Bek A, Lazzarino M, Maksymov I, Liberale C, Andreani LC, Di Fabrizio E (2010) Nanoscale chemical mapping using three-dimensional adiabatic compression of surface plasmon polaritons. Nat Nanotechnol 5:67–72
4. Babadjanyan AJ, Margaryan NL, Nerkararyan Kh V (2000) Superfocusing of surface polaritons in the conical structure. J Appl Phys 87:3785–3788
5. Vaccaro L, Aeschimann L, Staufer U, Herzig HP, Dandliker R (2003) Propagation of the electromagnetic field in fully coated near-field optical probes. Appl Phys Lett 83:584–586
6. Ding W, Andrews SR, Maier SA (2007) Internal excitation and superfocusing of surface plasmon polaritons on a silver-coated optical fiber tip. Phys Rev A 75:063822
7. Neacsu CC, Bergewer S, Olmon RL, Saraf LV, Ropers C, Raschke MB (2010) Near-field localization in plasmonic superfocusing: a nanoemitter on a tip. Nano Lett 10:592–596; Gramotnev DK, Vogel MW, Stockman MI (2008) Optimized nonadiabatic nanofocusing of plasmons by tapered metal rods. J Appl Phys 104:034311
8. Lee JS, Han S, Shirdel J, Koo S, Sadiq D, Lienau C, Park N (2011) Superfocusing of electric or magnetic fields using conical metal tips: effect of mode symmetry on the plasmon excitation method. Opt Express 19:12342–12347
9. Proietti Zaccaria R, Alabastri A, De Angelis F, Das G, Liberale C, Toma A, Giugni A, Razzari L, Malerba M, Sun HB, Di Fabrizio E (2012) Fully analytical description of adiabatic compression in dissipative polaritonic structures. Phys Rev B 86:035410
10. Proietti Zaccaria R, De Angelis F, Toma A, Razzari L, Alabastri A, Das G, Liberale C, Di Fabrizio E (2012) Surface plasmon polariton compression through radially and linearly polarized source. Opt Lett 37:545–547
11. Corio P, Brown SDM, Marucci A, Pimenta MA, Kneipp K, Dresselhaus G, Dresselhaus MS (2000) Surface-enhanced resonant Raman spectroscopy of single-wall carbon nanotubes adsorbed on silver and gold surfaces. Phys Rev B 61:13202–13211
12. Davis TJ, Gomez DE, Vernon KC (2010) Evanescent coupling between a Raman-active molecule and surface plasmons in ensembles of metallic nanoparticles. Phys Rev B 82:205434
13. Fazio B, D'Andrea C, Bonaccorso F, Irrera A, Calogero G, Vasi C, Gucciardi PG, Allegrini M, Toma A, Chiappe D, Martella C, Buatier de Mongeot F (2011) Re-radiation

enhancement in polarized surface-enhanced resonant raman scattering of randomly oriented molecules on self-organized gold nanowires. ACS Nano 5:5945–5956

14. Chou SY, Ding W (2013) Ultrathin, high-efficiency, broad-band, omniacceptance, organic solar cells enhanced by plasmonic cavity with subwavelength hole array. Opt Express 21:A60–A76

15. Ojea-Jime'nez I, Lo'pez X, Arbiol J, Puntes V (2012) Citrate-coated gold nano-particles as smart scavengers for mercury(II) removal from polluted waters. ACS Nano 6:2253–2260

16. Harris C, Kamat PV (2010) Photocatalytic events of CdSe quantum dots in confined media. Electrodic behavior of coupled platinum nanoparticles. ACS Nano 4:7321–7330

17. Persano A, De Giorgi M, Fiore A, Cingolani R, Manna L, Cola A, Krahne R (2010) Photoconduction properties in aligned assemblies of colloidal CdSe/CdS nanorods. ACS Nano 4:1646

18. Vasilantonakis N, Terzaki K, Sakellari I, Purlys V, Gray D, Soukoulis CM, Vamvakaki M, Kafesaki M, Farsar M (2012) Three-dimensional metallic photonic crystals with optical bandgaps. Adv Mater 24:1101

19. Christ A, Zentgraf T, Kuhl J, Tikhodeev SG, Gippius NA, Giessen H (2004) Optical properties of planar metallic photonic crystal structures: experiment and theory. Phys Rev B 70:125113

20. Neubrech F, Weber D, Katzmann J, Huck C, Toma A, Di Fabrizio E, Pucci A, Härtling T (2012) Infrared optical properties of nanoantenna dimers with photochemically narrowed gaps in the 5 nm regime. ACS Nano 6:7326

21. Razzari L, Toma A, Shalaby M, Clerici M, Proietti Zaccaria R, Liberale C, Marras S, Al-Naib IAI, Das G, De Angelis F, Peccianti M, Falqui A, Ozaki T, Morandotti R, Di Fabrizio E (2011) Extremely large extinction efficiency and field enhancement in terahertz resonant dipole nanoantennas. Opt Express 19:26088

22. Eigler D (1990) A new role for the STM. Science 250:1340–1341

23. Mock JJ, Barbic M, Smith DR, Schultz DA, Schultz S (2002) Shape effects in plasmon resonance of individual colloidal silver nanoparticles. J Chem Phy 116:6755–6759

24. Dasary SSR, Singh AK, Senapati D, Yu H, Ray PC (2009) Gold nanoparticle based label-free SERS probe for ultrasensitive and selective detection of trinitrotoluene. J Am Chem Soc 131:13806–13812

25. Alvarez-Puebla RA, Zubarev ER, Kotov NA, Liz-Marzan LM (2012) Self-assembled nanorod supercrystals for ultrasensitive SERS diagnostics. Nano Today 7:6–9

26. Sans V, Moskalenko A, Wilson K, Kozhevin V, Yavsin D, Kuzmin I, Gurevich S, Lapkin A (2011) SE(R)RS devices fabricated by a laser electrodispersion method. Analyst 136:3295–3302

27. Toma A, Chiappe D, Boragno C, Buatier de Mongeot F (2010) Self-organized ion-beam synthesis of nanowires with broadband plasmonic functionality. Phys Rev B 81:165436

28. Belardini A, Larciprete MC, Centini M, Fazio E, Sibilia C, Chiappe D, Martella C, Toma A, Giordano M, Buatier de Mongeot F (2011) Circular dichroism in the optical second-harmonic emission of curved gold metal nanowires. Phys Rev Lett 107:257401

29. Fazio B, D'Andrea C, Bonaccorso F, Irrera A, Calogero G, Vasi C, Gucciardi PG, Allegrini M, Toma A, Chiappe D, Martella C, Buatier de Mongeot F (2011) Re-radiation enhancement in polarized surface-enhanced resonant Raman scattering of randomly oriented molecules on self-organized gold nanowires. ACS Nano 5:5945

30. Chung AJ, Huh YS, Erickson D (2011) Large area flexible SERS active substrates using engineered nanostructures. Nanoscale 3:2903–2908

31. Kumar A, Hwang JH, Kumar S, Nam JM (2013) Tuning and assembling metal nanostructures with DNA. Chem Commun 49:2597–2609

32. Qiu T, Chu PK (2008) Self-selective electroless plating: an approach for fabrication of functional 1D nanomaterials. Mater Sci Eng R 61:59–77

33. Gao J, Tang F, Ren J (2005) Electroless nickel deposition on amino-functionalized silica spheres. Surf Coat Technol 200:2249–2252

34. Goia D, Matijevic E (1998) Preparation of monodispersed metal particles. New J Chem 22:1203–1215

35. Peng K, Zhu J (2004) Morphological selection of electroless metal deposits on silicon in aqueous fluoride solution. Electrochim Acta 49:2563–2568

36. Yang Y, Shi J, Kawamura G et al (2008) Preparation of Au-Ag, Ag-Au core-shell bimetallic nanoparticles for surface-enhanced Raman scattering. Scr Mater 58:862–865

37. Ye W, Chengmin S, Jifa T et al (2008) Self-assembled synthesis of SERS-active silver dendrites and photoluminescence properties of a thin porous silicon layer. Electrochem Commun 10:625–629

38. Palermo V, Jones D (2001) Morphological changes of the Si [100] surface after treatment with concentrated and diluted HF. Mater Sci Semicon Proc 4:437–441

39. Yae S, Nasu N, Matsumoto K et al (2007) Nucleation behavior in electroless displacement deposition of metals on silicon from hydrofluoric acid solutions. Electrochim Acta 53:35–41

40. Ye W, Chang Y, Ma C et al (2007) Electrochemical investigation of the surface energy: effect of the HF concentration on electroless silver deposition onto p-Si (111). Appl Surf Sci 253:3419–3424

41. Luk'yanchuk B, Zheludev NI, Maier SA et al (2010) The Fano resonance in plasmonic nanostructures and metamaterials. Nat Mater 9:707–715

42. Tao AR, Habas S, Yang P (2008) Shape control of colloidal metal nanocrystals. Small 4:310–325

43. Le Ru E, Etchegoin PG, Grand J et al (2008) Surface enhanced Raman spectroscopy on nanolithography-prepared substrates. Curr Appl Phys 8:467–470

44. Coluccio ML, Das G, Mecarini F et al (2009) Silver-based surface enhanced Raman scattering (SERS) substrate fabrication using nanolithography and site selective electroless deposition. Microelectron Eng 86:1085–1088

45. Das G, Mecarini F, Gentile F et al (2009) Nano-patterned SERS substrate: application for protein analysis vs. temperature. Biosens Bioelectron 24:1693–1699

46. Zhang X, Yonzon C, Duyne R (2006) Nanosphere lithography fabricated plasmonic materials and their applications. J Mater Res 21:1083–1092

47. De Angelis F et al (2011) Emerging fabrication techniques for 3D nano-structuring in plasmonics and single molecule studies. Nanoscale 3:2689–2696

48. Ashkin A (1970) Acceleration and trapping of particles by radiation pressure. Phys Rev Lett 24:156–158

49. Emiliani V (2005) Wave front engineering for microscopy of living cells. Opt Express 13(5):1395–1405

50. Cojoc D et al (2004) Multiple optical trapping by means of diffractive optical elements. Jpn J Appl Phys 43(6B):3910–3915

51. Garbin V et al (2007) Changes in microbubble dynamics near a boundary revealed by combined optical micromanipulation and high-speed imaging. Appl Phys Lett 90:114103

52. Cojoc D et al (2007) Properties of the force exerted by filopodia and lamellipodia and the involvement of cytoskeletal components. PLoS One 2(10):e1072

53. Sun HB, Kawata S (2004) Two-photon photopolymerization and 3D lithographic microfabrication, in advances in polymer science: NMR, 3-D analysis, photopolymerization, vol 170. Springer, Berlin, pp 169–273

54. Maruo S et al (2003) Force-controllable, optically driven micromachines fabricated by single-step two-photon microstereolithography. J Microelectromech Syst 12:533–539

55. Liberale C et al (2010) Micro-optics fabrication on top of optical fibers using two-photon lithography. IEEE Photonics Technol Lett 22:474–476

56. Takada K et al (2005) Improved spatial resolution and surface roughness in photopolymerization-based laser nanowriting. Appl Phys Lett 86:071122

57. Fuchs R (1975) Theory of the optical properties of ionic crystal cubes. Phys Rev B 11(4):1732–1740
58. Chirumamilla M et al (2012) Optimization and characterization of Au cuboid nanostructures as a SERS device for sensing applications. Microelectron Eng 97:189–192
59. Kreibig U, Vollmer M (1995) Optical properties of metal clusters, vol 25. Springer, Berlin
60. Kelly KL et al (2002) The optical properties of metal nanoparticles: the influence of size, shape, and dielectric environment. J Phys Chem B 107(3):668–677
61. Banaee MG, Crozier KB (2010) Mixed dimer double-resonance substrates for surface-enhanced Raman spectroscopy. ACS Nano 5(1):307–314
62. Chu Y, Banaee MG, Crozier KB (2010) Double-resonance plasmon substrates for surface-enhanced Raman scattering with enhancement at excitation and stokes frequencies. ACS Nano 4(5):2804–2810
63. Gopinath A et al (2009) Deterministic aperiodic arrays of metal nanoparticles for surface-enhanced Raman scattering (SERS). Opt Express 17(5):3741–3753
64. Das G et al (2012) Fabrication of large-area ordered and reproducible nanostructures for SERS biosensor application. Analyst 137(8):1785–1792
65. Rakic AD et al (1998) Optical properties of metallic films for vertical-cavity optoelectronic devices. Appl Opt 37(22):5271–5283
66. Johansson P, Xu H, Käll M (2005) Surface-enhanced Raman scattering and fluorescence near metal nanoparticles. Phys Rev B 72(3):035427
67. Witten T, Sander L (1981) Diffusion-limited aggregation, a kinetic critical phenomenon. Phys Rev Lett 47:1400–1403
68. Zhang Z, Lagally M (1997) Atomistic process in the early stages of thin-film growth. Science 276:377–383
69. Dawkins R, Ben-Avraham D (2001) Computer simulations of diffusion-limited reactions. Comput Sci Eng 3:72–76
70. Gentile F, Coluccio M, Toma A et al (2012) Electroless deposition dynamics of silver nanoparticles clusters: a diffusion limited aggregation (DLA) approach. Microelectron Eng 98:359–362
71. Witten T, Sander L (1983) Diffusion-limited aggregation. Phys Rev B 27:5686–5697
72. Hill SC, Alexander JID (1997) Modified diffusion-limited aggregation simulation of electrodeposition in two dimensions. Phys Rev E 56:4317–4327
73. Wu H, Lattuada M, Sandkuhler P et al (2003) Role of sedimentation and buoyancy on the kinetics of diffusion limited colloidal aggregation. Langmuir 19:10710–10718
74. Persson M, Yasuda H, Albergel J et al (2001) Modeling plot scale dye penetration by a diffusion limited aggregation (DLA) model. J Hydrol 250:98–105
75. Howells AR, Hung L, Chottiner GS et al (2002) Annealing of defects in crystals. Solid State Ion 150:53–62
76. Qiu T, Wu X, Siu G et al (2005) Self-assembled growth and green emission of gold nano whiskers. Appl Phys Lett 87:223115
77. Kuhn A, Argoul F (1995) Diffusion-limited kinetics in thin-gap electroless deposition. J Electroanal Chem 397:93–104
78. Qiu T, Wu X, Mei Y et al (2005) Self-organized synthesis of silver dendritic nanostructures via an electroless metal deposition method. Appl Phys A 81:669–671
79. Liu F-M, Green M (2004) Efficient SERS substrates made by electroless silver deposition into patterned silicon structures. J Mater Chem 14:1526–1532
80. Saltzmann M (2001) In drug delivery, vol pp. Oxford University Press, Oxford
81. Decuzzi P, Gentile F, Granaldi A et al (2007) Flow chamber analysis of size effects in the adhesion of spherical particles. Int J Nanomedicine 2:689–696
82. Haynes WM (1998) CRC handbook of chemistry and physics. CRC Press, Boulder
83. Gentile F, Battista E, Accardo A et al (2011) Fractal structure can explain the increased hydrophobicity of nanoporous silicon films. Microelectron Eng 88:2537–2540

84. Gentile F, Rocca RL, Marinaro G et al (2012) Differential cell adhesion on mesoporous silicon substrates. ACS Appl Mater 4:2903–2911

85. Meakin P (1984) Diffusion controlled deposition on surfaces: cluster size distribution, interface exponents, and other properties. Phys Rev B 30:4207–4214

86. Racz Z, Vicsek T (1983) Diffusion controlled deposition: cluster statistics and scaling. Phys Rev Lett 51:2382–2385

87. Gentile F, Moretti M, Limongi T et al (2012) Direct imaging of DNA fibers: the visage of double helix. Nano Lett 12:6453–6458

88. Han W, Byun M, Lin Z (2011) Assembling and positioning latex nanoparticles via controlled evaporative self-assembly. J Mater Chem 21:16968

89. Hejazi V, Nosonovsky M (2012) Wetting transitions in two-, three-, and four-phase systems. Langmuir 28:2173–2180

90. Cui Y (2001) Nanowire nanosensors for highly sensitive and selective detection of biological and chemical species. Science 293:1289–1292

91. Accardo A, Tirinato L, Altamura D, Sibillano T, Giannini C, Riekel C, Di Fabrizio E (2013) Superhydrophobic surfaces allow probing of exosome self organization using X-ray scattering. Nanoscale 5:2295–2299

92. Berry SM, Pabba S, Crest J et al (2011) Characterization and modeling of direct-write fabrication of microscale polymer fibers. Polymer 52:1654–1661

93. De Angelis F, Gentile F, Mecarini F et al (2011) Breaking the diffusion limit with super-hydrophobic delivery of molecules to plasmonic nanofocusing SERS structures. Nat Photonics 5:682–687

94. Su B, Wang S, Wu Y et al (2012) Small molecular nanowire arrays assisted by superhydrophobic pillar-structured surfaces with high adhesion. Adv Mater 24:2780–2785

95. Accardo A, Gentile F, Mecarini F et al (2010) In situ X-ray scattering studies of protein solution droplets drying on micro- and nanopatterned superhydrophobic PMMA surfaces. Langmuir 26:15057–15064

96. Tucker TJ (1961) Behavior of exploding gold wires. J Appl Phys 32:1894

97. Willander M, Nur O, Zhao QX et al (2009) Zinc oxide nanorod based photonic devices: recent progress in growth, light emitting diodes and lasers. Nanotechnology 20:332001

98. Xu S, Wang ZL (2011) One-dimensional ZnO nanostructures: solution growth and functional properties. Nano Res 4:1013–1098

99. Atanasova P, Thomas Weitz R, Gerstel P et al (2009) DNA-templated synthesis of ZnO thin layers and nanowires. Nanotechnology 20:365302

100. Demming A, Brongersma M, Kim D-S (2012) Plasmonics in optoelectronic devices. Nano-technology 23:440201

101. Willets KA, Van Duyne RP (2007) Localized surface plasmon resonance spectroscopy and sensing. Annu Rev Phys Chem 58:267–297

102. Liu N, Tang ML, Hentschel M et al (2011) Nanoantenna-enhanced gas sensing in a single tailored nanofocus. Nat Mater 10:631–636

103. Toma A, Das G, Chirumamilla M et al (2012) Fabrication and characterization of a -nanoantenna-based Raman device for ultrasensitive spectroscopic applications. Microelectron Eng 98:424–427

104. De Angelis F, Proietti Zaccaria R, Francardi M et al (2011) Multi-scheme approach for efficient surface plasmon polariton generation in metallic conical tips on AFM-based cantilevers. Opt Express 19:22268–22279

105. Biagioni P, Huang JS, Hecht B (2012) Nanoantennas for visible and infrared radiation. Rep Prog Phys 75:024402

106. Huang J-S, Kern J, Geisler P et al (2010) Mode imaging and selection in strongly coupled nanoantennas. Nano Lett 10:2105–2110

107. Panaro S, Toma A, Proietti Zaccaria R et al (2013) Design and top-down fabrication of metallic L-shape gap nanoantennas supporting plasmon-polariton modes. Microelectron Eng. doi:10.1016/j.mee.2013.02.014

108. Chen K-P, Drachev VP, Borneman JD et al (2010) Drude relaxation rate in grained gold nanoantennas. Nano Lett 10:916–922
109. Stockman MI (2004) Nanofocusing of optical energy in tapered plasmonic waveguides. Phys Rev Lett 93(13):137404(1)–137404(4)
110. Tormen M, Romanato F, Altissimo M et al (2004) Three-dimensional micro- and nanostructuring by combination of nanoimprint and X-ray lithography. J Vac Sci Technol B 22(2):766–770
111. Romanato F, Businaro L, Vaccari L et al (2003) Fabrication of 3D metallic photonic crystals by X-ray lithography. Microelectron Eng 67:479–486
112. Krauss TF, DeLaRue RM, Brand S (1996) Two-dimensional photonic-bandgap structures operating at near-infrared wavelengths. Nature 383:699–702
113. Vlasov YA, Bo XZ, Sturm JC et al (2001) On-chip natural assembly of silicon photonic bandgap crystals. Nature 414:289–293
114. Noda S, Fujita M, Asano T (2007) Spontaneous-emission control by photonic crystals and nanocavities. Nat Photonics 1:449–458
115. Van Dorp WF, Van Someren B, Hagen CW et al (2005) Approaching the resolution limit of nanometer-scale electron beam-induced deposition. Nanoletters 5(7):1303–1307
116. Gentile F, Das G, Coluccio ML et al (2010) Ultra low concentrated molecular detection using super hydrophobic surface based biophotonic devices. Microelectron Eng 87:798–801
117. Anker JN et al (2008) Biosensing with plasmonic nanosensors. Nat Mater 7:442
118. Shegai T et al (2012) Directional scattering and hydrogen sensing by bimetallic Pd–Au nanoantennas. Nano Lett 12:2464–2469
119. Parkhutik VP, Shershulsky VI (1992) Theoretical modelling of porous oxide growth on aluminium. J Phys D Appl Phys 25:1258
120. Das G et al (2012) Surface enhanced Raman scattering substrate based on gold-coated anodic porous alumina template. Microelectron Eng 97:383
121. Salerno M, Patra N, Cingolani R (2009) Use of ionic liquid in fabrication, characterization, and processing of anodic porous alumina. Nanoscale Res Lett 4:865
122. Vogel E, Gbureck A, Kiefer W (2000) Vibrational spectroscopic studies on the dyes cresyl violet and coumarin. J Mol Struct 177:550–551
123. Kudelski A (2005) Raman studies of rhodamine 6G and crystal violet sub-monolayers on electrochemically roughened silver substrates: do dye molecules adsorb preferentially on highly SERS-active sites? Chem Phys Lett 414:271
124. Mondal B, Saha SK (2010) Fabrication of SERS substrate using nanoporous anodic alumina template decorated by silver nanoparticle. Chem Phys Lett 497:89
125. Jensen L, Schatz GC (2006) Resonance Raman scattering of rhodamine 6G as calculated using time-dependent density functional theory. J Phys Chem A 110:5973

Metal Oxide Nanocrystals and Their Properties for Application in Solar Cells

20

Ashish Dubey, Jiantao Zai, Xuefeng Qian, and Qiquan Qiao

Metal oxides have been of interest in processing, synthesis, characterization, and fabrication in both polymer-inorganic hybrid and dye-sensitized solar cells. TiO_2 [1–5], ZnO [6–9], CuO [10], and Nb_2O_5 [11] have been used as effective charge transport medium in solar cells. Different morphologies of these metal oxides have been synthesized for better charge transport across solar cells. These metal oxide nanostructures are chosen to provide large interfacial area and enhance charge transport across active layer. Metal oxide-based inorganic nanostructures can also improve environmental stability to cells, which is a major cause of degradation in cell performance. In this section, commonly used metal oxides (e.g., TiO_2, ZnO, Nb_2O_5, and CuO) will be discussed for their role in fabrication of polymer solar cells.

Processing and Synthesis of Metal Oxide Nanostructures

In the past decades, metal oxide nanostructures have attracted great interest due to their potential applications in optoelectronics. Controlling the size and shape of nanostructures is crucial in developing novel properties in nanoscience research. Considerable efforts have been devoted in obtaining various nanostructures such as nanoparticles, nanospheres, nanorings, nanopolyhedrons, nanorods, nanowires, nanobelts, and nanosheets [12, 13], which showed that nanostructure properties and device performance greatly depend on their size, morphology, composition,

Both Ashish Dubey and Jiantao Zai made equal contribution to this work.

A. Dubey • Q. Qiao (✉)
Department of Electrical Engineering and Computer Sciences, Center for Advanced Photovoltaics, DEH 219, South Dakota State University, Brookings, SD, USA
e-mail: ashish.dubey@sdstate.edu; qiquan.qiao@sdstate.edu

J. Zai • X. Qian
School of Chemistry and Chemical Engineering, State Key Laboratory of Metal Matrix Composites, Shanghai Jiao Tong University, Shanghai, China
e-mail: zaijiantao@sjtu.edu.cn; xfqian@sjtu.edu.cn

and surface properties that can be tuned by synthetic methods. Numerous techniques have been developed to synthesize metal oxide nanostructures with a wide range of compositions, sizes, sophisticated crystallite shapes, and complex assembly properties. Although vapor-phase processing has been successfully employed for the preparation of metal oxide nanostructures, especially for one-dimensional nanostructures [14–17], solution-based chemical (wet chemistry) synthesis methods have become more versatile with regard to the controlled variation of structural, compositional, and morphological features. In fact, solution-based chemical synthesis such as sol–gel [18–22], chemical (co)precipitation [23], hydrothermal [24–28], combustion [29, 30], spray pyrolysis [31], microemulsion [25, 26, 32, 33–46], and electrospinning [24–28] has received considerable attention since they offer the possibilities to control homogeneity, purity of phase, size distribution, surface area, and microstructure uniformity. In this work, we will discuss general synthesis methods that are used to prepare several important semiconductors, such as TiO_2, ZnO, Nb_2O_5, CuO, and others with different nanostructures.

TiO_2

Historically, Fujishima and Honda reported electrochemical water splitting property on a TiO_2 electrode in 1972 [45, 47, 48], and Brian O'Regan introduced high surface area TiO_2 films in dye-sensitized solar cells in 1991 [49, 50]. TiO_2 is one of the most extensively studied materials with more than 80,000 publications over the past 5 years based on the database, web of knowledge. TiO_2, a large-band gap semiconductor, is known to be a very useful nontoxic, environmentally friendly, corrosion-resistant material used as pigment, paint, cosmetics, and catalyst. It has been widely studied with applications in photocatalysts, biosensors, and dye-sensitized solar cells (DSSCs) due to its unique optical and chemical properties [13, 34, 36, 47, 49, 51–55]. As a photocatalyst with large surface area, TiO_2 facilitates diffusion of photoinduced electrons and holes towards the surface before their recombination. TiO_2 having high dielectric constant and refractive index has also been widely used as optical coatings, beam splitters and antireflection coatings. In addition, TiO_2 has also been reported in use as humidity, hydrogen, and oxygen sensors [56–60]. TiO_2 has three crystalline polymorphs including anatase, rutile, and brookite. Rutile is a thermodynamically stable phase with smaller band gap than anatase. This section focuses on the recent progresses in the synthesis of TiO_2 nanostructures such as nanoparticles, nanorods, nanotubes, nanofibers, and various doping in TiO_2 nanostructures.

Nanoparticle

The anatase TiO_2 nanoparticles have been one of the most widely studied among various nanostructures with high surface area and strong absorption capacity. For industrial-scale production, the pyrolysis of $TiCl_4$ at high temperatures is used to produce Degussa P-25 TiO_2 nanoparticles. The laboratory scale synthetic approaches

to fabricate TiO_2 nanoparticles include sol–gel [61–65], hydrothermal [28, 63, 66], solvothermal [67, 68], chemical vapor deposition [16, 69, 70], and microemulsion [25, 26, 32]. Among them, hydrothermal is widely used for the production of small particles of TiO_2 [28, 63, 71–73]. TiO_2 nanoparticles can be synthesized by hydrothermal processing of either peptized precipitates of a titanium precursor with water [28] or titanium alkoxide in an acidic ethanol–water solution with particle sizes in the range of 7–25 nm by changing the concentration of Ti precursor and the solvents [63].

The sol–gel method from hydrolysis of a titanium precursor is another easy and widely used process to prepare TiO_2 nanoparticles. This process usually proceeds via a hydrolysis step of titanium alkoxide followed by condensation. A series of thorough studies have been conducted by Sugimoto et al. using the sol–gel method to prepare TiO_2 nanoparticles with different sizes and shapes by tuning the reaction parameters [74–78]. Under different pH conditions, the selective adsorption of shape controller on specific crystal planes of TiO_2 nanoparticles can tune the growth rate of these planes. Finally the size and shape is controlled by the growth rate in different crystal planes [74, 75]. Furthermore, the colloid dispersions of TiO_2 nanoparticles prepared by sol–gel method are efficient precursor to make various TiO_2 films on different substrates or nanostructures with various soft and hard templates [19, 21, 61, 73, 79–81].

Randomly Oriented and Highly Aligned Nanorods

TiO_2 nanorods can be used in novel photovoltaic devices including hybrid bulk heterojunction and dye-sensitized solar cells [82–84]. The synthesis of TiO_2 nanorods, especially arrays on the substrates, has attracted much attention. Weller et al. reported the controlled growth of high-aspect ratio anatase TiO_2 nanorods by hydrolysis of titanium tetraisopropoxide in oleic acid as surfactant at 80 °C [85]. Li et al. successfully synthesized the near monodisperse TiO_2 nanorods with their size, shape, and dispersibility controlled by adjusting reaction temperature, duration, and concentration of the reactants [68]. As previous mentioned, TiO_2 nanorods can be prepared by combining sol–gel method and anodic alumina membrane (AAM) template [34, 57]. TiO_2 nanorod arrays can be obtained by template-assisted sol–gel electrophoresis [18]. Direct oxidation of titanium metal plate with hydrogen peroxide can also produce crystalline TiO_2 nanorods [86]. For application in photovoltaic devices, developing a simple method to grow TiO_2 nanorod arrays on the transparent conductive substrates is important. The seed growth process is a commonly used method to prepare one-dimensional nanostructures on substrates. In order to prepare TiO_2 nanorod arrays, a TiO_2 polymeric sol prepared by sol–gel process was spin-coated on the fluorine-doped tin dioxide (FTO) substrate and then annealed as a seed layer, followed by the growth of nanorod arrays by hydrothermal method [42]. Aydil et al. invented a hydrothermal method for the first time to grow oriented, single-crystalline rutile TiO_2 nanorod films on FTO substrates (Fig. 20.1) by simply mixing hydrochloride with titanium precursors [87]. The acidity, concentration, additives of surfactants, processing temperature, and time were used to optimize the diameter, length, and density of the nanorods.
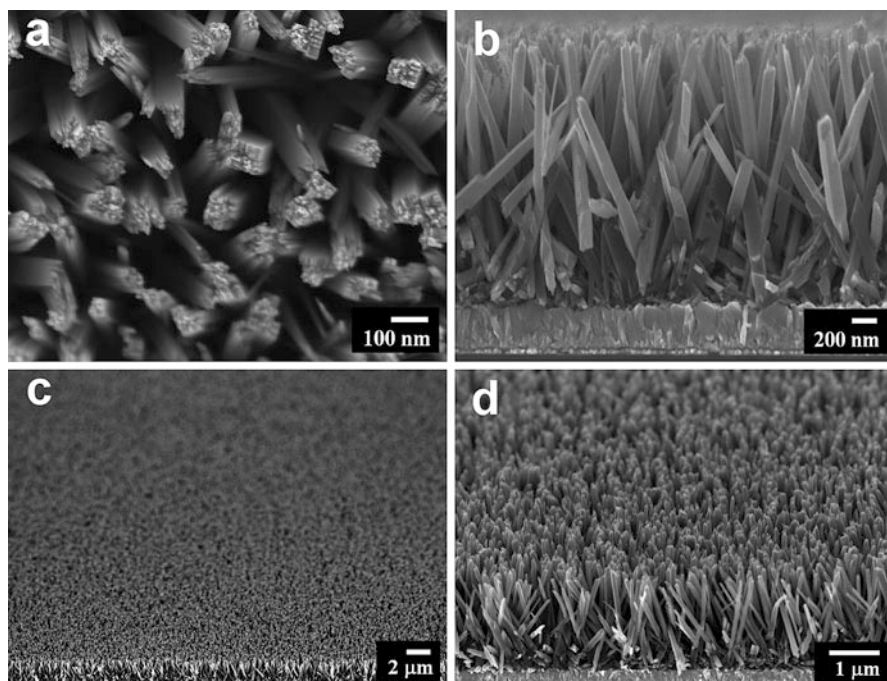
Fig. 20.1 FESEM images of oriented rutile TiO_2 nanorod film grown on FTO substrate in 30 mL of deionized water, 30 mL of hydrochloric acid, and 1 mL of titanium butoxide at 150 °C for 20 h. (**a**) Top view, (**b**) cross-sectional view, (**c**) and (**d**) tilted cross section (Reprinted (adapted) with permission from Ref. [87]. Copyright (2009) American Chemical Society.)

Nanotubes

The first titania nanotubes were probably synthesized by Hoyer through a template-assisted electrochemical deposition method in 1996 [88]. Since then, template-assisted methods [20, 89] and others including hydro-/solvothermal methods with or without templates [20, 24, 80, 90–92] and anodic oxidation method [89, 93, 94] have been reported. The hydrothermal method has been widely used to prepare TiO_2 nanotubes since Kasuga et al. reported that the hydrothermal treatment of TiO_2 particles in NaOH resulted in the formation of anatase TiO_2 nanotubes with large surface areas in 1998 [80]. Teng et al. further studied the structural features of nanotubes obtained by NaOH treatment on TiO_2 with different posttreatments [90]. Today, this method is widely used for preparing TiO_2 nanotubes. Crystallized TiO_2 nanotube arrays can be obtained by anodic oxidation of titanium foil and annealed at high temperature [43, 89, 93, 94]. The length and diameter of the TiO_2 nanotubes can be controlled over a wide range with an applied potential from 1 to 25 V in optimized phosphate/HF electrolytes. Depositing Ti film on the transparent conductive substrates, followed by an anodic oxidation process, has become a typical method to grow TiO_2 nanotube arrays [41, 44, 95, 96].

Nanofibers

TiO_2 nanofibers can be fabricated by the template-assisted sol–gel method with TiO_2 sol and porous alumina membranes or 'track-etched' polycarbonate filters as templates [20]. The template method is usually complex, cost- and time-consuming. Su et al. developed a soft hydrothermal chemical process via the reactions of amorphous TiO_2 gel (or commercial $TiOSO_4$ particles) and NaOH solution to synthesize TiO_2 nanofibers with high surface area [97]. Today, TiO_2 nanofibers can be conveniently prepared by electrospinning an alcohol solution that contains a polymer of high molecular weight and a titanium alkoxide precursor. Calcination in a subsequent step leads to the formation of polycrystalline nanofibers made of anatase TiO_2 with controllable diameters and interesting porous structures (Fig. 20.2) [56, 98–102]. Figure 20.2 shows extremely long TiO_2/polymer composite nanofibers (a) can be produced by electrospinning method, and the anatase TiO_2 nanofibers (b) with a diameter around 50 nm can be easily obtained by the calcination of these composite nanofibers.

Doping in TiO_2 Nanostructures

As a wide band gap semiconductor, TiO_2 can only utilize the ultraviolet light in solar spectrum. In order to extend its optical absorption to visible light region, doping metals or nonmetals into TiO_2 is well studied. Doping TiO_2 will mainly maintain TiO_2 crystal structure, but generate some favorable changes in their electronic and optical properties [12]. Typically, substitution of Ti^{4+} cations in TiO_2 with other transition metals is much easier than replacing O^{2-} anions with other anions due to the differences in charge states and ionic radii.

Three types of methods are typically used to dope TiO_2 nanostructures: wet chemistry, high-temperature treatment, and ion implantation on TiO_2 nanostructures. Wet chemistry usually realizes the doping by adding metal ion dopants to the titanium precursor, and then the mixed solution undergoes similar processes as the synthesis of pure TiO_2 nanostructures. Choi et al. successfully prepared TiO_2 nanoparticles doped with 21 different metal ions by sol–gel method and found the presence of metal ion dopants significantly influenced the photoreactivity, charge carrier recombination rates, and interfacial electron-transfer rates [103]. Nagaveni et al. performed a systematic study of W, V, Ce, Zr, Fe, and Cu ion-doped anatase TiO_2 nanoparticles by a solution combustion method and found that the solid solution formation was limited to a narrow range of concentrations of the dopant ions [30]. Li et al. synthesized highly crystalline and near monodisperse TiO_2 nanoparticles and nanorods doped by Sn, Fe, Co, and Ni ions by well-controlled solvothermal reactions [68]. Anpo et al. prepared TiO_2 nanoparticles doped with Cr and V ions with an ion implantation method. Plasma-enhanced CVD, ion beam-induced CVD, and radiation-frequency (RF) thermal plasma are also used to prepare metal-doped TiO_2 nanoparticles [12].

Some nonmetal elements such as B, C, N, F, S, Cl, and Br have also been successfully doped into TiO_2 nanostructures. Annealing the TiO_2 nanostructures under their corresponding gas flow is commonly used to synthesize nonmetal-doped TiO_2 nanostructures [12]. For example C- and F-doped TiO_2 nanomaterials can be
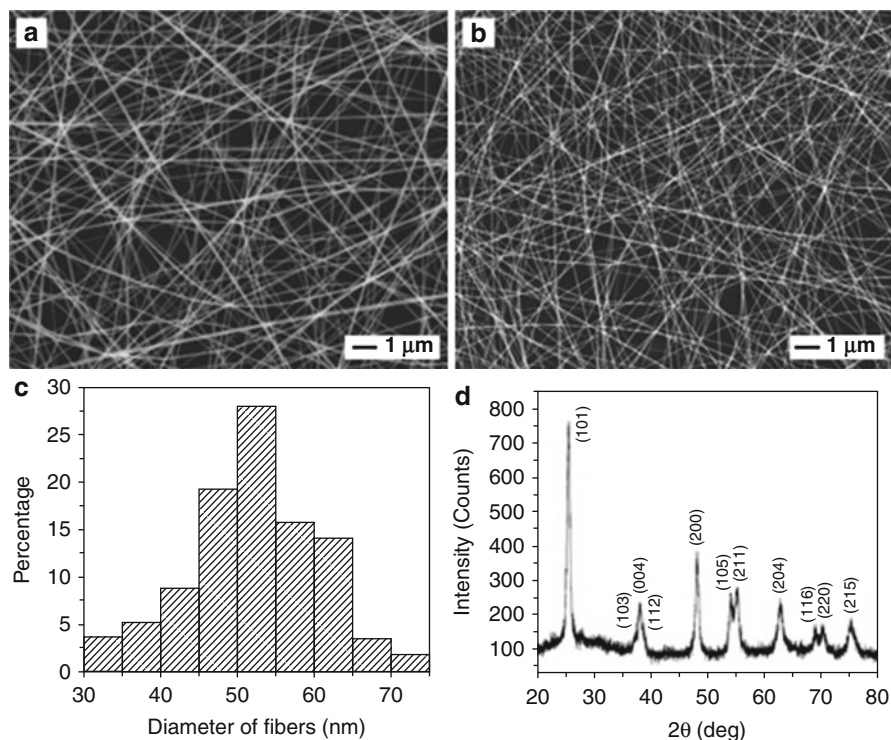
Fig. 20.2 (**a**) SEM image of TiO$_2$/PVP nanofibers that were electrospun from an ethanol solution containing Ti(OiPr)$_4$ (0.1 g/mL) and PVP (0.03 g/mL). The electric field strength was 1 kV/cm. (**b**) SEM image of the same sample after it had been calcined in air at 500 °C for 3 h. (**c**) Histogram showing the size distribution of nanofibers contained in the calcined sample. The size distribution was obtained from the SEM images of about 100 nanofibers. (**d**) XRD pattern of the same calcined sample. All diffraction peaks can be indexed to those of the anatase phase of titania (Reprinted (adapted) with permission from Ref. [101]. Copyright (2003) American Chemical Society.)

synthesized by heating TiO$_2$ under CO and hydrogen fluoride gas flow, respectively [104, 105]. Hydrolysis of titanium precursors in the solvent-containing dopants has also been reported. *N*-doped TiO$_2$ nanomaterials have been synthesized by the hydrolysis of titanium precursors in a water/amine mixture, followed by posttreatment of TiO$_2$ sol with amines [39, 106]. *S*-doped TiO$_2$ nanomaterials were synthesized by mixing TTIP with ethanol containing thiourea [107]. Cl$^-$ and Br$^-$ co-doped nanomaterials were synthesized by adding TiCl$_4$ to ethanol containing HBr [108].

ZnO

ZnO is a technologically important and environmental-friendly semiconductor with many remarkable properties, such as a direct wide band gap of 3.37 eV, large excitonic binding energy, high electron mobility, large piezoelectric constants, high
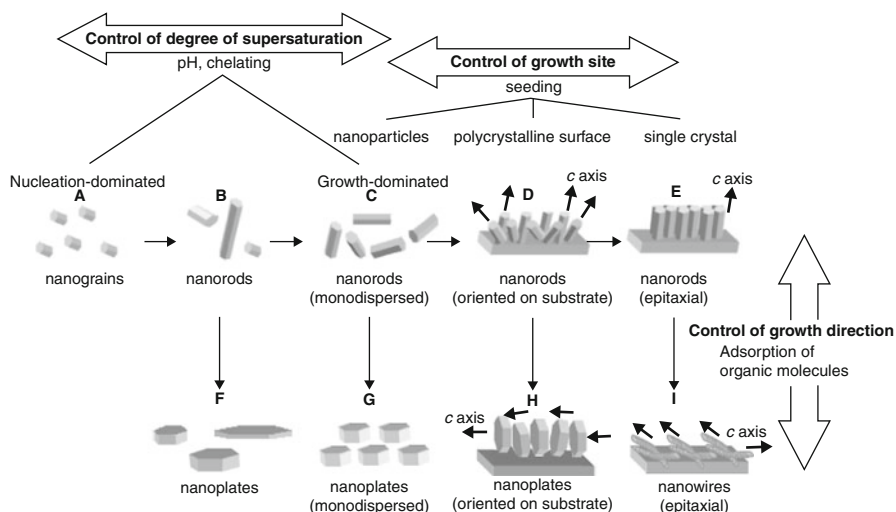
Fig. 20.3 Schematic illustration of the effects of the guiding parameters for the morphological design of ZnO crystals in solutions (Reproduced with permission from Ref. [119])

nonlinear optical coefficients, and radiation hardness. ZnO can be used in many applications including thin film transistors [109], sensors [110], solar cells [38, 111–115], UV photodetectors [116], and piezoelectric power generators [117, 118]. Because the ZnO properties determining the performance of ZnO-derived devices strongly depend on the size and shape, precise control of the morphology of ZnO nanostructures is of importance. Recently, wet chemistry attracted a lot of attention for its advantages such as low cost, low energy consumption, ease of large-scale production, and controllability of the morphology. And a wide variety of crystalline ZnO nanostructures and films were prepared using various solutions containing different chemicals, additives, and seeds or substrates by aqueous solution-based processing. Kawano [119] reviewed various morphologies of ZnO nanostructures and their dependence on preparation conditions including the source chemicals, the role of seeds or substrates, and the presence of organic molecules as a shape modifier. Figure 20.3 shows a schematic illustration of the effects of the guiding parameters. Under a high degree of supersaturation, fine grains are produced through a high rate of nucleation. On the other hand, nanorods elongated in the c direction can be obtained through gradual crystal growth with a low rate of the nucleation under a low degree of supersaturation. The presence of seeds could control the size distribution and crystal orientation. The ZnO nanostructures are basically controlled by tuning the growth rate, growth site, and growth direction. In addition, the degree of the supersaturation, the presence of seeds, and the adsorption of additives are other essential parameters. Many approaches including chemical vapor deposition [120], sputtering [121], sol–gel routes [31], and electrodeposition [46] have also been investigated as the size- and morphology-controlled synthesis method to prepare ZnO crystals.
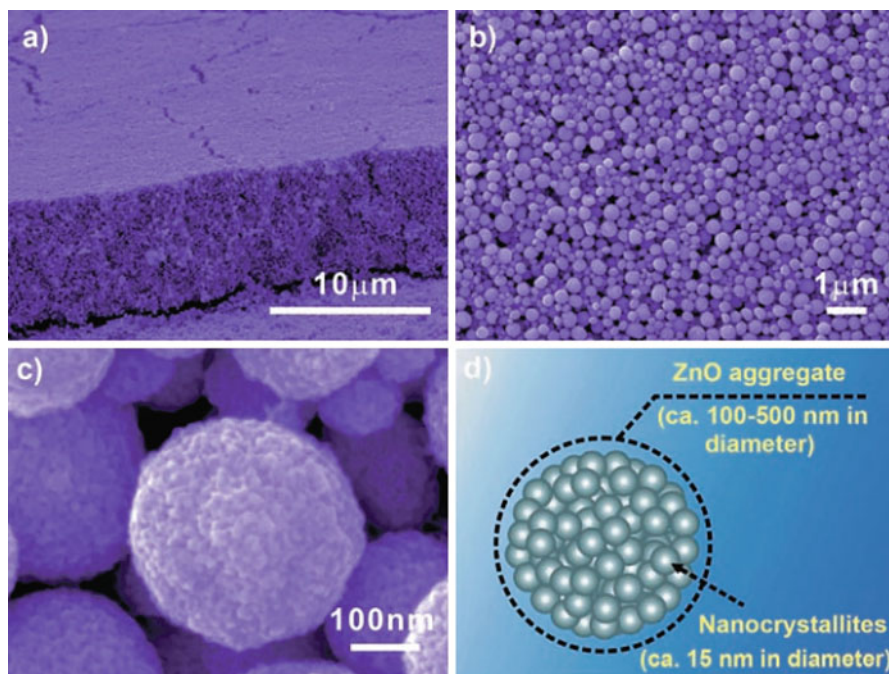
Fig. 20.4 Morphology and structure of the ZnO aggregate film: (**a**) SEM image of the cross section of the ZnO aggregate film, (**b**) SEM image of the top view of the ZnO film consisting of polydisperse aggregates, (**c**) magnified SEM image of an individual ZnO aggregate, and (**d**) schematic diagram illustrating the microstructure of aggregated ZnO comprising closely packed nanocrystallites (Reproduced with permission from Ref. [127])

Nanoparticles

Anderson et al. performed the synthesis of ZnO quantum dots (3–6 nm) by a sol–gel method with the addition of LiOH into an ethanolic zinc acetate solution [22]. They also studied the factors that influence the rate of particle growth [22]. Searson synthesized ZnO nanoparticles with different size by precipitation from solutions using $Zn(CH_3CO_2)_2$ and NaOH in a series of *n*-alkanols from ethanol to 1-hexanol [122]. ZnO nanoparticles were also been synthesized by ultrasonic irradiation of an aqueous-alcoholic/aqueous-alcoholic-ethylenediamine solution of zinc nitrate and sodium hydroxide [123]. Imai et al. prepared ZnO nanoparticles with size of 30–40 nm by dropping base solutions to Zinc salts solution under 60 °C [124]. Nanoparticles and superstructures of aggregated ZnO nanoparticles were also prepared by surfactant-assisted solvothermal method, where the anions and types of surfactants greatly affected the ZnO structures [125, 126]. Zhang et al. synthesized polydisperse ZnO aggregates by the hydrolysis of zinc precursor in polyol medium at 160 °C [127]. And then, a well-stacked ZnO porous film on FTO (Fig. 20.4) is fabricated by using
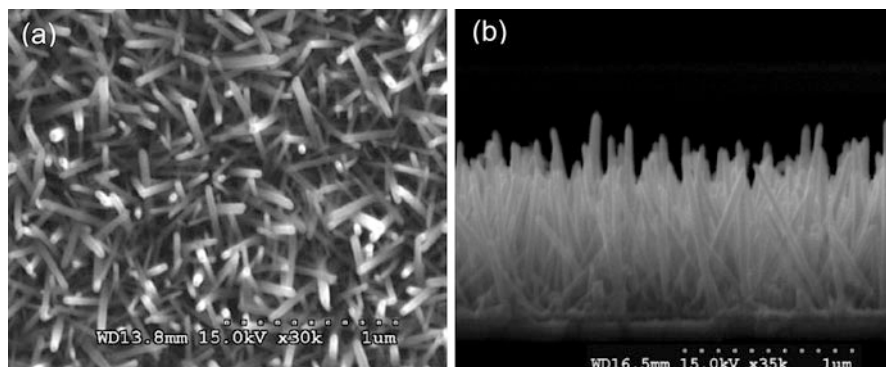
Fig. 20.5 (**a**) Top view and (**b**) cross-section SEM image of nd-ZnO (Reprinted (adapted) with permission from Ref. [114]. Copyright (2010) American Chemical Society.)

a drop-cast method. The film is assembled by spherical ZnO aggregates with different diameters, which consists of packed nanocrystallites. Spin coating of ZnO sol combined with calcinations is a common process to prepare thin film of ZnO nanoparticles on various substrates. Magnetron sputtering [121], pulsed laser deposition [17], and spray pyrolysis [128, 129] were also utilized to prepare ZnO nanoparticle films.

Randomly Oriented or Highly Aligned Nanorods

Chemical vapor deposition (CVD) is an efficient method to prepare ZnO nanorods on substrates. The partial oxygen pressure and chamber pressure are parameters that influence the growth mechanism and govern the final ZnO structure [130]. According to the epitaxial crystalline growth mechanism, ZnO nanorods can grow on (100) sapphire at a 30° angle to the substrate [131]. Lee et al. fabricated well-aligned, single-crystalline ZnO nanowires on GaAs substrates by metal-organic CVD [132]. Low-temperature growth routes on fused silica or Si substrates have also been reported [133]. Electrochemical deposition is another technique for achieving uniform and large area synthesis of ZnO nanostructures [46]. Growth of ZnO nanostructures can occur on a general substrate, flat or curved, without any seeds, as long as the substrate is conductive [37]. Under an external electric field, higher nanowire alignment and stronger adhesion to the substrate have been observed [37]. Vayssieres invented an aqueous method without template and surfactant to grow ZnO nanowires and oriented nanorod arrays [134]. Seed growth via a solution-based method is a typical process to prepare ZnO nanoarrays with different diameter, length, and density [114, 115, 135, 136]. ZnO nanocrystal seeds are coated onto cleaned fluorine-doped tin oxide (FTO) substrates firstly. And then the substrates that were immersed into a mixed solution of Zn-precursor, surfactant, and controlled-released bases underwent a chemical bath process to grow ZnO nanoarrays. And calcinations are usually used to improve the crystallinity of the products. Figure 20.5 shows the morphology of ZnO nanoarrays synthesized based on the

seed growth method by Yu et al. [114] The average diameter and length of the individual nanorods are ~ 40 nm and 1 μm, respectively.

Nanotower

Growth of ZnO nanocolumns on alumina substrates via oxidation of ZnS in a tube furnace at 950 °C has been reported [137]. The substrates were kept apart from the source at a lower temperature. The synthesized nanocolumns show a layered structure and become gradually thinner. This was attributed to be a result of a gradually decreasing supply of ZnO vapor. Qian et al. [138] developed a novel solution-based method to grow ZnO nanotower on the different substrates including glass, quartz, and polyethylene terephthalate (PET). The towerlike ZnO crystal arrays (Fig. 20.6a–c) were obtained in a reaction mixture solution containing zinc salt, ammonia, ammonium salt, and thiourea. The orientation of these tower like crystals could be controlled by the contents of these reactants at 95 °C. Other methods including CVD [139, 140], MOCVD [15], carbon thermal reduction method [141], and seed growth combined with hydrothermal processes have also been utilized to prepare ZnO nanotower.

Nanoflower

Qian et al. [138] also found that the flower-like ZnO arrays (Fig. 20.6d) can be obtained at 85 °C in the towerlike ZnO reaction solution system. Zhu et al. [142] synthesized flowerlike ZnO by a simple microwave-assisted solution phase approach using an ionic liquid (1-n-butyl-3-methyl imidazolium tetrafluoroborate). Gao et al. [143] performed flowerlike ZnO nanostructures on Si substrate from aqueous solution by the hexamethylenetetramine-assisted thermolysis of zinc-ethylenediamine complex at 95 °C for 1 h. Adschiri et al. [144] identified that a biomolecule, peptide, could recognize and generate ZnO nanoparticles to assemble into a highly ordered flower-type structure. Further researches indicate simply tuning the type and concentration of Zn-precursor/bases used in solution routes, ZnO flowers will be obtained [145–147]. In addition, hydrothermal [27, 148–150], eletrodeposition [33], and CVD methods [139, 151] are also used for the synthesis of ZnO nanoflowers.

Doping in ZnO Nanostructures

By controlling the doping level of ZnO, its electrical properties can be changed from insulator through n-type semiconductor to metal while maintaining optical transparency that makes it unique as a low-cost transparent electrode in flat-panel displays and solar cells to replace In-doped SnO_2 [31, 152, 153]. Mn-doped ZnO and Fe-, Co-, or Ni-alloyed ZnO were predicted to stabilize high-Curie-temperature ferromagnetism [154]. P-type doping in ZnO is also possible by substituting either group-I elements such as Li, Na, and K for Zn sites or group-V elements including N, P, and As for O sites [155]. Alloying ZnO with MgO (Eg = 7.7 eV) enables widening of band gap of ZnO and have been considered as a suitable material as barrier layers [156, 157]. However, when alloyed with CdO (Eg = 2.3 eV), it will narrow the band gaps to even the visible spectrum [158, 159]. The doping of ZnO films is usually utilized by CVD [158],
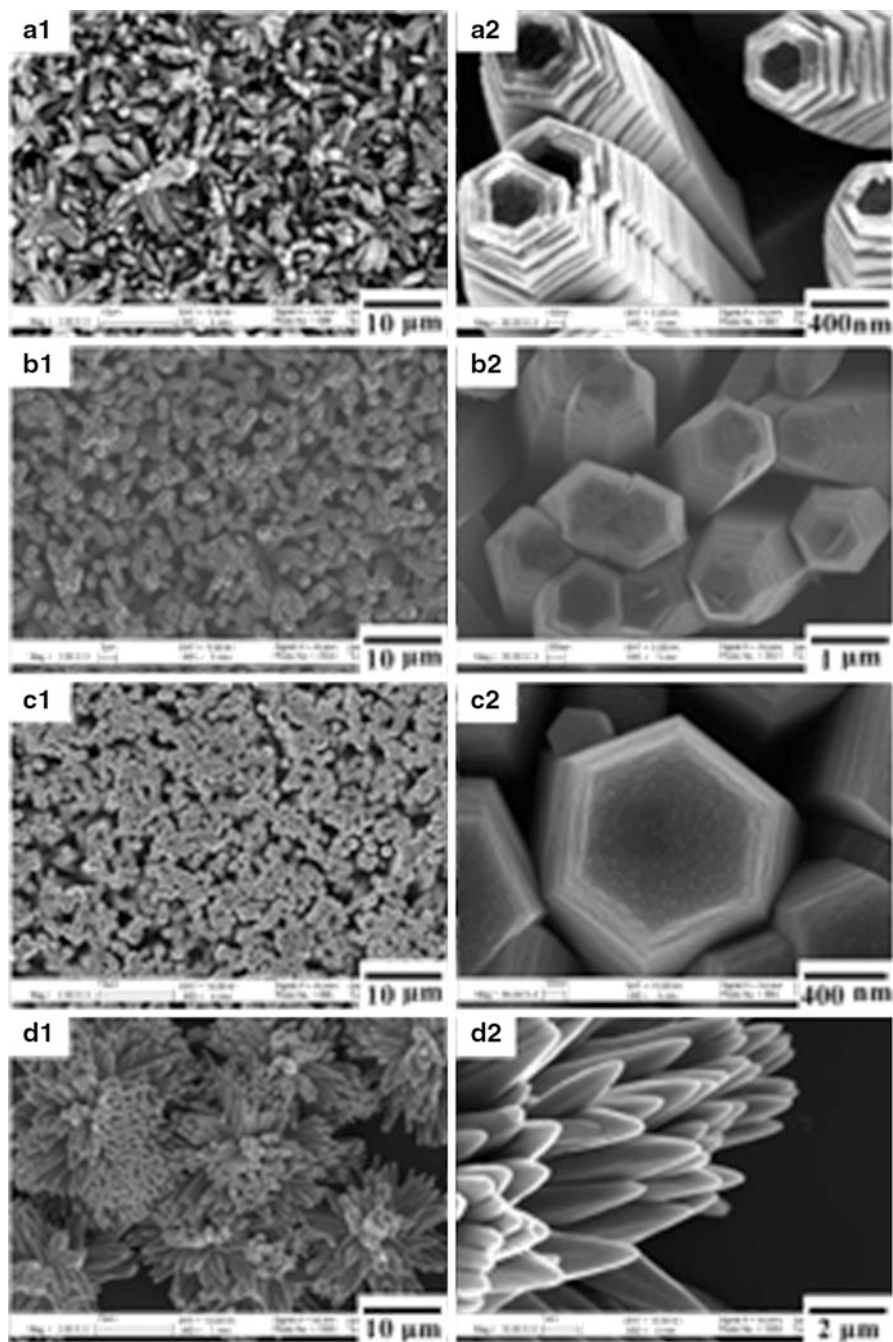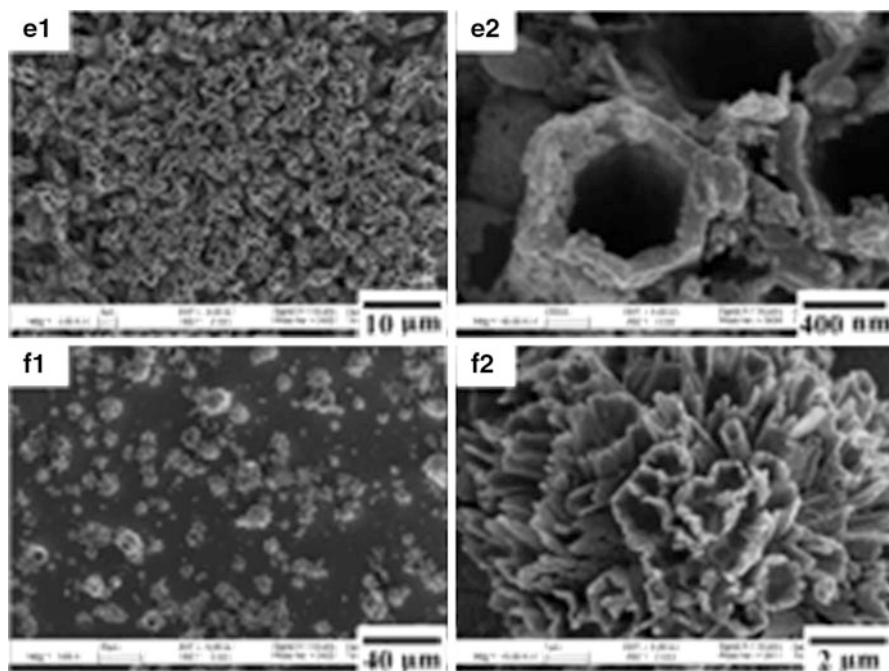
Fig. 20.6 (continued)

Fig. 20.6 FESEM images of the as-prepared towerlike, flowerlike, and tubelike ZnO arrays grown on glass substrate: (**a**–**c**) towerlike ZnO with general, better, and best orientation, (**d**) flowerlike ZnO, and (**e**, **f**) tubelike ZnO with high density and low density (Reprinted (adapted) with permission from Ref. [138]. Copyright (2004) American Chemical Society.)

MOCVD [14], molecular beam epitaxy [156], atomic layer deposition [160], and sputtering method [157]. Sol–gel process can be used to dope both ZnO film [31] and nanopowder [161]. The thermal decomposition of metal acetylacetonate precursors in a nonoxygen and nonpolar solvent is another method to prepare doped ZnO nanopowders, even the nanoink, a stable ZnO nanoparticle dispersion in the solvent [153].

Nb_2O_5 Nanoparticles

Nb_2O_5 is widely used in catalysts, gas sensors, electrochromic devices, and optical filters [162]. Up to now, several processes have been reported to synthesize Nb_2O_5 nanoparticles. Uekawa et al. prepared 4.5 nm sized Nb_2O_5 nanoparticles by heating the peroxoniobic acid sol obtained from the peptization of the acid precipitate with the H_2O_2 aqueous solution [163]. Zhou et al. prepared porous Nb_2O_5 nanoparticles via a solution-based method combined with calcination without the assistance of any surfactant [162]. Buha et al. synthesized Nb_2O_5 nanocrystals with size of 18–35 nm using a nonaqueous sol–gel route based on the solvothermal reaction
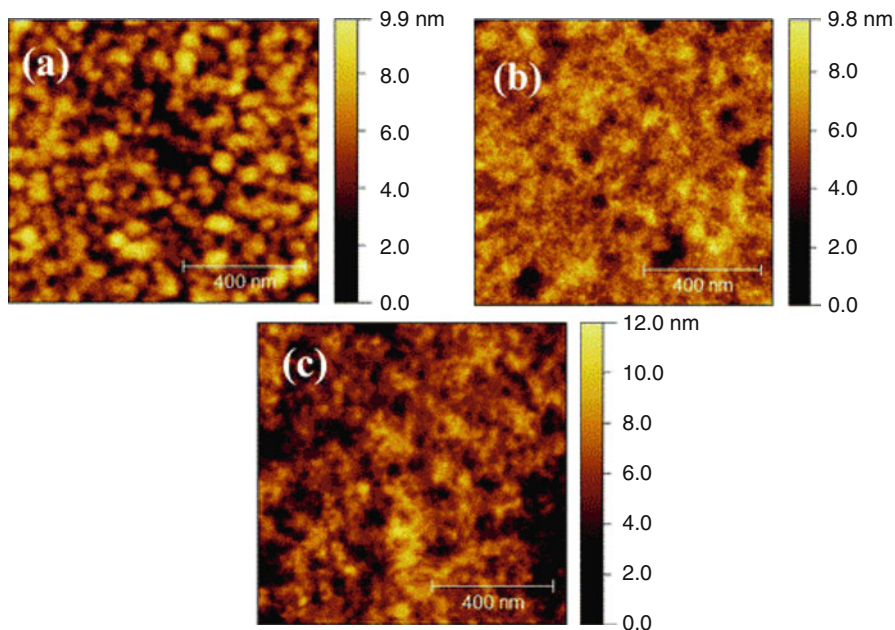
Fig. 20.7 Atomic force microscopy (AFM) topography image of (**a**) MDMO-PPV:PCBM active layer, (**b**) Nb_2O_5 ETL deposited on top of the MDMO-PPV:PCBM active layer, and (**c**) the pH neutral PEDOT:PSS HTL on top of the Nb_2O_5 layer (Reproduced with permission from Ref. [11])

of the corresponding metal chlorides with benzyl alcohol [164]. Recently, Qiao group grew Nb_2O_5 nanoparticles film by spin-coating the Nb_2O_5 sol–gel solution prepared by mixing the niobium ethoxide ($Nb(OC_2H_5)_5$) precursor with ethanol and acetic acid at room temperature and used the layer as a new electron transport layer for double junction polymer solar cells [11]. In particular, the preparation of Nb_2O_5 layer only takes half an hour and can be done at room temperature in an air atmosphere. When deposited by spin coating, the Nb_2O_5 sol–gel solution exhibited a high attachability on the polymer–fullerene active layer. Then the spin-coated film got oxidized quickly to form the Nb_2O_5 layer (Fig. 20.7).

CuO

As a p-type semiconductor, CuO exhibits a narrow band gap (1.2 eV) and shows wide applications in the field of emission materials, catalysts [165], gas sensors, magnetic storage media, electronics, and solar cells.

CuO Nanoparticles
Liu et al. prepared highly stable CuO nanoparticles with size of 2–4 nm in diameter (Fig. 20.8) by heating aqueous $Cu(CH_3COO)_2$ and urea solution in the presence of
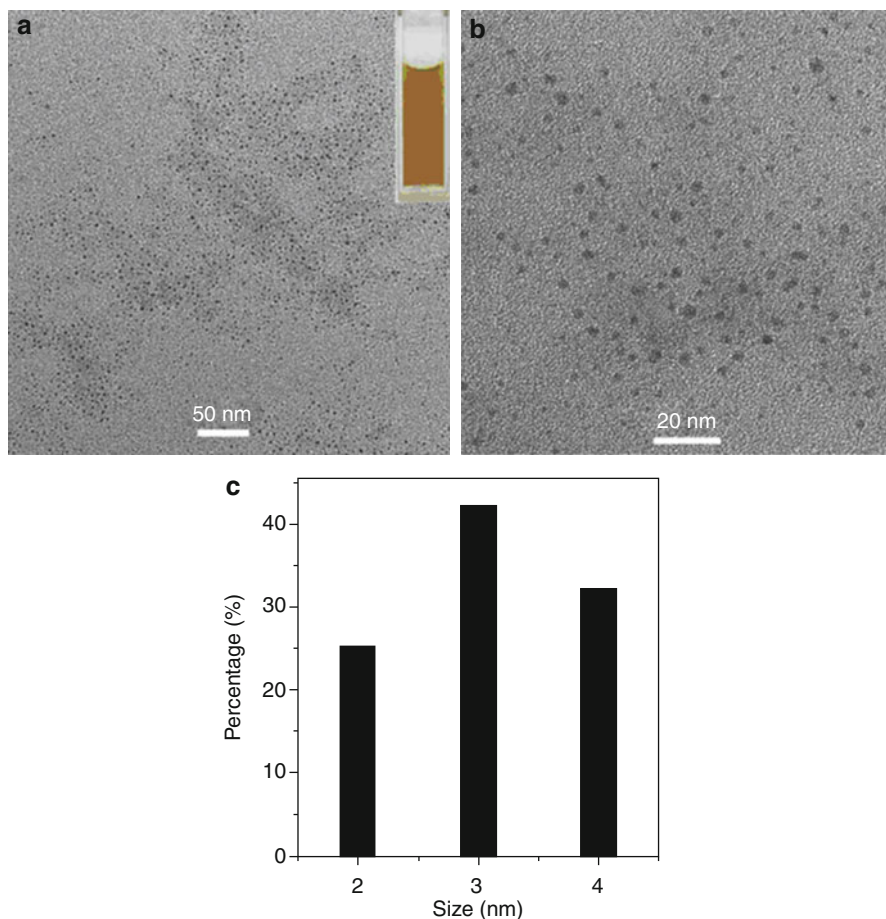
Fig. 20.8 (**a**) Low, (**b**) HRTEM images, and (**c**) their corresponding particle size distribution histogram of the products (inset: the photograph of CuO dispersion in water) (Reproduced with permission from Ref. [166])

poly[(2-ethyldimethylammonioethyl methacrylate ethyl sulfate)-co-(1-vinylpyr-rolidone)] (PQ11) [166]. Wang et al. performed CuO nanoparticles with an average size of ca. 4 nm by microwave irradiation, using copper (II) acetate and sodium hydroxide as the starting materials and ethanol as the solvent [167]. Applerot et al. also reported a sonochemical method to synthesize CuO nanoparticles [168]. Solid-state synthesis [169], green synthesis via starch as surfactant [165], simple precipitation method [23, 170], and thermal decomposition [171] have also been used to prepare CuO nanoparticles.

CuO Hollow Spheres

Hollow nanostructures have been prepared to increase their surface area and reduce density for applications in drug delivery, chemical sensors, photonic devices, and

lightweight filler. A variety of methods have been developed to prepare nanostructures with hollow interiors [35, 172, 173]. Zeng et al. found that CuO hollow dandelion-like architectures by a one-pot hierarchical organizing scheme rely primarily on geometric constraints of building blocks [172]. Zhu et al. prepared a CuO hierarchical hollow nanostructure (Fig. 20.9), assembled by nanosheets, in *n*-octanol/aqueous liquid system through a microwave approach [174]. Controlled experiments revealed that both bubble and interface play key roles in determining the self-assembly process of CuO hierarchical hollow nanostructures. The morphology/size of building blocks and final products could be readily tuned by adjusting reaction parameters. Kong et al. synthesized CuO hollow nanospheres with an average diameter of 400 nm and shell thickness of 40 nm via a thermal oxidation strategy with Cu_2O solid nanospheres as the precursor [35]. The formation of CuO hollow nanospheres mainly result from the Kirkendall effect in the temperature-dependent experiments. Park et al. [175] synthesized uniform Cu_2O nanocubes by a one-pot polyol process, and the Cu_2O nanocubes were converted to polycrystalline CuO hollow nanostructures through a sequential dissolution–precipitation process, by adding aqueous ammonia solutions in air.

CuO Nanowires

Among various metal oxides, CuO has been extensively studied as a p-type metal oxide semiconductor [40, 176]. Jiang et al. described a vapor-phase approach to the facial synthesis of CuO nanowires supported on the surfaces of various copper substrates that include grids, foils, and wires [177]. Hansen et al. introduced and provided details on a large-scale, cost-effective pathway to fabricating ultrahigh dense CuO nanowire arrays by thermal oxidation of Cu substrates in oxygen ambient [178, 179]. The CuO nanowires that are produced by heating copper foil at 500 °C in a pure O_2 gas flow for 150 min feature an average length and diameter of ∼15 μm and ∼200 nm, respectively. Umar et al. demonstrated the preparation of a large-scale vertical array of single-crystalline CuO nanowires on different material surfaces [180]. The procedure simply involved a room-temperature liquid–solid growth process of attached CuO nanoseeds on ITO surface in the mixed aqueous solution of $Cu(CH_3COO)_2$ and NH_3. The field emission scanning electron microscopy (FESEM) image analysis indicated that these nanowires feature uniform size with tiny structures that have diameters and lengths in the range of 10 and 100 nm, respectively, and tend to form a bundle-like structure at the top end of the wires as shown in Fig. 20.10.

Applications of Metal Oxides in Solar Cells

Organic and organic/inorganic hybrid solar cells have attracted a lot of interest due to their solution-based processing and low cost [181–195]. Figure 20.11 shows the calculated 3D contour plots of polymer LUMO, polymer band gap, and
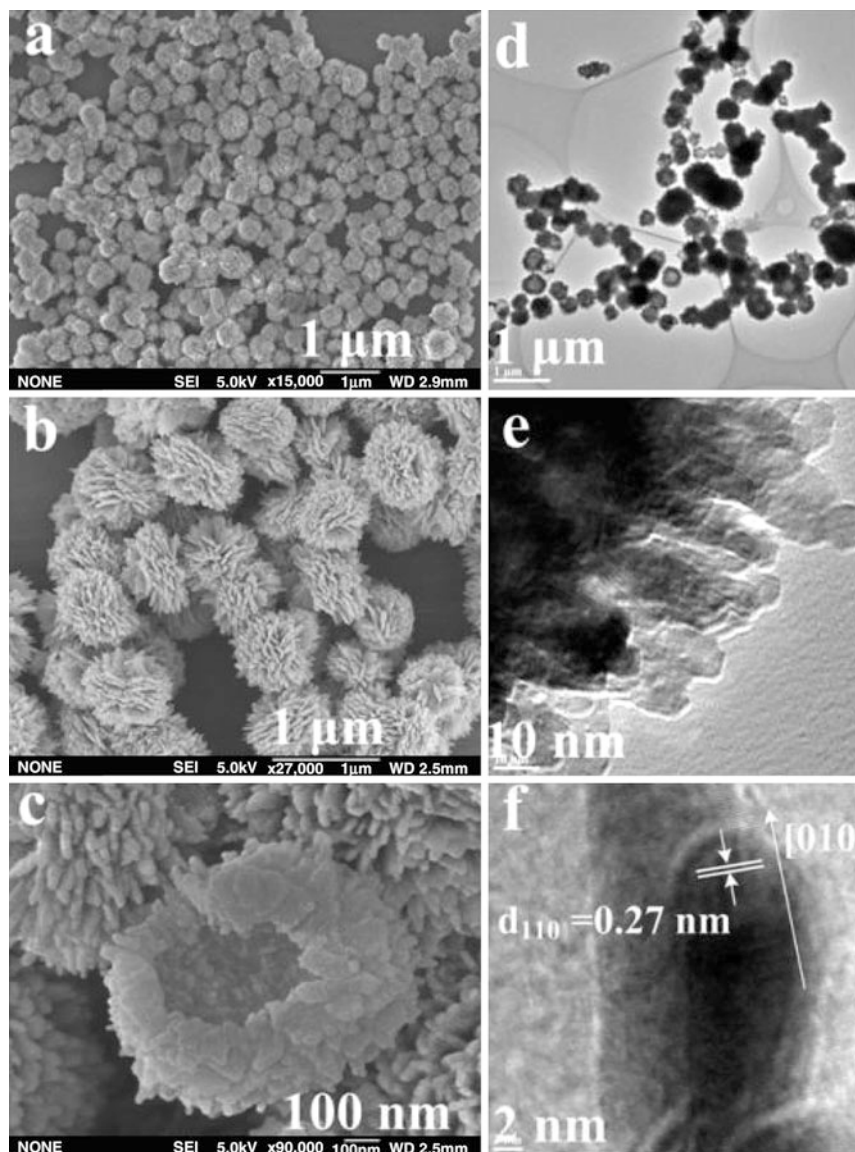
Fig. 20.9 SEM and TEM images of CuO obtained: (**a**) low-magnification SEM image, (**b**) enlarged SEM image, (**c**) FESEM image, (**d**) low-magnification TEM image, (**e**) enlarged TEM image, and (**f**) HRTEM image (Reprinted from Ref. [174], Copyright (2010), with permission from Elsevier.)

cell efficiency with three typical inorganic acceptors of (a) TiO_2, (b) ZnO, and (c) CdSe. It can be seen that the polymer band gaps are almost the same at $\sim$1.5 eV; however, their LUMO and HOMO energy levels are different depending on what acceptor materials will be used [188].
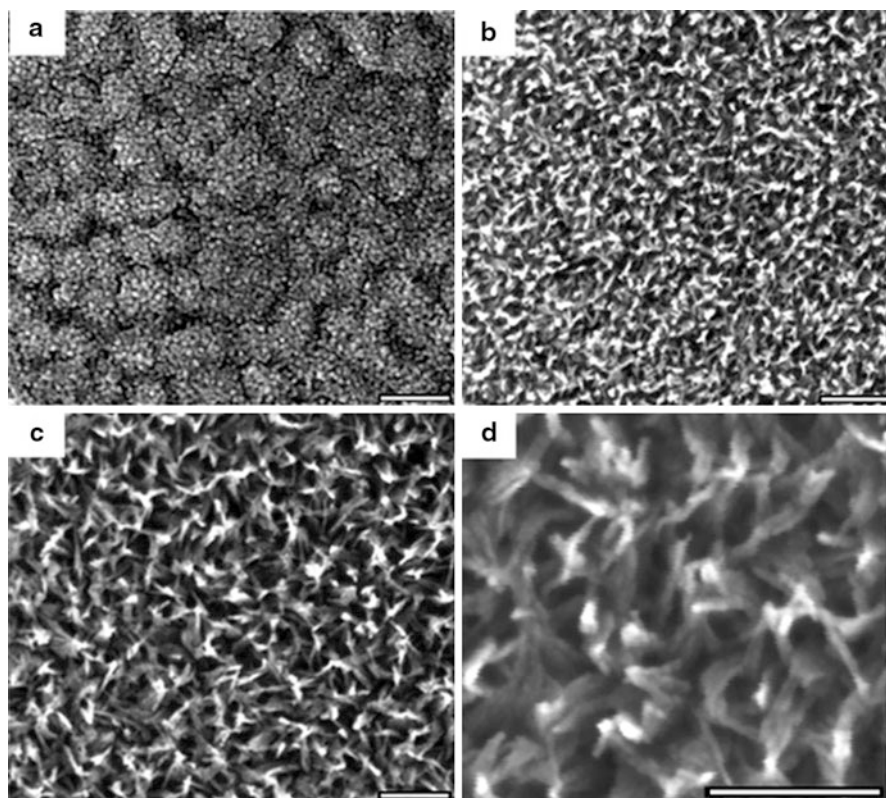
Fig. 20.10 (**a**) FESEM image of CuO nanoseed particles prepared using an alcohothermal method for 2 h at 250 °C; (**b**, **c**) FESEM images of CuO NWs grown at different growth periods in the mixed aqueous solution of 10 mM $Cu(CH_3COO)_2$ and 12 mM NH_3 for (**b**) 2 and (**c**) 15 h at room temperature (25 °C); (**d**) high-magnification image of (**c**). Scale bars are 100 nm (Reprinted (adapted) with permission from Ref. [180]. Copyright (2007) American Chemical Society.)

Titanium Dioxide (TiO$_2$)

Different nanostructures (e.g., nanoparticles, nanotubes, and nanofibers) of TiO_2 have been employed for fabricating efficient solar cells. Kwong et al. in 2003 reported the use of TiO_2 nanoparticle with poly(3-hexylthiophene) (P3HT) to make a nanocomposite film acting as an active layer [196]. Photoluminescence spectrum of active layer films showed quenching of P3HT emission for all different concentrations of TiO_2 which was mixed with P3HT. Cells made from 50 % and 60 % TiO_2 concentrations showed improved performance than those made with TiO_2 concentrations as 40 % (lowest) and 70 % (highest). Poor performance for lower concentration (40 %) of TiO_2 was attributed to recombination of dissociated charges, whereas higher concentration (70 %) of TiO_2 led to poor film quality. Solvent selection for mixing
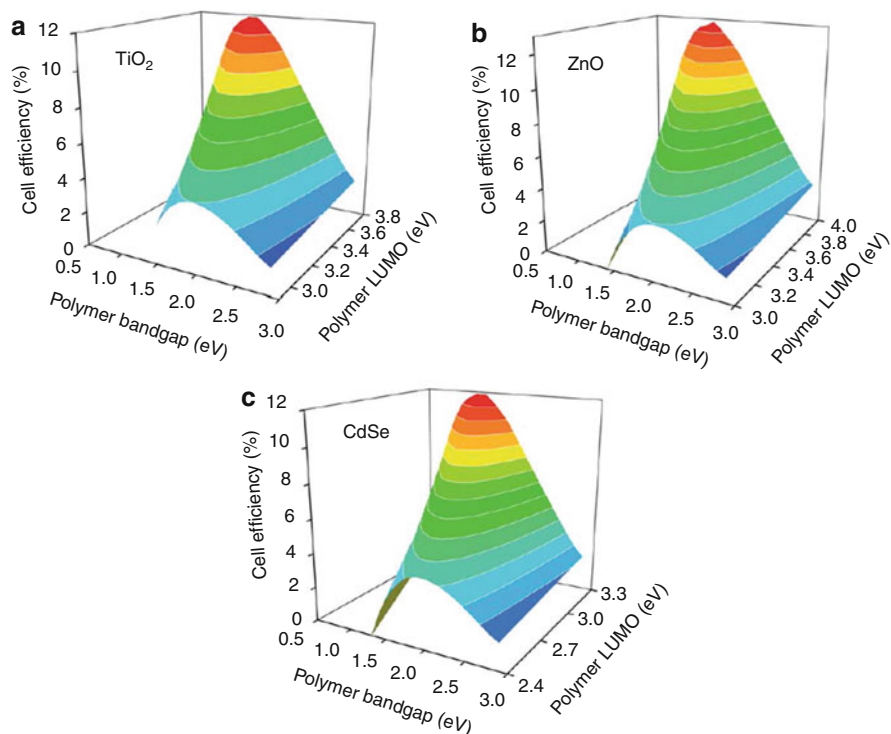
Fig. 20.11 Calculated relationship between polymer band gap (E_g), polymer LUMO, and cell efficiency in single junction hybrid solar cells with three representative inorganic acceptors of (a) TiO$_2$, (b) ZnO, and (c) CdSe. The efficiency was calculated with IPCE = 65 %, FF = 60 % under AM 1.5 with an incident light intensity of 100 mW cm^{-2}. (Reproduced from Ref. [188] with permission from The Royal Society of Chemistry)

TiO$_2$ and P3HT also affected the performance of fabricated cell. Cell fabricated with 60 % TiO$_2$, using xylene as solvent gave best performance. Qiao et al. also used TiO$_2$ nanoparticles to blend with a water soluble polymer (PTEBS) and demonstrated potential to develop environmentally friendly solar cells [82, 197–199]. Yang et al. studied the effect of adding TiO$_2$ nanotubes into P3HT:PCBM blend on device performance in 2010 [200]. Conventional device structure was fabricated with device structure as glass/ITO/PEDOT:PSS/P3HT:PCBM:TiO$_2$/LiF/Al (Fig. 20.12a). Active layer films were prepared by adding TiO$_2$ nanotubes in P3HT:PCBM solution, followed by sonication for 30 min, in order to disperse it uniformly. The solution was then stirred and spin-coated on top of PEDOT:PSS, followed by thermal deposition of LiF (1 nm) and Al (100 nm). Finally the device fabricated was annealed at 150 °C for different time period to optimize morphology of active layer.

From Fig. 20.12b, it was observed that TiO$_2$ nanotube aggregates are made from many individual nanotube each having diameter of ∼10 nm. The TiO$_2$ aggregates as a whole had diameter of 300–600 nm, which was much larger than the films

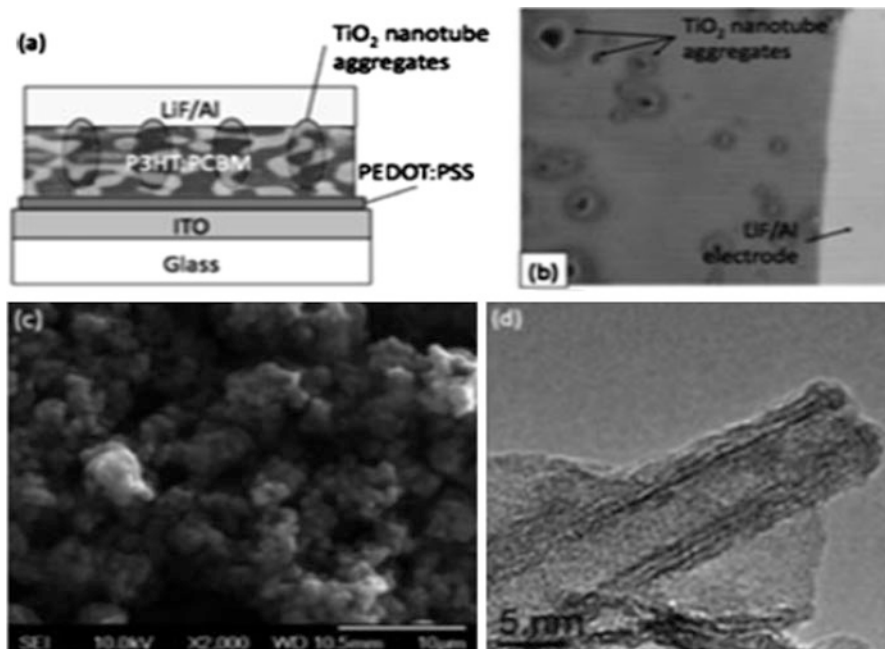**Fig. 20.12** (**a**) Device structure of TiO$_2$ nanotube-based solar cells, (**b**) optical image of fabricated solar cell surface taken at × 500, (**c**) SEM micrograph of TiO$_2$ nanotubes, and (**d**) TEM micrograph of TiO$_2$ nanotubes (Reproduced from Ref. [200] with permission from The Royal Society of Chemistry)

made from P3HT:PCBM (140 nm). The surface roughness of active layer film therefore increased after adding TiO$_2$ nanotube aggregates. J-V curves of the control sample without TiO$_2$ aggregates annealed for 9 min showed an efficiency of 2.8 %, whereas device with TiO$_2$ aggregates annealed for 5 min showed an efficiency of 3 % with an open circuit voltage (V$_{oc}$) of 0.68 V, short circuit current (J$_{sc}$) of 0.60, and power conversion efficiency (PCE) of 3.2 %.

Liao et al. reported hybrid solar cells made from nanostructured arrays of TiO$_2$/P3HT in 2012 [201]. The hybrid cell was modified by introducing Z907 and D149 dye molecule showing enhancement in device performance. Introduction of dye molecules enhanced light absorption and improved the TiO$_2$ nanostructure/P3HT interface. Dye molecule acted as a bridge to link TiO$_2$ and P3HT, where the dye carboxylic group links with hydrophilic TiO$_2$ and the dye aryl group connects with hydrophobic P3HT. Rutile TiO$_2$ nanorod (NR) nanoarrays and nanodendrite (ND) structure were used with P3HT to fabricate hybrid solar cells. TiO$_2$ NR and ND structures were modified by treating it with TiCl$_4$ to form nanoparticles on NR and ND surface, thus increasing the surface area. Figure 20.13 shows top and cross-sectional SEM micrograph of TiO$_2$ nanorods treated with TiCl$_4$. TiO$_2$ NR and ND structure act as electron acceptor and provide transport pathway in TiO$_2$/P3HT-based hybrid cell. Two types of device were fabricated: one without any dye modification and the other with dye attached onto both TiO$_2$ NR and TiO$_2$ ND.
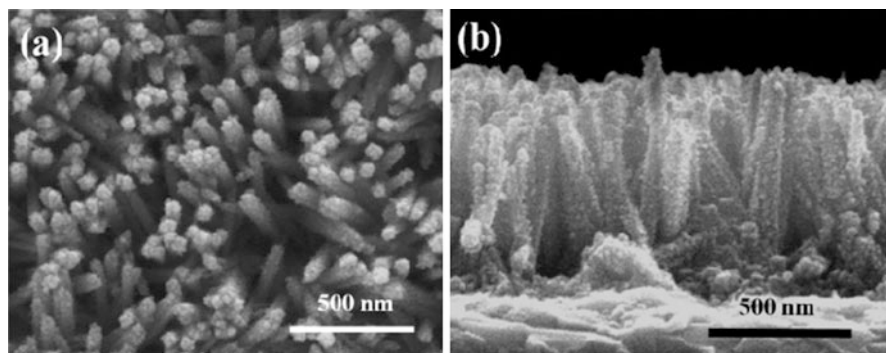
Fig. 20.13 (**a**) Top view and (**b**) cross-sectional TiO$_2$ nanorod SEM images of TiCl$_4$ treated TiO$_2$ NR (Reprinted (adapted) with permission from Ref. [201]. Copyright (2012) American Chemical Society.)
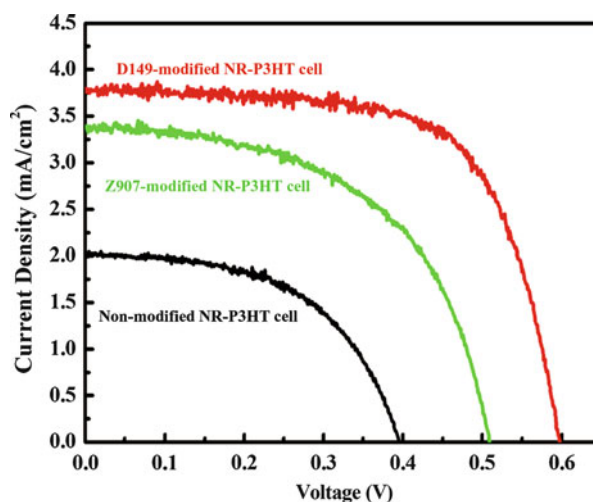

Fig. 20.14 J-V plot for non-modified, Z907 dye modified, D149 dye modified TiO$_2$ NR array-/P3HT-based hybrid cell (Reprinted (adapted) with permission from Ref. [201]. Copyright (2012) American Chemical Society.)

J-V characteristics of non-modified TiO$_2$ NR/P3HT solar cells showed poor device performance with efficiency of 0.43 %. The Z907 and D149 dye modified cells exhibited higher efficiency at 0.94 % for Z907 and 1.58 % for D149. The devices were made by using 650 nm thick TiO$_2$ nanorod arrays. Figure 20.14 shows device performance without and with dyes attached onto TiO$_2$ as surface modifier.

Further enhancement in solar cell performance was observed by using 1.5 μm thick TiO$_2$ NR array and 1.5 μm thick ND array with D149 dye modification. J-V curves showed a significant performance improvement with increasing thickness of TiO$_2$ nanostructured array with TiO$_2$ ND (1.5 μm)–P3HT-based cell showing highest power conversion efficiency at 3.12 % (Fig. 20.15).

Xu et al. in 2012 studied charge transfer in P3HT–TiO$_2$ nanorod composite by photoluminescence quenching [83]. Three different samples were prepared: In first
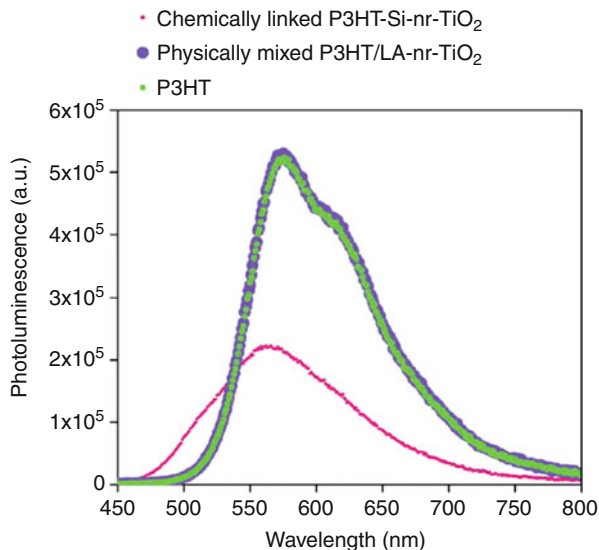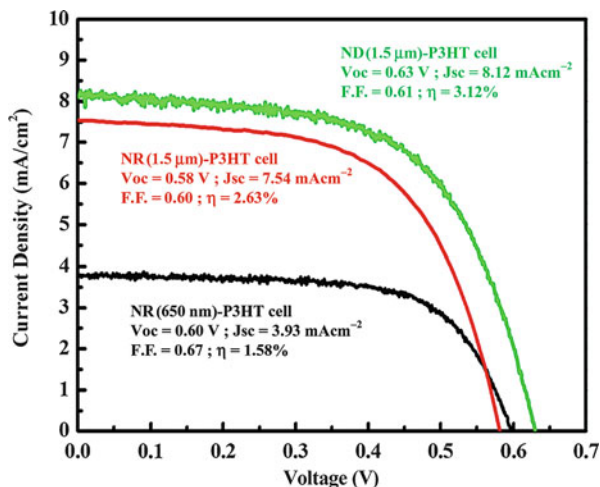
Fig. 20.16 Photoluminescence spectra of chemically linked P3HT–Si–nr–TiO$_2$, physically mixed P3HT/LA–nr–TiO$_2$, and pristine P3HT. The measurement was taken at excitation wavelength of 420 nm (Reproduced from Ref. [83] with permission from The Royal Society of Chemistry)

sample P3HT was chemically linked with TiO$_2$ nanorod (nr) by a linker triethoxy-2-thienylsilane (P3HT–Si–nr–TiO$_2$), second sample was composite of P3HT and TiO$_2$ (P3HT/LA–nr–TiO$_2$), made by physical mixing of P3HT and linoleic acid (LA) capped TiO$_2$ nanorods, and third sample was pristine P3HT itself. Steady state photoluminescence quenching spectra of all three samples were recorded (Fig. 20.16). Photoluminescence quenching was observed in P3HT chemically

linked with TiO_2 nanorods, which was attributed to charge transfer occurring between P3HT and TiO_2 nanorods, whereas physically mixed P3HT–TiO_2 nanorods showed overlap of PL spectrum with pristine P3HT spectrum, indicating no charge transfer occurring in P3HT–TiO_2 composite.

ZnO

ZnO, an n-type material, is used as electron acceptor along with electron-donating polymer in fabricating organic–inorganic hybrid solar cell. ZnO acts as electron transport layer with good electron mobility and is solution processable and environmentally stable. Beek et al. in 2006 reported hybrid solar cells made from blend of ZnO nanoparticles and P3HT with efficiency $\sim$ 0.9 % [7]. Hau et al. in 2008 reported inverted polymer solar cell utilizing ZnO as electron transport layer [202]. Charge collection in inverted solar cell is reverse of regular device structure, in which electrons are collected at front electrode, and holes are collected at back metal electrode. Regular device with structure of ITO/PEDOT:PSS/P3HT:PCBM/LiF/Al and inverted cell with structure of ITO/ZnO/P3HT:PCBM/PEDOT:PSS/Ag were fabricated and tested. Inverted P3HT:PCBM blend (1:0.6 by weight) with a film thickness of 200 nm achieved an efficiency of $\sim$3.5 %. Regular device structure gave an efficiency of $\sim$2.4 %. Fill factor for both device structures was comparable, but J_{sc} and V_{oc} were higher in inverted devices, partly attributed to high interfacial area provided by ZnO nanoparticle layer.

Stability studies of conventional and inverted device were carried out by keeping them in ambient condition and measuring their performance for 40 days. In regular device, it was observed that cell efficiency reduced to less than half of its original value in 1 day and got totally degraded after 4 days (Fig. 20.17a). On the other hand, inverted device was found to be highly stable for 40 days (Fig. 20.17b). All the device parameters remained comparable except J_{sc}, which slightly decreased. In inverted cells, silver electrode can form silver oxide layer in air and thus increase its work function to -5.0 eV. The work function then matches better with HOMO of PEDOT:PSS that is -5.1 eV. Inset of Fig. 20.17a shows the diode behavior in dark condition. The current density at 2 V on the J-V curves of fresh regular solar cells is 2 orders higher that of solar cells left in air for 4 days. However, inverted device shows a much higher stability with V_{oc} and FF remaining almost the same, while J_{sc} decreases slightly. Their dark condition J-V curves are also comparable as shown in inset of Fig. 20.17b.

In 2013, Ka et al. studied the ZnO annealing effects on performance of inverted solar cells [203]. Devices fabricated with ZnO annealed at a low temperature of 80 °C exhibited an efficiency of 3.6 % that is comparable to devices processed at higher annealing temperatures. Several characterization results concluded that the optimum efficiency at low temperature annealing was attributed to improvement in band energy alignment, crystallinity, and relative ZnO amount. Device structures and their J-V curves under different ZnO annealing temperatures are shown in
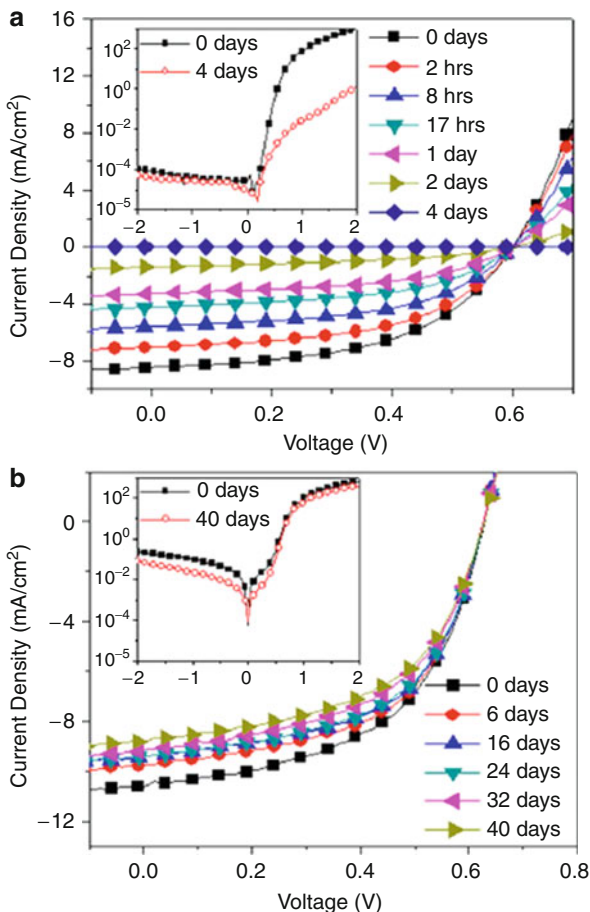
Fig. 20.18. For devices with annealing temperatures (T_a) at 25 °C and 60 °C, J-V curve shows S-shape in nature, indicating inefficient and/or unbalanced electron and hole transport to electrodes, therefore leading to cell efficiency (η) lower than 0.2 %. When the annealing temperature increased to 70 °C, the J-V characteristics improve a lot, leading to a J_{sc} of 9.7 mA/cm^2, V_{oc} of 0.59 V, FF of 0.49, and η of 2.6 %. When further increased to 80 °C or above, device efficiency increased to 3.61 % with a higher fill factor at 0.61. Further increase in ZnO annealing temperature (T_a) to 90 °C and 150 °C resulted in similar device performance as observed for T_a = 80 °C (Fig. 20.18).

Xu et al. in 2013 fabricated organic–inorganic hybrid solar cells and studied donor–acceptor interface by Kelvin probe force microscopy [189]. Cell structure consisted of ITO/ZnO/P3HT/Ag, where two different structures of ZnO (nanoridges and nanorods) were used as active layer for fabricating two different
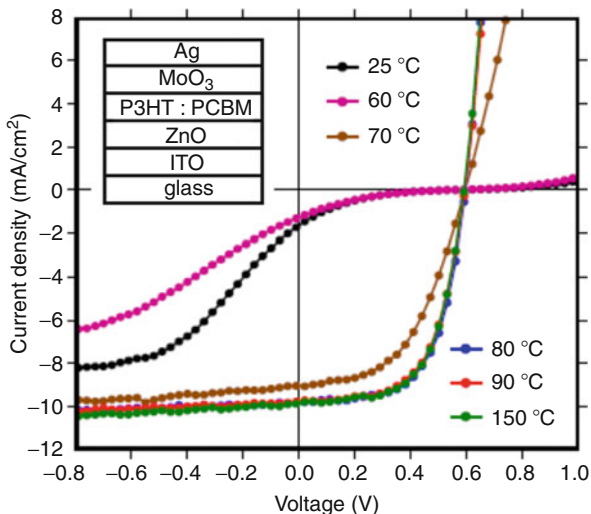
cells. P3HT was spin casted on ZnO films, followed by annealing at 150 °C, for 10 min. Topography and interface studies of ZnO/P3HT films were studied by atomic force microscope (AFM) and Kelvin probe force microscopy (KPFM). Topography of ZnO nanoridge films showed wrinkled shaped morphology which was attributed to stress relaxation caused by slow drying process of film (Fig. 20.19). Surface potential (SP) across the interface of P3HT/ZnO was studied by KPFM, which showed higher SP value for P3HT and lower SP value for ZnO nanoridge region (Fig. 20.19). Surface potential of the interface was measured under dark and illuminated condition. A 0.1 V difference in SP was seen under dark condition and 0.25 V difference under illuminated condition and was attributed to light response of P3HT and ZnO (Fig. 20.19). P3HT shows better light response in comparison to ZnO; therefore, P3HT exhibited higher surface potential than ZnO, allowing a favorable path for electron transfer to ZnO.

Nb_2O_5

Nb_2O_5 is new in the list of oxides, towards which researchers have been showing interest to use as electron transport layer for solar cells. In 2011, Wiranwetchayan et al. reported the use of Nb_2O_5 in fabricating inverted solar cells [204]. A thin film of Nb_2O_5 was introduced in between fluorine-doped tin oxide (FTO) and active layer (P3HT:PCBM) with device structure as glass/FTO/Nb_2O_5/P3HT:PCBM/ PEDOT/Ag. The sol of Nb_2O_5 was used for spin coating a thin film of Nb_2O_5 on FTO, followed by annealing at 450 °C for 1 h to make it crystalline.

Photovoltaic response of the devices without and with Nb_2O_5 was studied. The devices without Nb_2O_5 showed no photovoltaic response; however, devices having a thin film of Nb_2O_5 exhibited an efficiency of 2.7 %. Dependence of film thickness on device efficiency was also studied. The efficiency decreased to zero with increasing thickness. This was attributed to the Nb_2O_5 film thickness increasing more than tunneling path length. As conduction band of Nb_2O_5 is higher than the
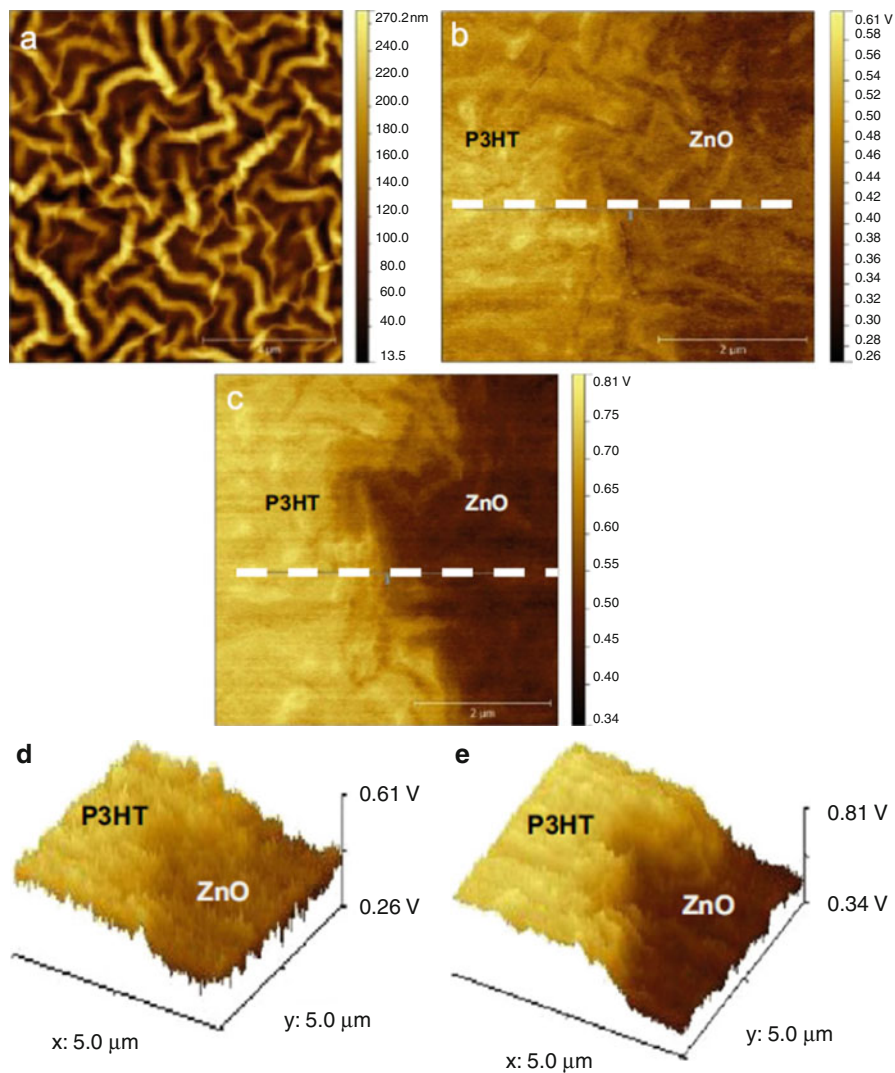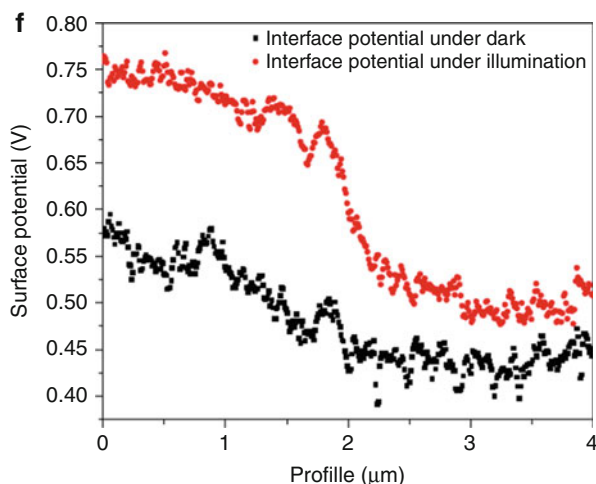

Fig. 20.19 (continued)

Fig. 20.19 (**a**) AFM image showing ZnO nanoridge topography; surface potential image of P3HT/ZnO film in (**b**) dark condition and (**c**) illuminated condition; 3D SP image of P3HT/ZnO film in (**d**) dark condition and (**e**) illuminated condition; cross-section profile of SP in the film (Reproduced with permission from Ref. [189])

LUMO of PCBM, therefore it shows little probability of electron transfer from PCBM to Nb_2O_5. However, Nb_2O_5-based device showed an efficiency of 2.7 %, suggesting that electron transport to electrode takes place through tunneling. Therefore, as film thickness increased, tunneling distance also increased, thus inhibiting electron transport to the electrode.

Later in 2012, Siddiki et al. reported use of Nb_2O_5 as electron transport layer in double junction polymer solar cell [11]. Double junction polymer solar cell was fabricated with structure shown in Fig. 20.20a. Nb_2O_5 was used as an interfacial layer for electron transport between front and back cell. 25 nm thick Nb_2O_5 film showed >90 % transmittance in the visible region. J-V characteristics of double junction cell and individual cells are shown in Fig. 20.20b. Device efficiency of double junction cell was found to be 0.8 % with a V_{oc} of 1.3 V, which was higher than individual front and back cells. The J_{sc} of double junction solar cell is less than the individual cells. The series resistance was also found to be increased in the double junction cell. The decrease in J_{sc} and increase of series resistance were possibly caused by two factors: (1) mismatch in current between front and back cells and (2) barrier formed at the interfacial layer between the two cells. The higher V_{oc} indicated Nb_2O_5 can be used as electron transport layer in double junction polymer solar cells. Simulation results showed that device performance using Nb_2O_5 could be improved by current matching of individual cells and reducing series resistance.

Fig. 20.20 (a) Device structure of double junction polymer solar cells and (b) J-V plots of front cell, back cell, double junction solar cell (Reproduced from Ref. [11], with permission from the PCCP Owner Societies.)
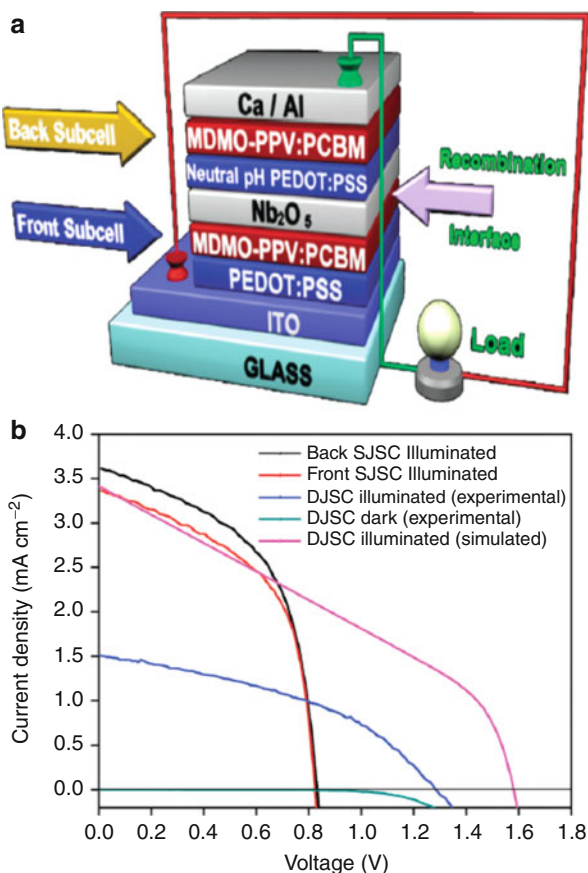
CuO

Copper oxide has been recently used as interfacial layer to improve the stability in polymer solar cells. Wang et al. in 2011 fabricated polymer bulk heterojunction solar cells by introducing CuO_x layer in between cathode and P3HT:PCBM [10]. Two device structures were fabricated: one with a thin layer (~5 nm) of CuO_x which was deposited by thermal evaporation in a structure of ITO/PEDOT:PSS/P3HT:PCBM/CuO_x/Al and the other was a bilayer of CuO_x and LiF in a device structure of ITO/PEDOT:PSS/P3HT:PCBM/LiF/CuO_x/Al and ITO/PEDOT:PSS/P3HT:PCBM/CuO_x/LiF/Al.

The thickness of LiF was 0.6 nm. The devices without CuO_x interfacial layer showed an efficiency of 1.5 %, while that using CuO_x as interfacial layer exhibited a similar efficiency but a higher J_{sc} and lower V_{oc}. Decrease in V_{oc} was attributed to the high work function of CuO_x in comparison to aluminum. On the other hand,

devices fabricated using a bilayer of CuO_x/LiF showed improvement in V_{oc}. Introduction of CuO_x improved device stability, but did not show improvement in device performance. Device stability was monitored by keeping the devices made without and with CuO_x in air. Devices without CuO_x layer showed ~50 % efficiency decrease after 3 h in air, which was mainly due to decrease in J_{sc}. The devices made using CuO_x/LiF exhibited a 40 % efficiency increase, which was probably due to increase in V_{oc} and FF when kept in air. The increase in V_{oc} and FF was attributed to the oxidation of CuO_x in air, leading to increase in shunt resistance and reduction of quenching of excitons and charge carriers occurring at the metal cathode. Device with CuO_x layers retained ~80 % of the initial efficiency after 240 h and ~50 % after 500 h. Therefore, it was concluded that use of LiF and CuO_x improved charge collection and increased V_{oc} and FF of devices.

Conclusion

General synthesis methods of common nanomaterials including TiO_2, ZnO, Nb_2O_5, and CuO with 0D, 1D, 2D, and 3D hierarchical nanostructures and their applications in solar cells have been reviewed in this chapter. Although laboratory-based synthesis methods have been extensively developed, there are still few methods that can realize large-scale, low-cost, and environmental-friendly synthesis processing, especially for the synthesis of some specific structures, such as TiO_2 and ZnO nanoarrays. However, applications usually require metal oxides have special structures with aimed properties. For TiO_2 and ZnO films used in polymer-inorganic hybrid solar cells as efficient electron transport layer, high crystallinity and surface area are required to facilitate charge separation and transport. Thus, design of ideal structures with large-scale synthesis capability is one of the largest missions of inorganic synthetic chemistry. Nanostructured metal oxides have played an important role in improving polymer-inorganic hybrid solar cell performance. These inorganic metal oxides possess high charge mobility, solution processability, and are environmentally stable. Therefore introduction of metal oxides into solar cells has led to improvement in performance of polymer-inorganic hybrid solar cells. Nanostructured metal oxides have brought new design and properties in fabricating solar cells.

References

1. Alparslan Z, Kosemen A, Ornek O et al (2011) TiO_2-based organic hybrid solar cells withMn^{+2} doping. Int J Photoenergy
2. Breeze AJ, Schlesinger Z, Carter SA (2001) Charge transport in TiO_2/MEH-PPV polymer photovoltaics. Phys Rev B 64(125205):1–9

3. Bouclé J, Chyla S, Shaffer MSP et al (2008) Hybrid solar cells from a blend of poly (3-hexylthiophene) and ligand-capped TiO_2 nanorods. Adv Funct Mater 18(4):622–633

4. Chang C-H, Huang T-K, Lin Y-T et al (2008) Improved charge separation and transport efficiency in poly(3-hexylthiophene)–TiO_2 nanorod bulk heterojunction solar cells. J Mater Chem 18(19):2201–2207

5. Liang S, Zhu G, Wenbin G, Chen T, Xindong Z, Caixia L, Weiyou C, Shengping R, Zhicheng Z (2008) Performance improvement of TiO_2/P3HT solar cells using CuPc as a sensitizer. Appl Phys Lett 92(7):073307

6. Beek WJE, Slooff LH, Wienk MM et al (2005) Hybrid ZnO: polymer bulk heterojunction solar cells from a ZnO precursor. In: Organic photovoltaics VI. SPIE

7. Beek W, Wienk M, Janssen R (2006) Hybrid solar cells from regioregular polythiophene and ZnO nanoparticles. Adv Funct Mater 16(8):1112–1116

8. Beek WJE, Wienk MM, Janssen RAJ (2005) Hybrid bulk heterojunction solar cells: blends of ZnO semiconducting nanoparticles and conjugated polymers. In: Organic photovoltaics VI. SPIE

9. Kuwabara T, Kawahara Y, Yamaguchi T et al (2009) Characterization of inverted-type organic solar cells with a ZnO layer as the electron collection electrode by ac impedance spectroscopy. ACS Appl Mater Interfaces 1(10):2107–2110

10. Wang M, Xie F, Xie W et al (2011) Device lifetime improvement of polymer-based bulk heterojunction solar cells by incorporating copper oxide layer at Al cathode. Appl Phys Lett 98(18):183304

11. Siddiki MK, Venkatesan S, Qiao Q (2012) Nb_2O_5 as a new electron transport layer for double junction polymer solar cells. Phys Chem Chem Phys 14(14):4682–4686

12. Chen X, Mao SS (2007) Titanium dioxide nanomaterials: synthesis, properties, modifications, and applications. Chem Rev 107(7):2891–2959

13. Chen H, Nanayakkara C, Grassian V (2012) Titanium dioxide photocatalysis in atmospheric chemistry. Chem Rev 112(11):5919–5948

14. Biswas P, Kundu S, Banerji P (2013) A study on electrical transport vis-a-vis the effect of thermal annealing on the p-type conductivity in arsenic-doped MOCVD grown ZnO in the temperature range 10–300 K. J Alloys Compd 552:304–309

15. Liu CY, Zhang BP, Binh NT et al (2006) Temperature dependence of structural and optical properties of ZnO films grown on Si substrates by MOCVD. J Cryst Growth 290(2):314–318

16. Pradhan SK, Reucroft PJ, Yang FQ et al (2003) Growth of TiO_2 nanorods by metalorganic chemical vapor deposition. J Cryst Growth 256(1–2):83–88

17. Liu B, Hu Z, Che Y et al (2008) Growth of ZnO nanoparticles and nanorods with ultrafast pulsed laser deposition. Appl Phys A Mater Sci Process 93(3):813–818

18. Limmer SJ, Seraji S, Wu Y et al (2002) Template-based growth of various oxide nanorods by sol-gel electrophoresis. Adv Funct Mater 12(1):59–64

19. Antonelli DM, Ying JY (1995) Synthesis of hexagonally packed mesoporous TiO_2 by a modified sol-gel method. Angew Chem Int Ed 34(18):2014–2017

20. Lakshmi BB, Patrissi CJ, Martin CR (1997) Sol-gel template synthesis of semiconductor oxide micro- and nanostructures. Chem Mater 9(11):2544–2550

21. Yanan F, Zhengguo J, Weijiang X et al (2008) Ordered macro-mesoporous nc-TiO_2 films by sol-gel method using polystyrene array and triblock copolymer bitemplate. J Am Ceram Soc 91(8):2676–2682

22. Spanhel L, Anderson MA (1991) Semiconductor clusters in the sol-gel process: quantized aggregation, gelation, and crystal growth in concentrated zinc oxide colloids. J Am Chem Soc 113(8):2826–2833

23. Rahnama A, Gharagozlou M (2012) Preparation and properties of semiconductor CuO nanoparticles via a simple precipitation method at different reaction temperatures. Opt Quant Electron 44(6–7):313–322

24. Bavykin DV, Parmon VN, Lapkin AA et al (2004) The effect of hydrothermal conditions on the mesoporous structure of TiO_2 nanotubes. J Mater Chem 14(22):3370–3377

25. Andersson M, Osterlund L, Ljungstrom S et al (2002) Preparation of nanosize anatase and rutile TiO_2 by hydrothermal treatment of microemulsions and their activity for photocatalytic wet oxidation of phenol. J Phys Chem B 106(41):10674–10679

26. Wu MM, Long JB, Huang AH et al (1999) Microemulsion-mediated hydrothermal synthesis and characterization of nanosize rutile and anatase particles. Langmuir 15(26):8822–8825

27. Guixiang D, Lidong Z, Yan F et al (2012) Controllable synthesis of ZnO architectures by a surfactant-free hydrothermal process. Mater Lett 73:86–88

28. Yang J, Mei S, Ferreira JMF (2001) Hydrothermal synthesis of TiO_2 nanopowders from tetraalkylammonium hydroxide peptized sols. Mater Sci Eng C-Biomimetic Supramol Syst 15(1–2):183–185

29. Patil KC, Aruna ST, Ekambaram S (1997) Combustion synthesis. Curr Opin Solid State Mater Sci 2(2):158–165

30. Nagaveni K, Hegde MS, Madras G (2004) Structure and photocatalytic activity of $Ti_{1-x}M_xO_{2\pm\delta}$ (M = W, V, Ce, Zr, Fe, and Cu) synthesized by solution combustion method. J Phys Chem B 108(52):20204–20212

31. Jimenez-Gonzalez AE, Urueta JAS, Suarez-Parra R (1998) Optical and electrical characteristics of aluminum-doped ZnO thin films prepared by solgel technique. J Cryst Growth 192(3–4):430–438

32. Cong Y, Zhang J, Chen F et al (2007) Synthesis and characterization of nitrogen-doped TiO_2 nanophotocatalyst with high visible light activity. J Phys Chem C 111(19):6976–6982

33. Elias J, Levy-Clement C, Bechelany M et al (2010) Hollow Urchin-like ZnO thin films by electrochemical deposition. Adv Mater 22(14):1607–+

34. Roy P, Berger S, Schmuki P (2011) TiO_2 nanotubes: synthesis and applications. Angew Chem Int Ed 50(13):2904–2939

35. Kong M, Zhang W, Yang Z et al (2011) Facile synthesis of CuO hollow nanospheres assembled by nanoparticles and their electrochemical performance. Appl Surf Sci 258(4):1317–1321

36. Kafi AKM, Wu G, Chen A (2008) A novel hydrogen peroxide biosensor based on the immobilization of horseradish peroxidase onto Au-modified titanium dioxide nanotube arrays. Biosens Bioelectron 24(4):566–571

37. Izaki M, Watanabe M, Aritomo H et al (2008) Zinc oxide nano-cauliflower array with room temperature ultraviolet light emission. Cryst Growth Des 8(4):1418–1421

38. Xu J, Yang X, Yang QD et al (2012) Arrays of CdSe sensitized ZnO/ZnSe nanocables for efficient solar cells with high open-circuit voltage. J Mater Chem 22(26):13374–13379

39. Sakthivel S, Janczarek M, Kisch H (2004) Visible light activity and photoelectrochemical properties of nitrogen-doped TiO_2. J Phys Chem B 108(50):19384–19387

40. Zhang X, Wang G, Zhang W et al (2008) Seed-mediated growth method for epitaxial array of CuO nanowires on surface of Cu nanostructures and its application as a glucose sensor. J Phys Chem C 112(24):8856–8862

41. Kongkanand A, Tvrdy K, Takechi K et al (2008) Quantum dot solar cells. Tuning photoresponse through size and shape control of CdSe-TiO_2 architecture. J Am Chem Soc 130(12):4007–4015

42. Cho IS, Chen Z, Forman AJ et al (2011) Branched TiO_2 nanorods for photoelectrochemical hydrogen production. Nano Lett 11(11):4978–4984

43. Zhang Z, Zhang L, Hedhili M et al (2013) Plasmonic gold nanocrystals coupled with photonic crystal seamlessly on TiO_2 nanotube photoelectrodes for efficient visible light photoelectrochemical water splitting. Nano Lett 13(1):14–20

44. Zhu K, Neale NR, Miedaner A et al (2007) Enhanced charge-collection efficiencies and light scattering in dye-sensitized solar cells using oriented TiO_2 nanotubes arrays. Nano Lett 7(1):69–74

45. Fujishima A, Honda K (1972) Electrochemical photolysis of water at a semiconductor electrode. Nature 238(5358):37–38

46. Zeng HB, Cui JB, Cao BQ et al (2010) Electrochemical deposition of ZnO nanowire arrays: organization, doping, and properties. Sci Adv Mater 2(3):336–358

47. Fujishima A, Zhang X, Tryk DA (2008) TiO_2 photocatalysis and related surface phenomena. Surf Sci Rep 63(12):515–582

48. Inoue T, Fujishima A, Konishi S et al (1979) Photoelectrocatalytic reduction of carbon dioxide in aqueous suspensions of semiconductor powders. Nature 277(5698):637–638

49. Law M, Greene LE, Johnson JC et al (2005) Nanowire dye-sensitized solar cells. Nat Mater 4(6):455–459

50. O'Regan B, Gratzel M (1991) A low-cost, high-efficiency solar cell based on dye-sensitized colloidal TiO_2 films. Nature 353(6346):737–740

51. Senthilarasu S, Peiris TAN, Jorge G-C et al (2012) Preparation of nanocrystalline TiO_2 electrodes for flexible dye-sensitized solar cells: influence of mechanical compression. J Phys Chem C 116:19053–19061

52. Bao S-J, Li CM, Zang J-F et al (2008) New nanostructured TiO_2 for direct electrochemistry and glucose sensor applications. Adv Funct Mater 18(4):591–599

53. Sakthivel S, Kisch H (2003) Daylight photocatalysis by carbon-modified titanium dioxide. Angew Chem Int Ed 42(40):4908–4911

54. Su W, Zhang Y, Li Z et al (2008) Multivalency iodine doped TiO_2: preparation, characterization, theoretical studies, and visible-light photocatalysis. Langmuir 24(7):3422–3428

55. Varley J, Janotti A, Van de Walle C (2011) Mechanism of visible-light photocatalysis in nitrogen-doped TiO_2. Adv Mater 23(20):2343–2347

56. Li Z, Zhang H, Zheng W et al (2008) Highly sensitive and stable humidity nanosensors based on LiCl doped TiO_2 electrospun nanofibers. J Am Chem Soc 130(15):5036–+

57. Lu C, Chen Z (2009) High-temperature resistive hydrogen sensor based on thin nanoporous rutile TiO(2) film on anodic aluminum oxide. Sensor Actuat B-chem 140(1):109–115

58. Lu HF, Li F, Liu G et al (2008) Amorphous TiO(2) nanotube arrays for low-temperature oxygen sensors. Nanotechnology 19(40)

59. Yang L, Luo S, Cai Q et al (2010) A review on TiO_2 nanotube arrays: fabrication, properties, and sensing applications. Chin Sci Bull 55(4–5):331–338

60. Zhang Y, Fu W, Yang H et al (2008) Synthesis and characterization of TiO(2) nanotubes for humidity sensing. Appl Surf Sci 254(17):5545–5547

61. Kim JY, Kim SH, Lee HH et al (2006) New architecture for high-efficiency polymer photovoltaic cells using solution-based titanium oxide as an optical spacer. Adv Mater 18(5):572–+

62. Kokubo T, Kim HM, Kawashita M (2003) Novel bioactive materials with different mechanical properties. Biomaterials 24(13):2161–2175

63. Chae SY, Park MK, Lee SK et al (2003) Preparation of size-controlled TiO_2 nanoparticles and derivation of optically transparent photocatalytic films. Chem Mater 15(17):3326–3331

64. Yu JC, Yu JG, Ho WK et al (2002) Effects of F-doping on the photocatalytic activity and microstructures of nanocrystalline TiO_2 powders. Chem Mater 14(9):3808–3816

65. Carp O, Huisman CL, Reller A (2004) Photoinduced reactivity of titanium dioxide. Prog Solid State Chem 32(1–2):33–177

66. Cot F, Larbot A, Nabias G et al (1998) Preparation and characterization of colloidal solution derived crystallized titania powder. J Eur Ceram Soc 18(14):2175–2181

67. Pinna N, Niederberger M (2008) Surfactant-free nonaqueous synthesis of metal oxide nanostructures. Angew Chem Int Ed 47(29):5292–5304

68. Li XL, Peng Q, Yi JX et al (2006) Near monodisperse TiO_2 nanoparticles and nanorods. Chem Eur J 12(8):2383–2391

69. Shah SI, Li W, Huang CP et al (2002) Study of Nd3+, Pd2+, Pt4+, and Fe3+ dopant effect on photoreactivity of TiO_2 nanoparticles. Proc Natl Acad Sci USA 99:6482–6486

70. Chen C-A, Chen Y-M, Huang Y-S et al (2009) Synthesis and characterization of well-aligned anatase TiO_2 nanocrystals on fused silica via metal-organic vapor deposition. Cryst Eng Comm 11(11):2313–2318

71. Yang HG, Sun CH, Qiao SZ et al (2008) Anatase TiO(2) single crystals with a large percentage of reactive facets. Nature 453(7195):638-U4

72. Li GS, Li LP, Boerio-Goates J et al (2005) High purity anatase TiO_2 nanocrystals: near room-temperature synthesis, grain growth kinetics, and surface hydration chemistry. J Am Chem Soc 127(24):8659–8666

73. Burnside SD, Shklover V, Barbe C et al (1998) Self-organization of TiO_2 nanoparticles in thin films. Chem Mater 10(9):2419–2425

74. Sugimoto T, Zhou XP, Muramatsu A (2003) Synthesis of uniform anatase TiO_2 nanoparticles by gel-sol method 3. Formation process and size control. J Colloid Interface Sci 259(1):43–52

75. Sugimoto T, Zhou XP, Muramatsu A (2003) Synthesis of uniform anatase TiO_2 nanoparticles by gel-sol method 4. Shape control. J Colloid Interface Sci 259(1):53–61

76. Sugimoto T, Zhou XP, Muramatsu A (2002) Synthesis of uniform anatase TiO_2 nanoparticles by gel-sol method – 1. Solution chemistry of Ti(OH)(n)((4-n)+) complexes. J Colloid Interface Sci 252(2):339–346

77. Sugimoto T, Zhou XP (2002) Synthesis of uniform anatase TiO_2 nanoparticles by the gel-sol method – 2. Adsorption of OH- ions to Ti(OH)(4) gel and TiO_2 particles. J Colloid Interface Sci 252(2):347–353

78. Sugimoto T, Okada K, Itoh H (1997) Synthesis of uniform spindle-type titania particles by the gel-sol method. J Colloid Interface Sci 193(1):140–143

79. Fu G, Vary P, Lin C-T (2005) Anatase TiO_2 nanocomposites for antimicrobial coatings. J Phys Chem B 109(18):8889–8898

80. Kasuga T, Hiramatsu M, Hoson A et al (1998) Formation of titanium oxide nanotube. Langmuir 14(12):3160–3163

81. Zhong ZY, Yin YD, Gates B et al (2000) Preparation of mesoscale hollow spheres of TiO_2 and SnO_2 by templating against crystalline arrays of polystyrene beads. Adv Mater 12(3):206-+

82. Qiao QQ, McLeskey JT (2005) Water-soluble polythiophene/nanocrystalline TiO_2 solar cells. Appl Phys Lett 86(15):153501

83. Xu T, Yan M, Hoefelmeyer JD et al (2012) Exciton migration and charge transfer in chemically linked P3HT-TiO_2 nanorod composite. RSC Adv 2(3):854–862

84. Kang SH, Choi S-H, Kang M-S et al (2008) Nanorod-based dye-sensitized solar cells with improved charge collection efficiency. Adv Mater 20(1):54-+

85. Cozzoli PD, Kornowski A, Weller H (2003) Low-temperature synthesis of soluble and processable organic-capped anatase TiO_2 nanorods. J Am Chem Soc 125(47):14539–14548

86. Wu J-M (2004) Low-temperature preparation of titania nanorods through direct oxidation of titanium with hydrogen peroxide. J Cryst Growth 269(2–4):347–355

87. Liu B, Aydil ES (2009) Growth of oriented single-crystalline rutile TiO_2 nanorods on transparent conducting substrates for dye-sensitized solar cells. J Am Chem Soc 131(11):3985–3990

88. Hoyer P (1996) Formation of a titanium dioxide nanotube array. Langmuir 12(6):1411–1413

89. Daoai W, Tianchang H, Litian H et al (2009) Microstructured arrays of TiO_2 nanotubes for improved photo-electrocatalysis and mechanical stability. Adv Funct Mater 19

90. Tsai C, Teng H (2006) Structural features of nanotubes synthesized from NaOH treatment on TiO_2 with different post-treatments. Chem. Mater 18(2):367–373

91. Lan Y, Gao XP, Zhu HY et al (2005) Titanate nanotubes and nanorods prepared from rutile powder. Adv Funct Mater 15(8):1310–1318

92. Tian ZRR, Voigt JA, Liu J et al (2003) Large oriented arrays and continuous films of TiO_2-based nanotubes. J Am Chem Soc 125(41):12384–12385

93. Macak JM, Tsuchiya H, Schmuki P (2005) High-aspect-ratio TiO_2 nanotubes by anodization of titanium. Angew Chem Int Ed 44(14):2100–2102

94. Jan MM, Cordt Z, Brian JR et al (2009) Ordered ferroelectric lead titanate nanocellular structure by conversion of anodic TiO_2 nanotubes. Adv Mater 21:3121–3125

95. Mor GK, Shankar K, Paulose M et al (2006) Use of highly-ordered TiO_2 nanotube arrays in dye-sensitized solar cells. Nano Lett 6(2):215–218

96. Bavykin DV, Friedrich JM, Walsh FC (2006) Protonated titanates and TiO_2 nanostructured materials: synthesis, properties, and applications. Adv Mater 18(21):2807–2824

97. Yuan ZY, Zhou WZ, Su BL (2002) Hierarchical interlinked structure of titanium oxide nanofibers. Chem Commun 2(11):1202–1203

98. Joshi P, Zhang L, Davoux D et al (2010) Composite of TiO_2 nanofibers and nanoparticles for dye-sensitized solar cells with significantly improved efficiency. Energy Environ Sci 3(10):1507–1510

99. Qidong T, Xingzhong Z, Feng Y (2010) Hybrid solar cells based on poly(3-hexylthiophene) and electrospun TiO_2 nanofibers with effective interface modification. J Mater Chem 20:7366–7371

100. Drew C, Liu X, Ziegler D et al (2003) Metal oxide-coated polymer nanofibers. Nano Lett 3(2):143–147

101. Li D, Xia YN (2003) Fabrication of titania nanofibers by electrospinning. Nano Lett 3(4):555–560

102. Li D, Xia YN (2003) Rapid fabrication of titania nanofibers by electrospinning. In: Cao G, Xia Y, Braun PV (eds) Nanomaterials and their optical applications. pp 17–24

103. Choi W, Termin A, Hoffmann MR (1994) The role of metal ion dopants in quantum-sized TiO_2: correlation between photoreactivity and charge carrier recombination dynamics. J Phys Chem 98(51):13669–13679

104. Gole JL, Stout JD, Burda C et al (2003) Highly efficient formation of visible light tunable $TiO_{2-x}N_x$ photocatalysts and their transformation at the nanoscale. J Phys Chem B 108(4):1230–1240

105. Park JH, Kim S, Bard AJ (2005) Novel carbon-doped TiO_2 nanotube arrays with high aspect ratios for efficient solar water splitting. Nano Lett 6(1):24–28

106. Burda C, Lou Y, Chen X et al (2003) Enhanced nitrogen doping in TiO_2 nanoparticles. Nano Lett 3(8):1049–1051

107. Ohno T (2004) Preparation of visible light active S-doped TiO_2 photocatalysts and their photocatalytic activities. Water Sci Technol 49(4):159–163

108. Luo H, Takata T, Lee Y et al (2004) Photocatalytic activity enhancing for titanium dioxide by co-doping with bromine and chlorine. Chem Mater 16(5):846–849

109. Hsieh CY, Lu ML, Chen JY et al (2012) Single ZnO nanowire-PZT optothermal field effect transistors. Nanotechnology 23(35)

110. Yang M, Kim HC, Hong SH (2012) DMMP gas sensing behavior of ZnO-coated single-wall carbon nanotube network sensors. Mater Lett 89:312–315

111. Xu CK, Wu JM, Desai UV et al (2012) High-efficiency solid-state dye-sensitized solar cells based on TiO_2-coated ZnO nanowire arrays. Nano Lett 12(5):2420–2424

112. Tingting X, Qiquan Q (2011) Conjugated polymer–inorganic semiconductor hybrid solar cells. Energy Environ Sci 4:2700–2720

113. Shangke P, Tingting X, Swaminathan V et al (2012) Direct growth of CdSe nanorods on ITO substrates by co-anchoring of ZnO nanoparticles and ethylenediamine. J Nanopart Res 14:1115

114. Xie Y, Joshi P, Darling SB et al (2010) Electrolyte effects on electron transport and recombination at ZnO nanorods for dye-sensitized solar cells. J Phys Chem C 114(41):17880–17888

115. Tingting X, Swaminathan V, David G et al (2013) Study of polymer/ZnO nanostructure interfaces by Kelvin probe force microscopy. Sol Energy Mater Sol Cells 108:246–251

116. Afsal M, Wang CY, Chu LW et al (2012) Highly sensitive metal-insulator-semiconductor UV photodetectors based on ZnO/SiO_2 core-shell nanowires. J Mater Chem 22(17):8420–8425

117. Gao PX, Song JH, Liu J et al (2007) Nanowire piezoelectric nanogenerators on plastic substrates as flexible power sources for nanodevices. Adv Mater 19(1):67–+

118. Soomro MY, Hussain I, Bano N et al (2012) Piezoelectric power generation from zinc oxide nanowires grown on paper substrate. Phys Status Solidi-R 6(2):80–82

119. Kawano T, Imai H (2010) Nanoscale morphological design of ZnO crystals grown in aqueous solutions. J Ceram Soc Jpn 118(1383):969–976
120. Wang XD, Summers CJ, Wang ZL (2004) Large-scale hexagonal-patterned growth of aligned ZnO nanorods for nano-optoelectronics and nanosensor arrays. Nano Lett 4(3):423–426
121. Chen JJ, Gao Y, Zeng F et al (2004) Effect of sputtering oxygen partial pressures on structure and physical properties of high resistivity ZnO films. Appl Surf Sci 223(4):318–329
122. Hu Z, Oskam G, Searson PC (2003) Influence of solvent on the growth of ZnO nanoparticles. J Colloid Interface Sci 263(2):454–460
123. Yadav RS, Mishra P, Pandey AC (2008) Growth mechanism and optical property of ZnO nanoparticles synthesized by sonochemical method. Ultrason Sonochem 15(5):863–868
124. Kawano T, Imai H (2006) Fabrication of ZnO nanoparticles with various aspect ratios through acidic and basic routes. Cryst Growth Des 6(4):1054–1056
125. Distaso M, Klupp Taylor RN, Taccardi N et al (2011) Influence of the counterion on the synthesis of ZnO mesocrystals under solvothermal conditions. Chemistry 17(10):2923–2930
126. Jézéquel D, Guenot J, Jouini N et al (1995) Submicrometer zinc oxide particles: elaboration in polyol medium and morphological characteristics. J Mater Res 10(01):77–83
127. Zhang Q, Chou T, Russo B et al (2008) Aggregation of ZnO nanocrystallites for high conversion efficiency in dye-sensitized solar cells. Angew Chem Int Ed 47(13):2402–2406
128. Shinde SS, Korade AP, Bhosale CH et al (2013) Influence of tin doping onto structural, morphological, optoelectronic and impedance properties of sprayed ZnO thin films. J Alloys Compd 551:688–693
129. Chen Y-Y, Hsu J-C, Lee C-Y et al (2013) Influence of oxygen partial pressure on structural, electrical, and optical properties of Al-doped ZnO film prepared by the ion beam co-sputtering method. J Mater Sci 48(3):1225–1230
130. Ramgir NS, Late DJ, Bhise AB et al (2006) ZnO multipods, submicron wires, and spherical structures and their unique field emission behavior. J Phys Chem B 110(37):18236–18242
131. Ng HT, Chen B, Li J et al (2003) Optical properties of single-crystalline ZnO nanowires on m-sapphire. Appl Phys Lett 82(13):2023–2025
132. Lee WN, Jeong MC, Myoung JM (2004) Fabrication and application potential of ZnO nanowires grown on GaAs(002) substrates by metal-organic chemical vapour deposition. Nanotechnology 15(3):254–259
133. Ramsdale CM, Greenham NC (2002) Ellipsometric determination of anisotropic optical constants in electroluminescent conjugated polymers. Adv Mater 14(3):212–+
134. Vayssieres L (2003) Growth of arrayed nanorods and nanowires of ZnO from aqueous solutions. Adv Mater 15(5):464–466
135. Greene LE, Law M, Tan DH et al (2005) General route to vertical ZnO nanowire arrays using textured ZnO seeds. Nano Lett 5(7):1231–1236
136. Xu TT, Chen QL, Lin DH et al (2011) Self-assembled thienylsilane molecule as interfacial layer for ZnO nanowire/polymer hybrid system. J Photonics Energy 1(1):011107
137. Hu P, Liu YQ, Wang XB et al (2003) Tower-like structure of ZnO nanocolumns. Chem Commun 3(11):1304–1305
138. Wang Z, Qian XF, Yin J et al (2004) Large-scale fabrication of tower-like, flower-like, and tube-like ZnO arrays by a simple chemical solution route. Langmuir 20(8):3441–3448
139. Liang Y, Zhang X, Qin L et al (2006) Ga-assisted synthesis and optical properties of ZnO submicron- and nanotowers. J Phys Chem B 110(43):21593–21595
140. Xiao J, Zhang X, Zhang G (2008) Field emission from zinc oxide nanotowers: the role of the top morphology. Nanotechnology 19(29):295706
141. Wang F, Cao L, Pan A et al (2007) Synthesis of tower-like ZnO structures and visible photoluminescence origins of varied-shaped ZnO nanostructures. J Phys Chem C 111(21):7655–7660

142. Wang WW, Zhu YJ (2004) Shape-controlled synthesis of zinc oxide by microwave heating using an imidazolium salt. Inorg Chem Commun 7(9):1003–1005

143. Gao XD, Li XM, Yu WD (2005) Flowerlike ZnO nanostructures via hexamethylenetetramine-assisted thermolysis of zinc-ethylenediamine complex. J Phys Chem B 109(3):1155–1161

144. Umetsu M, Mizuta M, Tsumoto K et al (2005) Bioassisted room-temperature immobilization and mineralization of zinc oxide – the structural ordering of ZnO nanoparticles into a flower-type morphology. Adv Mater 17(21):2571–+

145. Li P, Liu H, Zhang Y-F et al (2007) Synthesis of flower-like ZnO microstructures via a simple solution route. Mater Chem Phys 106(1):63–69

146. Wahab R, Ansari SG, Kim YS et al (2007) Low temperature solution synthesis and characterization of ZnO nano-flowers. Mater Res Bull 42(9):1640–1648

147. Peng WQ, Qu SC, Cong GW et al (2006) Synthesis and structures of morphology-controlled ZnO nano- and microcrystals. Cryst Growth Des 6(6):1518–1522

148. Xie Q, Dai Z, Liang HB et al (2005) Synthesis of ZnO three-dimensional architectures and their optical properties. Solid State Commun 136(5):304–307

149. Sun F, Qiao X, Tan F et al (2012) Fabrication and photocatalytic activities of ZnO arrays with different nanostructures. Appl Surf Sci 263:704–711

150. Fang Z, Tang K, Shen G et al (2006) Self-assembled ZnO 3D flowerlike nanostructures. Mater Lett 60(20):2530–2533

151. Ye CH, Fang XS, Hao YF et al (2005) Zinc oxide nanostructures: Morphology derivation and evolution. J Phys Chem B 109(42):19758–19765

152. Ozgur U, Alivov YI, Liu C et al (2005) A comprehensive review of ZnO materials and devices. J Appl Phys 98(4):41301

153. Tran VT, Shinya M (2010) Synthesis of high-quality Al-doped ZnO nanoink. J Appl Phys 107:014308

154. Pearton SJ, Heo WH, Ivill M et al (2004) Dilute magnetic semiconducting oxides. Semicond Sci Technol 19(10):R59–R74

155. Park CH, Zhang SB, Wei SH (2002) Origin of p-type doping difficulty in ZnO: the impurity perspective. Phys Rev B 66(7):073202(1-3)

156. Matsumoto Y, Murakami M, Jin ZW et al (1999) Combinatorial laser molecular beam epitaxy (MBE) growth of Mg-Zn-O alloy for band gap engineering. Jpn J Appl Phys Part 2 38(6AB):L603–L605

157. Liu W-S, Chen W-K, Hsueh K-P (2013) Transparent conductive Ga-doped $Mg_xZn_{1-x}O$ films with high optical transmittance prepared by radio frequency magnetron sputtering. J Alloys Compd 552:255–263

158. Wan Q, Li QH, Chen YJ et al (2004) Positive temperature coefficient resistance and humidity sensing properties of Cd-doped ZnO nanowires. Appl Phys Lett 84(16):3085–3087

159. Wang YS, Thomas PJ, O'Brien P (2006) Optical properties of ZnO nanocrystals doped with Cd, Mg, Mn, and Fe ions. J Phys Chem B 110(43):21412–21415

160. Fernandes GE, Lee D-J, Kim JH et al (2013) Infrared and microwave shielding of transparent Al-doped ZnO superlattice grown via atomic layer deposition. J Mater Sci 48(6):2536–2542

161. Kumar S, Chen CL, Dong CL et al (2013) Structural, optical, and magnetic characterization of Co and N co-doped ZnO nanopowders. J Mater Sci 48(6):2618–2623

162. Zhou Y, Qiu Z, Lü M et al (2008) Preparation and characterization of porous Nb_2O_5 nanoparticles. Mater Res Bull 43(6):1363–1368

163. Uekawa N, Kudo T, Mori F et al (2003) Low-temperature synthesis of niobium oxide nanoparticles from peroxo niobic acid sol. J Colloid Interface Sci 264(2):378–384

164. Buha J, Arcon D, Niederberger M et al (2010) Solvothermal and surfactant-free synthesis of crystalline Nb_2O_5, Ta_2O_5, HfO_2, and Co-doped HfO_2 nanoparticles. Phys Chem Chem Phys 12(47):15537–15543

165. Suramwar NV, Thakare SR, Karade NN et al (2012) Green synthesis of predominant (1 1 1) facet CuO nanoparticles: Heterogeneous and recyclable catalyst for N-arylation of indoles. J Mol Catal A Chem 359:28–34

166. Liu S, Tian J, Wang L et al (2012) A simple route for preparation of highly stable CuO nanoparticles for nonenzymatic glucose detection. Catal Sci Technol 2(4):813–817

167. Wang H, Xu J-Z, Zhu J-J et al (2002) Preparation of CuO nanoparticles by microwave irradiation. J Cryst Growth 244(1):88–94

168. Applerot G, Lellouche J, Lipovsky A et al (2012) Understanding the antibacterial mechanism of CuO nanoparticles: revealing the route of induced oxidative stress. Small 8(21):3326–3337

169. Vidyasagar CC, Naik YA, Venkatesh TG et al (2011) Solid-state synthesis and effect of temperature on optical properties of Cu–ZnO, Cu–CdO and CuO nanoparticles. Powder Technol 214(3):337–343

170. Sun L, Zhang Z, Wang Z et al (2005) Synthesis and characterization of CuO nanoparticles from liquid ammonia. Mater Res Bull 40(6):1024–1027

171. Premkumar T, Geckeler KE (2006) A green approach to fabricate CuO nanoparticles. J Phys Chem Solids 67(7):1451–1456

172. Liu B, Zeng HC (2004) Mesoscale organization of CuO nanoribbons: formation of "dandelions". J Am Chem Soc 126(26):8124–8125

173. Chang Y, Teo JJ, Zeng HC (2004) Formation of colloidal CuO nanocrystallites and their spherical aggregation and reductive transformation to hollow Cu_2O nanospheres. Langmuir 21(3):1074–1079

174. Zhu J, Qian X (2010) From 2-D CuO nanosheets to 3-D hollow nanospheres: interface-assisted synthesis, surface photovoltage properties and photocatalytic activity. J Solid State Che 183(7):1632–1639

175. Park JC, Kim J, Kwon H et al (2009) Gram-scale synthesis of Cu_2O nanocubes and subsequent oxidation to CuO hollow nanostructures for lithium-ion battery anode materials. Adv Mater 21(7):803–807

176. Cheng S-L, Chen M-F (2012) Fabrication, characterization, and kinetic study of vertical single-crystalline CuO nanowires on Si substrates. Nanoscale Res Lett 7(1):119

177. Jiang X, Herricks T, Xia Y (2002) CuO nanowires can be synthesized by heating copper substrates in air. Nano Lett 2(12):1333–1338

178. Hansen BJ, Kouklin N, Lu G et al (2010) Transport, Analyte detection, and opto-electronic response of p-type CuO nanowires. J Phys Chem C 114(6):2440–2447

179. Hansen BJ, Lu G, Chen J (2008) Direct oxidation growth of CuO nanowires from copper-containing substrates. J Nanomater 2008:1–7

180. Umar AA, Oyama M (2007) A seed-mediated growth method for vertical array of single-crystalline CuO nanowires on surfaces. Cryst Growth Des 7(12):2404–2409

181. Siddiki M, Li J, Galipeau D et al (2010) A review on polymer multijunction solar cells. Energy Environ Sci 3:867–883

182. Siddiki MK, Venkatesan S, Galipeau D et al (2013) Kelvin probe force microscopic imaging of the energy barrier and energetically favorable offset of interfaces in double-junction organic solar cells. ACS Appl Mater Interfaces 5(4):1279–1286

183. Siddiki MK, Venkatesan S, Wang M et al (2013) Materials and devices design for efficient double junction polymer solar cells. Sol Energy Mater Sol Cells 108:225–229

184. Taranekar P, Qiao Q, Jiang J et al (2007) Hyperbranched conjugated polyelectrolyte bilayers for solar cell applications. J Am Chem Soc 129(29):8958–8959

185. Xie Y, Bao Y, Du J et al (2012) Understanding of morphology evolution in local aggregates and neighboring regions for organic photovoltaics. Phys Chem Chem Phys 14:10168–10177

186. Xie Y, Li Y, Xiao L et al (2010) Femtosecond time-resolved fluorescence study of P3HT/PCBM blend films. J Phys Chem C 114(34):14590–14600

187. Xu T, Chen Q, Lin D-H et al (2011) Self-assembled thienylsilane molecule as interfacial layer for ZnO nanowire/polymer hybrid system. J Photonics Energy 1(1):011107

188. Xu T, Qiao Q (2011) Conjugated polymer-inorganic semiconductor hybrid solar cells. Energy Environ Sci 4(8):2700–2720

189. Xu T, Venkatesan S, Galipeau D et al (2013) Study of polymer/ZnO nanostructure interfaces by kelvin probe force microscopy. Sol Energy Mater Sol Cells 108:246–251

190. Xu T, Yan M, Hoefelmeyer J et al (2011) Exciton migration and charge transfer in chemically linked P3HT-TiO$_2$ nanorod composite. RSC Adv 2(3):854–862
191. Zhang W, Wang H, Chen B et al (2012) Oleamide as a self-assembled cathode buffer layer for polymer solar cells: the role of the terminal group on the function of the surfactant. J Mater Chem 22(45):24067–24074
192. Li J, Yan M, Xie Y et al (2011) Linker effects on optoelectronic properties of alternate donor–acceptor conjugated polymers. Energy Environ Sci 4:4276–4283
193. Shao S, Zheng K, Pullerits T et al (2012) Enhanced performance of inverted polymer solar cells by using poly(ethylene oxide)-modified ZnO as an electron transport layer. ACS Appl Mater Interfaces 5(2):380–385
194. Yunfei Zhou FSR, Yuan Y, Schleiermacher H-F, Niggemann M, Urban GA, Krüger M (2010) Improved efficiency of hybrid solar cells based on non-ligand-exchanged CdSe quantum dots and poly(3-hexylthiophene). Appl Phys Lett 96(1):013304
195. Yunfei Zhou ME, Veit C, Zimmermann B, Rauscher F, Niyamakom P, Yilmaz S, Dumsch I, Allard S, Scherf U, Krüger M (2011) Efficiency enhancement for bulk-heterojunction hybrid solar cells based on acid treated CdSe quantum dots and low bandgap polymer PCPDTB-T. Sol Energy Mater Sol Cells 95(4):1232–1237
196. Kwong CY, Choy WCH, Djurisic AB et al (2004) Poly(3-hexylthiophene): TiO$_2$ nanocomposites for solar cell applications. Nanotechnology 15(9):1156–1161
197. Qiao Q, Beck J, James J, McLeskey T (2005) Photovoltaic devices from self-doped polymers. In: Organic photovoltaics VI. SPIE
198. Qiao Q, Su L, Beck J et al (2005) Characteristics of water soluble polythiophene: TiO$_2$ composite and its application in photovoltaics. J Appl Phys 98(10):094906
199. Qiao Q, Xie Y, McLeskey JJT (2008) Organic/inorganic polymer solar cells using a buffer layer from all-water-solution processing. J Phys Chem C 112(26):9912–9916
200. Yang P, Zhou X, Cao G et al (2010) P3HT:PCBM polymer solar cells with TiO$_2$ nanotube aggregates in the active layer. J Mater Chem 20(13):2612–2616
201. Liao W-P, Hsu S-C, Lin W-H et al (2012) Hierarchical TiO$_2$ nanostructured array/P3HT hybrid solar cells with interfacial modification. J Phys Chem C 116(30):15938–15945
202. Hau SK, Yip H-L, Baek NS et al (2008) Air-stable inverted flexible polymer solar cells using zinc oxide nanoparticles as an electron selective layer. Appl Phys Lett 92(25):253301–253303
203. Ka Y, Lee E, Park SY et al (2013) Effects of annealing temperature of aqueous solution-processed ZnO electron-selective layers on inverted polymer solar cells. Org Electron 14(1):100–104
204. Wiranwetchayan O, Liang Z, Zhang Q et al (2011) The role of oxide thin layer in inverted structure polymer solar cells. Mater Sci Appl 2:1697–1701

Carbon Nanomaterials: A Review

21

Nitin Choudhary, Sookhyun Hwang, and Wonbong Choi

Keywords

Carbon nanomaterials • Carbon nanotubes • Graphene • Synthesis and applications

Introduction

For almost three decades now, fullerenes (0D), carbon nanotubes (1D), and graphene (2D) carbon nanomaterials have attracted significant attention due to their unique electronic, optical, thermal, mechanical, and chemical properties and provided researchers the opportunity to significant advances in fundamental and applied science and the development of disruptive technologies and applications [1–3]. Today, the materials research community continues to discover and harness new low-dimensional graphitic carbon allotropes, perhaps at a historically unprecedented rate. In this context, carbon nanotubes (CNTs) and, more recently, graphene have become versatile platforms for new materials research and device architectures and are finding their way into nearly every facet of the research world, including conductive polymers, transparent electrodes, chemical sensors, high-frequency devices, optoelectronic sensors, alternative energy, and bio-inspired systems, to name a few [4, 5].

At the same time, researchers from diverse disciplines are pushing the frontiers of these materials by developing innovative arrays of ribbon, hybrid, functionalized, doped, and heterostructures often resulting in dramatically new scientific and engineering directions. Figure 21.1 shows the significant growth in the number of publications and patents on graphene and CNTs in the last decade. It is clear from the figure that since 2006, CNT and graphene production capacity have been increased drastically, and the annual number of journal publications and issued patents continues to

N. Choudhary • S. Hwang • W. Choi (✉)

Department of Materials Science and Engineering, University of North Texas, Denton, TX, USA
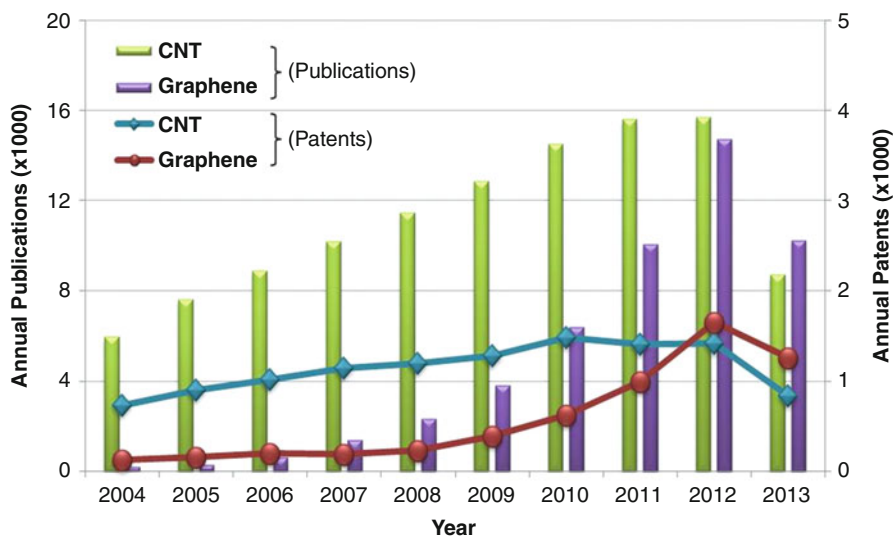e-mail: wonbong.choi@unt.edu

Fig. 21.1 Trend in the number of publications and patents based on CNTs and graphene (Ref: Scifinder (http://scifinder.cas.org), US Patent & Trademark Office (http://patft.uspto.gov/), 07/23/2013)

grow. Although graphene is, from a technological point of view, less mature than nanotubes, a significant progress has been made in recent years.

The present study will focus on the synthesis, properties, and applications of graphene and CNTs in detail. This includes the synthesis methods like exfoliation and cleavage, thermal chemical vapor deposition techniques, plasma-enhanced chemical vapor deposition techniques, chemical methods, thermal decomposition of SiC, and thermal decomposition on other substrates, while the synthesis methods for CNTs include unzipping CNTs and other methods. We will also focus on the electrical, mechanical, and thermal properties of CNTs and graphene. The practical applications like electronics (FET), gas and biosensors, transparent electrodes, energy, battery, and solar cells will also be discussed in detail.

Properties of Carbon Nanomaterials

Properties of Carbon Nanotubes (CNTs)

Carbon nanotubes (CNTs) can be viewed as seamless cylinders rolled by graphene sheets. Single-walled carbon nanotube (SWNT) is composed of one graphene sheet, whereas multiwalled carbon nanotube (MWNT) is composed of multiple graphene sheets (Fig. 21.2a) [6]. The structure of SWNTs can be described by the circumference vector or chiral vector C_h, which is defined by $C_h = n \cdot a_1 + m \cdot a_2$ where a_1 and a_2 are the unit vectors in the hexagonal graphene lattice and n and m are the

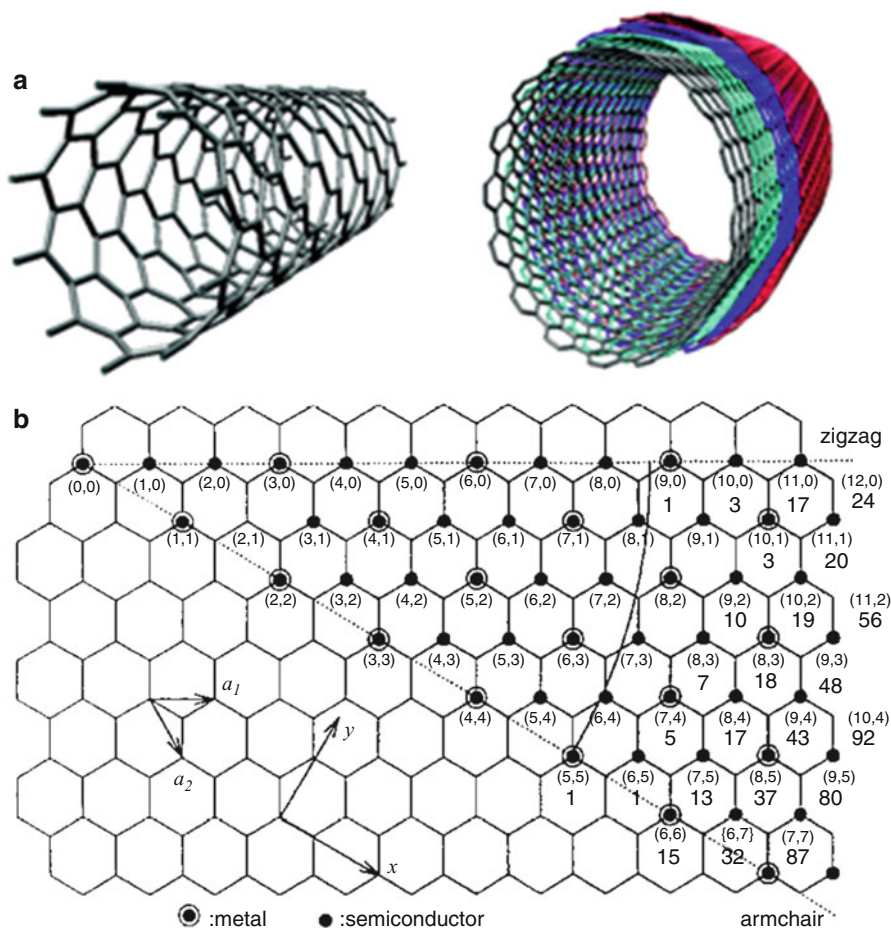**Fig. 21.2** (**a**) Schematics of carbon nanotubes, (*left*) single-walled CNT (SWNT) and (*right*) multiwalled CNT (MWCNT). (**b**) Possible vectors specified by the pairs of integers (*n*, *m*) for general carbon nanotubes, including zigzag, armchair, and chiral nanotubes. The *encircled dots* denote metallic nanotubes, while the small dots are for semiconducting nanotubes (Reprinted with permission from Foldvari et al. [6]. Copyright 2008: Elsevier, and Dresselhaus et al. [7]. Copyright 1995: Elsevier)

integers defined by the chiral vector $\mathbf{C_h}$ as shown in Fig. 21.2b [7]. SWNTs show semiconducting or metallic behavior depending on their chiral angle θ and integer (n, m). Basically, if n − m = 3q, the SWNT is metallic. If n − m ≠ 3q, the SWNT resembles a semiconductor with band gap where q is an integer. Zigzag (θ = 0°)-structured and armchair (θ = 30°)-structured SWNTs are shown in figure.

The electronic structure of CNTs is usually described on the basis of band structure of graphene. The band structure and Brillouin zone of graphene is as shown in Fig. 21.3a [8]. The valence band (π-bonding) and the conduction band (π*-bonding) touch at six points that lie at the Fermi energy. The momentum along the
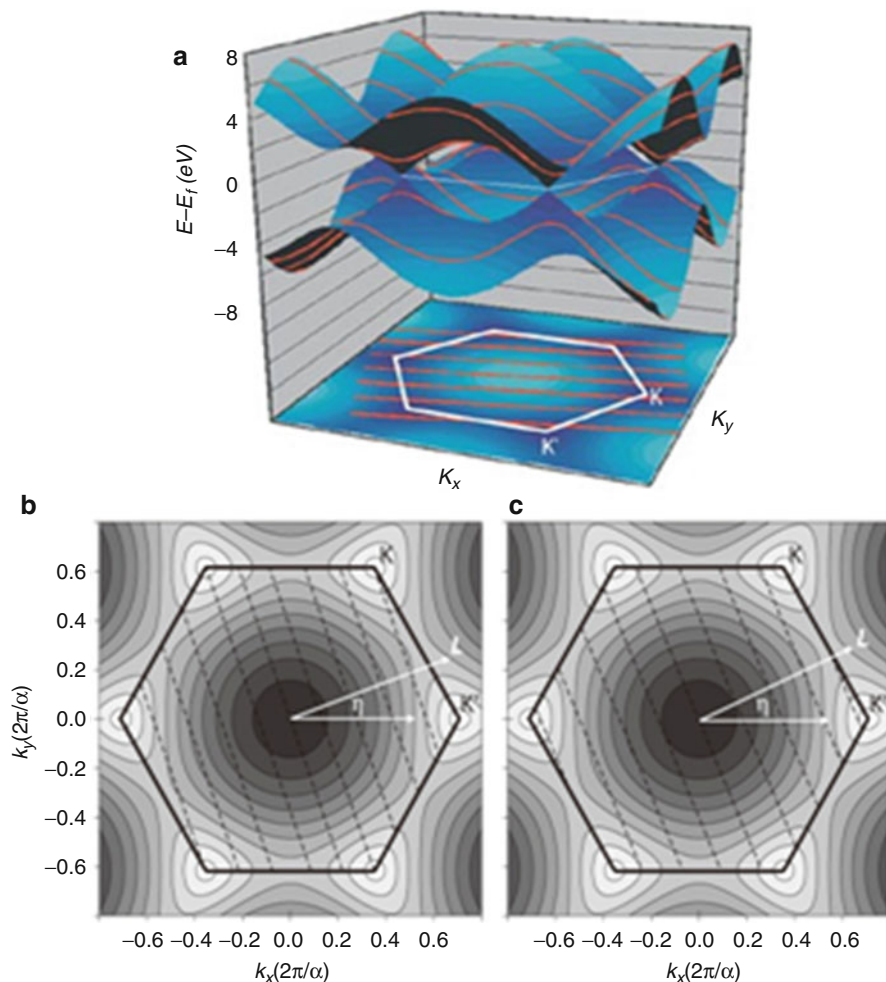
Fig. 21.3 (**a**) Band structure (*top*) and Brillouin zone (*bottom*) of graphene. (**b**) Allowed wavevector lines cross the K (or K') point, the nanotube is metallic. (**c**) If the lines do not pass through the K (or K') point, it is semiconducting (Reprinted by permission from Macmillan Publishers Ltd: *Nature Nanotechnology* [8]. Copyright 2007 and *NPG Asia Materials* [9]. Copyright 2009)

circumferential direction in SWNTs is limited and quantized, which leads to the formation of a set of discrete energy sub-bands for each nanotube (red parallel lines in the bottom Brillouin zone in Fig. 21.3a). When the allowed wave vector lines cross the K (or K') point, the nanotube is metallic (Fig. 21.3b) [9]; whereas it is semiconducting when the lines does not pass through the K (or K') point (Fig. 21.3c) [9]. Depending on their chirality (n, m), the energy band gap of semiconducting SWNTs is known to be proportional to the inverse of tube diameter, i.e., $Eg \approx 0.9$ eV/diameter (nm) [7].

Electrical Properties

As noted above, carbon nanotubes with n – m $\neq$ 3×integer, the SWNT resembles a semiconductor with band gap that is inversely proportional to the tube's diameter. The electrical nature of SWNT depends sensitively on the chiral vector (**C**) and diameter, little variations in **C** and diameter alters their band structure dramatically as discussed in Fig. 21.2 and Fig. 21.3. CNTs have been attracted for use as electronic components such as FET channel and interconnect due to their unique properties of the highest current density, ballistic transport, ultrahigh thermal conductivity, and extremely high mechanical strength [10]. The current density of CNTs has been reported as high as 10^9 A/cm^2 [11], which is two to three orders of magnitudes higher than that for Cu, and to exhibit a ballistic transport along the tube, which may be the solution to the high-resistance problem in scaled-down interconnect [12]. Also, conventional metal interconnect (vias) needs a barrier layer, which results in an increase in resistance and in process complexity, but CNT interconnect does not need barrier layers [13].

The Fermi velocity v_F of metallic CNTs equals that of metals ($v_F \approx 9 \times 10^7$ cm s^{-1}) and an electron mean free path l_{fmp} for the electrons of at least 1 μm. However, due to the low density of states, the resistivity is only of the order of that of the best metals (∼1 Ω cm) despite the huge mean free path. The conductance of an ideal ballistic nanotube is $4e^2/h \approx 155$ S or about 6.5 kΩ [14]; therefore, additional series resistances need to be added for the contact resistance RC and the Drude-like length-dependent resistance $h/(4e^2)(L/l_{fmp})$ which accounts for additional backscattering for a nanotube with length L. For multiwalled CNTs, each individual shell can contribute to the conductance, and larger diameters can add additional channels to the conductance. Experimentally, F. Kreupl et al. [15] reported the growth of single nanotubes at lithographically defined locations (vias) for the use of CNTs as future interconnects. They reported that in the 20-nm node, a current density of 5×10^8 A cm^{-2} and a resistance of 7.8 kΩ could be achieved for a single multiwalled CNT vertical interconnect, which exceed the achievable values for metals, whereas the obtained resistance of 7.8 kΩ should be lowered by 2 orders of magnitude to compare with theoretical values for copper. In 2006, Y. Awano research group [16] demonstrated the feasibility of CNT vias as inter-connects. To reduce the thermal budget and to make the CNT growth compatible with Si LSI process, a hot-filament chemical vapor deposition (HFCVD) was utilized. The resulting vertically aligned MWNTs were grown at ∼420 °C, and the smallest CNT via achieved was ∼160 nm (Fig. 21.4).

The measured electrical property of the CNT vias, i.e., resistance, was ∼0.59 Ω, and the estimated current capability of 2 μm via with high-density tightly packed CNTs was ∼6,270 mA which was higher than the values of ITRS requirements. No degradation of the current was noticed from the reliability studies of the CNT vias performed for ∼125 h at room temperature. The current level for the reliability tests was maintained at ∼100 mA [17] (Fig. 21.5).

The first field-effect transistor (FET) based on SWNT was demonstrated in 1998 [18, 19]. The structure of these early CNT–FETs was very simple. The SWCNT was positioned so as to bridge two metal electrodes, the source and drain of the
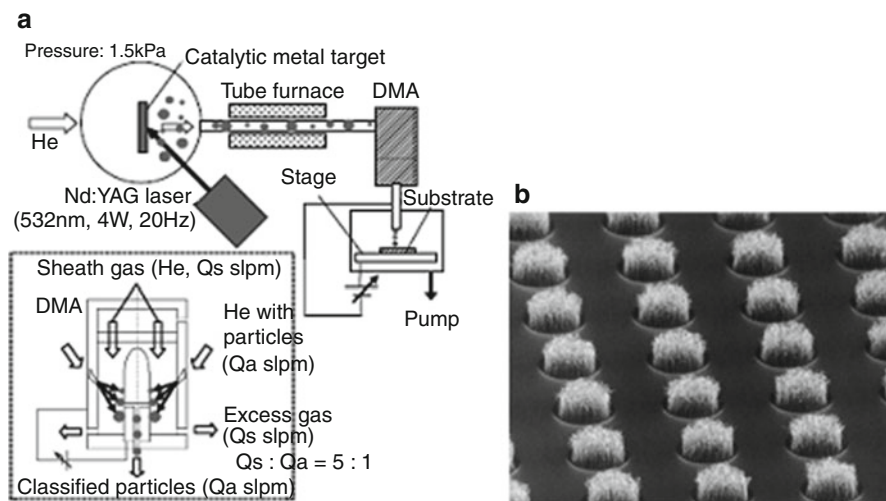
a

b

Fig. 21.4 (**a**) Catalyst metal particle generation and deposition system. (**b**) MWNT via array grown by HFCVD (Reprinted with permission from Awano et al. [16]. Copyright (2006): John Wiley and Sons)
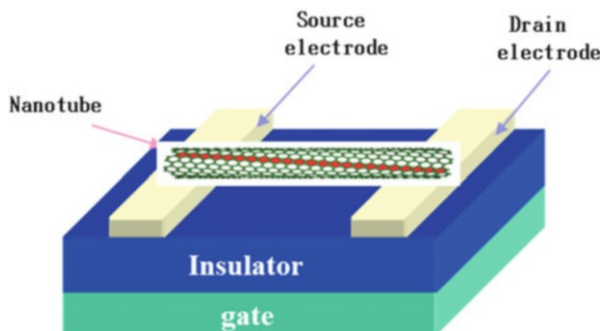

Fig. 21.5 A schematic of SWCNT–FET where a SWCNT is bridged between two metal electrodes

FET, and the silicon wafer itself as a back gate. These CNT–FETs acted as unipolar p-type FETs with on/off current switching ratios of 10^5 but a low transconductance, $g_m = dI_{sd}/dV_{gs}$ of about 10^{-9} A V^{-1}, which was due to the large contact resistance of CNT/electrodes. To approach the performance limit of CNT–FETs, it is essential to integrate ballistic semiconducting nanotube channel with ohmic contact and high-dielectric-constant gate oxide, which has been studied by many researchers reported [20]. By integration of high-κ ZrO_2 as top-gate oxide, the CNT–FET outperforms the state-of-the-art Si MOSFET, showing subthreshold swings (70 mV per decade), high transconductance (dI/dVg) of 12 μS per tube, and high mobility 3,000 cm^{2}V^{-1} s^{-1} [21].

Such CNTs had hope to use as future nanoelectronic devices. However the intrinsic drawbacks of SCNTs need to be overcome for their use in the nanoelectronic device application, which are summarized as shown below: (1) Transport in SWNTs is sensitive to scattering by adsorbed impurities, background gases, and trapped charges at the gate oxide/CNT interface, (2) difficulty in creating uniform energy band gap in s-SWNTs, (3) the intrinsic high contact resistance between SWNT and metal, and (4) integration issue of SWNT for large-scale production.

Mechanical Properties

Carbon nanotubes are the strongest and stiffest materials yet discovered in terms of tensile strength and elastic modulus, respectively. This strength results from the covalent sp^2 bonds formed between the individual carbon atoms [22]. A large number of theoretical and experiments techniques have been performed to determine the mechanical properties of CNTs. In 1996, Treacy et al. [23] determined Young's modulus of multiwalled CNTs by measuring the amplitude of intrinsic vibrations of the nanotubes in the transmission electron microscope. The average value of Young's modulus was found to be 1.8 TPa. Apart from the uncertainties in accurate measurement of the nanotubes' length, the tubes were not able to strain at will. Similarly, Krishnan et al. [24] used this technique to measure Young's modulus of SWNTs, and the average value was found to be 1.25 TPa. Later in 2000, Yu et al. [25] utilized tensile testing by using atomic force microscope (AFM) tips to measure Young's modulus of CNTs, and the value of Young's modulus was found to be between 0.27 and 0.95 TPa. At the same time, Salvetat [26] and Yu et al. [27] studied the mechanical response of bundles of SWNTs under tensile loading, and the values of elastic modulus were 0.6 and 1.002 TPa, respectively. Hence, a large discrepancy was observed in the experimental values of CNTs which was attributed to the lack of proper direct measuring techniques, inadequacy in preparing the good quality samples, and extreme limitations on the specimen size [28]. The large variation in experimental data encouraged researchers to pursue atomistic modeling and analytical and numerical types of modeling and simulations in order to understand their mechanical behavior and to justify the observation of experimental data [29–31]. However, a large discrepancy in Young's modulus was obtained and was attributed to the different assumptions, models, force field parameters, and different tube thicknesses. Consequently, the study of the mechanical properties of CNTs is still an ongoing process.

The applications of CNTs as reinforcing material for the development of an entirely new class of composites show the great potentials of CNT-based composites as well as the enormous challenges in the development of such nanocomposites. Qian et al. [32] has demonstrated that just 1 % (by weight) of CNTs added to a polyester resin can significantly enhance the stiffness of the resulting composite between 36 % and 42 % and the tensile strength by 25 %. Figure 21.6 shows the homogeneous distribution of MWNTs in polystyrene matrices with nanotubes of 33.6-nm average diameter. Inset of figure shows the loading of nanotubes over different length scales, and it shows the standard deviation (a measure of the

Fig. 21.6 TEM image showing the homogenous distribution of MWNT in polystyrene matrix. The inset is the MWNT weight fraction as a function of length scale (Reprinted with permission from Qian et al. [32]. Copyright (2000): American Institute of Physics)
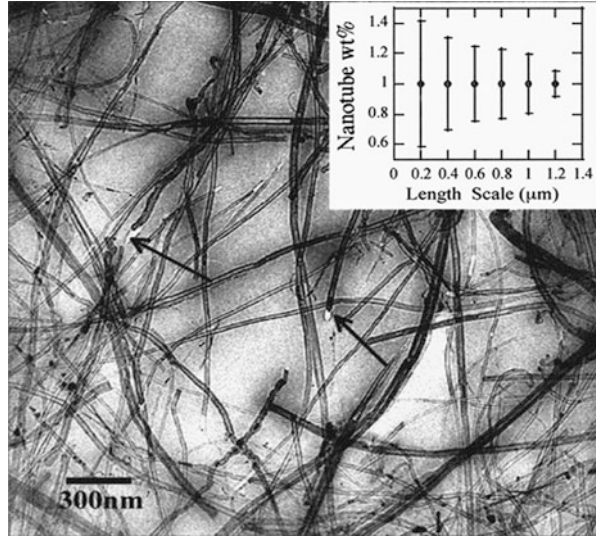
homogeneity) decreases to 0.08 wt% from the average 1 wt% at a length scale of 1.2 mm. In a similar work by Xu et al. [33], they prepared a thin-film epoxy composite by adding 0.1 wt% MWCNTs and showed that the elastic modulus increased up to 20 %. For the better application of CNTs in composites, the choice of the CNT diameter, its length and morphology, strong interactions, and good dispersion of the CNTs with the matrix are the critical factors for bringing about the best of the CNTs' mechanical properties. Shanmugharaj et al. [34] studied that surface fictionalization of MWCNTs by acid treatment helped in improving the interaction of CNT and rubber composites and enhanced the tensile strength of the composite by 20–30 % as compared to the nonfunctionalized CNT/rubber composites. Insufficient dispersion of CNTs into the matrix may result in voids or vacancies that do not improve the mechanical properties of composites [35]. Choi et al. [36] have used the cup-stacked CNT (CSCNT) to prepare the epoxy nanocomposites and found that addition of 5 wt% CSCNT improved Young's modulus by 20–30 %. Due to the exposed edge sites at the sidewall of the tube, cup-stacked CNTs (CSCNTs) are considered to have a good affinity to the matrix. By using CNTs in composites, in addition to the excellent mechanical properties, we can improve or implement other properties such as electric and thermal conductivity or an electromagnetic shielding function. These additional characteristics can add extra value to the CNT composites and can justify the additional costs incurred by their use. However, much work still needed to be done before the potentials of the CNT-based composites can be fully realized in real engineering applications. Computational approaches, based on the molecular dynamics (MD) approach (for smaller scales) and continuum mechanics approach (for larger scales), can play significant roles in the areas of characterizing CNT-based composites [37].

Fig. 21.7 (**a**) Electrical
(I–V) characteristics of
a suspended SWNT with
$L = 2.6$ m and $d = 1.7$ nm
measured at ambient
temperatures from 250 to
400 K and (**b**) extracted
values of thermal
conductivity versus average
SWNT temperature from
fitting the high-bias I–V data
(Reprinted with permission
from Pop et al. [41].
Copyright 2006: American
Chemical Society)
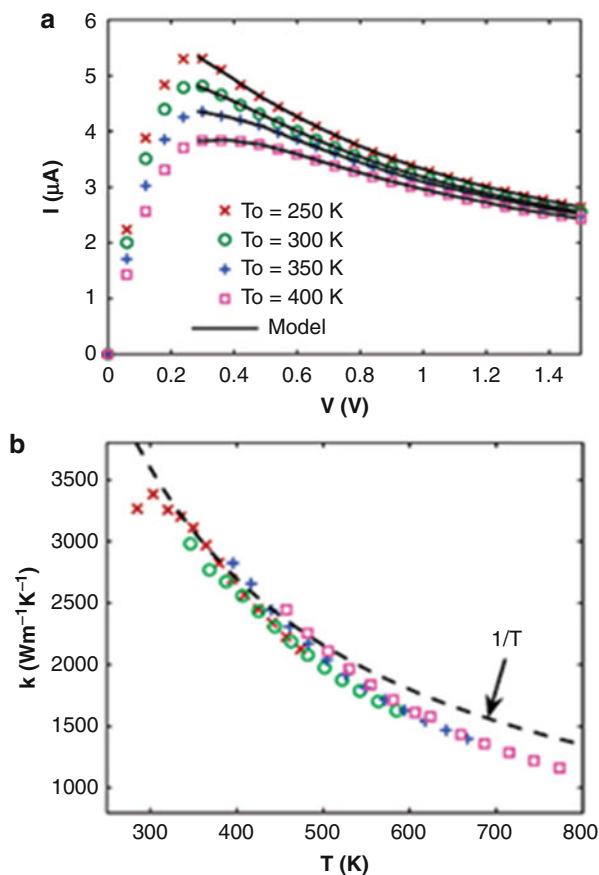
Thermal Properties

Carbon nanotubes have sparked great scientific and engineering interest because of
their outstanding thermal properties. Consequently, they have been proposed for
thermal management devices as a thermal interface material [38, 39]. Thermal
transport in CNTs can be dominated by the intrinsic properties of the strong sp^2
lattice, rather than by phonon scattering on boundaries or by disorder, giving rise to
extremely high thermal conductivity (K) values. Kim et al. [40] observed thermal
conductivity more than 3,000 Wm^{-1} K^{-1} in SWNTs using a microfabricated
suspended device at room temperature. In another experiment by Pop et al. [41]
in 2006, they determined the K of suspended metallic single-walled carbon nano-
tube (SWNT) from its high-bias I–V characteristics (Fig. 21.7). They found a ther-
mal conductivity nearly equal to 3,500 Wm^{-1} K^{-1} at room temperature for a SWNT
of length 2.6 μm and diameter 1.7 nm. On the other hand, Berber et al. [42] used
molecular dynamics and theoretically determined the value of $K \sim 6{,}600$ WmK^{-1}.
In other theoretical studies by Che et al. [43] and Donadio et al. [44], the value of

K for CNTs was found to be 3,000 and 7,000 WmK^{-1}, respectively. Thus, there is a substantial scattering in the reported room temperature K values for CNTs ranging from $\sim$1,100 to $\sim$7,000 WmK^{-1}. The commonly reported values for individual CNTs are $\sim$3,000 W mK^{-1} for MWCNTs [40] and $\sim$3,500 W mK^{-1} for SWCNTs [41] at room temperature. The highest K values obtained in the experiments could be attributed to the ballistic transport regime achieved in some CNTs. These values are above the bulk-graphite limit of $\sim$2,000 WmK^{-1}. Thus, CNTs are nanostructures where heat transport is not mostly limited by the extrinsic effects, such as boundary scattering, like in many semiconductor nanowires with rough interfaces.

The thermoelectric power defined by TEP $= \Delta V/\Delta T$, where V is thermoelectric voltage and T is temperature, is of great interest in understanding transport due to its extreme sensitivity to the change of electronic structure at the Fermi level [45, 46]. When a bias is applied across a single tube, the temperature gradient will be built up along the tube axis through joule heating. TEP for a single metallic or semiconducting tube follows linear temperature dependence with positive and negative slope, respectively, for p- and n-dope tube. Its room temperature value is around 280 μV K^{-1} for a semiconducting SWNT and 80 μV K^{-1} for a MWNT [47]. Thermoelectric properties vary significantly from sample to sample for filmed and bundled SNWTs and MWNTs. The thermoelectric measurements with SWCNTs revealed a Seebeck coefficient of $\sim$42 μV K $-$ 1 at room temperature, which is about an order of magnitude higher than that of graphite or metals, suggesting that electron transport is not ballistic [48]. They also showed that the measured thermal conductance G_p in SWCNTs was found to increase with temperature from 0.7×10^{-9} WK^{-1} or $\sim$7 g_0 at 110 K to 3.8×10^{-9} WK^{-1} or $\sim$14 g_0 at room temperature, where $g_0 \approx (9.456 \times 10^{-9}$ WK$^{-2})$.

Properties of Graphene

Graphene is one of the most exciting materials being invested today, not only out of academic curiosity but also with potential applications. Graphene is considered as the fundamental building block for graphitic carbon-based nanomaterials of all other dimensions. It can be wrapped up into zero-dimensional (0D) fullerenes, rolled into one-dimensional (1D) nanotubes, and stacked into three-dimensional (3D) graphite. Figure 21.8 illustrates the schematic diagram demonstrating that graphene is the mother of all graphitic forms [49]. It is a fascinating new nanocarbon possessing single, bi-, or few layers of carbon atoms forming six-membered rings. A single-layer graphene is defined as a single two-dimensional hexagonal sheet of carbon atoms (Fig. 21.9a) [50]. Bilayer and few-layer graphene has 2 and 3 to 10 layers of such two-dimensional sheets, respectively. In bi- and few-layer graphene, C atoms can be stacked in different ways, generating hexagonal or AA stacking, Bernal or AB stacking, and rhombohedral or ABC stacking (Fig. 21.9b, c) [50].
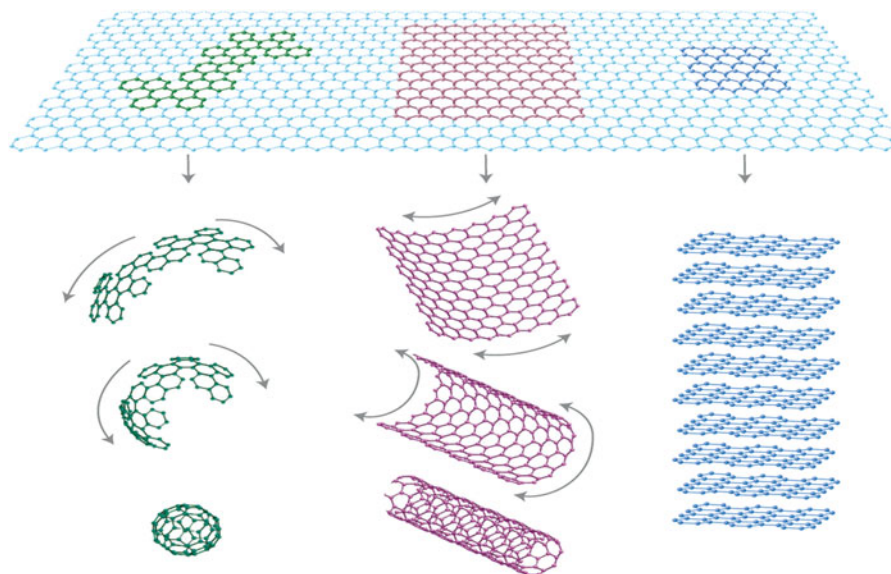
Fig. 21.8 Schematic diagram showing that graphene can be wrapped to form 0D fullerenes, rolled to form 1D CNTs, or stacked to form 3D graphite (Reprinted by permission from Macmillan Publishers Ltd: *Nature Materials* [49]. Copyright 2007)

Fig. 21.9 (**a**) Graphene structure of single two-dimensional hexagonal sheet of carbon atoms, (**b**) bilayer, and (**c**) tri (few)-layer stacking sequences (Reprinted with permission from Macmillan Publishers Ltd: *Nature Physics* [50]. Copyright 2011)

Graphene has a hybridized sp^2 bonding. It has three in-plane σ bonds/atom and π orbitals perpendicular to the plane. While the strong σ bonds work as the rigid backbone of the hexagonal structure, the out-of-plane π bonds control interaction between different graphene layers [51].

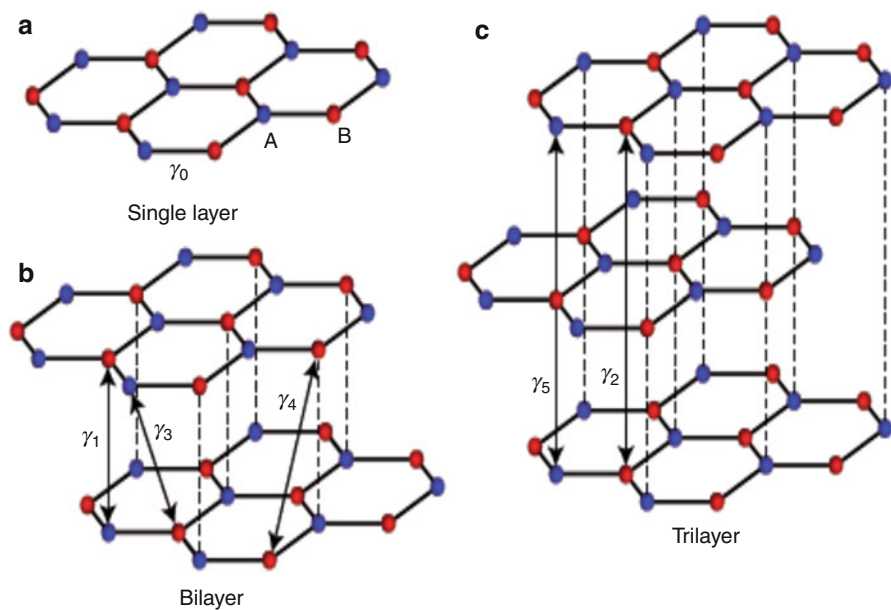Intrinsic graphene is characterized as a semimetal or zero-gap semiconductor, and its unique electronic properties produce an unexpectedly high opacity for an atomic monolayer, with a startlingly low absorption ratio of 2.3 % of white light. Electrical characterization has shown remarkably high electron mobility at room temperature, with experimentally reported values in excess of 20,000 $cm^2\,V^{-1}\,s^{-1}$. The corresponding resistivity of the graphene sheet would be 10^{-6} Ω cm, less than the resistivity of silver, the lowest resistivity substance known at room temperature. Graphene nanoribbons (GNRs), with zigzag or armchair configuration, show different electrical property; the zigzag GNRs are metallic, while armchairs can be either metallic or semiconductor. The energy band gap of armchair GNRs are inversely proportional to the width.

Mechanical Properties of Graphene

The discovery of graphene in 2004 has triggered enormous research interests around the world due to its extraordinary mechanical properties. Graphene received the title of 'strongest material ever' after the confirmation of its sustaining breaking strength of 42 N m^{-1} and a Young's modulus of 1.0 ± 0.1TPa by Lee et al. [52] in 2008. It has been experimentally demonstrated that graphene surpasses the graphite and carbon nanotubes in enhancing Young's modulus and tensile strength of nanocomposites [53, 54]. The superior mechanical strength of graphene could be attributed to its two-dimensional geometry, high surface-to-volume ratio, and the associated stronger interface interaction. In addition to the experimental findings, several theoretical works like ab initio [55], tight binding [56], molecular dynamics simulations [57], and semiempirical models [58] have been carried to confirm the main mechanical features of the graphene. Aluru et al. [59, 60] used molecular dynamics (MD) simulations to investigate the mechanical properties of graphene under uniaxial tension and shear strain. They found that size, chirality, temperature, and strain rate exert significant influences on the fracture strength of graphene. Similarly, Pei et al. [61] and Zheng et al. [62] employed MD simulations to investigate the mechanical properties of the graphene functionalized with hydrogen and other chemical groups.

Due to its light weight, high stiffness, high electron mobility, and flexibility, graphene is getting higher interest as a building block component in nanoelectromechanical systems (NEMS) applications, including sensing and signal processing. Bunch et al. [63] have demonstrated graphene electromechanical resonators exhibiting charge sensitivities down to 8×10^{-4} electrons per root Hz at room temperature, highlighting the potential of graphene for NEMS applications. The appearance of high-frequency NEMS is tempting enough for us to consider the co-integration of the NEMS and conventional silicon electronic devices because we expect such hybrid systems enhance scaling of functional density and performance while simultaneously reducing the power dissipation
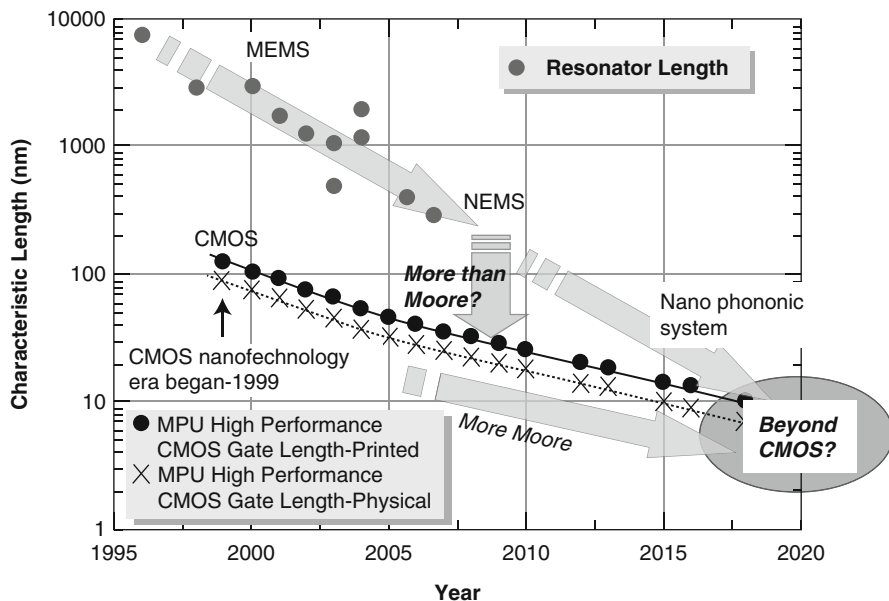
Fig. 21.10 Trend of MEMS/NEMS downscaling along with CMOS miniaturization (Reprinted with permission from Mizuta et al. [65]. Copyright (2009): JAMRIS)

beyond the conventional CMOS-based systems. In addition, recent emergence of superior graphene-based NEMS (GNEMS) provides more choice of building blocks for the hybrid systems [64]. Figure 21.10 shows the silicon NEMS downscaling trend. One foresees two possibilities; graphene for more Moore or graphene for more than Moore by combining GNEMS with graphene transistor [65].

Graphene nanoribbons (GNRs), resulting from the finite termination of graphene into quasi one-dimensional ribbonlike structures with two different possible edge geometries, namely, zigzag and armchair, possess intriguing electronic and mechanical properties [66]. They are termed as zigzag graphene nanoribbons (ZGNRs) and armchair graphene nanoribbons (AGNRs), respectively. The unconventional electronic and mechanical properties of GNRs are mainly due to their edge shapes and characteristic sizes, particularly when their width is shorter than 100 nm [67]. It has been shown that the transport and electronic features of GNRs can be effectively tuned as a function of strain [68, 69]. Ribbons with armchair edge symmetry can undergo a metal–semiconductor transition as mechanical strain increases, whereas zigzag ribbons exhibit a more robust transport behavior against stretching. Very small values of strain are sufficient to open an energy gap in AGNRs, confirming that their electronic character is sensitive to mechanical stress. In this sense armchair edge ribbons are more suitable for engineering electromechanical devices in comparison to zigzag geometry.

Fig. 21.11 Electronic band
structure of single-layer
graphene (Reprinted with
permission from Katsnelson
et al. [72]. Copyright (2007):
Elsevier)
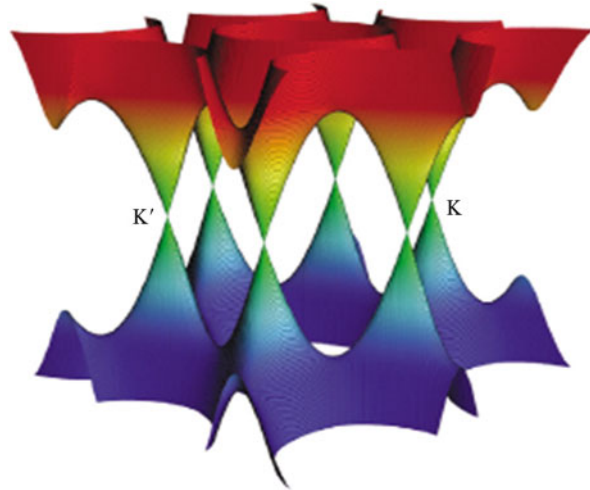
Electrical Properties of Graphene

One of the hottest areas of graphene research focuses on the intrinsic electronic
properties as how electrons flow through a one-atom-thick sheet under the influence
of various external forces [70, 71]. Graphene is great conductor, and thereby
electrons are able to flow through graphene more easily than through even copper.
The electrons travel through the graphene sheet as if they carry no mass, as fast as
just one hundredth that of the speed of light. Single-layer graphene (SLG) is unique
in electronic structure, as it shows band overlap in two conical points (K and K') in
the Brillouin zone (Fig. 21.11) [72]. The charge carriers in this structure, known as
massless Dirac fermions, are electrons losing their rest mass, m_o, and can best be
described by (2 + 1)-dimensional Dirac equations. Thus, SLG is expected to show
some unusual properties, as compared with metals and semiconductors and typical
of a semimetal. Single-layer graphene exhibits a strong ambipolar electric field
effect such that charge carriers can be tuned continuously between electrons and
holes in concentrations up to 10^{13} cm^{-2}, and room temperature mobilities of
10,000 cm^2 V^{-1} s^{-1} can be induced by applying gate voltage [73]. Anomalous
(half-integer) quantum Hall Effect (QHE), at low temperature and room tempera-
ture, has also been reported for this structure [74, 75]. These unusual properties of
SLG have made it suitable for applications in electronics, as well as one of the most
suitable materials for studying basic quantum physics phenomena.

Bilayer graphene shows a gapless state with parabolic bands touching at K and
K', in contrast to conical bands of SLG. Thus, bilayer graphene is considered as
a gapless semiconductor. In contrast to single-layer graphene, charge carriers in
bilayer graphene have finite mass and called massive Dirac fermions. The structure
also shows an anomalous QHE but different from that of single-layer graphene, and
as a result, it remains metallic at the neutrality points [76]. However, application of
a gate voltage can change the carrier concentration and introduces symmetry
between the two layers. This results in formation of a semiconducting gap and

restoration of normal QHE [77]. However, Zhou et al. have shown that an energy band gap of ~0.26 eV is produced in graphene, when it is epitaxially grown on SiC substrate [78]. Such a structure, with a finite band gap, makes graphene more suitable for application in electronics industries. It was found that the band gap decreases with increasing number of layers and approaches zero, as the structure has more than four layers. This substrate-induced band gap opening was proposed to be caused by graphene–substrate interaction and breaking of sublattice symmetry. In a related study, it was claimed that graphene, epitaxially grown on C-terminated surface of 4H-SiC, has a different stacking sequence [79]. As a result, the structure, irrespective of its number of layers (up to ~10 layers thick), shows an electronic structure similar to that of single-layer graphene and behaves like SLG. Thus, synthesis methods play an important role in determining the structure and properties of graphene. In an interesting application of gaseous molecule adsorption on epitaxially grown graphene surface, it was shown that a controlled molecular treatment (by gases like H_2 and NO_2) can trigger a reversible metal-to-insulator transition in single and bilayer graphene [80, 81]. Treatment of graphene sheets by atomic hydrogen is known to produce insulating or semiconducting graphane, a two-dimensional hydrocarbon structure. Moreover, single and bilayer graphene shows very high transparency for light waves in the range of ultraviolet to infrared, making it suitable for applications as transparent electrode in solar cells [82].

Analysis of the band structure of few-layer graphene (FLG) shows no gap. The structure becomes increasingly metallic with more number of layers in it [83]. FLG shows very high surface area, almost comparable to that of single-layer graphene. Interlayer coupling in few-layer graphene (FLG) leads to a dramatic change of this electronic structure, with the emergence of hyperbolically dispersing bands [70, 84]. Further, the electronic properties of FLG are predicted to be highly sensitive to the crystallographic stacking sequence. Mak et al. [85] claimed that different electronic spectra of FLG with same number of layers arises from the existence of two stable polytypes of FLG, namely, Bernal (AB) stacking and rhombohedral (ABC) stacking. The decoration of FLG with metallic nanoparticles also becomes necessary to make the structure more suitable for usage in electronics-, optics-, and biotechnology-related applications. FLG was found to be easily decorated with Pt, Ag, and Au nanoparticles, in a single-step chemical process. Such decoration enhances its application in optoelectronics [86].

Thermal Properties of Graphene

Graphene has more than 100-fold anisotropy of heat flow between the in-plane and out-of-plane directions. The in-plane thermal conductivity of graphene at room temperature is among the highest of any known material, about 2,000–4,000 Wm^{-1} K^{-1} for freely suspended samples [87, 88]. The very high room temperature thermal conductivity (κ) of single-layer graphene is mainly due to the acoustic phonons [89]. The high κ is attributed to the absence of crystal defects and suppression of Umklapp processes as the number of layers are reduced, i.e., long mean free path of phonons [90]. The phonon branches of graphene can be

grouped as in-plane (LA, TA, LO, and TO) whereas out-of-plane (flexural) modes (ZA and ZO). On the other hand, the out-of-plane heat flow is limited by weak van der Waals coupling [91]. Despite its high room temperature value for freely suspended samples, the in-plane thermal conductivity of graphene decreases significantly when this 2D material is in contact with a substrate or confined into graphene nanoribbons (GNRs). Nonetheless, κ of graphene supported by SiO_2 has been measured as $\sim$600 $Wm^{-1} K^{-1}$, that of SiO_2-encased graphene was measured as $\sim$160 $Wm^{-1} K^{-1}$, and that of supported GNRs was estimated as $\sim$80 $Wm^{-1} K^{-1}$ [92–94]. This behavior is not unexpected, given that phonon propagation in an atomically thin graphene sheet is likely to be very sensitive to surface or edge perturbations. For SiO_2 supported graphene, the decrease in thermal conductivity occurs as a result of the coupling and scattering of all graphene phonons with substrate vibrational modes [95]. Measurements on few-layer graphene, with the number of layers ranging between 2 and 10, show the dimensional crossover from two dimensions to bulk-like behavior, and the crossover is assigned to the interlayer coupling of low-energy phonons and enhanced Umklapp scatterings and κ drops from 2,800 to 1,300 $Wm^{-1} K^{-1}$ [90].

When graphene is confined into GNRs that are narrower than the intrinsic phonon mean free path ($W \leq \lambda_0$), phonon scattering with boundaries and edge roughness further reduces the thermal conductivity compared to the case of suspended and SiO_2-supported graphene [96]. Similar to the electronic states in GNRs, only standing wave solutions are allowed perpendicular to the ribbon axis [97]. The effect of disorder in the edge shape of GNRs increases with decreasing ribbon width and suppresses thermal conductivity strongly for GNRs having width of 20 nm or below. The thermal conductivity of GNRs with sub-20-nm widths was measured as 1,000 $Wm^{-1} K^{-1}$ [98, 99]. Since the thermal measurements of graphene are challenging because of its atomic thinness, modeling and simulation have played a key role in developing an understanding of graphene properties. Existing methods for modeling thermal transport in graphene and GNRs that include atomistic techniques such as molecular dynamics (MD), non-equilibrium Green's functions (NEGF), and Boltzmann transport equation (BTE) simulations have provided atomistic insights into graphene heat flow and have also predicted novel routes to tailor the thermal properties of nanostructured graphene materials [98, 100, 101].

Synthesis of Carbon Nanomaterials

Synthesis of CNT

Carbon nanotubes (CNTs), first discovered by S. Iijima [102] in 1991, are allotropes of carbon with a cylindrical nanostructure, having diameter of nanometer order but length in micrometers. CNT is configurationally equivalent to a two-dimensional graphene sheet rolled into a tube. Owing to their extraordinary structural, electrical, and mechanical properties, carbon nanotubes (CNTs) offer promising applications

in the fields ranging from electronics to biotechnology including field emitters, scanning probes, sensors, nanoelectronics, and drug delivery devices [103–105]. There are two main types of carbon nanotubes that can have high structural perfection. Single-walled nanotubes (SWNT) consist of a single graphite sheet seamlessly wrapped into a cylindrical tube. Multiwalled nanotubes (MWNT) comprise an array of nanotubes one concentrically placed inside another like rings of a tree trunk (Fig. 21.2). Here, we will discuss the three main techniques used for the synthesis of carbon nanotubes like arc discharge, laser ablation, and chemical vapor deposition.

Arc Discharge

The carbon arc discharge method, initially used to produce C60 fullerenes, is one of the oldest and perhaps the easiest method to produce CNTs. This method creates CNTs through arc vaporization of two carbon rods placed end to end, separated by approximately 1 mm, in an enclosure that is usually filled with inert gas at low pressure [106]. SWNTs are produced in the presence of transition metal catalyst which plays a significant role in the process yield. In this, an arc discharge of hydrogen or argon atmosphere, the anode is made as a composition of graphite and a metal such as Ni, Fe, Co, and Pd or mixtures of Co, Fe, and Ni with other elements like Co–Ni, Fe–Ni, and Ni–Cu. For the first time, S. Iijima and T. Ichihashi found the SWNTs of 1 nm in sootlike deposits formed in a carbon arc chamber similar to that used for fullerene production [107]. In a similar process, many groups described Co catalyzed growth of SWNT [108]. One of the most utilized catalysts for SWNTs synthesis is nickel. Seraphin et al. [109] studied the catalytic role of Ni, Pd, and Pt in the formation of carbon nanoclusters using DC arc discharge operated at 28 V, 70 A, and under a 550 Torr He atmosphere. They found out that nickel-filled anode stimulated the growth of SWNTs. A similar method was used by Saito et al. [110] who reported SWNTs growing radially from Ni fine particles. The arc discharge method is still in use for SWNTs synthesis but usually with new approaches. Chen et al. [111] produced high-purity SWNTs by a hydrogen DC arc discharge method with evaporation of carbon anode containing 1 % Fe catalyst in H_2–Ar mixture gas. Fan et al. [112] successfully discovered a cheap method to produce high-purity SWNTs with diameter of about 1.2 nm. They used an argon DC arc discharge from charcoal as carbon source and FeS (20 wt%) as catalyst. In another work, Wang et al. [113] incorporated Mo into Ni/Y–He and Fe–Ar/H_2, which are two typical arc systems. They observed that addition of Mo increased the yield of soot manifolds. They also noticed a considerable increment in the purity of SWNTs Fe–Ar/H_2 system with the addition of Mo.

On the other hand, MWNTs are produced in the absence of a catalyst. The most utilized methods use DC arc discharge between two graphite usually water-cooled electrodes in a chamber filled with helium at subatmospheric pressure. Ebbesen and Ajayan [106] reported large-scale synthesis of MWNT by a variant of the standard arc discharge technique under He atmosphere. Under certain conditions, a pure nanotube and nanoscale particles in high yield were obtained. The purity and yield was found to be dependent on the gas pressure in the reaction vessel. In a different

Fig. 21.12 Schematic diagram of laser ablation (Reprinted with permission from Smalley et al. [119]. Copyright (1995): Elsevier)
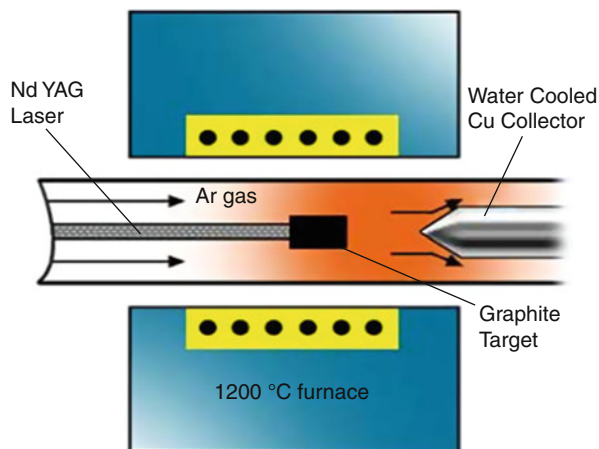
work by Shimotani et al. [114], they studied the synthesis of MWNTs under He, ethanol, acetone, and hexane atmosphere at various pressures. They observed that arc discharges in these organic atmospheres produce approximately two times MWNTs as compared to those in the He atmosphere. Jiang et al. [115] demonstrated the arc discharge growth of CNTs in NH_3 atmosphere and found no significant difference of the shapes and the structures between NH_3 atmosphere and other atmospheres such as He and H_2. Apart from DC arc discharge, Parkansky et al. [116] reported single-pulse arc production of near vertically oriented MWNTs on the Ni/glass samples using a graphite counter electrode in ambient air. Contrary to a gas atmosphere, Jung et al. [117] reported high-yield synthesis of MWNTs by arc discharge in liquid nitrogen. Similarly, Guo et al. [118] synthesized high-quality MWNTs in water between pure graphite electrodes.

However this technique produces a large amount of complex components such as metal particle, amorphous carbon, and multi-shell and requires further purification to separate the CNTs from the soot and the residual catalytic metals present in the crude product. There are several techniques like oxidation, acid treatment, annealing, ultrasonication, and microfiltration which may be used separately or combined with each other to improve the purification and to remove different impurities at the same time.

Laser Ablation

The laser ablation method for the synthesis of carbon nanotubes was first developed by Smalley's group in 1995 [119]. In this technique, a pulsed laser is made to strike at graphite target in a high-temperature reactor in the presence of inert gas such as helium which vaporizes a graphite target. The produced CNTs are condensed and collected on a water-cooled target (Fig. 21.12) [119]. The typical yield of CNTs in this process is up to 70 %. This method has several advantages of high-quality and high-purity CNTs production, diameter control, investigation of growth dynamics,

and the production of new materials. The properties of CNTs prepared by laser ablation depend on various parameters like laser energy fluence, peak power, repetition rate and oscillation wavelength, composition of the target material, chamber pressure, chemical composition of the buffer gas, substrate, and distance between the target and the substrates. Lebel et al. [120] synthesized SWNTs using the UV-laser (KrF excimer) ablation of a graphite target appropriately doped with Co/Ni metal catalyst. In their work, they tested as-prepared SWNTs as a reinforcing agent of polyurethane. Kusaba and Tsunawaki [121] used XeCl excimer laser with the oscillation wavelength of 308 nm to irradiate a graphite containing Co and Ni at various temperatures, and they found that laser ablation at 1,623 K produced the highest yield of SWNTs with the diameter between 1.2 and 1.7 nm and the length of 2 mm or above. Zhang et al. [122] showed the influence of CO_2 laser power (400–900 W) on the shape and size of CNTs. They obtained a slight increment in the diameter of SWNTs with increasing laser power. They also showed that the shape of CNTs changed from bamboo-like to bundle-like when power was increased from 500 to 900 W, respectively. Stramel et al. [123] have successfully applied commercial MWNTs and MWNTs–polystyrene targets (PSNTs) for deposition of composite thin films onto silicon substrates using PLD with a pulsed, diode pumped, Tm:Ho:LuLF laser (a laser host material LuLF ($LuLiF_4$) is doped with holmium and thulium in order to reach a laser light production in the vicinity of 2 mm). They found that usage of pure MWNTs targets gives rise to a thin film containing much higher-quality MWNTs compared to PSNTs targets. Scott et al. [124] revealed that the carbon which serves as feedstock for SWNT's formation not only comes from the direct ablation of the target but also from carbon particles suspended in the reaction zone.

Despite the production of some high-quality CNTs, laser ablation suffers from the disadvantages of high cost needed to produce laser, and a large-scale production is not feasible due to its requirement of very large graphite target, and thereafter, better purification steps are needed to separate the tubes from unwanted form of carbon or catalysts.

Chemical Vapor Deposition

Due to the high-temperature preparation and limitations on the volume of the sample prepared in relation to the size of carbon source, both arc discharge and laser ablation techniques have now been replaced by gas-phase techniques such as low-temperature chemical vapor deposition (CVD) [125, 126]. CVD is the catalytic decomposition of gaseous carbon molecules such as methane, carbon monoxide, and acetylene (placed in a gas phase) into reactive atomic carbon with the aid of supported transition metal catalysts in a high-temperature furnace. The synthesis is achieved by breaking the gaseous carbon molecules, such as and sometime helped by plasma to enhance the generation of atomic carbon [127]. This carbon will get diffused towards substrate, which is coated with catalyst, and nanotubes grow over this metal catalyst. Temperature used for synthesis of nanotube is in the 650–900 °C range, and the typical yield is ∼30 % [128, 129]. However, other CVD techniques, like oxygen-assisted CVD [130], hot filament (HFCVD) [131], microwave plasma

(MPECVD) [132], or radio-frequency CVD (RF-CVD) [133], are also frequently used. But catalytic CVD is considered to be an economically viable process for large-scale and quite pure CNTs production compared with laser ablation. The main advantages of CVD are easy control of the reaction course and high purity of the obtained material [134].

The most frequently used catalysts are transition metals, primarily Fe, Co, or Ni [135], and the frequently used carbon source, most preferred in CVD, are hydrocarbons such as methane, ethane, ethylene, acetylene, xylene, and eventually their mixture, isobutene or ethanol [125]. In the case of gaseous carbon source, the CNTs growth efficiency strongly depends on the reactivity and concentration of gas-phase intermediates produced together with reactive species and free radicals as a result of hydrocarbon decomposition. Commonly used substrates are Ni, Si, SiO_2, Cu, Cu/Ti/Si, stainless steel, or glass, rarely $CaCO_3$; graphite and tungsten foil or other substrates were also tested [136, 137]. Zhu et al. [138] reported a CVD synthesis of DWNTs over supported metal catalysts decomposed from Fe and Co on mesoporous silica. Similarly, Ramesh et al. [139] succeeded in high-yield selective CVD synthesis of DWNTs over Fe/Co loaded high-temperature stable mesoporous silica. The choice of catalyst, its preparation, composition, and morphology play an important role in the CNT's growth. Therefore, its preparation is also a crucial step in CNTs synthesis. Flahaut et al. [140] prepared catalysts by the combustion route using urea or citric acid as the fuel. They found that the milder combustion conditions obtained in the case of citric acid can either limit the formation CNTs with fewer walls, depending on the catalyst composition. Fotopoulos and Xanthakis [141] stated in their report that in order to produce SWNTs, the size of the nanoparticle catalyst must be smaller than about 3 nm. Zhang et al. [142] prepared MWNTs with diameters of 40–60 nm by the catalytic decomposition of methane at 680 °C for 120 min, using nickel oxide–silica binary aerogels as the catalyst. In another work by Li et al. [143], well-aligned MWNTs were synthesized on a large area of Ni-deposited SiO_2/Si substrates via the pyrolysis of C_2H_2 using the thermal CVD technique at 900 °C. He found that NH_3 pretreatment was very crucial to control the surface morphology of catalytic metals and thus to achieve the vertical alignment of CNTs. In addition, Cui et al. [144] synthesized thin-walled, open-ended, and well-aligned N-doped CNTs on the quartz slides using acetonitrile as the carbon source and ferrocene as the catalyst.

Synthesis of Graphene

The realization of single-layer graphene to extract from bulk graphite by Novoselov et al. in 2004 [73, 145] has driven explosive scientific studies on graphene physics and chemistry. Although there have been numerous efforts to produce graphene, utilization of graphene in many applications requires systematic optimization of preparation techniques to obtain selective single or bilayer growth, as well as highly crystalline and large area. Several routes have been proposed to

prepare single-layer graphene so far, such as thermal- or plasma-enhanced chemical vapor deposition (CVD), SiC sublimation, exfoliation of graphite, and other processes. In this section, an overview of existing graphene synthesis methods will be presented.
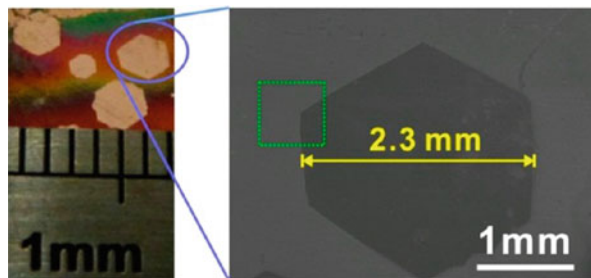
Thermal CVD

Chemical vapor deposition (CVD) has emerged as an important method for the preparation and production of large-area and high-quality graphene for various applications since the method was first reported in 2008/2009 [146–150]. The successful demonstration of a 30-in. graphene sheet by roll-to-roll and CVD methods have brought graphene research much closer to commercial production of large-scale applications [151]. Recent CVD method could provide large-scale and uniform graphene, but graphene by CVD contains grain boundaries that can weaken the material and degrade its electrical properties [152]. Large-size grain growth can be achieved controlling nucleation site density on a metal substrate, especially Cu [153]. Therefore, reducing the nucleation density is a feasible route to prepare large-size single-crystal graphene domains. Various approaches have been reported that graphene grain growth on Cu is not only determined by the quality of Cu substrate and its pretreatment method but also the growth parameters such as a precursor concentration, pressure, temperature, and growth time.

During the growth reaction, the metal substrate not only works as a catalyst to lower the energy barrier of the reaction but also determines the graphene growth mechanism, which ultimately affects the quality of graphene [154]. The surface morphology of the Cu substrate can be controlled by polishing methods, for example, chemical–mechanical polishing [155] and electrochemical polishing [156], which led to suppress the density of nuclei. On the other hand, graphene morphology is affected by the crystallographic orientation of Cu substrate [157, 158], but the orientation relationship between graphene grains and the different grains of Cu foil still remains unclear. The recently developed recipe for single-layer and large-size graphene was first introduced by Li et al. [150] and employs a low-pressure mixture of methane and hydrogen flowing over Cu substrate heated to a temperature up to 1,000 °C. Wang et al. [159] has obtained the large single-crystal graphene, measured to be about 0.16 mm^2, suppressed nucleation site on Cu foil by pregrowth longtime annealing at 1,045 °C for 3 h under atmospheric pressure. Yan et al. [160] have synthesized large single-crystal hexagonal monolayer graphene by a controlled chamber pressure CVD system. Using this system, high-pressure annealing at 1,500 Torr and 1,077 °C (closer to melting temperature of Cu) for 7 h with a H$_2$ flow was applied, and the growth of subcentimeter-sized (around ∼0.23 cm) graphene was obtained on electrochemical polished Cu foil by extremely low concentration of CH$_4$ shown in Fig. 21.13. And graphene growth on Cu substrate is strongly dependent on H$_2$, suggested a partial pressure of H$_2$ 200–400 times that of CH$_4$ [161].

The recent achievements in graphene growth by thermal CVD have corroborated reproducibility of high-quality graphene on a centimeter-scale substrate. The performance of obtained graphene is comparable to that of exfoliated graphene,

Fig. 21.13 Optical and SEM images of as-produced graphene domains on Cu. After growth, the Cu foils were heated in air for 1 min at 215 °C to visualize graphene (Reprinted with permission from Z. Yan et al. [160]. Copyright (2012): ACS Nano)

and these developments provide new routes for large-scale application of graphene. However, the understanding of the optimum growth parameters by thermal CVD is still unclear. Therefore, new approaches beyond existing techniques are necessary for controlling graphene properties and its potential applications.

PECVD

Plasma-enhanced chemical vapor deposition (PECVD) offers another route of graphene growth. The first report of the production of single-to-few-layer graphene by CVD involved a radio-frequency PECVD system to synthesize graphene on various substrates without any catalyst or special substrate treatment where graphene sheets were produced from a gas mixture of 5–100 % CH_4 in H_2, at 900 W power and 680 °C substrate temperature [162, 163]. Several studies have been reported the growth of high-quality large-area graphene using plasma-enhanced methods with different plasma sources lower temperature. Nandamura et al. [164] have reported remote plasma-assisted growth of graphene films on Ni surfaces with CH_4 and H_2 at 650–700 °C for 1 min, and they suggested that remote plasma can eliminate the orientation effect of the electrical field on the grown film. With the radio-frequency PECVD, the graphene is grown on Ni thin-film-coated SiO_2/Si substrate at 200 W and 650 °C for 30 s, and the grown graphene consists of different regions with 1–3 layers [165]. Kim and coworkers [166] have demonstrated high-quality centimeter-scale graphene film by microwave plasma CVD at lower temperature from 750 °C down to 450 °C. The obtained monolayer graphene films have achieved the overall transparency of 89 % and low sheet resistances ranging from 59 to 1855 $\Omega \, sq^{-1}$ regardless of the temperatures. Kalita et al. [167] have obtained triangular-shaped nanographene domains with sizes of 80–100 nm in length on Si and SiO_2 substrates between 400 °C and 560 °C by surface wave plasma CVD and studied their application in photovoltaic devices.

Compared with thermal CVD, PECVD possesses a unique advantage of additional high-density reactive gas atoms and radicals, facilitating low-temperature and rapid synthesis. However, because the growth of graphene by PECVD is a recent development and a fundamental aspect of PECVD, that is, the effect of plasma on graphene synthesis resulting in a synthesis behavior different from that of thermal CVD, has not been addressed in detail yet, further systematic research is
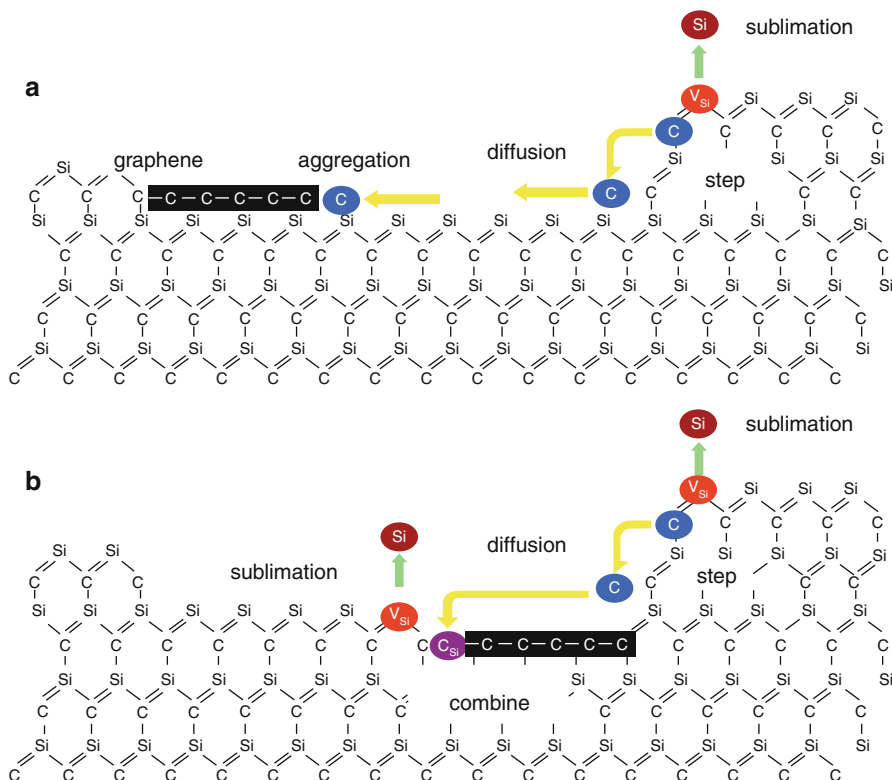
Fig. 21.14 Schematic of the graphene growth atomic process models on SiC (0001): (**a**) on top graphene case and (**b**) embedded graphene case (Reprinted with permission from H. Kageshima et al. [169]. Copyright (2012): J Phys: Condens Matter)

required. It remains a challenge to develop a simple, effective, and reproducible method to synthesize low-cost, high-quality, and large-area graphene at relatively low temperature.

SiC Sublimation

Another method of obtaining graphene is the epitaxial growth on single-crystal silicon carbide (SiC) heated to high temperatures (>1,100 °C) under low pressure ($\sim 10^{-6}$ Torr) to reduce it to graphene [168]. When SiC is annealed in high temperature, Si atoms selectively sublimate from the surface, because the melting temperature of Si is around 1,100 °C, while that of C is around 3,650 °C. This makes the surface rich in C. Figure 21.14 shows the atomic process model of graphene growth on SiC (0001) [169]. The graphitization of SiC by Si sublimation during high-temperature (2,050–2,150 °C) vacuum annealing was demonstrated in 1962 [170] and has been steadily studied [71, 168, 171, 172]. Many important graphene properties have been identified in graphene produced by this method,

for example, the electronic band structure has been first visualized in this material [171, 172]. There are some theoretical approaches for the growth of epitaxial graphene on the SiC surface by assuming Si sublimation from the surface [173–175]. Hibino and coworkers have established a method of evaluating the number of graphene layers grown on SiC digitally using low-energy electron microscopy (LEEM) to investigate the reflectivity from graphitized SiC (0001) [169, 175, 176]. They used nominally flat 6H-SiC (0001) wafers (n type, 0.02–0.2 Ω cm) and found that the samples are fully graphitized by annealing under higher than 1×10^{-8} Torr at 1,450 °C [175]. They succeed in growing monolayer graphene in an Ar environment, as well as bilayer graphene uniformly on a micrometer scale in ultrahigh vacuum. Multilayer graphene grown on the C face involves domains with different azimuthal orientation, and annealing in an Ar environment significantly enlarges the domain size [176].

Because SiC is a wide band gap semiconductor, graphene devices operable at room temperature can be fabricated directly on top of it. The issue of SiC sublimation method is that crystal size could be a major cost impediment for large-scale production, and it is difficult to exfoliate or transfer graphene from SiC to another substrate due to the strong cohesive strength of the graphene/SiC interface and the extreme chemical stability of SiC. Till now, the effect of interface is well understood, and future research should be focused on understanding this issue. With the knowledge about growth mechanism and interface effects and the ability to effectively control the number of layers, this method is set to be used industrially to produce wafer-scale graphene.

Exfoliation

Exfoliation method uses mechanical and chemical energy to break weak bonds between graphene sheets and isolate individual graphene sheets from others. In 2004, the Manchester group obtained graphene by micro-mechanical alleviation of graphite using the scotch tape method which is the popular method of mechanical cleavage that has been explored for separation of graphene [73, 145]. The exfoliated graphene cannot be produced in large scale, at most ∼100 μm typically, and a lot of debris or graphite flakes are generated together near the graphene in this process. After the exfoliation using scotch tape, the thick graphite flakes can be eliminated by heating at 350 °C for 30 min and sonication in acetone which does not cause any chemical contamination [177]. Very recently, Jayasena et al. [178] reported a wedge-based mechanical exfoliation machining technique to produce few-layer graphene. An ultra-sharp single-crystal diamond wedge is inserted between graphene layers in the highly ordered pyrolytic graphite (HOPG) to cause exfoliation and produce few-layer graphene shown in Fig. 21.15. Since it is not easy to observe the process in situ during the exfoliation, molecular dynamics simulations help to understand separation, folding, and shearing of graphene layers. Mechanical exfoliation process is found to be very reliable and easy and thus attracted the immediate attention of the scientific community, but repeated peeling is needed to achieve single-layer graphene, and it is still difficult to predict the number of peelings required.
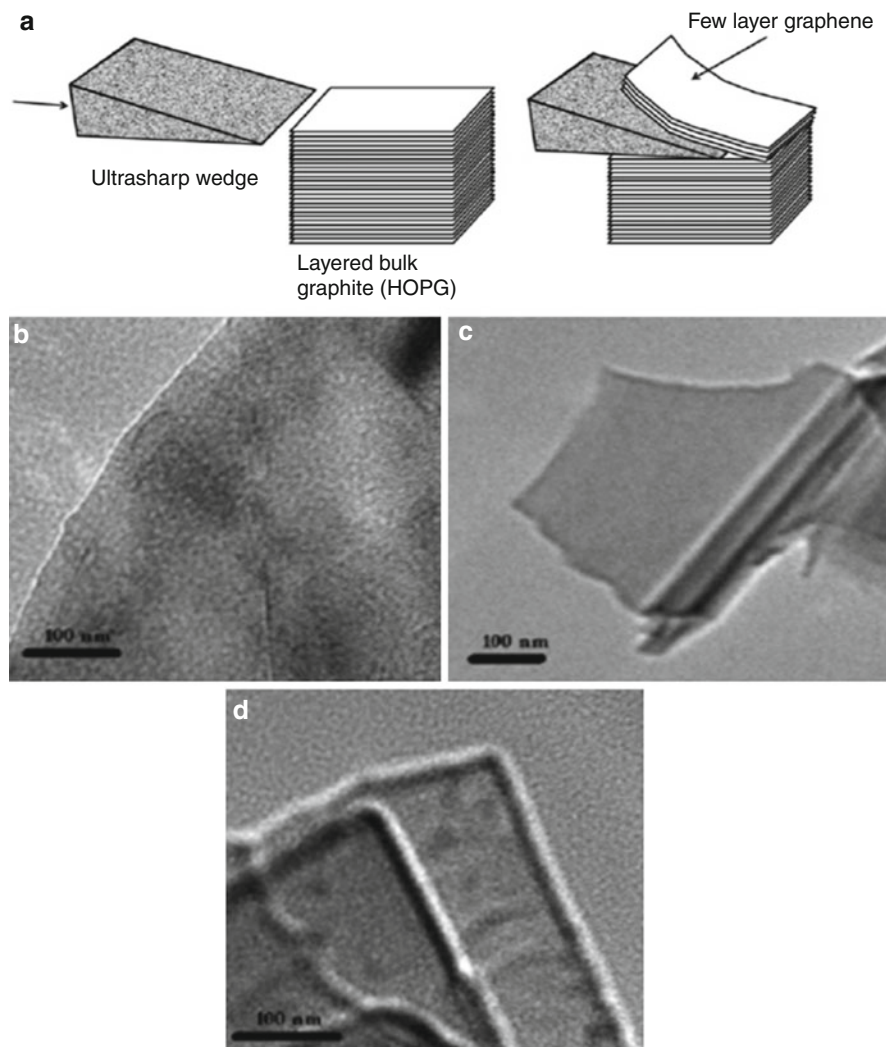
Fig. 21.15 (**a**) Schematic diagram for wedge-based mechanical exfoliation of a few layers of graphene, (**b**) flat separated, (**c**) folded, and (**d**) sheared few-layer graphene (Reprinted with permission from B. Jayasena et al. [178] Copyright (2013): Nanotechnology)

Graphite can also be chemically exfoliated in liquid environments exploiting ultrasounds to extract individual layers. Modified Hummers method [179] is most commonly used to produce well-dispersed graphite oxide (GO) solution. This method generally involves three steps: (1) dispersion of graphite in a solvent, (2) exfoliation via chemical reaction, and (3) purification, usually carried out by ultracentrifugation. Solvents ideal to disperse graphene are those that minimize the

interfacial tension between the liquid and graphene flakes [180]. Some researchers have suggested different re-intercalation and dispersion methods to prevent the oxidation of graphene [181–184]. In a little different approach, GO is exposed to a thermal treatment to expand or to exfoliate it via oxygen removal from GO. The GO is suddenly heated by inserting it in a preheated furnace [185, 186]. Under this type of heat treatment, GO gets exfoliated into graphene sheets. Graphene prepared by thermal exfoliation method contains some oxygen functionalities and is often termed as functionalized graphene sheet. But this process requires a rapid heating ($>2,000\ ^\circ C\ min^{-1}$) up to $1,050\ ^\circ C$. The thermal method is believed to be a green method in which no hazardous reductants are used, but it is still difficult to thermally reduced GO under mild conditions. Improvements have been accomplished by post-heating at low temperature ($100–150\ ^\circ C$) [187, 188] or by thermochemical treatment at $300\ ^\circ C$ [189]. The methods described here enable the production of liquid colloids of graphene sheets that can be easily spin-cast and sprayed on multiple substrates without the need of high-temperature processes and are scalable and low cost. Current challenges may be controlling the number of layers and minimizing impurity levels into an industrial-scale production level.

Others

Molecular beam epitaxy (MBE) is widely used and well suited for the deposition and growth of compound semiconductors. It was used to grow graphene layers with high-purity carbon sources on a variety of substrates such as SiC [190], Si [191], Ni [192], and h-BN [193], in the $400–1,100\ ^\circ C$ range. Since MBE is a thermal process, the carbon is expected to be deposited in the amorphous or nanocrystalline phase. Compared to other methods, it is unlikely that MBE can be used to grow single-layer graphene of high enough quality. With future optimizations, therefore, it may be possible to use this technique to downscale towards two-dimensional film growth and produce large-area single-crystal graphene sheets.

Graphene can be also produced from unzipping carbon nanotubes (CNTs) by controlled oxidation reaction [194, 195]. Kosynkin et al. [196] obtained oxidized graphene nanoribbons by suspending CNTs in concentrated sulfuric acid followed by treatment with 500 wt% $KMnO_4$ for 1 h at room temperature and 1 h at $55–70\ ^\circ C$. As-prepared nanoribbons are poor conductors because of the oxidized edges and planes; however, their conductivity can be improved either by chemical reduction using N_2H_4 or by annealing in H_2. In another study, graphene nanoribbons were produced by Ar plasma etching of CNTs, partially embedded in a PMMA film [197]. Recently a clean method of hot water steam reaction has been developed for the production of graphene nanoribbons from CNTs with mild synthesis conditions and without any toxic reagents [198]. When the temperature rises from $150\ ^\circ C$ to $200\ ^\circ C$, water steam molecules have higher activity and more opportunities to be adsorbed on CNTs and then cause CNTs unzipping. This new process route of unzipping CNTs creates possibilities of synthesizing graphene in a substrate-free manner and producing large-scale, well-aligned semiconducting graphene nanoribbons.

Applications of Carbon Nanomaterials

Carbon Nanotubes (CNTs)

Electronics

As the electronic device scales down, the conventional CMOS technology will reach its scaling limit in the near future [199]. New materials and novel device concepts have been proposed for further device miniaturization. Carbon nanotubes have been considered as one of the most promising candidates for nanoelectronics application owing to their nearly ballistic transport, lack of surface dangling bonds and strong C–C covalent bonding, compatibility with high-k dielectrics, and band gap dependency on diameter and chiral vectors [200, 201]. Because of their nanoscale cross section, electrons propagate only along the tube's axis, and electron transport involves quantum effects. As a result, carbon nanotubes are frequently referred to as one-dimensional conductors. The maximum electrical conductance of a single-walled carbon nanotube is $2G_0$, where $G_0 = 2e^2/h$ is the conductance of a single ballistic quantum channel [21]. To approach the performance limit of CNT-based electronic devices, it is essential to integrate ballistic semiconducting nanotube channel with ohmic contact and high-dielectric-constant gate oxide, which has been pursued aggressively by many research groups [10, 202, 203]. With the development of first CNT transistor in 1998 [18], a large number of devices like SWNT–FET with a threshold swing of 60 mV decade^{-1}, CNT-based radios, and SWNT FETs with sub-10-nm channel lengths with a normalized current density of 2.41 mA μm^{-1} have been made with a greater performance than those obtained for silicon devices [204–206]. Although it is hard to control the CNT diameter, density, and chirality for the production of CNT microelectronics over large areas, there have been attempts to pattern transistors with tens to thousands of SWNT films for more practical applications. Cao et al. [207] fabricated transistors using horizontally aligned CNT arrays on plastic substrates. They were able to achieve high mobilities of 80 cm^2 V^{-1} s^{-1}, subthreshold slopes of 140 mV decade^{-1}, and on/off ratios as high as 10^5. Similarly, Park et al. [208] assembled a high density of carbon nanotube transistors in a conventional semiconductor fabrication line and then electrically tested more than 10,000 devices in a single chip.

Nowadays, CNT thin-film transistors (TFTs) are gaining attention for driving organic light-emitting diode (OLED) displays due to their high mobility than amorphous silicon (1 cm^2 V^{-1} s^{-1}) and can be deposited by low-temperature, non-vacuum methods [209]. Sun et al. [210] demonstrated flexible CNT TFTs with a mobility of 35 cm^2 V^{-1} s^{-1} and an on/off ratio of 6 × 10^6. McCarthy et al. [211] developed vertical CNT FET showing enough current output to drive OLEDs at low voltage, enabling red–green–blue emission by the OLED through a transparent CNT network. Owing to their low scattering, high current-carrying capacity, and resistance to electromigration, CNTs could replace copper in microelectronic interconnects. Recently, complementary metal–oxide–semiconductor (CMOS)-compatible 150-nm-diameter interconnects with a single CNT–contact-hole resistance of 2.8 kΩ were demonstrated on full 200-mm-diameter wafers [212].

Field Emission

CNTs have been considered as preferred field emitters due to their geometrical high aspect ratio (i.e., the ratio of diameter/length), low threshold voltage, good emission stability, and long emitter lifetime [213, 214]. The increased sensitivity of CNTs to electrical fields can be used in gas ionization sensors, high-frequency (>200 MHz) vacuum microelectronics, flat panel display, and X-ray generation [215–218]. The field enhancement factor (β), which is the ratio of the electric field at the CNT tip and the macroscopic electric field, can be as high as 3,000, lower turn-on voltages (<10 V μm^{-1}), and larger currents (up to 10 μA from a single MWNT) and current densities ($\sim$4 A cm^{-2}) make them useful for practical applications [213, 219]. Although SWNTs showed excellent field emission performance, they were simply degraded at high emission current [220]. In this sense, DWNTs and/or thin MWNTs have been examined as the best field-emitting materials because they were shown to have a low threshold voltage comparable to SWNTs and a better structural stability compared to SWNTs [221, 222]. Hiraoka et al. [223] successfully fabricated a DWNT forest using Ni-based alloys with Cr or Fe as catalysts and then measured the field emission from such a CNT/buckypaper cathode to an anode. Their results showed a homogeneous emission from the DWNT electrode as a result of the good electrical contact between the DWNTs and the grid substrate.

Charlier et al. [224] have demonstrated experimentally and theoretically that doping of boron (B) in MWNTs exhibits enhanced field emission (turn-on voltages at ca. 1.4 V μm^{-1}) when compared to pure carbon MWNTs (turn-on voltages at ca. 3 V μm^{-1}). It could be attributed to the presence of B atoms at the nanotubes tips, which results in an increased density of states close to the Fermi level. Theoretical tight-binding and ab initio calculations demonstrate that the work function of B-doped SWNT is much lower (1.7 eV) than that observed in pure carbon MWNTs. Similarly, it has been demonstrated that bundles of N-doped MWNTs are able to emit electrons at relatively low turn-on voltages (2 V μm^{-1}) and high current densities (0.2–0.4 A cm^{-2}) [225]. N-doped MWNTs have also shown excellent field emission properties at 800 K; experimental work functions of 5 eV and emission currents of ca. 100 nA were obtained at ±10 V [226].

One of the important factors in a CNT-based field emitter is the interface resistance. Metallic CNTs grown a metallic (highly conducting) substrate, along with a conducting interface between the CNTs and the substrate, could offer better emission response. Following this principle, interface-controlled MWCNT-based emitter structure was prepared on copper substrates, and the device was found to offer very good emission response [227]. It showed a low turn-on field of $\sim$0.5 V μm^{-1}, high rms emission current of 6.7 mA at low excitation field of 1.6 V μm^{-1}, excellent stability, and very high field enhancement ($\sim$10,700). This CNT-on-Cu emitter device has shown much higher emission current as compared to similar CNT structures grown on Si substrates.

Field emission properties of thin MWNTs could be interesting as these have intermediate structural properties of single- (SWNTs) and multiwalled (MWNTs) carbon nanotubes. The aspect ratio of the synthesized thin MWNTs is $\sim$1,500, and the
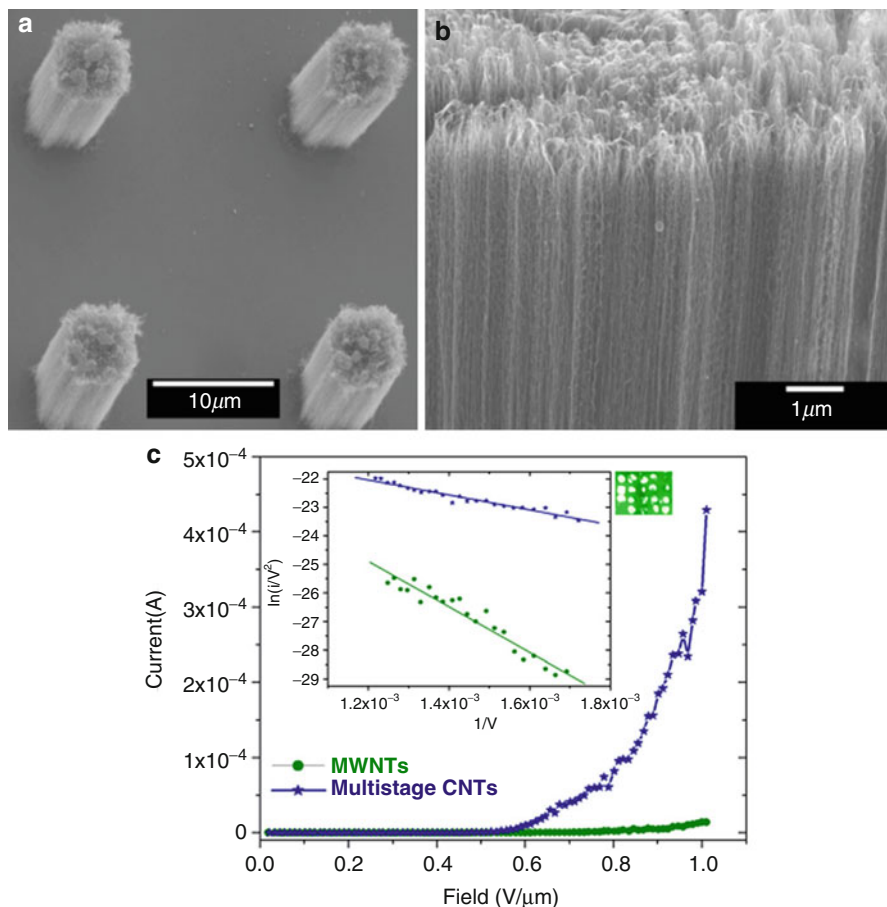
Fig. 21.16 (**a**, **b**) SEM images of the multistage MWCNT emitter. (**c**) Field emission enhancement of the multistage emitter, as compared to MWCNT array emitter [228, 229]

turn-on field is $\sim$1.0 V μm^{-1} with a field enhancement factor of $\sim$9,300 with high emission stability [228]. We obtained $\sim$7.5 times increase in emission current when an electron micro-channel plate (MCP) was placed between cathode and anode. Further enhancement at high emission current level will be achieved by introducing a ceramic-based MCP system. A multistage MWCNT emitter, SWCNT, or thin MWCNT emitters on top of MWCNT emitters were also found to increase the field emission response [229]. Such a novel structure offered very low turn-on field ($\sim$0.4 V μm^{-1}) and very high field enhancement ($\sim$26,200). Figure 21.16 presents the basic structure and electron emission response of this emitter structure.

Energy Applications

Because of their unique high electrical conductivity, good chemical stability, and highly accessible surface area, carbon nanotubes have been utilized in

various electrochemical energy storage systems like supercapacitors, Li-ion batteries, solar cells, and fuel cells [230, 231]. Li-ion batteries are the source of energy for most of the portable electronic devices, and they are expected to play an important role in hybrid automobiles, too. Current research trends in Li-ion batteries are focused on enhancing its capacity, lifetime, and safety. A number of new materials have been proposed as cathode and anode of next-generation Li-ion batteries. Graphite offers excellent stability as an anode in Li-ion batteries, and most commercial Li-ion batteries use graphite as the anode material. However, theoretical specific capacity of graphite being low (372 mAh g^{-1}) [232], ample opportunity exists for development of new anode materials. We have proposed interface-controlled, directly grown multiwalled carbon nanotubes (MWCNT) onto copper current collector, as a new anode structure for Li-ion batteries [233]. This novel structure is expected to offer exciting properties owing to many reasons: (a) In contrast to the past studies, which used raw CNTs and polymeric binders, our structure has directly grown CNTs on Cu current collector, thus avoiding the polymeric binders completely leading to offer potential to be used for high-temperature application; (b) CNTs are not reported to have any kind of expansion/contraction problem (like Si and SnO$_2$), so structural degradation during long cycles is avoided. (c) Direct growth on current collector ensures that each CNT is well bonded, and thus all of them contribute to the capacity and stability of the battery. (d) High specific surface area of CNTs allows more Li-ion intercalation, leading to more capacity. (e) Interface control, as proposed in this study, offers to form an ohmic contact and strong bonding between the CNTs and substrate, further helping in efficient charge transport. (f) Finally, the anode consisting MWCNTs grown on Cu foil can be very easily fabricated by two-step process – catalyst deposition by sputtering and CNT growth by thermal chemical vapor deposition (CVD) [234].

However, many research groups suggested the potential of CNTs to be used as the electrodes in lithium-ion batteries (LIBs) because of their increased reversible capacity up to 1,000 mAh g^{-1}, but a large hysteresis, the absence of a voltage plateau, and the large reversible capacity that were observed in a typical hard carbon limited the use of nanotubes as the electrode material in LIBs [235–237]. On the other hand, CNTs have been well commercialized as filler for the anode materials used in LIBs. Endo et al. [238] demonstrated that homogeneously dispersed carbon nanotubes in synthetic graphite (ca. 3 wt%) give rise to a continuous conductive network as well as a mechanically strong electrode, resulting in a doubled energy efficiency of LIBs. For energy storage devices other than batteries, supercapacitors have been extensively and actively investigated because they are able to store and deliver energy rapidly and efficiently for a long life cycle via a simple charge separation process. An et al. [239] observed a SWNT electrode exhibiting the maximum capacitance of ca. 180 F g^{-1} and a power density in the range of 6.5–7 Wh kg^{-1}. Also, Veen et al. [212] have shown remarkable performance for supercapacitors deploying forest-grown SWNTs that are binder- and additive-free; an energy density of

16 Wh kg^{-1} and a power density of 10 kW kg^{-1} were obtained for a 40-F supercapacitor with maximum voltage of 3.5 V.

The use of CNTs as a catalyst support can potentially reduce Pt usage by 60 % compared with carbon black for fuel cells, and doped CNTs may enable fuel cells that do not require Pt [240, 241]. Carbon nanotubes can be a good material for forming bulk heterojunctions in organic solar cells to reduce undesired carrier recombination and enhance resistance to photo oxidation [242]. Their high aspect ratio allows formation of a percolating network of nanotubes at low doping levels in a polymer composite, and as one-dimensional nanostructures, nanotubes are also ideal for electron transport as they exhibit quasiballistic features [243]. In the long run, photovoltaic technologies may incorporate CNT–Si heterojunctions and leverage efficient multiple-exciton generation at p–n junctions formed within individual CNTs [244]. In the nearer term, commercial photovoltaics may incorporate transparent SWNT electrodes.

Biological Applications

In recent years, efforts have also been devoted to exploring the potential biological applications of CNTs as motivated by their interesting size, shape, and structure, as well as attractive, unique intrinsic physical, and chemical properties [245, 246]. The optical properties of nanotubes impart promising advantages to their use in imaging applications within live cells and tissues. SWNTs are highly absorbing materials with strong optical absorption in the NIR range due to E11 optical transitions and thus can be utilized for photothermal therapy and photoacoustic imaging [247, 248]. Semiconducting SWNTs with small band gaps on the order of 1 eV exhibit photoluminescence in the near-infrared (NIR) range. The emission range of SWNTs is 800–2,000 nm, which covers the biological tissue transparency window, and is therefore suitable for biological imaging [249]. Nanotube fluorescence was also used to image SWNT in tissue sections as well as measure their concentration in blood [250]. SWNTs also have unique resonance-enhanced Raman signatures for Raman detect ion/imaging, with large scattering cross sections for single tubes [251]. The intrinsic physical properties of SWNTs can be utilized for multimodality imaging and therapy.

CNTs have received a lot of attention as potential drug delivery vehicles due to their higher surface to surface area to volume which gives them potential to be conjugated with more functional agents and accommodate higher loadings of therapeutic agents [245, 252, 253]. They are readily internalized by the cells, first by binding of their tips to receptors on the cell membrane. This enables transfection of molecular cargo attached to the CNT walls or encapsulated inside the CNTs [254]. Liu et al. [255] showed that the cancer drug doxorubicin was loaded at up to 60 wt% on CNTs compared with 8–10 wt% on liposomes. Cargo release can be triggered by using near-infrared radiation. However, for use of free-floating CNTs, it will be critical to control the retention of CNTs within the body and prevent undesirable accumulation, which may result from changing CNT surface chemistry [256]. The introduction of foreign DNA to cells is another major area for therapeutic delivery using carbon nanotubes. Cai et al. [257] used nanotube spearing,
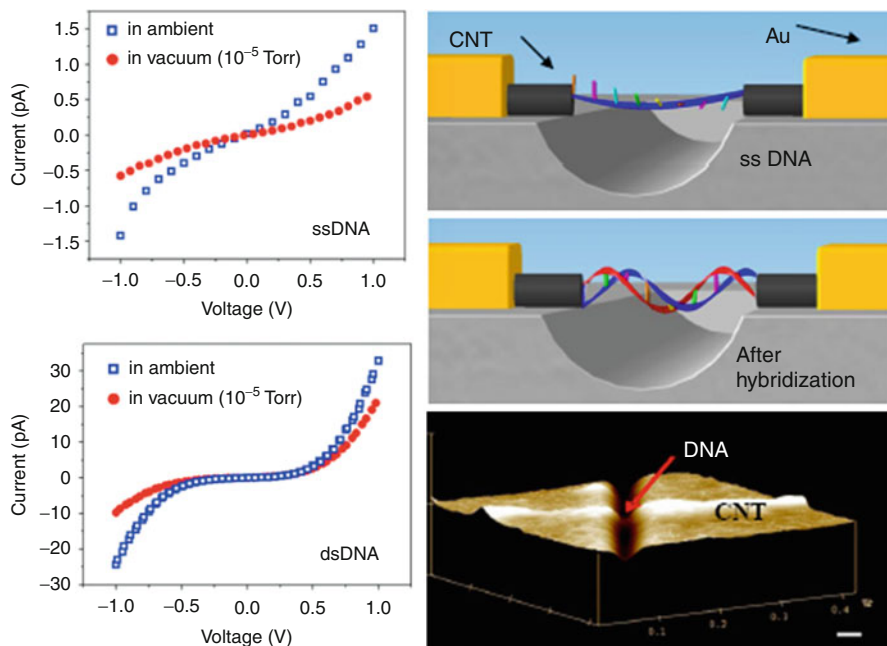
Fig. 21.17 (*Right column*) Schematic CNT nanoelectrode with single- (*top*) and double- (*middle*) strand DNA attached between the electrode pairs and AFM image of DNA attachment between CNT electrodes (*bottom*). (*Left column*) Their conductance data, before (*top*) and after (*bottom*) hybridization [258, 259]

utilizing the magnetic properties of nickel-embedded single-walled carbon nanotubes (SWNTs), to deliver DNA plasmid vectors containing the sequence for EGFP (a fluorescent protein) to Bal17 and mouse splenic B cells, which are nondividing cells and therefore notoriously difficult to transfect. They observed expression of EGFP in the cells, whereas a vector without EGFP did not show any detectable fluorescence. Potential CNT toxicity remains a concern, although it is emerging that CNT geometry and surface chemistry strongly influence biocompatibility, and therefore CNT biocompatibility may be engineerable.

Further, development of novel and sensitive DNA biosensor based on CNTs for future analyte detection is a genuine possibility. Identification of DNA using CNTs has been pursued in the past, motivated by the prospects of using carbon nanotubes as a unique electrode material. This study overcomes the challenge of electronic detection of single-molecule DNA through the exploitation of CNT nanoelectrodes. CNTs functionalized with a carboxylic acid group (MWNTs–COOH) for covalent DNA immobilization and enhanced hybridization detection is adopted [258, 259] (Fig. 21.17). The MWCNT–COOH-modified nanoelectrodes are fabricated, and oligonucleotides with the 5′-amino group are covalently bonded to the carboxyl group of carbon nanotubes. The hybridization reaction on the electrode is monitored by change in charge transport through the DNA. Compared with previous

DNA sensors with oligonucleotides directly incorporated on carbon electrodes, this carbon nanotube-based assay with its large surface area and good charge transport characteristics dramatically increases DNA attachment quantity and complementary DNA detection sensitivity.

Future medical acceptance of CNTs requires deeper understanding of immune response, along with definition of exposure standards for different use cases including inhalation, injection, ingestion, and skin contact.

Graphene

Electronics

One of the best device applications of graphene is in field-effect transistors (FETs) [73, 260]. Being a zero-gap semiconductor, graphene cannot be directly utilized for FET applications. For the transistor applications, graphene should be in the form of quasi one-dimensional (1D) structure, with narrow widths and atomically smooth edges. Such structures, termed as graphene nanoribbons (GNRs), are predicted to exhibit band gaps useful for room temperature FET applications, with excellent switching speed and high carrier mobility [67, 261, 262]. In addition to the 2D confinement due to its structure, electrons in graphene are further confined by the formation of nanoribbons. The width confinement is expected to result in the split of original 2D energy dispersion of graphene into a number of 1D modes. Due to this splitting, some 1D modes may not pass through the intersection point of the conduction and valence bonds, depending on the boundary conditions. Thus, the qausi-1D GNRs become semiconductors with finite energy band gap [67, 261, 262]. Band gaps up to 400 meV have been introduced by patterning graphene into GNRs. Figure 21.18 demonstrates GNR FETs fabricated on SiO_2/Si substrates [263]. Although band gaps have been demonstrated in GNRs, these were observed to be quite different from those of graphene, in terms of carrier mobility and fabrication challenges [264]. Band gap has also been achieved through application of electric fields to bilayer graphene structures. However, these gaps have been observed to be less than 400 meV and lead to significant tunneling between bands [260, 265]. For the FET application, several researchers have demonstrated various methods to fabricate GNRs including chemical and lithographic methods. Lithographic patterning has led to fabrications of GNRs with width 20–30 nm [266].

Since the first experimental demonstration of graphene-based FETs, several theoretical studies have been reported to predict the performance of GNR FETs as functions of theirs edge roughness, chirality, chemical doping, carrier scattering, and contacts [267–269]. In addition, various models have also been developed to predict the performance of GNR FETs [270, 271]. The theoretical studies provide a better understanding about the performance of GNR-based FETs characteristics; furthermore, they can be valuable tools for designing efficient FETs. Even though the potential of graphene FETs have been demonstrated, it might take several years to fabricate commercially viable logic devices from graphene, due to its various intrinsic difficulties.
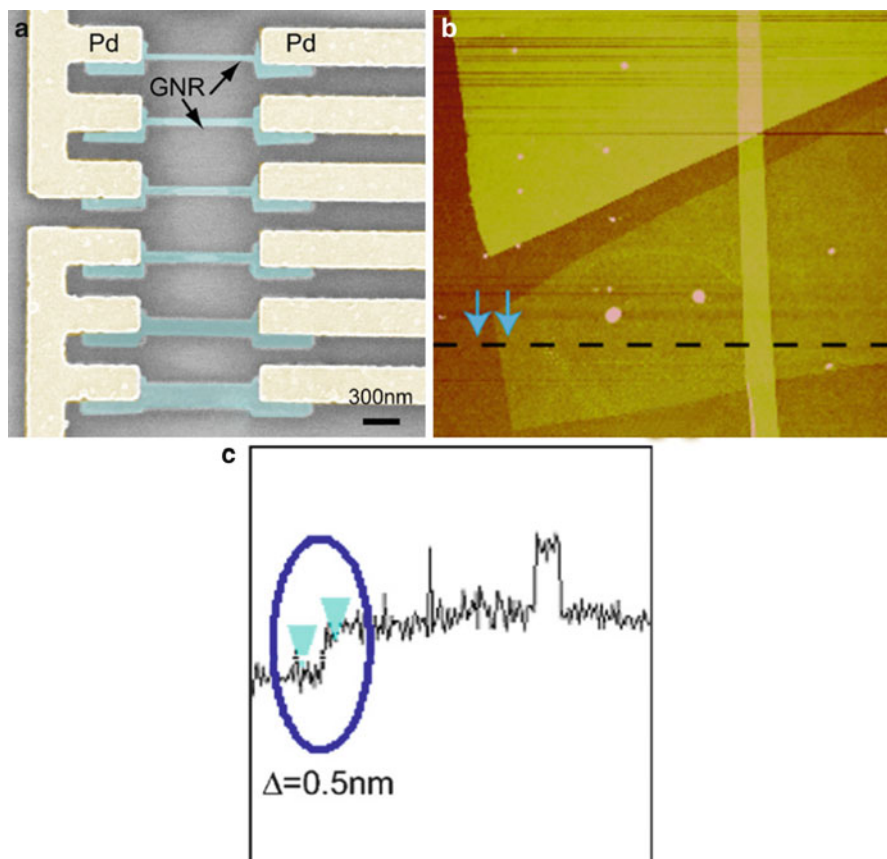
Fig. 21.18 (**a**) SEM picture of GNR devices fabricated on a 200-nm SiO$_2$ substrate with width from top to bottom: 20, 30, 40, 50, 100, and 200 nm. (**b**) AFM image of a SLG before lithographic process, (**c**) cross-sectional measurement of AFM which provides the thickness of the graphene (Reprinted with permission from Chen et al. [263]. Copyright 2007: Elsevier)

The extraordinary thermal, chemical, and mechanical stability of graphene, combined with its high transparency and atomic layer thickness, makes it an ideal candidate for transparent conducting electrode applications. Therefore, the most soon-to-be realized application of graphene would be next-generation transparent conductive electrode. Monolayer graphene is highly conductive and highly transparent (absorb only 2.3 % of white light); K. Kim et al. reported 80 % transmittance from the graphene grown on a 300-nm-thick nickel layer, corresponding to 6–10 graphene layers [149]. The transmittance was increased up to 93 % by further reducing the growth time and nickel thickness, resulting in formation of thinner graphene film. Wang et al. [272] have reported application of graphene-based transparent electrodes for dye-sensitized solar cell (DSSC) with a good transparency of 70 % over 1,000–3,000 nm, with good conductivity of 550 S cm^{-1}.

Currently, the touch screen and electrode fields are dominated by the use of indium tin oxide (ITO). The practical application of graphene electrodes in optoelectronic devices is limited by its low work function (∼4.4 eV) and high sheet resistance. Recently Han et al. [273] have tackled both problems, i.e., low work function and high sheet resistance and demonstrated the fabrication of OLEDs with transparent graphene electrodes that are not only flexible but outperforms OLEDs with ITO-based electrodes. Graphene films have also been implemented to make flexible organic solar cells working as anodes with a better performance at harsh bending condition as compared to their counterparts using ITO electrodes [274]. Researchers have found that the conductivity of graphene on flexible substrates has outstanding stability even after hundreds of bending cycles [275].

RF

The combination of the unique properties of graphene with new device concepts and nanotechnology can overcome some of the main limitations of traditional radio-frequency electronics in terms of maximum frequency, linearity, and power dissipation. The main figure of merit considered so far in order to assess graphene performance for RF applications is the cutoff frequency f_T [276], i.e., the frequency at which the short-circuit current gain is unity, and in the last few years, we have seen a fast increase in the frequency performance of graphene transistors. Moon et al. [277] reported on the fabrication of GFETs grown on SiC substrates with a $f_T = 4.2$ GHz in self-aligned devices with a gate length of 1 μm. A record power gain cutoff frequency (f_{max}) value of 14 GHz was reported for these devices. Y. M. Lin from IBM reported non-self-aligned devices fabricated on graphene flakes with an intrinsic f_T of 100 GHz [278]. To reduce the access resistances in these non-self-aligned devices, a substrate voltage was applied to induce carriers in the access regions. In spite of significant recent progress, the absence of band gap in graphene can indeed have a negative impact in graphene short-channel devices, where transport is quasiballistic and drift velocity saturation cannot occur and interband tunneling suppresses the output differential resistance r_o, the intrinsic voltage gain A_v, and therefore f_{max}. Recently, Szafranek et al. [279] have shown with experiments and simulation that a larger r_o and A_v can be obtained by using bilayer graphene. The reason is that by applying an electric field perpendicular to the bilayer graphene plane, it is possible to induce a small band gap of 100–200 meV which is sufficient to significantly improve saturation of the device output characteristics.

The intriguing ambipolar nature of graphene together with its high mobility allows completely new nonlinear devices for radio frequency (RF) and mixed-signal applications, such as full-wave rectifiers, frequency doublers, and mixers, and truly distinguishes it from other semiconductor materials [280, 281]. The V-shaped current–voltage (I–V) transfer characteristic of graphene ambipolar transistors closely resembles that of an ideal full-wave rectifier [70, 281]. With a single graphene device, it is therefore possible to realize full-wave rectification with zero-volt threshold voltage. Graphene ambipolar transistors can also be used for frequency doubling [281], by biasing the gate to the minimum conduction point and

superimposing a sinusoidal input signal to the gate. Electrons and holes conduct in alternative half cycles to produce an output signal at the drain, whose fundamental frequency is twice that of the input. Wang et al. [282] tested a top-gate graphene field-effect transistor-based frequency doubler in order to gauge its performance. They were able to show that a graphene-based frequency doubler can provide more than 90 % converting efficiency, while the corresponding value is not larger than 30 % for conventional frequency doubler. Numerous communication systems rely on electromechanical devices, such as filters, resonators, and RF switches. The miniaturization of these devices will strongly affect the development of future communication systems. The ultimate limit to this miniaturization is represented by graphene electromechanical devices, which are only one atom thick. Chen et al. [64] fabricated monolayer graphene nanomechanical resonators with operating frequencies in the 50–80 MHz frequency range. These devices showed quality factors of $\sim 1 \times 104$ at low temperatures (5 K). It has been predicted that graphene's ability to withstand ultrahigh strains, up to ~ 25 % in nanoindentation experiments, will allow increasing the resonance frequency of these devices above the gigahertz range while maintaining a robust signal level. Milaninia et al. [283] developed a switch comprising two polycrystalline graphene films grown by CVD. The top film is pulled into contact with the bottom one by applying a voltage of 5 V between the layers, and the contact is broken after removing the voltage due to restoring mechanical forces. It is expected that the graphene–graphene contact will be more robust than the traditional metal–metal contact, which will significantly increase the reliability of future DC and RF switches.

Sensor: Gas, Biosensor, and Mechanical Sensor

Graphene has potential application for a large number of gas, bio-, and mechanical sensors. The operating principle of graphene gas or bioelectronic sensors is based on the change of graphene's electrical conductivity (σ) due to adsorption of molecules on graphene surface [52]. Due to 2D structure and large surface exposure, very high conductivity, few crystal defects, and ease of making ohmic contacts with graphene aid to increase its sensitivity up to single atom or molecular level detection [74, 76, 145]. For the first time, Schedin et al. [284] reported good graphene sensing properties towards NO_2, NH_3, H_2O, and CO. They showed that graphene sensing properties were fully recoverable after exposure to the analyte of interest, by vacuum annealing at 150 °C or by illumination to UV for short time. In another work by Fowler et al. [285] in addition to NO_2 and NH_3, dinitrotoluene (DNT), a volatile compound found in explosives, was also detected (Fig. 21.19). The sensing mechanism was primarily attributed to charge transfer at the graphene surface. DNT sensing mechanism was similar to that of NO_2, i.e., electron withdrawing, and the limit of detection of DNT was reported to be 28 ppb, which is well below the room temperature vapor pressure of DNT, i.e., 173 ppb. In another related study by Sundaram et al. [286], graphene surface was chemically modified by electrodeposition of Pd nanoparticles. The electrodeposition of Pd on graphene was observed to improve the response of graphene sensors to H_2 detection, as Pd has good affinity towards H_2 detection. Also, Lu et al. [287] reported that
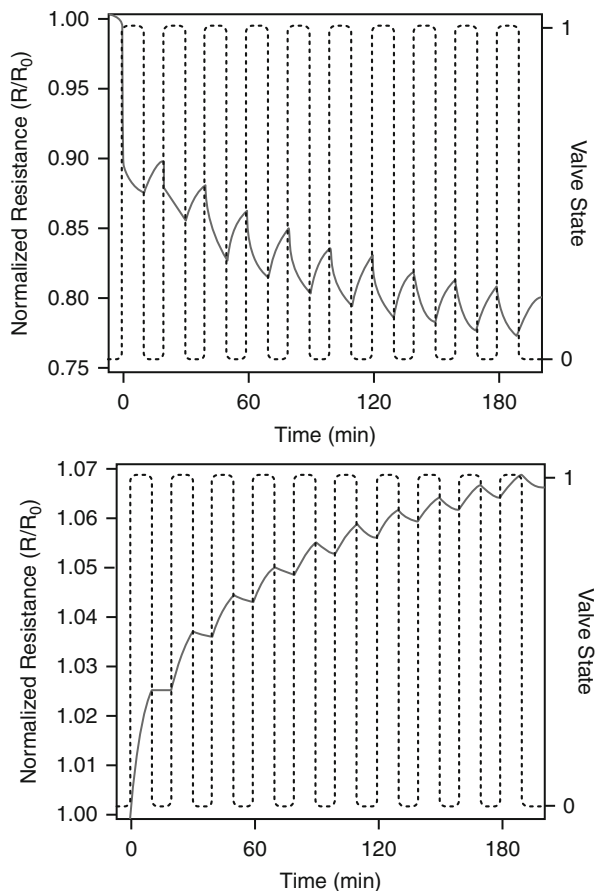
hydrazine-reduced GO sensors are more effective than thermally reduced GO for the detection of NO$_2$ and NH$_3$. Huang et al. [288] also showed that graphene nanoribbons could detect NH$_3$ at very low concentrations.

In addition to gas sensing, Shan et al. [289] demonstrated biosensing, i.e., glucose properties of graphene. With glucose oxidase (GOD) as an enzyme model, they constructed a novel polyvinylpyrrolidone-protected graphene/polyethylenimine-functionalized ionic liquid/GOD electrochemical biosensor. Through the sensor, they reported direct electron transfer of GOD, demonstrating graphene's potential application for fabrication of glucose sensors. A linear response up to 14 mM of glucose was observed in their work. In addition to biosensing application for glucose detection, Alwarappan et al. [290] has demonstrated that graphene electrodes exhibited a superior biosensing performance than CNTs towards dopamine detection in the presence of common interfering agents, such as ascorbic acid and serotonin. In another work by Li et al. [291],

a nanocomposite film sensing platform, based on the Nafion graphene, was used for determination of Cd^{2+} by anodic stripping voltammetry (ASV). The nanocomposite film has demonstrated advantages of graphene and the ionic exchange capacity of Nafion, which enhanced the sensitivity of Cd^{2+} assay. For most of the gas and bioelectronic sensor applications, graphene synthesized by various methods was deposited on Si or Si/SiO_2 substrates, and electrical contacts were prepared with Au/Ti or other metals, which provide good adhesion and ohmic contact with graphene [285, 286, 289].

Nowadays, graphene has become a potential candidate for strain sensor because of its good mechanical properties [52, 292]. Enormous efforts have been devoted to exploration of its many applications in the field of science and engineering; however, there are very few investigations to explore the applications of graphene for testing the devices subjected to strain/stress and pressure effects. Lee et al. [293] reported the piezo-resistance response of graphene and the graphene-based strain sensor with a gauge factor of 6.1. The zigzag-type graphene electrodes with 300-μm-wide and 140-mm-long conducting paths were patterned on a polydimethylsiloxane (PDMS) substrate. They found that the resistance increases from ∼492 to ∼522 kΩ with an applied strain up to 1 %. Fu et al. [294] fabricated a strain sensor based on monolayer graphene on a flexible PDMS substrate. A high sensitivity value (γ) of 151 showed that the device has promising applications in sensor, switches, and gauges. Furthermore, Wang et al. [295] showed that graphene can be used under high strain over 30 % using fully reversible structural geometry. Recently, Smith et al. [296] demonstrated piezoelectric pressure sensors based on suspended graphene membranes with direct electrical signal readout. The high sensitivity of the piezoresitive graphene pressure sensor is measured to be 3.95 $\mu V\ V^{-1}\ mmHg^{-1}$ which outperforms conventional piezoresitive Si-based and CNT-based pressure sensors reported in literature [297, 298].

Field Emission

Graphene, consisting of a single- or few-layer graphite layers, has a very high aspect ratio (thickness to lateral size ratio), and a dramatically enhanced local electric field is expected at its edges and has high potential for field emission (FE) applications [299, 300]. FE is an electron emission process in which electrons are emitted from a material under the application of high electric field. The simplest way to create such a field is by field enhancement at the tip of a sharp object. To take advantage of high field enhancement, graphene sheets, i.e., single or few layers, need to be erected on the substrates. Except for graphene synthesis by MW–PECVD method, almost all other methods result in flat graphene layers on substrates [301, 302]. Eda et al. [303] have recently fabricated a graphene/polymer composite thin film for achieving a field enhancing structure, required for FE applications. The FE cathodes by Eda et al. were prepared from graphene, synthesized from graphite oxide (GO), and dissolved in polystyrene by spin coating it on to silicon substrates. Relatively better FE was observed from films prepared at spin coating speed of 600 rpm; the turn-on electric field (E_{to}) in such sample was ∼4 V μm^{-1}, and the field enhancement factor (β) was ∼1,200. In another
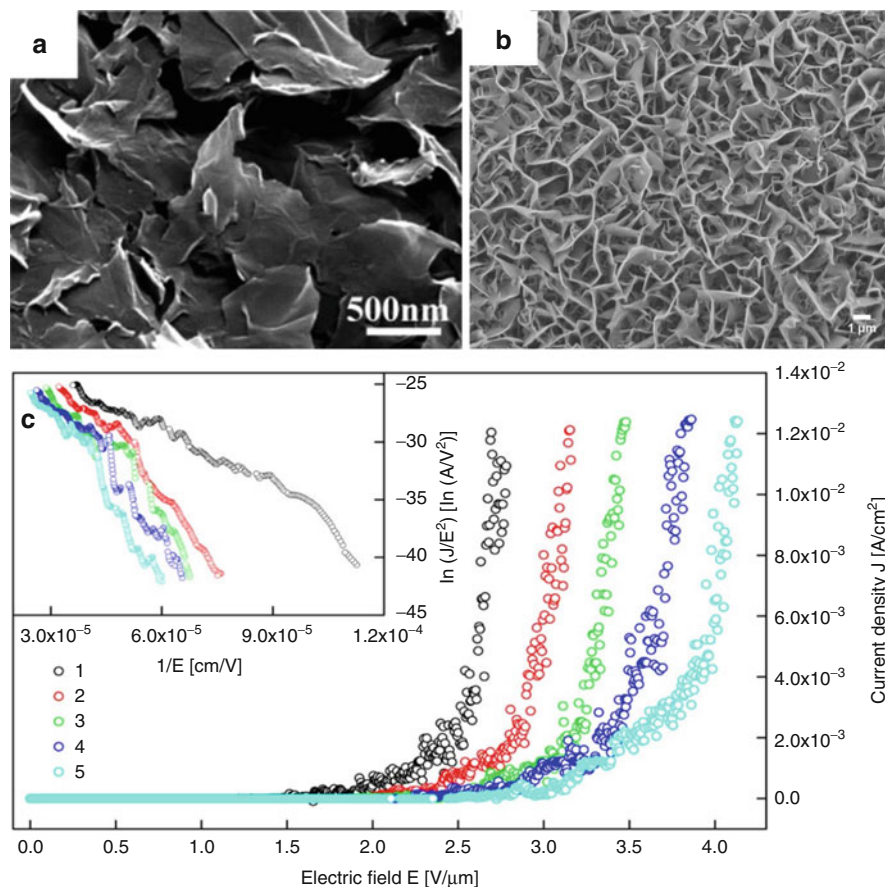
Fig. 21.20 (**a**) High-magnification SEM image of the graphene film deposited in the ITO-coated glass for 1 min at an applied field of 160 V by EPD using a 0.1 mg mL^{-1} graphene suspension as electrolyte. (**b**) SEM image showing top view of FLG synthesized by MW–PECVD. (**c**) Current density as a function of applied electric field for FLG grown on silicon with gas ratio H$_2$/CH$_4$ = 8/1. *Inset* shows the same data plotted according to the Fowler–Nordheim relation (Reprinted with permission from Malesevic et al. [301]. Copyright (2008): American Institute of Physics, and Wu et al. [304]. Copyright (2009): Wiley-VCH Verlag GmbH & Co.)

work by Wu et al. [304] single-layer graphene film was prepared by electrophoretic deposition (EPD) method. Graphene films, prepared by exfoliation of graphite, were dispersed in isopropyl alcohol, and the resulting solution was deposited onto indium tin oxide (ITO)-coated glass substrates by EPD (Fig. 21.20a). Graphene cathodes prepared by this method demonstrated an E$_{to}$ of 2.3 V μm^{-1} and a β of ~3,700. Choi et al. [232, 305] have demonstrated all-graphene-based flexible and transparent field emission device for the first time. Graphene electrodes were prepared by transferring the graphene grown (by thermal CVD) on copper foil onto

a polyethylene terephthalate (PET) substrate. Hot press lamination and chemical etching process was followed for transferring the graphene on to the transparent flexible substrates. The all-graphene transparent and flexible field emitter structure showed appreciable field emission current and high field enhancement factor. Although these research works have demonstrated methods to prepare graphene films for FE applications on flexible and other substrates, these methods may not be suitable to achieve high FE currents, in the order of few mA-A, required for high current applications.

This issue may probably be addressed by MW–PECVD method demonstrated by Malesevic et al. [301], to fabricate vertically aligned few-layer graphene (FLG) FE cathodes on titanium and silicon (Fig. 21.20b). FLG was synthesized by MW–PECVD with H_2 and CH_4 precursor gases, at 700 °C. The quality of FLG films was observed to be dependent on the ratio of H_2/CH_4 gases; best quality was achieved when the ratio was 8:1. Graphene cathodes prepared by this method demonstrated an E_{to} of 1 V μm^{-1}, β of ∼7,500 and a current density of 14 mA cm^{-2} (Fig. 21.20c). The advantage of this method is direct synthesis of graphene on metallic substrates creating ohmic contact, which is essential for FE applications. The drawback of this method is the limited scope to control the FLG density, which can cause field-screening effect. On the other hand, Watcharotone et al. [306] and Babenko et al. [307] have also theoretically addressed filed emission from graphene films. The theoretical works describe the importance of field enhancement factor and role of defects in graphene field emission. In summary, the enthusiasm for FE of graphene is justified by its unique properties. However, due to FE durability at high electric field and vacuum stability in a fabricated device, it might take a while to demonstrate a real FE device, which can reach the market.

Energy Applications

Due to its high surface area and ability to facilitate electrons or hole transfer along its two-dimensional surface, graphene has been a promising material for energy storage devices. There have been several reports on graphene-based electrodes for rechargeable lithium-ion batteries (RLBs) [308, 309]. Graphite, the most commonly used anode material in RLBs, has been replaced by graphene for its superior electrical conductivity, high surface area, and chemical tolerance. Lithium-ion battery has been a key component of handheld devices due to its renewable and clean nature. To meet the increasing demand for lithium-ion batteries with higher energy density and durability, new electrode materials with higher capacity and stability have been developed. Paek et al. [310] demonstrated a reversible capacity of 810 mAh/g in SnO_2-decorated graphene nanosheets with a significant improvement in its cycling performance as compared to bare SnO_2 nanoparticles. Wang et al. [311] have shown self-assembled TiO_2 graphene hybrid nanostructure to enhance high-rate performance of electrochemical active material. Xie et al. [312] synthesized a SnSb nanocrystal/graphene hybrid nanostructure by a facile one-step solvothermal route which can be used as a potential high-capacity anode material for lithium-ion battery. Xiao and his coworkers demonstrated a novel air electrode consisting of an unusual hierarchical arrangement of

functionalized graphene sheets (with no catalyst) which delivered an exceptionally high capacity of 15,000 mAh g^{-1} (highest value ever reported) [313].

Graphene materials have also been used in fuel cells and solar cells. Graphene has been identified as a catalyst support for oxygen reduction and methanol oxidation in case of a fuel cell configuration [314, 315]. In particular, platinum nanoparticles supported on graphene sheets were found to exhibit a higher electrochemical surface area and oxygen reduction reaction (ORR) activity and better stability than the commercial platinum catalyst [316]. Jafri et al. [317] used graphene nanoplatelets and nitrogen-doped graphene nanoplatelets as supports for platinum nanoparticles to construct proton-exchange membrane fuel cells with power densities of 4,400 W cm^{-2} and 3,900 W cm^{-2}, respectively. The better performance of the nitrogen-doped graphene nanoplatelets was attributed to pyrrolic nitrogen defects acting as anchoring sites for carbon–catalyst binding and increasing electrical conductivity. Graphene-based materials have been used as both window electrode and counter electrode in dye-sensitized solar cells [318, 319]. Graphene-doped conducting polymers (PEDOT:PSS) and P3HT have shown better power consumption efficiency (4.5 %) than cells with PEDOT:PSS as counter electrode (2.3 %) [320].

Graphene is a near-zero band gap material, due to high mobility and electrical conductivity of graphene; the junction of graphene/n-type semiconductor heterojunction can be considered as an efficient Schottky junction. In this context, graphene–Si [321], graphene–single CdS nanowire (NW), and Schottky junction solar cell [322] have been reported so far. In dye-sensitized solar cells, the counter electrode (CE) is an essential constituent, which injects electrons into the electrolyte to catalyze triiodide reduction (I$_3^-$ to I$^-$) after charge injection from the photo-oxidized dye [323–326]. Platinum (Pt) is widely used as a counter electrodes for DSSC owing to its excellent catalytic activity and low resistance. However, due to high cost, low abundance, and low chemical inertness, replacing Pt with other materials is becoming a fundamental issue for DSSC. In this context, graphene has several advantages for being a potential counter electrode material for solar cells: high electrical conductance, high thermal conductivity, ultrahigh transmittance, and excellent mechanical properties. In particular, graphene exhibited remarkable transparency in the entire solar spectrum including infrared (IR) region.

Das et al. [327] showed the functionalization of large-scale CVD graphene using fluorine (F$^-$ ions) ions with higher catalytic activity towards triiodide reduction compared to pristine graphene. The PCE of the DSSC showed ~2.56 % with corresponding VOC, JSC, and Fill Factor (FF) of 0.66 mV, 10.9 mA cm^{-2}, and 35.9 %, respectively (Fig. 21.21). Similarly, HNO$_3$-doped graphene showed the enhancement in the electro-catalytic activities of graphene with DSSC efficiency of ~3.21 % as shown in Fig. 21.21 [328, 329]. The cell performance is lower than the expected, and this is due to the lower FF, which causes potential voltage drop at the graphene/FTO interface. Therefore, it has been well demonstrated that functionalized graphene is more effective than pristine graphene in order to enhance the kinetics of I^{3-} reduction at cathode.

Recently, several reports on graphene have highlighted the potential of this material to be used for hydrogen storage and raise new hopes for the development

Fig. 21.21 Schematic of surface functionalized graphene counter electrodes for sensitized solar cells, and its J–V curve of DSSCs consists with different PG- and CoS-deposited graphene counter electrodes (Reprinted with permission from Das et al. [328]. Copyright (2012): Elsevier)
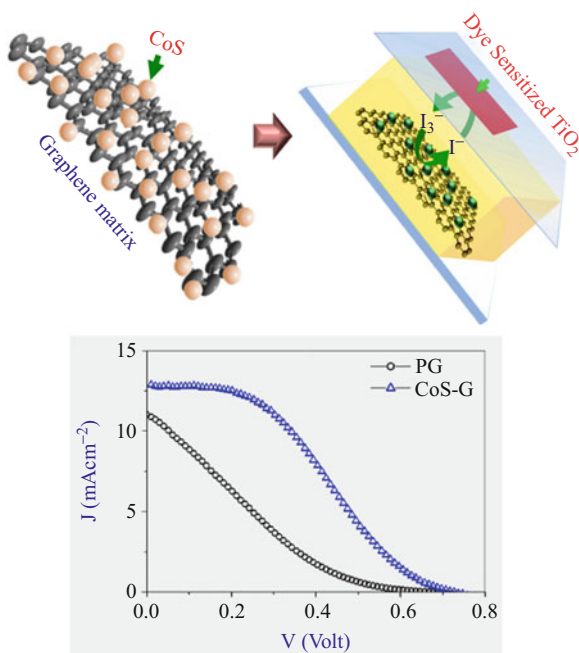
of efficient solid-state hydrogen storage device. The sp^2 covalent bonding arrangement of carbon atoms in the honeycomb structure allows efficient binding to hydrogen atoms. Graphene has taken center stage in the field of hydrogen storage due to its high surface area and vast possibilities of chemical functionalization [52, 330]. Graphene was successfully isolated in 2004 and first considered as a material for hydrogen storage in 2005 [145]. Sofo et al. [331] in 2007 discussed the possible routes for synthesizing graphane and its potential applications as a hydrogen storage materials and its stability on the basis of first-principles total energy calculations. The spark came in 2009 when hydrogen-passivated graphene, graphane, was first demonstrated [80]. Graphane is graphene with atomic hydrogen chemically bonded to each graphene lattice atom. Since then, a large number of theoretical and experimental studies have been published to increase the interaction between molecular hydrogen and graphene. The predicted theoretical gravimetric densities are around 5–8 wt%, lower than some of the current materials but well above the standards set by the DoE for 2015 [332]. Ao et al. [333] predicted a very high storage capacity of 13.79 wt% with average adsorption energy −0.193 eV/H$_2$ of a graphene layer with Al-adsorbed on both sides. In a DFT simulation by Beheshti et al. [334] the hydrogen adsorption and storage on Ca-decorated, B-doped graphene were explored. They showed that double-sided Ca-decorated graphene doped with individual boron atoms of 12 wt% can theoretically reach a gravimetric capacity of 8.38 wt% hydrogen. In 2009, Balog et al. [335] published STM results on monolayer graphene on SiC (0001) showing that hydrogen adsorbs along the superstructure and that hydrogen adsorbs in dimer configurations. Recently, Goler et al. [336] presented

an experiment exploiting the curvature of graphene for adsorption and desorption of atomic hydrogen on graphene. They show that by controlling the curvature, one could possibly control uptake and release of hydrogen, which is also in agreement with the theoretical models [337, 338].

Composites

The unique physical properties of graphene render the development of graphene composites and their potential applications in the field of ultracapacitors and batteries for energy storage and fuel cell and solar cell for energy generation. The first graphene-based composite (graphene/polystyrene) was reported in 2006 by Ruoff and coworkers [339]. Their main observation was low percolation threshold, which they had computed to be 0.1 vol% of graphene for the composite. At present most of the composites based on graphene use reduced graphene oxide (RGO), which is obtained by the exfoliation and chemical reduction of graphite oxide (GO), a graphite derivative. Of several methods prescribed, modified Hummers method has mostly been used to synthesize graphite oxide by treating graphite with strong mineral acids [340, 341]. Graphene has been successfully used as a filler material, similar to the CNT in polymers. Rafiee et al. [54] studied and compared the mechanical properties of epoxy nanocomposites with graphene platelets and carbon nanotubes at a nanofiller weight fraction of 0.1 ± 0.002 %. The results showed about 31 % increment in Young's modulus and 40 % in tensile strength of graphene nanocomposites as compared to 3 % in Young's modulus and 14 % in tensile strength for carbon nanotubes. Several nanoparticles of metals, metal oxides, and other inorganic compounds like Au, Ag, TiO_2, and Fe_3O_4 have been made into a composite structure with graphene using ex situ and in situ hybridization techniques to further enhance their properties [342–344]. Several research groups have reported the synthesis of graphene/inorganic material composites on different substrates using physical vapor deposition, chemical vapor deposition, and atomic layer deposition techniques [345–347]. Among them, CVD or chemical vapor deposition process has more advantages, e.g., inexpensive, controllable, and high deposition rate.

One of the main practical applications of graphene-based composites is in batteries and ultracapacitors for energy storage. Graphene and its composites with different metal oxide nanostructures, e.g., SnO_2, Co_3O_4, MnO_2, and Fe_3O_4, make hybrid electrodes which provide excellent conductivity with large active surface area that allows the nanoparticles to participate more efficiently in Li/electron diffusion during discharge/charge cycles and hence increase its specific capacity [348, 349]. Though graphene has been used as the electrode materials of supercapacitors, graphene composited with different metal oxides, e.g., ZnO, Co_3O_4, RuO_2, has also been used to enhance the effect. The metal oxide nanoparticles contribute to the energy storage, and the RGO sheets provide the capacitance by the electron double-layer mechanism at the carbon surface. The RGOs also create the conducting network for the nanoparticles [348, 350]. Wu and others [351] had worked on graphene/metal oxide hybrid electrode, to improve the energy density of the supercapacitor while maintaining its high power density. They had used graphene as negative electrode and MnO_2

nanowire/graphene composite as positive electrode and observed high energy density, which is the square of the operating voltage across the cell. This asymmetric capacitor system showed much higher energy density ($\sim$30.4 Wh kg^{-1}) in comparison to the symmetric one. The large effective area of graphene makes it a possible candidate for fuel cell applications. Dong et al. [352] demonstrated an enhanced efficiency for methanol and ethanol electrooxidations when Pt/graphene composite sheets were used as catalyst supports for direct methanol and ethanol fuel cells. In addition, nitrogen-doped graphene, with higher conductivity, has also been used for the fuel cell applications [353]. This enhanced electronic conductivity essentially increases the electro-catalytic activities of N–RGO–Pt catalysts. The graphene-based polymer composites have been incorporated as electrodes, electron, and hole transports for photovoltaic device applications [275, 354].

Summary

This review aims to present an overview of recent advancement of research in carbon nanomaterials – carbon nanotubes and graphene – in the areas of synthesis, properties, and applications, such as electronics, heat transport, field emission, sensors, composite, and energy. Graphene, a monolayer of sp^2-bonded carbon atoms in a honeycomb lattice, created a surge in research activities during last 10 years owing to its high current density, ballistic transport, chemical inertness, high thermal conductivity, optical transmittance, and super hydrophobicity at nanometer scale. Graphene is considered to be one of the miracle materials in the twenty-first century.

In a sense, graphene is more attractive than its allotrope, carbon nanotubes (CNTs), since the 2-dimensional form of graphene is much better, from the fabrication and application point of view, than 1-dimensional CNTs. Utilizing its extremely high mobility (200,000 cm^2 V^{-1} s^{-1} in compare with 1,400 cm^2 V^{-1} s^{-1} for Si), stand-alone high-frequency transistor with a cutoff frequency as high as 300 GHz could be designed. On the other hand, electromigration problem in interconnects could be avoided with high current capacity (108 A cm^{-2}) and low resistance (1 $\mu\Omega$-cm: 35 % less than Cu) of graphene. Graphene heat pad has shown good promise owing to its high thermal conductivity (5 kW mK^{-1} – 10 times larger than Cu and Al). Graphene can also be a strong candidate for replacement of ITO as a transparent electrode (which is a necessity as earth crust has very low reserve of Indium). Graphene could have over 90 % of transparency and 30 Ω sq^{-1} of sheet resistivity, making it most suitable for transparent conducting electrode applications. Graphene has an extraordinary mechanical strength/weight ratio exceeding that of any known material. Graphene also has the highest surface-to-volume ratio, utilizing two-side surfaces. Thus, graphene-based chemical sensors can be used to detect explosives in luggage and volatile organic compounds in air, by converting chemical reactions into electrical signals. Graphene might revolutionize battery technologies, where it can be used as a superconductive membrane between battery's poles. This battery could supply a huge energy for a short period of time.

However, one problem is that graphene does not have a band gap, which is a prerequisite for a semiconductor. Furthermore, graphene transistor is very difficult to turn off, with an on/off ratio as high as 1,000 at room temperature. To open a stable band gap of ~1 eV, it is necessary to make graphene ribbons smaller than 2 nm wide with single atom precision. Variation in width of a graphene sheet results in deviation of band gap energy. Mobility of graphene is severely degraded if the ribbon edges are rough and if the substrate underneath is not flat. In turn, reproducibility issues are challenging for the success of future graphene nanoelectronics. Graphene grown by chemical vapor method is not a single crystal, due to unavoidable occurrence of nucleation and growth during the process. This leads to degradation and variation in properties of graphene-based electronic devices. So, it seems that graphene's promise in next-generation electronics is not easily achievable. Its future may lie elsewhere such as passive devices and/or components less sensitive on variation of its energy band gap. Graphene was manufactured in the 2-D stable form through an easy and reproducible process in 2004 – just 9 years ago. Thus, we need some patience for the materialization of our dream in the application of nanocarbon materials – CNTs and graphene. Lots of research efforts should be made until some big breakthroughs happen with CNTs and graphene.

References

1. Kroto HW, Heath JR, O' Brien SC, Curl SC, Smalley RE (1985) C_{60}: buckministerfullerene. Nature 318:162–163
2. Ajayan PM (1999) Nanotubes from carbon. Chem Rev 99:1787–1800
3. Huang X, Yin Z, Wu S, Qil X, He Q, Zhang Q, Yan Q, Boey F, Zhang H (2011) Graphene-based materials: synthesis, characterization, properties, and applications. Small 7:1876–1902
4. Choi W, Lahiri I, Seelaboyna R, Kang Y (2010) Synthesis of Graphene and its applications: a review. Crit Rev Solid State Mat Sci 35:52–71
5. Choi W, Lee J-W (2011) Graphene: synthesis and applications. CRC Press, Boca Raton, Publication Date: October 11 (2011). ISBN 10: 1439861870, 13: 978-1439861875
6. Foldvari M, Bagonluri M (2008) Carbon nanotubes as functional excipients for nanomedicines: I. Pharmaceutical properties. Nanomed Nanotech Biol Med 4(173)
7. Dresselhaus MS, Dresselhaus G, Saito R (1995) Physics of carbon nanotubes. Carbon 33:883–891
8. Avouris P, Chen Z, Perebeinos V (2007) Carbon-based electronics. Nat Nanotechnol 2(10):605
9. Ando T (2009) The electronic properties of graphene and carbon nanotubes. NPG Asia Mater 1(1):17–21
10. Anantram MP, Leonard F (2006) Physics of carbon nanotube electronic devices. Rep Prog Phys 69:507–561
11. Yao Z, Kane CL, Dekker C (2000) High-field electrical transport in single-wall carbon nanotubes. Phys Rev Lett 84:2941–2944
12. Kong J, Yenilmez E, Tombler TW, Kim W, Dai H, Laughlin RB, Liu L, Jayanthi CS, Wu SY (2001) Quantum interference and ballistic transmission in nanotube electron waveguides. Phys Rev Lett 87:106801
13. Awano Y, Sato S, Nihei M, Sakai T, Ohno Y, Mizutani T (2010) Carbon nanotubes for VLSI: interconnect and transistor applications. Proc IEEE 98(12)

14. Kreupl F, Graham AP, Duesberg GS, Steinhögl W, Liebau M, Unger E, Hönlein W (2002) Carbon nanotubes in interconnect applications. Microelectron Eng 64:399–408
15. Kreupl F, Graham AP, Liebau M, Duesberg GS, Seidel R, Unger E (2004) Carbon nanotubes for interconnect applications. In: Electron devices meeting, IEDM technical digest. IEEE International, pp 683–686
16. Awano Y, Sato S, Kondo D, Ohfuti M, Kawabata A, Nihei M, Yokoyama N (2006) Carbon nanotube via interconnect technologies: size-classified catalyst nanoparticles and low-resistance ohmic contact formation. Phys Stat Sol (a) 203:3611–3616
17. Horibe M, Nihei M, Kondo D, Kawabata A, Awano Y (2005) Carbon nanotube growth technologies using tantalum barrier layer for future ULSIs with Cu/low-k interconnect processes. Jpn J Appl Phys 44:5309
18. Tans S, Verschueren A, Dekker C (1998) Room-temperature transistor based on a single carbon nanotubes. Nature (London) 393(49)
19. Martel R, Schmidt T, Shea HR, Hertel T, Avouris P (1998) Single- and multi-wall carbon nanotube field-effect transistors. Appl Phys Lett 73:2447
20. McEuen PL, Fuhrer MS, Park H (2002) Single-walled carbon nanotube electronics. IEEE Trans Nanotechnol 1:78–85
21. Javey A, Kim H, Brink M, Wang Q, Ural A, Guo J, Mcintyre P, Mceuen P, Lundstrom M, Dai H (2002) High-κ dielectrics for advanced carbon nanotube transistors and logic gates. Nat Mater 1:241
22. Robertson DH, Brenner DW, Mintmire JW (1992) Energetics of nanoscale graphitic tubules. Phys Rev B 45:12592
23. Treacy MM, Ebbesen TW, Gibson JM (1996) Exceptionally high Young's modulus observed for individual carbon nanotubes. Nature 38:678–680
24. Krishnan A, Dujardin E, Ebbesen TW, Yianilos PN, Treacy MMJ (1998) Young's modulus of single-walled nanotubes. Phys Rev B 58:14013
25. Yu MF, Lourie O, Dyer MJ, Moloni K, Kelly TF, Ruoff RS (2000) Strength and breaking mechanism of multi-walled carbon nanotubes under tensile load. Science 287:637
26. Salvetat JP, Briggs GAD, Bonard JM, Bacsa RR, Kulik AJ, Stockli T, Burnham NA, Forro L (1999) Elastic and shear moduli of single-walled carbon nanotube ropes. Phys Rev Lett 82:944
27. Yu MF, Files BF, Arepalli S, Ruoff RS (2000) Tensile loading of ropes of single wall carbon nanotubes and their mechanical properties. Phys Rev Lett 84:5552
28. Shokrieh MM, Rafiee R (2010) A review of the mechanical properties of isolated carbon nanotubes and carbon nanotube composites. Mech Comp Mater 46:2
29. Lu Q, Bhattacharya B (2005) The role of atomistic simulations in probing the small-scale aspects of fracture – a case study on a single-walled carbon nanotubes. Eng Fract Mech 72:2037–2071
30. Rafii-Tabar H (2004) Computational modelling of thermo-mechanical and transport properties of carbon nanotubes. Phys Rep 390:235–452
31. Bathe KJ (1997) Finite element procedures. Prentice-Hall, New Delhi, pp 1–14
32. Qian D, Dickey E, Andrews R, Rantell T (2000) Load transfer and deformation mechanisms in carbon nanotube-polystyrene composites. Appl Phys Lett 76:2868–2870
33. Xu X, Thwe MM, Christopher S, Liao K (2002) Mechanical properties and interfacial characteristics of carbon-nanotube-reinforced epoxy thin films. Appl Phys Lett 81:2833
34. Shanmugharaj AM, Bae JH, Lee KY, Noh WH, Lee SH, Ryu SH (2007) Physical and chemical characteristics of multiwalled carbon nanotubes functionalized with aminosilane and its influence on the properties of natural rubber composites. Comp Sci Technol 67:1813
35. Xiao KQ, Zhang LC (2004) The stress transfer efficiency of a single-walled carbon nanotube in epoxy matrix. J Mater Sci 39:4481
36. Choi Y-K, Gotoh Y, Sugimoto K, Song S-M, Yanagisawa T, Endo M (2005) Processing and characterization of epoxy nanocomposites reinforced by cup-stacked carbon nanotubes. Polymer 46(11489)

37. Liu YJ, Chen XL (2003) Continuum models of carbon nanotube-based composites by the BEM. Electron J Bound Element 1:316–335
38. Biercuk MJ, Llaguno MC, Radosavljevic M, Hyun JK, Johnson AT, Fischer JE (2002) Carbon nanotube composites for thermal management. Appl Phys Lett 80:2767–2769
39. Huang H, Liu CH, Wu Y, Fan S (2005) Aligned carbon nanotube composite films for thermal management. Adv Mater 17:1652–1656
40. Kim P, Shi L, Majumdar A, Mc Euen PL (2001) Thermal transport measurement of individual multiwalled nanotubes. Phys Rev Lett 87:215502
41. Pop E, Mann D, Wang Q, Goodson K, Dai H (2006) Thermal conductance of an individual single-wall carbon nanotube above room temperature. Nano Lett 6:96–100
42. Berber S, Kwon Y-K, Tomanek D (2000) Unusually high thermal conductivity of carbon nanotubes. Phys Rev Lett 84:4613–4616
43. Che J, Cagin T, Goddard WA (2000) III thermal conductivity of carbon nanotubes. Nanotechnology 11:65–69
44. Donadio D, Galli G (2007) Thermal conductivity of isolated and interacting carbon nanotubes: comparing results from molecular dynamics and the Boltzmann transport equation. Phys Rev Lett 99:255502
45. Hone J, Ellwood I, Muno M, Mizel A, Cohen ML, Zettl A, Rinzler AG, Smalley RE (1998) Thermoelectric power of single-walled carbon nanotubes. Phys Rev Lett 80:1042–1045
46. Bradley K, Jhi S-H, Collins PG, Hone J, Cohen ML, Louie SG, Zettl A (2000) Is the intrinsic thermoelectric power of carbon nanotubes positive ? Phys Rev Lett 85:4361–4364
47. Li W, Lu L, Lin ZD, Pan ZW, Xie SS (1999) Linear specific heat of carbon nanotubes. Phys Rev B 59:R9015
48. Yu CH, Shi L, Yao Z, Li DY, Majumdar A (2005) Thermal conductance and thermopower of an single-wall carbon nanotubes. Nano Lett 5:1842–1846
49. Geim AK, Novoselov KS (2007) The rise of graphene. Nat Mater 6:183–191
50. Freitag M (2011) Graphene: trilayers unraveled. Nat Phys 7:596–597
51. Hass J, de Heer WA, Conrad EH (2008) The growth and morphology of epitaxial multilayer graphene. J Phys Cond Matter 20:323202
52. Lee C, Wei X, Kysar JW, Hone J (2008) Measurement of the elastic properties and intrinsic strength of monolayer graphene. Science 321:385–388
53. Ramanathan T, Abdala AA, Stankovich S, Dikin DA, Herrera-Alonso M, Piner RD, Adamson DH, Schniepp HC, Chen X, Ruoff RS, Nguyen ST, Aksay IA, Prud'Homme RK, Brinson LC (2008) Functionalized graphene sheets for polymer nanocomposites. Nat Nanotechnol 3:327–331
54. Rafiee MA, Rafiee J, Wang Z, Song H, Yu ZZ, Koratkar N (2009) Enhanced mechanical properties of nanocomposites at low graphene content. ACS Nano 3:3884–3890
55. Liu F, Ming P, Li J (2007) Ab initio calculation of ideal strength and phonon instability of graphene under tension. Phys Rev B 76:064120
56. Pereira VM, Castro Neto AH, Peres NMR (2009) Tight-binding approach to uniaxial strain in graphene. Phys Rev B 80:045401
57. Xu Z (2009) Graphene nanoribbons under tension. J Compd Theor Nanosci 6(625)
58. Lu Q, Huang R (2010) Effect of edge structure on elastic modulus and fracture of graphene nanoribbons under uniaxial tension. arXiv:1007. 3298
59. Zhao H, Min K, Aluru NR (2009) Size and chirality dependent elastic properties of graphene nanoribbons under uniaxial tension. Nano Lett 9:3012–3015
60. Min K, Aluru NR (2011) Mechanical properties of graphene under shear deformation. Appl Phys Lett 98:013113
61. Pei QX, Zhang YW, Shenoy VB (2010) A molecular dynamics study of the mechanical properties of hydrogen functionalized graphene. Carbon 48:898–904
62. Zheng QB, Geng Y, Wang SJ, Li ZG, Kim JK (2010) Effects of functional groups on the mechanical and wrinkling properties of graphene sheets. Carbon 48:4315–4322

63. Bunch JS, van der Zande AM, Verbridge SS, Frank IW, Tanenbaum DM, Parpia JM, Craighead HG (2007) Electromechanical resonators from graphene sheets. Science 315:490–493

64. Chen C, Rosenblatt S, Bolotin KI, Kalb W, Kim P, Kymissis I, Stormer HL, Heinz TF, Hone J (2009) Performance of monolayer graphene nanomechanical resonators with electrical readout. Nat Nanotech 4:861

65. Mizuta H, Ramirez MAG, Tsuchiya Y, Nagami T, Sawai S, Oda S, Okamoto M (2009) Multi-scale simulation of hybrid silicon nano-electromechanical (NEM) information systems. J Autom Mobile Robot Intell Syst 3:58

66. Dutta S, Pati SK (2010) Novel properties of graphene nanoribbons: a review. J Mater Chem 20:8207–8223

67. Han MY, Ozyilmaz B, Zhang Y (2007) Energy band gap engineering of graphene nanoribbons. Phys Rev Lett 98:206805

68. Erdogan E, Popov I, Rocha CG, Cuniberti G, Roche S, Seifert G (2011) Engineering carbon chains from mechanically stretched graphene-based materials. Phys Rev B 83:041401 (R)

69. Topsakal M, Ciraci S (2010) Elastic and plastic deformation of graphene, silicene, and boron nitride honeycomb nanoribbons under uniaxial tension: a first-principles density-functional theory study. Phys Rev B 81:024107

70. Castro Neto AH, Guinea F, Peres NMR, Novoselov KS, Geim AK (2009) The electronic properties of graphene. Rev Modern Phys 81:109

71. Berger C, Song Z, Li T, Li X, Ogbazghi AY, Feng R, Dai Z, Marchenkov AN, Conrad EH, First PN, de Heer WA (2004) Ultrathin epitaxial graphite: 2D electron gas properties and a route toward graphene-based nanoelectronics. J Phys Chem 108:19912–19916

72. Katsnelson MI (2007) Graphene: carbon in two dimensions. Mat Today 10:20–27

73. Novoselov KS, Geim AK, Morozov SV, Jiang D, Zhang Y, Dubonos SV, Grigorieva IV, Firsov AA (2004) Electric field effect in atomically thin carbon films. Science 306:666–669

74. Novoselov KS, Geim AK, Morozov SV, Jiang D, Katsnelson MI, Grigorieva IV, Dubonos SV, Firsov AA (2005) Two-dimensional gas of massless Dirac fermions in graphene. Nature 438:197

75. Novoselov KS, Jiang Z, Zhang Y, Morozov SV, Stormer HL, Zeitler U, Maan JC, Boebinger GS, Kim P, Geim AK (2007) Room-temperature quantum Hall effect in graphene. Science 315:1379

76. Novoselov KS, McCann E, Morozov SV, Fal'ko VI, Katsnelson MI, Zeitler U, Jiang D, Schedin F, Geim AK (2006) Unconventional quantum Hall effect and Berry's phase of 2π in bilayer graphene. Nat Phys 2:177

77. McCann E (2006) Asymmetry gap in the electronic band structure of bilayer graphene. Phys Rev B 74:161403

78. Zhou SY, Gweon G-H, Fedorov AV, First PN, de Heer WA, Lee D-H, Guinea F, Castro Neto AH, Lanzara A (2007) Substrate-induced bandgap opening in epitaxial graphene. Nat Mater 6:770

79. Hass J, Varchon F, Millan-Otoya JE, Sprinkle M, Sharma N, de Heer WA, Berger C, First PN, Magaud L, Conrad EH (2008) Why multilayer graphene on 4H-SiC(0001) behaves like a single sheet of graphene. Phys Rev Lett 100:125504

80. Elias DC, Nair RR, Mohiuddin TMG, Morozov SV, Blake P, Halsall MP, Ferrari AC, Boukhvalov DW, Katsnelson MI, Geim AK, Novoselov KS (2009) Control of graphene's properties by reversible hydrogenation: evidence for graphene. Science 323:610

81. Zhou SY, Siegel DA, Fedorov AV, Lanzara A (2008) Metal to insulator transition in epitaxial graphene induced by molecular doping. Phys Rev Lett 101:086402

82. Peres NMR (2009) The electronic properties of graphene and its bilayer. Vacuum 83:1248

83. Morozov SV, Novoselov KS, Schedin F, Jiang D, Firsov AA, Geim AK (2005) Two-dimensional electron and hole gases at the surface of graphite. Phys Rev B 72:201401

84. McCann E, Fal'ko VI (2006) Landau-level degeneracy and quantum hall effect in a graphite bilayer. Phys Rev Lett 96:086805

85. Mak KF, Shan J, Heinz TF (2010) Electronic structure of few-layer graphene: experimental demonstration of strong dependence on stacking sequence. Phys Rev Lett 104:176404

86. Muszynski R, Seger B, Kamat PV (2008) Decorating graphene sheets with gold nanoparticles. J Phys Chem C 112:5263

87. Chen S, Wu Q, Mishra C, Kang J, Zhang H, Cho K, Cai W, Balandin AA, Ruoff RS (2012) Thermal conductivity of isotopically modified graphene. Nat Mater 11:203

88. Cai W, Moore AL, Zhu Y, Li X, Chen S, Shi L, Ruoff RS (2010) Thermal transport in suspended and supported monolayer graphene grown by chemical vapor deposition. Nano Lett 10:1645–1651

89. Saito K, Nakamura J, Natori A (2007) Ballistic thermal conductance of a graphene sheet. Phys Rev B 76:115409

90. Ghosh S, Bao W, Nika DL, Subrina S, Pokatilov EP, Lau CN, Balandin AA (2010) Dimensional crossover of thermal transport in few-layer graphene. Nat Mater 9:555–558

91. Schabel MC, Martins JL (1992) Energetics of interplanar binding in graphite. Phys Rev B 46:7185

92. Liao AD, Wu JZ, Wang XR, Tahy K, Jena D, Dai HJ, Pop E (2011) Thermally limited current carrying ability of graphene nanoribbons. Phys Rev Lett 106:256801

93. Seol JH, Jo I, Moore AL, Lindsay L, Aitken ZH, Pettes MT, Li XS, Yao Z, Huang R, Broido D, Mingo N, Ruoff RS, Shi L (2010) Two-dimensional phonon transport in supported graphene. Science 328:213

94. Jang W, Chen Z, Bao W, Lau CN, Dames C (2010) Thickness-dependent thermal conductivity of encased graphene and ultrathin graphite. Nano Lett 10:3909

95. Qiu B, Ruan X (2012) Reduction of spectral phonon relaxation times from suspended to supported graphene. Appl Phys Lett 100:193101

96. Aksamija Z, Knezevic I (2011) Lattice thermal conductivity of graphene nanoribbons: anisotropy and edge roughness scattering. Appl Phys Lett 98:141919

97. Yamamoto T, Watanabe K (2004) Empirical-potential study of phonon transport in graphitic ribbons. Phys Rev B 70:245402

98. Li W, Sevincli H, Cuniberti G, Roche S (2010) Phonon transport in large scale carbon-based disordered materials: implementation of an efficient order-N and real-space Kubo methodology. Phys Rev B 82:041410 (R)

99. Murali R, Yang Y, Brenner K, Beck T, Meindl JD (2009) Breakdown current density of graphene nano ribbons. Appl Phys Lett 94:243114-1-3

100. Ong ZY, Pop E (2011) Effect of substrate modes on thermal transport in supported graphene. Phys Rev B 84:075471

101. Huang Z, Fisher TS, Murthy JY (2010) Simulation of phonon transmission through graphene and graphene nanoribbons with a Green's function method. J Appl Phys 108:094319

102. Iijima S (1991) Helical microtubules of graphitic carbon. Nature 354:56

103. Dai H, Hafner JH, Rinzler AG, Colbert DT, Smalley RE (1996) Nanotubes as nanoprobes in scanning probe microscopy. Nature 384:147

104. Mahar B, Laslau C, Yip R, Sun Y (2007) Development of carbon nanotube-based sensors – a review. IEEE Sens J 7:266

105. Bianco A, Kostarelos K, Prato M (2005) Applications of carbon nanotubes in drug delivery. Curr Opin Chem Biol 9:674–679

106. Ebbesen TW, Ajayan PM (1992) Large-scale synthesis of carbon nanotubes. Nature 358:220–222

107. Iijima S, Ichihashi T (1993) Single-shell carbon nanotubes of 1-nm diameter. Nature 363:603–605

108. Journet C, Maser WK, Bernier P, Loiseau A, Lamy De La Chapelle M, Lefrant S, Deniard P, Lee R, Fischer JE (1997) Large-scale production of single-walled carbon nanotubes by the electric-arc technique. Nature 388:756–758

109. Seraphin S, Zhou D, Jiao J, Minke MA, Wang S, Yadav T, Withers JC (1994) Catalytic role of nickel, palladium, and platinum in the formation of carbon nanoclusters. Chem Phys Lett 217:191–198

110. Saito Y, Okuda M, Fujimoto N, Yoshikawa T, Tomita M, Hayashi T (1994) Single-wall carbon nanotubes growing radially from Ni fine particles formed by arc evaporation. Jpn J Appl Phys 33:L526–L529

111. Chen B, Zhao X, Inoue S, Ando Y (2010) Fabrication and dispersion evaluation of single-wall carbon nanotubes produced by FH-arc discharge method. J Nanosci Nanotechnol 10:3973–3977

112. Fan WW, Zhao J, Lv YK, Bao WR, Liu XG (2010) Synthesis of SWNTs from charcoal by arc-discharging. J Wuhan Univ Technol Mater Sci Ed 25:194–196

113. Wang HF, Li ZH, Inoue S, Ando Y (2010) Influence of Mo on the growth of single-walled carbon nanotubes in arc discharge. J Nanosci Nanotechnol 10:3988–3993

114. Shimotani K, Anazawa K, Watanabe H, Shimizu M (2001) New synthesis of multi-walled carbon nanotubes using an arc discharge technique under organic molecular atmospheres. Appl Phys A Mater Sci Process 73:451–454

115. Jiang Y, Wang H, Shang XF, Li ZH, Wang M (2009) Influence of NH_3 atmosphere on the growth and structures of carbon nanotubes synthesized by the arc-discharge method. Inorg Mater 45:1237–1239

116. Parkansky N, Boxman RL, Alterkop B, Zontag I, Lereah Y, Barkay Z (2004) Single-pulse arc production of carbon nanotubes in ambient air. J Phys D Appl Phys 37:2715–2719

117. Jung SH, Kim MR, Jeong SH, Kim SU, Lee OJ, Lee KH, Suh JH, Park CK (2003) High-yield synthesis of multi-walled carbon nanotubes by arc discharge in liquid nitrogen. Appl Phys A Mater Sci Process 76:285–286

118. Guo JJ, Wang XM, Yao YL, Yang XW, Liu XG, Xu BS (2007) Structure of nanocarbons prepared by arc discharge in water. Mater Chem Phys 105:175–178

119. Guo T, Nikolaev P, Thess A, Colbert DT, Smalley RE (1995) Catalytic growth of single-walled manotubes by laser vaporization. Chem Phys Lett 243:49–54

120. Lebel LL, Aissa B, El Khakani MA, Therriault D (2010) Preparation and mechanical characterization of laser ablated single-walled carbon-nanotubes/polyurethane nanocomposite microbeams. Comp Sci Technol 70:518–524

121. Kusaba M, Tsunawaki Y (2006) Production of single-wall carbon nanotubes by a XeCl excimer laser ablation. Thin Solid Films 506:255–258

122. Zhang H, Ding Y, Wu C, Chen Y, Zhu Y, He Y, Zhong S (2003) The effect of laser power on the formation of carbon nanotubes prepared in CO_2 continuous wave laser ablation at room temperature. Phys B 325:224–229

123. Stramel AA, Gupta MC, Lee HR, Yu J, Edwards WC (2010) Pulsed laser deposition of carbon nanotube and polystyrene-carbon nanotube composite thin films. Opt Lasers Eng 48:1291–1295

124. Scott CD, Arepalli S, Nikolaev P, Smalley RE (2001) Growth mechanisms for single-wall carbon nanotubes in a laser-ablation process. Appl Phys A 72:573–580

125. Kumar M, Ando Y (2010) Chemical vapor deposition of carbon nanotubes: a review on growth mechanism and mass production. J Nanosci Nanotechnol 10:3739–3758

126. Ren ZF, Huang ZP, Wang DZ, Wen JG, Xu JW, Wang JH, Calvet LE, Chen J, Klemic JF, Reed MA (1999) Growth of a single freestanding multiwall carbon nanotube on each nanonickel dot. Appl Phys Lett 75:1086

127. Meyyappan M (2009) A review of plasma enhanced chemical vapour deposition of carbon nanotubes. J Phys D Appl Phys 42:213001

128. Ren ZF, Huang ZP, Xu JW, Wang JH, Bush P, Siegel MP, Provencio PN (1998) Synthesis of large arrays of well-aligned carbon nanotubes on glass. Science 282:1105–1107

129. Masako Y, Rie K, Takeo M, Yoshimasa O, Susumu Y, Etsuro O (1995) Specific conditions for Ni catalyzed carbon nanotube growth by chemical vapor deposition. Appl Phys Lett 67:2477–2479

130. Byon HR, Lim H, Song HJ, Choi HC (2007) A synthesis of high purity single-walled carbon nanotubes from small diameters of cobalt nanoparticles by using oxygen-assisted chemical vapor deposition process. Bull Korean Chem Soc 28:2056–2060

131. Chen YM, Zhang HY (2011) In: Bu JL, Jiang ZY, Jiao S (eds) The super-capacitor properties of aligned carbon nanotubes array prepared by radio frequency plasma-enhanced hot filament chemical vapor deposition. Advanced Materials Research 150–151:1560–1563

132. Kim HD, Lee JH, Choi WS (2011) Direct growth of carbon nanotubes with a catalyst of nickel nanoparticle-coated alumina powders. J Korean Phys Soc 58:112–115

133. Xu Y, Dervishi E, Biris AR, Biris AS (2011) Chirality-enriched semiconducting carbon nanotubes synthesized on high surface area MgO-supported catalyst. Mater Lett 65:1878–1881

134. Zhu YJ, Lin TJ, Liu QX, Chen YL, Zhang GF, Xiong HF, Zhang HY (2006) The effect of nickel content of composite catalysts synthesized by hydrothermal method on the preparation of carbon nanotubes. Mater Sci Eng B 127:198–202

135. Lee O, Jung J, Doo S, Kim SS, Noh TH, Kim KI, Lim YS (2010) Effects of temperature and catalysts on the synthesis of carbon nanotubes by chemical vapor deposition. Met Mater Int 16:663–667

136. Afolabi AS, Abdulkareem AS, Mhlanga SD, Iyuke SE (2011) Synthesis and purification of bimetallic catalysed carbon nanotubes in a horizontal CVD reactor. J Exp Nanosci 6:248–262

137. Dumpala S, Jasinski JB, Sumanasekera GU, Sunkara MK (2011) Large area synthesis of conical carbon nanotube arrays on graphite and tungsten foil substrates. Carbon 49:2725–2734

138. Zhu J, Yudasaka M, Iijima S (2003) A catalytic chemical vapor deposition synthesis of double-walled carbon nanotubes over metal catalysts supported on a mesoporous material. Chem Phys Lett 380:496–502

139. Ramesh P, Okazaki T, Taniguchi R, Kimura J, Sugai T, Sato K, Ozeki Y, Shinohara H (2005) Selective chemical vapor deposition synthesis of double-wall carbon nanotubes on mesoporous silica. J Phys Chem B 109:1141–1147

140. Flahaut E, Laurent C, Peigney A (2005) Catalytic CVD synthesis of double and triple-walled carbon nanotubes by the control of the catalyst preparation. Carbon 43:375–383

141. Fotopoulos N, Xanthakis JP (2010) A molecular level model for the nucleation of a single-wall carbon nanotube cap over a transition metal catalytic particle. Diamond Relat Mater 19:557–561

142. Zhang DS, Shi LY, Fang JH, Dai K, Li XK (2006) Preparation and desalination performance of multiwall carbon nanotubes. Mater Chem Phys 97:415–419

143. Li G (2010) Synthesis of well-aligned carbon nanotubes on the NH_3 pretreatment Ni catalyst films. Russ J Phys Chem A 84:1560–1565

144. Cui T, Lv RT, Kang FY, Hu Q, Gu JL, Wang KL, Wu DH (2010) Synthesis and enhanced field-emission of thin-walled, open-ended, and well-aligned N-doped carbon nanotubes. Nanoscale Res Lett 5:941–948

145. Novoselov KS, Jiang D, Schedin F, Booth TJ, Khotkevich VV, Morozov SV, Geim AK (2005) Two-dimensional atomic crystals. Proc Natl Acad Sci USA 102:10451

146. Yu OK, Lian J, Siriponglert S, Li H, Chen YP, Pei SS (2008) Graphene segregated on Ni surfaces and transferred to insulators. Appl Phys Lett 93:113103

147. De Arco LG, Zhang Y, Kumar A, Zhou C (2009) Synthesis, transfer, and devices of single and few-layer graphene by chemical vapor deposition. IEEE Trans Nanotechnol 8:135

148. Reina A, Jia X, Ho J, Nezich D, Son H, Bulovic V, Dresselhaus MS, Kong J (2009) Large area, few-layer graphene films on arbitrary substrates by chemical vapor deposition. Nano Lett 9:30

149. Kim KS, Zhao Y, Jang H, Lee SY, Kim JM, Kim KS, Kim KS, Ahn J-H, Kim P, Choi J-Y, Hong BH (2009) Large-scale pattern growth of graphene films for stretchable transparent electrodes. Nature 457:706

150. Li X, Cai W, An J, Kim S, Nah J, Yang D, Piner R, Velamakanni A, Jung I, Tutuc E, Banerjee SK, Colombo L, Ruoff RS (2009) Large-area synthesis of high-quality and uniform graphene films on copper foils. Science 324:1312

151. Bae S, Kim H, Lee Y, Xu X, Park J-S, Zheng Y, Balakrishnan J, Lei T, Kim HR, Song YI, Kim Y-J, Kim KS, Ozyilmaz B, Ahn J-H, Hong BH, Iijima S (2010) Roll-to-roll production of 30-inch graphene films for transparent electrodes. Nat Nanotechnol 5:574

152. Yu Q, Jauregui LA, Wu W, Colby R, Tian J, Su Z, Cao H, Liu Z, Pandey D, Wei D, Chung TF, Peng P, Guisinger NP, Stach EA, Bao J, Pei S-S, Chen YP (2011) Control and characterization of individual grains and grain boundaries in graphene grown by chemical vapour deposition. Nat Mater 10:443

153. Kim H, Mattevi C, Calvo MR, Oberg JC, Artiglia L, Agnoli S, Hirjibehedin CF, Chhowalla M, Saiz E (2012) Activation energy paths for graphene nucleation and growth on Cu. ACS Nano 6:3614

154. Vlassiouk I, Fulvio P, Meyer H, Lavrik N, Dai S, Datskos P, Smirnov S (2013) Large scale atmospheric pressure chemical vapor deposition of graphene. Carbon 54:58

155. Han GH, Gunes F, Bae JJ, Kim ES, Chae SJ, Shin H-J, Choi J-Y, Pribat D, Lee YH (2011) Influence of copper morphology in forming nucleation seeds for graphene growth. Nano Lett 11:4144

156. Luo Z, Lu Y, Singer DW, Berck ME, Somers LA, Goldsmith BR, Johnson ATC (2011) Effect of substrate roughness and feedstock concentration on growth of wafer-scale graphene at atmospheric pressure. Chem Mater 23:1441

157. Tao L, Lee J, Holt M, Chou H, McDonnell SJ, Ferrer DA, Babenco MG, Wallace RM, Banerjee SK, Ruoff RS, Akinwande D (2012) Uniform wafer-scale chemical vapor deposition of graphene on evaporated Cu (111) film with quality comparable to exfoliated monolayer. J Phys Chem C 116:24068

158. Murdock AT, Koos A, Britton TB, Houben L, Batten T, Zhang T, Wilkinson AJ, Dunin-Borkowski RE, Lekka CE, Grobert N (2013) Controlling the orientation, edge geometry, and thickness of chemical vapor deposition graphene. ACS Nano 7:1351

159. Wang H, Wang G, Bao P, Yang S, Zhu W, Xie X, Zhang W-J (2012) Controllable synthesis of submillimeter single-crystal monolayer graphene domains on copper foils by suppressing nucleation. J Am Chem Soc 134:3627

160. Yan Z, Lin J, Peng Z, Sun Z, Zhu Y, Li L, Xiang C, Samuel EL, Kittrell C, Tour JM (2012) Toward the synthesis of wafer-scale single-crystal graphene on copper foils. ACS Nano 6:9110

161. Vlassiouk I, Regmi M, Fulvio R, Dai S, Datskos P, Eres G, Smirnov S (2011) Role of hydrogen in chemical vapor deposition growth of large single-crystal graphene. ACS Nano 5:6069

162. Wang J, Zhu M, Outlaw RA, Zhao X, Manos DM, Holloway BC (2004) Synthesis of carbon nanosheets by inductively coupled radio-frequency plasma enhanced chemical vapor deposition. Carbon 42:2867

163. Wang JJ, Zhu MY, Outlaw RA, Zhao X, Manos DM, Holloway BC, Mammana VP (2004) Free-standing subnanometer graphite sheets. Appl Phys Lett 85:1265

164. Nandamuri G, Roumimov S, Solanki R (2010) Remote plasma assisted growth of graphene films. Appl Phys Lett 96:154101

165. Qi JL, Zheng WT, Zheng XH, Wang X, Tian HW (2011) Relatively low temperature synthesis of graphene by radio frequency plasma enhanced chemical vapor deposition. Appl Surf Sci 257:6531

166. Kim Y, Song W, Lee SY, Jeon C, Jung W, Kim M, Park C-Y (2011) Low-temperature synthesis of graphene on nickel foil by microwave plasma chemical vapor deposition. Appl Phys Lett 98:263106

167. Kalita G, Kayastha MS, Uchida H, Wakita K, Umeno M (2012) Direct growth of nanographene films by surface wave plasma chemical vapor deposition and their application in photovoltaic devices. RSC Advances 2:3225

168. Sutter P (2009) How silicon leaves the scene. Nat Mater 8:171
169. Kageshima H, Hibino H, Tanabe S (2012) The physics of epitaxial graphene on SiC(0001). J Phys: Condens Matter 24:314215
170. Badami DV (1962) Graphitization of α-silicon carbide. Nature 193:569
171. Zhou SY, G–H G, Graf J, Fedorav AV, Spataru CD, Diehl RD, Kopelevich Y, D–H L, Louie SG, Lanzara A (2006) First direct observation of dirac Fermions in graphite. Nat Phys 2:595
172. Ohta T, Bostwick A, McChesney JL, Seyller T, Horn K, Rotenberg E (2007) Interlayer interaction and electronic screening in multilayer graphene investigated with angle-resolved photoemission spectroscopy. Phys Rev Lett 98:206802
173. Kageshima H, Hibino H, Yamaguchi H, Nagase M (2011) Theoretical study on epitaxial graphene growth by Si sublimation from SiC (0001) surface. Jpn J Appl Phys 50:095601
174. Dmitriev AN, Cherednichenko DI (2011) Formation of graphene layers by vacuum sublimation of silicon carbide using a scanning heat source. Semiconductors 45:1656
175. Hibino H, Kageshima H, Maeda F, Nagase M, Kobayasi Y, Yamaguchi H (2008) Microscopic thickness determination of thin graphite films formed on SiC from quantized oscillation in reflectivity of low-energy electrons. Phys Rev B 77:075413
176. Hibino H, Tanabe S, Mizuno S, Kageshima H (2012) Growth and electronic transport properties of epitaxial graphene on SiC. J Phys D:Appl Phys 45:154008
177. Kim K, Park J, Kim C, Choi W, Seo Y, Ahn J, Park I-S (2012) Removing graphite flakes for preparing mechanically exfoliated graphene sample. Micro Nano Lett 7:1133
178. Jayasena B, Reddy CD, Subbiah S (2013) Separation, folding and shearing of graphene layers during wedge-based mechanical exfoliation. Nanotechnology 24:205301
179. Cai D, Song M (2007) Preparation of fully exfoliated graphite oxide nanoplatelets in organic solvents. J Mater Chem 17:3678
180. Israelachvili J (2011) Intermolecular and surface force, 3rd edn. Academic, Boston
181. Paredes JI, Villar-Rodil S, Martinez-Alonso A, Tascon JMD (2008) Graphene oxide dispersions in organic solvents. Langmuir 24:10564
182. Liu W, Wang JN (2011) Direct exfoliation of graphene in organic solvents with addition of NaOH. Chem Commun 47:6888
183. Pei S, Cheng H-M (2012) The reduction of graphene oxide. Carbon 50:3210
184. Srivastava PK, Ghosh S (2013) Eliminating defects from graphene monolayers during chemical exfoliation. Appl Phys Lett 102:043102
185. Schniepp HC, J–L L, McAllister MJ, Sai H, Alonso MH, Adamson DH, Prud'homme RK, Car R, Saville DA, Aksay IA (2006) Functionalized single graphene sheets derived from splitting graphite oxide. J Phys Chem B 110:8535
186. McAllister MJ, Li JL, Adamson DH, Schnlepp HC, Abdalam AA, Liu J, Aksay IA (2007) Single sheet functionalized graphene by oxidation and thermal expansion of graphite. Chem Mater 19:4396
187. Chen W, Yan L (2010) Preparation of graphene by a low-temperature thermal reduction at atmosphere pressure. Nanoscale 2:559
188. Liu X, Kim H, Guo LJ (2013) Optimization of thermally reduced graphene oxide for an efficient hole transport layer in polymer solar cells. Organ Electron 14:591
189. Park O-K, Hahm MG, Lee S, Joh HI, Na SI, Vajtai R, Lee JH, Ku B-C, Ajayan PM (2012) In situ synthesis of thermochemically reduced graphene oxide conducting nanocomposites. Nano Lett 12:1789
190. Al-Temimy A, Riedl C, Starke U (2009) Low temperature growth of epitaxial graphene on SiC induced by carbon evaporation. Appl Phys Lett 95:231907
191. Hackley J, Ali D, DiPasquale J, Demaree JD, Richardson CJK (2009) Graphitic carbon growth on Si(111) using solid source molecular beam epitaxy. Appl Phys Lett 95:133114
192. Garcia JM, He R, Jiang MP, Yan J, Pinczuk A, Zuev YM, Kim KS, Kim P, Baldwin K, West KW, Pfeiffer LN (2010) Multilayer graphene films grown by molecular beam deposition. Solid State Commun 150:809

193. Garcia JM, Wurstbauer U, Levy A, Pfeiffer LN, Pinczuk A, Plaut AS, Wang L, Dean CR, Buizza R, Van Der Zande AM, Hone J, Watanabe K, Taniguchi T (2012) Graphene growth on h-BN by molecular beam epitaxy. Solid State Commun 152:975

194. Li J-L, Kudin KN, McAllister MJ, Prud'homme RK, Aksay IA, Car P (2006) Oxygen-driven unzipping of graphitic materials. Phys Rev Lett 96:176101

195. Ajayan PM, Yakobson BI (2006) Oxygen breaks into carbon world. Nature 441:818

196. Kosynkin DV, Higginbotham AL, Sinitskii A, Lomeda JR, Dimiev A, Price BK, Tour JM (2009) Longitudinal unzipping of carbon nanotubes to form graphene nanoribbons. Nature 458:872

197. Jiao L, Zhang L, Wang X, Diankov G, Dai H (2009) Narrow graphene nanoribbons from carbon nanotubes. Nature 458:877

198. Zhuang N, Liu C, Jia L, Wei L, Cai J, Guo Y, Zhang Y, Hu X, Chen J, Chen X, Tang Y (2013) Clean unzipping by steam etching to synthesize graphene nanoribbons. Nanotechnology 24:325604

199. Iwai H (2009) Roadmap for 22 nm and beyond. Microelectron Eng 86:1520–1528

200. Wang C, Takei K, Takahashi T, Javey A (2013) Carbon nanotube electronics–moving forward. Chem Soc Rev 42:2592

201. Charlier J-C, Blase X, Roche S (2007) Electronic and transport properties of nanotubes. Rev Mod Phys 79:677–732

202. Javey A, Guo J, Wang Q, Lundstrom M, Dai H (2003) Ballistic carbon nanotube transistors. Nature 424:654–657

203. Bradley K, Gabriel JCP, Star A, Gruner G (2003) Short-channel effects in contact-passivated nanotube chemical sensors. Appl Phys Lett 83:3821

204. Ionescu AM, Riel H (2011) Tunnel field-effect transistors as energy-efficient electronic switches. Nature 479:329

205. Jensen K, Weldon J, Garcia H, Zettl A (2007) Nanotube radio. Nano Lett 7:3508

206. Franklin AD, Luisier M, Han SJ, Tulevski G, Breslin CM, Gignac L, Lundstrom MS, Haensch W (2012) Sub – 10 nm carbon nanotube transistor. Nano Lett 12:758

207. Cao Q, Rogers JA (2009) Ultrathin films of single-walled carbon nanotubes for electronics and sensors: a review of fundamental and applied aspects. Adv Mater 21:29

208. Park H, Afzali A, Han S-J, Tulevski GS, Franklin AD, Tersoff J, Hannon JB, Haensch W (2012) High-density integration of carbon nanotubes via chemical self-assembly. Nat Nanotechnol 7:787–791

209. Snow ES, Campbell PM, Ancona MG, Novak JP (2005) High-mobility carbon-nanotube thin film transistors on a polymeric substrate. Appl Phys Lett 86:033105

210. Sun DM, Timmermans MY, Tian Y, Nasibulin AG, Kauppinen EI, Kishimoto S, Mizutani T, Ohno Y (2011) Flexible high-performance carbon nanotube integrated circuits. Nat Nanotechnol 6:156

211. McCarthy MA, Liu B, Donoghue EP, Kravchenko I, Kim DY, So F, Rinzler AG (2011) Low-voltage, low-power, organic light-emitting transistors for active matrix displays. Science 332:570

212. van der Veen MH, Vereecke B, Sugiura M, Kashiwagi Y, Ke X, Cott DJ, Vanpaemel JKM, Vereecken PM, Gendt SD, Huyghebaert C, Tökei Z (2012) Electrical and structural characterization of 150 nm CNT contacts with Cu damascene top metallization. In: Paper presented at the 2012 I.E. international interconnect technology conference (IITC), San Jose, 4 to 6 June 2012

213. Rinzler AG, Hafner JH, Nikolaev P, Nordlander P, Colbert DT, Smalley RE, Lou L, Kim SG, Tománek D (1995) Unraveling nanotubes: field emission from an atomic wire. Science 269:1550–1553

214. Saito Y, Uemura S (2000) Field emission from carbon nanotubes and its applications to electron sources. Carbon 38:169–182

215. Modi A, Koratkar N, Lass E, Wei B, Ajayan PM (2003) Miniaturized gas ionization sensors using carbon nanotubes. Nature 424:171

216. Bower C, Zhu W, Shalom D, Lopez D, Chen LH, Gammel PL, Jin S (2002) On-chip vacuum microtriode using carbon nanotube field emitters. Appl Phys Lett 80:3820
217. Choi WB, Jin YW, Kim HY, Lee SJ, Yun MJ, Kang JH, Choi YS, Park NS, Lee NS, Kim JM (2001) Electrophoresis deposition of carbon nanotubes for triode-type field emission display. Appl Phys Lett 1547:78
218. Choi WB, Lee YH, Chung DS, Lee NS, Kim JM (2000) Field emission from 4.5″ single-walled and multi-walled carbon nanotube films. J Vac Sci Tech B 18(2):1054–1058
219. Cheng Y, Zhou O (2003) Electron field emission from carbon nanotubes. CR Phys 4:1021
220. Bonard JM, Salvetat JP, Stockli T, Deheer WA, Forro L, Chatelain A (1998) Field emission from single-wall carbon nanotube film. Appl Phys Lett 73:918–920
221. Seko K, Kinoshita J, Saito Y (2005) In situ transmission electron microscopy of field-emitting bundles of double wall carbon nanotubes. Jpn J Appl Phys 44:L743–L745
222. Son Y-W, Oh S, Ihm J, Han S (2005) Field emission properties of double-wall carbon nanotubes. Nanotechnol 16:125–128
223. Hiraoka T, Yamada T, Hata K, Futaba DN, Kurachi H, Uemura S, Yumura M, Iijima S (2006) Synthesis of single and double walled carbon nanotubes forests on conducting metal foils. J Am Chem Soc 128:13338–13339
224. Charlier J-C, Terrones M, Baxendale M, Meunier V, Zacharia T, Ru-pesinghe NL, Hsu WK, Grobert N, Terrones H, Amaratunga GAJ (2002) Enhanced electron field emission in B-doped carbon nanotubes. Nano Lett 2:1191
225. Golberg D, Dorozhkin PS, Bando Y, Dong ZC, Tang CC, Uemura Y, Grobert N, Reyes-Reyes M, Terrones H, Terrones M (2003) Structure, transport and field-emission properties of compound nanotubes: CNx vs. BNCx (x < 0.1). Appl Phys A Mater 76:499
226. Doytcheva M, Kaiser M, Reyes-Reyes M, Terrones M, de Jonge N (2004) Electron emission from individual nitrogen-doped multi-walled carbon nanotubes. Chem Phys Lett 396:126
227. Lahiri I, Seelaboyina R, Hwang JY, Banerjee R, Choi W (2010) Enhanced field emission from multi-walled carbon nanotubes grown on pure copper substrate. Carbon 48:1531–1538
228. Seelaboyina R, Huang J, Choi WB (2006) Enhanced field emission of thin-multiwall carbon nanotubes by electron multiplication from microchannel plate. Appl Phys Lett 88:194104
229. Seelaboyina R, Bodepalli S, Noh K, Jeon M, Choi W (2008) Enhanced field emission from aligned multistage carbon nanotube emitter arrays. Nanotechnology 19:065605
230. Dai L, Chang DW, Baek J-B, Lu W (2012) Carbon nanomaterials for advanced energy conversion and storage. Small 8:1130
231. Evanoff K, Khan J, Balandin AA, Magasinski A, Ready WJ, Fuller TF, Yushin G (2012) Towards ultrathick battery electrodes: aligned carbon nanotube-enabled architecture. Adv Mater 24:533
232. Verma VP, Das S, Lahiri I, Choi W (2010) Large-area graphene on polymer film for flexible and transparent anode in field emission device. Appl Phys Lett 96:203108
233. Lahiri I, Oh SW, Hwang JY, Cho S, Sun YK, Banerjee R, Choi W (2010) High capacity and excellent stability of lithium ion battery anode using interface-controlled binder-free multiwall carbon nanotubes grown on copper. ACS Nano 4(6):3440–3446
234. Lahiri I, Das S, Kang C, Choi W (2011) Application of carbon nanostructures – energy to electronics. JOM 63:70
235. Leroux F, Metenier K, Gautier S, Frackowiak E, Bonnamy S, Beguin F (1999) Electrochemical insertion of lithium in catalytic multi-walled carbon nano-tubes. J Power Sources 81:317–322
236. Claye AS, Fischer JE, Huffman CB, Rinzler AG, Smalley RE (2000) Solid-state electrochemistry of the Li single wall carbon nanotube system. J Electrochem Soc 147:2845–2852
237. Sato M, Noguchi A, Demachi N, Oki N, Endo M (1994) A mechanism of lithium storage in disordered carbons. Science 264:556–558
238. Endo M, Kim YA, Hayashi T, Nishimura K, Matsushita T, Miyashita K, Dresselhaus MS (2001) Vapor-grown carbon fibers (VGCFs) basic properties and battery application. Carbon 39:1287–1297

239. An KH, Kim WS, Park YS, Moon JM, Bae DJ, Lim SC, Lee YS, Lee YH (2001) Electro-chemical properties of high-power supercapacitors using single-walled carbon nanotube electrodes. Adv Funct Mater 11:387–392

240. Matsumoto T, Komatsu T, Arai K, Yamazaki T, Kijima M, Shimizu H, Takasawab Y, Nakamura J (2004) Reduction of Pt usage in fuel cell electrocatalysts with carbon nanotube electrodes. Chem Commun 2004:840–841

241. Goff AL, Artero V, Jousselme B, Tran PD, Guillet N, Métayé R, Fihri A, Palacin S, Fontecave M (2009) From hydrogenases to noble metal -free catalytic nanomaterials for H_2 production and uptake. Science 326:1384–1387

242. Lee JM, Park JS, Lee SH, Kim H, Yoo S, Kim SO (2011) Selective electron-or hole-transport enhancement in bulk-heterojunction organic solar cells with N-or B-doped carbon nanotubes. Adv Mater 23:629

243. Xu ZH, Wu Y, Hu B, Ivanov IN, Geohegan DB (2005) Carbon nanotubes effects on electroluminescence and photovoltaic response in conjugated polymers. Appl Phys Lett 87:263118

244. Gabor NM, Zhong Z, Bosnick K, Park J, McEuen PL (2009) Extremely efficient multiple electron – hole pair generation in carbon nanotube photodiodes. Science 325:1367

245. Kam NWS, Jessop TC, Wender PA, Dai HJ (2004) Nanotube molecular transporters: internalization of car bon nanotube-protein conjugates into mammalian cells. J Am Chem Soc 126:6850–6851

246. Bianco A, Kostarelos K, Partido CD, Prato M (2005) Biomedical applications of functionalised carbon nanotubes. Chem Commun 5:571–577

247. Kam NWS, O'Connell M, Wisdom JA, Dai H (2005) Carbon nanotubes as multifunctional biological transporters and near-infrared agents for selective cancer cell destruction. Proc Natl Acad Sci USA 102:11600–11605

248. Zerda ADL, Zavaleta C, Keren S, Vaithilingam S, Bodapati S, Liu Z, Levi J, Ma T-J, Oralkan O, Cheng Z (2008) Photoacoustic molecular imaging in living mice utilizing targeted carbon nanotubes. Nat Nanotech 3:557–562

249. Welsher K, Liu Z, Daranciang D, Dai H (2008) Selective probing and imaging of cells with single walled carbon nanotubes as near-infrared fluorescent molecules. Nano Lett 8:586–590

250. Cherukuri P, Gannon CJ, Leeuw TK, Schmidt HK, Smalley RE, Curley SA, Weisman RB (2006) Mammalian pharmacokinetics of carbon nanotubes using intrinsic near-infrared fluorescence. Proc Natl Acad Sci USA 103:18882–18886

251. Heller DA, Baik S, Eurell TE, Strano MS (2005) Single-walled carbon nanotube spectros-copy in live cells: towards long-term labels and optical sensors. Adv Mater 17:2793–2799

252. Kam NWS, Liu Z, Dai HJ (2005) Functionalization of carbon nanotubes via cleavable disulfide bonds for efficient intracellular delivery of siRNA and potent gene silencing. J Am Chem Soc 127:12492–12493

253. Roy S, Vedala H, Prasad V, Choi W (2006) Vertically aligned multiwall carbon nanotube bioprobes on silicon platform for cholesterol detection. Nanotechnology 17:S14–S18

254. Hong SY, Tobias G, Jamal KTA, Ballesteros B, Boucetta HA, Perez SL, Nellist PD, Sim RB, Finucane C, Mather SJ, Green ML, Kostarelos K, Davis BG (2010) Filled and glycosylated carbon nanotubes for in vivo radioemitter localization and imaging. Nat Mater 9:485

255. Liu Z, Sun X, Ratchford NN, Dai H (2007) Supramolecular chemistry on water-soluble carbon nanotubes for drug loading and delivery. ACS Nano 1(1):50–56

256. Bianco A, Kostarelos K, Prato M (2011) Making carbon nanotubes biocompatible and biodegradable. Chem Commun 47:10182

257. Cai D, Mataraza JM, Qin ZH, Huang Z, Huang J, Chiles TC, Carnahan D, Kempa K, Ren Z (2005) Highly efficient molecular delivery into mammalian cells using carbon nanotube spearing. Nat Method 2:449–454

258. Roy S, Vedala H, Roy A, Kim D, Doud M, Mathee K, Shin H, Shimamoto N, Prasad V, Choi W (2008) Direct electrical measurements on single-molecule genomic DNA using single-walled carbon nanotubes. Nano Lett 8:26–30

259. Vedala H, Roy S, Doud M, Mathee K, Choi W (2008) The effect of environmental factors on the electrical conductivity of a single oligo-DNA molecule measured using single-walled carbon nanotube nanoelectrodes. Nanotechnology 19:265704

260. Meric I, Han MY, Young AF, Ozyilmaz B, Kim P, Shepard KL (2008) Current saturation in zero-bandgap, top-gated graphene field-effect transistors. Nat Nanotechnol 3:654–659

261. Barone V, Hod O, Scuseria GE (2006) Electronic structure and stability of semiconducting graphene nanoribbons. Nano Lett 6:2748

262. Liang GC, Neophytou N, Nikonov DE, Lund-strom MS (2007) Performance projections for ballistic graphene nanoribbon field-effect transistors. IEEE Trans Electron Dev 54:677

263. Chen Z, Lin YM, Rooks MJ, Avouris P (2007) Graphene nano-ribbon electronics. Physica E 40:228

264. Obradovic B, Kotlyar R, Heinz F, Matagne P, Rakshit T, Giles MD, Stettler MA (2006) Analysis of graphene nanoribbons as a channel material for field-effect transistors. Appl Phys Lett 88:142102

265. Ohta T, Bostwick A, Seyller T, Horn K, Rotenberg E (2006) Controlling the electronic structure of bilayer graphene. Science 313:951

266. Bai J, Duan X, Huang Y (2009) Rational fabrication of graphene nanoribbons using a nanowire etch mask. Nanoletters 9:2083

267. Tseng F, Unluer D, Holcomb K, Stan MR, Ghosh AW (2009) Diluted chirality dependence in edge rough graphene nanoribbons field-effect transistors. Appl Phys Lett 94:223112

268. Farmer DB, Mojarad RG, Perebeinos V, Lin YM, Tulevski GS, Tsang JC, Avouris P (2009) Chemical doping and electron–hole conduction asymmetry in graphene devices. Nanoletters 9:388

269. Ouyang Y, Wang X, Dai H, Guo J (2008) Carrier scattering in graphene nanoribbon field-effect transistors. Appl Phys Lett 92:243124

270. Ryzhii V, Ryzhii M, Otsuji T (2008) Thermionic and tunneling transport mechanisms in graphene field-effect transistors. Phys Stat Sol (a) 205(1527)

271. Ryzhii V, Ryzhii M, Satou A, Otsuji T (2008) Current–voltage characteristics of a graphene-nanoribbon field-effect transistor. J Appl Phys 103:094510

272. Wang X, Zhi L, Mullen K (2008) Transparent, conductive graphene electrodes for dye-sensitized solar cells. Nanoletters 8:323

273. Han T-H, Lee Y, Choi MR, Woo SH, Bae SH, Hong BH, Ahn JH, Lee TW (2012) Extremely efficient flexible organic light emitting diodes with modified graphene anode. Nat Photonics 6:105–110

274. Gomez DAL, Zhang Y, Schlenker CW, Ryu K, Thompson ME, Zhou C (2010) Continuous, highly flexible, and transparent graphene films by chemical vapor deposition for organic photovoltaics. ACS Nano 4:2865

275. Li S, Tu KH, Lin CC, Chen CW, Chhowalla M (2010) Solution-process-able graphene oxide as an efficient hole transport layer in polymer solar cells. ACS Nano 4:3169

276. Liao L, Lin Y-C, Duan X (2010) High speed graphene transistors with a self-aligned nanowire gate. Nature 467:305

277. Moon JS, Curtis D, Hu M, Wong D, McGuire C, Campbell PM, Jernigan G, Tedesco JL, VanMil B, Myers-Ward R, Eddy C Jr, Gaskill DK (2009) Epitaxial-graphene RF field-effect transistors on Si-face 6H-SiC substrates. IEEE Electron Device Lett 30:650–652

278. Lin Y-M, Dimitrakopoulos C, Jenkins KA, Farmer DB, Chiu H-Y, Grill A, Avouris P (2010) 100-GHz transistors from wafer-scale epitaxial graphene. Science 327:662

279. Szafranek BN, Fiori G, Schall D, Neumaier D, Kurz H (2012) Current saturation and voltage gain in bilayer graphene field effect transistors. Nano Lett 12:1324

280. Rangel NL, Gimenez A, Sinitskii A, Seminario JM (2011) Graphene signal mixer for sensing applications. J Phys Chem C 115(24):12128–12134

281. Wang H, Nezich D, Kong J, Palacios T (2009) Graphene frequency multipliers. IEEE Electron Device Lett 30:547–549

282. Wang Z, Zhang Z, Xu H, Ding L, Wang S, Peng L-M (2010) A high-performance top-gate graphene field-effect transistor based frequency doubler. Appl Phys Lett 96:173104
283. Milaninia KM, Baldo MA, Reina A, Kong J (2009) All graphene electromechanical switch fabricated by chemical vapor deposition. Appl Phys Lett 95:183105
284. Schedin F, Geim AK, Morozov SV, Hill EW, Blake P, Katsnelson MI, Novoselov KS (2007) Detection of individual gas molecules adsorbed on graphene. Nat Mater 6:652
285. Fowler JD, Allen MJ, Tung VC, Yang Y, Kaner RB, Weiller BH (2009) Practical chemical sensors from chemically derived graphene. ACS Nano 3:201
286. Sundaram RS, Navarro CG, Balasubramaniam K, Burghard M, Kern K (2008) Electrochemical modification of graphene. Adv Mater 20:3050
287. Lu J, Do I, Drzal LT, Worden RM, Lee I (2008) Nanometal-decorated exfoliated graphite nanoplatelet based glucose biosensors with high sensitivity and fast response. ACS Nano 2:1825–1832
288. Huang B, Li Z, Liu Z, Zhou G, Hao S, Wu J, Gu B-L, Duan W (2008) Adsorption of gas molecules on graphene nanoribbons and its implication for nanoscale molecule sensor. J Phys Chem C 112:13442–13446
289. Shan C, Yang H, Song J, Han D, Ivaska A, Niu L (2009) Direct electrochemistry of glucose oxidase and biosensing for glucose based on graphene. Anal Chem 81:2378
290. Alwarappan S, Erdem A, Liu C, Li CZ (2009) Probing the electrochemical properties of graphene nanosheets for biosensing applications. J Phys Chem C 113:8853
291. Li J, Guo S, Zhai Y, Wang E (2009) Nafion–graphene nanocomposite film as enhanced sensing platform for ultrasensitive de-termination of cadmium. Electrochem Commun 11(1085)
292. Bae S-H, Lee Y, Sharma BK, Lee HJ, Kim J-H, Ahn J-H (2013) Graphene-based transparent strain sensor. Carbon 51:236–242
293. Lee Y, Bae S, Jang H, Jang S, Zhu S-E, Sim SH, Song Y, Hong BH, Ahn J-H (2010) Wafer-scale synthesis and transfer of graphene films. Nano Lett 10(2):490–493
294. Fu X-W, Liao Z-M, Zhou JX, Zhou YB, Wu HC, Zhang R (2011) Strain dependent resistance in chemical vapor deposition grown graphene. Appl Phys Lett 99(21):213107
295. Wang Y, Yang R, Shi Z, Zhang L, Shi D, Wang E, Zhang G (2011) Super-elastic graphene ripples for flexible strain sensors. ACS Nano 5(5):3645–3650
296. Smith AD, Niklaus F, Paussa A, Vaziri S, Fischer AC, Sterner M, Forsberg F, Delin A, Esseni D, Palestri P, Palestri P, Palestri P, Ostling M, Lemme MC (2013) Electromechanical piezoresistive sensing in suspended graphene membranes. Nano Lett 13:3237–3242
297. Hierold C, Jungen A, Stampfer C, Helbling T (2007) Nano electromechanical sensors based on carbon nanotubes. Sens Actuators A 136(1):51–61
298. Kalvesten E, Smith L, Tenerz L, Stemme G (1998) The first surface micromachined pressure sensor for cardiovascular pressure measurements. In Proceedings 11th Annu. Int. Workshop on Micro Electro Mech Syst 574–579
299. Lee SW, Lee SS, Yang EH (2009) A study on field emission characteristics of planar graphene layers obtained from a highly oriented pyrolyzed graphite block. Nanoscale Res Lett 4:1218–1221
300. Koh ATT, Foong YM, Pan L, Sun Z, Chua DHC (2012) Effective large-area free-standing graphene field emitters by electrophoretic deposition. Appl Phys Lett 101:183107
301. Malesevic A, Kemps R, Vanhulsel A, Chowdhury MP, Volodin A, Haesendonck CV (2008) Field emission from vertically aligned few-layer graphene. J Appl Phys 104:084301
302. Geim AK, Kim P (2008) Carbon wonderland. Sci Am 298:90
303. Eda G, Unalan HE, Rupesinghe N, Amartunga GAJ, Chhowalla M (2008) Field emission from graphene based composite films. Appl Phys Lett 93:233502
304. Wu ZS, Pei S, Ren W, Tang D, Gao L, Liu B, Li F, Liu C, Cheng HM (2009) Field emission from single layer graphene films prepared by electrophoretic deposition. Adv Mater 21:1756
305. Lahiri I, Verma VP, Choi W (2011) An all-graphene based transparent and flexible field emission device. Carbon 49(5):1614–1619

306. Watcharotone S, Ruoff RS, Read FH (2008) Possibilities for graphene for field emission: modeling studies using the BEM. Phys Procedia 1:71

307. Babenko AY, Dideykin AT, Eidelman ED (2009) Graphene ladder: a model of field emission center on the surface of loose nanocarbon materials. Phys Solid State 51:435

308. Yoo E, Kim J, Hosono E, Zhou H, Kudo T, Honma I (2008) Large reversible li storage of graphene nanosheet families for use in rechargeable lithium ion batteries. Nano Lett 8:2277

309. Xiang HF, Li ZD, Xie K, Jiang JZ, Chen JJ, Lian PC, Wu JS, Yud Y, Wang HH (2012) Graphene sheets as anode materials for Li-ion batteries: preparation, structure, electrochemical properties and mechanism for lithium storage. RSC Adv 2:6792–6799

310. Paek S-M, Yoo EJ, Honma I (2009) Enhanced cyclic performance and lithium storage capacity of SnO_2/graphene nanoporous electrodes with three dimensionally delaminated flexible structure. Nano Lett 9:72

311. Wang D, Choi D, Li J, Yang Z, Nie Z, Kou R, Hu D, Wang C, Saraf LV, Zhang J, Aksay IA, Jiu J (2009) Self-assembled TiO_2-graphene hybrid nanostructures for enhanced Li-ion insertion. ACS Nano 3:907

312. Xie J, Song W, Zheng Y, Liu S, Zhu T, Cao G, Zhao X (2011) Preparation and Li-storage properties of SnSb/graphene hybrid nanostructure by a facile one-step solvothermal route. Int J Smart Nano Mat 2(4):261–271

313. Xiao JD, Mei D, Li X, Xu W, Wang D, Graff GL, Bennett WD, Nie Z, Saraf LV, Aksay IA, Liu J, Zhang JG (2011) Hierarchically porous graphene as a lithium-air battery electrode. Nano Lett 11(11):5071–5078

314. Xu C, Wang X, Zhu J (2008) Graphene-metal particle nanocomposites. J Phys Chem C 112:19841–19845

315. Seger B, Kamat PV (2009) Electrocatalytically active graphene-platinum nanocomposites. Role of 2-D carbon support in PEM fuel cells. J Phys Chem C 113:7990–7995

316. Kou R, Shao YY, Wang DH, Engelhard MH, Kwak JH, Wang J, Viswanathan VV, Wang CM, Lin YH, Wang Y, Aksay IA, Liu J (2009) Enhanced activity and stability of Pt catalysts on functionalized graphene sheets for electrocatalytic oxygen reduction. Electrochem Commun 11:954

317. Jafri RI, Rajalakshmi N, Ramaprabhu S (2010) Nitrogen doped graphene nanoplatelets as catalyst support for oxygen reduction reaction in proton exchange membrane fuel cell. J Mater Chem 20:7114

318. Wu J, Becerril HA, Bao Z, Liu Z, Chen Y, Peumans P (2008) Organic solar cells with solution-processed graphene transparent electrodes. Appl Phys Lett 92:263302–263304

319. Eda G, Lin YY, Miller S, Chen CW, Su WF, Chhowalla M (2008) Transparent and conducting electrodes for organic electronics from reduced graphene oxide. Appl Phys Lett 92:233305–233307

320. Hong W, Xu Y, Lu G, Li C, Shi G (2008) Transparent graphene/PEDOT-PSS composite films as counter electrodes of dye-sensitized solar cells. Electrochem Comm 10:1555–1558

321. Li X, Zhu H, Wang K, Cao A, Wei J, Li C, Jia Y, Li Z, Li X, Wu D (2010) Graphene-on-silicon schottky junction solar cells. Adv Mater 22:2743–2748

322. Ye Y, Dai Y, Dai L, Shi Z, Liu N, Wang F, Fu L, Peng R, Wen X, Chen Z, Liu Z, Qin G (2010) High-oerformance single CdS nanowire (nanobelt) schottky junction solar cells with Au/Graphene Schottky electrodes. ACS Appl Mater Interfaces 2:3406–3410

323. Gratzel M (2001) Photoelectrochemical cells. Nature 414:338–344

324. Grätzel M (2004) Conversion of sunlight to electric power by nanocrystalline dye-sensitized solar cells. J Photochem Photobiol A Chem 164:3–14

325. Trancik JE, Barton SC, Hone J (2008) Transparent and catalytic carbon nanotube films. Nano Lett 8:982–987

326. Li GR, Wang F, Jiang QW, Gao XP, Shen PW (2010) Carbon nanotubes with titanium nitride as a low-cost counter-electrode material for dye-sensitized solar cells. Angew Chem Int Ed 49:3653–3656

327. Das S, Sudhagar P, Verma V, Song D, Ito E, Lee SY, Kang YS, Choi W (2011) Amplifying charge-transfer characteristics of graphene for triiodide reduction in dye-sensitized solar cells. Adv Funct Mater 21:3729–3736

328. Das S, Sudhagar P, Nagarajan S, Ito E, Lee SY, Kang YS, Choi W (2012) Synthesis of graphene-CoS electro-catalytic electrodes for dye sensitized solar cells. Carbon 50:4815–4821

329. Das S, Sudhagar P, Ito E, Lee DY, Nagarajan S, Lee SY, Kang YS, Choi W (2012) Effect of HNO_3 functionalization on large scale graphene for enhanced tri-iodide reduction in dye-sensitized solar cells. J Mater Chem 22:20490–20497

330. Li D, Müller MB, Gilje S, Kaner RB, Wallace GG (2008) Processable aqueous dispersions of graphene nanosheets. Nat Nanotechnol 3:101

331. Sofo JO, Chaudhari AS, Barber GD (2007) Graphane: a two dimensional hydrocarbon. Phys Rev B 75:153401

332. U.S. Department of Energy. Energy efficiency and renewable energy. http://www1.eere.energy.gov/hydrogenandfuelcells/storage/current_technology.html

333. Ao ZM, Peeters FM (2010) High-capacity hydrogen storage in Al-adsorbed graphene. Phys Rev B 81:205406

334. Beheshti E, Nojeh A, Servati PA (2011) A first-principles study of calcium-decorated, boron-doped graphene for high capacity hydrogen storage. Carbon 49:1561–1567

335. Balog R, Jørgensen B, Wells J, Lægsgaard E, Hofmann P, Besenbacher F, Hornekær L (2009) Atomic hydrogen adsorbate structures on graphene. J Am Chem Soc 131:8744–8745

336. Goler S, Coletti C, Tozzini V, Piazza V, Mashoff T, Beltram F, Pellegrini V, Heun S (2013) Influence of graphene curvature on hydrogen adsorption: toward hydrogen storage devices. J Phys Chem C 117:11506–11513

337. Tozzini V, Pellegrini V (2011) Reversible hydrogen storage by controlled Buckling of graphene layers. J Phys Chem C 115:25523–25528

338. Boukhvalov DW, Katsnelson MI (2009) Enhancement of chemical activity in corrugated graphene. J Phys Chem C 113:14176–14178

339. Stankovich S, Dikin DA, Dommett GHB, Kohlhaas KM, Zimney EJ, Stach EA, Piner RD, Nguyen ST, Ruoff RS (2006) Graphene-based composite materials. Nature 442:282

340. Dreyer DR, Park S, Bielawski CW, Ruoff RS (2010) The chemistry of graphene oxide. Chem Soc Rev 39:228–240

341. Chen T, Zeng B, Liu JL, Dong JH, Liu XQ, Wu Z, Yang XZ, Li ZM (2009) High throughput exfoliation of graphene oxide from expanded graphite with assistance of strong oxidant in modified Hummers method. J Phys: Conf Ser 188:012051

342. Zhou X, Huang X, Qi X, Wu S, Xue C, Boey FYC, Yan Q, Chen P, Zhang H (2009) In situ synthesis of metal nanoparticles on single-layer graphene oxide and reduced graphene oxide surfaces. J Phys Chem C 113:10842

343. Liu J, Bai H, Wang Y, Liu Z, Zhang X, Sun DD (2010) Self-assembling TiO_2 nanorods on large graphene oxide sheets at a two-phase interface and their anti-recombination in photocatalytic applications. Adv Funct Mater 20:4175–4181

344. Shen J, Hu Y, Shi M, Li N, Ma H, Ye M (2010) One step synthesis of graphene oxide – magnetic nanoparticle composite. J Phys Chem C 114:1498–1503

345. Zhou H, Qiu C, Liu Z, Yang H, Hu L, Liu J, Yang H, Gu C, Sun L (2010) Thickness-dependent morphologies of gold on N-layer graphenes. J Am Chem Soc 132:944–946

346. Yu K, Lu G, Mao S, Chen K, Kim H, Wen Z, Chen J (2011) Selective deposition of CdSe nanoparticles on reduced graphene oxide to understand photoinduced charge transfer in hybrid nanostructures. ACS Appl Mater Interfaces 3:2703–2709

347. Meng X, Geng D, Liu J, Banis MN, Zhang Y, Li R, Sun X (2010) Non-aqueous approach to synthesize amorphous/crystalline metal oxide-graphene nanosheet hybrid composites. J Phys Chem C 114:18330–18337

348. Wang H, Cui L-F, Yang Y, Casalongue HS, Robinson JT, Liang Y, Cui Y, Dai H (2010) Mn_3O_4 – graphene hybrid as a high-capacity anode material for lithium Ion batteries. J Am Chem Soc 132:13978–13980

349. Yang S, Feng X, Ivanovici S, Mullen K (2010) Fabrication of graphene-encapsulated oxide nanoparticles: towards high-performance anode materials for lithium storage. Angew Chem Int Ed 49:8408–8411

350. Wang D, Kou R, Choi D, Yang Z, Nie Z, Li J, Saraf LV, Hu D, Zhang J, Graff GL, Liu J, Pope MA, Aksay IA (2010) Ternary self-assembly of ordered metal oxide – graphene nanocomposites for electrochemical energy storage. ACS Nano 4:1587–1595

351. Wu Q, Xu Y, Yao Z, Liu A, Shi G (2010) Supercapacitors based on flexible graphene/polyaniline nanofiber composite films. ACS Nano 4:1963–1970

352. Dong L, Gari RRS, Li Z, Craig MM, Hou S (2010) Graphene-supported platinum and platinum–ruthenium nanoparticles with high electrocatalytic activity for methanol and ethanol oxidation. Carbon 48:781–787

353. Zhang L-S, Liang X-Q, Song W-G, Wu Z-Y (2010) Identification of the nitrogen species on N-doped graphene layers and Pt/NG composite catalyst for direct methanol fuel cell. Phys Chem Chem Phys 12:12055–12059

354. Yu D, Yang Y, Durstock M, Baek J-B, Dai L (2010) Soluble P3HT-grafted graphene for efficient bilayer – heterojunction photovoltaic devices. ACS Nano 4:5633–5640

Carbon Nanostructures for Enhanced Photocatalysis for Biocidal Applications

22

Georgios Pyrgiotakis

Keywords

Carbon Nanotubes • Photocatalysis • Sol-gel • Titania

Introduction

In the last few decades, the demand for safer environmental conditions has increased dramatically. The burden of infectious diseases worldwide, related to contamination via contact with contaminated surfaces (fomites), is a growing issue. Globally, these infections are linked to an estimated 1.7 million deaths a year from diarrheal disease and 1.5 million deaths from respiratory infections [1]. Apart from hospitals, the problem has become a growing liability at places where food is prepared and handled [2], where there is a growing risk associated with the cross-contamination of edible goods and where large amounts are handled by a single facility [3]. Already many *E. coli* and *Salmonella* outbreaks have been recorded and linked to single a facility [2, 4, 5]. The problem of cross-contamination via surfaces can also be traced, in smaller scale, to households where common areas can accumulate pathogens that can potentially become a threat, especially to more sensitive population groups [6]. There are also biological threats in forms of dangerous epidemic outbreaks (Ebola and SARS) and biological warfare weapons (anthrax and smallpox). The need for effective and efficient disinfection is driving the industry in the development of a wide range of products. These products can currently be divided into three major categories:

- **Chemical disinfectants:** Chemical-based disinfectants are currently the majority of the commercial disinfectants, and they have been used for the longest time. Most of them are chlorine-, alcohol-, or ammonium-based products. They are in liquid form and therefore are limited to surfaces. The majority

G. Pyrgiotakis
Department of Environmental Health, Harvard School of Public Health, Boston, USA
e-mail: gpyrgiot@hsph.harvard.edu

is used to disinfect contaminated surfaces and not as a prevention of contamination. Although their use is relatively simple and easy, they can still be dangerous if they are misused. Gases can also be used for the disinfection. However, the use of other disinfection methods which are based on the use of biocidal gases such ethylene oxide [7], hydrogen peroxide [8], ozone [9], and chlorine dioxide [10] also has limitations associated with toxicity [11] potential material damage, and in some instances downtime of the space or equipment being treated.

- **Radiation-based disinfection:** Radiation is a very effective technique since it can immediately inactivate the majority of the contaminants without damaging the surroundings [9, 12, 13]. Still however, the use is limited since it usually requires expensive equipment and under certain conditions, exposure to the used radiation can be proved dangerous [9, 14].

- **Passive disinfectants:** Passive disinfectants are characterized as those that do not require a certain application (chemicals) or operation (radiation), but constantly purify and clean surfaces, air, and water. Current air disinfection technologies, such as the use of upper-room UV-C irradiation (Ultraviolet 254 nm), [9, 12] high efficiency particulate (HEPA), and air filtration [15], have shortcomings. UV is associated with health risks [14, 16], requires the upper-room installation of UV fixtures, and relies on a well-mixed air concept. HEPA filters remove bacteria and viruses from the air effectively, but there are excessive costs associated with the energy needed to move air through the filter, and for filter replacement [17]. In addition, they do not deactivate the contaminants; so, if they are not replaced regularly, they can become a source of contamination rather than disinfection medium.

One of the most promising and rapidly emerging means of disinfection is photocatalysis, which does not share any of the shortcomings of the aforementioned methods. Photocatalysis is the type of reaction that takes place on the surface of a certain type of material in the presence of a very specific range of radiation [18]. There is a large selection of materials that can display this type of reaction, but the most widely used is titanium dioxide, TiO_2, or titania. Titania in addition to the high efficiency is cheap and environmentally safe, already used widely as pigment and food additive. However, there are significant limitations, which constrain the wider range of applications. Among them, the most notable is the relative low efficiency as compared to the chemical techniques.

In the last decade, one of the methods that has gained a great deal of attention is the combination of titania with various carbon structures such as carbon nanotubes (CNT). One of the most important carbon materials (after diamond) is the carbon nanotube, discovered in 1991 [19]. Their unique properties arise from their structure. Although they possess a large number of unique properties, probably, the most outstanding are their electric properties. In addition, their needle-like shape results in very high specific surface area. Both characteristics (electric properties and high surface area) are essential to the enhancement of photocatalysis, as will be evident in this chapter.

In this book chapter, we outline the major principles of photocatalysis and we examine the methods that have been developed to enhance it. In addition, we

discuss the major properties of the carbon nanostructures such as single and multiwall carbon nanotubes (SWNT and MWNT, respectively) and fullerenes and polyhydroxyl fullerenes (C_{60} and PHF) and how they can be combined with titania in a form of novel nanostructured materials to enhance the photocatalysis.

Photocatalysis

As described earlier, the term "photocatalysis" is a surface reaction that results in "lysis" (Greek for breakdown) molecules in the presence of light. However, the term "photocatalysis" is still under debate since strictly the term implies the initiation of reactions in the presence of light only, something that is not accurate in the case of semiconductor photocatalysis, since in this case, the presence of the semiconductor is equally important [20].

The first report on photocatalytic activity was by Becquerel in 1839, when he observed voltage and electric current on a silver chloride electrode when it was immersed in electrolyte solution in the presence of sunlight [21]. Generally speaking, all semiconductors can display photocatalytic properties, but usually, the oxides and compound semiconductors are demonstrating significantly better results [22–25]. The ability of a semiconductor to undergo photocatalytic oxidation is governed by the band energy positions of the semiconductor and redox potentials of the acceptor species. The latter is thermodynamically required to be below (more positive than) the conduction band potential of the semiconductor [24, 26]. The potential level of the donor needs to be above (more negative than) the valence band position of the semiconductor in order to donate an electron to the vacant hole. Figure 22.1 shows some of the most popular semiconductor photocatalysts represented with their band energy positions. Among them, TiO_2 is the most popular as it is efficient, effective, requires shallow UV radiation, is very cheap to manufacture, environmentally safe, and easily incorporated with other materials. Since 1972, when the ability to split the water under UV radiation was first discovered [27], there has been great work in understanding the mechanism and the reactions that take place.

Basic Principles

Figure 22.2 schematically represents the steps of photocatalysis. Initially when a photon of proper energy ($h\nu \geq E_g$) strikes the surface of the semiconductor, it generates an electron hole pair (h^+–e^-). Both electron and holes either recombine or migrate to the surface, where, they proceed with chemical reactions. The holes are generating OH• and the electrons H_2O_2. A very important factor for those processes is the required time. These reactions are summarized, with the estimated time required for each one [28], measured with laser flash photolysis [29, 30]:
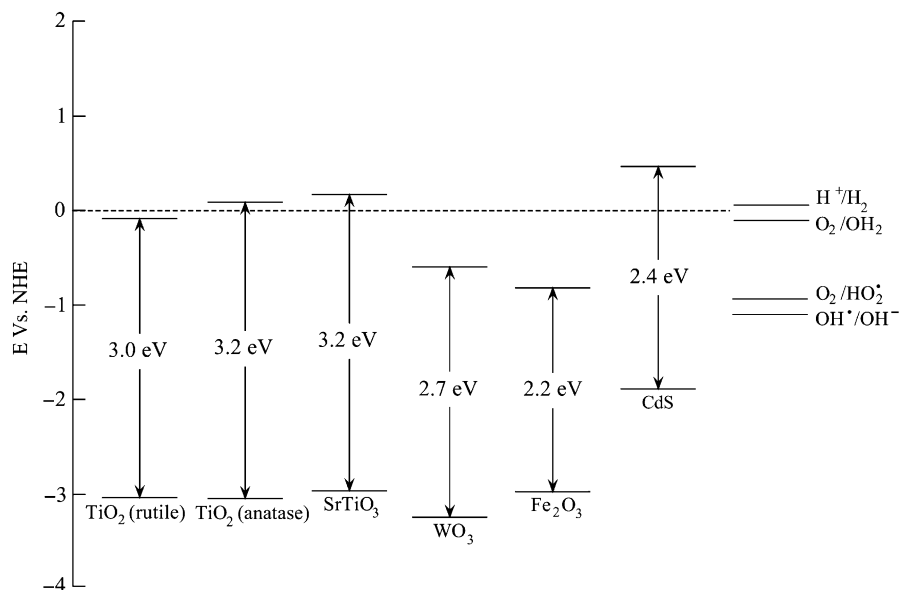
Fig. 22.1 Schematic diagram representing the main photocatalysts with their band-gap energy. In order to photo-reduce a chemical species, the conductance band of the semiconductor must be more negative than the reduction potential of the chemical species; to photo-oxidize a chemical species, the potential of the valence band has to be more positive than the oxidation potential of the chemical species. The energies are shown for pH 0
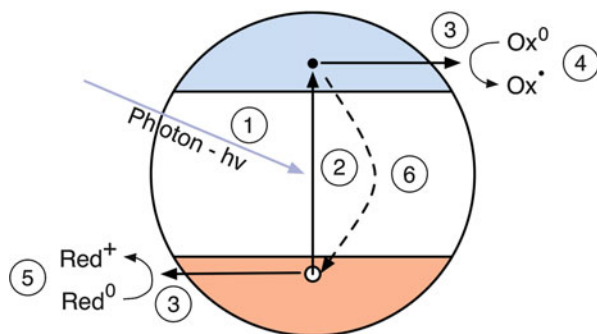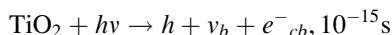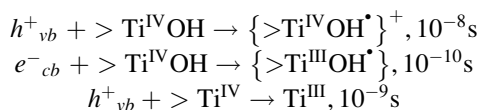

Fig. 22.2 Schematic representation of the reactions taking place in titania. (*1*) Light strikes the semiconductor. (*2*) An electron–hole pair is formed. (*3*) Electrons and holes are migrating to the surface. (*4*) The holes initiate reduction, leading to CO_2, Cl^- H^+, H_2O. (*5*) The conduction band initiate the oxidation. (*6*) electron and holes recombination to heat or light

- Charge-carrier generation

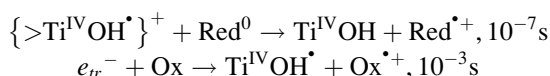$$TiO_2 + hv \rightarrow h + v_b + e^-{}_{cb}, 10^{-15}s$$

- Charge-carrier trapping

$$h^+{}_{vb} + > Ti^{IV}OH \rightarrow \{>Ti^{IV}OH^\bullet\}^+, 10^{-8}s$$
$$e^-{}_{cb} + > Ti^{IV}OH \rightarrow \{>Ti^{III}OH^\bullet\}, 10^{-10}s$$
$$h^+{}_{vb} + > Ti^{IV} \rightarrow Ti^{III}, 10^{-9}s$$

- Charge-carrier recombination
  $e^-{}_{cb} + \{Ti^{IV}OH^\bullet\}^+ \rightarrow Ti^{IV}OH, 10^{-7}s$ – The electrons inactivate the holes
  $h^+{}_{vb} + \{Ti^{III}OH\} \rightarrow Ti^{IV}OH, 10^{-8}s$ – The holes inactivate the electrons
- Charge-carrier recombination

$$\{>Ti^{IV}OH^\bullet\}^+ + Red^0 \rightarrow Ti^{IV}OH + Red^{\bullet+}, 10^{-7}s$$
$$e_{tr}{}^- + Ox \rightarrow Ti^{IV}OH^\bullet + Ox^{\bullet+}, 10^{-3}s$$

According to the above mechanism, the overall quantum efficiency depends on two major types of reactions: the carrier recombination and the $OH^\bullet/H_2O_2$ generation. The dominant reaction is the recombination of the e^- and h^+ (1 ns), followed by the reduction reaction (10 ns) and oxidation (1 ms). Since the recombination is also assisted by the localized crystal defects, the remaining carriers are not enough for an efficient photocatalytic reaction, resulting in a low efficient photocatalytic material.

Methods for Enhancing Photocatalytic Reactions

Before we discuss the enhancement of the photocatalysis with the advanced carbon nanocomposites, it is important to investigate the leading mechanisms of that can be used to enhance the photocatalytic reactions. Since 1972, there has been extensive work toward all three types of photocatalytic enhancement with the titania/semiconductor and titania/metal coupling more dominant since they are easier to achieve.

Time-wise the oxidation coming from the holes is the fastest degrading reaction [30]. It is reasonable therefore to favor this reaction over the reduction reaction initiated by the electrons. Since the mechanism that is responsible for the reduced efficiency is the recombination between the h^+ and e^-, all the previous research has focused on either scavenging the electrons away from the system to prevent recombination, or just retarding the recombination so that the holes will generate $OH^\bullet$ [22, 24, 26, 28]: namely, the most common ways are the doping of titania, the coupling with a metal, and the coupling with a semiconductor.

Doping of Titania

A great deal of work has been done the last few decades to dope titania with transition metals, N [31] and C [32, 33]. In general, transition metals are incorporated into the structure of titania and occupy substitutional or interstitial lattice positions. It is a very common defect in the case of semiconductors since it generates trap levels in the band-gap. Figure 22.3a shows the electronic structure of titania before the doping. After the doping (Fig. 22.3b), the band-gap has been modified with the addition of the trapping levels. The trap levels are usually located slightly below the lower edge of the conduction band and usually are in a form of a narrow band.

There are several advantages to this modification. Before the modification, the required photon energy had to satisfy the condition $h\nu \geq E_g$. After the modification, the required energy is going to be $h\nu \geq (E_g - E_t)$ where E_t is the lower edge of the trapping level band. In addition, the electrons that are excited at those levels are trapped, and the holes have sufficient time for $OH^\bullet$ generation. Even in the case that $h\nu \geq E_g$ and the electron is excited to the conduction band, then during the de-excitation process the electron is going to be transitioned from the conduction band to the trap levels and then to the valence band which again retards the recombination and therefore increases the overall efficiency. This process is subjected to a series of quantum mechanics dictated rules that will allow it or not, but generally, the trap levels generated by the transition metals C and N are satisfying these rules.

The most common transition metals used are Fe^{+3}, Cr^{+3}, and Cu^{+2}. Fe^{+3} doping of titania has been shown to increase the quantum efficiency for the reduction of N_2 [34–36] and methylviologen [34] and to inhibit the electron hole recombination [29, 30, 37]. In the case of phenol degradation, Scalfani et al. [35] and Palmisano et al. [38] reported that Fe^{+3} had little effect on the efficiency. Enhanced photoreactivity for water splitting and N_2 reduction have been reported with Cr^{+3} [38–41] doping, while other reports mention the opposite result. Negative effects have been also reported with the Mo and V doping, while Grätzel and Howe reported inhibition of electron hole recombination [42]. Finally, Karakitsou and Verykios noted a positive effect on the efficiency by doping of titania with cations of higher valency than Ti^{+4} [43]. Butler and Davis [44] and Fujihira et al. [45] reported that Cu^+ can also inhibit recombination.
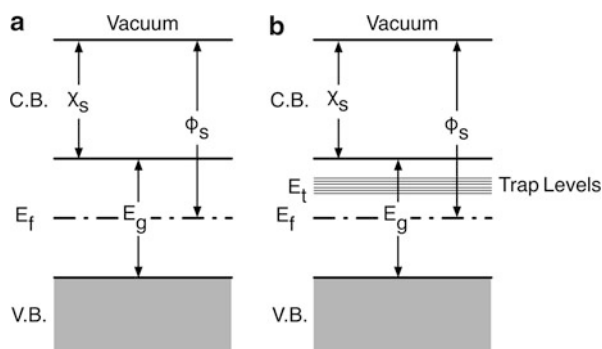

Fig. 22.3 Titania band structure (**a**) before and (**b**) after doping. The transition metals are interstitial or substitutional defects in the structure of titania and generate trapping levels in the band-gap

Coupling with a Metal

In photocatalysis, the addition of metals can affect the overall efficiency of the semiconductor by changing the semiconductor's surface properties. The addition of metal, which is not chemically bonded to the TiO_2, can selectively enhance the generation of holes by scavenging away the electrons. The enhancement of the photocatalysis by metal was first observed using the Pt/TiO_2 system [46, 47] by increasing the split of H_2O to H_2 and O_2. In particular cases, the addition of metal can affect the reaction products.

Figure 22.4 demonstrates the effect on titania band structure when titania is coupled with a metal. In general, when a semiconductor that has work function φ_s is compared with a metal with work function of $\varphi_m > \varphi_s$, the Fermi level of the semiconductor, E_f^s, is higher than the Fermi level of the metal E_f^m (Fig. 22.4a). So when the two materials are brought into contact (Fig. 22.4b), there will be electrons flowing from the semiconductor to the metal until the two Fermi energy levels come to equilibrium. The electrons transition will generate an excess of positive charge that creates an upward band bending. This bending creates a small barrier (in the order of 0.1 eV) that excited electrons can cross and be transported to the metal. From the moment the electrons migrate to the metal, it is not possible to cross back since the barrier for this action is larger, and therefore, the electrons will remain in the metal.

The earliest work on titania metal was the Pt/TiO_2 electrode for the split of water [46, 47]. Currently, one of the most effective metal/TiO_2 interface is achieved by colloidal suspension [48]. It was found that in the case of Pt/TiO_2 system, the Pt particles are gathered in the form of clusters on the surface of TiO_2 [49]. Other metals have also been investigated. Ag has been found to increase the efficiency [50]. Other transition metals such as Cr^{+3} negatively modify the surface by creating recombination sites. Although in principle all metals can be used, noble metals are
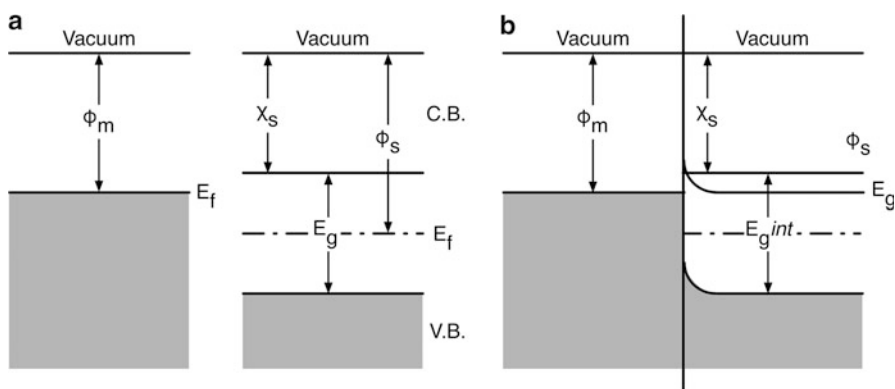

Fig. 22.4 The principles of rectifying contact between titania ($E_g = 3.2$ eV) and a metal with work function (φ_m), in this example 5 eV, greater than the affinity (χ_s) of titania. (**a**) Before the contact, and (**b**) after the contact, where a barrier is formed to prevent the electrons of crossing back to the semiconductor. The E_{int} is the Fermi level if titania is an intrinsic semiconductor and E_f is the Fermi level as an oxygen-deficient material
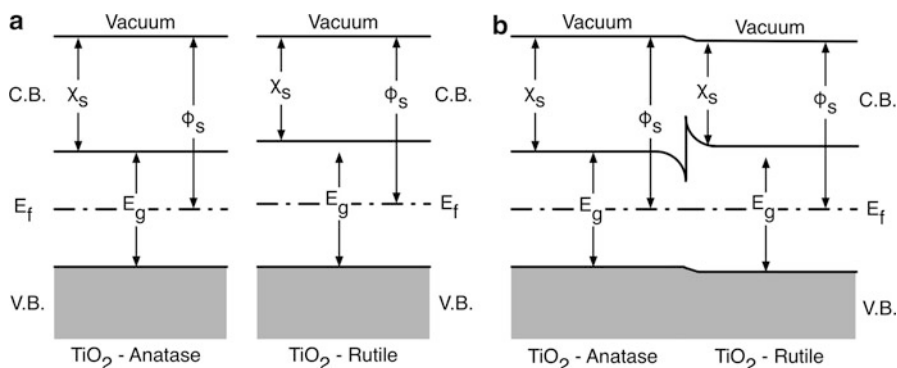
Fig. 22.5 The principles of rectifying contact between anatase (α) titania ($E_g = 3.2$ eV) and rutile (r) titania ($Erg = 3.0$ eV). (**a**) Before the contact and (**b**) after the contact, where a barrier is forming to prevent the electrons created in anatase crossing to the utile. On the other hand, holes created into anatase can migrate to rutile. So the couple of anatase − rutile is creating an effective electron–hole separation

preferred since they have higher work function and better conductivity. In all cases, high solids loading will affect the kinetics of the system, the light distribution, and eventually decrease the overall efficiency [48]. Although composite materials with TiO_2 coatings have been attempted, the relatively inert surface of the metals does not allow for a chemical bonding, resulting in flaking off of the titania coating.

Coupling with a Semiconductor
Coupling a semiconductor with a photocatalyst is a very interesting way of assisting the photocatalysis. Figure 22.5 demonstrates the principles of the TiO_2 coupling with another semiconductor. When two semiconductors are brought together, as in the previous case, the Fermi levels tend to balance, so electrons are flowing from the semiconductor with the highest Fermi level to the semiconductor with the lowest.

This charge transfer will create an excess of positive charge to the semiconductor that had the highest Fermi level and an excess of negative charge to the semiconductor that had the lowest energy (Fig. 22.5b). In the example in Fig. 22.5, the cases of anatase and rutile (both crystal phases of TiO_2) are examined as they are one of the most successful photocatalytic nanocomposites. By light illumination, $e^- - h^+$ pairs are generated in both semiconductors. The barrier that forms separates the electrons in the conduction band, but at the valence band, the holes are free to move, and based on the energy diagram, they move from the semiconductor with the larger gap to the one with the smaller. In this case, the composite material is acting as a charge separator. The holes are gathered in the rutile where they create an excess of holes, and despite the fact that the recombination is still the main process, the excess of holes will be enough to photo-oxidize the organic molecules.

In addition, semiconductors can be used as a hole or electron injector. In order to achieve optimum results, a candidate semiconductor has to satisfy the following criteria.

- Have a proper band-gap
- Have a proper position of the Fermi energy level
- Have proper relative position of the conduction and valence band to the vacuum level

The combination of the band-gap and Fermi level will determine if there are holes or electrons that will be transported and toward which direction. Thus, in order for a semiconductor coupled with titania to enhance the photocatalysis, the semiconductor has to have very specific properties. This is the reason that this technique, despite its simplicity, ease of manufacturing, and very promising results, is not very widely applied. Systems that have been developed are the TiO_2/CdS [51], TiO_2/RuO_2 [52, 53], and anatase-TiO_2/rutile-TiO_2 [54, 55]. The last one is a system commercially available from Degussa, known as Aeroxide P25, and is the most powerful commercial, particulate, photocatalytic system [55]. The excellent and uniform properties have established it as benchmark material to compare photocatalytic efficiencies.

Carbon Nanotubes

Carbon nanotubes were discovered by Iijima [56] in 1991 and since their discovery, they have attracted a great deal of attention due to the exceptional electric [57], thermal, and mechanical properties [58]. Iijima reported the creation of multiwall carbon nanotubes (MWNT) with outer diameter up to 55 Å and inner diameter down to 23 Å. Since that time, extensive theoretical and experimental research for the past decade has led to the creation of a rapidly developing research field. In 1993, Bethune et al. [59] reported the discovery of the single-wall nanotubes (SWNT). The very small diameter of the single nanotubes and the very big length makes them to behave as quantum wires, giving them very interesting properties. Due to the fact that the SWNT usually contains a small number of carbon atoms (usually < 102), they have attracted almost all the theoretical work. They possess some remarkable electronic, mechanical, and thermal properties that are related mainly to their diameter and chirality. Due to their importance and relevance to the photocatalysis, the electronic properties will be discussed in more detail later.

Structure

The CNTs can be thought as rolled graphene sheets that are held by the bonding of the sp^2 orbital. However, due to the curvature of the tube, the σ and π bonds are going to be re-hybridized. The new structure pushes σ bonds out of the plane, all at the same direction (toward the center of the tube). To compromise the charge shift, the π bond will be delocalized to the direction outside the tube. This configuration will make the tubes mechanically stronger and electrically and thermally more conducting than graphite. The flexibility of the σ bond allows the incorporation of topological defects, such as pentagons or heptagons, that allow the formation of caps, bend, toroidal, or helical tubes.

The direction the graphene sheet is "rolled" to produce the nanotubes is referred to as chirality. Without going into detail, it should be mentioned that the chirality essentially defines the amount of the deformations the orbitals undergo which further define the type of nanotubes. It is beyond the scope of the chapter to get into detail on the types and the related notation that is used, but we can mention the zigzag type tubes and the armchair, names directly related to the rolling direction. Although the properties that arise are very interesting, it is beyond the scope of the book chapter. The interested reader can find more information elsewhere [19, 60, 61].

Electronic Properties

Their unique electronic properties are attributed to the different quantum confinement of electrons. We can see three different directions that based on the geometry it will result in, or not confinement. (i) In the radial direction, electrons are confined by the monolayer thickness of the graphene sheet. (ii) Around the circumference of the nanotube, periodic boundary conditions come into play. (iii) Finally the direction parallel to the axis, since it is considered infinite, there is no confinement. The last one defines the conductivity of the SWNT. The longitudinal confinements largely depend on the chirality of the nanotube. Regarding the SWNT conductivity, 1/3 of the zigzag nanotubes are conducting, meaning they do not have any band-gap and the electrons are free to move toward any direction. On the other hand, the armchairs are all conducting.

However, the multiwall nanotubes are very different as they behave as a wire, regardless of the chirality of the bundle tubes or their number. The estimated conductance follows the simple relation [62];

$$\sigma = \sigma_0 M = \left(\frac{2e^2}{h}\right) M$$

For the case of the MWNT, the value of M is significantly bigger than for the SWNT to account for more conducting channels. In addition, the multilayer structure increases the probability to have armchair or zigzag tubes that will increase the conductivity. While the diameter is increasing, the electrons on the tube are less confined and the electron distribution resembles more the structure of graphite. This is due to the rehybridization of the σ and π orbitals, that is less intense and the tubular structure approaches more the graphite structure. This basically means that while the tube diameter increases, the energy gap is diminishing even for the semiconducting tubes. So in general, MWNTs are in their majority conducting and behave as nanowires. But, there are still chances that the tubes will be semiconducting, depending always on the arrangement of the tubes, certain crystal defects, and purity.

Although these properties are essential for the success or failure of the photocatalytic composites, they are often overlooked, either because they are not considered important or because it is very hard to control them.

Synthesis

There is a tremendous amount of research that has been done for the last 30 years in the field of the carbon nanotube growth. However, the majority of the methods are still based on the two leading methods that have been widely used the arc discharge and the CVD. The method of production is essential in the photocatalytic composites as it impacts directly the structure and the quality of the nanotubes.

Arc Discharge

In general, carbon nanotubes that are produced with carbon vapor that is being created by the arc discharge have fewer defects compared to other techniques. The reason for that is the high growth process temperature that ensures perfect annealing that eliminates most of the defects. The MWNTs that are produced via arc discharge are perfectly straight. The fewer defects have an immediate dramatic impact on the tube properties such as electric and mechanical. One of the main disadvantages is the limited yield that this method has. Besides the low yield, it is a highly time-consuming process. So in general, if a high yield of nanotubes is required, this method is not recommended; on the contrary, if more defined and better properties are required, then arc discharge is a very good solution [63].

Thermal- or Plasma-Enhanced CVD

Since the application field of the nanotubes is growing, the demand for higher yield production methods is also growing. One of the most promising techniques is the chemical vapor deposition (CVD). The apparatus for CVD-grown nanotubes is simple, which is also reducing a lot of the cost of the production. The growth rates can be controlled precisely and can go from a few nm/min up to 5 μm/min. Moreover, metal catalyst can further assist the yield. In addition, the nanotubes that are CVD grown have a lot of structural defects due to the low synthesis temperature during the growth process. An approach to improve this is annealing the tubes, which will reduce the defects but in no case will have the same results as the arc discharge [63]. The purification of the tubes in this case is a necessity since they contain metal catalyst and different amorphous carbon structures.

There are many ways to purify the tubes: hydrothermal treatment [64], H_2O-plasma oxidation [65], acid oxidation [66], dispersion and separation by micro-filtration [67], and high-performance liquid chromatography [68].

Carbon Nanotubes–TiO$_2$ Composites

It is obvious from the previous discussion regarding the photocatalysis and the CNTs, that the combination of MWNTs or SWNTs and TiO_2, in one composite will deliver a new material with high photocatalytic efficiency.

Both MWNTs and SWNTs have a variety of electronic properties useful for photocatalytic enhancement. MWNTs can behave as metals, exhibiting metallic conductivity. Alternatively, the SWNTs can exhibit semiconducting properties

which is a well-documented mechanism to enhance photocatalysis (discussed in the previous section). However, in addition to the intrinsic electronic properties and the CNT have also a very high surface area. Since photocatalysis is a surface reaction, more surface means more efficiency. In addition, CNTs due to their black color can further assist the photocatalysis by further increasing the amount of the adsorbed light. As explained, TiO_2 requires UV light in order to excite an electron with enough energy to overcome the band-gap. The UV spectrum represents only 5 % of the available total sunlight spectrum. Being able to use a larger portion of the spectrum of natural sunlight for photocatalysis is an important aspect for commercialization of the technology as UV usage is not always recommended [69].

Beyond the surface area and the higher adsorption, the surface of the CNTs can be tailored to increase specificity toward particular pollutants (molecular or biological) through the attachment of specific surface groups. When purified via acid treatment, CNTs formed alcohol, keto, and acid moieties on their surfaces. These groups can be further modified to improve adsorption of specific species, an advantage over activated carbons that are typically nonselective and have a lower pollutant-degradation rate due to the degradation of all species (benign and pollutant) present [70].

Synthesis Routes of the CNT–TiO$_2$ Composites

The precise control required to achieve the nanothin layer of titania on the MWNTs limits the methods that the CNT/TiO$_2$ can be synthesized. The most common method is the sol–gel chemistry [69, 71–77], which not only provides the precise control but also creates the strong adhesion due to the bonding between the coating and the MWNTs, a very important parameter for reasons that will be obvious later. In addition, there are reports where the coating has been synthesized via the hydrothermal method, which can have much higher yield, very important for commercialization of the composite [71, 78–80].

The variations in the synthesis method can also be seen on the structure of the final product. In one case, there is the formation of a uniform thin coating of titania around the MWNTs. In this case, the MWNTs' surface acts as a catalyst to initiate the nucleation of the TiO$_2$ formation, resulting in a thin uniform layer thickness. Alternatively, there is the formation of the titania nanoparticles on the surface of the nanotubes which is actually one of the most common configurations. This is typically achieved by nucleating and growing titania on dispersed CNTs in a liquid medium. A drawback is the formation of free titania nanoparticles instead of only those on the surface of nanoparticles.

The sol–gel coating of CNTs is performed in a liquid medium, alcohol, or water, based on the sol–gel reactions [69, 72, 73, 81]. Therefore, one of the biggest challenges is the proper dispersion of the CNTs. Improper dispersion will result in coating MWNTs aggregates instead of the single MWNTs. This is not a trivial task since the graphite sheet of the MWNTs is hydrophobic, making this task almost impossible. Sun and Gao [82] developed a method to increase hydrophilicity of CNTs dispersible in water via heating in an ammonia atmosphere at 600 °C. Other

methods use surface charges stemming from acid groups that were introduced by treatments in hot oxidizing mineral acids [73, 77, 83]. This process results in the generation of –OH and –COOH groups on the surface of the nanotubes. These groups make the CNTs hydrophilic making them dispersible in water and in addition act as nucleation points for the coating to initiate.

For sol–gel, the most common precursors are the various metal alkoxides, $(R–O–)_4Ti$. The most common characteristic of the titanium alkoxide precursors is their high reactivity with water to yield TiO_2, which in general is amorphous at room temperature with small seeds of anatase phase. The reactivity controls the speed of the reactions and therefore the uniformity of the coating. Faster reaction rates usually result in large particle-size distributions of the primary particles. The addition of acids or bases is one possibility to change the reaction rate [69, 72, 73, 81]. The reactivity is controlled primarily from the chain length of the alkoxide with longer chain resulting in slower reaction. The most common precursor is titanium isopropoxide [69, 72, 77], since it combines several desirable characteristics. It readily dissolves in alcohols and is not overly sensitive to humidity. An alternative is titanium butoxide [73, 78], which is even less sensitive to humidity; however, its higher viscosity may cause problems when dissolving it in ethanol at high concentrations. There are also reports where titanium ethoxide was used, but it is preferred for the formation of TiO_2 particles on the surface of the nanotubes, since the precise control of the reaction is very hard [71]. Alternatives to the titanium alkoxides in sol–gel are titanium tetrachloride [53] and titanium oxysulfate ($TiOSO_4$) [78], which have been used in the past for the synthesis of TiO_2 rutile and anatase particles, respectively. These precursors can be used in water, but this requires the CNTs to be dispersed in water, which can be challenging. Recently, CNTs have also been coated via hydrothermal methods [53, 71, 78–80] using mostly titanium tetrachloride [53] and $TiOSO_4$ [78].

Regardless of the chosen conditions and chemistry, the final material is mostly amorphous TiO_2 with seeds of anatase. It is therefore required a heat treatment to fully crystallize the coating. It usually occurs in nitrogen atmosphere at 300–500 °C to avoid the burnout of the CNTs and the phase transformation from anatase to rutile respectively [84]. It is worth mentioning that the coating of single-wall nanotubes was reported only recently [85, 86]. Single-wall CNT coatings are of importance since the electronic properties of tubes are better defined than in multiwalled CNTs. This will allow for better experiments to verify the proposed mechanisms.

A relatively new method of preparing such composites is the filter-mat or fiber-form via the electrospinning method [75, 77, 87]. Such methods produce mm to m long fibers with 40–100 nm in diameter. Typically, a fiber mat is formed, which is currently explored for a variety of catalytic applications. Such methodologies again involve chemistries very similar to the sol–gel route. One of the major differences is the addition of a polymer to form the backbone of the structure. Huey and Sigmund [88] have measured the mechanical properties of such fibers. The modulus of elasticity was found to be above 250 GPa for the CNT reinforced anatase nanofibers, which is significantly higher compared to less than 100 GPa, which was found for the electrospun pure anatase nanofibers. As electrospray is widely used for coatings of surfaces this method has a great potential.

Mechanisms of Photocatalysis Enhancement in CNT–TiO$_2$ Composites

Beyond the obvious, high surface area, the high surface energy (leading to higher adsorption), and the enhancement of light adsorption, there is a number of prevailing theories used to explain the enhancement of the photocatalytic properties of CNT–TiO$_2$ composites.

One mechanism, proposed by Wang et al. [80], states that the CNTs act as sensitizers and transfer electrons to the TiO$_2$. The photogenerated electrons are then injected into the conduction band of the TiO$_2$, allowing for the formation of superoxide radicals by adsorbed molecular oxygen. Once this occurs, the positively charged nanotubes remove an electron from the valence band of the TiO$_2$, leaving a hole. The now positively charged TiO$_2$ can then react with adsorbed water to form hydroxyl radicals.

Another mechanism, proposed by Pyrgiotakis, is a based on the theories described above as methods for the enhancement coupling with a metal or a semiconductor following the mechanisms explained in the related theory (Figs. 22.4 and 22.5). A high-energy photon excites an electron from the valence band to the conduction band of TiO$_2$. As discussed the recombination of the hole and electron is the dominant mechanism. The nanotubes especially those that have metallic properties can accept the photogenerated electrons, leaving the holes in the TiO$_2$ to take part in redox reactions. However, according to the theory of photocatalysis, the work function is a critical parameter to the creation of the rectifying contact. Table 22.1 compares the work function of the nanotubes to the work function of other traditional metals among which are Pt and Au, both used to improve photocatalysis. Carbon nanotubes compare very well with the other metals, since they are only slightly below Au. Therefore, the utilization of carbon nanotubes as the core of the photocatalytic composite is expected to enhance the photocatalysis since it has the ability to increase the efficiency by both methods mentioned earlier, high specific area and metallic properties. In addition, as it was discussed earlier, carbon can act as a dopant to the titania structure.

Table 22.1 Electron affinity and work function for metals, used to create rectifying contact with titania in order to increase the photocatalytic efficiency, compared to the carbon nanotubes

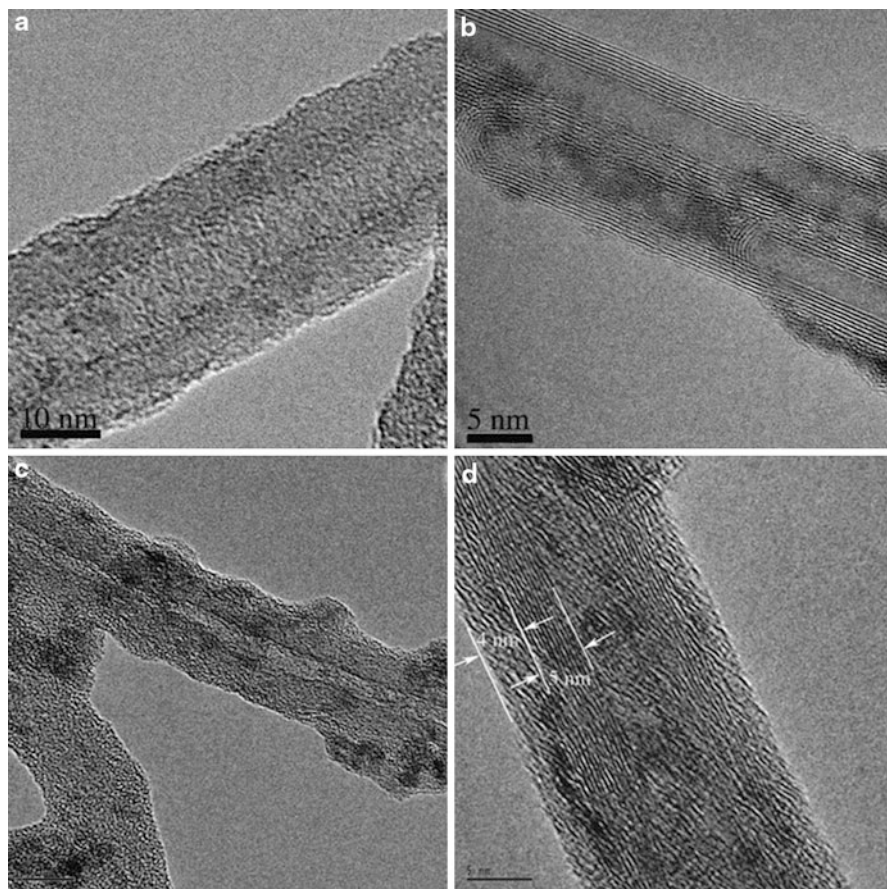| Element	Work function (φ) [eV]	Electron affinity (χ) [eV]
Pt	5.55	2.128
Au	5.38	2.309
Ag	4.63	1.302
Al	4.17	0.441
C (amorphous)	5.00	1.263
SWNTs	4.78–5.10	2.65
MWNTs	4.80–5.05	2.840

Fig. 22.6 The (**a**) CVD and (**b**) arc-discharge MWNTs post acid treatment. The same tubes after the coating: (**c**) CVD and (**d**) arc discharge

In this scheme, the carbon can generate trap levels in the band-gap that can change the transition of the electrons trapping them for short period of time. This gives time to the hole to lead the reduction reaction.

Although according to above mechanisms, all CNT–TiO$_2$ composites should preform based on this mechanism, this is not the case, as these systems are more complex. There are two parameters that are very important for the CNT–TiO$_2$ composite to work. The most essential parameter is the electronic configuration of the CNTs. It was shown by Pyrgiotakis that although CVD and arc-discharge-synthesized CNTs appear to have the same properties, number of tubes, diameter, etc., their core electronic properties are drastically different (Fig. 22.6a, b) [89]. As it was described in section "Electronic Properties", the electronic properties of the nanotubes depend on the coherence of the various layer of the MWNT.

The catalyst-assisted CVD-grown MWNTs result in a more random growth, while the lower temperature of the reactor prevents the various defects to self-correct. This results in a large number of defects that compromise the electrical properties of the MWNTs. Although at macroscopic level, those defects do not significantly impact their usage, this become essential at the nanoscale level. In the case of photocatalysis, the electrons need to transit to the underlying MWNT. If, however, there are defects, the electrons' ability to transfer to the MWNT is reduced, impacting significantly the photocatalyitc ability of the CNT–TiO_2 composites. This was proved experimentally by Pyrgiotakis where both arc discharge- and CVD-grown MWNTs were coated with TiO_2 via sol–gel processes. Although both nanocomposites were structurally similar under the TEM, the photocatalytic activity was ten higher for the arc discharge MWNT compared to the CVD-grown nanotubes. However, even in the case of the CVD-grown MWNTs, the enhanced photocatalytic activity can still occur mainly due to the fact that the tubes still provide an electron depository, carbon doping, high surface area, higher light adsorption, and higher pollutant adsorption.

In addition to the quality of the MWNTs, there is an equally important parameter; the carbon–oxygen–titanium bond. This bond serves two different purposes: From one side, this bond can activate the carbon as dopant for the titania, similar to carbon-doped titania, and on the other side, it is a channel to transfer the electrons to the MWNT. A composite that does not have this bond will be missing the dopant mechanism and will have significantly reduced ability to transport the electrons. Pyrgiotakis confirm the presence of Ti–O–C bonds in both types of nanocomposites with X-Ray photoelectron spectroscopy (XPS) [90], Raman Spectroscopy and Fourier-transform infrared spectroscopy (FTIR) [89]. In addition to the confirmation of the bond, Raman spectroscopy confirmed that arc-discharge-synthesized CNTs must have a higher electrical conductivity and fewer defects. This is also supported by transmission electron microscopy (TEM) images of the nanocomposites. The bond was later confirmed by Wang et al. in composites synthesized via the hydrothermal process [80].

Conclusion

Titania and carbon nanotubes composites are very promising solution for a wide range of biocidal applications. As it was evident from the discussion, the various properties of the nanotubes are among the main reasons that the nanotubes can assist the photocatalysis when they are in colloidal suspension. However, the application of a thin TiO_2 coating on the carbon nanotubes is not enough to yield very high photocatalytic efficiency. As it was shown, the bond (C−O−Ti) created between the MWNTs and the TiO_2 is essential for the creation of a highly reliable photocatalytic material [90]. The bond makes the underlined carbon atoms dopants to the structure of titania and provides a channel for the electrons to diffuse to the nanotube. However, the metallic nature of the carbon nanotubes is equally critical as the bond. Overall, carbon in the form of carbon nanotubes can be a very

promising way to enhance the photocatalysis, but the carbon nanotubes must be very well defined, with distinct structure and good electrical properties.

Over the years, this work was expanded and now similar nanocomposites are made with other forms of carbon such as fullerenes [91], polyhydroxyl fullerenes (PHF) [92], and graphene [93]. Although due to the size of the fullerenes, the fullerenes are applied as a coating to titania, the main principles remain the same. However, large concentration of fullerenes can affect the light adsorption, compromising the photocatalytic reaction. Krishna et al. showed that the ideal mass ratio is 0.001 C_{60}/TiO_2 [92]. For the case of the graphene, small titania particles are nucleating on the surface and the process is similar to the nanotubes. However, the exposed graphene can be a chemical magnet for contaminants attracting them, further increasing the overall efficiency [94].

References

1. Osseiran N, Hartl G (2006) WHO | Almost a quarter of all disease caused by environmental exposure. WHO 14:159–167 and 188
2. Mead PS, Slutsker L, Dietz V, McCaig LF, Bresee JS, Shapiro C et al (1999) Food-related illness and death in the United States. Emerg Infect Dis 5:607–625
3. Luber P, Brynestad S, Topsch D, Scherer K, Bartelt E (2006) Quantification of campylobacter species cross-contamination during handling of contaminated fresh chicken parts in kitchens. Appl Environ Microbiol 72:66–70
4. World Health Organization (2008) Foodborne disease outbreaks: guidelines for investigation and control. World Health Organization, Geneva, Switzerland
5. Redmond EC, Griffith CJ, Slader J, Humphrey TJ (2004) Microbiological and observational analysis of cross contamination risks during domestic food preparation. Br Food J 106:581–597
6. Scott E (1999) Hygiene issues in the home. Am J Infect Control 27:S22–S25
7. Chang FM, Sakai Y, Ashizawa S (1973) Bacterial pollution and disinfection of the colonofiberscope. II. Ethylene oxide gas sterilization. Am J Dig Dis 18:651–658
8. Krause J, McDonnell G, Riedesel H (2001) Biodecontamination of animal rooms and heat-sensitive equipment with vaporized hydrogen peroxide. Contemp Top Lab Anim Sci 40:18–21
9. Kujundzic E, Matalkah F, Howard CJ, Hernandez M, Miller SL (2006) UV air cleaners and upper-room air ultraviolet germicidal irradiation for controlling airborne bacteria and fungal spores. J Occup Environ Hyg 3:536–546
10. Taylor RH, Falkinham JO, Norton CD, LeChevallier MW (2000) Chlorine, chloramine, chlorine dioxide, and ozone susceptibility of *Mycobacterium avium*. Appl Environ Microbiol 66:1702–1705
11. Connor AJ, Laskin JD, Laskin DL (2012) Ozone-induced lung injury and sterile inflammation. Role of toll-like receptor 4. Exp Mol Pathol 92:229–235
12. Lai KM, Burge HA, First MW (2004) Size and UV germicidal irradiation susceptibility of *Serratia marcescens* when aerosolized from different suspending media. Appl Environ Microbiol 70:2021–2027
13. McDevitt JJ, Rudnick SN, Radonovich LJ (2012) Aerosol susceptibility of influenza virus to UV-C light. Appl Environ Microbiol 78:1666–1669
14. Zaffina S, Camisa V, Lembo M, Vinci MR, Tucci MG, Borra M et al (2012) Accidental exposure to UV radiation produced by germicidal lamp: case report and risk assessment. Photochem Photobiol 88:1001–1004

15. Mead K, Johnson DL (2004) An evaluation of portable high-efficiency particulate air filtration for expedient patient isolation in epidemic and emergency response. Ann Emerg Med 44:635–645

16. Kligman LH, Akin FJ, Kligman AM (1985) The contributions of UVA and UVB to connective tissue damage in hairless mice. J Invest Dermatol 84:272–276

17. Adal KA, Anglim AM, Palumbo CL, Titus MG, Coyner BJ, Farr BM (1994) The use of high-efficiency particulate air-filter respirators to protect hospital workers from tuberculosis. A cost-effectiveness analysis. N Engl J Med 331:169–173

18. Suppan P (1994) Chemistry and light. The Royal Society of Chemistry, Cambridge, UK

19. Dresselhaus M, Dresselhaus G, Saito R (1995) Physics of carbon nanotubes. Carbon 33:883–891

20. Gupta SM, Tripathi M (2011) An overview of commonly used semiconductor nanoparticles in photocatalysis. High Energy Chem 46:1–9

21. Becquerel E (1839) Mçmoire sur les effets électriques produits sous l'influence des rayons solaires. Comptes Rendus De l'Academie Des Sciences 9:561–567

22. Fox MA, Dulay MT (1996) Acceleration of secondary dark reactions of intermediates derived from adsorbed dyes on irradiated TiO_2 powders. J Photochem Photobiol A 98:91–101

23. Intra P, Tippayawong N (2008) An overview of differential mobility analyzers for size classification of nanometer-sized aerosol particles. Songklanakarin J Sci Technol 30:243–256

24. Linsebigler AL, Lu G, Yates JT (1995) Photocatalysis on TiO_2 surfaces: principles, mechanisms, and selected results. Chem Rev 95:735–758

25. Kühn KP, Chaberny IF, Massholder K, Stickler M, Benz VW, Sonntag H-G et al (2003) Disinfection of surfaces by photocatalytic oxidation with titanium dioxide and UVA light. Chemosphere 53:71–77

26. Mills G, Hoffmann MR (1993) Photocatalytic degradation of pentachlorophenol on TiO_2 particles - identification of intermediates and mechanism of reaction. Environ Sci Technol 27:1681–1689

27. Fujishima A, Honda K (1972) Electrochemical photolysis of water at a semiconductor electrode. Nature 238:37–40

28. Hoffmann MR, Martin ST, Choi WY, Bahnemann DW (1995) Environmental applications of semiconductor photocatalysis. Chem Rev 95:69–96

29. Martin ST, Herrmann H, Hoffmann MR (1994) Time-resolved microwave conductivity. Part 1. Quantum-sized TiO_2 and the effect of adsorbates and light-intensity on charge-carrier dynamics. J Chem Soc-Faraday Trans 90:3323–3330

30. Martin ST, Herrmann H, Choi WY, Hoffmann MR (1994) Time-resolved microwave conductivity. Part 2. TiO_2 photoreactivity and size quantization. J Chem Soc-Faraday Trans 90:3315–3322

31. Khan SUM, Al-Shahry M, Ingler WB (2002) Efficient photochemical water splitting by a chemically modified n-TiO_2. Science 297:2243–2245

32. Irie H, Watanabe Y, Hashimoto K (2003) Carbon-doped anatase TiO_2 powders as a visible-light sensitive photocatalyst. Chem Lett 32:772–773

33. Sakthivel S, Kisch H (2003) Daylight photocatalysis by carbon-modified titanium dioxide. Angew Chem Int Ed 42:4908–4911

34. Moser J, Gratzel M, Gallay R (1987) Inhibition of electron–hole recombination in substitutionally doped colloidal semiconductor crystallites. Helv Chim Acta 70:1596–1604

35. Sclafani A, Palmisano L, Schiavello M (1992) Phenol and nitrophenols photodegradation carried out using aqueous TiO_2 anatase dispersions. Abstracts of Papers of the Amercian Chemical Society. 203:132–ENVR

36. Soria J, Conesa JC, Augugliaro V, Palmisano L, Schiavello M, Sclafani A (1991) Dinitrogen photoreduction to ammonia over titanium-dioxide powders doped with ferric ions. J Phys Chem 95:274–282

37. Choi WY, Termin A, Hoffmann MR (1994) Effects of metal-ion dopants on the photocatalytic reactivity of quantum-sized TiO_2 particles. Angew Chem Int Ed 33:1091–1092

38. Palmisano L, Augugliaro V, Sclafani A, Schiavello M (1988) Activity of chromium-ion-doped titania for the dinitrogen photoreduction to ammonia and for the phenol photodegradation. J Phys Chem 92:6710–6713

39. Herrmann JM, Disdier J, Pichat P (1984) Effect of chromium doping on the electrical and catalytic properties of powder titania under UV and visible illumination. Chem Phys Lett 108:618–622

40. Mu W, Herrmann JM, Pichat P (1989) Room-temperature photocatalytic oxidation of liquid cyclohexane into cyclohexanone over neat and modified TiO_2. Catal Lett 3:73–84

41. Sun B, Reddy EP, Smirniotis PG (2005) Effect of the Cr^{6+} concentration in Cr-incorporated TiO_2-loaded MCM-41 catalysts for visible light photocatalysis. Appl Catal B-Environ 57:139–149

42. Grätzel M (1999) Mesoporous oxide junctions and nanostructured solar cells. Curr Opin Colloid Interface Sci 4:314–321

43. Karakitsou KE, Verykios XE (1993) Effects of altervalent cation doping of TiO_2 on its performance as a photocatalyst for water cleavage. J Phys Chem 97:1184–1189

44. Butler EC, Davis AP (1993) Photocatalytic oxidation in aqueous titanium-dioxide suspensions - the influence of dissolved transition-metals. J Photochem Photobiol A 70:273–283

45. Fujihira M, Satoh Y, Osa T (1982) Heterogeneous photocatalytic reactions on semiconductor-materials. 3. Effect of Ph and Cu^{2+} ions on the photo-Fenton type reaction. Bull Chem Soc Jpn 55:666–671

46. Sato S, White JM (1980) Photo-decomposition of water over $Pt-TiO_2$ catalysts. Chem Phys Lett 72:83–86

47. Sato S, White JM (1980) Photoassisted reaction of CO_2 with H_2O on $Pt-TiO_2$. Abstracts of Papers of the American Chemical Society. 179:75–COLL

48. Bahnemann D, Bockelmann D, Goslich R (1991) Mechanistic studies of water detoxification in illuminated TiO_2 suspensions. Solar Energy Mater 24:564–583

49. Pichat P, Mozzanega MN, Disdier J, Herrmann JM (1982) Pt content and temperature effects on the photocatalytic H-2 production from aliphatic-alcohols over Pt TiO_2. Nouveau J De Chimie-New J Chem 6:559–564

50. Sclafani A, Mozzanega MN, Pichat P (1991) Effect of silver deposits on the photocatalytic activity of titanium-dioxide samples for the dehydrogenation or oxidation of 2-propanol. J Photochem Photobiol A 59:181–189

51. Gopidas KR, Bohorquez M, Kamat PV (1990) Photoelectrochemistry in semiconductor particulate systems.16. Photophysical and photochemical aspects of coupled semiconductors - charge-transfer processes in colloidal Cds-TiO_2 and Cds-Agi systems. J Phys Chem 94:6435–6440

52. Duonghong D, Borgarello E, Gratzel M (1981) Dynamics of light-induced water cleavage in colloidal systems. J Am Chem Soc 103:4685–4690

53. Xia X-H, Jia Z-J, Yu Y, Liang Y, Wang Z, Ma L-L (2007) Preparation of multi-walled carbon nanotube supported TiO_2 and its photocatalytic activity in the reduction of CO_2 with H_2O. Carbon 45:717–721

54. Hurum DC, Gray KA, Rajh T, Thurnauer MC (2005) Recombination pathways in the Degussa P25 formulation of TiO_2: surface versus lattice mechanisms. J Phys Chem B 109:977–980

55. Sun B, Smirniotis PG (2003) Interaction of anatase and rutile TiO_2 particles in aqueous photooxidation. Catal Today 88:49–59

56. Iijima S (1991) Helical microtubules of graphitic carbon. Nature 354:56–58

57. Mintmire J, White C (1995) Electronic and structural properties of carbon nanotubes. Carbon 33:893–902

58. Ruoff R, Lorents D (1995) Mechanical and thermal properties of carbon nanotubes. Carbon 33:925–930

59. Bethune DS, Klang CH, de Vries MS, Gorman G, Savoy R, Vazquez J et al (1993) Cobalt-catalysed growth of carbon nanotubes with single-atomic-layer walls. Nature 363:605–607

60. Dresselhaus MS (2003) Carbon nanotubes. Carbon 33:1–2

61. Dresselhaus M (1998) New tricks with nanotubes. Nature 391:19–20
62. Frank S, Poncharal P, Wang ZL, de Heer WA (1998) Carbon nanotube quantum resistors. Science 280:1744–1746
63. Meyyappan M (2004) Carbon nanotubes: science and applications. CRC, Boca Raton
64. Tohji K, Takahashi H, Shinoda Y (1997) Purification procedure for single-walled nanotubes. J Phys Chem 101:1974–1978
65. Huang S, Dai L (2002) Plasma etching for purification and controlled opening of aligned carbon nanotubes. J Phys Chem B 106:3543–3545
66. Chiang IW, Brinson BE, Smalley RE, Margrave JL, Hauge RH (2001) Purification and characterization of single-wall carbon nanotubes. J Phys Chem B 105:1157–1161
67. Bandow S, Rao AM, Williams KA, Thess A, Smalley RE, Eklund PC (1997) Purification of single-wall carbon nanotubes by microfiltration. J Phys Chem B 101:8839–8842
68. Zhao B, Hu H, Niyogi S, Itkis ME, Hamon MA, Bhowmik P et al (2001) Chromatographic purification and properties of soluble single-walled carbon nanotubes. J Am Chem Soc 123:11673–11677
69. Wang W, Serp P, Kalck P, Faria J (2005) Visible light photodegradation of phenol on MWNT-TiO$_2$ composite catalysts prepared by a modified sol–gel method. J Mol Catal A 235:194–199
70. Carp O, Huisman CL, Reller A (2004) Photoinduced reactivity of titanium dioxide. Prog Solid State Chem 32:33–177
71. Jitianu A, Cacciaguerra T, Benoit R, Delpeux S, Beguin F, Bonnamy S (2004) Synthesis and characterization of carbon nanotubes-TiO$_2$ nanocomposites. Carbon 42:1147–1151
72. Wang W, Serp P, Kalck P, Faria J (2005) Photocatalytic degradation of phenol on MWNT and titania composite catalysts prepared by a modified sol–gel method. Appl Catal B-Environ 56:305–312
73. Zhu Z, Zhou Y, Yu H, Nomura T, Fugetsu B (2006) Photodegradation of humic substances on MWCNT/Nanotubular-TiO$_2$ composites. Chem Lett 35:890–891
74. Kuo C-S, Tseng Y-H, Lin H-Y, Huang C-H, Shen C-Y, Li Y-Y et al (2007) Synthesis of a CNT-grafted TiO$_2$ nanocatalyst and its activity triggered by a DC voltage. Nanotechnology 18:465607
75. Hu G, Meng X, Feng X, Ding Y, Zhang S, Yang M (2007) Anatase TiO$_2$ nanoparticles/carbon nanotubes nanofibers: preparation, characterization and photocatalytic properties. J Mater Sci 42:7162–7170
76. Rincón A, Pulgarin C (2003) Photocatalytical inactivation of *E. coli*: effect of (continuous-intermittent) light intensity and of (suspended-fixed) TiO$_2$ concentration. Appl Catal B-Environ 44:263–284
77. Aryal S, Kim CK, Kim K-W, Khil MS, Kim HY (2008) Multi-walled carbon nanotubes/TiO$_2$ composite nanofiber by electrospinning. Mater Sci Eng C 28:75–79
78. Yen C-Y, Lin Y-F, Hung C-H, Tseng Y-H, Ma C-CM, Chang M-C et al (2008) The effects of synthesis procedures on the morphology and photocatalytic activity of multi-walled carbon nanotubes/TiO$_2$ nanocomposites. Nanotechnology 19:045604
79. Byrappa K, Dayananda AS, Sajan CP, Basavalingu B, Shayan MB, Soga K et al (2008) Hydrothermal preparation of ZnO:CNT and TiO$_2$:CNT composites and their photocatalytic applications. J Mater Sci 43:2348–2355
80. Wang Q, Yang D, Chen D, Wang Y, Jiang Z (2007) Synthesis of anatase titania-carbon nanotubes nanocomposites with enhanced photocatalytic activity through a nanocoating-hydrothermal process. J Nanopart Res 9:1087–1096
81. Luo X, Zha C, Luther-Davies B (2005) Preparation and optical properties of titania-doped hybrid polymer via anhydrous sol–gel process. J Non Cryst Solids 351:29–34
82. Sun J, Gao L (2003) Development of a dispersion process for carbon nanotubes in ceramic matrix by heterocoagulation. Carbon 41:1063–1068
83. Zhu Z, Sun M, Guo Y, Li Y (2007) Effect of phosphorylation on peptidyl-prolyl imide bond cis/trans isomerization of peptides with xaa-pro motif. Prog Biochem Biophys 34:585–594

84. Lee S-W, Sigmund WM (2003) Formation of anatase TiO_2 nanoparticles on carbon nanotubes. Chem Commun 6:780–781
85. Ahmmad B, Kusumoto Y, Somekawa S, Ikeda M (2008) Carbon nanotubes synergistically enhance photocatalytic activity of TiO_2. Catal Commun 9:1410–1413
86. Ahmmad B, Kusumoto Y, Ikeda M, Somekawa S, Horie Y (2007) Photocatalytic hydrogen production from diacids and their decomposition over mixtures of TiO_2 and single walled carbon nanotubes. J Adv Oxidation Technol 10:415–420
87. Kedem S, Schmidt J, Paz Y, Cohen Y (2005) Composite polymer nanofibers with carbon nanotubes and titanium dioxide particles. Langmuir 21:5600–5604
88. Huey BD, Sigmund W (2007) The application of scanning probe microscopy in materials science studies. JOM 59:11–11
89. Pyrgiotakis G (2006) Titania carbon nanotube composites for enhanced photocatalysis. University of Florida
90. Pyrgiotakis G, Sigmund WM (2010) X-Ray photoelectron spectroscopy of anatase-TiO_2 coated carbon nanotubes. Solid State Phenom 162:163–177
91. Yu J, Ma T, Liu G, Cheng B (2011) Enhanced photocatalytic activity of bimodal mesoporous titania powders by C60 modification. Dalton Trans 40:6635
92. Krishna V, Noguchi N, Koopman B, Moudgil B (2006) Enhancement of titanium dioxide photocatalysis by water-soluble fullerenes. J Colloid Interface Sci 304:166–171
93. Ma W, Han D, Zhang N, Li F, Wu T, Dong X et al (2013) Bionic radical generation and antioxidant capacity sensing with photocatalytic graphene oxide–titanium dioxide composites under visible light. Analyst 138:2335–2342
94. Lee E, Hong J-Y, Kang H, Jang J (2012) Synthesis of TiO_2 nanorod-decorated graphene sheets and their highly efficient photocatalytic activities under visible-light irradiation. J Hazard Mater 219–220:13–18

Electrospun Functional Nanofibers and Their Applications in Chemical Sensors and Li-Ion Batteries

23

Il-Doo Kim, Seon-Jin Choi, and Won-Hee Ryu

Introduction to Electrospun Functional Nanofibers

One-dimensional nanobuilding blocks such as nanowires, nanotubes, and nanofibers have been widely studied due to their fascinating electronic transport characteristics, high surface-to-volume ratios, and quantum confinement effect. More recently, as one of the most efficient techniques for the realization of nonwoven fiber networks, the electrospinning method has attracted much attention. With a number of materials explored, such as polymers, metals, ceramics, and their composites, nanofiber structures with a large surface area, a high degree of porosity, and controlled surface functionalities have been prepared by the electrospinning route. Polymeric nanofibers or metal salt precursor/polymer composite fibers, which are on the order of several tens of hundreds of nanometers, are collected via the electrical charging of a suspended droplet of polymer solution with/without an inorganic precursor. During the electrospinning process, a hemispherical surface of the droplet at the end of the needle is pulled to form a Taylor cone. When the repulsive electrical force is large enough to overcome the surface tension of the Taylor cone by increasing the applied electric field, a charged jet of the solution is ejected from the Taylor cone. Subsequently, the unstable and rapid whipping jet evaporates the solvent and falls down in the shape of a thin nanofiber on the collector, as illustrated in Fig. 23.1.

In particular, metallic and metal-oxide nanofibers are easily synthesized by a subsequent heat treatment of metal salt precursor/polymer composite fibers in

I.-D. Kim (✉) • S.-J. Choi • W.-H. Ryu
Department of Materials Science and Engineering, Korea Advanced Institute of Science and Technology (KAIST), Yuseong-gu, Daejeon, Republic of Korea
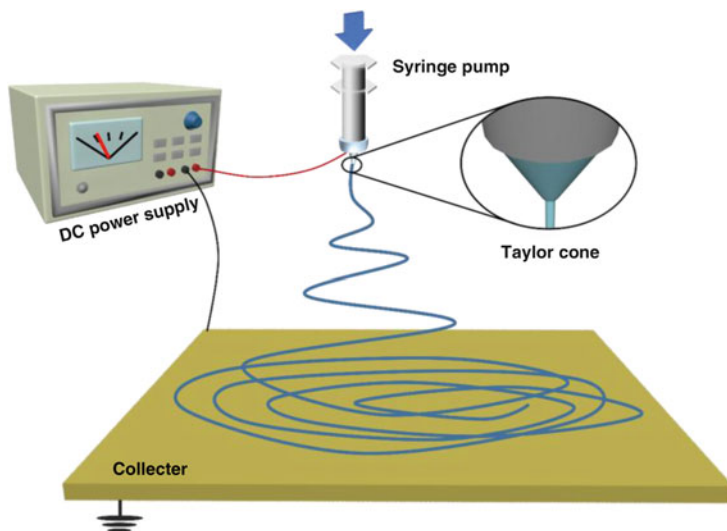e-mail: idkim@kaist.ac.kr

Fig. 23.1 Schematic illustration of electrospinning process

a reducing or oxidizing atmosphere. Thus, the phases, microstructures, and morphologies of the resulting electrospun inorganic fibers are significantly governed by key electrospinning parameters, including the needle diameter, solution feeding rate, strength of the electric field, polymer solubility/viscosity, surface tension, and dielectric constant of the solvents. Therefore, careful control of the processing parameters is very important to explore a variety of nanofiber materials with unique microstructures, such as hollow tubes as well as polycrystalline, porous, and core–shell structures.

In addition, the possibility of large-scale production via the utilization of a multi-nozzle (>10,000 pieces) system and the simplicity of the process make this process very attractive and are now opening up new commercial markets for various applications. These applications include the filtration of liquids/gases, active electrode materials for electrochemical cells, chemical sensors, nanofiber-reinforced composites, photo-electrodes for dye-sensitized solar cells, oxygen evolving catalysts and biomedical applications for enzyme immobilization, wound dressing, and in work related to tissue-engineering-based drug release. In this chapter, we address recent progress pertaining to electrospun nanofibers and their applications, which are mostly focused on chemical sensors and anode materials for Li-ion batteries.

Electrospun Chemical Gas Sensors

Several studies have undertaken the development of highly sensitive gas sensors using wide bandgap semiconducting metal oxides (SMOs) such as SnO_2, WO_3, ZnO, TiO_2, and In_2O_3 as n-type SMOs and CuO, NiO, Co_3O_4, and Cr_2O_3 as p-type SMOs. Hazardous environmental gas detection studies involving CO, CO_2, NO,

and NO$_2$ and explosive gas detection results with H$_2$ and CH$_4$ have been achieved using chemical gas sensors. In general, n-type sensing materials have been mainly utilized for chemical gas sensors due to their high electron mobility levels. Inherently, p-type SMOs possess relatively low hole conduction mobility levels (e.g., 0.2 cm^2 V^{-1} s^{-1} for NiO), which markedly hinders the rapid recognition of the electrical conductivity change when the target gases are adsorbed on gas sensing layers [1]. In chemical gas sensors, the selection and synthesis of gas sensing materials are very important because the intrinsic properties of SMOs and their morphologies can significantly affect the precise detection of analyte gases, particularly in terms of the gas sensitivity and selectivity. Gas responses are mainly involved in surface reactions of SMOs; thus, nanostructures with high surface areas and high levels of porosity have been adopted as highly sensitive gas sensing layers. More recently, besides the environmental detection of chemical gas sensors, medical applications for diagnoses of diseases via the detection of H$_2$S, acetone, toluene, and NH$_3$ in exhaled breath were introduced using SMOs.

In this part, we introduce the operating principles of gas sensors and the recent progress in the area of chemical sensor development using 1-D metal-oxide nanofibers. In addition, the microstructural evolution of 1-D metal-oxide nanofibers and the catalytic decoration effect are discussed.

Dilemmas Associated with Thin-Film Sensors

Among the various SMOs, such as ZnO, TiO$_2$, WO$_3$, and SnO$_2$, tin oxide (SnO$_2$) with a bandgap of 3.7 eV has been one of the most studied sensing materials since the 1980s due to its high carrier mobility (160 cm^2 V^{-1} s^{-1}) [1, 2]. Regarding the basic principles of gas sensing, which are governed by electrical property changes through the gas–solid interaction, sensing materials with increased surface-to-volume ratios are crucial to achieve highly sensitive gas sensors. Conventionally, thin-film and thick-film SMOs layers are prepared by RF sputtering and screen-printing and/or the drop-coating of a paste including metal-oxide particles followed by a high-temperature calcination step to eliminate binders and solvents to provide good electrical contact between the sensing layers and the substrate [3–6]. Although thin-film sensors have several advantages, such as miniaturization due to the simple microfabrication process and the capability of mass production, thin-film layers are typically very dense such that a sensing reaction between the sensing layers and target gases mainly occurs on the surface of the sensing layers, which is detrimental to the high gas response due to the limited surface reaction. With advanced synthetic methods and fabrication technologies, it is possible to explore a variety of 1-D nanobuilding blocks with very high surface-to-volume ratios. Sensing materials with 1-D nanobuilding blocks have been proposed with several synthetic methods, such as a catalyst-promoted vapor phase [7, 8], a template-assisted method [9], a hydrothermal method [10], and an electrospinning approach [11]. Among these approaches, as one of the most promising synthetic routes, the electrospinning method has been suggested.
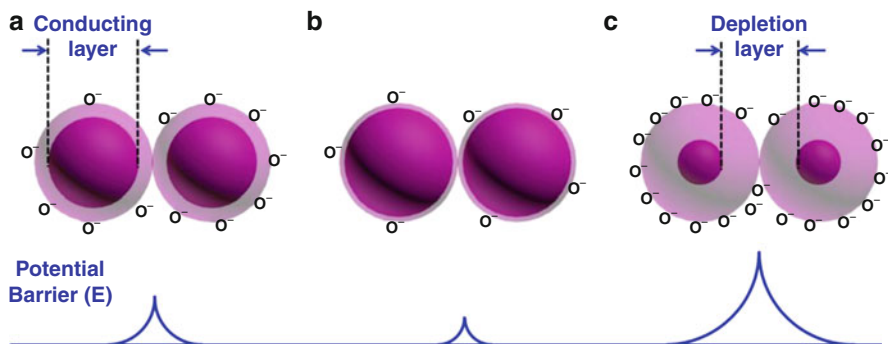
Fig. 23.2 Basic gas sensing mechanism of semiconductor metal oxide

Operating Principle

The basic principle of chemiresistive gas sensors is based on the electrical conductivity change of SMOs upon exposure to oxidizing (NO, NO_2, Cl_2) or reducing (CO, CO_2, N_2, H_2, NH_3, H_2S, CH_3COCH_3, $C_6H_5CH_3$) gases as compared to the base resistance (R_{air}) of SMOs in air. As illustrated in Fig. 23.2a, when SMOs are exposed in air at an elevated temperature, the oxygen gas in the air, which possesses a high electronegativity value, can be adsorbed on the outer surface of the SMOs. These chemisorbed oxygen molecules attract electrons from the conduction bands of SMOs and then form O_2^-, O^-, or O^{2-} species [12, 13]. As a result, an electron depletion region at the outer surface of the SMOs is formed, allowing potential barriers to be generated at the interface between two SMO particles (Fig. 23.2a). When n-type SMOs are exposed to reducing gases such as H_2 or CO, chemisorbed oxygen species can be vaporized according to the equation

$$H_2 + O^- \rightarrow H_2O + e^- \tag{23.1}$$

During this reaction, electrons which were adsorbed on oxygen gas can return to the conduction band of the SMOs, leading to an increase in the level of conductivity with the elimination of surface-adsorbed oxygen accompanied by a decreased potential barrier (Fig. 23.2b). In contrast, with exposure to oxidizing gases such Cl_2, given the high electron affinity value of Cl_2, electron depletion layers are more deeply created, resulting in a large decrease in the conductivity of SMOs (Fig. 23.2c). When an oxidizing gas is introduced to n-type SMOs, the concentration of surface-adsorbed oxygen will increase, which extends the surface space-charged region. Accordingly, potential barriers preventing an electron from passing through the SMO grains will be higher than that of its initial state, resulting in a decrease in the conductivity of the SMOs (Fig. 23.2c). P-type SMOs present precisely the opposite behavior in terms of the conductivity change when reducing and oxidizing gases are exposed. Therefore, effective thickness modulation of the electron depletion layers is a key parameter to improve the gas response characteristics.

Electrospun Semiconducting Metal-Oxide Nanofibers

Among the various fabrication methods used for 1-D nanostructures, electrospinning is very powerful and versatile route to form highly porous SMOs with 1-D nanostructures. 1-D SMOs with a variety of morphologies have been achieved by controlling electrospinning processing parameters such as the needle size and heat treatment temperature for metal salt precursor/polymer composite fibers, by induced phase separation between inorganic precursors and polymers, and by controlling the flow rates. In addition, a polymeric templating route combined with the physical vapor deposition (PVD) of metal-oxide layers has been suggested to produce hollow thin-walled structures. Figure 23.3 shows typical electrospun 1-D nanostructures which are optimized for applications in chemical sensors. Polycrystalline SnO_2 nanofibers were synthesized by a subsequent calcination step at 500 °C for 1 h, followed by the electrospinning of $Sn(Ac)_4$/poly(vinyl acetate) (PVAc, $M_w = 1,300,000$ g mol^{-1}) composite fibers (Fig. 23.3a) [14]. In addition, porous WO_3 fibers were prepared via an electrospinning route using WCl_6/polyvinylpyrrolidone (PVP, Mw = 1,300,000 g mol^{-1}) composite fibers (Fig. 23.3b) [15]. More recently, quaternary p-type metal-oxide $SrTi_{0.65}Fe_{0.35}O_{3-\sigma}$ nanofibers were successfully synthesized and used for oxygen sensors (Fig. 23.3c) [16]. Hence, by manipulating a mixed solution of various inorganic precursors and matrix polymers, one can explore a variety of n-type or p-type SMOs nanofibers with a polycrystalline nature. Polymers are easily decomposed via high-temperature calcination and thus can be used as a sacrificial template. Figure 23.3d shows thin-walled WO_3 hemitubes which were fabricated by the polymeric fiber-templating route [17]. Sacrificial fiber templates were synthesized by electrospinning, and WO_3 thin films were deposited onto polymer fibers followed by high-temperature calcination, resulting in the formation of thin-walled WO_3 hemitubes. The thickness of the WO_3 hemitubes was controlled by controlling the RF sputtering time of the WO_3 thin films. Phase separation between the inorganic precursors and the polymers often induces highly porous nanofibers because a polymer-rich domain is converted to open pores after the calcination step, as shown in the porous Zn_2SnO_4 nanofiber in Fig. 23.3e [18]. Highly porous Zn_2SnO_4 fibers showed threefold higher ethanol sensitivity as compared to conventional solid Zn_2SnO_4 fibers. Thin-wall assembled SnO_2 tubes with a number of elongated pores were synthesized via electrospinning controlled by the variation of the flow rate (Fig. 23.3f) [19]. Highly porous SnO_2 tubes showed a fivefold higher acetone response compared to dense SnO_2 fiber in a humid atmosphere similar to an oral cavity. An accurate detection of acetone in exhaled breath provides useful information for the real-time diagnosis of diabetes [19]. In the following section, we discuss the effects of processing parameters.

Hollow Metal-Oxide Nanofibers

SMOs with a large surface area and high porosity can enhance the gas response because the reaction between the gas molecules and the sensing layers mainly occurred on the surface of the SMOs. Thus, several promising approaches have been proposed to increase the surface area of 1-D SMOs nanostructures further.
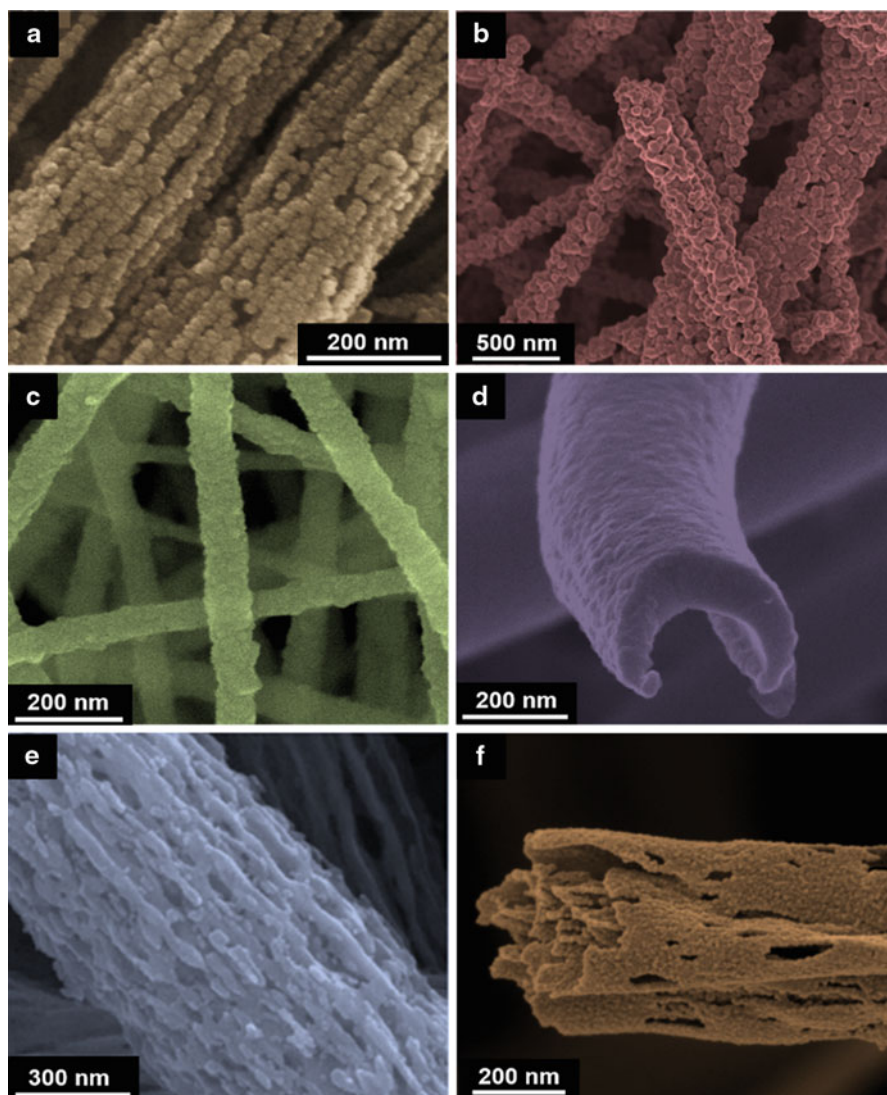
Fig. 23.3 1-D metal-oxide nanostructures synthesized by electrospinning routes: (**a**) SnO_2 nanofibers (Reprinted with permission from Ref. [14]. Copyright (2010), Springer). (**b**) WO_3 nanofibers (Reprinted with permission from Ref. [15]. Copyright (2012), Springer). (**c**) $SrTi_{0.65}Fe_{0.35}O_{3-\sigma}$ nanofibers (Reprinted with permission from Ref. [16]. Copyright (2012), Wiley). (**d**) Hollow WO_3 hemitube (Reprinted with permission from Ref. [17]. Copyright (2012), American Chemical Society). (**e**) Porous Zn_2SnO_4 nanofiber (Reprinted with permission from Ref. [18]. Copyright (2011), Royal Society of Chemistry). (**f**) Thin-wall assembled SnO_2 fiber. (Reprinted with permission from Ref. [19]. Copyright (2012), Wiley)

For example, hollow and porous SMO nanofibers were synthesized using modified electrospinning by controlling (i) the induced phase separation between the inorganic precursor and polymer [20–24], (ii) a co-electrospinning approach using dual spinnerets [25–27], and (iii) a polymeric templating route combined with physical- and chemical-vapor deposition [17, 28–34].

(i) Induced Phase Separation

To induce phase separation between an inorganic precursor and a polymer, processing parameters such as the ratio of the inorganic precursor and polymer, the annealing temperature, and the effectiveness of the solvent evaporation process should be optimized. As one example, a hollow tube structure can be formed by controlling the relative ratio between the inorganic precursor and polymer as well as the subsequent annealing temperature followed by electrospinning. At a certain compositional ratio between the inorganic precursor and polymer, phase-separated fibers can be formed, leading to core–shell structures. In the core and shell of electrospun fibers, polymers and inorganic precursors predominantly exist due to the induced phase separation between the inorganic precursor and polymer. In addition, an appropriate annealing temperature is important to achieve hollow nanotubes. At exceedingly low and high temperatures, solid nanowire structures form. Meanwhile, a nanotube structure can be formed at appropriate temperatures when the reaction rate in the inner site of the fibers is faster, resulting in the expansion of the inner particles.

Effective solvent evaporation during the electrospinning process can also produce a hollow nanotube structure, as shown in Fig. 23.4 [24]. A ZnO hollow nanofiber was achieved by rapid solvent evaporation assisted by distilled water and ethanol. Distilled water can induce ionization between the Zn^{2+} and Ac^- of $Zn(Ac)_2 \cdot 2H_2O$, and ethanol promotes solvent evaporation and phase separation between Zn^{2+} and a polymer (PVP), which forms an inner polymer (PVP) and outer Zn^{2+}-rich region (Fig. 23.4a). After high-temperature calcination, the inner polymer decomposes, and the outer Zn^{2+} precursors are oxidized, resulting in the formation of hollow ZnO tubes (Fig. 23.4b, c).

Hollow ZnO nanotubes showed higher responses (the gas response of acetone at 100 ppm = 67.7 at 220 °C) while maintaining a reduced optimum operating temperature compared to that (gas response of acetone at 100 ppm = approx. 20 at 270 °C) of solid ZnO nanofibers (Fig. 23.4d). Highly selective detection for acetone gas was also investigated with a minor response toward the other gases, i.e., ethanol, toluene, methanol, CO, NO_2, NH_3, and CH_4 (Fig. 23.4e). Besides simple binary nanotubes, multiple composite hollow nanotubes using an induced phase separation method have been explored, such as SnO_2-ZnO for toluene [21] and In_2O_3-CeO_2 for H_2S and acetone sensing [23].

(ii) Co-electrospinning Route

A hollow nanotube can be synthesized by co-electrospinning using coaxial jets, as illustrated in Fig. 23.5 [26]. The basic principle of co-electrospinning is to use of two immiscible liquids through two-capillary spinneret. Two viscous liquids were loaded into the inner (core of mineral oil) and outer (shell of polyvinyl pyrrolidone (PVP)/Ti $(OiPr)_4$) capillaries (Fig. 23.5a). Then, while applying high voltage between the metallic needle and the collector in a process identical to that of conventional
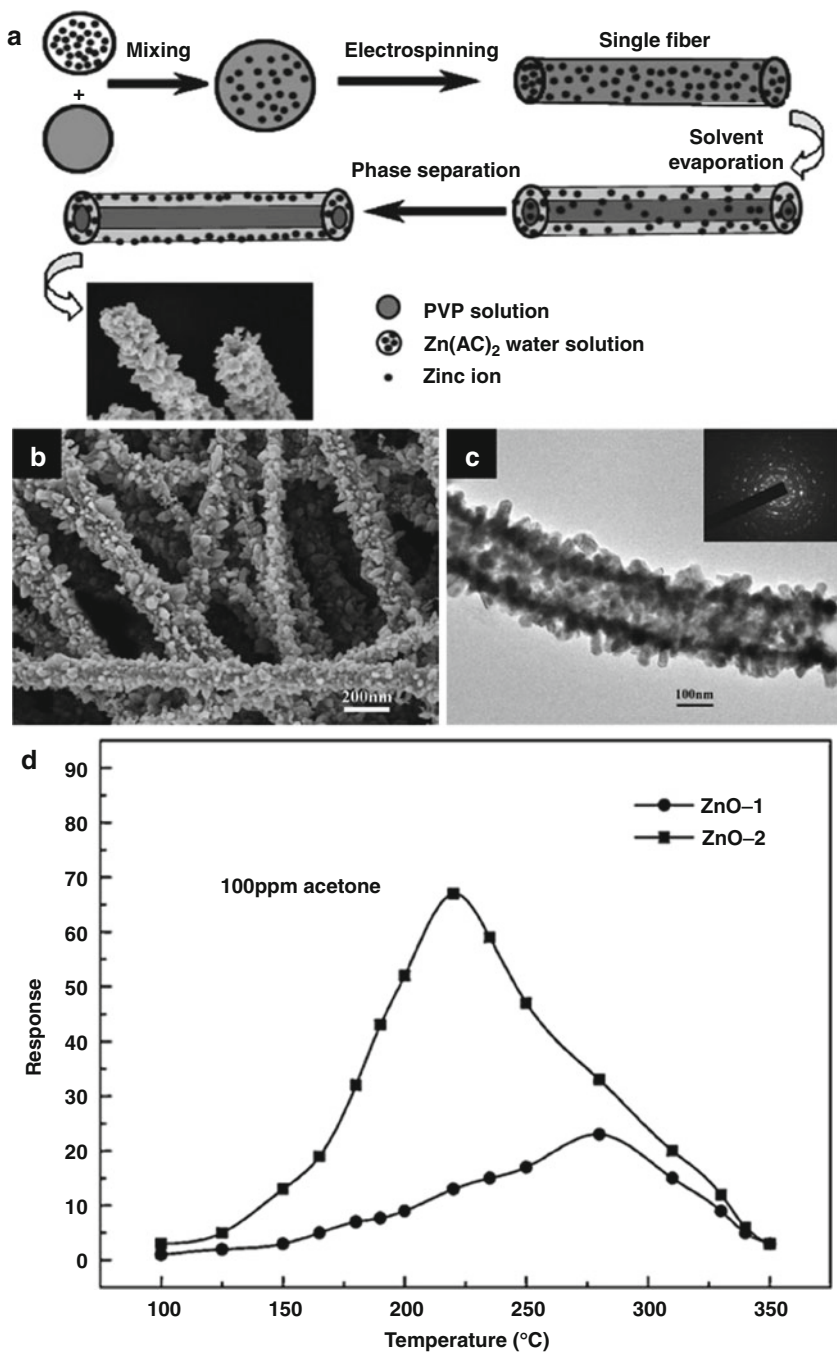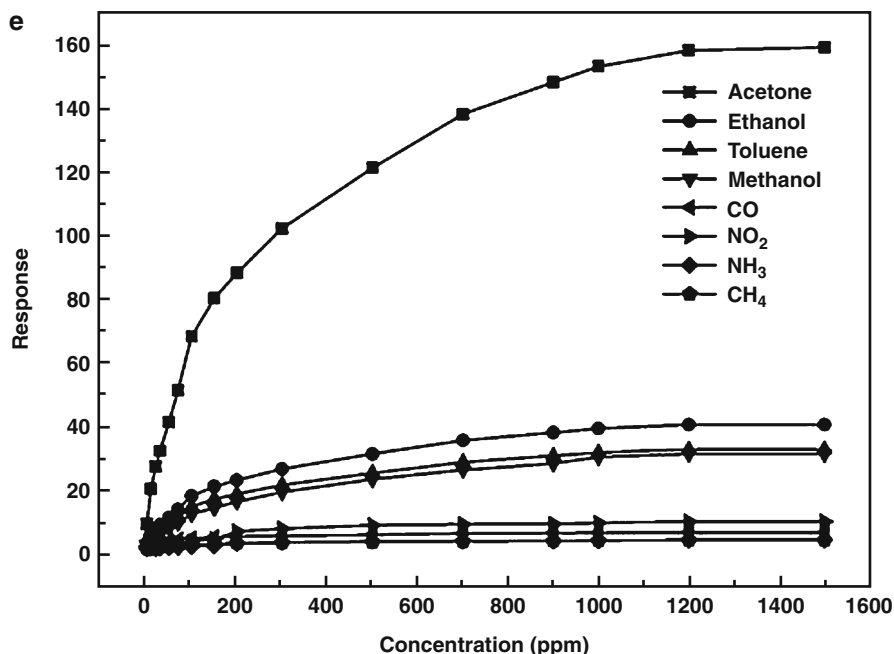
Fig. 23.4 (continued)

Fig. 23.4 (**a**) Schematic illustration of hollow ZnO nanotube formation, (**b**) SEM image of the fabricated hollow ZnO nanotubes, (**c**) TEM image of a hollow ZnO nanotube, (**d**) acetone response of solid ZnO nanofibers (ZnO-1) and hollow ZnO nanotubes (ZnO-2) in the temperature ranges of 100–350 °C with 100 ppm of acetone, and (**e**) selective sensing characteristics of hollow ZnO nanotubes with a variety of target gases with a gas concentration range of 1–1,500 ppm at 220 °C (Reprinted with permission from Ref. [24]. Copyright (2011), Elsevier)

single-nozzle electrospinning, nanofibers were formed with a core (mineral oil)–shell (PVP/Ti(OiPr)$_4$) structure. Finally, PVP and mineral oil were decomposed and crystallized TiO$_2$ was formed by a high-temperature calcination process, thus resulting in a thin-walled TiO$_2$ nanotube (Fig. 23.5b). The diameter of the hollow nanofibers can be modulated by control of the feeding rate of the core (oil) phase. The fundamental mechanism of forming a hollow nanotube structure by co-electrospinning is the viscous dragging and/or contact friction force, which stretch the inner oil core. The electrospinning of the shell solution is mainly accomplished by electrostatic repulsion between the metallic needle and the collector, as in conventional electrospinning. On the other hand, the inner oil phase was stretched by the sheer stress applied by the shell solution during elongation. Hollow TiO$_2$ nanofibers and heterostructured hollow NiO-ZnO nanotubes were fabricated by co-electrospinning for the detection of CO [25] and H$_2$S [27], respectively.

(iii) Polymeric Fiber-Templating Route

Not only the direct formation of hollow nanotube structures by electrospinning but also an electrospinning process combined with PVD process can lead to hollow nanofibers [30]. Polymeric nanofibers as a sacrificial template were produced by an
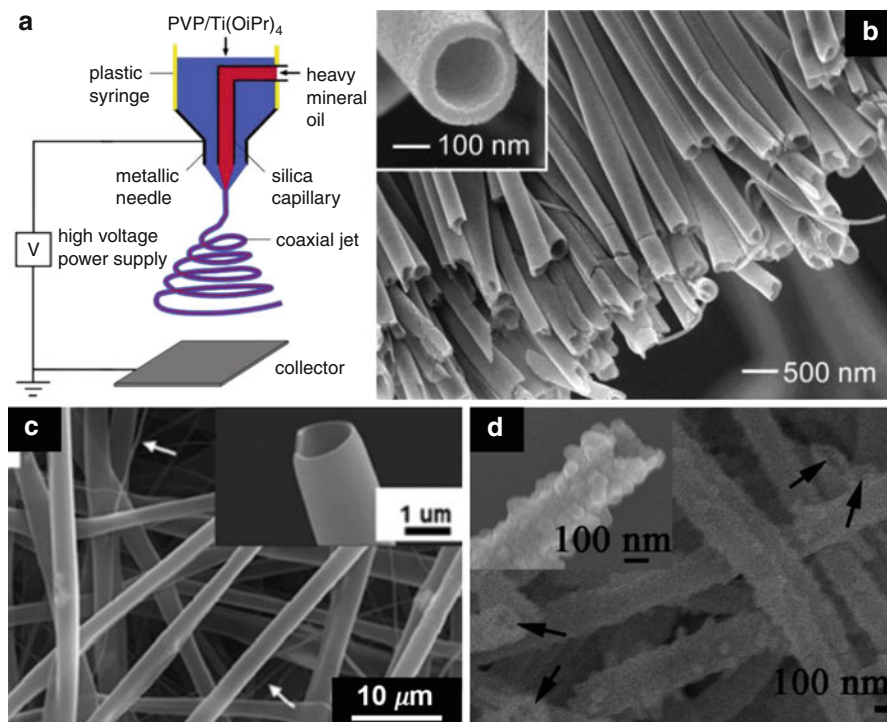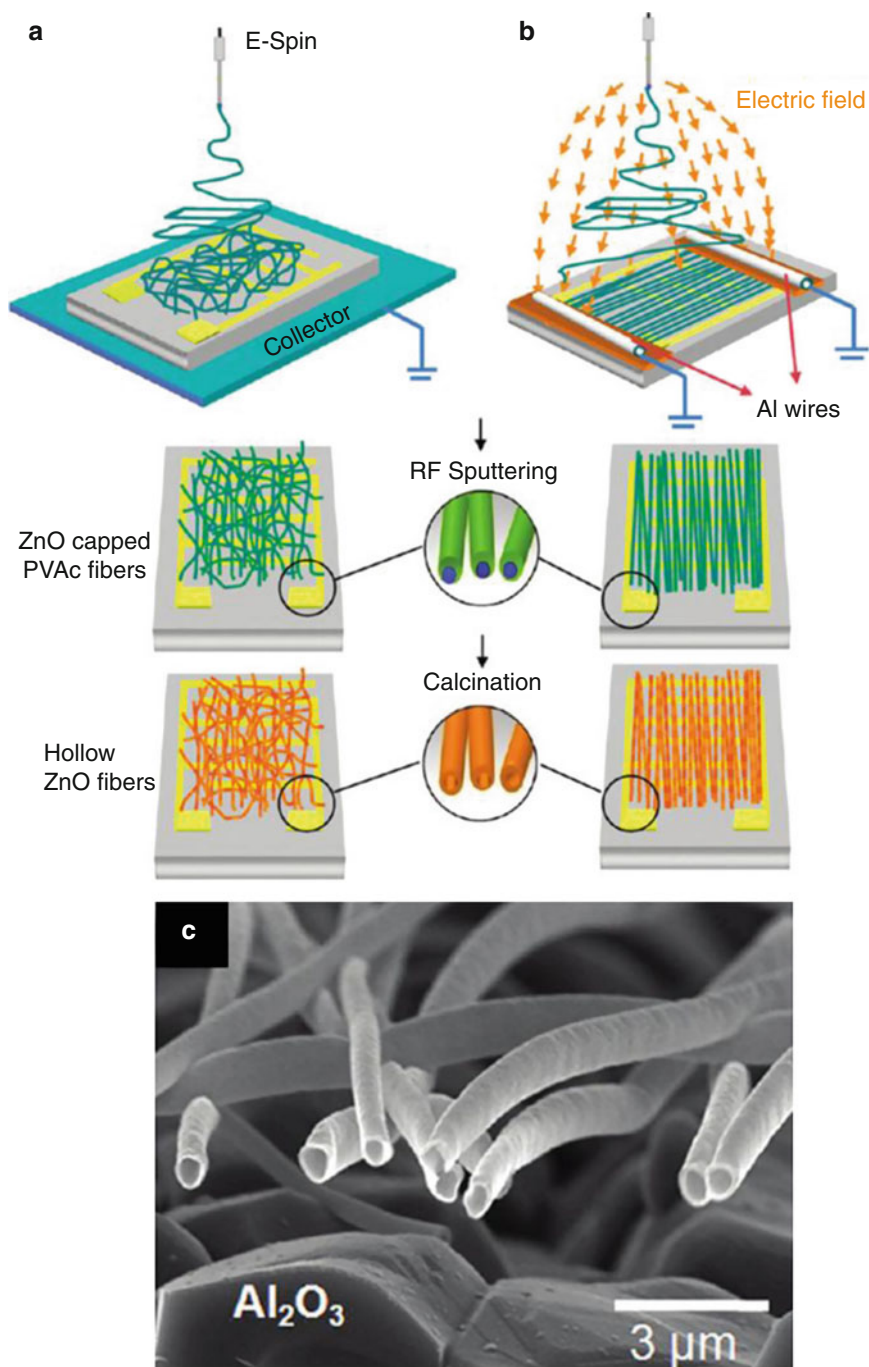
Fig. 23.5 (**a**) Schematic illustration of the co-electrospinning method. (**b**) SEM image of an aligned array of hollow TiO$_2$ nanofibers (Reprinted with permission from Ref. [26]. Copyright (2004), American Chemical Society). (**c**) Hollow TiO$_2$ fibers prepared by coaxial electrospinning for CO detection (Reprinted with permission from Ref. [25]. Copyright (2011), Elsevier). (**d**) NiO-ZnO heterostructured hollow nanotubes for H$_2$S detection (Reprinted with permission from Ref. [27]. Copyright (2012), American Chemical Society)

electrospinning process, as illustrated in Fig. 23.6a, b. Here, the polymeric nanofibers were collected both in the form of nonwoven fibers and quasi-aligned fibers. Then, ZnO was deposited on the polymeric fiber template using RF sputtering, which forms ZnO (shell)-coated polymer nanofibers (core). Finally, hollow ZnO nanofibers were obtained through high-temperature calcination. During the calcination process, the inner core polymer was decomposed and the outer shell of ZnO was further oxidized into crystallized ZnO while forming hollow nanotubes (Fig. 23.6c). For the close observation of the hollow ZnO nanotubes, a focused ion beam (FIB) was utilized (Fig. 23.6d). It was found that the fabricated hollow ZnO nanotubes showed elliptical tubular cross sections with asymmetric wall thicknesses. The top wall was the thickest part, 105–107 nm, with a thinner thicknesses at the sidewalls (80–85 nm) and the thinnest part at the bottom side (37–47 nm). The asymmetric wall thicknesses were attributed to the hydrodynamics of the fluxes of the Zn^{2+} and O^{2-} ions sputtered from the ZnO target, considering the partial shadow effect introduced by the 3-D structure of the polymeric fibers. The critical advantage
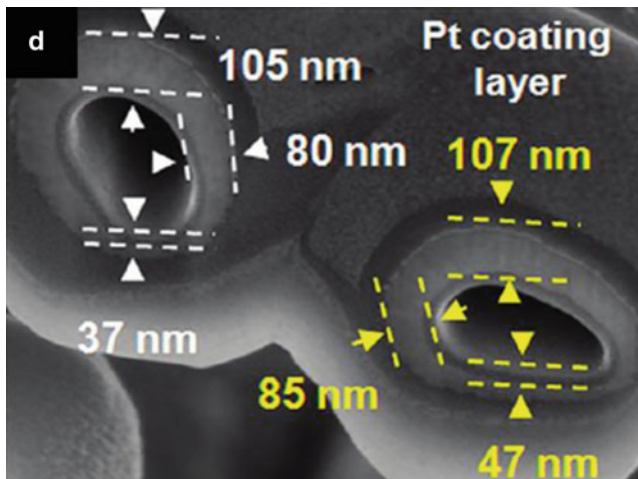
Fig. 23.6 (continued)

Fig. 23.6 Schematic illustration of the fabrication of hollow ZnO nanofibers: (**a**) random networks and (**b**) quasi-aligned networks, (**c**) SEM image of hollow ZnO nanofibers on an Al_2O_3 substrate, and (**d**) focused ion beam (*FIB*) cross-sectional observation of hollow ZnO nanofibers (Reprinted with permission from Ref. [30]. Copyright (2009), American Chemical Society)

when fabricating hollow nanotubes using an electrospun fibrous template with the PVD method is the relatively free selection of materials. A variety of hollow tubular structures can be formed by simply changing the sputtering target material.

Three different samples were prepared to identify the NO_2 sensing characteristics: a random type, a quasi-aligned type of hollow ZnO nanofibers, and ZnO thin film. During the sensing characterization process, the sensitivity (R/R_0) was monitored when NO_2 gas was exposed to the samples with concentration ranges of 2–10 ppm at a temperature of 350 °C (Fig. 23.7). It was distinctively revealed that the hollow ZnO nanotubes were more sensitive to NO_2 gas as compared to the ZnO thin film. Hollow ZnO nanotubes showed a stable response down to 2 ppm, while the thin ZnO film did not respond below 8 ppm with low sensitivity at a higher concentration of NO_2 compared to the hollow ZnO nanofibers. The higher sensitivity of the hollow ZnO nanotubes was attributed to the increased oxygen adsorption sites on the surface, which resulted in the high resistivity changes compared to thin ZnO film. It is important to note that quasi-aligned hollow ZnO nanofibers showed approximately twofold higher sensitivity than random hollow ZnO nanofibers. The sensitivity enhancement of the quasi-aligned fibers most likely resulted from the improved gas transport properties and the more distinctive 1-D characteristic of the electronic transport along the aligned fibers compared to random counterparts. This demonstrated that the alignment technique can significantly improve the gas sensitivity.

Hollow nanotubes with an open tubular structure, i.e., a hemitube shape, were demonstrated using a RF-sputtered WO_3-coated electrospun polymeric fiber template followed by high-temperature calcination [17]. When the deposition time is not long enough to cover the bottom side, a hemitube structure can be obtained
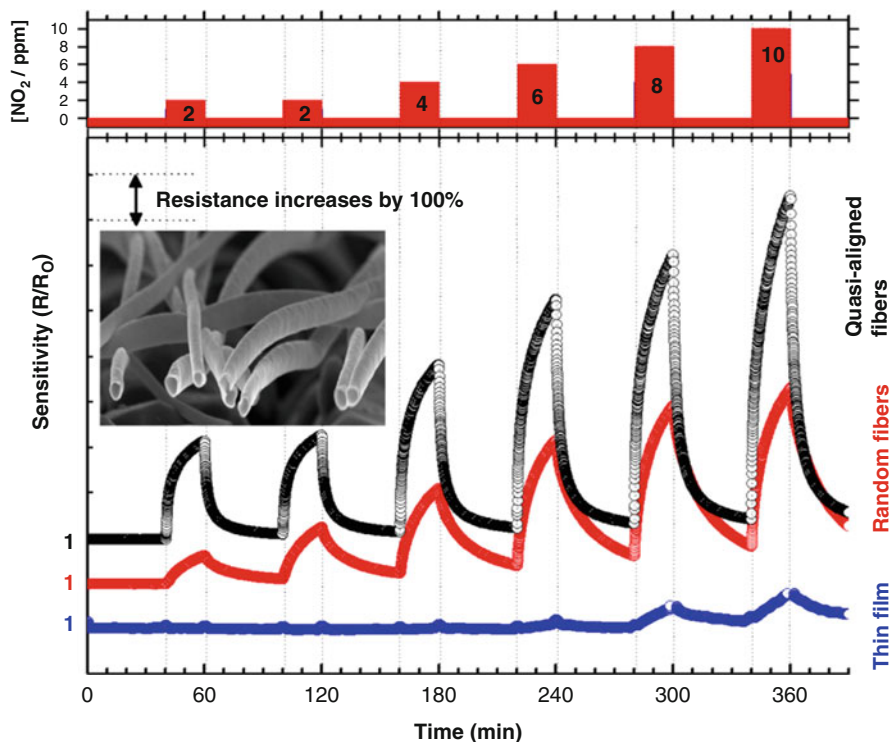
Fig. 23.7 The resistance response R/R_0 during cyclic exposure to increasing NO_2 concentrations at 350 °C of sensors composing a network of nonaligned (*red*) or quasi-aligned hollow ZnO fibers (*black*) with a reference ZnO thin-film sensor (*blue*) (Reprinted with permission from Ref. [30]. Copyright (2009), American Chemical Society)

after decomposing the inner polymer templates. It was noted that the wall thickness can be easily controlled by varying the deposition time. Here, a longer deposition time could form WO_3 hemitubes with a relatively thick (121 nm) top wall thickness compared to WO_3 hemitubes having a thinner top wall thickness (58.6 nm), as obtained by the shorter deposition time (Fig. 23.7a, b). A detailed structural investigation was undertaken by a TEM analysis in which the hemitubular nature of the thin-walled WO_3 films was clearly verified (Fig. 23.7c).

To verify the volatile organic compound sensing characteristics via the detection of H_2S, a gas sensing test was performed in a highly humid atmosphere (85 RH%). Hollow WO_3 hemitubes having a thick top wall thickness (121 nm) and a thin top wall thickness (58.6 nm) were prepared to compare the H_2S sensing performance levels (Fig. 23.8a–c). WO_3 nanoparticles were also tested as a reference (Fig. 23.8d). Hollow WO_3 hemitubes having a thin top wall thickness showed the highest response among the test samples with stable response down to 120 ppb (Fig. 23.8d). The gas response (R_{air}/R_{gas} at 2 ppm H_2S) of the 58.6 nm thick WO_3 hemitubes was 6.76, which indicates 1.94 and 2.72 times higher

responses than those of the 121 nm thick WO_3 hemitube- and WO_3 nanoparticle-based sensors, respectively. The increased H_2S responses of the hollow WO_3 hemitubes were mainly due to the increased surface area (approximately π times) compared to the dense thin films, leading to an enhanced surface reaction of the hemitube structure through its accommodation of a large number of O^- adsorption sites. The selective sensing characteristics were investigated with H_2S,
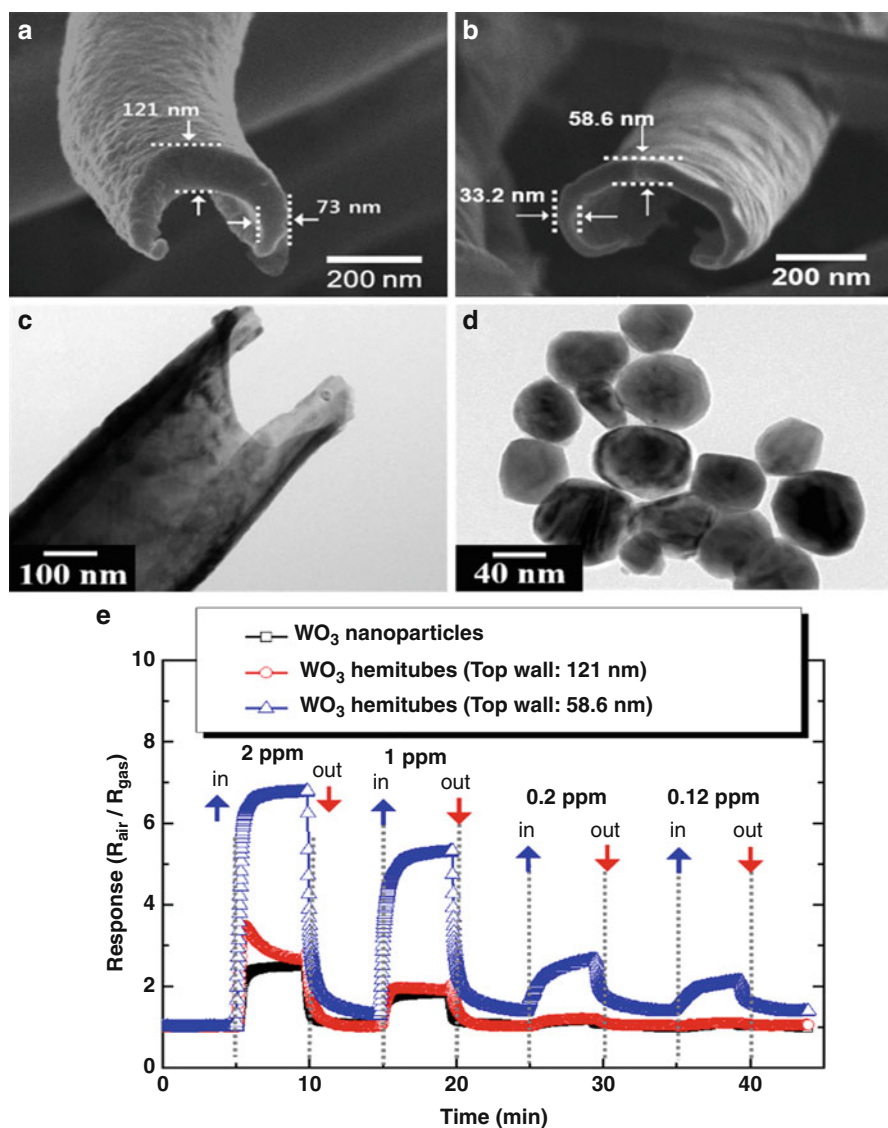

Fig. 23.8 (continued)
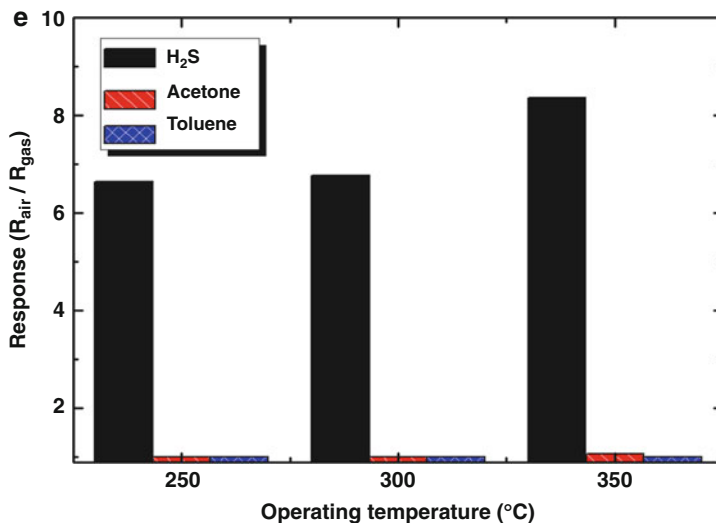
Fig. 23.8 SEM image of WO$_3$ hemitubes with different top wall thicknesses of (**a**) 121 nm and (**b**) 58.6 nm. (**c**) TEM image of a WO$_3$ hemitube, (**d**) gas response (R$_{air}$/R$_{gas}$) toward H$_2$S with gas concentration ranges of 0.12–2 ppm at a temperature of 300 °C, and (**e**) gas response (R$_{air}$/R$_{gas}$) of WO$_3$ hemitubes with a top wall thickness of 121 nm toward H$_2$S, acetone, and toluene in the temperature range of 250–350 °C (Reprinted with permission from Ref. [17]. Copyright (2012), American Chemical Society)

acetone, and toluene gases in the temperature range of 250–350 °C (Fig. 23.8e). The result revealed that highly selective H$_2$S-sensing performance was achieved in a wide operating temperature range.

Micro-Phase Separation-Assisted Porous Metal-Oxide Nanofibers

Highly porous fibers can be achieved by controlling various factors such as the miscibility of the polymer [35–37], the humidity [38], the liquid–liquid miscibility [39, 40], the phase-separation-inducing agent [41], the solubility difference between the precursors and polymers [42, 43], and the use of volatile solvents [44, 45]. Among these measures, micro-phase separation electrospinning via flow rate control is one of the simplest and most versatile methods for fabricating very highly porous surfaces of nanofibers with large pore distributions [19].

Controlling the flow rate of the solvents during the electrospinning process can generate a porous surface with a large pore distribution. Components consist of tin (IV) acetate, poly(vinyl acetate) (PVAc, M$_w$ = 500,000 g mol^{-1}), DMF, and acetic acid with the generation of poor compatibility between tin (IV) acetate and PVAc in the DMF solvent to create porous structures after the oxidation of the Sn precursor and the decomposition of immiscible polymers. The flow rates of the successive electrospinning steps were adjusted to 5 μL min^{-1}, 15 μL min^{-1}, and 25 μL min^{-1}. The as-spun fibers produced with a low flow rate (5 μL min^{-1}) showed a smooth surface morphology with homogeneously mixed polymers and tin precursors

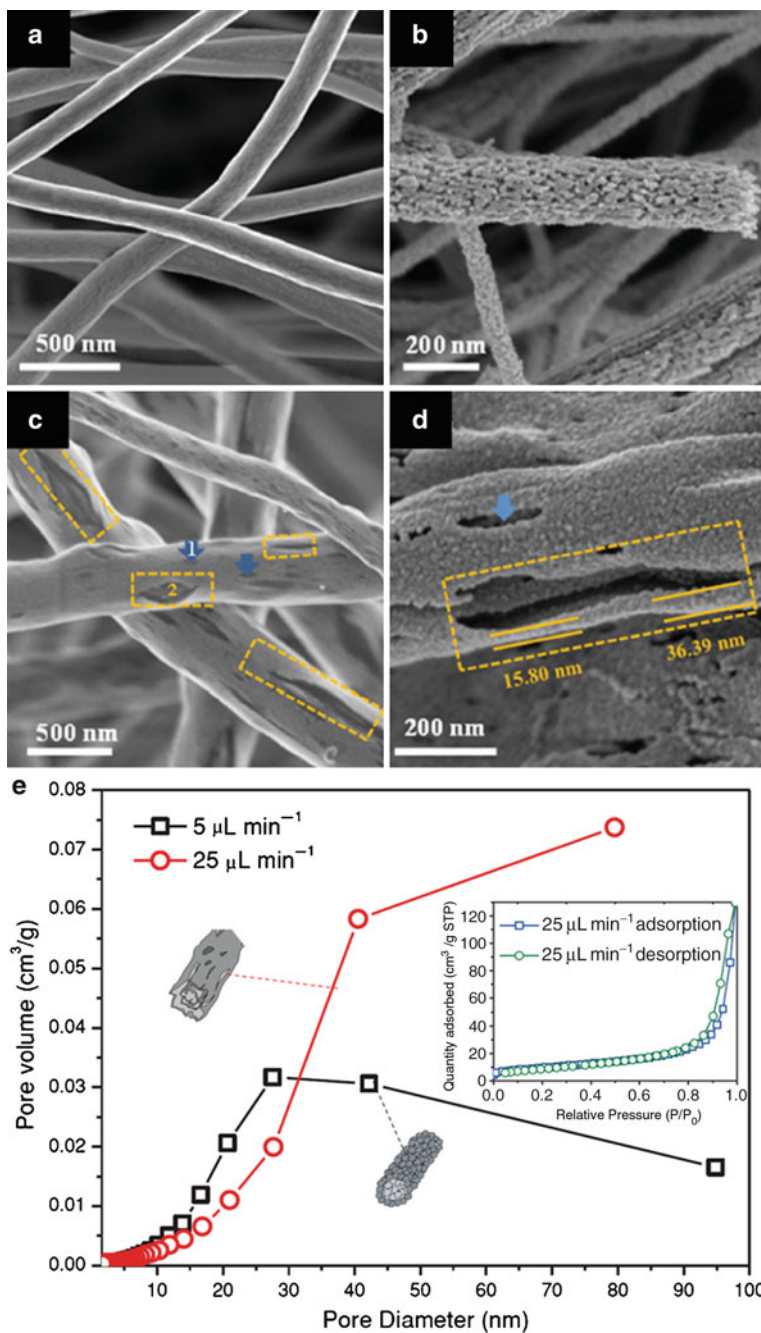**Fig. 23.9** (**a**) SEM image of as-spun fibers prepared at a low flow rate (5 μL min^{-1}), (**b**) SEM image of fibers calcined at 500 °C showing (**a**) densely packed SnO$_2$ fibers, (**c**) SEM image of

inside (Fig. 23.9a). On the other hand, a wide range of carved valleys was observed on the as-spun fibers prepared at high flow rates (25 $\mu L \ min^{-1}$), as shown in Fig. 23.9c. After high-temperature calcination, highly porous SnO_2 fibers having elongated open pores and consisting of large voids between the inner walls were obtained (Fig. 23.9d). Fibers produced with a low flow rate showed a densely packed fibrous surface consisting of small SnO_2 grains (Fig. 23.9b). As shown in Fig. 23.9e, the densely packed SnO_2 fibers contained mesopores that were mainly distributed in the range of 10–30 nm which originated mainly from the small SnO_2 nanoparticles. In contrast, the pore distribution of thin-wall assembled SnO_2 fibers mainly existed on a larger scale ($>$30 nm), which can be understood by the elongated open pores and large voids between the walls inside the fibers. The thin-wall assembled SnO_2 fibers showed a higher response to acetone gas with stable response characteristics at a low concentration of acetone compared to densely packed SnO_2 fibers (Fig. 23.10). The thin-wall assembled SnO_2 fibers showed a fivefold higher acetone response ($R_{air}/R_{gas} - 1 = 6.12$ at 3 ppm) compared to that (1.22 at 3 ppm) of densely packed SnO_2 fibers. The increased response of the thin-wall assembled SnO_2 fibers can be explained by the enhanced reaction kinetics on the SnO_2 surface due to the high porosity and additional diffusion pathways.

Phase separation between two types of inorganic precursors, i.e., $Zn(OAc)_2$-$Sn(OAc)_4$ and polymer, i.e., PVAc, induced highly porous Zn_2SnO_4 nanofibers with a lotus-root-like morphology (Fig. 23.11a) [18]. Various small pores were distributed in the Zn_2SnO_4 fibers. In contrast, densely packed Zn_2SnO_4 fibers with a smooth surface were synthesized with the $Zn(OAc)_2$-$Sn(OAc)_4$ precursor and PVP composites followed by an identical calcination procedure (Fig. 23.11b). The distinctive morphology change was ascribed to the immiscible behavior between the Zn-Sn precursor and the polymer. A Zn-Sn precursor-rich domain and a PVAc-rich domain were effectively separated, and the PVAc-rich domain was converted to voids after the calcination step, which resulted in highly porous Zn_2SnO_4 fibers. On the other hand, the better miscibility of the Zn-Sn precursor/PVP composites led to dense Zn_2SnO_4 fibers.

The gas responses (R_{air}/R_{gas}) were investigated using porous and dense Zn_2SnO_4 fibers at an operating temperature of 450 °C with 100 ppm of H_2, CO, and C_2H_5OH (Fig. 23.11c). Markedly enhanced C_2H_5OH sensing characteristics ($R_a/R_g = 300$) were presented with porous Zn_2SnO_4 fibers compared to that ($R_a/R_g = 80$) of a dense sample. The increased C_2H_5OH response was attributed to the large surface area (29.02 $m^2 \ g^{-1}$) and highly porous structure of the sample compared to the sample (11.06 $m^2 \ g^{-1}$) with the dense structure, thus enabling facile gas penetration into the fibers and an effective surface reaction. In addition, highly selective properties were revealed with negligible responses toward H_2 and CO (Fig. 23.11c).

Fig. 23.9 (continued) as-spun fibers prepared at a high flow rate (25 $\mu L \ min^{-1}$), (**d**) SEM image of fibers calcined at 500 °C showing (**c**) highly porous with thin-wall assembled SnO_2 fibers, and (**e**) Brunauer–Emmett–Teller (*BET*) measurement to determine the pore volume distribution of densely packed SnO_2 fibers (5 $\mu L \ min^{-1}$) and thin-wall assembled SnO_2 fibers (25 $\mu L \ min^{-1}$) (Reprinted with permission from Ref. [19]. Copyright (2012), Wiley)

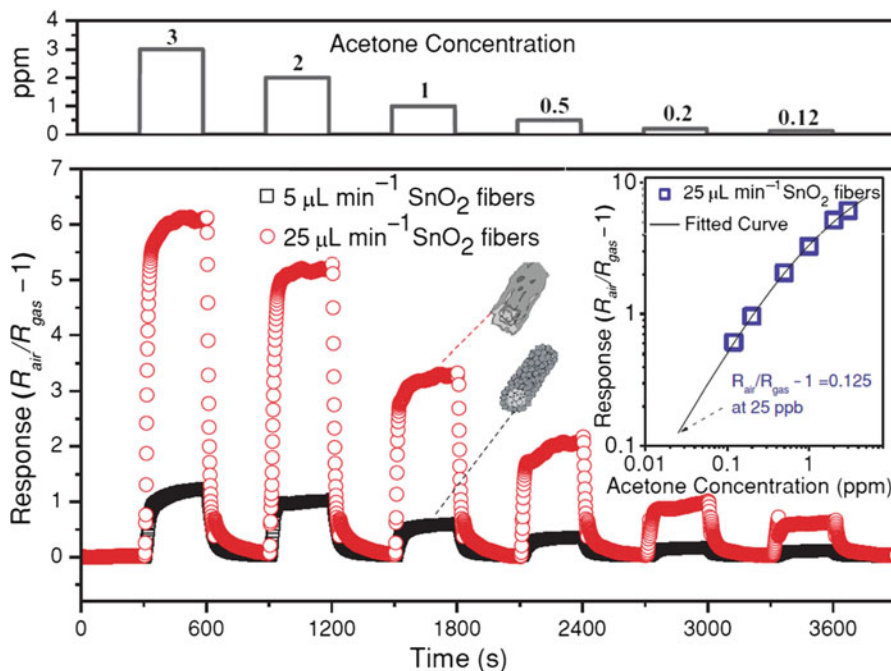**Fig. 23.10** Morphological effect on the acetone sensing characteristic using SnO_2 fibers with densely packed SnO_2 fibers (5 μL min^{-1}) and thin-wall assembled SnO_2 fibers (25 μL min^{-1}). The limit of detection of acetone using thin-wall assembled SnO_2 fibers showed that a response (R_{air}/R_{gas} − 1) of 0.125 was anticipated with an acetone concentration of 25 ppb. The acetone gas was introduced from 3 to 0.12 ppm with a stabilized temperature of 400 °C in an atmosphere with a relative humidity of 80 % (Reprinted with permission from Ref. [19]. Copyright (2012), Wiley)

Electrospun Semiconducting Metal-Oxide Nanofibers with Catalytic Additives

Catalytic addictive decoration on the sensing materials was feasibly applied in SMOs, and the sensing performances were evaluated. From the catalytic additive effect on the sensing performance, enhanced sensitivity and improved selectivity were achieved [17, 46]. In addition, reduced operating temperatures with maximum response to a target gas were also identified [15, 47, 48]. Thus far, a number of catalysts have been employed, such as noble metals, i.e., Pt, Pd, Ru, Au, and Ag, or metal/metal oxides such as Co, Co_3O_4, Cu, Al, and NiO as well as even graphene-based materials. The roles of catalytic additives differ depending on the individual catalyst, and several roles come into effect simultaneously regarding the effect on the sensing characteristics. One dominant role of the catalytic additive effect is grain size control [49–51]. As shown in Fig. 23.12a, the reduced grain size of SnO_2 promoted the gas responses to H_2 and CO, which resulted from the increased electron depletion region. This grain size effect on the sensing performance is generally true for all SMOs as well as SnO_2. It is also known that some additives
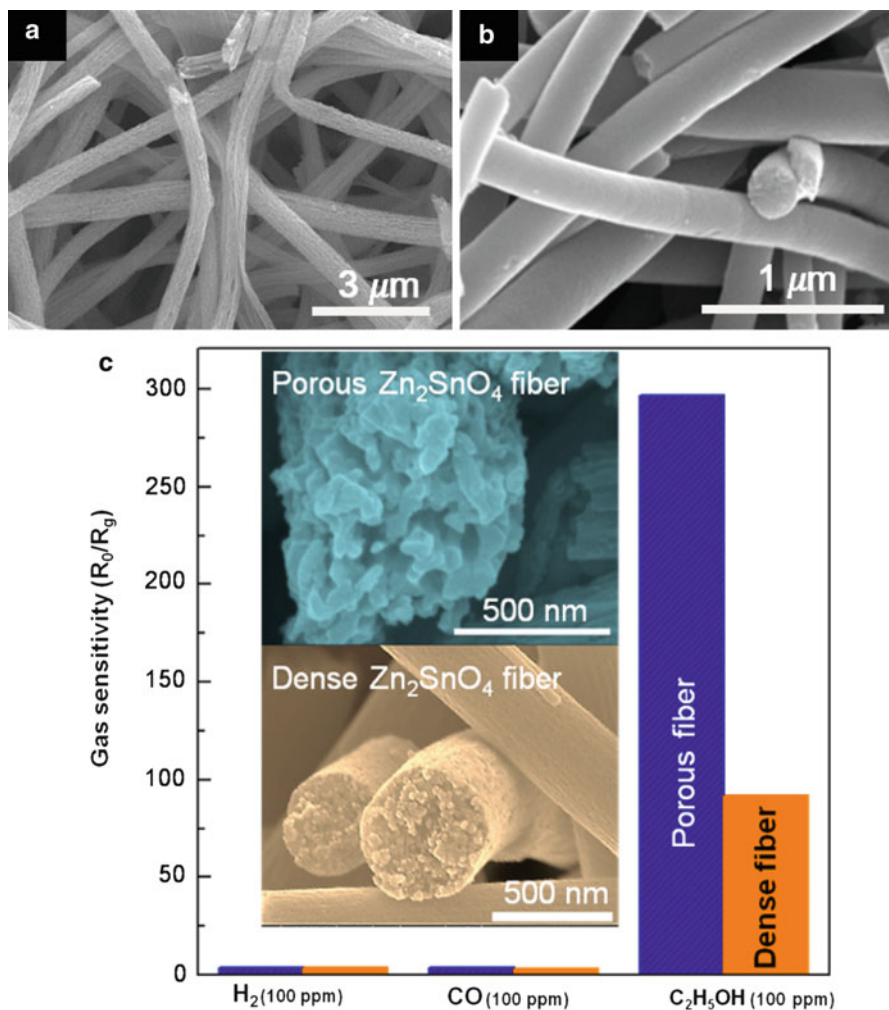
Fig. 23.11 (**a**) SEM image of Zn_2SnO_4 fibers calcined at 700 °C (reference, PVP matrix), (**b**) SEM images of Zn_2SnO_4 fibers calcined at 700 °C (PVAc matrix), (**c**) gas responses to 100 ppm of CO, H_2, and C_2H_5OH at an operating temperature of 450 °C (Reprinted with permission from Ref. [18]. Copyright (2011), Royal Society of Chemistry)

maintain a very small crystal size, whereas others accelerate the grain growth, as shown in Fig. 23.12b. With the stabilized crystal size under high-temperature calcination, additive-impregnated SnO_2 can be prepared with a high mechanical strength and with a reduced crystal size, resulting in a highly sensitive sensor. The crystal size effect on the gas sensitivity toward 800 ppm H_2 was investigated with a number of additives impregnated with SnO_2 at temperatures of 300 °C and 400 °C (Fig. 23.12c). A catalytic additive can be decorated either by mechanically mixing
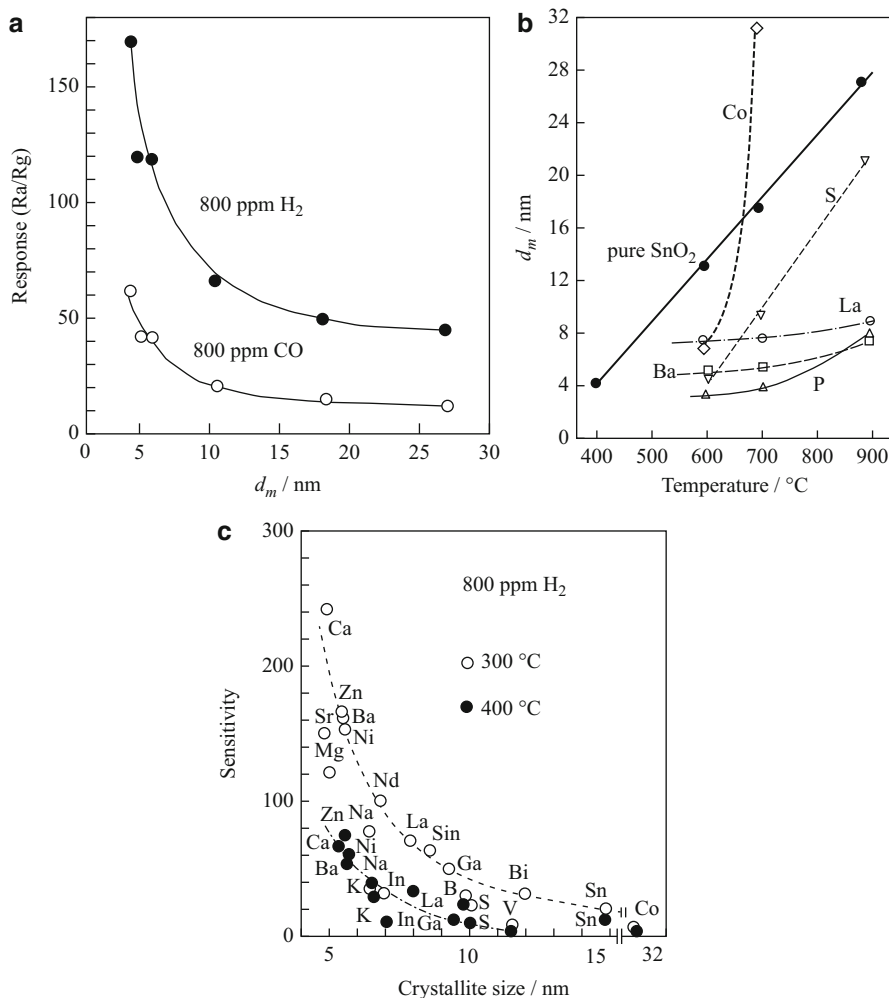
Fig. 23.12 (**a**) Grain size effect on the sensing response (R_a/R_g) to 800 ppm H_2 and 800 ppm CO at 300 °C, (**b**) grain size of pure SnO_2 and foreign additive-impregnated SnO_2 after calcination at various temperatures, and (**c**) gas sensitivity of additive-impregnated SnO_2 toward 800 ppm H_2 at 300 °C and 400 °C (Reprinted with permission from Ref. [49]. Copyright (1991), Elsevier)

with electrospun fibers in the form of nanoparticles or by dissolving into a solvent for electrospinning in the form of a catalytic precursor. The former method includes Pt-functionalized WO_3 hemitubes and Pt-functionalized SnO_2 nanofibers, as shown in Fig. 23.13a, b. In this case, the catalyst can be decorated on the surface of the SMOs. In the latter case, the catalytic precursor can be imbedded into the electrospun fibers as well as precipitated on the surface. After the calcination process, electrospun fibers with reduced crystal sizes and oxidized catalysts were observed, most likely enhancing the gas sensing performance [50–52]. One example is Pd-loaded SnO_2 nanofibers,
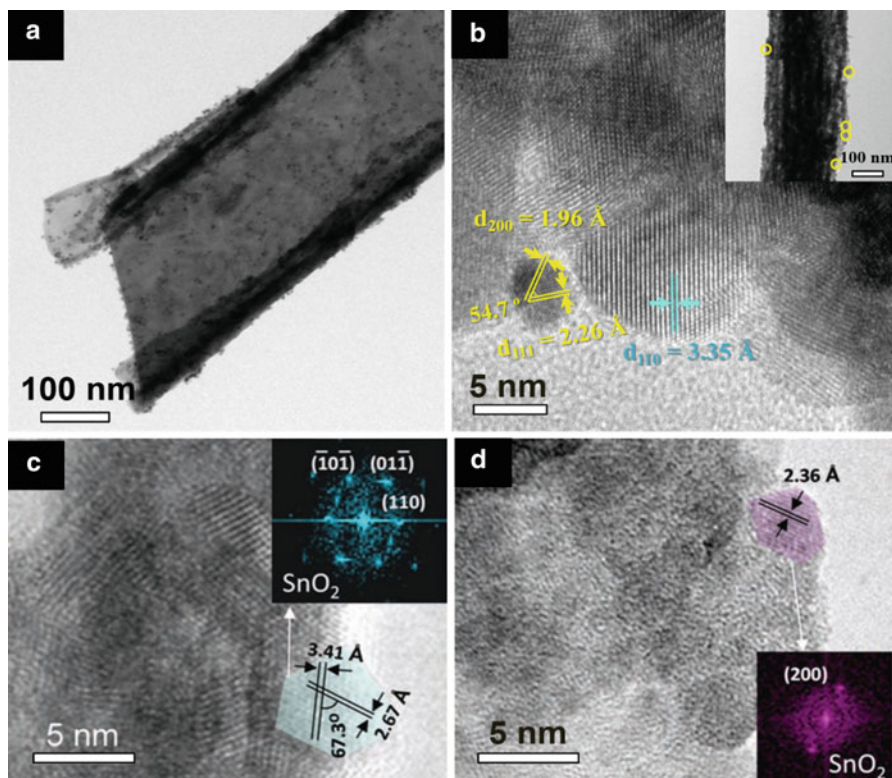
Fig. 23.13 (**a**) TEM image of a Pt-functionalized WO_3 hemitube, (**b**) HRTEM image of a Pt-functionalized SnO_2 nanofiber, (**c**) HRTEM image of pristine SnO_2 nanofiber calcined at 450 °C, and (**d**) HRTEM image of 40 mol% Pd-loaded SnO_2 fiber calcined at 450 °C (Reprinted with permission from Ref. [50]. Copyright (2010), Wiley)

which showed a decreased grain size from 5 nm with an unloaded SnO_2 fiber to 3 nm with 40 mol% Pd-loaded SnO_2 fibers after being calcined at 450 °C (Fig. 23.13c, d). A similar tendency was observed in specimens calcined at 600 °C [50].

Another well-known role regarding the catalytic additive effect is chemical and electronic sensitization, as summarized in Table 23.1 [49, 53]. Chemical sensitization is based on the spillover effect. During chemical sensitization by a catalytic additive, gas molecules are dissociated and diffused onto the semiconductor surface. The diffused molecules react with surface-adsorbed oxygen (O^-) and reduce the concentration of adsorbed oxygen, which results in a change in the resistivity. Pt is the typical catalytic additive in this type of sensitization. On the other hand, electronic sensitization is generated by the direct electronic interaction between the additive and the semiconductor. The electronic state of the catalytic additive is changed by the surrounding atmosphere, which can promote direct electron exchange and thus resistivity changes. Pd and Ag are typical catalytic additives for electronic sensitization, which can be easily oxidized to PdO and Ag_2O and

Table 23.1 Proposed catalytic additive effect on the sensing mechanism: chemical and electronic sensitization (Reprinted with permission from Ref. [49]. Copyright (1991), Elsevier)

	Chemical sensitization	Electronic sensitization
Role of additives	Activation of gas followed by spilling over	Acceptor of electrons
Origin of resistance change	Change in surface oxygen concentration	Change in redox state of addictive

returned to a metallic form in a reducing atmosphere. A number of studies have demonstrated enhanced sensing response and selectivity levels by means of catalytic additive decoration on electrospun fibers such as Pt-SnO_2 nanofibers [19], Pd-SnO_2 hollow nanofibers [52], Pd-SnO_2 nanofibers [54], and Co-ZnO nanofibers [55], which were promoted by either chemically or electronically sensitization. It is still expected that numerous catalytic additives will be studied with electrospun metal-oxide nanofibers to characterize gas sensing properties for environmental and medical applications.

Electrospun Nanofibers for Anode Electrodes in Li-Ion Batteries

Global concern about environmental pollution and the exhaustion of fossil fuels has recently motivated many researchers to seek alternative fuels and renewable energy sources, such as solar energy, wind energy, and tidal energy. In most cases, the alternative fuels and renewable energy sources should be stored for future use whenever and wherever is desired because the energy sources are highly dependent on the area, time, and weather. Therefore, highly efficient energy conversion and storage methods have been considered as an essential step prior to the delivery and use of these types of energy sources [1–5]. As important electrochemical power sources, lithium-ion batteries, fuel cells, and electrochemical supercapacitors have been widely used [6]. In particular, special attention has been paid to Li-ion batteries with high energy density levels [56, 57]. Recent Li-ion battery applications are expanding their usage area from portable devices to large-scale vehicles and smart grids [58, 59]. Extensive energy resources obtained from multiple energy sources such as solar, hydrogen,

wind, and fossil fuel sources are often constrained by the limited capable energy density of conventional Li-ion batteries systems. The electrode materials comprising Li-ion batteries dominantly determine their electrochemical performance [60]. Thus, the development of new electrode materials and breakthroughs in the synthesis of electrode materials, rather than incremental changes, hold the key to the realization of next-generation Li-ion batteries [61, 62].

Thus far, 1-D nanostructured materials have attracted much interest in recent years as high-capacity anode components in Li-ion batteries, especially owing to their unusual mechanical, electrical, and electrochemical properties endowed by confining the dimensions of certain materials as well as their combinations of bulk and surface properties and how they affect the overall behavior of these materials [61, 63]. Conventional Li-ion batteries have electrodes that are composed of powders containing millimeter-sized particles, with the electrolyte trapped within the millimeter-sized pores of a polypropylene separator [63]. Although lithium-ion batteries have a high energy density, a low-power outcome (slow charge–discharge) is common with these batteries. The intrinsic diffusivity (ca. 10^{-8} cm^2 s^{-1}) of Li ions in a solid state is very low and is considered as an inevitable limitation during the intercalation and deintercalation process [63].

On the other hand, 1-D nanomaterials significantly improve the power capability and kinetic properties due to large surface area as well as the short lithium diffusion length (t = L^2/D; t, reaction time; L, Li$^+$ diffusion length; D, diffusion coefficient). In addition, nanostructures provide structural relaxation against internal stress during lithium insertion and deinsertion cycling [61]. Recent studies of nanomaterials for Li-ion batteries have focused on next-generation cathode (LiM$_2$O$_4$, LiMPO$_4$, Li$_2$MnO$_3$·LiMO$_2$, Li$_2$MSiO$_4$; M = Mn, Ni, Co, Fe) and anode (Li-metal alloys, conversion-reaction anodes, intercalation compounds) materials with higher operating voltage windows and capacities, as well as excellent thermal and structural stability. Particularly, the development of nanoarchitectured anode materials with high power and capacity levels has introduced the possibility for significant improvements in conventional Li-ion batteries. Related to this, we address the potential advantages of electrospun nanofibers, which are especially optimized for applications in high-capacity anodes for Li-ion batteries.

High-Capacity Anode Materials

Lithium (Li) metal is an attractive material for use as the anode in Li-ion batteries because this metal is lighter than any other metals and has not only a low anode potential (-3.045 vs. SHE) but also a high specific capacity (3,860 mAh g^{-1}) [64, 65]. In fact, Li metal has been widely used as the anode material in primary Li batteries for more than two decades. However, Li metal is still not used in commercially rechargeable Li-ion batteries due to dendrite formation of the lithium

metal, which brings about serious problems in terms of safety and cycleability [66]. Many researchers have endeavored to commercialize rechargeable lithium metal batteries by suppressing the growth of lithium dendrites [67, 68]. In spite of the extensive effort of many researchers, it is known that Li-metal anodes are not currently suitable for use in rechargeable Li batteries [66].

Therefore, several candidates to replace the Li metal anode have been suggested, as follows: (1) carbonaceous materials, (2) Li-metal alloy, (3) conversion-reaction metal oxides, and (4) intercalation compounds. Recently, noticeable improvements of each classified anode material were reported by the introduction of 1-D nanofibers prepared by electrospinning. Continuous and long 1-D nanofibers prepared by the electrospinning method can facilitate charge transport characteristics and electrolyte penetration, offering multifunctional properties (e.g., improved Li-ion conductivity, a 1-D electron pathway, and numerable reaction sites with Li) for the anode materials of Li-ion batteries. In this chapter, we discuss facile and versatile synthetic methods for preparing such classes of 1-D nanofibers and investigate their effects on the electrochemical performance of Li-ion batteries.

Electrospun Carbon Nanofibers

Li ions can be intercalated into carbon, and the resulting lithiated carbons exhibit a sufficiently negative operating potential close to that of a Li-metal anode. The reversible intercalation/deintercalation reactions overcome the problem of dendrite formation of the lithium and provide dramatic improvements in terms of safety and cycleability. The charge and discharge reactions are described as follows:

$$C + x\text{Li}^+ + xe^- \leftrightarrow \text{Li}_x\text{C} \tag{23.2}$$

Graphite as a conventional carbonaceous anode is a typical layered compound that consists of hexagonal graphene sheets of sp^2-carbon atoms with covalent bonding. The graphene sheets are weakly bonded together by van der Waals forces into an ABAB, a stacking sequence along the c-axis. However, the low specific capacity (372 mAh g^{-1}) of graphite has driven the research to replace it with new carbonaceous materials. Furthermore, the Li-ion transport rates of graphite anodes are always less than 10^{-6} cm^2 s^{-1}, which results in a limited power density of the Li-ion batteries [69]. Carbon fiber anodes such as vapor-grown carbon fiber (VGCF) and electrospun carbon nanofiber (CNF) have been introduced to improve the electrochemical performance of carbonaceous anodes. VGCF can be produced by exposing a metal catalyst particle (e.g., Fe) with a diameter of few nanometers to a carbon-based gas. On the other hand, CNF can easily be made through the electrospinning of a polymer (e.g., PAN) and a subsequent calcination treatment under a reducing atmosphere. Figure 23.14 shows the typical morphologies of electrospun PAN fiber and CNF.
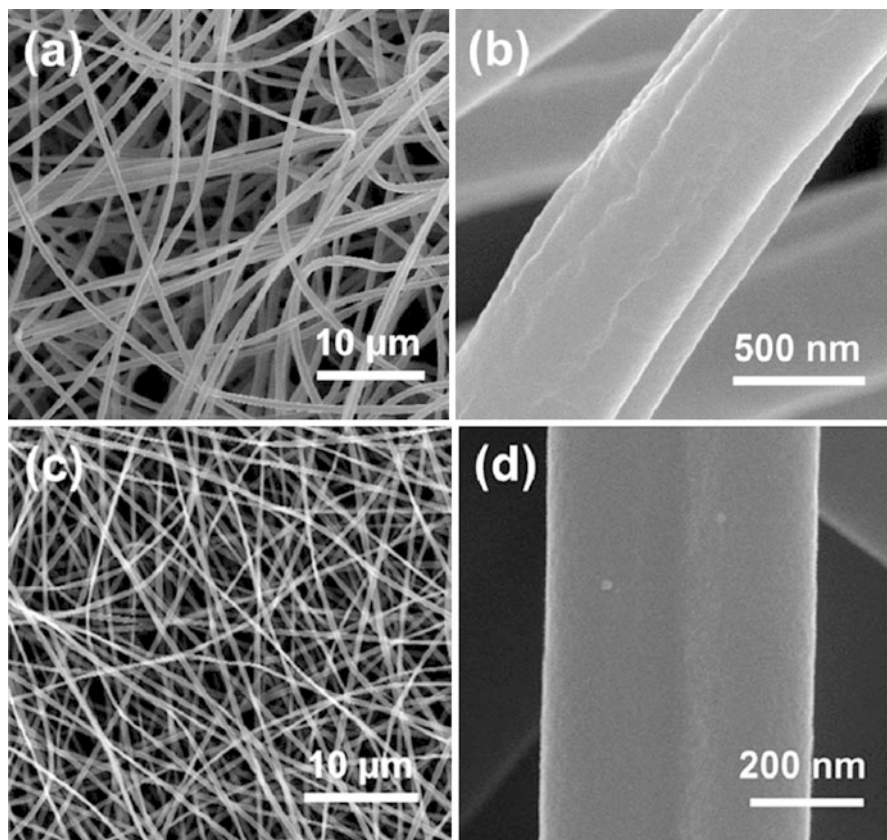
Fig. 23.14 SEM images of (**a**, **b**) as-spun NFs with PAN polymer prepared by electrospinning and (**c**, **d**) pristine CNFs obtained from the calcination of the as-spun fiber with different levels of magnification (Reprinted with permission from Ref. [70]. Copyright (2013), Royal Society of Chemistry)

Generally, a higher calcination temperature of the PAN precursor fiber helps to create CNF with higher electronic conductivity. For example, PAN-based CNF calcined at 1,000 °C exhibits a capacity that exceeds 400 mAh g^{-1} and improved rate capability compared to a conventional graphite anode due to its particular structural features, with a highly disordered structure, defects, and dangling bonds for additional Li reaction sites (Fig. 23.15) [71]. To improve the electrochemical performance of CNFs further, porous CNFs via an electrospinning and subsequent carbonization process were recently reported. For example, Lee et al. reported hollow CNFs synthesized by means of the coaxial electrospinning of sacrificial styrene-co-acrylonitrile (core) and poly(acrylonitrile) (shell) solutions and a subsequent thermal treatment, as shown in Fig. 23.16 [72]. The hollow CNFs exhibited improved electrochemical performance due to the many reaction sites related to their higher specific surface area and larger pore volume compared to nonporous (dense) CNFs [72–75].

Fig. 23.15 Variation of reversible capacities (rate capability) for nanofiber webs thermally treated at 700, 1,000, and 2,800 °C at discharge current densities of 30, 50, and 100 mA g^{-1}, respectively (Reprinted with permission from Ref. [71]. Copyright (2006), Wiley)
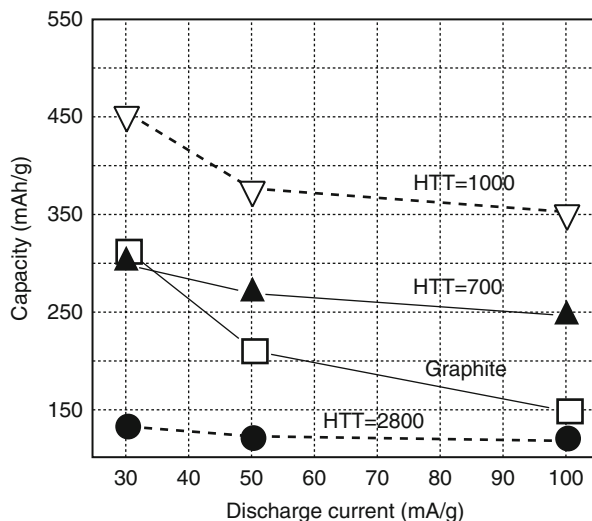
Electrospun Metallic Alloy Nanofibers

To overcome the low capacity of the graphite anode (372 mAh g^{-1}), electrochemical alloying reactions of Li with various metals have been widely studied since the 1970s [76–78]. A number of binary alloy systems have been considered, including Li-Sb [79], Li-Sn [80], Li-Pb [81], Li-Si [82], and Li-Ge [83]. The Li-metal (Li-M) alloy exhibits a high theoretical capacity originating from the acceptance of multiple Li ions per metal ion (e.g., $Li_{4.4}Si$, ~4,200 mAh g^{-1}; $Li_{4.4}Sn$, ~992 mAh g^{-1}; $Li_{4.4}Ge$, 1,600 mAh g^{-1}) [84–86]. However, it shows severe capacity fading due to mechanical failures of the active material caused by large amounts of volume expansion/shrinkage of approximately ~300 % (Si, 297 %; Sn, 257 %) during the repeated discharge–charge reactions [87, 88]. In order to overcome these problems, various approaches have been applied, such as (1) the use of binary alloys (e.g., Si-M, Sn-M alloy), (2) functional nanostructures, and (3) Si or Sn dispersion in active and/or inactive matrices as the buffer phase. First, the introduction of a 1-D nanostructure for metallic alloy anodes has been considered as a feasible approach. A 1-D nanostructured metallic alloy anode provides less volume variation, empty space in the structure for stress relaxation, and facile 1-D Li ion and electron pathways [89–91]. Therefore, functional composite structures with 1-D nanofiber morphologies synthesized by electrospinning also exhibit good electrochemical performance. Nanotubular alloying metal anodes, which are easily made by means of electrospinning methods such as the dual-nozzle electrospinning method and with electrospun template nanofiber, provide an open structure with a hollow interior for stress relaxation against severe volume changes during charging–discharging [92–94]. For example, a double-walled Si nanotube (DWSiNTs) anode in which the inner wall is active silicon and the outer wall is
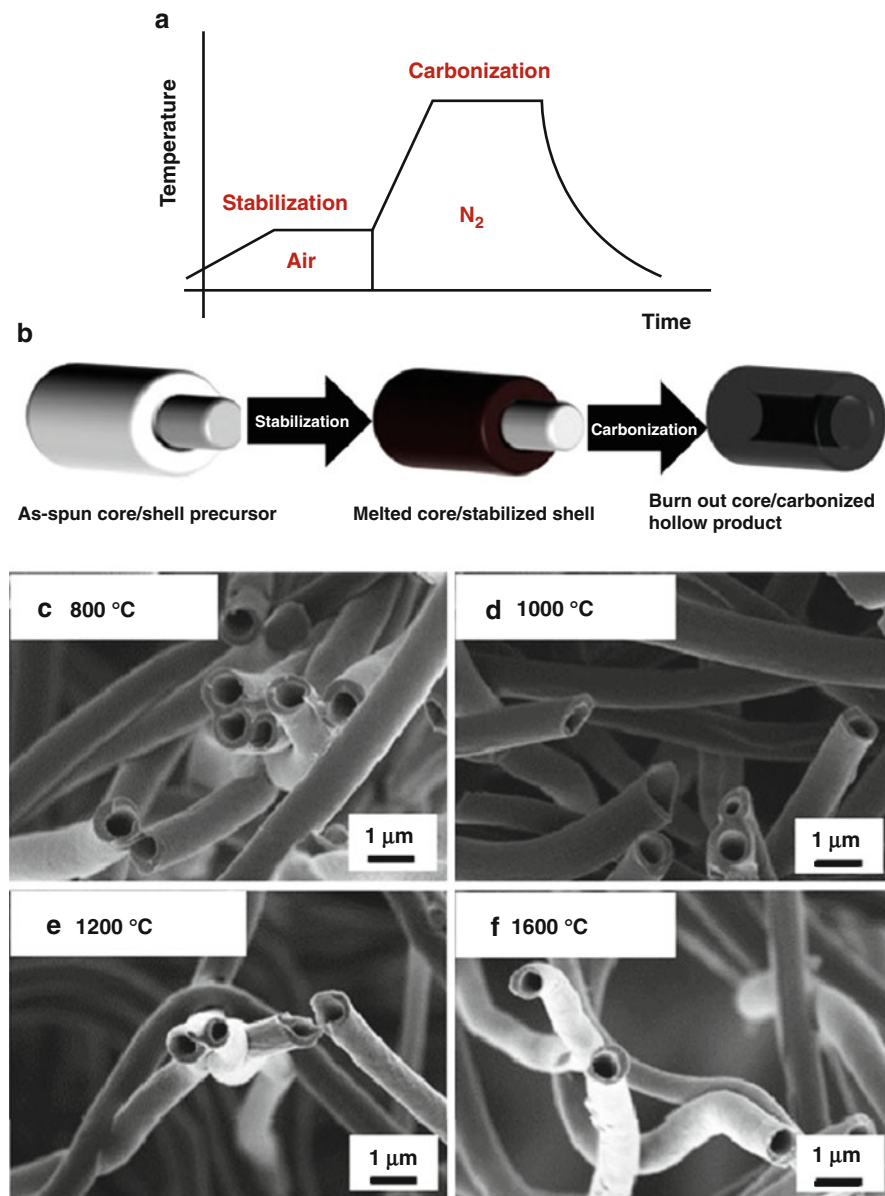
Fig. 23.16 (**a**) Schematic thermal treatment profile; (**b**) structural evolution during thermal treatment; SEM images of hollow carbon nanofibers (HCNFs) carbonized at various carbonization temperatures: (**c**) 800, (**d**) 1,000, (**e**) 1,200, and (**f**) 1,600 °C (Reprinted with permission from Ref. [72]. Copyright (2012), Elsevier)
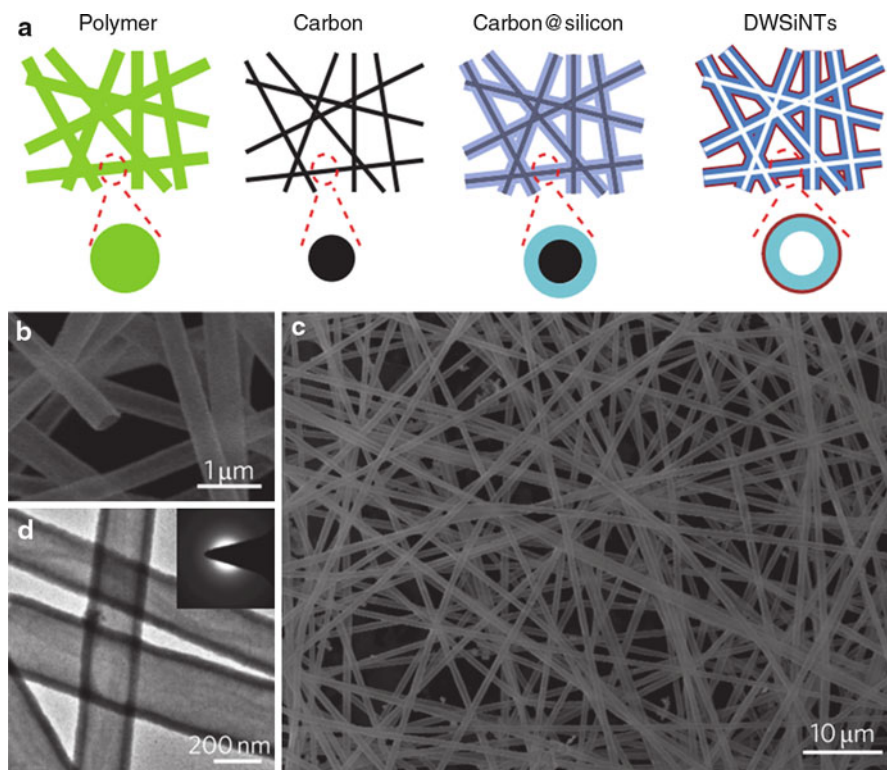
Fig. 23.17 (**a**) Schematic of the fabrication process of DWSiNTs. Polymer nanofibers (*green*) were first made by electrospinning. The polymer fibers were then carbonized and coated with silicon (*blue*) using a CVD method. By heating the sample in air at 500 °C, the inner carbon templates (*black*) were selectively removed, leaving continuous silicon tubes with a SiOx mechanical constraining layer (*red*). (**b**, **c**) SEM images of synthesized DWSiNTs at high and low magnification, respectively. (**d**) TEM image of DWSiNTs, showing the uniform hollow structure with smooth tube walls (Reprinted with permission from Ref. [94]. Copyright (2012), Nature)

confining SiO_x can be fabricated via an electrospun CNF template (Fig. 23.17). The SiO_x on the outer surface prevents direct contact with the electrolyte, meaning that the inner surface of the Si nanotube is not exposed to the electrolyte, resulting in a stable SEI layer. In addition, the mechanically rigid outer wall can allow an inward expansion into the hollow space for the inner Si. Tubular Si- or Sn-based nanofibers facilitate electrolyte diffusion into the inner space and 1-D charge transfer through the thin wall of the hollow nanofiber. The tailored Si nanotube exhibits long cycling (6,000 cycles with 88 % capacity retention) and high specific capacities ($\sim$2,971 mAh g^{-1} at 0.2 °C) [94].

Another way to improve the performance of metallic alloy anode is to use dispersed nanosized metal particles within the carbon nanofibers. The carbon nanofibers in the composite structures act as structural buffers, particle stabilizers,

and electroactive materials, eliminating the need for binding or conducting additives. Si or Sn nanoparticles, which are spatially dispersed in the CNFs, demonstrate better electrochemical properties compared to bulk Si or Sn anodes [95–100]. For example, Yu et al. reported Sn@carbon nanoparticles encapsulated in bamboo-like hollow carbon nanofibers prepared by the pyrolysis of coaxially electrospun nanofibers (Fig. 23.18) [95]. During coaxial electrospinning, two viscous liquids were simultaneously fed through the inner (tributyltin (TBT) and a mineral oil solution) and outer (polyacrylonitrile solution) capillaries, respectively. After soaking to extract the mineral oil in *n*-octane, the Sn nanoparticles encapsulated in the bamboo-like hollow carbon nanofibers were prepared after pyrolysis at 1,000 °C. The unique nanofiber structure exhibited a high reversible capacity of 737 mAh g^{-1} and excellent cycleability for 200 cycles owing to the high Sn long content (~70 wt% Sn) and the appropriate free space to relieve internal stress caused by volume changes of the Sn nanoparticles.

Similarly, Hwang et al. reported a unique core–shell nanofiber structure composed of Si NPs (core) and carbon (shell) (Fig. 23.19) [100]. The core Si NPs perfectly wrapped by the carbon shell resolve various problems with the Si anode, such as pulverization, insufficient contact between the Si and carbon conductors, and an unstable SEI layer, thereby exhibiting outstanding cell performance, as defined by a capacity of 1,384 mAh g^{-1}, an improved rate capability at 3 C, and superb cycleability for 300 cycles without a loss of capacity. The improvements of Si or Sn anodes in terms of the reversible capacity and cycle stability were mainly attributable to the unique morphological features, specifically the hybrid nanofiber networks realized through the diverse shapes of the surrounding agents.

Electrospun Metal-Oxide Nanofibers for Conversion Reaction Anode

The practical utilization of alloying reaction anodes such as Si and Sn has been severely handicapped by the intrinsic major volume changes associated with the (de)alloying process, which result in the introduction of large strains in the particles of the active material. Therefore, recent interests have focused on a new reactivity concept with the reversible electrochemical reaction of lithium with transition metal oxides, according to what is conventionally referred to as a 'conversion reaction', generalized as follows:

$$M_a X_b + (b \cdot n)\text{Li} \leftrightarrow aM + b\text{Li}_n X \qquad (23.3)$$
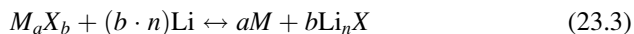
Here, M denotes the transition metal (e.g., Co, Mn, Fe, Ni, Cu, and V) and X refers to the anion species (e.g., O, F, and S). Among various types of conversion reaction anodes, transition metal oxides have received much attention because metal-oxide anodes can store more than two Li ions per transition metal ion through a conversion reaction, leading to a higher capacity compared to that of graphite (C$_6$Li). However, unlike an intercalation reaction which Li$^+$ ions are inserted
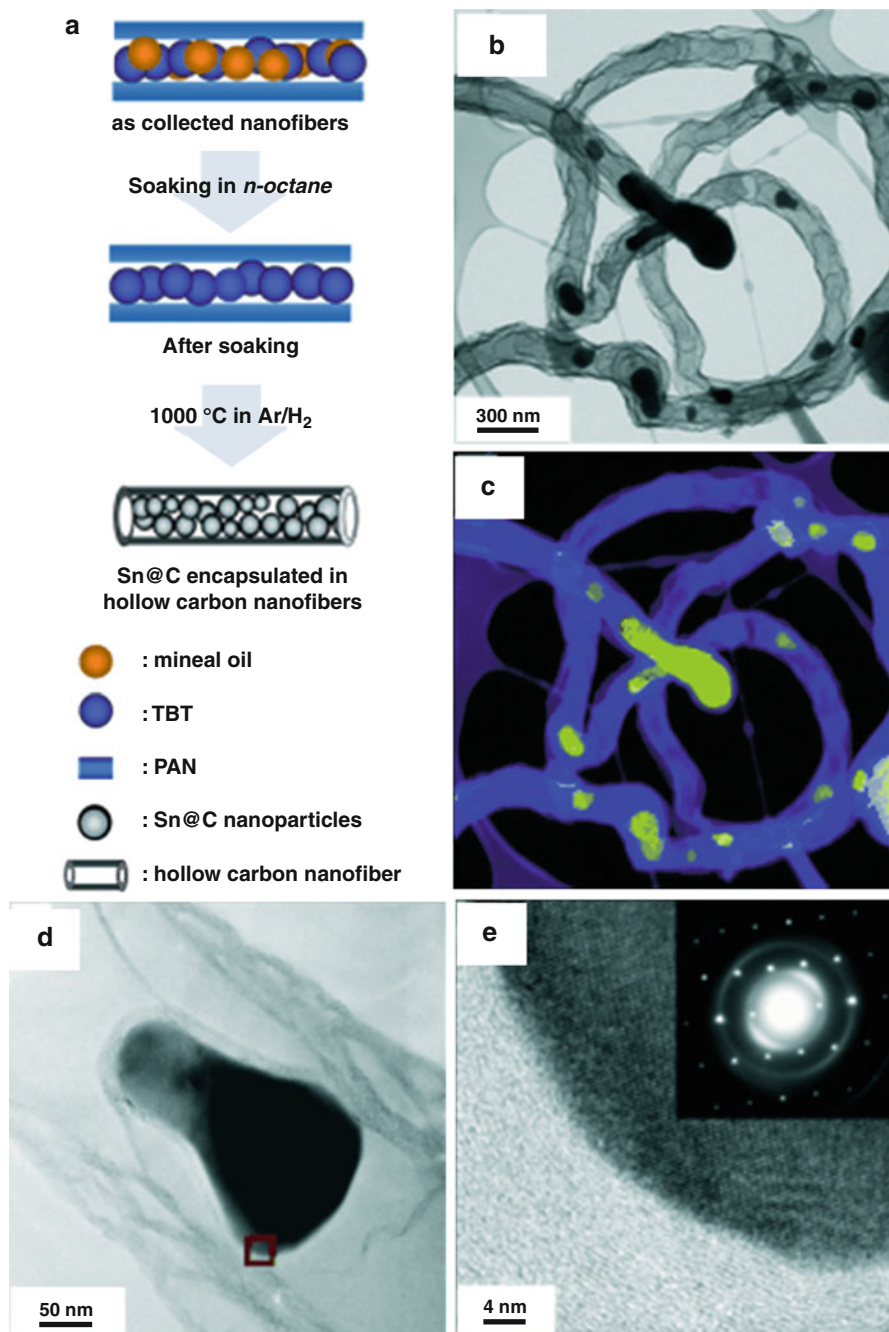
Fig. 23.18 (**a**) Schematic illustration of the preparation of Sn@carbon nanoparticles encapsulated in hollow carbon nanofibers; (**b**) TEM micrograph of pyrolyzed nanofibers obtained by

and extracted in a structurally consistent host matrix, conversion-reaction anode materials are known to undergo large amounts of polarization due to the repeated structural reorganization of lattices [101]. In addition, the electronic conductivity of bulk metal-oxide particles is too low to provide high-rate capability. Therefore, 1-D carbon nanofibers encapsulating conversion-reaction metal-oxide nanoparticles are a promising structure for high-capacity anode materials. Thus far, the diameters and morphologies of 1-D conversion-reaction materials have been designed to offer a high surface area, fast Li^+-ion diffusion, a facile electron pathway, and good strain accommodation [102, 103]. Many types of metal-oxide materials (MnO_x, CoO, Co_3O_4, Fe_2O_3, Fe_3O_4, MoO_2, NiO, CuO, $ZnCo_2O_4$, and $ZnFe_2O_4$) have been designed for 1-D nanofibers prepared via electrospinning methods [70, 104–114]. The surface areas and specific morphologies of 1-D metal-oxide nanofibers are important to determine the electrochemical performances because a larger surface area of the 1-D nanofiber can provide many reaction sites in the Li and electrode–electrolyte contact area. For example, 1-D hollow metal-oxide (α-Fe_2O_3) nanofibers can improve the cell performance due to the increased surface area realized by the additional inner space (Fig. 23.20).

The low electronic conductivity of conversion-reaction anodes, which leads to poor rate capability, has been improved by networks of 1-D metal-oxide nanostructures combined with a highly conductive carbon matrix. Therefore, electrospun CNF has been widely used as affordable component of hybrid composite structures [115, 116]. Effectively interconnected conductive carbon species with metal oxides allow facile electron transport and relieve internal stress for structural reorganization during the charging and discharging processes. Thus far, many studies related to 1-D metal oxide/CNF composites prepared via electrospinning have been conducted in an effort to improve the electrochemical properties of metal oxides [70, 104, 111, 115, 117–119]. Tiny metal-oxide nanoparticles (e.g., CoO, MnO_2, and Fe_2O_3) were often interconnected with highly conductive CNF. Recently, Ryu et al. reported that CoO nanoparticles embedded in porous CNFs can be successfully synthesized via one-step electrospinning and subsequent calcination in an inert atmosphere (Fig. 23.21) [70]. The CoO nanoparticles perfectly wrapped by porous CNFs delivered a high theoretical capacity of 1,381 mAh g^{-1}, excellent cycleability for 100 cycles, and a high-rate capability even at a rate of 20 C because (i) the nanosized CoO particles reversibly react with Li ions according to the reaction of CoO + $2Li^+$ + 2e $\leftrightarrow$ Li_2O + Co, and (ii) the conductive CNF backbones as an active phase provide a 1-D electron transport path [70].

Fig. 23.18 (continued) calcining the composite in Ar/H_2 at 1,000 °C for 5 h; (**c**) elemental mapping of the nanofibers showing the chemical distribution of carbon (*blue*) and tin (*yellow*); (**d**) electron micrograph of an isolated Sn@carbon nanoparticle encapsulated in a hollow carbon nanofiber; and (**e**) HRTEM and SAED (*inset*) images of the region marked in (**d**) indicating the presence of single-crystalline metallic tin and graphitic carbon (Reprinted with permission from Ref. [95]. Copyright (2009), Wiley)
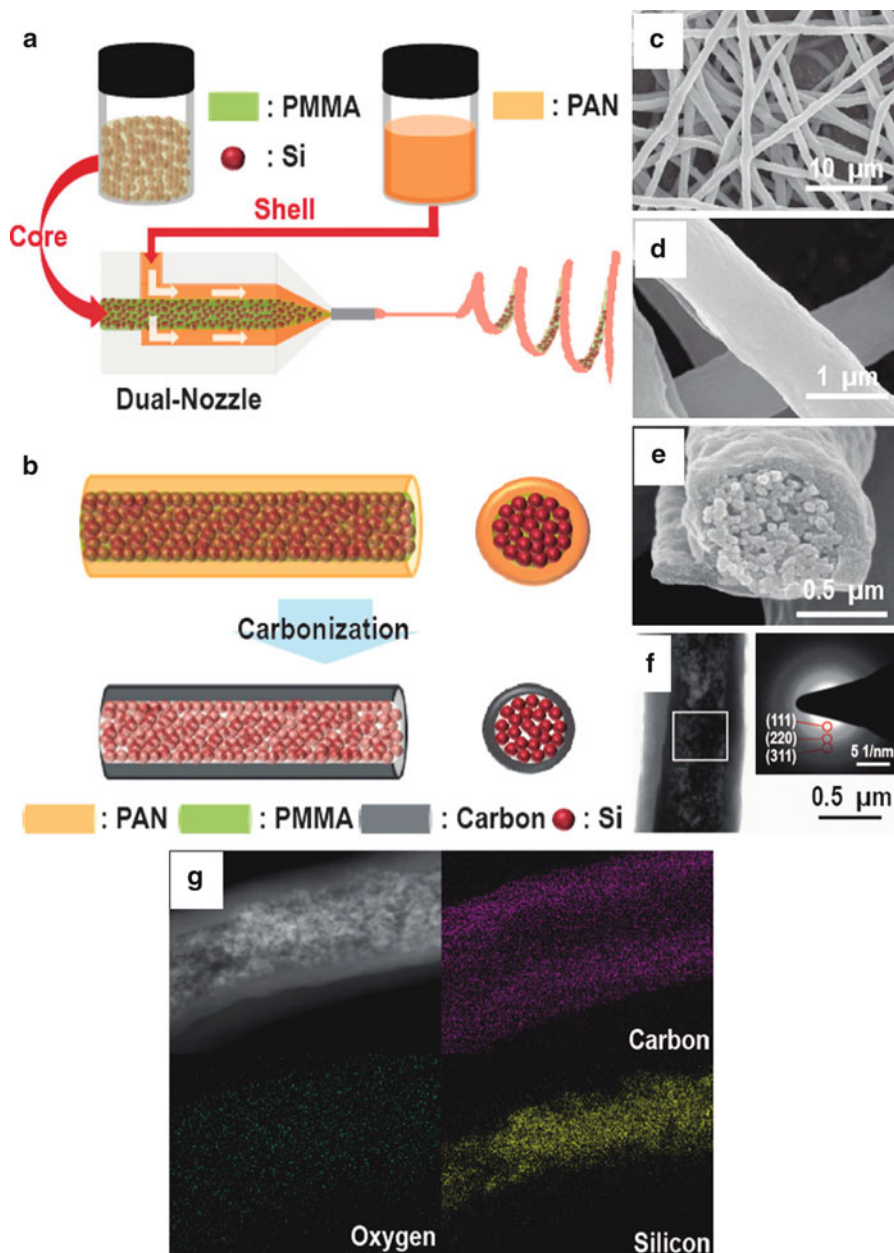
Fig. 23.19 Schematic illustration of the electrospinning and carbonization steps: (**a**) The electrospinning process using a dual nozzle. PMMA solutions containing Si NPs and the PAN solution were injected into the core and shell channels of the nozzle, respectively. (**b**) After electrospinning, stabilization and carbonization steps were employed to complete the core−shell 1-D fibers consisting of Si NPs−carbon, respectively. Characterization of the Si NP@Carbon
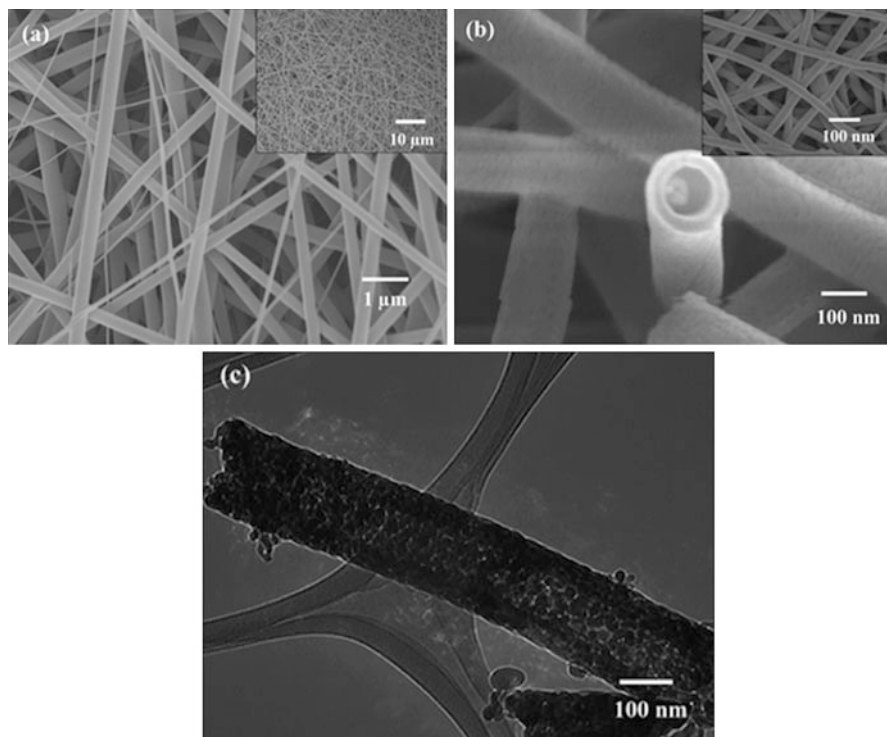
Fig. 23.20 (**a**) FESEM images of Fe(acac)$_3$–PVP composite fibers under higher magnification, the inset shows lower magnification; (**b**) FESEM images of α-Fe$_2$O$_3$ hollow fibers under higher magnification with the inset showing lower magnification; and (**c**) TEM image of α-Fe$_2$O$_3$ hollow fibers (Reprinted with permission from Ref. [106]. Copyright (2012), Royal Society of Chemistry)

Electrospun Intercalation Compounds (Li$_4$Ti$_5$O$_{12}$, TiO$_2$, TiNb$_2$O$_7$)

Studies of new anode materials have been done with intercalation compounds based on metal oxides, in contrast to a graphite anode. In this range of materials, titanium oxide (TiO$_2$) and lithium titanate, (Li$_4$Ti$_5$O$_{12}$) are the representative anode materials for Li-ion batteries [120–122]. Intercalation host materials offer accommodation sites for Li ions without significant structural changes (zero strain). Unlike alloying reactions and conversion reactions, intercalation

Fig. 23.19 (continued) core−shell 1-D fibers. SEM images of Si NP@Carbon at (**c**) low and (**d**) high magnification levels. (**e**) A cross-sectional SEM view of a single Si NP@Carbon indicating that the core full of Si NPs is wrapped by a carbon shell. (**f**) A TEM image of a single Si NP@Carbon. (Inset) SAED pattern of the region in the white box with the diffraction rings indexed. (**g**) A STEM image of a single Si NP@Carbon fiber (*top left*) as well as EDAX elemental mappings for carbon, oxygen, and silicon (Reprinted with permission from Ref. [100]. Copyright (2012), American Chemical Society)

reactions can easily occur with redox reactions of transition metal components (e.g., Ti^{4+}/Ti^{3+}) [123]. Therefore, it has been found that an intercalation reaction assures stable cycling performance and excellent rate capability compared to other types of reactions with Li ions. However, the number of electrons involved in the insertion
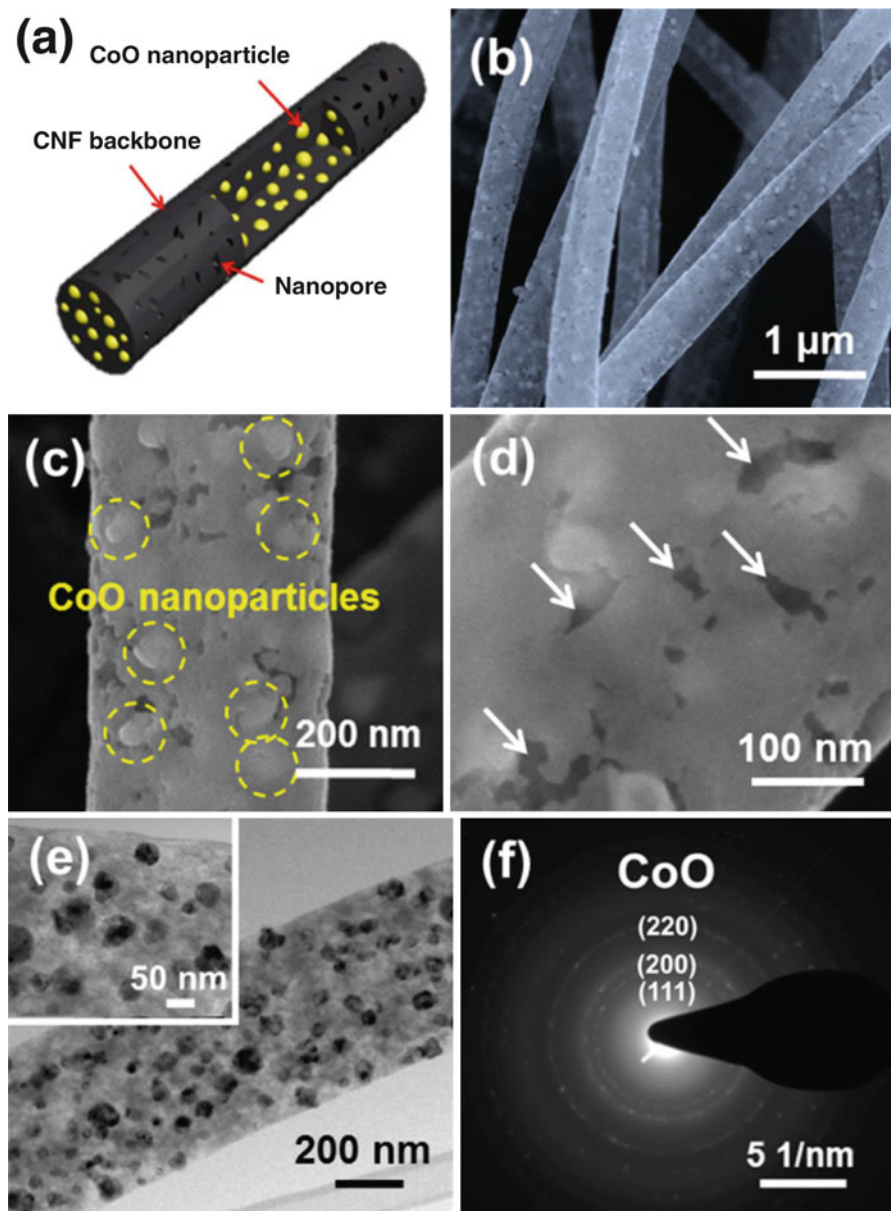

Fig. 23.21 (continued)
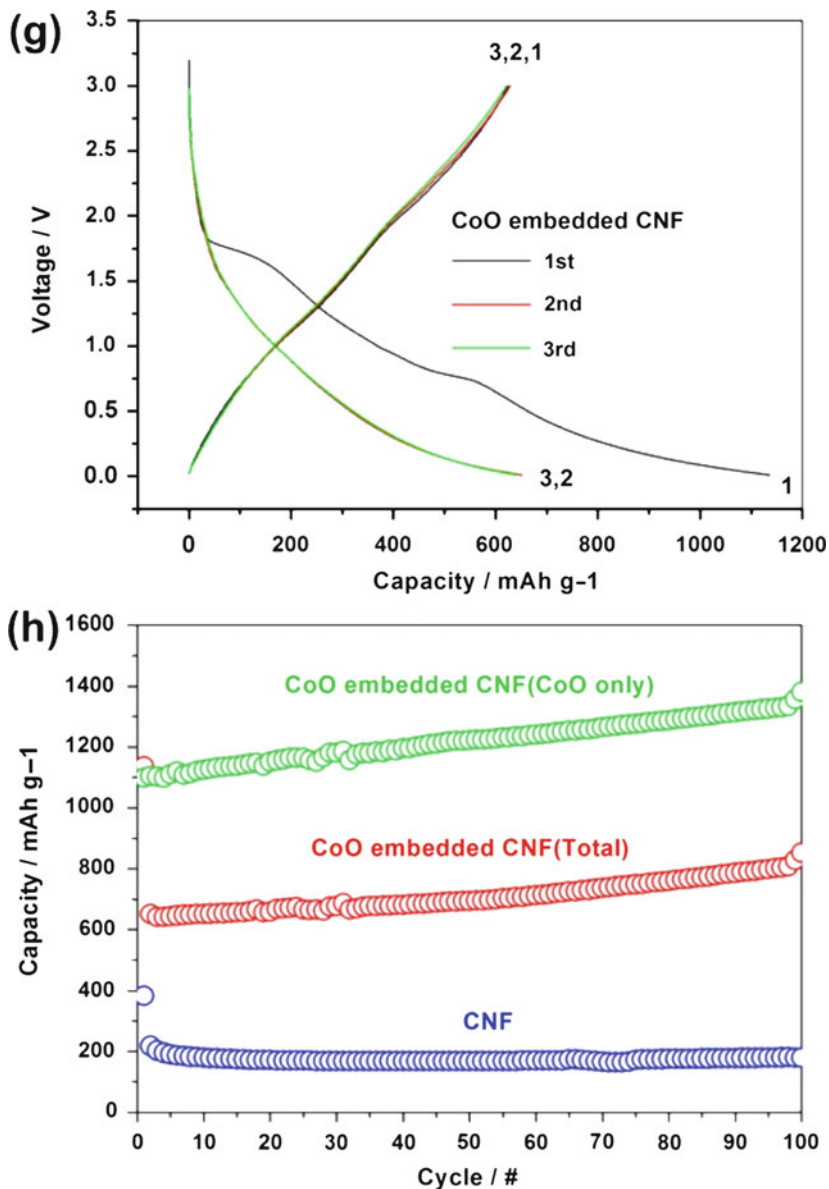
Fig. 23.21 (**a**) Schematic illustration of CoO embedded CNF; SEM images of (**b**–**d**) CoO embedded CNF calcined at 700 °C; (**e**) HRTEM images and (**f**) SAED pattern of the CoO embedded CNF; (**g**) charge–discharge curves of CoO embedded CNF; and (**h**) cycle performance of the CNF and CoO embedded CNF (calculated from the total weight of the entire active material or only CoO) for 100 cycles (Reprinted with permission from Ref. [70]. Copyright (2013), Royal Society of Chemistry)

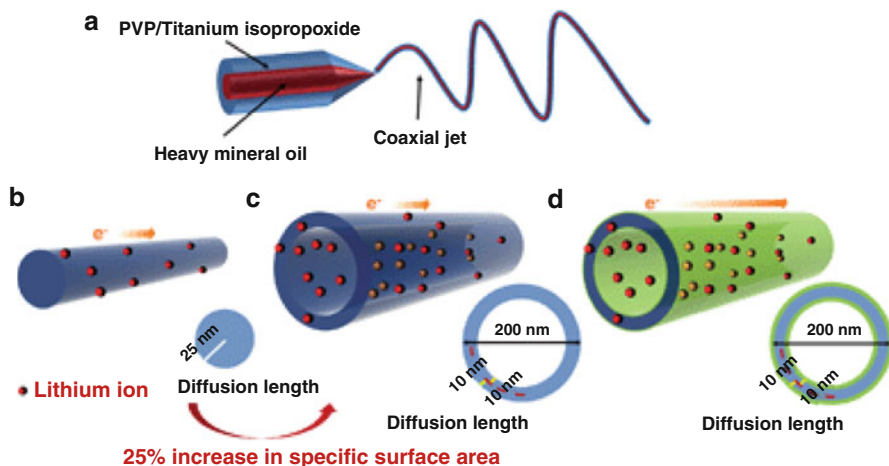**Fig. 23.22** (**a**) Schematic illustrations of a coaxial electrospinning spinneret using a dual nozzle, (**b**) TiO_2 nanofibers, (**c**) TiO_2 hollow nanofibers, and (**d**) nitridated TiO_2 hollow nanofibers (Reprinted with permission from Ref. [128]. Copyright (2011), Royal Society of Chemistry)

reaction is generally less than one per Li because Li can only be accommodated into the vacant sites of the frameworks in these intercalation compounds [124, 125]. Therefore, insertion reaction-based metal-oxide anodes have relatively low specific capacities ($Li_4Ti_5O_{12}$, 175 mAh g^{-1}; anatase TiO_2, 167 mAh/g). To maximize the electrochemical performances of titanium oxide (TiO_2) and lithium titanate ($Li_4Ti_5O_{12}$), 1-D electrospun nanofiber structures based on these materials have been suggested. Beyond smooth nanofibers, there have been many attempts to synthesize electrospun TiO_2 nanofibers with various morphological evolution processes [126, 127]. Han et al. attempted to synthesize 1-D TiO_2 hollow nanofibers by coaxial electrospinning using a Ti/PVP precursor solution and mineral oil (Fig. 23.22) [128]. The unique hollow geometry, consisting of inner and outer surfaces, allows for vigorous lithium-ion access due to the substantial increase in the interfacial area between the electrolyte and the electrode material and the shorter diffusion length of the Li ions compared to that of a simpler nanofiber structure, which led to an improvement in the kinetics of lithium ions. In addition, conductive agents such as carbon were combined with TiO_2 anode materials to improve the electrical conductivity and thus achieve full electrode utilization [129–131]. Recently, Nam et al. reported that metallic Ag or Au nanoparticle-embedded TiO_2 nanofibers can be prepared via a one-step electrospinning process using Ag or Au containing a Ti/PVP precursor solution [132]. The highly conductive Ag or Au agents embedded in the TiO_2 nanofiber enable rapid Li-ion diffusion and electron transfer.

$Li_4Ti_5O_{12}$ with a spinel-framework structure has shown promising electrochemical properties with structural and chemical stability. Because the insulating characteristic of $Li_4Ti_5O_{12}$ originates from the electronic structure

Fig. 23.23 (continued)
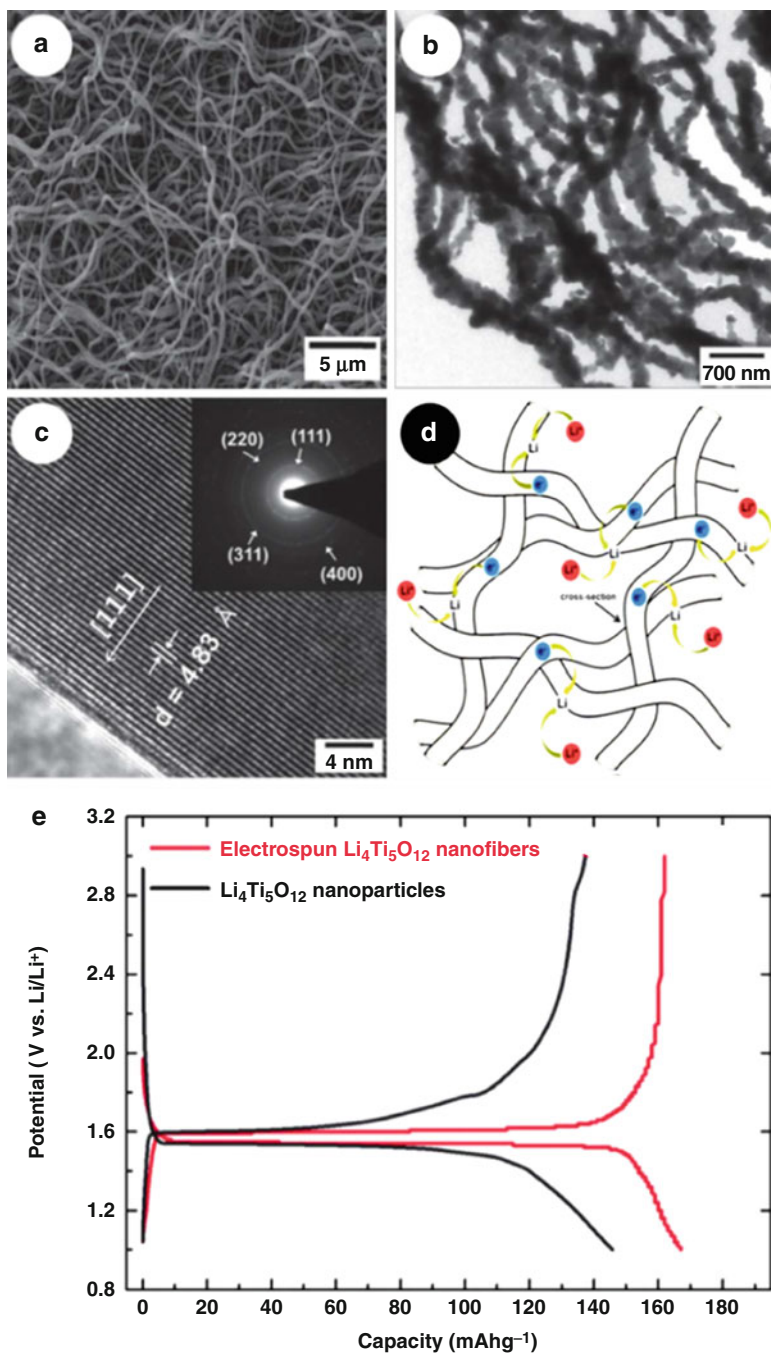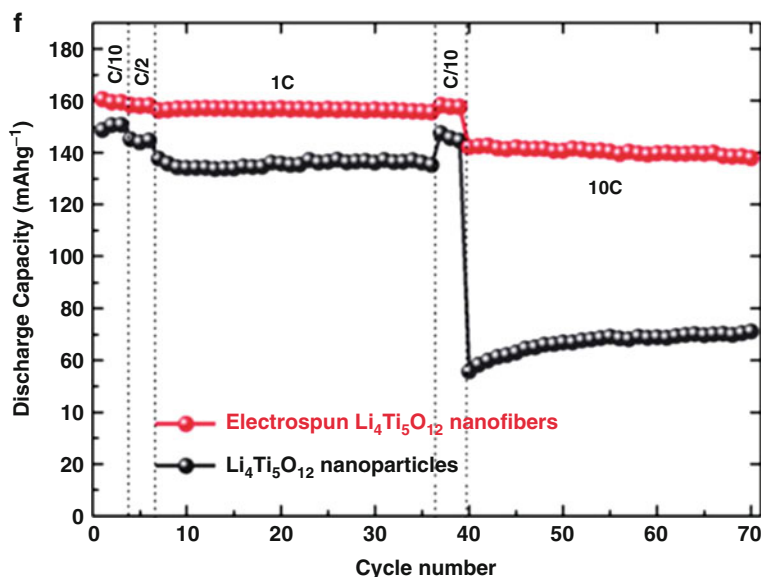
Fig. 23.23 (**a**) SEM image and (**b**) TEM image of electrospun $Li_4Ti_5O_{12}$ nanofibers; (**c**) high-resolution TEM image indicated the d-spacings and the axes of the (111) planes (inset: selected area electron diffraction pattern (*SAED*) of electrospun $Li_4Ti_5O_{12}$ nanofibers); (**d**) a schematic diagram of the facilitated Li ion and electron transfer in electrospun $Li_4Ti_5O_{12}$ nanofibers; (**e**) the initial galvanostatic charge–discharge curves at 0.1 C; and (**f**) capacity retention amounts when conducting charge–discharge cycles at various current rates (Reprinted with permission from Ref. [134]. Copyright (2012), Royal Society of Chemistry)

Fig. 23.24 (**a**) TEM images of $TiNb_2O_7$ nanofibers. (**b**) Charge–discharge curves of $TiNb_2O_7$ nanofibers at various rates (Reprinted with permission from Ref [141]. Copyright (2013), Wiley)

(bandgap energy level, 2 eV), $Li_4Ti_5O_{12}$ is often used in applications for large-scale devices such as energy storage s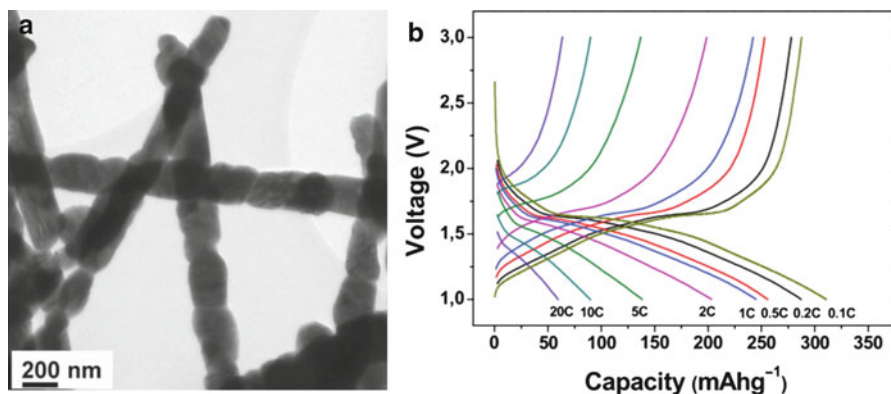ystems (ESSs) and electric vehicles (EVs) [133, 134]. In particular, for high-current applications, developing energy-storage electrodes with excellent cycleability and capacity retention characteristics at high charge–discharge rates is a critical issue. Related to this, 1-D $Li_4Ti_5O_{12}$ nanofibers offering more reaction sites on the surface and a shorter diffusion length for Li^+ insertion have also been designed by electrospinning methods [134–139]. Jo et al. reported that the high crystalline $Li_4Ti_5O_{12}$ nanofibers with a diameter of 300 nm can deliver improved capacity and excellent rate capability at 10 C (Fig. 23.23) [134].

Ti-based intercalation compounds such as TiO_2 and $Li_4Ti_5O_{12}$ which react only by a redox reaction of Ti^{4+}/Ti^{3+} have low theoretical capacity levels. Related to this Goodenough et al. recently invented $TiNb_2O_7$ as a new anode framework with a high theoretical capacity of $387.6 \, mAh \, g^{-1}$ [140]. Five of Li ions can be reversibly inserted into the (110) plane of the $TiNb_2O_7$ according to five electron transfer reactions (Ti^{4+}/Ti^{3+}, Nb^{5+}/Nb^{3+}). However, the development of rechargeable Li-ion batteries with $TiNb_2O_7$ as an anode has been limited due to its low electronic conductivity and ionic conductivity, which restricts the electrochemical kinetics. Recently, $TiNb_2O_7$ nanofiber prepared by the electrospinning of Ti and Nb precursors and subsequent calcination at 1,000 °C was reported, as shown in Fig. 23.24 [141]. The $TiNb_2O_7$ nanofibers delivered a high reversible capacity of $280 \, mAh \, g^{-1}$, which is related to the favorable kinetics properties stemming from the 1-D nanostructure and the absence of a SEI layer due to the higher operating voltage of 1.65 V.

Future Prospects

Electrospinning is a powerful technique that can be used to fabricate 1-D structures with high surface-to-volume ratios. Numerous materials, including metals, metal oxides, and polymers, have been successfully synthesized by means of electrospinning. These materials have been applied in various areas, including gas sensors and Li-ion batteries, as mentioned in this chapter. For further optimization of the gas sensor and Li-ion battery performances, the morphologies, material compositions, and structures have been controlled by a number of methods, such as induced phase separation, coaxial electrospinning of the core–shell structure, a templating route for hollow nanofibers, and catalyst functionalization inside or outside of the electrospun fibers. It is clear that material characterization by designing and fabricating new types of electrospun nanofibers will be attempted. In addition, the effort to create desirable structures for specific applications will continue with other fabrication methods such as PVD or CVD in conjunction with electrospinning. Regarding the versatility to synthesize various nanobuilding blocks and opportunities for the selection of diverse materials using electrospinning, upcoming efforts to improve the performance levels of gas sensors and Li-ion batteries will be highly promising.

References

1. Yamazoe N, Sakai G, Shimanoe K (2003) Oxide semiconductor gas sensors. Catal Surv Asia 7(1):63–75
2. Szklarski Z, Zakrzewska K, Rekas M (1989) Thin oxide-films as gas sensors. Thin Solid Films 174:269–275
3. Sberveglieri G, Benussi P, Coccoli G, Gropelli S, Nelli P (1990) Reactively sputtered indium tin oxide polycrystalline thin-films as NO and NO_2 gas sensors. Thin Solid Films 186(2):349–360
4. Nanto H, Minami T, Takata S (1986) Zinc-oxide thin-film ammonia gas sensors with high-sensitivity and excellent selectivity. J Appl Phys 60(2):482–484
5. Advani GN, Jordan AG (1980) Thin-films of SnO_2 as solid-state gas sensors. J Electron Mater 9(1):29–49
6. Oyabu T (1982) Sensing characteristics of SnO_2 thin-film gas sensor. J Appl Phys 53(4):2785–2787
7. Singh N, Gupta RK, Lee PS (2011) Gold-nanoparticle-functionalized In_2O_3 nanowires as CO gas sensors with a significant enhancement in response. ACS Appl Mater Interfaces 3(7):2246–2252
8. Wang ZL (2009) ZnO nanowire and nanobelt platform for nanotechnology. Mater Sci Eng R 64(3–4):33–71
9. Li X, Wang Y, Lei Y, Gu Z (2012) Highly sensitive H_2S sensor based on template-synthesized CuO nanowires. RSC Adv 2(6):2302
10. Mai L, Xu L, Gao Q, Han C, Hu B, Pi Y (2010) Single beta-$AgVO_3$ nanowire H_2S sensor. Nano Lett 10(7):2604–2608
11. Kim ID, Rothschild A (2011) Nanostructured metal oxide gas sensors prepared by electrospinning. Polym Adv Technol 22(3):318–325
12. Watson J (1984) The tin oxide gas sensor and its applications. Sens Actuator 5(1):29–42
13. Morrison SR (1987) Mechanism of semiconductor gas sensor operation. Sens Actuator 11(3):283–287
14. Kim ID, Jeon EK, Choi SH, Choi DK, Tuller HL (2010) Electrospun SnO_2 nanofiber mats with thermo-compression step for gas sensing applications. J Electroceram 25(2–4):159–167
15. Shin J, Choi SJ, Youn DY, Kim ID (2012) Exhaled VOCs sensing properties of WO_3 nanofibers functionalized by Pt and IrO_2 nanoparticles for diagnosis of diabetes and halitosis. J Electroceram 29(2):106–116
16. Choi S-H, Choi S-J, Min BK, Lee WY, Park JS, Kim I-D (2013) Facile synthesis of p-type perovskite $SrTi_{0.65}Fe_{0.35}O_{3-\delta}$ nanofibers prepared by electrospinning and their oxygen-sensing properties. Macromol Mater Eng 298:521–527
17. Choi SJ, Lee I, Jang BH, Youn DY, Ryu WH, Park CO, Kim ID (2013) Selective diagnosis of diabetes using Pt-functionalized WO_3 hemitube networks as a sensing layer of acetone in exhaled breath. Anal Chem 85(3):1792–1796
18. Choi SH, Hwang IS, Lee JH, Oh SG, Kim ID (2011) Microstructural control and selective C_2H_5OH sensing properties of Zn_2SnO_4 nanofibers prepared by electrospinning. Chem Commun 47(33):9315–9317
19. Shin J, Choi S-J, Lee I, Youn D-Y, Park CO, Lee J-H, Tuller HL, Kim I-D (2013) Thin-wall assembled SnO_2 fibers functionalized by catalytic Pt nanoparticles and their superior exhaled-breath-sensing properties for the diagnosis of diabetes. Adv Funct Mater 23:2357–2367

20. Xu L, Dong B, Wang Y, Bai X, Liu Q, Song H (2010) Electrospinning preparation and room temperature gas sensing properties of porous In_2O_3 nanotubes and nanowires. Sens Actuators B 147(2):531–538
21. Wei S, Zhang Y, Zhou M (2011) Toluene sensing properties of SnO_2–ZnO hollow nanofibers fabricated from single capillary electrospinning. Solid State Commun 151(12):895–899
22. Zhang ZY, Li XH, Wang CH, Wei LM, Liu YC, Shao CL (2009) ZnO hollow nanofibers: fabrication from facile single capillary electrospinning and applications in gas sensors. J Phys Chem C 113(45):19397–19403
23. Xu L, Song H, Dong B, Wang Y, Chen J, Bai X (2010) Preparation and bifunctional gas sensing properties of porous In_2O_3-CeO_2 binary oxide nanotubes. Inorg Chem 49(22):10590–10597
24. Wei S, Zhou M, Du W (2011) Improved acetone sensing properties of ZnO hollow nanofibers by single capillary electrospinning. Sens Actuators B 160(1):753–759
25. Zhang J, Choi S-W, Kim SS (2011) Micro- and nano-scale hollow TiO_2 fibers by coaxial electrospinning: preparation and gas sensing. J Solid State Chem 184(11):3008–3013
26. Li D, Xia YN (2004) Direct fabrication of composite and ceramic hollow nanofibers by electrospinning. Nano Lett 4(5):933–938
27. Xu L, Zheng R, Liu S, Song J, Chen J, Dong B, Song H (2012) NiO@ZnO heterostructured nanotubes: coelectrospinning fabrication, characterization, and highly enhanced gas sensing properties. Inorg Chem 51(14):7733–7740
28. Cho NG, Yang DJ, Jin M-J, Kim H-G, Tuller HL, Kim I-D (2011) Highly sensitive SnO_2 hollow nanofiber-based NO_2 gas sensors. Sens Actuators B 160(1):1468–1472
29. Cho S, Kim D-H, Lee B-S, Jung J, Yu W-R, Hong S-H, Lee S (2012) Ethanol sensors based on ZnO nanotubes with controllable wall thickness via atomic layer deposition, an O_2 plasma process and an annealing process. Sens Actuators B 162(1):300–306
30. Choi SH, Ankonina G, Youn DY, Oh SG, Hong JM, Rothschild A, Kim ID (2009) Hollow ZnO nanofibers fabricated using electrospun polymer templates and their electronic transport properties. ACS Nano 3(9):2623–2631
31. Cho NG, Kim ID (2011) NO_2 gas sensing properties of amorphous $InGaZnO_4$ submicron-tubes prepared by polymeric fiber templating route. Sens Actuator B Chem 160(1):499–504
32. Cho NG, Woo HS, Lee JH, Kim ID (2011) Thin-walled NiO tubes functionalized with catalytic Pt for highly selective C_2H_5OH sensors using electrospun fibers as a sacrificial template. Chem Commun 47(40):11300–11302
33. Park JY, Choi SW, Kim SS (2010) A synthesis and sensing application of hollow ZnO nanofibers with uniform wall thicknesses grown using polymer templates. Nanotechnology 21(47):475601
34. Kim WS, Lee BS, Kim DH, Kim HC, Yu WR, Hong SH (2010) SnO_2 nanotubes fabricated using electrospinning and atomic layer deposition and their gas sensing performance. Nanotechnology 21(24):245605
35. Bognitzki M, Frese T, Steinhart M, Greiner A, Wendorff JH, Schaper A, Hellwig M (2001) Preparation of fibers with nanoscaled morphologies: electrospinning of polymer blends. Polym Eng Sci 41(6):982–989
36. Han SO, Son WK, Cho DW, Youk JH, Park WH (2004) Preparation of porous ultra-fine fibres via selective thermal degradation of electrospun polyetherimide/poly(3-hydroxybutyrate-co-3-hydroxyvalerate) fibres. Polym Degrad Stab 86(2):257–262
37. Peng M, Li DS, Shen L, Chen Y, Zheng Q, Wang HJ (2006) Nanoporous structured submicrometer carbon fibers prepared via solution electrospinning of polymer blends. Langmuir 22(22):9368–9374
38. Pai CL, Boyce MC, Rutledge GC (2009) Morphology of porous and wrinkled fibers of polystyrene electrospun from dimethylformamide. Abstr Pap Am Chem S 238
39. Han SO, Son WK, Youk JH, Lee TS, Park WH (2005) Ultrafine porous fibers electrospun from cellulose triacetate. Mater Lett 59(24–25):2998–3001
40. Nayani K, Katepalli H, Sharma CS, Sharma A, Patil S, Venkataraghavan R (2012) Electrospinning combined with nonsolvent-induced phase separation to fabricate highly porous and hollow submicrometer polymer fibers. Ind Eng Chem Res 51(4):1761–1766

41. Hong YL, Chen XS, Jing XB, Fan HS, Gu ZW, Zhang XD (2010) Fabrication and drug delivery of ultrathin mesoporous bioactive glass hollow fibers. Adv Funct Mater 20(9):1503–1510
42. Shengyuan Y, Peining Z, Nair AS, Ramakrishna S (2011) Rice grain-shaped TiO_2 mesostructures – synthesis, characterization and applications in dye-sensitized solar cells and photocatalysis. J Mater Chem 21(18):6541
43. Wang W, Zhou JY, Zhang SS, Song J, Duan HG, Zhou M, Gong CS, Bao Z, Lu BA, Li XD, Lan W, Xie EQ (2010) A novel method to fabricate silica nanotubes based on phase separation effect. J Mater Chem 20(41):9068–9072
44. Bognitzki M, Czado W, Frese T, Schaper A, Hellwig M, Steinhart M, Greiner A, Wendorff JH (2001) Nanostructured fibers via electrospinning. Adv Mater 13(1):70–72
45. Casper CL, Stephens JS, Tassi NG, Chase DB, Rabolt JF (2004) Controlling surface morphology of electrospun polystyrene fibers: effect of humidity and molecular weight in the electrospinning process. Macromolecules 37(2):573–578
46. Morrison SR (1987) Selectivity in semiconductor gas sensors. Sens Actuator 12(4):425–440
47. Tong MS, Dai GR, Gao DS (2001) Surface modification of oxide thin film and its gas-sensing properties. Appl Surf Sci 171(3–4):226–230
48. Lin HM, Hsu CM, Yang HY, Leeb PY, Yang CC (1994) Nanocrystalline WO_3-based H_2S sensors. Sens Actuat B Chem 22(1):63–68
49. Yamazoe N (1991) New approaches for improving semiconductor gas sensors. Sens Actuator B Chem 5(1–4):7–19
50. Yang DJ, Kamienchick I, Youn DY, Rothschild A, Kim ID (2010) Ultrasensitive and highly selective gas sensors based on electrospun SnO_2 nanofibers modified by Pd loading. Adv Funct Mater 20(24):4258–4264
51. Dong KY, Choi JK, Hwang IS, Lee JW, Kang BH, Ham DJ, Lee JH, Ju BK (2011) Enhanced H_2S sensing characteristics of Pt doped SnO_2 nanofibers sensors with micro heater. Sens ActuatOR B Chem 157(1):154–161
52. Choi J-K, Hwang I-S, Kim S-J, Park J-S, Park S-S, Jeong U, Kang YC, Lee J-H (2010) Design of selective gas sensors using electrospun Pd-doped SnO_2 hollow nanofibers. Sens Actuators B 150(1):191–199
53. Matsushima S, Teraoka Y, Miura N, Yamazoe N (1988) Electronic interaction between metal additives and tin dioxide in tin dioxide-based gas sensors. Jpn J Appl Phys 27(10):1798–1802
54. Zhang H, Li Z, Liu L, Xu X, Wang Z, Wang W, Zheng W, Dong B, Wang C (2010) Enhancement of hydrogen monitoring properties based on Pd–SnO_2 composite nanofibers. Sens Actuators B 147(1):111–115
55. Liu L, Li SC, Zhuang J, Wang LY, Zhang JB, Li HY, Liu Z, Han Y, Jiang XX, Zhang P (2011) Improved selective acetone sensing properties of Co-doped ZnO nanofibers by electrospinning. Sens Actuator B Chem 155(2):782–788
56. Tarascon JM, Armand M (2001) Issues and challenges facing rechargeable lithium batteries. Nature 414(6861):359–367
57. Winter M, Brodd RJ (2004) What are batteries, fuel cells, and supercapacitors? Chem Rev 104(10):4245–4269
58. Tarascon JM (2010) Key challenges in future Li-battery research. Philos T R Soc A 368(1923):3227–3241
59. Jeong G, Kim YU, Kim H, Kim YJ, Sohn HJ (2011) Prospective materials and applications for Li secondary batteries. Energy Environ Sci 4(6):1986–2002
60. Whittingham MS (2004) Lithium batteries and cathode materials. Chem Rev 104(10):4271–4301
61. Arico AS, Bruce P, Scrosati B, Tarascon JM, Van Schalkwijk W (2005) Nanostructured materials for advanced energy conversion and storage devices. Nat Mater 4(5):366–377
62. Goodenough JB, Kim Y (2010) Challenges for rechargeable Li batteries. Chem Mater 22(3):587–603
63. Bruce PG, Scrosati B, Tarascon JM (2008) Nanomaterials for rechargeable lithium batteries. Angew Chem Int Ed 47(16):2930–2946
64. JrO B (1999) Handbook of battery materials. Wiley-VCH, Weinheim/New York

65. Inaba M, Ogumi Z (2001) Up-to-date development of lithium-ion batteries in Japan. IEEE Electr Insul M 17(6):6–20
66. Schalkwijk WAV, Scrosati B (2002) Advances in lithium-ion batteries. Kluwer/Plenum, New York
67. Takehara Z (1997) Future prospects of the lithium metal anode. J Power Sources 68(1):82–86
68. Peled E, Golodnitsky D, Ardel G, Eshkenazy V (1995) The Sei model – application to lithium polymer electrolyte batteries. Electrochim Acta 40(13–14):2197–2204
69. Persson K, Sethuraman VA, Hardwick LJ, Hinuma Y, Meng YS, van der Ven A, Srinivasan V, Kostecki R, Ceder G (2010) Lithium diffusion in graphitic carbon. J Phys Chem Lett 1(8):1176–1180
70. Ryu WH, Shin J, Jung JW, Kim ID (2013) Cobalt(II) monoxide nanoparticles embedded in porous carbon nanofibers as a highly reversible conversion reaction anode for Li-ion batteries. J Mater Chem A 1(10):3239–3243
71. Kim C, Yang KS, Kojima M, Yoshida K, Kim YJ, Kim YA, Endo M (2006) Fabrication of electrospinning-derived carbon nanofiber webs for the anode material of lithium-ion secondary batteries. Adv Funct Mater 16(18):2393–2397
72. Lee BS, Son SB, Park KM, Yu WR, Oh KH, Lee SH (2012) Anodic properties of hollow carbon nanofibers for Li-ion battery. J Power Sources 199:53–60
73. Liu BX, Yu YH, Chang J, Yang XJ, Wu DZ, Yang XP (2011) An enhanced stable-structure core-shell coaxial carbon nanofiber web as a direct anode material for lithium-based batteries. Electrochem Commun 13(6):558–561
74. Chen YM, Lu ZG, Zhou LM, Mai YW, Huang HT (2012) In situ formation of hollow graphitic carbon nanospheres in electrospun amorphous carbon nanofibers for high-performance Li-based batteries. Nanoscale 4(21):6800–6805
75. Lee BS, Son SB, Park KM, Lee G, Oh KH, Lee SH, Yu WR (2012) Effect of pores in hollow carbon nanofibers on their negative electrode properties for a lithium rechargeable battery. ACS Appl Mater Interfaces 4(12):6701–6709
76. Dey AN (1971) Electrochemical alloying of lithium in organic electrolytes. J Electrochem Soc 118(10):1547–1549
77. Huggins RA (1999) Lithium alloy negative electrodes. J Power Sources 81:13–19
78. Park CM, Kim JH, Kim H, Sohn HJ (2010) Li-alloy based anode materials for Li secondary batteries. Chem Soc Rev 39(8):3115–3141
79. Weppner W, Huggins RA (1978) Thermodynamic properties of intermetallic systems lithium-antimony and lithium-bismuth. J Electrochem Soc 125(1):7–14
80. Wen CJ, Huggins RA (1981) Thermodynamic study of the lithium-tin system. J Electrochem Soc 128(6):1181–1187
81. Besenhard JO, Yang J, Winter M (1997) Will advanced lithium-alloy anodes have a chance in lithium-ion batteries? J Power Sources 68(1):87–90
82. Boukamp BA, Lesh GC, Huggins RA (1981) All-solid lithium electrodes with mixed-conductor matrix. J Electrochem Soc 128(4):725–729
83. Stjohn MR, Furgala AJ, Sammells AF (1982) Thermodynamic studies of Li-Ge alloys – application to negative electrodes for molten-salt batteries. J Electrochem Soc 129(2):246–250
84. Wen CJ, Huggins RA (1981) Chemical diffusion in intermediate phases in the lithium-silicon system. J Solid State Chem 37(3):271–278
85. Goward GR, Taylor NJ, Souza DCS, Nazar LF (2001) The true crystal structure of $Li_{17}M_4$ (M=Ge, Sn, Pb)-revised from $Li_{22}M_5$. J Alloy Compd 329(1–2):82–91
86. Lupu C, Mao JG, Rabalais JW, Guloy AM, Richardson JW (2003) X-ray and neutron diffraction studies on "$Li_{4.4}Sn$". Inorg Chem 42(12):3765–3771
87. Yang HB, Fu PP, Zhang HF, Song YJ, Zhou ZX, Wu MT, Huang LH, Xu G (2007) Amorphous Si film anode coupled with $LiCoO_2$ cathode in Li-ion cell. J Power Sources 174(2):533–537

88. Kepler KD, Vaughey JT, Thackeray MM (1999) $Li_xCu_6Sn_5$ ($0 < x < 13$): An intermetallic insertion electrode for rechargeable lithium batteries. Electrochem Solid State 2(7):307–309

89. Li H, Huang XJ, Chen LQ, Wu ZG, Liang Y (1999) A high capacity nano-Si composite anode material for lithium rechargeable batteries. Electrochem Solid State 2(11):547–549

90. Kang K, Lee HS, Han DW, Kim GS, Lee D, Lee G, Kang YM, Jo MH (2010) Maximum Li storage in Si nanowires for the high capacity three-dimensional Li-ion battery. Appl Phys Lett 96(5)

91. Cui LF, Yang Y, Hsu CM, Cui Y (2009) Carbon-silicon core-shell nanowires as high capacity electrode for lithium ion batteries. Nano Lett 9(9):3370–3374

92. Yoo JK, Kim J, Jung YS, Kang K (2012) Scalable fabrication of silicon nanotubes and their application to energy storage. Adv Mater 24(40):5452–5456

93. Li LM, Yin XM, Liu SA, Wang YG, Chen LB, Wang TH (2010) Electrospun porous SnO_2 nanotubes as high capacity anode materials for lithium ion batteries. Electrochem Commun 12(10):1383–1386

94. Wu H, Chan G, Choi JW, Ryu I, Yao Y, McDowell MT, Lee SW, Jackson A, Yang Y, Hu LB, Cui Y (2012) Stable cycling of double-walled silicon nanotube battery anodes through solid-electrolyte interphase control. Nat Nanotechnol 7(5):309–314

95. Yu Y, Gu L, Wang CL, Dhanabalan A, van Aken PA, Maier J (2009) Encapsulation of Sn@carbon nanoparticles in bamboo-like hollow carbon nanofibers as an anode material in lithium-based batteries. Angew Chem Int Ed 48(35):6485–6489

96. Kim D, Lee D, Kim J, Moon J (2012) Electrospun Ni-added SnO_2-carbon nanofiber composite anode for high-performance lithium-ion batteries. ACS Appl Mater Interfaces 4(10):5408–5415

97. Bonino CA, Ji LW, Lin Z, Toprakci O, Zhang XW, Khan SA (2011) Electrospun carbon-tin oxide composite nanofibers for use as lithium ion battery anodes. ACS Appl Mater Interfaces 3(7):2534–2542

98. Zou L, Gan L, Lv RT, Wang MX, Huang ZH, Kang FY, Shen WC (2011) A film of porous carbon nanofibers that contain Sn/SnO_x nanoparticles in the pores and its electrochemical performance as an anode material for lithium ion batteries. Carbon 49(1):89–95

99. Yu Y, Gu L, Zhu CB, van Aken PA, Maier J (2009) Tin nanoparticles encapsulated in porous multichannel carbon microtubes: preparation by single-nozzle electrospinning and application as anode material for high-performance Li-based batteries. J Am Chem Soc 131(44):15984–15985

100. Hwang TH, Lee YM, Kong BS, Seo JS, Choi JW (2012) Electrospun core-shell fibers for robust silicon nanoparticle-based lithium ion battery anodes. Nano Lett 12(2):802–807

101. Guo YG, Hu JS, Wan LJ (2008) Nanostructured materials for electrochemical energy conversion and storage devices. Adv Mater 20(15):2878–2887

102. Li YG, Tan B, Wu YY (2008) Mesoporous Co_3O_4 nanowire arrays for lithium ion batteries with high capacity and rate capability. Nano Lett 8(1):265–270

103. Kim SW, Lee HW, Muralidharan P, Seo DH, Yoon WS, Kim DK, Kang K (2011) Electrochemical performance and ex situ analysis of $ZnMn_2O_4$ nanowires as anode materials for lithium rechargeable batteries. Nano Res 4(5):505–510

104. Ji LW, Toprakci O, Alcoutlabi M, Yao YF, Li Y, Zhang S, Guo BK, Lin Z, Zhang XW (2012) Alpha-Fe_2O_3 nanoparticle-loaded carbon nanofibers as stable and high-capacity anodes for rechargeable lithium-ion batteries. Acs Appl Mater Interfaces 4(5):2672–2679

105. Wang B, Cheng JL, Wu YP, Wang D, He DN (2012) Porous NiO fibers prepared by electrospinning as high performance anode materials for lithium ion batteries. Electrochem Commun 23:5–8

106. Chaudhari S, Srinivasan M (2012) 1D hollow alpha-Fe_2O_3 electrospun nanofibers as high performance anode material for lithium ion batteries. J Mater Chem 22(43):23049–23056

107. Cherian CT, Sundaramurthy J, Kalaivani M, Ragupathy P, Kumar PS, Thavasi V, Reddy MV, Sow CH, Mhaisalkar SG, Ramakrishna S, Chowdari BVR (2012) Electrospun alpha-Fe_2O_3 nanorods as a stable, high capacity anode material for Li-ion batteries. J Mater Chem 22(24):12198–12204

108. Luo W, Hu XL, Sun YM, Huang YH (2012) Electrospun porous $ZnCo_2O_4$ nanotubes as a high-performance anode material for lithium-ion batteries. J Mater Chem 22(18):8916–8921

109. Teh PF, Sharma Y, Pramana SS, Srinivasan M (2011) Nanoweb anodes composed of one-dimensional, high aspect ratio, size tunable electrospun $ZnFe_2O_4$ nanofibers for lithium ion batteries. J Mater Chem 21(38):14999–15008

110. Lin Z, Ji LW, Woodroof MD, Zhang XW (2010) Electrodeposited MnO_x/carbon nanofiber composites for use as anode materials in rechargeable lithium-ion batteries. J Power Sources 195(15):5025–5031

111. Wang L, Yu Y, Chen PC, Zhang DW, Chen CH (2008) Electrospinning synthesis of C/Fe_3O_4 composite nanofibers and their application for high performance lithium-ion batteries. J Power Sources 183(2):717–723

112. Yang G, Li YH, Ji HM, Wang HY, Gao P, Wang L, Liu HD, Pinto J, Jiang XF (2012) Influence of Mn content on the morphology and improved electrochemical properties of Mn_3O_4 vertical bar MnO@carbon nanofiber as anode material for lithium batteries. J Power Sources 216:353–362

113. Ding YH, Zhang P, Long ZL, Jiang Y, Huang JN, Yan WJ, Liu G (2008) Synthesis and electrochemical properties of Co_3O_4 nanofibers as anode materials for lithium-ion batteries. Mater Lett 62(19):3410–3412

114. Sahay R, Kumar PS, Aravindan V, Sundaramurthy J, Ling WC, Mhaisalkar SG, Ramakrishna S, Madhavi S (2012) High aspect ratio electrospun CuO nanofibers as anode material for lithium-ion batteries with superior cycleability. J Phys Chem C 116(34):18087–18092

115. Ji LW, Medford AJ, Zhang XW (2009) Porous carbon nanofibers loaded with manganese oxide particles: formation mechanism and electrochemical performance as energy-storage materials. J Mater Chem 19(31):5593–5601

116. Jung KN, Lee JI, Yoon S, Yeon SH, Chang W, Shin KH, Lee JW (2012) Manganese oxide/carbon composite nanofibers: electrospinning preparation and application as a bi-functional cathode for rechargeable lithium-oxygen batteries. J Mater Chem 22(41):21845–21848

117. Ji LW, Lin Z, Medford AJ, Zhang XW (2009) In-situ encapsulation of nickel particles in electrospun carbon nanofibers and the resultant electrochemical performance. Chem Eur J 15(41):10718–10722

118. Ji LW, Zhang XW (2009) Manganese oxide nanoparticle-loaded porous carbon nanofibers as anode materials for high-performance lithium-ion batteries. Electrochem Commun 11(4):795–798

119. Wang B, Cheng JL, Wu YP, Wang D, He DN (2013) Electrochemical performance of carbon/Ni composite fibers from electrospinning as anode material for lithium ion batteries. J Mater Chem A 1(4):1368–1373

120. Deng D, Kim MG, Lee JY, Cho J (2009) Green energy storage materials: nanostructured TiO_2 and Sn-based anodes for lithium-ion batteries. Energy Environ Sci 2(8):818–837

121. Kubiaka P, Geserick J, Husing N, Wohfahrt-Mehrens A (2008) Electrochemical performance of mesoporous TiO_2 anatase. J Power Sources 175(1):510–516

122. Liu B, Deng D, Lee JY, Aydil ES (2010) Oriented single-crystalline TiO_2 nanowires on titanium foil for lithium ion batteries. J Mater Res 25(8):1588–1594

123. Nuspl G, Yoshizawa K, Yamabe T (1997) Lithium intercalation in TiO_2 modifications. J Mater Chem 7(12):2529–2536

124. Zhu GN, Wang YG, Xia YY (2012) Ti-based compounds as anode materials for Li-ion batteries. Energy Environ Sci 5(5):6652–6667

125. Ryu WH, Nam DH, Ko YS, Kim RH, Kwon HS (2012) Electrochemical performance of a smooth and highly ordered TiO_2 nanotube electrode for Li-ion batteries. Electrochim Acta 61:19–24

126. Luo W, Hu XL, Sun YM, Huang YH (2012) Surface modification of electrospun TiO_2 nanofibers via layer-by-layer self-assembly for high-performance lithium-ion batteries. J Mater Chem 22(11):4910–4915

127. Lu HW, Zeng W, Li YS, Fu ZW (2007) Fabrication and electrochemical properties of three-dimensional net architectures of anatase TiO_2 and spinel $Li_4Ti_5O_{12}$ nanofibers. J Power Sources 164(2):874–879

128. Han H, Song T, Bae JY, Nazar LF, Kim H, Paik U (2011) Nitridated TiO_2 hollow nanofibers as an anode material for high power lithium ion batteries. Energy Environ Sci 4(11):4532–4536

129. Zhao BT, Cai R, Jiang SM, Sha YJ, Shao ZP (2012) Highly flexible self-standing film electrode composed of mesoporous rutile TiO_2/C nanofibers for lithium-ion batteries. Electrochim Acta 85:636–643

130. Zhang X, Kumar PS, Aravindan V, Liu HH, Sundaramurthy J, Mhaisalkar SG, Duong HM, Ramakrishna S, Madhavi S (2012) Electrospun TiO_2-graphene composite nanofibers as a highly durable insertion anode for lithium ion batteries. J Phys Chem C 116(28):14780–14788

131. Zhu PN, Wu YZ, Reddy MV, Nair AS, Chowdari BVR, Ramakrishna S (2012) Long term cycling studies of electrospun TiO_2 nanostructures and their composites with MWCNTs for rechargeable Li-ion batteries. RSC Adv 2(2):531–537

132. Nam SH, Shim HS, Kim YS, Dar MA, Kim JG, Kim WB (2010) Ag or Au nanoparticle-embedded one-dimensional composite TiO_2 nanofibers prepared via electrospinning for use in lithium-ion batteries. ACS Appl Mater Interfaces 2(7):2046–2052

133. Zaghib K, Simoneau M, Armand M, Gauthier M (1999) Electrochemical study of $Li_4Ti_5O_{12}$ as negative electrode for Li-ion polymer rechargeable batteries. J Power Sources 81:300–305

134. Jo MR, Jung YS, Kang YM (2012) Tailored $Li_4Ti_5O_{12}$ nanofibers with outstanding kinetics for lithium rechargeable batteries. Nanoscale 4(21):6870–6875

135. Choi HS, Kim T, Im JH, Park CR (2011) Preparation and electrochemical performance of hyper-networked $Li_4Ti_5O_{12}$/carbon hybrid nanofiber sheets for a battery-supercapacitor hybrid system. Nanotechnology 22(40)

136. Guo BK, Li Y, Yao YF, Lin Z, Ji LW, Xu GJ, Liang YZ, Shi Q, Zhang XW (2011) Electrospun $Li_4Ti_5O_{12}$/C composites for lithium-ion batteries with high rate performance. Solid State Ion 204:61–65

137. Li HS, Shen LF, Zhang XG, Nie P, Chen L, Xu K (2012) Electrospun hierarchical $Li_4Ti_{4.95}Nb_{0.05}O_{12}$/carbon composite nanofibers for high rate lithium ion batteries. J Electrochem Soc 159(4):A426–A430

138. Wang L, Xiao QZ, Li ZH, Lei GT, Zhang P, Wu LJ (2012) Synthesis of $Li_4Ti_5O_{12}$ fibers as a high-rate electrode material for lithium-ion batteries. J Solid State Electrochem 16(10):3307–3313

139. Zhu N, Liu W, Xue MQ, Xie ZA, Zhao D, Zhang MN, Chen JT, Cao TB (2010) Graphene as a conductive additive to enhance the high-rate capabilities of electrospun $Li_4Ti_5O_{12}$ for lithium-ion batteries. Electrochim Acta 55(20):5813–5818

140. Han JT, Huang YH, Goodenough JB (2011) New anode framework for rechargeable lithium batteries. Chem Mater 23(8):2027–2029

141. Tang K, Mu XK, van Aken PA, Yu Y, Maier J (2013) "Nano-Pearl-String" $TiNb_2O_7$ as anodes for rechargeable lithium batteries. Adv Energy Mater 3(1):49–53

Mesoporous Transition Metal Oxide Ceramics

24

Massey de Los Reyes and Peter Majewski

Development of Porous Materials

One of the most important milestones in the history and applicability of porous materials is the discovery of zeolites and porous silicates. Accompanying a large family of crystalline aluminosilicates, zeolites were first discovered by a Swedish mineralogist Axel Fredrik Cronstedt in 1756 who found that upon heating a tectosilicate mineral called 'silbite', the material was observed to froth releasing bouts of steam, thus the name *zeo* for boiling and *lithos* or *lite* for stone [1, 2]. Within a few years of this breakthrough, the ion-exchange properties were noted, although the ability to absorb small molecules and organics was not discovered until the early 1900s [3]. Studies of the adsorption and diffusion of organic molecules such as benzene and chloroform on zeolites by J. W. McBain in 1932 lead to the recognition of the potential for separating molecules using zeolites, and hence the expression 'molecular sieve' was coined [4]. This term was used to describe a class of materials that exhibit high surface areas and selective sorption properties through the screening of molecules of different size through inherent micro porosity (i.e., pores no bigger than 5 Å) [5]. Between 1949 and 1953 the large upscale synthesis of a new class of commercialized zeolites A(LTA), X(FAU), and Y(FAU) was undertaken by Milton and Breck and the name Linde Molecular Sieves (LMS) was announced in 1954,

M. de Los Reyes
Australian Nuclear Science and Technology Organization, Lucas Heights, Australia

P. Majewski (✉)
Division of Information Technology, Engineering and the Environment, School of Engineering,
Mawson Institute, University of South Australia, Mawson Lakes, Australia
e-mail: Peter.Majewski@unisa.edu.au

representing one of the most important industrial zeolites used today [6]. Within the last 50 years, approximately 150 new structures have been developed and characterized, including a family of aluminophosphates and silicoaluminophosphonates, with the practical applications of these zeolites still expanding [7–9].

Despite the many important applications of zeolites, most especially for industrial catalysis (i.e., catalytic cracking, dewaxing), a continued interest to expand the pore size of zeotype materials remained. With much effort focused upon breaking through the micropore size domain into the mesoporous and macroporous regions, increasing demands of industry and also new insights gained from fundamental research have expanded zeolite applications [10, 11]. Of particular interest was the cracking of high molecular weight hydrocarbons. Other uses included (i) a separation tool for heavy metals and radionuclides, (ii) the encapsulation of complexes for drug delivery, and (iii) the introduction of nanometer-sized particles within zeolites for electronic and optical applications [12–15].

Since it was thought that organic templates used in zeolite synthesis affected the gel chemistry of the materials by filling out the voids in the growing solid, many attempts at increasing the pore size made use of large template molecules. It was not until 1982 when researchers from the Union Carbide Corporation in New York first synthesized a so-called 'ultra large pore molecular sieve' $AlPO_4$-8 containing 14-membered rings that a new class of molecular sieve materials came into fruition [16]. These three-dimensional crystalline aluminophosphate phases have uniform pore dimensions ranging from about 3 to 10 Å and are capable of making size selective separations of molecular species. Not only did this break with traditional views of zeolites and zeolite chemistry, but it also paved the way for further studies into other large pore molecular sieves, including VPI-5 with an 18-tetrahedral ring opening and cloverite and JDF-20 with a 20-membered ring opening [17–19]. Although zeolites still attract considerable attention for numerous applications, their inherently poor thermal and radiation stabilities, weak acidity, and small pore sizes brought about a need for research into a new branch of materials, namely, the breakthrough of mesoporous molecular sieves.

Mesoporous carbon, namely, activated carbon, is also widely used, e.g., as filter material and molecular sieve. It is obtained via combustion, partial combustion, or thermal decomposition from a variety of carbonaceous raw materials such as wood charcoal, grain hulls, and nutshells. Typically, conventional activated carbons possess surface areas and pore volumes in the range 10–200 m^2/g and 0.1–0.5 cm^3/g, respectively [20].

Organized Mesoporous Materials

The fabrication of a new branch of organized mesoporous silica molecular sieves pioneered by Kresge et al. of the Mobil Oil Research and Development Corporation in early 1992 opened a new field of research in materials science [21]. Breaking past the long-standing pore-size constraints of microporous zeolites, members
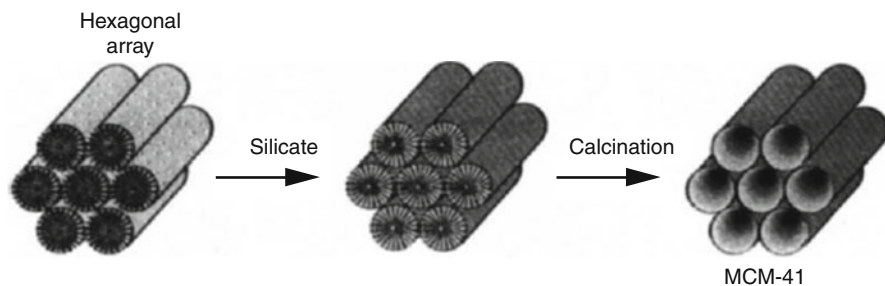
Fig. 24.1 A schematic representation of the MCM-41 liquid crystal templating mechanism using silicate ions with polar groups of quaternary ammonium cations. Calcination burns off original organic material, leaving hollow cylinders [21] (Reprint with permission from Nature Publishing Group)

of this family, designated MCM-41, were first observed through transmission electron micrographs from aluminosilicate sol-gels through liquid crystal or 'supramolecular templating' of quaternary ammonium surfactants (Fig. 24.1) [21]. The synthetic paradigm shift from the synthesis of microporous zeolites to mesoporous silicates was the use of molecular aggregates as opposed to single-molecule templates. That is, in zeolite synthesis a single molecule creates the channel shape or directs the structure. In the case of supramolecular templating, the channels are created by large molecular aggregates afforded by amphiphilic molecules such as surfactants. This synthesis procedure gave rise to hexagonally shaped mesophases with pore diameters ranging from 20 to 100 Å, surface areas above 1,000 m^2/g, and pore volumes of 0.79 cm^3/g. By the simple change in the length of the surfactant, molecule used or the silica source (e.g., fused silica, colloidal silica, tetraethylorthosilicate (TEOS)), the diameter and shape of the mesoporous structure could be controlled [22, 23]. Some refined phases, such as MCM-48 and MCM-50, were also reported in earlier publications [24, 25]. From the early days of periodic mesoporous material synthesis, revolutionary developments have been achieved in the synthesis, characterization, and application of these materials, stimulating the search beyond silica-based materials to other mesostructured compositions, particularly transition metal oxides and mixed metal oxides. Huo and co-workers at the University of California developed the first stable examples in 1994 [26, 27].

The synthesis of mesoporous transition metal oxides containing zinc, aluminum, and tungsten was performed and based on the cooperative formation of inorganic-organic interfaces through 'charge density matching' that minimized both the organic van der Waals interactions and the inorganic-organic charge to allow the formation of the resulting mesostructure [26, 27]. Many other materials containing titanium, zirconium, and manganese oxides as well as rare earth metals followed suit, using different synthetic pathways such as nanocasting, nanocrystalline templating, and self-assembly [28–30]. Periodic mesoporous materials have also been synthesized based on the 'bottom up' strategy using block
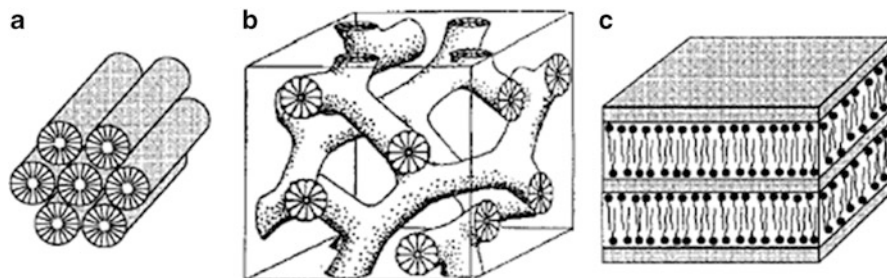
Fig. 24.2 An example of three different mesoporous structures: (**a**) hexagonal, (**b**) cubic bicontinuous, and (**c**) lamellar [36] (Reprint with permission from American Chemical Society)

copolymer structure-directing agents such as Pluronic P123 and Brij 58 [31]. By varying the chemical composition, structural properties, and reaction conditions, it has been possible to attain a remarkable range of porous structures (Fig. 24.2). Such structures offer significant potential in molecular adsorption studies, not only due to the cost-effectiveness of the material but also because the structures have the capability and variability to impart different size constraints to incoming 'guest species'. Particularly for large biomolecules in bioadsorption and biocatalysts, mesoporous structures, unlike zeolites, have pores that can be manipulated in size [32–35].

For these and other related applications such as battery electrodes and capacitors, mesoporous carbonaceous materials are also of interest, following a similar trend of previously inherent microporosity that has broken into the mesoporous regime in the last decade [37–40].

## Sol–Gel Synthesis of Transition Metal Oxides

Innovative synthesis techniques and the flexibility to alter composition and structure are essential for the novelty of mesoporous materials where designing intricate inorganic structures are modelled by rational synthetic pathways [37]. One of the most established techniques administered in this area is sol–gel synthesis. It offers many advantages over other conventional preparation methods due to (i) lower processing temperatures, (ii) smaller production costs, and (iii) precise control over the chemical homogeneity that can manipulate the size and shape of materials [38]. Basically, the sol–gel method involves both the hydrolysis and condensation of metallic and nonmetallic molecular precursors via inorganic polymerization. The precursors may either be an aqueous solution of an inorganic salt, organometallic compound, or metal alkoxide. Aqueous solutions of transition metal alkoxides can involve a number of molecular species, those of which are affected by the oxidation state, pH, and concentration [39]. Such reactions are generally described as [40].

Table 24.1 Molecular complexity of titanium and zirconium tetravalent metal alkoxides

Alkoxide M(OR)$_4$ (R = OPr, OEt)	Ti(OR)$_4$	Zr(OR)$_4$
Covalent radius (Å)	1.32	1.45
Coordination/oxidation state (N-Z)^a	2	3
Molecular complexity^b	2.9	3.6
Positive partial charge on M (δ)	+0.63	+0.65

^{a}Coordination/oxidation stat (N-Z): N is the number of water molecules covalently bound to cation M$^+$Z- charge on a particular cation or anion
^{b}In this context 'molecular complexity' of a metal oxide is where essential aspects of a molecule (geometry, topology, symmetry) are taken together and rated for its complexity. Data taken from [41]
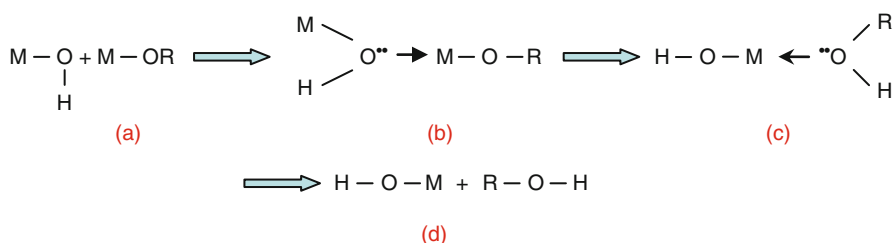
Fig. 24.3 A four-step hydrolysis process for transition metal alkoxides

$$\text{M-OR} + \text{H}_2\text{O} \rightarrow \text{M-OH} + \text{ROH (hydrolysis)} \qquad (24.1)$$

$$\text{M-OH} + \text{RO-M} \rightarrow \text{M-O-M} + \text{ROH (condensation)} \qquad (24.2)$$

The formation of condensed species commonly arises within these reactions, essentially producing oxopolymers and/or hydrous oxides $MO_n \times H_2O$ after excess water is added. Unlike silicate precursors such as $Si(OR)_4$, transition metal alkoxides ($M(OR)_n$) possess inherently high chemical reactivities which are often difficult to control due to rapid hydrolysis kinetics. This, in large part, is due to their smaller electronegativities. Transition metals themselves also have higher positive partial charges, making them more reactive (Table 24.1). Complexants or catalysts are sometimes used to slow down the rate of hydrolysis which prevents the final products from forming precipitates instead of gels. This is especially applied to binary mixed metal oxides whose hydrolysis kinetics are significantly different from one another [41].

Commonly, a four-step mechanism is proposed for metal alkoxide hydrolysis (Fig. 24.3) [42, 43]:

In the first instance (a), hydrolysis is initiated by the nucleophilic addition of a water molecule to a positively charged metal atom M. This then lends to (b) a 'transition state' where the coordination number of M increases by one. At the same time a proton transfer creates an intermediate (c). This proton then transfers to a neighboring negatively charged oxygen atom from an adjacent OR group.
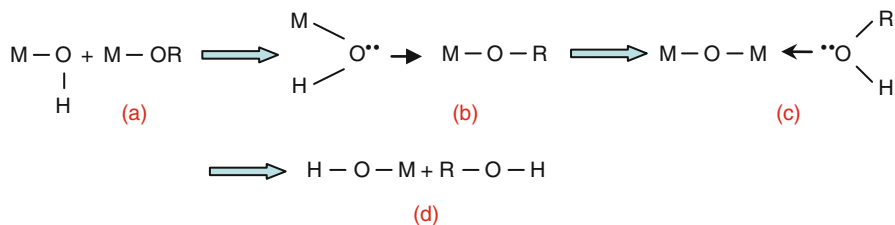
Fig. 24.4 The condensation (alcoxolation) of transition metal oxides

The departure of a leaving group, which should be the most positively charged species, also occurs in (c). The process (a) to (d) undergoes a nucleophilic substitution mechanism [40]. The thermodynamics of this reaction will be highly favored depending on the nucleophilic character of the entering molecule, electrophilic character of the metal atom, and the coordination unsaturation of the metal atom in the alkoxide [44]. Three different mechanisms have also been considered for condensation reactions generally incorporating alcoxolation, oxolation, and olation.

The first step in a condensation reaction occurs similarly to hydrolysis, although M replaces H in the first instance (Fig. 24.4) [40]. With oxolation, the leaving group is a water molecule and with olation either water or ROH leaves, depending on the concentration of water in the medium [42, 43]. Alcoxolation is a reaction where a bridging oxo group is formed through the elimination of an alcohol molecule [40]:

Here, the mesostructure assembly is very rapid, but the shape of the walls is not defined until the condensation of the metal oxides is complete. The removal of remaining liquid after this process usually requires drying through heat or solvent extraction and is generally accompanied by the shrinkage and densification of the gel. Solvent removal is also needed to promote further polycondensation and enhance the gel's structural properties [45]. The final product is usually an amorphous xerogel, although by manipulating the calcination temperature, crystal structures can also be obtained.

Mesostructure Formation with Amphiphilic Structure-Directing Agents (Anionic Carboxylates and Block Copolymer Templates)

Self-assembled amphiphilic templates have played an important role in tailoring the pore size and morphology of mesoporous materials due to their lyophilic (solvent loving) and lyophobic (solvent hating) bifunctional constituents [46]. In general, the formation of a surfactant involves the creation of micelles (microphases), where lyophobic chains sequester inside aggregates (a supramolecular array formed upon self-assembly of surfactant molecules) and lyophilic groups lie toward the solvent phase to minimize contact between the two incompatible ends [47]. Surfactants associate into micelles (micellation) in large part due to the surfactant concentration, the structure of the surfactant, and the temperature at which micelles are formed. This is termed the critical micelle concentration (CMC). At low surfactant
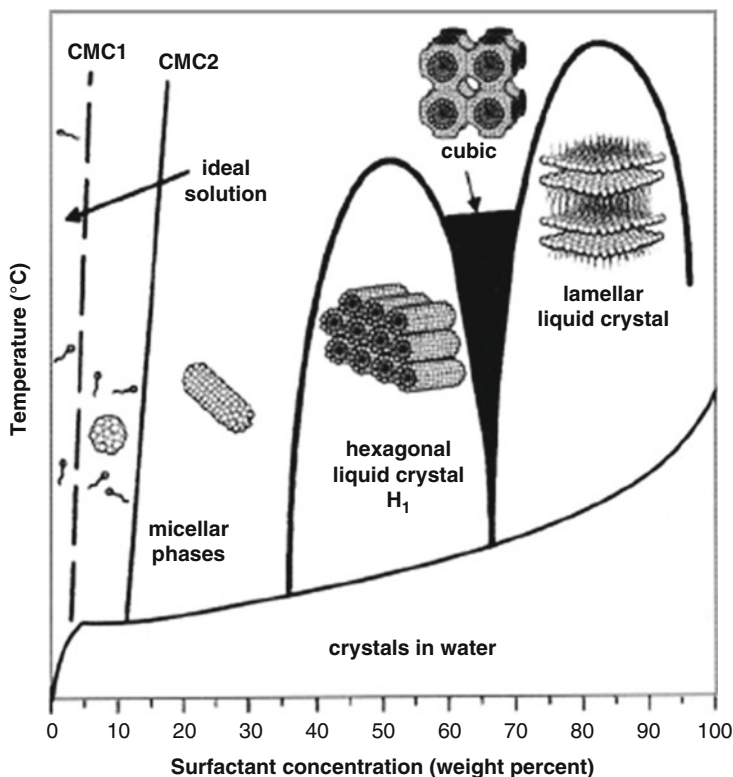
Fig. 24.5 An example of surfactant self-assembly using a schematic phase diagram for the template cetyltrimethylammonium bromide (*CTAB*) in water [36] (Reprint with permission from American Chemical Society)

concentrations, amphiphilic surfactants are present as free molecules either dissolved in aqueous solution or adsorbed at interfaces [48]. Slightly above this concentration (the first critical micelle concentration (CMC1)), individual surfactant molecules form small spherical-like aggregates. Beyond the second CMC (CMC2), surfactants not only assemble into micelles forming spheres but also cylindrical structures or rod-like micelles, with lyophilic parts maintaining contact with the aqueous phase while also shielding the lyophobic parts within the structures interior (Fig. 24.5) [49]. Adding more surfactant simply produces more micelles over a considerable concentration range rather than further growth of existing micelles. Details of this procedure may differ for other systems, although generally this scheme is valid for most depending on the surfactant used [50]. Amphiphilic molecules are associated physically, not chemically, and for this reason the size and shape of surfactants can be manipulated easily by responding to small changes in concentration, salt content, temperature, pH, and counterions in solution [51].

The way in which organic surfactants and inorganic species interact also plays a crucial role in the assembly of mesophases, with resulting structures strongly dependant on the charge of the surfactant, charge on the inorganic species, and the presence of any mediating ions. Cooperative mechanisms for the formation of mesostructures are generally based on specific electrostatic interactions between inorganic precursors (I) and surfactant head groups (S), and so far, as many as six to eight of these mechanisms have been identified to date (Fig. 24.6) [52, 53]. Apart from charge-matching mechanisms (which include reverse charge matching (i.e., S^+I^- and S^-I^+)) and like-charged surfactant/inorganic ions mediated through ions of opposite charge ($S^+X^-I^+$, X = halides or $S^-M^+I^-$, M = alkali metal ions), synthesis pathways have also been extended to neutral (S^0) or nonionic surfactants (N^0) [54]. Anionic long-chain carboxylic acid surfactants are a classic example of charge matched structure-directing agents used in sol–gel synthesis that have been found to act as simple complexants which retard the hydrolysis kinetics of metal alkoxides by decreasing their functionality through the partial substitution of O-R ligands [55]. This also eliminates the need for solvents, mitigating competition between carboxylates and alcohols for the complexation of metal centers and thus enabling control over hydrolysis kinetics [56].

Japanese researchers from the University of Chiba were among the first to investigate the use of carboxylic acids as surfactants for metal oxides, producing mesoporous TiO_2 using stearic acid ($C_{17}H_{35}CO_2H$) surfactants to generate pore diameters between 50 and 150 Å simply by altering the metal-to-surfactant ratio [58]. Takenaka et al followed suit using a variety of straight-chain alkylcarboxylates [$CH_3(CH_2)nCOOH$: $n = 0$–20] for the preparation of TiO_2 mesophases (Fig. 24.7) [59]. From Fourier transform infrared (FTIR) spectra, they found that strong complexation occurred between the carboxylate group and $Ti(OR)_4$ inorganic precursor, generating a 2:2 complex between them. Low-angle XRD patterns also evidenced these materials having a lamellar-type pore assembly as the structures grew in alkyl chain length [59]. In 1999, Antonelli utilized carboxylic acid surfactants for the preparation of hexagonally packed mesoporous zirconia through ligand-assisted templating [60]. Like Takenaka et al, Antonelli also found that varying the chain length of the surfactant also varied the pore size of ZrO_2 from micro to meso. After aging for a week at 150 °C in the absence of water, it was found from X-ray Diffraction (XRD) analysis that the pore structure was retained upon template removal with sulfuric acid in methanol. Further synthesis beyond TiO_2 and ZrO_2 using carboxylic acids has also been reported for other transition metal oxides including Al_2O_3 [61, 62].

Use of nonionic amphiphiles (block copolymers) to prepare metal oxide mesophases has also been well accepted as their ability to participate in hydrogen bonding with inorganic frameworks makes them easier to dissociate [54]. These amphiphiles also have the capability to produce both larger pore sizes (150–400 Å) and thicker walls that are affordable, nontoxic, and easy to remove from the metal oxide framework by thermal treatment or solvent extraction [63]. Pioneering works by Tanev and associates were the first to bring about this idea of using a nonionic surfactant template, dodecylamine (DDA, $C_{12}H_{27}N$), as a porogen to create
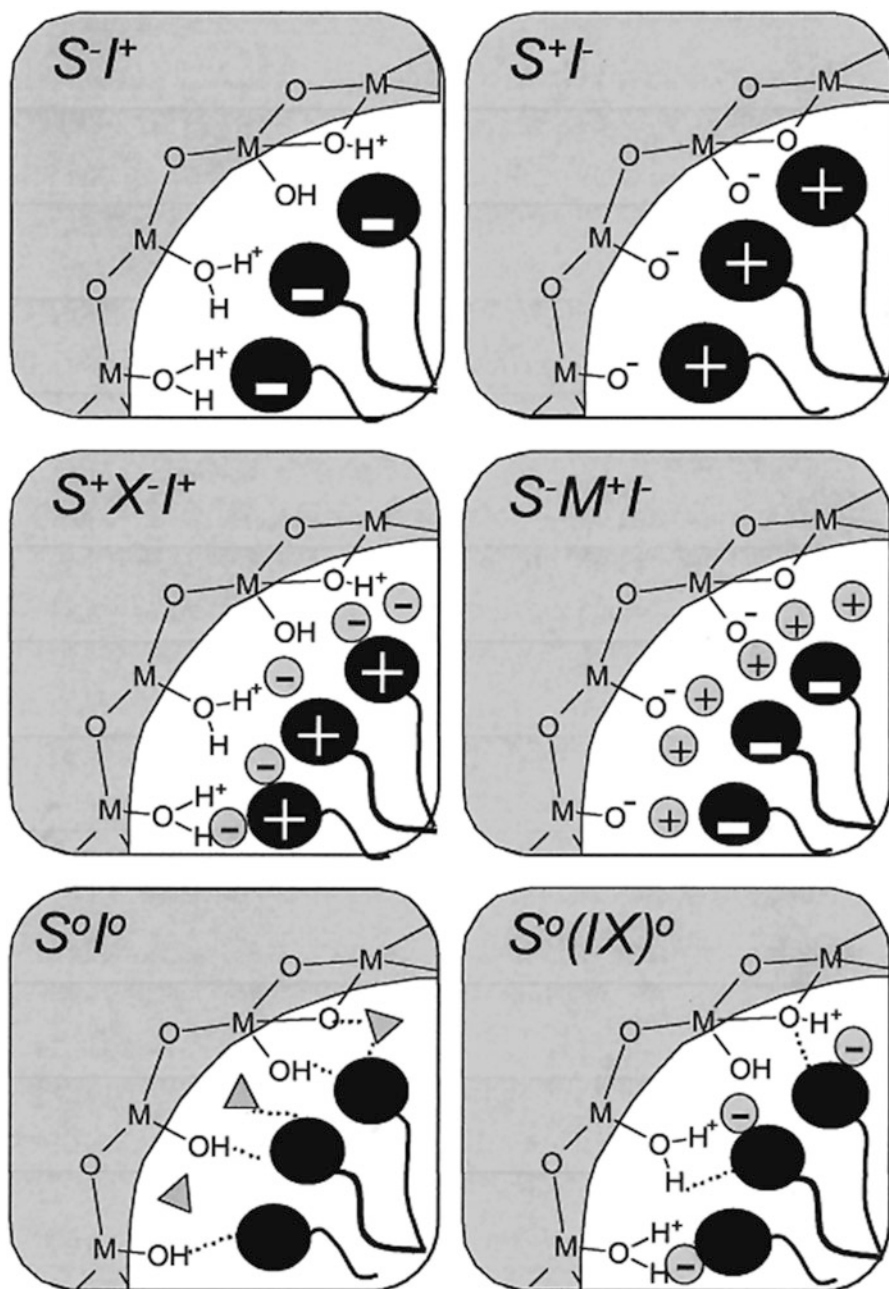
Fig. 24.6 An illustration of the different types of inorganic-surfactant interfaces. S represents the surfactant model, I the metal oxide framework. M^+ and X^- are corresponding counterions. Solvent molecules are not shown, except for the case of I^0S^0 depicted as triangles for hydrogen bonding interactions [57] (Reprint with permission from American Chemical Society)

Fig. 24.7 A schematic representation of the complex structure between carboxylates (RCOO$^-$) and titanium tetravalent alkoxides (Ti(OR)$_4$) [58] (Reprint with permission from Springer)
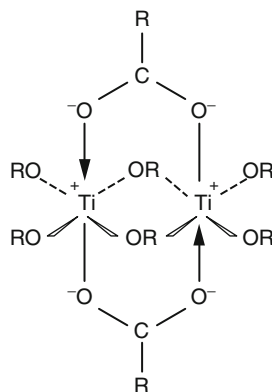
mesoporous silicates in neutral media [53]. Yang et al extended this technique to mesoporous transition metal oxides TiO$_2$, ZrO$_2$, Al$_2$O$_3$, WO$_3$, and HfO$_2$ as well as mixed metal oxides SiTiO$_4$, ZrTiO$_4$, and Al$_2$TiO$_5$ using amphiphilic poly (alkylene oxide) block copolymers as structure-directing agents in nonaqueous solution [64]. In the same year, Yang et al employed Pluronic F127 (EO$_{106}$PO$_{70}$EO$_{106}$) block copolymer templates for the synthesis of SiO$_2$, Nb$_2$O$_5$, and TiO$_2$, successfully resulting in materials of hierarchical ordering with tuneable length scales ranging from 10 nm to several micrometers [65]. A summary of these block copolymer surfactants can be found in a few recent reviews [66–69].

Block copolymers have also been extensively used in the preparation of thin film titanate-based materials using the so-called 'evaporation-induced self-assembly' method. In this approach, the evaporation of solvent and the ingress of water vapor occur simultaneously [70–75]. One of the first studies that aimed to reduce the hydrolysis of highly reactive transition metal oxides during the evaporation-induced self-assembly of surfactants was by Luca and co-workers [76]. The syntheses of mesostructured vanadates using ethanol soluble cetyl trimethylammonium vanadate salts were carried out in ethanol solvent with the controlled introduction of water.

Template Removal

The effective removal of amphiphilic surfactants has been shown to largely depend on the interaction between the template, inorganic matrix, and the ability of the matrix to accommodate, interact with, or adapt to the template. This close association is generally facilitated by the flexibility of inorganic networks (with low structural constraints), by small inorganic oligomers, and by the radius of curvature of the template used [77]. Ideally, when templates are removed either by calcination, solvent extraction, or precipitation, these templates leave voids whose size, arrangement in space, and symmetry are indicative of the surfactant structure. Figure 24.8 shows an example of some transmission electron micrographs (TEM) of non-siliceous mesopores after template removal.
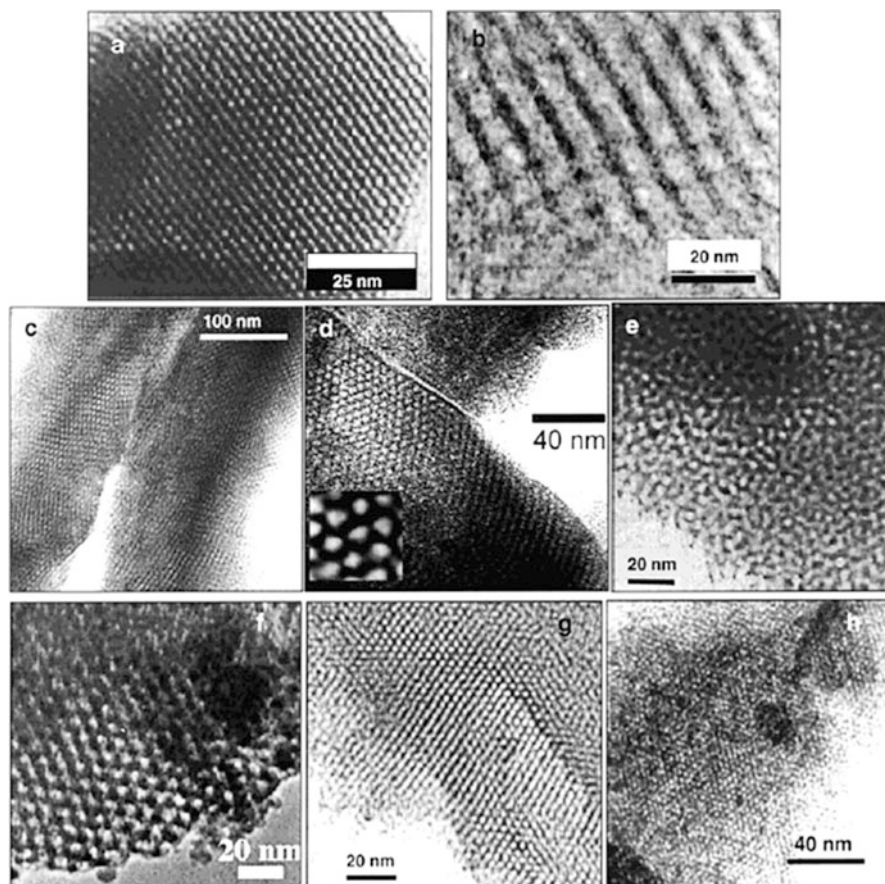
Fig. 24.8 TEM micrographs of non-silica phases: (**a**) dodecylamine-templated Nb_2O_5, (**b**) diblock copolymer-templated ($EO_{75}BO_{45}$) cubic ZrO_2, (**c**) ZrO_2 hexagonal hybrid film, (**d**) TiO_2 hexagonal film, (**e**) Zr/Si mixed oxide, (**f**) triblock copolymer-templated hexagonal SnO_2 oxide, (**g**) hybrid TiO_2/CTAB composite, (**h**) same as (**g**), calcined to 350 °C [57] (Reprint with permission from American Chemical Society)

Modification of the Mesoporous Network: Organic Surface Functionalization

Another step into the development of mesoporous materials involves the ability to alter their physical and chemical properties by incorporating suitable organic functionalities onto and within the matrix. Specifically for ion-exchange applications, these materials are termed 'composite' or ion-exchange type 'hybrid mesoporous materials'. To date, the bulk of the literature has focused primarily on the functionalization of mesoporous SiO_2-based materials, silicas, and

polysiloxanes, with transition metal oxides under researched mainly due to their chemical complexities. Pioneering research into organic functionalization was first reported by Feng and associates, where cross-linked mercaptopropylsilane monolayers were introduced onto internal pore surfaces of MCM-41 and called 'self-assembled monolayers on mesoporous supports' (SAMMS) [78]. Solid-state nuclear magnetic resonance (NMR) spectroscopy found that cross-linked mono-layers of mercaptopropylsilane were bound to mesoporous silica via covalent bonds, resulting in surface monolayer coverage of up to 79 %. Similar systems were also described by Mercier and Pinnavaia [79]. Liu and co-workers also reported on the functionalization of mercaptopropylsilane monolayers on SBA-15 [80]. Depending on the concentration of mercaptopropylsilane, the Santa Barbara group found that they could systematically vary the surface coverage of these functional molecules from 10 % to 100 % density depending on the application. One of the first groups to functionalize organic monolayers onto transition metal oxide surfaces was that of Cosnier et al who immobilized glucose oxidase (GOD) proteins onto mesoporous TiO_2 films for the amperomet-ric detection of glucose and found that successful chemical cross-linking between the surface and monolayer occurred using stationary potential patterns [81]. It was not until many years later that the functionalization of transition metal oxides had been further contemplated, with Mutin and co-workers the first to anchor organ-ophosphorous acids (phosphoric, phosphonic, and phosphinic) onto microporous TiO_2 and ZrO_2 using sol–gel processing and surface modification [82]. Crepaldi and co-workers then grafted organic molecules onto mesoporous zirconia films using dibenzoylmethane, phenylphosphonic acid, and ferrocene-carboxylic acid [83]. The modification of mesoporous titania surfaces with orthophosphates was also reported in the same year [84]. Subsequent research oriented toward applications in drug delivery, acid–base catalysis, and electrochemical sensors using transition metal oxides Fe_2O_3 and Al_2O_3 then followed [85–87]. Generally, anchoring functional molecules onto mesoporous materials draws analogy from the preparation of self-assembled monolayers (SAMs) on colloidal substrates, although with considerably more complexity as the functional molecules must be able to access the interior surface of the pore channels without prematurely hydrolyzing or condensing within themselves [88]. Moreover, internal pore surfaces are far from regular and defect free as might be the case for flat gold or silicon substrates with low surface roughness. Compared to flat substrates, the geometry of mesopores are quite unique and can influence the formation of surface molecular structures due to pore architecture and composition. Pores should also be large enough not only to accommodate surface functional groups but also for accessible diffusion inside pores to allow for further functionalization. The two most applied methods for the surface modification of mesoporous materials are direct co-condensation and post-synthetic grafting. Studies using lithography, radiation, molecular imprinting, or vapor phase functionalization have also been utilized, though will not be part of this review [89, 90].

Synthesis: Grafting and Direct Co-condensation

An approach more commonly seen in literature is grafting. In this context, grafting is a post-synthetic technique that places functional molecules onto prefabricated mesoporous materials after surfactant removal. In general, the grafting procedure is carried out through molecular anchoring onto surface hydroxyl groups as organics are known to chemisorb well onto these sites by way of covalent bonding with oxygen atoms [91]. This method of modification also has the added advantage that, under the synthetic conditions used, the mesostructure of the starting phase is usually retained despite the reduction in pore diameter. Depending on the pore morphology and hydroxyl group distribution, grafting may lead to different quantities of organic molecules bound to the surface [92]. Figure 24.9 is a classic example of the grafting process that occurs in mesoporous silica using alkoxysilanes. If preferential functionalization takes place at pore openings during the initial stages of synthesis, this maybe a slight disadvantage for the grafting technique as diffusion of molecules into the pores can be impaired, leading to a heterogeneous distribution of organic groups and the possibility of lower surface coverage.

Indeed, the conditions governing the distribution of surface-grafted molecules can be quite complex, especially in a monolithic material where long diffusion paths are involved. Grafting does, however, offer the remarkable advantage of structurally improved and hydrolytically more stable functional groups than other techniques.
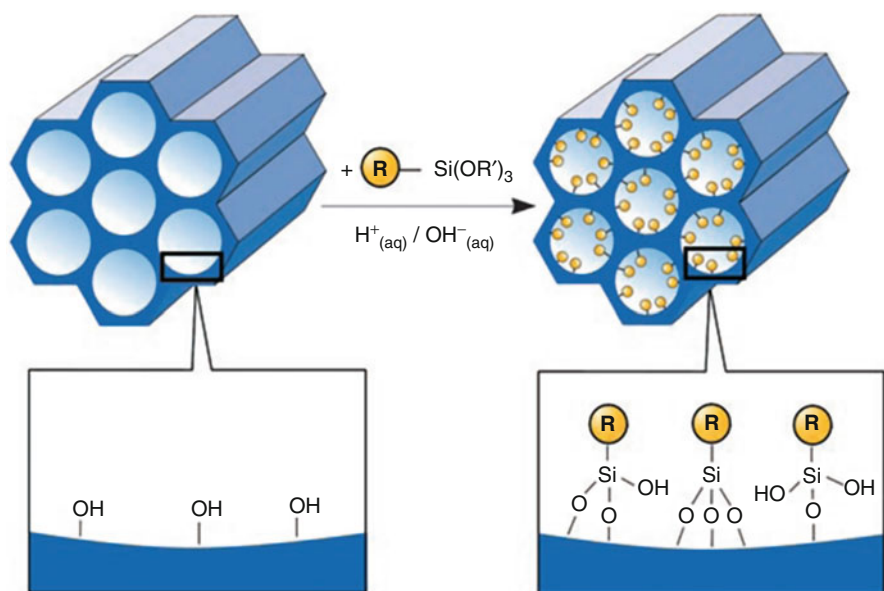

Fig. 24.9   An example of the grafting technique used for organic modification of mesoporous silica phases with terminal organosilanes [93] (Reprint with permission from John Wiley and Sons)
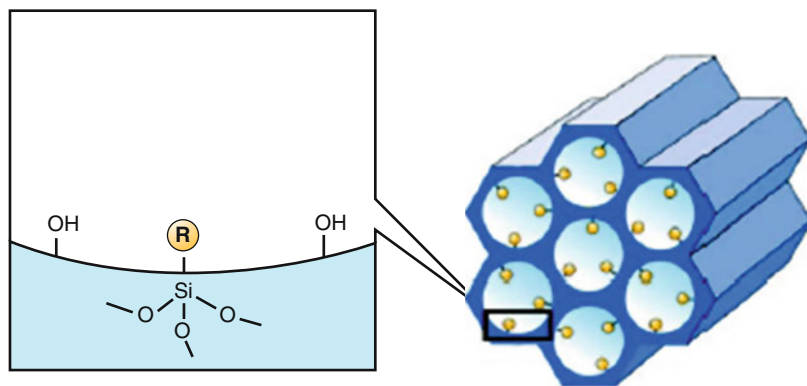
Fig. 24.10 Resulting mesoporous silica phase using the co-condensation method (one-pot synthesis) for organic surface modification [93] (Reprint with permission from John Wiley and Sons)

Regardless of homogeneity, materials made this way have proved to be good candidates for selective adsorption of heavy metals and heterogeneous catalysis [94–96].

An alternative method to grafting is direct co-condensation (also called one-pot synthesis), which is a technique where all the components making up the desired material are concurrently introduced [97]. During the co-assembly process, functional groups that contain hydrophobic ligands (organosilicates or alkyl groups in the case of transition metal oxides) may serve as cosurfactants and insert the ligands into the hydrophobic micellar cores, resulting in preferential ligand distribution along the metal oxide/surfactant interface [98]. The hybrid materials offer functional groups that are directly incorporated into the walls of the host and their connectivity anticipated as one with [M]-R (M = metal oxide or Si, R = functional group) bonds reaching out of the walls instead of [M]-O-R when using the grafting method. Accordingly, after extraction of the surfactant, the interior pore surface is decorated with organic moieties (Fig. 24.10).

The greatest advantage of one-pot synthesis is the production of materials with a relatively uniform distribution of functional groups with fewer synthesis steps and fewer reagents. While this is advantageous, Radu et al did present a specific drawback in which the method is yet to reach above 25 % coverage without destroying the structural integrity and long-range periodicity [99]. It has been advised that the precursors must be chosen carefully to avoid possible phase separation and M-C bond cleavage during the synthesis and surfactant removal process [99].

## Anchoring Phosphonic Acid Molecules onto Surfaces

There are many possible functional groups that can be incorporated onto mesoporous materials, with many alternatives still being introduced and researched to meet various application requirements.

Fig. 24.11 The bonding modes of a phosphonate unit onto metal oxide surfaces
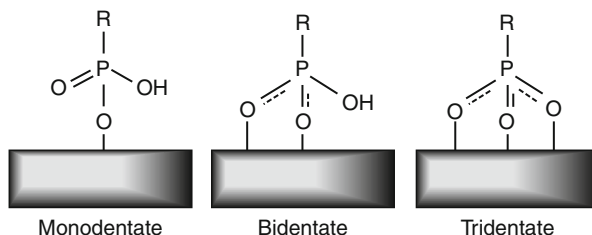
In this review, we will focus on the recent developments of phosphonate and phosphonic acid functionalized mesoporous materials, with emphasis on their ion-exchange properties and applications within the nuclear industry. Aliev and co-workers were among the first to design covalently anchored phosphonate and phosphonic acid groups onto mesoporous silica materials with the view to apply them in separation processes [100]. In this study, organosilica phosphonates $[(EtO)_3Si(CH_2)_3PO(OEt)_2]$ and $[(EtO)_3Si(CH_2)_2PO(OEt)_2]$ were used to introduce phosphonate and phosphonic acid functionalities onto mesoporous silica, resulting in high surface areas and narrow pore size distributions. The same characteristics were also described by Corriu and co-workers for ordered phosphonic acid functionalized SBA-15 [101], with additional hydrothermal stability achieved. Hu et al covalently attached diphenylphosphinoethyl ligands onto mesoporous silica by direct co-condensation but found that increased ligand concentration disordered the mesostructure [102]. In a recent study, Dudarko and co-workers demonstrated that 1-dodecylamine could be used as a template for the fabrication of mesoporous silicas with phosphorus-containing functional groups of composition $\equiv Si(CH_2)_2P(O)(OC_2H_5)_2$ and $\equiv Si(CH_2)_2P(O)(ONa)CH_3$ (1.6 mmol/g) [103]. The mesoporous framework had, however, a nonuniform particle shape and size, with structures less ordered than that of classic mesoporous silicas such as MCM-41. It has been reported by Gao and associates that the difference between functional groups deposited onto high surface area substrates versus planar substrates is the surface curvature, which may effect the efficiency of chain packing or cross-linking at the interfacial region [104]. They also found that long-chain phosphonic acids having much larger pK_as would not condense with surface silanols. Nevertheless, phosphonic acids are known to bind strongly to transition metal oxide surfaces, especially ZrO_2 and TiO_2. The relative instability of phosphonates grafted to silicates possibly arises due to the sensitivity of Si-O-P bonds toward hydrolysis [82]. In general, phosphonic acids may form three M-O-P bonds with metal oxide surfaces (Fig. 24.11).

Linking phosphonic acid moieties onto oxide surfaces involves the formation of M-O-P bonds by heterocondensation of surface hydroxyl groups with those of POX (X = H, ethyl, alkyl) through complexation of the phosphoryl oxygen to the surface metal atoms [82]. Heterocondensation is kinetically favored, owing to the protonation of the leaving alkoxy group by the acidic P-OH groups as summarized below:

$$M\text{-}O\text{-}R + P\text{-}O\text{-}H \rightarrow M\text{-}O^+(H)\text{-}R + P\text{-}O^- \rightarrow M\text{-}O\text{-}P + R\text{-}OH \qquad (24.3)$$
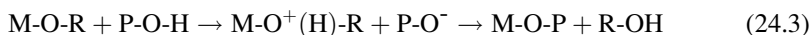
Hydrogen bonds between surface hydroxyl groups and residual P-OH and P = O groups may also be involved [105]. The bonding mode (-mono, -bi, -tridentate) of organophosphorous molecules likely depends on the nature of both the molecule and the metal oxide surface, and on the conditions of the surface modification.

Ion Exchange for Nuclear Applications

The first extensive investment into the development of ion-exchange systems and their use in separation processes was for nuclear applications [106]. The birth and growth of the nuclear industry in the 1950s due to World War II stimulated fundamental research in this area, more so for materials that remained stable above 150 °C as well as high radiation fields. The research conducted in these early years showed that certain ion-exchange materials had quite elevated selectivity for certain metal ions and this opened the way for applications in metal recovery from exhausted solutions and aquatic pollution control [107]. Since then, applications of ion exchangers to radionuclides and metal recovery have increased enormously, now including such widely different fields such as the isolation of tracers from target materials, separation of activities in neutron activation analysis, and the general analysis of solution chemistry and waste disposal [108–111]. Although literature deems solid inorganic ion-exchange materials as crucial for separations, organic ion exchangers have also played a major role as they have proven to be reliable and effective for the control of both the chemistry and radiochemistry of liquid streams in nuclear power plants. Another major development in recent times is the coupling of both inorganic and organic ion exchangers to form 'hybrids'. These composite ion-exchange materials are increasingly important due to their extraordinary properties, combining their characteristics to obtain a synergism between the two components [112]. These materials have gained much interest owing to their remarkable change in properties (including mechanical, electrical, and magnetic), compared to pure organic frameworks or inorganic solids. In addition to combining their distinct characteristics, new or enhanced phenomena can also arise as a result of the intercalation between organic and inorganic components [113–116]. Within this context, the fabrication of a new class of hierarchical porous materials with added organic functionality has attracted favorable interest. Their high surface areas, accessible porosity, and tailorable surface functional groups have made them ideal for host-guest encapsulation of metal ions and radionuclides. Studies on the metal/radionuclide adsorption properties of these materials are governed mostly by siliceous frameworks [6–12], with only a handful at best by modified metal oxide matrices comprised of titanium, alumina, and zirconium [13–15]. Such hybrid mesoporous ion exchangers can be made by several routes including blending in situ polymerization and molecular self-assembly, with the latter being the most prominent synthesis route.

Counterion Association

The mechanism by which a counterion associates with an ion exchanger, particularly with surface functional groups on solid matrices, is important for identifying factors that determine the selectivity of an ion exchanger to a specific ion. Earlier theories and recent investigations have elucidated the electrostatic interactions created through ion-pair formation as the most likely mode for the interaction between counterions and surface functional groups. Research of Helfferich suggests that provided electroneutrality is maintained, counterions are free to move within the charged matrix of the solid, with no counterions permanently bound to the surface [117]. In fact, counterions exist in the region of the solid's surface where the potential energy between the two ions of opposite charges (counterion and charged site on the solid) is likely to be at a minimum, with such conditions favoring the formation of ion pairs [118]. Figure 24.12 (B) represents a schematic illustration of the formation of an ion pair between an anion X^- and cation Y^+. Here (A) depicts two types of ions in a matrix held together by an ionic bond. It then goes to show in (B) that oppositely charged ions Y^+ and X^- are involved in an ion-pair interaction with one another and remain close due to intermolecular forces present. Even in the presence of solvent molecules (C), the ion pair can continue to subsist, provided that the intermolecular forces between the ions are adequately strong. When the solvent effects overcome intermolecular forces, ion-pair dissociation can occur, leaving ions dissociated (D) [119].

When water molecules surround ions in solution, this effect is known as hydration. Hydration influences ion-pair formation between counterions and functional groups on solid matrices by weakening electrostatic interactions that are caused by primary ionic forces. Water molecules in close proximity to the charged ion will become ordered and form a shell around the ion [120]. Figure 24.13 displays an example of the hydration effects that occur between the interaction of counterions and functional groups. Here A and B$^-$ represent both the solid matrix and functional group respectively.

Generally, ion C^+ is expected to have a stronger localized charge and therefore more hydrated in aqueous solution compared to ion D^+. Consequently for C^+, the interaction between surface functional groups is compromised due to hydration. Conversely, the less hydrated ion D^+, which also has a smaller ionic radius, can be attracted more strongly to the functional groups B^-. Basically, the degree of exchange available can be correlated to the quantity of

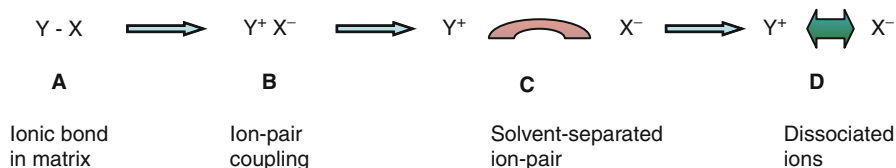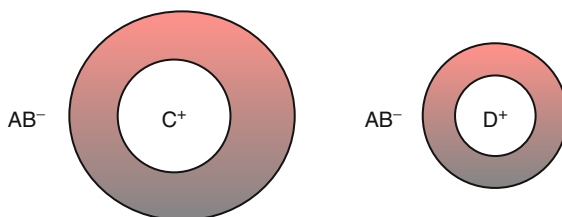| Y - X	⟹	$Y^+ X^-$	⟹	Y^+ ⌒ X^-	⟹	Y^+ ⬌ X^-
A		**B**		**C**		**D**
Ionic bond in matrix		Ion-pair coupling		Solvent-separated ion-pair		Dissociated ions

Fig. 24.12 A schematic illustration of ion-pair formation in ion exchange

Fig. 24.13 Counterion-functional group interactions due to the effects of hydration

hydrated ions, meaning, the higher the charge density of the ion, the larger the hydration sphere and the greater shielding of the charge [118]. Thus, small highly charged ions that surround water molecules are much more likely to be exchanged than large, lower charged ions. In actual fact, lower charged ions can break the structure of large volumes of water, although they do not have enough charge density to tightly bind the nearest water molecules [121].

Ion-Exchange Materials with Chelating Anchor Groups: Polyphosphonates and Iminodiacetic Acid

Perhaps the most useful of organic molecules anchored onto solid supports (particularly for the ion-exchange and sorption of metal ions) are chelating ligands (also called chelating agents or multidentate ligands). These molecules are a special class of compounds, possessing the ability to link with specific metal atoms through coordinate bonds that result in the formation of a complex compound or ring structure [122]. The most common and widely used chelating agents are those that coordinate to metal ions through oxygen or nitrogen donor atoms which are electron-donor elements. Typical structure complexes are octahedral (coordination number (CN) of 6), tetrahedral (CN = 4), or square planar (CN = 4) [123]. The choice of any chelating group is dependant on several factors, most especially the pH range, ionic strength of the solution, and the presence of other complex-forming species likely to compete for coordination sites [123]. One of the first complexing agents industrially manufactured was nitrilotriacetic acid (NTA) in 1936, followed by ethylene diamine tetra-acetate (EDTA) in 1939 which was used for applications in scale inhibition, corrosion, and laundry detergents [124]. With a great many chelating agents marketed to date, polyphosphonic acids have shown to have excellent chelating capacity compared to other inorganic phosphates and have the added advantage of being chemically stable and tolerant of hydrolysis [125]. One well-recognized example of a polyphosphonic acid chelator is ATMP (also called NTMP) nitrilotris (methylenephosphonic acid) (Fig. 24.14).

A structural analogue of NTA, ATMP functional groups have been found to bind to a variety of solid surfaces, including minerals, transition metal oxides, and epoxy resins such as Epikote 828 and Dequest® 2000 (Solutia, Newport) [126–128]. ATMP is commonly used in industrial water cooling systems and oilfield water

Fig. 24.14 The structure of chelating ligand nitrilotris (methylenephosphonic acid) (*ATMP*)
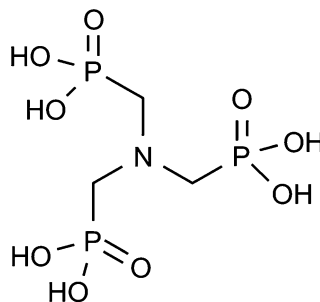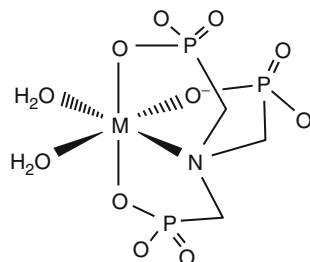

Fig. 24.15 An ideal octahedral structure of metal-ATMP complexes [134], (Reprint with permission from Elsevier)

pipelines to decrease scale formation, desalination, and corrosion inhibition for metallic equipment due to its excellent chelation properties and low threshold inhibition [129]. It can also be used as a chelating agent in the woven and dyeing industries as a surface treatment agent for metals [130].

Recently it has also been found that ATMP coordinates well to surfaces of mesoporous materials and successfully used as a metal adsorbent material for Cu(II), Hg(II), Cd(II), U(VI), and other radionuclides [131–133]. Depending on the interaction type, ATMP ligands surrounding a metal center ideally coordinate with both deprotonated phosphoryl oxygens and an N-central donor atom, creating an octahedral coordination structure (Fig. 24.15). If one or two phosphonates are unavailable for binding due to surface attachment, phosphonate oxygens from ATMP can still create a six membered chelate with many metal ions.

Another well-known polyphosphonate chelator is the carbon substituted pyrophosphate analogue 4-amino,1-hydroxy,1,1-bisphosphonic acid (HABDP), also called alendronate or alendronic acid (Fig. 24.16).

Recognized considerably in nuclear medicine and pharmaceutical products, HABDP is a potent inhibitor of osteoclast-mediated bone resorption and has been extensively studied in the treatment of bone disorders such as Paget's disease, malignant hypercalcemia, immobilization of osteopatia, and postmenopausal osteoporosis by mechanisms that involve calcium mobilization, actin-cytoskeleton reorganization, and the inhibition of neutral phosphatases [135–138]. It is also known to complex with Fe(III) and Cu(II) ions forming chromophoric complexes [139, 140]. Like ATMP, HABDP participates in metal complex formation as well as

Fig. 24.16 Molecular
structure of chelate
4-amino,1-hydroxy,1,1-bis-
phosphonic acid (*HABDP*)
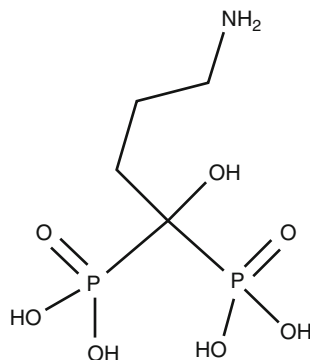
mononuclear and binuclear complexes containing four-membered metal chelate rings. If the oxygen donors are from two different phosphonic acid groups, a six-membered chelate ring will be formed. In addition to four- and six-membered rings, a variety of neutral and protonated metal chelates may also be present [141]. Currently, research has been undertaken on the modification of mesoporous SBA-15 supports with HABDP molecules for application in drug delivery systems due to the advanced bioactive character of silica and HABDP's ability to repair bone defects [142, 143]. Apart from ATMP and HABDP, 1-hydroxy ethylidene-1,1-diphosphonic acid (HEDP) is another known chelate, forming stable six-membered rings with metal ions such as Cd(II) and Pb(II) when anchored onto mesoporous titanium dioxide supports [132].

Chelates bearing an iminodiacetate (IDA) functional group have also been found to have wide applications in catalysis and remediation, owing to their favorably strong adsorption properties for a variety of metal ions. This functional group has been found in many chelating ion-exchange resins; Chelex-100 with a poly(styrene-divinylbenzene) support (Bio-Rad Lab, USA), MetPac CC-1 with a highly cross-linked macroporous poly(styrene-divinylbenzene) support (Dionex, USA), and Prosep IDA as a controlled pore glass material (Bioprocessing, UK). Although they possess the same iminodiacetate functional group, the variation in support material and spacer arm between functional groups and polymer supports results in performance differences in the absorptivity and selectivity of metal ions [144]. N-(Phosphonomethyl)iminodiacetic acid (PIDC) is a multidentate organic ligand with interesting and flexible coordination properties. Apart from the two carboxylic acid groups and a central N-donor atom, this molecule contains a phosphonate group capable of coordinating to several metal centers and the ability to eliminate available coordination sites (Fig. 24.17) [145].

Metal centers can easily be trapped inside three five-membered rings formed by the two carboxylates and the phosphonate group, plus the central N-atom (Fig. 24.18). This was first investigated by Crans et al for the trapping of vanadium centers in catalysis applications [146].

Fig. 24.17 The chemical structure of chelating ligand *N*-(phosphonomethyl) iminodiacetic acid (*PIDC*)
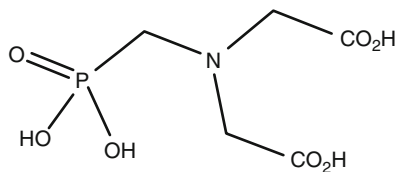

Fig. 24.18 Schematic representation of the three five-membered chelate rings formed by PIDC with metal centers. *Arrows* indicate available coordination sites [147] (Reprint with permission from Elsevier)
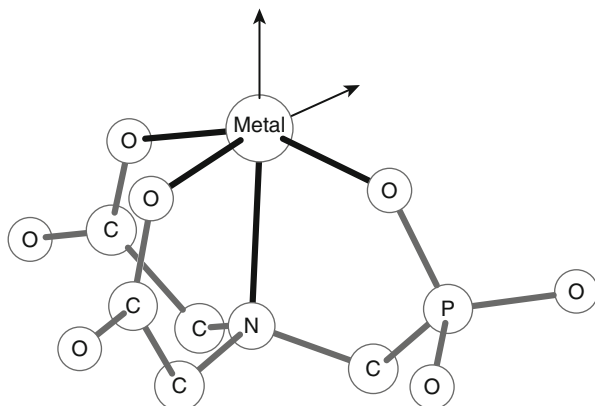
The Application of Functionalized Mesoporous Materials as Sequestering Agents: Actinides, Lanthanides, and Radionuclides

The separation of heavy metal ions or radioactive materials from aqueous streams has been one of the most significant technological problems to date, the solution of which is severely thwarted by the presence of a large excess of competing ionic species. Therefore, the potential for the adsorption and separation of these toxic substances needs to be specific enough to discriminate the ions of interest (heavy metal ions, radionuclides) from other more plentiful benign ions present. Contamination of water streams by transition metals, complex metals, and radioactive compounds remains a major concern in the field of environmental remediation. These materials enter the environment through a variety of avenues that include mining, coal-fired power plants, and industrial processing plants [148, 149]. Furthermore, some natural waters contain naturally high concentration levels of metal species. The presence of even low concentrations (ppb) of some heavy metals or radioactive substances in natural water systems can have a harmful effect on both wildlife and humans. At such low concentrations however, samples often require pre-concentration before analysis can be undertaken. As mentioned in section 'Mesostructure Formation with Amphiphilic Structure-Directing Agents (Anionic Carboxylates and Block Copolymer Templates)', ion exchange or adsorption of these contaminant ions onto solid substrates provides one of the most effective

means for adsorption, separation, and removal of trace pollutants from aqueous streams. A wide variety of novel materials can be prepared through the chemical modification of ordered mesoporous materials. It is the characteristics of these materials, such as their versatility and environmental safety, that make them attractive alternatives to traditional adsorbent materials such as activated carbon and zeolites [150].

The design of mesostructured ion exchangers/adsorbents for the removal of actinides and radionuclides from aqueous solutions is a subject that has not been thoroughly explored. Much has been learned in terms of metal-ligand interactions from actinide solvent extraction studies, as well as those studies aimed at designing chelating ligands to remove actinides from biological systems [151]. Actinides in aqueous solution can be present as solids, colloids, or solvated mono or polynuclear species. The presence of these species is regulated by thermodynamic and kinetic laws and is sensitive to parameters such as cation/anion concentration, ionic strength, liquid–solid phase equilibria, and oxidation-reduction potential [152]. Electrostatic interaction, steric effects, and the number of water molecules in the hydration sphere about the actinide cation are the primary influences on the structure of the complexes [152]. As radionuclide sorption is influenced by the charge of the cations as well as by steric effects, sorption strength follows the same trend as complexation. These factors must be considered when designing functional materials. The important point is that the speciation of the nuclide profoundly influences its solubility, mobility, and toxicity [153].

To date, few mesoporous systems have been applied for the use of heavy metal ion and radionuclide uptake especially on an industrial scale. Ju et al prepared ordered anion-exchange hybrid mesoporous silicas for thorium uptake from process waste streams [154]. The thorium adsorption was to be far more selective in the hybrid mesoporous material compared to a popular organic commercial anion-exchange resin containing quaternary ammonium. Birnbaum et al synthesized carbamoylphosphonate mesoporous silanes for the selective sequestration of actinides [155]. They found this material presented distribution coefficients of approximately 20, 000 for Pu (IV) under conditions of pH $<$ 1 and high nitrate concentrations (approximately 99.5 % removed from solution). Sportsman et al. found that dodecanethiol functionalization of mesoporous Poretics membranes showed effective removal of many actinide species (Cs, Sr, Am and Pu), estimating around 70–80 % removal in acidic (HNO_3) solution [156]. Recently, Yantasee et al functionalized mesoporous silicas with diphosphonic acid (DiPhos), acetamide phosphonic acid (AcPhos), propionamide phosphonic acid (Prop-Phos), and 1-hydroxy-2-pyridinone (1,2-HOPO) for the selective removal of a number of lanthanides (La, Ce, Pr, Nd, Eu, Gd, and Lu) from both natural waters and acidic aqueous solution and found that over 95 % of 100 g/L of Gd in dialysate was removed by the Prop-Phos mesoporous silica after 1 min and 99 % in 10 min [157]. These particular functionalized mesoporous materials could also be regenerated with a 0.5 M HCl wash without losing the binding properties.

The Influence of Gamma Irradiation on the Ion-Exchange Properties of Phosphonic Acid Functionalized Mesoporous Zirconium Titanium Oxide

As an understanding of the sequestration ability of these hybrid mesoporous materials grows, their resistance and behavior toward ionizing radiation fields are yet to be investigated extensively. This is an important factor as exposure to unavoidable cumulative radiation may either alter or potentially damage the physical and chemical properties of hybrid mesoporous structures, which ultimately leads to the futility of the materials ion-exchange performance [158]. Reports on the behavior of surface functionalized organic monolayers toward ionizing radiation [159–161], especially organophosphorous derivatives [162–164], have not been studied widely. Huai-Yu et al observed the behavior of both unbound and bound phosphonates to gamma irradiation at 77 K and found that radicals formed at different radiation doses [165]. Carboxyethyl phosphonic and phenylphosphonic acids on layered zirconium phosphonates were also investigated for their resistance to γ-radiation, where it was found that materials containing phenyl rings provided more stability to the framework at a total dose of 3×10^6 Gy [166, 167]. Other reports on organophosphorous resistance to ionizing radiation include work on α-zirconium and α-titanium phosphates, evidencing that high radiation doses of 6.6×10^5 Gy and 3.1×10^6 Gy did not alter their structure or ion-exchange properties [168, 169].

Preliminary investigations conducted by the authors on the gamma irradiation effects of phosphonate functionalized zirconium titanium mesoporous oxides found the same trend, where the rate of damage caused by gamma radiation (having doses of 0.29, 0.58, and 2 MGy) seemed to decrease above 0.58 MGy and materials appeared to sustain their structure much better than those irradiated at a lower dose. Specifically when trialled as adsorbents for the uptake and extraction of ^{153}Gd, these functionalized mesoporous materials experienced a decrease in adsorption
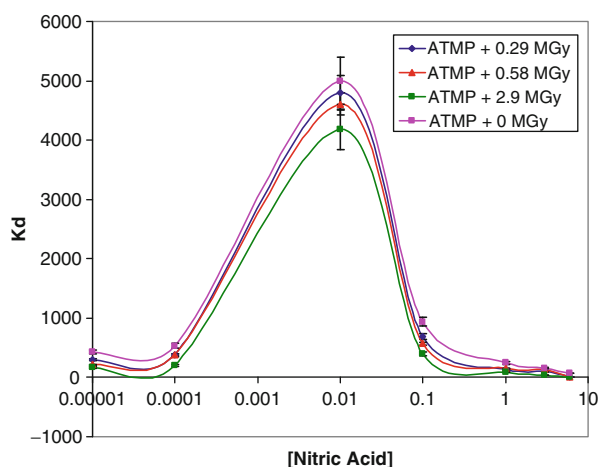

Fig. 24.19 Distribution coefficients (Kd) for carrier-free ^{153}Gd radiotracer (mL/g) measured for γ-irradiated ATMP functionalized mesoporous zirconium titanium oxides across a range of nitric acid concentrations (0.00001–6 M). All corresponding un-irradiated P-ZrTi-*0.33* materials are included [170]

efficiency when subjected to gamma irradiation. The ATMP functionalized materials showed the best adsorption due to the potential it had to bind to more ions with three phosphonate groups as opposed to molecules bearing only one phosphonate group (Fig. 24.19).

References

1. Bekkum HV, Flanigen EM, Jansen JC (1991) Introduction to zeolite science and practice. Elsevier, Amsterdam, Netherlands
2. Cundy CS, Cox PA (2003) The hydrothermal synthesis of zeolites: history and development from the earliest days to the present time. Chem Rev 103:663–702
3. Szostak R (1998) Molecular sieves. Springer, New York, USA
4. van der Waal J, van Bekkum H (1998) Molecular sieves; multifunctional microporous materials in organic synthesis. J Porous Mat 5:289–303
5. Flanigen EM (2005) Molecular sieve zeolites: an industrial research success story. Res Technol Manage 48:29–33
6. Sherman JD (1999) Synthetic zeolites and other microporous oxide molecular sieves. Proc Natl Acad Sci USA 96:3471–3478
7. Schmidt I, Madsen C, Jacobsen CJH (2000) Confined space synthesis. A novel route to nanosized zeolites. Inorg Chem 39:2279–2283
8. Caro J, Noack M, Kölsch P, Schäfer R (2000) Zeolite membranes – state of their development and perspective. Micropor Mesopor Mat 38:3–24
9. Millini R, Perego C (2009) The role of molecular mechanics and dynamics methods in the development of zeolite catalytic processes. Top Catal 52:42–66
10. Davis ME, Lobo RF (1992) Zeolite and molecular sieve synthesis. Chem Mater 4:756–768
11. Wilson ST, Lok BM, Messina CA, Cannan TR, Flanigen EM (1982) Aluminophosphate molecular sieves: a new class of microporous crystalline inorganic solids. J Am Chem Soc 104:1146–1147
12. Balkus KJ, Gabrielov AG (1995) Zeolite encapsulated metal complexes. J Incl Phenom Macro 21:159–184
13. Erdem E, Karapinar N, Donat R (2004) The removal of heavy metal cations by natural zeolites. J Colloid Interface Sci 280:309–314
14. Beecroft LL, Ober CK (1997) Nanocomposite materials for optical applications. Chem Mater 9:1302–1317
15. Ramamurthy V, Eaton DF, Caspar JV (1992) Photochemical and photophysical studies of organic molecules included within zeolites. Acc Chem Res 25:299–307
16. Wilson ST, Lok BM, Flanigen EM (1982) Crystalline metallophosphate compositions. US Patent 4310440
17. Casci J (1994) The preparation and potential applications of ultra-large pore molecular sieves: a review, Advanced zeolite science and applications. Elsevier, Amsterdam, Netherlands, pp 329–356
18. De Man AJM, Van Santen RA, Vogt ETC (1992) Modeling of AlPO4-8, VPI-5, and related structures. J Phys Chem 96:10460–10466
19. Davis ME (1991) Grand openings for cloverite. J Incl Phenom Macro 11:283–285
20. Marsh H, Rodríguez-Reinoso F (2006) Activated carbon. Elsevier, Amsterdam
21. Kresge CT, Leonowicz ME, Roth WJ, Vartuli JC, Beck JS (1992) Ordered Mesoporous molecular sieves synthesized by a liquid-crystal template mechanism. Nature 359:710–712
22. Vartuli JC, Schmitt KD, Kresge CT, Roth WJ, Leonowicz ME, McCullen SB, Hellring SD, Beck JS, Schlenker JL (1994) Effect of surfactant/silica molar ratios on the formation of mesoporous molecular sieves: inorganic mimicry of surfactant liquid-crystal phases and mechanistic implications. Chem Mater 6:2317–2326

23. Cheng C, He H, Zhou W, Klinowski J (1995) Crystal morphology supports the liquid crystal formation mechanism for the mesoporous molecular sieve MCM-41. Chem Phys Lett 244:117–120

24. Alfredsson V, Anderson MW (1996) Structure of MCM-48 revealed by transmission electron microscopy. Chem Mater 8:1141–1146

25. Tanev PT, Pinnavaia TJ (1996) Biomimetic templating of porous lamellar silicas by vesicular surfactant assemblies. Science 271:1267–1269

26. Huo Q, Margolese DI, Ciesla U, Demuth DG, Feng P, Gier TE, Sieger P, Firouzi A, Chmelka BF (1994) Organization of organic molecules with inorganic molecular species into nanocomposite biphase arrays. Chem Mater 6:1176–1191

27. Huo Q, Margolese DI, Ciesla U, Feng P, Gier TE, Sieger P, Leon R, Petroff PM, Schüth F, Stucky GD (1994) Generalized synthesis of periodic surfactant/inorganic composite materials. Nature 368:317–321

28. Antonelli DM, Ying JY (1995) Synthesis of hexagonally packed mesoporous TiO by a modified sol–gel method. Angew Chem Int Ed 34:2014–2017

29. Boyse RA, Ko EI (1996) Preparation and characterization of zirconia-phosphate aerogels. Catal Lett 38:225–230

30. Tian Z, Tong W, Wang J, Duan N, Krishnan VV, Suib SL (1997) Manganese oxide mesoporous structures: mixed-valent semiconducting catalysts. Science 276:926–930

31. Moller K, Bein T (1998) Inclusion chemistry in periodic mesoporous hosts. Chem Mater 10:2950–2963

32. Ciesla U, Schüth F (1999) Ordered mesoporous materials. Micropor Mesopor Mat 27:131–149

33. Schuth F (2001) Non-siliceous mesostructured and mesoporous materials. Chem Mater 13:3184–3195

34. Taguchi A, Schüth F (2005) Ordered mesoporous materials in catalysis. Micropor Mesopor Mat 77:1–45

35. Hartmann M (2005) Ordered mesoporous materials for bioadsorption and biocatalysis. Chem Mater 17:4577–4593

36. Raman NK, Anderson MT, Brinker CJ (1996) Template-based approaches to the preparation of amorphous, nanoporous silicas. Chem Mater 8:1682–1701

37. Voss R, Thomas A, Antonietti M, Ozin GA (2005) Synthesis and characterization of highly amine functionalized mesoporous organosilicas by an "all-in-one" approach. J Mater Chem 15:4010–4014

38. Choi D, Yang S (2003) Effect of two-step sol–gel reaction on the mesoporous silica structure. J Colloid Interface Sci 261:127–132

39. Wold A, Dwight K (1993) Solid state chemistry. Springer, New York, USA

40. Livage J, Henry M, Sanchez C (1988) Sol–gel chemistry of transition metal oxides. Prog Solid State Ch 18:259–341

41. Turova NY (2002) The chemistry of metal alkoxides. Springer, New York, USA

42. Bradley DC (1989) Metal alkoxides as precursors for electronic and ceramic materials. Chem Rev 89:1317–1322

43. Sakka S, Kamiya K (1982) The sol–gel transition in the hydrolysis of metal alkoxides in relation to the formation of glass fibers and films. J Non-Cryst Solids 48:31–46

44. Livage J, Sanchez C (1992) Sol–gel chemistry. J Non-Cryst Solids 145:11–19

45. Ding X, Qi Z, He Y (1995) Effect of hydrolysis water on the preparation of nano-crystalline titania powders via a sol–gel process. J Mater Sci Lett 14:21–22

46. Xia H, Liu X, Zhang K (2008) Nano-architecture by molecular structure-directing agent. Chem Mater 20:2432–2434

47. Evans DF, Wennerström H (1999) The colloidal domain. Wiley-VCH, New York, USA

48. Rosen MJ (2004) Surfactants and interfacial phenomena. Wiley, Hoboken, USA

49. Palmqvist AEC (2003) Synthesis of ordered mesoporous materials using surfactant liquid crystals or micellar solutions. Curr Opin Colloid In 8:145–155

50. Attard GS, Corker JM, Göltner CG, Henke S, Templer RH (1997) Liquid-crystal templates for nanostructured metals. Angew Chem Int Ed 36:1315–1317
51. Renzo FD, Galarneau A, Trens P, Fajula F (2004) Ordered mesoporous oxides: micelle-templated materials. ChemInform 35:1311–1395
52. Beck JS, Vartuli JC (1996) Recent advances in the synthesis, characterization and applications of mesoporous molecular sieves. Curr Opin Solid State Mater Sci 1:76–87
53. Tanev PT, Pinnavaia TJ (1995) A neutral templating route to mesoporous molecular sieves. Science 267:865–867
54. Soler-Illia GJDAA, Crepaldi EL, Grosso D, Sanchez C (2003) Block copolymer-templated mesoporous oxides. Curr Opin Colloid In 8:109–126
55. Liu F, Weng-hua Z, Shuo-kui H, Lian-sheng [1] W, Zheng Z (1996) Hydrolysis kinetics of phenylthio-carboxylates. Chemosphere 32:1691–1697
56. Luca V, Bertram WK, Widjaja J, Mitchell DR, Griffith CS, Drabarek E (2007) Synthesis of mesoporous zirconium titanates using alkycarboxylate surfactants and their transformation to dense ceramics. Micropor Mesopor Mat 103:123–133
57. Soler-Illia GJDAA, Sanchez C, Lebeau B, Patarin J (2002) Chemical strategies to design textured materials: from microporous and mesoporous oxides to nanonetworks and hierarchical structures. Chem Rev 102:4093–4138
58. Takenaka S, Takahashi R, Sato S, Sodesawa T (2000) Structural study of mesoporous titania prepared from titanium alkoxide and carboxylic acids. J Sol–gel Sci Techn 19:711–714
59. Sato S, Oimatsu S, Takahashi R (1997) Pore size regulation of TiO2 by use of a complex of titanium tetraisopropoxide and stearic acid. Chem Commun 12:2219–2220
60. Antonelli DM (1999) Synthesis and mechanistic studies of sulfated meso- and microporous zirconias with chelating carboxylate surfactants. Adv Mater 11:487–492
61. Arpornpong N, Charoensaeng A, Sabatini D, Khaodhiar S (2010) Ethoxy carboxylate extended surfactant: micellar, adsorption and adsolubilization properties. J Surfactants Deterg. doi:10.1007/s11743-010-1179-6
62. Vaudry F, Khodabandeh S, Davis ME (1996) Synthesis of pure alumina mesoporous materials. Chem Mater 8:1451–1464
63. Yang P, Zhao D, Margolese DI, Chmelka BF, Stucky GD (1999) Block copolymer templating syntheses of mesoporous metal oxides with large ordering lengths and semicrystalline framework. Chem Mater 11:2813–2826
64. Yang P, Zhao D, Margolese DI, Chmelka BF, Stucky GD (1998) Generalized syntheses of large-pore mesoporous metal oxides with semicrystalline frameworks. Nature 396:152–155
65. Yang P, Deng T, Zhao D, Feng P, Pine D, Chmelka BF, Whitesides GM, Stucky GD (1998) Hierarchically ordered oxides. Science 282:2244–2246
66. Harnley IW (2003) Nanostructure fabrication using block copolymers. Nanotechnology 14:R39
67. Smarsly B, Antonietti M (2006) Block copolymer assemblies as templates for the generation of mesoporous inorganic materials and crystalline films. Eur J Inorg Chem 206:1111–1119
68. Chen D, Li Z, Wan Y, Tu X, Shi Y, Chen Z, Shen W, Yu C, Tu B, Zhao D (2006) Anionic surfactant induced mesophase transformation to synthesize highly ordered large-pore mesoporous silica structures. J Mater Chem 16:1511–1519
69. Li M, Ober CK (2006) Block copolymer patterns and templates. Mater Today 9:30–39
70. Brinker CJ, Lu Y, Sellinger A, Fan H (1999) Evaporation-induced self-assembly: nanostructures made easy. Adv Mater 11:579–585
71. Brezesinski T, Smarsly B, Iimura K, Grosso D, Boissière C, Amenitsch H, Antonietti M, Sanchez C (2005) Self-assembly and crystallization behavior of mesoporous, crystalline HfO$_2$ thin films: a model system for the generation of mesostructured transition-metal oxides. Small 1:889–898
72. Grosso D, Babonneau F, Sanchez C, GDeAA S-I, Crepaldi E, Albouy P, Amenitsch H, Balkenende A, Brunet-Bruneau A (2003) A first insight in the mechanisms involved in the

self-assembly of 2D-hexagonal templated SiO_2 and TiO_2 mesostructured films during dip-coating. J Sol–gel Sci Techn 26:561–565

73. Grosso D, Cagnol F, Soler-Illia G, Crepaldi E, Amenitsch H, Brunet-Bruneau A, Bourgeois A, Sanchez C (2004) Fundamentals of mesostructuring through evaporation-induced self-assembly. Adv Funct Mater 14:309–322

74. Gibaud A, Grosso D, Smarsly B, Baptiste A, Bardeau JF, Babonneau F, Doshi DA, Chen Z, Brinker CJ, Sanchez C (2003) Evaporation-controlled self-assembly of silica surfactant mesophases. J Phys Chem B 107:6114–6118

75. Soler-Illia GJDAA, Louis A, Sanchez C (2002) Synthesis and characterization of mesostructured titania-based materials through evaporation-induced self-assembly. Chem Mater 14:750–759

76. Luca V, Hook JM (1997) Study of the structure and mechanism of formation through self-assembly of mesostructured vanadium oxide. Chem Mater 9:2731–2744

77. Kleitz F (2002) Ordered mesoporous materials: template removal, frameworks and morphology. PhD thesis, Ruhr-Universität Bochum

78. Feng X, Fryxell GE, Wang L, Kim AY, Liu J, Kemner KM (1997) Functionalized monolayers on ordered mesoporous supports. Science 276:923–926

79. Mercier L, Pinnavaia TJ (1998) Heavy metal ion adsorbents formed by the grafting of a thiol functionality to mesoporous silica molecular sieves: factors affecting Hg(II) uptake. Environ Sci Technol 32:2749–2754

80. Liu J, Feng X, Fryxell GE, Wang L, Kim AY, Gong M (1998) Hybrid mesoporous materials with functionalized monolayers. Adv Mater 10:161–165

81. Cosnier S, Gondran C, Senillou A, Grätzel M, Vlachopoulos N (1997) Mesoporous TiO_2 films: new catalytic electrode fabricating amperometric biosensors based on oxidases. Electroanal 9:1387–1392

82. Mutin PH, Guerrero G, Vioux A (2003) Organic–inorganic hybrid materials based on organophosphorus coupling molecules: from metal phosphonates to surface modification of oxides. C R Chim 6:1153–1164

83. Crepaldi EL, Soler-Illia GJDAA, Grosso D, Sanchez C, Albouy P (2001) Design and post-functionalisation of ordered mesoporous zirconia thin films. Chem Commun 11:1582–1583

84. Vichi FM, Tejedor-Tejedor MI, Anderson MA (2000) Effect of pore-wall chemistry on proton conductivity in mesoporous titanium dioxide. Chem Mater 12:1762–1770

85. Kapoor S, Girish TS, Mandal SS, Gopal B, Bhattacharyya AJ (2010) Inhibition of a protein tyrosine phosphatase using mesoporous oxides. J Phys Chem B 114:3117–3121

86. Das SK, Kapoor S, Yamada H, Bhattacharyya AJ (2009) Effects of surface acidity and pore size of mesoporous alumina on degree of loading and controlled release of ibuprofen. Micropor Mesopor Mat 118:267–272

87. Huang Z, Tang F (2005) Preparation, structure, and magnetic properties of mesoporous magnetite hollow spheres. J Colloid Interface Sci 281:432–436

88. Sanchez C, Soler-Illia GJDAA, Ribot F, Grosso D (2003) Design of functional nano-structured materials through the use of controlled hybrid organic–inorganic interfaces. C R Chim 6:1131–1151

89. Fan H, Lu Y, Stump A, Reed ST, Baer T, Schunk R, Perez-Luna V, Lopez GP, Brinker CJ (2000) Rapid prototyping of patterned functional nanostructures. Nature 405:56–60

90. Juan FD, Ruiz-Hitzky E (2000) Selective functionalization of mesoporous silica. Adv Mater 12:430–432

91. Jia M, Seifert A, Berger M, Giegengack H, Schulze S, Thiel WR (2004) Hybrid mesoporous materials with a uniform ligand distribution: synthesis, characterization, and application in epoxidation catalysis. Chem Mater 16:877–882

92. Mbaraka IK, Shanks BH (2006) Acid strength variation due to spatial location of organosulfonic acid groups on mesoporous silica. J Catal 244:78–85

93. Hoffmann F, Cornelius M, Morell J, Fröba M (2006) Silica-based mesoporous organic–inorganic hybrid materials. Angew Chem Int Ed 45:3216–3251

94. Brunel D, Cauvel A, Fajula F, DiRenzo F (1995) MCM-41 type silicas as supports for immobilized catalysts, zeolites: a refined tool for designing catalytic sites. Proceedings of the international zeolite symposium. Elsevier, pp 173–180

95. Sayari A, Kruk M, Jaroniec M, Moudrakovski IL (1998) New approaches to pore size engineering of mesoporous silicates. Adv Mater 10:1376–1379

96. Wight AP, Davis ME (2002) Design and preparation of organic − inorganic hybrid catalysts. Chem Rev 102:3589–3614

97. Park SS, Ha C (2006) Organic–inorganic hybrid mesoporous silicas: functionalization, pore size, and morphology control. Chem Rec 6:32–42

98. Shi J, Hua Z, Zhang L (2004) Nanocomposites from ordered mesoporous materials. J Mater Chem 14:795–806

99. Radu DR, Lai C, Huang J, Shu X, Lin VS (2005) Fine-tuning the degree of organic functionalization of mesoporous silica nanosphere materials via an interfacially designed co-condensation method. Chem Commun 14:1264–1266

100. Aliev A, Ou DL, Ormsby B, Sullivan AC (2000) Porous silica and polysilsesquioxane with covalently linked phosphonates and phosphonic acids. J Mater Chem 10:2758–2764

101. Corriu RJP, Leclercq D, Mutin PH, Sarlin L, Vioux A (1998) Nonhydrolytic sol–gel routes to layered metal(IV) and silicon phosphonates. J Mater Chem 8:1827–1833

102. Hu W, Yuan C, Li S (2002) Synthesis of hindered alkyl phosphonates and phosphonic and phosphinic acids. Chin Chem Lett 3:167–170

103. Dudarko O, Mel'nyk I, Zub Y, Chuiko A, Dabrowski A (2006) Template-directed synthesis of mesoporous silicas containing phosphonic acid derivatives in the surface layer. Inorg Mater 42:360–367

104. Gao W, Dickinson L, Grozinger C, Morin FG, Reven L (1996) Self-assembled monolayers of alkylphosphonic acids on metal oxides. Langmuir 12:6429–6435

105. Mutin PH, Guerrero G, Vioux A (2005) Hybrid materials from organophosphorus coupling molecules. J Mater Chem 15:3761–3768

106. Moyer BA (2009) Ion exchange and solvent extraction. CRC Press, Boca Raton, USA

107. Colella C (1996) Ion exchange equilibria in zeolite minerals. Miner Deposita 31:554–562

108. Marinin DV, Brown GN (2000) Studies of sorbent/ion-exchange materials for the removal of radioactive strontium from liquid radioactive waste and high hardness groundwaters. Waste Manag 20:545–553

109. Killey RWD, McHugh JO, Champ DR, Cooper EL, Young JL (1984) Subsurface cobalt-60 migration from a low-level waste disposal site. Environ Sci Technol 18:148–157

110. Hou X, Dahlgaard H, Rietz B, Jacobsen U, Nielsen SP, Aarkrog A (1999) Determination of chemical species of iodine in seawater by radiochemical neutron activation analysis combined with ion-exchange preseparation. Anal Chem 71:2745–2750

111. Vaaramaa K, Lehto J (2003) Removal of metals and anions from drinking water by ion exchange. Desalination 155:157–170

112. Xu T (2005) Ion exchange membranes: state of their development and perspective. J Membr Sci 263:1–29

113. Moon J, Kim K, Jung C, Shul Y, Lee E (2000) Preparation of organic–inorganic composite adsorbent beads for removal of radionuclides and heavy metal ions. J Radioan Nucl Ch 246:299–307

114. Helfferich FG (1995) Ion exchange. Courier Dover, New York, USA

115. Muraviev D, Gorshkov VI, Warshawsky A (1999) Ion exchange. CRC Press, Boca Raton, USA

116. De Bokx PK, Boots HMJ (1989) The ion-exchange equilibrium. J Phys Chem 93:8243–8248

117. Helfferich F (1965) Ion-exchange kinetics. V. Ion exchange accompanied by reactions. J Phys Chem 69:1178–1187

118. Marcus Y, SenGupta AK (2004) Ion exchange and solvent extraction. CRC Press, Boca Raton, USA

119. Buckingham AD (1957) A theory of ion-solvent interaction. Discuss Faraday Soc 24:151–157
120. Essington ME (2004) Soil and water chemistry. CRC Press, Boca Raton, USA
121. Nightingale ER (1959) Phenomenological theory of ion solvation. Effective radii of hydrated ions. J Phys Chem 63:1381–1387
122. Volesky B (1990) Biosorption of heavy metals. CRC Press, Boca Raton, USA
123. Zagorodni AA (2007) Ion exchange materials. Elsevier, Amsterdam, Netherlands
124. Knepper TP (2003) Synthetic chelating agents and compounds exhibiting complexing properties in the aquatic environment. Trends Anal Chem 22:708–724
125. Valsami-Jones E (2004) Phosphorus in environmental technologies. IWA Publishing, London, UK
126. Ahearn JS, Davis GD (1989) Improved durability of aluminum adhesive bonds with phosphonic acid inhibitors. J Adhes 28:75
127. Matienzo LJ, Shaffer DK, Moshier WC, Davis GD (1986) Environmental and adhesive durability of aluminium-polymer systems protected with organic corrosion inhibitors. J Mater Sci 21:1601–1608
128. Thi Xuan Hang T, Truc TA, Nam TH, Oanh VK, Jorcin J, Pébère N (2007) Corrosion protection of carbon steel by an epoxy resin containing organically modified clay. Surf Coat Technol 201:7408–7415
129. Gu Y, Yeung AT, Koenig A, Li H (2009) Effects of chelating agents on zeta potential of cadmium-contaminated natural clay. Sep Sci Technol 44:2203
130. Schwartz M (2008) Smart materials. CRC Press, Boca Raton, USA
131. Ma T, Zhang X, Yuan Z (2009) Hierarchical meso-/macroporous aluminum phosphonate hybrid materials as multifunctional adsorbents. J Phys Chem C 113:12854–12862
132. Ma T, Zhang X, Yuan Z (2009) High selectivity for metal ion adsorption: from mesoporous phosphonated titanias to meso-/macroporous titanium phosphonates. J Mater Sci 44:6775–6785
133. Sizgek GD, Griffith CS, Sizgek E, Luca V (2009) Mesoporous zirconium titanium oxides. Part 3. Synthesis and adsorption properties of unfunctionalized and phosphonate-functionalized hierarchical polyacrylonitrile-F-127-templated beads. Langmuir 25:11874–11882
134. Nowack B (2008) Chelating agents and the environment. Environ Pollut 153:1–20
135. Chesnut CH, McClung MR, Ensrud KE, Bell NH, Genant HK, Harris ST, Singer FR, Stock JL, Yood RA, Delmas PD, Kher U, Pryor-Tillotson S, Santora AC (1995) Alendronate treatment of the postmenopausal osteoporotic woman: effect of multiple dosages on bone mass and bone remodeling. Am J Med 99:144–152
136. Tucci JR, Tonino RP, Emkey RD, Peverly CA, Kher U, Santora AC II (1996) Effect of three years of oral alendronate treatment in postmenopausal women with osteoporosis. Am J Med 101:488–501
137. Yasui T, Fujita K, Sasaki S, Iguchi M, Hirota S, Nomura S, Azuma Y, Ohta T, Kohri K (1998) Alendronate inhibits osteopontin expression enhanced by parathyroid hormone-related peptide (PTHrP) in the rat kidney. Urol Res 26:355–360
138. Roelofs AJ, Thompson K, Gordon S, Rogers MJ (2006) Molecular mechanisms of action of bisphosphonates: current status. Clin Cancer Res 12:6222s–6230s
139. Kuljanin J, Jankovic I, Nedeljkovic J, Prstojevic D, Marinkovic V (2002) Spectrophotometric determination of alendronate in pharmaceutical formulations via complex formation with Fe(III) ions. J Pharm Biomed Anal 28:1215–1220
140. Ostović D, Stelmach C, Hulshizer B (1993) Formation of a chromophoric complex between alendronate and copper(II) ions. Pharm Res 10:470–472
141. Kontturi M, Peräniemi S, Vepsäläinen JJ, Ahlgrén M (2005) X-ray diffraction study of bisphosphonate metal complexes: Mg and Ca complexes of (dichloromethylene) bisphosphonic acid P, P'-diisopropyl ester. Polyhedron 24:305–309

142. Balas F, Manzano M, Horcajada P, Vallet-Regí M (2006) Confinement and controlled release of bisphosphonates on ordered mesoporous silica-based materials. J Am Chem Soc 128:8116–8117

143. Nieto A, Balas F, Colilla M, Manzano M, Vallet-Regí M (2008) Functionalization degree of SBA-15 as key factor to modulate sodium alendronate dosage. Micropor Mesopor Mat 116:4–13

144. Gao Y, Oshita K, Lee K, Oshima M, Motomizu S (2002) Development of column-pretreatment chelating resins for matrix elimination/multi-element determination by inductively coupled plasma-mass spectrometry. Analyst 127:1713–1719

145. Mao J, Clearfield A (2002) Metal carboxylate-phosphonate hybrid layered compounds: synthesis and single crystal structures of novel divalent metal complexes with N-(phosphonomethyl)iminodiacetic acid. Inorg Chem 41:2319–2324

146. Crans DC, Jiang F, Boukhobza I, Bodi I, Kiss T (1999) Solution characterization of vanadium (V) and -(IV) N-(phosphonomethyl)iminodiacetate complexes: direct observation of one enantiomer converting to the other in an equilibrium mixture. Inorg Chem 38:3275–3282

147. Shi F, Almeida Paz FA, Girginova PI, Mafra L, Amaral VS, Rocha J, Makal A, Wozniak K, Klinowski J, Trindade T (2005) Hydrothermal synthesis, structural characterisation and magnetic behaviour of hybrid complexes of N-(phosphonomethyl)iminodiacetate. J Mol Struct 754:51–60

148. Papastefanou C (2010) Escaping radioactivity from coal-fired power plants (CPPs) due to coal burning and the associated hazards: a review. J Environ Radioact 101:191–200

149. Babel S, Kurniawan TA (2003) Low-cost adsorbents for heavy metals uptake from contaminated water: a review. J Hazard Mater 97:219–243

150. Galarneau A (2001) Zeolites and mesoporous materials at the dawn of the 21st century. Elsevier, Amsterdam, Netherlands

151. Eccles H (1995) Removal of heavy metals from effluent streams -why select a biological process? Int Biodeter Biodegr 35:5–16

152. Choppin GR (2006) Actinide speciation in aquatic systems. Mar Chem 99:83–92

153. Moulin V, Moulin C (2001) Radionuclide speciation in the environment: a review. Radiochimica Acta 89:773

154. Ju YH, Webb OF, Dai S, Lin JS, Barnes CE (2000) Synthesis and characterization of ordered mesoporous anion-exchange inorganic/organic hybrid resins for radionuclide separation. Ind Eng Chem Res 39:550–553

155. Birnbaum JC, Busche B, Lin Y, Shaw WJ, Fryxell GE (2002) Synthesis of carbamoylphosphonate silanes for the selective sequestration of actinides. Chem Commun 11:1374–1375

156. Sportsman KS, Bluhm EA, Abney KD (2005) Removal of actinides from acidic solution via carrier-mediated facilitated transport across mesoporous substrates with nanoengineered surfaces: thiol self-assembled monolayers with D(tBu)ΦD(iBu)CMPO – ligands. Sep Sci Technol 40:709–719

157. Yantasee W, Fryxell GE, Addleman RS, Wiacek RJ, Koonsiripaiboon V, Pattamakomsan K, Sukwarotwat V, Xu J, Raymond KN (2009) Selective removal of lanthanides from natural waters, acidic streams and dialysate. J Hazard Mater 168:1233–1238

158. Weber W, Ewing R, Catlow C, Diaz de la Rubia T, Hobbs L, Kinoshita C, Matzke H, Motta A, Nastasi M, Salje E, Vance E, Zinkle S (1998) Radiation effects in crystalline ceramics for the immobilization of high-level nuclear waste and plutonium. J Mater Res 13:1434–1484

159. Kim TK, Yang XM, Peters RD, Sohn BH, Nealey PF (2000) Chemical modification of self-assembled monolayers by exposure to soft X-rays in air. J Phys Chem B 104:7403–7410

160. Feulner P, Niedermayer T, Eberle K, Schneider R, Menzel D, Baumer A, Schmich E, Shaporenko A, Tai Y, Zharnikov M (2004) Strong temperature dependence of irradiation effects in organic layers. Phys Rev Lett 93:178302

161. Zharnikov M, Frey S, Heister K, Grunze M (2000) Modification of alkanethiolate monolayers by low energy electron irradiation: dependence on the substrate material and on the length and isotopic composition of the alkyl chains. Langmuir 16:2697–2705

162. Mincher B, Modolo G, Mezyk S (2009) Review article: the effects of radiation chemistry on solvent extraction 3: a review of actinide and lanthanide extraction. Solvent Extr Ion Exc 27:579–606

163. Wagner R, Kinderman E, Towle L (1959) Radiation stability of organophosphorous compounds. J Ind Eng Chem 51:45–46

164. Chiarizia R, Horwitz E (2000) Radiolytic stability of some recently developed ion exchange and extraction chromatographic resins containing diphosphonic acid groups. Solvent Extr Ion Exc 18:109–132

165. Huai-Yu S, Zhi-Zhong W, Yao-Huan C, Yong-Hai H, Qi-Zhong W, Jin-Tai C, Ren-Zhong L (1989) A study of the radiation chemistry of phosphorous compounds. Int J Radiat Appl Inst Pt C Radiat Phys Ch 33:585–597

166. Allcock HR, Hofmann MA, Ambler CM, Lvov SN, Zhou XY, Chalkova E, Weston J (2002) Phenyl phosphonic acid functionalized poly[aryloxyphosphazenes] as proton-conducting membranes for direct methanol fuel cells. J Membr Sci 201:47–54

167. Alberti G, Costantino U, Szirtes L (1997) Effect of ionising radiation on intercalation compounds and organic derivatives of zirconium phosphates I. Effect of irradiation on carboxyethylphosphonic and phenylphosphonic acids and on the corresponding layered zirconium phosphonates. Radiat Phys Chem 50:369–376

168. Shakshooki S, Szirtes L, Dehair A, Elmismary Y, Haraga S, Benfaid N, Benhamed A, Maiof A (1988) Mixed insoluble acidic salts of tetravalent metals V. Effect of gamma radiation and drying temperature on granular mixed zirconium-titanium phosphates. J Radioan Nuclear Ch 121:185–193

169. Szirtes L, Megyeri J, Riess L, Kuzmann E, Havancsák K (2005) Swift heavy ion and gamma-ray irradiation of various double metal phosphates. Radiat Phys Chem 73:39–44

170. De Los Reyes M, Majewski P, unpublished data

Properties of Ferroic Nanomaterials

25

Jennifer S. Andrew

Introduction

There exist three main types of ferroic ordering, ferroelectric, ferromagnetic, and ferroelastic, which relates the type of applied field that can be used to control the spontaneously polarized state. Figure 25.1 shows these types of ferroic ordering, where an applied electric, magnetic, or stress field can be used to control an electric polarization, magnetization, or strain, respectively. Furthermore, multiferroic materials exist, which couple two different types of ferroic behavior, leading to additional levels of ordering. For example, in a ferroelectric ferromagnetic multiferroic, an applied magnetic field can be used to control the polarization, or an applied electric field can be used to control the magnetization. The goal of this book chapter will be to review the bulk properties of ferroelectric and ferromagnetic materials. Once the bulk properties are understood, the fundamental science behind the unique nanoscale behavior of these materials will be discussed. In this chapter, the properties of bulk and nanoscale ferromagnetic materials will be discussed, followed by a discussion of the unique applications these nanomaterials are employed in. Next, the bulk and nanoscale properties of ferroelectric materials will be presented. Lastly, a summary will be provided.

J.S. Andrew

Department of Materials Science and Engineering, University of Florida, Gainesville, FL, USA
e-mail: jandrew@mse.ufl.edu

Fig. 25.1 The types of
ferroic ordering where an
applied magnetic, electric, or
stress field results in a
spontaneous magnetization,
polarization, or strain,
respectively. When multiple
types of ferroic ordering are
coupled new types of
behavior arise, including
piezoelectricity,
magnetoelectricity, and
magnetoelasticity
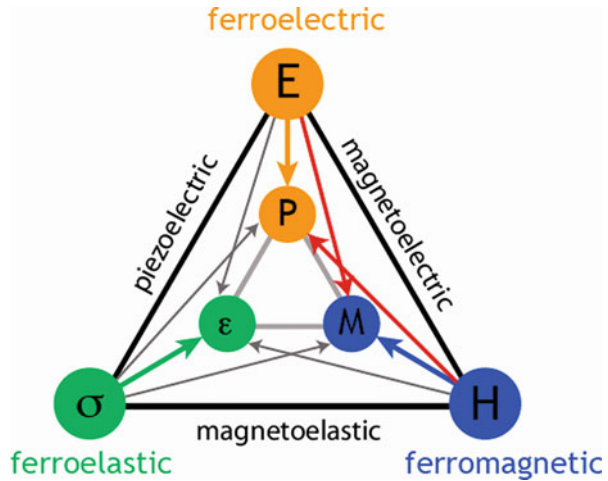
Ferromagnets

Bulk Behavior

Here, a brief description of the properties of bulk ferromagnetic materials will be presented; for a more thorough discussion, please refer to several outstanding textbooks on magnetism [1, 2]. A ferromagnetic material exhibits a spontaneous magnetic moment, even in the absence of a magnetic field. Figure 25.2a shows how the magnetic dipoles order in a ferromagnetic material, while Fig. 25.2b shows the variation in overall magnetization in an applied magnetic field. Samples, as-synthesized in the laboratory, will typically have no net magnetization, due to the formation of domains, which are oriented such that the overall energy of the sample is minimized. However, once a positive magnetic field is applied to the sample, these domains will try to align and orient with the magnetic field until the magnetic moment of the sample increases to a saturation value, known as the saturation magnetization, M_s. The saturation magnetization corresponds to the state where all the magnetic dipoles and domains are aligned parallel to one another and to the external field. When the applied field is removed, the magnetization decreases from the saturation value to a remnant value, M_r. The coercive field, Hc, is the field required to return the magnetization to zero. If a negative magnetic field is applied, the magnetization will again increase to its saturation value, and the dipoles and domains will align parallel to one another and in the opposite direction from the positive field.

The properties of the hysteresis loop are material dependent and are determined by the intrinsic properties of a given material. In most magnetic materials the magnetic properties are anisotropic. This means that it is easier to magnetize samples along certain crystallographic directions, referred to as the easy axes. Materials with a greater degree of anisotropy have fewer magnetically easy axes and tend to require larger fields to achieve the saturation magnetization value as well as higher coercive
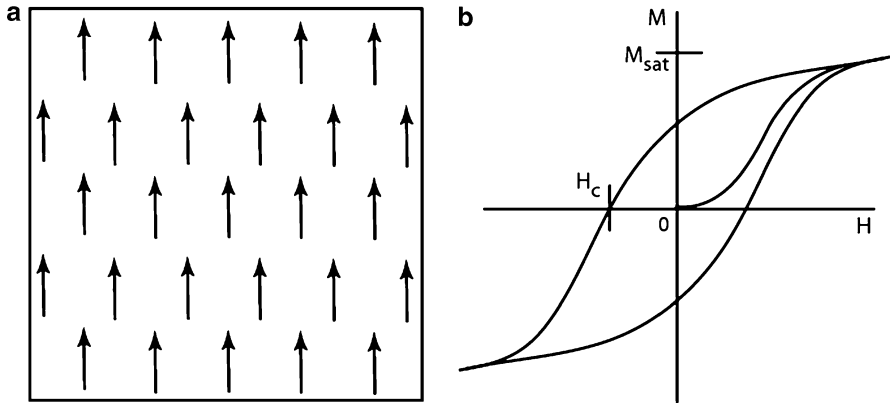
Fig. 25.2 Schematic ordering of (**a**) magnetic moments and (**b**) magnetization behavior for a ferromagnetic material

fields. These highly anisotropic ferromagnetic materials are referred to as hard magnets, whereas ferromagnetic materials with low degrees of anisotropy are referred to as soft magnets. It is easy to distinguish between hard and soft magnetic materials by the shape of their hysteresis loops. Hard magnetic materials are characterized by broad, square-shaped hysteresis loops, whereas soft magnetic materials have narrow hysteresis loops. The shape of their hysteresis loops dictates applications. The broad loop of hard magnetic materials provides two stable magnetic states, which can be used for memory applications. The area within a hysteresis loop is equivalent to the energy required to switch between the two magnetic states and describes the energy lost when a material is rapidly switched between the two magnetic states. In memory applications, where hard magnets are typically employed, loss is not an issue. However, soft magnetic materials find applications in dc power applications, such as transformer cores, where low hysteresis loss is important.

Ferromagnetic behavior, like many material properties, is temperature dependent. Ferromagnetic materials undergo a phase transition from a high-temperature paramagnetic phase (Fig. 25.3), where the magnetic moments within the sample are randomly oriented as a result of thermal motion, to a low-temperature ferromagnetic phase, where the dipole moments order parallel to one another. This transition from ferromagnetic to paramagnetic behavior occurs at the Curie temperature, T_c. Above the Curie temperature, the thermal energy, kT, is greater than the energy aligning the magnetic moments, which results in the random alignment of the magnetic moments and paramagnetic behavior exhibited above this temperature.

Nanoscale Ferromagnetic Materials

Now, that the macroscale behavior of ferromagnetic materials has been established, it is time to investigate how size affects magnetic properties. As outlined above,
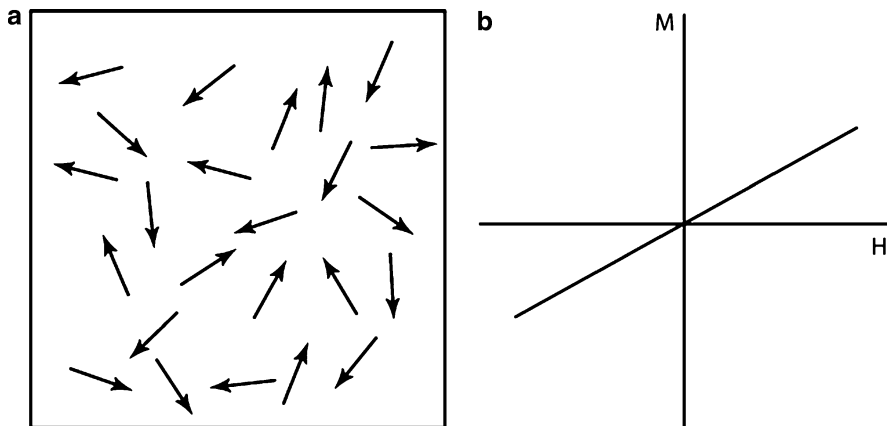
Fig. 25.3 Schematic ordering of (**a**) magnetic moments and (**b**) magnetization behavior for a paramagnetic material

bulk magnetic materials form domains in order to minimize their magnetostatic energy. Magnetic materials are characterized by their response, magnetization (M), to an applied field. When a ferromagnetic material is exposed to an applied magnetic field, H, hysteresis behavior is exhibited. Each time the material is subjected to one complete cycle, there is a corresponding loss of energy, hysteresis loss, in the form of heat that is equal to the area within the hysteresis loop. However, for sufficiently small particles, the formation of domains becomes energetically unfavorable, and the particles become ahysteretic.

Louis Néel was probably the first to predict the properties of single-domain ferromagnetic nanoparticles [3]. Néel revealed that when ferromagnetic particles are below a critical size, their hysteresis behavior disappears and they become superparamagnetic. In other words, the particles are single domain and are capable of rotating freely in an applied field, as for the case of an ideal paramagnet, while maintaining the high magnetic moment characteristic of a ferromagnet. Superparamagnetic behavior can be explained in terms of energetics as the point where thermal energy (kT) exceeds the energy (ΔE) required to reverse the magnetization direction. The energy to reverse the magnetization direction is directly related to the magnetocrystalline anisotropy energy (K) and the particle volume (V). This direct proportionality between ΔE and the particle volume is what leads to the unique behavior of small magnetic nanoparticles. Mathematically, the relaxation time (τ) for the overall magnetization of a particle can be expressed as an activated process [4]:

$$\tau = \tau_0 \exp\left(\frac{\Delta E}{kT}\right) = \tau_0 \exp\left(\frac{KV}{kT}\right), \tag{25.1}$$

where τ_0 is a pre-exponential and has values between 10^{-11} and 10^{-12} s for noninteracting particles [5, 6]. The superparamagnetic limit is therefore a function of particle size and the degree of magnetocrystalline anisotropy, a material parameter.

Fig. 25.4 Superparamagnetic limit for several common magnetic oxides and metals. Adapted from Ref. {7}. These limits depend on material properties, including magnetocrystalline anisotropy
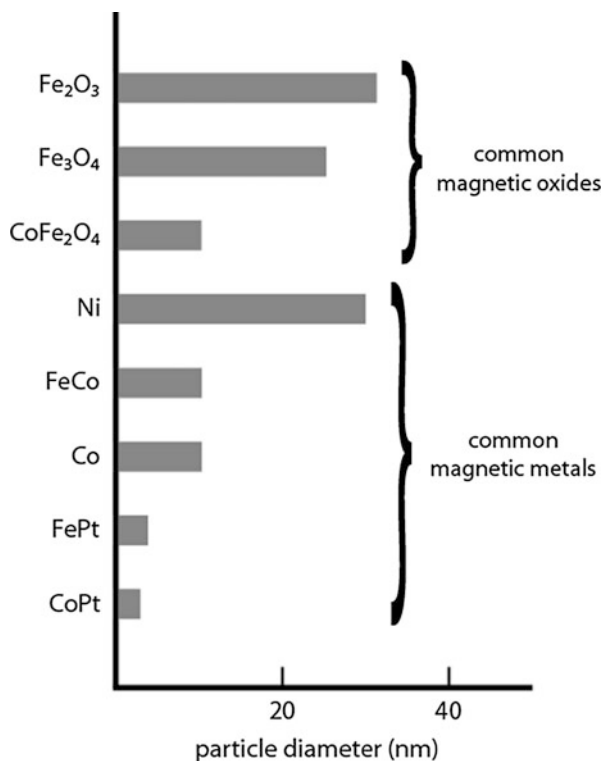
Therefore, it is anticipated that softer bulk ferromagnets can maintain superparamagnetic behavior up to larger sizes. In general, the upper limit for superparamagnetic behavior ranges from a few nanometers up to 50 nm depending on material properties, including magnetocrystalline anisotropy (Fig. 25.4) [7].

Superparamagnets exhibit no hysteresis on domain switching and maintain a high saturation magnetization (Fig. 25.5). In order to maintain this superparamagnetic behavior, the nanoparticles must be non-interacting. Magnetic nanoparticle isolation can be accomplished by surrounding the nanoparticle with an organic shell, or capping ligand, which can be used to control interparticle spacing and thereby interactions. The total magnetization of N noninteracting magnetic nanoparticles can be given by the following Langevin function:

$$M = mN\left(\frac{mH}{kT}\right) = \coth\left(\frac{mH}{kT}\right) - \frac{kT}{mH} \tag{25.2}$$

where m is the moment of an individual particle.

Nanoscale superparamagnetic materials are typically synthesized via wet chemistry techniques. The most common methods include aqueous co-precipitation [8–11] and thermal decomposition of metal-organic precursors in high-boiling-point solvents [12–16]. Figure 25.6 shows a representative transmission electron microscope
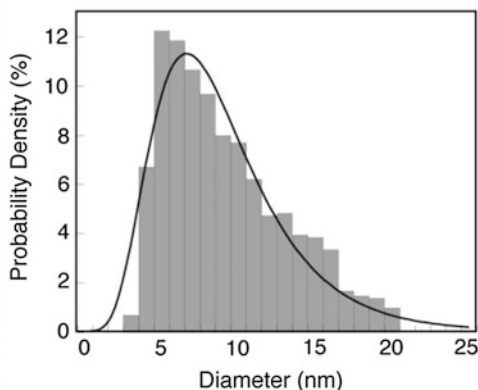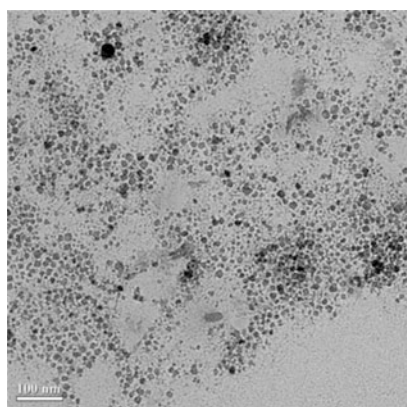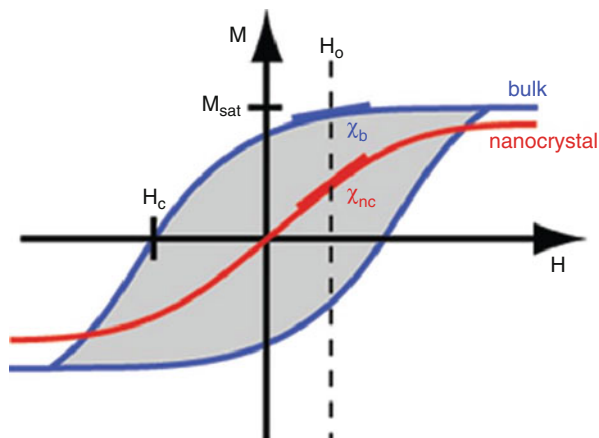
Fig. 25.6 Transmission electron microscope (TEM) image and corresponding histogram for Ni0.5Zn0.5Fe2O4 particles prepared via aqueous co-precipitation

image and a particle size distribution for particles prepared via aqueous coprecipitation. Particles prepared via aqueous coprecipitation typically have an average size between 8 and -10 nm. Synthesis via thermal decomposition of metal-organic precursors results in the formation of monodisperse particles, and the size of the particles can be increased by performing the synthesis in a higher-boiling-point solvent (Fig. 25.7) [13].

Figure 25.8 shows a typical hysteresis loop for a superparamagnetic $Ni_{0.5}Zn_{0.5}Fe_2O_4$ nanoparticle prepared via aqueous coprecipitation at a temperature of 305 K. The lack of hysteresis in the magnetization measurements verifies the superparamagnetic behavior of the nanoparticles. It is, however, important to note that the saturation magnetization for the nanoparticles is much lower than the 70 emu/g of bulk $Ni_{0.5}Zn_{0.5}Fe_2O_4$. This decrease could be the result of a number of effects, including a magnetically "dead" layer on the surface of the nanoparticles.
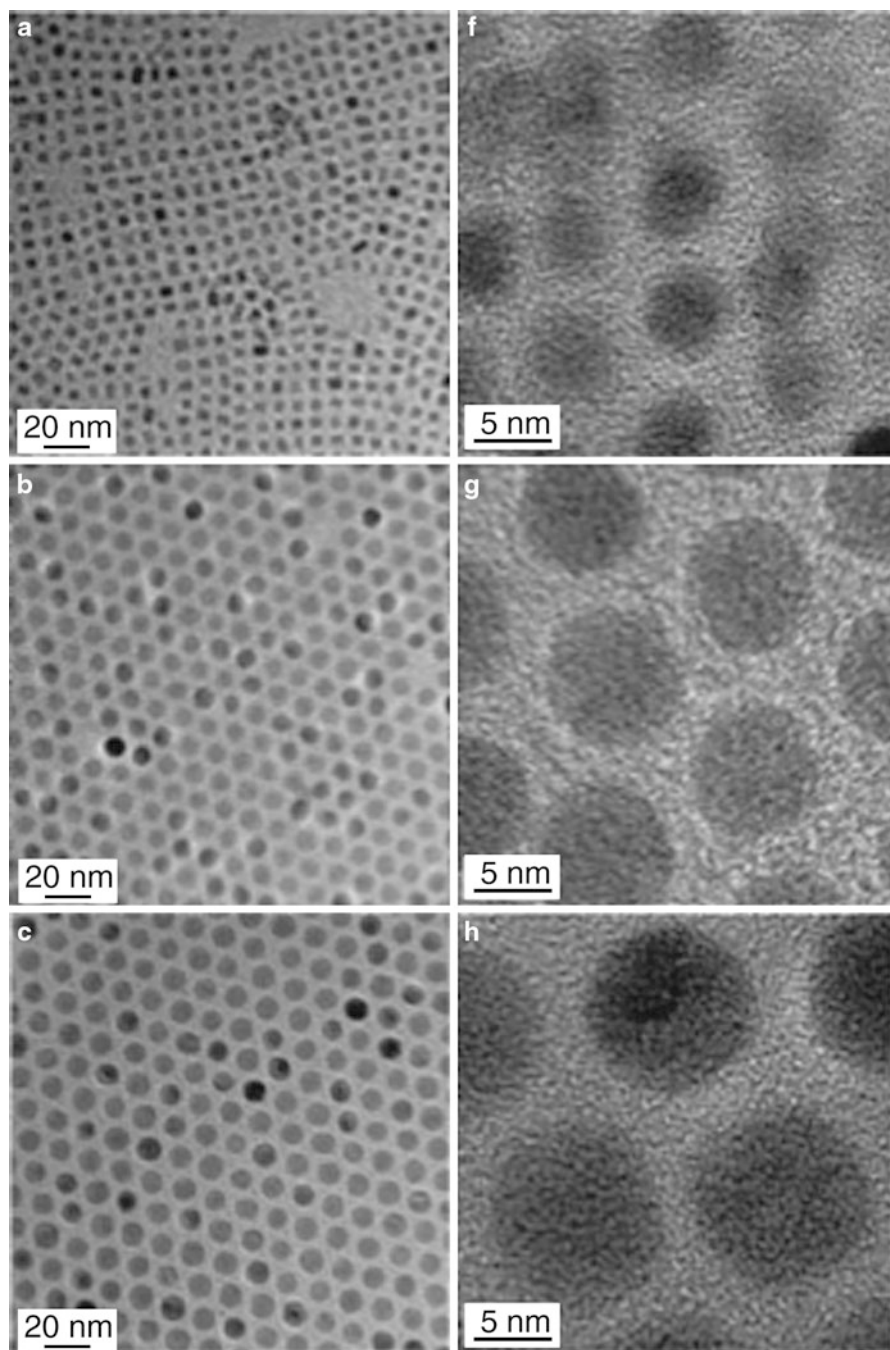
Fig. 25.7 (continued)
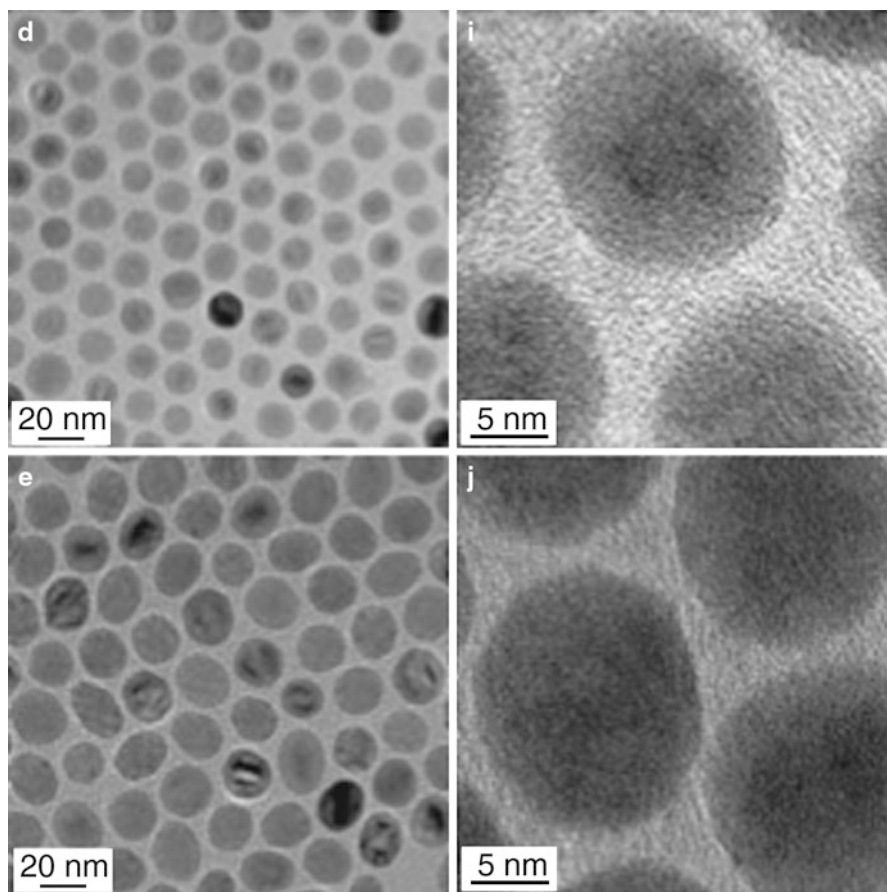
Fig. 25.7 TEM images of monodisperse iron oxide nanocrystals formed from thermal decomposition in a range of high-boiling-point solvents. (**a**) 5 nm particles, 1-hexadecene $T_b = 274\ °C$, (**b**) 9 nm, octyl ether $T_b = 287\ °C$, (**c**) 12 nm, 1-octadecene $T_b = 315\ °C$, (**d**) 16 nm, 1-eicosene $T_b = 330\ °C$, (**e**) 22 nm, triocty lamine $T_b = 365\ °C$, and (**f–j**) corresponding HRTEM images [14] (Reprinted with permission from *Nature Publishing Group*)

The bonding at the surface of the nanoparticle is different than in the bulk and may contain defects, and these defects affect the alignment of the spins at the surface resulting in this so-called magnetic "dead" layer [17]. Another possible effect can be attributed to the fact that an increase in lattice parameter is typically observed in these nanomaterials compared with bulk [18]. The magnetic ordering in these materials occurs via the superexchange interaction, which is dependent on the distance between neighboring cations. It follows that if the lattice parameter increases, so does the distance between the cations, decreasing the superexchange interactions and therefore the saturation magnetization of the ferrite nanoparticles.

The decrease in saturation magnetization can also be explained by the cation distribution in $Ni_{0.5}Zn_{0.5}Fe_2O_4$ nanoparticles. In order to get the maximum

Fig. 25.8 A representative hysteresis loop taken at 305 K for Ni0.5Zn0.5Fe2O4 nanoparticles, revealing superparamagnetic behavior
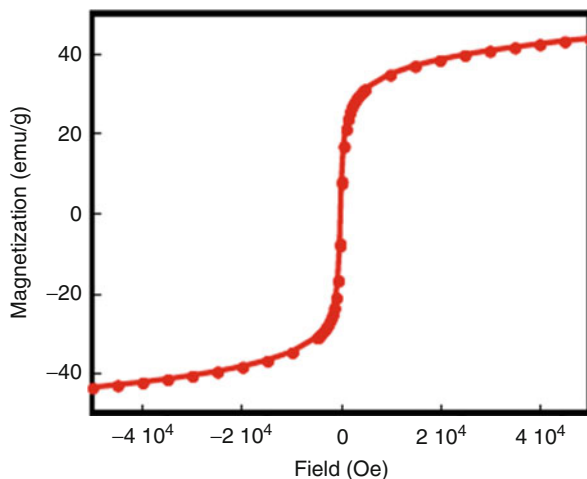
enhancement of magnetic properties in the mixed ferrite, the Zn^{2+} cations must replace the Fe^{3+} cations on the tetrahedral sites [19]. However, during synthesis there may not be enough time for this rearrangement to fully occur, resulting in a decrease in the observed saturation magnetization compared to bulk. Additionally, during aqueous coprecipitation, hydroxyl groups may be incorporated that may also lead to a decrease in the overall saturation magnetization by either increasing the lattice parameter or interfering with the cation distribution. It is most likely a combination of all of these effects that results in the overall decrease in saturation magnetization of ferrite nanoparticles compared to bulk values.

Applications of Superparamagnetic Particles

One of the key aspects of a nanomaterial is that they exhibit properties unique to the nanoscale, due to quantum confinement. The unique properties of magnetic nanoparticles have opened up new uses in medical and power applications. The following sections will seek to highlight some key results in these areas; however, for a complete review, the author suggests the reader to look at the following review articles [5, 6, 20].

Medical Applications

Magnetic nanoparticles are attractive for medical applications for a variety of reasons. Because the particles are magnetic, they can be directed to a desired location with the pull of an external magnet. This is particularly relevant for sensing applications, including the labeling of cells and their subsequent magnetic separation [21–23]. Frequently, in biology it is desired to separate out certain moieties for sensing applications, e.g., the detection of an antibody or biomarker. One method to accomplish this is to use a magnetic nanoparticle that is surface functionalized such that it will bind with the biomolecule of interest; these magnetically functionalized nanoparticles can then

Fig. 25.9 Schematic of a magnetic particle functionalized for biological applications. A magnetic nanoparticle core is coated with a biocompatible shell (SiO2, polymer) which can be further functionalized by an organic linker to an active molecule capable of targeting or binding with a desired biological moiety
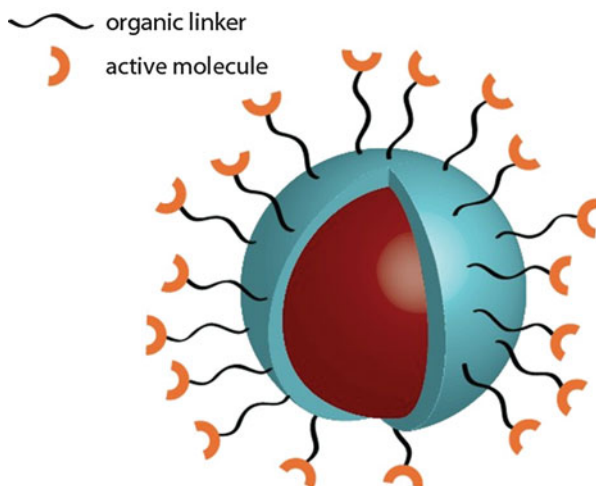
be separated out using an applied magnetic field. Synthesized magnetic nanoparticles can be rendered biocompatible through coating with polyethylene glycol (PEG), dextran, or other biocompatible molecules [10, 11, 13, 24–26]. Figure 25.9 shows a schematic biocompatible magnetic particle, where a magnetic core is surrounded by an organic coating (surfactant, dextran, silica), which can be further functionalized with an active molecule (e.g., drug, antibody, targeting peptide) via an organic linker. Due to the ease in pulling out magnetic particles with the external magnet, this can be used to detect low-volume amounts of the desired biomolecule and aid in the development of sensitive assays, including magnetic enzyme-linked immunosorbent assays (ELISAs) [27, 28].

Magnetic targeting has also been discussed as a way to deliver drugs to a desired location in the body. Although magnetic targeting is limited by the field strengths that are required, it may still find use for regions with limited blood flow [5, 6] or near the surface of the body.

Another key application of magnetic nanoparticles in medicine is their use in hyperthermia treatment of cancer. In hyperthermia treatment the ability of magnetic nanoparticles to generate heat in response to an applied alternating magnetic field is employed to locally heat and kill cancerous cells. The success of magnetic hyperthermia therapy is based on the idea that the cancerous cells are less robust than the surrounding healthy tissue and will thereby be killed by the increased heat, while the surrounding healthy tissue is spared. In hyperthermia, a ferrofluid of colloidally stable magnetic particles is subjected to an alternating magnetic field. When this ferrofluid is exposed to the alternating magnetic field, the particles will align with the field using one of the two mechanisms. Some of the particles will physically rotate in order to align with the field, and this is referred to as Brownian rotation. In other particles, Néel relaxation will occur, in which the moment within the particle will rotate to align with the field. Both Brownian and Néel rotation mechanisms are described by their characteristic relaxation times, τ_b and τ_n,

respectively. Hysteresis is observed when these relaxation times are longer than the period of reversal of the alternating magnetic field, which generates localized heating. The details of the mechanisms behind this heating are described in the literature by Rosensweig [29].

The effectiveness of a nanoparticle for hyperthermia applications depends on the amount of heat generated when it is placed in an alternating field. In order to compare different nanoparticles, or ferrofluids based on them, a figure of merit referred to as the specific absorption rate (SAR) values is reported. The units for SAR are $W\ g^{-1}$, and values up to 211 $W\ g^{-1}$ ferrite have been reported. A recent review by Sharifi et al. outlines some of the recent advances in high SAR values reported for ferrite-based materials [30].

Power Applications

As mentioned above, one key characteristic of ferromagnetic materials is the hysteresis response of magnetization in an applied magnetic field. Each time the magnetic field is cycled, the area within the loop is lost in the form of heat. However, superparamagnetic materials maintain the high saturation magnetization of a ferromagnet, without thermal loss on switching. This makes superparamagnetic nanoparticles relevant for power applications as a method to minimize loss. Due to the lack of hysteresis loss on switching, superparamagnetic nanoparticles could be incorporated in dc-dc power converters. Other relevant sources for loss in magnetic materials are eddy currents, which are formed when a conductive material is placed in an alternating magnetic field. Selecting magnetic oxides, which are insulators, can minimize eddy current losses. However, there are several design challenges in incorporating nanoparticles into real engineering devices. In order to gain the benefits of superparamagnetic nanoparticles in dc-dc power converters, the particles must remain below the critical size for superparamagnetic behavior and must be noninteracting [31]. Therefore, processing routes must be selected that avoid coarsening of the particles. Porosity will also negatively affect device performance, by driving down the overall magnetic properties of the device [32]. Naughton et al. were able to overcome some of these processing challenges by coating superparamagnetic $Ni_{0.5}Zn_{0.5}Fe_2O_4$ nanoparticles with a silica shell. These particles were then consolidated and sintered to form dense toroids (Fig. 25.10) [31]. They found that by increasing the thickness of the silica shell, the losses of the resultant device could be improved, at the cost of overall magnetic properties. However, in forming fully dense composites, Naughton et al. were unable to avoid coarsening, and their composites ($Ni_{0.5}Zn_{0.5}Fe_2O_4$-SiO_2) began to display ferromagnetic properties and losses at high frequencies (Fig. 25.11).

Superparamagnetic nanoparticles also find use as magnetic field sensors with high sensitivity. The requirements for a magnetic field sensor are to respond to experience a linear response to an applied magnetic field, be a hysteretic, and lastly sensitive to small changes in the magnetic field [20]. As outlined previously, one key aspect of superparamagnetic nanoparticles is their lack of hysteresis behavior, making them excellent candidate materials as magnetic field sensors. As shown in Fig. 25.6, superparamagnetic nanoparticles have high magnetic susceptibilities,
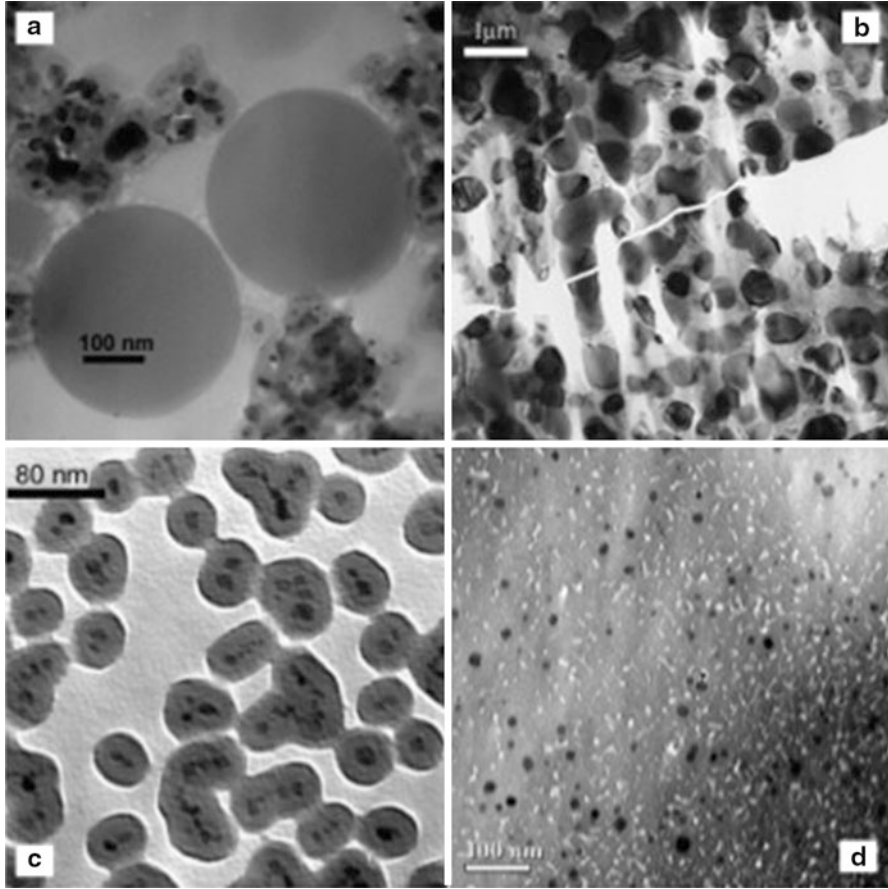
Fig. 25.10 TEM micrographs of Ni-Zn ferrite nanoparticles silica coated under poor (**a**) and improved conditions (**c**) and their resultant microstructures after sintering at 1100°C, (**b**, **f**). The more uniform silica coating in C produces a composite with limited nanoparticle coarsening (**d**). (Reproduced with permission from Ref. [33])

thereby making them sensitive to small changes in magnetic fields. As a result of this high susceptibility and a hysteretic behavior, superparamagnetic nanoparticles can also act as highly sensitive magnetic field sensors.

Ferroelectrics

Bulk Behavior

Ferroelectrics get their name, not because they contain iron but because many of their properties, specifically their response to an applied electric field, behave

Fig. 25.11 Real (*solid line*) and imaginary (*dashed line*) components of the complex permeability spectrum of (**a**) Ni-Zn ferrite nanoparticles with no silica coating and the resultant sintered toroids and (**b**) of Ni-Zn ferrite particles with a 1 nm silica shell after sintering for 1 h at the temperatures indicated (Reproduced with permission from Ref. [33])
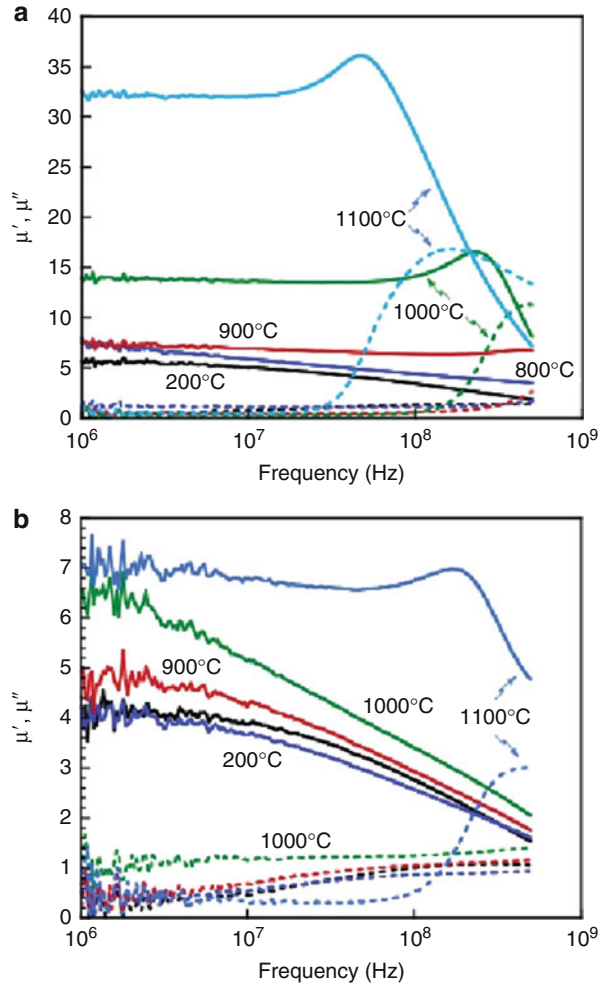
analogously to those of ferromagnetic materials in an applied magnetic field. Ferroelectric materials have a permanent dipole moment and an overall electronic polarization that is not necessarily zero in the absence of an electric field. Similar to ferromagnetic materials, ferroelectric materials contain domains and their polarization, P, shows a hysteretic response to an applied electric field (E). Ferroelectric materials also undergo a phase transition from a high-temperature paraelectric phase, where the net polarization is zero in the absence of an applied field, but can be induced by an applied electric field, to a low-temperature ferroelectric phase with a spontaneous polarization. For ferroelectric materials this phase transition is coincident with a structural phase transition. The temperature at which this phase transition occurs is also known as the Curie temperature, T_c, and the permittivity, ε, follows Curie-Weiss behavior:

Fig. 25.12 Schematic of (**a**) permittivity and (**b**) lattice parameters as a function of temperature for ferroelectric material (e.g., $BaTiO_3$, $PbTiO_3$)
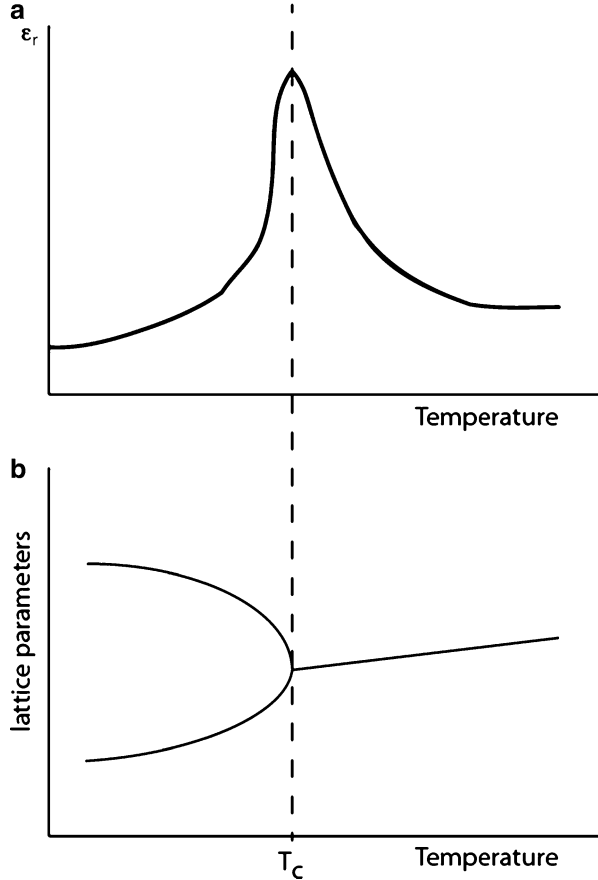
$$\varepsilon_r = \frac{c}{T - T_C} \qquad (25.3)$$

C is the Curie constant and is specific to the material of interest and T is temperature. As seen in Eq. 25.3, the permittivity diverges at the Curie temperature, when the dipole moments spontaneously align, even in the absence of an electric field (Fig. 25.12).

The most extensively studied ferroelectric materials belong to a class of materials in the perovskite structure of the form ABO_3 (Fig. 25.13). The cubic perovskite structure, shown in Fig. 25.8a, is characterized by a small cation, B, that sits at the center of octahedra formed by oxygen anions. The large, A, cations are located at the unit cell corners. This cubic perovskite is the high-temperature paraelectric phase, and the polarization behaves linearly with applied electric field. However, below the Curie temperature the unit cell undergoes a structural distortion to a non-centrosymmetric tetragonal perovskite phase (Fig. 25.13b), where the center (B) cation shifts off center.
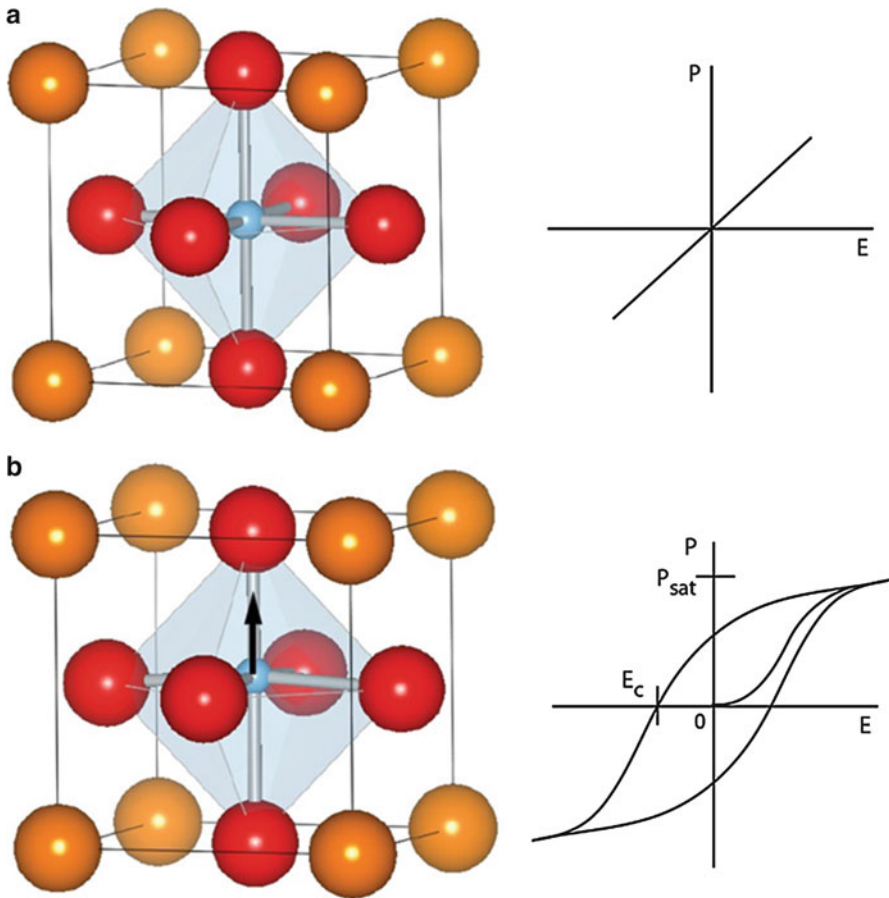
Fig. 25.13 The (**a**) cubic and (**b**) tetragonal perovskite crystal structure and their corresponding polarization (*P*) response to an applied electric field (*E*), where the small B cation (*blue*) is in the middle of the oxygen octahedra (*red*), and the large A cations (*orange*) occupy the corners of the unit cell. The *black arrow* in (**b**) is to guide the eye to notice that the B cation has gone off center

This off-center shift of the B cation is responsible for the spontaneous polarization of the ferroelectric phase. Analogous to ferromagnetic materials, as synthesized ferroelectric materials typically have no net polarization due to the formation of domains. When an electric field is applied, these domains similarly align and reorient themselves with the applied field, resulting in hysteresis behavior (Fig. 25.13b). As a positive electric field is applied, the polarization increases to a saturation value, known as the saturation polarization, P_s, where all dipoles are aligned parallel to one another and the applied field. When the field is removed, the polarization decreases to a remnant value, P_r, and a coercive field, E_c, is required to return the polarization to zero.

Nanoscale Ferroelectric Materials

It is anticipated that below some critical size single-domain ferroelectric or superparaelectric particles should be realized. Similar to ferromagnets there should exist some lower size limit at which it will become energetically unfavorable for a multi-domain structure to exist [33]. At this point, the ferroelectric should exhibit superparaelectric behavior, where the energy losses on switching go to zero while maintaining a high polarization. However, to date no superparaelectric free-standing nanoparticles have been reported.

Ferroelectricity is directly related to crystal structure and requires a non-centrosymmetric structure. This direct link between crystal structure and ferroelectricity leads to some problems. For small particles the tetragonal crystal structure becomes energetically unfavorable, resulting in a transformation to a cubic or pseudo-cubic structure and subsequently a loss of ferroelectric behavior. There are many reports of just such a lower size limit in the literature, but no single theory seems capable of accounting for these size effects. Differing theories center on surface effects of small particles and the large defect concentrations in small ferroelectric particles. However, for all ferroelectric materials, as the particle size decreases, the particles will no longer undergo a transition from a cubic to a tetragonal crystal structure; in other words the Curie temperature goes below room temperature. The particle size below which the particle no longer exhibits this transition to a tetragonal crystal system and ferroelectric behavior is dependent on the material system but occurs for all ferroelectric materials. In $BaTiO_3$, a prototypical ferroelectric, the Curie temperature begins to drop for particles below 200 nm [34]. However, for the case of $PbTiO_3$, another perovskite-based ferroelectric, the Curie temperature remains near the bulk value until $\sim$50 nm (Fig. 25.14) [33, 35].

One of the theories for the lack of ferroelectric behavior in nanoparticles of ferroelectric materials is due to the presence of a depolarizing field as a result of surface charges. Ferroelectric behavior inherently involves dipoles or a separation of positive and negative charges (Fig. 25.15). At some point these charge separations will reach an external surface, resulting in surface charges. These surface charges will result in the formation of a depolarizing field. Bulk ferroelectric materials form domains in order to reduce these depolarizing fields. However, for sufficiently small particles, the formation of a domain wall becomes energetically unfavorable. The size effects of ferroelectric behavior have been described by Mehta et al., and they showed that the depolarizing field (E_d) for a perfectly insulating, homogenously poled ferroelectric, where the polarization charge is localized on the surface of the material, can be given by [32, 34].

$$E_d = \frac{P(1 - \theta)}{\varepsilon_0 \varepsilon_r} \qquad (25.4)$$

P is the saturation polarization of the ferroelectric and θ is a size-dependent parameter,
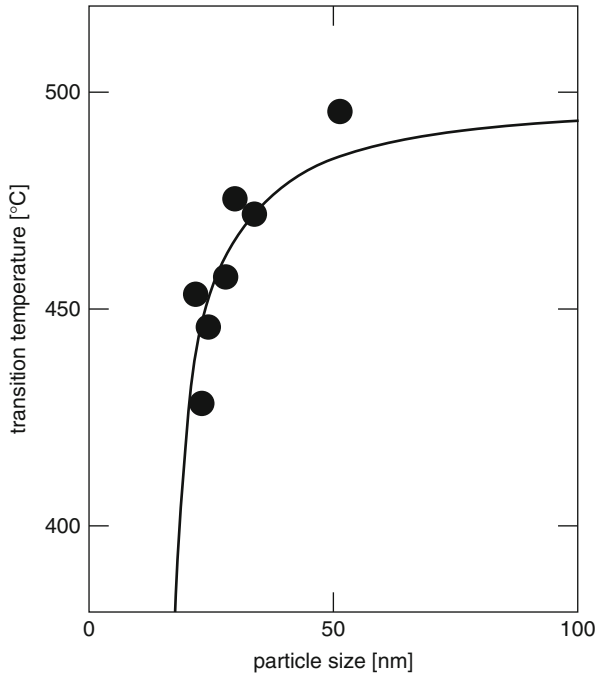
Fig. 25.14 Transition temperature of PbTiO$_3$ as a function of particle diameter (Reprinted with permission from Ref. [35])
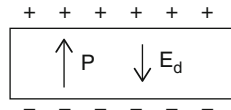
Fig. 25.15 Schematic representation of surface charges as a result of polarization terminating on the surface, for example, in a single-domain ferroelectric particle. These surface charges will lead to a depolarizing field, making the ferroelectric behavior unstable for small particles

$$\theta = \frac{L}{2\varepsilon_r C + L} \tag{25.5}$$

where L is the characteristic size of the ferroelectric material, or the distance separating oppositely charged surfaces as a result of spontaneous polarization, and C is a constant that is dependent on the material in contact with the charged ferroelectric surface. ε_r and εo are the relative permittivity of the material and the permittivity of free space, respectively. The above equations (Eqs. 25.4 and 25.5) reveal that as the particle size or L decreases, the magnitude of the depolarizing field increases, making ferroelectric behavior increasingly unstable for small particle sizes.

Summary

Although at the bulk scale ferromagnetic and ferroelectric materials behave analogously to one another in an applied magnetic or electric field, respectively, their behaviors differ dramatically at the nanoscale. These differences can be directly related to the fundamental processes that govern magnetic and electronic properties of materials. For the case of both ferromagnetic and ferroelectric materials, there will exist a critical size below which the formation of domains becomes energetically unfavorable due to the energy cost of forming a domain wall. In the case of ferromagnetic materials, this results in the formation of single-domain particles that are capable of rotating freely in the absence of an applied magnetic field, exhibiting superparamagnetic behavior. However, single-domain ferroelectric particles are energetically unfavorable due to the nature of electric fields. A single-domain ferroelectric particle leads to the formation of positive and negative charges at the surface of the particle, which generates a depolarizing field that precludes ferroelectric behavior at the nanoscale. Additionally, for ferroelectric behavior to occur, a material must have a non-centrosymmetric crystal structure. For very small ferroelectric particles, a cubic or pseudo-cubic structure is energetically more stable, once again precluding the existence of a single-domain ferroelectric or superparaelectric particle. Because of the unique superparamagnetic properties of magnetic nanoparticles, they find numerous new applications spanning electronics to medicine.

References

1. Spaldin NA (2010) Magnetic materials: fundamentals and applications. Cambridge University Press, New York
2. Cullity BD, Graham CD (2008) Introduction to magnetic materials. IEEE Press, Piscataway
3. Neel L (1953) Thermoremanent magnetization of fine powders. Rev Mod Phys 25(1):293–296
4. Brown J, Fuller W (1963) Thermal fluctuations of a single-domain particle. Phys Rev 130(5):1677
5. Pankhurst Q, Connolly J, Jones S, Dobson J (2003) Applications of magnetic nanoparticles in biomedicine. J Phys D Appl Phys 36:R167
6. Pankhurst Q, Thanh N, Jones S, Dobson J (2009) Progress in applications of magnetic nanoparticles in biomedicine. J Phys D Appl Phys 42:224001
7. Krishnan KM (2010) Biomedical nanomagnetics: a spin through possibilities in imaging, diagnostics, and therapy. IEEE Trans Magn 46(7):2523–2558
8. Massart R (1981) Preparation of aqueous magnetic liquids in alkaline and acidic media. IEEE Trans Magn MAG-17:1247–1248
9. Massart R, Dubois E, Cabuil V, Hasmonay E (1995) Preparation and properties of monodisperse magnetic fluids. J Magn Magn Mater 149:1–5
10. Andrew JS, Clarke DR (2008) Enhanced ferroelectric phase content of polyvinylidene difluoride fibers with the addition of magnetic nanoparticles. Langmuir 24:8435–8438
11. Andrew JS, Mack JJ, Clarke DR (2008) Electrospinning of polyvinylidene difluoride-based nanocomposite fibers. J Mater Res 23:105–114
12. Lee J-H, Huh Y-M, Jun Y-W, Seo J-W, Jang J-T, Song H-T, Kim S, Cho E-J, Yoon H-G, Suh J-S, Cheon J (2007) Artificially engineered magnetic nanoparticles for ultra-sensitive molecular imaging. Nat Med 13(1):95–99

13. Park J, An K, Hwang Y, Park J-G, Noh H-J, Kim J-Y, Park J-H, Hwang N-M, Hyeon T (2004) Ultra-large-scale syntheses of monodisperse nanocrystals. Nat Mater 3(12):891–895

14. Park J, Joo J, Kwon SG, Jang Y, Hyeon T (2007) Synthesis of monodisperse spherical nanocrystals. Angew Chem Int Ed 46:4630–4660

15. Park J, Lee E, Hwang NM, Kang MS, Kim SC, Hwang Y, Park JG, Noh HJ, Kini JY, Park JH, Hyeon T (2005) One-nanometer-scale size-controlled synthesis of monodisperse magnetic iron oxide nanoparticles. Angew Chem Int Ed 44(19):2872–2877

16. Kinsella JM, Ananda S, Andrew JS, Grondek JF, Chien M-P, Scadeng M, Gianneschi NC, Ruoslahti E, Sailor MJ (2011) Enhanced magnetic resonance contrast of Fe_3O_4 nanoparticles trapped in a porous silicon nanoparticle host. Adv Mater 23(36):H248–H253

17. Leslie-Pelecky DL, Rieke RD (1996) Magnetic properties of nanostructured materials. Chem Mater 8:1770–1783

18. Tsunekawa S, Ishikawa K, Li Z-Q, Kawazoe Y, Kasuya A (2000) Origin of anomalous lattice expansion in oxide nanoparticles. Phys Rev Lett 85:3440–3443

19. Smit J, Wijn H (1959) Ferrites: physical properties of ferromagnetic oxides in relation to their technical applications. Philips, Eindhoven

20. Cowburn RP (2002) Magnetic nanodots for device applications. J Magn Magn Mater 242:505–511

21. Riehemann K, Schneider SW, Luger TA, Godin B, Ferrari M, Fuchs H (2009) Nanomedicine–challenge and perspectives. Angew Chem Int Ed Engl 48(5):872–897

22. Herr JK, Smith JE, Medley CD, Shangguan DH, Tan WH (2006) Aptamer-conjugated nanoparticles for selective collection and detection of cancer cells. Anal Chem 78(9):2918–2924

23. Perez JM, Josephson L, O'loughlin T, Hogemann D, Weissleder R (2002) Magnetic relaxation switches capable of sensing molecular interactions. Nat Biotechnol 20(8):816–820

24. Park J, Kang E, Bae CJ, Park J-G, Noh H-J, Kim J-Y, Park J-H, Park HM, Hyeon T (2004) Synthesis, characterization, and magnetic properties of uniform-sized MnO nanospheres and nanorods. J Phys Chem B 108:113594–113598

25. Park J-H, Von Maltzahn G, Zhang L, Derfus AM, Simberg D, Harris TJ, Ruoslahti E, Bhatia SN, Sailor MJ (2009) Systematic surface engineering of magnetic nanoworms for in vivo tumor targeting. Small 5:694–700

26. Park J-H, Von Maltzahn G, Zhang L, Schwartz MP, Ruoslahti E, Bhatia SN, Sailor MJ (2008) Magnetic iron oxide nanoworms for tumor targeting and imaging. Adv Mater 20:1630–1635

27. Fan AP, Lau CW, Lu JZ (2005) Magnetic bead-based chemiluminescent metal immunoassay with a colloidal gold label. Anal Chem 77(10):3238–3242

28. Tang DP, Yuan R, Chal YQ (2008) Ultrasensitive electrochemical immunosensor for clinical immunoassay using thionine-doped magnetic gold nanospheres as labels and horseradish peroxidase as enhancer. Anal Chem 80(5):1582–1588

29. Rosensweig RE (2002) Heating magnetic fluid with alternating magnetic field. J Magn Magn Mater 252:370–374

30. Sharifi I, Shokrollahi H, Amiri S (2012) Ferrite-based magnetic nanofluids used in hyperthermia applications. J Magn Magn Mater 324(6):903–915

31. Naughton B, Majewski P, Clarke D (2007) Magnetic properties of nickel-zinc ferrite toroids prepared from nanoparticles. J Am Ceram Soc 90(11):3547–3553

32. Lakhtakia A, Mackay T (2004) Size–dependent Bruggeman approach for dielectric–magnetic composite materials. Int J Electron Commun 58(1):1–3

33. Rudiger A, Shnueller T (2005) Nanosize ferroelectric oxides- tracking down the superpara-electric limit. Appl Phys A-Mater Sci Process 80:1247–1255

34. Mehta RR, Silverman BD, Jacobs JT (1973) Depolarization fields in thin ferroelectric films. J Appl Phys 44(8):3379–3385

35. Ishikawa K, Yoshikawa K, Okada N (1988) Size effect on the ferroelectric phase transition in $PbTiO_3$ ultrafine particles. Phys Rev B 37(10):5852–5855

Segregation-Induced Low-Dimensional Surface Structures in Oxide Semiconductors

26

A. J. Atanacio, Tad Bak, Dewei Chu, Mihail Ionescu, and
Janusz Nowotny

Keywords

Segregation • Surface structure • Bidimensional surface layer • Oxide
semiconductors

Introduction

Nanomaterials have been commonly considered in terms of nano-size solids, which
exhibit different shapes and sizes. It has been shown that the properties of the nano-
size solids depend profoundly on their shapes and sizes. The related morphology is
determined by the applied experimental procedures. Therefore, the nano-size
solids with reproducible properties may be achieved when the applied processing
procedures are reproducible. This appears to be difficult.

A.J. Atanacio

Solar Energy Technologies, School of Computing, Engineering and Mathematics, University of
Western Sydney, Penrith, NSW, Australia

Australian Nuclear Science and Technology Organisation, Kirrawee DC, NSW, Australia

T. Bak • J. Nowotny (✉)
Solar Energy Technologies, School of Computing, Engineering and Mathematics, University of
Western Sydney, Penrith, NSW, Australia
e-mail: j.nowotny@uws.edu.au

D. Chu
University of New South Wales, School of Materials Science and Engineering, Sydney, NSW,
Australia

M. Ionescu
Australian Nuclear Science and Technology Organisation, Kirrawee DC, NSW, Australia

The present chapter considers low-dimensional structures, which are formed at interfaces of solids, such as external surfaces and grain boundaries. Therefore, the shape of these structures is consistent with the shape of the interfaces, while their thickness is limited to several lattice layers [1]. The driving force of their formation is an excess of interface energy. The local properties of these structures are determined by the thermodynamic factor related to the excess of energy at the interface.

The present work considers the low-dimensional structures, which are formed at external surfaces of TiO_2-based semiconductors in contact with the gas phase or liquid phase. It is shown that the local properties of these structures have a profound influence on catalytic and photocatalytic performance. Therefore, the progress in photocatalysis is determined by the progress in the science of materials interfaces.

Surface properties of crystalline solids are different from those of the bulk phase in terms of chemical composition, structure, and the related electrical properties [1–3]. The difference results from the excess of surface energy leading to surface segregation of selected lattice elements. When the concentration of these elements at the surface surpasses a certain critical value, then the surface layer undergoes a structural transition leading to the formation of a quasi-isolated surface structure, which is distinctively different from that of the bulk phase.

The characterization of the surface structures is difficult due to their thickness that is limited to 1–2 lattice layers. Application of rapidly developed modern surface-sensitive techniques indicates that the surface structures exhibit extraordinary properties [1]. The resulting progress in surface science of nonstoichiometric compounds indicates that segregation results in the formation of low-dimensional surface structures, which are distinctively different from the bulk phase. Therefore, solids should be considered in terms of the so-called *onion-like* model, involving the bulk phase that is enveloped by a thin surface layer. Consequently, the reactivity of solids with gases and liquids is determined by the properties of nano-size surface structure rather than the bulk phase. Better understanding of the local properties of these structures is essential in better understanding of the mechanism of catalytic and photocatalytic reactions, which take place at the surface.

The surface structures are not autonomous. These structures are in contact with the bulk phase on one side and the gas phase, or the liquid phase, on the other side. Therefore, the local properties of these structures are influenced by chemical composition of both phases forming the interface.

The local properties of surface structures of oxide materials are determined by oxygen activity in the gas phase, bulk phase composition, and the kinetics of the interactions between the two phases. At lower temperatures, the interactions are limited to physical adsorption of oxygen. As the temperature increases, the interactions at the gas/solid interface involve oxygen chemisorptions and its incorporation into the lattice leading to a change in oxygen nonstoichiometry.

At elevated temperatures, when the lattice elements become sufficiently mobile, selected lattice species segregate to the surface leading to the formation of the surface structures. At elevated temperatures, these structures are in equilibrium with both the bulk phase and the gas phase.

In the case of metal oxides, the most important property of the gas phase is oxygen activity. However, the properties of the surface structures of oxide semiconductors during their performance as a photocatalyst at room temperature should be considered in terms of the oxide/water interface. The properties of the related surface structures are influenced by the chemical activity of protons in water.

The present work is focused on the surface structures for TiO_2-based semiconductors which exhibit promising properties for solar energy conversion [4]. The related surface structures are considered in terms of their formation during processing at the gas/solid interface and their performance at the liquid/solid interface. The formation of surface structures is considered in terms of the segregation-induced enrichment of the surface layer in point defects, which are the atomic size lattice imperfections.

Postulation of the Problem

The performance of oxide semiconductors in water purification and water splitting is determined by their reactivity with water leading to total or partial water oxidation, which may be represented by the following respective reactions [5, 6]:

$$2H_2O + 4h^\bullet \rightarrow O_2 + 4H^+ \tag{26.1}$$

$$H_2O + h^\bullet \rightarrow OH^\bullet + H^+ \tag{26.2}$$
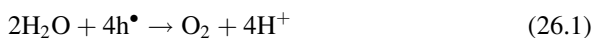
where $h^\bullet$ is an electron hole, H^+ is proton, and OH* is the hydroxyl radical (both in the aqueous solution). As seen, progress of the water oxidation reactions (26.1) and (26.2) depends on the light-induced activity of electron holes and the related chemical potential of electrons at the surface of anodic sites:

$$\mu_n = \mu_n^o + RT \ln n \tag{26.3}$$

$$\mu_h = \mu_h^o + RT \ln p \tag{26.4}$$

where n and p denote the concentration of electrons and holes.

The advantage of oxide semiconductors as promising photocatalysts, over alternative semiconductors, is their good resistance to corrosion and photocorrosion in water. In consequence, their performance in water is stable over an extensive period of time. The research aims at the modification of their properties in order to enhance the energy conversion efficiency in order to achieve the efficiency

level that is required for commercialization. The ultimate aim of the research is to enhance the selectivity of water oxidation towards the mechanism (26.1) or (26.2).

The most commonly applied research strategy is the modification of composition by a change of nonstoichiometry, either through oxidation and reduction or the incorporation of ions of different size and valency. The latter process results in the formation of solid solutions. The resulting experimental data are usually considered in terms of theoretical models describing the effect of composition on performance. It is important to note that photocatalytic performance is determined by the local semiconducting properties of the outermost surface layer and the related charge transfer. Therefore, appropriate interpretation of the photocatalytic performance requires knowledge of the local properties of this layer, rather than bulk properties.

The interpretation of the effect of segregation on properties of metal oxides is complex. The first complication is strong concentration gradients, which are formed in the segregation-induced surface layer. There has been an accumulation of the segregation- induced data indicating that the segregation-induced enrichment results in strong concentration gradients [1]. Awareness is growing that the outermost surface layer undergoes structural transitions when the segregation-induced enrichment surpasses a certain critical value. The latter effect results in the formation of low-dimensional quasi-isolated surface structures, which exhibit outstanding properties. In this respect, the following questions can be formulated:

- What are the local composition and the structure of the surface layer?
- What is the thickness of the surface layer?
- What is the reactivity of the surface layer with the surrounding phase, such as gas phase of the liquid phase?

The present work is an attempt in addressing these questions using the experimental data for TiO_2 and its solid solutions. The overview on the experimental evidence is preceded by a brief analysis of the Gibb's isotherm describing adsorption and segregation at interfaces.

Definition of Basic Terms

Composition of Interfaces

The surface of solids has a tendency to change the chemical composition as a result of adsorption and segregation [1–3]. Both segregation and adsorption can be considered in terms of the same concept of the Gibb's equation describing the relationship between the surface excess concentration Γ (in moles per square meter) and the bulk concentration. For a two-component system, the difference between surface and bulk concentration may be represented by the Gibb's adsorption isotherm:

$$\Gamma_2 = -\frac{1}{RT}\frac{\partial\gamma}{\partial\ln a_2} \tag{26.5}$$

where γ is the surface tension and a is the activity. The larger the reduction of γ (caused by addition of a_2), the larger the surface excess. In this case, segregation is considered as adsorption of species derived from the solid phase.

Another approach concerns nonstoichiometric compounds, such as metal oxides. In this case, surface composition may be considered in terms of the formation energy of defects at interfaces. This energy depends on the crystal field and the related environment in the lattice. As a consequence, the concentration of defects at the surface differs from that in the bulk phase. The lattice charge neutrality requires that the surface charge, induced by the increased concentrations of defects in the surface layer, is compensated by the space charge in the sublayer. The resulting electric field is the driving force for the transport of charged lattice species leading to the formation of a surface layer. The charge neutrality in this case must be considered in terms of Poisson's equation.

The present work considers the effect of segregation of lattice elements, including both intrinsic and extrinsic defects, in TiO_2 and its solid solutions. The description of the related effects is preceded by definition of defect disorder and the related semiconducting properties. The derived theoretical models are valid for all nonstoichiometric oxides.

Bulk Defect Disorder and Related Semiconducting Properties

Defects play a key role in variety of surface phenomena where annealing to high temperatures is necessary, for example, in bulk-assisted reoxidation, in restructuring and reconstruction processes, and adsorption of sulfur and other compounds. The relationship between bulk defects and surface structure of rutile (110) has been systematically investigated. The bulk structure of reduced TiO_2 crystals is quite complex with a various types of defects such as doubly charged oxygen vacancies, Ti^{3+} and Ti^{4+} interstitials, and planar defects. The defect structure varies with oxygen deficiency which depends on temperature, oxygen activity, impurities, etc.

It has been documented that either metal oxides, which are free of defects, are not reactive or their reactivity is low [7]. The present section considers point defects in titanium dioxide, TiO_2; its solid solutions with donor- and acceptor-type elements; and their effect on reactivity with oxygen, hydrogen, water, and bacteria, as well as reported bits of evidence on the effect of segregation on the formation of low-dimensional surface structures.

Titanium dioxide involves three types of ionic defects: oxygen vacancies, titanium interstitials and titanium vacancies, as well as electronic defects.

Table 26.1 The Kröger-Vink [8] and the traditional notations of defects for TiO_2

Traditional notation	Description	Kröger-Vink notation
Ti_{Ti}^{4+}	Ti_{Ti}^{4+} ion in the titanium lattice site	Ti_{Ti}^{X}
Ti_{Ti}^{3+}	Ti_{Ti}^{3+} ion in the titanium lattice site (quasi-free electron)	e'
V_{Ti}	Titanium vacancy	V_{Ti}''''
Ti_i^{3+}	Ti_i^{3+} in the interstitial site	$Ti_i^{\bullet\bullet\bullet}$
Ti_i^{4+}	Ti_i^{4+} in the interstitial site	$Ti_i^{\bullet\bullet\bullet\bullet}$
O_O^{2-}	O_O^{2-} ion in the oxygen lattice site	O_O^{X}
V_O	Oxygen vacancy	$V_o^{\bullet\bullet}$
O_O^{-}	O_O^{-} ion in oxygen lattice site (quasi-free electron hole)	$h^{\bullet}$

Table 26.2 Basic defect equilibria in TiO_2 [9], where n and p denote concentrations of electrons and electron holes, respectively, $p(O_2)$ is oxygen activity, K_1, K_2, K_3 and K_4 denote the equilibrium constants, and ΔH^o and ΔS^o denote the enthalpy and entropy terms, respectively

Defect reaction	Equilibrium constant	ΔH^O [kJ/mol]	ΔS^O [J/(mol K)]
1 $O_O^X \Leftrightarrow V_O^{\bullet\bullet} + 2e' + \frac{1}{2}O_2$	$K_1 = [V_O^{\bullet\bullet}]n^2p(O_2)^{1/2}$	493.1	106.5
2 $Ti_{Ti}^X + 2O_O^X \Leftrightarrow Ti_i^{\bullet\bullet\bullet} + 3e' + O_2$	$K_2 = [Ti_i^{\bullet\bullet\bullet}]n^3p(O_2)$	879.2	190.8
3 $Ti_{Ti}^X + 2O_O^X \Leftrightarrow Ti_i^{\bullet\bullet\bullet\bullet} + 4e' + O_2$	$K_3 = [Ti_i^{\bullet\bullet\bullet\bullet}]n^4p(O_2)$	1,025.8	238.3
4 $O_2 \Leftrightarrow [V_{Ti}''''] + 4h^{\bullet} + 2O_O^X$	$K_4 = [V_{Ti}''''^{\bullet\bullet\bullet\bullet}]p^4p(O_2)^{-1}$	354.5	−202.1
5 $nil \Leftrightarrow e' + h^{\bullet}$	$K_i = np$	222.1	44.6
$\ln K = [(\Delta S^\circ)/R] - [(\Delta H^\circ)/RT]$			

The diffusion mechanism for various defects is also quite different, e.g., oxygen migrates via a site exchange mechanism, while excess Ti diffuses through the crystal as interstitial atoms.

The list of predominant defects in TiO_2, including the traditional notation and the Kröger-Vink notation [8], is in Table 26.1.

The defects in crystals must satisfy the charge neutrality condition, which for pure TiO_2 may be represented in the following form:

$$2[V_o^{\bullet\bullet}] + 3[Ti_i^{\bullet\bullet\bullet}] + 4[Ti_i^{\bullet\bullet\bullet\bullet}] + p = n + 4[V_{Ti}''''] \tag{26.6}$$

where the symbols of defects are defined in Table 26.1, the square brackets denote concentrations, and n and p denote concentrations of electrons and electron holes. The point defects may react with other defects within the same structure forming defect clusters and larger defect aggregates. The reactions between TiO_2 and oxygen, leading to the formation of defects, may be represented by defect equilibria, which are shown in Table 26.2.

Combination of the equilibrium constants in Table 26.2 and the charge neutrality (26.6) leads to the relationship between the concentration of electrons and oxygen activity:

$$n^5 + An^4 - K_i n^3 - 2K_1 P^{1/2} n^2 - 3K_2 P^{-1} n - 4K_3 P^{-1} = 0 \qquad (26.7)$$

where

$$P = p(O_2) \qquad (26.8)$$

K_1, K_2, K_3, and K_i are the equilibrium constants that are defined in Table 26.2 [9] and the term A represents the effective concentration of acceptors:

$$A = 4\left[V_{Ti}''''\right] + [A'] - [D^\bullet] \qquad (26.9)$$

As seen, the term A considers titanium vacancies in a similar manner as acceptor-type external defects. The reason for such treatment is that titanium vacancies are practically immobile, and therefore, in the first approximation, the concentration of titanium vacancies is practically independent of oxygen activity. Equation (26.6) may be used in derivation of defect disorder diagrams, which are valid for the bulk phase. Figure 26.1 represents the defect disorder diagram of TiO_2 at 1,273 K at constant concentration of titanium vacancies [10]. The diagram becomes more complicated when TiO_2 is in equilibrium with respect to both oxygen vacancies, which are fast defects, and titanium vacancies, which are very slow defects [11, 12]. Then defect disorder may be represented in terms of the diagram shown in Fig. 26.2.

The defect diagrams represented in Figs. 26.1 and 26.2 represent the bulk phase where the charge neutrality represented by Equation (26.5) applies. The concentration of defects in the surface layer is entirely different from that of the bulk phase as a result of segregation. The effect of segregation on the formation of low-dimensional surface structures is considered below.

The diagram in Fig. 26.1 can be used for the determination of the concentration of electronic charge carriers and the related chemical potential. The related Fermi level is shown in the upper part of Fig. 26.1. As seen, imposition of controlled oxygen activity may lead to a change in Fermi level by 1.1 eV. As seen, reactivity of TiO_2 and the related charge transfer may be modified by a change in oxygen activity. An additional change in reactivity may be achieved by the incorporation of aliovalent ions forming donors and acceptors.

Surface Versus Bulk Defect Disorder

Intrinsic Defects

The diagram in Fig. 26.1 represents the concentration of both ionic and electronic defects as a function of oxygen activity for pure TiO_2. In thermodynamic equilibrium the concentrations of all defects in the bulk phase are spacially uniform

Fig. 26.1 Effect of oxygen activity on the concentration of defects for pure TiO$_2$ at 1,248 K, derived at constant concentration of titanium vacancies (*lower part*) and Fermi level (*upper part*) (Reproduced with permission from T. Bak, Oxide Semiconductors, Res. Rep., 2010, Copyright T Bak, 2010)
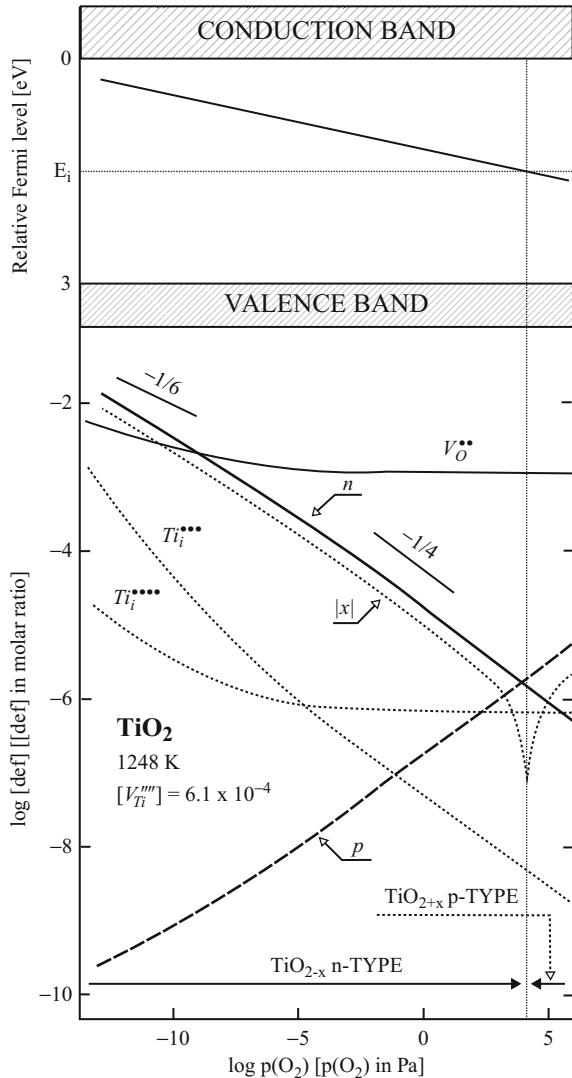
and determined only by the temperature and oxygen activity. For example, the concentration of oxygen vacancies can be expressed as follows:

$$\left[V_O^{\bullet\bullet}\right] = Cp(O_2)T \tag{26.10}$$

where C is a parameter related to defect disorder.

The picture is different in the proximity of interfaces where the crystal structure is affected by the excess of surface energy, resulting in the transport of lattice species to/from the interfaces and leading to a decrease of surface energy. This phenomenon is termed segregation. The present work is focused on the surface segregation.

Fig. 26.2 Full defect disorder of pure TiO$_2$ at 1,248 K (Reproduced with permission from T. Bak, Oxide Semiconductors, Res. Rep., 2010, Copyright T Bak, 2010)
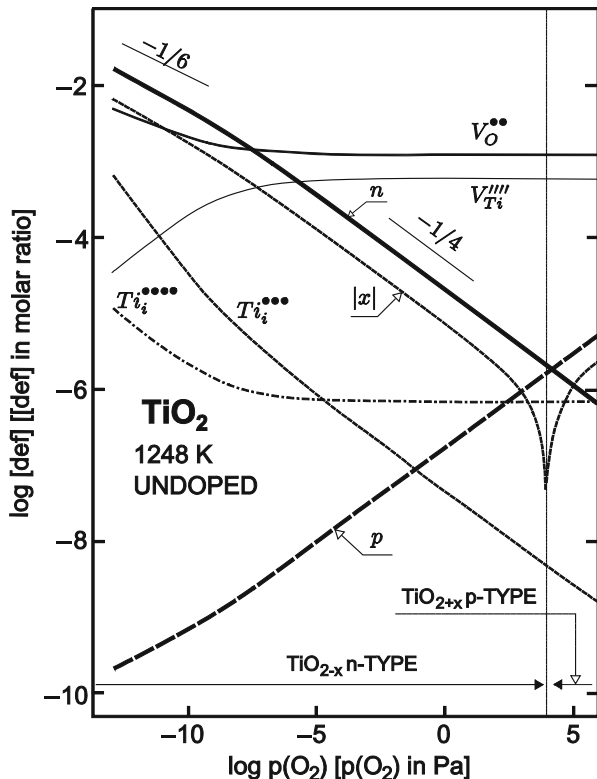
The predominant defects in TiO$_2$ in reducing conditions are oxygen vacancies. When their concentration is low, oxygen vacancies may be considered as a solid solution in the TiO$_2$ crystal. Then the defects, and the related defect equilibria, may be considered using the mass action law. As the formation of oxygen vacancies at the surface results in lattice relaxation and a decrease of surface tension, their concentration within the surface layer is elevated as it represented schematically in Fig. 26.3. In this case, the concentration of oxygen vacancies, and the related nonstoichiometry, is a function of the distance from the surface, in addition of the remaining parameters of temperature and oxygen activity:

$$\left[V_O^{\bullet\bullet}\right] = C'(\xi)Tp(O_2) \tag{26.11}$$

where ξ is the distance from the surface. The picture becomes different when TiO$_2$ is exposed to oxidizing conditions. Then concentration of oxygen vacancies is comparable to the concentration of titanium vacancies (Fig. 26.2). In this case the surface is enriched in these defects, which results in a stronger decrease in surface tension.

Fig. 26.3 Schematic representation of bulk versus surface oxygen nonstoichiometry of TiO$_2$ (Reprinted with permission from J. Nowotny, T. Bak, M.K. Nowotny, L.R. Sheppard. Titanium dioxide for solar-hydrogen I. Functional properties. International Journal of Hydrogen Energy. 2007; 32:2609–2629. Copyright 2007 International Association for Hydrogen Energy)
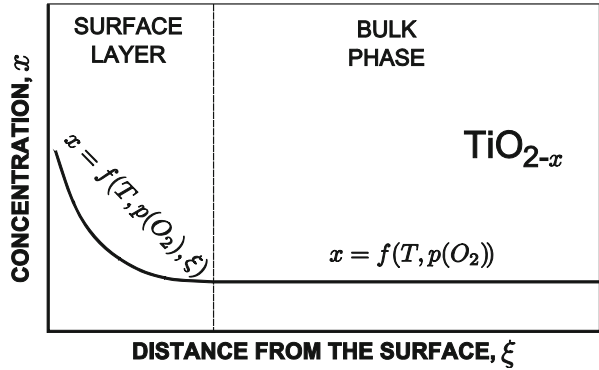
Fig. 26.4 Schematic representation of the concentration of electrons at grain boundary of TiO$_2$ [13] (Reproduced with permission from T. Bak, Oxide Semiconductors, Res. Rep., 2010. Copyright T Bak, 2010)
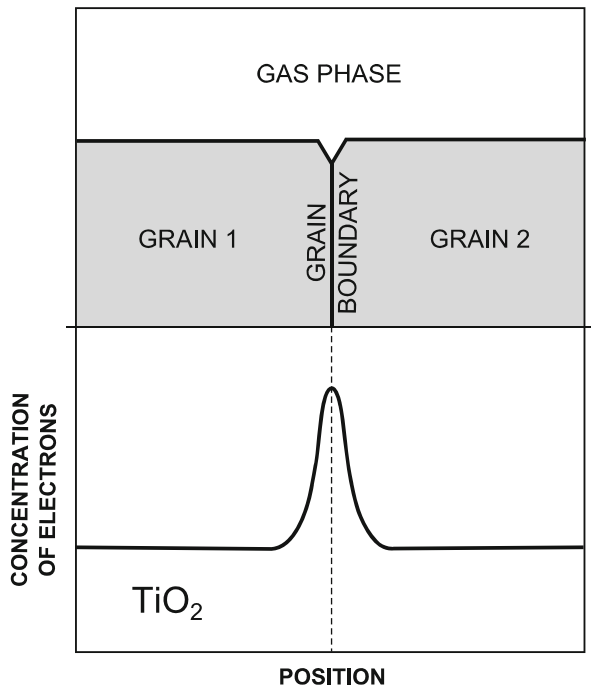
Recent studies of the authors show that the concentration of electrons at grain boundaries of TiO$_2$ is much larger than that in the bulk phase (Fig. 26.4) [13]. Assuming that this effect is valid also for the external surface, one may expect that the surface layer in oxidizing conditions is mainly enriched in donor-type defects, such as oxygen vacancies [14].

Recent studies of Tao et al. [15] confirmed experimentally that the surface of pure TiO$_2$ exhibits a two-dimensional structure, which is distinctively different

Fig. 26.5 Schematic representation of bulk versus surface bandgap of TiO$_2$ [15]

TiO$_2$-type surface structure (E$_g$ = 2.1 eV)

DISTANCE FROM THE SURFACE

TiO$_2$ bulk phase (E$_g$ = 3.0 eV)
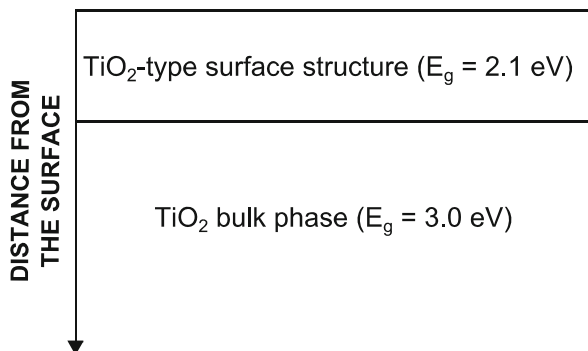
Fig. 26.6 Effect of oxygen activity on iron segregation for Fe-doped TiO$_2$ at 1,673 K [16] (Reprinted from Solid State Ionics, 72, A. Bernasik, M. rekas, M. Sloma, W. Weppner, Electrical surface versus bulk properties of Fe-doped TiO$_2$ single crystals, 12–18, Copyright (1994), with permission from Elsevier)

Fe-doped TiO$_2$
0.5 at% Fe
Single crystal
Annealing conditions:
T = 1400 K
t = 20 h
Bernasik et al., 1994

Oxidising

Reducing

INTENSITY RATIO [Fe/Ti]

DEPTH FROM THE SURFACE [nm]
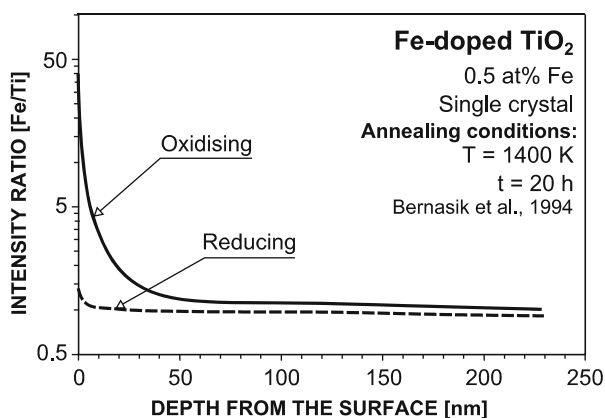
from that of the bulk phase. This structure is confined to the topmost surface layer with some relaxations of atoms in the lower layers. The difference concerns the electronic structure. It has been shown that the local bandgap of this layer is 2.1 eV compared to 3.0 eV in the bulk phase as it is schematically represented in Fig. 26.5.

Solid Solutions

The studies of surface vs. bulk composition of TiO$_2$ and its solid solutions with a range of ions, such as iron [16], niobium [17, 18], antimony [19], yttrium [20], and indium [21], indicate that these ions exhibit a strong segregation to the surface. It has been also documented that the segregation-induced enrichment is profoundly influenced by oxygen activity.

The studies of Bernasik et al. [16] show that iron segregates to the surface of Fe-doped TiO$_2$. As seen in Fig. 26.6, the segregation-induced enrichment factor in reducing environment is insignificant. However, imposition of oxidizing conditions results in an increase of the iron enrichment factor, which at the outermost surface

Fig. 26.7 Schematic representation of Ti-doped Fe_2O_3 surface layer formed on Fe-doped TiO_2
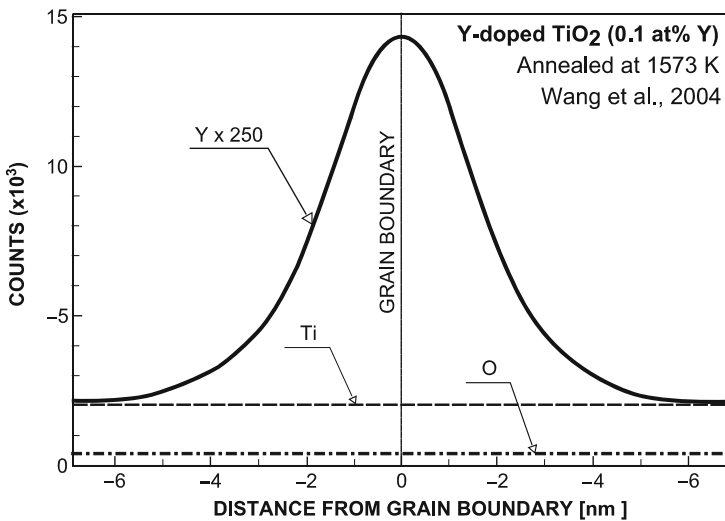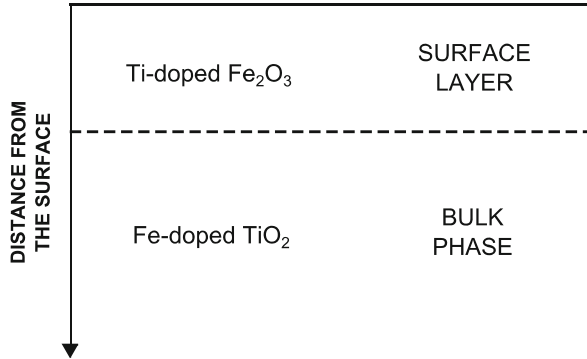
Fig. 26.8 Change of composition across grain boundary of Y-doped TiO_2 [20] (Reprinted from Acta Materialia, 52, Q. Wang, G. Lian, E. Dickey, Grain boundary segregation in yttrium-doped polycrystalline TiO_2, 809–820, Copyright (2004), with permission from Elsevier)

layer is approximately f = 40. The extent of the enrichment in the latter case indicates that the outermost surface layer may be considered as Ti-doped Fe_2O_3, as it is schematically represented in Fig. 26.7, rather than Fe-doped TiO_2.

Wang et al. [20] reported that yttrium segregates to grain boundaries of Y-doped TiO_2. As seen in Fig. 26.8, the concentration of yttrium at the grain boundary is distinctively higher compared to the bulk, while the concentration profiles of the host lattice elements remain constant.

A number of reports consider segregation of niobium for Nb-doped TiO_2 [18–25]. Pang and Wynblatt [17] reported the grain boundary segregation of niobium in Nb-doped TiO_2. As seen in Fig. 26.9, the concentration profiles of niobium and titanium across the grain boundary of Nb-doped TiO_2 indicate
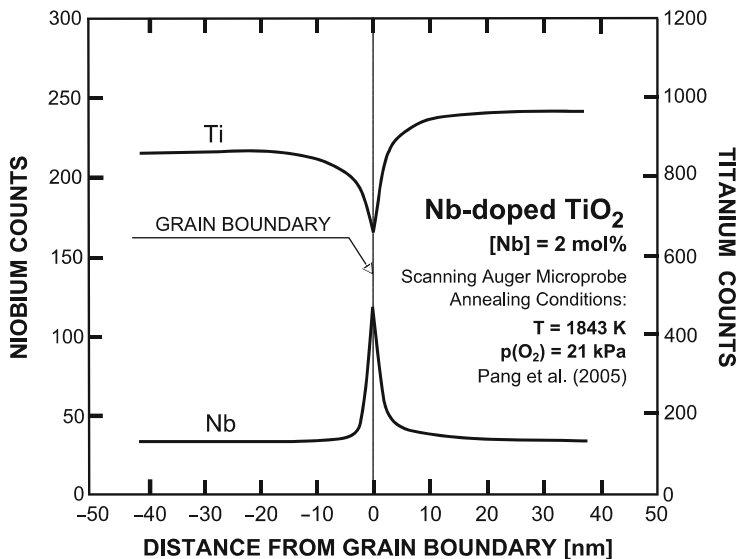
Fig. 26.9 Change of composition across grain boundary of Nb-doped TiO_2 [17] (Reprinted from Microscopy and Microanalysis, 11, Y. Pang, N.T. Nuhfer, P. Wynblatt, Segregation of Nb to TiO_2 grain boundaries, 1726–1727 (Suppl 2), Copyright (2005), with permission from Cambridge University Press)

niobium enrichment and titanium depletion. This effect is consistent with the substitution mechanism of niobium incorporation into titanium sites.

Atanacio et al. [21] reported the effect of the gas phase on surface vs. bulk composition of In-doped TiO_2 using secondary ion mass spectrometry, SIMS, and Rutherford backscattering, RBS. The related data are shown in Figs. 26.10 and 26.11. As seen from the SIMS data, the segregation-induced enrichment in indium results in a structural transition of the outermost surface layer leading to the formation of a quasi-isolated surface structure [21] (Fig. 26.12).

The derived theoretical model indicates that the surface layer exhibits entirely different structure than that of the bulk phase and resembles the In_2TiO_5-type structure. It has been also shown that the subsurface layer, which is interfacing the surface structure and the bulk phase, involves In-doped TiO_2 where indium is predominantly incorporated into interstitial sites as it is shown in Fig. 26.13.

Reactivity at the TiO_2/H_2O Interface

The effect of processing on properties of TiO_2-based semiconductors is commonly studied when the specimen is in contact with the gas phase at room temperature or at elevated temperatures. However, the TiO_2-based photoelectrodes and photocatalysts operate in aqueous environments. It has been shown by Norby [26]

Fig. 26.10 SIMS data representing the segregation-induced concentration profile of indium for In-doped TiO$_2$ [21]. (Reprinted with permission from A.J. Atanacio, T. Bak, J. Nowotny, ACS Applied Materials & Interfaces 4 (2012) 6626–6634. Copyright 2012 American Chemical Society)
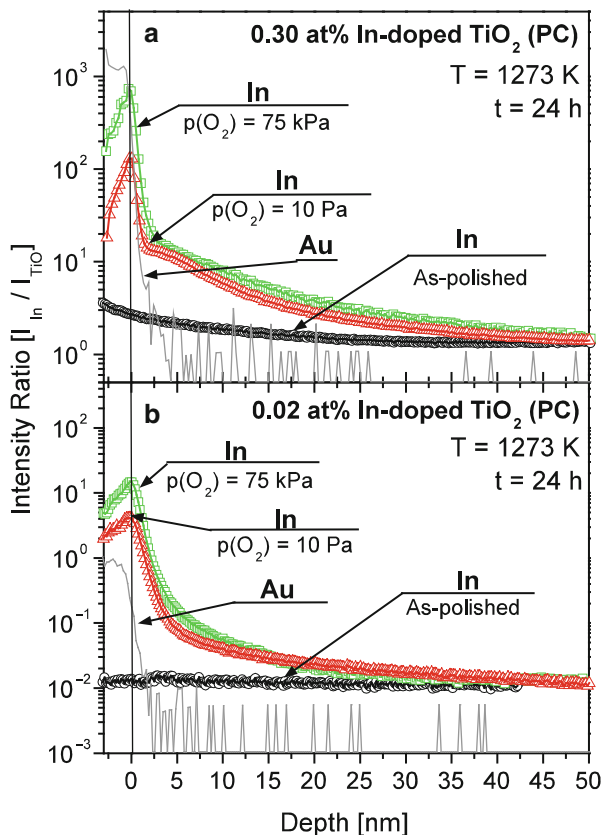
that the reactivity of water with TiO$_2$ results in the formation of a low-dimensional structure of titanic acid, which is formed according to the reaction:

$$2H_2O + TiO_2 \leftrightarrow H_4TiO_4 \qquad (26.12)$$

Therefore, TiO$_2$ in contact with water results in the formation of a H$_4$TiO$_4$ surface structure, which on one side is in contact with water and on the other side with TiO$_2$, as it is represented schematically in Fig. 26.14. The stability range of the H$_4$TiO$_4$ structure is limited to lower and moderate temperatures for n-type TiO$_2$ (Fig. 26.15). Imposition of light results in an increase of electron holes and leads to removal of protons and decomposition of the surface structure. Alternative species in water include OH$^-$ions; hydroxyl radicals, OH*; hydrogen peroxide, H$_2$O$_2$; superoxide, O$_2^-$; as well as protons, H$^+$. These species may be adsorbed on the surface of TiO$_2$ leading to imposition of the surface charge, which depends on their valency and the dipole moment. The only species which can incorporate into the TiO$_2$ lattice are protons, which exhibit high mobility even at room temperature.
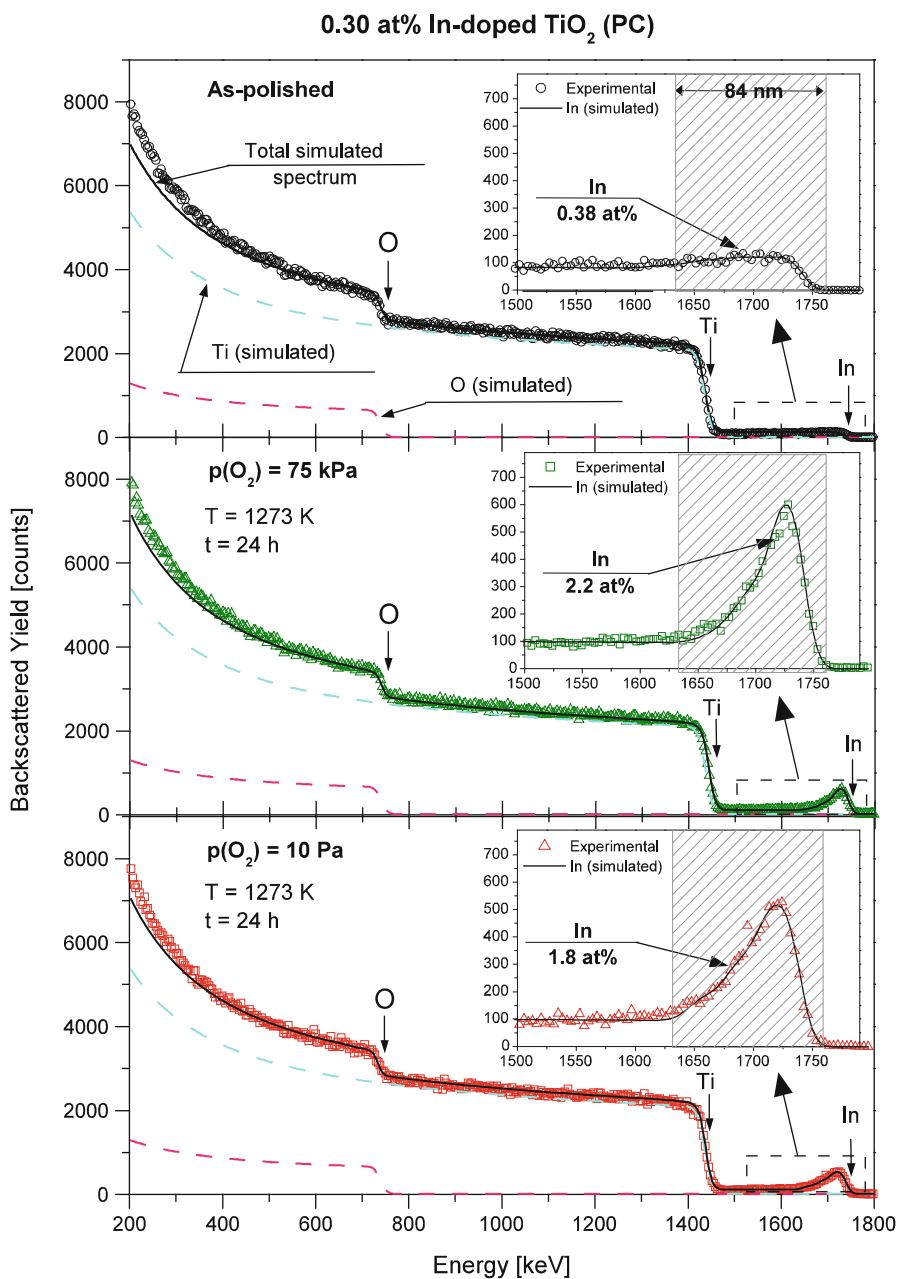
Fig. 26.11 RBS data representing the segregation-induced concentration profile of indium for In-doped TiO$_2$ [21] (Reprinted with permission from A.J. Atanacio, T. Bak, J. Nowotny, ACS Applied Materials & Interfaces 4 (2012) 6626–6634. Copyright 2012 American Chemical Society)

Fig. 26.12 Schematic representation of the segregation-induced concentration profile of indium for In-doped TiO_2 and resulting theoretical model [21] (Reprinted with permission from A.J. Atanacio, T. Bak, J. Nowotny, ACS Applied Materials & Interfaces 4 (2012) 6626–6634. Copyright 2012 American Chemical Society)

INDIUM CONCENTRATION ➝

DISTANCE FROM THE SURFACE

In_2TiO_5-type surface structure

Negatively charged surface layer

Bulk phase

DONOR-TYPE MECHANISM

ACCEPTOR-TYPE MECHANISM
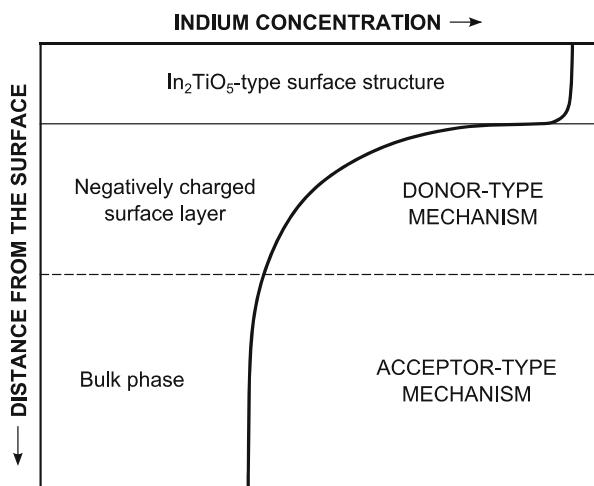
Fig. 26.13 Schematic representation of surface versus bulk defect disorder model of In-doped TiO_2

DISTANCE FROM THE SURFACE

SURFACE STRUCTURE

In_2TiO_5

SUBLAYER

$\{V_{Ti}''''In_i^{\bullet\bullet\bullet}\}'$

BULK PHASE

In-doped TiO_2

$\{In_{Ti}'\}$
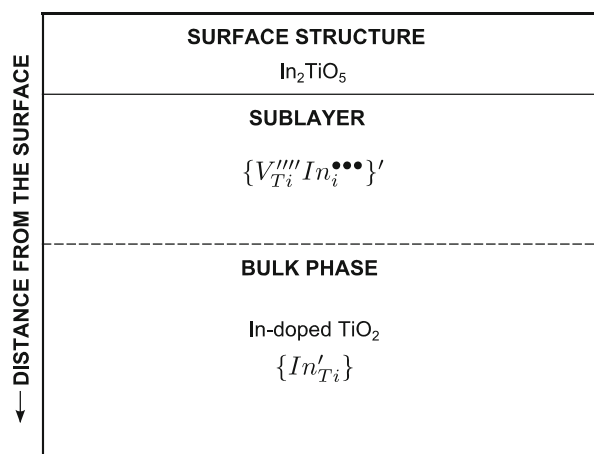
Reconstructions Under Reducing and Oxidizing Conditions

The effect of reducing and oxidizing conditions has been studied using a range of surface techniques, including low energy electron diffraction (LEED), Auger electron spectroscopy, (AES), ion scattering spectroscopy (ISS), and scanning transition microscopy (STM). The most common reconstruction of TiO_2 (110) in reducing condition was considered in terms of missing bridging oxygen rows or added Ti_2O_3 rows. It has been observed that application of oxidizing conditions results in the transport of titanium interstitials towards the surface where they react with oxygen leading to building up new TiO_2 lattice layers [27].

Fig. 26.14 Schematic
representation of the
water/TiO$_2$ interface

LIQUID PHASE

H$_2$O

SURFACE STRUCTURE

H$_4$TiO$_4$

BULK PHASE

TiO$_2$
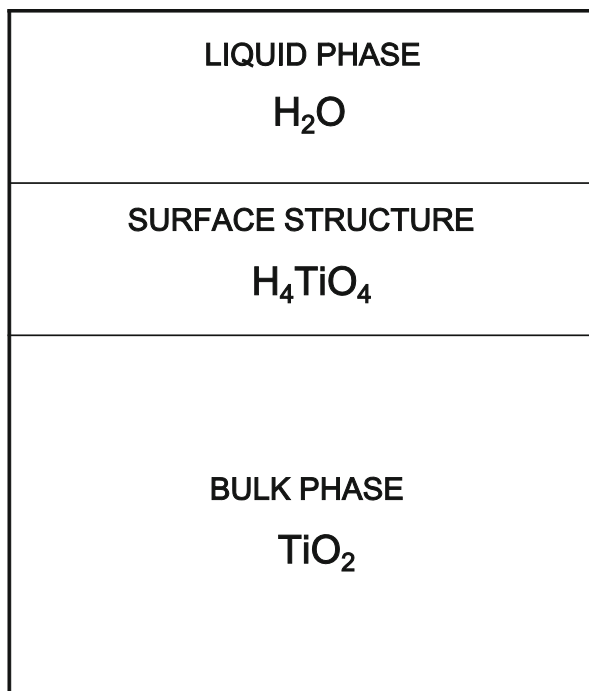
So far, little is known about the local properties of the low-dimensional surface
structures, LDSS. However, owing to the importance of the LDSS in photocatalytic
performance, there have been efforts to identify the local properties of this layer.
Moreover, the established effects of segregation of selected lattice elements may be
used for surface engineering in order to impose desired surface composition. The
established effect of oxygen activity on the extent of segregation may be used to
engineer the specific surface compositions, which are required to achieve desired
properties.

Conclusions

The reported experimental data and the derived theoretical models indicate that the
surface layer of oxide materials is stabilized in the form of a low-dimensional
surface structure, which is entirely different from that in the bulk phase in terms of
chemical composition, crystalline structure, and the related semiconducting
properties. Therefore, oxide materials can be considered in terms of an
onion-type model, which is represented schematically in Fig. 26.16. According to
this model, solids consist of a homogeneous bulk phase (BP); a quasi-isolated
surface layer, which is termed the low-dimensional surface structure (LDSS); and
a transition layer (TL) between the two BP and LDSS. The function of the TL is
to accommodate the entirely different properties of LDSS and BP within one system.
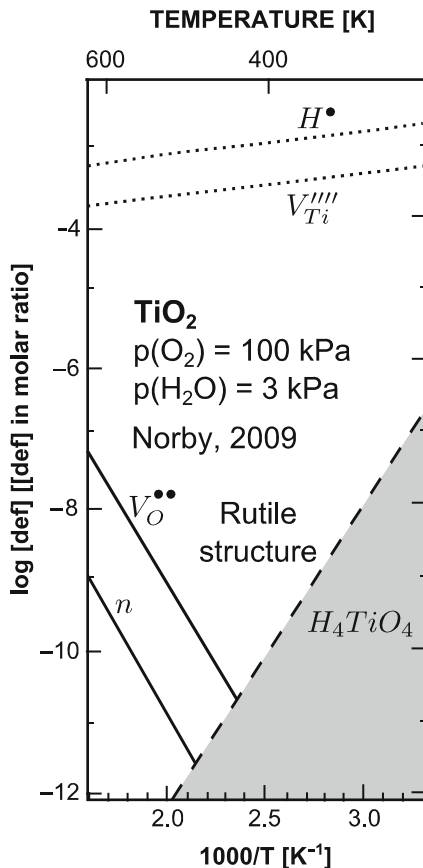
The thickness of the LDSS is limited to 1–2 lattice layers. It exhibits chemical composition, which is entirely different than that of the BP. When the segregation-induced enrichment of the surface layer exceeds its solubility limit, then a structural transition leads to the formation of an entirely new structure. The photocatalytic reactions, including light absorption and the light-induced chemical reactions at the solid/liquid interface, take place at the LDSS, which is predominantly responsible for the photocatalytic properties.

The function of the TL is to integrate the LDSS and the BS together in the form of one system. Therefore, the TL exhibits the concentration gradients, which are consistent with the LDSS on one side and the BP on the other side. This layer exhibits solubility limit which is much larger than that of the bulk phase [1].

The bulk phase is well defined in terms of its homogeneous chemical composition and may be represented by its defect disorders. The semiconducting properties of this phase are relatively easy to determine experimentally.

Fig. 26.16 Schematic representation of the onion-type model of nonstoichiometric compounds showing homogeneous bulk phase and low-dimensional surface structure
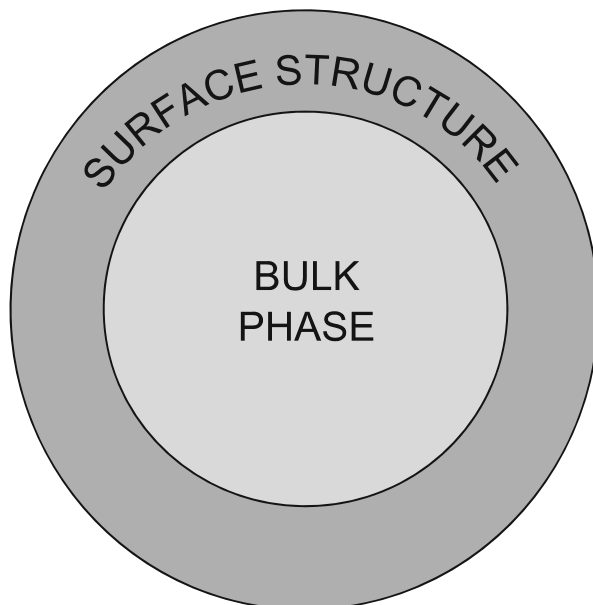
References

1. Nowotny J (1991) Science of ceramic interfaces. Elsevier, Amsterdam, pp 79–204
2. Cabanes J, Cabane F (1991) Science of ceramic interfaces. Elsevier, Amsterdam, pp 1–40
3. Wynblatt P, McCune RC (1988) Surface and near surface chemistry of oxide materials. Elsevier, Amsterdam, pp 247–275
4. Fujishima A, Honda K (1972) Nature 238:37–38
5. Bak T, Nowotny J, Sucher NJ, Wachsman E (2011) J Phys Chem C 115:15711
6. Bak T, Nowotny J, Sucher NJ, E Wachsman E (2012) Adv Appl Cer 111:4–15
7. Henrich VE, Cox PA (1994) The surface science of metal oxides. Cambridge University Press, Cambridge, pp 316–317
8. Kroger FA, Vink HJ (1956) In: Seitz F, Turnbull D (eds) Solid state physics. Academic, New York, pp 273–301
9. Nowotny J (2012) Oxide semiconductors for solar energy conversion. CRC, Boca Raton
10. Bak T, Nowotny J, Nowotny MK (2006) Defect disorder of TiO_2. J Phys Chem B 110:21560–21567
11. Nowotny MK, Bak T, Nowotny J (2006) Electrical properties of TiO_2 single crystal. III. Equilibration kinetics and chemical diffusion. J Chem Phys B 110:16293–16301
12. Nowotny MK, Bak T, Nowotny J (2006) Electrical properties of TiO_2 single crystal. IV. Prolonged oxidation and chemical diffusion. J Chem Phys B 110:16302–16308
13. Bak T, Chu D, Francis A, Li W, Nowotny J. Concentration of electrons at grain boundaries in TiO_2 (Rutile). Impact on charge transport and reactivity. Catalysis Today (in submission)
14. Nowotny J, Bak T, Burg T, Nowotny MK, Sheppard LR (2007) Effect of grain boundaries on semiconducting properties of TiO_2 at elevated temperatures. J Phys Chem C 111:9769–9778
15. Tao J, Luttrell T, Batzill M (2011) Nature Chem 3:296–300
16. Bernasik A, Rekas M, Sloma M, Weppner W (1994) Solid State Ion 72:12
17. Pang Y, Nuhfer T, Wynblatt P (2005) Microsc Microanal 11:1726–1727

18. Nakajima T, Sheppard LR, Prince KE, Nowotny J, Ogawa T (2007) Adv Appl Cer 106:82–88
19. Gulino A, Condirelli GG, Fragalh I, Egdell RG (1995) Appl Surf Sci 90:289
20. Wang Q, Lian G, Dickey EC (2004) Acta Mater 52:809
21. Atanacio A, Bak T, Nowotny J (2012) ACS Appl Mater Interfaces 4:6626–6634
22. Zaitzev V, Moon J, Tagaki H, Awano M (2000) Adv Powder Technol 11:211
23. Tsunashima M, Muraoka K, Akiyama K, Toyama N (1998) Sikizai (Japan) 71:297
24. Akiyama K, Toyama N (1998) J Am Ceram Soc 81:1071
25. Atashbar MZ, Sun HT, Gong B, Wlodarski W, Lamb R (1998) Thin Solid Films 326:238
26. Norby T (2009) MRS Bull 34:923–928
27. Diebold U (2003) Surf Sci Rep 48:88–89

Biofunctionalization of Nanoporous Alumina Substrates

27

Thomas D. Lazzara, Andreas Janshoff, and Claudia Steinem

Keywords

Anodic aluminum oxide • Optical waveguide spectroscopy • Pore-spanning membranes • Protein recognition • Silane chemistry

Introduction

Porous materials are 3-D structures with a significantly larger surface area compared to 2-D flat surfaces and can be prepared with a range of different pore dimensions. The international pure and applied chemistry (IUPAC) has established a nomenclature for porous materials based on the average pore diameter d_0: microporous ($d_0 < 2$ nm), mesoporous (2 nm $< d_0 < 50$ nm), and macroporous materials ($d_0 > 50$ nm). Recently, many *bottom-up* approaches have been used to develop materials that lie at the interface between mesoporous and macroporous, commonly referred to as nanoporous to describe their pore dimensions of 0.2 nm $< d_0 < 100$ nm. A number of different nanoporous materials have been studied as potential platforms for high-sensitivity sensor devices [1],

T.D. Lazzara (✉)
Institute of Organic and Biomolecular Chemistry, University of Göttingen, Göttingen, Germany

Polytechnique Montreal, 2900 boul, Édouard–Montpetit, Université de Montréal Campus 2500, Montréal, Québec, Canada
e-mail: thomas.lazzara@gmail.com

A. Janshoff
Institute of Physical Chemistry, University of Göttingen, Göttingen, Germany
e-mail: ajansho@gwdg.de

C. Steinem
Institute of Organic and Biomolecular Chemistry, University of Göttingen, Göttingen, Germany
e-mail: csteine@gwdg.de; claudia.steinem@chemie.uni-goettingen.de

or to enhance physical properties such as photosensitivity [2, 3] or catalytic efficiency [4]. As yet, only few examples have been given, in which nanoporous hybrid materials have been generated for biological applications [5–9]. Because nanoporous materials have pore dimensions that are commensurable with small organic compounds and biomolecules, these substrates provide unique opportunities for high-sensitivity biodetection, improved analyte retention/capture, tailored nanofiltration systems, and for the development of creative platforms to study the biophysical properties of proteins, lipid membranes, and cells.

Anodic Aluminum Oxide

Anodic aluminum oxide (AAO) is a nanoporous material that is of significant interest because of its simple and reliable method of fabrication and its mechanical stability. The predictability of its 3-D structure greatly facilitates theoretical simulations and calculations. Furthermore, the porous structure also facilitates biofunctionalization in aqueous solution. Nanoporous AAO [10–13] is a self-ordered material having non-intersecting, hexagonally ordered cylindrical pores that run straight through the film thickness and whose monodisperse interpore distance λ_{C-C} (Fig. 27.1) can be adjusted between 10 and 420 nm by choosing the right acid (sulfuric acid, oxalic acid, phosphoric acid) in combination with the applied anodization potential (19–160 V) as detailed in Li et al. [14].

AAO has been a preferred candidate for novel sensing platforms owing to the achievable 1–3 orders in magnitude increased surface area. For AAO with $d_0 = 60$ nm, the surface area of a 25-μm deep AAO is about 600 times larger than that of a flat surface. The main advantage of AAO over isotropic porous networks comes from its well-ordered structure that can be used to more easily and reliably predict the amount of deposited materials and the expected adsorption-desorption properties that ensue. In many practical industrial applications, the use of nanopores has been toward more efficient size-selective molecular and macromolecular filtering [15–18]. AAO has been used for size-dependent filtration applications that have proven effective to separate proteins [19], DNA [20], and large macromolecules [21]. Sensing applications rely on the increased instrumental response associated with probing a porous material, as opposed to a flat surface [22–26]. Novel 1-D and 3-D materials have also been produced by the negative replication of the structure of a first sacrificial nanoporous material, a technique referred to as template-replication. AAO has been extensively used to produce a variety of metals, inorganic and polymer nanorods [27–29] and nanotubes [30] of various axis ratios, by controlling both, pore depth and pore diameter of the cylindrical nanopores. Most importantly, because the size of AAO's nano-structured features are below the scattering limit of visible light, optical characterization of nanoporous material properties becomes possible by direct confocal and epi-fluorescence microscopy to investigate
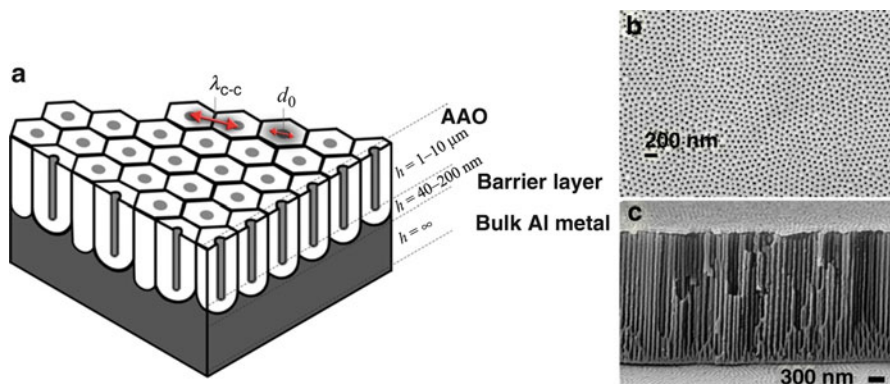
Fig. 27.1 (**a**) 3-D schematic of the self-ordered anodic aluminum oxide (*AAO*) material that is produced by electrochemical anodization of bulk Al metal. Anodization conditions control the parameters: lattice constant ($\lambda_{C\text{-}C}$) and pore diameter (d_0). (**b**) Scanning electron microscopy (*SEM*) image (ca. 50 nm of Au evaporated for imaging) shows the ordered pores AAO, $d_0 = 55$ nm. (**c**) SEM cross-section image of AAO film showing parallel cylindrical nanopores

phenomena occurring within the substrate, or by optical thin-film analysis techniques such ellipsometry, optical waveguide spectroscopy, and thin-film reflectometry.

Preparation of AAO

The preparation of AAO thin-films amenable for optical thin-film analysis conventionally requires the anodization of a layer of high quality Al deposited by vacuum [31, 32] or electrochemical techniques [33]. The deposition of high purity Al films with a minimum thickness of 0.5–1 μm and low surface roughness is required for spatially uniform pore initiation during anodization but may be technically demanding [33, 34]. To produce AAO in a two-step anodization process, even thicker films are necessary [35]. Although pore ordering by mechanical or lithographic pre-texturing of the Al thin-film surface is possible [36], the pre-texturing process generally requires e-beam or ion-beam lithography and sample areas are limited. Furthermore, depending on the mechanical and electrochemical stability of the interface between the deposited Al film and the substrate, high voltage anodization for producing lattice constants larger than 100 nm [13], or for hard anodization [37], becomes problematic. Thus, we have refined a procedure to readily produce highly ordered mounted AAO thin-films on solid supports. They are prepared according to the scheme shown in Fig. 27.2. First, anodization is performed following common procedures for bulk Al after polishing (Fig. 27.2, step 1) [13]. Anodization in oxalic acid produces AAO films with a lattice constant of about 100 nm, which allows optical waveguide measurements with

Fig. 27.2 Preparation scheme for AAO thin-films on different surfaces
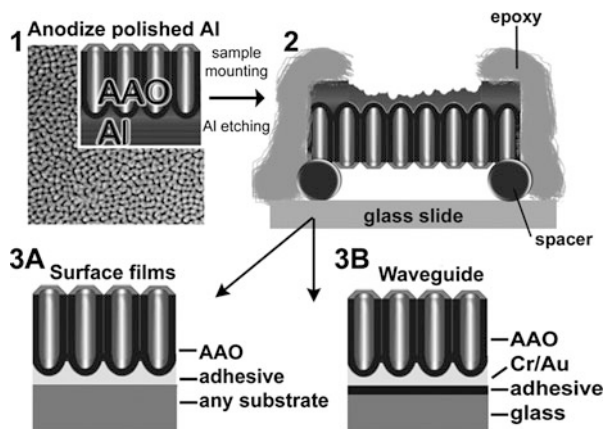
wavelengths in the visible range. After anodization, the unreacted Al is selectively etched to obtain free-standing AAO films (Fig. 27.2, step 2). After the etching is completed, the pure AAO membrane is mounted (Fig. 27.2, step 3), barrier layer side down, over a substrate coated with an adhesive either directly (Fig. 27.2, step 3A), or after evaporation of a thin chromium/gold layer onto the AAO barrier layer (Fig. 27.2, step 3B), which is required for optical waveguide spectroscopy.

Optical Waveguide Spectroscopy

Nanoporous materials with pore diameters below the scattering limit (<100 nm) are optically transparent and thus, it becomes possible to monitor processes occurring within the pore interior by thin-film optical characterization methods relying on the measurement of optical thickness variations. Optical waveguide spectroscopy (OWS) is an experimental technique that is used to analyze the optical waveguide modes that are excited in a thin-film slab waveguide mounted in the Kretschmann configuration (Fig. 27.3) [38–42].

It is a highly sensitive yet experimentally simple technique for independently characterizing the thickness and refractive index ($n = \sqrt{\varepsilon}$) of optically transparent thin-films [42, 43]. In recent years, OWS has also been explored for in situ monitoring of processes occurring within AAO [44, 45] and other nanoporous templates [41, 46–48] at sub-nanometer sensitivities. The nano-porosity ensures that scattering losses are minimal for optical waveguiding at visible or longer wavelengths, and that effective medium theory (EMT) can be applied to quantify processes occurring within the nanoporous AAO structure based on refractive index responses [49, 50]. In this regard, the ordered cylindrical pore morphology of AAO membranes lends itself to a simple EMT description using the Maxwell-Garnett approach [44, 45, 50]. The dielectric constant of AAO (ε_{AAO}) that is measured by OWS includes contributions from the alumina, the pore-filling medium (e.g. buffer),

Fig. 27.3 Schematic of the
optical waveguide
spectroscopy (*OWS*) setup
used to measure propagating
waveguide modes, from
which ε_{AAO}, and the thickness
can be extracted. The
reflectivity **R** is measured as
a function of the incidence
angle θ. The idealized field
distributions of several guided
modes are shown. The
excitation of these modes is
detected as sharp minima in
the **R**(θ) curve
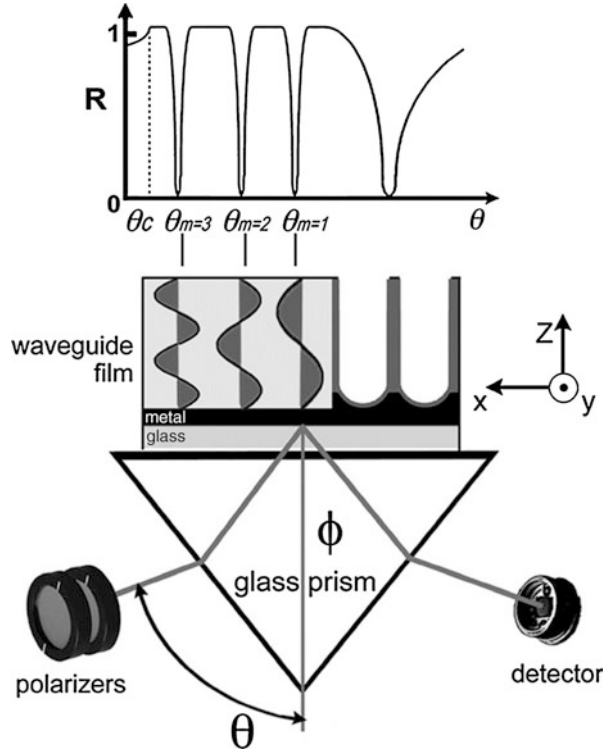
and any organic thin layer coating the pore surfaces. ε_{AAO} has anisotropic
components that are described by the infinite, prolate ellipsoid approximation
within the Maxwell-Garnett theory, and well-described elsewhere [41, 44, 51]:

$$\varepsilon_{\text{AAO}}^{\perp} = \varepsilon_{\text{alumina}} + f_{\text{pore}} \left(\varepsilon_{\text{pore}} - \varepsilon_{\text{alumina}} \right) \tag{27.1}$$

$$\varepsilon_{\text{AAO}}^{//} = \varepsilon_{\text{alumina}} + \frac{\varepsilon_{\text{alumina}} + \tfrac{1}{2} \left(1 + f_{\text{pore}} \right) \left(\varepsilon_{\text{pore}} - \varepsilon_{\text{alumina}} \right)}{\varepsilon_{\text{alumina}} + \tfrac{1}{2} \left(1 - f_{\text{pore}} \right) \left(\varepsilon_{\text{pore}} - \varepsilon_{\text{alumina}} \right)} \tag{27.2}$$

$\varepsilon_{\text{AAO}}^{\perp}$ and $\varepsilon_{\text{AAO}}^{//}$ are, respectively, the dielectric constant components normal and
parallel to the AAO membrane surface, f_{pore} is the pore volume fraction within the
AAO, $\varepsilon_{\text{alumina}} = 2.68$ is the dielectric constant of bulk anodic aluminum oxide at
$\lambda = 632.8$ nm, and $\varepsilon_{\text{pore}}$ is the (effective) dielectric constant within the pores. For
a blank AAO film in water, $\varepsilon_{\text{pore}} = \varepsilon_{\text{buffer}} = 1.78$. With the addition of an organic
film on the internal pore surfaces, the volume within the pores is occupied by
a combination of the organic material and the pore filling buffer. After applying
Eqs. 27.1 and 27.2 for the organic-filled AAO pores, recursive use with a new
effective $\varepsilon_{\text{pore}}'$ for the pore interior provides ε_{AAO} after molecular adsorption.

Anodic Aluminum Oxide as Porous Substrates for Protein Adsorption

Many realizations of biosensor devices and setups are based on the specific binding of proteins on receptor-functionalized surfaces [52–56]. Researchers usually seek to quantify the interaction with the surface in terms of rate constants (adsorption and desorption rate) or association/dissociation constants (adsorption isotherms) to determine the protein concentration in the bulk phase or the binding affinity to the corresponding ligand. In this case, knowledge of mass transport limitations depending on the design of the experimental setup is pivotal to obtain trustworthy data allowing the determination of biologically relevant interaction parameters [57, 58].

While the adsorption behavior of molecules and macromolecules at planar interfaces is well described [57–60], the growing number of applications involving mesoporous and macroporous substrates requires a comprehensive investigation of the factors governing macromolecular adsorption within functionalized porous substrates [22, 61–66]. Porous TiO_2, SiO_2, or Al_2O_3 have recently been investigated as sensor devices to detect protein adsorption on functionalized pore-walls [1, 22, 24, 67–70]. Particularly relevant in this context is anodic aluminum oxide that allows adjustment of pore diameters over a wide range [10, 13, 14, 71]. Some studies have provided insight into how various parameters, such as ionic strength [72] particle size [73, 74], and porosity [75], modify the binding efficiency and the transport within porous substrates. However, there is a fundamental need to elucidate which parameters are accessible from a biosensor readout based on porous substrates.

We found that the adsorption in AAO pores is largely explained in terms of boundary layer theory [73, 76], i.e., adsorption kinetics are predominately driven by the flux into the pores [7]. Consequently, the large porous surface area behaves as a perfect sink for protein binding, which results in a depletion of the solution and produces a so-called stationary Lévêque boundary layer [76].

Assuming that entry into the pores is the rate-limiting step of protein adsorption on the pore walls, a stationary boundary layer will be established, as found for perfect sink conditions ($c(y = 0) = c_{wall} = 0$) on flat surfaces. This means that proteins entering the pores experience numerous surface contacts, which increases the apparent rates of adsorption and justifies approximate "perfect sink" conditions for porous media [7].

Finite element simulations show the validity of boundary layer theory for "perfect sink" conditions with a large parameter space (Fig. 27.4). Only at very low rate constants ($k_{ad} < 10^{-3} \mathrm{m^3 mol^{-1} s^{-1}}$), the flux becomes nonstationary and adsorption follows Langmuir kinetics. At the end ($x = L$) of the adsorption area, the constant flux into the pores can be estimated to be approximately:

$$j = D \left(\frac{\partial c(L,0)}{\partial y} \right)_{wall} = \frac{D}{\delta(L)} (c_b - c_{wall}) = \frac{D}{\delta(L)} c_b \qquad (27.3)$$

with D, the diffusion constant and the diffusion layer thickness δ at $x = L$:
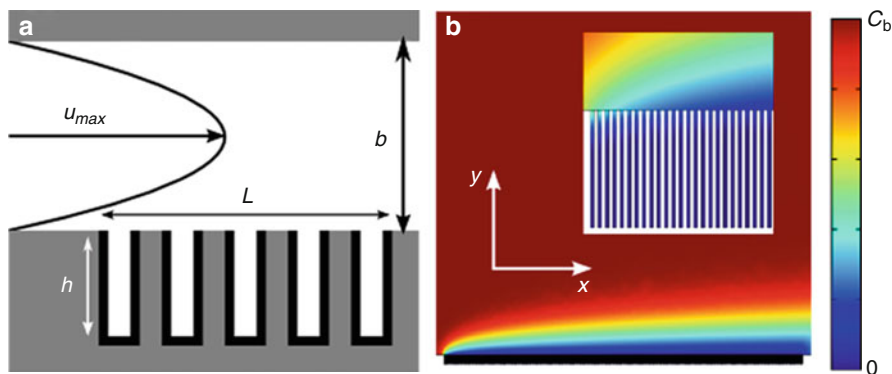
Fig. 27.4 (**a**) Flow cell geometry used for finite element simulations and optical waveguide spectroscopy studies of protein adsorption. For the simulations, equally spaced pores with $R_{\text{pore}} = 25$ nm and $h = 3.2$ μm along a distance of $L = 120$ μm were used. The flow chamber has a height of $2b = 0.5$ mm with a maximum flow velocity of u_{max} at the center of the flow cell. (**b**) Stationary concentration profile obtained from finite elements simulations taken after 60 s. c_b is the bulk concentration [7]

$$\delta(L) = 1.475 \left(\frac{DbL}{u_{\text{max}}} \right)^{\frac{1}{3}} \tag{27.4}$$

Consequently, the surface concentration at $x = L$ and the corresponding surface concentration $\Gamma(t)$ is increasing linearly with time:

$$\Gamma(L, 0, t) \cong 0.68 \left(\frac{u_{\text{max}} D^2}{bL} \right)^{\frac{1}{3}} \frac{R_{\text{pore}}}{2h} c_b t \tag{27.5}$$

The area ratio between pore entry area (πR^2_{pore}) and overall surface area of a single pore ($2\pi R_{\text{pore}} h$) needs to be taken into account, because the flux into the pores (molecules per pore entry area and time) relates to a different area than the rate of adsorption (molecules per *wall-area* and time). This explains why the kinetics is apparently slower with increasing surface area.

In conclusion, replacing a flat adsorbing surface with porous media has one important consequence for kinetics of protein adsorption on the pore walls. The walls of the pores essentially act as a reacting wall (perfect sink), which produces a stationary concentration profile (depletion layer) that renders adsorption entirely controlled by mass transport into the pores. Porous media are essentially a realization of a perfect sink with respect to boundary layer theory producing the identical concentration profile expected for a flat surface with adsorbing boundary conditions. As a consequence, rate constants of adsorption can only be determined for very low affinity to the pore walls.
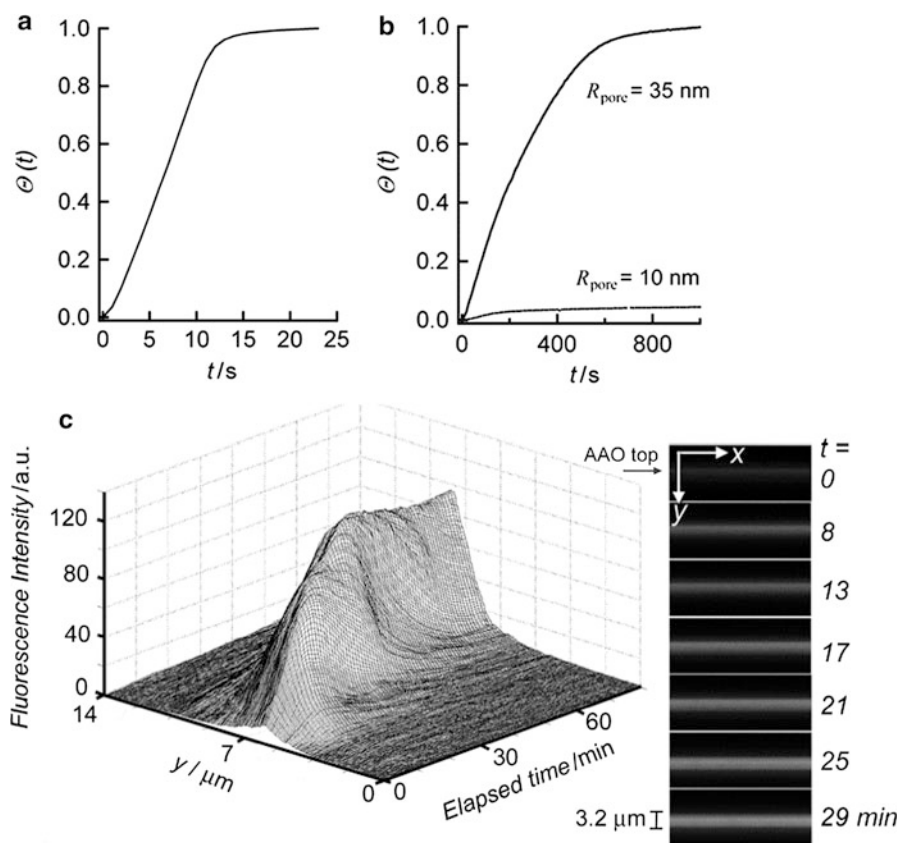
Fig. 27.5 (**a**) Adsorption kinetics of avidin ($c_b = 1.5$ μM) on a flat negatively charged gold surface measured by SPR. (**b**) Avidin adsorption kinetics on AAO with $h = 3.2$ μm as a function of R_{pore}. Pores with $R_{pore} = 10$ nm are not filled with avidin. (**c**) *Left hand side*: time evolution of fluorescence intensity, across the y-direction, of avidin ($c_b = 0.45$ μM) adsorbing onto AAO ($R_{pore} = 32.5$ nm, $h = 3.2$ μm). *Right-hand side*: vertical slices (y-direction) taken at different times showing the fluorescence increasing across the AAO thickness [7]

Verification of the theoretical considerations was obtained from protein adsorption experiments on AAO employing optical waveguide spectroscopy. The cylindrical pores were adjusted to a desired pore radius $R_{pore} \geq 10$ nm. The electrostatically driven adsorption kinetics of avidin [77] on the AAO pore walls were monitored by watching the change in the average dielectric constant following the angular shift of a high order TM waveguide mode [44]. Generally, a substantially slower kinetics within the porous matrix in comparison to flat surfaces was found (Fig. 27.5a). The adsorption of avidin ($c_b = 1.5$ μM) on a planar gold surface functionalized with negatively charged mercaptohexadecanoic acid, measured by surface plasmon resonance (SPR), takes about 10 s, which translates into $k_{ad} \approx 200$ m^{3}mol^{-1}s^{-1}, while adsorption within a porous substrate

($R_{pore} = 35$ nm, $h = 3.2$ μm) takes about 60 times longer (Fig. 27.5b). Also, the change in surface concentration with time is approximately linear over a long time period (500–600 s) until the pore wall surfaces eventually saturate with proteins. As argued above, the almost linear regime is predominately governed by the constant flux of protein molecules into the pores due to a stationary diffusion boundary layer that forms as a result of protein depletion. In fact, it is straightforward to show that the avidin flux into an individual pore is only a few proteins per pore per second.

OWS adsorption kinetics (Fig. 27.5a, b) can be confirmed with time-resolved confocal laser scanning fluorescence microscopy (CLSM) since AAO thin-films are sufficiently transparent. The fluorescence increase (y-direction) with time was essentially linear (Fig. 27.5c), as observed for the adsorption kinetics measured by OWS. Experiments carried out with different pore radii suggest that the pore radius needs to be adjusted to be larger than 20 nm to be filled with avidin.

Biofunctionalization of Porous Alumina Substrates

A range of chemical strategies are available to chemically modify solid and porous substrates, effectively producing a new surface that has a different chemistry and therefore different interfacial properties than the original surface. For example, a hydrophobic modification of oxide surfaces with a single molecular layer of alkyl-molecules changes the wetting properties of the surface, which becomes water-repellant. Coinage metals [78–84], polymers [85–87], and inorganic or metal oxide [88–94] substrates can be functionalized by the formation of functional monolayers through surface reactions such as silanizations [88–90, 95], reactive plasma treatments [96, 97], thiols [78, 79, 81–83, 98–101], and phosphonate chemistry [102–104]. For other applications, one may require charged moieties, reactive monomers, bio-recognition elements, protein-covered or polymer-coated surfaces. All require tailored surface modification strategies. For AAO, a number of different functionalization strategies have been described including wet chemical approaches comprising self-assembly processes with silanes (ethoxy-, methoxysilanes), phosphonates, organic acids, and layer-by-layer deposition, polymer grafting, sol–gel processing as well as electrochemical and electroless deposition [105]. Apart from wet chemical approaches, gas-phase surface modification techniques are used to enhance stability and add functionalities encompassing thermal vapor metal deposition, chemical vapor deposition (CVD), plasma processing and polymerization, and atomic layer deposition (ALD). As a neat untreated AAO surface suffers from chemical instability in aqueous acidic environment, functionalization of the AAO surface is particularly advantageous as it passivates the surface and makes it, thus, more stable in aqueous solutions on a long term basis.

The alteration of the surface chemistry then allows the subsequent covalent attachment of proteins, recognition of ligands, single stranded DNA, polysaccharides, and other relevant biological material through a range of simple

bioconjugation strategies. By using silane chemistry, it is possible to functionalize anodic aluminum oxide while maintaining its optical transparency required for optical thin-film characterization methods. This strategy creates a homogeneous functionalization of the porous material, such that the entire surface is covered with the same groups, i.e., both the pore rims and the pore interior.

Orthogonal Silanization of AAO

While a homogeneous deposition of molecules on OH-terminated AAO surfaces is rather straightforward using silane chemistry, tailored micro-patterned chemistry is more demanding, but essential for designing locally addressable areas on substrates. A number of selective functionalization strategies have been developed for flat surfaces [106–108]. However, porous 3-D substrates still remain a challenge for orthogonal functionalization even though they are highly desirable for high-sensitivity bifunctional detection platforms and the formation of pore-spanning membrane systems. In the past, we have shown that orthogonal functionalization of porous substrates can be achieved by directly depositing a gold metal layer on the substrate, which then allows pore-rim modification using functional thiols designed to direct the formation of lipid membranes [8, 109]. However, for anodic aluminum oxide with pore diameters below the scattering limit, the attractive advantage of optical transparency is lost when a metal is deposited onto the porous film. Hence, this strategy prevents the study of processes occurring within the porous network using optical thin-film methods such as OWS. To circumvent this problem, silane- based orthogonal functionalizations of AAO appear to be attractive [110–112], but challenging to implement because spatial selectivity is difficult to achieve. Few examples are given in literature to address this issue. Voelcker and coworkers [105] reported on a silane-based strategy to functionalize the aluminum surface before the anodization process that generates AAO, which results in a selective functionalization of the pore rims. In this procedure, the deposited molecules must endure the anodization process, as well as pore widening in acidic solution. Thus, it is not suited for functional moieties that are moisture- or pH-sensitive. Sailor and coworkers [113] produced porous silicon that was etched in a two-step process, which was hydrophobically functionalized after the first step to produce a membrane with dual-functionality. Kilian et al. [114] used surface tension and capillary forces to facilitate or prevent pore-interior functionalization. A porous membrane with hydrophilic pore rims and a hydrophobic pore-interior surface was achieved using plasma-polymerization of a fluorocarbon layer, followed by detachment from the solid-support generating hydrophilic rims at the bottom side [115].

We have developed a two-step process involving an evaporated thin gold film to protect the underlying surface functionality of the pore-rim surface to generate orthogonal functionalization of AAO [116]. Subsequent treatment with oxygen plasma of the modified AAO membrane removed the unprotected organic functional groups, i.e., the pore-interior surface. After gold removal, the substrate
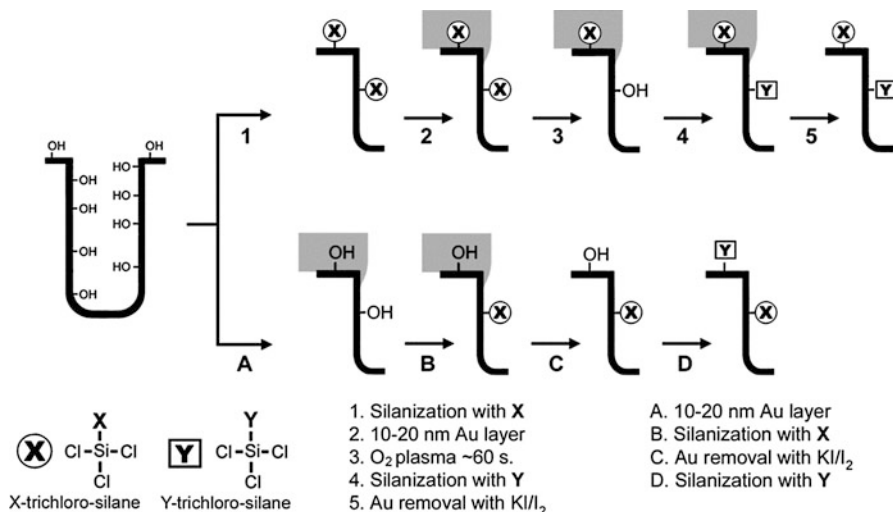
Fig. 27.6 Two experimental protocols (1–5 and A–D) to prepare AAO substrates with dual-functionality using a thin Au layer as a protective mask. Thermally evaporated gold is used to prevent the underlying AAO pore-rim functionalization from oxidation during O_2 plasma treatment and from any further chemical reactions. The final AAO substrates, after step 5 or step D, have different pore-rim versus pore-interior functionalities and, most importantly, remain optically transparent [116].

became optically transparent, and displayed two distinct generated surface functionalities, one at the pore rims and another at the pore-interior surface. The general procedure is depicted in Fig. 27.6.

Selective Deposition of Hybrid-Solid Supported Lipid Membranes

According to the two procedures depicted in Fig. 27.6, AAO substrates with a hydrophobic dodecyltrichlorosilane (C_{12}-TCS) layer at different positions (Fig. 27.7a) were prepared to be able to deposit lipid monolayers atop the C_{12}-TCS monolayer. Substrate **1** was functionalized at the pore-rim and pore-interior surfaces with C_{12}-TCS. Substrate **2** was prepared according to steps A–D (Fig. 27.6), resulting in pore rims that are hydrophilic and without functionalization and pore-interiors that are hydrophobic after silanization with C_{12}-TCS. Substrate **3** is the inverse of **2**, with hydrophobic pore rims, prepared by following steps 1–5 (Fig. 27.6). Substrate **4** was subjected to O_2 plasma treatment, rendering it hydrophilic. To deposit a lipid monolayer on the hydrophobic C12-TCS monolayer, the substrates were immersed in a suspension of fluorescently labeled small unilamellar vesicles (SUVs) composed of 1-palmitoyl-2-oleoyl-*sn*-glycero-3-phosphocholine (POPC). SUVs are known to adhere strongly on different hydrophobic functionalities and can rupture to form hybrid solid-supported lipid

Fig. 27.7 (**a**) Schematic representation of AAO substrates differing in their orthogonal surface functionalities. Small unilamellar vesicles (*SUVs*) composed of POPC are expected to interact differently with these surfaces. (**b**) Fluorescence images of the substrates with $d_0 = 75$ nm and $h = 3.8\,8\,\mu m$ mu;m after addition of SUVs are shown. The *left side* shows CLSM fluorescence cross-sectional *Y-Z* plane images for AAO substrates **1–4**. The images on the *right* are *top X-Y* plane epi-fluorescence images of substrates **1** (*top image*) and **3** (*bottom image*) under identical exposure conditions showing the increased fluorescence intensity of **1** due to lipids adsorbed on the entire AAO surface vs. only atop for **3**. (**c**) Fluorescence recovery after photobleaching (*FRAP*) experiments on substrate **1** and **2**, to which SUVs doped with Bodipy DHPE were added [116]
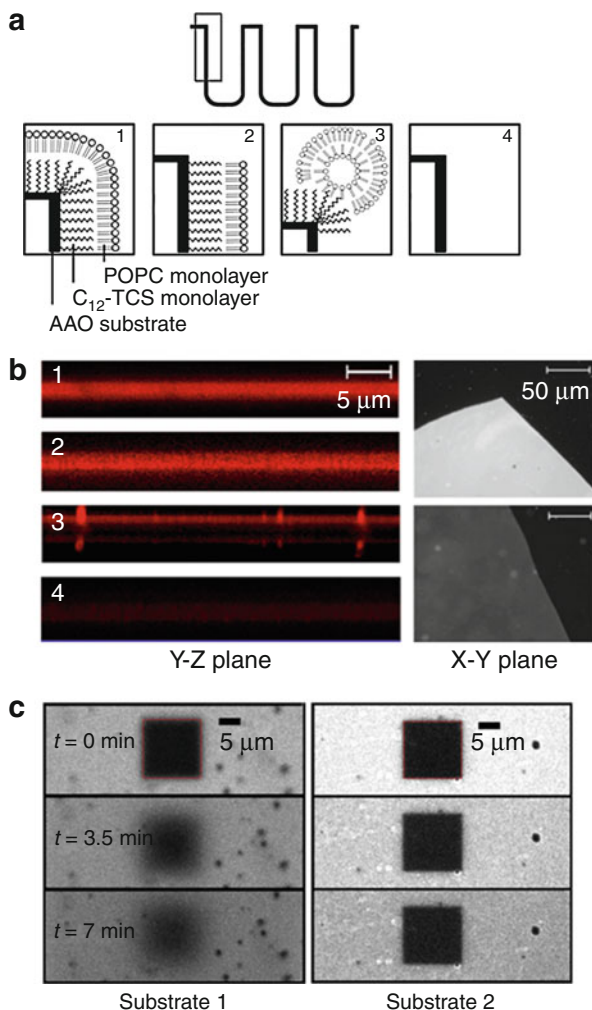
monolayers, while they do not adsorb on native hydrophilic Al_2O_3 surfaces [117]. By means of 3-D confocal laser scanning microscopy images of substrates **1–4**, the position of the fluorescently labeled lipids was determined (Fig. 27.7b, left side). For substrate **1** and **2**, fluorescence images show that the lipids line the pore-interiors throughout the AAO. For substrate **3**, fluorescence is not observed in the pore interior but only atop, which is attributed to surface adsorbed vesicles. Substrate **4** does not show any significant fluorescence as expected for a non-functionalized substrate. Epifluorescence images of substrates **1** and **3** (Fig. 27.7b, right side) show that hybrid solid-supported lipid membranes formed within the AAO pore-interiors (substrate **1**, top image), which increases significantly the overall fluorescence intensity compared to only surface adsorbed
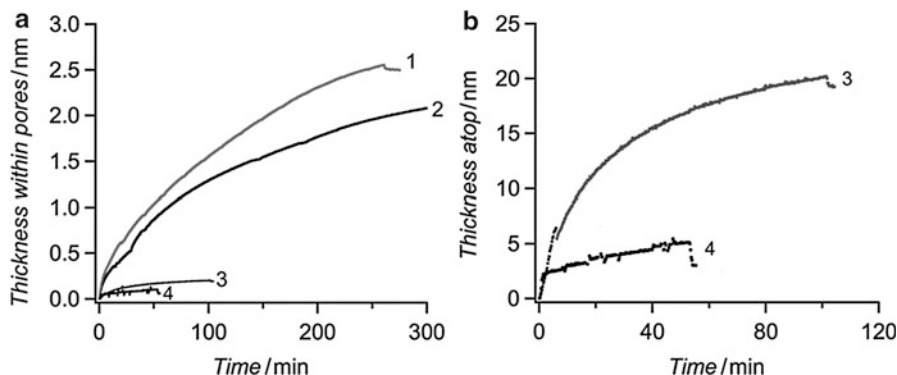
Fig. 27.8 (**a**) Kinetics of POPC SUV interaction with the differently functionalized substrates (**1–4**) presented in Fig. 27.7 measured using OWS. The overall dielectric constant of the AAO membrane with $d_0 = 75$ nm and $h = 3.8\ 8$ μm increases due to the deposition of a 2.0–2.5-nm phospholipid monolayer within the pores for substrates **1** and **2**, which is not observed for substrates **3** and **4**. (**b**) The atop deposition of vesicles is much larger for substrate **3** than for **4**, because only the hydrophobic pore rims of substrate **3** interact strongly with SUVs [116]

lipids (substrate **3**, bottom image). Fluorescence recovery after photobleaching (FRAP) experiments further corroborated the notion that only for substrate **1**, a continuous monolayer with laterally mobile lipids has been formed, whose fluorescence intensity recovers after a square region was photobleached (Fig. 27.7c, substrate **1**). In contrast, no recovery was observed for substrate **2** within the time scale of the experiment. In this case (Fig. 27.7c, substrate **2**), the pore rims are not covered with lipids but are composed of Al_2O_3 serving as a barrier for the lipids to laterally move and therefore, fluorescence recovery is not expected.

As the functionalized AAO substrates are optically transparent, not only 3-D confocal laser scanning fluorescence microscopy can be applied to monitor processes that occur in the interior of the pores but also optical waveguide spectroscopy, which provides the kinetics of the lipid monolayer deposition process (Fig. 27.8) and whether lipids adsorb only atop the AAO or within the pores. If lipids adsorb within the pores, a uniform increase in the AAO dielectric constant can be observed as significantly large and uniform positive angular shifts in all of the waveguide modes. If vesicle adsorption only takes place atop the AAO film, only the higher order modes slightly shift while the lower order modes remain unchanged. OWS measurements of substrates **1** and **2** demonstrate that a dielectric layer with a thickness of about 2.0–2.5 nm has been adsorbed on the either fully functionalized (**1**) or inner-pore wall (**2**) functionalized AAO substrate. This change in thickness supports the notion of the formation of a hybrid solid-supported lipid bilayer obtained by spreading of the SUVs on the hydrophobic C_{12}-TCS monolayer. In the case of substrates **3** and **4**, no significant interior deposition was observed, indicated by the very small change in optical thickness. However, for substrate **3**, a significant atop SUV deposition with a thickness change of about 25 nm was observed, which was considerably larger than that observed for substrate **4**,

which was only about 2 nm. This result confirms that intact SUVs adhere only on the hydrophobic monolayer on the pore rims, while they did not bind to native Al_2O_3 surfaces. The vesicles do not spread due to the limited contact area with the substrate. The results clearly demonstrate that a selective functionalization of the AAO substrates is feasible.

Surface Functionalization of Nanoporous Alumina for Protein Recognition

Controlling the number and distribution of multiple receptor molecules at the surface of porous materials is not always a straightforward task, because the composition of reactive solution species rarely translates into equivalent surface functionalization ratios and homogeneous distributions of receptors. Alternatives to covalent coupling schemes involve using multifunctional silanes, mixtures of silanes, or macromolecules to control the surface properties of a material through electrostatic or molecular recognition interactions. For example, proteins such as avidin and streptavidin can be used to cover a surface with biotin active sites, which are subsequently modified with different ratios of biotinylated molecules. A much more interesting approach is to create multifunctional lipid monolayers, with the advantage that receptor molecules embedded in a lipid mono-layer are laterally mobile and become homogeneously distributed. In addition to the advantage of mobility, lipid membranes with specific compositions also allow clustering around nucleation points or even reversible domain formation, which are properties that cannot be achieved using covalent coupling schemes. Modification of solid planar hydrophobic surfaces with lipid monolayers by the Langmuir-Blodgett technique [118] or liposome spreading [119, 120] has been extensively investigated with the aim to reproduce the complex composition of natural lipid membranes. Similarly, the formation of a hydrophobic C_{12}-TCS monolayer on AAO can be advantageously used to produce functional monolayers by reproducing the complex mixture of liposomes and even cellular membranes through a phospholipid-transfer mechanism.

Streptavidin Binding to Biotin Functionalized AAO Substrates

To deposit different surface densities of biotin molecules on the AAO substrate, the AAO was first silanized with dodecyltrichlorosilane (C_{12}-TCS) to obtain a hydrophobic alkyl self-assembled monolayer, and then POPC SUVs doped with different mole fractions of biotin-DOPE lipids were spread on the AAO surface in order to transfer the lipid composition of the liposome directly onto the AAO surface [121]. Kinetic OWS measurements of the vesicle spreading process showed that POPC SUVs continued spreading until the AAO surface was completely saturated with a lipid monolayer, measuring about 2.3 ± 0.2 nm in thickness in agreement with a lipid monolayer lining the pore-interior surface, as well as the

Fig. 27.9 Streptavidin thickness after binding to the lipid monolayer containing different fractions of biotinylated lipid. The amount of adsorbed protein can be tuned by varying the biotin-DOPE content of SUVs, while this cannot be achieved by direct covalent surface modifications
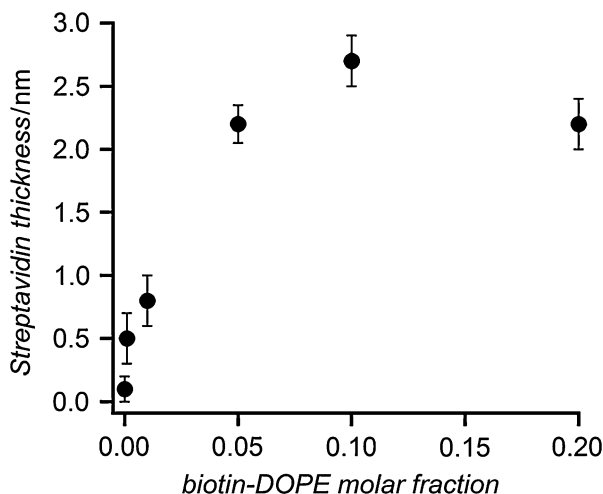
pore-rim surface. As the dielectric response increase due to adsorbed material is directly proportional to the occupied volume fraction of this material, it is a direct measure of surface coverage. It turned out that spreading of POPC SUVs on the hydrophobic AAO surface containing different mole fractions of biotin-DOPE results in the same lipid monolayer thickness of 2.4 ± 0.2 nm in agreement with a lipid monolayer lining the entire AAO pore depth, which is independent of the biotin content. The notion that the lipids are mobile within the monolayer was proven by FRAP experiments.

The amount of streptavidin adsorbed to the lipid-modified AAO surfaces was directly proportional to the biotin-DOPE mole fraction of the SUVs, as shown in Fig. 27.9. In agreement with the work of Spinke et al. [122] and Lopez and coworkers [123], the highest streptavidin surface coverage was obtained when using a biotin-DOPE to POPC ratio of 9:1. In our experiments, using 10 mol% biotin-DOPE gave a protein layer thickness about 15 % greater than working with a 5 % or 20 % biotin-DOPE lipid monolayer content.

When biotin was covalently linked to the AAO substrate by first silanizing the AAO with aminopropyl-triethoxysilane, followed by coupling to a heterobifunctional biotin linker, the amount of adsorbed streptavidin was estimated by OWS to be approximately 2.3 ± 0.2 nm in thickness. This corresponded to about 50 % surface coverage of a tightly packed protein layer, considering that the protein measures $4.5 \times 4.5 \times 5.8$ nm^3. The surface density of proteins achieved by this covalent coupling method is similar to the maximum surface coverage obtained for streptavidin bound to biotin-DOPE doped POPC monolayers [121].

Besides kinetics information obtained by time-resolved OWS experiments, streptavidin adsorption on biotin-DOPE doped lipid monolayers can be readily monitored by fluorescence microscopy. To detect the lipid monolayer, vesicles were fluorescently labeled with 0.3 mol% Bodipy DHPE and streptavidin was labeled with the dye atto-633. The evolution of protein adsorption of a 0.2 μM

Fig. 27.10 CLSM fluorescence profiles cross-section scans (in *z*-direction) taken at progressive times showing the evolution of streptavidin adsorption (0.2 μM) on a 10 mol% biotin-DOPE containing POPC lipid monolayer on hydrophobic AAO ($d_0 = 75$ nm, $h = 10$ μm) [121]
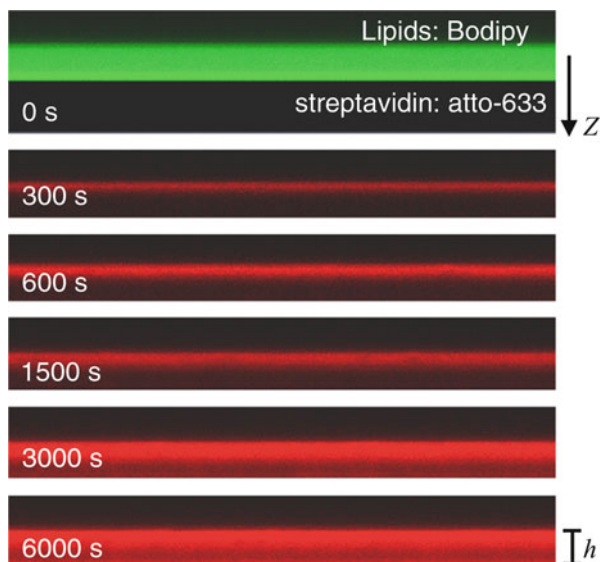
atto-633-labeled streptavidin solution can be studied using time-resolved confocal laser scanning microscopy by acquiring a *z*-profile scan of the AAO cross section (Fig. 27.10). Before addition of streptavidin, the Bodipy fluorescence of the lipids is visible across the entire AAO depth, which demonstrates the entire AAO surface is covered with a lipid monolayer. Addition of fluorescently labeled streptavidin results in the evolution of an increased fluorescence within the 10-μm depth of AAO (Fig. 27.10). Adsorption proceeded from near the pore entrance and continued until the entire pore depth *h* was saturated with streptavidin.

Protein Multilayer Formation Within AAO Nanopores

The results presented in section "Streptavidin Binding to Biotin Functionalized AAO Substrates" demonstrate that the biofunctionalized AAO can serve as a detection platform for either the label-free or the fluorescently labeled detection of protein adsorption on a lipid monolayer covering the porous surface. Owing to the nanometer-sized pores, it is well conceivable that macromolecular complexation within the pores, i.e., the binding of a second protein layer on top of the first one, could be prevented. To analyze this, protein multilayers composed of streptavidin and biotinylated-bovine serum albumin (BSA) were built onto the biotin-DHPE doped lipid monolayer. The result shown in Fig. 27.11 demonstrates that the amount of protein from a second streptavidin (2.1 nm) layer onto the biotinylated-BSA layer was similar to the amount initially deposited from the first streptavidin layer on the lipid surface (2.2 nm). Our experiments therefore showed that with sufficiently large pores ($d_0 > 60$ nm), the detection of
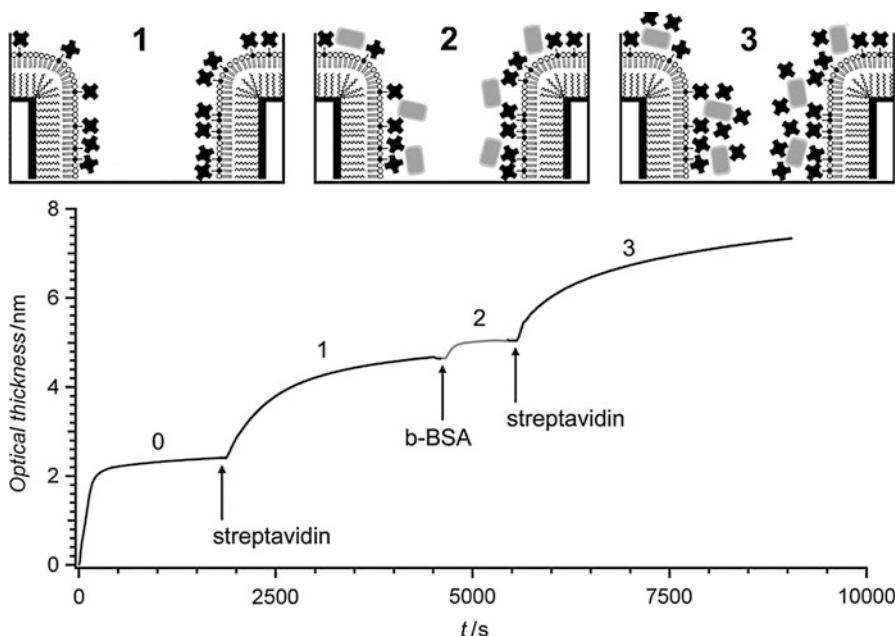
Fig. 27.11 Kinetic OWS measurements of lipid POPC monolayer formation containing 20 mol % biotin-DOPE (0), followed by streptavidin adsorption (1), then biotinylated-BSA (13 biotin per protein) (2), and finally a second layer of streptavidin (3). The pores remained accessible after AAO functionalization with a lipid monolayer (0) since step (3) shows as much deposition as step (1). Above are shown schematic representations of the different steps of the measurement. The sample used had pore diameters $d_0 = 65$ nm

biomacromolecular complexion is indeed possible, without steric hindrance inside the pores. This is particularly useful for the development of ELISA type assays, where large antibodies, which are often labeled, are used for biomarker detection.

Direct Protein Extraction from Cell Lysates

As demonstrated in section "Protein Multilayer Formation Within AAO Nanopores", AAO substrates can be functionalized with continuous, laterally mobile and highly repelling membranes that can be functionalized with mobile receptors for proteins recognition [121]. In contrast to a planar 2-D surface, the AAO surface area of a 3.5-µm thick sample ($d_0 = 75$ nm) is about 80 times larger. This large surface area of membrane-coated AAO can be used to monitor the purification of proteins directly from cell lysates in situ and in a time-resolved manner. To demonstrate this, a DOGS-NTA(Ni) lipid was embedded in a 1,2-dioleoly-*sn*-glycero-3-phosphocholine (DOPC) lipid monolayer to capture histidine-tagged proteins directly from a raw cell lysate. As a test protein, a hexahistidine-tagged protein termed PIGEA14 was used, which is composed of 126 amino acids and has a molecular weight of 14 kDa [124].
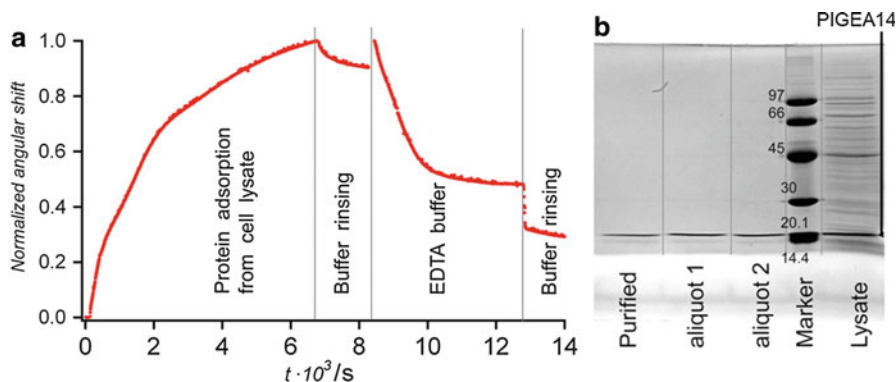
Fig. 27.12 (**a**) Time-resolved OWS measurement of His-tag-labeled PIGEA14 protein adsorption on a 10 mol% DOGS-NTA(Ni) lipid monolayer directly from a cell lysate solution. The protein was collected using a TRIS elution buffer containing 50 mM EDTA. (**b**) SDS-PAGE gel showing that only the 14 kDa PIGEA14 protein was extracted from the cell lysate using the purification scheme. Columns from *left-to-right* are: purified protein using regular techniques, two replica measurements of the experimental extraction using DOGS-NTA(Ni) on a AAO ($d_0 = 75$ nm, $h = 10$ μm), marker bands (kDa units), and cell lysate. The cell lysate contained a range of different proteins, while the aliquots only contained PIGEA14 [121]

DOPC SUVs containing 10 mol% of DOGS-NTA(Ni) lipids were first spread on AAO, initially silanized with C_{12}-TCS. The kinetics of the protein adsorption process on the functionalized AAO after addition of the cell lysate was then monitored by OWS (Fig. 27.12a). The angular shift corresponds to a captured 1.8-nm protein layer. Assuming full surface coverage of the lipid monolayer with proteins about 2 nm in diameter, the AAO surface capture efficiency, for the particular geometry of the AAO tested, was approximately 3.5 nMcm^{-2}. While the adsorption of the protein took about 2 h, elution of the protein using 50 mM EDTA buffer took only about 10–15 min. A control experiment using a DOPC lipid monolayer shows that some material from the cell lysate adsorbs nonspecifically in agreement with the observed 0.2-nm thickness that remains after rinsing with EDTA containing buffer. Of note, the presented method allows us to monitor and control the adsorption and desorption at a sub-nanometer surface coverage. The same experiment was repeated on a larger scale using AAO with a surface area of 25 mm^2 ($d_0 = 75$ nm) measuring $h = 10$ μm in order to collect a larger amount of proteins to characterize its purity by SDS PAGE analysis (Fig. 27.12b). In fact, the purity of two extracted protein samples using nanoporous AAO (identified as the aliquot samples 1, 2) was similar to a sample purified using standard columns containing Ni(NTA) gels (identified as the purified sample).

The use of functionalized, high surface area AAO demonstrates that this material can in fact effectively be used to extract biomacromolecules from complex fluid mixtures such as cell lysates and could be extended to blood and serum samples. The porous structure of AAO has the inherent advantage that sub-100 nm pores advantageously block many of the large biological particulates and cells that

typically will interfere with a planar surface, such that the active surface lying within the nanopores remains exposed only to components that are sufficiently small to enter within the pores, i.e., proteins, antibodies, small molecules, RNA, and short-stranded DNA, for example.

Pore-Spanning Lipid Membranes

In recent years, pore-spanning membranes have attracted more and more attention as an alternative to membranes attached to planar solid supports. Pore-spanning membranes are exposed to two aqueous compartments, above and below the membrane. For AAO, these aqueous compartments can have distinct compositions and can be adjusted independently of each other, i.e., the liquid environment within the pores and the bulk solution above the membrane lying on the pores. We can thus separate attoliter- to picoliter-sized compartments from the external aqueous environment [5, 6, 8, 9, 125–135].

Generally, two types of pore-spanning lipid membranes have been developed over the years. Depending on the functionalization of the underlying porous material, they are termed hybrid pore-spanning membranes (Fig. 27.13a) and supported pore-spanning membranes (Fig. 27.13b). Hybrid pore-spanning membranes are based on hydrophobic self-assembled monolayers (SAMs) chemisorbed on, for instance, gold-covered porous substrates [6, 8, 133]. In these systems, a lipid bilayer is formed over the pores, while only a lipid monolayer is produced on the SAM. One preparation strategy is to spread phospholipids dissolved in n-decane on a hydrophobic SAM composed of, e.g., octanethiol or cholesterylpolyethyleneoxythiol (CPEO$_3$).
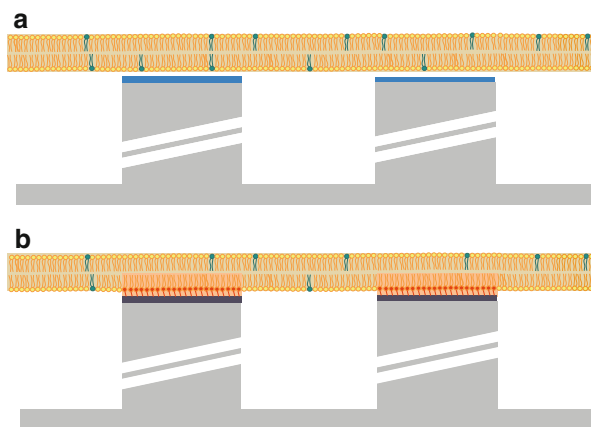
Fig. 27.13 Different systems of pore-spanning lipid bilayers termed supported and hybrid pore-spanning membranes. (**a**) Illustration of a supported pore-spanning bilayer prepared on hydrophilic porous substrates. (**b**) Illustration of a hybrid pore-spanning membrane. A self-assembly layer is formed atop the porous substrate prior to membrane deposition either via painting of lipids or spreading of giant liposomes [132]
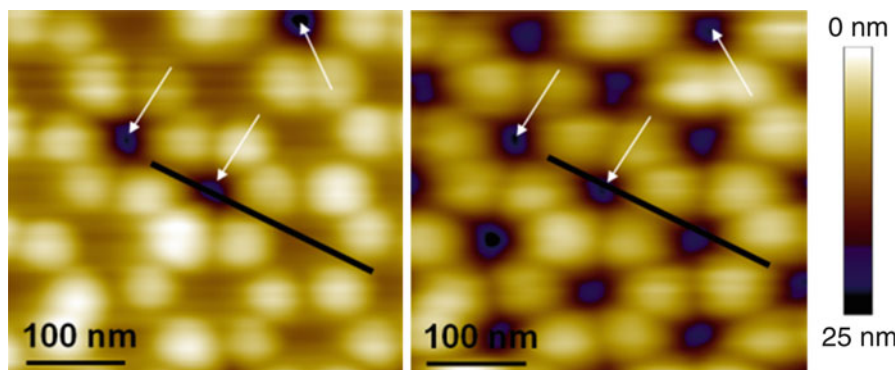
Fig. 27.14 Visualization of pore-spanning bilayers by AFM (contact mode in aqueous solution). *Left*: Pores covered by a DODAB bilayer imaged at low forces (0.9 nN). The *arrows* indicate uncovered pores. *Right*: Same region imaged at larger forces (2.7 nN) emphasizing that the membranes are pushed into the pores [135]

Another approach results in solvent-free hybrid pore-spanning membranes by spreading of unilamellar vesicles on a hydrophobic monolayer [9]. In contrast, supported pore-spanning membranes (Fig. 27.13b) are continuous, i.e., the membranes that are formed have a double phospholipid leaflet structure throughout. These are formed on hydrophilic porous substrates floating on a thin aqueous layer, regardless whether covering rims or holes [130, 131]. Either preparation technique has its merits and drawbacks as detailed below.

A method to detect individual pore-spanning membranes on nanoporous alumina is atomic force microscopy (AFM), as it provides the lateral resolution, which is not given by conventional or confocal optical microscopy. A typical AFM image of a pore-spanning membrane is shown in Fig. 27.14.

Here the nanoporous AAO is covered with a dioctadecylammonium bromide (DODAB) bilayer, which electrostatically adheres to mercaptopropionic acid functionalized gold-coated pore rims [127, 128, 135]. To produce pore-spanning membranes without compromising the nanoporous AAO transparency, silane chemistry is required to selectively functionalize the top surface of the alumina substrate. The silanization has to be localized on the pore rims to ensure that membranes cover the pores and do not line the inner pore walls.

Preparation of Pore-Spanning Membranes on Transparent AAO Substrates

Hybrid Pore-Spanning Membranes

For generating pore-spanning membranes following preparation protocols based on vesicle spreading, the surface must be sufficiently reactive so that it induces liposome rupture, while simultaneously avoiding the rupture of the pore-spanning part [136, 137]. Furthermore, the surface chemistry inside the pores and on the pore
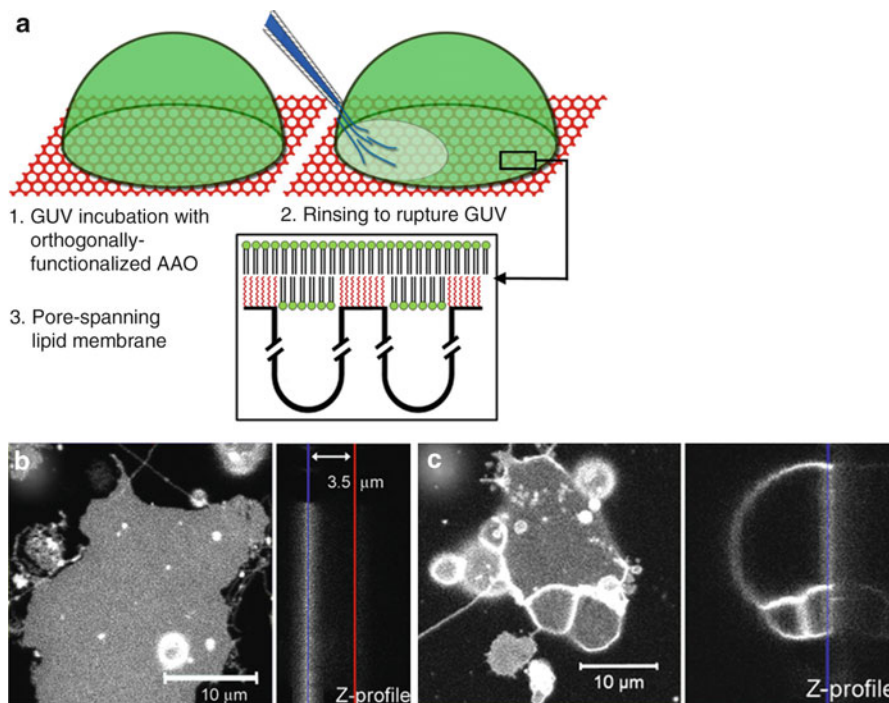
Fig. 27.15 (**a**) Illustration of the steps leading to the formation of hybrid pore-spanning lipid membranes on orthogonally functionalized AAO with hydrophobic pore rims obtained from silanization with C_{12}-TCS following Fig. 27.6. (**b**) Confocal fluorescent image of a giant unilamellar POPC vesicle on an orthogonal functionalized AAO substrate ($d_0 = 65$ nm and $h = 3.5$ μm) with C_{12}-TCS on the pore rims: *X-Y* plane (*left*) and Z-profile (*right*). (**c**) Confocal fluorescent image of a hybrid lipid membrane patch formed by the rupture of flattened POPC GUVs: the membrane, which is visible in the *X-Y* focal plane (*left*) and the Z-profile (*right*) shows that the fluorescence is localized atop the AAO, not within the AAO. The *blue line* indicates the *top* of the 3.5-μm-thick substrate, while the *red line* indicates the *bottom* [116]

rims needs to be distinct to avoid coverage of the pore walls with lipids [138–140]. Silane-based surface modifications have the particular advantage that fluorescence near the functionalized surface is not quenched, in contrast to metals, where quenching occurs up to 15 nm away from the surface [141, 142]. Using the silane-based functionalization presented in Fig. 27.7, porous AAO substrate with a selective hydrophobic functionalization of the pore rims using C_{12}-TCS can be prepared (see substrate **3**, Fig. 27.7) [116]. Giant unilamellar vesicles (GUVs), composed of POPC and labeled with Texas Red DHPE, can rupture on this functionalized AAO substrate, forming a pore-spanning hybrid lipid membrane, as illustrated in Fig. 27.15.

When AAO was not orthogonally functionalized, as for substrate **1** (see Fig. 27.7), where the entire AAO surface was hydrophobic, the volume beneath the measured patch was fluorescent throughout the thickness of the AAO due to lateral lipid diffusion within the membranes lining the pore walls, as observed in the results

obtained with SUVs incubated with substrate **1**. FRAP experiments confirmed that a continuous lipid monolayer is formed atop the AAO surface.

Continuous Pore-Spanning Membranes

While hybrid pore-spanning membranes have the advantage of being easily prepared on porous substrates, they are considerably pre-stressed because of the hydrophobic nature of the pore-rim tethering [109]. By using hydrophilic surfaces obtained, for instance, through the deposition of SiO_2 directly onto a gold surface [143], or directly using porous SiO_2 obtained by lithographical means [136, 144, 145], fluid bilayer membranes can be achieved.

We developed a method that allows nanoporous AAO substrates to be coated with a thin hydroxyl-terminated film at the interface between the nanoporous AAO and the bulk solution. The functionalized AAO substrates allow rupturing of POPC GUVs forming pore-spanning bilayer patches with laterally mobile lipids. The optical transparency of the alumina substrate enabled us to visualize the entrapment of fluorescent molecules within the attoliter-sized compartments by confocal microscopy.

Phosphocholine lipid vesicles adhere only weakly and do not rupture on untreated or plasma-treated (oxygen or argon plasma) AAO surfaces. Therefore, chemical surface functionalization of AAO is required to generate a hydrophilic surface that induces liposome rupture, while simultaneously ensuring that the substrate remains optically transparent [131]. To generate the required functionality on the AAO substrates, they were first silanized with mercaptopropyltriethoxysilane followed by evaporation of a thin gold layer (10–20 nm). The gold layer served as a protective mask that prevented the removal of the pore-rim surface functionalization as shown in Fig. 27.6 [116]. The sample was then treated with O_2 and Ar plasma, removing the organosilane functionalization from the non-protected pore-interior surface [146, 147]. Afterward, the gold layer was removed by I_2/KI and the substrate was oxidized for a short period in O_2 plasma. The substrates were then incubated with GUVs composed of POPC to form pore-spanning membranes (Fig. 27.16a).

In comparison to SUVs, the large surface area of GUVs allows them to deform and form large flat areas at the interface with the substrate, which form the pore-spanning membrane (Fig. 27.15b). To obtain accessible pore-spanning membrane patches, the adsorbed vesicle needs then to be gently rinsed until it ruptures. The remaining membrane patch is effectively the bottom of the GUV, which interacted with the hydrophobic pore rims. The fluorescence of these pore-spanning membranes originates solely from the top of the functionalized 3.5-μm-thick AAO substrate, which indicates that the lipids are localized in the atop focal plane.

In Fig. 27.16b, a typical noncircular patch is shown from rupture near the liposome's side, varying slightly from a heart-shape. Owing to the AAO transparency, z-stacks taken with confocal laser scanning fluorescence microscopy allowed us to show that pore-spanning membranes were formed, in contrast to membranes lining the pore-interior. The confocal z-stack image shown in Fig. 27.16c demonstrates that the fluorescence is only localized atop the AAO substrate, indicating that the membranes are localized only atop the AAO, as
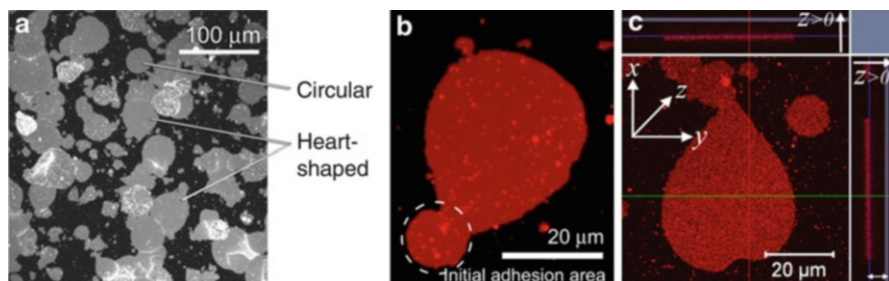
Fig. 27.16 (**a**) Pore-spanning lipid bilayer patches obtained by the rupture of giant unilamellar POPC vesicles doped with 1 mol% Texas Red DHPE on functionalized AAO substrates. (**b**) Enlarged view of a heart-shaped lipid membrane patch, formed by vesicle rupture. (**c**) Confocal z-stack image illustrating the formation of a pore-spanning membrane atop functionalized AAO ($d_0 = 60$ nm, $h = 3.5$ μm) [131]

expected for pore-spanning membranes; the double arrow shows the AAO thickness and the blue line marks the pore bottoms. Spread POPC GUVs display an average mobile fraction of 90 ± 5 %, and a diffusion coefficient of 3.8 ± 0.8 μm^2/s. The small immobile fraction indicates that both, the top and bottom leaflet of the bilayer, are mobile, while the diffusion coefficient is characteristic for a continuous solvent-free fluid lipid bilayer on a hydrophilic surface [148, 149].

Ruptured GUVs on AAO effectively separate thousands of individual attoliter-sized compartments (nanopores) from the outer medium [131]. The individually covered pores are isolated from each other because of the cylindrical geometry and because the AAO pores are closed at the substrate bottom. The insulating properties of the lipid bilayer patches are shown by excluding macromolecules from entering and adsorbing into the nanopores. Pore-spanning membranes composed of POPC and doped with Texas Red DHPE were first formed and then, fluorescently labeled avidin (Alexa-488 avidin) was added, which electrostatically adsorbed on the AAO porous surface. Fluorescence images revealed that in the regions, where pore-spanning membranes were formed, no avidin could be detected [131]. In contrast, the areas that were not covered by a membrane showed a bright green fluorescence because of protein adsorption onto the inner pore walls (Fig. 27.17). Figure 27.17b (ii) envisions the protein deposition. Figure 27.17c shows two different focal plane views: at the top AAO interface with the bulk solution, where the lipid membrane is formed (top image) and within the AAO, where no fluorescence was observed since neither lipids nor proteins were present within the buffer-filled AAO nanopores (bottom image). The z-projections clearly show that (1) the lipid fluorescence from the pore-spanning membrane is located at the top AAO surface only, (2) avidin can diffuse throughout the depth of the AAO substrate, and (3) fluorescently labeled proteins are excluded from entering the pores that are covered by a pore-spanning lipid bilayer.
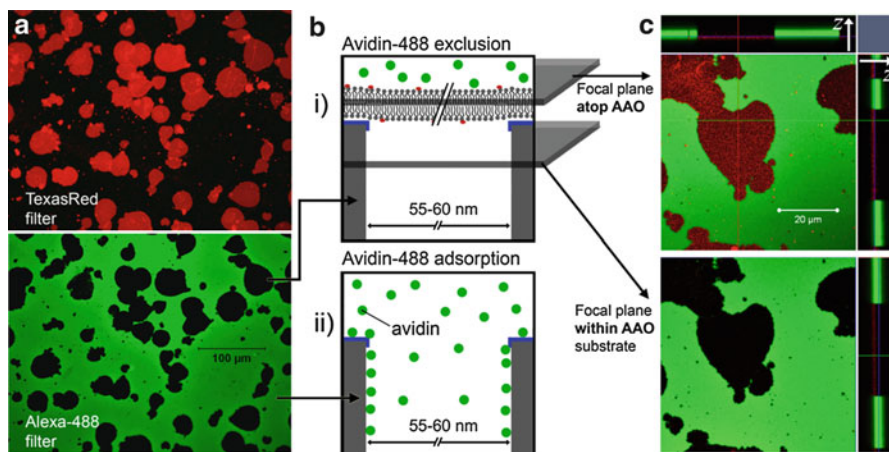
Fig. 27.17 (**a**) CLSM images of AAO with POPC pore-spanning membranes (*top image: red filter*) that exclude Alexa-488 avidin from entering the pores (*bottom image: green filter*), fluorescence in same area, but recorded using two filters. The protein is either excluded (*dark*) or adsorbed within unblocked nanopores (*green*). Pore-spanning membrane fluorescence correlates with the absence of protein fluorescence. (**b**) Two scenarios: (i) pore-spanning membrane blocks avidin entrance within pores and (ii) adsorption in uncovered pores. (**c**) Composite *z*-stack images (total *z*-distance: 15 μm) of a pore-spanning POPC bilayer preventing avidin entrance into the underlying pores (*black areas*). *Top image*: lipid membrane is located at the interface between the AAO and the bulk solution, showing both Texas Red DHPE and Alexa-488 avidin fluorescence in the overlay. *Bottom image*: taken within the center focal plane of the AAO film, where Texas Red DHPE fluorescence is no longer observed. *Top* and *right side* images are line profiles (shown in *top frame*) in the *z*-direction and clearly show that the membrane prevents the fluorescently labeled proteins from entering the pores [131]

Since the pore-spanning membranes served as a permeability barrier, they can be used to entrap small water-soluble molecules inside the pores, which do not adsorb onto the pore walls. Pore-spanning membranes were produced by spreading Texas Red DHPE doped POPC GUVs on the functionalized AAO surface in the presence of pyranine dye (10 mM) in buffer. Fluorescence images (Fig. 27.18) demonstrate that in the regions, where pore-spanning membranes were formed, pyranine molecules remained entrapped within the pores. In areas where the membrane was not pore-spanning but still remained on the pore rims, the Texas Red DHPE fluorescence was still visible, but the pyranine fluorescence was absent, because pyranine was removed from the pores during rinsing. Z-stacks also showed the fluorescence distribution in the vertical direction across these patches (Fig. 27.18).

Since the cylindrical pores of AAO are not interconnected, each cylindrical pore is physically isolated from its neighbor. Therefore, the pyranine fluorescence in photobleached area with encapsulated pyranine dyes does not recover with time (Fig. 27.18c). Interestingly, the pyranine fluorescence images also show that adjacent membrane patches show interfacial faults.
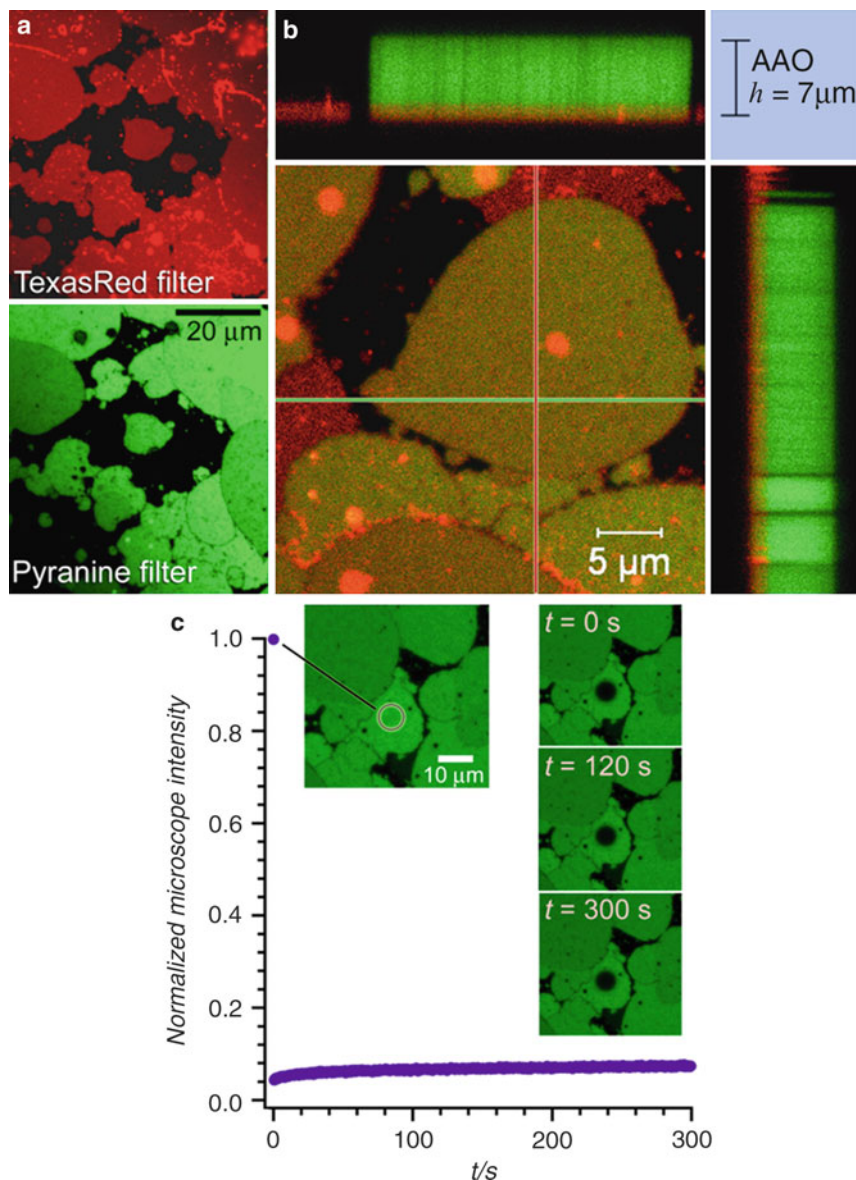
Fig. 27.18 (a) 2-D confocal fluorescence images of pore-spanning POPC lipid membranes with pyranine entrapped in the AAO pores. The pyranine fluorescence (*bottom, green*) correlates with the position of the POPC membranes (*top, red*). (**b**) 3-D *z*-stack image of the membrane encapsulating dye molecules within the cylindrical nanopores of AAO ($h = 7$ μm). Only membrane-covered pores can entrap the pyranine dye. (**c**) Fluorescence recovery of the interior of the bleached nanoporous area filled with pyranine dye. Each nanopore is isolated from its neighbors and therefore, the fluorescence cannot recover. Inset shows the lack of fluorescence recovery at $t = 0$, 120 and 300 s (*right*) [131]

Pore-spanning lipid membrane platforms open new possibilities for standardized and rapid on-chip screening of drug candidate or target analyte screening. One can imagine testing the effect of different constituents (such as target peptides, oligonucleotides, and small molecules) on the physical integrity of membranes and membrane-bound components such as peripheral proteins and transmembrane channels.

Concluding Remarks

Porous alumina is a versatile material providing a very large surface area. It is rather stable in aqueous solution and can serve as an optical waveguide, which makes this material well suited for biochemical/biophysical and bioanalytical applications. To produce an appropriate sensing surface, tailor-made surface functionalization strategies are required and there is still a need for the development of orthogonal biocompatible surface functionalization methods. Owing to their nanometer-sized pores, pore-spanning membranes prepared on porous alumina substrates can generate sealed attoliter-sized compartments, which offers new possibilities for rapid on-chip screening assays comprising molecular recognition events coupled to transport across membranes.

References

1. Alvarez SD, Li CP, Chiang CE, Schuller IK, Sailor MJ (2009) Acs Nano 3:3301–3307
2. Haberkorn N, Gutmann JS, Theato P (2009) Acs Nano 3:1415–1422
3. Haberkorn N, Lechmann MC, Sohn BH, Char K, Gutmann JS, Theato P (2009) Macromol Rapid Commun 30:1146–1166
4. Lee J, Orilall MC, Warren SC, Kamperman M, Disalvo FJ, Wiesner U (2008) Nat Mat 7:222–228
5. Horn C, Steinem C (2005) Biophys J 89:1046–1054
6. Kepplinger C, Höfer I, Steinem C (2009) Chem Phys Lipids 160:109–113
7. Lazzara TD, Mey I, Steinem C, Janshoff A (2011) Anal Chem 83:5624–5630
8. Schmitt EK, Vrouenraets M, Steinem C (2006) Biophys J 91:2163–2171
9. Schmitt EK, Weichbrodt C, Steinem C (2009) Soft Matter 5:3347–3353
10. O'Sullivan JP, Wood GC (1970) Proc R Soc Lond A 317:511–543
11. Mikulskas I, Juodkazis S, Tomasiunas R, Dumas JG (2001) Adv Mater 13:1574
12. Martin CR (1994) Science 266:1961–1966
13. Nielsch K, Choi J, Schwirn K, Wehrspohn RB, Gösele U (2002) Nano Lett 2:677–680
14. Li AP, Müller F, Birner A, Nielsch K, Gösele U (1998) J Appl Phys 84:6023–6026
15. Bowen WR, Sharif AO (1996) Proc R Soc Lond A 452:2121–2140
16. Chen W, Yuan JH, Xia XH (2005) Anal Chem 77:8102–8108
17. Han JY, Fu JP, Schoch RB (2008) Lab Chip 8:23–33
18. Jiang XQ, Mishra N, Turner JN, Spencer MG (2008) Microfluid Nanofluid 5:695–701
19. Roy P, Dey T, Lee K, Kim D, Fabry B, Schmuki P (2010) J Am Chem Soc 132:7893–7895
20. Vlassiouk I, Krasnoslobodtsev A, Smirnov S, Germann M (2004) Langmuir 20:9913–9915
21. Wang Y, Angelatos AS, Dunstan DE, Caruso F (2007) Macromolecules 40:7594–7600
22. Bonanno LM, Kwong TC, DeLouise LA (2010) Anal Chem 82:9711–9718

23. Hotta K, Yamaguchi A, Teramae N (2010) Anal Chem 82:6066–6073
24. Schwartz MP, Alvarez SD, Sailor MJ (2007) Anal Chem 79:327–334
25. Wang ML, Meng GW, Huang Q, Li MT, Li ZB, Tang CL (2011) Analyst 136:278–281
26. Yamaguchi A, Hotta K, Teramae N (2009) Anal Chem 81:105–111
27. Schmid G (2002) J Mater Chem 12:1231–1238
28. Metzger RM, Konovalov VV, Sun M, Xu T, Zangari G, Xu B, Benakli M, Doyle WD (2000) IEEE Trans Magn 36:30–35
29. Zhang ZB, Ying JY, Dresselhaus MS (1998) J Mat Res 13:1745–1748
30. Hou SF, Wang JH, Martin CR (2005) Nano Lett 5:231–234
31. Lei Y, Cai WP, Wilde G (2007) Prog Mater Sci 52:465–539
32. Rabin O, Herz PR, Lin YM, Akinwande AI, Cronin SB, Dresselhaus MS (2003) Adv Funct Mat 13:631–638
33. Biring S, Tsai K-T, Sur UK, Wang Y-L (2008) Nanotechnology 19:015304
34. Lita AE, Sanchez JJE (1999) J App Phys 85:876
35. Masuda H, Fukuda K (1995) Science 268:1466–1468
36. Masuda H, Hasegwa F, Ono S (1997) J Electrochem Soc 144:L127–L130
37. Chu SZ, Wada K, Inoue S, Isogai M, Yasumori A (2005) Adv Mater 17:2115
38. Kovacs GJ, Scott GD (1978) Appl Opt 17:3314–3322
39. Aust EF, Knoll W (1993) J Appl Phys 73:2705–2708
40. Hickel W, Knoll W (1990) Appl Phys Lett 57:1286–1288
41. Kim DH, Lau KHA, Robertson JWF, Lee OJ, Jeong U, Lee JI, Hawker CJ, Russell TP, Kim JK, Knoll W (2005) Adv Mater 17:2442
42. Knoll W (1998) Annu Rev Phys Chem 49:569–638
43. Dürr M, Menges G, Knoll W, Yasuda A, Nelles G (2007) Appl Phys Lett 91:021113–021115
44. Lau KHA, Tan LS, Tamada K, Sander MS, Knoll W (2004) J Phys Chem B 108:10812–10818
45. Lau KHA, Duran H, Knoll W (2009) J Phys Chem B 113:3179–3189
46. Cameron PJ, Jenkins ATA, Knoll W, Marken F, Milsom EV, Williams TL (2008) J Mater Chem 18:4304–4310
47. Fujimaki M, Rockstuhl C, Wang XM, Awazu K, Tominaga J, Ikeda T, Ohki Y, Komatsubara T (2007) Microelectron Eng 84:1685–1689
48. Reimhult E, Kumar K, Knoll W (2007) Nanotechnology 18:275303
49. Egan WG, Aspnes DE (1982) Thin Solid Films 89:249–262
50. Foss CA, Tierney MJ, Martin CR (1992) J Phys Chem 96:9001–9007
51. Kim DH, Lau KHA, Joo W, Peng J, Jeong U, Hawker CJ, Kim JK, Russell TP, Knoll W (2006) J Phys Chem B 110:15381–15388
52. Casero E, Vazquez L, Parra-Alfambra AM, Lorenzo E (2010) Analyst 135:1878–1903
53. Endo T, Kerman K, Nagatani N, Takamura Y, Tamiya E (2005) Anal Chem 77:6976–6984
54. Janshoff A, Galla HJ, Steinem C (2000) Angew Chem Int Ed 39:4004–4032
55. McPhillips J, Murphy A, Jonsson MP, Hendren WR, Atkinson R, Hook F, Zayats AV, Pollard RJ (2010) ACS Nano 4:2210–2216
56. Shi HQ, Tsai WB, Garrison MD, Ferrari S, Ratner BD (1999) Nature 398:593–597
57. Schuck P (1997) Ann Rev Biophys Biomol Struct 26:541–566
58. Schuck P, Minton AP (1996) Anal Biochem 240:262–272
59. Rabe M, Verdes D, Seeger S (2011) Adv Colloid Interface Sci 162:87–106
60. Schuck P (1997) Curr Opin Biotechnol 8:498–502
61. Carrasquilla C, Li Y, Brennan JD (2011) Anal Chem 83:957–965
62. DeLouise LA, Miller BL (2004) Anal Chem 76:6915–6920
63. Feng L, Musto CJ, Kemling JW, Lim SH, Zhong W, Suslick KS (2010) Anal Chem 82:9433–9440
64. Qiao YH, Wang D, Buriak JM (2007) Nano Lett 7:464–469
65. Gopinath SCB, Awazu K, Fujimaki M, Sugimoto K, Ohki Y, Komatsubara T, Tominaga J, Gupta KC, Kumar PKR (2008) Anal Chem 80:6602–6609
66. Lawrie JL, Jiao Y, Weiss SM (2010) IEEE Trans 9:596–602

67. Dancil KPS, Greiner DP, Sailor MJ (1999) J Am Chem Soc 121:7925–7930
68. Mun KS, Alvarez SD, Choi WY, Sailor MJ (2010) ACS Nano 4:2070–2076
69. Trivinho-Strixino F, Guerreiro HA, Gomes CS, Pereira EC, Guimaraes FEG (2010) Appl Phys Lett 97
70. Walt DR (2009) ACS Nano 3:2876–2880
71. Li FY, Zhang L, Metzger RM (1998) Chem Mater 10:2470–2480
72. Lazzara TD, Lau KHA, Abou-Kandil AI, Caminade AM, Majoral JP, Knoll W (2010) ACS Nano 4:3909–3920
73. Bird RB, Stewart WE, Lightfoot EN (2001) Transport Phenomena, 2nd edn. Wiley, New York
74. Deen WM, Bohrer MP, Epstein NB (1981) AlChE J 27:952–959
75. Huang CJ, Dostalek J, Knoll W (2010) Biosens Bioelectron 26:1425–1431
76. Probstein RF (2003) Physicochemical hydrodynamics: an introduction. Wiley, Hoboken
77. Wolny PM, Spatz JP, Richter RP (2009) Langmuir 26:1029–1034
78. Bain CD, Biebuyck HA, Whitesides GM (1989) Langmuir 5:723–727
79. Bain CD, Troughton EB, Tao YT, Evall J, Whitesides GM, Nuzzo RG (1989) J Am Chem Soc 111:321–335
80. Dubois LH, Nuzzo RG (1992) Ann Rev Phys Chem 43:437–463
81. Dubois LH, Zegarski BR, Nuzzo RG (1993) J Chem Phys 98:678–688
82. Laibinis PE, Whitesides GM, Allara DL, Tao YT, Parikh AN, Nuzzo RG (1991) J Am Chem Soc 113:7152–7167
83. Schreiber F (2000) Prog Surf Sc 65:151–256
84. Sellers H, Ulman A, Shnidman Y, Eilers JE (1993) J Am Chem Soc 115:9389–9401
85. Gombotz WR, Guanghui W, Horbett TA, Hoffman AS (1991) J Biomed Mater Res 25:1547–1562
86. Liston EM, Martinu L, Wertheimer MR (1993) J Adhes Sci Technol 7:1091–1127
87. Tran Y, Auroy P (2001) J Am Chem Soc 123:3644–3654
88. Brzoska JB, Benazouz I, Rondelez F (1994) Langmuir 10:4367–4373
89. Brzoska JB, Shahidzadeh N, Rondelez F (1992) Nature 360:719–721
90. Fadeev AY, McCarthy TJ (2000) Langmuir 16:7268–7274
91. Nanci A, Wuest JD, Peru L, Brunet P, Sharma V, Zalzal S, McKee MD (1998) J Biomed Mater Res 40:324–335
92. Oner D, McCarthy TJ (2000) Langmuir 16:7777–7782
93. Ozin GA (1992) Adv Mater 4:612–649
94. Weetall HH (1993) Appl Biochem Biotechnol 41:157–188
95. Fadeev AY, McCarthy TJ (1999) Langmuir 15:3759–3766
96. Kobayash H, Bell AT, Shen M (1974) Macromolecules 7:277–283
97. Medard N, Soutif JC, Poncin-Epaillard F (2002) Surf Coat Technol 160:197–205
98. Biebuyck HA, Whitesides GM (1993) Langmuir 9:1766–1770
99. Hubbard JB, Silin V, Plant AL (1998) Biophys Chem 75:163–176
100. Plant AL (1993) Langmuir 9:2764–2767
101. Ron H, Matlis S, Rubinstein I (1998) Langmuir 14:1116–1121
102. Kelley TW, Boardman LD, Dunbar TD, Muyres DV, Pellerite MJ, Smith TYP (2003) J Phys Chem B 107:5877–5881
103. Templeton MK, Weinberg WH (1985) J Am Chem Soc 107:97–108
104. Templeton MK, Weinberg WH (1985) J Am Chem Soc 107:774–779
105. Mutalib Md Jani A, Anglin EJ, McInnes SJP, Losic D, Shapter JG, Voelcker NH (2009) Chem Commun 3062–3064
106. Gorton L (2005) Biosensors and modern biospecific analytical techniques, 1st edn. Elsevier, Amsterdam
107. Soriaga MP, Stickney J, Bottomley LA, Kim Y-G (2002) Thin films: preparation, characterization applications, 1st edn. Springer, New York

108. Wilbur JL, Whitesides GM (1999) Chapter 8: Self-assembly and self-assembled monolayers in micro- and nanofabrication. In: Timp GL (ed) Nanotechnology. Springer, New York, pp 331–353
109. Mey I, Stephan M, Schmitt EK, Müller MM, Ben Amar M, Steinem C, Janshoff A (2009) J Am Chem Soc 131:7031–7039
110. Hobler C, Bakowsky U, Keusgen M (2010) Phys Status Solidi A 207:872–877
111. Popat KC, Mor G, Grimes CA, Desai TA (2004) Langmuir 20:8035–8041
112. Velleman L, Triani G, Evans PJ, Shapter JG, Losic D (2009) Microporous Mesoporous Mater 126:87–94
113. Sailor MJ, Link JR (2005) Chem Commun 1375–1383
114. Kilian KA, Bocking T, Gaus K, Gooding JJ (2008) Angew Chem Int Ed 47:2697–2699
115. Brevnov DA, Barela MJ, Brooks MJ, Lopez GP, Atanassov PB (2004) J Electrochem Soc 151:B484–B489
116. Lazzara TD, Kliesch TT, Janshoff A, Steinem C (2011) ACS Appl Mater Interfaces 3:1068–1076
117. Fliniaux O, Elie-Caille C, Pantigny J, Bourdillon C (2005) Electrochem Commun 7:697–702
118. Tamm LK, McConnell HM (1985) Biophys J 47:105–113
119. Plant AL (1999) Langmuir 15:5128–5135
120. Brian AA, McConnell HM (1984) PNAS 81:6159–6163
121. Lazzara T, Behn D, Kliesch T-T, Janshoff A, Steinem C (2012) J Coll Int Sci 366:57–63
122. Spinke J, Liley M, Schmitt FJ, Guder HJ, Angermaier L, Knoll W (1993) J Chem Phys 99:7012–7019
123. Perez-Luna VH, O'Brien MJ, Opperman KA, Hampton PD, Lopez GP, Klumb LA, Stayton PS (1999) J Am Chem Soc 121:6469–6478
124. Hidaka S, Konecke V, Osten L, Witzgall R (2004) J Biol Chem 279:35009–35016
125. Carnarius C, Kreir M, Krick M, Methfessel C, Moehrle V, Valerius O, Brüggemann A, Steinem C, Fertig N (2012) J Biol Chem 287:2877–2886
126. Drexler J, Steinem C (2003) J Phys Chem B 107:11245–11254
127. Hennesthal C, Drexler J, Steinem C (2002) Chem Phys Chem 3:885–889
128. Hennesthal C, Steinem C (2000) J Am Chem Soc 122:8085–8086
129. Janshoff A, Steinem C (2012) Supported lipid bilayers: intelligent surfaces for ion channel recordings. In: Textor M (ed) Intelligent surfaces: polymer coatings for applications in bio-related and life sciences. Wiley, pp 141–182
130. Kocun M, Lazzara TD, Steinem C, Janshoff A (2011) Langmuir 27:7672–7680
131. Lazzara TD, Carnarius C, Kocun M, Janshoff A, Steinem C (2011) ACS Nano 5:6935–6944
132. Mey I, Steinem C, Janshoff A (2012) J Mater Chem 22:19348–19356
133. Römer W, Steinem C (2004) Biophys J 86:955–965
134. Schmitt EK, Nurnabi M, Bushby RJ, Steinem C (2008) Soft Matter 4:250–253
135. Steltenkamp S, Müller MM, Deserno M, Hennesthal C, Steinem C, Janshoff A (2006) Biophys J 91:217–226
136. Jonsson P, Jonsson MP, Hook F (2010) Nano Lett 10:1900–1906
137. Bhattacharya J, Kisner A, Offenhäusser A, Wolfrum B (2011) Beilstein J Nanotechnol 2:104–109
138. Suzuki K, Masuhara H (2005) Langmuir 21:6487–6494
139. Pfeiffer I, Seantier B, Petronis S, Sutherland D, Kasemo B, Zach M (2008) J Phys Chem B 112:5175–5181
140. Pfeiffer I, Petronis S, Koper I, Kasemo B, Zach M (2010) J Phys Chem B 114:4623–4631
141. Liebermann T, Knoll W (2000) Colloids Surf A-Physicochem Eng Asp 171:115–130
142. Vasilev K, Knoll W, Kreiter M (2004) J Chem Phys 120:3439–3445
143. Im H, Wittenberg NJ, Lesuffleur A, Lindquist NC, Oh SH (2010) Chem Sci 1:688–696

144. Worsfold O, Voelcker NH, Nishiya T (2006) Langmuir 22:7078–7083
145. Cunin F, Milhiet PE, Anglin E, Sailor MJ, Espenel C, Le Grimellec C, Brunel D, Devoisselle JM (2007) Ultramicroscopy 107:1048–1052
146. Aronsson BO, Lausmaa J, Kasemo B (1997) J Biomed Mater Res 35:49–73
147. Raiber K, Terfort A, Benndorf C, Krings N, Strehblow HH (2005) Surf Sci 595:56–63
148. Castellana ET, Cremer PS (2006) Surf Sci Rep 61:429–444
149. Stelzle M, Miehlich R, Sackmann E (1992) Biophys J 63:1346–1354

Computational Materials Science of Bionanomaterials: Structure, Mechanical Properties and Applications of Elastin and Collagen Proteins

28

Anna Tarakanova, Shu-Wei Chang, and Markus J. Buehler

Keywords

Materiomics • Elastin • Collagen • Hierarchical structure • Elasticity • Inverse temperature transition • Osteogenesis imperfecta (OI)

Introduction

Elastin and collagen can be thought of as complementary structural protein materials, having balanced roles in the function of the extracellular matrix. Elastin adds to the extensibility, while the more abundant collagen protein forms a robust framework within essential tissues. Here, we review the hierarchical structure of each protein, with an emphasis on mechanical signature and behavior. For elastin, we focus on the molecular and fiber level structure and mechanical properties that have been identified thus far, noting a missing fibril scale that has yet to be well-characterized. We go on to examine the molecular origins of two unique properties of elastin, namely, its ability to extend beyond multiple times its resting length and its unusual propensity to fold under higher temperatures, an effect known as the inverse temperature transition.

These authors Anna Tarakanova and Shu-Wei Chang contributed equally to this work

A. Tarakanova • S.-W. Chang
Laboratory for Atomistic and Molecular Mechanics (LAMM), Department of Civil and Environmental Engineering, Massachusetts Institute of Technology, Cambridge, MA, USA

M.J. Buehler (✉)
Laboratory for Atomistic and Molecular Mechanics (LAMM), Department of Civil and Environmental Engineering, Massachusetts Institute of Technology, Cambridge, MA, USA

Center for Computational Engineering, Massachusetts Institute of Technology, Cambridge, MA, USA
e-mail: mbuehler@mit.edu

Both qualities render elastin an excellent template material for novel biomaterial applications and drug delivery devices, for example. In the section on collagen, we present recent finding of the molecular and fibril-scale signature of the protein, highlighting its multilevel hierarchy. We then outline a detailed case study of the disease *osoteogenesis imperfecta*, identifying molecular level origins and implications. We conclude with a section on applications and future directions in the study of these two important biomaterials.

Elastin

Tropoelastin: Precursor Molecule of Elastin

Elastin is an important extracellular matrix protein that is found in a wide range of tissues, including the skin, lung, heart, and arteries [1–4]. It is highly elastic, providing reversible deformability and recoil, with an ability to extend beyond several times its resting length and reversibly return to its original state, undergoing a lifetime of extension and compression cycles with minimal degradation. Elastic fibers are composed of a proteinaceous scaffold made up of several different proteins including fibrillins, fibulins, and glycoproteins, which acts as the base onto which elastin protein aggregates and assembles [5]. Elastin protein is made up of cross-linked soluble tropoelastin molecules, secreted from smooth muscle cells and fibroblasts, which are catalyzed by lysyl oxidase to make larger globules that assemble onto the scaffold (Fig. 28.1) [6].
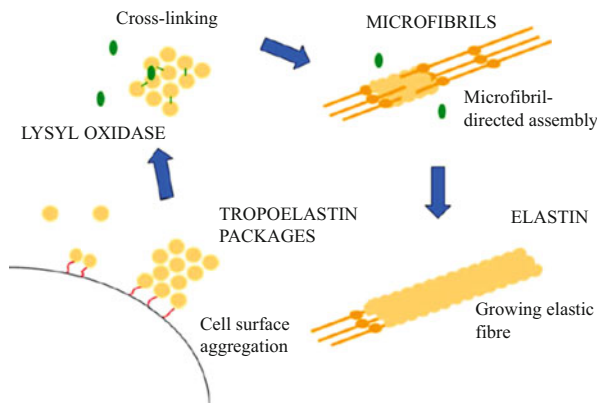
Fig. 28.1 Assembly mechanism of elastic fibers from tropoelastin molecules. Tropoelastin molecules assemble into larger globules, which are cross-linked with lysyl oxidase, forming larger clusters. Tropoelastin clusters assemble on microfibril scaffolds, forming a growing elastic fiber (Reprinted from Journal of Cellular Physiology, Kozel, B.A., et al., *Elastic fiber formation*: *A dynamic view of extracellular matrix assembly using timer reporters*, 2006. **207**(1): p. 87–96 with permission from Elsevier [6])
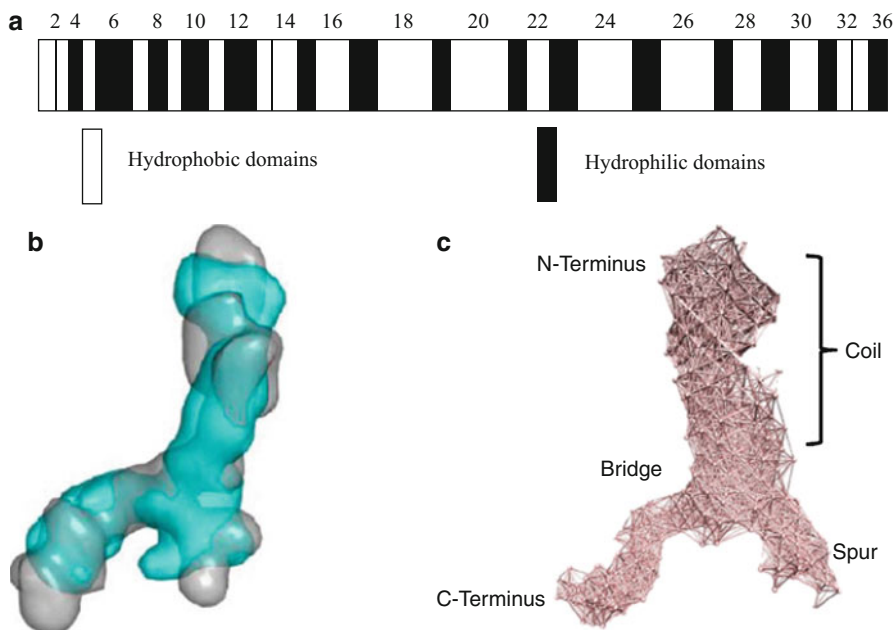
Fig. 28.2 (**a**) Structure of human tropoelastin gene with alternating hydrophobic and hydrophilic domains (Reprinted from Journal of Structural Biology, Wise, S.G., et al., *Specificity in the coacervation of tropoelastin*: *solvent exposed lysines*, 2005. **149**(3): p. 273–281 with permission from Elsevier [70]) (**b**) Averaged superimposed tropoelastin structures from small-angle x-ray (*blue*) and neutron (*gray*) scattering profiles (Reprinted with permission from [7]) (**c**) Full-length tropoelastin model (Adapted from [71])

Tropoelastin, elastin's soluble precursor molecule, is encoded by a single gene [5]. The most common isoform of tropoelastin is a 60 kDa molecule, consisting of 698 amino acids, composed of alternating hydrophilic and hydrophobic domains (Fig. 28.2a). Hydrophilic domains are involved in cross-linking, while the hydrophobic domains are believed to play a key part in the entropic elasticity of elastin. Hydrophobic domains are rich in glycine, alanine, valine, and proline residues, often occurring in repeating motifs of PGV, GVA, and GGV [5]. Hydrophilic domains are rich in lysines, which undergo irreversible cross-linking.

The globular structure of tropoelastin has recently been determined with small-angle x-ray and neutron scattering (Fig. 28.2b) [7]. Tropoelastin is an extended asymmetric molecule, with a 16-nm end-to-end distance and a width between 3 and 7.5 nm from its most narrow to its widest region. The N-terminus sits at the top of an extended cylinder of the molecular body. The cylinder contains an amorphous coiled region responsible for the elasticity of the molecule. Below the coil, the molecule splices into a spur region, thought to contain exons 20–24, which is
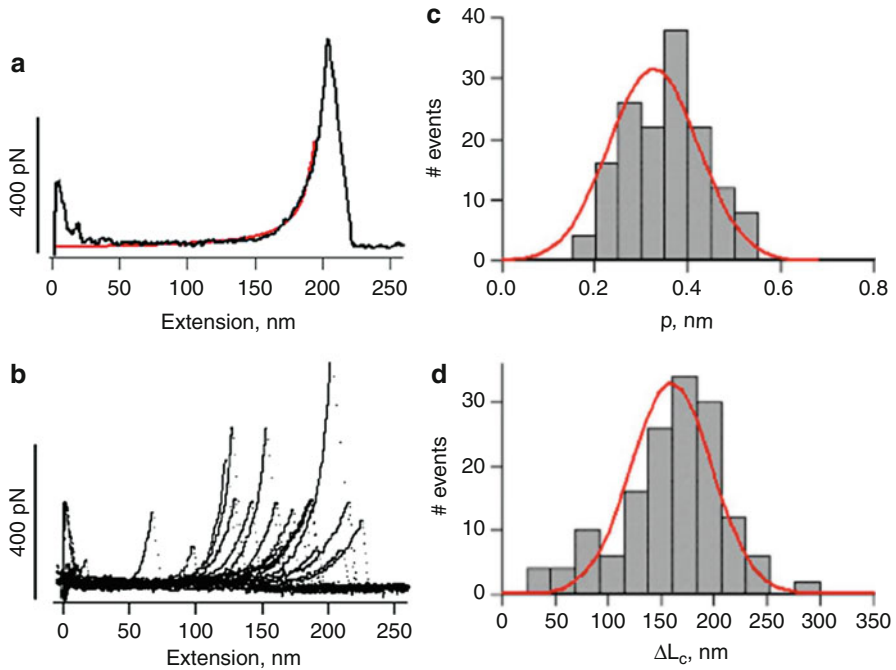
Fig. 28.3 (**a**) Sample single-molecule force-extension curve, with the *red line* representing worm-like chain model of a polymer with contour length of 211 nm and persistence length 0.38 nm. (**b**) 17 force-extension curves for stretching of tropoelastin molecules. (**c**) Frequency histogram for persistence length and (**d**) contour lengths, for 158 samples (Reprinted with permission from [7], Copyright (2011) National Academy of Sciences, U.S.A.)

connected to the cell-binding C-terminus foot region through a bridge, a highly exposed region, predisposed to cross-linking. The C-terminus region of tropoelastin has been found to be highly conserved across mammalian species (Fig. 28.2c) [7].

The mechanical signature of tropoelastin, that can reversibly extend to several times its resting length of 20 nm, with minimal energy loss, is a key factor in the overall superior mechanical properties of elastic fibers. Single tropoelastin molecules have been characterized by using atomic force microscopy, where molecules were stretched and relaxed sequentially (Fig. 28.3a, b). The force-extension patterns of tropoelastin molecules fit well to a worm-like chain model, with a persistence length of 0.36 calculated for an average contour length of 166 nm, suggesting high molecular elasticity (Fig. 28.3c, d). The Young's modulus was calculated to be approximately 3 kPa [7].

Elastic Fibers: Structure and Mechanical Properties

Elastin fibers are the largest structural unit composing tissues. Water-swollen elastic fibers are approximately 1–8 μm in diameter (Fig. 28.4a) [5, 8]. Elastic
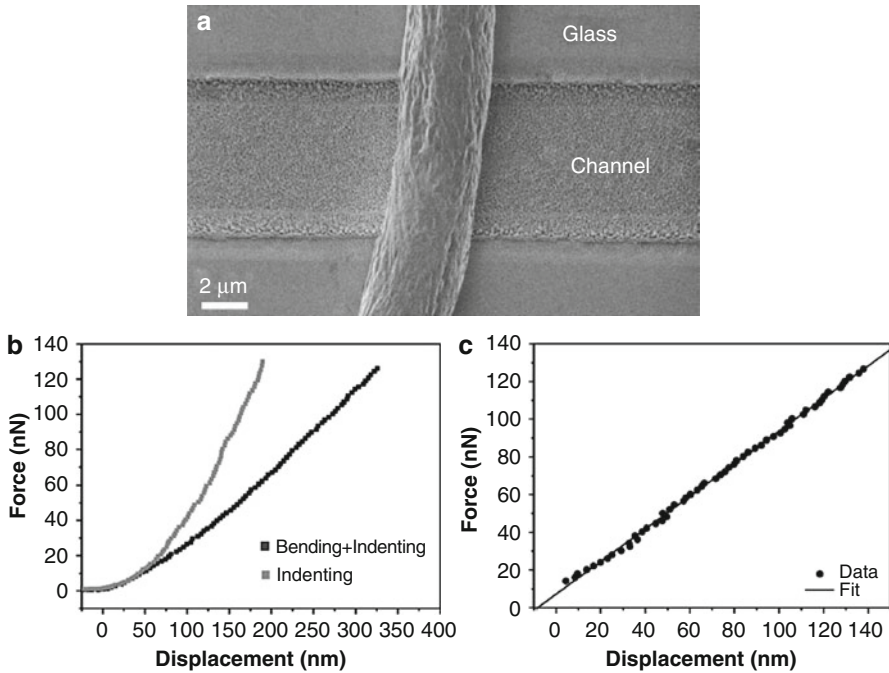
Fig. 28.4 (**a**) SEM image of an elastic fiber in a micro-channel of a glass substrate. (**b**) Force-displacement curve for indenting elastic fiber on the glass substrate (*black*) and bending the fiber in the middle, with indentation. (**c**) Force-displacement curve representing bending only (Reprinted from Biomaterials, Koenders, M.M.J.F., et al., *Microscale mechanical properties of single elastic fibers*: *The role of fibrillin-microfibrils*, 2009. **30**(13): p. 2425–2432 with permission from Elsevier [11])

fibers have been observed to be twisted and straight, arranged as interwoven networks or as flattened sheets, depending on tissue type [8]. Elastin networks can generally be found in connective tissue, while dense tissue such as the aorta is composed of flattened elastin sheets, or elastic laminae [8]. Elastin fibers have been extensively studied, with various studies identifying a supramolecular fibrillar organization within fibers. Scanning electron microscope (SEM) studies have found that elastin fibers from bovine fetal and adult samples are composed of fibrils 100–130 nm in diameter, where thickening occurs during maturation [9, 10]. Thicker fibrils in adult tissue may be due to aggregation of smaller filaments onto the fibrils. Further down the length-scale hierarchy, filaments of about 1 nm up to 8 nm have been observed within fibrils, arranged parallel to the main fiber axis, and sometimes exhibiting helical or twisted configuration with some cross-bridging [9]. Variable sizes were observed depending on whether a stretched or relaxed configuration was considered, with smaller sizes corresponding to stretched configurations [9]. Stretched filaments also showed better alignment than relaxed filaments.

Elastic tissue and fiber mechanics have been well studied, but substructure filaments and fibrils are yet to be characterized as a result of the difficulty in isolating these substructures, due to high levels of cross-linking and their propensity to aggregate. Macro-mechanical testing has been used for years to study elastin-rich tissue samples. Studies from dog, sheep, and pig aorta determined the Young's modulus of the elastic fiber-rich tissue to be in the range of 0.1–0.8 MPa [11–13]. The Young's modulus of single elastin fibers was first determined from bovine ligamentum nuchae samples to be in the range of 0.4–1.2 MPa, by using a microtesting apparatus attached to a polarizing microscope [14]. A later study comparing fibrillin-rich and fibrillin-free elastin fibers revealed a similar Young's modulus of 0.90 and 0.79 MPa, respectively, though the statistical difference was not significant, signifying that scaffolding microfibrils do not significantly influence the mechanical properties of single elastic fibers [11]. Here, a tip-less Atomic Force Microscope (AFM) cantilever was used to bend freely suspended fibers on a microchanneled substrate. A displacement from bending and local indentation was induced by exerting a force at the middle point of the channel, and the modulus was determined by subtracting the force-displacement curve derived from local indentation only (Fig. 28.4b, c). A linear force-displacement curve was found for fibers with and without microfibrils [11].

Entropic Origins of Elastin's Elasticity

Three prevalent hypotheses have guided the understanding of elastin's elasticity for the past half century: the classical theory of rubber elasticity, the hydrophobic effect, and librational entropic mechanisms [1]. Initially, elastin's superb elasticity was attributed to the classical theory of rubber elasticity, first proposed by Hoeve and Flory [15]. This model assumed that elastin was a single-phase system with randomly configured polymeric chains which assume a highest entropy at lowest end-to-end extension, such that any displacement from this highest entropy state is responsible for the elastic restoring force [15, 16]. This model failed to explain certain elements key to elastin's performance, such as the requirement for water [17].

Computationally intensive molecular dynamics (MD) simulation studies began to shift away from the rubber elasticity viewpoint, first with Urry's proposal of an alternative librational elasticity mechanism, suggesting that the elastic restoring force originates from a reduction in available configuration space upon extension as the peptide segments are stretched [18]. Chang and Urry first conducted molecular dynamics studies on the elastomeric polypentapeptide $(VPGVG)_7$ [19], finding that the total energy was lower by 15 kcal/mol for the relaxed state than for the extended state, which was primarily attributed to the difference in the van der Waals term, and could be explained by the greatly reduced side chain interactions in the extended state. They found that the number of accessible amplitudes of torsional libration in the linker residues bridging different segments was reduced as the structure was extended, suggesting a librational entropic mechanism.
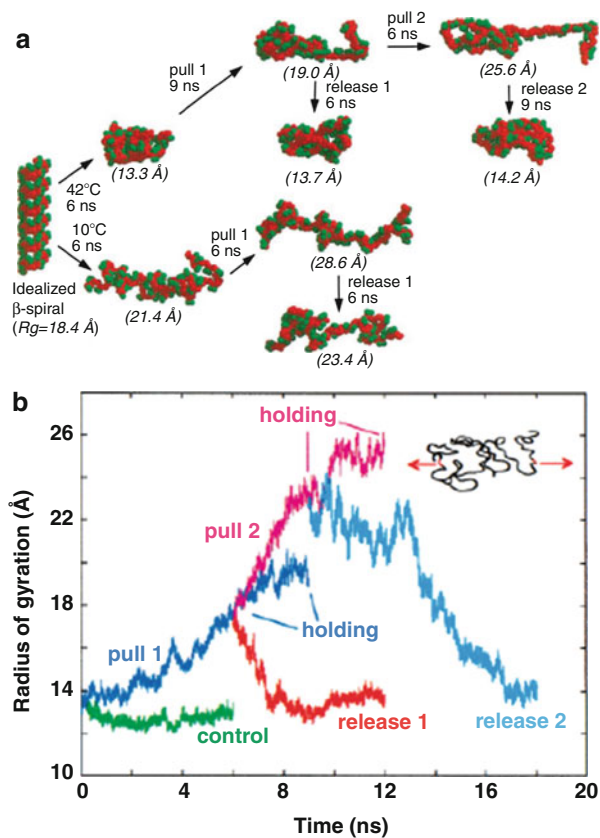
The second alternative idea was suggested by Gosline [20] proposing that the hydrophobic effect guided protein-water interactions, accounting for elastin's elasticity. Wasserman studied elastin-like polypeptide $(VPGVG)_{18}$, concluding that hydrophobic interactions in the initial regimes of elastic stretching contribute to elastin entropy at low extensions, but that librational mechanisms are more significant at longer extensions [21]. Further studies have since yielded further evidence against the original classic rubber elasticity proposal. Li et al. carried out MD simulations in explicit water for the same elastin-like polypeptide $(VPGVG)_{18}$ but with longer trajectory lengths, at two different temperatures, 10 °C and 42 °C (Fig. 28.5a) [22]. They found that the extended state of the peptide at both temperatures had a large solvent-accessible surface area and a low number of hydrophobic contacts in the extended state. Upon release, the surface area and the number of hydration waters decreased, while the number of interchain contacts increased (Fig. 28.5b). Their finding suggested that the orientational entropy of the water, rather than the number of main-chain polar hydration waters as well as the release of hydration waters, is responsible for the

elasticity of the system. Altogether, these studies point to a dual entropic effect to describe elastin's elasticity: a combination of the hydrophobic entropic effect and a librational entropic effect [19, 21–26].

Inverse Temperature Transition of Elastin

Another fundamental property of elastin and elastin-like peptides (ELPs) is its propensity to fold to a more stable configuration with higher temperatures, an effect termed an inverse temperature transition (ITT) [1]. Several studies have observed filament formation in aqueous solution upon increasing temperature in elastin fragments and in ELPs [27, 28]. From these observations, elastin and ELPs have been suggested as effective candidates for "biomolecular machines," converting chemical, electrical, and particularly thermal signals into other forms of energy, such as reversible contraction [29].

Several computational studies have looked at elastin's ITT. Li et al. studied the ITT using the elastin-like polypeptide, $(VPGVG)_{18}$, considering dynamics at seven temperatures ranging from 7 °C to 42 °C (Fig. 28.6a) [30]. At higher temperatures solvent-accessible surface area of the polypeptide and the number of hydration

10 °C, 6 ns MD

Idealized β-spiral $(VPGVG)_{18}$

42 °C, 6 ns MD
Expelled waters in magenta
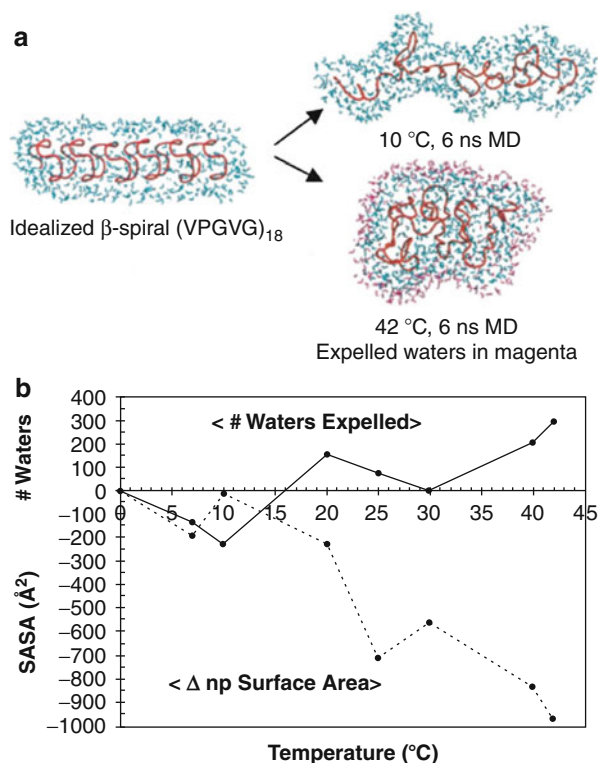
Fig. 28.6 (**a**) Conformational change resulting from an inverse temperature transition. 6 ns trajectories are recorded for the same starting structure at temperatures of 10 °C and 42 °C. (**b**) The number of expelled waters increases, while the surface area exposed to hydration decreases as temperature increases beyond the transition temperature (Reprinted from the Journal of Molecular Biology, Li, B., D.O. Alonso, and V. Daggett, *The molecular basis for the inverse temperature transition of elastin*, 2001. **305**(3): p. 581–92 with permission from Elsevier [30])

waters decreased, while intra-chain contacts increased, as had been observed in the released state of the polypeptide following extension in elasticity studies (Fig. 28.6b).

Marx et al. considered the elastin-like octapeptide GVG(VPGVG), finding a two-state system near the transition temperature [31]. They showed that at low temperatures, strong peptide/water interactions stabilize open conformations, while an increase in temperature above transition decreases the stability of the extended state but has less effect on the folded conformation. The folded conformation is stabilized by intermolecular hydrogen bonds as well as by an entropic increase in backbone fluctuation, though eventually the highly dynamic system unfolds at still higher temperatures [31].

Based on elastin's unique inverse temperature transition, several studies have explored the effect of directly manipulating elastin-like polypeptides to probe their capacity to act as molecular switch systems [1]. MD simulations of wild-type chymotrypsin inhibitor 2 (CI2) and variants containing elastin-like turns were performed at 10 °C and 40 °C, with a result yielding wild-type CI2 that was more stable at 10 °C, while both of the variant forms were more stable at 40 °C [23]. This suggests that elastin-like peptides could be used to stabilize target proteins, for example. Arkin and Bilsel [32, 33] considered the effects of single-residue substitutions in the elastin-like sequence VPGXG as well as the polypeptide length as a governing factor influencing the transition temperature. They found that the ITT was highly dependent on residue specificity and polypeptide length, identifying switchable parameters for tuning materials. These studies confirm the validity and applicability of the unique quality of elastin to undergo an inverse temperature transition, opening an important new direction in material design to create controllably mutable elastin-based materials.

Collagen

Structure of Collagen Molecules

Collagen is the most abundant protein in the vertebrate and, like elastin, the basic component of connective tissues. It provides mechanical strength and biological functions for connective tissues [34–37]. A collagen molecule consists of three chains stacked alongside forming a triple helix structure, as shown in Fig. 28.7. Each chain of a collagen molecule consists of amino acids and has a characteristic repeating sequence of $(Gly\text{-}X\text{-}Y)_n$. The spheres in Fig. 28.7 represent the alpha-carbon atoms of Gly residues, which are mostly located within the center of a collagen molecule. The triple helix structure is stabilized by hydrogen bonds between each chain. About 28 types of collagen have been identified while type I collagen, which is found in tendon, skin, teeth, cornea, and bone, is the most abundant collagen in the human body. A type I collagen molecule has a length of about 300 nm with a radius of approximately 1.6 nm.
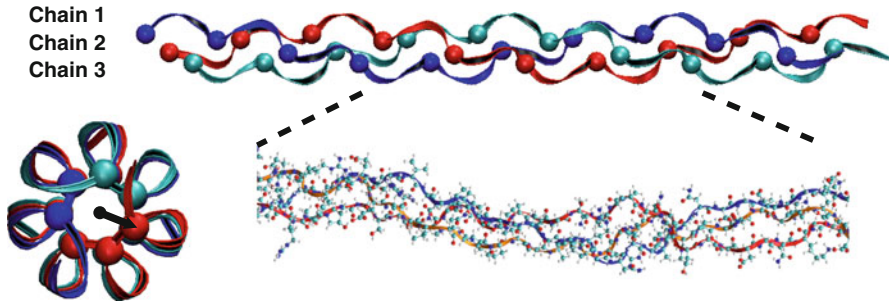
Fig. 28.7 Molecular structure of a collagen molecule, which consists of three chains forming a triple helix structure. Each chain is plotted with one color, and the spheres represent the alpha-carbon atoms of glycine residues. The collagen molecule has a characteristic sequence of $(Gly-X-Y)_n$. The triple helix structure is stabilized by interchain hydrogen bonds

The collagen molecule is a heterogeneous structure along its twisting axis due to the variation of amino acid sequence. The variation of sequence is crucial for varied biological functions along each segment of the collagen molecule. A collagen molecule has a varying unit height of ∼0.853 nm for imino-rich regions and ∼0.865 nm for amino-rich regions [38]. Triple helix builders, such as GENCOLLAGEN [39] and THeBuScr [40], have been developed recently to create idealized atomic coordinates by using sequence information of collagen. Variation of sequence also affects the thermal stability of local conformation of a collagen molecule. Persikov et al. have developed a thermal stability calculator for collagen based on experimental measurements [41]. Figure 28.8 shows examples of relative thermal stability profiles for full-length type I and type II collagen molecules. It identifies a nonuniform distribution of thermal stability along the entire length of the molecule. The highest thermal stability are found at the N- and C-terminals, which impacts the mechanical and biological properties. For example, the two regions with low stability in the type I collagen molecule (indicated by arrows in the figure) are identified to be the cross-linking sites.

Hierarchical Structure of Collagen-Based Tissues

Collagen molecules are the basic building blocks of connective tissue, having a hierarchical structure as illustrated in Fig. 28.9. Collagen molecules, produced by cells, are stacked together in a characteristic *D*-period to form collagen fibrils which have diameters of ∼100 nm. Collagen fibrils are the basic components of collagen fiber which forms connective tissues. The orientation of collagen fibrils varies in different connective tissues to provide particular mechanical and biological functions. In tendon and bone, collagen fibrils align mostly parallel
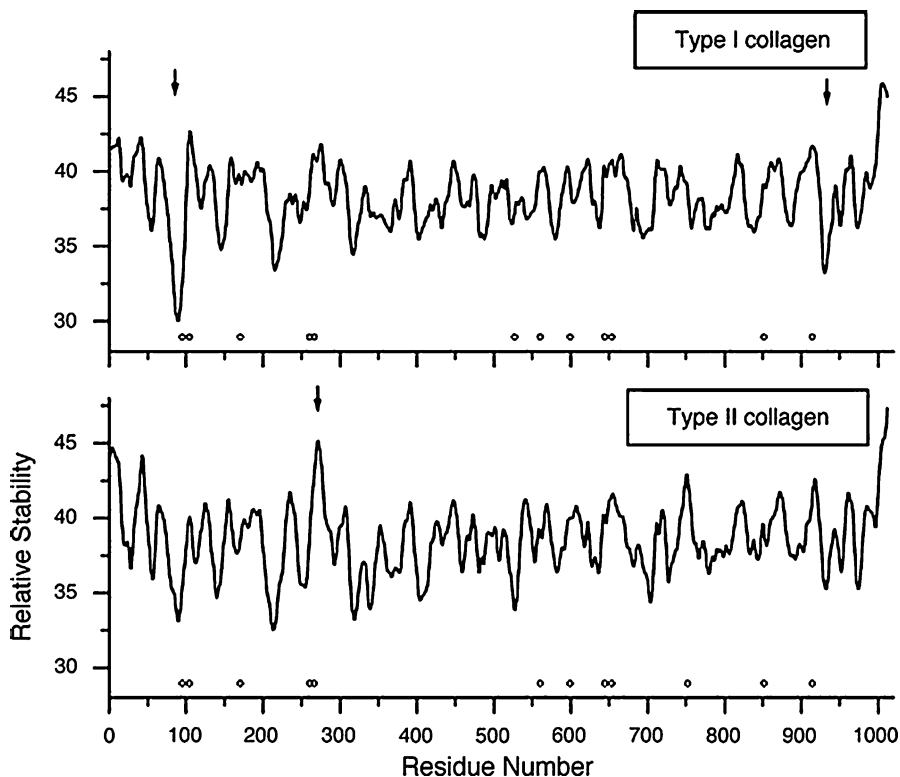
Fig. 28.8 Calculated relative thermal stability of type I and type II collagen along the twisting axis. Collagen molecule is a heterogeneous material along its length. The variation of sequence impacts its material and biological properties (Reprinted from [41] with permission)

to each other to provide mechanical strength in the axial direction of the tissue. In the cornea, collagen fibrils align radially to form a membrane structure. Alignment also varies across animals species to provide specific biomechanical properties [42].

Structure of the Collagen Fibril

Recently, the in situ structure of the full-length type I collagen fibril (Protein Data Bank identification code 3HR2) has been revealed [43], as shown in Fig. 28.10. The collagen fibril has a triclinic unit cell with dimensions $a \sim 40.0$ Å, $b \sim 27.0$ Å, $c \sim 678$ Å, $\alpha \approx 89.2^{\circ}$, $\beta \approx 94.6^{\circ}$, $\gamma \approx 105.6^{\circ}$. A fibril has a gap region with a length of 0.54 D and an overlap region with a length of 0.46 D (Fig. 28.10). Here D (~ 67 nm) denotes the length of the D-period of collagen fibril. Overlap and gap regions have different biological properties. The cell interaction domain of
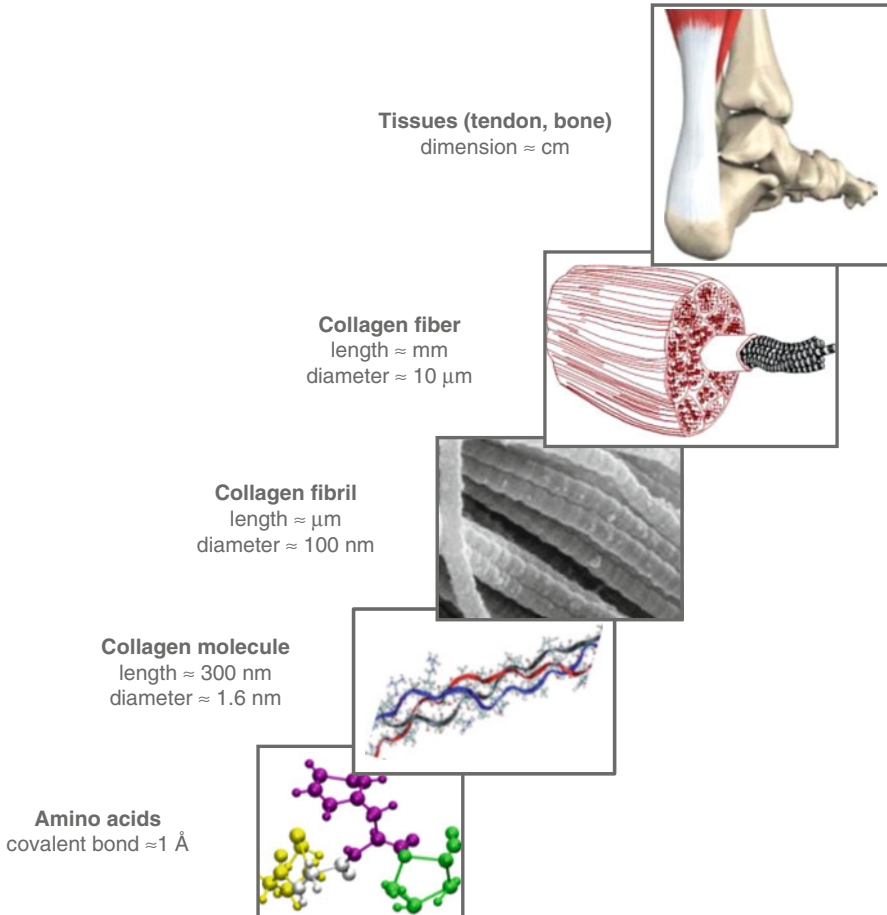
Fig. 28.9 Hierarchical structure of collagenous tissues, from the atomistic level to the tissue level. Collagen molecules pack to form collagen fibrils with diameter of ∼100 nm. Connective tissues such as tendon and bone consist of collagen fibers, formed by bundles of collagen fibrils (Reprinted with permission from Gautieri, A., et al., *Hierarchical structure and nanomechanics of collagen microfibrils from the atomistic scale up*. Nano Letters, 2011. **11**(2): p. 757–66. Copyright 2011 American Chemical Society)

collagen has been linked to the overlap region, while tissue mineralization occurs in the gap region [44]. The length of the *D*-period of the collagen fibril has slightly different values for different tissues. The *D*-period is about 67 nm for tendon and bone which contains primarily type I collagen. Skin, which contains about 15 % type III and 85 % type I collagen, has been shown to have a slightly shorter *D*-period of ∼65 nm [45–47].
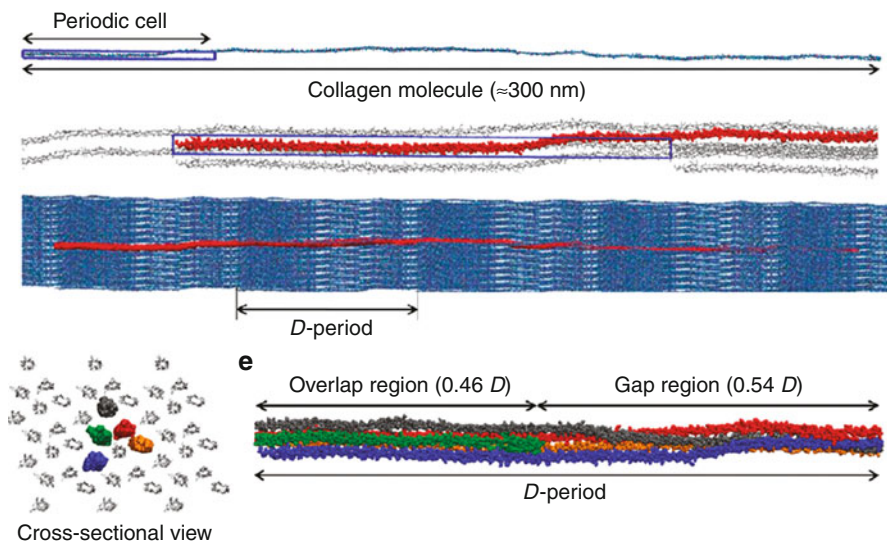
Fig. 28.10 A periodic cell of a collagen fibril model. Collagen molecules packing in a specific arrangement form a *D*-period of ∼67 nm, which contains an overlap region and a gap region. The in situ structure of full-length type I collagen fibril is revealed by Orgel et al. [72]. The figure shows a full atomistic model of human collagen fibril, which is reprinted with permission from Gautieri, A., et al., *Hierarchical structure and nanomechanics of collagen microfibrils from the atomistic scale up*. Nano Letters, 2011. **11**(2): p. 757–66. Copyright 2011 American Chemical Society

Collagen Mechanics

Mechanical Properties of a Single Collagen Molecule

A typical force-displacement curve of a single collagen molecule is shown in Fig. 28.11. For mechanical forces below 14 pN, a collagen molecule is flexible and behaves in a worm-like chain behavior [48–50]. This is the entropic elasticity regime of a collagen molecule, where the molecule exhibits large strain which may play a role in cell signaling. Collagen molecules have persistence lengths in the range of 10–15 nm, depending on collagen type. Mechanical tests using optical tweezers have shown a persistence length of 14.5 ± 0.73 nm for type I collagen [51] and a persistence length of 11.2 ± 8.4 nm for type II collagen [49]. Atomistic simulations have predicted a similar range of the persistence length of collagen [50, 52]. Although the worm-like chain model can describe the force-displacement curve of a collagen molecule quite well overall, the collagen molecule is known to feature nonuniform deformation throughout its length due to the variations of sequence.

The mechanical properties of a collagen molecule vary along its twisting axis, and the local conformations are known to change and have different biological functions [44]. There exist micro-unfolding regions in a collagen
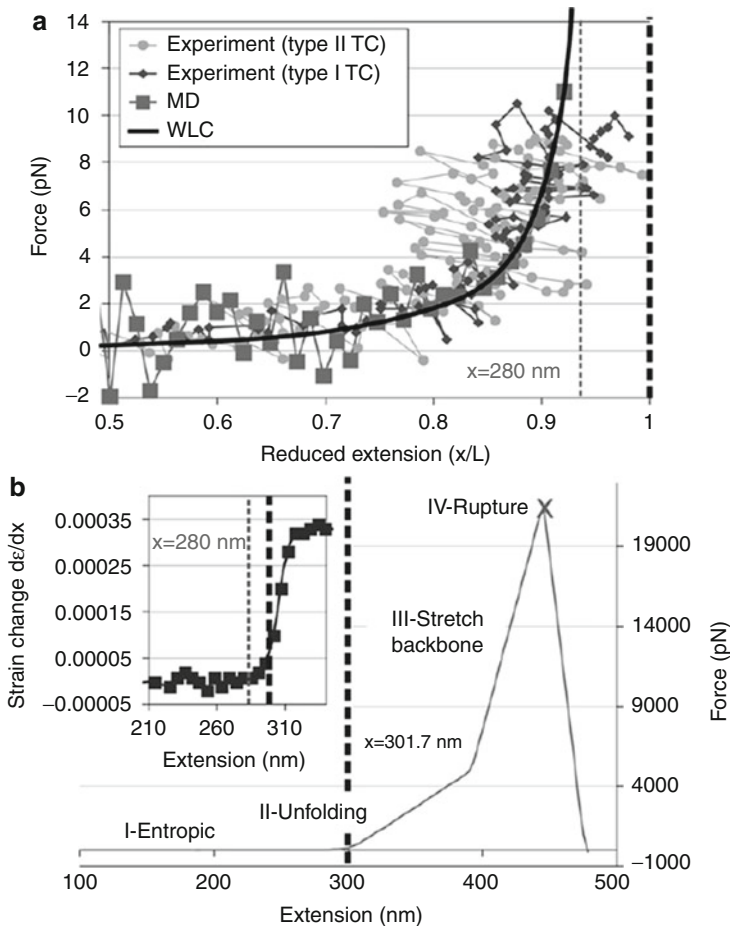
Fig. 28.11 Mechanical response of a single collagen molecule. When exposed to a mechanical force below ∼14 pN, the collagen molecule behaves like a flexible worm-like chain with a persistence length of ∼10–15 nm. This is the entropic elasticity regime of a collagen molecule. When mechanical force is larger than ∼14 pN, there are three regimes in a force-displacement curve of a collagen molecule. The collagen molecule is uncurling first followed by stretching backbone covalent bonds and then rupture (Reprinted from Biophysical Journal, Buehler, M.J. and S.Y. Wong, *Entropic Elasticity Controls Nanomechanics of Single Tropocollagen Molecules.*, 2007. **93**(1): p. 37–43., Copyright 2007, with permission from Elsevier [50])

molecule [52–54]. Micro-unfolding regions are thought to be important for biological functions such as collagen degradation. When a collagen molecule is stretched in the entropic elasticity regime, the mechanical force induces larger deformations in the micro-unfolding regions (as they are softer), while only inducing small deformation for regions that have higher thermal stability [53]. The mechanical response of a collagen molecule in the entropic elasticity regime is likely relevant

for its biological functions. For example, recent studies have shown that low mechanical force in the order of pN is sufficient to alter the collagen degradation rate greatly [55–57].

Once a collagen molecule is pulled out of the entropic elasticity regime, there are three other regimes [50]. Firstly, the collagen molecule undergoes uncurling through its entire length. In this regime, the collagen molecule is likely to feature a more uniform strain distribution since micro-unfolding regions have already been stretched [53]. Earlier experimental and computational studies revealed that the Young's modulus of a collagen molecule is in the range of 3–9 GPa [51, 53, 58–62]. Further stretching a collagen molecule will induce stretching of the backbone of each chain, resulting in a markedly stiffer response. In the last regime, a collagen molecule is ruptured if it is deformed beyond its strength.

Mechanical Properties of Collagen Fibrils

The mechanical response of collagen fibrils is distinct from collagen molecules. The mechanical features of a collagen microfibril obtained from a molecular model are shown in Fig. 28.12. For a hydrated collagen fibril, two regimes have been

Fig. 28.12 (a) Mechanical response of a hydrated and dehydrated collagen fibril. A dehydrated collagen fibril has a linear stress–strain curve, while a hydrated collagen fibril has two regimes. In the first regime of a hydrated collagen, the collagen fibril exhibits nonlinear relations, while in the second regime, the collagen fibril, it is stiffer and has a linear stress–strain relation. (b) Young's modulus of single collagen molecules and collagen fibrils obtained from various experimental and computational studies (Reprinted with permission from Gautieri, A., et al., *Hierarchical structure and nanomechanics of collagen microfibrils from the atomistic scale up*. Nano Letters, 2011. **11**(2): p. 757–66. Copyright 2011 American Chemical Society)
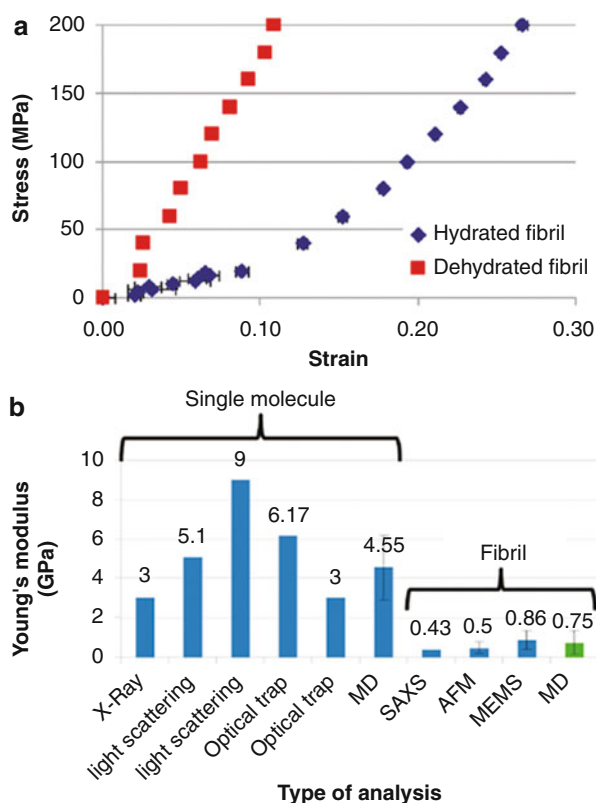
identified in the stress–strain curve. In the first regime (strain below ∼10 % and stress below ∼50 MPa), the collagen fibril has a nonlinear and softer mechanical response. The end-to-end distance of a collagen molecule within the fibril is increased in this region, which suggests that the micro-unfolding domains are stretched. The extensibility of a collagen fibril in this regime is important for cell-matrix interactions and for many biological functions. Once the stress in a collagen fibril reaches ∼50 MPa, the end-to-end distance of a collagen molecule reaches its contour length, indicating that it has been straightened. Atomistic simulations have revealed that the straightening of a collagen molecule happens primary in the gap region [62]. Beyond this point, the stress–strain curve of a collagen fibril enters the second regime which has a linear behavior. Because the collagen molecule has been straightened, the collagen fibril becomes stiffer in this regime (Fig. 28.12).

A hydrated collagen fibril has a Young's modulus of ∼300 MPa at small strain and a modulus of ∼1.2 GPa at large strain [62], while a dehydrated fibril has a larger modulus of ∼2 GPa independent of the applied stress. Figure 28.12b shows values of the Young's modulus of collagen molecules and fibrils from various experimental studies and molecular simulations. A collagen fibril has been found to have a smaller modulus ∼0.4–0.9 GPa compared with a single collagen molecule, which features a modulus ∼3–9 GPa. These data suggest a strong scale and environment dependence of collagen properties.

Mutations and Diseases in Collagen-Based Tissues

Single-residue mutations in collagen molecules have been identified and associated with various diseases. For example, *osteogenesis imperfecta* (OI), which is known as brittle bone disease, is a rare genetic disorder of collagenous tissues. The OI mutation is caused primarily by a replacement of the Gly residue in the repeating $(Gly-X-Y)_n$ triplets. In brittle bone disease, mutations at a single-molecule level alter the material properties of collagenous tissue at macroscale. As of now, several mutation locations and types along the entire collagen molecule have been identified and classified into severe, moderate, and mild disease conditions, as shown in Fig. 28.13 [63].

Although it remains unclear how a mutation of a collagen molecule could lead to a change in the material property of collagenous tissues, recent studies have revealed that mutations in the molecule cause changes in its structure and mechanical properties [64] at the molecular level. The OI mutations are found to disrupt the triple helix structure of the collagen molecule in the vicinity of the mutation. The unfolding of the triple helix structure at the mutation site results from the disruption of interchain hydrogen bonds. The severity of structure disruption is found to depend on mutation phenotype (Fig. 28.14).
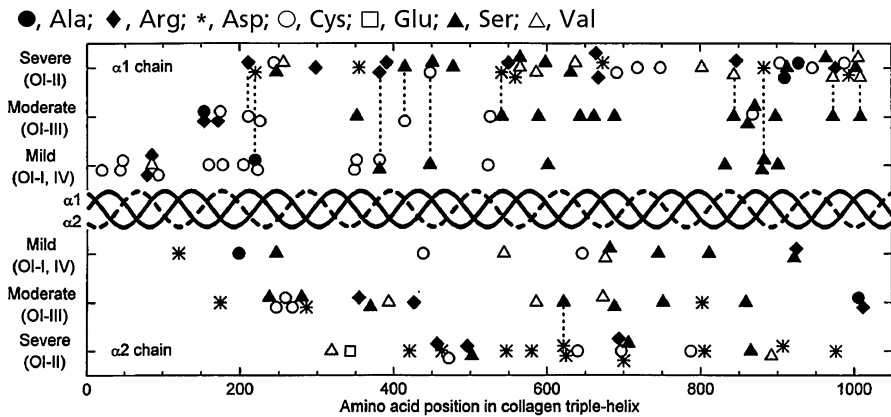
Fig. 28.13 Mutations throughout the entire type I collagen molecule which have be identified to cause severe, moderate, and mild OI (Reprinted from [63], Copyright (2000) National Academy of Sciences, U.S.A.)

There is a strong correlation with the severity of the phenotype and the interchain distance at energy minimum. Experimental studies have shown that the severity of the phenotype can be correlated to the decrease of melting temperature of the collagen molecule, indicating that the reduction of thermal stability caused by the OI mutation is a critical aspect to understand brittle bone disease. The OI mutations have also been shown to cause reductions in the Young's modulus of collagen molecules [65].

The change in the chemical composition of collagen molecules not only affects the properties at the single collagen molecule level (Fig. 28.14) but also alters the properties of collagen tissues. The *osteogenesis imperfecta* mouse model, *oim*, is also caused by mutations in the collagen molecule. In the case of *oim* mutations, the alpha-2 chain of the collagen molecule is replaced by an alpha-1 chain, resulting in a homotrimer molecule. Experimental studies of *oim* mice bone and tendon have shown reduced mechanical strength compared to normal mice. As shown in Fig. 28.15a, material properties of 1-year-old mice have been measured to examine the severity of phenotype [66]. The *oim/oim* mice are found to have significant reductions of their failure torque and torsional stiffness compared with normal bone. On the other hand, experimental studies of mouse tail tendon have shown that the *oim* mouse fiber from tail tendon has a higher denaturation temperature compared with normal mice (Fig. 28.15b) [67], indicating that the mutation alters the packing of collagen molecules. These data suggests that the material properties of collagen molecules, which are controlled by their chemical compositions, have a great impact on larger-scale structure and mechanical properties of collagen-based tissues.

Fig. 28.14 Atomistic simulations on the structural alterations causing by OI mutations. (*Panel a*) shows the atomistic simulation model. (*Panel b*) shows the selected mutation site. (*Panel c*) shows the mutation types which have been studied. The figure on the *right* shows the correlation between OI phenotype and collagen unfolding (Reprinted from [64])
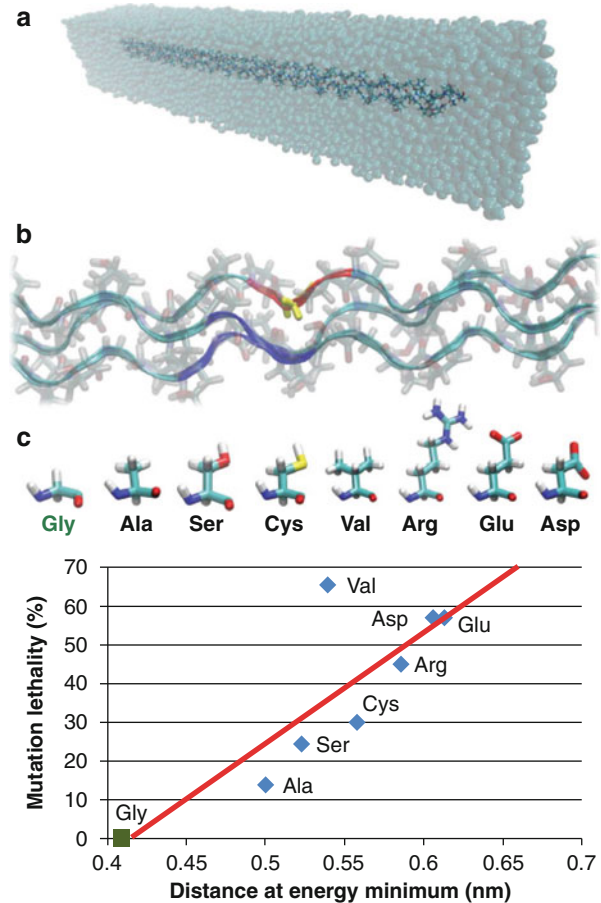
Conclusions and Applications

The structure, superb mechanical properties, and unique biological properties of elastin and collagen proteins make them distinctive biomaterials. Applications of elastin-based and collagen-based biomaterials are numerous. Elastin can be used to create tunable electrospun elastin fiber scaffolds for large-scale tissue repair; elastin hydrogels are ideal for creating biodegradable matrices for drug delivery; elastin-based synthetic fibers can be used as prototypes for tissue engineering and artificial arteries [4]. Elastin-based tissue replacements are in high demand as elastin's low thrombogenicity, capacity for favorable cell interactions, and blood compatibility make it an ideal candidate for dermal and vascular substitutes for tissue regeneration [68]. Artificial collagen-based materials hold great opportunity in many biological and pathological applications [69]. For example, collagen sponges have been used to improve in vitro growth of many types of tissue. A molecular level
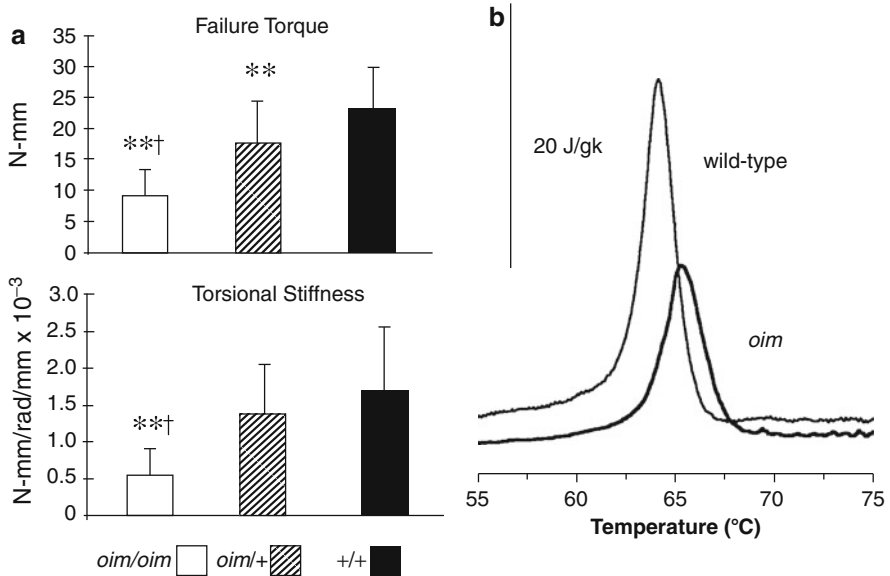
Fig. 28.15 (**a**) Failure torque and torsional stiffness of bone from *oim* and normal mice (Reprinted from [66] with permission). (**b**) Thermograms of tail tendon of wild-type and *oim* mice in water. The *oim* mice fibers have higher denaturation temperature, indicating that the mutation alters the packing of collagen molecules (Reprinted from *J. Mol. Biol.*, Miles, C.A., et al., The role of alpha2 chain in the stabilization of the collagen type I heterotrimer: a study of the type I homotrimer in oim mouse tissues, 2002. **321**: p. 797–805., Copyright 2002, with permission from Elsevier [67])

understanding, with the help of computational studies of these outstanding functionalities, holds great promise for tissue engineering applications and development of new, nature-inspired biomaterials, even surpassing material properties of elastin and collagen.

References

1. Tarakanova A, Buehler MJ (2013) Molecular modeling of protein materials: case study of elastin. Modelling and Simulation in Materials Science and Engineering 21(6):063001
2. Rosenbloom J et al (1995) Structure of the elastin gene. Ciba Foundation Symposium 192: The Molecular Biology and Pathology of Elastic Tissues 59–80
3. Debelle L, Alix AJP (1999) The structures of elastins and their function. Biochimie 81(10):981–994
4. Wise SG, Mithieux SM, Weiss AS (2009) Engineered tropoelastin and elastin-based biomaterials. Adv Protein Chem Struct Biol 78:1–24
5. Muiznieks LD, Weiss AS, Keeley FW (2010) Structural disorder and dynamics of elastin. Biochem Cell Biol Biochim Biol Cell 88(2):239–250
6. Kozel BA et al (2006) Elastic fiber formation: a dynamic view of extracellular matrix assembly using timer reporters. J Cell Physiol 207(1):87–96

7. Baldock C et al (2011) Shape of tropoelastin, the highly extensible protein that controls human tissue elasticity. Proc Natl Acad Sci USA 108(11):4322–4327

8. Ushiki T (2002) Collagen fibers, reticular fibers and elastic fibers. A comprehensive understanding from a morphological viewpoint. Arch Histol Cytol 65(2):109–126

9. Pepe A, Bochiechio B, Tamburro AM (2007) Supramolecular organization of elastin and elastin-related nanostructured biopolymers. Nanomedicine 2(2):203–218

10. Kewley MA, Steven FS, Williams G (1977) Presence of fine elastin fibrils within elastin fiber observed by scanning electron-microscopy. J Anat 123:129–134

11. Koenders MMJF et al (2009) Microscale mechanical properties of single elastic fibers: the role of fibrillin-microfibrils. Biomaterials 30(13):2425–2432

12. Lillie MA, David GJ, Gosline JM (1998) Mechanical role of elastin-associated microfibrils in pig aortic elastic tissue. Connect Tissue Res 37(1–2):121–141

13. Sherebrin MH (1983) Mechanical anisotropy of purified elastin from the thoracic aorta of dog and sheep. Can J Phys Pharmacol 61(6):539–545

14. Aaron BB, Gosline JM (1981) Elastin as a random-network elastomer – a mechanical and optical analysis of single elastin fibers. Biopolymers 20(6):1247–1260

15. Hoeve CA, Flory PJ (1974) The elastic properties of elastin. Biopolymers 13(4):677–686

16. Hoeve CA, Flory PJ (1958) The elastic properties of elastin. J Am Chem Soc 80:6523–6526

17. Partridge SM (1962) Elastin. Adv Protein Chem 17:227–302

18. Urry DW, Venkatachalam CM (1983) A librational entropy mechanism for elastomers with repeating peptide sequences in helical array. Int J Quantum Chem 10:81–93

19. Chang DK, Urry DW (1988) Molecular dynamics calculations on relaxed and extended states of the polypentapei'tide of elastin. Chem Phys Lett 147(4):395–400

20. Gosline JM, Yew FF, Weisfogh T (1975) Reversible structural-changes in a hydrophobic protein, elastin, as indicated by fluorescence probe analysis. Biopolymers 14(9):1811–1826

21. Wasserman ZR, Salemme FR (1990) A molecular dynamics investigation of the elastomeric restoring force in elastin. Biopolymers 29:1613–1631

22. Li B, Daggett V (2001) Hydrophobic hydration is an important source of elasticity of elastin. J Am Chem Soc 123:11991–11998

23. Li B, Alonso DOV, Daggett V (2002) Stabilization of globular proteins via introduction of temperature-activated elastin-based switches. Structure 10(7):989–998

24. Huang JX et al (2012) On the inverse temperature transition and development of an entropic elastomeric force of the elastin mimetic peptide [LGGVG](3,7). J Chem Phys 136(8):085101

25. Rauscher S et al (2006) Proline and Glycine control protein self-organization into elastomeric or amyloid fibrils. Structure 14(11):1667–1676

26. Ma X et al (2012) Thermal hysteresis in the backbone and side-chain dynamics of the elastin mimetic peptide [VPGVG](3) by H-2 NMR. J Phys Chem B 116(1):555–564

27. Cox BA, Starcher BC, Urry DW (1973) Coacervation of α-elastin results in fiber formation. Biochim Biophys Acta 317:209–213

28. Urry DW (1988) Entropic elastic processes in protein mechanisms.1. elastic structure due to an inverse temperature transition and elasticity due to internal chain dynamics. J Protein Chem 7(1):1–34

29. Urry DW (1995) Elastic biomolecular machines. Sci Am 272(1):64–69

30. Li B, Alonso DO, Daggett V (2001) The molecular basis for the inverse temperature transition of elastin. J Mol Biol 305(3):581–592

31. Rousseau R et al (2004) Temperature-dependent conformational transitions and hydrogen-bond dynamics of the elastin-like octapeptide GVG(VPGVG): a molecular-dynamics study. Biophys J 86(3):1393–1407

32. Arkin H, Bilsel M (2010) Conformational transition in elastin polypeptide with different residue length. AIP Conf Proc 1203:1211–1216

33. Arkin H, Bilsel M (2009) Conformational transition in elastin polypeptide with different residue length. In: 7th international conference of the Balkan physical union, vols 1 and 2. 1203:1211–1216

34. Fratzl P (ed) (2008) Collagen: structure and mechanics. Springer, New York
35. Buehler MJ, Yung YC (2009) Deformation and failure of protein materials in physiologically extreme conditions and disease. Nat Mater 8(3):175–188
36. Rainey J, Wen C, Goh M (2002) Hierarchical assembly and the onset of banding in fibrous long spacing collagen revealed by atomic force microscopy. Matrix Biol 21(8):647–660
37. Eppell SJ et al (2006) Nano measurements with micro-devices: mechanical properties of hydrated collagen fibrils. J R Soc Interface 3(6):117–121
38. Rainey J, Goh M (2002) A statistically derived parameterization for the collagen triple-helix. Protein Sci 11(11):2748–2754
39. Huang CC et al (1998) The object technology framework: an object-oriented interface to molecular data and its application to collagen. Pac Symp Biocomput 349–361
40. Rainey J, Goh M (2004) An interactive triple-helical collagen builder. Bioinformatics 20(15):2458–2459
41. Persikov AV, Ramshaw JAM, Brodsky B (2005) Prediction of collagen stability from amino acid sequence. J Biol Chem 280(19):19343–19349
42. Boote C et al (2008) Collagen organization in the chicken cornea and structural alterations in the retinopathy, globe enlarged (rge) phenotype – an X-ray diffraction study. J Struct Biol 161(1):1–8
43. Orgel JPRO et al (2006) Microfibrillar structure of type I collagen in situ. Proc Natl Acad Sci 103(24):9001–9005
44. Sweeney SM et al (2008) Candidate cell and matrix interaction domains on the collagen fibril, the predominant protein of vertebrates. J Biol Chem 283(30):21187–21197
45. Brodsky B, Eikenberry EF, Cassidy K (1980) An unusual collagen periodicity in skin. Biochim Biophys Acta Protein Struct 621(1):162–166
46. Stinson RH, Sweeny PR (1980) Skin collagen has an unusual d-spacing. Biochim Biophys Acta Protein Struct 621(1):158–161
47. Gathercole LJ, Shah JS, Nave C (1987) Skin-tendon differences in collagen D-period are not geometric or stretch-related artefacts. Int J Biol Macromol 9(3):181–183
48. Sun YL, Luo ZP, An KN (2001) Stretching short biopolymers using optical tweezers. Biochem Biophys Res Commun 286(4):826–830
49. Sun YL et al (2004) Stretching type II collagen with optical tweezers. J Biomech 37(11):1665–1669
50. Buehler MJ, Wong SY (2007) Entropic elasticity controls nanomechanics of single tropocollagen molecules. Biophys J 93(1):37–43
51. Sun YL et al (2002) Direct quantification of the flexibility of type I collagen monomer. Biochem Biophys Res Commun 295(2):382–386
52. Chang S-W, Sandra J, Shefelbine SJ, Buehler MJ (2012) Structural and mechanical differences between collagen homo- and heterotrimers: relevance for the molecular origin of brittle bone disease. Biophys J 102(3):640–648
53. Chang S-W et al (2012) Molecular mechanism of force induced stabilization of collagen against enzymatic breakdown. Biomaterials 33(15):3852–3859
54. Bodian DL et al (2011) Molecular dynamics simulations of the full triple helical region of collagen type I provide an atomic scale view of the protein's regional heterogeneity. Pac Symp Biocomput 193–204
55. Adhikari AS, Chai J, Dunn AR (2011) Mechanical load induces a 100-fold increase in the rate of collagen proteolysis by MMP-1. J Am Chem Soc 133(6):1686–1689
56. Adhikari AS, Glassey E, Dunn AR (2012) Conformational dynamics accompanying the proteolytic degradation of trimeric collagen I by collagenases. J Am Chem Soc 134(32):13259–13265
57. Camp RJ et al (2011) Molecular mechanochemistry: low force switch slows enzymatic cleavage of human type I collagen monomer. J Am Chem Soc 133(11):4073–4078
58. Hofmann H et al (1984) Localization of flexible sites in thread-like molecules from electron-micrographs – comparison of interstitial, basement-membrane and intima collagens. J Mol Biol 172(3):325–343

59. Sasaki N, Odajima S (1996) Stress–strain curve and Young's modulus of a collagen molecule as determined by the X-ray diffraction technique. J Biomech 29(5):655–658
60. Cusack S, Miller A (1979) Determination of the elastic-constants of collagen by brillouin light-scattering. J Mol Biol 135(1):39–51
61. Harley R et al (1977) Phonons and elastic-moduli of collagen and muscle. Nature 267(5608):285–287
62. Gautieri A et al (2011) Hierarchical structure and nanomechanics of collagen microfibrils from the atomistic scale up. Nano Lett 11(2):757–766
63. Beck K et al (2000) Destabilization of osteogenesis imperfecta collagen-like model peptides correlates with the identity of the residue replacing glycine. Proc Natl Acad Sci 97(8):4273–4278
64. Gautieri A et al (2012) Osteogenesis imperfecta mutations lead to local tropocollagen unfolding and disruption of H-bond network. RSC Advances 2(9):3890–3896
65. Gautieri A et al (2009) Molecular and mesoscale mechanisms of osteogenesis imperfecta disease in collagen fibrils. Biophys J 97(3):857–865
66. Camacho NP et al (1999) The material basis for reduced mechanical properties in oim mice bones. J Bone Miner Res 14(2):264–272
67. Miles CA et al (2002) The role of alpha2 chain in the stabilization of the collagen type I heterotrimer: a study of the type I homotrimer in oim mouse tissues. J Mol Biol 321:797–805
68. Waterhouse A et al (2011) Elastin as a nonthrombogenic biomaterial. Tissue Engr Part B-Rev 17(2):93–99
69. Glowacki J, Mizuno S (2008) Collagen scaffolds for tissue engineering. Biopolymers 89(5):338–344
70. Wise SG et al (2005) Specificity in the coacervation of tropoelastin: solvent exposed lysines. J Struct Biol 149(3):273–281
71. Tarakanova A, Weiss A, Buehler MJ (2013) Elastic network model of tropoelastin implicated bridge region in assembly and cell-binding (In Preparation)
72. Orgel JPRO et al (2006) Microfibrillar structure of type I collagen in situ. Proc Natl Acad Sci USA 103(24):9001–9005

Handbook of Nanomaterials Properties: Siliceous Nanobiomaterials

29

Wei Han, Linnea K. Ista, Gautam Gupta, Linying Li, James M. Harris, and Gabriel P. López

---

Keywords

Silica • Hybrid material • Encapsulation • Biomimetic • Bionanomaterial • Nanobiomaterial

---

Introduction

In the scope of silica materials across the breadth of research and technology, perhaps one of the most active and exciting research areas is that of siliceous nanobiomaterials – materials forged at the interface of silica and biomaterials that give rise to and augment a multitude of biotechnological applications. In the development of these hybrid silica nanomaterials, taking cues from both the short term in early silica research to the long term in nature itself itself, the main rationale

---

W. Han (✉) • L. Li • J.M. Harris
NSF Research Triangle Materials Research Science and Engineering Center, Durham, NC, USA

Department of Biomedical Engineering, Duke University, Durham, NC, USA
e-mail: wei.han@duke.edu

L.K. Ista
Center for Biomedical Engineering, Department of Chemical and Nuclear Engineering, University of New Mexico, Albuquerque, NM, USA

G. Gupta
Center for Integrated Nanotechnologies, Los Alamos National Laboratory, Los Alamos, NM, USA

G.P. López
NSF Research Triangle Materials Research Science and Engineering Center, Durham, NC, USA

Department of Biomedical Engineering, Duke University, Durham, NC, USA

Department of Mechanical Engineering and Materials Science, Duke University, Durham, NC, USA
e-mail: gabriel.lopez@duke.edu

for the application of silica has been to enhance functionality through the adaptation and exploitation of properties inherent to silica materials and chemistry. In fact, siliceous nanobiomaterials are not a human creation: Silica interactions with cells and other biological entities are ancient and ubiquitous. Stromatolites, Earth's earliest fossils, consist of bacteria within silica-containing mineral matrices as an early example of biomineralization. Even today diatoms and radiolarian sponges employ silica shells for protection. Incorporation of siliceous components within nanobiomaterials has mainly been motivated by properties and attributes of silica that have made it a valuable research tool for decades. Silica is readily formed by hydrolysis and condensation of simple silicate precursors (e.g., tetramethyl orthosilicate, TMOS, and tetraethyl orthosilicate, TEOS). In addition, silica materials can be tuned in size, porosity, and pore size by controlling reaction rates and chemistries. Silica also provides good mechanical strength while being compatible for biological applications. Lastly, silica and its precursors are relatively inexpensive materials and provide for ease of production and scale-up.

In order to provide a fair introduction to the material covered within this chapter, it is necessary to also provide definitions for common terms within this topic. Siliceous materials are defined as those that are composed of, incorporate, or are derived from silica. Biomaterials, encompassing a wide range of materials, can be defined as naturally derived materials as well as materials found to be compatible for biological applications. The latter includes a wide array of synthetic components such as metals, polymers, and other nonbiological molecules, particularly those used in biotechnological or medical applications. Finally, we define siliceous nanobiomaterials as materials incorporating silica and containing features on the nanoscopic scale for biotechnological applications; for example, these can include nanoscopic particles of various constructs, materials containing nanoscopic porosity, ultrathin films, and hybrid nanocomposite materials.

Within this chapter, we aim to cover areas of research within siliceous nanobiomaterials that provide innovative and interesting properties toward applications across many research fields. We begin by exploring the vast arena of surface modification of silica. In particular, modification of surface properties of silica nanoparticles has received much interest due to its applicability in biotechnological research. Next, we investigate enzymatic immobilization within silica matrices and onto silica surfaces. We move then to study siliceous biomineralization and biologically inspired silica hybrid nanobiomaterials, a particularly active research area of the past decade. Subsequently, we explore hybrid materials containing both silica and lipid bilayers. Finally, we cover siliceous encapsulation of living cells and tissues. While we do not pretend that the contents of this chapter encompass all silica nanomaterial research and technology, we trust the examples of material properties of siliceous nanobiomaterials will provide the reader with a general rationale of why these materials have been developed and analyzed, and why they are attractive in research applications today.

Surface Modification of Silica and Silica Nanoparticles

Throughout decades of research, numerous examples have shown that silanol groups on silica surfaces can facilitate easy surface modification with different functional groups for subsequent bioconjugation, greatly increasing their versatility. In addition, nanoparticles (NPs) have proven to be ideal biomolecular hosts, as they have large surface areas and can be easily suspended in aqueous solution. Silica NPs that have biological entities coupled to their surfaces can be used in biosensing, bioassays, enzymatic immobilization (see next section), and drug or gene delivery [1–5]. However, particle aggregation and nonspecific binding of biomolecules to NPs remain a challenge in developing these biofunctionalized silica NPs. Surface modification of silica NPs is usually performed to improve their colloidal properties, and to facilitate the immobilization of biomolecules. For instance, modifying NP surfaces with various functional groups (e.g., carboxylate, octadecyl, polyethylene glycol (PEG)) can increase the repulsive forces between the particles in solution [6, 7], and hence improve the dispersibility and stability of silica NPs, as well as provide the reaction sites for further bioconjugation [8–10]. This section will serve to highlight key examples of properties of silica nanomaterials that can be augmented through various surface modification methodologies.

Surface Modification Techniques

Surface modification of silica is often achieved via covalent conjugation, sol–gel processing, polymerization processes, self-assembly methods, physical absorption, or metal coatings. These methods aim to change surface charge, dispersibility, and wettability of silica materials and therefore avoid aggregation and increase specific binding capacity.

1. Sol–gel processes and organosilane coupling

   Silica NPs with various reactive groups can be produced by using different silane coupling reagents for cohydrolysis or post-coating [8, 10–13]. For instance, thiol-modified silica NPs were achieved by co-hydrolyzing organosilane (3-mercaptopropyl) trimethoxysilane (MPTMS) and TEOS [1]. Similarly amine-modified silica NPs were successfully prepared by acid-catalyzed sol–gel reactions of TEOS and 3-aminopropyl trimethoxysilane (APTMS) [14, 15]. An alternative method is to introduce the desired functional groups to silica surfaces via the treatment of organosilane compounds containing specific, desired groups. For example, silica particles were treated with (3-aminopropyl)-triethoxysilane (APTES) to obtain amine-modified surfaces [16]. After surface functionalization, biochemical-coupling reactions between suitable groups on particle surfaces and biomolecules can be used to tether biological entities to silica surfaces. Some common bioconjugation schemes are carbodiimide chemistry, disulfide-coupling chemistry, and succinimidyl ester hydrolysis chemistry (Fig. 29.1). For instance, thiol-modified NPs can be directly coupled to disulfide-modified oligonucleotides [17].
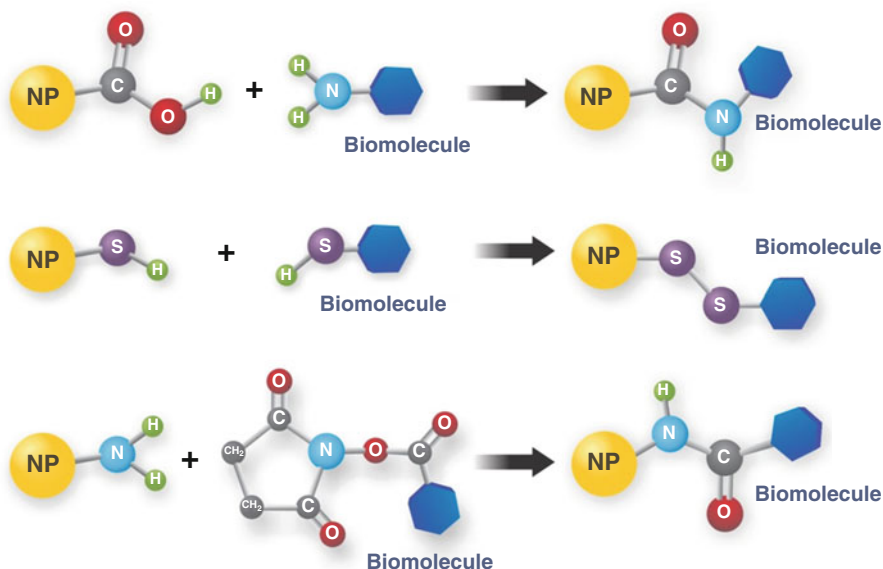
Fig. 29.1 Bioconjugation schemes for the biomolecules immobilization

2. Polymerization processes

   It has been shown that various polymers can be used to modify silica surfaces via polymerization for biomaterials applications, perhaps most notably to suppress protein absorption. A number of methods have been used to produce polymer-coated particles, including monomer adsorption onto particles followed by subsequent polymerization, heterocoagulation-polymerization, and emulsion polymerization [18]. Tsukagoshi et al. [19] have successfully prepared silica NPs with dense polymer chain layers using surface-initiated atom transfer radical polymerization (ATRP). These polymer-modified silica particles have demonstrated good resistance to protein adsorption. In addition, PEG-functionalized silica NPs showed improved biomolecule recognition efficiency and increased specific binding affinity [20].

3. Affinity interaction

   Biological moieties can also be attached to nanoparticle surfaces via affinity interaction. The interaction between phospholipid bilayer vesicles and silica nanoparticle surfaces can produce bilayer adsorption from vesicles onto silica surfaces, under certain experimental conditions that depend on temperature, pH, ionic strength, etc. [21, 22]. For instance, it has been demonstrated that, at low temperature, a low affinity exists between neutral phospholipids and silica surfaces; however, an increased affinity between silica and phospholipid bilayers can be achieved when Tris is used as the buffer, the pH is below 7.4, and the temperature is above the phase transition temperature for the phospholipid bilayer [23].
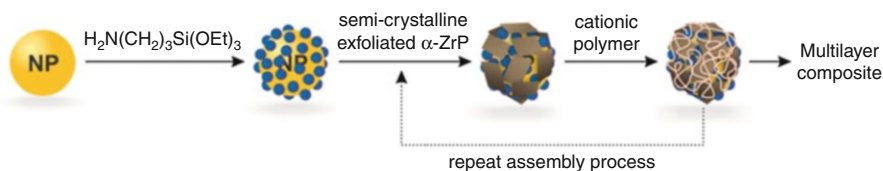
Fig. 29.2 Schematic procedure for the preparation of the composite multilayers on silica particle surface (Figure adapted from [24])

Biomolecules and polyelectrolytes from solution can be deposited onto oppositely charged silica particle surfaces through electrostatic interactions. For instance, alternating adsorption of exfoliated zirconium phosphate sheets and charged polymer onto APTES-modified silica particles was reported by Keller et al. [24]. This self-assembly method is highly promising to fabricate composites with controllable composition and thickness (Fig. 29.2).

In addition, affinity interactions between silica surfaces and proteins that contain charged domains can also localize proteins onto silica surfaces. Several silica-binding proteins have recently been identified and used to target proteins onto silica substrates in a one-step process. For instance, the L2 protein-fusion [25] strongly binds to silica surfaces. Because most site-specific immobilization techniques of biomolecules mentioned above require pretreatment of silica surfaces by surface modification, proteins that contain silica-binding tags are highly desirable to simplify the surface modification process.

4. Metal coating strategies

Metal nanoshell composites have attracted intense interest due to their tunable optical properties. Oldenburg et al. [26] fabricated gold-coated silica particles via self-assembly of gold NPs onto amine-modified silica particle surfaces. By changing the relative sizes of the silica core and metal shell, these particles demonstrated an obvious optical resonance shift. Moreover, mesoporous silica nanoparticles (MSNs) modified with gadolinium complexes exhibited high magnetic resonance relaxivities, which can be used as highly efficient magnetic resonance imaging contrast agents [27].

Application of Surface-Modified Silica Nanomaterials

Bioconjugated silica NPs have been widely used in biomedical applications, such as biodetection as well as gene delivery. Silica NPs modified with DNA/RNA molecules have been widely exploited as probes for DNA hybridization detection and DNA bioassays [28]. Fluorescent silica NPs with high luminescence and photostability were designed and applied to increase the fluorescence signal and to enhance oligonucleotide detection sensitivity [28]. Sub-femtomolar concentration detection limits in DNA analytes have been achieved using a sandwich hybridization assay based on tetramethylrhodamine (TMR)-doped silica NPs [29].

In addition, immunoassays based on enzyme- or antibody-conjugated silica particles have also been developed; Lin et al. [30] reported a sandwich-type electrochemical immunoassay with poly(guanine)-functionalized silica NPs as labels of secondary antibodies. A sensitive and simple electrochemical immunoassay based on horseradish peroxidase (HRP)-doped silica particles has also been employed for the detection of human serum IgGs [31]. In addition, protein and nucleic acid-functionalized silica NPs have been widely used for the preparation of biosensors as labels for signal amplification and to improve detection sensitivity [32, 33]. For example, an H_2O_2 biosensor using HRP-encapsulated silica particles was constructed by Wang et al. [34]. Avidin/streptavidin has also been immobilized onto silica surface. The resulting avidin/streptavidin-coated silica particles can bind to biotinylated recognition molecules, like biotinylated glutamate dehydrogenase which is used as a biosensor for glutamate detection [35]. Biomolecule-conjugated silica NPs containing high intensity of dyes have also demonstrated good sensitivity and high specificity in protein microarray analysis. Dye-doped silica NPs have served as fluorescent labels for sensitive detection of protein biomarkers in protein microarrays [4, 11, 20]. For instance, tris(2,2'-bipyridyl)ruthenium(II) chloride hexahydrate (Rubpy) doped silica NPs modified with secondary anti-IL-6 antibodies were used to detect biomarker IL-6 in a protein microarray [11].

Surface-functionalized silica NPs have also shown significant promise as gene delivery carriers to deliver DNA into target cells or tissues [2], because of their low toxicity, high transfection efficiency, and good biocompatibility [36]. An efficient non-viral gene carrier based on cationic silica NPs was developed and applied to transfer DNA into plants [37] and mouse lungs [38]. Mesoporous silica nanoparticles are also attractive as effective gene therapy carriers due to the high uptake efficiencies by both animal and plant cells, and the ability to control release [3, 39].

In addition, silica NPs are also promising candidates for improved drug-delivery systems [2]. As with other applications, the rich breadth of silica chemistry allows for many manipulations to optimize the physiochemical property of silica NPs (e.g., surface charge, size, morphology), and hence to control the release rate, minimize opsonization, and increase blood circulation rate. Drug molecules can be either encapsulated within silica or covalently bound to the silica surface. Moreover, introduction of biorecognition entities to silica particle surfaces facilitates localized delivery and release of biomedical agents. For instance, modification with hydrophilic polymers, like PEG or polyethylene oxide (PEO) [40], can decrease the natural immune response. Wang et al. [21] fabricated PEGylated-phospholipid modified silica particles with superior solubility in phosphate-buffered saline and significantly lower nonspecific binding. These particles also exhibited an enhanced cellular uptake in cancer cells and no apparent cytotoxic effect in vivo.

Outlook

Silica nanomaterials allow easy and efficient surface modifications, as well as precise size and composition control, making it possible to obtain desirable

properties for a variety of biological applications. Future research will continue to optimize the property of existing silica conjugates, and to develop complex nanoparticle-incorporated biological systems for use in bioanalytical applications, biosensing, targeted therapeutics, and medical diagnostics.

Biomineralization and Biologically Inspired Silica Hybrid Materials

In the historical overview of siliceous nanomaterial research and knowledge, one of the most important sources of exploration and advancement has been through the study of biomineralization from living organisms. Through natural and evolutionary forces, numerous species of life on different orders of complexity have developed simple, rapid, and elegant techniques to synthesize silica from simple precursors [41–45]. In diatoms and sponges, two of the best characterized sources of biosilica, nanoscopically ornate silica deposits are driven through processes under biological conditions, including aqueous solvents, low temperatures and neutral pH [41, 42, 46–48] and leading to high interest and extensive research in the mechanisms for biosilica generation for the past decade. Indeed the discovery of biological entities such as proteins and peptides, and the biomimetic and biologically inspired synthetic molecules that have additionally come as a result of these works have allowed for the development of new materials with controllable composition, size, porosity, and formation rate with various applications [44].

Silaffins

Silaffins, or peptides with silica affinity, were first isolated by Kroger et al. [46] from the diatom *Cylindrotheca fusiformis*. Upon study of the cell walls of the diatom and isolation of numerous polypeptides, three heavily modified peptides were show to have the ability to precipitate silica from silicic acid: silaffin-1A, -1B, and -2. With further genomic analysis, silaffin-1A and -1B were determined to be processed forms of a larger precursor protein sil1p, containing seven homologous peptide sequences (R1–R7) with repeat positively charged lysine and arginine residues (Table 29.1).

Lysine residues were further posttranslationally modified with polyamines. A notable property of these isolated silaffin peptides is their ability to template the deposition of silica from precursors at a remarkable rate; clusters of spherical silica particles could be formed in sizes of up to 700 nm in diameter within a few minutes. In addition, the amount of silica is proportional to the concentration of silaffin added, allowing for another degree of potential control. Lastly, a synthetic version of the R5 peptide also precipitated silica with activity at neutral pH. The discoveries of this work led researchers to believe that the long-chain polyamine (LCPAs) modifications of silaffins play a key role in their silica-precipitating behavior and that synthetic and biomimetic fabrications could potentially be useful

Table 29.1 Silaffin peptides from *C. fusiformis*. Adapted from [46]

Peptide	Amino acid sequence
R1	SSKKSGSYYSYGTKKSGSYSGYSTKKSASRRIL
R2	SSKKSGSYSGYSTKKSGSRRIL
R3, R5, R7	SSKKSGSYSGSKGSKRRIL
R4, R6	SSKKSGSYSGSKGSKRRNL

for silica materials applications. In later work [49], it was also determined that the serines of silaffins were also posttranslationally modified with phosphate groups, imparting a zwitterionic nature to the peptides. Specifically, silaffin-1A, a peptide without phosphorylation, does not have the silica-precipitating characteristics when in a buffer without phosphate, while a fully modified silaffin maintains the property. Taken together, the evidence supported the conclusion that these peptides allowed for silica deposition through a self-assembly process [42, 49] in which electrostatic interactions allowed for a higher ordered structure of silaffins to form and upon which silica precursors condense.

In addition, properties of the formed silica were found to be controlled by another silaffin, silaffin-2 [50]. Unlike other silaffins, which had numerous positively charged long-chain polyamine modifications necessary for silica precipitation, silaffin-2 has numerous modifications that provide an anionic character, including residues with phosphate, sulfate, and glucuronic acid modifications. Reactions containing both silaffin-1A (or LCPAs) and silaffin-2 in differing proportions can control silica pore sizes from tens up to hundreds of nanometers [44, 50]; this is thought to be due to the interactions of the highly negative silaffin 2 occluding and interacting with the higher order assemblies from silaffin-1A. The findings of silaffins within *C. fusiformis* and their silica-precipitating abilities were also corroborated by silaffins found in *Thalassiosira pseudonana*, another diatom with ornate silica walls. In this work [51], researchers found that, although silaffins in *T. pseudonana* were not compositionally homologous to those in *C. fusiformis*, they maintain similar posttranslational modifications of lysines as well as phosphorylation modifications, and provide the same structural template for the condensation of silica. In addition, regulatory silaffins in both species are modified by sulfation and glycosylation.

The property of the silaffin peptides that causes the formation of silica from silicic acid precursors in a controlled and rapid manner has led to numerous applications, many employing the biomimetic R5 silaffin peptide. As discussed previously, encapsulation of enzymes and other biological entities within silica has been shown to confer numerous advantages, including stabilization and protection from adverse conditions [43, 44, 52–54]. By employing silaffin-inspired techniques such as co-incubating an enzyme with R5 silaffin [52] or concatenation of silaffin with enzyme at the genetic level [54], the resultant immobilized enzymes retained enzymatic activity while exhibiting significantly improved thermal stability. Lastly R5 has also been used in facile holographic patterning of silica [55].

Fig. 29.3 Scanning electron micrographs of (**a**) isolated silica spicules (×130) and (**b**) axial filaments (×1,000) from *Tethya aurantia* (Reprinted with permission from [47])
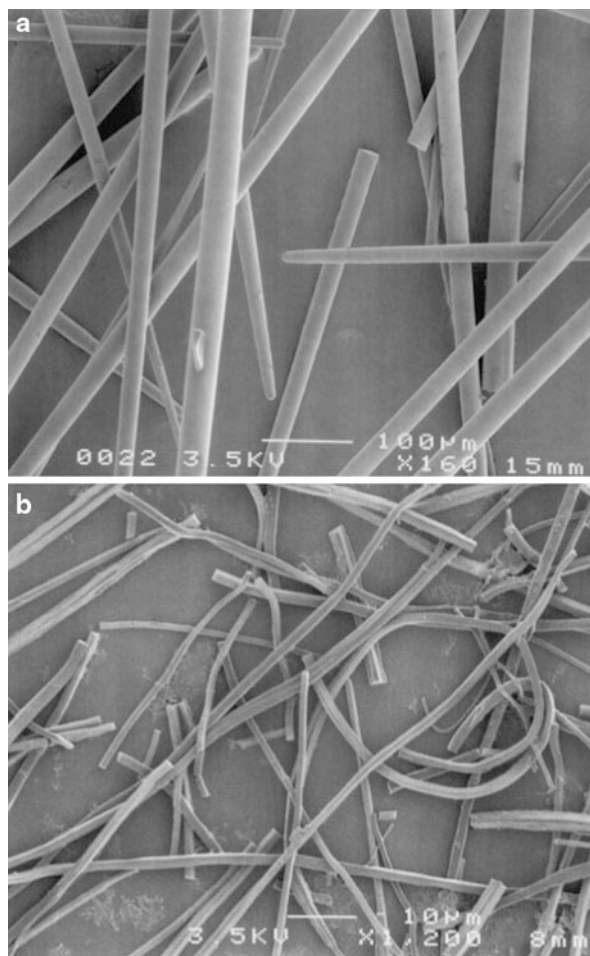
Silicateins

Silicateins, as the name suggests, are a class of proteins that have able to catalyze the formation of silica from silicic acid precursors first discovered in the spicules of the sea sponge *Tethya aurantia* [41, 43, 44, 47, 56]. The key distinction between silicateins and silaffins is that silicateins are proteins with demonstrated enzymatic activity for the polycondensation of silica, while silaffins only template the deposition of silica with favorable electrostatic interactions. The first isolation of the major fraction of the silicatein subunits, silicatein α, was performed by Shimizu et al. (Fig. 29.3) [47] and followed directly by the in vitro work of Cha et al. [56], who proposed an active site of serine, histidine, and asparagine. In addition, it was proposed that the mechanism for the catalyzed reaction occurs through an nucleo-philic attack of precursors such as tetraethoxysilane (TEOS) through the serine

hydroxyl and histidine imidazole groups (the asparagine acts to support and stabilize the intermediate products) [43, 56]. In addition, silicateins have also been isolated in other sponges, *Lubromirskia baicalensis and Suberites somuncula*, and show a large degree of homology, especially with respect to the active site and proposed enzymatic mechanism [57].

Due to the enzymatic nature of silicateins, many applications for this protein have stemmed from the ability to control the silica-precipitating activity and rate through concentration and amount of the enzyme. For instance, Rai and Perry [58] showed that silica film properties such as thickness, roughness, and contact angle are determined by silicatein pre-adsorption onto surfaces and can be controlled by degree of adsorption as well as reaction time. The coverage of silicatein on the surface was controlled by silicatein immobilization to a gold surface adsorbed with by either cystamine or cysteamine and through the cross-linking agent glutardialdehyde (GDA). While silicatein adsorbed nonspecifically and minimally to the gold surface or gold with either cystamine or cysteamine, the addition of glutardialdehyde provided a high level of surface coverage with silicateins. In addition, more silicatein was able to be loaded onto the gold-cystamine-glutardialdehyde surface. By ramping the concentration of adsorbed silicateins, ranging from 10 to 30 ng/cm^2, it was possible to linearly increase the thickness of silica film formed from 20 to over 90 nm, respectively, and also increase the average roughness from approximately 1 to greater than 5 nm, respectively. This work showed how silicateins can affect changes in silica film properties. In addition, silicateins have also been attributed to imbuing self-healing capabilities to silica materials [59]. As previously mentioned, silica encapsulation of enzymes retains enzymatic activity while providing stabilizing and protective forces for the encapsulated entity. Because silicatein itself is an enzyme, when entrapped in silica such as in sponge spicules or for any applications, the ability for silicatein to catalyze the formation of silica is prolonged significantly. These properties make silicatein an attractive potential partner for the formation of silica through biomineralization.

Outlook

The study of siliceous materials developed through biomineralization as well as biologically inspired methodologies has increased dramatically over the last decade or so. Novel strategies for the rapid and controlled formation of silica using mild conditions in pH, temperature, and solvent have allowed increased applications in areas such as drug delivery, biosensing, and fabrication of hybrid materials. By understanding further the processes and mechanisms under which these silica structures are formed, as well as taking advantages of the attractive features of biomimetic and biologically inspired strategies, these techniques have started to expand into many other areas of research, including complex biotechnological applications.

Lipid Bilayer–Based Hybrid Siliceous Nanomaterials

Cell membranes of almost all organisms are primarily composed of lipid bilayers (phospholipids, glycolipids and sterols) that are embedded with transmembrane proteins. These membranes act as a physical barrier between the cytoplasm and the extracellular environment and perform numerous functions including selective transport of solutes, cellular signaling, antibody recognition, and energy harvesting [60, 61]. High specificity of transmembrane proteins toward various solutes along with self-assembly properties of phospholipids has made them indispensible choice for numerous applications including drug delivery [62–65], biosensing for drug discovery, medical diagnosis and environmental monitoring [66], chemical and biological warfare agent sequestration [67], and actuator development [68]. However, to date, there has been a lack of realistic lipid-based sensors or devices primarily due to lack of stability of these fragile systems. Numerous technologies have been proposed to stabilize lipid bilayer systems including disaccharides such as trehalose [69, 70], PEG [71, 72], agarose [73], and sol-gels [74–81].

Encapsulation of biological entities such as enzymes, antibodies, and bacterial cells using sol–gel technologies has been well established and documented; however, the encapsulation of lipid bilayer–based systems (liposomes, planar lipid bilayers, and multi-lipid bilayers) as well as mammalian cells still remains in its infancy. This is primarily due to a lack of stability of the lipid bilayer under conventional sol–gel techniques that involve use of acids for hydrolysis and co-solvents such as ethanol and the strong interaction of silica with lipid-head groups. However, over last decade, several strategies have emerged that have successfully demonstrated the encapsulation of lipid-based systems using modified sol–gel routes, sodium silicate as precursor, and a chemical vapor deposition (CVD) route. Here, we will focus on the synthesis and functional properties of hybrid silica materials made using (a) liposomes (b) supported lipid bilayer, and multilayers. Before we investigate these hybrid materials in detail, a brief introduction to phospholipids and their properties is presented below. Phospholipids are amphipathic molecules that have a head group that is hydrophilic and a lipophilic tail that is hydrophobic in nature, as shown in Fig. 29.4a. In aqueous solution, lipids arrange in the form of a lipid bilayer ($\sim$5 nm in thickness), as shown in Fig. 29.4b, due to the hydrophobic effect. Unlike surfactants that tend to form micelles, lipids form bilayers due to their packing factor (g) of 1 [82, 83]:

$$g = v_c/a_0 l_c = 1 \text{ (for most phospholipids)}$$

where v_c = chain volume, a_0 = area of head group, l_c = critical chain length.

Liposome-Silica Hybrids

Liposomes, also known as lipid vesicles or protocells, are defined as closed lipid bilayer structures that have an aqueous compartment (Fig. 29.4b). They were discovered by Bangham et al. [84] in 1965 and have been explored for optical
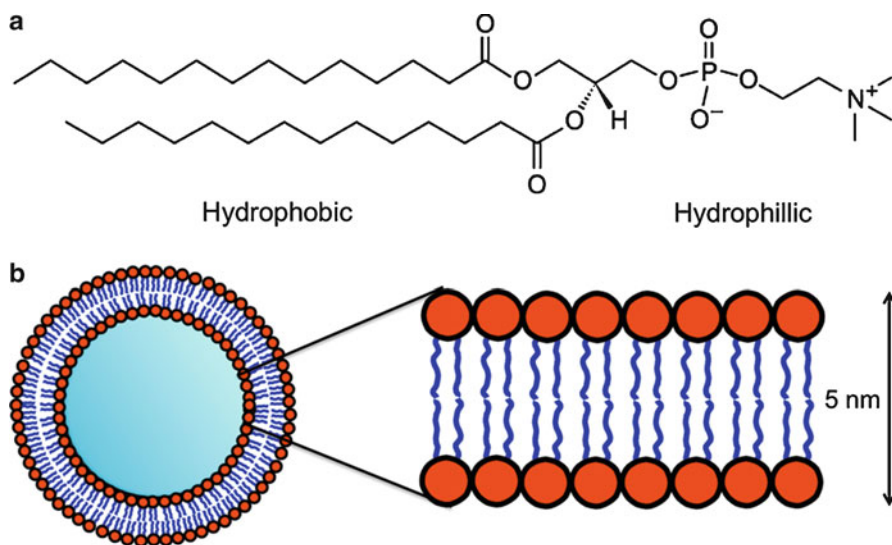
Fig. 29.4 (**a**) Structure of lipid molecule 1,2-dimyristol-sn -glycero-3-phosphocholine (**b**) Structure of a liposome (typically 100 nm in size obtained by extrusion) and a magnified view of the lipid bilayer. *Red* "heads" are hydrophilic in nature and *blue* "tails" are hydrophobic in character

sensing [74, 75], targeted drug delivery [62–64], and ultrasound contrast agents [85]. Typically, an aqueous solution containing lipids (∼1 mg/ml) is subjected to sonication or extrusion. The resulting solution obtained generally has a controlled size population of lipid vesicles. Optically transparent silica gels containing immobilized liposomes were first reported by Sasaki et al. [74] followed by several other groups. An aqueous solution containing liposomes (with or without additives, e.g. glycerol) is added to a buffered hydrolyzed silica solution resulting in rapid gelation and bulk encapsulation of liposomes [86].

A substantial challenge in synthesizing hybrid biomaterials is that the individual components must maintain the properties of interest within the whole. Therefore, the primary properties that need to be conserved for realization of lipid-silica devices include intact lipid membranes, similar lipid phase transition temperature, and diffusion of lipid molecules in the bilayer. Additional properties these hybrid materials gain include increased stability of liposomes, controlled pore size of silica allowing selective transport, faster response time for analytes and optical transparency, which is essential for spectroscopic techniques.

The phase transition temperature (gel to liquid) of liposomes is typically maintained after encapsulation in silica using aqueous routes [76, 77]. Time resolved fluorescence and leaching studies indicate increased stability of liposomes in silica monoliths for several months. Liposomes enhanced with surface recognition groups immobilized in silica gels have been shown to have up to 4–50 times faster response time for faster detection of metal ions due to ionic attraction with the anionic silicate surface [74]. Montemagno et al. [78] achieved a significant
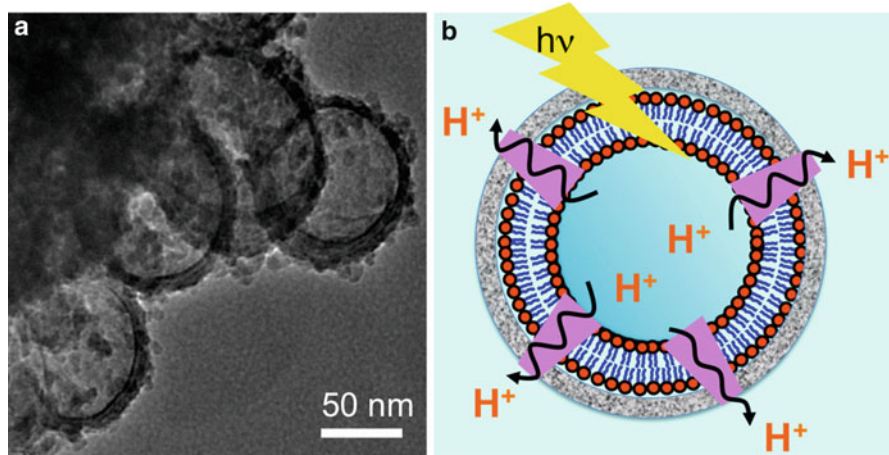
Fig. 29.5 (**a**) TEM image of silica coated liposome obtained using CVD silica process. (**b**) Schematic of encapsulation of proteoliposome containing bacteriorhodopsin (*purple*) using a CVD process. Upon excitation with light, bacteriorhodopsin pumps proton outside of liposomes

advancement in functional silica-based nanobiomaterials, where they clearly demonstrated the effective immobilization of proteoliposomes (bacteriorhodopsin and F_0F_1-ATP synthase containing vesicles) to demonstrate the synthesis of ATP.

Although liposome-bulk gels have been demonstrated in prototype sensor applications, drug-delivery applications have not been achieved due to the bulk gelation, resulting in poor transport characteristics. To this challenge, Sylvie et al. were the first to develop a thin coating of silica around the liposomes [87]. They demonstrated the effective triggered release of hydrophilic drugs with change in pH. Recently, we have developed a CVD approach that was used to coat a thin layer of silica around liposomes and proteoliposomes [80, 81]. This technique does not involve the use of acids or co-solvents. Typically, a solution containing liposomes is exposed to silica precursor (TMOS) at room temperature for desired time. Silica preferentially accumulates around phospholipid assemblies because of favorable electrostatic interaction and hydrogen bonding between silica-associated silanol groups and polar head groups of phospholipid assembly. The conservation of proteoliposome structure upon encapsulation was probed by examining the light-activated proton pumping capability of liposomes containing the purple membrane, as shown in Fig. 29.5b.

Supported Lipid Bilayers and Multilayers

Screening for drugs or other reagents using a lipid bilayer platform can be ideally achieved using a stable bilayer structure over a period of time, fluidic behavior, and active embedded transport proteins. We have reported the stabilization of solid-supported lipid bilayer using a CVD process as described above [80, 81]. Fluidity was measured using a fluorescence recovery after photobleaching (FRAP)
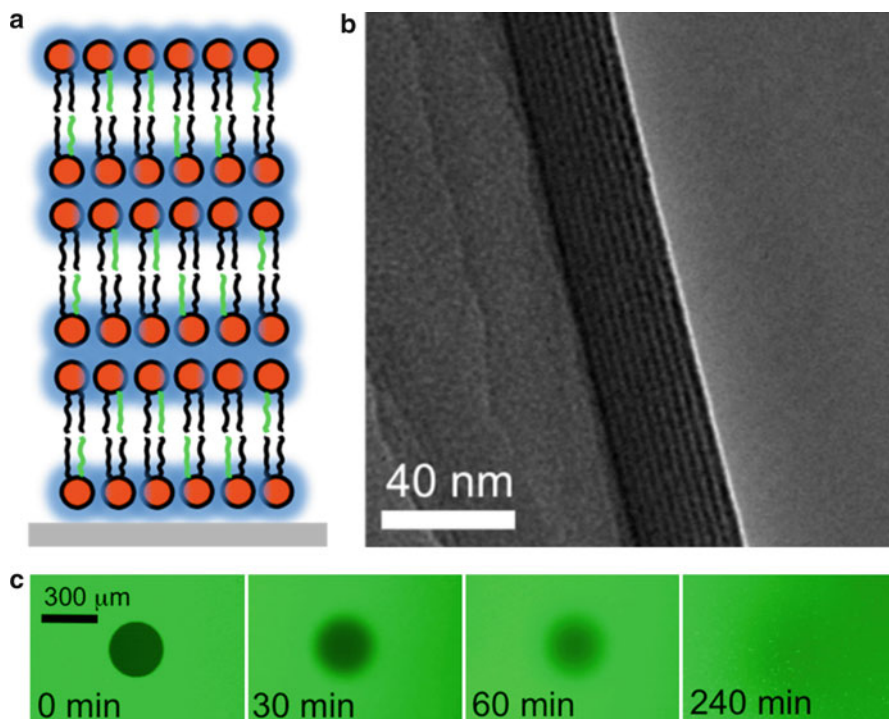
Fig. 29.6 (**a**) Structure of multi-lamellar lipid silica assembly. *Blue* regions show condensed silica on lipid head groups. (**b**) TEM micrograph of a POPC-silica multi-lamellar assembly synthesized at 37 °C. (**c**) Selected fluorescence images from typical sequences of POPC-silica obtained immediately after bleaching

technique, which clearly demonstrated no change in diffusion coefficient ($D = 2.8 \pm 0.5 \ \mu m^2/s$) of lipid bilayer before and after silica encapsulation. These results indicate that there is minimal change in phase transition temperature for lipid molecules. This result suggests that the silica encapsulation of supported lipid bilayers can yield laterally diffusive assemblies while potentially enhancing the stability (to at least 1 month) to allow a greater flexibility of manipulation than is typical for untreated lipid bilayers, which are notoriously fragile. Secondly, the unique nature of CVD process results in a thin silica coating and therefore may allow for successful protein interactions with ligands.

In addition to single lipid bilayers, complex multi-lamellar structures play a critical role in native biological systems such as the myelin sheath. However, rapid delamination of the lipid multilayers from the substrates in water has precluded the use of lipid multilayers as simple models of the myelin sheath. We have recently demonstrated a one-step synthesis, where spin-coated lamellar lipid assemblies are exposed to silica vapors resulting in formation of robust functional assemblies, as shown in Fig. 29.6a (2–40 bilayers). Silica precursors penetrate these multilayers and hydrolyze and condense at the lipid-head group region.

Fig. 29.6b shows a TEM image of resulting alternative lipid-silica structure. Importantly, sequential FRAP images show that lipids can maintain their characteristic fluidity after silica incorporation. These materials are not only stable in aqueous solution, but also stable in air for several months.

Outlook

In a nutshell, phospholipid-silica materials are promising materials for next generation devices and drug delivery, and possess superior properties including stability and functionality. However, more research is clearly required to obtain a fundamental understanding of their structure-function relationships that can develop continuously during storage due to the long-term continuation of polycondensation reactions that form silica. Moreover, it is necessary to pursue the further understanding of the lipid-silica interface for realization of goal of successful immobilization of viable cells.

Encapsulation of Biological Materials in Nanoporous Silica

Enzymes and cells are capable, literally, of transforming the world. The number of biochemical transformations available throughout the natural world is nearly unlimited, life having evolved to fill every available biochemical niche, no matter how extreme, over the last 3.5 billion years. Unfortunately, the niches that these entities fill and the niches in which we would find them most useful are not always compatible. Encapsulation offers a means by which they can be stabilized for useful application in biotechnology.

The processes by which silica is used for encapsulation are legion, as are the reports of their optimization; therefore, we emphasize the functional properties of encapsulation. Optimized functional properties of silica hybrid materials include structural integrity and longevity, containment, and systematic complexity. The silicate bond is thermodynamically robust, resulting in a high degree of not only mechanical strength, but resistance to chemical degradation [14, 88–90]. As a result, silica-encapsulated proteins and cells are likely to stay intact. For proteins, successful encapsulation allows for potential retention of activity in addition to positive attributes such as protection from various forms of degradation.

Cells also experience increased longevity; for example, diatoms, considered the living prototype of encapsulated cells, show increased viability and photosynthetic longevity when further encapsulated in nonbiological silica [91]. Increased longevity has been observed, from several weeks [92, 93], to several months [80] or longer. Encapsulated cells form a monolithic material, and the cells remain, more or less, where they are originally located. This property not only allows for recovery, and in some cases, reuse, of the cells [92], but also prevents contamination from competing cells and unwanted release of cells into the environment. Additionally, the containment seems to often times increase the efficiency of metabolic activity.

Encapsulation does impose some changes on enzymes and cells, as examples have shown. Many enzymes are not suitable for encapsulation using traditional sol–gel techniques due to loss of function [89, 94] or stability due to the presence of alcohols from processing; however, these can be circumvented using different precursors (e.g. silicates) [95] or modified encapsulation conditions [14, 90]. Cells are unable to divide within the silica matrix. This means that the metabolic processes available to them are not likely to be those involved in primary metabolism (i.e., active growth), but those associated with stationary, quiescent, or biofilm growth. In fact, quorum sensing activity, essential for maintenance of a biofilm, increases upon encapsulation of single cells [96, 97].

Encapsulation of Enzymes

The encapsulation of enzymes extends back decades to work in enzymatic encapsulation in sol–gel matrices [98]. Silica encapsulation of enzymes mainly aids in restricting the motion of protein segments due to interactions with other molecules [99] by providing stabilization within the relatively rigid silica matrix and its hydrated surface as well as providing a physical barrier from proteolysis and/or denaturants. There have been numerous examples of successful encapsulation of enzymes to gain favorable properties. In many cases, a key property of encapsulation of enzymes that is affected is enhanced stability with a tradeoff of decreased activity, most likely due to slower transport of biomolecules into the matrix or unreachable enzyme [90]. For the most part, however, the silica matrix enhances enzyme stability at both high temperature and extreme pH [100]. In other highlights, researchers showed that certain characteristics of the silica matrix and enzymes dictate the addition of other additives to maintain and enhance the properties of the enzyme-silica hybrid. For instance, Chen et al. [101] studied the encapsulation of three oxidases in silica gels – glucose oxidase, lactate oxidase, and glycolate oxidase – and found that, while lactate oxidase and glycolate oxidase did not experience enhancement of function, glucose oxidase improved in stability by over 200 times at temperatures greater than 60 °C. In accompanying work, Heller and Heller [94] determined that charge interactions play a key role in the maintenance of activity for both enzymes. Specifically, the interaction of positively charged residues, which are necessary for lactate oxidase and glycolate oxidase function, with anionic silanols within the silica matrix prevented enzyme function and stability unlike glucose oxidase, which is charge balanced. However, when these enzymes were complexed with bases, balancing their channel charger, they each also retained activity while experiencing thermal stability enhancement of over 100 times at high temperature [101].

Enhancement of stability against changes in pH was highlighted by Frenkel-Mullerad and Avnir with alkaline phosphatase [102]; effectively, the authors explained that the thin layer of hydration surrounding the enzyme does not afford large external changes in pH to penetrate within the matrix to a large degree.

A simplistic view of the enzymatic encapsulation within silica can be seen as the matrix providing a solid, rigid support for enzymes, while the enzymes inhabit pores within and are supported by the matrix. In addition, while substrates are able to reach their reaction sites, proteases and other denaturants of the enzyme may not. Encapsulation of enzymes within these matrices can therefore maintain the function of enzymes while enhancing their stability. These studies, combined with the biomimetic strategies covered previously, provide an excellent framework for previous research in enzymatic encapsulation.

Organelles and Subcellular Structures

The majority of metabolic activity in eukaryotes is carried out in membrane-bound organelles that derive energy from relief of ion partition. The major types of these organelles, chloroplasts and mitochondria, are largely self-contained systems, and are thought to have originated from free-living cells encapsulated by a larger cell. It is not surprising, therefore, that they make attractive targets for stand-alone encapsulation.

Thylakoids are the membrane-bound compartments common to both chloro-plasts and cyanobacteria and contain the photosystems responsible for conver-sion of light to chemical energy and generate reducing power for carbon fixation and production of value-added chemicals, such as fatty acids, isoprene, and hydrogen. As such, they are of particular interest in green energy production [103]. Advances in silica-based immobilization of thylakoids have resulted in preservation of not only the water-splitting activity [104], but carbon fixation [105], for periods of up to 1 month. The same techniques used to preserve these structures have also resulted in short-term (7 day) preservation of intact chloro-plasts [104]. A functional biofuel incorporating encapsulated thylakoids on the anode (electron donating) and laccase on the cathode was recently reported [106], paving the way for deployable systems in the near future. A similar device with an air cathode has been developed for a self-powered herbicide biosensor. Photocatalytic subcellular components from other organisms have also been encapsulated in silica, preserving their photoactivity. In addition to bacteriorho-dopsin containing purple membranes from Halobacteria, chlorosomes from *Chloroflexus aurantiacus* [80] and the reaction center from *Rhodobacter sphaeroides* have also been successfully encapsulated, thus expanding the rep-ertoire of light and other environmental conditions that can be produced. While mitochondria may seem similarly likely candidates for exploitation of non-photosynthetic metabolism, either as anodic material for biofuel cells [107] or as biosensors [108], published accounts of their immobilization are limited to those of microsomes containing cytochrome b complexes [109]. Recently, however, Minteer and coworkers have shown the encapsulation of *Saccharomyces cerevisiae* on carbon electrodes with preserved metabolic activity after several weeks as shown by interaction with a metabolically sensitive dye.

Microbes and Biofilms

Not surprisingly single celled organisms are also used in many of the same applications as their organelle cousins, namely, for energy production and biosensing. Biofuel cells containing encapsulated algae and cyanobacteria have been described by a variety of laboratories and have been extensively reviewed [103–105, 110, 111]. Whole cells, being already stabilized by polymeric carbohydrate cell wells, are more robust than either membrane-bound chloroplasts or essentially unprotected thylakoids and require no purification [103]. However, because whole cells do not have direct access to reduced NADPH produced during photosynthesis, external redox shuttles must be added to the system [103]. Encapsulated cells are also spatially fixed, thus limiting cell division, and thus, overall photosynthetic longevity. Given that most microalgae and cyanobacteria have a phototactic response, allowing them to seek optimal light conditions, their inability to move may reduce photosynthetic efficiency. Taken together, these limitations have directed researchers to more frequently use encapsulated chloroplasts and thylakoids for biofuel cells based on electron transfer.

Whole cell photosynthesis, however, can be used for energy production in cases where metabolites are used as fuel. Encapsulated cyanobacterium *Synechocystis* sp. PCC 6803 has been shown to be very efficient in hydrogen production, which is significantly enhanced when the cells are encapsulated [112]. In this case, the steric constraint preventing the cells from dividing works to the cells' advantage, as it obviates the need for photosystem (PS) II (responsible for carbon fixation); photosystem I still operates as normal, resulting in excess amounts of the reduced electron carrier NADPH. In fact, transcriptomic analysis of this organism post encapsulation shows an upregulation of genes involved in PS I electron acceptor synthesis [113]. The need for regeneration of oxidized $NADP^+$ is relieved by a chloroplast-associated hydrogenase, resulting in production of H_2 equal to or greater than that found in free growing cells [112]. Similarly, in eukaryotic algae, such constraint and loss of PSII activity can lead to the reduction of gold salts, leading to production of biologically generated gold nanoparticles (Fig. 29.7) [114].

The example of gold nanoparticle production by reduction of metallic salts by algae suggests that other, more reactive metal oxides may also be removed using encapsulated organisms in the process of bioremediation of heavy metals. Encapsulated yeast cells, in particular, have proven to be effective at biosorption of heavy metal contaminants [115]. Biological reduction of hexavalent chromium was recently demonstrated in sol–gel-derived beads encapsulating a natural soil isolate of *Burkholdia* sp. The bacterial-bead hybrids were demonstrated to reduce hexavalent chromium from liquid medium as efficiently as free-living cells, while withstanding much higher concentration of Cr VI [116]. In addition, the beads could be regenerated by a simple washing step and exhibited equal removal efficiency even after 5 cycles of use and regeneration, obviating the need for regrowth of cultures. Cr VI removal was even more efficient in sterile soil, further illustrating the utility and portability of encapsulated bacteria. Bioremediation can also be accomplished using contaminants as metabolic electron donors.
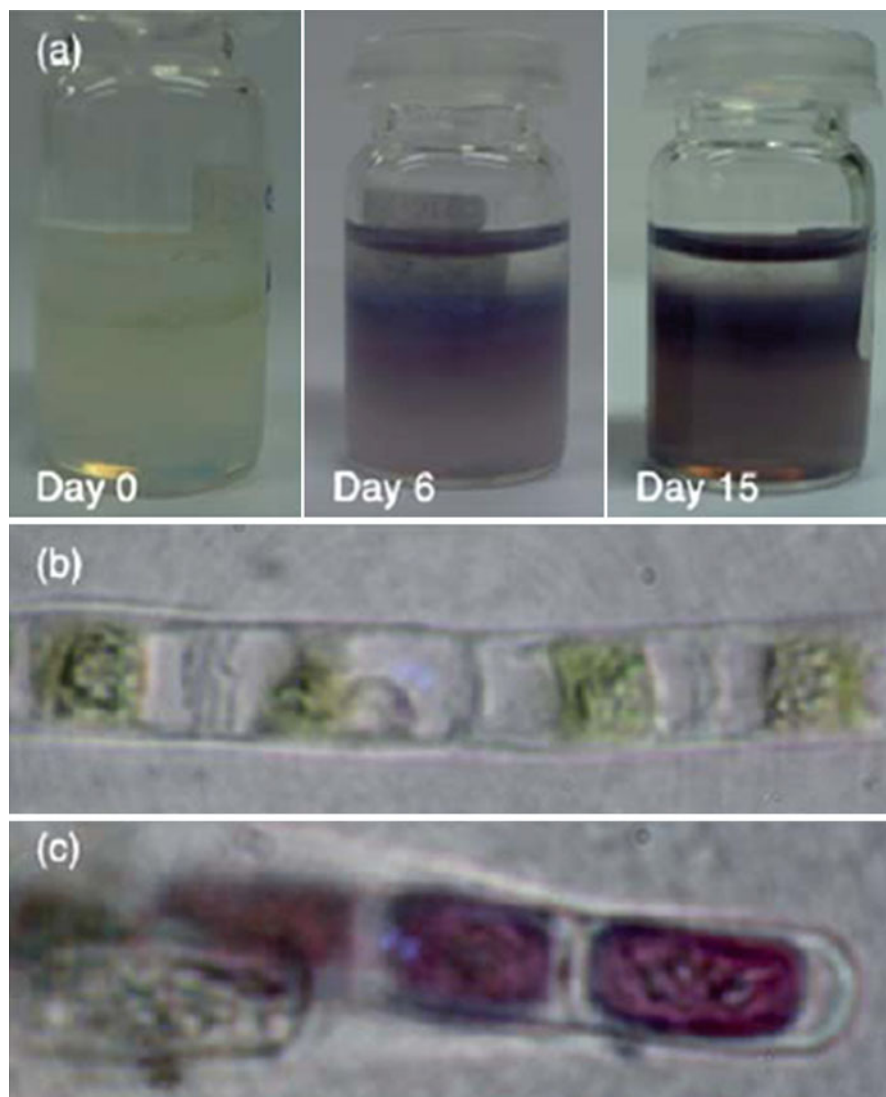
Fig. 29.7 (**a**) Evolution with time of silica gels encapsulating *Klebsormidium faccidum* cells after HAuCl₄ addition. (**b**, **c**) Optical microscopy images of encapsulated cells before and after gold reduction (Reprinted with permission from [114])

Encapsulation of several genera of soil bacteria has demonstrated an increased ability to oxidize phenolic compounds [117, 118] and formaldehyde [119]. Fungi incorporated into silica-alginate beads have found potential application in degradation of waste Kraft mill pulp [120] and wastewater for olive oil production [121]. In a unique material combining physical contaminant removal with biological processing, cells of the methylotroph, *Acinetobacter venetianu*, were

encapsulated onto commercially available, petroleum absorbent hair mats. Encapsulated cells outperformed both physisorbed cells and abiotic mats in the removal of medium chain hydrocarbons under laboratory conditions [122].

The current emphasis on global climate change has made it desirable to mitigate CO_2 emissions from all facets of modern life. While the emphasis for biological CO_2 removal has been on trees, microorganisms (microalgae, cyanobacteria, and autotrophic bacteria) play a substantial role in CO_2 fixation [111]. Encapsulated microorganisms may also have their role to play, therefore, in technology for CO_2 removal. Encapsulated *Chlorella vulgaris* and *Botryococcus braunii* have been shown to retain both their photosynthetic and carbon fixing abilities several months after encapsulation [93]. Moreover, these encapsulated algae demonstrated the ability to excrete polymers into interstitium between the cell and the surrounding silica, suggesting that they will be able to remove CO_2 while retaining their ability to produce value-added products (e.g., *B. braunii* produces a compound with antitumor activity). Encapsulated microbes also show promise for direct production of commercially viable products, as in *Haematococcus pluvialis*, a microalga that produces the yellow food coloring astaxanthin [92]. Under current commercial production, a *H. pluvialis* culture actively produces astaxanthin for 5 days. In contrast, encapsulation of the microalga allows for continuous 40-day production. Additionally, the dye is held in the silica matrix and can be easily extracted using organic solvents, compared to the current method, which destroys the cells, requiring recultivation. The encapsulated cells, however, survive organic extraction, resulting in an eightfold increase in the amount of astaxanthin produced from a single "culture." In addition, a fourfold increase in the extractable astaxanthin is also obtained from the encapsulated cells, resulting in even greater production efficiency [92].

Combining bioremediation and energy production is possible with dissimilatory metal-reducing bacteria, such as *Shewanella* sp. and *Geobacter* sp. [123, 124]. Both genera are able to utilize a wide variety of metabolic electron donors and electron acceptors during both primary and secondary metabolism, enabling them to be effective both in oxidative and reductive bioremediation. Because these organisms undergo anaerobic respiration in which metals can be the terminal electron acceptors, they are also able to donate electrons directly to an electrode; thus, both genera have been extensively explored as anodic biomaterials for microbial biofuel cells [123, 124]. In both applications, it is not the single cell, but a multicellular, phenotypically developed biofilm that is required for optimal bioactivity [125]. Encapsulation of *S. oneidensis* biofilms as hybrid material anodes has been particularly successful (Fig. 29.8) [126], having shown to be functional when environmentally deployed [127]. Both biofilms formed artificially (i.e., by encapsulating planktonic bacteria onto an anode surface) and those formed over time by natural processes have been encapsulated in silica [128], with the latter showing superior electron transfer. The electrical activity of these hybrid materials is long lived; a laboratory sample prepared for one of these manuscripts [126] was still electrically active 6 months after preparation.

A unique method in which monocultures *Pseudomonas aeruginosa* and *Nitrosomonas europaea* were allowed to direct encapsulation during biofilm
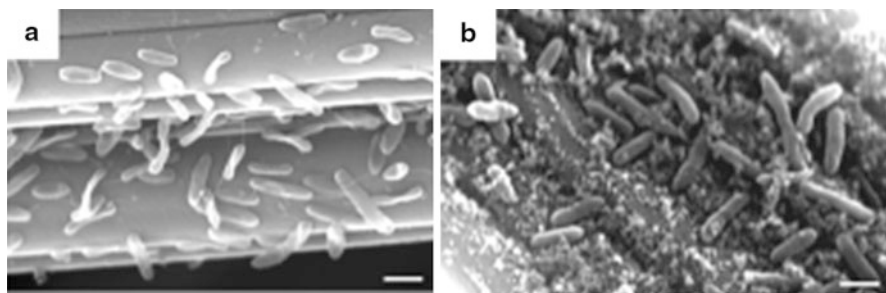
Fig. 29.8 SEM of *S. oneidensis* biofilms on graphite felt electrodes (**a**) in the absence and (**b**) in the presence of silica matrix. Scale bars are 1 μm (Reprinted with permission from [126])

formation [129] resulted in biofilms with very similar morphology to unencapsulated biofilms, with physiological activity (glucose uptake, nitrate oxidation, and oxygen consumption) unchanged over periods of up to 90 days with increased resistance to removal from the attachment substrates. Given the usefulness of these organisms in bioremediation (*P. aeruginosa*) and wastewater treatment (*N. europaea*), encapsulation of these biofilms represents the opportunity to deploy preformed, encapsulated biofilms at contamination sites with decreased risk of release of foreign bacteria.

Metabolic response is also exploited for biosensors incorporating microbial cells, allowing them to detect more specific properties than toxicity that is common for organelles [130]. Genetic manipulation is also relatively easy in microbes, allowing for both a greater range of detectable compounds and larger number of engineered cellular responses [130]. Sol–gel encapsulation has shown great promise in integration of whole cells into biohydbrid sensing devices [131]. One of the more successful endeavors in this regard is the successful encapsulation of a strain of *Escherichia coli* that has been genetically engineered to produce green fluorescent protein in response to cadmium [132]. Both viability and some degree of bioluminescence were retained for up to 1 month post encapsulation. Encapsulated genetically modified yeast have also been successfully used as biosensors. *Saccharomyces cerevisiae* genetically modified to express yellow fluorescent protein in response to galactose were encapsulated in silica with polyglycerol [133]. The resultant hybrid material exhibited long-term (60-day) survival; they also produced a bioluminescence response similar to free-living cells upon exposure to galactose. One interesting aspect of this particular study was that cells encapsulated during stationary phase fared better than logarithmic-phase cells; additionally, inclusion of growth medium during the encapsulation process had a deleterious effect on the cells [133].

Mammalian Cells and Tissues

Mammalian cells present a special challenge for silica encapsulation. Similar to organelles, the lack of a protective cell wall makes them more vulnerable to damage

during the encapsulation process. Less obvious is the fact that mammalian cell growth and function often requires attachment to surfaces [131]. Related to the requirement for attachment is that successful functionality requires cells that are attached one to another, rather than as single entities; thus, preservation of the extracellular matrix (ECM) is also vital. Nonetheless, the last several years have seen the successful incorporation of both attached and unattached mammalian cells within modified silica systems. The modifications usually include organic hydrogels, such as alginate or addition of osmoprotectants, to maintain cell stability [88] and polymeric scaffolds (collagen, chitosan), to support attachment [131]. An example of successful encapsulation of nonadhered cells is that of hybridoma cells, resulting in successful production of antibodies from the hybrid material [134]. Unconstrained by cell walls, the hybridoma cells were able to multiply within the matrix and increased cell number threefold from the original inoculum under the best conditions; cells were viable for 10 days. Antibodies were successfully released from entrapped cells after 10 min post encapsulation, and maximum levels of release were achieved after 8 h and persisted for 2 days, indicating that the encapsulation process did not induce significant changes in the functional phenotype of the cells. The antibodies exhibited normal activity [134]. An example of successful encapsulation of adhered cells was demonstrated by the preparation of a hybrid material incorporating human dermal fibroblasts which are predicted to have applications in ulcer treatment and other skin replacement therapies [135]. An obvious advantage of encapsulated fibroblast/scaffold materials is their resistance to stomach acid, which would be extremely deleterious to unencapsulated cells. Metabolic activity of the cells was confirmed by their ability to reduce a tetrazolium dye known to react with enzymes active in glycolysis for up to 3 weeks (in comparison, cells growing under normal cell culture conditions would exhibit such activity for 1–2 weeks). The ability to reorganize the collagen scaffold, a key feature of cells suitable in wound healing applications, was retained in those samples exposed to the lowest concentration of silane precursor.

Silica is also an attractive encapsulation matrix for cell therapy, which requires implantation into the human body; in addition to their mechanical strength, silica gels are largely biocompatible and resistant to immune response, thus delaying or eliminating the foreign body response [136], allowing for a greater number of encapsulated cells or tissues to be deployed. Cultured human hepatocarcinoma cells have been encapsulated in silica-alginate hybrid materials [137]. These cells showed a 60-day survival rate in vitro and were still able to secrete human albumin, demonstrating phenotypic preservation [137]. Recently, these beads were implanted subcutaneously and intramuscularly into rat models [138]. After 1 month of implantation, little inflammatory response was observed, whereas some rejection response was observed for those materials implanted near blood vessels [138]. No functional analysis of the implanted materials was performed. Another target for cell therapy is the incorporation of stem cells. Mesenchymal stem cells (MCSs), for example, are able to differentiate into bone, cartilage, or fat, depending on their chemical milieu; in the presence of growth factors from plasma, these cells become osteoblasts, and are thus are a potential source for bone

replacement therapy. A system combining human MCSs and platelet cells in a silica-alginate gel has been developed and examined in vitro [139]. Both cell types were viable up to 4 days, and protein production was sustained throughout the entire time. Although the differentiation of MSCs into osteoblasts was not tested, this study represents a major step toward cell-based therapy and the ultimate goal of mammalian cell encapsulation: immobilization of whole tissues.

Tissue encapsulation has been most well studied for possible transplantation of pancreatic islet cells for in situ diabetes treatment [140]. One major challenge in transplanting islets or islet cells is that it requires an allograft (i.e., donor material from another) often unrelated, person, resulting in ultimate rejection of the transplanted cells and further pancreatic damage [140]. For reasons cited above, silica encapsulation is attractive because it would isolate the transplanted cells from an immune response. The first successful encapsulation of and transplantation of intact mouse islet tissue was accomplished in the late 1990s [141]. Although cited extensively by many of the other works discussed herein, further development of this process has not been pursued, other than a report of encapsulation of individual islets 5 years later [142], further developments have not been forthcoming. Recently, however, intact rat ovarian follicles were encapsulated in silica alkoxide–generated matrices [143]. Cell viability persisted for 9 days, although the production of progesterone, although initially approaching those of unencapsulated follicles, fell off rapidly after 3 days. Estradiol production, however, was similar to those of control cells starting at 3 days. Although these results suggest a partial phenotypical disruption upon encapsulation, the normal levels of estradiol suggest that these or similar materials could be used in cell-mediated hormone replacement therapy [143].

Outlook

As is the case for the methodology for cellular encapsulation, the literature is replete with speculation on the use of silica-encapsulated cells for energy production, bioremediation, and medicine. Because the number of successfully encapsulated cell types has been burgeoning in the last decade, the potential for technological impact is huge. For most unicellular organisms and many mammalian cells, the impact on phenotype upon encapsulation is minimal and the cells are kept together and are easily retrievable; therefore, silica-cellular (or subcellular) materials offer enormous research potential in the study the various "omics," particularly within natural settings. Encapsulated cells could be placed into an environment, left unattended, and retrieved at a later time, allowing for longer-term studies (and less risk of environmental contamination) than is currently possible. Because soluble metabolites are often produced in greater abundance than in free-living cells, metabolomic examination of these products becomes more feasible. From a microbiological standpoint, the limits imposed by the nonculturability of the majority of the earth's microorganisms can be relieved by in situ encapsulation of organisms and communities; combined with general genomic information, the three dimension organization and, perhaps, functionality of unculturable organisms can

be approached. Practically, as envisioned for cell therapy, a variety of cell types can be implanted into environments where they are not normally found without fear of site contamination with foreign organisms that might negatively impact ecosystems. Most exciting, however, is the ability to use communities of cells, either as encapsulated tissues or biofilms, themselves as hybrid materials, taking advantage of the emergent properties of the collective.

Conclusion

Siliceous nanomaterials and material hybrids containing silica are attractive in research because silica has been determined to be compatible with and improve numerous existing systems. In addition, the fabrication and property characterization of silica at the nanoscale have both deep roots in history as well as a multitude of more recent advances, contributing to the large body of work in siliceous nanomaterials research. Indeed, the ability to finely tune silica properties and apply them toward functional systems provides a robust framework for creating useful nanomaterials for biological applications and beyond.

References

1. Tanaka S, Nishiyama N, Oku Y, Egashira Y, Ueyama K (2004) Nano-architectural silica thin films with two-dimensionally connected cage-like pores synthesized from vapor phase. J Am Chem Soc 126(15):4854–4858
2. Kneuer C, Sameti M, Bakowsky U, Schiestel T, Schirra H, Schmidt H, Lehr CM (2000) A nonviral DNA delivery system based on surface modified silica-nanoparticles can efficiently transfect cells in vitro. Bioconjug Chem 11:926–932
3. Slowing II, Trewyn BG, Giri S, Lin VS-Y (2007) Mesoporous silica nanoparticles for drug delivery and biosensing applications. Adv Funct Mater 17:1225–1236
4. Wang L, Wang K, Santra S, Zhao X, Hilliard LR, Smith JE, Wu Y, Tan W (2006) Watching silica nanoparticles glow in the biological world. Anal Chem 78:646–654
5. Guerrero-Martínez A, Pérez-Juste J, Liz-Marzán LM (2010) Recent progress on silica coating of nanoparticles and related nanomaterials. Adv Mater (Deerfield Beach, Fla) 22:1182–1195
6. Bagwe RP, Yang C, Hilliard LR, Tan W (2004) Optimization of dye-doped silica nanoparticles prepared using a reverse microemulsion method. Langmuir: ACS J Surf Colloids 20:8336–8342
7. Santra S, Yang H, Dutta D, Stanley JT, Holloway PH, Tan W, Moudgil BM, Mericle RA (2004) TAT conjugated, FITC doped silica nanoparticles for bioimaging applications. Chem Commun (Camb) 21:2810–2811

8. Zheng M, Davidson F, Huang X (2003) Ethylene glycol monolayer protected nanoparticles for eliminating nonspecific binding with biological molecules. J Am Chem Soc 125:7790–7791

9. Lin P-C, Chou P-H, Chen S-H, Liao H-K, Wang K-Y, Chen Y-J, Lin C-C (2006) Ethylene glycol-protected magnetic nanoparticles for a multiplexed immunoassay in human plasma. Small (Weinheim an der Bergstrasse, Germany) 2:485–489

10. Bagwe RP, Hilliard LR, Tan W (2006) Surface modification of silica nanoparticles to reduce aggregation and nonspecific binding. Langmuir: ACS J Surf Colloids 22:4357–4362

11. Wu H, Huo Q, Varnum S, Wang J, Liu G, Nie Z, Liu J, Lin Y (2008) Dye-doped silica nanoparticle labels/protein microarray for detection of protein biomarkers. Analyst 133:1550–1555

12. Hiramatsu H, Osterloh FE (2003) pH-controlled assembly and disassembly of electrostatically linked CdSe–SiO_2 and Au–SiO_2 nanoparticle clusters. Langmuir 19 (17):7003–7011

13. Zhao X, Kopelman R (1996) Mechanism of organosilane self-assembled monolayer formation on silica studied by second-harmonic generation. J Phys Chem 100:11014–11018

14. Avnir D, Coradin T, Lev O, Livage J (2006) Recent bio-applications of sol–gel materials. J Mater Chem 16(11):1013–1030

15. Chang K-C, Lin C-Y, Lin H-F, Chiou S-C, Huang W-C, Yeh J-M, Yang J-C (2008) Thermally and mechanically enhanced epoxy resin-silica hybrid materials containing primary amine-modified silica nanoparticles. J Appl Polym Sci 108:1629–1635

16. Patel K, Angelos S, Dichtel WR, Coskun A, Yang Y-W, Zink JI, Stoddart JF (2008) Enzyme-responsive snap-top covered silica nanocontainers. J Am Chem Soc 130:2382–2383

17. Hilliard LR, Zhao X, Tan W (2002) Immobilization of oligonucleotides onto silica nanoparticles for DNA hybridization studies. Anal Chim Acta 470:51–56

18. Hall SR, Davis SA, Mann S (2000) Cocodensation of organosilica hybrid shells on nanoparticle templates: A direct synthetic route to functionalized core-shell colloids. Langmuir 16(3):1454–1456

19. Tsukagoshi T, Kondo Y, Yoshino N (2007) Protein adsorption on polymer-modified silica particle surface. Colloids Surf B Biointerfaces 54:101–107

20. Wang L, Lofton C, Popp M, Tan W (2007) Using luminescent nanoparticles as staining probes for Affymetrix GeneChips. Bioconjug Chem 18(3):610–613

21. Wang L-S, Wu L-C, Lu S-Y, Chang L-L, Teng I-T, Yang C-M, Ho J-AA (2010) Biofunctionalized phospholipid-capped mesoporous silica nanoshuttles for targeted drug delivery: improved water suspensibility and decreased nonspecific protein binding. ACS Nano 4:4371–4379

22. Rapuano R, Carmona-Ribeiro AM (2000) Supported bilayers on silica. J Colloid Interface Sci 226:299–307

23. Moura SP, Carmona-Ribeiro AM (2005) Biomimetic particles: optimization of phospholipid bilayer coverage on silica and colloid stabilization. Langmuir: ACS J Surf Colloids 21:10160–10164

24. Keller SW, Johnson SA, Brigham ES, Yonemoto EH, Mallouk TE (1995) Photoinduced charge separation in multilayer thin films grown by sequential adsorption of polyelectrolytes. J Am Chem Soc 117(51):12879–12880

25. Taniguchi K, Nomura K, Hata Y, Nishimura T (2007) The Si-tag for immobilizing proteins on a silica surface. Biotechnol Bioeng 96:1023–1029

26. Oldenburg SJ, Averitt RD, Westcott SL, Halas NJ (1998) Nanoengineering of optical resonances. Chem Phys Lett 288:243–247

27. Taylor KML, Kim JS, Rieter WJ, An H, Lin W, Lin W (2008) Mesoporous silica nanospheres as highly efficient MRI contrast agents. J Am Chem Soc 130:2154–2155

28. Zhou X, Zhou J (2004) Improving the signal sensitivity and photostability of DNA hybridizations on microarrays by using dye-doped core-shell silica nanoparticles. Anal Chem 76:5302–5312

29. Zhao X, Tapec-Dytioco R, Tan W (2003) Ultrasensitive DNA detection using highly fluorescent bioconjugated nanoparticles. J Am Chem Soc 125:11474–11475
30. Wang J, Liu G, Wu H, Lin Y (2008) Sensitive electrochemical immunoassay for 2,4,6-trinitrotoluene based on functionalized silica nanoparticle labels. Anal Chim Acta 610:112–118
31. Zhong Z, Li M, Xiang D, Dai N, Qing Y, Wang D, Tang D (2009) Signal amplification of electrochemical immunosensor for the detection of human serum IgG using double-codified nanosilica particles as labels. Biosens Bioelectron 24:2246–2249
32. Coradin T, Allouche J, Boissière M, Livage J (2006) Sol–gel biopolymer/silica nanocomposites in biotechnology. Curr Nanosci 2:219–230
33. Coradin T, Boissière M, Livage J (2006) Sol–gel chemistry in medicinal science. Curr Med Chem 13:99–108
34. Wang G-H, Zhang L-M (2006) Using novel polysaccharide-silica hybrid material to construct an amperometric biosensor for hydrogen peroxide. J Phys Chem B 110:24864–24868
35. Tapec R, Zhao XJ, Tan W (2002) Development of organic dye-doped silica nanoparticles for bioanalysis and biosensors. J Nanosci Nanotechnol 2:405–409
36. Luo D, Saltzman WM (2005) Nonviral gene delivery: thinking of silica. Gene Ther 13:585–586
37. Torney F, Trewyn BG, Lin VS-Y, Wang K (2007) Mesoporous silica nanoparticles deliver DNA and chemicals into plants. Nat Nanotechnol 2:295–300
38. Ravi Kumar MNV, Sameti M, Mohapatra SS, Kong X, Lockey RF, Bakowsky U, Lindenblatt G, Schmidt H, Lehr CM (2004) Cationic silica nanoparticles as gene carriers: synthesis, characterization and transfection efficiency in vitro and in vivo. J Nanosci Nanotechnol 4:876–881
39. Giri S, Trewyn BG, Lin VSY (2007) Mesoporous silica nanomaterial-based biotechnological and biomedical delivery systems. Nanomedicine (Lond) 2:99–111
40. Rathbone MJ, Hadgraft J, Roberts MS (2003) Modified-release drug delivery technology. In: Rathbone MJ, Hadgraft J, Roberts MS (eds), Drugs and the Pharmaceutical Sciences, vol 126, Marcel Dekker, Inc
41. Schroder H, Wang X, Tremel W, Ushijima H, Muller W (2008) Biofabrication of biosilica-glass by living organisms. Nat Prod Rep 25(3):455–474
42. Hildebrand M (2008) Diatoms, biomineralization processes, and genomics. Chem Rev 108(11):4855–4874
43. Dickerson M, Sandhage K, Naik R (2008) Protein- and peptide-directed syntheses of inorganic materials. Chem Rev 108(11):4935–4978
44. Patwardhan S (2011) Biomimetic and bioinspired silica: recent developments and applications. Chem Commun 47(27):7567–7582
45. Patwardhan S, Clarson S (2002) Silicification and biosilicification. Silicon Chem 1(3):207–214
46. Kröger N, Deutzmann R, Sumper M (1999) Polycationic peptides from diatom biosilica that direct silica nanosphere formation. Science 286(5442):1129–1132
47. Shimizu K, Cha J, Stucky G, Morse D (1998) Silicatein α: cathepsin L-like protein in sponge biosilica. Proc Natl Acad Sci USA 95(11):6234–6238
48. Wenzl S, Hett R, Richthammer P, Sumper M (2008) Silacidins: highly acidic phosphopeptides from diatom shells assist in silica precipitation in vitro. Angew Chem 120(9):1753–1756
49. Kröger N, Lorenz S, Brunner E, Sumper M (2002) Self-assembly of highly phosphorylated silaffins and their function in biosilica morphogenesis. Science 298(5593):584–586
50. Poulsen N, Sumper M, Kröger N (2003) Biosilica formation in diatoms: characterization of native silaffin-2 and its role in silica morphogenesis. Proc Natl Acad Sci USA 100(21):12075–12080
51. Poulsen N, Kröger N (2004) Silica morphogenesis by alternative processing of silaffins in the diatom *Thalassiosira pseudonana*. J Biol Chem 279(41):42993–42999

52. Luckarift H, Spain J, Naik R, Stone M (2004) Enzyme immobilization in a biomimetic silica support. Nat Biotechnol 22(2):211–213

53. Sano K-I, Minamisawa T, Shiba K (2010) Autonomous silica encapsulation and sustained release of anticancer protein. Langmuir 26(4):2231–2234

54. Marner WD, Shaikh AS, Muller SJ, Keasling JD (2009) Enzyme immobilization via silaffin-mediated autoencapsulation in a biosilica support. Biotechnol Prog 25(2):417–423

55. Brott L, Naik R, Pikas D, Kirkpatrick S, Tomlin D, Whitlock P, Clarson S, Stone M (2001) Ultrafast holographic nanopatterning of biocatalytically formed silica. Nature 413(6853):291–293

56. Cha J, Shimizu K, Zhou Y, Christiansen S, Chmelka B, Stucky G, Morse D (1999) Silicatein filaments and subunits from a marine sponge direct the polymerization of silica and silicones in vitro. Proc Natl Acad Sci USA 96(2):361–365

57. Müller W, Boreiko A, Wang X, Belikov SI, Wiens M, Grebenjuk VA, Schloßmacher U, Schröder HC (2007) Silicateins, the major biosilica forming enzymes present in demosponges: protein analysis and phylogenetic relationship. Gene 395(1–2):62–71

58. Rai A, Perry C (2009) Facile fabrication of uniform silica films with tunable physical properties using silicatein protein from sponges. Langmuir 26(6):4152–4159

59. Müller W, Wang X, Jochum K, Schröder H (2013) Self-healing, an intrinsic property of biomineralization processes. IUBMB Life 65(5):382–396

60. Nagle JF, Tristram-Nagle S (2000) Structure of lipid bilayers. Biochim Et Biophys Acta 1469(3):159–195

61. Nagle JF, Zhang RT, TristramNagle S, Sun WJ, Petrache HI, Suter RM (1996) X-ray structure determination of fully hydrated L(alpha) phase dipalmitoylphosphatidylcholine bilayers. Biophys J 70(3):1419–1431

62. Lian T, Ho RJ (2001) Trends and developments in liposome drug delivery systems. J Pharm Sci 90(6):667–680

63. Allen TM, Cullis PR (2004) Drug delivery systems: entering the mainstream. Science 303(5665):1818–1822

64. Fielding RM (1991) Liposomal drug delivery. Clin Pharmacokinet 21(3):155–164

65. Drummond DC, Meyer O, Hong K, Kirpotin DB, Papahadjopoulos D (1999) Optimizing liposomes for delivery of chemotherapeutic agents to solid tumors. Pharmacol Rev 51(4):691–744

66. Ottenbacher D, Kindervater R, Gimmel P, Klee B, Jähnig F, Göpel W (1992) Developing biosensors with pH-ISFET transducers utilizing lipid bilayer membranes with transport proteins. Sens Actuators B 6(1):192–196

67. Bayley H, Braha O, Gu LQ (2000) Stochastic sensing with protein pores. Adv Mater 12(2):139–142

68. Nicolini C (1995) From neural chip and engineered biomolecules to bioelectronic devices: an overview. Biosens Bioelectron 10(1):105–127

69. Eleutheria EC, de Araujo PS, Panek AD (1993) Role of the trehalose carrier in dehydration resistance of *Saccharomyces cerevisiae*. Biochim Biophys Acta (BBA)-Gen Subj 1156(3):263–266

70. Albertorio F, Chapa VA, Chen X, Diaz AJ, Cremer PS (2007) The α, α-$(1 \rightarrow 1)$ linkage of trehalose is key to anhydrobiotic preservation. J Am Chem Soc 129(34):10567–10574

71. Richter RP, Brisson AR (2005) Following the formation of supported lipid bilayers on mica: a study combining AFM, QCM-D, and ellipsometry. Biophys J 88(5):3422–3433

72. Albertorio F, Diaz AJ, Yang T, Chapa VA, Kataoka S, Castellana ET, Cremer PS (2005) Fluid and air-stable lipopolymer membranes for biosensor applications. Langmuir 21(16):7476–7482

73. Kang X-f, Cheley S, Rice-Ficht AC, Bayley H (2007) A storable encapsulated bilayer chip containing a single protein nanopore. J Am Chem Soc 129(15):4701–4705

74. Yamanaka SA, Charych DH, Loy DA, Sasaki DY (1997) Solid phase immobilization of optically responsive liposomes in sol–gel materials for chemical and biological sensing. Langmuir 13(19):5049–5053

75. Nguyen T, McNamara KP, Rosenzweig Z (1999) Optochemical sensing by immobilizing fluorophore-encapsulating liposomes in sol–gel thin films. Anal Chim Acta 400(1):45–54

76. Besanger T, Zhang Y, Brennan JD (2002) Characterization of fluorescent phospholipid liposomes entrapped in sol–gel derived silica. J Phys Chem B 106(41):10535–10542

77. Keeling-Tucker T, Brennan JD (2001) Fluorescent probes as reporters on the local structure and dynamics in sol–gel-derived nanocomposite materials. Chem Mater 13(10):3331–3350

78. Luo T-JM, Soong R, Lan E, Dunn B, Montemagno C (2005) Photo-induced proton gradients and ATP biosynthesis produced by vesicles encapsulated in a silica matrix. Nat Mater 4(3):220–224

79. Gupta G, Atanassov P, Lopez GP (2006) Robust hybrid thin films that incorporate lamellar phospholipid bilayer assemblies and transmembrane proteins. Biointerphases 1(1):6–10

80. Gupta G, Rathod SB, Staggs KW, Ista LK, Oucherif KA, Atanassov PB, Tartis MS, Montano GA, Lopez GP (2009) CVD for the facile synthesis of hybrid nanobiomaterials integrating functional supramolecular assemblies. Langmuir 25(23):13322–13327

81. Gupta G, Iyer S, Leasure K, Virdone N, Dattelbaum AM, Atanassov PB, López GP (2013) Stable and fluid multilayer phospholipid–silica thin films: mimicking active multi-lamellar biological assemblies. ACS Nano. doi:10.1021/nn401123p

82. Israelachvili JN, Mitchell DJ, Ninham BW (1976) Theory of self-assembly of hydrocarbon amphiphiles into micelles and bilayers. J Chem Soc, Faraday Trans 2(72):1525–1568

83. Israelachvili JN, Mitchell DJ (1975) A model for the packing of lipids in bilayer membranes. Biochim Biophys Acta (BBA)-Biomembr 389(1):13–19

84. Bangham A, Standish M, Watkins J (1965) Diffusion of univalent ions across the lamellae of swollen phospholipids. J Mol Biol 13(1):238–IN227

85. Alkan-Onyuksel H, Demos SM, Lanza GM, Vonesh MJ, Klegerman ME, Kane BJ, Kuszak J, McPherson DD (1996) Development of inherently echogenic liposomes as an ultrasonic contrast agent. J Pharm Sci 85(5):486–490

86. Dwivedi N, Arunagirinathan M, Sharma S, Bellare J (2010) Silica-coated liposomes for insulin delivery. J Nanomater 2010:34

87. Bégu S, Pouëssel AA, Lerner DA, Tourné-Péteilh C, Devoisselle JM (2007) Liposil, a promising composite material for drug storage and release. J Control Release 118(1):1–6

88. Oliver AE (2012) Dry state preservation of nucleated cells: progress and challenges. Biopreserv Biobank 10(4):376–385

89. Jin W, Brennan JD (2002) Properties and applications of proteins encapsulated within sol–gel derived materials. Anal Chim Acta 461(1):1–36

90. Avnir D, Braun S, Lev O, Ottolenghi M (1994) Enzymes and other proteins entrapped in sol–gel materials. Chem Mater 6(10):1605–1614

91. Gautier C, Livage J, Coradin T, Lopez PJ (2006) Sol–gel encapsulation extends diatom viability and reveals their silica dissolution capability. Chem Commun 44:4611–4613

92. Fiedler D, Hager U, Franke H, Soltmann U, Böttcher H (2007) Algae biocers: astaxanthin formation in sol–gel immobilised living microalgae. J Mater Chem 17:261–266

93. Rooke JC, Leonard A, Sarmento H, Meunier CF, Descy JP, Su BL (2011) Novel photosynthetic CO2 bioconvertor based on green algae entrapped in low-sodium silica gels. J Mater Chem 21(4):951–959

94. Heller J, Heller A (1998) Loss of activity or gain in stability of oxidases upon their immobilization in hydrated silica: significance of the electrostatic interactions of surface arginine residues at the entrances of the reaction channels. J Am Chem Soc 120(19):4586–4590

95. Gill I, Ballesteros A (1998) Encapsulation of biologicals within silicate, siloxane, and hybrid sol–gel polymers: an efficient and generic approach. J Am Chem Soc 120(34):8587–8598

96. Baca HK, Carnes EC, Ashley CE, Lopez DM, Douthit C, Karlin S, Brinker C (2011) Cell-directed-assembly: directing the formation of nano/bio interfaces and architectures with living cells. BBA-Gen Subj 1810(3):259–267

97. Carnes EC, Lopez DM, Donegan NP, Cheung A, Gresham H, Timmins GS, Brinker C (2010) Confinement-induced quorum sensing of individual *Staphylococcus aureus* bacteria. Nat Chem Biol 6(1):41–45

98. Braun S, Rappoport S, Zusman R, Avnir D, Ottolenghi M (1990) Biochemically active sol–gel glasses: the trapping of enzymes. Mater Lett 10(1):1–5

99. Martinek K, Klibanov AM, Goldmacher VS, Berezin IV (1977) The principles of enzyme stabilization I. Increase in thermostability of enzymes covalently bound to a complementary surface of a polymer support in a multipoint fashion. Biochim Biophys Acta (BBA) Enzymol 485(1):1–12

100. Ellerby L, Nishida C, Nishida F, Yamanaka S, Dunn B, Valentine J, Zink J (1992) Encapsulation of proteins in transparent porous silicate glasses prepared by the sol–gel method. Science 255(5048):1113–1115

101. Chen Q, Kenausis GL, Heller A (1998) Stability of oxidases immobilized in silica gels. J Am Chem Soc 120(19):4582–4585

102. Frenkel-Mullerad H, Avnir D (2005) Sol–gel materials as efficient enzyme protectors: preserving the activity of phosphatases under extreme pH conditions. J Am Chem Soc 127(22):8077–8081

103. Meunier CF, Yang XY, Rooke JC, Su BL (2011) Biofuel cells based on the immobilization of photosynthetically active bioentities. ChemCatChem 3(3):476–488

104. Meunier CF, Van Cutsem P, Kwon YU, Su BL (2009) Investigation of different silica precursors: design of biocompatible silica gels with long term bio-activity of entrapped thylakoids toward artificial leaf. J Mater Chem 19(24):4131–4137

105. Meunier CF, Dandoy P, Su BL (2010) Encapsulation of cells within silica matrixes: towards a new advance in the conception of living hybrid materials. J Colloid Interface Sci 342(2):211–224

106. Rasmussen M, Shrier A, Minteer SD (2013) High performance thylakoid bio-solar cell using laccase enzymatic biocathodes. Phys Chem Chem Phys 15(23):9062–9065

107. Minteer SD, Atanassov P, Luckarift HR, Johnson GR (2012) New materials for biological fuel cells. Mater Today 15(4):166–173

108. Maltzman SL, Minteer SD (2012) Mitochondrial-based voltammetric sensor for pesticides. Anal Methods-UK 4(5):1202–1206

109. Sakai-Kato K, Hasegawa T, Takaoka A, Kato M, Toyo'oka T, Utsunomiya-Tate N, Kawanishi T (2011) Controlled structure and properties of silicate nanoparticle networks for incorporation of biosystem components. Nanotechnology 22(20):205702

110. Jenkins JS, Flickinger MC, Velev OD (2013) Engineering cellular photocomposite materials using convective assembly. Materials 6(5):1803–1825

111. Dickson DJ, Ely RL (2013) Silica sol–gel encapsulation of cyanobacteria: lessons for academic and applied research. Appl Microbiol Biotechnol 97(5):1809–1819

112. Dickson DJ, Page CJ, Ely RL (2009) Photobiological hydrogen production from *Synechocystis* sp. PCC 6803 encapsulated in silica sol–gel. Int J Hydrog Energy 34:204–215

113. Dickson DJ, Luterra MD, Ely RL (2012) Transcriptomic responses of *Synechocystis* sp. PCC 6803 encapsulated in silica gel. Appl Microbiol Biotechnol 96(1):183–196

114. Sicard C, Brayner R, Margueritat J, Hemadi M, Coute A, Yepremian C, Djediat C, Aubard J, Fievet F, Livage J, Coradin T (2010) Nano-gold biosynthesis by silica-encapsulated micro-algae: a "living" bio-hybrid material. J Mater Chem 20(42):9342–9347

115. Al-Saraj M, Abdel-Latif MS, El-Nahal I, Baraka R (1999) Bioaccumulation of some hazardous metals by sol–gel entrapped microorganisms. J Non-Cryst Solids 248(2–3):137–140

116. Alvarez GS, Foglia ML, Camporotondi DE, Tuttolomondo MV, Desimone MF, Diaz LE (2011) A functional material that combines the Cr(VI) reduction activity of *Burkholderia* sp. with the adsorbent capacity of sol–gel materials. J Mater Chem 21(17):6359–6364

117. Khongkhaem P, Intasiri A, Luepromchai E (2011) Silica-immobilized *Methylobacterium* sp. NP3 and *Acinetobacter* sp. PK1 degrade high concentrations of phenol. Lett Appl Microbiol 52(5):448–455

118. Pannier A, Mkandawire M, Soltmann U, Pompe W, Bottcher H (2012) Biological activity and mechanical stability of sol–gel-based biofilters using the freeze-gelation technique for immobilization of *Rhodococcus ruber*. Appl Microbiol Biotechnol 93(4):1755–1767

119. Habibi A, Vahabzadeh F (2013) Degradation of formaldehyde at high concentrations by phenol-adapted *Ralstonia eutropha* closely related topink-pigmented facultative methylotrophs. J Environ Sci Health A 48:279–292

120. Duarte K, Justino CIL, Pereira R, Panteleitchouk TSL, Freitas AC, Rocha-Santos TAP, Duarte AC (2013) Removal of the organic content from a bleached kraft pulp mill effluent by a treatment with silica-alginate-fungi biocomposites. J Environ Sci Health A 48(2):166–172

121. Duarte KR, Freitas AC, Pereira R, Pinheiro JC, Goncalves F, Azaari H, El Azzouzi M, Zrineh A, Zaydoun S, Duarte AC, Rocha-Santos TAP (2012) Treatment of olive oil mill wastewater by silica-alginate-fungi biocomposites. Water Air Soil Pollut 223(7):4307–4318

122. Luckarift HR, Sizemore SR, Farrington KE, Fulmer PA, Biffinger JC, Nadeau LJ, Johnson GR (2011) Biodegradation of medium chain hydrocarbons by *Acinetobacter venetianus* 2AW immobilized to hair-based adsorbent mats. Biotechnol Prog 27(6):1580–1587

123. El-Naggar MY, Finkel SE (2013) Live wires. The Scientist 27:38–43

124. Lovley DR (2011) Live wires: direct extracellular electron exchange for bioenergy and the bioremediation of energy-related contamination. Energy Environ Sci 4(12):4896–4906

125. Nealson KH, Finkel SE (2011) Electron flow and biofilms. MRS Bull 36(5):380–384

126. Luckarift HR, Sizemore SR, Roy J, Lau C, Gupta G, Atanassov P, Johnson GR (2010) Standardized microbial fuel cell anodes of silica-immobilized *Shewanella oneidensis*. Chem Commun 46(33):6048–6050

127. Strack G, Luckarift HR, Sizemore SR, Nichols RK, Farrington KE, Wu PK, Atanassov P, Biffinger JC, Johnson GR (2013) Power generation from a hybrid biological fuel cell in seawater. Bioresour Technol 128:222–228

128. Roy JN, Luckarift HR, Lau C, Falase A, Garcia KE, Ista LK, Chellamuthu P, Ramasamy RP, Gadhamshetty V, Wanger G, Gorby YA, Nealson KH, Bretschger O, Johnson GR, Atanassov P (2012) A study of the flavin response by *Shewanella* cultures in carbon-limited environments. RSC Adv 2(26):10020–10027

129. Jaroch D, McLamore E, Zhang W, Shi J, Garland J, Banks MK, Porterfield DM, Rickus JL (2011) Cell-mediated deposition of porous silica on bacterial biofilms. Biotechnol Bioeng 108(10):2249–2260

130. Ben-Yoav H, Melamed S, Freeman A, Shacham-Diamand Y, Belkin S (2011) Whole-cell biochips for bio-sensing: integration of live cells and inanimate surfaces. Crit Rev Biotechnol 31(4):337–353

131. Blondeau M, Coradin T (2012) Living materials from sol–gel chemistry: current challenges and perspectives. J Mater Chem 22(42):22335–22343

132. Ghach W, Etienne M, Billard P, Jorand FPA, Walcarius A (2013) Electrochemically assisted bacteria encapsulation in thin hybrid sol–gel films. J Mater Chem B 1(7):1052–1059

133. Harper JC, Lopez DM, Larkin EC, Economides MK, McIntyre SK, Alam TM, Tartis MS, Werner-Washburne M, Brinker C, Brozik SM, Wheeler DR (2011) Encapsulation of *S. cerevisiae* in poly(glycerol) silicate derived matrices: effect of matrix additives and cell metabolic phase on long-term viability and rate of gene expression. Chem Mater 23(10):2555–2564

134. Desimone MF, De Marzi MC, Alvarez GS, Mathov I, Diaz LE, Malchiodi EL (2011) Production of monoclonal antibodies from hybridoma cells immobilized in 3D sol–gel silica matrices. J Mater Chem 21(36):13865–13872

135. Desimone MF, Helary C, Mosser G, Giraud-Guille MM, Livage J, Coradin T (2010) Fibroblast encapsulation in hybrid silica-collagen hydrogels. J Mater Chem 20(4):666–668

136. Leonard A, Dandoy P, Danloy E, Leroux G, Meunier CF, Rooke JC, Su BL (2011) Whole-cell based hybrid materials for green energy production, environmental remediation and smart cell-therapy. Chem Soc Rev 40(2):860–885

137. Dandoy P, Meunier CF, Michiels C, Su BL (2011) Hybrid shell engineering of animal cells for immune protections and regulation of drug delivery: towards the design of "Artificial Organs". Plos One 6(6):e20983
138. Dandoy P, Meunier CF, Leroux G, Voisin V, Giordano L, Caron N, Michiels C, Su BL (2013) A hybrid assembly by encapsulation of human cells within mineralised beads for cell therapy. Plos One 8(1):e54683
139. Gimeno-Fabra M, Peroglio M, Eglin D, Alini M, Perry CC (2011) Combined release of platelet-rich plasma and 3D-mesenchymal stem cell encapsulation in alginate hydrogels modified by the presence of silica. J Mater Chem 21(12):4086–4089
140. O'Sullivan ES, Vegas A, Anderson DG, Weir GC (2011) Islets transplanted in immunoisolation devices: a review of the progress and the challenges that remain. Endocr Rev 32(6):827–844
141. Pope EJA, Braun K, Peterson CM (1997) Bioartificial organs. 1. Silica gel encapsulated pancreatic islets for the treatment of diabetes mellitus. J Sol–gel Sci Technol 8(1–3):635–639
142. Boninsegna S, Bosetti P, Carturan G, Dellagiacoma G, Dal Monte R, Rossi M (2003) Encapsulation of individual pancreatic islets by sol–gel SiO2: a novel procedure for perspective cellular grafts. J Biotechnol 100(3):277–286
143. Catalano PN, Bourguignon NS, Alvarez GS, Libertun C, Diaz LE, Desimone MF, Lux-Lantos V (2012) Sol–gel immobilized ovarian follicles: collaboration between two different cell types in hormone production and secretion. J Mater Chem 22(23):11681–11687

High-Throughput Screening for the Production of Biomaterials: A New Tool for the Study of the Interactions Between Materials and Biological Species

30

Si Amar Dahoumane, Blake-Joseph Helka, Mathieu Artus, Brandon Aubie, and John D. Brennan

Keywords

High-throughput screening (HTS) • Combinatorial chemistry (CombiChem) • Automated synthesis • Contact printing • Non-contact printing • Biomaterial libraries • Microarrays • Biointerface • Biosensors

Introduction

Predicting a rapid development of new preparation and characterization techniques in the near future, Prof. Wilhem M. Maier wrote, in 1999: "Combinatorial chemistry presents a unique chance for the development of new materials and catalysts, and its major task, at least in the academic environment, should be the discovery of new materials and not the fine-tuning and optimization of known materials" [1]. More than a decade later, these methodologies, used initially for the discovery of new drugs, have been applied to the synthesis of a wide range of organic and inorganic materials [2].

Combinatorial chemistry methodologies, also known as CombiChem, allow the fast and efficient generation of a huge number of compounds, starting from a relatively small number of initial reagents. Perhaps one of the most famous uses of CombiChem was the solid-phase peptide synthesis method developed by Merrifield [3]. Since this early example, researchers have developed numerous tools and techniques permitting the rapid and efficient screening and

S.A. Dahoumane • B.-J. Helka • M. Artus • J.D. Brennan (✉)
Department of Chemistry and Chemical Biology, McMaster Univeristy, Hamilton, ON, Canada
e-mail: sa.dahoumane@gmail.com; helkab@mcmaster.ca; artus.mathieu@gmail.com; brennanj@mcmaster.ca

B. Aubie
Biointerfaces Institute, McMaster University, Hamilton, ON, Canada
e-mail: aubiebn@mcmaster.ca

characterization of a wide range of different products. These techniques are gathered under the term "high-throughput screening" or HTS. CombiChem and HTS are, nowadays, interchangeable. However, at their origin, CombiChem referred to the way the experiment was designed, that is, a combination of structures and reagents was used and parameters were tuned to optimize yields, while HTS referred to the tools used to carry out that experiment, characterize the library of compounds, and rapidly assess compound properties [4].

The aim of this chapter is to focus on recent developments in the use of CombiChem and HTS for the production and characterization of biomaterials and biointerfaces, with a focus on microscale synthesis methods based on microarrays and nanoparticles, and the tools used for their characterization. Typical biomaterials include organic materials prepared from cross-linked polymers, inorganic materials, such as sol-gel derived silica materials used for the entrapment of cells and proteins, and hybrids made of organic-inorganic mixtures. We will also focus on the interaction between these materials and biological entities. The interface between the inert material and the active biological component determines their potential applications, such as coatings or sensors. Several reviews have been written in the field of fabrication of biomaterials through HTS and CombiChem methodologies. Peptide libraries are discussed by Henderson et al., while DNA and protein microarray fabrication and use are described by Wu et al. [5, 6]. These topics will not be further discussed here. More relevant to this chapter is the recent review by Hook et al. which describes the fabrication of polymer microarrays and the assessment of their biological responses [7]. Additional reviews written by Webster et al., Meredith et al., Kohn et al., and Mei et al. describe the synthesis of polymer libraries, via HTS methodologies, and their main biological applications [2, 4, 8, 9]. Su et al. have discussed the use of the CombiChem techniques in the synthesis of nanomaterials, and the methods used to functionalize their surfaces to address biological criteria such as cell targeting and reduction of cytotoxicity [10]. More recently, the review written by Potyrailo et al. discussed extensively the generation of material libraries of all kinds among which a large section is dedicated to biomedical materials [11]. From these reviews, one can note that HTS approaches are typically used to identify two key classes of biomaterials; bioactive materials, which are used for biosensors, solid-phase small molecule screening platforms, wound dressings, control of cell adhesion or differentiation or active release of compounds, and "stealth" or biologically inert materials that are used for applications such as implants, blood storage media, or ophthalmic coatings. In this chapter, we focus primarily on bioactive materials, but provide some examples of stealth materials that are emerging for selected applications.

Principles of CombiChem and HTS

The strength of CombiChem methodologies lies in their ability to generate thousands of new materials in a relatively short time by taking advantage of full automation of experiments and using chemical approaches that minimize intermediate species and

Fig. 30.1 Illustration of the philosophy of the coupled CombiChem and HTS
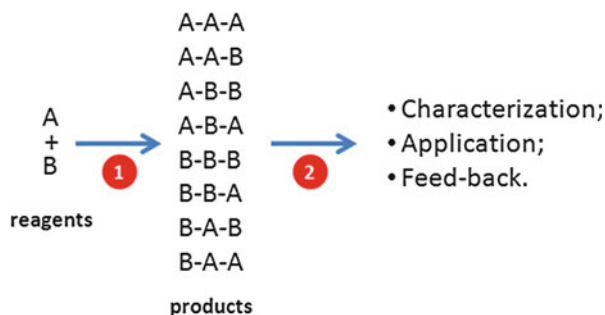
side products. For instance, starting from two monomers, there are $2^3 = 8$ ways of producing trimers (ignoring side products). CombiChem allows one to examine each of the different possible ways of mixing both of the monomers (Fig. 30.1, step 1). Then HTS synthesis tools, such as liquid-handling robots and microarray printers, allow the production of all the possible combinations. Following synthesis, the physicochemical and biological properties of these products are assessed using HTS characterization tools, such as fluorescence and optical microscopies, fluorescence spectroscopy, x-ray photoelectron spectroscopy (XPS), time-of-flight secondary ion mass spectrometry (ToF-SIMS), Fourier transform infrared spectroscopy (FTIR), Raman spectroscopy, etc. Once the different properties are investigated, the interaction of each material with a biological species, which can be cells, nucleic acids, or proteins, for instance, is studied (Fig. 30.1, step 2). This last step provides researchers with new insights into the materials, and allows "hits" to be used as leads for subsequent HTS studies to improve material properties by changing one or several reagents and/or tuning one or a number of experimental parameters.

Importance and Applications of Biomaterials

For the purposes of this chapter, we define biomaterials as compositions that are either stand-alone materials that interact with biological species, or materials that are composed of both a hosting material and a hosted biological entity. The material can be organic in nature, such as biopolymers or synthetic polymers, inorganic materials such as sol-gel derived silica, or hybrid organic-inorganic materials such as thin film surfaces or nanoparticles capped with a polymeric layer. These materials can be used as surfaces for the binding of small biomolecules or cells, or for the entrapment of these biological entities within three-dimensional networks.

As noted in Table 30.1, biomaterials have found numerous applications in different fields. Such materials have been used as biocompatible coatings for the attachment of a biological target (usually a protein or nucleic acid), or as biocompatible porous media to obtain active or passive controlled drug release. In addition, biomaterials can be used as coating for prostheses, bioactive materials for biosensors, surfaces to control cell adhesion, differentiation and growth, and as selective extraction or separation media. HTS and CombiChem provide the tools

Table 30.1 A summary of various materials amenable to high-throughput synthesis and their potential applications

Biomaterial	Format	Application(s)	References
Polymer	Microarray	1. Polymer-cell interaction (adhesion promotion or inhibition)	[12–15]
		2. Study of the relationship between cell adhesion and the different chemical functionalities of the polymer library	[16–19]
		3. Control of stem cell growth and fate	[20–24]
		4. 3D biomimetic scaffolds for tissue engineering	[23]
		5. Polymer-protein affinity assays	[25, 26]
		6. Drug formulation	[27]
Sol-gel	Microarrays	1. Identification of the optimal materials that retain protein/enzyme activity	[28–30]
		2. Study of the interaction between aptamers and sol-gel entrapped small molecules	[31]
		3. Biosensors	[32–34]
Particles	Organic and inorganic	1. Cell factorization	[35]
		2. Gene delivery	[36, 37]
		3. MRI contrast agents	[38]
		4. Protein-specific binding	[39, 40]
		5. Biomolecule delivery/release	[41]

for the synthesis of thousands of materials and the assessment of their different physical and chemical properties. The use of these methods is both cost- and time-effective and allows identification of important material trends and applications. Furthermore, HTS and CombiChem methodologies have allowed the design of such materials in a systematic way, compared to the tedious on-at-a-time approaches to discovery that occurred before the advent of the aforementioned techniques. Table 30.1 summarizes some of the most recent applications in the field of bio-materials, the format used for providing high-throughput synthesis and screening, and some of their applications. It should be noted that the table is not exhaustive, and is meant to serve as an introductory reference to methods in HTS of bio-materials and their applications. The applications outlined in Table 30.1 are described in more detail in the section "Examples of High-Throughput Studies of Biomaterials".

Production Tools

Parallel development in assay miniaturization and material handling automation has allowed translation of conventional bench-top techniques to production tools amenable to HTS methodologies. While assay miniaturization and automation can stand alone as independent concepts in HTS, one could imagine a scenario where both principles are combined to increase overall throughput. The focus of this section

however will be focused toward highlighting key concepts related to automation and assay miniaturization (microarray formation) as independent concepts.

Robotic Handling

With respect to automation, today's standards are based upon fully customizable work decks with integration of stand-alone plate readers and material handling systems. Such systems can be equipped with solid-phase synthesis stations, magnetic separation systems, integrated centrifuges, weigh stations, and other items that extend the utility of such systems beyond simple liquid handling. Such systems are capable of handling volumes from 0.5 μL to several mL and masses from μg to grams, with additional options for heating, cooling, and shaking, depending on required material/assay parameters. These fully automated decks are capable of running for extended periods without the need for human intervention, and can produce or screen several thousand materials per hour. A key design advantage of such systems is the ability to work with standard microwell plates based on 96-, 384-, 1536-, and even 3456-well formats, with the ability to utilize specialized assay-specific plates depending on the particular application. Importantly, such systems can be used for very high-throughput formulation studies using syringe- or pipette-based liquid handing, including the ability to perform multistep synthesis, or can be used to prepare source plates for secondary formulation methods using contact or non-contact microarraying (see below). These systems can also aid in high-throughput assaying of either microplate or microarray platforms, using integrated readers within the deck.

Microarray Fabrication

Building on the material production capabilities of automated liquid-handling workstations, microarrays stand out within the literature as an optimal platform for both high-throughput synthesis and characterization. Generally defined as a method for the production of highly ordered patterns, microarrays are commonly produced using several methods including but not limited to, photo-, soft-, or nano-lithography and contact or non-contact printing. Each method is capable of producing arrays consisting of thousands to tens of thousands of "spots" per standard microscope slide (25 mm × 75 mm). For this chapter however, only microarray formation through contact (pin-printing) and non-contact (ink-jet) printing will be discussed as these methods relate to the most common methods utilized within the literature for the production and evaluation of biomaterial microarrays. It should also be noted that this section will only focus on technical aspects related to the two printing modalities. Subsequent sections will address the relevant literature related to the composition of biomaterial arrays and application of microarrays. For more detailed reviews related to printing technologies, the authors recommend one of several excellent reviews [42–45]. Independent of printing method, the aim of each
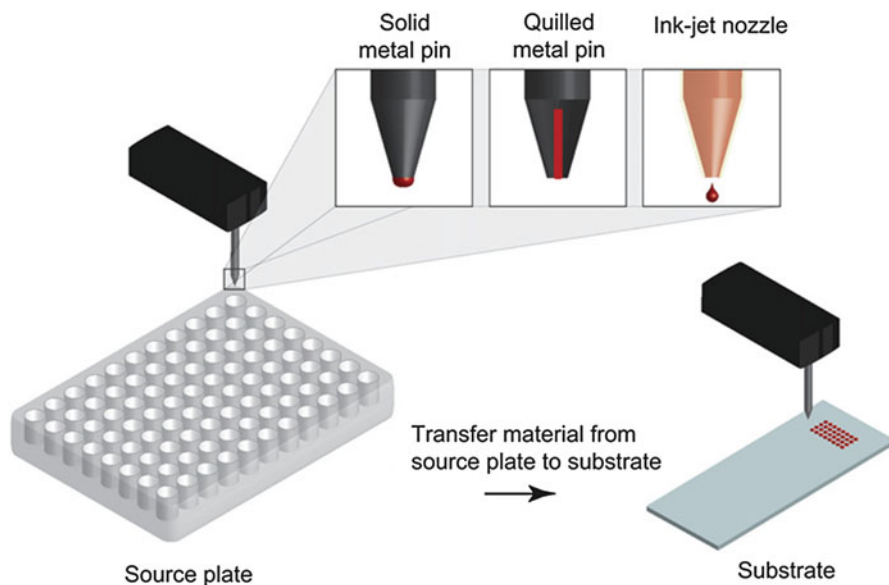
Fig. 30.2 Schematic representation of different print heads used for microarray formation. *Red* is used to represent spotting solutions, which are collected from a source plate and deposited onto a substrate (*slide*) by means of a printing pin (*solid* or *quilled*) or ink-jet nozzle (Pending Copyright permission [7])

technique is the efficient production of homogeneous, (uniform spot size) high-density arrays with high precision and accuracy. Further shared among several printing modalities is control and movement of the "print head" through a power driven XYZ stage.

Contact Pin-Printing

As the name implies, contact pin-printing refers to microarrays formed through the direct contact between a "printing" pin and the substrate. Typically, pins are either solid or quilled (containing a slit which acts as a reservoir, Fig. 30.2). With respect to solid pins, the deposited spot size and shape will be directly linked to the shape and size of the pin. For quilled pins, slit width will influence the size of the spot, while the shape of the slit reservoir will influence the volume deposited for each spot [42]. Pins are typically metallic and will allow for deposition of spots ranging from one hundred to a few hundred microns in diameter. Recently, silicon-based pins have been developed which allow for greater dimensional control and smaller deposited spot volumes [46]. Unfortunately, the robustness of silicon-based pins often results in inconsistent spotting from pin-induced fractures in substrate coatings [42]. Other important parameters related to producing quality contact arrays remain independent of the pin itself. Environmental factors (temperature and humidity), and instrumental (print head travel speed and contact time) and solution (viscosity and surface tension) properties determine the "printability" of any given

solution. The combination of environmental, instrumental, and solution-based factors which determine printability of materials makes contact printing methods highly versatile and well suited for printing a range of chemically stable solutions. Many research groups have been utilizing contact printing as a method to prepare microarrays of polymers such acrylates, acrylamides, and urethanes, which generally require UV irradiation or addition of an initiator after printing to form and fix the polymer materials to the substrate surface [12, 17]. For less stable polymers, an alternative approach can be utilized wherein a pre-screening and selection approach is used to first identify materials that are printable (i.e., do not polymerize in the pin), followed by production of a more limited microarray of materials using a contact printer [28, 29].

Non-contact (Ink-jet) Printing

In contrast to contact printing methods, non-contact (ink-jet) printing relates to a much larger and more diverse class of printing techniques. The two main types of non-contact printing methods involved in microarray production utilize thermal and piezoelectric dispensing and either continuous or drop on demand methods, where continuous refers to a steady stream of expelled droplets. Both thermal and piezoelectric printing methods form drops through the prorogation of pressure within the fluid-containing chamber. Differences relate to the means used to produce drops through the creation of "pressure pulses". In thermal printing, solution in direct contact with a heater, which raises the solution above the boiling point (up to 300 °C), forms and deforms bubbles in solution, generating the required pressure pulse. In contrast, piezoelectric printing produces pressure pulses through direct mechanical action using a piezoelectric material (commonly a crystal or ceramic) as an actuator [42, 44, 45]. As piezoelectric printing methods are more tunable than thermal printing methods, material microarrays are most often produced using piezoelectric printing robots, including both polymer and sol-gel derived microarrays [30, 47]. The size of the expelled drops ranges from low to mid-hundred picoliter volumes, which determines the size of the on-array spot. Alteration of drop volume, and thus spot size, can be accomplished by altering the size of the nozzle orifice, or by altering the pressure pulse through precise control of pulse duration and voltage. Aside from nozzle constraints (size and applied pulse duration and/or voltage), spotting solution properties are important factors that determine the printability of a material. For example, solutions that are too viscous (typically greater than 20 mPa*s) will inhibit printing. Failed printing due to materials clogging the nozzle orifice is also a characteristic of ink-jet printing [42]. Temperature and humidity also have significant effects (as compared to contact printing methods), on the printability of materials and final spot shape and size, due to evaporation of small drop sizes [48]. However, the advantage of small drop sizes is the ability to perform "drop-in-drop" printing. In this technique, multiple nozzles are used in parallel to initially spot and subsequently respot solutions over each other [49]. Taking advantage of this method, it may be possible to print materials that are reactive in nature (such as sol-gel derived materials), which would normally

be considered unprintable owing to rapid polymerization upon mixing (akin to separately printing components A and B or an epoxy rather than mixing these prior to printing, as is required for contact printing).

Characterization Techniques

HTS methodologies provide powerful and rapid tools for the production of large numbers of new biomaterials per day. However, this comes with a significant challenge in the need to rapidly evaluate different properties of this large number of biomaterials. While it is impossible to fully characterize thousands of biomaterials within a reasonable amount of time, it is possible to extract a substantial amount of useful information from a library of biomaterials, as illustrated in Fig. 30.3. To do so, it is critical that the fastest and simplest test be carried out initially, typically using parallel imaging techniques based on optical, confocal, or fluorescence microscopies. This initial information, though it has "low information content" and lacks the ability to give insight on the chemical or mechanical properties, provides the means to rapidly identify potential "lead biomaterials" or compatible surfaces. This first step of the characterization process provides the highest throughput and can provide data on >1,000 biomaterials arrayed on glass slides or within microtiter plates in a matter of hours. For some materials, such as sol-gel derived materials, the initial florescence imaging method can provide useful information on printability, spot uniformity and reproducibility, adhesion to the surface, and assay compatibility. This information can be used to select lead materials, which can dramatically reduce the number of materials that must be characterized using slower methods that have higher information content [23].

More advanced characterization of lead materials can take many forms, including evaluation of chemical or mechanical properties, examination of bioactivity of entrapped biologicals (enzyme activity, DNA hybridization, etc.), or interactions between biomaterials and biological entities, such as proteins, nucleic acids, or cells, using a wide range of spectroscopic (i.e., surface plasmon resonance (SPR), XPS, Raman, FTIR, etc.), mass spectrometric (matrix-assisted laser desorption/ionization mass spectrometry (MALDI-MS), ToF-SIMS), or physicochemical methods (contact angle, surface charge, electron microscopy, atomic force microscopy). Among these techniques, some give chemical information, others physical properties. Importantly, many of these methods operate under high vacuum (MALDI-MS, ToF-SIMS, XPS) and thus are more suitable for providing a snapshot of a biomaterial or biomolecular interaction, while others, such as FTIR, SPR, or Raman, can operate under ambient or even physiological conditions and provide real-time data on the nature of biomaterials and interactions. However, even when operated in an imaging mode (which is possible for SPR, Raman, FTIR, XPS, MALDI-MS, or ToF-SIMS), the sample preparation and need to slowly raster over the sample can require up to several days to read a full microarray. When used strictly to probe lead materials following initial screening, these methods can provide a wealth of information in a "medium-throughput" format. As an example
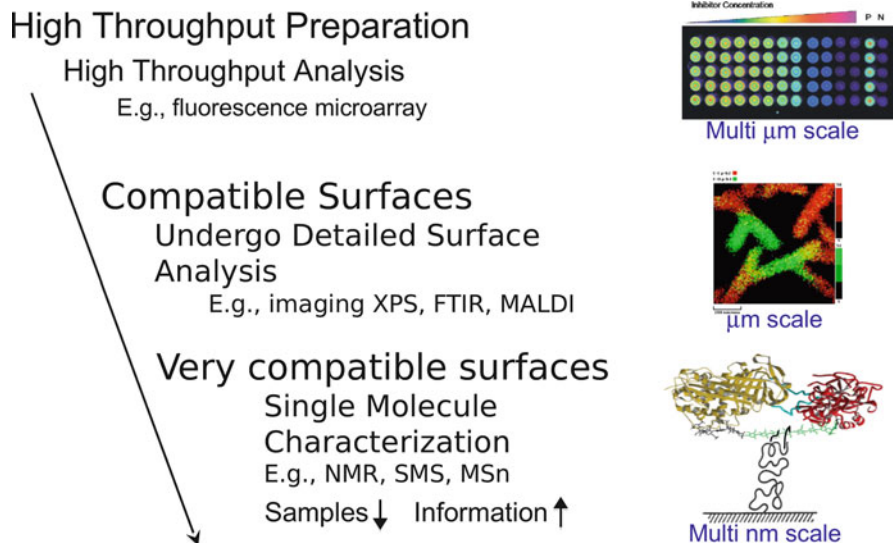
Fig. 30.3 Illustration of the general principle of the parallel high-throughput synthesis and characterization. As the number of the samples drops down, the amount of extracted information goes up

of this medium-throughput approach, Davies and coworkers analyzed the surface chemistry of 576 polymers with three techniques, XPS, ToF-SIMS, and water contact angle (WCA) measurements, though this required a total of 6 days [50]. These techniques, however, provided high information content on the biomaterials, including elemental and functional group composition of the biomaterial surfaces that could be correlated to the polarity of the material. Using principal component analysis (see below), these data provided a predictive model for biomaterial properties that could be used to control cell adhesion.

In terms of specific chemical information, methods such as XPS and ToF-SIMS provide information on the surface properties of biomaterials. Low resolution XPS provides a quantitative analysis of the chemical elements present in the top 10 nm of the sample, while high resolution XPS can elucidate the different functional groups present in this layer, such as alkyl, alcohol, amine, or carboxylic acids. Complementary to XPS, ToF-SIMS analysis, which is a destructive method, provides information on the top few molecular layers of the sample, to a depth of $\sim$1 nm, and gives a quantitative analysis of the elements present at the interface and the molecular entities they form [51]. For information on the chemical properties of the bulk material, methods such as FTIR and Raman imaging can be utilized (Fig. 30.4) [23]. These methods provide data on the nature of the chemical groups present in the sample, and can give relative amounts of different functional groups within the material. It is also possible to screen, in a high-throughput
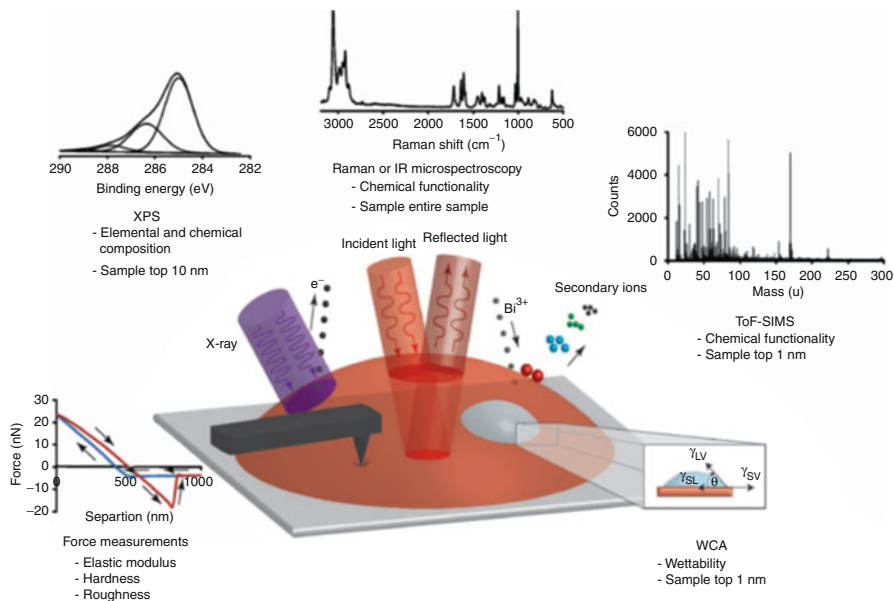
Fig. 30.4 Schematic illustration of the most common high-throughput characterization techniques used for the screening of the properties of polymer-based microarrays [7]

manner, the wettability of a polymer library, or the adhesion and adsorption of a protein or cell onto a polymer microarray using AFM (atomic force microscopy) [26, 52].

As the number of the samples decreases, more accurate and time-consuming techniques can be implemented on the most promising biomaterials. Among these analytical techniques, one can utilize NMR (nuclear magnetic resonance), imaging SPR, and MALDI-MS. In theory, NMR can be applied to virtually any atoms with a spin number different from zero. This method provides detailed information on the chemical environment of an atom and can be used with both liquid phase and solid-state materials (i.e., magic angle spinning (MAS) or double rotation (DOR) experiments). For structural elucidation of macromolecules, which are hard to obtain in a crystalline form, or for other amorphous materials, like silica, NMR is among the most informative characterization techniques [53, 54].

Surface plasmon resonance imaging or microscopy, SPRi, can be used to monitor, in a high-throughput manner, in real time and label-free, interactions between arrayed biomaterials and biomolecules, such as DNA and proteins [55]. SPRi can be used to monitor on and off rates of biological species interacting with materials. From this, thermophysical data such as association and dissociation constants can be obtained. However, SPRi has the disadvantage of being unable to identify the components that adsorb from a mixture. Fortunately, one can take advantage of its nondestructive working principles. As such, SPRi can be coupled to other techniques, such as MALDI-MS, to perform further analyses [56]. MALDI-MS can be used to identify

proteins that have adsorbed, using either the conventional "bottom-up" approach involving tryptic digestion on the surface, or more recently with "top-down" approaches to directly fragment and sequence proteins that are adsorbed to surfaces. This is particularly useful when studies involve adsorption of unknown proteins from complex matrixes. Thus, by combining SPRi and MALDI, one can obtain both thermodynamic and kinetic data, as well as protein identity.

Data Analysis

Principal Component Analysis

Characterizing how the chemical and physical properties of a surface correlate with the desired functional response is a key part of identifying lead biomaterials. Combining multiple measurements from the same or multiple characterization techniques produces high-dimensional datasets that are hard to analyze and visualize. Two commonly employed methods for simplifying and understanding such datasets are principal component analysis (PCA) and regression analysis, especially partial least squares (PLS) regression. Principal component analysis is a commonly employed statistical method for reducing high-dimensional datasets to lower dimensionality with minimal loss of information [57]. Given a set of N-dimensional data points (N different axes of measurement), PCA iteratively computes a complementary set of N orthogonal vectors as linear combinations of the original variables (axes). The first computed vector, or principal component (PC), is in the direction of highest variance within the dataset. The second PC, orthogonal to the first, is in the direction of the highest *remaining* variance, and so on. By projecting each data point onto a subset of PCs that account for the most variance, the dimensionality of the dataset can be reduced without substantial loss of information and inform about the actual complexity of a dataset (Fig. 30.5a, b). For example, a dataset of 10 different measurements could be described with only one or two PCs if the majority of measurements are correlated. Furthermore, the distance of a PC axis from the originally measured variable axes provides information about which features are responsible for the most chemical heterogeneity. When PCA is performed on variables with different units, care must be taken to scale measurements in some way to ensure that a comparison of variances is well founded.

Explaining the mechanisms underlying successful versus unsuccessful biomaterials is critical for optimizing future iterations of material synthesis. Predictive models of biomaterial characteristics are often employed to form hypotheses of which properties are important for synthesizing an optimal biomaterial. In simple cases, a linear regression analysis will generate a predictive model of a desired observed property (e.g., enzyme activity) as a linear function of material properties; however, a linear regression model will fail to capture interactions of material properties. Principal component regression (PCR) builds a linear model from the reduced dimensionality PCs acquired from PCA. That is, the desired
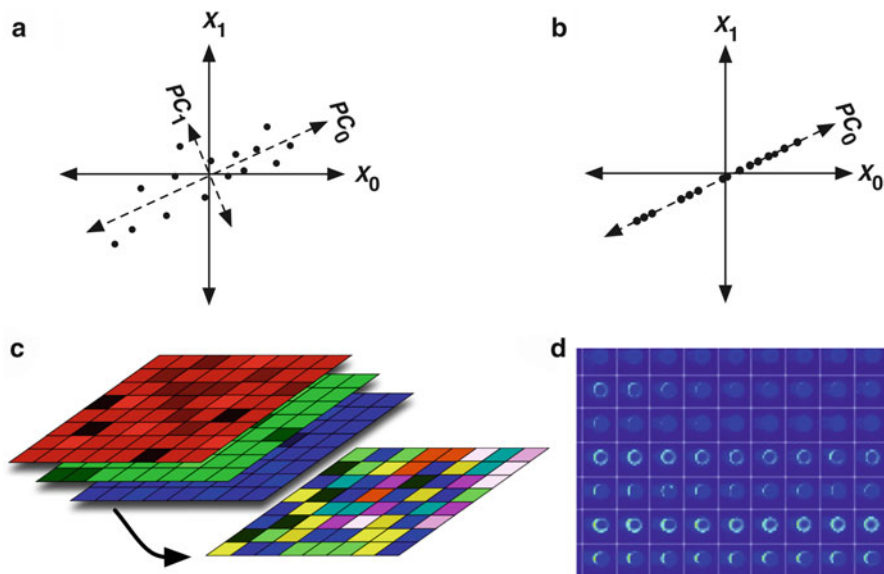
Fig. 30.5 Illustrations of data analysis techniques. (**a**) Principal component analysis on 2D data measured on two axes, X_0 and X_1. PCA analysis generates two new axes, PC_0 and PC_1, orthogonal to the original axes, with PC_0 in the direction of the highest variance. (**b**) The same data as in (**a**) but with reduced dimensionality (from 2 dimensions down to 1 dimension). Note how the majority of variance in the data is still preserved. (**c**) Image data consists of an array of pixels made of *N*-dimensional data points (shown as *red*, *green*, and *blue* layers). Composed together gives a multichannel image. (**d**) Example image of a fluorescing microarray with a defined grid from image analysis software

observed variable, *Y*, can be written as a linear function of PCs with coefficients that minimize the error between predicted and observed values ($Y = b_0 + b_1.PC1 + b_2.PC2 + \ldots$). If the PCs can be interpreted in an informative way, then one can calculate the optimal coefficients, $b_0, b_1, b_2, \ldots$, for producing the desired outcome of *Y* and thus determine the optimal material synthesis procedure. Partial least squares (PLS) regression, developed by Swedish statistician Wold Herman, is similar to PCA in that it produces a linear model from latent variables that are orthogonal combinations of the original variables except that the factors (axes) in PLS are determined as a function of variance in both the measured *and* the response variable [57–59]. As a result, PLS regression models can have predictive capabilities on par with PCA models while using fewer explanatory variables (lower dimensionality).

Image-Based Data Analysis

Image-based characterization techniques are increasingly being used in spectroscopy to map the local and global compositional properties of a sample [60].

Image-based analysis can also be adapted for multivariate analysis across multiple instruments and analysis techniques. An *image* is typically a 2D array of *N*-dimensional data points (pixels) where each dimension represents a particular measurement at that location of the sample. For visualization of related measurements (e.g., the concentration of different compounds), the values can be mapped to a specific numerical range (e.g., 0–1 or 0–255) and then assigned a color channel: red, green, or blue (Fig. 30.5c). Such visualizations make it easy to observe compound distribution and co-localizations across an image. For example, a compound concentration image map could be combined with an enzyme activation map (observed via fluorescence) to determine sample compositions that favor enzyme activity.

Recent advances in high resolution image-based analysis with SPR, Raman, FTIR, XPS, MALDI, and TOF-SIMS (see above) allow images to be used as a common data encapsulation device for cross technique multivariate analysis. Analysis software can be general purpose, agnostic to the particular measurement at hand, allowing for powerful cross-analysis insights to be gained. Image analysis procedures are easily extendable to microarray analysis by imaging the entire sample array, both the sample and the background area, then using microarray analysis software to define a grid pattern over the image (Fig. 30.5d). Independent analysis within each grid region (spot) can then be performed as though each region was individual sample characterized independently. Microarray image analysis can easily be performed in parallel across multiple processors for fast and automated analysis.

Examples of High-Throughput Studies of Biomaterials

As noted above, high-throughput screening methodologies were first applied to the synthesis of peptide libraries. Since then, the use of these methodologies has undergone significant development and is currently a very useful and efficient technique that has been applied in the fabrication of a wide range of materials, including organic and bio-organic materials, nanomaterials, and hybrid organic-inorganic materials. Among organic materials, the production of polymer libraries has attracted the most attention. Biochips, comprised of arrays of inorganic or organic-inorganic hybrids, have also been an area of intense research, with one of the key goals being production of materials that support production of 3D protein or cell microarrays. For nanoparticles, it is possible to generate libraries, such as peptides, on the surface of beads [61]. Each of these examples is discussed in more detail below.

Organic and Bio-organic Materials

Organic Polymer Libraries
The group lead by Langer was the first group to report on the semi-automated screening of polymer libraries [62]. Prior to this, the same group carried out

a manual screening for the synthesis of transfection polymer-based vectors for gene delivery [63, 64]. These findings opened up a new era in the field of polymer-based library synthesis using CombiChem and HTS techniques. This domain is currently the subject of interest of several groups.

The nature, number, and rate of mixing of the premixed polymers or monomers have been thoroughly investigated as these parameters confer to the so-produced polymers their physical, mechanical, and chemical properties which underpin the potential applications of these materials. Among these parameters, those that are often evaluated include the Young's modulus, the hydrophobicity/hydrophilicity, the wettability, the biocompatibility, adhesion, and adherence. Once this is completed, the material is then screened for a given application, such as retention of immobilized protein activity, resistance to protein or cell binding, selective recruitment of desired proteins, or selective differentiation of stem cells.

The diversity of starting monomers or polymers has made polymer-based microarrays an expanding area in the field of biomaterials. It is possible to build microarrays starting from different monomers belonging to the same class, like diacrylates, two different monomers belonging to two different classes, such as diacrylates and amines, or with three different monomers belonging to three different classes like methacrylates, acrylamide, and acrylates [14, 62, 65]. The same trend has been observed when the starting reagents are polymers. For instance, the group led by Bradley has produced polymer microarrays by printing the same polymer, such as polystyrene or a blend of two different polymers from different classes, like poly(ethylenimine), poly(ethylene oxide), and poly(vinyl acetate) [23]. Mixing different polyols with different diisocyanates is the only example of a polymer made from the reaction of a polymer with a monomer [66]. But in this case, a chain extender, that is, another monomer, was used.

Depending on the desired application, these libraries can be produced at the gram-scale level or in a microarray format [36, 65]. Generally, the printed spots of polymers are hemisphere-shaped. However, it is possible to design cross-linked lines of polymer forming a grid network [67]. The most widely used procedure in the building of polymer arrays involves starting from different monomers, these chemical entities may be premixed before being printed or spotted directly onto the support [19]. As an example of the first approach, Anderson et al. used a liquid-handling robot to premix a series of acrylate monomers (Fig. 30.6) [65]. As this polymerization involves a free radical mechanism, and therefore requires the absence of oxygen, the process was carried out in an atmosphere of humid argon with less than 0.1 % of O_2 present. To perform the printing onto epoxy-coated glass slides, they had to add 25 % of dimethyl formamide to the pre-formed polymer to reduce the viscosity, increase the washing and preprinting steps, and modify the pin speed and size. The polymerization occurred after the slides were exposed for ~10 s to long wavelength UV irradiation. The group led by Bradley contact printed the same polymer (polyacrylate) onto agarose-coated glass slides. Instead of using UV irradiation, the synthesis of the polyacrylates was carried out in the presence of an initiator [18]. Using fluorescence imaging, this polymer library was screened to assess platelet attachment, as this is a key initial process in blood coagulation and
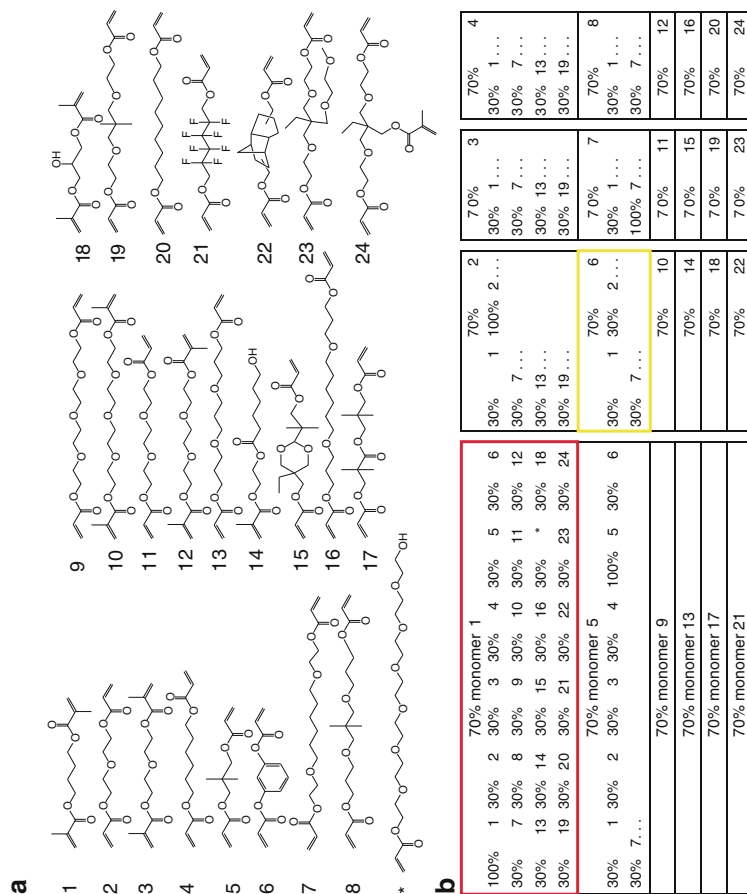
Fig. 30.6 (a) List of the monomers used for the fabrication of polymer-based microarrays; and (b) the composition of each monomer mixed pairwise in all the possible combinations, monomer 17 excepted (replaced by * in order to increase the hydrophilicity) (Adapted from Anderson et al. [65])

wound healing. A total of 12 polyacrylates displayed higher or similar binding compared to collagen-coated surfaces, and improved the activation state of the platelets. As a result, these promising polyacrylate formulations could be used in wound-healing applications [18]. In addition to premixing monomers, it is also possible to directly premix polymers in order to synthesize co-polymer-based microarrays [17]. For example, Anderson et al. prepared a series of poly (lactide-co-glycolide) materials by printing combinations of monomers onto arrays and examining stem cell adhesion and growth on the polymer microarray.

The Bradley group reported on the fabrication of arrays of polymer gradients using a non-contact printer. To do so, acrylate and acrylamide monomers were printed onto a pre-treated glass slide, on a drop-by-drop basis, in N-methyl-2-pyrrolidone (NMP, the solvent), in the presence of 1,4-butanediol acrylate in NMP (a cross-linker) and 1-hydroxycyclohexyl phenyl ketone in NMP, which acted as a photo initiator [68]. Prior to UV radiation, the glass was compressed by another fluorous-coated glass, leading to the merging of the spots and giving rise to the gradients. To ensure complete polymerization, these slides were heated overnight at 50 °C and then rinsed to remove any non-polymerized moieties. Such gradients allowed for rapid identification of polymer compositions that were optimal for binding either suspended or adherent cell lines.

Hydrogels Nanoarrays and Microarrays

Hydrogels are networks made of natural or synthetic polymeric chains that are hydrophilic and in some cases form colloidal gels dispersed in water. Hydrogels are superabsorbent, and can contain over 99 % water. The hydrophilicity of the polymeric chains makes the hydrogels generally biocompatible, and thus, hydrogels find numerous applications in the biomedical field [69]. These applications include, among others, wound care, drug delivery, tissue engineering, and injectable polymeric systems.

An interesting feature of such materials is their ability to form very high resolution structures. As an example, a field-emission gun scanning electron microscope (FEG-SEM) was used for high resolution electron beam rastering by Saaem et al. to design hydrogel-based protein nanoarrays [70]. A thin film of monoamine terminated PEG (PEG-NH$_2$) was first deposited onto a glass slide, followed by irradiation with a 2 keV electron beam to create the nanoarrays. The resulting material was then cross-linked to a target protein, taking advantage from the presence of the amine moieties. The formation of the so-designed arrays was monitored using fluorescence and SEM imaging. In 2008, the group led by Bradley used an ink-jet printer to elaborate hydrogel microarrays [47]. The arrays were prepared in two ways. The first one consisted of the spotting of premixed monomers followed by their polymerization. The second method consisted of the printing of a series of monomers and the overprinting of another series of monomers, which was followed by the in situ formation of the hydrogels. The same group reported in 2009 the non-contact printing fabrication of microarrays of over 2000 hydrogels [71]. Two monomers, in different molar ratios, were spotted onto a glass slide and left to polymerize, in situ, in the presence of an initiator. Among all these

combinations, 23 were identified as "hits" for the binding of HeLa cells. Further evaluation showed that only three compositions could bind HeLa cells efficiently at 37 °C and release them upon cooling. This was reported as the first temperature-dependent ON/OFF attachment switch for cells. It is also possible to produce protein-based and peptide-based hydrogel microarrays by similar methods, which were used to examine kinase activity in cell lysates [72, 73].

Hybrid Organic-Inorganic Materials

The sol-gel process has been used extensively for the immobilization of a large number of biological species within inorganic matrices, in a mild and efficient manner. Among these biological hosts, a wide variety of proteins, DNA aptamers, and cells including yeast, bacteria, plant, micro-algae, and mammalian cells have been entrapped in silica monoliths without any major loss or alteration of biological activity. Perhaps one of the most exciting advances is the use of sol-gel based materials to form protein microarrays [74–78]. The earliest examples of protein arrays used contact spotting of proteins directly onto a surface (2D arrays), as exemplified by the work of Macbeath et al. in 2000 [79]. These platforms were used to study protein-protein interactions, and to screen protein kinase substrates and protein targets. Snyder et al. extended this work in 2001 to the fabrication of protein microarrays containing the whole yeast proteome, and since this time, a wide range of studies have appeared on the production of 2D protein arrays using contact printing or non-contact spotting of proteins [79–81].

The versatility of the sol-gel process has also allowed the design of 3D protein microarrays as well as arrays of aptamers (see below) and membrane proteins [82]. In each case, the material can be tuned so that the pores of the inorganic network offer the entrapped biological enough space to retain functionality. The addition of glycerol or sugars to the sol-gel composition prevents the dehydration of the immobilized biomolecules [30]. These capabilities make sol-gel materials well suited for the production of high-density and active 3D protein or cell microarrays. Given the large number of starting reagents involved in matrix synthesis, such as silica precursors, additives and buffers, and the experimental parameters to be tuned, such as the concentration of each reagent, the ionic strength and the pH of the buffer, the development of sol-gel derived protein microarrays is one area where a CombiChem/HTS approach is ideally suited.

At this time, there are only a few groups around the world that are working on sol-gel derived protein microarrays and thus, the number of published papers is limited. The group led by Clark published some of the earliest papers in the area, and reported on the design of enzyme-based microarrays using a micro-patterning method or an ink-jet printer [83–85]. In the first two papers, the enzyme was entrapped within sol-gel derived materials, while cytochrome P450 was encapsulated within alginate for the last example. The same team designed a metabolizing enzyme toxicity assay chip (Metachip). This chip consisted of two components: MTMS (methyltrimethoxysilane) sol-gel entrapped human cytochrome P450 (CYP)

microarrays and a cancer cell monolayer [82]. The overprinting of a lead compound, or a prodrug, on the sol-gel spots resulted in catalysis and the release of active metabolites. Then, the cancer cell monolayer was stamped onto the P450 sol-gel based microarrays and left to incubate for 6 h at 37 °C. After this incubation step, the cell monolayer was examined using a live/dead test kit, demonstrating that CYP microarrays could convert nontoxic prodrugs into a cytotoxic chemotherapeutic drug. While ∼13 % of cell death was observed in spots containing no CYP, almost all cancer cells died upon contact with CYP microarrays.

One of the first examples of utilizing an HTS approach for formulation of an optimized sol-gel material was reported by Cho et al. in 2002 [32]. In this work, the authors screened 900 organic polymer or sol-gel formulations via pin-printing of materials as a microarray, with two desired outcomes. In the first screen, materials were selected based on their ability to degrade and release keratinocyte growth factor (KGF), which is a key component in wound healing. In the second screen, tetramethoxysilicate-based sol-gel materials were screened for their ability to retain the activity of the anti-fluorescein antibody. In each case, a large number of "hits" were identified (i.e., up to 80 % of materials showed some activity for entrapped antibodies), and it was noted that some of the active compositions identified would not have been likely to be generated using a rational design approach.

Much more extensive sol-gel material screening studies have been carried out by the group of Kim, who has examined methods to prepare protein and aptamer microarrays via a screening approach involving non-contact printing of sol-gel polymers with entrapped biological moieties. Initial work involved the screening of 100,000 sol-gel based materials for the fabrication of protein chips by combining seven silicate monomers, two intermediates, six additives, and three buffer conditions [30]. Of these, ∼700 combinations proved to be amenable to formation of microarrays (good adhesion, spot morphology, and optical properties) and a subset of seven materials were found to be optimal to retain the activity of the entrapped proteins. Such materials were utilized for both antibody microarrays and for entrapment of cyclin T to study protein-protein interactions. These materials also proved to be amenable to the selection of RNA aptamers from a random library using immobilized hepatitis C virus (HCV) proteins in a protein chip format, and for subsequent immobilization of the identified optimal aptamer for detection of HCV [86, 87]. A similar high-throughput material screening study was performed to identify optimal materials for entrapment of DNA or RNA aptamers, and these materials were subsequently utilized to produce aptamer chips for protein capture, with on-chip tryptic digestion followed by ESI mass spectrometry for protein identification [88, 89].

Our research group has examined the use of sol-gel based materials as a platform for development of antibody and enzyme microarrays. Early work utilized a low-throughput screening approach to evaluate a limited number of materials, mainly focusing on those materials that retained biological activity for a small selection of biomolecules [90, 91]. These were previously identified from studies of protein activity using bulk materials, and were then examined for the ability to be
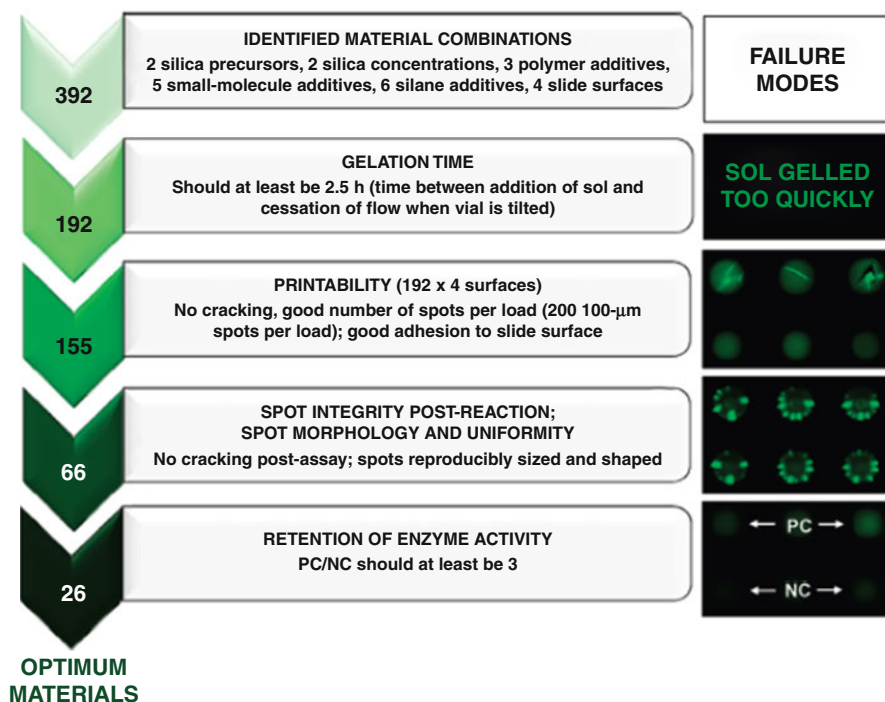
Fig. 30.7 Illustration of the approach followed for the design of sol-gel based AChE microarrays [29]

adapted for printing microarrays. While successful, these materials did not permit printing of large-scale arrays owing to issues with short gelation times [92]. A more recent study evaluated high-throughput screening of sol-gel based materials for production of enzyme microarrays, which were subsequently used as a platform for nanovolume screening of small molecule libraries to identify enzyme inhibitors, as shown in Fig. 30.7 for the case of acetylcholinesterase (AChE) [28, 29]. A total of ~2,000 material/surface combinations were evaluated to identify suitable formulations. Sols were first evaluated for gelation time, with those having a 2.5 h or longer gelation time moving to the second stage based on the ability to allow printing of high-density arrays within this time frame. These formulations were then screened for printability, adhesion to the supporting substrate, shape and size uniformity of the spots, and absence of cracking. Materials that passed this stage were screened for assay compatibility, and those that moved forward from this stage were finally screened for retention of the enzymatic activity. Ultimately, 26 materials provided activity for entrapped AChE, while only 2 of these 26 proved to be able to retain the activity of a set of four kinases. This demonstrates that the ability of the sol-gel materials to maintain enzyme activity is dependent on the protein, although even labile proteins such as kinases can be stabilized when appropriate materials are used.

Organic and Inorganic Particles

The use of inorganic nanomaterials in the biomedical field has attracted a lot of attention over the past two decades. By exploiting their unique optical or magnetic properties, and their highly adaptable porosity and surface chemistry, these materials can be used as sensing agents, drug or biomolecule carriers, imaging agents, as therapeutics for diseases such as cancer, or as agents to deactivate biological species such as bacteria [93–96]. Traditionally, chemists examine a set of experimental parameters to produce the desired nanomaterials, which can be made of inorganic, hybrid, or polymeric materials. However, this time- and energy-consuming approach allows the screening of only a few limited parameters. Once the materials are fabricated, their properties are screened using standard techniques (UV-vis, XRD, XPS, Magnetometer, etc.) and their potential applications are assessed. However, in recent years, HTS tools, mainly liquid-handling robots, have made it is possible to synthesize tens to hundreds of materials at a time and characterize their properties rapidly in order to assess their potential usage in the biomedical field. These tools can also be used to identify the optimal capping agents needed to improve nanoparticle stability, functionality, and addressability when used for multiplexing.

Recently, several papers reporting the production of nanomaterials using combinatorial methods have been published. For instance, polymeric particles are particularly interesting for drug, gene, or small molecule delivery. They exist in a wide range of formulations and molecular weights and can be adapted to the host therapeutic agents. However, this wide range of chemical combinations are impossible to explore with standard laboratory syntheses. It is thus important to utilize high-throughput synthesis and screening methods to produce nanoparticles with desired properties [37, 62, 97–101]. As an example, Siegwart et al. used a high-throughput method for the synthesis, characterization, and screening of core-shell polymeric nanoparticles (Fig. 30.8) [37]: 1,536 nanoparticles (16 block co-polymers × 96 amines) were synthesized with liquid-handling robotics in glass vials in a 96 well-plate format (Fig. 30.8a). These particles were then tested for complexation and delivery of siRNA (small interfering RNA, short double stranded RNA molecules that can knock down expression of a specific gene). This work demonstrates the great utility of high-throughput synthesis formulation.

Automated synthesis of polymer particles can also be conducted with a contact pin printer. Acharya et al. synthesized PLGA (poly(lactide-co-glycolide)) microparticles loaded with 216 compositions of hydrophobic fluorescent molecules. The different content of dyes (coumarin, rhodamine, and cyanine) simulates varying loads of drugs in polymer particles [100]. At first, the dyes were printed in a 384-well plate. After that, the polymer precursors were added to the medium with a multichannel pipette to generate nanoparticles via oil-in-water emulsion. Combined with HT microarray printing, the so-produced 216 particles were evaluated against dendritic cells for drug delivery. This experiment was conducted within a few days and proved that with HT techniques, optimized delivery systems can be achieved in a short timescale [102].
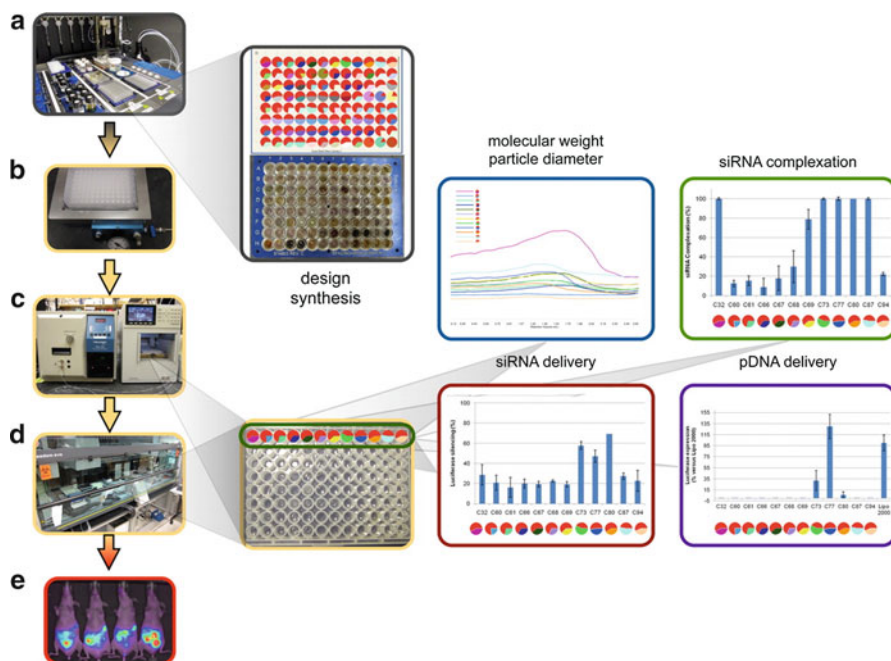
Fig. 30.8 A typical example of polymers particles synthesized and characterized in a high-throughput manner [37]

Although HT synthesis has proven to be a promising technique for biopolymer particle design, its application in the field of inorganic particles is more limited. In most of the cases, the nanoparticles are obtained with a low material/volume yield, and a synthesis conducted using a microarray printing method, for example, will not give enough products. It is also worth noting that the main tools for characterizing inorganic particles, such as solid-state NMR, XRD, and TEM, are not amenable to high-throughput analysis of nanoparticles. However, certain atoms, like silicon or vanadium with a high rate of condensation, can form oxides or hydroxides over a wide range of conditions. Indeed, sol-gel type synthesis of silica particles with a high product/volume yield using mild conditions can be easily run using an automated synthesis platform. For example, Tse et al. reported on the synthesis of mesoporous silica doped with gadolinium as an MRI contrast agent [38]. The properties of the obtained materials were similar to those of materials obtained in larger batch syntheses and proved that HT synthesis is a reliable technique for material preparation. The authors reported a size polydispersity slightly higher than that obtained using bulk synthesis methods, but this may be related to the local variation of parameters such as surfactant concentration or calcination temperature due to the location in the furnace. With bigger batch sizes, these kinds of variations remain unnoticed due to a mass averaging effect [46].

Conclusion and Perspectives

The use of HTS and CombiChem methodologies has allowed the rapid expansion of the biomaterial field by the generation of libraries consisting of thousands of materials in a time- and cost-effective manner. While the CombiChem/HTS approach originated in the pharmaceutical industry as a means for more rapid lead discovery, this method has now been successfully adapted to produce a range of polymeric material libraries, mainly based on microarrays, by combining a number of available starting monomers that can lead to biocompatible materials that are suitable for a range of applications. The microarray platform takes advantage from the ability to design high-density arrays of varying composition, which can be rapidly characterized by a range of established and emerging imaging methods and analyzed using advanced multi-parametric regression and image analysis techniques. The ability to generate and assay large numbers of biomaterials in a short time has led to the discovery of a range of materials with improved performance in applications as diverse as resistance of bacterial attachment, control of cell adhesion or differentiation, retention of protein activity, improved drug release properties, or resistance to nonspecific binding of proteins. When combined with advanced data analysis tools, the output of HTS studies also provides an efficient way to create new fundamental knowledge about parameters that influence material performance in a given application.

Over the coming years, it is likely that the number of materials-based HTS studies will grow, the types of materials examined by such methods will expand, and that new applications of biomaterials HTS will emerge to address issues related to biosensor performance, implantable devices, and coatings that are resistant to biofouling or biofilm formation, among many others. In addition, as has been the case for genomics and proteomics data, the wealth of new biomaterials and biointerface data will create the need for a standardized repository to store, catalog, and allow mining of this data so as to glean the maximum amount of useful information from the HTS studies. Such a resource will be critical to understanding the factors controlling material-biological interactions, and could serve as a global focal point for biomaterials and biointerface research.

References

1. Maier WF (1999) Combinatorial chemistry – challenge and chance for the development of new catalysts and materials. Angew Chem Int Ed 38:1216–1218
2. Webster DC (2008) Combinatorial and high-throughput methods in macromolecular materials research and development. Macromol Chem Phys 209:237–246
3. Lowe G (1995) Combinatorial chemistry. Chem Soc Rev 24:309–317
4. Meredith JC (2009) Advances in combinatorial and high-throughput screening of biofunctional polymers for gene delivery, tissue engineering and anti-fouling coatings. J Mater Chem 19:34–45
5. Wu P, Castner DG, Grainger DW (2008) Diagnostic devices as biomaterials: a review of nucleic acid and protein microarray surface performance issues. J Biomater Sci Polym Ed 19:725–753

6. Henderson G, Bradley M (2007) Functional peptide arrays for high-throughput chemical biology based applications. Curr Opin Biotechnol 18:326–330
7. Hook AL, Anderson DG, Langer R et al (2010) High throughput methods applied in biomaterial development and discovery. Biomaterials 31:187–198
8. Mei Y, Gerecht S, Taylor M et al (2009) Mapping the interactions among biomaterials, adsorbed proteins, and human embryonic stem cells. Adv Mater 21:2781–2786
9. Kohn J, Welsh WJ, Knight D (2007) A new approach to the rationale discovery of polymeric biomaterials. Biomaterials 28:4171–4177
10. Su G, Yan B (2010) Nano-combinatorial chemistry strategy for nanotechnology research. J Comb Chem 12:215–221
11. Potyrailo R, Rajan K, Stoewe K et al (2011) Combinatorial and high-throughput screening of materials libraries: review of state of the art. ACS Comb Sci 13:579–633
12. Hook AL, Chang CY, Yang J et al (2012) Combinatorial discovery of polymers resistant to bacterial attachment. Nat Biotechnol 30:868–875
13. Pernagallo S, Diaz-Mochon JJ, Bradley M (2009) A cooperative polymer-DNA microarray approach to biomaterial investigation. Lab Chip 9:397–403
14. Pernagallo S, Wu M, Gallagher MP et al (2011) Colonising new frontiers – microarrays reveal biofilm modulating polymers. J Mater Chem 21:96
15. Wu M, Bridle H, Bradley M (2012) Targeting Cryptosporidium parvum capture. Water Res 46:1715–1722
16. Pickering H, Wu M, Bradley M et al (2012) Analysis of Giardia lamblia interactions with polymer surfaces using a microarray approach. Environ Sci Technol 46:2179–2186
17. Anderson DG, Putnam D, Lavik EB et al (2005) Biomaterial microarrays: rapid, microscale screening of polymer–cell interaction. Biomaterials 26:4892–4897
18. Hansen A, McMillan L, Morrison A et al (2011) Polymers for the rapid and effective activation and aggregation of platelets. Biomaterials 32:7034–7041
19. Yang J, Mei Y, Hook AL et al (2010) Polymer surface functionalities that control human embryoid body cell adhesion revealed by high throughput surface characterization of combinatorial material microarrays. Biomaterials 31:8827–8838
20. Mei Y, Saha K, Bogatyrev SR et al (2010) Combinatorial development of biomaterials for clonal growth of human pluripotent stem cells. Nat Mater 9:768–778
21. Fisher OZ, Khademhosseini A, Langer R et al (2009) Bioinspired materials for controlling stem cell fate. Acc Chem Res 43:419–428
22. Hay DC, Pernagallo S, Diaz-Mochon JJ et al (2011) Unbiased screening of polymer libraries to define novel substrates for functional hepatocytes with inducible drug metabolism. Stem Cell Res 6:92–102
23. Khan F, Tare RS, Kanczler JM et al (2010) Strategies for cell manipulation and skeletal tissue engineering using high-throughput polymer blend formulation and microarray techniques. Biomaterials 31:2216–2228
24. Tare RS, Khan F, Tourniaire G et al (2009) A microarray approach to the identification of polyurethanes for the isolation of human skeletal progenitor cells and augmentation of skeletal cell growth. Biomaterials 30:1045–1055
25. Roska RLW, Lama TGS, Hennes JP et al (2009) Small molecule-based binding environments: combinatorial construction of microarrays for multiplexed affinity screening. J Am Chem Soc 131:16660–16662
26. Taylor M, Urquhart AJ, Anderson DG et al (2008) A methodology for investigating protein adhesion and adsorption to microarrayed combinatorial polymers. Macromol Rapid Commun 29:1298–1302
27. Scoutaris N, Hook AL, Gellert PR et al (2012) ToF-SIMS analysis of chemical heterogenities in inkjet micro-array printed drug/polymer formulations. J Mater Sci Mater Med 23:385–391
28. Ge X, Lebert JM, Monton MRN et al (2011) Materials screening for sol–gel-derived high-density multi-kinase microarrays. Chem Mater 23:3685–3691

29. Monton MRN, Lebert JM, Little JRL et al (2010) A sol–gel-derived acetylcholinesterase microarray for nanovolume small-molecule screening. Anal Chem 82:9365–9373

30. Kim S, Kim Y, Kim P et al (2006) Improved sensitivity and physical properties of sol–gel protein chips using large-scale material screening and selection. Anal Chem 78:7392–7396

31. Ahn J-Y, Lee S, Jo M et al (2012) Sol–gel derived nanoporous compositions for entrapping small molecules and their outlook toward aptamer screening. Anal Chem 84:2647–2653

32. Cho EJ, Tao Z, Tehan EC et al (2002) Multianalyte pin-printed biosensor arrays based on protein-doped xerogels. Anal Chem 74:6177–6184

33. Doong R-a, Lee P-S, Anitha K (2010) Simultaneous determination of biomarkers for Alzheimer's disease using sol–gel-derived optical array biosensor. Biosens Bioelectron 25:2464–2469

34. Tsai H-c, Doong R-a (2005) Simultaneous determination of pH, urea, acetylcholine and heavy metals using array-based enzymatic optical biosensor. Biosens Bioelectron 20:1796–1804

35. Bible E, Chau DYS, Alexander MR et al (2009) Attachment of stem cells to scaffold particles for intra-cerebral transplantation. Nat Protoc 4:1440–1453

36. Anderson DG, Peng W, Akinc A et al (2004) A polymer library approach to suicide gene therapy for cancer. Proc Natl Acad Sci USA 101:16028–16033

37. Siegwart DJ, Whitehead KA, Nuhn L et al (2011) Combinatorial synthesis of chemically diverse core-shell nanoparticles for intracellular delivery. Proc Natl Acad Sci USA 108:12996–13001

38. Tse NM, Kennedy DF, Moffat BA et al (2012) High-throughput preparation of hexagonally ordered mesoporous silica and gadolinosilicate nanoparticles for use as MRI contrast agents. ACS Comb Sci 14:443–450

39. Zhang B, Xing Y, Li Z et al (2009) Functionalized carbon nanotubes specifically bind to α-chymotrypsin's catalytic site and regulate its enzymatic function. Nano Lett 9:2280–2284

40. Zhou H, Mu Q, Gao N et al (2008) A nano-combinatorial library strategy for the discovery of nanotubes with reduced protein-binding, cytotoxicity, and immune response. Nano Lett 8:859–865

41. Petersen LK, Sackett CK, Narasimhan B (2010) Novel, high throughput method to study in vitro protein release from polymer nanospheres. J Comb Chem 12:51–56

42. Barbulovic-Nad I, Lucente M, Sun Y et al (2006) Bio-microarray fabrication techniques – a review. Crit Rev Biotechnol 26:237–259

43. Calvert P (2001) Inkjet printing for materials and devices. Chem Mater 13:3299–3305

44. de Gans BJ, Duineveld PC, Schubert US (2004) Inkjet printing of polymers: state of the art and future developments. Adv Mater 16:203–213

45. Derby B (2010) Inkjet printing of functional and structural materials: fluid property requirements, feature stability, and resolution. Annu Rev Mater Res 40(40):395–414

46. Tsai J, Kim CJ (2002) Second joint embs-bmes conference 2002, vols 1–3. Conference proceedings. pp 1632–1633

47. Zhang R, Liberski A, Khan F, et al (2008) Inkjet fabrication of hydrogel microarrays using in situ nanolitre-scale polymerisation. Chem Commun 11: 1317–1319

48. Taylor M, Urquhart AJ, Zelzer M et al (2007) Picoliter water contact angle measurement on polymers. Langmuir 23:6875–6878

49. Gutmann O, Kuehlewein R, Reinbold S et al (2005) Fast and reliable protein microarray production by a new drop-in-drop technique. Lab Chip 5:675–681

50. Urquhart AJ, Anderson DG, Taylor M et al (2007) High throughput surface characterisation of a combinatorial material library. Adv Mater 19:2486–2491

51. Dietrich PM, Horlacher T, Gross T et al (2010) Surface analytical characterization of carbohydrate microarrays. Surf Interface Anal 42:1188–1192

52. Thaburet J-F, Mizomoto H, Bradley M (2004) High-throughput evaluation of the wettability of polymer libraries. Macromol Rapid Commun 25:366–370

53. Castellani F, van Rossum B, Diehl A, Schubert M, Rehbein K, Oschkinat H (2002) Structure of a protein determined by solid-state magic-angle-spinning NMR spectroscopy. Nature 420:23–26

54. Lippmaa E, Maegi M, Samoson A et al (1980) Structural studies of silicates by solid-state high-resolution silicon-29 NMR. J Am Chem Soc 102:4889–4893

55. Spoto G, Minunni M (2012) Surface plasmon resonance imaging: what next? J Phys Chem Lett 3:2682–2691

56. Bellon S, Buchmann W, Gonnet F et al (2009) Hyphenation of surface plasmon resonance imaging to matrix-assisted laser desorption ionization mass spectrometry by on-chip mass spectrometry and tandem mass spectrometry analysis. Anal Chem 81:7695–7702

57. Davies MC, Alexander MR, Hook AL et al (2010) High throughput surface characterization: a review of a new tool for screening prospective biomedical material arrays. J Drug Target 18:741–751

58. Wold H (1966) Multivariate analysis. Academic, New York, pp 391–420

59. Yeniay O, Goktas A (2002) A comparison of partial least squares regression with other prediction methods. Hacettepe J Math Stat 31:99–111

60. Juan AD, Tauler R, Dyson R et al (2004) Spectroscopic imaging and chemometrics: a powerful combination for global and local sample analysis. TrAC, Trends Anal Chem 23:70–79

61. Xu Q, Lam KS (2003) Protein and chemical microarrays-powerful tools for proteomics. J Biomed Biotechnol 2003:257–266

62. Anderson DG, Lynn DM, Langer R (2003) Semi-automated synthesis and screening of a large library of degradable cationic polymers for gene delivery. Angew Chem Int Ed Engl 42:3153–3158

63. Akinc A, Lynn DM, Anderson DG et al (2003) Parallel synthesis and biophysical characterization of a degradable polymer library for gene delivery. J Am Chem Soc 125:5316–5323

64. Lynn DM, Anderson DG, Putnam D et al (2001) Accelerated discovery of synthetic transfection vectors: parallel synthesis and screening of a degradable polymer library. J Am Chem Soc 123:8155–8156

65. Anderson DG, Levenberg S, Langer R (2004) Nanoliter-scale synthesis of arrayed biomaterials and application to human embryonic stem cells. Nat Biotechnol 22:863–866

66. Mant A, Tourniaire G, Diaz-Mochon JJ et al (2006) Polymer microarrays: identification of substrates for phagocytosis assays. Biomaterials 27:5299–5306

67. Liberski A, Zhang R, Bradley M (2009) Inkjet fabrication of polymer microarrays and grids – solving the evaporation problem. Chem Commun 48: 334–336

68. Hansen A, Zhang R, Bradley M (2012) Fabrication of arrays of polymer gradients using inkjet printing. Macromol Rapid Commun 33:1114–1118

69. Gulrez SKH, Al-Assaf S, Phillips GO (2011) Hydrogels: methods of preparation, characterisation and applications. In: Carpi A (ed) Progress in molecular and environmental bioengineering – from analysis and modeling to technology applications. InTech, Rijeka. ISBN 978-953-307-268-5

70. Saaem I, Papasotiropoulos V, Wang T et al (2007) Hydrogel-based protein nanoarrays. J Nanosci Nanotechnol 7:2623–2632

71. Zhang R, Liberski A, Sanchez-Martin R et al (2009) Microarrays of over 2000 hydrogels – identification of substrates for cellular trapping and thermally triggered release. Biomaterials 30:6193–6201

72. Ghosh G, Yan X, Lee AG et al (2010) Quantifying the sensitivities of EGF receptor (EGFR) tyrosine kinase inhibitors in drug resistant non-small cell lung cancer (NSCLC) cells using hydrogel-based peptide array. Biosens Bioelectron 26:424–431

73. Brueggemeier SB, Wu D, Kron SJ et al (2005) Protein-acrylamide copolymer hydrogels for array-based detection of tyrosine kinase activity from cell lysates. Biomacromolecules 6:2765–2775

74. Inama L, Diré S, Carturan G et al (1993) Entrapment of viable microorganisms by SiO_2 sol–gel layers on glass surfaces: trapping, catalytic performance and immobilization durability of Saccharomyces cerevisiae. J Biotechnol 30:197–210

75. Nassif N, Bouvet O, Noelle Rager M et al (2002) Living bacteria in silica gels. Nat Mater 1:42–44

76. Pressi G, Toso R, Monte R et al (2003) Production of enzymes by plant cells immobilized by sol–gel silica. J Sol–gel Sci Technol 26:1189–1193

77. Sicard C, Brayner R, Margueritat J et al (2010) Nano-gold biosynthesis by silica-encapsulated micro-algae: a "living" bio-hybrid material. J Mater Chem 20:9342–9347

78. Muraca M, Vilei MT, Zanusso GE et al (2002) SiO_2 entrapment of animal cells: liver-specific metabolic activities in silica-overlaid hepatocytes. Artif Organs 26:664–669

79. Macbeath G, Schreiber SL (2000) Printing proteins as microarrays for high-throughput function determination. Science 289:1760–1763

80. Zhu H, Bilgin M, Bangham R et al (2001) Global analysis of protein activities using proteome chips. Science 293:2101–2105

81. Delehanty JB, Ligler FS (2003) Method for printing functional protein microarrays. Biotechniques 34:380–385

82. Lee M-Y, Park CB, Dordick JS et al (2005) Metabolizing enzyme toxicology assay chip (MetaChip) for high-throughput microscale toxicity analyses. Proc Natl Acad Sci USA 102:983–987

83. Park CB, Clark DS (2002) Sol–gel encapsulated enzyme arrays for high-throughput screening of biocatalytic activity. Biotechnol Bioeng 78:229–235

84. Sukumaran SM, Potsaid B, Lee M-Y et al (2009) Development of a fluorescence-based, ultra high-throughput screening platform for nanoliter-scale cytochrome P450 microarrays. J Biomol Screen 14:668–678

85. Kim YD, Park CB, Clark DS (2001) Stable sol–gel microstructured and microfluidic networks for protein patterning. Biotechnol Bioeng 73:331–337

86. Lee S, Kim YS, Jo M et al (2007) Chip-based detection of hepatitis C virus using RNA aptamers that specifically bind to HCV core antigen. Biochem Biophys Res Commun 358:47–52

87. Kwon J-a, Lee H, Lee KN et al (2008) High diagnostic accuracy of antigen microarray for sensitive detection of hepatitis C virus infection. Clin Chem 54:424–428

88. Ahn J, Cho M, Lee S et al (2008) Sol–gel material optimization for aptamer biosensors. Mol Cell Toxicol 4:100–105

89. Ahn JY, Lee SW, Kang HS et al (2010) Aptamer microarray mediated capture and mass spectrometry identification of biomarker in serum samples. J Proteome Res 9:5568–5573

90. Rupcich N, Brennan JD (2003) Coupled enzyme reaction microarrays based on pin-printing of sol–gel derived biomaterials. Anal Chim Acta 500:3–12

91. Rupcich N, Nutiu R, Li Y et al (2005) Entrapment of fluorescent signaling DNA aptamers in sol–gel-derived silica. Anal Chem 77:4300–4307

92. Rupcich N, Goldstein A, Brennan JD (2003) Optimization of sol–gel formulations and surface treatments for the development of pin-printed protein microarrays. Chem Mater 15:1803–1811

93. Hirsch LR, Stafford RJ, Bankson JA et al (2003) Nanoshell-mediated near-infrared thermal therapy of tumors under magnetic resonance guidance. Proc Natl Acad Sci USA 100:13549–13554

94. Gupta AK, Gupta M (2005) Synthesis and surface engineering of iron oxide nanoparticles for biomedical applications. Biomaterials 26:3995–4021

95. Ferrari M (2005) Cancer nanotechnology: opportunities and challenges. Nat Rev Cancer 5:161–171

96. Davis ME, Chen ZG, Shin DM (2008) Nanoparticle therapeutics: an emerging treatment modality for cancer. Nat Rev Drug Discov 7:771–782

97. Bosman AW, Heumann A, Klaerner G et al (2001) High-throughput synthesis of nanoscale materials: structural optimization of functionalized one-step star polymers. J Am Chem Soc 123:6461–6462

98. Akinc A, Zumbuehl A, Goldberg M et al (2008) A combinatorial library of lipid-like materials for delivery of RNAi therapeutics. Nat Biotechnol 26:561–569

99. Zhang Y, Liu S, Wang L et al (2012) Novel use of poly (3, 4-ethylenedioxythiophene) nanoparticles for fluorescent nucleic acid detection. ACS Comb Sci 14:191

100. Acharya AP, Lewis JS, Keselowsky BG (2013) Combinatorial co-encapsulation of hydrophobic molecules in poly(lactide-co-glycolide) microparticles. Biomaterials 34:3422–3430

101. Thorstenson JB, Petersen LK, Narasimhan B (2009) Combinatorial/high throughput methods for the determination of polyanhydride phase behavior. J Comb Chem 11:820–828

102. Acharya AP, Clare-salzler MJ, Keselowsky BG (2009) A high-throughput microparticle microarray platform for dendritic cell-targeting vaccines. Biomaterials 30:4168–4177

Mapping the Stiffness of Nanomaterials and Thin Films by Acoustic AFM Techniques

31

Stefan Zauscher, Zehra Parlak, and Qing Tu

Introduction

Nanomaterials and thin films are an integral part of many devices [1–7] and biological structures [8–10], and the detailed knowledge of their mechanical properties, such as elasticity, hardness, and friction behavior, is necessary for their successful integration into devices and to understand their biological functions. Both the topographical and elastic properties of nanomaterials and many thin films are often heterogeneous which requires techniques that can map the distribution of these properties with nanometer lateral resolution. However, the nanometer scale dimensions and the requirement of applying low forces for determining mechanical responses present significant challenges for common micromechanical characterization approaches.

The atomic force microscope (AFM) is an instrument that provides exquisite force control while mapping the surface topography with nanoscale resolution [11]. AFMs use micro-fabricated cantilever beams with a sharp tip to touch the surface and typically employ piezoelectric actuators to displace the surface relative to the cantilever tip for imaging [11]. A range of forces acting between the tip and the surface affect the cantilever deflection, which can be measured by several techniques, including laser light reflection [11], interferometry [12, 13], or measurement of the piezoresistance [14]. To accurately map the surface topography, the AFM feedback loop uses a control parameter, typically the DC contact force in contact mode AFM or the RMS of the cantilever vibration in intermittent contact mode AFM. Even though the initial reason

S. Zauscher (✉) • Z. Parlak • Q. Tu

Department of Mechanical Engineering and Material Science, Duke University,
Durham, NC, USA
e-mail: zauscher@duke.edu; zehra.parlak@duke.edu; qing.tu@duke.edu

for measuring force was to provide a feedback signal during imaging, researchers soon realized that measuring force also provides access to the nanomechanical properties of nanomaterials and thin films, including biological surfaces [10], biomolecular coatings, polymer mixtures [15–17], and nanocomposites [18].

In this chapter we focus on advances in the use of acoustic AFM techniques [19–22] for mapping the elasticity of nanomaterials and thin films. Acoustic AFMs inherently work in contact mode, i.e., the contact force between the tip and the surface is kept constant while scanning. However, a high-frequency vibration is added to the tip–sample contact, and the cantilever's response to this vibration is used to determine the elastic properties of the sample. Here, we specifically focus on three acoustic AFM techniques: (1) force modulation microscopy (FMM), (2) ultrasonic force microscopy (UFM), and (3) contact resonance atomic force microscopy (CR-AFM). We review the theoretical background of each of these techniques, their limitations, and their application to mapping the elastic properties of nanomaterials and thin films.

Introduction to Nanoscale Contact Mechanics

In acoustic AFM, the amplitude and phase of the high-frequency vibration of the cantilever is detected and converted into the contact stiffness that arises from the tip–surface interaction. To extract surface elastic material properties, the contact stiffness can be interpreted by a variety of contact mechanics models [23–25]. For the purpose of this review, we explain the contact mechanics in the framework of the Hertzian contact model, the simplest model describing the AFM tip–surface contact. Although the assumptions of the Hertz model, such as frictionless and nonconforming surfaces, lack of adhesion, small strains, and interaction of homogeneous bodies [26, 27], are not always realized in AFM imaging of nanomaterials and thin films, this model provides a useful and simple description of the tip's contact with the surface.

The AFM tip is assumed to be a spherical indenter with a radius of curvature, R_t, that touches a surface with a radius of curvature, R_s. The indenter contacts the surface with a contact force F, giving rise to a circular contact area. The radius of this contact area, a_c, which also defines the theoretical lateral resolution in AFM imaging, is

$$a_c = \sqrt[3]{\frac{3FR}{4E^*}}, \tag{31.1}$$

where R is the reduced radius of curvature and E^* is the reduced indentation modulus. R is a simple function of R_t and R_s:

$$\frac{1}{R} = \frac{1}{R_t} + \frac{1}{R_s}. \tag{31.2}$$

As Eq. 31.2 suggests, for very high R_s values, i.e., flat surfaces, R converges to R_t. E^* is defined as

$$\frac{1}{E^*} = \frac{1-v_t^2}{E_t} + \frac{1-v_s^2}{E_s}, \tag{31.3}$$

where E_t and E_s are the Young's moduli and v_t and v_s are the Poisson ratios of the tip and sample, respectively. With the contact force F pressing the two bodies together, a deformation, δ, occurs in the contact region:

$$\delta = \frac{a_c^2}{R} = \sqrt[3]{\frac{9F^2}{16RE^{*2}}}. \tag{31.4}$$

Equation 31.4 shows that the relationship between F and δ is nonlinear; however, it is possible to linearize this relationship around a constant contact force, such as is used in contact mode AFM, to obtain the contact stiffness:

$$k^* = -\frac{\partial F}{\partial \delta} = \frac{3F}{2\delta} = \sqrt[3]{6FRE^{*2}}. \tag{31.5}$$

Because F is kept constant by the feedback loop during acoustic AFM and because R also does not change, mapping k^* is sufficient to determine E^* and hence the elasticity of the surface.

Layered Materials

Combining the Hertzian contact model with stiffness measurements by acoustic AFM can provide E_s for a bulk material. However, if the sample is heterogeneous, such as is often the case in thin layers, the measured E_s is the apparent indentation modulus, which reflects the surface and subsurface contributions [20, 22, 28–32]. Studies show that for a soft thin film, the stress and displacement field generated by the contact can penetrate to a depth up to seven times the contact radius; e.g., when the contact radius is 10 nm on a soft thin film, the film thickness should be at least 70 nm on a stiff substrate to render substrate stiffness contributions ineffective [30, 32–34].

Many elasticity measurement techniques, including microindentation, nanoindentation, and AFM, use layered material contact models to determine the actual indentation modulus of a thin film from the measured, apparent contact stiffness. To properly deconvolute the apparent contact stiffness with these models, one needs to know the thickness of the film, details about its bonding or adhesion to the supporting substrate, and the substrate stiffness.

Finite-element modeling (FEM) of an AFM tip in contact with a layered material is a powerful method for the analysis of layered material configurations [31, 32, 35–39]. FEM can account for bonding of a thin film to the substrate [39] for the presence of interfacial defects [39]

Fig. 31.1 The ratio of surface elastic modulus and thin film elastic modulus is plotted as a function of the applied force for different film thicknesses. In this calculation, a thin film with elastic modulus, E_{top} = 1 GPa, and a supporting substrate with elastic modulus of 100 GPa and a tip radius of 10 nm are assumed. Thinner films appear stiffer than thicker films for a constant force [46] (Reproduced with permission by the American Chemical Society)
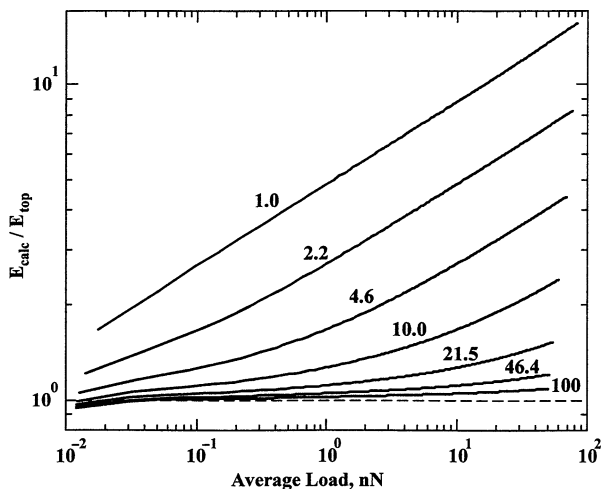
and for inclusions in the thin film layer [31, 32]. Even though finite-element models are quite powerful, they are also computationally expensive and time-consuming.

Analytical methods developed for layered material contacts [29, 40–44] usually are limited to simple contact geometries [43], but they are typically easy to implement. Analytical methods can account for bonding of the thin film to the substrate [43], multiple thin film layers [29], and transitions in the thin film layers by using a fitting parameter [29, 42].

Semi-analytical methods combine recursive algorithms [37, 45] or finite-element-like modeling of the layers [46] with analytical expressions of the layered material contact. A semi-analytical method, developed by Akhremitchev et al. [46], even accounts for the effects of the tip shape on the indentation modulus. This method has also been applied successfully in the analysis of acoustic AFM data. As expected, it shows that the thinner the layer or the higher the force, the more the substrate will affect the stiffness measurement (Fig. 31.1). Another semi-analytical method, developed by Yaralioglu et al. [37], is specifically designed for acoustic AFM techniques and harnesses the propagation of waves generated by the vibrating contact to determine substrate stiffness. This method is effective for analyzing organic and inorganic thin films [45] and the effects of interfacial defects on stiffness [30].

Stiffness Measurements with Acoustic AFM

To measure the contact stiffness sensitively with AFM, two parameters are critically important, the ratio of cantilever to substrate stiffness and the signal to noise ratio of the measurement. The selection of the cantilever stiffness is

a compromise between the demand to image a sample without causing surface damage, which generally favors a cantilever with much lower stiffness than that of the substrate, and the need to measure contact stiffness sensitively, which favors a cantilever stiffness that is matched to that of the substrate. In time-resolved measurement techniques, such as used in recording conventional force–distance curves or in pulsed-force mode [47, 48], forces on the cantilever are acquired over a certain time period which adds noise over a broad frequency range to the cantilever deflections. This broadband noise reduces the sensitivity of the measurement. Especially for stiffness measurements on thin films and nanomaterials, this noise issue is compounded by the only small stiffness variation which arises from the significant contribution to the overall contact stiffness from the supporting substrate. Performing stiffness measurements in a narrow frequency range can thus effectively reduce noise and enhance sensitivity. One way of doing this is to supply a sinusoidal vibration to either the cantilever or the sample, when the cantilever is in static contact with the surface, and to then detect the cantilever deflection response to this vibrational excitation using a phase-locked loop. As the feedback loop for topography imaging is typically low-pass filtered around 1–2 kHz, vibration frequencies higher than this limit do not interfere with topography imaging and yet provide information about the tip–surface interaction.

In the next section we review several AFM techniques that are based on tracking the small, dynamic excitations of the cantilever in contact with the surface. Collectively these methods are called acoustic AFM. Furthermore, we outline how these methods can be applied for measuring the stiffness of nanomaterials and thin films. Specifically, we describe three variants of acoustic AFM: (1) force modulation microscopy (FMM), (2) ultrasonic force microscopy (UFM), and (3) contact resonance atomic force microscopy (CR-AFM).

Force Modulation Microscopy

FMM Working Principle

Force modulation microscopy (FMM), one of the earliest acoustic AFM techniques [21, 49], combines stiffness mapping capability on nanomaterials with ease of implementation. It uses a transducer under the sample or in the cantilever holder to induce high-frequency, sinusoidal vibrations of the sample or cantilever, respectively, and uses a lock-in amplifier to monitor the high-frequency vibration coupled to the cantilever. The resulting amplitude and phase data are then mapped concurrently with the topographic image data, collected in contact mode (Fig. 31.2). FMM is known for its high-contrast amplitude and phase images that reflect differences in contact stiffness on the sample surface. The ability to map contact stiffness with high contrast is largely due to the narrow noise bandwidth of the lock-in detection technique. Furthermore, if the sample surfaces allow, cantilevers with spring constants that are matched to the contact stiffness are selected to maximize sensitivity.
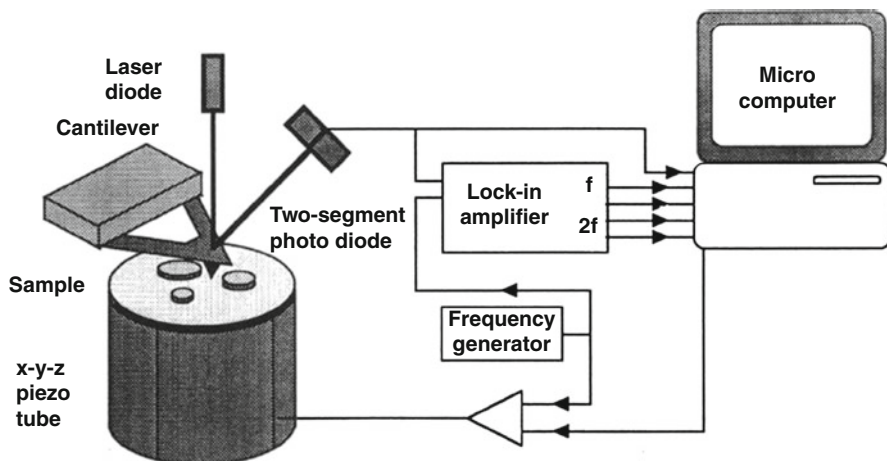
Fig. 31.2 FMM setup with sample modulation [49] (Reproduced with permission by the Biophysical Society)
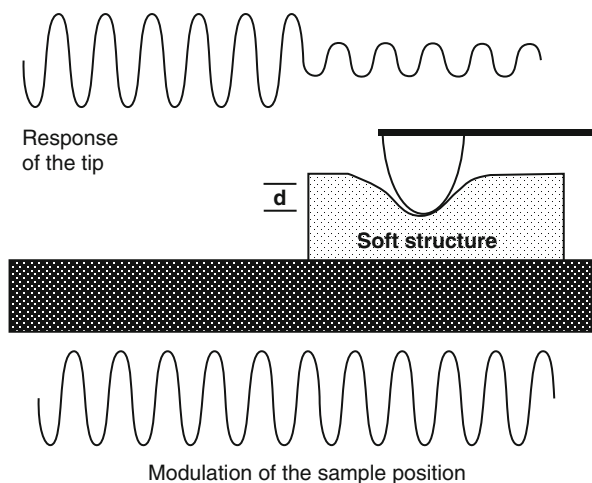
Fig. 31.3 Contrast generation in FMM. Most of the sample modulation transfers to the cantilever when imaging a stiff sample, while higher indentation on soft sample decreases the coupled modulation on the cantilever [49] (Reproduced with permission by the Biophysical Society)

In FMM, the vibrational indentation on a stiff surface is small and causes little attenuation in the vibration amplitude transferred to the cantilever. On the other hand, a soft surface is indented more (Eq. 31.4) and hence attenuates the resulting cantilever vibration amplitude. Consequently, lower amplitudes in a FMM amplitude image generally represent softer surfaces (Fig. 31.3) [49–51]. FMM vibration frequencies are often chosen to lie between 5 and 25 kHz. The lower frequency limit is determined by the imaging feedback loop frequency cutoff and by the scan rate and desired image resolution, which define

the time available to obtain the cantilever amplitude and phase signal at each image location. The upper frequency limit is defined by the cantilever resonance frequencies.

FMM Data Analysis

For quantitative stiffness mapping, an analysis approach originally developed by Radmacher et al. can be used [49]. In this analysis, the AFM cantilever and the contact are represented by two springs in series, with spring constants k_c and k^* for the cantilever and contact, respectively. The effects of cantilever mass and damping are assumed to be small, an assumption that holds true whenever the modulation frequency is much lower than the first contact resonance frequency. In addition, the modulation amplitude has to be very small compared to the static cantilever deflection for the contact to behave linear elastically, i.e., it can be represented by a linearized spring.

The contact and cantilever experience the same amount of force modulation since the force has to be in equilibrium, and this force modulation is a function of cantilever deflection and indentation:

$$F_{ac} = k_c(u_0 \sin \omega t - \delta) = k^* \delta, \qquad (31.6)$$

where u_0 is the sample vibration amplitude given by the piezoelectric transducer and $\omega = 2\pi f$ is the excitation frequency. Equation 31.6 can be rearranged to relate cantilever vibration amplitude (u_c) to the contact stiffness [51]:

$$u_c = (u_0 \sin \omega t - \delta) = \frac{u_0 k^*}{k^* + k_c} \sin \omega t. \qquad (31.7)$$

Equation 31.7 shows how much the cantilever deflects when the contact is modulated by u_0. The cantilever vibration amplitude (u_c) is high on stiff samples (large k^*) and low on soft samples (small k^*) (Fig. 31.3). On viscoelastic materials, which have significant phase delay to sinusoidal driving forces, k^* becomes a complex quantity. A complex k^* introduces a phase difference between the sample modulation and cantilever vibration response.

FMM Imaging Examples

A range of nanomaterials, including self-assembled monolayers, biopolymers, and polymers, have been imaged with FMM in air (see Table 31.1). FMM is sufficiently sensitive to detect the elasticity variations caused by patterning of self-assembled alkanethiols on gold [52, 55]. Similar to thiolated molecules on gold, octadecyl-triethoxysilane (OTE) patterns on mica surfaces also show significant elasticity variations in FMM images [57, 58]. Furthermore, tris(8-hydroxyquinolinato) aluminum(III) (AlQ$_3$), which is used for organic light-emitting devices, has been patterned as a molecularly thin film and the stiffness distribution on this sample has been imaged with FMM [59]. The organization of block-copolymer chains such as

Table 31.1 Nanomaterials and thin films imaged by acoustic AFM techniques

		FMM	UFM	CR-AFM
Self-assembled monolayers	Air	Alkanethiols [52]	Sexithiophene(T6) [53]	N-octyldimethylchlorosilane (ODS) [54]
		Octadecanethiols [55]	Polystyrene/poly(butyl methacrylate) [56]	
		Octadecyltriethoxysilane (OTE) [57, 58]		
		Tris(8-hydroxyquinolinato) aluminum (III) (AlQ3) [59]		
		quercetin-3-O-palmitate (QP)/dimyristoylphosphatidylcholine (DMPC) [60]		
	Fluid	Alkanethiols [52, 61]	Thiolipid Langmuir–Blodgett (LB) film [62]	
		Octadecyltriethoxysilane (OTE) [57, 58]		
Polymers		Poly (vinylidenefluoride–trifluoroethylene) (PVDF–TrFE) [63]	Rubber-toughened polymethylmethacrylate (PMMA) [64]	Tetravinylsilane [66]
		Polyaniline–polyacrylic acid (PANI/PAA) [67]	Agarose/polyacrylamide (PAAm) interpenetrating polymer hydrogels [65]	Poly(3-hexylthiophene)/ phenyl-C61-butyric acid methyl ester (P3HT/PCBM) [15]
				Polystyrene/polypropylene (PS/PP) [16, 68]
		Epoxy fiber [69]		Poly(methyl methacrylate) (PMMA) [70]
				Polystyrene (PS) [70, 71] poly(methyl methacrylate)/ styrene–butadiene–styrene PMMA/SBS [72]
				Photoresist [37, 45]

Biomaterials	Air	Glycolipids [8, 73]	Eye α-crystalline proteins [62]	Vascular cells [74]
			Peptide-loaded lipid bilayer liposomes and synthetic human amyloid fibers [75]	Enamel [76]
				DNA [77]
	Fluid	Proteins [61]	Nerve cells [78]	
Nanostructures			Carbon fibers in epoxy matrix [79]	Epoxy with nanoparticles [80]
			Rubber inclusions in PMMA matrix [79]	Nanoparticles [31, 84]
			Al/divinylsiloxane-bis-benzocyclobutene (BCB) [81]	Nanowhiskers [85]
			BCB, Al, and TiN nanostructures [82]	Nanotubes [86]
			Glass-PET nanocomposite [83]	Piezoelectric domain boundaries [87–89]
Inorganic thin films			GaSb-InAs and GaAs-Al$_x$Ga$_{1-x}$As supper lattice [62] PET-SiO$_x$ [62]	Tin selenide (SnSe$_x$) [90]
				Clay minerals [91]
				Nanoferrite crystals [92]
				Aluminum [37]
				Tungsten [30, 37, 45]
				Copper [30, 45]
				SiO$_2$ [30, 93]
				Niobium [94]
				Nickel [95]
				Gold/Si interface [30, 96]
				Highly oriented pyrolytic graphite (HOPG) [22]
				Silicon [32, 34, 97]
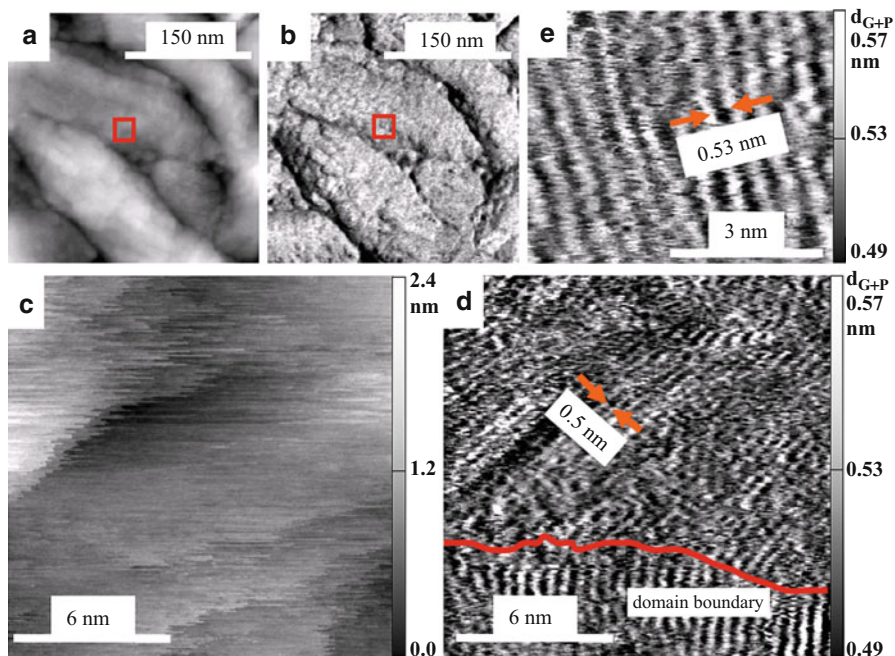
Fig. 31.4 PVDF-TrFE film on graphite: (**a**) topography (300 × 300 nm), (**b**) FMM amplitude image, (**c**) topography (15 × 15 nm), and (**d**–**e**) FMM amplitude images collected with different scan speeds. Domain boundaries and stripe-like structure of the thin film can be observed in FMM [63] (Reproduced with permission by IOP Publishing)

poly(vinylidenefluoride–trifluoroethylene) (PVDF–TrFE)) on graphite (Fig. 31.4) causes periodic stiffness variations that can be observed by FMM imaging [63]. Similarly, FMM was used to investigate structural details and the stiffness distribution in polyaniline (PANI)–polyacrylic acid (PAA) composite thin films [67]. Phase-separated glycolipids in lipid mono- and bilayers [8, 73] were imaged by FMM to examine the elasticity of the different glycolipid phases. Similarly, phase separation in quercetin-3-O-palmitate (QP)/dimyristoylphosphatidylcholine (DMPC) Langmuir–Blodgett monolayers was studied with FMM. This phase separation results in spiral-like, sub-micrometer domains with less than 0.3 nm height. FMM's high lateral resolution was used to map the elasticity distribution on these spiral-like nanostructure in air [60].

When excitation frequencies are chosen sufficiently below the contact resonance frequency, FMM performs well also in liquid environments. The ability to operate FMM in liquids enables imaging of hydrated, self-assembled monolayers, where FMM can reveal stiffness differences due to differences in molecular packing and the presence of domain boundaries, on areas that otherwise do not show any

topographic or surface chemical differences (Table 31.1) [52, 61]. Furthermore, FMM can map the elasticity variations in protein molecules patterned on gold surfaces (Fig. 31.5) [61]. FMM also works in nonaqueous liquids, for example, octadecyltriethoxysilane (OTE) patterns on mica surfaces have been imaged with FMM in butanol [57, 58].

Parameter Selection Process and Limitations

While many experiments and analytical studies showed that softer regions on a sample give rise to lower amplitudes, there also have been reports that showed the opposite. For example, FMM imaging on phase-separated surfactant and DPPC monolayers yielded higher amplitudes on the fluid-like DPPC regions, which are supposed to be softer [73]. This unexpected result was even more pronounced when the amplitude of the high-frequency modulation was increased. In another study, changing the frequency reversed the amplitude and phase contrast on OTE monolayers on mica [57]. These contradicting results arise from nonlinear deformation of the contact and the details of the cantilever dynamics [61, 98]. For example, researchers that image organic thin films or nanomaterials typically reduce the contact force to avoid sample damage, but thus unknowingly also increase contact nonlinearity. Similarly, the vibration amplitude is typically increased, which inadvertently also increases contact nonlinearity. For quantitative analysis it is thus important to verify that FMM is performed in a linear regime. This can be done by monitoring the second harmonic of the cantilever vibration. Since the frequency content does not change, and only amplitude and phase are affected in a linear system, the appearance of a second harmonic at twice the fundamental vibration frequency is a clear sign of contact nonlinearity. To minimize the effects of cantilever dynamics, vibration frequencies that are much lower than the cantilever resonances must be selected. At low frequencies, the cantilever system behaves quasi-static, and Eq. 31.7 becomes applicable. Finally, keeping the actuation frequency under a few hundred Hz precludes imaging but allows for acquisition of quantitative viscoelastic information from single-point measurements [83, 99].

Summary and Outlook

When used properly, FMM is a powerful technique for mapping the stiffness of nanomaterials and thin films. To obtain reliable elasticity mapping on a surface, a cantilever with stiffness similar to that of the surface has to be selected, the actuation frequency should be kept much lower than the contact resonance frequency, and contact nonlinearities need to be avoided by keeping the vibration amplitude much smaller than the static cantilever deflection. Recent experimental developments using magnetic actuation of the cantilever mitigate some of the uncertainties in the actuation amplitude [69, 100]. Additionally, new analysis approaches are emerging that take into account effects of cantilever dynamics and thus allow a more quantitative and consistent stiffness mapping of soft nanomaterials.
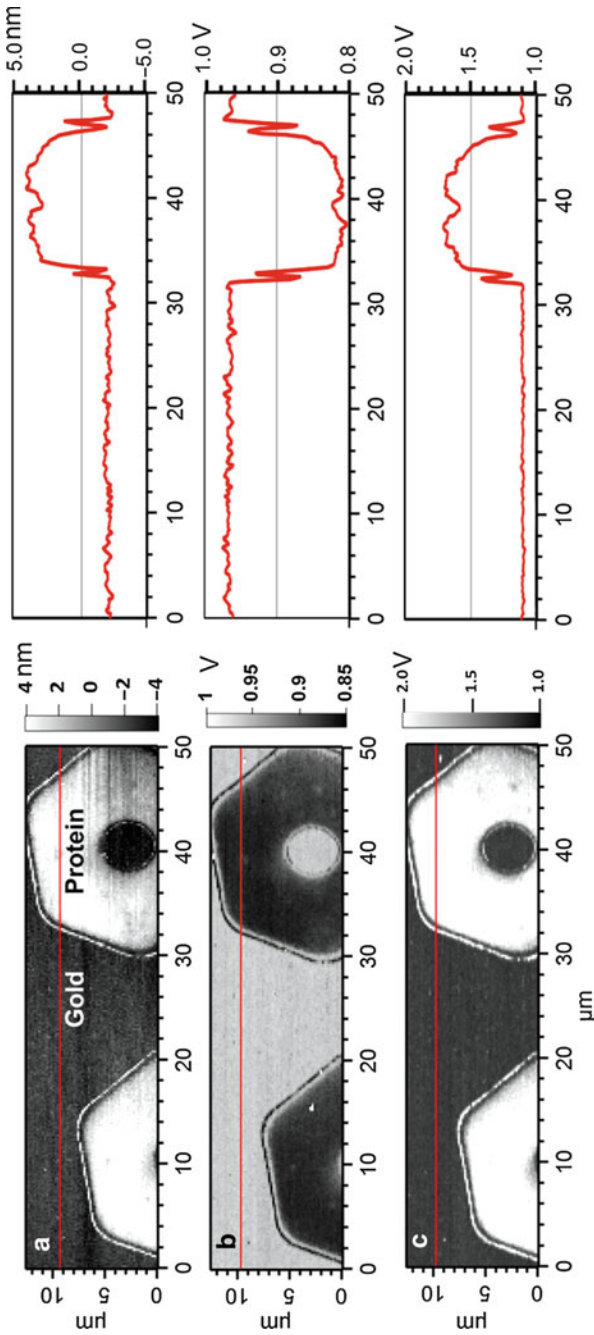
Fig. 31.5 FMM images (*left*) and corresponding section views (*right*) of surface-tethered protein molecules patterned on gold. (**a**) Topography, (**b**) amplitude, and (**c**) phase images [61] (Reproduced with permission by Beilstein Journals)

Ultrasonic Force Microscopy (UFM)

UFM Working Principle

Ultrasonic force microscopy (UFM) [101] uses the dynamic stiffening of the cantilever at ultrasonic frequencies to match the contact stiffness and thus extends the range of contact stiffness that can be measured by FMM. In addition, UFM works in a frequency range that is much higher than that of FMM and is thus able to probe the high-frequency dynamics of the elastic interaction between the tip and sample [102]. In UFM, a transducer vibrates the sample with frequencies in the ultrasonic range, i.e., much higher than the first contact resonance frequency and away from any eigen frequencies of the cantilever. By avoiding resonance [101], the cantilever tip periodically indents the material according to the chosen, amplitude-modulated excitation (Fig. 31.6).

Figure 31.6a shows a typical nonlinear force–indentation curve of a material which has distinct adhesion hysteresis during approach and retraction of the cantilever probe tip. For a certain set-point contact force (F_{set}), a threshold amplitude (A_1) exists, above which the tip jumps out of contact with the sample. This force jump causes an additional deflection and leads to a measurable deviation between the average force on the cantilever and the set-point force (Fig. 31.6b).

For mapping the elastic properties of the substrate surface, three conditions need to be fulfilled: (i) the modulation frequency should be high enough to allow for a complete amplitude sweep within the residence time at each location during the raster scan of the surface; (ii) at any point in the raster scan, the maximum amplitude should be larger than the threshold amplitude; and (iii) to avoid any ambiguous results due to the unconventional use of the lock-in amplifier in the amplitude modulation (i.e., the original and the detected signal is not a sinusoidal wave), the modulation waveform needs to have zero amplitude for half its cycle and needs to be linearly ramped over the other half [62, 79]. Furthermore, to extract stiffness information from the amplitude data, three assumptions are made: (i) a threshold amplitude can be identified, (ii) the threshold amplitude depends on the applied normal force, and (iii) the cantilever is not resonating at the applied ultrasonic frequency [79].

UFM Data Analysis

The average force during the vibration cycle is obtained from the feedback error and can be expressed as

$$F_{am}(A, \delta) = \frac{1}{T} \int^{T} F(\delta - A \sin \omega t) dt, \tag{31.8}$$

where δ is the initial indentation and A, $\omega = \frac{2\pi}{T}$, and T are the amplitude, the circular frequency, and the period of the excitation, respectively. The threshold amplitude at which the cantilever jumps out of contact depends on both the elasticity of the material and the cantilever-surface adhesion. When the cantilever reaches
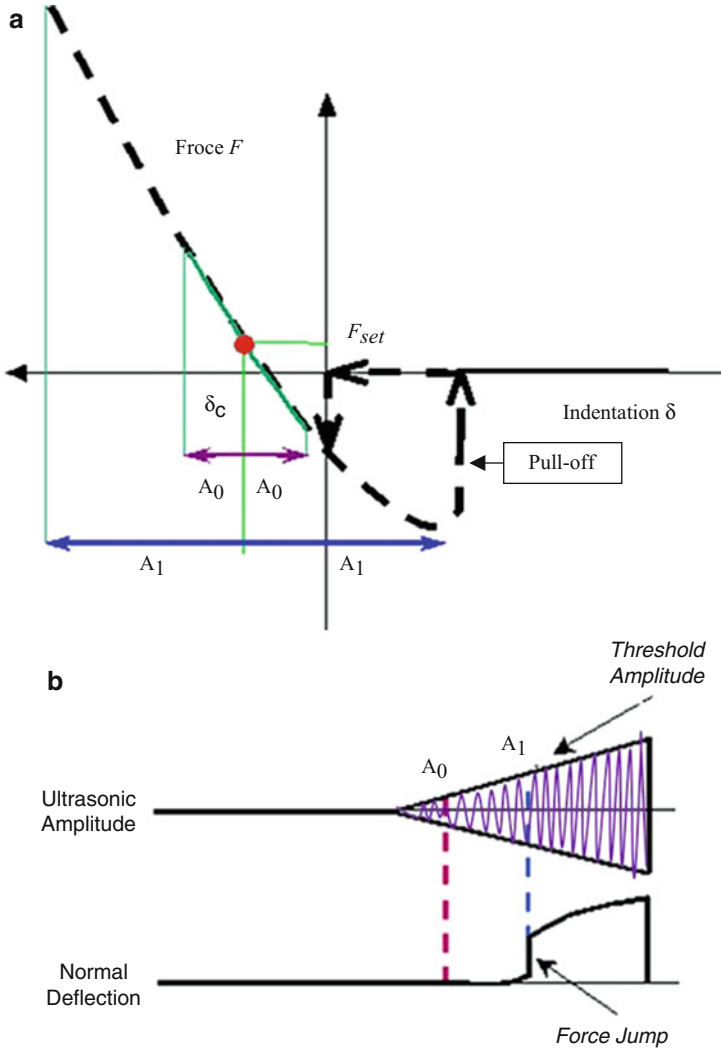
Fig. 31.6 (**a**) Force plotted as a function of indentation for approach and retraction (indicated by the *arrows*), showing adhesion hysteresis. (**b**) The corresponding oscilloscope traces of ultrasound detection, showing a force jump at the threshold amplitude [53] (Reproduced with permission by Elsevier)

mechanical equilibrium, a new equilibrium deflection of the cantilever is obtained as well as a corresponding indentation depth according to Eq. 31.9:

$$F_{am}\left(A, \delta_{eq}\right) = k_c z_{eq}. \tag{31.9}$$

Using this equilibrium condition, the force–indentation relation is obtained and the reduced modulus can be extracted with a model of the tip–sample contact.

Fig. 31.7 Schematic showing (**a**) the contrast mechanism in UFM where, at the same set point, a stiffer material (1) will give a lower threshold amplitude than a softer material (2) and (**b**) differential UFM where threshold amplitude values (A_1 and A_2) are measured for different normal forces (F_1 and F_2) and yield the contact stiffness as $S_{eff}(F_{av}) = (F_2 - F_1)/(A_2 - A_1)$ [103] (Reproduced with permission by Springer Verlag)
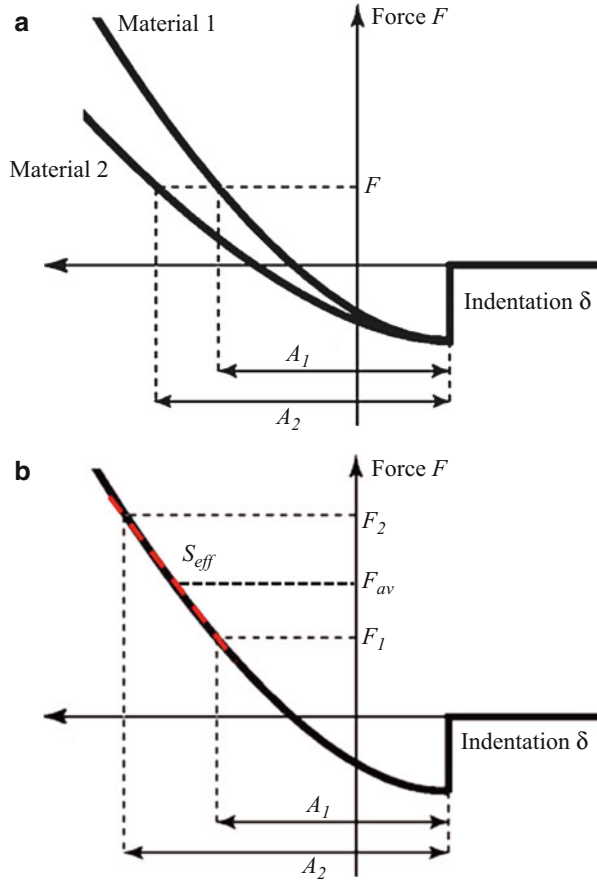
Typically, on a stiffer material, the indentation depth and the threshold amplitude are smaller for any applied normal force, compared to those on a softer sample (Fig. 31.7). For a stiffer material this translates into a larger, average force, i.e., a stiffer material will appear brighter in a deflection image. Another way to map surface stiffness is to use so-called differential UFM (Fig. 31.7b) [104], in which the contact stiffness is determined with two different set points.

UFM Imaging Examples

The power of UFM lies in its versatility to map stiffness differences in nanomaterials ranging from very stiff crystalline solids, including semiconductors and metals, to very soft materials, like polymers and even cells (Table 31.1). For example, UFM provided high-contrast images that reveal the periodicity of GaSb-InAs and GaAs-Al_xGa_{1-x}As superlattices [62]. Here, UFM was sufficiently sensitive to detect a 6 % difference in the elastic modulus (E_{GaSb} = 88 GPa vs. E_{InAs} = 82 GPa). Nanoscale aluminum damascene
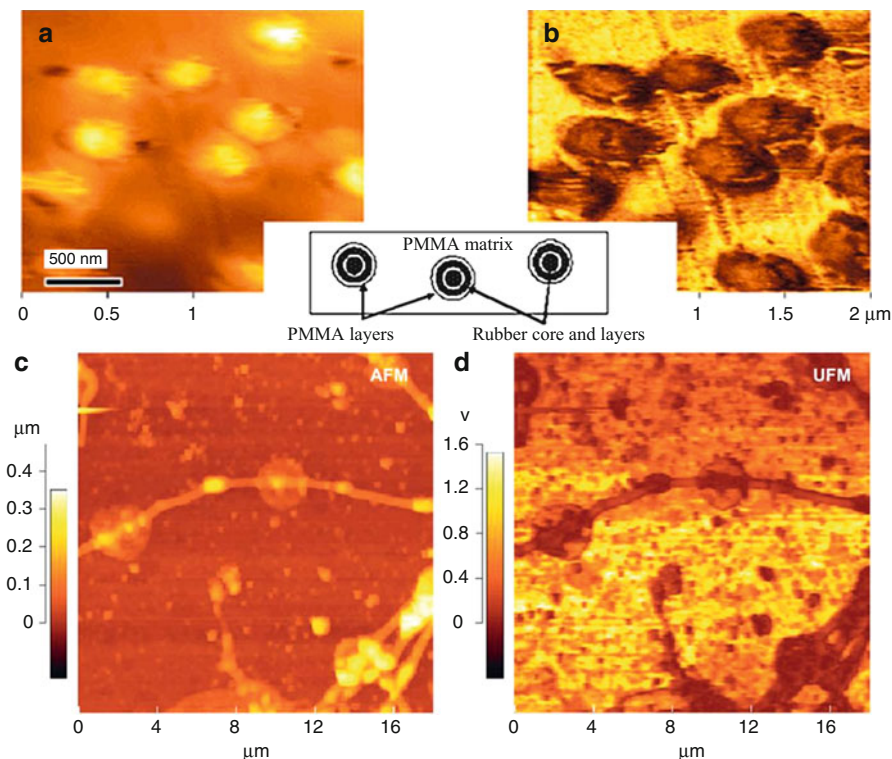
Fig. 31.8 (**a**) Topography and (**b**) UFM images of a compliant sample made of injection-molded PMMA (E_{PMMA} = 4.5 GPa) with spherical PMMA–rubber inclusions (E_{rubber} < 0.1 GPa) [105] (Reproduced with permission by Springer Verlag). (**c**) AFM and (**d**) UFM images of fixed nerve cells in solution that appear as protruding lines in the topographic image *left* [78] (Reproduced with permission by Annual Reviews)

interconnect structures of Al and TiN in divinylsiloxane-bis-benzocyclobutene (BCB) were imaged by UFM [81]. Applied to a copolymer system, UFM imaging revealed the segment density distribution in a polystyrene and poly(butyl methacrylate) absorption layer on SiO_2 [56], and the domain structure of sub-monolayer thick sesquithiophene films [53]. UFM stiffness mapping was also applied to reveal structural details of injection-molded polymer-matrix composites. Specifically, in injection-molded poly(methyl methacrylate) (PMMA) with spherical PMMA–rubber inclusions, UFM showed that the inclusions have a layered structure and are softer than the matrix (Figs. 31.8a, b) [105]. UFM has also been used to image very soft biological materials on stiff substrates with high lateral resolution, including α-crystalline proteins on freshly cleaved mica [62], peptide-loaded lipid bilayer liposomes, and human amyloid fibers on mica [75]. Nanoscale elasticity maps of agarose/polyacrylamide interpenetrating polymer hydrogels (IPHs) were generated by UFM to visualize the phase-separated domains in these IPHs [65].

UFM also functions in liquid, as demonstrated by the high-contrast stiffness mapping of nerve cells in aqueous buffer solutions (Figs. 31.8c, d) [78]. Finally, subsurface delaminations and nanoscale internal structures, which can influence the contact stiffness, can be revealed by UFM. For instance, sub-micrometer delaminations at the polymer–metal interface of flexible circuits [106], at polyethylene terephthalate (PET)–SiO$_x$ interfaces [62], and in nanocomposites consisting of brittle glass and PET [83] have all been detected and mapped with UFM.

Limitations and Problems

Although UFM has been widely employed to characterize the mechanical properties of a wide variety of materials and micro/nanostructures, the specific working requirements of this technique limit its more widespread use. First, UFM is not well suited for characterizing viscoelastic materials, where the indentation is time-dependent, because the phase information is generally not used [104]. Second, in UFM, the force versus indentation curve is determined by a combination of the elastic properties of the sample and the tip–sample interactions. Thus, surface adhesion and topography affect image contrast and hence quantitative analysis [107]. For example, one assumption made for UFM image contrast interpretation (see also UFM working principles) is that adhesion forces do not vary much over the imaging area, and image contrast is only caused by elasticity differences of the surface [79]. This renders UFM less effective for quantitative imaging of some polymeric nanostructures and thin films, such as solvent-swollen polymer brushes and hydrated hydrogel thin films. For instance, in a monolayer Langmuir–Blodgett film made of two phases, solid and fluid, the UFM images show reverse contrast, i.e., they appear stiffer in fluid areas and softer in solid areas, due to the presence of liquid increasing the local adhesion [62]. Furthermore, abrupt changes in surface topography can increase or decrease the contact area. This influences the threshold amplitude and thus directly affects image contrast and consequently the interpretation of surface mechanical properties.

Summary

Ultrasonic force microscopy is useful for imaging a broad range of nanomaterials and thin films supported by a stiff substrate. This is due to the dynamic stiffening of the cantilever at frequencies much higher than the resonant frequency of the tip–sample contact. If the excitation is amplitude modulated, the tip will lose contact at a threshold amplitude. This threshold amplitude reflects the nonlinear force–indentation curve of the material. In UFM this nonlinearity of the tip–sample contact is used, in conjunction with an appropriate contact mechanics model, to extract the sample stiffness. Although UFM has been used to characterize a wide variety of materials exhibiting a wide range of stiffness, the technique is not well suited to characterize materials with viscoelastic properties, surfaces with highly varied adhesive properties, or abrupt topographic changes.

Contact Resonance Atomic Force Microscopy (CR-AFM)

CR-AFM Working Principles

Contact resonance atomic force microscopy (CR-AFM) uses high-frequency vibrations to determine the stiffness of a sample from the contact resonance frequency. An AFM cantilever typically has several free-resonance modes whose frequencies depend on the cantilever properties (i.e., stiffness and geometry) and the surrounding environment (e.g., gas or liquid). As the cantilever comes in contact with the surface, its dynamic deflection behavior is changed, and the cantilever behaves as if there is a spring attached to the cantilever tip. This spring reflects the contact stiffness. The contact thus affects cantilever vibration and determines the mode shapes of the resonating cantilever [107, 108]. Compared with soft contacts, stiffer contacts restrain the tip motion more and increase the contact resonance frequencies [109]. To induce high-frequency vibrations, an ultrasonic transducer is typically placed under the sample [109] or in the cantilever holder [110, 111]. As small-amplitude, high-frequency vibrations are coupled to the cantilever in contact with the substrate surface, the cantilever amplifies these vibrations if they are close to the contact resonances. The amplitude of these cantilever vibrations is then detected with a lock-in amplifier.

In the early years of CR-AFM, which is also known as atomic force acoustic microscopy (AFAM) or ultrasonic atomic force microscopy (UAFM), the contact resonances were detected by sweeping the frequency and detecting the amplitude responses at each raster location of the image. Due to the need to acquire and store large amounts of data, this was a slow process. This difficulty has been overcome by the development of dual AC resonance tracking (DART) [77]. In DART mode, vibrations at two frequencies, one below (f_1) and one above (f_2) a contact resonance frequency, are used and their amplitudes are detected with two lock-in amplifiers (Fig. 31.9). To detect and center the resonance frequency, the frequency controller then shifts f_1 and f_2 so that the cantilever vibration at each of these frequencies has the same amplitude, which means the contact resonance frequency lies halfway between f_1 and f_2 for a symmetric resonance curve. In addition to the contact resonance, the quality factor of the resonance can be extracted from phase information obtained using DART. With this method, it is now much easier to implement CR-AFM and to map contact resonance frequencies on a surface quickly.

CR-AFM is particularly well suited to measure the contact stiffness of nanomaterials because the cantilever stiffness can be matched dynamically to the stiffness of the material. Since each resonance mode of the cantilever has a different effective length, and this length gets shorter as higher vibrational modes are used, the dynamic cantilever stiffness also increases. It is thus possible to select a resonance mode that best matches the stiffness of the contact [107]. As a result, one can image a wide range of materials with the same cantilever just by changing the contact resonance mode. For example, the defects in a stiff, synthetic diamond film can be detected by CR-AFM with higher contrast and sensitivity when imaged at the second resonance mode compared to the first mode, as shown in Fig. 31.10 [112]. In addition, CR-AFM has a small noise

Fig. 31.9 (**a**) Contact resonance frequency imaging using DART. (**b**) Two lock-in amplifier detects the response of the cantilever at two different frequencies to determine the contact resonance frequency [77] (Reproduced with permission by IOP Publishers)
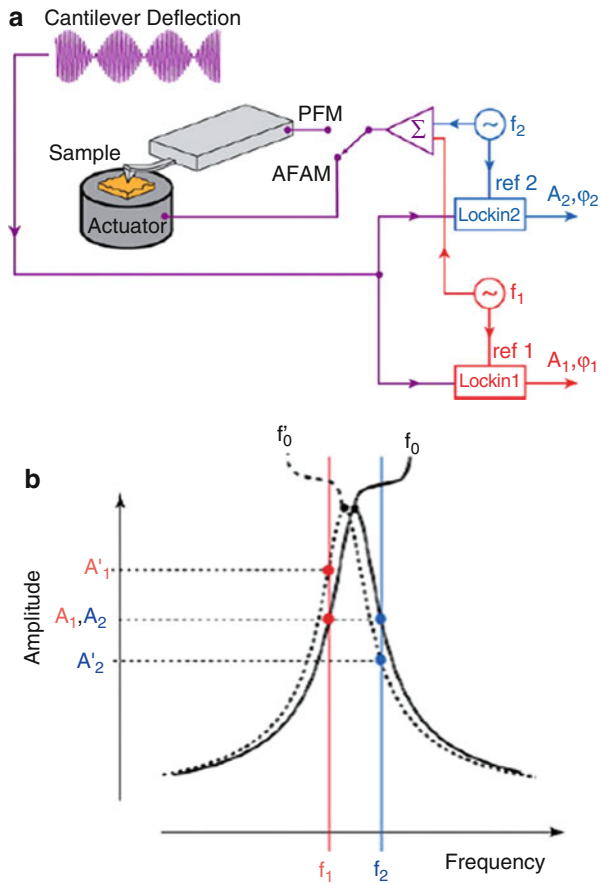
bandwidth, which it owes to the phase-locked loop detection that is common in acoustic AFM methods. This further enhances the sensitivity to small variations in sample stiffness.

CR-AFM Data Analysis

The quantitative analysis of CR-AFM resonance data requires understanding of the dynamics of a cantilever in contact with the surface. Since the contact behaves as a spring attached to the tip, it affects the boundary condition of the cantilever and the mode shape of the cantilever for each resonance mode. There are, however, multiple vibrational modes that satisfy the same boundary conditions. Each mode, n, has a complex wave number, k_n, to satisfy the contact stiffness and damping condition at the tip. When the contact does not have any viscoelastic losses, k_n is real [16, 68, 70, 71].

To calculate the contact stiffness and contact damping, the resonance frequency and the quality factor of the cantilever have to be determined when the cantilever is free (f_n^0 and Q_n^0) and when it is in contact (f_n^c and Q_n^c). These parameters are
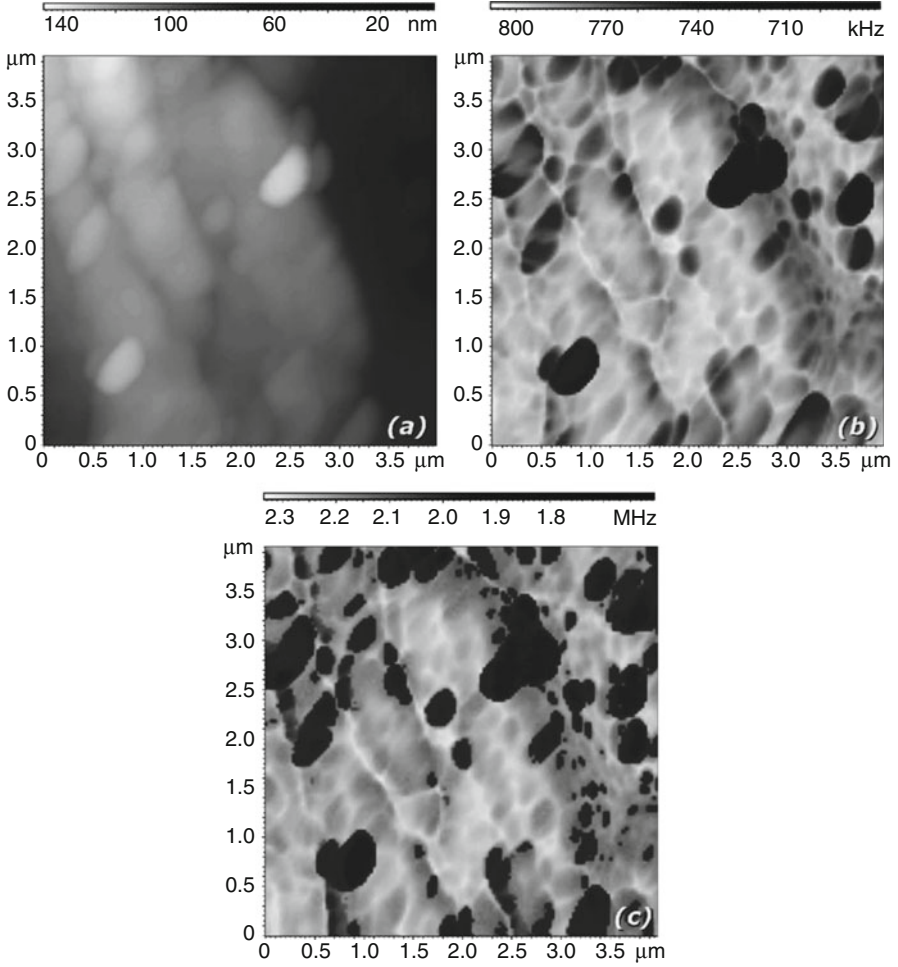
Fig. 31.10 Diamond-like carbon film imaged with CR-AFM. (**a**) Topography, (**b**) first contact resonance frequency, (**c**) second contact resonance frequency [112] (Reproduced with permission by American Institute of Physics)

then used to determine $k_n L$, where L is the cantilever length. Since k_n is generally complex, $k_n L$ can be separated into real and imaginary parts, $k_n L = a_n + i b_n$:

$$a_n = a_n^0 L \left(f_n^c / f_n^0 \right), \tag{31.10a}$$

$$b_n = a_n \left(\frac{2\pi f_n^c - 2\pi f_n^0 Q_n^c / Q_n^0}{8\pi f_n^c Q_n^c} \right), \tag{31.10b}$$

where $a_n^0 L$ is the root of the characteristic equation for the corresponding free mode and equals 1.8751, 4.6941, or 7.8548 for the first three modes of a rectangular

cantilever. After obtaining k_nL, it is possible to calculate the contact stiffness, k^*, and contact damping, c, by the following equation:

$$3\frac{k^*}{k_c} + ic\sqrt{\frac{3}{k_c m}}(k_nL)^2 = \frac{(\lambda_nL)^3[1 + \cos k_nL \cosh k_nL]}{\sinh k_nL \cos k_nL - \sin k_nL \cosh k_nL}, \tag{31.11}$$

where m is the cantilever mass and c is the contact damping constant. The real part of the reduced elastic modulus, $E^{*'}$, can then be determined once k^* is known. Similarly, the loss modulus, $E^{*''}$, can be determined using c,

$$E^{*''} = \frac{\pi c f_c^n}{a_c}. \tag{31.12}$$

Although Eq. 31.11 is for a beam with a tip on its very end, more complicated versions of this equation are available for cantilevers with tip offset [16].

CR-AFM Imaging Examples

The strength of CR-AFM for nanomaterial stiffness measurement lies in its ability to yield quantitative information [16, 70, 71, 109, 113]. By acquiring the contact resonance frequencies and quality factors at each pixel of a topography image and by using an appropriate contact mechanics model, both the Young's modulus and the viscoelastic loss modulus of a material can be mapped with nanometer lateral resolution.

CR-AFM has been applied to map the elastic properties of a broad range of organic and polymeric thin films [15, 16], including plasma-deposited, thin tetravinylsilane layers [66], spin-coated polystyrene/polypropylene (PS/PP) films [16, 68], and a poly(methyl methacrylate)/styrene–butadiene–styrene (PMMA/SBS) mixture (Fig. 31.11) [72]. CR-AFM images of PS/PP thin films, for example, show that even though PS and PP have similar elastic moduli, their loss moduli differ greatly [16]. CR-AFM has also been used to characterize the stiffness of nanostructured polymers including silica nanoparticles in an epoxy matrix [31, 80], of nanowhiskers [85], of carbon nanotubes [86], and of biomaterials [74], such as enamel [76], cell walls [114], and even single DNA strands [77]. Furthermore, the effect of humidity and UV exposure on the surface energy of self-assembled monolayers (SAMs) has been studied using CR-AFM, by mapping differences in contact stiffness [54] (Table 31.1).

Table 31.1 shows that CR-AFM is especially useful for mapping stiff materials. For example, CR-AFM revealed the stiffness variations of the domain boundaries in piezoelectric materials [87–89]. Furthermore, CR-AFM imaging of nanostructured tin selenide ($SnSe_x$) ultrathin films revealed the different phases of SnSe and $SnSe_x$ nanocrystals [90]. The stiffness of clay minerals [91] and nanoferrite crystals oxidized at varying temperatures [92] was also examined with CR-AFM. The high stiffness sensitivity of CR-AFM is harnessed for investigating thin films used in semiconductor technology, such as photoresists [37, 45], aluminum [37], tungsten [30, 37, 45], copper [30, 32, 45], silicon dioxide [30, 93],

Fig. 31.11 PMMA/SBS mixture imaged by CR-AFM. The contact resonance frequency is lower on SBS regions and higher in PMMA regions, demonstrating that SBS is softer than PMMA [72] (Reproduced with permission from Springer Verlag)
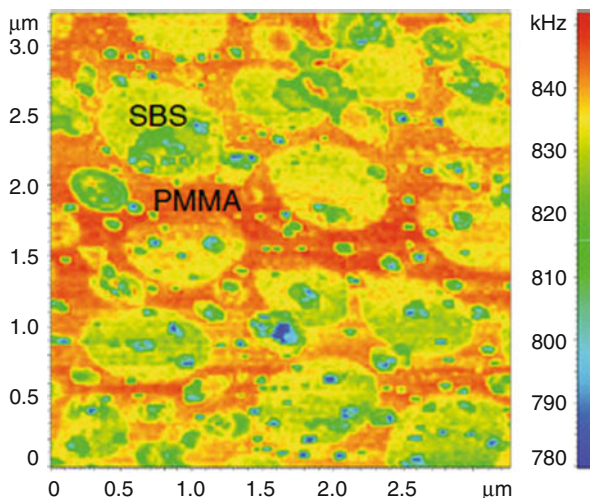
niobium [94], and nickel [95]. In addition, several CR-AFM studies have focused on detecting subsurface defects under thin films [22, 30, 34, 96, 97] and nanoscale subsurface inclusions and voids [31, 32, 34, 84].

Limitations

Since the initial challenges of data acquisition and analysis in CR-AFM have been resolved, the technique is increasingly used for the determination of the elastic properties of nanomaterials. However, because the contact resonances are very sensitive to stiffness changes, scan speed needs to be selected carefully as friction affects tip wear and thus the contact geometry [115]. Even though CR-AFM is sensitive and quantitative, its application for imaging samples in liquid environments is limited, because contact resonances are dampened and a quantitative analysis is not yet available.

Summary

CR-AFM has large potential for sensitive stiffness mapping of nanomaterials and a widespread of applications. CR-AFM has been demonstrated on composite polymer films, polymers with nanostructures, inorganic thin films, biomaterials, and self-assembled monolayers. To date, however, CR-AFM is largely confined to measurements in air, as analytical descriptions of contact resonance in liquids are still missing, and viscous damping of the cantilever resonances decrease the sensitivity of the method.

Summary and Outlook

Acoustic AFM methods map the stiffness of nanomaterials and thin films concurrently with the sample topography, by detecting the vibrational response of

a microcantilever using a phase-locked loop. Acoustic AFM techniques have been used to characterize the stiffness of self-assembled monolayers, polymers, biomaterials, nanostructures, and inorganic thin films. The materials imaged by each acoustic AFM technique differ due to the different capabilities and stiffness ranges available with each technique. FMM is mostly used for qualitative imaging of organic thin layers and soft nanostructures in air and liquid. UFM, which can be used in air and in liquid, is sensitive to stiffer materials and mostly performed on nanomaterials that have both soft and stiff regions. On the other hand, CR-AFM is a quantitative technique with a wide stiffness detection range, which has been mostly applied to inorganic thin films, crystalline nanostructures, and dry organic materials in air.

Nevertheless, acoustic AFM methods also have drawbacks that are related to the necessary imaging of the samples in contact mode. For example, small topographical features effectively decrease the contact area which leads to errors in the determination of the contact stiffness. Furthermore, acoustic AFM methods assume that the adhesion forces are small and uniform across the sample surface. Variations in the adhesion force directly affect the applied contact force during imaging, which leads to variations in the measured contact stiffness. Additional complications arise for thin films or thin-layered materials, where the film's or layer's stiffness is convoluted by the stiffness of the substrate material. When such materials are imaged with two different forces, different elastic moduli are obtained. This complicates the analysis of contact stiffness measurements on such materials. Although acoustic AFM has been introduced more than 20 years ago, the different methods are still in a phase of development to address some of the drawbacks mentioned above. For example, the increasingly faster data acquisition ability developed over the last couple of years has allowed significant progress in imaging, such as realized by DART. Furthermore, novel ways of directly exciting the tip–sample contact, for example, by magnetic actuation, have improved the sensitivity of the methods. To address the issue of adhesion variation, some recent studies combined acoustic AFM methods with pulsed-force mode AFM [116, 117]. With this combination of imaging modes, the interaction forces on the surface were measured in real time, and lateral forces were minimized. This allowed for even more accurate stiffness detection on soft materials. The operation of acoustic AFM methods in fluids has been challenging due to the fluid-damped cantilever dynamics. Work is currently ongoing to better understand the dynamics of a cantilever in contact with the sample surface while immersed in a fluid.

References

1. Li G, Zhu R, Yang Y (2012) Polymer solar cells. Nat Photon 6(3):153–161
2. Klauk H (2010) Organic thin-film transistors. Chem Soc Rev 39(7):2643–2666

3. Kaltenbrunner M, White MS, Glowacki ED, Sekitani T, Someya T, Sariciftci NS, Bauer S (2012) Ultrathin and lightweight organic solar cells with high flexibility. Nat Comm 3:770–776

4. Sekitani T, Zschieschang U, Klauk H, Someya T (2010) Flexible organic transistors and circuits with extreme bending stability. Nat Mater 9(12):1015–1022

5. Kim DK, Lai YM, Diroll BT, Murray CB, Kagan CR (2012) Flexible and low-voltage integrated circuits constructed from high-performance nanocrystal transistors. Nat Comm 3:1216–1225

6. Lipomi DJ, Vosgueritchian M, Tee BC, Hellstrom SL, Lee JA, Fox CH, Bao Z (2011) Skin-like pressure and strain sensors based on transparent elastic films of carbon nanotubes. Nat Nanotechnol 6(12):788–792

7. Stuart MAC, Huck WTS, Genzer J, Muller M, Ober C, Stamm M, Sukhorukov GB, Szleifer I, Tsukruk VV, Urban M, Winnik F, Zauscher S, Luzinov I, Minko S (2010) Emerging applications of stimuli-responsive polymer materials. Nature Mater 9(2):101–113

8. Menke M, Künneke S, Janshoff A (2002) Lateral organization of G M1 in phase-separated monolayers visualized by scanning force microscopy. Eur Biophys J 31(4):317–322

9. Pan J, Tristram-Nagle S, Nagle JF (2009) Effect of cholesterol on structural and mechanical properties of membranes depends on lipid chain saturation. Phys Rev E 80(2):021931-12

10. Picas L, Rico F, Scheuring S (2012) Direct measurement of the mechanical properties of lipid phases in supported bilayers. Biophys J 102(1):L01–L03

11. Binnig G, Quate CF, Gerber C (1986) Atomic Force Microscope. Phys Rev Lett 56(9):930–933

12. Yaralioglu GG, Atalar A, Manalis SR, Quate CF (1998) Analysis and design of an interdigital cantilever as a displacement sensor. J Appl Phys 83(12):7405–7415

13. Rugar D, Mamin HJ, Guethner P (1989) Improved fiber-optic interferometer for atomic force microscopy. Appl Phys Lett 55(25):2588–2590

14. Kim YS, Nam HJ, Cho SM, Hong JW, Kim DC, Bu JU (2003) PZT cantilever array integrated with piezoresistor sensor for high speed parallel operation of AFM. Sensor Actuat a-Phys 103(1–2):122–129

15. Karagiannidis P, Kassavetis S, Pitsalidis C, Logothetidis S (2011) Thermal annealing effect on the nanomechanical properties and structure of P3HT:PCBM thin films. Thin Solid Films 519(12):4105–4109

16. Killgore JP, Yablon DG, Tsou AH, Gannepalli A, Yuya PA, Turner JA, Proksch R, Hurley DC (2011) Viscoelastic property mapping with contact resonance force microscopy. Langmuir 27(23):13983–13987

17. Schön P, Bagdi K, Molnár K, Markus P, Pukánszky B, Julius Vancso G (2011) Quantitative mapping of elastic moduli at the nanoscale in phase separated polyurethanes by AFM. Eur Polym J 47(4):692–698

18. Cuenot S, Fretigny C, Demoustier-Champagne S, Nysten B (2004) Surface tension effect on the mechanical properties of nanomaterials measured by atomic force microscopy. Phys Rev B 69(16):165410-1–165410-5

19. Rabe U, Kester E, Arnold W (1999) Probing linear and non-linear tip-sample interaction forces by atomic force acoustic microscopy. Surf Interface Anal 27(5–6):386–391

20. Yamanaka K, Ogiso H, Kolosov O (1994) Ultrasonic force microscopy for nanometer resolution subsurface imaging. Appl Phys Lett 64(2):178–180

21. Maivald P, Butt HJ, Gould SAC, Prater CB, Drake B, Gurley JA, Elings VB, Hansma PK (1991) Using force modulation to image surface elasticities with the atomic force microscope. Nanotechnology 2(2):103–106

22. Tsuji T, Yamanaka K (2001) Observation by ultrasonic atomic force microscopy of reversible displacement of subsurface dislocations in highly oriented pyrolytic graphite. Nanotechnology 12(3):301–307

23. Bhushan B (2005) Nanotribology, Nanomechanics, and Material Characterization. Nanotribology and nanomechanics: an introduction, vol xxviii. Springer, Berlin, 1148 p

24. Prokopovich P, Perni S (2011) Comparison of JKR-and DMT-based multi-asperity adhesion model: Theory and experiment. Colloid Surf A 383(1):95–101

25. Maugis D (1992) Adhesion of spheres: the JKR-DMT transition using a Dugdale model. J Colloid Interf Sci 150(1):243–269

26. Johnson KL (2003) Normal contact of elastic solids – Hertz theory. In: Contact mechanics. Cambridge University Press, Cambridge, pp 84–106

27. Johnson KL, Kendall K, Roberts AD, Proc R (1971) Surface energy and contact of elastic solids. Soc Lon Ser-A 324(1558):301–303

28. Hurley DC, Kopycinska-Muller M, Langlois ED, Kos AB, Barbosa N (2006) Mapping substrate/film adhesion with contact-resonance-frequency atomic force microscopy. Appl Phys Lett 89(021311):1–3

29. Kovalev A, Shulha H, Lemieux M, Myshkin N, Tsukruk VV (2003) Nanomechanical probing of layered nanoscale polymer films with atomic force microscopy. J Mater Res 19(3):716–728

30. Sarioglu AF, Atalar A, Degertekin FL (2004) Modeling the effect of subsurface interface defects on contact stiffness for ultrasonic atomic force microscopy. Appl Phys Lett 84(26):5368–5370

31. Killgore JP, Kelly JY, Stafford CM, Fasolka MJ, Hurley DC (2011) Quantitative subsurface contact resonance force microscopy of model polymer nanocomposites. Nanotechnology 22(17):175706-6

32. Parlak Z, Degertekin FL (2008) Contact stiffness of finite size subsurface defects for atomic force microscopy: Three-dimensional finite element modeling and experimental verification. J Appl Phys 103(11):114910–114918

33. Parlak Z, Degertekin LF (2013) Quantitative subsurface imaging by acoustic AFM techniques. Acoustic scanning probe microscopy. Springer, Berlin Heidelberg pp 417–436

34. Striegler A, Koehler B, Bendjus B, Roellig M, Kopycinska-Mueller M, Meyendorf N (2011) Detection of buried reference structures by use of atomic force acoustic microscopy. Ultramicroscopy 111(8):1405–1416

35. Clifford CA, Seah MP (2009) Nanoindentation measurement of Young's modulus for compliant layers on stiffer substrates including the effect of Poisson's ratios. Nanotechnology 20(14):145708

36. Batog GS, Baturin AS, Bormashov VS, Sheshin EP (2006) Calculation of the thicknesses and elastic properties of thin-film coatings using atomic-force acoustic microscopy data. Tech Phys 51(8):1084–1089

37. Yaralioglu GG, Degertekin FL, Crozier KB, Quate CF (2000) Contact stiffness of layered materials for ultrasonic atomic force microscopy. J Appl Phys 87(10):7491–7496

38. Onaran AG, Balantekin M, Lee W, Hughes WL, Buchine BA, Guldiken RO, Parlak Z, Quate CF, Degertekin FL (2006) A new atomic force microscope probe with force sensing integrated readout and active tip. Rev Sci Instrum 77(2):023501–023507

39. Gao H, Chiu C-H, Lee J (1992) Elastic contact versus indentation modeling of multi-layered materials. Int J Solids Struct 29(20):2471–2492

40. Tsukruk VV, Huang Z, Chizhik SA, Gorbunov VV (1998) Probing of micromechanical properties of compliant polymeric materials. J Mater Sci 33(20):4905–4909

41. Tsukruk VV, Sidorenko A, Gorbunov VV, Chizhik SA (2001) Surface nanomechanical properties of polymer nanocomposite layers. Langmuir 17(21):6715–6719

42. Shulha H, Kovalev A, Myshkin N, Tsukruk VV (2004) Some aspects of AFM nanomechanical probing of surface polymer films. Eur Polym J 40(5):949–956

43. Dimitriadis EK, Horkay F, Maresca J, Kachar B, Chadwick RS (2002) Determination of elastic moduli of thin layers of soft material using the atomic force microscope. Biophys J 82(5):2798–2810

44. Lin DC, Horkay F (2008) Nanomechanics of polymer gels and biological tissues: A critical review of analytical approaches in the Hertzian regime and beyond. Soft Matter 4(4):669–682

45. Crozier KB, Yaralioglu GG, Degertekin FL, Adams JD, Minne SC, Quate CF (2000) Thin film characterization by atomic force microscopy at ultrasonic frequencies. Appl Phys Lett 76(14):1950–1952

46. Akhremitchev BB, Walker GC (1999) Finite sample thickness effects on elasticity determination using atomic force microscopy. Langmuir 15(17):5630–5634

47. Rosa-Zeiser A, Weilandt E, Hild S, Marti O (1997) The simultaneous measurement of elastic, electrostatic and adhesive properties by scanning force microscopy: pulsed-force mode operation. Meas Sci Tech 8(11):1333–1338

48. Marti O, Holzwarth M, Beil M (2008) Measuring the nanomechanical properties of cancer cells by digital pulsed force mode imaging. Nanotechnology 19(38):384015–384017

49. Radmacher M, Tillmann RW, Gaub HE (1993) Imaging viscoelasticity by force modulation with the atomic force microscope. Biophys J 64(3):735–742

50. Nie HY, Motomatsu M, Mizutani W, Tokumoto H (1996) Local elasticity measurement on polymers using atomic force microscopy. Thin Solid Films 273(1):143–148

51. Arnold W (2012) Force modulation in atomic force microscopy. In: Encyclopedia of nanotechnology. Springer, Netherlands pp 876–884

52. Bar G, Rubin S, Parikh AN, Swanson BI, Zawodzinski TA, Whangbo MH (1997) Scanning force microscopy study of patterned monolayers of alkanethiols on gold. Importance of tip−sample contact area in interpreting force modulation and friction force microscopy images. Langmuir 13(3):373–377

53. Dinelli F, Albonetti C, Kolosov OV (2011) Ultrasonic force microscopy: Detection and imaging of ultra-thin molecular domains. Ultramicroscopy 111(4):267–272

54. Hurley DC, Kopycinska-Muller A, Julthongpiput D, Fasolka MJ (2006) Influence of surface energy and relative humidity on AFM nanomechanical contact stiffness. Appl Surf Sci 253(3):1274–1281

55. Price WJ, Leigh SA, Hsu SM, Patten TE, Liu G-Y (2005) Measuring the size dependence of Young's modulus using force modulation atomic force microscopy. J Phys Chem A 110(4):1382–1388

56. Bliznyuk VN, Lipatov YS, Ozdemir N, Todosijchuk TT, Chornaya VN, Singamaneni S (2007) Atomic force and ultrasonic force microscopy investigation of adsorbed layers formed by two incompatible polymers: Polystyrene and poly(butyl methacrylate). Langmuir 23(26):12973–12983

57. Jourdan JS, Cruchon-Dupeyrat SJ, Huan Y, Kuo PK, Liu GY (1999) Imaging nanoscopic elasticity of thin film materials by atomic force microscopy: Effects of force modulation frequency and amplitude. Langmuir 15(19):6495–6504

58. Kiridena W, Jain V, Kuo PK, Liu G-Y (1997) Nanometer-scale elasticity measurements on organic monolayers using scanning force microscopy. Surf Interface Anal 25(6):383–389

59. Cavallini M, Murgia M, Biscarini F (2001) Patterning a conjugated molecular thin film at submicron scale by modified microtransfer molding. Nano Lett 1(4):193–195

60. Bruno P, Laura S, Giovanni M (2003) Dynamic scanning force microscopy investigation of nanostructured spiral-like domains in Langmuir–Blodgett monolayers. Nanotechnology 14(2):245–249

61. Zhang J, Parlak Z, Bowers CM, Oas T, Zauscher S, Beilstein J (2012) Mapping mechanical properties of organic thin films by force-modulation microscopy in aqueous media. Nanotechnology 3(1):464–474

62. Dinelli F, Castell MR, Ritchie DA, Mason NJ, Briggs GAD, Kolosov OV (2000) Mapping surface elastic properties of stiff and compliant materials on the nanoscale using ultrasonic force microscopy. Philos Mag A-Phys Condens Matter Struct Defect Mech Prop 80(10):2299–2323

63. Kimura K, Kobayashi K, Yamada H, Matsushige K (2007) High resolution molecular chain imaging of a poly(vinylidenefluoride–trifluoroethylene) crystal using force modulation microscopy. Nanotechnology 18(30):305504–305506

64. Porfyrakis K, Kolosov OV, Assender HE (2001) AFM and UFM surface characterization of rubber-toughened poly(methylmethacrylate) samples. J Appl Polym Sci 82(11):2790–2798

65. Fernandez E, Hernandez R, Cuberes MT, Mijangos C, Lopez D (2010) New hydrogels from interpenetrated physical gels of agarose and chemical gels of polyacrylamide: Effect of relative concentration and crosslinking degree on the viscoelastic and thermal properties. J Polym Sci Pt B-Polym Phys 48(23):2403–2412

66. Cech V, Trivedi R, Skoda D (2011) Mechanical properties of individual layers in a-SiC:H multilayer film. Plasma Process Polym 8(12):1107–1115

67. Hu H, Saniger JM, Bañuelos JG (1999) Thin films of polyaniline–polyacrylic acid composite by chemical bath deposition. Thin Solid Films 347(1–2):241–247

68. Yablon DG, Gannepalli A, Proksch R, Killgore J, Hurley DC, Grabowski J, Tsou AH (2012) Quantitative viscoelastic mapping of polyolefin blends with contact resonance atomic force microscopy. Macromolecules 45(10):4363–4370

69. Xu X, Koslowski M, Raman A (2012) Dynamics of surface-coupled microcantilevers in force modulation atomic force microscopy–magnetic vs. dither piezo excitation. J Appl Phys 111(5):054303–054303-5

70. Yuya PA (2008) Contact-resonance atomic force microscopy for viscoelasticity. J Appl Phys 104(7):074916–074917

71. Yuya PA, Hurley DC, Turner JA (2011) Relationship between Q-factor and sample damping for contact resonance atomic force microscope measurement of viscoelastic properties. J Appl Phys 109(11):113528-5

72. Passeri D, Rossi M, Tamburri E, Terranova ML (2013) Mechanical characterization of polymeric thin films by atomic force microscopy based techniques. Anal Bioanal Chem 405(5):1463–1478

73. Deleu M, Nott K, Brasseur R, Jacques P, Thonart P, Dufrêne YF (2001) Imaging mixed lipid monolayers by dynamic atomic force microscopy. BBA-Biomembranes 1513(1):55–62

74. Zhang B, Cheng Q, Chen M, Yao W, Qian M, Hu B (2012) Imaging and analyzing the elasticity of vascular smooth muscle cells by atomic force acoustic microscope. Ultrasound Med Biol 38(8):1383–1390

75. Grishin I, Tinker C, Allsop D, Robson A, Kolosov O (2012) Nanoscale SPM characterisation of nacre aragonite plates and synthetic human amyloid fibres. NSTI-Nanotech 2012 3:110–113

76. Zhao W, Cao C, Korach CS (2011) Measurement of structural variations in enamel nanomechanical properties using quantitative atomic force acoustic microscopy. Time dependent constitutive behavior and fracture/failure processes,. Springer, New York vol 3. pp 373–381

77. Gannepalli A, Yablon DG, Tsou AH, Proksch R (2011) Mapping nanoscale elasticity and dissipation using dual frequency contact resonance AFM. Nanotechnology 22(35):355705–355708

78. Huey BD (2007) AFM and acoustics: fast, quantitative nanomechanical mapping. In: Annual review of materials research. Annual Reviews, Palo Alto, pp 351–385

79. Dinelli F, Assender HE, Takeda N, Briggs GAD, Kolosov OV (1999) Elastic mapping of heterogeneous nanostructures with ultrasonic force microscopy (UFM). Surf Interface Anal 27(5–6):562–567

80. Preghenella M, Pegoretti A, Migliaresi C (2006) Atomic force acoustic microscopy analysis of epoxy-silica nanocomposites. Polym Testing 25(4):443–451

81. Geer RE, Kolosov OV, Briggs GAD, Shekhawat GS (2002) Nanometer-scale mechanical imaging of aluminum damascene interconnect structures in a low-dielectric-constant polymer. J Appl Phys 91(7):4549–4555

82. Kolosov OV, Grishin I, Jones R (2011) Material sensitive scanning probe microscopy of subsurface semiconductor nanostructures via beam exit Ar ion polishing. Nanotechnology 22(18):185702–185707

83. McGuigan AP, Huey BD, Briggs GAD, Kolosov OV, Tsukahara Y, Yanaka M (2002) Measurement of debonding in cracked nanocomposite films by ultrasonic force microscopy. Appl Phys Lett 80:1180–1183

84. Kimura K, Kobayashi K, Matsushige K, Yamada H (2013) Imaging of Au nanoparticles deeply buried in polymer matrix by various atomic force microscopy techniques. Ultramicroscopy 133:41–49

85. Alvarado-Rivera J, Munoz-Saldanal J, Castro-Beltran A, Quintero-Armenta JM, Almaral-Sanchez JL, Ramirez-Bon R (2007) Hardness and wearing properties of SiO2-PMMA hybrid coatings reinforced with Al2O3 nanowhiskers. Phys Status Solid C 4(11):4254–4259

86. Passeri D, Rossi M, Alippi A, Bettucci A, Terranova M, Tamburri E, Toschi F (2008) Characterization of epoxy/single-walled carbon nanotubes composite samples via atomic force acoustic microscopy. Physica E 40(7):2419–2424

87. Rabe U, Kopycinska M, Hirsekorn S, Saldaña JM, Schneider GA, Arnold W (2002) High-resolution characterization of piezoelectric ceramics by ultrasonic scanning force microscopy techniques. J Phys D Appl Phys 35(20):2621–2635

88. Tsuji T, Ogiso H, Akedo J, Saito S, Fukuta K, Yamanaka K (2004) Evaluation of domain boundary of piezo/ferroelectric material by ultrasonic atomic force microscopy. Jpn J Appl Phys 43(5B):2907–2913

89. Kopycinska M, Ziebert C, Schmitt H, Rabe U, Hirsekorn S, Arnold W (2003) Nanoscale imaging of elastic and piezoelectric properties of nanocrystalline leadcalcium titanate. Surf Sci 532:450–455

90. Passeri D, Rossi M, Alippi A, Bettucci A, Manno D, Serra A, Filippo E, Lucci M, Davoli I (2008) Atomic force acoustic microscopy characterization of nanostructured seleniumtin thin films. Supperlattice Micros 44(4–5):641–649

91. Prasad M, Kopycinska M, Rabe U, Arnold W (2002) Measurement of Young's modulus of clay minerals using atomic force acoustic microscopy. Geophys Res Lett 29(8):13-1–13-4

92. Kester E, Rabe U, Presmanes L, Tailhades P, Arnold W (2000) Measurement of Young's modulus of nanocrystalline ferrites with spinel structures by atomic force acoustic microscopy. J Phys Chem Solids 61(8):1275–1284

93. Cunfu H, Gaimei Z, Bin W, Zaiqi W (2010) Subsurface defect of the SiOx film imaged by atomic force acoustic microscopy. Opt Laser Eng 48(11):1108–1112

94. Hurley DC, Kopycinska-Müller M, Kos AB, Geiss RH (2005) Quantitative elastic-property measurements at the nanoscale with atomic force acoustic microscopy. Adv Eng Mater 7(8):713–718

95. Kopycinska-Muller M, Geiss RH, Muller J, Hurley DC (2005) Elastic-property measurements of ultrathin films using atomic force acoustic microscopy. Nanotechnology 16:703–709

96. Hurley DC, Kopycinska-Muller M, Langlois ED, Kos AB, Barbosa N (2006) Mapping substrate/film adhesion with contact-resonance-frequency atomic force microscopy. Appl Phys Lett 89(2):021911-1–021911-3

97. Robert L, Cretin B (1999) Determination of the observation depth in scanning microdeformation microscopy. Surf Interface Anal 27(5–6):568–571

98. Arinero R, Leveque G (2003) Vibration of the cantilever in force modulation microscopy analysis by a finite element model. Rev Sci Instrum 74(1):104–111

99. Nia Hadi T, Han L, Li Y, Ortiz C, Grodzinsky A (2011) Poroelasticity of cartilage at the nanoscale. Biophys J 101(9):2304–2313

100. Mazeran P-E, Loubet J-L (1997) Force modulation with a scanning force microscope: an analysis. Tribol Lett 3(1):125–132

101. Kolosov O, Yamanaka K (1993) Nonlinear detection of ultrasonic vibrations in an atomic force microscope. Jpn J Appl Phys Part 2 Lett 32(8A):L1095–L1098

102. Kolosov O, Briggs A, Yamanaka K, Arnold W (1996) Nanoscale imaging of mechanical properties by ultrasonic force microscopy (UFM). In: Tortoli P, Masotti L (eds) Acoustical imaging. Springer, New York, pp 665–668

103. Passeri D, Bettucci A, Rossi M (2010) Acoustics and atomic force microscopy for the mechanical characterization of thin films. Anal Bioanal Chem 396(8):2769–2783

104. Dinelli F, Biswas SK, Briggs GAD, Kolosov OV (2000) Measurements of stiff-material compliance on the nanoscale using ultrasonic force microscopy. Phys Rev B 61(20):13995–14006
105. Kolosov O, Briggs A (2013) Ultrasonic force microscopies. In: Marinello F, Passeri D, Savio E (eds) Acoustic scanning probe microscopy. Springer, Berlin/Heidelberg, pp 261–292
106. Nalladega V, Sathish S, Brar AS (2006) Nondestructive evaluation of submicron delaminations at polymer/metal interface in flex circuits. In: Thompson DO, Chimenti DE (eds) Review of progress in quantitative nondestructive evaluation, vol 25a, b. American Institute of Physics, Melville, pp 1562–1569
107. Rabe U, Janser K, Arnold W (1996) Vibrations of free and surface-coupled atomic force microscope cantilevers: Theory and experiment. Rev Sci Instrum 67(9):3281–3293
108. Turner JA, Hirsekorn S, Rabe U, Arnold W (1997) High-frequency response of atomic-force microscope cantilevers. J Appl Phys 82(3):966–979
109. Rabe U, Amelio S, Kester E, Scherer V, Hirsekorn S, Arnold W (2000) Quantitative determination of contact stiffness using atomic force acoustic microscopy. Ultrasonics 38(1–8):430–437
110. Yamanaka K, Nakano S (1998) Quantitative elasticity evaluation by contact resonance in an atomic force microscope. Appl Phys A-Mater 66:S313–S317
111. Yamanaka K, Noguchi A, Tsuji T, Koike T, Goto T (1999) Quantitative material characterization by ultrasonic AFM. Surf Interface Anal 27(5–6):600–606
112. Passeri D, Bettucci A, Germano M, Rossi M, Alippi A (2006) Local indentation modulus characterization of diamondlike carbon films by atomic force acoustic microscopy two contact resonance frequencies imaging technique. Appl Phys Lett 88:121910–121913
113. Wagner H, Bedorf D, Küchemann S, Schwabe M, Zhang B, Arnold W, Samwer K (2011) Local elastic properties of a metallic glass. Nat Mater 10(6):439–442
114. Nair SS, Wang S, Hurley DC (2010) Nanoscale characterization of natural fibers and their composites using contact-resonance force microscopy. Compos Part A-Appl S 41(5):624–631
115. Killgore JP, Geiss RH, Hurley DC (2011) Continuous measurement of atomic force microscope tip wear by contact resonance force microscopy. Small 7(8):1018–1022
116. Parlak Z, Degertekin FL (2010) Combined quantitative ultrasonic and time-resolved interaction force AFM imaging. Rev Sci Instrum 81(12):013703-1–013703-4
117. Killgore JP, Hurley DC (2012) Pulsed contact resonance for atomic force microscopy nanomechanical measurements. Appl Phys Lett 100(5):053104-4

Nanomaterials as Antimicrobial Agents

32

Martin Malmsten

Introduction

Despite continuing progress in pharmaceutics, biomaterials, and medical procedures, but also in hygiene products, water purification, and food processing, infection remains a large source of illness and mortality. Current antimicrobial therapeutics, e.g., tetracycline, β-lactam, aminoglycoside, macrolide, and quinolone antibiotics, as well as widely used antiseptic agents, e.g., chlorhexidine, triclosan, and quaternary ammonium compounds, are facing problems with increasing resistance development [1]. Thus, there is a growing need for novel antibiotics, as well as antimicrobial formulations, in a range of contexts, e.g., as coating of medical devices or in personal care products. Here, nanoparticles and nanoscale self-assembly structures offer interesting opportunities [2]. Apart from scalability, low cost, and versatility, such materials offer advantages related to presently undeveloped resistance, lower toxicity to the environment than traditional antibiotics, as well as longer duration. Antimicrobial nanomaterials may therefore provide an alternative to low molecular weight antimicrobial and antiseptic agents in a range of applications.

Polymers, Lipids, and Surfactants

Many factors affect the antimicrobial properties of polymers, including molecular weight, hydrophobicity, charge, and amphiphilicity. Similar to antimicrobial

---

M. Malmsten

Department of Pharmacy, Uppsala University, Uppsala, Sweden
e-mail: martin.malmsten@farmaci.uu.se

peptides, antimicrobial polymers are frequently positively charged, since this facilitates binding to, and rupture of, negatively charged bacteria membranes [3, 4]. As a result of direct membrane rupture being the main mode of action of such polymers, their antimicrobial effect depends on charge density and distribution, type of positively charged groups in the polymer, and counterion identity [5]. However, also hydrophobic interactions may play a major role in driving polymer charges to the bacteria membrane surface and to facilitate membrane packing disruption, particularly at high ionic strength, where electrostatic interactions are screened [4, 6]. Apart from linear polymers, cationic dendrimers are of interest as antimicrobials due to high surface charge, e.g., for efficient drug complexing or for direct membrane disruption of bacteria. In addition, dendrimers have been found to display potent antiviral effects when functionalized with entities capable of complexing with cell or viral receptors to interfere with cell-virus interactions, including initial virus-cell binding. The antiviral action of dendrimers thus occurs early in the infection process, and demonstrates promising potency, e.g., against HIV, influenza virus, respiratory syncytial virus (RSV), and measles virus [7].

While cationic polymers find use as antimicrobials in a host of applications, many applications of such systems require incorporation of antibiotics and low molecular weight antiseptics. Since the antimicrobial action for such systems stems primarily from the incorporated compounds, the matrix-forming polymer need not possess antimicrobial properties itself, allowing the polymer system to be designed to offer other advantages, such as responsive gelation, controlled degradation, and drug release rate, as well as low toxicity and favorable tissue integration. For example, poly(ethylene oxide)/poly(propylene oxide) (PEO/PPO) block copolymers display a dramatic temperature-induced thickening, caused by a transition from a micellar solution to a (disordered) cubic phase [8]. Employing this, Esposito et al. investigated Lutrol 407 as delivery system for tetracycline in the treatment of periodontitis, and found promising performance [9]. Formulations for such localized treatments need to be easily administered, e.g., by syringe or as a spray, so that it efficiently fills all cavities. After administration, the formulation should solidify for good bioadhesion and localization. After releasing its drug cargo, the formulation should either self-disintegrate or be easy to remove. Similarly, Chiapetta et al. incorporated the antiviral drug efavirenz into PEO/PPO block copolymer hydrogels in pediatric anti-HIV treatment. This Class II compound is poorly soluble in water, but efficiently solubilized in PEO/PPO block copolymer micelles, resulting in improved and less varying oral bioavailability [10].

As for polymers, nanoscale structures formed by surfactants and polar lipids offer functional advantages for antimicrobial and antiviral therapies, including improved solubility of sparingly soluble drugs, reduction of drug hydrolysis, control of release rate, and improved bioavailability. As cationic surfactants and lipids bind readily to bacterial membranes and destabilize these, such compounds are antimicrobial also when molecularly distributed, exemplified, e.g., by the widely used antiseptic benzalkonium chloride [11]. Investigating these effects, Yang et al. studies the antimicrobial activity of fatty acids of different acyl chain

lengths, i.e., lauric acid ($C_{12:0}$), palmitic acid ($C_{16:0}$), and oleic acid ($C_{18:1}$) [12]. Of these, lauric acid was found to give the strongest bactericidal activity. In an effort to increase the effective solubility of lauric acid and its antimicrobial potency, these authors incorporated lauric acid into phosphatidylcholine (PC)/cholesterol liposomes, and found that the liposomes could fuse with membranes of *P. acnes*, thereby providing these liposomes with antimicrobial effect, the extent of which increased with the lauric acid content of the liposomes. Analogously, Huang et al. found oleic acid–loaded PC/cholesterol liposomes to able to fuse with bacterial membranes, thereby promoting bacterial killing [13]. In vivo, these liposomes were effective in curing skin infections caused by methicillin-resistant *S. aureus* (MRSA), at the same time showing good biocompatibility in skin toxicity evaluations.

Ag, Au, and Cu Nanoparticles

The last decade has seen a dramatically increased interest in Ag nanoparticles as an antimicrobial and antiseptic agent. Ag has the highest bactericidal activity of all known metal nanoparticles, increasing with decreasing particle size [14], and also displays size- and stabilizer-dependent antiviral effects (Fig. 32.1) [15]. Ag (as well as Au and Cu) nanoparticles cause antimicrobial effects by several mechanisms, including direct membrane rupture, binding to sulfhydryl groups of metabolic enzymes, and binding to microbial DNA. Such nanoparticles also generate reactive oxygen species, in turn causing bacterial enzyme and lipid oxidation. Due to these multiple modes of action, resistance development against Ag nanoparticles and related systems is precluded due to the requirement of multiple mutations. Nevertheless, resistance development in bacteria has been found also against silver compounds [16].

Furthermore, Ag nanoparticles have been extensively investigated as a composite component. For example, Thomas et al. investigated Ag nanoparticle formation from $AgNO_3$ in poly(acrylamide-co-acrylic acid) matrices [17]. For such systems, the antibacterial potency increased with the concentration of $AgNO_3$, the acrylic acid content (promoting Ag^+ binding and Ag nanoparticle nucleation), and decreasing particle size (i.e., larger surface area). Similarly Ozay et al. prepared composite particles by emulsion polymerization of 4-vinylpyridine [18]. While the hydrogel particles displayed modest antibacterial activity on *E. coli*, *P. aeruginosa*, *S. aureus*, and *B. subtilis*, incorporation of Ag or Cu nanoparticles substantially increased antibacterial potency. Furthermore, Marsich et al. investigated chitosan hydrogels containing Ag and Au nanoparticles, and found that Au-containing hydrogels, but not Ag-containing ones, displayed considerable toxicity, evidenced by LDH release for MG63 and HepG2 eukaryotic cells [19]. In addition, cytofluorometry demonstrated increased cell death caused by reactive oxygen species, as well as thicker (inflammation-related) capsule formation around such composite hydrogels after subcutaneous administration in mice. Considering the importance of factors such as particle size, shape, and stabilizing agent for nanoparticle toxicity, however, further work on these issues is needed.

Fig. 32.1 Antiviral activity of Ag nanoparticles against HIV-I virus. Shown are data on HIV-I-mediated syncytium formation in MT-2 cells for three different surface coatings of the Ag nanoparticles. Mean particle sizes for the carbon-, PVP-, and BSA-modified nanoparticles were around 16 nm, 7 nm, and 3 nm, respectively (Redrawn from [15])
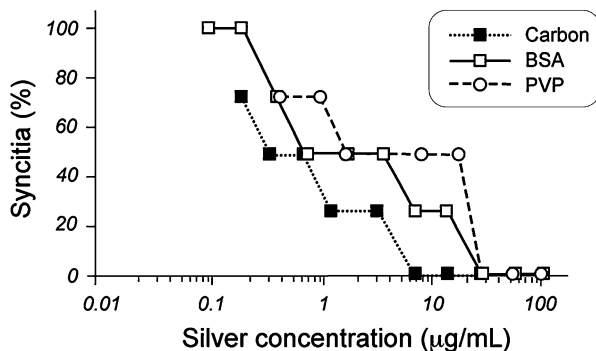
Through suitable design, antimicrobial composites of Ag nanoparticles can be provided with additional beneficial properties, including reduction of cell adhesion, coagulation, and complement activation. For example, Zan et al. prepared poly (vinyl alcohol) (PVA) hydrogel films on biodegradable poly(L-lactic acid) (PLLA), which were subsequently loaded with Ag nanoparticles [20]. The resulting composites displayed potent antimicrobial activity against *E. coli*, but also a reduced HeLa cell adhesion. The latter effect, likely due to a low electrostatic potential and high water content (resulting in low electrostatic and van der Waals interactions with the cells, respectively), is attractive in applications where tissue integration is not desired (e.g., catheters). In addition, antimicrobial and other drugs can be readily adsorbed at the surface of Ag and Au nanoparticles for additional functionality [21], allowing large drug loads due to the small size of these nanoparticles. Release of the adsorbed drug can be controlled, e.g., through simple desorption induced by a change in pH or ionic strength, by light exposure for drugs covalently bound to the nanoparticles through photolabile linking groups, or through reduction of thiol links used for drug chemisorption.

There have also been studies of the antimicrobial properties of Au/Ag hybrid systems. For example, Dos Santos et al. reported on the use of citrate-capped Au/Ag-alloy nanoparticles, combined with conventional antibiotics [22]. Presence of such alloy nanoparticles considerably decreased the dose of antibiotics needed for antimicrobial effect, both in rich medium suspension and under biofilm-like conditions. Somewhat related, Fan et al. investigated magnetic core-gold shell nanoparticles for surface-enhanced Raman spectroscopy (SERS) detection and photothermal destruction of bacteria. Thus, photoexcitation of anti-MDR *Salmonella* DT104-conjugated nanoparticles was found to cause local heating in the immediate surroundings of the nanostructure, and result in the specific destruction of MDR bacteria [23]. Localized heating for antimicrobial treatment by Au nanoparticles was investigated also by Kojic et al., aiming at improved infection management in ischemic, avascular, and necrotic tissues [24]. Since drug uptake into abscesses is limited by the dense capsule wall and limited vascularity, conventional antibiotics require high plasma concentrations to overcome the

Fig. 32.2 (a) Effect of Au nanoparticle concentration (given as mixing ratio, where 40 corresponds to a concentration of 8.75 nM) on the temperature increase caused by illumination. (b) Effect of illumination intensity on the antimicrobial effect of Au nanoparticles against *S. aureus* (as observed by the size of the clearance zone) (Redrawn from [24])
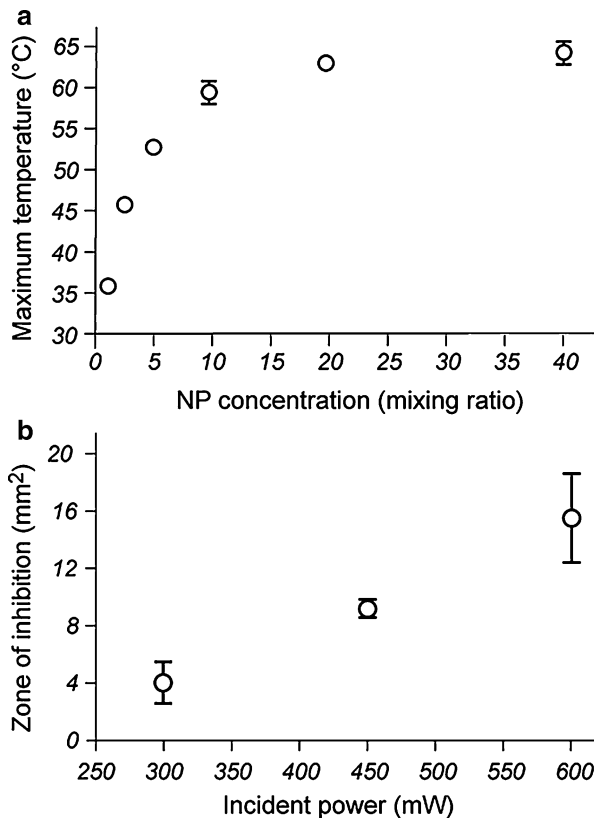
penetration barrier, in turn resulting in dose-limiting toxicity. To address these obstacles, laser-induced heating of Au nanoparticles embedded in an injectable silk-protein hydrogel was investigated, showing that a single 10-min laser treatment of a subcutaneous infection in mice was sufficient to achieve potent bactericidal effects, at preserved tissue architecture (Fig. 32.2).

TiO$_2$ and Related Materials

In analogy to Ag, Au, and Cu nanoparticles, a number of metal oxide and related nanoparticles display antimicrobial properties, either on their own or on light/magnetic field exposure, including TiO$_2$, ZnO, Fe$_2$O$_3$/Fe$_3$O$_4$, CeO$_2$, ZnS, and CdSe [2, 5]. Of these, TiO$_2$ been particularly extensively investigated due to the photocatalytic nature of this material. The photocatalysis of TiO$_2$, which depends on factors such as crystal structure, morphology, and crystallite size, is caused by UV-induced generation of hydroxyl radicals, and is able to oxidize essential bacterial components such as proteins, polysaccharides, lipids, and nucleic acids. This causes TiO$_2$, particularly in its anatase form, to be strongly antimicrobial when

exposed to near-UV light [25]. Investigating these effects, Chen et al. incorporated TiO_2 nanoparticles in polyurethane, and found efficient antimicrobial effect against *S. aureus*, *E. coli*, and *P. aeruginosa* [26]. Furthermore, the effect of this composite against full-thickness wounds in rats was significantly better than that of a commercial benchmark material. The importance of direct membrane action for the antimicrobial action of these materials was demonstrated by Schwegman et al. for iron oxide nanoparticles, who found both binding and killing to follow the z-potential contrast between the bacteria and nanoparticles [27]. Direct morphological damage on bacteria was furthermore observed by Fang et al. for TiO_2, ZnO, and CeO_2, while ZnO nanoparticles were also demonstrated to cause bacterial stress through release of Zn^{2+} ions [28]. Somewhat related, Hajipour et al. investigated the antimicrobial effects of ZnO, CuO, NiO, and Sb_2O_3 against *E. coli*, *B. subtilis*, and *S. aureus*, and noted CuO to display the highest potency, followed by ZnO, NiO, and Sb_2O_3 [29].

In addition, composite materials containing Ag and TiO_2 nanoparticles have attracted attention as antimicrobial/antiviral agents. Such systems were found, e.g., by Yuan et al. [30], to have dual antimicrobial effects. In the dark, such systems display antibacterial properties due to released silver ions. In the presence of UV light, an enhancement of this effect occurs, due to the generation of antibacterial superoxide anions and peroxide species. Similarly, Akhavan prepared Ag-TiO_2 composite films and found synergistic UV-triggered antimicrobial effects, paralleled by the release of Ag^+ [31], while Karunakaran et al. investigated Cu-doped TiO_2 nanoparticles, and found potent UV-triggered antimicrobial properties against *E. coli* [32]. Composite antimicrobial materials were investigated also by Chen et al., who studied antibody-conjugated Fe_3O_4/TiO_2 core/shell nanoparticles to allow selective antibacterial activity, e.g., against *S. aureus*, *S. saprophyticus*, and *S. pyogenes* [26]. These authors also found, however, that Fe_3O_4/TiO_2 core/shell nanoparticles can be used directly, i.e., without antibodies, as affinity probes for trapping pathogenic bacteria for photokilling under UV illumination. Several pathogenic bacteria, including *H. influenzae*, *E. cloacae*, *A. baumannii*, and *S. pyogenes*, including antibiotic-resistant strains such as *A. baumannii* (PDRAB) and methicillin-resistant *S. aureus* (MRSA), were used to demonstrate the approach (Fig. 32.3). Similarly, Yu et al. investigated alumina-coated Fe_3O_4 magnetic nanoparticles as photothermal agents to selectively kill bacteria under near-infrared (NIR) illumination [33]. The temperature of such nanoparticle suspension under NIR illumination increased by 20 °C over 5 min, while functionalization of the alumina coating of the nanoparticles allows targeting them toward bacteria. In addition, the magnetic properties of the Fe_3O_4/alumina nanoparticles allow conjugated target species to aggregate at a specific location under a magnetic field. The cell growth of nosocomial bacteria, including antibiotics-resistant bacterial strains, was effectively inhibited.

Quantum dots (QDs) are nanocrystals formed by semiconductor materials, displaying high quantum yield, resistance to photobleaching, and tunable photoluminescence, making them potentially powerful tools in a range of biomedical applications. Their wider application in this area has, however, been hampered

Fig. 32.3 Plots of the survival ratio (%) of methicillin-resistant *S. aureus* (MRSA) as a function of time in the dark (control/dark) and under UV light irradiation (control/UV), as well as in the presence of Fe$_3$O$_4$/TiO$_2$ nanoparticles in the dark (Fe$_3$O$_4$/TiO$_2$/dark) and under illumination (Fe$_3$O$_4$/TiO$_2$/ UV) (Redrawn from [26])
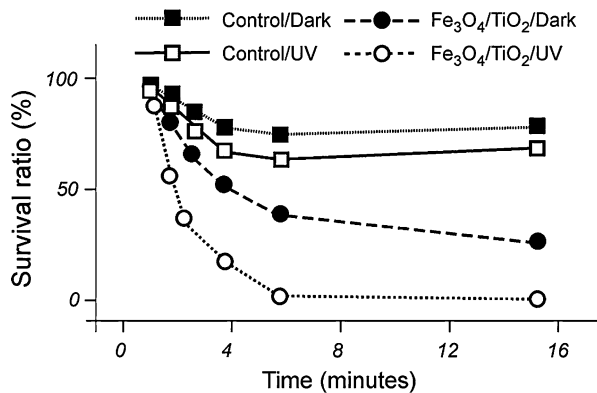
by the toxicity displayed by many QDs. Thus, released metal ions from QDs (e.g., Cd^{2+}) cause acute toxicity effects, as well as accumulation-related toxicity in liver and other tissues, with a half-time of many years. Furthermore, several QDs (e.g., CdSe) display considerable cytotoxicity under UV radiation [21]. In this context, the development of Cd-free QDs such as InAs/InP/ZnSe or InAs/ZnSe opens up some opportunities. In addition, the toxicity displayed by unmodified QDs can be reduced by various surface coatings. As an example of the investigation of QDs as antimicrobial agents, Luo et al. investigated cooperative antibacterial effects of rocephin and CdTe QDs against *E. coli* [34]. FTIR, photoluminescence, and detection of reactive oxygen species indicated that CdTe QDs and rocephin form a stable antimicrobial complex, while colony-forming capability and inhibition zone assays showed the antibiotic action of CdTe QDs-rocephin complex to be better than the superposition of those of the CdTe QDs and rocephin components. Moreover, the fluorescence intensity of CdTe QDs and the optical density of *E. coli* suspensions showed a good linear relationship, allowing dynamic monitoring of the bacterial concentration during the antibacterial process. Moreover, Lu et al. investigated QD-induced growth inhibition of bacteria and its photophysical mechanism, and found QDs to effectively inhibit bacterial growth [35]. Based on results from a cytochrome c reduction assay, photoluminescence, and UV-visible spectrometry, a photophysical mechanism involving a polypeptide or amino acid adsorption-mediated fluorescence and reactive oxygen species quenching process was proposed as the origin of the antimicrobial effect. Furthermore, Geraldo et al. investigated single-walled aluminosilicate nanotubes (SWNT) as template for in situ growth of mercaptopropionic acid–capped CdTe QDs [36]. Based on FTIR and TEM, noncovalent QD functionalization of SWNT was demonstrated. The antimicrobial activities of the QD-coated SWNT toward *S. typhimurium*, *A. baumannii*, and *P. aeruginosa* were demonstrated by growth inhibition tests, demonstrating that CdTe QDs/SWNT hybrid compound may have potential as an antimicrobial agent against heavy metal-resistant bacteria. Analogously, Neelgund et al. reported on antimicrobial nanohybrids composed of multiwalled carbon nanotubes (MWCNTs) with deposited CdS and Ag2S QDs

through amine terminated PAMAM dendrimers [37]. The antibacterial activity of the nanohybrids was evaluated against *E. coli*, *P. aeruginosa* and *S. aureus* and the results compared to that of carboxylated MWCNTs, PAMAM, PAMAM-grafted MWCNTs, and CdS and Ag2S QDs. It was found that the antimicrobial action of MWCNTs was enhanced by grafting of PAMAM, which was further improved with immobilization of CdS and Ag2S QDs.

Fullerenes

Also known as "bucky-balls," fullerenes originated from carbon-60 (C60), forming a hollow sphere 1 nm in diameter. Functionalization improves fullerene water solubility, although aggregate formation may occur. Such aggregates are toxic to microorganisms, e.g., interacting with proteins and DNA. Functionalized fullerenes have several attractive features as antimicrobial agents. For example, they have a higher photostability and generate more hydroxyl radical and superoxide than alternative photosensitizers. In addition, they are selective for microbes over mammalian cells. Addressing these effects, Huang et al. investigated the concentration-dependent microbial killing by fullerenes, and correlated this to the ability of the fullerenes to partition into bacterial membranes (expressed as logP) [38]. For *S. aureus*, *E. coli*, and *P. aeruginosa*, a good correlation was observed, demonstrating the importance of membrane insertion for the antimicrobial activity of the fullerenes investigated. In addition, however, considerable photoactivation was demonstrated (Fig. 32.4a, c). Moreover, Kumar et al. investigated a series of fullerene derivatives of s-triazine [39]. These compounds were screened for their antibacterial activity against *S. aureus*, *B. subtilis*, *B. pumilis*, *E. coli*, *P. aeruginosa*, and *K. pneumonia*, and found to display activities against these strains comparable to that of the benchmark antibiotic ciprofloxacin. In addition, Lu et al. reported that C60 fullerene functionalized by dimethylpyrrolidinium groups (BF6) is a highly active broad-spectrum antimicrobial photosensitizer in vitro when combined with white-light illumination [40]. These authors also investigated the relevance of the high in vitro activity for in vivo therapeutic effects in two mouse models. In doing so, an excisional wound on the mouse back was contaminated with one of two bioluminescent Gram-negative species, *P. mirabilis* and *P. aeruginosa*. Both showed light-dependent reduction of bioluminescence from the wound, not observed in control groups. Furthermore, fullerene-mediated photodynamic therapy of mice infected with *P. mirabilis* led to 82 % survival compared with 8 % survival without treatment (Fig. 32.4c).

The antimicrobial activity of fullerenes extends to antiviral effects as well. For example, Marchesan et al. [41] developed a series of bis-fulleropyrrolidines-containing ammonia groups, and investigated their antiviral activity against HIV-1 and HIV-2. It was found that positive charges in proximity to the carbon cage were necessary for antiviral activity, while bulky polar chains were shown to induce cytotoxicity and reduce potency. Interestingly, none of the compounds showed inhibitory activity against DNA and RNA viruses other than HIV. Similarly,

Fig. 32.4 (**a**) Killing curves for *E. coli* with increasing concentrations of fullerene (BF1) in dark and after illumination, as well as (**b**) correlation between membrane partitioning (expressed as logP) and the concentration fullerene required to result in 99 % bacterial killing. (Redrawn from [38].) Shown in (**c**) are results on fullerene (BF6)-based photodynamic therapy of mice infected with *P. mirabilis* (Redrawn from [40])
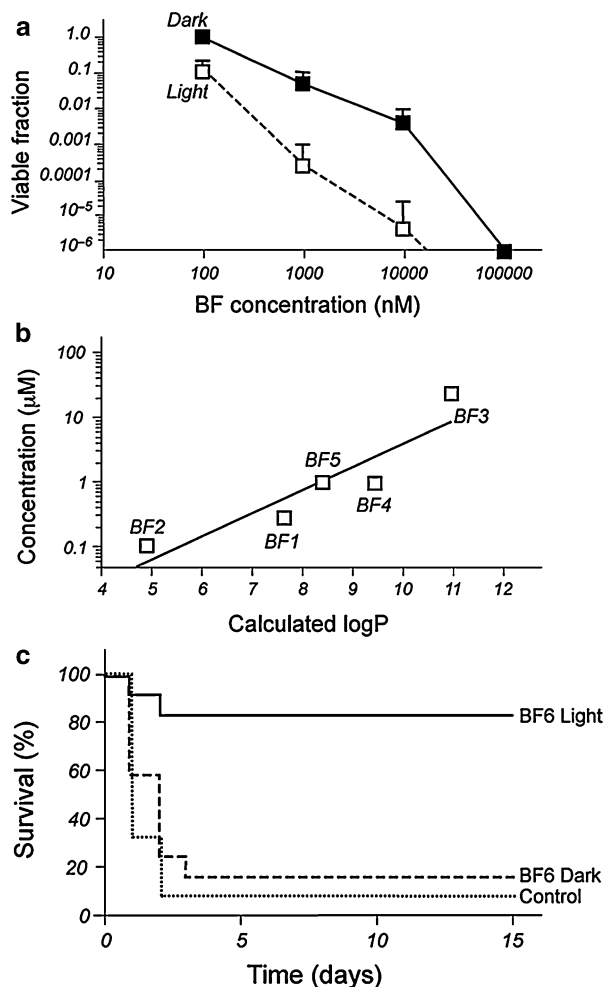
Kornev et al. reported pronounced antiviral activity in vitro, particularly against human immune-deficiency virus (HIV) and influenza A virus (subtypes H1N1 and H3N2), for a series of C70 derivatives, while Toshima et al. found a fullerene-sugar hybrid to degrade HIV-1 protease upon irradiation with long-wavelength UV light or visible light [42]. Finally, we note that Chae et al. compared C60 fullerenes with single-wall (SWNT) and multi-wall (MWNT) carbon nanotubes regarding ROS production and inactivation of *V. fischeri* under UV-A irradiation [43]. It was found that ROS production and microbial inactivation increases with decreasing nano-particle size, and decreased in the order C60 > SWNT > MWNT. In addition, however, Lyon reported nC60 to exert also ROS-independent oxidative stress in bacteria, based on protein oxidation, changes in cell membrane potential, and interruption of cellular respiration [44].

Carbon Nanotubes

While their main application in nanomedicine so far lies in biosensors rather than as therapeutics, carbon nanotubes (CNTs) are receiving increasing interest also as delivery systems. Non-modified CNT is colloidally unstable in aqueous solution, flocculating to inhomogeneous bundles. As a result of this, they display (length dependent) toxicity, e.g., causing acute pulmonary toxicity and induction of inflammatory reactions and granulomas. In contrast, (some) functionalized CNTs have been found to cause limited inflammation after subcutaneous administration, to be well tolerated following i.v. and i.p. injection, as well as after oral administration [21]. Thus, surface modification of CNTs is of critical importance for their biomedical application. Single-walled carbon nanotubes (SWNTs) have been found to be strongly antimicrobial, partially due to direct membrane action. However, oxidation by SWNT plays an important role as well, as demonstrated by Vecitis et al. from studies of well-characterized SWNT of similar dimensions, but with different electronic structure (i.e., metallic versus semiconducting) [45]. Thus, antimicrobial effect against *E. coli* was found to increase with an increasing fraction of metallic SWNTs, paralleled by an increase in glutathione oxidation, indicating the importance of oxidative stress. In parallel, SEM images of *E. coli* in contact with SWNTs demonstrated electronic structure–dependent morphological changes. From this, a three-step mechanism was proposed, i.e., (i) initial SWNT/bacteria contact, (ii) cell membrane perturbation, and (iii) electronic structure–dependent bacterial oxidation (Fig. 32.5).

Zardini et al. investigated multiwalled carbon nanotubes functionalized with arginine and lysine and their antimicrobial activity [46]. Based on minimum inhibitory concentration and radial diffusion assays, the antibacterial potency decreased in the order: arginine > lysine > pristine MWCNTs. The functionalized MWCNTs were especially effective against Gram-negative bacteria (e.g., *E. coli* and *S. typhimurium*), but also against a resistant *S. aureus* strain. The enhanced antibacterial activity was attributed to electrostatic adsorption of bacteria membrane due to positive charges of the functional groups on MWCNTs surface. Similarly, carbon nanotubes may be modified with cationic polymers to enhance their antimicrobial activity. For example, Aslan et al. investigated the antimicrobial activity of SWNT surface modified through layer-by-layer assembly of cationic poly(L-lysine) (PLL) and poly(L-glutamic acid) (PGA), terminated with a cationic PLL layer, observing significantly higher inactivation of *E. coli* and *S. epidermidis* for the modified SWNTs [47]. Somewhat analogously, Murugan et al. investigated MWCNTs functionalized with either amphiphilic poly(propyleneimine) dendrimer or Ag nanoparticles, observing good activity against *B. subtilis*, *S. aureus*, and *E. coli* [48].

In another approach, Qi et al. modified MWNTs by covalent immobilization of the antibiotic cefalexin in order to increase its antimicrobial potency, and found this to be twice as high as that of pristine MWNTs against *S. aureus* and *B. subtilis* [49]. Moreover, MWNT-cefalexin deposited film effectively inhibited cell adhesion. Analogously, Wu et al. demonstrated that the antifungal potency of

Fig. 32.5 Loss of *E. coli*
viability (**a**) and glutathione
(**b**) versus time upon exposure
to SWNTs of various fraction
metallic nanotubes. In (**a**),
dashed lines correspond to
negative controls (Redrawn
from [45])
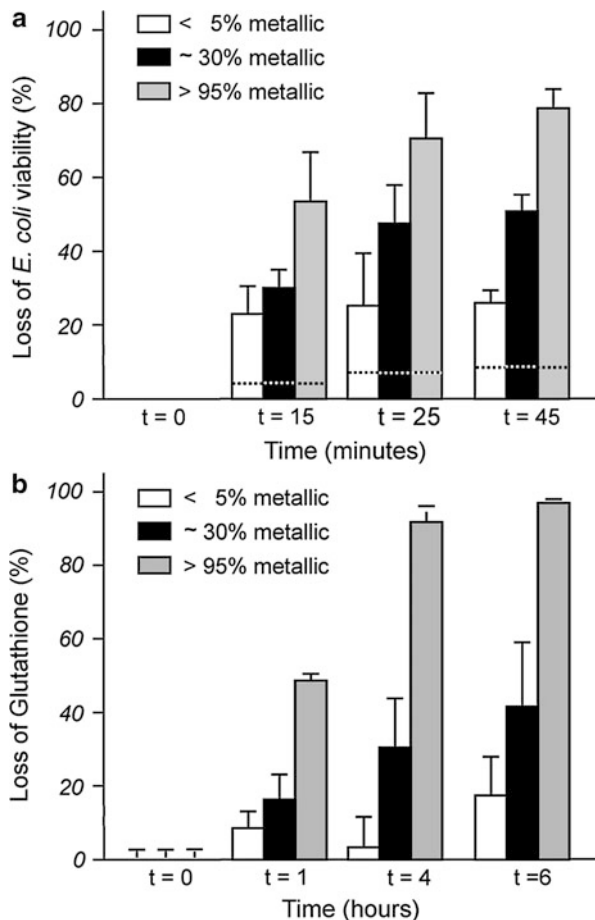
amphotericin B could be drastically enhanced when this drug is attached to carbon
nanotubes [50]. The origin of this boosting effect is unclear, but may be due to
nanotube modification of amphotericin B internalization into the fungi. Somewhat
related, Pantarotto et al. conjugated carbon nanotubes with a peptide from the foot-
and-mouth disease virus, and found the peptide-functionalized carbon nanotube to
display high antibody responses with virus-neutralizing capacity [51]. Similarly,
Benincasa et al. conjugated amphotericin B to carbon nanotubes, and investigated
their antifungal activity against a collection of reference and clinical fungal strains
[52]. Based on minimum inhibition concentrations, these conjugates were found to
perform either comparably or better than the drug itself. Importantly, resistant
Candida strains were found to be susceptible to the CNT conjugates, and no toxic
effects were observed in Jurkat cells at antifungal concentrations. Since the com-
pounds show a major permeabilizing effect on the tested fungal strains only after
extended incubation, direct membrane permeabilization was suggested not to be the
main mode of action of these conjugates.

Graphene

As for carbon nanotubes, the main interest of graphene in nanomedicine lies in biosensors and diagnostics. However, an increasing number of studies have reported on the potential use of graphene in drug delivery [21]. Considering its extended structure, an obvious concern with graphene in this context is its biodistribution after administration, relating to both efficacy and toxicity. Like carbon nanotubes, dispersions of unmodified graphene sheets in aqueous solution are not colloidally stable. Instead, graphene oxide (GO) is generally used as drug carrier, frequently after additional surface modification. In contrast to unmodified graphene, both GO and polymer-modified GO display small particle size and drastically improved stability in aqueous solution. Investigating graphene as an antimicrobial material, Liu et al. compared the antibacterial activity of graphite (Gt), graphite oxide (GtO), graphene oxide (GO), and reduced graphene oxide (rGO)) toward *E. coli* [53]. Under similar concentration and incubation conditions, the antimicrobial potency of these materials decreased in the order GO > rGO > Gt > GtO. Graphene nanosheets were furthermore demonstrated to disrupt cell membranes, while no production of reactive oxygen species was detected. Nevertheless, these materials can oxidize glutathione, conductive rGO and Gt more so than insulating GO and GtO. Based on this, a three-step antimicrobial mechanism was suggested, including initial cell deposition, causing membrane stress by direct contact with sharp nanosheets, in turn initiating superoxide anion-independent oxidation. Addressing the effect of graphene dimensions on its antimicrobial activity, Liu et al. studied the antibacterial activity of GO sheets differing in lateral size by more than 100 times, and found larger GO sheets to display stronger antibacterial activity against *E. coli* than smaller ones [54]. As the GO sheets investigated were all well dispersed and their oxidation capacity toward glutathione similar, the size-dependent antibacterial activity is not due to differences in aggregation state or oxidation capacity. AFM analysis shows that large GO sheets cover bacteria more efficiently, precluding proliferation once fully covered, resulting in the viability loss observed. In contrast, small GO sheets are less efficient in effectively covering and isolating bacteria from its surrounding. As noted by Sawangphruk et al. for *F. oxysporum*, *A. niger*, and *A. oryzae*, graphene oxide possesses similar antifungal properties, inhibiting mycelial growth [55].

Graphene has also been investigated as an antimicrobial component in composite films. For example, Santos et al. investigated composites of poly(*N*-vinylcarbazole) (PVK) and graphene in solution and thin films [56]. The antimicrobial properties of PVK-graphene films, as well as solution conjugates, were investigated for *E. coli* and *B. subtilis*. Microbial growth, metabolic, and live/dead assays all showed fewer viable and active bacteria than after exposure to either PVK or graphene alone. The toxicity of the conjugates on NIH 3 T3 cells was evaluated using the MTS cell proliferation assay, showing ≈80 % cell viability Similarly, Carpio et al. investigated a PVK-graphene oxide (GO) nanocomposite regarding antimicrobial effects on both planktonic microbes and biofilms, but also regarding toxicity against NIH 3 T3 fibroblasts [57]. The antibacterial effects were

evaluated against two Gram-negative (*E. coli* and *C. metallidurans*) and two Gram-positive (*B. subtilis* and *R. opacus*) bacteria. The results show the PVK-GO nanocomposite to have higher antimicrobial potency than pristine GO. In suspension, the nanocomposite effectively encapsulated bacteria, causing reduced microbial metabolic activity and cell death. In parallel, PVK-GO did not show any significant cytotoxicity to fibroblast cells. Alternatively, graphene can be used as carrier for other antimicrobial agents. For example, Nguyen et al. investigated graphene decorated with Ag nanoparticles [58]. Highly dispersed nanoparticles of varying size and shape were adhered to graphene sheets. The composites showed high antibacterial activities against *E. coli*, *L. anguillarum*, *B. cereus*, and *S. aureus*. Similarly, Das et al. investigated Ag nanoparticles deposited on graphene oxide and noted inhibition of growth kinetics particularly for *P. aeruginosa* [59].

Mesoporous Silica and Related Materials

Due to well-defined pores in the nm range, mesoporous materials are interesting for control of loading and release of guest molecules, with obvious opportunities in drug delivery. While such materials may be formed by a number of materials, e.g., alumina, silica, titania, and zirconia, mesoporous silica has attracted particular attention in the context of drug delivery. Such materials offer advantages related to, e.g., good physical and chemical stability, high loading capacity, and opportunities for controlled drug release. In addition, mesoporous silica has been found to be relatively "nontoxic" and biocompatible, although depending on dose and administration route. As with other nanoscale materials, mesoporous silica and related materials can be rendered antimicrobial by cationic surface modification. For example, Botequim et al. investigated antimicrobial nanoparticles based on silica nanoparticles coated with a quaternary ammonium cationic surfactant, didodecyldimethylammonium bromide (DDAB) [60]. At saturation, DDAB forms a bilayer at the silica surface, as confirmed by z-potential measurements, thermogravimetry, and diffuse reflectance infrared analyses, with limited desorption, the latter inferred from the observation of no measurable loss of antimicrobial activity for 60 days. In line with this, antimicrobial activity does not require surfactant leaching, but is instead based on localized action at the modified silica surface.

With an overall ambition to contribute to the development of multifunctional bioactive scaffolds, combining angiogenesis capacity, osteostimulation, and antibacterial properties for regenerating lost bone tissues, Wu et al. prepared Cu-containing mesoporous bioactive glass scaffolds with interconnective large pores and mesopore channels [61]. The scaffolds, as well and their ionic extracts, were found to stimulate hypoxia-inducible factor-1a and vascular endothelial growth factor expression in human bone marrow stromal cells. In addition, they promoted osteogenic differentiation of bone marrow cells by improving their bone-related gene expression. Furthermore, the scaffolds displayed sustained release of incorporated ibuprofen and significantly reduced bacteria viability. Addressing the

related indication of bone infections, Molina-Manso et al. investigated mesoporous silica (SBA-15) as carrier for vancomycin, rifampicin, and linezolid, either alone or in combination [62]. Of the drugs investigated, vancomycin displayed the highest activity after loading and release, followed by linezolid. The results also show that SBA-15 bioceramics may be of interest for local release of antibiotics of interest, e.g., for bone infection. Similarly, Park et al. investigated MCM-41 and SBA-15 mesoporous silica for the controlled release of the natural antimicrobial compound allyl isothiocyanate (AITC) [63]. Controlled release of AITC was found to be determined by the pore size distribution of these materials. Thus, SBA-15 initially displayed "burst release," with 65 % desorbed in the first 12 h, compared to 20 % for MCM-41. The antimicrobial activity of released AITC against *E. coli*, *B. cereus*, and *P. anomola* was found to be unaffected by the adsorption/desorption process. In addition to low molecular weight antimicrobials, mesoporous silica offers opportunities as carriers for macromolecular antimicrobials, including low antimicrobial peptides and proteins. For example, Izquierdo-Barba et al. investigated the incorporation of the antimicrobial peptide LL-37, as well as low molecular weight antimicrobial chlorhexidine, into mesoporous silica [64]. The mesoporous silica released LL-37 and chlorhexidine slowly, the rate controlled, e.g., through incorporation of SH groups in the pore walls. Mesoporous silica containing either LL-37 or chlorhexidine displayed potent bactericidal properties against both *S. aureus* and *E. coli*, and the material containing LL-37 also very low cell toxicity.

The antimicrobial activity of mesoporous silica extends also to antifungal effects. For example, Paulo et al. covalently immobilized the antifungal drug amphotericin B (AmB) into silica nanoparticles, and observed fungicidal against several strains of *Candida* sp., mainly by contact [65]. Surfaces functionalized by antifungal nanocoatings based on AmB-loaded silica nanoparticles displayed no hemolytic or cytotoxic effects. Finally, mesoporous silica may also be used as carrier for antimicrobial nanoparticles. For example, Carmona et al. investigated mesoporous silica (SBA-15) with silver nanoparticles attached to their pore walls, and found a strong bactericidal effect on antibiotic-resistant and biofilm-forming *S. aureus* [66]. Similarly, Yang et al. loaded Ag nanoparticles onto the interior wall of a mesoporous silica capsules, and found potent antibacterial activity against *E. coli*, which can be maintained for several months [67]. Thus, the mesoporous structure is able to prevent the Ag nanoparticles from aggregation, keeping the inherent activity of individual Ag nanoparticles, but also releasing Ag^+ ions, thereby resulting in the high antibacterial durability observed.

Clays and Related Materials

Clays constitute a family of layered materials consisting of either positively or negatively charged layers with charge-balancing counterions between them. Through ion-exchange, considerable amounts of guest molecules (including drugs) can bind to the basal planes with little resistance to incorporation from a confining 3D structure. Investigating the role of surface modification of such

systems, Wang et al. modified montmorillonite to generate nanosilicate platelets, using either cationic, nonionic, or anionic surfactants [68]. All modified platelets showed less cytotoxicity than pristine montmorillonite, and those modified with either a cationic or an anionic surfactant also showed good antimicrobial activities against *S. aureus* and *E. coli*. Composites of the modified platelets with poly (urethane) were characterized for cell attachment and proliferation, antimicrobial activity, and in vivo biocompatibility. Somewhat related, Wu et al. investigated the antimicrobial properties and influence factors of clay minerals intercalated by tetradecyl tributyl phosphonium bromide (TDTB) on antimicrobial effects [69]. The results showed that montmorillonite-TDTB inhibited the growth of *E. coli* and *S. aureus* effectively. It was found that the antimicrobial activities of these materials depended on the several factors, including the amount TDTB released, and the size and z-potential of the loaded nanoparticles. Thus, higher antimicrobial activity was observed at higher amount TDTB released and higher z-potential, but also at nanoparticle-bacteria size matching. Demonstrating the potential of clays for achieving delivery advantages, Eversdijk et al. incorporated different (model) biocides in Nanofil clay and evaluated the resulting materials for antifungal activity [70]. Intercalation was found to prolong biocide release, controllable by the surface modification used. Even after exposure for up to 45 days in artificial rain tests, gypsum samples containing biocide/clay composites did not show fungal growth, whereas gypsum containing pure biocide lost its antifungal activity after 7 days. The possibilities to obtain sustained antimicrobial effects by incorporating antibiotics in clays and related systems seem to be system specific, however. Thus, Chakraborti et al. investigated Mg-Al (carbonate) layered double hydroxides as carriers for the antibiotics tetracycline, doxorubicin, 5-fluorouracil, vancomycin, and sodium fusidate, together with the antimicrobial performance of these systems against *S. epidermidis* [71]. With the exception of doxorubicin, burst release was observed, with little further drug release after 4 days. Dispersion of drug/clay complexes in poly(lactic-co-glycolic acid) films, on the other hand, resulted in a reduced burst release and in a sustained release for many weeks.

Demonstrating the translation of the antimicrobial potency of antibiotics-loaded clays, Hesse et al. investigated LDH as carrier for ciprofloxacin for the treatment of chronic otitis [72]. Male New Zealand White rabbits were implanted with middle ear prostheses coated with ciprofloxacin-loaded LDH. One group was infected with *P. aeruginosa* directly after implantation, while another was infected 1 week after implantation. Clinical outcome, blood counts, histological analyses, and microbiological examination showed excellent antimicrobial activity for the group microbially challenged directly after implantation, while the effect was reduced when infection was performed 1 week after implantation, indicating a need for further prolonging drug release for optimal performance of these materials.

As with many other nanomaterials, antimicrobial activity of clays can be induced or improved also by the incorporation of other antimicrobial nanomaterials. Here, Ag nanoparticles have attracted particular interest. For example, Chen et al. reported on Ag nanoparticles deposited on layered double hydroxide (LDH) films [73]. In the presence of LDH, Ag^+ can be readily reduced to metallic

Ag nanoparticles in aqueous solution, resulting in Ag nanoparticle deposition at the LDH surface. The composite coating was found to exhibit durable antimicrobial activity against both Gram-negative (*E. coli* and *P. aeruginosa*) and Gram-positive (*B. subtilis* and *S. aureus*) bacteria, effectively inhibiting bacterial growth and preventing biofilm formation. Furthermore, Su et al. investigated Ag nanoparticles supported on silicate platelets, and found strong antibacterial activity on a number of pathogens, including methicillin-resistant *S. auerus* and Ag^+-resistant *E. coli* [74]. These nanohybrids were found to effectively encapsulate bacteria. Through platelet localization, Ag nanoparticles are furthermore concentrated and colloidaly stabilized, resulting in stronger biocidal effect than silver nitrate on silver-resistant bacteria. Addressing the toxicity of Ag/clay hybrids, Lin et al. investigated fully exfoliated nanosilicate platelets as carrier and dispersing agent for Ag nanoparticles [75]. Not only antimicrobial activity, but also biocompatibility and immunological response of the resulting hybrids were evaluated. The results showed the hybrids to cause only mild inflammatory response, as well as good antibacterial activity. The hybrids were also embedded in poly(ether)urethane to further increase biocompatibility. The resulting composites were nontoxic to mouse skin fibroblasts, while simultaneously exhibiting potent bacterial growth reduction.

Remotely Addressable Nanoparticles

Apart from metal nanoparticles, susceptible to light-induced heating caused by surface plasmons, a number of nanomaterials are addressable by external fields. For example, iron oxide nanoparticles (IONPs) are magnetic Fe_3O_4 or Fe_2O_3 nanocrystals which can interact with external magnetic fields, offering various opportunities in nanomedicine, e.g., as contrast agents in MRI, for magnetic hyperthermal therapies, or as magnetically triggerable drug delivery systems. For biomedical applications, IONPs have to be surface modified to increase their colloidal stability, and to reduce adverse interactions with the biological system. Although chemical reactions and coordination binding can be readily done (achieved, e.g., by silanization and catechol binding, respectively), the dominating surface modification strategy is through hydrophilic polymers. Investigating such systems as antimicrobial agents, Chen et al. reported on Fe_3O_4/TiO_2 core/shell magnetic nanoparticles for photoinduced antimicrobial effects [26]. In these hybrid nanoparticles, titanium has a dual role, i.e., for light-induced generation of oxidative stress and reactive oxygen species, but also as affinity substrate for bacteria. Due to their Fe_3O_4 core, these nanoparticles are readily localized at a small spot under external magnetic field, thereby increasing treatment outcome and reducing damage to nontarget cells. The results show that Fe_3O_4/TiO_2 core/shell magnetic nanoparticles target pathogenic bacteria and effectively inhibit their growth under low-intensity UV irradiation. Similarly, Zhang et al. investigated Ag nanoparticle-decorated Janus nanorods, i.e., hetero-nanostructures with a superparamagnetic Fe_3O_4 head and a mesoporous SiO_2 tail [76]. Through this, Janus particles can combine individual components without sacrificing their magnetic and mesoporous

properties. The decorated nanorods displayed good magnetic sensitivity, bacteria binding of high affinity, and effective and long-term antimicrobial activity.

Furthermore, metal or magnetic nanoparticles may be incorporated in temperature-responsive hydrogels, thereby allowing light- or magnetically induced heating to result in deswelling transitions, and in squashing release of incorporated drugs [77]. Using this approach for hyaluronic acid modified with N-isopropyl acrylamide, and magnetic iron nanoparticles, Ekici et al. demonstrated temperature-triggered release of the antibacterial drug sulfamethoxazole [78]. In addition to iron particles in combination with a magnetic field, localized heat generation may be obtained with metal (e.g., Au) nanoparticles, utilizing the generation of surface plasmons on the interaction of such nanoparticles with light. Combined with a thermally responsive hydrogel, optical triggering of hydrogel swelling and drug release may thus be obtained.

Nanoparticles of heavy elements (e.g., gold and bismuth), have a large cross-section for X-ray absorption and photoelectron generation, and can therefore be used as radiosensitizers to enhance the (local) radiation dose for bacterial killing. Employing this approach, Luo et al. reported on nanoparticle-enhanced X-ray irradiation for combating multidrug resistant (MDR) bacteria [79]. In doing so, antibody-modified bismuth nanoparticles were introduced into bacterial culture to specifically target *P. aeruginosa*. On low-intensity X-ray irradiation, using a setup mimicking a deeply buried wound in humans, up to 90 % of MDR *P. aeruginosa* was killed in the presence of bismuth nanoparticles, compared to 6 % in their absence, an effect due to the bismuth nanoparticles enhancing the localized X-ray dose. In addition, no significant effects on HeLa and MG-63 cells were observed under these conditions. Since X-rays can easily penetrate human tissue, the approach has potential for eradication of deeply buried MDR bacteria in vivo (Fig. 32.6).

Lanthanide-doped upconversion nanoparticles (UCN) are interesting for a range of biomedical applications, including as cancer therapy, biolabeling, fluorescence and magnetic resonance imaging, and drug delivery. The interest in UCNs stems from the better tissue penetration displayed by near-infrared (NIR) compared to visible light, making such nanoparticles widely addressable also in deep tissue. Addressing this in the context of antimicrobials, Wang et al. investigated Er^{3+}-Yb^{3+}-Fe^{3+} tridoped TiO_2 nanoparticles, as well as its antimicrobial activity against *A. hydrophia* [80]. Bactericidal killing was found to be 65 % under 980-nm laser irradiation, while the corresponding Fe^{3+}-TiO_2 and Er^{3+}-Yb^{3+}-TiO_2 nanoparticles were inefficient against *A. hydrophia*. The initial energy applied in the photocatalytic antibacterial process is supplied by the upconversion emission of Er^{3+} and Yb^{3+} and the codoping of Fe^3, which intensifies the light absorption intensity and enlarges the absorption range. Because of the strong penetrability of near-infrared, this kind of material may be used in photodynamic therapy to kill bacteria or tumors directly. Similarly, Lim et al. reported on $NaYF4$:Yb/Er^{3+} upconversion nanoparticles as antiviral agents [81]. These UCNs act as carriers of incorporated photosensitizers, but also transduce NIR radiation to visible emissions appropriate for excitation of the attached photosensitizers, in turn resulting in ROS generation and viral damage. The UCNs were

Fig. 32.6 (**a**) HeLa cell
viability after exposure to
bismuth nanoparticles of
different concentration.
Shown in (**b**) and (**c**) is
P. aeruginosa bacterial count
and live/dead fraction at
different concentrations of
bismuth nanoparticles and
after X-ray treatment
(Redrawn from [79])
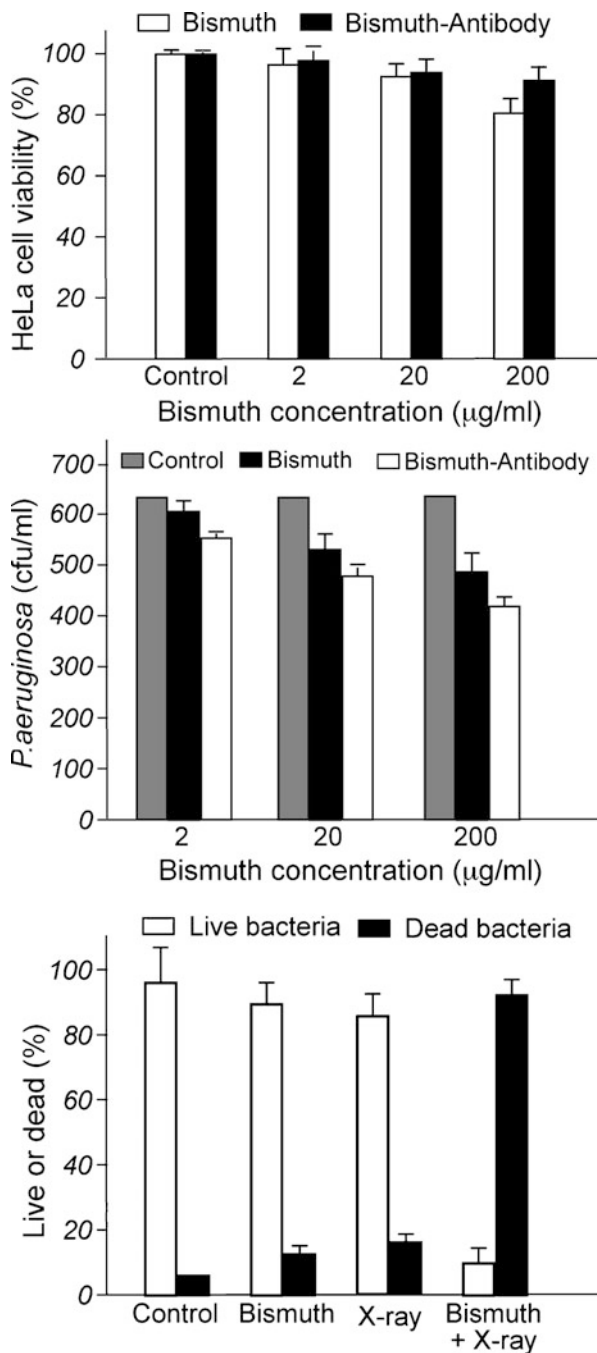
found to effectively reduce virus concentrations in vitro, with no clear pathogenicity in murine model and good specificity to infected cells, thus presenting an interesting approach for the treatments of virus-associated infections, lesions, and cancers, also in deep tissue.

Outlook

While less investigated and understood than conventional antibiotics and antiseptics, the importance of nanoscale antimicrobial agents is likely to increase during the coming years. Such systems offer opportunities both on their own through direct bacterial membrane action, generation of oxidative stress, cation release, or combinations of these. They also provide controlled, extended, and triggerable release of incorporated antibiotics and related compounds. In addition, many nanoparticle-based antimicrobial systems are addressable with external fields (e.g., NIR, visible light, X-rays, and magnetic fields), providing additional opportunities for both triggered nanoparticle action and drug release at the site of action and in a dose-on-demand setup. This also opens up new opportunities for dual function applications, e.g., in theranostics, where individual drug-containing particles are used for disease localization/diagnosis, triggered drug release, and monitoring of therapeutic outcome. Having said that, the spectrum width of antimicrobial nanomaterials remains poorly understood, and there is a need for investigations of the performance of such systems against a much wider range of strains, as regularly done, e.g., for antibiotics. Also toxicity aspects of such systems are relatively poorly understood, and further investigations are needed also in this context. Furthermore, resistance development needs to be given further attention, so that the rapidly increasing everyday use of antimicrobial nanomaterials does not result in uncontrolled resistance development.

References

1. Coates ARM, Halls G, Hu Y (2011) Novel classes of antibiotics or more of the same? Br J Pharmacol 163:184–194
2. Huh AJ, Kwon YJ (2011) "Nanoantibiotics": a new paradigm for treating infectious diseases using nanomaterials in the antibiotics resistant era. J Control Release 156:128–145
3. Kenawy ER, Worley SD, Broughton R (2007) The chemistry and applications of antimicrobial polymers: a state-of-the-art review. Biomacromolecules 8:1359–1384
4. Strömstedt AA, Ringstad L, Schmidtchen A, Malmsten M (2010) Interaction between amphiphilic peptides and phospholipid membranes. Curr Opin Colloid Interface Sci 15:467–478
5. Malmsten M (2011) Antimicrobial and antiviral hydrogels. Soft Matter 7:8725–8736
6. Malmsten M (2006) Soft drug delivery systems. Soft Matter 2:760–769
7. du Toit LS, Pillay V, Choonara YE (2010) Nano-microbiocides: challenges in drug delivery, patient ethics, and intellectual property in the war against HIV/AIDS. Adv Drug Del Rev 62:532–546

8. Scherlund M, Malmsten M, Holmqvist P, Brodin A (2000) Thermosetting microemulsions and mixed micellar solutions as drug delivery systems for periodontal anesthesia. Int J Pharm 194:103–116

9. Esposito E, Carotta V, Scabbia A, Trombelli L, D'Antona P, Menegatti E, Nastruzzi C (1996) Comparative analysis of tetracycline-containing dental gels: poloxamer and monoglyceride-based formulations. Int J Pharm 142:9–23

10. Chiappetta DA, Hocht C, Taira C, Sosnik A (2010) Efavirenz-loaded polymeric micelles for pediatric anti-HIV pharmacotherapy with significantly higher oral bioavailability. Nanomedicine 5:11–23

11. Murguia MC, Cristaldi MD, Porto A, Di Conza J, Grau RJ (2008) Synthesis, surface-active properties, and antimicrobial activities of new neutral and cationic trimeric surfactants. J Surf Deterg 11:41–48

12. Yang D, Pornpattananangkl D, Nakatsuji T, Chan M, Carson D, Huang CM, Zhang L (2009) The antimicrobial activity of liposomal lauric acids against Propionibacterium acnes. Biomaterials 30:6035–6040

13. Huang CM, Chen CH, Pornananangkul D, Zhang L, Chan M, Hsieh MF, Zhang L (2011) Eradication of drug resistant *Staphylococcus aureus* by liposomal oleic acids. Biomaterials 32:214–221

14. Sharma VK, Yngard RA, Lin Y (2009) Silver nanoparticles: green synthesis and their antimicrobial activities. Adv Colloid Interface Sci 145:83–96

15. Elechiguerra JL, Burt JL, Morones JR, Camacho-Bragado A, Gao X, Lara HH, Yacaman MJ (2005) Interaction of silver nanoparticles with HIV-I. J Nanobiotechnol 3:1–10

16. Silver S (2003) Bacterial silver resistance: molecular biology and uses and misuses of silver compounds. FEMS Microbiol Rev 27:341–353

17. Thomas V, Yallapu MM, Sreedhar B, Bajpai SK (2007) A versatile strategy to fabricate hydrogel-silver nanocomposites and investigation of their antimicrobial activity. J Colloid Interface Sci 315:389–395

18. Ozay O, Akcali A, Otkun MT, Silan C, Atkas N, Sahiner N (2010) P(4-VP) based nanoparticles and composites with dual action as antimicrobial materials. Colloids Surf B 79:460–466

19. Marsich E, Travan A, Donati I, Di Luca A, Benincasa M, Crosera M, Paoletti S (2011) Biological response of hydrogels embedding gold nanoparticles. Colloids Surf B 83:331–339

20. Zan X, Kozlov M, McCarthy TJ, Su Z (2011) Covalently attached, silver-doped poly(vinyl alcohol) hydrogel film on poly(L-lactic acid). Biomacromolecules 11:1082–1088

21. Malmsten M (2013) Inorganic nanomaterials as delivery systems for proteins, peptides, DNA, and siRNA. Curr Opin Colloid Interface Sci 18(5):468–480

22. Moriera dos Santos M, Joao Queiroz M, Baptista PV (2012) Enhancement of antibiotic effects via gold:silver-alloy nanoparticles. J Nanopart Res 14(859):1–8

23. Fan Z, Senapati D, Khan SA, Singh AK, Hamme A, Yust B, Sardar D, Ray PC (2013) Popcorn-shaped magnetic core-plasmonic shell multifunctional nanoparticles for the targeted magnetic separation and enrichment, label-free SERS imaging, and photothermal destruction of multidrug-resistant bacteria. Chem Eur J 19:2839–2847

24. Kojic N, Pritchard EM, Tao H, Brenckle MA, Mondia JP, Panilatis B, Omenetto F, Kaplan DL (2012) Focal infection treatment using laser-mediated heating of injectable silk hydrogels with gold nanoparticles. Adv Funct Mater 22:3793–3798

25. Baram N, Starosvetsky D, Starovetsky J, Epshtein M, Armon R, Ein-Eli Y (2011) Photocatalytic inactivation of microorganisms using nanotubular TiO_2. Appl Catal B 101:212–219

26. Chen WJ, Chen YC (2010) Fe_3O_4/TiO_2 core/shell magnetic nanoparticle-based photokilling of pathogenic bacteria. Nanomedicine 5:1585–1593

27. Schwegmann H, Feitz AJ, Frimmel FH (2010) Influence of the zeta potential on the sorption and toxicity of iron oxide nanoparticles on *S. cerevisiae* and *E. Coli*. J Colloid Interface Sci 347:43–48

28. Fang X, Yu R, Li B, Somasundaran P, Chandran K (2010) Stresses exerted by ZnO, CeO$_2$ and anastase TiO$_2$ nanoparticles on the *Nitrosomas europaea*. J Colloid Interface Sci 348:329–334

29. Hajipour MJ, Fromm KM, Ashkarran AA, de Aberasturi DJ, Ruiz de Larramendi I, Rojo T, Serpooshan V, Parak WJ, Mahmoudi M (2012) Antibacterial properties of nanoparticles. Trends Biotechnol 30:499–511

30. Yuan W, Ji J, Fu J, Shen J (2008) A facile method to construct hybrid multilayered films as a strong and multifunctional antibacterial coating. J Biomed Mater Res B 85B:556–563

31. Akhavan O (2009) Lasting antibacterial activities of Ag-TiO$_2$/Ag/a-TiO$_2$ nanocomposite thin film photocatalysts under solar lights irradiation. J Colloid Interface Sci 336:117–124

32. Karunakaran C, Abiramasundari G, Gomathisankar P, Manikandan G, Anandi V (2010) Cu-doped TiO$_2$ nanoparticles for photocatalytic disinfection of bacteria under visible light. J Colloid Interface Sci 352:68–74

33. Yu TJ, Li PH, Tseng TW, Chen YC (2011) Multifunctional Fe$_3$O$_4$/alumina core/shell MNPs as photothermal agents for targeted hyperthermia of nosocomial and antibiotic-resistant bacteria. Nanomedicine 6:1353–1363

34. Luo Z, Wu Q, Zhang M, Li P, Ding Y (2011) Cooperative antimicrobial activity of CdTe quantum dots with recephin and fluorescence menitoring for Escherichia coli. J Colloid Interface Sci 362:100–106

35. Lu ZS, Li CM, Bao HF, Qiao Y, Bao QL (2009) Photophysical mechanism for quantum dots-induced bacterial growth inhibition. J Nanosci Nanotechnol 9:3252–3255

36. Geraldo DA, Arancibia-Miranda N, Villagra NA, Mora GC, Arrantia-Perez R (2012) Synthesis of CdTe QDs/single-walled aluminosilicate nanotubes hybrid compound and their antimicrobial activity on bacteria. J Nanopart Res 14(1286):1–9

37. Neelgund GM, Oki A, Luo Z (2012) Antimicrobial activity of CdS and Ag$_2$S quantum dots immobilized on poly(amidoamine) grafted carbon nanotubes. Colloids Surf B 100:215–221

38. Huang L, Terakawa M, Zhiyentayev T, Huang YY, Sawayama Y, Jahnke A, Tegos GP, Wharton T, Hamblin MR (2010) Innovative cationic fullerenes as broad-spectrum light activated antimicrobials. Nanomedicine 6:442–452

39. Kumar A, Menon SK (2009) Fullerene derivatized s-triazine analogues as antimicrobial agents. Eur J Med Chem 44:2178–2183

40. Lu Z, Dai T, Huang L, Kurup DB, Tegos GP, Jahnke A, Wharton T, Hamblin MR (2010) Photodynamic therapy with a cationic functionalized fullerene rescues mice from fatal wound infections. Nanomedicine 5:1525–1533

41. Marchesan S, Da Ros T, Spalluto G, Balzarini J, Prato M (2005) Anti-HIV properties of actionic fullerene derivatives. Bioorg Med Chem Lett 15:3615–3618

42. Kornev AB, Peregudov AS, Martynenko VM, Balzarini J, Hoorelbeke B, Troshin PA (2011) Synthesis and antiviral activity of highly water-soluble polycarboxylic derivatives of [70]fullerene. Chem Commun 47:8298–8300

43. Chae SR, Therezien M, Budarz JF, Wessel L, Lin S, Xiao Y, Wiesner MR (2011) Comparison of the photosensitivity and bacterial toxicity of spherical and tubular fullerenes of variable aggregate size. J Nanopart Res 13:5121–5127

44. Lyon DY, Alvarez PJJ (2008) Fullerene water suspension (nC$_{60}$) exerts antibacterial effects via ROS-independent protein oxidation. Environ Sci Technol 42:8127–8132

45. Vecitis CD, Zodrow KR, Kang S, Elimelech M (2012) Electronic-structure-dependent bacterial cytotoxicity of single-walled carbon nanotubes. ACS Nano 4:5471–5479

46. Zardini HZ, Amiri A, Shanbedi M, Maghrebi MM, Banaidam M (2012) Enhanced antibacterial activity of amino acids-functionalized multi walled carbon nanotubes by a simple method. Colloids Surf B 92:196–202

47. Aslan S, Deneufchatel M, Hashimi S, Li N, Pfefferle LD, Elimelech M, Pauthe E, Van Tassel PR (2012) Carbon nanotube-based antimicrobial biomaterials formed via layer-by-layer assembly with polypeptides. J Colloid Interface Sci 388:268–273

48. Murugan E, Vimala G (2011) Effective functionalization of multiwalled carbon nanotube with amphiphilic poly(propyleneimine) dendrimer carrying silver nanoparticles for better dispersability and antimicrobial activity. J Colloid Interface Sci 357:354–365

49. Qi X, Gunawan P, Xu R, Chang MW (2012) Cefalexin-immobilized multi-walled carbon nanotubes show strong antimicrobial and anti-adhesion properties. Chem Eng Sci 84:552–556

50. Wu W, Wieckowski S, Pastorin G, Benincasa M, Klumpp C, Briand JP, Gennaro R, Prato M, Bianco A (2005) Targeted delivery of amphotericin B to cells by using functionalized carbon nanotubes. Angew Chem Int Ed 44:6358–6362

51. Pantarotto D, Partidos CD, Hoebeke Brown JF, Kramer E, Briand JP, Muller S, Prato M, Bianco A (2003) Immunization with peptide-functionalized carbon nanotubes enhances virus-specific neutralizing antibody responses. Chem Biol 10:961–966

52. Benincasa M, Pacor S, Wu W, Prato M, Bianco A, Gennaro R (2011) Antifungal activity of amphotericin B conjugated to carbon nanotubes. ACS Nano 5:199–208

53. Liu S, Zeng YH, Hofmann M, Burcombe E, Wei J, Jiang R, Kong J, Chen Y (2011) Antibacterial activity of graphite, graphite oxide, grapheme oide, and reduced graphene oxide: membrane and oxidative stress. ACS Nano 5:6971–6980

54. Liu S, Hu M, Zeng TH, Wu R, Jiang R, Wei J, Wang L, Kong J, Chen Y (2012) Lateral dimension-dependent antibacterial activity of grapheme oxide sheets. Langmuir 28:12364–12372

55. Sawangphruk SMP, Chiochan P, Sangsri T, Siwayaprahm P (2012) Synthesis and antifungfal activity of reduced graphene oxide nanosheets. Carbon 50:5156–5161

56. Santos CM, Mangadlao J, Ahmed F, Leon A, Advincula RC, Rodrigues DF (2012) Graphene nanocomposite for biomedical applications: fabrication, antimicrobial, and cytotoxic investigations. Nanotechnology 23:395101, 1–10

57. Carpio IEM, Santos CM, Wei X, Rodrigues DF (2012) Toxicity of a polymer-graphene oxide composite against bacterial planktonic cells, biofilms, and mammalian cells. Nanoscale 4:4746–4756

58. Nguyen VH, Kim BK, Jo YL, Shim JJ (2012) Preparation and antibacterial activity of silver nanoparticles-decorated grapheme composites. J Supercrit Fluids 72:28–35

59. Das MR, Sharma RK, Saikia R, Kale VS, Shelke MV, Sengupta P (2011) Synthesis of silver nanoparticles in an aqueous suspension of graphene oxide sheets and its antimicrobial activity. Colloids Surf B 83:16–22

60. Botequim D, Maia J, Lino MMF, Lopes LMF, Simones PN, Ilharco LM, Ferreira L (2012) Nanoparticles and surfaces presenting antifungal, antibacterial, and antiviral properties. Langmuir 28:7646–7656

61. Wu C, Zhou Y, Xu M, Han P, Chen L, Chang J, Xiao Y (2013) Copper-containing mesoporous bioactive glass scaffolds with multifunctional properties of angiogenesis capacity, osteostimulation, and antibacterial activity. Biomaterials 34:422–433

62. Molina-Manso D, Manzano M, Doadrio JC, Del Prado G, Ortiz-Perez A, Vallet-Regi M, Gomez-Barrena E, Esteban J (2012) Usefulness of SBA-15 mesoporous ceramics as a delivery system for vancomycin, rifampicin and linezolid: a preliminary report. Int J Antimicrob Agents 40:252–256

63. Park SY, Barton M, Pendleton P (2011) Mesoporous silica as a natural antimicrobial carrier. Colloids Surf A 385:256–261

64. Izquierdo-Barba I, Vallet-Regi M, Kupferschmidt N, Terasaki O, Schmidtchen A, Malmsten M (2009) Incorporation of antimicrobial compounds in mesoporous silica film monolith. Biomaterials 30:5729–5736

65. Paulo CSO, Vidal M, Ferreira LS (2010) Antifungal nanoparticles and surfaces. Biomacromolecules 11:2810–2817

66. Carmona D, Lalueza P, Balas F, Arruebo M, Santamaria J (2012) Mesoporous silica loaded with peracetic acid and silver nanoparticles as a dual-effect, highly efficient bactericidal agent. Micropor Mesopor Mater 161:84–90

67. Yang H, Liu Y, Shen Q, Chen L, You W, Wang X, Sheng J (2012) Mesoporous silica microcapsule-supported Ag nanoparticles fabricated via nano-assembly and its antibacterial properties. J Mater Chem 22:24132–24138

68. Wang MC, Lin JJ, Tseng HJ, Hsu SH (2012) Characterization, antimicrobial activities, and biocompatibility of organically modified clays and their nanocomposites with polyurethane. ACS Appl Mater Interfaces 4:338–350

69. Wu T, Xie AG, Tan SZ, Cai X (2011) Antimicrobial effects of quarternary phosphonium salt intercalated clay minerals on *Escherichia coli* and *Staphylococci aureus*. Colloids Surf B 86:232–236

70. Eversdijk J, Erich SLF, Hermanns SPM, Adan OCG, De Bolle M, de Meyer K, Bylemans D, Bekker M, ten Cate AT (2012) Development and evaluation of a biocide release system for prolonged antifungal activity and finishing materials. Progr Org Coat 74:640–644

71. Chakraborti M, Jackson JK, Plackett D, Gilchrist SE, Burt HM (2012) The application of layered double hydroxide clay (LDH)-poly(lactide-co-glycolic acid) (PLGA) film composites for the controlled release of antibiotics. J Mater Sci Mater Med 23:1705–1713

72. Hesse D, Badar M, Bleich A, Smoczek A, Glage S, Kieke M, Behrens P, Müller PP, Esser KH, Stieve M, Prenzler NK (2013) Layered double hydroxides as efficient drug delivery systems of ciprofloxacin in the middle ear: an animal study in rabbits. J Mater Sci Mater Med 24:129–136

73. Chen C, Gunawan P, Lou XW, Xu R (2012) Silver nanoparticles deposited layered double hydroxide nanoporous coatings with excellent antimicrobial activities. Adv Funct Mater 22:780–787

74. Su HL, Lin SH, Wei JC, Pao IC, Chiao SH, Huang CC, Lin SZ, Lin JJ (2011) Novel nanohybrids of silver particles on clay platelets for inhibiting silver-resistant bacteria. PLoS One 6(e21125):1–10

75. Lin JJ, Lin WC, Li SD, Lin CY, Hsu SH (2013) Evaluation of the antibacterial activity and biocompatibility for silver nanoparticles immobilized on nano silica platelets. ACS Appl Mater Interfaces 5:433–443

76. Zhang L, Luo Q, Zhang F, Zhang DM, Wang YS, Sun YL, Dong WF, Liu JQ, Huo QS, Sun HB (2012) High performance magnetic antimicrobial Janus nanorods decorated with Ag nanoparticles. J Mater Chem 22:23741–23744

77. Malmsten M, Bysell H, Hansson P (2010) Biomacromolecules in microgels – opportunities and challenges for drug delivery. Curr Opin Colloid Interface Sci 15:435–444

78. Ekici S, Ilgin P, Yilmaz S, Aktas N, Sahiner N (2011) Temperature and magnetic field responsive hyaluronic acid particles with tunable physical and chemical properties. Appl Surf Sci 257:2669–2676

79. Luo Y, Hossain M, Wang C, Qiao Y, An J, Ma L, Su M (2013) Targeted nanoparticles for enhanced X-ray radiation killing of multidrug-resistant bacteria. Nanoscale 5:687–694

80. Wang W, Shang Q, Zheng W, Yu H, Feng X, Wang Z, Zhang Y, Li G (2010) A novel near-infrared antibacterial material depending on the upconverting property of Er^{3+}-Yb^{3+}-Fe^{3+} tridoped TiO_2 nanopowder. J Phys Chem C 114:13663–13669

81. Lim ME, Lee YL, Zhang Y, Chu JJH (2012) Photodynamic inactivation of viruses using upconversion nanoparticles. Biomaterials 33:1912–1920

Nanomechanics of Single Biomacromolecules

33

Qing Li, Zackary N. Scholl, and Piotr E. Marszalek

Introduction

Biopolymers such as nucleic acids, proteins, and polysaccharides play diverse biological functions and are components of various materials. Nucleic acids encode hereditary information and instructions for protein synthesis. In addition, the unique hybridization properties of nucleic acids provide building blocks of nanomaterials, nanomachines, and nanosensors [1–13] and are considered as a viable platform for highly parallel biological computing [14–18]. Proteins mainly perform enzymatic reactions and participate in cellular signal transduction and communication but also play critical structural and mechanical roles (e.g., supporting cell shape and elasticity) and are natural components of bioadhesives, biocomposites [19, 20], and bio-fibers like collagen [21] and silk [22–24]. Natural, synthetic, and hybrid proteins have recently been exploited for development of new biomaterials with rationally tuned elastic properties [25–29]. Polysaccharides, either alone or as components of glycoproteins or peptidoglycans that are exploited for energy storage, participate in molecular recognition between biomolecules and also play important structural roles, e.g., in the cell wall of plants and

These authors contributed equally to this work

Q. Li (✉) • P.E. Marszalek
Department of Mechanical Engineering and Materials Science, Center for Biologically Inspired Materials and Material Systems, and Duke University, Durham, NC, USA
e-mail: ql24@duke.edu; pemar@duke.edu

Z.N. Scholl
Program in Computational Biology and Bioinformatics, Duke University, Durham, NC, USA
e-mail: zns@duke.edu

bacteria and as components of hydrogels and biofilms [30, 31]. They are also components of many natural and semisynthetic materials (e.g., paper, cotton, rayon).

The mechanical properties of individual biomacromolecules and their nanostructures are critically important for their biological and other functions. For example, the mechanics of the DNA double helix plays an important role during cell division, DNA replication, DNA damage repair, and transcription of DNA information onto RNA [32]. The mechanics of protein networks, such as present in the extracellular matrix, is essential for cell shape, cell flexibility, and binding interactions between cells (cell adhesion) [33–70]. Also, muscle elasticity is partially determined and regulated by the elastic properties of giant modular proteins [71–76]. The mechanics of polysaccharide chains (such as cellulose chains and fibers) is important in providing rigidity to cellular structures (e.g., wood), and the flexibility of sugar rings is exploited in molecular recognition between sugars and lectins and is important for enzymatic reactions such as glycolysis [77]. The combined mechanics of proteins and polysaccharides is exploited in biohydrogels such as those lubricating joints [78–81]. Since these biomacromolecules are also used as building blocks for various nanostructures and nanomachines, the characterization of their mechanical properties is of considerable significance to nanotechnology. The progress in directly measuring mechanical properties of individual biomacromolecules paralleled the development of a variety of single-molecule visualization, manipulation, and characterization techniques. This chapter will briefly introduce the most popular single-molecule manipulation techniques and will review the nanomechanical properties of individual biomacromolecules determined using these methods.

Polymer Elasticity and Techniques to Study the Mechanical Properties of Single Polymer Molecules

The mechanical properties of individual biomacromolecules are typically examined by means of single-molecule force spectroscopy (SMFS) techniques [73, 82–89]. In SMFS, individual macromolecules or their fragments are attached to a substrate and to a force probe and stretched (by separating the two), and their extension and tension are accurately measured [90]. The relationship between the applied force (tension) and extension that describes molecule's elasticity has been coined a force spectrogram. Biomacromolecules covered in this chapter are polymeric in nature so they are composed of many identical or similar units (monomers). For this reason, the primary source of their elasticity is entropic in origin [91–94]. The entropy is at its maximum in equilibrium and is gradually decreased when the polymer ends are separated and the monomers are forced to align with the direction of the stretching force. Fully stretched polymers would have just a single configuration so their configurational entropy would be zero and attaining such a state would require an infinite force [94, 95]. However, even before such high forces are generated entropically, the chemical and physical bonds within the polymeric structure gradually extend according to their own stiffness and the polymer exhibits the

enthalpic elasticity that results in continually increasing the contour length of the polymer (overstretching) [73, 96]. The enthalpic elasticity may also manifest itself as an abrupt transition in the force–extension relationship typically in the form of a force peak or a force plateau, when individual bonds or their groups undergo a discrete conformational force-induced transition that results in an abrupt lengthening of the polymer [73, 83, 96–99].

Atomic Force Microscopy (AFM)

Advantages: Excellent length resolution, low-high force range (5–10,000 pN), and constant-velocity or constant-force conditions are available, no need for specialized attachment.

   Disadvantages: Cantilever spring constants are difficult to determine accurately [100, 101], not suitable for probing events at low forces (<5 pN).

   AFM was invented in 1986 by Binning, Quate, and Gerber [102, 103] on the basis of an earlier invention of the scanning tunneling microscope (STM) [104, 105]. AFM was initially applied primarily as an imaging tool, but soon its power for mechanical manipulation of individual biomolecules was realized [106]. In SMFS measurements by AFM, molecules are attached at their termini or at random positions to a substrate and to the AFM tip, either specifically through chemical bonds or using ligand–receptor specificity (e.g., avidin–biotin) or even nonspecifically through physisorption [90]. The molecules that formed a bridge between substrate and the tip may be stretched in solution, which is of significance to measurements on biomacromolecules. The stretching process is controlled by means of a highly precise piezoelectric actuator that moves the sample away from the AFM tip or vice versa. The force experienced by the molecule (its tension) is determined through monitoring the bending of the AFM cantilever, which is followed by a split photodiode that measures the position of a laser beam reflected off of the cantilever and projected onto the diode. Force and length resolutions of SMFS measurements by AFM are on the order of 1 pN and < 1 nm. The main advantages of AFM as a force spectrometer are its superb length resolution, the ability to stretch short molecules, and the ability to apply small forces (piconewton order) and uniquely also very large forces (tens of nanonewtons). Also, AFM force spectrometers are fast and allow large loading rates (force/time) that are of importance when studying lifetimes of intermolecular bonds. SMFS by AFM are typically carried out under constant extension rate [73] or force clamp conditions [107].

Optical Tweezers

Advantages: Excellent force resolution and excellent length resolution at low forces (0.1–100 pN).

   Disadvantages: Requires functionalized biopolymers to tether to bead

   Optical tweezers [108–111] use a focused laser light to create a potential well that traps dielectric objects, as first observed by A. Ashkin in 1970 [112]. An appropriately surface-functionalized micron-size dielectric bead (e.g., coated with avidin) can be used to attach to it a terminally functionalized biopolymer (e.g., biotin-labeled DNA) and can be captured by an optical trap. The other end of the

molecule can be attached to a surface or to another bead kept, e.g., in a glass pipette by suction. The molecule is stretched by moving the surface or the second bead away from the optical trap (e.g., by means of piezoelectric actuator). A microscope-based video system accurately monitors the position of the first bead relative to the center of the optical trap to determine the applied force, while the translation of the second bead is accurately measured to determine the molecule extension. Optical tweezers provide superb force and length resolution on the order of <0.1 pN and <1 nm and are widely used in SMFS of DNA and proteins.

Magnetic Tweezers

Advantages: Excellent force resolution at low and medium forces (0.01–100 pN), simple method for applying torque

   Disadvantages: Requires functionalized biopolymers to tether to bead

   Magnetic tweezers use micron-size superparamagnetic beads, which develop a net magnetic moment in an external magnetic field and are pulled by a magnetic force that is proportional to the field gradient [113–115]. Similar to optical tweezers, a molecule of interest can be tethered between a surface (bead) and a superparamagnetic bead and stretched by an external magnetic field. Forces on the order of 0.01–100 pN can be easily exerted by magnetic tweezers [94]. In addition to stretching, magnetic tweezers provide a very simple means to apply a torque to the molecule of interest allowing it to be rotated and coiled [113, 116–118].

Biomembrane Force Probe

Advantages: High precision in spring constant measurement, excellent force range (0.01–1,000 pN)

   Disadvantages: Limited to probing molecules that appear on (or are introduced to) the cell surface

   In the biomembrane force probe assay (BFP), a small glassy bead is biochemically "glued" to a pressurized membrane capsule (e.g., red blood cell membrane) that is held by a pipette through a controlled amount of suction [41]. Different negative pressures result in different membrane tension, so the probe stiffness can be easily controlled (by the pressure) and forces on the order of 0.01–1,000 pN can be generated. The bead itself is decorated at low surface density with molecules of interest that are brought to contact to their cognate receptors, presented on another cell. By forming contacts between the bead and the surface of the investigated cell, specific bonds between ligands (presented on the bead) and receptor (presented on the cell surface) are formed and then ruptured by moving the bead away from the cell surface. In this way bonds' strength and lifetimes can be accurately measured. Forces and extensions are determined via optical microscopy by the amount of deformation of the membrane transducer and the position of the glassy bead. Typical resolution is <0.5 pN and <5 nm [41, 119].

Nanopore Techniques

Advantages: Capabilities to uniquely measure size and charge of molecules

   Disadvantages: Method not fully developed

Molecules pass through a nanometer-size pore in a membrane separating two compartments to which a potential gradient is applied and transiently block the ionic current flowing through the pore producing characteristic current blockage fingerprints. These current patterns can be used to infer various molecular properties of the traversing molecules, such as size and charge. It was proposed that natural or solid-state nanopores could be used to sequence long DNA strands, because characteristic blockage currents are different for different nucleobases [120–122]. Electric field-driven passage of charged biomacromolecules such as nucleic acids or uncharged but terminally functionalized with a charged "leader" (e.g., a short piece of DNA) molecules such as proteins can also be used to examine mechanical properties of traversing molecules. This is because in most cases these molecules are too bulky to pass through the pore and need to be stretched and unfolded before they will fit into a narrow pore [123, 124]. For direct measurements of the force applied to a molecule traversing a nanopore, its end can be attached a bead whose position can be accurately monitored in a force measuring optical trap [122].

Flow Techniques

Advantages: Readily simulate physiological flow conditions

Disadvantages: Requires careful calibration of flow to determine forces

Mechanical properties of biomacromolecules can also be studied by stretching them in an elongational flow [125, 126]. This can be achieved either directly due to the coupling of the flowing fluid with the molecule of interest or indirectly by attaching one end of the molecule to a surface and the other to a micron-size bead which then experiences a hydrodynamic force [127]. Also, to limit unwanted interactions between the molecule and the surface during flow measurements, a magnetic bead attached to the molecule of interest can be levitated magnetically while subjected to a horizontal hydrodynamic force [128].

Particle Tether

Advantage: Simple, inexpensive system suitable to various microscopy methods. The system does not involve external forces.

Disadvantage: Low spatial resolution

The tethered particle motion experiments (TPM) were first started by Jeff Gelles and colleagues in the early 1990s to study transcription by single RNA polymerase molecule [129, 130]. This method has been used to study DNA looping [131–142], DNA transposition [143], promoter sequences bending [144], and site-specific recombination [145, 146]. In a typical tethered particle experiment, a single polymer molecule is tethered between the microscope coverslip surface and a microsphere through specific binding [147]. Brownian motion of the bead is restricted to a semispherical region by the tethered polymer molecule and can be captured by an optical microscopy. Variance in travelling scope of the particle gives information about change in the length of the tethered polymer. TPM has the advantage of simple implementation, easy combination with optical and magnetic tweezers, and straightforward data analysis methods. However, TPM has low time

resolution caused by the time cost by the probe to explore the region limited by the polymer tether [148]. Attempts to improve the accuracy of TPM include investigation of the volume effects of the bead [149, 150], suppression of the Brownian motion of the bead [151], simultaneous tracing of hundreds of single molecules by biochip [152], and development of proper data analysis approaches to obtain reliable kinetic parameters from TPM measurements [148, 153, 154].

A detailed comparison of these various single-molecule manipulation techniques along with the description of their advantages and limitations can be found in a number of review articles [155–159].

Applications

In its force measuring mode, AFM is typically used to stretch and relax DNA, proteins, and sugars either in isolation or also on living cells [83, 86, 87, 160] to study their elasticity, mechanical, unfolding, refolding, and binding behaviors. At low forces (<20 pN) AFM force spectra capture the characteristic highly nonlinear entropic elasticity of biomacromolecules. At higher forces various deviations from the purely entropic elasticity are frequently observed [82]. These deviations are indicative of structural and conformational transitions induced by force that on the experimental time scale are either reversible or irreversible. For example, using AFM-based SMFS the elasticity of individual titin molecules that govern the passive elasticity of muscle was characterized in various force regimes [73]. It was found that the entropic alignment of titin immunoglobulin and fibronectin-type domains occurs at low stretching forces, and at higher forces, these domains reversibly unfold providing an extra length to the muscle when needed [75]. In addition AFM is frequently used to probe the strength of the interactions between various biomolecules including receptors and ligands pairs [43, 60, 161]. Optical tweezers are frequently used to examine the elasticity of biopolymers at low forces, and OT measurements can be set up to exploit the nanomechanical properties of biomacromolecules (such as DNA) [96] to study the mechanochemical behaviors of various enzymes that process these molecules (e.g., DNA and RNA polymerases) [162]. OT measurements can also be used to follow near equilibrium folding/ unfolding behavior of proteins, either alone [163] or while interacting with ligands [164]. Magnetic tweezers found many applications to study torsional elastic properties of DNA and to follow the work of special DNA enzymes that affect coiling properties of DNA (such as gyrases) [165, 166]. BFP techniques were found particularly suited for measuring receptor–ligand interactions on live cells [167]. Nanopore techniques are used to study folding properties of biomacromolecules and to examine the interactions between various biomolecules, and they are continuously improved for DNA sequencing applications [122, 123, 168]. Flow techniques are used for biopolymer elasticity measurements and in conjunction with fluorescence video microscopy are being applied to follow the interactions between various biomacromolecules (e.g., DNA–protein interactions) [128].

Atomic Force Microscopy (AFM)

AFM Instrumentation

The schematic of an AFM instrument is shown in Fig. 33.1.

The principle of the AFM is conceptually simple: a small cantilever is first calibrated and then deflection of the cantilever during the stretching of an attached molecule is measured to precisely determine forces (from one to thousands of piconewtons) using Hooke's law. Cantilever deflection is measured and recorded by tracking voltage signal output from multi-segment photodiode detector (quadrant detector module in most recent design). The final signal used to convert to force recording is

$$V = \Delta V_{BT}/\Sigma$$

where ΔV_{BT} is the voltage difference between top and bottom area of the photodiode and Σ is the voltage sum from both areas. V is usually multiplied by an operational amplifier to improve the signal to noise ratio. The position of the sample is accurately controlled by a piezo actuator via a feedback–control loop with 0.2–0.5 nm resolution. These piezo actuator stages are usually equipped with
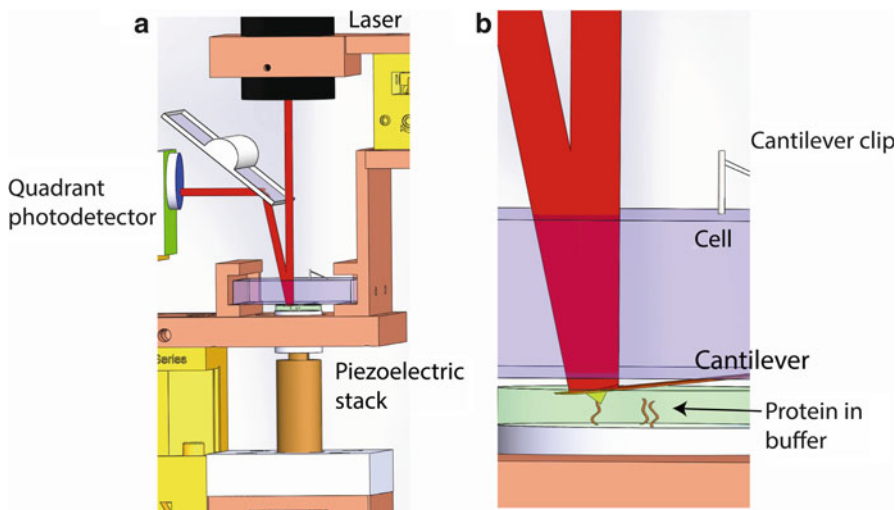
Fig. 33.1 (**a**) Schematic of an AFM instrument and (**b**) closeup of the cell containing the cantilever and probing the substrate. A laser probes the cantilever deflection which is detected using the difference between the top and bottom of a quadrant photodetector. The cantilever is suspended in a quartz cell over a substrate (clean glass or freshly evaporated gold) that has a drop of solution with the molecule of interest. A piezoelectric stack on the bottom controls the 3D movement of the substrate to contact the cantilever and then move away at constant force or constant velocity. Nonspecific attachment will allow the molecule (*red lines*) to attach to the cantilever and stretch the molecule of interest

capacitive or strain-gauge position sensors. The sensor signal output from the piezo controller is converted into distance using the voltage constant of the piezo,

$$\Delta z = C\Delta V$$

where C is the constant measured and given by piezo actuator factory specifications, Δz is the movement of the piezo, and ΔV is the sensor voltage signal output of the piezo actuator.

Cantilever calibration is based on thermal noise method (one of dynamic deflection methods proposed by Hutter and Bechhoefer [169]). In this method, the cantilever and the tip are treated together as a simple harmonic oscillator with one degree of freedom. Thermal fluctuations are considered as the only motion of the oscillator with the Hamiltonian

$$H = \frac{p^2}{2m} + \frac{1}{2}k_c q^2.$$

According to the equipartition theorem,

$$< \frac{1}{2}k_c q^2 > = \frac{1}{2}k_B T$$

where k_B is the Boltzmann's constant, k_C is the spring constant of the oscillator, T is the absolute temperature, and q is the displacement of the oscillator. Therefore, k_C can be obtained by measuring the mean-square spring displacement $< q^2 >$ due to thermal fluctuations at room temperature. This measurement is performed in the frequency domain by taking the power spectral density of the fluctuations of the photodiode signal δV (Fig. 33.2 is a representative power spectrum).
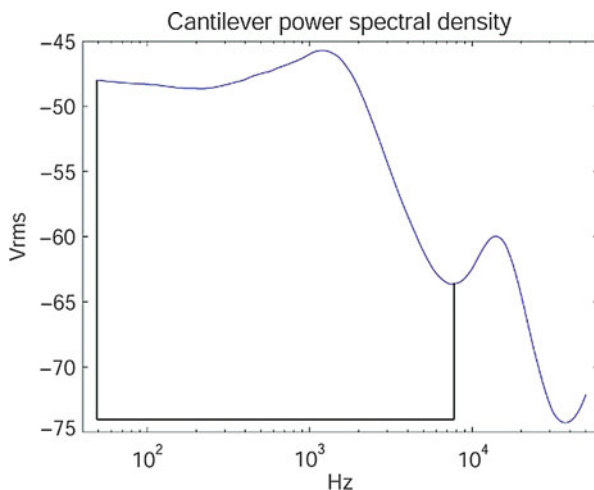
Fig. 33.2 A typical power spectral density curve of the photodiode signal thermal fluctuations. Frequencies are shown in their natural logarithm (dB) and signals are displayed in Vrms. Integration interval is between the *black lines*

Fig. 33.3 Force spectrum. Voltage difference ΔV and piezo movement Δz used for slope calculation are shown in the graph
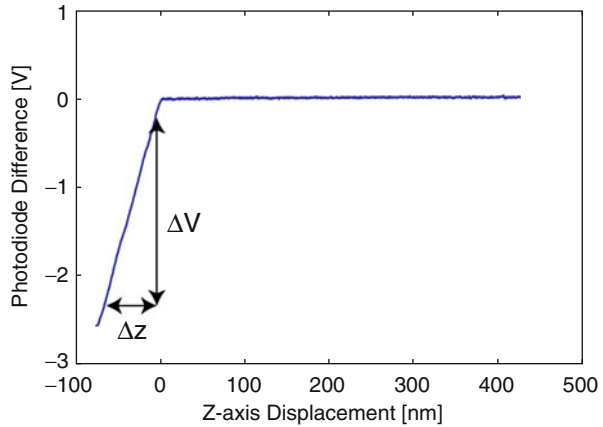
The integration is performed according to Parseval's equality

$$
< \delta V^2 > = \frac{\int\limits_{a}^{b} \delta V^2(t)dt}{\int\limits_{a}^{b} dt} = \frac{\int\limits_{a'}^{b'} FT^2(\delta V)df}{ENBW}
$$

where FT(δV) is the Fourier transform of δV and ENBW is the equivalent noise bandwidth of the spectrum. Integration of the power spectrum is usually done in an interval close to the resonance frequency of the cantilever such as depicted in Fig. 33.2.

To finally convert the photodiode voltage signal into force, a force spectrum is acquired by moving the sample vertically using the piezo, while the position of the piezo and resulting cantilever deflection are recorded simultaneously (Fig. 33.3).

Then the slope of the deflection versus piezo position is

$$
\text{slope} = \Delta z / \Delta V
$$

Thus, the voltage signal from the photodiode, V, is interpreted to force by the following formula

$$
F = k_c * V * \text{slope} = \frac{k_B T}{< \delta V^2 > * \text{slope}^2} * V * \text{slope}
$$

where T is room temperature (usually 300 K).

Sample Preparation

The sample is prepared simply by depositing the molecule of interest in the relevant substrate. Substrates commonly used for AFM single-molecule force spectroscopy experiments are gold or glass. In the most basic experiment, molecules attach to the surface and the tip nonspecifically. Since the attachment is nonspecific, the location that the molecule absorbs to the tip and substrate is random. To circumvent the random attachment, there have been methods developed to control attachment to the surface and tip, like thiol chemistry [170], HaloTag7 immobilization [171], Strep-Tag immobilization [172], and Ni–NTA functionalization [173]. In any kind of immobilization, it is important to have a positive control to differentiate between single- and multi-molecular AFM stretching experiments. Generally, only about 1 % of the data is usable. For protein unfolding experiments, a positive control can be designed by flanking the unknown protein of interest by previously characterized protein with known properties so that their presence indicates the recording is of a single molecule of interest (e.g., flanking unknown proteins by I27 domains of titin, which have a characteristic unfolding force of $\sim$200 pN and a contour length increment of $\sim$28 nm).

Stock solutions containing biomacromolecule (i.e., DNA, protein, polysaccharide) are usually diluted to 10–1,000 nM and incubated on the substrate for a period of time ranging from a few minutes to overnight. Appropriate incubation time and substrate choice are empirical and the ideal incubation case would allow the formation of a monolayer of the molecule on the substrate. Usually proteins are incubated on gold or functionalized glass for half an hour, DNAs are incubated on gold for more than 4 h, and polysaccharides are incubated on glass overnight. After incubation, the samples are usually washed several times before used for AFM pulling experiments to remove excess molecules that are not tethered to the surface of the substrates.

Experimental Procedure

AFM pulling experiments are carried out by gently moving the substrate relative to the cantilever tip through voltage applied to the piezo. The piezo can either control the height of the substrate relative to an immobilized cantilever or control the height of the cantilever relative to an immobilized substrate. Here we describe the procedure using nomenclature for the former method (as depicted in Fig. 33.1). There are two modes of motion for each pulling cycle (Fig. 33.4). In the up mode, initially the
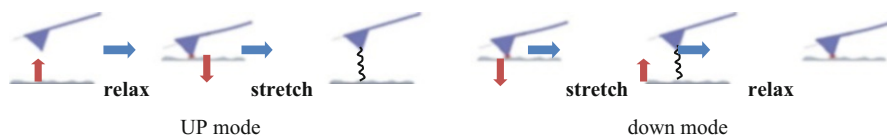

Fig. 33.4 Up mode versus down mode. *Red arrow* indicates the moving direction of the substrate; *blue arrow* indicates the process

tip rests above the surface; the pulling measurement starts with the substrate moving up first to bring into contact with the tip under a voltage ramp generated by the computer and then descending to the original position. While in the down mode, at first the tip presses slightly onto the substrate; the substrate begins to move down to leave the tip; and after that, the substrate reverts to the origin. The stretching traces in both modes are obtained when the substrate departs from the tip; accordingly the relaxing traces are acquired in the other half of the cycle.

Sometimes after the first cycle of pulling experiment, the cantilever tip still holds the molecule, which can be judged by discrepancy of the stretching trace tail from the horizontal line, since loss of the molecule would generate a horizontal baseline at the end of the stretching trace. Then refolding experiments can be realized by decreasing the pulling size to the desired length to stretch and relax the molecule for another several cycles.

Force–extension curves obtained from the AFM pulling experiments are selected first with several criteria and later analyzed with freely jointed chain (FJC) [73] or worm-like chain (WLC) [174] model for polymer elasticity. The FJC model considers the polymer chain segments (Kuhn segments) to be statistically independent. Assume that the elastic response of the polymer to the applied external force is purely entropic, then the extension $< x >$ (instant end-to-end distance of the polymer projected on the direction of the force) as a function of the applied force is

$$< x > = L_c \left(\coth \frac{F l_k}{k_B T} - \frac{k_B T}{F l_k} \right)$$

where L_c is the contour length of the molecule, l_k is Kuhn segment length of the polymer, T is the temperature, and k_B is the Boltzmann's constant. In reality, molecules are often overstretched so that enthalpic contributions to the extension originated from bending of covalent bond angles and elongation of covalent bonds have to be taken into account. The revised version of the FJC model is

$$< x > = L_c \left(\coth \frac{F l_k}{k_B T} - \frac{k_B T}{F l_k} \right) \left(1 + \frac{F}{k_{\text{segment}} L_c / N} \right)$$

where k_{segment} is the so-called segment elasticity that includes all the enthalpic effects and N is the number of segments contained in the polymer chain.

The WLC model treats the polymer as an irregularly curved filament. In this model, the force versus extension $< x >$ relation is given by

$$F(< x >) = \frac{k_B T}{l_p} \left[\frac{1}{4} \left(1 - \frac{< x >}{L_c} \right)^2 + \frac{< x >}{L_c} - \frac{1}{4} \right]$$

where L_c is the contour length of the molecule and l_p is the persistent length of the polymer which equals one-half of l_k. In AFM studies, proteins are usually described using the WLC model, while DNA and sugar are depicted by revised FJC model.

The selection criteria for the force extension curve use a combination of heuristics. Often a reference fingerprint pattern of the unfolding for a protein is used. The fingerprint is obtained from a recording that has a number of force–extension recordings with enough unfolding events of the flanking protein handles and the correct initial contour length before the first unfolding. The theoretical value for initial contour length which precedes the first unfolding peak of the reference protein can be calculated out by the estimated length of the proteins when in their native form.

Protein Mechanics

Protein Unfolding

The sequence of amino acids in a protein encodes the unique three-dimensional structure which is attained through folding. Properly folded proteins are important for their function. The determination of the folding pattern of proteins from the amino acid sequence to the 3D structure is an important problem in biology. Proteins are characterized by their 3D structure, their function, and also by their dynamic processes such as unfolding and folding rates and progression to the native state. The folding and unfolding processes are stochastic although not all conformational transitions are equally possible as the energy landscape (the space of all conformations and associated free energies) is not flat. Each protein state has an energetic contribution from configurational entropy and enthalpy from forming hydrogen bonding or electrostatic networks. The states of the protein are also subject to environmental factors such as temperature and concentration of denaturants and mechanical forces, which all contribute to the energy landscape. Since it is currently experimentally unfeasible to monitor all possible order parameters, the multidimensional landscape of protein folding is often studied by looking at a single-order parameter (e.g., N–C extension, GdmCl concentration, percent of native contacts) which then describes a small part of the entire energy landscape. When proteins are perturbed using force, such as using AFM-SMFS, the order parameter is along the extension of protein, between the tethered ends (usually N–C extension). The relevant parameters that characterize protein unfolding by AFM-SMFS are the unfolding force, the contour length increment, the unfolding rate, the refolding rate, and the distance to the transition state. These properties for a wide variety of proteins are tabulated in Table 33.1 and each of these properties is discussed below, in detail.

A protein, upon mechanical unfolding (Fig. 33.5) by AFM or other SMFS tool, adopts an unstructured chain of amino acids that behave in a worm-like chain manner in which their bonds tend to line up with the vector of the pulling direction

Table 33.1 Compiled parameters for the unfolding of various proteins. The Protein Data Bank (PDB) code indicates the representative structure used to determine native state lengths and native contacts and fold type. The mean unfolding force, Fu, is determined from the comparable loading rates. Proteins with information about intrinsic unfolding rates, k_u^0; intrinsic folding rates (as determined by double-pulse protocol), k_f^0; and the distance to transition state, x_b, are included for respective proteins

Protein	References	PDB	F_u^a [pN]	ΔL_c [nm]	# aa	Fold type	k_u^0 [s^{-1}]	x_b [nm]	k_f^0 [s^{-1}]
Ankyrin repeat	[178–180]	2QYJ [181]	25–50	10.5–12.4	33	α			
Armadillo repeat	[182, 183]	2Z6H [184]	20–80	6.7, 15, 29.2	44	α			
Barnase	[185]	1A2P [186]	70	38	110	α/β			
Calmodulin	[187]	1CLL [188]	14	25,18.7	148	α	0.02	2	2×10^5
Cold-shock protein	[189]	1G6P [190]	78	23.5	64	β	1.5×10^{-2}	0.49	
Dihydrofolate reductase	[191]	1DLS [192]	82	67.4	186	α			
E2lip3 N–41	[176]	1QJO [193]	175	10	41	β	7.6×10^{-3}	0.29	
E2lip3 N–C	[176]	1QJO [193]	0	N/A	75	β			
Enhanced yellow fluorescent protein (EYFP) wild type	[194]	1YFP [195]	69	16,54	238	α/β			
EYFP circular permutant 145	[194]	N/A	68,103	13,57	238	α/β			
EYFP circular permutant 174	[194]	N/A	57,112	7,56	238	α/β			
Fibrinogen	[196]	N/A	90	23	112	α/β			
Protein G, B1 domain (GB1)	[197, 198]	2QMT [199]	178	17.7	56	α/β	3.9×10^{-2}	0.17	720
GB1 4,51- > His	[200]		120	17.7	56	α/β	1.2×10^{-1}	0.2	
GB1 6,53- > His	[200]		119	17.7	56	α/β	1.4×10^{-1}	0.2	
GB1 8,55- > His	[200]		160	17.7	56	α/β	2.9×10^{-2}	0.2	
Green fluorescent protein (3–212)	[201, 202]	1B9C [203]	105	77	227	α/β	7×10^{-2}	0.28	
HaloTag7	[171]	1BN6 [204]	106	66	187	α/β			

(continued)

Table 33.1 (continued)

Protein	References	PDB	F_u^a [pN]	ΔL_c [nm]	# aa	Fold type	k_u^0 [s^{-1}]	x_b [nm]	k_f^0 [s^{-1}]
Huntington elongation factor 3 protein phosphatase 2A and the yeast Kinase TOR1 (HEAT) repeat	[182]	1B89 [205]	20–75	5.8–16.1	29	α			
Ig rod domains of filamin from Dictyostelium discoideum (ddFLN4)	[206, 207]	N/A	62.9, 52.5	14.4, 16.6	98	β	0.28, 0.33	0.4, 0.52	55, 179
Kettin actin-binding region	[208]		193	30.1			9×10^{-3}	0.17	
Leucine rich (LR) repeat	[182]	2Q4G [209]	20–50		28	α/β			
Leucine zipper	[210]		10–15		43–95	α			
Maltose-binding protein	[211]	1ANF [212]	22,51, 25,20	22.6, 15.9, 42, 47.9	370	α/β	1.4×10^{-3}, 5.9×10^{-2}, 1000,10	2.3, 0.66,0.2, 0.38	
Myomesin	[213]	1R15 [214]	75	30	109	α/β			
Myosin coiled coil	[215, 216]		22–30 (plateau)	150–315		α			
Nebulin	[217]		220–1000	75–200	~6669	α			
NuG2 (protein G variant)	[218]	1MI0 [219]	105	15	56	α/β	3.1×10^{-2}	0.25	
Polycystin-1 (human) wild type	[220]	1B4R [221]	176		86	β	9.8×10^{-4}	0.25	
Polycystin-1 (human) mutant R57L	[220]		143		86	β	2.6×10^{-2}	0.24	
Polycystin-1 (human) mutant V59H	[220]		127		86	β	6.9×10^{-2}	0.22	
Polycystin-1 (human) mutant G43S	[220]		54		86	β	2.3×10^{-1}	0.31	

Name	Ref	PDB							
Projectin	[208]		90, 170	30.1			$7 \times 10^{-2}/0.3 \times 10^{-3}$	0.1/0.2	15
Polycystin-1 (human) mutant T36C	[220]		79		86	β	0.7×10^{-1}	0.32	
Protein L	[222]	1HZ6 [223]	136	18.6	60	α	5×10^{-2}	0.22	
Scaffoldin c1C	[224]	1G1K [225]	430	48.5	144	β	1.1×10^{-4}	0.14	
Scaffoldin c2A	[224]	1ANU [226]	285	48.6	144	β	2.1×10^{-2}	0.15	
Scaffoldin c7A	[224]	1AOH [227]	562	49.3	144	β	6×10^{-6}	0.13	
Streptococcus pyogenes (Spy) 0128 E117A	[228]	3B2M [229]	172	52	142	β			
Streptococcus pyogenes (Spy) 0128 E258A	[228]	3B2M [229]	250	50	142	β			
Staphylococcal nuclease	[230]	2SNS [231]	26.3	47	149	α/β			
Small ubiquitin-related modifier 1	[232]	1A5R [233]	129	24.1	97	α/β	1.15×10^{-3}	0.51	
Small ubiquitin-related modifier 2	[232]	1WM3 [234]	122	24.1	93	α/β	5×10^{-3}	0.33	
Spectrin	[33, 65, 235, 236]	1S35 [237]	30	31.7	106	α	3.3×10^{-5}	1.7	
Synaptotagmin C2A	[238]	2R83 (140–265) [239]	51	39.6	126	β			
Synaptotagmin C2B	[238]	2R83 [239]	106	43	150	α/β			
T4 lysozyme	[240]	1 L63 [241]	64	55	103	α	5.5×10^{-2}	0.75	
Tenascin fibronectin domains all	[242]		138	24.7	88–92	β	4.6×10^{-4}	0.3	42, 0.5
Tenascin fibronectin type III domains	[243]	1TEN [244]	128	32.4	92	β			

(continued)

Table 33.1 (continued)

Protein	References	PDB	F_u^a [pN]	ΔL_c [nm]	# aa	Fold type	k_u^0 [s^{-1}]	x_b [nm]	k_f^0 [s^{-1}]
Titin Ig27	[245]	1WAA [246]	200	28.5	89	β	3.3×10^{-4}	0.25	1.2
Titin kinase	[247]	1TKI [248]	40–120	9.1, 28.6, 7.3, 10.1, 7.5, 16.4, 58.3	344	α/β			
Titin-like protein TTN-1 Ig domain	[249]		85	30		β	5×10^{-2}	0.35	
Titin-like protein TTN-1 Ig/Fn domain	[249]		111	31		β	1.4×10^{-2}	0.35	
Titin-like protein TTN-1 kinase	[249]	1KOA [250]	83, 52	67, 97		α/β	4×10^{-2}	0.6	
Top7	[251]	1QYS [252]	150	29	92	α/β	6×10^{-2}	0.21	
Ubiquitin	[232, 253]	1UBQ [254]	188–203	24	76	α/β	8×10^{-3}	0.19	
Ubiquitin (48-C)	[253]		85	7.8	28	α/β			

[a]Note that these unfolding force values should be considered with care as they represent only the mean of many experiments. Force measurements between experiments may differ by up to 20 % due to uncertainty in the measurement of the spring constant of the cantilever [101]
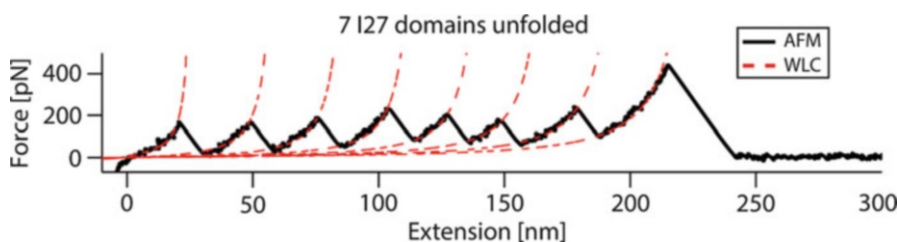
Fig. 33.5 Typical force–extension plot of the unfolding of a polyprotein consisting of seven I27 domains from the titin protein (also called I91 domains). Each peak corresponds to an unfolding event of a single domain. The unfolding force for each domain is ∼200 pN. The dashed red line indicates a family of worm-like chain fits with a contour length spacing of 28.5 nm between unfolding events

with greater probability at higher force. Polyproteins will have several unfolding events as each protein domain contributes an unfolding event. The contour length distance between two unfolding events – as measured by the worm-like chain model – and the 3D crystal structure can be used to determine total extension of an amino acid at high force. For instance, the unfolding of a single I27 protein domain produces a contour length increment of 28.5 nm before the next unfolding event (Fig. 33.5). Before the rupturing of the single domain, it is assumed that the polyproteins have completely aligned with the pulling vector in their native state so that the extended chain distance is comprised of the increase in contour length (28.5 nm) plus the distance between the N-terminus and C-terminus of the protein in the native state, as measured by a NMR or X-ray crystal structure model (4 nm for IgI27). Thus, the total length 28.5 nm + 4 nm = 32.5 nm divided by the number of amino acids, 89, gives the distance of a fully extended single amino acid unit of IgI27, which is 3.65 Å. The mean length of a fully extended amino acid unit determined from the corresponding proteins in Table 33.1 with their corresponding PDB structures is 3.64 ± 0.04 Å (mean ± SE, n = 27). The consistency between these measurements then allows for the contour length increment, ΔL_c, to be an important indicator of the number of amino acids unfolding within each unfolding event, if the protein structure is known, by inverting the previous calculation.

The unfolding force, F_u, for proteins ranges from as low as 5 pN up to 500 pN. The nonzero unfolding force is the result of proteins resisting unfolding due to an energy barrier between the unfolded and folded state along the particular pathway. The likelihood of unfolding increases exponentially with applied force because of thermal activation of bond rupturing so that the unfolding force is logarithmically dependent on the loading rate (cantilever stiffness x pulling velocity) [175]. The model derived from this concept, called the Bell–Evans–Ritchie model, interprets the log-linear dependence of the loading rate with force as an image of an energy barrier at a fixed location along the pathway. The intrinsic unfolding rate, k_u^0, can then be determined by relating natural logarithm of the loading rate, r, to the most likely unfolding force, F_u, with the formula
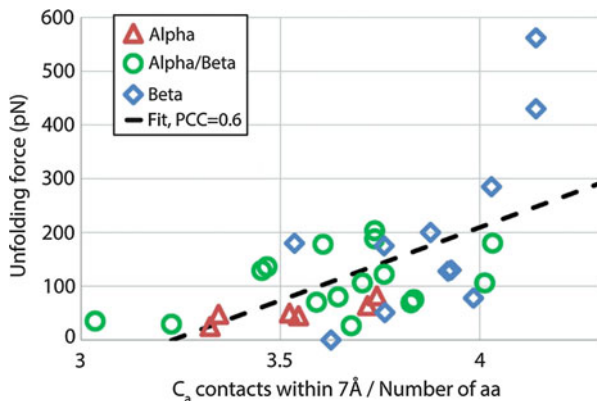
$$F_u(r) = \frac{k_b T}{x_b} \ln\left(\frac{r x_b}{k_u^0 k_b T}\right).$$

This model incorporates the parameter x_b, which corresponds to the distance to the fixed location along the pathway from the unfolding state and the top of the barrier (the transition state). The experiments to determine these parameters are often referred to as "dynamic force spectroscopy" which simply involves performing pulling experiments at many loading rates (differing speeds and varying strengths of cantilever spring constants) to get enough data to reliably fit the parameters in the Bell–Evans–Ritchie model.

The intrinsic folding rate of proteins, k_f^0, can be determined using a polyprotein and a "double-pulse" protocol. In this experiment, a polyprotein is unfolded during the first pulse and the number of unfolded modules determined. Then, after waiting a time t, a second pulse is applied and the number of modules unfolded is counted. The modules unfolded in the second pulse were able to refold during the time delay t. Thus, the proportion of the refolded protein modules out of the total unfolded modules in the first pulse can be plotted against the time delay t and fit to an exponential function to determine the intrinsic folding rate for each module, k_f^0. The 3D structure and geometry of the pulling vectors also affects the unfolding force of proteins [176, 177]. However, most proteins unfolded from the N-terminus to the C-terminus have an unfolding force that correlates with contact density and their specific fold type (Fig. 33.6).

It would be useful to determine the unfolding parameters of proteins from pulling experiments through computer simulations and purely theoretic means since many proteins already have a 3D structure available and experimental setups can be time intensive and costly. The atomistic detail of molecular dynamic simulations also provides insightful explanations for unfolding and folding phenomena. The analogous computer simulation to the experimental force spectroscopy experiment is steered molecular dynamics [255]. Steered molecular

Table 33.2 Tabulated peak unfolding forces from steered molecular dynamic simulations with explicit water and comparable force fields (OPLS-AA or CHARM22 or AMBER99). Unfolding forces were compared at a pulling speed of 100 A/ns. Unfolding forces from simulations performed at other were extrapolated to 100 A/ns using unfolding force peaks from at least three different speeds fitted using log-linear regression (in accordance with Bell–Evans–Ritchie model where unfolding force depends on the logarithm of speed)

Protein	References	Simulated peak unfolding force [pN]
Barnase	[256]	1048[a]
Fibronectin III domain	[257, 258]	1231[a]
NI6C	[259]	245[b]
Scaffoldin c1C	[224]	2253[a]
Scaffoldin c2A	[224]	1420[a]
Scaffoldin c7A	[224]	2236[a]
Spectrin	[260]	457[a]
Titin I27	[224, 251, 261]	1460
Top7	[251]	1050
Ubiquitin (48-C)	[253]	1400
Ubiquitin (N–C)	[253]	2000

[a]Extrapolated to 100 A/ns using several speeds
[b]5A/ns

dynamics consists of a solvated protein model (determined from X-ray crystallography or NMR) that is fixed at one end and pulled at constant velocity or constant force on the other. These simulations do not reach the quasi-equilibrium conditions of the actual experiments because of limitations in computing time. Thus, the unfolding of proteins in steered molecular dynamics simulations are performed at speeds that are orders of magnitude faster. Table 33.2 lists the simulated peak unfolding force determined from the steered molecular dynamic simulations. Even though computer simulations are done at much higher speeds, there is a good correlation between the experimental results of the unfolding force and the theoretical unfolding force determined through simulation, as shown in Fig. 33.7.

Protein–Ligand Complex Unfolding

Proteins bind to cofactors and other proteins which can have an effect on their mechanical stability (as perturbed from the N to C extension) as tabulated in Table 33.3. In all cases the unfolding force is increased upon binding with the exception of titin kinase in which a new separate unfolding event occurred in the presence of ligand. Dr. Hongbin Li and colleagues exploited the difference between apo- and bound force spectra of proteins and measured the dissociation constant of proteins with their ligands by counting the proportion of bound proteins based on their unfolding force [30, 72, 73]. Surprisingly, the dissociation constants for

Fig. 33.7 Correlation between unfolding forces as performed by steered molecular dynamics (y-axis; from Table 33.2) and experimentally determined by atomic force microscopy (x-axis from Table 33.1). The correlation between the datasets is 0.84 determined by the Pearson correlation coefficient
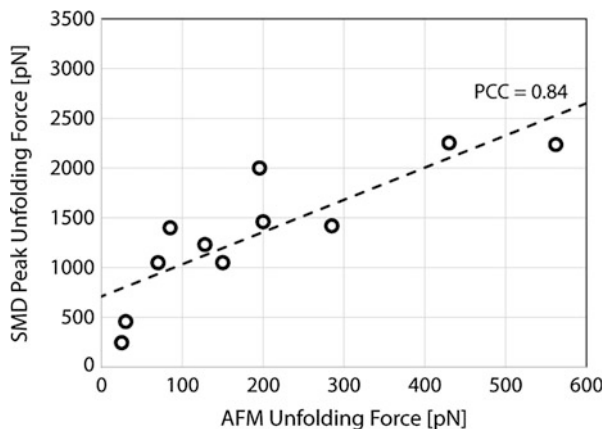

Table 33.3 Protein unfolding characteristics when bound to their respective ligands. The fold increase indicates the increase in the mean unfolding force from the unfolding force tabulated in Table 33.1. The dissociation constant, Kd, was measured from SMFS experiments for some protein–ligand combinations and compared to the bulk measure dissociation constant (*italics*)

Protein	References	Ligand	F_u increase [fold increase]	K_d [M] (*bulk K_d [M]*)
Calmodulin	[187]	10 μM Mas peptide	1.4×	
DHFR	[191]	19 μM–1.2 mM MTX	2.9×	
DHFR	[191]	180 μM DHF	3.1×	
DHFR	[191]	210 μM NADPH	3.4×	
GB1 4,51- > His	[200]	4 mM Ni^{2+}	1.7×	
GB1 6,53- > His	[200, 262]	4 mM Ni^{2+}	2.0×	9.8×10^{-5} (*2.6×10^{-4}*)
GB1 8,55- > His	[200]	4 mM Ni^{2+}	1.4×	
GB1	[263]	hFc antibody	1.5×	2.2×10^{-6} (*5×10^{-10}–5×10^{-7}*)
Maltose-binding protein (53–141)	[264]	Maltose	1.1×	
NuG2	[263]	hFc antibody	2.0×	1.3×10^{-5} (*5×10^{-10}–5×10^{-7}*)
Staphylococcal nuclease	[230]	Deoxythymidine 3',5'-bisphosphate	1.9×	
Titin kinase	[247]	ATP	N/A[a]	3.5×10^{-4} (*2.4×10^{-4}*)

[a]Instead of increasing unfolding force, an additional peak appears

proteins and their antibodies are lower than when measured with traditional experimental methods, while the dissociation constants for metal ions or small molecules are comparable. The differences between the SMFS measured dissociation constant and the bulk measured constant may be due to the mechanical perturbations required in SMFS, but more research in this area is needed.

Protein–Ligand Unbinding

The model for measuring the energy barrier between the folded state and the unfolded state of proteins can also be applied to the energy barrier between the bound and unbound state of proteins with their ligand. In these experiments the protein is conjugated to the tip and the ligand is conjugated to a surface. Pulling experiments are then performed and all the unbinding forces are recorded and tabulated in a histogram. The control experiment where there is no ligand conjugated to the surface serves as a distribution of nonspecific binding forces. Performing measurements at varying loading rates can determine the unbinding rate using the Bell–Evans–Ritchie model discussed in Section IIIA which can be used to extrapolate a dissociation constant for a protein and its ligand. The unbinding forces for several protein–ligand complexes and their dissociation constants (when known) are shown in Table 33.4. The unbinding forces range from 30 pN to 250 pN. The association constants (inverse of the dissociation constant) are positively correlated with the binding force as shown in Fig. 33.8.

Protein-Based Nanomaterials

The properties of proteins lend themselves to be useful building blocks for nanomaterials. Individual proteins can be selected based on mechanical strength and elastic characteristics and then fused at the DNA level into polyproteins. These polyproteins can then be linked via thiol chemistry or protein chemistry into biomaterials. Hongbin Li and colleagues tested this idea by building a protein-based elastomeric hydrogel ring constructed from a network of polyprotein GB1 domains [283]. The properties of the material can then be easily tuned by changing the composition of the polyproteins. Such materials are useful for developing scaffolds for tissue engineering.

DNA

The behavior of DNA under force has been studied for over 30 years using a variety of techniques. Single-molecule methods have allowed for precise characterization of DNA under force which revealed mechanical transitions that occur during unwinding and melting of the DNA helix [32, 284–292]. The origin of these transitions is still under study. One of the first DNA molecules studied is the λ phage dsDNA molecule, composed of 48,502 bp. When force is exerted on both ends of the molecule, it stretches and the force increases following the worm-like chain model very closely at forces below 50 pN. The force–extension profile is salt dependent, and measurements in 10 mM Na+ typically indicate a persistence length of ∼60 nm and an elastic modulus of ∼800 pN as shown in Table 33.5.

The λ phage DNA, along with other types of double-stranded DNA and single-stranded DNA/RNA, has been shown to undergo overstretching transitions when

Table 33.4 Tabulated unbinding forces for protein–ligand rupture events from SMFS. SMFS can also be used to determine the experimental dissociation constant, K_d, from single molecules perturbed by force (in contrast to the dissociation constant measured from a bulk sample in italic)

Protein–ligand	References	Unbinding force [pN]	K_d [M] (*bulk K_d [M]*)
Alpha-synuclein/alpha-synuclein (with spermidine)	[265]	60	
Amyloid β-40 peptide/amyloid β-40 peptide	[266]	100	
Amyloid β-42 peptide/amyloid β-42 peptide	[267]	41, 47 (with Cu^{2+})	
Antifluorescein Fv fragment/fluorescein	[268]	160	2.4×10^{-9} (*1.1×10^{-9}*)
Antilysozyme Fv fragment/lysozyme	[269]	55	(*3.7×10^{-9}*)
Anti-Sendai antibody/Sendai bacteriorhodopsin	[270]	126	
Azurin/cytochrome c551	[271]	95	(*1×10^{-5}*)
Biotin–avidin	[272]	80	(*1×10^{-15}*)
Cadherin/cadherin X-dimer	[273, 274]	35	(*1×10^{-4}*)
Cadherin/cadherin strand-swapped dimer	[274]	55	
ExpG protein/DNA target sequence	[275]	75	
HSA (human serum albumin)/anti-HSA	[276]	244	
Ni^{2+}-NTA/histidine peptide	[277]	38	(*1.4×10^{-8}*)
p53/azurin	[278]	75	6×10^{-6} (*3.3×10^{-8}*)
P-selectin/ligand	[279]	115	5.5×10^{-8} (*6×10^{-8}*)
RNase inhibitor/angiogenin	[280]	78,156	(*5×10^{-7}, 7×10^{-16}*)
Streptavidin/biotin	[172]	253	(*1×10^{-14}*)
Strep-Tactin/Strep-tag II	[280, 281]	40–48,74	(*1×10^{-6}*)
Titin Z1 and Z2 dimerization	[282]	700	

stretched beyond 15 pN up to 1800 pN. The origin of these transitions is still a subject of study. The transition forces and gain in extension (as determined by normalized extensions) are shown in Table 33.6.

Sugars

Entropic Elasticity and Force-Induced Conformational Transitions of Polysaccharides

AFM proved very valuable for characterizing the mechanical properties of many polysaccharides and enabled observations of unique force-driven transitions in the sugar rings [73, 83, 98, 308–310]. For AFM measurements, a polysaccharide sample

Fig. 33.8 The unbinding
force at similar load rates for
proteins and their ligands
correlates with the bulk
measured association constant
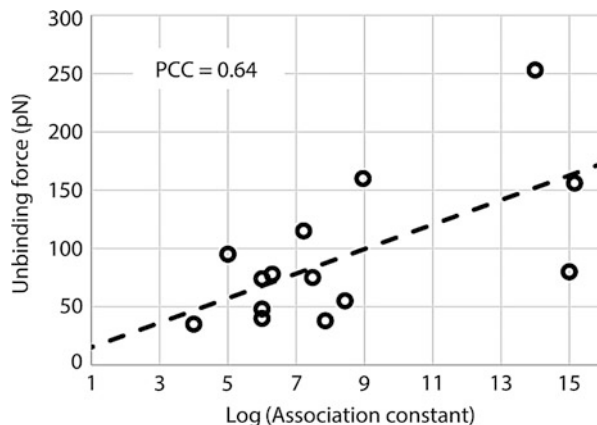(inverse of dissociation
constant)

Table 33.5 Basic properties of λ phage DNA as studied by a variety of nanomolecular techniques

Method	References	Ionic strength [mM Na+]	Persistence length[a] [nm]	Elastic modulus [pN]
SMFS-laser tweezers	[293–295]	9–10	53–67	452–1008
Magnetic tweezers	[296]	10	53	869
AFM compression	[297]	N/A	N/A	700
SMFS-AFM	[298]	N/A	N/A	558

[a]These values should be treated with caution as the exact value of the persistence length of dsDNA is a matter of controversy, and the newest study [299] suggests that this value may be significantly lower than the values shown in the table

is dissolved in water or another appropriate solvent at a wide range of concentrations ranging from 0.001 % to 20 % (w/w). A small drop of the solution (e.g., 50–100 µl) is placed on a clean substrate (glass, gold) and the molecules are allowed to adsorb to the substrate for several hours. The nonattached or weakly attached molecules are then removed from the surface by vigorous washing of the substrate. The molecules that strongly adsorbed to the substrate can then be lifted from it by the AFM tip and stretched in solution so their extension and tension can be accurately measured [90].

While some polysaccharides display the entropic elasticity that is typical of many structurally simple polymers at all forces (e.g., cellulose [308, 311]), some polysaccharides follow this behavior only at low forces, and at higher forces they show marked deviations from the entropic elasticity (e.g., amylose, dextran, pectin [83, 312]). These deviations are caused by force-induced conformational transitions within the sugar rings (e.g., chair–boat transitions in α-D-glucopyranose [98]), within the bonds connecting neighboring rings (e.g., bond flips in pustulan [313, 314]) or by force-induced separation of polysaccharide chains in multichain molecular structures (e.g., xanthan [315, 316]). Generally, when sugar monomers are connected by equatorial glycosidic linkages that lay in the plane of the sugar ring
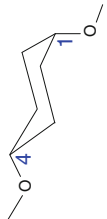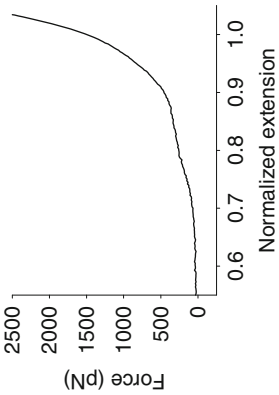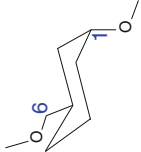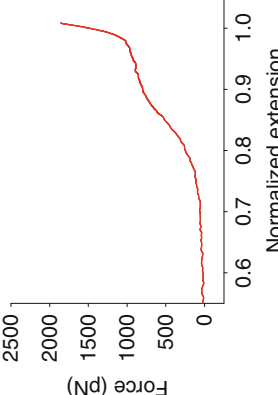
Table 33.6 Properties of nucleic acid polymers when perturbed by forces up to 1.8nN. Nomenclature: poly(dA) stands for a polymer of polydeoxyadenylic acid, or a single-stranded DNA molecule composed only of adenines whereas poly(A) stands for a polymer of polyadenylic acid, which consists of a single-stranded RNA molecule composed of adenines. Similarly, poly(dGdC)poly(dCdG) stands for a double-stranded DNA composed of CG repeats. Overstretching percent refers to the percent fraction of the plateau relative to the initial length

Nucleic acid	References	Canonical form[a]	1st plateau [pN]	Overstretching [%]	2nd plateau [pN]	Overstretching [%]
Poly(dA)	[300, 301]	B-helix	23	80	113	16
Poly(A)	[302, 303]	A-helix	24	80	-	-
Poly(C)	[303]	A-helix	25	~50	-	-
Poly(dT)	[300]	Unstructured	-	-	-	-
Poly(U)	[303]	Unstructured				
dsDNA (e.g., lambda phage DNA)	[96, 284, 286, 288, 289, 304–306]	B-helix	65–105	70	150–450	10–20
Poly(dGdC) poly(dCdG)	[305, 306]	B-helix	65–95	70	300–450	20
Poly(dG) poly(dC)	[306]	A-helix	70	70	-	-
Poly(dA) poly(dT)	[306]	B'-helix	70	70	-	-
Poly(dAdT) poly(dTdA)	[304, 305]	D-helix	35	-	-	-

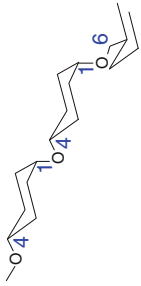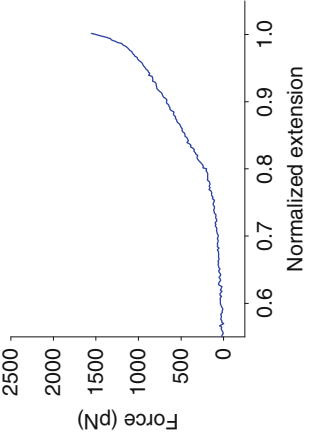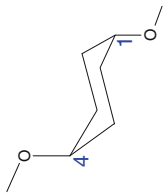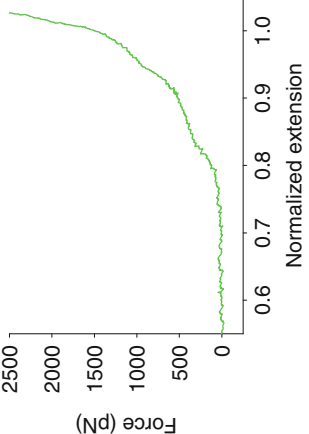[a]See reference [307] for specific characteristics of DNA helixes

(as in cellulose), the elasticity of these polysaccharides is primarily entropic in nature and force spectra are quite simple. When monomers are connected by axial bonds (that are perpendicular to the plane of the sugar ring), the elasticity of those polysaccharides frequently displays interesting features (deviations) from the entropic elasticity that manifest themselves as pronounced force plateaus. Those plateaus were interpreted as indicative of force-induced transitions of the sugar ring from a low-energy conformation to a high-energy conformation that provides an increased separation of the consecutive glycosidic oxygen atoms and thus increases the contour length of the chain. Force bond rotations (flips) that occur over an energy barrier (such as in 1,6 linked polysaccharides) typically produce linear relationships between force and extension. Unwinding of helical structures (such as in xanthan) typically produces a long plateau in the force extension data and is typically associated with pronounced hysteresis between the stretching and relaxing part of the force–extension spectrum that reports strand separation in multiple helices. Table 33.7 compiles most of the known elasticity profiles (force spectrums) of various natural polysaccharides measured by AFM, in solution, on isolated molecules. The elasticity profiles of a number of polysaccharides measured directly on cell surfaces, from which they protrude, may be found through the references in a recent review [83].

Table 33.7 Table of sugars and their corresponding chemical structures and force spectra as determined by atomic force microscopy

Polysaccharide	Chemical structure	Force spectrum	References
Amylose	α-1,4 D-glucopyranose		[98, 309, 311, 317–322]
Dextran	α−1,6 D-glucopyranose		[73, 98, 317, 323]

(*continued*)

Table 33.7 (continued)

Polysaccharide	Chemical structure	Force spectrum	References
Pullulan	[2(α-1,4) + α1,6]ₙ D-glucopyranose		[98, 317]
Pectin	α-1,4 D-galactopyranuronic acid		[308]

Cellulose   β-1,4 d-glucopyranose   [308, 311, 316]
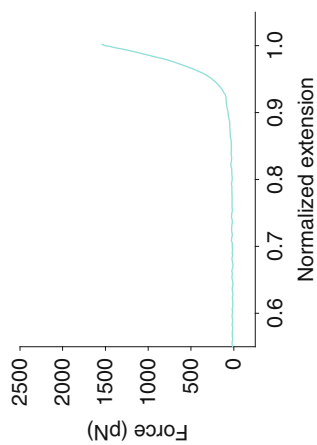
Beta-galactan   β-1,4 d-galactopyranose   [324]
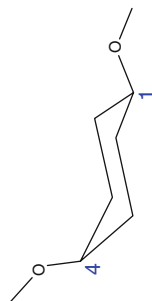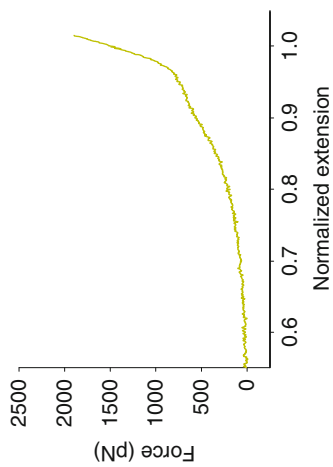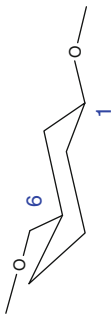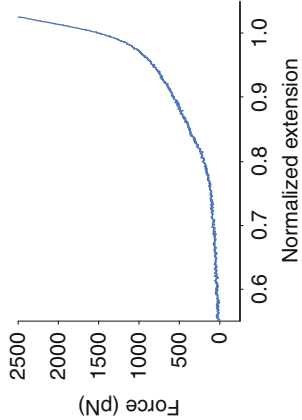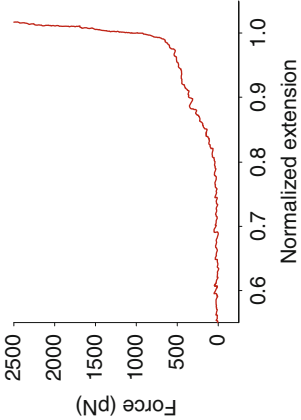
Table 33.7 (continued)

Polysaccharide	Chemical structure	Force spectrum	References
Pustulan	β-1,6 D-glucopyranose		[313]
Carrageenan λ	[(α-1,3) + (β1,4)]n D-galactopyranose		[317, 325]

Carrageenan ι
(iota)

$[(\alpha-1,3) + (\beta1,4)]$n D-galactopyranose
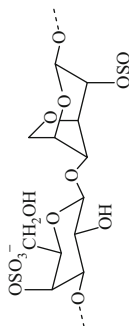
[325]
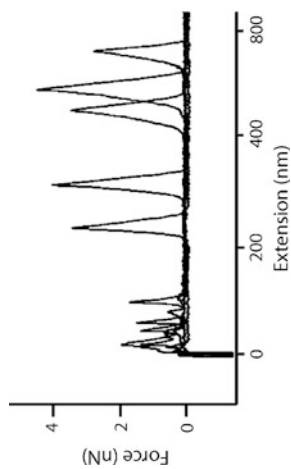
Alginate
Poly(GM)

(Poly GM; 40 %G + 60 %M): α-1,4 L-glucopyranuronic
acid (G) + β-1,4 D-mannuropyranuronic acid (M)
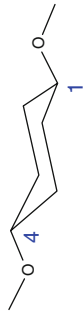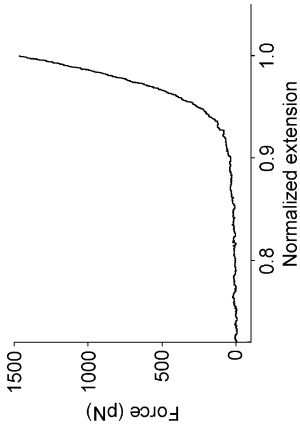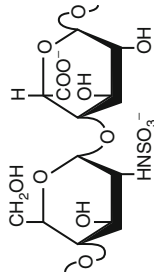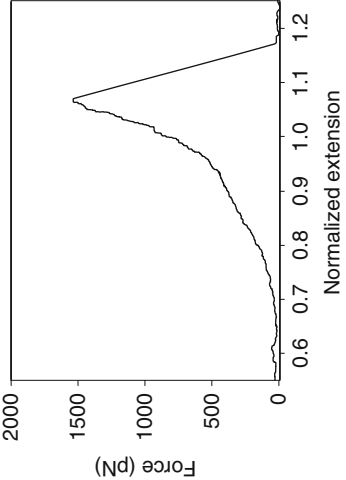
[312]

(*continued*)

Table 33.7 (continued)

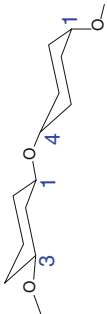| Polysaccharide	Chemical structure	Force spectrum	References
Alginate Poly(M)	β-1,4 D-mannuropyranuronic acid		[312]
Heparin	Uronic acid, and α glucose-amine or α galactosamine sugar linked by α (1,4) or β (1,3) linkages		[311, 326]

| Curdlan | β-(1,3)-linked D-glucose | [327] |
| Xanthan | A linear cellulosic backbone of (1,4)-β-D-glucose substituted with a trisaccharide side chain O-β-D mannopyranosyl-(1,4)-O-β-D-glucopyranosyl-uronic acid-(1,2)-6-O-acetyl-α-D-mannopyranosyl at the C-3 of alternate glucose residues of the main chain | [316] |
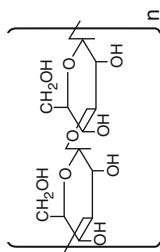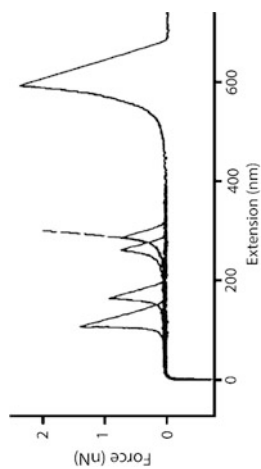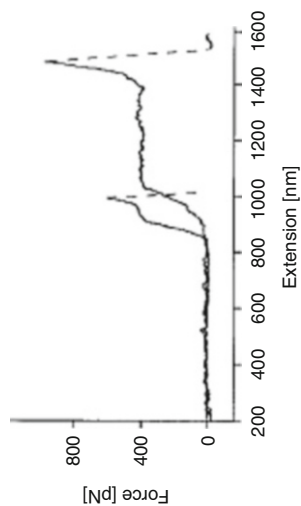
Outlook and Conclusion

The development of single-molecule manipulation techniques over the last 20 years enabled direct measurements of the mechanical properties of individual biomacro-molecules. The number of biopolymers tested is steadily increasing and many fundamental observations and measurements were already repeated on the same systems by independent groups and verified. The data about types of elasticity and force-induced structural transitions obtained this way is invaluable for deciphering molecular mechanisms supporting life processes and for using these biopolymers in nanobiotechnology. Standardization of measurement conditions, automation of measurements [328] and analysis, and improvements of the accuracy of force sensors calibration [329] will continue to increase the quantity and reliability of single-molecule characterization measurements.

References

1. Seeman NC (2003) DNA in a material world. Nature 421(6921):427–431
2. Seeman NC (2005) From genes to machines: DNA nanomechanical devices. Trends Biochem Sci 30(3):119–125. doi:10.1016/j.tibs.2005.01.007
3. Seeman NC (2007) An overview of structural DNA nanotechnology. Mol Biotechnol 37(3):246–257. doi:10.1007/s12033-007-0059-4
4. Seeman NC (2010) Nanomaterials based on DNA. Annu Rev Biochem 79:65–87. doi:10.1146/annurev-biochem-060308-102244
5. Seeman NC, Belcher AM (2002) Emulating biology: building nanostructures from the bottom up. Proc Natl Acad Sci USA 99(Suppl 2):6451–6455. doi:10.1073/pnas.221458298
6. Ito Y, Fukusaki E (2004) DNA as a 'nanomaterial'. J Mol Catal B: Enzym 28(4–6):155–166. doi:10.1016/j.molcatb.2004.01.016
7. Zhang SG (2003) Fabrication of novel biomaterials through molecular self-assembly. Nat Biotechnol 21(10):1171–1178. doi:10.1038/nbt874
8. Gothelf KV, LaBean TH (2005) DNA-programmed assembly of nanostructures. Org Biomol Chem 3(22):4023–4037. doi:10.1039/b510551j
9. Davis JT, Spada GP (2007) Supramolecular architectures generated by self-assembly of guanosine derivatives. Chem Soc Rev 36(2):296–313. doi:10.1039/b600282j
10. Bath J, Turberfield AJ (2007) DNA nanomachines. Nat Nanotechnol 2(5):275–284. doi:10.1038/nnano.2007.104
11. Aldaye FA, Palmer AL, Sleiman HF (2008) Assembling materials with DNA as the guide. Science 321(5897):1795–1799. doi:10.1126/science.1154533
12. Zhang DY, Seelig G (2011) Dynamic DNA nanotechnology using strand-displacement reactions. Nat Chem 3(2):103–113. doi:10.1038/nchem.957
13. Pinheiro AV, Han D, Shih WM, Yan H (2011) Challenges and opportunities for structural DNA nanotechnology. Nat Nanotechnol 6(12):763–772. doi:10.1038/nnano.2011.187
14. Adleman LM (1994) Molecular computation of solutions to combinatorial problems. Science 266(5187):1021–1024. doi:10.1126/science.7973651
15. Adleman LM (1998) Computing with DNA. Sci Am 279(2):54–61

16. Braich RS, Chelyapov N, Johnson C, Rothemund PWK, Adleman L (2002) Solution of a 20-variable 3-SAT problem on a DNA computer. Science 296(5567):499–502. doi:10.1126/science.1069528

17. Liu QH, Wang LM, Frutos AG, Condon AE, Corn RM, Smith LM (2000) DNA computing on surfaces. Nature 403(6766):175–179

18. Benenson Y, Adar R, Paz-Elizur T, Livneh Z, Shapiro E (2003) DNA molecule provides a computing machine with both data and fuel. Proc Natl Acad Sci USA 100(5):2191–2196. doi:10.1073/pnas.0535624100

19. Smith BL, Schaffer TE, Viani M, Thompson JB, Frederick NA, Kindt J, Belcher A, Stucky GD, Morse DE, Hansma PK (1999) Molecular mechanistic origin of the toughness of natural adhesives, fibres and composites. Nature 399(6738):761–763

20. Thompson JB, Kindt JH, Drake B, Hansma HG, Morse DE, Hansma PK (2001) Bone indentation recovery time correlates with bond reforming time. Nature 414(6865):773–776

21. Gutsmann T, Fantner GE, Kindt JH, Venturoni M, Danielsen S, Hansma PK (2004) Force spectroscopy of collagen fibers to investigate their mechanical properties and structural organization. Biophys J 86(5):3186–3193. doi:S0006-3495(04)74366-0 [pii], doi:10.1016/S0006-3495(04)74366-0

22. Oroudjev E, Soares J, Arcdiacono S, Thompson JB, Fossey SA, Hansma HG (2002) Segmented nanofibers of spider dragline silk: atomic force microscopy and single-molecule force spectroscopy. Proc Natl Acad Sci USA 99(14):9606. doi:10.1073/pnas.132282899 (Proc Natl Acad Sci USA 99:6460)

23. Oroudjev E, Soares J, Arcdiacono S, Thompson JB, Fossey SA, Hansma HG (2002) Segmented nanofibers of spider dragline silk: atomic force microscopy and single-molecule force spectroscopy. Proc Natl Acad Sci USA 99:6460–6465. doi:10.1073/pnas.082526499

24. Oroudjev EM, Hansma HG (2002) AFM and force spectroscopy of recombinant spider dragline silk protein nanofibers. Biophys J 82(1):41A–42A

25. Cao Y, Li H (2007) Polyprotein of GB1 is an ideal artificial elastomeric protein. Nat Mater 6(2):109–114, http://www.nature.com/nmat/journal/v6/n2/suppinfo/nmat1825_S1.html

26. Cao Y, Li H (2008) Engineered elastomeric proteins with dual elasticity can be controlled by a molecular regulator. Nat Nanotechnol 3(8):512–516

27. Li HB, Cao Y (2010) Protein Mechanics: from single molecules to functional biomaterials. Acc Chem Res 43(10):1331–1341. doi:10.1021/ar100057a

28. Lv S, Dudek DM, Cao Y, Balamurali MM, Gosline J, Li H (2010) Designed biomaterials to mimic the mechanical properties of muscles. Nature 465(7294):69–73, http://www.nature.com/nmat/journal/v6/n2/suppinfo/nmat1825_S1.html

29. Kim M, Wang C-C, Benedetti F, Rabbi M, Bennett V, Marszalek PE (2011) Nanomechanics of Streptavidin hubs for molecular materials. Adv Mater 23(47):5684–5688. doi:10.1002/adma.201103316

30. Robyt JF (1998) Essentials of carbohydrate chemistry. Springer-Verlag, New York, p 163

31. Rao VSR, Qasba PK, Balaji PV, Chandrasekaran R (1998) Conformation of carbohydrates. Harwood Academic Publishers, The Netherlands

32. Bustamante C, Bryant Z, Smith SB (2003) Ten years of tension: single-molecule DNA mechanics. Nature 421(6921):423–427

33. Bao G, Suresh S (2003) Cell and molecular mechanics of biological materials. Nat Mater 2(11):715–725. doi:10.1038/nmat1001

34. Bennett V, Baines AJ (2001) Spectrin and Ankyrin-based pathways: Metazoan inventions for integrating cells Into tissues. Physiol Rev 81(3):1353–1392

35. Benoit M, Gaub HE (2002) Measuring cell adhesion forces with the atomic force microscope at the molecular level. Cells Tissues Organs 172(3):174–189

36. Deguchi S, Ohashi T, Sato M (2006) Tensile properties of single stress fibers isolated from cultured vascular smooth muscle cells. J Biomech 39(14):2603–2610

37. del Rio A, Perez-Jimenez R, Liu RC, Roca-Cusachs P, Fernandez JM, Sheetz MP (2009) Stretching single talin rod molecules activates vinculin binding. Science 323(5914):638–641. doi:10.1126/science.1162912

38. Emerson RJ IV, Camesano TA (2004) Nanoscale investigation of pathogenic microbial adhesion to a biomaterial. Appl Environ Microbiol 70(10):6012–6022. doi:10.1128/aem.70.10.6012-6022.2004

39. Evans E (2001) Probing the relation between force – Lifetime – and chemistry in single molecular bonds. Annu Rev Biophys Biomol Struct 30:105–128. doi:10.1146/annurev.biophys.30.1.105

40. Evans E, Ritchie K (1997) Dynamic strength of molecular adhesion bonds. Biophys J 72(4):1541–1555

41. Evans E, Ritchie K, Merkel R (1995) Sensitive force technique to probe molecular adhesion and structural linkages at biological interfaces. Biophys J 68(6):2580–2587

42. Evans EA, Calderwood DA (2007) Forces and bond dynamics in cell adhesion. Science 316(5828):1148–1153. doi:10.1126/science.1137592

43. Florin E, Moy V, Gaub H (1994) Adhesion forces between individual ligand-receptor pairs. Science 264(5157):415–417. doi:10.1126/science.8153628

44. Grashoff C, Hoffman BD, Brenner MD, Zhou R, Parsons M, Yang MT, McLean MA, Sligar SG, Chen CS, Ha T, Schwartz MA (2010) Measuring mechanical tension across vinculin reveals regulation of focal adhesion dynamics. Nature 466(7303):263–266. doi:http://www.nature.com/nature/journal/v466/n7303/abs/nature09198.html#supplementary-information

45. Hanley W, McCarty O, Jadhav S, Tseng Y, Wirtz D, Konstantopoulos K (2003) Single molecule characterization of P-selectin/ligand binding. J Biol Chem 278(12):10556–10561

46. Helenius J, Heisenberg CP, Gaub HE, Muller DJ (2008) Single-cell force spectroscopy. J Cell Sci 121(11):1785–1791. doi:10.1242/jcs.030999

47. Kienberger F, Ebner A, Gruber HJ, Hinterdorfer P (2006) Molecular recognition imaging and force spectroscopy of single biomolecules. Acc Chem Res 39(1):29–36. doi:10.1021/ar050084m

48. Krammer A, Craig D, Thomas WE, Schulten K, Vogel V (2002) A structural model for force regulated integrin binding to fibronectin's RGD-synergy site. Matrix Biol 21(2):139–147

49. Krammer A, Lu H, Isralewitz B, Schulten K, Vogel V (1999) Forced unfolding of the fibronectin type III module reveals a tensile molecular recognition switch. Proc Natl Acad Sci USA 96(4):1351–1356

50. Leckband D, Prakasam A (2006) Mechanism and dynamics of cadherin adhesion. Ann Rev Biomed Eng 8(1):259–287, 10.1146/annurev.bioeng.8.061505.095753

51. Leckband D, Sivasankar S (2012) Cadherin recognition and adhesion. Curr Opin Cell Biol 24(5):620–627. doi:10.1016/j.ceb.2012.05.014

52. Leckband D, Sivasankar S (2012) Biophysics of cadherin adhesion. In: Harris T (ed) Adherens junctions: from molecular mechanisms to tissue development and disease, vol 60, Subcellular biochemistry. Springer, Netherlands, pp 63–88. doi:10.1007/978-94-007-4186-7_4

53. Lee H, Scherer NF, Messersmith PB (2006) Single-molecule mechanics of mussel adhesion. PNAS 103(35):12999–13003. doi:10.1073/pnas.0605552103

54. Li F, Redick SD, Erickson HP, Moy VT (2003) Force measurements of the α5β1 integrin–fibronectin interaction. Biophys J 84(2):1252–1262. doi:10.1016/s0006-3495(03)74940-6

55. Litvinov RI, Shuman H, Bennett JS, Weisel JW (2002) Binding strength and activation state of single fibrinogen-integrin pairs on living cells. Proc Natl Acad Sci 99(11):7426–7431. doi:10.1073/pnas.112194999

56. Liu W, Montana V, Parpura V, Mohideen U (2009) Single molecule measurements of interaction free energies between the proteins within binary and ternary SNARE complexes. J Nanoneuroscience 1(2):120–129. doi:10.1166/jns.2009.1001

57. Liu Y, Pinzón-Arango PA, Gallardo-Moreno AM, Camesano TA (2010) Direct adhesion force measurements between E. coli and human uroepithelial cells in cranberry juice cocktail. Mol Nutr Food Res 54(12):1744–1752. doi:10.1002/mnfr.200900535

58. Liu Y, Strauss J, Camesano TA (2008) Adhesion forces between *Staphylococcus epidermidis* and surfaces bearing self-assembled monolayers in the presence of model proteins. Biomaterials 29(33):4374–4382. doi:10.1016/j.biomaterials.2008.07.044

59. Ludwig M, Moy VT, Rief M, Florin EL, Gaub HE (1994) Characterization of the adhesion force between avidin-functionalized Afm tips and biotinylated agarose beads. Microscop Microanal Microstruct 5(4–6):321–328

60. Marshall BT, Long M, Piper JW, Yago T, McEver RP, Zhu C (2003) Direct observation of catch bonds involving cell-adhesion molecules. Nature 423(6936):190–193

61. Ng SP, Billings KS, Ohashi T, Allen MD, Best RB, Randles LG, Erickson HP, Clarke J (2007) Designing an extracellular matrix protein with enhanced mechanical stability. Proc Natl Acad Sci USA 104(23):9633–9637. doi:10.1073/pnas.0609901104

62. Rakshit S, Zhang Y, Manibog K, Shafraz O, Sivasankar S (2012) Ideal, catch, and slip bonds in cadherin adhesion. Proc Natl Acad Sci 109(46):18815–18820. doi:10.1073/pnas.1208349109

63. Rico F, Chu C, Abdulreda MH, Qin Y, Moy VT (2010) Temperature modulation of integrin-mediated cell adhesion. Biophys J 99(5):1387–1396. doi:10.1016/j.bpj.2010.06.037

64. Rico F, Chu C, Moy VT (2011) Force-clamp measurements of receptor–ligand interactions atomic force microscopy in biomedical research. In: Braga PC, Ricci D (eds) Methods in molecular biology, vol 736. Humana Press, New York, pp 331–353. doi:10.1007/978-1-61779-105-5_20

65. Rief M, Pascual J, Saraste M, Gaub HE (1999) Single molecule force spectroscopy of spectrin repeats: low unfolding forces in helix bundles. J Mol Biol 286(2):553–561

66. Thomas WE, Trintchina E, Forero M, Vogel V, Sokurenko EV (2002) Bacterial adhesion to target cells enhanced by shear force. Cell 109(7):913–923

67. Thomas WE, Vogel V, Sokurenko E (2008) Biophysics of catch bonds. Annu Rev Biophys 37(1):399–416. doi:10.1146/annurev.biophys.37.032807.125804

68. van Roy F, Berx G (2008) The cell-cell adhesion molecule E-cadherin. Cell Mol Life Sci 65(23):3756–3788. doi:10.1007/s00018-008-8281-1

69. Vogel V (2006) Mechanotransduction involving multimodular proteins: converting force into biochemical signals. Annu Rev Biophys Biomol Struct 35:459–488. doi:10.1146/annurev.biophys.35.040405.102013

70. Wojcikiewicz EP, Abdulreda MH, Zhang X, Moy VT (2006) Force spectroscopy of LFA-1 and its ligands, ICAM-1 and ICAM-2. Biomacromolecules 7(11):3188–3195. doi:10.1021/bm060559c

71. Erickson HP (1994) Reversible unfolding of fibronectin type-III and immunoglobulin domains provides the structural basis for stretch and elasticity of titin and fibronectin. Proc Natl Acad Sci USA 91:10114–10118

72. Erickson HP (1997) Stretching single protein molecules: titin is a weird spring. Science 276(5315):1090–1092. doi:10.1126/science.276.5315.1090

73. Rief M, Oesterhelt F, Heymann B, Gaub HE (1997) Single molecule force spectroscopy on polysaccharides by atomic force microscopy. Science 275(5304):1295–1297. doi:10.1126/science.275.5304.1295

74. Kellermayer MSZ, Smith SB, Granzier HL, Bustamante C (1997) Folding-unfolding transitions in single titin molecules characterized with laser tweezers. Science 276(5315):1112–1116

75. Li HB, Linke WA, Oberhauser AF, Carrion-Vazquez M, Kerkviliet JG, Lu H, Marszalek PE, Fernandez JM (2002) Reverse engineering of the giant muscle protein titin. Nature 418(6901):998–1002

76. Tskhovrebova L, Trinick J, Sleep JA, Simmons RM (1997) Elasticity and unfolding of single molecules of the giant muscle protein titin. Nature 387(6630):308–312

77. Davies GJ, Mackenzie L, Varrot A, Dauter M, Brzozowski AM, Schülein M, Withers SG (1998) Snapshots along an enzymatic reaction coordinate: analysis of a retaining β-glycoside hydrolase. Biochemistry 37(34):11707–11713. doi:10.1021/bi981315i

78. Kim IL, Mauck RL, Burdick JA (2011) Hydrogel design for cartilage tissue engineering: a case study with hyaluronic acid. Biomaterials 32(34):8771–8782. doi:10.1016/j.biomaterials.2011.08.073

79. Hills BA (2000) Boundary lubrication in vivo. Proc Inst Mech Eng H 214(1):83–94. doi:10.1243/0954411001535264

80. Hui AY, McCarty WJ, Masuda K, Firestein GS, Sah RL (2012) A systems biology approach to synovial joint lubrication in health, injury, and disease. Wiley Interdiscip Rev Syst Biol Med 4(1):15–37. doi:10.1002/wsbm.157

81. Coles JM, Chang DP, Zauscher S (2010) Molecular mechanisms of aqueous boundary lubrication by mucinous glycoproteins. Curr Opin Colloid Interface Sci 15(6):406–416. doi:10.1016/j.cocis.2010.07.002

82. Fisher TE, Marszalek PE, Fernandez JM (2000) Stretching single molecules into novel conformations using the atomic force microscope. Nat Struct Mol Biol 7(9):719–724

83. Marszalek PE, Dufrene YF (2012) Stretching single polysaccharides and proteins using atomic force microscopy. Chem Soc Rev 41(9):3523–3534. doi:10.1039/c2cs15329g

84. Puchner EM, Gaub HE (2009) Force and function: probing proteins with AFM-based force spectroscopy. Curr Opin Struct Biol 19(5):605–614. doi:S0959-440X(09)00135-3 [pii], doi:10.1016/j.sbi.2009.09.005

85. Dufrene YF, Evans E, Engel A, Helenius J, Gaub HE, Muller DJ (2011) Five challenges to bringing single-molecule force spectroscopy into living cells. Nat Meth 8(2):123–127

86. Muller DJ, Dufrene YF (2008) Atomic force microscopy as a multifunctional molecular toolbox in nanobiotechnology. Nat Nanotechnol 3(5):261–269. doi:10.1038/nnano.2008.100

87. Muller DJ, Helenius J, Alsteens D, Dufrene YF (2009) Force probing surfaces of living cells to molecular resolution. Nat Chem Biol 5(6):383–390. doi:10.1038/nchembio.181

88. Hansma PK (2006) Molecular mechanics of single molecules. Structure 14(3):390–391

89. Viani MB, Schaffer TE, Paloczi GT, Pietrasanta LI, Smith BL, Thompson JB, Richter M, Rief M, Gaub HE, Plaxco KW, Cleland AN, Hansma HG, Hansma PK (1999) Fast imaging and fast force spectroscopy of single biopolymers with a new atomic force microscope designed for small cantilevers. Rev Sci Instrum 70(11):4300–4303

90. Rabbi M, Marszalek P (2008) Probing polysaccharide and protein mechanics by atomic force microscopy. In: Selvin PR, Ha T (eds) Single-molecule techniques: a laboratory manual. Cold Spring Harbor Laboratory Press, Cold Spring Harbor, pp 371–394

91. Flory PJ (1953) Principles of polymer chemistry. Cornell University Press, Ithaca

92. Flory PJ (1989) Statistical Mechanics of Chain Molecules. Hanser Publishers, New York

93. Bustamante C, Marko JF, Siggia ED, Smith S (1994) Entropic elasticity of lambda-phage dna. Science 265(5178):1599–1600

94. Smith SB, Finzi L, Bustamante C (1992) Direct mechanical measurements of the elasticity of single DNA-molecules by using magnetic beads. Science 258(5085):1122–1126

95. Bustamante C (1994) Entropic elasticity of [lambda]-phage DNA. Science 265:1599–1600

96. Smith SB, Cui YJ, Bustamante C (1996) Overstretching B-DNA: the elastic response of individual double-stranded and single-stranded DNA molecules. Science 271(5250):795–799

97. Marszalek PE, Lu H, Li HB, Carrion-Vazquez M, Oberhauser AF, Schulten K, Fernandez JM (1999) Mechanical unfolding intermediates in titin modules. Nature 402(6757):100–103

98. Marszalek PE, Oberhauser AF, Pang YP, Fernandez JM (1998) Polysaccharide elasticity governed by chair-boat transitions of the glucopyranose ring. Nature 396(6712):661–664

99. Strick TR, Dessinges MN, Charvin G, Dekker NH, Allemand JF, Bensimon D, Croquette V (2003) Stretching of macromolecules and proteins. Rep Prog Phys 66(1):1–45

100. Frentrup H, Allen MS (2011) Error in dynamic spring constant calibration of atomic force microscope probes due to nonuniform cantilevers. Nanotechnology 22(29):295703

101. Burnham N, Chen X, Hodges C, Matei G, Thoreson E, Roberts C, Davies M, Tendler S (2003) Comparison of calibration methods for atomic-force microscopy cantilevers. Nanotechnology 14(1):1

102. Binnig G, Quate CF, Gerber C (1986) Atomic force microscope. Phys Rev Lett 56(9):930–933

103. Rugar D, Hansma P (1990) Atomic force microscopy. Physics Today 43(10):23–30

104. Binnig G, Rohrer H, Gerber C, Weibel E (1982) Tunneling through a controllable vacuum gap. Appl Phys Lett 40(2):178–180

105. Binnig G, Rohrer H, Gerber C, Weibel E (1983) 7x7 reconstruction on Si(111) resolved in real space. Phys Rev Lett 50(2):120–123

106. Hansma P, Elings V, Marti O, Bracker C (1988) Scanning tunneling microscopy and atomic force microscopy: application to biology and technology. Science 242:209–216

107. Oberhauser AF, Hansma PK, Carrion-Vazquez M, Fernandez JM (2001) Stepwise unfolding of titin under force-clamp atomic force microscopy. Proc Natl Acad Sci USA 98(2):468–472

108. Moffitt JR, Chemla YR, Smith SB, Bustamante C (2008) Recent advances in optical tweezers. Annu Rev Biochem 77:205–228. doi:10.1146/annurev.biochem.77.043007.090225

109. Visscher K, Block SM (1998) Versatile optical traps with feedback control. Molecular Motors and the Cytoskeleton, Pt B 298:460–489

110. Mehta AD, Rief M, Spudich JA, Smith DA, Simmons RM (1999) Single-molecule biomechanics with optical methods. Science 283(5408):1689–1695

111. Moffitt JR, Chemla YR, Izhaky D, Bustamante C (2006) Differential detection of dual traps improves the spatial resolution of optical tweezers. PNAS 103(24):9006–9011. doi:10.1073/pnas.0603342103

112. Ashkin A (1970) Acceleration and trapping of particles by radiation pressure. Phys Rev Lett 24(4):156–159. doi:10.1103/PhysRevLett.24.156

113. De Vlaminck I, Dekker C (2012) Recent advances in magnetic tweezers. Annu Rev Biophys 41:453–472

114. Lipfert J, Kerssemakers JWJ, Jager T, Dekker NH (2010) Magnetic torque tweezers: measuring torsional stiffness in DNA and RecA-DNA filaments. Nat Methods 7(12):977–980. doi:10.1038/nmeth.1520

115. Lipfert J, Hao XM, Dekker NH (2009) Quantitative modeling and optimization of magnetic tweezers. Biophys J 96(12):5040–5049. doi:10.1016/j.bpj.2009.03.055

116. Strick T, Allemand JF, Croquette V, Bensimon D (2000) Twisting and stretching single DNA molecules. Prog Biophys Mol Biol 74(1–2):115–140. doi:10.1016/s0079-6107(00)00018-3

117. Strick TR, Allemand JF, Bensimon D, Bensimon A, Croquette V (1996) The elasticity of a single supercoiled DNA molecule. Science 271(5257):1835–1837

118. Strick TR, Allemand JF, Bensimon D, Croquette V (1998) Behavior of supercoiled DNA. Biophys J 74(4):2016–2028

119. Simson DA, Ziemann F, Strigl M, Merkel R (1998) Micropipet-based pico force transducer: in depth analysis and experimental verification. Biophys J 74(4):2080–2088

120. Deamer DW, Akeson M (2000) Nanopores and nucleic acids: prospects for ultrarapid sequencing. Trends Biotechnol 18(4):147–151. doi:10.1016/S0167-7799(00)01426-8

121. Kasianowicz JJ, Brandin E, Branton D, Deamer DW (1996) Characterization of individual polynucleotide molecules using a membrane channel. Proc Natl Acad Sci 93(24):13770–13773

122. Dekker C (2007) Solid-state nanopores. Nat Nanotechnol 2(4):209–215. doi:10.1038/nnano.2007.27

123. Rodriguez-Larrea D, Bayley H (2013) Multistep protein unfolding during nanopore translocation. Nat Nanotechnol 8(4):288–295. doi:10.1038/nnano.2013.22

124. Dudko OK, Mathé J, Meller A (2010) Chapter twenty-one – nanopore force spectroscopy tools for analyzing single biomolecular complexes. In: Nils GW (ed) Methods in enzymology, vol 475. Academic Press, New York, pp 565–589. doi:10.1016/S0076-6879(10)75021-7

125. Perkins TT, Smith DE, Chu S (1997) Single polymer dynamics in an elongational flow. Science 276(5321):2016–2021
126. Perkins TT, Smith DE, Larson RG, Chu S (1995) Stretching of a single tethered polymer in a uniform-flow. Science 268(5207):83–87. doi:10.1126/science.7701345
127. Davenport RJ, Wuite GJL, Landick R, Bustamante C (2000) Single-molecule study of transcriptional pausing and arrest by E-coli RNA polymerase. Science 287(5462):2497–2500. doi:10.1126/science.287.5462.2497
128. Kim SJ, Blainey PC, Schroeder CM, Xie XS (2007) Multiplexed single-molecule assay for enzymatic activity on flow-stretched DNA. Nat Methods 4(5):397–399. doi:10.1038/nmeth1037
129. Schafer DA, Gelles J, Sheetz MP, Landick R (1991) Transcription by single molecules of RNA polymerase observed by light microscopy. Nature 352(6334):444–448. doi:10.1038/352444a0
130. Yin H, Landick R, Gelles J (1994) Tethered particle motion method for studying transcript elongation by a single RNA polymerase molecule. Biophys J 67(6):2468–2478. doi:10.1016/S0006-3495(94)80735-0
131. Finzi L, Gelles J (1995) Measurement of lactose repressor-mediated loop formation and breakdown in single DNA molecules. Science 267(5196):378–380
132. van den Broek B, Vanzi F, Normanno D, Pavone FS, Wuite GJ (2006) Real-time observation of DNA looping dynamics of Type IIE restriction enzymes NaeI and NarI. Nucleic Acids Res 34(1):167–174. doi:10.1093/nar/gkj432
133. Vanzi F, Broggio C, Sacconi L, Pavone FS (2006) Lac repressor hinge flexibility and DNA looping: single molecule kinetics by tethered particle motion. Nucleic Acids Res 34(12):3409–3420. doi:10.1093/nar/gkl393
134. Wong OK, Guthold M, Erie DA, Gelles J (2008) Interconvertible lac repressor-DNA loops revealed by single-molecule experiments. PLoS Biol 6(9):e232. doi:10.1371/journal.pbio.0060232
135. Han L, Garcia HG, Blumberg S, Towles KB, Beausang JF, Nelson PC, Phillips R (2009) Concentration and length dependence of DNA looping in transcriptional regulation. PLoS One 4(5):e5621. doi:10.1371/journal.pone.0005621
136. Rutkauskas D, Zhan H, Matthews KS, Pavone FS, Vanzi F (2009) Tetramer opening in LacI-mediated DNA looping. Proc Natl Acad Sci USA 106(39):16627–16632. doi:10.1073/pnas.0904617106
137. Zurla C, Manzo C, Dunlap D, Lewis DE, Adhya S, Finzi L (2009) Direct demonstration and quantification of long-range DNA looping by the lambda bacteriophage repressor. Nucleic Acids Res 37(9):2789–2795. doi:10.1093/nar/gkp134
138. Chen YF, Milstein JN, Meiners JC (2010) Protein-mediated DNA loop formation and breakdown in a fluctuating environment. Phys Rev Lett 104(25):258103
139. Chen Y-F, Milstein J, Meiners J-C (2010) Femtonewton entropic forces can control the formation of protein-mediated DNA loops. Phys Rev Lett 104(4):048301
140. Johnson S, Linden M, Phillips R (2012) Sequence dependence of transcription factor-mediated DNA looping. Nucleic Acids Res 40(16):7728–7738. doi:10.1093/nar/gks473
141. Laurens N, Rusling DA, Pernstich C, Brouwer I, Halford SE, Wuite GJ (2012) DNA looping by FokI: the impact of twisting and bending rigidity on protein-induced looping dynamics. Nucleic Acids Res 40(11):4988–4997. doi:10.1093/nar/gks184
142. Manzo C, Zurla C, Dunlap DD, Finzi L (2012) The effect of nonspecific binding of lambda repressor on DNA looping dynamics. Biophys J 103(8):1753–1761. doi:10.1016/j.bpj.2012.09.006
143. Pouget N, Turlan C, Destainville N, Salomé L, Chandler M (2006) IS911 transpososome assembly as analysed by tethered particle motion. Nucleic Acids Res 34(16):4313–4323
144. Tolic-Norrelykke SF, Rasmussen MB, Pavone FS, Berg-Sorensen K, Oddershede LB (2006) Stepwise bending of DNA by a single TATA-box binding protein. Biophys J 90(10):3694–3703. doi:10.1529/biophysj.105.074856

145. Mumm JP, Landy A, Gelles J (2006) Viewing single lambda site-specific recombination events from start to finish. EMBO J 25(19):4586–4595. doi:10.1038/sj.emboj.7601325

146. Fan HF (2012) Real-time single-molecule tethered particle motion experiments reveal the kinetics and mechanisms of Cre-mediated site-specific recombination. Nucleic Acids Res 40(13):6208–6222. doi:10.1093/nar/gks274

147. Monico C, Capitanio M, Belcastro G, Vanzi F, Pavone FS (2013) Optical methods to study protein-DNA interactions in vitro and in living cells at the single-molecule level. Int J Mol Sci 14(2):3961–3992

148. Vanzi F, Sacconi L, Pavone FS (2007) Analysis of kinetics in noisy systems: application to single molecule tethered particle motion. Biophys J 93(1):21–36. doi:10.1529/biophysj.106.094151

149. Segall DE, Nelson PC, Phillips R (2006) Volume-exclusion effects in tethered-particle experiments: bead size matters. Phys Rev Lett 96(8):088306

150. Milstein JN, Chen YF, Meiners JC (2011) Bead size effects on protein-mediated DNA looping in tethered-particle motion experiments. Biopolymers 95(2):144–150. doi:10.1002/bip.21547

151. Fan H-F, Li H-W (2009) Studying RecBCD Helicase translocation along Ç-DNA using tethered particle motion with a stretching force. Biophys J 96(5):1875–1883

152. Plenat T, Tardin C, Rousseau P, Salome L (2012) High-throughput single-molecule analysis of DNA-protein interactions by tethered particle motion. Nucleic Acids Res 40(12):e89. doi:10.1093/nar/gks250

153. Beausang JF, Zurla C, Manzo C, Dunlap D, Finzi L, Nelson PC (2007) DNA looping kinetics analyzed using diffusive hidden Markov model. Biophys J 92(8):L64–L66

154. Manzo C, Finzi L (2010) Quantitative analysis of DNA-looping kinetics from tethered particle motion experiments. Methods Enzymol 475:199–220. doi:10.1016/S0076-6879(10)75009-6

155. Bustamante C, Macosko JC, Wuite GJL (2000) Grabbing the cat by the tail: manipulating molecules one by one. Nat Rev Mol Cell Biol 1(2):130–136

156. Neuman KC, Nagy A (2008) Single-molecule force spectroscopy: optical tweezers, magnetic tweezers and atomic force microscopy. Nat Methods 5(6):491–505. doi:10.1038/nmeth.1218

157. Giannotti MI, Vancso GJ (2007) Interrogation of single synthetic polymer chains and poly-saccharides by AFM-based force spectroscopy. Chemphyschem 8(16):2290–2307. doi:10.1002/cphc.200700175

158. Greenleaf WJ, Woodside MT, Block SM (2007) High-resolution, single-molecule measurements of biomolecular motion. Annu Rev Biophys Biomol Struct 36(1):171–190. doi:10.1146/annurev.biophys.36.101106.101451

159. Tinoco I, Li PTX, Bustamante C (2006) Determination of thermodynamics and kinetics of RNA reactions by force. Quart Rev Biophys 39(4):325–360. doi:10.1017/S0033583506004446

160. Dufrêne Y, Hinterdorfer P (2008) Recent progress in AFM molecular recognition studies. Pflügers Arch 456(1):237–245. doi:10.1007/s00424-007-0413-1

161. Moy VT, Florin EL, Gaub HE (1994) Adhesive forces between ligand and receptor measured by Afm. Colloid Surf A-Physicochem Eng 93:343–348

162. Wuite GJL, Smith SB, Young M, Keller D, Bustamante C (2000) Single-molecule studies of the effect of template tension on T7 DNA polymerase activity. Nature 404(6773):103–106

163. Onoa B, Dumont S, Liphardt J, Smith SB, Tinoco I, Bustamante C (2003) Identifying kinetic barriers to mechanical unfolding of the T-thermophila ribozyme. Science 299(5614):1892–1895

164. Stigler J, Ziegler F, Gieseke A, Gebhardt JCM, Rief M (2011) The complex folding network of single calmodulin molecules. Science 334(6055):512–516. doi:10.1126/science.1207598

165. Koster DA, Croquette V, Dekker C, Shuman S, Dekker NH (2005) Friction and torque govern the relaxation of DNA supercoils by eukaryotic topoisomerase IB. Nature 434(7033):671–674. doi:10.1038/nature03395

166. Gore J, Bryant Z, Stone MD, Nollmann MN, Cozzarelli NR, Bustamante C (2006) Mechanochemical analysis of DNA gyrase using rotor bead tracking. Nature 439(7072):100–104

167. Merkel R, Nassoy P, Leung A, Ritchie K, Evans E (1999) Energy landscapes of receptor-ligand bonds explored with dynamic force spectroscopy. Nature 397(6714):50–53. doi:10.1038/16219

168. Dudko OK, Mathe J, Szabo A, Meller A, Hummer G (2007) Extracting kinetics from single-molecule force spectroscopy: nanopore unzipping of DNA hairpins. Biophys J 92(12):4188–4195. doi:10.1529/biophysj.106.102855

169. Hutter JL, Bechhoefer J (1993) Calibration of atomic-force microscope tips. Rev Sci Instrum 64:1868

170. Hinterdorfer P, Dufrêne YF (2006) Detection and localization of single molecular recognition events using atomic force microscopy. Nat Methods 3(5):347–355

171. Taniguchi Y, Kawakami M (2010) Application of HaloTag protein to covalent immobilization of recombinant proteins for single molecule force spectroscopy. Langmuir 26(13):10433–10436

172. Wong J, Chilkoti A, Moy VT (1999) Direct force measurements of the streptavidin–biotin interaction. Biomol Eng 16(1):45–55

173. Kienberger F, Kada G, Gruber HJ, Pastushenko VP, Riener C, Trieb M, Knaus HG, Schindler H, Hinterdorfer P (2000) Recognition force spectroscopy studies of the NTA-His6 bond. Single Molecules 1(1):59–65

174. Bustamante C, Marko J, Siggia E, Smith S (1994) Entropic elasticity of lambda-phage DNA. Science 265:1599–1601

175. Merkel R, Nassoy P, Leung A, Ritchie K, Evans E (1999) Energy landscapes of receptor–ligand bonds explored with dynamic force spectroscopy. Nature 397(6714):50–53

176. Brockwell DJ, Paci E, Zinober RC, Beddard GS, Olmsted PD, Smith DA, Perham RN, Radford SE (2003) Pulling geometry defines the mechanical resistance of a beta-sheet protein. Nat Struct Biol 10(9):731–737. doi:10.1038/nsb968

177. Dietz H, Rief M (2006) Protein structure by mechanical triangulation. Proc Natl Acad Sci USA 103(5):1244–1247

178. Lee W, Zeng X, Zhou H-X, Bennett V, Yang W, Marszalek PE (2010) Full reconstruction of a vectorial protein folding pathway by atomic force microscopy and molecular dynamics simulations. J Biol Chem 285(49):38167–38172. doi:10.1074/jbc.M110.179697

179. Li L, Wetzel S, Pluckthun A, Fernandez JM (2006) Stepwise unfolding of ankyrin repeats in a single protein revealed by atomic force microscopy. Biophys J 90(4):L30–L32. doi:10.1529/biophysj.105.078436

180. Lee G, Abdi K, Jiang Y, Michaely P, Bennett V, Marszalek PE (2006) Nanospring behaviour of ankyrin repeats. Nature 440(7081):246–249. doi:nature04437 [pii]. doi:10.1038/nature04437

181. Merz T, Wetzel SK, Firbank S, Pluckthun A, Grutter MG, Mittl PR (2008) Stabilizing ionic interactions in a full-consensus ankyrin repeat protein. J Mol Biol 376(1):232–240. doi:10.1016/j.jmb.2007.11.047

182. Kim M, Abdi K, Lee G, Rabbi M, Lee W, Yang M, Schofield CJ, Bennett V, Marszalek PE (2010) Fast and forceful refolding of stretched alpha-helical solenoid proteins. Biophys J 98(12):3086–3092. doi:10.1016/j.bpj.2010.02.054

183. Valbuena A, Vera Andrés M, Oroz J, Menéndez M, Carrión-Vázquez M (2012) Mechanical properties of β-catenin revealed by single-molecule experiments. Biophys J 103(8):1744–1752. doi:10.1016/j.bpj.2012.07.051

184. Xing Y, Takemaru K, Liu J, Berndt JD, Zheng JJ, Moon RT, Xu W (2008) Crystal structure of a full-length beta-catenin. Structure 16(3):478–487. doi:10.1016/j.str.2007.12.021

185. Best RB, Li B, Steward A, Daggett V, Clarke J (2001) Can non-mechanical proteins withstand force? Stretching barnase by atomic force microscopy and molecular dynamics simulation. Biophys J 81(4):2344–2356. doi:10.1016/S0006-3495(01)75881-X

186. Martin C, Richard V, Salem M, Hartley R, Mauguen Y (1999) Refinement and structural analysis of barnase at 1.5 A resolution. Acta Crystallogr D Biol Crystallogr 55(Pt 2):386–398

187. Junker JP, Ziegler F, Rief M (2009) Ligand-dependent equilibrium fluctuations of single calmodulin molecules. Science 323(5914):633–637. doi:10.1126/science.1166191

188. Chattopadhyaya R, Meador WE, Means AR, Quiocho FA (1992) Calmodulin structure refined at 1.7 Å resolution. J Mol Biol 228(4):1177–1192

189. Hoffmann T, Tych KM, Brockwell DJ, Dougan L (2013) Single-molecule force spectroscopy identifies a small cold shock protein as being mechanically robust. J Phys Chem B 117(6):1819–1826. doi:10.1021/jp310442s

190. Kremer W, Schuler B, Harrieder S, Geyer M, Gronwald W, Welker C, Jaenicke R, Kalbitzer HR (2001) Solution NMR structure of the cold-shock protein from the hyperthermophilic bacterium *Thermotoga maritima*. Eur J Biochem 268(9):2527–2539

191. Ainavarapu SRK, Li L, Badilla CL, Fernandez JM (2005) Ligand binding modulates the mechanical stability of dihydrofolate reductase. Biophys J 89(5):3337–3344

192. Lewis WS, Cody V, Galitsky N, Luft JR, Pangborn W, Chunduru SK, Spencer HT, Appleman JR, Blakley RL (1995) Methotrexate-resistant variants of human dihydrofolate reductase with substitutions of leucine 22 Kinetics, crystallography, and potential as selectable markers. J Biol Chem 270(10):5057–5064

193. Tang L, Whittingham JL, Verma CS, Caves LS, Dodson GG (1999) Structural consequences of the B5 histidine –> tyrosine mutation in human insulin characterized by X-ray crystallography and conformational analysis. Biochemistry 38(37):12041–12051

194. Perez-Jimenez R, Garcia-Manyes S, Ainavarapu SRK, Fernandez JM (2006) Mechanical unfolding pathways of the enhanced yellow fluorescent protein revealed by single molecule force spectroscopy. J Biol Chem 281(52):40010–40014

195. Wachter RM, Elsliger MA, Kallio K, Hanson GT, Remington SJ (1998) Structural basis of spectral shifts in the yellow-emission variants of green fluorescent protein. Structure 6(10):1267–1277

196. Brown André E, Litvinov RI, Discher DE, Weisel JW (2007) Forced unfolding of coiled-coils in fibrinogen by single-molecule AFM. Biophys J 92(5):L39–L41

197. Cao Y, Lam C, Wang M, Li H (2006) Nonmechanical protein can have significant mechanical stability. Angew Chem 118(4):658–661

198. Cao Y, Li H (2007) Polyprotein of GB1 is an ideal artificial elastomeric protein. Nat Mater 6(2):109–114

199. Nieuwkoop AJ, Wylie BJ, Franks WT, Shah GJ, Rienstra CM (2009) Atomic resolution protein structure determination by three-dimensional transferred echo double resonance solid-state nuclear magnetic resonance spectroscopy. J Chem Phys 131(9):095101. doi:10.1063/1.3211103

200. Cao Y, Yoo T, Li H (2008) Single molecule force spectroscopy reveals engineered metal chelation is a general approach to enhance mechanical stability of proteins. Proc Natl Acad Sci 105(32):11152–11157

201. Abu-Lail NI, Ohashi T, Clark RL, Erickson HP, Zauscher S (2006) Understanding the elasticity of fibronectin fibrils: unfolding strengths of FN-III and GFP domains measured by single molecule force spectroscopy. Matrix Biol 25(3):175–184

202. Dietz H, Rief M (2004) Exploring the energy landscape of GFP by single-molecule mechanical experiments. Proc Natl Acad Sci USA 101(46):16192–16197

203. Battistutta R, Negro A, Zanotti G (2000) Crystal structure and refolding properties of the mutant F99S/M153T/V163A of the green fluorescent protein. Proteins 41(4):429–437

204. Newman J, Peat TS, Richard R, Kan L, Swanson PE, Affholter JA, Holmes IH, Schindler JF, Unkefer CJ, Terwilliger TC (1999) Haloalkane dehalogenases: structure of a Rhodococcus enzyme. Biochemistry 38(49):16105–16114

205. Ybe JA, Brodsky FM, Hofmann K, Lin K, Liu SH, Chen L, Earnest TN, Fletterick RJ, Hwang PK (1999) Clathrin self-assembly is mediated by a tandemly repeated superhelix. Nature 399(6734):371–375. doi:10.1038/20708

206. Schwaiger I, Kardinal A, Schleicher M, Noegel AA, Rief M (2003) A mechanical unfolding intermediate in an actin-crosslinking protein. Nat Struct Mol Biol 11(1):81–85

207. Schwaiger I, Schleicher M, Noegel AA, Rief M (2004) The folding pathway of a fast-folding immunoglobulin domain revealed by single-molecule mechanical experiments. EMBO Rep 6(1):46–51

208. Bullard B, Garcia T, Benes V, Leake MC, Linke WA, Oberhauser AF (2006) The molecular elasticity of the insect flight muscle proteins projectin and kettin. Proc Natl Acad Sci USA 103(12):4451–4456

209. Johnson RJ, McCoy JG, Bingman CA, Phillips GN Jr, Raines RT (2007) Inhibition of human pancreatic ribonuclease by the human ribonuclease inhibitor protein. J Mol Biol 368(2):434–449. doi:10.1016/j.jmb.2007.02.005

210. Bornschlögl T, Rief M (2006) Single molecule unzipping of coiled coils: sequence resolved stability profiles. Phys Rev Lett 96(11):118102

211. Bertz M, Rief M (2008) Mechanical unfoldons as building blocks of maltose-binding protein. J Mol Biol 378(2):447–458

212. Quiocho FA, Spurlino JC, Rodseth LE (1997) Extensive features of tight oligosaccharide binding revealed in high-resolution structures of the maltodextrin transport/chemosensory receptor. Structure 5(8):997–1015

213. Berkemeier F, Bertz M, Xiao S, Pinotsis N, Wilmanns M, Grater F, Rief M (2011) Fast-folding alpha-helices as reversible strain absorbers in the muscle protein myomesin. Proc Natl Acad Sci USA 108(34):14139–14144. doi:10.1073/pnas.1105734108

214. Pinotsis N, Lange S, Perriard JC, Svergun DI, Wilmanns M (2008) Molecular basis of the C-terminal tail-to-tail assembly of the sarcomeric filament protein myomesin. EMBO J 27(1):253–264. doi:10.1038/sj.emboj.7601944

215. Schwaiger I, Sattler C, Hostetter DR, Rief M (2002) The myosin coiled-coil is a truly elastic protein structure. Nat Mater 1(4):232–235. doi:10.1038/nmat776

216. Kaiser CM, Bujalowski PJ, Ma L, Anderson J, Epstein HF, Oberhauser AF (2012) Tracking UNC-45 chaperone-myosin interaction with a titin mechanical reporter. Biophys J 102(9):2212–2219

217. Yadavalli VK, Forbes JG, Wang K (2009) Nanomechanics of full-length nebulin: an elastic strain gauge in the skeletal muscle sarcomere. Langmuir 25(13):7496–7505. doi:10.1021/la9009898

218. Cao Y, Kuske R, Li H (2008) Direct observation of Markovian behavior of the mechanical unfolding of individual proteins. Biophys J 95(2):782–788

219. Nauli S, Kuhlman B, Le Trong I, Stenkamp RE, Teller D, Baker D (2002) Crystal structures and increased stabilization of the protein G variants with switched folding pathways NuG1 and NuG2. Protein Sci 11(12):2924–2931

220. Ma L, Xu M, Forman JR, Clarke J, Oberhauser AF (2009) Naturally occurring mutations alter the stability of polycystin-1 polycystic kidney disease (PKD) domains. J Biol Chem 284(47):32942–32949

221. Bycroft M, Bateman A, Clarke J, Hamill SJ, Sandford R, Thomas RL, Chothia C (1999) The structure of a PKD domain from polycystin-1: implications for polycystic kidney disease. EMBO J 18(2):297–305

222. Brockwell DJ, Beddard GS, Paci E, West DK, Olmsted PD, Smith DA, Radford SE (2005) Mechanically unfolding the small, topologically simple protein L. Biophys J 89(1):506

223. O'Neill JW, Kim DE, Baker D, Zhang KY (2001) Structures of the B1 domain of protein L from Peptostreptococcus magnus with a tyrosine to tryptophan substitution. Acta Crystallogr D Biol Crystallogr 57(Pt 4):480–487

224. Valbuena A, Oroz J, Hervás R, Vera AM, Rodríguez D, Menéndez M, Sulkowska JI, Cieplak M, Carrión-Vázquez M (2009) On the remarkable mechanostability of scaffoldins and the mechanical clamp motif. Proc Natl Acad Sci 106(33):13791–13796

225. Spinelli S, Fierobe HP, Belaich A, Belaich JP, Henrissat B, Cambillau C (2000) Crystal structure of a cohesin module from Clostridium cellulolyticum: implications for dockerin recognition. J Mol Biol 304(2):189–200. doi:10.1006/jmbi.2000.4191

226. Shimon LJ, Bayer EA, Morag E, Lamed R, Yaron S, Shoham Y, Frolow F (1997) A cohesin domain from *Clostridium thermocellum*: the crystal structure provides new insights into cellulosome assembly. Structure 5(3):381–390

227. Tavares GA, Béguin P, Alzari PM (1997) The crystal structure of a type I cohesin domain at 1.7 Å resolution. J Mol Biol 273(3):701–713

228. Alegre-Cebollada J, Badilla CL, Fernández JM (2010) Isopeptide bonds block the mechanical extension of pili in pathogenic *Streptococcus pyogenes*. J Biol Chem 285(15):11235–11242

229. Kang HJ, Coulibaly F, Clow F, Proft T, Baker EN (2007) Stabilizing isopeptide bonds revealed in gram-positive bacterial pilus structure. Science 318(5856):1625–1628

230. Wang C-C, Tsong T-Y, Hsu Y-H, Marszalek PE (2011) Inhibitor binding increases the mechanical stability of *Staphylococcal Nuclease*. Biophys J 100(4):1094–1099. doi:10.1016/j.bpj.2011.01.011

231. Cotton FA, Hazen EE, Legg MJ (1979) *Staphylococcal nuclease*: proposed mechanism of action based on structure of enzyme—thymidine 3′, 5′-bisphosphate—calcium ion complex at 1.5-Å resolution. Proc Natl Acad Sci 76(6):2551–2555

232. Kotamarthi HC, Sharma R, Koti Ainavarapu SR (2013) Single-molecule studies on PolySUMO proteins reveal their mechanical flexibility. Biophys J 104(10):2273–2281

233. Bayer P, Arndt A, Metzger S, Mahajan R, Melchior F, Jaenicke R, Becker J (1998) Structure determination of the small ubiquitin-related modifier SUMO-1. J Mol Biol 280(2):275–286

234. Huang WC, Ko TP, Li SSL, Wang AHJ (2004) Crystal structures of the human SUMO-2 protein at 1.6 Å and 1.2 Å resolution. Eur J Biochem 271(20):4114–4122

235. Randles LG, Rounsevell RWS, Clarke J (2007) Spectrin domains lose cooperativity in forced unfolding. Biophys J 92(2):571–577. doi:10.1529/biophysj.106.093690

236. Law R, Carl P, Harper S, Dalhaimer P, Speicher DW, Discher DE (2003) Cooperativity in forced unfolding of tandem spectrin repeats. Biophys J 84(1):533–544

237. Kusunoki H, MacDonald RI, Mondragón A (2004) Structural insights into the stability and flexibility of unusual erythroid spectrin repeats. Structure 12(4):645–656

238. Fuson KL, Ma L, Sutton RB, Oberhauser AF (2009) The c2 domains of human synaptotagmin 1 have distinct mechanical properties. Biophys J 96(3):1083–1090

239. Fuson KL, Montes M, Robert JJ, Sutton RB (2007) Structure of human synaptotagmin 1 C2AB in the absence of Ca2+ reveals a novel domain association. Biochemistry 46(45):13041–13048

240. Peng Q, Li H (2008) Atomic force microscopy reveals parallel mechanical unfolding pathways of T4 lysozyme: evidence for a kinetic partitioning mechanism. Proc Natl Acad Sci 105(6):1885–1890

241. Nicholson H, Anderson D, Dao Pin S, Matthews B (1991) Analysis of the interaction between charged side chains and the. alpha.-helix dipole using designed thermostable mutants of phage T4 lysozyme. Biochemistry 30(41):9816–9828

242. Oberhauser AF, Marszalek PE, Erickson HP, Fernandez JM (1998) The molecular elasticity of the extracellular matrix protein tenascin. Nature 393(6681):181–185

243. Ng SP, Rounsevell RW, Steward A, Geierhaas CD, Williams PM, Paci E, Clarke J (2005) Mechanical unfolding of TNfn3: the unfolding pathway of a fnIII domain probed by protein engineering, AFM and MD simulation. J Mol Biol 350(4):776–789

244. Leahy DJ, Hendrickson WA, Aukhil I, Erickson HP (1992) Structure of a fibronectin type III domain from tenascin phased by MAD analysis of the selenomethionyl protein. Science 258(5084):987–991

245. Carrion-Vazquez M, Oberhauser AF, Fowler SB, Marszalek PE, Broedel SE, Clarke J, Fernandez JM (1999) Mechanical and chemical unfolding of a single protein: a comparison. Proc Natl Acad Sci 96(7):3694–3699

246. Stacklies W, Vega MC, Wilmanns M, Grater F (2009) Mechanical network in titin immunoglobulin from force distribution analysis. PLoS Comput Biol 5(3):e1000306. doi:10.1371/journal.pcbi.1000306

247. Puchner EM, Alexandrovich A, Kho AL, Hensen U, Schäfer LV, Brandmeier B, Gräter F, Grubmüller H, Gaub HE, Gautel M (2008) Mechanoenzymatics of titin kinase. Proc Natl Acad Sci 105(36):13385–13390

248. Mayans O, van der Ven PF, Wilm M, Mues A, Young P, Fürst DO, Wilmanns M, Gautel M (1998) Structural basis for activation of the titin kinase domain during myofibrillogenesis. Nature 395(6705):863–869

249. Greene DN, Garcia T, Sutton RB, Gernert KM, Benian GM, Oberhauser AF (2008) Single-molecule force spectroscopy reveals a stepwise unfolding of *Caenorhabditis elegans* giant protein kinase domains. Biophys J 95(3):1360–1370

250. Kobe B, Heierhorst J, Feil SC, Parker MW, Benian GM, Weiss KR, Kemp BE (1996) Giant protein kinases: domain interactions and structural basis of autoregulation. EMBO J 15(24):6810–6821

251. Sharma D, Perisic O, Peng Q, Cao Y, Lam C, Lu H, Li H (2007) Single-molecule force spectroscopy reveals a mechanically stable protein fold and the rational tuning of its mechanical stability. Proc Natl Acad Sci 104(22):9278–9283

252. Kuhlman B, Dantas G, Ireton GC, Varani G, Stoddard BL, Baker D (2003) Design of a novel globular protein fold with atomic-level accuracy. Science 302(5649):1364–1368

253. Carrion-Vazquez M, Li H, Lu H, Marszalek PE, Oberhauser AF, Fernandez JM (2003) The mechanical stability of ubiquitin is linkage dependent. Nat Struct Mol Biol 10(9):738–743

254. Vijay-Kumar S, Bugg CE, Cook WJ (1987) Structure of ubiquitin refined at 1.8 Å resolution. J Mol Biol 194(3):531–544

255. Isralewitz B, Gao M, Schulten K (2001) Steered molecular dynamics and mechanical functions of proteins. Curr Opin Struct Biol 11(2):224–230

256. Neumann J, Gottschalk K-E (2009) The effect of different force applications on the protein-protein complex barnase-barstar. Biophys J 97(6):1687–1699

257. Gao M, Craig D, Lequin O, Campbell ID, Vogel V, Schulten K (2003) Structure and functional significance of mechanically unfolded fibronectin type III1 intermediates. Proc Natl Acad Sci 100(25):14784–14789

258. Krammer A, Lu H, Isralewitz B, Schulten K, Vogel V (1999) Forced unfolding of the fibronectin type III module reveals a tensile molecular recognition switch. Proc Natl Acad Sci 96(4):1351–1356

259. Lee W, Strümpfer J, Bennett V, Schulten K, Marszalek PE (2012) Mutation of conserved histidines alters tertiary structure and nanomechanics of consensus ankyrin repeats. J Biol Chem 287(23):19115–19121. doi:10.1074/jbc.M112.365569

260. Paramore S, Voth GA (2006) Examining the influence of linkers and tertiary structure in the forced unfolding of multiple-repeat spectrin molecules. Biophys J 91(9):3436–3445

261. Paci E, Karplus M (2000) Unfolding proteins by external forces and temperature: the importance of topology and energetics. Proc Natl Acad Sci USA 97(12):6521–6526

262. Cao Y, Er KS, Parhar R, Li H (2009) A force spectroscopy based single molecule metal binding assay. Chemphyschem 10(9–10):1450–1454

263. Cao Y, Balamurali M, Sharma D, Li H (2007) A functional single-molecule binding assay via force spectroscopy. Proc Natl Acad Sci 104(40):15677–15681

264. Bertz M, Rief M (2009) Ligand binding mechanics of maltose binding protein. J Mol Biol 393(5):1097–1105

265. Krasnoslobodtsev AV, Peng J, Asiago JM, Hindupur J, Rochet J-C, Lyubchenko YL (2012) Effect of spermidine on misfolding and interactions of alpha-synuclein. PLoS One 7(5):e38099

266. Kim B-H, Palermo NY, Lovas S, Zaikova T, Keana JF, Lyubchenko YL (2011) Single-molecule atomic force microscopy force spectroscopy study of Aβ-40 interactions. Biochemistry 50(23):5154–5162

267. Lv Z, Condron MM, Teplow DB, Lyubchenko YL (2013) Nanoprobing of the effect of Cu2+ cations on misfolding, interaction and aggregation of amyloid β peptide. J Neuroimmune Pharmacol 8(1):262–273

268. Schwesinger F, Ros R, Strunz T, Anselmetti D, Güntherodt H-J, Honegger A, Jermutus L, Tiefenauer L, Plückthun A (2000) Unbinding forces of single antibody-antigen complexes correlate with their thermal dissociation rates. Proc Natl Acad Sci 97(18):9972–9977

269. Berquand A, Xia N, Castner DG, Clare BH, Abbott NL, Dupres V, Adriaensen Y, Dufrêne YF (2005) Antigen binding forces of single antilysozyme Fv fragments explored by atomic force microscopy. Langmuir 21(12):5517–5523

270. Kienberger F, Kada G, Mueller H, Hinterdorfer P (2005) Single molecule studies of antibody–antigen interaction strength versus intra-molecular antigen stability. J Mol Biol 347(3):597–606

271. Bonanni B, Kamruzzahan A, Bizzarri A, Rankl C, Gruber H, Hinterdorfer P, Cannistraro S (2005) Single molecule recognition between cytochrome C 551 and gold-immobilized azurin by force spectroscopy. Biophys J 89(4):2783–2791

272. De Paris R, Strunz T, Oroszlan K, Güntherodt H-J, Hegner M (2000) Force spectroscopy and dynamics of the biotin-avidin bond studied by scanning force microscopy. Single Molecules 1(4):285–290

273. Baumgartner W, Hinterdorfer P, Ness W, Raab A, Vestweber D, Schindler H, Drenckhahn D (2000) Cadherin interaction probed by atomic force microscopy. Proc Natl Acad Sci 97(8):4005–4010

274. Leckband D, Sivasankar S (2012) Cadherin recognition and adhesion. Curr Opin Cell Biol 24(5):620–627

275. Bartels FW, Baumgarth B, Anselmetti D, Ros R, Becker A (2003) Specific binding of the regulatory protein ExpG to promoter regions of the galactoglucan biosynthesis gene cluster of *Sinorhizobium meliloti* − a combined molecular biology and force spectroscopy investigation. J Struct Biol 143(2):145–152

276. Hinterdorfer P, Kienberger F, Raab A, Gruber HJ, Baumgartner W, Kada G, Riener C, Wielert-Badt S, Borken C, Schindler H (2000) Poly (ethylene glycol): an ideal spacer for molecular recognition force microscopy/spectroscopy. Single Molecules 1(2):99–103

277. Schmitt L, Ludwig M, Gaub HE, Tampe R (2000) A metal-chelating microscopy tip as a new toolbox for single-molecule experiments by atomic force microscopy. Biophys J 78(6):3275–3285

278. Taranta M, Bizzarri AR, Cannistraro S (2008) Probing the interaction between p53 and the bacterial protein azurin by single molecule force spectroscopy. J Mol Recognit 21(1):63–70

279. Fritz J, Katopodis AG, Kolbinger F, Anselmetti D (1998) Force-mediated kinetics of single P-selectin/ligand complexes observed by atomic force microscopy. Proc Natl Acad Sci 95(21):12283–12288

280. Kim M, Wang CC, Benedetti F, Marszalek PE (2012) A nanoscale force probe for gauging intermolecular interactions. Angew Chem 124(8):1939–1942

281. Tang J, Ebner A, Badelt-Lichtblau H, Völlenkle C, Rankl C, Kraxberger B, Leitner M, Wildling L, Gruber HJ, Sleytr UB (2008) Recognition imaging and highly ordered molecular templating of bacterial S-layer nanoarrays containing affinity-tags. Nano Letters 8(12):4312–4319

282. Garcia-Manyes S, Badilla CL, Alegre-Cebollada J, Javadi Y, Fernández JM (2012) Spontaneous dimerization of titin protein Z1Z2 domains induces strong nanomechanical anchoring. J Biol Chem 287(24):20240–20247. doi:10.1074/jbc.M112.355883

283. Lv S, Dudek DM, Cao Y, Balamurali M, Gosline J, Li H (2010) Designed biomaterials to mimic the mechanical properties of muscles. Nature 465(7294):69–73

284. Cluzel P, Lebrun A, Heller C, Lavery R, Viovy J-L, Chatenay D, Caron F (1996) DNA: an extensible molecule. Science 271:792–794

285. Cocco S, Yan J, Leger J-F, Chatenay D, Marko JF (2004) Overstretching and force-driven strand separation of double-helix DNA. Phys Rev E 70(1):011910

286. Leger J, Romano G, Sarkar A, Robert J, Bourdieu L, Chatenay D, Marko J (1999) Structural transitions of a twisted and stretched DNA molecule. Phys Rev Lett 83(5):1066

287. Strick T, Dessinges M, Charvin G, Dekker N, Allemand J, Bensimon D, Croquette V (2003) Stretching of macromolecules and proteins. Rep Prog Phys 66(1):1

288. van Mameren J, Gross P, Farge G, Hooijman P, Modesti M, Falkenberg M, Wuite GJ, Peterman EJ (2009) Unraveling the structure of DNA during overstretching by using multicolor, single-molecule fluorescence imaging. Proc Natl Acad Sci 106(43):18231–18236

289. Williams MC, Rouzina I, Bloomfield VA (2002) Thermodynamics of DNA interactions from single molecule stretching experiments. Acc Chem Res 35(3):159–166

290. Williams MC, Rouzina I, McCauley MJ (2009) Peeling back the mystery of DNA overstretching. Proc Natl Acad Sci 106(43):18047–18048

291. Williams MC, Wenner JR, Rouzina I, Bloomfield VA (2001) Entropy and heat capacity of DNA melting from temperature dependence of single molecule stretching. Biophys J 80(4):1932–1939

292. Bustamante C, Smith SB, Liphardt J, Smith D (2000) Single-molecule studies of DNA mechanics. Curr Opin Struct Biol 10(3):279–285

293. Baumann CG, Smith SB, Bloomfield VA, Bustamante C (1997) Ionic effects on the elasticity of single DNA molecules. Proc Natl Acad Sci 94(12):6185–6190

294. Wang MD, Yin H, Landick R, Gelles J, Block SM (1997) Stretching DNA with optical tweezers. Biophys J 72(3):1335–1346

295. Wenner JR, Williams MC, Rouzina I, Bloomfield VA (2002) Salt dependence of the elasticity and overstretching transition of single DNA molecules. Biophys J 82(6):3160

296. Chiou C-H, Huang Y-Y, Chiang M-H, Lee H-H, Lee G-B (2006) New magnetic tweezers for investigation of the mechanical properties of single DNA molecules. Nanotechnology 17(5):1217

297. Goodman RP, Schaap IA, Tardin CF, Erben CM, Berry RM, Schmidt CF, Turberfield AJ (2005) Rapid chiral assembly of rigid DNA building blocks for molecular nanofabrication. Science 310(5754):1661–1665

298. Morii T, Mizuno R, Haruta H, Okada T (2004) An AFM study of the elasticity of DNA molecules. Thin Solid Films 464:456–458

299. Vafabakhsh R, Ha T (2012) Extreme bendability of DNA less than 100 base pairs long revealed by single-molecule cyclization. Science 337(6098):1097–1101

300. Ke C, Humeniuk M, S-Gracz H, Marszalek PE (2007) Direct measurements of base stacking interactions in DNA by single-molecule atomic-force spectroscopy. Phys Rev Lett 99(1):018302–018304

301. W-s C, Chen W-H, Chen Z, Gooding AA, Lin K-J, Kiang C-H (2010) Direct observation of multiple pathways of single-stranded DNA stretching. Phys Rev Lett 105(21):218104

302. Ke C, Loksztejn A, Jiang Y, Kim M, Humeniuk M, Rabbi M, Marszalek PE (2009) Detecting solvent-driven transitions of poly (A) to double-stranded conformations by atomic force microscopy. Biophys J 96(7):2918–2925

303. Seol Y, Skinner GM, Visscher K, Buhot A, Halperin A (2007) Stretching of homopolymeric RNA reveals single-stranded helices and base-stacking. Phys Rev Lett 98(15):158103

304. Rief M, Clausen-Schaumann H, Gaub HE (1999) Sequence-dependent mechanics of single DNA molecules. Nat Struct Mol Biol 6(4):346–349

305. Clausen-Schaumann H, Rief M, Tolksdorf C, Gaub HE (2000) Mechanical stability of single DNA molecules. Biophys J 78(4):1997–2007

306. Lee G, Rabbi M, Clark RL, Marszalek PE (2007) Nanomechanical fingerprints of UV damage to DNA. Small 3(5):809–813

307. Saenger W (1984) Principles of nucleic acid structure, vol 7. Springer-Verlag, New York

308. Marszalek PE, Pang YP, Li HB, El Yazal J, Oberhauser AF, Fernandez JM (1999) Atomic levers control pyranose ring conformations. Proc Natl Acad Sci USA 96(14):7894–7898

309. Zhang QM, Lee GR, Marszalek PE (2005) Atomic cranks and levers control sugar ring conformations. J Phys Condens Matter 17(18):S1427–S1442

310. Zhang QM, Marszalek PE (2006) Solvent effects on the elasticity of polysaccharide molecules in disordered and ordered states by single-molecule force spectroscopy. Polymer 47(7):2526–2532

311. Li HB, Rief M, Oesterhelt F, Gaub HE, Zhang X, Shen JC (1999) Single-molecule force spectroscopy on polysaccharides by AFM – nanomechanical fingerprint of alpha-(1,4)-linked polysaccharides. Chem Phys Lett 305(3–4):197–201
312. Lee W, Zeng X, Yang W, Marszalek PE (2012) Mechanics of polysaccharides. In: Anne-Sophie Duwez NW (ed) Molecular manipulation with atomic force microscopy. CRC Press, Boca Raton/London/New York
313. Lee G, Nowak W, Jaroniec J, Zhang Q, Marszalek PE (2004) Nanomechanical control of glucopyranose rotamers. J Am Chem Soc 126(20):6218–6219
314. Lee G, Nowak W, Jaroniec J, Zhang Q, Marszalek PE (2004), Molecular dynamics simulations of forced conformational transitions in 1,6-linked polysaccharides. Biophys J, 87(3):1456–1465.
315. Li H, Rief M, Oesterhelt F, Gaub HE (1999) Force spectroscopy on single xanthan molecules. Appl Phys A-Mater Sci Process 68(4):407–410
316. Li HB, Rief M, Oesterhelt F, Gaub HE (1998) Single-molecule force spectroscopy on Xanthan by AFM. Adv Mater 10(4):316–319
317. Marszalek PE, Li HB, Fernandez JM (2001) Fingerprinting polysaccharides with single-molecule atomic force microscopy. Nat Biotechnol 19(3):258–262
318. Marszalek PE, Li HB, Oberhauser AF, Fernandez JM (2002) Chair-boat transitions in single polysaccharide molecules observed with force-ramp AFM. Proc Natl Acad Sci USA 99(7):4278–4283
319. Zhang Q, Jaroniec J, Lee G, Marszalek PE (2005) Direct detection of inter-residue hydrogen bonds in polysaccharides by single-molecule force spectroscopy. Angew Chem Int Ed 44(18):2723–2727
320. Zhang Q, Lu Z, Hu H, Yang W, Marszalek PE (2006) Direct detection of the formation of V-Amylose helix by single molecule force spectroscopy. J Am Chem Soc 128(29):9387–9393
321. Zhang Q, Marszalek PE (2006) Solvent effects on the elasticity of polysaccharide molecules in disordered and ordered states by single-molecule force spectroscopy. Polymer 47(7):2526–2532
322. Lu ZY, Nowak W, Lee GR, Marszalek PE, Yang WT (2004) Elastic properties of single amylose chains in water: a quantum mechanical and AFM study. J Am Chem Soc 126(29):9033–9041
323. Lee G, Nowak W, Jaroniec J, Zhang Q, Marszalek PE (2004) Molecular dynamics simulations of forced conformational transitions in 1,6-linked polysaccharides. Biophys J 87(3):1456–1465
324. Zhang QM, Marszalek PE (2006) Identification of sugar isomers by single-molecule force spectroscopy. J Am Chem Soc 128(17):5596–5597
325. Xu Q, Zhang W, Zhang X (2002) Oxygen bridge inhibits conformational transition of 1,4-linked -galactose detected by single-molecule atomic force microscopy. Macromolecules 35(3):871–876
326. Marszalek PE, Oberhauser AF, Li HB, Fernandez JM (2003) The force-driven conformations of heparin studied with single molecule force microscopy. Biophys J 85(4):2696–2704
327. Zhang L, Wang C, Cui S, Wang Z, Zhang X (2003) Single-molecule force spectroscopy on curdlan: unwinding helical structures and random coils. Nano Lett 3(8):1119–1124. doi:10.1021/nl034298d
328. Struckmeier J, Wahl R, Leuschner M, Nunes J, Janovjak H, Geisler U, Hofmann G, Jähnke T, Müller DJ (2008) Fully automated single-molecule force spectroscopy for screening applications. Nanotechnology 19(38):384020
329. Churnside AB, Sullan RMA, Nguyen DM, Case SO, Bull MS, King GM, Perkins TT (2012) Routine and timely sub-picoNewton force stability and precision for biological applications of atomic force microscopy. Nano Lett 12(7):3557–3561

Properties of DNA

34

Ronnie Pedersen, Alexandria N. Marchi, Jacob Majikes,
Jessica A. Nash, Nicole A. Estrich, David S. Courson, Carol K. Hall,
Stephen L. Craig, and Thomas H. LaBean

Keywords

DNA • Deoxyribonucleic acid • Properties • Structural DNA nanotechnology
• Self-assembly

Introduction

This chapter is targeted towards researchers both inside and outside the field of
nanomaterials. For those without experience in DNA-based nanotechnology, it will
serve as an introduction to important concepts, background, and properties of DNA
as a biopolymer, a chemical, a material, and a medium for nanofabrication and
molecular computation. For specialists in DNA nanotech, this chapter will serve as
a review and reminder of the most important properties of DNA, hopefully provid-
ing fresh insights to enhance problem solving and new viewpoints leading to novel
research directions.

R. Pedersen
Duke University, Durham, NC, USA

A.N. Marchi
Department of Biomedical Engineering, Duke University, Durham, NC, USA

J. Majikes • J.A. Nash • N.A. Estrich • D.S. Courson • T.H. LaBean (✉)
Department of Materials Science and Engineering, North Carolina State University,
Raleigh, NC, USA
e-mail: thlabean@ncsu.edu

C.K. Hall
Department of Chemical and Biomolecular Engineering , North Carolina State University,
Raleigh, NC, USA

S.L. Craig
Chemistry Department, Duke University, Durham, NC, USA

Table 34.1 Dimensions of DNA

	dsDNA (B form) [1, 2]	ssDNA [3]
Pitch (nm)	3.36	
Repeat length: BP/turn	10.5	
Helix width (nm)	2.2–2.6	
Major groove width (nm)	1.17	
Major groove depth (nm)	0.87	
Minor groove width (nm)	0.57	
Minor groove depth (nm)	0.75	
Rise/BP (nm)	0.33	0.6
Charge/length (e⁻/nm)	6	1.66
Persistence length (nm)	50	1.5–3

The use of DNA as a nanoscale construction material has come to be known as structural DNA nanotechnology – in order to differentiate it from the field of biotechnology, in which DNA is used to encode genetic information for altering living cells, for example, by reprogramming them to produce novel or transplanted proteins. The primary goal of structural DNA nanotechnology is to exploit complementary base pairing in order to program the self-assembly of molecules into supramolecular complexes with desired properties. In separate sections, we will examine the properties of DNA from the following points of view: chemical, mechanical, biological, optical, electrical, informational, and structural.

Chemical Properties of DNA

The importance of DNA for biological processes cannot be overstated. It is a biological polymer with a simple, yet robust information-encoding system. DNA's fundamental structure leads to efficient replication and transmission of encoded genetic information. DNA has also been recognized as a unique material for various nanotechnology applications (see section 'DNA as a Self-Assembling Construction Material' below). A fundamental understanding of DNA starts at the level of chemical structure and properties.

Basic Structure

Most people are familiar with the double-helical model of a double-stranded DNA molecular complex (dsDNA). In this chapter, unless otherwise stated, we will discuss this canonical DNA structure (right-handed, B-form DNA). Specific dimensions and feature sizes of B-form dsDNA as well as ssDNA are summarized in Table 34.1. The other common helix forms include A- and Z-form (see Fig. 34.1). A-form dsDNA resembles the double-helical form of RNA, is often seen in dehydrated samples of DNA, and has a shorter, more-compact helix than B-form dsDNA. Z-form dsDNA has a left-handed helix and is promoted under solution
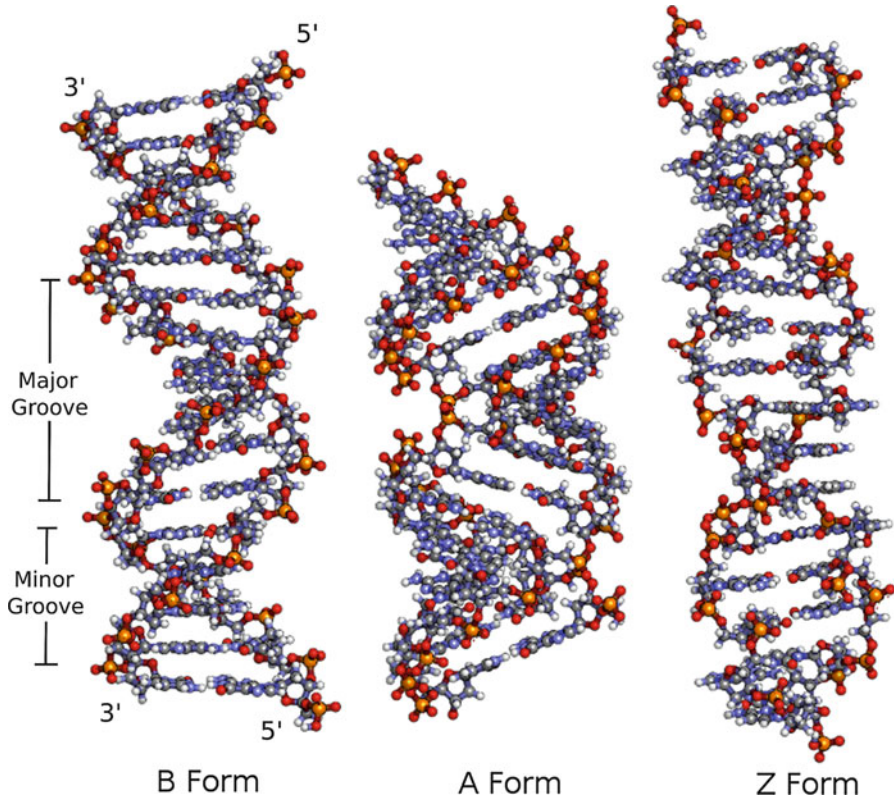
Fig. 34.1 The three most common types of DNA helices. B-form DNA is right-handed, with 10.5 base pairs per helical turn. It is the normal, expected form of dsDNA under physiological-like solution conditions. The narrower *minor groove* and wider *major groove* are indicated. A-form DNA is also right-handed and has a shorter more-compact helix with 10 bases per turn. Z-DNA is left-handed and slightly stretched with 12 bases per full turn of the helix

conditions involving certain salts (especially hexamminecobalt chloride) or by high torsional strain of the helix [1].

The fundamental unit of the DNA polymer is the nucleotide monomer. It consists of three covalently linked chemical motifs: an aromatic nucleobase, a deoxyribose sugar, and a phosphate group. Nucleobases are divided into two classes: pyrimidines and purines (Fig. 34.2). The canonical purines are adenine (A) and guanine (G) and the canonical pyrimidines are cytosine (C) and thymine (T). Numerous other nucleobases, including uracil (U) which replaces thymine in RNA, are found in natural and synthetic systems but they will not be addressed here. In dsDNA, nucleobases on opposite antiparallel backbone strands interact with one another to form 'Watson-Crick' hydrogen bonding base pairs. Adenine forms two stable hydrogen bonds with thymine, and guanine forms three stable hydrogen bonds with cytosine. The base-pairing hydrogen bonds provide the specificity for strand-strand hybridization, while the hydrophobic (π-π) base stacking provides the
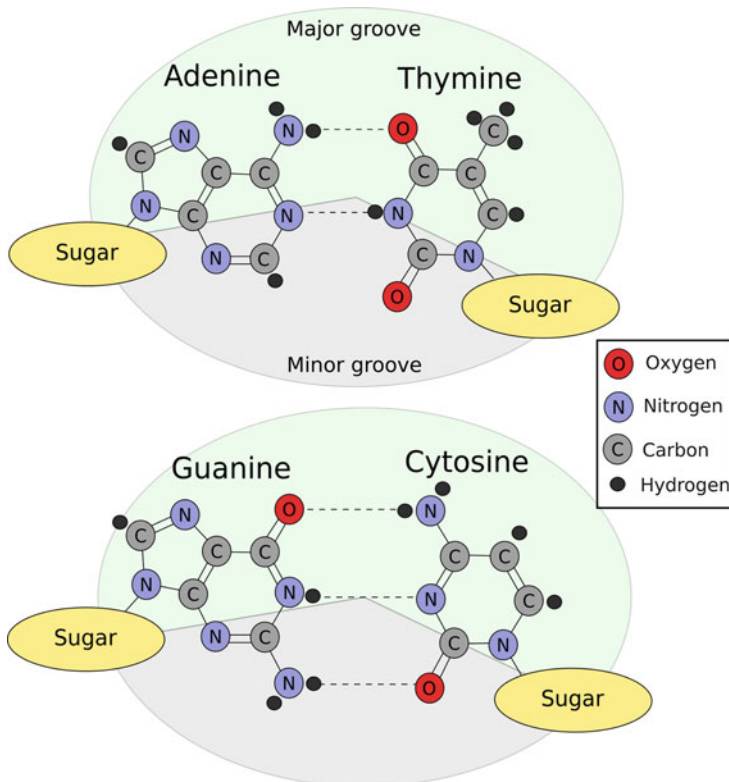
Fig. 34.2 The nucleobases on the *left* are purines; those on the *right* are pyrimidines. The *dotted lines* indicate Watson-Crick hydrogen bonding pairs. DNA helices have major and minor grooves; the latter is defined as the side of the helix the sugars are bound on, the lower half in this figure

energetic driving force [1, 4]. Although G-C pairs contribute greater stabilization free energy to dsDNA than do A-T pairs, this is due to their base stacking interactions rather than to the additional hydrogen bond in a G-C pair, as often mistakenly stated. The strength of base stacking interactions is evidenced by the tendency of assembled DNA structures consisting of multiple, blunt-ended helices to stack their ends and cluster next to one another on surfaces [5–7].

The DNA backbone consists of alternating ribose sugars and phosphate groups (see Fig. 34.3). The ribose sugar is connected to the nucleobase at the 1′ carbon position of the sugar; the phosphate bridges the 5′ and 3′ positions of alternating sugars. Directionality of the sugar-phosphate backbone in ssDNA stems from this asymmetry in bonding; thus, the molecule will have distinct termini, noted as the 5′ and 3′ ends. Formation of a dsDNA complex from two ssDNA molecules requires alignment of two strands with (mostly) complementary sequences in an antiparallel orientation with respect to their backbones. Parallel backbone orientation prevents proper hydrogen bonding between the bases as well as significant loss of aromatic base stacking that is seen in well-ordered B-form dsDNA [1].

Fig. 34.3 A ribose sugar is depicted bounded by two phosphate groups. The *upper* group is bound to the 5′ carbon and the *lower* to the 3′ carbon. The 5′ to 3′ direction of the strand runs down the page. The base is bound to the 1′ carbon
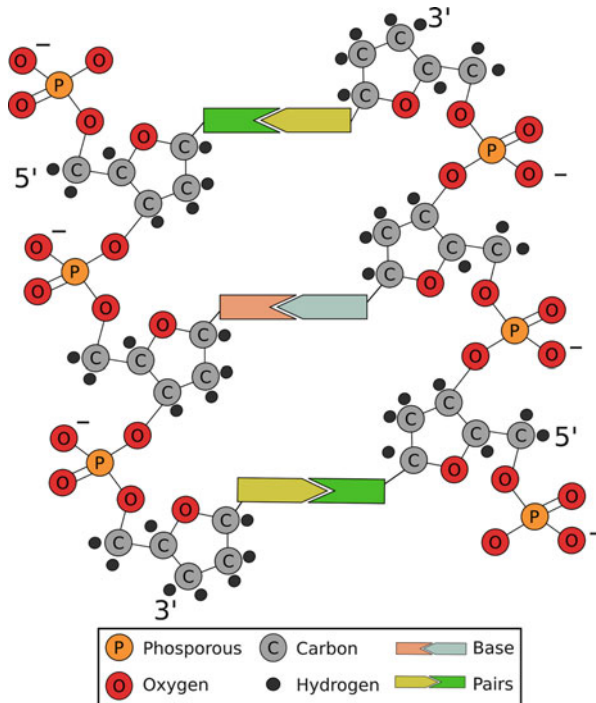
Noncanonical Hydrogen Bonding

Despite the normal base-pairing rules stated above, nucleic acids are capable of forming noncanonical hydrogen bonding arrangements, with both parallel and antiparallel backbone orientations. The majority of these, however, cannot hydrogen bond along a continuous helix. Ionization of functional groups in nucleobases can provide further opportunities for noncanonical bonding; at low or high pH, the N, NH, OH, and CO groups which participate in hydrogen bonding can become protonated or deprotonated, allowing for a variety of hydrogen bonding pairs. These arrangements are relatively rare in physiological pH ranges (between 4 and 9) and are less stable than well-formed duplex. Two of these structures which are of particular interest due to their stability and use in self-assembling DNA nanomaterials are the G-quartet and the I-motif. The G-quartet motif consists of four guanine nucleobases as depicted in Fig. 34.4. G-quartets were discovered with parallel chain directions but can form in a variety of parallel and antiparallel configurations [8, 9]. Multiple, stacked, G-quartets are often referred to as G-quadruplexes.

The I-motif is similar to the G-quartet and consists of C groups intercalating and hydrogen bonding diagonally between strands as shown in Fig. 34.4 [10]. The I-motif is only stable at low pH when the cytosine nucleobases are protonated [10, 11]. In contrast, G-quartets are as stable as dsDNA but with significantly slower
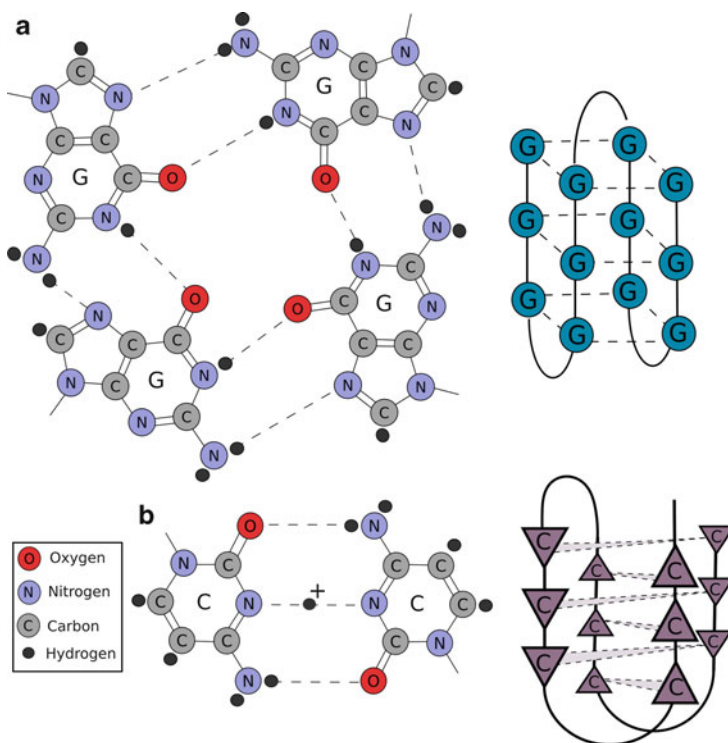
Fig. 34.4 Examples of noncanonical base pairing. (**a**) A G-quartet is depicted with hydrogen bonding between four guanine nucleobases. An example of G-quadruplex is shown with a single strand of DNA folding into the full structure. (**b**) An I-motif is depicted with two protonated cytosine nucleobases. The cytosines intercalate vertically to maximize base stacking

unfolding kinetics [8, 12]. Both G-quartets and I-motifs have been exploited for their potential in nanotechnology applications [11, 13–16].

Major and Minor Grooves

The rungs (bases) of the dsDNA ladder do not protrude from the rails (sugar-phosphate backbone) and join at 180°. Rather, the rungs are bent at an angle of about 146° on one side and 214° on the other, when looking down the helix axis. As shown in Fig. 34.2, the sides of the bases closest to the sugars form the minor groove, and the side farthest from the sugar forms the major groove (see also Fig. 34.1 for wider view of the two grooves). The major and minor grooves play significant roles in the behavior of dsDNA. As the phosphate groups are slightly negatively charged, the minor groove has a significantly higher negative charge density than the major groove. This charge density encourages salts, and some positively charged proteins, to bind to dsDNA along the minor groove without AT/GC sequence specificity [17, 18].

Further, bending the helix increases the negative charge density at the bent region. As the helices bend, intertwine, or simply enter into proximity, electrostatic screening is necessary to accommodate the charges. This is particularly true for nanotechnology purposes as many helices must be in very close proximity for successful self-assembly during annealing.

Thermal Melting and Annealing

Determination of the melting temperature (T_m) of a dsDNA complex into its constituent ssDNA molecules requires experimental measurement via techniques such as differential scanning calorimetry (DSC) or ultraviolet absorption spectroscopy (UV–vis, discussed in optical properties section). An approximate melting temperature can be predicted based solely on the nucleobase sequences with a variety of formulas. Most of these formulas assume specific conditions such as buffer composition and DNA concentration. Use of approximate melting temperatures instead of direct empirical measurement can be useful when working with nanotechnology applications where sample sizes may be exceedingly small or expensive.

Predictive equations for T_m are parameterized from experimental data and typically are algebraic relationships addressing information such as AT/GC content, strand length, salt concentration, and pH [19, 20]. In general, A-T pairs contribute less to the enthalpy of melting than do G-C pairs, ensuring that the T_m changes with AT/GC content. Numerous programs and websites are freely available to calculate the melting temperature of dsDNA under typical solution conditions and will often compare multiple predictive formulae [21]. Base pair mismatches between strands lower stability and therefore the T_m, of the resulting dsDNA. The degree of this change can vary depending on the type of mismatch and local sequence but is typically between 0.6 °C and 1.5 °C for each 1 % sequence mismatch [22]. Steric hindrance due to molecular crowding or surface interactions may also affect T_m [23]. In nanotechnology applications, this can be especially relevant, particularly in situations requiring dense strand packing on surfaces. Steric concerns are often addressed via the addition of ssDNA spacers (consisting of only T or A residues) between functional groups such as thiols or biotin moieties and the sequence responsible for specific binding [24, 25].

Salt Effects

As mentioned above, the formation of dsDNA from ssDNA creates a region of increased negative charge density around the minor groove. This increase in charge density is unfavorable without the presence of counterions that screen the backbone charges and improve the energetics of duplex formation [1, 26]. Counterions are especially important for systems that rely on DNA for self-assembly where many of the helices wind up being close together. Holliday junctions, which are one of the most common motifs used in DNA nanotechnology (see section

Fig. 34.5 Variations of T_m for solutions of DNA as a function of divalent metal ion concentration [1]: This figure illustrates the importance of cation choice for buffers; the binding locations of divalent cations are often dependent on concentration and drastically effect dsDNA stability
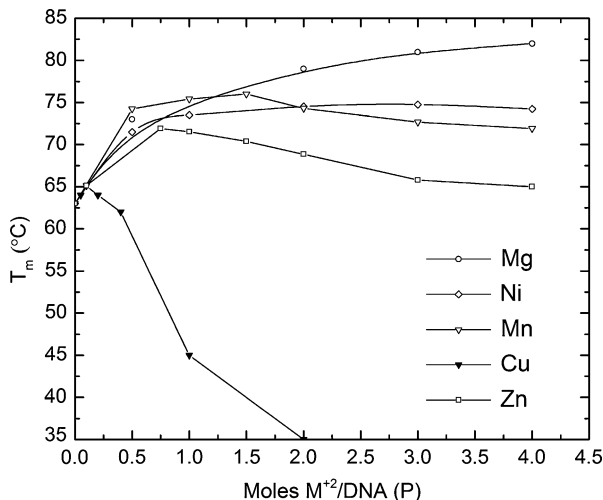
'Holliday Junctions' below), prefer divalent ions [27]. It is for this reason that most buffers used in DNA nanotechnology applications carefully control the concentration of divalent cations, such as Mg^{2+}.

Monovalent cations such as Na^+ typically increase the stability of B-DNA up to a concentration of ∼1 M. The T_m generally increases linearly with $\log[Na^+]$. Above 1 M, the T_m of dsDNA is decreased by additional monovalent ions. Monovalent cations typically coordinate with the phosphate of the DNA backbone [28]. Divalent cations such as Mg^{2+} show evidence of site-selective binding to the negatively charged phosphates along the DNA strand. However, unlike monovalent cations, divalent cations can also bind to the nucleobases. This can result in destabilization of the helix, and decreased T_m, at higher salt concentrations. Figure 34.5 shows the change in DNA melting temperature that is brought about by varying the concentration of several divalent cations [1, 29].

Solvent Effects

Typically, the addition of organic solvents to water reduces the stability of dsDNA and decreases the T_m roughly linearly with solvent concentration [30]. In particular, formamide has a fairly linear effect on T_m, which changes by ∼0.62–0.72 °C per % formamide content [1, 31]. This decrease in T_m with formamide has been attributed to increasingly favorable base/solvent interactions and has been used as a substitute for thermal denaturation in the annealing of DNA nanostructures, allowing self-assembly to occur without thermal cycling [32, 33]. Solvent effects are also exploited during DNA purification. The most common method by far is ethanol precipitation. Other methods exist, however, including the use of alkaline solutions to separate circular dsDNA from linear, using cetyltrimethylammonium bromide (CTAB) in low ionic strength solution [34, 35].

Changes in pH within the range 5–9 have a negligible effect on the melting/annealing of dsDNA systems [36, 37]. Below pH 4, the nucleobases become protonated, interfering with hydrogen bonding and making the unhybridized single strand more hydrophilic. At significantly higher pH, the G and T bases become deprotonated, thus preventing Watson-Crick hydrogen bonding. As such, high and low pH can rapidly denature dsDNA.

Backbone Cleavage

The dsDNA backbone can be readily cleaved by hydrolysis of the phosphodiester bond between the phosphate and ribose groups. The mechanism is that of an addition-elimination reaction. During hydrolysis, the phosphorus is attacked and becomes the center of a trigonal bipyramidal intermediate that subsequently eliminates phosphate. In the hydrolysis, the oxygen attached to the 3′ of the sugar is the leaving group, and it is in-line from the attacking group. Base catalysis accelerates the addition step by virtue of increasing the concentration of the attacking hydroxide ion. Acid catalysis accelerates the elimination step, during which the leaving oxygen is protonated to become a hydroxyl. Metal catalysis encourages cleavage by neutralizing the negative charge of the intermediate state. The end result is a 3′ hydroxyl group separated from a 5′ phosphate. This, and the requirement of many nucleases for divalent cations, is why, for long-term storage, DNA should be stored in buffer that includes chelating agents like EDTA and be buffered at neutral pH [1].

Chemical Cross-Linking and Modification of DNA

Many chemicals are available to chemically cross-link dsDNA so that single strands become covalently linked. A common cross-linker is psoralen, a heterocyclic compound which intercalates between two nucleobases. When hit with a photon of 300–400 nm, psoralen will form a covalent cross-link if the nucleobase pairs above and below it have pyrimidines on opposite sides of the dsDNA [38]. Glutaraldehyde and formaldehyde are used to form cross-links to lysine residues in proteins [1]. Unsaturated aldehydes [39], cisplatin, and nitrogen mustards [40] have also been used to form interstrand chemical cross-links.

During chemical synthesis, DNA can also be chemically modified to provide various capabilities such as additional chemical linkages, attachment of fluorophores, or nuclease resistance. Chemical linkers are often placed at the 5′ and 3′ positions. Chemical linkers include thiols or amines for binding to metals or other surfaces, alkynes and azides for click chemistry, as well as biotin labels for strong, non-covalent binding with avidin protein. Nonnatural nucleobase incorporation as well as other chemical modifications can be used for a variety of purposes.

Synthesis

In recent years, a dramatic reduction in the price of custom synthetic DNA oligonucleotides has made it feasible for researchers to buy specific DNA strands for applications from nanotechnology to whole gene synthesis. The synthesis of DNA is typically performed via solid-phase phosphoramidite chemistry. In this method, the 3′ terminal monomer is attached to a solid support (typically silica), and then, the next monomer (with a protected 5′ end) is attached to the 5′ end of the first monomer. The 5′-OH of the first monomer and the 3′-phosphoramidite of the second monomer join to make a phosphite diester, which is then oxidized to a phosphate diester, followed by deprotection of the 5′ group of the second monomer. The cycle is repeated until the desired molecule is synthesized. Many advances have been made in this area, particularly in using ink-jet printers to perform the reactions on micron-sized spots on glass or plastic surfaces for rapid, automated synthesis [1, 41–44].

Mechanical Properties of DNA

DNA is a biological polymer that has many unique physical and chemical properties and serves a critical and central role in the function of all known life. For the purposes of this discussion, it is important to remember that there are several different types of molecular and atomic interactions that give DNA its properties including, but not limited to, covalent bonding between atoms in a strand, hydrogen bonding between bases on opposite strands, stacking interactions between bases on the same strand, and solvent interactions. Measurements of DNA mechanical properties must be interpreted with this diverse interaction set in mind.

Curvature and Flexibility

Despite typically being depicted as a rigid rod, DNA can be bent without breaking. Indeed, in the cellular context, it is almost always found in tightly bent and wound conformations. To illustrate this, the extended length of the DNA in a single human cell is between 1.5 and 3.0 m [45], while a typical cell volume is between 200 and 2,730 μm^3 [46]. For a cell volume of 200 μm^3 and a DNA length of 3 m, assuming cells are cubes with side ∼6 μm in length and the DNA is not limited to a smaller nucleus, a single DNA would have to be bent 500,000 times. Another way of approaching the problem is to consider the cylindrical volume of a DNA strand 3 m in length. If we assign B-form DNA a diameter of 2.0 nm [47], the volume of the DNA alone would be ∼90 μm^3. When one considers that the nucleus of a cell typically occupies less than half the volume of the cell, and that much of the cellular DNA must be accessible to the cell at all times, the compaction problem becomes truly staggering. DNA achieves much of this compaction through wrapping around protein oligomers called histones, which have diameters of 10 nm [48]. Despite the

large distortions due to twist and writhe as the DNA packs tightly against these proteins, we are aware of no reports of DNA undergoing material failure as a result of histone packaging.

Theoretical Models of DNA Elasticity and Force-Induced Transitions

Two widely used models that describe the solution structure and molecular mechanics of ssDNA and dsDNA are the freely jointed chain (FJC) model and the wormlike chain (WLC) model [49]. The simplest forms of both models do not directly describe the details of the chain such as base sequence, hydrogen bonding, and helical twist. For the FJC model, a polymer chain is approximated by stiff monomers of a fixed length whose orientations are completely independent of one another. In comparison, for the WLC model, the polymer is approximated as a rigid rod that bends smoothly in response to thermal fluctuations [49, 50]. Due to π-π stacking of the nucleobases and electrostatic repulsions along the sugar-phosphate backbone, dsDNA is a relatively stiff polymer [51]. Thus, the WLC model is better suited to describe the flexibility and force extension behavior of dsDNA than the FJC model.

Predictions of DNA stretching behavior based on these models can be compared to experimental data from single-molecule force extension studies in which one end of the DNA strand is fixed while the other end is pulled. At low forces, extension and force scale linearly; the behavior is well described by both the FJC and WLC models. Because of DNA's stiffness, the forces needed to elongate a strand past its linear regime are very low compared to conventional synthetic polymers [51]. At intermediate forces, the extension curve becomes nonlinear and the more complicated WLC model predicts stretching. For an in-depth review of these models, the reader is referred to the literature [49–52].

When end-to-end tensile forces reach 60–70 pN, dsDNA undergoes a force-induced transition from B-form to the so-called S-form DNA. The generally accepted structure of S-form DNA is based on computer simulations, although the specific structure might depend on the specific attachment points [53]. The B-to-S transition results in a roughly 2.2-fold extension in DNA contour length, beyond which high-energy enthalpic distortions in bond angles are necessary for further extension.

We point out that high forces are only achieved in long dsDNA helices, because short oligomers will dissociate under force. This force-induced duplex melting is a kinetic phenomenon, in which the applied force helps to surmount the activation barrier for duplex dissociation. As such, the force at which dissociation occurs is time scale dependent, but it also depends on dsDNA stability (and hence the same factors of temperature, salt and salt concentration, and sequence discussed above). Additional mechanical properties, such as the torsional stiffness of dsDNA and its interplay with tensile properties, have been studied in recent years, and a full review of dsDNA mechanics is outside the scope of this chapter. The interested reader is referred to recent reviews on the topic [49]. Because nanotechnological

applications of DNA often involve a structural component, it is reasonable to assume that these applications will involve mechanical forces.

Computational Methods to Describe Nucleic Acids

Computational methods are useful for understanding complex behavior of macro-molecules such as their structures and dynamics in solution. The type of information desired will dictate the method used. Molecular dynamic (MD) simulations allow for dynamic properties and interactions within systems to be studied. Other methods, such as Monte Carlo, may be used for structure prediction [54].

For MD simulations, software programs such as AMBER (Assisted Model Building with Energy Refinement) [55] have sets of force fields for the simulation of biomolecules, particularly proteins and nucleic acids. MD may be performed at the atomic level. However, these simulations are computationally expensive; therefore, large systems are often coarse grained. This means that components of the molecule are replaced with less complicated but approximately equivalent models. For example, a DNA base may be replaced by a single pseudo-atom that mimics the behavior of that base. However, it must be assured that the coarse graining accurately represents the system. For an overview of this topic, the reader is referred to the review listed in [54].

A notable example of a computational program relevant to DNA nanotechnology is the program CanDo (computer-aided engineering for DNA origami) [56]. CanDo uses a finite element method to predict the solution structure of DNA origami assemblies (see section 'DNA Scaffolded Origami' below). Double-stranded DNA is approximated as a homogenous elastic rod with mechanical parameters taken from experimental measurements. DNA origami structures are modeled as bundles of rods that are rigidly constrained to their nearest neighbor at specific crossover points. This program currently accounts for bend, twist, and stretch stiffness of DNA. CanDo accurately predicts flexibility and solution shape for many DNA origami nanostructues. However, the model's predictive ability is currently limited to designs on a square or honeycomb lattice and does not consider sequence effects.

Biological Properties of DNA

DNA is the primary information carrier in biology. Its role can be summed up in the *central dogma* which states that DNA codes for DNA and for RNA and RNA codes for protein. That DNA codes for DNA is evident in the way that hereditary information is passed on from parent to progeny. To understand what the rest of the dogma means, we have to know that RNA (ribonucleic acid) is a molecule structurally similar to DNA except it has a hydroxyl group at the $2'$ ribose position. A given DNA sequence will thus have a complementary RNA sequence to which it can anneal. In this way, a piece of DNA sequence – such as a gene – can be

transcribed into a complementary RNA sequence, which can then be translated into a specific protein. Proteins are biological polymers made from 20 types of amino acids, and for any triplet of nucleobases (a codon), the genetic code specifies a specific amino acid. Proteins are the structural and catalytic 'machines' of living cells and thus determine the actions and makeup of the cell. In the following, we will look at how the properties of DNA are intimately tied to its role as the information carrier in living cells.

DNA in Cells and in Molecular Cloning

The central dogma is a universal characteristic of all life as we know it. However, when considering the biological properties of DNA in more detail, we have to differentiate between the major classifications of life. Biologists group different forms of life based on their similarity and relationship. Humans are distinct from apes but more closely related to them than they are to dogs. All three are distinct from plants and again these four share characteristics distinct from an *Escherichia coli* bacterium. At the very root of the classification of life, we find three so-called domains. These are Archaea, Bacteria, and Eucarya with members of Eucarya often referred to as eukaryotes [57]. Members of all three domains have the cell as the basic unit of life. A cell is a lipid membrane encapsulating the molecular machinery required for executing the central dogma. One defining feature of eukaryotes is that they have an additional internal lipid compartment, the nucleus, encapsulating their DNA. This is distinct from Archaea and Bacteria, and for this reason and others, these two domains have often been grouped together as prokaryotes [58]. In the following, we will be primarily concerned with common features and will only distinguish between eukaryotes and Bacteria, disregarding the interesting but less studied Archaea.

In Bacteria, the entire genomic sequence is usually a single circular dsDNA condensed in one area of the cell. For *E. coli*, the size of this molecule is 4.6 Mb (million base pairs). In addition, Bacteria often have smaller auxiliary pieces of dsDNA called plasmids. These are smaller circular molecules that can be replicated independently and transferred between different Bacteria and thus can be used to transfer genetic traits such as antibiotic resistance. This is at the heart of molecular cloning and biotechnology. By inserting a gene of interest in a plasmid and 'transfecting' it into a bacterium, the gene will then be replicated as the cell divides.

This technique is made possible by the use of restriction endonucleases which are a class of enzymes that cleave DNA at specific sequences. Type II endonucleases typically cleave palindromic sequences, meaning sequences that read the same backward and forward. In the context of DNA, this is understood in the way that the sequence that reads $5'$ to $3'$ on one strand reads the same in the $5'$ to $3'$ direction on the complementary strand. By convention, genetic sequences are written $5'$ to $3'$ (see section 'Chemical Properties of DNA' above for a description of DNA chain directionality). For example, the restriction endonuclease *Eco*RI recognizes the sequence $5'$-G · AATTC-$3'$ and cleaves the backbone of both the written strand

and the identical complementary strand (between the G and A). This creates a duplex with a short overhang (4 bases, in this case) called a sticky end. If a genetic sequence is cut from a genome with a certain restriction enzyme and mixed with purified plasmids cut with the same enzyme, the sticky ends will be complementary and can bridge the cut plasmid by hybridizing sticky ends to sticky ends.

Endonucleases typically hydrolyze the oxygen-phosphorus bond on the 5′ side of the phosphorus, meaning that the 3′ end of the product will have a hydroxyl group and the 5′ end will terminate at the phosphate group. This configuration allows for ligase enzyme to covalently ligate the backbone once the sticky ends have annealed. Ligation can be prevented by removing the phosphate on the 5′ end with phosphatase enzyme.

Eukaryotic cells have larger genomes than Bacteria, from tens of millions of base pairs (bp) to more than 100 billion bp, distributed on several different DNA molecules termed chromosomes. These excessively long DNA molecules are organized on several different hierarchical levels during the cell cycle with the most compacted form visible through light microscopy during S phase as irregular X shapes. The first step of organization is achieved by spooling DNA onto alkaline proteins called histones. This creates a unit called a 'nucleosome' containing 146 bp that is visible in electron microscopy as beads on a string.

Compaction of DNA by histones plays an important role in regulating gene expression as more compact DNA are less available for RNA polymerases to bind. Another level of transcriptional control observed in some vertebrates – but not all eukaryotes – is based on methylation of cytosine on carbon 5. This chemical modification of DNA generally serves to repress genetic expression. Both histone-mediated compaction and methylation can change during a cell's life cycle but can also be passed on through several generations. Thus, the effective genetic expression is altered without altering the underlying DNA sequence.

DNA Replication

The most important biological aspect of DNA's structure is arguably the ability to accurately transmit genetic information to offspring. As noted by Watson and Crick in their seminal paper from 1953, the double-helical structure immediately suggests a mechanism for DNA replication. This mechanism is based on a semiconservative scheme where unwinding of the double helix allows each single strand to function as a template for the synthesis of new strands. Completion of a round of replication thus results in two helices, each containing one strand carried over from the parent duplex and one newly synthesized strand. If we consider this scheme, we can identify three processes that need to occur. The duplex needs to unwind. The resulting supercoil needs to be alleviated. And finally, new strands need to be synthesized using the parent strands as templates. Each of these processes is catalyzed by a different group of enzymes.
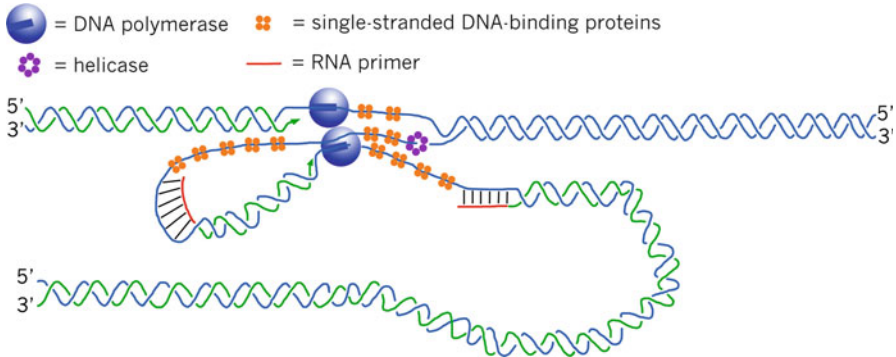
Fig. 34.6 Schematic representation of replication fork. The DNA duplex is unwound by a helicase enzyme that moves along the lagging strand. Single-stranded DNA-binding proteins bind to the newly unwound duplex preventing reannealing. Two core polymerases associate in a large complex consisting of several different subunits (not shown). The polymerases can only synthesize in the 5′ to 3′ direction by adding nucleotides to a 3′ end but both move in the same direction along the parent duplex. This is accomplished by looping the lagging strand and synthesizing it in the fragments. Each fragment is initiated with an RNA primer that is subsequently replaced with DNA (Adapted from [59])

In bacterial cells, replication is initiated at a specific site on the genome called the origin. Starting at this site, helicase enzymes hydrolyze adenosine triphosphate (ATP) in order to peel the single strands apart, while single-stranded DNA-binding proteins bind the single strands and help prevent reannealing. The bubble created this way has two junctions called replication forks, and helicases run processively along the DNA in both directions extending the loop (see Fig. 34.6). In both circular prokaryotic and large eukaryotic genomes, this process results in supercoiling which is alleviated by topoisomerase enzymes.

In both prokaryotes and eukaryotes, topoisomerase enzymes are divided into type I and type II. Type I works by cleaving just one of the two strands creating what is called a nick in the backbone (a single-strand break). This is accomplished by a nucleophilic attack from a tyrosine hydroxyl group on a phosphorus atom in the sugar-phosphate backbone creating a transient covalent bond between enzyme and DNA. With the backbone nicked, either the duplex can now perform a controlled rotation or the intact single strand can be passed through the nick depending on the enzyme. Type II topoisomerases cleave both DNA strands of a duplex using two tyrosine residues. By holding the ends in place, a different part of the duplex is allowed to pass through the break, thus releasing or introducing supercoil. This reaction cycle is completed with ATP hydrolysis.

DNA polymerase is the primary enzyme responsible for DNA replication; however, it only catalyzes the addition of deoxynucleoside triphosphates (dNTP) to the 3′ end of a growing strand using exposed single strand as a template for dNTP selection. This has two implications. The first is that a short primer strand is needed for DNA polymerase to work. A primer is synthesized by a primase enzyme and consists of RNA which is later excised and replaced with DNA. The second

implication is that DNA polymerase only works in the 5′ to 3′ direction as the 3′-OH group makes a nucleophilic attack on the α-phosphate of the incoming dNTP. This results in a semidiscontinuous replication scheme where the two strands are replicated in different ways. One strand, called the leading strand, is initiated with one primer and extends continuously as the parent duplex is unwound. The other strand, called the lagging strand, can only be synthesized in short fragments as the synthesis is in the opposite direction of the moving replication fork. These short fragments are called Okazaki fragments and are 1,000–2,000 nucleotides long in *E. coli* and 100–200 fragments long in eukaryotes.

Besides catalyzing addition of dNTPs, all DNA polymerases in *E. coli* also have 3′ to 5′ exonuclease activity meaning that they can excise nucleotides in this direction. This is done when a noncomplementary nucleotide is erroneously added to the growing chain, thus improving the fidelity with which replication occurs. In *E. coli*, the specific polymerase responsible for substituting the RNA primers with DNA is called polymerase I. This enzyme also contains 5′ → 3′ exonuclease activity enabling it to extend from a nick by excising nucleotides on the 5′ side as it moves along. It can thereby remove the RNA primers, and subsequently, ligase can covalently link the fragments.

Polymerase Chain Reaction

A synthetic form of DNA replication that has been of paramount importance is the polymerase chain reaction (PCR) technique. This method reliably amplifies miniscule amounts of DNA in a test tube within hours. This is accomplished by using a heat-stable polymerase and adding a large excess of both forward and reverse primers to a DNA target. Cycling between melting the duplex DNA, annealing primers, and letting the polymerase extend results in an exponential replication of the sequence bordered by the primers (see Fig. 34.7). (1) In the first step, a mixture of target DNA, nucleotides, primers, and heat-stable polymerase is heated to 94 °C in order to melt the target duplex. Heat-stable polymerase – such as *Taq* polymerase from the bacterium *Thermus aquaticus* – prevents the enzyme from denaturing during this step. (2) In the second step, the temperature is lowered to allow the primers to anneal to the target single-stranded DNA. The forward primer anneals to the 3′ end of the template strand and the reverse primer anneals to the 3′ end of the complementary strand. The temperature chosen may depend on the melting temperature of the primers but will typically be around 55 °C. The high concentration of primers prevents the target DNA from reforming a duplex. (3) In the third step, the temperature is raised to the optimum working temperature of the polymerase. For *Taq*, this is 72 °C. The polymerase then extends the primers in the 5′ to 3′ direction.

The first round of replication results in the new strands that extend beyond the region bordered by the primers in the 5′ direction. Subsequent rounds of replication from newly synthesized strands generate a sequence defined by primer location.
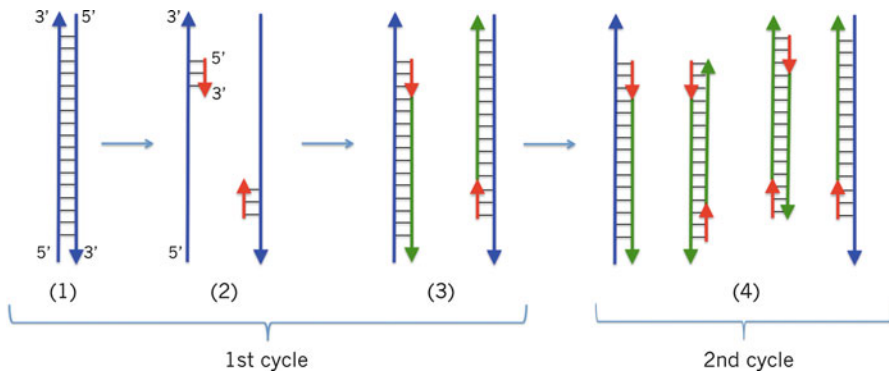
Fig. 34.7 Polymerase chain reaction consists of several repeating cycles, all producing a set of copies of a desired sequence. All cycles consist of 3 steps: denaturing, annealing, and extension. The figure illustrates the 3 steps in the first cycles. *1* The sample is denatured at a high temperature. *2* Lowering of the temperature allows for the primers to anneal. *3* In the final step, the temperature is raised enough to allow the heat-stable polymerase to function but not so much that the primers denature. *4* The newly formed duplexes then function as substrates for subsequent cycles resulting in an exponential increase of sequence copies

Transcription and Translation

Transcription is the process of synthesizing messenger RNA (mRNA) molecules based on the sequence of genes on a DNA molecule. Analogous to DNA replication, this is accomplished by an RNA polymerase that reads the template sequence in the 3′ to 5′ direction and synthesizes an mRNA molecule in the 5′ to 3′ direction. One of the sharp differences between prokaryotes and eukaryotes is the fact that there is only one known RNA polymerase in prokaryotes but three distinct RNA polymerases are known in eukaryotes. This is mirrored in the fact that eukaryotes have more complex RNA-mediated control of expression.

In *E. coli*, RNA polymerase associates with transcription factor proteins to initiate transcription of a gene. For this to occur, the transcription complex recognizes a specific sequence by binding non-covalently to the individual nucleobases. Both strands in a genome contain genetic information. In the context of a specific gene, the strand that is being 'read' by the polymerase – the complementary strand – is called the noncoding strand or the antisense strand. The strand that is identical in sequence to the resulting mRNA is called the coding strand or the sense strand.

Transcription is terminated when reaching a specific sequence, sometimes through the association of additional protein factors. The mRNA is processed by ribosomes where amino acids linked to transfer RNAs (tRNA) complementary to specific codons (nucleotide triplets) are transferred to a growing polypeptide chain. The final product is a protein specified by the original gene sequence in the DNA molecule.

Genetic Recombination

As the information carrier of life, DNA need not only facilitate accurate transmission of information but also allow for genetic diversity, the substrate of evolution. One process attributing to this is homologous recombination which is the recombination of two different DNA duplexes with a stretch of identical sequence. In other words, two different DNA duplexes exchanged their binding partners and then they are cleaved and the pieces recombined. Different organisms have different enzymatic pathways facilitating this process but one common feature is the formation of a Holliday junction (see section 'DNA as a Self-Assembling Construction Material' and Fig. 34.9 below). This four-arm junction illustrates the topological diversity of DNA that makes it suitable not only as a carrier of information but also as a nanometer-scale building material.

Optical Properties of DNA

DNA molecules typically interact with electromagnetic radiation typically through the absorption of photons causing excitation of electrons from one state to another. This absorbed energy is then lost either by emission of photons, dissipation as heat, or alteration of chemical bonding.

Simple Absorbance

Different atomic structures preferentially absorb different wavelengths of radiation. To understand the optical properties of DNA, first, one must be familiar with the chemical structure (discussed in section 'Chemical Properties of DNA', above). Different wavelengths are preferentially absorbed by the backbone phosphates (near IR), the conjugated electron systems that make up the bases (260 nm), and other groups in other biological polymer systems such as aromatic side chains in proteins (254–280 nm) and peptide bonds in polypeptide backbones (190–230 nm). Investigators routinely use optical properties to gain useful insight into the structure and concentration of the organic molecules being observed.

The most widely exploited optical property of DNA is its characteristic absorption at 260 nm. Molecules change absorption based on sequence composition and number of bases present. Any particular sequence will show a characteristic absorbance spectrum, making the assignment of an extinction coefficient simple. This provides a means of determining DNA concentration via an absorption measurement. Protein, one of the most common contaminants of DNA solutions, typically displays significant absorption at 280 nm; therefore, the ratio of absorbance

at 260–280 nm is a crude measure of the purity of a DNA sample. Note that RNA shows a similar absorbance profile to DNA, so RNA contamination is more difficult to detect.

Hyper-/Hypochromicity

Interestingly, ssDNA and dsDNA have different characteristic absorptions. A dsDNA helix shows less absorbance at 260 nm than does a sample containing the same concentration of the two-component ssDNA strands. This property of increasing absorbance during the transition from double-stranded to single-stranded forms is called hyperchromicity. The inverse property of going from high to low absorbance when reannealing ssDNA into dsDNA is termed hypochromicity. Because DNA can be denatured via heat or solute conditions, this change in absorbance with respect to base pairing has proved experimentally useful. The most common application of this principle is seen in DNA melting studies, where a solution of DNA is heated steadily while the absorbance is monitored. As molecules in duplex form begin to separate, the absorbance starts to rise. When all the molecules have denatured, a maximum absorbance is reached. Further addition of heat or denaturant at this point will not change the absorbance. Similarly, as a solution is cooled, the DNA molecules will rehybridize, and generally, the population will retrace the absorbance versus temperature curve created during heating, although some hysteresis may be observed.

Light-Induced Chemical Modification

When DNA is exposed to high-energy light, absorbed photons can cause chemical modifications. The most well-documented and characterized chemical modifications due to light are the formation of pyrimidine dimers, 6–4 photoproducts, and abasic sites under UV exposure (UVB [315–280 nm], UVC [280–100 nm]). This is highly relevant for biological processes, since UVB radiation from the sun penetrates the ozone and causes 50–100 of these modifications per second per exposed skin cell [60]. These modifications must then be corrected by the cell's DNA repair machinery, or else modifications may be propagated and lead to disease including melanoma. Interestingly, these modifications disrupt base pairing, leading to a localized decrease in DNA backbone rigidity. It is this increased backbone flexibility that DNA repair enzymes use to identify modified bases rather than directly assessing the condition of the base [61]. These modifications are rarely intentionally exploited in the laboratory setting; however, many laboratory techniques, including assessing concentration via 260 nm measurement and visualizing DNA bands in a gel on a UV box, will cause these types of modifications. This is one of the many reasons that laboratory workers are encouraged to routinely sequence their DNA stocks if they are performing experiments in which specific sequence is critical.

Electrical Properties of DNA

In this section, we will discuss the electrical properties of DNA, including early debate of whether DNA is an insulator, semiconductor, conductor, or even a superconductor; the conclusion of this debate; and a discussion of possible conduction mechanisms, as well as underlying measurement difficulties.

Investigation of the electrical properties of DNA began in the late 1950s, in which experimenters tested the conductivity or lack thereof in DNA. While some researchers incorrectly found DNA to be insulating, in 1962, Eley et al. reported that bulk DNA samples act as a semiconductor when compressed between platinum electrodes and resistance is measured under vacuum [62]. They theorized that the base-pair units of DNA are 'arranged like a pile of coins along the helix axis', supposing that 'a DNA molecule might behave as a one-dimensional aromatic crystal and show a n-electron conductivity down the axis', and, furthermore, that the orbital overlap of the bases along the axis of the helix could be sufficient to promote conductivity. More sophisticated experiments were performed to further investigate the conductivity of DNA, in one case, even claiming superconductivity [63].

More precise measurements of DNA conductivity have been made by producing a small voltage across two well-separated parts of a DNA molecule and measuring the electric current while under vacuum so as to avoid contact with anything other than the sample. Although different experiments report different band gap values, these variations in results are likely due to the quality of DNA and the types of electrodes used. To circumvent these issues, chemists have focused on the photochemical aspects of well-defined oligonucleotide assemblies in solution rather than physically measuring resistance in dry samples [64].

In 1999, Fink noted that, while experiments conclusively show that DNA molecules are molecular conductors, the mechanism that allows the transport of charge is not well defined [65]. Eley presented a model for electron transfer through DNA, which is based on overlap between the π-orbitals in adjacent base pairs [61]. Because of imperfections or irregularities in base-pair sequences, localization of charge carriers and the reduction of the transfer rate of electrons make measurements of conductivity difficult [66].

A few models exist to describe the possible mechanisms for electron transport through DNA. One model suggests electronic interactions between the bases in the DNA molecule, leading to a molecular band where the electronic states are delocalized over the entire length of the molecule. In this model, electrons can tunnel between the bound donor and acceptor. This tunneling from electrode to electrode is often ruled out, as separating the electrodes a distance larger than what is probable for tunneling still yields large conductivity [64, 66–68]. Another model suggests sequential hopping between localized states. This could involve hopping between discrete base orbitals or hopping from domain to domain, skipping several bases at a time (Fig. 34.8) [64, 66–68]. One example would be incoherent hopping through low-potential regions of the stacked base pairs, for example, over guanines, which are the most easily oxidized bases [69].

Fig. 34.8 Representations of three current opinions in structural biology of the mechanisms by which charge transports through DNA. (**a**) Charge tunnels all the way from the donor to the acceptor. (**b**) Charge hopping between discrete molecular orbitals from the donor to the acceptor. (**c**) Charge hopping from domain to domain on its way from the donor to the acceptor. Broken lines represent domains at which electrons tend to collect (Adapted from [64])
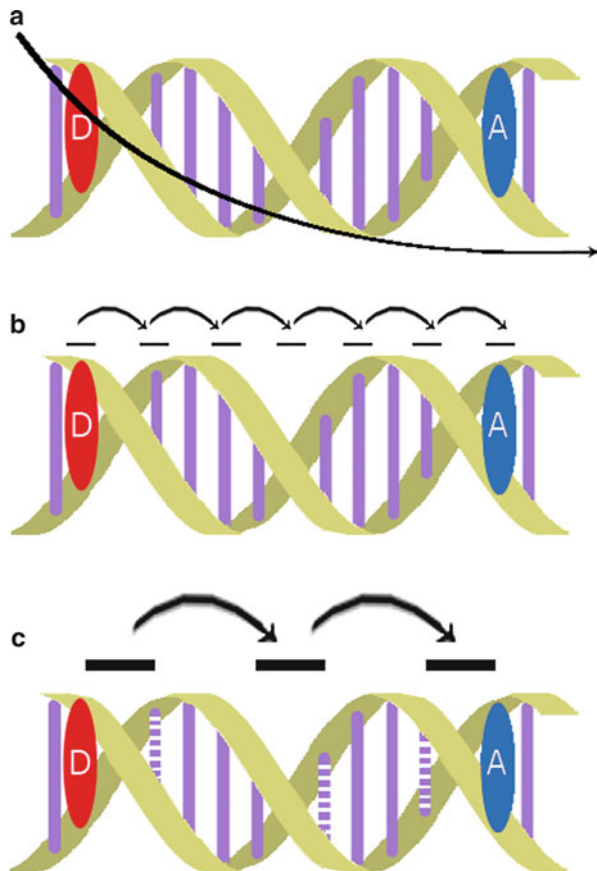
With these ideas as to how charge is transported, many underlying measurement difficulties arise. For example, in the case where there are stacks of high-barrier, flexible base pairs, such as long A-T tracts, the stacking dynamics become less than ideal, as does the charge transport. Such a situation would require a buildup of charge before the barrier can be surpassed. To avoid these situations, one can replace these high-potential sites with lower-potential sites, like guanine, as mentioned above [69, 70].

Furthermore, there are fundamental difficulties that must be considered, including DNA as a biological sample – only conducting well in biologically relevant conditions such as the presence of water and ions. As such, nanostructured devices constructed with DNA will be fragile and easily perturbed [69, 70]. Also, Genereux points out that charge transport across many DNA sequences occurs too fast for measurement. In such situations, rapid charge recombination will occur. To prevent this, an extended adenine tract can be added at the site of injection [69].

While it has become clear that DNA has electrical conduction properties ranging between a semiconductor and conductor, it is apparent that the magnitude of the

DNA conduction is dependent on many factors, including the quality of DNA, environment in which conductance is measured, the length of DNA across which voltage is applied, as well as the individual bases in a particular DNA strand. The realization that DNA holds conductive electrical properties allows the possibility of incorporating DNA into nanoelectronic devices.

Information Encoding in DNA

Since DNA is the genetic material of all known free-living organisms, and since it is through this material that hereditary information is passed from generation to generation, it is obvious that DNA is an excellent medium for the storage and propagation of information. Separation of the complementary strands of the double helix, followed by template-directed polymerization (as described in section 'Biological Properties of DNA', above), provides an elegant mechanism for making copies of genetic information for passing to successive generations of cells and organisms. In addition, it has been noted that nonbiological information can be recorded in DNA, starting with the first demonstration of a DNA-based computer [71] and leading to recent results showing efficient information propagation using self-assembling DNA nanostructures as seed crystals [72].

This may lead one to inquire what amount of information can be encoded within the nucleobase sequence of a DNA molecule. Information theory and coding theory have established that the maximum amount of information (the maximum number of bits per symbol) that a series of letters or symbols can encode is equivalent to the base-two logarithm of the size of the alphabet [73]. Therefore for DNA, with an alphabet of four bases, the maximum information density is $\log_2 4 = 2$ bits of information per nucleotide base in the sequence. This is a maximum because less than two bits of information will be encoded if the exact identity of all the bases is not required in order to specify the function of the sequence, as, for example, the third position in the codons of protein-coding genes since GGN codes for a glycine residue and CCN codes for proline (where N can be any of the four bases), regardless of the identity of the base in the third position. No information is recorded in this so-called wobble position of these codons. Likewise, highly variable sites in protein or regulatory genes, as well as sites that allow compensatory mutations in base-paired stem regions of self-folding RNA structures, will each contain less than the maximum possible information density.

A variety of methods have been used to estimate the information density within different classes of biological sequences including protein-protein and protein-DNA interaction motifs and secondary structure elements in RNA and protein molecules [74, 75]. For example, a six-base recognition site for a restriction enzyme that requires an exact match would be said to hold twelve bits of information. Human-designed DNA sequence libraries for use in DNA-based computing have been created with information densities on the order of 1 bit per 10 or 20 bases in order to maximize the difference (Hamming distance) between neighboring

sequence words [76]. This provides sets of distinct words that can be reliably annealed with their complements to form hydrogen-bonded, base-pairing couples without significant probability of mispairing with incorrect words. We have therefore observed natural and artificial DNA sequences with information contents between 2.0 and 0.05 bits per nucleotide residue.

DNA as a Self-Assembling Construction Material

The chemical, mechanical, and biological properties of dsDNA, as discussed in the previous sections of this chapter, describe a stable and relatively stiff biopolymer that is perfect for the self-assembly of functional architectures for bottom-up fabrication at the nanometer scale. Nucleic acid molecules are readily programmable and have predictable intermolecular interactions. Their extensive biological study has led to marked advances in synthesis and modification methods. The sequence of a DNA molecule can be read by other nucleic acids and proteins, which leads to specific manipulation and modification by a large number of enzymes. The objective of structural DNA nanotechnology is to take the unique properties of DNA, which make it such a great molecule for genetic material, and exploit them for the precise positioning of functional materials.

Holliday Junctions

In its natural, biological state, DNA is a double-helical, topologically linear molecule that does not have the structural integrity for a basic unit of a construction material. Instead, nanoscale materials and devices must be built from a rigid unit capable of branching off into multiple directions. The most biologically famous branched unit of DNA is the Holliday junction: an intermediate structure during genetic recombination where four strands of DNA associate to form four double-helical arms [77]. The naturally occurring Holliday junction is unstable. The homologous symmetry of the sequences involved in the arms of the junction allows for branch migration, junction elimination, and formation of two separate linear double-stranded complexes. In 1982, Nadrian Seeman generated oligonucleotide sequences to form immobile junctions, incapable of branch migration [78]. This development spurred the use of DNA as a structural material for nanotechnology.

The structure of the four-armed Holliday junction in solution was a subject of debate since its first discovery. Of the many isomeric conformations that the four arms could adopt in solution, the junction strongly prefers a particular crossover configuration where each pair of arms base-stacks to form two helical domains with a bias towards these helices running antiparallel to each other [79]. Multi-arm junctions, with 3–8 double-helical arms, form single tiles [78]. Tile arms may terminate with several single-stranded residues (sticky ends) that can link with a neighboring tile with complementary sticky ends via Watson-Crick base pairing. High-fidelity sticky-ended

association and the long persistence length of double-stranded nucleic acids allow for the prediction of intermolecular interactions between each tile component and of the local structure of the hybridized product. These Holliday junction-based tiles were expected to be a key unit for forming 2-dimensional periodic DNA lattices. However, Holliday and multi-arm junctions are too flexible to produce large-scale DNA networks [80]. Instead, the conformational flexibility of multi-arm tile architectures has been exploited to produce three-dimensional objects including cubes, truncated octahedra, octahedra, tetrahedra, dodecahedra, buckyballs, and icosahedra [81–84].

Double-Crossover Constructs

Forming long-range DNA networks requires structurally rigid basic building blocks. To generate stiffer DNA tiles, the so-called double-crossover motif was fashioned. In this structure, two neighboring DNA helices are joined at two junction sites where two strands are exchanged between the neighboring duplexes [85]. There are five strand-routing isomers of DNA double-crossover supramolecular complexes that vary in their neighboring helix orientation (parallel or antiparallel), the number of helical half-turns between each crossover point (odd or even), and, for those with an odd number of half-turns, the excess groove between each crossover point (major groove or minor groove) [86]. Of these five isomers, DAE, the double-crossover complex with an antiparallel orientation and an even number of helical half-turns between each crossover point, proved to be the most stable and, thus, suitable for nanoconstruction [86]. Figure 34.9 illustrates the differences between a single DNA helix, a Holliday junction between two helices, and two helices connected by double crossovers.

Tile and Lattice Assemblies

The rigid antiparallel double-crossover motif (DAE) was a breakthrough achievement for the production of large lattices. DAE tiles self-assemble into periodic networks via sticky-end sequence recognition. The rigid DAE motif is used extensively to form 2-dimensional lattices and 3-dimensional objects [87–89]. Different variations of DAE tiles form distinct semi-infinite two-dimensional periodic lattices. Rigid tile assemblies including triple-crossover complexes, paranemic crossover molecules, bulged 3-arm triangular constructions, tensegrity designs, and other geometries have been employed for structure formation [27, 90–96]. Additionally, surface-assisted anneals have proven to stabilize more flexible systems that would otherwise be incapable of forming larger lattices in solution [97, 98]. Two tile systems are shown in Fig. 34.10 with their corresponding lattices.

The tile systems described above are engineered to propagate endlessly with dimensions predicated on the thermodynamics of the annealed system. To this end, DNA tile systems that self-assemble into finite-sized arrays have been established.
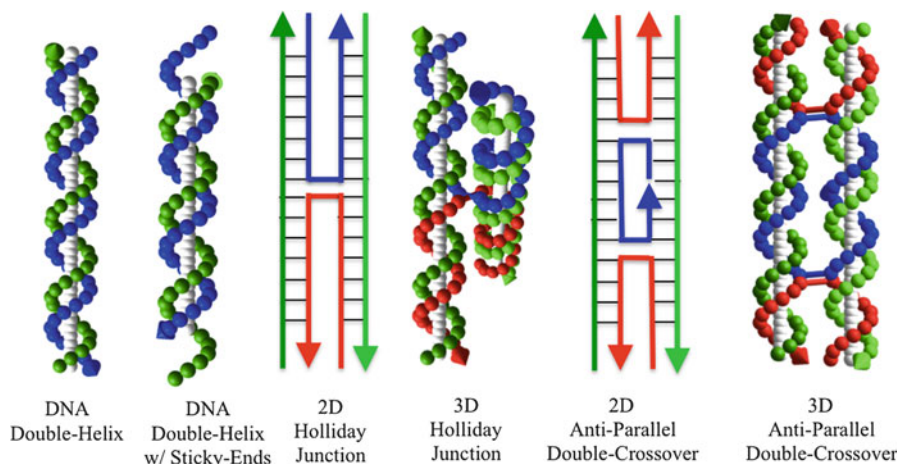
Fig. 34.9 Basic DNA constructions used for DNA structural nanotechnology. The double-helical structure is displayed terminating with and without unpaired regions (sticky ends). A DNA Holliday junction structure is shown in two and three dimensions to exhibit the flexibility about the crossover section. The double-crossover construction fixes the position of the two helices to be parallel, as shown in the three-dimensional representation

Some of these finite-sized nanoarrays use hierarchical assembly methods (anneals set up to progressively build upon single tiles to the desired size) to promote cost-efficiency and full addressability [99–102]. The ultimate network topology of the nanoarrays is predictable based on sequence specificity, local geometry, and flexibility. Thus, flexible tiles can create lattices with inherent curvature that can roll up into DNA nanotubes [103–108]. DNA-based networks are useful for the site-specific organization of inorganic nanomaterials (such as nanoparticles, nanorods, and nanowires) and organic molecules (such as proteins, dyes, aptamers, and antibodies) for electronic, photonic, chemical, and biomedical applications [109–112].

DNA Scaffolded Origami

The previously reviewed tile-based method was made possible by the rigidity of the antiparallel double-crossover motif. This construct places two helices almost parallel to each other. In 2006, Paul Rothemund expanded this motif by specifically positioning many helices with multiple double crossovers [5]. Each helix is comprised of a long, biologically derived single strand of DNA, termed the 'scaffold' strand (e.g., M13mp18 ssDNA), bound to numerous, short, chemically synthesized ssDNA molecules, termed 'staple' strands, designed to tether neighboring helices (Fig. 34.11a, b). Rothemund named this method DNA scaffolded origami since the staple strands fold the scaffold strand into a desired shape.
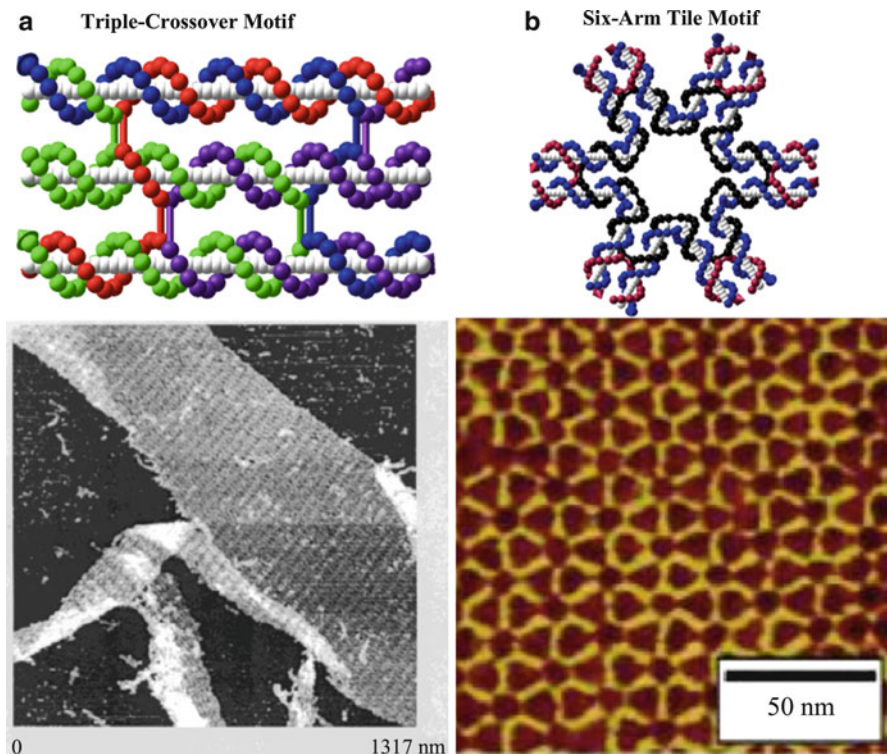
Fig. 34.10 Example of tile constructions and AFM of corresponding lattice formation. (**a**) The triple-crossover tile further illustrates the use of double crossovers to impose rigidity. (**b**) The six-arm, or six-point-star, tile forms 2D arrays with sticky-ended motifs

The DNA origami scheme allows for the realization of more sophisticated constructions while simplifying structure formation. Origami is formed by mixing a scaffold strand with a molar excess (over 5 times more than scaffold) of staple strands. Since its basis is a long scaffold strand, origami eliminates the necessity for exact stoichiometry between all staple strands involved in the structure. In Rothemund's original origami designs, staple strands form crossovers every 32 bases along each helix. This spacing enforces three helical turns between crossovers, which corresponds to an average twist density of 10.67 base pairs per turn. Varying the number of bases between crossovers imposes torque along the helix-parallel axis. Placing crossovers in precise positions between helices controls the global curvature of two- and three-dimensional objects (Fig. 34.11f) [113–115].

With the goals of increasing the dimensions of objects and expanding the surface area available for functionalization, methods to increase the size of origami structures have been explored. Since the length of the scaffold strand ultimately determines the total size of DNA origami structures, the first inclination is to increase the size of the scaffold. However, it is difficult to develop long, single strands of DNA biologically. Synthetic PCR techniques have been attempted, but
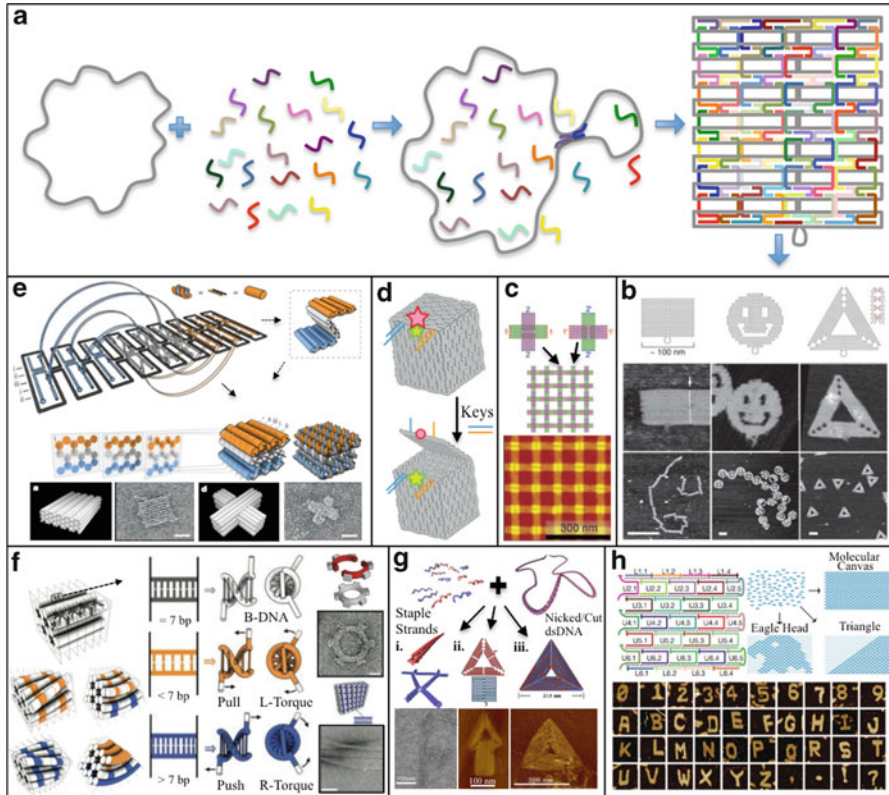
Fig. 34.11 DNA scaffolded origami. (**a**) Schematic shows how DNA origami is constructed by folding a long scaffold strand with hundreds of short oligonucleotides, whose sequences determine the final structure. (**b**) The same scaffold strand can be folded into many different two-dimensional shapes. (**c**) DNA origami tiles are patterned into crystalline two-dimensional arrays. (**d**, **e**) Three-dimensional constructions are also possible. (**f**) By manipulating the DNA helical twist, structures can exhibit global curvature and twisting. (**g**) In an effort to increase the functional surface area of origami, double-stranded scaffolds can also be used to form (*i*) two separate shapes, (*ii*) heterodimeric shapes, and (*iii*) one unified shape. (**h**) The complete elimination of the scaffold strand is achieved by utilizing single strands of DNA forming tiles with half-crossovers

structure formation yield is low [116]. Methods to fold origami from double-stranded scaffold sources have been achieved by the addition of chemical denaturing agents (Fig. 34.11g) [32, 43, 117, 118]. Other approaches for scaling-up origami include linking origami structures together via staple sequence recognition along edges, shape complementarity, base stacking interactions at helix ends, and predefined lattices with sticky-end interactions (Fig. 34.11c) [6, 119–125]. Analogous two-dimensional molecular canvases have also been created from single-stranded tiles (Fig. 34.11h). Structures are built from 3 × 7 nm tiles made from 42-base synthetic DNA strands that organize to form repetitive half-crossovers.

This method eliminates the requirement for a single-stranded scaffold, while maintaining the ability to construct nanostructures with complex two-dimensional shapes.

The advent of origami has simplified structure formation based on DNA [126, 127]. Even novices of the DNA nanotechnology field can easily design two- or three-dimensional objects (Fig. 34.11d, e) [128]. The practicality of this method makes DNA origami readily utilizable for applications in many fields including supramolecular assembly, biomedical engineering, and nanofabrication [129–134].

Structure Design Programs

As structural DNA nanotechnology progresses, designs become larger and more elaborate. The original tiled structures were designed by hand or with the assistance of short, quick computational scripts that were not generalized for wider design problems [78]. The drive towards greater complexity has compelled researchers to develop simple programs where users may define shapes and sequences, and appropriate complementary sequences are produced [77–80]. With the rising interest in DNA origami, software has been developed to simplify the design of two- and three-dimensional structures following the origami architecture constraints [135–137].

Also, computational models (see section 'Computational Methods to Describe Nucleic Acids' above) can predict origami shapes and their flexibilities in solution based on the mechanical properties of DNA and crossover formation [56].

Conclusion

In this chapter, we have presented information on the chemical, mechanical, biological, optical, electrical, informational, and structural properties of DNA. We have also introduced the reader to the use of DNA as a nanoscale construction material within the field of structural DNA nanotechnology. While these topics are large and the space here is brief, we hope that this introduction will help direct interested readers to further resources within the scientific literature.

References

1. Bloomfield VA, Crothers DM, Tinoco I (2000) Nucleic acids: structures, properties, and functions. University Science Books, Sausalito
2. Mandelkern M, Elias JG, Eden D, Crothers DM (1981) The dimensions of DNA in solution. J Mol Biol 152(1):153–161. doi:10.1016/0022-2836(81)90099-1
3. Murphy MC, Rasnik I, Cheng W, Lohman TM, Ha TJ (2004) Probing single-stranded DNA conformational flexibility using fluorescence spectroscopy. Biophys J 86(4):2530–2537
4. Yakovchuk P, Protozanova E, Frank-Kamenetskii MD (2006) Base-stacking and base-pairing contributions into thermal stability of the DNA double helix. Nucleic Acids Res 34(2):564–574

5. Rothemund PW (2006) Folding DNA to create nanoscale shapes and patterns. Nature 440(7082):297–302
6. Woo S, Rothemund PW (2011) Programmable molecular recognition based on the geometry of DNA nanostructures. Nat Chem 3(8):620–627
7. Yan H et al (2003) Directed nucleation assembly of DNA tile complexes for barcode-patterned lattices. Proc Natl Acad Sci USA 100(14):8103–8108
8. Davis JT (2004) G-quartets 40 years later: from 5′-GMP to molecular biology and supra-molecular chemistry. Angew Chem Int Ed Engl 43(6):668–698
9. Sen D, Gilbert W (1988) Formation of parallel four-stranded complexes by guanine-rich motifs in DNA and its implications for meiosis. Nature 334(6180):364–366
10. Gehring K, Leroy JL, Gueron M (1993) A tetrameric DNA structure with protonated cytosine.cytosine base pairs. Nature 363(6429):561–565
11. Phan AT, Mergny JL (2002) Human telomeric DNA: G-quadruplex, i-motif and Watson-Crick double helix. Nucleic Acids Res 30(21):4618–4625
12. Lane AN et al (2008) Stability and kinetics of G-quadruplex structures. Nucleic Acids Res 36(17):5482–5515
13. Laisne A, Pompon D, Leroy JL (2010) [C7GC4]4 association into supra molecular i-motif structures. Nucleic Acids Res 38(11):3817–3826
14. Lin Z et al (2011) DNA nanotechnology based on polymorphic G-Quadruplex. Prog Chem 23(5):974–982
15. Liu D, Balasubramanian S (2003) A proton-fuelled DNA nanomachine. Angew Chem Int Ed Engl 42(46):5734–5736
16. Sondermann A et al (2002) Assembly of G-Quartet based DNA superstructures (G-Wires). AIP Conf Proc 640(1):93–98
17. Afek A et al (2011) Nonspecific transcription-factor-DNA binding influences nucleosome occupancy in yeast. Biophys J 101(10):2465–2475
18. Jen-Jacobson L et al (2000) Thermodynamic parameters of specific and nonspecific protein-DNA binding. Supramol Chem 12:143–160
19. Howley PM et al (1979) A rapid method for detecting and mapping homology between heterologous DNAs. Evaluation of polyomavirus genomes. J Biol Chem 254(11):4876–4883
20. Schildkraut C (1965) Dependence of the melting temperature of DNA on salt concentration. Biopolymers 3(2):195–208
21. Kibbe WA (2007) OligoCalc: an online oligonucleotide properties calculator. Nucleic Acids Res 35(Web Server issue):W43–6
22. Wetmur JG (1991) DNA probes: applications of the principles of nucleic acid hybridization. Crit Rev Biochem Mol Biol 26(3–4):227–259
23. Harris NC, Kiang CH (2006) Defects can increase the melting temperature of DNA-nanoparticle assemblies. J Phys Chem B 110(33):16393–16396
24. Maye MM et al (2010) Switching binary states of nanoparticle superlattices and dimer clusters by DNA strands. Nat Nanotechnol 5(2):116–120
25. Knorowski C, Travesset A (2012) Dynamics of DNA-programmable nanoparticle crystallization: gelation, nucleation and topological defects. Soft Matter 8:12053–12059
26. Sponer J, Leszczynski J, Hobza P (1996) Nature of Nucleic acid–base stacking: nonempirical ab initio and empirical potential characterization of 10 stacked base dimers. Comparison of stacked and H-bonded base pairs. J Phys Chem 100(13):5590–5596
27. Mao C, Sun W, Seeman NC (1999) Designed two-dimensional DNA holliday junction arrays visualized by atomic force microscopy. J Am Chem Soc 121(23):5437–5443
28. Izatt RM, Christensen JJ, Rytting JH (1971) Sites and thermodynamic quantities associated with proton and metal ion interaction with ribonucleic acid, deoxyribonucleic acid, and their constituent bases, nucleosides, and nucleotides. Chem Rev 71(5):439–481
29. Eichhorn GL, Shin YA (1968) Interaction of metal ions with polynucleotides and related compounds. XII. The relative effect of various metal ions on DNA helicity. J Am Chem Soc 90(26):7323–7328

30. Hickey DR, Turner DH (1985) Solvent effects on the stability of A7u7p. Biochemistry 24(8):2086–2094
31. McConaughy BL, Laird CD, McCarthy BJ (1969) Nucleic acid reassociation in formamide. Biochemistry 8(8):3289–3295
32. Hogberg B, Liedl T, Shih WM (2009) Folding DNA origami from a double-stranded source of scaffold. J Am Chem Soc 131(26):9154–9155
33. Jungmann R et al (2008) Isothermal assembly of DNA origami structures using denaturing agents. J Am Chem Soc 130(31):10062–10063
34. Cleaver JE, Boyer HW (1971) Solubility and dialysis limits of DNA oligonucleotides. Biochem Biophys Acta 262:116–124
35. Tan SC, Yiap BC (2009) DNA, RNA, and protein extraction: the past and the present. J Biomed Biotechnol 2009:574398
36. Blake RD (2006) Denaturation of DNA. In: Encyclopedia of molecular cell biology and molecular medicine. Wiley-VCH Verlag GmbH & Co, Germany
37. Bloomfield VA, Crothers DM, Tinoco I (1974) Physical chemistry of nucleic acids. In: Nucleic acids: structures, properties, and functions. Harper and Row, New York
38. Shi Y et al (1990) Applications of psoralens as probes of nucleic acid structure and function. In: Morrison H (ed) Bioorganic photochemistry, vol 1, Photochemistry and the nucleic acids. Wiley, New York
39. Stone MP et al (2008) Interstrand DNA cross-links induced by alpha, beta-unsaturated aldehydes derived from lipid peroxidation and environmental sources. Acc Chem Res 41(7):793–804
40. Kohn KW, Spears CL, Doty P (1966) Inter-strand crosslinking of DNA by nitrogen mustard. J Mol Biol 19(2):266–288
41. Lausted C et al (2004) POSaM: a fast, flexible, open-source, inkjet oligonucleotide synthesizer and microarrayer. Genome Biol 5(8):R58
42. Quan J et al (2011) Parallel on-chip gene synthesis and application to optimization of protein expression. Nat Biotechnol 29(5):449–452
43. Marchi AN et al (2013) One-Pot assembly of a Hetero-dimeric DNA Origami from chip-derived staples and Double-Stranded Scaffold. ACS Nano 7(2):903–910
44. Saaem I et al (2010) In situ synthesis of DNA microarray on functionalized cyclic olefin copolymer substrate. ACS Appl Mater Interfaces 2(2):491–497
45. Lehninger AL (1975) Biochemistry. Worth, New York
46. Zhao L et al (2008) Intracellular water-specific MR of microbead-adherent cells: the HeLa cell intracellular water exchange lifetime. NMR Biomed 21(2):159–164
47. Bansal M (2003) DNA structure: revisiting the Watson-Crick double helix. Curr Sci 85(11):1556–1563
48. Kornberg RD (1974) Chromatin structure: a repeating unit of histones and DNA. Science 184(4139):868–871
49. Bustamante C et al (2000) Single-molecule studies of DNA mechanics. Curr Opin Struct Biol 10(3):279–285
50. Rubinstein M, Colby RH (2003) Ideal chains, in polymer physics. Oxford University Press, Oxford/New York, pp xi, 440
51. Marko JF, Siggia ED (1995) Stretching DNA. Macromolecules 28:8759–8770
52. Strick T et al (2000) Twisting and stretching single DNA molecules. Prog Biophys Mol Biol 74(1–2):115–140
53. Balaeff AA, Craig SL, Beratan DN (2011) B-DNA to zip-DNA: simulating a DNA transition to a novel structure with enhanced charge-transport characteristics. J Phys Chem A 115(34):9377–9391
54. Sim AY, Minary P, Levitt M (2012) Modeling nucleic acids. Curr Opin Struct Biol 22(3):273–278
55. Salomon-Ferrer R, Case DA, Walker RC (2013) An overview of the Amber biomolecular simulation package. WIREs Comput Mol Sci 3:198–210

56. Kim DN et al (2012) Quantitative prediction of 3D solution shape and flexibility of nucleic acid nanostructures. Nucleic Acids Res 40(7):2862–2868
57. Woese CR, Kandler O, Wheelis ML (1990) Towards a natural system of organisms – proposal for the domains archaea, bacteria, and eucarya. Proc Natl Acad Sci USA 87(12):4576–4579
58. Sapp J (2006) Two faces of the prokaryote concept. Int Microbiol 9(3):163–172
59. Karp C (2004) Cell and molecular biology: concepts and experiments. Wiley, Hoboken
60. Goodsell DS (2001) The molecular perspective: ultraviolet light and pyrimidine dimers. Oncologist 6(3):298–299
61. Perry JJP et al (2010) Structural dynamics in DNA damage signaling and repair. Curr Opin Struct Biol 20(3):283–294
62. Eley DD, Spivey DI (1962) Semiconductivity of organic substances. Trans Faraday Soc 58:411–415
63. Kasumov AY et al (2001) Proximity-induced superconductivity in DNA. Science 291:280–282
64. Boon EM, Barton JK (2002) Charge transport in DNA. Curr Opin Struct Biol 12(3):320–329
65. Fink HW, Schonenberger C (1999) Electrical conduction through DNA molecules. Nature 398:407–410
66. Porath D et al (2000) Direct measurement of electrical transport through DNA molecules. Nature 403:635–638
67. Jortner J et al (1998) Charge transfer and transport in DNA. Proc Natl Acad Sci USA 95:12759–12765
68. Grozema FC, Berlin YA, Siebbeles LDA (1999) Sequence dependent charge transfer in donor-DNA-acceptor systems: a theoretical study. Int J Quantum Chem 75:1009–1016
69. Genereux JC, Barton JK (2009) Molecular electronics: DNA charges ahead. Nat Chem 1:106–107
70. Kawai K et al (2009) Sequence independent and rapid long-range charge transfer through DNA. Nat Chem 1:156–159
71. Adleman LM (1994) Molecular computation of solutions to combinatorial problems. Science 266(5187):1021–1024
72. Schulman R, Yurke B, Winfree E (2012) Robust self-replication of combinatorial information via crystal growth and scission. Proc Natl Acad Sci USA 109(17):6405–6410
73. Apter MJ, Wolpert L (1965) Cybernetics and development. I. Information theory. J Theor Biol 8(2):244–257
74. Adami C (2004) Information theory in molecular biology. Phys Life Rev 1:3–22
75. Schneider TD (2010) A brief review of molecular information theory. Nano Commun Netw 1(3):173–180
76. Marathe A, Condon AE, Corn RM (2001) On combinatorial DNA word design. J Comput Biol 8(3):201–219
77. Holliday R (2007) A mechanism for gene conversion in fungi. Genet Res 89(5–6):285–307
78. Seeman NC (1982) Nucleic acid junctions and lattices. J Theor Biol 99(2):237–247
79. Fu TJ, Tse-Dinh YC, Seeman NC (1994) Holliday junction crossover topology. J Mol Biol 236(1):91–105
80. Petrillo ML et al (1988) The ligation and flexibility of four-arm DNA junctions. Biopolymers 27(9):1337–1352
81. Goodman RP et al (2005) Rapid chiral assembly of rigid DNA building blocks for molecular nanofabrication. Science 310(5754):1661–1665
82. He Y et al (2008) Hierarchical self-assembly of DNA into symmetric supramolecular polyhedra. Nature 452(7184):198–201
83. Seeman NC (1996) The design and engineering of nucleic acid nanoscale assemblies. Curr Opin Struct Biol 6(4):519–526
84. Zhang C et al (2008) Conformational flexibility facilitates self-assembly of complex DNA nanostructures. Proc Natl Acad Sci USA 105(31):10665–10669

85. Fu TJ, Seeman NC (1993) DNA double-crossover molecules. Biochemistry 32(13):3211–3220
86. Li X et al (1996) Antiparallel DNA double crossover molecules as components for nanoconstruction. J Am Chem Soc 118:6131–6140
87. Majumder U et al (2011) Design and construction of double-decker tile as a route to three-dimensional periodic assembly of DNA. J Am Chem Soc 133(11):3843–3845
88. Malo J, Mitchell JC, Turberfield AJ (2009) A two-dimensional DNA array: the three-layer logpile. J Am Chem Soc 131(38):13574–13575
89. Reishus D et al (2005) Self-assembly of DNA double-double crossover complexes into high-density, doubly connected, planar structures. J Am Chem Soc 127(50):17590–17591
90. LaBean TH et al (2000) Construction, analysis, ligation, and self-assembly of DNA triple crossover complexes. J Am Chem Soc 122(9):1848–1860
91. Liu D et al (2004) Tensegrity: construction of rigid DNA triangles with flexible four-arm DNA junctions. J Am Chem Soc 126(8):2324–2325
92. Qi J, Li X, Seeman NC (1996) Ligation of triangles built from bulged 3-arm DNA branched junctions. J Am Chem Soc 118(26):6121–6130
93. Rothemund PW, Papadakis N, Winfree E (2004) Algorithmic self-assembly of DNA Sierpinski triangles. PLoS Biol 2(12):e424
94. Shen Z et al (2004) Paranemic crossover DNA: a generalized holliday structure with applications in nanotechnology. J Am Chem Soc 126(6):1666–1674
95. Yang X et al (1998) Ligation of DNA triangles containing double crossover molecules. J Am Chem Soc 120(38):9779–9786
96. Zhang X et al (2002) Paranemic cohesion of topologically-closed DNA molecules. J Am Chem Soc 124(44):12940–12941
97. Hamada S, Murata S (2009) Substrate-assisted assembly of interconnected single-duplex DNA nanostructures. Angew Chem Int Ed Engl 48(37):6820–6823
98. Sun X et al (2009) Surface-mediated DNA self-assembly. J Am Chem Soc 131(37):13248–13249
99. Liu Y, Ke Y, Yan H (2005) Self-assembly of symmetric finite-size DNA nanoarrays. J Am Chem Soc 127(49):17140–17141
100. Park SH et al (2006) Finite-size, fully addressable DNA tile lattices formed by hierarchical assembly procedures. Angew Chem Int Ed Engl 45(5):735–739
101. Pistol C, Dwyer C (2007) Scalable, low-cost, hierarchical assembly of programmable DNA nanostructures. Nanotechnology 18(12):125305
102. Schulman R, Winfree E (2007) Synthesis of crystals with a programmable kinetic barrier to nucleation. Proc Natl Acad Sci USA 104(39):15236–15241
103. Ke Y et al (2006) A study of DNA tube formation mechanisms using 4-, 8-, and 12-helix DNA nanostructures. J Am Chem Soc 128(13):4414–4421
104. Kuzuya A et al (2007) Six-helix and eight-helix DNA nanotubes assembled from half-tubes. Nano Lett 7(6):1757–1763
105. Liu D et al (2004) DNA nanotubes self-assembled from triple-crossover tiles as templates for conductive nanowires. Proc Natl Acad Sci USA 101(3):717–722
106. Mitchell JC et al (2004) Self-assembly of chiral DNA nanotubes. J Am Chem Soc 126(50):16342–16343
107. Rothemund PW et al (2004) Design and characterization of programmable DNA nanotubes. J Am Chem Soc 126(50):16344–16352
108. Yin P et al (2008) Programming DNA tube circumferences. Science 321(5890):824–826
109. Lo PK, Metera KL, Sleiman HF (2010) Self-assembly of three-dimensional DNA nanostructures and potential biological applications. Curr Opin Chem Biol 14(5):597–607
110. Samano EC et al (2011) Self-assembling DNA templates for programmed artificial biomineralization. Soft Matter 7:3240–3245

111. Simmel FC (2007) Towards biomedical applications for nucleic acid nanodevices. Nanomedicine (Lond) 2(6):817–830
112. Teller C, Willner I (2010) Functional nucleic acid nanostructures and DNA machines. Curr Opin Biotechnol 21(4):376–391
113. Dietz H, Douglas SM, Shih WM (2009) Folding DNA into twisted and curved nanoscale shapes. Science 325(5941):725–730
114. Han D et al (2011) DNA origami with complex curvatures in three-dimensional space. Science 332(6027):342–346
115. Ke Y, Voigt NV, Gothelf KV, Shih WM (2012) Multilayer DNA origami packed on hexagonal and hybrid lattices. J Am Chem Soc 134:1770–1774
116. Zhang H et al (2012) Folding super-sized DNA origami with scaffold strands from long-range PCR. Chem Commun (Camb) 48:6405–6407
117. Liu W et al (2011) Crystalline two-dimensional DNA-origami arrays. Angew Chem Int Ed Engl 50(1):264–267
118. Yang Y et al (2012) DNA origami with double-stranded DNA as a unified scaffold. ACS Nano 6(9):8209–8215
119. Endo M et al (2010) Programmed-assembly system using DNA jigsaw pieces. Chemistry 16(18):5362–5368
120. Endo M et al (2011) Two-dimensional DNA origami assemblies using a four-way connector. Chem Commun 47:3213–3215
121. Li Z et al (2010) Molecular behavior of DNA origami in higher-order self-assembly. J Am Chem Soc 132(38):13545–13552
122. Rajendran A et al (2011) Programmed two-dimensional self-assembly of multiple DNA origami jigsaw pieces. ACS Nano 5(1):665–671
123. Rangnekar A et al (2012) Increased anticoagulant activity of thrombin-binding DNA aptamers by nanoscale organization on DNA nanostructures. Nanomedicine 8(5):673–681
124. Zhao Z, Liu Y, Yan H (2011) Organizing DNA origami tiles into larger structures using preformed scaffold frames. Nano Lett 11(7):2997–3002
125. Zhao Z, Yan H, Liu Y (2010) A route to scale up DNA origami using DNA tiles as folding staples. Angew Chem Int Ed Engl 49(8):1414–1417
126. Torring T et al (2011) DNA origami: a quantum leap for self-assembly of complex structures. Chem Soc Rev 40(12):5636–5646
127. Gothelf KV (2012) LEGO-like DNA structures. Science 338:1159–1160
128. Castro CE et al (2011) A primer to scaffolded DNA origami. Nat Methods 8(3):221–229
129. Hung AM, Noh H, Cha JN (2010) Recent advances in DNA-based directed assembly on surfaces. Nanoscale 2(12):2530–2537
130. Li H, Labean TH, Leong KW (2011) Nucleic acid-based nanoengineering: novel structures for biomedical applications. Interface Focus 1(5):702–724
131. McLaughlin CK, Hamblin GD, Sleiman HF (2011) Supramolecular DNA assembly. Chem Soc Rev 40(12):5647–5656
132. Shih WM, Lin C (2010) Knitting complex weaves with DNA origami. Curr Opin Struct Biol 20(3):276–282
133. Smith D et al (2013) Nucleic acid nanostructures for biomedical applications. Nanomedicine (Lond) 8(1):105–121
134. Zhang G et al (2013) DNA nanostructure meets nanofabrication. Chem Soc Rev 42(7):2488–2496
135. Andersen ES (2010) Prediction and design of DNA and RNA structures. N Biotechnol 27(3):184–193
136. Andersen ES et al (2008) DNA origami design of dolphin-shaped structures with flexible tails. ACS Nano 2(6):1213–1218
137. Douglas SM et al (2009) Rapid prototyping of 3D DNA-origami shapes with caDNAno. Nucleic Acids Res 37(15):5001–5006

Aptamer-Functionalized Nanomaterials for Biological and Biomedical Applications

35

Yike Huang and Yong Wang

Keywords

Nucleic acid aptamer • Nanomaterial • Biosensor • Drug delivery • Cell imaging

---

Introduction

Nanomaterials can be developed to acquire unique optical [1], magnetic [2], electronic [3] and biological properties [4, 5]. Therefore, they hold great potential for biological and biomedical applications of various fields such as molecular detection, intracellular signaling assessment, cell/tissue imaging, and targeted drug delivery. For example, quantum dots (QD) have been extensively studied for tissue imaging and multiplex detection of biological samples as they have lower photobleaching thresholds than organic fluorophores with broad absorption/emission profiles [6, 7]. Magnetic nanoparticles (e.g., ferrite colloids, magnetite (Fe_3O_4) and maghemite (γ-Fe_2O_3)) have been used as a contrast agent for magnetic resonance imaging (MRI) because they exhibit a resonating response to a magnetic field [8, 9]. In addition to chemical compounds, pure metals (e.g., gold [10]) can also be developed into nanomaterials with desired functionalities. Although a diverse array of nanomaterials can be developed using different chemistries, they usually do not have the capability of recognizing target molecules, cells, or tissues with high binding strength and specificity. Therefore, it is often necessary to functionalize nanomaterials with affinity biomolecules such as nucleic acid aptamers.

Nucleic acid aptamers are DNA or RNA oligonucleotides identified using a method called systematic evolution of ligands by exponential enrichment (SELEX) (Fig. 35.1) [11, 12]. The SELEX process starts with the generation of a library

---

Y. Huang (✉) • Y. Wang

Pennsylvanian State University, University Park, PA, USA

e-mail: yikehuang.zju@gmail.com; yxwbio@engr.psu.edu; yongwang@engr.uconn.edu
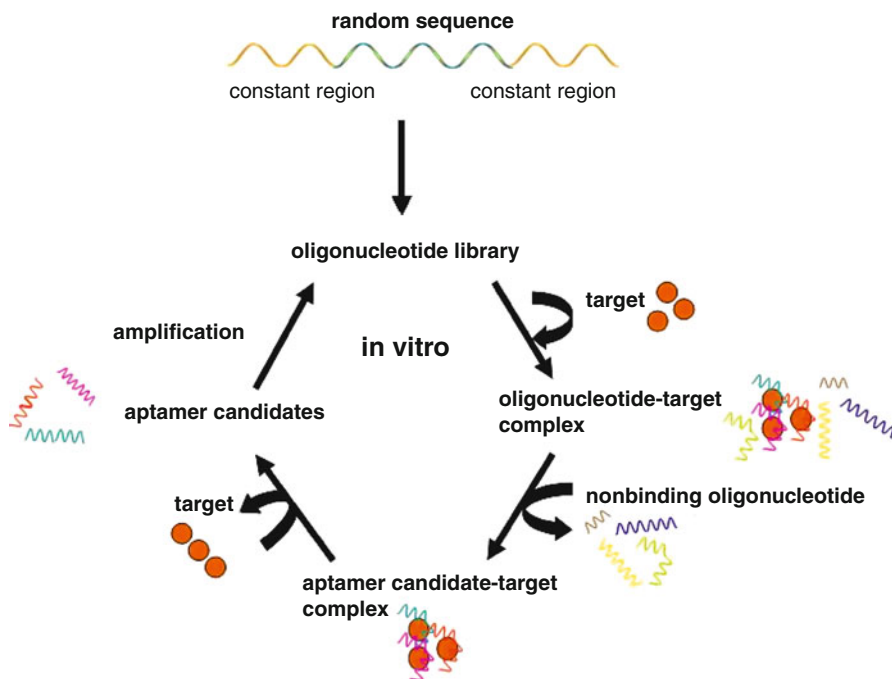
Fig. 35.1 Schematic illustration of the SELEX procedure for the identification of nucleic acid aptamers

containing billions of oligonucleotides. In the screening process, target molecules are first incubated in the library. During the incubation, a small fraction of oligonucleotide sequences bind to the target. These binding sequences will be subsequently separated from those unbound sequences, and amplified to obtain an enriched library for a new round of selection/amplification cycle [13, 14]. After 8–15 rounds of selection [15], high affinity oligonucleotides (aptamers) can be identified. The identified aptamers can be further truncated to eliminate nucleotides that do not play the role of binding to the target [16, 17]. Nucleic acid aptamers identified via SELEX have numerous advantages over other affinity ligands. First, they can interact with target molecules or cells with high affinity and specificity [18, 19]. The binding affinities of most aptamers against their targets are comparable to those of antibodies for antigens [20]. However, antibodies are produced in vivo or from in vitro cell culture [21, 22], whereas aptamers are obtained and synthesized without the involvement of living organism. Thus, the identification and synthesis of aptamers are easier than those of antibodies. In addition, aptamers are tolerant of harsh conditions [23]. Thus, they can be chemically modified or conjugated to a solid support without losing their binding functionality. Their small size is also beneficial to the development of novel nanotechnology tools [24]. Because of these characteristics, nucleic acid aptamers have recently attracted significant attention in a variety of fields. In this chapter, the discussion is focused

on how aptamers and nanomaterials are integrated for novel biological and biomedical applications including molecular detection, cell imaging, cell isolation, and drug delivery.

Molecular Detection

Surface-Enhanced Raman Scattering (SERS)

The intensity of the Raman signal increases when molecules are absorbed on metal surfaces. This phenomenon is called surface-enhanced Raman scattering (SERS) [25, 26]. Based on this mechanism, aptamer-functionalized nanomaterials have been designed to detect target molecules. For instance, a SERS detector was fabricated via the formation of aptamer/target/aptamer–gold nanoparticles (AuNPs) sandwich [27]. Specifically, AuNPs were labeled by Raman reporters and the electromagnetic hot spots were fabricated by deposition of Ag nanoparticles (AgNPs) on AuNPs. The two aptamers [17, 28] were anchored on an Au substrate and AuNPs, respectively. In the presence of the target molecule (e.g., thrombin) that has two distinct binding sites for each aptamer [29], the Raman signal increased due to AuNPs approaching the substrate. An alternative approach was studied by using a partially hybridized double-stranded DNA (dsDNA) aptamer AuNPs and a flat Au substrate [30] (Fig. 35.2). In this approach, the small space between AuNPs and the Au substrate is a SERS hot spot. A partially hybridized double-stranded DNA aptamer is anchored to the Au substrate. One strand is tethered to the AuNP, while the other strand contains the binding sequence to recognize the target molecule. On the addition of an analyte (e.g., adenosine), the double-stranded DNA is partially dissociated due to the binding of the analyte to the aptamer. Thus, it increases molecular flexibility and allows the AuNPs functionalized with Raman reporter molecules to approach the Au substrate more closely. As a result, it leads to the field enhancement within the hot spot and the signal intensity is amplified.
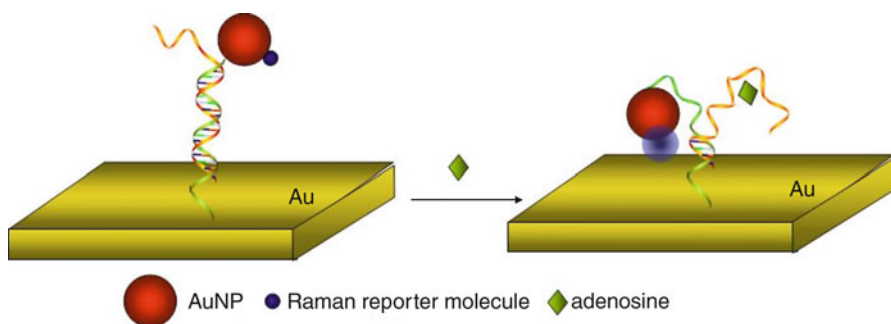

Fig. 35.2 A SERS system for the detection of adenosine using aptamer-functionalized AuNPs

Fluorescence Sensing

Because of the unique optical properties, QDs have been functionalized with aptamers to detect thrombin [31]. When the aptamer-functionalized QD binds to the thrombin, the charge transfer occurs from amine groups on the target protein to the QD, which results in a fluorescence quenching. Based on this method, the thrombin was detected with high specificity and sensitivity. Importantly, this assay could be accomplished within 1 min. The limit of detection was 1 nM. It is also important to emphasize that this method worked effectively even in the sample containing a large amount of interfering proteins. Fluorescence resonance energy transfer (FRET) is a phenomenon showing the excitation energy of the donor transferred to the acceptor via an induced dipole-induced dipole interaction [32]. The efficiency of energy transfer is a function of the distance between donor and acceptor. A small change in distance will lead to the energy transfer significantly. Therefore, FRET is extremely sensitive [33, 34]. Aptamer-functionalized nanomaterials, thus, have been developed to detect molecules via FRET. The first aptamer-QD FRET-based probe was reported in 2005 using thrombin aptamer as a model [35]. The aptamer conjugated on QD was hybridized with a complementary DNA labeled with quencher. In the absence of thrombin, the fluorescent signal of QDs was quenched due to the close proximity to the quenchers and the energy transfer from the quantum dot to the quencher. However, in the presence of thrombin, thrombin will induce the conformational change of the hybridized aptamer and compete against the complementary DNA. Resultantly, the complementary DNA will fall off from the QD. Because the quencher was conjugated with the complementary DNA, the dissociation of the complementary DNA will lead to the recovery of the fluorescent signal. The signal intensity is affected by the concentration of thrombin. Thus, this method, in principle, can be applied to the detection of protein targets in the solution.

In addition to QDs, carbon nanomaterials such as graphene and graphene oxide have also been studied for highly sensitive and specific molecular detection via FRET since they are good energy acceptors [36]. For example, Chang et al. reported graphene FRET system functionalized with a thrombin aptamer [37]. In this system, the thrombin aptamer is non-covalently absorbed on graphene that induces fluorescence quenching of the dye tethered to the aptamer. When thrombin is added into the system, the formation of the aptamer-thrombin complexes leads to the dissociation of the complex from the graphene due to very weak interaction of the complex with graphene. Thus, the dye leaves from graphene, which gives rise to the fluorescence recovery. This method exhibits high sensitivity and specificity in detecting thrombin in blood with a limit of detection as low as 31.3 nM. Similarly, aptamer-functionalized QDs can be integrated with graphene oxide (GO) for the molecular detection [38].

In addition to the detection of proteins, aptamer-functionalized nanomaterials can be applied to the detection of small molecular weight drugs using FRET. Freeman et al. reported a cocaine detection system that involves two nucleic acid sequences [39]. One nucleic acid sequence was used to modify the QDs; the other nucleic acid sequence was functionalized with a dye molecule. Both nucleic acid oligonucleotides have aptamers as one critical fragment in their sequences.
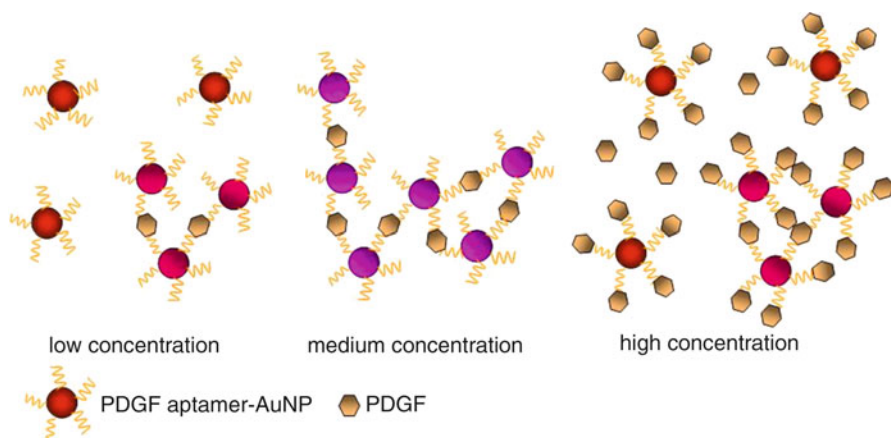
Fig. 35.3 A sandwich assay for visual detection of PDGF

These two sequences have defined regions to form intermolecular duplexes. However, in the absence of cocaine, they are not stable. In contrast, in the presence of cocaine, the supramolecular cocaine-aptamer complex is synergistically stabilized and self-assembled. It results in the FRET process between the QD and the dye acceptor, decreasing the luminescence of the QD and increasing the fluorescence of the dye. The decrease in the luminescence intensity of the QDs can be used to determine the cocaine within a low limit of detection of 1 μM.

Colorimetric Assays for Visual Detection

Visual detection is important since it minimizes or eliminates the necessity of using expensive and complicated instruments. One strategy for applying nanoparticles to visual detection is based on the variation of the distance of gold nanoparticles. The surface plasmon resonance (SPR) is a resonant coherent oscillation of the free electrons at the surface of nanoparticles. When this distance among individual AuNPs decreases to be less than the diameter of AuNPs, the red-to-purple color change can occur [40]. It provides an opportunity of using AuNPs for visual detection.

A typical example is a system established with four key components: gold nanoparticles, two DNAs for nanoparticle functionalization, and a linker DNA bearing an aptamer [41]. In the absence of target molecules, the DNA-functionalized AuNPs are assembled by the linker DNA. This assembly-induced aggregation leads to the generation of a faint purple color in solution. In the presence of target molecules, the conformation of the linker DNA is changed. Resultantly, the two DNA molecules used for nanoparticle functionalization are dissociated. It causes the disassembly of AuNPs to give rise to a color change. Instead of inducing the dissociation of nanoparticles by analytes, another detecting system was established by using analytes as a cross-linker to assemble nanoparticles (Fig. 35.3) [42]. This system has been
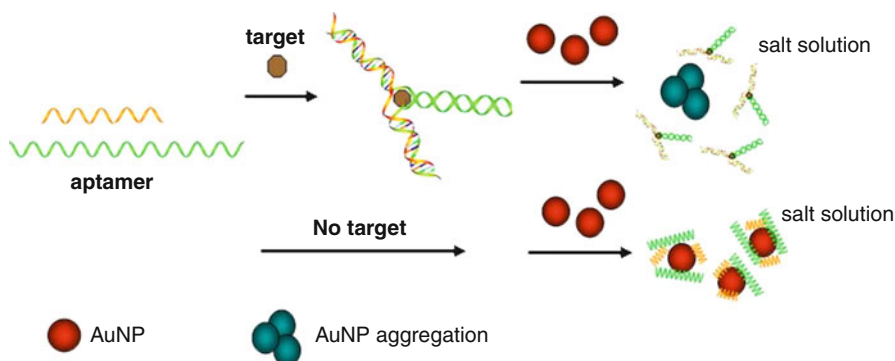
Fig. 35.4 Scheme of the visual detection using aptamer containing two engineered ssDNA pieces at high salt concentration

studied to detect platelet-derived growth factor-BB (PDGF-BB). At low PDGF concentrations, no obvious nanoparticle aggregation occurred, presumably due to the low degree of cross-linking. When the concentration of PDGF increased to a threshold level, the color changed. It indicates that PDGF molecules act as bridges to link aptamer-AuNPs together. However, while the concentration of PDGF is high enough to saturate the surface of aptamer-AuNPs, the aggregation disappeared again.

Nanoparticle aggregation is not only controlled by DNA molecules and analytes, but also salts. Studies have shown that the presence of NaCl above a certain concentration can induce AuNPs to aggregate. It is because NaCl decreases the electrostatic repulsion between nanoparticles. However, the highly negatively charged DNA that spontaneously binds to the AuNPs can effectively stabilize AuNPs against salt-induced aggregation [43]. An aptamer containing two single-stranded DNA (ssDNA) pieces (Fig. 35.4) [44] and a random-coil-like ssDNA aptamer [45] have been used to stabilize the AuNPs in the high concentration NaCl solution. In the presence of the target analyte, the ssDNA lose their affinity in binding to AuNPs because of the formation of aptamer-target complex. As a result, salt is able to induce AuNPs to aggregate. The aggregation leads to a red-to-blue color change. This method has shown some promise for molecular detection.

At low salt concentrations, both ssDNA and dsDNA can prevent aggregation of AuNPs [46]. The method, thus, can be further developed using a positively charged polyelectrolyte. Fan Xia et al. employed single-stranded probe DNA, unmodified gold nanoparticles, and a positively charged polyelectrolyte to develop an approach to detect many target molecules including DNA, proteins, and small molecules [47]. In this approach, positively charged polyelectrolytes efficiently sequester ssDNA dsDNA or 'folded' DNA from AuNPs. This sequestration leads to the aggregation of AuNPs and color change if the target molecule does not present in the system. When this approach was used to detect DNA, the limit of detection reached the picomolar level (Fig. 35.5).
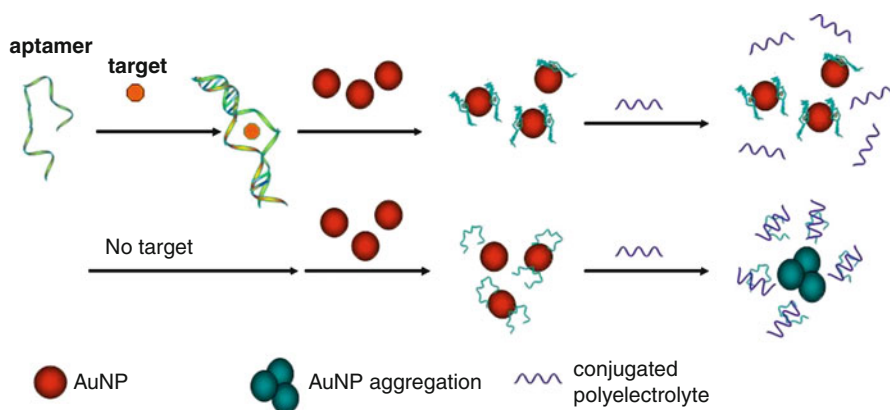
Fig. 35.5 Scheme of the visual detection using a nanoparticle-based polyelectrolyte system at a low salt concentration. The analytes can be DNAs, proteins, and small molecules

Electronic Methods

The aptamer-target binding event can affect the potential changes of the gate of a field-effect transistor (FET), enabling the sensing of target molecules. Maya Zayats and coworkers demonstrated that the FET-based system can detect adenosine with a limit of detection at $50\,\mu M$ [48]. In this approach, the Al_2O_3 gate surface was functionalized with the adenosine aptamer. A complementary nucleic acid sequence was hybridized with the aptamer to increase the negative charge on the gate surface. The presence of adenosine induces the conformational change of the aptamer and the dissociation of the complementary sequence. The displacement of the complementary sequence affects the local charge density on the gate surface. It results in the transduction of the signal of adenosine. In addition to small molecules such as adenosine, this approach has also been studied to examine large biomolecules. For instance, an aptamer-functionalized single-walled carbon nanotube (SWCNT) FET device was demonstrated to detect thrombin with the limit of detection at 10 nM [49]. Similarly, Kenzo Maehashi and coworkers developed a device to monitor immunoglobulin E (IgE) based on an aptamer-functionalized carbon nanotube FET [50]. The limit of detection reached 250 pM. In contrast, it is difficult to replace the aptamer with the antibody to realize the similar detection because of the large size of the antibody.

Though many studies rely on the use of one aptamer for analyzing an individual analyte, others have been focused on using two aptamers and one nanoparticle. For instance, two thrombin aptamers are used to functionalize a Pt nanoparticle (PtNP) and a gold electrode to develop a single detection system [51]. The PtNP functions as a catalyst to reduce H_2O_2 to produce currents. These two aptamers bind to the same protein target but two different regions. The presence of the target protein will induce the formation of a thrombin-aptamer-PtNP sandwich complex on the electrode. The system has been demonstrated to detect thrombin with a limit of detection at 1 nM. In addition to the detection of single analytes, the electronic methods can be

applied to multiplex detection. For instance, Jacob A. Hansen et al. reported a highly sensitive system to detect two proteins, thrombin and lysozyme [52]. In this approach, two aptamers are conjugated to the Au substrate and two proteins are conjugated with two different types of QDs. The aptamers on the substrate are used to capture the corresponding protein–QD conjugates. When free thrombin and lysozyme are added into the system, these proteins will replace the protein–QD conjugates. The electrochemical detection of the remaining QDs on the substrate is used to quantify the amount of free proteins. This approach has a potential to satisfy the low power, size, and cost requirements of molecular detection.

The electronic methods as mentioned above do not involve any amplification reaction. An ultrasensitive detection method has been studied based on aptamer-rolling circle amplification (aptamer-RCA) [53]. In this method, a capture antibody is immobilized on the electrode surface. After the analyte is captured by the antibody, the aptamer will be subsequently captured by this analyte. The whole procedure will lead to the formation of an antibody-analyte-aptamer sandwich. Because the aptamer is functionalized with a primer sequence, this sandwich can initiate an in situ RCA isothermal reaction. This reaction will lead to the generation of a long DNA chain with many repeating sites for the hybridization of probes and the accumulation of enzymes (e.g., alkaline phosphatase). After the substrates are added into the system, the enzymatic catalysis will initiate a multiple-step reaction that will lead to the deposition of silver to the electrode surface for the linear sweep voltammetric measurement. This method can provide a limit of detection as low as 10 fM.

Cell Analysis

The ability to diagnose a disease at the early stage is crucial to the development of timely treatment strategies. To this end, aptamers have been selected to recognize abnormal cells and tissues. However, not all aptamers have high binding affinities. To increase the binding affinity, multiple aptamers can be conjugated to a nanoparticle to acquire multivalency. In addition, as mentioned before, nanomaterials have their unique functionalities as contrast agents and fluorescence provider. In certain conditions, nanomaterials can also protect aptamers while free aptamers can be degraded by nucleases. Therefore, great efforts have been made to develop aptamer-functionalized nanoparticles for cell imaging, cell detection, and intracellular analysis.

In Vivo Cell Imaging

Sgc8c aptamer [54] was selected against the PTK7 receptor that is overexpressed on CCRF-CEM cells (human acute lymphoblastic leukemia). It has been used as a model to functionalize numerous nanoparticles for cell imaging. For instance, Huang et al. used this aptamer to functionalize Au-Ag nanorods (Au/Ag NRs) [55]. The results showed that approximately 80 aptamers could be conjugated to one

nanorod. The large number of aptamers on one NR led to the production of a much stronger fluorescence signal than an individual dye-labeled aptamer. The flow cytometry result showed that the NR labeled cells exhibited fluorescence intensity 300 times more than those labeled with individual aptamers.

Wang et al. used sgc8c aptamer to functionalize lipid-based nanobubbles, a contrast agent to study ultrasound-mediated CCRF-CEM cell imaging [56]. The A10 aptamer [57] that was selected against prostate-specific membrane antigen (PSMA), a well-known prostate cancer tumor marker, was studied to functionalize QDs for imaging [58]. The aptamer-QD conjugates showed specific targeting to both fixed and live cells expressing PSMA. In addition to single-modality imaging, nanoparticles can be designed to satisfy the need of multimodal imaging. A recent study showed that a composite nanoparticle could be synthesized with a cobalt-ferrite core and a silica shell containing rhodamine and radioisotope [59]. The surface of this nanoparticle was functionalized with AS1411 aptamer [60] that recognize nucleolin (NCL) overexpressed by numerous cancer cells. This multifunctional nanoparticle was demonstrated to have the potential for concurrent fluorescence imaging, radionuclide imaging, and MRI in vivo.

However, it is important to note that these novel aptamer-functionalized nanomaterials have not been tested in vivo though they were originally designed for in vivo cell imaging. Thus, more work is needed to understand their pharmacokinetics and pharmacodynamics.

Ex Vivo Cell Detection

A two-nanoparticle system has been studied for cell detection [61]. The two nanoparticles included a fluorescent dye-doped nanoparticle and a magnetic nanoparticle. The aptamer-functionalized fluorescent nanoparticle was used to bind to target cells and to produce fluorescence signals. The aptamer-functionalized magnetic nanoparticle also bound target cells. However, this nanoparticle was used for the magnet-mediated cell separation from the cell mixture. The limit of detection of this two-nanoparticle system was approximately 250 cells. This method can be further optimized by varying the nanoparticle size and the conjugation chemistry [62]. Moreover, because of high binding affinity and specificity, multiple aptamers can be used to functionalize multiple nanoparticles for the multiplex detection of cancer cells [63].

The use of two-nanoparticle system for cell isolation and detection needs time-consuming operations and large instruments. To simplify the detection, a colorimetric assay was developed [64]. Because the surface of a cancer cell has a large number of specific cell receptors, the distance of aptamer-functionalized nanoparticles targeting these receptors can be very short. The short distance of AuNPs can induce a color change. In addition, this color change is a function of cell number. Thus, the AuNP assembly on the cell surface has been used as a colorimetric assay for the detection of cancer cells. The results showed that 1,000 cells could be detected by naked eyes.

Aptamer-functionalized nanoparticles can also be integrated into simple devices for cell detection. For instance, nanoparticles and a strip biosensor have been
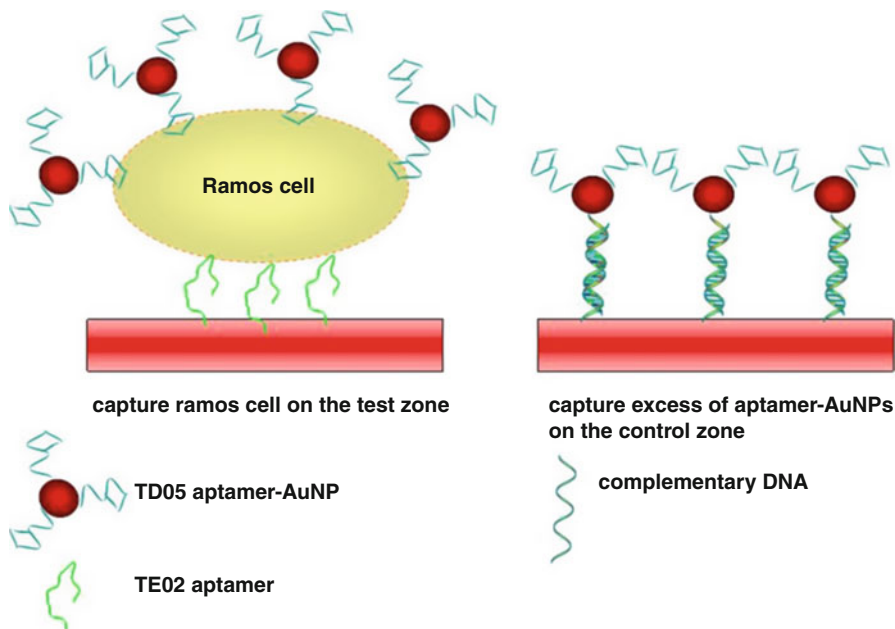
Fig. 35.6 An aptamer-nanoparticle strip biosensor for the detection of cancer cells

integrated to develop a nanoparticle strip biosensor (ANSB) [65]. The ANSB harnesses the advantages of both aptamers and AuNPs. In this ANSB assay, two aptamers (TD05,TE02) that can bind to target Ramos cells were immobilized on the surface of AuNPs and the test zone of the ANSB, respectively. When the cell suspension meets aptamer-functionalized AuNPs, target cells will form cell-AuNP complexes with aptamer-functionalized AuNPs. With the running solution along the strip, the complexes will eventually migrate to the test zone and they will be captured on the test zone due to the interactions of target cells and the secondary aptamer. The accumulation of AuNPs in the test zone will produce a characteristic red band for the observation (test line). In addition, the free aptamer-functionalized AuNPs will continue to flow to the control zone where the complementary DNA of the aptamer will capture AuNPs to form a second red band (control line). The limit of detection can reach 4,000 cells. The optical intensity of the test line can be quantitatively measured by using a portable strip reader (Fig. 35.6).

Intracellular Analysis

The ability to detect molecules inside a cell will provide deep insights into the life of the cell and the fundamental molecular mechanisms. Aptamer-functionalized nanomaterials have been studied as a promising tool for real-time monitoring of intracellular molecules. For example, an aptamer-functionalized AuNP has been

applied to achieve this goal using ATP as a model [66]. In this approach, a fluorophore-labeled oligonucleotide hybridizes with the aptamer immobilized on the AuNP surface. The AuNP is used to quench the fluorescence of the fluorophore. ATP can induce the conformational change of the aptamer. Resultantly, the fluorophore-labeled oligonucleotide falls off from the AuNP and the fluorescence signal can be detected. Similarly, carboxyfluorescein (FAM) labeled aptamers and graphene oxide nanosheet (GONS) were also studied to monitor the intracellular APT in real time based on FRET [67]. In the absence of the target molecule, the aptamer is attached to the surface of GONS through intermolecular hybridization and the fluorescence of FAM was quenched because of FRET between GONS and FAM. In the presence of the target molecule (e.g., ATP), the aptamer is released from the GONS surface and the fluorescence signal is recovered. One concern with these systems is nuclease degradation. Interestingly, GONS plays a role of protecting the aptamers in the cells. In addition to using nanoparticles as a quencher, studies have also been carried out to use porous polyacrylamide nanoparticles only as a carrier to deliver aptamers into the cells. This carrier can allow rapid diffusion of ATP into the particles to interact with the aptamer while retaining the aptamer in the matrix and protecting it from intracellular degradation [68]. The two ends of the aptamer are labeled with a fluorophore and a quencher. The target molecule (ATP) can induce the structural change of the aptamer and trigger the separation of the fluorophore from the quencher to produce the signal.

Drug Delivery

Nanomaterials can be used for not only imaging and separation, but also for therapy. As a drug delivery vehicle, nanomaterials need to carry drugs with high payload, protect drugs from degradation, and release drugs at the right location at the right rate. In addition, nanomaterials need to be well suspended or dissolved in aqueous solutions for systemic transport in the blood circulation [69]. Nanomaterials that can satisfy these needs hold great potential for the treatments of various human diseases. In the past few decades, most efforts were focused on nanomaterial-mediated cancer therapy. Because solid tumors usually have leaky microvasculature, nanomaterials with certain sizes can be delivered into solid tumors via the enhanced permeation and retention (EPR) effect [5]. In addition, nanomaterials can be tuned to acquire desired properties to escape from the reticuloendothelial system (RES) such as liver and spleen that usually play an important role in capturing and clearing foreign nanoparticles from the blood stream. For instance, polyethyleneglycol (PEG) can be grafted on the nanomaterial surface to eliminate the uptake by the RES system [70, 71] and to enhance nanomaterial delivery into tumors. Although nanomaterials can be delivered into tumors via the passive EPR effect, it has been believed that the conjugation of molecular recognition elements to nanomaterials will provide an active way of drug delivery. Therefore, great efforts have been recently made to develop aptamer-functionalized nanomaterials for drug delivery and cancer therapy.

Aptamer-Functionalized Polymeric Nanomaterials

The first aptamer-functionalized nanoparticle for cancer therapy was reported in 2004 by Farokhzad et al. [72]. This nanoparticle was made of poly(lactic acid)-block-polyethylene glycol (PEG) copolymer, with carboxylic acid as a terminal functional group using a emulsification method. The carboxylic acid was activated to react with the amino group of A10 aptamer. The results showed that the functionalized nanoparticles specifically recognized the prostate LNCaP cells overexpressing PSMA rather than control cells not expressing PSMA. In a following study, this research group used aptamer-functionalized nanoparticles to encapsulate docetaxel (Dtxl) [73]. After a single intratumoral injection of the nanoparticles, complete tumor reduction was observed in five of seven mice bearing LNCaP xenograft. All of these mice survived during the 109-day test. In contrast, two of seven mice receiving non-functionalized nanoparticles had complete tumor reduction and 57 % survived during the same period of time. The group of mice treated with only Dtxl only had a survivability of 14 %. These results clearly demonstrate the great potential of using aptamer-functionalized nanoparticles for cancer therapy.

In addition to the emulsification method, studies have also been carried out to use polymer self-assembly to develop nanoparticles. For instance, the self-assembly of a triblock copolymer and a diblock copolymer was used to develop nanoparticles [74]. The copolymers were composed of end-to-end linkage of poly (lactic-co-glycolic-acid) (PLGA), PEG, and a modified A10 aptamer. The specific advantage of this method is that the uptake of nanoparticles by the LNCaP cells can be controlled by adjusting the density of aptamers on the nanoparticle surface. However, the results also indicate that the high density of aptamers may increase nanoparticle accumulation in the liver and spleen presumably, because PEG is shielded by the aptamers on the nanoparticle surface. Therefore, this study shows that it is important to balance the amount of aptamers and PEG molecules on the surface of nanoparticles for targeted drug delivery in cancer therapy.

Nanomaterials can be developed with not only synthetic polymers but also lipids. A aptamer-functionalized liposome was developed with a lipid membrane composed of hydrogenated soy phosphatidylcholine (HSPC) cholesterol (Chol), methoxypoly-(ethyleneglycol)-distearoyl-phosphatidyl-ethanolamine (MPEGDSPE), and maleimide-terminated PEG-DSPE (MalPEG) [75]. The sgc8 aptamer was covalently conjugated to the liposome through the PEG spacer. The result showed that the aptamers improved the stability of the liposomes and targeting specificity. A similar study was also carried out by Yanrong Wu et al. [76] The DNA aptamer was conjugated to a simple lipid tail phosphomidite with diacyl chains through a PEG linker that was inserted between the aptamer and the lipid. By using this conjugate, a promising aptamer-based micelle was developed. This micelle showed 45-fold enhancement in binding to target cells.

Aptamer-Functionalized Multifunctional Nanomaterials

In addition to using nanomaterials as a drug vehicle, nanomaterials can be designed to be responsive to physical stimuli [10]. For instance, gold nanoparticles are responsive to light and can produce heat locally. A photoactivatable drug release system was synthesized using AuNPs functionalized with both sgc8c aptamers and hairpin DNAs [77]. AuNPs support the DNA molecules and receive the input photoenergy; the sgc8c aptamer functions as the affinity ligand to recognize target cancer cells; and the hairpin DNAs function as a depot to load drugs. This multifunctional AuNP releases doxorubicin upon illumination with a continuous-wave laser. The in vitro cell culture study showed that cancer cells could be killed more than 80 %. Kang et al. integrated Au/Ag NRs and cross-linked polyacrylamide gel shells to develop a similar drug delivery platform [78]. When exposed to near-infrared light irradiation, the photothermal effect of the Au/Ag NRs resulted in a rapid rise in the temperature of the hydrogel and consequently fast release of the encapsulated payload with high controllability. Au nanorods and a mesoporous silica material were also integrated to develop similar aptamer-functionalized nanomaterials for drug delivery [79].

Integrated Imaging and Therapy

Great attention has recently been paid to the development of nanomaterials that have the functionalities of both imaging and therapy. The successful development of multifunctional nanomaterials will allow for synchronous disease diagnose and therapy. For instance, the A10 aptamer has been used to functionalize a CdSe/ZnS QD for cancer imaging and therapy [80]. The A10 aptamer played a dual role of recognizing tumor cells and carrying doxorubicin. Based on the mechanism of FRET, QD is quenched by doxorubicin and doxorubicin is quenched by aptamer. After QDs are delivered into the target cancer cells, doxorubicin is gradually released via two potential mechanisms. One is the passive dissociation of doxorubicin from the aptamer; the other is the active degradation of the aptamer by nuclease [81]. After the release, the fluorescence of both QD and doxorubicin is activated (Fig. 35.7). Similarly, a superparamagnetic iron oxide nanoparticle was functionalized with the A10 aptamer [82]. The magnetic nanoparticles act as an MRI contrast agent, and the aptamers function as the target ligand and the carrier of doxorubicin. The results showed the high nuclear magnetic resonance (NMR) sensitivity of the nanoparticles in examining PSMA+ cells. In addition, the nanoparticles showed high specificity to PSMA+ prostate cancer cells compared to the free drugs that did not differentiate PSMA+ and PSMA− cell lines. The same concept could also be tuned to the integrated computed tomography (CT) imaging and drug delivery [83]. Nanomaterials can be further optimized to acquire more functions. For instance, studies have been carried out to integrate
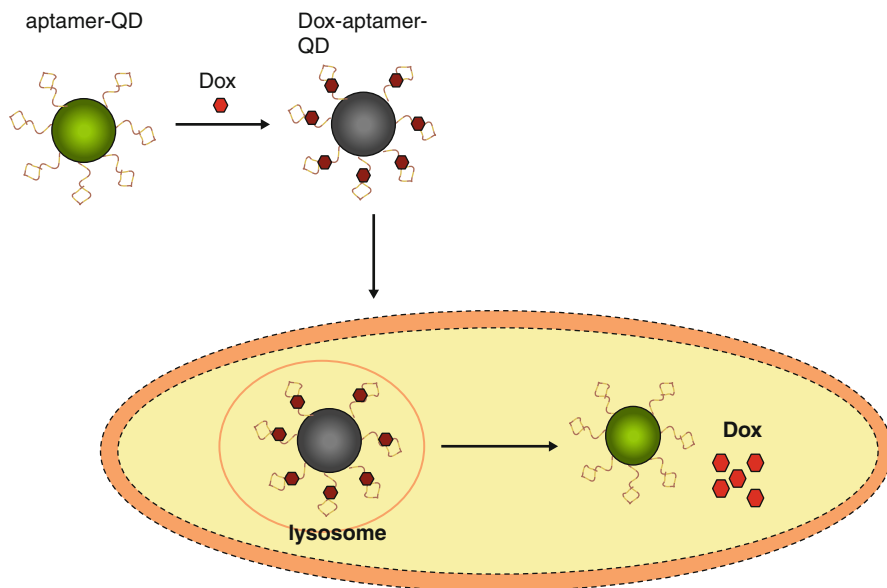
Fig. 35.7 A multifunctional nanoparticle for integrated imaging and therapy

magnetic separation with fluorescence imaging and photothermal destruction [84]. However, most of these studies were pursued in vitro. Therefore, it is important to test the effectiveness of these novel multifunctional nanomaterials in animals.

References

1. Alivisatos AP (1996) Semiconductor clusters, nanocrystals, and quantum dots. Science 271(5251):933–937
2. Lu AH et al (2007) Magnetic nanoparticles: Synthesis, protection, functionalization, and application. Angew Chem Int Ed 46(8):1222–1244
3. Xia YN et al (2003) One-dimensional nanostructures: synthesis, characterization, and applications. Adv Mater 15(5):353–389
4. Hillaireau H, Couvreur P (2009) Nanocarriers' entry into the cell: relevance to drug delivery. Cell Mol Life Sci 66(17):2873–2896
5. Dobrovolskaia MA, McNeil SE (2007) Immunological properties of engineered nanomaterials. Nat Nanotechnol 2(8):469–478
6. Medintz IL et al (2005) Quantum dot bioconjugates for imaging, labelling and sensing. Nat Mater 4(6):435–446
7. Chan WCW, Nie SM (1998) Quantum dot bioconjugates for ultrasensitive nonisotopic detection. Science 281(5385):2016–2018
8. Reddy LH et al (2012) Magnetic nanoparticles: design and characterization, toxicity and biocompatibility, pharmaceutical and biomedical applications. Chem Rev 112(11):5818–5878
9. Pouliquen D et al (1991) Iron-oxide nanoparticles for use as an MRI contrast agent – pharmacokinetics and metabolism. Magn Reson Imaging 9(3):275–283

10. Boisselier E, Astruc D (2009) Gold nanoparticles in nanomedicine: preparations, imaging, diagnostics, therapies and toxicity. Chem Soc Rev 38(6):1759–1782
11. Ellington AD, Szostak JW (1990) Invitro selection of RNA molecules that bind specific ligands. Nature 346(6287):818–822
12. Ellington AD, Szostak JW (1992) Selection in vitro of single-stranded-DNA molecules that fold into specific ligand-binding structures. Nature 355(6363):850–852
13. Daniels DA et al (2003) A tenascin-C aptamer identified by tumor cell SELEX: systematic evolution of ligands by exponential enrichment. Proc Natl Acad Sci USA 100(26):15416–15421
14. Wilson DS, Szostak JW (1999) In vitro selection of functional nucleic acids. Annu Rev Biochem 68:611–647
15. Lou X et al (2009) Micromagnetic selection of aptamers in microfluidic channels. Proc Natl Acad Sci USA 106(9):2989–2994
16. Stoltenburg R et al (2007) SELEX-a (r)evolutionary method to generate high-affinity nucleic acid ligands. Biomol Eng 24(4):381–403
17. Bock LC et al (1992) Selection of single-stranded-DNA molecules that bind and inhibit human thrombin. Nature 355(6360):564–566
18. Tuerk C, Gold L (1990) Systematic evolution of ligands by exponential enrichment – RNA ligands to bacteriophage-T4 DNA-polymerase. Science 249(4968):505–510
19. Morris KN et al (1998) High affinity ligands from in vitro selection: complex targets. Proc Natl Acad Sci USA 95(6):2902–2907
20. Jayasena SD (1999) Aptamers: an emerging class of molecules that rival antibodies in diagnostics. Clin Chem 45(9):1628–1650
21. Chames P et al (2009) Therapeutic antibodies: successes, limitations and hopes for the future. Br J Pharmacol 157(2):220–233
22. Evan GI et al (1985) Isolation of monoclonal-antibodies specific for human c-myc proto-oncogene product. Mol Cell Biol 5(12):3610–3616
23. Iliuk AB et al (2011) Aptamer in bioanalytical applications. Anal Chem 83(12):4440–4452
24. Song SP et al (2008) Aptamer-based biosensors. Trends Analyt Chem 27(2):108–117
25. McNay G et al (2011) Surface-Enhanced Raman Scattering (SERS) and Surface-Enhanced Resonance Raman Scattering (SERRS): a review of applications. Appl Spectrosc 65(8):825–837
26. Nie SM, Emery SR (1997) Probing single molecules and single nanoparticles by surface-enhanced Raman scattering. Science 275(5303):1102–1106
27. Wang Y et al (2007) SERS opens a new way in aptasensor for protein recognition with high sensitivity and selectivity. Chem Commun (48):5220–5222
28. Tasset DM et al (1997) Oligonucleotide inhibitors of human thrombin that bind distinct epitopes. J Mol Biol 272(5):688–698
29. Padmanabhan K et al (1993) The strucure of alpha-thrombin inhibited by a 15-mer single-stranded-DNA aptamer. Journal of Biological Chemistry 268(24): 17651–17654
30. Kim NH et al (2010) Aptamer-mediated surface-enhanced Raman spectroscopy intensity amplification. Nano Lett 10(10):4181–4185
31. Choi JH et al (2006) Aptamer-capped nanocrystal quantum dots: a new method for label-free protein detection. J Am Chem Soc 128(49):15584–15585
32. Jares-Erijman EA, Jovin TM (2003) FRET imaging. Nat Biotechnol 21(11):1387–1395
33. Ha T et al (1996) Probing the interaction between two single molecules: Fluorescence resonance energy transfer between a single donor and a single acceptor. Proc Nat Acad Sci USA 93(13):6264–6268
34. Clapp AR et al (2004) Fluorescence resonance energy transfer between quantum dot donors and dye-labeled protein acceptors. J Am Chem Soc 126(1):301–310
35. Levy M et al (2005) Quantum-dot aptamer beacons for the detection of proteins. Chembiochem 6(12):2163–2166
36. Morales-Narvaez E et al (2012) Simple forster resonance energy transfer evidence for the ultrahigh quantum dot quenching efficiency by graphene oxide compared to other carbon structures. Carbon 50(8):2987–2993

37. Chang H et al (2010) Graphene fluorescence resonance energy transfer aptasensor for the thrombin detection. Anal Chem 82(6):2341–2346
38. Dong H et al (2010) Fluorescence resonance energy transfer between quantum dots and graphene oxide for sensing biomolecules. Anal Chem 82(13):5511–5517
39. Freeman R et al (2009) Self-assembly of supramolecular aptamer structures for optical or electrochemical sensing. Analyst 134(4):653–656
40. Ghosh SK, Pal T (2007) Interparticle coupling effect on the surface Plasmon resonance of gold nanoparticles: from theory to applications. Chem Rev 107(11):4797–4862
41. Liu J, Lu Y (2006) Preparation of aptamer-linked gold nanoparticle purple aggregates for colorimetric sensing of analytes. Nat Protoc 1(1):246–252
42. Huang CC et al (2005) Aptamer-modified gold nanoparticles for colorimetric determination of platelet-derived growth factors and their receptors. Anal Chem 77(17):5735–5741
43. Rosi NL, Mirkin CA (2005) Nanostructures in biodiagnostics. Chem Rev 105(4):1547–1562
44. Zhang J et al (2008) Visual cocaine detection with gold nanoparticles and rationally engineered aptamer structures. Small 4(8):1196–1200
45. Wang L et al (2006) Unmodified gold nanoparticles as a colorimetric probe for potassium DNA aptamers. Chem Commun (36):3780–3782
46. Li HX, Rothberg L (2004) Colorimetric detection of DNA sequences based on electrostatic interactions with unmodified gold nanoparticles. Proc Natl Acad Sci USA 101(39):14036–14039
47. Xia F et al (2010) Colorimetric detection of DNA, small molecules, proteins, and ions using unmodified gold nanoparticles and conjugated polyelectrolytes. Proc Natl Acad Sci USA 107(24):10837–10841
48. Zayats M et al (2006) Label-free and reagentless aptamer-based sensors for small molecules. J Am Chem Soc 128(42):13666–13667
49. So HM et al (2005) Single-walled carbon nanotube biosensors using aptamers as molecular recognition elements. J Am Chem Soc 127(34):11906–11907
50. Maehashi K et al (2009) Aptamer-based label-free immunosensors using carbon nanotube field-effect transistors. Electroanalysis 21(11):1285–1290
51. Golub E et al (2009) Electrochemical, photoelectrochemical, and surface Plasmon resonance detection of cocaine using supramolecular aptamer complexes and metallic or semiconductor nanoparticles. Anal Chem 81(22):9291–9298
52. Hansen JA et al (2006) Quantum-dot/aptamer-based ultrasensitive multi-analyte electrochemical biosensor. J Am Chem Soc 128(7):2228–2229
53. Zhou L et al (2007) Aptamer-based rolling circle amplification: a platform for electrochemical detection of protein. Anal Chem 79(19):7492–7500
54. Shangguan D et al (2006) Aptamers evolved from live cells as effective molecular probes for cancer study. Proc Natl Acad Sci USA 103(32):11838–11843
55. Huang YF et al (2008) Cancer cell targeting using multiple aptamers conjugated on nanorods. Anal Chem 80(3):567–572
56. Wang CH et al (2011) Aptamer-conjugated nanobubbles for targeted ultrasound molecular imaging. Langmuir 27(11):6971–6976
57. Lupold SE et al (2002) Identification and characterization of nuclease-stabilized RNA molecules that bind human prostate cancer cells via the prostate-specific membrane antigen. Cancer Res 62(14):4029–4033
58. Chu TC et al (2006) Labeling tumor cells with fluorescent nanocrystal-aptamer bioconjugates. Biosens Bioelectron 21(10):1859–1866
59. Hwang do W et al (2010) A nucleolin-targeted multimodal nanoparticle imaging probe for tracking cancer cells using an aptamer. J Nucl Med 51(1):98–105
60. Bates PJ et al (1999) Antiproliferative activity of G-rich oligonucleotides correlates with protein binding. J Biol Chem 274(37):26369–26377
61. Herr JK et al (2006) Aptamer-conjugated nanoparticles for selective collection and detection of cancer cells. Anal Chem 78(9):2918–2924

62. Medley CD et al (2011) Aptamer-conjugated nanoparticles for cancer cell detection. Anal Chem 83(3):727–734
63. Smith JE et al (2007) Aptamer-conjugated nanoparticles for the collection and detection of multiple cancer cells. Anal Chem 79(8):3075–3082
64. Medley CD et al (2008) Gold nanoparticle-based colorimetric assay for the direct detection of cancerous cells. Anal Chem 80(4):1067–1072
65. Liu GD et al (2009) Aptamer-nanoparticle strip biosensor for sensitive detection of cancer cells. Anal Chem 81(24):10013–10018
66. Zheng D et al (2009) Aptamer Nano-flares for Molecular Detection in Living Cells. Nano Lett 9(9): 3258–3261
67. Wang Y et al (2010) Aptamer/graphene oxide nanocomplex for in situ molecular probing in living cells. J Am Chem Soc 132(27):9274–9276
68. Nielsen LJ et al (2010) Aptamers embedded in polyacrylamide nanoparticles: a tool for in vivo metabolite sensing. Acs Nano 4(8):4361–4370
69. Allen TM, Cullis PR (2004) Drug delivery systems: entering the mainstream. Science 303(5665):1818–1822
70. Cho KJ et al (2008) Therapeutic nanoparticles for drug delivery in cancer. Clin Cancer Res 14(5):1310–1316
71. Gref R et al (1994) Biodegradable long-circulating polymeric nanospheres. Science 263(5153):1600–1603
72. Farokhzad OC et al (2004) Nanopartide-aptamer bioconjugates: a new approach for targeting prostate cancer cells. Cancer Res 64(21):7668–7672
73. Farokhzad OC et al (2006) Targeted nanoparticle-aptamer bioconjugates for cancer chemotherapy in vivo. Proc Natl Acad Sci USA 103(16):6315–6320
74. Gu F et al (2008) Precise engineering of targeted nanoparticles by using self-assembled biointegrated block copolymers. Proc Natl Acad Sci USA 105(7):2586–2591
75. Kang HZ et al (2010) A liposome-based nanostructure for aptamer directed delivery. Chem Commun 46(2):249–251
76. Wu Y et al (2010) DNA aptamer-micelle as an efficient detection/delivery vehicle toward cancer cells. Proc Natl Acad Sci USA 107(1):5–10
77. Luo YL et al (2011) Release of photoactivatable drugs from plasmonic nanoparticles for targeted cancer therapy. Acs Nano 5(10):7796–7804
78. Kang HZ et al (2011) Near-infrared light-responsive core-shell nanogels for targeted drug delivery. Acs Nano 5(6):5094–5099
79. Yang XJ et al (2012) Near-infrared light-triggered, targeted drug delivery to cancer cells by aptamer gated nanovehicles. Adv Mater 24(21):2890–2895
80. Bagalkot V et al (2007) Quantum dot - aptamer conjugates for synchronous cancer imaging, therapy, and sensing of drug delivery based on bi-fluorescence resonance energy transfer. Nano Lett 7(10):3065–3070
81. Soontornworajit B, Wang Y (2011) Nucleic acid aptamers for clinical diagnosis: cell detection and molecular imaging. Anal Bioanal Chem 399(4):1591–1599
82. Wang AZ et al (2008) Superparamagnetic iron oxide nanoparticle-aptamer bioconjugates for combined prostate cancer imaging and therapy. ChemMedChem 3(9):1311–1315
83. Kim D et al (2010) A drug-loaded aptamer-gold nanoparticle bioconjugate for combined CT imaging and therapy of prostate cancer. Acs Nano 4(7):3689–3696
84. Fan Z et al (2012) Multifunctional plasmonic shell-magnetic core nanoparticles for targeted diagnostics, isolation, and photothermal destruction of tumor cells. Acs Nano 6(2):1065–1073

Electrical and Optical Enhancement Properties of Metal/Semimetal Nanostructures for Metal Oxide UV Photodetectors

Shayla Sawyer and Dali Shao

Introduction

UV photodetectors have been investigated for various commercial and military applications, such as secure space-to-space communications, pollution monitoring, water sterilization, flame sensing, and early missile plume detection [1]. To date, epitaxially grown or bulk wide bandgap semiconductors such as GaN, AlN, AlGaN, C (diamond), and SiC have been used for ultraviolet detection [2–12]. Fabrication of devices from these materials is often expensive with intricate processes. Also organic semiconductor materials are an attractive alternative [13, 14], though they lack the carrier mobility of inorganic semiconductors. Metal oxide semiconductor nanomaterials have the advantages of low processing cost, ease of fabrication, a large surface-to-volume ratio with carrier and photon confinement, and amenability to surface functionalization for hybrid inorganic–organic configurations. Furthermore, the unique combination of the carrier transport mechanism and oxygen adsorption/desorption processes on the nanostructures surface leads to a high internal gain. However, they also lead to slow transient response with response time on the order of seconds.

Significant enhancement of photodetector performance can be enabled by layers of metal/semimetal nanostructures. The trade-off between sensitivity and time response may be significantly reduced with careful design of metallic nanostructures relative to metal oxide active regions. The primary mechanisms for enhancement include surface plasmon resonance and carrier transfer to highly conductive materials. Details of the fundamental concepts, parameters of influence, and comparisons of enhanced devices are presented.

S. Sawyer (✉) • D. Shao
Electrical, Computer, and Systems Engineering Department, Rensselaer Polytechnic Institute, Troy, NY, USA
e-mail: sawyes@rpi.edu

Metal Oxide UV Photodetector

Materials

Metal oxides have been developed with a range of quantum confinement options from bulk, single crystals to 0D quantum dots. Much attention has been placed on nanoscale dimensions. For ultraviolet detection, ZnO has led the way as the most prominent semiconductor among the metal oxides, though In_2O_3, SnO_2, Ga_2O_3, WO_3, and CeO_2 are all viable materials for either solar-blind or visible-blind applications. Table 36.1 shows their basic properties.

Detection Mechanism

The mechanism for ultraviolet detection and subsequent carrier transport for metal oxide nanostructures is the cause of the high photocurrent-to-dark-current ratio characteristic of these materials. A significant change of conductance upon the UV illumination can be described by the following semiquantitative model as described in Wu et al. [15] (Fig. 36.1):

$$G = G_0 \, \exp\left(-\frac{q\psi_s}{kT}\right)$$

The activation energy, $q\psi_s$, is located in the interspace between nanocrystals, k is the Boltzmann constant, and T is the absolute temperature. Electrons must overcome the barrier $q\psi_s$; thus, the conductance is exponentially dependent on the barrier height. In the dark, due to the affinity between the oxygen molecules and electrons, oxygen molecules adsorb onto metal oxide surface and capture nearby electrons to form negatively charged oxygen ion layer. This process can be represented by

$$O_2(g) + e^- \rightarrow O_2^-(ad)$$
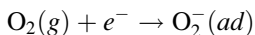
As a result, a depletion layer is formed near the surface of metal oxide and the barrier height increases, which results in reduced carrier concentration and low conductance. For low-dimensional metal oxide materials, this effect can be extremely strong due to the high surface-to-volume ratio, and the depletion region created in the oxygen adsorption process can extend throughout the entire film. Upon exposure to light with photon energy above the bandgap of the metal oxide, electron–hole pairs are generated.

$$h\upsilon \rightarrow e^- + h^+$$
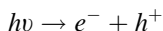
The photogenerated holes migrate to the surface of metal oxide and discharge the negatively charged adsorbed oxygen ions through surface electron–hole recombination.

Table 36.1 Summary of metal oxides for ultraviolet detection

Metal oxides	Crystal structure	Bandgap (eV)	Spectrum[a]
ZnO	Hexagonal	3.37	UV A
In$_2$O$_3$	Cubic/rhombohedral	3.5–3.7	UV A (direct)
		2.9	Blue (indirect)
SnO$_2$	Tetragonal	3.6	UV A
Ga$_2$O$_3$	Monoclinic	4.2–4.9	UV B-UV C
WO$_3$	Monoclinic	3.3	UV A
CeO$_2$	Cubic	3.2	UV A

[a]Ultraviolet A (3.10–3.94 eV, 400–315 nm), ultraviolet B (3.94–4.43 eV, 315–280 nm), ultraviolet C (4.43–12.4 eV, 280–100 nm)
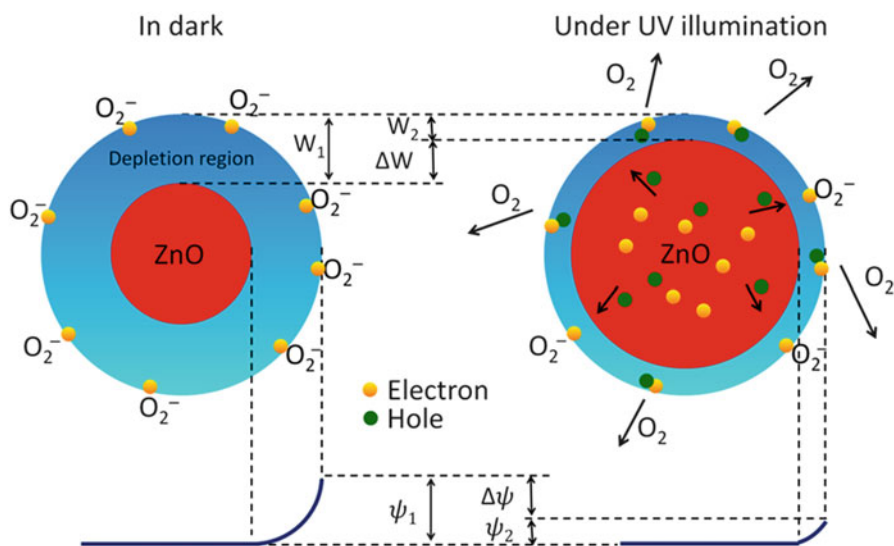
Fig. 36.1 Depletion region and potential barrier for (**a**) UV off and (**b**) UV on (Modified from [15])

$$h^+ + O_2^-(ad) \rightarrow O_2(g)$$
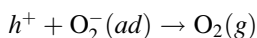
The barrier and depletion width decreases, and thus, the photocurrent exponentially increases until saturation.

The strong influence of surface effects on the high internal gain also results in a slow transient response. The slow decay time can be attributed to the persistent photoconductivity (PPC) phenomenon. Prades et al. discuss the origin and models for PPC in ZnO nanowires specifically through the principle that can be applied to all metal oxide nanostructures [16]. Two opposite models are proposed. The first is due to bulk defects between shallow and deep energy levels, while the second is

a pure surface effect with the capture of electrons by surface states. The relative persistence of conductance, G, is defined as $\frac{\Delta G}{G_0}$ where G_0 is the initial value in darkness. For the metal oxide nanowire, the electron–hole pairs created by UV photons give a photoresponse (ΔG_{ph}) with excess carriers (Δn, Δp):

$$\Delta G_{ph} \propto \Delta n = \Delta p = \frac{g}{1/\tau_{bulk} + 1/\tau_{surf}}$$

where g is the photogeneration rate of carriers per unit volume and τ_{bulk} and τ_{surf} are the lifetimes of photocarrier recombination in the bulk and at the surface. When surface states dominate, which is the case with nanostructures, oxygen adsorbs on the surface to separate holes from electrons forming a built-in potential. The recombination rate is significantly reduced and strongly dependent on oxygen content in air.

Photodetector Figures of Merit

Commonly used figures of merit for photodetectors are summarized in Table 36.1. Responsivity and normalized detectivity are both measures of detector sensitivity. Responsivity is essentially a measure of the effectiveness of the detector to take a given light input and convert it to current. The responsivity can be expressed by

$$R = \frac{i_{out}(\lambda, f)}{P_{in}} \quad \text{A/W}$$

where i_{out} is the photogenerated current of the detector, measured in amperes (A), and P_{in} is the incident radiation power, measured in watts (W).

Noise-equivalent power (NEP) is another basic indicator of the performance of a photodetector, which is defined as the signal power that gives a signal-to-noise ratio of one in a one hertz output bandwidth. The NEP can be expressed by the following equation:

$$NEP = \frac{i_n}{R}$$

where the i_n is the noise current in the unit of A/Hz$^{1/2}$ and the R is the responsivity in the unit of A/W.

The term normalized detectivity (D^*) is proportional to the reciprocal of the NEP and is independent of the detector area. It is therefore a popular measure of the intrinsic merit of a photodetector material:

$$D^* = \frac{\sqrt{A \times \Delta f}}{NEP} \quad \text{Jones} \left(cm\sqrt{Hz}/W \right)$$

where A is the active area in cm^{-2} and Δf is the operating bandwidth in hertz (unity: 1Hz). On the assumption that noise current is dominated by shot noise in the dark current $\left(i_n = i_{shot} = \sqrt{2qi_{dc}\Delta f} \right)$,

$$D^* = R\sqrt{\frac{A}{2qi_{dc}}} \quad \text{Jones}$$

where i_{dc} is dark current.

The dark current is measured current under dark conditions. When divided by the active area of the device, it becomes dark current density. Often a photocurrent-to-dark-current ratio is defined for a given bias.

The quantum efficiency (QE or η) is another measure of the effectiveness of the radiant energy producing electrical current in a detector. It is the ratio of photogenerated carriers and incident photons.

$$\eta = \frac{i_{out}}{q} \times \frac{hv}{P_{in}} (100) \ \%$$

The relationship between η and R is defined by the following equation:

$$R = \frac{\eta\lambda(\mu m)}{1.24} \quad (A/W)$$

Internal gains are defined by the ratio of photogenerated carriers to absorbed photons, while external gains are defined by the ratio of photogenerated carriers to incident photons. Overall the gain of a photodetector defines the number of electron–hole pairs produced from one photon.

The time or transient response of photodetectors is defined in both rise time and fall time. The incident light source is switched on and off at a sufficient frequency to determine the detector's ability to respond to pulsed light. Rise time is measured between 10 % and 90 % as current increases, while fall time is measured between 90 % and 10 % as current decreases.

Detector types for ultraviolet detection using metal oxides include photoconductors (PC), photodiodes (PD), metal–semiconductor–metal (MSM), metal insulator semiconductor (MIS), and field effect transistors (FET). Figure 36.2 shows schematics of device structures.

Performance Comparison

ZnO Photodetectors

ZnO materials possess various attractive characteristics for ultraviolet optoelectronic devices with reported bandgap values ranging from 3.2 to 3.4 eV, a large excitonic binding energy (60 meV), high radiation harness, amenability to wet chemical etching, and a relatively low growth temperature.
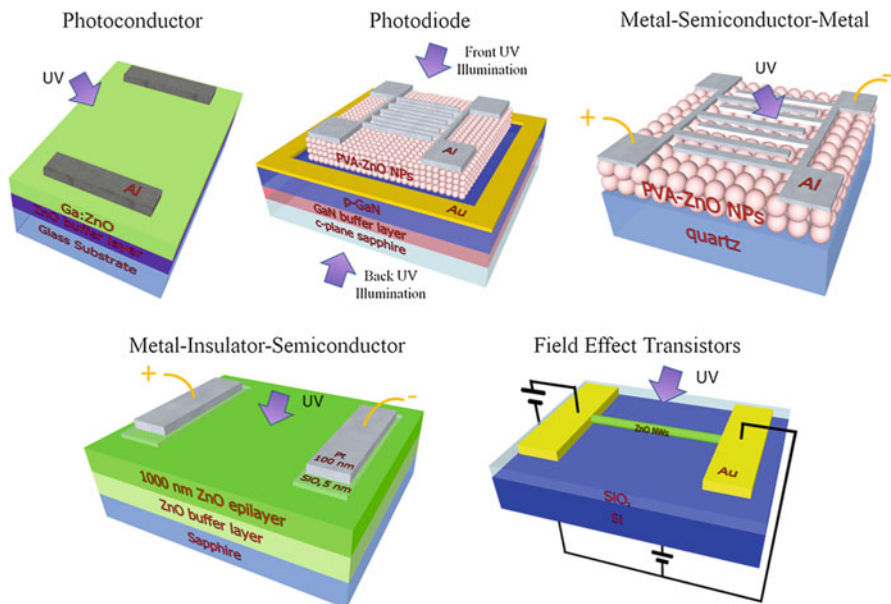
Fig. 36.2 Device design examples of ultraviolet photodetectors (Modified from [17–21])

Table 36.2 compares devices for metal oxides using selected figures of merit. Thin films have been developed by various deposition techniques including RF magnetron sputtering [22], molecular beam epitaxy (MBE), metalorganic chemical vapor deposition (MOCVD), pulsed laser deposition (PLD), and the sol–gel process. In 2000 and 2001, Liu et al. developed metal–semiconductor–metal and Schottky UV photodetectors with high-quality, epitaxially grown, ZnO thin films using MOCVD [23, 24]. Yang et al., in 2002, were the first to discover extreme sensitivity to ultraviolet light with ZnO nanowires (1D nanostructures), grown using a vapor phase transport process [25]. In 2007, Soci et al. investigated the inherent internal gain mechanism and consequential slow transient response of ZnO nanostructures [26]. Solution-processed colloidal nanoparticles (0D nanostructures) were developed by Jin et al. in 2008. The existence of persistent photoconduction found in solution-processed hybrid inorganic–organic nanostructures resulting in slower response time was investigated by Li et al. (Table 36.3).

Sawyer et al. explored surface passivation, increasing photocurrent sensitivity, for high-quality ZnO nanocrystals made by top-down wet-chemical etching technique developed by Dutta et al. [36, 38].

Other Metal Oxide UV Photodetectors

Research has expanded detection wavelengths throughout the UV range with materials such as indium oxide (In_2O_3), tin dioxide (SnO_2), gallium oxide ($\beta\text{-}Ga_2O_3$), and cerium oxide or ceria (CeO_2). Though typically the detection

Table 36.2 Photodetector figures of merit

Figure-of-Merit	Symbol/ acronym	Unit	Definition
Responsivity	R	A/W	Photocurrent divided by incident optical power
Normalized detectivity	$D*$	$\mathrm{cm}\,\frac{\sqrt{\mathrm{Hz}}}{\mathrm{W}}$ (Jones)	Measure of detector sensitivity that enables comparison even when detector area and bandwidth are different
Dark current	I_d	A	Current in the absence of light
Dark-current density	J_d	A cm^{-2}	Current divided by device active area in the absence of light
UV photogenerated current to dark current ratio	UV/dark ratio	*Unitless*	
External quantum efficiency	EQE or η	%	The ratio of photogenerated carriers to photon incident on the device
Internal gain	G_{int}	*Unitless*	Ratio of photogenerated carriers to photon absorbed
External gain	G_{ext}	*Unitless*	Ratio of photogenerated carriers to photon incident $G_{ext} = \eta \times G_{int}$
Noise-equivalent power	NEP	$\mathrm{W}/\sqrt{\mathrm{Hz}}$	Minimal detectable power, the optical signal in watts at which the electrical signal of noise ratio is unity when the bandwidth is limited to 1 Hz
Response time or transient response	t_r *rise time*	s	Amount of time required for current to rise from 10 % to 90 % of maximum current
	t_f *fall time*		Amount of time required for current to fall from 90 % to 10 % of maximum current

mechanisms are the same, physical properties of each material vary which contribute to differences in device performance.

Tin-doped indium oxide (ITO) is a pervasive material in electronics and photonics for its use as a transparent conducting electrode. However, the electronic and optical properties of undoped indium oxide, In_2O_3, especially in nanostructure form, have only recently been investigated. In 2001, Liang et al. were among the first to measure the semiconducting properties of In_2O_3 nanofibers grown by gold-seeded vapor–liquid–solid (VLS) mechanism [39]. Since then, nanowires, nanotowers, nanopyramids, and colloidal nanoparticles have been characterized for their electronic and optical properties [39–47]. However, the complete photoresponse including responsivity and time response of an In_2O_3 ultraviolet photodetector was only recently investigated [48]. A maximum responsivity of 11 A/W was observed at 340 nm, and the rise and fall times were 1,100 and 3,200 s, respectively.

Tin oxide (SnO_2) materials were historically researched for use as a conductive electrode and antireflective coating due to its transparency to visible light. As a wide bandgap material (3.6 eV), its potential as an ultraviolet detector has been explored with the creation of FETs and photoconductors using SnO_2 nanowire,

Table 36.3 Performance comparison of ZnO photodetectors

Ref.	Year	λ (nm)	Responsivity (A W⁻¹)	Dark current (A)	Area (cm²)	D^* (cm. Hz$^{0.5}$. W^{-1})	Time response (s)		Device type	Material
							Rise time	Fall time		
[23]	2000	300–373	400	4.50×10^{-7}	–	–	1×10^{-6}	1.5×10^{-6}	MSM	Epitaxial thin film MOCVD
[24]	2000	300–385	1.5	1×10^{-9}	1.77×10^{-4}	1.12×10^{12}	1.2×10^{-8}	5×10^{-8}	MSM	Epitaxial thin film MOCVD
[26]	2007	245–385	3.33×10^4	10^{-9}	3×10^{-7}	2.04×10^{13}	~50	>100	PC	Nanowires
[27]	2008	370–395	61	1.2×10^{-10}	3.14×10^{-2}	1.91×10^{15}	25	120	MSM	Colloidal nanoparticles
[22]	2007	300–384	2,069	2.22×10^{-6}	8.85×10^{-3}	2.31×10^{14}	–	–	MSM	Thin film grown by RF sputtering
[17]	2008	300–400	8.9×10^{-2}	4.11×10^{-7}	4×10^{-4}	4.91×10^9	–	–	MSM	Epi layer grown by RF plasma-assisted MBE (Omni Vac) on sapphire (0001) substrates
			8.3×10^{-3}	2.22×10^{-10}	4×10^{-4}	1.97×10^{10}	–	–	MIS	
[28]	2008	300–400	0.18	1.8×10^{-5} (A/cm²)		7.5×10^{10}	–	–	–	Nanorods
[29]	2008	300–420	0.68	9.4×10^{-7} (A/cm²)		1.24×10^{12}	<0.2	<0.2	PD	Nanoparticles
[30]	2009	325–375	12.5	–		–	–	–	–	Nanoparticles
[31]	2009	310–450	1×10^{-4}	4×10^{-13}	1.2×10^{-4}	3.06×10^9	48	0.9	PC	Nanoparticles

Ref	Year	Range							Type	Description
[32]	2009	115–400	3.3×10^{-10}	4.1×10^{-9}	4×10^{-6}	18.22	>1,000 ms	–	MSM	Lateral nanowires on a ZnO: Ga/glass template
[33]	2009	300–370	0.011	4.32×10^{-9}	0.24	1.45×10^{11}	–	–	MSM	Nanowires
[34]	2009	400–600	1.5×10^{-5}	–	–	–	–	–	PC	ZnO-infiltrating CQD films
[15]	2010		4.29×10^{-5}	2.23×10^{-9}	25	8.03×10^{9}	–	–	PC	Nanowires and nanoparticles
[35]	2010	200–425	0.02287	2×10^{-9} (A/cm^2)		9.04×10^{11}	1	–	PD	Polymer/nanoparticle bilayer
[36]	2010	200–380	0.33	4.88×10^{-12}	7.85×10^{-3}	2.34×10^{13}	100	25	PC	PVA-coated colloidal nanoparticles
[18]	2010	200–380	731.42	2.91×10^{-12}	6.24×10^{-3}	5.98×10^{16}	0.6	8	MSM	Colloidal nanoparticles
[19]	2013	320–380	1.19×10^{-4}	4.2×10^{-13}	7.85×10^{-3}	2.88×10^{10}	0.025	0.05	PD	Back-illuminated p-GaN/ZnO nanoparticle heterojunction diode
[37]	2013	365	6.83×10^{1}	6.83×10^{-9}		1.46×10^{15}	0.034	0.132	PC	Nanorods passivated by TOPO

nanobelts, and nanonets. These materials were fabricated using the vapor–liquid–solid process [49–51], laser ablation [52], and thermal evaporation [53]. A SnO_2 nanonet photoconductor was fabricated using a colloid crystal polymer template which forms a 2D ordered semiconducting nanofilm with hole sizes that can be adjusted by the mean diameter of the polymer colloidal spheres. Though responsivity characterization for ultraviolet photodetectors has not yet been reported, FET devices demonstrated on/off ratios of 10^3 and 10^5 with nanowire and nanobelts, respectively [52, 53]. High gain values have also been reported for the photoconductor devices up to 1.32×10^7 for SnO_2 nanowires [49, 50].

Solar-blind detection below 290 nm has been demonstrated with β-Ga_2O_3. Its bandgap has been reported with values between 4.2 and 4.9 eV. Photodetectors were fabricated using thermal evaporation and a single-step chemical vapor deposition process. In recent work, a bridged nanowire photoconductor demonstrated a high 250–280 nm rejection ratio of 2×10^4 and a high photocurrent-to-dark-current ratio of 3×10^4 [54]. In comparison to In_2O_3- and ZnO-based photodetectors, the bridged β-Ga_2O_3 NWs photoconductor can achieve much faster transient response with decay times less than 20 ms. The fast transient response is attributed to the extremely low electron density of β-Ga_2O_3 NWs in dark environment, which significantly suppressed the formation of surface states that originate from oxygen adsorption process [55, 56]. Therefore, the PPC phenomenon was greatly reduced in that oxygen adsorption has a nearly negligible effect on conductance.

Ceria or cesium oxide CeO_2 and tungsten oxide WO_3 are lesser-known metal oxides for UV detection. Ceria have reported bandgap values of 3.2 eV and 3.3 eV, respectively. Both were developed as nanowire devices [57–59] and possess similar high gain values and longtime responses as In_2O_3 and ZnO materials (Table 36.4).

Nanostructures for Performance Enhancement

Research to improve sensitivity and transient response of photodetectors is being pursued across the UV, visible, and infrared (IR) wavelength regions. To date, much of the research has focused on wavelengths from the visible to IR region. Until only recently investigations of enhancement for shorter UV wavelengths begun [61]. Mechanisms for performance enhancement can be categorized as either plasmonic interactions with an electric field induced by metal/semimetal nanostructures or carrier transfer from metal oxide active regions to highly conductive materials. Surface plasmon resonance (SPR) and carrier transfer concepts are described below with examples of nanostructures and performance comparisons.

Surface Plasmon Resonance Mechanisms

Metallic nanostructures absorb light due to the coherent oscillation of conduction band electrons induced by the interacting electromagnetic field. An incident

Table 36.4 Performance comparison of In_2O_3, SnO_2, β-Ga_2O_3, CeO_2, and WO_3

Ref.	Year	λ (nm)	Responsivity ($A\,W^{-1}$)	UV-to-dark-current ratio	Dark current (A)	Area (cm^2)	D^* (cm. $Hz^{0.5}.W^{-1}$)	Time response (s)		Type	Material
								Rise time	Fall time		
[44]	2012	280–470	1.82	1.2×10^2	1.8×10^{-9}	7.85×10^{-3}	6.72×10^{12}	35	48	PC	In_2O_3-milled nanorods
[48]	2012	250–500	11	80	1.0×10^6	6.24×10^{-3}	1.54×10^{12}	500	1,600	MSM	In_2O_3 PVA-coated nanoparticles
[52]	2003	–	–	1×10^3	$\sim 3.8 \times 10^{-8}$	$\sim 3.8 \times 10^{-11}$	–	–	–	FET	SnO_2 nanowires
[53]	2007	–	–	1×10^5	4.0×10^{-10}	–	–	–	–	FET	SnO_2 nanobelts
[60]	2012	210–630	–	3.5	6.55×10^{-5}	–	–	>50 s	>50 s	PC	SnO_2 nanonets
[50]	2008	–	–	10^5	3.2×10^{-8}	–	–	–	–	PC	SnO_2 nanowires
[56]	2006	254	–	6.67×10^2	1.5×10^{-11}	–	–	0.22	0.09	PC	β-Ga_2O_3 nanowires
[54]	2010	254	–	3.0×10^4	2.0×10^{-13}	–	–	–	< 0.02	PC	Bridged β-Ga_2O_3 nanowires
[59]	2007	254	–	40	2.50×10^{-10}	–	–	30	300	PC	CeO_2 nanowires
[58]	2011	375	–	–	–	–	–	3	20	FET	WO_3 nanowires
[57]	2010	280–320	–	1.5×10^2	1.00×10^{-10}	–	–	100	150	PC	WO_3 nanowire

photon coupled to the electron oscillations results in an absorption band. This is known as surface plasmon resonance (SPR). Figure 36.3 demonstrates this phenomenon in detail [62]. Polarization within the metal sphere is induced by the incoming light where the separation of free electrons with respect to the ionic core results in the need for a force to restore the system. The dipolar oscillation of electrons is the surface plasmon oscillation. The size, shape, distance between nanostructures, and material all have an effect on the resonant wavelength. The electromagnetic interaction with metal gratings was first documented in 1902 by R. Wood [63]. The Mie Theory, developed in 1908, begins to create a working model for the optical properties that result with isolated metal nanoparticles. Specifically, it is a mathematical description of the scattering of electromagnetic reaction by spherical particles in a continuous medium [64]. Fano et al. first described plasmons from incident electromagnetic radiation on metallic gratings as "superficial waves traveling with momentum along the surface of the grating and exponentially damped in the normal direction" [65]. In the review article by Ghosh et al., the assumptions, application, and limitations of the Mie Theory for plasmonic systems are thoroughly analyzed [64]. For isolated nanoparticles less than 100 nm in diameter, the Mie Theory can be reduced to the following relationship:

$$\sigma_{ext} = 9 \frac{\omega}{c} \epsilon_m^{3/2} V \frac{\epsilon_2(\omega)}{[\epsilon_1(\omega) + 2\epsilon_m]^2 + [\epsilon_2(\omega)]^2}$$

where $V = (4\pi/3)R^3$ is the volume of the spherical particle, ω is the angular frequency of the exciting light, c is the velocity of light, and ϵ_m and $\epsilon_1(\omega) + i\epsilon_2(\omega)$ are the dielectric functions of the surrounding medium and the material itself, respectively. The resonance condition is fulfilled when $\epsilon_1(\omega) = -2\epsilon_m$ if ϵ_2 is small or weakly dependent on ω. Nanoparticles larger than 100 nm require a correction factor that results in the broadening and red-shifting of the resonance frequency. Non-spherical nanoparticles also require a correction factor to more accurately predict the resonant frequency.

There is an ongoing debate about the exact mechanism responsible for enhancement in grating structures. Crouse and Keshavareddy weighed the significance of electromagnetic modes responsible for transmittance peaks including horizontally oriented surface plasmons (HSPs), Wood-Rayleigh (WR) anomalies, vertical surface resonances (VSRs), diffracted modes, and cavity modes (also called waveguide modes) [66]. Most agree that HSPs should be minimized as it has a converse affect on enhancement.

Ebbessen et al. were the first to discover enhanced optical transmission from sub-wavelength hole arrays [67]. This work spawned studies of 1D and 2D nanoarrays with slits, gratings, resonant cavities, and holes for the performance improvement of photodetectors [66, 68–76]. Collin et al. investigated the strong confinement of light by a resonant cavity on an MSM photodetector using

Fig. 36.3 Surface plasmon resonance (SPR) of spherical nanometal particle. A dipole oscillates in phase with the electric field of the incoming light (Modified from [62])
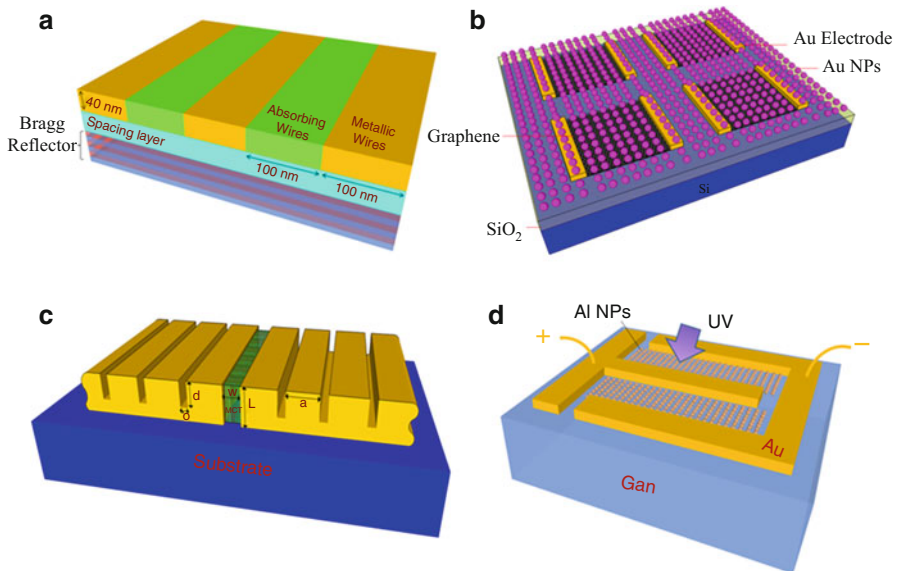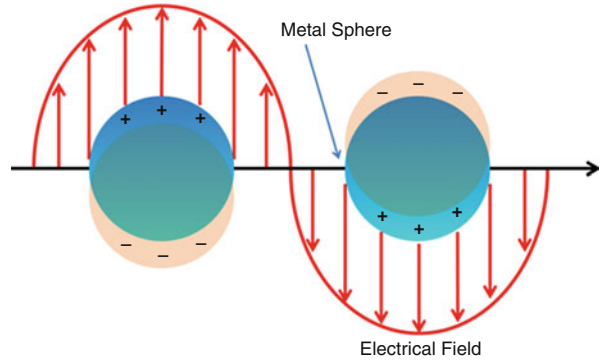

Fig. 36.4 Examples of metal nanostructures to induce surface plasmon resonance. (**a**) Alternating metal–semiconductor gratings on a Bragg reflector (Modified from [74]). (**b**) Graphene photodetector enhanced by gold nanoparticle arrays (Modified from [77]). (**c**) Nanoslit metal grating (Modified from [79]). (**d**) Aluminum nanoparticles on GaN photodetector (Modified from [78])

alternating metal–semiconductor gratings on a multilayer Bragg reflector [74]. A graphene photodetector was enhanced by gold nanoparticle arrays [77]. Plasmonic enhancement in the UV range was achieved by Butan et al. using aluminum nanoparticles deposited on a GaN MSM photodetector [78]. Schematic designs of the enhancement structures are shown in Fig. 36.4. Table 36.5 is a cross section of the experimental research results for plasmonic enhancement for various photodetectors.

Table 36.5 Surface plasmon-enhanced photodetectors across UV–vis–IR spectrum

Ref.	Year	Plasmonic structure	Material (semiconductor/metal plasmonic)	Device structure	λ (nm)	Enhancement factor
[76]	1998	Island nanoparticles	Si/Au	SOI-MSM	Near-IR (800 nm)	18× photocurrent enhancement
[80]	2002	Metallic gratings	Ge/Au	MSM	IR	8× absorption enhancement factor
[74]	2004	Metal–semiconductor grating	GaAs/alternating Ag and GaAs	MSM	IR	9× enhancement of external quantum efficiency
[77]	2011	Nanoparticle array	Graphene/Au	MGM*	Green-Red (530–633 nm)	Order of magnitude improvement in QE >800 % increase in photocurrent
[81]	2006	Nanoslit(s)	HgCdTe/Au	–	Mid-IR (10 μm)	1 slit 10× enhancement factor 20 periods 250× enhancement factor
[82]	2005	Nanoparticles	Si/Au	PN junction diode	Red (640 nm)	50–80 % increase in photocurrent
[78]	2012	Nanoparticle array	GaN/Al	MSM	UV (340 nm)	50 % enhancement in QE

*Average photocurrent enhancement
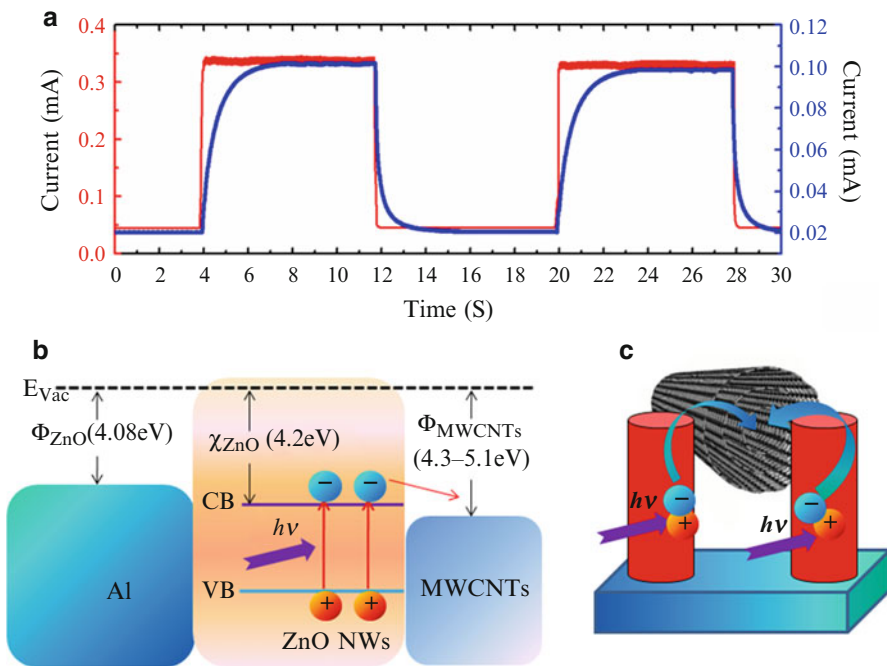
Fig. 36.5 Transient response of photodetector with MWCNT (*red*) and without MWCNT (*blue*) (**b**) Energy band diagram of Al/ZnO NWs/MWCNT system. (**c**) Carrier transport process of ZnO NWs/MWCNT interface (Republished with permission from [98])

Carrier Transfer Mechanisms

It is well known that the photoresponse of metal oxide materials is sensitive to film thickness, deposition temperature, annealing treatments, and doping. It has been shown that aspects of device performance can therefore be improved by optimizing these parameters [83–88]. Further enhancement with the addition of metal/semi-metal layers is an approach to circumvent issues inherent to most metal oxides attributed to the slow chemisorption of oxygen molecules [16].

In 2007, Yadav et al. were the first to study the interfacial charge-transfer kinetics between ultrathin layers of different metals with a metal oxide thin film [89]. In this work, enhanced photoresponse was due to the effective transfer of electrons from the metal to ZnO at the interface, and the injected charge carriers compensate the surface states and increase the photoconductivity. The UV/dark current ratio improved by more than $5\times$ with Te/ZnO bilayer. Nevertheless, the rise and fall times significantly increased, demonstrating the common trade-off in photodetectors. Tzeng et al. continued the concept of interfacial charge transfer by modifying the interface using Ag nanoparticles. The photocurrent-to-dark-current contrast ratio increased by almost 74 times. The decay time was reduced from 824 to 36 s, and the rise time was also reduced from $\sim$151 to 4 s after depositing Ag NPs [90]. These results are

Table 36.6 Carrier transfer enhancement of UV photodetectors

Ref.	Year	Carrier transfer enhancement material	Semiconductor material	Device structure	λ (nm)	Enhancement factor
[92]	2010	Embedded graphene layer	ZnO QD-polymer		365 nm	~330× photocurrent
[89]	2007	Metal thin sheet: Te, Au, Pb, Cu, Sn, Al	ZnO thin film	Bilayer	365 nm	5× UV/dark current ratio (Te)
[90]	2012	Ag NP	ZnO NW		365 nm	74× UV/dark current ratio
						37× faster rise time
						23× faster fall time
[101]	2013	Graphene core-shell	ZnO NP	PC	335 nm	3 orders of magnitude rise and fall time improvement
[98]	2013	MWCNT	ZnO NW/p-Si	PD	335 nm	3× improvement responsivity
						23× faster rise time
						18× faster fall time
[94]	2013	Graphene core–shell	WO_3	MSM	340 nm	100× faster time response
[99]	2012	Graphene QD	ZnO NP	MSM	335 nm	2× improvement responsivity
						50× faster rise time
						37× faster fall time

attributed to the formation of AgO_x at the interface between Ag and ZnO, which increased the Schottky barrier height and led to a significant enhancement in the charge-transfer kinetics near the interface of ZnO and AgO_x.

Carbon nanomaterials, specifically carbon nanotubes (CNTs) and graphene, have been investigated in hybrid nanocomposites to provide improved charge separation and subsequent carrier transport [91–97]. CNT hybrid materials have proven to be a versatile electrode for fuel-cell, photodetector, and supercapacitor applications for their solution processable fabrication, high conductivity, mechanical flexibility and strength, and dimension variability. Recently, Shao et al. demonstrated a multiwalled carbon nanotube (MWCNT)/ZnO NW/p-Si photodiode with rise and fall times of 0.09 s and 0.08 s, respectively. This is at least 20 times faster than ZnO NW/p-Si photodiode without using MWCNTs. In addition to improved transient response, the maximum responsivity of the photodiode employing MWCNTs enhanced by three times, which can reach to 4.7 A/W for UV light (365 nm) at 2 V bias [98]. The improved performance is explained by the band diagram in Fig. 36.5. Electrons transfer from ZnO to MWCNTs because it is energetically favorable to do so. Due to the semimetallic property of the MWCNTs, the composite structure has much better conductivity than the bare ZnO NWs array. This effectively improved the carrier transport and collection efficiency.

Graphene has many unique properties including high carrier transport mobility, superior mechanical properties, excellent chemical stability, larger surface area than CNTs, and low cost. Thin graphene sheet layers, quantum dots, and core-shells are common structures for nanocomposites with metal oxides for improved carrier transport [93, 94, 97, 99]. Graphene-CdS quantum dot nanocomposites were explored through facile fabrication processes by Wu et al. and Cao et al. as methods to enhance conductivity of quantum dot layers. Williams et al. were among the first to create graphene metal oxide nanocomposites for conductivity improvement [100]. Recently, graphene quantum dots, synthesized by the hydrothermal method, were used to enhance the performance of ZnO-based ultraviolet photodetectors through the preferential carrier transfer to the more conductive material [99]. The rise and fall times reduced from longer than 3 s each to 0.06 s and 0.08 s, respectively, while a high responsivity of >450 A/W at 375 nm was maintained [99]. Similar results were obtained with a ZnO NPs-graphene core-shell structure [94, 101] (Table 36.6).

Summary

Metal oxides and their nanostructures have many advantages for ultraviolet detection including low cost, a high surface-to-volume ratio, and a large internal gain mechanism. A long transient response due to the adsorption of oxygen on the semiconductor surface limits performance. Metal and semimetal nanostructures can improve overall performance by inducing surface plasmon resonance or allowing the transfer of carriers to more conductive material.

References

1. Blank TV, Gol'dberg YA (2003) Semiconductor photoelectric converters for the ultraviolet region of the spectrum. Semiconductors 37:999–1030
2. Zhang SK, Wang WB, Shtau I, Yun F, He L, Morkoc H, Zhou X, Tamargo M, Alfano RR (2002) Back-illuminated GaN/AlGaN heterojunction ultraviolet photodetector with high internal gain. Appl Phys Lett 81(25):4862–4864. doi:10.1063/1.1526166
3. Xu GY, Salvador A, Kim W, Fan Z, Lu C, Tang H, Morkoc H, Smith G, Estes M, Goldenberg B, Yang W, Krishnankutty S (1997) High speed, low noise ultraviolet photodetectors based on GaN p-i-n and AlGaN(p)-GaN(i)-GaN(n)structures. Appl Phys Lett 71(15):2154–2156
4. Chen X, Zhu H, Cai J, Wu Z (2007) High-performance 4H-SiC-based ultraviolet p-i-n photodetector. J Appl Phys 102(2):024505. doi:10.1063/1.2747213
5. Whitfield MD, Chan SSM, Jackman RB (1996) Thin film diamond photodiode for ultraviolet light detection. Appl Phys Lett 68(3):290–292. doi:10.1063/1.116062
6. Walker D, Monroy E, Kung P, Wu J, Hamilton M, Sanchez FJ, Diaz J, Razeghi M (1999) High-speed, low-noise metal–semiconductor–metal ultraviolet photodetectors based on GaN. Appl Phys Lett 74(5):762. doi:10.1063/1.123303
7. Osinsky A, Gangopadhyay S, Gaska R, Williams B, Khan MA, Kuksenkov D, Temkin H (1997) Low noise p-π-n GaN ultraviolet photodetectors. Appl Phys Lett 71(16):2334. doi:10.1063/1.120023

8. Monroy E, Omnès F, Calle F (2003) Wide-bandgap semiconductor ultraviolet photodetectors. Semicond Sci Technol 18(4):R33–R51

9. Liao M, Koide Y, Alvarez J (2005) Thermally stable visible-blind diamond photodiode using tungsten carbide Schottky contact. Appl Phys Lett 87(2):022105-022105-022103. doi:10.1063/1.1992660

10. Li J, Fan ZY, Dahal R, Nakarmi ML, Lin JY, Jiang HX (2006) 200 nm deep ultraviolet photodetectors based on AlN. Appl Phys Lett 89(21):213510–213513

11. Chen X, Yang W, Wu Z (2006) Visible blind p–i–n ultraviolet photodetector fabricated on 4H-SiC. Microelectron Eng 83(1):104–106. doi:http://dx.doi.org/10.1016/j.mee.2005.10.034

12. Chen Q, Khan MA, Sun CJ, Yang JW (1995) Visible-blind ultraviolet photodetectors based on GaN p-n junctions. Electron Lett 31(20):1781–1782. doi:10.1049/el:19951190

13. Cárdenas JR, de Vasconcelos EA, de Azevedo WM, da Silva EF, Pepe I, da Silva AF, Ribeiro SS, Silva KA (2008) A conducting polymer–silicon heterojunction as a new ultraviolet photodetector. Appl Surf Sci 255(3):688–690. doi:http://dx.doi.org/10.1016/j.apsusc.2008.07.038

14. Yu G, Pakbaz K, Heeger AJ (1994) Semiconducting polymer diodes: large size, low cost photodetectors with excellent visible–ultraviolet sensitivity. Appl Phys Lett 64(25):3422. doi:10.1063/1.111260

15. Wu JM, Chen YR, Lin YH (2011) Rapidly synthesized ZnO nanowires by ultraviolet decomposition process in ambient air for flexible photodetector. Nanoscale 3(3):1053–1058. doi:10.1039/c0nr00595a

16. Prades JD, Hernandez-Ramirez F, Jimenez-Diaz R, Manzanares M, Andreu T, Cirera A, Romano-Rodriguez A, Morante JR (2008) The effects of electron–hole separation on the photoconductivity of individual metal oxide nanowires. Nanotechnology 19(46):465501. doi:10.1088/0957-4484/19/46/465501

17. Young SJ, Ji LW, Chang SJ, Liang SH, Lam KT, Fang TH, Chen KJ, Du XL, Xue QK (2008) ZnO-based MIS photodetectors. Sens Act A: Phys 141(1):225–229. doi:10.1016/j.sna.2007.06.003

18. Qin L, Shing C, Sawyer S (2011) Metal–Semiconductor–Metal ultraviolet photodetectors based on zinc-oxide colloidal nanoparticles. IEEE Electron Device Lett 32(1):51–53

19. Qin L, Shao D, Shing C, Sawyer S (2013) Wavelength selective p-GaN/ZnO colloidal nanoparticle heterojunction photodiode. Appl Phys Lett 102(7):071106. doi:10.1063/1.4793210

20. Campos LC, Guimarães MHD, Goncalves AMB, de Oliveira S, Lacerda RG (2013) ZnO UV photodetector with controllable quality factor and photosensitivity. AIP Advances 3(2):022104. doi:10.1063/1.4790633

21. Shinde SS, Rajpure KY (2011) High-performance UV detector based on Ga-doped zinc oxide thin films. Appl Surf Sci 257(22):9595–9599. doi:10.1016/j.apsusc.2011.06.073

22. Bi Z, Zhang J, Bian X, Wang D, Zhang X, Zhang W, Hou X (2008) A high-performance ultraviolet photoconductive detector based on a ZnO film grown by RF sputtering. J Electron Mater 37(5):760–763

23. Liu Y, Gorla CR, Liang S, Emanetoglu N, Lu Y, Shen H, Wraback M (2000) Ultraviolet photodetectors based on epitaxial ZnO films grown by MOCVD. J Electron Mater 29(1):69–74

24. Liang S, Sheng H, Liu YG, Huo Z, Lu Y, Shen H (2001) ZnO schottky ultraviolet photodetectors. J Cryst Growth 22:110–113

25. Kind H, Yun H, Messer B, Law M, Yang P (2002) Nanowire ultraviolet photodetectors and optical switches. Adv Mater 14(2):158–160

26. Soci C, Zhang A, Xiang B, Dayeh SA, Aplin DPR, Park J, Bao XY, Lo YH, Wang D (2007) ZnO nanowire UV photodetectors with high internal gain. Nano Lett 7(4):1003–1009

27. Jin Y, Wang J, Sun B, Blakesley JC, Greenham NC (2008) Solution-processed ultraviolet photodetectors based on colloidal ZnO nanoparticles. Nano Lett 8(6):1649–1653

28. Lin Y-Y, Chen C-W, Yen W-C, Su W-F, Ku C-H, Wu J-J (2008) Near-ultraviolet photode-tector based on hybrid polymer/zinc oxide nanorods by low-temperature solution processes. Appl Phys Lett 92(23):233301. doi:10.1063/1.2940594

29. Li H-G, Wu G, Shi M-M, Yang L-G, Chen H-Z, Wang M (2008) ZnO/poly (9,9-dihexylfluorene) based inorganic/organic hybrid ultraviolet photodetector. Appl Phys Lett 93(15):153309. doi:10.1063/1.3003881

30. Venkataprasad Bhat S, Vivekchand SRC, Govindaraj A, Rao CNR (2009) Photolumi-nescence and photoconducting properties of ZnO nanoparticles. Solid State Commun 149(13–14):510–514. doi:10.1016/j.ssc.2009.01.014

31. Jun JH, Seong H, Cho K, Moon B-M, Kim S (2009) Ultraviolet photodetectors based on ZnO nanoparticles. Ceram Int 35(7):2797–2801. doi:10.1016/j.ceramint.2009.03.032

32. Lu C-Y, Chang S-P, Chang S-J, Hsueh T-J, Hsu C-L, Chiou Y-Z, Chen IC (2009) A lateral ZnO nanowire UV photodetector prepared on a ZnO: Ga/glass template. Semicond Sci Technol 24(7):075005. doi:10.1088/0268-1242/24/7/075005

33. Chen KJ, Hung FY, Chang SJ, Young SJ (2009) Optoelectronic characteristics of UV photodetector based on ZnO nanowire thin films. J Alloys Compd 479(1–2):674–677. doi:10.1016/j.jallcom.2009.01.026

34. Pourret A, Guyot-Sionnest P, Elam JW (2009) Atomic layer deposition of ZnO in quantum dot thin films. Adv Mater 21(2):232–235. doi:10.1002/adma.200801313

35. Li H, Fan C, Wu G, Chen H, Wang M (2010) Solution-processed hybrid bilayer photode-tectors with rapid response to ultraviolet radiation. J Phys D Appl Phys 43(42):425101. doi:10.1088/0022-3727/43/42/425101

36. Qin L, Shing C, Sawyer S, Dutta PS (2011) Enhanced ultraviolet sensitivity of zinc oxide nanoparticle photoconductors by surface passivation. Opt Mater 33(3):359–362. doi:10.1016/j.optmat.2010.09.020

37. Rostami A, Dolatyari M, Amini E, Rasooli H, Baghban H, Miri S (2013) Sensitive, fast, solution-processed ultraviolet detectors based on passivated zinc oxide nanorods. Chemphyschem: A Eur J Chem Phys Phys Chem 14(3):554–559. doi:10.1002/cphc.201200660

38. Sharma S, Tran A, Nalamasu O, Dutta PS (2006) Spin-coated ZnO thin films using ZnO nano-colloid. J Electron Mater 35(6):1237–1240

39. Liang C, Meng G, Lei Y, Phillipp F, Zhang L (2001) Catalytic growth of semiconducting In2O3 nanofibers. Adv Mater 13(17):1330–1333

40. Gali P, Kuo F-L, Shepherd N, Philipose U (2012) Role of oxygen vacancies in visible emission and transport properties of indium oxide nanowires. Semicond Sci Technol 27(1):015015. doi:10.1088/0268-1242/27/1/015015

41. Guha P, Kar S, Chaudhuri S (2004) Direct synthesis of single crystalline In[sub 2]O[sub 3] nanopyramids and nanocolumns and their photoluminescence properties. Appl Phys Lett 85(17):3851. doi:10.1063/1.1808886

42. Jean S-T, Her Y-C (2010) Growth mechanism and photoluminescence properties of In2O3 nanotowers. Cryst Growth Des 10(5):2104–2110. doi:10.1021/cg9011839

43. Li C, Zhang D, Han S, Liu X, Tang T, Zhou C (2003) Diameter-controlled growth of single-crystalline In2O3 nanowires and their electronic properties. Adv Mater 15(2):143–146

44. Qin L, Dutta PS, Sawyer S (2012) Photoresponse of indium oxide particulate-based thin films fabricated using milled nanorods grown by the self-catalytic vapor–liquid–solid process. Semicond Sci Technol 27(4):045005. doi:10.1088/0268-1242/27/4/045005

45. Shao D, Qin L, Sawyer S (2013) Optical properties of polyvinyl alcohol (PVA) coated In2O3 nanoparticles. Opt Mater 35(3):563–566. doi:10.1016/j.optmat.2012.10.026

46. Zhang D, Li C, Han S, Liu X, Tang T, Jin W, Zhou C (2003) Electronic transport studies of single-crystalline In[sub 2]O[sub 3] nanowires. Appl Phys Lett 82(1):112. doi:10.1063/1.1534938

47. Zhang D, Li C, Han S, Liu X, Tang T, Jin W, Zhou C (2003) Ultraviolet photodetection properties of indium oxide nanowires. Appl Phys A: Mater Sci Process 77(1):163–166. doi:10.1007/s00339-003-2099-3

48. Shao D, Qin L, Sawyer S (2012) Near ultraviolet photodetector fabricated from polyvinyl-alcohol coated In2O3 nanoparticles. Appl Surf Sci 261:123–127. doi:10.1016/j.apsusc.2012.07.111

49. Hu L, Yan J, Liao M, Wu L, Fang X (2011) Ultrahigh external quantum efficiency from thin SnO2 nanowire ultraviolet photodetectors. Small 7(8):1012–1017. doi:10.1002/smll.201002379

50. Lin C-H, Chen R-S, Chen T-T, Chen H-Y, Chen Y-F, Chen K-H, Chen L-C (2008) High photocurrent gain in SnO[sub 2] nanowires. Appl Phys Lett 93(11):112115. doi:10.1063/1.2987422

51. Mathur S, Barth S, Shen H, Pyun JC, Werner U (2005) Size-dependent photoconductance in SnO2 nanowires. Small 1(7):713–717. doi:10.1002/smll.200400168

52. Liu Z, Zhang D, Song H, Li C, Tang T, Jin W, Liu X, Lei B, Zhou C (2003) Laser ablation synthesis and electron transport studies of tin oxide nanowires. Adv Mater 15(20):1754–1757

53. Chen Y, Zhu C, Cao M, Wang T (2007) Photoresponse of SnO2 nanobelts grown in situ on interdigital electrodes. Nanotechnology 18(28):285502. doi:10.1088/0957-4484/18/28/285502

54. Li Y, Tokizono T, Liao M, Zhong M, Koide Y, Yamada I, Delaunay J-J (2010) Efficient assembly of bridged β-Ga2O3 nanowires for solar-blind photodetection. Adv Funct Mater 20(22):3972–3978. doi:10.1002/adfm.201001140

55. Feng P, Xue XY, Liu YG, Wan Q, Wang TH (2006) Achieving fast oxygen response in individual β-Ga[sub 2]O[sub 3] nanowires by ultraviolet illumination. Appl Phys Lett 89(11):112114. doi:10.1063/1.2349278

56. Feng P, Zhang JY, Li QH, Wang TH (2006) Individual β-Ga[sub 2]O[sub 3] nanowires as solar-blind photodetectors. Appl Phys Lett 88(15):153107. doi:10.1063/1.2193463

57. Huang K, Zhang Q, Yang F, He D (2010) Ultraviolet photoconductance of a single hexagonal WO3 nanowire. Nano Res 3(4):281–287. doi:10.1007/s12274-010-1031-3

58. Li L, Zhang Y, Fang X, Zhai T, Liao M, Sun X, Koide Y, Bando Y, Golberg D (2011) WO3 nanowires on carbon papers: electronic transport, improved ultraviolet-light photodetectors and excellent field emitters. J Mater Chem 21(18):6525. doi:10.1039/c0jm04557h

59. Fu XQ, Wang C, Feng P, Wang TH (2007) Anomalous photoconductivity of CeO[sub 2] nanowires in air. Appl Phys Lett 91(7):073104. doi:10.1063/1.2771090

60. Chen H, Hu L, Fang X, Wu L (2012) General fabrication of monolayer SnO2 nanonets for high-performance ultraviolet photodetectors. Adv Funct Mater 22(6):1229–1235. doi:10.1002/adfm.201102506

61. Qiaoqiang G, Liangcheng Z, Dierolf V, Bartoli FJ (2009) UV plasmonic structures: direct observations of UV extraordinary optical transmission and localized field enhancement through nanoslits. IEEE Photonics J 1(4):245–253. doi:10.1109/jphot.2009.2035998

62. Liang A, Liu Q, Wen G, Jiang Z (2012) The surface-plasmon-resonance effect of nanogold/silver and its analytical applications. TrAC Trends Anal Chem 37:32–47. doi:10.1016/j.trac.2012.03.015

63. Wood RW (1902) On a remarkable case of uneven distribution of light in a diffraction grating spectrum. Philos Mag 4(21):396–402

64. Ghosh SK, Pal T (2007) Interparticle coupling effect on the surface plasmon resonance of gold nanoparticles: form theory to applications. Chem Rev 107:4797–4862

65. Fano U (1941) The theory of anomalous diffraction gratings and of quasi-stationary waves on metallic surfaces (Sommerfeld's waves). J Opt Soc Am 31:213–222

66. Crouse D, Keshavareddy P (2005) Role of optical and surface plasmon modes in enhanced transmission and applications. Opt Express 13(20):7760–7771

67. Ebbesen TW, Lezec HJ, Ghaemi HF, Thio T, Wolff PA (1998) Extraordinary optical transmission through sub-wavelength hole arrays. Nature 391:667–669

68. Crouse D (2005) Numerical modeling and electromagnetic resonant modes in complex grating structures and optoelectronic device applications. IEEE Trans Electron Devices 52(11):2365–2373

69. Treacy M (2002) Dynamical diffraction explanation of the anomalous transmission of light through metallic gratings. Phys Rev B 66(19):195105. doi:10.1103/PhysRevB.66.195105

70. Collin S, Pardo F, Tessier R, Pelouard J-L (2002) Horizontal and vertical surface resonances in transmission metallic gratings. J Opt A: Appl Opt 4:5154–5160

71. Barbara A, Quémerais P, Bustarret E, Lopez-Rios T (2002) Optical transmission through subwavelength metallic gratings. Phys Rev B 66(16):161403. doi:10.1103/PhysRevB.66.161403

72. García-Vidal F, Martín-Moreno L (2002) Transmission and focusing of light in one-dimensional periodically nanostructured metals. Phys Rev B 66(15):155412. doi:10.1103/PhysRevB.66.155412

73. Cao Q, Lalanne P (2002) Negative role of surface plasmons in the transmission of metallic gratings with very narrow slits. Phys Rev Lett 88(5):057403. doi:10.1103/PhysRevLett.88.057403

74. Collin S, Pardo F, Teissier R, Pelouard J-L (2004) Efficient light absorption in metal–semiconductor–metal nanostructures. Appl Phys Lett 85(2):194. doi:10.1063/1.1771467

75. Collin SP, Pardo F, Pelouard J-L (2003) Resonant-cavity-enhanced subwavelength metal–semiconductor–metal photodetector. Appl Phys Lett 83(8):1521. doi:10.1063/1.1604942

76. Stuart HR, Hall DG (1998) Island size effects in nanoparticle-enhanced photodetectors. Appl Phys Lett 73(26):3815. doi:10.1063/1.122903

77. Liu Y, Cheng R, Liao L, Zhou H, Bai J, Liu G, Liu L, Huang Y, Duan X (2011) Plasmon resonance enhanced multicolour photodetection by graphene. Nat Commun 2:579. doi:10.1038/ncomms1589

78. Butun S, Cinel NA, Ozbay E (2012) LSPR enhanced MSM UV photodetectors. Nanotechnology 23(44):444010. doi:10.1088/0957-4484/23/44/444010

79. Porto JA, Garcia-Vidal FJ, Pendry JB (1999) Transmission resonances on metallic gratings with very narrow slits. Phys Rev Lett 83(14):2845–2848

80. Burc S, Tidin O, Okyay K (2012) Plasmonic nanoslit array enhanced metal–semiconductor–metal optical detectors. IEEE Photon Technol Lett 324(7):548–550

81. Yu Z, Veronis G, Fan S, Brongersma ML (2006) Design of midinfrared photodetectors enhanced by surface plasmons on grating structures. Appl Phys Lett 89(15):151116. doi:10.1063/1.2360896

82. Schaadt DM, Feng B, Yu ET (2005) Enhanced semiconductor optical absorption via surface plasmon excitation in metal nanoparticles. Appl Phys Lett 86(6):063106. doi:10.1063/1.1855423

83. Zhang DH (1995) Fast photoresponse and the related change of crystallite barriers for ZnO films deposited by RF sputtering. J Phys D Appl Phys 28:1273–1277

84. Studenikin SA, Golego N, Cocivera M (2000) Carrier mobility and density contributions to photoconductivity transients in polycrystalline ZnO films. J Appl Phys 87(5):2413. doi:10.1063/1.372194

85. Bikowski A, Ellmer K (2013) Electrical transport in hydrogen-aluminium Co-doped ZnO and Zn1 − xMgxO films: relation to film structure and composition. J Appl Phys 113(5):053710. doi:10.1063/1.4790314

86. Li Y, Huang Q, Bi X (2013) The change of electrical transport characterizations in Ga doped ZnO films with various thicknesses. J Appl Phys 113(5):053702. doi:10.1063/1.4789985

87. Lee JY, Choi YS, Kim JH, Park MO, Im S (2002) Optimizing n-ZnO/p-Si heterojunctions for photodiode applications. Thin Solid Films 403–404:553–557

88. Shao D, Yu M, Lian J, Sawyer S (2012) Heterojunction photodiode fabricated from hydrogen treated ZnO nanowires grown on p-silicon substrate. Appl Phys Lett 101(21):211103. doi:10.1063/1.4767679

89. Yadav HK, Sreenivas K, Gupta V (2007) Enhanced response from metal/ZnO bilayer ultraviolet photodetector. Appl Phys Lett 90(17):172113. doi:10.1063/1.2733628

90. Tzeng S-K, Hon M-H, Leu I-C (2012) Improving the performance of a Zinc Oxide nanowire ultraviolet photodetector by adding silver nanoparticles. J Electrochem Soc 159(4):H440. doi:10.1149/2.088204jes

91. Yang M-H, Liang T, Peng Y-C, Chen Q (2007) Synthesis and characterization of a nanocomplex of ZnO nanoparticles attached to carbon nanotubes. Acta Phys-Chim Sin 23(2):145–151

92. Yang HY, Son DI, Kim TW, Lee JM, Park WI (2010) Enhancement of the photocurrent in ultraviolet photodetectors fabricated utilizing hybrid polymer-ZnO quantum dot nanocomposites due to an embedded graphene layer. Org Electron 11(7):1313–1317. doi:10.1016/j.orgel.2010.04.009

93. Wu J, Bai S, Shen X, Jiang L (2010) Preparation and characterization of graphene/CdS nanocomposites. Appl Surf Sci 257(3):747–751. doi:10.1016/j.apsusc.2010.07.058

94. Shao D, Yu M, Lian J, Sawyer S (2013) Ultraviolet photodetector fabrication from WO3 nano-disks/graphene nanocomposite material. Nanotechnology 24:295701. doi:10.1088/0957-4484/24/29/295701

95. Robel I, Bunker BA, Kamat PV (2005) Single-walled carbon nanotube-CdS nanocomposites as light-harvesting assemblies: photoinduced charge-transfer interactions. Adv Mater 17(20):2458–2463. doi:10.1002/adma.200500418

96. Hou Y, Cheng Y, Hobson T, Liu J (2010) Design and synthesis of hierarchical MnO2 nanospheres/carbon nanotubes/conducting polymer ternary composite for high performance electrochemical electrodes. Nano Lett 10(7):2727–2733. doi:10.1021/nl101723g

97. Cao A, Liu Z, Chu S, Wu M, Ye Z, Cai Z, Chang Y, Wang S, Gong Q, Liu Y (2010) A facile one-step method to produce graphene-CdS quantum dot nanocomposites as promising optoelectronic materials. Adv Mater 22(1):103–106. doi:10.1002/adma.200901920

98. Shao D, Yu M, Lian J, Sawyer S (2013) Heterojunction photodiode fabricated from multiwalled carbon nanotube/ZnO nanowire/p-silicon composite structure. Appl Phys Lett 102(2):021107. doi:10.1063/1.4776691

99. Dali S, Sawyer S, Tao H, Mingpeng Y, Jie L (2012) Photoconductive enhancement effects of graphene quantum dots on ZnO nanoparticle photodetectors. In: Lester Eastman conference on high performance devices (LEC), Brown University, Providence RI, 7–9 Aug 2012, pp 1–4. doi:10.1109/lec.2012.6410972

100. Williams G, Seger B, Kamat PV (2008) TiO2-graphene nanocomposites UV-assisted photocatalytic reduction of graphene oxide. ACS Nano 2(7):1487–1491

101. Shao D, Yu M, Sun T, Lian J, Sawyer S (2013) High responsivity, fast ultraviolet photodetector fabricated from ZnO nanoparticle-graphene core/shell structure. Nanoscale 5:3664–3667

Photothermal Properties of Hollow Gold Nanostructures for Cancer Theranostics

37

Liangran Guo, Yajuan Li, Zeyu Xiao, and Wei Lu

Keywords

Hollow gold nanostructures • Gold nanocages • Hollow gold nanospheres • Hollow gold nanoshells • Cancer theranostics • Photothermal

Introduction

Cancer is the leading cause of death in developed countries and the second leading cause of death in developing countries [1]. It is estimated that the number of cancer-related deaths worldwide will reach 12 million in 2030 [1]. The challenges of manipulating cancers, including early diagnosis, effective treatment, and real-time monitoring of therapeutic efficacy, need to be relieved or modified in urgent [2]. Over the past decade, with the advances in nanotechnology and the requirement for personalized medicine [3], great attention has been focused on the development of nanoparticle-based theranostics, i.e., the combination of diagnostics and therapeutics in single nanoparticles. A variety of nanoplatforms have been used as theranostic agents, such as gold (Au) nanoparticles, silicon nanoparticles, and carbon nanotubes.

L. Guo • Y. Li
Department of Biomedical and Pharmaceutical Sciences, College of Pharmacy,
The University of Rhode Island, Kingston, RI, USA

Z. Xiao
David H. Koch Institute for Integrative Cancer Research, Massachusetts Institute of Technology,
Cambridge, MA, USA

W. Lu (✉)
Department of Biomedical and Pharmaceutical Sciences, College of Pharmacy,
The University of Rhode Island, Kingston, RI, USA

School of Pharmacy, Fudan University, Shanghai, China
e-mail: weilu@uri.edu

Fig. 37.1 Hollow Au nanostructures can be modified with a wide variety of functional moieties for different purposes
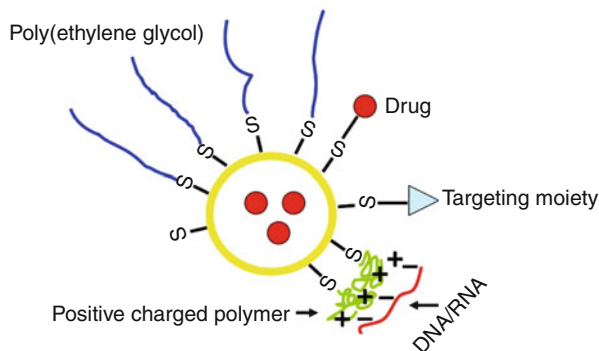
In particular, Au nanoparticles have emerged as well-established theranostic agents due to their unique optical and surface chemical properties. Upon the light irradiation, Au nanoparticles can strongly absorb and scatter light at specific resonant wavelengths, a phenomenon defined as localized surface plasmon resonance (LSPR) [4]. The absorbed light is then transformed into heat, a process known as the photothermal effect. This local heating can increase the temperature of surrounding tissues to above 42 °C, leading to the irreversible cellular damage [5]. As such, the generated heat can be used to directly kill cancer cells or trigger the release of drugs from loaded nanoparticles [5]. The LSPR effects rely on the size, morphology, and local environment of the Au nanoparticles. This observation allows for tuning the LSPR features of Au nanoparticles for multiple purposes. For example, the Au nanoparticles used in vivo should have LSPR peaks in near-infrared (NIR) region ranging from 700 to 900 nm, where the light can deeply penetrate the soft tissues due to the negligible light absorption by hemoglobin and water [6]. Only those Au nanoparticles with hollow structures [7–10] or specific nonspherical morphologies (e.g., rod, star) have LSPR peaks in the NIR region [6, 11–13]. We usually define those Au nanoparticles as Au nanostructures.

Hollow Au nanostructures possess the following advantages compared to other nanoplatforms: (i) Their nonreactive and bio-inert characteristics are adaptable to in vivo applications [14, 15], and (ii) the strong Au–thiolate (Au–S, 50 kcal/mol) interaction enables the surface of Au nanostructures to be easily functionalized for differential applications (Fig. 37.1) [16]. As such, hollow Au nanostructures are promising theranostic agents for cancer imaging and therapy [17]. In this chapter, we provide an up-to-date review on the applications of hollow Au nanostructures in cancer theranostics, with emphasis on the synthesis methods, cancer imaging, and therapy. The hollow Au nanostructures discussed in this chapter include Au nanocages (AuNC), hollow Au nanospheres (HAuNS), and hollow Au nanoshells (HAuNSH).

AuNC

AuNC, invented by Xia's group, are a kind of nanostructures [6] characterized by hollow interiors and ultrathin and porous walls. Compared to solid Au nanoparticles, AuNC show a series of characteristics suitable for cancer theranostic applications as follows: (i) They have uniform and tunable morphologies with the controllable wall thickness in the range of 2–10 nm and precise accuracy of 0.5 nm [6]; (ii) they have tunable LSPR peaks, adaptable to the specific requirement for in vitro and in vivo applications; and (iii) their wall can be incorporated with other metals to maneuver optical properties [6].

Synthesis

AuNC can be prepared through galvanic replacement reaction between $HAuCl_4$ solution and silver (Ag) nanostructures as sacrificing templates [18–20]. The galvanic reaction can be presented in the following equation:

$$3Ag_{(s)} + AuCl^-_{4(aq)} \rightarrow Au_{(s)} + 3Ag^+_{(aq)} + 4Cl^-_{(aq)} \tag{37.1}$$
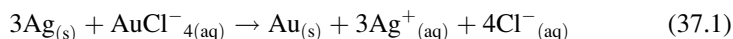
This is a spontaneous reaction, as the reduction potential of $AuCl^-_4$/Au (1.00 V vs. SHE) is more positive than that of Ag^+/Ag (0.80 V vs. SHE). Among various nanostructures, Ag nanocubes are the most suitable templates for AuNC synthesis because they can be prepared as monodisperse samples with controllable size between 30 and 200 nm [21]. With the single crystal Ag nanocubes as sacrificing templates, the derived AuNC essentially exhibit single crystal characteristic and show stronger mechanical strength than the polycrystalline forms [21]. The mechanism involved in galvanic reaction in aqueous media has been investigated or reviewed in previous publications [20, 22]. These studies show that AuNC are formed through three major steps in this reaction: (i) the initiation and preliminary continuation of replacement reaction which results in the formation of partially hollow structure, (ii) the formation of nanoboxes with walls composed of smooth and uniform Au/Ag alloy, and (iii) the formation of pores due to the initiation of dealloying process, in which Ag atoms are selectively oxidized [21]. Through above mechanism, the Ag nanocube-based galvanic replacement reaction runs like a titration. Given a certain amount of Ag nanocubes, the stage of reaction depends on the added volume of $HAuCl_4$ solution. Therefore, the dimensions, pore sizes, and densities of prepared AuNC are well controllable through changing the molar ratio between Ag nanocubes and $AuCl_4$ solutions (Fig. 37.2). Notably, during the nanostructures changing from Ag nanocubes to AuNC, their LSPR peak is continuously shifted toward longer wavelengths (from 400 nm to approximately 900 nm) [21]. Owing to the extremely large absorption cross section, AuNC could be used as potential contrast agents for cancer imaging modalities and coupling agents for cancer photothermal therapy (PTT).
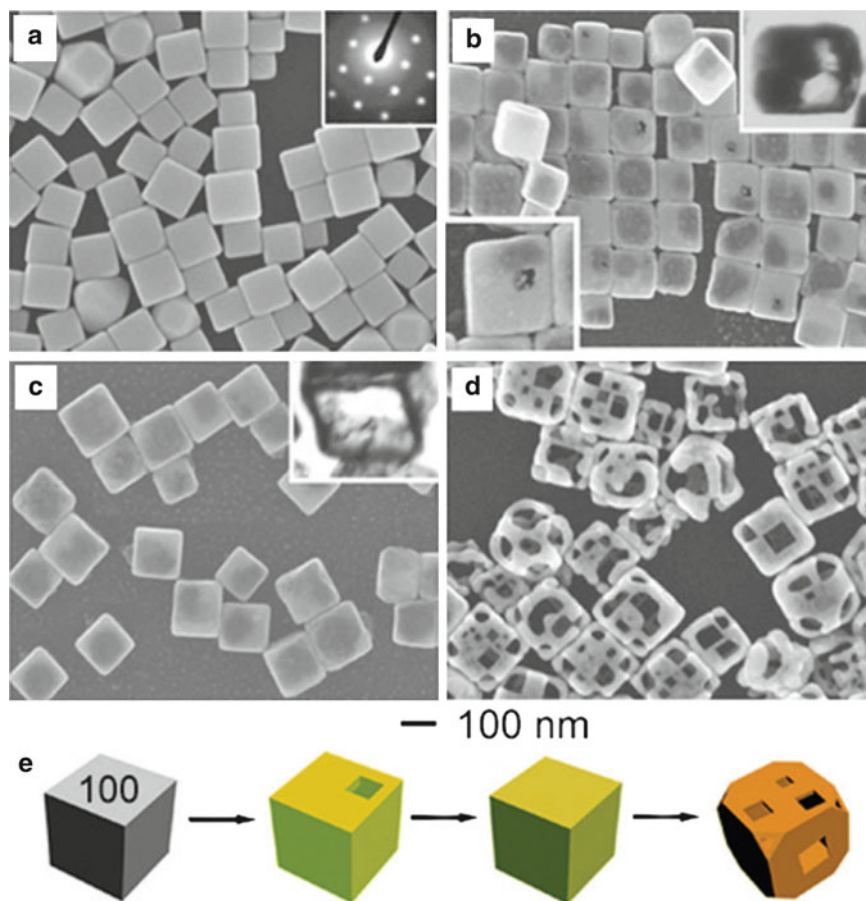
Fig. 37.2 The stage of Ag nanocube-based galvanic replacement depends on the added volume of HAuCl$_4$ solution. (**a**) SEM image of pure Ag nanocubes without adding HAuCl$_4$ solution; they are single crystals as shown by electron diffraction (inset). (**b**) SEM image of galvanic replacement reaction products after adding 0.30 mL of 1 mM HAuCl$_4$ solution to 5 mL of 0.8 mM Ag nanocube suspension; a pinhole (lower inset) has been formed in this step and TEM image (upper inset) of a microtomed sample shows the early hollowing out. (**c**) SEM image of galvanic replacement reaction products after adding 0.50 mL of HAuCl$_4$ solution to the above amount of Ag nanocubes; the formation of nanobox with walls composed of Ag/Au alloy. The hollow cavity is shown by TEM image (inset). (**d**) SEM image of formed AuNC after adding 2.25 mL of HAuCl$_4$ solution to Ag nanocubes. (**e**) Graphic summary of three stages of AuNC formation. The color change indicates the different composition of the product in each step (Reproduced with permission from Ref. [22]. Copyright 2008 American Chemical Society)

Imaging and Diagnosis

Up to date, AuNC have been used as contrast agents in various imaging modalities, such as optical coherence tomography (OCT) or spectroscopic optical coherence
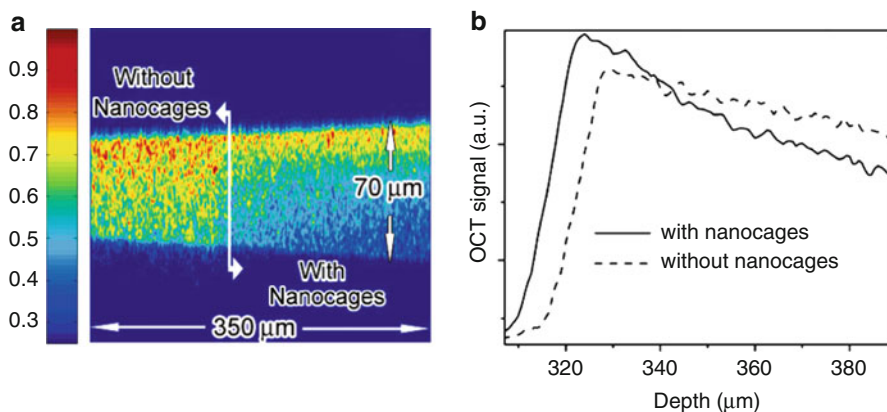
Fig. 37.3 The study of using AuNC as contrast agent for OCT imaging. (**a**) The OCT image of a gelatin phantom with (*right portion*) and without AuNC (*left portion*). The phantom was embedded with 1 mg/mL of TiO$_2$ to mimic the background scattering of soft tissues. (**b**) Plot of OCT signals as a function of phantom depth. The signal of AuNC-contained gelatin phantom decays faster than non-contained one (Reproduced with permission from Ref. [25], copyright 2005 American Chemical Society)

tomography (SOCT), photoacoustic tomography (PAT), and multiphoton luminescence-based detection. The detailed applications are described in the following:

OCT and SOCT

OCT and SOCT can provide high-resolution cross-sectional imaging of the internal microstructure in biological samples by measuring backscattered or backreflected light [23, 24]. One challenge for using OCT or SOCT is the difficulty to detect tumors in early stages or morphologically or optically similar to surrounding normal tissues. To improve their imaging capabilities, various light-scattering and absorption materials have been developed as contrast agents. Among them, AuNC are an ideal kind of contrast agents for cancer OCT or SOCT imaging because of their controllable size, tunable light absorption in the NIR region, easiness of modification with tumor-targeting ligands, and improved tumor accumulation due to the enhanced permeability and retention (EPR) effect [6].

To investigate the potential of AuNC as a class of contrast agents for OCT or SOCT imaging, Chen et al. prepared AuNC with the dimensions on the scale of 36.7 nm and LSPR peak tuned to 800 nm [25]. The phantom samples which can mimic the scattering background of biological tissues were used for OCT imaging. The experiment was conducted using a 7-fs Ti:sapphire laser (center wavelength, 825 nm; bandwidth, 155 nm). Figure 37.3 showed that the tissue phantom added with AuNC displayed strong light attenuation due to the strong absorption of the AuNC. In another study, Cang et al. demonstrated the enhanced contrast of AuNC in both OCT and SOCT imaging [26], convincing the feasibility of AuNC served as contrast agents for OCT and SOCT.

PAT

PAT is a cross-sectional or three-dimensional imaging technology based on the photoacoustic effect. It combines the merits of both optical and ultrasonic imaging methods, thus providing high structure and functional information in vivo [27]. To achieve precise visualization and delineation of structures in biological tissues, signal needs to be enhanced by using contrast agents [27], such as AuNC.

Kim, C et al. evaluated PAT contrast enhancement on B16 melanomas using nontargeted and tumor-targeted AuNC [28]. The AuNC prepared in that study have an outer edge length of 46 nm and a wall thickness of 7 nm. The tumor-targeted AuNC were obtained by modifying with $[Nle^4,_D-Phe^7]-\alpha$-melanocyte-stimulating hormone which binds to melanoma-overexpressed α-MSH receptors. Two groups of tumor-bearing mice (Fig. 37.4a, e) were systematically administered with nontargeted and targeted AuNC, respectively. Before the injection, control images of melanoma (Fig. 37.4b, f) were acquired by using microscopic systems for detecting melanoma (10 MHz, 778 nm) and blood vessels (50 MHz, 570 nm). PAT imaging was obtained from both groups of mice 3 and 6 h after injection. As shown in Fig. 37.4b–d, f–h, the PAT signal in the melanoma-bearing mice was reached to 36 % in the targeted AuNC group and reached to 14 % in the nontargeted AuNC group. In addition, PAT had also been performed on the cerebral cortex of rats using AuNC as an optical contrast agent [29]. The enhanced optical contrast was observed for identifying the vasculature in the cerebral cortex. In another study, AuNC were proved to be an effective PTA contrast agent for detection of sentinel lymph nodes in rats [30]. These results indicated the feasibility of using AuNC as contrast agents in PTA imaging.

Multiphoton Luminescence-Based Detection

As mentioned above, the tumor-targeted AuNC can bind to the receptors expressed in tumor cells and subsequently undergo the cellular uptake. To investigate the receptor-mediated endocytosis process of targeted AuNC, the common method is to quantitatively measure the concentration of Au accumulated in the cells by using inductively coupled plasma mass spectrometry (ICP-MS). However, the technique needs to digest cell samples containing Au with aqua regia which is a time-consumable process [31]. Alternatively, optical imaging might get the results quicker. It is known that solid Au emits photon luminescence (PL) under the laser irradiation, resulting from the recombination of photoexcited electrons in the s-p conduction band with holes in the d-band [6, 32]. In terms of Au nanostructures, this emission will be significantly enhanced given the laser lays in resonance with the LSPR peak in a two-photon configuration [6]. Au nanorods with LSPR peak in NIR region have been used as contrast agents for 2PL imaging of tumor cells [33]. Similarly, 2PL imaging is also an effective method to measure the AuNC accumulation through the cellular uptakes [31, 34]. For example, Au et al. investigated the U87MGwtEGFR cellular uptake of AuNC modified with monoclonal anti-epidermal growth factor receptor (EGFR) which can bind to EGFR expressed in U87MGwtEGFR cells [31]. As shown in Fig. 37.5a, the green color means the PL collected

Fig. 37.4 The PAT images of B16 melanomas using tumor-targeted AuNC ([Nle^4, $_D$-Phe^7]-α-MSH-AuNC) and non-targeted AuNC. (**a**, **e**) Photographs of melanoma-bearing mice injected with tumor-targeted AuNC (**a**) and non targeted AuNC (**e**), respectively. (**b**–**d**) PAT images of B16 melanomas before and after i.v. injection of tumor-targeted AuNC. (**f**–**h**) PAT images of B16 melanomas before and after i.v. injection of non-targeted AuNC (Reproduced with permission from Ref [28], copyright 2010 American Chemical Society)
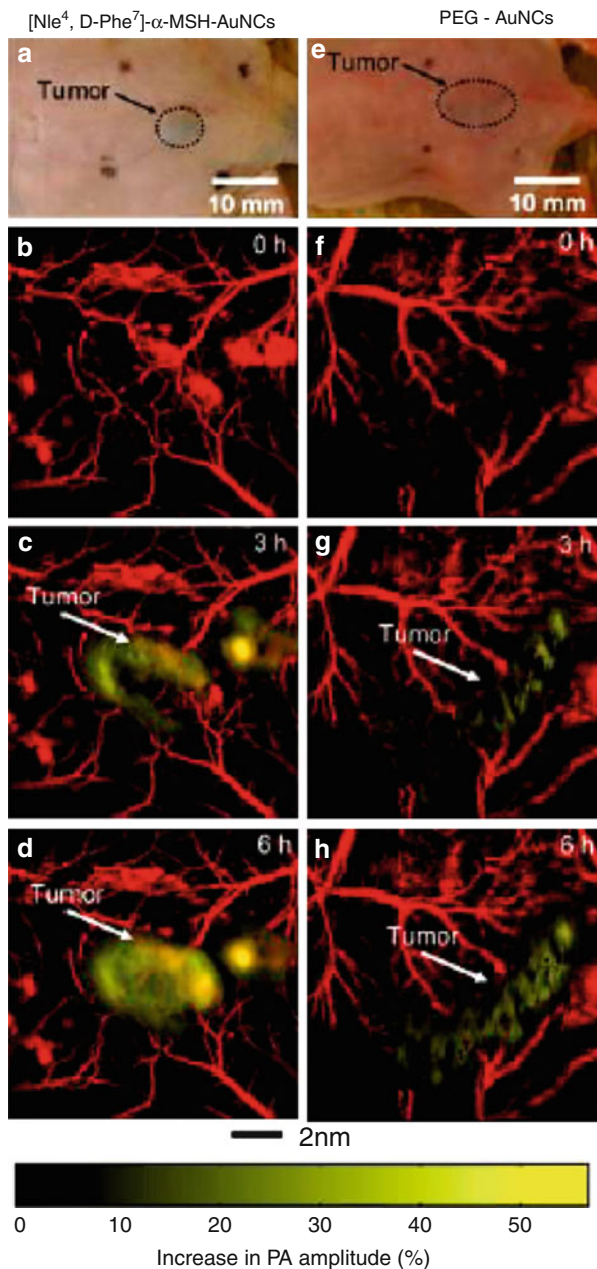
from the AuNC in the range of 500–550 nm, while the red color represents fluorescence from FM4-64 dye (a marker for cell membrane and endosome) collected in the range of 650–700 nm (Fig. 37.5b). Figure 37.5c is the superimposition of Fig. 37.5a, b, indicating the intracellular location of surface modified
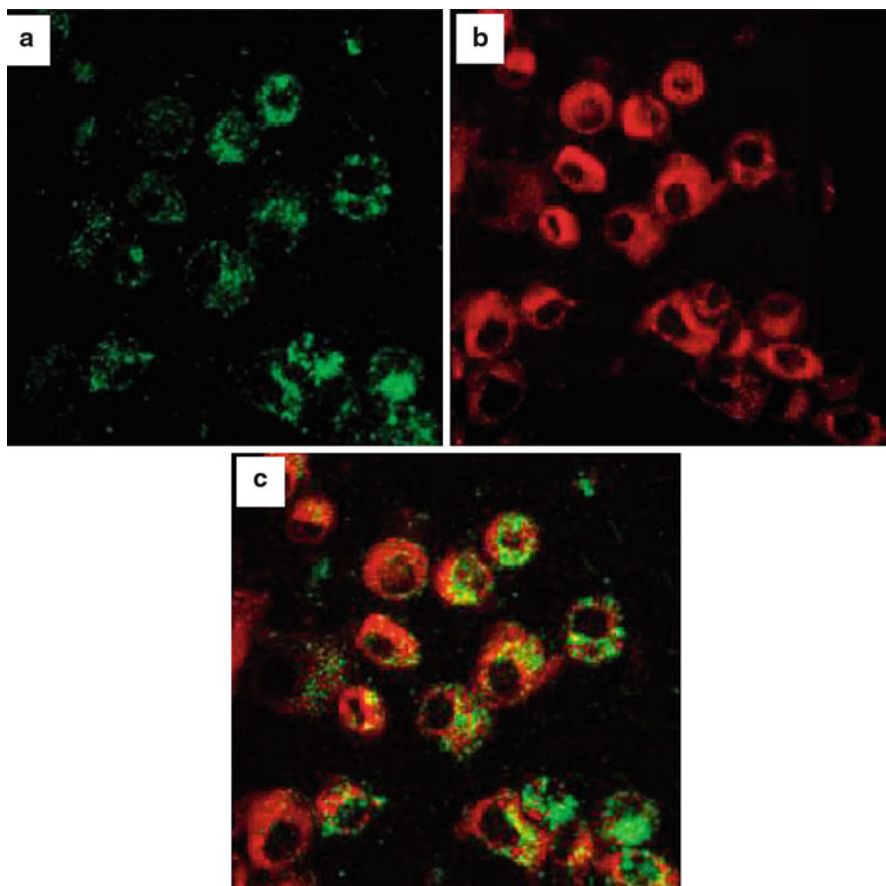
Fig. 37.5 Cellular location of AuNC detected through 2PL. The U87MGwtEGFR cells were incubated with anti-EGFR modified AuNC and FM4-64 dye for 3 h. (**a**) PL collected from anti-EGFR modified AuNC. (**b**) *Red fluorescence* collected from FM4-64 dye, indicating the location of cell membrane and endosomes. (**c**) Overlap of (**a**) and (**b**), indicating that majority of anti-EGFR modified AuNC were colocalized with FM4-64 (Reproduced with permission from Ref. [31], copyright 2010 American Chemical Society)

AuNC [31]. The PL from AuNC provides a convenient way to evaluate their cellular location using two-photon microscopy.

Notably, heat is generated in 2PL imaging, mainly due to the overlap of its excitation wavelength with the LSPR peak of AuNC [35]. To overcome this limitation, 3PL imaging was developed by using Au/Ag alloyed nanocages as the contrast agents. This method takes advantages of its excitation wavelength far away from the LSPR peak, thus resulting in less heat generation during the imaging. Tong et al. compared the cytotoxicity effects in 2PL and 3PL imaging method. The cells were incubated under the same time period and irradiated using the same laser power. After 90-s irradiation, significant cell damage (e.g., membrane
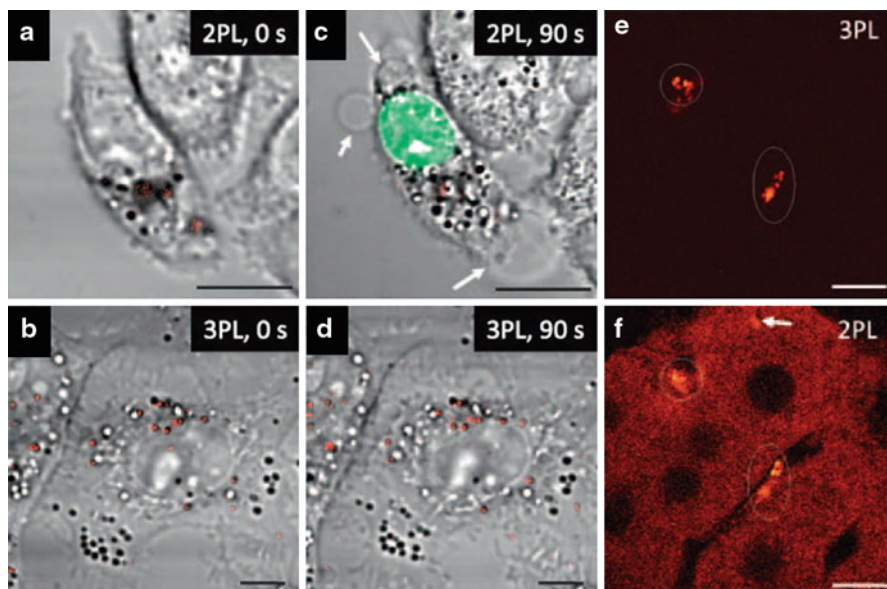
Fig. 37.6 The study of 2PL and 3PL imaging of AuNC (49 % Ag/51 % Au) in KB cells (**a–d**) and liver tissue (**e, f**). 3PL imaging showed significant less cell damage and can clearly identify the AuNC in the liver compared to 2PL imaging. (**a, b**) 2PL (**a**) and 3PL (**b**) image of Au/Ag nanocages (*red*) in KB cells before laser scanning; (**c**) 2PL image of KB cells after 90s laser scanning (760 nm femtosecond laser). 2PL image after laser scanning showed much difference from that before laser scanning. The heat generated leads to membrane blebbing (*arrowed*) and compromised membrane integrity indicated by ethidium bromide labeling (*green*); (**d**) 3PL image of KB cells after 90s laser scanning (1,290 nm femtosecond laser). No obvious cell damage was observed after laser scanning compared to (**b**); (**e**) 3PL imaging for identifying AuNC (49 % Ag/51 % Au, *white circles*) in liver tissue; (**f**) 2PL imaging for indentifying AuNC in liver tissue. Scale bars: 10 μm (Reproduced with permission from Ref. [35], copyright 2010 Wiley-VCH Verlag GmbH & Co)

blebbing and compromised plasma integrity) was observed in 2PL imaging, but not in 3PL imaging (Fig. 37.6) [35]. Additionally, 3PL imaging can be used to determine the distribution of AuNC in vivo. As shown in Fig. 37.6e, the nanocages distributed in the liver were shown as bright dots in the 3PL image, clearly distinguished from the dark surrounding background. This information is hardly acquired by 2PL image, as both nanocages and hepatocytes can emit fluorescence in the emission wavelength (Fig. 37.6f).

Therapeutics Applications

PTT

Due to the LSPR effects as described above, AuNC can be used for photothermal therapy. Both passively and actively targeted AuNC have been developed for this

purpose. The former relies on the leaky vasculature surrounding tumors by EPR effects, and the latter is achieved by modifying AuNC with tumor-targeted molecules. In this section, we will introduce PTT using these two kinds of targeted AuNC.

Au et al. quantitatively investigated the in vitro photothermal effect of AuNC on SK-BR-3 cells, a well-characterized breast cancer cell line [36]. The AuNC were conjugated with anti-HER2 monoclonal antibodies which can specifically bind to EGFR 2 overexpressed in SK-BR-3 cells. In this study, SK-BR-3 cells were incubated with AuNC for 3 h and then irradiated with a Ti:sapphire laser (wavelength, 805 nm; bandwidth, 54 nm) with a spot size of 2 mm. After laser treatment, the cells were harvested at different time point for flow cytometry analysis. Some factors such as laser exposure time, laser power density, and cells' response to laser exposure were systemically investigated. The result indicated that these parameters should be properly set up as they all have important influences to photothermal effect of AuNC [36].

The in vivo photothermal effect was also investigated [37]. Two groups of tumor-bearing mice were i.v. injected with PEGylated AuNC and saline, respectively. Seventy-two hours after injection, the tumor was exposed to the laser treatment (0.7 W/cm^2) for 10 min (Fig. 37.7a), and the thermographic images were captured during this treatment (Fig. 37.7b–i). The temperature in tumor site, which is the key factor for PTT, was record at a serial of time points (Fig. 37.7j). For the mice injected with PEGylated AuNC, the tumor temperature increased rapidly up to 50 °C within 1 min, while that of the mice injected with saline showed no obvious increase.

The tumor response to laser treatment, reflected by metabolic activity, was evaluated by using [^{18}F] fluorodeoxyglucose (^{18}F-FDG) positron emission tomography (PET). The tumor metabolism of saline- or AuNC-injected mice was measured with ^{18}F-FDG PET/CT imaging before and after laser treatment. No obvious differences were found in either saline-treated (Fig. 37.8a) or AuNC-treated mice (Fig. 37.8b) before laser treatment. After 24-h irradiation, the metabolic activity of the tumor injected with AuNC (Fig. 37.8d) significantly reduced compared to the tumor injected with saline (Fig. 37.8c). To minimize the variation, the signal of the treated tumor was normalized to that of the untreated tumor in the same mouse in each time point. As shown in Fig. 37.8e, after laser treatment, the normalized value of AuNC-injected mice decreased 70 %, while that of saline injected mice show no obvious change.

Controlled Drug Release

Due to the hollow cavity of AuNC, drugs can be loaded inside for chemical therapy. In addition, the unique optical property of AuNC allows for the real-time monitoring of drug release at the target of interest. In the following, we summarize recent studies and present as the following [38–40].

In one study, AuNC were loaded with drugs, and their surface was covered with poly (N-isopropylacrylamide) (pNIPAAm) [38], a kind of smart polymer that can sensitively change its formation upon the temperature variations [41]. Once exposed to the laser, the generated heat causes the polymer chains collapsed, resulting in drug release via the exposed pores on the AuNC (Fig. 37.9a). Briefly,

Fig. 37.7 (**a**) One of the tumor-bearing mice used for photothermal treatment. Each mouse was i.v. injected with 100 μL PEGylated AuNC (9×10^{12} particles/mL) or saline. Seventy-two hours after injection, the tumor on the right frank was irradiated by the diode laser at 0.7 W/cm^2. *Dash circle*: tumor site treated with laser; *black arrow*: position of i.v. injection. (**b–e**) Thermographic images of mice injected with PEGylated AuNC. (**f–i**) Thermographic images of mice injected with saline. (**b, f**) 1 min, (**c, g**) 3 min, (**d, h**) 5 min, and (**e, i**) 10 min. (**j**) Plots of tumor temperature as a function of laser exposure time. Bars: 1 cm (Reproduced with permission from Ref [37], copyright 2010 Wiley-VCH Verlag GmbH & Co)
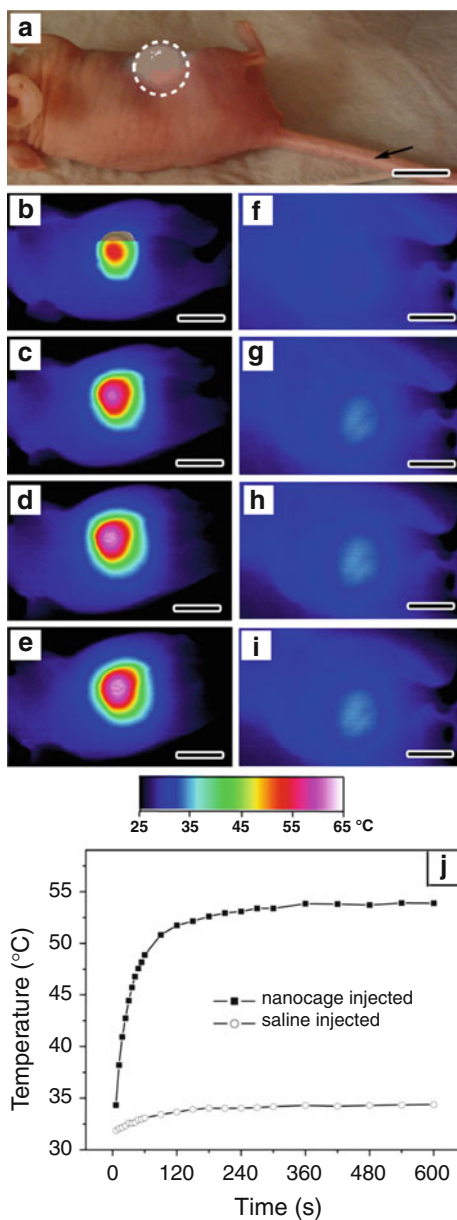
the pNIPAAm-co-pAAm, a copolymer with a low critical solution temperature (LCST) of 39 °C, was covalently anchored to the surface of AuNC through Au–thiolate linkage. Transmission electron microscope (TEM) observation indicates that the pNIPAAm-co-pAAm formed a uniform coating of 3 nm thickness (Fig. 37.9b). To demonstrate the laser-controlled release of effectors from

Fig. 37.8 ^{18}F-FDG PET images of mice receiving treatment of "PEGylated AuNC + laser" or "saline + laser." (**a**) The PET image of a mouse injected with saline before laser. (**b**) The PET image of a mouse injected with PEGylated AuNC before laser treatment. (**c**) The PET image of a mouse injected with saline after laser treatment. (**d**) The PET image of a mouse injected with PEGylated AuNC after laser treatment. *White arrows*: tumors exposed to the diode laser at a power density of 0.7 W/cm^2 for 10 min. (**e**) Ratios of laser-treated tumor (*right tumor*) to nontreated tumor (*left tumor*) in terms of ^{18}F-FDG standardized uptake value. (*, $P < 0.001$) (Reproduced with permission from Ref. [37], copyright 2010 Wiley-VCH Verlag GmbH & Co)
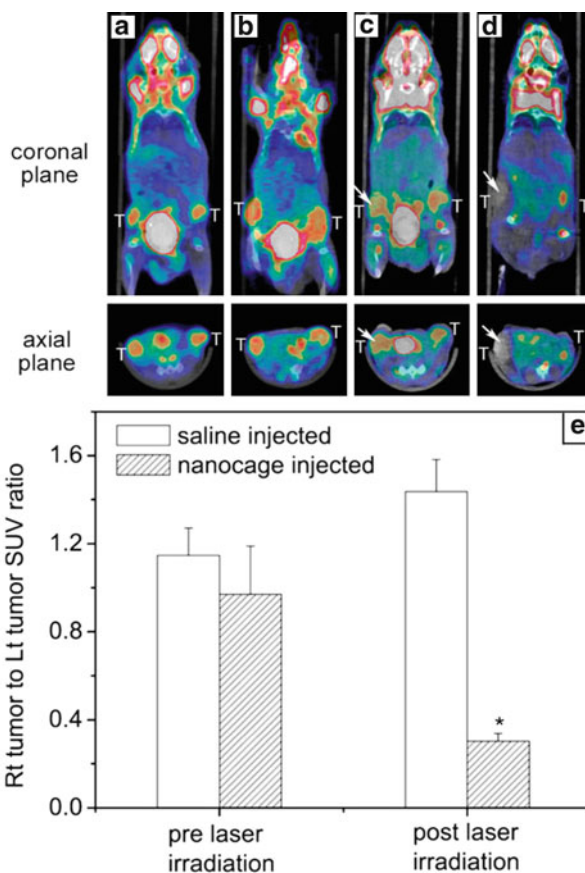
copolymer-coated AuNC, a dye was loaded inside this AuNC followed by different laser irradiation periods. As shown in Fig. 37.9c, more dye molecules were released with the increase of laser irradiation time. The authors further extended this study with doxorubicin (DOX) as a model drug. Similarly, most of DOX was released with the laser treatment which was supported by the following cytotoxic study in vitro. As shown in Fig. 37.9d, with the increase of irritation time, more cancer cell death was observed due to the laser-triggered release of DOX. In contrast, laser irradiation alone or laser irritation of DOX-free AuNC resulted in a slight cell death. This type of AuNC actually combine the PTT with chemotherapy, showing promising antitumor effect compared to single treatment alone.

Li et al. designed another similar nanoplatform based on the AuNC loaded with a dye (Rhodamine 6G) in hollow cavity and covered with pNIPAAm-co-pAAm outside [39]. Different from above study, the dye release from AuNC can be controlled by high-intensity focused ultrasound (HIFU). HIFU treatment can raise the tissue temperature to a cytotoxic level much faster than conventional heating [42], thus greatly increasing the drug release rate. The result in this study indicated
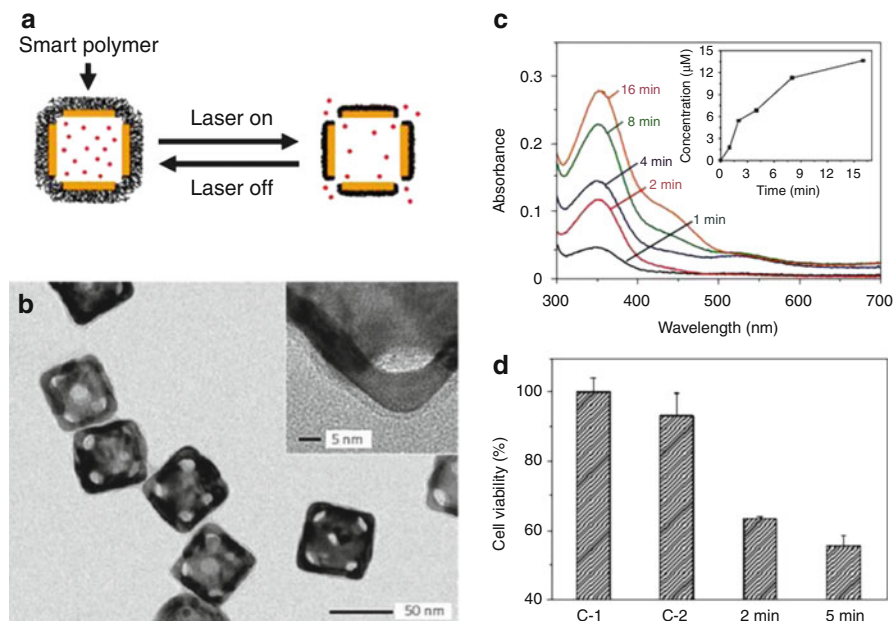
Fig. 37.9 (**a**) Schematic illustration of smart polymer-coated AuNC. Upon laser treatment, the generated heat will result in collapse of smart polymer and therefore release the pre-loaded effectors. When stopping the laser treatment, the smart polymer will go back to the extended conformation and terminate the drug release. (**b**) TEM images of AuNC whose surface was covered with copolymer, pNIPAAm-co-pAAm. The magnified TEM image (inset) shows the corner of AuNC was covered with the copolymer. (**c**) Controlled release of the dye from the AuNC covered by a copolymer with a LCST at 39 °C. The AuNC were treated with a NIR laser (10 mW/cm^2) for different time length. (**d**) Breast cancer cell viability after different treatments: (C-1) Cells were treated with laser for 2 min without AuNC; (C-2) Cells were treated with laser for 2 min with DOX-free AuNC; (2 min) Cells were treated with the laser for 2 min in the presence of DOX-loaded AuNC; (5 min) Cells were treated with the laser for 5 min in the presence of DOX-loaded AuNC (Reproduced with permission from Ref. [38], copyright 2009 Nature Publishing Group)

that most of the dye was released within 10-min exposure to HIFU. Recently, HIFU was reported to use in a theranostic system based on AuNC, showing the promising ability to both enhance the contrast of PA imaging and control the dye (Rhodamine 6G) release from this system [40]. These results taken together convince the feasibility of AuNC used as carriers for controlling drug release.

Hollow Au Nanospheres (HAuNS)

HAuNS are characterized by small size (outer diameter, 30–50 nm), spherical shape, and hollow interior nanostructures with strong and tunable absorption [9, 43–46]. Considerable reports suggest that HAuNS are a promising kind of conducting agent for cancer imaging and therapy [9, 43–46].

Synthesis

Up to date, two major methods are reported for synthesizing HAuNS. The first is based on a process where a thin Au shell is initially formed on the surface of sacrificial templates, followed by the removal of the inside template [47]. The second relies on the direct Au deposition on the preformed vesicles followed by the removal of vesicles [48]. The detailed methods are described below.

In the first method, HAuNS were synthesized using Co nanoparticles as sacrificial template [47]. In brief, Co particles were firstly prepared through the reaction between $CoCl_2$ and $NaBH_4$ in citric acid solution. This reaction should be proceeding with the protection of Argon, therefore avoiding the oxidation of the Co nanoparticles. The prepared Co nanoparticles were then added to the $AuCl_4$ solution with stirring to generate the HAuNS. The equation for the second reaction can be presented as below:

$$3Co + 2AuCl_4^- = 2Au + 3Co^{2+} + 8Cl^- \tag{37.2}$$
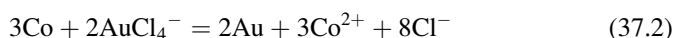
As the reduction potential of the $AuCl_4^-$/Au redox couple (0.994 V vs. SHE) is much higher than that of the Co^{2+}/Co redox couple (-0.277 V vs. SHE), this reaction also proceeds spontaneously [47]. Added with Co nanoparticles, aqueous Au ion will be deposited to solid Au atoms in the nanoparticle surface and solid Co will switch to the Co ions. With the continuation of reaction, the deposited Au atoms begin to nucleate, grow up to very small Au particles, and finally form a thin shell surrounding the Co nanoparticles [49]. After Au ions were totally deposited as Au shell, the solid core inside will continually be oxidized by H^+ until its disappearance, leading to the formation of HAuNS (Fig. 37.10a). During this process, the shell thickness grow inward, and the outer diameter should be determined by the size of Co nanoparticles, while the inner diameter can be controlled by adding different amount of Au salt [49]. The detailed mechanisms for synthesis of HAuNS have been systemically investigated [47, 50]. Figure 37.10b indicates that the absorption peak of HAuNS can be tuned from visible spectrum to NIR region through varying the particle size and wall thickness [50].

In the second method, HAuNS can be synthesized through a simple one-step reaction [48]. As described, 20 mL of 10 mmol/L Bu_4PBr aqueous solution was mixed with 2.0 mL of 5.0 mmol/L $HAuCl_4$ aqueous solution under stirring. Several minutes later, a certain amount of KBH_4 aqueous solution was added, and the whole system was kept under vigorous string until no gas was generated. The HAuNS were obtained by centrifugation and washed with deionized water. The mechanism of this reaction is illustrated in Fig. 37.10c. Firstly, in aqueous solution, the Bu_4PBr undergoes hydrolysis, resulting in the Br^- and Bu_4P^+ ions. Meanwhile, the Bu_4P^+ can automatically form vesicles [51] that were used as sacrificial templates in the following steps. Secondly, after adding $HAuCl_4$ to Bu_4PBr solution, the $AuBr_4^-$ complex is formed and subsequently accumulated on both the inner and the outer surfaces of the vesicles through electrostatic interaction. Thirdly, after adding KBH_4, the reduction reaction between $AuBr_4^-$ and KBH_4 results in the formation
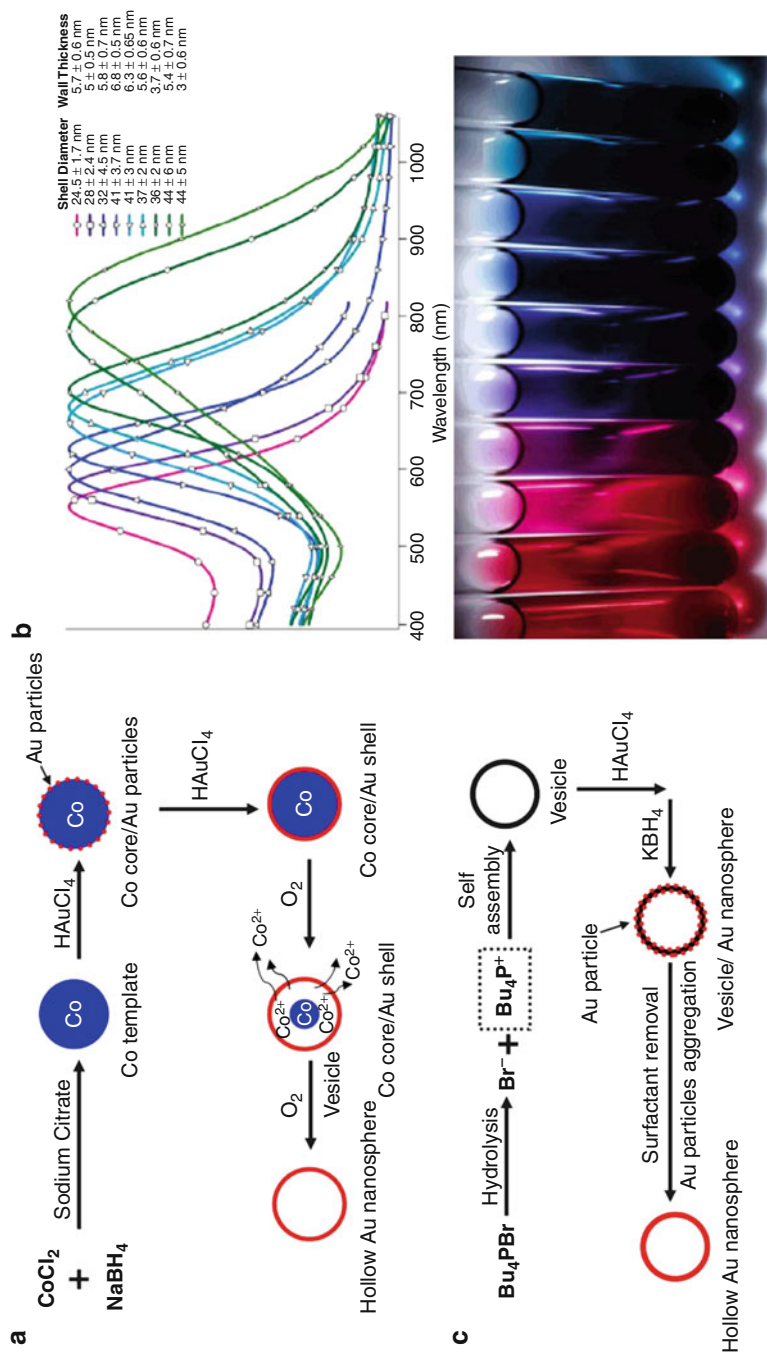
Fig. 37.10 Schematic illustration of HAuNS synthesis using Co nanoparticles (**a**) and vesicles (**c**) as sacrificial templates. (**b**) The absorption peaks of HAuNS with different shell diameters and wall thicknesses (*up panel*) and the color range of various HAuNS tested in the *up panel* (*low panel*). The most *left* sample is solid Au nanoparticle, and the others are HAuNS. (**b**) (Reproduced with permission from Ref. [50], copyright 2006 American Chemical Society)

of small Au particles on both sides of the vesicle surface. Lastly, the HAuNS can be formed through aggregation of small Au particles and removal of vesicles. The HAuNS produced in this method are also tunable, since the shell thickness can be controlled via adjusting the reaction temperature.

Imaging and Diagnosis

Lu et al. investigated the usage of HAuNS for PAT in orthotropic mouse xenograft model of glioma [43]. In order to increase the tumor accumulation, the PEGylated HAuNS (PEG-HAuNS) were modified with cyclic RGD peptides (RGD-PEG-HAuNS). The choice of RGD for cancer imaging is due to its high binding affinity to integrin receptors such as $\alpha_v\beta_3$ receptors overexpressed in human U87 glioma cells [52]. The mice used in this study were inoculated with U87 cells (transfected with luciferase gene) in the brain. At day 8, the tumor-bearing mice were i.v. injected with RGD-PEG-HAuNS or PEG-HAuNS and subjected to PAT imaging 24 h later. As a control, mice were also imaged before the injection. In Fig. 37.11, precontrast PAT can only detect the brain vasculature. It is hard to locate the brain tumor because of the low signal-to-background ratio. In contrast, PAT can clearly demonstrate the location of brain tumor after injection of RGD-PEG-HAuNS, while there was no significant modification in identifying the brain tumor for the mice injected with PEG-HAuNS. This result suggests that RGD-PEG-HAuNS can specifically accumulate in the tumor and reach an enhanced PAT imaging. In addition, the HAuNS used for PAT images can identify the brain vasculature with greater clarity and detail in living mice [45].

PTT

HAuNS can serve as photothermal coupling agents. To achieve tumor-targeted delivery, Lu et al. prepared PEG-HAuNS modified with NDP-MSH (NDP-MSH-PEG-HAuNS), a molecule targeting melanoma cells [46]. Three groups of mice were inoculated with B16/F10 cells in both flanks of the abdomen and injected with "NDP-MSH-PEG-HAuNS," "PEG-HAuNS," or "saline." The tumor in one side of each mouse received laser treatment (808 nm, 0.5 W/cm^2, 1 min) at 4 h after injection. Twenty-four hours posttreatment, the tumors were collected for histological evaluation. The result suggests that NDP-MSH-PEG-HAuNS plus laser induces greater necrosis than other treated groups (Fig. 37.12). The necrosis area was more than eight times bigger than that of "PEG-HAuNS plus laser" group.

Melancon et al. investigated the PTT of bare HAuNS and anti-EGFR monoclonal antibody (C225)-conjugated HAuNS (C225-HAuNS) both in vitro and in vivo [53]. Human squamous carcinoma A431 cells overexpressing EGFR were treated with NIR laser alone, C225-HAuNS alone, IgG-HAuNS plus NIR laser, and C225-HAuNS plus laser. The result indicates that C225-HAuNS plus laser induced most cell death compared to other groups (Fig. 37.13a). Morphologically, the A431
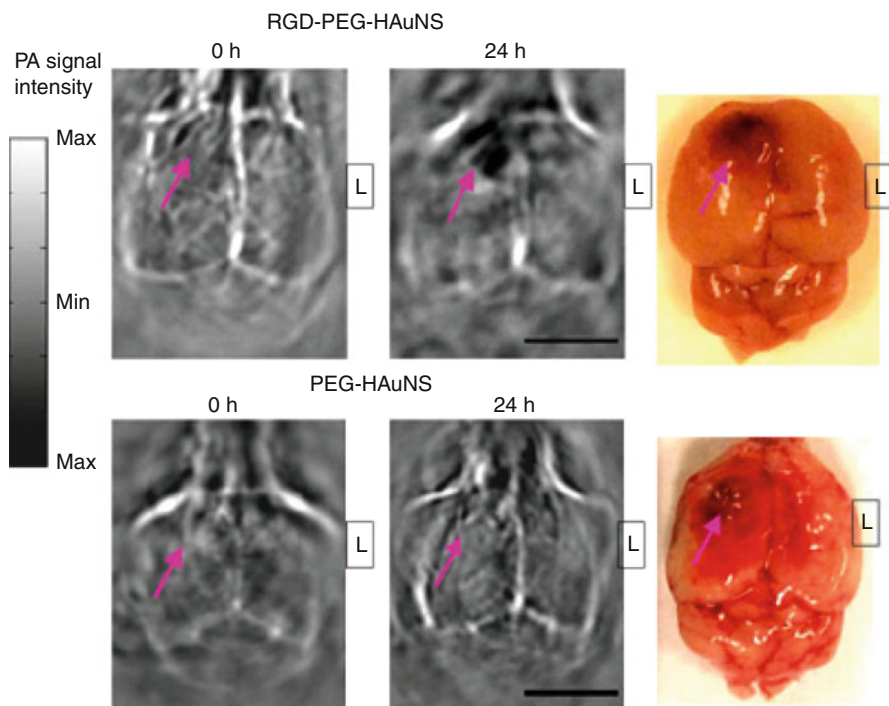
Fig. 37.11 Grey images: PAT images of U87 gliomas inoculated in mouse brains. The images were captured before (0 h) and after (24 h) i.v. injection of PEG-HAuNS or RGD-PEG-HAuNS. Scale Bar, 5 mm. Color images: the tumor location of U87 glioma in mouse brains. *Arrows*, locations of tumors; L, *left* (Reproduced with permission from Ref. [43], copyright: 2011 American Association for Cancer Research)

cells without treatment were polygonal and crowded (Fig. 37.13b), showing almost no staining of EthD-1. However, only a few rounded cells were observed after C225-HAuNS plus laser treatment. In addition, several cells were positively stained with EthD-1, indicating the lost of cellular integrity. These results suggest that HAuNS are promising photothermal coupling agents for both in vitro and in vivo applications.

Controlled Drug Release

Despite its antitumor effect, one major challenge in PTT is the incomplete cell killing, mainly due to the nonuniform heat distribution inside the tumor [44, 54]. Tumor cells surrounding large blood vessels are relatively resistant to PTT, as part of heat can be removed by circulating blood [44, 54–56]. At this condition, the combination of chemotherapy with PTT in one drug carrier provides a choice to resolve the problem. You et al. developed a novel tumor-targeted

NDP-MSH-PEG-HAuNS+ Laser · PEG-HAuNS + Laser · Saline + Laser · Saline Control
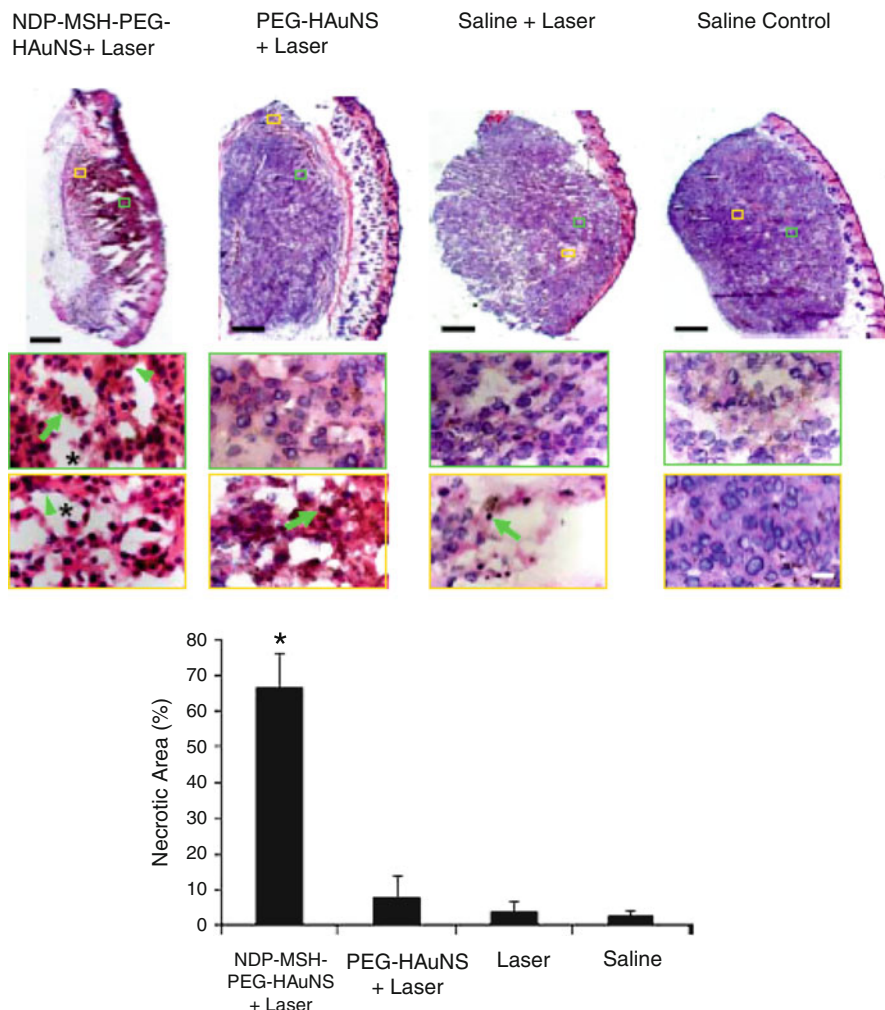
Fig. 37.12 H&E staining of mice tumors after each treatment. Scale Bar, 500 μm. Magnified photographs indicate that NDP-MSH-PEG-HAuNS plus laser induced more cell death as characterized by obvious karyolysis (*arrowheads*), extensive pyknosis (*arrows*), cytoplasmic acidophilia, and degradation of the extracellular matrix (*asterisks*). Bar, 50 μm. The percentage of necrotic area in the tumor was shown in the most *low panel*. *, $P < 0.05$. (n = 5) (Reproduced with permission from Ref. [46], copyright: 2009 American Association for Cancer Research)

HAuNS whereby DOX was loaded inside the cavity (T-DOX-HAuNS) [54]. The targeting moiety, cyclic peptide c(TNYL-RAW), can selectively bind to EphB4 receptor which is overexpressed in many tumor cells lines [57–59]. Upon laser irradiation, this tumor-targeted nanoplatform mediated PTT and DOX release for chemotherapy. The in vitro cell uptake study demonstrated that T-DOX-HAuNS
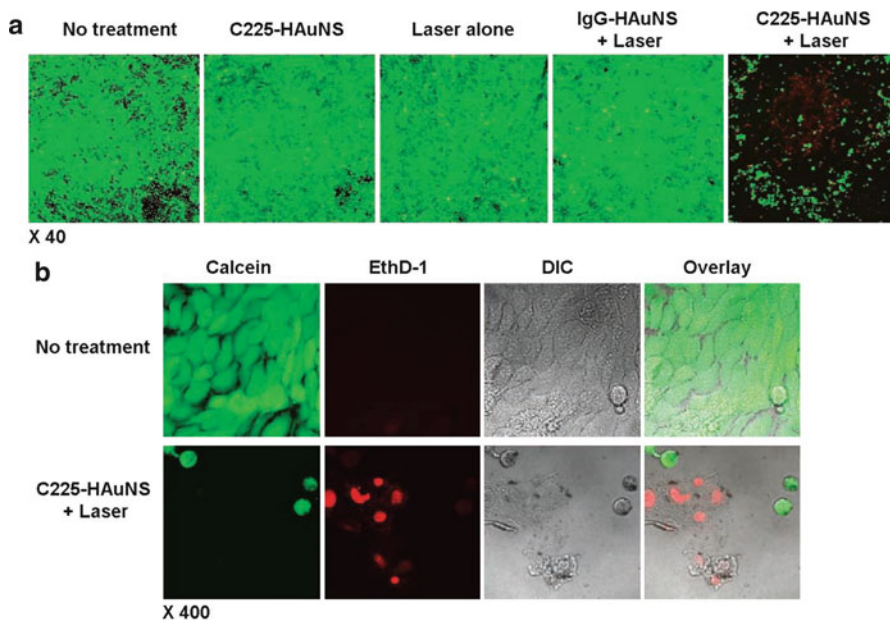
Fig. 37.13 (**a**) The A431 cell viability analysis after each treatment. Significant decrease of *green color* was observed after treating with C225-HAuNS plus NIR laser, meaning majority of cells in this group were dead. (**b**) Images of cells receiving no treatment or C225-HAuNS plus laser at higher magnification. The cells treated with C225-HAuNS plus laser showed rounded morphology and were positively stained with EthD-1, indicating the cell death and lost of cellular integrity. *DIC* differential interference contrast (Reproduced with permission from Ref. [53], copyright: 2008 American Association for Cancer Research)

were readily taken up by the HeLa cells overexpressing EphB4 receptors. Fluorescence observation indicates that DOX remained inside the HAuNS after T-DOX-HAuNS were internalized. Next, authors investigated the laser-triggered release property of DOX from T-DOX-HAuNS in vivo through the radio-labeled DOX and HAuNS, respectively. Figure 37.14a showed ^{3}H-DOX was effectively released and dispersed in HAuNS site after NIR laser irradiation. In contrast, ^{3}H-DOX without laser treatment was mostly colocalized with ^{111}In-HAuNS in the tumor. The following in vivo study, as shown in Fig. 37.14b, demonstrated that the T-DOX-HAuNS significantly suppressed tumor growth compared to other treatments. Similarly, another study showed the possibility of using PTT and DOX for combination therapy [60].

In another example, the biodegradable and biocompatible poly(lactide-co-glycolide) acid (PLGA) microspheres were combined with HAuNS as photothermal coupling agent and paclitaxel (PTX) as an anticancer drug [61]. The structure of PTX-loaded HAuNS-containing microspheres (PTX/HAuNS-MS) was shown in Fig. 37.15a. PTX is uniformly dispersed in the microspheres, while HAuNS form as clusters in the inner water phase. Importantly, PTX/HAuNS-MS can generate
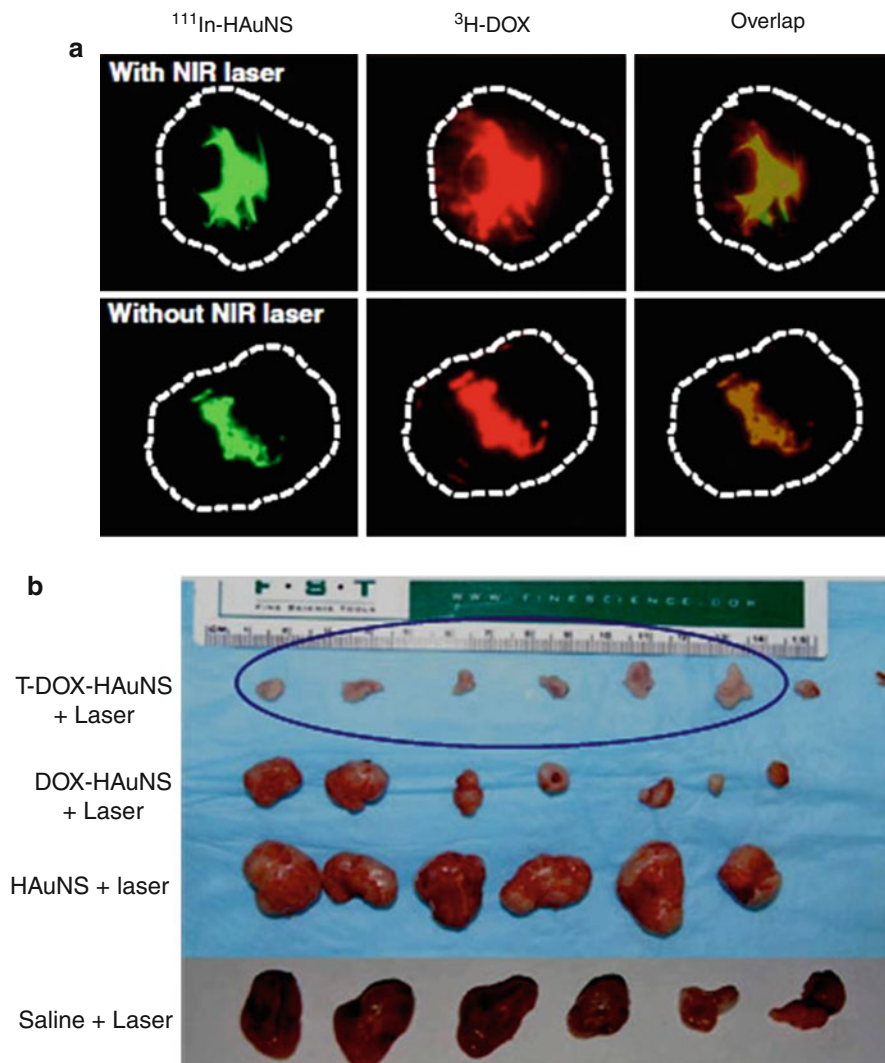
Fig. 37.14 (**a**) In vivo DOX release in the Hey tumor which was triggered by laser irradiation on T-DOX-HAuNS. The position of ^{111}In-HAuNS and ^{3}H-DOX was shown by *green* and *red* signals, respectively. The tumor border was indicated by *white broken circle*. (**b**) Photograph of tumors collected from mice receiving different treatment. Tumors of saline plus laser group were collected on day 9 and that of other groups were collected on day 22. The tumors growth of mice treated with T-DOX-HAuNS were totally suppressed and only scar tissues in the tumor site were photographed in the *blue circle* (Reproduced with permission from Ref. [54], copyright: 2012 American Association for Cancer Research)
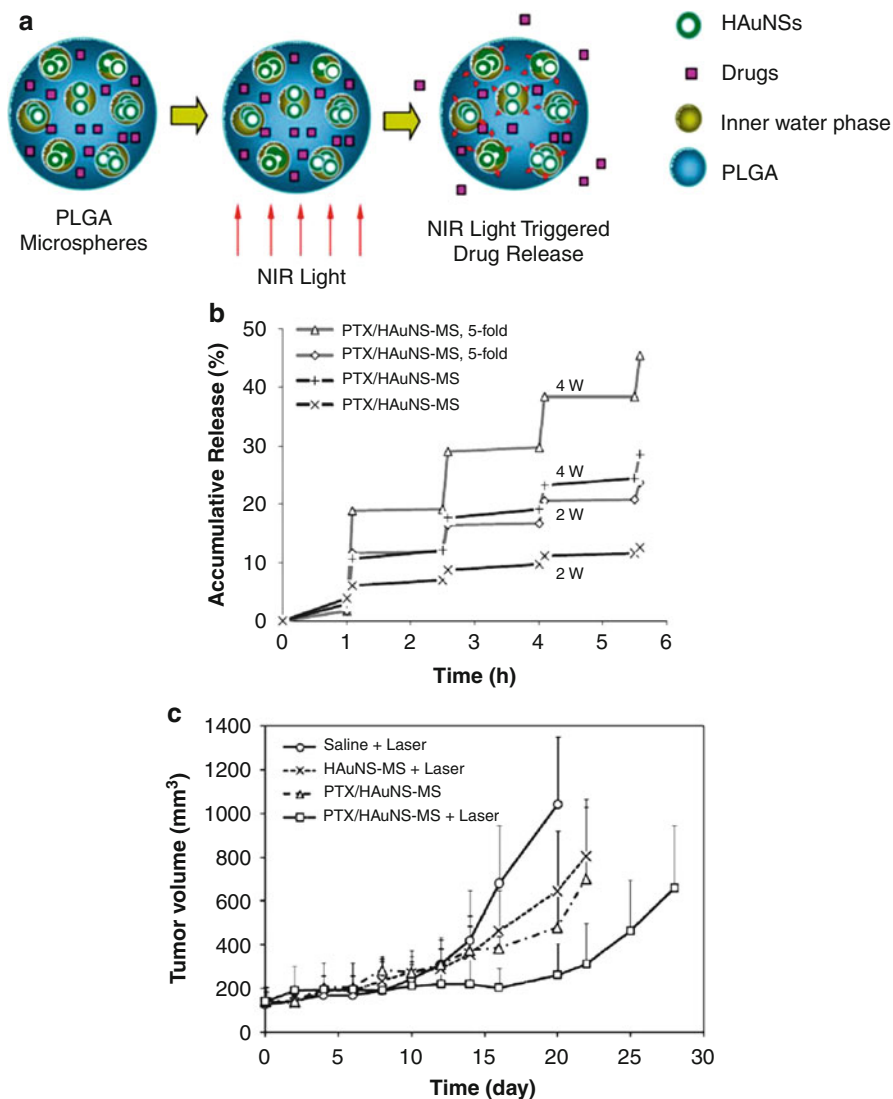
Fig. 37.15 (**a**) Schematic illustration of PTX/HAuNS-MS composition and laser controlled drug release from microspheres. (**b**) Accumulated release of PTX from PTX/HAuNS-MS with the laser irradiation. ($\diamond$ and Δ), PTX/HAuNS-MS containing 4.7×10^{10} HAuNS/mg PLGA received laser treatment at 2 W ($\diamond$) and 4 W (Δ). ($\times$ and +) PTX/HAuNS-MS containing 9.4×10^{9} HAuNS/mg PLGA received laser treatment at 2 W ($\times$) and 4 W (+). (**c**) In vivo antitumor effect of various treatments on U87 gliomas-bearing nude mice (Reproduced with permission from Ref. [61], copyright: 2010 Wiley-VCH Verlag GmbH & Co)
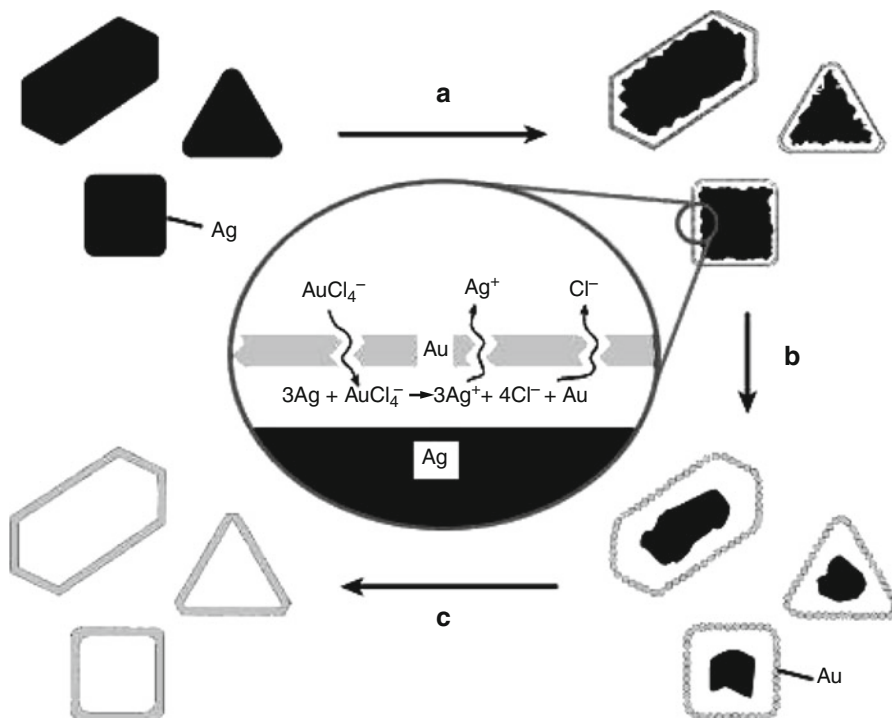
Fig. 37.16 The formation process of HAuNSH via galvanic replacement reaction between Ag nanoparticles and HAuCl$_4$ solution. There are three possible steps involved in this reaction. (**a**) The deposition of Au atoms to the surface of Ag template; (**b**) Au atoms start to nucleate, grow and finally melt into a Au shell; (**c**) depletion of Ag template and the refluxing at high temperature to generate highly crystalline HAuNSH (Reproduced with permission from Ref. [63], copyright: 2002 American Chemical Society)

comparable heat with bare HAuNS at the same concentration. Moreover, this laser-induced heat is able to control the PTX release from PTX/HAuNS-MS, depending on the laser power and HAuNS concentration (Fig. 37.15b). The in vivo study showed that PTX/HAuNS-MS plus laser induced a significant tumor growth delay compared to "saline + laser," "HAuNS-MS + laser," or "PTX/HAuNS-MS" (Fig. 37.15c), showing that biodegradable PLGA microspheres containing HAuNS and antitumor drugs can be used for targeted therapy for the tumor where the photothermal effect and drug release are controlled via laser irradiation. Lu et al. reported the laser-induced NF-κB downregulation through a tumor-targeting HAuNS loaded with siRNA recognizing NF-κB p65 subunit [9]. Up on the laser treatment, the gene siRNA can be efficiently delivered and transfected due to the photothermal effect.
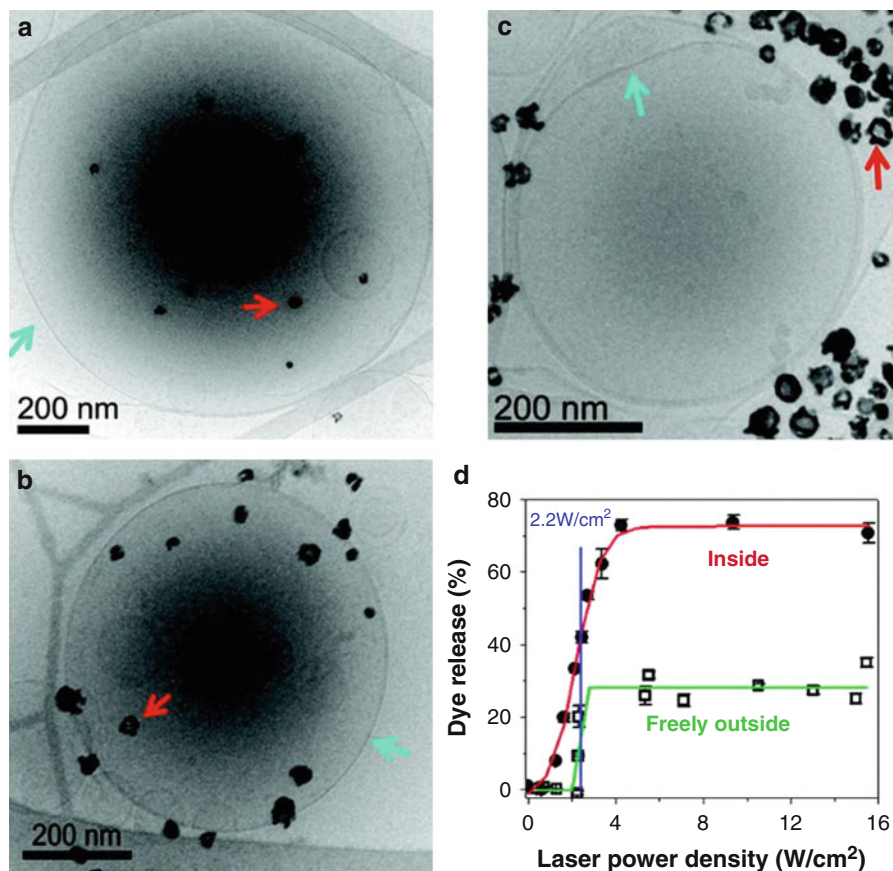
Fig. 37.17 Cryo-EM images of HAuNSH-containing liposomes. HAuNSH are encapsulated inside (**a**), tethered to (**b**), dispersed outside of the liposomes (**c**). (*red arrows*: HAuNSH; *blue arrows*: liposomes). (**d**) CF release cures from HAuNSH-containing liposomes triggered by laser irradiation (Reproduced with permission from Ref. [64], copyright: 2008 American Chemical Society)

Hollow Au Nanoshells (HAuNSH)

HAuNSH, characterized by hollow interiors with a thin Au shell, have several advantages, such as unique optical properties, easy synthesis, and smooth and highly crystalline walls [62]. Different from HAuNS, the shell morphology of HAuNSH is not restricted to the sphere shape but relies on the shape of the templates [62]. Currently, the major method for synthesizing HAuNSH is galvanic replacement reaction between Ag nanoparticles and $HAuCl_4$ solution, a method similar to AuNC and well investigated by Sun et al. [63].

Synthesis

The galvanic replacement reaction for synthesizing HAuNSH is the same to Eq. 37.1. Figure 37.16 illustrates the reaction steps involved in the formation of HAuNSH. At the beginning of this reaction, Au atoms are deposited to the surface of Ag nanoparticles. As the reaction progresses, Au atoms start to nucleate, grow, and finally melt into a Au shell surrounding Ag template. This thin shell is incomplete at early stage, as both $HAuCl_4$ and AgCl diffuse across this shell [62, 63]. The reaction at this time needs a refluxing at a high temperature, in which the Au shell can reconstruct to form closed and highly crystalline structures. It is obvious that the HAuNSH obtained in this method showed a similar morphology to the Ag template and the void size is determined by the template dimension [62, 63]. In terms of the shell thickness, it accounts approximately one tenth of the lateral dimension of sacrificing Ag template as more molar Ag is consumed than Au in this reaction [63].

Applications in Cancer Theranostics

Several studies reported the potential of using HAuNSH as cancer theranostic agents. Wu et al. reported that HAuNSH can induce a rapid liposome release under NIR laser irradiation [64]. HAuNSH can be encapsulated within liposomes, tethered to the liposome membrane, or dispersed in inner water phase (Fig. 37.17a–c). To test the liposome release property, a fluorescent dye, 6-carboxyfluorescein (CF), was encapsulated inside the liposomes as a water soluble drug. As shown in Fig. 37.17d, when the laser power reach a threshold ($1.5 \ W/cm^2$), the drug release can be initiated. While above $4.3 \ W/cm^2$, the laser irradiation can induce a fast and high amount of drug release. In contrast, the laser irradiation cannot trigger the CF release from liposomes without HAuNSH. The instant drug release may be due to the temporal disruption of lipid membrane induced by the heat [64]. This system thus overcomes the slow release profile of liposomes as drug carriers [65].

Braun et al. investigated the gene silencing capabilities of HAuNSH–siRNA conjugates [7]. That study indicated that gene silencing can be achieved through laser-induced release of siRNAs from HAuNSH. Similar to the study by Lu et al., HAuNSH are a new kind of candidate mediating gene therapy for tumor.

Summary

In this review, we mainly summarized the preparation methods and theranostic applications of hollow Au nanostructures. We did not include herein the investigations regarding their cellular uptake pathway and in vivo biodistribution, though they represent interesting research directions [66]. Notably, no published data discussed the long-term metabolism of hollow Au nanostructures in vivo, the better understanding of which may facilitate their clinical translation.

Currently, two gold-based nanoparticles are investigated in the clinical trials and have shown promising results: One is solid gold nanoparticles used for tumor necrosis factor alpha (TNF) delivery [67], and the other is Au nanoshell for PTT of tumor [68]. Although several challenges needs to be addressed, such as their biosafety and efficacy [69], we are optimistic regarding the future clinical translation of hollow Au nanostructures for theranostic applications.

References

1. http://www.cancer.gov/researchandfunding/priorities/global-research-activities. Accessed on 15 March 2013
2. Young J, Figueroa E, Drezek R (2012) Tunable nanostructures as photothermal theranostic agents. Ann Biomed Eng 40:438–459
3. MacKay JA, Li ZB (2010) Theranostic agents that co-deliver therapeutic and imaging agents? preface. Adv Drug Deliv Rev 62:1003–1004
4. Chen J, Yang M, Zhang Q, Cho EC, Cobley CM et al (2010) Gold nanocages: a novel class of multifunctional nanomaterials for theranostic applications. Adv Funct Mater 20:3684–3694
5. Cobley CM, Au L, Chen J, Xia Y (2010) Targeting gold nanocages to cancer cells for photothermal destruction and drug delivery. Expert Opin Drug Deliv 7:577–587
6. Xia Y, Li W, Cobley CM, Chen J, Xia X et al (2011) Gold nanocages: from synthesis to theranostic applications. Acc Chem Res 44:914–924
7. Braun GB, Pallaoro A, Wu G, Missirlis D, Zasadzinski JA et al (2009) Laser-activated gene silencing via gold nanoshell-siRNA conjugates. ACS Nano 3:2007–2015
8. Khan SA, Kanchanapally R, Fan Z, Beqa L, Singh AK et al (2012) A gold nanocage-CNT hybrid for targeted imaging and photothermal destruction of cancer cells. Chem Commun (Camb) 48:6711–6713
9. Lu W, Zhang G, Zhang R, Flores LG 2nd, Huang Q et al (2010) Tumor site-specific silencing of NF-kappaB p65 by targeted hollow gold nanosphere-mediated photothermal transfection. Cancer Res 70:3177–3188
10. Wang Y, Xu J, Xia X, Yang M, Vangveravong S et al (2012) SV119-gold nanocage conjugates: a new platform for targeting cancer cells via sigma-2 receptors. Nanoscale 4:421–424
11. Hao F, Nehl CL, Hafner JH, Nordlander P (2007) Plasmon resonances of a gold nanostar. Nano Lett 7:729–732
12. Senapati D, Singh AK, Khan SA, Senapati T, Ray PC (2011) Probing real time gold nanostar formation process using two-photon scattering spectroscopy. Chem Phys Lett 504:46–51
13. Vu L, Ramos J, Potta T, Rege K (2012) Generation of a focused poly(amino ether) library: polymer-mediated transgene delivery and gold-nanorod based theranostic systems. Theranostics 2:1160–1173
14. Lewinski N, Colvin V, Drezek R (2007) Cytotoxicity of nanoparticles. Small 4:26–49
15. Murphy CJ, Gole AM, Stone JW, Sisco PN, Alkilany AM et al (2008) Gold nanoparticles in biology: beyond toxicity to cellular imaging. Acc Chem Res 41:1721–1730
16. Love JC, Estroff LA, Kriebel JK, Nuzzo RG, Whitesides GM (2005) Self-assembled mono-layers of thiolates on metals as a form of nanotechnology. Chem Rev 105:1103–1170
17. Choi KY, Liu G, Lee S, Chen X (2012) Theranostic nanoplatforms for simultaneous cancer imaging and therapy: current approaches and future perspectives. Nanoscale 4:330–342
18. Chen J, McLellan JM, Siekkinen A, Xiong Y, Li ZY et al (2006) Facile synthesis of gold-silver nanocages with controllable pores on the surface. J Am Chem Soc 128:14776–14777

19. Lu XM, Tuan HY, Chen JY, Li ZY, Korgel BA et al (2007) Mechanistic studies on the galvanic replacement reaction between multiply twinned particles of Ag and HAuCl4 in an organic medium. J Am Chem Soc 129:1733–1742

20. Sun YG, Xia YN (2004) Mechanistic study on the replacement reaction between silver nanostructures and chloroauric acid in aqueous medium. J Am Chem Soc 126:3892–3901

21. Chen J, Wiley B, Li Z, Campbell D, Saeki F et al (2005) Gold nanocages: engineering their structure for biomedical applications. Adv Mater 17:2255–2261

22. Skrabalak SE, Chen J, Sun Y, Lu X, Au L et al (2008) Gold nanocages: synthesis, properties, and applications. Acc Chem Res 41:1587–1595

23. Fujimoto JG, Pitris C, Boppart SA, Brezinski ME (2000) Optical coherence tomography: an emerging technology for biomedical imaging and optical biopsy. Neoplasia 2:9–25

24. Huang D, Swanson EA, Lin CP, Schuman JS, Stinson WG et al (1991) Optical coherence tomography. Science 254:1178–1181

25. Chen J, Saeki F, Wiley BJ, Cang H, Cobb MJ et al (2005) Gold nanocages: bioconjugation and their potential use as optical imaging contrast agents. Nano Lett 5:473–477

26. Cang H, Sun T, Li Z-Y, Chen J, Wiley BJ et al (2005) Gold nanocages as contrast agents for spectroscopic optical coherence tomography. Opt Lett 30:3048–3050

27. Li W, Brown PK, Wang LV, Xia Y (2011) Gold nanocages as contrast agents for photoacoustic imaging. Contrast Media Mol Imaging 6:370–377

28. Kim C, Cho EC, Chen J, Song KH, Au L et al (2010) In vivo molecular photoacoustic tomography of melanomas targeted by bioconjugated gold nanocages. ACS Nano 4:4559–4564

29. Yang XM, Skrabalak SE, Li ZY, Xia YN, Wang LHV (2007) Photoacoustic tomography of a rat cerebral cortex in vivo with au nanocages as an optical contrast agent. Nano Lett 7:3798–3802

30. Song KH, Kim CH, Cobley CM, Xia YN, Wang LV (2009) Near-infrared gold nanocages as a new class of tracers for photoacoustic sentinel lymph node mapping on a rat model. Nano Lett 9:183–188

31. Au L, Zhang Q, Cobley CM, Gidding M, Schwartz AG et al (2010) Quantifying the cellular uptake of antibody-conjugated Au nanocages by two-photon microscopy and inductively coupled plasma mass spectrometry. ACS Nano 4:35–42

32. Mooradian A (1969) Photoluminescence of metals. Phys Rev Lett 22:185–187

33. Durr NJ, Larson T, Smith DK, Korgel BA, Sokolov K et al (2007) Two-photon luminescence imaging of cancer cells using molecularly targeted gold nanorods. Nano Lett 7:941–945

34. Wang H, Huff TB, Zweifel DA, He W, Low PS et al (2005) In vitro and in vivo two-photon luminescence imaging of single gold nanorods. Proc Natl Acad Sci USA 102:15752–15756

35. Tong L, Cobley CM, Chen J, Xia Y, Cheng JX (2010) Bright three-photon luminescence from gold/silver alloyed nanostructures for bioimaging with negligible photothermal toxicity. Angew Chem Int Ed Engl 49:3485–3488

36. Au L, Zheng DS, Zhou F, Li ZY, Li XD et al (2008) A quantitative study on the photothermal effect of immuno gold nanocages targeted to breast cancer cells. ACS Nano 2:1645–1652

37. Chen J, Glaus C, Laforest R, Zhang Q, Yang M et al (2010) Gold nanocages as photothermal transducers for cancer treatment. Small 6:811–817

38. Yavuz MS, Cheng Y, Chen J, Cobley CM, Zhang Q et al (2009) Gold nanocages covered by smart polymers for controlled release with near-infrared light. Nat Mater 8:935–939

39. Li W, Cai X, Kim C, Sun G, Zhang Y et al (2011) Gold nanocages covered with thermally-responsive polymers for controlled release by high-intensity focused ultrasound. Nanoscale 3:1724–1730

40. Moon GD, Choi S-W, Cai X, Li W, Cho EC et al (2011) A new theranostic system based on gold nanocages and phase-change materials with unique features for photoacoustic imaging and controlled release. J Am Chem Soc 133:4762–4765

41. Hoffman AS (2012) Hydrogels for biomedical applications. Adv Drug Deliv Rev 54:3–12

42. Zhou Y-F (2011) High intensity focused ultrasound in clinical tumor ablation. World J Clin Oncol 2:8
43. Lu W, Melancon MP, Xiong C, Huang Q, Elliott A et al (2011) Effects of photoacoustic imaging and photothermal ablation therapy mediated by targeted hollow gold nanospheres in an orthotopic mouse xenograft model of glioma. Cancer Res 71:6116–6121
44. You J, Zhang G, Li C (2010) Exceptionally high payload of doxorubicin in hollow gold nanospheres for near-infrared light-triggered drug release. ACS Nano 4:1033–1041
45. Lu W, Huang Q, Ku G, Wen X, Zhou M et al (2010) Photoacoustic imaging of living mouse brain vasculature using hollow gold nanospheres. Biomaterials 31:2617
46. Lu W, Xiong C, Zhang G, Huang Q, Zhang R et al (2009) Targeted photothermal ablation of murine melanomas with melanocyte-stimulating hormone analog–conjugated hollow gold nanospheres. Clin Cancer Res 15:876–886
47. Liang H-P, Wan L-J, Bai C-L, Jiang L (2005) Gold hollow nanospheres: tunable surface plasmon resonance controlled by interior-cavity sizes. J Phys Chem B 109:7795–7800
48. Meng Q, Li H, Yang H, Li H (2010) Synthesis of hollow gold nanospheres and their applications in surface-enhanced Raman scattering and DNA biosensor. Chinese J Chem 28:2015–2019
49. Melancon MP, Zhou M, Li C (2011) Cancer theranostics with near-infrared light-activatable multimodal nanoparticles. Acc Chem Res 44:947–956
50. Schwartzberg AM, Olson TY, Talley CE, Zhang JZ (2006) Synthesis, characterization, and tunable optical properties of hollow gold nanospheres. J Phys Chem B 110:19935–19944
51. Zhang X, Li D (2006) Metal-compound-induced vesicles as efficient directors for rapid synthesis of hollow alloy spheres. Angew Chem Int Ed 118:6117–6120
52. Zhan C, Qian J, Feng L, Zhong G, Zhu J et al (2011) Cyclic RGD-poly (ethylene glycol)-polyethyleneimine is more suitable for glioblastoma targeting gene transfer in vivo. J Drug Target 19:573–581
53. Melancon MP, Lu W, Yang Z, Zhang R, Cheng Z et al (2008) In vitro and in vivo targeting of hollow gold nanoshells directed at epidermal growth factor receptor for photothermal ablation therapy. Mol Cancer Ther 7:1730–1739
54. You J, Zhang R, Xiong C, Zhong M, Melancon M et al (2012) Effective photothermal chemotherapy using doxorubicin-loaded gold nanospheres that target EphB4 receptors in tumors. Cancer Res 72:4777–4786
55. Lee S-M, Kim HJ, Ha Y-J, Park YN, Lee S-K et al (2012) Targeted chemo-photothermal treatments of rheumatoid arthritis using gold half-shell multifunctional nanoparticles. ACS Nano 7:50–57
56. Liu Z, Fan AC, Rakhra K, Sherlock S, Goodwin A et al (2009) Supramolecular stacking of doxorubicin on carbon nanotubes for in vivo cancer therapy. Angew Chem Int Ed 48:7668–7672
57. Kumar S, Masood R, Spannuth W, Singh J, Scehnet J et al (2007) The receptor tyrosine kinase EphB4 is overexpressed in ovarian cancer, provides survival signals and predicts poor outcome. British J Cancer 96:1083–1091
58. Nakamoto M, Bergemann AD (2002) Diverse roles for the Eph family of receptor tyrosine kinases in carcinogenesis. Microsc Res Tech 59:58–67
59. Stephenson S-A, Slomka S, Douglas EL, Hewett PJ, Hardingham JE (2001) Receptor protein tyrosine kinase EphB4 is up-regulated in colon cancer. BMC Mol Biol 2:15
60. You J, Zhang R, Zhang G, Zhong M, Liu Y et al (2011) Photothermal-chemotherapy with doxorubicin-loaded hollow gold nanospheres: a platform for near-infrared light-triggered drug release. J Control Release 158:319–328
61. You J, Shao R, Wei X, Gupta S, Li C (2010) Near-infrared light triggers release of paclitaxel from biodegradable microspheres: photothermal effect and enhanced antitumor activity. Small 6:1022–1031
62. Sun Y, Mayers B, Xia Y (2003) Metal nanostructures with hollow interiors. Adv Mater 15:641–646

63. Sun Y, Mayers BT, Xia Y (2002) Template-engaged replacement reaction: a one-step approach to the large-scale synthesis of metal nanostructures with hollow interiors. Nano Lett 2:481–485
64. Wu G, Mikhailovsky A, Khant HA, Fu C, Chiu W et al (2008) Remotely triggered liposome release by near-infrared light absorption via hollow gold nanoshells. J Am Chem Soc 130:8175–8177
65. Abraham SA, Waterhouse DN, Mayer LD, Cullis PR, Madden TD et al (2005) The liposomal formulation of doxorubicin. Methods Enzymol 391:71
66. Guo L, Panderi I, Yan DD, Szulak K, Li Y, et al (2013) A comparative study of hollow copper sulfide nanoparticles and hollow gold nanospheres on degradability and toxicity. ACS Nano 7:8780–8793.
67. http://www.cytimmune.com/go.cfm?do=Page.View&pid=14
68. http://www.nanospectra.com/technology/aurolasetherapy.html
69. Papasani MR, Wang G, Hill RA (2012) Gold nanoparticles: the importance of physiological principles to devise strategies for targeted drug delivery. Nanomedicine 8:804–814

Properties of DNA-Capped Nanoparticles   **38**

Wenjuan Yang, Yi Chen, and Wenlong Cheng

Material Properties

DNA-capped nanoparticles are a new class of multifunctional materials by combining unique properties of nanomaterials and unique properties of DNA molecules. They can serve as building blocks to construct highly ordered super-structures with precise periodicity and complexity [1]. In particular, it is critical to develop methodologies to construct structurally well-defined assemblies ("artificial molecules" [2, 3], "artificial polymers" [4, 5], "supracrystals" [6–11]) to be used in future materials and devices. The structural diversity and sequence programmability of DNA make it a powerful tool for designing such future materials with unprecedented properties [12, 13].

Unique Propertimees of Nanoparticles

Nanoparticles or artificial atoms [1] have unique optical, electrical, magnetic, and catalytic properties different from their corresponding bulk phase materials, representing an exciting route to engineer materials at nanoscopic dimensions. Substantial research efforts have been directed to synthesize various nanoparticles including plasmonic nanoparticles, quantum dots, and magnetic nanoparticles.

W. Yang • Y. Chen • W. Cheng (✉)
Department of Chemical Engineering, Faculty of Engineering, Monash University, Clayton, VIC, Australia

The Melbourne Centre for Nanofabrication, Clayton, VIC, Australia
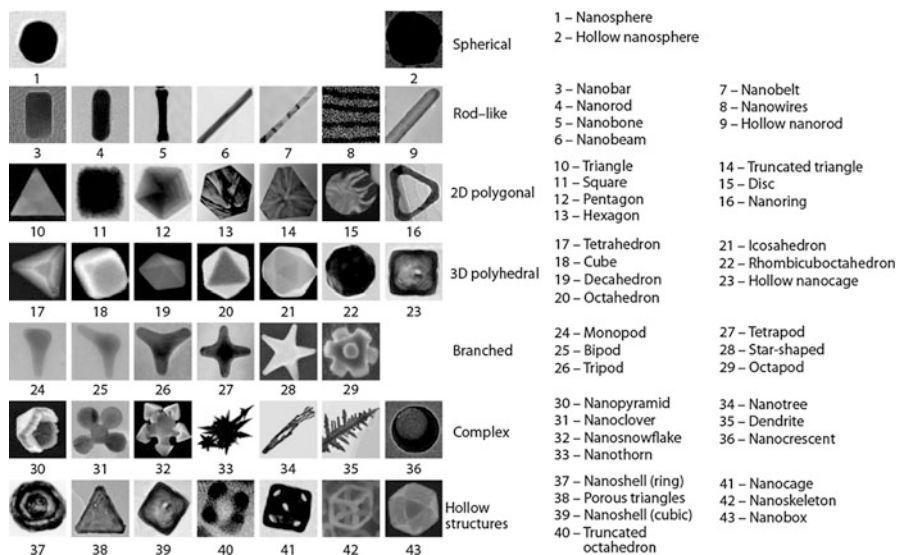e-mail: wenlong.cheng@monash.edu

| | | 1 – Nanosphere
2 – Hollow nanosphere | |
| Spherical | | | |

| | | 3 – Nanobar
4 – Nanorod
5 – Nanobone
6 – Nanobeam | 7 – Nanobelt
8 – Nanowires
9 – Hollow nanorod |
| Rod–like | | | |

| | | 10 – Triangle
11 – Square
12 – Pentagon
13 – Hexagon | 14 – Truncated triangle
15 – Disc
16 – Nanoring |
| 2D polygonal | | | |

| | | 17 – Tetrahedron
18 – Cube
19 – Decahedron
20 – Octahedron | 21 – Icosahedron
22 – Rhombicuboctahedron
23 – Hollow nanocage |
| 3D polyhedral | | | |

| | | 24 – Monopod
25 – Bipod
26 – Tripod | 27 – Tetrapod
28 – Star-shaped
29 – Octapod |
| Branched | | | |

| | | 30 – Nanopyramid
31 – Nanoclover
32 – Nanosnowflake
33 – Nanothorn | 34 – Nanotree
35 – Dendrite
36 – Nanocrescent |
| Complex | | | |

| | | 37 – Nanoshell (ring)
38 – Porous triangles
39 – Nanoshell (cubic)
40 – Truncated octahedron | 41 – Nanocage
42 – Nanoskeleton
43 – Nanobox |
| Hollow structures | | | |

Fig. 38.1 A plasmonic "periodic table" of nanoparticles. Reprinted with permission from [1]. Copyright Nature Publishing Group

These nanoparticles possess unique size-, shape-, and composition-dependent properties, leading to a wide spectrum of applications in miniaturized optical [14] and electronic devices [15, 16], sensors [17] and photonic circuits [18], and medical diagnostics and therapeutics [19, 20]. As far as interfacing with biological species such as DNA, plasmonic nanoparticles have attracted major attention due to their unique optical properties, facile surface chemistry, and high biocompatibility and stability. In this section, we briefly summarize the various synthetic strategies for synthesizing nanoparticles with a focus on metal nanoparticles.

Properties of Metal Nanoparticles

Metal nanoparticles possess unique light-mater interactive properties due to localized surface plasmon resonance, therefore, also termed as plasmonic nanoparticles. Two key parameters influencing properties of plasmonic nanoparticles are size and shape. The cost-effective way to synthesize plasmonic nanoparticles is by wet chemical techniques [21]. Careful optimization of synthesis conditions allows rational control over nanoparticle sizes and morphologies [22]. Figure 38.1 summarizes various protocols developed so far for controlling size, shape, and material composition [1]. Note that geometric order in each row from left to right and in each column from top to bottom is evident.

Among various shapes, nanosphere is relatively easy to synthesize because it represents thermodynamically lowest energy state. By using citrate-based approach, plasmonic nanospheres with a wide size range of 2 and 100 nm can be obtained even though they become more polydisperse when size is above 50 nm [23]. In an alternative way, seed-mediated growth method could improve the

monodispersity of larger-sized nanoparticles [24]. Typically, small gold nanoparticles (AuNPs, ∼5 nm) were prepared as seeds, followed by seed-guided nucleation and growth in cetyltrimethylammonium bromide (CTAB) solution. This approach successfully restricted the size distribution (∼10–15 %) of the resulted products, but a substantial secondary population of smaller nanoparticles is formed apart from growth of the seeds. This could be overcome with an agent capable of selectively reducing gold only when in proximity to particle seeds. In a typical method, hydroquinone is used as reducing agent, which improved monodispersity and shape consistency in the 50–175-nm size range [25]. Furthermore, large nanoparticles with diameters of >200 nm can also be fabricated, which have developed the synthesized AuNPs into a greater size range and better size and shape dispersion.

As for synthesis of anisotropic nanoparticles, control over nucleation and growth typically is achieved by using organic ligands [21, 22]. In particular, seed-mediated growth approach has proven to be a powerful approach to synthesize monodispersed gold nanorods with tunable aspect ratio [26]. It was found that the crystalline structures of the seeds and the presence/absence of $AgNO_3$ influence the nucleation and growth [27]. In addition, seed-mediated approach has also been used to synthesize many other shapes such as triangular gold nanoprisms [28].

A fascinating aspect of metal nanoparticles is that their optical properties are highly tunable by structural parameters such as size and shape, as well as material composition and the surrounding dielectric environment [29, 30]. The origin of surface plasmon resonance (SPR) is from the coherent collective oscillations of conduction electrons induced by electromagnetic radiation [31]. Gustav Mie was the first to develop theoretical understanding of SPR of metal nanoparticles [32], which can predict the plasmonic properties of spherical metallic nanoparticles as a function of size and dielectric environments [33]. Substantial additional research efforts have sought to understand interparticle plasmonic coupling using spherical-shaped nanoparticles as a model system [34]. Strong near-field coupling between adjacent particles occurs when edge-to-edge interparticle spacing is less than 2.5 times the particle diameter, which results in enhanced electric fields that are confined to small regions between nanoparticles and decay quickly with increasing distance [35]. As a general qualitative design principle [1], plasmonic resonance frequencies of spherical nanoparticles red-shift with increasing peak intensities as particle size increases; the resonance frequencies of non-spherical particles red-shift with increasing corner sharpness and particle anisotropy, and the intensity of the resonance peak increases if charges separate with mirror symmetry; the resonance modes increase with the number of ways that the particle can be polarized. Those general properties of plasmonic nanoparticles are extremely useful to designing desired plasmonic nanostructures for various applications.

Properties of Semiconductor Nanoparticles

Semiconductor nanocrystals, also known as quantum dots (QDs), possess tunable fluorescent properties due to adjustable bandgaps by varying particle sizes [36]. A number of synthetic approaches have been developed for tailoring fluorescent

properties and biocompatibility of QDs for various applications in optoelectronics and biology [37, 38]. Particularly, pyrolysis of organometallic precursors of Cd has been established as a powerful approach to synthesize monodisperse cadmium chalcogenide (CdX, X = S/Se/Te) [39]. Refining QD sizes can be achieved by controlling suitable injection and growth temperature. Organics ligands such as alkylphosphonic acids or alkyl amines are required to stabilize CdX QDs for further application in biotechnology [40–42]. In addition, core-shell QDs were also successfully obtained, which facilitated bioconjugation and improved stability and lowered toxicity allowing their applications as multicolor biomarkers [43, 44].

The appealing fluorescent properties of QDs originate from their energy bandgaps and absorption onsets dependent on particle size, therefore, tunable in a wide range spectrum from visible to infrared regions [45]. In particular, the emission wavelength of QDs can be continuously tuned by programming particle sizes, and a single light source can be used for simultaneous excitation of all different-sized QDs [46]. The excitation wavelength can be set for various purposes below the bandgap energy; the photoluminescence bands are narrow, important for multiplexed detection. In addition, QDs exhibit stable emission and broad absorption bands, multiphoton absorption cross sections, considerable brightness, and exceptional photostability. The above characteristics of QDs render them ideal candidates for applications in biotechnology [47], such as high-resolution cellular imaging, in vivo observation of cell trafficking, tumor targeting, and cancer diagnostics [43].

Properties of Magnetic Nanoparticles

Magnetic nanoparticles are a class of nanomaterials with magnetic properties. Such particles commonly consist of magnetic elements (iron, nickel, cobalt, etc.). In special cases, gold nanoparticle can also exhibit weak magnetic properties. Magnetic nanoparticles have shown attractive applications in pharmaceutical and biomedical sciences [48]. They can be used as drug delivery carrier to transport drugs to desired locations followed by controlled release by an external magnetic field.

Among various magnetic nanoparticles, ferrite nanoparticles attracted most intensive attention. Once their size reduces to sub-100 nm range, they exhibit superparamagnetic properties which can prevent their self-agglomeration [49]. This is because superparamagnetic property is only activated when exposed to an external magnetic field, without remanent magnetization when field is removed [50]. Ferrite nanoparticles possess excellent biocompatibility and biodegradability, leading to their applications in the biomedical and cancer diagnostics.

Unique Properties of DNA

DNA is a unique genetic material which virtually exists in almost all known living organisms and viruses. A DNA strand contains a phosphate-deoxyribose backbone and four types of bases: adenine (A), thymine (T), cytosine (C), and guanine (G). The programmability of DNA molecules originates from highly specific

Watson-Crick base-pairing interactions, namely, A binds to T by forming two hydrogen bonds and C binds to G by forming three hydrogen bonds. Thus, when two DNA strands have complementary sequences, a duplex with a helix structure will form under right conditions. This process is reversible; double-stranded DNA (dsDNA) can be denatured into two single-stranded DNA (ssDNA) typically by heating or exposure to high pH. Because G-C pairing is stronger than A-T pairing, dsDNA with more G-C pairings is more stable against heating and pH [51]. Structurally, dsDNA has a width of about 2 nm, with a base separation of 0.34 nm and helical periodicity of 3.5 nm per turn.

Beyond its traditional role in biology as genetic information carrier, DNA is emerging as a unique building material at the nanoscale. This led to the birth of DNA nanotechnology. ssDNA is very flexible with a persistence length of 0.7 nm; however, dsDNA has a persistence length of about 50 nm. Thus, the rigidity and flexibility of DNA can be easily tailored [52]. Programmable structure design can be performed by controlling the rigidity and flexibility by a combination of ssDNA and dsDNA. For example, the rigid dsDNA can be linked by relatively flexible ssDNA strands to form stable motifs. DNA can be made even more rigid by forming double-crossover (DX) tiles [53, 54], triple-crossover (TX) tiles [55], and paranemic-crossover (PX) tiles [56]. Indeed, structural DNA design has been established with aid of computer program. In particular, "DNA origami" [57] can be designed by folding hundreds of short staple strands into almost arbitrary microscale topological 2D and 3D shapes [58] (Fig. 38.2).

Apart from the structural design, a rich toolkit is available for precise manipulation and modification of DNA. For example, replication of DNA can be achieved via the polymerase chain reaction, an amplification technology that exponentially increases the amount of a specific DNA sequence. DNA strands can be cut at desire sites by using endonucleases function and exonucleases function. By using other enzymes, covalent connection, elongation, and degradation of DNA can all be achieved.

Self-Assembling Properties of DNA-Capped Nanoparticles

Combination of novel properties of nanomaterials and unique properties of DNA provides an exciting route to design multifunctional self-assembled materials for various applications [59]. This requires precise synthetic strategy to make DNA-nanoparticle conjugates as well as development of highly ordered assemblies. We begin with various approaches for the synthesis of DNA-capped nanoparticles.

Synthesis of DNA-Nanoparticle Conjugates

Synthesis of DNA-capped nanoparticles dates back to the pioneering work reported by Alivisatos and Mirkin in 1996. However, the fundamental synthesis methods for the basic building blocks are notably different: the former focus on mono-DNA conjugate, whereas the later focus on multi-DNA conjugate. As reported by Alivisatos and co-workers, the assembly of spatially defined dimer and trimer structures was mainly conducted by mono-conjugation with careful rational design
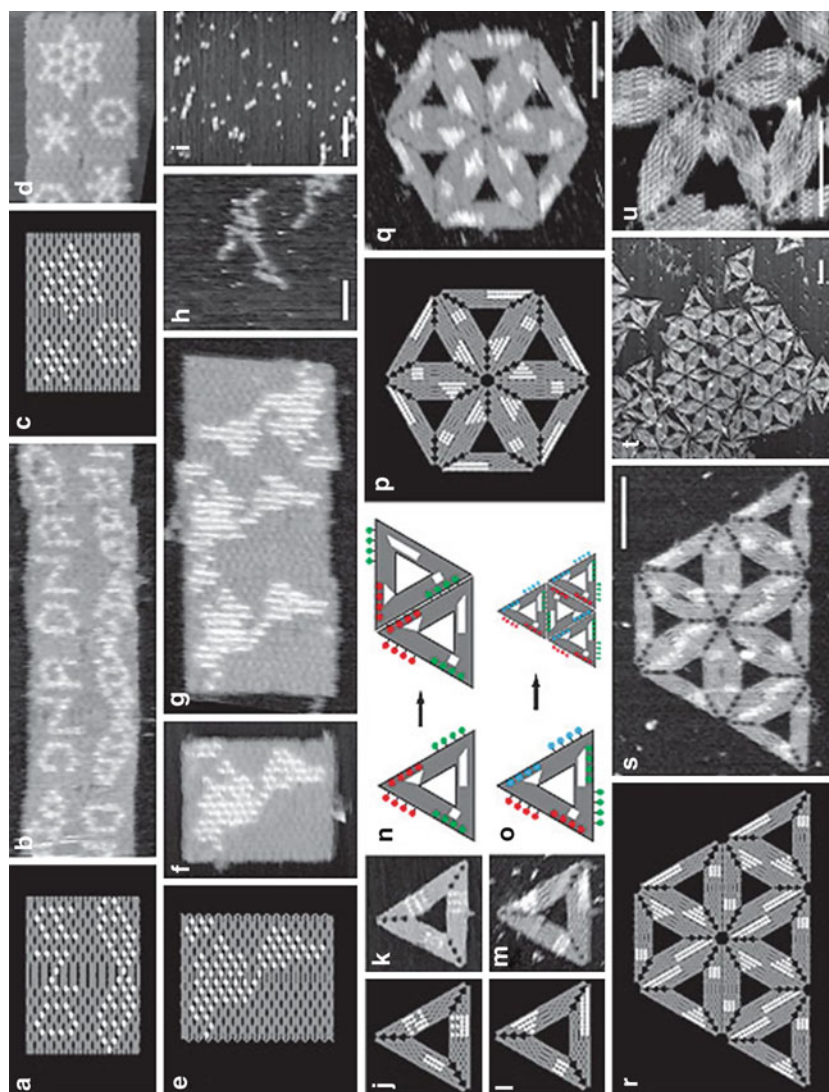
Fig. 38.2 Complex shapes from DNA origami. Reprinted with permission from [57]. Copyright Nature Publishing Group

and substantial purification techniques (functionalized DNA-AuNPs conjugates with one oligonucleotide attached on each particle) [2]. In this method, sulfhydryl-terminated ssDNA was coupled with an excess of monomaleimido-functionalized gold nanoparticles. Although mono-conjugates can be produced in this process, the yield is generally very low (<30 %). Further purification of the DNA-AuNPs conjugates by gel electrophoresis or HPLC is required. Hence, the mobility of DNA-AuNPs conjugates was thoroughly studied by analyzing the critical role of the surface charge of nanoparticles [60]. It was found that the properties of particle dominated the electrophoretic mobility, and well-defined conjugates (1–5 DNA ligands per nanoparticle) can be achieved by gel electrophoresis [61]. In addition, the length of DNA strand and size of nanoparticles can also affect mobility.

Multiple DNA strands could be attached to specific sites on nanoparticle surfaces, leading to the formation of site-specific DNA-nanoparticle conjugates. Such conjugates are more likely to be used as functional building blocks to construct anisotropic nanoassemblies such as satellite, cat paw, and dendrimer-like heterostructures. In one example, the asymmetric DNA-AuNPs conjugation was achieved by using magnetic microparticles as geometric restriction templates [62]. In this method, the microparticle facilitated the separation and purification of the anisotropically functionalized nanoparticles. In addition, site-specific DNA-nanoparticle conjugates can also be formed by utilizing a solid support with a stepwise surface-encoding strategy [63]. This method proved higher efficiency and yield of dimers than the conventional solution-based reactions. Through repeated assembly and disassembly at surface, well-defined dimer clusters and Janus nanoparticles could generate remarkably high yields (70–83 %).

DNA strands can also be attached in a site-specific manner to gold nanorods. For the original gold nanorods, cetyltrimethylammonium bromide (CTAB) molecules are preferentially bound on the sides rather than to the ends of the nanorods [64]. Consequently, thiolated DNA are more likely to attach exclusively to the ends of nanorods where CTAB concentrations are low.

Apart from the mono-conjugation and site-specific conjugation, multiple DNA strands can be covalently attached to a single nanoparticle, which can be termed as multi-DNA conjugates. The synthesis of multi-DNA conjugates requires rational design of the DNA sequences, ligand density, ionic strength, and hybridization temperatures [65].

Ordered Nanoparticle Assemblies

Various DNA-nanoparticle conjugates can be used to construct structurally well-defined nanoarchitectures, which possess new properties not possessed by individual nanoparticles or corresponding bulk solids.

Assemblies Through DNA Hybridization

Highly specific Watson-Crick base-pairing forces allow for programming material synthesis at the nanoscale. Mono-DNA-conjugated nanoparticles have opened a powerful pathway to heterodimeric and heterotrimeric nanostructures [66]. By carefully designing the complementary ssDNA sequences, the relative spatial

arrangement of AuNPs could be controlled through Watson-Crick base-pairing interactions. The product was generally needed to be purified using gel electrophoresis to improve the yield.

Multicomponent nanoassemblies could also be constructed by the hybridization strategy. For example, high-yield fabrication for ultrasensitive SERS-active Au-Ag core-shell nanodumbbells was obtained, and the interparticle spacing was able to be controlled [67]. In conjunction with polymerase chain reaction (PCR), structurally complex assemblies could be obtained by adjusting the density of primer DNA molecules on the nanoparticle surface and the number of PCR cycles [68].

Multi-DNA-conjugated nanoparticles can be used to construct 3D super-assemblies [9, 10]. The DNA sequences substantially affected the crystallization process, leading to different lattice structures including face-centered-cubic or body-centered-cubic crystal structures as revealed by synchrotron-based small-angle X-ray scattering (SAXS) as shown in Fig. 38.3. This clearly indicates synthetically programmable colloidal crystallization is possible. Temperature programming played a critical role in forming highly ordered 3D assemblies, and the crystalline assemblies formed reversibly during heating and cooling cycles as revealed by SAXS studies. Furthermore, basic design rules were formulated in guiding the design of DNA-programmed nanoparticle assembly, which can predict crystallographic symmetry, and interparticle distances [69, 70]. Remarkably, by applying hollow DNA nanostructures as 3D spacer, voids could be selectively placed into a lattice structure. This led to diverse lattice structures such as AB2 type, simple hexagonal, graphite type, AB6 type, and "lattice X" [71]. This includes the lattice not existing in nature.

Due to the structural plasticity of DNA and the reversibility of their conjugations, a distance-dependent plasmonic response [72] and in situ conformational changes using molecular stimuli could be achieved [73]. Specifically, controllable switching of interparticle distances (in the range of 15–25 %) can be realized by using a reconfigurable DNA device that acts as an interparticle linkage [3].

Besides the synthetically tunable length and programmable properties of DNA, the shapes of nanoparticle also strongly influenced the crystallization of DNA-capped nanoparticles. By using anisotropic building blocks, multi-dimensional assemblies including 1D lamellar assemblies of gold nanoprisms, 2D assemblies of vertical-aligned gold nanorods, and 3D crystals of gold rhombic dodecahedra can be constructed [8]. These structures were not observed with spherical particles, which provides fundamental insights into shape-dependent DNA hybridization effects on the superlattice dimensionality, crystallographic symmetry, and phase behavior.

DNA has also been used to program the assembly of the quantum dots. DNA-capped quantum dots were synthesized by a one-pot process with tunable number densities of DNA strands [74]. In a typical method, the DNA ligands with three domains were designed [75]: a phosphorothioate domain for binding to quantum dots, a spacer, and a DNA-binding domain contains phosphodiester linkages. The binding domain of DNA shows high affinity for the cations of the metal chalcogenide semiconductor quantum dot and thus capped to the surface of
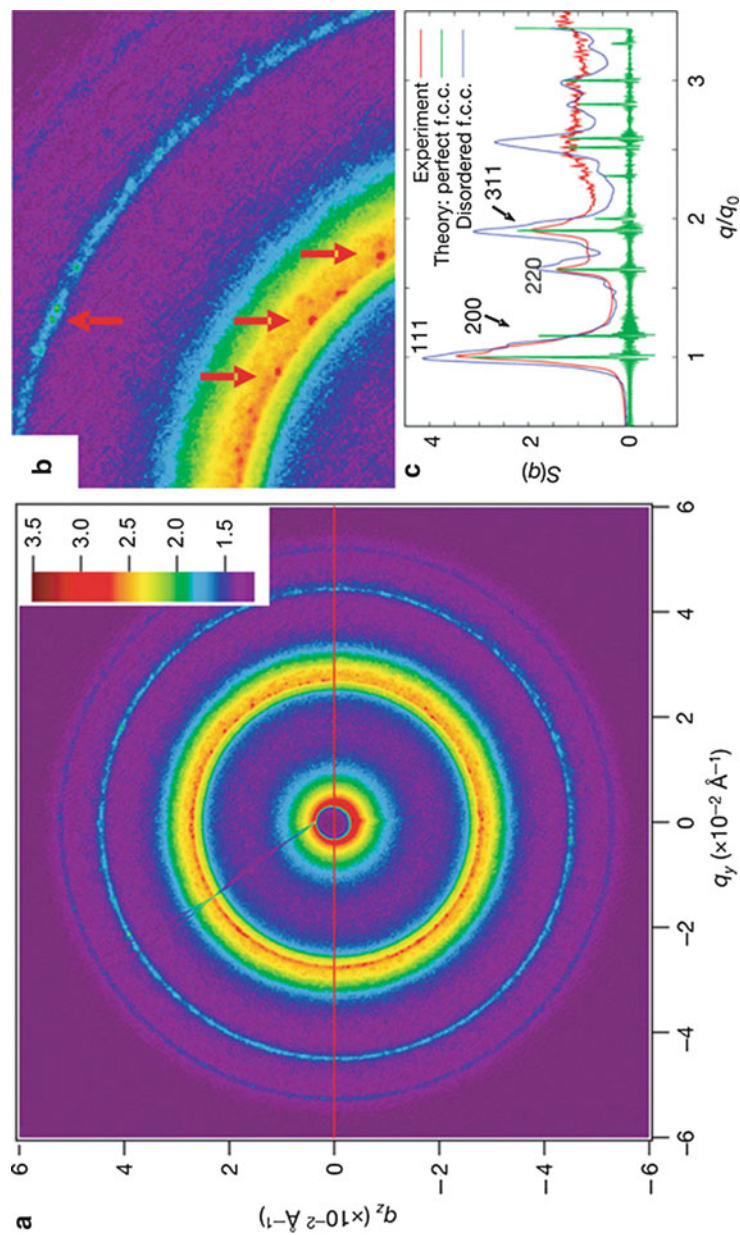
Fig. 38.3 Synchrotron-based small-angle X-ray patterns of DNA-based nanoparticle crystals. Reprinted with permission from [9]. Copyright Nature Publishing Group

the quantum dot. The spacer then acts as an unbound section for specific conjugation with a complementary strand from other quantum dots. Such DNA-capped quantum dots can then be used as building blocks for assemblies, including cross-shaped complexes containing three different types of dots [76]. Well-defined photophysical studies quantified energy transfer among the constituent QDs. By controlling of pH, the conformation of the assemblies can be reversibly switched through turning on and off the energy transfer between the QDs.

Assemblies Through Dry-DNA-Ligand Mediation

Using Watson-Crick base pairing to program material synthesis is a major research activity. However, the use of DNA strands can go beyond specific hybridization. In a different route, DNA has been used in a drying-mediated self-assembly process to guide the assembly of freestanding monolayered DNA-nanoparticle superlattice membranes [77]. Such freestanding structures have not been achieved with base-pairing-based strategy. This process involved the spatial confinement of a holy substrate fabricated by top-down lithography and highly ordered nanoparticle arrays formed under unusually low ionic strength without the requirement of specific Watson-Crick base pairing. Compared to alkyl ligands, molecular lengths of DNA ligands can be controlled over a much large size regime, enabling tailoring of both structural and functional properties over a wide window. Remarkably, these plasmonic coupling properties were not easily achieved with base-pairing-based strategy in which particle-to-particle spacing is generally too large and ordered domains are limited to small area.

Dry-DNA-ligand-based approach can be combined with top-down lithography to obtain nanoscale structures with micrometer-sized molds [78]. In addition, this combined top-down and bottom-up strategy is able to rationally control over the local nucleation and growth of the nanoparticle superlattices, leading to a versatile structure with high degrees of internal order, such as single particle-width corrals, single particle-thickness microdiscs, and submicrometer-sized "supracrystals." Notably, these patterned superlattices can be addressed by micropatterned electrode arrays, suggesting potential applications in bottom-up nanodevices.

Different from the base-pairing forces driving the crystallization of DNA-capped nanoparticles, the drying-mediated crystallization of DNA-capped nanoparticles is entropy driven [11]. During water evaporation, the forces exerted on the DNA corona gradually increase and resulted in a smooth and uniform deformation of the DNA corona. By synchrotron-based SAXS, a general entropic spring model for the drying-mediated crystallization of DNA-capped nanoparticles was established. In addition, the crystallization time in the soft-crystallization process is programmable by taking advantage of the fine and wide tunability of DNA length. In an extended fundamental study, the crystalline Gibbs monolayers of DNA-capped nanoparticle were found to form at the air/water interface [79] (Fig. 38.4). The spatial crystallization was characterized by grazing-incidence SAXS in specific configurations and predicted the interparticle spacing programmability by adjusting both ionic strength and DNA sequence length.
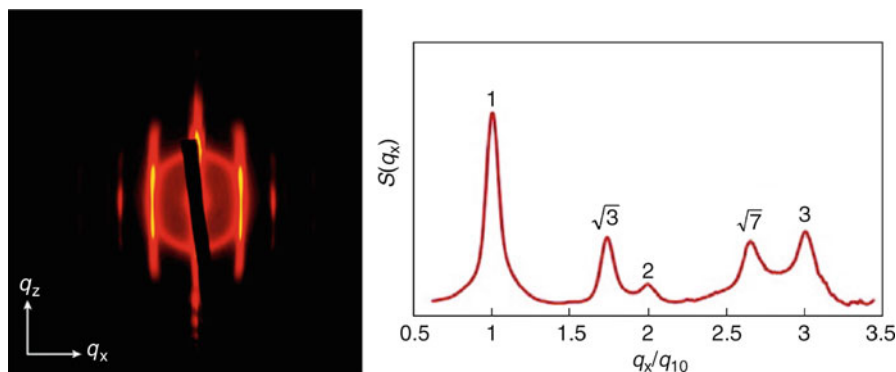
Fig. 38.4 Example spectrum showing a high degree of crystalline order (N = 7, [NaCl] = 500 mM). The relative positions of the Bragg peaks with respect to the first-order peak indicate a simple hexagonal lattice. Reprinted with permission from [79]. Copyright American Chemical Society Publications

Assemblies Through DNA Template

The emerging structural DNA nanotechnology provides a rich toolkit on synthesizing rigid DNA structures, such as DNA tiles/frames, and origami, which can be used to template the assembly of nanoparticles. Generally speaking, the design is based on the following two steps: (1) design the DNA tiles/origami with capture strands at predetermined locations and (2) hybridization of DNA-capped nanoparticles with capture strands at the designed sites [80]. As an example, 3D tubular assemblies of gold nanoparticles including stacked rings, single spirals, double spirals, and nested spiral tubes have been achieved with DNA tile-templated self-assembly [74]. The different conformations of tubular structure and chiralities could be controlled by size-dependent steric repulsions among nanoparticles. Four different DNA double-crossover (DX) tiles have been used to template the DNA-modified nanoparticles into closely packed rows with precisely defined regular inter-row spacings [81]. By using the similar method, 2D periodic pattern and rhombic lattice arrangement were realized [82].

By careful sequence design of DNA geometries, various nonlinear structures could form and were used to control the placement of nanoparticles. In particular, pyramidal plasmonic assemblies were reported [83], in which the tetrahedral symmetry of DNA pyramids enabled the formation of chiral nanostructures with four different-sized nanoparticle at each tip. Gel electrophoresis purification was used to separate the pyramids and further confirmed by transmission electron microscope (TEM).

Unlike interweaving various DNA chains into a rigid scaffold, dynamic DNA templates can be created with functional single-stranded and cyclic form [84]. This template guided the selective attachment of mono-DNA-conjugated nanoparticles with different diameters on the complementary arms of DNA templates. Interestingly, post-assembly named "write/erase" method is shown by selectively
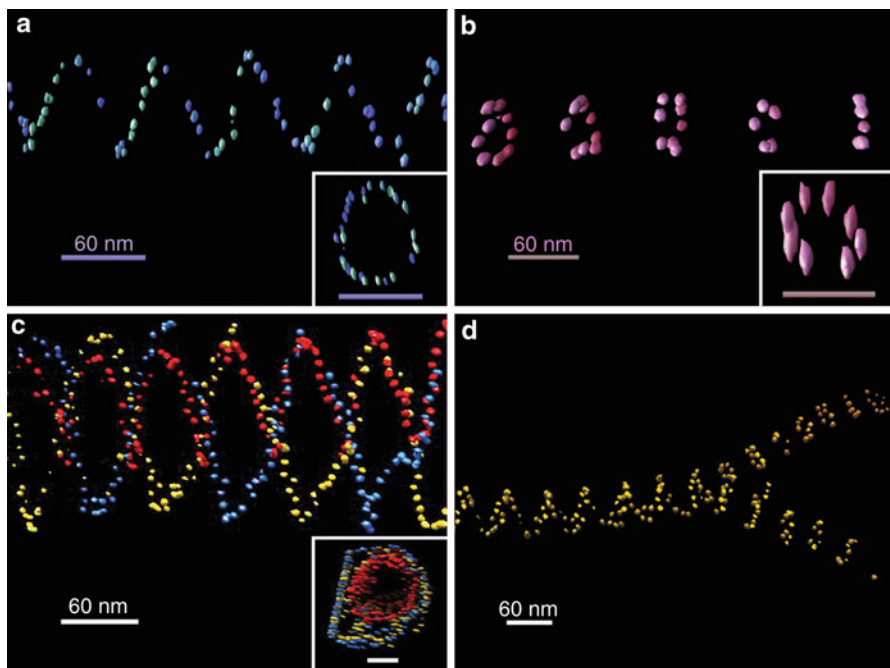
Fig. 38.5 Representative 3D structures of nanoparticle tubes reconstructed from cryoelectron tomographic imaging. Reprinted with permission from [74]. Copyright AAAS

removing one particle from triangles of three AuNPs clusters, followed by replacement of another nanoparticle onto the specific site.

By using DNA origami folding technique [58] or rationally designed DNA geometries [85], more complex nanostructures could be obtained. DNA origami has attracted much attention to the field of DNA nanotechnology since the landmark work established by Rothemund [57]. Different from the conventional crossover strategy that uses single building blocks to construct larger structures in a "two-step" process, DNA origami provides a versatile and simple "one-pot" method to create fully addressable DNA nanostructures by using short staple DNA strands to fold a single-stranded genomic DNA into geometrically desired nanopatterns [80]. Multiple clusters and Ag-Au heterodimers have been obtained by DNA origami templated assembly [80]. More complex structures such as helical plasmonic assemblies could be obtained from origami method (Fig. 38.5). Apart from symmetrical spheres, positioning of gold nanorods was also achieved forming discrete, well-ordered assemblies [86].

The assembly property of DNA-capped nanoparticles could be combined with top-down lithography. The versatile method for integrating top-down lithography with bottom-up DNA-programmed self-assembly is a potential future nanofabrication strategy for plasmonic circuitry, data storage, diagnostic assays,

and optoelectronics [87]. Various lithographic techniques are proved to be efficient in patterning and depositing plasmonic nanocrystals on DNA-functionalized surfaces [88–91], also including patterning of DNA tiles and origami as templates to guide the assembly of plasmonic nanocrystals. In a typical method, repeated patterning of large-area arrays of ssDNA-capped gold nanoparticle was achieved by a soft-lithographic subtraction printing process [92]. Spatially ordered 2D arrays were constructed by large-area patterning of DNA-capped nanoparticles through the site-selective deposition of triangular DNA origami onto lithographically patterned substrates [93]. Precise binding of AuNPs to each DNA structure was achieved and formed macroscopic arrays with characteristic length scales ranging from a few to several hundreds of nanometers. In addition, different patterns, such as multiple triangles with alternating left and right orientations, were also formed and suggested a new way to rationally create not just periodic arrays but complex networks [94].

Sensing Properties

Plasmonic Sensing

Noble metal nanoparticles such as gold and silver nanoparticles have attracted considerable attention due to their unique optical properties [12, 95–97]. Under a certain frequency of light, the conduction electrons of the noble metal nanoparticles can experience a coherent oscillation, which is known as localized surface plasmon resonance (LSPR). The LSPR for certain metals including gold, silver, and copper can occur in visible range of spectra, which gives rises to the unique colors by naked eyes. Remarkably, the LSPR properties are tunable by adjusting particle sizes, shapes, interparticle spacing of the nanoparticle, and composition of the nanoparticles (Fig. 38.1) [98, 99]. In particular, the gold plasmon band generally shifts to red as the interparticle spacing decreases. Upon the hybridization of DNA, gold nanoparticles aggregate, substantially reducing interparticle spacing. Consequently, a red shift of the plasmon band is usually observed. The plasmonic properties of DNA-capped nanoparticles have been widely used in biological diagnostics.

In the Mirkin's seminal work [65], two batches of colloidal gold nanoparticles were modified with two different sequences of oligonucleotides A and B through robust covalent Au-S linkage. In the presence of a target DNA which had sequences partially complementary to the red strand A and the blue strand B, gold nanoparticles could be linked together into 3D aggregates by the known Watson-Crick base-pairing interactions if the system temperature was lower than the characteristic DNA melting temperature (Fig. 38.6a). The formation of aggregates was reversible, and aggregates could be dissolved into discrete particles if the system temperature was increased above the characteristic DNA melting temperature. Remarkably, the discrete particles and the aggregates exhibit distinct optical properties, and the former was red and latter was blue (Fig. 38.6b). The origin of the
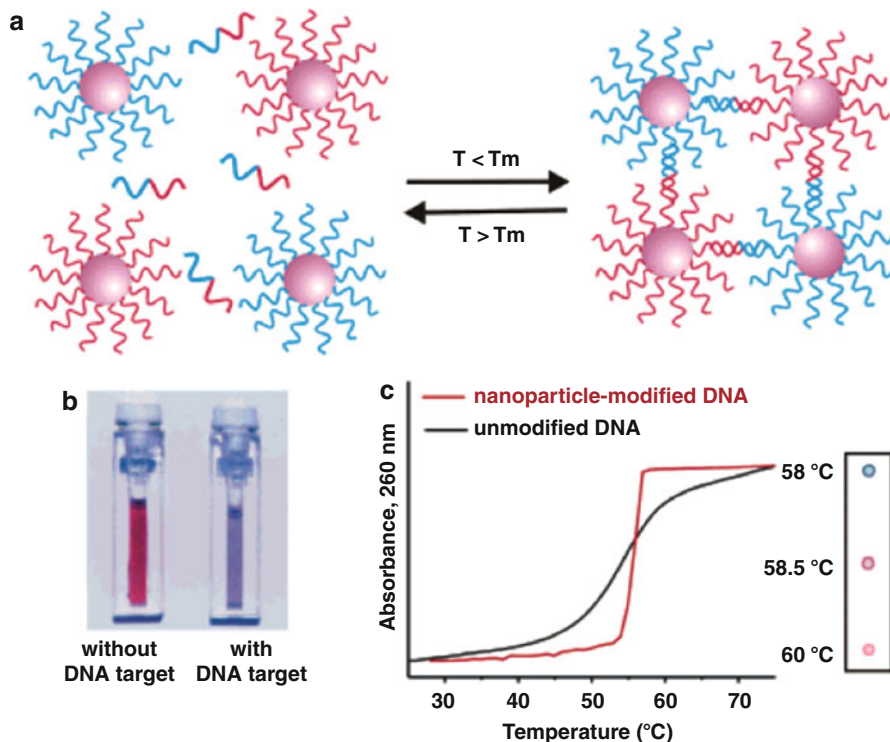
Fig. 38.6 Colorimetric sensors of DNA. (**a**) Schematic of target DNA-mediated aggregation of gold nanoparticles. Note that half of target DNA strand is complementary to the *red* strand a and the other half is complementary to *blue* strand b. (**b**) Without target DNA, gold nanoparticles are discrete, exhibiting *red color*; in the presence of target DNA, gold nanoparticles aggregate leading to the color change from *red* to *blue*. (**c**) The melting profiles for free DNA strands (*dark line*) and DNA strands associated with gold nanoparticles (*red line*). Reprinted with permission from [98]. Copyright American Chemical Society Publications

phenomena was due to LSPR in which the coupling interactions among adjacent nanoparticles in aggregates led to blue color, whereas the coupling interactions were absent in dispersed particle solution. This colorimetric detection method is an easy and cost-efficient strategy potentially applicable in future point-of-care diagnostics [98].

Interestingly, compared with free DNA strands, the melting profiles of DNA strands associated with gold nanoparticles exhibited sharper melting points in a narrower temperature window (Fig. 38.6c). Nanoparticle-modified DNA and unmodified DNA were compared in a temperature/time dissociation experiment in which temperature was cycled between 0 °C and 80 °C. Interestingly, it was observed that the characteristic DNA absorbance at 260 nm for
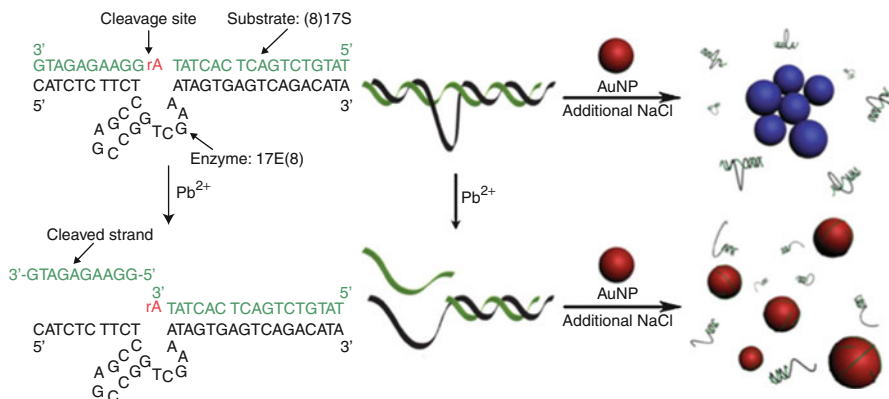
Fig. 38.7 A label-free plasmonic sensor. DNAzyme contains an enzymes strand (17E (8)), a substrate strand ((8)17S), and a cleavage site. The ssDNA is released from the cleavage site in the presence of the Pb^{2+}, and this ssDNA bonds on the surface of gold nanoparticles, which can result in dissolution of aggregates into discrete gold nanoparticles. Corresponding to this, solution color changes from *blue* to *red*. Reprinted with permission from [107]. Copyright Wiley

nanoparticle-modified DNA changed sharply when temperature changed; however, unmodified DNA exhibited a gradual transition. The sharp melting transition properties are advantageous in biodiagnostics, under right conditions, even the single base-pair mismatches can be discriminated [100, 101].

Perhaps inspired by colorimetric DNA detection method, plasmonic nanoparticles were also employed to the detection of protein [102, 103], small molecules [104], and metal ions [105]. Almost all of these are based on red-to-blue changes for sensing targets. Particularly, as for DNA, a labeling step is usually required to covalently attach DNA molecules to nanoparticle surfaces. In a different design strategy, a label-free plasmonic sensor was fabricated based on blue-to-red transition for detection of metallic ions [106]. The design principle was based on different adsorption properties of dsDNA and ssDNA on gold nanoparticles. Compared with dsDNA, ssDNA is mechanically flexible and can be easily adsorbed onto gold nanoparticle surfaces.

Lu's group reported a label-free method to detect the lead ion [107]. Their plasmonic sensor was based on gold nanoparticles and DNAzyme (DNAzyme is a unique DNA sequence but can be cleaved specifically by lead ions). In the absence of lead ions, DNAzyme kept its double helix exhibiting weak binding to gold nanoparticle surfaces; therefore, nanoparticles are ill-protected with tendency to aggregate. When lead ions were added, DNAzyme was cleaved, forming ssDNA which could bind to gold nanoparticle surfaces. The ssDNA binding enhanced electrostatic repulsion between gold nanoparticles, hence, rendered aggregates to dissolve, forming dispersed particle solution. Corresponding to the structural changes, the solution color changed from blue to red (Fig. 38.7). Beyond heavy

metal ions, DNA label-free-based plasmonic sensors could be extended to detect specific DNA [108] and RNA [109] and mercury ions [110], potassium ions [111], cocaine [112], thrombin [113], and adenosine [114].

13-nm-diameter gold nanoparticles were heavily used in colorimetric diagnostics as it has many advantages such as facile sample preparation, high stability, and high specificity; however, the sensitivity was usually very low. In the later developments, 50-nm-diameter gold nanoparticles were synthesized and used. It was found the sensitivity could be improved to between 5pM and 5nM [115]. Notably, this was still lower than the fluorophore-based assay [116]. Nevertheless, this was fairly good given the simplicity of the colorimetric approaches.

The colorimetric sensitivity could be improved by silver enhancement in a process called scanometric detection [117]. This assay takes the exquisite selectivity advantage of the aggregating of oligonucleotide-modified gold nanoparticles into a glass chip-based system. Silver which traditionally is used to protein-conjugated gold nanoparticles for signal amplification [118, 119] was successfully used for DNA detection. It was found that two orders of magnitude higher than dominant fluorophore-based assay could be achieved. In a typical scanometric detection for DNA, there were three components: a separate oligonucleotide-modified glass slide, an oligonucleotide-modified gold nanoparticle probe, and a target DNA [117]. Firstly, the target DNA hybridized with the oligonucleotide on the glass slide, and then oligonucleotide-modified gold nanoparticle probe hybridized with the DNA target. In this process a sandwich-like structure was formed, with the target DNA in the middle and gold nanoparticles and glass slide on both sides. Afterwards, this sandwich structure was treated with silver enhancing chemicals containing silver ions and hydroquinone. The reduction of the silver ions was catalyzed by gold nanoparticles, which amplified the signal substantially (Fig. 38.8). Normally when the target concentration was lower than 100pM, the color change could not be visible. In the scanometric detection system, the limit of target concentrations could be as low as 50fM, almost 100-times sensitivity over Cy3-labeled assays.

It is known that LSPR is highly dependent on interparticle spacing which could be used as nanoscale rulers to "measure" biological events. An excellent example was to employ plasmonic ruler to detect the target DNA. It was based on the principle that when the distances between two metal particles change, the peak of plasmon resonance wavelength changed as well [72]. In this study, a ssDNA links two gold nanoparticles by covalent Au-S bonding at the 5' end and biotin streptavidin binding at the 3' end. In the presence of a complementary strand, the hybridization occurred leading to increase of interparticle spacing. This change can be detected by the blueshift of plasmon band (Fig. 38.9).

The one advantage of the plasmon ruler method is that it offers the real-time imaging capabilities. Note that conventional fluorophore-based assay usually suffers from photobleaching and photoblinking effects, limiting their use in real-time studies. In contrast, plasmonic properties do not have limit of time scale, and one can keep observing plasmonic structures virtually for unlimited time. The other advantage is that plasmonic ruler can sense much longer distance than traditional
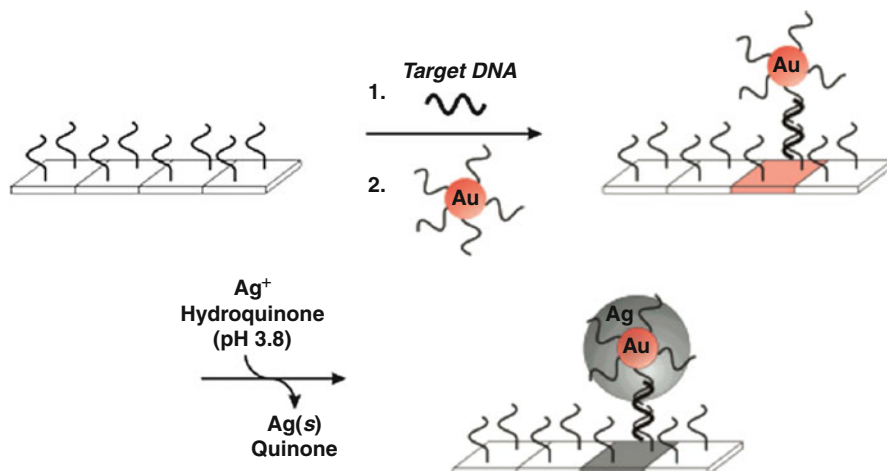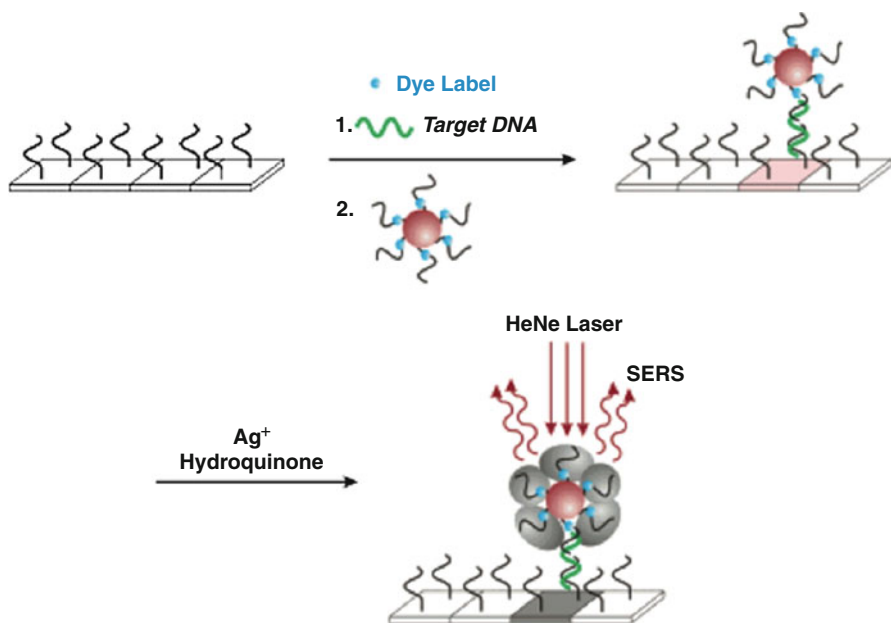
Fig. 38.8 Schematic of scanometric sensor for DNA detection. Capture DNA strands are immobilized onto glass slide; report DNA strands are attached to gold nanoparticle surfaces. In the presence of target DNA strands, nanoparticles anchor to glass surface. Furthermore, silver electroless-deposition solution is applied to coat gold nanoparticles in order to enhance visibility in a scanner. Reprinted with permission from [117]. Copyright AAAS

Fig. 38.9 Plasmonic ruler sensor for DNA detection. When a ssDNA strand linking two gold nanoparticles hybridizes with its complementary oligonucleotides, the distance of two gold nanoparticles increases due to enhancing persistence length. Corresponding to the distance changes, LSPR band shifts to *blue*. Reprinted with permission from [72]. Copyright Nature Publishing Group
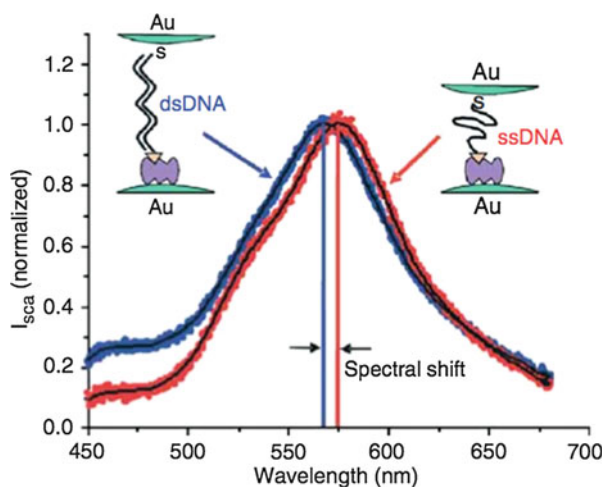
fluorescent resonance energy transfer (FRET) method. Up to about 20 nm could be measured up by typical plasmonic ruler, which is about twice the distance achieved by FRET approach. However, sizes of the particles used for plasmonic ruler are generally large (20–30 nm) which limits their use for in vivo applications.

SERS Sensing

Surface-enhanced Raman scattering (SERS) has proved to be a highly sensitive diagnostic method in analytical chemistry [120–124]. Chemicals usually have characteristic fingerprint SERS peaks which are ideal for multiplex detection. Although the fluorophore-based assays are also able to achieve multiplex detection, there are a few drawbacks such as spectral overlapping and nonuniform photobleaching [125, 126]. SERS detection can potentially overcome all those limitations.

Experimentally, it was demonstrated that it is possible to detect multiple DNA targets simultaneously [127, 128]. In one example, the gold nanoparticles were functionalized with six commercially available Raman dye-labeled oligonucleotides [128]. In the presence of DNA target and capture strands on substrate, the Raman dye-labeled oligonucleotides could be anchored to substrate surfaces. Apparently, this is similar to the process in scanometric detection forming a sandwich-like structure, followed by silver enhancement (Fig. 38.10). The key advancement of this approach was that multiple Raman dyes were involved, allowing multiple targets to be detected simultaneously. Compared to conventional

Fig. 38.10 Schematic of SERS-based DNA detection. Capture DNA strands are immobilized onto glass slide; report DNA strands are dye-labeled and attached to gold nanoparticle surfaces. In the presence of target DNA strands, nanoparticles anchor to glass surface. Furthermore, silver electroless-deposition solution is applied to coat gold nanoparticles in order to enhance SERS sensitivity. Reprinted with permission from [128]. Copyright AAAS

fluorescence-based methodologies, this approach offered sufficiently high sensitivities and multiplexing capabilities without typical photobleaching issues inherent in fluorescence-based technologies [129]. The downside of this approach was the low reproducibility as Raman signals are affected by both physical and chemical factors. In addition to Raman dyes, the sizes of nanoparticles, the interparticle distance, and their ordering arrangements affected enhancement factors substantially. This may render the practical uses challenging.

The reproducibility and sensitivity of SERS detection could be improved by using novel plasmonic nanoparticles. In a different approach, Lim et al. applied gap-tailorable gold-silver core-shell nanodumbbells (GSNDs) for SERS detection of DNA [67]. In this demonstration, a large gold nanoparticle was functionalized with Raman-active Cys3 dye-tagged DNA with sequences complementary to half of the target DNA; a small gold nanoparticle was functionalized with DNA with sequences complementary to the other half of the target DNA. Thus, in the presence of DNA targets, a dimeric structure was formed, which was followed by silver coating for signal enhancement (Fig. 38.11) [67]. The significance of this work is that it offers a high-yield synthetic method to produce highly reproducible plasmonic nanostructures for SERS-based detection. Due to the signals coming from the single plasmonic nanostructures, this method could be potentially used to detect the single molecules. It was observed that the calculated enhancement factor for the GSND was 2.7×10^{12}, which is large enough for single-molecular detection.

Electrochemical Sensing

The conductivity and redox properties of nanoparticles have been applied to electrochemical detection of DNA [130]. Silver-enhanced nanoparticle sandwich assays can also be used for the electrical detection of DNA (Fig. 38.12) [131]. Mirkin et al. have developed a DNA detection assay which utilized the conductivity changes generated by the binding of oligonucleotides. In this assay, the sandwich detection structure is positioned between two electrodes. If there is no target DNA, there will be no current flow across the electrode gap. When the target DNA is present, the gold nanoparticle probes and catalytically deposited silver will recruit as well, there will be current flow across the electrode gap. The sensitivity of this assay is as high as 500 fmol and with mutation selectivity factor of 100,000:1.

Ozsoz et al. utilized the redox properties of gold nanoparticles for the detection of DNA [132]. In their study, target DNA was immobilized onto pencil graphite electrode (PGE), and probe DNA is modified with Au nanoparticle. When target DNA hybridized with complementary probes, oxidation signal of gold nanoparticles was measured by using differential pulse voltammetry (DPV), which is around +1.20 V in their study. This assay has been developed by silver enhancement and modification of gold nanoparticles with electrochemically active groups [133–135].

Li et al. designed an electrochemical detection of DNA using aggregation of Au nanoparticles on electrodes coupled with integration of

Fig. 38.11 Schematic of the GSNDs sensor for ultrasensitive DNA detection. *Top*: A small gold nanoparticle is functionalized with DNA with sequences complementary to half of the target DNA, and a large gold nanoparticle is functionalized with Raman-active Cys3 dye-tagged DNA with sequences complementary to the other half of the target DNA. A dimeric structure is formed in the presence of DNA targets. Then a silver-enhancing solution is used to coat gold surfaces to amplify the SERS signal. Reprinted with permission from [67]. Copyright Nature Publishing Group
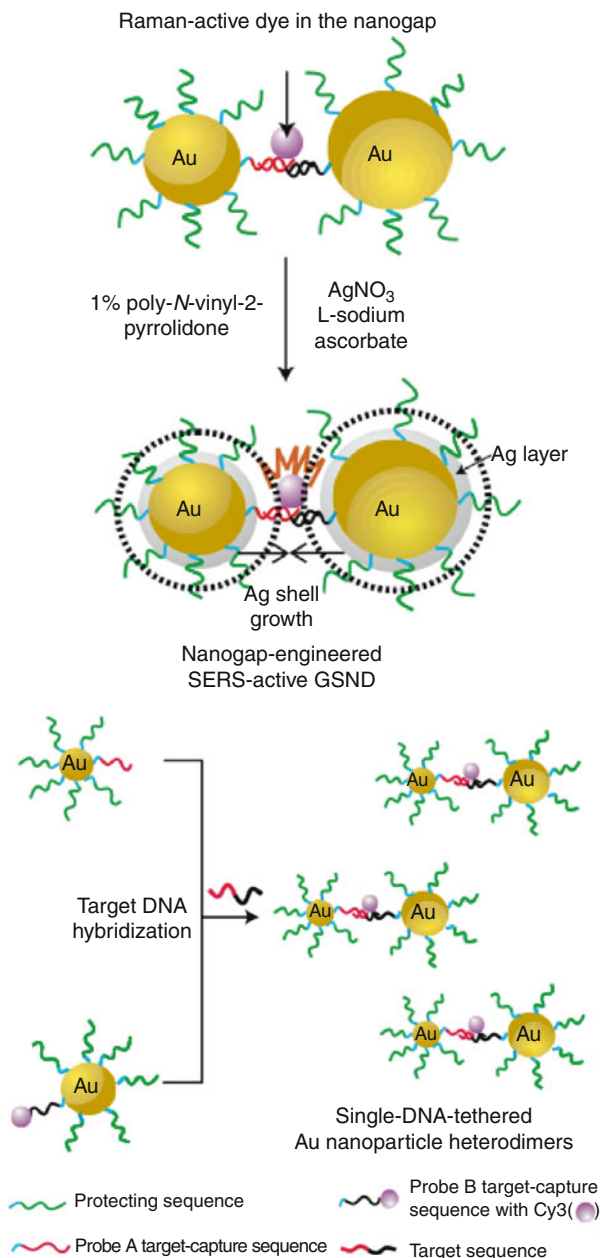
methylene blue into DNA-cross-linked structure [136]. The methylene blue performs as electrochemical indicator for the formation of DNA-cross-linked structure, and the Au nanoparticles assemblies assist electrical contact of methylene blue.
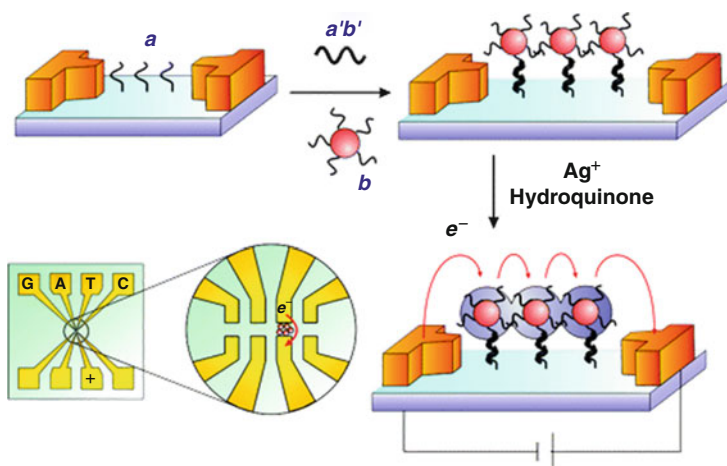
Fig. 38.12 Electrical detection of DNA. Reprinted with permission from [131]. Copyright AAAS

Magnetic Sensing

Magnetic nanoparticles, such as ferri nanoparticles, are a major class of nanomaterials. These nanoparticles have the ability to utilize magnetic attraction, which can be used for separation. Due to the properties of magnetic nanoparticles, DNA-capped magnetic nanoparticles also have great potential in diagnostic field.

A new assay, called bio-bar-code amplification (BCA), utilized the magnetic properties and greatly improved the detection limit of DNA-capped nanoparticles. Practically speaking, the scanometric detection has potential application in food safety and environment monitoring. However, the current detection still requires tedious target amplification steps such as sample concentration, cell culture, and PCR amplification. The BCA assay, which combines silver enhancement and an additional indirect target amplification assay, reaches detection limits of the PCR assay (Fig. 38.13) [137]. There are two components to the BCA assay: oligonucleotide-modified gold nanoparticles and single-component oligonucleotide-modified magnetic microparticles. In the presence of target DNA, the gold nanoparticles and the magnetic microparticles form sandwich structures that are magnetically separated from solution and washed to remove the hybridized bar-code DNA. The bar codes are detected by scanometric assay, and the detection sensitivity can be as low as 500 zM ($zM = 10^{-21}$ M). This BCA assay provides a sensitivity that is comparable to that of PCR-based approaches and without the need for enzymatic amplification.
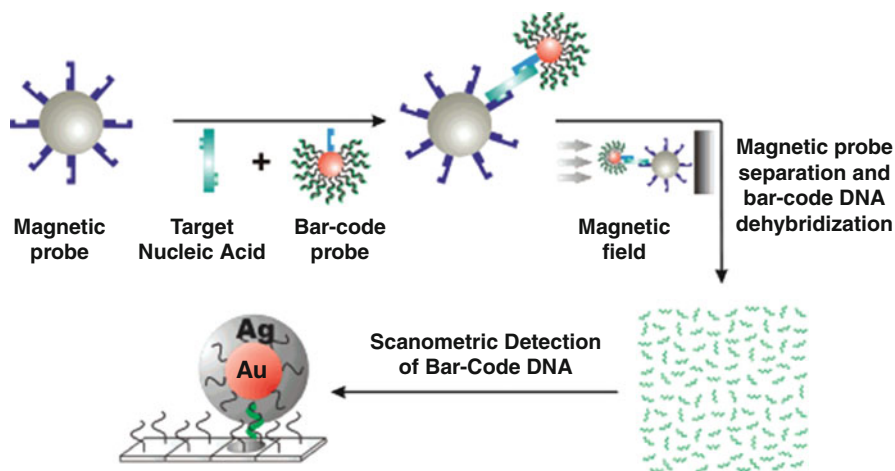
Fig. 38.13 Nanostructure-based bio-bar-code amplification scheme. Reprinted with permission from [137]. Copyright American Chemical Society Publications

Fluorescent Sensing

Quantum dots are inorganic fluorophores that are usually made up of CdSe and ZnS. They emit fluorescent light when irradiated with a UV light. The size of the dots determines the frequency of light emitted. Quantum dots own many significant properties compared with conventional fluorescent markers in biodetection assays, such as broad excitation spectra, sharp emission spectra, and easily tunable emission.

Nie et al. reported the application of DNA-modified quantum dots in multiplexed DNA detection (Fig. 38.14) [125]. In their study, target DNA was labeled with a fluorophore and oligonucleotide-modified microbeads with quantum dots designed to emit at various specified wavelengths. Different signature fluorescence spectra are achieved by embedding different ratios of quantum dots into microbeads. Optical spectroscopy yields both the coding and target signals. The coding signals identify the DNA sequence, whereas the target signal indicates the presence of the sequence. When the DNA probe hybridizes with target DNA, both the coding and target signals can be simultaneously read at the single-bead level.

Zhang et al. reported an ultrasensitive nanosensor utilizing fluorescence resonance energy transfer (FRET) (Fig. 38.15) [138]. This nanosensor has two probes for the target DNA. One probe is labeled with biotin, which can conjugate with quantum dots, so is called capture probe. Another probe has Cy5 fluorophore and is called reporter probe. With the presence of target DNA, target DNA will hybridize with both reporter probe and capture probe. Then some of the hybrids will be captured by single quantum dot, which brings the Cy5 fluorophore and quantum dots into close proximity, leading to fluorescence emission from the acceptors by means of FRET on illumination of the donor. This assay is capable of detecting approximately 50 copies or less amount of target DNA.
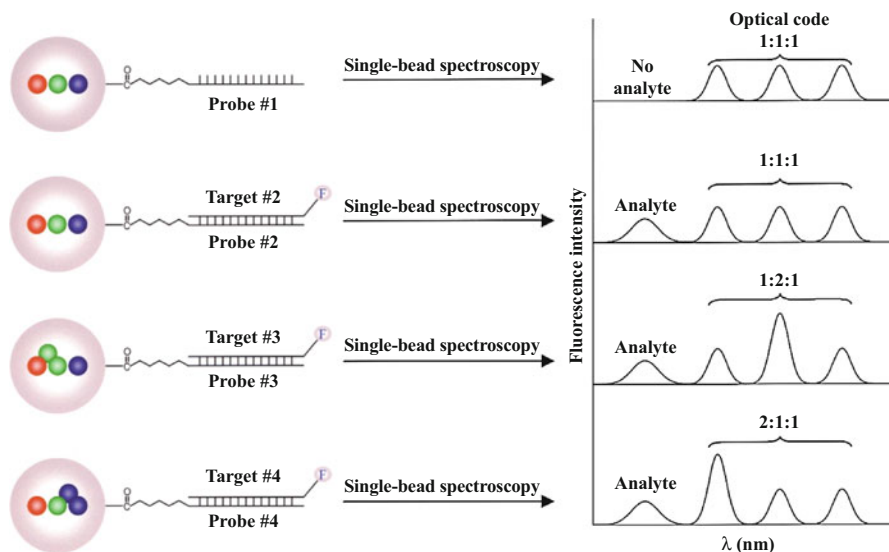
Fig. 38.14 Quantum dots in multiplexed DNA detection. Reprinted with permission from [124]. Copyright Nature Publishing Group
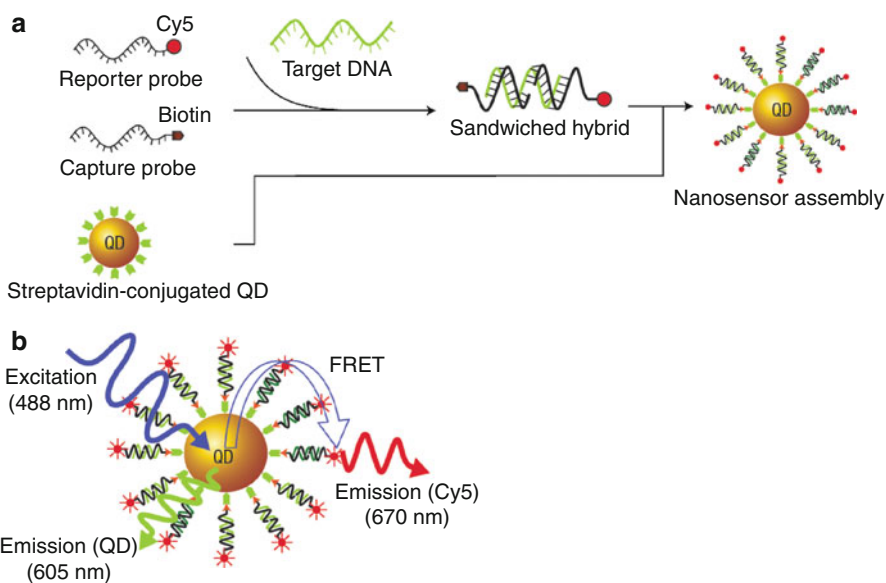

Fig. 38.15 Quantum dots in DNA detection. Reprinted with permission from 138. Copyright Nature Publishing Group

Drug-Carrying Properties

Antisense gene therapy is a potentially powerful tool in the treatment of genetic disorders or infections, which aims to turn off a specific gene in a cell. Antisense refers to nucleic acid which is designed to be complementary to a specific gene sequence. Once the antisense agents bind to target messenger RNA (mRNA), gene pathway would be blocked, which either disables or induces the degradation of the target mRNA [139]. The process of antisense therapy involves two steps; first, the antisense agents are delivered into target cells or the cell nucleus, and second, the antisense RNA strands bind with complementary mRNA (Fig. 38.16).

Because of the negative charge properties of both nucleic acid and cell membrane, it is hard for high concentration of nucleic acid to enter into the cell without the help of transfection vehicle. Conventionally, positively charged polymers are designed as transfection materials. Although this method has been employed for more than 20 years to downregulate gene expression and achieved some dramatic successes, there are some obstacles limiting its development such as efficiency, toxicity, and stability of transfection [140, 141].

In recent years, nanoparticles, such as gold nanoparticles, are employed as carriers of nucleic acids for gene regulation. These hybrid nanostructures pose remarkable properties that make them extremely attractive as intracellular gene regulation agents. In the next, we aim to cover the properties of DNA-capped nanoparticles and its application for targeted drug delivery.
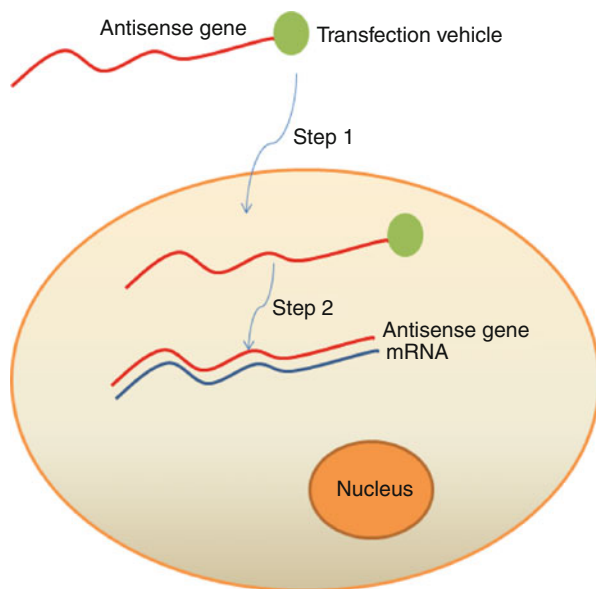

Fig. 38.16 The process of antisense therapy. First, the antisense agents are delivered into target cells or the cell nucleus with the help of transfection vehicle, and second, antisense RNA strands bind with complementary mRNA. Once the antisense agents bind to target messenger RNA (mRNA), gene pathway would be blocked, which either disables or induces the degradation of the target mRNA

High Drug Delivery Efficacy

One amazing property about polyvalent nanoparticle conjugates is that this negatively charged structure can enter cells without the help of transfection agents. An uptake efficiency of more than 99 % was demonstrated for various cell types, including macrophage, cervical carcinoma, fibroblast, and kidney cell lines [142–146].

It was found that these oligonucleotide-capped nanoparticles have higher affinity to complementary nucleic acids than their unmodified oligonucleotide counterparts, exhibit high cellular uptake, and can introduce oligonucleotides more effectively than conventional transfection agents [142–146]. In Markin's study, antisense sequences are designed to be complementary with the mRNA sequences than coding for enhanced green florescent protein (EGFP) expressed in mouse cell line. The surfaces of 13-nm gold nanoparticles are conjugated to two different groups of antisense oligodeoxynucleotides, respectively. One group is about 40–45 strands and functionalized by four thiol terminated, another group is about 110–120 strands and modified by only one thiol terminated (Fig. 38.17). The former conjugates with tetrathiol-functionalized oligonucleotides can constantly bind to its complementary sequence, which is approximately similar to the unmodified
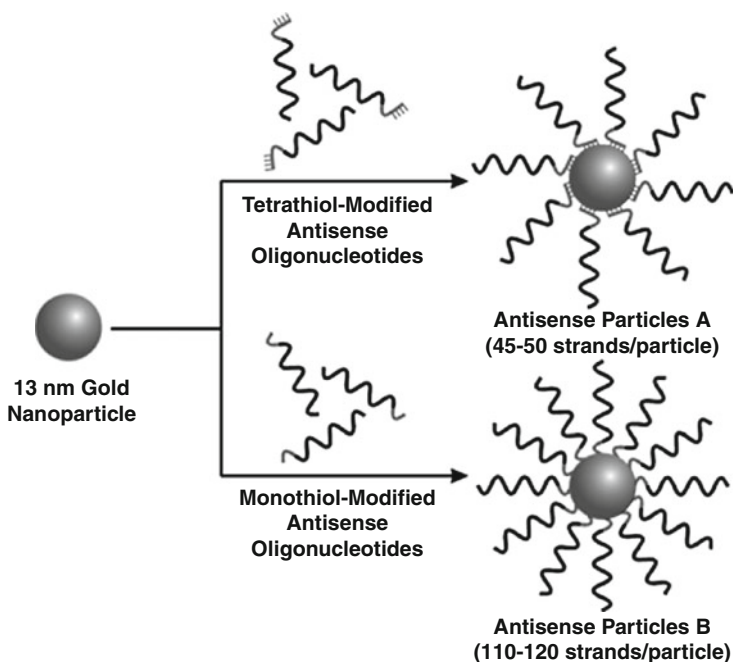

Fig. 38.17 Preparations of antisense Au NPs. 13-nm gold nanoparticles were functionalized with two groups of antisense oligodeoxynucleotides respectively. Reprinted with permission from [144]. Copyright AAAS
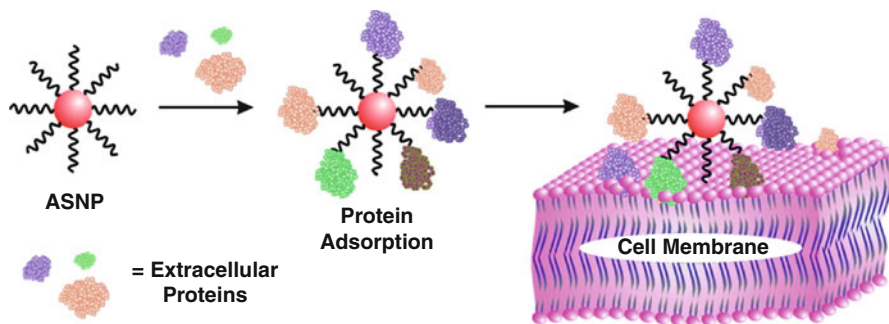
Fig. 38.18 Proposed scheme for antisense nanoparticle (ASNP) cellular uptake. Upon addition to the media, ASNP binds extracellular proteins and allows it to interface with the cellular membrane. Reprinted with permission from [149]. Copyright American Chemical Society Publications

nucleotide, whereas latter conjugates with monothiol-modified oligonucleotides possess high affinity that is 35 orders of oligonucleotides before modification. This is mainly because high oligonucleotide packing densities facilitate the nucleotide association [147].

On the basis of electrostatic repulsion rule, the negatively charged polyvalent nanoparticle conjugates cannot enter into a cell, as the cell member is negatively charged as well. Polyvalent nanoparticle conjugates that enter cell directly cannot be explained according to the simple electrostatic repulsion rule. Unlike the most common delivery systems which require co-carrier such as cationic lipids and polymers, the uptake of DNA-capped nanoparticles do not require co-carrier and follow different mechanism. The uptake depended on several factors, such as oligonucleotide density, concentration of nanoparticles, and the cell type. Cellular uptake is highly dependent on the number of oligonucleotides immobilized on each antisense nanoparticle. The higher density of the oligonucleotide loading on the surface of the particles leads to greater uptake. Another reason why this negatively charged polyvalent nanoparticle structure can enter into the cell is because it complexes with the positively charged protein in cell membrane and then enters into the cell. It was found that the number of proteins per particle correlates with particle uptake. Because cells will readily recognize certain proteins [148], Giljohann et al. hypothesized that the interaction of antisense nanoparticles with proteins is also a possible mechanism of recognition and their subsequent uptake (Fig. 38.18) [149].

High Stability

The stability of nucleic acid in the cell is a significant factor for the success of intracellular gene regulation. Usually, nucleic acid can be degraded by nucleases in
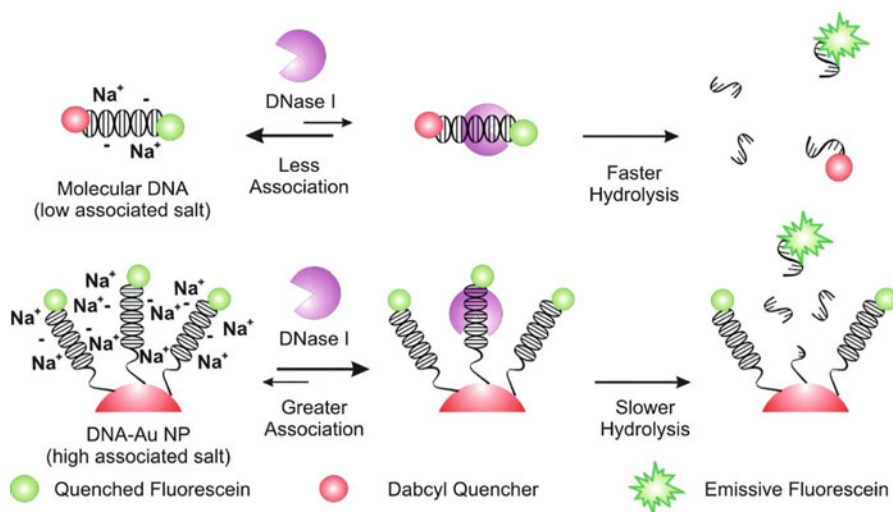
Fig. 38.19 Proposed mechanism for polyvalent nanoparticle-induced DNA stability. Reprinted with permission from [145]. Copyright American Chemical Society Publications

cell. Traditionally, the stability of nucleic acid can be increased through chemical modification [150] or electrostatic interaction [151, 152]. However, these materials can be toxic at high concentration or degraded intracellularly [153].

To investigate the intracellular stability of nucleic acid for polyvalent gold nanoparticle nucleic acid, gold nanoparticle was conjugated to nucleic acid terminated with fluorophores; thus the nucleic acid can be tracked within the cell [144]. The study shows that the oligonucleotides remain chemically attached to the particle while inside the cell. Although oligonucleotide degradation still occurs in the cell, their degradation rates are negligible compared with particle-free oligonucleotides.

Further investigations reveal that electric charge and local salt are the main factors that correlate with nuclease stability of DNA-capped nanoparticle [145]. Seferos et al. investigated the apparent stability of DNA toward nucleases that results when they are arranged in a dense monolayer on a nanoparticle surface. In their study, various nanoparticle properties such as surface density and charge have been investigated, and they found that electric charge and local salt are the main factors that correlate with the increased nuclease stability of DNA-AuNPs. They found that negatively charged surfaces of the nanoparticles and resultant high local salt concentrations are responsible for enhanced stability. Enzyme-catalyzed DNA hydrolysis is modeled in two steps: enzyme association and DNA hydrolysis. The high surface charge resulting in increased associated salts is postulated to be the origin of DNA stability and the slower enzymatic hydrolysis (Fig. 38.19) [145].

Low Toxicity

Besides considering the stability after uptake, the cytotoxicity is also another significant aspect for the application of polyvalent gold nanoparticle nucleic acid for gene regulation. In more than 50 tested cell types, no differences were found in cellular morphology or cell viability between nanoparticle-treated and untreated control cells [144].

Later, a study investigated the immune response of macrophages after exposed to polyvalent oligonucleotides-capped gold nanoparticles [154]. Cellular innate immune response protects cell from harmful foreign agent invasion. Foreign nucleic acids can also be recognized as harmful foreign agent and removed from the cell and/or cause immune responses. In this study, they employ interferon-β as an indicator of innate immune response to investigate the immune response of polyvalent oligonucleotide-capped gold nanoparticles. It was found that densely functionalized, oligonucleotide-modified nanoparticles are significantly less (up to a 25-fold decrease) when compared to the same DNA sequence with lipoplex as transfection vehicle. They also found that magnitude of this effect is inversely proportional to the density of oligonucleotide. It is because that foreign oligonucleotide is responsible for the immune response, while the local surface environment of the particle, particularly high charge density, can inhibit the immune response. So the net effect is that gold nanoparticle shows a significantly lower cellular immune response than conventional DNA transfection materials in nucleic acid delivery.

To date, oligonucleotide-capped gold nanoparticle conjugates have not been reported to be responsible for any detectable toxicity associated with cultured mammalian cells or mouse models. In spite of the fact that cellular response to gold nanoparticles is significant, when these same nanoparticles are covalently attached with nucleic acids, no cellular response was shown [155–158].

Theranostics

Multifunctionality of nanoparticles allows for the design of theranostic drug delivery system in which therapeutics and diagnostics can be combined. It is desirable to have one nanoparticle structure with both of these functions so that we can visualize and quantify mRNA binding while it is working for gene therapy. Mirkin's group designed and synthesized such polyvalent DNA-nanoparticle conjugate that has both functions of DNA diagnostics and gene therapy. This nanoparticle structure is called a nanoflare (Fig. 38.20) [146, 159]. There are two components to the nanoflare construct: oligonucleotide-modified gold nanoparticles that can recognize an mRNA target and a second short oligonucleotide sequence terminated with fluorophore. In the nanoflare construct, the short oligonucleotide hybridizes with the longer sequence, though DNA hybridization fluorophore is held close to the gold nanoparticle and quenches its fluorescence. When this nanoflare construct enters into the cell and meets the target mRNA, oligonucleotide on the nanoparticle would bind to the target mRNA and replace the flare sequence, which releases the fluorophore from the nanoparticle and fluorescent again. This offers an approach of
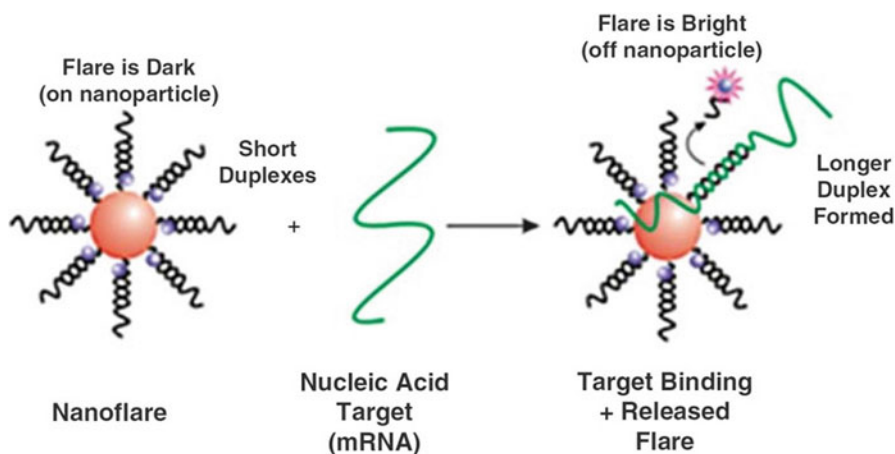
Fig. 38.20 Schematic diagram of a nanoflare binding to its target mRNA and releasing a fluorophore-labeled flare. Reprinted with permission from [161]. Copyright Materials Research Society

quantitatively measuring the intracellular mRNA concentration while one is affecting gene regulation. In their study, it is observed that the target binding and response of the nanoflare is able to recognize single base-pair mismatches. Furthermore, this nanoflare construct is capable of depleting mRNA levels by as much as 92 % ± 4 in a dose and sequence-dependent manner, consistent with enzymatic degradation of targeted mRNA. This nanoflare construct offers the intracellular gene diagnostics and regulation in a single material.

Although molecular beacons can also achieve the same results, it is found that the background led by nuclease activity is enormous so we cannot use this approach effectively in an intracellular assay [160]. One advantage of nanoflare construct is that one can create new cell-screening assays, where cell populations are differentiated in real time with cell counting and imaging equipment [161]. Moreover, these new detection strategies are expected to combine the concurrent developments in nanoparticle-based therapeutics, which potentially will lead to new opportunities in personalized medicine.

References

1. Tan SJ et al (2011) Building plasmonic nanostructures with DNA. Nat Nanotechnol 6:268–276
2. Alivisatos AP et al (1996) Organization of "nanocrystal molecules" using DNA. Nature 382(6592):609–611
3. Maye MM et al (2010) Switching binary states of nanoparticle superlattices and dimer clusters by DNA strands. Nat Nanotechnol 5:116–120
4. Nie Z et al (2007) Self-assembly of metal-polymer analogues of amphiphilic triblock copolymers. Nat Mater 6(8):609–614

5. Liu K et al (2010) Step-growth polymerization of inorganic nanoparticles. Science 329(5988):197–200

6. Pileni M-P (2007) Self-assembly of inorganic nanocrystals: fabrication and collective intrinsic properties. Acc Chem Res 40(8):685–693

7. Heitsch AT et al (2010) GISAXS characterization of order in hexagonal monolayers of FePt nanocrystals. J Phys Chem C 114(34):14427–14432

8. Jones MR et al (2010) DNA-nanoparticle superlattices formed from anisotropic building blocks. Nat Mater 9(11):913–917

9. Park SY et al (2008) DNA-programmable nanoparticle crystallization. Nature 451:553–556

10. Nykypanchuk D et al (2008) DNA-guided crystallization of colloidal nanoparticles. Nature 451:549–552

11. Cheng WL et al (2010) Probing in real time the soft crystallization of DNA-capped nanoparticles. Angew Chem Int Ed 49:380–384

12. Gao Y, Tang Z (2011) Design and application of inorganic nanoparticle superstructures: current status and future challenges. Small 7(15):2133–2146

13. Jones MR et al (2011) Templated techniques for the synthesis and assembly of plasmonic nanostructures. Chem Rev 111(6):3736–3827

14. Schuller JA et al (2010) Plasmonics for extreme light concentration and manipulation. Nat Mater 9(3):193–204

15. Shipway AN, Katz E, Willner I (2000) Nanoparticle arrays on surfaces for electronic, optical, and sensor applications. Chem Phys Chem 1(1):18–52

16. Ozbay E (2006) Plasmonics: merging photonics and electronics at nanoscale dimensions. Science 311(5758):189–193

17. Anker JN et al (2008) Biosensing with plasmonic nanosensors. Nat Mater 7(6):442–453

18. Maier SA et al (2003) Local detection of electromagnetic energy transport below the diffraction limit in metal nanoparticle plasmon waveguides. Nat Mater 2(4):229–232

19. Lal S, Clare SE, Halas NJ (2008) Nanoshell-enabled photothermal cancer therapy: impending clinical impact. Acc Chem Res 41(12):1842–1851

20. Yavuz MS et al (2009) Gold nanocages covered by smart polymers for controlled release with near-infrared light. Nat Mater 8(12):935–939

21. Grzelczak M et al (2008) Shape control in gold nanoparticle synthesis. Chem Soc Rev 37(9):1783–1791

22. Xia Y et al (2009) Shape-controlled synthesis of metal nanocrystals: simple chemistry meets complex physics? Angew Chem Int Ed 48(1):60–103

23. Frens G (1973) Controlled nucleation for the regulation of the particle size in monodisperse gold suspensions. Nat Phys Sci 241:20–22

24. Jana NR, Gearheart L, Murphy CJ (2001) Seeding growth for size control of 5–40 nm diameter gold nanoparticles. Langmuir 17(22):6782–6786

25. Perrault SD, Chan WCW (2009) Synthesis and surface modification of highly monodispersed, spherical gold nanoparticles of 50–200 nm. J Am Chem Soc 131(47):17042–17043

26. Nikoobakht B, El-Sayed MA (2003) Preparation and growth mechanism of gold nanorods (NRs) using seed-mediated growth method. Chem Mater 15(10):1957–1962

27. Busbee BD, Obare SO, Murphy CJ (2003) An improved synthesis of high-aspect-ratio gold nanorods. Adv Mater 15(5):414–416

28. Millstone JE et al (2005) Observation of a quadrupole plasmon mode for a colloidal solution of gold nanoprisms. J Am Chem Soc 127(15):5312–5313

29. Liz-Marzán LM (2005) Tailoring surface plasmons through the morphology and assembly of metal nanoparticles. Langmuir 22(1):32–41

30. Kelly KL et al (2002) The optical properties of metal nanoparticles: the influence of size, shape, and dielectric environment. J Phys Chem B 107(3):668–677

31. Mulvaney P (1996) Surface plasmon spectroscopy of nanosized metal particles. Langmuir 12(3):788–800

32. Mie G (1908) Beiträge zur optik trüber medien, speziell kolloidaler metallösungen. Ann Phys 330(3):377–445
33. Link S, El-Sayed MA (1999) Size and temperature dependence of the plasmon absorption of colloidal gold nanoparticles. J Phys Chem B 103(21):4212–4217
34. Wiley BJ et al (2006) Maneuvering the surface plasmon resonance of silver nanostructures through shape-controlled synthesis. J Phys Chem B 110(32):15666–15675
35. Su KH et al (2003) Interparticle coupling effects on plasmon resonances of nanogold particles. Nano Lett 3(8):1087–1090
36. Alivisatos AP (1996) Semiconductor clusters, nanocrystals, and quantum dots. Science 271(5251):933–937
37. Brus LE (1984) Electron–electron and electron–hole interactions in small semiconductor crystallites: the size dependence of the lowest excited electronic state. J Chem Phys 80(9):4403–4409
38. Katari JEB, Colvin VL, Alivisatos AP (1994) X-ray photoelectron spectroscopy of CdSe nanocrystals with applications to studies of the nanocrystal surface. J Phys Chem 98(15):4109–4117
39. Murray CB, Norris DJ, Bawendi MG (1993) Synthesis and characterization of nearly monodisperse CdE (E = sulfur, selenium, tellurium) semiconductor nanocrystallites. J Am Chem Soc 115(19):8706–8715
40. Peng ZA, Peng X (2000) Formation of high-quality CdTe, CdSe, and CdS nanocrystals using CdO as precursor. J Am Chem Soc 123(1):183–184
41. Talapin DV et al (2001) Highly luminescent monodisperse CdSe and CdSe/ZnS nanocrystals synthesized in a hexadecylamine − trioctylphosphine oxide − trioctylphospine mixture. Nano Lett 1(4):207–211
42. Qu L, Peng ZA, Peng X (2001) Alternative routes toward high quality CdSe nanocrystals. Nano Lett 1(6):333–337
43. Bruchez M et al (1998) Semiconductor nanocrystals as fluorescent biological labels. Science 281(5385):2013–2016
44. Chan WCW, Nie S (1998) Quantum dot bioconjugates for ultrasensitive nonisotopic detection. Science 281(5385):2016–2018
45. Medintz IL et al (2005) Quantum dot bioconjugates for imaging, labelling and sensing. Nat Mater 4(6):435–446
46. Sargent EH (2005) Infrared quantum dots. Adv Mater 17(5):515–522
47. Biju V, Itoh T, Ishikawa M (2010) Delivering quantum dots to cells: bioconjugated quantum dots for targeted and nonspecific extracellular and intracellular imaging. Chem Soc Rev 39(8):3031–3056
48. Laurent S et al (2008) Magnetic iron oxide nanoparticles: synthesis, stabilization, vectorization, physicochemical characterizations, and biological applications. Chem Rev 108(6):2064–2110
49. Reddy LH et al (2012) Magnetic nanoparticles: design and characterization, toxicity and biocompatibility, pharmaceutical and biomedical applications. Chem Rev 112(11):5818–5878
50. Haun JB et al (2010) Magnetic nanoparticle biosensors. Wiley Interdiscip Rev Nanomed Nanobiotechnol 2(3):291–304
51. Yang D et al (2010) Novel DNA materials and their applications. Wiley Interdiscip Rev Nanomed Nanobiotechnol 2(6):648–669
52. LaBean TH, Li H (2007) Constructing novel materials with DNA. Nano Today 2(2):26–35
53. Winfree E et al (1998) Design and self-assembly of two-dimensional DNA crystals. Nature 394(6693):539–544
54. Reishus D et al (2005) Self-assembly of DNA double-double crossover complexes into high-density, doubly connected, planar structures. J Am Chem Soc 127(50):17590–17591
55. Liu Y et al (2005) Aptamer-directed self-assembly of protein arrays on a DNA nanostructure. Angew Chem Int Ed 44(28):4333–4338

56. Yan H et al (2002) A robust DNA mechanical device controlled by hybridization topology. Nature 415(6867):62–65
57. Rothemund PWK (2006) Folding DNA to create nanoscale shapes and patterns. Nature 440(7082):297–302
58. Han D et al (2011) DNA origami with complex curvatures in three-dimensional space. Science 332(6027):342–346
59. Luo D (2003) The road from biology to materials. Materials Today 6(11):38–43
60. Zanchet D et al (2002) Electrophoretic and structural studies of DNA-directed Au nanoparticle groupings. J Phys Chem B 106(45):11758–11763
61. Zanchet D et al (2000) Electrophoretic isolation of discrete Au nanocrystal/DNA conjugates. Nano Lett 1(1):32–35
62. Xu X et al (2006) Asymmetric functionalization of gold nanoparticles with oligonucleotides. J Am Chem Soc 128(29):9286–9287
63. Maye MM et al (2009) Stepwise surface encoding for high-throughput assembly of nanoclusters. Nat Mater 8(5):388–391
64. Nie Z et al (2008) "Supramolecular" assembly of gold nanorods end-terminated with polymer "pom-poms": effect of pom-pom structure on the association modes. J Am Chem Soc 130(11):3683–3689
65. Mirkin CA et al (1996) A DNA-based method for rationally assembling nanoparticles into macroscopic materials. Nature 382(6592):607–609
66. Loweth CJ et al (1999) DNA-based assembly of gold nanocrystals. Angew Chem Int Ed 38(12):1808–1812
67. Lim D-K et al (2010) Nanogap-engineerable Raman-active nanodumbbells for single-molecule detection. Nat Mater 9(1):60–67
68. Chen W et al (2009) Nanoparticle superstructures made by polymerase chain reaction: collective interactions of nanoparticles and a new principle for chiral materials. Nano Lett 9(5):2153–2159
69. Macfarlane RJ et al (2010) Establishing the design rules for DNA-mediated colloidal crystallization. Angew Chem Int Ed 49(27):4589–4592
70. Macfarlane RJ et al (2011) Nanoparticle superlattice engineering with DNA. Science 334(6053):204–208
71. Auyeung E et al (2012) Synthetically programmable nanoparticle superlattices using a hollow three-dimensional spacer approach. Nat Nanotechnol 7(1):24–28
72. Sonnichsen C et al (2005) A molecular ruler based on plasmon coupling of single gold and silver nanoparticles. Nat Biotechnol 23(6):741–745
73. Sebba D, LaBean T, Lazarides A (2008) Plasmon coupling in binary metal core-satellite assemblies. Appl Phys B 93(1):69–78
74. Sharma J et al (2009) Control of self-assembly of DNA tubules through integration of gold nanoparticles. Science 323(5910):112–116
75. Hinds S et al (2005) Nucleotide-directed growth of semiconductor nanocrystals. J Am Chem Soc 128(1):64–65
76. Tikhomirov G et al (2011) DNA-based programming of quantum dot valency, self-assembly and luminescence. Nat Nanotechnol 6(8):485–490
77. Cheng WL et al (2009) Free-standing nanoparticle superlattice sheets controlled by DNA. Nature materials 8(6):519–525
78. Cheng WL et al (2008) Nanopatterning self-assembled nanoparticle superlattices by moulding microdroplets. Nat Nanotechnol 3(11):682–690
79. Campolongo MJ et al (2011) Crystalline Gibbs monolayers of DNA-capped nanoparticles at the Air–liquid interface. ACS Nano 5(10):7978–7985
80. Pal S et al (2010) DNA-origami-directed self-assembly of discrete silver-nanoparticle architectures. Angew Chem Int Ed 49(15):2700–2704
81. Le JD et al (2004) DNA-templated self-assembly of metallic nanocomponent arrays on a surface. Nano Lett 4(12):2343–2347

82. Zheng J et al (2006) Two-dimensional nanoparticle arrays show the organizational power of robust DNA motifs. Nano Lett 6(7):1502–1504

83. Mastroianni AJ, Claridge SA, Alivisatos AP (2009) Pyramidal and chiral groupings of gold nanocrystals assembled using DNA scaffolds. J Am Chem Soc 131(24):8455–8459

84. Aldaye FA, Sleiman HF (2007) Dynamic DNA templates for discrete gold nanoparticle assemblies: control of geometry, modularity, write/erase and structural switching. J Am Chem Soc 129(14):4130–4131

85. Pinheiro AV et al (2011) Challenges and opportunities for structural DNA nanotechnology. Nat Nanotechnol 6(12):763–772

86. Pal S et al (2011) DNA directed self-assembly of anisotropic plasmonic nanostructures. J Am Chem Soc 133(44):17606–17609

87. Hung AM, Noh H, Cha JN (2010) Recent advances in DNA-based directed assembly on surfaces. Nanoscale 2(12):2530–2537

88. Gates BD et al (2005) New approaches to nanofabrication: molding, printing, and other techniques. Chem Rev 105(4):1171–1196

89. Perl A, Reinhoudt DN, Huskens J (2009) Microcontact printing: limitations and achievements. Adv Mater 21(22):2257–2268

90. Salaita K, Wang Y, Mirkin CA (2007) Applications of dip-pen nanolithography. Nat Nanotechnol 2(3):145–155

91. Maune HT et al (2010) Self-assembly of carbon nanotubes into two-dimensional geometries using DNA origami templates. Nat Nanotechnol 5(1):61–66

92. Noh H et al (2009) 50 nm DNA nanoarrays generated from uniform oligonucleotide films. ACS Nano 3(8):2376–2382

93. Hung AM et al (2010) Large-area spatially ordered arrays of gold nanoparticles directed by lithographically confined DNA origami. Nat Nanotechnol 5(2):121–126

94. Kershner RJ et al (2009) Placement and orientation of individual DNA shapes on lithographically patterned surfaces. Nat Nanotechnol 4(9):557–561

95. Hutter E, Fendler JH (2004) Exploitation of localized surface plasmon resonance. Adv Mater 16(19):1685–1706

96. Chen Y et al (2013) Mechanically strong, optically transparent, giant metal superlattice nanomembranes from ultrathin gold nanowires. Adv Mater 25(1):80–85

97. Ng KC et al (2012) Free-standing plasmonic-nanorod super lattice sheets. ACS Nano 6(1):925–934

98. Rosi NL, Mirkin CA (2005) Nanostructures in biodiagnostics. Chem Rev 105(4):1547–1562

99. Cheng WL, Dong SJ, Wang EK (2004) Two- and three-dimensional Au nanoparticle/CoTMPyP self-assembled nanostructured materials: film structure, tunable electrocatalytic activity, and plasmonic properties. J Phys Chem B 108(50):19146–19154

100. Elghanian R et al (1997) Selective colorimetric detection of polynucleotides based on the distance-dependent optical properties of gold nanoparticles. Science 277(5329):1078–1081

101. Storhoff JJ et al (1998) One-pot colorimetric differentiation of polynucleotides with single base imperfections using gold nanoparticle probes. J Am Chem Soc 120(9):1959–1964

102. Pavlov V et al (2004) Aptamer-functionalized Au nanoparticles for the amplified optical detection of thrombin. J Am Chem Soc 126(38):11768–11769

103. Huang CC et al (2005) Aptamer-modified gold nanoparticles for colorimetric determination of platelet-derived growth factors and their receptors. Anal Chem 77(17):5735–5741

104. Liu J, Lu Y (2005) Fast colorimetric sensing of adenosine and cocaine based on a general sensor design involving aptamers and nanoparticles. Angew Chem Int Ed Engl 45(1):90–94

105. Liu JW, Lu Y (2003) A colorimetric lead biosensor using DNAzyme-directed assembly of gold nanoparticles. J Am Chem Soc 125(22):6642–6643

106. Li HX, Rothberg LJ (2004) Label-free colorimetric detection of specific sequences in genomic DNA amplified by the polymerase chain reaction. J Am Chem Soc 126(35):10958–10961

107. Wang ZD, Lee JH, Lu Y (2008) Label-free colorimetric detection of lead ions with a nanomolar detection limit and tunable dynamic range by using gold nanoparticles and DNAzyme. Adv Mater 20(17):3263–3267

108. Li HX, Rothberg L (2004) Colorimetric detection of DNA sequences based on electrostatic interactions with unmodified gold nanoparticles. Proc Natl Acad Sci USA 101(39):14036–14039

109. Li HX, Rothberg L (2005) Detection of specific sequences in RNA using differential adsorption of single-stranded oligonucleotides on gold nanoparticles. Anal Chem 77(19):6229–6233

110. Liu CW et al (2008) Detection of mercury(II) based on Hg(2+)-DNA complexes inducing the aggregation of gold nanoparticles. Chem Commun 19:2242–2244

111. Wang LH et al (2006) Unmodified gold nanoparticles as a colorimetric probe for potassium DNA aptamers. Chem Commun 36:3780–3782

112. Zhang J et al (2008) Visual cocaine detection with gold nanoparticles and rationally engineered aptamer structures. Small 4(8):1196–1200

113. Wei H et al (2007) Simple and sensitive aptamer-based colorimetric sensing of protein using unmodified gold nanoparticle probes. Chem Commun 36:3735–3737

114. Zhao WA et al (2007) Simple and rapid colorimetric biosensors based on DNA aptamer and noncrosslinking gold nanoparticle aggregation. Chembiochem 8(7):727–731

115. Reynolds RA, Mirkin CA, Letsinger RL (2000) A gold nanoparticle/latex microsphere-based colorimetric oligonucleotide detection method. Pure Appl Chem 72(1–2):229–235

116. Storhoff JJ et al (2005) Labels and detection methods. In: Microarray technology and its applications. Springer, Berlin/Heidelberg, pp 147–179

117. Taton TA, Mirkin CA, Letsinger RL (2000) Scanometric DNA array detection with nanoparticle probes. Science 289(5485):1757–1760

118. Hacker GW (1989) Colloidal gold: principles, methods, and applications, vol 1. Academic, San Diego

119. Zehbe I et al (1997) Sensitive in situ hybridization with catalyzed reporter deposition, streptavidin-nanogold, and silver acetate autometallography – detection of single-copy human papillomavirus. Am J Pathol 150(5):1553–1561

120. Petry R, Schmitt M, Popp J (2003) Raman spectroscopy – a prospective tool in the life sciences. Chemphyschem 4(1):14–30

121. Graham D et al (2008) Control of enhanced Raman scattering using a DNA-based assembly process of dye-coded nanoparticles. Nat Nanotechnol 3(9):548–551

122. Kneipp K, Kneipp H, Kneipp J (2006) Surface-enhanced Raman scattering in local optical fields of silver and gold nanoaggregatess – from single-molecule Raman spectroscopy to ultrasensitive probing in live cells. Acc Chem Res 39(7):443–450

123. Li JF et al (2010) Shell-isolated nanoparticle-enhanced Raman spectroscopy. Nature 464(7287):392–395

124. Nie SM, Emery SR (1997) Probing single molecules and single nanoparticles by surface-enhanced Raman scattering. Science 275(5303):1102–1106

125. Han MY et al (2001) Quantum-dot-tagged microbeads for multiplexed optical coding of biomolecules. Nat Biotechnol 19(7):631–635

126. Kneipp K et al (1999) Ultrasensitive chemical analysis by Raman spectroscopy. Chem Rev 99(10):2957–2976

127. Macaskill A et al (2007) Quantitative surface-enhanced resonance Raman scattering of phthalocyanine-labelled oligonucleotides. Nucleic Acids Res 35(6):e42

128. Cao YC, Jin R, Mirkin CA (2002) Nanoparticles with Raman spectroscopic fingerprints for DNA and RNA detection. Science 297(5586):1536–1540

129. Faulds K et al (2004) SERRS as a more sensitive technique for the detection of labelled oligonucleotides compared to fluorescence. Analyst 129(7):567–568

130. Katz E, Willner I, Wang J (2004) Electroanalytical and bioelectroanalytical systems based on metal and semiconductor nanoparticles. Electroanalysis 16(1–2):19–44

131. Park SJ, Taton TA, Mirkin CA (2002) Array-based electrical detection of DNA with nanoparticle probes. Science 295(5559):1503–1506
132. Ozsoz M et al (2003) Electrochemical genosensor based on colloidal gold nanoparticles for the detection of factor V Leiden mutation using disposable pencil graphite electrodes. Anal Chem 75(9):2181–2187
133. Cai H et al (2002) Electrochemical detection of DNA hybridization based on silver-enhanced gold nanoparticle label. Anal Chim Acta 469(2):165–172
134. Wang J et al (2003) Amplified voltammetric detection of DNA hybridization via oxidation of ferrocene caps on gold nanoparticle/streptavidin conjugates. Anal Chem 75(15):3941–3945
135. Baca AJ et al (2004) Attachment of ferrocene-capped gold nanoparticle-streptavidin conjugates onto electrode surfaces covered with biotinylated biomolecules for enhanced voltammetric analysis. Electroanalysis 16(1–2):73–80
136. Li D et al (2007) Amplified electrochemical detection of DNA through Au nanoparticles on electrodes and the incorporation into the DNA-crosslinked structure. Chem Commun 34:3544–3546
137. Nam JM, Stoeva SI, Mirkin CA (2004) Bio-bar-code-based DNA detection with PCR-like sensitivity. J Am Chem Soc 126(19):5932–5933
138. Zhang CY et al (2005) Single-quantum-dot-based DNA nanosensor. Nat Mater 4(11):826–831
139. Crooke ST (2004) Progress in antisense technology. Annu Rev Med 55:61–95
140. Lebedeva I, Stein CA (2001) Antisense oligonucleotides: promise and reality. Annu Rev Pharmacol Toxicol 41:403–419
141. Lv H et al (2006) Toxicity of cationic lipids and cationic polymers in gene delivery. J Control Release 114(1):100–109
142. Patel PC et al (2008) Peptide antisense nanoparticles. Proc Natl Acad Sci USA 105(45):17222–17226
143. Seferos DS et al (2007) Locked nucleic acid-nanoparticle conjugates. Chembiochem 8(11):1230–1232
144. Rosi NL et al (2006) Oligonucleotide-modified gold nanoparticles for intracellular gene regulation. Science 312(5776):1027–1030
145. Seferos DS et al (2009) Polyvalent DNA nanoparticle conjugates stabilize nucleic acids. Nano Lett 9(1):308–311
146. Prigodich AE et al (2009) Nano-flares for mRNA regulation and detection. ACS Nano 3(8):2147–2152
147. Jin R et al (2003) What controls the melting properties of DNA-linked gold nanoparticle assemblies? J Am Chem Soc 125(6):1643–1654
148. Ryser HJ (1968) Uptake of protein by mammalian cells: an underdeveloped area. The penetration of foreign proteins into mammalian cells can be measured and their functions explored. Science 159(3813):390–396
149. Giljohann DA et al (2007) Oligonucleotide loading determines cellular uptake of DNA-modified gold nanoparticles. Nano Lett 7(12):3818–3821
150. Ng PS, Bergstrom DE (2005) Alternative nucleic acid analogues for programmable assembly: hybridization of LNA to PNA. Nano Lett 5(1):107–111
151. He XX et al (2003) Bioconjugated nanoparticles for DNA protection from cleavage. J Am Chem Soc 125(24):7168–7169
152. Han G, Martin CT, Rotello VM (2006) Stability of gold nanoparticle-bound DNA toward biological, physical, and chemical agents. Chem Biol Drug Des 67(1):78–82
153. Amiji MM (2004) Polymeric gene delivery: principles and applications. CRC Press, Boca Raton
154. Massich MD et al (2009) Regulating immune response using polyvalent nucleic acid-gold nanoparticle conjugates. Mol Pharm 6(6):1934–1940

155. Clift MJ et al (2008) The impact of different nanoparticle surface chemistry and size on uptake and toxicity in a murine macrophage cell line. Toxicol Appl Pharmacol 232(3):418–427
156. Goodman CM et al (2004) Toxicity of gold nanoparticles functionalized with cationic and anionic side chains. Bioconjug Chem 15(4):897–900
157. Hauck TS, Ghazani AA, Chan WC (2008) Assessing the effect of surface chemistry on gold nanorod uptake, toxicity, and gene expression in mammalian cells. Small 4(1):153–159
158. Alkilany AM et al (2009) Cellular uptake and cytotoxicity of gold nanorods: molecular origin of cytotoxicity and surface effects. Small 5(6):701–708
159. Seferos DS et al (2007) Nano-flares: probes for transfection and mRNA detection in living cells. J Am Chem Soc 129(50):15477–15479
160. Wang K et al (2009) Molecular engineering of DNA: molecular beacons. Angew Chem Int Ed Engl 48(5):856–870
161. Mirkin CA (2010) The polyvalent gold nanoparticle conjugate-materials synthesis, biodiagnostics, and intracellular gene regulation. MRS Bulletin 35(7):532–539

Properties of Quantum Dots: A New Nanoprobe for Bioimaging

39

Chunyan Li, Bohua Dong, and Qiangbin Wang

Introduction

Quantum dots (QDs) are semiconductor nanoparticles with diameters ranging typically from 1 to 10 nm, comprising some hundreds to a few thousands of atoms of II and VI elements (e.g., CdSe and CdTe) or group III and V elements (e.g., InAs and InP). Bulk semiconductors are materials with a relatively small band gap between the valence and conduction bands; electron (e^-) in them can be excited from the valence to the conduction band by supplying an amount of energy, leaving a hole (h^+) in the valence band. In certain cases, relaxation of an electron leads to the release of band gap energy in the form of light (fluorescence). As a result of their small size that is usually below the dimensions corresponding to a bound electron–hole pair (exciton), the electronic and optical properties of QDs change with respect to the bulk material. In particular, the band gap and quantization of the energy levels to discrete values increase with decreasing particle size. This phenomenon has been discovered in the early 1980s and is commonly called "quantum confinement effect" [1, 2].

One of the most important consequences of quantum confinement is the possibility to tune the fluorescence wavelength of QDs by changing their size. Besides size-controlled fluorescence, the QDs have other unique photophysical properties, such as high-fluorescence quantum yields; high molar extinction coefficients [3, 4]; broad absorption with narrow, symmetric emission peak; large effective Stokes shifts; and high photostability [5–8]. These unique properties have made QDs potential candidates in many applications, especially for biomedical field; the QDs have become one of the dominant classes of imaging probes.

C. Li • B. Dong • Q. Wang (✉)
Division of Nanobiomedicine, Suzhou Institute of Nano-Tech and Nano-Bionics, Chinese Academy of Sciences, Suzhou, Jiangsu, China
e-mail: qbwang2008@sinano.ac.cn

QDs, as highly fluorescent probes, play an important role in bioimaging due to better sensitivity, longer stability, good biocompatibility, and minimum invasiveness. QD-based ex vivo nanosensors and in vivo imaging are both critical for future optimization in theranostics. Ex vivo diagnostics in combination with in vivo diagnostics can markedly impact future cancer patient management by providing a synergistic approach that neither strategy can provide alone. After further development and validation, QD-based approaches (both ex vivo nanosensor and in vivo imaging) will eventually be able to predict which patients will likely respond to a specific disease therapy and monitor their response to personalized therapy. With their capacity to provide enormous sensitivity, throughput, and flexibility, QDs have the potential to profoundly impact patient management in the future.

Preparation and Surface Functionalization of Quantum Dots (QDs)

The synthesis of QDs was first reported in 1982 by Efros [9] and Ekimov [10] who prepared semiconductor nanocrystals and microcrystals in glass matrices. Since then, a wide variety of methods have been developed for the fabrication of QDs in different media, including organic solvents, aqueous solution, and molecular films deposition onto solid substrates [11–15]. Generally, these approaches to synthesis of QDs can be divided into two main classifications: the top-down approach and bottom-up approach. In the first approach, some physics technologies are used to reduce the size of a bulk semiconductor to obtain the nanometer-sized material, for example, nanolithography, lithography, and electrochemical cave. For the second approach, an important fabrication of QDs is colloidal synthesis in which the molecular or ionic precursors react together in solution media to produce the QDs as colloids. So far, the colloidal method has become the most popular route for synthesis of QDs with controlled sizes and optical and electronic properties. This chapter will focus on the colloid synthesis and surface functionalization of QDs and their unique optical properties. In the following sections, the colloid synthesis of QDs will be divided into two categories: organic method and aqueous method, which are two main methods to synthesize QDs with desirable optical properties. The surface functionalizations of QDs including water solubilization and biofunctionalization are reviewed in the next section. Finally, an important strategy involving one-step in situ preparation and functionalization of QDs is introduced.

Organic Method

The breakthrough in preparing high-quality QDs with excellent optical properties came up when Bawendi and coworkers [16] developed the famous synthesis strategy involving organometallic synthesis in hot coordinating solvents, which
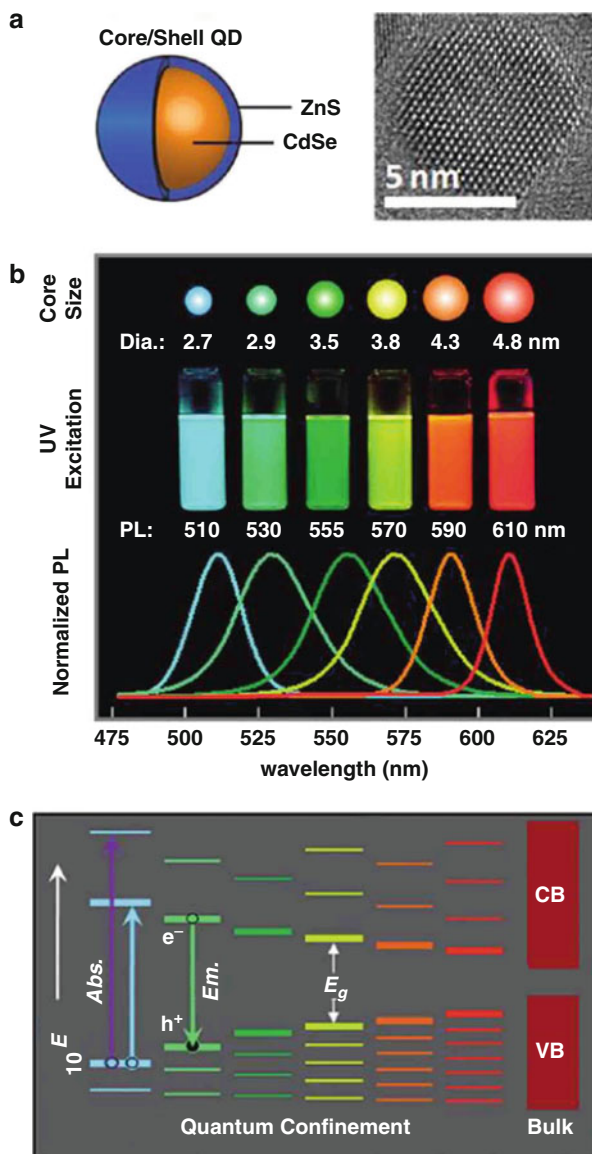
yielded QDs with highly crystalline, narrow size distributions and controlled
morphology. From then on, the synthetic chemistry of QDs advanced quickly,
generating several classic Cd-based QDs including CdSe, CdS, CdTe, and their
core-shell structure QDs with varied morphology, sizes, and structures that were
then used in wide application fields due to their unique optical properties. By
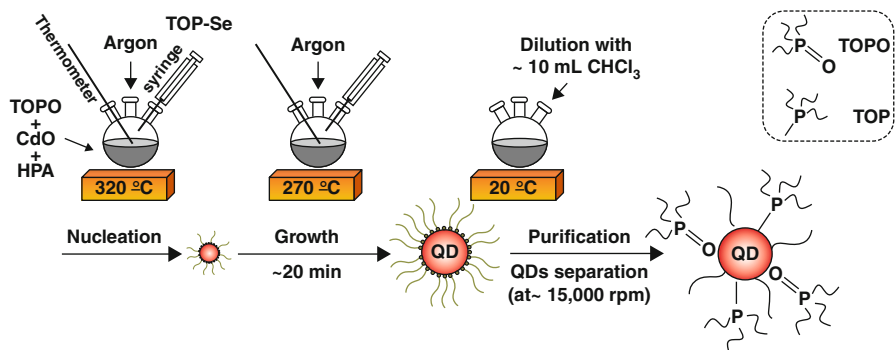controlling the size of QDs, their band gap and optical properties could be turned
due to the quantum size effect, as shown in Fig. 39.1.

Fig. 39.2 Schematic illustration of a typical synthesis process of CdSe QDs by organic method (Reproduced with permission from [18], Copyright © 2007, Elsevier)

The synthesis of highly monodisperse QDs by this organic method is based on the decomposition of molecular precursors. Under vigorous stirring and the absence of moisture and oxygen, an appropriate metallic or organometallic precursor (e.g., cadmium, zinc, or mercury species) is rapidly injected into the corresponding chalcogen precursor (e.g., selenium, sulfur, or tellurium species) in a coordinating organic solvent at high temperatures. The typical synthesis route for CdSe QDs is showed in Fig. 39.2. The nucleation process of QDs takes place rapidly, and the QDs then begin further growth. The type and ratios of the starting solvent/ligand mixtures, reaction temperature, reaction time, and aging period could strongly influence on the growth kinetics, which further decided the size and morphology of the obtained QDs [19, 20], as shown in Fig. 39.3.

Although the organometallic synthesis is very effective route for the synthesis of high-quality QDs, some disadvantages still exist in this period. For example, this method often involves complicated procedures and air-free manipulation and used some toxic and expensive precursor and surfactants like Cd(CH$_3$)$_2$, tri-n-octylphosphine oxide (TOPO), and tri-n-octylphosphine (TOP), resulting in the limitation of large-scale synthesis and a concern for environment. In 2001, Peng et al. used CdO instead of Cd(CH$_3$)$_2$ as cadmium precursor to synthesize CdSe, CdS, and CdTe QDs [21], which was regarded as a significant step forward. Since then, some other modified routes were developed for green synthesis of QDs. In 2005, Cao group proposed phosphine-free synthesis methods for CdSe QDs [22]. They used selenium powder as the precursor in a one-step reaction: selenium powder becomes soluble in 1-octadecene (ODE) above 190 °C and starts to react with the cadmium myristate Cd precursor at higher temperatures. This phosphine-free synthetic route does not require the injection of precursors into the hot reaction medium and is therefore more facile and green. Specially, the as-synthesized QDs processed narrow distribution and zinc blende crystal structure. The temporal evolution of the optical properties of the CdSe QDs during synthesis is shown in Fig. 39.4.
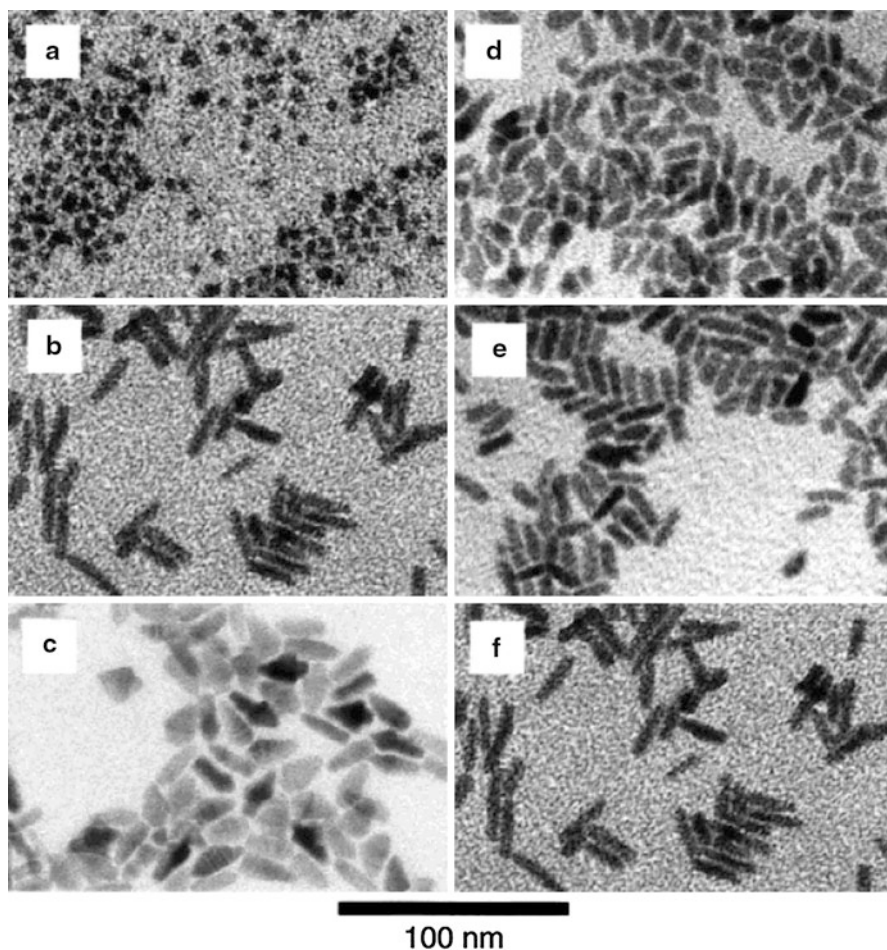
Fig. 39.3 TEM images of the single-injection experiments. All of the surfactant ratio experiments (**a–c**) used an injection volume of 2.0 mL of stock solution. The surfactant ratio was increased from (**a**) 8 to (**b**) 20 to (**c**) 60 % HPA in TOPO. For the injection volume experiments (**d–f**), 20 % HPA in TOPO was used, as it was found to provide optimal rod growth conditions. The injection volumes used were (**d**) 1.0, (**e**) 1.5, and (**f**) 2.0 mL. Greater injection volume favors rod growth (**d–f**) (Reproduced with permission from [19], Copyright © 2000, American Chemical Society)

Recently, a so-called single-source precursor method based on organic synthesis has been proved to be very facile and highly effective for generating many nanocrystals including QDs. The single-source precursor contained both the desired metal and corresponding chalcogen elements, which can decompose under a certain temperature to yield QDs. In 2010, Wang group used Ag(DDTC) [$(C_2H_5)_2NCS_2Ag$] as single-source precursor to prepare high-quality Ag_2S QDs (Fig. 39.5) [23]. The obtained Ag_2S QDs exhibited excellent NIR-II emission indicating their potential application in biomedical fields. Nowadays, organic
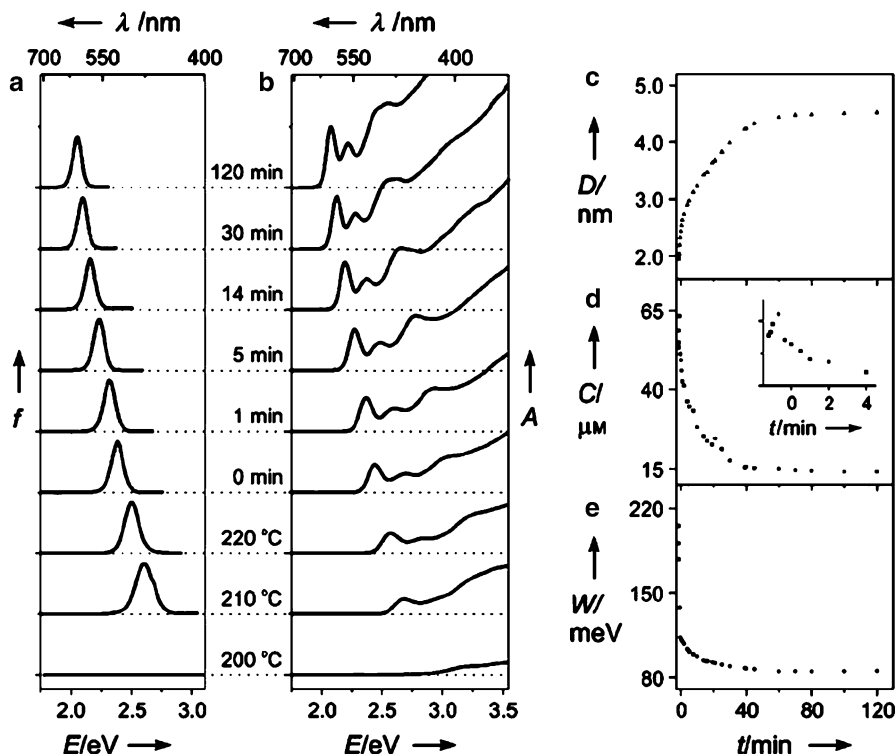
Fig. 39.4 Temporal evolution of (**a**) the fluorescence (F) spectrum, (**b**) the absorption spectrum, (**c**) the diameter (D) of the nanocrystals, (**d**) (and *inset*) the concentration (C) of the nanocrystals, and (**e**) full width at half maximum (FWHM) of the fluorescence spectrum during the CdSe synthesis (Reproduced with permission from [22], Copyright © 2006, John Wiley and Sons)

method and their modified routes have been proved to be an effective strategy for the controlled preparation of high-quality QDs. By controlling the size and composition, the photoluminescence (PL) spectrum of QDs can be tuned from UV-visible to NIR-II region involving the several classic QDs (CdS, CdSe, CdTe, PbS, Ag_2S, PbSe, etc.), indicating their potential applications in bioimaging field.

Aqueous Method

Compared with the organic method, the synthesis of QDs in aqueous solution is more facile and environmentally friendly, and the prepared QDs possess good water solubility and biological compatibility showing their superiority to the hydrophobic QDs synthesized by organometallic method. Thus, the synthesis of QDs by an aqueous route is studied and developed rapidly. Generally, the QDs synthesized by aqueous method are CdTe QDs. Weller et al. first reported the synthesis and characterization of thiol-stabilized CdTe QDs in 1996 [24].
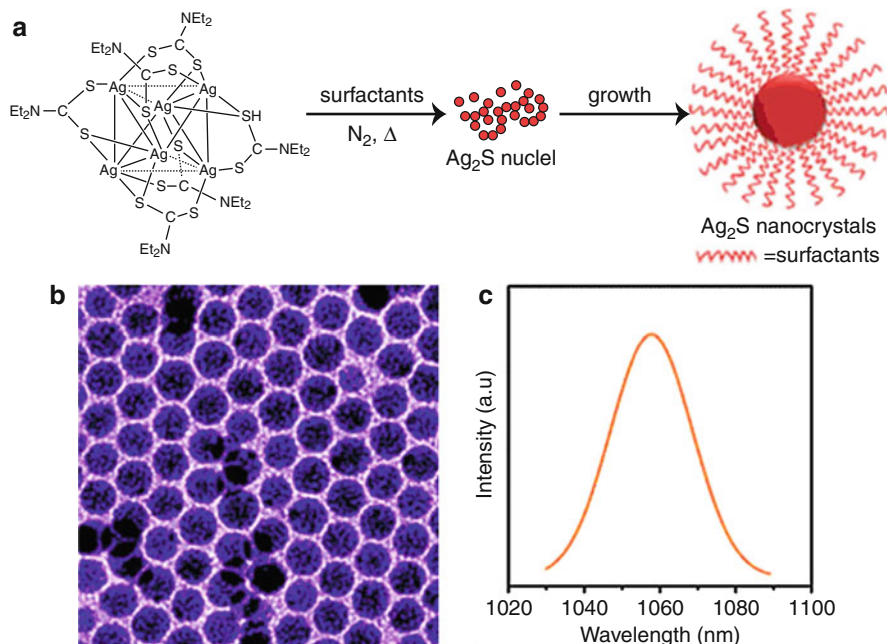
Fig. 39.5 Scheme of synthesis from a single-source precursor of Ag(DDTC) (**a**) TEM images (**b**) and PL spectrum of Ag_2S NIR QDs (**c**) (Reproduced with permission from [23], Copyright © 2010, American Chemical Society)

In their synthesis, $Cd(ClO_4)_2 \cdot 6H_2O$ is dissolved in water, and an appropriate amount of the thiol stabilizer is added under stirring, followed by adjusting the pH by NaOH solution. The solution is placed in a flask fitted with a septum and valves and is deaerated by N_2 bubbling. Under stirring, H_2Te gas as Te source is injected into above solution by slow nitrogen flow. CdTe precursors are formed at the stage of Te precursor addition, and then nucleation and growth of CdTe QDs proceed upon refluxing at appropriate temperature. A schematic drawing of typical synthesis route for CdTe QDs is shown in Fig. 39.6.

The PL quantum yield and wavelength of CdTe QDs prepared by the aqueous method can be controlled by parameters during the synthesis, such as precursor concentration, Cd/thiol stabilizer, the ratio of Cd/Te, and pH value. By choosing a different thiol stabilizer, the optical properties of CdTe QDs could also be tuned. For example, PL spectra of TGA-capped CdTe QDs are tunable in the range of 500–700 nm, while those of MPA-capped QDs are tunable between 530 and 800 nm [26]. Typical absorption and PL spectra of size-selected fractions of TGA- and MPA-capped CdTe QDs are shown in Fig. 39.7. In later years, many groups focus their work on the aqueous synthesis of QDs and contribute their effort on the improving the method to obtain high-quality water-soluble QD. Some other new types of QDs including HgTe, $Cd_xHg_{1-x}Te$, ZnSe, and ZnSe:Mn [27–30]
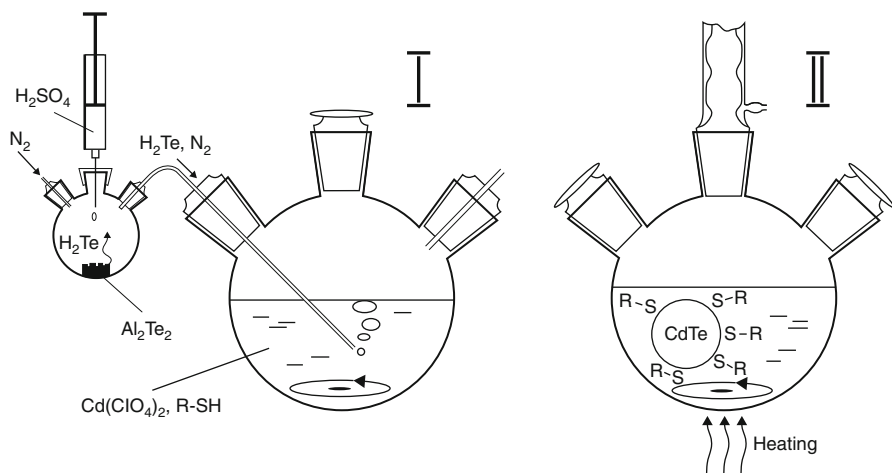
Fig. 39.6 Schematic presentation of the synthesis of thiol-capped CdTe nanocrystal by aqueous method (Reproduced with permission from [25], Copyright © 2002, American Chemical Society)
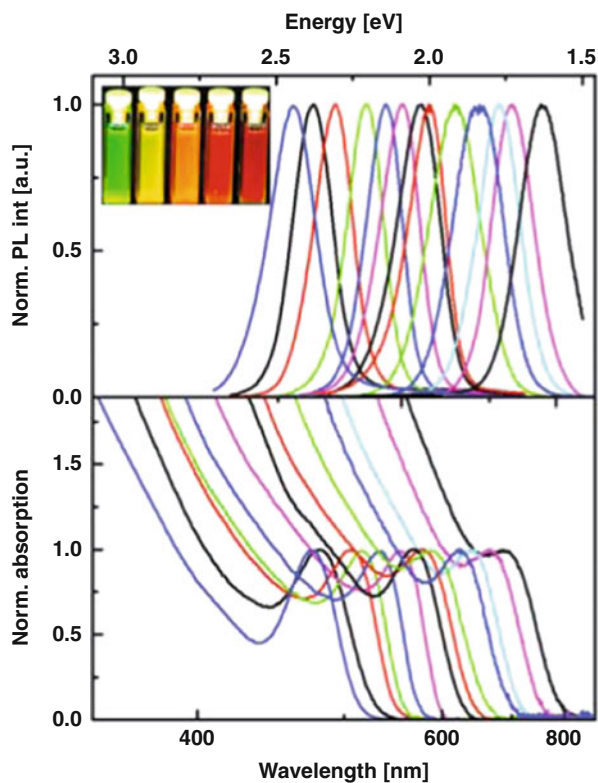

Fig. 39.7 A set of typical PL and absorption spectra of TGA-capped and MPA-capped CdTe QDs with tuned PL emission range from visible to near-infrared. The *inset* shows a photograph of emitting CdTe QDs under UV lamp excitation (Reproduced with permission from [26], Copyright © 2007, American Chemical Society)

are also synthesized and studied. Although the QDs prepared by aqueous method usually are water-soluble and can be directly used for biomedical applications, it has to be noted that these QDs still disadvantage, such as low PL QYs or poor crystallinity due to the low-temperature reaction system.

Surface Functionalization of QDs

Unlike the QDs synthesized in aqueous medium having good water solubility, the high-quality QDs are prepared using organic method and have no intrinsic aqueous solubility due to the surface hydrophobic ligands. Thus, in order to be used for biological application, these hydrophobic QDs must be made water-soluble. Up to now, several different approaches have been developed to impart the hydrophobic QDs with good water solubility, including ligand exchange, encapsulating the hydrophobic QDs with amphiphilic molecules, which are shown in Fig. 39.8.

The first approach involves the substitution of hydrophobic surface groups of QDs with hydrophilic ones through ligand exchange. The used hydrophilic ligands have to present both a surface-anchoring group (e.g., thiol) to bind to the surface of QDs and a hydrophilic end group (e.g., carboxyl or hydroxyl) to achieve water solubility. To date, mercaptoacetic acid (MAA), mercaptopropionic acid (MPA), and 11-mercaptonudecanoic acid (MUA) [32–34] have successfully been employed to replace the original hydrophobic ligands to transfer the QDs into water. However, these mono-thiol ligands tend to detach from the QD surface causing QD aggregation, which will compromise the fluorescence efficiency and photochemical stability of QDs. To improve long-term stability of QDs, using dithiol ligands instead of mono-thiol ligands is proposed. The dithiol ligand dihydrolipoic acid (DHLA) was used for the preparation of water-soluble QDs with long-term stability [35–37]. The DHLA ligands provide stable interactions with the QD surfaces due to the bidentate chelate effect of the dithiol groups. Other thiol-containing materials, such as cysteine and peptides, were also used as exchanged ligand to synthesize water-soluble QDs [37, 38].

A more robust ligand exchange approach involves formation of polymerized silica shells on the QD surface [39, 40]. In this procedure, for example, 3-(mercaptopropyl) trimethoxysilane (MPS) is used to displace the native organic molecules. And then, silanol groups are hydrolyzed and linked with each other producing stable and compact silica/siloxane shell that will render QDs soluble in intermediate polar solvents (e.g., methanol or dimethyl sulfoxide). After further reaction with bifunctional methoxy compounds, the obtained QDs coated with silica shell could be soluble in aqueous media. Silica has the advantage of being transparent, chemically robust, and opening the possibility for a wide variety of surface functionalization thanks to their large number of available functional trimethoxy- and triethoxysilanes.

The alternative approach to make QDs water-soluble is to preserve the native organic coating and encapsulate the hydrophobic QDs with amphiphilic molecules such as
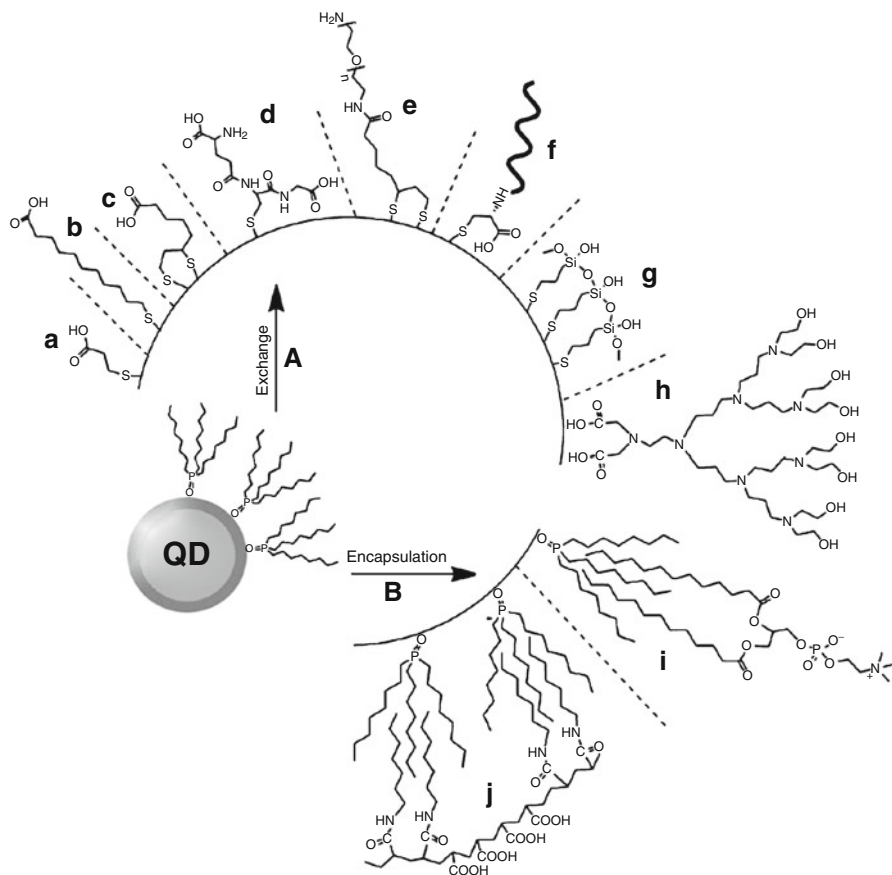
Fig. 39.8 Modification of semiconductor QDs with functional encapsulating layers for water solubilization and preservation of luminescence properties and/or secondary covalent modification of the surface with biomolecules. (**a**) Exchange of the organic encapsulating layer with a water-soluble layer; (*a–d*) thiolated or dithiolated functional monolayers, (*e*) glutathione layer, (*f*) cysteine-terminated peptide, (*g*) thiolated siloxane, (*h*) carboxylic acid-functionalized dendrone. (**b**) Encapsulation of QDs stabilized with an organic encapsulating layer in functional bilayer films composed of (*i*) a phospholipid encapsulating layer and (*j*) a diblock copolymer (Reproduced with permission from [31], Copyright © 2008, John Wiley and Sons)

polymers or phospholipids [41, 42]. The hydrophobic part of this molecule interacts with alkyl chain of surface ligands, while the hydrophilic chain faces outwards, rendering the QDs water-soluble. This coating does not disturb the surface passivation layer; thus, the obtained water-soluble QDs retained their optical properties after transfer to aqueous media.

For their application in bioimaging and therapy, including tumor-targeted imaging, multimodal imaging, and photodynamic therapy (PDT), the conjugation of QDs with different biomolecules including proteins, peptides, nucleic acids, or other biomolecules is required. Several approaches have been developed for

conjugation of QDs with biological molecules, which have been reviewed by recent important papers [35, 36]. Generally, the conjugation approaches can be divided into two categories: noncovalent and covalent conjugation [43].

One of the most simple and effective way of linking biomolecules to QDs is covalent bond formation between reactive functional groups. By activating the carboxyl groups on the QD surface in a 1-ethyl-3-(3-dimethylaminopropyl) carbodiimide hydrochloride (EDC) and N-hydroxysuccinimide sodium salt (sulfo-NHS) in buffer, carboxyl-terminated QDs can react with biological molecules containing amine groups, such as antibodies, diamino PEG, FA-chitosan, and DNA. This conjugation is also widely used to link proteins to QDs, because it does not require additional chemical modification of proteins, retaining their natural structure [43]. However, this method still has limitations, for example, the molecular orientation of the attached proteins cannot be controlled; moreover, the EDC reaction often produces intermediate QD aggregation due to cross-linking between numerous reactive sites on QDs and proteins [44]. Another common covalent bonding method is the conjunctions of amine-terminated QDs with sulfhydryl coupling. For example, after the reduction by dithiothreitol (DTT), the antibodies have sulfhydryl groups which could be conjugated to amine-terminated QDs, using heterobifunctional cross-linkers, such as succinimidyl 4-(N-maleimidomethyl) cyclohexane-1-carboxylate (SMCC). This reaction yields stable QD-ligand complexes with controlled ligand orientation.

Besides covalent bonding to organic capping ligands of QDs, biomolecules coating polyhistidine tags (HIS) or thiol groups can bind directly the surface of QDs via coordination with metal atoms of the QDs. For example, by adding a HIS tag to proteins, antibodies, short peptides, and DNA, these biomolecules can be assembly linked to the surface of QDs. It has to be noted that the obtained QDs usually exhibit reduced PL QYs and stability, due to the direct interaction of biomolecules with QDs surface.

Another noncovalent conjugation involves the electrostatic interaction between the positively charged biomolecules and the negatively charged QD shell. For example, the protein was engineered with a positively charged domain (e.g., polyhistidine) and then interacted electrostatically with the negatively charged surface of the QDs. The conjugated QDs prepared by this method exhibit good water solubility and high QYs; however, this approach is often limited to conjugation of specific ligands. Moreover, these conjugated QDs are not suitable for application in complex biological environment, as electrostatic interactions generally are not specific and strong enough.

One-Step In Situ Preparation and Functionalization of QDs

As mentioned in the above section, various strategies have been developed to obtain QDs with water solubility and bioconjugates, either by ligand exchange, silica coating, encapsulation of amphiphilic molecules, or noncovalent and covalent bioconjugation methods, but these usually require multiple steps to obtain the final

products with desired functionalization. Recently, Wang et al. develop a new and simple method of in situ preparation and functionalization of CdSe QDs and surface passivation by a thin ZnS shell in a single step [45]. This one-step in situ preparation and surface functionalization method is shown in Fig. 39.9, which illustrates the scheme of QD preparation (Fig. 39.9b) and its comparison to the conventional ligand exchange method (Fig. 39.9a). In this new method, the starting oleylamine-capped CdSe QDs were firstly synthesized, and then the CdSe/ZnS core-shell QDs capped with MPA are achieved in a single step by in situ ZnS shell formation and ligand capping. This method avoids a second-step ligand exchange after the core-shell formation and preserved high QY of the QDs with good water solubility and photostability. Furthermore, the obtained CdSe/ZnS core-shell QDs are functionalized by MPA, allowing the biomolecules with a thiol group (e.g., antibody) to be directly conjugated with QDs in a single step.

Wang et al. further develop a simple and robust one-step method for creating stable, water-soluble QDs with desirable bioconjugates [46]. The process of QD functionalization with DNA is illustrated in Fig. 39.10. The starting oleylamine-capped CdSe QDs were prepared by low-temperature synthesis method [47, 48]. Coating of the CdSe core with a ZnS shell and capping of the surface with thiolated DNA oligonucleotides are achieved in a single-step one-pot reaction by mixing the oleylamine-capped QD core with Zn^{2+}, S^{2-}, and thiolated DNA all dissolved in dimethyl sulfoxide (DMSO). This new strategy is devised so that direct capping of QDs with thiolated DNA oligonucleotides could be achieved during the formation of core-shell QDs. This in situ functionalization of QDs with DNA avoids the cross-linking chemistry or the second-step ligand exchange after core-shell formation, which is more simple and efficient. The results demonstrate that a high DNA density on the QD surface is achieved and the high QY and stability of the QDs are preserved. Furthermore, many other types of biomolecules carrying a thiol or other ligands (e.g., peptides containing cysteine residues) could also be conjugated on the surface of QDs; thus, this simple and robust approach provides a broad range of QD bioconjugates for biomedical applications.

Unquestionably, there have been great progresses in the surface engineering and biofunctionalization of QDs. With the development of stable and biofunctional QD probes with high PL QY and tuned optical window from UV-visible to NIR-II region, these materials will provide exciting opportunities for biomedical applications including biomedical imaging, detection, and nanotherapy.

QD Probes for In Vitro Applications

Since the first demonstration of the biomedical potential of QDs in 1998 [32, 39], QD-based research has increased exponentially. In the last decade, QD-based probes have found numerous applications where traditional organic dyes and fluorescent proteins were previously the only tools available. And QDs have also
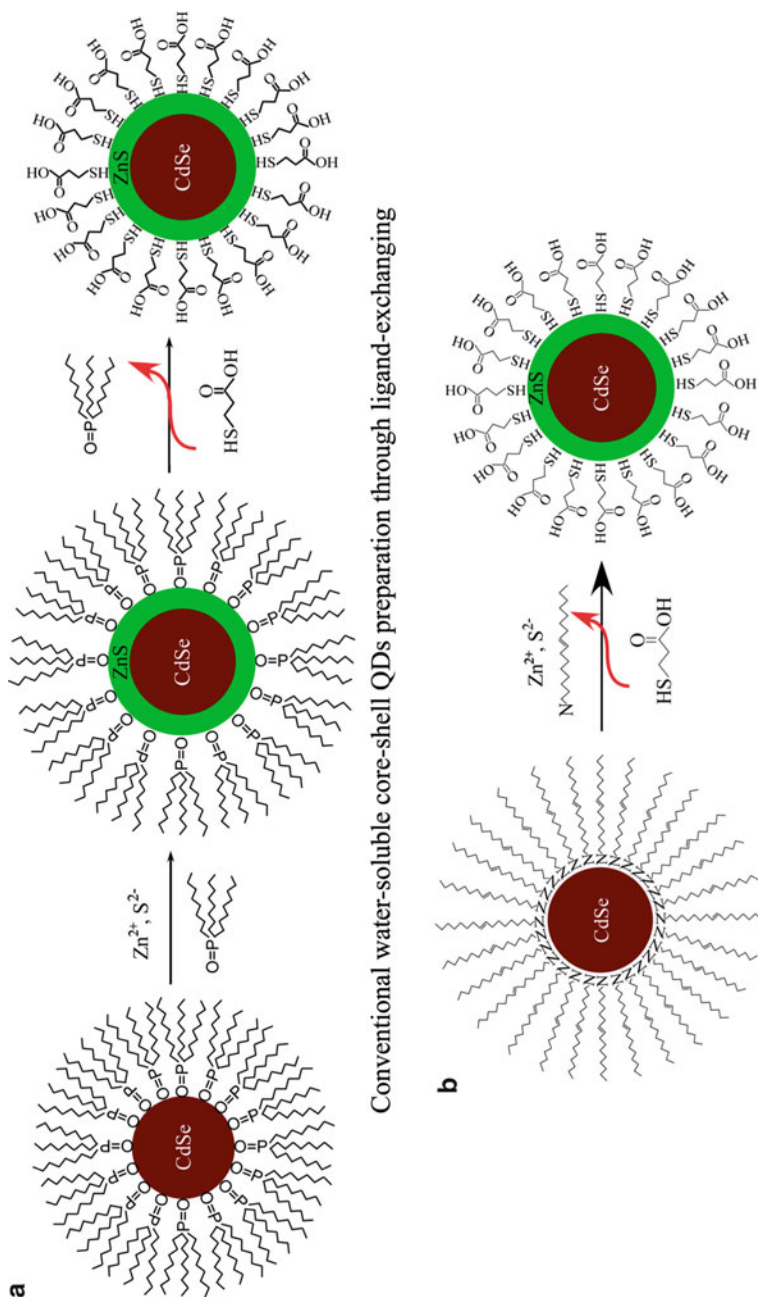
Fig. 39.9 Preparation of MPA-capped CdSe/ZnS core-shell QDs through **(a)** the conventional two-step surface passivation and ligand exchange method and **(b)** one-step in situ surface functionalization method (Reproduced with permission from [45], Copyright © 2007, American Chemical Society)
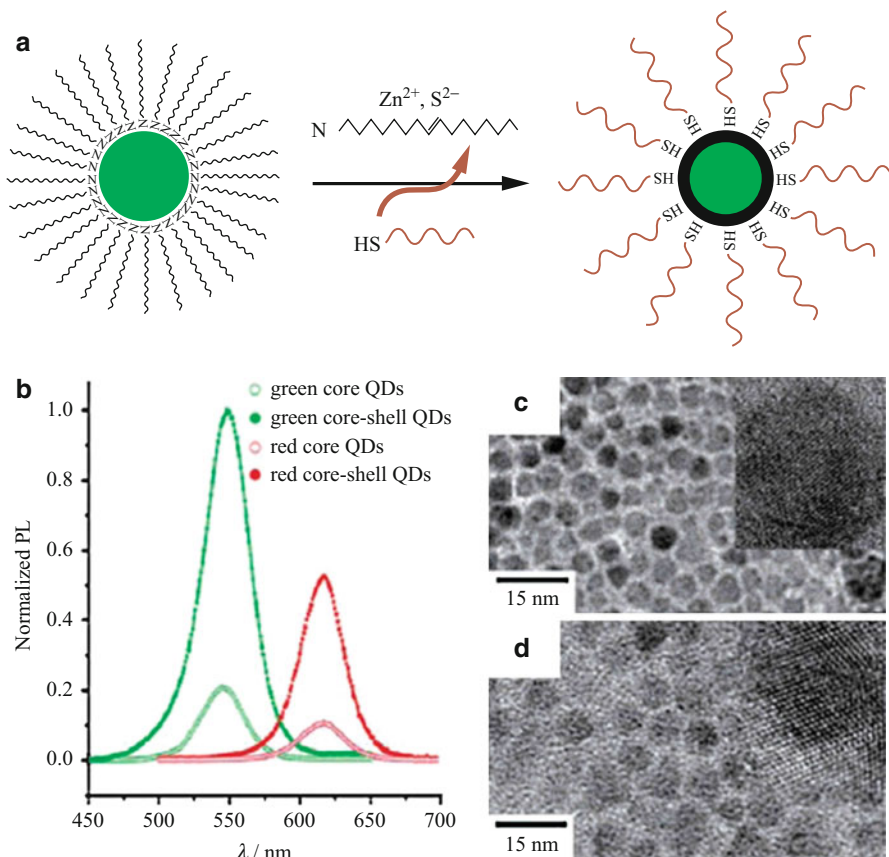
Fig. 39.10 (**a**) One-step in situ DNA functionalization of CdSe/ZnS core-shell QDs. (**b**) PL spectra of CdSe core QDs and the DNA-capped CdSe/ZnS core-shell QDs. Both the *green* and *red* QDs show a significant increase of the QY after growth of the ZnS shell and DNA capping, simultaneously. The intensities were normalized by *green* CdSe/ZnS core-shell QDs. (**c**, **d**) TEM images of *green* and *red* core-shell QDs, respectively. Higher magnification images of individual *dots* are shown in the insets (Reproduced with permission from [46], Copyright © 2008, WILEY-VCH Verlag GmbH☐Co. KGaA, Weinheim)

allowed for complicated and difficult multiplexed cellular imaging and in vitro applications which were previously impossible given the limitations of fluorescent dyes and proteins. The major advantage of QDs is their strong resistance to photobleaching for a long period of time, which permits acquisition of images with good contrast and signal intensity. Most QDs are much brighter than organic dyes due to the combination of higher extinction coefficients and higher quantum yields. In addition, significant improvements in QD synthesis, surface engineering, and biofunctionalization techniques permit QDs to use in a vast number of in vitro and cell-based applications.

Cellular Labeling

In recent years, QDs have been receiving increased attention for its implications in the area of cellular labeling. Various subcellular components and molecules of the cell have been labeled and visualized with biofunctionalized QDs, such as the mitochondria, Golgi apparatus, endoplasmic reticulum, microtubules, cell membrane, nucleic acids, proteins, ions, and metabolites [49–53]. Different types of QDs have been delivered into live cells through various approaches such as endocytosis [54], peptide-induced transport [55], and microinjection [56]. Wu et al. reported the utility of QD-streptavidin and QD-antibody bioconjugates for labeling of membrane-associated Her2 receptor and of a nuclear antigen in breast cancer cells (Fig. 39.11) [57]. Using the same strategy, different membrane proteins and receptors of cells have also been labeled with QDs including prostate-specific membrane antigen (PSMA), HER kinases, glycine receptors, serotonin transport proteins, P-glycoprotein, and band 3 protein [44, 54, 58–61]. Derfus et al. reported that the CdSe/ZnS QDs conjugated with localization sequence peptides which can target the nucleus and mitochondria in living cells [62]. In addition, besides mammalian cells, biologically conjugated quantum dots can also be used for labeling of microorganisms. The conjugated CdSe QDs were used for strain and metabolism-specific microbial labeling for a wide variety of bacteria and fungi [63]. Similarly, Kloepfer et al. reported that lectin-coated QDs were used to label gram-positive bacteria [64].

Notably, compared with organic dyes, QDs with excellent photostability are not only useful for quantitative analysis and three-dimensional reconstructions but also suitable for monitoring cellular dynamics such as movement, differentiation, and fate [54, 56, 60, 65]. Jaiswal et al. have utilized QD endocytic uptake and specific cell surface labeling of P-glycoprotein transporters over the course of 14 h [54]. It shows that the QDs within the endosomes of live HeLa cells and *Dictyostelium discoideum* amoebae could be monitored over a week with negligible loss of QD fluorescence. Osaki et al. have also studied the cellular endocytosis with different sizes of CdSe QD-conjugated sugar balls with different sizes [66]. They compared the particle sizes ranging from 5 to 50 nm and found that endocytosis was highly size dependent.

Fluorescent In Situ Hybridization (FISH)

Fluorescent in situ hybridization (FISH) is a powerful technique for the study of structural cytology of the cell nucleus, which can visualize and map cellular genetic material in order to quantify gene copy numbers in cancer cells that have abnormal gene amplification [67, 68]. Based on specific base pairing, DNA or oligonucleotides which have been modified with QDs as a fluorescent probe can retain their ability to form complementary sequences [56, 69–73]. Tholouli et al. reported the preparation of QD-oligonucleotide probes by biotin-streptavidin linkage for FISH-based studies of mRNA [74]. Compared with organic dyes, the QDs display
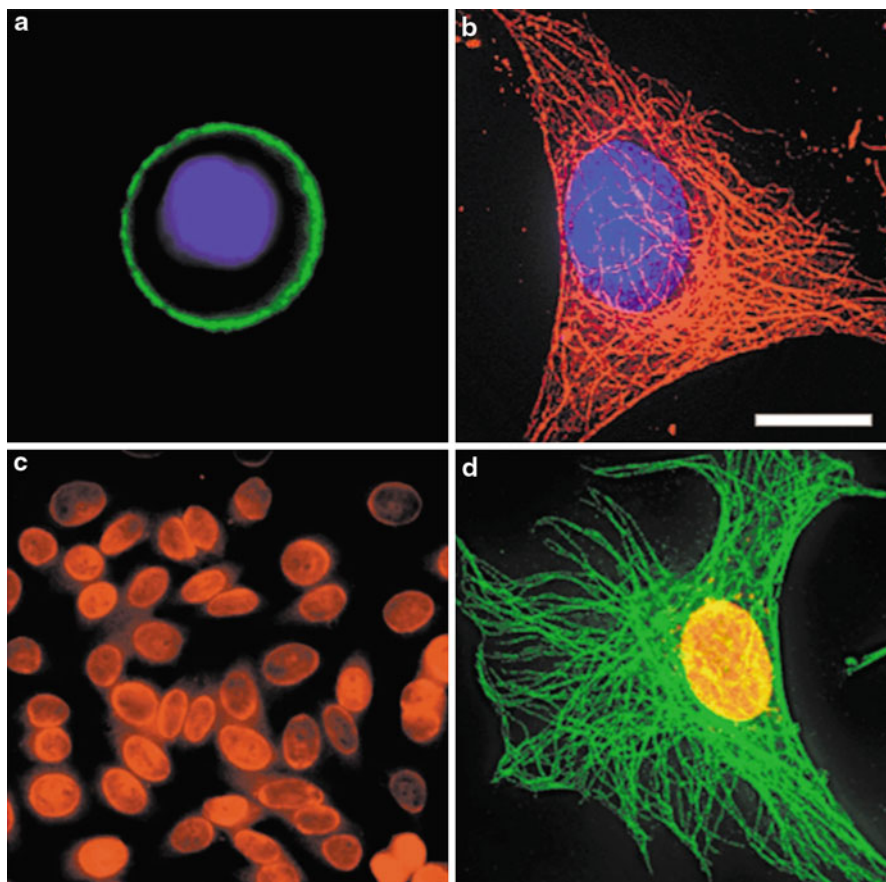
Fig. 39.11 Immunofluorescent labeling of cancer cells using QD probes. (**a**) QD-labeled secondary IgG (*green*) for labeling of membrane-associated Her2 receptors. (**b**) Microtubules were labeled with monoclonal anti-α-tubulin antibody, biotinylated anti-mouse IgG, and QD 630-streptavidin (*red*). (**c**) QD 630-streptavidin to label nuclear antigens. (**d**) Microtubules and the nuclear antigens were labeled with two different QD probes. The nuclei are counterstained with Hoechst 33342 (*blue*) in A and B (Reproduced with permission from [57], Copyright © 2003, Nature Publishing Group)

significantly brighter and more photostable fluorescence signals which allow for more stable and quantitative uses of FISH for research and clinical applications (Fig. 39.12) [73]. In addition, it has also been reported that the fluorescence intensity of QD-streptavidin-based FISH probes varied according to the pH of the final incubation buffer [75]. However, the exact mechanism of this varying fluorescence has yet to be clarified. Recently, direct multicolor imaging of multiple subnuclear genetic sequences using QD-based FISH probes was achieved in *Escherichia coli* [76].
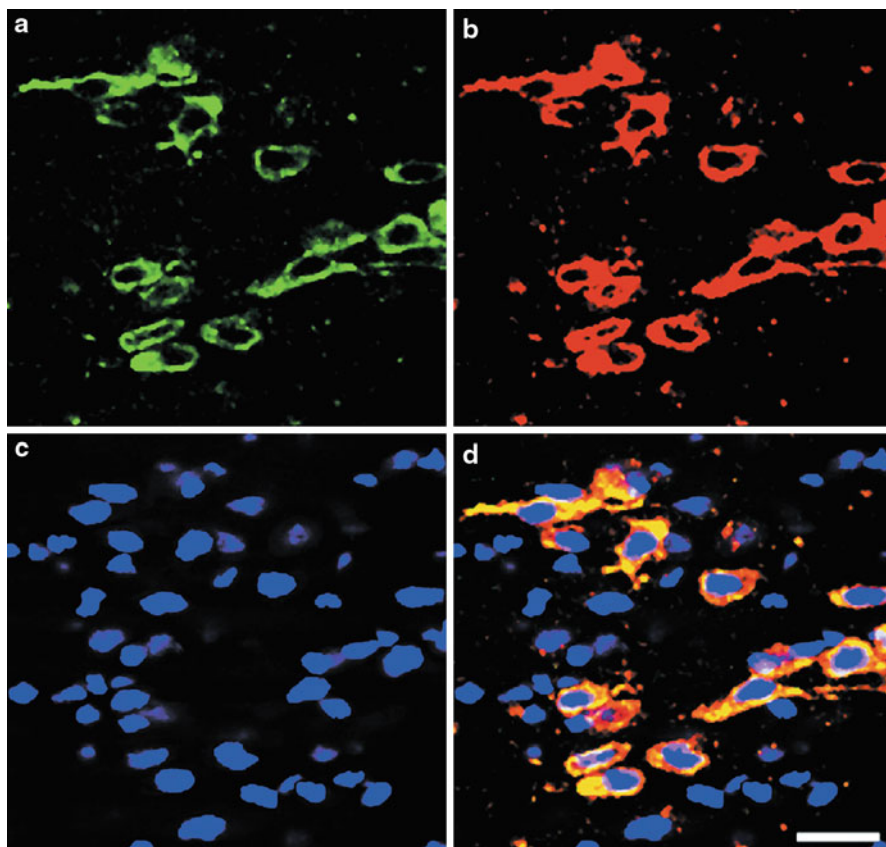
Fig. 39.12 Double labeling FISH using QD probes. *Vmat2* mRNA was detected with both QD525 (**a**) and QD585 (**b**) probes. DAPI (**c**) staining and overlayed images (**d**) are also shown Scale bar, 20 μm (Reproduced with permission from [73], Copyright © 2005, Oxford University Press)

Fluorescence Resonance Energy Transfer (FRET)

Fluorescence resonance energy transfer (FRET) is unique in generating fluorescence signals sensitive to molecular conformation, association, and separation in the 1–10 nm range, a scale correlating to the size of biological macromolecules. It is suited to measuring changes in distance, rather than absolute distances, making it appropriate for measuring protein conformational changes, monitoring protein interactions, and assaying of enzyme activity. These are several distinct advantages of using QDs for FRET applications. Firstly, narrow, size-tunable emission of QDs increases the spectral overlap with a specific acceptor dye. Secondly, compared with organic fluorophores, QDs have high-emission quantum yields and have chemical stability and photostability. Thirdly, FRET efficiency can be significantly improved
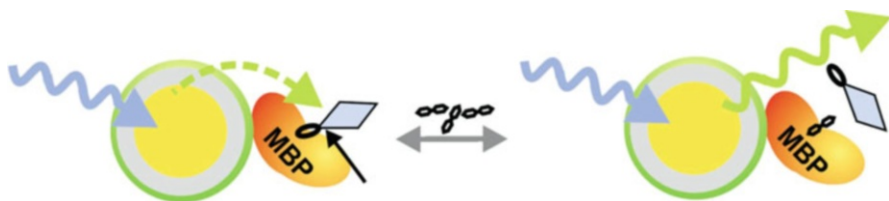
Fig. 39.13 Schematic illustration of QD-based FRET. QD560 is surrounded by an average of ∼10 MBP moieties; a single MBP is shown for simplicity. Formation of QD-MBP-β-CD-QSY9 (maximum absorption ∼565 nm) results in quenching of QD emission. Added maltose displaces β-CD-QSY9 from the sensor assembly, giving rise to an increase in direct QD emission (Reproduced with permission from [36], Copyright © 2003, Nature Publishing Group)

by adjusting the proportion of donors and acceptors [36, 77]. Bawendi et al. first reported QDs for FRET application [78]; since then numerous studies have demonstrated the use of QD-based FRET in biological systems [33, 36, 77, 79–85]. Medintz et al. designed two maltose-binding assays based on FRET from CdSe/ZnS QDs to the organic dye acceptors or through a two-step FRET mechanism that overcomes inherent QD donor-acceptor distance limitations (Fig. 39.13) [36]. Similarly, Shi et al. reported quantum dots FRET-based protease sensors by using QDs as fluorescence resonance energy transfer donors [85].

FRET analysis using QDs can provide qualitative molecular association information and has great potential as nanoscale biosensors, but there are also intrinsic limitations with QDs for FRET applications. Among them, the heterogeneity in QD size is the major problem which can affect the precision of single-molecule FRET analysis. Single QD blinking can also significantly affect FRET efficiency and accuracy [86]. In addition, QDs are superior FRET donors compared with organic dyes, but they are not ideal FRET acceptors [87]. Most of biosensor systems involved FRET, where QDs acted as donors and organic fluorophores acted as acceptors [36, 85].

Other Applications of QDs In Vitro

In addition to the above mentioned functions, QDs have also been employed for other applications. "phagokinetic tracks" is a useful method for studying cell motile behavior [88]. Assaying the level of tumor cell motility is an excellent indicator of metastatic potential. Parak et al. have developed an efficient and sensitive two-dimensional cell motility assay to image the phagokinetic uptake of colloidal CdSe/ZnS/SiO$_2$ semiconductor nanocrystals [89]. When cells move across a thin, homogeneous layer of QDs, they engulf and uptake the nanocrystals and leave behind a fluorescent-free trail (Fig. 39.14). By measuring the ratio of trail area to cell area, we have discovered that it is possible to distinguish between noninvasive and invasive cancer cells lines. This technique has the potential to be used as a rapid, robust, and quantitative in vitro measure of metastatic potential.

Conjugation of luminescent quantum dots with antibodies has also been used for co-immunoprecipitation and Western blot analysis (Fig. 39.15) [90–92]. Compared
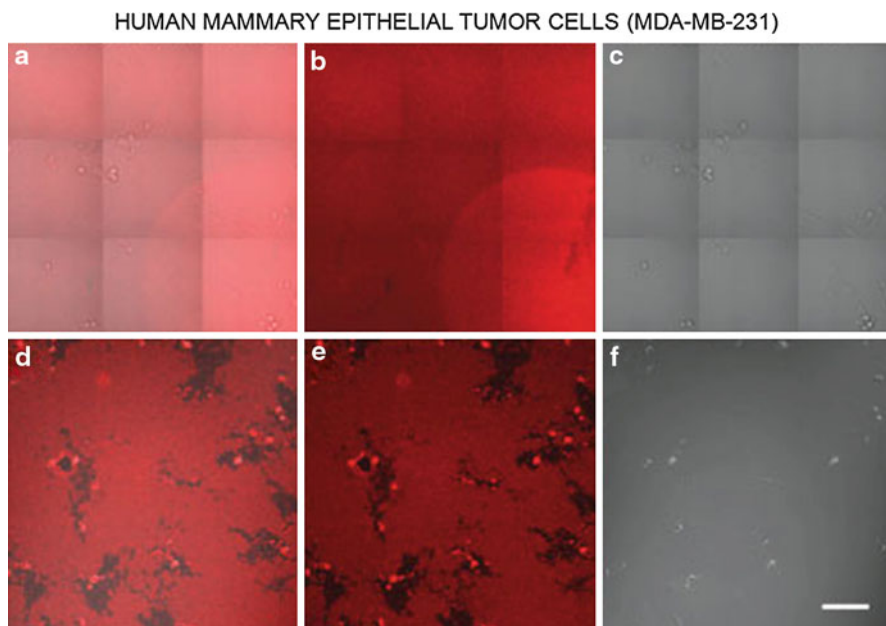
HUMAN MAMMARY EPITHELIAL TUMOR CELLS (MDA-MB-231)

Fig. 39.14 Phagokinetic tracks of human mammary epithelial tumor cells (MDA-MB-231) based on CdSe/ZnS/SiO$_2$ QDs (Reproduced with permission from [89], Copyright © 2002, John Wiley and Sons)
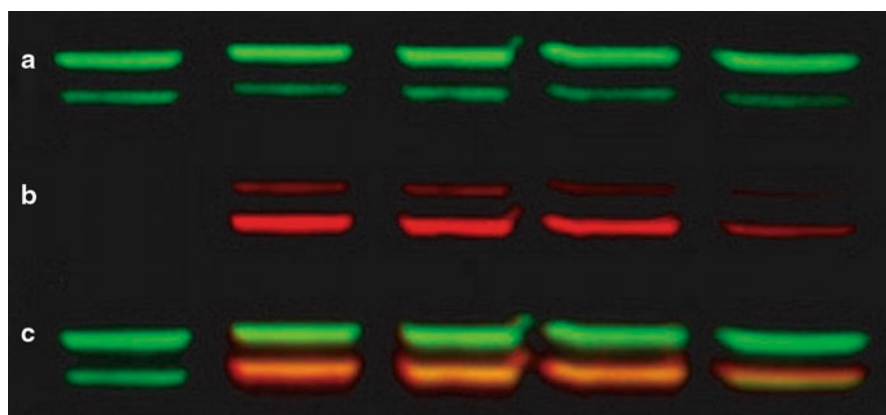

Fig. 39.15 Western blot of two proteins (**a**, **b**) using two QD-antibody conjugates. Overlay of the two images is shown in (**c**) (Reproduced with permission from [92], Copyright © 2005, Nature Publishing Group)

with traditional methods, QD-based probes can allow for simpler and faster image acquisition and quantification. In addition, QDs have also been used for fluorescence-activated cell sorting [93–97], tracking RNA interference [98], as well as detecting bacteria [99].

QD Probes for In Vivo Applications

In vivo fluorescence imaging promises to obtain more biological information on anatomical structure and mechanism of action at the whole-body level, which was more than what traditional in vitro imaging can attain. One of the main objectives of QD-based research is to eventually translate QDs for use in clinical applications such as high-resolution multiplexed vascular imaging and intraoperative image guidance in human body. Compared with the imaging in vitro, QDs as fluorescence probes for in vivo imaging need to overcome many challenges in complex organisms, such as toxicity, biodistribution, interaction with biomolecules, pharmacokinetics, as well as deep-tissue imaging. Experimental studies have revealed that two tissue optical windows exist for QD imaging in living animals (Fig. 39.16), one at 650–950 nm and another at 1,000–1,350 nm [100, 101]. QDs that emit in the NIR region are suitable for in vivo applications due to low tissue absorption, scattering, and tissue autofluorescence in this region which leads to high photon penetration in tissues [102, 103]. Significant improvements in QD synthesis, surface engineering, and biofunctionalization techniques combined with their photostability and brightness have made QDs powerful tools for in vivo imaging.

Cell Trafficking

Utilization of QDs for real-time cell tracking is one of the near future appealing applications. To reduce the photobleaching and nonspecific adsorption, single QD has been encapsulated in phospholipid block-copolymer micelles for embryo imaging [56]. After conjugation with DNA, QDs were directly injected into Xenopus embryos and QDs were found to be diffusely distributed throughout the cell during early stages of development while at later stages they mainly resided in cell nuclei. The fluorescence signal of QDs could be followed to the tadpole stage with little or no
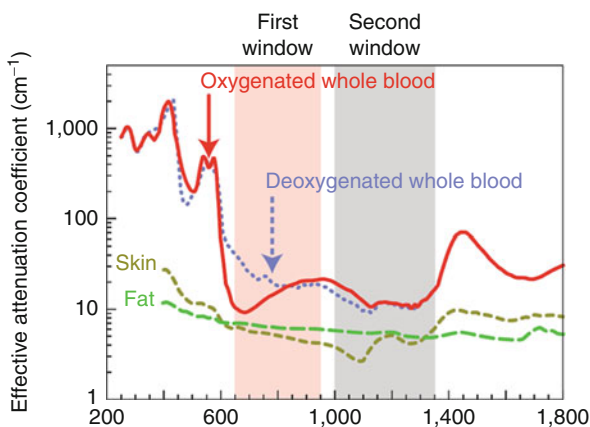

Fig. 39.16 Two optical windows in biological tissues (Reproduced with permission from [101], Copyright © 2009, Nature Publishing Group)

indication of cytotoxicity. QDs were also reported to have high fluorescent yield and robust photostability for successful imaging of zebrafish embryos [104]. In both studies, QDs were used as contrast agents in living organisms to demonstrate the efficacy of QDs for long-term studies. These findings have provided useful techniques in the fields of embryology, cell biology, as well as disease phenotyping and diagnosis.

Tracking cell migration (stem cells, tumor cells, leukocyte, etc.) will provide useful insights into the behaviors of the transplanted cells in vivo and the pathogenesis of diseases. QDs have also been used as cell markers to study extravasation in living mice. Simon et al. have utilized quantum dot nanocrystals as a fluorescent live cell tracker probe to dynamically track cancer cells after intravenous injection and observe that they extravasated into lung tissue [105]. The results show that QD-labeled cancer cells can permit in vivo imaging despite tissue autofluorescence. These QD-labeled cells could also be used to analyze the distribution of tumor cells in organs and tissues and to track different populations of cells. By using multiphoton laser excitation, five different populations of cells have been simultaneously identified.

Lymph Node Mapping

The sentinel lymph node (SLN) is one that first receives lymphatic drainage from the site of the primary tumor, and the sentinel node biopsy is very important for identifying the metastasis of cancer cells. To this end, identification of the SLNs has become a routine examination for cancer patients. However, evaluation of the lymphatic system is not easy due to the presence of complicated fine structures and the complexity of the physical structures of living organisms. Using QDs as fluorescent probes, NIR type II CdTe/CdSe QDs emitted at 850 nm were injected intradermally into live mice and pigs, respectively [106]. The results show that these QDs can rapidly migrate to local sentinel lymph nodes (SLNs) with negligible background signal, which permit image-guided resection of a one-centimeter deep lymph node in a pig (Fig. 39.17). This is the first demonstration of NIR QD-guided surgery by means of both the spectroscopic properties and the size effects of QDs. Since then, identification and resection of SLN in various locations of the body during operation have also been reported in mice [107, 108], rats [109–111], and large animals [112–114]. Besides SLNs, the potential of QDs for lymphatic system imaging has also been investigated. Zimmer et al. reported that small size (HD <10 nm) enables QD probes to escape SLN and travel along the lymphatic system to distant lymph nodes [107]. Using these QDs with tunable emission from 694 to 812 nm, they have achieved sequential mapping of up to 5 lymph nodes following subcutaneous injection.

Furthermore, multiplexed imaging is a useful strategy for simultaneous recognition of different organisms. The multicolor nature of QD probes makes it possible to investigate separate vascular systems in a multiplexed manner, providing insight into the intricate blood and lymph circulation networks within organs and tissues. The multiplexing capability of QDs has been exploited for in vivo imaging of 5 different lymphatic basins in mice (Fig. 39.18). Following intracutaneous injection of 5 types
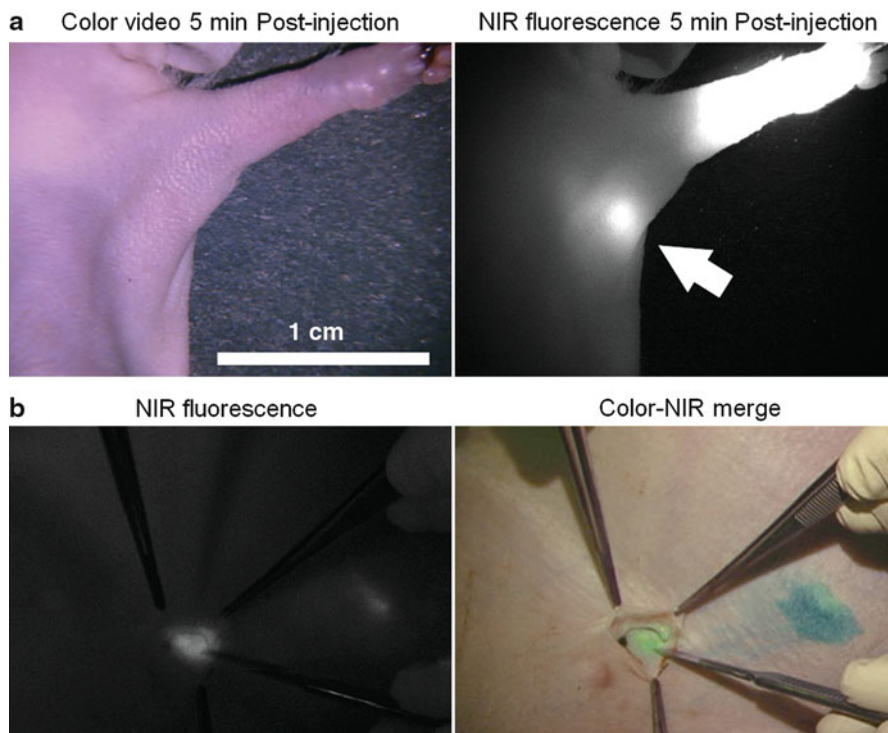
Fig. 39.17 Sentinel lymph node mapping using QDs. (**a**) Images of a mouse injected intradermally with type II NIR QDs in the left paw. (**b**) SLN resection using fluorescence image guidance in the pig (Reproduced with permission from [106], Copyright © 2004, Nature Publishing Group)

of polymer-coated carboxy QDs ranging in emission wavelength from 565 to 800 nm (HD 15–19 nm) into the paws, ears, and chin of mice, Kobayashi et al. have monitored the transport of QDs through lymphatic networks and accumulation in SLNs [115]. Further passage of QD probes to secondary draining lymph nodes was significantly inhibited, possibly due to nonspecific binding between negatively charged QD coating and proteins resulting in an increase in probe size. Recently, it was demonstrated that QDs injected into model tumors rapidly migrated to SLNs [116]. PEG-coated QDs with terminal carboxyl, amino, or methoxyl groups all similarly migrated from the tumor to surrounding lymph nodes. Passage from the tumor through lymphatics to adjacent nodes could be dynamically visualized through the skin, and at least two nodes could be typically defined. Imaging during necropsy confirmed QD confinement to the lymphatic system and demonstrated tagging of SLNs for pathology. Examination of the SLNs identified by QD localization showed that several of them contained metastatic tumor foci.

SLN mapping using QDs overcomes the limitations of currently available methods and provides highly sensitive, real-time image-guided dissection, which may permit potential mapping of SLNs and lymphatic flow in patients.
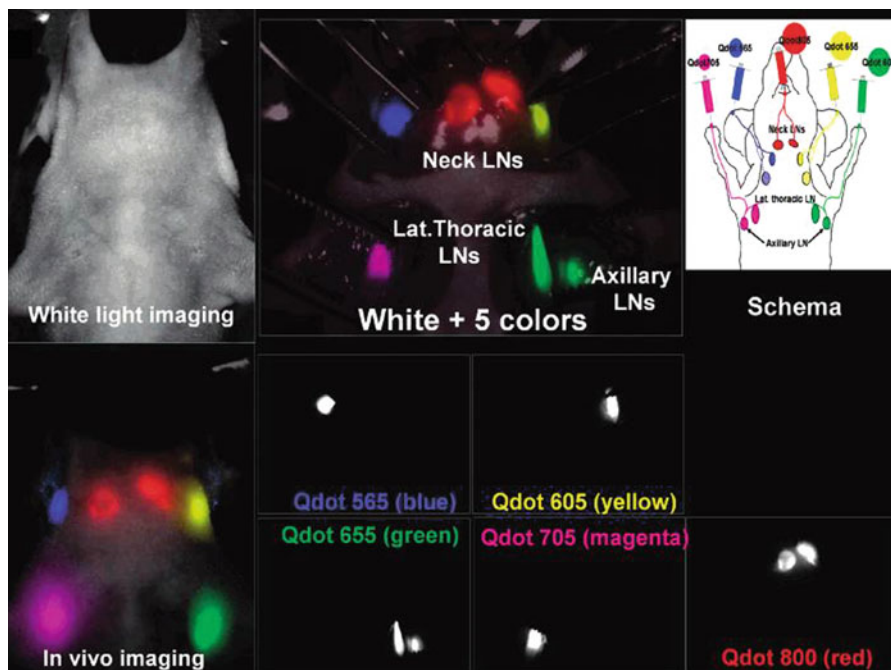
Fig. 39.18 Multiplexed in vivo and ex vivo imaging of different SLNs using QD probes (Reproduced with permission from [115], Copyright © 2007, American Chemical Society)

Vasculature Imaging

Changes in vascularization and vascular dysfunction have been implicated in many diseases, such as cardiovascular and kidney disease, as well as in many cancers. Vascular imaging provides information about the number and spacing of vessels, permeability of the vasculature, and functional abnormalities of the vessels. With such a great potential, the major design focus in engineering of QD contrast agents for vascular imaging should be placed on synthesis of non-fouling and possibly biodegradable coatings that will efficiently protect the QD core, evade RES uptake and renal filtration for the duration of experiment, and then enable eventual particle degradation and excretion. Further, engineering of fluorescence imaging systems suitable for deep-tissue in vivo imaging will be indispensable for the success of QD-based angiography.

Larson et al. have demonstrated the value of QD probes for the dynamic imaging of the blood vasculature of the skin and adipose tissue in live mice [117]. The relatively large size and high stability of polymer-encapsulated QDs have provided bright and persistent fluorescence contrast after intravenous injection. Visualization of blood vessels in the chick chorioallantoic membrane, a popular model for studying various aspects of blood vessel development such as angiogenesis, was recently achieved with QDs [118].

Two-photon imaging of vasculature through the skin of living mice has been reported with water-soluble CdSe/ZnS QDs [117]. QDs were dynamically observed in capillaries as deep as several hundred micrometers, and no blinking in solution was observed on the nanosecond to millisecond time scale. Compared to conventional methods using 70-kD FITC-dextran, QDs provided significantly more information at the same depth. Stroh et al. have combined two-photon intravital microscopy, blue-emitting QDs encapsulated in PEG-phospholipid micelles, and a transgenic mice model with GFP-expressing perivascular cells to study the morphology of the tumor vasculature [119]. Following systemic administration, QDs highlight the vessel boundary providing a clear picture of tumor vessel morphology while resisting extravasation for at least 30 min. In another report, coronary vasculature was imaged in vivo and the effects of tissue absorbance, scatter, and thickness on the performance of QDs were analyzed when embedded in biological tissue [100]. Using multiphoton microscopy, QDs can differentiate tumor vessels from perivascular cells and matrix better than traditional fluorescently labeled dextran vessel markers [119]. Multiphoton microscopy through gradient index lenses has also been used for minimally invasive, subcellular resolution imaging of cortical layer and hippocampus several millimeters deep in anesthetized live animals [120]. NIR CdMnTe/Hg QDs have been used for deep-tissue in vivo optical imaging [121]. QDs were grown in aqueous solution and coated with bovine serum albumin. After either subcutaneous or intravenous injection, these QDs were used as angiographic contrast agents for vessels surrounding and penetrating murine squamous cell carcinoma in mice. No significant photobleaching or degradation of QDs was observed even after an hour of continuous excitation. The stability of QDs combined with their time resolution of optical detection makes them attractive candidates for pharmacokinetic imaging studies.

In Vivo Targeted Imaging Using QDs

Targeted imaging of the specific organ or disease site (e.g., tumors) is important for disease diagnosis and therapy. However, QD-based targeted imaging in vivo remains a significant challenge due to the relatively large overall size (typically about 20 nm in diameter), short circulation time, the lack of specificity in heterogeneous physiological conditions, as well as pervasive foreign-particle clearance mechanisms. Recently, a series of tumor-specific probes have been reported for in vivo imaging. Based on the specific recognition of ligand-acceptor and antigen-antibody interactions, QDs conjugated with peptides, antibodies, and folic acid have been able to realize targeted imaging.

Peptide-Conjugated QDs Some small peptides can provide better cellular uptake and tissue penetration when introduced in vivo. The pioneering report first demonstrated in vivo targeting of QD conjugates employing peptides as the targeting ligands [122]. Peptide-conjugated QDs were injected into the tail veins of MDA-MB-435 breast carcinoma xenograft-bearing nude mice. Three different sequence peptides were tested: CGFECVRQCPERC (denoted as GFE) which binds to membrane dipeptidase on the endothelial cells [123, 124],

KDEPQRRSARLSAK-PAPPKPEPKPKKAPAKK (denoted as F3) which preferentially binds to blood vessels and tumor cells in various tumors [125], and CGNKRTRGC (denoted as LyP-1) which recognizes lymphatic vessels and tumor cells in certain tumors [126]. Since the QD used in this study emits in the visible range which is not optimal for in vivo imaging, ex vivo histological analyses were carried out to show that QDs were specifically directed to the tumor vasculature and organ targets by the surface peptide molecules. A high level of PEG substitution on the QDs was found to be important to reduce nonselective accumulation in the RES, thereby increasing the circulation half-life and targeting efficiency. QD-F3 colocalizes with blood vessels in tumor tissue and QD-LyP-1 was also accumulated in tumor tissue but did not colocalize with the blood vessel marker. QD-F3 and QD-LyP-1 (of different emission wavelengths) injected into the same tumor mouse targeted different structures in the tumor tissue, showing that QDs can be targeted in vivo with a high level of specificity. This pioneering report first demonstrated the feasibility of specific targeting of QD in vivo and opened up a new field of QD-based research.

The arginine-glycine-aspartic acid (RGD) peptide has a high affinity for the $\alpha_v\beta_3$ integrin receptor which plays an important role in tumorigenesis and metastasis. Cai et al. reported the first in vivo targeted imaging of tumor vasculature using polymer-encapsulated NIR CdTe/ZnS core-shell QDs functionalized with cyclic RGD (arginine-glycine-aspartic acid) peptides for targeting integrin $\alpha_v\beta_3$ [127], which is highly expressed on activated endothelial cells and tumor cells but is not readily detectable in resting endothelial cells and most normal organ systems following systemic administration in tumor-bearing mice [128, 129]. Arginine-glycine-aspartic acid (RGD; potent integrin $\alpha_v\beta_3$ antagonist) containing peptides was conjugated to QD705 (emission maximum at 705 nm) and QD705-RGD exhibited high-affinity integrin $\alpha_v\beta_3$ specific binding in cell culture and ex vivo. In vivo NIR fluorescence (NIRF) imaging was carried out on athymic nude mice bearing subcutaneous integrin $\alpha_v\beta_3$-positive U87MG human glioblastoma tumors (Fig. 39.19) [127]. Tumor fluorescence intensity reached a maximum at 6 h postinjection with good contrast. The size of QD705-RGD ($\sim$20 nm) prevented efficient extravasation; thus, QD705-RGD mainly targeted tumor vasculature instead of tumor cells. Immunofluorescence staining of the tumor vessels confirmed that the majority of the QD fluorescence signal in the tumor colocalizes with the tumor vessels. Successful in vivo tumor imaging using QD conjugates has introduced new perspectives for targeted NIRF imaging and may aid in cancer detection and management including image-guided surgery. This probe may also have great potential as a universal NIRF probe for detecting tumor vasculature in living subjects.

Antibody-Conjugated QDs Due to the high affinity of antigen to antibody, their interaction is the most important strategy of targeted recognition for luminescence bioimaging. QDs modified with antibodies are used for targeted delivery to cancer cells. Angiogenic tumors produce vascular endothelial growth factor [130–132], which hyperpermeabilizes tumor neovasculature and causes leakage of circulating macromolecules and nanoparticles. Subsequent macromolecule or nanoparticle accumulation occurs since tumors lack an effective lymphatic drainage system.
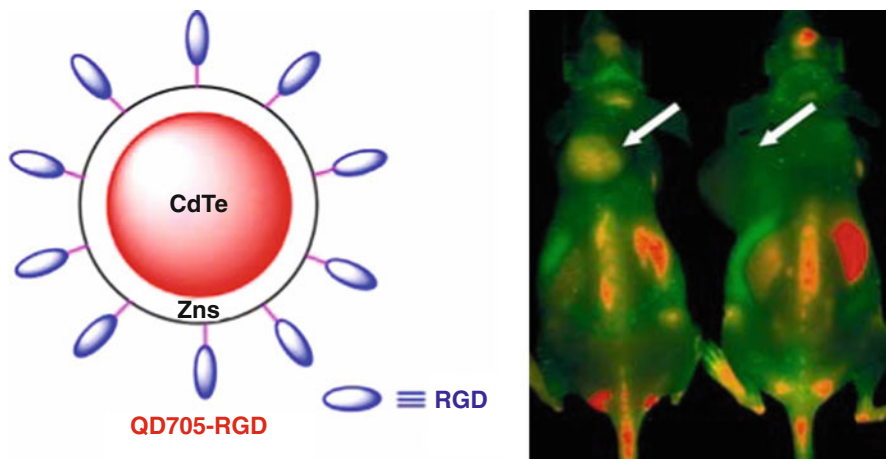
Fig. 39.19 RGD peptide-conjugated QD705 successfully targets the tumor vasculature in vivo. Mouse on the *left* was injected with QD705-RGD and the mouse on the *right* was injected with QD705. *Arrows* indicate tumors (Reproduced with permission from [127], Copyright © 2006, American Chemical Society)

Gao et al. demonstrated the use of ABC triblock copolymer-coated QDs for prostate cancer targeting and imaging in live animals [59]. Based on spectral imaging techniques which can discriminate fluorescence signals of QDs from tissue autofluorescence [133, 134], intravenously injected probes were found to accumulate in the tumor site (Fig. 39.20) [59]. Yu et al. reported that QDs were linked to anti-AFP (alpha-fetoprotein, a marker for hepatocellular carcinoma cell lines) antibody for in vivo tumor targeting and imaging [135]. It was reported that active tumor targeting and spectroscopic hepatoma imaging were achieved using an integrated fluorescence imaging system. The heterogeneous distribution of the QD-based probe in the tumor was also evaluated by a site-by-site measurement method. However, there is not enough experimental evidence to support the view whether or not the targeting ligands were actually attached to the QD. Therefore, the conclusion that the tumor contrast observed was mainly from active rather than passive targeting was ambiguous.

In addition, tracking a single QD conjugated with tumor-targeting antibody in tumors of living mice was achieved using a dorsal skinfold chamber and a high-speed confocal microscope with a high-sensitivity camera [136].

Folic Acid-Labeled QDs for In Vivo Tumor Targeting. Folic acid (FA) as a targeting agent has attracted wide attention, due to its high stability, non-immunogenic character, and ability to conjugate with a wide variety of molecules. Moreover, folate receptors (FR) are overexpressed in a broad spectrum of malignant tumors and are only minimally distributed in normal tissues, which are an attractive target for selective delivery of imaging agents to tumor cells. On the basis of the high affinity of FA and FR, several FA-modified QDs have been developed for targeted imaging in vivo. Chen et al. reported that the folate-conjugated
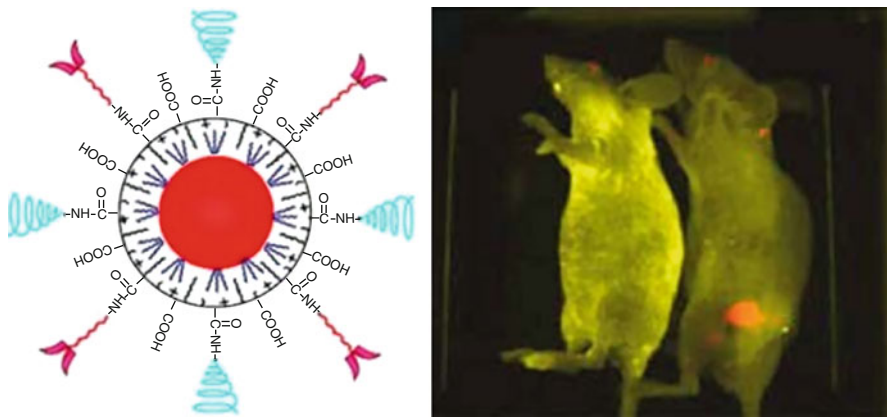
Fig. 39.20 Antibody-conjugated QDs for in vivo cancer targeting and imaging. Mouse on the *left* was a control (Reproduced with permission from [59], Copyright © 2004, Nature Publishing Group)

CdHgTe QDs that emitted at 790 nm can be high targeting affinity and sensitivity for in vivo early tumor diagnosis in S180 tumor beard mouse model [137]. Xue et al. synthesized the CdSe QDs with folate-polyethylene glycol (FA-PEG) coating for targeted imaging of tumors overexpressing the folate receptor (FR) [138].

It is worth mentioning that besides active targeting methods by conjugating specific ligands, the enhanced permeability and retention (EPR) effect in tumor vasculature can also realize nanomaterial enrichment. Wang group has successfully developed the PEG-functionalized Ag_2S QDs which emit at 1,200 nm for the tumor imaging of small animals with maximum penetration depth and high feature fidelity [139]. This kind of NIR-II-emitting QDs can escape from phagocytes in the RES and circulate through the blood vessels with a long half-life, which can be used to detect tumors with a high signal-to-background ratio through passive tumor targeting (Fig. 39.21).

Other Applications of QDs In Vivo

Nerve system is vital to life. QDs can also be employed for nerve preservation and therapy of nerve-relative diseases. Diffusion within the extracellular space (ECS) of the brain is necessary for chemical signaling and for neurons and glia to access nutrients and therapeutic agents [140, 141]. Integrative optical imaging was employed to show that water-soluble QDs diffuse within the ECS of adult rat neocortex in vivo [142]. This report could improve the modeling of neurotransmitter spread after spillover and ectopic release while establishing size limits for diffusion of drug delivery vectors such as viruses, liposomes, and nanoparticles in brain ECS. Santra et al. reported that TAT (a cell-penetrating peptide)-conjugated CdS:Mn/ZnS quantum dots (QDs), intra-arterially delivered to a rat brain, rapidly
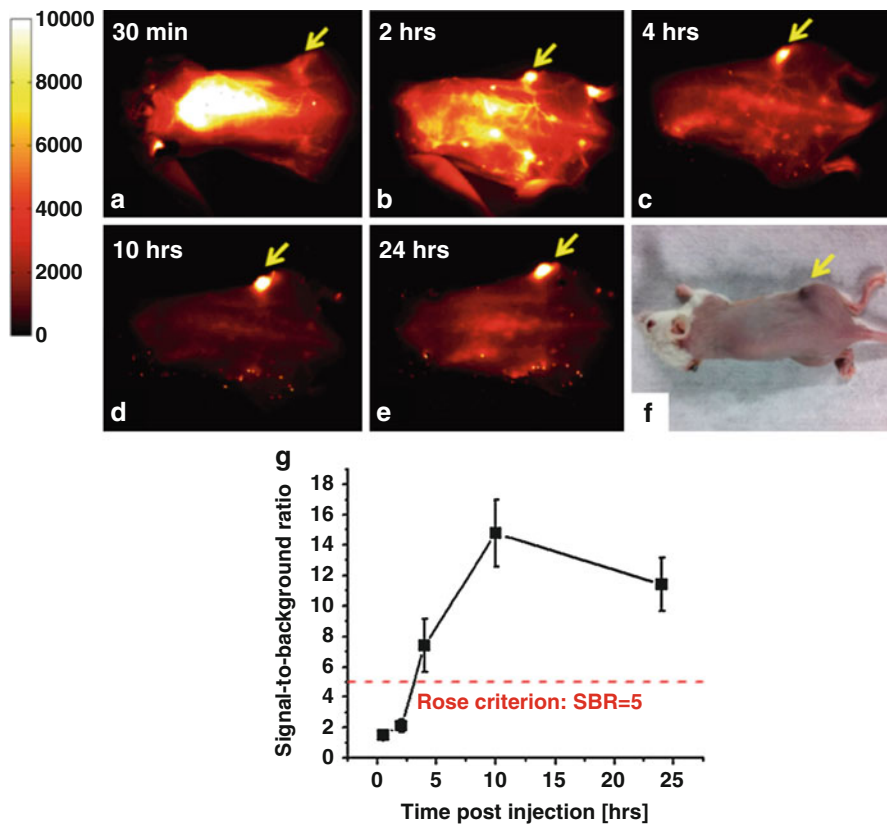
Fig. 39.21 (**a–e**) Time course imaging of a xenograft 4T1 tumor with high uptake of NIR-II 6PEG-Ag$_2$S QDs. (**f**) A color photo of the same mouse at 24 h p.i. (**g**) Signal of tumor-to-background ratio (TBR) (Reproduced with permission from [139], Copyright © 2012, John Wiley and Sons)

(within a few minutes) labeled the brain tissue without manipulating the blood–brain barrier (BBB) [143]. In addition, intravenously injected QDs were shown to be taken up by macrophages and localize to experimental glioma in a rat model using optical detection [144].

Current biomedical imaging techniques, including MRI, PET, and CT, are vital in the diagnosis of various diseases. Each imaging modality has its own merits and disadvantages, and a single technique does not possess all the required capabilities for comprehensive imaging. Therefore, multimodal imaging probes based on QDs are quickly becoming important tools for state-of-the-art biomedical research, clinical diagnostics, and therapeutics [145]. In addition, on the basis of three-photo imaging, Hyeon et al. reported on high-resolution in vitro and in vivo imaging by combining three-photo excitation of ZnS nanocrystals and visible emission from Mn$^+$ dopants. The large three-photon cross section of the nanocrystals enabled targeted cellular imaging under high spatial resolution, approaching the theoretical limit of three-photon excitation [146].

Conclusion and Perspectives

This chapter has described recent developments of preparation, surface modification, biofunction of QDs, and their applications in bioimaging. QDs as biological probes have lived up to much of their initially promoted potential for in vitro and in vivo imaging. Since the pioneer works of QDs for biological applications by the Alivisatos group and the Nie group [32, 39], numerous breakthroughs in QD technology have gave rise to the recent success of in vivo imaging of QDs in live animals. QDs have been perceived as technological marvels with characteristics that could greatly improve biological imaging and therapy. Future development of improved QD-based biological probes for in vivo optical imaging is promising for both basic science and clinical applications. Although QDs provide a class of exciting new fluorescent probes that opens up many opportunities for bioimaging, there are several issues remaining to require concerted effort for success:

1. Biotoxicity. One of the major issues that hinder the application of QDs to human being is the concern about their safety. There have been many serious questions and concerns raised regarding the cytotoxicity of inorganic QDs containing Cd, Se, Zn, Te, Hg, and Pb. For the future application in biomedical area, the preparation of nontoxicity QDs should be paid more attention.

2. Size effect. For in vivo applications, QDs need to overcome the nanospecific uptake by the reticuloendothelial system (RES) organs. In general, bigger QDs can be quickly removed from blood system by the RES, such as the liver and spleen and bone, but smaller particles can escape from phagocytes in the RES and prolong the blood circulation in the body. In addition, tumor vasculatures are typically quite leaky; bigger size does not permit efficient delivery. Thus, design and development of smaller and decent biocompatible QDs is a tendency in real applications.

3. Surface modification. The surface of QDs plays an important role in controlling the PL efficiency and bioconjugation with biomolecules. For nanosize QDs, the presence of large defects on the surface is attributed to the non-radiative decay, corresponding to weak PL emission. Moreover, the surface properties (including surface ligands, functional groups, and zeta potential) of QDs are related to the reaction activity, coordination ability, and stability of the nanoparticles. Therefore, further understanding of the surface chemistry of QDs is required.

4. Tissue penetration depth. Although the superior brightness and photostability of QDs made them attractive candidates for in vivo animal imaging, most of the current QDs still emit within the visible range. The ideal QDs for deep tissue imaging, that is, high-quality QDs with near-infrared-emitting properties are not yet widely available. Theoretical modeling studies indicate that two spectral windows are excellent for in vivo QD imaging, one at 650–950 nm and another at 1,000–1,350 nm. NIR-II imaging technique provides anatomical and hemodynamic information and surpasses the need to use multiple imaging modalities to obtain equivalent data, owing to reduced tissue scattering and deeper anatomical penetration of NIR-II over shorter wavelengths, thus significantly extending potential human applications. In addition to high-quality NIR QDs,

multiphoton fluorescence microscopy and novel illuminating mechanisms such as bioluminescence energy transfer can all be used to achieve deeper tissue penetration.

References

1. Henglein A (1982) Photo-degradation and fluorescence of colloidal-cadmium sulfide in aqueous-solution. Ber Der Bunsen-Ges-Phys Chem Chem Phys 86(4):301–305
2. Rossetti R, Nakahara S, Brus LE (1983) Quantum size effects in the redox potentials, resonance Raman-spectra, and electronic-spectra of CdS crystallites in aqueous-solution. J Chem Phys 79(2):1086–1088
3. Dabbousi BO, Rodriguez Viejo J, Mikulec FV, Heine JR, Mattoussi H, Ober R et al (1997) (CdSe)ZnS core-shell quantum dots: synthesis and characterization of a size series of highly luminescent nanocrystallites. J Phys Chem B 101(46):9463–9475
4. Leatherdale CA, Woo WK, Mikulec FV, Bawendi MG (2002) On the absorption cross section of CdSe nanocrystal quantum dots. J Phys Chem B 106(31):7619–7622
5. Niemeyer CM (2001) Nanoparticles, proteins, and nucleic acids: biotechnology meets materials science. Angew Chem-Int Ed 40(22):4128–4158
6. Murphy CJ (2002) Optical sensing with quantum dots. Anal Chem 74(19):520a–526a
7. Parak WJ, Gerion D, Pellegrino T, Zanchet D, Micheel C, Williams SC et al (2003) Biological applications of colloidal nanocrystals. Nanotechnology 14(7):R15–R27
8. Alivisatos P (2004) The use of nanocrystals in biological detection. Nat Biotechnol 22(1):47–52
9. Efros AL, Efros AL (1982) Interband absorption of light in a semiconductor sphere. Sov Phys Semicond-USSR 16(7):772–775
10. Ekimov AI, Onushchenko AA (1982) Quantum size effect in the optical-spectra of semiconductor micro-crystals. Sov Phys Semicond-USSR 16(7):775–778
11. Mansur HS, Grieser F, Marychurch MS, Biggs S, Urquhart RS, Furlong DN (1995) Photoelectrochemical properties of Q-state CdS particles in arachidic acid Langmuir-Blodgett-films. J Chem Soc-Faraday Trans 91(4):665–672
12. Mansur HS, Grieser F, Urquhart RS, Furlong DN (1995) Photoelectrochemical behavior of Q-state $CdS_xSe_{(1-x)}$ particles in arachidic acid Langmuir-Blodgett-films. J Chem Soc-Faraday Trans 91(19):3399–3404
13. Mansur HS, Vasconcelos WL, Grieser F, Caruso F (1999) Photoelectrochemical behaviour of CdS "Q-state" semiconductor particles in 10,12-nonacosadiynoic acid polymer Langmuir-Blodgett films. J Mater Sci 34(21):5285–5291
14. Alivisatos AP (1996) Semiconductor clusters, nanocrystals, and quantum dots. Science 271(5251):933–937
15. Crouch D, Norager S, O'Brien P, Park JH, Pickett N (2003) New synthetic routes for quantum dots. Philos Trans Royal Soc Math Phys Eng Sci 361(1803):297–310
16. Murray CB, Norris DJ, Bawendi MG (1993) Synthesis and characterization of nearly monodisperse CdE (E = sulfur, selenium, tellurium) semiconductor nanocrystallites. J Am Chem Soc 115(19):8706–8715
17. Algar WR, Susumu K, Delehanty JB, Medintz IL (2011) Semiconductor quantum dots in bioanalysis: crossing the valley of death. Anal Chem 83(23):8826–8837
18. Costa-Fernandez JM, Pereiro R, Sanz-Medel A (2006) The use of luminescent quantum dots for optical sensing. Trac-Trends Anal Chem 25(3):207–218
19. Manna L, Scher EC, Alivisatos AP (2000) Synthesis of soluble and processable rod-, arrow-, teardrop-, and tetrapod-shaped CdSe nanocrystals. J Am Chem Soc 122(51):12700–12706
20. Peng ZA, Peng XG (2001) Mechanisms of the shape evolution of CdSe nanocrystals. J Am Chem Soc 123(7):1389–1395

21. Peng ZA, Peng XG (2001) Formation of high-quality CdTe, CdSe, and CdS nanocrystals using CdO as precursor. J Am Chem Soc 123(1):183–184

22. Yang YA, Wu HM, Williams KR, Cao YC (2005) Synthesis of CdSe and CdTe nanocrystals without precursor injection. Angew Chem-Int Ed 44(41):6712–6715

23. Du YP, Xu B, Fu T, Cai M, Li F, Zhang Y et al (2010) Near-infrared photoluminescent Ag_2S quantum dots from a single source precursor. J Am Chem Soc 132(5):1470–1471

24. Rogach AL, Katsikas L, Kornowski A, Su DS, Eychmuller A, Weller H (1996) Synthesis and characterization of thiol-stabilized CdTe nanocrystals. Ber Bunsen-Ges-Phys Chem Chem Phys 100(11):1772–1778

25. Gaponik N, Talapin DV, Rogach AL, Hoppe K, Shevchenko EV, Kornowski A et al (2002) Thiol-capping of CdTe nanocrystals: an alternative to organometallic synthetic routes. J Phys Chem B 106(29):7177–7185

26. Rogach AL, Franzl T, Klar TA, Feldmann J, Gaponik N, Lesnyak V et al (2007) Aqueous synthesis of thiol-capped CdTe nanocrystals: state-of-the-art. J Phys Chem C 111(40):14628–14637

27. Rogach AL, Harrison MT, Kershaw SV, Kornowski A, Burt MG, Eychmuller A et al (2001) Colloidally prepared CdHgTe and HgTe quantum dots with strong near-infrared luminescence. Phys Status Solidi B-Basic Res 224(1):153–158

28. Koktysh DS, Gaponik N, Reufer M, Crewett J, Scherf U, Eychmuller A et al (2004) Near-infrared electroluminescence from HgTe nanocrystals. Chem Phys Chem 5(9):1435–1438

29. Osipovich NP, Shavel A, Poznyak SK, Gaponik N, Eychmuller A (2006) Electrochemical observation of the photoinduced formation of alloyed ZnSe(S) nanocrystals. J Phys Chem B 110(39):19233–19237

30. Wang C, Gao X, Ma Q, Su XG (2009) Aqueous synthesis of mercaptopropionic acid capped Mn^{2+}-doped ZnSe quantum dots. J Mater Chem 19(38):7016–7022

31. Gill R, Zayats M, Willner I (2008) Semiconductor quantum dots for bioanalysis. Angew Chem-Int Ed 47(40):7602–7625

32. Chan WCW, Nie SM (1998) Quantum dot bioconjugates for ultrasensitive nonisotopic detection. Science 281(5385):2016–2018

33. Willard DM, Carillo LL, Jung J, Van Orden A (2001) CdSe-ZnS quantum dots as resonance energy transfer donors in a model protein-protein binding assay. Nano Lett 1(9):469–474

34. Wang SP, Mamedova N, Kotov NA, Chen W, Studer J (2002) Antigen/antibody immunocomplex from CdTe nanoparticle bioconjugates. Nano Lett 2(8):817–822

35. Mattoussi H, Mauro JM, Goldman ER, Anderson GP, Sundar VC, Mikulec FV et al (2000) Self-assembly of CdSe-ZnS quantum dot bioconjugates using an engineered recombinant protein. J Am Chem Soc 122(49):12142–12150

36. Medintz IL, Clapp AR, Mattoussi H, Goldman ER, Fisher B, Mauro JM (2003) Self-assembled nanoscale biosensors based on quantum dot FRET donors. Nat Mater 2(9):630–638

37. Pinaud F, King D, Moore HP, Weiss S (2004) Bioactivation and cell targeting of semiconductor CdSe/ZnS nanocrystals with phytochelatin-related peptides. J Am Chem Soc 126(19):6115–6123

38. Iyer G, Pinaud F, Tsay J, Weiss S (2007) Solubilization of quantum dots with a recombinant peptide from *Escherichia coli*. Small 3(5):793–798

39. Bruchez M, Moronne M, Gin P, Weiss S, Alivisatos AP (1998) Semiconductor nanocrystals as fluorescent biological labels. Science 281(5385):2013–2016

40. Gerion D, Pinaud F, Williams SC, Parak WJ, Zanchet D, Weiss S et al (2001) Synthesis and properties of biocompatible water-soluble silica-coated CdSe/ZnS semiconductor quantum dots. J Phys Chem B 105(37):8861–8871

41. Yu WW, Chang E, Falkner JC, Zhang JY, Al-Somali AM, Sayes CM et al (2007) Forming biocompatible and nonaggregated nanocrystals in water using amphiphilic polymers. J Am Chem Soc 129(10):2871–2879

42. Nikolic MS, Krack M, Aleksandrovic V, Kornowski A, Forster S, Weller H (2006) Tailor-made ligands for biocompatible nanoparticles. Angew Chem-Int Ed 45(39):6577–6580

43. Zrazhevskiy P, Sena M, Gao XH (2010) Designing multifunctional quantum dots for bioimaging, detection, and drug delivery. Chem Soc Rev 39(11):4326–4354

44. Medintz IL, Uyeda HT, Goldman ER, Mattoussi H (2005) Quantum dot bioconjugates for imaging, labelling and sensing. Nat Mater 4(6):435–446

45. Wang QB, Xu Y, Zhao XH, Chang Y, Liu Y, Jiang LJ et al (2007) A facile one-step in situ functionalization of quantum dots with preserved photoluminescence for bioconjugation. J Am Chem Soc 129(20):6380–6381

46. Wang QB, Liu Y, Ke YG, Yan H (2008) Quantum dot bioconjugation during core-shell synthesis. Angew Chem Int Ed 47(2):316–319

47. Wang QB, Iancu N, Seo DK (2005) Preparation of large transparent silica monoliths with embedded photoluminescent CdSe@ZnS core/shell quantum dots. Chem Mater 17(19):4762–4764

48. Wang QB, Seo DK (2006) Synthesis of deep-red-emitting CdSe quantum dots and general non-inverse-square behavior of quantum confinement in CdSe quantum dots. Chem Mater 18(24):5764–5767

49. Hanaki K, Momo A, Oku T, Komoto A, Maenosono S, Yamaguchi Y et al (2003) Semiconductor quantum dot/albumin complex is a long-life and highly photostable endosome marker. Biochem Biophys Res Commun 302(3):496–501

50. Chen FQ, Gerion D (2004) Fluorescent CdSe/ZnS nanocrystal-peptide conjugates for long-term, nontoxic imaging and nuclear targeting in living cells. Nano Lett 4(10):1827–1832

51. Kaul Z, Yaguchi T, Kaul SC, Hirano T, Wadhwa R, Taira K (2003) Mortalin imaging in normal and cancer cells with quantum dot immuno-conjugates. Cell Res 13(6):503–507

52. Mansson A, Sundberg M, Balaz M, Bunk R, Nicholls IA, Omling P et al (2004) In vitro sliding of actin filaments labelled with single quantum dots. Biochem Biophys Res Commun 314(2):529–534

53. Ishii D, Kinbara K, Ishida Y, Ishii N, Okochi M, Yohda M et al (2003) Chaperonin-mediated stabilization and ATP-triggered release of semiconductor nanoparticles. Nature 423(6940):628–632

54. Jaiswal JK, Mattoussi H, Mauro JM, Simon SM (2003) Long-term multiple color imaging of live cells using quantum dot bioconjugates. Nat Biotechnol 21(1):47–51

55. Mattheakis LC, Dias JM, Choi YJ, Gong J, Bruchez MP, Liu JQ et al (2004) Optical coding of mammalian cells using semiconductor quantum dots. Anal Biochem 327(2):200–208

56. Dubertret B, Skourides P, Norris DJ, Noireaux V, Brivanlou AH, Libchaber A (2002) In vivo imaging of quantum dots encapsulated in phospholipid micelles. Science 298(5599):1759–1762

57. Wu XY, Liu HJ, Liu JQ, Haley KN, Treadway JA, Larson JP et al (2003) Immunofluorescent labeling of cancer marker Her2 and other cellular targets with semiconductor quantum dots. Nat Biotechnol 21(1):41–46

58. Michalet X, Pinaud FF, Bentolila LA, Tsay JM, Doose S, Li JJ et al (2005) Quantum dots for live cells, in vivo imaging, and diagnostics. Science 307(5709):538–544

59. Gao XH, Cui YY, Levenson RM, Chung LWK, Nie SM (2004) In vivo cancer targeting and imaging with semiconductor quantum dots. Nat Biotechnol 22(8):969–976

60. Dahan M, Levi S, Luccardini C, Rostaing P, Riveau B, Triller A (2003) Diffusion dynamics of glycine receptors revealed by single-quantum dot tracking. Science 302(5644):442–445

61. Rosenthal SJ, Tomlinson A, Adkins EM, Schroeter S, Adams S, Swafford L et al (2002) Targeting cell surface receptors with ligand-conjugated nanocrystals. J Am Chem Soc 124(17):4586–4594

62. Derfus AM, Chan WCW, Bhatia SN (2004) Intracellular delivery of quantum dots for live cell labeling and organelle tracking. Adv Mater 16(12):961–966

63. Kloepfer JA, Mielke RE, Nadeau JL (2005) Uptake of CdSe and CdSe/ZnS quantum dots into bacteria via purine-dependent mechanisms. Appl Environ Microbiol 71(5):2548–2557

64. Kloepfer JA, Mielke RE, Wong MS, Nealson KH, Stucky G, Nadeau JL (2003) Quantum dots as strain- and metabolism-specific microbiological labels. Appl Environ Microbiol 69(7):4205–4213

65. Tokumasu F, Dvorak J (2003) Development and application of quantum dots for immuno-cytochemistry of human erythrocytes. J Microsc-Oxf 211:256–261

66. Osaki F, Kanamori T, Sando S, Sera T, Aoyama Y (2004) A quantum dot conjugated sugar ball and its cellular uptake on the size effects of endocytosis in the subviral region. J Am Chem Soc 126(21):6520–6521

67. Nath J, Johnson KL (1998) Fluorescence in situ hybridization (FISH): DNA probe production and hybridization criteria. Biotech Histochem 73(1):6–22

68. Nath J, Johnson KL (2000) A review of fluorescence in situ hybridization (FISH): current status and future prospects. Biotech Histochem 75(2):54–78

69. Mitchell GP, Mirkin CA, Letsinger RL (1999) Programmed assembly of DNA functionalized quantum dots. J Am Chem Soc 121(35):8122–8123

70. Mahtab R, Harden HH, Murphy CJ (2000) Temperature- and salt-dependent binding of long DNA to protein-sized quantum dots: thermodynamics of "inorganic protein"-DNA interactions. J Am Chem Soc 122(1):14–17

71. Lakowicz JR, Gryczynski I, Gryczynski Z, Nowaczyk K, Murphy CJ (2000) Time-resolved spectral observations of cadmium-enriched cadmium sulfide nanoparticles and the effects of DNA oligomer binding. Anal Biochem 280(1):128–136

72. Gerion D, Parak WJ, Williams SC, Zanchet D, Micheel CM, Alivisatos AP (2002) Sorting fluorescent nanocrystals with DNA. J Am Chem Soc 124(24):7070–7074

73. Chan PM, Yuen T, Ruf F, Gonzalez-Maeso J, Sealfon SC (2005) Method for multiplex cellular detection of mRNAs using quantum dot fluorescent in situ hybridization. Nucleic Acids Res 33(18):e161

74. Tholouli E, Hoyland JA, Di Vizio D, O'Connell F, MacDermott SA, Twomey D et al (2006) Imaging of multiple mRNA targets using quantum dot based in situ hybridization and spectral deconvolution in clinical biopsies. Biochem Biophys Res Commun 348(2):628–636

75. Xiao Y, Telford WG, Ball JC, Locascio LE, Barker PE (2005) Semiconductor nanocrystal conjugates, FISH and pH. Nat Methods 2(10):723

76. Wu SM, Zha X, Zhang ZL, Xie HY, Tian ZQ, Peng J et al (2006) Quantum-dot-labeled DNA probes for fluorescence in situ hybridization (FISH) in the microorganism *Escherichia coli*. Chem Phys Chem 7(5):1062–1067

77. Clapp AR, Medintz IL, Mauro JM, Fisher BR, Bawendi MG, Mattoussi H (2004) Fluorescence resonance energy transfer between quantum dot donors and dye-labeled protein acceptors. J Am Chem Soc 126(1):301–310

78. Kagan CR, Murray CB, Bawendi MG (1996) Long-range resonance transfer of electronic excitations in close-packed CdSe quantum-dot solids. Phys Rev B 54(12):8633–8643

79. Medintz IL, Trammell SA, Mattoussi H, Mauro JM (2004) Reversible modulation of quantum dot photoluminescence using a protein-bound photochromic fluorescence resonance energy transfer acceptor. J Am Chem Soc 126(1):30–31

80. Nagasaki Y, Ishii T, Sunaga Y, Watanabe Y, Otsuka H, Kataoka K (2004) Novel molecular recognition via fluorescent resonance energy transfer using a biotin-PEG/polyamine stabilized CdS quantum dot. Langmuir 20(15):6396–6400

81. Oh E, Hong MY, Lee D, Nam SH, Yoon HC, Kim HS (2005) Inhibition assay of bio-molecules based on fluorescence resonance energy transfer (FRET) between quantum dots and gold nanoparticles. J Am Chem Soc 127(10):3270–3271

82. Patolsky F, Gill R, Weizmann Y, Mokari T, Banin U, Willner I (2003) Lighting-up the dynamics of telomerization and DNA replication by CdSe-ZnS quantum dots. J Am Chem Soc 125(46):13918–13919

83. Clapp AR, Medintz IL, Mattoussi H (2006) Forster resonance energy transfer investigations using quantum-dot fluorophores. Chem Phys Chem 7(1):47–57

84. Medintz IL, Clapp AR, Brunel FM, Tiefenbrunn T, Uyeda HT, Chang EL et al (2006) Proteolytic activity monitored by fluorescence resonance energy transfer through quantum-dot-peptide conjugates. Nat Mater 5(7):581–589

85. Shi LF, De Paoli V, Rosenzweig N, Rosenzweig Z (2006) Synthesis and application of quantum dots FRET-based protease sensors. J Am Chem Soc 128(32):10378–10379

86. Hohng S, Ha T (2005) Single-molecule quantum-dot fluorescence resonance energy transfer. Chem Phys Chem 6(5):956–960

87. Clapp AR, Medintz IL, Fisher BR, Anderson GP, Mattoussi H (2005) Can luminescent quantum dots be efficient energy acceptors with organic dye donors? J Am Chem Soc 127(4):1242–1250

88. Albrechtbuehler G (1977) Phagokinetic tracks of 3 t3 cells - parallels between orientation of track segments and of cellular structures which contain actin or tubulin. Cell 12(2):333–339

89. Parak WJ, Boudreau R, Le Gros M, Gerion D, Zanchet D, Micheel CM et al (2002) Cell motility and metastatic potential studies based on quantum dot imaging of phagokinetic tracks. Adv Mater 14(12):882–885

90. Liu HY, Vu TQ (2007) Identification of quantum dot bioconjugates and cellular protein co-localization by hybrid gel blotting. Nano Lett 7(4):1044–1049

91. Bakalova R, Zhelev Z, Ohba H, Baba Y (2005) Quantum dot-based western blot technology for ultrasensitive detection of tracer proteins. J Am Chem Soc 127(26):9328–9329

92. Ornberg RL, Harper TF, Harper H (2005) Western blot analysis with quantum dot fluorescence technology: a sensitive and quantitative method for multiplexed proteomics. Nat methods 2:79–81

93. Gao XH, Nie SM (2004) Quantum dot-encoded mesoporous beads with high brightness and uniformity: rapid readout using flow cytometry. Anal Chem 76(8):2406–2410

94. Shah LS, Clark PA, Moioli EK, Stroscio MA, Mao JJ (2007) Labeling of mesenchymal stem cells by bioconjugated quantum dots. Nano Lett 7(10):3071–3079

95. Chattopadhyay PK, Price DA, Harper TF, Betts MR, Yu J, Gostick E et al (2006) Quantum dot semiconductor nanocrystals for immunophenotyping by polychromatic flow cytometry. Nat Med 12(8):972–977

96. Perfetto SP, Chattopadhyay PK, Roederer M (2004) Seventeen-colour flow cytometry: unravelling the immune system. Nat Rev Immunol 4(8):648–655

97. Ferrari BC, Bergquist PL (2007) Quantum dots as alternatives to organic fluorophores for *Cryptosporidium* detection using conventional flow cytometry and specific monoclonal antibodies: lessons learned. Cytom Part A 71A(4):265–271

98. Chen AA, Derfus AM, Khetani SR, Bhatia SN (2005) Quantum dots to monitor RNAi delivery and improve gene silencing. Nucleic Acids Res 33(22):e190

99. Edgar R, McKinstry M, Hwang J, Oppenheim AB, Fekete RA, Giulian G et al (2006) High-sensitivity bacterial detection using biotin-tagged phage and quantum-dot nanocomplexes. Proc Natl Acad Sci USA 103(13):4841–4845

100. Lim YT, Kim S, Nakayama A, Stott NE, Bawendi MG, Frangioni JV (2003) Selection of quantum dot wavelengths for biomedical assays and imaging. Mol Imaging 2(1):50–64

101. Smith AM, Mancini MC, Nie SM (2009) Bioimaging second window for in vivo imaging. Nat Nanotechnol 4(11):710–711

102. Frangioni JV (2003) In vivo near-infrared fluorescence imaging. Curr Opin Chem Biol 7(5):626–634

103. Reich G (2005) Near-infrared spectroscopy and imaging: basic principles and pharmaceutical applications. Adv Drug Deliv Rev 57(8):1109–1143

104. Rieger S, Kulkarni RP, Darcy D, Fraser SE, Koster RW (2005) Quantum dots are powerful multipurpose vital labeling agents in zebrafish embryos. Dev Dyn 234(3):670–681

105. Voura EB, Jaiswal JK, Mattoussi H, Simon SM (2004) Tracking metastatic tumor cell extravasation with quantum dot nanocrystals and fluorescence emission-scanning microscopy. Nat Med 10(9):993–998

106. Kim S, Lim YT, Soltesz EG, De Grand AM, Lee J, Nakayama A et al (2004) Near-infrared fluorescent type II quantum dots for sentinel lymph node mapping. Nat Biotechnol 22(1):93–97

107. Zimmer JP, Kim SW, Ohnishi S, Tanaka E, Frangioni JV, Bawendi MG (2006) Size series of small indium arsenide-zinc selenide core-shell nanocrystals and their application to in vivo imaging. J Am Chem Soc 128(8):2526–2527

108. Kim SW, Zimmer JP, Ohnishi S, Tracy JB, Frangioni JV, Bawendi MG (2005) Engineering InAsxP1-x/InP/ZnSe III-V alloyed core/shell quantum dots for the near-infrared. J Am Chem Soc 127(30):10526–10532

109. Parungo CP, Colson YL, Kim SW, Kim S, Cohn LH, Bawendi MG et al (2005) Sentinel lymph node mapping of the pleural space. Chest 127(5):1799–1804

110. Parungo CP, Soybel DI, Colson YL, Kim SW, Ohnishi S, DeGrand AM et al (2007) Lymphatic drainage of the peritoneal space: a pattern dependent on bowel lymphatics. Ann Surg Oncol 14(2):286–298

111. Frangioni JV, Kim SW, Ohnishi S, Kim S, Bawendi MG (2007) Sentinel lymph node mapping with type-II quantum dots. Methods Mol Biol 374:147–159

112. Soltesz EG, Kim S, Laurence RG, DeGrand AM, Parungo CP, Dor DM et al (2005) Intraoperative sentinel lymph node mapping of the lung using near-infrared fluorescent quantum dots. Ann Thorac Surg 79(1):269–277

113. Parungo CP, Ohnishi S, Kim SW, Kim S, Laurence RG, Soltesz EG et al (2005) Intraoperative identification of esophageal sentinel lymph nodes with near-infrared fluorescence imaging. J Thorac Cardiov Surg 129(4):844–850

114. Soltesz EG, Kim S, Kim SW, Laurence RG, De Grand AM, Parungo CP et al (2006) Sentinel lymph node mapping of the gastrointestinal tract by using invisible light. Ann Surg Oncol 13(3):386–396

115. Kobayashi H, Hama Y, Koyama Y, Barrett T, Regino CAS, Urano Y et al (2007) Simultaneous multicolor imaging of five different lymphatic basins using quantum dots. Nano Lett 7(6):1711–1716

116. Ballou B, Ernst LA, Andreko S, Harper T, Fitzpatrick JAJ, Waggoner AS et al (2007) Sentinel lymph node imaging using quantum dots in mouse tumor models. Bioconjugate Chem 18(2):389–396

117. Larson DR, Zipfel WR, Williams RM, Clark SW, Bruchez MP, Wise FW et al (2003) Water-soluble quantum dots for multiphoton fluorescence imaging in vivo. Science 300(5624):1434–1436

118. Smith JD, Fisher GW, Waggoner AS, Campbell PG (2007) The use of quantum dots for analysis of chick CAM vasculature. Microvasc Res 73(2):75–83

119. Stroh M, Zimmer JP, Duda DG, Levchenko TS, Cohen KS, Brown EB et al (2005) Quantum dots spectrally distinguish multiple species within the tumor milieu in vivo. Nat Med 11(6):678–682

120. Levene MJ, Dombeck DA, Kasischke KA, Molloy RP, Webb WW (2004) In vivo multiphoton microscopy of deep brain tissue. J Neurophysiol 91(4):1908–1912

121. Morgan NY, English S, Chen W, Chernomordik V, Russo A, Smith PD et al (2005) Real time in vivo non-invasive optical imaging using near-infrared fluorescent quantum dots. Acad Radiol 12(3):313–323

122. Michalet X, Pinaud FF, Bentolila LA, Tsay JM, Doose S, Li JJ et al (2005) Peptide-coated semiconductor nanocrystals for biomedical applications. Genet Eng Opt Probes Biomed Appl III 5704:57–68

123. Rajotte D, Ruoslahti E (1999) Membrane dipeptidase is the receptor for a lung-targeting peptide identified by in vivo phage display. J Biol Chem 274(17):11593–11598

124. Rajotte D, Arap W, Hagedorn M, Koivunen E, Pasqualini R, Ruoslahti E (1998) Molecular heterogeneity of the vascular endothelium revealed by in vivo phage display. J Clin Invest 102(2):430–437

125. Porkka K, Laakkonen P, Hoffman JA, Bernasconi M, Ruoslahti E (2002) A fragment of the HMGN2 protein homes to the nuclei of tumor cells and tumor endothelial cells in vivo. Proc Natl Acad Sci USA 99(11):7444–7449

126. Laakkonen P, Porkka K, Hoffman JA, Ruoslahti E (2002) A tumor-homing peptide with a targeting specificity related to lymphatic vessels. Nat Med 8(7):751–755

127. Cai WB, Shin DW, Chen K, Gheysens O, Cao QZ, Wang SX et al (2006) Peptide-labeled near-infrared quantum dots for imaging tumor vasculature in living subjects. Nano Lett 6(4):669–676

128. Cai W, Chen X (2006) Anti-angiogenic cancer therapy based on integrin alphavbeta3 antagonism. Anti-Cancer Agents Med Chem 6(5):407–428

129. Cai WB, Rao JH, Gambhir SS, Chen XY (2006) How molecular imaging is speeding up antiangiogenic drug development. Mol Cancer Ther 5(11):2624–2633

130. Cai WB, Chen K, Mohamedali KA, Cao QZ, Gambhir SS, Rosenblum MG et al (2006) PET of vascular endothelial growth factor receptor expression. J Nucl Med 47(12):2048–2056

131. Cai WB, Chen XY (2007) Multimodality imaging of vascular endothelial growth factor and vascular endothelial growth factor receptor expression. Front Biosci 12:4267–4279

132. Ferrara N (2004) Vascular endothelial growth factor: basic science and clinical progress. Endocr Rev 25(4):581–611

133. Levenson RM (2004) Spectral imaging and pathology: seeing more. Lab Med 35(4):244–252

134. Mansfield JR, Gossage KW, Hoyt CC, Levenson RM (2005) Autofluorescence removal, multiplexing, and automated analysis methods for in-vivo fluorescence imaging. J Biomed Opt 10(4):41207

135. Yu XF, Chen LD, Li KY, Li Y, Xiao S, Luo X et al (2007) Immunofluorescence detection with quantum dot bioconjugates for hepatoma in vivo. J Biomed Opt 12(1):014008

136. Tada H, Higuchi H, Wanatabe TM, Ohuchi N (2007) In vivo real-time tracking of single quantum dots conjugated with monoclonal anti-HER2 antibody in tumors of mice. Cancer Res 67(3):1138–1144

137. Chen HY, Li L, Cui SS, Mahounga D, Zhang J, Gu YQ (2011) Folate conjugated CdHgTe quantum dots with high targeting affinity and sensitivity for in vivo early tumor diagnosis. J Fluoresc 21(2):793–801

138. Xue B, Deng DW, Cao J, Liu F, Li X, Akers W et al (2012) Synthesis of NAC capped near infrared-emitting CdTeS alloyed quantum dots and application for in vivo early tumor imaging. Dalton Trans 41(16):4935–4947

139. Hong GS, Robinson JT, Zhang YJ, Diao S, Antaris AL, Wang QB et al (2012) In vivo fluorescence imaging with Ag_2S quantum dots in the second near-infrared region. Angew Chem Int Ed 51(39):9818–9821

140. Nicholson C (2005) Factors governing diffusing molecular signals in brain extracellular space. J Neural Transm 112(1):29–44

141. Nicholson C, Chen KC, Hrabetova S, Tao L (2000) Diffusion of molecules in brain extracellular space: theory and experiment. Prog Brain Res 125:129–154

142. Thorne RG, Nicholson C (2006) In vivo diffusion analysis with quantum dots and dextrans predicts the width of brain extracellular space. Proc Natl Acad Sci USA 103(14):5567–5572

143. Santra S, Yang H, Stanley JT, Holloway PH, Moudgil BM, Walter G et al (2005) Rapid and effective labeling of brain tissue using TAT-conjugated CdS: Mn/ZnS quantum dots. Chem Commun 25:3144–3146

144. Muhammad O, Popescu A, Toms SA (2007) Macrophage-mediated colocalization of quantum dots in experimental glioma. Methods Mol Biol 374:161–171

145. Louie AY (2010) Multimodality imaging probes: design and challenges. Chem Rev 110(5):3146–3195

146. Yu JH et al (2013) High-resolution three-photon biomedical imaging using doped ZnS nanocrystals. Nat Mater 12:359–366

Dental Composites Reinforced with Ceramic Whiskers and Nanofibers

40

Xiaoming Xu and Hockin H. K. Xu

Introduction

Dental composites have been widely used in dentistry to restore tooth cavities due to their esthetics and direct-filling capabilities [1, 2]. However, nearly half of all dental restorations fail within 10 years with fracture and secondary caries as the main reasons for failure, and replacing the failed restorations consumes 50–70 % of the average dentist's practice time [3–7]. Extensive studies have significantly improved the mechanical and physical properties as well as the handling characteristics of dental composites [8–14]. These previous studies have investigated and improved the fillers, resin compositions, filler-matrix bonding, and cure conditions. Further enhancements are needed for dental composites to overcome brittle fracture and high failure rates in large-sized, stress-bearing posterior restorations, especially those that involve the replacement of tooth cusps.

Another important aspect in reducing restoration failure is to inhibit secondary caries at the tooth-restoration margins. One approach is the development and application of fluoride-releasing dental materials. Fluoride is a well-documented

X. Xu (✉)

Division of Biomaterials, Department of Comprehensive Dentistry & Biomaterials, Louisiana State University Health Sciences Center School of Dentistry, New Orleans, LA, USA
e-mail: xxu@lsuhsc.edu; xiaomingxu@hotmail.com

H.H.K. Xu

Biomaterials & Tissue Engineering Division, Department of Endodontics, Prosthodontics and Operative Dentistry, University of Maryland School of Dentistry, Baltimore, MD, USA
e-mail: hxu@umaryland.edu

anticaries agent. Water fluoridation and the use of fluoride-containing toothpaste have contributed to the reduction of dental caries in the past 40 years. However, current commercial fluoride-releasing dental composites containing F-releasing glass filler particles have very low fluoride-releasing and recharge capabilities, while glass ionomers (GI) and resin-modified glass ionomers (RMGI), which have high fluoride release, have low mechanical properties [15]. The early attempts to increasing fluoride release by incorporating soluble fluoride salts (e.g., NaF, SnF_2) in dental composites have yielded the materials with poor mechanical properties due to the porosity formed after the dissolution of fluoride salts [16]. Recently, X. Xu, et al. [17–23] have developed several fluoride-exchange (fluoride-releasing) monomers. Using together with fluoride-releasing fillers and antibacterial monomer, they can significantly increase fluoride release and recharge capability of the composite while minimizing the reduction of mechanical properties [21, 22].

Another approach to reduce secondary caries is to incorporate calcium phosphates (CaP) or calcium fluoride (CaF_2) particles into composites to render them bioactive. The CaP composites were capable of releasing Ca and P ions which could remineralize the tooth lesions [24–26]. Previous studies developed traditional CaP composites with particle sizes of 1–55 μm, yielding relatively low mechanical properties that were inadequate for bulk restoratives [24, 25]. More recently, a spray-drying technique produced calcium phosphate and calcium fluoride nanoparticles with sizes of about 50–100 nm, which were incorporated into dental resins [27]. In particular, nanoparticles of amorphous calcium phosphate (NACP) were synthesized with a mean particle size of 116 nm, and dental nanocomposites containing CaP nanoparticles have many advantages over the composites with micrometer-sized CaP particles [28–30]. They release high levels of cavity-fighting ions at low filler levels, thus making room in the resin matrix for significant amounts of reinforcement fillers and leading to enhanced mechanical properties.

In general, dental composites, particularly those containing and releasing anticaries agents, have insufficient strength and fracture toughness. One of the most effective methods to reinforce dental composites is to incorporate various high-strength, high-modulus fibers into the material. Since the early 1990s, fiber-reinforced composites (FRCs) have been extensively studied [31–34]. Long continuous fibers with high strength and modulus, in the form of unidirectional fibers, woven fibers, or braided ribbons, have been incorporated into the polymer matrix. Ultra-high-molecular-weight polyethylene (UHMWPE, 18–35 μm), Kevlar (aramid), carbon fibers, and glass fibers have been used with varying degrees of success. The most commonly used fiber is silane-treated, monomer-preimpregnated glass fiber. The properties of the fibers commonly used in FRC and some commercial ceramic oxide fibers are listed in Table 40.1.

Fiber-reinforced composites have shown significant increase of mechanical properties over conventional particle-reinforced dental composites. For example, FRCs have flexure strength 200∼500 MPa, fiber posts 800∼1,600 MPa, compared to 80∼130 MPa for conventional dental composites. The influence of fiber type, wetting (bonding) agents, and orientation on the mechanical properties of FRC has been studied [35–38]. FRCs have been used as posts

Table 40.1 Properties of common fibers used in FRCs and some commercial ceramic fibers

Property	Chemical composition (%)	Crystal phase	Tensile strength (GPa)	Tensile modulus (GPa)	Ref.
E-glass	SiO_2 52-56, CaO 15-25, Al_2O_3 12-16, B_2O_3 5-11	_	3.4	72	[31, 44]
S-glass	_	_	4.5	85	[31]
Carbon	C	_	2.4–3.3	230–390	[31]
Spectra 900	Polyethylene	_	2.6	117	[31]
Nextel^{TM} 610	>99 Al_2O_3	α-Al_2O_3	3.3	373	[45]
Nextel^{TM} 650	89 Al_2O_3, 10 ZrO_2, 1 Y_2O_3	α-Al_2O_3+ cubic ZrO_2	2.5	358	[45]
Nextel^{TM} 720	85 Al_2O_3, 15 SiO_2	α-Al_2O_3+ mullite	2.1	260	[45]

(e.g., C-Post^{TM} and FibreKor^{TM} post) and prosthodontic restorations, such as inlays [39], crowns [40], and fixed partial dentures (FPD) [41]. However, the fabrication of such fiber-reinforced composite restorations is technique sensitive and time consuming, and they are very difficult to use for direct restoration of dental cavities. In addition, some of the fiber materials such as Kevlar and E-glass have shown unsatisfactory chemical stability, i.e., they have substantial decomposition after prolonged water immersion [42–44]. Nowadays, the only significant commercial application of FRCs in dental clinics is fiber posts.

The applications of short glass fibers [46–48] in dental composites as direct-filling materials have been studied. A commercial dental composite, Alert (Jeneric/Pentron), containing coarse glass fibers (diameter ∼10 μm) has been reported to have significant higher fracture toughness and modulus but equal or lower flexure strength than other packable composites (Surefil, Prodigy, Z-100) [46, 47]. Another similar composite, DC-Tell (DCS Dental, Finland), also contains 38 % short (<200 μm) glass fibers with composition similar to E-glass and has high initial flexure strength (297 MPa, dry samples), but it decreased 66 % after storage in water for 3 months [48]. In general, these short fiber-reinforced dental composites have shown different degrees of improvement in mechanical properties and fracture toughness, but their chemical stability, esthetics, and handling properties are often unsatisfactory. For example, Alert is a very tough resin and difficult to handle in clinic.

Properties of Ceramic Whiskers and Nanofibers

Ceramic whiskers are single-crystalline ceramics. For example, the scanning electron micrographs of silicon nitride and silicon carbide whiskers are shown in Fig. 40.1 [49]. The silicon nitride whiskers (β-Si_3N_4) (UBE Industries,
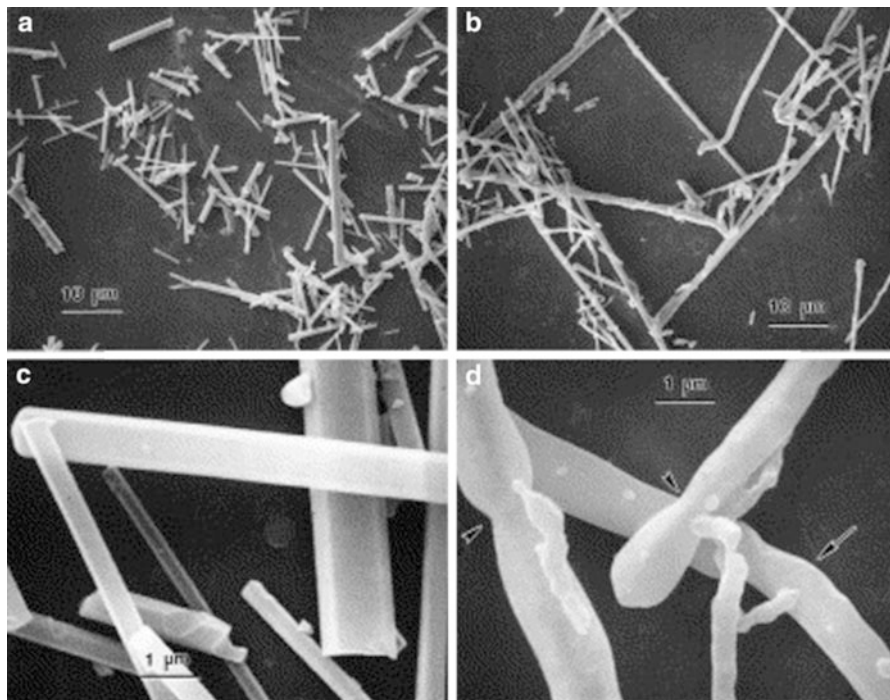
Fig. 40.1 (**a**) and (**b**) are SEM images of silicon nitride and silicon carbide whiskers, respectively. (**c**) Silicon nitride whiskers were straight with smooth surfaces. (**d**) Some of the silicon carbide whiskers were bent (*long arrow*), and some had diameters that varied along their lengths (*short arrows*) (Adapted from Ref. [49], with permission)

New York, NY) are relatively straight with smooth surfaces (Fig. 40.1a and c) and have diameters ranging from about 0.1–2 μm (mean = 0.4 μm) and lengths ranging from 2 to 30 μm (mean = 5 μm). The silicon carbide whiskers (Advanced Refractory Technologies, Buffalo, NY) have diameters ranging from about 0.1–3 μm with a mean of approximately 0.7 μm and lengths ranging from about 2 to nearly 100 μm with a mean of approximately 14 μm (Fig. 40.1b). Some of the silicon carbide whiskers were bent, and some had diameters varying along their lengths (Fig. 40.1d). Ceramic whiskers have very high tensile strength. Silica nitride whiskers, for example, have a tensile strength of about 50 GPa [50], more than 10 times that of glass fibers.

Ceramic oxide fibers are long polycrystalline fibers. They usually have high mechanical properties and toughness. The mechanical properties of some commercial ceramic oxide fibers are listed in Table 40.1. They also have superior chemical stability (inertness), resisting acid, and alkaline attacks, even at high temperatures (700–1,000 °C). Coarse (7–20 μm) ceramic oxide fibers, including yttria-stabilized zirconia (YSZ) and alumina fibers, have been produced commercially and used as

Table 40.2 Physical properties of some ceramic oxides [51]

Compound	Mineral name	Chemical formulae	Hardness (Mohs' scale)	Refractive index
α-Alumina	Corundum	Al_2O_3	9	1.761
Aluminum silicate	Andalusite	Al_2OSiO_4	7.5	1.64
Aluminum silicate	Mullite	$3Al_2O_3 \cdot 2SiO_2$	–	1.638
Silica	Quartz	SiO_2	7	1.544
Zirconia	Baddeleyite	ZrO_2	6.5	2.13
Zirconium orthosilicate	Zircon	$ZrSiO_4$	7.5	1.94
Silicon carbide	Moissanite	SiC	9.5	2,648
Silicon nitride	–	Si_3N_4	–	2.2

heat insulation materials, catalysts, etc. Table 40.2 lists the names, chemical formulae, and hardness and refractive index of some common ceramic oxides as well as SiC and Si_3N_4. Alumina and zirconia ceramics have been increasingly used in all-ceramic prosthodontic restorations (crowns, bridges, and veneers). Therefore, ceramic oxide fibers may be good candidates for fiber-reinforced dental composites.

One drawback of ceramic whiskers and fibers as reinforcement elements in dental composites is their high refractive index (Table 40.2). The mismatch of refractive indices with resin matrix (1.53) causes severe light scattering, which makes the composite opaque and reduces the degree of polymerization conversion and the depth of cure. For example, the dental composites containing a significant amount of SiC or Si_3N_4 whickers cannot be light cured. They can only be heat cured or chemical cured [49, 52–57].

Recently, the nanofibers of zirconia-based ceramics – ZrO_2-Y_2O_3 (ZY), ZrO_2-SiO_2 (ZS), and ZrO_2-Y_2O_3-SiO_2 (ZYS) – and silica-rich SiO_2-ZrO_2-Y_2O_3 have been fabricated by reactive sol-gel electrospinning and calcination [58, 59]. Figure 40.2 shows the morphologies of various ceramic nanofibers. The ZY nanofibers have a "sausage-like" morphology because of the grained structure due to formation of tetragonal crystalline phase, while ZS and ZYS nanofibers calcinated at 1,200 °C have smooth surfaces. The ZS nanofibers calcinated at 1,400 °C have a rougher surface than those calcinated at 1,200 °C but did not show grain structure.

The dental composite reinforced with 2.5 % or 5 % ZS or ZYS nanofibers can be cure by either heat of dental curing light, and they have shown significant (20–40 %) increase in flexural strength and toughness [60]. However, the composites appear opaque, and the degree of polymerization conversion decreases with increase of fiber content. The silica-rich SiO_2-ZrO_2-Y_2O_3 nanofibers containing 85 % silica have been fabricated using an improved coaxial reactive electrospinning method, and the dental composite containing such ceramic nanofibers has shown similar reinforcement effect but significantly improved translucency and esthetics [59]. More details will be described in later sections.
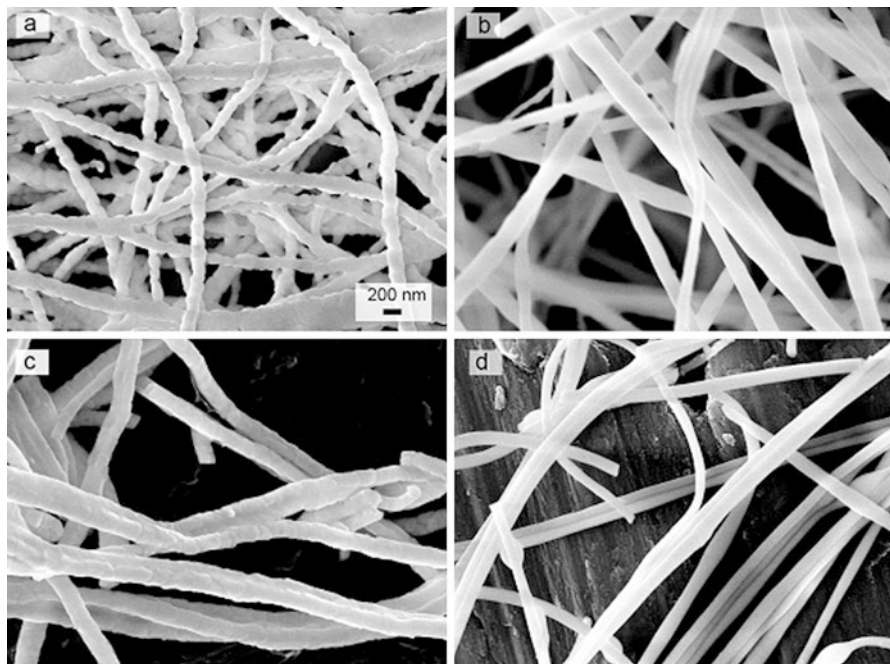
Fig. 40.2 SEM images of (**a**) ceramic ZrO_2-Y_2O_3 nanofibers (molar ratio 96/4) calcinated at 1,200 °C, (**b**) ceramic ZrO_2-SiO_2 (molar ratio 80/20) nanofibers calcinated at 1,200 °C, (**c**) ceramic ZrO_2-SiO_2 nanofibers calcinated at 1,400 °C, and (**d**) ceramic ZrO_2-Y_2O_3-SiO_2 nanofibers (molar ratio 76.8/3.2/20) calcinated at 1,200 °C. (All fibers are electrospun from the sol containing 1.5 M ZrO_2 and 1.5 % PEO. All images have magnification of 50,000) (Adapted from Ref. [57], with permission)

Dental Composites Reinforced with Ceramic Whiskers

Dental Composite Reinforced with Si_3N_4 Whiskers

Although SiC and Si_3N_4 whiskers have high strength and modulus, their surfaces are inert and smooth. Consequently, they cannot be directly treated with a silane coupling agent, and they have low retention in the polymer matrix. One solution to this problem is to fuse them with silica nanoparticles and then treat resulting material with a silane coupling agent. Xu, HH et al. have successfully used this method in a series of reports on the whisker-reinforced dental composites [49, 51–56]. Their mechanical properties and in vitro wear have been tested.

Nano-sized silica (Aerosil OX50, Degussa, Ridgefield, NJ) with particle sizes of approximately 40–100 nm was used. Silicon nitride whiskers (β-Si_3N_4, UBE, New York, NY) were used with diameters of 0.1–2 μm (mean = 0.4 μm) and lengths of 2–30 μm (mean = 5 μm). The whiskers were mixed with silica at

Fig. 40.3 Fracture toughness (K_{IC}) of whisker composite. (**a**) SEM micrograph of nano-silica-fused whisker after fusion at 800 °C. The nano-silica particles (*S*) were indicated by the arrow, and "*W*" designates the whisker. (**b**) K_{IC} vs. whisker filler level (mean ± sd; $n = 6$). Dissimilar letters indicate values that are significantly different ($p < 0.05$). (**c**) K_{IC} was measured by using a single-edge V-notched beam method with a sharp notch. An indirect inlay/onlay composite (Concept, Ivoclar, Amherst, NY) was referred to as inlay/onlay control. An indirect prosthetic composite (Artglass, Heraeus Kulzer GmbH, Germany) was referred to as prosthetic control (Adapted from Ref. [23] with permission)
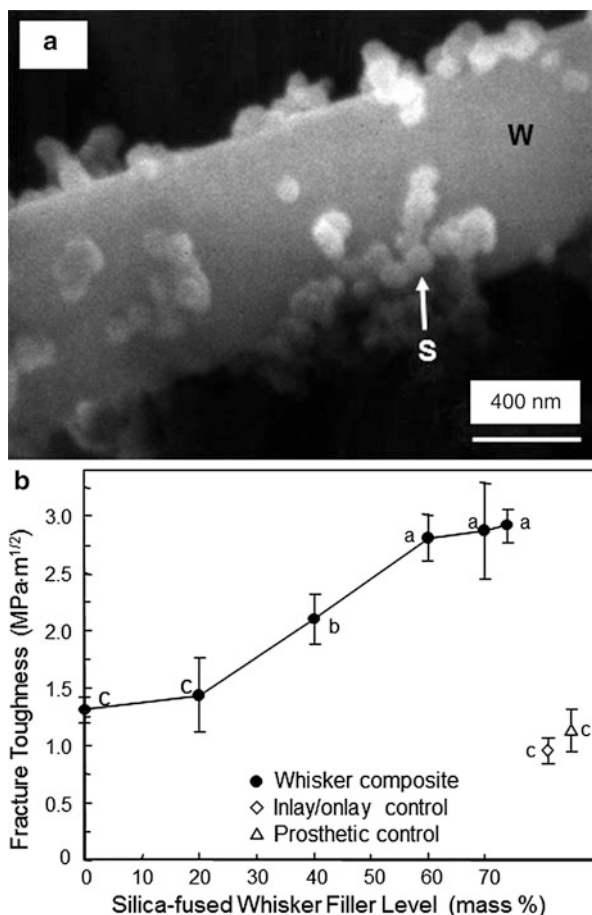
a whisker-to-silica mass ratio of 2:1. The mixed powder was heated in a furnace at 800 °C for 30 min to fuse the nano-silica onto the whiskers. The powder was silanized via 4 % 3-methacryloxypropyltrimethoxysilane and 2 % *n*-propylamine in cyclohexane. The silanized powder was mixed with a resin monomer of mass fractions of 48.965 % of an oligomeric urethane derivative of BisGMA (NCO/BisGMA, Caulk/Dentsply, Milford, DE), 48.965 % triethylene glycol dimethacrylate (TEGDMA), 2 % benzoyl peroxide, and 0.07 % 4-methoxyphenol. The following filler level mass fractions (%) were used: 0 (unfilled resin), 20, 40, 60, 70, and 74. For fracture toughness test, the paste was placed in steel molds of $2 \times 2 \times 25$ mm and heat cured in an oven at 120 °C for 30 min. For wear testing, the paste was placed in mold cavities of 4 mm diameter and 3 mm depth and cured in the same manner. Specimens were immersed in water at 37 °C for 24 h prior to testing.

Figure 40.3a shows a representative SEM micrograph of the nano-silica-fused whiskers. Figure 40.3b plots the fracture toughness. Fracture toughness (mean ± sd; $n = 6$) at a silica-fused whisker filler mass fraction of 74 % was
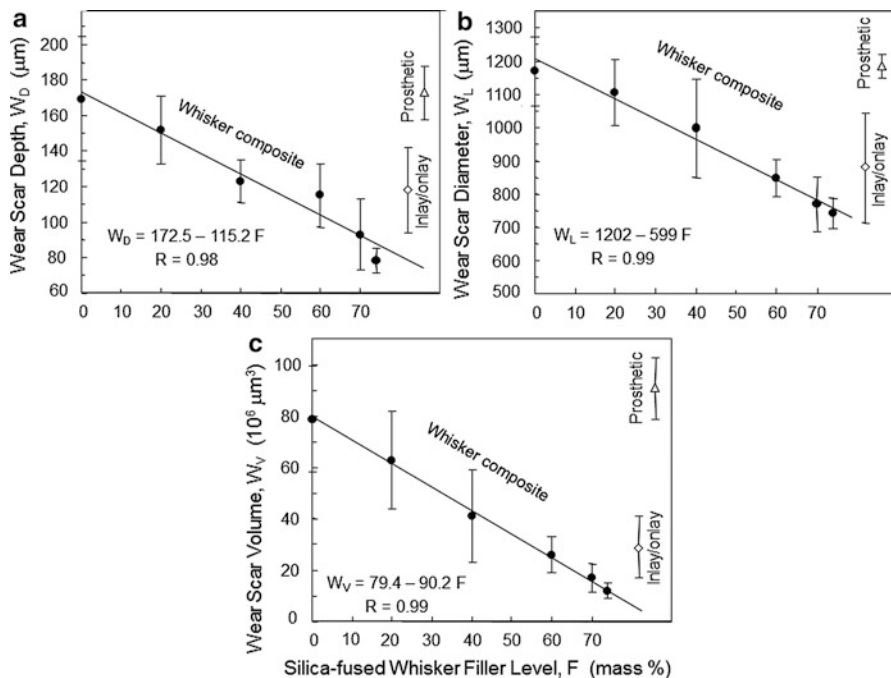
Fig. 40.4 Three-body wear: (**a**) wear scar depth W_D, (**b**) wear scar diameter W_L, and (**c**) wear scar volume W_V versus whisker filler level F (mean $\pm$ sd; $n = 6$). Data for the prosthetic and inlay/onlay composite controls were included in each plot near the right axis. The line through the data was the linear best fit with the equation with correlation coefficient R (Adapted from Ref. [23] with permission)

2.92 $\pm$ 0.14 MPa $\cdot$ m$^{1/2}$, significantly higher than those at filler levels from 0 % to 40 %; 1.13 $\pm$ 0.19 MPa $\cdot$ m$^{1/2}$ for a commercial prosthetic composite; and 0.95 $\pm$ 0.11 MPa $\cdot$ m$^{1/2}$ for a commercial inlay/onlay composite ($p < 0.05$).

A four-station wear apparatus (Caulk/Dentsply, Milford, DE) was used to test the wear resistance of the composites [61]. Each specimen was surrounded by a brass ring filled with a water slurry containing 63 % mass fraction of polymethyl methacrylate (PMMA) beads of a mean particle size of 44 μm. A carbide steel pin with a tip diameter of approximately 3 mm was loaded onto the specimen submerged in the slurry of PMMA beads in each of the four stations. A maximum load of 76 N was used, and each specimen was subject to 4×10^5 wear cycles. Figure 40.4 plots wear scar depth, diameter, and volume vs. silica-fused whisker filler level. Increasing the whisker filler level significantly decreased the amount of wear ($p < 0.05$). The line in each plot is a linear best fit to the data for the whisker composites, with correlation coefficients R of 0.98, 0.99, and 0.99 for wear depth, diameter, and volume, respectively. In (A), the whisker composite at a filler mass fraction of 74 % had a wear depth of (77.7 $\pm$ 6.9) μm, significantly less than 118.0 $\pm$ 23.8 μm of the inlay/onlay control and 172.5 $\pm$ 15.4 μm of the prosthetic

control ($p < 0.05$). The wear volume (C) of the whisker composite at 74 % filler mass fraction was 12.1 ± 3.2 (10^6 μm^3), not significantly different from 29.3 ± 11.9 (10^6 μm^3) of the inlay/onlay control, both of which were significantly less than 91.2 ± 11.8 (10^6 μm^3) of the prosthetic control ($p < 0.05$). Therefore, increasing the nano-silica-fused whisker filler level significantly increased the composite K_{IC} and wear resistance. The high resistance to wear and high fracture toughness may help extend the use of whisker composite to larger stress-bearing posterior restorations involving cusps.

Whisker-Reinforced Dental Composites Containing CaP Nanoparticles

Nano-sized dicalcium phosphate anhydrous (DCPA, CaHPO$_4$) particles were prepared via a spray-drying process [62]. Briefly, a solution was prepared by dissolving 1.088 g of DCPA (J.T. Baker, Phillipsburg, NJ) in 1 L of an acetic acid at 16 mmol/L concentration to obtain a Ca and PO$_4$ ionic concentration of 8 mmol/L. The solution was sprayed through a nozzle (PNR America, Poughkeepsie, NY) that was situated on the top of a heated glass column. An electrostatic precipitator (MistBuster, Air Quality Engineering, Minneapolis, MN) was connected to the lower end of the column and drew air from the column to create a steady flow of air/mist. The water/volatile acid was evaporated into the dry, heated column and expelled from the precipitator into an exhaust hood. The dried particles were collected by the electrostatic precipitator. Transmission electron microscopy (TEM) revealed agglomerated particles with individual particles having a size of approximately 50 nm [62]. The XRD pattern had peaks corresponding to DCPA. The BET measurement yielded a specific surface area of 18.6 m^2/g [24].

Three groups of specimens were tested (Fig. 40.5). A 3×3 design was used with three resins (direct filling with HEMA; direct filling without HEMA; indirect heat cured without HEMA) and three DCPA-to-whisker mass ratios (1:2, 1:1, 2:1) (designated as "D:W"). The Ca and P ion release increased with time and then reached a plateau with further increase in time. The ion release also increased with the DCPA-to-whisker mass ratio. The composite with HEMA (D:W = 2:1) had higher release than other composites ($p < 0.05$). For group 1 at 56 d, the total ionic P concentration reached 1.95 ± 0.13 mmol/L, 0.98 ± 0.05 mmol/L, and 0.43 ± 0.07 mmol/L, at D:W = 2:1, 1:1, and 1:2, respectively. The corresponding Ca concentrations reached 0.68 ± 0.07 mmol/L, 0.38 ± 0.05 mmol/L, and 0.27 ± 0.01 mmol/L, respectively [62].

Whisker-CaP Composite with Different Filler Levels

The effects of different filler levels of ceramic whiskers on the mechanical properties and ion release of whisker-CaP composites have been studied [63]. Silicon nitride whiskers (β-Si$_3$N$_4$, UBE) were mixed with nano-silica (Aerosil OX50) at
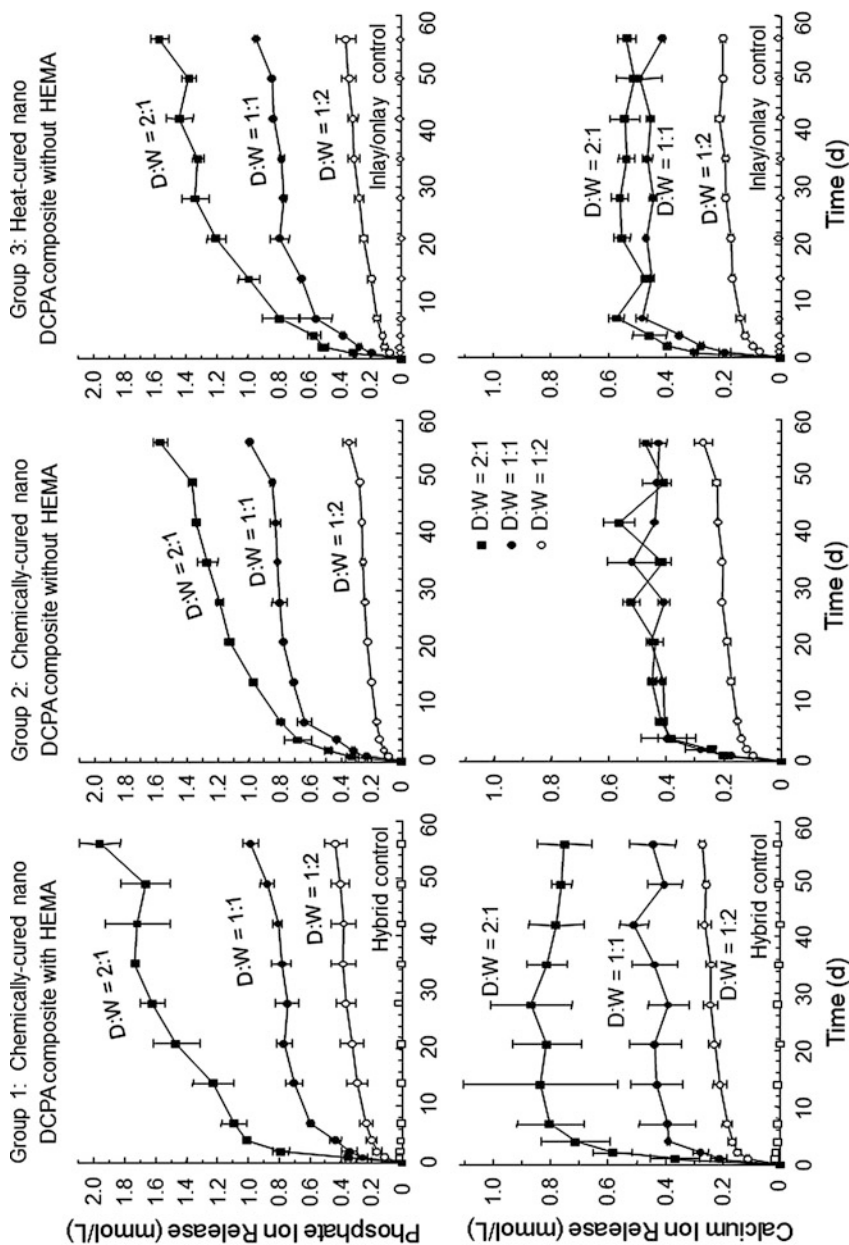
Fig. 40.5 (continued)

a whisker-to-silica mass ratio of 5:1. The mixture was heated in a furnace at 800 °C for 30 min to fuse the silica onto the whiskers. The powder was then silanized. The fillers consisted of nano-silica-fused whiskers and nano-DCPA at an intermediate DCPA-to-whisker mass ratio of 1:1. To fabricate the composites with different filler levels, the (DCPA+whiskers)/(DCPA+whiskers+resin) mass fractions in the resin were 0 %, 30 %, 40 %, 50 %, 60 %, 65 %, 70 %, and 75 %.

The Ca and P ion release from these composites is shown in Fig. 40.6. The ion release significantly increased with increasing the filler level ($p < 0.05$). In addition, the ion release increased with time and then started to plateau. At 56 days, the released Ca ion concentration (mean $\pm$ sd; $n = 3$) was 0.65 $\pm$ 0.02 mmol/L with 75 % fillers, significantly higher than 0.59 $\pm$ 0.02 mmol/L with 70 % fillers, and 0.39 $\pm$ 0.03 mmol/L with 65 % fillers ($p < 0.05$). The corresponding P ion concentrations were 2.29 $\pm$ 0.07 mmol/L, 1.92 $\pm$ 0.14 mmol/L, and 1.26 $\pm$ 0.09 mmol/L, at filler levels of 75 %, 70 %, and 65 %, which were significantly different from each other ($p < 0.05$). The new nanocomposites with substantial Ca and P ion release possessed mechanical properties matching those of a commercial stress-bearing and non-releasing composite [63]. Therefore, the nano-DCPA-whisker composite may have both stress-bearing and caries-inhibiting capabilities, a combination not yet available in current dental restorative materials.

Dental Composites Reinforced with Ceramic Nanofibers

Dental Composite Reinforced with ZrO-Y$_2$O$_3$-SiO$_2$ Ceramic Nanofibers

As mentioned above, dental composites reinforced with ceramic SiC and Si$_3$N$_4$ whisker have high strength and toughness, but they have a serious drawback: they cannot be light cured due the high refractive index of the whiskers. The mismatch of refractive index with the resin matrix causes severe light scattering, makes the composite opaque, and reduces the degree of polymerization conversion and the depth of cure. One possible solution is to use nanofibers of high-strength ceramics such zirconia or alumina. The hypothesis is as follows: if the diameter of the fiber is less than half of the wavelength of curing light (e.g., blue light at 470 nm), i.e., <230 nm, the refraction of the visible light will be greatly reduced and the translucency and esthetics of the material will be improved. However,

Fig. 40.5 Ion release from the whisker-reinforced CaP composites (mean $\pm$ sd; $n = 4$). The nano-DCPA-to-whisker mass ratio was designated as D:W. For each group, two-way ANOVA showed significant effects of D:W and immersion time, with a significant interaction between the two parameters ($p < 0.05$). Increasing the D:W ratio significantly increased the P and Ca ion concentrations ($p < 0.05$). At each D:W, increasing the immersion time significantly increased the P and Ca ion concentrations. The hybrid control and inlay/onlay control had no detectable release (Adapted from Ref. [24] with permission)

Fig. 40.6 Ion release from nano-DCPA-whisker composites versus filler level and immersion time: (**a**) Ca ion release and (**b**) total ionic P release. The symbols on the x-axis represent the hybrid control (TPH, Caulk/ Dentsply) and the unfilled resin that had no Ca or P ion release. Each value is mean $\pm$ sd; $n = 3$. *Lines* connect the data points for visual clarity (Adapted from Ref. [25] with permission)
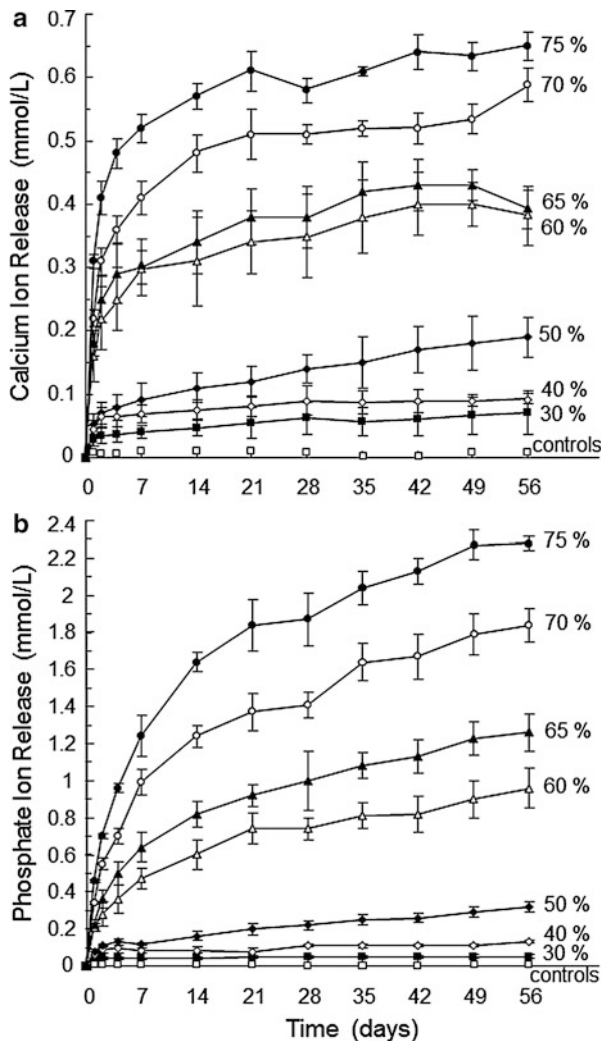
zirconia and alumina are inert and nonreactive to silane coupling agents. Therefore, incorporation of silica into ceramic nanofibers would enhance surface treatment by silane and reduce refractive index of the nanofibers.

Recently, Xu X. et al. have fabricated the nanofibers of zirconia-based ceramics, ZrO_2-Y_2O_3 (ZY, Z/Y = 96/4 mol%), ZrO_2-SiO_2 (ZS, Z/S = 90/10, or 80/20 mol%), and ZrO_2-Y_2O_3-SiO_2 (ZYS, Z/Y/S = 76.8/3.2/20 mol%), using reactive sol-gel electrospinning and calcination (Fig. 40.2) [58]. The mean diameters of ZS ceramic nanofibers varied from 102 to 272 nm and increased with ZrO_2 sol concentration (1–2 M). X-Ray diffraction analysis of the ceramic nanofibers calcinated at different

temperatures shows that ZY and ZYS calcinated between 800 °C to 1,400 °C have pure tetragonal ZrO_2 Phase. The ZS nanofibers calcinated between 800 to 1,200 °C have pure tetragonal ZrO_2, while those calcinated at 1,400 °C have 99 % monoclinic ZrO_2. No crystalline silica or silicates were detected from ZS and ZYS nanofibers. Therefore, the ZS and ZYS nanofibers are composite ceramic nanofibers consisting of tetragonal zirconia and amorphous silica [58].

The experimental ceramic nanofiber-reinforced dental composites have been formulated [60] with different amounts (0, 2.5, 5.0, and 7.5 wt%) of silanized ceramic nanofibers and glass filler particles (mean diameter of 0.8 μm, Caulk/Dentsply) (total filler content of 70 wt%) and 29 % of dental monomer mixture (11.6 % BisGMA, 11.6 % EBPADMA, and 5.8 % HDDMA). The heat-cured composites contain 1 % benzyl peroxide (BPO) as initiator, and the light-cured composites contained 1 % of mixed photoinitiators (0.14 % camphorquinone (CQ), 0.59 % ethyl 4-dimethylaminobenzoate (4E), and 0.27 % phenylbis (2,4,6-trimethyl benzoyl)phosphine oxide (PO)). Both ZS1 (zirconia/silica 90/10) and ZS2 (zirconia/silica 80/20) nanofibers were used. These composites were either heat cured (110 °C for 2 h in an oven) or light cured (80 s with an Optilux 501 dental curing light (Kerr Corp, Orange, CA)) and tested for flexural strength (FS), flexural modulus (FM), and energy at break (EAB) at 24 h, 3 months, and 6 months. The results are shown in Fig. 40.7 and Fig. 40.8 [60].

For the heat-cured composite containing 2.5 % ZS1 nanofibers tested at 24 h, both FS and EAB increased significantly over the control by 28.7 % ($p = 0.004$) and 64.87 % ($p = 0.029$), respectively (Fig. 40.7), while the FM increased only by 6.29 %, which was not statistically significant ($p = 0.145$). When ZS1 nanofiber content was increased to 5 %, there was no significant change in the mean FS ($p = 0.815$), FM ($p = 0.946$), and EAB ($p = 0.996$) compared with HC2.5 %.

After 3 or 6 months storage of control (HC) and HC2.5 % specimens in 37 °C deionized water, FS and EAB of both composites did not change significantly (Fig. 40.7). This was a significant improvement over the glass fiber-reinforced dental composites as reported in [48]. The mean EAB of HC2.5 % was nearly double that of controls at both 3 months ($p = 0.053$) and 6 months ($p = 0.019$). This result indicated that ceramic nanofibers can increase the composite's long-term resistance to fracture.

Light-cured dental composites are more widely used in the dental clinic for direct restorations. Therefore, it is more important to study the influence of nanofibers on mechanical properties of light-cured dental composites. Figure 40.8 shows the FS and EAB of light-cured dental composites after 24 h or 6 months storage in 37 °C deionized water. At 24 h, the composite containing 2.5 % ZS fiber (LC(2.5 %) and 5.0 % ZS nanofibers (LC(5.0 %)) had significantly higher FS and EAB than that of the control composite and were similar to the corresponding heat-cured control composite. After 6 months storage in 37 °C deionized water, the FS and EAB of the control composite decreased but not significantly ($p = 0.852, 0.327$, respectively). There was no significant change in the FS
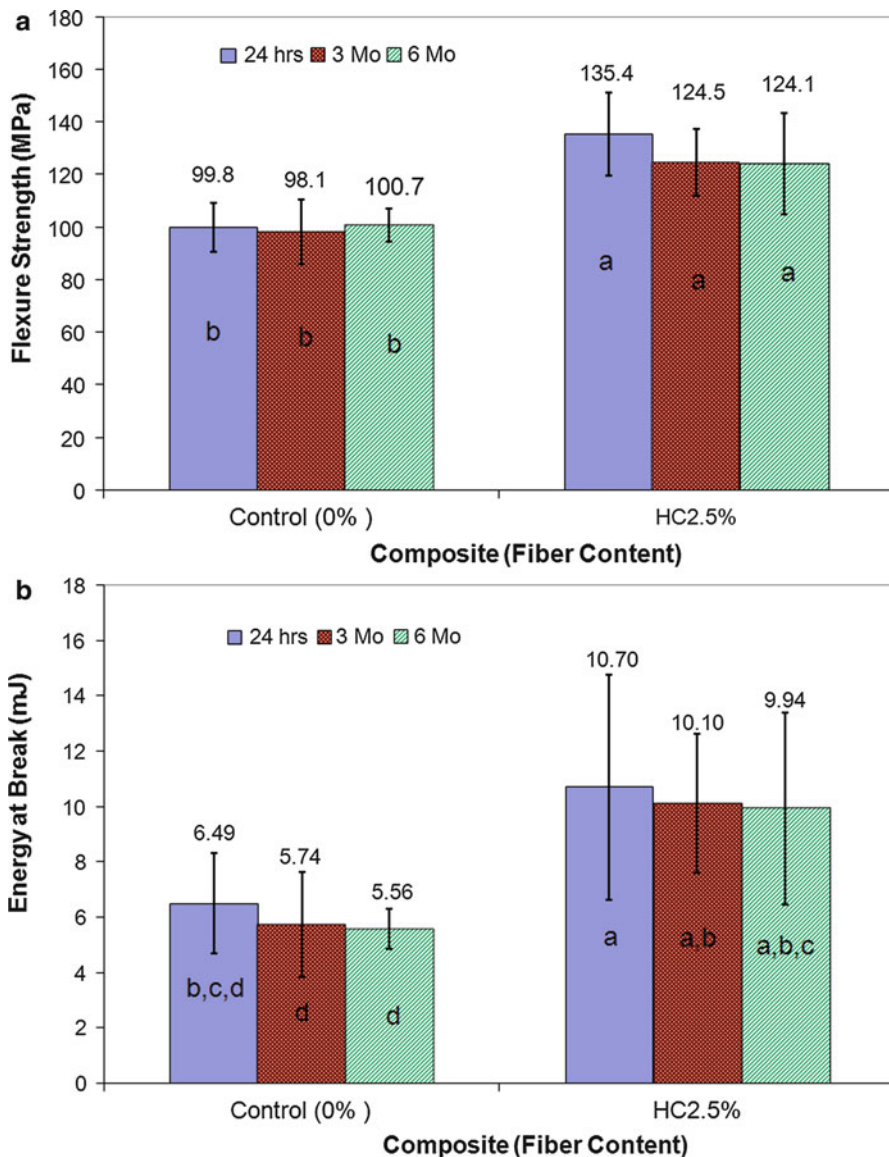
Fig. 40.7 (**a**) Flexural strength (*FS*) and (**b**) energy at break (*EAB*) of heat-cured dental composite with 0 % and 2.5 % ZS1 ceramic nanofibers after immersion in water for 24 h, 3 months, and 6 months [60]

($p = 0.999$) or EAB ($p = 0.999$) of ZS2-reinforced composites (LC(2.5 %)), and they were higher than the control composite (for FS $p < 0.001$ and for EAB $p = 0.001$). The FS and EAB of LC(5.0 %) decreased (for FS, $p = 0.005$, for EAB, $p = 0.067$), but the FS was significantly higher than that of the control
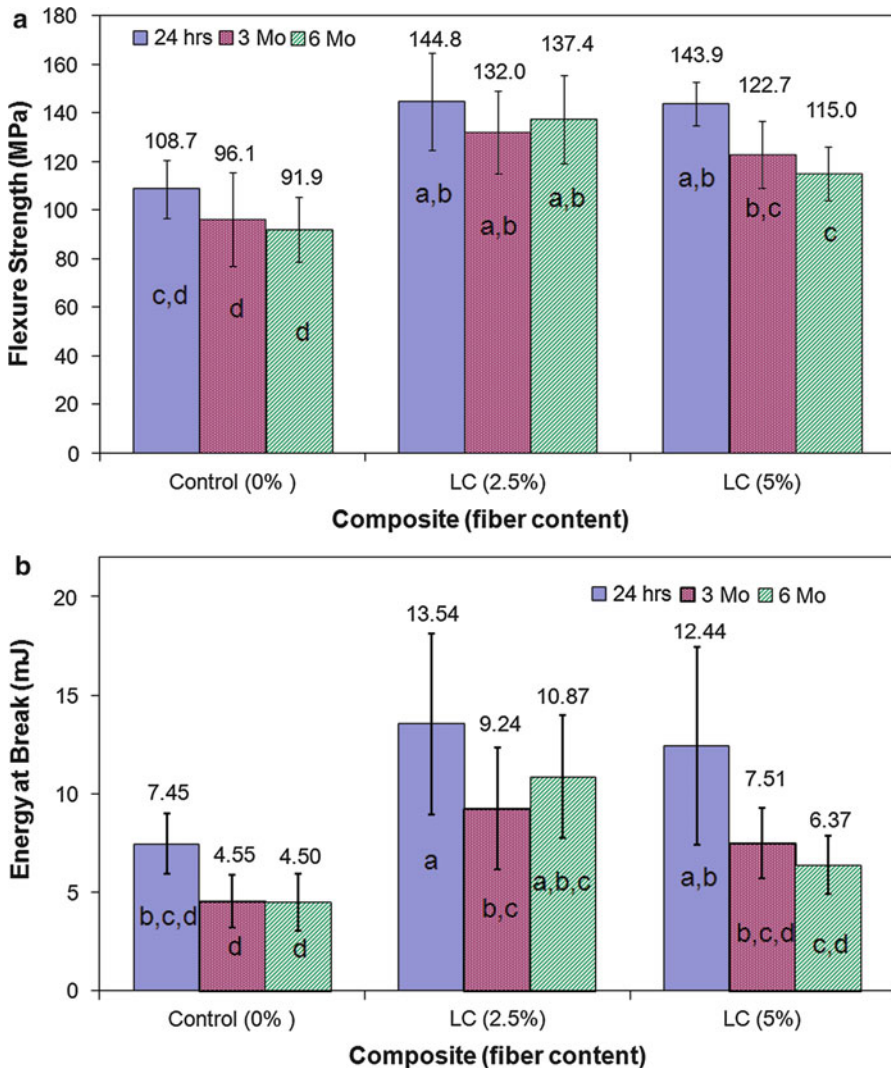
Fig. 40.8 (**a**) Flexural strength and (**b**) energy at break of light-cured dental composite with 0 %, 2.5 %, and 5.0 % ZS2 ceramic nanofibers after immersion in water for 24 h, 3 months, and 6 months [60]

composites ($p = 0.03$), while the EAB was not significantly different ($p = 0.949$). The decrease of FS and EAB for LC(5.0 %) is probably due to the lower degree of conversion caused by increased light scattering, which in turn lead to the leaching out of more uncured monomers. The light-cured composite containing 2.5 % ZYS (zirconia/yttria/silica 76.3/3.6/20) exhibited the highest mean FS (146.4 ± 10.3 MPa), which was 42.3 % higher than that of the control composite. The addition of more

ZS2 nanofibers (7.5 %) to the composite decreased FS slightly compared to LC (5.0 %), but the value was still higher than that of control composites without nanofibers.

Influence of ZS Nanofibers on Degree of Conversion (DC) and Translucence

Figure 40.9 shows the DC of monomers in the light-cured control composite and experimental composites. Through the efforts of reducing the diameter of the ceramic fiber to the nanoscale (<200 nm) and incorporating the amorphous silica in the ceramic nanofibers, the ceramic nanofiber-reinforced composites can be light cured with acceptable DC (62–75 %), which was a significant improvement over the composites reinforced with SiC and Si_3N_4 whiskers, which could not be light cured [49, 52–57]. On the other hand, due to the high refractive index of the zirconia, the refractive indices of the ZS nanofiber-reinforced composites increase with increasing content of ZS nanofibers, while the translucence, as determined by transmittance at 470 nm matching the wavelength of dental curing light, decreases with the increasing content of ZS nanofibers, as shown in Fig. 40.10. Therefore, the DC of the composites decreases with increasing content of the ceramic nanofibers as shown in Fig. 40.9. The reduction in DC may lead to lower mechanical properties, as shown in the case of composite containing 7.5 % ZS2 nanofibers. It can also increase the elution of uncured monomers, which in turn will cause a reduction in the mechanical properties of the composite after immersion in water for 6 months, as demonstrated by composite EXP2(LC).

The above results indicate that impregnation of ZS ceramic nanofibers in light-cured dental composites may have two opposite effects: a fiber reinforcing effect and a weakening effect due to the decrease of DC and the formation of fiber bundles. Therefore, the content of ceramic nanofibers in the composite needs to be optimized in order to tune the composites' mechanical properties. Our experimental results indicate that the suitable content of ZS or ZYS nanofibers in a dental composite is in the range 2.5–5.0 %.

Influence of ZS Nanofibers on Fracture Toughness

Fracture toughness (FT) reflects the resistance to crack propagation from an initiating flaw in materials. This property is very important in dental composites because bulk fracture is one of the main reasons for a shorter life of composites compared to amalgams. Therefore, FT of light-cured dental composites reinforced by nanofibers was tested. When 2.5 % ZS2 nanofibers were added to the composites, FT increased significantly ($1.24 \ MPa \cdot m^{1/2}$) over the control composite ($1.08 \ MPa \cdot m^{1/2}$) ($p < 0.05$), but further increase in the fiber content (5.0 % or 7.5 %) did not lead to significant change
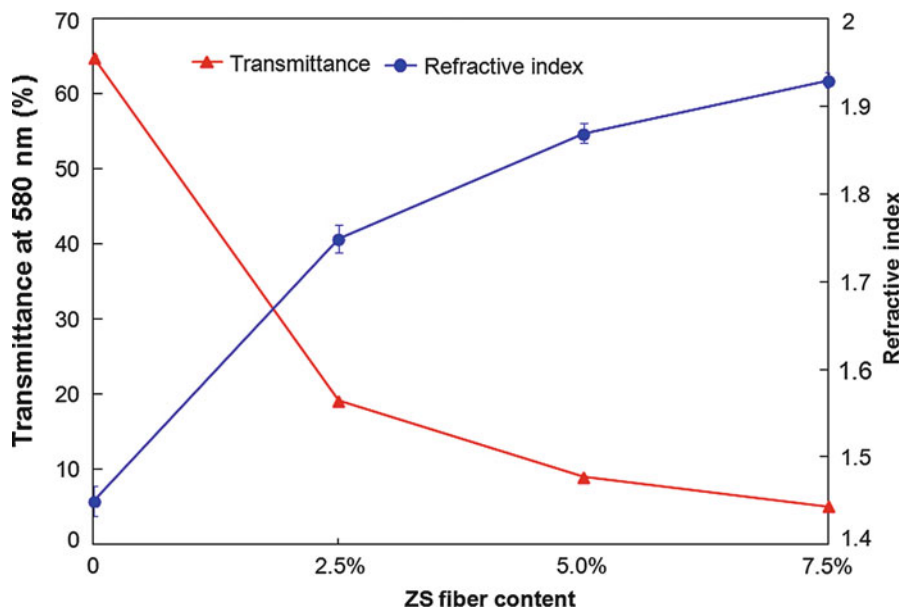
Fig. 40.9 Influence of ZS nanofibers content (0, 2.5 %, 5.9 %, and 7.5 %) on the degree of conversion (groups with the same letter do not have significant difference ($p > 0.05$)) (Adapted from Ref. [60] with permission)

in FT (1.25 or 1.28 MPa • $m^{1/2}$)($p > 0.05$) [60]. It is interesting to compare this result with whisker-reinforced dental composites (Fig. 40.3). The latter had no significant change in FT when whisker content was below 20 %, and FT increase significantly when the whisker content increased above 20 % up to 70 %.

Dental Composite Reinforced with Silica-Rich SiO₂-ZrO-Y₂O₃ Ceramic Nanofibers with Improved Translucency

Although the zirconia-rich ZS and ZYS nanofibers could reinforce the light-cured dental composites and improve their mechanical properties, they still have a problem of light scattering and opacity due to the mismatch of refractive index between the ceramic fiber and resin matrix. This leads to the reduction of degree of conversion and limitation of fiber content in the composite. In a tempt to solve this problem, Li et al. recently fabricated silica-rich SiO_2-ZrO_2-Y_2O_3 nanofibers containing 62–96 mol% silica using a coaxial reactive electrospinning technology [59]. They used a spin-on-glass (SOG, IC1-200 from Futurrex Inc., Southlake, TX, USA) solution containing 10 % siloxane polymer and 4 % poly(vinylpyrrolidone) (PVP) as the source of silica and injected it through an outer (main) tubing of the electrospinning device, and injected the zirconia-yttria sol prepared as previously
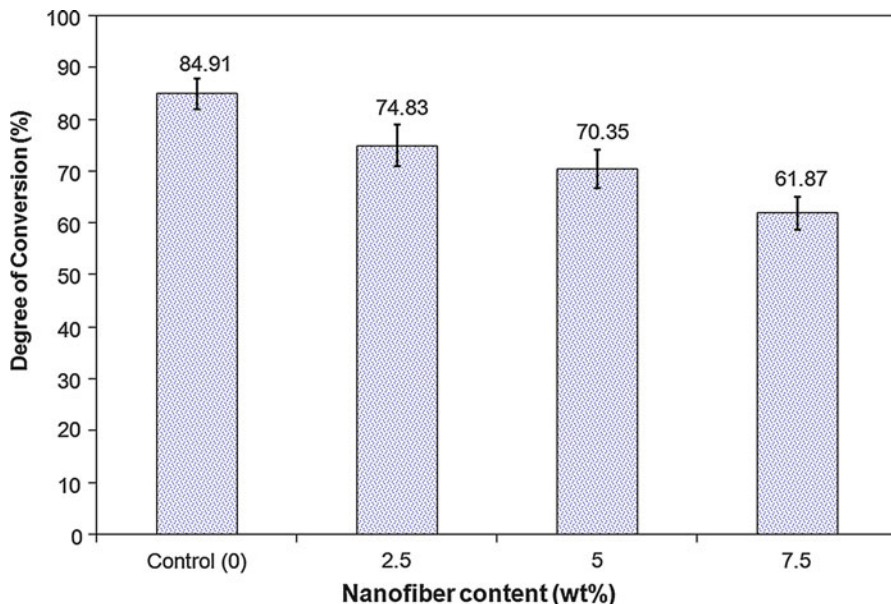
Fig. 40.10 Refractive index and transmittance of ZS nanofiber-reinforced composites with different fiber contents (Adapted from Ref. [60] with permission)

reported [58] with 1 % PEO through an inner (smaller) tubing. The two solutions were mixed at the tip of the spinneret and undergone electrospinning. After calcination at 75 °C, the silica-rich silica-zirconia-yttria (SZY) ceramic nanofibers (mean diameter of 290 nm) were obtained. The nanofibers with various Si/Zr ratios can be readily fabricated by adjusting the flow rate ratio of the two solutions. The pure silica nanofibers were also fabricated under the same conditions (without the zirconia-yttria solution).

Dental composites containing 2.5 % and 5 % of the SZY (Si/Zr: 85/15 mol) ceramic nanofibers and 2.5t% silica nanofibers were formulated and tested for FS, FM, refractive index, and transmittance at wavelength (300–1,100nm) and compared with control (no fiber) and composite containing 2.5 % and 5 % ZYS (zirconia/yttria/silica 76.3/3.6/20) nanofibers. The results showed that the composite containing 2.5 % SZY nanofibers exhibited the highest flexural strength (145.3 $\pm$ 10.6 MPa), an improvement of 41.6 % compared to the control composite. This value is also very similar to that (142.7 $\pm$ 17.1 MPa) of the composite containing 2.5 % ZYS nanofibers [60]. Further increase of SZY nanofiber contents (e.g., 5 %) slightly decreased composites flexural strength to 131.3 $\pm$ 10.1 MPa although it is still significantly higher than that of the control composite (102.6 $\pm$ 12.0 MPa) ($p < 0.05$). Incorporation of 2.5 % pure silica nanofibers in the dental composite can also increase its flexural strength and modulus. But its flexural strength (122.6 $\pm$ 13.0 MPa) was significantly lower than that of 2.5 % SZY nanofiber-reinforced composite ($p < 0.05$), although they have similar improved flexural modulus.

The dental composites containing 2.5 % SYZ nanofibers has a similar refractive index (1.537 ± 0.017) as the composite containing 2.5 % silica nanofibers (1.522 ± 0.015) $(p > 0.05)$; both are significantly lower than that of composite with 2.5 % ZYS nanofiber (1.692 ± 0.009) $(p < 0.05)$. Similarly, the composite with 5.0 % SZY nanofibers has a lower refractive index (1.605 ± 0.023) than that with 5.0 % ZYS nanofiber (1.783 ± 0.003) $(p < 0.05)$. The light transmittances (at 580 nm) of the composites reinforced by 2.5 % silica, 2.5 % SZY, or 5.0 % SZY nanofibers $(54.31 \pm 0.15, 47.12 \pm 0.01, 25.92 \pm 0.06,$ respectively) are higher than those with 2.5 % or 5.0 % ZYS nanofibers $(28.45 \pm 0.04$ and $17.28 \pm 0.21,$ respectively). Overall, the composites reinforced with silica-rich SZY nanofiber have much improved light transmittance and visual appearance over the composites reinforced by the same amount of zirconia-rich zirconia-yttria-silica (ZYS) nanofibers. Therefore, the silica-rich SZY ceramic nanofibers (with high Si/Zr ratio) are preferred reinforcement materials for dental composites. A small amount (2.5 %) of such nanofibers can significantly improve mechanical properties of dental composites while largely maintaining its translucency and esthetics.

Conclusion

Silicon carbide or nitride whiskers and zirconia-based ceramic nanofibers have high strength and toughness and excellent chemical stability. They can significantly increase the mechanical properties, fractural toughness, and wear resistance of dental composites. They can compensate the reduction of the mechanical properties caused by the incorporation of antibacterial and anticariogenic agents and monomers in the composites and therefore provide opportunity to develop new anticariogenic dental materials for longer service life. Due to their high refractive index, however, the dental composites reinforced with these materials either cannot be light cured or have reduced degree of photopolymerization conversion. It is also difficult to disperse the ceramic nanofibers uniformly in the highly viscose resin matrix, thus limiting the fiber content and reinforcement effect. Silica-rich silica-zirconia-yttria nanofiber seems a preferred reinforcement element, which provides the composite with better translucency as well as enhanced mechanical properties. Although they have not been discussed in this chapter, other fibrous materials with low refractive index (better matching that of resin), such as clay nanotubes [64] and cellulose nanowhiskers [65], are also being studied as reinforcement elements for dental composites and have shown interesting results.

References

1. Demarco FF, Correa MB, Cenci MS, Moraes RR, Opdam NJ (2012) Longevity of posterior composite restorations: not only a matter of materials. Dent Mater 28:87
2. Ferracane JL (2011) Resin composite – State of the art. Dent Mater 27:29
3. National Institute of Dental and Craniofacial Research (2009) Dental resin composites and caries. NIDCR announcement # 13-DE-102
4. Deligeorgi V, Mjor IA, Wilson NH (2001) An overview of reasons for the placement and replacement of restorations. Prim Dent Care 8:5
5. Frost PM (2002) An audit on the placement and replacement of restorations in a general dental practice. Prim Dent Care 9:31
6. Mjor IA, Moorhead JE, Dahl JE (2000) Reasons for replacement of restorations in permanent teeth in general dental practice. Int Dent J 50:361
7. Sakaguchi RL (2005) Review of the current status and challenges for dental posterior restorative composites: clinical, chemistry, and physical behavior considerations. Dent Mater 21:3
8. Bayne SC, Thompson JY, Swift EJ Jr, Stamatiades P, Wilkerson M (1998) An audit on the placement and replacement of restorations in a general dental practice. J Am Dent Assoc 129:567
9. Coelho-De-Souza FH, Camacho GB, Demarco FF, Powers JM (2008) Fracture resistance and gap formation of MOD restorations: influence of restorative technique, bevel preparation and water storage. Oper Dent 33:37
10. Drummond JL (2008) Degradation, fatigue, and failure of resin dental composite materials. J Dent Res 87:710
11. Lim BS, Ferracane JL, Sakaguchi RL, Condon JR (2002) Reduction of polymerization contraction stress for dental composites by two-step light-activation. Dent Mater 18:436
12. Lu H, Stansbury JW, Bowman CN (2005) Impact of curing protocol on conversion and shrinkage stress. J Dent Res 84:822
13. Samuel SP, Li S, Mukherjee I, Guo Y, Patel AC, Baran G, Wei Y (2009) Mechanical properties of experimental dental composites containing a combination of mesoporous and nonporous spherical silica as fillers. Dent Mater 25:296
14. Watts DC, Marouf AS, Al-Hindi AM (2003) Photo-polymerization shrinkage-stress kinetics in resin-composites: methods development. Dent Mater 19:1
15. Xu X, Burgess JO (2003) Compressive strength, fluoride release and recharge of fluoride-releasing materials. Biomaterials 24:2451–2461
16. Arends J, Dijkman GEHM, Dijkman AG (1995) Adv Dent Res 9:367
17. Xu X, Burgess JO, Ding X, Ling L (2004) Fluoride-releasing compositions. US Patent 6,703,518, 9 Mar 2004
18. Xu X, Ling L, Ding X, Burgess JO (2004) Synthesis and characterization of a novel fluoride-releasing dimethacrylate monomer and its dental composite. J Polym Sci Part A: Polym. Chem 42:985–998
19. Xu X, Ding X, Ling L, Burgess JO (2005) Synthesis and characterization of novel fluoride-releasing monomers 2. Dimethacrylates containing bis(aminodiacetic acid) and their ternary zirconium-fluoride complexes. J Polym Sci Part A: Polym Chem 43:3153–3166
20. Xu X, Ling L, Wang R, Burgess JO (2006) Formulation and characterization of a novel fluoride-releasing dental composite. Dent Mater 22:1014–1023
21. Ling L, Xu X, Choi GY, Billodeaux D, Guo G, Diwan RM (2009) Novel F-releasing composite with improved mechanical property. J Dent Res 88:83–88
22. Wang Y, Samoei GK, Lallier TE and Xu X (2012) Synthesis and charaterization of new antibacterial fluoride-releasing monomer and dental composite. ACS Maco Letters 2(1):59–62

23. Xu X, Shailaja J (2012) Fluoride-releasing compositions. US Patent #8,217,173, 10 July 2012
24. Dickens SH, Flaim GM, Takagi S (2003) Mechanical properties and biochemical activity of remineralizing resin-based Ca-PO$_4$ cements. Dent Mater 19:558
25. Langhorst SE, O'Donnell JN, Skrtic D (2009) In vitro remineralization of enamel by polymeric amorphous calcium phosphate composite: quantitative microradiographic study. Dent Mater 25:884
26. Weir MD, Chow LC, Xu HH (2012) Remineralization of demineralized enamel via calcium phosphate nanocomposite J Dent Res 91:979
27. Xu HH, Weir MD, Sun L, Moreau JL, Takagi S, Chow LC, Antonucci JM (2010) Nano DCPA-whisker composites with high strength and Ca-PO$_4$ release. J Dent Res 89:19
28. Xu HH, Moreau JL, Sun L, Chow LC (2011) Nanocomposite containing amorphous calcium phosphate nanoparticles for caries inhibition. Dent Mater 27:762
29. Moreau JL, Sun L, Chow LC, Xu HH (2011) J Biomed Mater Res B Appl Biomater 98:80
30. Xu HH, Weir MD, Sun L (2007) Dental nanocomposites with Ca-PO$_4$ release: effects of reinforcement, dicalcium phosphate particle size and silanization. Dent Mater 23:1482
31. Freilich M, Meiers J, Duncan and Goldberg AJ (1999) Fiber-reinforced dental composites in clinic dentistry. Quintessence Publishing, Chicago, pp 9–21 (Chap 2)
32. Goldberg AJ, Burstone CJ (1992) The use of continuous fiber reinforcement in dentistry. Dent Mater 8(3):197–202
33. Freilich MA, Karmaker AC, Burstone CJ, Goldberg AJ (1998) Development and clinical applications of a light polymerized fiber-reinforced composite. J Prosth Dent 80(3):311–318
34. Vallittu PK (1998) Compositional and weave pattern analyses of glass fibers in dental polymer fiber composites. J Prosth Dent 7(3):170–176
35. Ellakwa AE, Shortall AC, Shehata MK, Marquis PM (2002) Influence of bonding agent composition on flexural properties of an ultra-high molecular weight polyethylene fiber-reinforced composite. Oper Dent 27(2):184–191
36. Ellakwa AE, Shortall AC, Marquis PM (2002) Influence of fiber type and wetting agent on the flexural properties of an indirect fiber reinforced composite. J Prosth Dent 88(5):485–490
37. Freilich MA, Duncan JP, Alarcon EK, Eckrote KA, Goldberg AJ (2002) The design and fabrication of fiber-reinforced implant prostheses. J Prosth Dent 88(4):449–454
38. Eckrote KA, Burstone CJ, Freilich MA, Messer GE, Goldberg AJ (2003) Shear in flexure of fiber composites with different end supports. J Dent Res 82(4):262–266
39. Monaco C, Ferrari M, Miceli GP, Scotti R (2003) Clinical evaluation of fiber-reinforced composite inlay FPDs. Int J Prosth 16(3):319–325
40. Ellakwa A, Thomas GD, Shortall AC, Marquis PM, Burke FJ (2003) Fracture resistance of fiber-reinforced composite crown restorations. Am J Dent 16(6):375–380
41. Behr M, Rosentritt M, Handel G (2003) Fiber-reinforced composite crowns and FPDs: a clinical report. Int J Prosth 16(3):239–243
42. Lassila LV, Nohrstrom T, Vallittu PK (2002) The influence of short-term water storage on the flexural properties of unidirectional glass fiber-reinforced composites. Biomaterials 23(10):2221–2229
43. Cal NE, Hersek N, Sahin E (2000) Water sorption and dimensional changes of denture base polymer reinforced with glass fibers in continuous unidirectional and woven form. Int J Prosth 13(6):487–493
44. Vallittu PK (2000) Effect of 180-week water storage on the flexural properties of E-glass and silica fiber acrylic resin composite. Int J Prosth 13(4):334–339
45. Wilson DM, Visser LR (2002) High performance oxide fibers for metal and ceramic composites. In: Processing of fibers & composites conference, Barga, 22 May 2002
46. Kelsey WP, Latta MA, Shaddy RS, Stanislav CM (2000) Physical properties of three packable resin-composites restorative materials. Oper Dent 25:331–335
47. Knobloch LA, Kerby RE, Seghi R, Berlin JS, Clelland N (2002) Fracture toughness of packable and conventional composite materials. J Prosth Dent 88(3):307–313

48. Lastumäki TM, Lassila LVJ, Vallittu PK (2001) Flexural properties of the bulk fiber-reinforced composite DC-tell used in fixed partial dentures. Int J Prosth 14(1):22–26
49. Xu HH, Quinn JB, Smith DT, Guiseppetti AA, Eichmiller FC (2003) Effects of different whiskers on the reinforcement of dental resin composites. Dent Mater 19:359–367
50. Iwanaga H, Kawai C (1998) J Am Ceram Soc 81:773–776
51. Lide DR (ed) (2001) CRC handbook of chemistry and physics, 82nd edn. CRC Press, Boca Raton
52. Xu HH, Martin TA, Antonucci JM, Eichmiller FC (1999) Ceramic whisker reinforcement of dental resin composites. J Dent Res 78(2):706–712
53. Xu HH, Eichmiller FC, Antonucci JM, Flaim GM (2000) Single-crystalline ceramic whisker-reinforced carboxylic acid-resin composites with fluoride release. Oper Dent 25(2):90–97
54. Xu HH (2000) Whisker-reinforced heat-cured dental resin composites: effects of filler level and heat-cure temperature and time. J Dent Res 79(6):1392–1397
55. Xu HH, Quinn JB (2001) Effect of silicon carbide whisker-silica heat treatment on the reinforcement of dental resin composites. J Biomed Mater Res 58(1):81–87
56. Xu HH, Quinn JB, Smith DT, Antonucci JM, Schumacher GE, Eichmiller FC (2002) Dental resin composites containing silica-fused whiskers – effects of whisker-to-silica ratio on fracture toughness and indentation properties. Biomaterials 23(3):735–742
57. Xu HH (2003) Long-term water-aging of whisker-reinforced polymer-matrix composites. J Dent Res 82(1):48–52
58. Xu X, Guo G, Fan Y (2010) Fabrication and characterization of dense zirconia and zirconia-silica ceramic nanofibers. J Nanosci Nanotechnol 10(9):5672–5679
59. Li S, Zhang JF, Xu X (2012) Dental composite reinforced by zirconia–silica ceramic nanofibers with improved translucency. Dent Mater 28(Suppl 1):e49–e50
60. Guo G, Fan Y, Zhang JF, Hagan J, Xu X (2012) Novel dental composites reinforced with zirconia–silica ceramic nanofibers. Dent Mater 28:360–368
61. Xu HH, Quinn JB, Giuseppetti AA (2004) Wear and mechanical properties of nano-silica-fused whisker composites. J Dent Res 83:930
62. Xu HH, Sun L, Weir MD, Antonucci JM, Takagi S, Chow LC, Peltz M (2006) Nano DCPA-whisker composites with high strength and Ca-PO$_4$ release. J Dent Res 85:722
63. Xu HH, Weir MD, Sun L, Takagi S, Chow LC (2007) Effect of calcium phosphate nanoparticles on Ca-PO$_4$ composites. J Dent Res 86:378
64. Zhong S, Zhang JF, Wu R, Xu X (2013) Mechanical properties of dental composites reinforced with halloysite nanotubes. J Dent Res 92(Special Issue A). Abstract 1923
65. Xu X, Wu R, Zhang J, Wang Y, Costin S, Fan Y, Hagan J (2012) Antibacterial dental composites reinforced by tunicate cellulose whiskers. J Dent Res 91(Special Issue A). AADR abstract 1201

Elastic, Viscoelastic, and Fracture Properties of Bone Tissue Measured by Nanoindentation

41

Do-Gyoon Kim and Kathy L. Elias

Keywords

Nanoindentation • Bone • Indentation elastic modulus • Indentation viscosity • Dynamic mechanical analysis • Continuous stiffness measurement

Quantity and Quality of Bone

Bone is a load-bearing organ. The mechanical properties of bone control its ability to support weight and locomotive muscular activities [1, 2]. Bone quantity has been considered to be the best surrogate for the mechanical properties of bone. As bone is not a solid material with numerous pores for blood supply, it is obvious that an increase in bone porosity will result in a reduction of the quantity of bone. There are two types of bone, cortical and trabecular, with differing levels of porosity ranging from 5–10 % to 75–95 %, respectively. At the organ level, long tubular bones primarily consist of cortical bone, while vertebrae have a greater proportion (60–80 %) of trabecular bone. The porosity of bone also changes as a result of bone diseases, such as osteoporosis [3]. Clinically, bone mineral density (BMD) is used to assess bone quantity. The osteoporotic population has a lower BMD and an associated higher fracture history than healthy people. As BMD has a strong positive correlation with bone strength, it is not surprising that less BMD is associated with a higher fracture risk in osteoporotic bone [4, 5]. However, a substantial overlap in the associated values of BMD was found between osteoporotic patients who had experienced bone fracture and those who did not, suggesting that bone quantity alone is not able to explain the mechanical properties of bone [6, 7].

The quantity of bone is described by bone mass and volume fraction. On the other hand, bone quality can be estimated by parameters including morphology,

D.-G. Kim (✉) • K.L. Elias

Division of Orthodontics, College of Dentistry, The Ohio State University, Columbus, OH, USA
e-mail: kim.2508@osu.edu; elias.18@osu.edu

microstructure, and tissue mineral density (TMD) [8, 9]. While BMD accounts for the mineral content within an apparent volume of bone, including bone tissue, marrow, and porosity, TMD represents the hard tissue mineral content of bone [10]. The morphology of bone changes through growth, regeneration at a defect site, and disease. Bone modeling and remodeling are involved in these processes. Bone remodeling is initiated by activation of bone resorption cells, called osteoclasts, which remove preexisting bone tissue. The removed regions can be filled with new bone tissue produced by bone-forming cells, called osteoblasts. While activation, resorption, and formation are chained together in bone remodeling, resorption and formation are uncoupled in bone modeling, which undergoes only activation-resorption or activation-formation. Bone loss or gain that arises from an imbalance between resorption and formation in the process of bone remodeling and bone modeling leads to morphological changes in bone [11]. The formation of new bone begins when the osteoblasts produce collagen and mineral to build bone tissue (Fig. 41.1a) [12]. The mineral is deposited in the collagen framework. Following the initial formation, bone tissue progressively matures through the addition of more mineral into the more organized collagen fibrils (Fig. 41.2) [13, 14]. It was indicated that bone tissue is rapidly mineralized up to 70 % of its final mineral content within 1 week after initiation of bone formation [13]. However, the rest of the mineralization process takes much longer and can last many years [13, 15]. These bone tissues that are produced during different periods of time result in variability of the TMD of bone (Fig. 41.1b). As bone modeling forms new tissue or removes both new (less mineralized) and preexisting (more mineralized) bone tissue, and bone remodeling produces new tissue following the removal of preexisting tissue [13, 16, 17], the alteration of TMD distribution can be accelerated by active bone modeling and remodeling. It was observed that estrogen deficiency in postmenopausal osteoporotic patients stimulates active bone remodeling, giving rise to less trabecular bone volume fraction and number, and mean TMD, but higher variability of TMD than in people with no evidence of bone disease [18]. The mechanical properties of trabecular bone were also significantly lower for postmenopausal osteoporotic patients. These observations indicate that alteration of bone composition at the tissue level plays an important role in determining the mechanical behavior of bone at the macro-level.

Bone is composed of approximately 30 % water, 40 % mineral, and 30 % organic collagen at the tissue level [1]. The composition of bone varies in different animals depending on the age of the bone tissue. The mineral portion consists of mostly hydroxyapatite crystals ($Ca_{10}(PO_4)_6(OH)_2$), and the collagen portion is predominantly type I with a triple-helix structure of protein (Fig. 41.2). The elastic modulus of hydroxyapatite was determined to be 114 GPa [19] and that of collagen fibrils was measured to be up to 0.2 GPa [20], while that of bone tissue ranged from 16.6 to 26.6 GPa (Table 41.1). As bone tissue matures, the size of the crystals and the perfection of the minerals increase, and cross-linking in the collagen stabilizes, leading to changes in mineral-collagen interactions and the fragility of bone [14]. It has been widely accepted that the mineral component of bone tissue has more control over the elastic and plastic properties, and the collagen component is mostly
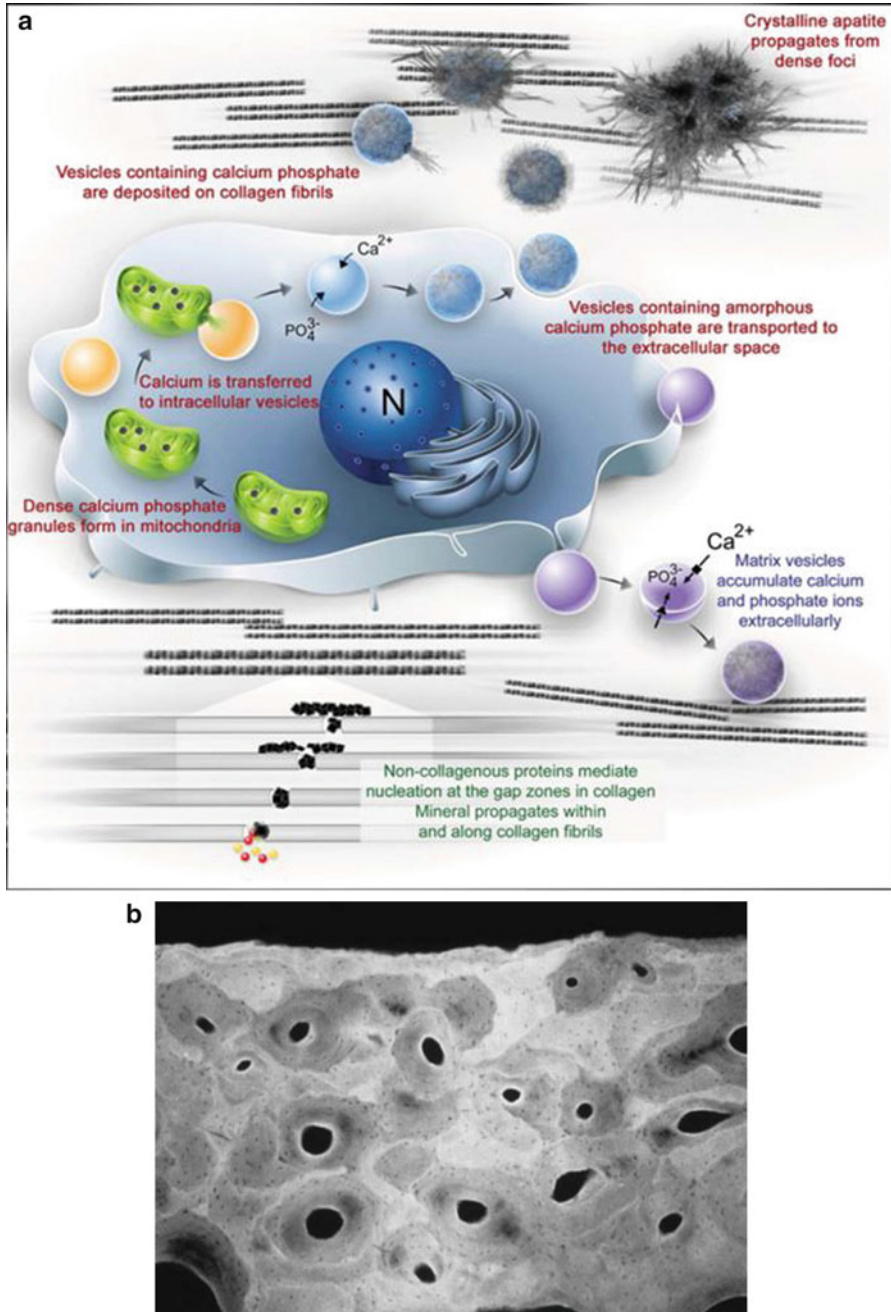
Fig. 41.1 (**a**) Osteoblasts deposit collagen and mineral to build bone matrix [12], and (**b**) variability of bone mineralization resulted from bone remodeling at different time points [77]
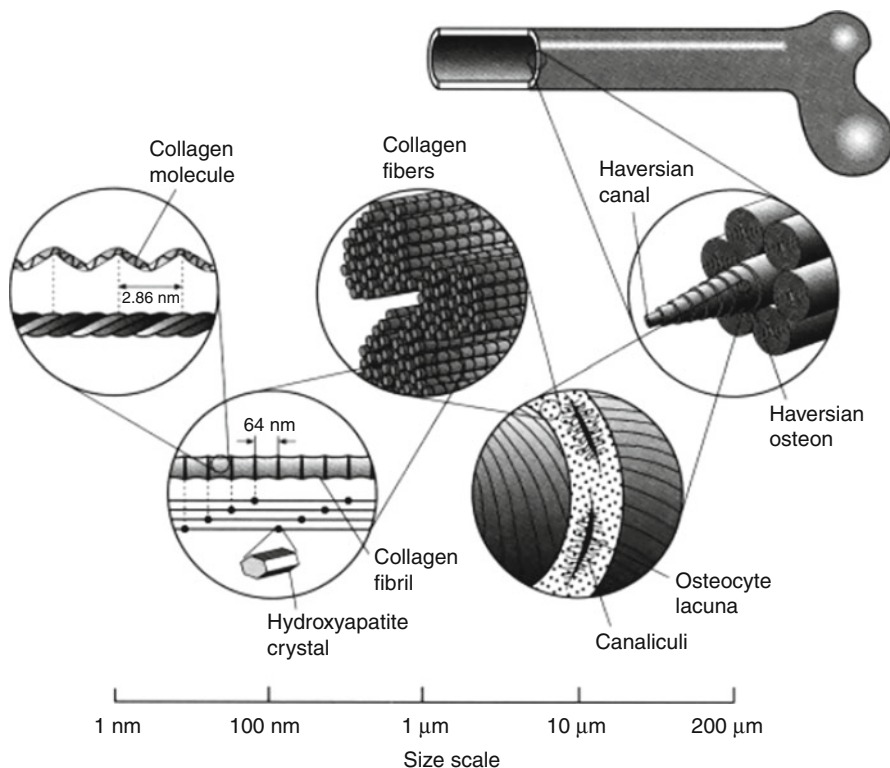
Fig. 41.2 Hierarchical structure of bone at different scales [78]

Table 41.1 Conditions of nanoindentation for bone tissue

Conditions		Species	Site	Elastic modulus (GPa)	Plastic hardness (GPa)	Ref
Embedding	No	Human	Femur cortical	22.8±7.9	0.53±0.17	[24]
	Embedding			21.5±7.2	0.53±0.16	
Dehydration	Wet	Bovine	Femur cortical	21.1±2.0	0.58±0.05	[35]
	Dry			24.4±2.2	0.68±0.10	
Displacement rate	5 nm/s	Human	Femur cortical	17.5±0.5[a]	0.42±0.12[a]	[24]
	10 nm/s			18.6±4.2[a]	0.52±0.15[a]	
Indentation depth	250 nm	Human	Femur cortical	23.5±10.0[a]	0.75±0.72[a]	[24]
	500 nm			22.8±7.9[a]	0.62±0.32[a]	
Holding period	30 s	Human	Tibia cortical	25.3±3.1	–	[30]
	1,000 s			26.6±2.1	–	
Anisotropy	Longitudinal	Human	Tibia cortical	22.4±1.2	0.62±0.04	[44]
	Transverse			16.6±1.1	0.56±0.03	

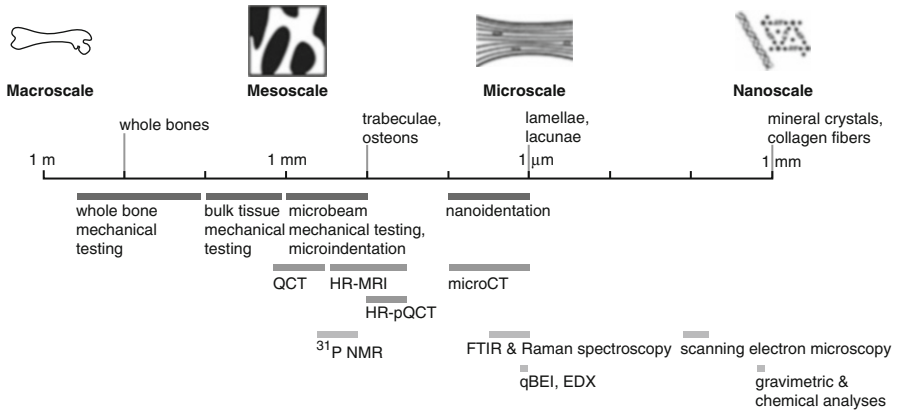[a]Approximated based on graphs in the cited article

Fig. 41.3 Mechanical (*dark gray bars*), geometric/microarchitectural (*medium gray bars*), and compositional (*light gray bars*) technologies are listed based on their approximate length scale of analysis at the hierarchical structure of bone [22]

responsible for the viscoelastic properties [14, 21]. Thus, interactions between these components determine the mechanical behavior of bone at the tissue level. The composition of bone changes through active biological activities triggered by bone disease and regeneration at healing sites. In particular, as a composite of hydroxyapatite and collagen fibril is a basic building block of bone tissue, alteration of its composition is responsible for mechanobiologic response of the local bone matrix, which directly controls the activities of bone cells. As the dimension of this composite is in the nano-range (Fig. 41.2), assessment of mechanical properties at the nano-level provides critical baseline information that can help understand the underlying mechanism of bone complications. Unfortunately, the gauge length of a traditional mechanical testing machine, which is coarser than a millimeter scale, was not able to assess the mechanical properties of the nano-composite materials in bone tissue (Fig. 41.3) [22].

Introduction of Nanoindentation to Bone Tissue Mechanics

Basic Principles of Nanoindentation

Oliver and Pharr introduced nanoindentation as a way to measure the mechanical properties of materials on the nanoscale using the pyramidal Berkovich indenter [23]. Figure 41.4 shows the typical nanoindentation machines and a microscopic image of the pyramidal shape of the indentation impression on bone tissue [24]. Nanoindentation elastic modulus and plastic hardness were estimated using the indentation load and displacement curve (Fig. 41.5).

Fig. 41.4 (**a**) A typical
nanoindentation machine and
(**b**) a microscopic image of
indentation sites on the
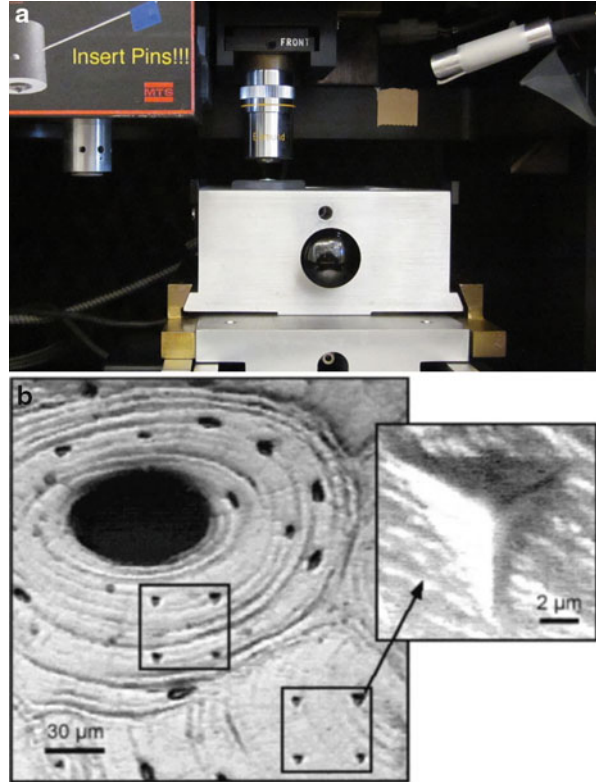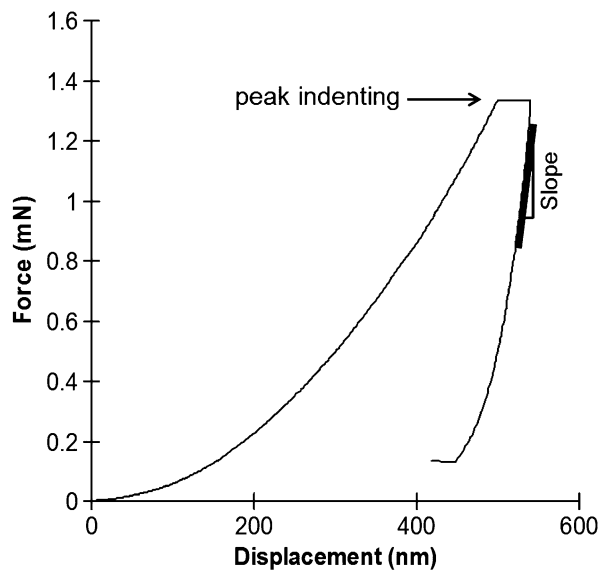osteonal and interstitial bone
tissue [24]

Fig. 41.5 A typical
nanoindentation load and
displacement curve. The
nanoindentation hardness is
measured at the peak
indenting load, and the
nanoindentation elastic
modulus is assessed using the
slope at the early unloading
curve

The hardness was obtained by Eq. 41.1:

$$H = \frac{P_{max}}{A}$$

(41.1)

where P_{max} is the peak indenting load. The indenter contact area (A) was assessed using an area shape function (Eq. 41.2) [25]:

$$A = 24.5h^2 + C_1h + C_2h^{1/2} + C_3h^{1/4} + C_4h^{1/8} + C_5h^{1/16} + C_6h^{1/32} + C_7h^{1/64} + C_8h^{1/128}$$

(41.2)

where $C_0 \ldots C_8$ are constants for the shape function obtained during calibration [26]. The indenting depth (h) can be estimated using Eq. 41.3:

$$h = h_{max} - \varepsilon \frac{P_{max}}{S}$$

(41.3)

where ε is a constant representing the indenter geometry, with $\varepsilon = 0.75$ for the Berkovich indenter [27]. Equation 41.2 was able to estimate the projected contact area of the indenter as a function of indenting depth (h) without taking a high-resolution microscopic image for the hardness impression [26]. Based on the elastic contact mechanics, a method to compute elastic modulus was developed using the slope (S) during the early unloading curve of the indentation load–displacement curve (Fig. 41.5 and Eq. 41.4):

$$S = \frac{dP}{dh} = \beta \frac{2}{\sqrt{\pi}} E_r \sqrt{A}$$

(41.4)

where S is the experimental stiffness of the unloading curve; β is the shape factor, which is 1.034 for the pyramidal Berkovich indenter; E_r is the reduced modulus; and A is the projected contact area estimated using Eq. 41.2 [26]. The E_r was input into Eq. 41.5 to compute the elastic modulus:

$$\frac{1}{E_r} = \frac{(1 - v_s^2)}{E_s} + \frac{(1 - v_i^2)}{E_i}$$

(41.5)

where the indices s and i refer to the sample and the indenter material, respectively, and v is Poisson's ratio. The reduced modulus accounted for elastic displacements of both specimen and indenter. For a diamond indenter, values of $E_i = 1{,}141$ GPa and $v_i = 0.07$ are typically used. Poisson's ratio for bone is generally assumed to be 0.3 [24, 25].

The nanoindentation machine should be calibrated for its compliance and for the indenter area function for the indenter using indentation testing of fused silica [26]. It was indicated that the fused silica does not provide pileup error around the contact impression, providing a reference for the calibration. With an ideal calibration, the reference values (E = 72 GPa with v = 0.17) of fused silica will be measured, and the indenter contact area, estimated based on Eq. 41.2, will be identical to the experimentally measured contact area.

Preparation of Bone Specimen for Nanoindentation

Rho performed many of the first nanoindentation studies of bone tissue [28]. Following his pioneering work, various procedures for the preparation of bone specimens have been developed depending on the study objectives. Polishing the indentation surface of the specimen is the most important step to successfully obtaining greater nanoindentation accuracy. Figure 41.4b shows an acceptable bone specimen surface for nanoindentation. An example procedure for bone specimen preparation is described below.

First, the soft tissue surrounding the bone is removed. A bone section is made using a low-speed saw with a diamond blade under water irrigation to prevent frictional heat damage on the bone surface. The surface of each slice is polished continuously using 2,400 grit SiC paper on a rotary wheel (Ecomet, Buehler, Lake Bluff, IL) and then on a napless cloth with diluted 1 and 0.3 μm alumina oxide pastes. All polishing processes are performed under wet conditions. The specimens are then sonicated in deionized water, and fresh specimens can be stored at $-20\,^\circ$C until nanoindentation. After thawing, the specimens are glued onto a holder and mounted on a sample tray that is to be placed in the receiving table of the nanoindenter. The indentation sites are precisely located under a nanoindenter light microscope that is calibrated for the distance from the indenter tip. The specimen is located to the determined indentation position using a high-resolution motorized stage, as programmed by the operating software.

Conditions of Nanoindentation for Bone Tissue

Many technical challenges that can influence nanoindentation measurements of bone specimens are listed in Table 41.1. The nanoindentation testing conditions for bone specimens may be optimized based on a comprehensive review of the individual testing variables which are summarized here.

Embedding Effect

A bone specimen was embedded in an epoxy such as polymethyl methacrylate (PMMA) to provide support for fragile cancellous networks and to allow for the sample to be polished to a flat surface in preparation for nanoindentation. However, it was indicated that the embedding process may alter the properties of bone tissue due to infiltration and heat generated from exothermal polymerization [29, 30]. Thus, it was recommended to not indent close to the resin [30]. While it was observed that there was no effect on the nanoindentation values from the embedding [24], the nanoindentation hardness significantly increased when a low-viscosity epoxy resin was used [29]. However, all other types of resin material did not have an effect on the nanoindentation values. In addition, recent nanoindentation studies obtained comparable nanoindentation values for both cortical and trabecular bone tissues without embedding [31–34]. These findings suggest that embedding is not necessary if an appropriate method is developed to prepare the bone specimens.

Dehydration Effect

It is difficult to identify the precise microscopic location for nanoindentation of bone tissue if moisture exists on the surface of the specimen when viewing it under a nanoindentation microscope. As such, dry bone specimens were prepared for many nanoindentation studies [28, 35–37]. However, it has been well accepted that dehydration has a significant effect on the mechanical properties of bone, by increasing the modulus and decreasing the toughness [38]. Many studies indicated that dehydrated bone specimens, when compared to wet specimens, had values of nanoindentation modulus and hardness that were 9.7–22.6 % and 12.2–56.9 % greater, respectively [24, 35, 39]. It is anticipated that a bone specimen's mechanical properties would be a better representation of the physiological properties when measured in a hydrated state. A special irrigation setup was developed to have a physiological buffer solution that provides moisture in the vascular channels of the bone [24, 31].

Indention Site Selection

As the indentation method is based on the assumption of a semi-infinite half-space solid, indentations performed close to any defect may cause an error when computing the elastic modulus [23, 25]. Bone has many pores in the size range of about 10 μm, the average diameter of osteocyte lacunae, to about 50 μm, the average diameter of a Haversian canal (Fig. 41.2). Although nanoindentation is known to be a method of measuring the material properties of bone at the submicron level, the projected area on the specimen is actually larger than the micron level. For the Berkovich indenter, indenting to a depth of 500 nm affects the surface of the specimen in a diameter up to about 5 μm [24]. As such, it is recommended to carefully determine the location of each indentation so as not to be interrupted by those defects. In fact, it was also indicated that the distance between indentation sites and pores could significantly influence measures of hardness [40]. To date, the distance between nanoindentation sites used for bone specimens has ranged from 15 μm, with up to 1 μm of depth for a trabecular bone sample from a pig mandible [41], to 50 μm, with up to 500 nm of depth for a cortical bone sample from a dog femur [34]. However, few studies have been performed to investigate the direct effect of inter-indentation distance on the nanoindentation values of bone specimens.

Loading and Unloading Displacement Rate

While nanoindentation testing is operated under force control, many experiments have utilized a feedback method that converts testing to its corresponding displacement control [26]. Usually, nanoindentation has been performed using the same loading and unloading rate. A conventional compressive test for human bones at the macro-level showed that their strength increases with higher compressive strain rates [42]. This result was interpreted because bone is a viscoelastic material that has a time-dependent mechanical response to loading. It was observed that the nanoindentation elastic modulus of human cortical bone has a significant positive power relationship with indentation strain rate [30]. Interestingly, the power relationship coefficient (0.059) was similar to that (0.06) of the conventional test using macro-level cancellous bones. Recently, the displacement rate dependency of nanoindentation elastic modulus was

found for both trabecular and cortical bones [43]. It was also found that the nanoindentation modulus and hardness of human femoral cortical bone, analyzed at a 5 nm/s displacement rate, were significantly lower than those measured at 10 nm/s, where no difference was found when rates were higher than 10 nm/s [24].

Indentation Depth

As the displacement resolution of nanoindentation is as high as 0.04 nm [44], the values of nanoindentation measurement are influenced by the surface irregularities present in each bone specimen. Nanoindentation elastic modulus was found to be higher when the surface of trabecular bone specimens was more smoothly polished (7–15 nm root mean square (RMS)) when compared to a rougher surface (33–35 nm RMS) [45]. Investigators also observed that increasing maximum indentation load, which corresponds to indentation depth, decreased indentation modulus independent of the surface roughness of a trabecular bone specimen. Another study observed no effect of the maximum indentation load on the modulus and hardness of human femoral trabecular bone [29]. In yet another study, indenting depth had negative correlations with indentation modulus and hardness for both bovine trabecular and cortical bone at a low range of indenting depth (from 75 to 185 nm) [43]. However, indenting deeper than 500 nm substantially reduced the variance of both modulus and hardness of human femoral cortical bone tissue [24]. As bone tissue has heterogeneous properties, it is likely that load-controlled indenting may not reach a consistent depth between indentation sites, which may not provide stable nanoindentation values at some locations.

Holding Period for Elastic Modulus of Bone Specimen

Many studies observed a time-dependent viscoelastic creep displacement during the holding period at the constant peak load of nanoindentation for bone tissue [30, 33, 43, 46]. Creep behavior was taken into consideration as it may produce negative modulus values unless it is eliminated prior to unloading [30, 35]. It was suggested that the testing of each bone specimen include repetition or delayed indentations prior to unloading in order to remove the effects of viscoelastic behavior [24, 30]. As a result, the repetition and delays during the indentation holding period did not have a significant effect on modulus and hardness [24, 30]. However, the creep response during the holding period provided an important source for measuring the viscoelastic property of bone tissue [32, 33].

Anisotropy

Bone grows in the load-bearing direction [47]. Bone modeling and remodeling control this biological adaptation by changing the morphology and composition of bone tissue. It has been accepted that bone at the organ level has stronger mechanical properties in the longitudinal direction than in the transverse direction [1, 48]. Nanoindentation values at the tissue level of bone followed the anisotropy of mechanical properties at the organ level, having higher modulus and hardness in the longitudinal direction [25, 44].

**Table 41.2** Nanoindentation values of bone tissue at the hierarchical bone levels

Bone levels	Species	Bone types	Elastic modulus (GPa)	Plastic hardness (GPa)	Ref
Anatomical sites	Human	Femoral diaphysis osteon	19.47±1.63	0.63±0.06[a]	[49]
		Distal radius osteon	17.0±1.7[a]	0.56±0.07[a]	
Microstructure	Human	Femoral osteon	15.11±2.2	0.51±0.10	[50]
		Femoral interstitial	16.13±2.2	0.55±0.07	
		Femoral trabecular	11.10±2.4	0.44±0.14	
Tissue age	Dog	Femoral new osteon	8.06±4.61	0.19±0.14	[33]
		Femoral old osteon	12.80±5.51	0.35±0.20	
Trabecular region	Rat	Vertebral marginal	18.02±7.72	0.62±0.34	[31]
		Vertebral core	20.84±6.46	0.72±0.35	

[a]Approximated based on graphs in the cited article

Nanoindentation Elastic Modulus and Plastic Hardness of Bone Tissue in the Hierarchical Bone Levels

Nanoindentation modulus accounts for the reversible elastic response of bone tissue, while hardness represents its resistance to plastic deformation. Many nanoindentation studies consistently observed a strong positive correlation between the elastic modulus and the plastic hardness of bone tissue [24, 39, 49]. These mechanical properties of bone tissue likely vary between anatomical sites where differing degrees of bone modeling and remodeling occur [1, 2, 47]. For example, the cortical bone of human femoral diaphyses had significantly higher nanoindentation modulus and hardness than distal radii [49] (Table 41.2). On the other hand, differences in nanoindentation modulus and hardness values between cortical and trabecular bone tissues at the same anatomical site were higher than differences in those values between cortical bone tissues from different anatomical sites. It has been consistently observed that the osteonal and interstitial tissue of cortical bone has significantly higher nanoindentation modulus and hardness than trabecular bone tissue, independent of anatomical site, age, and gender [39, 44, 50]. These findings indicated that the mechanical properties of bone tissue change at the local microstructural level more than at the organ level. Bone modeling and remodeling occur more frequently in trabecular bone than in cortical bone, replacing about 5 % of cortical bone and 25 % of trabecular bone each year [1]. The changing degree and timing of bone modeling and remodeling produce the heterogeneous composition of bone tissue (Fig. 41.1b). In a previous study, in vivo calcein-labeled new osteons in a dog femur were observed using an epifluorescent microscope (Fig. 41.6) [33]. In dog femurs, the nanoindentation modulus and hardness of newly formed (less mineralized) osteons were significantly lower than those of preexisting (more mineralized) old osteons [33, 34]. Trabecular bone tissue in a marginal region has lower values of nanoindentation modulus and hardness than trabecular bone tissue in a core region

Fig. 41.6 (**a**) Bright-field light microscope and (**b**) fluorescent microscope images for osteons at the indentation location. The newly forming bone tissue was identified by calcein labels [33]
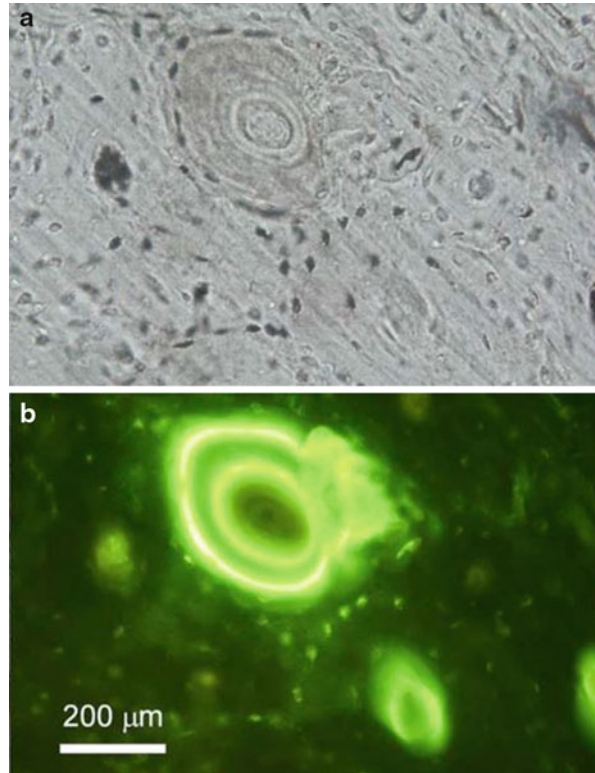
for humans and other animal models [31, 51, 52]. This result was explained as follows: the marginal region of trabecular bone, which directly contacts bone marrow, likely has more chance to be modeled and remodeled, producing more new bone tissue with less mineral density than the core region. The strong positive correlation between the nanoindentation modulus and TMD supported these observations [41, 52].

Nanoindentation Viscoelastic Properties of Bone Tissue

To date, relatively few studies have been performed that observe the viscoelastic properties of bone tissue, in contrast to the large number of studies observing the elastic and plastic properties of bone tissue.

A differential model was developed to describe the displacement curve during nanoindentation [53–55]. This model was created to describe a full range of viscous-elastic–plastic (VEP) responses during indentation. The VEP constitutive differential equation includes each of the three terms (Eq. 41.6):
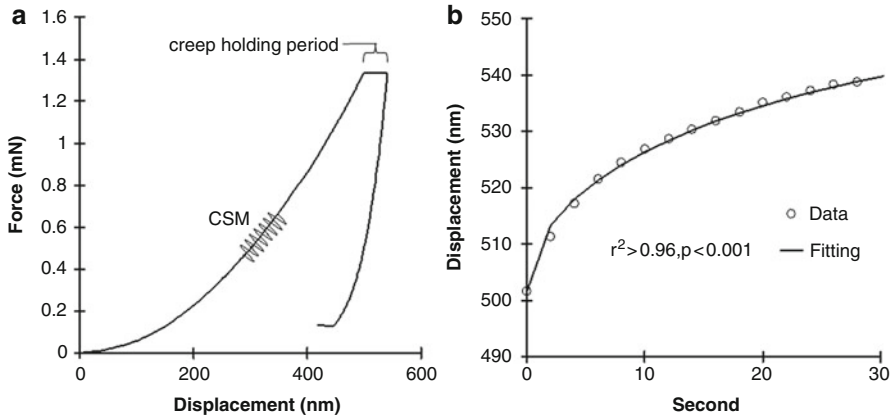
Fig. 41.7 (a) A typical nanoindentation curve with continuous stiffness measurement (CSM) and holding period and (b) the creep curve with an excellent curve fitting [31–33, 46]

$$\frac{dh}{dt} = \frac{dh_v}{dt} + \frac{dh_e}{dt} + \frac{dh_p}{dt}$$

$$= \frac{P^{1/2}}{\left(\alpha_3 \eta_Q\right)^{1/2}} + \frac{1}{P^{1/2}} \frac{dP}{dt} \frac{1}{2\left(\alpha_2 E'\right)^{1/2}} + \frac{1}{P^{1/2}} \frac{dP}{dt} \frac{1}{2\left(\alpha_1 H\right)^{1/2}} \tag{41.6}$$

where h is displacement, P is indenting load, and quadratic viscosity (μ_Q) is identified as the product of a geometry term, α_3, and a material property: $\mu_Q = \alpha_3 \eta_Q$. Applicability of this equation was examined for mineralized tissues and healing bone at the implant interface [54, 55].

Kim et al. introduced the traditional viscoelastic Voigt model to describe the creep curve during the holding period of nanoindentation testing for bone tissue [32, 33]. In these studies, creep was obtained as the displacement for the 30 s holding period at peak loading (Fig. 41.7a). The creep displacement-time curve was fitted using the following equation (Eq. 41.7):

$$h^2(t) = \frac{\pi}{2} p_{\max} \cot \alpha \left[\frac{1}{E_2} \left(1 - e^{-tE_2/\eta} \right) \right] \tag{41.7}$$

where h(t) is indentation creep displacement (nm) as a function of time, α is an equivalent cone semi-angle (70.3°) to the face angle of the Berkovich indenter (65.27°) [56], E_2 is an elastic element of the Voigt model (GPa), and η is the indentation viscosity (GPaS) term. This equation represents two elements of the Voigt model in which an elastic spring and a viscous dashpot are linked in parallel [56]. Excellent fitting has been obtained for all nanoindentation creep curves from bone tissue ($r^2 > 0.96$, $p < 0.001$) (Fig. 41.7b). The Voigt equation can be applied to the analysis of any nanoindentation data that includes the holding period. This equation makes it possible to obtain elastic modulus, viscoelastic viscosity, and

Fig. 41.8 Strong positive correlations between nanoindentation modulus and viscosity were significantly different between mandibles and vertebrae (ANCOVA, p < 0.001) [31]
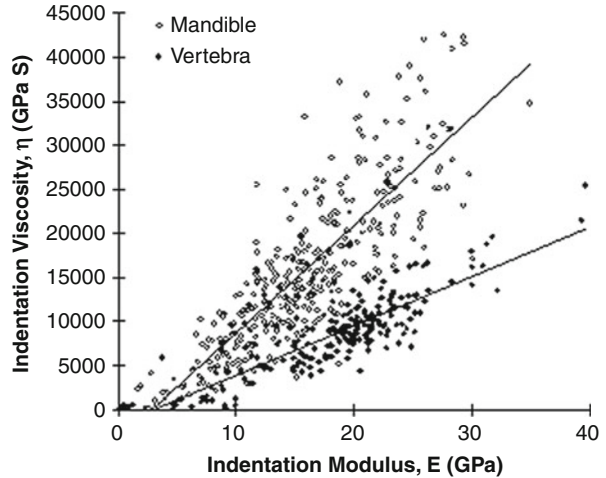
plastic hardness together using the same nanoindentation curve. Strong positive correlations were found between indentation viscosity, modulus, and hardness independent of bone tissue age [32, 33].

Following its introduction, the Voigt model has been successfully utilized to describe nanoindentation viscoelastic behavior for various types of bone [31, 37, 43, 46, 57, 58]. Strong correlations were found between nanoindentation viscosity and modulus and hardness between different types of bone tissues [31, 58]. However, the slopes of the correlations were significantly different between different anatomical sites (Fig. 41.8). These findings suggested that the different correlation slopes between bone tissue properties can reflect changes of bone material composition that support different functional demands at those anatomical sites.

Dynamic nanoindentation was also utilized as another approach to obtain the viscoelastic property of bone tissue [59]. An oscillation load of 60 μN (corresponding to a displacement of up to 3 nm) at 10–200 Hz was superposed on the constant load of 500 μN during a holding period of nanoindentation for a human vertebral trabecular bone sample. A longer 90 s holding period was needed in the previous study [59]. Energy dissipation capacity (tan δ) was computed by Eq. 41.8:

$$\tan \delta = \frac{E''}{E'} = \frac{[\omega C_s (1 + v)\sqrt{\pi}]/\sqrt{A(\mathrm{h}_c)}}{[K_s (1 + v)\sqrt{\pi}]/\sqrt{A(\mathrm{h}_c)}} = \frac{\omega C_s}{K_s} \tag{41.8}$$

where δ is the phase angle that can be determined by computing the phase difference between force and displacement during oscillation, E'' is the loss modulus, E' is the storage modulus, ω is the frequency, C_s is the damping coefficient of a specimen, K_s is the stiffness of the tip-specimen contact, v is Poisson's ratio of the specimen, and A is the nanoindentation contact area as a function of indenting depth (h_c). As a result, a relatively low tan δ was measured at the bone tissue area, which consisted of highly ordered, collagen-rich bone tissue lamellae. Recently,

this method was utilized to identify a larger viscoelastic response from newer bone tissue regions with higher collagen content [60].

Alternatively, tan δ can be assessed by continuous stiffness measurements (CSM) that use the oscillatory response during nanoindentation loading [27]. Oscillatory force, corresponding to 2 nm of displacement, is applied at 45 Hz. After CSM, the remainder of the regular nanoindentation testing, including the holding and unloading periods, continues. Then, tan δ is computed using Eq. 41.9:

$$\tan \delta = \frac{\omega C}{\left(S^{-1} + K_f^{-1}\right)^{-1} + K_s - m\omega^2} \tag{41.9}$$

where δ is again the phase angle between the force and displacement signals, ω is the frequency of the oscillation, ωC is the damping due to air in the gaps between the capacitor plates, S is the contact stiffness, K_f is the stiffness of the indenter frame, K_s is the spring constant for the leaf springs that support the indenter, and m is the mass of the indenter. This CSM method does not require any additional steps beyond the regular nanoindentation process to obtain the modulus, viscosity, and hardness. Thus, it is a very useful method for investigating the relationships between conventional nanoindentation parameters and the capacity of energy dissipation by including only one cycle of indentation at the same specimen site.

Limitations of Nanoindentation for Bone Specimens

This review focused on displacement-based nanoindentation conditions, while the indenter is operated by load control. This is because the depth of the indentations should be enough to obtain stable indentation measures. As such, the loading rate was also determined using the corresponding displacement rate.

While the elastic, viscoelastic, and plastic properties of bone tissue were reviewed here, indentation work, which can be computed as the area under the loading and unloading indentation curve, is also important for computing the plasticity index [30, 61].

Bone specimens are essentially damaged during the rigorous preparation process. Mineral loss and destruction of collagen likely occur, and microcracks may develop, all of which result in deterioration of bone tissue properties. Thus, it is recommended that one use the same preparation procedure every time in order to ensure a direct comparison of the absolute values of nanoindentation between specimens.

The contact mechanics were applied to obtain nanoindentation modulus based on the assumption of an isotropic semi-infinite half-space solid [23, 25]. However, bone is an anisotropic composite material, and it includes many pores and microcracks. Although these inherent irregularities likely influence the computation of the nanoindentation modulus, if indenting is performed carefully so as to

avoid the defects, the resulting errors will not be significant enough to exceed the variation of modulus within the same type of bone tissue. Further studies are needed to validate or modify the current computations for the modulus of bone tissue.

At high indenting loads (up to 700 μN), post-indentation damages, including mechanical denaturation of collagen fibrils, disruption of interfibrillar interfaces, and slices through the thickness of individual fibrils, were found to lead to microcracks within and outside the indented regions [62, 63]. This damage during indenting is critical to accurately assess the viscoelastic and elastic properties during the holding and unloading periods following nanoindentation loading. Finite element analysis indicated a 21–48 % overestimation for the elastic modulus of bone tissue based on Eq. 41.5.

The high spatial resolution of nanoindentation enables the examination of the mechanical properties of bone tissue at the submicron level. However, it is obvious that the values obtained from such small indentations are not capable of representing the properties of an entire bone tissue region of interest. It would be helpful to increase the number of indentations in an array in order to obtain representative values of the targeted region [60].

Application of Nanoindentation for Bone Tissue Analysis

Nanoindentation can be utilized to examine the mechanical properties of any bone region that changes its material composition. The compositional parameters that have an effect on the mechanical properties of bone tissue included TMD distribution, mineral-to-matrix ratio, collagen quantity and quality, calcium-phosphate (Ca/P) ratio, and mineral crystallinity [21, 64–66]. Recently, it was found that the mineral-to-matrix ratio explained 54 % and 62 % of the variation in nanoindentation modulus and hardness of rat cortex, respectively [67]. A new bone tissue region of the rat femur with a higher collagen content had a larger nanoindentation energy dissipation capacity [60].

The compositional changes have been observed in diseased and aging bone. Distribution of calcium concentration varies between healthy, diseased, and treated bones (Fig. 41.9) [13], and intrinsic collagen content declines with aging [21, 68]. It was observed that collagen interfibrillar pyrrole cross-links decrease with osteoporosis [21]. The Ca/P ratio had a positive relationship with bone loss, providing less Ca/P for osteoporotic bone [69]. Many studies observed that antiresorptive agents (bisphosphonates) used to treat osteoporosis change the composition of bone tissue [65, 70, 71]. For instance, risedronate, a type of bisphosphonate, decreases mineral crystallinity and the collagen cross-link ratio after 3 and 5 years of treatment [65]. Thus, assessment of the changing bone tissue properties around bone cells is important to obtain an understanding of the mechanism in the progress of those bone diseases.

Active bone modeling and remodeling give rise to drastic alteration of bone tissue composition. Rigorous implantation surgery inherently damages bone adjacent to the implant [72, 73]. Then, active bone remodeling is stimulated to remove
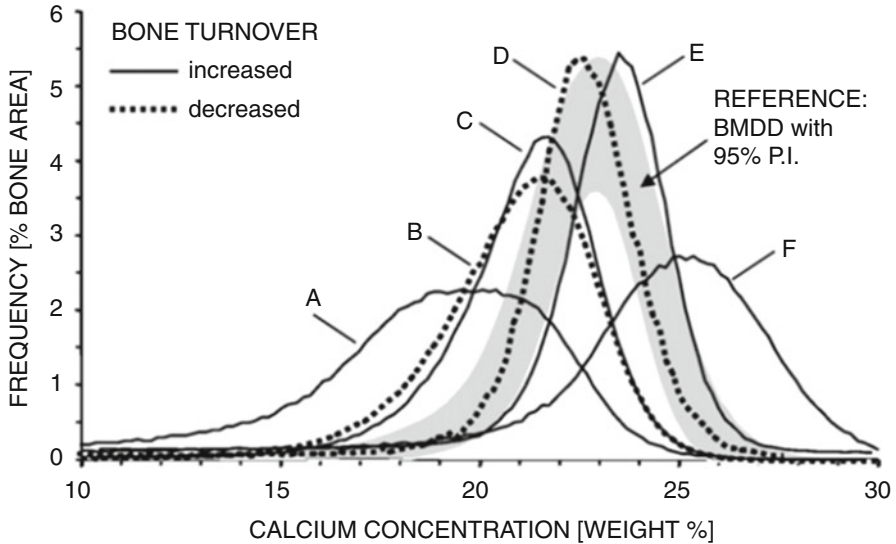
Fig. 41.9 Distribution of calcium concentration between healthy, diseased, and treated bones. *A* osteomalacia (celiac disease), *B* idiopathic osteoporosis, *C* postmenopausal osteoporosis, *D* postmenopausal osteoporosis treated with bisphosphonates, *E* osteogenesis imperfecta type I of a child, *F* postmenopausal osteoporosis treated with NaF [13]

the damaged old bone tissue and form new bone tissue at the implant interface [72]. Active bone modeling and remodeling are also observed during new bone regeneration in a graft or scaffold used to fill in a significant defect site from bone injury [74, 75]. As stem cells have the ability to self-renew and differentiate into specialized cell types, stem cell therapy has been suggested as an ideal resource for bone regeneration [75, 76]. For these therapies, bone maturation following new bone formation plays an important role in determining the ability of the newly regenerating bone to resist loading. Nanoindentation can successfully provide direct mechanical measures to validate the alteration of the material composition of bone.

Conclusion

Nanoindentation has been widely used to obtain the mechanical properties of bone tissue at the nano-level. Based on results from the previous studies, it is recommended that an ideal condition of nanoindentation on a specimen of bone tissue would be to indent faster than 10 nm/s loading/unloading displacement rate up to deeper than 500 nm while keeping more than 15 µm inter-indentation distance on a well-polished non-embedded wet bone specimen. To date, most of nanoindentation studies for bone have utilized this technology in determining elastic modulus and plastic hardness of mineralized tissues. Recent results indicated

that nanoindentation can be applied to assess viscoelastic properties of bone tissue. Combined together, these findings contribute to advance the current knowledge of bone biology and mechanics by providing more detailed information to understand a fundamental mechanism of mechanobiologic response of bone to elastic, viscoelastic, and plastic loading during daily activities.

References

1. Martin RB, Burr DB, Sharkey NA (1998) Skeletal tissue mechanics. Springer, New York, p 79
2. Carter DR, Beaupre GS (2001) Skeletal function and form: mechanobiology of skeletal development, aging, and regeneration. Cambridge University Press, Cambridge
3. Seeman E (2003) Pathogenesis of osteoporosis. J Appl Physiol 95:2142–2151
4. Keaveny TM, Morgan EF, Niebur GL, Yeh OC (2001) Biomechanics of trabecular bone. Annu Rev Biomed Eng 3:307–333
5. Kopperdahl DL, Keaveny TM (1998) Yield strain behavior of trabecular bone. J Biomech 31:601–608
6. McCreadie BR, Goldstein SA (2000) Biomechanics of fracture: is bone mineral density sufficient to assess risk? J Bone Miner Res 15:2305–2308
7. Heaney RP (2003) Is the paradigm shifting? Bone 33:457–465
8. Seeman E, Delmas PD (2006) Bone quality – the material and structural basis of bone strength and fragility. N Engl J Med 354:2250–2261
9. Hernandez CJ, Keaveny TM (2006) A biomechanical perspective on bone quality. Bone 39:1173–1181
10. Renders GA, Mulder L, van Ruijven LJ, van Eijden TM (2006) Degree and distribution of mineralization in the human mandibular condyle. Calcif Tissue Int 79:190–196
11. Seeman E (2003) Reduced bone formation and increased bone resorption: rational targets for the treatment of osteoporosis. Osteoporos Int 14(Suppl 3):S2–S8
12. Boonrungsiman S, Gentleman E, Carzaniga R, Evans ND, McComb DW, Porter AE, Stevens MM (2012) The role of intracellular calcium phosphate in osteoblast-mediated bone apatite formation. Proc Natl Acad Sci USA 109:14170–14175
13. Roschger P, Paschalis EP, Fratzl P, Klaushofer K (2008) Bone mineralization density distribution in health and disease. Bone 42:456–466
14. Ruppel M, Miller L, Burr D (2008) The effect of the microscopic and nanoscale structure on bone fragility. Osteoporos Int 19:1251–1265
15. Boivin G, Meunier PJ (2003) Methodological considerations in measurement of bone mineral content. Osteoporosis Int 14(Suppl 5):S22–S27; discussion S27–28
16. Yao W, Cheng Z, Koester KJ, Ager JW, Balooch M, Pham A, Chefo S, Busse C, Ritchie RO, Lane NE (2007) The degree of bone mineralization is maintained with single intravenous bisphosphonates in aged estrogen-deficient rats and is a strong predictor of bone strength. Bone 41:804–812
17. Roschger P, Gupta HS, Berzlanovich A, Ittner G, Dempster DW, Fratzl P, Cosman F, Parisien M, Lindsay R, Nieves JW, Klaushofer K (2003) Constant mineralization density distribution in cancellous human bone. Bone 32:316–323
18. Busse B, Hahn M, Soltau M, Zustin J, Puschel K, Duda GN, Amling M (2009) Increased calcium content and inhomogeneity of mineralization render bone toughness in osteoporosis: mineralization, morphology and biomechanics of human single trabeculae. Bone 45:1034–1043
19. Gilmore RS, Katz JL (1982) Elastic properties of apatites. J Mater Sci 17:1131–1141
20. Grant CA, Brockwell DJ, Radford SE, Thomson NH (2009) Tuning the elastic modulus of hydrated collagen fibrils. Biophys J 97:2985–2992
21. Burr DB (2002) The contribution of the organic matrix to bone's material properties. Bone 31:8–11

22. Donnelly E (2011) Methods for assessing bone quality: a review. Clin Orthop Relat Res 469:2128–2138
23. Oliver WC, Pharr GM (1992) An improved technique for determining hardness and elastic modulus using load and displacement-sensing indentation systems. J Mater Res 7:1564–1583
24. Hoffler CE, Guo XE, Zysset PK, Goldstein SA (2005) An application of nanoindentation technique to measure bone tissue Lamellae properties. J Biomech Eng 127:1046–1053
25. Roy ME, Rho JY, Tsui TY, Evans ND, Pharr GM (1999) Mechanical and morphological variation of the human lumbar vertebral cortical and trabecular bone. J Biomed Mater Res 44:191–197
26. Oliver WC, Pharr GM (2004) Measurement of hardness and elastic modulus by instrumented indentation: advances in understanding and refinements to methodology. J Mater Res 19:3–20
27. Li XD, Bhushan B (2002) A review of nanoindentation continuous stiffness measurement technique and its applications. Mater Charact 48:11–36
28. Rho JY, Tsui TY, Pharr GM (1997) Elastic properties of human cortical and trabecular lamellar bone measured by nanoindentation. Biomaterials 18:1325–1330
29. Mittra E, Akella S, Qin YX (2006) The effects of embedding material, loading rate and magnitude, and penetration depth in nanoindentation of trabecular bone. J Biomed Mater Res A 79:86–93
30. Fan Z, Rho JY (2003) Effects of viscoelasticity and time-dependent plasticity on nanoindentation measurements of human cortical bone. J Biomed Mater Res 67A:208–214
31. Kim DG, Huja SS, Navalgund A, D'Atri A, Tee B, Reeder S, Ri Lee H (2013) Effect of estrogen deficiency on regional variation of a viscoelastic tissue property of bone. J Biomech 46:110–115
32. Kim DG, Huja SS (2008) Nanoindentation viscosity of osteonal bone matrix is associated with degree of mineralization. Trans Orthop Res Soc 33:297
33. Kim DG, Huja SS, Lee HR, Tee BC, Hueni S (2010) Relationships of viscosity with contact hardness and modulus of bone matrix measured by nanoindentation. J Biomech Eng 132:024502
34. Huja SS, Beck FM, Thurman DT (2006) Indentation properties of young and old osteons. Calcif Tissue Int 78:392–397
35. Rho JY, Pharr GM (1999) Effects of drying on the mechanical properties of bovine femur measured by nanoindentation. J Mater Sci Mater Med 10:485–488
36. Zhang J, Niebur GL, Ovaert TC (2008) Mechanical property determination of bone through nano- and micro-indentation testing and finite element simulation. J Biomech 41:267–275
37. Wu Z, Ovaert TC, Niebur GL (2012) Viscoelastic properties of human cortical bone tissue depend on gender and elastic modulus. J Orthop Res 30:693–699
38. Reilly DT, Burstein AH (1974) Review article. The mechanical properties of cortical bone. J Bone Joint Surg Am 56:1001–1022
39. Zysset PK, Guo XE, Hoffler CE, Moore KE, Goldstein SA (1999) Elastic modulus and hardness of cortical and trabecular bone lamellae measured by nanoindentation in the human femur. J Biomech 32:1005–1012
40. Johnson WM, Rapoff AJ (2007) Microindentation in bone: hardness variation with five independent variables. J Mater Sci Mater Med 18:591–597
41. Mulder L, Koolstra JH, den Toonder JM, van Eijden TM (2008) Relationship between tissue stiffness and degree of mineralization of developing trabecular bone. J Biomed Mater Res A 84:508–515
42. Carter DR, Hayes WC (1977) The compressive behavior of bone as a two-phase porous structure. J Bone Joint Surg 59-A:954–962
43. Isaksson H, Nagao S, Malkiewicz M, Julkunen P, Nowak R, Jurvelin JS (2010) Precision of nanoindentation protocols for measurement of viscoelasticity in cortical and trabecular bone. J Biomech 43:2410–2417

44. Rho JY, Roy ME 2nd, Tsui TY, Pharr GM (1999) Elastic properties of microstructural components of human bone tissue as measured by nanoindentation. J Biomed Mater Res 45:48–54
45. Donnelly E, Baker SP, Boskey AL, van der Meulen MC (2006) Effects of surface roughness and maximum load on the mechanical properties of cancellous bone measured by nanoindentation. J Biomed Mater Res A 77:426–435
46. Kim DG, Hueni S, Tee BC, Lee H, Huja SS (2009) Effect of nanoindentation holding periods on correlation between viscosity and modulus of bone matrix. BMES Fall meeting, Pittsburgh, p 1256
47. van der Meulen MCH, Huiskes R (2002) Why mechanobiology?: a survey article. J Biomech 35:401–414
48. Novitskaya E, Chen PY, Lee S, Castro-Cesena A, Hirata G, Lubarda VA, McKittrick J (2011) Anisotropy in the compressive mechanical properties of bovine cortical bone and the mineral and protein constituents. Acta Biomater 7:3170–3177
49. Hoffler CE, Moore KE, Kozloff K, Zysset PK, Brown MB, Goldstein SA (2000) Heterogeneity of bone lamellar-level elastic moduli. Bone 26:603–609
50. Hoffler CE, Moore KE, Kozloff K, Zysset PK, Goldstein SA (2000) Age, gender, and bone lamellae elastic moduli. J Orthop Res 18:432–437
51. Tjhia CK, Odvina CV, Rao DS, Stover SM, Wang X, Fyhrie DP (2011) Mechanical property and tissue mineral density differences among severely suppressed bone turnover (SSBT) patients, osteoporotic patients, and normal subjects. Bone 49:1279–1289
52. Mulder L, Koolstra JH, den Toonder JMJ, van Eijden TMGJ (2007) Intratrabecular distribution of tissues stiffness and mineralization in developing trabecular bone. Bone 41:256–265
53. Oyen ML, Cook RF (2003) Load–displacement behavior during sharp indentation of viscous-elastic–plastic materials. J Mater Res 18:139–150
54. Oyen ML, Ko CC (2007) Examination of local variations in viscous, elastic, and plastic indentation responses in healing bone. J Mater Sci Mater Med 18:623–628
55. Oyen ML (2006) Nanoindentation hardness of mineralized tissues. J Biomech 39:2699–2702
56. Fischer-Cripps AC (2004) A simple phenomenological approach to nanoindentation creep. Mater Sci Eng A-Struct Mater Prop Microstruct Process 385:74–82
57. Kim DG, Kwon HJ, Han JS, Kim D, Lee B, Park C (2013) Change of viscoelastic property at bone-implant interface in healing. IADR #3736
58. Kim D-G, Huja SS, Hueni S, Tee BC, Lee H (2010) Relationship between elastic modulus and viscosity of bone matrix is strong independent of species, anatomical sites, and types of bone. Trans Ortho Res Soc 56:645
59. Donnelly E, Williams RM, Downs SA, Dickinson ME, Baker SP, van der Meulen MCH (2006) Quasistatic and dynamic nanomechanical properties of cancellous bone tissue relate to collagen content and organization. J Mater Res 21:2106–2117
60. Pathak S, Swadener JG, Kalidindi SR, Courtland HW, Jepsen KJ, Goldman HM (2011) Measuring the dynamic mechanical response of hydrated mouse bone by nanoindentation. J Mech Behav Biomed Mater 4:34–43
61. Raghavan M, Sahar ND, Kohn DH, Morris MD (2012) Age-specific profiles of tissue-level composition and mechanical properties in murine cortical bone. Bone 50:942–953
62. Tai K, Qi HJ, Ortiz C (2005) Effect of mineral content on the nanoindentation properties and nanoscale deformation mechanisms of bovine tibial cortical bone. J Mater Sci Mater Med 16:947–959
63. Tai K, Dao M, Suresh S, Palazoglu A, Ortiz C (2007) Nanoscale heterogeneity promotes energy dissipation in bone. Nat Mater 6:454–462
64. Morris MD, Mandair GS (2011) Raman assessment of bone quality. Clin Orthop Relat Res 469:2160–2169
65. Hofstetter B, Gamsjaeger S, Phipps RJ, Recker RR, Ebetino FH, Klaushofer K, Paschalis EP (2012) Effects of alendronate and risedronate on bone material properties in actively forming trabecular bone surfaces. J Bone Miner Res 27:995–1003

66. Tzaphlidou M (2008) Bone architecture: collagen structure and calcium/phosphorus maps. J Biol Phys 34:39–49
67. Donnelly E, Boskey AL, Baker SP, van der Meulen MC (2010) Effects of tissue age on bone tissue material composition and nanomechanical properties in the rat cortex. J Biomed Mater Res A 92:1048–1056
68. Bailey AJ, Sims TJ, Ebbesen EN, Mansell JP, Thomsen JS, Mosekilde L (1999) Age-related changes in the biochemical properties of human cancellous bone collagen: relationship to bone strength. Calcif Tissue Int 65:203–210
69. Kourkoumelis N, Balatsoukas I, Tzaphlidou M (2012) Ca/P concentration ratio at different sites of normal and osteoporotic rabbit bones evaluated by Auger and energy dispersive X-ray spectroscopy. J Biol Phys 38:279–291
70. Bala Y, Depalle B, Farlay D, Douillard T, Meille S, Follet H, Chapurlat R, Chevalier J, Boivin G (2012) Bone micromechanical properties are compromised during long-term alendronate therapy independently of mineralization. J Bone Miner Res 27:825–834
71. Donnelly E, Meredith DS, Nguyen JT, Gladnick BP, Rebolledo BJ, Shaffer AD, Lorich DG, Lane JM, Boskey AL (2012) Reduced cortical bone compositional heterogeneity with bisphosphonate treatment in postmenopausal women with intertrochanteric and subtrochanteric fractures. J Bone Miner Res 27:672–678
72. Garetto LP, Chen J, Parr JA, Roberts WE (1995) Remodeling dynamics of bone supporting rigidly fixed titanium implants: a histomorphometric comparison in four species including humans. Implant Dent 4:235–243
73. Brunski JB (1999) In vivo bone response to biomechanical loading at the bone/dental-implant interface. Adv Dent Res 13:99–119
74. Kallai I, Mizrahi O, Tawackoli W, Gazit Z, Pelled G, Gazit D (2011) Microcomputed tomography-based structural analysis of various bone tissue regeneration models. Nat Protoc 6:105–110
75. Pellegrini G, Seol YJ, Gruber R, Giannobile WV (2009) Pre-clinical models for oral and periodontal reconstructive therapies. J Dent Res 88:1065–1076
76. Rios HF, Lin Z, Oh B, Park CH, Giannobile WV (2011) Cell- and gene-based therapeutic strategies for periodontal regenerative medicine. J Periodontol 82:1223–1237
77. Boivin G, Meunier PJ (2002) The degree of mineralization of bone tissue measured by computerized quantitative contact microradiography. Calcif Tissue Int 70:503–511
78. Asefa T, Yoshina-Ishii C, MacLachlan MJ, Ozin GA (2000) New nanocomposites: putting organic function "inside" the channel walls of periodic mesoporous silica. J Mater Chem 10:1751–1755

Modulating Protein Adhesion and Conformation with Block Copolymer Surfaces

42

Scott R. Schricker, Manuel Palacio, and Bharat Bhushan

Keywords

Block Copolymer • AFM • Protein Adsorption • Protein Conformation • Nanostructured Surfaces

Introduction

Nanotechnology and nanostructured materials have a wide variety of applications in biotechnology and biomedicine. One of the more interesting applications of nanostructured materials is the control of the host response commonly referred to as biocompatibility. For many biomaterials, it is sufficient for host to have a minimal or virtually no response to be bioinert. Permanent implants such bone cements, dental implants, artificial joints, stents, and heart valves are all examples of materials that are considered bioinert or where it is important for them to be bioinert. In reality, no foreign material is completely bioinert, and this often leads to complications or failure of biomaterials. Designing materials that minimize the host response is very important and the focus of a great deal of research. However, in the past couple of decades, it has been the focus of biomaterial research to elicit a positive response, for instance, a bone

S.R. Schricker (✉)
Section of Restorative, Prosthetic and Primary Care Dentistry, The Ohio State University, Columbus, OH, USA
e-mail: schricker.1@osu.edu

M. Palacio
Western Digital
e-mail: manuel.palacio@gmail.com

B. Bhushan
Nanoprobe Laboratory for Bio- & Nanotechnology and Biomimetics (NLBB), The Ohio State University, Columbus, OH, USA
e-mail: bhushan.2@osu.edu

implant that is osteoconductive and can induce healing. The field of tissue engineering is an example of biomaterials that are designed to induce regeneration that leads to functional tissues. Nanostructure has become one of the important methods to control biocompatibility and elicit an appropriate host response.

Nanostructures have been widely used in biomaterials and as tools to study the material–host interface. Nanostructured biomaterials can be broadly classified into two main categories: (1) top-down or engineered materials generated by electrospinning, lithography, soft lithography, or e-beam lithography or (2) bottom-up or self-assembled materials, liquid crystals, block copolymers, self-assembled monolayers, and peptide nanofibers. Many of these materials are inspired by biological structures, such as bone and teeth, which are nanostructured materials. Nanotechnology has been harnessed to control biomaterial properties such as mechanical properties, degradation properties, and biological properties. The ability of nanostructured block copolymers to control the molecular and cellular level biological response will be the focus of this article.

Block copolymers are widely used in many applications including biomaterials. The physical, mechanical, degradation, and biological properties of biomaterials can be controlled and manipulated by modulating the chemistry and morphology of block copolymers. The ability of block copolymers to phase separate into a variety of micro- and nanoscale patterns allows them to interact with biological systems at a molecular level. Block copolymers are well known in the biomaterial field to control nonspecific protein absorption and degradation properties. In addition to the previously mentioned nonspecific biological interactions, there is a growing recognition that block copolymers can be used to control specific biological responses. This can be through recognition of the self-assembled patterns, or using these patterns to control the spacing of biologically active ligands. The first section of this article will provide background information on the protein–material interactions on a biomaterial surface, nanostructured biomaterials, block copolymer, and block copolymer-based biomaterials. This will be followed by a detailed discussion of the ability of block copolymers to control biological responses. The focus of this article is on synthetic block copolymers, though some peptide containing block copolymers will be discussed.

The Biomaterial–Host Interface

The biomaterial–host interface is a complex environment that is not completely understood at a molecular level. Protein adsorption to a biomaterial surface is thought to govern the host response to the biomaterial [1–6]. The distribution of these proteins and their conformation are thought to play a significant role in the biological response. Many studies have suggested that the chemistry and morphology of the biomaterial surface will regulate the characteristics of this intervening protein layer [2, 4, 7–12]. A consequence of an ill-defined, random coating is often a negative host response including inflammation and poor integration [13]. An example of the effects of protein conformation is depicted in Fig. 42.1. Fibronectin (Fn) is an extracellular matrix (ECM) protein that contains the RGD peptide sequence that promotes cellular

Fig. 42.1 Depiction of fibronectin adsorbing to either a hydrophilic or a hydrophobic surface. On the hydrophilic surface, the protein will retain a more 'normal' conformation and display the RGD binding epitope. Conversely, on the hydrophobic surface, the fibronectin will change its conformation, and the RGD binding epitope will no longer be available for binding
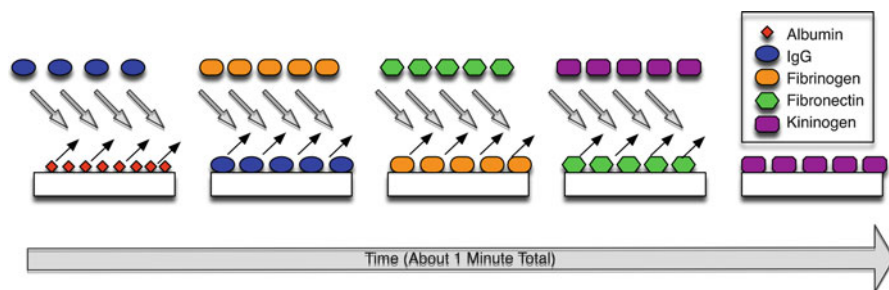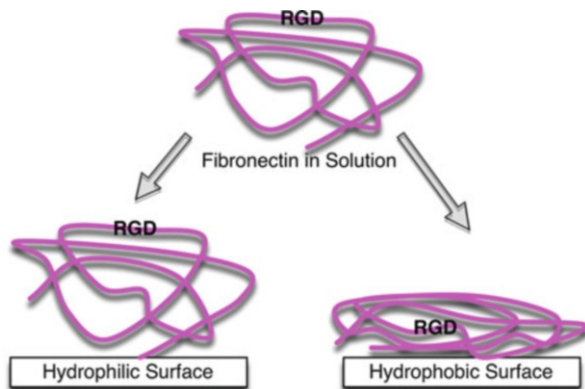

Fig. 42.2 Depiction of the 'Vroman effect'. As a biomaterial surface comes into contact with blood, a series of protein adsorptions and desorptions take place. Initially, albumin will adsorb to the surface and is then displaced by immunoglobulin G (*IgG*). Over the time course of approximately 1 min, IgG is displaced by fibrinogen, fibronectin, and high molecular weight kininogen

binding. Studies have demonstrated that on hydrophilic surface, Fn will maintain a physiological conformation and express the RGD group to promote cellular adhesion. However, on a hydrophobic surface, Fn will denature and the RGD group will be buried in the interior of the protein inhibiting cellular adhesion.

Additionally, the biomaterial surface is dynamic with respect to protein absorption, and existing adsorbed proteins can be displaced and replaced [14–18]. This is known as the Vroman effect, and in general it is thought that lower molecular weight proteins are initially absorbed to the surface and displaced with larger proteins. The time frame of this process is seconds to minutes, and it is also been demonstrated that the surface chemistry will affect this process. Figure 42.2 depicts a potential Vroman process. It is important to note that the exact nature of the process is very complex and still not completely characterized and Fig. 42.2 is only an idealized depiction.

The control of the adsorbed protein layer is thought to be important to controlling the biocompatibility of a biomaterial. Hydrophilic surfaces and attaching polyethylene glycol (PEG) have been known to reduce protein absorption and promote biocompatibility. Another strategy involves preabsorbing proteins on

a biomaterial surface prior to implantation [19–21]. While this has shown potential, the preadsorbed protein layer can also experience a variety of environmental insults: biological, chemical, and mechanical [22–26]. Mechanical degradation can result from wear forces caused by micromotion of the biomaterial or abrasive forces. The degradation of the preadsorbed protein layer can reduce the long-term efficacy and biocompatibility of a biomaterial. Recent work has also demonstrated that nanomorphology – both non-defined, such as roughness, and highly defined, such as patterns generated by lithography – will influence protein adsorption and conformation and cellular response [27–32]. Many other additional concepts have been used; however, the focus for this article will be nanostructured materials particularly block copolymers.

Nanostructured Biomaterials

The ability of nanostructures or nanomorphology to control cellular behavior is well discussed in the literature [27–32]. While there are many ways to generate irregular nanoscale features such as roughness [33–35], there are only a few methods for generating highly defined nanostructures. Most of the techniques are based on some form of lithography [36], soft lithography [37–39], e-beam etching [40, 41], dip-pen [42, 43], or conventional lithography [44, 45]. Self-assembled methodologies such as peptide amphiphiles [46, 47], dendrimers [48], and liquid crystals [49] are also utilized to generate regular nanostructures. Despite their well-documented ability to generate nanostructured patterns, there are relatively few examples of block copolymers generating bioactive surfaces [50–56]. Block copolymers have typically been used to generate micelles for drug delivery [57–59] or as a method to control biodegradation or surface energy [60]. Relatively recent synthetic methodologies such as RAFT polymerization and 'click' chemistry have greatly expanded the ability and ease of generating a large variety of block copolymers.

Nanotechnology has the potential to manipulate properties and interfaces at a molecular level and in a controlled manner. Biological systems already utilize nanostructure to control mechanical properties, such as the well-defined nanostructures found in teeth and hard tissue. The extracellular matrix that regulates cell behavior is nanostructured, so it is not surprising that synthetic nanomorphology is known to affect the behavior of cells in both in vivo and in vitro models. Many of the general effects of nanostructure, roughness, shape, and spacing on cell behavior are known. Innovation in synthetically generated nanostructures will result from the ability to rationally control and easily generate nanostructures. Because many of the principles that govern biological response to synthetic nanostructures are not known, the ability to easily and systematically generate nanostructures is important.

Self-assembled monolayers (SAMs) have been widely used to study protein absorption and conformation on a surface. SAMs are well-defined nanostructures and have end groups that can be manipulated to control the chemistry of the surface. While not necessarily practical as a biomaterial, SAMs are important tools to study protein behavior on a surface and can provide data on how a protein will behave on similar

biomaterial surfaces. A series of papers [3, 4, 11] describes the effect of the SAMs with different end groups on fibronectin conformation and subsequent cellular adhesion. Four end groups were utilized: CH_3, OH, COOH, and NH_2. The conformation assays demonstrated that the OH-functionalized SAMs induced the absorbed Fn to have a more natural conformation. This was evidenced by the Fn having the most binding sites available. Subsequent assays demonstrated that the Fn on the OH-functionalized SAMs had better binding to integrins and produced improved cellular adhesion. This work is an example of well-defined nanostructured materials being used to control protein conformation and control subsequent cell response.

Block Copolymers

Block copolymers are specific type of copolymer system such that each monomer is homopolymerized to create chemically distinct domains that are covalently linked. The effective result is two or more homopolymers that are covalently linked as in the poly(styrene-b-butadiene) example shown in Fig. 42.3. Linear block copolymers can be arranged as diblocks or triblocks, and many multiblock copolymers are also known. It is common to refer to blocks by letter, so that diblocks are A-B block copolymers and triblocks can be designated as A-B-C block copolymers. There are many variations; a two-component system could have an arrangement of A-B, A-B-A, B-A-B, or A-B-A-B with many other possible permutations. Block copolymers can also have nonlinear architectures such as graft systems and star systems to name a few.

High molecular weight polymers of different chemistries are often immiscible, and as a result the individual blocks in a block copolymer will phase separate to minimize energetic interactions. The covalently bound blocks will phase separate into patterns, with examples of bulk morphology shown in Fig. 42.4. The morphology of the block copolymer systems is dependent on many factors including the monomer ratio, architecture, and chemistry of the blocks, and many additional morphologies are known. Patterned surfaces can be created by casting thin films on a substrate. The ability of block copolymers to phase separate has found many useful applications. For instance, combining a high-modulus block with an elastomeric block will result in a strong but tough polymer [61–65]. Applications that require precise structural control such as electronics, membranes [66], or nanoparticle templating [67] utilize block copolymers. The precise structural control is an example of bottom-up self-assembly. Small changes in the chemistry of the block copolymers can result in material with different morphology and properties.

A variety of polymerization methods are used to synthesize block copolymers, and many systems are useful without a high degree of control over the individual blocks. However, many applications, such as electronics and biological, require well-defined block copolymer morphology. This can only be achieved by controlling the molecular weight and architecture of the individual blocks through 'living' polymerizations. Cationic and anionic polymerizations have long been used to create well-defined blocks and architectures [68–70]. With the development of ring-opening metathesis polymerization (ROMP) [71, 72] and the 'living'
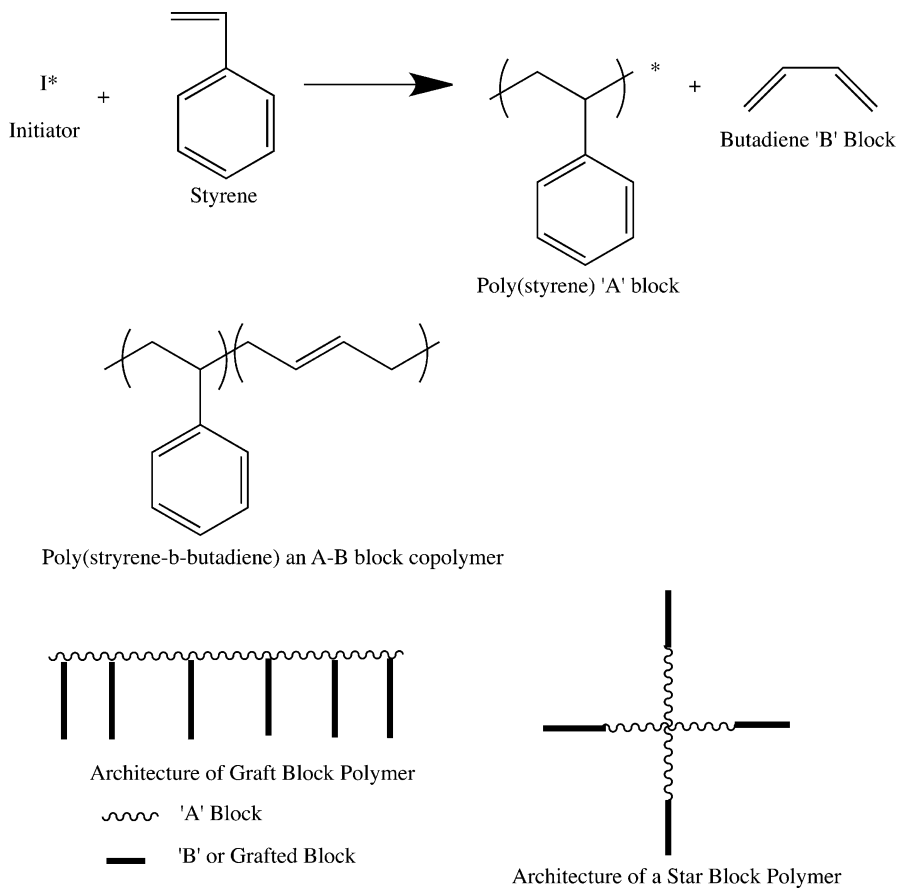
Fig. 42.3 Examples of block copolymer architecture and chemistry
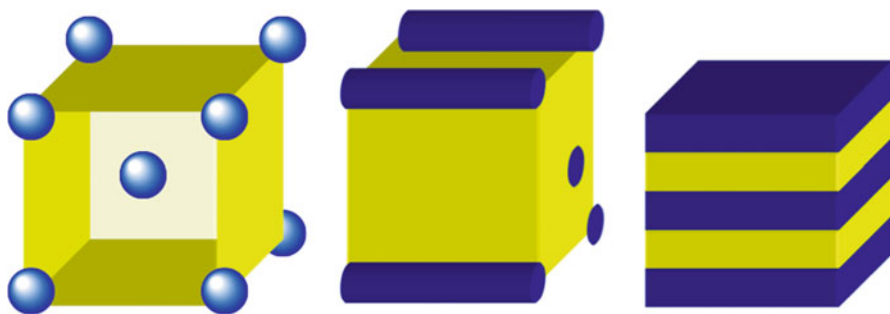

Fig. 42.4 Examples of block copolymer morphologies: spherical, cylindrical, and lamellar

free radical polymerizations [73–75], a wider variety of polymer chemistries could be utilized. Both ROMP and 'living' free radical polymerizations tolerate functional groups and do not require meticulous reaction conditions. Combined with ligation chemistry such as 'click' chemistry [76–78], a wide variety of architectures and chemistries can be obtained.

Techniques to Measure Protein Adhesion and Conformation on a Surface

Many techniques are available to measure protein adhesion on a biomaterial surface. The assays can range from studying the bulk weight gain in a material using a microbalance, surface spectroscopy to highly sophisticated methods using antibodies that can quantify different protein types and profiles. The different techniques often reflect the variety of models that can be used to study protein–biomaterial interactions. For instance, the difference in protein adsorption may be sufficient to determine if adding polyethylene glycol to a surface has the desired effect. This is similar to modeling vascular grafts and blood contact, where reducing protein adsorption of any type is thought to be beneficial. By contrast, if the purpose of the material is cellular adhesion, then the amount of fibronectin absorption on a surface will be of interest. Several different techniques that are discussed in this article will be briefly described in this section, and it is not intended as a comprehensive review of surface characterization.

Quartz Crystal Microbalance (QCM)

A quartz crystal microbalance (QCM) is a common technique used to measure protein adsorption to a surface. Quartz crystal will vibrate with a specific frequency, and this frequency will be affected by materials absorbed on the surface. In order to model protein absorption on biomaterials, thin films of biomaterials such as polystyrene can be cast on the surface of the quartz crystal. The QCM can then measure the protein adsorbed on the cast polymer surface. The basic mathematical relationship between the absorbed protein and the crystal frequency is given by the Sauerbrey equation [79, 80]:

$$\Delta f = -n\Delta m C^{-1}$$

where f is the frequency, m is the mass, n is the overtone number, and C is a constant given in ng cm^{-2} Hz^{-1}.

Another version of the Sauerbrey equation is [81]

$$\Delta m = -\frac{p_q l_q}{f_o} \frac{\Delta f}{n}$$

where instead of a constant, p_q is the specific density, l_q is the thickness of the quartz crystal, and f_o is the fundamental resonance frequency.

The result is that the observed frequency of the quartz crystal changes as proteins adhere to the surface. The caveats to this technique are that the mass of the water associated with the proteins will affect the frequency and that the viscoelastic properties of the protein will affect the observed frequency. QCM has been used to model different protein absorption phenomena such as the activation of complement on a polystyrene surface [79, 80] or the adsorption of fibronectin on a polysiloxane surface [6].

Ellipsometry

Surface spectroscopy is another powerful tool to measure protein adsorption on a biomaterial surface. Fourier transform infrared spectroscopy (FTIR), ellipsometry, and XPS are all examples of spectroscopic techniques that have been used to characterize the protein–biomaterial interaction. Ellipsometry and FTIR were some of the earliest tools used to characterize protein absorption on a biomaterial surface. Ellipsometry utilized polarized monochromatic light to detect changes to a surface. Figure 42.5 demonstrates the basic configuration of an ellipsometry experiment.

The polarization of the light source will be adjusted until the sample is linearly polarized, and the analyzer will be adjusted until it is opaque to the polarized light. Through a series of calculations [82], a sample thickness can be determined. Based on the known density of proteins, the amount of protein absorbed on the surface can be determined by the following relationship [83]:

$$\Gamma \ \left(ng \ mm^{-2}\right) = K \ x \ thickness \ (nm)$$

where K is an approximation of protein density given at 1.2 (g ml^{-1}) in air and 1.35 (g ml^{-1}) for water [82]. Figure 42.6 adapted from Elwing et al. is a representative graph from an ellipsometry experiment. It is noteworthy that this allows for monitoring protein absorption in real time, including desorption from the surface and the ability to measure antibody absorption to a surface. Antibodies can be used in combination with ellipsometry to quantify specific proteins being adsorbed from a mixture or to quantify protein conformation.

FTIR

Fourier transform infrared spectroscopy (FTIR) characterizes materials by measuring the adsorption of infrared radiation that corresponds to specific functional groups. In order to characterize a surface, an ATR (attenuated total reflectance) configuration is often used. The sample is placed on a diamond (other types are also known) crystal, and the infrared radiation will internally reflect within the crystal. The infrared radiation at the surface of diamond will interact with the surface of the sample, resulting in the characterization of the surface chemistry. FTIR has been
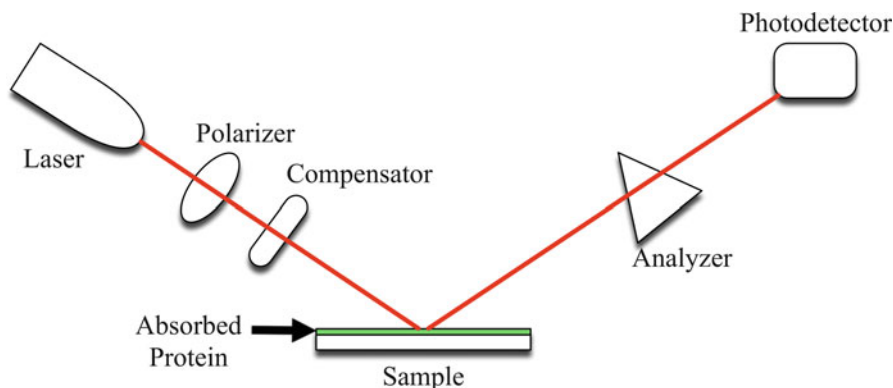
Fig. 42.5 Generic depiction of an ellipsometer evaluating a protein on a surface
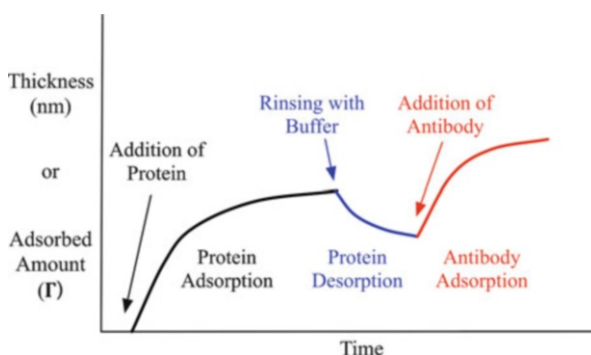

Fig. 42.6 This is a representative graph of an ellipsometer experiment adapted from Elwing et al. [83]. It is important to note that this allows for the monitoring of protein adsorption in real time and allows subsequent events to take place. The sequence depicted is the depositing of the protein followed by an equilibrium plateau. The excess protein was washed away, and the surface reestablished equilibrium. The antibody was added and then reached equilibrium at. In every step of this sequence, ellipsometry was able to quantify the protein absorbed to the surface as a function of time

widely used to characterize surfaces, and it is possible to quantify the adsorbed proteins. By measuring the molar absorptivity of the protein in a transmission FTIR experiment, the amount of adsorbed protein can be calculated [84].

XPS or ESCA

X-ray photoelectron spectroscopy (XPS) is a powerful technique that is used to characterize surfaces and is used to characterize proteins on biomaterial surfaces. This technique is also known as ESCA (electron spectroscopy for chemical analysis)

and is based on the photoelectron effect. This technique has been thoroughly reviewed [85–87], and the basic concept is that X-rays will force the ejection of electrons from elements on the surface of a material. The basic equation that governs this process is

$$E = hv - BE - \phi$$

where E is the observed kinetic energy of the electron that is emitted upon irradiation with the X-ray source. The energy of the X-ray source is given by hv, ϕ is the constant that varies from instrument to instrument, and BE is the binding energy of the electron. BE is the unknown and provides the surface chemical information.

By measuring the energy of the ejected electrons, the elemental composition of a surface can be determined. In addition, binding and ionization states can also be determined due to the fact that energy of an electron will vary depending on its orbitals and type of bonding. This allows for the collection of highly detailed chemical information about the surface and proteins adsorbed on the surface. By varying the angle of the sample relative to the source, information about the thickness of the adsorbed protein layer can be obtained. Imagine an X-ray source that is perpendicular to a surface vs. at 30° angle to the surface. The 30° angle will be more shallow and capture more information about the upper layers of the surface. This technique is also useful for studying conformation changes in proteins. Proteins that denature will have a different elemental surface composition than proteins that have not denatured. The major disadvantage of this technique, from the standpoint of characterizing proteins, is that it must be performed in high vacuum.

Antibodies Coupled with AFM

Antibodies are widely used to specifically detect proteins in biochemistry and medicine. Antibodies are very specific and can selectively detect a desired protein from a mixture. Proteins adsorbed onto a biomaterial surface can also be characterized by antibodies. A mixture of proteins can be deposited on a surface followed by the adsorption of the antibody specific to one of the proteins. After washing off the unbound antibodies, the protein in question can be quantified by measuring the bound antibodies (Fig. 42.7). Antibodies are typically paired with a tag that will aid in the quantification. The tag can be fluorescent, radioactive, or a metal cluster or nanoparticle that can be detected by AFM or electron microscopy. The quantification is almost always relative, and absolute measures are difficult.

In an alternate method, an antibody can be covalently bound to an AFM tip. As the AFM scans the surface, a higher adhesion force will indicate that the antibody is specifically interacting with the protein of interest. This allows for the quantification and spatial distribution of the protein of interest. The advantage of AFM is that this experiment can be performed in aqueous media under physiological conditions.
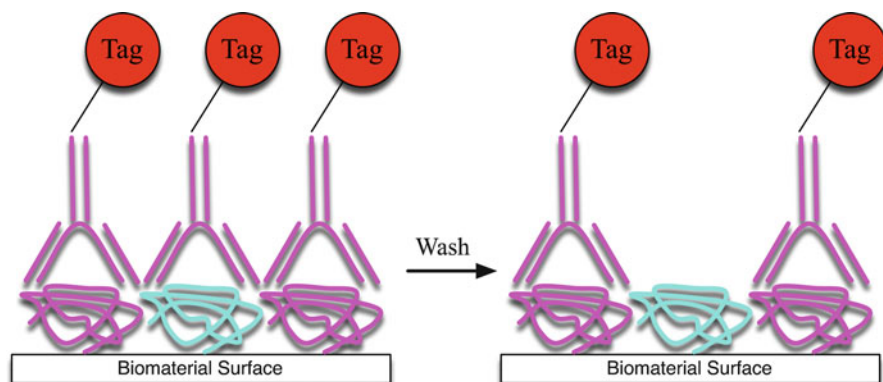
Fig. 42.7 The tagged antibody will selectively bind to the purple protein on a biomaterial surface. After washing, the unbound antibody is removed, leaving the tagged antibody bound to only the purple protein. The tag can be used to quantity the purple protein adsorbed to the biomaterial surface

The AFM-antibody pairing can also be used to detect protein conformation. The antibody does not bind to the entire protein but rather specific sections or epitopes. Misfolding of a protein can cause the epitopes to become unavailable for binding. For instance, if a protein is adsorbed onto a hydrophobic surface, it can denature and cause its binding epitope to become buried in the protein. Since this epitope is no longer expressed on the surface, the antibody will no longer selectively bind to the protein. This phenomenon can be harnessed to determine if a given surface will affect the conformation of a protein. After a protein is adsorbed to a surface, the antibody-modified AFM tip will scan the surface. A strong binding action will indicate that the antibody is binding to the epitope and that the protein is in a native conformation. Averaging the adhesion across the surface will provide information about the protein conformation. This technique is an indirect measure, and it is useful for comparing surfaces rather than obtaining an absolute value.

In summary, many techniques exist to characterize proteins that are adsorbed onto a biomaterial surface. Clearly, no one technique can completely characterize the interactions between proteins and a surface. Each experiment provides a different set of information and has its own set of advantages and disadvantages. The ease of use and availability of equipment will also be a factor in determining which technique is the most useful.

Block Copolymers as Biomaterials

Block copolymers have been widely used as biomaterials to control biological response. Two instructive examples of harnessing block copolymers to control nonspecific interactions are their use in drug delivery micelles and as degradable

scaffolds. Amphiphilic block copolymers are known to form micelles and have been utilized to deliver drugs and therapeutic agents [57–59, 88–90].

For example, a polyethylene glycol (PEG)–polycaprolactone (PCL) block copolymer was used to deliver taxol [91]. The self-assembly properties of the block copolymer created a core–shell micelle with the hydrophobic PCL as the core and the PEG as the hydrophilic shell. This core–shell configuration allowed for taxol encapsulation at the core, with the PEG providing protection from protein adsorption and increasing circulation time. The diameter and drug loading were controlled by adjusting the molecular weight of the block copolymer as a whole and of the individual blocks. An additional advantage of this core–shell architecture is the ability to put targeting moieties on the surface. For instance, folate-conjugated drug delivery micelles were synthesized to increase the uptake in cancer cells [92]. The folate functional groups improved the uptake of the micelles in an in vitro cell culture model. The individual blocks can also provide functionality to other types of drug delivery systems such as the incorporation of a polyethylenimine block [93]. This cationic block allowed for the incorporation of plasmid DNA in the micelle, suggesting the potential for gene delivery.

Block copolymers have also been used to modify the properties of the poly (lactic acid-co-glycolic acid) (PLGA) family of degradable scaffolds [94–96]. PEG blocks were incorporated in PLGA polymers and had the expected effect of increasing water sorption and increasing the degradation rate. One interesting finding was that at higher levels of PEG content, the crystallinity of the block copolymer increased, presumably due to the increase in chain mobility due to the flexible PEG segments. In addition, PEG blocks have also been demonstrated to resist nonspecific protein adsorption [97]. Beyond modulating bulk properties, various blocks have also been used to add functionality and modify the properties of PLGA polymers. For example, a block of pH-sensitive sulfamethazine was added to the ends of a degradable polymer to control gelation behavior. This functional block copolymer would form a gel under physiological conditions but not at elevated temperature or basic pH [98]. A block of semiconducting poly(aniline) was incorporated into a poly(lactic acid) polymer to introduce an electroactive character to the polymer. Poly(aniline) is widely studied as a conducting polymer and is known to biodegrade and act as a tissue engineering scaffold [99].

There are many other examples of block copolymers modulating the properties of biomaterials. The previous section contained only examples of what could be accomplished by incorporating functional polymer blocks in biomaterials. However, the focus of this review is to examine how block copolymer morphology can be used to elicit a specific biological response. Initially, the discussion will involve how block copolymer morphology will be used to control the biological response on a molecular level, namely protein adhesion and conformation. Subsequently, patterning of biologically active molecules by block copolymers will be reviewed followed by a discussion of anti-thrombogenic block copolymers.

Block Copolymers and Protein Adhesion

Proteins adsorbed on a biomaterial surface are thought to govern the response of the host [1–3, 5, 6]. In a highly complex and not completely understood process, proteins will nonspecifically coat a biomaterial surface upon implantation. The host will react to this protein layer, specifically to the types of proteins and their conformation [14–18]. So controlling the specific interaction between the proteins and a biomaterial surface will lead to improved biomaterials and control over the host response. In addition to the nonspecific coating, there is also the 'Vroman effect' [17, 18, 23, 100] which affects the protein profile on a biomaterial surface. Over time the initially deposited proteins are displaced from the surface with other, often larger, proteins. The chemistry of the biomaterial surface is also thought to affect this process. The systems discussed in this section deal with attempts to control the interaction of specific proteins with a surface rather than general resistance to protein absorption [101–104].

Fundamental Studies of Protein Adsorption to Acrylate Block Copolymers

An important aspect to describing block copolymer–protein interactions is to separate the contributions from the chemical composition and the morphology of the block copolymer surface. The surface morphology is highly dependent on the chemical composition and arrangement of the blocks. In addition, changing the chemical composition of the polymer could affect the interaction with a protein. A method to address this problem is to synthesize a series of block copolymers and a random copolymer of the same chemical composition. So the only difference will be the block copolymer morphology independent of chemical composition. For example, given a block copolymer system where the A and B monomers have an equal mole ratio, the block can be arranged in many different ways: A-B, A-B-A, B-A-B, and A-B-A-B. Each configuration will have a different surface morphology but the same chemistry. So it should be possible to determine the effect of morphology on proteins, independent of chemistry.

In studies by Palacio et al. [50–53, 105–107] a series of block copolymers was synthesized by RAFT polymerization followed by 'click' coupling reaction as shown in Fig. 42.8. This powerful combination is widely used in the synthesis of block copolymers [76–78, 108–111]. Table 42.1 lists the polymers that were synthesized: the hydrophobic block is methyl methacrylate (MMA), and the hydrophilic block is either acrylic acid (AA) or 2-hydroxyethyl methacrylate (HEMA).

The block copolymers were synthesized in a diblock A-B configuration and triblock A-B-A configuration with the random copolymer serving as a control. The block copolymers were cast on silicon wafers and annealed with heat and humidity. The morphology of the block copolymers was imaged by AFM in both height and phase mode. It was verified that the diblock had a different surface morphology compared to the triblock copolymer (Fig. 42.9) and that the random copolymer and
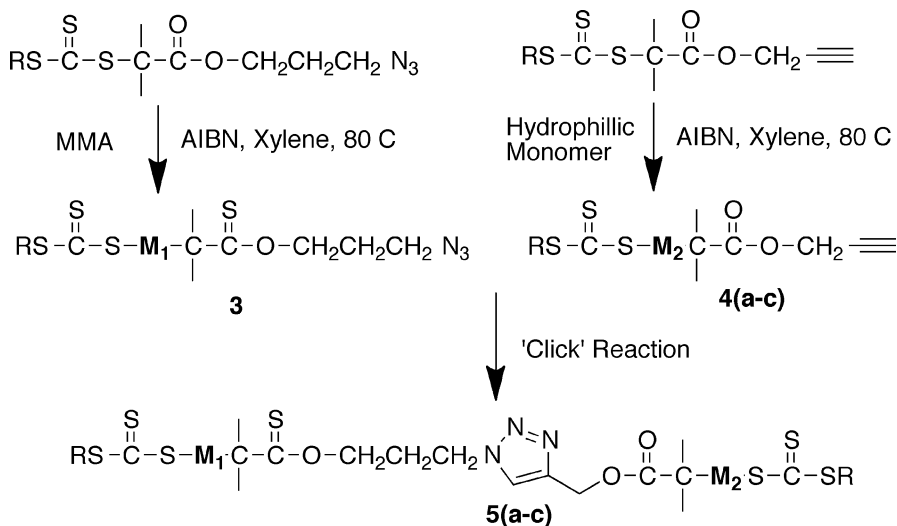
Fig. 42.8 Synthesis of block copolymers through RAFT and click chemistry [50]. *MMA* methyl methacrylate; hydrophilic monomer is either acrylic acid (AA) or 2-hydroxyethyl methacrylate (*HEMA*), dimethylacrylamide (*DMA*); **3** (M_1 = PMMA) and **4a** (M_2 = PAA); **4b** (M_2 = PHEMA); **4c** (M_2 = PDMA); **5a** (M_1 = PMMA, M_2 = PAA) **5b** (M_1 = PMMA, M_2 = PHEMA) **5c** (M_1 = PMMA, M_2 = PDMA)

Table 42.1 Molecular weight and glass transition data for acrylate block copolymers (Taken from Schricker et al. [50])

Polymer	Molecular weight (kg mol^{-1})[a]	Polydispersity	Glass transition (°C)
PMMA-N$_3$ (**3**)	6.4	1.03	103, 115
PAA-Alky (**4a**)	6.8	1.20	110
PDMA-Alky (**4b**)	5.9	1.10	82
PHEMA-Alky (**4c**)	8.1	1.06	48
PMMA-b-PAA (**5a**)	12.2	1.10	103, 115
PMMA-b-PDMA (**5b**)	11.7	1.23	80, 98
PMMA-b-PHEMA (**5c**)	14.3	1.09	45, 105

[a]Measured by GPC in DMF at 60 °C

homopolymers had a homogenous surface morphology. In addition, the contact angle of the diblock and triblock PAA–PMMA polymers are similar (Fig. 42.10), so differences can be attributed to the morphology rather than the surface hydrophilicity.

The protein adhesion was measured with AFM tips modified with the protein of interest. The block copolymer surfaces were imaged in phosphate buffer solution (PBS) or in an acidic buffer. The data was averaged over the area scanned, and a higher force recorded by the AFM was interpreted as the protein more strongly adhering to the block copolymer surface. The results are shown in Table 42.2.
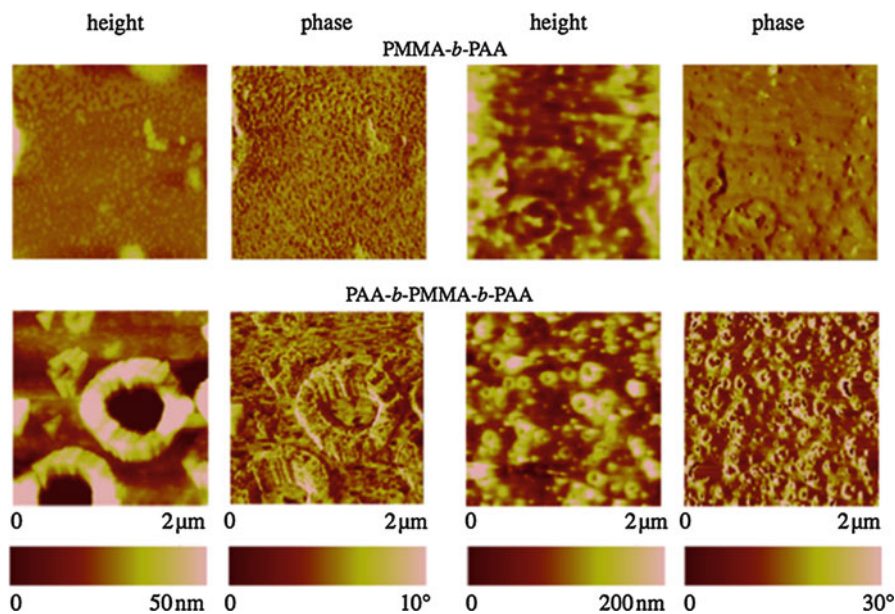
Fig. 42.9 Morphology of a PAA–PMMA diblock and triblock copolymer. Taken from Palacio et al. [51]

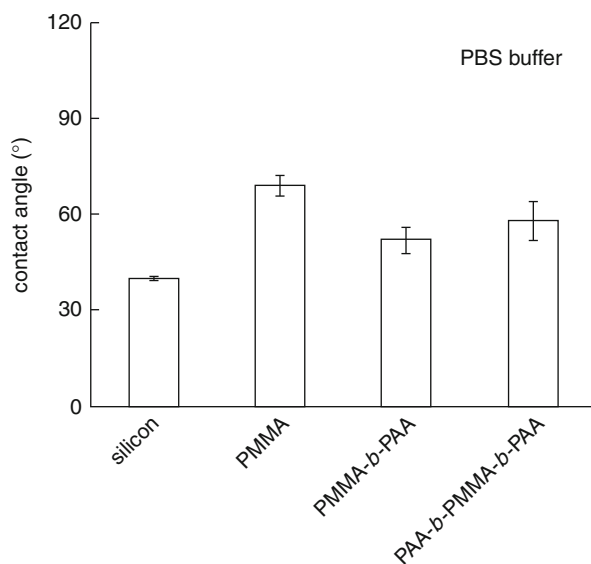**Fig. 42.10** Contact angle of PAA–PMMA block copolymers. Taken from Palacio et al. [51]

It is clear that the block copolymer morphology has an effect on protein adhesion. However, the effect varies based on the protein and the conditions. There is almost no effect for collagen at either neutral or acidic pH. For fibronectin and BSA, there is an increase in adhesion for the diblock and triblock PMMA–PAA compared to the

Table 42.2 Summary of the measured adhesive force [52]

| | Adhesive force (nN) | | | | | |
| | Fibronectin | | BSA | | Collagen | |
Material	(pH 7.4)	(pH 6.2)	(pH 7.4)	(pH 6.2)	(pH 7.4)	(pH 6.2)
PMMA	1.0 ± 0.1	0.7 ± 0.3	2.2 ± 0.2	2.7 ± 0.3	2.4 ± 0.2	3.2 ± 0.2
PMMA-co-PAA (1/1)[a]	1.4 ± 0.2	2.2 ± 0.9	2.6 ± 0.6	3.4 ± 0.7	2.6 ± 0.4	3.9 ± 0.8
PMMA-b-PAA (1/1)	1.6 ± 0.9	3.5 ± 1.3	2.9 ± 1.0	4.0 ± 0.8	3.2 ± 0.5	4.7 ± 1.1
PAA-b-PMMA-b-PAA (1/2/1)	2.1 ± 0.5	3.7 ± 0.8	4.8 ± 0.4	6.5 ± 0.4	3.8 ± 0.9	5.2 ± 0.7
PMMA-co-PHEMA (1/1)[a]	1.6 ± 0.3	3.4 ± 0.4	1.6 ± 0.4	4.2 ± 0.6	3.6 ± 0.8	5.1 ± 0.6
PMMA-b-PHEMA (1/1)	3.0 ± 0.2	4.4 ± 0.9	3.8 ± 0.4	3.7 ± 0.7	3.9 ± 0.7	5.0 ± 0.6
PMMA-b-PHEMA-b-PMMA (1/2/1)	4.2 ± 0.3	4.6 ± 1.0	3.3 ± 0.2	3.7 ± 0.4	4.0 ± 0.8	4.5 ± 1.0

[a]Random copolymer

random copolymer at acidic pH but not at neutral pH. The opposite effect is seen with the PMMA–HEMA polymer series. It is thought that because PAA has an ionizable group, the charge experienced by the protein will change at acidic pH. This demonstrates that block copolymer morphology can influence protein adhesion. The effect is dependent on the protein and the conditions of the experiment. This suggests that surfaces can be tuned for specific proteins and conditions.

The conformation of fibronectin (Fn) was measured on the polymer surfaces using an AFM technique. Protein conformation on a biomaterial surface can have a profound effect on the cellular response [2, 6]. In particular, fibronectin has been widely studied because it contains epitopes that bind to cellular receptors [112]. If the fibronectin at a biomaterial surface maintains a natural conformation, then it will elicit a positive cellular response. However, if Fn denatures on the surface, then the binding epitopes are not displayed which inhibits cellular binding. So antibodies to Fn were covalently attached to AFM tips to measure the conformation of Fn on a block copolymer surface. Fn is deposited on the polymer surface in PBS followed by scanning the surface with the antibody-modified AFM tip. It is expected that if the Fn is in a more natural conformation, then a specific interaction between the Fn and the antibody will occur. This will be registered by the AFM as an adhesion event, and the greater the average adhesion of the Fn-coated surface, the more natural the Fn conformation. The adhesion results are shown in Fig. 42.11.

The data demonstrates that fibronectin on the triblock copolymer surfaces has the greatest interaction with the antibody-functionalized tip. This is true for both the PMMA-b-AA and PMMMA-b-HEMA. The interpretation of this data is that the fibronectin is in a more natural conformation of the triblock copolymer surfaces and
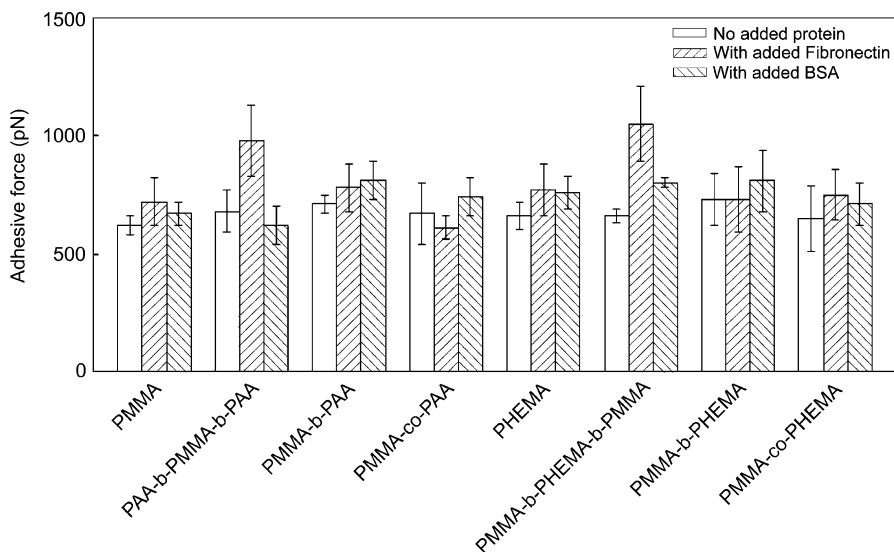
Fig. 42.11 Adhesive force between an AFM tip functionalized with anti-Fn antibodies and block copolymer surfaces incubated with an Fn solution [107]

Table 42.3 XPS data of fibronectin absorbed on polymer surfaces [106]

	O/C		N/C		S/C	
	90°	30°	90°	30°	90°	30°
PMMA	0.35	0.33	0.10	0.10	0.002	0.003
PAA-b-PMMA-b-PAA	0.48	0.27	0.05	0.05	0.006	0.003
PMMA-b-PAA	0.40	0.36	0.03	0.03	0.004	0.0001
PMMA-r-PAA (random)	0.92	0.57	0.12	0.11	0.004	0.005

has stronger adhesive interactions with the antibody. A subsequent XPS study (Table 42.3) demonstrates that the elemental profile for the triblock copolymer is different than the other copolymer surfaces, suggesting that the conformation of the protein is affected by the surface.

Several other methacrylate/acrylate systems have been explored to control protein adhesion. Phase-separated mixtures of PMMA and PS were studied for protein adhesion using X-ray photoemission electron spectroscopy [113–115]. While not strictly a block copolymer, these mixture phase separate to form patterns that are similar to those found in block copolymers. A 28:72 (w/w) ratio of polymethyl methacrylate (PMMA) to polystyrene (PS) was cast on a silicon substrate, and human plasma fibrinogen (HPF) was deposited on the surface. One of the interesting findings of this study was that the HPF absorbed to the PS component rather than the PMMA component but only when deposited from an ionic buffer solution. When deposited from a water or low ion solution, the HPF would localize at the interface between the PMMA and the PS [113]. Further studies
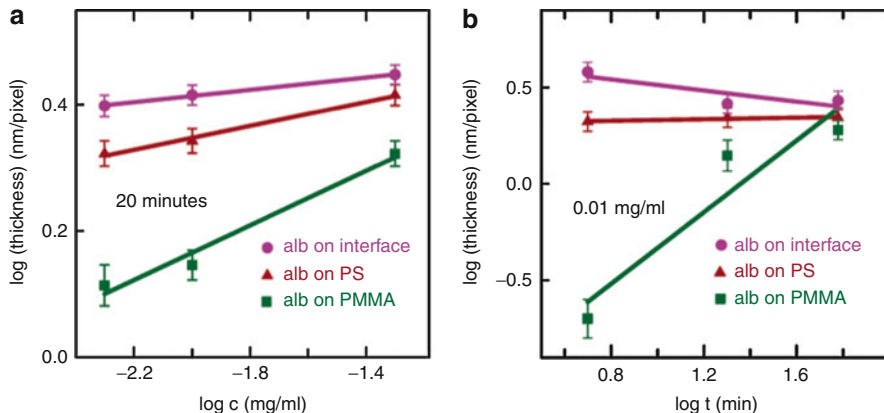
Fig. 42.12 Thickness of albumin on different components of a demixed PS–PMMA system (Taken from Li et al. [115])

focused on the absorption of albumin on the PMMA–PS surfaces under different conditions. Albumin will deposit on different regions of the surface depending on the concentration and time. Measurements taken after 20 min indicate that at low concentrations the albumin will selectively absorb at the polymer interface, but at higher concentrations the absorption on the PMMA and PS components will increase (Fig. 42.12) [115]. Similarly, at a given concentration, the albumin would start absorbing at the interface at the initial time point and at latter time points absorb on the PMMA and PS components. The effect of pH on the localization was also evaluated, and the effect is shown on a series of pie charts in Fig. 42.13. At slightly basic and acid conditions, the absorption profile was different than at neutral and highly acidic and basic pH. This is thought to result from changes in the albumin conformation as a function of pH [114].

There are many other studies that have focused on the use of block copolymers to control protein absorption. George et al. described a series of poly(styrene-b-ethylene oxide) polymers that could control the adsorption of proteins from FBS [54], and Kang et.al. described PDMS–poly(glutamate) block copolymer to control Fn and BSA adhesion. A poly(MMA-b-AA) was described that would increase the adhesion of mucin, a glycoprotein, that is useful for controlling bacterial adhesion [116]. A polyrotaxane block copolymer was described to control protein absorption. Additionally, this system used host–guest chemistry with a cyclodextrin-containing polymer to create a dynamic surface [117, 118].

Block Copolymers and Protein Patterning

Another innovative method to control biological response is to use block copolymer self-assembly to pattern biologically functional proteins. The block copolymer could drive patterning through selective adsorption or could involve a peptide

Fig. 42.13 Distribution of albumin coverage as a function of pH (Taken from Li et al. [114])
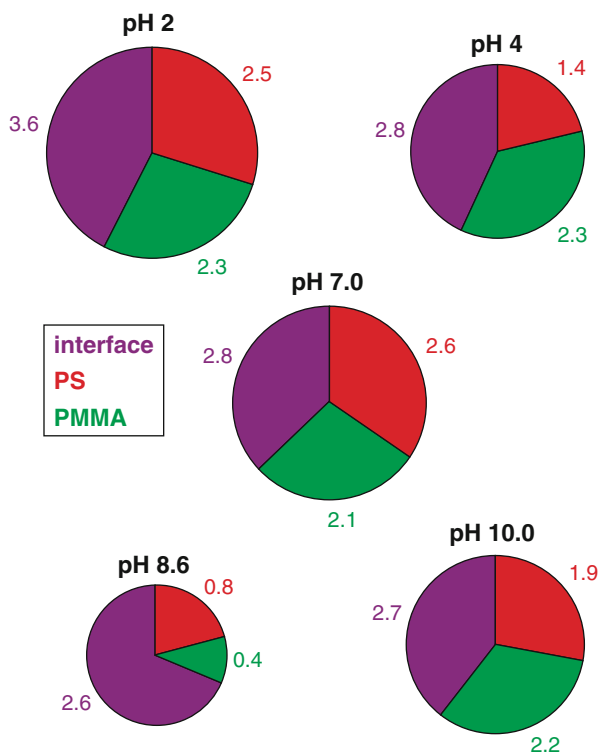
that is covalently attached to either the A or B block of a diblock copolymer. This is a powerful methodology as it is known that spacing and distribution of peptides will affect a biological response [119].

Kumar et al. reported that in a polystyrene (PS)–polymethyl methacrylate (PMMA) block copolymer, surface proteins such as IgG and protein G will preferentially absorb to the PS block [120]. Further work demonstrated that spatially arranged proteins could retain their catalytic activity [121]. Utilizing the PS-b-PMMA system, a variety of proteins including horseradish peroxidase, mushroom tyrosinase, and enhanced green fluorescent protein were patterned on the block copolymer surfaces. Colorimetric assays demonstrated that these enzymes retained their activity and could have applications in protein arrays. While the application does not involve controlling a cellular response, it demonstrates that absorbed proteins have the potential to retain their activity. This group also demonstrated the versatility of block copolymers by using solvent to change the block copolymer morphology and hence the distribution and spacing of the proteins [122]. A PS-b-poly(vinyl pyridine) (PVP) block copolymer was used, and the morphology was modulated as demonstrated as shown in Fig. 42.14. So by treating the block copolymer with ethanol, its morphology will change, and it can be further altered by treatment with toluene. The spatial

Fig. 42.14 The morphology of the PS-b-PVP block copolymer can be modulated by changing the solvent conditions (Taken from Kumar et al. [122])
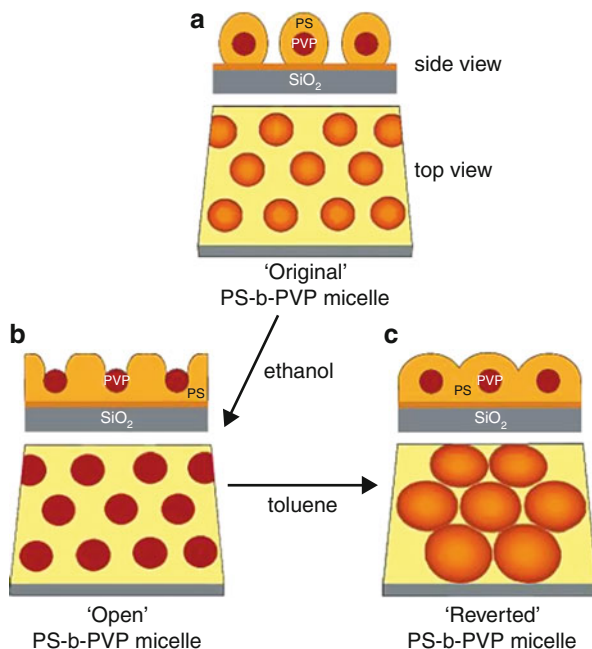
relationship of the absorbed proteins could be controlled because of their preference for the polystyrene block.

Work by Liu et.al demonstrates that albumin and fibronectin (Fn) can be patterned on block copolymer surfaces of polystyrene (PS) and polyisoprene (PI) [123, 124]. One polymer was a PS(45)-b-PI(46) and the other was a PS(65)-b-PI(26) where the parentheses denote the Mn x 1,000. When cast at a thickness of approximately 18 nm, the PS(45)-b-PI(46) will form a circular pattern, while the PS (65)-b-PI(26) will form a more stripped pattern. The proteins would selectively absorb on the more hydrophobic polystyrene block and follow the patterns of the block copolymers. The fibronectin pattern is shown in Fig. 42.15 with c and d showing the stripped pattern and with e and f showing the circular pattern. When Chinese hamster ovary cells were cultured on the respective surfaces, the circular patterned Fn had better cell coverage and density compared to the stripped Fn pattern. These studies demonstrate another mechanism to control block copolymer morphology, film thickness. Varying the block copolymer morphology will control protein patterning and subsequently control cellular behavior.

Work by George et al. developed a system such that proteins or peptide sequences can be covalently bound to a block copolymer and be spatially arranged. A PS-b-poly(ethylene oxide) (PEO) polymer was synthesized with a terminal maleimide functionality (Fig. 42.16) [54]. This allows a cystine amino acid residue to covalently bind to the maleimide after the block copolymer film has been formed, allowing for functionalization by a peptide or a protein. In this study, the block
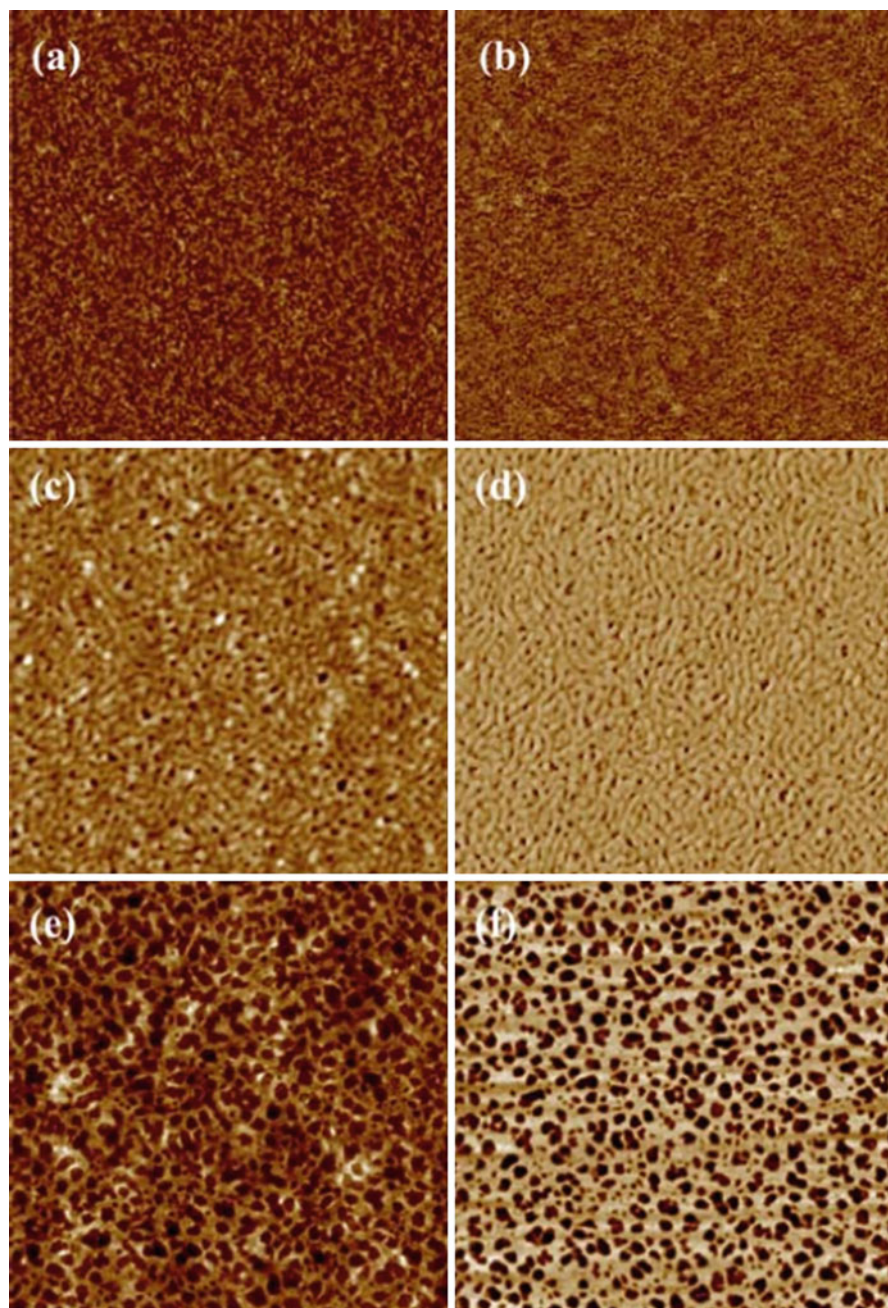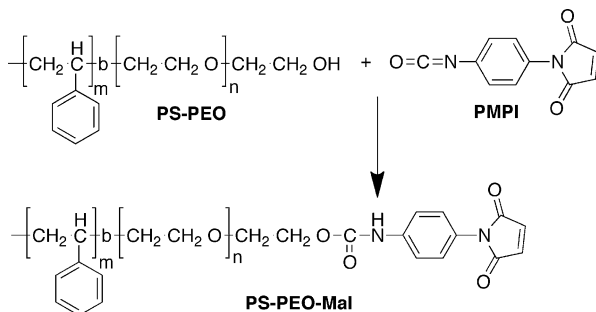
Fig. 42.15 Demonstrates that the Fn assumes the same pattern as the underlying block copolymer substrate (Taken from Liu et al. [124])

Fig. 42.16 PS-b-PEO block copolymer with a maleimide functionality (Adapted from George et al. [55])

copolymers were functionalized with an RGD binding sequence, a fibronectin fragment, and an RGE nonbinding peptide. It was found that the RGD-modified block copolymer improved cellular adhesion compared to the nonbinding control. Further, by changing the concentration of the block copolymer, the spacing and patterning of the peptide sequences could be controlled. In another study, George et al. extended this concept by forming porous three-dimensional scaffolds from block copolymers [56], thus creating nanostructured block copolymer in a configuration that is useful for tissue engineering. This highlights another advantage of block copolymer generated morphology, ease of processing. The nature of a block copolymer allows for processing into a variety of shapes such that the surface is nanostructured. It would be very challenging to generate a 3-D structure with a nanostructured surface through traditional lithographic techniques.

Applications of Block Copolymers to Antithrombogenic Materials

Some of the earliest applications of block copolymers as biomaterials are their use as antithrombogenic materials. This is also one of the most prominent applications of block copolymers to clinical materials. Early work focused on segmented polyurethanes, a block copolymer with a soft and a hard segment with a generic structure shown in Fig. 42.17. The soft segment will have a flexible group such as R = polyethylene oxide or polybutadiene. The hard segment is often aromatic with a typical R′ = 4,4′-diaminodiphenylmethane. Many other chemistries exist and the structures can be depicted in a variety of methods. However, the general concept is that the hard and soft segments will phase separate, affecting the mechanical and biological properties. In order to evaluate the biological properties, the protein adsorption and conformation on polyurethane surfaces have been extensively studied. Protein adsorption is thought to govern platelet adhesion and development of thrombosis [125–130].

Work by Stupp et al. [130] studied the substrate effect on the surface chemistry of polyurethane block copolymers (with a PEO soft segment) and their subsequent effect on fibronectin adsorption. A polyurethane block copolymer was cast on a glass or a polyethylene terephthalate substrate. FTIR reveled that the surface
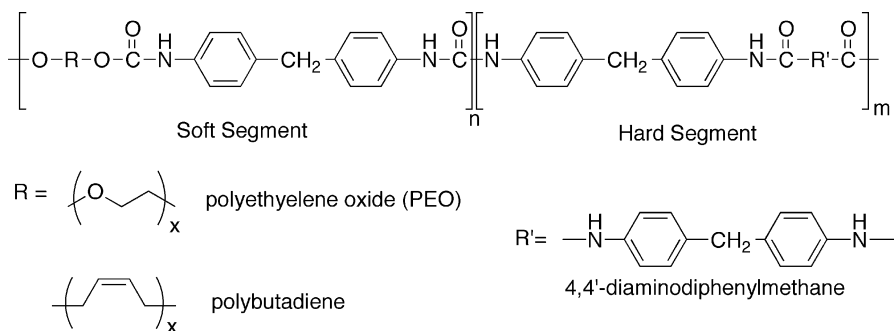
Fig. 42.17 Depiction of segmented polyurethane containing soft and hard segments

chemistry of the polyurethane film was altered, due to the different substrates, resulting in different adsorption levels for the fibronectin. Subsequent studies have examined the role of polyurethane chemistry in more detail. Fibronectin was adsorbed onto a polyurethane block copolymer surface, in work by Goodman et al. [129] that contained two hydrophobic segments: a soft segment based on polybutadiene and a hard segment with aromatic structures. Using gold-labeled antibodies, it was determined that the fibronectin was preferentially adsorbed to the soft segment. The authors discussed the possibility that this observation could be due to conformation changes in the fibronectin on the different segments. However, they hypothesized that fibronectin was adsorbing on the soft segment.

A study by Pitt et al. [126] describes the dynamic adsorption of fibronectin on polyurethane (PUU) block copolymers with different soft segments. The soft segments are polyethylene oxide (PEO), polytetramethylene oxide (PTMO), and polydimethylsiloxane (PDMS). The polymers were placed in a flow cell with a fibronectin solution, and the surface coverage was measured by FTIR. The adsorption was linear for the first minute, and the overall results are depicted in Table 42.4. It is clear from the results that the block copolymer surfaces had an effect on the protein adsorption. In addition to the adsorbed protein, many parameters were calculated from the data: Q is the ratio of the experimental adsorption rate to the diffusion-controlled absorption rate; from this Φ, a dimensionless rate constant is derived as well as K, a first-order irreversible adsorption parameter; and finally θ is a ratio of sites occupied by fibronectin and empty sites. All the parameters follow a trend such that the PEO–PUU has the least fibronectin adsorption. Given that PEO would produce the most hydrophilic surface and that PEO is often used to prevent protein adsorption, this is not a surprising result. Clearly, the block copolymer composition can be manipulated to control the interaction with a dynamic protein solution.

A study by Groth et al. [131] examined the effect of varying the relative amount of the hard segment of a polyurethane on the mechanical and biological properties. The hard segment content was varied by changing the ratio of the hard segment (4,4′ diphenylmethane diisocyanate) to the soft segment (polytetramethylene glycol).

Table 42.4 Absorption parameters of fibronectin on three polyurethanes with different soft segment (Reproduced from Pitt et al. [126])

Surface	Adsorbed at 120 min (μg/cm^2)	Q	Φ	K (cm/s)	θ
PDMS–PUU	0.42	0.82	5.5	4.8×10^{-4}	3.9×10^{-6}
(95 % CI)	$0.40 < \Gamma < 0.44$	$0.66 < Q < 0.98$	$2.0 < \Phi < 68$	$(1.7 < K < 59) \times 10^{-4}$	$(1.4 < \theta < 59) \times 10^{-6}$
PTMO–PUU	0.37	0.60	1.5	1.3×10^{-4}	1.1×10^{-6}
(95 % CI)	$0.32 < \Gamma < 0.42$	$0.48 < Q < 0.72$	$0.71 < \Phi < 3.0$	$(0.62 < K < 2.6) \times 10^{-4}$	$(5.1 < \theta < 21) \times 10^{-7}$
PEO–PUU	0.27	0.34	0.29	2.5×10^{-5}	2.1×10^{-7}
(95 % CI)	$0.16 < \Gamma < 0.38$	$0.25 < Q < 0.43$	$0.14 < \Phi < 0.53$	$(1.2 < K < 4.6) \times 10^{-5}$	$(1.0 < \theta < 3.8) \times 10^{-7}$

Fig. 42.18 Albumin adsorption on segmented polyurethanes with varying hard segment content. The *x*, *o*, and *filled circle* represent different series of polyurethanes with different urethane-to-urea ratios (Taken from Groth et al. [131])

Fig. 42.19 Fibrinogen adsorption on segmented polyurethanes with varying hard segment content. The *x*, *o*, and *filled circle* represent different series of polyurethanes with different urethane-to-urea ratios (Taken from Groth et al. [131])
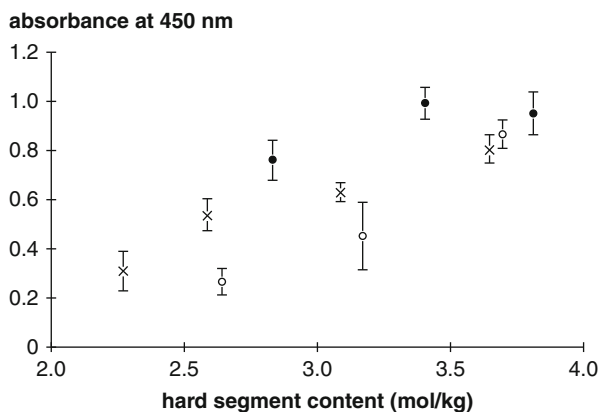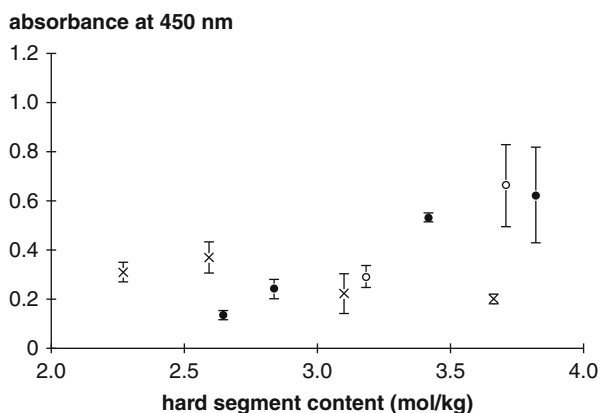

The ratio of hard segment content ranged from 1.5 to 3.0 mol/kg. The contact angle was identical for all the formulations, so this was not a significant factor in controlling the protein adhesion or biological response. While many properties were measured, the protein adhesion of albumin and fibrinogen is shown in Fig. 42.18 and Fig. 42.19. In general, an increase in hard segment content resulted in an increase in protein adhesion for both the proteins evaluated. Subsequent cell adhesion studies also reflected a similar trend. Similar work was also done by Wu et al. [127] demonstrating that the block copolymer chemistry has a significant effect on protein and platelet adhesion. This further demonstrates the ability of block copolymer chemistry to control protein adhesion and regulate a biological response.

Many other block copolymers have been used as antithrombogenic materials. A-B-A block copolymer of a polyamino acid and polydimethylsiloxane was studied for thrombus formation [132]. The block copolymers resisted thrombus formation compared to controls, and composition influenced the levels of thrombus formation. Work by Mori and Funatsu [133, 134] also examined the use of a polystyrene–poly (γ-benzyl-L-glutamate) block copolymer. One of the interesting findings of this

Fig. 42.20 Thrombus as a function of poly(γ-benzyl-L-glutamate) (Taken from Funatsu et al. [133])
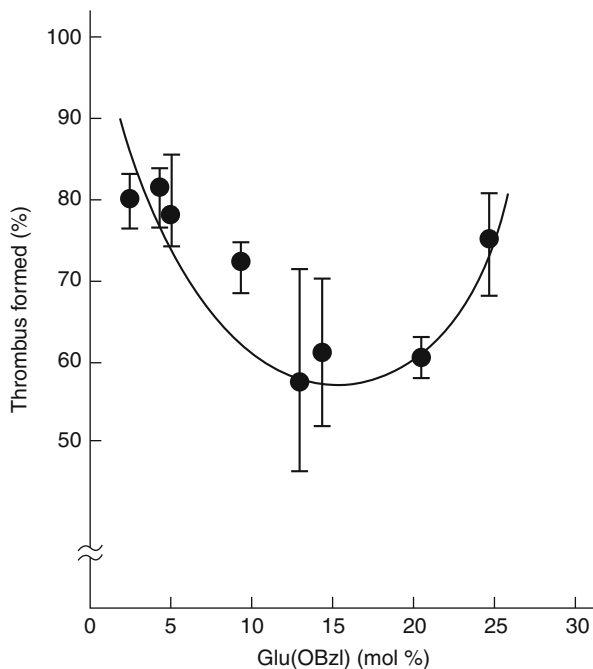
work was that there was an optimal composition to resist both thrombosis and protein adsorption. Figure 42.20 demonstrates that an optimal composition for thrombosis resistance is about 13 % of poly(γ-benzyl-L-glutamate) with increasing thrombosis and higher and lower compositions. This appears to correlate with the protein adsorption and degree and denaturation data in Table 42.5. Minima are found at about 13 % poly(γ-benzyl-L-glutamate) composition for adsorption and degree of denaturation. An example of a block copolymer that was tested clinically comes from Rubens et al. [135] An A-B-A block copolymer of polycaprolactone–polydimethylsiloxane–polycaprolactone was shown to have better resistance to thrombosis compared to a standard commercial bypass material.

Conclusions

The microstructure and nanostructure of block copolymers have the potential to control many properties of biomaterials. By manipulating the chemistry of block copolymer, it is possible to control the resulting morphology and surface chemistry. The domain size allows for molecular-level interactions between proteins and the surface or cell receptors and the surface. This allows for control of protein adsorption and conformation on the surface with the potential to create a desirable protein adsorption profile. The patterning of the block copolymer domains also allows for periodic spacing of bioactive ligands on the surface. These features allow the block

Table 42.5 Protein adhesion and conformation on polystyrene–poly(γ-benzyl-L-glutamate) block copolymers (Adapted from Funatsu et al. [133])

| Block copolymer | Bovine serum albumin | | Bovine-γ-globulin | | Bovine plasma fibrinogen | |
	Total adsorption ($\mu g/cm^2$)	Denatured (%)	Total adsorption ($\mu g/cm^2$)	Denatured (%)	Total adsorption ($\mu g/cm^2$)	Denatured (%)
P[Glu (OBzl)]/ PST-2.3	6.02	46.5	6.67	68.2	2.86	37.8
P[Glu (OBzl)]/ PST-4.2	8.77	46.3	8.22	71.4	3.55	41.4
P[Glu (OBzl)]/ PST-5.0	10.04	39.8	12.88	56.5	6.41	20.1
P[Glu (OBzl)]/ PST-9.3	12.14	0	2.42	55.4	2.83	14.8
P[Glu (OBzl)]/ PST-13.0	7.83	0	2.53	56.9	2.37	12.4
P[Glu (OBzl)]/ PST-14.6	10.81	0	2.77	54.2	2.08	14.4
P[Glu (OBzl)]/ PST-20.2	18.52	22.1	4.53	60.7	1.92	15.6
P[Glu (OBzl)]/ PST-24.2	14.31	36.8	4.87	61.8	2.25	15.1

copolymer surfaces to control the cell response. As a greater understanding of the block copolymer–protein interface evolves, more potential applications for block copolymer-based biomaterials will be developed.

References

1. Lhoest JB, Detrait E, van den Bosch de Aguilar P, Bertrand P (1998) Fibronectin adsorption, conformation, and orientation on polystyrene substrates studied by radiolabeling, XPS, and ToF SIMS. J Biomed Mater Res 41:95–103
2. Garcia AJ, Vega MD, Boettiger D (1999) Modulation of cell proliferation and differentiation through substrate-dependent changes in fibronectin conformation. Mol Biol Cell 10:785–798
3. Keselowsky BG, Collard DM, Garcia AJ (2003) Surface chemistry modulates fibronectin conformation and directs integrin binding and specificity to control cell adhesion. J Biomed Mater Res A 66:247–259
4. Keselowsky BG, Collard DM, Garcia AJ (2004) Surface chemistry modulates focal adhesion composition and signaling through changes in integrin binding. Biomaterials 25:5947–5954

5. Barrias CC, Martins MC, Almeida-Porada G, Barbosa MA, Granja PL (2009) The correlation between the adsorption of adhesive proteins and cell behaviour on hydroxyl-methyl mixed self-assembled monolayers. Biomaterials 30:307–316
6. Giamblanco N, Yaseen M, Zhavnerko G, Lu JR, Marletta G (2011) Fibronectin conformation switch induced by coadsorption with human serum albumin. Langmuir 27:312–319
7. Dekker A, Reitsma K, Beugeling T, Bantjes A, Feijen J, van Aken WG (1991) Adhesion of endothelial cells and adsorption of serum proteins on gas plasma-treated polytetrafluoroethylene. Biomaterials 12:130–138
8. Nimeri G, Lassen B, Golander CG, Nilsson U, Elwing H (1994) Adsorption of fibrinogen and some other proteins from blood plasma at a variety of solid surfaces. J Biomater Sci Polym Ed 6:573–583
9. Nuttelman CR, Mortisen DJ, Henry SM, Anseth KS (2001) Attachment of fibronectin to poly (vinyl alcohol) hydrogels promotes NIH3T3 cell adhesion, proliferation, and migration. J Biomed Mater Res 57:217–223
10. Collier TO, Anderson JM (2002) Protein and surface effects on monocyte and macrophage adhesion, maturation, and survival. J Biomed Mater Res 60:487–496
11. Lan MA, Gersbach CA, Michael KE, Keselowsky BG, Garcia AJ (2005) Myoblast proliferation and differentiation on fibronectin-coated self assembled monolayers presenting different surface chemistries. Biomaterials 26:4523–4531
12. Lord MS, Cousins BG, Doherty PJ, Whitelock JM, Simmons A, Williams RL, Milthorpe BK (2006) The effect of silica nanoparticulate coatings on serum protein adsorption and cellular response. Biomaterials 27:4856–4862
13. Wilson CJ, Clegg RE, Leavesley DI, Pearcy MJ (2005) Mediation of biomaterial-cell interactions by adsorbed proteins: a review. Tissue Eng 11:1–18
14. Vroman L, Adams AL (1969) Findings with the recording ellipsometer suggesting rapid exchange of specific plasma proteins at liquid/solid interfaces. Surf Sci 16:438–446
15. Vroman L (1987) Methods of investigating protein interactions on artificial and natural surfaces. Ann N Y Acad Sci 516:300–305
16. Fang F, Szleifer I (2001) Kinetics and thermodynamics of protein adsorption: a generalized molecular theoretical approach. Biophys J 80:2568–2589
17. Jung SY, Lim SM, Albertorio F, Kim G, Gurau MC, Yang RD, Holden MA, Cremer PS (2003) The Vroman effect: a molecular level description of fibrinogen displacement. J Am Chem Soc 125:12782–12786
18. Krishnan A, Siedlecki CA, Vogler EA (2004) Mixology of protein solutions and the Vroman effect. Langmuir 20:5071–5078
19. Black J (1999) Biological performance of materials: fundamentals of biocompatibility. CRC Press, New York
20. Wise DL (2000) Biomaterials and bioengineering handbook. Marcel Dekker, New York
21. Sousa SR, Lamghari M, Sampaio P, Moradas-Ferreira P, Barbosa MA (2008) Osteoblast adhesion and morphology on TiO_2 depends on the competitive preadsorption of albumin and fibronectin. J Biomed Mater Res A 84:281–290
22. Ratner BD, Hoffman AS, Schoen FJ, Lemons JE (2004) Biomaterials science: an introduction to materials in medicine. Academic, San Diego
23. Turbill P, Beugeling T, Poot AA (1996) Proteins involved in the Vroman effect during exposure of human blood plasma to glass and polyethylene. Biomaterials 17:1279–1287
24. Bhushan B, Tokachichu DR, Keener MT, Lee SC (2006) Nanoscale adhesion, friction and wear studies of biomolecules on silicon based surfaces. Acta Biomater 2:39–49
25. Bhushan B, Joo Kwak K, Gupta S, Lee SC (2008) Nanoscale adhesion, friction and wear studies of biomolecules on silane polymer-coated silica and alumina-based surfaces. J R Soc Interface 6:719–733
26. Bhushan B, Joo Kwak K, Gupta S, Lee SC (2009) Nanoscale adhesion, friction and wear studies of biomolecules on silane polymer-coated silica and alumina-based surfaces. J R Soc Interface 6:719–733

27. Khang D, Carpenter J, Chun YW, Pareta R, Webster TJ (2008) Nanotechnology for regenerative medicine. Biomed Microdevices 12:575–587
28. Engel E, Michiardi A, Navarro M, Lacroix D, Planell JA (2008) Nanotechnology in regenerative medicine: the materials side. Trends Biotechnol 26:39–47
29. Khang D, Lu J, Yao C, Haberstroh KM, Webster TJ (2008) The role of nanometer and sub-micron surface features on vascular and bone cell adhesion on titanium. Biomaterials 29:970–983
30. Khang D, Liu-Snyder P, Pareta R, Lu J, Webster TJ (2009) Reduced responses of macrophages on nanometer surface features of altered alumina crystalline phases. Acta Biomater 5:1425–1432
31. Kantawong F, Burchmore R, Gadegaard N, Oreffo RO, Dalby MJ (2009) Proteomic analysis of human osteoprogenitor response to disordered nanotopography. J R Soc Interface 6:1075–1086
32. Pareta RA, Reising AB, Miller T, Storey D, Webster TJ (2010) An understanding of enhanced osteoblast adhesion on various nanostructured polymeric and metallic materials prepared by ionic plasma deposition. J Biomed Mater Res A 92:1190–1201
33. Webster TJ, Ejiofor JU (2004) Increased osteoblast adhesion on nanophase metals: Ti, Ti6Al4V, and CoCrMo. Biomaterials 25:4731–4739
34. Eisenbarth E, Velten D, Muller M, Thull R, Breme J (2006) Nanostructured niobium oxide coatings influence osteoblast adhesion. J Biomed Mater Res A 79:166–175
35. Wang CC, Hsu YC, Su FC, Lu SC, Lee TM (2009) Effects of passivation treatments on titanium alloy with nanometric scale roughness and induced changes in fibroblast initial adhesion evaluated by a cytodetacher. J Biomed Mater Res A 88:370–383
36. Blattler T, Huwiler C, Ochsner M, Stadler B, Solak H, Voros J, Grandin HM (2006) Nanopatterns with biological functions. J Nanosci Nanotechnol 6:2237–2264
37. Mele E, Pisignano D (2009) Nanobiotechnology: soft lithography. Prog Mol Subcell Biol 47:341–358
38. Kim EJ, Boehm CA, Fleischman AJ, Muschler GF, Kostov YV, Roy S (2009) Modulating human connective tissue progenitor cell behavior on cellulose acetate scaffolds by surface microtextures. J Biomed Mater Res A 90:1198–1205
39. Qin D, Xia Y, Whitesides GM (2010) Soft lithography for micro- and nanoscale patterning. Nat Protoc 5:491–502
40. Hart A, Gadegaard N, Wilkinson CD, Oreffo RO, Dalby MJ (2007) Osteoprogenitor response to low-adhesion nanotopographies originally fabricated by electron beam lithography. J Mater Sci Mater Med 18:1211–1218
41. Dalby MJ, Gadegaard N, Wilkinson CD (2008) The response of fibroblasts to hexagonal nanotopography fabricated by electron beam lithography. J Biomed Mater Res A 84:973–979
42. Huo F, Zheng Z, Zheng G, Giam LR, Zhang H, Mirkin CA (2008) Polymer pen lithography. Science 321:1658–1660
43. Huang L, Braunschweig AB, Shim W, Qin L, Lim JK, Hurst SJ, Huo F, Xue C, Jang JW, Mirkin CA (2010) Matrix-assisted dip-pen nanolithography and polymer pen lithography. Small 6:1077–1081
44. Diehl KA, Foley JD, Nealey PF, Murphy CJ (2005) Nanoscale topography modulates corneal epithelial cell migration. J Biomed Mater Res A 75:603–611
45. Karuri NW, Nealey PF, Murphy CJ, Albrecht RM (2008) Structural organization of the cytoskeleton in SV40 human corneal epithelial cells cultured on nano- and microscale grooves. Scanning 30:405–413
46. Sargeant TD, Rao MS, Koh CY, Stupp SI (2008) Covalent functionalization of NiTi surfaces with bioactive peptide amphiphile nanofibers. Biomaterials 29:1085–1098
47. Greenfield MA, Palmer LC, Vernizzi G, de la Cruz MO, Stupp SI (2009) Buckled membranes in mixed-valence ionic amphiphile vesicles. J Am Chem Soc 131:12030–12031

48. Peterca M, Imam MR, Leowanawat P, Rosen BM, Wilson DA, Wilson CJ, Zeng X, Ungar G, Heiney PA, Percec V (2010) Self-assembly of hybrid dendrons into doubly segregated supramolecular polyhedral columns and vesicles. J Am Chem Soc 132:11288–11305

49. Yu H, Li J, Shishido A, Iyoda T, Ikeda T (2007) Control of regular nanostructures self-assembled in an amphiphilic diblock liquid-crystalline copolymer. Mol Cryst Liq Cryst 478:271–281

50. Schricker S, Palacio M, Thirumamagal BT, Bhushan B (2010) Synthesis and morphological characterization of block copolymers for improved biomaterials. Ultramicroscopy 110:639–649

51. Palacio M, Schricker S, Bhushan B (2010) Morphology and protein adsorption characteristics of block copolymer surfaces. J Microsc 240:239–248

52. Palacio M, Schricker S, Bhushan B (2011) Bioadhesion of various proteins on random, diblock, and triblock copolymer surfaces and the effect of pH conditions. J R Soc Interface 8:630–640

53. Schricker SR, Palacio ML, Bhushan B (2011) Protein adhesion of block copolymer surfaces. Colloid Polym Sci 289:219–225

54. George PA, Donose BC, Cooper-White JJ (2009) Self-assembling polystyrene-block-poly (ethylene oxide) copolymer surface coatings: resistance to protein and cell adhesion. Biomaterials 30:2449–2456

55. George PA, Doran MR, Croll TI, Munro TP, Cooper-White JJ (2009) Nanoscale presentation of cell adhesive molecules via block copolymer self-assembly. Biomaterials 30:4732–4737

56. George PA, Quinn K, Cooper-White JJ (2010) Hierarchical scaffolds via combined macro- and micro-phase separation. Biomaterials 31:641–647

57. Kwon GS, Kataoka K (1995) Block copolymer micelles as long-circulating drug vehicles. Adv Drug Deliv Rev 16:295–309

58. Rösler A, Vandermeulen GWM, Klok HA (2001) Advanced drug delivery devices via self-assembly of amphiphilic block copolymers. Adv Drug Deliv Rev 53:95–108

59. Adams ML, Lavasanifar A, Kwon GS (2003) Amphiphilic block copolymers for drug delivery. J Pharm Sci 92:1343–1355

60. Ajami-Henriquez D, Rodriguez M, Sabino M, Castillo RV, Muller AJ, Boschetti-de-Fierro A, Abetz C, Abetz V, Dubois P (2008) Evaluation of cell affinity on poly(L-lactide) and poly (epsilon-caprolactone) blends and on PLLA-b-PCL diblock copolymer surfaces. J Biomed Mater Res A 87:405–417

61. Choi SH, Lodge TP, Bates FS (2010) Mechanism of molecular exchange in diblock copolymer micelles: hypersensitivity to core chain length. Phys Rev Lett 104:047802

62. Grubbs RB, Dean JM, Bates FS (2001) Methacrylic block copolymers through metal-mediated living free radical polymerization for modification of thermosetting epoxy. Macromolecules 34:8593–8595

63. Hillmyer MA, Lipic PM, Hajduk DA, Almdal K, Bates FS (1997) Self-assembly and polymerization of epoxy resin-amphiphilic block copolymer nanocomposites. J Am Chem Soc 119:2749–2750

64. Ruiz-Pérez L, Royston GJ, Fairclough JPA, Ryan AJ (2008) Toughening by nanostructure. Polymer 49:4475–4488

65. Serrano E, Martin MD, Tercjak A, Pomposo JA, Mecerreyes D, Mondragon I (2005) Nanostructured thermosetting systems from epoxidized styrene butadiene block copolymers. Macromol Rapid Comm 26:982–985

66. Kim JK, Yang SY, Lee Y, Kim Y (2010) Functional nanomaterials based on block copolymer self-assembly. Prog Polym Sci 35:1325–1349

67. Rozenberg BA, Tenne R (2008) Polymer-assisted fabrication of nanoparticles and nanocomposites. Prog Polym Sci 33:40–112

68. Fetters LJ (1969) Synthesis of block polymers by homogeneous anionic polymerization. J Polym Sci Pol Sym 26(1):1–35

69. Hillmyer M (1999) Block copolymer synthesis. Curr Opin Solid St Mater Sci 4:559–564
70. Kennedy JP (1979) Sequential copolymers by ionic polymerizations. Die Makromol Chem 3:1–16
71. Riegler S, Slugovc C, Trimmel G, Stelzer F (2004) Block copolymers via ROMP–awakening the sleeping beauty. Macromol Symp 217(1):231–246
72. Lynn DM, Kanaoka S, Grubbs RH (1996) Living ring-opening metathesis polymerization in aqueous media catalyzed by well-defined ruthenium carbene complexes. J Am Chem Soc 118:784–790
73. Chiefari J, Chong YKB, Ercole F, Krstina J, Jeffery J, Le TPT, Mayadunne RTA, Meijs GF, Moad CL, Moad G (1998) Living free-radical polymerization by reversible addition – fragmentation chain transfer: the RAFT process. Macromolecules 31:5559–5562
74. Lai JT, Filla D, Shea R (2002) Functional polymers from novel carboxyl-terminated trithiocarbonates as highly efficient RAFT agents. Macromolecules 35:6754–6756
75. Matyjaszewski K, Tsarevsky NV (2009) Nanostructured functional materials prepared by atom transfer radical polymerization. Nat Chem 1:276–288
76. O'Reilly RK, Joralemon MJ, Lui W, Hawker CJ, Wooley KL (2005) Combination of RAFT and click chemistry for the synthesis of core functionalized nanoparticles. Polym Prepr (Am Chem Soc Div Polym Chem) 46:183–184
77. Quémener D, Davis TP, Barner-Kowollik C, Stenzel MH (2006) RAFT and click chemistry: a versatile approach to well-defined block copolymers. Chem Commun 2006:5051–5053
78. Ranjan R, Brittain WJ (2007) Tandem RAFT polymerization and click chemistry: an efficient approach to surface modification. Macromol Rapid Comm 28:2084–2089
79. Andersson J, Ekdahl KN, Larsson R, Nilsson UR, Nilsson B (2002) C3 adsorbed to a polymer surface can form an initiating alternative pathway convertase. J Immunol 168:5786–5791
80. Andersson J, Ekdahl KN, Lambris JD, Nilsson B (2005) Binding of C3 fragments on top of adsorbed plasma proteins during complement activation on a model biomaterial surface. Biomaterials 26:1477–1485
81. Tang Y, Liu G, Yu C, Wei X, Zhang G (2008) Chemical oscillation induced periodic swelling and shrinking of a polymeric multilayer investigated with a quartz crystal microbalance. Langmuir 24:8929–8933
82. Tengvall P, Lundstrom I, Liedberg B (1998) Protein adsorption studies on model organic surfaces: an ellipsometric and infrared spectroscopic approach. Biomaterials 19:407–422
83. Elwing H (1998) Protein absorption and ellipsometry in biomaterial research. Biomaterials 19:397–406
84. Chittur KK (1998) FTIR/ATR for protein adsorption to biomaterial surfaces. Biomaterials 19:357–369
85. Ratner BD (1983) Surface characterization of biomaterials by electron spectroscopy for chemical analysis. Ann Biomed Eng 11:313–336
86. Merrett K, Cornelius RM, McClung WG, Unsworth LD, Sheardown H (2002) Surface analysis methods for characterizing polymeric biomaterials. J Biomater Sci Polym Ed 13:593–621
87. Kingshott P, Andersson G, McArthur SL, Griesser HJ (2011) Surface modification and chemical surface analysis of biomaterials. Curr Opin Chem Biol 15:667–676
88. Kumar N, Ravikumar MNV, Domb AJ (2001) Biodegradable block copolymers. Adv Drug Deliv Rev 53:23–44
89. Rosler A, Vandermeulen GW, Klok HA (2012) Advanced drug delivery devices via self-assembly of amphiphilic block copolymers. Adv Drug Deliv Rev 53:95–108
90. Ranade SV, Richard RE, Helmus MN (2005) Styrenic block copolymers for biomaterial and drug delivery applications. Acta Biomater 1:137–144
91. Kim SY, Lee YM (2001) Taxol-loaded block copolymer nanospheres composed of methoxy poly(ethylene glycol) and poly(epsilon-caprolactone) as novel anticancer drug carriers. Biomaterials 22:1697–1704

92. Prabaharan M, Grailer JJ, Pilla S, Steeber DA, Gong S (2009) Folate-conjugated amphiphilic hyperbranched block copolymers based on boltorn H40, poly(L-lactide) and poly(ethylene glycol) for tumor-targeted drug delivery. Biomaterials 30:3009–3019

93. Tian HY, Deng C, Lin H, Sun J, Deng M, Chen X, Jing X (2005) Biodegradable cationic PEG-PEI-PBLG hyperbranched block copolymer: synthesis and micelle characterization. Biomaterials 26:4209–4217

94. Dorati R, Genta I, Colonna C, Modena T, Pavanetto F, Perugini P, Conti B (2007) Investigation of the degradation behaviour of poly (ethylene glycol-co-d, l-lactide) copolymer. Polym Degrad Stab 92:1660–1668

95. Ferruti P, Penco M, D'Addato P, Ranucci E, Deghenghi R (1995) Synthesis and properties of novel block copolymers containing poly(lactic-glycolic acid) and poly(ethyleneglycol) segments. Biomaterials 16:1423–1428

96. Penco M, Marcioni S, Ferruti P, D' Antone S, Deghenghi R (1996) Degradation behaviour of block copolymers containing poly(lactic-glycolic acid) and poly(ethylene glycol) segments. Biomaterials 17:1583–1590

97. Lucke A, Tessmar J, Schnell E, Schmeer G, Gopferich A (2000) Biodegradable poly(D, L-lactic acid)-poly(ethylene glycol)-monomethyl ether diblock copolymers: structures and surface properties relevant to their use as biomaterials. Biomaterials 21:2361–2370

98. Shim WS, Kim JH, Park H, Kim K, Chan Kwon I, Lee DS (2006) Biodegradability and biocompatibility of a pH- and thermo-sensitive hydrogel formed from a sulfonamide-modified poly(epsilon-caprolactone-co-lactide)-poly(ethylene glycol)-poly(epsilon-caprolactone-co-lactide) block copolymer. Biomaterials 27:5178–5185

99. Huang L, Hu J, Lang L, Wang X, Zhang P, Jing X, Wang X, Chen X, Lelkes PI, Macdiarmid AG, Wei Y (2007) Synthesis and characterization of electroactive and biodegradable ABA block copolymer of polylactide and aniline pentamer. Biomaterials 28:1741–1751

100. Noh H, Vogler EA (2007) Volumetric interpretation of protein adsorption: competition from mixtures and the Vroman effect. Biomaterials 28:405–422

101. Jeong JH, Lim DW, Han DK, Park TG (2000) Synthesis, characterization and protein adsorption behaviors of PLGA/PEG di-block co-polymer blend films. Colloids Surf B Biointerfaces 18:371–379

102. Lee JH, Kopecek J, Andrade JD (1989) Protein-resistant surfaces prepared by PEO-containing block copolymer surfactants. J Biomed Mater Res 23:351–368

103. Schroen C, Stuart MAC, Van Der Voort MK, Van der Padt A, van't Riet K (1995) Influence of preadsorbed block copolymers on protein adsorption: surface properties, layer thickness, and surface coverage. Langmuir 11:3068–3074

104. Grafahrend D, Calvet JL, Klinkhammer K, Salber J, Dalton PD, Moller M, Klee D (2008) Control of protein adsorption on functionalized electrospun fibers. Biotechnol Bioeng 101:609–621

105. Schricker SR, Palacio MLB, Bhushan B (2011) Antibody sensed protein surface conformation. Mater Today 14:616–621

106. Palacio MLB, Schricker SR, Bhushan B (2012) Protein conformation changes on block copolymer surfaces detected by antibody-functionalized AFM tips. J Biomed Mater Res A 100A:18–25

107. Palacio MLB, Schricker SR, Bhushan B (2012) Block copolymer arrangement and composition effects on protein conformation using atomic force microscope-based antigen-antibody adhesion. J Biomed Mater Res A 100A:978–988

108. Zhu J, Zhu X, Kang ET, Neoh KG (2007) Design and synthesis of star polymers with hetero-arms by the combination of controlled radical polymerizations and click chemistry. Polymer 48:6992–6999

109. Ranjan R, Brittain WJ (2007) Combination of living radical polymerization and click chemistry for surface modification. Macromolecules 40:6217–6223

110. Gondi SR, Vogt AP, Sumerlin BS (2007) Versatile pathway to functional telechelics via RAFT polymerization and click chemistry. Macromolecules 40:474–481

111. Pressly ED, Amir RJ, Hawker CJ (2011) Rapid synthesis of block and cyclic copolymers via click chemistry in the presence of copper nanoparticles. J Polym Sci Pol Chem 49:814–819

112. Slater JH, Frey W (2008) Nanopatterning of fibronectin and the influence of integrin clustering on endothelial cell spreading and proliferation. J Biomed Mater Res A 87:176–195

113. Morin C, Hitchcock AP, Cornelius RM, Brash JL, Urquhart SG, Scholl A, Doran A (2004) Selective adsorption of protein on polymer surfaces studied by soft X-ray photoemission electron microscopy. J Electron Spectrosc Relat Phenom 137:785–794

114. Li L, Hitchcock AP, Cornelius R, Brash JL, Scholl A, Doran A (2008) X-ray microscopy studies of protein adsorption on a phase segregated polystyrene/polymethylmethacrylate surface. 2. Effect of pH on site preference. J Phys Chem B 112:2150–2158

115. Li L, Hitchcock AP, Robar N, Cornelius R, Brash JL, Scholl A, Doran A (2006) X-ray microscopy studies of protein adsorption on a phase-segregated polystyrene/polymethyl methacrylate surface. 1. Concentration and exposure-time dependence for albumin adsorption. J Phys Chem B 110:16763–16773

116. Nikonenko NA, Bushnak IA, Keddie JL (2009) Spectroscopic ellipsometry of mucin layers on an amphiphilic diblock copolymer surface. Appl Spectrosc 63:889–898

117. Inoue Y, Ye L, Ishihara K, Yui N (2012) Preparation and surface properties of polyrotaxane-containing tri-block copolymers as a design for dynamic biomaterials surfaces. Colloids Surf B Biointerfaces 89:223–227

118. Seo JH, Kakinoki S, Inoue Y, Yamaoka T, Ishihara K, Yui N (2012) Designing dynamic surfaces for regulation of biological responses. Soft Matter 8:5477–5485

119. Huang J, Grater SV, Corbellini F, Rinck S, Bock E, Kemmerer R, Kessler H, Ding J, Spatz JP (2009) Impact of order and disorder in RGD nanopatterns on cell adhesion. Nano Lett 9:1111–1116

120. Kumar N, Hahm JI (2005) Nanoscale protein patterning using self-assembled diblock copolymers. Langmuir 21:6652–6655

121. Kumar N, Parajuli O, Dorfman A, Kipp D, Hahm JI (2007) Activity study of self-assembled proteins on nanoscale diblock copolymer templates. Langmuir 23:7416–7422

122. Kumar N, Parajuli O, Hahm JI (2007) Two-dimensionally self-arranged protein nanoarrays on diblock copolymer templates. J Phys Chem B 111:4581–4587

123. Liu D, Wang T, Keddie JL (2009) Protein nanopatterning on self-organized poly(styrene-b-isoprene) thin film templates. Langmuir 25:4526–4534

124. Liu D, Abdullah CAC, Sear RP, Keddie JL (2010) Cell adhesion on nanopatterned fibronectin substrates. Soft Matter 6:5408–5416

125. Huang SL, Chao MS, Ruaan RC, Lai JY (2000) Microphase separated structure and protein adsorption of polyurethanes with butadiene soft segment. Eur Polym J 36:285–294

126. Pitt WG, Weaver DR, Cooper SL (1993) Fibronectin adsorption kinetics on phase segregated polyurethaneureas. J Biomater Sci Polym Ed 4:337–346

127. Wu Y, Simonovsky FI, Ratner BD, Horbett TA (2005) The role of adsorbed fibrinogen in platelet adhesion to polyurethane surfaces: a comparison of surface hydrophobicity, protein adsorption, monoclonal antibody binding, and platelet adhesion. J Biomed Mater Res A 74:722–738

128. Takahara A, Tashita J, Kajiyama T, Takayanagi M (1985) Effect of aggregation state of hard segment in segmented poly (urethaneureas) on their fatigue behavior after interaction with blood components. J Biomed Mater Res 19:13–34

129. Goodman SL, Simmons SR, Cooper SL, Albrecht RM (1990) Preferential adsorption of plasma proteins onto apolar polyurethane microdomains. J Colloid Interface Sci 139:561–570

130. Stupp SI, Kauffman JW, Carr SH (1977) Interactions between segmented polyurethane surfaces and the plasma protein fibrinogen. J Biomed Mater Res 11:237–250

131. Groth T, Klosz K, Campbell EJ, New RRC, Hall B, Goering H (1995) Protein adsorption, lymphocyte adhesion and platelet adhesion/activation on polyurethane ureas is related to hard segment content and composition. J Biomater Sci Polym Ed 6:497–510

132. Kumaki T, Sisido M, Imanishi Y (1985) Antithrombogenicity and oxygen permeability of block and graft copolymers of polydimethylsiloxane and poly(alpha-amino acid). J Biomed Mater Res 19:785–811

133. Funatsu E, Mori A, Wu SK, Imanishi Y (1988) Block copolymerization of styrene using azo-containing poly (γ-benzyl l-glutamate) initiator and interaction of the block copolymers with blood. Polymer 29:177–183

134. Mori A, Ito Y, Sisido M, Imanishi Y (1986) Interaction of polystyrene/poly (γ-benzyl l-glutamate) and poly (methyl methacrylate)/poly (γ-benzyl l-glutamate) block copolymers with plasma proteins and platelets. Biomaterials 7:386–392

135. Rubens FD, Labow RS, Lavallee GR, Watson MI, Robblee JA, Voorhees ME, Nathan HJ (1999) Hematologic evaluation of cardiopulmonary bypass circuits prepared with a novel block copolymer. Ann Thorac Surg 67:689–696, discussion 696–8

Nanofillers in Restorative Dental Materials 43

Sarah S. Mikhail, Shereen S. Azer, and Scott R. Schricker

Introduction

The main objective of dental therapy is to improve the quality of life of dental patients by relieving pain, enhancing masticatory efficiency, and improving speech and appearance. To accomplish these goals, the selection of dental restorative materials has always posed a challenge for practitioners. Over the years, research in dentistry has focused on developing and innovating materials and modifying their properties to enhance their clinical performance. An ideal dental restorative material should possess the following: (1) adequate strength to withstand the chewing forces (mastication) that result in continuous cyclic loading, particularly in the back (posterior) region of the mouth, where the maximum biting force may reach ∼800 Newtons (N) in bruxers [1]; (2) ease of manipulation of the restorative material by clinicians and laboratory personnel; (3) tissue biocompatibility and stability in the oral environment; and (4) in certain situations where esthetics is a concern, such as in the anterior (front) region of the mouth, optical properties play a major role in the selection of a particular restorative material.

S.S. Mikhail (✉) • S.S. Azer • S.R. Schricker
Division of Restorative, Prosthetic and Primary Care Dentistry, The Ohio State University College of Dentistry, Columbus, OH, USA
e-mail: mikhail.9@osu.edu; azer.1@osu.edu; schricker.1@osu.edu

Introduction to Composites

Over the years dental composite resin restorations have been appealing to clinicians due to the rising concerns of mercury in amalgam restorations and the heightened awareness of the population for esthetics. An optimal restoration should not only provide perfect color match but in addition behave in a similar manner to tooth structure with respect to mechanical and physical characteristics. As the paradigm of direct restoratives shifted from amalgams to tooth-colored composite materials, clinicians were confronted with several physical barriers such as dimensional stability (the coefficient of thermal expansion and polymerization shrinkage), wear resistance, surface roughness, as well as mechanical barriers such as flexural strength and fracture toughness. Other limitations of dental composites are the manipulation and application parameters which often controls physical properties (such as consistency, flow, and viscosity) and influence the integrity of the final restoration. The added challenges of an aggressive oral environment characterized by abrupt temperature changes, continuous pH fluctuations, heavy masticatory forces, oral bacterial flora, and enzymatic degradation should be taken into account. For decades, composite resin materials have been improving to provide superior optical properties while maintaining, often improving, resistance to degradation during service. Currently available products vary in color [2], translucency [3], and many clinically important mechanical properties [4]. A challenge to the clinician is to select the material which will best satisfy the requirements of the restoration and will remain in service to the satisfaction of the patient.

Composite refers to a material having two or more components. The basic components of a final cured dental resin-based composite are:

1. Organic phase of a polymeric matrix derived from a base monomer mainly bisphenol-A-glycidyl methacrylate (Bis-GMA) and a diluent comonomer such as triethyleneglycol dimethacrylate (TEGDMA) to reduce viscosity.
2. Inorganic phase of filler particles dispersed within the matrix.
3. Silane coupling agent bonding the fillers to the resinous matrix as shown in Fig. 43.1 [5].

Fig. 43.1 Schematic illustration of cured dental composite resin with the 3 basic components. The silane coupling agent bonds the fillers and the polymer matrix in dental composites
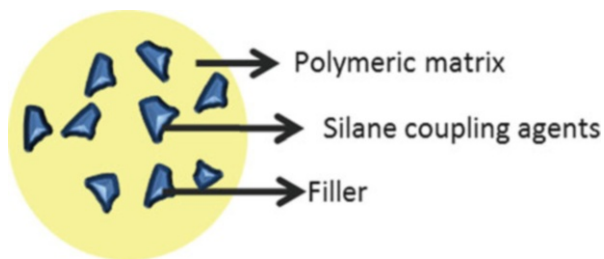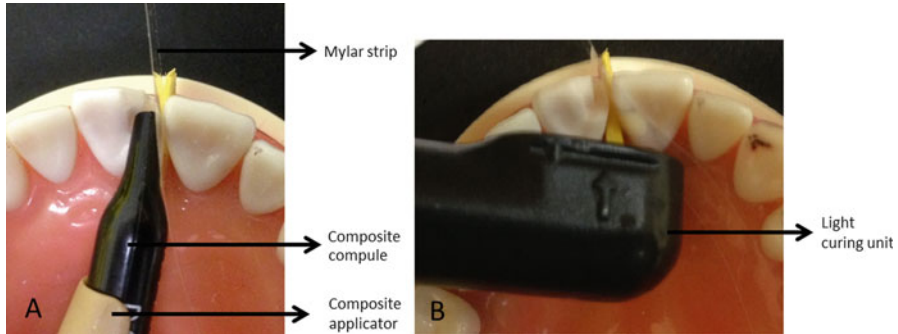
Fig. 43.2 (**a**) Application of dental composite resin in a cavity. (**b**) Light curing of dental composite resin

Application of Composites and Physical Characteristics

The goal of end-use parameters is to facilitate handling characteristics which in turn affect chairside operating time and quality of the final restoration however; they impart certain physical limitations on dental composites:

1. Dental composites are moisture-sensitive materials; hence, their application has to be in a dry operation field under rubber dam isolation. They are considered as bonded restorations where an adhesive system is needed prior to their placement (see adhesives section 'Dental Adhesive Systems'). Most current direct dental resin composites are photo-initiated. Unlike the limited working time of amalgam, composite curing through visible light permits adequate working time to build up the lost tooth structure before initiating the curing process. Dental composites possess a paste-like consistency and are packaged in compules, applied by the clinician via a composite applicator and manipulated by hand instruments in the cavity, Fig. 43.2a.

   Prior to curing appropriate consistency and viscosity of these materials (particularly flowable composites) is of great importance to offer the dentist ease of workability of the uncured composite and at the same time provide adequate flow to wet and adapt to cavity walls and margins without void formation. However, composites are shear-thinning materials; they become less resistant to flow under greater shearing forces, for instance, during dispensing from the applicator. Nevertheless, viscosity of composites greatly impacts the mobility of monomer species during curing, and a low viscosity will increase the degree of conversion (DC) of the monomers, resulting in less residual monomers in the resinous polymeric network (DC = breakage of double bonds to single bonds) [6]. Viscosity of these materials depends on the type of monomers used [7], the level of filler loading [8], and the aspect ratio of the fillers used.

Fig. 43.3 (a) Schematic illustration of a cross linked polymer after the breakage of C = C leaving pendant methacrylate groups (Adapted from Ferracane [5]) (b) Schematic representation of polymerization stresses on cavity walls

Other handling properties are stickiness and slumping resistance. An ideal composite material should have low stickiness on steel instruments and sufficient stickiness on tooth structure so that it remains in the cavity and is not pulled back by the steel instrument [9]. In general, stickiness increases from room temperature 23 °C to body temperature 37 °C, and composite resin has higher stickiness on dentin (dental tissue that constitutes the main bulk of the tooth and lies between the enamel/cementum layer and the pulp tissue) than on the metal instruments [10]. Slumping resistance means retaining the material position and shape under its own weight. It is a more complex property that depends on the material's viscoelastic properties and is highly correlated to viscous modulus of the uncured composite [11].

2. Once the original shape of the tooth is roughly restored, visible light is directed on the composite and photo curing takes place within less than a minute, forming a rigid solid mass, Fig. 43.2b. The visible light initiates free radical polymerization reaction, breaking the carbon double bonds of the monomers to form single bonds. This results in linking individual monomers to obtain a cross-linked polymer network, Fig. 43.3a [5]. The double-bond breakage is associated with bulk contraction compromising the dimensional stability of the restoration. This is denoted as polymerization shrinkage ranging from <1 to 6 % for current composites. Polymerization shrinkage and the generated stresses during curing

will cause internal deformation on the cavity margins of the tooth structure [12, 13], Fig. 43.3b. This endangers marginal integrity of restoration, leading to microleakage [14], recurrent decay, and postoperative sensitivity [15]. The polymerization stresses can also compromise the composite–tooth structure bond [16].

For a specific volume of composite, increasing the filler content reduces the amount of resin, resulting in less volumetric shrinkage, so less stress is generated on the cavity walls. Attempts to increase filler levels by incorporation of submicron particles were behind the exploration of nanosized fillers to lessen shrinkage. Conversely, filler overloading will dramatically increase viscosity, affecting handling and manipulation properties as well as lowering degree of conversion [17].

3. Finally the restoration is finished with carbide finishing burs and polished to accomplish enamel-like luster and reduce surface energy of restoration. Poorly finished composite restoration results in an undesirable rough dull surface.

Surface Roughness Associated with Finishing and Polishing

Surface roughness is a surface property that contributes to bacterial adhesion, plaque accumulation, and staining/discoloration. It also contributes to a poor lustrous finish of anterior composites. Moreover, surface roughness can impact coefficient of friction and increase occlusal wear of posterior composites. A wide variety of finishing and polishing techniques with descending grades of abrasiveness (coarse= > medium= > fine= > ultrafine abrasives) have been proposed to reduce surface roughness [18].

Although studies [18, 19] have shown that mylar strip/matrix, Fig. 43.4 [20], produces the best surface finish and smoothness, polishing and finishing procedures are still crucial to minimize the resin-rich phase of the superficial layer that lies against the mylar strip. This polymer-rich layer is softer than the bulk composite, compromising mechanical properties and wear resistance and encouraging plaque accumulation. Because oxygen precludes complete polymerization of this layer, it is referred to as oxygen-inhibited layer. Finishing and polishing of composites is also important to remove excess flash of material, replicate natural anatomy of the tooth, and restore proximal contacts and occlusion. Unfortunately during finishing and polishing, the resin and the filler do not abrade uniformly because the difference in hardness between the soft resin and the filler particles results in rougher surfaces compared to that of the mylar matrix. Figure 43.5 is a summary of the effects of an increase in surface roughness.

Bacterial Adhesion

Most bacteria survive when they adhere to the hard surfaces (teeth, filling materials, and dental implants), Fig. 43.6 [21]. During bacterial adhesion the roughness and the free energy of the surfaces play a key role; thereby both parameters justify the demand for smooth surfaces with a low surface free energy in order to prevent plaque formation [22, 23]. It has been proposed that 0.2 μm is the threshold for surface roughness beyond
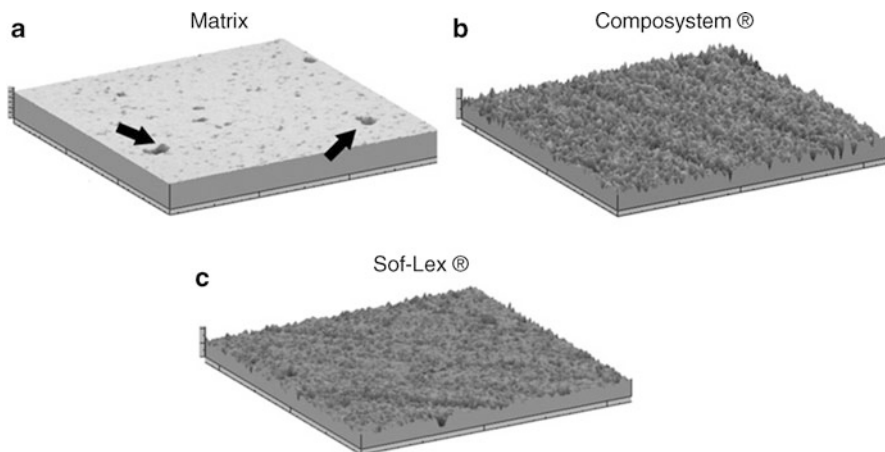
Fig. 43.4 Dental composite unpolished and polished with two polishing systems. 3D roughness images of the tested composites obtained by optical profilometry. (**a**) Composite unpolished/Mylar matrix showed few air voids *black arrows*. (**b**) Composite polished with Coposystem. (**c**) Composite polished with Soflex discs. Polished specimens presented rougher surfaces with some grooves left by the abrasives (From Janus [20])

Fig. 43.5 Representation showing the effect of surface roughness on bacterial adhesion, gloss retention and staining

which bacterial adhesion and colonization can occur [24]. The bacteria at the bottom of surface irregularities are protected against shear forces (from tongue or food), establishing a strong attachment [25]. Plaque accumulation which is initiated by bacterial adhesion and biofilm formation could thereby increase the risk of gingival inflammation and recurrent caries if the threshold level is exceeded.
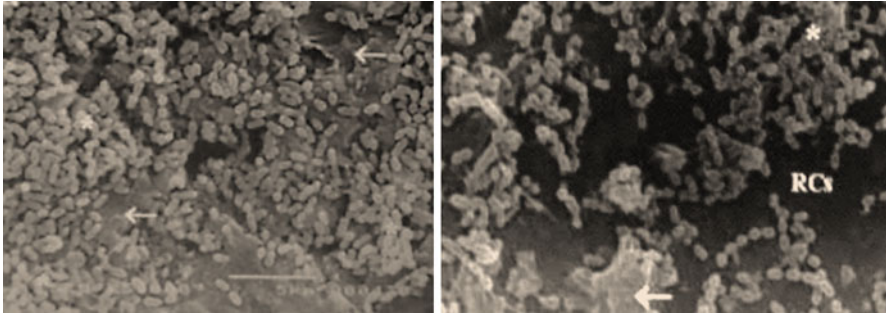
Fig. 43.6 SEM micrographs of resin composite surface (RC) with *arrows* indicating extracelluar matrix produced by bacteria called glucan and *asterisks* indicationg bacterial biofilm clusters (From Ono [21])

(a) Gingival Inflammation: The formation and maturation of plaque on the surface of enamel or restorative materials could affect the adjacent gingival tissue and initiate an inflammatory host response. This occurs only if plaque is not removed. Weitman et al. showed that plaque accumulation on finished composite was higher than natural tooth structure [26]. Despite the variation in surface roughness of composites and enamel, there was no clinical significant difference in development of plaque-induced gingivitis between the two for patients with adequate oral hygiene. If a patient presents with poor oral hygiene, then periodontal complications may be expected regardless of surface texture of restorative materials [27].

(b) Among the causative factors of recurrent caries are bacterial adhesion and plaque formation on surface of composite resin. *Streptococcal mutans* are cariogenic pathogens responsible for dental caries which commences with demineralization of tooth structure when *S. mutans* harbored in mature plaque produces lactic acid and lowers pH around the enamel. Since there is a linear correlation between surface roughness and bacterial adhesion, the rougher the surface and the more contact time, the higher the adhesion forces of streptococcal strains caused by hydrophobic interactions between protein ligands and composite interface, Fig. 43.7 [28]. Ionescu et al. concluded that resin matrix and filler particles on the surface of resin-based composites strongly influence *S. mutans* biofilm formation in vitro, suggesting that polishing is useful to minimize resin matrix exposure to reduce biofilm formation on the surface of resin-based composites [29].

Initial Gloss/Gloss Retention

Reflection of light in a specular direction by a surface is defined as gloss. According to the American Dental Association (ADA) professional product review, 40–60 GU was identified as a typical desired gloss [30]. High-gloss material accomplishes a more natural appearance by blending with the adjacent teeth better than the ones
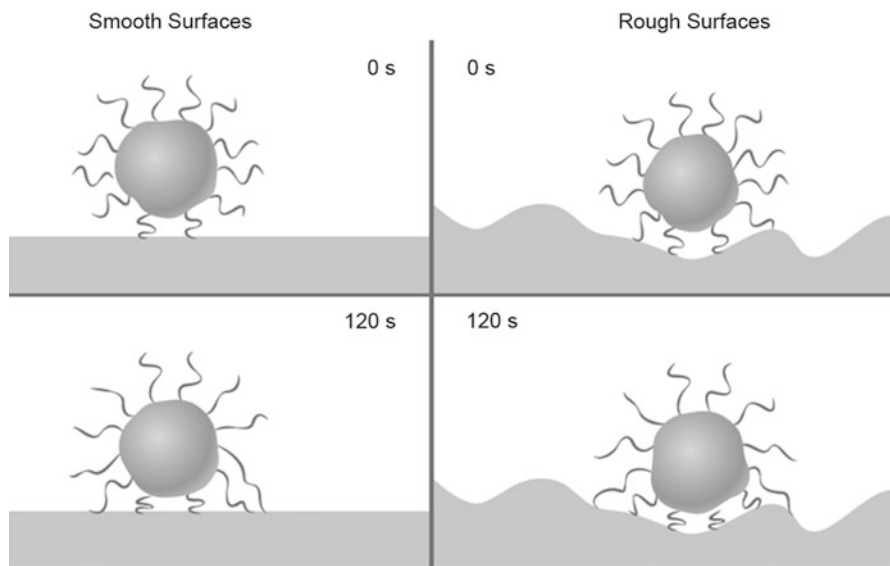
Fig. 43.7 Schematic diagram of Streptococcal adhesion forces to resin composite surfaces that increase with increasing surface roughness and contact time due to larger contact areas and more binding sites (Adapted from Mei [28])

with lower gloss. Increasing the gloss of resin composites involves a smooth surface restoration. It has been stated that when the surface roughness is increased, the susceptibility of a surface to discoloration and the degree of random reflection of light increase, both of which will cause a decline in gloss [31], affecting the esthetic outcome of a restoration [32]. The abrasive medium and pressure applied during polishing and the polishing time affect the gloss values [18, 33–35]. Additionally, surface roughness from toothbrushing and food abrasion decreases gloss [36]. Investigations concluded that dental composites with smaller filler particles show higher initial gloss values and retain a glossier surface for an extended period of time [37].

Fillers

Dental restorative composite resins are generally classified according to filler size distribution (Table 43.1), filler shape [38], and location of use and, more recently, according to their resin matrix. The filler size classification, however, remains the most widely used. Several properties of dental composites are improved by incorporation of fillers: (1) Fillers act as reinforcing particles, raising flexural strength. (2) They act as crack deflectors in low modulus resin matrix, thus increasing fracture resistance. (3) Increasing the levels of fillers would occupy more space, leading to a reduction in the mass fractions of monomers. Consequently this diminishes

Table 43.1 Dental composite classification according to filler size

Dental resin composite classification according to filler distribution

Type of composite	Filler size	Loading (wt%)	Comments
Macrofill	10–100 μm	60–65 %	Outdated, fillers dislodged leaving rough surface after polishing
Midifill (conventional)	8–10 μm		Very good mechanical and physical properties but a rough finish and polishability were draw backs
SPF: small particle filler	0.1–3.0 μm		Small fine glass particles were introduced. More filler loading. Polishability was still a drawback. Did also contain nanoparticles in their htybrid types
Microfill	0.02–0.04 μm	40–60 %	Incorporated colloidal silica overcoming polishability problem
Nanofilled	0.005–0.075 μm		Offers high translucency, high polish, large surface area limits loading
Hybrids	Mixture of particle sizes and types		Has the advantages of nano (micro) sized filler but maintains high filler loading. Example: nanomidi hybrid
Heterogeneous	Pre-polymerized		Pre-polymerize nano (micro) sized fillers in resin to increase loading. Often used in combination with hybrid technology

dimensional instability (polymerization shrinkage/coefficient of thermal expansion). In return, the stresses developed from polymerization shrinkage or thermal expansion on cavity margins are reduced. (4) Fillers reduce water sorption that results in softening of the resin matrix. (5) Fillers can modify the viscosity of dental composites before curing to provide good handling properties. (6) They provide the required radiopacity of composites by incorporation of heavy metals.

Advances in the filler loading, type, and size have tremendously aided in achieving a more natural appearance for composite resin restorations [39]. With the evolution of nanotechnology, nanosized (submicron) fillers have been incorporated into the dental composite resin systems by several manufacturers. Optical [40], polishing, and wear characteristics [41] were improved, while mechanical properties remained at least comparable to conventional composites [42–46].

Surface Roughness and Filler Size

During finishing and polishing, surface roughness results from the creation of residual defects and surface flaws caused by debonding of glass fillers and from scratch lines left by abrasives of greater size. Cracks and pits are of critical clinical relevance as it has been reported to create niche for bacterial colonization. The filler particle type, size distribution, and loading influence the polishability of composites [47].
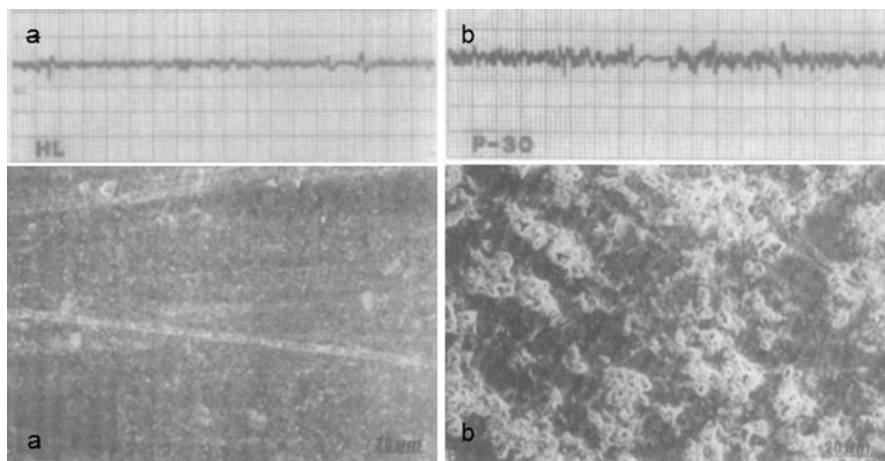
Fig. 43.8 (**a**) Roughness profilometry and SEM image of a microfill composite with nanofillers <0.1 μm after polishing. (**b**) Roughness profilometry and SEM image after polishing of a conventional composite containing larger fillers ∼2 μm in size (From Tijan [48])
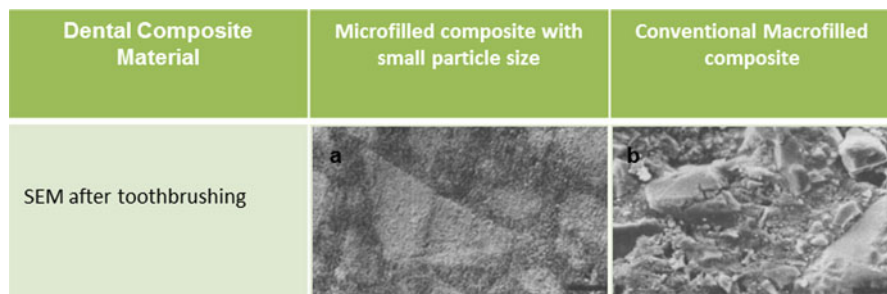

Fig. 43.9 SEM micrographs of two dental composites after toothbrushing (From van Dijken [53])

Composites with larger filler particles exhibited a significantly higher surface roughness values (R_a) than those with smaller filler particles (<1 μm); lower levels of surface roughness correlate to the smaller filler particle sizes, Fig. 43.8 [48].

It is also clinically significant to determine the performance of restorative materials as a consequence of toothbrush abrasion [49, 50], different dentifrices [51] polishing pastes, food abrasion, and occlusal wear which are daily physical processes that influence surface roughness and decrease gloss over time, thus affecting the desired optical characteristics of a restoration. All polished surfaces are abraded by toothbrushing [52]. Investigations found that brushing increased surface roughness on all polished composite surfaces [53, 54], but the degree of roughness is dependent on brushing load and time as well [55]. Figure 43.9a [53] shows that the microfilled resin accomplished a smooth surface with a more uniform abrasion due to nanosized softer particles within its organic matrix. However, resins coupled with

large fillers showed high roughness values with preferential resin loss and larger, harder particles protruding from the surface after toothbrushing, Fig. 43.9b [53]. Since a correlation between filler size and surface roughness has been established, a great theoretical advantage of nanostructured composites should be that they retain their polished surfaces over the course of time [54].

Nanofillers in Dentistry

In order to withstand the oral environment, reinforcement of dental restorative materials is primarily achieved by the addition of fillers. *Nanofillers* and their various applications have been currently investigated in dental materials research. The introduction of nanofillers, which are commonly used in medicine and engineering (such as *nanofibers* and *nanotubes*), into the world of dentistry has been attempted experimentally with limited clinical application in restorative dentistry to date.

Experimental Nanofillers

(I) *Nanofibers* are elongated fibrous filaments that possess high elastic modulus and high strength properties. They consist of organic polymers, silica, carbon, and glass fibers and have several morphologies such as short fibers or a continuous network. In addition, they can be arranged in either a random or an orderly fashion. Nanofibers are processed by "electrospinning," which is a process that does not yield impurities [56]. In this process, a polymer solution is charged by an electric field and is then forced through a small needlelike opening being attracted towards a target. As the material approaches the target, it is drawn into fibers with nanoscale diameters [57]. Investigations conducted on nanofibers to reinforce the polymeric matrix have shown dramatic improvements in flexural strength, fracture toughness, and elastic modulus of the reinforced material.

Some inherent features of nanofibers limit their use in dental applications, for example, they exhibit high viscosity with increased loading due to their high aspect ratio. In a current study, increasing the hydroxyapatite (HAP) nanofibers mass fraction beyond 10 % did not improve the biaxial flexural strength (BFS) of the resin material, Table 43.2 [58]. The HAP nanofibers may be uniformly distributed in the dental resins at a low loading rate up to 5 %, leading to improvement in their mechanical properties. However, as the mass fraction increases, nanofibers seem to bundle up forming "defect points" exhibiting a lack of homogenous dispersion within the matrix due to their high viscosity resulting in decreased flexural strength (Fig. 43.10) [58].

In order to lower the total volumetric shrinkage rate of dental composite resins, manufacturers tend to incorporate at least 60 % wt. inorganic fillers to enhance marginal adaption and prevent microleakage [59]. In order to achieve low shrinkage and improve the handling characteristics of dental composites, the addition of other inorganic fillers (such as silica particles) besides the HAP

Table 43.2 Biaxial flexural strength of resin with consecutive increase in nanofiber content (From Chen [58])

Mean biaxial flexural strength of BisGMA/TEGDMA dental resins incrementally filled with various mass fractions of HAP nanofibers

HAP mass fraction	Mean strength	Standard deviation	ANOVA
0 %	100.3	2.4	Control
5 %	112.6	5.9	
10 %	122.3	4.4	
20 %	80.4	5.7	
40 %	41.7	10.4	
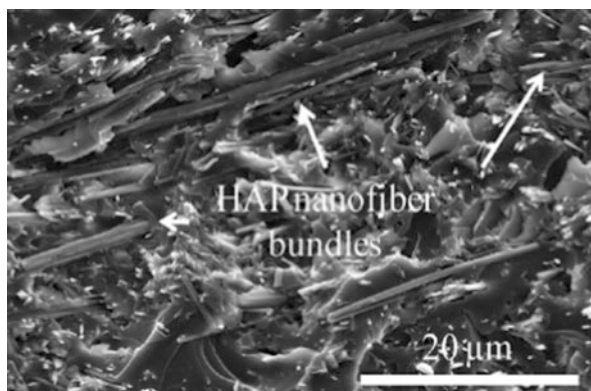
Fig. 43.10 Bundling of hydroxyapatite nanofibers (From Chen [58])

nanofibers is necessary. It was reported that the addition of 57 % wt. silica particles of size 0.7 μm and 2 % wt. silane coupling agent as fillers to an experimental composite system together with 3 % mass fractions HAP nanofibers dramatically increased the flexural strength of composite from 90.6 MPa (control) to 124.2 MPa [58]. Similarly, it was found that partial replacement of the glass fillers by ceramic Zr–Si nanofibers with mass fractions of 2.5 and 5 % wt. significantly improved the flexural strength of nanofiber-reinforced composites from 102.6 MPa (control) to 143.2 and 141.9 MPa, respectively, which is ∼40 % higher than that of the control [60]. Furthermore, fracture toughness increased from 1.08 to 1.24MN/m$^{1.5}$ after the addition of 2.5 % Zr–Si nanofibers to the studied composites [60].

(II) *Nanowhiskers (NW)*: Similar to nanofibers, they are nanometric elongated rodlike fillers characterized by high strength, low density, high elastic modulus, and high melting point. These fillers are developed from natural (cellulose, chitin) or artificial (carbon, ceramic) materials. The strength of nanowhiskers is about 10 times that of the nanofibers, and their aspect ratio is smaller (short and stubby). Ceramic nanofibers are polycrystalline or amorphous, whereas nanowhiskers are well-defined, one-dimensional monocrystalline fibers. The properties of a fiber-reinforced composite are usually anisotropic and heterogeneous depending on the fiber orientation. Conversely,

Fig. 43.11 SEM micrograph of a rough tortuous fracture surface with multiple cracks in nanowhisker reinforced-resin indicated by *black arrows* (From Xu [62])
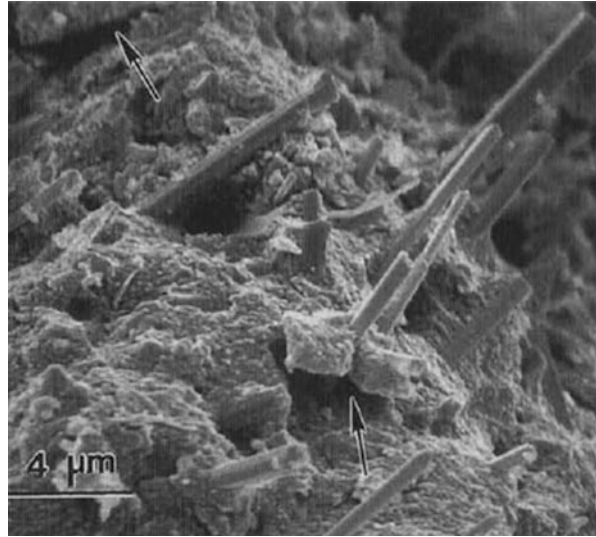
whisker composites are relatively isotropic and are more suitable for contact and wear applications. Since wear resistance has been a concern for the longevity of dental composite resins, whisker-reinforced nanocomposites are a more promising candidate for clinical research. They have proven to be excellent in microcrack bridging to prevent crack propagation [61, 62] as shown in Fig. 43.11 [62].

Compared to silica particulate type fillers, experimental silicon nitride whiskers (β-Si$_3$N$_4$) lack sufficient surface SiO$_2$ with silanol groups to effectively interact with silane coupling agents. As a consequence, composites coupled with these fillers, even when silanized, were found to be mechanically inferior to similar composites formulated with silanized glass fillers. Additionally, whisker entanglement is a commonly encountered problem in composite manufacturing [63, 64]. Mixing the whiskers with silica particles has the potential benefit of (1) dispersing the whiskers away from each other to minimize whisker entanglement and (2) forming a bimodal distribution with improved filler packing. Efforts of fusing submicrometer silica glass particles onto the individual whiskers to facilitate silanization of the whisker and to enhance whisker retention in the matrix by providing rougher whisker surfaces have been attempted [65]. Fusing nanosilica particles onto silicon nitride whiskers at 800 °C significantly improved the composite's mechanical properties over similar composites utilizing silanized untreated whiskers or whiskers silanized after the thermal oxidative treatments. The composite properties, however, became inferior at a fusion temperature of 1,000 °C likely as a result of whisker degradation at this temperature. Because of the mismatch of the refractive indices between the whiskers (SiC 2.65 and Si$_3$N$_4$ 2.2) and polymer resin (1.53), high opacity (light-scattering effect) of the whisker-reinforced composites could make them esthetically unacceptable [65].

(III) **Carbon Nanotubes (CNT)**: Nanotubes are hollow cylinders ranging from 1 to 30 nm (smaller than nanofibers) in size whereby carbon atoms are bonded by strong covalent forces within individual tubes and weak van der Waals forces between the tubes. The major limitations of CNT include poor solubility and dispersion in a resinous matrix as they tend to form bundles or rope-like structures because of the strong interaction between carbon atoms. Thus, CNT require chemical dispersants and sophisticated treatments to attain homogenous dispersion in a polymeric matrix. Due to their high processing cost, they might be less cost-effective to utilize in dental composites. They also lack interfacial adhesion to the matrix; hence, they need to be silanized. In addition, because of the graphite nature of the bundles, they undergo slide in a polymeric matrix and hence do not exhibit their outstanding mechanical properties. The combination of high aspect ratio, small size, high strength and stiffness, low density, high conductivity, and high flexibility makes carbon nanotubes perfect candidates for the production of nanocomposite materials in tissue-engineered bone scaffolds. To date, CNT have not been utilized in clinical restorative dentistry.

For the past 40 years, polymethyl methacrylate (PMMA) has been the acrylic resin material of choice for denture bases. They exhibit good physical properties, low water sorption, low density, and good esthetic resemblance to soft tissues. Their mechanical properties, however, are far from ideal, having a low cyclic flexural fatigue resistance [66] and a low impact strength that could make this material fracture with long-term use or under sudden impact. A CNT-reinforced denture base material was designed to improve flexural strength, fracture toughness, and impact resistance [67]. Despite the dramatic improvement in mechanical properties, it was not implemented in clinical dentistry due to black discoloration, resulting in poor esthetics. Reinforcing dental composite resin with silanized CNT did indeed enhance the flexural strength [68]. However, their dark color remained, limiting their application in composite resin restorations for it would be difficult to achieve the desired natural tooth structure shades and translucency.

Transparent nanotubes sheets have been recently developed to overcome the discoloration drawback of the CNT [69]. The halloysite nanotubes (HNT) allow uniform distribution in a small amount (1–2.5 % mass fractions of HNT) of well-separated, silanized HNTs into Bis-GMA/TEGDMA dental composite resins. This formulation could result in substantial improvements in the material's mechanical properties [70]. The values for flexural strength, elastic modulus, and work of fracture of unfilled composite are 90.4 ± 8.2 MPa, 2.0 ± 0.2 GPa, and 28.2 ± 3.0 kJ/m^2, respectively. Whereas the measured values of flexural strength, elastic modulus, and work of fracture for resin filled with 2.5 % HNT were all increased significantly to 132.2 ± 9.0 MPa, 2.6 ± 0.2 GPa, and 61.7 ± 5.1 kJ/m^2, the improvements were 46.2 %, 30.0 %, and 118.8 %, respectively [70].

(IV) **Nanoclay (Lamellar Silicate)**: The incorporation of nanoscale layered silicates, as montmorillonite (MMT), into polymers has attracted great attention due to their ability to improve mechanical, thermal, and barrier properties of nanocomposites because of their high aspect ratio and lamellar

Fig. 43.12 SEM image of a large agglomerate of the MMT vinyl observed in dental resins containing 16 wt% of the clay (From Discacciati [72])
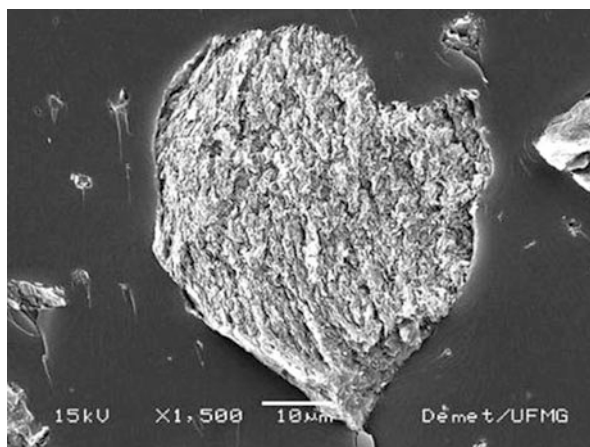
morphology [71]. These layered silicates consist of stacked silicate sheets separated by a regular spacing called gallery. They are classified in a dental composite as intercalated or exfoliated phases. Intercalated state is when the polymer chains are inserted into the gallery space between the individual layers of the silicates, maintaining the well-ordered multilayer structure of the silicate. Exfoliated state is the structure where the interaction between the individual silicate layers no longer exists. Because exfoliated nanocomposites imply higher phase homogeneity and interfacial area than the intercalated structure, the exfoliated structure is usually more desirable in enhancing the mechanical properties in dental resin composites.

Inserting these nanocomponents into dental resins could lead to materials with improved wear resistance under masticatory attrition. The hydrophilic nature of the silicate structure restricts their dispersion, thus a hydrophobic surface modification is desirable. Chemical modification of the clays with species containing polar groups was found to produce materials with a larger concentration of exfoliated layers than when MMT with highly hydrophobic vinyl species were used; Fig. 43.12 [72]. This result can be explained by the fact that dental resin has polar groups (such as ether linkages) within its structure that can interact with polar units grafted on the surface of clay. The shortcoming is that even with dental resins filled with clay concentrations as high as 16 % weight ratio, only a small fraction could be exfoliated due to the spatial limitations of the silicate-layered structure. Hand mixing of the clay into the resin did not apply high shear forces, leading to partially exfoliated clay particles [72].

Commercial Nanofillers

Particulate Nanofillers: Particulate nanofillers are very different from traditional fillers, and they require a shift from a top-down to a bottom-up manufacturing approach. Today, particles of the mechanically strong composites (such as macrofills, hybrids, and microhybrids) start as dense, large particles and are comminuted to small

particle sizes using milling procedures. However, such manufacturing techniques usually cannot reduce the filler particle size below 100 nm. To overcome this hurdle, synthetic chemical processes such as sol–gel method produce building blocks on a molecular scale. Particulate nanofillers include amorphous nanosilica, titanium dioxide nanoparticles, and zirconia–silica nanoclusters.

Amorphous Colloidal Nanosilica

Amorphous nanosilica is the most commonly utilized nanosized filler in contemporary dental composites. Colloidal silica is fine monodispersed amorphous nonporous solid silica particles with nanometric size range from 1 to 1,000 nm.

Advantages of Colloidal Nanosilica

1. Primary particles of colloidal silica are almost spherical and nanosized during their manufacturing process. Unlike CNT and nanofibers that belong to high aspect ratio fillers, spherical nanosilica has an aspect ratio of almost 1 which may assume isotropic properties.
2. Colloidal nanosilica can be used in relatively small quantities as *cofillers* together with larger-size fillers to achieve higher packing capacity in hybrid-type composites, thus serving as reinforcement for several polymer systems [73].
3. They can "fill in" the regions between the larger particles, allowing for larger volume fractions of filler, resulting in reduced polymerization shrinkage.
4. Another advantage of using nanoparticles in hybrid composites is that these thixotropic particles prevent large filler settling [74].
5. They are denser and thus more resistant to water sorption and permeability than mesoporous silica.
6. Amorphous silica does not possess health hazards like the crystalline quartz which has been associated with silicosis.

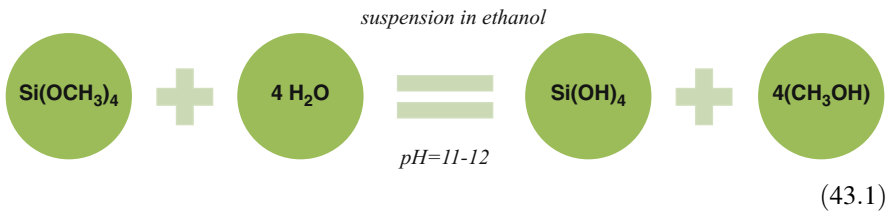## Disadvantages of Colloidal Nanosilica

If high loading levels of the discrete nanosilica particles is required in resin systems, manufacturers and practitioners are faced with three main drawbacks:

1. Because of the high specific area to volume ratio of the nanosilica, they have a tendency to agglomerate if their loading level increases which could prevent homogenous dispersion. High surface tension and their tendency to form interparticle hydrogen bonding cause agglomeration of silica in a polymeric matrix to form larger secondary particles in the micron scale which is always a hurdle because it reduces interaction and dispersability of the nanosilica in polymeric systems.
2. The rise in specific area and its corresponding thickening effect due to the presence of the agglomerated fillers limit handling properties of composite paste; they tend to be sticky and may slump during their application.
3. Deaggregation of secondary particles is very difficult even under a high shear stress, and this would limit the nanoparticles to a relatively low filler level. Otherwise, surface treatment of the discrete nanosilica particles would be a compelling demand if higher contents are required.
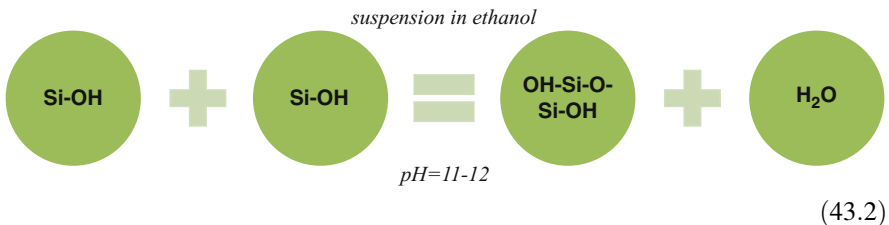
Synthesis of Amorphous Colloidal Silica-Based Nanofillers

There are various methods to prepare colloidal silica by sol–gel method including ion exchange of sodium silicate known as water glass [75], hydrolysis and condensation of tetraethoxyorthosilicates known as Stöber method, direct oxidation of silicon, and milling and peptization of fumed silica or silica gel [76]. This section will focus on the Stöber method which is widely mentioned in the dental literature. Chemical structure of colloidal silica manufactured by sol–gel method is silicon dioxide in the form of a polymer SiO_2 with siloxane bridges in the bulk and surface (vinyl) silanol groups (Si–OH) oriented in a random fashion. The silanol groups characterize the interfacial chemistry and surface properties of nanosilica grains. Macroscopically, the product of this multistep manufacturing process is an amorphous white powder that differs from the naturally occurring or synthetic crystalline quartz or tridymite. The motivation for sol–gel method is primarily for the high purity of silica, homogeneity in particle size with a narrow distribution range, and the lower processing temperatures associated with the process compared with traditional glass melting or ceramic powder methods [77]. The Stöber method is a continuous and simultaneous hydrolysis and polycondensation processes of tetraethoxyorthosilicate (TEOS) or silicon tetralkoxide (SiR_4) in aqueous alcohol solution with a catalyst (base/acid) under mild conditions to form a homogenous monodispersed colloidal silica polymer of Si–O–Si with siloxane bridges. This process is catalyzed by an acid (HCl) or a base (NH_3).

1. Hydrolysis: In this step silanol is formed by hydrolysis, Eq. 43.1:

$$\text{Si(OCH}_3)_4 \; + \; 4\,H_2O \; \underset{pH=11\text{-}12}{\overset{\text{suspension in ethanol}}{=\!=\!=}} \; \text{Si(OH)}_4 \; + \; 4(CH_3OH) \tag{43.1}$$

2. Condensation: This step involves formation of siloxane linkages, Eq. 43.2:

$$\text{Si-OH} \; + \; \text{Si-OH} \; \underset{pH=11\text{-}12}{\overset{\text{suspension in ethanol}}{=\!=\!=}} \; \text{OH-Si-O-Si-OH} \; + \; H_2O \tag{43.2}$$

3. Aging step to achieve a silica gel network.
4. Drying step to remove pore liquid from the gel structure and change the silica gel to amorphous powdered silica [77]. A well-controlled drying process leads to the formation of well-dispersed particles, whereas drying in the presence of water can

result in agglomeration phenomena. Agglomeration will reduce the filler loading in polymer systems, leading to compromised thermomechanical properties.

Milling and dispersion of pyrogenic/fumed silica is sometimes used in the manufacture of nanofillers in dentistry, so it is worth mentioning. The properties of the colloidal silica prepared by this route largely depend on the primary aggregates of fumed silica and not on the milling and peptization process. It was found that the primary particles are interconnected by high cohesive forces which are difficult to separate and disperse. Fumed/pyrogenic silica formation is by a thermal process called pyrolysis where tetrachlorosilane/alkoxysilane is exposed to high temperature (1,500 °C) flame hydrolysis in the presence of H_2 and O_2, leading to formation of dry pure colloidal silica and hydrogen chloride. Difficulty to control the size, morphology, and compositional phase has restricted the use of pyrolysis [78]. In addition, the price of the silica source and the energy requirements are limiting factors.

Physicochemical Properties of Synthetic Amorphous Silica (by Sol–Gel Method)

(i) **Shape and Size**: The effect of various synthesis parameters such as types of silicon alkoxides (silica source) and alcohols (solvent), ammonia (catalyst) concentration, and reaction temperature and pH are critical to the particle size and shape of the silica particles. Each step in the sol–gel method should be thoroughly optimized to achieve the desired particle shape and size. The effects of the shape, size, and other properties of nanosilica on restorative dental materials will be discussed in section 'Nanostructured Dental Composite Resin'.

Shape: With sol–gel method the silica would attain amorphously and entropically a spherical shape, reaching a minimum interfacial surface area. A spherical shape has an aspect ratio almost close to one. The smaller the aspect ratio, the more material could be used to attain *percolation threshold* and the higher the filler content in dental composite which can be beneficial in many ways. The larger the particle size, the more irregular the shape of the silica-based fillers. Without ammonia, particles did not exhibit a spheroidal shape. Surfactants [79], electrolytes, and organic acids control the shape of silica nanoparticles during processing.

Size: Under the controlled parameters of the sol–gel method, reproducibility of the particle size ranging from 10 to 100 nm is expected. Kim and coworkers demonstrated that the increase in particle size was due to the increase in ammonia and TEOS and a decrease in water concentration as shown in Figs. 43.13 and 43.14, respectively [80]. The smaller the particle size, the higher the surface area to weight ratio and the more Si–OH (hydroxyl groups) are on the surface for interfacial interaction.

Methanol would be the solvent of choice for silica particles with diameter from 5 to 50 nm, while nanosilicas above 50 nm are synthesized utilizing ethanol as a solvent. Ethanol forms larger particle size; this is because the nuclei created in ethanol solvent are larger than those created in methanol
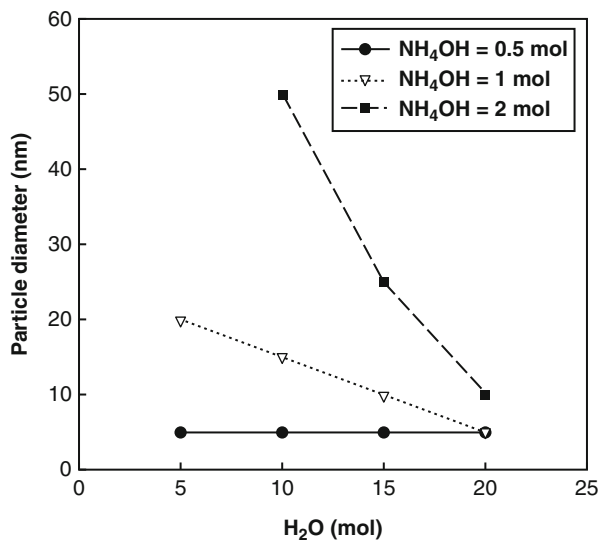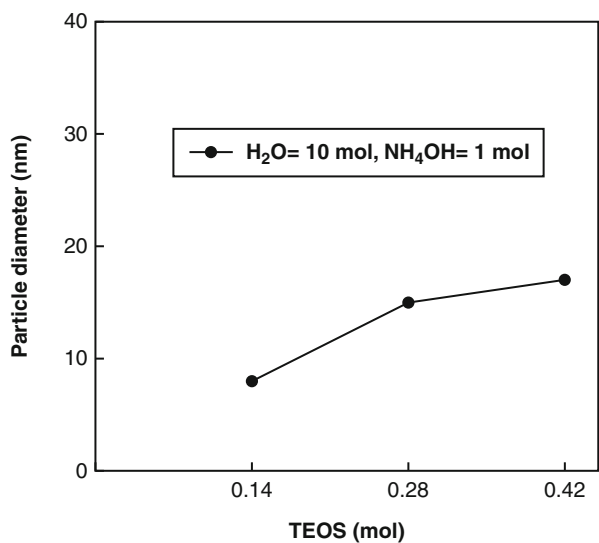
because the supersaturation ratio of the hydrolyzed monomer in ethanol is lower than that in methanol solvent. Figure 43.15 shows TEM micrographs of silica nanoparticles with particle size >25 nm produced by using ethanol as a solvent [80]. When ethanol was used as a solvent, nearly monodispersed and spherical nanoparticles were formed with particle size larger than 25 nm without aggregation.

However, aggregates of silica nanoparticles having a network structure began to form when their size was below about 25 nm. The smaller the nuclei that form,
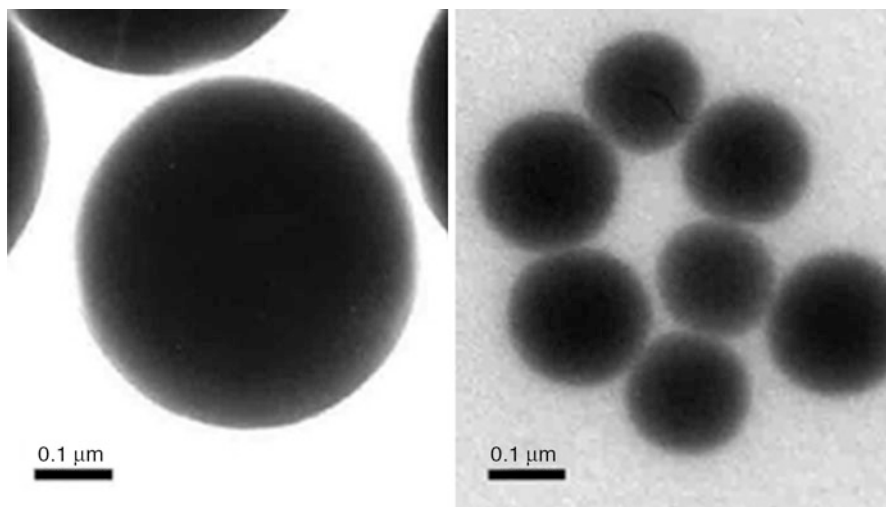
Fig. 43.15 TEM microphotographs of the silica nanoparticles (450 and 150 nm respectively) synthesized by using ethanol as a solvent (From Kim [80])
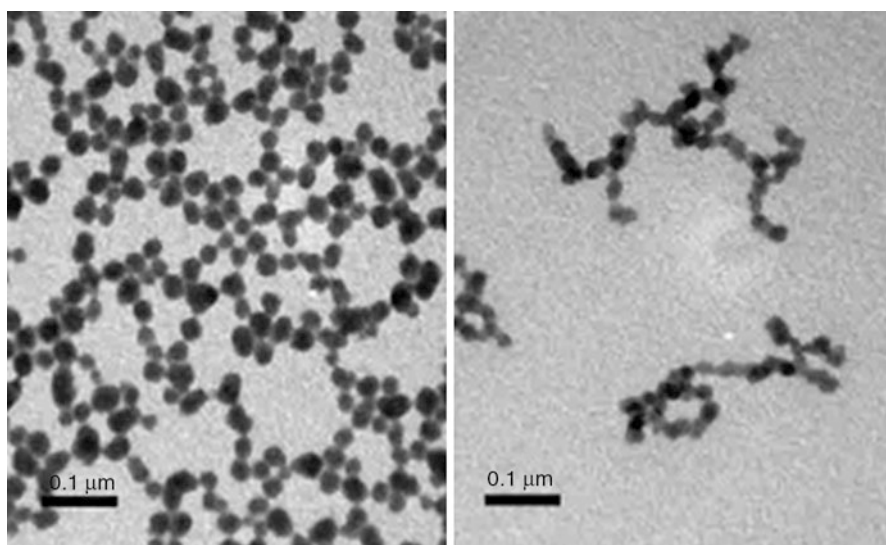

Fig. 43.16 TEM microphotographs of the silica nanoparticles (25 and 20 nm respectively) synthesized by using methanol as a solvent (From Kim [80])

the more particles are produced. Since small particles have a higher surface tension than large particles, they easily aggregate to make their surface more stable. For such reasons, silica particles below about 25 nm formed a network structure caused by aggregation as shown in Fig. 43.16 [80].

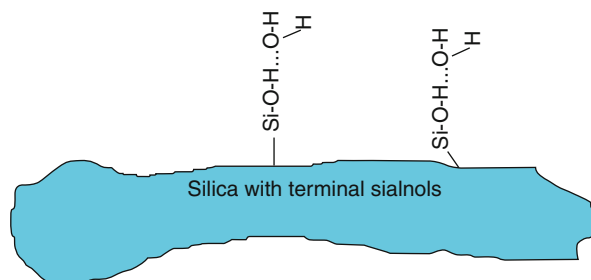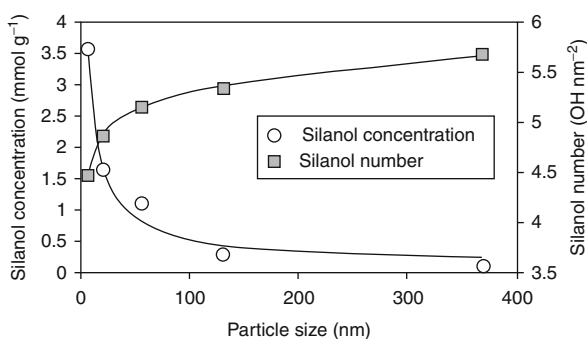**Fig. 43.17** Schematic diagram of bulk silica that has terminal OH groups forming hydrogen bonds with water

Fig. 43.18 Variation of silanol concentration and silanol number with particle size (From Rahman [81])

(ii) ***Surface Properties of Nanosilica***: Several practical applications depend on the adsorption properties of silica where the surface chemistry of nanosilica dictates the interfacial interactions. The sol–gel process produces nanosilica with surface silanol groups. The OH terminal group gives the silanol its hydrophilic nature and will interact with water and form hydrogen bonds as shown in Fig. 43.17. This gives silica its excellent water adsorption property. The hydrophilicity of silica increases with the number of surface silanol groups. Pyrogenic silica manufactured by high-temperature flame decomposition is completely dehydroxylated, forming strong covalent Si–O–Si bonds that are hydrophobic in nature.

The extent of chemical modification of silica such as grafting of organo-functional groups highly depends on the concentration of silanol groups per grams of silica (OH). The number of silanol groups per unit area of silica provides information regarding the distribution of silanol groups on the silica surface [81]. The concentration of silanol increased ~12 times as the particle size reduced from ~130 to ~7 nm, Fig. 43.18 [81]. The same trend was observed for the specific surface area (SSA), Fig. 43.19 [81]. The concentration of silanol groups increases with the decrease in the particle size which is interrelated to the SSA. The increase in the SSA and Si–OH at smaller particle size renders the smaller silica nanoparticles suitable for being utilized as fillers in advanced nanocomposites.

(iii) ***Thermal Properties***: Upon thermal treatment, the hydrophilic surface gradually changes to hydrophobic surface by irreversible elimination of a pair of

Fig. 43.19 Variation of BET specific surface area with particle size (From Rahman [81])
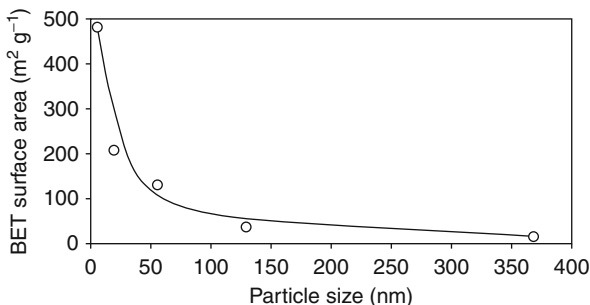
adjacent hydroxyls. In crystalline materials the hydrophobic species are more stable than that in the amorphous ones. Quartz remains as hydrophilic after degassing at 1,073 K, whereas, pyrogenic silica (AEROSIL) can become hydrophobic upon degassing at 673 K [82]. Feng et al. studied the rate of adsorption and desorption of water on silica surface [83]. The silica surface becomes hydrophobic on heating in vacuum, but it becomes hydrophilic immediately on contact with water at low temperature. Due to the high covalent bond energy in Si–O, silica has very good thermal stability and low coefficient of thermal expansion. Chen et al. showed that the addition of nanosilica to new epoxy resin material increased decomposition temperature (5 % wt. loss) up to about 30 °C. Furthermore, the coefficient of thermal expansion was significantly reduced from 123 μm/m °C^{-1} for the epoxy resin with no nanofiller to 49 μm/m °C^{-1} for the epoxy resin with 55.64 wt% nanosilica [84].

(iv) ***Mechanical Properties***: In contrast, amorphous silica is more flexible than the crystalline counterparts and the brittle glass particles, thus enhancing wear resistance. They also act as reinforcements in various polymer systems to improve strength [85].

(v) ***Surface Modification***: The nanosized silica has high surface area occupied by silanol groups which gives colloidal amorphous silica its hydrophilic nature. Incompatibility between the hydrophilic silica fillers and the hydrophobic functional groups of the resin-based composites renders silanization an essential step for optimal wetting of nanosilica and grafting it within the polymeric matrix. According to Plueddemann [86], besides adhesion, the silane coupling agent reduces the inhibitory effect of fillers on the cure of resin by reducing viscosity. Under ideal conditions, coupling agents provide a good stress distribution between the flexible continuous organic phase and the stiffer dispersed filler [87], thus protecting the filler from fracture. This would strengthen the boundary layer of resin, not only enhancing resin properties at the resin–filler interface but also [88] positively affecting the overall mechanical properties [89, 90] like fracture toughness [91, 92] and chemical resistance of composite systems [93].

Silane coupling agents are bifunctional molecules usually organosilanes that have terminal functional groups. One group is a hydrolytically active silicon-based
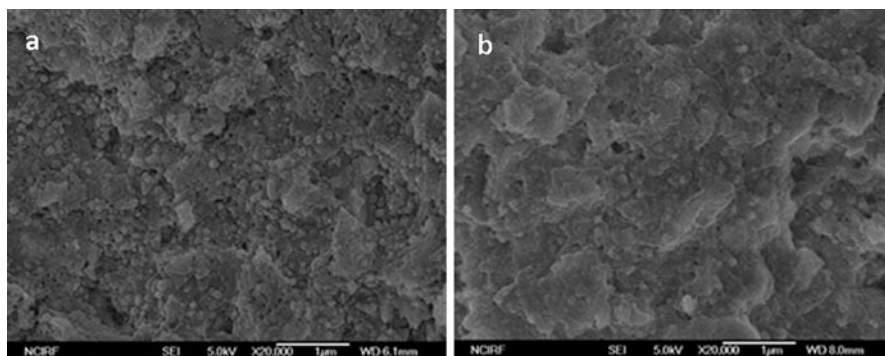
Fig. 43.20 (**a**) Dental composite containing untreated silica nanoparticles. (**b**) Dental composite containing surface treated silica nanoparticles (From Kim [80])

group, SiX_3, which condenses with the silanol group of the silica filler to form siloxane bridges. The other R group is a nonhydrolyzable organic radical that covalently bonds to resin by graft copolymerization imparting desired characteristics. Thus, they react with both inorganic and organic substrates by complex hydrolysis–condensation reactions to form a hybrid organic–inorganic structure [94].

(vi) *Silanization of Silica*: The absence of impurities in colloidal silica positively influences silane adsorption mechanism. Besides, the large specific surface area per weight ratio implies the presence of more OH groups improving the interfacial bond between filler–silane agent.

Interfacial Adhesion of Silica in Dental Composites

Kim et al. showed the surface-treated particles were better adhered to the polymer matrix. As Fig. 43.20b shows, fewer nanoparticles are visible after surface treatment (because they are covered by the matrix) [80] than that is seen in Fig. 43.20a. There are also fewer black holes in the matrix in Fig. 43.20b. Black holes are, indication of pullout of poorly attached particles. Thus, interfacial adhesion between silica particles and resin matrix was enhanced by using silanized silica nanoparticles [80].

Dispersion of Silica Particles in Dental Composites

Kim et al. showed that the dispersion of treated particles in the resin matrix was much better than that of untreated particles. Composites prepared from the untreated particles contained particle aggregates, while those prepared from the treated particles did not contain particle aggregates as shown in Fig. 43.21 [80].

Hydrolytic Degradation of Silane–Silica Interface

3-Methacryloxypropyltrimethoxysilane (MPTMS) is the most commonly used silane in dental restorative composites; see Fig. 43.22a [95]. The organic portion of MPTMS which reacts with dimethacrylate monomer during photopolymerization has
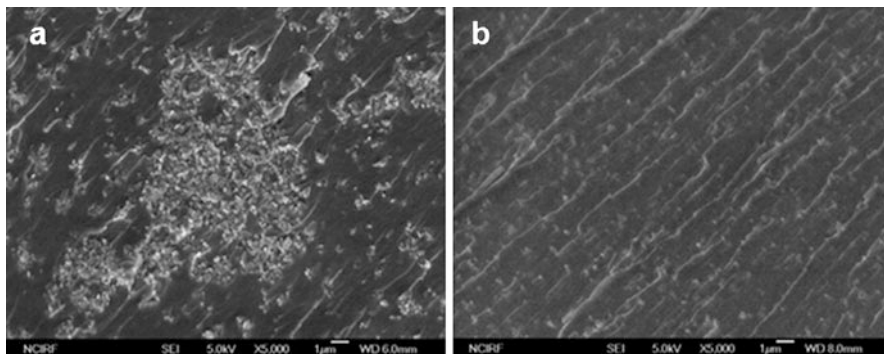
Fig. 43.21 (**a**) Composites prepared by using untreated silica nanoparticles showing agglomeration. (**b**) Composites prepared by using surface treated silica nanoparticle are well dispersed (From Kim [80])
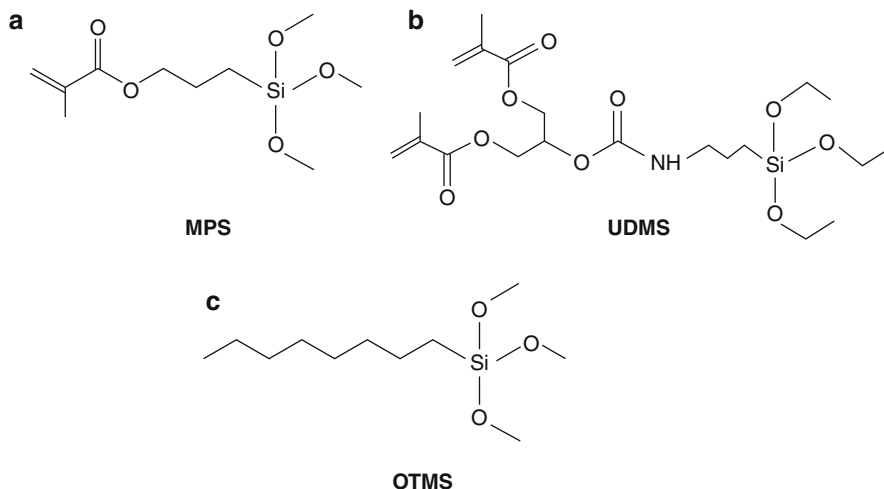

Fig. 43.22 Chemical structure of three silane coupling agents. (**a**) MPS 3-methacryloxypropyltrimethoxy silane. (**b**) UDMS Urethane dimethacrylate silane. (**c**) OTMS Octyltrimethoxy silane (From Karabela [95])

a carbon–carbon covalent bond that forms between the silane and the resin matrix. These bonds are more stable to hydrolysis than the silicon–oxygen covalent bond created between the resin and the silane coupling agent where the covalent bond has an ionic character. Therefore, the hydrolytic stability of MPS is a major concern [94]. In the oral environment absorption of water by dental composites takes place, which leads to the breakdown of Si–O bond interface between the silane and the inorganic phase [96]. The debonded filler–silane interface will facilitate water migration into the interior layer of resin composite.

Karabela et al. suggested that silane structure used for the silanization of nanosilica has an effect on the water sorption and solubility of composites [95]. Urethane dimethacrylate silane (UDMS) (see Fig. 43.22b [95]) is a polar silane with two methacrylate groups, which in turn cross-links with the resin matrix and also has the hydrophilic urethane group (–NHCOO–) bonds. For this reason UDMS composites showed the highest water sorption due to the hydrophilic nature of urethane groups which form strong hydrogen bonds with the water molecules, stronger than those formed between ester groups and water. UDMS showed the least solubility due to cross-linking between the polymer chains which decreases the solubility of the polymer network. Octyltrimethoxysilane (OTMS) is a nonpolar hydrophobic nonreactive silane used to improve handling characteristics of uncured resin pastes; see Fig. 43.22c [95]. It cannot react covalently with the dimethacrylate monomers, because it has no methacrylate group, but interacts through weak van der Waals interactions [74]. OTMS composite absorbed a smaller amount of water than MPS composite because of the presence of the hydrophobic and nonpolar OTMS. It showed the highest solubility because it did not covalently bond with the resin and was effectively forced out of the polymer network during photopolymerization, resulting in phase separation.

Fourier Transform Infrared Spectroscopy (FTIR) Spectrum of Amorphous Silica

The findings by Söderholm and coworkers suggest that the amount of silane needed for filler treatment depends on the number of isolated OH left on the filler surface [97]. These results were confirmed in FTIR spectrum by Karabela et al. [98]. The FTIR spectrum of the nanosilica is shown in Fig. 43.23 [95].

Before silanization (solid line) absorption bands due to the surface silanol groups (Si–OH) are shown which are principally of two types: (a) free Si–OH corresponding to a sharp absorption band at $3{,}740\ \mathrm{cm}^{-1}$ and (b) adjacent silanols in which hydrogen bonds to each other and/or absorbs water corresponding to a broad region at $3{,}600\ \mathrm{cm}^{-1}$. Silica also showed an absorption band at $1{,}870\ \mathrm{cm}^{-1}$, which is attributed to the siloxane linkages in the bulk of the silica and is unaffected by the surface modification, and a band at $1{,}630\ \mathrm{cm}^{-1}$ due to the structure of the bulk silica [99].

After silanization (dotted line) the peak at $3{,}740\ \mathrm{cm}^{-1}$ disappears due to condensation of Si–OH. In addition two peaks are apparent, one at $1{,}720\ \mathrm{cm}^{-1}$ due to the free carbonyl $(-C = O)$ stretching vibration and another at $1{,}470\ \mathrm{cm}^{-1}$ due to the double-bond $C = C$ of the methacrylate group of the silane agent. The peak at $1{,}700\ \mathrm{cm}^{-1}$, characteristic of the carbonyl groups forming hydrogen bonds with the silica hydroxyls, was almost completely overlapped by the strong peak at $1{,}720\ \mathrm{cm}^{-1}$.

Thermogravimetric Analysis (TGA) of Silica

The thermal degradation of polymers and thermogravimetric analysis is one way to determine the weight percentage of silaned nanosilica (fillers) available in commercial dental composites. Figure 43.24 a and b below is TGA curve and its corresponding differential TGA (DTGA) curve of prepared composites containing different amounts of silane coupling agents [100]. The graphs indicated a three-step
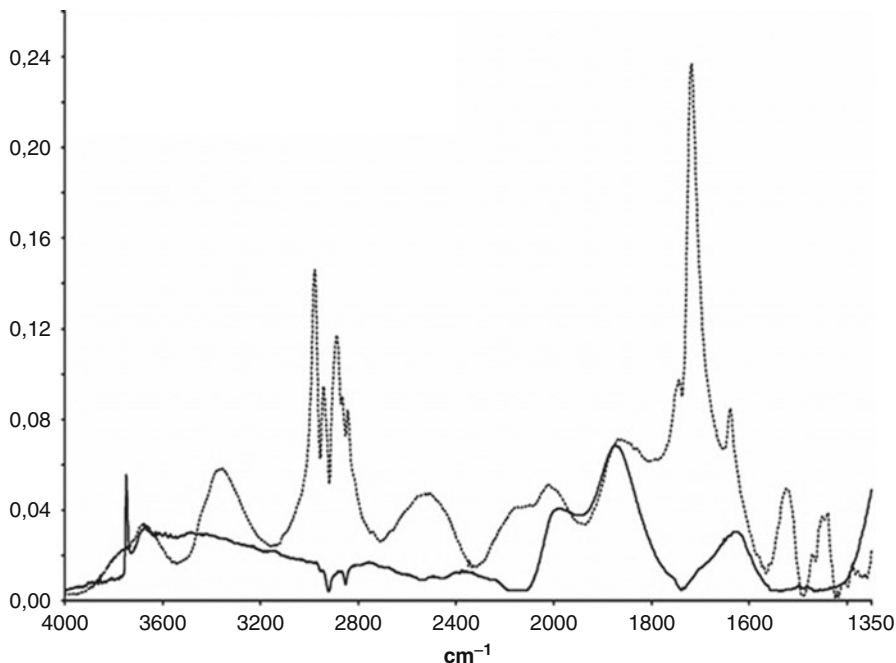
Fig. 43.23 Infrared absorption curves of: nanosilica (*solid line*) and silanized nanosilica (*dotted line*) (From Karabela [95])

degradation process. The first two steps are related to the thermal degradation of the neat polymeric matrix of prepared composites and the decomposition of the silane, one around 210–350 °C and the other one from 350 to 490 °C, while the third step around 490–770 °C is due to condensation of surface silanols of silica [100]. It was also concluded that the composite with the lowest amount of silane has the highest amount of free surface silanol groups which have condensed, in return giving the highest weight loss followed by the other four composites, which showed similar percentage weight loss as shown in Fig. 43.24b [100].

Titanium Dioxide Nanoparticles (TiO$_2$ NP)

These nanoparticles are photocatalysts; they use light photons to activate redox reactions, forming free radicals OH in the presence of water, giving TiO$_2$ NP its superhydrophilicity property. TiO$_2$ has a high elastic modulus of 230 Gpa. TiO$_2$ NPs have been used as additives in dental materials for their radiopacity to match the opaque properties of teeth [101], but using TiO$_2$ NPs to enhance the mechanical properties of dental resins has not been successful due to the inconsistent agglomeration of TiO$_2$ NPs [102]. Many methods have been attempted to facilitate their dispersion in organic solvent by modifying the TiO$_2$ surface with different reagents including surfactants [103] and acids [104]. TiO$_2$ nanoparticles have been experimented in small fractions in dental resin. TiO$_2$ nanoparticles were coated

Fig. 43.24 TGA (**a**) and DTGA (**b**) curves of prepared nanocomposites with varying amounts of silane coupling agents (From Sideridou [100])
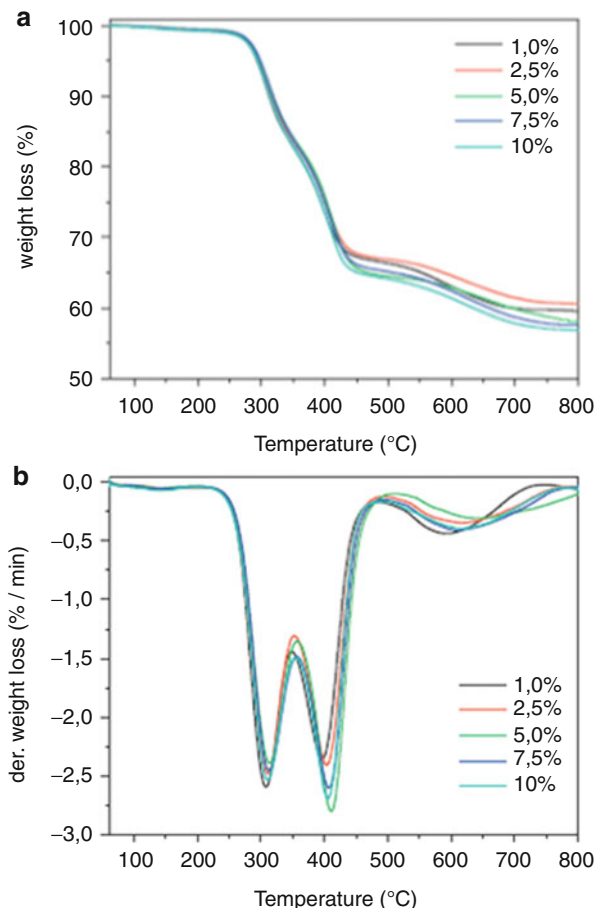
with the organosilane allyltriethoxysilane. 1 % weight ratio of modified TiO_2 showed improved microhardness value and moderate improvement in flexural strength [105]. The modified TiO_2 particles have better dispersion in the matrix and tend to form smaller clusters than the unmodified particles that form larger aggregates. These results were similar to another study by Sun et al. [106]. Another downside to TiO_2 NP is their extensive radiopacity if larger aggregates are formed. Yu et al. showed that increasing TiO_2 even to 0.1 % would substantially decrease translucency and cause a color change beyond acceptability limits for dental composite resins [101].

Zirconia/Silica Nanoparticles

With the sol–gel procedure, a mixture of metal oxides could be prepared in order to match the refractive index of the polymeric matrix [107]. Silica sols enable the synthesis of custom-made agglomerates called nanoclusters, which were synthesized from a silica sol and a zirconyl salt. The formed zirconia–silica nanoparticles are not clusters in the sense of a chemical definition but are a specific kind of

agglomerates. Nevertheless, the dental nanocomposites based on them showed high translucency, high polish, and polish retention similar to microfill composites, while physical properties and mechanical strength were equivalent to commercial hybrid composites.

Nanostructured Dental Composite Resin

Nanofillers in Dental Composite Material

Problems with the early composite formulations, such as percentage of filler and particle size leading to high wear rates, loss of anatomic form, and poor polishability, convinced researchers that early composite formulations were unacceptable for restoring posterior teeth [108]. The increase of the filler loading percentage, the modification and reduction on the particle size, and their better distribution in the resin matrix contributed to the reduction of wear rates and to the improvement of the surface smoothness of these restorative materials [109, 110].

Types of Composites with Nanofillers

Under continual heavy masticatory loading in the oral environment, unlike amalgam restorations, large posterior composite restorations are subjected to occlusal wear and cyclic fatigue especially for patients with parafunctional habits (bruxers, clenchers). In order to lengthen the life expectancy of resin composites, manufacturers strive to enhance the wear resistance of dental composites which has always been a concern. Occlusal wear occurring on the surface of teeth or restorations are categorized as abrasive wear or attrition wear. In vitro wear is quantified by profilometry through volume loss of material and maximum wear depth [111].

Attrition refers to the direct contact of opposing cusps on the occlusal surface of a restoration observed in centric contact areas. It is usually related to fatigue phenomena. Abrasive wear is a three-body behavior encountered when the food bolus is compressed between antagonists as abrading particles of food slide over the restoration surface in noncontact areas. This type of wear is characterized by the preferential loss of resin matrix where the relatively soft organic matrix between the filler particles is gradually removed, leading to protrusion of the particles from the surface. Left unsupported, fillers are easily pulled out, leaving a layer of unprotected resin. This layer quickly erodes away and the wear cycle continues in a similar manner [112].

For a fixed volume fraction of fillers, several studies concluded that the use of fine and ultrafine particles would reduce the wear process of resin restorations. One theory supporting this phenomenon is that smaller filler particles would reduce the interparticle spacing because smaller filler particles are more closely packed and the resin between the fillers becomes protected from further abrasion by adjacent particles. This "protection theory" was hypothesized as the early

Fig. 43.25 SEM image of a microfilled composite with well-delineated facets in occlusal contact area (From Lutz [118])
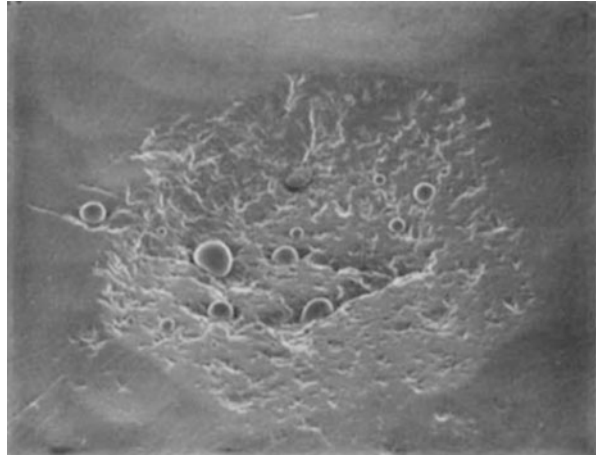
Traditional homogenous Microfilled composites as *Concept* showed higher abrasion wear resistance and maintained a smoother surface finish than the older midifill and hybrid composites even with lower filler loadings [113, 114]. However, it is worth saying that the wear behavior of resin composites does not solely depend on the particle size. Other factors characterize the wear pattern such as type of filler, filler loading, degree of conversion of the resin [115], resin composition, and interfacial adhesion between the filler and the resin [116].

Homogenous Microfilled Composites

(i) *Wear Resistance*: Colloidal nanosized fillers (40–50 nm) used in the formulation of many microfilled composite resins are embedded in the surface, and they do not get easily worn away by an oscillating antagonist as compared to larger particles. This would minimize the interparticle spacing, thus "protecting" the resin between the particles from abrasive action. This implies that microfills have higher abrasive wear resistance in occlusal free areas [117, 118] and where low generalized sliding wear exists in anterior regions [119]. Nevertheless, this theory was not applicable in wear-prone areas where continuous application of localized stresses is appreciable such as the intraoral cuspal contact area [120]; microfilled composites have low filler levels such that the small primary filler particles and resin matrix are abraded off together during heavy occlusal wear. Scanning electron micrographs of microfilled composites with low abrasive wear usually reveal a smooth surface, whereas in attrition areas rough surface is evident. Figure 43.25 shows that SEM image of an in vivo microfill composite in a contact area was different from surrounding occlusal free surface [118].

(ii) Various studies showed enamel asperities caused by loose composite filler particles during the wear process observed macroscopically as parallel scratches on the cusp surfaces [121–123]. The materials having reduced silanation levels and larger particle size fillers produced an increased amount of enamel wear [122]. Hence, another benefit of microfilled composite is the
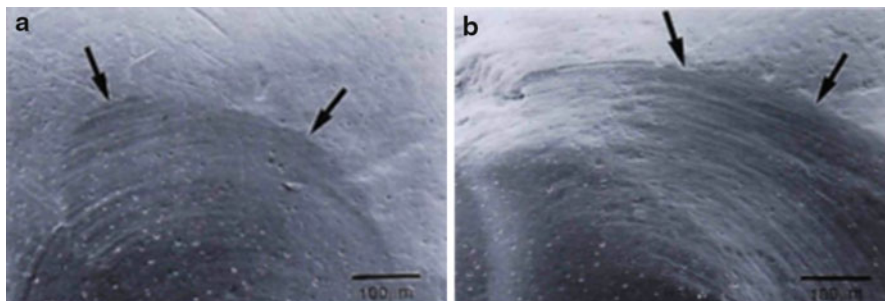
Fig. 43.26 SEM images (**a**) Enamel surface worn by microfilled composite containing nanosilica (**b**) Enamel surface worn by a conventional composite containing quartz particles (From Suzuki [122])

consistent results of low opposing enamel (antagonist) wear, while conventional composites and hybrids with various glass fillers can significantly increase the opposing cusp wear [123]. The presence of nanosilica particles in microfill with lower hardness values than other glass fillers (*descending hardness values*: quartz in conventional composites > barium silicate > silica) is the primary reason for lower wear rate on opposing enamel as shown in Fig. 43.26 [122]. Silux Plus, a microfill, demonstrated the least amount of enamel and composite wear. This then was followed by Herculite, the fine-particle composite resin containing the barium silicate glass. The next greatest amount of wear was generated by the composite resin containing the larger filler particles of barium silicate (Ful-Fil). The quartz-filled posterior composite resin, Clearfil, created the most extensive wear of the opposing enamel, Table 43.3 [122].

(iii) *Polishability*: Moreover, microfilled composites are polished to a high gloss and provide a smoother surface finish than conventional hybrids as seen in Fig. 43.8 [48, 124]. The studies relate smooth surface finish and gloss to the ultrafine inorganic SiO_2 particles incorporated in a homogenous polymeric matrix. Their small dimensions (100–500 A) enable a smooth polish with low R_a values, indicating small irregularities. A glossy surface is obtained because the ultimate grains are so small that the scratches left behind are finer than the wavelength of visible light and are undetectable.

(iv) *Toothbrush Abrasion*: Microfill was observed to have the highest toothbrush abrasion resistance and retained the smoothest surface [49, 53]; refer to Fig. 43.9.

However, the mechanical properties of homogenous microfill, such as flexural strength, are insufficient for posterior restorations because of reduced filler concentrations (23–52 % by weight) compared to 78 % weight of fillers in conventional composites. As a result, microfilled composites have higher thermal expansion, higher water sorption with dimensional changes [125], and possibly greater polymerization shrinkage. These drawbacks create concerns of microleakage, marginal fractures [126], and marginal discoloration and the potential for secondary caries. Meanwhile, higher volume ratio of nanosized fillers is counteracted by particle agglomerations and thicker consistency (viscosity problems) due to the high

Table 43.3 Enamel and composite wear of four composites (Adapted from Suzuki [122])

Means (standard deviations) of surface area of wear facets on enamel and composites tested (mm^2)		
Product	Enamel	Composite
Silux plus	0.40 (0.01)	2.36 (0.02)
Ful-fil	2.67 (0.14)	2.93 (0.08)
Herculite	1.51 (0.03)	2.38 (0.04)
Clearfil photoposterior	4.02 (0.01)	4.55 (0.04)

specific area of the colloidal nanofillers. Agglomeration is undesirable in particulate composite resin because inhomogenous dispersion of nanostructures will lead to anisotropic properties [127]. Therefore, microfills were indicated in anterior regions where esthetics and smoothness is of primary importance.

Heterogeneous Microfilled Composites

To enhance the overall filler loading of microfilled composites for optimizing mechanical properties without particle aggregation and lowering polymerization shrinkage of a composite, prepolymerized resin fillers (inorganic/organic filler – PPRF) are cured, ensuring complete polymerization and higher degree of conversion (DC), and then grinded and incorporated in the uncured resin matrix and hence the name ***Heterogeneous Microfilled Composites***.

Nevertheless, it was later realized that the bond strength between the prepolymerized fillers and the matrix resin is weak and subject to stress fracture and microcracking. Therefore, they did not show adequate durability due to their low fatigue resistance under heavy occlusal contacts; thus, heterogeneous composites were also contraindicated in posterior region of the oral cavity just like homogenous microfill. Furthermore, their filler loading capacity was relatively low, leading to significantly low mechanical properties; see Table 43.4 [38]. Composites filled solely with prepolymerized particles showed the lowest filler content; composites that contain round filler particles had the highest filler content. Composites that contained prepolymerized filler particles exhibited significantly lower flexural strength, flexural modulus, and hardness values than composites that contained round, irregular-shaped particles or a combination of prepolymerized and irregular-shaped particles.

Microhybrid Composites

In an attempt to overcome the shortcomings of microfill composite, ***microhybrid composites*** containing a distribution of particles of varying sizes (average particle size <1 μm) were developed to improve mechanical properties as well as maintain good surface polishability of the microfill [128]. The average filler size in microhybrid composites has been reduced to less than 1 μm to achieve polishability while retaining higher filler loading. A certain filler size distribution is usually necessary to get high filler loading in microhybrid composites [129]. Fillers in most microhybrid composites are mostly ground glass particles whose morphology is irregular; see Fig. 43.27 of two microhybrids [130].

Table 43.4 Flexural strength, flexural modulus and Vickers hardness values of composites with different filler morphology (Adapted from Kim [38])

Mechanical properties of studied composites				
Product	Filler morphology	Flexural strength (MPa)	Flexural modulus (GPa)	Vickers hardness (VHN)
Metafil CX	Prepolymerized particles	75(2)[IH]	3.4 (0.6)[I]	26(1)[I]
Silux plus		59(2)[G]	6.8(0.4)[G]	49(3)[H]
Heliomolar radiopaue		78(3)[H]	5.5(0.4)[H]	36(2)[I]
Palfique esthelite		74(2)[H]	6.7(0.5)[G]	57(3)[G]
Aelitefil	Irregular-shaped particles	123(2)[B]	11.6(1.2)[BC]	89(5)[c]
Charisma		113(3)[DEF]	10.2(0.9)[DE]	79(4)[DE]
Herculite XR		125(3)[AB]	10.4(0.9)[DE]	77(4)[E]
Hepolite		109(3)[F]	11.4(1.2)[BCD]	56(2)[G]
TPH		116(4)[DC]	9.6(0.8)[E]	60(2)[G]
Veridonfil		114(3)[DE]	11.6(0.9)[B]	64(3)[F]
Photoclearfil	Prepolymerized + irregular shaped particles	80(2)[G]	8.4(1.0)[F]	63(2)[F]
Pertac-hybrid		109(3)[EF]	11(0.9)[CD]	81(3)[D]
Z100	Round particles	129(5)[A]	15(1.3)[A]	117(5)[A]
Palfique toughwell		120(3)[BC]	12.3(1.3)[B]	101(4)[B]

Data superscripted with capital letters denote statistically insignificant differences within each column
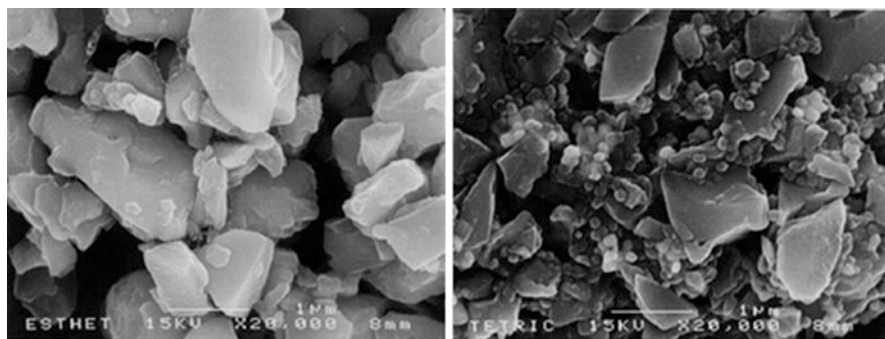
Fig. 43.27 SEM micrographs of Irregular inorganic filler particles in microhybrid composites (*left*: Esthet X Improved; *right*: Tetric Ceram) (From Lu [130])

Atomic force microscopy showed detailed surface topography of a hybrid, microhybrid, and microfilled composite, respectively, as shown in Fig. 43.28 [131]. Hybrid has a strong irregular surface with distinct sharp projections and filler dislodgement, while a moderate irregular surface was obtained for the microhybrid. Microfilled composite demonstrated a low surface profile interrupted
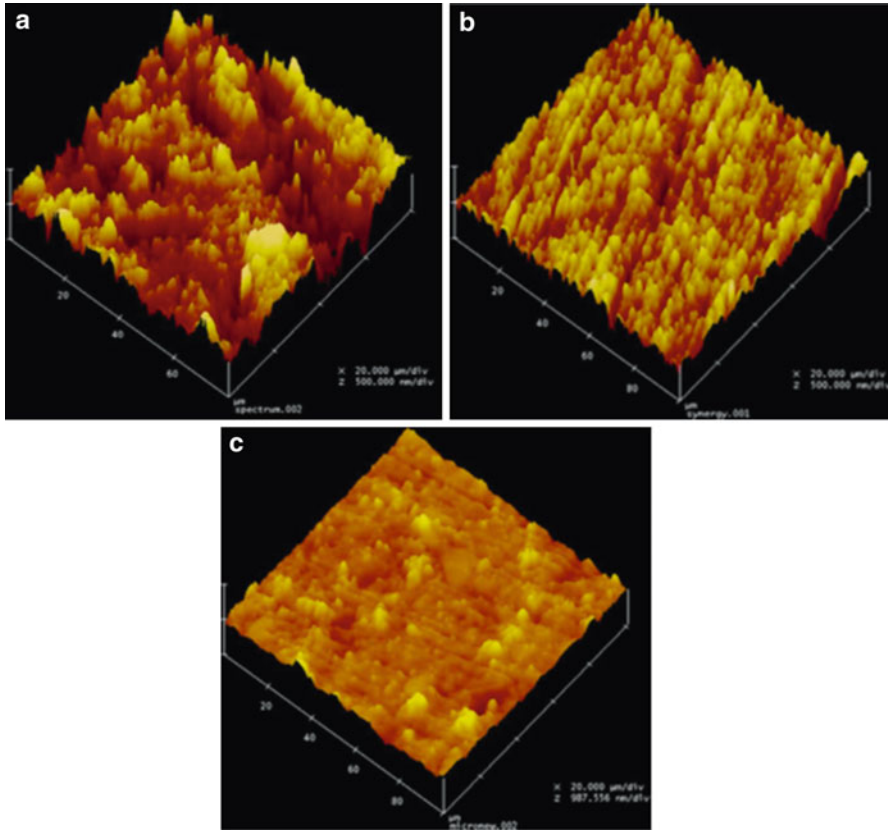
Fig. 43.28 Atomic force microscopy images (**a**) Hybrid. (**b**) Microhybrid. (**c**) Microfill (From Kakaboura [131])

by rounded shinny projections on surface. The surface texture of the microfilled is such due to the predominantly amorphous silica. Certain microhybrids will have roughness values very comparable to microfill because of the narrow distribution of the submicron particle size, for example, Point 4, whereas other microhybrids will show rougher surface texture due to a broader distribution of the submicron particle size and a slightly larger average particle size, for example, Esthet X (DENTSPLY Caulk, Milford, DE) and Synergy Duo (Coltene/Whaledent, Mahwah, NJ) [131]. However, neither microfill nor microhybrid materials provide the optimal combination of strength and surface finish desired for dental restorative composites.

Contemporary Nanocomposites
Amorphous spherical nanosilica approximately 0.04 μm (40 nm), which have been incorporated into microfill composites and in some hybrids, acted as the predecessors to contemporary nanocomposites that were recently introduced to the market. Nanocomposites may be available as ***nanofilled*** or ***nanohybrid*** composites.
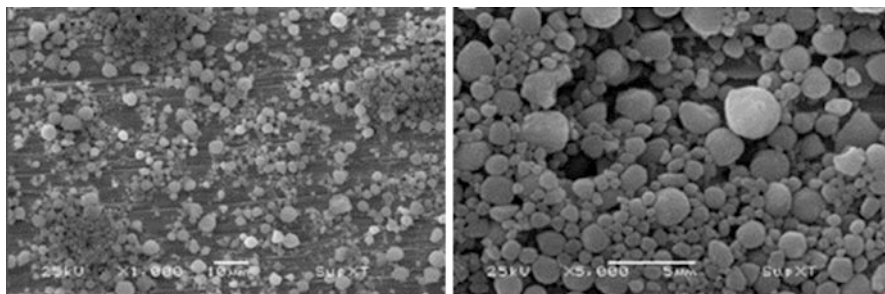
Fig. 43.29 SEM images of Supreme XT nanofilled: *round-shaped* clusters are observed, although the magnification is not sufficient to accurately observe the individual nanosized particles (From Moraes [54])
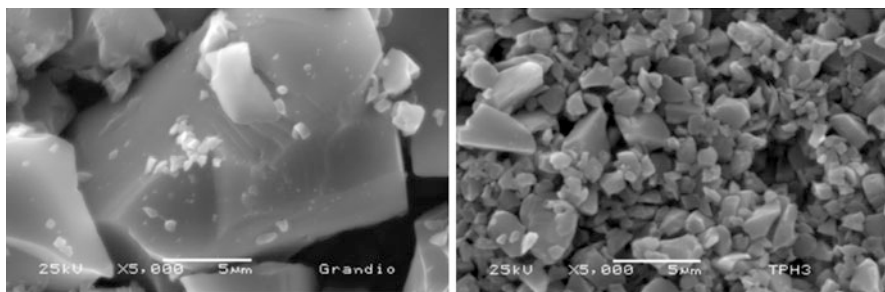

Fig. 43.30 SEM images of inorganic filler of nariohybrids (*left*: Grandio with very large, irregular-shaped particles mixed with medium fillers *Right*: TPH3 with irregular-shaped small and medium particles) (From Moraes [54])

(A) *Nanofilled Composites (Nanofills)*

Nanofills contain both nanosized monodispersed filler particles called nanomers (average size 20–75 nm) and agglomerations of these particles known as "nanoclusters," Fig. 43.29 [54]. The nanomers are silica particles below the wavelength of light offering favorable polishability and high translucency. The nanoclusters are partially sintered agglomerates of spherical zirconia and silica nanomers with average size ∼0.7 μm (range 1.6–0.4 μm). Unlike microfill and hybrid systems, the presence of nanoclusters in selected nanocomposites provides a distinct reinforcing mechanism, resulting in significant improvements to the material's strength and reliability [44, 132, 133].

(B) *Nanohybrid Composites*

This class of dental composites varies widely among manufacturers, Fig. 43.30 [54]. They contain discrete spherical nanoparticles ranging in size from 50 to 100 nm and milled glass particles, and in many instances large prepolymerized filler particles are added. Some may also include nanoclusters.

Nanohybrid composites are capable of having an increased overall filler loading capacity which is a characteristic of all hybrid systems. The compressive strength,
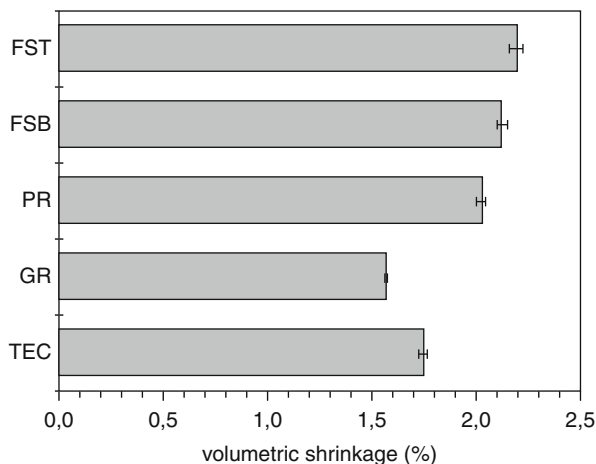
hardness, flexural strength, and elastic modulus increase with the amount of inorganic fraction, while the polymerization shrinkage decreases [134–136]. The nanosized fillers are capable of occupying the spaces between the larger particles allowing for more dense packing, yielding a dental composite with higher filler volume fraction and a homogenous distribution comparable to that of microhybrid composites [137]. Additionally, the nanospherical shape in a mixture of different sizes geometrically favors the incorporation of more inorganic fillers in the resin matrix, which will raise the fracture strength because stresses tend to develop at sharp edges of the irregularly shaped fillers [38, 138]. Theoretically speaking, when nanofillers are added to the resin matrix, a greater amount of fillers can ultimately be incorporated in the resin matrix. However, caution should be exercised to avoid nanoparticle overfilling in order to minimize agglomeration and increase in viscosity.

Consequently, unlike nanofills, this increase in filler content in nanohybrids results in a lower proportion of resin matrix with significant reduction in polymerization shrinkage [132] as well as improved physical properties [138–140], Fig. 43.31 and Table 43.5 [132]. Grandio, a nanohybrid, contains the least amount of organic matrix and more filler loading (13.0 wt%), thereby showing the lowest shrinkage among the composites tested, whereas Filtek Supreme, a nanofill, contains the most (30.0 wt%) organic, displaying a surge in shrinkage. Notice that the shrinkage does not solely depends on filler capacity. It is also affected by the degree of conversion which in return depends on the type of monomer used, for instance, Bis-GMA (bisphenol A-glycidyl methacrylate) and UDMA (urethane dimethacrylate) have lower degree of conversion (DC) than TEGMA.

Additionally, the small size of the filler particles improves the optical properties of the composite material because their diameter is a fraction of the wavelength of visible light, they do not practically scatter or absorb visible light, and the human eye is incapable of detecting them. Moreover, the submicron-size structures offer adequate polishability. Thus, nanohybrid systems are marketed as universal composites that can be utilized as anterior and/or posterior restorations. They are

Table 43.5 Summary of the filler ratios of five composites (nanohybrids and nanofills) (Adapted from Sideridou [132])

Summary of total filler loading by weight (wt) and volume (vol%) for five commercial dental composite resin systems

Composite resin	Classification	Total filler content	
		Weight percent (wt%)	Volume percent (vol%)
Tetric evo ceram (TEC)	Nanohybrid	82–83	82.5
Grandio (GR)	Nanohybrid	87.0	71.4
Protofill-nano (PR)	Nanohybrid	81.9	
Filtek supreme body (FSB)	Nanofill	79.0	59.5
Filtek supreme translucent (FST)	Nanofill	70.0	57.5

claimed to exhibit favorable physical and mechanical properties, particularly when used in tooth locations of high stress concentration. In this respect, they perform similar to hybrid composites while also maintaining the desirable characteristics of adequate wear resistance, luster, and polishability of the microfill composites due to the presence of the nanomeric fillers, resulting in high esthetic qualities [141–143].

Physical Properties of Contemporary Nanocomposites

(i) *Polishability*: It is believed that filler particle size is one factor which will influence surface roughness [144], particularly when microfill composites that contain fillers less than 100 nm were found to render smooth polished surfaces than hybrids [48].

(a) *Surface Roughness*: Microfills, as described previously, displayed the smoothest surface after finishing and polishing. When contemporary nanofill composite roughness was compared to that of microfill, they showed similar surface texture and were not significantly different after various finishing and polishing techniques [18, 141] as shown in Fig. 43.32 [18].

Senawongse et al. demonstrated that nanofill resin composites with nanoclusters demonstrated smoother surfaces after polishing in contrast to nanohybrids and microhybrids, due to the presence nanoscale-size fillers within the nanoclusters [145]. These results confirmed the findings of Turssi (2005) and da Costa (2007) [18, 146]. Once polished, the polymer-rich matrix on the surface is wiped away, exposing large irregularly shaped particles of nanohybrid and microhybrid composite resins, reflecting rougher surface than the nanofill. Conversely, nanohybrids like Premise (Kerr, Orange, CA) that contain a narrower submicron particle size distribution were shown to exhibit the smoothest surface finish within the nanohybrid and microhybrid composite groups, imparting similar polishability to nanofills, Table 43.6 [145]. Janus et al. also concluded that
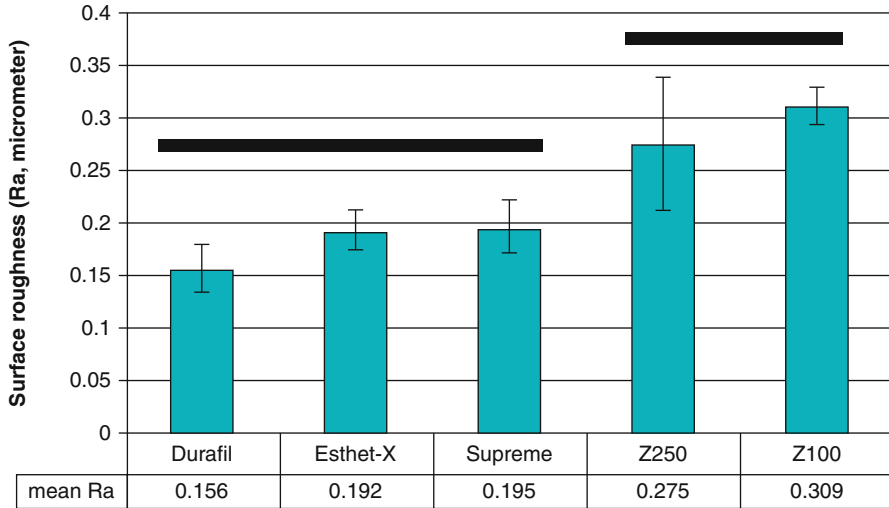
Fig. 43.32 Surface roughness of the resin composites. Microfill (Durafill), Nanofill (Supreme), Microhybrid (Z100, Z250, Esthet-X) Resin composites or polishing systems with the same *black bar* are not statistically different (From da Costa [18])

among the newer generations of nanocomposites, nanofilled Filtek Supreme (3 M ESPE, St. Paul, MN) composites exhibited the least roughness after polishing even though AFM showed that dislodgement of the whole nanoclusters was possible but is localized in certain regions shown in Fig. 43.33 [20].

(b) *Initial Gloss*: Diffuse reflectance decreases with composites filled with smaller particles, and surfaces appear glossier [147, 148].

Da Costa et al. demonstrated that after polishing, nanofill (Filtek Supreme) maintained surface gloss with most polishing systems as the microfill (Durafill) did, but the former presented a decline in gloss with few polishing techniques perhaps attributed to the pluck out of nanoclusters [149]. The nanohybrid (Premise) did not significantly show better luster than the microhybrid (Esthet X and Z250) in most situations, Table 43.7 [149]. Nevertheless, all composites are within clinically acceptable range.

(ii) *Wear Resistance*: Microfills incorporating nanosized fillers <0.1 μm showed good resistance to wear as described earlier; therefore, it was hypothesized that increasing the levels of submicron fillers would increase wear resistance in contemporary nanocomposites. Nanoclusters provide nanocomposites with adequate wear resistance. Unlike glass particles that completely exfoliate, they partially shear off as the nanosized particles that make up the cluster break apart, thus protecting the resin in between. Turssi et al. concluded that nanofill (Supreme) containing nanoclusters performed similarly to microfill

Table 43.6 Mean surface roughness of different composites after exposure to (a) mylar matrix, (b) polished with abrasive disk, (c) polished with silicone bur, (d) toothbrush abrasion (Adapted from Senawongse [145])

Mean surface roughness (μm) and standard deviations (S.D.) of resin composites				
Resin composite	Under mylar strip/matrix	Abrasive disc	Silicone bur	Tooth brushing
Microhybrids				
Clearfil AP-X	0.022 (0.005)[a]	0.145 (0.025)[f]	0.103 (0.049)[e]	0.299 (0.116)[i]
tetric ceram filtek	0.024 (0.003)[a,b,c]	0.065 (0.015)[b,c,d,e]	0.054 (0.013)[a,b,c,d]	0.235 (0.074)[h]
Z250	0.017 (0.002)[a]	0.105 (0.027)[e]	0.040 (0.012)[a,b,c]	0.148 (0.010)[f]
Nanofills				
Filtek Z350	0.017 (0.003)[a]	0.020 (0.003)[a,b]	0.020 (0.003)[a,b]	0.051 (0.009)[a,b,c,d]
Filtek supreme XT (dentin shade)	0.016 (0.003)[a]	0.038 (0.017)[a,b,c]	0.038 (0.009)[a,b,c]	0.052 (0.016)[a,b,c,d]
Filtek supreme XT (transparent shade)	0.020 (0.04)[a,b]	0.029 (0.005)[a,b,c]	0.038 (0.006)[a,b,c]	0.183 (0.081)[f,g]
Esthelite sigma	0.021(0.002)[a,b]	0.054 (0.009)[a,b,c,d]	0.049 (0.041)[a,b,c,d]	0.369 (0.115)[j]
Nanohybrids				
Tetric evo ceram	0.029 (0.009)[a,b,c]	0.051 (0.013)[a,b,c,d]	0.085 (0.017)[d,e]	0.428 (0.071)[k]
Ceram X	0.018 (0.003)[a]	0.069 (0.012)[c,d,e]	0.088 (0.010)[d,e]	0.411 (0.031)[k]
Premise	0.026 (0.003)[a,b,c]	0.057 (0.014)[a,b,c,d]	0.035 (0.009)[a,b,c]	0.207 (0.057)[g,h]

Same superscript letters demonstrate no significant differences between the groups

(Heliomolar) regarding abrasive wear resistance, with no significant improvement over the latter, Table 43.8 [150]. These findings were corroborated by another study which showed a significant improvement in wear resistance over microhybrids [151].

Nevertheless, conflicting results were observed when in vitro wear behavior of nanohybrid composite was compared to that of microfill. Some nanohybrids presented with a significant reduction in wear resistance which was attributed to detachment of large glass particles (Grandio, VOCO, Sunnyside, NY) during wear, leaving more resin exposed. Others have very minute nanoparticles that did not provide any load support and were abraded easily by irregularities in the opposing cusps (CeramX). Some nanohybrids with narrower distribution of particle size (<1 μm) have shown adequate wear resistance (Premise) comparable to microfill (Heliomolar) and nanofill (Supreme) [150, 151].

(a) *Surface Roughness*: SEM images in attrition sites, Fig. 43.34, displayed nanofilled composite (image b) with a lower surface roughness than microfill (Heliomolar) [150]. This smoother surface is due to presintered nanoclusters which did not result in stress fractures or particle plucking. This may be due to micromechanical interlocking of the resin penetrating within the sintered agglomerated structures. Heliomolar (image e) showed the highest roughness when compared with other nanofilled, nanohybrid, and microhybrid composites especially in attrition zones due to the
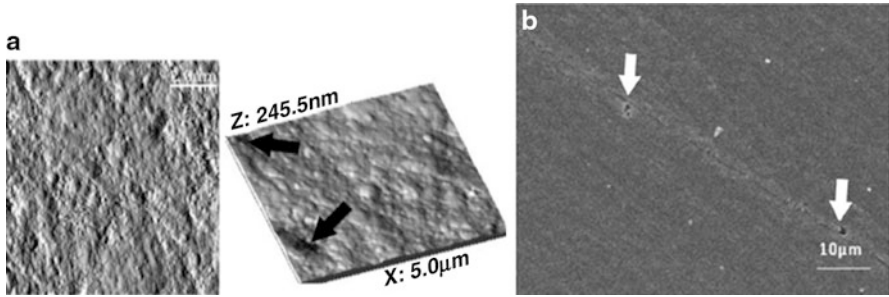
Fig. 43.33 (**a**) AFM image of a nanofilled composite with *black arrows* showing few plucked out nanoclusters. (**b**) SEM image nanofilled composite with *white arrows* indicating voids *left* by plucked out fillers (From Janus [20])

Table 43.7 Average gloss values for microfill (Durafill) nanofill (Filtek Supreme), microhybrid (Z250, Esthet-X) and nanohybrid (Premise) after finishing/polishing with three systems (Enhance Flex NST Sof-lex and Super-Snap) (Adapted from da Costa [149])

Average Gloss values (GU) and standard deviation (S.D.) for five resin composite material and three finishing and polishing systems

Resin/polishing systems	Enhance flex NST	Sof-lex	Super-snap
Filtek supreme	44.57[b/C] (1.04)	63.6[a/A] (1.43)	64.22[a/A] (1.08)
Durafil	65[a/A] (2.5)	58.02[a/A] (2.4)	58.62[a/A] (2.86)
Premise	57.57[b/AB] (0.75)	60.96[a,b/A] (1.24)	65.60[a/A] (1.0)
Z250	51.38[b/B] (2.17)	57.0[a,b/A] (0.84)	62.60[a/A] (1.61)
Esthet-X	58.76[a/AB] (0.94)	61.82[a/A] (1.20)	62.47[a/A] (1.22)

Values with same superscript are not significantly different. Lowercase superscripts refer to the rows (polishing systems within composites). Uppercase superscripts refer to the columns (composite within polishing system)

Table 43.8 Means for volumetric loss, flexural strength, and flexural fatigue limit for nanofill (supreme), microfill (heliomolar) and nanohybrids (premise, grandio, ceram-X-mono) (Adopted from Turssi [150])

Means and standard deviations (S.D.) of volumetric loss, flexural strength and flexural fatigue limit

Composite material	Volumetric loss (mm^3)	Flexural strength (MPa)	Flexural fatigue limit (MPa)
Supreme	0.398 (0.152)[a]	116.5 (12.0)[ab]	49.6 (3.8)[a]
Premise	0.550 (0.233)[a]	101.9 (10.2)[bc]	43.4 (6.9)[b]
Heliomolar	0.593 (0.220)[a]	91.9 (11.3)[c]	52.7 (1.0)[a]
Grandio	0.900 (0.242)[b]	120.9 (12.2)[a]	52.6 (7.4)[a]
Ceram-X-mono	1.628 (0.240)[c]	98.0 (12.1)[c]	43.6 (3.9)[b]

Means indicated by different letters are significantly different
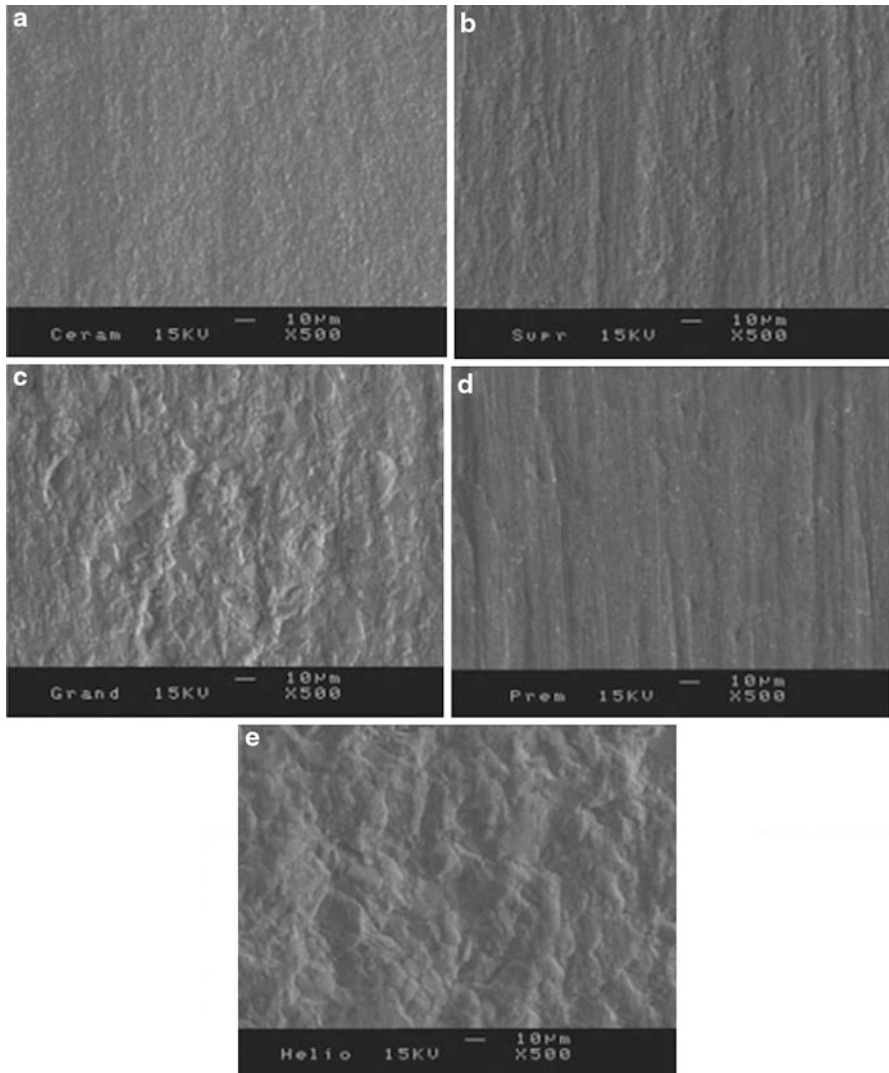
Fig. 43.34 SEM micrographs of the worn surface (attrition region) of the composites tested: (**a**) Ceram-X mono, (**b**) Filtek Supreme, (**c**) Grandio, (**d**) Premise and (**e**) Heliomolar (From Turssi [150])

"pluck out" effect of the prepolymerized resin filler at the resin matrix interface (PPRF) [150, 151]. Moreover, they possess a low filler loading capacity.

In attrition regions, Fig. 43.34, nanohybrids with large particles (image c) show high surface roughness due to their debonding, and the ones with nanomeric size (image a) had smoother surfaces, whereas nanohybrids that contain PPFR revealed intermediate surface irregularities (image d) [150].

Fig. 43.35 Gloss values after 400,000 cycles of generalized wear simulation for different composite resin materials (From Lee [36])
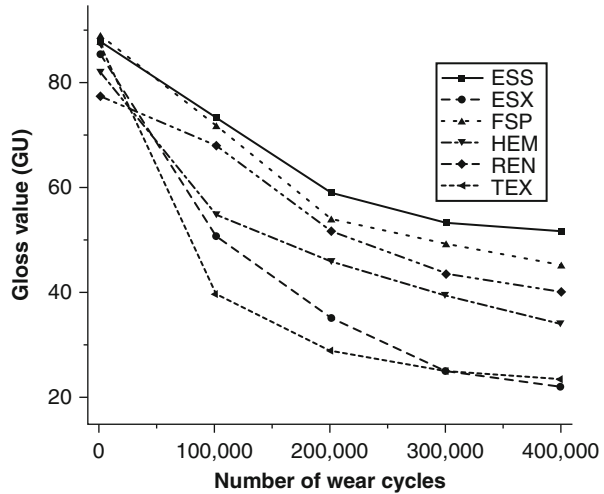
(b) *Gloss Retention*: Lee 2005 observed that gloss decreased significantly among all studied composites after 400,000 cycles of generalized wear simulation which correlated with 3 years of in vivo wear behavior [36]. Although the gloss values at baseline were similar for all 6 composite resins (77.3–88.7 GU), the post-wear simulation values differed visually by composite resin (22.1–51.5 GU). This study concluded that composite with submicron spherical particles (ESS(<0.2 μm)) produced the glossiest surface because they reflected more light than irregular particles, while nanofill (FSP) and microfill (HEM, REN) showed the least change in gloss over microhybrid composites (TEX, ESX) that had larger filler particles after 400,000 cycles of generalized wear testing, Fig. 43.35 [36]. Similar results were reported by da Costa (2007) [18].

(iii) *Optical Properties*: Recently, filler particles of sizes between 5 and 100 nm are being manufactured [141]. Because these filler sizes are below the wavelengths (380–780 nm) of visible light, nanofilled composites provide favorable translucency, polishability, and surface-gloss retention [41, 152, 153]. It has also been reported that nanomeric particles, such as found in Filtek Supreme Translucent (FST) with average sizes between 20 and 75 nm (below the wavelengths of visible light), allow these materials to exhibit high translucency [133]. This is a desirable feature to mimic the translucency of enamel during composite layering clinical procedures. Conventional hybrid composites often contain filler particles which range in size from 8,000 to 30,000 nm which exhibit a mismatch in the refractive index when compared to the resin matrix. These large filler particles will scatter the light, resulting in an unavoidable reduction in translucency. The translucency of FST exceeded that of microfill which has always been known to possess adequate optical characteristics, Fig. 43.36 [133].

Fig. 43.36 Optical effect of nanocomposite material (FST) versus that of the other types of composite materials (From Mitra [133])

Visual Opacity of Nanocomposite

Hybrid		Microfill		FST	
0	11.7	22.3	11.9	22.6	100
100	88.3	77.7	88.1	77.4	0
.3 (0.1)	87.4 (0.1)	93.3 (0.1)	94.6 (0.2)	94.5 (0.3)	96.8 (0.

(iv) *Resistance to Toothbrush Abrasion*

    (a) *Surface Roughness*: Nanofilled composites showed the highest retention of smoothness after toothbrush abrasion due to the presence of the nanoclusters [54, 145] (not reaching roughness threshold) [145], whereas irregularly shaped particles present in nanohybrid composites did not maintain smoothness. Senawongse et al. found that nanohybrids demonstrated higher roughness levels >0.2 μm after toothbrush abrasion. This might have been due to the pluck out of prepolymerized resin fillers incorporated in some nanohybrids [145]. Nanohybrids like Premise contain a narrower size distribution of fillers with average filler size of 0.4–0.6 μm which would reflect a smooth surface close to that of nanofill, while nanohybrids, which have a broader distribution, have higher R_a values. SEM micrographs showed dislodgement of PPRF from some nanohybrids, which might explain the significant increase in roughness [145].

    (b) *Gloss Retention*: Nanofilled composites such as Filtek Supreme Standard and Filtek Supreme Translucent with higher levels of nanomeric structures, and zirconia–silica nanoclusters were shown to provide better gloss rentention than hybrid and microfilled composites after 500 cycles of tooth abrasion, Fig. 43.37 [133].

(v) *Depth of Cure*: Filler particles have been shown to scatter the curing light [154]. Light penetration would not be significantly affected for the nanofill composite, because the particles are too small to scatter the light. However, in a recent study, the agglomerated nanofillers present in nanofilled composites (Filtek Supreme) exhibited a high surface area approaching wavelength of the curing light, thus maximizing scattering and explaining the decrease of depth of cure (DC) at the full depth of the cavity (roughly 2 mm) [155]. The microhybrid composite (Z250) proved to be homogeneously cured at 2 mm thickness, presenting only a slightly lower DC at the bottom surface, but not enough to significantly reduce its hardness, Table 43.9 [155].

(vi) *Slumping Resistance*: Figure 43.38 shows, among the three tested composites, that the nanofill (Z350) exhibited the highest slumping resistance (SR) due to its high viscous modulus as the SR is correlated to viscosity [11]. The high slumping resistance index (SRI) was related to the unique mix of 20 nm silica nanoparticles and agglomerated nanoclusters, which are 0.6–1.4 μm in size, not available in the other two studied hybrid composites [11].
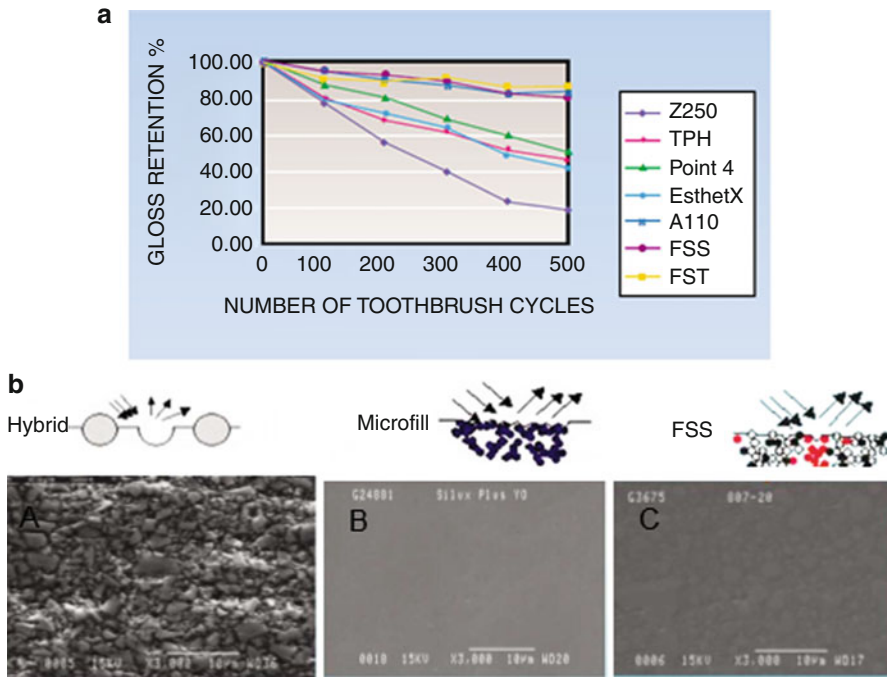
Fig. 43.37 (**a**) Gloss retention of nanocomposites (*FSS* Filtek Supreme Standard, *FST* Filtek Supreme Translucent) as compared with other composites Microhybrid (Z250: Filtek Z250,TPH: TPH Spectrum, Point 4: Point 4 EsthetX: EsthetX). Microfill (A110): Filtek A110. (**b**) SEM images of toothbrush-abraded surfaces of restorative dental composites. A Hybrid. B Microfill. C FSS (nanofill) (From Mitra [133])

Mechanical Properties of Nanostructured Composites

Contemporary nanocomposite resins exhibit mechanical properties comparable to universal hybrids [145, 155]. They were shown to exhibit adequate strength and stiffness to withstand loading and thus were indicated for posterior restorations.

(a) *Elastic modulus* is a measure of stiffness. Dental restorative materials must withstand masticatory forces in the oral cavity. The elastic moduli play a major role in the longevity of the restoration. A composite with low modulus deforms more than the tooth structure under functional forces. Eventually, the tooth likely suffers a catastrophic fracture or fail at the restoration–tooth bond interface. Additionally, a high elastic modulus is required to withstand cuspal strain resulting from the polymerization process [156]. The elastic modulus of most posterior composites is lower than the elastic modulus of dental tissues (enamel, 94GPa; dentin, 19GPa), which makes them less satisfactory to be used as posterior restorative materials. Material selection for restoring posterior teeth (molars and premolars) does not depend on elastic modulus alone. Other physical and mechanical properties such as strength, resistance to wear and

Table 43.9 Values for hardness and degree of conversion for a nanofill (filtelk supreme) and a microhybrid (Filtek 250) (Adapted From Rodrigues [155])

Mean (S.D.) values for hardness (H) and degree of conversion (DC) of the top and bottom surfaces, and statistical groupings				
	Filtek Z250™		Filtek supreme™	
	Top	Bottom	Top	Bottom
H (MPa)	6.4 (0.2)a	5.7 (0.3)b	5.9 (0.2)b	4.4 (0.1)c
DC (%)	46.8 (2.8)a	44.2 (5.3)a	46.6 (2.8)a	38 (2.3)b

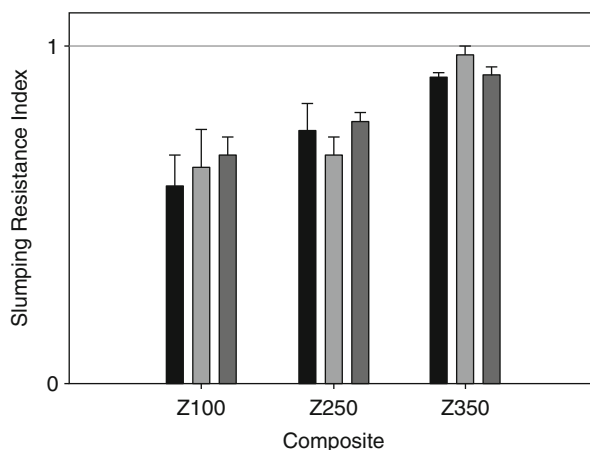Same letters in the same line indicate no statistical differences between groups

Fig. 43.38 Slumping resistance index (SRI) of nanofill (Z350) and two hybrid sustems (Z100 and Z250) (From Lee [11])

chemical stability to water sorption and enzymatic degradation, and esthetics should also be considered.

The nanosized filler-containing composites exhibit different elastic properties among them, and this implies that filler size is not the only parameter that affects the elastic behavior of dental composites. Some materials exhibit higher modulus than others most likely because of compositional differences, such as variations in filler loading, the type of resin component in each material, quality of silane coupling agent, and degree of cure. Previous studies reported that the filler loading has more impact on elastic modulus [157, 158]. For example, within the tested nanohybrid group, Grandio had the highest filler load of 71.4 % by volume and therefore showed the highest elastic modulus close to that of dentin. The dynamic and static elastic modulus of nanohybrid (Grandio) and nanofill (Supreme) superseded some microhybrids. Microfilled composites showed the least elastic modulus, Fig. 43.39 [138]. The high rigidity renders nanocomposites suitable for posterior composites.

(b) *Hardness (H)* is the resistance of a material to indentation or penetration described in microhardness (Knoop or Vickers) or nanohardness values. It is
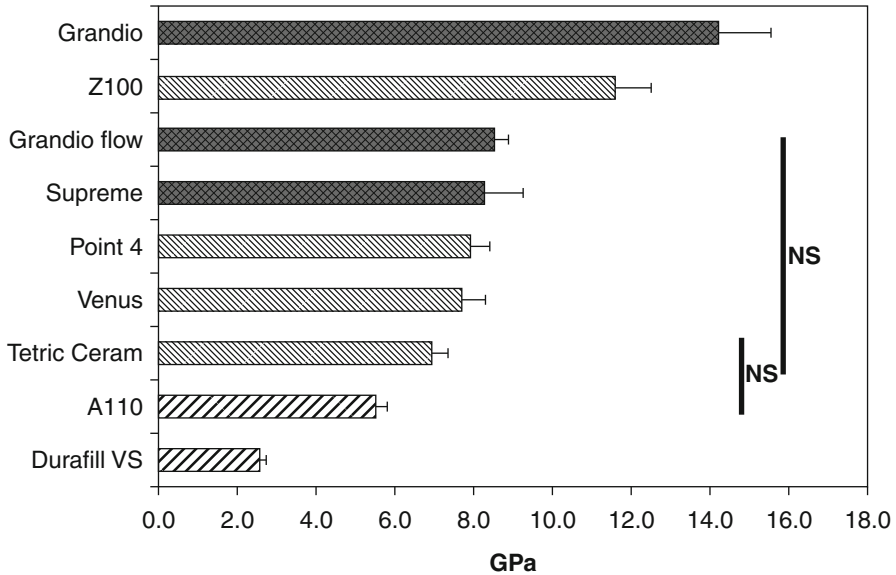
Fig. 43.39 Static moduli of elasticity of the composite materials: Nanohybrid (Grandio, Grandio flow), Nanofill (Supreme), Microhybrid (Point 4, Venus, Tetric Ceram), Microfill (A110, Durafill VS) *Vertical bars* connect materials that are not statistically significant (From Buen [138])

usually associated with the depth of polymerization [159]. Additionally, studies found a correlation between the filler loading and the hardness values [38, 160]. Microfill composites showed the least hardness values due to lower filler loading, while hybrids (microhybrids and nanohybrids) showed higher values due to greater filler levels. Among the hybrids, some nanohybrids performed better than others in regard to hardness when compared to microhybrids due to variability in parameters such as packing capacity, resin formulation, and degree of conversion.

As for nanofill composites when compared to microhybrids (Filtek Z250), the latter exhibited higher filler wt % (78.5 %) than the nanofill (73.2 %), which might explain its higher *H* values [155] as shown in Table 43.9.

(c) *Flexural strength* of nanocomposites whether nanofilled (Supreme) or nanohybrid (Grandio, Grandio Flow) demonstrated a significant improvement in flexural strength over microfilled composites (A110, Durafill VS) which had the poorest mechanical properties and was comparable to other hybrids (Point 4, Tetric Ceram, Z100) used for posterior composite restorations as seen Fig. 43.40 [138]. Some hybrid composites that incorporated filler less than 1 μm showed mechanical properties very similar to conventional hybrids. Nanohybrids with spherical particles <1 μm showed high flexural strengths. A spherical shape found in Point 4 and Supreme does not only allow an increased filler load in composites [161] but also enhances their fracture
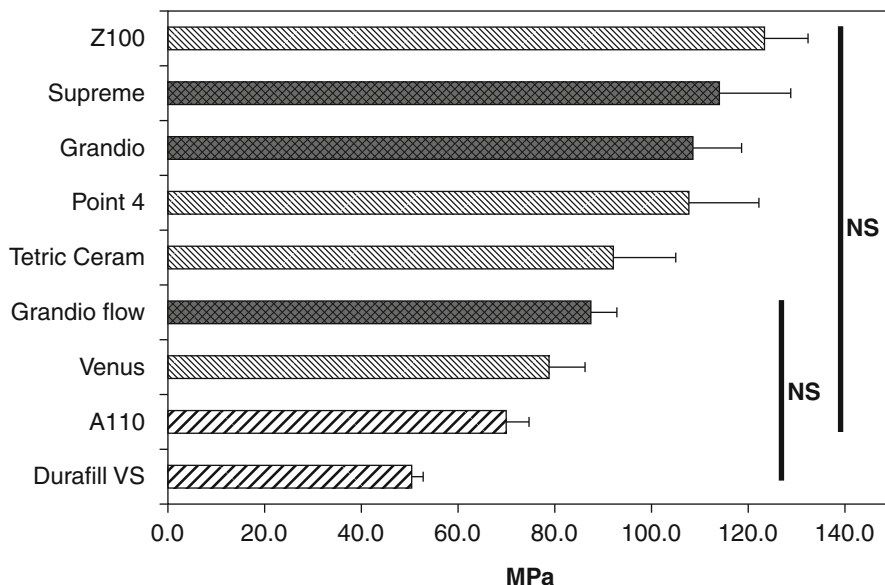
Fig. 43.40 Flexural strength of the materials tested: Nanohybrid (Grandio, Grandio flow), Nanofill (Supreme), Microhybrid (Point 4, Venus, Tetric Ceram), Microfill (A110, Durafill VS). *Vertical bars* connect materials that are not statistically significant (From Buen [138])

strength since mechanical stresses tend to concentrate on the corners of the filler particles [162].

(d) *Fracture toughness (K_{Ic})* is a measure of a material's ability to resist crack propagation from an existing flaw which correlates to intraoral chipping and marginal breakdown [163]. Several reports observed a significant improvement of K_{Ic} by increasing the filler volume [92, 164, 165] but to a level where they do not act as defect points. The presence of a closely spaced disperse phase in a brittle material like composites may increase both its fracture strength σ_f and fracture energy because filler particles act as crack deflectors during crack propagation [166]. Studies revealed a significantly higher K_{Ic} for commercial hybrid composites in comparison to microfill composites, the latter having a lower filler content [38, 167].

Rodrigues et al. found that nanofill (Filtek Supreme: SU) composite exhibited similar results for the σ_f and K_{Ic} to that of microhybrid (Filtek Z250: Z2) composites which might be the result of the relatively high filler content in both composites shown in Table 43.10 [155]. The disperse phase of both composites is composed of spherical-shaped particles which might have contributed to the similar fracture behavior of both composites. Spherical-shaped particles are associated not only with a higher filler levels but also with a reduction of stress concentration typically found in angles, corners, and protuberances of irregular-shaped filler particles, thus improving the fracture behavior of the material [145, 168]. The average values of critical defect size distribution (m) are similar for both composites, reflecting similar K_{Ic} for both composites.

Table 43.10 Summary of mean values of flexural strength, weibull modulus, characteristic strength, critical crack size, fracture toughness, measured either by fractography analysis (FA) or by the single edge notch beam (SENB) method for a microhybrid (Z2) and a nanofill (SU) (Adapted from Rodrigues [155])

Mean (S.O.) for flexural strength (σ_f), weibull modulus and standard error, characteristic strength (σ_0) and standard error, fracture toughness (K_{IC}) measured by FA and SENB, critical crack size (c) and fracture origins for tested composites

Material	σ_f (MPa)	m	σ_0 (MPa)	K_{IC} FA (Mpa$^{0.5}$)[a]	K_{IC} SENB (Mpa m$^{0.5}$)a	c (μm)	Fracture origin (%)[b]
Z2 (microhybrid)	140.7 (19.9)	7.6 (1.3)	149.5 (3.8)	1.5 (0.4)A a (25)	1.5 (2.2)A a (15.4)	68 (34)	SF (93); IF (7)
SU (nanofill)	135.7 (15.3)	9.7 (1.5)	142.5 (2.8)	1.5 (0.5)A a (30.7)	1.3 (0.02)A b (1.9)	76 (38)	SF (93); IF (3)

Capital letters refer to statistical groupings in the line, and small letters refer to statistical groupings in the column. Different letters indicate statistical differences between groups
[a]Values in brackets are the coefficient of variation (CV)
[b]SF: surface flaw; IF: internal flaw

Furthermore, in a recent study, the agglomerated nanocluster-type filler in Filtek Supreme identified different mechanical properties compared with fused spheroidal fillers and particles with an irregular morphology. Upon loading to failure the nanocluster provided distinct multiple fractures which may enhance tolerance to local dresses and cluster deformation providing reinforcement to the resin matrix as seen in Fig. 43.41 [169]. The incorporation of nanocluster filler into the resin matrix of the nanofilled systems may alter the failure mechanisms due to the infiltration of the silane coupling agent around and within the minute gaps of the agglomerated structure producing an interpenetrating composite [169].

Dental Adhesive Systems

Introduction

Adhesive systems are utilized with dental composite resin to facilitate bonding to tooth structure (enamel and dentin). An adequate adhesive resin–tooth structure bond will withstand the generated stresses during polymerization of composite resin at the adhesive interface and minimize the drawbacks of these deleterious forces as described earlier. Ever since it has been reported that the physical and mechanical properties of dental resin composites increase with an increase in filler content [39, 170], researchers experimented raising filler loading of adhesive systems as well in an attempt to enhance their physical and mechanical properties. Commercial adhesives are applied by several strategies as shown in Table 43.11.

Application of Bonding Agent
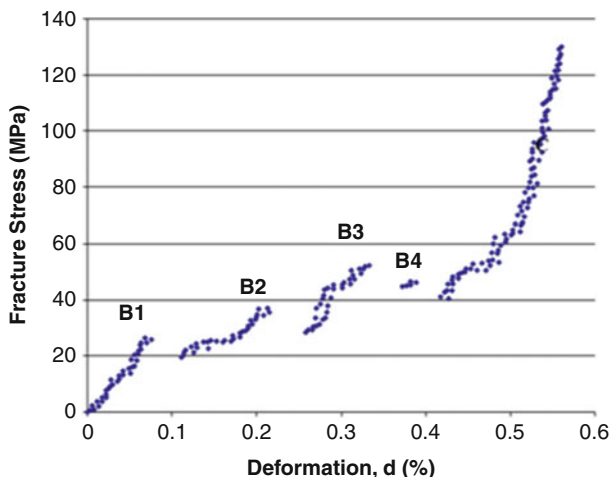As a gold standard dentists should follow the manufacturer's application protocol. The following are general steps:

Fig. 43.41 Stress deformation curves showing multiple distinct fractures during loading to failure of Nanofill (Filltek Supreme Body FSB) "nanocluster". Curves labeled 'B1' corresponds to the first fracture and 'B2–4' related to further fractures of the particle or cluster (From Curtis [169])

Table 43.11 Various strategies for different dental adhesive agents

Different adhasion technIques	
Etch and rinse	*3-step or multibottle*: *etchant + primer + adhesive*
	2-step: *etchant + (primer and adhesive in 1 bottle)*
Self-etching	*2-step*: *acidic primer + adhesive*
	All-in-one: (*etchant, primer, adhesive in one bottle*)

1. Before dental composite resin is inserted, the cavity walls are acid etched/conditioned with 37 % phosphoric acid or acidic primer. This will demineralize the enamel/dentin exposing collagenous network as shown in Fig. 43.42 [171].
2. Then copious air–water is sprayed for 15–20 s to remove the irritant etchant. In self-etching technique, steps 2, 3, and 4 are skipped.
3. Next the cavity is dried with light stream of air or blotted gently. Excessive drying is not recommended since it will collapse the extended collagen network, limiting wetting and compromising the interfacial bond and marginal integrity of resin composites.
4. Since dried dentin will still contain around 20 % water, a primer, an integral component of the adhesive system, that acts as a hydrophilic agent (usually 2-hydroxyethylmethacrylate – HEMA) is applied to provide a low contact angle and reduce surface tension between adhesive and dentin.
5. This is followed by adhesive resin application if they (primer and adhesive) are in separate bottles, lightly air-dried. Finally resin is photo cured for 10 s.
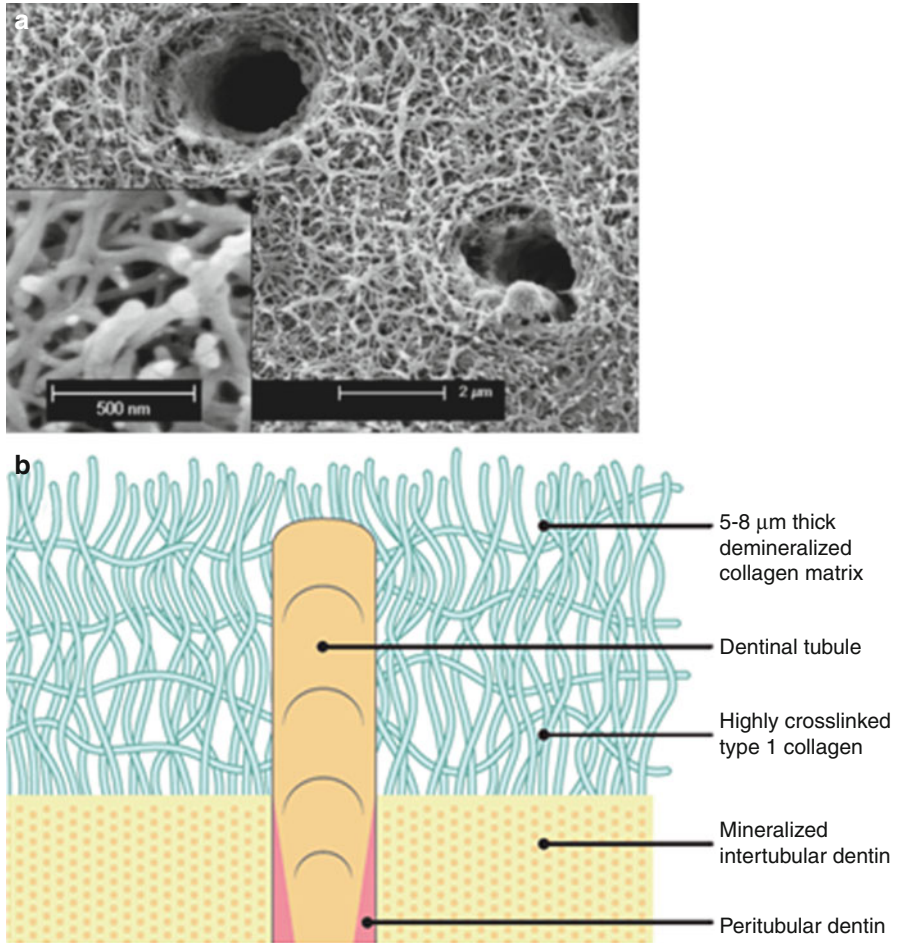
Fig. 43.42 (**a**) Scanning electron micrograph of acid-etched dentin showing two dentinal tubules containing remnants of peritubular dentin matrix. High magnification of branching collagen fibrils (75 nm in diameter) separated by interfibrillar spaces that serve as channels for resin infiltrations during bonding. (**b**) Simplified illustration of demineralized dentin created by an etch-and-rinse adhesive leaving collagen fibrils exposed to form a hybrid layer. A dentinal tubule is shown to illustrate its presence (Adapted from Pashley [171])

Mechanism of Bonding

Current adhesive systems that use Etch and Rinse or the self-etching approach characteristically bond by the formation of a *hybrid layer*. The hybrid layer is a bicomposite layer composed of resin tags micromechanically interlocked within collagen fibrils producing resin-impregnated dentin. After dentin conditioning with 37 % phosphoric acid, intertubular dentin decalcifies up to a 3–5 μm thickness apically, leaving nanoscale porosities with a size ~12.1 and 19.8 nm after applying solvent (water/ethanol available in the adhesive bottle) [172, 173]. Resin monomers

interpenetrate the submicron spaces within the collagen fibrils of the etched dentin, envelope, and entangle the fibrils after the resin polymerizes, Fig. 43.43. Adequate resin–dentin bond is crucial for long-term stability of composite restoration. To achieve a strong bond, adequate wetting of the dentin substrate by the adhesive agent is warranted.

Bond Strength of Hybrid Layer

Etching demineralizes dentin and depletes hydroxyapatite crystals, leading to a reduction in dentin's tensile properties [175]. However, resin infiltration into the demineralized collagen network helps to regain and even improve the strength of the mineral-depleted dentin by formation of strong hybrid layer [176]. Nevertheless, over time the hybrid layer undergoes hydrolytic degradation due to water sorption and degradation of insoluble collagen fibrils by matrix metalloproteinases (MMP). This results in less retention between the resin tags and the collagen network, leading to a dramatic mechanical decrease in microtensile bond strength (μTBS). Interfacial debonding and marginal failure are also likely to occur if the values of polymerization stresses exceed the adhesive bond strength. This will result in deleterious effects of microleakage, postoperative sensitivity, pulpal irritation, and secondary caries which were early drawbacks of adhesive systems of dental resin composites. Since then research to eliminate water and/or ethanol in primer and adhesive bottles to create solvent-free adhesives and to incorporate fillers had been launched to improve the long-term use and durability of adhesive systems.

Fillers in Dental Adhesives

Improving the bond strength of adhesive agents by adding fillers is one of several ways to improve interfacial bond strength between the composite resin and dentin [177]. To obtain an optimal increase in bond strength is multifactorial where size, shape, filler loading, and the filler surface properties are all considered. Traditional adhesive systems were filler-free materials unlike the composite resin restoration which by definition always contained fillers. Currently, there are numerous reasons to add filler particles to the dental adhesive resins. The low tensile strength and low elastic modulus of unfilled adhesives act as a weak junction between the overlying composite resin and the mineralized dentin underneath. Although adding fillers was thought to reinforce the adhesive layer, the filler loading capacity of the adhesive is not as high as in composite resins because a highly viscous resin would prevent interdiffusion into interfibrillar gaps. Furthermore, fillers would increase the adhesive layer thickness even after air thinning [178]. Appropriate thickness of adhesives is recommended to ensure complete polymerization of the resin adhesive; a thin adhesive layer may lack complete polymerization because of the oxygen inhibition effect. Due to its low elastic modulus, adhesive layer possesses a stress-absorbing potential and high strain capacity to relieve the contraction
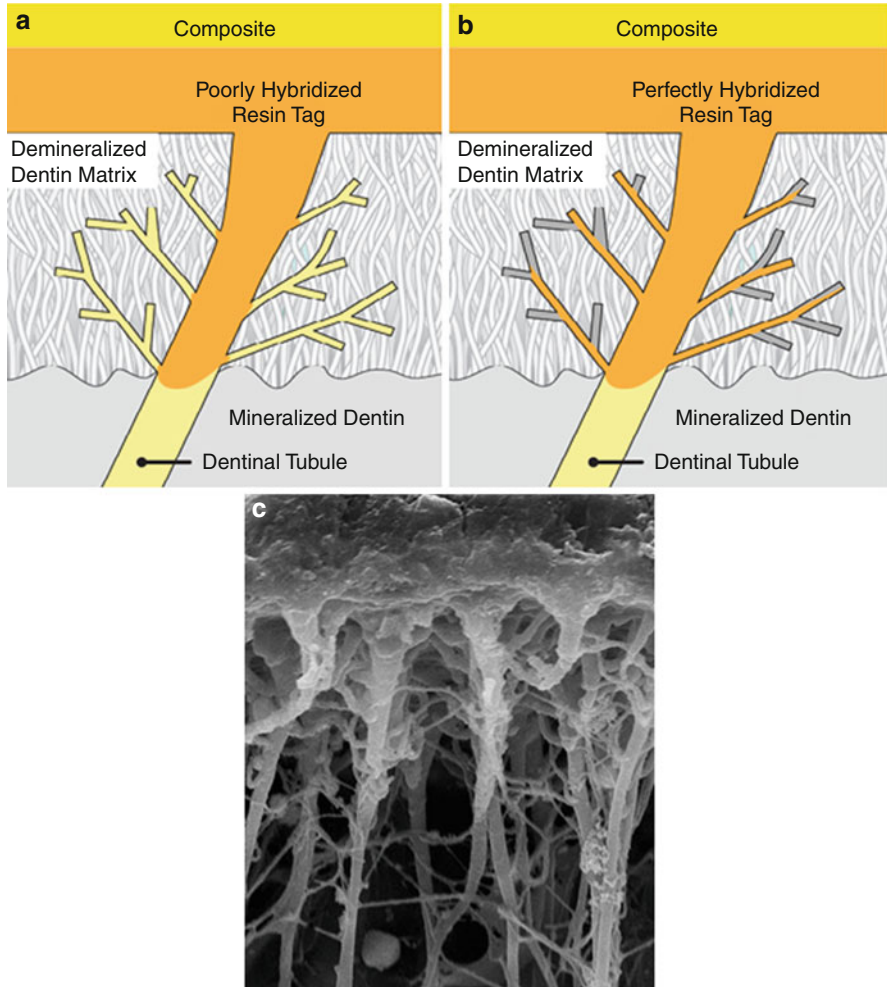
Fig. 43.43 Schematic diagram of (**a**) Poor hybridization of resin tags in etched dentin saturated with water; the resin could not displace water in the lateral tubules of tubules in the hybrid layer. (**b**) Optimal hybridization of resin tags in etched dentin saturated with ethanol; the resin dissolved the ethanol in lateral branches (Reproduced from Sauro et al. [174]) (**c**) SEM image of a perfectly hybridized layer (Courtesy of David Lafuente, DDS, MS, School of Dentistry, University of Costa Rica with permission)

stresses developed during composite resin polymerization [179]; thicker layers absorb greater stresses [180]. Moreover, specific silicate glasses may provide fluoride-releasing properties for remineralization (fluoro-alumino silicate); others would serve as radiopacifiers for differential diagnosis with secondary caries under an old-standing restoration as necessary.

Fig. 43.44 TEM micrograph of the resindentin interface of Prime and bond group. Electrondense nanofillers are concentrated at the adhesive (A) layer and around the tubular orifice (*arrow*) and could also be seen in this dentinal tubule (T), Absence of nanofillers from the hybrid layer (H) is evident. U: unaltered dentin demineralized (From Tay [176])
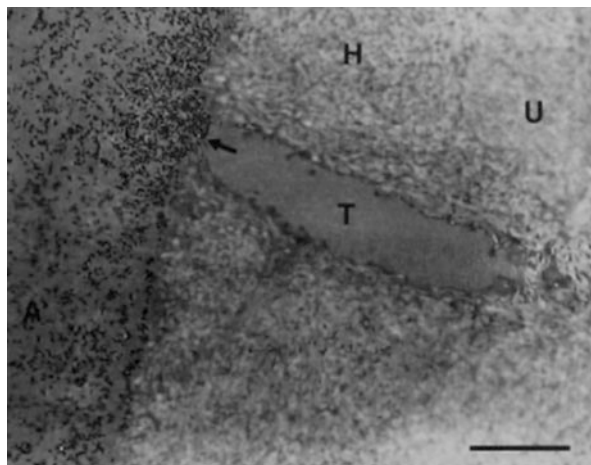
Nanofillers in Dental Adhesive Systems

Since the filler size is critical to the wetting properties of the adhesive resins, most proprietary adhesive systems contain pure silicon dioxide either colloidal silica or pyrogenic silica. Early attempts to increase bond quality and efficacy were by incorporation of micrometric particles of silica in bonding agents. But the filler particles did not penetrate the hybrid layer [181] but rather accumulate around the boundaries of either the adhesive or the tubular layer. Although it acted as a shock-absorbing layer between the hybrid layer and the composite, this reinforced polymer layer did not play a role in enhancing the bond strength.

Developments have been recently introduced in dental adhesive systems to incorporate nanometric silica fillers to form particle-reinforced hybrid layer and resin tags, improving mechanical properties particularly bond strength. For instance, an innovative Prime & Bond NT by DENTSPLY incorporated 7 nm fumed silica fillers, but transmission electron microscopy (TEM) postulated that nanofillers were congested at the dentinal tubule orifices and within the adhesive layer and did not impregnate the collagen network. This was indicative that primary particles have the tendency to accumulate and form micrometric clusters which are too big to infiltrate the collagen mesh, Fig. 43.44 [176]. It has been suggested that the residual solvent existing within the dentin (5 vol.% water or ethanol) [182, 183] will produce filler aggregation. In order to avoid clustering, the nanofillers have to be physically and chemically stabilized by surface treatments.

Recently, Adper Single Bond 2 commercial adhesive system with 5 nm silanated nanosilica was introduced. Recent work showed microtensile strength statistically highest in the group with the 5 nm fillers compared to the other groups as shown in Table 43.12 [184]. SEM displayed the same group of nanofillers that impregnated the hybrid layer as seen in Fig. 43.45 [184].

Table 43.12 Mean values for microtensile bond strength (μTBS) and standard deviations (±SD) for different adhesives (Adapted from Di Hipólito [184])

Means for microtensile bond strength (μTBS) for four commercial adhesives				
Adhesive system	Adper single bond	OptiBond solo plus	Prime & bond NT	Adper single bond 2
Bond Strength (MPa)	$34.68 \pm 7.61b$	$33.33 \pm 5.64b$	$28.59 \pm 7.08b$	$42.64 \pm 11.44a$

Means indicated by different letters are significantly different
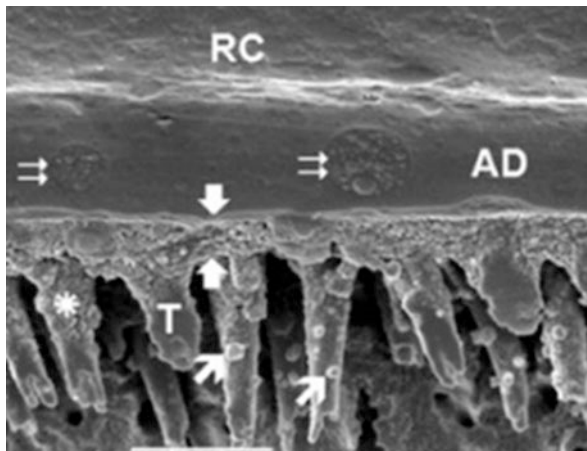
Fig. 43.45 SEM image showing the morphologic aspect of the bonding zone formed by the adhesive system Adper Single Bond 2 (SB2). Hybridization extended down to tubular walls at the initial portion of some resin tags (*asterisk*). The hybrid layer formed by Adper Single Bond 2 showed a atypical granular front, and round grains (*white arrows*) at the medium third of some resin tags indicating infiltration of nanofillers. Globular structures formed by the grouping of small "vesicles" of polyalkenoic acid (*double white arrows*), can be observed in the adhesive layer (AD) of SB2. RC: resin composite (From Di Hipólito [184])

Limitations of Nanofillers in Adhesives

1. The primary particles must be sufficiently stabilized to prevent them from aggregating during storage and/or application of the adhesive solution, forming "filler clusters" that are too large to infiltrate the interfibrillar spaces.
2. The difference in molecular weight between the nanofillers and the solvated resin monomer imparts different diffusion rate which may preclude complete infiltration of the nanofillers into demineralized dentin zone, even if the interfibrillar spaces are fully extended [185].
3. The interfibrillar spaces within the demineralized collagen network may contain a hydrogel of residual ground substance, proteoglycans, and noncollagenous proteins that may physically impede the infiltration of the nanofillers [186].

Surface Modification of Nanofillers

Chemical Stabilization: Zeta potential (ζ) is an electric charge of particles in colloidal systems when they are at an interface and in a "shear plane." If particles have a neutral zeta potential, they tend to cluster. Keeping the nanoparticles under a negative zeta potential to impose electrostatic repulsion forces between the surfaces could stabilize particles and prevent clustering. It was proven that solvent evaporation and temperature increase during polymerization and presence of residual water and/or ethanol will put nanofillers in a neutral zeta potential, thereby causing entanglement [187] as Fig. 43.46 shows [183]. Surface silanization is the most utilized method in dentistry to prevent the agglomeration of nanoparticles. Treating the particles with appropriate ratio of organosilanes and the replacement of 70 % of the surface silanol groups with siloxane groups will produce hydrophobic silica [188] and negatively charges the particles [189]. This allows for a uniform/homogenous dispersion of nanoparticles in the adhesive resin after polymerization. Hydrophobized silica has dimethylsilyl ($-Si-(CH_3)_2-$) and trimethylsilyl ($-Si-(CH_3)_3$) groups at the surface.

Hydrophilic Nanofillers

Most of the nanofillers used in the three-step Etch and Rinse adhesives are hydrophobic in nature because they are added to the adhesive bottle that has more hydrophobic monomers such as MMA. Conversely, in one-step self-etching adhesive system, both hydrophobic MMA and hydrophilic HEMA monomers are present in one bottle. Research studies incorporated hydrophilic silica nanofillers with Si–OH, hoping to disperse more homogeneously under wet conditions. Results showed that hydrophilic nanofillers did not achieve desirable results with respect to µTBS especially when filler loading increased to 3 % as seen in Table 43.13 [190]. Nanofiller content did not affect degree of conversion, and the flexural strength tended to increase with increasing nanofiller content. The MTBS appeared to increase when up to 1.0 wt% of the nanofillers were added, and the test groups were not statistically significant. When 3.0 wt% of the nanofillers were added, the MTBS decreased significantly. The hydrophilic silica seemed to form large clusters once applied to wet dentin, prohibiting a hybrid layer formation [190].

Future Research

Caries Preventive Nanocomposites: Secondary caries is the recurrence of tooth decay under existing restoration and is cited as the most frequent reason for the replacement of previous restorations [191]. More than half of the restorations placed annually are replacements which could cost about $5 billion/year in the USA alone [192]. The sustained release of fluoride (F) ions could be a substantial benefit for a dental restoration, because fluoride could enrich enamel or dentin to remineralize and enhance reprecipitation of calcium and phosphate. F-releasing restorative materials include glass ionomers, resin-modified glass ionomers, compomers, and resin composites [193–195]. However, the inferior mechanical
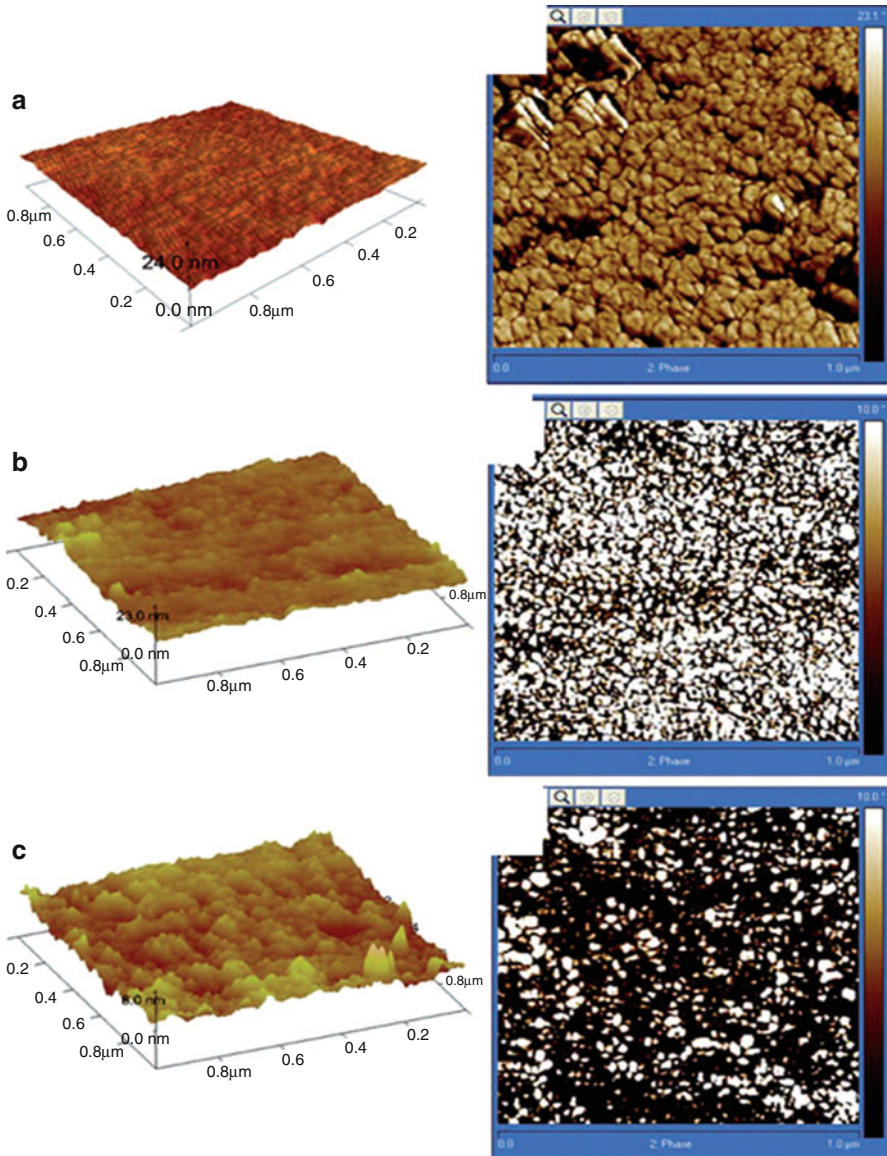
Fig. 43.46 AFM images (**a**) Solvent free adhesives. (**b**) Adhesive saturated with 5 % ethanol. (**c**) Adhesive saturated with 5 % water. The addition of solvents (water or ethanol) increases cluster formation whose size is above the measurements of the interfibrillar demineralized spaces (From Osorio [183])

properties of glass-ionomer and resin-modified glass-ionomer materials have limited their use [196]. A novel group of nanoparticles has been recently developed for caries prevention. CaPO$_4$- and CaF$_2$-containing nanocomposites yielded prolonged F-release and stress-bearing properties [197].

Table 43.13 Degree of conversion (DC) of a thin coating of the experimental adhesives, flexural strength (FS) of bulk specimens made from the solvent-removed experimental one-bottle adhesives and microtensile bond strength (MTBS) to the dentin with varying filler content (Adapted from Kim [190])

Degree of conversion (DC) of experimental adhesives, flexural strength (FS) of the solvent-removed bulk adhesives and the microtensile bond strength (MTBS) of the adhesives to wet occlusal dentin					
Filler content (wt %)	0	0.5	1.0	3.0	p Value
DC (%)	46.14 (7.73)	48.13 (5.85)	44.56 (9.69)	43.25 (11.02)	0.835
FS (MPa)	89.78 (6.21)[bc]	88.77 (3.87)[c]	96.35 (4.41)[a]	94.31 (4.51)[ab]	0.011
MTBS (MPa)	27.45 (6.86)[ab]	33.57 (10.42)[a]	29.51 (11.69)[ab]	23.88 (7.97)[b]	0.025

Means indicated by different letters are significantly different

Polyvinylsiloxane Impression Material: Alginate was one of the oldest dental materials that incorporated a high content of silica. In a recent study, polyvinylsiloxane, a dental impression material, was formulated with the variation of loading combination of six types of fillers including nanosized fumed silica. The test group in which a quarter of quartz was replaced with fumed silica showed the most ideal working and setting time for clinical use. Combining the fumed nanosilica was effective in increasing the viscosity, tensile strength, and maximum percentage of strain [198].

Bioactive Nanosilica: Silicon dioxide or silica (SiO_2) is a component of bioactive glasses and is found to have an apatite-forming ability in body fluid. The ability of silica to induce apatite formation has been evaluated. Hench proposed that a combination of high pH and repolymerizing SiO_2 from surface Si–OH groups was sufficient to induce CaO and P_2O_5 from body fluids and precipitate apatite layer [199]. Later, it was proposed that silica gel forms an essential step in the formation and mineralization of hard tissues; the abundant silanol groups (Si–OH) on the surface of silica gel are responsible for apatite formation [200]. It was found that crystalline hydroxyapatite was formed on/in nanosilica scaffolds after 7 and 14 days of biomineralization [201]. Most composite materials are used to produce specific strength, stiffness, or toughness properties that match the natural bone. The cortical bone has a wide range of mechanical properties (7–30 GPa Young's modulus, 50–150 MPa tensile strength, and 1–3 % elongation at fracture). Therefore, nanospheres can be dispersed throughout a continuous matrix to induce porosity and improve mechanical properties of a bulk scaffold for reinforcement and as drug delivery vehicles [202]. These scaffolds were also found to be highly biocompatible. They may also serve as excellent candidates for bone tissue regeneration and socket preservation after teeth extraction in periodontal surgeries.

Denture Teeth: An important physical property of denture teeth is wear resistance. Microfilled composite denture teeth have been used to overcome the shortcoming of porcelain [203] (brittleness, lack of retention to denture base, abrasion to opposing teeth) as well as PMMA denture teeth (low wear resistance). Although nanocomposite denture teeth did not show significant differences in wear resistance and hardness when compared to microfilled composite teeth and cross-linked acrylic teeth, they performed better when compared to conventional acrylic teeth [204]. Nanocomposite denture teeth could be promising due to the high impact resistance and antistaining feature [205].

Prophy Pastes and Surface Roughness: Nanoparticles in slurry pastes for polishing were investigated to smooth teeth specimens and to remove *Streptococcus mutans* bacterial attachments. Nanosilica polished the enamel surface, attaining nanometric levels of smoothness, which was found to achieve less R_a values than that of professional fine polishing pastes. The bacterial removal was easier from the surfaces polished with silica nanoparticles than rougher ones. Future research should focus on how would that smooth surface affect the remineralization process and the time frame for plaque to reform [206].

Summary

For the last five decades, dental composites have become more diverse materials with expanded range of functions, putting high expectations on the materials' properties and their clinical performance. Further research of these materials includes increase in mechanical properties such as strength and fracture resistance, reduction in polymerization shrinkage, novel adhesion strategies to tooth surfaces, the inclusion of cariostatic agents and remineralizing compounds, and a customized interaction with the changing pH in the oral environment, as in smart polymers.

Filler size and shape are only two of several parameters affecting the overall properties of composite resins. More investigations are needed to improve the quality and formulation of composites filled with experimental nanofillers to implement them in commercial composite resin systems. The development of nanosilica has made its way in several dental materials and has particularly led to significant improvements in clinical behavior of contemporary nanocomposites, becoming referred to as universal composites. Their use in large- or small-size cavities and as anterior or posterior restorations may facilitate the practitioner's selection of material.

References

1. Calderon Pdos S, Kogawa EM, Lauris JR et al (2006) The influence of gender and bruxism on the human maximum bite force. J Appl Oral Sci 14:448–453
2. Aguilar FG, Roberti Garcia Lda F, Cruvinel DR et al (2012) Color and opacity of composites protected with surface sealants and submitted to artificial accelerated aging. Eur J Dent 6:24–33
3. Schmeling M, DE Andrada MA, Maia HP et al (2012) Translucency of value resin composites used to replace enamel in stratified composite restoration techniques. J Esthet Restor Dent 24:53–58
4. Craig RG, Powers JM, Sakaguchi RL (2006) Chapter 9 Resin composite restorative materials. In: Craig's restorative dental materials, 12th edn. Mosby Elsevier, St Louis, pp 189–212
5. Ferracane JL (1995) Current trends in dental composites. Crit Rev Oral Biol Med 6:302–318
6. Ruyter IE (1982) Methacrylate-based polymeric dental materials: conversion and related properties. Summary and review. Acta Odontol Scand 40:359–376
7. Lee JH, Um CM, Lee IB (2006) Rheological properties of resin composites according to variations in monomer and filler composition. Dent Mater 22:515–526

8. Taylor DF, Kalachandra S, Sankarapandian M et al (1998) Relationship between filler and matrix resin characteristics and the properties of uncured composite pastes. Biomaterials 19:197–204

9. Al-Sharaa KA, Watts DC (2003) Stickiness prior to setting of some light cured resin-composites. Dent Mater 19:182–187

10. Ertl K, Graf A, Watts D, Schedle A (2010) Stickiness of dental resin composite materials to steel, dentin and bonded dentin. Dent Mater 26:59–66

11. Lee I-B, Chang J, Ferracane J (2008) Slumping resistance and viscoelasticity prior to setting of dental composites. Dent Mater 24:1586–1593

12. Suliman AH, Boyer DB, Lakes RS (1994) Polymerization shrinkage of composite resins: comparison with tooth deformation. J Prosthet Dent 71:7–12

13. Meredith M, Setchell DJ (1997) In vitro measurement of cuspal strain and displacement in composite restored teeth. J Dent 25:331–337

14. Ferracane JL, Mitchem JC (2003) Relationship between composite contraction stress and leakage in Class V cavities. Am J Dent 16:239–243

15. Eick JD, Welch FH (1986) Polymerization shrinkage of posterior composite resins and its possible influence on postoperative sensitivity. Quintessence Int 17:103–111

16. Davidson CL, De Gee AJ, Feilzer A (1984) The competition between the composite-dentin bond strength and the polymerization contraction stress. J Dent Res 63:1396–1399

17. Chung KH, Greener EH (1990) Correlation between degree of conversion, filler concentration and mechanical properties of posterior composite resins. J Oral Rehabil 17:487–494

18. da Costa J, Ferracane J, Paravina R et al (2007) The effect of different polishing systems on surface roughness and gloss of various resin composites. J Esthet Restor Dent 19:214–226

19. Yap AU, Lye KW, Sau CW (1997) Surface characteristics of tooth-colored restoratives polished utilizing different polishing systems. Oper Dent 22:260–265

20. Janus J, Fauxpoint G, Arntz Y et al (2010) Surface roughness and morphology of three nanocomposites after two different polishing treatments by a multitechnique approach. Dent Mater 26:416–425

21. Ono M, Nikaido M, Ikeda M et al (2007) Surface properties of resin composite materials relative to biofilm formation. Dent Mater J 26:613–622

22. Quirynen M (1994) The clinical meaning of the surface roughness and the surface free energy of intra-oral hard substrata on the microbiology of the supra- and subgingival plaque: results of in vitro and in vivo experiments. J Dent 22:13–16

23. Quirynen M, Bollen CML (1995) The influence of surface roughness and surface-free energy on supra- and subgingival plaque formation in man. A review of the literature. J Clin Periodontol 22:1–14

24. Bollen CM, Lambrechts P, Quirynen M (1997) Comparison of surface roughness of oral hard materials to the threshold surface roughness for bacterial plaque retention: a review of the literature. Dent Mater 13:258–269

25. Quirynen M, Marechal M, Busscher HJ et al (1990) The influence of surface free energy and the surface roughness on early plaque accumulation. J Clin Periodontol 17:138–144

26. Weitman RT, Eames WB (1975) Plaque accumulation on composite surfaces after various finishing procedures. J Am Dent Assoc 91:101–106

27. van Dijken JW, Sjöström S, Wing K (1987) The effect of different types of composite resin fillings on marginal gingiva. J Clin Periodontol 14:185–189

28. Mei L, Busscher HJ, van der Mei HC, Ren Y (2011) Influence of surface roughness on streptococcal adhesion forces to composite resins. Dent Mater 27:770–778

29. Ionescu A, Wutscher E, Brambilla E et al (2012) Influence of surface properties of resin-based composites on in vitro *Streptococcus mutans* biofilm development. Eur J Oral Sci 120:458–465

30. ADA Professional Product Review (2010) Polishing systems 5(1):2–16

31. Watanabe T, Miyazaki M, Moore BK (2006) Influence of polishing instruments on the surface texture of resin composites. Quintessence Int 37:61–67

32. Lu H, Roeder LB, Lei L, Powers JM (2005) Effect of surface roughness on stain resistance of dental resin composites. J Esthet Restor Dent 17:102–108
33. Paravina RD, Roeder L, Lu H, Vogel K, Powers JM (2004) Effect of finishing and polishing procedures on surface roughness, gloss and color of resin-based composites. Am J Dent 17:262–266
34. Stoddard JW, Johnson GH (1991) An evaluation of polishing agents for composite resins. J Prosthet Dent 65:491–495
35. Waheeb N, Silikas N, Watts D (2012) Initial polishing time affects gloss retention in resin composites. Am J Dent 25:303–306
36. Lee YK, Lu H, Oguri M, Powers JM (2005) Changes in gloss after simulated generalized wear of composite resins. J Prosthet Dent 94:370–376
37. Furuse AY, Kathryn Gordon K, RodriguesF SN, Watts DC (2008) Colour-stability and gloss-retention of silorane and dimethacrylate composites with accelerated aging. J Dent 36:945–952
38. Kim KH, Ong JL, Okuno O (2002) The effect of filler loading and morphology on the mechanical properties of contemporary composites. J Prosthet Dent 6:642–649
39. Li Y, Swartz ML, Phillips RW et al (1985) Effect of filler content and size on properties of composites. J Dent Res 64:1396–1401
40. Terry DA (2004) Direct applications of a nanocomposites resin system. Part 1. The evolution of contemporary composite materials. Pract Proced Aesthet Dent 16:417–422
41. Palaniappan S, Elsen L, Lijnen I, Peumans M, Van Meerbeek B, Lambrechts P (2010) Three-year randomised clinical trial to evaluate the clinical performance, quantitative and qualitative wear patterns of hybrid composite restorations. Clin Oral Investig 14:441–458
42. Visvanathan A, Ilie N, Hickel R et al (2007) The influence of curing times and light curing methods on the polymerization shrinkage stress of a shrinkage-optimized composite with hybrid-type prepolymer fillers. Dent Mater 23:777–784
43. Chen MH (2010) Update on dental nanocomposites. J Dent Res 89:549–560
44. Curtis AR, Palin WM, Fleming GJ, Shortall AC, Marquis PM (2009) The mechanical properties of nanofilled resin-based composites: the impact of dry and wet cyclic pre-loading on bi-axial flexure strength. Dent Mater 25:188–197
45. Krämer N, Reinelt C, Richter G et al (2009) Nanohybrid vs. fine hybrid composite in Class II cavities: clinical results and margin analysis after four years. Dent Mater 25:750–759
46. Rodrigues SA Jr, Ferracane JL, Della Bona A (2008) Flexural strength and Weibull analysis of a microhybrid and a nanofill composite evaluated by 3- and 4-point bending tests. Dent Mater 24:426–431
47. Jordan RE (1986) Esthetic composite bonding: techniques and materials, 1st edn. BC Decker, Philadelphia
48. Tijan AH, Chan CA (1989) The polishability of posterior composites. J Prosthet Dent 61:138–146
49. Kanter J, Koski RE, Martin D (1982) The relationship of weight loss to surface roughness of composite resins from simulated toothbrushing. J Prosthet Dent 47:505–513
50. Goldstein GR, Lerner T (1991) The effect of toothbrushing on a hybrid composite resin. J Prosthet Dent 66:498–500
51. Settembrini L, Penugonda B, Fisher E (1993) Dentifrices abrasiveness on microfill composite resin and dentin: a comparative study. J Clin Dent 4:55–60
52. Tanoue N, Matsumura H, Atsuta M (2000) Wear and surface roughness of current prosthetic composites after toothbrush/dentifrice abrasion. J Prosthet Dent 84:93–97
53. van Dijken JW, Ruyter IE (1987) Surface characteristics of posterior composites after polishing and toothbrushing. Acta Odontol Scand 45:337–346
54. Moraes RR, Gonçalves Lde S, Lancellotti AC et al (2009) Nanohybrid resin composites: nanofiller loaded materials or traditional microhybrid resins? Oper Dent 34:551–557

55. Heintze SD, Forjanic M, Ohmiti K, Rousson V (2010) Surface deterioration of dental materials after simulated toothbrushing in relation to brushing time and load. Dent Mater 26:306–319

56. Subbiah T, Bhat GS, Tock RW et al (2005) Electrospinning of nanofibers. J Appl Polym Sci 96:557–569

57. Doshi J, Reneker DH (1995) Electrospinning process and applications of electrospun fibers. J Electrost 35:151–160

58. Chen L, Yu Q, Wang Y, Li H (2011) BisGMA/TEGDMA dental composite containing high aspect-ratio hydroxyapatite nanofibers. Dent Mater 27:1187–1195

59. Pamela S, Stein JS, Haubenreicb JE, Osborne PB (2005) Composite resin in medicine and dentistry. J Long-Term Eff Med Implant 15:641–654

60. Guo G, Fan Y, Zhang JF et al (2012) Novel dental composites reinforced with zirconia-silica ceramic nanofibers. Dent Mater 28:360–368

61. Xu HH, Quinn JB, Giuseppetti AA (2004) Wear and mechanical properties of nano-silica-fused whisker composites. J Dent Res 83:930–935

62. Xu HH (2000) Whisker-reinforced heat-cured dental resin composites: effects of filler level and heat-cure temperature and time. J Dent Res 79:1392–1397

63. Hood PE, Pickers JO (1984) Silicon carbide whisker composites. US patent 4,463,058

64. Hirata Y, Matsushita S, Nakagama S et al (1989) Rheological properties and consolidation of the suspension in the alumina powder-silicon nitride whisker system. J Ceram Soc Jpn 97:866–871

65. Xu HH, Martin TA, Antonucci JM, Eichmiller FC (1999) Ceramic whisker reinforcement of dental resin composites. J Dent Res 78:706–712

66. Ruyter IE, Svendsen SA (1980) Flexural properties of denture base polymers. J Prosthet Dent 43:95–104

67. Jagger DC, Jagger RC, Allen SM, Harrison H (2002) An investigation into the transverse and impact strength of "high strength" denture base acrylic resins. J Oral Rehabil 29:263–267

68. Zhang F, Xia Y, Xu L, Gu N (2008) Surface modification and microstructure of single-walled carbon nanotubes for dental resin-based composites. J Biomed Mater Res B Appl Biomater 86:90–97

69. Zhang M, Fang S, Zakhidov AA et al (2005) Strong, transparent, multifunctional, carbon nanotube sheets. Science 19:1215–1219

70. Chen Q, Zhaoa Y, Wu W et al (2012) Fabrication and evaluation of Bis-GMA/TEGDMA dental resins/composites containing halloysite nanotubes. Dent Mater 28:1071–1079

71. Lan T, Kaviratna PD, Pinnavaia TJ (1996) Epoxy self-polymerization in smectite clays. J Phys Chem Solid 57:1005–1010

72. Discacciati JAC, Oréfice RL (2007) Structural analysis on photopolymerized dental resins containing nanocomponents. J Mater Sci 42:3883–3893

73. Reynaud E, Jouen T, Gauthier C et al (2001) Nanofillers in polymeric matrix. Polymer 42:8759–8768

74. Wilson KS, Zhang K, Antonucci JM (2005) Systematic variation of interfacial phase reactivity in dental nanocomposites. Biomaterials 26:5095–5103

75. Tsai MS, Huang PY, Yang CH (2006) Formation mechanisms of colloidal silica via sodium silicate. J Nanoparticle Res 8:943–949

76. Lim HM, Lee J, Jeong JH et al (2010) Comparative study of various preparation methods of colloidal silica. Engineering 2:998–1005

77. Hench' LL, West JK (1990) The sol-gel process. Chem Rev 90:33–72

78. Klabunde KJ (2001) Nanoscale materials in chemistry. Wiley-Interscience, New York

79. Wang Z, Zhao J, Ding X, Yu K (2005) Synthesis of silica nanocubes by sol-gel method. Mater lett 59:4013

80. Kim JW, Kim LU, Kim CK (2007) Size control of silica nanoparticles and their surface treatment for fabrication of dental nanocomposites. Biomacromolecules 8:215–222

81. Rahman IA, Vejayakumaran P, Sipaut CS et al (2009) Size-dependent physicochemical and optical properties of silica nanoparticles. Mater Chem Phys 114:328–332

82. Parida SK, Dash S, Patel S, Mishra BK (2006) Adsorption of organic molecules on silica surface. Adv Colloid Interface Sci 121:77–110

83. Feng A, McCoy BJ, Munir ZA, Cagliostro DE (1996) Water adsorption and desorption kinetics on silica insulation. J Colloid Interface Sci 180:276–284

84. Chen MH, Chen CR, Hsu SH et al (2006) Low shrinkage light curable nanocomposite for dental restorative material. Dent Mater 22:138–145

85. Rahim TNA, Mohamad D, Ismail AR, Akil HMD (2011) Synthesis of nanosilica fillers for experimental dental nanocomposites and their characterisations. J Phys Sci 22: 93–105

86. Plueddemann EP (1982) Silane coupling agents. Pleunam Press, New York, p 167

87. Calais JG, Söderholm KJ (1998) Influence of filler type and water exposure on flexural strength of experimental composite resin. J Dent Res 67:836–840

88. Mohsen NM, Craig RG (1995) Effect of silanation of fillers on their dispersability by monomer systems. J Oral Rehabil 22:183–189

89. Chen TM, Brauer GM (1982) Solvent effects on bonding organo-silane to silica surfaces. J Dent Res 61:1439–1443

90. Jones DW, Rizkalla AS, Sutow EJ et al (1990) Effect of silane treatment on elastic moduli & poisson's ratio of experimental composites. J Dental Res 69:207. Abstract # 787

91. Broutman LJ, Sahu S (1971) The effect of interfacial bonding on the toughness of glass filled polymers. Mater Sci Eng 8:98–107

92. Ferracane JL, Berge HX, Condon JR (1998) In vitro aging of dental composites in water – effect of degree of conversion, filler volume, and filler/ matrix coupling. J Biomed Mater Res 42:465–472

93. Karmaker A, Prasad A, Sarkar NK (2007) Characterization of adsorbed silane on fillers used in dental composite restoratives and its effect on composite properties. J Mater Sci Mater Med 18:1157–1162

94. Antonucci JM, Dickens SH, Fowler BO et al (2005) Chemistry of silanes: interfaces in dental polymers and composites. J Res Natl Inst Stand Technol 110:541–558

95. Karabela M, Sideridou ID (2008) Effect of the structure of silane coupling agent on sorption characteristics of solvents by dental resin-nanocomposites. Dent Mater 24:1631–1639

96. Söderholm KJ (1981) Degradation of glass filler in experimental composites. J Dent Res 60:1867–1875

97. Söderholm JM, Shang SW (1993) Molecular orientation of silane at the surface of colloidal silica. J Dent Res 72:1050–1054

98. Karabela MM, Sideridou ID (2011) Synthesis and study of properties of dental resin composites with different nanosilica particles size. Dent Mater 27:825–835

99. Chen TM, Brauer GM (1982) Solvent effects on bonding organo-silane to silica surfaces. J Dent Res 61:1439–1443

100. Sideridou ID, Karabela MM (2009) Effect of the amount of 3-methacryloxypropyltrimethoxy-silane coupling agent on physical properties of dental resin nanocomposites. Dent Mater 25:1315–1324

101. Yu B, Ahn JS, Lim JI, Lee YK (2009) Influence of TiO_2 nanoparticles on the optical properties of resin composites. Dent Mater 25:1142–1147

102. Klapdohr S, Moszner N (2005) New inorganic components for dental filling composites. Monatshefte für Chemie 136:21–45

103. Frankamp BL, Fischer NO, Hong R et al (2006) Surface modification using cubic silsesquioxane ligands. Facile synthesis of water-soluble metal oxide nanoparticles. Chem Mater 18:956–959

104. Vo DQ, Kim EJ, Kim S (2009) Surface modification of hydrophobic nanocrystals using short-chain carboxylic acids. J Colloid Interface Sci 337:75–80

105. Xia Y, Zhang F, Xie H, Gu N (2008) Nanoparticle-reinforced resin-based dental composites. J Dent 36:450–455

106. Sun J, Forster AM, Johnson PM et al (2011) Improving performance of dental resins by adding titanium dioxide nanoparticles. Dent Mater 27:972–982

107. Taira M, Toyooka H, Miyawaki H, Yamaki M (1993) Studies on radiopaque composites containing ZrO_2-SiO_2 fillers prepared by the sol-gel process. Dent Mater 9:167–171

108. Leinfelder KF, Sluder TB, Santos JFF et al (1980) Five-year clinical evaluation of anterior and posterior restorations of composite resin. Oper Dent 5:57–65

109. Wendt SL Jr, Leinfelder KF (1994) Clinical evaluation of a posterior composite resin: 3-year results. Am J Dent 7:207–211

110. Reis AF, Giannini M, Lovadino JR et al (2002) The effect of six polishing systems on the surface roughness of two packable resin-based composites. Am J Dent 15:193–197

111. Mitchell CA, Pintado MR, Douglas WH (2002) Iatrogenic tooth abrasion comparisons among composite materials and finishing techniques. J Prosthet Dent 88:320–328

112. Condon JR, Ferracane JL (1997) Factors effecting dental composite wear in vitro. J Biomed Mater Res 38:303–313

113. Jørgensen KD, Hørsted P, Janum O et al (1979) Abrasion of class 1 restorative resins. Scand J Dent Res 87:140–145

114. Bayne SC, Taylor DF, Heymann HO (1992) Protection hypothesis for composite wear. Dent Mater 8:305–309

115. Ferracane JL, Mitchem JC, Condon JR, Todd R (1997) Wear and marginal breakdown of composites with various degrees of cure. J Dent Res 76:1508–1516

116. Condon JR, Ferracane JL (1997) In vitro wear of composite with varied cure, filler level, and filler treatment. J Dent Res 76:1405–1411

117. Knibbs PJ, Smart ER (1992) The clinical performance of a posterior composite resin restorative material, Heliomolar R.O®:3-year report. J Oral Rehabil 19:231–237

118. Lutz F, Phillips RW, Roulet JF, Setcos JC (1984) In vivo and in vitro wear of potential posterior composites. J Dent Res 63:914–920

119. Rice SL, Bailey WF, Wayne SF et al (1984) Comparative in vitro sliding-wear study of conventional, microfilled, and light-cured composite restoratives. J Dent Res 63:1173–1175

120. Fan PL, Powers JM, Craig RG (1979) In vitro wear of microfilled and visible light-cured composites. J Dent Res 58:2116–2119

121. Clelland NL, Villarroel SC, Knobloch LA, Seghi RR (2003) Simulated oral wear of packable composites. Oper Dent 28:830–837

122. Suzuki S, Leinfelder KF (1993) Wear of enamel cusps opposed by posterior composite resin. Quintessence Int 24:885–890

123. Jagger DC, Harrison A (1995) An in vitro investigation into the wear effects of selected restorative materials on enamel. J Oral Rehabil 22:275–281

124. Lambrechts P, Vanherle G (1982) Observation and comparison of polished composite surfaces with the aid of SEM and profilometer. J Oral Rehabil 9:169–182

125. Braden M, Causton B (1976) Water at sorption and solubility of composite filling materials. J Dent Res 55:730–732

126. Lambrechts P, Ameye C, Vanherle G (1982) Conventional and microfilled composite resins. Part II: chip fractures. J Prosthet Dent 48:527–538

127. Braem M, Van Doren VE, Lambrechts P, Vanherle G (1987) Determination of young's modulus of dental composites: a phenomenological model. J Mater Sci 22:2037–2042

128. Summitt JB (2006) Fundamentals of operative dentistry a contemporary approach, 3rd edn. Quintessence, Chicago

129. Cross M, Douglas WH, Fields RP (1983) The relationship between filler loading and particle size distribution in composite resin technology. J Dent Res 62:850–852

130. Lu H, Lee YK, Oguri M, Powers JM (2006) Properties of a dental resin composite with a spherical inorganic filler. Oper Dent 31:734–740

131. Kakaboura A, Fragouli M, Rahiotis C, Silikas NJ (2007) Evaluation of surface characteristics of dental composites using profilometry, scanning electron, atomic force microscopy and gloss-meter. J Mater Sci Mater Med 18:155–163

132. Sideridou ID, Karabela MM, Vouvoudi EC (2011) Physical properties of current dental nanohybrid and nanofill light-cured resin composites. Dent Mater 27:598–607

133. Mitra SB, Wu D, Holmes BN (2003) An application of nanotechnology in advanced dental materials. J Am Dent Assoc 134:1382–1390

134. St Germain H, Swartz ML, Phillips RW, Moore BK, Roberts TA (1985) Properties of microfilled composite resins as influenced by filler content. J Dent Res 64:155–160

135. Ikejima I, Nomoto R, McCabe JF (2003) Shear punch strength and flexural strength of model composites with varying filler volume fraction, particle size and silanation. Dent Mater 19:206–211

136. Moszner N, Salz U (2001) New developments of polymeric dental composites. Prog Polym Sci 26:535–576

137. Schmidt C, Ilie N (2012) The mechanical stability of nano-hybrid composites with new methacrylate monomers for matrix compositions. Dent Mater 28:152–159

138. Beun S, Glorieux T, Devaux J et al (2007) Characterization of nanofilled compared to universal and microfilled composites. Dent Mater 23:51–59

139. Bauer F, Sauerland V, Ernst H, Glasel HJ et al (2003) Preparation of scratch and abrasion resistant polymeric nanocomposites by monomer grafting onto nanoparticles. Macromol Chem Phys 204:375–383

140. Baroudi K, Saleh AM, Silikas N, Watts DC (2007) Shrinkage behaviour of flowable resin-composites related to conversion and filler-fraction. J Dent 35:651–655

141. Moszner N, Klapdohr S (2004) Nanotechnology for dental composites. Int J Nanotechnol 1:130–156

142. Duke ES (2001) Finishing and polishing techniques for composite resins. Compend Contin Educ Dent 22:392–396

143. Yap AU, Yap SH, Teo CK, Ng JJ (2004) Comparison of surface finish of new aesthetic restorative materials. Oper Dent 29:100–104

144. Strassler H (1990) Polishing composite resins to perfection depends on the filler. Dent Off 10:9–10

145. Senawongse P, Pongprueksa P (2007) Surface roughness of nanofill and nanohybrid resin composites after polishing and brushing. J Esthet Restor Dent 19:265–273; discussion 274–275

146. Turssi CP, Ferracane JL, Serra MC (2005) Abrasive wear of resin composites as related to finishing and polishing procedures. Dent Mater 21:641–648

147. Takanashi E, Kishikawa R, Ikeda M et al (2008) Influence of abrasive particle size on surface properties of flowable composites. Dent Mater J 27:780–786

148. Nanbu T, Tani Y (1979) Study of surface gloss of composite restorative materials. Dent Mater J 35:421–430

149. da Costa JB, Goncalves F, Ferracane JL (2011) Comparison of two-step versus four-step composite finishing/polishing disc systems: evaluation of a new two-step composite polishing disc system. Oper Dent 36:205–212

150. Turssi CP, Ferracane JL, Ferracane LLJ (2006) Wear and fatigue behavior of nano-structured dental resin composites. J Biomed Mater Res B Appl Biomater 78:196–203

151. Yesil ZD, Alapati S, Johnston W, Seghi RR (2008) Evaluation of the wear resistance of new nanocomposite resin restorative materials. J Prosthet Dent 99:435–443

152. Powers JM, Wataha JC (2008) Dental materials properties and manipulation, 9th edn. Mosby Elsevier, St Louis, p 82

153. Ergücü Z, Türkün LS, Aladag A (2008) Color stability of nanocomposites polished with one-step systems. Oper Dent 33:413–420

154. Turssi CP, Ferracane JL, Vogel K (2005) Filler features and their effects on wear and degree of conversion of particulate dental resin composites. Biomaterials 26:4932–4937

155. Rodrigues SA Jr, Scherrer SS, Ferracane JL, Della Bona A (2008) Microstructural characterization and fracture behavior of a microhybrid and a nanofill composite. Dent Mater 24:1281–1288

156. Sabbagh J, Vreven J, Leloup G (2002) Dynamic and static moduli of elasticity of resin-based materials. Dent Mater 18:64–71

157. Papadogiannis DY, Lakes RS, Papadogiannis Y et al (2008) The effect of temperature on the viscoelastic properties of nano-hybrid composites. Dent Mater 24:257–266

158. Braem M, Lambrechts P, Van Doren V, Vanherle G (1986) The impact of the composite structure on its elastic response. J Dent Res 65:648–653

159. Rueggeberg FA, Craig RG (1988) Correlation of parameters used to estimate monomer conversion in a light-cured composite. J Dent Res 67:932–937

160. Chung KH (1990) The relationship between composition and properties of posterior resin composites. J Dent Res 69:852–856

161. Bayne S, Heymann H, Swift E (1994) Update on dental composites restorations. J Am Dent Assoc 25:687–701

162. Suzuki S, Leinfelder KF, Kawai K, Tsuchitani Y (1995) Effect of particle variation on wear rates of posterior composites. Am J Dent 8:173–178

163. Tyas MJ (1990) Correlation between fracture properties and clinical performance of composite resins in Class IV cavities. Aust Dent J 35:46–49

164. Ferracane JL, Antonio RC, Matsumoto H (1987) Variables affecting the fracture toughness of dental composites. J Dent Res 66:1140–1145

165. Kim KH, Park JH, Imai Y, Kishi T (1994) Microfracture mechanisms of dental resin composites containing spherically-shaped filler particles. J Dent Res 73:499–504

166. Lange FF (1970) The interaction of a crack front with a second-phase dispersion. Philos Mag 22:983–992

167. Kim KH, Park JH (1991) Fracture behavior of dental composite resins. Bio-Med Mater Eng 1:45–57

168. Sabbagh J, Ryelandt L, Bacherius L et al (2004) Characterization of the inorganic fraction of resin composites. J Oral Rehabil 31:1090–1101

169. Curtis AR, Palin WM, Fleming GJ, Shortall AC, Marquis PM (2009) The mechanical properties of nanofilled resin-based composites: characterizing discrete filler particles and agglomerates using a micromanipulation technique. Dent Mater 25:180–1877

170. Braem M, Finger W, Van Doren VE, Lambrechts P, Vanherle G (1989) Mechanical properties and filler fraction of dental composites. Dent Mater 5:346–348

171. Pashley DH, Tay FR, Breschic L et al (2011) State of the art etch-and-rinse adhesives. Dent Mater 27:1–16

172. Osorio E, Toledano M, Aguilera FS, Tay FR et al (2010) Ethanol wet bonding technique sensitivity assessed by AFM. J Dent Res 89:1264–1269

173. Tay FR, Pashley DH, Kapur RR et al (2007) Bonding BisGMA to dentin – a proof-of-concept for hydrophobic dentin bonding. J Dent Res 86:1034–1039

174. Sauro S et al (2009) Two-photon laser confocal microscopy of micropermeability of resin-dentin bonds made with water or ethanol wet bonding. J Biomed Mater Res Part B Appl Biomater 90B:327–337

175. Sano H, Takatsu T, Ciucchi B, Russell CM, Pashiey DH (1995) Tensile properties of resin-infiltrated demineralized human dentin. J Dent Res 74:1093–1102

176. Tay FR, Mouldings KM, Pashley DH (1999) Distribution of nanofillers from a simplified-step adhesive in acid-conditioned dentin. J Adhes Dent 2:103–117

177. Fanning DE, Wakefield CW, Robbins JW, Bagley AL (1995) Effect of a filled adhesive on bond strength in three dentinal bonding systems. Gen Dent 13:256–262

178. Pashley EL, Agee KA, Pashley DH, Tay FR (2002) Effects of one versus two applications of an unfilled, all-in-one adhesive on dentine bonding. J Dent 30:83–90

179. Kemp-Scholte CM, Davidson CL (1990) Complete marginal seal of Class V resin composite restorations effected by increased flexibility. J Dent Res 69:1240–1243

180. Labella R, Lambrechts P, Van Meerbeek B, Vanherle G (1999) Polymerization shrinkage and elasticity of flowable composites and filled adhesives. Dent Mater 15:128–137
181. Van Meerbeek B, Conn LJ Jr, Duke ES et al (1996) Correlative transmission electron microscopy examination of nondemineralized and demineralized resin-dentin interfaces formed by two dentin adhesive systems. J Dent Res 75:879–888
182. Spencer P, Wang Y (2002) Adhesive phase separation at the dentin interface under wet bonding conditions. J Biomed Mater Res 62:447–456
183. Osorio E, Toledano M, Yamauti M et al (2012) Differential nanofiller cluster formations in dental adhesive systems. Microsc Res Tech 75:749–757
184. Di Hipólito V, Reis AF, Mitra SB et al (2012) Interaction morphology and bond strength of nanofilled simplified-step adhesives to acid etched dentin. Eur J Dent 6:349–360
185. Eick JD, Robinson SJ, Byerley TJ et al (1995) Scanning transmission electron microscopy/energy-dispersive spectroscopy analysis of the dentin adhesive interface using a labeled 2 hydroxyethyl analogue. J Dent Res 74:1246–1252
186. Lindén LA, Källskog O, Wolgast M (1995) Human dentine as a hydrogel. Arch Oral Biol 40:991–1004
187. De Monredon-Senani S, Bonhomme C, Ribot F, Babonneau F (2009) Covalent grafting of organoalkoxysilanes on silica surfaces in water-rich medium as evidence by ^{29}Si NMR. J Sol-Gel Sci Technol 50:152–157
188. Michael G, Fench H (1993) "Basic characteristics of AEROSIL", Technical bulletin pigments, number 11, 4th ed. Degussa AG, Frankfurt, pp 5–80
189. Bagwe RP, Hilliard LR, Tan W (2006) Surface modification of silica nanoparticles to reduce aggregation and non-specific binding. Langmuir 22:4357–4362
190. Kim JS, Cho BH, Lee IB et al (2005) Effect of the hydrophilic nanofiller loading on the mechanical properties and the microtensile bond strength of an ethanol- based one-bottle dentin adhesive. J Biomed Mater Res B Appl Biomater 72B:284–291
191. Mjör IA, Moorhead JE, Dahl JE (2000) Reasons for replacement of restorations in permanent teeth in general dental practice. Int Dent J 50:361–366
192. Jokstad A, Bayne S, Blunck U, Tyas M, Wilson N (2001) Quality of dental restorations. FDI Commission Project 2–95. Int Dent J 51:117–158
193. Glasspoole EA, Erickson RL, Davidson CL (2001) A fluoride-releasing composite for dental applications. Dent Mater 17:127–133
194. Itota T, Nakabo S, Narukami T et al (2005) Effect of two-step adhesive systems on inhibition of secondary caries around fluoride-releasing resin composite restorations in root dentine. J Dent 33:147–154
195. Xu X, Burgess JO (2003) Compressive strength, fluoride release and recharge of fluoride-releasing materials. Biomaterials 24:2451–2461
196. Sidhu SK, Sherriff M, Watson TF (1997) In vivo changes in roughness of resin-modified glass ionomer materials. Dent Mater 13:208–213
197. Xu HH, Moreau JL, Sun L et al (2010) Novel CaF_2 nanocomposite with high strength and fluoride ion release. J Dent Res 89:739–745
198. Choi JH, Kim MK, Woo HG, Song HJ, Park YJ (2011) Modulation of physical properties of polyvinylsiloxane impression materials by filler type combination. J Nanosci Nanotechnol 11:1547–1550
199. Hench LL, Wilson J (1986) Biocompatibility of silicates for medical use. Ciba Found Symp 121:231–246
200. Li P, Ohtsuki C, Kokubo T et al (1993) Effects of ions in aqueous media on hydroxyapatite induction by silica gel and its relevance to bioactivity of bioactive glasses and glass-ceramics. J Appl Biomater 4:221–229
201. Madhumathi K, Kumara S, Kavyaa KC et al (2009) Novel chitin/nanosilica composite scaffolds for bone tissue engineering applications. Int J Biol Marcomol 45:289–292

202. Boissard CI, Bourban PE, Tami AE et al (2009) Nanohydroxyapatite/poly(ester urethane) scaffold for bone tissue engineering. Acta Biomater 5:3316–3327
203. O'brien WJ (1997) Dental materials and their selection, 2nd edn. Quintessence, Chicago
204. Suzuki S (2004) In vitro wear of nanocomposite of denture teeth. J Prosthodont 13:238–243
205. Stober T, Henninger M, Schmitter M et al (2010) Three-body wear of resin denture teeth with and without nanofillers. J Prosthet Dent 103:108–117
206. Gaikwad RM, Sokolov I (2008) Silica nanoparticles to polish tooth surfaces for caries prevention. J Dent Res 87:980–983

Nanostructured Multiphase Polymer Networks

44

Carmem S. Pfeifer

Introduction

One of the most commonly used approaches to obtain polymeric materials with micro- and nanoscale features is the use of polymer blends. The first patent for a polymer blend was filed in 1846 and consisted of a mixture of natural rubber with gutta-percha (T. Hancock, English Patent, No. 11,147). Since then, the increasing demand for improved mechanical and optical properties, as well as the need to control polymerization shrinkage and stress in the plastics industry, has led to tremendous developments in terms of multicomponent polymeric materials [18, 43, 59, 69]. At a molecular level, thermoplastic polymer blends can form homogeneous or heterogeneous structures, in which case nano- or micro-sized domains can be formed. The formation of homogeneous and heterogeneous mixtures, as well as the size of the domains in heterogeneous structures, can be controlled through modifications in the composition or in the processing temperature. Of particular interest are the multiphase systems, where there is a potential for polymeric network structure-related reinforcement to occur. For example, for polystyrene and polybutadiene blends, the polybutadiene phase acts as a toughening agent, decreasing the brittleness of polystyrene [83]. One of the biggest challenges with such blends is determining their miscibility and controlling nano- and micro-phase formation through processing to achieve useful products [1, 24, 25, 70]. There are other, more sophisticated mechanisms of multicomponent system formation including thermosetting materials. Block copolymers can be added to a blend to act as compatibilizers and improve the interaction between incompatible phases [75]. Block copolymers can also be designed to self-assemble upon polymerization of a secondary monomer matrix, forming micelles [52] or other structures [68].

C.S. Pfeifer
Oregon Health and Science University, School of Dentistry, Portland, OR, USA
e-mail: pfeiferc@ohsu.edu

Another approach to achieve heterogeneity is to sequentially or simultaneously polymerize a mixture of monomers, which can be initially miscible or immiscible, polymerizable through a similar or dissimilar mechanism (e.g., radical and cationic) [8, 14, 42]. The inclusion of an inert [74] or functionalized prepolymer phase [50] to a secondary monomer matrix has also been used, with favorable shrinkage and stress outcomes [50]. These heterogeneity formation strategies may give rise to either the copolymerizations or the formation of interpenetrating polymer networks (IPNs), as will be discussed later.

In terms of property tailoring capabilities, for example, ternary phase terpolymers have been demonstrated to increase toughening of polymeric structures through a synergistic combination of the physical properties of each individual micro- or nano-sized phase ([45]; Zhang et al. 2012). Particularly for toughness, this can, for example, be achieved through crystallinity induction in block copolymers, a structural feature driven by phase separation [34]. Other examples include shrinkage reductions obtained with phase-separated materials that are far greater than would have been predicted based on the simple monomer conversion [57, 74]. In that case, the addition of non-functionalized pre-polymerized particles leads to separation, and volume accommodation due to void formation or even less noticeable increases in free volume at the nanoscale domain interfaces contribute less macroscopic deformation [37–40, 74]. In summary, if judiciously designed, the properties of the resulting heterogeneous materials can be superior to the simple prediction of the additive contributions of each component.

IPNs can be created sequentially or simultaneously, and that usually is accomplished through distinct, non-interfering polymerization mechanisms [15, 44] that allow temporal control of the sequence of network formation [4]. For example, when combining monomers that produce polymers of different moduli, by designing the higher modulus phase to polymerize first, diffusion challenges are imposed to the second lower modulus component, in an effect known as IPN vitrification, which may lead to smaller phase-separated nano-sized domains to be formed, as evidenced by narrower tan delta peaks [4, 8]. The effect of monomer reactivity in the phase-separation behavior has also been demonstrated in hybrid polymerizations of methacrylate and vinyl esters, accomplished through a single free-radical mechanism [35]. Methacrylates are two orders of magnitude more reactive than vinyl esters, showing a strong tendency to homopolymerization. This means that the less reactive monomer starts polymerizing in a diffusion-restricted environment, and a two-stage kinetic profile is observed, along with phase separation [35].

One approach that has received relatively little attention involves homogeneous monomer mixtures displaying marginal compatibility that engage in a common copolymerization process to create heterogeneous copolymers through polymerization-induced phase separation (PIPS). In copolymerizations, the degree of miscibility depends mainly on the solubility parameter, secondary intermolecular interactions (such as hydrogen bonding – [83]), and the relative concentration of each component [77]. In a simple example of a binary mixture of monomers A and B, as the polymerization progresses, the free energy of mixing increases and the coil size of the propagating radical decreases in the poor reaction medium, jeopardizing

segmental diffusion [23, 54]. For all monomeric mixtures, especially the ones leading to the formation of cross-linked networks, the possibility for diffusion of the A-rich phase then depends on the constraint imposed by gelation of the B-rich phase [84]. The resulting domain structure (dispersed phase or co-continuous) correlates with the portion of the phase diagram from where the initial mixture starts to polymerize [16] but also depends on the reaction kinetics [44, 71]. Therefore, thermodynamic and kinetic considerations (processing conditions) control the potential extent of stress relaxation (or void formation) at the domain interfaces, the overall volumetric shrinkage [71], and mechanical properties (Zhang et al. 2012).

This chapter will focus on materials in which at least one component is actively polymerizing during phase separation, in such a way that phase-separated structures derived from polymer melts will not be discussed. These reactions are extremely useful to generate polymeric structures with advantageous properties, such as controlled polymerization shrinkage and stress, increased toughness, and tailorable optical properties, which find applications in many fields – biomedical in situ applications, drug delivery, inks and coatings, molded parts, etc.

Phase Morphology and Interfaces

Solutions and Mixtures

Thermodynamics and reaction kinetics are the factors governing phase formation in polymerizing systems. Miscibility defines the flow behavior and the type of mechanism of phase formation [71] and is determined by a delicate balance of enthalpic and entropic forces. In particular, the entropic term is to a great extent responsible for miscibility. The temperature also plays an important role. It is not the intention of this chapter to provide a comprehensive explanation on the laws of thermodynamics and chemical equilibria. However, a general overview of some fundamental concepts is essential to the understanding of phase development as well as of the mechanisms that can be used to control phase formation.

In general terms, at the equilibrium, the Gibbs free energy of mixing is given by: $G = H - TS$, where H is the heat content (or enthalpy), T is the absolute temperature, and S is the entropy. The change in G can be written as:

$$dG = VdP - SdT + \Sigma_i \mu_i dn_i; \qquad\qquad \mu_i = (\partial G / \partial n_i)_{P, T, n_j}$$

where n_i represents the number of moles of the substance i having the chemical potential μ_i. The free energy, enthalpy, entropy, and chemical potential of mixing are respectively defined as the difference:

$$\Delta F_m = F - F_0; \qquad\qquad F \equiv G, H, S, \mu_i$$

where F and F_0 represent the mixture and pure state, respectively [71].

In a mixture of molecules A and B, the entropy of mixing (ΔS_{mix}) depends on the mole fraction of each component (x_A and x_B, respectively). If A and B are completely immiscible, there is no change in entropy and $\Delta S_{mix} = 0$. If the two substances mix in a random order, the entropy increases according to the mole fraction of A and B. In other words, mixing and entropy must increase in tandem, and entropy is the driving force for mixing. In an ideal solution, the free energy of mixing is given by $\Delta G_{mix} = -T \Delta S_{mix}$ and involves no change in energy or other entropies due to changes in volume, structuring, or ordering in the solution. In practice, very few solutions are close to ideal. In a simple lattice model, the total energy of mixing is the sum of the contact interactions of noncovalent bonds of all the pair of nearest neighbors in the mixture (i.e., interactions of the types AA, BB, or AB). Even if one cannot precisely determine the count of AB contacts, an assumption can be made, called the mean-field approximation. In this approximation, for any given numbers of A and B molecules, the particles are mixed as randomly and uniformly as possible, which gives us a way to estimate the count of AB contacts. This assumes that the self-attractions of AA or BB are as strong as the interaction AB, which does not always hold. Nevertheless, the Bragg-Williams mean-field approximation is often a reasonable first approximation. In the regular solution model, described by Hildebrand in 1929, $\Delta G_{mix} > 0$ indicates thermodynamic instability, and the components are immiscible. Conversely, if $\Delta G_{mix} < 0$, the components are miscible. This does not take into consideration the possibility for phase separation, in which the components partition in phases with different compositions. However, the model is the starting point to understand the phenomenon [16].

Another parameter to consider is the chemical potential, which is obtained by the derivative of the ΔG_{mix} equation. In very general terms, the chemical potential can be expressed as

$$\mu = \mu^0 + kT \, ln \, \gamma x$$

where k is the Boltzmann's constant, T is the temperature, γ is the activity coefficient, μ^0 is the standard state chemical potential, and x is the mole fraction of the different components. In practice, this equation describes two tendencies driving particle movement. First, A particles tend to leave regions of high A concentration and move towards regions of low A concentrations to gain mixing entropy (described by the term $kT \, ln \, \gamma x$). Second, A particles are attracted to regions or phases for which they have high chemical affinity (described by μ^0). In turn, the energetic parameter χ_{AB} (or the Flory-Huggins parameter, which is dimensionless) describes the energetic cost of beginning with the pure states A and B and transferring one B into a medium of pure A's and one A into a medium of pure B's. According to the Hildebrand's principle, for most systems, the AB affinity is weaker than the AA and BB affinities, so usually $\chi_{AB} > 0$ (or immiscible). The quantity χ_{AB} also contributes to the interfacial free energy between two materials and can be estimated from interfacial tension experiments [16].

Fig. 44.1 Phase diagram and solutions exemplifying each composition at temperature T_0. χ' indicates the concentration of B that saturates liquid A, and χ'' is concentration of B at which A saturates B. T_c is the critical temperature (Adapted from Dill and Bromberg [16])
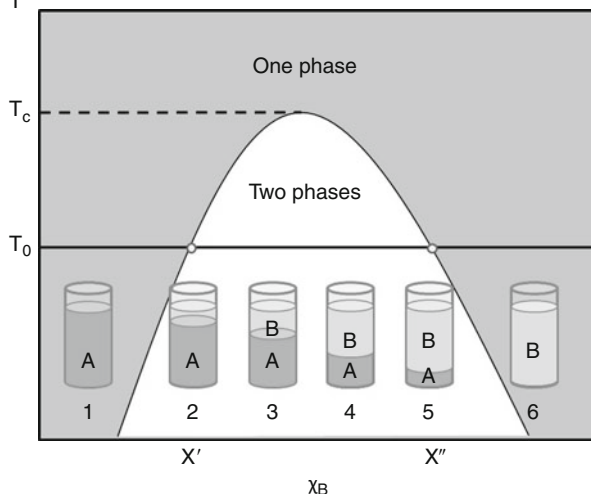
Phase Transitions

Phase diagrams describe which conditions of relative mole fractions of components A and B result in single or multiple phases as a function of temperature. An illustrative example is given for water and oil in Fig. 44.1. Phase separations are driven by the tendency to lower the free energy. The lattice model predicts that at high temperatures, where the free energy of mixing is dominated by the entropic component, solutions mix to gain translational entropy. At low temperatures, where the free energy is dominated by the energy (enthalpy), solutions form different phases because AA and BB attractions are stronger compared to AB attractions. The free energy of mixing ΔF_{mix} for a mixture of A and B can be written as:

$$\frac{\Delta G_{mix}}{NkT} = x \ln x + (1-x) \ln (1-x) + \chi_{AB} x (1-x)$$

where the NkT term represents the product of the degrees of freedom in the lattice model, the Boltzmann's constant, and the temperature [16]. From this equation, the graphs in Fig. 44.2 are derived, with the $\frac{\Delta G_{mix}}{NkT}$ term as a function of composition. Varying the temperature changes the balance of mixing forces. As can be seen from these graphs, when the temperature is high (a), the graph is concave upwards, meaning that the system is more stable as a single phase (miscible). When the temperature is lowered for the same system (b), the graph function is concave downwards and the free energy function has two minima ($\chi_{AB} > 2$), which means the system is more stable as two phases (immiscible). It is, therefore, possible to predict the composition of the two phases by calculating the tangent of each graph [16].
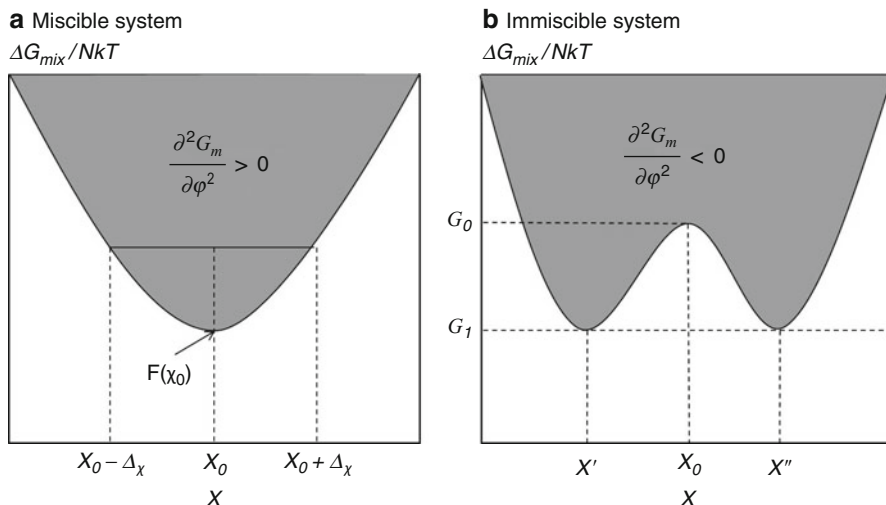
a Miscible system

$\Delta G_{mix}/NkT$

b Immiscible system

$\Delta G_{mix}/NkT$

Fig. 44.2 (**a**) If a system's free energy (ΔG_{mix}) is concave upwards, the system is miscible. (**b**) For compositions (in this case, near $\chi = \chi_0$) where ΔG_{mix} is concave downwards, systems are immiscible (Adapted from Dill and Bromberg [16])

Further, from the $\frac{\Delta G_{mix}}{NkT}$ and *composition* graphs built for a range of temperatures (Fig. 44.3a), where $T_1 < T_{crit}$, it is possible to then obtain a combined graph of temperature and composition (3b and 3c), or the phase diagram for that particular system. The compositions inside the dashed line (or coexistence curve) are immiscible and in the grayish area are miscible. The peak temperature represents the critical point for phase separation of a system in equilibrium.

From Dill and Bromberg [16], "In summary, when χ_{AB} is small (less than 2), corresponding to high temperature, the disaffinity of A for B is small, and the entropic tendency to mix is greater than the energetic tendency to separate. The free energy function is concave upward for all compositions. However, if the disaffinity of A for B is strong ($\chi_{AB} >> 0$, or $T \rightarrow 0$), AA and BB attractions are stronger than AB attractions. The energetic affinities overwhelm the mixing entropy so there is a phase separation. Very dilute solutions are miscible, despite the strong disaffinities, because there is large mixing entropy at those compositions."

It is noteworthy that some solutions (be that polymer/polymer or monomer/polymer or monomer/monomer solutions) present a lower critical solution temperature (LCST), i.e., phase separation is observed upon an increase in temperature. This is more common for polymer/polymer blends. The upper critical solution temperature (UCST – phase separation is observed upon a decrease in temperature), to which emphasis was given in this chapter, has been associated with small-molecule solutions.

(a) Free energies of mixing at a series of temperatures
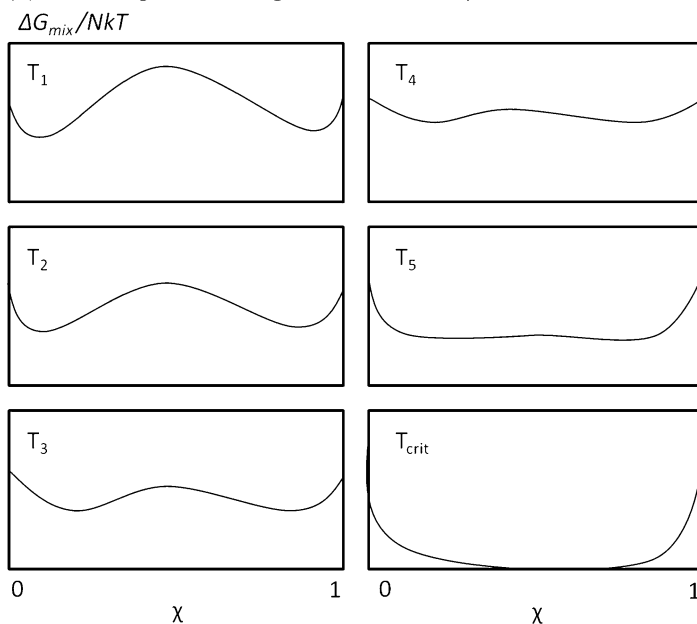
$\Delta G_{mix}/NkT$

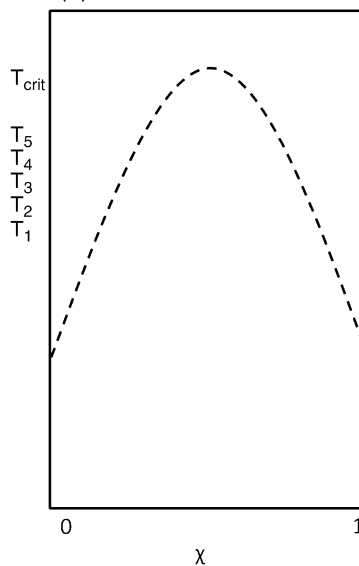(b) Free energies from (a) combined
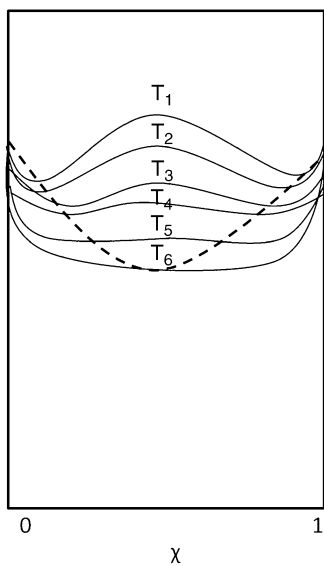
(c) Inverted dashed curve from (b)

Fig. 44.3 Use of the lattice model to compute the phase diagram. The *dashed curve* represents the two minima in $\Delta G_{mix}/NkT$ against χ for each temperature. Inside the *dashed curve* is the two-phase region (Adapted from Dill and Bromberg [16])

Fig. 44.4 Phase diagram showing one- or two-phase regions and metastable region (M). At M, the system is unstable. If perturbations are small, the system is single phase; if perturbations are large, the system is two phase. The spinodal and binodal curves meet at the critical point (Adapted from Dill and Bromberg [16])
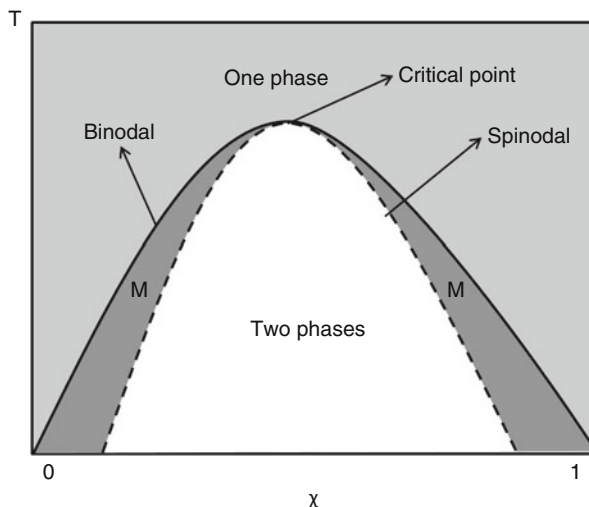
Mechanisms of Phase Separation

So far, we have described systems in equilibrium, meaning the system has reached its lowest level of entropy and was left unperturbed for a long time. In practice, multicomponent mixtures are often in a metastable state, as, for example, in a supersaturated solution. In those cases, there are regions of local stability, more markedly for compositions surrounding the coexistence curve (also called binodal curve, obtained from the first derivative of the free energy function). The limit of metastability is identified by the spinodal curve, given by a condition on the second derivative of the free energy function, as represented in the graph in Fig. 44.4 [16]. In the metastable region (M), the system remains in one single phase if external perturbations are kept to a minimum or separate into two phases if enough energy is provided to the system to cause demixing. The critical point is where coexisting phases merge, identified at the intersection of the binodal and spinodal curves (much like the eutectic point in the Sn/Pb alloys) [2].

In a simple binary system, phase separation occurs from either the metastable or the immiscible regions, according to the composition of the starting mixture at a given temperature. In the metastable region between the binodal and spinodal lines, the phase separation requires some kind of energy transfer to occur (change in temperature or polymerization, as will be discussed in detail in the following sections). This energy can be the initiation of polymerization, as will be discussed later. In the immiscible region, no external stimulus is required, and the phase separation happens spontaneously. Due to fluctuation of density within the metastable region, the spinodal line is only a diffuse boundary. Based on the mean-field theory, discussed previously, two types of quenching from a homogeneous state must be distinguished: (1) to the metastable and (2) to the spinodal region [29, 79].

For a non-polymerizing material with an upper critical solution temperature (UCST; Fig. 44.4), lowering the temperature of a given miscible composition above the binodal

and into the metastable region leads to phase separation by localized fluctuation of concentration (or density), in a mechanism known as nucleation and growth (NG). For this process to be possible, an initial expenditure of energy is necessary. This is the activation energy of nucleation, and after that is overcome, further phase separation happens spontaneously. The droplets that are formed grow by diffusion of macromolecules into the nucleated domains, in a process known as ripening. Finally, the system goes through coalescence coarsening, determined by the interphase energy balance [26]. This process can be stopped at any stage through stabilizing mechanisms to control droplet size. The other quenching mechanism is spinodal decomposition (SD). For the same material described above, lowering the temperature at a faster rate from the binodal into the spinodal region causes delocalized fluctuations in density (or concentrations), leading to long-range spontaneous phase separation. While in the ND mechanism the composition of the separated domains remains constant, with only the size and size distribution of droplets changing with time, in the SD mechanism both the size and composition depend on the phase-separation times. Three stages of growth can be identified [63]: diffusion, liquid flow, and coalescence (Fig. 44.5).
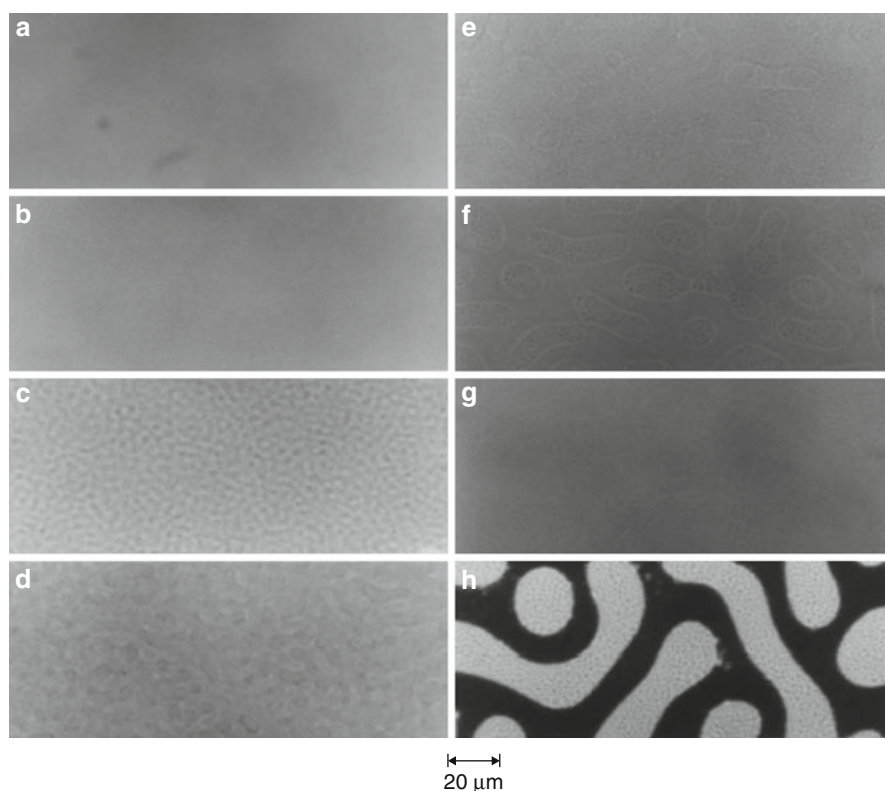

Fig. 44.5 Optical micrographs following the cure of resin A with 9 % saturated polyester at 32 °C. Gel time: 40.8 min. (**a–h**) are snapshots at different phases of the reaction (h > 5 h) (From Li et al. 2000)

The diffusion stage is very short, and diameter of the domains is inversely proportional to the variation in temperature (ΔT) used to drive the separation. The size and distribution of the domains follow a Gaussian distribution during the liquid flow stage and depart from that relationship as the process matures into the coalescence stage.

Of greater interest for this chapter are polymerizing systems. During a polymerization, the entropic contribution (ΔS_{mix} in the Gibbs free energy equation explained earlier) is constantly negative as the monomer converts to polymer and the number of molecules decreases, favoring phase separation [12, 21]. The enthalpic component (ΔH_{mix}) varies according to the system; the polymerization of vinyl bonds is exothermic ($\Delta H \text{ mix} < 0$), but the interactions of neighboring molecules may contribute positively or negatively to the enthalpy. If the resulting $\Delta G_{mix} > 0$, and assuming diffusion is permitted, both an ND mechanism from the binodal and an SD mechanism from the spinodal may take place. The SD mechanism yields a co-continuous phase structure that is interconnected ([5, 53]; Li and Lee 2000; [8]) and has been correlated with better control of phase formation and tailoring of shrinkage (Li and Lee 2000), stress, and mechanical properties [64, 76]. The influence of diffusional limitations to phase separation imposed by network formation in polymerizing systems will be discussed in the following section.

Reaction Kinetics in Polymerization-Induced Phase-Separation (PIPS) Systems

As discussed so far, phase diagrams assume systems in equilibrium, in which maximum diffusion has been allowed to happen towards the thermodynamic stability [22]. In polymerizing systems, not only is the thermodynamic component determinant to phase formation, but also the kinetics of polymerization and network formation, more specifically gelation, play a role [11]. The gel point has been defined either as the first instance in the polymerization when one macromolecule spans the entire vessel or when the system experiences a significant drop in fluidity [54]. If the onset of gelation is observed too early in conversion, further polymerization is hindered by limitation of diffusion of macro-radicals, and usually the final conversion attained is low [13]. This depends on the monomer system; for example, the typical gel-point conversion in free-radical polymerized methacrylates is only a few percent [62], while for thiolenes, which polymerize through a step-growth mechanism, gelation has been observed at conversions as high as 90 % [7]. In terms of phase separation, there are two possible scenarios, depending on the system. Typically, for cross-linked systems, if gelation occurs too early in conversion, diffusion of compatible phases may be prohibited, thus preventing phase separation despite any thermodynamic instability [22]. On the other hand, for certain polymer-dispersed liquid crystals, network formation physically drives incompatible phases apart, analogous to the squishing of water from a sponge [33], meaning that phase separation actually starts after the network has been established. This will be further explored later in this chapter.

   The ability to control the phase formation and its relationship with the gelation of the network is important to expand the potential applications of phase separating systems and harness all its advantages. For example, in many applications, the control of polymerization shrinkage is crucial to the quality and longevity of the polymeric structure, such as in the molded parts and coatings industries, in electronics, and in biomedical fields. One approach that has been used for several years is the induction of phase separation by the addition of pre-polymerized additives [31, 32, 72–74]. One study has shown that polyethylene glycol dimethacrylate networks modified by the addition of pre-polymerized beads of polymethyl methacrylate show significantly less shrinkage than it would have been predicted [74]. The same results have been reported for polyesters [31, 32] and polystyrene modified by urethanes [37–40]. In some cases, the mechanism for shrinkage reduction has been correlated with void formation at the domain interface, which reduces the net dimensional change [74]. This is usually the case in systems where coarse phase separation is observed, which may be deleterious for some applications where the water sorption and solubility and mechanical properties under fatigue are important [74]. However, it is possible to obtain more controllable phase separation and tailor domain size and structure to achieve shrinkage and stress reduction through relaxation at the interface between the domains ([37, 38]; Li and Lee 2000; [39, 40]). This can be achieved, for example, in interpenetrating thermoset networks, by sequential or simultaneous polymerization of networks of different stiffness [4, 8, 14]. Vinyl ester/epoxy hybrids are a fairly common example of IPNs formed quasi-simultaneously via non-interfering reactions (free radical and polyaddition, respectively), used for mutual mechanical reinforcement [30]. Some authors investigated networks formed by the photopolymerization of a low-modulus methacrylate (polyethylene glycol dimethacrylate) and the thermopolymerization of a rigid epoxy (diglycidyl ether of bisphenol A) [4]. By controlling the phase that polymerizes first, it is possible to control not only the size and distribution of the domains but also the composition of the different domains [4]. When the epoxy resin is allowed to polymerize first, the network goes through a phenomenon known as "IPN vitrification," which causes a reduction of segmental mobility and, hence, of the reactivity of the methacrylate groups. This results in phase separation of the dimethacrylate components from the developing epoxy network and a localized increase in the dimethacrylate concentration in its own domains. Evidence for phase separation can be observed by a broadening of the tan delta peaks in the DMA plots, as shown in Fig. 44.6, with clear indication of the influence of sequence of polymerization on the Tg of materials with essentially the same initial monomeric composition [4]. In terms of dimensional changes, having a low-Tg phase surrounding a higher-Tg phase during its polymerization allows for accommodation of the strain generated by the shrinkage of the latter. This allows for reduction of net shrinkage without the presence of voids at the interface of the domains [12, 13].

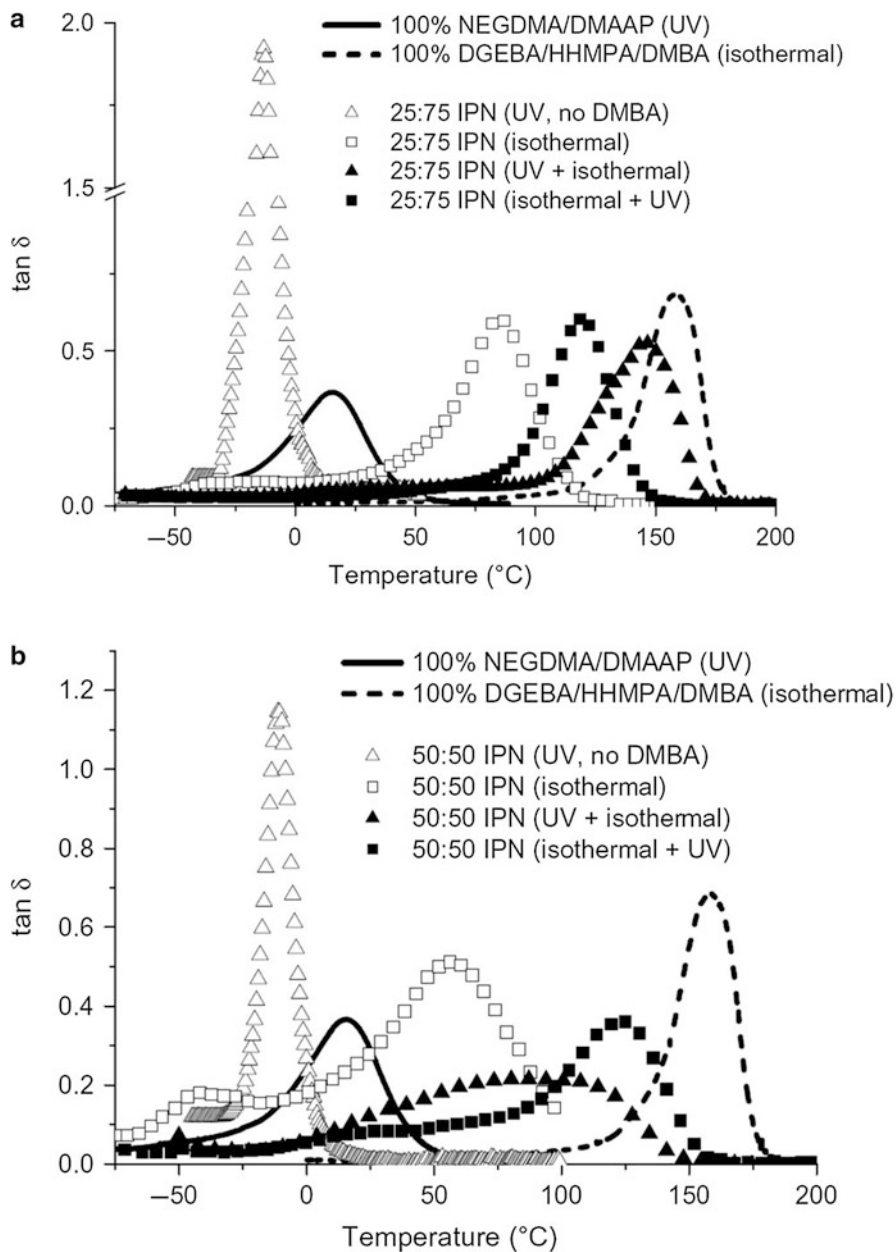**Fig. 44.6** (**a**) Tan δ versus temperature for the photocured NEGDMA/DMAAP, thermally cured DEGBA/HHMPA/DMPA, and 25:75 NEGDMA/DMAAP:DEGBA/HHMPA/DMPA IPNs using various curing schedules. (**b**) Tan δ versus temperature for the photocured NEGDMA/DMAAP, thermally cured DEGBA/HHMPA/DMPA, and 50:50 NEGDMA/DMAAP:DEGBA/HHMPA/DMPA IPNs using various curing schedules (From Chen and Cook [4])

Gelation and Onset of Phase Separation

Thermodynamic miscibility of the two components within an IPN is governed by the Gibbs free energy of mixing, as previously exposed. As the polymerization proceeds, the molecular weight of the different components increases, which lowers the entropy of mixing and reduces the miscibility which may lead to phase separation. The morphology of the network is mainly controlled by the volume fractions of the components, the thermodynamics of mixing, and the kinetics of network interpenetration. Thus, the morphology is controlled by the specific order and rate of gelation of each component and the rate of diffusion of the monomers and oligomers [12, 13]. Even though it is more common for phase separation to occur before gelation, there are examples in which gelation precedes phase separation. Each mechanism will be discussed separately in the following paragraphs.

When polymerizing systems with compositions falling in the metastable region of the phase diagrams (between the spinodal and binodal; Fig. 44.4), the most common situation is for gelation to arrest phase separation, which means the resulting morphology is stabilized by gelation [78]. In other words, even if there is thermodynamic instability past gelation, diffusion of macromolecular chains to allow for rearrangement in phase-separated domains is impeded by network formation. This has been demonstrated in a study using IR-coupled rheometry for a methacrylate network to which pre-polymerized methyl methacrylate was added [67]. In that study, the decrease in light transmission through a sample (used as an indication of onset of phase separation, as will be discussed later) took place earlier in conversion than did the gel point (as determined by rheometry). In practical terms, this means that the onset and extent of phase separation can be controlled by reaction kinetics, so that the domain size and separation mechanism (nucleation and growth and spinodal decomposition) can be tailored through control not only of the composition but also (and perhaps more practically) of the reaction temperature or irradiance (in the case of photopolymerized systems), as will be discussed later.

Some polymer-dispersed liquid crystals (PDLCs), used in monitors and other applications, represent examples in which phase separation may take place after gelation. For linear polymerizations, the increasing size of the polymer molecules results in phase separation of the liquid crystal, because no cross-linked network is present. When cross-linked systems are used, gelation may occur very early in conversion, and an infinite network is present almost from the start of the reaction. In this case, phase separation can be induced by the increasing elasticity of the swollen network during polymerization. At phase separation, the polymer network deswells due to increasing cross-linking and a new phase appears, in a mechanism analogous to a sponge being squished. Afterwards, the coalescence of the LC droplets is impeded by the cross-links in the matrix or the vitrification of the network [3]. That way, phase diagrams of pure liquids and cross-linked polymer differ from those of the liquid/linear polymers in that phase separation occurs between a swollen network and a pure liquid rather than between polymer-poor and polymer-rich phases (liquid-liquid demixing). In fact, the conversion-phase diagrams indicate that the phase separation in that case happens through a liquid-gel

mechanism [60, 61]. Indeed, for a system containing one type of liquid crystal (K15) and mono-/di-acrylates as the monomer phase, the onset of phase separation (as determined by the onset of turbidity in the sample) was observed at conversions approximately 10 % higher than the vitrification point (as defined by the conversion at maximum rate of reaction) [60, 61]. This percentage is even higher (up to 80 %) for compositions with a higher concentration of liquid crystal. The conversion-phase diagrams are obviously expected to vary according to the polymerization conditions (e.g., temperature and irradiance) and monomer used, since the primary kinetic chain length plays a major role in the gel point [48]. The practical implications of these effects may be perceived in the morphologies and contrast ratios of PDLCs [60] or organoclay-modified materials [56].

Control of Phase Formation: Same and Dissimilar Polymerization Mechanisms

Several approaches to control phase formation can be used. The most commonly used relies on orthogonal dual-cure systems that result in interpenetrating polymer networks (IPNs). This approach has some advantages, such as the ease of control of the sequence in which each network is being polymerized. Moreover, by judiciously choosing the moduli of each phase, it is possible to control the phase structure. One practical example has been described for a system comprised of methacrylate and epoxy monomers polymerized through a light- and a thermo-induced mechanism, respectively [14]. In this specific case, the epoxy component was selected to have higher modulus. If this component was allowed to polymerize first (or if present in greater concentration), less heterogeneous materials were formed due to a lack of mobility in the system. If the cure order is reversed, a more homogeneous material is formed, resulting in residual unreacted epoxy monomers residing in the preformed methacrylate phase [4, 8, 12]. In another study, methacrylate and vinyl ethers were used as the radical/cationic species, both initiated by a UV source, in a one pot methodology [41, 42]. In such cases, the wavelength of the initiating light can be modulated to concurrently or sequentially polymerize one type of monomer or the other, with dramatic effects on reaction kinetics [41], and on the effect of water concentration on network formation [42].

In purely methacrylate systems, as, for example, in networks modified by the addition of pre-polymerized particles, the phase composition can be modulated by controlling the relative solubility of the particle on the matrix [37, 38; 39, 40], the additive concentration [73], and the potential of the additive to covalently engage with the surrounding network [50, 51]. The use of hyperbranched prepolymers has been described as a way to avoid gelation in polymer-dispersed liquid crystals and to control phase formation through the judicious selection of additives of different Tgs at different concentrations [80]. All those approaches require the pre-polymerization of the additive. More recently, one approach was described to induce separation from purely free-radical systems on the basis of polymerization-driven instability [58]. The use of homogeneous combinations of marginally

compatible monomers that engage in direct copolymerization with a progression into a thermodynamically unstable mixture of monomers and copolymer due to an increase in the free energy of mixing has been described [58]. The initial degree of compatibility of any two given monomers depends, among other factors, on steric constraints (such as the presence of aromatic rings, either in the backbone or as substitutions, favoring π-π interactions) [44, 68] and the strength of intermolecular interactions, particularly hydrogen [68, 84] and halogen bonding (as is the case with nanostructured fluorinated block copolymers) [47]. The increased segmental packing density (which translates into reduced free volume) given by hydrogen-bonding interactions has been shown to improve miscibility in IPNs composed of polyurethanes (used as low-profile additives) and epoxy resins [84]. Without the addition of prepolymers, the influence of hydrogen-bonding interactions on the phase-separation behavior has also been demonstrated in hybrid networks formed by 2-hydroxyethyl methacrylate and vinyl ethers, although in this case, the fact that only one of the monomers presented hydrogen-bonding capability led to an increase in the Flory-Huggins χ-parameter, therefore favoring phase separation [66].

The combination of radical/cationic polymerizations has been used in the preparation of a number of hybrid structures, such as block, graft, or random copolymers [19, 20, 27, 46, 49], and to obtain IPNs. Those materials have been proposed for use in many industrial applications. For in situ biomedical applications, some of these formulations are not adequate, especially those involving thermo-activation such as for epoxies, since the increase in temperature could be potentially harmful to surrounding tissues, besides the need for polymerization times far longer than clinically practical. In addition, the use of thermo-activated systems in general produces greater internal stresses due to post-polymerization curing contraction effects that can generate poorly controlled micro-/macro-void formation in phase-separated polymers. Alternatively, the use of photopolymerizable systems, either purely free-radical [67, 73, 74] or free-radical/cationic hybrids [41], has the advantage of room-temperature processing, which limits the temperature rise to the exotherm of the reaction. Moreover, the polymerization can be started on demand after the material is in place.

Control of Phase Formation: Kinetics of Polymerization

Other than composition and sequence of network activation, another resource to control phase separation is through reaction kinetics [8]. Evidence has been presented for the impact of reaction kinetics on macromolecular diffusion and gelation, ultimately dictating final polymer structure and properties in all methacrylate systems, without the addition of prepolymers [58]. Processing conditions such as temperature [73, 74], irradiance (for photopolymerizable systems) [36], and initiator concentration [42] are of key importance in determining phase-separation behavior since they directly control reaction kinetics and onset of gelation. In thermally polymerized materials, temperature has two distinct and, more often than not, antagonist effects. Increasing temperatures may favor miscibility in incompatible monomers due to increased entropy. On the other hand, especially for IPNs, it likely leads to higher

polymerization rate and greater conversion prior to gelation [6, 9, 10], which is expected to favor phase separation [4]. This effect is likely to be less important in direct copolymerization routes, where higher temperatures may actually compatibilize monomers by improving miscibility and limiting long-range diffusion by reducing the time to gel-based mobility restriction. Photopolymerization then emerges as an advantageous technique, since it provides a means to control reaction kinetics independent of temperature. In free-radical polymerizations, rate of polymerization (R_p) is proportional to irradiance, meaning that higher irradiances are prone to cause diffusion restriction at an earlier stage in conversion, in a mechanism analogous to the early gelation of the most rigid phase for epoxy/PEGDMA systems shown elsewhere [4]. In other words, higher irradiance levels more quickly lock the structure in place (whether homogeneous or heterogeneous), and conversion progresses locally within each phase (if heterogeneity is present), with little opportunity for further compositional rearrangement (as predicted by [55]). This is a very convenient approach to control domain size [44].

One study evaluated the influence of irradiance on reaction kinetics of heterogeneous systems composed of one glassy dimethacrylate (BisGMA) and one rubbery monomethacrylate (isodecyl methacrylate), all photopolymerized via the same free-radical mechanism [58]. For selected compositions, the reaction kinetics profile presented two stages at lower irradiances, which is indicative of two phases reacting at different rates. The composition with the highest concentration of the rubbery monomer did not show vitrification (as would have been demonstrated by a plateau in conversion [58], in spite of the very high conversion (80–90 %). At lower irradiance, the reaction medium sustains relatively higher mobility over a longer time scale potentially allowing greater development of the IDMA-rich and BisGMA-rich domains in terms of both structure and composition. For the materials polymerized at higher irradiance as expected, both conversion and rate of polymerization were higher than with the other irradiance levels, except for the material containing 90 mol% monomethacrylate, whose maximum conversion was 10–17 % lower. For this formulation, a rapid increase in conversion caused by the polymerization of BisGMA-rich phases is followed by a second slower stage of the reaction, again without a plateau region. The absence of a peak in the rate of polymerization curve in this section means that the Trommsdorff effect was suppressed, similar to what was observed in another study where the secondary phase was also a monomethacrylate [65]. For all other formulations, higher irradiance led to reduced conversion at vitrification, which translates into more modest opportunity for diffusion and therefore, less domain rearrangement and comparatively more homogeneous materials. Indeed, the extent of phase separation, as determined by light transmission reduction, was slightly lower compared to the ones obtained at lower irradiances (at similar final conversion), which indicates a better match in refractive index among the different phases [28], possibly due to closer domain compositions and possibly smaller domain dimensions. Since all these materials form homogeneous, clear mixtures in the monomeric state, these findings suggest that even higher irradiances would be necessary to

completely avoid phase separation through an earlier onset of gelation. Thermodynamic driving forces seem to have been predominant in controlling heterogeneity, such as the higher interaction parameter (χ) and ΔGm for poly-BisGMA/IDMA or even the greater exotherm expected at higher reaction rates.

Experimental Evidence of Phase Separation

Several experimental procedures can be used to determine the onset and extent of phase separation in polymeric systems. This chapter will name the two most common ones.

Turbidity

The light transmission ability of polymers is of particular interest in photonics, especially for polymer-dispersed liquid crystals. According to the Rayleigh scattering theory, light or other electromagnetic radiation is scattered by particles much smaller than the wavelength of light. Therefore, light scattering (or light transmission) through a sample is a commonly used technique not only to infer the onset of heterogeneity formation in polymers but also to estimate domain size and distribution [17, 36]. In general, the turbidity has been correlated to the cube of the domain size and to the fourth power of the incident wavelength, and these relationships need to be adjusted for much bigger droplets due to anomalous diffraction [36]. This means that one can estimate the size of the domain based on the wavelength it scatters the most. However, although commonly used to study phase separation [71], the lack of turbidity (or the observation of transparency) in a blend does not necessarily mean that the system has a single phase, because blends with a small difference in the refractive indices of the components, domain sizes less than a micrometer, or low-volume fractions of one of the phases can also be transparent [71]. The refractive index of different phases and the order at which they polymerize also plays a role in light transmission [17]. The refractive index increases with polymerization, so it is expected that at the maximum light transmission reduction, either phases capable of scattering the incident light are being formed or the refractive index mismatch between the phase that polymerizes first and the surrounding monomeric phases is being observed. The latter explains the light transmission recovery observed in some systems after a maximum drop in transmission is observed [67].

Presence of Multiple Thermal Transitions (in DSC Experiments, or Tan Delta Peaks in DMA)

Dynamic mechanical thermal analysis is a common and useful technique to study the glass transition temperatures and thus phase separation of IPNs [14], provided that the individual components of the IPN have clearly defined and well-separated Tgs.

When those conditions are met, it is even possible to determine the composition of each phase, as has been demonstrated for a methacrylate system [67].

Summary

This chapter is intended to serve as a reference for the mechanisms of phase formation in heterogeneous networks, when used as a way to produce materials with micro- and nanoscale features. The presence of such features can be tailored by the starting material composition, as well as processing conditions, to optimize properties of interest. Examples include, but are not limited to, toughening in polymeric networks, shrinkage and stress reduction for a number of applications, and optical properties optimization, markedly refractive index. Heterogeneous networks with nanoscale features are a great example of the versatility of polymeric materials, justifying their use in an increasing number of applications.

References

1. Abolhasani MM, Guo Q et al (2013) Poly(vinylidene fluoride)-acrylic rubber partially miscible blends: phase behavior and its effects on the mechanical properties. J Appl Polym Sci 130:1247
2. Anusavice KJ, Shen C et al (2013) Phillip's science of dental materials. Elsevier, St. Louis
3. Boots HMJ, Kloosterboer JG et al (1996) Polymerization-induced phase separation. 1. Conversion-phase diagrams. Macromolecules 29(24):7683–7689
4. Chen F, Cook WD (2008) Curing kinetics and morphology of IPNs from a flexible dimethacrylate and a rigid epoxy via sequential photo and thermal polymerization. Eur Polym J 44(6):1796–1813
5. Chou YC, Lee LJ (1994) Reaction-induced phase separation during the formation of a polyurethane-unsaturated polyester interpenetrating polymer network. Polym Eng Sci 34(16):1239–1249
6. Cook WD (1993) Photopolymerization kinetics of oligo (ethylene oxide) and oligo (methylene) oxide dimethacrylates. J Poly Sci Part A Poly Chem 31(4):1053–1067
7. Cook WD, Chen F et al (2010) Photo-plasticity in thiol-ene network polymers – a review. Macromol Symp 291–292(1):50–65
8. Cook WD, Chen F et al (2006) Effect of curing order on the curing kinetics and morphology of bisGMA/DGEBA interpenetrating polymer networks. Poly Int 55(9):1027–1039
9. Daronch M, Rueggeberg FA et al (2005) Monomer conversion of pre-heated composite. J Dent Res 84(7):663–667
10. Daronch M, Rueggeberg FA et al (2006) Polymerization kinetics of pre-heated composite. J Dent Res 85(1):38–43
11. de Leon RD, Morales G et al (2010) Phenomenon of phase inversion in high impact polystyrene: physico-chemical, rheological and morphological study in the presence of chain transfer agent and using different tapered block copolymers as the precursor rubber. Poly Eng Sci 50(2):373–383
12. Dean K, Cook WD (2002) Effect of curing sequence on the photopolymerization and thermal curing kinetics of dimethacrylate/epoxy interpenetrating polymer networks. Macromolecules 35(21):7942–7954

13. Dean K, Cook WD et al (2001) Near-infrared and rheological investigations of epoxy-vinyl ester interpenetrating polymer networks. Macromolecules 34(19):6623–6630

14. Dean KM, Cook WD et al (2006) Small angle neutron scattering and dynamic mechanical thermal analysis of dimethacrylate/epoxy IPNs. Eur Polym J 42(10):2872–2887

15. Derrough SN, Rouf C et al (1993) Investigations for obtaining semiinterpenetrating polymer networks based on monomers of different reactivity toward radicals. J Appl Polym Sci 48(7):1183–1188

16. Dill KA, Bromberg S (2003) Molecular driving forces. Statistical thermodynamics in chemistry and biology. Garland Science, New York

17. Doane JW, Vaz NA et al (1986) Field controlled light scattering from nematic microdroplets. Appl Phys Lett 48(4):269–271

18. Dou R, Wang W et al (2013) Effect of core-shell morphology evolution on the rheology, crystallization, and mechanical properties of PA6/EPDM-g-MA/HDPE ternary blend. J Appl Polym Sci 129(1):253–262

19. Erdogan T, Bernaerts KV et al (2005) Preparation of star block co-polymers by combination of cationic ring opening polymerization and atom transfer radical polymerization. Des Monomers Poly 8(6):705–714

20. Erdogan T, Hizal G et al (2006) A new strategy for the preparation of multiarm star-shaped polystyrene via a combination of atom transfer radical polymerization and cationic ring-opening polymerization. Des Monomers Poly 9(4):393–401

21. Flory PJ (1941) Thermodynamics of high polymer solutions. J Chem Phys 9(8):660–661

22. Flory PJ (1944) Thermodynamics of heterogeneous polymer solutions. J Chem Phys 12(3):114–115

23. Flory PJ (1953) Principles of polymer chemistry. Cornell University Press, Ithaca

24. Frederix C, Beauchene P et al (2013) Kinetics of the non-isothermal fusion-welding of unlike ethylene copolymers over a wide crystallinity range. Polymer (UK) 54(11):2755–2763

25. Hashemi Doulabi A, Mirzadeh H et al (2013) Interaction and miscibility study of fumarate-based macromers with chitosan. Mater Chem Phys 139(2–3):515–524

26. Hashimoto T, Takebe T et al (1986) Apparatus to measure small-angle light scattering profiles of polymers under shear flow. Poly J 18(2):123–130

27. Hizal G, Sakar D et al (2005) Synthesis of tri-arm star di-block co-polymer containing poly (tetrahydrofuran-b-methyl methacrylate) arms via combination of cationic ring-opening polymerization and photosensitized free radical polymerization routes. Des Monomers Poly 8(6):609–617

28. Howard B, Wilson ND et al (2010) Relationships between conversion, temperature and optical properties during composite photopolymerization. Acta Biomater 6(6):2053–2059

29. Kammer HW, Inoue T et al (1989) Upper and lower critical solution temperature behaviour in polymer blends and its thermodynamic interpretation. Polymer 30(5):888–892

30. Karger-Kocsis J (2005) Simultaneous interpenetrating network structured vinylester/epoxy hybrids and their use in composites. In: Harrats C, Thomas S, Groeninckx G (eds) Micro- and nanostructured multiphase polymer blend systems. Taylor and Francis, Boca Raton, pp 273–293

31. Khoun L, Chaudhuri RI et al (2011) Effect of low-profile additives on thermo-mechanical properties of glass fiber-reinforced unsaturated polyester composites. J Reinf Plast Compos 30(9):815–823

32. Khoun L, Palardy G et al (2011) Relation between volumetric changes of unsaturated polyester resin and surface finish quality of fiberglass/unsaturated polyester composite panels. Polym Compos 32(9):1473–1480

33. Kloosterboer JG, Serbutoviez C et al (1996) Monitoring of polymerization-induced phase separation by simultaneous photo-d.s.c./turbidity measurements. Polymer 37(26):5937–5942

34. Koo CM, Wu L et al (2005) Microstructure and mechanical properties of semicrystalline-rubbery-semicrystalline triblock copolymers. Macromolecules 38(14):6090–6098

35. Lee TAIY, Cramer NB et al (2009) (Meth) Acrylate Vinyl Ester Hybrid Polymerizations. J Poly Sci Part A Poly Chem 47(10):2509–2517

36. Li W, Cao H et al (2008) Control of the microstructure of polymer network and effects of the microstructures on light scattering properties of UV-cured polymer-dispersed liquid crystal films. J Polym Sci B 46(19):2090–2099

37. Li W, Lee LJ (2000) Low temperature cure of unsaturated polyester resins with thermoplastic additives. II. Structure formation and shrinkage control mechanism. Polymer 41(2):697–710

38. Li W, Lee LJ (2000) Low temperature cure of unsaturated polyester resins with thermoplastic additives: I. Dilatometry and morphology study. Polymer 41(2):685–696

39. Li W, Lee LJ et al (2000) Low temperature cure of unsaturated polyester resins with thermoplastic additives III. Modification of polyvinyl acetate for better shrinkage control. Polymer 41(2):711–717

40. Li W, Sheller N et al (2000) Morphology and ordering behavior of a poly(styrene)-b-poly (ferrocenyldimethylsilane) diblock copolymer. Polymer 41(2):719–724

41. Lin Y, Stansbury JW (2003) Kinetics studies of hybrid structure formation by controlled photopolymerization. Polymer 44(17):4781–4789

42. Lin Y, Stansbury JW (2005) The impact of water on photopolymerization kinetics of methacrylate/vinyl ether hybrid systems. Poly Adv Technol 16(2–3):195–199

43. Lin Y, Tan Y et al (2013) Casting solvent effects on molecular dynamics of weak dynamic asymmetry polymer blend films via broadband dielectric spectroscopy. J Membr Sci 439:20–27

44. Lipatov YS (2007) Interfacial regions in the phase-separated interpenetrating networks. Polym Bull 58(1):105–118

45. Liu X, Deng J et al (2012) Amphiphilic triblock terpolymers consisting of poly(n-hexyl isocyanate) and poly(ethylene glycol): preparation and characterization. Polymer (UK) 53(25):5717–5722

46. Lynd NA, Meuler AJ et al (2008) Polydispersity and block copolymer self-assembly. Prog PolymSci (Oxf) 33(9):875–893

47. Martinelli E, Agostini S et al (2008) Nanostructured films of amphiphilic fluorinated block copolymers for fouling release application. Langmuir 24(22):13138–13147

48. Matsumoto A (1995) Free-radical crosslinking polymerization and copolymerization of multivinyl compounds. Adv Polym Sci 123:41–80

49. McCormick CL, Lowe AB (2004) Aqueous RAFT polymerization: recent developments in synthesis of functional water-soluble (Co)polymers with controlled structures. Acc Chem Res 37(5):312–325

50. Moraes RR, Garcia JW et al (2011) Control of polymerization shrinkage and stress in nanogel-modified monomer and composite materials. Dent Mater 27(6):509–519

51. Morães RR, Garcia JW et al (2012) Improved dental adhesive formulations based on reactive nanogel additives. J Dent Res 91(2):179–184

52. Nguyen PT, Wiesenauer EF et al (2013) Effect of composition and nanostructure on CO_2/N_2 transport properties of supported alkyl-imidazolium block copolymer membranes. J Membr Sci 430:312–320

53. Nishi T, Wang TT et al (1975) Thermally induced phase separation behavior of compatible polymer mixtures. Macromolecules 8(2):227–234

54. Odian G (2004) Principles of polymerization. Wiley, Hoboken

55. Okay O, Yilmaz Y et al (1999) Heterogeneities during the formation of poly(sodium acrylate) hydrogels. Polym Bull 43(4–5):425–431

56. Owusu-Adom K, Guymon CA (2008) Photopolymerization kinetics of poly(acrylate)-clay composites using polymerizable surfactants. Polymer 49(11):2636–2643

57. Patel MP, Braden M et al (1987) Polymerization shrinkage of methacrylate esters. Biomaterials 8(1):53–56

58. Pfeifer CS, Szczepanski CR et al (2011) Heterogeneous methacrylate networks: reaction kinetics, compositional drift and network formation. Dent Mater 27(S1):e43

59. Privas E, Leroux F et al (2013) Preparation and properties of blends composed of lignosulfonated layered double hydroxide/plasticized starch and thermoplastics. Carbohydr Polym 96(1):91–100
60. Serbutoviez C, Kloosterboer JG et al (1997) Polymerization-induced phase separation III. Morphologies and contrast ratios of polymer dispersed liquid crystals. Liq Cryst 22(2):145–156
61. Serbutoviez C, Kloosterboer JG et al (1996) Polymerization-induced phase separation. 2. Morphology of polymer-dispersed liquid crystal thin films. Macromolecules 29(24):7690–7698
62. Siddaramaiah, Barcia FL et al (2007) Rheological, mechanical, and morphological studies of epoxy/poly(methyl methacrylate) semi-interpenetrating polymer networks. J Appl Polym Sci 106(6):3808–3815
63. Siggia ED (1979) Late stages of spinodal decomposition in binary mixtures. Phys Rev A 20(2):595–605
64. Sonnenschein MF, Wendt BL (2013) Design and formulation of soybean oil derived flexible polyurethane foams and their underlying polymer structure/property relationships. Polymer (UK) 54(10):2511–2520
65. Soulé ER, Borrajo J et al (2005) Kinetics of the free-radical polymerization of isobornyl methacrylate in the presence of polyisobutylenes of different molar masses. Macromolecules 38(14):5987–5994
66. Stansbury JW, Trujillo-Lemon M et al (2005) Conversion-dependent shrinkage stress and strain in dental resins and composites. Dent Mater 21(1):56–67
67. Szczepanski CR, Pfeifer CS et al (2012) A new approach to network heterogeneity: polymerization induced phase separation in photo-initiated, free-radical methacrylic systems. Polymer (UK) 53(21):4694–4701
68. Tang C, Lennon EM et al (2008) Evolution of block copolymer lithography to highly ordered square arrays. Science 322(5900):429–432
69. Tian W, Kong J et al (2013) Temperature-responsive property of star poly((N, N-dimethylamino)ethyl methacrylate) with hyperbranched core: effect of core-shell architecture and β-cyclodextrin grafted via covalent bond or ionic electrostatic attraction. Soft Mater 11(3):272–280
70. Ulum S, Holmes N et al. (2013) The role of miscibility in polymer: fullerene nanoparticulate organic photovoltaic devices. Nano Energy
71. Utracki LA (1989) Polymer alloys and blends: thermodynamics and rheology. Hanser, New York
72. Vaessen DM, McCormick AV et al (2002) Effects of phase separation on stress development in polymeric coatings. Polymer 43(8):2267–2277
73. Velázquez R, Ceja I et al (2004) Morphology–composition–processing relationships in poly (methyl methacrylate)–polytriethylene glycol dimethacrylate shrinkage-controlled blends. J Appl Polym Sci 91(2):1254–1260
74. Velázquez R, Sánchez F et al (2000) Synthesis of shrinkage-controlled acrylic copolymers. J Appl Polym Sci 78(3):586–591
75. Vilay V, Mariatti M et al (2011) Effect of PEO-PPO-PEO copolymer on the mechanical and thermal properties and morphological behavior of biodegradable poly (L-lactic acid) (PLLA) and poly (butylene succinate-co-L-lactate) (PBSL) blends. Polym Adv Technol 22(12):1786–1793
76. Vonka M, Kosek J (2012) Modelling the morphology evolution of polymer materials undergoing phase separation. Chem Eng J 207–208:895–905
77. Williams RJJ, Rozenberg BA et al (1997) Reaction-induced phase separation in modified thermosetting polymers. Adv Polym Sci 128:95–156
78. Yamagishi FG, Miller LJ et al. (1986) Morphological control in polymer-dispersed liquid crystal film matrices. Proc SPIE 1080 Liq Cryst Chem Phys Appl 1080(24)
79. Yamanaka K, Takagi Y et al (1989) Reaction-induced phase separation in rubber-modified epoxy resins. Polymer 30(10):1839–1844

80. Yang Q, Chung TS et al (2009) Rheological investigations of linear and hyperbranched polyethersulfone towards their as-spun phase inversion membranes' differences. Polymer 50(2):524–533
81. Zhang H, Yang S et al (2012) Preparation of PNHMPA/PEG interpenetrating polymer networks gel and its application for phase change fibers. J Appl Polym Sci 129:1563
82. Zhang W, Zhang J et al (2012) Effect of core-shell structured modifier ACR on ASA/SAN/ ACR ternary blends. J Mater Sci 47(12):5041–5049
83. Zhu LD, Yang HY et al (2013) Submicrometer-sized rubber particles as "craze-bridge" for toughening polystyrene/high-impact polystyrene. J Appl Polym Sci 129(1):224–229
84. Zhu YC, Wang B et al (2006) Investigation of the hydrogen-bonding structure and miscibility for PU/EP IPN nanocomposites by PALS. Macromolecules 39(26):9441–9445